

SMART 2025

Smart Structures and Materials

Editors: Michael Krommer
Manfred Nader
Martin Schagerl



PROCEEDINGS

SMART 2025 - Smart Structures and Materials

Proceedings of the 11th ECCOMAS Thematic Conference on Smart Structures and Materials

Johannes Kepler University Linz, Austria
July 1-3, 2025

Edited by:

Michael Krommer
Johannes Kepler University Linz, Austria

Manfred Nader
Linz Center of Mechatronics, Linz, Austria

Martin Schagerl
Johannes Kepler University Linz, Austria

SMART 2025 - Smart Structures and Materials
Michael Krommer, Manfred Nader, Martin Schagerl
First Edition, May 2026
ISBN: XXX-XXX-XXXXX-X-X
© The Author(s) 2025

Preface

The ECCOMAS Thematic Conference on Smart Structures and Materials (SMART 2025) took place July 1-3, 2025 at the Johannes Kepler University (JKU) in Linz, Austria. SMART 2025 was the 11th bi-annual conference in a series of successful international conferences previously held in Poland (2003, 2007), Portugal (2005, 2009, 2015), Germany (2011), Italy (2013), Spain (2017), France (2019) and Greece (2023). SMART 2025 was co-organized by the Institute of Technical Mechanics and the Institute of Structural Lightweight Design at JKU and by the Linz Center of Mechatronics.

After SMART 2023 in Patras, Greece had reached a new high in terms of number of presentations and participants, SMART 2025 had a slightly lower number of presentations and participants; however, maintining the numbers from previous editions before SMART 2023 in Greece. SMART 2025 attained a robust international content of approximately 150 presentations and 174 participants form 22 countries. Besides a strong European participation with diverse contributions from almost all European countries (142), international participants come from the Americas (9) and from Asia (23). Approximatetly 35% of the participants were graduate and doctoral students.

The overall quality of the presented papers was very good and the discussions were intense and productive, which is already an important characteristic of this Thematic Conference. The excellent quality of plenary lectures (3 from accademia and 1 from a research center) provided to the participants a vision of the state-of-the art, future trends in smart structures technology and current and future applications. 9 invited lectures by internationally re-known experts in the field of smart structures and materials presented in the special session *A Tribute to Professor Carlos Mota Soares* further contributed to the excellent scientific quality of SMART 2025.

The topics of the conference ranged from smart structures with embedded sensors and actuator for real time monitoring and control for machine elements and robotics to vibration control strategies using piezoelectric transducers and multi-physics materials. In the field of modelling, design and testing of smart materials and structures research on composite structures, non-linear modelling and numerical methods was strongly represented. The particular field of smart materials was covered through smart and architected composites, functional and non-linear metamaterials, and active polymers. Going beyond these traditional topics of the ECCOMAS SMART conference series, SMART 2025 included numerous mini-symposia and special sessions in the field of Structural Health Monitoring, a mini-symposium on Symbiotic Mechatronics, a mini-symposium on Adaptive and Compliant Engineering Structures and a special session on Smart and Sustainable Sensor Technologies Using Cellulosic and Wood Substrates.

As chairmen of SMART 2025 and editors of the present proceedings we wish to thank the presenters and the plenary lecturers, the active members of the Scientific Committee, the Mini-Symposium and Special Session organizers, the chairwomen and chairmen, our colleagues in the Local Organizing Committee, and our Ph.D. and graduate student volunteers.

The present proceedings include a total of 132 full length papers, which were presented at SMART 2025. We thank all authors for their contributions and we sincerely wish that the proceedings will be very useful to academic and industrial researchers, to engineers and to graduate students engaged in the highly active topic of smart structures and materials.

Linz
April 2026

Michael Krommer
Manfred Nader
Martin Schagerl

Contents

Part I SPECIAL SESSION - A TRIBUTE TO PROFESSOR CARLOS MOTA SOARES
Aurelio Araujo, Ayech Benjeddou

Full 3D Effective Properties of Piezoelectric d_{31} MFC: Validation by Detailed Finite Element Analyses of Experimented Free Smart Hybrid Honeycomb Sandwich 3
Ayech Benjeddou, Marcelo A. Trindade

Adaptive Petal Polymer Reflector for Cubesat Applications 15
Carl Johan G. Nielsen, Gonçalo Rodrigues, André Preumont

Fractal-Inspired Phononic Crystal for Waves and Vibrations Suppression 23
Wiesław Ostachowicz, Sourava Prasad Mishra, Paweł Kudela

Finite Element Evaluation of Effective Damping Properties of d_{31} Piezoelectric Macro-Fibre Composites 33
Marcelo A. Trindade, Ayech Benjeddou

Advanced Tailored Kinematic Models for Multi-Field Analysis of Laminated Structures 45
Enrico Zappino, Erasmo Carrera, Daniele Scano

Part II MS 01 - SMART SYSTEMS AND CONTROL STRATEGIES FOR VIBRATION ATTENUATION USING PIEZOELECTRIC TRANSDUCERS
Marta Berardengo, Jan Høgsberg, Boris Lossouarn, Stefano Manzoni

Magnetostrictive Shunt versus Piezoelectric Shunt: A Comparison 59
Marta Berardengo, Marco Mercato, Stefano Manzoni

Switching Shunts using Fuzzy Logic for Vibration Mitigation of Smart Flexible Structures . . . 69
Maria-Styliani Daraki, Aikaterini Smarianaki, Konstantinos Marakakis, Georgia A. Foutsitzi, Georgios E. Stavroulakis

A Nonlinear Saturating Amplifiers Circuit for Piezoelectric Vibration Control of Flexible Mechanical System 81
Kevin Dekemele, Christophe Giraud-Audine, Olivier Thomas

Artificial intelligence using adaptive strategy for distributed control on a smart beam 93
Maryne Febvre, Jonathan Rodriguez, Simon Chesné, Manuel Collet

Comparison of Two Fully-Passive Multimodal Damping Techniques: Multi-Branch Shunts and Interconnected Piezoelectric Networks 113
Pierre Flament, Boris Lossouarn, Éric Ramond, Pascal Audrain, Jean-François Deü

Potential of Piezoelectric Energy Harvesting for Road Bridges 125
Thomas Furtmüller

Adaptive Resonant Piezoelectric Shunt Using Tunable Inductance 137
Arthur Haudeville, Adrien Queste, Christophe Giraud-Audine, Boris Lossouarn, Xavier Amandolese, Olivier Thomas

A Unified Tuning Method for Piezoelectric Vibration Damping by Positive Position Feedback Control 149
Jan Høgsberg, Amirali Sadeqi, Niels Leergaard Pedersen, Ayech Benjeddou

Band Gap Control and Vibration Attenuation in Periodic Piezoelectric Meta-Structures 161
Ali Hosseinkhani, Eduard Rohan

Eigenfrequency Adaptivity of Locally Resonant Metamaterial Resonators using Piezoelectric Elements with Negative Capacitance Shunts 173
Stefan Janssen, Gabriel Konda Rodrigues, Leopoldo Pisanelli Rodrigues de Oliveira, Carlos De Marqui Jr., Claus Claeys, Elke Deckers

Piezoelectric Patch with Self-Tuning Analogue Shunt Circuit for Vibration Control 185
Gabriel Konda Rodrigues, Leopoldo Pisanelli Rodrigues de Oliveira, Paolo Gardonio

Embedded Piezoelectric Shear Actuators as Inertial Systems for Vibration Control in Metallic Structures 195
Sherif Okda, Sneha Rupa Nampally, Mauro Fontana, Sven Herold, Rainer Nordmann, Stephan Rinderknecht, Tobias Melz

Experimental Calibration of Digital Piezoelectric Shunts: Practical Considerations, Parameter Estimation and Dielectric Losses 205
Jens Damholt Richardt, Boris Lossouarn, Jan Høgsberg, Jean-François Deü

A Semi-Active Metastructure System for Vibroacoustic Isolation 217
Giorgos M. Sarmas, Ilias A. Tsakonas, Dimitris K. Dimitriou, Nikolaos A. Chrysochoidis, Dimitris A. Saravanos, Christoforos S. Rekatsinas

A Nonlinear Piezoelectric Shunt Absorber with 2:1 Internal Resonance and Saturation 229
Olivier Thomas, Christophe Giraud-Audine, Zein A. Shami

Part III MS 02 - ADVANCED MODELLING, DESIGN AND TESTING OF SMART COMPOSITE STRUCTURES
Aurelio Araujo, Enrico Zappino

Materials informatics approaches for the layering of smart composites 239
Adrian Ehrenhofer, Thomas Wallmersperger

A novel Multistable Sandwich Hinge Design with a Flexible Honeycomb Core 251
Abhijeet Kumar, Anoop Singh Bagri, Yuvraj Singh, Suranjan Kumar, Subham Sekhar Mandal, Ayan Haldar, Pralay Maiti

Multimodal optimization for effective vibration reduction using passive shunt damping 263
Pedro A. Magalhaes, Aurelio L. Araujo, Jose F. A. Madeira

Integration of piezoelectric transducers in hydrofoils made of composite materials 275
Antoine Morvan, Boris Lossouarn, Y. Watine, Jean-François Deü

New finite element for piezoelectric modeling of plates and shells structures 287
Olivier Polit, Michele D'Ottavio, Philippe Vidal

Advanced Multi-Field Modeling for the Virtual Manufacturing of Layered Structures with Embedded Sensors 301
Enrico Zappino, Marco Petrolo

Part IV MS 03 - SYMBIOTIC MECHATRONICS
Manfred Nader, Sven Herold, Alexander Büchner

Condition Monitoring of the Human Arterial System by Modal Analysis of Blood Flow Rates 315
Florian Brunnmayr, Gudrun Mikota, Peter Benedikt, Georg Hagleitner

High Frequency Dipole Magnetic Field For Vacuum Magnetic Birefringence 327
Dominik Freller, Gerald Jungmayr, Robert Santner, Laura Roberts, Aldo Ejlli, Guido Mueller

Low Temperature Effects on Guided Wave Structural Health Monitoring Signals 339
Shankar Galiana Blanch, Bhooshit Patel, Maria Moix-Bonet, Daniel Schmidt, Peter Wierach

A Digital Twin for Vibration and Fault Monitoring in Power Plant Turbogenerators 349
Hendrik Holzmann, Vincent Rachor, Georg Stoll, Rainer Nordmann, Sven Herold

Modeling the Human as a Control Component in Power Tool Systems: A Case Study on Chainsaw Operation 361
Helena Käppeler, Stefan C. Schlanderer, Edmund Marth, Gerd Bramerdorfer

Performance Evaluation of MS-SLAM in Indoor Environments 373
Daniel Louback S. Lubanco, Ahmed Hashem, Markus Pichler-Scheder, Thomas Schlechter, Reinhard Feger, Andreas Stelzer

A Comprehensive Review of Prior Art in Bearingless Induction Machine - Part I: Control . . . 381
Stefan Mallinger, Wolfgang Gruber

Assessment of Ecometrics in Engineering Workflows 393
Hubert Mitterhofer, Stefan Fragner

Data acquisition and evaluation for condition monitoring of a cutting tool 405
Kurt Pichler, Christian Helmel, Gerhard Kaineder, Robert Schlosser, Veronika Putz

Holistic Simulation Model for optimizing Piezoelectric Bone Conduction Implant with SyMSpace 417
Alexander Reininger, Lukas Grasböck, Daniel Reischl, Julia Lieber, Armin Stockhammer, Kathrin Sonntag

Design and Experimental Characterization of Rotatory Magnetorheological Actuators 427
Thomas Wiener, Christina Offenzeller, Bernhard Jakoby

Hotspot Temperature Modeling for the Online Condition Monitoring of PMSMS With Jumble Windings 437
Daniel Wöckinger, Magdalena Schaber, Gerd Bramerdorfer

Part V MS 04 - SMART MATERIALS, SENSORS, ACTUATORS AND CONTROL FOR MACHINE ELEMENTS AND ROBOTICS
Thomas Wallmersperger, Markus Vorrath, Karsten Stahl, Eckhard Kirchner

Numerical Investigations of the Asymmetric Energy Landscape in Cantilever Bistable Piezoelectric Energy Harvesters 451
Danish Bashir, P. M. Anilkumar, Ayan Haldar, Sven Scheffler, B. N. Rao, Raimund Rolfes

Development of a Shape-Adaptive Robot Gripper using Magnetorheological Fluids and Additively Manufactured Cylinders 463
Jennifer J. Blöchle, Thomas M. Wendt, Thomas Seifert

Experimental investigation of a novel sensor-integrating jaw coupling for data acquisition . . . 475
Arthur Ewert, Johannes D. M. Menning, Artem Prokopchuk, Thomas Rosenlöcher, E.-F. Markus Vorrath, Thomas Wallmersperger, Berthold Schlecht

Structural Integrated Supercapacitors 487
Sebastian Geier, Jan Petersen, Peter Wierach

High Load Shape Memory Alloy Actuators: Design, Development and Application in Production Engineering 499
Andreas Hofer, Kai Thüsing, Kenny Pagel, Welf-Guntram Drossel

Systematic Conceptualization of Soft Sensors 511
Florian Koetz, Michel Fett, Eckhard Kirchner

A Parametric Study on Magnetic Force Effects in Enhancing the Dynamic Response of Vibration Energy Harvester 523
Kishor Kumar, Amit Tyagi

Numerical Study of the Impact of Manufacturing Deviations on the Performance of a Bi-directional Piezoelectric Motor 537
Paul Marter, Sascha Eisenträger, Ryan Orszulik, Daniel Juhre

Numerical investigation of wear effects on sensor-integrating jaw couplings 551
Johannes D. M. Menning, Arthur Ewert, Artem Prokopchuk, Berthold Schlecht, E.-F. Markus Vorrath, Thomas Wallmersperger

Correlation between Temperature Changes and Magnetstriction Effect of Magnetoactive Foam 565
Nur Azmah Nordin, Nurul Nadia Senin, Saiful Amri Mazlan, Mohd Aidy Faizal Johari, Abdullah Yasser Abd Fatah

Bidirectional Evolutionary Structural Optimization for Enhanced Design of SMA Superelastic Structures and Actuators 577
Sefa Oksuz, Darren Hartl

Small-Scale Energy Harvesting using Piezoelectric Paints 589
Ismael Payo, César García-Asensio, José García-Delgado

Part VI MS 05 - ADAPTIVE AND COMPLIANT ENGINEERING STRUCTURES
Malte von Scheven, Renate Sachse, Alexander Hasse

Stability Analysis of Adaptive Funicular Structures 603
Andres Felipe Guerra Riaño, Péter L. Várkonyi

Design of a Thermoresponsive Shading System with shape memory material 613
Weifeng He, Aniket Pal, Thomas Wortmann, Maria Matheou

Efficient Design of Compliant Mechanisms Using Multi-Objective Optimization 625
Alexander Humer, Sebastian Platzer

Proof of Concept for a Damage Localization Strategy in Beams through Stiffness Modulation 639
Arka P. Reksowardojo, Ann C. Sychterz

Stiffness Adjustment of Compliant Mechanisms via Prestress Considering Large Deformations 651
Stephanie Seltmann, Alexander Hasse

Retrofitting a Tied-Arch Bridge with Adaptive Elements 663
Axel Trautwein, Amelie Zeller, Spasena Dakova, Christina Tarín, Oliver Sawodny, Manfred Bischoff

Static Shape Control of Slender Structures: An Overview and a Classification of Control Laws 671
Péter L. Várkonyi, Andres Felipe Guerra Riaño

Part VII MS 06 - FUNCTIONAL AND NON-LINEAR METAMATERIALS
Andrea Bergamini, Bart Van Damme, Nikolaos Karathanasopoulos

Electro-Mechanical Coupling in Compliant Dielectric Elements with Bias Voltage 681
Andrea E. Bergamini, Alexandre Brun d'Arre, Patrick Danner, Dorina Opris, Bart Van Damme

Metamaterial Inspired Vibration Damping System for Rotors 691
Ankur Dwivedi, Tanuj Gupta, Bishakh Bhattacharya

Inverse design of the Acoustic Black Hole Metabeam using Tandem Neural Network 705
Pratham Khairnar, Ankur Dwivedi, Aman Sengar, Bishakh Bhattacharya

Wave Propagation in Phononic Beam Structure with Periodically Varying Cross-Section in Presence of Crack 719
Subhasish Sarkar, Srinivasan Gopalakrishnan

On the Global Dynamics of Metaimpactor Lattices using Physics-Enhanced Machine Learning 731
Rui Zhang, Marcus Haywood-Alexander, Oleg Gendelman, Sami Masri, Eleni Chatzi, Vasilis Dertimanis

Part VIII MS 07 - RECENT ADVANCES IN NON-LINEAR MODELING AND NUMERICAL METHODS FOR SMART MATERIALS AND STRUCTURES
Alexander Humer, Michael Krommer, Astrid Pechstein

Application of Rate-type Variational Formulations and Scalable Linear Solvers to the Thermo-Chemo-Mechanical Modeling of Hydrogels 745
Akshay B Jeeja, Bjoern Kiefer, Stefan Prüger, Oliver Rheinbach, Friederike Röver

Characterization of the Dynamic Behavior of Soft Elastomers Using a Shaker Testbed 757
Mario Kunzemann, Andreas Brandl, Astrid Pechstein, Alexander Humer

On the Integration of Multiple Load Protocols for Parameter Identification and Calibration of Superelastic Shape Memory Alloy Models Using Artificial Neural Networks 771
Niklas Lenzen, Florian Kolisch, Sven Klinkel

Ferroelectric Polarization of bimorph piezoelectric plates - an accurate equivalent single-layer approach 783
Astrid Pechstein, Alexander Humer, Michael Krommer

Part IX MS 08 - STRUCTURAL CONTROL AND HEALTH MONITORING
Grzegorz Mikułowski, Olivier Bareille, Łukasz Jankowski

A Case Study in Semi-Active Structural Control Based on Multi-Agent Reinforcement Learning 801
Aleksandra Barbay, Dominik Pisarski, Grzegorz Mikułowski, Bartłomiej Błachowski, Łukasz Jankowski

Verification of a Combined SHM/CM System on a 2.4 MW Wind Turbine 813
Lukas Bonekemper, Marcel Wiemann, Benedikt Wüllner, Herbert Friedmann, Peter Kraemer

Singularity Detection by K-Space Identification in Plate-like-Structures - Location Index Evaluation 827
Thomas Brion, Xi Li, Pascal Fossat, Mohamed Ichchou, Olivier Bareille, Abdelmalek Zine

Active Control of Vibration Energy Transmission in an Inhomogeneously Damped Plate 837
Alexander Büchner, Hans Peter Monner

Design and Analysis of a Robust Hybrid Tuned Mass Damper System for Structural Vibration Control: Active Synthesis of Multiple TMD 847
Simon Chesné, Jonathan Rodriguez

Numerical and Experimental Investigation of Novel Control Methods for Self-Adaptive Shock-Absorbers 857
Cezary Graczykowski, Grzegorz Mikułowski, Rafał Wiszowaty, Michał Niedzielczyk, Rami Faraj

Localization of Impacts on Thin-Walled Structures by Recurrent Neural Networks: End-to-End Learning from Real-World Data 869
Alexander Humer, Lukas Grasböck, Ayech Benjeddou

Unified and Governing Equation for Passive Vibration Control of Buildings via Pole Allocation 881
Yoshiki Ikeda

Extreme Vibration Mitigation and Structural Health Monitoring under Impulse Loads 893
Mohammad Shamim Miah, Werner Lienhart

Vibration attenuation in a semi-passive frame based on reinforcement learning algorithm . . . 905
Grzegorz Mikułowski, Dominik Pisarski, Błażej Popławski, Łukasz Jankowski

Smart Pneumatic Airbag-Type Energy Absorber - Design and Development 917
Blazej Poplawski, Jan Stoppel, Mariusz Ostrowski, Rafał Wiszowaty, Rami Faraj

Development and Implementation of a Combined SHM/CM System to Identify Yield Losses of a 2.4MW Wind Turbine 929
Marcel Wiemann, Lukas Bonekemper, Benedikt Wüllner, Herbert Friedmann, Peter Kraemer

Simulation of time series of a 2.4 MW wind turbine for the development of CM/SHM methods 943
Benedikt Wüllner, Marcel Wiemann, Lukas Bonekemper, Herbert Friedmann, Peter Kraemer

Part X MS 09 - ADVANCES IN ACTIVE POLYMERS INNOVATIONS AND APPLICATIONS
Eric Monteiro, Nazih Mechbal, Ingrid Graz

Optimization of omnidirectional piezoelectric polymer transducers for high-purity selective excitation of Lamb wave modes 959
Hao Dong, Pierre Margerit, Marc Rébillat, Mickaël Pruvost, Nazih Mechbal

Characterization of electromechanical properties of Electroactive Polymer Actuators for Soft Robots in mini-invasive surgery 975
Imane Ferradj, Eric Monteiro, Damien Thuau, Sebastien Roland, Nazih Mechbal

Weather-Induced Degradation in Magnetorheological Elastomers: Tropical Climatic Conditions on The Rheological and Mechanical Properties 985
Mohd Aidy Faizal Johari, Saiful Amri Mazlan, Nur Azmah Nordin, Nur Amirah Farhana Rahimin, Rehnupreya Hentry Viension

An Active Silicone Foam Mat for Medical Applications 997
Florian Poltschak, Rene Preuer, Ingrid Graz

Bioinspired Particle-Filled Silicone Foams for Soft Sensors and Actuators 1009
Rene Preuer, Evrim Burkut, Dan Kytyr, Ingrid Graz

Dielectric elastomer actuator-zipping actuator hybrid concept 1025
Rafal Ziembicki, Astrid Pechstein, Alexander Humer, Ingrid Graz

Part XI SS 01 - STRUCTURAL HEALTH MONITORING SYSTEMS FOR FIBER COMPOSITE AND HYBRID STRUCTURES
Kai-Uwe Schröder, Tobias Schalm, Martin Schagerl, Christoph Kralovec

Guided Wave-Based Damage Monitoring of Pinned Hybrid Composite-Titanium Joints 1039
Christoph Humer, Christoph Kralovec, Andreas Dengg, Martin Schagerl

Model- and a-priori knowledge-based acoustic emission data fusion for atmospheric corrosion identification on aluminum aircraft structures 1051
Christoph Kralovec, Thomas Erlinger, Christoph Humer, Martin Schagerl

Optimized Placement of Distributed Optic Fiber Sensors for Structural Health Monitoring via the Modified Constitutive Relation Error 1063
José Andrés Pérez Orozco, Ludovic Chamoin, Julien Cortial, Maya de Buhan, Bruno Soulier

Lessons Learned in Developing a Convolutional Neural Network to Identify Damage Modes in Type-IV Composite Overwrapped Pressure Vessels 1075
Finja Carlotta Rentzsch Holm, Tobias Schalm, Finn Eggers, Kai-Uwe Schröder

Robotically Automated Tap Testing for Damage Detection in Filament-Wound CFRP Tubes . . 1087
Tobias Schalm, Linus Wermert, Kai-Uwe Schröder

A hybrid Piezo / Temperature Sensor for Production and Structural Health Monitoring of Composite Structures - development and lessons learned 1097
Michael Scheerer, Zoltan Simon, Michael Marischler, Bernhard Rittenschober

Part XII SS 02 - SHM-INFORMED STRATEGIES AND THEIR USE FOR LIFETIME EXTENSION OF STRUCTURES
Luis David Avendaño-Valencia, Stefano Manzoni

Damage Detection and Filtering of EOV Effects by Monitoring Piezoelectric Coupling 1111
Marta Berardengo, Matteo Brambilla, Stefano Manzoni

Vibration-Based Robust Detection of Gear Incipient Faults under Different Speeds and Loads via a Cloud of Functional Models 1121
Dimitrios M. Bourdalos, John S. Sakellariou

Modeling and damage detection in systems with multiple operational regimes through a Bayesian Multi-Model time series approach 1133
Casper Aaskov Drangsfeldt, Luis David Avendaño-Valencia, Marie Lützen

A Deep Neural Network Framework for the Prediction of Ice Mass Accumulation on Wind Turbine Blades 1145
Paola Guevara, Jawad Fayaz, Rodrigo Astroza

Monitoring-based Identification of Corrosion in Steel Structures 1157
Yasemin Kurtis, Antonina Kosikova, Konstantinos Vlachas, Rosalba Ferrari, Andrew W. Smyth, Eleni Chatzi

A Frequency-Domain Framework for Sensor Fault Diagnosis in Vibration-Based SHM: Application to a Population of Composite Aerostructures under Operational Uncertainity . . .1169
Ioannis E. Saramantas, Ilias A. Iliopoulos, Sampetai S. Koen, John S. Sakellariou, Spilios D. Fassois, Dimitrios N. Serpanos

Performance of Frequency-Based Fatigue Methods Using Realistic Power Spectral Densities .1183
Jack Rahbek Steengaard, Luis David Avendaño-Valencia, Marie Lützen, Mikkel Løvenskjold Larsen

Part XIII SS 03 - VIBRATION CONTROL THROUGH MULTIPHYSICS MATERIALS
Paolo Gardonio, Stefano Manzoni, Emiliano Rustighi

An Investigation of Structural Stress in Active Acoustic Black Holes 1197
Jordan Cheer, Archie Keys

Morphing Aircraft Wing Structure for the Application of 3D Shock Control Bumps 1209
Sven Christian Künnecke, Martin Radestock, Hans Peter Monner

Multi-Frequency Adaptive Tuned Mass Dampers Through Intelligent Materials 1225
Stefano Manzoni, Marta Berardengo, Francescantonio Lucá

Self-Tuning Vibration Absorber Made With In-Vacuo Structured Fabrics 1235
Lisa Ortis, Daniel Casagrande, Paolo Gardonio, Emiliano Rustighi, Ciro Malacarne, Matteo Perini

A Modeling Study of Elastic Properties of Structured Fabrics under Vacuum Pressure 1247
Emiliano Rustighi, Davide Raffaele, Paolo Gardonio, Ciro Malacarne, Matteo Perini

Bending Performance of Polymer Auxetic to Non-Auxetic Lattice Gradient Beams 1257
Neeraj Sharma, Kshitij Kumar Yadav

Part XIV SS 04 - SMART AND SUSTAINABLE SENSOR TECHNOLOGIES USING CELLULOSIC AND WOOD SUBSTRATES
Arunjunai Raj Mahendran, Martin Riegler, Claudia Pretschuh

Prospects and challenges of monitoring moisture uptake in wood samples with acoustic emissions 1269
Mehieddine Derbas, Alexander Schneider, Martin Riegler

Real-Time Cure Monitoring of Thermoset Resin Using Printed Paper Sensors 1279
Nitin Gupta, Günter Wuzella, Arunjunai Raj Mahendran, Martin Kaltenbrunner

Porous Smart Paper Sensors for Structural Health Monitoring in Composites 1287
Christian Koren, Arunjunai Raj Mahendran

Exploring the applicability of printed sensors for deformation detection in wooden laminates . 1295
Sebastian Platzer, Astrid Pechstein, Alexander Humer, Michael Krommer

New Approaches to Sensor Fabrication on Wooden Substrates and Cellulosic Paper 1305
Claudia Pretschuh, Arunjunai Raj Mahendran

Simulation of Surface Energy to Identify Optimum Laser Parameters for LIG on Wood 1315
Martin Riegler, Mehieddine Derbas, Christian Hueber

Enhancing the Properties of Smart Sustainable Materials Through Atmospheric Plasma Deposition of Bio-Based Coatings 1323
Judith Sinic, Christoph Jocham, Arunjunai Raj Mahendran, Kamal Baba, François Loyer, Nicolas Boscher

Part XV SS 05 - SMART AND ARCHITECTED COMPOSITES AND STRUCTURES
Wael Zaki, Marwan El-Rich

Characterization of Electrically Conductive Polymers Integrated in Additively Manufactured Parts for Sensing 1333
Giorgio De Pasquale, Ferdinando Ursi

Integration of Shape Memory Alloy Wires into Additive Fabricated Structures for Robotic Grippers 1345
Alexander Dierle, Thomas M. Wendt, Thomas Seifert

Numerical Prediction of Effective Functional Behavior of Mg-NiTi Strut-Architected Interpenetrating Phase Composites 1357
Shahzaib Ilyas, Marwan El-Rich, Mohamad Khalil, Wael Zaki

Effect of topological hybridization on the elastic isotropy of three-dimensional lattice metamaterials 1367
Mohamed M. Naji, Rashid K. Abu Al-Rub, Imad Barsoum, Wael Zaki

Part XVI SS 06 - SMART STRUCTURES AND SENSING TECHNOLOGIES FOR REAL-TIME MONITORING
Mehdi Ghommem, Abdessattar Abdelkefi

Explainable sensor fault diagnosis for structural health monitoring 1379
Heba Al-Nasser, Kosmas Dragos, Kay Smarsly

A Machine Learning Framework for Predicting Moisture Effects on Active Sensory Piezoelectric Flax Composite Laminates 1391
Vassilis Gkatsis, Antigoni Barouni, Nikolaos A. Chrysochoidis, Georgios Giannakopoulos, Christoforos S. Rekatsinas

In-situ Monitoring of Electrochemically Generated μm-sized Corrosion Pits Growth in Aluminum Thin Plates using Lamb Waves 1405
Cyril Nicard, Marc Rébillat, Olivier Devos, Mohamed El May, Nazih Mechbal

Damage Localization and Quantification Using Meta-Lens for Signal Enhancement 1417
Jiahui Shi, Gabriele Cazzulani, Claudio Sbarufatti

On the Use of Piezoelectric Flags for Fluid Flow Sensing 1429
Dheeraj Tripathi, Mehdi Ghommem, Abdessattar Abdelkefi, Lotfi Romdhane

Part XVII GS - GENERAL SESSIONS
Michael Krommer, Manfred Nader, Martin Schagerl

Finite Element Modelling and Experimental Validation of Endovascular Nitinol Stents: A Pathway to Additive Manufacturing Optimization 1441
Alberto Bellelli, Farzaneh Hoseini, Luke Mizzi, Andrea Spaggiari

Prototype of a cable-actuated lightweight canopy system installed with thin-film photovoltaics 1453
Eftychios G. Christoforou, Eleftherios G. Vourkos, Panayiota Dimitriou, Rafaela Agathokleous, Andreas Müller, Marios C. Phocas

Design of a morphing winglet trailing edge with fluid actuation - Design process and experimental results 1463
Ralf Keimer, Michael Schäfer, Srinivas Vasista

A Time Series Global Model Method for Random Vibration Modeling and Generation in Rotating Machinery under any Operating Speed 1473
Xenofon D. Konstantinou, Dimitrios M. Bourdalos, Kyriakos Kritikakos, John S. Sakellariou, Spilios D. Fassois, Josef Koutsoupakis, George Karyofyllas, Dimitrios Giagopoulos

Multiphysics Modelling of an Active Coupled Helmholtz-Resonator-Cantilever Sound Absorber 1485
Felix Langfeldt

Development of a Tow-steered Composite Design Tool for Morphing Applications 1497
Jared Lilly, Darren Hartl

Wave Propagation Analysis of Sigmoid Functionally Graded Square lattice Structures Using Dynamic Stiffness Method and Wittrick-Williams Algorithm 1509
Mudit Mishra, Sandeep Kumar

Lightweight 3D Auxetic Metamaterials 1523
Luke Mizzi, Krzysztof K. Dudek, Mandy Leconte, Andrea Frassineti, Andrea Spaggiari, Gwen Ulliac, Muamer Kadic

Auxetic Mechanical Metamaterials Designed using Missing/Added Ribs in Hexagonal Tessellation 1535
Reza Moghimimonfared, Andrea Spaggiari, Luke Mizzi

Magnetometer-based Particle Filter with enhanced velocity input for GPS-independent navigation of UAV 1545
Dominik Pisarski, Rami Faraj, Robert Konowrocki, Błażej Popławski, Łukasz Jankowski

A stationary return mapping scheme for the simulation of elastic-plastic bending of axially moving structures with non-material finite elements 1557
Jakob Scheidl, Stefan Ramsauer

Test results of HyTEM a Morphing Trailing edge Demonstrator 1569
Jan Tikalsky, Martin Radestock

Index 1581

Part I
SPECIAL SESSION - A TRIBUTE TO PROFESSOR CARLOS MOTA SOARES

Aurelio Araujo, Ayech Benjeddou

XI ECCOMAS Thematic Conference on Smart Structures and Materials - SMART 2025
M. Krommer, M. Nader and M. Schagerl (Eds)

Received: 29 April 2025 / Revised: 29 August 2025 / Accepted: 7 October 2025
© The Author(s) 2025

Full 3D Effective Properties of Piezoelectric d_{31} MFC: Validation by Detailed Finite Element Analyses of Experimented Free Smart Hybrid Honeycomb Sandwich

Ayech Benjeddou, Marcelo A. Trindade

Abstract. The purpose of this contribution is to provide a *validation* of the recently proposed *full* 3D effective *Electro-Mechanical* (EM) dataset of the *Piezo-Electric* (PE) *transverse* mode (d_{31}) *Macro-Fiber Composite* (MFC) transducer through *detailed* finite element analyses of an *experimented* free *smart hybrid honeycomb* sandwich with a *surface-bonded* PE d_{31}MFC patch. Depending on the faces and core *quadrangular* or *triangular* meshes, less than 6% deviation was found for *short-circuit* and *open-circuit* frequencies of the first three EM *coupled* modes.

Key words: Full 3D electromechanical properties, PE d_{31} MFC, Detailed FE analysis, Modal analysis, Smart hybrid honeycomb sandwich.

1 INTRODUCTION

Thanks to their main feature, the conformability, *transverse mode* (d_{31}) *Piezo-Electric* (PE) *Macro-Fiber Composites* (MFC) are nowadays popularly used for sensing [1], actuation [2], control [3,4], health monitoring [1] and energy harvesting [5]. While their multilayer *hybrid* (multi-materials) construction does not pose particular difficulty in experimental applications, their use for 3-Dimensional (3D) simulations is rather challenging. Indeed, only *partial* 3D electromechanical (EM) properties of the *multilayer* d_{31} MFC were available [2,3,5,6] until the recent *extension* [7] of the *Average Quantities-based Homogenization* (AQH) *Finite Element*

Ayech Benjeddou
Institut Supérieur de Mécanique de Paris (ISAE-SUPMECA), France
e-mail: benjeddou@isae-supmeca.fr

Ayech Benjeddou
Roberval Laboratory, Université de Technologie de Compiègne (UTC), France
e-mail: ayech.benjeddou@utc.fr

Marcelo A. Trindade
Sao Carlos School of Engineering, University of Sao Paulo, Sao Carlos, SP, Brazil
e-mail: trindade@sc.usp.br

(FE) procedure [6] for computing the *full 3D dataset* that includes the earlier missing *transverse shear* EM properties. The latter were formerly completed using either the values of the piezoceramic (PZT) fiber material [5] or those of the active layer (PZT fibers + Epoxy matrix) [8]. However, due to the *anisotropy* of the MFC material *effective behavior*, using nil missing values in 3D FE simulation leads to very poorly predicted zeros of the smart structure (MFC + host) application's frequency response function (FRF), as shown in [8].

On the other hand, while MFC combination with metallic, mainly Aluminum (Al) [2], or laminated composite, often Carbon Fiber Reinforced Polymer (CFRP) [8], hosts is common, that with *honeycomb* sandwiches is scarce. Indeed, a careful literature search has led to only two references [1,4]: One [1] has experimented a d_{31} MFC patch on a honeycomb sandwich made of CFRP [1] (no further details were given on the skins/core construction). The other [4] experimented *longitudinal* response mode (d_{33}) MFC patches on a *hybrid* honeycomb sandwich made of [0/90] CFRP laminated skins and Aramid (Nomex®) core. Here, for the patches' maximum/minimum strain-based locations, the host structure was modelled as a laminate for which the skins and core were considered as a *transversely equivalent isotropic* material with no variation along the thickness. No material dataset was given for the used d_{33} MFC patches.

Due to its *multilayer* construction, the d_{31} MFC is homogenized using FE approaches that exploit its constituents' material EM properties for computing its effective ones. As the multilayer construction, material and geometric details are mostly not known, generic material data and construction dimensions reverse engineering are used for the FE computations. Therefore, it is necessary to validate the reached effective dataset. The most followed approach is to compare to the manufacturer data and literature-homogenized ones. However, the former are incomplete and the latter use different computation inputs, such as the material and geometric data, representative volume element (RVE), FE mesh, software, etc…, hence not comparable. Consequently, there is a need to validate the homogenized data through test-model correlation of a smart structure application's measured outputs. Examples are: cantilever aluminum beam *actuation* using a d_{31} MFC patch [2], *active elasticity control* of a d_{31} MFC patch using a negative capacitance shunt [3], strain *energy harvesting* from a substrate (not defined) on which is bonded a d_{31} MFC patch [5], and *active vibration control* of a composite boom using a d_{31} MFC actuator/sensor pair [8].

Therefore, this contribution has the main aim to complement originally the above-analyzed literature by investigating the validation of the presently *unique* 3D *full* material dataset of the multilayer PE d_{31} MFC [7]. For this purpose, *detailed* FE approach [9]-based *short-circuit* (SC) and *open-circuit* (OC) *modal* analyses, using ANSYS® Mechanical APDL via a developed C^{++} application, are correlated for their SC/OC frequency outputs with those from earlier *experimental impedance analyses* (EIA) of a free *smart hybrid honeycomb sandwich* [10]. The latter is made of an Al core and *woven* Glass Fiber Reinforced Plastic (GFRP) skins on which a PE d_{31} MFC patch is bonded. Hence, in the following section 2, the SC/OC frequencies extracted from the EIA of the smart hybrid honeycomb sandwich and the FE AQH-induced 3D *full* dataset of the multilayer PE d_{31} MFC are first recalled from [10] and [7], respectively. Then, inspired from [9], section 3 presents the *detailed* FE models, simulations and test-model correlation of the host and smart hybrid honeycomb sandwich, leading to the validation of the 3D *full* material dataset of the PE d_{31} MFC. Finally, conclusions are given as a closure.

2 SMART HYBRID HONEYCOMB SANDWICH BENCHMARK

The smart structure application, used here as a benchmark for the validation of the FE AQH-induced full 3D material dataset, is a free smart *hybrid* honeycomb sandwich, typically used as a trim panel in aircraft interiors. It is composed of an Al regular *hexagonal* honeycomb core sandwiched between *woven* GFRP skins on which a PE d_{31} MFC large patch is surface-bonded. This benchmark was used earlier [10] for the EIA-based evaluation of the related effective EM coupling coefficient. Here, the resonant/anti-resonant frequencies, used for the EMCC evaluation, are considered as experimental references for, respectively, the SC/OC natural frequencies computed using the FE AQH-induced full 3D material dataset as input to the later described detailed FE approach for modelling the bare and smart sandwich panels. Figure 1 shows (a) EIA test setup and (b) a zoom on the *free* boundary conditions (BCs) realization.

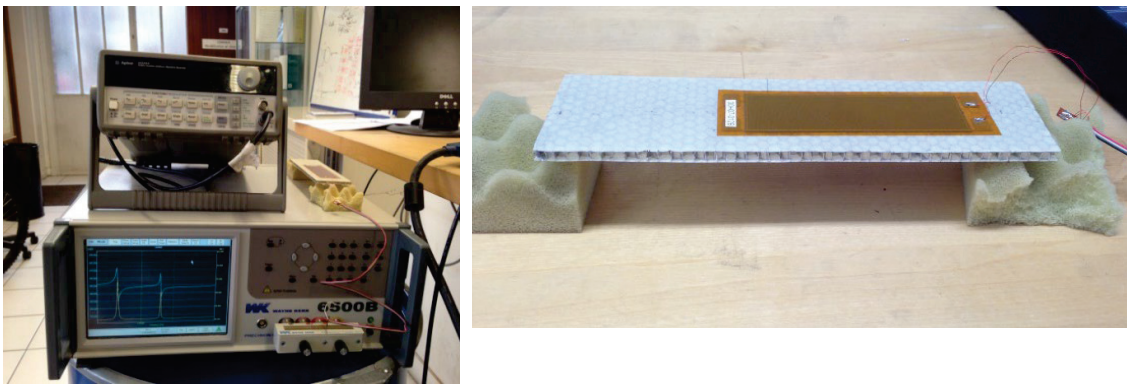

(a) EIA test setup (b) Zoom on the free BCs

Figure 1: EIA test setup (a) and free BCs realization (b) [10].

2.1 EIA-extracted SC/OC frequencies of the smart hybrid honeycomb sandwich

The SC (f_{SC}) and OC (f_{OC}) natural frequencies of the free smart hybrid honeycomb sandwich were extracted (Table 1) from the surface-bonded PE d_{31} MFC patch's *capacitance module* and *phase* of the *voltage-to-current ratio* (FRF), displayed on a WK 6500B *impedance analyzer* (Figure 1a). They approximate, respectively, the resonant (f_r) and anti-resonant (f_a) frequencies.

Table 1: EIA-extracted SC/OC frequencies (Hz) of the free smart hybrid honeycomb sandwich.

EM *coupled* Mode	f_r, f_{SC}	f_a, f_{OC}
1	600.00	618.07
2	1502.92	1523.39
3	2751.82	2788.52
4	4184.76	4242.32
5	6981.76	7089.31
6	7722.69	7850.82
7	7988.71	8061.02
8	8170.71	8319.28

It is worthy to mention that the EIA-displayed FRFs can show only the EM *coupled* modes. As the *in-plane bending* and *torsion* modes are EM *uncoupled*, only the FE computed SC/OC frequencies associated to the *transverse bending* modes-type can be compared to the extracted experimental SC/OC values shown in Table 1. This requires not only to consider the FE modal analyses SC/OC frequency outputs but also to check the *type* (transverse bending, in plane bending or torsion) of their corresponding modes.

2.2 FE AQH-induced 3D full EM dataset of the multilayer d_{31} MFC

The 3D *full* EM material properties of the *multilayer* d_{31} MFC were obtained by extending the FE AQH approach [6] to consider the *missing transverse shear* PE and dielectric (DE) coefficients [7]. The same 5-layer construction (Figure 2a) and RVE (Figure 2b), were used.

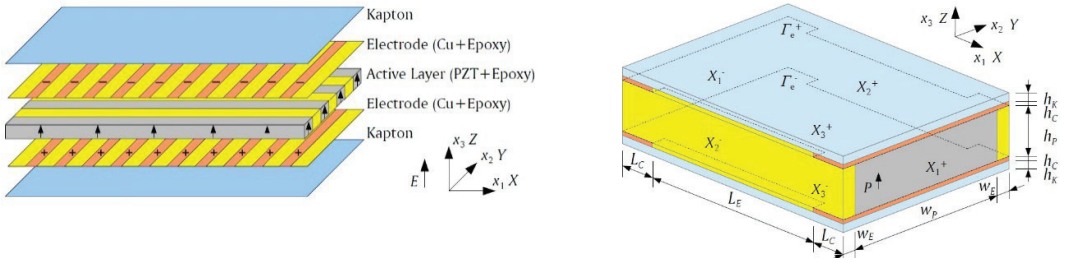

(a) 5-layer construction (b) RVE

Figure 2: d_{31} MFC 5-layer construction (a) and RVE (b) used in the extended [7] FE AQH approach [6].

However, few *additional local problems* were introduced to cover the missing coefficients, namely the shear response mode-related PE and DE ones, which are e_{15}, e_{24}, ϵ_{11}^S, ϵ_{22}^S, in the e-form, or d_{15}, d_{24}, ϵ_{11}^T, ϵ_{22}^T, in the d-form. Table 2 lists the resulting *engineering* 3D full EM dataset in both e-form and d-form, since either of them can be used as material inputs to an FE software, such as the ANSYS® Mechanical APDL used here for implementing the FE AQH. Nevertheless, only the e-form dataset will be used in the later-presented detailed FE approach for its validation via the modal analyses of above-presented smart hybrid honeycomb sandwich.

Table 2: e-form and d-form full 3D material dataset of multilayer PE d_{31} MFC.

SC *elastic* coefficients		*e-form* PE & DE coefficients		*e-form* PE & DE coefficients	
Y_1^E (GPa)	31.37	e_{31} (C/m^2)	-6.03	d_{31} (pC/N)	-172.3
Y_2^E (GPa)	19.69	e_{32} (C/m^2)	-3.44	d_{32} (pC/N)	-133.2
Y_3^E (GPa)	9.02	e_{33} (C/m^2)	1.48	d_{33} (pC/N)	308.9
G_{23}^E (GPa)	2.16	e_{15} (C/m^2)	0.81	d_{15} (pC/N)	334.9
G_{31}^E (GPa)	2.42	e_{24} (C/m^2)	0.47	d_{24} (pC/N)	219.3
G_{12}^E (GPa)	5.33	$\epsilon_{11}^S/\epsilon_0$	988.6	$\epsilon_{11}^T/\epsilon_0$	1019.3
ν_{12}^E (-)	0.36	$\epsilon_{22}^S/\epsilon_0$	24.1	$\epsilon_{22}^T/\epsilon_0$	24.1
ν_{23}^E (-)	0.37	$\epsilon_{33}^S/\epsilon_0$	1181.7	$\epsilon_{33}^T/\epsilon_0$	1573.3
ν_{13}^E (-)	0.42	ϵ_0 (pF/m)	8.854	ϵ_0 (pF/m)	8.854

3 DETAILED FE MODELS, SIMULATIONS AND CORRELATIONS

3.1 Hybrid honeycomb sandwich host structure

The honeycomb sandwich panel, having the geometric and material properties shown in Table 3, is modelled using a similar methodology to the practical detailed FE approach [9]. The latter is based on a *Graphical User Interface* (GUI) that generates a *commands script* for a FE software (ANSYS® Mechanical APDL). Beside the main characteristic of the skins and core cell walls *individual meshes*, the generated script contains all other data and commands for the pre-processing, solution (modal) and post-processing (outputs) steps needed by a FE analysis.

Table 3: Hybrid honeycomb sandwich panel geometric and materials properties [9]

Sandwich*	Length (L)	Width (l)	Thickness (H)	Length cells (N_L)	Width cells (N_l)
	18.3 cm	5.2 cm	4.6 mm	25 (*counted*)	10 (*counted*)
Core	Cell length (A)	Cell width (B)	Cell wall thickness (t)	Double wall thickness (2t)	Cell side (a)
	*6 mm	*5.2 mm	*45 µm	*90 µm	*3 mm
	Material	Thickness (h)	Young's (E_c)	Poisson's (ν_c)	Density (ρ_c)
	Aluminum	*4.2 mm	**70 GPa	**0.3	**2815 Kg/m^3
Faces	Material	Thickness (t_{fg})	Young's (E_f)	Poisson's (ν_f)	Density (ρ_f)
	Composite	*155 µm	***19 GPa	**0.17	***2200 Kg/m^3

* *Measured*. ** *Assumed* as generic data. *** *Identified* via test-FE correlation.

The main new features of the present detailed FE approach are: (i) a specifically developped C^{++} *application* (Visual Studio 2022), instead of the earlier Matlab® GUIDE function-based GUI for generating the commands script; (ii) the skins and core cell walls are *automatically meshed* in ANSYS® while, earlier, each core cell wall was meshed prior to ANSYS® by a single element and those of the skins use a minimum number of elements that cover top and bottom areas of the core hexagonal cells; iii) the geometric models of the skins are defined by only their corner nodes while, formerly, their geometries were extruded from the top and bottom geometric nodes of the core, prior to meshing the three layers (skins and core). Here, the core in-plane geometry (Figure 3a) is obtained by repeating the elementary cell shown in Figure 3b.

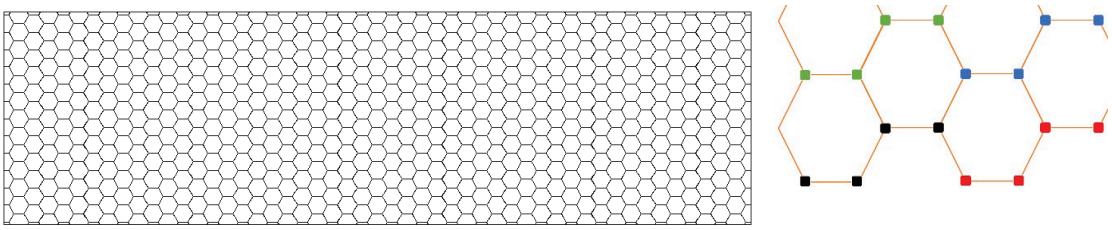

(a) In-plane geometry of the core (b) Elementary cell

Figure 3: The core in-plane geometry (a) created by repeating an elementary cell (b).

Noticeably, as ANSYS® has archived its SHELL63 element used in [9], it is replaced here

by SHELL181 element, as recommended in ANSYS® documentation. Besides, the geometries induced by the detailed FE approach [9] led to *saw teeth-like lateral edges* of the sandwich that were necessary to make straight as are the actual ones while here, by the new design approach, there is no need for this meshing complexity, as the edges are 'naturally' straight. Moreover, due to manufacturing geometric defaults of the sandwich panel assembly, the use of the counted 25 hexagonal cells of 3 mm radius in the length leads to a longer panel, while using the latter radius value leads to 21 cells only along the length. For this reason, to use the 25 cells as a dimension input, a homothetic factor of 4/5 was used in [9] to cover a closer value to the actual length. Here, 2.44 mm hexagonal cell radius is used to cover the counted 25 cells. Table 4, comparing the two cell radii-induced fundamental mode frequency with the measured one, via a drop test, of the sandwich panel, shows clearly the very good accuracy (0.56 % error) of the reduced radius. It can be also noticed that using a homothetic factor with the length actual cells number (25) recovers the results of the saw teeth edges with a length of reduced 21 cells. The closest (0.07 % error) value to the experiment is obtained using the latter cell number and 3-node triangular (T3) FE for closing the saw teeth-like lateral edges.

Table 4: Fundamental frequency variation with the sandwich panel modelling method.

Method	Model	Frequency (Hz)	Error* (%)
Test		560.00	reference
Present (SHELL181)	21 cells (3 mm)	576.73	2.99
	25 cells (2.44mm)	563.13	0.56
[9] (SHELL63)	21 cells (3 mm, *saw teeth*-like lateral edges)	567.52	1.34
	21 cells (3 mm, added T3 FE-*straight* lateral edges)	560.40	0.07
	25 cells (3 mm, added T3 FE-*straight* lateral edges & *homothetic* factor)	567.61	1.36

* Error (%) = 100*(FE-test)/test

The results from [9] in Table 4 were obtained using a *mapped* mesh as described above. However, the present ones were obtained using an *automatic* mesh with a 4-node quadrangular (Q4) element size of 2 mm, shown in Figure 4a in comparison to that of 5 mm (Figure 4b). It corresponds to the minimum error (0.56%) with the drop test fundamental frequency (Figure 5a) in the cost of a dense mesh of 20496 elements (Figure 5b). Nevertheless, it is retained for the next sub-section and its validation results with the present methodology.

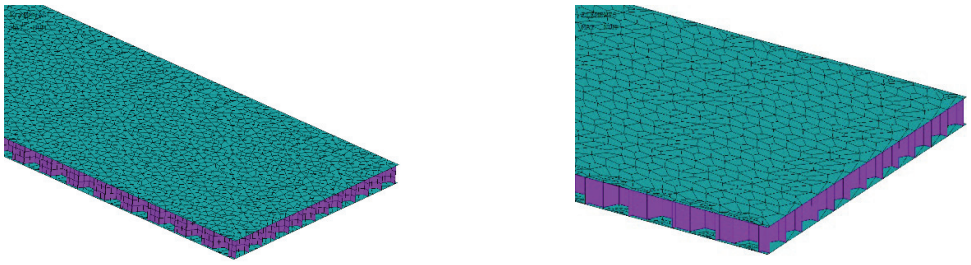

(a) Element size 2 mm (20496 FE) (b) Element size 5 mm (7570 FE)

Figure 4: Hybrid honeycomb sandwich Q4 FE mesh with element size 2 mm (a) and 5 mm (b).

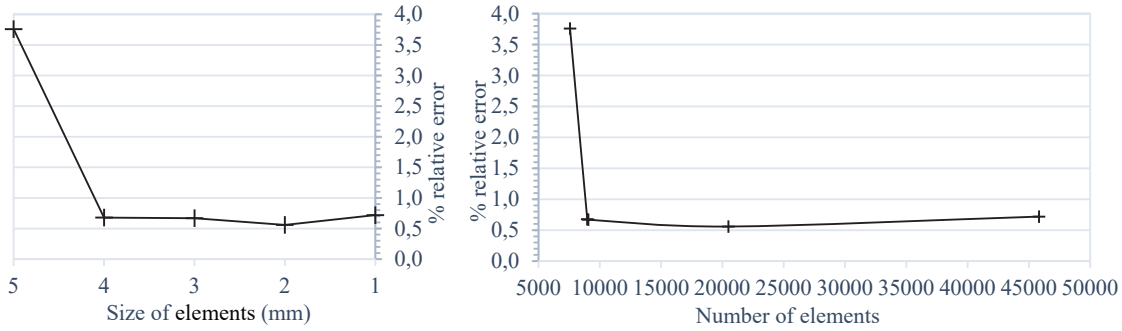

(a) Element size (mm) (b) Element number

Figure 5: Element size (a) and number (b) of the mesh *convergence* analysis.

Besides, all results of Table 4 were obtained using Q4 FE-based meshes. The use of a T3 FE-based mesh for all layers, within the present methodology, led to a much less accurate (5.26 % error) fundamental frequency (589.48 Hz) as can be seen in Table 5. This may be because T3 *option* is a *degeneration* of the Q4 SHELL181, which is '*not recommended*' by ANSYS®. Table 5 shows other combinations of skin/core/skin Q4- and T3-based meshes, but clearly, the most accurate (0.56 % error) mesh is the Q4/Q4/Q4 followed by the T3/Q4/T3 (1.57 % error).

Table 5: Fundamental frequency variation with the skin/core/skin FE mesh.

Method	Skin/core/skin FE mesh (2 mm)	Frequency (Hz)	Error* (%)
Test		560.00	reference
Present (SHELL181, 25 cells, 2.44 mm)	Q4/Q4/Q4	563.13	0.56
	T3/T3/T3	589.48	5.26
	T3/Q4/T3	568.78	1.57
	Q4/T3/Q4	578.23	3.25

* Error (%) = 100*(FE- test)/test

The fundamental mode, superposed to the non-deformed honeycomb sandwich, is illustrated in Figure 6 with the Q4/Q4/Q4 most accurate mesh, hence *retained* for the next sub-section.

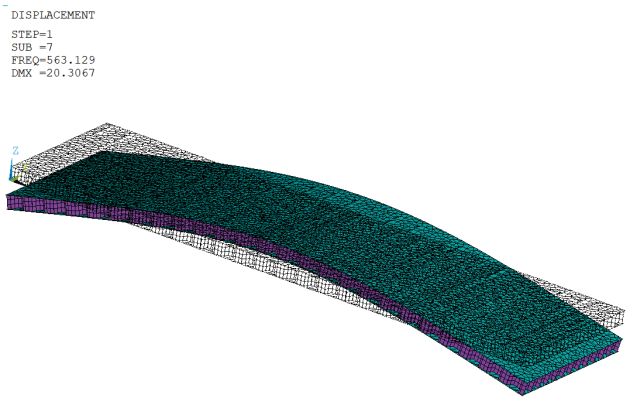

Figure 6: Superposed fundamental mode shape and non-deformed honeycomb sandwich (Q4/Q4/Q4 mesh).

3.2 Hybrid honeycomb sandwich smart structure

In the C^{++} application, first, the four corners model the geometry of d_{31} MFC patch (having an active area of 85 x 28 mm^2 and thickness of 0.3 mm) and its bottom-left node defines its location (30 mm from an edge of the sandwich and *width-centered*) on the sandwich top skin. Then, in replacement of SOLID5 used in [9], which was archived, the d_{31} MFC patch mesh in ANSYS® uses the 6-node *prismatic* (P6) FE *option* of the 8-node hexahedral (H8) SOLID225 one, which cannot be used for an *automatic* mesh. Thanks to its three quadrangular and two triangular faces, the prismatic FE can be *automatically* compatible with Q4 and T3 meshes of the top skin. The other two options of 4-node *tetrahedral* and 5-node *pyramid* FEs are '*not recommended*' by ANSYS®. Figure 7 shows one of the smart hybrid honeycomb sandwich meshes used in the hereafter validation results.

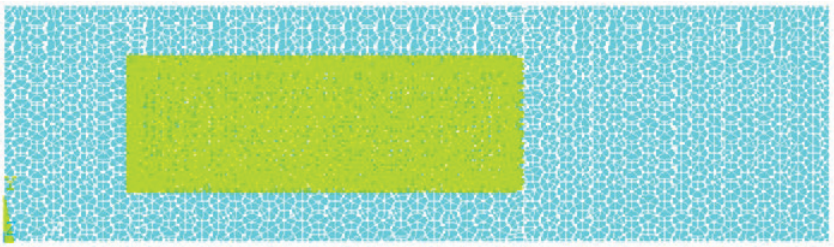

Figure 7: Top view of the free smart hybrid honeycomb sandwich Q4/Q4/Q4/P6 2mm-size mesh.

First, Table 6 shows a comparison of the first three EM *coupled* modes' frequencies and their variations with those of the EIA test (Table 1), obtained with the C^{++} application four-mesh options of the smart hybrid honeycomb sandwich when the d_{31} MFC patch electrodes are in SC electric connection. The most accurate mesh is that with Q4/Q4/Q4, except for the fundamental mode where Q4/T3/Q4 performs better. The second most accurate mesh is the T3/Q4/T3, which also performs less than Q4/T3/Q4 for the fundamental mode.

Table 6: EM coupled FE SC frequencies and variations with EIA test (Table 1) and skin/core/skin FE mesh.

Skin/core/skin FE mesh (2 mm)	Order of EM coupled mode	7		9		11	
		Freq. (Hz)	Error (%)	Freq. (Hz)	Error (%)	Freq. (Hz)	Error (%)
Q4/Q4/Q4		587.44	-2.09	1501.62	**-0.03**	2796.23	**1.61**
T3/T3/T3		611.95	1.99	1565.09	4.19	2912.24	5.83
T3/Q4/T3		592.21	*1.30*	1514.36	*0.82*	2820.16	*2.48*
Q4/T3/Q4		602.26	**0.38**	1539.98	2.52	2866.55	4.17

* Error (%) = 100*(FE- test)/test

Then, Table 7 shows the comparison of the first three EM *coupled* modes' frequencies and their variations with those of the EIA test (Table 1), obtained with the C^{++} application four-mesh options of the smart hybrid honeycomb sandwich when the d_{31} MFC patch electrodes are in OC electric connection with enforced *equipotential* (EP) constraints. Here, Q4/Q4/Q4 and T3/Q4/T3 behave similarly in the sense that each one is the most accurate for one mode, performs secondly for another mode and less than T3/T3/T3 for the fundamental mode.

Table 7: EM coupled FE OC frequencies and variations with EIA test (Table 1) and skin/core/skin FE mesh.

Skin/core/skin FE mesh (2 mm)	Order of EM coupled mode	7		9		11	
		Freq. (Hz)	Error (%)	Freq. (Hz)	Error (%)	Freq. (Hz)	Error (%)
Q4/Q4/Q4		590.01	-4.54	1506.82	*-1.09*	2805.44	**0.61**
T3/T3/T3		614.70	**-0.54**	1570.65	3.10	2922.11	4.79
T3/Q4/T3		594.82	-3.76	1519.64	**-0.25**	2829.54	*1.47*
Q4/T3/Q4		604.91	*2.13*	1545.35	1.44	2876.08	3.14

* Error (%) = 100*(FE- test)/test

As guessed earlier, on one hand, the FE EM *coupled* modes are transverse (x-z) ones. For confirmation, those (of order 7, 9, 11) compared in Tables 6 and 7 are shown in Figure 8.



(a) First (FE order 7) transverse (x-z) mode.

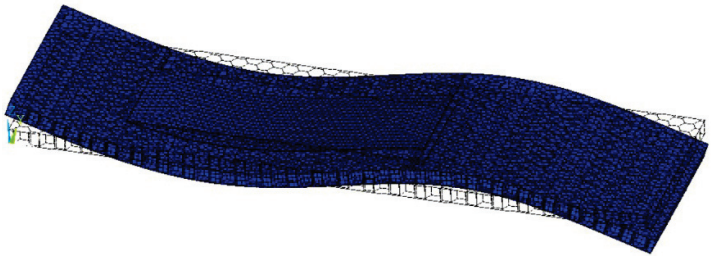

(b) Second (FE order 9) transverse (x-z) mode.

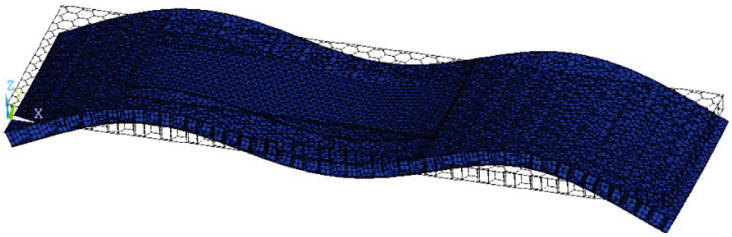

(c) Third (FE order 11) transverse (x-z) mode.

Figure 8: First three FE EM *coupled* modes of the free *smart* hybrid honeycomb sandwich.

On the other hand, the FE EM *uncoupled* modes are *torsion* ones and are shown in Figure 9 for those (of order 8 and 10) not appearing in Tables 6 and 7.

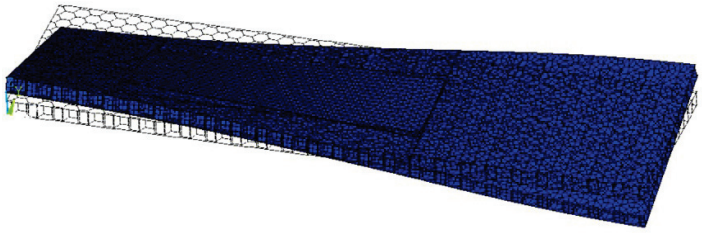

(a) First (FE order 8) *torsion* mode.

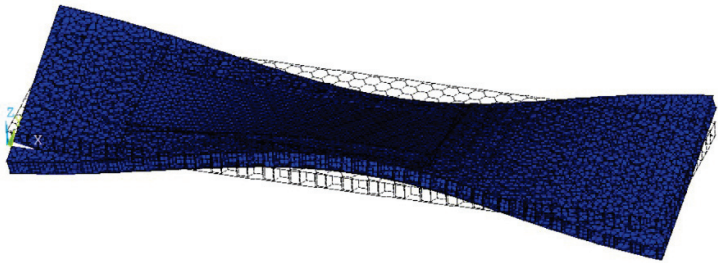

(b) Second (FE order 10) *torsion* mode.

Figure 9: First two FE EM *uncoupled* modes of the free *smart* hybrid honeycomb sandwich.

4 CONCLUSIONS

The presently *unique* 3D *full* EM material properties dataset of the *multilayer* (5-layer) d_{31} MFC [7] has been validated against drop test [9] and EIA tests (Table 1) [10] of a *free* hybrid honeycomb sandwich, as a *host* structure and *smart* (with surface-bonded d_{31} MFC) one. Both structures were modelled by a detailed FE approach [9]-like *new* methodology, which was implemented via a *C*$^{++}$ *application* new GUI that generates *commands* scripts, as input files for ANSYS® Mechanical APDL FE *modal* analyses. It was found that, for the *host* structure, the comparison of the only experimentally available *fundamental* mode frequency, a maximum 5.26 % error was obtained for the four configurations of Q4 and T3 *automatically* meshed skin/core/skin sandwich. Besides, for the *smart* structure with the same four mesh configurations of the host while the d_{31} MFC patch always meshed with P6 FEs, maximum errors of 5.83 % and 4.79 % were obtained, respectively, for the SC and OC (with EP constraints) MFC patch electrodes. Therefore, these good results clearly validate the presently *unique* 3D *full* EM material properties dataset of the *multilayer* (5-layer) d_{31} MFC [7].

ACKNOWLEDGEMNTS

The first author is grateful to the support of the COMET-K2 *Symbiotic Mechatronics Center*, of the *Linz Center of Mechatronics*, funded by the Austrian federal government and state of Upper Austria. He is also thankful to his Master students for their help in designing (M. Hussain) and enhancing (T. L'Horset) the C^{++} application, within their respective design office projects under the author's guidance.

REFERENCES

[1] M. Rebillat, M. Guskov, E. Balmès, and N. Mechbal, "Simultaneous influence of static load and temperature on the electromechanical signature of piezoelectric elements bonded to composite aeronautic structures," *ASME Journal of Vibration and Acoustics*, vol. 138, art. no. 064504, 2016.

[2] M. P. Saravanan, K. Marimuthu, and K. Jayabal, "Characteristic investigation of macro fiber composite structure using FE model," *Archives of Metallurgy and Materials*, vol. 66, no. 4, pp. 1059-1066, 2021.

[3] K. Steiger, and P. Mokrý, "Finite element analysis of the macro fiber composite actuator: macroscopic elastic and piezoelectric properties and active control thereof by means of negative capacitance shunt circuit," *Smart Materials and Structures*, vol. 24, art. no. 025026, 2015.

[4] A. Zippo, G. Ferrari, M. Amabili, M. Barbieri, and F. Pellicano, "Active vibration control of a composite sandwich plate," *Composite Structures*, vol. 128, pp. 100–114, 2015.

[5] Y. Kuang, and M. Zhu, "Evaluation and validation of equivalent properties of macro fibre composites for piezoelectric transducer modelling," *Composites Part B*, vol. 158, pp. 189-197, 2019.

[6] M. A. Trindade, and A. Benjeddou, "Finite element characterisation of multilayer d_{31} piezoelectric macro-fibre composites," *Composite Structures*, vol. 151, pp. 47-57, 2016.

[7] M. A. Trindade, and A. Benjeddou, "Finite element evaluation of full 3D effective properties of d_{31} piezoelectric macro-fibre composites," In *Proceedings of the Eighth International Conference on Smart Materials and Nanotechnology in Engineering*, M. Ghommem, A. Benjeddou, J. Leng and A. Abdelkefi (eds.), pp. 52-61, 2024.

[8] A. Deraemaeker, S. Benelechi, A. Benjeddou, and A. Preumont, "Analytical and numerical computation of homogenized properties of MFCs : application to a composite boom with MFC actuators and sensors," In *Proceedings of the III ECCOMAS Thematic Conference on Smart Structures and Materials*, W. Ostachowicz, J. Holnicki-Szulc, C. Mota Soares et al. (eds.), CD-ROM, 2007.

[9] A. Benjeddou, and M. Guerich, "Free-vibration of actual aircraft and spacecraft hexagonal honeycomb sandwich panels: a practical detailed FE approach," *Advances in Aircraft and Spacecraft Science*, vol. 6, no. 2, pp. 169-187, 2019.

[10] A. Benjeddou, "Experimental evaluation of the effective electromechanical coupling of a vibrating aircraft-type hybrid honeycomb sandwich panel with bonded piezoelectric d_{31} macro-fibre composite (MFC) patch," In *Proceedings of the Eighth International Conference on Smart Materials and Nanotechnology in Engineering*, M. Ghommem, A. Benjeddou, J. Leng and A. Abdelkefi (eds.), pp. 62-69, 2024.

XI ECCOMAS Thematic Conference on Smart Structures and Materials - SMART 2025
M. Krommer, M. Nader and M. Schagerl (Eds)

Received: 21 March 2025 / Revised: 5 October 2025 / Accepted: 7 October 2025
© The Author(s) 2025

Adaptive Petal Polymer Reflector for Cubesat Applications

Carl Johan G. Nielsen, Gonçalo Rodrigues, André Preumont

Key words: CubeSat, PVDF-TrFE, Piezoelectric Polymers, Deployable Space Telescope, Petal Reflector, Shape Control, Optical Communication.

Abstract Flexible ultra-thin deployable reflectors are the subject of increasing interest because they combine a low areal density with the capability to deploy to sizes significantly larger than their stowed size, allowing a better resolution and a better signal quality. The present study is targeted at cube-sats; the idea consists of having a petal polymer primary reflector, folded during the launch, which unfolds elastically in orbit thanks to a linear translation mechanism. To improve the surface figure accuracy, the system is actively controlled with an array of integrated piezoelectric polymer actuators (PVDF-TrFE). The project "Advanced Multilayer Adaptive Thin Shell" (AMATS) is supported by ESA-ESTEC. The paper presents the work done to date that is relevant to the topic of the conference and discusses the problems encountered because of the space thermal environment.

1 INTRODUCTION

So far, most optical systems operating in space are using rigid primary reflectors. More recent space projects tend to substitute large spacecraft with LEO constellations of smaller ones that are cheaper and mass producible. Ultimately, CubeSats could be used for Earth observation or inter-satellite laser communication (e.g. [1, 2]) if it were not limited by the image resolution in Earth observation and the transmission gain in laser communication, both of which depend critically on the size of the telescope aperture [3] (constrained below 10 cm for CubeSats). This has led to considering foldable primary light-collecting surfaces. Various CubeSats prototypes with rigid petal reflectors are being considered (e.g. [4, 5]). See also [6] for a review of deployable space optics.

Figure 1 shows an interesting concept where the primary light-collecting mirror consists of four rigid petals fitting within the volume of a 1.5 U CubeSat; the deployed configuration consists of 4 square rigid panels of 9×9 cm^2. According to [7], high deployment repeatability and active control with piezoelectric motors (3 per petal) driven by image sharpness optimization on tip, tilt and piston of each individual petal allows to improve the resolution by a factor 3 (compared to a single circular monolithic mirror fitting in the CubeSat), leading to a spatial resolution in the visible of 1 m at 500 km.

An alternative solution, considered in this study, consists of a petal flexible polymer reflector of spherical shape as illustrated in Figure 2. The petals are stowed in the CubeSat body during the launch and then deployed on orbit by opening the sides and extending the secondary mirror boom. The surface figure accuracy after deployment is actively improved thanks to an array of piezoelectric polymer actuators [8,9] used to compensate for thermal, viscoelastic and manufacturing errors.

Carl Johan G. Nielsen & André Preumont
Université Libre de Bruxelles, Laboratory of System Analysis and Automatic Control, 50, Av. F.D.Roosevelt 1050 Brussels, Belgium, e-mail: andre.preumont@ulb.be

Gonçalo Rodrigues
ESA/ESTEC, Structures Section (TEC-MSS), Keplerlaan 1, PO Box 299, NL-2200 AG Noordwijk, The Netherlands, e-mail: goncalo.rodrigues@esa.int

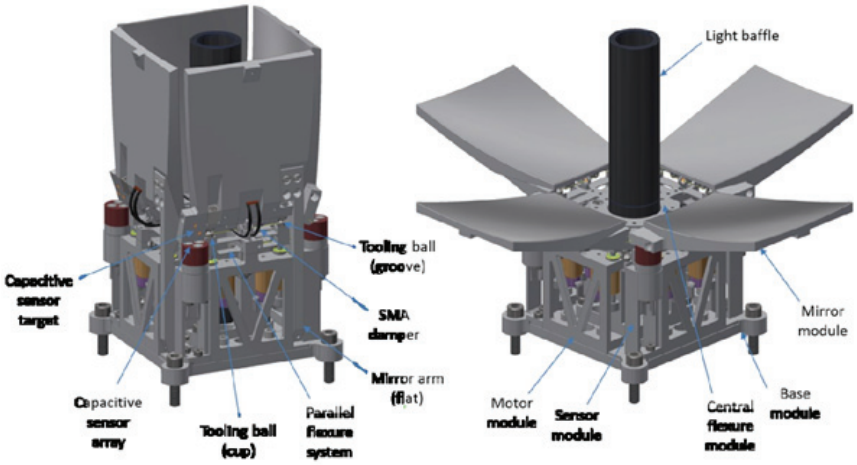

Figure 1: Active deployable primary mirrors fitting in a 1.5 U CubeSat. Folded (left) and deployed (right) configurations [5, 7].

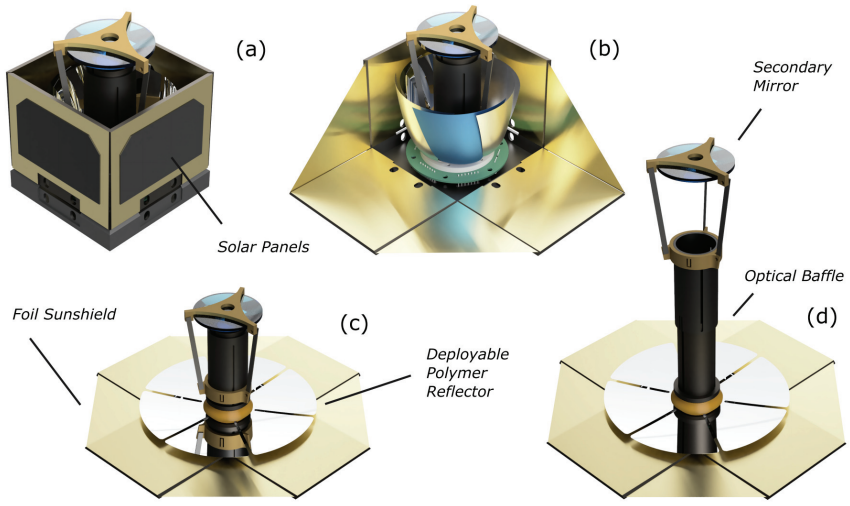

Figure 2: CAD rendering of a One-unit CubeSat adaptive deployable petal telescope with a primary mirror of 160 mm. (a) Folded configuration. (b) With 2 sides deployed showing the folded petal primary mirror. (c) Secondary mirror deployed. (d) All sides open, primary mirror and solar blanket deployed.

2. ACTIVE CONTROL

Active control of a polymer shell with an array of piezoelectric polymer (PVDF-TrFe) was demonstrated in an earlier project [8]. However, it appeared that, because of the large CTE of the PVDF (140 10^{-6} K^{-1}), a single layer design (Figure 3a) was not possible due to the thermal sensitivity (thermal disturbances are the most critical disturbance in the space environment and even small thermal gradients would rapidly lead to large deformations that cannot be compensated by active control). The control layer must therefore be thermally balanced by a symmetric layer with equal CTE (Figure 3b) [9]. PVDF-TrFe (acting passively) was selected

for the thermal balancing layer; the two layers of equal thickness are deposited simultaneously by dip coating.

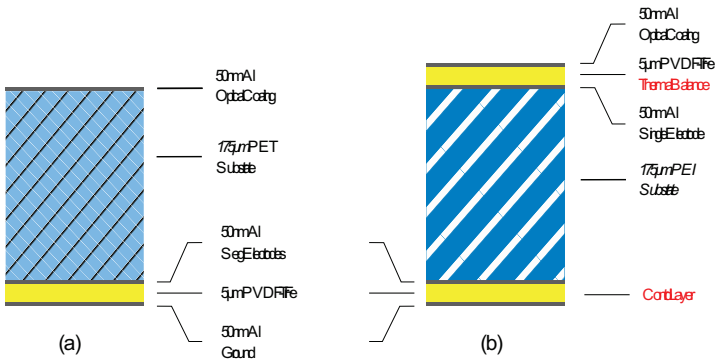

Figure 3: (a) Single layer configuration. (b) Thermally balanced configuration.

The potential benefit of active control and the influence of the electrode layout is illustrated by the following simulations. The spherical reflector has an outside diameter of 160 mm and a radius of curvature of 850 mm; the central support where the reflector is clamped has a diameter of 45 mm. The material data are those of Table 1. Figure 4 considers the gravity deformations introduced when the reflector is in vertical position (for laboratory metrology); from left to right, the figure displays the gravity aberration without control, the residual error after control (the residual RMS error is indicated in the figure) and the electrode voltage map. The upper figure corresponds to 6 electrodes per petal and the bottom one to 12 electrodes per petal. One sees that, with 6 electrodes per petal, the RMS error within a pupil extending from a diameter of 60 mm to 150 mm (indicated by dashed circles) is reduced from 55 µm to 2.4 µm while it is reduced to 1.2 µm with 12 electrodes per petal. Figure 5 illustrates the control of a thermal gradient of +/- 10°K. With 6 electrodes, the RMS residual error within the pupil is reduced from 5.7 µm to 0.44 µm. The residual error drops to 0.23 µm with 12 electrodes per petal. The voltages remain moderate

Table 1: Material and Layer properties used in simulations.

Function	Material	Thickness	Young's modulus (GPa)	Poisson's ratio	CTE (10^{-6}/°K)	d31 (10^{-6} µm/V)
Optical Coating	Al	50 nm	68	0.32	23	–
Thermal balance	PVDF	5 µm	2.5	0.34	140	15
Single Electrode	Al	50 nm	68	0.32	23	–
Substrate	PEI	175 µm	2.9	0.38	56	–
Patterned Electrodes	Al	50 nm	68	0.32	23	–
Patterned Electrode	PVDF	5 µm	2.5	0.34	140	15
Ground electrode	Al	50 nm	68	0.32	23	–

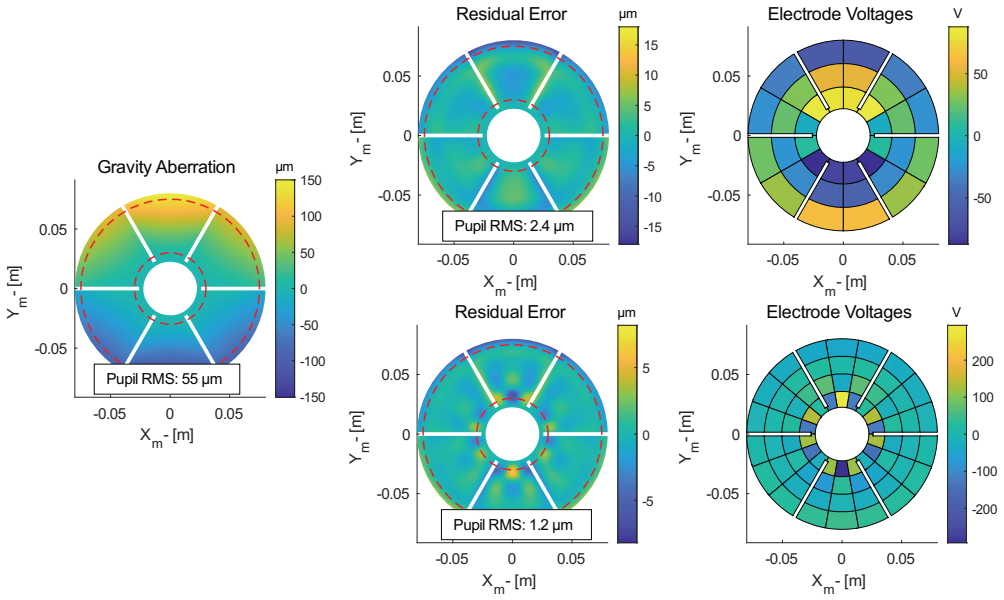

Figure 4: Control of the gravity deformation when the reflector is in vertical position. The remaining aberration over the pupil (from d=60 mm to d=150 mm indicated by dashed red circles) of the reflector is 2.4 μm with 6 electrodes per petal and it is reduced to 1.2 μm with 12 electrodes per petal.

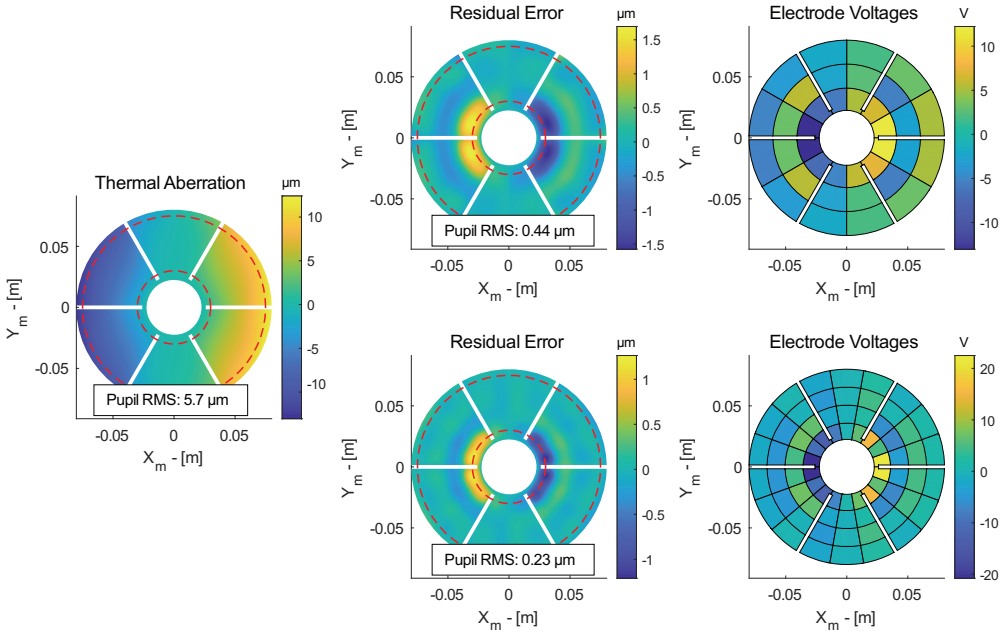

Figure 5: Control of a thermal gradient of +/- 10°K. The reflector is clamped on the inner circle. The RMS error in the pupil is reduced from 5.7 μm to 0.44 μm with 6 electrodes per petal and it drops to 0.23 μm with 12 electrodes per petal.

Figure 6 shows the importance of having the same thermal expansion behaviour for the reflector and its central support. The figure compares the thermal deformations induced by a uniform temperature increase of 10°K when the thermal expansion of the central support is not allowed (top) and when the CTE of the central support matches that of the reflector (bottom). Similarly, Figure 7 illustrates the importance of having a good thermal balance; the figure shows the thermal deformations for a uniform temperature increase of 10°K when the CTE of the central support matches that of the reflector but there is a 5 % mismatch between the thickness of the control layer (4.75 µm) and the thermal balancing layer (5 µm). The comparison with the bottom part of Figure 6 where the two layers have the same thickness (5 µm) highlights the need for a careful thermal balance.

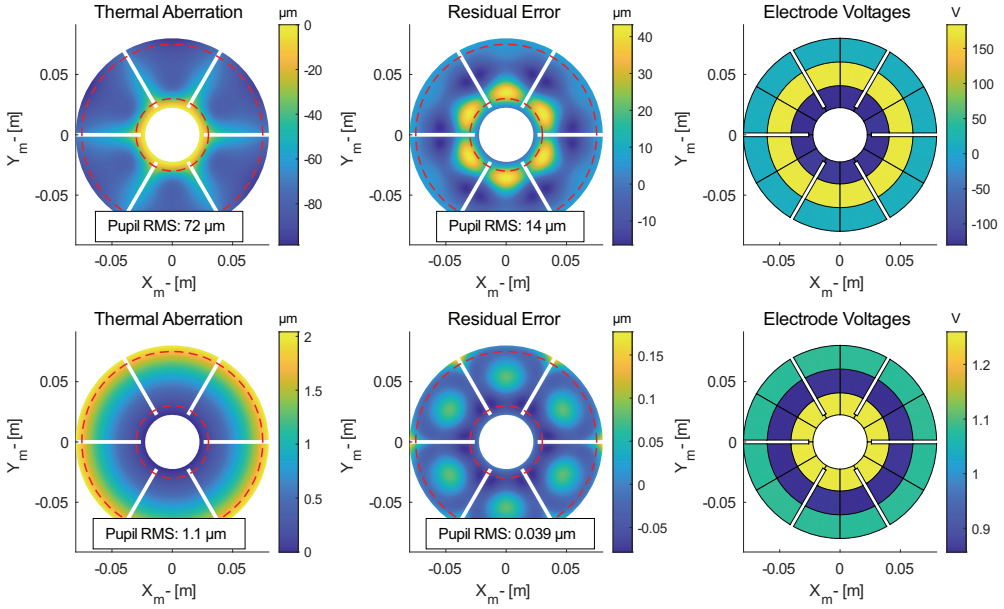

Figure 6: Uniform temperature increase of 10°K, 6 electrodes per petal. Influence of the CTE of the central clamp support. In the top figure, the thermal expansion of the central support is not allowed. In the bottom figure, the CTE of the central support matches that of the reflector.

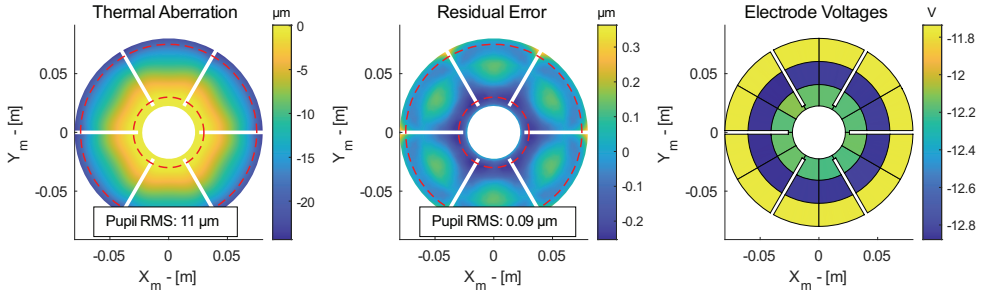

Figure 7: Sensitivity to the thermal balance. Uniform thermal field of 10°K. The thermal balancing layer thickness is t=5 µm while the control layer thickness is t=4.75 µm. This figure is to be compared with Figure 6 (bottom).

3. DEMONSTRATOR

Figure 8 shows the main features of the demonstrator under manufacturing. Both the reflector substrate and the plastic clamp are made of the same material (PEI Ultem 1000), to minimize the effect of thermal differential expansion on the surface figure. All the electrodes (36 control electrodes plus ground) are connected to the to the PCB by spring-loaded POGO connectors. The spherical shell consists of 7 layers as described in Figure 9, with the properties of Table 1. The thermal balance layer and the active control layer are made simultaneously by dipcoating of the piezoelectric material (PVDF-TrFe); they are both polarized to keep internal stresses symmetrical. The demonstrator is being manufactured by our partner in this project, MateriaNova (Mons, Belgium).

4. SCOTS METROLOGY

Measuring the surface figure error of a spherical reflector alone during the development phase and assessing the control performance before assembling the telescope is a challenging task requiring special equipment. The SCOTS (Software Configurable Optical Testing System) developed at the University of Arizona [10] appears to provide a fast and satisfactory solution to this problem. Figure 10 shows the setup showing screen, reflector, camera, and control electronics [11]. The shape of the reflector is found from the distortion of the reflected pattern. With the screen near the centre of curvature, the errors in the shape are highly amplified. The metrology has been found satisfactory for the project.

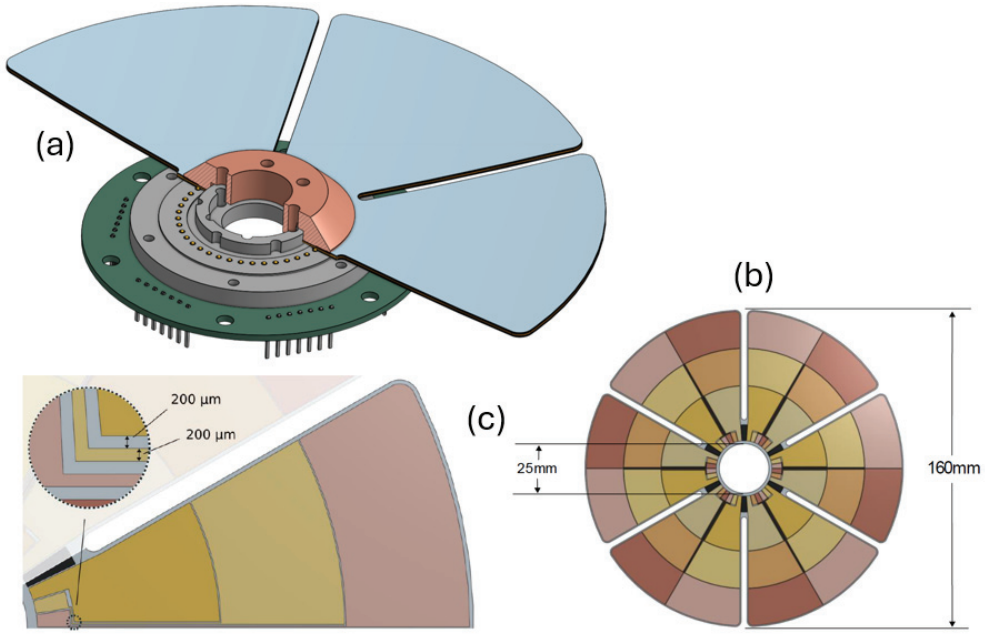

Figure 8: Demonstrator design. (a) Exploded view showing the overall design of the PCB (green), bottom clamp (grey), top clamp (light-red) and reflector (light-blue). The POGO connectors (yellow) connect the PCB to the reflector electrodes (the thickness of the reflector is exaggerated). (b) Layout of the control electrodes, 6 electrodes per petal. (c) Details of 3 control electrodes on half a petal and their conducting tracks coming from the central support.

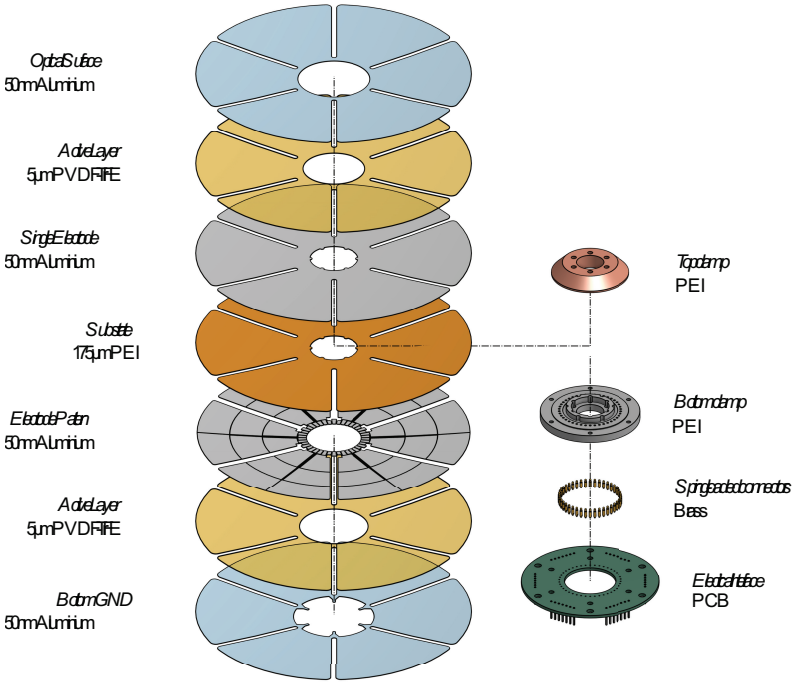

Figure 9: Exploded view of the layers making up the reflector and electrical clamp assembly. The material properties are given in Table 1.

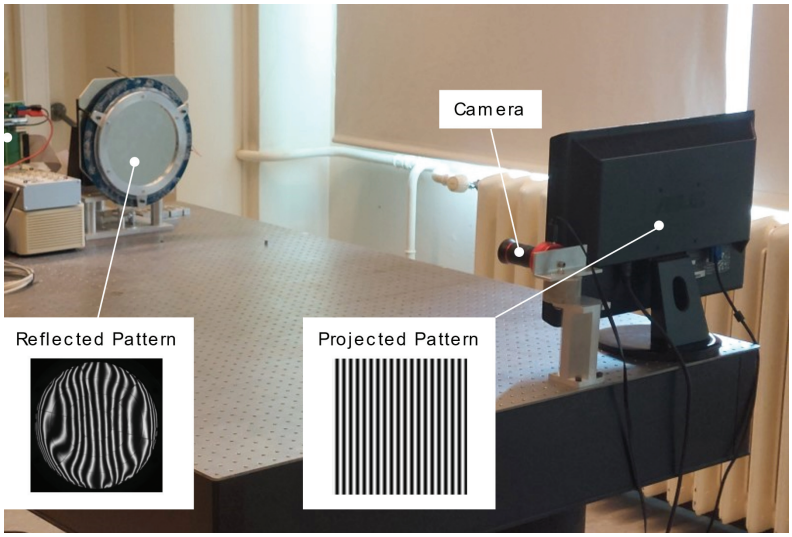

Figure 10: SCOTS metrology: Experimental configuration for measuring the surface figure of a spherical shell, showing screen, reflector, camera, and control electronics. The shape of the reflector is found from the distortion of the reflected pattern.

5. VISCOELASTIC DEFORMATIONS

The polymer petal reflector is subject to creep during the storage period in folded configuration before the launch, and relaxation once deployed in orbit. Numerical and experimental studies are underway:

1. to demonstrate that the stress level created by the large displacements during the folding do not reach the threshold where permanent strains will appear, so that the reflector remains in the viscoelastic regime (handled numerically with a multibranch Maxwell model [12]).
2. To predict viscoelastic deformations over a period including all phases of folding and deployment, to estimate the residual shape aberration in deployed configuration and to verify that it remains within the range of the active shape control.

Experiments monitoring the relaxation post deployment are also in preparation with the SCOTS metrology.

6. ACKNOWLEDGEMENTS

The design and manufacture of the multilayer petal demonstrator is under the responsibility of our project partner MateriaNova (Mons). The authors wish to thank Thomas Godfroid, Damien Robert and Julie Passion for their friendly collaboration.

REFERENCES

[1] JIN, H., LIM, J., KIM, Y., KIM, S. (2013). Optical Design of a Reflecting Telescope for CubeSat. Journal of the Optical Society of Korea, 17(6), 533-537.

[2] GUELMAN, M., KOGAN, A., KAZARIAN, A., LIVNE, A., ORENSTEIN, M., MICHALIK, H, ARNON, S. (2004). Acquisition and pointing control for inter-satellite laser communications. IEEE Transactions on Aerospace and Electronic Systems, Vol.40. No 4, 1239 - 1248.

[3] BOONE B.G. et al. Optical Communications Development for Spacecraft Applications, JOHNS HOPKINS APL TECHNICAL DIGEST, VOLUME 25, NUMBER 4, pp.306-315 (2004)

[4] CHAMPAGNE, J. et al., CubeSat image resolution capabilities with deployable optics and current imaging technology, in 28th Annual AIAA/USU Conf. Small Satellites, (2014).

[5] SCHWARTZ, N. et al., A segmented deployable primary mirror for earth observation from a CubeSat platform, in Proc. AIAA/USU Conf. Small Satell., vol. SSC16, p. SSC16-WK-23 (2016).

[6] VILLALBA, V., KUIPER, H. and GILL, E., Review on thermal and mechanical challenges in the development of deployable space optics. J. of Astronomical Telescopes, Instruments, and Systems, 6(1), 010902 (2020), doi: 10.1117/1.JATIS.6.1.010902

[7] SCHWARTZ, N. et al., High resolution deployable CubeSat prototype, Proc. SPIE 11443, Space Telescopes and Instrumentation 2020.

[8] WANG, K.; GODFROID, T.; ROBERT, D.; PREUMONT, A. Adaptive shell spherical reflector actuated with PVDF-TrFE thin film strain actuators. *Actuators* 2021, 10, 7.

[9] NIELSEN, C.J.G.; TIAN, D.; WANG, K.; PREUMONT, A. Adaptive Deployable Thin Spherical Shell Reflectors. Actuators **2022**, 11, 198. https://doi.org/10.3390/act11070198.

[10] PENG SU, ROBERT E. PARKS, LIRONG WANG, ROGER P. ANGEL, and JAMES H. BURGE, "Software configurable optical test system: a computerized reverse Hartmann test," Appl. Opt. 49, 4404-4412 (2010)

[11] NIELSEN, C.J.G.; PREUMONT, A. Adaptive Petal Reflector: In-Lab Software Configurable Optical Testing System Metrology and Modal Wavefront Reconstruction. Sensors **2023**, 23, 7316. https://doi.org/10.3390/s23177316

[12] GERADIN, M.; NIELSEN, C.J.G.; PREUMONT, A., Numerical simulation of the folding and deployment of a polymer reflector. Submitted for publication in Multibody System Dynamics.

XI ECCOMAS Thematic Conference on Smart Structures and Materials - SMART 2025
M. Krommer, M. Nader and M. Schagerl (Eds)

Received: 2 April 2025 / Revised: 30 August 2025 / Accepted: 7 October 2025
© The Author(s) 2025

Fractal-Inspired Phononic Crystal for Waves and Vibrations Suppression

Wiesław Ostachowicz, Sourava Prasad Mishra, Paweł Kudela

Abstract. Phononic crystals are manufactured structures having unique properties not commonly found in nature. Their behaviour can be tuned by the selection of material composition and structural topology. In this paper, we are exploring fractal-inspired phononic crystals. In particular, we consider a part of the Julia set fractal. The fractal intensity along the third axis is thresholded at several levels. It results in unique 2D shapes of various porosity levels that are next extruded into the third dimension. This is considered as a unit cell of two-phase phononic crystal. However, for simplification isotropic solid phase and air phase are considered only in numerical simulations. Parametric studies takes into account porosity and thickness to unit cell size ratio revealing the existence of band gaps. The analysed parameters strongly affects the mid-gap frequency and band gap width. It is shown that these parameters can be tuned to achieve the widest possible band gap for a selected cell size. The band gap is a frequency range at which waves and vibrations are suppressed. Therefore, such a phononic crystal can potentially be applied as a passive protective barrier against unwanted waves and vibrations. We are focusing our attention especially on ultrasonic waves. In the future, active manipulation of the metamaterial structure, e.g. by using shaper memory alloys, can be considered for creating a smart barrier.

Key words: Fractal, Metamaterial, Vibrations Suppression, Waves Suppression, Smart Barrier

1 INTRODUCTION

Phononic crystals (PnC) are architected structures composed of periodically placed unit cells, created to exhibit unique properties when subjected to acoustic waves of specific frequencies. They have found widespread application in noise suppression [1], medical ultrasound imaging [2], vibration isolation [3], acoustic cloaking [4], energy harvesting [5], and others. PnC are well known due to the presence of bandgaps (BG) [6], a frequency range in which ultrasonic waves are attenuated from transmission through these materials. The bandgap frequency range can

Wiesław Ostachowicz & Sourava Prasad Mishra & PawełKudela
Institute of Fluid Flow Machinery, Polish Academy of Sciences 80-231 Gdansk, Poland,
e-mail: wieslaw@imp.gda.pl, smishra@imp.gda.pl, pk@imp.gda.pl

be adjusted within the full transmission range through topological and structural modifications. By optimizing such features, the band gap region is often explored to make materials useful for specific applications.

Bandgaps are created primarily using two naturally occurring phenomena, Bragg scattering [7, 8] and local resonance [9]. Sometimes, a combination of both phenomena is also used to create bandgaps in materials. Materials exhibiting these phenomena are known as phononic crystals and acoustic metamaterials, respectively, although these terms are used interchangeably in the literature of the subject. Bragg scattering occurs due to the periodic composition of a material, which causes constructive and destructive interference in the propagating wave and leads to bandgaps. The frequency range of these bandgaps is constrained to the wavelength of the incident wave and the periodic lattice constant of the material. In contrast, local resonance happens due to the presence of locally resonating structures in a material. These resonating structures obstruct the transmission of waves and result in bandgaps. Local resonance helps in creating small and low-frequency bandgaps, whereas Bragg scattering may result in wider bandgaps at higher frequencies.

One key factor in tuning bandgaps is the adjustment and optimization of the topology of a material. This is done by optimizing the volume of solid and introducing, e.g. air or liquid-filled cavities in the material. For a large-scale autonomous design of topologies, parametric methods in structural design are a preferred way. In this work, we are proposing the use of fractal sets [10] for the parametric design of phononic crystal topology. Fractals are mathematical structures created with self-similar repeating elements. They are created by recursively reiterating a structure many times at different scales. It is a naturally occurring pattern seen in trees, coastlines, snowflakes and many others. What makes them useful for PnC topology design is their algorithmic nature, which makes it accessible to generate shapes on different scale and their simple and yet complex structure. Some common fractal-generating techniques include the Koch snowflake, Cantor set, Menger sponge, Mandelbrot set, and Julia set. In this work, we are exploring the use of Julia set fractals for creating PnC topology design.

Efficient design of PnC or metamaterial structures is a complex and challenging process. First, it involves creating a sequence of unit cells followed by numerical or analytical verification of the bandgap through dispersion relation studies. The first step usually involves many cycles of trial and error, whereas the second stage is a computationally demanding process.

Fractal shapes consist of self-repeating structures in which subdivisions are an approximation of the larger geometrical shape. They are fine structures, and more details emerge as we increase the scale of measurement. One unique feature of fractal geometry is that they have a non-integer dimension, that is, the fractal dimension is mentioned as real numbers. Assume D as the dimension of a shape, where $D = 1$ for a line, $D = 3$ for a cube, and so forth. If we divide the line into two parts (N) of equal length (l) with $N = 2$ and $l = 3$, the dimension of the line will still be the same, as $D = 1$. The fractal dimension of any shape with N, l and D is given by $N = l^D$ or $D = \frac{ln(N)}{ln(l)}$ [11]. A Koch snowflake fractal is created by four parts of a line,

with each part being a third of the length of the original line. Which makes it's dimension to be $D = \frac{ln(4)}{ln(3)} = 1.26$. We can see the evolution of a star shape from a simple straight line in Figure 1. On the left is a straight line for illustration. In the middle is a simplest Koch snowflake fractal shape with four parts, each being one third the length of a line in left. On the right is a star shape created with three Koch snowflake shapes put together.

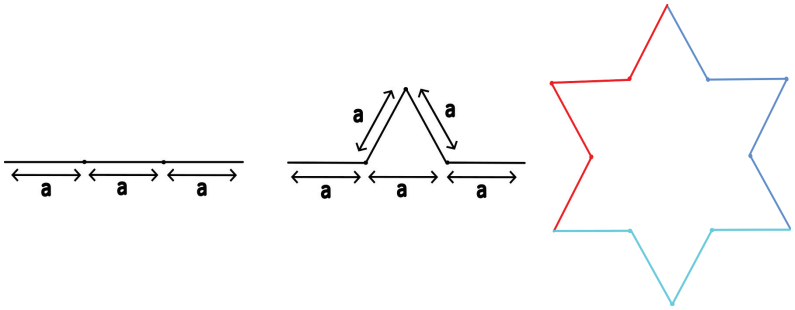

Figure 1: Formation of a star shaped *Koch snowflake* fractal, from a line. On the left, a straight line is divided into three equal segments, each of length a. In center, the same straight line is reconfigured into four parts, where each part is one-third of the total length of the original line. Right, joining three Koch snowflakes shapes to form a star shape.

2 METHODOLOGY

The starting point of our analysis is the Julia set fractal. The Julia set is named after the French mathematician Gaston Julia [12]. In particular we iterated over the following formulas:

$$\hat{z} = x + y \cdot 1i; \tag{1}$$

$$f(\hat{z}) = (\hat{z}^2 + c)/(\hat{z}^2 - c) \tag{2}$$

where constant c was kept fixed as $c = 0.7$, x and y are coordinates in range $[-1, 1]$, i is an imaginary part. It should be noted, that the interval range was selected to create an interesting unit cell geometry. The color bands were constrained by $|\hat{z}| \leq 2$ and the maximum number of iterations equals 50. In the next step, the resulting fractal $f(\hat{z})$, where $2 \leq f(\hat{z}) \leq 50$ was thresholded at levels $f(\hat{z}) \leq 3$, $f(\hat{z}) \leq 4$, $f(\hat{z}) \leq 5$ and $f(\hat{z}) \leq 6$ resulting in binary images of three porosity levels as shown in Figure 2. The black pixels represent solid material whereas white pixels represent air. These are unique, organic shapes which potentially can be fabricated by the additive manufacturing technique.

Subsequently, a MATLAB script was developed for automated detection of contours and subdivision of edges into discrete points. The detection of contours was aided by the *isocontour* function [13]. It computes the isocontour geometry for a 2D image and isovalue. To extract

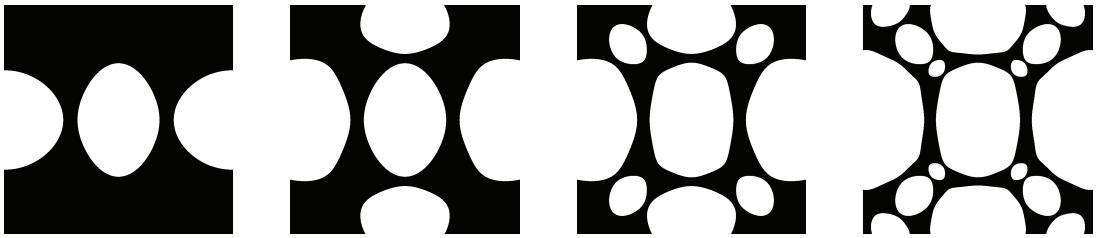

(a) Porosity level #1 (b) Porosity level #2 (c) Porosity level #3 (d) Porosity level #4

Figure 2: Julia set fractal representation of unit cell.

the isocontour geometry it uses marching squares and linear interpolation followed by sorting the contour geometry into separate sorted sets of points. The resulting points became vertices of boundaries used for creating geometry files in GMSH software [14] exported to *.step* files processed further in COMSOL Multiphysics software.

To understand how fractal shaped cavities help in the topological design of PnC, we perform the wavevector and eigenfrequency analysis of the unit cell. We investigate the wave propagation characteristics with respect to the dimensions of a unit cell to find bandgap in the range of 200 kHz to 1000 kHz. We assumed aluminum as a material of the unit cell used for calculations of dispersion diagrams. The material properties of aluminum are mentioned in Table 1.

Table 1: Material properties of aluminum

Density (ρ)	**Young's Modulus** (E)	**Poisson's ratio** (υ)
2700 kg/m^3	70 GPa	0.33

A unit cell dimensions typically consist of length, width and thickness. Typically, the values of length and width are treated as identical and referred to as lattice constant. In our studies we describe a unit cell with three parameters, lattice constant a, unit cell thickness H, and fractal porosity. The values of various geometrical parameters considered by us is mentioned in Table 2.

Figure 3a shows a basic unit cell structure with $a = 2$ mm, $H = 1a$ and porosity level #1. Unlike many classical structures, the unit cell considered by us (Figure 2 and Figure 3a) have reflection symmetry but do not have rotational symmetry. A tetrahedral mesh is created from the unit cell geometry as shown in Figure 3b. We computed the dispersion diagrams along the symmetric direction of first irreducible Brillouin zone along Γ –X –M – D – Γ path, where Γ is placed at $(0, 0)$, X at $(\pi/a, 0)$, M at $(\pi/a, \pi/a)$, and D at $(0, \pi/a)$ of a 2D Cartesian coordinates space. Band structures are computed as reduced wavevector k^* having components

Table 2: Unit cell parameters

Parameters	**Values**
Lattice constant (a)	2 mm
Thickness (H)	$1a$
Fractal porosity	
Level #1	30.7%
Level #2	50.5%
Level #3	61.4%
Level #4	72.1%

$k^* = [k_x a/\pi; k_y a/\pi]$ through Bloch-Floquet theorem and the finite element method.

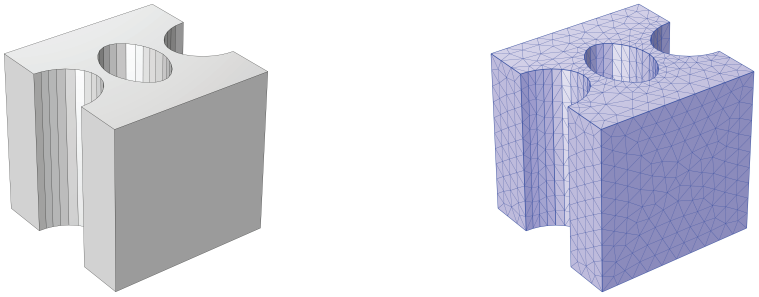

(a) A basic unit cell (b) Unit cell mesh

Figure 3: Unit cell representation (a) Unit cell geometry created using COMSOL Multiphysics software, and (b) Unit cell with tetrahedral meshing.

To get a better representation of the computed wave vectors, we color code them with a polarization value from 0 to 1. It is computed as shown in Equation 3 [15]. The polarization color code helps in understanding in-plane (closer to 0) and out-of-plane (closer to 1) wave displacement.

$$p = \frac{\int_v |u_z|^2 dV}{\int_v (|u_x|^2 + |u_y|^2 + |u_z|^2) dV} \tag{3}$$

3 RESULTS

For numerical analysis of unit cell, we explored a few variations of lattice constant and unit cell thickness values. Our initial experiment with lattice constant of $a = 8$ mm and thickness

$H = 0.5a$, did not yield any bandgap. After a few trials, we found some interesting bandgaps with lattice constant of $a = 2$ mm and thickness $H = 1a$. The dispersion relation from our numerical analysis is presented in Figure 4. The four figures correspond to levels of fractal porosity in a unit cell, with Figure 4a corresponding to the least porous unit cell and Figure 4d being the most porous. The design methodology of Julia set fractal and porosity level is discussed in section 2.

Figure 4 demonstrates the bandgaps seen through multiple unit cell designs in the frequency range 239 to 987 kHz with various unit cell configurations. Bandgaps with a range of more than 30 kHz are shaded with a gray rectangular box for visualization. We also list the minimum and maximum frequency value along with the relative bandgap width (RBW) in Table 3 for reference. RBW is calculated using Equation 4 for each bandgap region, where f_{min} is the starting frequency of a bandgap region, f_{max} is the maximum frequency and f_{mean} is the mid point of the frequency range of a bandgap, respectively.

$$RBG = \frac{f_{max} - f_{min}}{f_{mean}} \cdot 100\% \tag{4}$$

Figure 4a shows the dispersion relation vectors with fractal porosity level #1. In total we found 12 bandgaps from a unit cell having this configuration, five of which had a range of 30 kHz or more. The dispersion relation of a unit cell having a fractal porosity of level #2 is depicted in Figure 4b. One can identify 4 bandgaps for this unit cell, three of which have a range of more than 30 kHz. Figure 4c represents the unit cell dispersion relation and its corresponding fractal porosity level #3. It has 10 bandgaps with five having a range of 30 kHz or more. The dispersion relation, with fractal porosity level #4, is demonstrated in Figure 4d. Here we observe 11 bandgaps, with four of them above 30 kHz range.

4 CONCLUSION

In this article, we present the Julia fractal set as a parametric means of designing phononic crystal topology. We consider various porosity levels of the fractal set and use them to design the geometry of a phononic crystal unit cell. We then perform numerical analysis using COMSOL Multiphysics software to assess the eigenfrequencies and band structures. The results of numerical analysis are presented as dispersion diagrams with in-plane and out-of-plane polarisations and the corresponding bandgap ranges. Due to the ability of fractals to be created in different scales and the naturally occurring patterns they are a good choice for PC design. With the aid of additive manufacturing, it is possible to manufacture such geometries. The presence of multiple and wide bandgaps is encouraging to consider fractal topologies for phononic crystal design.

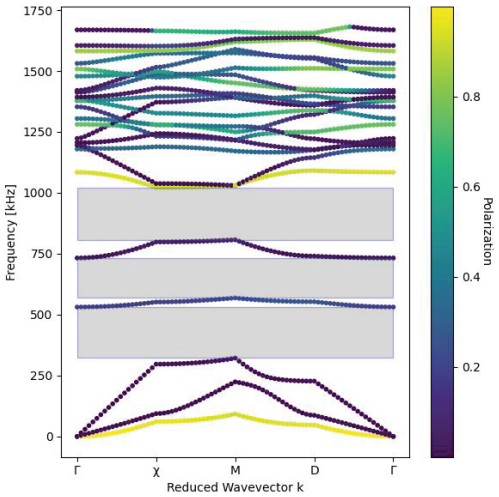

(a) Unit cell with fractal porosity level 1

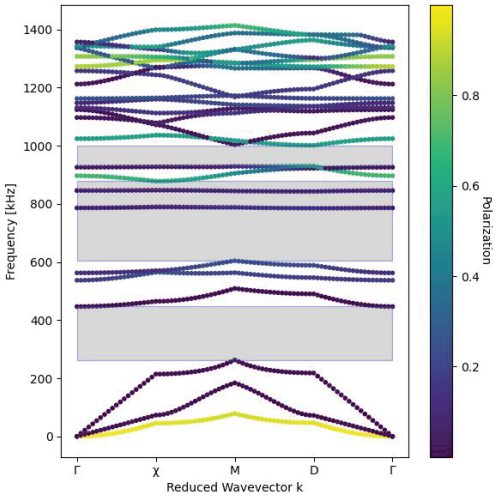

(b) Unit cell with fractal porosity level 2

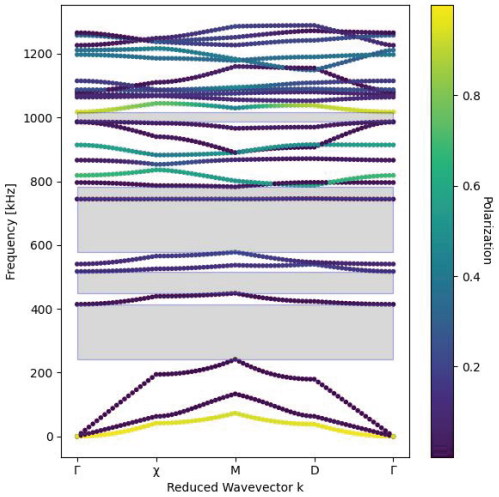

(c) Unit cell with fractal porosity level 3

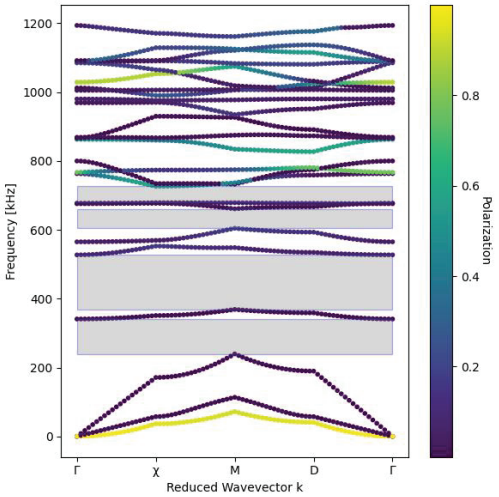

(d) Unit cell with fractal porosity level 4

Figure 4: Dispersion relation plots of four unit cells with varying level of fractal porosity. (a) porosity level 1, (b) porosity level 2, (c) porosity level 3, (d) porosity level 4.

Table 3: Bandgaps range of tested unit cells

Porosity level	Bandgap min-max (kHz)			RBG %
#1	241.86	to	414.33	53
	449.05	to	517.47	14
	577.92	to	744.18	25
	745.97	to	782.56	5
	987.01	to	1017.23	3
#2	321.79	to	531.26	49
	568.50	to	732.50	25
	807.16	to	1021.57	23
#3	263.06	to	446.79	52
	604.51	to	785.04	26
	789.91	to	842.85	6
	847.21	to	878.17	4
	930.45	to	1001.68	7
#4	239.73	to	340.99	35
	368.84	to	527.25	35
	604.38	to	661.16	9
	678.76	to	726.20	7

ACKNOWLEDGMENTS

We are very grateful to Marco Miniaci for feedback on an initial version of this manuscript. This project has received funding from the European Union's EU Framework Programme for Research and Innovation Europe Horizon (HORIZON TMA MSCA Doctoral Networks) under Grant Agreement No. 101119738 "MetacMed" (www.metacmed.eu). Views and opinions expressed are however those of the author(s) only and do not necessarily reflect those of the European Union. Neither the European Union nor the granting authority can be held responsible for them.

REFERENCES

[1] S. A. Cummer, "Selecting the direction of sound transmission," *Science*, vol. 343, no. 6170, pp. 495–496, 2014.

[2] S. Zhang, L. Yin, and N. Fang, "Focusing ultrasound with an acoustic metamaterial network," *Physical review letters*, vol. 102, no. 19, p. 194301, 2009.

[3] Z. Wang, Q. Zhang, K. Zhang, and G. Hu, "Tunable digital metamaterial for broadband

vibration isolation at low frequency," *Advanced materials*, vol. 28, no. 44, pp. 9857–9861, 2016.

[4] H. Chen and C. T. Chan, "Acoustic cloaking in three dimensions using acoustic metamaterials," *Applied physics letters*, vol. 91, no. 18, 2007.

[5] Z. Chen, B. Guo, Y. Yang, and C. Cheng, "Metamaterials-based enhanced energy harvesting: A review," *Physica B: Condensed Matter*, vol. 438, pp. 1–8, 2014.

[6] Y. Pennec, J. O. Vasseur, B. Djafari-Rouhani, L. Dobrzyński, and P. A. Deymier, "Two-dimensional phononic crystals: Examples and applications," *Surface Science Reports*, vol. 65, no. 8, pp. 229–291, 2010.

[7] S. Hedayatrasa, M. Kersemans, K. Abhary, M. Uddin, and W. Van Paepegem, "Optimization and experimental validation of stiff porous phononic plates for widest complete bandgap of mixed fundamental guided wave modes," *Mechanical Systems and Signal Processing*, vol. 98, pp. 786–801, 2018.

[8] F. Meseguer, M. Holgado, D. Caballero, N. Benaches, J. Sanchez-Dehesa, C. López, and J. Llinares, "Rayleigh-wave attenuation by a semi-infinite two-dimensional elastic-band-gap crystal," *Physical Review B*, vol. 59, no. 19, p. 12169, 1999.

[9] Z. Liu, X. Zhang, Y. Mao, Y. Y. Zhu, Z. Yang, C. T. Chan, and P. Sheng, "Locally resonant sonic materials," *science*, vol. 289, no. 5485, pp. 1734–1736, 2000.

[10] C. Bovill, *Fractal geometry in architecture and design*. Springer, 1996.

[11] F. M. Mwema, E. T. Akinlabi, O. P. Oladijo, O. S. Fatoba, S. A. Akinlabi, and S. Tălu, "Advances in manufacturing analysis: Fractal theory in modern manufacturing," in *Modern manufacturing processes*. Elsevier, 2020, pp. 13–39.

[12] G. Julia, "Mémoire sur l'iteration des fonctions rationnelles," *Journal de Mathématiques Pures et Appliquées*, vol. 8, pp. 47–245, 1918.

[13] D.-J. Kroon, "Isocontour," 2025. [Online]. Available: https://www.mathworks.com/matlabcentral/fileexchange/30525-isocontour

[14] C. Geuzaine and J.-F. Remacle, "Gmsh: A 3-D finite element mesh generator with built-in pre- and post-processing facilities," *International Journal for Numerical Methods in Engineering*, vol. 79, no. 11, pp. 1309–1331, sep 2009. [Online]. Available: http://doi.wiley.com/10.1002/nme.2579

[15] P. Kudela, A. Ijjeh, M. Radzienski, M. Miniaci, N. Pugno, and W. Ostachowicz, “Deep learning aided topology optimization of phononic crystals,” *Mechanical Systems and Signal Processing*, vol. 200, p. 110636, 2023.

XI ECCOMAS Thematic Conference on Smart Structures and Materials - SMART 2025
M. Krommer, M. Nader and M. Schagerl (Eds)

Received: 22 April 2025 / Revised: 26 August 2025 / Accepted: 7 October 2025
© The Author(s) 2025

Finite Element Evaluation of Effective Damping Properties of d_{31} Piezoelectric Macro-Fibre Composites

Marcelo A. Trindade, Ayech Benjeddou

Abstract. This work presents the evaluation of effective damping properties of a d_{31} piezoelectric Macro-Fibre Composite (MFC). This is important since it is well known that the softer elastomeric components of MFCs may induce non-negligible damping, while there are no studies attempting to evaluate or quantify the effective damping or loss factor of MFCs. This is done through an analogy with the Modal Strain Energy method in which an effective loss factor may be computed for each loading case. Then, for given damping properties of the MFC components, mainly the epoxy matrix, it is possible to quantify the effective damping properties of the MFC. It is shown that the d_{31} MFC effective loss factor may attain around 5%, particularly for transverse and in-plane shear loading modes, when the epoxy matrix transitions from glassy to rubbery state. Also, due to the epoxy softening, elastic stiffness and piezoelectric stress coefficients of the MFC may be substantially reduced.

Key words: Piezoelectric macro-fibre composites, damping, finite element homogenization

1 INTRODUCTION

Piezoelectric Macro-Fibre Composite (MFC) transducers have become very popular since they combine the conformability of epoxy-matrix composites and the electromechanical energy density of piezoceramic materials [1]. Since they are heterogeneous and made of several different materials (piezoceramic fibres, epoxy matrix, electrode and protective layers), a methodology is required to relate their effective properties with the individual ones of its components [2, 3]. Previous studies have shown that the effective properties depend not only on the active layer (piezoceramic fibres and epoxy matrix) but also on electrode and protective ones [4, 5].

In particular, it is well known that the softer elastomeric components of MFCs may induce non-negligible damping, while there are no studies attempting to evaluate or quantify the effective damping or loss factor of MFCs. Indeed, Placzek and Kokot [6] have shown that the

Marcelo A. Trindade
São Carlos School of Engineering, University of São Paulo, São Carlos, SP, Brazil
e-mail: trindade@sc.usp.br

Ayech Benjeddou
Institut Supérieur de Mécanique de Paris (ISAE-SUPMECA), France
e-mail: benjeddou@isae-supmeca.fr

Ayech Benjeddou
Roberval Laboratory, Université de Technologie de Compiègne (UTC), France
e-mail: ayech.benjeddou@utc.fr

energy harvesting performance of MFCs decreases significantly under increased operating temperatures. Lin et al. [7] have shown that the thermoelastic properties of the epoxy matrix were extremely important on the performance of piezoelectric fibre composites, since a temperature increase induced a decrease of free strain due to the deformation of the epoxy constituents. Also, the actuation capability were even more sensitive to temperature than free strain. Williams, Inman and Wilkie [1] have shown that the apparent transverse and in-plane shear moduli of MFCs can experience a decrease of up to 30% for increasing temperature in the epoxy matrix. Hence, the dependence of thermoelastic properties on temperature should be accounted for.

Meanwhile, for vibration-based applications, such as active or passive vibration control, shunted damping, energy harvesting and so on, the effective damping added by the MFC itself may be non-negligible and, thus, affects its effective performance when it is bonded to a host structure. Hence, this work presents the evaluation of effective damping properties of a d_{31} MFC. This is done through an analogy with the Modal Strain Energy (MSE) method [8] in which an effective loss factor may be computed for each loading case. Then, for given damping properties of the MFC components, mainly the epoxy matrix, it is possible to quantify the effective damping of the MFC. A parametric analysis is also performed to assess the effect of variations in the damping properties of the components.

2 EVALUATION OF d_{31} MFC EFFECTIVE ELECTROMECHANICAL PROPERTIES

2.1 Electromechanical constitutive equations of d_{31} MFC

The d_{31} MFC is composed of an active layer, made of piezoceramic macro-fibres embedded in an epoxy matrix, which is then fully covered by electrode and protective layers, as shown in Figure 1. The piezoceramic macro-fibres are poled along the x_3 (through-thickness) direction and their top (Γ_e^+) and bottom (Γ_e^-) surfaces are fully covered with an electrode layer, such that the dominant operation (response) mode is the d_{31} that couples longitudinal strain/stress (along direction x_1) and through-thickness electric field/displacement (direction x_3) (Figure 2).

Considering linear piezoelectricity, the general 3D constitutive equation for an orthotropic

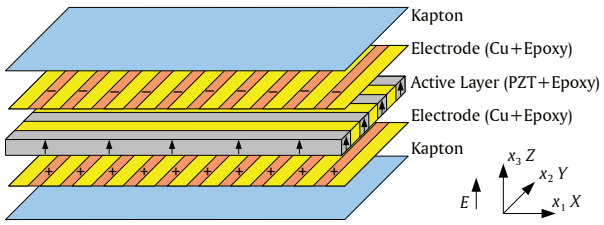

Figure 1: Schematic representation of a d_{31} MFC.

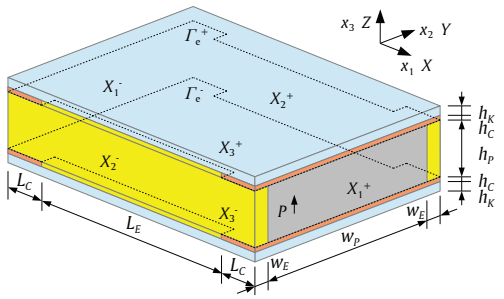

Figure 2: Representative volume element (RVE) of a d_{31} MFC.

piezoelectric material can be written as

$$\left\{\begin{array}{c} T_1 \\ T_2 \\ T_3 \\ T_4 \\ T_5 \\ T_6 \\ \hline D_1 \\ D_2 \\ D_3 \end{array}\right\} = \left[\begin{array}{ccc|ccc|ccc} c_{11}^E & c_{12}^E & c_{13}^E & 0 & 0 & 0 & 0 & 0 & -e_{31} \\ c_{12}^E & c_{22}^E & c_{23}^E & 0 & 0 & 0 & 0 & 0 & -e_{32} \\ c_{13}^E & c_{23}^E & c_{33}^E & 0 & 0 & 0 & 0 & 0 & -e_{33} \\ 0 & 0 & 0 & c_{44}^E & 0 & 0 & 0 & -e_{24} & 0 \\ 0 & 0 & 0 & 0 & c_{55}^E & 0 & -e_{15} & 0 & 0 \\ 0 & 0 & 0 & 0 & 0 & c_{66}^E & 0 & 0 & 0 \\ \hline 0 & 0 & 0 & 0 & e_{15} & 0 & \epsilon_{11}^S & 0 & 0 \\ 0 & 0 & 0 & e_{24} & 0 & 0 & 0 & \epsilon_{22}^S & 0 \\ e_{31} & e_{32} & e_{33} & 0 & 0 & 0 & 0 & 0 & \epsilon_{33}^S \end{array}\right] \left\{\begin{array}{c} S_1 \\ S_2 \\ S_3 \\ S_4 \\ S_5 \\ S_6 \\ \hline E_1 \\ E_2 \\ E_3 \end{array}\right\}, \quad (1)$$

where T_p and S_q, with $p,q = 1,\ldots,6$, stand for the six components of mechanical stress and strain vectors in Kelvin-Voigt notation. D_j and E_j denote the electric displacements and fields in direction x_j ($j = 1,2,3$). In the so-called e-form of the linear piezoelectric constitutive equations (1), c_{pq}^E, e_{jp} and ϵ_{jj}^S denote the short-circuit (SC) elastic stiffness (at constant electric fields), stress piezoelectric and blocked electric permittivity (at constant mechanical strains) coefficients. These constitutive equations can also be rewritten in the so-called d-form, in which material constants are s_{pq}^E, d_{jp} and ϵ_{jj}^T, the SC elastic compliance (at constant electric fields), strain piezoelectric and free electric permittivity (at constant mechanical stresses) coefficients.

The piezoelectric e_{31}/d_{31}, elastic c_{11}^E/s_{11}^E and dielectric $\epsilon_{33}^S/\epsilon_{33}^T$ coefficients are the most important properties to qualify these composite transducers as sensors and actuators. Nevertheless, due to the anisotropy induced by the composite construction, it is important to analyze other effective properties as well and, in particular, how the properties and behaviour of each composing material affect the effective properties and behavior of the resulting MFC.

2.2 FE homogenization procedure to evaluate the effective electromechanical properties

Previous works [5, 9] presented the evaluation of the effective electromechanical coefficients of a d_{31} MFC, using the so-called average quantity-based finite element (FE) homogenization technique proposed in [4]. This technique is based on the evaluation of the average stresses, strains, electric fields and electric displacements in a FE model of a Representative Volume Element (RVE) (Figure 2) of the MFC when subjected to properly chosen mechanical and electrical boundary and periodicity conditions.

For that, a set of local problems is defined, in which the MFC RVE is loaded and its response is used to compute the averaged quantities. Considering that the MFC behaves as an orthotropic piezoelectric material, the averaged quantities are then used to evaluate the effective elastic, piezoelectric and dielectric coefficients of the MFC. The local problems and the methodology to evaluate the effective properties are described in [5, 9].

To solve the local problems and evaluate the effective properties, a FE model was built in Ansys®, using 3D 20-Node coupled-field solid element (SOLID226) to mesh all volumes. This FE has the three displacement translations along the Cartesian coordinate system axes and the electric potential as nodal degrees of freedom. A mesh of 9900 finite elements was used

considering 25 divisions in x_1 direction (17 divisions for the Epoxy layer and 4 divisions for each electrode layer), 18 divisions in x_2 direction (14 divisions for the PZT fibre and 2 divisions for each Epoxy layer) and 22 divisions in x_3 direction (12 divisions for the PZT layer, 2 divisions for each electrode layer and 3 divisions for each protective layer). The dimensions considered for this RVE are $h_P = 180$ μm, $h_K = 40$ μm, and $h_C = 18$ μm, $L_E = 420$ μm, $L_C = 80$ μm, $w_E = 28.35$ μm and $w_P = 348.3$ μm. The material properties for the piezoceramic material Sonox P502, taken from [2], are: $s^E_{11} = s^E_{22} = 18.5$ pm^2/N, $s^E_{33} = 20.7$ pm^2/N, $s^E_{12} = -6.29$ pm^2/N, $s^E_{13} = -6.23$ pm^2/N, $s^E_{44} = s^E_{55} = 33.2$ pm^2/N, $s^E_{66} = 52.3$ pm^2/N, $d_{31} = d_{32} = -185$ pC/N, $d_{33} = 440$ pC/N, $d_{15} = d_{24} = 560$ pC/N, $\epsilon^T_{11} = \epsilon^T_{22} = 1950\epsilon_0$, $\epsilon^T_{33} = 1850\epsilon_0$. The material properties for the other constituents, taken from [3], are: Epoxy – $Y = 2.5$ GPa, $\nu = 0.42$ and $\epsilon = 4.25\epsilon_0$; Kapton – $Y = 2.5$ GPa, $\nu = 0.34$ and $\epsilon = 3.4\epsilon_0$; and Copper electrode – $Y = 110$ GPa, $\nu = 0.34$ and $\epsilon = 5\epsilon_0$, with $\epsilon_0 = 8.854$ pF/m.

Comparison of the evaluated full 3D effective coefficients of the d_{31} MFC with previous analytical results and data provided by the manufacturer (Smart Material Corp., [10]) has shown satisfactory coincidence [9]. It was then concluded that the 3D FE-evaluated effective electromechanical properties represent very well the actual (manufactured) d_{31} MFC.

Nevertheless, these analyses were performed considering linear elasticity and piezoelectricity. Other previous works have shown that nonlinear piezoelectricity of the piezoceramic macro-fibres may induce corresponding nonlinear behaviour of the MFC [5]. Similarly, it is worthwhile analyzing whether an anelastic behaviour of the epoxy matrix would induce a corresponding anelastic behaviour for the d_{31} MFC.

3 ANELASTIC BEHAVIOR OF EPOXY ADHESIVES

According to Williams [11], the first prototypes of d_{33} MFCs, developed by NASA, used epoxy adhesive Loctite® Durabond EA-E-120HP (manufactured by Henkel) for the matrix. These are composed of an epoxy resin with polyamide hardener, but not much information concerning its thermomechanical properties are available besides the fact that the glass transition temperature is around 90°C. The author mentioned that a satisfactory behaviour prediction was obtained using standard material properties for generic structural epoxy.

Other similar epoxy adhesives often used in fibre-reinforced composites are Araldite® 2019 (made by Huntsman) and Scotch-Weld® DP-460 (made by 3M). Their main thermomechanical properties are a maximum elastic modulus around 2.5 GPa and glass transition temperatures in the range 75-90°C. From the manufacturers' available data, the elastic modulus can indeed decrease significantly between the maximum value (in glassy state, low temperature) and the glass transition value (around the glass transition temperature). For Araldite® 2019, for instance, the elastic modulus varies from 2.4 GPa (at -40°C) to 0.4 GPa (at 80°C) [12].

For the prediction and simulation of the epoxy matrix behaviour in higher temperatures (intermediate/transition or rubbery states), one alternative is to model it as a temperature and frequency dependent viscoelastic material, such that its elastic modulus is replaced by a temperature and frequency dependent complex modulus

$$Y^*(\omega,T) = Y_R(\omega,T) + \mathrm{i}Y_I(\omega,T) = Y_R(\omega,T)[1+\mathrm{i}\eta(\omega,T)]. \tag{2}$$

where Y_R and η are known as the storage modulus and the loss factor, both dependent on operating temperature and frequency. The storage modulus usually transitions between a maximum value (in glassy state, for low temperature, or in instantaneous response, for high working frequencies) and a minimum value (in rubbery state, for high temperature, or in relaxed response, for low working frequencies). The loss factor is usually negligible for very low or very high temperature and frequencies and presents a maximum value after the glass transition temperature. However, as the glass transition temperature is frequency-dependent, the loss factor presents higher values within a frequency-range that depends on the temperature. Typical temperature and frequency dependences are represented in Figure 3, which was developed using a material model presented in [13] that was fitted to experimental dynamic mechanical analysis of an epoxy resin used for the production of glass-fibre-reinforced composites manufactured by Shanghai FRP Research Institute Co. Ltd.. This epoxy resin presents basic thermomechanical properties that are similar to those available for the epoxy resins used in MFCs.

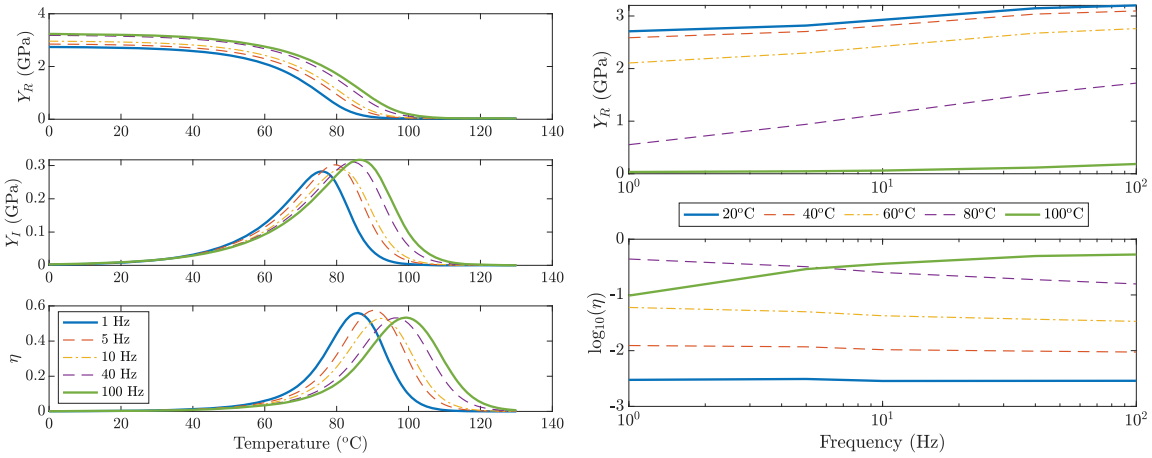

Figure 3: Temperature and frequency dependences of epoxy resin used for glass-fibre-reinforced composites based on a fitted material model proposed in [13].

For the present analysis, and based on this more detailed model, it is desired to perform a first quantification of the effect or importance of the viscoelastic behaviour, namely added damping and temperature and frequency dependences, of the epoxy matrix on the resulting MFC. In particular, it is noticeable that the material behaviour may be divided in three regions: glassy, intermediate and rubbery. In the glassy state, the resin presents a higher storage modulus and a smaller loss factor (stiffer and less damped). On the contrary, in the rubbery state, the resin presents a smaller storage modulus and a higher loss factor. The transition from a glassy state to a rubbery one may lead to a decrease of around 40% in the storage modulus (from 2.5 GPa to 1.5 GPa) and an increase of 15 times in the loss factor (from 1% to 15%) (Table 1 and Figure 4).

Table 1: Storage modulus and loss factor of the epoxy material for the three material states.

Property	Glassy	Intermediate	Rubbery
Y_R (GPa)	2.5	2.0	1.5
η_e (%)	1	8	15

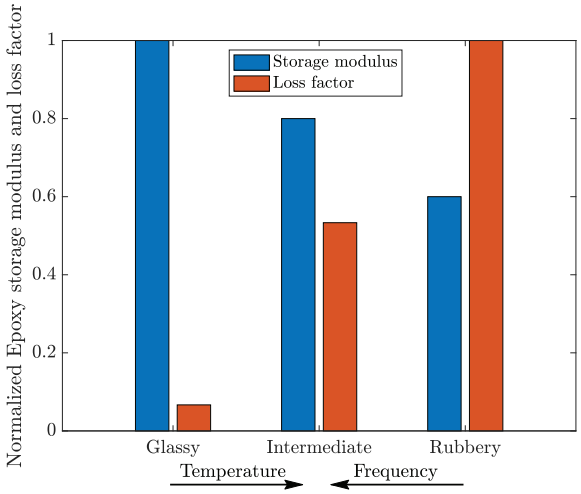

Figure 4: Relative values of storage modulus and loss factor for epoxy transitioning from glassy to rubbery state.

For the epoxy material considered in the present work (manufactured by Shanghai FRP Research Institute Co. Ltd. [13]), as a typical epoxy material used for fibre-reinforced composite, the so-called glassy state region is observed for temperatures below 45°C, for which the material behaviour is less frequency-dependent while, in the other two states, for temperatures above 45°C, the material is both temperature and frequency-dependent. The intermediate state is defined for temperature-frequency pairs in the range [55°C-1 Hz, 75°C-100 Hz]. The rubbery state is defined for temperature-frequency pairs in the range [65°C-1 Hz, 85°C-100 Hz]. Notice, however, that higher temperatures, above the glass transition temperature around 85°C, are not considered since the storage modulus reduces drastically, to below 0.5 GPa, and the loss factor can reach up to 60%.

4 EVALUATION OF d_{31} MFC EFFECTIVE LOSS FACTOR

Based on the previous observations, it is important to assess the effect of the loss factor of the epoxy matrix on the effective loss factor of a typical d_{31} MFC and, thus, to estimate the potential damping that may be induced when attaching a d_{31} MFC to a host structure.

For the evaluation of the d_{31} MFC effective loss factor, due to the epoxy matrix, it is hereby assumed that the only source of damping comes from the epoxy matrix. Also, to allow further numerical analyses, such as when attaching the MFC to a host structure, and assuming the complex modulus approach, it is chosen here to evaluate the effective loss factor induced in

each loading mode, leading to corresponding matrices of complex stiffness coefficients.

For that, an analogy with the well-known MSE method [8], in which the global structure's loss factor is approximated by the multiplication of the loss factor of a selected component and the fraction of strain energy in such component. In the MSE method, this computation is done for each vibration mode of interest (thus, a modal characteristic). Here, the MSE method is extended to the case of different loading modes of the MFC, instead of different vibration modes. Thus, the local problems used in previous works [5], for evaluating the effective elastic stiffness coefficients of the d_{31} MFC, are adapted to quantify the fraction of strain energy in the epoxy matrix in each loading mode.

Then, the effective loss factor η_i in the i-th loading mode is defined as

$$\eta_i = \eta_e f_i, \text{ with } f_i = \frac{U_{ei}}{U_i}, \tag{3}$$

where η_e is the epoxy matrix loss factor, U_{ei} and U_i are the strain energies in the epoxy matrix and in the MFC, respectively, and f_i is the fraction of the total strain energy contained in the epoxy matrix. In Ansys®, U_{ei} is obtained by summing the strain energies computed for elements of the FE model for the epoxy material for each loading mode i, while U_i follows the same procedure but for all elements of the FE model.

Since both storage modulus and loss factor of the epoxy matrix are frequency and temperature dependent, so are η_e and f_i in (3). Thus, the computation of the effective loss factors η_i should be done for each frequency and temperature of interest. In the present work, it is considered the three generic states defined in the previous section, namely glassy, intermediate and rubbery. Each state has pre-defined storage modulus Y_R and loss factor η_e for the epoxy matrix, as shown in Table 1.

As stated previously, the loading modes follow the local problems used to evaluate the elastic coefficients of the d_{31} MFC, which consist in inducing normal strains in longitudinal (along the piezoceramic fibres, defined as direction 1), transverse (perpendicular to the piezoceramic fibres in the MFC plane, defined as direction 2) and through-thickness (along the thickness of the MFC, defined as direction 3) directions, and shear strains in planes 23, 13 and 12 (defined, respectively, as local problems 4, 5 and 6).

A small modification is proposed here in the local problems 1, 2 and 3, removing the fixed displacements boundary conditions to better approximate the loss factor of the elastic moduli in each direction, Y_1, Y_2 and Y_3, such that they would be replaced by

$$Y_j^* = Y_{jR}(1 + \mathrm{i}\eta_j), \text{ for } j = 1,2,3. \tag{4}$$

For the shear modulus, local problems 4, 5 and 6 are used without modification, leading to corresponding complex shear moduli

$$G_k^* = G_{kR}(1 + \mathrm{i}\eta_k), \text{ for } k = 4,5,6. \tag{5}$$

where the Kelvin-Voigt notation is considered ($G_4^* \equiv G_{23}^*$, $G_5^* \equiv G_{13}^*$, $G_6^* \equiv G_{12}^*$).

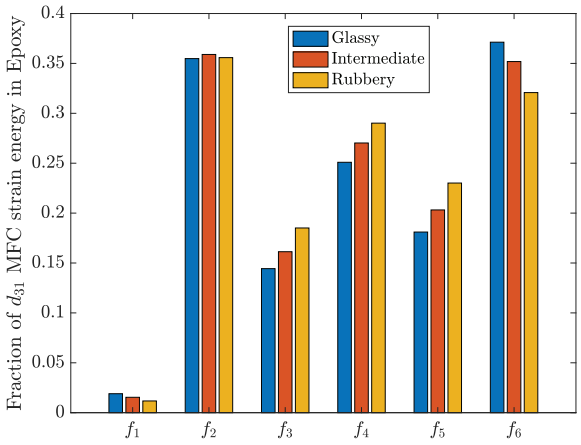

Figure 5: Fraction of strain energy contained in the epoxy matrix for each d_{31} MFC loading mode and epoxy state.

Figure 5 shows the fraction of strain energy contained in the epoxy matrix for each loading mode and epoxy state. It is noticeable that the epoxy strain energy fraction is much smaller in loading mode 1 (longitudinal), which is expected since in this case the normal stresses are concentrated in the stiffer PZT fibre and Copper electrode. On the other hand, the strain energy fraction is very important (higher than 30%) in loading modes 2 (transverse) and 6 (in-plane shear). In loading mode 2, most of the strain is concentrated in the softer epoxy matrix and the strain energy fraction does not depend much on the epoxy state. For the in-plane shear loading mode, the strain energy fraction decreases when the epoxy matrix transitions from glassy to rubbery states. As for the through-thickness (mode 3) and transverse shear (modes 4 and 5) loading modes, they lead to intermediate values for the strain energy fraction (between 15% and 30%), which all increase when the epoxy matrix transitions from glassy to rubbery states.

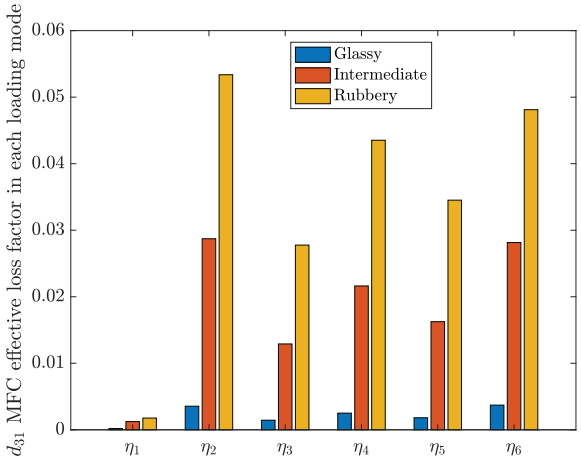

Figure 6: d_{31} MFC effective loss factors for each loading mode and epoxy state.

The d_{31} MFC effective loss factor for each loading mode and epoxy state, computed using (3), is presented in Figure 6. Since the epoxy loss factor increases substantially when the material transitions from glassy to rubbery state, as shown in the previous section, the d_{31} MFC effective loss factor in all loading modes also increases in this transition. For an epoxy matrix in glassy state, it is reasonable to admit that the effective loss factor is negligible (smaller than 0.4%). Nevertheless, even for an intermediate epoxy state, the loss factor is greater than 1% for all loading modes, with exception to loading mode 1 which, as expected, is not much affected by the epoxy matrix. The greater effective loss factors are observed for loading modes 2 (transverse) and 6 (in-plane shear), which attain 5.3% and 4.8% for a rubbery state and 2.9% and 2.8% for an intermediate one. Both transverse shear loading modes (4 and 5) may also present significant effective loss factor ($\sim$2% for intermediate state and $\sim$4% for rubbery one).

Table 2: Effective material properties of d_{31} MFC for the three epoxy matrix states (†: values obtained post-processing data provided in [10]).

Coefficient	Glassy	Intermediate	Rubbery	Manufacturer [10]
Y_1^{E*} (GPa) (η_1, %)	31.37 (0.02)	31.25 (0.12)	31.11 (0.18)	30.34 (–)
Y_2^{E*} (GPa) (η_2, %)	19.69 (0.35)	18.26 (2.87)	16.56 (5.34)	15.86 (–)
Y_3^{E*} (GPa) (η_3, %)	9.02 (0.14)	8.73 (1.29)	8.31 (2.78)	– (–)
G_{23}^{E*} (GPa) (η_4, %)	2.16 (0.25)	2.04 (2.16)	1.88 (4.35)	– (–)
G_{13}^{E*} (GPa) (η_5, %)	2.42 (0.18)	2.31 (1.63)	2.17 (3.45)	– (–)
G_{12}^{E*} (GPa) (η_6, %)	5.33 (0.37)	4.92 (2.82)	4.46 (4.81)	5.52 (–)
ν_{12}^{E}	0.36	0.35	0.35	0.31
ν_{23}^{E}	0.37	0.36	0.35	–
ν_{13}^{E}	0.42	0.42	0.42	–
$\epsilon_{11}^{T}/\epsilon_0$	1019.3	1019.7	1020.2	–
$\epsilon_{22}^{T}/\epsilon_0$	24.1	24.1	24.1	–
$\epsilon_{33}^{T}/\epsilon_0$	1573.3	1575.1	1576.9	1558.6
d_{31} (pC/N)	-172.3	-173.0	-173.6	-170
d_{32} (pC/N)	-133.2	-130.5	-126.3	–
d_{33} (pC/N)	308.9	309.1	308.9	–
d_{15} (pC/N)	334.9	335.6	336.3	–
d_{24} (pC/N)	219.3	221.8	225.1	–
e_{31} (C/m^2)	-6.03	-5.87	-5.70	–
e_{32} (C/m^2)	-3.44	-3.07	-2.63	–
e_{33} (C/m^2)	1.48	1.48	1.46	–
e_{15} (C/m^2)	0.81	0.78	0.73	–
e_{24} (C/m^2)	0.47	0.45	0.42	–
k_{31}^2 (%)	6.7	6.7	6.7	6.4†
k_{31}	0.26	0.26	0.26	0.25†

Besides the effective loss factor, the epoxy matrix state also affects other elastic, piezoelectric and dielectric coefficients mainly because of the change in the elastic modulus of the epoxy matrix. Thus, these properties are shown in Table 2. It is noticeable that all elastic stiffness co-

efficients decrease when the epoxy matrix transitions from glassy to rubbery states, as expected, particularly for the transverse normal modulus, transverse shear modulus in the plane 23 and in-plane shear modulus, which are reduced by up to 16%, 13% and 16%, respectively. One may also notice very small increase of the dielectric coefficients (less than 0.25%).

The piezoelectric strain coefficient d_{32} decreases by around 5% for the softer epoxy matrix (rubbery state), in comparison to the case of a glassy epoxy matrix, while d_{24} increases by less than 3% in the same scenario. The effect of a softer epoxy matrix is, however, much stronger for the piezoelectric stress coefficients, such that all of them are decreased for a softer epoxy matrix, particularly for the e_{32} which is decreased by more than 23%, while the coefficient e_{31} is decreased by 5.5%. Thus, the transition to a softer epoxy matrix should affect mostly the actuator performance of the MFC, while its effectiveness as a sensor is less influenced.

5 CONCLUSIONS

A methodology to evaluate the effective damping properties of d_{31} piezoelectric MFCs was presented. In particular, the effect of the anelastic behaviour of the epoxy matrix, common to the MFCs, was analyzed. The effective loss factor induced in the MFC was evaluated using an analogy with the well-known MSE method, but for each loading mode. It was found that, following the epoxy loss factor, which increases substantially when the material transitions from glassy to rubbery state, the d_{31} MFC effective loss factor in all loading modes also increases in this transition. The greater MFC effective loss factors were observed for loading modes 2 (transverse) and 6 (in-plane shear), which attain 5.3% and 4.8% for a rubbery state and 2.9% and 2.8% for an intermediate state. Both transverse shear loading modes (4 and 5) may also present significant effective loss factor.

It was also shown that the epoxy matrix state also affects other elastic, piezoelectric and dielectric coefficients mainly because of the change in the elastic modulus of the epoxy matrix. In fact, all elastic stiffness coefficients decrease when the epoxy matrix transitions from glassy to rubbery states, particularly for the transverse normal modulus, transverse shear modulus in the plane 23 and in-plane shear modulus, which are reduced by up to 16%, 13% and 16%, respectively. The effect of a softer epoxy matrix is also important for the piezoelectric stress coefficients, such that all of them are decreased for a softer epoxy matrix, particularly for the e_{32} which is decreased by more than 23%, while the coefficient e_{31} is decreased by 5.5%. Thus, the transition to a softer epoxy matrix should affect mostly the actuator performance of the MFC, while its effectiveness as a sensor is less influenced.

Notice that the use of static analyses only to estimate dynamic characteristics, such as damping, is based on the fact that the fraction of the strain energy contained in the epoxy matrix would be the same in a harmonic analysis. Nevertheless, this approach requires a set of static analyses for each temperature-frequency pair since the latter determines the epoxy properties that should be used in the static analyses. For practical applications, in which the MFC is bonded to a host structure, the actual energy dissipation, due to the MFC epoxy matrix, would then depend on the fraction of the strain energy contained in the MFC and on how the MFC is deformed. The here obtained results suggest that the effect of the viscoelastic behaviour of the MFC on its host

structure could be important when its application requires it to deform in transverse or shear modes. The complex moduli presented in this work could then be used to predict the effective damping added by the MFC to its host structure. This will be the focus of a future work.

ACKNOWLEDGEMENTS

Financial support of the National Institute of Science and Technology for Smart Structures in Engineering (INCT-EIE) and the National Council for Scientific and Technological Development (CNPq), grants 304954/2022-5 and 406148/2022-8, is gratefully acknowledged.

REFERENCES

[1] R. B. Williams, D. J. Inman, and W. K. Wilkie, "Temperature-dependent thermoelastic properties for macro fiber composite actuators," *Journal of Thermal Stresses*, vol. 27, pp. 903–915, 2004.

[2] A. Deraemaeker, H. Nasser, A. Benjeddou, and A. Preumont, "Mixing rules for the piezoelectric properties of macro fiber composites," *Journal of Intelligent Material Systems and Structures*, vol. 20, pp. 1475–1482, 2009.

[3] B. Kranz, A. Benjeddou, and W. G. Drossel, "Numerical and experimental characterizations of longitudinally polarized piezoelectric d_{15} shear macro-fiber composites," *Acta Mechanica*, vol. 224, no. 11, pp. 2471–2487, 2013.

[4] M. A. Trindade and A. Benjeddou, "Finite element homogenization technique for the characterization of d_{15} shear piezoelectric macro-fibre composites," *Smart Materials and Structures*, vol. 20, no. 7, 2011, art. no. 075012.

[5] ——, "Finite element characterisation of multilayer d_{31} piezoelectric macro-fibre composites," *Composite Structures*, vol. 151, pp. 47–57, 2016.

[6] M. Placzek and G. Kokot, "Modelling and laboratory tests of the temperature influence on the efficiency of the energy harvesting system based on MFC piezoelectric transducers," *Sensors*, vol. 19, 2019, art. no. 1558.

[7] X. Lin, H. Chen, Y. Ma, J. G. Fisher, S. Huang, D. Zhang, and X. Cheng, "Investigation of temperature sensitivity of actuation performance for piezoelectric fiber composites," *Ceramics International*, vol. 43, pp. 10 590–10 594, 2017.

[8] C. D. Johnson and D. A. Kienholz, "Finite element prediction of damping in structures with constrainted viscoelastic layers," *AIAA Journal*, vol. 20, no. 9, pp. 1284–1290, 1982.

[9] M. A. Trindade and A. Benjeddou, "Finite element evaluation of full 3D effective properties of d_{31} piezoelectric macro-fibre composites," in *Proceedings of the Eighth International Conference on Smart Materials and Nanotechnology in Engineering*, M. Ghommem, A. Benjeddou, J. Leng, and A. Abdelkefi, Eds., 2024, pp. 52–61.

[10] Macro-fibre composites technical data. Smart Material Corp. Accessed 14/04/2025. [Online]. Available: https://www.smart-material.com/MFC-product-propertiesV2.html

[11] R. B. Williams, "Nonlinear mechanical and actuation characterization of piezoceramic

fiber composites," Ph.D. Dissertation, Virginia Polytechnic Institute and State University, 2004.

[12] Araldite 2019 material model. Huntsman Advanced Materials. Accessed 25/03/2025. [Online]. Available: https://www.huntsman.com/products/araldite2000/araldite-2019

[13] J. Feng and Z. Guo, "Temperature-frequency-dependent mechanical properties model of epoxy resin and its composites," *Composites Part B*, vol. 85, pp. 161–169, 2016.

XI ECCOMAS Thematic Conference on Smart Structures and Materials - SMART 2025
M. Krommer, M. Nader and M. Schagerl (Eds)

Received: 19 April 2025 / Revised: 29 August 2025 / Accepted: 7 October 2025
© The Author(s) 2025

Advanced Tailored Kinematic Models for Multi-Field Analysis of Laminated Structures

Enrico Zappino, Erasmo Carrera, Daniele Scano

Abstract. This paper presents a novel methodology for constructing beam theories with fully customizable kinematic fields specifically designed for multi-layered composite piezoelectric structures. This work extends the most recent Carrera Unified Formulation implementations for multi-field analyses of piezoelectric structures, optimizing computational resources while maintaining accuracy. The proposed method applies Layer-Wise expansions where necessary, such as for the electric field, while employing Equivalent Single Layer formulations for fields that do not require piece-wise accuracy, like in-plane displacements. This tailored kinematic approach balances computational cost and accuracy, ensuring a more efficient yet precise structural analysis. This strategy is particularly effective for complex laminated structures, where different physical fields require varying levels of detail. Numerical analyses confirm the effectiveness of the approach, demonstrating its ability to provide accurate and efficient multi-field simulations. By selecting appropriate kinematic formulations for each field, the proposed method achieves high-fidelity modeling while significantly reducing computational costs.

Key words: Finite element method, higher-order theories, kinematic models, Unified Formulation, multifield analysis

1 INTRODUCTION

Piezoelectric materials exhibit a unique two-way energy conversion capability between mechanical and electrical domains. Certain crystals generate electrical charges when mechanically deformed - a linear relationship now known as the direct piezoelectric effect. The reciprocal phenomenon, termed the converse piezoelectric effect, describes mechanical deformation induced by applied electric fields. In smart structure applications, piezoelectric actuators exploit the converse effect to generate controlled strains. As demonstrated in seminal works by Crawley and Luis [1], Bailey and Hubbard [2], and Robbins and Reddy [3], these induced strains contribute additively to the total strain field of host structures. Notably, Crawley and Luis [1] developed a comprehensive analytical framework capable of modeling both surface-bonded and

Enrico Zappino & Erasmo Carrera & Daniele Scano
MUL2 Lab, Department of Mechanical and Aerospace Engineering, Politecnico di Torino, 10129 Turin, Italy
e-mail: enrico.zappino@polito.it, erasmo.carrera@poltio.it, daniele.scano@polito.it

embedded piezoelectric actuators in beam structures.
The work of Sarvanos and Heyliger [4] provides a comprehensive review and systematic classification of piezoelectric theories based on their underlying kinematic assumptions. To address the inherent limitations of analytical approaches, researchers have increasingly adopted finite element (FE) formulations for modeling piezoelectric composite structures. The active vibration control of smart structures has been investigated through both three-dimensional and reduced-order modeling approaches. While Dong *et al.* [5] employed 3D solid elements for plate analyses, numerous studies (e.g., Umesh and Ganguli [6]) have utilized classical Kirchhoff-Love theory, which neglects transverse shear deformation effects. To address this limitation, first-order shear deformation theory (FSDT) implementations (Kumar and Narayanan [7]; Vasques and Rodrigues [8]) have incorporated transverse shear effects. Moita *et al.* [9] developed an advanced triangular plate/shell element featuring 24 degrees of freedom and additional electrical potential degrees of freedom per piezoelectric layer. A third-order shear deformation theory is adopted. Beheshti-Aval *et al.* [10] introduced a three-node piezoelectric beam element based on a refined sinusoidal model that inherently accounts for transverse shear deformation without requiring shear correction factors. Finally, the Carrera Unified Formulation (CUF) has been introduced [11, 12]. This framework permits to generate beam and plate theories with the freedom to use the desired structural models.
The majority of existing studies adopt the Equivalent Single Layer (ESL) approach for modeling composite structures, where field variables are expressed independently of the laminate's layer count. For higher-fidelity analyses requiring through-thickness resolution, the Layer-Wise (LW) approach becomes necessary, assigning independent variables to each material layer. However, this enhanced accuracy comes at a substantially increased computational expense, prompting ongoing research to develop balanced efficiency-accuracy formulations. A notable contribution by Ballhause *et al.* [13] presents a unified electro-mechanical formulation for smart multilayered plates that encompasses both ESL and LW modeling paradigms and utilizes variable kinematic expansions up to fourth-order.
Recent research demonstrates the ability to create precise, customized models for predicting complex structural behaviour. However, traditional approaches require recalculating governing equations for each new theory. To address this, unified frameworks like Generalized Beam Theory [14] and the CUF have been developed, allowing flexible selection of multiple model types within a single framework. While existing methods show promise, they fail to evaluate the individual contributions of each term in the expansion. This study proposes a consistent formulation that enables users to choose theories with tailored precision. Given the importance of computational efficiency in structural analysis, the research seeks to balance accuracy and cost-effectiveness. Specifically, it investigates the combined use of ESL and LW approaches within unified structural models. This work extends the methodology proposed by Carrera and collaborators [15, 16, 17] for the pure mechanical cases.
This paper is organized as follows: (a) Section 2 presents the theoretical foundations of the Unified Formulation for beam structures and the approximations for the generalized displacements. (b) Section 3 derives the governing equations for piezoelectric materials within this

framework. (c) Section 4 demonstrates the methodology through a detailed stiffness matrix assembly procedure. (d) Section 5 presents numerical results validating the accurate prediction of both displacements and stress fields. (e) Section 6 summarizes key findings and discusses promising directions for future research.

2 CARRERA UNIFIED FORMULATION

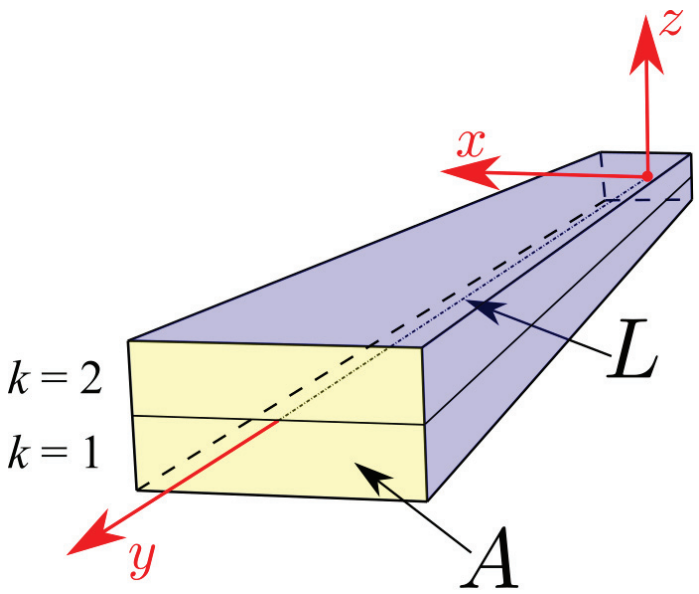

Figure 1: Reference systems for beam structures.

Figure 1 illustrate generic beam and the reference system. The upperscript k indicates the layer. The generalized electromechanical displacement vector field (with u_ϕ as the electric potential) may be expressed as follows:

$$\mathbf{u}^k(x,y,z) = \left\{ \; u_x^k(x,y,z), \quad u_y^k(x,y,z), \quad u_z^k(x,y,z), \quad u_\phi^k(x,y,z) \; \right\}^T \tag{1}$$

In the 1D beam formulation, the basis functions, $F_\tau(x,z)$, are defined over the $x-z$ plane. The following expressions can be utilized for each component:

$$f^k(x,y,z) = F_\tau^k(x,z) f_\tau^k(y), \qquad \tau = 1,2,...,M \tag{2}$$

The formulation employs Einstein's summation convention. This framework enables the displacement field to be expressed using general basis functions. To handle geometrically complex structures and diverse boundary conditions, the FEM is implemented.

$$
\begin{aligned}
u_x^k(x,y,z) &= N_i(y)F_{u_x\tau}^k(x,z)q_{x\tau i}^k \quad \text{with} \quad \tau = 1,\dots,M_{u_x} \quad i = 1,\dots,N_n \\
u_y^k(x,y,z) &= N_i(y)F_{u_y\tau}^k(x,z)q_{y\tau i}^k \quad \text{with} \quad \tau = 1,\dots,M_{u_y} \quad i = 1,\dots,N_n \\
u_z^k(x,y,z) &= N_i(y)F_{u_z\tau}^k(x,z)q_{z\tau i}^k \quad \text{with} \quad \tau = 1,\dots,M_{u_z} \quad i = 1,\dots,N_n \\
u_\phi^k(x,y,z) &= N_i(y)F_{u_\phi\tau}^k(x,z)q_{\phi\tau i}^k \quad \text{with} \quad \tau = 1,\dots,M_{u_\phi} \quad i = 1,\dots,N_n
\end{aligned}
\tag{3}
$$

The expansion functions $F_{u_x\tau}^k$, $F_{u_y\tau}^k$, $F_{u_z\tau}^k$, and $F_{u_\phi\tau}^k$ correspond to the generalized displacements $u_{x_\tau}^k$, $u_{y_\tau}^k$, $u_{z_\tau}^k$, and $u_{\phi_\tau}^k$ respectively, providing a basis for approximating these displacement components within the framework. The integers M_{u_x}, M_{u_y}, M_{u_z}, and M_{u_ϕ} denote the number of kinematic expansion terms for each displacement component. In this work, both Taylor and Lagrange expansions are adopted. The shape functions N_i and N_j discretize the solution domain, where N_n indicates the total number of shape functions per element. For comprehensive details on shape function for beams, see [18].
To proceed with the explanation, it is helpful to introduce a compact notation for both the real and virtual systems, as presented below:

$$
u_l^k = N_i F_{u_l\tau}^k q_{l_\tau i}^k \quad \text{with} \quad \tau = 1,\dots,M_{u_l} \quad \text{and} \quad i = 1,\dots,N_n \tag{4}
$$

$$
\delta u_m^k = N_j F_{u_m s}^k \delta q_{m_{sj}}^k \quad \text{with} \quad s = 1,\dots,M_{u_m} \quad \text{and} \quad j = 1,\dots,N_n \tag{5}
$$

where l and m can assume the values x, y, z, and ϕ.

3 GOVERNING EQUATIONS AND FINITE ELEMENT MATRICES

The electric field, $\mathbf{E}$, is first expressed as a 3×1 vector quantity:

$$
\mathbf{E}^k = \left\{ \begin{array}{ccc} E_x^k & E_y^k & E_z^k \end{array} \right\}^T = \left\{ \begin{array}{ccc} \partial_x & \partial_y & \partial_z \end{array} \right\}^T \phi^k \tag{6}
$$

The generalized strain vector, $\overline{\boldsymbol{\varepsilon}}$, is expressed in 9×1form as:

$$
\overline{\boldsymbol{\varepsilon}}^k = \left\{ \begin{array}{ccccccccc} \varepsilon_{xx}^k & \varepsilon_{yy}^k & \varepsilon_{zz}^k & \varepsilon_{yz}^k & \varepsilon_{xz}^k & \varepsilon_{xy}^k & E_1^k & E_2^k & E_3^k \end{array} \right\}^T = \overline{\mathbf{D}}\mathbf{u}^k \tag{7}
$$

where $\overline{\mathbf{D}}$ is the matrix of differential operators for small displacements and rotations. For more details, refer to [11, 12]. The coupled electromechanical constitutive relations (stress-charge form) are expressed in matrix notation as:

$$
\begin{aligned}
\boldsymbol{\sigma}^k &= \mathbf{C}^{kE}\boldsymbol{\varepsilon}^k - \mathbf{e}^{kT}\mathbf{E}^k \\
\boldsymbol{D}_e^k &= \mathbf{e}^k\boldsymbol{\varepsilon}^k + \boldsymbol{\chi}^{kS}\mathbf{E}^k
\end{aligned}
\tag{8}
$$

In this formulation, $\boldsymbol{D}_e^k$ indicates the electric displacement vector $\{D_x^k, D_y^k, D_z^k\}^T$, $\boldsymbol{\sigma}^k$ stands for the classical mechanical stress vector, $\mathbf{C}^{kE}$ is the 6×6 matrix for the material coefficients

evaluated at a constant electric field, and $\boldsymbol{\varepsilon}^k$ is the strain vector. The 3×3 $\boldsymbol{\chi}^{kS}$ is the dielectric permittivity matrix calculated at constant strain, and the 3×6 $\boldsymbol{e}^k$ is the piezoelectric stiffness coefficient matrix. Their complete expressions can be found in [18, 11, 12]. The generalized 9×1 stress vector can be seen as:

$$\overline{\boldsymbol{\sigma}}^k = \left\{ \begin{array}{cccccccccc} \sigma_{xx}^k & \sigma_{yy}^k & \sigma_{zz}^k & \sigma_{yz}^k & \sigma_{xz}^k & \sigma_{xy}^k & -D_1^k & -D_2^k & -D_3^k \end{array} \right\}^T \tag{9}$$

The constitutive equations is ow rewritten as follows

$$\overline{\boldsymbol{\sigma}}^k = \tilde{\mathbf{H}}^k \overline{\boldsymbol{\varepsilon}}^k \tag{10}$$

where

$$\tilde{\mathbf{H}}^k = \begin{bmatrix} C_{11}^{kE} & C_{12}^{kE} & C_{13}^{kE} & 0 & 0 & C_{16}^{kE} & -e_{11}^k & -e_{21}^k & -e_{31}^k \\ C_{21}^{kE} & C_{22}^{kE} & C_{23}^{kE} & 0 & 0 & C_{26}^{kE} & -e_{12}^k & -e_{22}^k & -e_{32}^k \\ C_{31}^{kE} & C_{32}^{kE} & C_{33}^{kE} & 0 & 0 & C_{36}^{kE} & -e_{13}^k & -e_{23}^k & -e_{33}^k \\ 0 & 0 & 0 & C_{44}^{kE} & C_{45}^{kE} & 0 & -e_{14}^k & -e_{24}^k & -e_{34}^k \\ 0 & 0 & 0 & C_{45}^{kE} & C_{55}^{kE} & 0 & -e_{15}^k & -e_{25}^k & -e_{35}^k \\ C_{61}^{kE} & C_{62}^{kE} & C_{63}^{kE} & 0 & 0 & C_{66}^{kE} & -e_{16}^k & -e_{26}^k & -e_{36}^k \\ e_{11}^k & e_{12}^k & e_{13}^k & e_{14}^k & e_{15}^k & e_{16}^k & \chi_{11}^{kS} & \chi_{12}^{kS} & 0 \\ e_{21}^k & e_{22}^k & e_{23}^k & e_{24}^k & e_{25}^k & e_{26}^k & \chi_{21}^{kS} & \chi_{22}^{kS} & 0 \\ e_{31}^k & e_{32}^k & e_{33}^k & e_{34}^k & e_{35}^k & e_{36}^k & 0 & 0 & \chi_{33}^{kS} \end{bmatrix} \tag{11}$$

Now, it is possible to derive the governing equations from the principle of virtual displacements, which states:

$$\delta L_{int} = \delta L_{ext} \tag{12}$$

For the internal work, δL_{int} is written down as follows:

$$\delta L_{int} = \int_{V^k} \delta \overline{\boldsymbol{\epsilon}}^{kT} \overline{\boldsymbol{\sigma}}^k \mathrm{d}V^k \tag{13}$$

where $\mathrm{d}V^k = \mathrm{d}x^k \mathrm{d}y^k \mathrm{d}z^k$.
Instead, the virtual external work, δL_{ext}, is evaluated as given below:

$$\delta L_{ext} = \int_{V^k} \delta \mathbf{u}^{kT} \mathbf{P}^k \mathrm{d}V^k = \int_{V^k} (\delta u_x^k P_x^k + \delta u_y^k P_y^k + \delta u_z^k P_z^k + \delta u_\phi^k P_\phi^k) \mathrm{d}V^k \tag{14}$$

Through systematic application of the kinematic displacement-strain relations, FE shape function approximations, and the electromechanical constitutive laws, the four coupled governing equations are derived in their final form:

$$\begin{aligned} \delta q_{x_{sj}}^k &: K_{u_x u_x s\tau ji}^k q_{x_{\tau i}}^k + K_{u_x u_y s\tau ji}^k q_{y_{\tau i}}^k + K_{u_x u_z s\tau ji}^k q_{z_{\tau i}}^k + K_{u_x u_\phi s\tau ji}^k q_{\phi_{\tau i}}^k = P_{u_x sj}^k \\ \delta q_{y_{sj}}^k &: K_{u_y u_x s\tau ji}^k q_{x_{\tau i}}^k + K_{u_y u_y s\tau ji}^k q_{y_{\tau i}}^k + K_{u_y u_z s\tau ji}^k q_{z_{\tau i}}^k + K_{u_y u_\phi s\tau ji}^k q_{\phi_{\tau i}}^k = P_{u_y sj}^k \\ \delta q_{z_{sj}} &: K_{u_z u_x s\tau ji}^k q_{x_{\tau i}}^k + K_{u_z u_y s\tau ji}^k q_{y_{\tau i}}^k + K_{u_z u_z s\tau ji}^k q_{z_{\tau i}}^k + K_{u_z u_\phi s\tau ji}^k q_{\phi_{\tau i}}^k = P_{u_x sj}^k \\ \delta q_{\phi_{sj}}^k &: K_{u_\phi u_x s\tau ji}^k q_{x_{\tau i}}^k + K_{u_\phi u_y s\tau ji}^k q_{y_{\tau i}}^k + K_{u_\phi u_z s\tau ji}^k q_{z_{\tau i}}^k + K_{u_\phi u_\phi s\tau ji}^k q_{\phi_{\tau i}}^k = P_{u_\phi sj}^k \end{aligned} \tag{15}$$

This work introduces a novel formulation of the Fundamental Nucleus (FN), where:

- The FNs $K^k_{u_m u_l s\tau ji}$ and $P^k_{u_m sj}$ are single scalar components;
- The theory requires only 16 independent scalar parameters for complete stiffness characterization (and 4 for the load array).

This represents a significant modification compared to traditional CUF implementations [11, 12] that employ 4×4 FN matrix. This contrasts with conventional CUF, which requires all variables to share the same expansion theory, often forcing unnecessary computational. The assembly across all nodes and elements results in the problem:

$$\mathbf{KU} = \mathbf{P} \tag{16}$$

Figure 2 demonstrates the systematic assembly procedure for the global stiffness matrix through

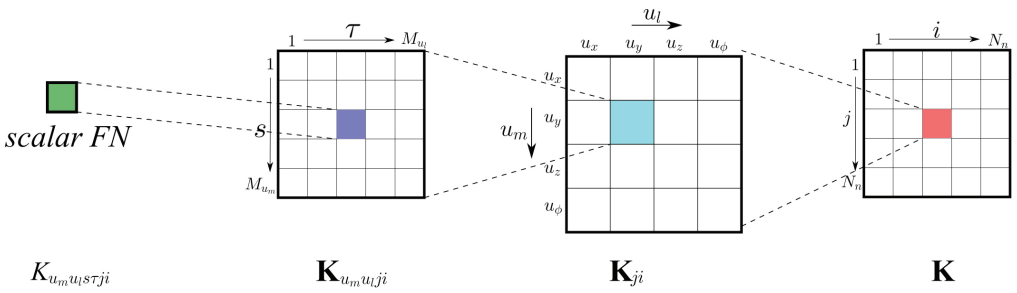

Figure 2: Assembly of the stiffness matrix, starting from the scalar fundamental nuclei.

three expansion stages. The invariant fundamental kernel is first developed through indices s and τ. The resulting submatrix undergoes expansion via displacement component indices u_m and u_l. Final expansion through nodal indices j and i generates the complete structural stiffness matrix.

4 ASSEMBLY

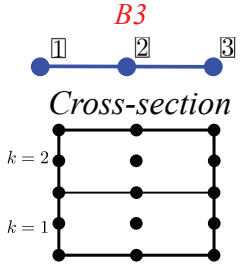

$$\text{TE1: } u_x = u_{x1} + xu_{x2} + zu_{x3} \qquad M_{u_x} = 3$$

$$\text{TE1: } u_y = u_{y1} + xu_{y2} + zu_{y3} \qquad M_{u_y} = 3$$

$$\text{TE1: } u_z = u_{z1} + xu_{z2} + zu_{z3} \qquad M_{u_z} = 3$$

$$\text{LE9: } u^k_\phi = F^k_1 u^k_{\phi 1} + F^k_2 u^k_{\phi 2} + F^k_3 u^k_{\phi 3} + F^k_4 u^k_{\phi 4} + F^k_5 u^k_{\phi 5} + F^k_6 u^k_{\phi 6} + F^k_7 u^k_{\phi 7} + F^k_8 u^k_{\phi 8} + F^k_9 u^k_{\phi 9} \qquad M_{u_\phi} = 15$$

Figure 3: Example of a beam element with a mixed ESL/LW model.

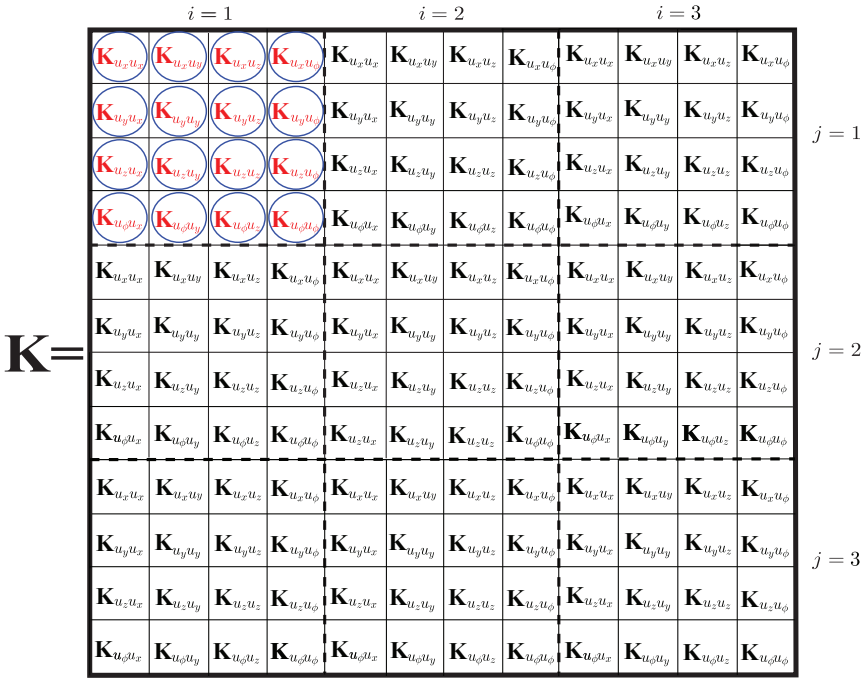

Figure 4: Assembly of the general stiffness matrix with total dimension 72×72.

This section presents the finite element matrix assembly for a multilayered beam element. As a representative example, the three-node element (B3) shown in Fig. 3 is considered, featuring two distinct material layers, a mixed ESL/LW kinematic formulation, and 72 total degrees of freedom. The displacement field employs linear Taylor expansions (TE1) for all components ($M_{u_x} = M_{u_y} = M_{u_z} = 3$), while the electric potential, ϕ, is discretized using two nine-node Lagrange expansions (LE9) with $M_{u_\phi} = 15$.
Figure 4 displays the assembled global stiffness matrix $\mathbf{K}$. While the formulation is presented specifically for the stiffness matrix (for conciseness), the methodology applies equally to the load vector $\mathbf{P}$. This scheme maintains model independence, though the actual matrix dimensions scale with the system's degrees of freedom. The stiffness matrix features a block structure where each sub-matrix $\mathbf{K}_{ji}$ decomposes into sixteen fundamental blocks $\mathbf{K}_{u_m u_l ji}$. For purely mechanical systems, this reduces to nine active sub-matrices, as detailed in Carrera *et al.* [16].

5 RESULTS

This section presents a comprehensive validation study through one canonical benchmarks, evaluating coupled electromechanical bending. The case study investigates a bimorph beam functioning as an actuator.

5.1 Acronym system

In the paper, a coherent acronym system is adopted to identify the structural theories. For instance, in the context of Lagrange-based expansions, the model LE9-LE9-LE9-LE9 indicates that all generalized displacement components are represented using bi-parabolic expansions. The number of Lagrange CUF elements employed for each material layer is explicitly stated. Moreover, mixed ESL/LW theories are utilized, enabling the formulation of refined models such as TE2-TE3-TE2-LE9, where different expansion types and orders are selectively applied to each component.

5.2 Polyvinylidene (PVDF) Bimorph Beam: Actuator Case

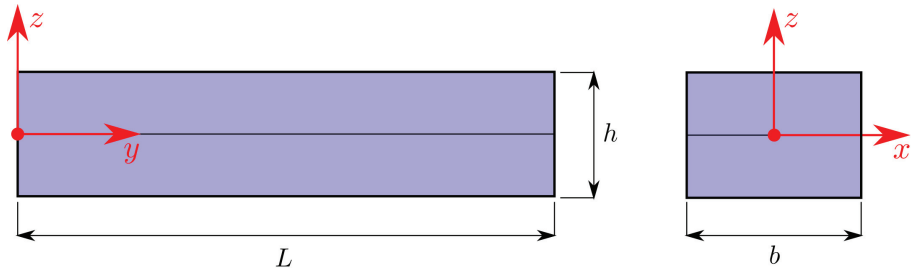

Figure 5: Geometrical properties of the bimorph beam.

A cantilever beam composed of two oppositely polarized Polyvinylidene (PVDF) layers is analyzed. The beam has a total thickness of 1 [mm], a length of 100 [mm], and a width of 5 [mm]. It is fixed on the left end, with an applied electric potential of 1 [V] across its thickness. The material properties are provided in Table 5.2. Note that the bimorph PVDF model excludes the piezoelectric constants e_{33} and e_{15}. The beam geometry is illustrated in Fig. 5. The present results are compared with three literature models. Miglioretti and Carrera [11] employed a uniform CUF-based expansion, while Tzou and Ye [19] used triangular shell elements with mechanical (FOSDT) and electrical degrees of freedom. Additionally, Chee *et al.* [20] implemented Hermitian beam elements with a layer-wise electric potential formulation. The deflection of the cantilever bimorph along its length is illustrated in Fig. 6. The present results demonstrate that it is convenient to use mixed ESL/LW, and they perfectly match the references.

6 CONCLUSIONS

This strategy is particularly effective for complex laminated structures, where different physical fields require varying levels of detail. Numerical analyses confirm the effectiveness of the approach, demonstrating its ability to provide accurate and efficient multi-field simulations. By selecting appropriate kinematic formulations for each field, the proposed method achieves high-fidelity modelling while significantly reducing computational costs. The benchmarks collectively verify the formulation's accuracy across both actuation and sensing configurations.

Table 1: Material properties for bimorph cantilever beam

PVDF		
Elastic modulus	2.00×10^9	Pa
Shear modulus	2.00×10^8	Pa
Mass density	2.00×10^3	Kg m^{-3}
Poisson ratio	0.29	—
e_{31} Piezo	0.046	Cm^{-2}
e_{32} Piezo	0.046	Cm^{-2}
Elec. perm. χ_{11}	1.06×10^{-10}	Fm^{-1}
Elec. perm. χ_{22}	1.06×10^{-10}	Fm^{-1}
Elec. perm. χ_{33}	1.06×10^{-10}	Fm^{-1}

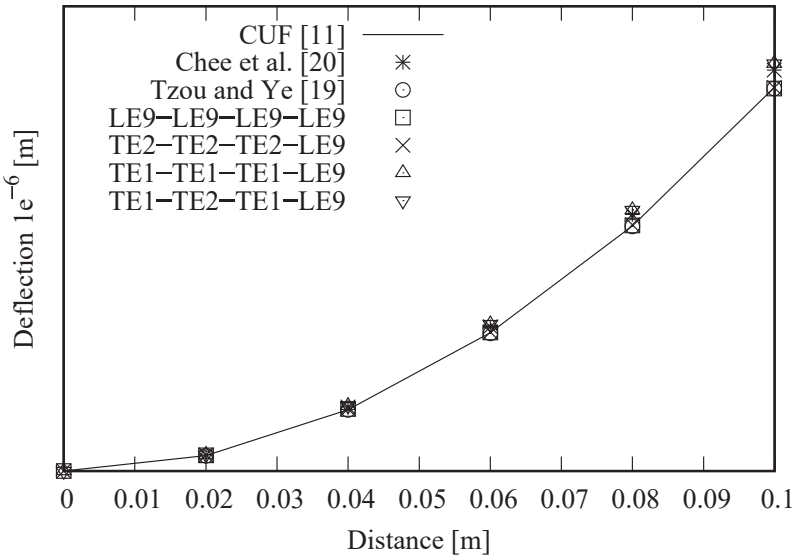

Figure 6: Deflection of the bimorph cantilever along its length.

The proposed method is particularly promising for applications requiring extensive simulations, such as wave propagation studies in health monitoring systems, where computational efficiency is crucial for real-time analysis and large-scale simulations.

REFERENCES

[1] E. F. Crawley and J. de Luis, "Use of piezoelectric actuators as elements of intelligent structures," *AIAA Journal*, vol. 25, no. 10, pp. 1373–1385, 1987. [Online]. Available: https://doi.org/10.2514/3.9792

[2] T. Bailey and J. E. Hubbard, "Distributed piezoelectric-polymer active vibration control of a cantilever beam," *Journal of Guidance, Control, and Dynamics*, vol. 8, no. 5, pp. 605–611, 1985. [Online]. Available: https://doi.org/10.2514/3.20029

[3] D. Robbins and J. Reddy, "Analysis of piezoelectrically actuated beams using a layer-wise displacement theory," *Computers & Structures*, vol. 41, no. 2, pp. 265–279, 1991. [Online]. Available: https://www.sciencedirect.com/science/article/pii/004579499190430T

[4] D. A. Saravanos and P. R. Heyliger, "Mechanics and computational models for laminated piezoelectric beams, plates, and shells," *Applied Mechanics Reviews*, vol. 52, no. 10, pp. 305–320, 10 1999. [Online]. Available: https://doi.org/10.1115/1.3098918

[5] X.-J. Dong, G. Meng, and J.-C. Peng, "Vibration control of piezoelectric smart structures based on system identification technique: Numerical simulation and experimental study," *Journal of Sound and Vibration*, vol. 297, no. 3, pp. 680–693, 2006. [Online]. Available: https://www.sciencedirect.com/science/article/pii/S0022460X06003087

[6] K. Umes and R. Ganguli, "Shape and vibration control of a smart composite plate with matrix cracks," *Smart Materials and Structures*, vol. 18, no. 2, p. 025002, dec 2008. [Online]. Available: https://dx.doi.org/10.1088/0964-1726/18/2/025002

[7] K. Ramesh Kumar and S. Narayanan, "The optimal location of piezoelectric actuators and sensors for vibration control of plates," *Smart Materials and Structures*, vol. 16, no. 6, p. 2680, nov 2007. [Online]. Available: https://dx.doi.org/10.1088/0964-1726/16/6/073

[8] C. Vasques and J. Dias Rodrigues, "Active vibration control of smart piezoelectric beams: Comparison of classical and optimal feedback control strategies," *Computers & Structures*, vol. 84, no. 22, pp. 1402–1414, 2006, composite Adaptive Structures: Modelling and Simulation. [Online]. Available: https://www.sciencedirect.com/science/article/pii/S0045794906000964

[9] J. M. Simões Moita, C. M. Mota Soares, and C. A. Mota Soares, "Active control of forced vibrations in adaptive structures using a higher order model," *Composite Structures*, vol. 71, no. 3, pp. 349–355, 2005, fifth International Conference on Composite Science and Technology. [Online]. Available: https://www.sciencedirect.com/science/article/pii/S0263822305002618

[10] S. Beheshti-Aval, M. Lezgy-Nazargah, P. Vidal, and O. Polit, "A refined sinus finite element model for the analysis of piezoelectric-laminated beams," *Journal of Intelligent Material Systems and Structures*, vol. 22, no. 3, pp. 203–219, 2011. [Online]. Available: https://doi.org/10.1177/1045389X10396955

[11] F. Miglioretti and E. Carrera, "Application of a refined multi-field beam model for the analysis of complex configurations," *Mechanics of Advanced Materials and Structures*, vol. 22, no. 1-2, pp. 52–66, 2015. [Online]. Available: https://doi.org/10.1080/15376494.2014.912365

[12] J. Najd, E. Zappino, E. Carrera, W. Harizi, and Z. Aboura, "A variable kinematic model for the prediction of capacitance variations in embedded PZT sensors," *Journal of Intelligent Material Systems and Structures*, vol. 34, no. 7, pp. 811–824, 2023. [Online]. Available: https://doi.org/10.1177/1045389X221121974

[13] D. Ballhause, M. D'Ottavio, B. Kröplin, and E. Carrera, "A unified formulation to assess multilayered theories for piezoelectric plates," *Computers & Structures*, vol. 83, no. 15, pp. 1217–1235, 2005, modelling of Smart Structures. [Online]. Available: https://www.sciencedirect.com/science/article/pii/S0045794905000271

[14] R. Schardt, "Eine Erweiterung der Technischen Biegetheorie zur Berechnung prismatischer Faltwerke," *Der Stahlbau*, vol. 35, pp. 161–171, 1966.

[15] E. Carrera and D. Scano, "Beam finite element models with node dependent kinematics and arbitrary displacement fields over the cross-section," *Mechanics of Advanced Materials and Structures*, 2025. [Online]. Available: https://doi.org/10.1080/15376494.2024.2434198

[16] E. Carrera, D. Scano, and E. Zappino, "Plate finite elements with arbitrary displacement fields along the thickness," *Finite Elements in Analysis and Design*, vol. 244, p. 104296, 2025. [Online]. Available: https://www.sciencedirect.com/science/article/pii/S0168874X24001902

[17] E. Carrera and D. Scano, "Complete variable kinematics CUF-based multilayered shell elements," in *16th World Congress on Computational Mechanics and 4th Pan American Congress on Computational Mechanics*, July 2024. [Online]. Available: https://www.scipedia.com/public/Carrera_Scano_2024a

[18] K. Bathe, *Finite Element Procedure*. Upper Saddle River, New Jersey, USA: Prentice hall, 1996.

[19] H. S. Tzou and R. Ye, "Analysis of piezoelastic structures with laminated piezoelectric triangle shell elements," *AIAA Journal*, vol. 34, no. 1, pp. 110–115, 1996. [Online]. Available: https://doi.org/10.2514/3.12907

[20] C. Y. K. Chee, L. Tong, and G. P. Steven, "A mixed model for composite beams with piezoelectric actuators and sensors," *Smart Materials and Structures*, vol. 8, no. 3, p. 417, jun 1999. [Online]. Available: https://dx.doi.org/10.1088/0964-1726/8/3/313

Part II

MS 01 - SMART SYSTEMS AND CONTROL STRATEGIES FOR VIBRATION ATTENUATION USING PIEZOELECTRIC TRANSDUCERS

Marta Berardengo, Jan Høgsberg, Boris Lossouarn, Stefano Manzoni

XI ECCOMAS Thematic Conference on Smart Structures and Materials - SMART 2025
M. Krommer, M. Nader and M. Schagerl (Eds)

Received: 9 April 2025 / Revised: 1 October 2025 / Accepted: 3 October 2025
© The Author(s) 2025

Magnetostrictive Shunt versus Piezoelectric Shunt: A Comparison

Marta Berardengo, Marco Mercato, Stefano Manzoni

Abstract. This paper treats the use of magnetostrictive shunt to the aim of vibration control when a primary system is excited by an external disturbance. It is shown that when the primary system is coupled with an magnetostrictive element surrounded by a coil, and this coil is shunted with a proper electric impedance, vibration reduction is achieved. To model the coupled system, an approach already used for piezoelectric shunt is employed, defining similar non-dimensional parameters which are then shown to drive the attenuation performance and the shunt tuning, exactly as for piezoelectric shunt. This model constitutes an improvement compared to the models available in the literature and shows that a strict parallelism exists between the two considered types of shunt control. Nevertheless, when practical applications are considered, it comes out that some adjustments are needed for the model of magnetostrictive shunt, mainly due to the magnetic losses in the shunted coil. This makes magnetostrictive shunt and piezoelectric shunt slightly different, and the paper proposes a possible upgrade for the model of magnetostrictive system. All the theoretical results related to magnetostrictive shunt are validated by means of a tailored set-up, focusing on the case of mono-modal control and using both resistive and resonant shunt. The work also defines which are the main limits of magnetostrictive shunt compared to piezoelectric shunt, and it resulted that the main limitations are primarily related to the inability to achieve optimal tuning when low frequency modes need to be attenuated. The proposed model of magnetostrictive shunt can also be used for other applications, such as, e.g., structural health monitoring.

Key words: Vibration control, Magnetostrictive shunt, Piezoelectric shunt, Resistive shunt, Resonant shunt

Marta Berardengo & Marco Mercato
Department of Mechanical, Energy, Management and Transportation Engineering, Universitá degli Studi di Genova, Via all'Opera Pia, 15a - 16145 Genoa, Italy
e-mail: marta.berardengo@unige.it

Stefano Manzoni
Department of Mechanical Engineering, Politecnico di Milano, Via La Masa, 1 - 20156 Milan, Italy, e-mail: stefano.manzoni@polimi.it

1 INTRODUCTION

The use of intelligent materials in the field of vibration control is gaining more and more attention because of the advantages provided by employing these types of materials. A very attractive approach when using intelligent materials is the so called shunt control where a proper electric network is connected to the material, obtaining a significant control action (e.g., [1, 2, 3, 4]). Different successful real applications are already described in the literature, especially considering piezoelectric shunt (e.g., [5, 6, 7, 8]). Magnetostrictive (MS) shunt is less considered in the literature but recently different works have analysed it [9, 10, 11, 12], evidencing its capability in providing good control performances.

This paper is aimed at showing similarities and differences among MS shunt and the piezoelectric shunt. Being the latter largely studied, the final aim is to evidence how control strategies developed for piezoelectric shunt can be used in the context of the MS shunt. Furthermore, the similarities between piezoelectric and MS shunt will be also useful for applying MS shunt in the context of structural health monitoring, since piezoelectric shunt has already been proven to be a reliable approach in this context [13].

The paper is structured as follows: Section 2 describes the models of the two shunt types, evidencing the similarities, then Section 3 presents some numerical simulations for analysing the control performance of MS shunt. Finally, Section 4 will discuss some practical issues which must be accounted for when using MS shunt, which are instead not significant in the context of piezoelectric shunt.

2 SHUNT MODELS

The system considered is the generic multi-degree-of-freedom system depicted in Fig. 1. The green rectangle named 'intelligent material' can be either a piezoelectric element or an MS element (surrounded by a coil).

Writing the equations of motion of the system and the equation of the electrical part, passing then in modal coordinates q_i (where q_i is the modal coordinate for the i-th mode, with $i = 1, .., G$), the following equations are obtained for the piezoelectric case [14, 15]

$$\ddot{q}_i(t) + 2\xi_i\omega_i\dot{q}_i(t) + \omega_i^2 q_i(t) - \chi_i V(t) = F_i(t), \quad \forall i \in \{1, \cdots, G\} \tag{1}$$

$$C_\infty V(t) - Q(t) + \sum_{i=1}^{G} \chi_i q_i(t) = 0 \tag{2}$$

and for the MS case [9]

$$\ddot{q}_i(t) + 2\xi_i\omega_i\dot{q}_i(t) + \omega_i^2 q_i(t) - \theta\phi_{i,1} I(t) = F_i(t), \quad \forall i \in \{1, \cdots, G\} \tag{3}$$

$$V(t) = R_\mathrm{c} I(t) + L_\mathrm{c}\dot{I}(t) + \bar{\theta}\sum_{i=1}^{G} \phi_{i,1}\dot{q}_i(t) \tag{4}$$

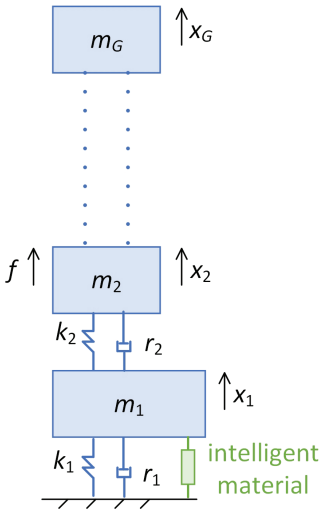

Figure 1: Schematic of a multi-degree-of-freedom system equipped with an intelligent material and excited by an external disturbance f.

where F_i is the modal force, ω_i is the i-th eigenfrequency (with either the piezoelectric element short-circuited or the coil open-circuited for the MS case), ξ_i is the associated non-dimensional damping ratio, V is either the voltage between the electrodes of the piezoelectric element or between the terminals of the coil, Q is the charge in one of the electrodes of the piezoelectric element ($-Q$ in the other), I is the current flowing in the coil, t is time, C_∞ is the capacitance of the piezoelectric element at constant strain (i.e., at infinite frequency, blocked capacitance), χ_i is a coupling coefficient describing the energy transfer between the i-th mode and the electrical part of the system based on the piezoelectric element, θ and $\bar{\theta}$ are constants depending on characteristics of the MS element and the associated coil, L_c is the coil inductance at constant strain, R_c is the associated inherent resistance of the coil, and, finally, $\phi_{i,1}$ is the eigenvector component of the i-th mode for the first degree of freedom (normalised to the unit modal mass and with the coil open-circuited).

To further elaborate equations (1) to (4) and show the similarities between the two types of shunt, a single-degree-of-freedom (SDOF) reduction can be performed.

According to [16], the SDOF reduction for the piezoelectric case leads to the following equations describing the dynamics of the system for $\Omega \simeq \omega_i$ (where Ω is the angular frequency):

$$\ddot{q}_i(t) + 2\xi_i\omega_i\dot{q}_i(t) + \omega_i^2 q_i(t) - \chi_i V t) = F_i(t) \tag{5}$$

$$C_{\mathrm{p},i}V(t) - Q(t) + \chi_i q_i(t) = 0 \tag{6}$$

where $C_{\mathrm{p},i}$ is the modal capacitance of the i-th mode, which allows accounting for the contribution of the out-of-band modes [17]. Considering the MS case, according to [9], the equations of the SDOF case are:

$$\ddot{q}_i(t) + 2\xi_i\omega_i\dot{q}_i(t) + \omega_i^2 q_i(t) - \theta\phi_{i,1}I(t) = F_i(t) \tag{7}$$

$$V(t) = R_{\mathrm{c}}I(t) + L_i\dot{I}(t) + \bar{\theta}\phi_{i,1}\dot{q}_i(t) \tag{8}$$

where L_i is the modal inductance of the i-th mode [9] and, also in this case, it is a quantity used to take into account the contribution of the out-of-band modes.

Equations (5) and (6) can be used to find the frequency response function (FRF) $H_i(\mathrm{j}\Omega) = q_i^{\mathrm{f}}/F_i^{\mathrm{f}}$ (superscript f indicates that the quantity is transformed in the frequency domain, while j is the imaginary unit) in case of specific shunt impedances Z_{sh} for piezoelectric shunt, by mixing them with the considered expression of Z_{sh}. The same can be performed for MS shunt with Eqs. (7) and (8). To evidence the similarities between piezoelectric and MS shunts, resistive and resonant shunts are considered, also because they are the most used types of shunt impedances in piezoelectric shunt.

2.1 Resistive shunt

When the shunt impedance is made from a simple resistance R, the FRF H_i can be expressed as:

$$H_i(\mathrm{j}\Omega) = \frac{1 + \mathrm{j}\tau\Omega}{\omega_i^2 - \Omega^2(1 + 2\xi_i\omega_i\tau) + \mathrm{j}\Omega(\hat{\omega}_i^2 + 2\xi_i\omega_i - \tau\Omega^2)} \tag{9}$$

where $\tau = C_{\mathrm{p},i}R$ for piezoelectric shunt while $\tau = L_i/(R_{\mathrm{c}} + R) = L_i/R_{\mathrm{tot}}$ for MS shunt. Furthermore, $\hat{\omega}_i$ is the i-th eigenfrequency of the system with either the piezoelectric element open-circuited or the coil surrounding the MS element short-circuited.

Since the FRF in case of resistive shunt has the same form for the two shunt types, the way to optimise the value of R for controlling the i-th mode can be directly derived by the theory of piezoelectric shunt: the optimal value of τ (named τ_{opt}) for controlling the ith mode is equal to [16]:

$$\tau_{\mathrm{opt}} = \sqrt{\frac{2}{\hat{\omega}_i^2 + \omega_i^2}} \tag{10}$$

Then, it is possible to calculate R using the corresponding link between τ and R for the considered shunt type, having estimated in advance the value of either $C_{\mathrm{p,i}}$ or L_i. The corresponding attenuation A_{dB} of the FRF amplitude peak is equal to [1]:

$$A_{\mathrm{dB}} = 20\log_{10}\frac{k_i^2 + 2\sqrt{2}\xi_i\sqrt{2 + k_i^2}}{4\xi_i\sqrt{1 - \xi_i^2}} \tag{11}$$

Here, the quantity k_i must be introduced. It is the modal coupling coefficient and it can be estimated in both the shunt types as [9]:

$$|k_i| \simeq \sqrt{\frac{\hat{\omega}_i^2 - \omega_i^2}{\omega_i^2}} \tag{12}$$

2.2 Resonant shunt

This subsection treats the case in which $Z_{\rm sh}$ is made from the series of a capacitance C and a resistance R for MS shunt and from the parallel between an inductance L and a resistance R for piezoelectric shunt.

In both the cases, the resulting FRF H_i is equal to:

$$H_i(\mathrm{j}\Omega) = \frac{-\Omega^2 + 2\mathrm{j}\xi_{\rm e}\omega_{\rm e}\Omega + \omega_{\rm e}^2}{\Omega^4 - \Omega^2 P_i + \omega_{\rm e}^2\omega_i^2 + 2\mathrm{j}\Omega p_i} \tag{13}$$

with

$$P_i = \omega_{\rm e}^2 + 4\xi_{\rm e}\xi_i\omega_{\rm e}\omega_i + \hat{\omega}_i^2 \tag{14}$$

$$p_i = [\xi_{\rm e}\omega_{\rm e}(\omega_i^2 - \Omega^2) + \xi_i\omega_i(\omega_{\rm e}^2 - \Omega^2)] \tag{15}$$

Furthermore, $\omega_{\rm e}$ and $\xi_{\rm e}$ for piezoelectric shunt are

$$\omega_{\rm e}^2 = 1/(C_{{\rm p},i}L) \tag{16}$$

$$\xi_{\rm e} = \frac{1}{2R}\sqrt{\frac{L}{C_{{\rm p},i}}} \tag{17}$$

and, for MS shunt, they are:

$$\omega_{\rm e}^2 = 1/(L_i C) \tag{18}$$

$$\xi_{\rm e} = \frac{R + R_{\rm c}}{2}\sqrt{\frac{C}{L_i}} = \frac{R_{\rm tot}}{2}\sqrt{\frac{C}{L_i}} \tag{19}$$

It is easy to demonstrate that a shunt impedance made from the parallel of a R and C for MS shunt leads to the same FRF related to a shunt impedance made from the series of R and L for piezoelectric shunt. This implies the possibility of finding optimal values for the shunt components and the corresponding attenuation performances with the approaches developed for piezoelectric shunt (see [18, 19]).

3 NUMERICAL ANALYSIS

The above formulations allows deriving the attenuation A_{dB} for both resonant and resistive shunt. As in the case of piezoelectric shunt, MS shunt offers attenuation performances depending on ξ_i and k_i. Figure 2 shows the resulting curves, which evidence the larger attenuation provided by resonant shunt.

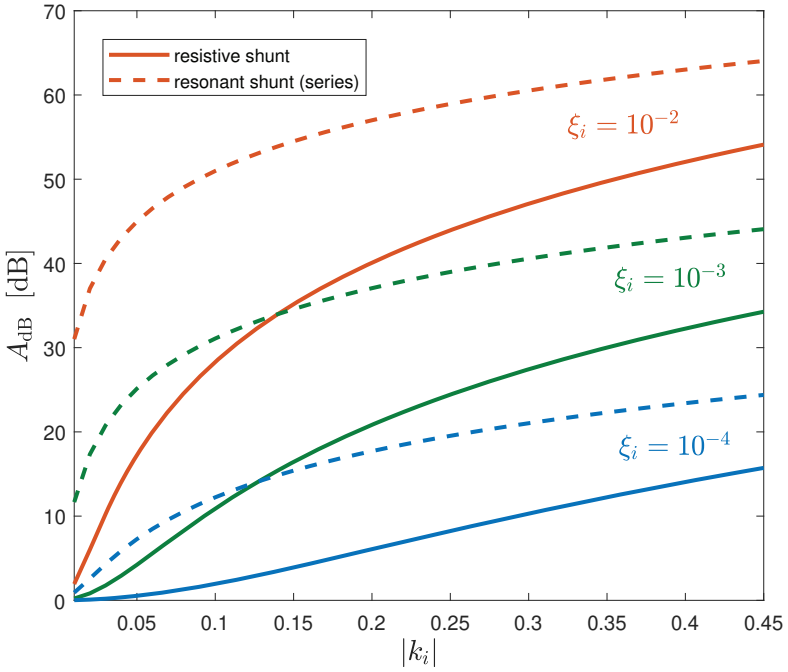

Figure 2: Trend of the attenuation (reduction of peak amplitude on a given mode) A_{dB} as function of the value of $|k_i|$ and for three different ξ_i values for resistive and resonant (series connection between R and C) MS shunt.

Furthermore, the above treatment allows deriving the optimal resistance values for piezoelectric and MS shunts in case of either resistive or resonant shunt. Figure 3a shows the trend of the optimal resistance for resistive shunt for different ω_i and $|k_i|$ values, while Fig. 3b provides the same information for resistive shunt. It results that the resistance values are much larger for piezoelectric shunt compared to MS shunt, making piezoelectric shunt better in terms of ease of implementation. Moreover, the value of the optimal resistance for MS shunt must account also for R_{c}. At low frequency, the optimal resistance can be larger than the value of R_{c}, implying the impossibility of reaching an optimal tuning of the shunt impedance.

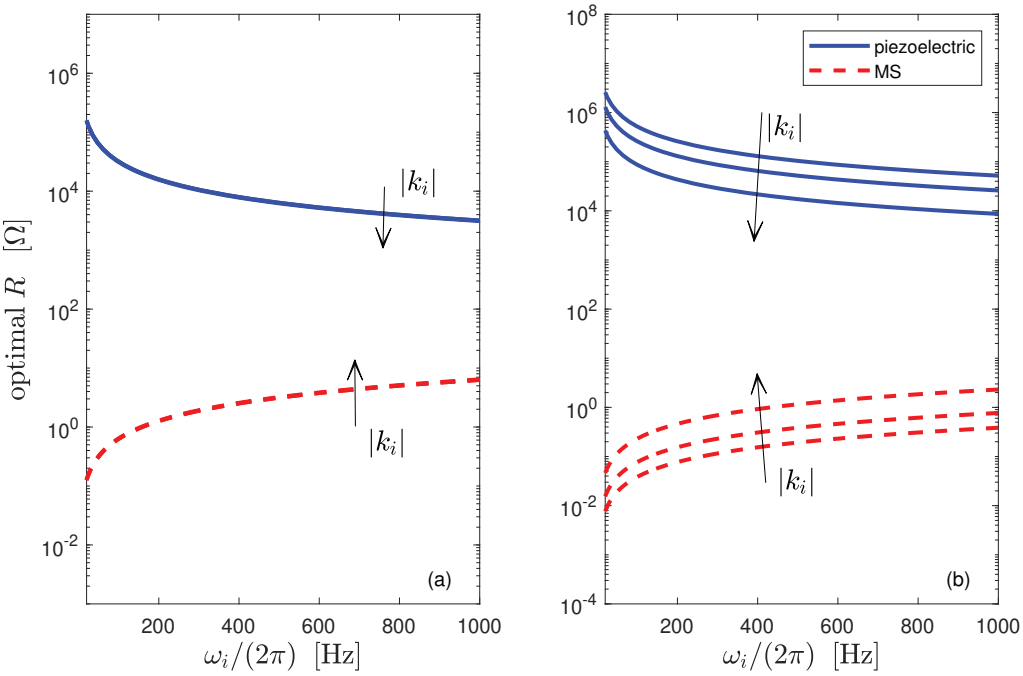

Figure 3: Trend of the optimal resistance as function of ω_i and for three different $|k_i|$ values (i.e., 0.05, 0.1 and 0.3) for resistive (a) and resonant (b) shunt in both piezoelectric and MS shunt. The shunt components are connected in series for MS shunt, and in parallel for piezoelectric shunt.

4 MAIN DIFFERENCE BETWEEN PIEZOELECTRIC AND MS SHUNT

The main difference between piezoelectric and MS shunt is related to the fact that the value of the modal inductance L_i must be adjusted to take into account the effect of magnetic losses of the coil. Indeed, considering as an example the equivalent inductance (measured on a set-up in the labs of Politecnico di Milano) of magnetostrictive material (obtained by inserting current in the coil and measuring the consequent voltage at the pins of the coil), a decreasing trend due to losses is present. When SDOF reductions are considered, it is possible to adjust the value of L_i as

$$\tilde{L}_i = L_i - \eta\omega_i \tag{20}$$

where η is a constant describing the descending trend around ω_i. A more detailed description of the problem is available in [9].

Conversely, the value of $C_{\mathrm{p},i}$ does not need any adjustment.

5 CONCLUSION

The paper has dealt with the parallelism between piezoelectric and MS shunt, showing that there is a common mathematical approach for describing both the approaches. The paper has also evidenced that there are some limits and issues (e.g., magnetic losses) associated to MS shunt which are not observed for piezoelectric shunt. The developed model of MS shunt will be useful not only for vibration control purposes but also for structural health monitoring applications of MS materials.

ACKNOWLEDGMENTS

This research has been supported by the project ”CHIMERA? - is there a CHance that Indexes and Measurements of the energy conversion Efficiency Reveal system Alterations?” funded by the European Union – Next Generation EU, M4C2 I1.1, through Progetti di Rilevante Interesse Nazionale (PRIN) 2022, grant n. 20225PKHWJ (CUP: D53D23003060006).

REFERENCES

[1] O. Thomas, J. Ducarne, and J. Deü, “Performance of piezoelectric shunts for vibration reduction,” *Smart Materials and Structures*, vol. 21, no. 1, 2012, 015008.

[2] J. D. Richardt, B. Lossouarn, J. Høgsberg, and J.-F. Deü, “Calibration of multiple shunted piezoelectric transducers with correction for residual modes and shunt interactions,” *JVC/Journal of Vibration and Control*, vol. 31, no. 1-2, p. 24 – 36, 2025.

[3] T. Wang, J. Dupont, and J. Tang, “On integration of vibration suppression and energy harvesting through piezoelectric shunting with negative capacitance,” *IEEE/ASME Transactions on Mechatronics*, vol. 28, pp. 2621 – 2632, 2023.

[4] P. Gardonio and G. K. Rodrigues, “Shunted piezoelectric patch adaptive vibration absorber set to maximise electric power absorption: A comparison between parallel and series rl-shunts,” *JVC/Journal of Vibration and Control*, vol. 31, no. 1-2, p. 37 – 50, 2025.

[5] H. Sun, Z. Yang, K. Li, B. Li, J. Xie, D. Wu, and L. Zhang, “Vibration suppression of a hard disk driver actuator arm using piezoelectric shunt damping with a topology-optimized pzt transducer,” *Smart Materials and Structures*, vol. 18, 2009, 065010.

[6] Y. Watine, B. Lossouarn, C. Gabillet, J.-A. Astolfi, and J.-F. Deü, “Mitigation of hydrofoil torsional flow induced vibrations by resonant piezoelectric shunt,” *Ocean Engineering*, vol. 313, 2024, 119598.

[7] B. Zhou, F. Thouverez, and L. D., “Vibration reduction of mistuned bladed disks by passive piezoelectric shunt damping techniques,” *AIAA Journal*, vol. 52, pp. 1194–1206, 2014.

[8] K. Zhou and Z. Hu, "Vibration suppression on the composite laminated plates subjected to aerodynamic and harmonic excitations based on the nonlinear piezoelectric shunt damping," *Applied Mathematical Modelling*, vol. 121, pp. 134–165, 2023.

[9] M. Berardengo, M. Mercato, and S. Manzoni, "Magnetostrictive shunt for vibration control and isolation: model, characteristics and similarities with piezoelectric shunt," *Smart Materials and Structures*, vol. 34, no. 1, 2025, 015043.

[10] Z. Deng, J. J. Scheidler, V. M. Asnani, and M. J. Dapino, "Shunted magnetostrictive devices in vibration control," *Smart Materials and Structures*, vol. 29, no. 10, 2020, 105007.

[11] E. Fukada, M. Date, and K. Sekigawa, "Vibration control by magnetostrictive actuator coupled with negative inductance circuits," *Japanese Journal of Applied Physics*, vol. 42, no. 11, pp. 7124–7128, 2003.

[12] J. J. Scheidler and V. M. Asnani, "Validated linear dynamic model of electrically-shunted magnetostrictive transducers with application to structural vibration control," *Smart Materials and Structures*, vol. 26, no. 3, 2017, 035057.

[13] M. Berardengo, M. Brambilla, A. Codina, N. Schena, and S. Manzoni, "Piezoelectric coupling as a feature sensitive to structural alterations," *Mechanical Systems and Signal Processing*, vol. 224, 2025, 112012.

[14] O. Thomas, J.-F. Deü, and J. Ducarne, "Vibration of an elastic structure with shunted piezoelectric patches: efficient finite-element formulation and electromechanical coupling coefficients," *International Journal of Numerical Methods in Engineering*, vol. 80, no. 2, pp. 235–268, 2009.

[15] J. Ducarne, O. Thomas, and J. Deü, "Placement and dimension optimization of shunted piezoelectric patches for vibration reduction," *Journal of Sound and Vibration*, vol. 331, no. 14, pp. 3286–3303, 2012.

[16] M. Berardengo, O. Thomas, C. Giraud-Audine, and S. Manzoni, "Improved resistive shunt by means of negative capacitance: new circuit, performances and multi mode control," *Smart Materials and Structures*, vol. 25, 2016, 075033.

[17] M. Berardengo, S. Manzoni, J. Høgsberg, and M. Vanali, "Vibration control with piezoelectric elements: The indirect measurement of the modal capacitance and coupling factor," *Mechanical Systems and Signal Processing*, vol. 151, 2021, 107350.

[18] K. Yamada, H. Matsuhisa, H. Utsuno, and K. Sawada, "Optimum tuning of series and parallel lr circuits for passive vibration suppression using piezoelectric elements," *Journal of Sound and Vibration*, vol. 329, no. 24, pp. 5036–5057, 2010.

[19] M. Berardengo, S. Manzoni, O. Thomas, and M. Vanali, "Guidelines for the layout and tuning of piezoelectric resonant shunt with negative capacitances in terms of dynamic compliance, mobility and accelerance," *Journal of Intelligent Material Systems and Structures*, vol. 32, no. 17, p. 2092 – 2107, 2021.

XI ECCOMAS Thematic Conference on Smart Structures and Materials - SMART 2025
M. Krommer, M. Nader and M. Schagerl (Eds)

Received: 22 March 2025 / Revised: 27 August 2025 / Accepted: 3 October 2025
© The Author(s) 2025

Switching Shunts using Fuzzy Logic for Vibration Mitigation of Smart Flexible Structures

Maria-Styliani Daraki, Aikaterini Smarianaki, Konstantinos Marakakis, Georgia A. Foutsitzi, Georgios E. Stavroulakis

Abstract. Shunted circuits are embedded in piezoelectric patches, which are attached to the host structure, forming a coupled electromechanical system capable of reducing vibrations by transforming kinetic energy into electrical energy and subsequently dissipating it within the electronic components. The aim of this work is to reduce vibrations using a switching damping control strategy. This approach suppresses structural vibrations by inverting the polarity of the displacement and velocity of a partially covered piezoelectric cantilever beam through a switched resonant shunt circuit. By applying the proposed control law, automatic adaptation of each system under study can be achieved. For comparison, the conventional shunted piezoelectric system with passive resonant circuits (without switches) is also considered. The results indicate a good agreement between the responses of the semi-active and passive techniques. As a further step, switches can be controlled by more general fuzzy logic tools, based on specific rules that account for structural and environmental conditions.

Key words: Piezoelectric elements, Switching shuts, Non-linear systems, Semi-active control method, Vibration damping.

Maria-Styliani Daraki & Konstantinos Marakakis & Georgios E. Stavroulakis
School of Production Engineering and Management, Technical University of Crete, GR-73100 Chania, Greece
e-mail: mdaraki1@tuc.gr, kmarakakis@tuc.gr, gestavroulakis@tuc.gr

Maria-Styliani Daraki
Technical University of Crete and Project: 101124439 - European University on Responsible Consumption and Production/EURECA-PRO 2.0 - ERASMUS-EDU-2023-EUR-UNIV, GR-73100 Chania, Greece
e-mail: eureca-pro@tuc.gr

Aikaterini Smarianaki
School of Electrical and Computer Engineering, Technical University of Crete, GR-73100 Chania, Greece
e-mail: asmarianaki@tuc.gr

Georgia A. Foutsitzi
Department of Informatics and Telecommunications, University of Ioannina, GR-47100 Arta, Greece
e-mail: gfouti@uoi.gr

1 INTRODUCTION

Plethora of different configurations have been developed for vibration attenuation, from active, passive, and semi-active until hybrid control methods [1], improving the span life of a structure and its resilience. Fuzzy control has gathered attention because it provides a way to implement non-linear control on systems with uncertainties [2]. Fuzzy controllers can also adapt and optimize their overall performance by taking into account changing operating conditions [3]. In the work of Tairidis [4] an optimization of resonant shunt piezoelectric circuits has been considered, along with an intelligent control system based on adaptive neuro-fuzzy techniques, for vibration reduction of smart composite structures.

A multitude of articles employ works by Clark [5] who uses the classical synchronized switch damping techniques. The SSDS method corresponds to the state-switching technique (the original switch shunt network). It is classified as a variable stiffness method in which piezoelectric elements are simply "synchronized" to the structural motion, where energy is spent on a form of state conversion [6], [7]. Switching between open-circuit, which represents a high stiffness state, and short or resistive circuit, which is the low stiffness state, is performed. The actuator is maintained in its high stiffness state as long a system movement is such that work can be performed on the actuator. The actuator is switched towards low stiffness state, to allow the dissipation of the stored energy in the circuit and consequently vibration suppression is attained [5].

Most of the synchronized switch damping techniques considered in the review article [6] have pointed out that the original control law was optimal for Single-frequency excitations. For this reason, in the last years, several synchronized switch damping techniques have appeared in the literature. The principal types of excitations are the bimodal and the broadband multimodal. This paper [6] evaluates the corresponding control laws based on different excitation cases as well as presents advantages and disadvantages of each strategy. Besides that, all the currently existing prototype multimodal synchronized switch damping on inductors (SSDI) control laws are considered. A new switching law that maximizes the energy dissipation for an bimodal excitation is introduced in [8]. The switching device is activated by the observer model while the switching takes place at the second non-resonant maxima. Berardengo et al. [9] addressed that the shunted circuit can have different configurations concerning the required type of control, i.e. single-modal, multi-modal and broadband.

Semi-active reduction of vibrations through piezo-benders and impendance shunts is reviewed in [9]. In particular, the contemporary focus is the utilization of the SSDI method in single mode control under random noise conditions. Kelley and Kauffman [10] are focusing on the consequences of deviation from the classical switch in semi-active systems which showcased the dependence of the optimal switching time on the forcing frequency. The work [10] analyzes in detail the damping characteristics of the SSDI method, as well as for this same method in [7] an optimal value of the quality factor of the electric circuit is found. In [11] the optimal settings of the parameters of the network for synchronized switched damping on inductors (SSDI) strategy is presented, together with the achieved corresponding maximal

damping performance. The main methods, which are used in the current work, mitigate the structural vibrations by checking the signs of the displacement and velocity of a partially covered piezoelectric cantilever beam utilizing a switched resonant shunt circuit. The objective of this paper is to examine and compare each of the switched piezoelectric damping techniques with the conventional resonant shunt damping technique. Here the topics of this research have been briefly introduced. In section 2 is summarized the FE and state-space models of the structure and states which are studied. After numerical simulations in MATLAB environment, the results of the adopted control strategy are presented in section 3 and a comparison is made. Finally, the highlights and the future perspectives of this work are given.

2 THEORETICAL PRESENTATION OF THE STRUCTURE WITH RESONANT CIRCUIT

A finite element model was developed to analyze the dynamic response of the laminated composite beam with piezoelectric patches on its surface. This model employs the super convergent finite element method developed by Foutsitzi et al. [12], and examined in detail in [12], [13]. In addition, a state-space representation is used to model the electromechanical response of the complete system in the case when a resonant shunt circuit is connected to the upper piezoelectric patch. A MATLAB code has been created and used to carry out the numerical experiments which are presented in the next section.

Summing up the coupled electromechanical equations are obtained, by substituting the linear constitutive equations of the piezoelectric layers into the energy expressions for the Hamilton's Principle and using standard finite element procedure.

$$\boldsymbol{M}_u\ddot{\boldsymbol{d}} + \boldsymbol{K}_u\boldsymbol{d} + \boldsymbol{\Theta}_1 v_1 + \boldsymbol{\Theta}_2 v_2 = \boldsymbol{F}_m \tag{1}$$

$$\boldsymbol{\Theta}_1^T\boldsymbol{d} + C_p v_1 = Q_1 \tag{2}$$

$$-\boldsymbol{\Theta}_2^T\boldsymbol{d} + C_p v_2 = Q_2 \tag{3}$$

In the equations (1) − (3), the symbol $\boldsymbol{d}$ represents the vector of the mechanical degress of freedom (DoF), $\boldsymbol{M}_u$ stands for the mass matrix of the system, $\boldsymbol{K}_u$ stands for the stiffness matrix, $\boldsymbol{F}_m$ corresponds to the mechanical force terms, $\boldsymbol{\Theta} = [\boldsymbol{\Theta}_1, \boldsymbol{\Theta}_2]$ denotes the electromechanical coupling matrix and C_p the piezoelectric capacitance. The elements of these matrices are not shown here for the purpose of conciseness.

In the case where both piezoelectric layers are shorted, the difference of the electric potential between their electrodes vanishes ($v_1 = v_2 = 0$). Therefore, the equation (1) becomes

$$\boldsymbol{M}_u\ddot{\boldsymbol{d}} + \boldsymbol{K}_u\boldsymbol{d} = \boldsymbol{F}_m \tag{4}$$

A representation of the system in state space form has been developed. The short-circuit equation (4) takes the form as shown below.

$$\dot{\boldsymbol{x}} = \boldsymbol{A}\boldsymbol{x} + \boldsymbol{B}\boldsymbol{w} \tag{5}$$
$$\boldsymbol{y} = \boldsymbol{C}\boldsymbol{x} + \boldsymbol{D}\boldsymbol{w}$$

where

$$\boldsymbol{A} = \begin{bmatrix} \boldsymbol{0} & \boldsymbol{I} \\ -\boldsymbol{M}_u^{-1}\boldsymbol{K}_u & \boldsymbol{0} \end{bmatrix}, \quad \boldsymbol{B} = \begin{bmatrix} \boldsymbol{0} \\ \boldsymbol{M}_u^{-1} \end{bmatrix} \tag{6}$$

$$\boldsymbol{x} = \begin{Bmatrix} \boldsymbol{d} \\ \dot{\boldsymbol{d}} \end{Bmatrix}, \quad \boldsymbol{w} = \{\boldsymbol{F}_m\} \tag{7}$$

The matrices, $\boldsymbol{C}$ and $\boldsymbol{D}$ depend on the choice of the observed inputs (placement of sensors, actuators).

The final electromechanical system of motion for a beam and piezoelectric element connected to the shunt circuit is:

$$\ddot{\boldsymbol{d}} = -\boldsymbol{M}_u^{-1}\boldsymbol{C}_d\dot{\boldsymbol{d}} - \boldsymbol{M}_u^{-1}\boldsymbol{K}_o\boldsymbol{d} - \boldsymbol{M}_u^{-1}C_p^{-1}(\boldsymbol{\Theta}_1 + \boldsymbol{\Theta}_2)q + \boldsymbol{M}_u^{-1}\boldsymbol{F}_m \tag{8}$$

$$\ddot{q} = -\frac{1}{LC_p}(\boldsymbol{\Theta}_1^T + \boldsymbol{\Theta}_2^T)\boldsymbol{d} - \frac{2}{LC_p}q - \frac{R}{L}\dot{q} \tag{9}$$

where

$$\boldsymbol{K_o} = \boldsymbol{K}_u + C_p^{-1}(\boldsymbol{\Theta}_1\boldsymbol{\Theta}_1^T + \boldsymbol{\Theta}_2\boldsymbol{\Theta}_2^T) \tag{10}$$

Using the extended state vector $\boldsymbol{x} = \left\{\boldsymbol{d}, \dot{\boldsymbol{d}}, q, \dot{q}\right\}^T$ the following state space form is obtained

$$\dot{\boldsymbol{x}}_{sh} = \boldsymbol{A}^{sh}\boldsymbol{x}_{sh} + \boldsymbol{B}^{sh}\boldsymbol{w}_{sh} \tag{11}$$

where the state matrices and the input vector are given by

$$\boldsymbol{A}^{sh} = \begin{bmatrix} \boldsymbol{0}_{N\times N} & \boldsymbol{I}_{N\times N} & \boldsymbol{0}_{N\times 1} & \boldsymbol{0}_{N\times 1} \\ -\boldsymbol{M}_u^{-1}\boldsymbol{K}_o & -\boldsymbol{M}_u^{-1}\boldsymbol{C}_d & -\boldsymbol{M}_u^{-1}C_p^{-1}(\boldsymbol{\Theta}_1^T + \boldsymbol{\Theta}_2^T) & \boldsymbol{0}_{N\times 1} \\ \boldsymbol{0}_{1\times N} & \boldsymbol{0}_{1\times N} & 0 & 1 \\ -\frac{1}{LC_p}(\boldsymbol{\Theta}_1^T + \boldsymbol{\Theta}_2^T) & \boldsymbol{0}_{1\times N} & -\frac{2}{LC_p} & -\frac{R}{L} \end{bmatrix} \tag{12}$$

and

$$\boldsymbol{B}^{sh} = \begin{bmatrix} \boldsymbol{0}_{N\times N} \\ \boldsymbol{M}_u^{-1} \\ \boldsymbol{0}_{1\times N} \\ \boldsymbol{0}_{1\times N} \end{bmatrix}, \qquad \boldsymbol{w}_{sh} = \{\boldsymbol{F}_m\} \tag{13}$$

The output can be defined by

$$\boldsymbol{y}_{sh} = \boldsymbol{C}^{sh}\boldsymbol{x}_{sh} + \boldsymbol{D}^{sh}\boldsymbol{w}_{sh} \tag{14}$$

The matrices, $\boldsymbol{C}^{sh}$ and $\boldsymbol{D}^{sh}$ depend on the choice of outputs. For example, if the output of interest is the tip displacement of a cantilever beam is discretized by N elements, and then the matrices, $\boldsymbol{C}^{sh}$ and $\boldsymbol{D}^{sh}$ are written as

$$\boldsymbol{C}^{sh} = [\boldsymbol{I}_{1\times N} \quad \boldsymbol{0}_{1\times N} \quad 0 \quad 0], \quad \boldsymbol{D}^{sh} = \boldsymbol{0} \tag{15}$$

where all the elements of the matrix $\boldsymbol{I}_{1\times N}$ are zero except for the $N-1$ element.

3 NUMERICAL RESULTS

In this paper, semi-active control is implemented through switched electronic circuits. By using switches - thereby reducing the operating time of the shunt circuit as a system of low energy consumption system - it is investigated whether the system with various switches can achieve the same performance or even better than a passive resonant $R-L$ shunt circuit in suppressing vibrations.

3.1 Activation - deactivation of a switch based on a specific law

In this work a sign check of the position and the velocity of the last node of the beam (transversal z-axis) is performed using the "ode23tb" integration method. When displacement and velocity have opposite signs then the shunt circuit is activated, and it is deactivated when they have the same sign. This control rule has been inspired by active control implemented with fuzzy resoning rules [14]. The shunt circuit consists of an inductor and resistor in a serial configuration. The system is schematically depicted in Figure 1. More general rules based on fuzzy inference can be used, although restricted experience exists and lack of comparison results.

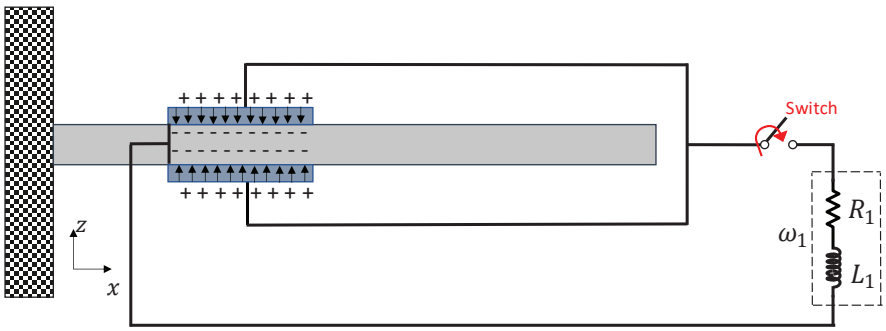

Figure 1: The beam model with the switched shunted circuit.

The first natural frequency of the system is equal to $\omega_{oc1} = 307.3\ {}^{\mathrm{rad}}/_{\mathrm{sec}}$ like as the excitation frequency. Due to switches the circuit is non-linear, therefore the electric circuit components resistance R, inductance L cannot be calculated by analytical expressions [15]. The following simulations are carried out using the appropriate calculated R, L values and are shown below (Table 1).

Table 1: Values of electrical circuit components of a non-linear switch shunted circuit for damping the first eigenfrequency.

	Resistance	**Inductance**
1st Eigenmode	$R_1 = 23661.5$ Ohm	$L_1 = 578.66$ H

The switch command strategy is now explained and follows the state-switched control law from Clark [5]. Two numerical experiments having a switch shunted circuit are carried out. In the first experiment – strait switch strategy, the activation of the circuit occurred when the velocity and the position of the last node of the beam have opposite signs for transverse displacement DoF while in the second – inverse switch strategy, when they have the same signs.

The results of the two tests are illustrated in Figure 2 (a), (b) along with a comparison to the passive $R-L$ circuit in Figure 2 (c). The three responses in Figures 2 (a)–(c) have been combined into one graph for easier comparisons, alongside the four responses are depicted in Figure 2 (d).

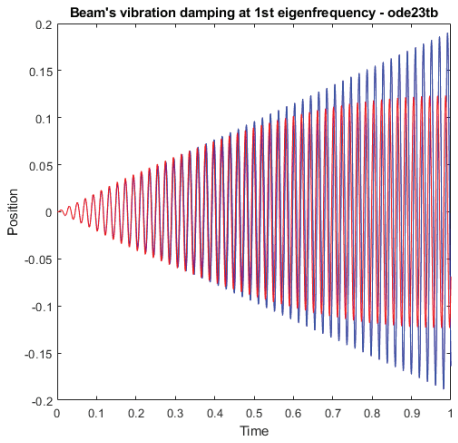

(a)

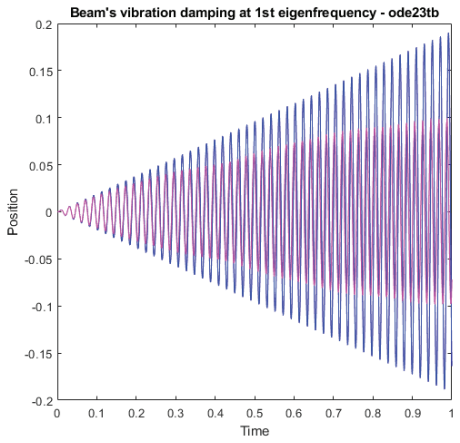

(b)

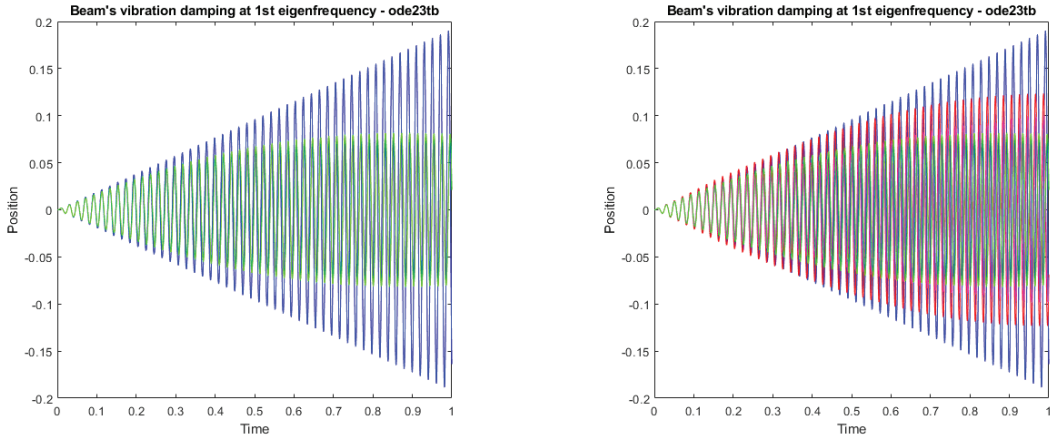

(c) (d)

Figure 2: Vibration attenuation of the first eigenfrequency having a switch shunted circuit: (a) the signs of velocity and position have opposite signs−red response vs blue: undamped (b) the signs of velocity and position have same signs−pink response vs blue: undamped (c) comparison by using passive resonant circuit−green response vs blue: undamped (d) Demonstration and comparison of the two switching damping techniques with the passive control strategy vs undamped.

It can be shown that the second experiment (Figure 2 (b)), where the circuit is activated when the velocity and position have the same sign, exhibits better damping compared to the first experiment (Figure 2 (a)). From the Figure 2 (d), the second experiment is able to exceed the efficiency of the passive $R-L$ shunt circuit and both of them can give a good dampening behaviour. According to the Figure 2 (d) it is noticed that, until the half of the simulation time, the second experiment (pink response) attenuates better than the passive control strategy (green response). Having the values from Table 1 the request for a very low value of the electric resonant period leads to using smaller inductors than those needed in passive inductive shunts, which greatly facilitates their application for vibrations of low frequencies [10]. As shown in [5], and confirmed through several numerical simulations, a properly tuned passive resonant shunt circuit significantly reduces vibrations. The tuning parameters were calculated according to [16].

The percentage of each controller's efficiency is presented in the next Table. The calculation has been done between the amplitude of open circuit terms and the three designed circuits under study divided by the amplitude of open circuit terms. Then, a comparison is performed between the different controllers until the end of the time (Table 2).

Table 2: Comparison Table of the different controller's efficiency around 1s.

Control strategy	Percentage around 1s
1. Strait switched circuit	35.1%
2. Inverse switched circuit	47.7%
3. Passive resonant circuit	57.4%

From Table 2, around the end of simulation time, it is detected that the Passive resonant circuit exceeds the performance in comparison to the other controllers with 57.4% percentage. Otherwise, around half of simulation time, it is noticed that the Inverse switched circuit dampens with 35.6% percentage and shows that the proposed control method can outperform the traditional controllers.

Having the circuit values from Table 1 and according to the formulas of [16] are computed the open and short circuit frequencies. Testing these for higher values of excitation frequencies, which is equivalent to $\omega_{oc1} = 434.51\ {}^{\mathrm{rad}}/_{\mathrm{sec}}$, has shown that neither the switched resonant circuit nor the passive resonant circuit give a good performance. The responses of second control law and passive are depicted on Fig. 3. Therefore the state-switched approach [5], which is used as an extend to the first and the second experiment, is more effective for off-resonance excitation, especially for lower frequencies, and is less responsive to variations in system parameters.

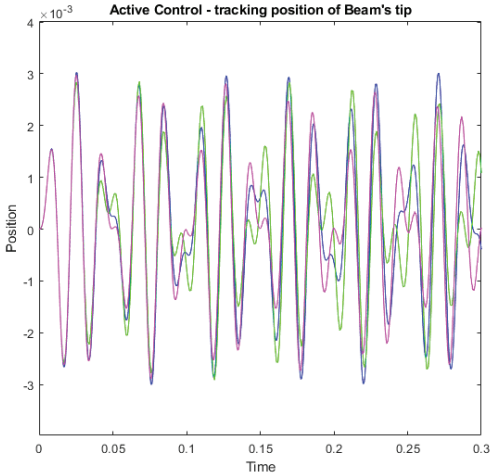

Figure 3: Time responses of second control law (pink), passive circuit (green) and undamped (blue) for time space [0, 0.3s].

The classical SSDS and SSDI electric circuit strategies like [7] are not considered in this work, since their ability to be extended to more general control strategies and multimode control is restricted. It was preferred the aforementioned method, because testing the SSD strategies in the presented system, as [7], they didn't give efficient results on vibration control.

4 CONCLUSIONS

In this work, a simplified switched shunted control strategy is implemented for reduction of structural vibrations under two examined conditions. A preliminary investigation was conducted by connecting a semi-active switched circuit to the host structure and its efficiency was compared with the passive circuit for attenuating the first eigenmode. The analysis shows that the results are comparable between the second control law and the passive resonant circuit. More specifically, the inverse switch circuit outperforms the other considered circuits up to half of simulation time, achieving a maximum amplitude reduction of 35.6% at 1 sec. The proposed controller can be considered as special cases of fuzzy rules, where the output is discrete and restricted to two states: closed or open circuit. A possible extension of this work could involve the application of fuzzy controllers [13], [17], incorporating variable resistance and inductance or enabling the activation of more complex circuits. Such an extension may be particularly relevant for shunted circuits with multiple branches, as in multimodal control.

AKNOWLEDMENT

"Co-funded by the ERASMUS+ Programme of the European Union" (Contract number: 101124439 — European University on Responsible Consumption and Production/EURECA-PRO 2.0 — ERASMUS-EDU-2023-EUR-UNIV).

EURECA • PRO
EUROPEAN UNIVERSITY

Funded by the European Union

REFERENCES

[1] L. Koutsoloukas, N. Nikitas, and P. Aristidou, "Passive, semi-active, active and hybrid mass dampers: A literature review with associated applications on building-like structures," *Developments in the Built Environment*, vol. 12, p. 100094, Dec. 2022, doi: 10.1016/j.dibe.2022.100094.

[2] G. Goswami and P. K. Goswami, "Energy Efficient ANFIS Supervised ShAPF for Harmonic Mitigation in PV based Micro-grid & Smart Electrical Systems," *Water and Energy International*, vol. 66r, no. 8, pp. 36–41, 2023.

[3] J. C. Collinger, J. A. Wickert, and L. R. Corr, "Adaptive Piezoelectric Vibration Control With Synchronized Switching," *Journal of Dynamic Systems, Measurement, and Control*, vol. 131, no. 4, p. 041006, July 2009, doi: 10.1115/1.3117189.

[4] G. K. Tairidis, "Vibration control of smart composite structures using shunted piezoelectric systems and neuro-fuzzy techniques," *Journal of Vibration and Control*, vol. 25, no. 18, pp. 2397–2408, Sept. 2019, doi: 10.1177/1077546319854588.

[5] W. W. Clark, "Vibration Control with State-Switched Piezoelectric Materials," *Journal of Intelligent Material Systems and Structures*, vol. 11, no. 4, pp. 263–271, Apr. 2000, doi: 10.1106/18CE-77K4-DYMG-RKBB.

[6] X. Han, M. Neubauer, and J. Wallaschek, "A review: The control strategies of synchronized switching damping technique," in *2011 IEEE International Conference on Mechatronics and Automation*, Beijing, China: IEEE, Aug. 2011, pp. 1657–1663. doi: 10.1109/ICMA.2011.5986372.

[7] J. Ducarne, O. Thomas, and J.-F. Deü, "Structural Vibration Reduction by Switch Shunting of Piezoelectric Elements: Modeling and Optimization," *Journal of Intelligent Material Systems and Structures*, vol. 21, no. 8, pp. 797–816, May 2010, doi: 10.1177/1045389X10367835.

[8] M. Neubauer, X. Han, and S. M. Schwarzendahl, "Enhanced switching law for synchronized switch damping on inductor with bimodal excitation," *Journal of Sound and Vibration*, vol. 330, no. 12, pp. 2707–2720, June 2011, doi: 10.1016/j.jsv.2011.01.003.

[9] M. Berardengo, S. Manzoni, M. Redaelli, and M. Vanali, "SSDI Technique Evolution to Improve Attenuation Performances with Random Disturbances," in *Topics in Modal Analysis, Volume 7*, R. Allemang, J. De Clerck, C. Niezrecki, and A. Wicks, Eds., in Conference Proceedings of the Society for Experimental Mechanics Series. , New York, NY: Springer New York, 2014, pp. 99–105. doi: 10.1007/978-1-4614-6585-0_10.

[10] C. R. Kelley and J. L. Kauffman, "Optimal switch timing for piezoelectric-based semi-active vibration reduction techniques," *Journal of Intelligent Material Systems and Structures*, vol. 28, no. 16, pp. 2275–2285, Sept. 2017, doi: 10.1177/1045389X17689934.

[11] M. Neubauer, X. Han, and J. Wallaschek, "On the maximum damping performance of piezoelectric switching techniques," *Journal of Intelligent Material Systems and Structures*, vol. 24, no. 6, pp. 717–728, Apr. 2013, doi: 10.1177/1045389X12445645.

[12] G. Foutsitzi, E. Hadjigeorgiou, C. Gogos, and G. Stavroulakis, "Modal shape control of smart composite beams using piezoelectric actuators," in *10th HSTAM International Congress on Mechanics*, Chania, Crete, Greece, May 2013.

[13] K. Marakakis, G. K. Tairidis, G. A. Foutsitzi, N. A. Antoniadis, and G. E. Stavroulakis, "New Optimal Design of Multimode Shunt-Damping Circuits for Enhanced Vibration Control," *Signals*, vol. 3, no. 4, pp. 830–856, Nov. 2022, doi: 10.3390/signals3040050.

[14] G. K. Tairidis and G. E. Stavroulakis, "Fuzzy and Neuro-fuzzy Control for Smart Structures," in *Computational Intelligence and Optimization Methods for Control Engineering*, vol. 150, M. J. Blondin, P. M. Pardalos, and J. Sanchis Sáez, Eds., in Springer Optimization and Its Applications, vol. 150. , Cham: Springer International Publishing, 2019, pp. 75–103. doi: 10.1007/978-3-030-25446-9_4.

[15] L. R. Corr and W. W. Clark, "Comparison of low-frequency piezoelectric switching shunt techniques for structural damping," *Smart Mater. Struct.*, vol. 11, no. 3, pp. 370–376, June 2002, doi: 10.1088/0964-1726/11/3/307.

[16] O. Thomas, J.-F. Deü, and J. Ducarne, "Vibrations of an elastic structure with shunted piezoelectric patches: efficient finite element formulation and electromechanical coupling coefficients," *Int. J. Numer. Meth. Engng*, vol. 80, no. 2, pp. 235–268, Oct. 2009, doi: 10.1002/nme.2632.

[17] G. Tairidis and G. Stavroulakis, *Introduction to Mechatronics*. 2024. doi: 10.57713/kallipos-318.

XI ECCOMAS Thematic Conference on Smart Structures and Materials - SMART 2025
M. Krommer, M. Nader and M. Schagerl (Eds)

Received: 27 March 2025 / Revised: 27 August 2025 / Accepted: 3 October 2025
© The Author(s) 2025

A Nonlinear Saturating Amplifiers Circuit for Piezoelectric Vibration Control of Flexible Mechanical System

Kevin Dekemele, Christophe Giraud-Audine, Olivier Thomas

Abstract. This work investigates the vibration control properties of a saturating shunt circuit for piezoelectric vibration control. The circuit is realized as a saturating operational amplifier that takes the induced piezoelectric voltage as input. Furthermore, an inductor and resistor are placed in series. Using complexification-averaging, an analytical form of the frequency response is derived by approximating the saturation by an arctangent. It is found that the vibration damping properties are similar to that of the piezo-electric nonlinear energy sink (NES) shunt circuit that consists of a cubic multiplication of the piezoelectric voltage. These properties are 1) Saturation of the host structure amplitude 2) an efficient quasi-periodic vibration regime, and 3) the appearance of an isolated response curve (IRC). The difference is that for the saturating circuit, the isolated response appears to the right of the host structures' resonance, while for the NES circuit, it results in an IRC to the left of this resonance. The analytical frequency response is compared to Runge-Kutta simulation for arctangent and non-smooth saturation, showing good agreement.

Key words: Piezoelectric Vibration Control, Shunt Circuit, Nonlinear circuit

1 INTRODUCTION

In vibration control, the nonlinear energy sinks (NES) devices are mechanical vibration absorbers that have a wider operational frequency bandwidth compared to linear counterparts as Tuned-Mass-Dampers [1]. This increased performance is attributed to the nonlinear spring, typically polynomial hardening. This hardening spring can be created by many mechanisms and is one of the main reasons this type of spring is common in investigations. In particular, the beneficial effects of the NES with a host system under harmonic excitation are a saturation of host system amplitude regardless of force magnitude, and an efficient quasi-periodic vibration regime called strongly modulated response (SMR). However, if the applied force is too large, an isolated resonance curve (IRC) appears to the left of the host system's natural frequency,

Kevin Dekemele
Department of Electromechanical, systems and metal engineering, Ghent University, 9052 Ghent, Belgium
e-mail: kevin.dekemele@ugent.be

Christophe Giraud-Audine & Olivier Thomas
L2EP, Univ. Lille, Centrale Lille, JUNIA LISPEN, Arts et Metiers Institute of Technology, LISPEN, F-59000 Lille, France

detrimental to the NES performance. In piezoelectrical vibration control, the common linear resistor-inductor (RL) shunt behaves similarly as a tuned-mass-damper [2] and similarly suffers from a limited effective frequency bandwidth. Although nonlinear shunt circuits have been investigated, they did not show the beneficial amplitude saturation and SMR response regime [3, 4, 5, 6, 7] Recently, a NES shunt circuit for piezoelectric vibration control was investigated and experimentally verified. It has the same behavior as a mechanical NES [8], that is, saturation of host system vibration amplitude, SMR, and the appearance of an IRC. The hardening characteristic was achieved by a cubic voltage law realized electronically by two analog multiplier components. The saturation effect of the host structure's amplitude was achieved near the open circuit resonance, but an IRC also appears to the left of this resonance. Although that work has shown an electronic NES is possible, in electronics, polynomial nonlinearities are not so common and was artificially created with the multiplier circuit. In this paper, we will investigate a saturating amplifier shunt circuit, a nonlinearity common in electronics yet challenging to realize as a mechanical mechanism. Some numerical investigations do exist for mechanical saturating stiffness, yet an experimental verification is still missing [9, 10]. We will derive the frequency response with complexification averaging and show that a saturation effect near the resonance also exist, this time near the short-circuited resonance. Around resonance, SMR also occurs. If the force magnitude is increased, an IRC appears, but unlike for the polynomial hardening circuit, this time to the right on the resonance instead of the left. For applications where excitation frequency ramps up, this property is especially interesting. The analytical frequency response is compared with the results from a multi-harmonic harmonic balancing toolbox and with the numerical results of a Runge-Kutta simulation of the full equations of motion.

2 THEORETICAL DESCRIPTION AND TUNING

2.1 EQUATIONS OF MOTION

The studied system is a linear elastic structure with a bonded piezoelectric patch, schematically shown in Figure 1a. The electrodes of the piezoelectric patch are shunted by a nonlinear circuit, consisting of a resistor, inductor and a nonlinear voltage source. The nonlinear voltage source under consideration in this work is a saturation nonlinearity, as shown in Figure 1b, which will be approximated by an arctangent in order to find an analytical solution.

The equations of motion (EOM) describing the dynamics of the coupled elastic structure, piezoelectric patch and shunt circuit is:

$$\begin{aligned} &\mathbf{M}\ddot{\mathbf{q}} + \mathbf{C}\dot{\mathbf{q}} + \mathbf{K}\mathbf{q} + \mathbf{\Theta}V = \mathbf{F}\cos(\omega t) \\ &C_p V - Q + \mathbf{\Theta}^T\mathbf{q} = 0 \\ &V + L\ddot{Q} + R\dot{Q} + V_{\text{nl}} = 0 \end{aligned} \tag{1}$$

where $\mathbf{q} \in \mathbb{R}^{n\times 1}$ is the modal displacement vector, $\mathbf{M}$, $\mathbf{C}$, $\mathbf{K}$ are the modal mass, modal damping and modal stiffness matrices, all $\in \mathbb{R}^{n\times n}$ and $\mathbf{F} \in \mathbb{R}^{n\times 1}$ is the modal force vector. On the piezoelectrical side, $\mathbf{\Theta} \in \mathbb{R}^{n\times 1}$ is the modal electromechanical coupling vector, V is the voltage over the piezo's electrodes, Q is the charge at the electrodes, C_p is the piezoelectrical

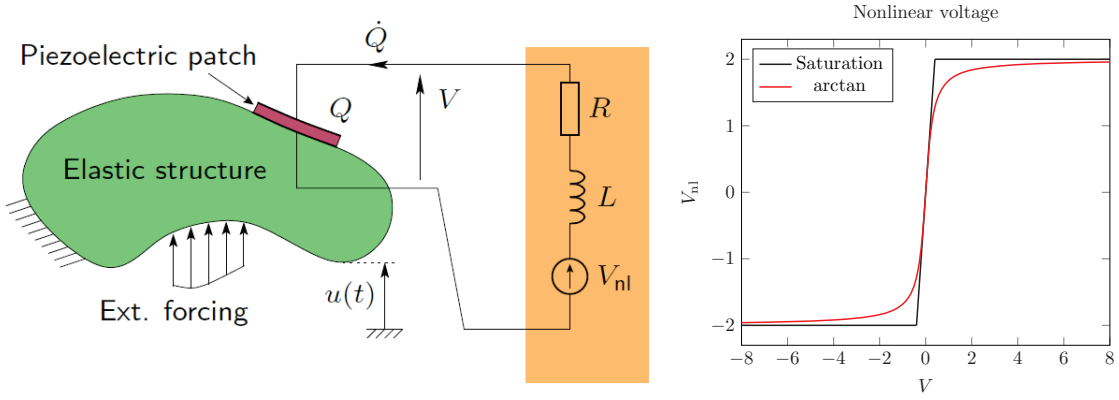

(a) (b)

Figure 1: The system under consideration (a) and the studied nonlinearity (b).

capacitance and R and L are the shunt's resistance and inductance. The nonlinear voltage source in the shunt is a saturating voltage, that can be approximated by a $\arctan$:

$$V_{\text{nl}} = \begin{cases} \beta_{\text{g}} V, & -\frac{V_{\text{sat}}}{\beta_{\text{g}}} < V < \frac{V_{\text{sat}}}{\beta_{\text{g}}} \\ V_{\text{sat}} & V > \frac{V_{\text{sat}}}{\beta_{\text{g}}} \\ -V_{\text{sat}} & V < -\frac{V_{\text{sat}}}{\beta_{\text{g}}} \end{cases} \approx V_{\text{sat}} \frac{2}{\pi} \arctan\left(\frac{\pi \beta_{\text{g}}}{2 V_{\text{sat}}} V\right) \tag{2}$$

The approximation of the saturation component by the smooth $\arctan$ voltage allows for an analytical derivation of the frequency response later on. ´

The dynamical behavior around a single linear mode is studied, which reduces (1) to the following equations of motion:

$$\begin{aligned} \ddot{q}_i + 2\zeta_i \omega_i \dot{q}_i + \omega_i^2 q_i + \frac{\theta_i}{m_i C_p} Q &= \frac{F_i}{m_i} \cos(\omega t) \\ \ddot{Q} + 2\zeta_e \omega_e \dot{Q} + \omega_e^2 Q + \frac{\theta_i}{L C_p} q_i + \frac{V_{\text{nl}}}{L} &= 0 \end{aligned} \tag{3}$$

where m_i is the modal mass of mode i, ω_i is the short-circuit eigenfrequency of mode i, ζ_i is the modal damping of mode i, θ_i is the modal electromechanical coupling of mode i, ω_e is the electrical eigenfrequency, and ζ_e the electrical damping coefficient. The last two are defined as:

$$\omega_e = \sqrt{\frac{1}{L C_p}} \quad \zeta_e = \frac{R}{2} \sqrt{\frac{C_p}{L}} \tag{4}$$

2.2 DIMENSIONLESS EQUATIONS

By defining the follwing dimensionless modal displacement, charge voltage and time:

$$\bar{q}_i = \frac{\sqrt{m_i}\omega_i}{\sqrt{C_p}} \frac{\pi\beta_{\mathrm{g}}}{2V_{\mathrm{sat}}} q_i, \quad \bar{Q} = \frac{\sqrt{L}\omega_i}{\sqrt{C_p}} \frac{\pi\beta_{\mathrm{g}}}{2V_{\mathrm{sat}}} Q, \quad \bar{V} = \frac{\pi\beta_{\mathrm{g}}}{2V_{\mathrm{sat}}} V, \quad \tau = \omega_i t, \tag{5}$$

Eq. (3) becomes:

$$\begin{aligned} &\bar{q}_i'' + 2\zeta_i \bar{q}_i' + \bar{q}_i + k_i r_i \bar{Q} = \bar{F}_i \cos(\Omega\tau) \\ &\bar{Q}'' + 2\zeta_e r_i \bar{Q}' + r_i^2 \bar{Q} + k_i r_i \bar{q}_i + \beta_{\mathrm{g}} r_i \arctan(\bar{V}) = 0 \end{aligned} \tag{6}$$

where

$$\circ' = \frac{d\circ}{d\tau} \quad r_i = \frac{\omega_e}{\omega_i} \quad \bar{F}_i = \frac{\pi\beta_{\mathrm{g}}}{2V_{\mathrm{sat}}} \frac{F_i}{\omega_i\sqrt{m_i}\sqrt{C_p}} \quad \Omega = \frac{\omega}{\omega_i} \quad k_i^2 = \frac{\theta_i^2}{\omega_i^2 C_p m_i} \tag{7}$$

In the next step, only the voltage is kept as electrical coordinate, where $\bar{Q}$ is eliminated by $\bar{V} = \left(k_i \bar{q}_i + r_i \bar{Q}\right)$:

$$\begin{aligned} &\bar{q}_i'' + 2\zeta_i \bar{q}_i' + (1 - k_i^2)\bar{q}_i + k_i \bar{V} = \bar{F}_i \cos(\Omega\tau) \\ &\bar{V}'' - k_i \bar{q}'' + 2\zeta_e r_i \left(\bar{V}' - k_i \bar{q}'\right) + r_i^2 \bar{V} + \beta_{\mathrm{g}} r_i^2 \arctan(\bar{V}) = 0 \end{aligned} \tag{8}$$

Opting for $\bar{V}$ as electrical variable allows for a closed form of the frequency response that is derived in the next section.

3 FREQUENCY RESPONSE

3.1 COMPLEXIFICATION AVERAGING (CxA)

The modal coordinate and piezoelectrical voltage are assumed to be in 1:1 resonance. The complex variables $A \in \mathbb{C}$ and $B \in \mathbb{C}$ of Manevitch are defined [11]:

$$2A(\tau)e^{j\tau} = \bar{q}_i - j\bar{q}_i' \quad 2B(\tau)e^{j\tau} = \bar{V} - j\bar{V}' \tag{9}$$

where $j = \sqrt{-1}$ is the imaginary unit. The original variables $\bar{q}_i$, $\bar{V}$ and their derivatives in functions of A and B are:

$$\begin{aligned} \bar{q}_i &= A(\tau)e^{j\Omega\tau} + A^*(\tau)e^{-j\Omega\tau} & \bar{V} &= B(\tau)e^{j\Omega\tau} + B^*(\tau)e^{-j\Omega\tau} \\ \bar{q}_i' &= j\Omega(A(\tau)e^{j\Omega\tau} - A^*(\tau)e^{-j\Omega\tau}) & \bar{V}' &= j\Omega(B(\tau)e^{j\Omega\tau} - B^*(\tau)e^{-j\Omega\tau}) \end{aligned} \tag{10}$$

The acceleration and second derivative of the voltage in the function of the new variables A and B is found by time derivation of (9) and using (10):

$$\bar{q}_i'' + \Omega^2 \bar{q}_i = j2\Omega A' e^{j\Omega\tau} \quad \bar{V}'' + \Omega^2 \bar{V} = j2\Omega B' e^{j\Omega\tau} \tag{11}$$

Substituting (10) and (11) into (8), and averaging over the first harmonic yields:

$$
\begin{aligned}
&2jA'\Omega + (1 - k_i^2 - \Omega^2)A + 2j\zeta_i\Omega A + k_i B = \frac{\bar{F}_i}{2} \\
&2jB'\Omega + (r_i^2 - \Omega^2)B - 2jA'\Omega k_i + \Omega^2 A k_i + 2\zeta_e r_i(j\Omega B - j\Omega A k_i) \\
&\qquad + \beta_g r_i^2 B \frac{\sqrt{4BB^* + 1} - 1}{2BB^*} = 0
\end{aligned} \tag{12}
$$

where the last term is found by projecting $\beta_g r_i^2 \arctan(B(\tau)e^{j\Omega\tau} + B^*(\tau)e^{-j\Omega\tau})$ on a Fourier series, and only keeping the first harmonic:

$$
\begin{aligned}
\frac{1}{2\pi}\int_0^{2\pi} f_{\bar{V}}(\bar{V})e^{-i\tau}d\tau &= \frac{\beta_g r_i^2}{2\pi}\int_0^{2\pi} \arctan\left(B(\tau)e^{j\Omega\tau} + B^*(\tau)e^{-j\Omega\tau}\right)e^{-i\tau}d\tau \\
&= \beta_g r_i^2 B \frac{\sqrt{4BB^* + 1} - 1}{2BB^*}
\end{aligned} \tag{13}
$$

3.2 STEADY-STATE EQUATIONS

The equations are studied in steady state, where $A' = B' = 0$. The complex variables A and B are written in their polar forms $A = \frac{a}{2}e^{j\alpha}$ and $B = \frac{b}{2}e^{j\beta}$, and the equation is split in real and imaginary parts. This procedure yields:

$$
\begin{aligned}
&(1 - k_i^2 - \Omega^2)a + k_i b\cos(\beta - \alpha) = \bar{F}_i\cos(-\alpha) \\
&2\zeta_i\Omega a + k_i b\sin(\beta - \alpha) = \bar{F}_i\sin(-\alpha) \\
&(r_i^2 - \Omega^2)b + \Omega^2 a k_i\cos(\alpha - \beta) + 2\zeta_e r_i k_i\Omega a\sin(\alpha - \beta) + 2\beta_g r_i^2\frac{\sqrt{b^2 + 1} - 1}{b^2} = 0 \\
&\Omega^2 a k_i\sin(\alpha - \beta) + 2\zeta_e r_i\Omega b - 2\zeta_e r_i k_i\Omega a\cos(\alpha - \beta) = 0
\end{aligned} \tag{14}
$$

Combining the third and fourth equation in (14) obtains a slow invariant manifold (SIM) that relates a and b:

$$
k_i^2\left(\Omega^4 + (2\zeta_e r_i\Omega)^2\right)a^2 = \left((2\zeta_e r_i\Omega)^2 + \left((\Omega^2 - r_i^2) - 2\beta_g r_i^2\frac{\sqrt{b^2 + 1} - 1}{b^2}\right)^2\right)b^2 \tag{15}
$$

An example of the SIM is shown in Figure 2. The minimum and maximum of he SIM are denoted as $[b_-, a_+]$ and $[b_+, a_-]$. These points are associated with the minimum and maximum amplitudes of a during SMR. The point on the right branch of the SIM where $a = a_+$ is $[b_{++}, a_-]$, where b_{++} is the maximum amplitude of b during SMR. Eliminating a from the third and fourth equation in (14) using the first two, yields a relation between the force $\bar{F}_i$ and b:

$$
\begin{aligned}
&b^2\left[\left(1 - k_i^2 - \Omega^2\right)\left(\left(r_i^2 - \Omega^2\right) + 2\beta_g r_i^2\frac{\sqrt{b^2 + 1} - 1}{b^2}\right) - \Omega^2 k_i^2 - 4\Omega^2\zeta_i\zeta_e r_i\right]^2 \\
&+ b^2\left[\left(1 - \Omega^2\right)2\Omega\zeta_e r_i + 2\zeta_i\Omega\left(\left(r_i^2 - \Omega^2\right) + 2\beta_g r_i^2\frac{\sqrt{b^2 + 1} - 1}{b^2}\right)\right] \\
&- (\bar{F}_i k_i)^2((2\Omega\zeta_e r_i)^2 + \Omega^4) = 0
\end{aligned} \tag{16}
$$

With equations (16) and (15), a frequency response is obtained, with examples on Figure 3 for various forcing amplitudes. To compute the stability of the solution, the eigenvalues of the Jacobian of (12) are computed. The full lines are stable solutions, while the dashed lines are unstable solutions. It can be seen that the host system amplitude a saturates on the line of a_+, which can be computed from the SIM for each frequency. Once the curve folds around this line, the Neimark-Sacker (NS) bifurcation makes the curve unstable, indicating a quasi-periodic response of the full EOM.

To verify the obtained analytical frequency response, it is compared to the result of a harmonic balancing (HB) continuation toolbox called MANLAB [12, 13]. The result of an HB of 30 harmonics is compared to the analytical result in Figure 4. Although they match quite well, the main difference is two side tongues, which are highlighted in the figure. According to the MANLAB, these are attributed mainly to the 3rd harmonic. Furthermore, a series of bifurcations (B) and NS (N) bifurcation suggests asymmetrical branches, which will have to be explored further in future works.

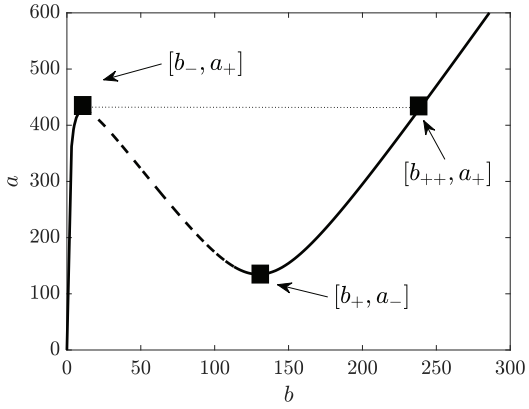

Figure 2: Examples a of a SIM for $k_i = \zeta_e = 0.2$, $r_i = 0.5$, $\zeta_i = 0.005$, $\Omega = 0.98$ and $\beta_g = 200$.

4 COMPARING RK SIMULATIONS AND WITH CXA FR

Here, the full EOM will be simulated with a sine sweep and compared to the analytical frequency response.

For $k_i = \zeta_e = 0.2$, $r_i = 0.5$, $\zeta_i = 0.005$,$\beta_g = 200$, the full dynamical equations are simulated with a force $\bar{F}_i = 20$ and forcing frequency $\Omega = 0.98$. Both the non-smooth saturating and the $\arctan$ voltage sources are simulated. The corresponding SIM is shown in Figure 5a, with the envelopes of the RK time simulations extracted from Figures 5b and 5c. This shows a quasi-periodic energy exchange between the mechanical coordinate $\bar{q}$ and the voltage $\bar{V}$. The a_+ and a_- do indeed well predict the maximum amplitude of the mechanical vibration in $\bar{q}$, while it is b_{++} and b_- that predict the maximum and minimum voltage. The RK simulation is now done for a whole frequency range in Figures 6 and 7. For each frequency, the minimum, maximum

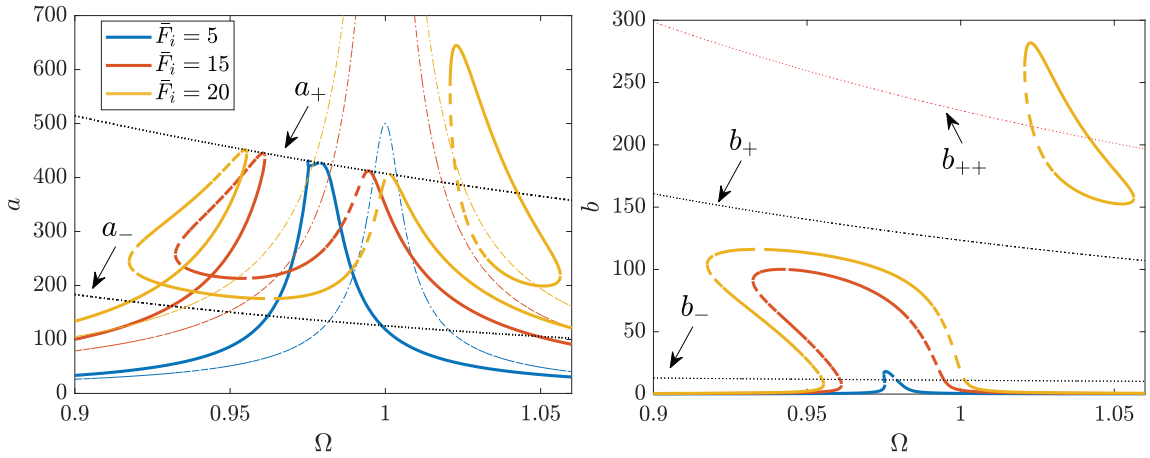

(a) (b)

Figure 3: Several frequency response for $k_i = \zeta_e = 0.2$, $r_i = 0.5$, $\zeta_i = 0.005$ and $\beta_g = 200$.

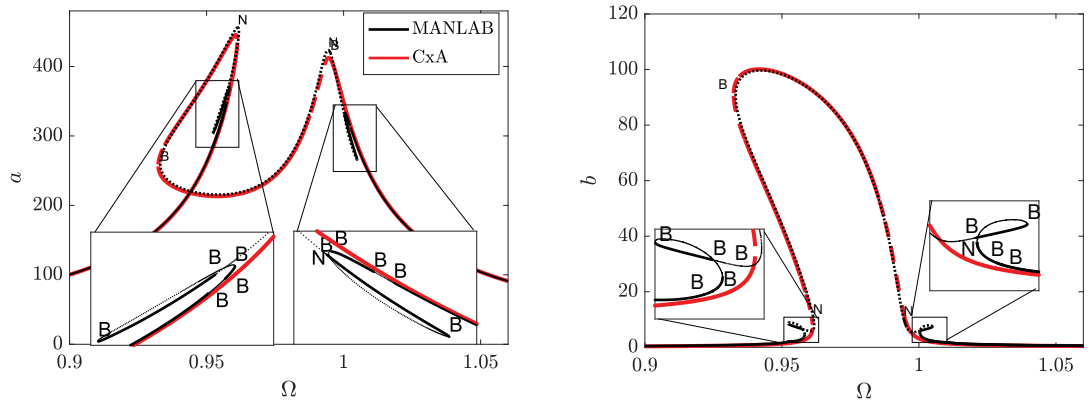

(a) (b)

Figure 4: Comparing the frequency response from CxA and MANLAB where $k_i = \zeta_e = 0.2$, $r_i = 0.5$, $\zeta_i = 0.005$,$\beta_g = 200$, $F_i = 15$ and $H = 30$

and RMS values are extracted and plotted on the FR computed from the CxA technique. Good correspondence is seen. Once $\bar{F}_i = 25$, the isola in the FR for a merges with the main branch, and the simulations reflect this.

5 CONCLUSION

This work has investigated the vibration mitigation performance of a saturating voltage source shunt in piezoelectric vibration control. An analytical form was found for the frequency response, and showed good correspondence to the frequency response found with a numerical harmonic balancing continuation toolbox. Similarly like a nonlinear energy sink shunt, the host structure amplitude saturates, there is strongly modulated response and an isolated response curve appears for high forcing. A sweep on the full equations of motion confirm this behavior. As a perspecive, a more thorough numerical investigation will be done to further investigated the bifurcations found in MANLAB that suggest assymetric solutions. Furthermore, an experimental verification will be done.

REFERENCES

[1] H. Ding and L.-Q. Chen, "Designs, analysis, and applications of nonlinear energy sinks," *Nonlinear Dynamics*, vol. 100, no. 4, pp. 3061–3107, 2020.

[2] O. Thomas, J. Ducarne, and J.-F. Deü, "Performance of piezoelectric shunts for vibration reduction," *Smart Materials and Structures*, vol. 21, no. 1, p. 015008, 2011.

[3] Z. A. Shami, C. Giraud-Audine, and O. Thomas, "A nonlinear piezoelectric shunt absorber with 2: 1 internal resonance: experimental proof of concept," *Smart Materials and Structures*, vol. 31, no. 3, p. 035006, 2022.

[4] ——, "A nonlinear tunable piezoelectric resonant shunt using a bilinear component: theory and experiment," *Nonlinear Dynamics*, vol. 111, no. 8, pp. 7105–7136, 2023.

[5] ——, "A nonlinear piezoelectric shunt absorber with a 2:1 internal resonance: Theory," *Mechanical Systems and Signal Processing*, vol. 170, p. 108768, 2022.

[6] O. Alfahmi and A. Erturk, "Programmable hardening and softening cubic inductive shunts for piezoelectric structures: Harmonic balance analysis and experiments," *Journal of Sound and Vibration*, vol. 571, p. 118029, 2024.

[7] T. M. Silva, M. A. Clementino, C. De Marqui Jr, and A. Erturk, "An experimentally validated piezoelectric nonlinear energy sink for wideband vibration attenuation," *Journal of Sound and Vibration*, vol. 437, pp. 68–78, 2018.

[8] K. Dekemele, C. Giraud-Audine, and O. Thomas, "A piezoelectric nonlinear energy sink shunt for vibration damping," *Mechanical Systems and Signal Processing*, vol. 220, p. 111615, 2024.

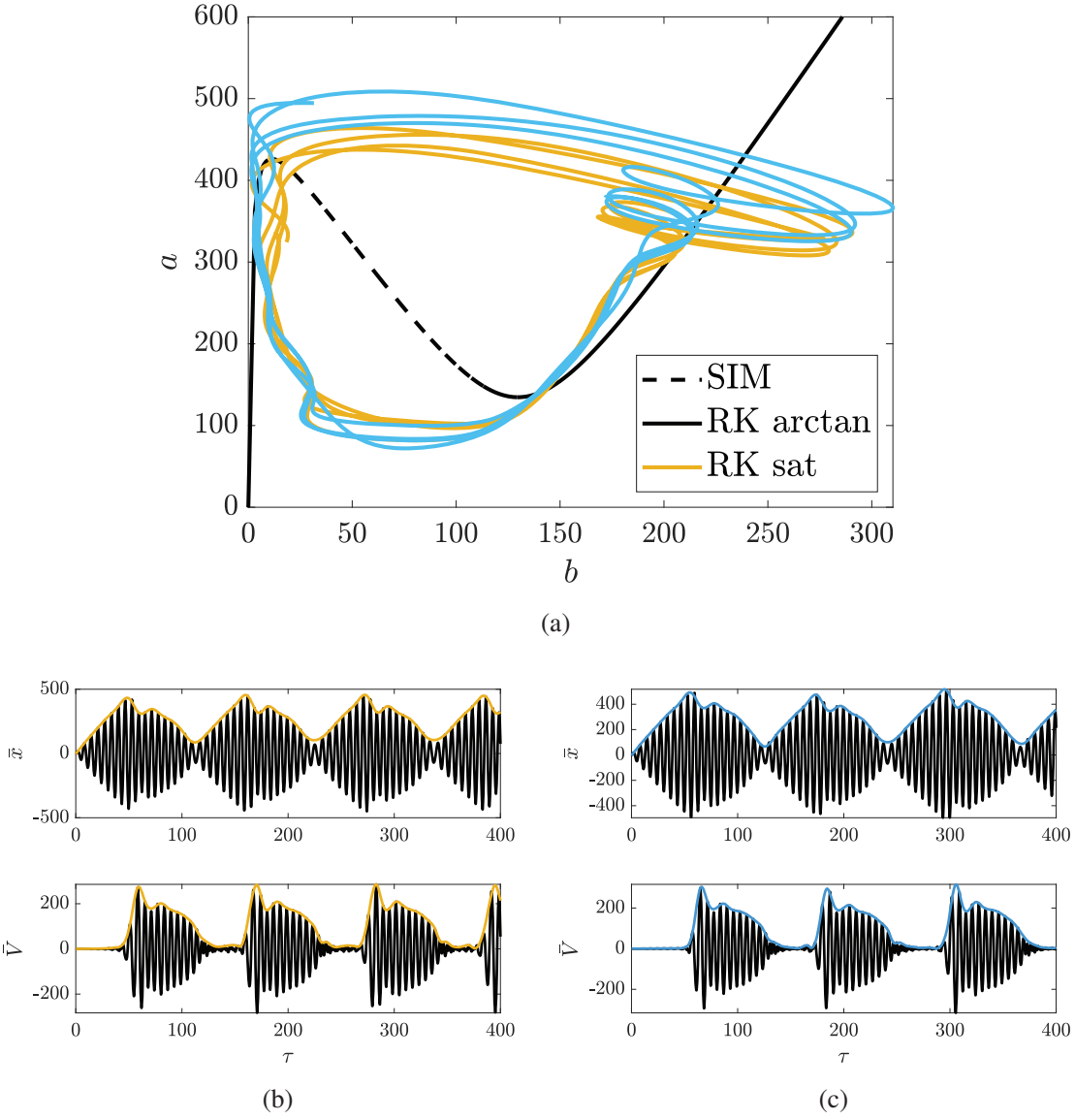

Figure 5: Time simulation for $k_i = \zeta_e = 0.2$, $r_i = 0.5$, $\zeta_i = 0.005$,$\beta_g = 200$, $\bar{F}_i = 20$ and $\Omega = 0.98$.

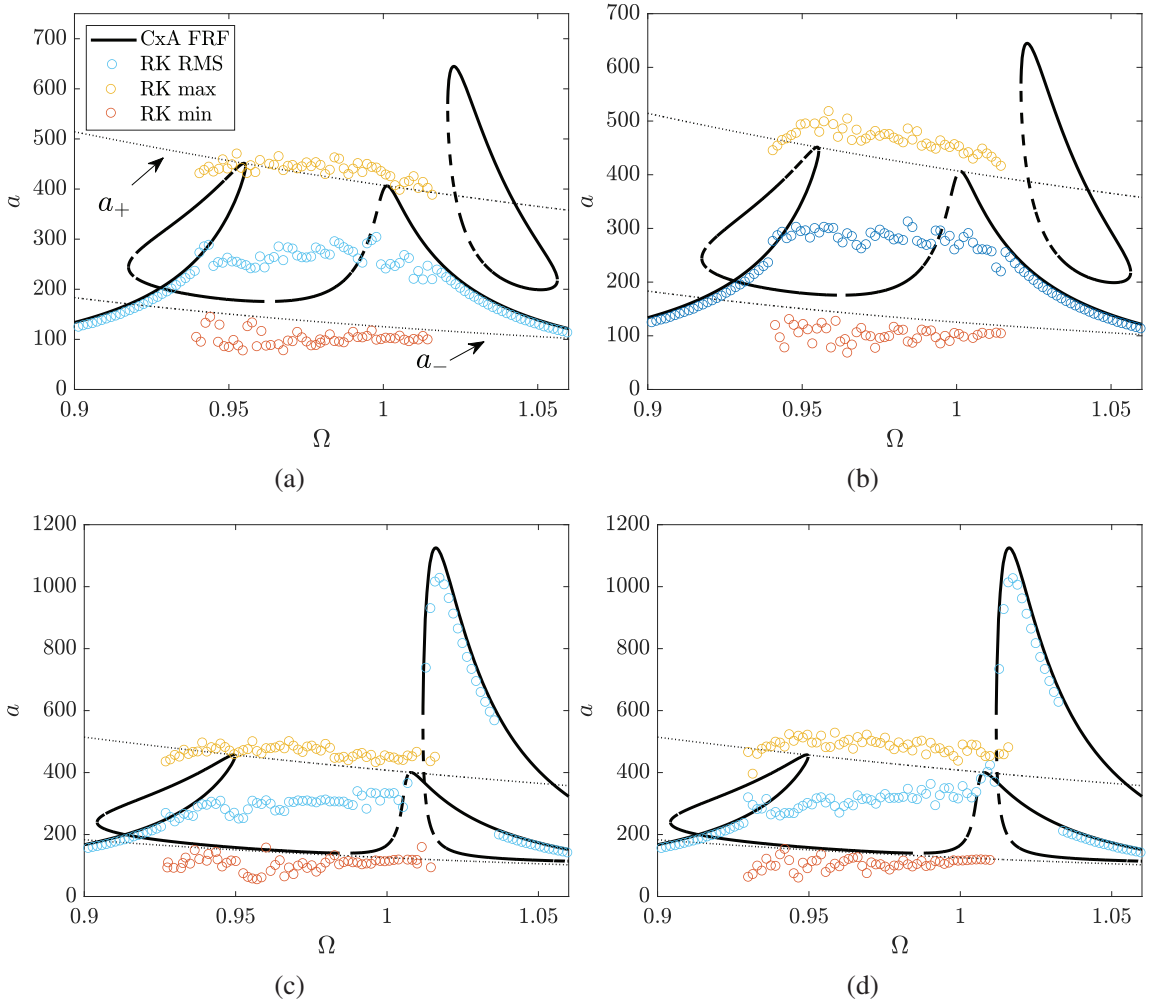

Figure 6: FRFs for a, left side is $\arctan$ and right side saturated voltage. (a)(b)$\bar{F}_i = 20$ (c)(d) $\bar{F}_i = 25$.

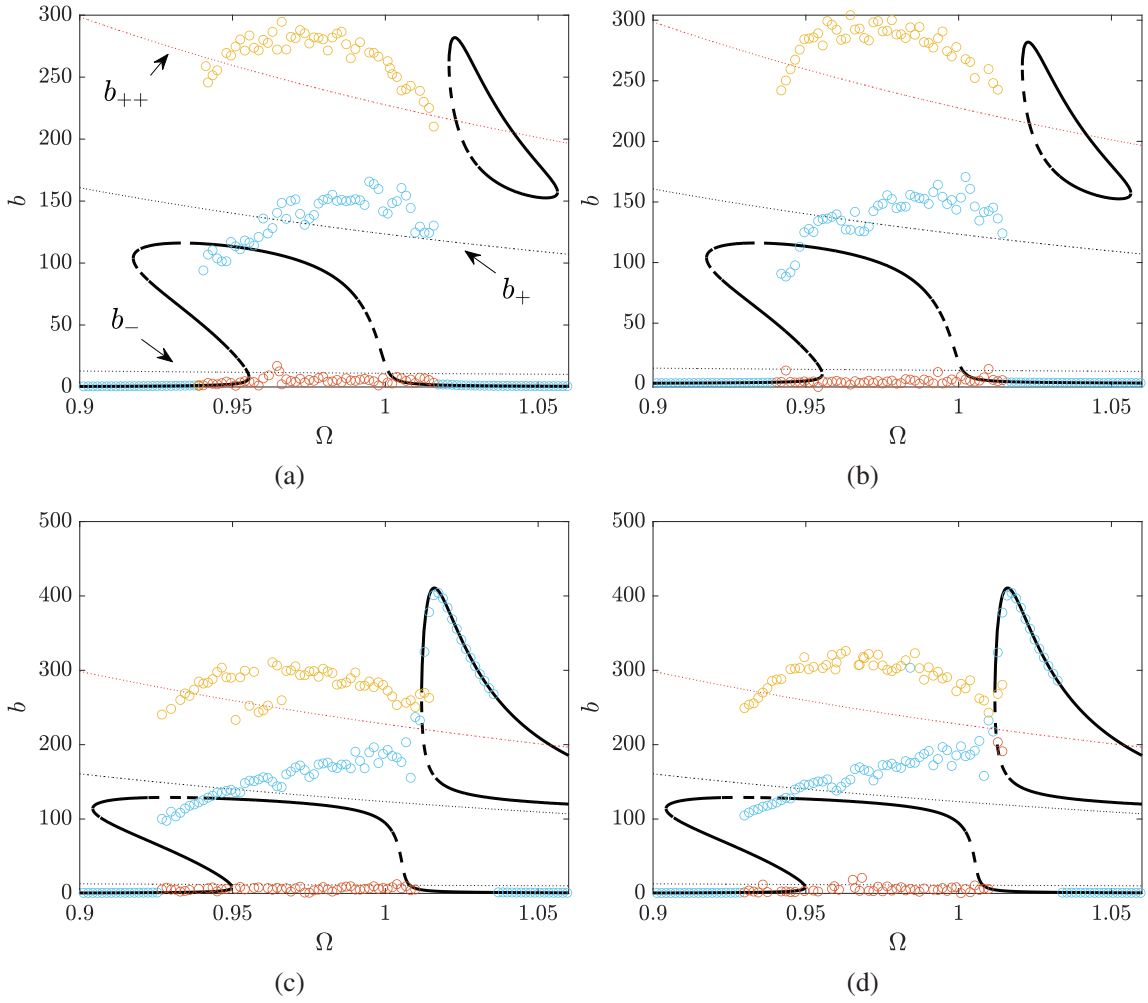

Figure 7: FR for b, left side is $\arctan$ and rightside saturated voltage. (a)(b)$\bar{F}_i = 20$ (c)(d) $\bar{F}_i = 25$

[9] K. Dekemele and G. Habib, "Inverted resonance capture cascade: modal interactions of a nonlinear energy sink with softening stiffness," *Nonlinear Dynamics*, pp. 1–23, 2023.

[10] S. Zhang, J. Zhou, H. Ding, K. Wang, and D. Tan, "Theoretical investigation on vibration mitigation in a system with fractional nonlinear energy sinks," *Nonlinear Dynamics*, pp. 1–23, 2024.

[11] L. Manevitch, "The description of localized normal modes in a chain of nonlinear coupled oscillators using complex variables," *Nonlinear Dynamics*, vol. 25, pp. 95–109, 2001.

[12] L. Guillot, B. Cochelin, and C. Vergez, "A taylor series-based continuation method for solutions of dynamical systems," *Nonlinear Dynamics*, vol. 98, no. 4, pp. 2827–2845, 2019.

[13] L. Guillot, A. Lazarus, O. Thomas, C. Vergez, and B. Cochelin, "A purely frequency based floquet-hill formulation for the efficient stability computation of periodic solutions of ordinary differential systems," *Journal of Computational Physics*, vol. 416, p. 109477, 2020.

XI ECCOMAS Thematic Conference on Smart Structures and Materials - SMART 2025
M. Krommer, M. Nader and M. Schagerl (Eds)

Received: 4 April 2025 / Revised: 29 August 2025 / Accepted: 3 October 2025
© The Author(s) 2025

Artificial intelligence using adaptive strategy for distributed control on a smart beam

Maryne Febvre, Jonathan Rodriguez, Simon Chesné, Manuel Collet

Abstract. Current research efforts are focused on the development of new generations of adaptive structures and systems composed of distributed composites integrating piezoelectric transducers. The proposed approaches focus on optimising a classical positive position feedback (PPF) for vibration mitigation of structures using distributed piezoelectric transducers. The challenge is to tune the control law parameters considering a large number of parameters, while ensuring stability and robustness to environmental variations. Artificial intelligence methods using neural networks are designed to consider a large number of inputs and outputs to represent complex problems. Considering a beam with three pairs of collocated piezoelectric transducers as a test bench, Deep Reinforcement Learning (DRL) strategies are implemented with the objective of vibration minimisation, focusing on the third bending mode as it is the most dominant. A pole-zero model is built from bench measurements to perform a trial-error process, allowing unstable control to be tested without damaging the bench. A step learning strategy is used to train the DRL on different minimisation target frequency bands, starting from the smallest to the largest. The result highlights the tuning adaptability to the target frequency band using DRL strategies. It also highlights the method's limitations regarding adaptation time and the structure instabilities.

Key words: Piezoelectric transducers, Deep Reinforcement Learning, Active Control, Distributive systems

1 INTRODUCTION

Smart materials, such as piezoelectric transducers, are being integrated into structures to provide adaptive behaviour with reduced additional mass. Current research efforts are focused on the development of new generations of adaptive structures and systems composed of distributed composites that integrate functional materials such as energy focusing with mechanical lenses [1], mechanical diodes [2] or mechanical insulators [3, 4]. These efforts aim to establish a set of methodological tools, numerical approaches, and technologies that will enable a fundamental advancement in the classical problem of active vibration control. Classical control laws, such

Maryne Febvre & Manuel Collet
CNRS, LTDS, Ecole Centrale de Lyon, UMR 5513, 69134 Ecully, France, e-mail: maryne.febvre@insa-lyon.fr

Maryne Febvre & Jonathan Rodriguez & Simon Chesne
INSA Lyon, CNRS, LaMCoS, UMR5259, 69621 Villeurbanne, France

as PID, LQG, H_∞ or positive position feedback (PPF) controllers, are efficient for performing vibration damping on piezoelectric structures, as detailed in the literature review by Aridogan et al. [5]. However, as the number of transducers on a structure increases, so does the number of control parameters that must be tuned. The smart structure evolves into a larger multi-input, multi-output (MIMO) system, requiring careful tuning to enhance vibration damping while maintaining stability. The optimization of all control parameters becomes increasingly difficult as system dimensions and complexity grow, especially when physical uncertainties are taken into account. To address this issue, researchers have explored reinforcement learning [6] methods to tune already existing forms of controllers in an autonomous way. Khal [7] works with an active mass drive (AMD) system on structures stressed with seismic events. Reinforcement learning is used with online tuning to determine the gains of a fuzzy PD controller. Experimental tests prove successful amplitude attenuation of the structural response amplitude in response to seismic perturbations. Panda et al. [8] propose to use Reinforcement Learning algorithm with policy gradient based method to tune a P and a PI controller, demonstrating the method's effectiveness in numerical simulations under harmonic excitation However, the application of RL for vibration mitigation in smart MIMO structures remains in its early stages, particularly in experimental test-bench scenarios.

This paper presents a methodology to autonomously compute the parameters of a PPF control law for a MIMO smart beam. The proposed strategy employs deep reinforcement learning (DRL) with the Trust Region Policy Optimization (TRPO) [9, 10, 11] algorithm to minimise oscillations within a target frequency range defined by a reward function. The approach is applied to a test bench beam equipped with three pairs of piezoelectric transducers. To train the DRL algorithm, a transfer function model is estimated from experimental test bench measurements. This study exploits the memory properties of neural networks to demonstrate their ability to adapt by progressively expanding the target frequency range during the staged training process.

2 PROBLEM FORMULATION

2.1 Structure Definition

The smart structure studied in Figure 1 consists of a steel beam of length L_b, width b_b and thickness h_b. Three identical pairs of piezoelectric transducers (PZT-PIC255) of length L_p, width b_p and thickness h_p are bonded to the beam. The top transducers Pa_1, Pa_2 and Pa_3 are used for actuation and Ps_1, Ps_2 and Ps_3 for sensing. All transducers are centered alongside of the beam main axis. The positions of the pairs of transducers are defined by the distances e_{p1}, e_{p2} and e_{p3}. The dimensions of the beam are given in Table 1.

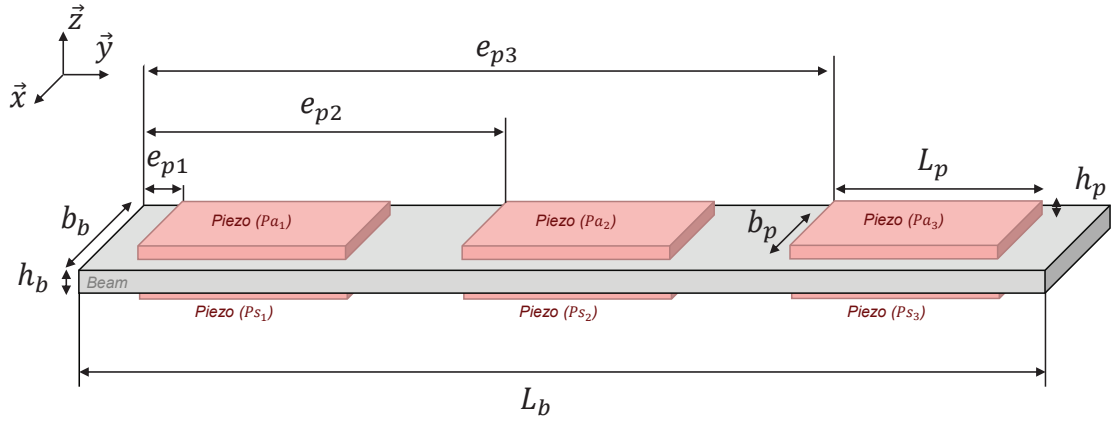

Figure 1: Beam dimensions diagram

Table 1: Setup dimensions

	Dimensions			Materials
	Name	Value	Unit	
Beam	L_b	400	[mm]	Steel
	b_b	60	[mm]	
	h_b	2	[mm]	
Piezoelectric Patch	L_p	61	[mm]	PI DuraAct Patch Transducer P-876.A15
	b_p	35	[mm]	
	h_p	1	[mm]	
	e_{p1}	70	[mm]	
	e_{p2}	169	[mm]	
	e_{p3}	269	[mm]	

2.2 Control Law Definition

A feedback control law $C(s)$ is implemented on the structure defined by the system $G(s)$, as shown in the block diagram Figure 2. Here $r = 0$ is the target signal, e the error, $u_d = [u_{d1}\ \ u_{d2}\ \ u_{d3}]^T$ the disturbances, $u_c = [u_{c1}\ \ u_{c2}\ \ u_{c3}]^T$ the control signals, $u = [u_1\ \ u_2\ \ u_3]^T$ the input drive signals of the system $G(s)$ from equation (4) and $y = [y_1\ \ y_2\ \ y_3]^T$ the respective system outputs.

One channel u is used to apply both the input disturbance and the control signals to the system. The signal $u_d(t)$ is a random noise $Rnd(t)$ with a sampling frequency F_s in Hz and a

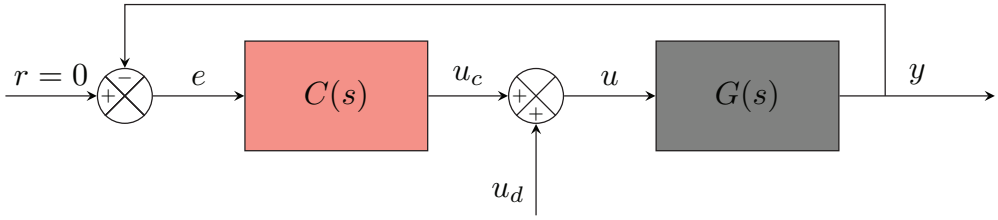

Figure 2: Control loop block diagram

second order filter with a cutoff frequency $F_c = 10000$ Hz, such as:

$$\begin{bmatrix} u_{d1}(t) \\ u_{d2}(t) \\ u_{d3}(t) \end{bmatrix} = \begin{bmatrix} Rnd(t) * \mathcal{L}^{-1}\{\left(\frac{2\pi F_c}{s+2\pi F_c}\right)^2\} \\ 0 \\ 0 \end{bmatrix} \tag{1}$$

Where $\mathcal{L}^{-1}$ is the inverse Laplace transform and $*$ being the temporal convolution.

The feedback control laws are implemented between each pair of collocated piezoelectric elements of the beam. Three PPF controllers are used such as:

$$C(s) = \begin{bmatrix} C_1(s) \\ C_2(s) \\ C_3(s) \end{bmatrix} = \begin{bmatrix} -K_1 \frac{1}{s^2+2\xi_1\omega_1 s+\omega_1^2} \\ -K_2 \frac{1}{s^2+2\xi_2\omega_2 s+\omega_2^2} \\ -K_3 \frac{1}{s^2+2\xi_3\omega_3 s+\omega_3^2} \end{bmatrix} \tag{2}$$

Where s is the Laplace variable of the transfer functions, K_i is the gain, ω_i is the filter frequency adapted to the target mode in $[rad.sec^{-1}]$ and ξ_i is the damping ratio of the control loop $i = \{1; 2; 3\}$.

2.3 Test bench setup

To satisfy the free boundary condition on the testbench, the beam is suspended with white parachute rubber bands at its four corners as shown in Figure 3. The main support is not shown in the picture and the electrical wires have been hidden for clarity.

The data acquisition setup implemented on the piezoelectric beam is shown in Figure 4. Here, y_1, y_2 and y_3 are the electric voltages measured at the piezoelectric transducers Ps_1, Ps_2 and Ps_3, respectively, and u_1, u_2 and u_3 are the electric voltages applied to the piezoelectric transducers Pa_1, Pa_2 and Pa_3, respectively. All devices used in the following experiments are listed in Table 2.



Figure 3: Experimental setup: beam with piezoelectric transducers (top view).

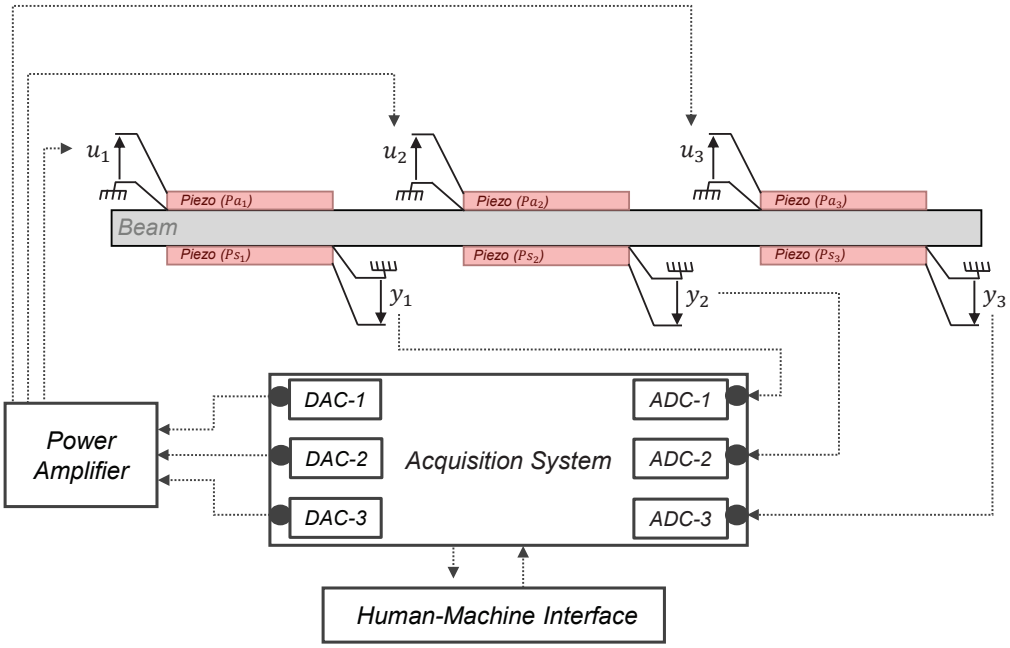

Figure 4: Experimental setup: data acquisition systems

2.4 System identification for a model building

An experimental model is built from the measurements. The input of the identification process is a band-limited noise $v(t)$. The noise power sent to the amplifier is equal to 0.1 with a sampling frequency $F_s = 10$ kHz, such as:

$$u(t) = Rnd(t) \tag{3}$$

Table 2: Experimental devices

Device	Brand	Reference	Sensitivity	Measuring Range
Acquisition System	DSPACE	DS1202	-	+/-50V
HMI	DSPACE	ControlDesk	-	-
Piezo transducers	PI	P-876.A15	0.64 µm/m/V	-250 to 1000 V
Power Amplifier	PI	DuraAct Piezo Amplifier	<10 mV	Input Voltage : -4 to 10 V Outpur Voltage : -100 to 250 V

Considering the MIMO system, the excitation is applied to the actuators one by one, while the others are short-circuited. Appendix A 7.1 provides measured transfer functions of the system.

The measured signals y_1, y_2 and y_3 are used to identify nine transfer functions $G_{i,j}$, where $i = \{1;2;3\}$ and $j = \{1;2;3\}$, defined by:

$$\begin{bmatrix} Y_1(s) \\ Y_2(s) \\ Y_3(s) \end{bmatrix} = \begin{bmatrix} G_{1,1}(s) & G_{2,1}(s) & G_{3,1}(s) \\ G_{1,2}(s) & G_{2,2}(s) & G_{3,2}(s) \\ G_{1,3}(s) & G_{2,3}(s) & G_{3,3}(s) \end{bmatrix} \begin{bmatrix} U_1(s) \\ U_2(s) \\ U_3(s) \end{bmatrix} \tag{4}$$

Where $Y_1(s)$, $Y_2(s)$, $Y_3(s)$ and $U(s)$ are the Laplace transforms of y_1, y_2, y_3 and u respectively. Pole and zero estimation is used to build the experimental model from the measured frequency response functions between 10 and 1000 Hz, such as:

$$G_{i=\{1;2;3\},j=\{1;2;3\}}(s) = \frac{\kappa}{s^{n_0}} \frac{\Pi_{i_z=1}^{n_z}(1 - z_{i_z}^{-1}s)}{\Pi_{i_p=1}^{n_p}(1 - p_{i_p}^{-1}s)} \tag{5}$$

Where $\kappa \in \mathbb{R}$ is a constant gain, $n_0 \in \mathbb{Z}$ is the number of null poles (integrator if $n_0 > 0$, derivative if $n_0 < 0$), $z_i \in \mathbb{C}$ zeros and $p_i \in \mathbb{C}$ poles of the system, $n_z \in \mathbb{N}$ the number of zeros and $n_p \in \mathbb{N}$ the number of poles, $G_{i,j}$ must be proper ($n_p + n_0 \geq n_z$).

Numerical transfer functions have 13 poles and 12 zeros, except for $G_{2,1}$ which has 14 poles and 13 zeros as needed to estimate the zeros between 450 and 700 Hz. The number of poles and zeros is not a multiple of the number of modes, but they are used to introduce phase shifting at low frequencies.

3 METHOD

During the lifetime of a structure, it is subject to variations of mechanical properties related to its operation (e.g.fatigue or damage) or to external environmental conditions (temperature, humidity...). The use of an adaptive method would allow the control parameters to be effectively adjusted to take account these variations. This study explores the properties of the DRL to adapt to changes in the environment by changing the reward definition.

3.1 Deep reinforcement learning

The methodology uses a reinforcement learning algorithm to tune a pre-defined control law on a smart structure. It does not use any database, but requires an environment to process trial errors and train an agent with multiple episodes. The environment is defined by the transfer function model of the beam defined in Equation 4. The main steps during an episode of the training are shown in Figure 5:

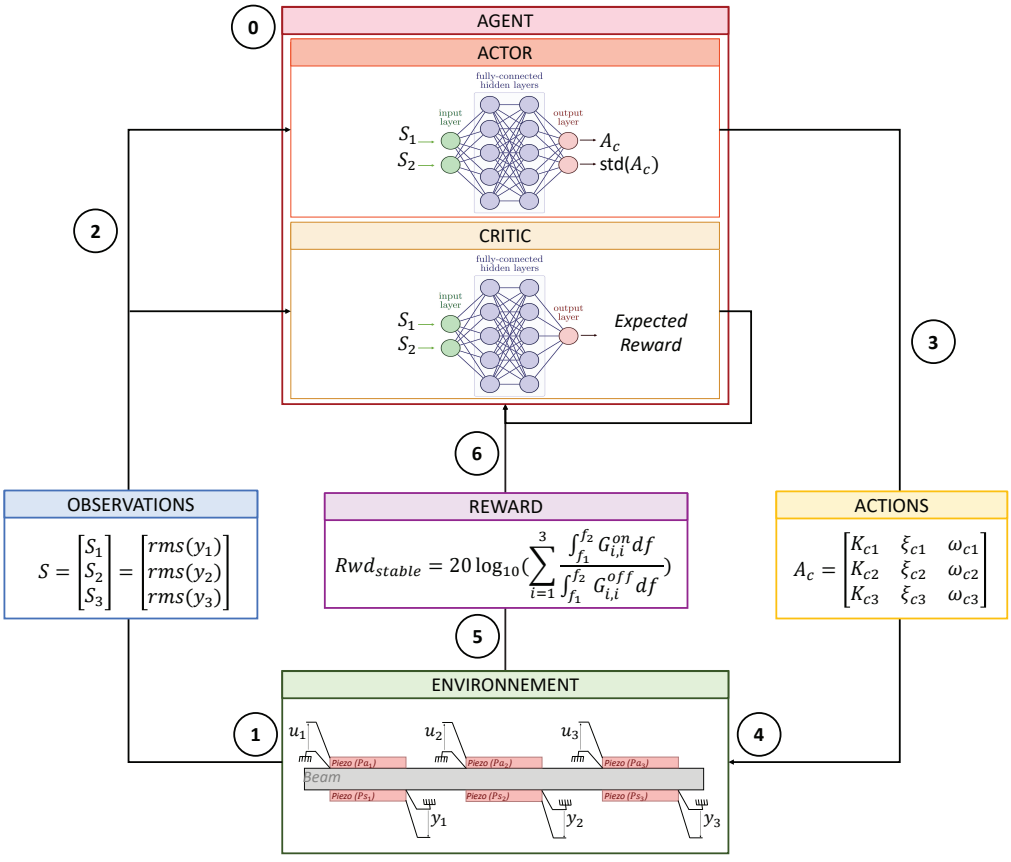

Figure 5: Deep Reinforcement Learning: Single-Episode Step Scheme for the Studied Smart System

- (0)-**Agent initialization**: The actor and the critic neural networks are initialized with random weight and bias. The neural networks properties are given in Appendix B 7.2.
- (1)-**Environment initialization**: The beam response to a white noise is simulated with the control off state.
- (2)-**Observation Computation**: The observations are calculated using chosen functions to convert the time domain data to representative values of the simulated environment.
- (3)-**Agent decision process**: The agent estimates an expected reward with the critic and an action value with the actor according with the input observations.
- (4)-**Environment running**: The beam response to a white noise is simulated with the control on set with PPF control law parameters chosen by the actor during step (3).
- (5)-**Reward computation**: The defined reward function is calculated using step (1) and step (4) simulations.
- (6)-**Agent update**: The actor and critic weights and biases are updated using TRPO algorithms [11], taking into account the expected reward from step (3) and the reward from step (6).

Then another episode is started at step (1) until the maximum number of episodes (here set to 5000) or a threshold reward (not used in this study) is reached.

3.2 Reward definition

The reward definition is designed with two objectives: firstly, to minimize the vibrations of the beam in a target frequency range and, secondly, to ensure the stability of the controlled structure. Inspired from the H_2 norm, it is defined using a frequency domain integration between f_1 and f_2 to consider only the dynamics of the poles associated with the bending mode in the target frequency band $j = \{1, 2, 3, 4\}$. It depends on the transfer functions $G_{1,1}$, $G_{2,2}$ and $G_{3,3}$ with control on or off, such as:

$$Rwd_{w_{bj}} = 20 \times log_{10} \sum_{i=1}^{3} \frac{\int_{f_1}^{f_2} G_{i,i}^{off}\, df}{\int_{f_1}^{f_2} G_{i,i}^{on}\, df} \tag{6}$$

This equation defines the reward for a stable controlled system where gain margins (Gm) are above 10 dB. For systems operating within a limited stability range ($Gm < 10dB$), a stability constraint is introduced into the reward definition with the gain margin, such as:

$$Rwd_{w_{bi}} = 20 \times log_{10} \sum_{i=1}^{3} \frac{\int_{f_1}^{f_2} G_{i,i}^{off}\, df}{\int_{f_1}^{f_2} G_{i,i}^{on}\, df} \times |\prod_{i=1}^{i=3}(\frac{Gm_{dB}^{i}}{10}))| \times |\prod_{i=1}^{i=3}(\frac{Pm_{deg}^{i}}{180}))| \tag{7}$$

Where Gm^i_{dB} is the gain margin of the loop $i = \{1, 2, 3\}$ when the other two controllers are applied to the system. In case of an unstable system, the reward is defined such as:

$$Rwd_{w_{bi}} = -1 \tag{8}$$

The aim is to estimate the capacity of the DRL to adapt to the control objective. The target frequency range is expanded as follows:

- Target frequency band w_{b1} from $f_1 = 350$ to $f_2 = 388$ Hz
- Target frequency band w_{b2} from $f_1 = 300$ to $f_2 = 388$ Hz
- Target frequency band w_{b3} from $f_1 = 220$ to $f_2 = 388$ Hz
- Target frequency band w_{b4} from $f_1 = 150$ to $f_2 = 388$ Hz

Target frequency bands w_{b1} to w_{b3} consider only the third bending mode but w_{b4} consider both the second and the third bending modes.

Figure 6 shows the defined reward $Rwd_{w_{b1}}$ variations with controllers gain parameters. Including the phase and the gain margin in the definition constrains the reward value when a controller is selected near the instability region. This includes more penalty in the reward for being close to the instability domain.

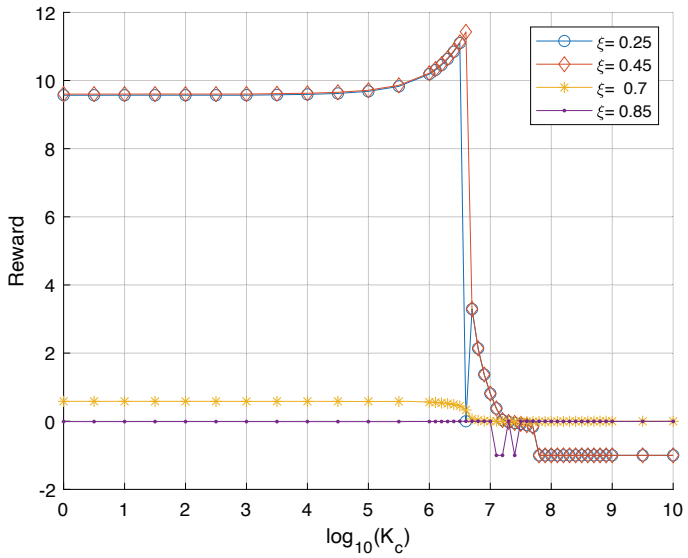

Figure 6: Reward $Rwd_{w_{b1}}$ variation with control law parameters set as identical for all control loops: $\omega_{1,2,3} = 380 \times 2\pi$ and $\xi = \xi_1 = \xi_2 = \xi_3$.

3.3 Stage Training Strategy

The numerical experiment is conducted considering 10 initialized NN known to offers a high probability of convergence according to the studied case. Figure 7 illustrates the strategy of stage training with reward variation from $Rwd_{w_{b1}}$ to $Rwd_{w_{b4}}$:

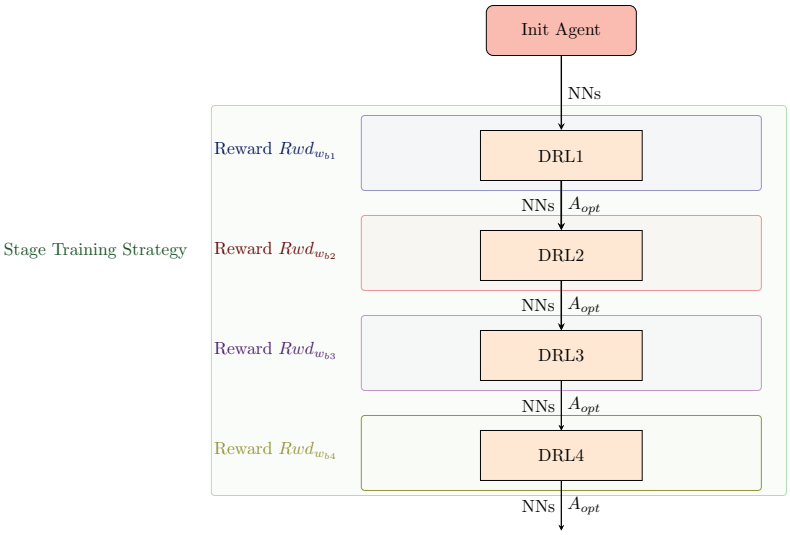

Figure 7: Flowchart: Training Stages

- The initial agent is trained during 5000 episodes with the goal of maximizing the reward $Rwd_{w_{b1}}$.
- Then the trained agent is again trained during 5000 episodes with the goal of maximizing the reward $Rwd_{w_{b2}}$.
- Finally, the same agent trained on reward $Rwd_{w_{b1}}$ is trained on reward $Rwd_{w_{b3}}$ and then on reward $Rwd_{w_{b4}}$.

4 RESULTS AND DISCUSSIONS

Positive Position Feedback (PPF) controllers function similarly to tuned mass dampers and are designed to attenuate vibrations of specific structural modes. Following Preumont's recommendations [12], a reference controller is designed to dampen the third bending mode at 380 Hz. All controllers are configured identically with $K_{1,2,3} = -400E3$, $\xi_{1,2,3} = 0.23$ and $\omega_{1,2,3} = 2387$. The corresponding reference reward value is used as an indicator during the DRL training phases.

Numerical experiment are conducted on the defined model from equation (4) to train the DRL agent with the objective defined by the reward equations (6-7-8). Figure 8 illustrates the training of the 10 initialised DRL Agents through different phases.

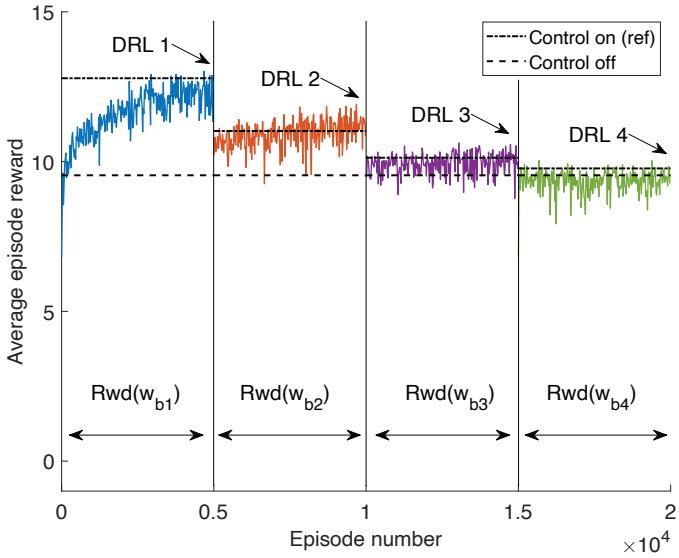

Figure 8: Reward Variations Over Episodes across Training Stages: Mean Over the 10 Agents

The changes in the target frequency band are indicated every 5000 episodes by vertical lines. The range of reward values, and therefore the maximum values that can be achieved, decreases as the range of target frequencies increases. DRL2 and DRL3 outperforms the reference controller performances faster (less than 1000 episodes) than DRL 1 (3000 episodes). These observations demonstrate the ability of the DRL to adapt controller tuning to a varying control objective. It also highlights the relationship between the adaptation time (number of episodes) and the variation in the environment to reach the updated optimum. Further calculations are required to quantify the variations in the environment with the number of episodes the DRL needs to adapt.

Table 5 in Appendix C 7.3 presents the parameter values of the 10 tuned controllers at the end of each training stage. The tuned controllers do not all converge to the same parameters. Trainings 1 and 8 fail to provide an improved solution compared to the uncontrolled case at each stage. Trainings 9 and 10 yield similar reward values at the end of DRL3 and DRL4, despite having distinctly different tuned parameters. Notably, the 9th solution achieves comparable performance using only two actuators, whereas the 10th utilizes all three. This demonstrates the method's ability to solve non-convex optimization problems, leading to multiple viable solutions. Incorporating optimal control criteria into the reward definition could further refine the approach and reduce the energy required to achieve a given vibration attenuation.

The tuned controller parameters evolve throughout the training stages, adapting to the target frequency range. However, due to discrepancies between the model and the test bench, some tuned controllers result in instabilities on the test bench that were not detected in the model. Controllers that remained stable during test bench validation are marked with a check symbol.

The controllers tuned according to each reward definition are tested on the transfer functions model (Figure 9a) and on the test-bench (Figure 9b). The effect of the controllers on the dynamics of the structure is shown focusing on the transfer functions of the first pair of collocated transducers.

The agent has tuned a set of controllers with effects on the system, adapted to the target frequency band. As the target frequency band increases, the controller parameters not only minimize the amplitude of the target mode but also influence the overall system response. This results in an increase in the amplitude of the third mode at 380 Hz as the target frequency band expands.

A zero is introduced between 300 and 350 Hz for target bands w_{b1}, w_{b2} and w_{b3} but it disappears with w_{b4}.

The amplitude of the second mode at 194 Hz remains unchanged for w_{b1} and w_{b2} but exhibits better damping with w_{b3} compared to w_{b4}. To better focus on mode damping, an improved reward function could minimize the peak amplitude of the transfer function response.

Differences between the model and test bench measurements can be observed, particularly in the amplitude at mode frequencies and the introduced zero dynamics. This difference may be due to test bench behaviour not accounted for in the model. However, the tuned controllers have a similar overall effect on both the model and test bench frequency response.

5 CONCLUSION

This study presented a reinforcement learning-based approach for autonomously tuning PPF controllers in a MIMO smart beam system. The results demonstrated the method's ability to find multiple solutions while adapting to different training stages with varying target frequency ranges, including multiple modes. The tuned controllers successfully mitigated vibrations on the test bench, highlighting the potential of deep reinforcement learning in optimizing vibration control systems, reducing the need for manual tuning, and enabling adaptive control in complex structures.

However, some tuned controllers exhibited instability on the test bench, emphasizing the need for improved modeling accuracy and robustness considerations. While the method effectively solves non-convex optimization problems, accessing multiple solutions requires running the algorithm multiple times. Also, the DRL strategy should be compared with other optimization algorithms to quantitatively assess its performance.

Future work could focus on incorporating optimal control criteria into the reward function to enhance energy efficiency and quantifying the algorithm's adaptability based on the rate of structural modifications.

By advancing data-driven control strategies, this research paves the way for more autonomous and efficient vibration mitigation techniques in smart structures.

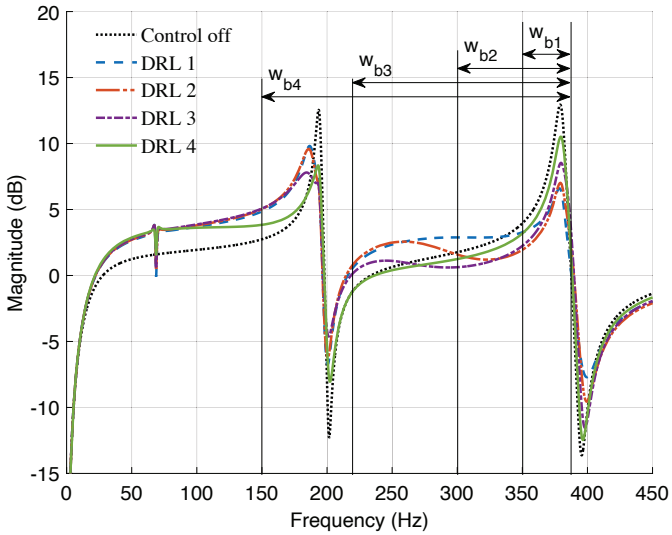

(a) Model

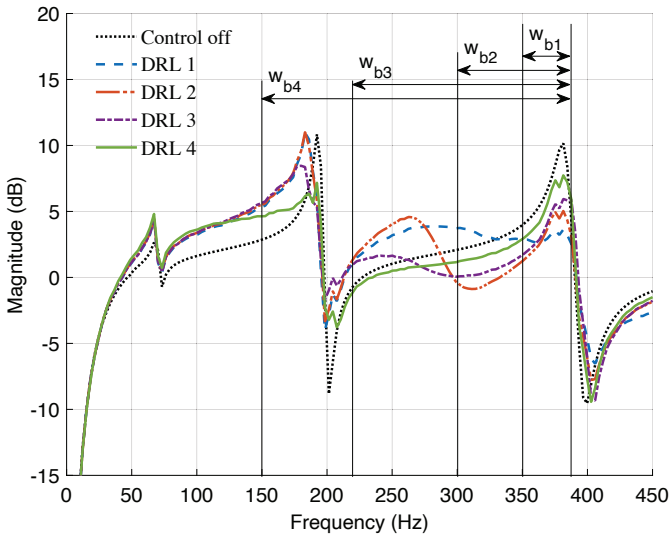

(b) Test-Bench

Figure 9: Bode plot from P_{a1} to P_{s1}: Mean Response of the 10 Tuned Controllers at Each Training Stage (Excluding Unstable Solutions on the Test Bench).

6 ACKNOWLEDGEMENTS

This work was supported by the LABEX CeLyA (ANR-10-LABX-0060) of Université de Lyon, within the program "Investissements d'Avenir" operated by the French National Research Agency (ANR).

REFERENCES

[1] K. Yi, M. Monteil, M. Collet, and S. Chesne, "Smart metacomposite-based systems for transient elastic wave energy harvesting," *Smart Materials and Structures*, vol. 26, no. 3, p. 035040, feb 2017.

[2] Y. Zheng, Z. Wu, X. Zhang, and K. W. Wang, "A piezo-metastructure with bistable circuit shunts for adaptive nonreciprocal wave transmission," *Smart Materials and Structures*, vol. 28, no. 4, p. 045005, mar 2019.

[3] J. Rodriguez, M. Collet, and S. Chesné, "Active vibration control on a smart composite structure using modal-shaped sliding mode control," *Journal of Vibration and Acoustics*, vol. 144, no. 2, feb 2022.

[4] H. Cudney, D. Inman, and Y. Oshman, "Distributed structural control using multilayered piezoelectric actuators," apr 1990.

[5] U. Aridogan and I. Basdogan, "A review of active vibration and noise suppression of plate-like structures with piezoelectric transducers," *Journal of Intelligent Material Systems and Structures*, vol. 26, no. 12, pp. 1455–1476, May 2015.

[6] R. S. Sutton and A. G. Barto, *Reinforcement Learning:An Introduction*, 1992.

[7] A. Khalatbarisoltani, "Online control of an active seismic system via reinforcement learning," vol. 26, p. e2298, 2019.

[8] J. Panda, M. Chopra, V. Matsagar, and S. Chakraborty, "An iterative gradient descent-based reinforcement learning policy for active control of structural vibrations," *Computers and Structures*, vol. 290, p. 107183, Jan. 2024.

[9] M. Febvre, J. Rodriguez, S. Chesne, and M. Collet, "Artificial Intelligence for Active Vibration Control Optimization on Smart Structures," ser. Smart Materials, Adaptive Structures and Intelligent Systems, vol. ASME 2023 Conference on Smart Materials, Adaptive Structures and Intelligent Systems, 09 2023, p. V001T04A001.

[10] ——, "Deep reinforcement learning for tuning active vibration control on a smart piezoelectric beam," *Journal of Intelligent Material Systems and Structures*, vol. 35, no. 14, pp. 1149–1165, 2024. [Online]. Available: https://doi.org/10.1177/1045389X241260976

[11] J. Schulman, S. Levine, P. Abbeel, M. Jordan, and P. Moritz, "Trust region policy optimization," in *Proceedings of the 32nd International Conference on Machine Learning*, ser. Proceedings of Machine Learning Research, F. Bach and D. Blei, Eds., vol. 37. Lille, France: PMLR, 07–09 Jul 2015, pp. 1889–1897.

[12] A. Preumont, *A. Vibration Control of Active Structures: An Introduction*. Springer Science and Business Media LLC, 2018, no. 4th Edition.

7 APPENDIX

7.1 Appendix A: Transfer Function Model

Figure 10 shows measurements made with successive actuation for some selected transfer functions. The first mode has a low dynamic considering the transfer functions $G_{1,1}$ (Figure 10a) and $G_{3,3}$ (Figure 10f) and is not estimated in the model. A zero amplitude measured at 0 Hz is explained by the use of piezoelectric sensors which do not measure the continuous component. A significant drop in coherence between non-collocated actuators and sensors occurs between 600 and 800 Hz (Figures 10d and 10g). In this frequency range, the model estimates zeros that are unreliable. Higher modes exist above the frequency of interest and may introduce control instabilities not considered in the model. Outside the frequency range, the sixth mode is estimated in $G_{1,3}$ (Figure 10b) and $G_{3,1}$ (Figure 10e). This allows phase fitting until 1000 Hz.

7.2 Appendix B: Hyperparameters and neural network size

The hyperparameters of the TRPO [11] algorithm govern the training process. Default parameters are used in this study since they are efficient enough, but tuning them will influence the learning efficiency of the actor and critic neural networks. Table 3 summarizes the most important hyperparameter values and their effect on training.

The Critic and Actor NNs dimensions used for this case are specified in Table 4. The dimensions of the NNs have been adjusted according to the previous results.

7.3 Appendix C: Tuned Controller Parameters

The proposed strategy trained 10 initialized agents to tune PPF controllers for minimizing vibrations within a target frequency range, which increases progressively from DRL1 to DRL4. The tuned parameters of the 10 PPF controllers at the end of each stage are listed in Table 5 along with their respective rewards. Their stability was tested on the test bench and is indicated with a check mark.

Table 3: Hyperparameter definition for TRPO algorithms

Hyperparameter	Name	Default value	Range values	Effect
Enthropy Loss Weigth	$w \in \mathbb{R}$	0.01	$\{0; 1\}$	It enhances agent exploration with high entropy loss.
Learning rate	$\alpha \in \mathbb{R}$	0.01	$\{0; \infty\}$	Training may lead to sub-optimal results or divergence if the learning rate is too high. If too low, training will take a long time to complete.
Discount Factor	$\gamma \in \mathbb{R}$	0.99	$\{0; 1\}$	In the learning process, it reduces the influence of the expected reward calculated by the critic.

Table 4: Actor and critic neural network definition

		Number of Neurons	
Layer	Name	Actor	Critic
Input	N_i	3	3
Hidden Layer 1	N_{hu}	25	25
Hidden Layer 2	N_{hu}	25	25
Hidden Layer 3	N_{hu}	25	25
Hidden Layer 4	N_{hu}	25	25
Output	No	9	1

Stage	Agent Number	K_1	K_2	K_3	ξ_1	ξ_2	ξ_3	Ω_1	Ω_2	Ω_3	Reward	T
	1	-16E3	0	0	0.13	0.05	0.1	6283	1607	6283	9.54	
	2	-16E3	-862E3	-543E3	0.41	0.46	0.11	6083	2039	2159	13.36	
	3	-1054E3	-2012E3	-3173E3	0.24	0.74	0.26	2215	4332	3747	14.19	
	4	-1054E3	-2012E3	-3173E3	0.24	0.74	0.26	2215	4332	3747	14.19	
DRL1	5	-113E3	-906E3	-894E3	0.73	0.32	0.95	2401	2371	1938	12.10	
	6	-4480E3	-51E3	-1203E3	0.6	0.68	0.31	4480	2632	2356	13.50	
	7	-943E3	-845E3	-833E3	0.18	0.1	0.16	2285	2309	2139	16.80	
	8	0	0	0	0.34	0.55	0.51	5194	4391	4174	9.54	
	9	-791E3	-1E3	-926E3	0.23	0.49	0.27	2287	2074	2104	14.13	
	10	-1993E3	-592E3	-2153E3	0.19	0.17	0.18	2996	2130	3151	14.99	
	1	-16E3	0	0	0.13	0.05	0.11	6283	1543	6283	9.54	
	2	-62E3	-722E3	-546E3	0.3	0.14	0.1	6042	2069	1952	12.41	
	3	-843E3	-397E3	-2516E3	0.16	0.40	0.52	2022	2176	3377	12.48	
	4	-843E3	-397E3	-2516E3	0.16	0.40	0.52	2022	2176	3377	12.48	
DRL2	5	-111E3	-817E3	-901E3	0.49	0.25	0.91	1729	2076	1955	11.26	
	6	-1975E3	-1E3	-692E3	0.66	0.65	0.14	2942	4186	1922	12.30	
	7	-839E3	-46E30	-648E3	0.15	0.08	0.13	2040	1995	1899	14.02	
	8	0	0	0	0.33	0.55	0.54	5270	4385	4199	9.54	
	9	-777E3	0	-736E3	0.17	0.66	0.15	2003	3041	1977	13.24	
	10	-1088E3	-419E3	-1688E3	0.28	0.1	0.3	2304	2029	2851	12.24	
	1	-16E3	0	0	0.13	0.05	0.18	6283	1181	6283	9.54	
	2	0	-515E3	-569E3	0.78	0.25	0.24	6264	1703	1941	10.49	
	3	-677E3	-419E3	-629E3	0.24	0.29	0.27	1870	1980	1801	11.16	
	4	-677E3	-419E3	-629E3	0.24	0.29	0.27	1870	1980	1801	11.16	
DRL3	5	-108E3	-475E3	-740E3	0.65	0.54	0.75	1209	1940	1788	10.33	
	6	-798E3	0	-534E3	0.35	0.03	0.15	1869	5876	1630	11.24	
	7	-517E3	-184E3	-466E3	0.15	0.07	0.18	1737	1525	1634	11.19	
	8	0	0	0	0.33	0.55	0.51	5242	4377	4178	9.54	
	9	-758E3	0	-543E3	0.26	0.95	0.19	1815	5249	1645	11.28	
	10	-656E3	-288E3	-499E3	0.25	0.06	0.2	1782	1681	1632	11.28	
	1	-16E3	0	0	0.13	0.05	0.33	6283	903	6283	9.54	
	2	0	-283E3	-492E3	1	0.13	0.97	6282	1280	1991	9.86	
	3	-434E3	0	-419E3	0.59	0.01	0.63	1397	6175	1421	10.30	
	4	-434E3	0	-419E3	0.59	0.01	0.63	1397	6175	1421	10.30	
DRL4	5	-92E3	-18E3	-61E30	0.58	0.22	0.81	881	2128	1683	10.07	
	6	-464E3	0	-475E3	0.39	0.22	0.99	1607	6151	1372	10.22	
	7	-295E3	0	-179E3	0.46	0.09	0.27	1277	2738	1036	10.29	
	8	0	0	0	0.31	0.55	0.56	5247	4376	4170	9.54	
	9	-865E3	0	-738E3	0.41	0.99	0.66	1985	6135	1744	10.26	
	10	-354E3	-50E3	-265E3	0.54	0.14	0.35	1283	2052	1214	10.35	

Table 5: PPF Control Law Values and Final Rewards for the 10 Initialized Agents Across Training Stages

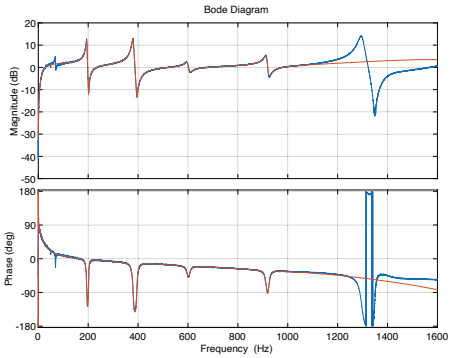

(a) $G_{1,1}$: From Pa_1 to Ps_1

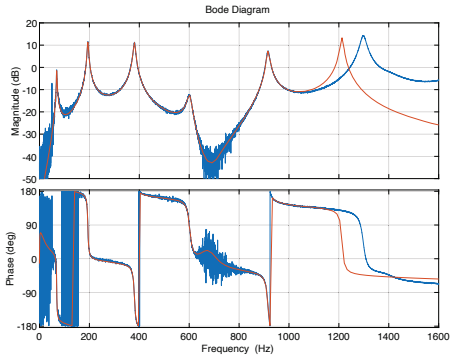

(b) $G_{3,1}$: From Pa_3 to Ps_1

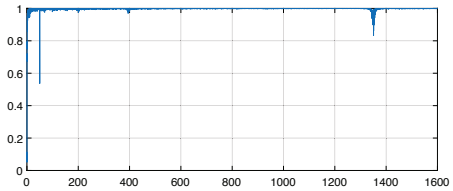

(c) Coherence: From Pa_1 to Ps_1

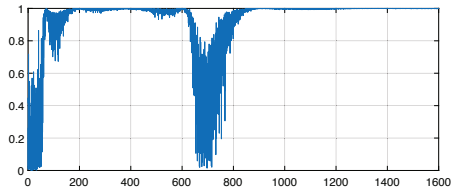

(d) Coherence: From Pa_3 to Ps_1

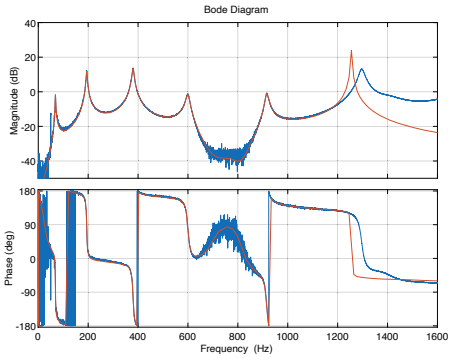

(e) $G_{1,3}$: From Pa_1 to Ps_3

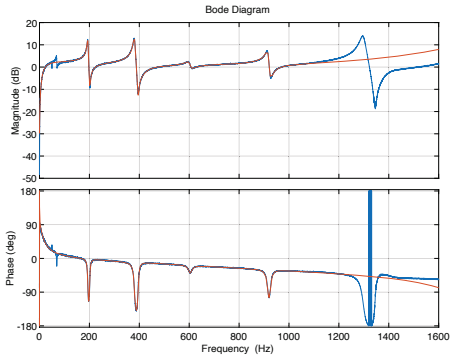

(f) $G_{3,3}$: From Pa_3 to Ps_3

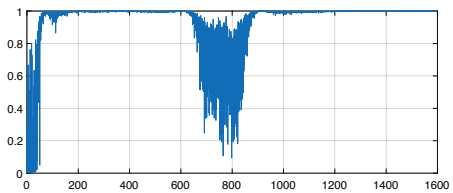

(g) Coherence: From Pa_3 to Ps_1

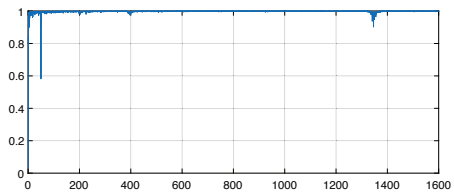

(h) Coherence: From Pa_3 to Ps_3

Figure 10: Bode and coherence plot with transfert function estimated from measurements (blue line) and the identified model (red line) between 0-1500 $[Hz]$

XI ECCOMAS Thematic Conference on Smart Structures and Materials - SMART 2025
M. Krommer, M. Nader and M. Schagerl (Eds)

Received: 23 April 2025 / Revised: 31 August 2025 / Accepted: 3 October 2025
© The Author(s) 2025

Comparison of Two Fully-Passive Multimodal Damping Techniques: Multi-Branch Shunts and Interconnected Piezoelectric Networks

Pierre Flament, Boris Lossouarn, Éric Ramond, Pascal Audrain, Jean-François Deü

Abstract. Multi-branch resonant piezoelectric shunt damping is an efficient method for mitigating the amplitude of multiple mechanical resonances. In this approach, one or several piezoelectric patches are connected to an electrical circuit designed to control several specific modes, enabling tailored management of broadband structural damping. However, the introduction of capacitors into the multi-branch shunts reduces the overall performance of the circuit. To overcome this limitation, interconnected piezoelectric networks have been proposed in the literature. This solution enhances performance by enabling each piezoelectric patch to contribute to the total coupling factor for each vibration mode. Based on recent studies, a method is introduced to define interconnected piezoelectric networks using a matrix formulation that optimally represents the multi-input multi-output behavior of the network, satisfying the optimal impedance equations. After numerical implementations on a benchmark blade structure, both techniques are compared by evaluating the fully interconnected optimal network with respect to the multi-branch shunts. Experimental results are also proposed to validate the numerical models and the subsequent comparison of performances between the two multimodal techniques.

Key words: Passive control, Multimodal vibration damping, Piezoelectricity, Multi-branch shunts, Interconnected piezoelectric networks, Coupling factors

1 INTRODUCTION

Piezoelectric shunt damping is an efficient vibration control technique that leverages the electromechanical coupling of piezoelectric materials to mitigate structural vibrations of a host structure. When subjected to strain, the material generates an electric field and deformation occurs when an electric field is applied. Thus, a piezoelectric transducer converts part of mechanical energy into electrical energy and can be dissipated through a properly tuned shunt circuit using resistive elements [1]. Introduced by Forward in 1979 [2] and theoretically formalized by Hagood and von Flotow in 1991 [3], these shunts can be resistive (R) or resonant (RL). Resonant shunts use inductive elements to create an electrical resonance

Pierre Flament & Éric Ramond & Pascal Audrain
Naval Group, Place Bruat, 50100, Cherbourg-en-Cotentin, France,
e-mail: pierre.flament@naval-group.com

Pierre Flament & Boris Lossouarn & Jean-François Deü
Laboratoire de Mecanique des Structures et Systemes Couples, Conservatoire national des arts et metiers, 292 rue Saint Martin, 75003, Paris, France

with the capacitance of the piezoelectric transducer. Optimized for damping around a specific mode, they may be insufficient for complex structures subjected to broadband excitations.

To damp multiple resonances simultaneously, multi-branch shunts have been proposed, where several electrical branches are connected to a single piezoelectric transducer, each tuned to a specific vibration mode. First introduced by Edberg *et al.* [4] in 1991 and generalized by Hollkamp [5] in 1994, several circuit topologies were proposed thereafter [6, 7], while these works have proven to be rather complex due to the interaction between the different resonant branches. More recently, Raze *et al.* [8] presented a summary of multi-branch shunts proposed in the literature with their respective optimal tuning rules. The potential of a purely passive realization is highlighted, mainly due to its inherent stability and cost-effectiveness [9]. The feasibility of using passive components has also been demonstrated by Lossouarn *et al.* [10], and a complete implementation on a complex structural geometry has been achieved by Flament *et al.* [11]. From his work [12], copper losses are considered through additional series resistors, dielectric losses are modeled using a frequency-dependent dynamic resistance, and iron losses are minimized through selection criteria to build tailor-made inductors. Although strengths and weaknesses are difficult to distinguish numerically [8], the current blocking shunt [13] has been shown to be more efficient and robust for a fully-passive application case [11]. However, a structure endowed with a single transducer may limit damping performance for certain modes, and the introduction of capacitors into the multi-branch shunts reduces the overall performance of the circuit [8]. In order to overcome this limitation, recent advances have explored the distribution of multiple transducers across a structure through an interconnected piezoelectric network, combining the electromechanical coupling factors between all transducers and modes when mechanical and electrical modal properties coincide [14]. Whereas comparisons between multi-branch shunts and networks are limited, pioneering studies show that networks offer superior performances [15]. Experimental validations have confirmed their effectiveness for various simple structures, such as beams [16]. To address complex structures, Raze *et al.* [17] developed a non-iterative, modal-based synthesis method for designing resonant electrical networks optimized for multimodal damping, ensuring realizability with passive components. Later, a matrix formulation was developed [18] to optimally represent the multi-input multi-output behavior of the network, satisfying the optimal impedance equation for the overall vibration reduction of the targeted resonances.

The objective of this work is to compare the vibration reduction performance of multi-branch shunts and interconnected piezoelectric networks applied to a complex geometry. The article is structured as follows. First, the benchmark structure is presented in Section 2. The current blocking shunt is then implemented in Section 3 while accounting for and incorporating parasitic losses associated with inductive components and piezoelectric patches. An optimal tuning strategy is thus proposed, aligning with the theoretical solution in the literature. Meanwhile, in Section 4, interconnected piezoelectric networks are implemented, and their performances are compared with that of the current blocking shunt. Finally, a fully-passive experimental validation is proposed for the current blocking shunt in Section 5.

2 BENCHMARK PIEZOELECTRIC STRUCTURE

2.1 Governing equations

Let us consider an elastic structure endowed with a piezoelectric patch characterized by a capacitance C_p and a parallel resistance R_p, connected to a shunt of impedance Z_s, as shown in Figure 1a. The governing equation of the coupled electromechanical system, incorporating mechanical damping, is derived from the strong formulation described by Thomas *et al.* [1]

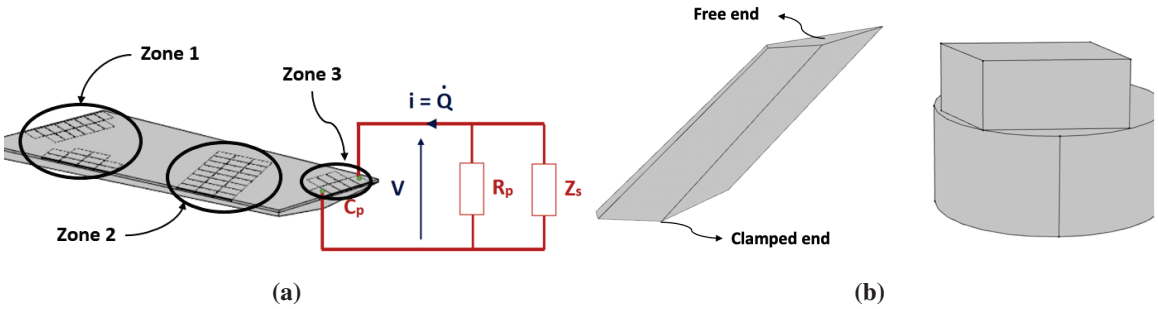

Figure 1: Benchmark piezoelectric structure: (a) electrical scheme of a piezoelectric patch of capacitance C_p and parallel resistance R_p connected to a shunt of impedance Z_s and (b) numerical model of the blade.

$$\begin{pmatrix} \mathbf{M}_m & \mathbf{0} \\ \mathbf{0} & \mathbf{0} \end{pmatrix} \begin{pmatrix} \ddot{\mathbf{U}} \\ \ddot{\mathbf{V}} \end{pmatrix} + \begin{pmatrix} \mathbf{C}_m & \mathbf{0} \\ \mathbf{0} & \mathbf{0} \end{pmatrix} \begin{pmatrix} \dot{\mathbf{U}} \\ \dot{\mathbf{V}} \end{pmatrix} + \begin{pmatrix} \mathbf{K}_{sc} & \mathbf{K}_c \\ -\mathbf{K}_c^T & \mathbf{K}_e \end{pmatrix} \begin{pmatrix} \mathbf{U} \\ \mathbf{V} \end{pmatrix} = \begin{pmatrix} \mathbf{F} \\ \mathbf{Q} \end{pmatrix}, \tag{1}$$

where $\mathbf{M}_m$, $\mathbf{K}_{sc}$, and $\mathbf{C}_m$ are the mechanical mass, stiffness (short-circuited), and damping matrices, respectively, each of size M $\times$ M. The electromechanical coupling matrix is denoted by $\mathbf{K}_c$ of size M $\times$ P and $\mathbf{K}_e$ is the diagonal matrix of the blocked capacitance of size P $\times$ P. Here, M and P are the numbers of mechanical degrees of freedom (dofs) and piezoelectric patches, respectively.

The system exhibits two different modal characteristics: its short-circuited configuration ($\mathbf{V} = \mathbf{0}$) and its open-circuited configuration ($\mathbf{Q} = \mathbf{0}$). The corresponding natural frequencies, denoted as ω_{sc} and ω_{oc}, along with their associated mode shapes $\mathbf{\Phi}_{sc}$ and $\mathbf{\Phi}_{oc}$, satisfy the eigenvalue problems formulated for each configuration at $\mathbf{F} = \mathbf{0}$, where $\mathbf{K}_{oc} = \mathbf{K}_{sc} + \mathbf{K}_c\mathbf{K}_e^{-1}\mathbf{K}_c^T$, given by

$$\mathbf{K}_{sc}\mathbf{\Phi}_{sc} - \omega_{sc}^2\mathbf{M}_m\mathbf{\Phi}_{sc} = \mathbf{0}, \tag{2}$$

$$\mathbf{K}_{oc}\mathbf{\Phi}_{oc} - \omega_{oc}^2\mathbf{M}_m\mathbf{\Phi}_{oc} = \mathbf{0}. \tag{3}$$

2.2 Finite element model and targeted modes

The benchmark piezoelectric structure under consideration represents a simplified model of a generic lifting surface, as described by Lossouarn [19], and clamped into a cylindrical block of 730 kg, as presented in Figure 1b, where fully detailed geometric data are provided in [19]. The blade and the cylindrical block are made of homogeneous and isotropic steel, characterized by a Young's modulus $E_s = 210$ GPa, a Poisson's ratio $\nu_s = 0.3$, and a density $\rho_s = 1780$ kg/m^3. The total weight is approximately 920 kg, with boundary conditions defined as follows: the end with the largest cross-section is rigidly fixed to a cylindrical block of 730 kg, while the opposite end is free. the blade is excited with a vertical pressure near the end of the trailing edge. This excitation is distributed to ensure a vertical force of 1 N at each measurement point within the designated area. Rayleigh damping is introduced based on the first and tenth vibration modes, with damping ratios ξ_1 = 0.2 % and ξ_{10} = 0.4 %, respectively. Three zones of piezoelectric patches are bonded to the upper surface and embedded within a 6.5 mm epoxy layer, following [19]. The epoxy has a Young's modulus $E_e = 3$ GPa, a Poisson's ratio $\nu_e = 0.3$, and a density $\rho_e = 1080$ kg/m^3. The piezoelectric material PIC255 is detailed in [9].

Table 1: Short and open-circuit eigenfrequencies and their corresponding electromechanical coupling factors of the first five bending modes and for the 3 zones from the finite element model.

Mode	f_{sc} (Hz)	$f_{oc,k}^{(1)}$ (Hz)	$f_{oc,k}^{(2)}$ (Hz)	$f_{oc,k}^{(3)}$ (Hz)	$\mathrm{k}_{c,k}^{(1)}$ (%)	$\mathrm{k}_{c,k}^{(2)}$ (%)	$\mathrm{k}_{c,k}^{(3)}$ (%)
1	88.62	88.80	88.66	88.62	6.28	2.94	0.24
2	295.32	295.54	295.79	295.34	3.84	5.61	1.25
5	650.98	651.05	651.16	651.27	1.52	2.38	2.99
7	1075.61	1075.61	1076.27	1077.06	0.17	3.49	5.19
10	1524.55	1524.55	1524.59	1528.88	0.21	0.71	7.54

The placement of the piezoelectric patches was initially designed to control bending modes 1, 2, and 10 [19]. The first five bending modes are targeted, where short and open-circuit frequencies are defined in Equations 2 and 3 and presented in Table 1. It is noted that f_{sc} are computed by short-circuiting all the piezoelectric patches and $f_{oc}^{(p)}$ by only open-circuiting the p-th piezoelectric patch, while the others remain short-circuited. The electromechanical coupling factor associated $k_c^{(p)}$ is directly linked to the efficiency of a piezoelectric transducer for vibration damping of the considered vibration mode. It is defined from the open- and short-circuit frequencies f_{oc} and f_{sc} [1], with i the index of the vibration modes and superscript (p) the number of the zone of patch, such as

$$k_{c,k}^{(p)} = \sqrt{\frac{f_{oc,k}^{(p)2} - f_{sc,k}^2}{f_{sc,k}^2}}. \tag{4}$$

3 FULLY-PASSIVE MULTIMODAL DAMPING TECHNIQUES

3.1 Parasitic losses

Since this work focuses on purely passive control, each targeted resonance is managed using passive inductors. The use of these components introduces parasitic losses [10], such as copper losses due to the non-negligible series resistance inherent in wire-wound inductors. Iron losses are also monitored, as they manifest as a frequency-dependent resistance value. Moreover, given the low coupling factors of the benchmark structure, the energy transfer between the mechanical and electrical domains results in increased heat dissipation within the piezoelectric patches [11], which also leads to consider dielectric losses. These losses can degrade the circuit's performance; therefore, they must be quantified and incorporated into the model to ensure optimal vibration reduction of the targeted resonances.

3.2 Multi-branch resonant piezoelectric shunts

Multi-branch resonant shunts extend the single-mode approach by adding multiple electrical branches in parallel to the piezoelectric patch. Each added branch is introduced with inductors and capacitors, allowing the control of several resonances simultaneously [5, 6]. Each branch can target a vibration mode thanks to the introduced capacitors but lead to reduced coupling factors of the circuit [8]. The degraded (effective) electromechanical coupling factors are given by

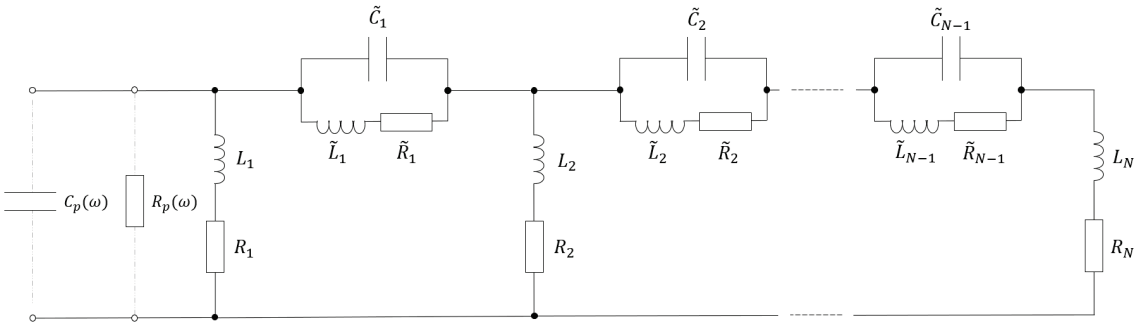

Figure 2: The proposed current blocking shunt circuit.

$$\kappa_{c,k}^{(p)2} = r_k^{(p)} k_{c,k}^{(p)2}, \quad r_k^{(p)} \geq 0, \sum_{k=1}^{N} r_k^{(p)} \leq 1, \tag{5}$$

where residues r_k serve as weighting factors assigned to each branch k, allowing a customized vibration performance control for each resonance.

The previous section highlighted that copper losses in a branch are included when an inductor is associated in series with a resistor. Since copper losses are often dominant in our applications, only this type of series configuration is considered. Consequently, the two selected solutions are the Hollkamp shunt and the current blocking shunt [8]. Despite comparable vibration reduction performance demonstrated both numerically and experimentally [8], and similar sensitivity to inductance variations [12], the current blocking shunt can offer an interesting advantage through its sequential tuning procedure for a fully-passive application case. It also provides greater resistive margins and typically requires smaller components, making it more efficient and robust for passive implementations [11]. Therefore, the current blocking shunt, illustrated in Figure 2, is adopted as the reference in the present study.

In its optimal configuration [8], inductors in the branches are coupled with series resistors, but not in the filters, accounting for only a portion of the copper losses. To fully consider them, additional series resistors are introduced in series with the filter inductors, resulting in $\tilde{R}\tilde{L}\tilde{C}$ filters. Dielectric losses are also modeled using a dynamic parallel resistor $R_p(\omega)$. Various types of passive inductors are available, and their selection is guided by the target (L, R) values and several feasibility criteria, aiming to minimize associated core losses and avoid nonlinear operating regimes [11].

The optimal admittance of the shunt $Y_s(s)$ is expressed as

$$Y_s(s) = \frac{1}{sL_1 + R_1} + \cfrac{1}{\cfrac{s\tilde{L}_1}{s^2\tilde{L}_1\tilde{C}_1 + 1} + \cfrac{1}{\cfrac{1}{sL_2 + R_2} + \cfrac{1}{\cfrac{s\tilde{L}_2}{s^2\tilde{L}_2\tilde{C}_2 + 1} + \cfrac{1}{\ddots + sL_N + R_N}}}}. \tag{6}$$

The aim is to compensate for the two parasitic losses thanks to an update of the inductors and resistors of the main branches, ensuring that the true admittance maintains the same level of performance as the optimal one. The optimal admittance of the shunt $Y_s^\star(s)$ considering parasitic losses is expressed as

$$Y_s^\star(s) = \frac{1}{R_p(\omega)} + \frac{1}{sL_1^\star + R_1^\star} + \cfrac{1}{\cfrac{s\tilde{L}_1 + \tilde{R}_1}{s^2\tilde{L}_1\tilde{C}_1 + s\tilde{R}_1\tilde{C}_1 + 1} + \cfrac{1}{\cfrac{1}{sL_2^\star + R_2^\star} + \cfrac{1}{\cfrac{s\tilde{L}_2 + \tilde{R}_2}{s^2\tilde{L}_2\tilde{C}_2 + s\tilde{R}_2\tilde{C}_2 + 1} + \cfrac{1}{\ddots + sL_N^\star + R_N^\star}}}}}, \quad (7)$$

where the compensation tuning procedure of $L_k^\star$ and $R_k^\star$ is fully described in [11, 12].

3.3 Interconnected piezoelectric networks

Interconnected piezoelectric networks offer another multimodal approach to mitigate vibration, overcoming certain limitations of the multi-branch strategy [15, 17]. Networks enable the combination of coupling factors generated by each piezoelectric patch for each vibration mode [18]. That allows to maximize the coupling factors of each structural mode and, in some cases, eliminate the need of additional capacitors in the network, which are often in charge of vibration reduction performance.

The governing equations of the interconnected piezoelectric network formulation are derived by applying the Ritz-Galerkin projection method to the electromechanical system presented in Equation (1). This is achieved by expressing $\mathbf{V}$ from Equation (1) in terms of $\mathbf{U}$ and $\mathbf{Q}$ and then pre-multiplying the first row of the reformulated electromechanical system by $\mathbf{\Phi}_{oc}$ with $\mathbf{U} = \mathbf{\Phi}_{oc}\mathbf{u}$, yielding

$$\begin{pmatrix} \mathbf{\Phi}_{oc}^T\mathbf{M}_m\mathbf{\Phi}_{oc} & \mathbf{0} \\ \mathbf{0} & \mathbf{0} \end{pmatrix} \begin{pmatrix} \ddot{\mathbf{u}} \\ \ddot{\mathbf{Q}} \end{pmatrix} + \begin{pmatrix} \mathbf{\Phi}_{oc}^T\mathbf{K}_{oc}\mathbf{\Phi}_{oc} & \mathbf{\Phi}_{oc}^T\mathbf{K}_c\mathbf{K}_e^{-1} \\ \mathbf{\Phi}_{oc}\mathbf{K}_c^T\mathbf{K}_e^{-1} & \mathbf{K}_e^{-1} \end{pmatrix} \begin{pmatrix} \mathbf{u} \\ \mathbf{Q} \end{pmatrix} = \begin{pmatrix} \mathbf{\Phi}_{oc}^T\mathbf{F} \\ \mathbf{V} \end{pmatrix}. \quad (8)$$

Let us consider a passive application [18], then the dynamic host system becomes

$$\begin{cases} (s^2\mathbf{I}_{N\times N} + \mathbf{\Omega}_{oc}^2)\eta_{oc} - \mathbf{\Gamma}\mathbf{\Phi}_p\eta_e = \mathbf{\Phi}_{oc}^T\mathbf{f} \\ (s^2\mathbf{\Omega}_e^{-2} + 2s\mathbf{Z}_e\mathbf{\Omega}_e^{-1} + \mathbf{I})\eta_e - \mathbf{\Phi}_p^T\mathbf{\Gamma}^T\eta_{oc} = 0 \end{cases}, \quad (9)$$

where s is the Laplace variable, $\mathbf{\Omega}_{oc} = \mathbf{diag}(\omega_{oc,1}, ..., \omega_{oc,N})$, $\mathbf{\Omega}_e = \mathbf{diag}(\omega_{e,1}, ..., \omega_{e,N})$, and $\mathbf{Z}_e = \mathbf{diag}(\xi_{e,1}, ..., \xi_{e,N})$ are the diagonal $N \times N$ matrices containing the mechanical natural frequencies in open-circuit configuration, the electrical natural frequencies, and the electrical damping ratios of the passive network, respectively. $\mathbf{\Phi}_{oc}$ are the eigenvectors of size $M \times N$ associated to the N considered eigenvalues, and $\mathbf{\Phi}_p$ are the electrical mode shapes of the passive network of size $N \times P$. Finally, $\mathbf{\Gamma} = -\mathbf{\Phi}_{oc}^T\mathbf{K}_c\mathbf{K}_e^{-1}$, η_{oc} and η_e are the mechanical and electrical vectors of modal coordinates. The objective is to calculate the state-space matrix model described in [18], given by

$$\mathbf{A}_e = \begin{pmatrix} \mathbf{0}_{N\times N} & \mathbf{I}_{N\times N} \\ -\mathbf{\Omega}_e^2(\mathbf{I} - \mathbf{\Phi}_p^T\mathbf{E}_p\mathbf{\Phi}_p) & -2\mathbf{\Omega}_e\mathbf{Z}_e \end{pmatrix}, \quad \mathbf{B}_e = \begin{pmatrix} \mathbf{0}_{N\times P} \\ \mathbf{\Omega}_e^2\mathbf{\Phi}_p^T \end{pmatrix}, \quad \mathbf{C}_e = \begin{pmatrix} \mathbf{0}_{P\times N} & \mathbf{\Phi}_p \end{pmatrix}, \quad (10)$$

where $\mathbf{A}_e$, $\mathbf{B}_e$, and $\mathbf{C}_e$ form the state-space model of the network.

The optimal admittance of the network [20] can be derived from Equation (10), as

Table 2: Comparison of the computed coupling factors with their corresponding residues and attenuation levels between three resonant shunts and the interconnected piezoelectric network for the modes 1, 2, and 10.

Mode	Patch	k_c (%)	r (%)	A_{multi} (dB)	K_c (%)	w	A_{net} (dB)
1	1	6.28	100	-22.2	6.89	1	-23.3
2	2	5.61	100	-23.1	6.91	1	-24.6
10	3	7.54	100	-17.9	7.55	1	-17.9

$$\mathbf{Y}_{net}(s) = \mathbf{C}_e(s\mathbf{I}_{2N\times 2N} - \mathbf{A}_e)^{-1}\mathbf{B}_e. \tag{11}$$

In order to tune the network, $\mathbf{C}_p$ is introduced into the tuning equations. By defining $\mathbf{E}_p = \mathbf{C}_p^{-1}$, using two singular value decompositions (SVD) [18], the electrical mode shapes of the network are equal to

$$\begin{cases} \mathbf{U}_D\mathbf{\Sigma}_D\mathbf{V}_D^T = \text{SVD}\left(\mathbf{E}_p\right) \\ \mathbf{U}_M\mathbf{\Sigma}_M\mathbf{V}_M^T = \text{SVD}\left(\mathbf{W}\mathbf{\Omega}_{oc}^{-1}\mathbf{\Gamma}\mathbf{V}_D\mathbf{\Sigma}_D^{-1/2}\right) \end{cases} \Rightarrow \quad \mathbf{\Phi}_p = \mathbf{V}_D\mathbf{\Sigma}_D^{-1/2}\mathbf{\Psi}, \tag{12}$$

where $\mathbf{W} = \mathbf{diag}(w_1, ..., w_N)$ with w_k representing the arbitrarily assigned control authority over the targeted modes and $\mathbf{\Psi} = \mathbf{V}_M\mathbf{U}_M^T$ the fully-passive realization criterion defined such that $\mathbf{I} - \mathbf{\Psi}^T\mathbf{\Psi} \succeq 0$. Then, the total electromechanical coupling factor of the network is given by [18]

$$K_{c,rk}^2 = \frac{\alpha_{rk}^2}{1-\alpha_{rk}^2}, \quad \text{with} \quad \alpha_{rk} = \frac{1}{\omega_{oc,k}}\|\gamma_r\phi_r\|, \tag{13}$$

with k the index of the structural resonance, γ_r and ϕ_r are the r-th row and column of $\mathbf{\Gamma}$ and $\mathbf{\Phi}_p$, respectively. Then, the components of the electrical matrices $\mathbf{\Omega}_e$ and $\mathbf{Z}_e$ of the network are calculated as

$$\omega_{e,k} = \sqrt{\frac{3K_{c,rk}^2 - 4r_{e,k} + 8}{4K_{c,rk}^2 + 4}}\omega_{oc,k}, \quad \xi_{e,k} = \sqrt{\frac{27K_{c,rk}^4 + 80K_{c,rk}^2 + 64 - 16r_{e,k}(4 + 3K_{c,rk}^2)}{\sqrt{2}(5K_{c,rk}^2 + 8)}}, \tag{14}$$

where $r_{e,k}$ is an intermediate parameter given in [17, 18]. To sum up, $\mathbf{\Omega}_e$ and $\mathbf{Z}_e$ can be build with Equation (14), which allows to compute Equation (10), enabling the calculation of the admittance matrix of the passive network given in Equation (11).

4 MULTI-BRANCH SHUNTS VS INTERCONNECTED PIEZOELECTRIC NETWORKS

4.1 Case study N = P

The case $N = P$, where $N = \text{rank}(\mathbf{\Phi_p})$, represents the simplest and most optimal scenario. Indeed, the problem is well-posed [18]. No additional capacitors are introduced into the network, thus preventing any degradation of the total coupling factors defined in Equation (13). Three classical resonant shunts are connected to each zone of patches as well as the associated interconnected network. FRF are presented in Figure 3. The different coupling factors k_c, K_c, and the attenuation levels A are presented in Table 2. The interconnected network solution enhances the coupling factors of modes 1 and 2. However, since mode 10 is exclusively coupled with zone 3, it does not exhibit any significant change.

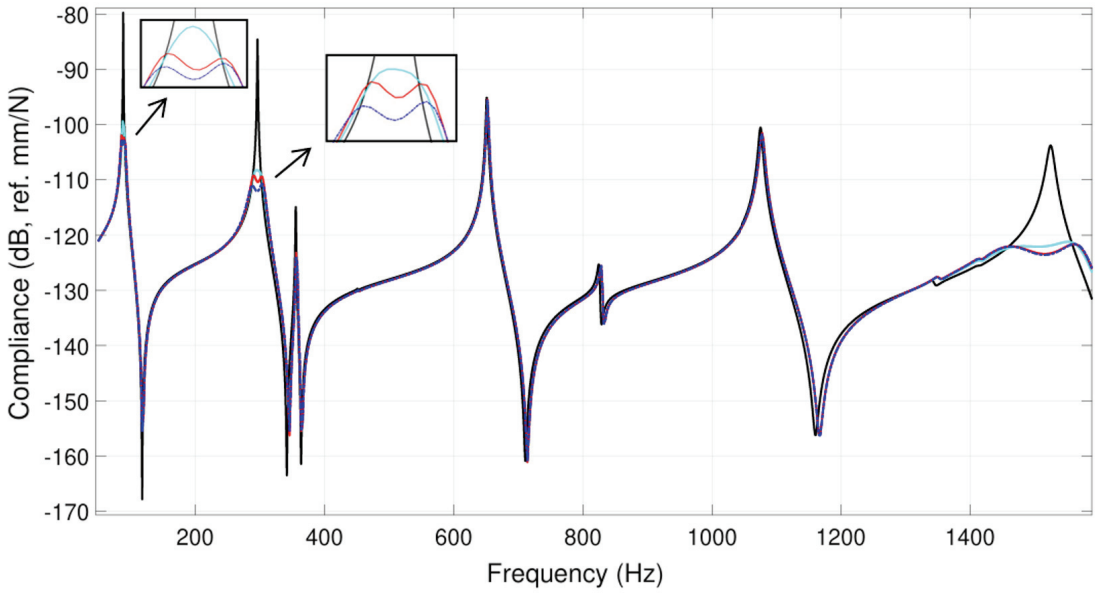

Figure 3: Numerical compliance in short-circuit (—), with three classical resonant shunts with the compensation of parasitic losses (—), without the compensation (—) and with the interconnected piezoelectric network (···) for the modes 1, 2, and 10.

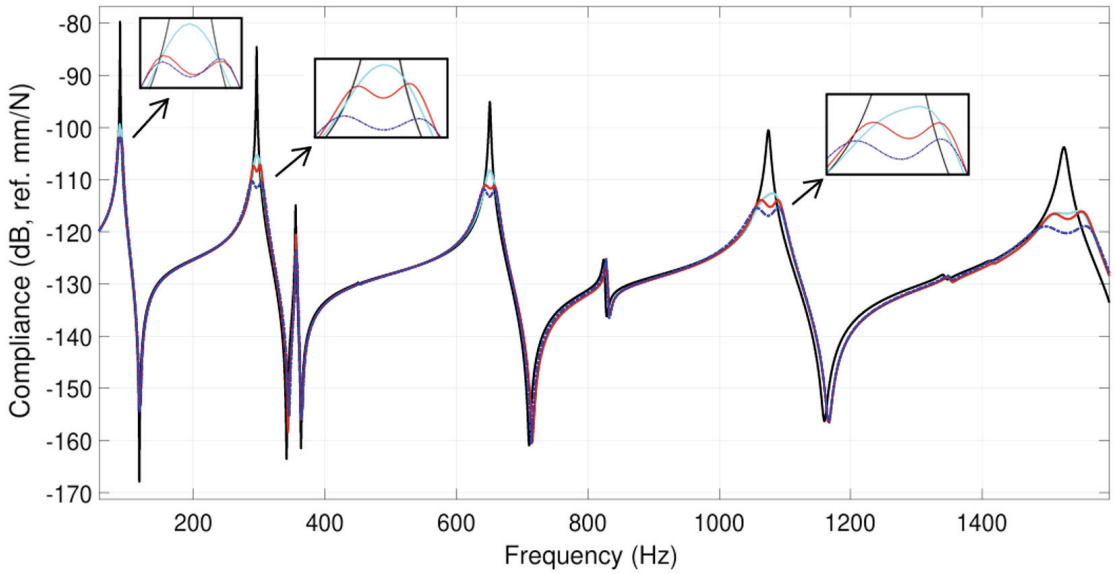

Figure 4: Numerical compliance in short-circuit (—), with three current blocking shunts with the compensation of parasitic losses (—), without the compensation (—) and with the interconnected piezoelectric network (···) for the first five bending modes.

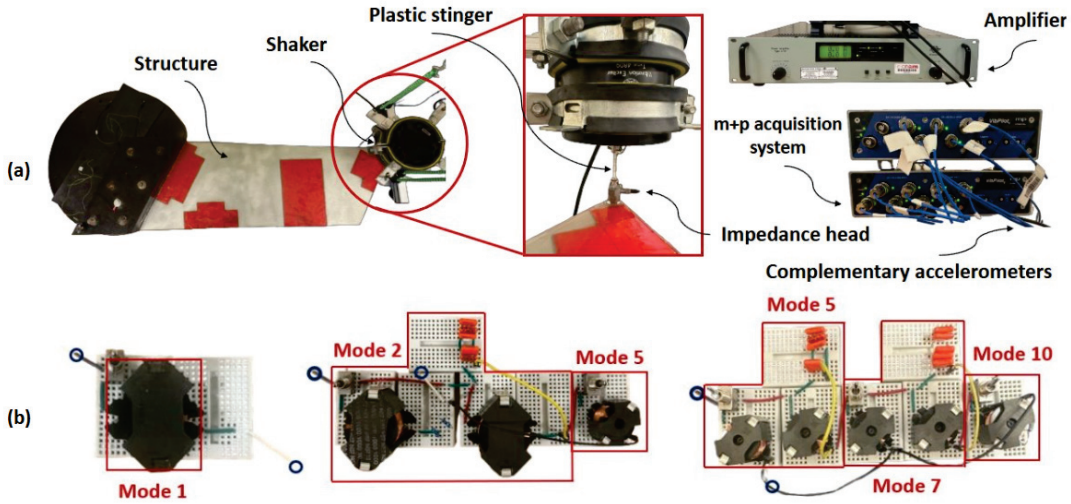

Figure 5: Experimental validation: (a) setup for the forced vibration analysis of the benchmark structure and (b) picture of the current blocking shunts - the targeted modes are highlighted with red boxes and connections to the piezoelectric patches are marked with blue circles.

4.2 Case study N > P

The case $N > P$, where $N > \text{rank}(\mathbf{\Phi_p})$, means that there are fewer transducers than targeted structural modes, and $\mathbf{\Phi_p}$ has more columns than rows. Therefore, internal dofs I have to be introduced to make the problem well-posed, as $I = N - \text{rank}(\mathbf{\Phi_p})$ [18]. Capacitors are then introduced into the network, and the total coupling factors are degraded. FRF are presented in Figure 4, where three current blocking shunts are connected to each patch as well as the associated interconnected network. The coupling factors κ_c and K_c and the attenuation levels A are presented in Table 3. The use of an interconnected piezoelectric network to target the first five bending modes provides greater vibration reduction compared to current blocking shunts. By selecting an appropriate weight vector w, the influence of each targeted mode can be selectively emphasized. In this case, to achieve performance at least comparable — and potentially superior — to that of the multi-branch shunts, the set of weights has been set to $w = [2, 2, 3, 1, 1]$.

5 EXPERIMENTAL VALIDATION

A fully-passive experimental validation is conducted for the first time on a well-known circuit architecture, which is the current blocking shunt. The objective was to validate the proposed compensation method to account for parasitic losses and the feasibility criteria developed in [11] for the fabrication of tailor-made inductors. To analyze the dynamics of the piezoelectric structure, an impedance head is glued at the free end, near the trailing edge. A plastic stinger is positioned between the impedance head and the shaker, ensuring alignment and enabling fine adjustments to achieve optimal orientation. The shaker, connected through an impedance head, is equipped with two sensors to measure the excitation force and the acceleration. Both signals are acquired through an m+p acquisition system and amplified accordingly. Eigenfrequency extraction is performed with the PolyFREQ algorithm. The experimental setup and the electrical circuits are presented in Figure 5. The FRF illustrated in Figure 6 is computed

Table 3: Comparison of the computed coupling factors with their corresponding residues and attenuation levels between three current blocking shunts and the interconnected piezoelectric network for the first five bending modes.

Mode	Patch	κ_c (%)	r (%)	A_{CB} (dB)	K_c (%)	w	A_{net} (dB)
1	1	6.28	100	-22.2	6.29	2	-22.2
2	2	4.45	60	-22.4	6.59	2	-25.8
5	2	1.51	40	-16	3.12	3	-17.2
5	3	2.14	50				
7	3	2.89	30	-13.7	3.57	1	-15.4
10	3	3.49	20	-12.5	4.97	1	-15

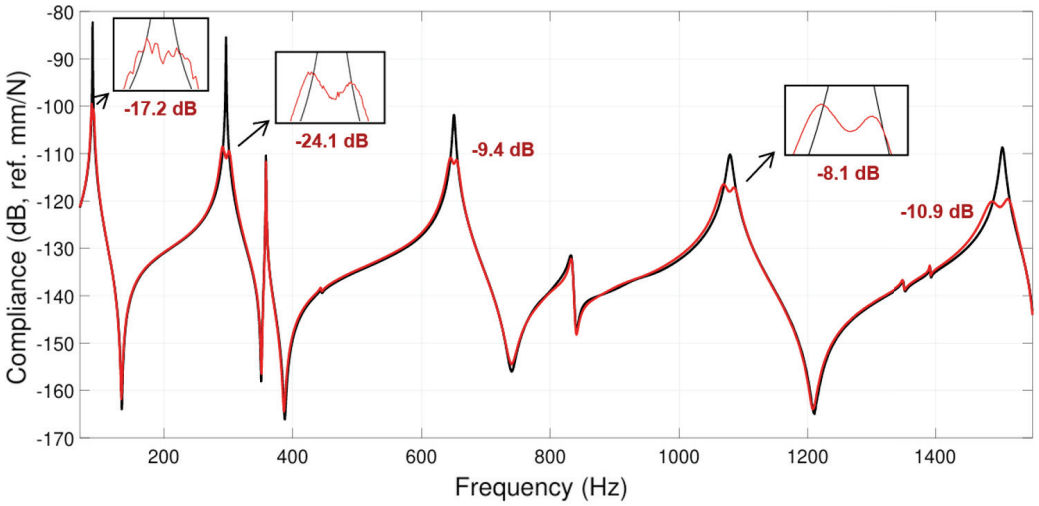

Figure 6: Experimental compliance in short-circuit (—) and with three current blocking shunts (—) with their respective attenuation levels for the first five bending modes.

using a processing block, with a complete acquisition comprising 10 blocks for a total duration of 40 seconds. The experimental FRF is consistent with the numerical model, with slightly lower attenuation levels due to weaker experimental coupling compared to the numerical predictions. Using purely inductive components, the vibration reduction profiles observed align with the optimal equal peaks behavior reported in the literature.

6 CONCLUSION

This study aims to compare the performance of multi-branch shunts and interconnected piezoelectric networks in the context of a fully-passive implementation. The different losses associated with passive inductors and piezoelectric patches are accurately quantified and implemented into the current blocking shunt — and multi-branch shunts in general — through a novel compensation method. The actual performance of the shunt is therefore in line with the expected theoretical performance, both numerically

and experimentally. Once this intermediate step is completed, interconnected piezoelectric networks once again demonstrate their superiority in terms of vibration reduction performance when compared to multi-branch shunts, yielding a gain between 1 and 4 dB on our benchmark structure depending on the mode to be controlled.

Future work will focus on describing the electrical network in a configuration of purely passive components, allowing fully-passive application of interconnected piezoelectric networks to any type of structure. Although this remains a challenge since explicit network topologies have not yet been derived, the electrical matrices of the network can be leveraged. Finally, the objective will be to implement a tuning correction that accounts for the same parasitic losses already considered into multi-branch shunts but applied to interconnected piezoelectric networks. Such a solution could be regarded as the most effective fully-passive approach for multimodal piezoelectric vibration damping.

ACKNOWLEDGMENTS

This work is part of a three-year Cifre doctoral project funded by Naval Group and the Agence de l'innovation de défense with supervision from the Conservatoire national des arts et métiers.

REFERENCES

[1] O. Thomas, J. Ducarne, and J.-F. Deü. Vibrations of an elastic structure with shunted piezoelectric patches: efficient finite element formulation and electromechanical coupling coeffients. *International Journal for Numerical Methods in Engineering*, 2009. https://doi.org/10.1002/nme.2632.

[2] R. L. Forward. Electronic damping of vibrations in optical structures. *Applied optics*, 18:690–7, 1979. https://doi.org/10.1364/AO.18.000690.

[3] N. W. Hagood and A. H. von Flotow. Damping of structural vibrations with piezoelectric materials and passive electrical networks. *Journal of Sound and Vibration*, 146:243–268, 1991. https://doi.org/10.1016/0022-460X(91)90762-9.

[4] D. L. Edberg, A. S. Bicos, and J. S. Fechter. On piezoelectric energy conversion for electronic passive damping enhancement. *Proceedings of Damping*, pages 717–724, 1991. https://contrails.library.iit.edu/item/163767.

[5] J. J. Hollkamp. Multimodal Passive Vibration Suppression with Piezoelectric Materials and Resonant Shunts. *Journal of Intelligent Material Systems and Structures*, 5:49–57, 1994. https://doi.org/10.1177/1045389X9400500106.

[6] S.-W. Wu. Method for Multiple Mode Piezoelectric Shunting with Single PZT Transducer for Vibration Control. *Journal of Intelligent Material Systems and Structures*, 9:991–998, 1998. https://doi.org/10.1177/1045389X9800901204.

[7] A. J. Fleming, S. Behrens, and S. O. R. Moheimani. Reducing the inductance requirements of piezoelectric shunt damping systems. *Smart Materials and Structures*, 12:57–64, 2003. https://doi.org/10.1088/0964-1726/12/1/307.

[8] G. Raze, J. Dietrich, and G. Kerschen. Tuning and performance comparison of multiresonant piezoelectric shunts. *Journal of Intelligent Material Systems and Structures*, 33(19):2470–2491, 2022. https://doi.org/10.1177/1045389X221088031.

[9] J. Ducarne. Modélisation et optimisation de dispositifs non-linéaires d'amortissement de structures par systèmes piézoélectriques commutés. *Conservatoire national des arts et metiers - CNAM*, 2009. https://theses.hal.science/tel-00464513v2.

[10] B. Lossouarn, M. Aucejo, J.-F. Deü, and B. Multon. Design of inductors with high inductance values for resonant piezoelectric damping. *Sensors and Actuators A: Physical*, 259:68–76, 2017. https://doi.org/10.1016/j.sna.2017.03.030.

[11] P. Flament, B. Lossouarn, É. Ramond, P. Audrain, and J.-F. Deü. Fully-passive implementation of multi-branch piezoelectric shunts for multimodal vibration damping. Manuscript in preparation, 2025.

[12] P. Flament, B. Lossouarn, É. Ramond, P. Audrain, and J.-F. Deü. Passive damping of several resonances using multi-branch resonant piezoelectric shunts. *INTER-NOISE and NOISE-CON Congress and Conference Proceedings*, 270(9):2207–2218, 2024. https://doi.org/10.3397/IN_2024_3151.

[13] A. Agneni, D. S. Matteoa, M. Francoa, and P. Gian Marioa. Multi-modal damping by shunted piezo-patches: Possible aeroelastic applications. *International Journal of Applied Electromagnetics and Mechanics*, 24:1–24, 2006. https://doi.org/10.3233/JAE-2006-709.

[14] S. Vidoli and F. dell'Isola. Modal coupling in one-dimensional electromechanical structured continua. *Acta Mechanica*, 141:37–50, 2000. https://doi.org/10.1007/BF01176806.

[15] R. Darleux. Development of analogous piezoelectric networks for the vibration damping of complex structures. *HESAM Université*, 2020. https://theses.hal.science/tel-02902755.

[16] B. Lossouarn, M. Aucejo, and J.-F. Deü. Multimodal vibration damping of a beam with a periodic array of piezoelectric patches connected to a passive electrical network. *Smart Materials and Structures*, 24:11, 2015. https://doi.org/10.1088/0964-1726/24/11/115037.

[17] G. Raze, J. Dietrich, B. Lossouarn, and G. Kerschen. Modal-based synthesis of passive electrical networks for multimodal piezoelectric damping. *Mechanical Systems and Signal Processing*, 176:109120, 2022. https://doi.org/10.1016/j.ymssp.2022.109120.

[18] G. Raze, J. Dietrich, B. Lossouarn, and G. Kerschen. Shunts vs networks: tuning and comparison of centralized and decentralized piezoelectric vibration absorbers. *Smart Materials and Structures*, 31:115006, 2022. https://doi.org/10.1088/1361-665X/ac92b0.

[19] B. Lossouarn. Optimal placement of thin piezoelectric patches for maximum modal coupling. *Journal of Intelligent Material Systems and Structures*, 35(20):1591–1605, 2024. https://doi.org/10.1177/1045389X241282054.

[20] C. Alexander and M. Sadiku. *Fundamentals of Electric Circuits Fourth Edition*. 2008.

XI ECCOMAS Thematic Conference on Smart Structures and Materials - SMART 2025
M. Krommer, M. Nader and M. Schagerl (Eds)

Received: 21 March 2025 / Revised: 7 July 2025 / Accepted: 3 October 2025
© The Author(s) 2025

Potential of Piezoelectric Energy Harvesting for Road Bridges

Thomas Furtmüller

Abstract. In this contribution energy harvesting from civil engineering structures, specifically road bridges, by means of piezoelectric discs is addressed. The piezo element is augmented by a Tuned Mass Damper assembly such that the thickness vibration mode is excited. Equations of motion of a four degree of freedom electromechanical model are derived, allowing for efficient numerical analyses. Transfer functions are derived from these equations in view of evaluating the electrical power output of the piezo element over a resistive load. The relevant parameters maximizing this power are revealed. Exemplarily, a three-span road bridge with realistic properties is subjected to randomly generated traffic based on real traffic data. It turns out that although the large mass of civil structures and the large forces acting on the structure might suggest a promising potential for piezoelectric energy harvesting, power output from a single piezo element remains rather small, even for optimally tuned parameters.

Key words: Energy harvesting, piezoelectricity, road bridges, Tuned Mass Damper

1 INTRODUCTION

Energy harvesting from vibrating structures by means of piezoelectric devices has been investigated for the last several years, as documented by several review papers, for instance [1]. In the present contribution, civil engineering structures are considered, specifically road bridges. The idea to harvest electric energy from these systems has been discussed recently. Another review article [2] summarizes approaches for energy harvesting from roadways and bridges. The authors conclude that photovoltaic energy harvesting currently is the most cost-efficient energy harvesting system while piezoelectric energy harvesting is still relatively expensive, but also not yet on a high enough technology readiness level.
In [3], vibrations of a Euler-Bernoulli beam due to travelling masses are considered. The obtained vibration responses are used for a cantilever-type piezoelectric energy harvester, however decoupled from the beam vibration. For a single concentrated mass traversing the bridge, the predicted rms power output is 8 mW. A cantilever beam piezoelectric energy harvester prototype for installation in roads and bridges is investigated in [4]. For each vehicle passing the

Thomas Furtmüller
Unit of Applied Mechanics, Universität Innsbruck, Technikerstr. 13, 6020 Innsbruck, Austria
e-mail: thomas.furtmueller@uibk.ac.at

prototype, 736 μW of power is generated. By theoretically upscaling the protoytpe, large potential for power generation is predicted, however without experimental validation. A case study of six piezoelectric energy harvesters installed in the pavement of a road bridge is presented in [5]. For a single truck passage, a peak power output of 113 mW and average power of 3 mW is reported.
In the present paper, the potential of a single piezoelectric energy harvester installed on a typical road bridge, considering realistically the time-varying excitation due to traffic is investigated based on numerical analyses. In section 2, the governing equations of the considered electromechanical system are derived. These are applied for a road bridge in section 3 with the aim of maximizing the power output.

2 PROBLEM STATEMENT

Consider a multi-span bridge, modeled as planar Euler-Bernoulli beam with mass per unit length ρA and bending stiffness EJ as shown in Fig. 1. Traffic loads across the bridge are considered by $k = 1, \dots n_f$ single forces $f_k = m_k g$ - corresponding to gravity loads of vehicles - traversing at constant speed v_k. At position x_p, a piezoelectric disc with thickness t_p and cross-section area A_p, connected in series with a linear elastic, viscously damped mass-spring-damper system (mass m_t, spring stiffness k_t, damping coefficient c_t, denoted TMD in the following), is attached to the structure. In Fig. 1, this sub-assembly is shown separated from the primary system through the internal force $f_p(t)$. A load resistance R_l is connected to the electrodes of the piezo disc, where the electric field $E(t)$ is induced due to deformation. $w(x,t)$ denotes the structural deflection as absolute displacement, while $w_p(t)$ is the relative deformation of the piezo disc with respect to $w(x_p,t)$ and $w_t(t)$ is the relative displacement of the sprung mass with respect to $w_p(t)$.

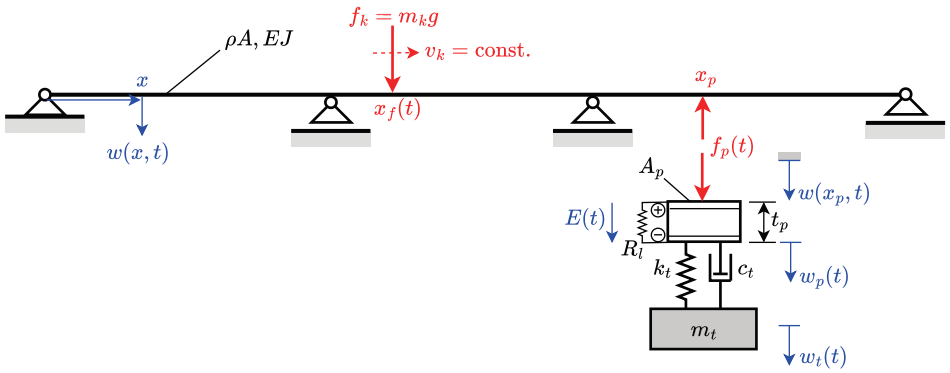

Figure 1: Electromechanical model of a bridge with attached Tuned Mass Damper-Piezoelectric energy harvester assembly

2.1 Equations of motion

Bending vibrations of the bridge beam are governed by Euler-Bernoulli beam theory according to

$$\rho A\ddot{w} + EJw_{,xxxx} = \delta\left(x - x_f\right) f_k - \delta\left(x - x_p\right) f_p \tag{1}$$

where $\dot{w}$ and $w_{,x}$ denote partial derivatives of w with respect to time and position, and $\delta(x)$ is Dirac's delta distribution. Introducing a Ritz ansatz in the form

$$w(x,t) = \varphi(x)y(t) \tag{2}$$

with shape function $\varphi(x)$ in Eq. (1), multiplying with φ and integration over the bridge length l discretizes the beam as modal single-degree-of-freedom oscillator with

$$m^*\ddot{y} + k^*y = \varphi_f f_k - \varphi_p f_p \quad \text{with} \quad m^* = \rho A \int_l \varphi(x)^2 \mathrm{d}x,\ k^* = EJ \int_l \varphi(x)\varphi(x)_{,xxxx}\mathrm{d}x \tag{3}$$

and abbreviations $\varphi_f = \varphi\left(x_f(t)\right),\ \varphi_p = \varphi\left(x_p\right)$. In the following, $m^* = 1$ is assumed, as obtained e.g. when φ is taken as mass-normalized mode shape of the bridge. Note that in this case the effective modal mass of the system at point x_p is [6]

$$m_{s,\text{eff}}\left(x_p\right) = \frac{1}{\varphi\left(x_p\right)^2} \tag{4}$$

With the natural frequency of the considered structural mode $\omega_s = \sqrt{k^*}$ and taking into account viscous damping through the damping ratio ζ_s, Eq. (3) reads

$$\ddot{y} + 2\zeta_s\omega_s\dot{y} + \omega_s^2 y = \varphi_f f_k - \varphi_p f_p \tag{5}$$

Conservation of momentum for the mass m_t yields with $\omega_t = \sqrt{k_t/m_t}$ and $\zeta_t = c_t/2m_t\omega_t$, and considering Eq. (2), after division by m_t

$$\ddot{w}_t + \ddot{w}_p + \varphi_p\ddot{y} + 2\zeta_t\omega_t\dot{w}_t + \omega_t^2 w_t = 0 \tag{6}$$

The internal force in the Kelvin-Voigt element is $f_t(t) = -f_p(t) = m_t\left(2\zeta_t\omega_t\dot{w}_t + \omega_t^2 w_t\right)$, which can be introduced in Eq. (5), rendering

$$\ddot{y} + 2\zeta_s\omega_s\dot{y} + \omega_s^2 y - \varphi_p m_t\left(2\zeta_t\omega_t\dot{w}_t + \omega_t^2 w_t\right) = \varphi_f f_k \tag{7}$$

For the piezo disc, uniaxial piezoelectric relations in e-form [7] are considered:

$$T(t) = c^E S(t) - eE(t) \quad \text{and} \quad D(t) = eS(t) + \varepsilon^S E(t) \tag{8}$$

For all quantities, indices 33 and 3, respectively, corresponding to the thickness-extensional deformation mode, are taken into account. In Eqs (8), the mechanical variables are stress T and

strain S, while the electrical variables are electric flux density D and electric field E. Material properties c^E, ε^S and e are the elastic stiffness at constant electric field, the permittivity at constant strain and the piezoelectric strain coefficient. Adapting the derivations outlined in [8], the variables can be written as

$$T(t) = -\frac{f_p(t)}{A_p} = \frac{m_t}{A_p}\left(2\zeta_t\omega_t\dot{w}_t + \omega_t^2 w_t\right) \quad E(t) = -\frac{v(t)}{t_p} \quad S(t) = \frac{w_p(t)}{t_p} \quad D(t) = \frac{q(t)}{t_p} \tag{9}$$

where $q(t)$ is the charge in the piezo disc. Substituting these relations in Eqs (8) yields, after multiplication with the cross-section area A_p

$$m_t\left(2\zeta_t\omega_t\dot{w}_t + \omega_t^2 w_t\right) - k_p w_p - \Theta v = 0 \quad \text{and} \quad \frac{v}{R_l} + C_p\dot{v} - \Theta\dot{w}_p = 0 \tag{10}$$

Here, $k_p = c^E A_p/t_p$, $C_p = \varepsilon^S A_p/t_p$ and $\Theta = eA_p/t_p$ are the piezo stiffness, capacitance and coupling cefficient. Note that Eq. $(10)_2$ has been obtained by taking the time derivative and inserting the current $\dot{q} = i = v/R_l$. Hence, the coupled electromechanical system is described by the equations of motion (6), (7) and (10) in terms of the four degrees of freedom $y(t)$, $w_p(t)$, $w_t(t)$ and $v(t)$.

2.2 Transfer functions

The Laplace transform of the degrees of freedom are denoted $\mathscr{L}\{y(t)\} = Y(s)$, and, accordingly, $W_p(s)$, $W_t(s)$ and $V(s)$. From Eq. $(10)_2$, a transfer function

$$V(s) = H_{VWp}(s)W_p(s) \quad \text{with} \quad H_{VWp}(s) = \frac{\Theta R_l s}{1+\tau_e s} \tag{11}$$

is obtained, where $\tau_e = C_p R_l$ is the time constant of the electric network. Substituting in the Laplace transform of Eq. $(10)_1$ yields

$$W_t(s) = H_{WtWp}(s)W_p(s) \quad \text{with} \quad H_{WtWp}(s) = \frac{k_p + \Theta H_{VWp}(s)}{m_t\left(2\zeta_t\omega_t s + \omega_t^2\right)} \approx \frac{k_p}{k_t} + \frac{\Theta^2 R_l s}{k_t\left(1+\tau_e s\right)} \tag{12}$$

where the approximation is valid for low damping values $\zeta_t \ll 1$. With the stiffness ratio $\kappa = k_p/k_t$, time constant $\tau_p = \Theta^2 R_l/k_t$ and time constant ratio $\gamma = \tau_e/\tau_p$, this transfer function can be written as

$$H_{WtWp}(s) = \kappa\frac{1+\tau_e(1+\gamma)s}{1+\tau_e s} \tag{13}$$

Using the definition above, the time constant ratio γ can be written equivalently by

$$\gamma = \frac{C_p k_t}{\Theta^2} = \frac{\varepsilon^S c^E}{e^2\kappa} \tag{14}$$

in terms of the piezo material properties ε^S, c^E and e. Since the ratio of these quantities in Eq. (14) is approximately one, $\gamma\kappa \approx 1$. Typically, $\kappa = k_p/k_t \gg 1$ holds, hence $\gamma \ll 1$ can be

assumed for practical setups. The Laplace transform of Eq. (6) gives the transfer function

$$W_p(s) = H_{WpY}(s)Y(s) \quad \text{with} \quad H_{WpY}(s) = \frac{-\varphi_p s^2}{H_{WtWp}(s)\left(s^2 + 2\zeta_t\omega_t s + \omega_t^2\right)} \tag{15}$$

Here, the approximation $1+1/H_{WtWp}(s) \approx 1$ has been used (due to $\kappa = k_p/k_t \gg 1$). With this approximation and discarding the second term of $H_{WtWp}(s)$ in Eq. (12), the Laplace transform of Eq. (7) yields, after inserting $W_t(s) = H_{WtWp}H_{WpY}(s)Y(s)$

$$Y(s) = H_{YF}(s)F(s) \quad \text{with} \quad H_{YF}(s) = \tag{16}$$
$$= \frac{s^2 + 2\zeta_t\omega_t s + \omega_t^2}{s^4 + 2\left(\zeta_s\omega_s + \zeta_t\omega_t\right)s^3 + \left(\omega_s^2 + \omega_t^2(1+m_t\varphi_p^2) + 4\zeta_t\zeta_s\omega_t\omega_s\right)s^2 + 2\omega_s\omega_t\left(\zeta_t\omega_s + \zeta_s\omega_t\right)}$$

i.e. a transfer function purely in terms of the mechanical properties. Note that in this equation, $\mu = m_t\varphi_p^2 = m_t/m_{s,\text{eff}}$ is the mass ratio between the TMD mass and the effective modal mass according to Eq. (4). Since in a practical setup, $\mu \ll 1$ holds, Eq. (16) then corresponds to a series connection of two single-degree-of-freedom transfer functions of the bridge mode and the TMD. In this case, optimal tuning of the TMD natural frequency to maximize its deformation corresponds to setting $\omega_t = \omega_s$ while minimizing the damping ratio ζ_t. In Eq. (16), $F(s) = \mathscr{L}\{\varphi_f(t)f_k\}$ is the Laplace transform of the modal load. Combining transfer functions in Eqs (11), (15) and (16), the transfer function relating external forces due to traffic and generated voltage in the piezo disc is obtained:

$$V(s) = H_{VF}(s)F(s) \quad \text{with} \quad H_{VF}(s) = H_{VWp}(s)H_{WpY}(s)H_{YF}(s) \tag{17}$$

The electrical power in the load resistance can then be computed as $P(s) = V(s)^2/R_l$.

2.3 Maximal power output

Evaluating H_{VWp} in Eq. (11) at the natural frequency of the structure ω_s gives the magnitude

$$|H_{VWp}(j\omega_s)| = \frac{\sqrt{\tau_e^2\Theta^2R_l^2\omega_b^4 + \Theta^2R_l^2\omega_s^2}}{1 + \left(\tau_e\omega_s\right)^2} = \frac{\Theta}{C_p}\frac{\eta}{\sqrt{1+\eta^2}} \quad \text{with} \quad \eta = \tau_e\omega_s \tag{18}$$

as dimensionless parameter relating the time constant of the electrical network and the structural natural frequency, i.e. a frequency ratio. Evaluating $|H_{VWp}(j\omega_s)|^2/R_l$ yields an expression for the electrical power in terms of the piezo deformation W_p at the structural natural frequency:

$$P(j\omega_s) = \frac{\Theta^2\omega_s}{C_p}\frac{\eta}{1+\eta^2}|W_p(j\omega_s)|^2 \tag{19}$$

As shown in Fig. 2, in terms of the frequency ratio the power is maximal at $\eta = 1$, i.e. matching load resistance $R_l = 1/C_p\omega_b$.

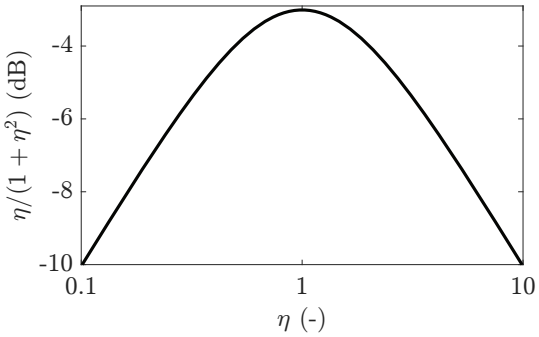

Figure 2: Maximum power output in terms of frequency ratio $\eta = \tau_e \omega_b$

$H_{WpY}(s)$ in Eq. (15) is a single-degree-of-freedom oscillator transfer function, scaled by $\varphi_p / H_{WtWp}(s)$. Hence, the output power (proportional to H^2_{WpY}) is inversely proportional to H^2_{WtWp}. Evaluating $H_{WtWp}(j\omega)$ at the structural frequency yields

$$|H_{WtWp}(j\omega_s)| = \kappa \frac{\sqrt{\left(1+\eta^2\left(1+\gamma\right)\right)^2 + \left(\eta\gamma\right)^2}}{1+\eta^2} = \kappa f(\eta,\gamma) \tag{20}$$

Fig. 3 shows the relevant function proportional to power, $1/f(\eta,\gamma)^2$ in terms of the dimensionless parameters η and γ. Here optimal values would be obtained at low values $\eta, \gamma \to 0$. If $\eta = 1$ is fixed, a value for γ as low as possible would minimize $|H_{WtWp}(j\omega_b)|$. Evaluating

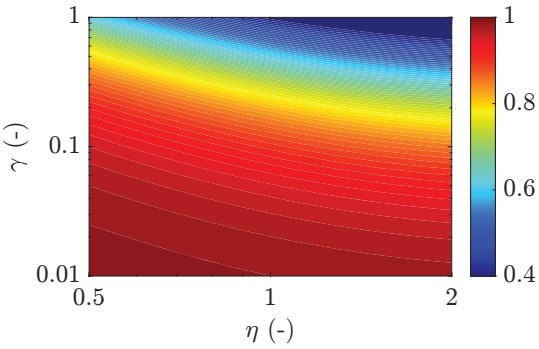

Figure 3: $1/f(\eta,\gamma)^2$ from Eq. (20) in (dB) in terms of frequency ratio $\eta = \tau_e \omega_b$ and time constant ratio $\gamma = \tau_p / \tau_e$

transfer function (16) for optimal tuning $\omega_s = \omega_t$ at that frequency yields $4\zeta_t\zeta_s\omega_s^4$ in the numerator. Combining all transfer functions, considering all above-mentioned approximations yields after some algebra for the power at the natural frequency of the bridge

$$P(j\omega_s) = \left(\frac{e}{c^E}\right)^2 \frac{R_l \mu m_t \omega_s^2}{16\zeta_t^2\zeta_s^2(1+\eta^2)} F(j\omega_s)^2 \tag{21}$$

The ratio of material properties in the first bracket is for typical piezoelectric materials in the order $e/c^E \approx 10^{-10}$ C/N, representing a major limitation of the maximum power. For a given material, Eq. (21) suggests that with increasing TMD mass m_t (which equivalently increases the mass ratio μ), the maximum power increases quadratically. Likewise, a decrease of the TMD damping ratio or an increase of the natural frequency ω_s yields a quadratic increase of the power. Note that $F(j\omega_s)$ is the Fourier transform of the modal load $\varphi_f(t)m_k g$, hence the last term in Eq. (21) has units of N^2/kg.

3 APPLICATION FOR A ROAD BRIDGE

3.1 Simulation model

In this section numerical studies on a three-span road bridge with equal span of 21 m are conducted where a single TMD-energy harvester is installed. Hence, the mechanical model of Fig. 1 applies. The model is based on ambient vibration tests of a real road bridge, from which the fundamental natural frequency and the acceleration level due to typical traffic was extracted. The parameters of the bridge model were then tuned to match these values, which led to a mass per unit length $\rho A = 20$ t/m, a bending stiffness $EJ = 33 \cdot 10^9$ Nm^2 and a modal damping ratio of $\zeta_s = 4$ %.

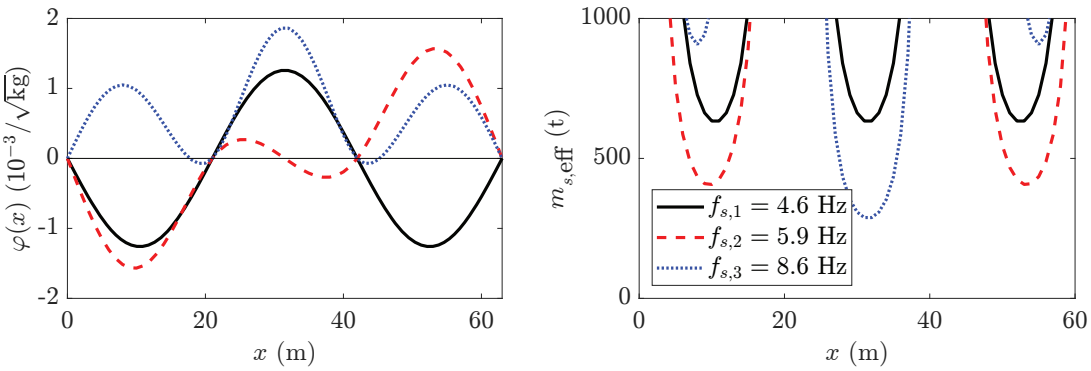

Figure 4: Mass-normalized modeshapes (left) and effective modal masses (right) fo the first three modes

In Fig. 4, the natural frequencies $f_{s,k}$ and (mass-normalized) modeshapes φ_k of the first three bending modes are shown. To place the TMD-piezo-assembly optimally, the effective modal masses $m_{s,\mathrm{eff}}$ along the bridge length is depicted on the right-hand side. In view of a maximum mass ratio μ, for the fundamental mode, the minimum effective modal mass is 633 t at the respective mid-spans. For the higher modes, smaller effective modal masses can be realized when considering optimal positions. Specifically, these are 407 t at the first or third field's midspan for mode 2 and 288 t at the second field's midspan for mode 3.
Traffic data publicly available [9] is used to generate one hour of random traffic across the bridge. Masses m_k and velocities v_k of both passenger cars and trucks are assumed normally distributed within typical ranges. Per hour, 350 passenger cars and 30 trucks cross the bridge.

Fig. 5 shows the simulated acceleration response of the bridge without attached TMD-piezo-assembly in terms of time history (left) and power spectral density (PSD, right). The first three modes are considered separately, and the vibration response is recorded at the respective positions of minimal effective modal masses according to Fig. 4. While for modes 1 and 2, the maximal spectral amplitude is approximately equal at the respective natural frequency (-52 dB re 1 m^2/s^4/Hz), for mode 3 the maximum amplitude is almost 10 dB less. Hence, considering Eq. 21 it is expected that maximum power output of the energy harvester can be achieved when the TMD is tuned to mode 2.

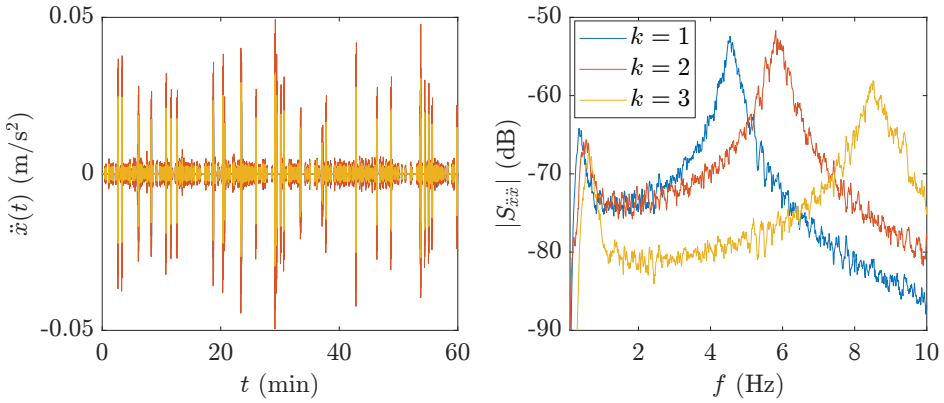

Figure 5: Acceleration time histories and PSDs from simulation of one hour traffic across the bridge for modes k =1, 2 and 3

3.2 Work per hour for simulated traffic

In the simulations presented here, properties of the piezoelectric disc are taken from [10]. To maximize power output, a low-capacitance disc of type PRYY-0886 (diameter 3 mm, thickness 2 mm) is chosen. The damping ratio of the TMD is set to $\zeta_t = 0.01$, while the natural frequency ω_t is tuned to either of the first three natural frequencies of the bridge ($\omega_b = \omega_t$). The load resistance is chosen such that $\eta = 1$. In this case, this yields $R_l = 620, 480$ and 330 MΩ. In Fig. 6, the cumulative work for one hour of simulated traffic for the piezo/TMD-assembly tuned to each of the three modes is shown. When a constant mass ratio $\mu = 0.1\,\%$ is considered, the TMD mass decreases with the mode number. Consequently, the maximum work is obtained for tuning to the first mode. On the other hand, when the TMD mass $m_t = 500$ kg is constant, the mass ratio increases with increasing mode number and tuning to the second mode yields the maximum work, as expected. However, for all considered cases the work per hour for a single piezo-disc remains below 4 μWh. This means that relevant electrical power and work, respectively can only be harvested by applying large arrays of piezo discs in parallel.

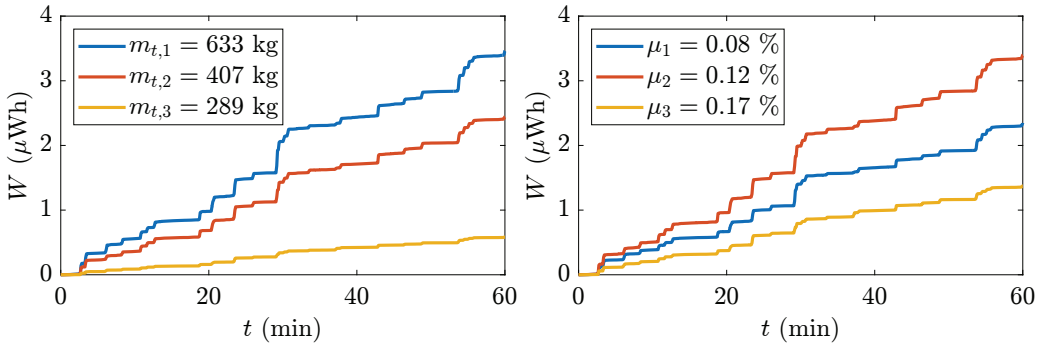

Figure 6: Cumulative work in the load resistance for one hour of simulated traffic, tuning to modes 1 (blue), 2 (red) and 3 (orange) with constant mass ratio $\mu = 0.1\,\%$ (left) and constant TMD mass $m_t = 500$ kg (right)

3.3 Optimal load resistance

In Fig. 7, results from a parametric study varying the tuning frequency ratio ω_t/ω_s and the time constant ratio η for the cumulative work after one hour are shown. All other parameter are kept the same as in the previous study, a constant TMD mass $m_t = 500$ kg is used for all three modes. It can be concluded from Fig. 7 that the maximum power is harvested for $\omega_t/\omega_s = 1$, which is expected due to the low mass ratio $\mu \ll 1$. On the other hand, optimal results are obtained for $\eta \approx 0.75$, i.e. load resistances lower than expected. Again, the maximal power is harvested when the TMD is tuned to mode 2 where the maximum cumulative work per hour is 5.3 μWh.

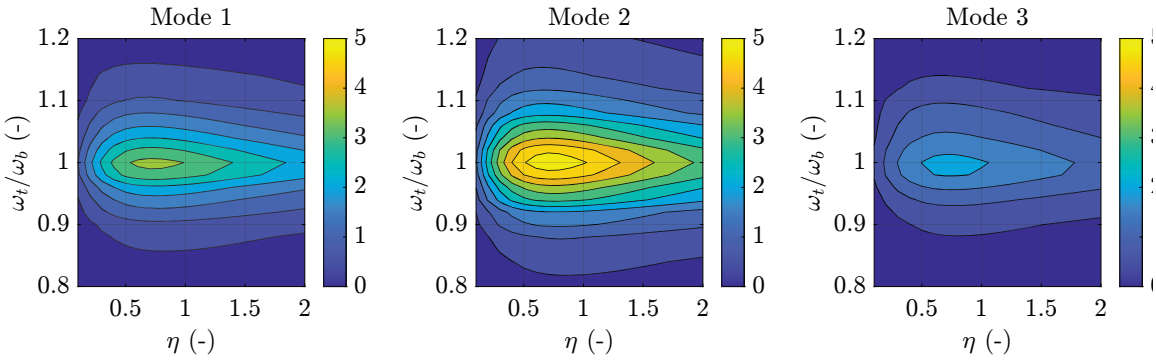

Figure 7: Work per hour for tuning to the first three modes, varying time constant $\eta = \omega_s \tau_e$ and tuning frequency ratio ω_t/ω_s, TMD mass $m_t = 500$ kg

The same parametric study is performed with an increase in the TMD mass by a factor of 10, i.e. $m_t = 5000$ kg. The results depicted in Fig. 8 show that optimal tuning occurs for $\omega_t/\omega_s = 1$ and $\eta \approx 0.75$ as in the previous study, however the optimal parameter range is wider. The mass ratio for the second mode is now 1.2 %, while the maximum cumulative work per hour is now 110 μWh, i.e. increased by a factor of approximately 20 with respect to the previous study. This

is in contrast to Eq. (21), which would suggest a quadratic increase in power due to the TMD mass change.

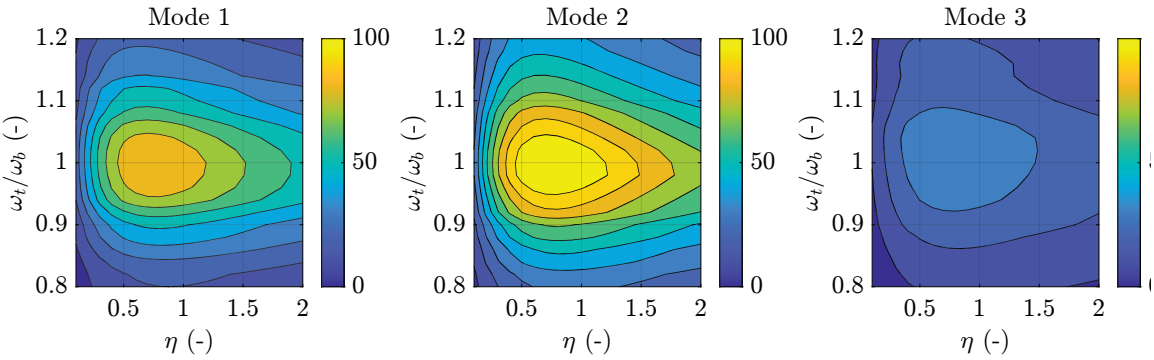

Figure 8: Work per hour for tuning to the first three modes, varying time constant $\eta = \omega_s \tau_e$ and tuning frequency ratio ω_t/ω_s, TMD mass $m_t = 5000$ kg

4 CONCLUSIONS

Piezoelectric energy harvesting from a road bridge subjected to traffic loads was considered by means of a linear four-degree-of-freedom electromechanical system which allows for fast computation of the bridge response and the voltage generated in the energy harvester. A bridge model based on real measurement data with realistic traffic loads was used to compute the cumulative work per hour in a resistive load connected to the piezo element. Although the large forces acting due to traffic and the large accelerated masses of both the bridge and a Tuned Mass Damper attached to the piezo disc might suggest a large potential for piezoelectric energy harvesting, the maximum work is a few μWh for a single energy harvester with 500 kg TMD attached to it. Hence, piezoelectric energy harvesting remains restricted to low-power applications like for instance self-powered sensors for bridge monitoring. For a practical application the number of piezo elements should be increased considerably.
By considering one vibration mode of the bridge at a time, it was shown that for the considered bridge, tuning the TMD natural frequency to the second natural frequency of the bridge yields the largest amount of harvested power. Furthermore, the optimal load resistance was significantly less than obtained by matching the electrical time constant of the harvester circuit to the inverse of the bridge natural frequency.

REFERENCES

[1] N. Sezer and M. Koc, “A comprehensive review on the state-of-the-art of piezoelectric energy harvesting,” *Nano Energy*, vol. 80, p. 105567, 2021.

[2] H. Wang, A. Jasim, and X. Chen, “Energy harvesting technologies in roadway and bridge

for different applications – a comprehensive review," *Applied Energy*, vol. 212, pp. 1083–1094, 2018.

[3] M. Karimi, A. H. Karimi, R. Tikani, and S. Ziaei-Rad, "Experimental and theoretical investigations on piezoelectric-based energy harvesting from bridge vibrations under travelling vehicles," *International Journal of Mechanical Sciences*, vol. 119, pp. 1–11, 2016.

[4] Y. Song, C. Yang, S. Hong, S. Hwang, J. Kim, J. Choi, S. Ryu, and T. Sung, "Road energy harvester designed as a macro-power source using the piezoelectric effect," *International Journal of Hydrogen Energy*, vol. 41, pp. 12 563–12 568, 2016.

[5] H. Xiong and L. Wang, "Piezoelectric energy harvester for public roadway: On-site installation and evaluation," *Applied Energy*, vol. 174, pp. 101–107, 2016.

[6] D. J. Ewins, *Modal Testing: Theory, Practice and Application*, 2nd ed. Baldock: Research Studies Press Ltd., 2000.

[7] T. Ikeda, *Fundamentals of Piezoelectricity*. New York: Oxford University Press, 1990.

[8] N. E. Du Toit, "Modeling and design of a MEMS piezoelectric vibration energy harvester. Master thesis, Massachusetts Institute of Technology (2005)."

[9] Traffic data region of Tyrol. [Online]. Available: https://verkehrsinformation.tirol.gv.at/web/html/vde.html

[10] Pi ceramic: Piezoceramic materials. [Online]. Available: https://www.piceramic.com/en/expertise/piezo-technology/piezoelectric-materials

XI ECCOMAS Thematic Conference on Smart Structures and Materials - SMART 2025
M. Krommer, M. Nader and M. Schagerl (Eds)

Received: 28 April 2025 / Revised: 24 June 2025 / Accepted: 3 October 2025
© The Author(s) 2025

Adaptive Resonant Piezoelectric Shunt Using Tunable Inductance

Arthur Haudeville, Adrien Queste, Christophe Giraud-Audine, Boris Lossouarn, Xavier Amandolese, Olivier Thomas

Abstract. Resonant piezoelectric shunts are highly effective for reducing vibrations of a structural natural mode. However, they require a fine tuning on the mechanical resonance to ensure that performances are optimal. This paper proposes a novel adaptive resonant piezoelectric shunt circuit and investigates its ability to adjust the value of the inductance. This circuit is thus used to vary the electrical frequency of the shunt and it proposes a robust strategy for vibration mitigation of a linear resonance. The principle involves incorporating a static converter controlled by a pulse-width modulation (PWM) circuit between the piezoelectric patch and the inductance. PWM is performed thanks to four-quadrant switches. It is demonstrated that the resonance frequency is linearly governed by the duty cycle of the PWM, with a range extending from zero hertz to the resonance frequency of the initial circuit. After numerical validation of the proposed circuit, a preliminary experimental validation is performed on a simple resonant LC circuit. It is observed that the resonance is indeed modified as expected. Some practical limitation yet appears, mainly due to the inductance internal resistance.

Key words: Resonant piezoelectric shunts, Adaptive shunt, Tunable inductance, Pulse-width modulation, Vibration mitigation

Arthur Haudeville & Adrien Queste & Christophe Giraud-Audine
Laboratoire d'Electrotechnique et d'Electronique de Puissance (L2EP), Univ. Lille, Arts et Metiers, Institute of Technology, Centrale Lille, Junia, ULR 2697, 8 Bd Louis XIV, 59000 Lille, France,
e-mail: christophe.giraud-audine@ensam.eu

Arthur Haudeville & Boris Lossouarn & Xavier Amandolese
Laboratoire de Mecanique des Structures et des Systemes Couples (LMSSC), Conservatoire national des arts et metiers (Cnam), 292 Rue Saint-Martin, 75000 Paris, France,
e-mail: boris.lossouarn@lecnam.net

Olivier Thomas
Laboratoire d'Ingenierie des Systemes Physiques et Numeriques (LISPEN), Ecole nationale superieure des arts et metiers (Ensam), 8 Bd Louis XIV, 59000 Lille, France,
e-mail: olivier.thomas@ensam.eu

1 INTRODUCTION

This work is part of the HYDRAVIB project where the aim is to perform hydrofoils' vibrations mitigation thanks to resonant piezoelectric shunts. Indeed, hydrofoils under a hydrodynamic flow are subjected to flow-induced vibrations [1], causing noise disturbances and structural fatigue. Resonant piezoelectric shunt circuits have been proven effective in mitigating vibrations of submerged hydrofoils [2, 3]. A typical passive resonant piezoelectric shunt consists of an electrical inductance L and resistance R connected in series, inducing an antiresonance effect on the mechanical response. However, optimal vibration suppression at a structural natural frequency demands precise tuning of both the resistance and inductance parameters [4]. Yet, in case of a structure under a hydrodynamic flow where a complex fluid-structure coupling operates, fixing values of R and L may resulting in weak performances of the shunt regarding the vibration mitigation. In marine applications, structures vibrating in hydrodynamic flows are prone to excitation across multiple natural frequencies due to time-varying flow velocities. Conventional approaches require a separate shunt circuit for each target natural frequency [5], a constraint that has motivated the development of adaptive shunt systems. Such systems aim to enhance robustness in complex dynamical systems and eliminate the need for multiple shunted circuits to suppress vibrations in case of sweeping excitation over multiple natural frequencies.

Adaptive shunt solutions, including electromagnetic [6, 7] or piezoelectric [8, 9] configurations, have been explored to emulate tunable electrical characteristics through active electronics. An alternative approach leverages standard PWM-based chopper circuits to achieve tunable resonant shunts. Demonstrated for electromagnetic systems [10], this method utilizes high-frequency switching to enable precise power modulation while avoiding complex active components. In this paper, this principle is adapted to modify the characteristics of the resonant RL piezoelectric shunt. Choppers of the electrical circuit modify the inductance value and so the electrical resonance frequency. The proof of concept is detailed in the next section with a simplified resonant electrical circuit. In a second step, the concept is extended to the model of a piezoelectric shunt coupled to the structure in the case of linear resonance. At last, an experimental validation of the PWM electronic circuits on a RLC circuit is performed.

2 PRINCIPLE OF A TUNABLE RESONANT CIRCUIT USING PWM

2.1 Average equivalent circuit

The operating principle of the adaptive shunt circuit is illustrated in Fig. 1. For simplicity, the piezoelectric patch is represented by an equivalent electrical circuit comprising a voltage source E in series with a capacitor C_P. Components L (inductance) and R (resistance) define the adaptive shunt, while R_L denotes the parasitic resistance of the inductance. The switches are assumed ideal (their practical implementation is addressed later) and are driven in a complementary manner, to achieve pulse-width modulation (PWM). During each switching period T_{PWM}, switch **A** conducts for a duration $\beta\, T_{\text{PWM}}$ (duty cycle β), connecting the piezoelectric patch to the inductance. For the remaining period, switch **B** conducts, disconnecting the patch and short-circuiting the inductance to interrupt power exchange between the components.

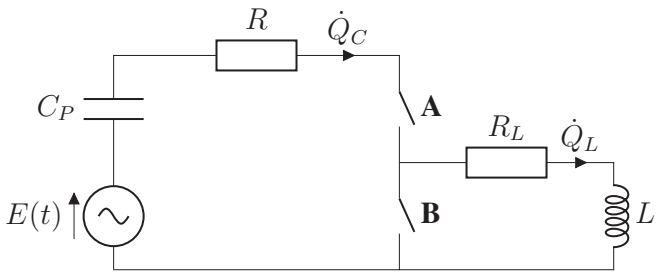

Figure 1: Simplified RLC circuit with tunable inductance thanks to the chopper with pulse-width modulation of the two switches.

Regarding the first configuration of the PWM, with the switch **A** closed and the switch **B** open, the electrical circuit is a classical RLC one with components in series and the Kirchhoff's law yields to

$$\begin{cases} L\dot{I}_L + (R + R_L)I_L + \dfrac{1}{C_P}Q_C = E\,, \\ \dot{Q}_C = I_L\,, \end{cases} \tag{1}$$

where Q_C is the electric charge in the capacitor and I_L is the current through the inductance. When the PWM operates in its second state (switch **A** open, switch **B** closed), a decaying current persists in the inductance branch (L). Kirchhoff's voltage law yields

$$\begin{cases} L\dot{I}_L + R_L I_L = 0\,, \\ \dot{Q}_C = 0\,. \end{cases} \tag{2}$$

Introducing the state vector $x = [I_L\ Q_C]^T$, Eq. (1, 2) can be written in the state-space form as $\dot{x}(t) = A_i\,x(t) + b_i\,u(t)$, for $i = \{1,\,2\}$, with $u = \{E\}_2^T$ the driving function and

$$A_1 = \begin{pmatrix} \frac{-(R+R_L)}{L} & \frac{-1}{LC_P} \\ 1 & 0 \end{pmatrix},\ b_1 = \begin{pmatrix} \frac{1}{L} \\ 0 \end{pmatrix} \quad \text{and} \quad A_2 = \begin{pmatrix} \frac{-R_L}{L} & 0 \\ 0 & 0 \end{pmatrix},\ b_2 = \begin{pmatrix} 0 \\ 0 \end{pmatrix}. \tag{3}$$

Considering the PWM pulsation much larger than the electrical pulsation of the circuit $\omega_{\text{PWM}} \gg \omega_e = 1/\sqrt{LC_P}$, it has been shown in [10] that the average state-space system can be written as

$$\dot{x}(t) \simeq \bar{A}\,x(t) + \bar{b}\,u(t) \quad \text{with} \quad \begin{cases} \bar{A} = \beta A_1 + (1-\beta)A_2\,, \\ \bar{b} = \beta b_1 + (1-\beta)b_2\,. \end{cases} \tag{4}$$

Then, the average dynamical equation of the RLC electrical circuit of Fig. 1 can be given as an equivalent resonant circuit as in the following expressions:

$$\frac{L}{\beta^2}\ddot{Q}_C + \frac{\beta R + R_L}{\beta^2}\dot{Q}_C + \frac{1}{C_P}Q_C = E\,, \tag{5}$$

where one can infer the equivalent electrical pulsation $\bar{\omega}_e$ and the electrical damping ζ_e:

$$\bar{\omega}_e = \frac{\beta}{\sqrt{LC_P}} = \beta\omega_e \,, \qquad \bar{\zeta}_e = \frac{R + R_L/\beta}{2}\sqrt{\frac{C_P}{L}} \,. \tag{6}$$

The PWM adjusts the electrical resonance of the circuit proportionally to the duty cycle β by modifying the effective value of the inductance L/β^2. Moreover, it appears that the PWM also impacts the electrical damping $\bar{\zeta}_e$ and so the resonance magnitude.

2.2 Tunable resonant electrical circuit

Thanks to Eq. (5), the Fourier transform of $E(t)$ is operated and the electrical admittance of the resonant circuit $\dot{Q}_C/E$ is given by

$$Y(\Omega) = \frac{j\,\Omega\,\breve{Q}_C}{\breve{E}} = \frac{j\,\Omega\,\bar{\omega}_e^2\,C_P}{\bar{\omega}_e^2 - \Omega^2 + 2j\bar{\zeta}_e\Omega\bar{\omega}_e} \,, \tag{7}$$

where j stand for the imaginary number and $\breve{\circ}(\Omega)$ denotes the Fourier transform of $\circ(t)$. Note that the resonance occurs at $\Omega = \bar{\omega}_e$ and one can deduce from Eq. (7) the theoretical maximal electrical admittance $Y_{\max} = \beta^2/(\beta R + R_L)$.

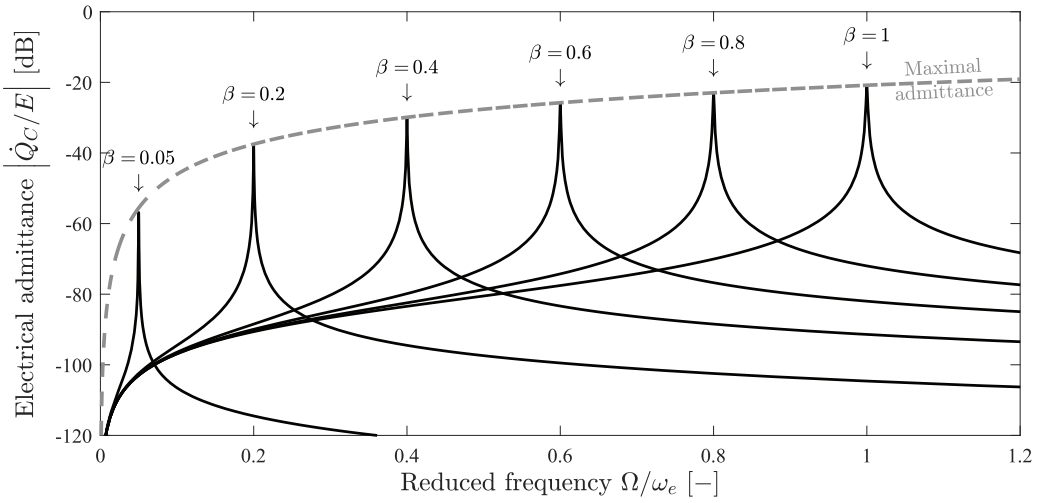

Figure 2: Modulus of the theoretical electrical admittance of Eq. (7), represented in solid lines (——), with $C_P = 40\,\mathrm{nF}$, $R = 10\,\Omega$, $R_L = 1\,\Omega$, $L = 2\,\mathrm{H}$ and a set of values β; The maximal admittance $Y_{\max}$, represented in dashed lines (- - -), is calculated by defining the duty cycle as $\beta = \Omega/\omega_e$.

Fig. 2 confirms the linear dependence of the electrical resonance frequency on the duty cycle β. Furthermore, the operating range spans the full normalized frequency spectrum ($\Omega \in [0,\, \omega_e]$, corresponding to $\beta \in [0,\, 1]$).

3 THEORY OF THE TUNABLE PIEZOELECTRIC SHUNT

3.1 Governing equations

The model of the electrical circuit is extended to include the vibrational dynamics of the underlying structure coupled through a piezoelectric patch. The mechanical displacement w of the structure is expended on the $N \in \mathbb{N}^*$ natural mode basis of the structure,

$$w(t) = \sum_{j=1}^{N} \Phi_j \, q_j(t) \ , \tag{8}$$

where Φ_j and $q_j(t)$ are the j-th mode shape and modal coordinate. As shown in Fig. 3, the piezoelectric patch is directly connected to the electrical resistance and the variable inductance. The variable inductance value is controlled with PWM as in Fig. 1 with two switches.

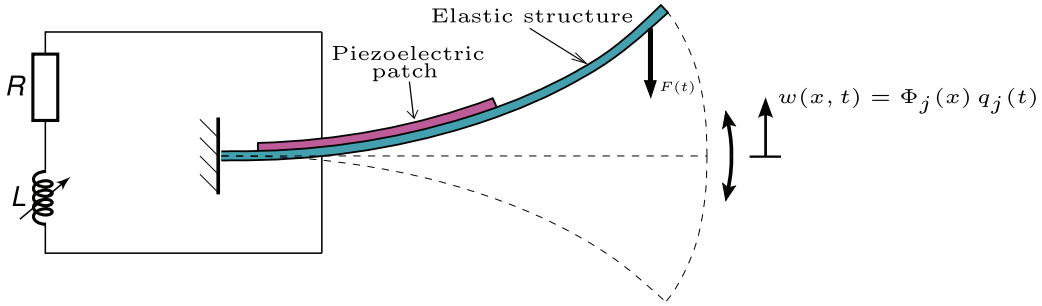

Figure 3: Vibrating elastic structure with a piezoelectric shunt composed of a tunable inductance with a resistance in series.

The state-space method used in the previous section yields to the following average electromechanical dynamic system:

$$\begin{cases} \ddot{q}_j + 2\zeta_j\omega_j\dot{q}_j + \hat{\omega}_j^2 q_j = \dfrac{F_j(t)}{m_j} + \dfrac{\chi_j}{m_j C_P} Q_C \qquad \forall j \in \{1, ..., N\} \ , \\ \ddot{Q}_C + \dfrac{\beta R + R_L}{L}\dot{Q}_C + \dfrac{\beta^2}{LC_P} Q_C = \dfrac{\beta^2}{LC_P} \displaystyle\sum_{j=1}^{N} \chi_j \, q_j \ , \end{cases} \tag{9}$$

where ζ_j, ω_j and m_j are the j-th modal damping ratio, pulsation (for the shunt in short-circuit) and modal mass of the structure, respectively. Accordingly to [11], we introduce the j-th piezoelectric coupling coefficient χ_j, the equivalent capacitance of the piezoelectric patch C_P and the electrical charge at the patch terminals Q_C. We also introduce the open-circuit natural pulsation of the j-th mode:

$$\hat{\omega}_j^2 = \omega_j^2 + \chi_j^2/(m_j C_P) \ . \tag{10}$$

3.2 Effect of the duty cycle on the mechanical resonance

Applying the Fourier transforms on the governing Eq. (9) in the frequency domain [12] and normalizing the modal forcing by the modal shape (such as $F_j = F$), for the modes $j \in \{1, ..., N\}$, it yields to

$$\begin{pmatrix} Z_1 & \cdots & 0 & -\chi_1/C_P \\ \vdots & \ddots & \vdots & \vdots \\ 0 & \cdots & Z_N & -\chi_N/C_P \\ \bar{\omega}_e^2\,\chi_1 & \cdots & \bar{\omega}_e^2\,\chi_N & -Z_e \end{pmatrix} \begin{pmatrix} \breve{q}_1 \\ \vdots \\ \breve{q}_N \\ \breve{Q}_C \end{pmatrix} = \begin{pmatrix} \breve{F} \\ \vdots \\ \breve{F} \\ 0 \end{pmatrix} , \tag{11}$$

where, as previously, $\breve{\circ}(\Omega)$ denotes the Fourier transform of $\circ(t)$, the equivalent electrical pulsation $\bar{\omega}_e$ and the equivalent electrical damping $\bar{\zeta}_e$ are defined in Eq. 6. Moreover, we introduce the modal impedance $Z_j\,\forall j \in \{1, ..., N\}$ and the electrical impedance of the system Z_e as

$$Z_j = m_j \left(\hat{\omega}_j^2 - \Omega^2 + 2j\zeta_j\omega_j\Omega\right) , \qquad Z_e = \bar{\omega}_e^2 - \Omega^2 + 2j\bar{\zeta}_e\bar{\omega}_e\Omega \, . \tag{12}$$

Solving the linear system of Eq. (11) leads to the generalized mechanical mobility of the tunable resonant piezoelectric shunt coupled to an elastic structure for all $j \in \{1, ..., N\}$:

$$H_j(\Omega) = \frac{j\,\Omega\,\breve{q}_j}{\breve{F}} = \frac{j\,\Omega\left(C_P\,Z_e\prod_{\substack{n=1\\n\neq j}}^{N} Z_n - \beta\,\bar{\omega}_e^2\sum_{\substack{n=1\\n\neq j}}^{N}\left[\chi_n\left(\chi_n - \chi_j\right)\prod_{\substack{m=1\\m\neq\{j,n\}}}^{N} Z_m\right]\right)}{C_P\,Z_e\prod_{n=1}^{N} Z_n - \beta\,\bar{\omega}_e^2\sum_{n=1}^{N}\left[\chi_n^2\prod_{\substack{m=1\\m\neq n}}^{N} Z_m\right]} \, . \tag{13}$$

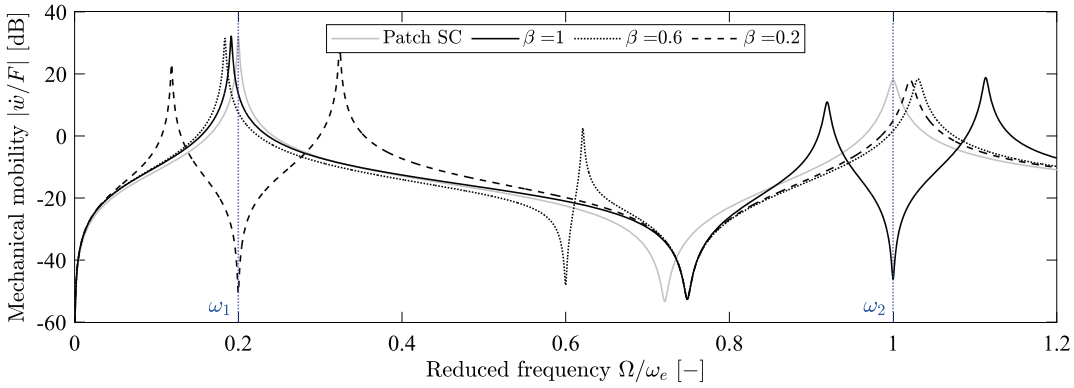

Figure 4: Modulus of the theoretical mechanical mobility of the elctromechanical system with the tunable inductance introduced in Fig. 3, about two modes of an arbitrary structure, $f_1 = 100\,\text{Hz}$ and $f_2 = 500\,\text{Hz}$, and for three values of the duty-cycle β; Electromechanical parameters of the structure have been arbitrary set to $\zeta_1 = \zeta_2 = 0.005$, $m_1 = m_2 = 4\,\text{g}$, $\chi_1 = \chi_2 = 8\,\text{mN.V}^{-1}$, $C_P = 40\,\text{nF}$, $L = 2.44\,\text{H}$, $R = 5\,\Omega$ and $R_L = 1\,\Omega$.

Direct interpretation of key properties from the transfer function in Eq. 13 poses analytic challenges. To address this, Fig. 4 illustrates a case study analyzing two mechanical modes of a generic structural configuration. The duty-cycle value is set to different values with two of them adjusted to align the antiresonance with the natural frequency of the structure (with the piezoelectric shunt in short-circuit configuration). Once again, one can observe the antiresonance position in frequency linearly depending of the duty-cycle value. The operating range of the antiresonance variation is also validated for a large band of the duty-cycle domain. Note that the usable duty-cycle domain is independent of the initial value of the inductance and the tunable shunt is expected to work regardless the electrical parameters values.

4 EXPERIMENTAL VALIDATION

4.1 Practical chopper design

In practice, to obtain switches functional in the four quadrants of the voltage/current plan, diodes and MOSFET are combined as in the scheme of Fig. 5 where zones **A** and **B** refers to the switches in Fig. 3. Voltages at the MOSFET source and gate are controlled by the driver which delivers two isolated control signals from the Digital Signal Processor (DSP). A simplified representation of the connections between the DSP, the driver and the MOSFET is given in Fig. 5.

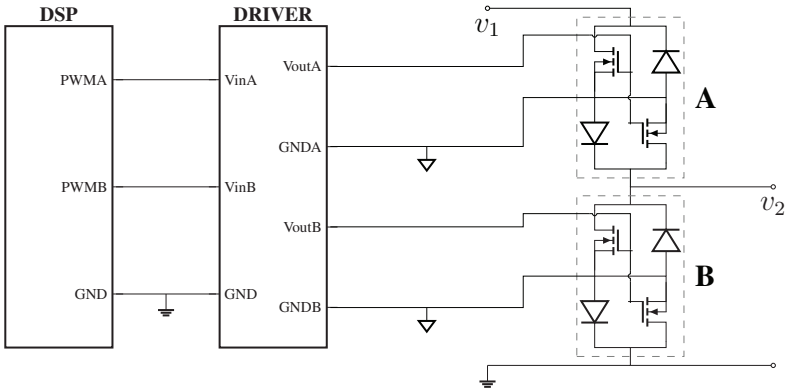

Figure 5: Practical 4-quadrants switches composed of two diodes and two MOSFET each; MOSFET are controlled by the driver with isolated control signals from ports PWMA and PWMB, the driver itself is managed by the Digital Signal Processor (DSP).

To prevent the chopper being in short-circuit during the transition state of the switches, the DSP also provide a dead-time of period T_{m} such as, in practice, the tunable shunt is monitored by the effective duty-cycle $\beta_{\mathrm{eff}} = \beta - T_{\mathrm{m}}/T_{\mathrm{PWM}}$ [10]. Here, the dead-time period is set such as $T_{\mathrm{m}}/T_{\mathrm{PWM}} = 0.004$.

4.2 Experimental setup

Prior to coupling the tunable shunt to an elastic structure, the core concept is experimentally validated using a simplified series RLC circuit (capacitor C and inductance L). The theoretical configuration of Fig. 1 is replicated experimentally, with the resistance R set to match the capacitor's internal resistance. A frequency-swept chirp signal, generated by a power amplifier driven by an m+p VibPilot controller, excites the circuit. Voltage measurements across the capacitor (V_C) and the RC branch (V_{in}) are acquired and processed in real time via the m+p VibPilot, as depicted in the experimental setup of Fig. 6(b). This preliminary step isolates the electrical resonance dynamics, ensuring unambiguous characterization before introducing mechanical coupling effects in subsequent structural tests.

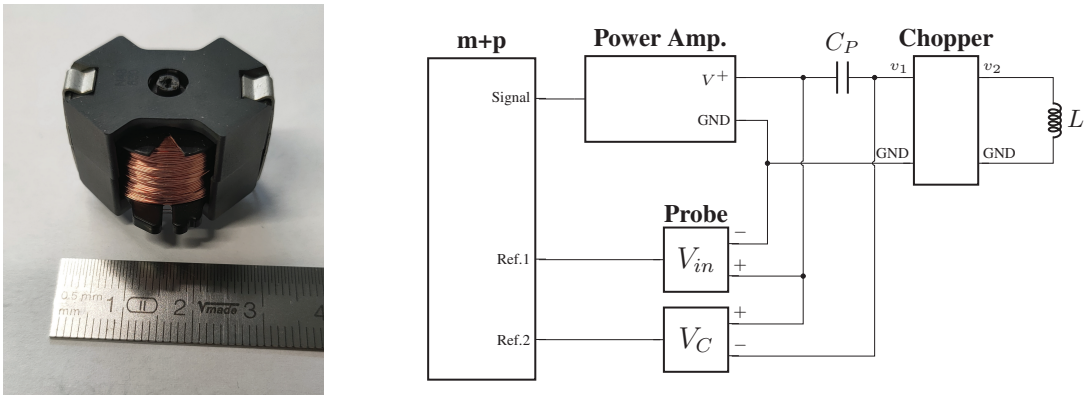

Figure 6: (a) Inductor made with a ferrite core for the experimental validation; (b) Scheme of the tunable LC circuit supplied by the power amplifier and with probes measuring the input voltage V_{in} and the voltage across the capacitor V_C.

The inductance is made of a coil of copper wire and a ferrite core as shown in Fig. 6(a). Commonly used for power applications, this kind of manufactured inductance allows reaching a value of $L = 1.06\,\text{H}$ and for an internal resistance of $R_L = 66\,\Omega$ (measured at $100\,\text{Hz}$). The electrical capacitor is chosen so that it has a low internal resistance and the electrical frequency f_e of the LC circuit is close to the firsts natural frequencies of the hydrofoil studied in the HYDRAVIB project ($\sim 100\,\text{to}\,1000\,\text{Hz}$). Then a capacitor of value $C_P = 660.2\,\text{nF}$ with an internal resistance $R_C = 3.33\,\Omega$ (measured at $100\,\text{Hz}$) is connected to the circuit. Regarding the expected frequency range of the electrical resonances, the switching frequency is set to $f_{\text{PWM}} = 2\,\text{kHz}$ which satisfies the 10:1 ratio requirement between the PWM frequency and the circuit's resonant frequency.

4.3 Assessment of the tuning performances

Thanks to the voltage signals measured across the capacitor and the RLC circuit, the electrical frequency response function (FRF) of V_c/V_{in} is drawn for different values of duty-cycle as seen in Fig. 7. First of all, it is shown that the electrical resonance frequency of the RLC circuit

is accurately modified in comparison to the theoretical results. Moreover, as expected from the theory, the resonance magnitude decrease with the duty-cycle even if experimental results show a greater magnitude reduction when the PWM is activated ($\beta \neq 1$).

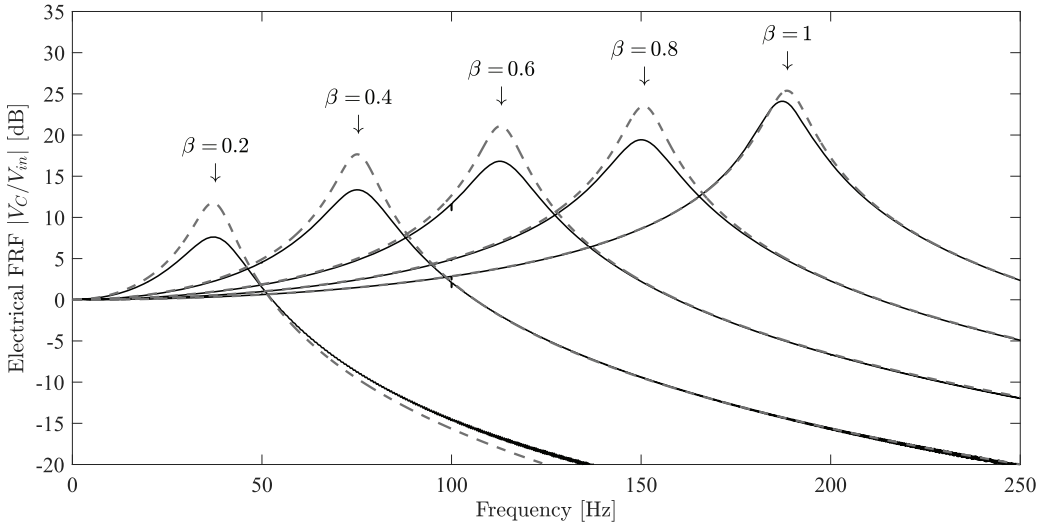

Figure 7: Modulus of the experimental electrical FRF V_c/V_{in}, represented in solid lines (——) of the tunable RLC circuit with $L = 1.06\,\text{H}$, $R_L = 66\,\Omega$, $C_P = 660.2\,\text{nF}$, $R = 3.33\,\Omega$ and for different values of β; Experimental data are compared to theoretical results, represented in dashed lines (- - -).

Experimental observations suggest the presence of a measurable parasitic resistance associated with the chopper circuit. While this phenomenon could theoretically originate from the switching components, its magnitude appears inconsistent with the low on-state resistance of the semiconductor devices, an apparent contradiction requiring further investigation. Systematic characterization of individual circuit elements will be necessary to isolate the underlying mechanism in future work.

5 CONCLUSIONS

Theoretical analyses presented in this work validate the tunable resonant shunt concept for both standalone RLC circuits and electromechanical coupled systems. The duty cycle β demonstrates precise control over the effective inductance, enabling targeted adjustment of the electrical resonance frequency (or antiresonance in coupled systems). Experimental validation on a simplified RLC circuit corroborates the theoretical framework, though measured responses exhibit unexpected over-damping. While preliminary evidence suggests switching losses in the chopper circuit as a plausible contributor, the exact source of this parasitic dissipation requires systematic characterization in future studies. Yet, even with a proper working tunable shunt, the theory suggests an increasing equivalent resistance while the duty-cycle decrease (refer to Eqs. (6) and (9)) and performance of the shunt may suffer when the duty-cycle β is set under 0.5 (risk of ending up with an over-resistive resonant shunt).

Future efforts will focus on two priorities: (1) implementing the tunable shunt on a piezoelectr coupled elastic structure to assess its vibration suppression capabilities under dynamic loading, and (2) experimental validation on a hydrofoil subjected to hydrodynamic flow to evaluate robustness in real-world marine environments. Concurrently, a detailed investigation into the origins of parasitic resistance (e.g., high-frequency eddy currents, PCB track impedance, or transient switching effects) will be conducted to resolve the observed damping discrepancy.

ACKNOWLEDGMENTS

The authors would like to express sincere gratitude to the *Agence de l'Innovation de Défense* (AID) and the *Agence Nationale de la Recherche* (ANR) for the support of the project HYDRAVIB (ANR-22-ASTR-0012).

REFERENCES

[1] M. Paidoussis, S. Price, and E. de Langre, *Fluid-Structure Interactions: Cross-Flow-Induced Instabilities*. Cambridge University Press, 2011.

[2] L. Pernod, B. Lossouarn, J. Astolfi, and J. Deü, "Vibration damping of marine lifting surfaces with resonant piezoelectric shunts," *Journal of Sound and Vibration*, vol. 496, p. 115921, 2021.

[3] Y. Watine, B. Lossouarn, C. Gabillet, J. A. Astolfi, and J. Deü, "Mitigation of hydrofoil torsional flow induced vibrations by resonant piezoelectric shunt," *Ocean Engineering*, vol. 313, p. 119598, 2024.

[4] O. Thomas, J. Ducarne, and J. Deü, "Performance of piezoelectric shunts for vibration reduction," *Smart Materials and Structures*, vol. 21, no. 1, p. 015008, 2012.

[5] J. F. Toftekær and J. Høgsberg, "Multi-mode piezoelectric shunt damping with residual mode correction by evaluation of modal charge and voltage," *Journal of Intelligent Material Systems and Structures*, vol. 31, no. 4, pp. 570–586, 2020.

[6] D. Niederberger, S. Behrens, A. Fleming, S. Moheimani, and M. Morari, "Adaptive electromagnetic shunt damping," *IEEE/ASME Transactions on Mechatronics*, vol. 11, no. 1, pp. 103–108, 2006.

[7] A. McDaid and B. Mace, "A self-tuning electromagnetic vibration absorber with adaptive shunt electronics," *Smart Materials and Structures*, vol. 22, no. 10, p. 105013, sep 2013.

[8] D. Niederberger, M. Morari, and S. Pietrzko, "Adaptive resonant shunted piezoelectric devices for vibration suppression," *Proc SPIE*, vol. 5056, 08 2003.

[9] Z. Shami, C. Giraud-Audine, and O. Thomas, "A nonlinear tunable piezoelectric resonant shunt using a bilinear component: theory and experiment," *Nonlinear Dynamics*, vol. 111, no. 8, pp. 7105–7136, 04 2023.

[10] M. Auleley, C. Giraud-Audine, H. Mahé, and O. Thomas, "Tunable electromagnetic resonant shunt using pulse-width modulation," *Journal of Sound and Vibration*, vol. 500, p. 116018, 2021.

[11] O. Thomas, J. F. Deü, and J. Ducarne, "Vibrations of an elastic structure with shunted piezoelectric patches: efficient finite element formulation and electromechanical coupling coefficients," *International Journal for Numerical Methods in Engineering*, vol. 80, no. 2, pp. 235–268, 2009.

[12] C. Close, D. Frederick, and J. Newell, *Modeling and Analysis of Dynamic Systems*. Wiley, 2001.

XI ECCOMAS Thematic Conference on Smart Structures and Materials - SMART 2025
M. Krommer, M. Nader and M. Schagerl (Eds)

Received: 22 April 2025 / Revised: 2 September 2025 / Accepted: 3 October 2025
© The Author(s) 2025

A Unified Tuning Method for Piezoelectric Vibration Damping by Positive Position Feedback Control

Jan Høgsberg, Amirali Sadeqi, Niels Leergaard Pedersen, Ayech Benjeddou

Abstract. Vibration damping of plate-like structures and panels can be effectively realized by active feedback control between a pair of piezoelectric patches or laminates. In the present work, active vibration damping is implemented by a Positive Position Feedback (PPF) control, for which the control gain governs the stability margin and attainable damping, while the filter time scale appears as the convenient tuning parameter. From an augmented modal representation, the so-called modal control coupling factor (MCCF) emerges as a governing coefficient in the derived closed-form expressions for optimal tuning and attainable damping. The accuracy of these design expressions is validated for vibration damping of a numerical cantilever beam.

Key words: Piezoelectric vibration damping, Active control, Positive Position Feedback (PPF)

1 INTRODUCTION

Positive Position Feedback (PPF) control has been extensively investigated for piezoelectric vibration control of flexible structures. The PPF control is introduced as an alternative to direct feedback methods in [1]. It is easily used for piezoelectric control systems, as it directly integrates strain by a second-order filter with desirable high-frequency roll-off properties. The PPF control format has also been applied to modal control in [2], for adaptive control in [3], while [4] provides a review of the earlier applications of PPF control for vibration damping.

The classic PPF format has been extended to more advanced control strategies. In [5], it is combined with a common proportional-derivative controller to improve stability margins, whereas in [6] it is implemented with a first-order velocity feedback control. More recently, a dedicated non-linear PPF control has been suggested for damping of nonlinear vibrations [7].

The tuning and design of PPF control has been approached by several paths. In the classic approach [1, 8], the second-order filter is used alone to secure effective high-frequency roll-off,

Jan Høgsberg, Amirali Sadeqi, Niels Leergaard Pedersen
Department of Civil and Mechanical Engineering, Technical University of Denmark, Koppels Alle Building 404, 2800 Kongens Lyngby, Denmark

Ayech Benjeddou
Roberval Laboratory, Université de Technologie de Compiègne (UTC), France

Ayech Benjeddou
Institut Supérieur de Mécanique de Paris, Saint Ouen, France

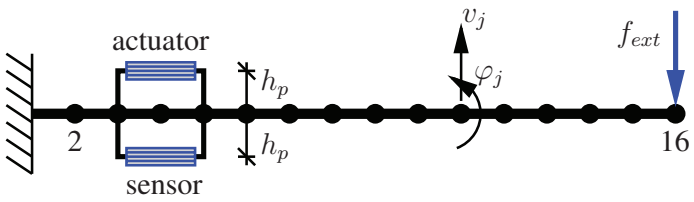

Figure 1: Numerical cantilever beam model with Euler-Bernoulli beam elements and transverse displacement v_j and rotation φ_j as the generalized nodal displacements for node j in $\mathbf{q}$. The sensor/actuator pair is located at nodes 3 and 5, while external loading is applied at the tip in node 16.

whereby the feedback gain is the only tunable parameter to ensure maximum damping. More recently, the potential resonant characteristics of the second-order filter have been utilized in [9, 10] to achieve vibration damping similar to that obtained by a resistive-inductive shunt. In the present work, the simpler first-order PPF control from [11, 8] is considered for vibration damping by a pair of symmetric piezoelectric patches on a cantilever beam. The equations of motion are presented in Section 2, while Section 3 derives the associated modal equations for a generic feedback function. The precise explicit design and tuning expressions are then derived in Section 4, followed by a numerical validation in Section 5. It is shown that the simple design expressions, containing the so-called modal control coupling factor (MCCF), provide close-to-optimal damping performance, even for a PPF design near the stability limit.

2 BEAM WITH PIEZOELECTRIC PAIR OF PATCHES

Figure 1 shows a benchmark cantilever beam with a pair of symmetrically placed piezoelectric patches, to be used in the present paper as a sensor-actuator pair for active vibration control. In the following, the upper-side patch is used for actuation (subscript $(\,)_a$), while the bottom-side patch is installed as a sensor (subscript $(\,)_s$). The cantilever beam is modelled by Euler-Bernoulli finite elements, with the transverse displacement v_j and rotation φ_j as the two nodal degrees of freedom (dofs). In its final form, the equation of motion can be written as

$$\mathbf{M}\ddot{\mathbf{q}} + \mathbf{C}\dot{\mathbf{q}} + \mathbf{K}\mathbf{q} + f_a\mathbf{b} = \mathbf{f}_{ext} \tag{1}$$

in which the force exerted by the piezoelectric actuator ($f_a = \theta V_a$) is proportional to the applied voltage V_a, with θ being the effective (structural) coupling coefficient. The vector $\mathbf{q}$ contains the nodal dofs, $\mathbf{M}$, $\mathbf{C}$ and $\mathbf{K}$ are the mass, damping and stiffness matrices, while $\mathbf{f}_{ext}$ is the external loading. As shown in Fig. 1, the piezo-pair is attached to the beam at two distinct nodes (n_1 and n_2). Because each patch has an offset h_p, the connectivity vector in (1) becomes

$$\mathbf{b}^T = [\,0,\,0,\,\ldots,\,\underbrace{0,\,-h_p}_{n_1},\,\ldots,\,\underbrace{0,\,h_p}_{n_2},\,\ldots,\,0,\,0\,] \tag{2}$$

with n_1 and n_2 depicting the two attachment nodes so that $\mathbf{b}^T\mathbf{q}$ defines the piezo deformation.

While the PPF control determines the actuator voltage V_a, the measured voltage V_s across the sensor patch's electrodes follows from the charge balance relation $Q_s = \theta \mathbf{b}^T \mathbf{q} + C_p^S V_s$, which for open-circuit sensor conditions, with vanishing charge ($Q_s = 0$), reduces to

$$V_s = -\frac{\theta}{C_p^S} \mathbf{b}^T \mathbf{q} \tag{3}$$

where C_p^S is the sensor-patch blocked capacitance. In the following, the piezoelectric patches' intrinsic damping and losses are assumed negligible, their inertia are added to the mass matrix $\mathbf{M}$, while their stiffness contributions are included in the stiffness matrix as

$$\mathbf{K} = \mathbf{K}_b + \left(2k_p + \frac{\theta^2}{C_p^S} \right) \mathbf{b}\mathbf{b}^T \tag{4}$$

where $\mathbf{K}_b$ is the stiffness matrix of the beam, k_p is the mechanical stiffness of a single patch, while θ^2 / C_p^S represents the piezoelectric stiffening from the open-circuited sensor-patch.

3 CLOSED-LOOP MODAL EQUATIONS

The PPF control is tuned to a specific vibration mode, assuming harmonic response at a given angular frequency ω. Thus, the equation of motion (1) is written in the frequency domain as

$$\left(-\omega^2 \mathbf{M} + i\omega \mathbf{C} + \mathbf{K} \right) \mathbf{q} + f_a \mathbf{b} = \mathbf{f}_{ext} \tag{5}$$

in which the response variables ($\mathbf{q}$, f_a and $\mathbf{f}_{ext}$) now represent frequency-domain amplitudes.

3.1 CONTROL TRANSFER FUNCTION

The feedback control from the sensor voltage V_s to the actuator voltage V_a is collocated and expressed by a linear filter equation, represented in the frequency domain by the relation

$$V_a = -H(\omega) V_s \tag{6}$$

where $H(\omega)$ is the control transfer function. The minus sign in (6) compensates for the sensor and actuator patches being placed on opposite sides of the beam. When eliminating $V_a = f_a / \theta$ and V_s by (3), the control equation is written in mechanical form as

$$f_a = H(\omega) \frac{\theta^2}{C_p^S} \mathbf{b}^T \mathbf{q} \tag{7}$$

whereby $H(\omega) \theta^2 C_p^S$ constitutes a frequency-dependent and complex stiffness from the PPF control. Thus, the coupled equations (5) and (7) constitute the final closed-loop equations.

3.2 MODAL EQUATIONS

The modal expansion is based on modes from the short-circuit (SC) eigenvalue problem

$$\left(-\omega_j^2\mathbf{M}+\mathbf{K}\right)\mathbf{u}_j=\mathbf{0} \tag{8}$$

obtained from (5) with vanishing actuator force $f_a = 0$ and no damping. For convenience, the mode shapes are all normalized to unit actuator amplitude, i.e. $\mathbf{b}^T\mathbf{u}_j = 1$. The linear combination of modes then represents the structural (physical) displacement vector with modal coordinates r_j,

$$\mathbf{q}=\sum_j \mathbf{u}_j r_j \tag{9}$$

Substitution of (9) into (5), followed by pre-multiplication with $\mathbf{u}_j^T$, gives the scalar equation

$$\left(-\omega^2 m_j + i\omega c_j + k_j\right) r_j + f_a = f_j \tag{10}$$

in which the modal mass, damping, stiffness and load are defined as

$$m_j=\mathbf{u}_j^T\mathbf{M}\mathbf{u}_j \quad , \quad c_j=\mathbf{u}_j^T\mathbf{C}\mathbf{u}_j \quad , \quad k_j=\mathbf{u}_j^T\mathbf{K}\mathbf{u}_j \quad , \quad f_j=\mathbf{u}_j^T\mathbf{f}_{ext} \tag{11}$$

where assumed orthogonal damping implies that the modal viscous coefficient can be expressed as $c_j = 2\zeta_j\omega_j m_j$ in terms of the modal damping ratio ζ_j and the natural angular frequency $\omega_j = \sqrt{k_j/m_j}$. Correspondingly, the control equation (7) is expressed in modal coordinates as

$$f_a = H(\omega)\frac{\theta^2}{C_p^S}\sum_j r_j \tag{12}$$

where the assumed normalization $\mathbf{u}_j^T\mathbf{b} = 1$ has been used to obtain both (10) and (12).

3.3 TARGET-MODE EQUATIONS

The control parameters in $H(\omega)$ are tuned to damp a targeted mode $j = s$. Initially, the modal summation in (12) is separated into the target term $j = s$ and the residual terms $j \neq s$. Then, the modal coordinate r_j is expressed by the modal equation (10) with $f_j = 0$, whereby

$$f_a = H(\omega)\frac{\theta^2}{C_p^S}\left(r_s+\sum_{j\neq s} r_j\right) = H(\omega)\frac{\theta^2}{C_p^S}\left(r_s - \underbrace{\sum_{j\neq s}\frac{1}{-\omega^2 m_j + i\omega c_j + k_j}}_{1/R_s(\omega)} f_a\right) \tag{13}$$

The summation over the other modes ($j \neq s$) defines the residual function $R_s(\omega)$, which can be included on the first left-hand side, so that the modal control equation (13) can be written as

$$\left(1 + H(\omega)k\,\frac{1}{R_s(\omega)}\right) f_a = H(\omega)k r_s \tag{14}$$

when introducing the piezoelectric stiffening $k = \theta^2/C_p^S$ as an apparent stiffness component.

The modal frequency response function (FRF) is derived by eliminating f_a between the actuator equation (14) and the modal equation in (10) for $j = s$. When normalizing the r_s/f_s ratio by the modal stiffness k_s, the FRF can be expressed as

$$\frac{r_s k_s}{f_s} = \frac{1 + H(\omega)\kappa \dfrac{k_s}{R_s(\omega)}}{\left(-\dfrac{\omega^2}{\omega_s^2} + 2i\zeta_s \dfrac{\omega}{\omega_s} + 1\right)\left(1 + H(\omega)\kappa \dfrac{k_s}{R_s(\omega)}\right) + H(\omega)\kappa} \tag{15}$$

in which the piezoelectric stiffening ratio

$$\kappa = \frac{k}{k_s} = \frac{\theta^2}{C_p^S k_s} \tag{16}$$

scales the control transfer function $H(\omega)$. In the following, the PPF control is tuned to maximum modal damping, governed by the characteristic equation

$$\left(-\frac{\omega^2}{\omega_s^2} + 1\right)\left(1 + H(\omega)\kappa \frac{k_s}{R_s(\omega)}\right) + H(\omega)\kappa = 0 \tag{17}$$

obtained from the denominator in (15) without structural damping ($\zeta_s = 0$). In the next Section 4, the simplest first-order PPF control is tuned by pole placement, using only (17).

4 POSITIVE POSITION FEEDBACK CONTROL

The present section considers the simple first-order PPF control for active vibration damping. The control equation is directly related to an equivalent mechanical damper model, from which expressions are derived for stability, optimal tuning and attainable damping.

4.1 CONTROL EQUATIONS

The simplest form of PPF control is obtained by the first-order filter equation [11, 8]

$$\tau \dot{V}_a + V_a = -gV_s \tag{18}$$

in which the two governing parameters are the time scale τ and the control gain g. In the frequency domain, the transfer function from (6) for the PPF filter in (18) is given as

$$H(\omega) = \frac{g}{1 + i\omega\tau} = \frac{g}{1 + (\omega\tau)^2} + i\,\frac{-g\tau\omega}{1 + (\omega\tau)^2} \tag{19}$$

Substitution into (7) gives the rheological mechanical model in Fig. 2, where the active stiffness

$$k_g = g\frac{\theta^2}{C_p^S} = gk \tag{20}$$

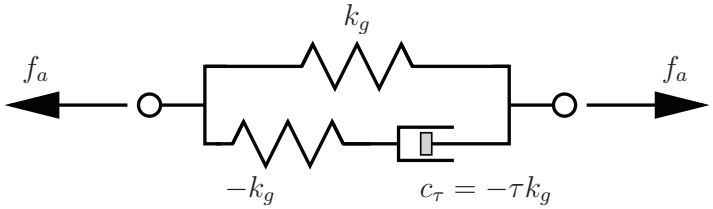

Figure 2: Equivalent mechanical (rheological) model of the filtered PPF control in (19) with active spring stiffness $\pm k_g$ and active viscous coefficient $c_\tau = -\tau k_g$.

is proportional to the control gain g, while the time scale τ governs the active viscous coefficient

$$c_\tau = -\tau k_g \tag{21}$$

It follows directly from (21) that k_g and thus g must be negative for the control to dissipate energy ($c_\tau > 0$). Furthermore, the imposed non-positive active stiffness (for $k_g \leq 0$) cannot make the resulting stiffness matrix singular, which requires that

$$k_g \geq k_{stab} = -\frac{1}{\mathbf{b}^T\mathbf{K}^{-1}\mathbf{b}} \qquad \Rightarrow \qquad k_{stab} \leq gk \leq 0 \tag{22}$$

see further details in [9]. The stability condition (22) requires collocation of the sensor/actuator pair [8] and therefore the symmetric placement of the patches in Fig. 1.

4.2 MODAL CONTROL COUPLING FACTOR (MCCF)

In contrast to the classical use of PPF control, the present approach identifies the time scale τ as the obvious tuning parameter. Thus, Fig. 3 shows the two limits of the mechanical damper model for infinite and vanishing τ, respectively. For $\tau \to \infty$ in (a), the viscous dashpot in Fig. 2 is rigid, whereby the two springs with stiffnesses $\pm k_g$ cancel. Hereby, the modal properties of the beam are determined by the fundamental eigenvalue problem in (8). In the opposite limit ($\tau \to 0$), the viscous dashpot vanishes, which prunes the lower branch in Fig. 2. This leaves the upper spring (k_g) in Fig. 3(b), determining the augmented eigenvalue problem

$$\left(\mathbf{K} + k_g\mathbf{b}\mathbf{b}^T - \hat{\omega}_j^2\mathbf{M}\right)\hat{\mathbf{u}}_j = \mathbf{0} \tag{23}$$

for the modal parameters denoted by $\hat{(\,)}$, representing the limit $\tau \to 0$.

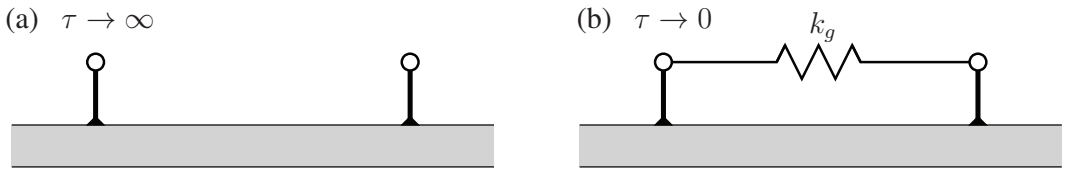

Figure 3: The equivalent mechanical damper model for (a) $\tau \to \infty$ and (b) $\tau \to 0$.

By substitution of the control transfer function (19) into (17), the target-mode characteristic equation can, after some re-organization, be written as

$$\left(-\frac{\omega^2}{\omega_s^2}+1\right)\left(1+i\frac{\omega}{\omega_s}\,\omega_s\tau+\kappa_g\,\frac{k_s}{R_s(\omega)}\right)+\kappa_g=0 \tag{24}$$

where the gain-stiffness ratio is defined as

$$\kappa_g=\frac{k_g}{k_s}=g\frac{k}{k_s}=g\kappa \tag{25}$$

The characteristic equation (24) is found to recover the fundamental solution $\omega=\omega_s$ when $\tau\to\infty$. In the opposite limit $\tau=0$, the characteristic equation (24) instead reduces to

$$\left(-\frac{\hat{\omega}_s^2}{\omega_s^2}+1\right)\left(1+\kappa_g\,\frac{k_s}{R_s(\omega)}\right)+\kappa_g=0 \tag{26}$$

when introducing the solution $\omega=\hat{\omega}_s$ from (23). The residual mode function $R_s(\omega)$ can now be determined from (26), conveniently expressed by the relation

$$-\frac{\kappa_g}{1+\kappa_g\,\dfrac{k_s}{R_s(\omega)}}=\frac{\omega_s^2-\hat{\omega}_s^2}{\omega_s^2}=K_s^2 \tag{27}$$

that defines the modal control coupling factor (MCCF) K_s^2 as the relative change between the square of the two limiting natural frequencies.

4.3 FREQUENCY SOLUTION AND OPTIMAL TUNING

By elimination of $\kappa_g k_s/R_s$ using (27), the characteristic equation (24) can be expressed as

$$\left(-\frac{\omega^2}{\omega_s^2}+1\right)\left(i\frac{\omega}{\omega_s}\,\omega_s\tau-\frac{\kappa_g}{K_s^2}\right)+\kappa_g=0 \tag{28}$$

A compact expression can be obtained by first isolating the former parenthesis, then expressing ω^2 relative to $\hat{\omega}_s^2$ and finally dividing this relative change by $\omega_s^2-\hat{\omega}_s^2$. When introducing K_s^2 from (27), this three-step procedure gives the final frequency solution

$$\frac{\omega^2-\hat{\omega}_s^2}{\omega_s^2-\hat{\omega}_s^2}=\frac{-i\dfrac{\omega}{\omega_s}\,\tau\omega_s\,\dfrac{K_s^2}{\kappa_g}}{1-i\dfrac{\omega}{\omega_s}\,\tau\omega_s\,\dfrac{K_s^2}{\kappa_g}}=\frac{i\dfrac{\omega}{\omega_s}\eta K_s^2}{1+i\dfrac{\omega}{\omega_s}\eta K_s^2} \tag{29}$$

based on the resulting damper parameter

$$\eta=-\frac{\tau\omega_s}{\kappa_g}=-\frac{\tau\omega_s}{g\kappa} \tag{30}$$

which represents a normalization of the time-scale $\tau\omega_s$ by the gain-stiffness ratio κ_g. It is directly verified that the frequency solution (29) recovers $\omega = \hat{\omega}_s$ for $\eta = 0$ and correspondingly $\omega = \omega_s$ for $\eta \to \infty$.

The damping ratio for the targeted mode $j = s$ can be derived from the frequency solution in (29) by applying the following approximations,

$$\zeta = \frac{\mathrm{Im}[\omega]}{|\omega|} \simeq \frac{\mathrm{Im}[\omega - \hat{\omega}_s]}{\frac{1}{2}(\omega_s + \hat{\omega}_s)} \simeq \frac{\mathrm{Im}[\omega^2 - \hat{\omega}_s^2]}{\frac{1}{2}(\omega_s + \hat{\omega}_s)^2} \simeq \tfrac{1}{2}K_s^2 \,\mathrm{Im}\left[\frac{\omega^2 - \hat{\omega}_s^2}{\omega_s^2 - \hat{\omega}_s^2}\right] \frac{\omega_s^2}{\left(\frac{1}{2}(\omega_s + \hat{\omega}_s)\right)^2} \tag{31}$$

where the final representation is obtained by approximating $\omega \simeq \frac{1}{2}(\omega_s + \hat{\omega}_s)$ and introducing the definition of the MCCF K_s^2 from (27). By substitution of the frequency solution (29) into the final expression in (31), the damping ratio becomes

$$\zeta \simeq \tfrac{1}{2}K_s^2 \,\frac{\eta K_s^2}{1 + (\eta K_s^2)^2} \frac{\omega_s^2}{\left(\frac{1}{2}(\omega_s + \hat{\omega}_s)\right)^2} \tag{32}$$

when assuming $\omega/\omega_s \simeq 1$ in the right-hand-side fraction of (29). This parametric expression in η attains its maximum value when $\eta K_s^2 = 1$, which gives the optimal time scale

$$\tau_{opt}\omega_s = -\frac{\kappa_g}{K_s^2} = -\frac{g\kappa}{K_s^2} = -\frac{g}{K_s^2}\frac{k}{k_s} = -\frac{g}{K_s^2}\frac{\theta^2}{C_p^S k_s} \tag{33}$$

and the maximum damping ratio

$$\zeta_{max} = \tfrac{1}{4}K_s^2 \,\frac{\omega_s^2}{\left(\frac{1}{2}(\omega_s + \hat{\omega}_s)\right)^2} \tag{34}$$

It is seen that τ_{opt} and ζ_{max} scale inversely and directly with K_s^2, respectively.

5 NUMERICAL EXAMPLE

The cantilever beam in Fig. 1 is discretized by 15 Bernoulli beam elements with v_j and φ_j as the nodal coordinates. The piezo pair is attached between nodes 3 and 5, whereby

$$\mathbf{b}^T = [\,0,\, 0,\, 0,\, 0,\, 0,\, h_p,\, 0,\, 0,\, 0,\, -h_p,\, 0,\, \ldots\, 0\,] \tag{35}$$

with the offset $\pm h_p$ inserted at the dofs 6 and 10, respectively. When installing the piezo pair, the natural frequency of the combined beam-piezo system in Fig. 1 can be determined by solving the eigenvalue problem (8).

5.1 MODAL CONTROL COUPLING FACTOR AND TUNING

For the present beam-control example, the piezoelectric actuator introduces the piezoelectric stiffening ratio $\kappa = 0.0382$ for the first mode shape normalized by $\mathbf{b}^T\mathbf{u}_1 = 1$. The MCCF can then be determined by (27), which for mode 1 is evaluated as

$$K_1^2 = \frac{\omega_1^2 - \hat{\omega}_1^2}{\omega_1^2} = 1 - \frac{\hat{\omega}_1^2}{\omega_1^2} \tag{36}$$

For the cantilever beam model in Fig. 1, the stability limit for the control gain g follows from the inequality in (22), which defines the stability limit by the inequality $k_g/k_{stab} < 1$, with the negative k_{stab} defined in (22). Table 1 gives the MCCF for different values of k_g/k_{stab}, ranging from 40% up to 80% of the stability limit. As the ratio $-K_1^2/\kappa_g \to 1$ in (27) when $1/R_s \to 0$, the increase relative to unity of $-K_1^2/\kappa_g$ in Table 1 describes the influence of including spill-over from residual modes in the tuning expression (33) for the time scale $\omega_1\tau$. Thus, as k_g approaches the stability limit k_{stab}, the ratio $-K_1^2/\kappa_g$ increases, whereby the optimal $\omega_1\tau$ reduces. Finally, the attainable damping ratio ζ_{max} associated with optimal tuning is derived by the explicit expression in (34). It is seen to increase significantly as $k_g/k_{stab} \to 1$.

k_g/k_{stab}	0.40	0.50	0.60	0.70	0.80
K_1^2	0.1052	0.1500	0.2093	0.2917	0.4140
$-K_1^2/\kappa_g$	1.3744	1.5671	1.8226	2.1775	2.7039
$\omega_1\tau$	0.7276	0.6381	0.5487	0.4592	0.3698
ζ_{max}	0.0278	0.0406	0.0586	0.0860	0.1328
ζ_{opt}	0.0284	0.0419	0.0615	0.0922	0.1471
$\max(\zeta)$	0.0286	0.0423	0.0623	0.0941	0.1532
$2\zeta_{max}\lvert q_{tip}^{max}\rvert/q_{tip}^0$	1.0180	1.0415	1.0753	1.1281	1.2231

Table 1: For vibration damping of mode $s = 1$: Modal control coupling factor (MCCF) K_1^2, MCCF relative to gain-stiffness ratio $-K_1^2/\kappa_g$, optimal time scale τ_{opt} and attainable damping ratios for different control gain ratios k_g/k_{stab}. The three mode 1 damping ratios are: The estimated maximum ζ_{max} from (34), the actual damping ratio ζ_{opt} for the optimal time scale in (33) and the actual maximum damping ratio $\max(\zeta)$ obtained by numerical search algorithm. The dynamic amplification of the beam tip displacement $|q_{tip}^{max}|/q_{tip}^0$ is normalized by the analytical result $1/(2\zeta_{max})$ for a single-mode structure.

5.2 ROOT LOCUS ANALYSIS

The actual attainable damping is found by performing a root locus analysis, in which the complex natural frequency ω is determined from $\tau = 0$ to ∞ in a complex plane diagram. The coupled equations (5) and (7) can, for H given in (19), be written in the state-space matrix form

$$(i\omega\mathbf{I} - \mathbf{A})\,\mathbf{z} = \mathbf{0} \tag{37}$$

for vanishing external loading and damping. The state-space vector $\mathbf{z} = [\,\mathbf{q}^T,\, i\omega\mathbf{q}^T, f_a\,]^T$ contains the control force f_a as an augmented variable, whereby the system matrix becomes

$$\mathbf{A} = \begin{bmatrix} \mathbf{O} & \mathbf{I} & \mathbf{0} \\ -\mathbf{M}^{-1}\mathbf{K} & \mathbf{O} & -\mathbf{M}^{-1}\mathbf{b} \\ (gk/\tau)\mathbf{b}^T & \mathbf{0}^T & -1/\tau \end{bmatrix} \tag{38}$$

with $\mathbf{O}$ and $\mathbf{I}$ being the zero and identity matrix, respectively.

Figure 4 shows the root loci, obtained by solving (37) for increasing values of τ and plotting the complex ω associated with the targeted mode $s = 1$. The five curves represent $k_g/k_{stab} =$

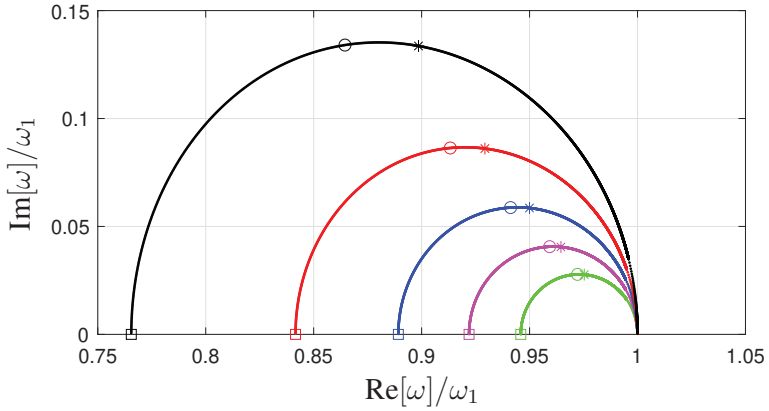

Figure 4: Root loci for $k_g/k_{stab} = 0.4$ (green), 0.5 (magenta), 0.6 (blue), 0.7 (red) and 0.8 (black). Markers represent ω for: τ_{opt} from (33) ($*$), actual optimum for $\max(\zeta)$ by numerical search ($\circ$) and $\hat{\omega}_1$ from (23) ($\square$).

0.4 (green), 0.5 (magenta), 0.6 (blue), 0.7 (red) and 0.8 (black), while the squares on the real axis represent $\hat{\omega}_1$ from (23), i.e. the natural frequency for $\tau \to 0$. The root loci in Fig. 4 are seemingly circular, with increasing diameter for increasing k_g/k_{stab}. The asterisks ($*$) represent the complex natural frequencies for the optimal tuning (τ_{opt}) derived in (33). The damping ratios for these optimal time scales are presented as ζ_{opt} in Table 1. They are seen to be slightly larger than the predicted ζ_{max} from (34). Furthermore, the circles ($\circ$) in Fig. 4 depict the complex roots associated with the actual maximum damping ratio, presented as $\max(\zeta)$ in Table 1. This maximum is simply chosen (by numerical search) as the complex root ω, along a given locus in Fig. 4, giving the largest damping ratio $\zeta = \text{Im}[\omega]/|\omega|$. For all practical purposes, the optimal time scale τ_{opt} results in damping ratios (ζ_{opt}, $*$) that are close to the actual maximum ($\max(\zeta)$, $\circ$). However, the explicit expression for ζ_{max} in (34) is only accurate up to moderate damping levels, while for the most aggressive cases with $k_g/k_{stab} = 0.70$ and 0.80 it underestimates the actual maximum by more than 10%.

5.3 FREQUENCY RESPONSE CURVES

The response mitigation performance of the PPF control can be investigated by a frequency response analysis, in which the external load vector $\mathbf{f}_{ext}$ is applied in the frequency domain equation (5). For the considered PPF control, it is convenient to utilize the previous state-space equation, from which the response vector can be directly determined as

$$\mathbf{z} = (i\omega\mathbf{I} - \mathbf{A})^{-1}\,\mathbf{f} \tag{39}$$

where the external load vector is directly constructed as $\mathbf{f} = [\,\mathbf{0}^T,\ (\mathbf{M}^{-\mathbf{1}}\mathbf{f}_{ext})^T\,, 0\,]^T$, in which $\mathbf{f}_{ext} = [\,0,\ 0,\ \ldots\ 0,\ f_{ext},\ 0\,]$ is an all-zero vector with f_{ext} in Fig. 1 added to the final node.

Figure 5(a) shows the tip deflection frequency amplitude q_{tip} divided by the corresponding static deflection with the piezoelectric actuator in SC conditions. As for the root locus analysis in Fig. 4, the five curves represent $k_g/k_{stab} = 0.4$ (green), 0.5 (magenta), 0.6 (blue), 0.7 (red)

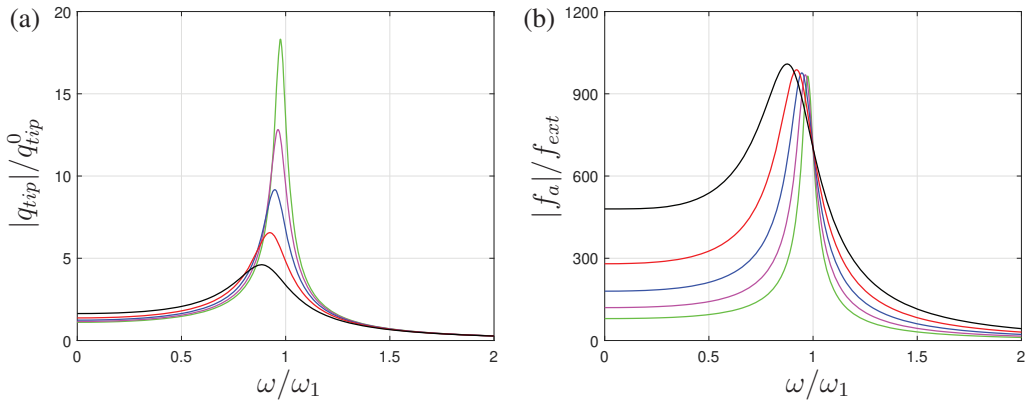

Figure 5: Frequency response curves for $k_g/k_{stab} = 0.4$ (green), 0.5 (magenta), 0.6 (blue), 0.7 (red) and 0.8 (black). (a) The dynamic amplification factor $|q_{tip}|/q^0_{tip}$ for the tip deflection, with q^0_{tip} being the static deflection obtained with short-circuited piezoelectric actuator. (b) The frequency amplitude of the piezoelectric actuator $|f_a|/f_{ext}$, normalized by the external force.

and 0.8 (black), and optimal τ from (33) or Table 1. It is seen that the resonance peak in Fig. 5(a) is reduced directly with the increased damping ratio obtained by k_g/k_{stab} approaching unity. In Table 1, the maximum value of the dynamic amplification curve $|q^{max}_{tip}|/q^0_{tip}$ in Fig. 5(a) is listed for each of the five cases. It is normalized by the theoretical estimate $1/(2\zeta_{max})$, whereby unity becomes a theoretical reference. For $k_g/k_{stab} = 0.4$ the ratio is close to unity, while for the aggressive control at $k_g/k_{stab} = 0.8$, the actual amplitude is 22% larger than the theoretical estimate. This shows that the attainable damping ratio from the PPF control can not be directly translated into a reduction in vibration amplitude, mainly because PPF control introduces apparent negative stiffness that alters the underlying mode shape used for modal expansion. The control effort of the patches is illustrated by the frequency curves for f_a in Fig. 5(b). It is seen that the improved response mitigation obtained by an increase in k_g/k_{stab} is not directly associated with a significant increase in peak control force. Instead, the operation by the PPF control yields a substantial increase in the low-frequency force limit, which explains the above-mentioned negative stiffness component.

6 CONCLUSIONS

Effective vibration mitigation of a cantilever beam is realized by active positive position feedback (PPF) control between a pair of piezoelectric patches. From the equivalent mechanical model of the closed-loop equations, the PPF control gain is found to directly govern the stability margin, while the filter time scale emerges as the obvious tuning control parameter, for which explicit design formulae are derived when introducing the modal control coupling factor (MCCF) to account for the spill-over from residual modes.

Acknowledgements

The results are obtained within the InTreCon project, supported by the Lundbeck Foundation.

REFERENCES

[1] J. L. Fanson and T. K. Caughey, "Positive position feedback control for large space structures," *AIAA Journal*, vol. 28, no. 4, pp. 717–724, 1990.

[2] S. Poh and A. Baz, "Active control of a flexible structure using a modal positive position feedback controller," *Journal of Intelligent Material Systems and Structures*, vol. 1, no. 3, pp. 273–288, 1990.

[3] A. Baz and J.-T. Hong, "Adaptive control of flexible structures using modal positive position feedback," *International Journal of Adaptive Control and Signal Processing*, vol. 11, no. 3, pp. 231–253, 1997.

[4] S. Hurlebaus and L. Gaul, "Smart structure dynamics," *Mechanical Systems and Signal Processing*, vol. 20, no. 2, pp. 255–281, 2006.

[5] Z.-C. Qiu, X.-M. Zhang, H.-X. Wu, and H.-H. Zhang, "Optimal placement and active vibration control for piezoelectric smart flexible cantilever plate," *Journal of Sound and Vibration*, vol. 301, no. 3-5, pp. 521–543, 2007.

[6] E. Omidi and N. Mahmoodi, "Hybrid positive feedback control for active vibration attenuation of flexible structures," *IEEE/ASME Transactions on Mechatronics*, vol. 20, no. 4, pp. 1790–1797, 2014.

[7] G. Zhao, A. Paknejad, G. Raze, A. Deraemaeker, G. Kerschen, and C. Collette, "Nonlinear positive position feedback control for mitigation of nonlinear vibrations," *Mechanical Systems and Signal Processing*, vol. 132, pp. 457–470, 2019.

[8] A. Preumont, *Vibration Control of Active Structures: An Introduction*. Springer, 2018.

[9] S. Krenk and J. Høgsberg, "Equal modal damping design for a family of resonant vibration control formats," *Journal of Vibration and Control*, vol. 19, no. 9, pp. 1294–1315, 2013.

[10] A. Paknejad, G. Zhao, M. Osée, A. Deraemaeker, F. Robert, and C. Collette, "A novel design of positive position feedback controller based on maximum damping and H_2 optimization," *Journal of Vibration and Control*, vol. 26, no. 15-16, pp. 1155–1164, 2020.

[11] J. R. Høgsberg and S. Krenk, "Linear control strategies for damping of flexible structures," *Journal of Sound and Vibration*, vol. 293, no. 1-2, pp. 59–77, 2006.

XI ECCOMAS Thematic Conference on Smart Structures and Materials - SMART 2025
M. Krommer, M. Nader and M. Schagerl (Eds)

Received: 31 March 2025 / Revised: 28 August 2025 / Accepted: 3 October 2025
© The Author(s) 2025

Band Gap Control and Vibration Attenuation in Periodic Piezoelectric Meta-Structures

Ali Hosseinkhani, Eduard Rohan

Abstract. Band gap frequency in periodic metamaterial structures is a well-known approach for noise and vibration attenuation. However, the common mechanisms for realizing band gaps, based on the Bragg scattering and the local resonance effect, cannot provide flexibility to change or tune band gaps according to the loading frequencies.
As a remedy to these limitations, we propose an extension of the conventional passive metamaterials by electroactive features provided due to integrated electroactive (piezoelectric) materials and external electrical circuits (EEC). These new design features bring more options for tuning band gaps and attenuating vibrations. Moreover, the EEC enables the introduction of non-local effects in the behavior of the continuum. In particular, the energy harvested due to the periodically distributed piezoelectric (PZ) sensors embedded in the metamaterial structure can be focused at distant "focal spots" to suppress the undesired vibrations. In this paper, we study how the band gap frequency ranges can be modified due to PZ segments embedded in the metamaterial periodic structure under the control using the EEC. Importantly, the proposed electroactive metamaterials are autonomous concerning the energy consumption, since only the harvested energy is used.
We consider examples of such electroactive metamaterials employed in the design of plate structures. The dispersion diagrams of the structures are evaluated, and the effects of the electrical circuit on band gap properties are examined. Vibration attenuation on the designed band gaps is investigated, and the results of the numerical simulations are compared to the analogous ones obtained for the band gap diagrams.

Key words: Periodic structure, piezoelectricity, external circuit, band gap, vibration attenuation.

Ali Hosseinkhani & Eduard Rohan
Department of Mechanics & NTIS New Technologies for Information Society, Faculty of Applied Sciences, University of West Bohemia in Pilsen, Univerzitni 22, 30100 Plzen, Czech Republic
e-mail: ahossein@kme.zcu.cz, Rohan@kme.zcu.cz

1 INTRODUCTION

Elastic wave propagation in solid media is an interesting and practical research area. Thanks to the emergence of metamaterials (MMs), control and manipulation of elastic waves have become feasible, and MMs open their path into several applications such as vibration and noise mitigation, high-quality imaging and sensing, high-efficient energy harvesting and etc. Anomalous wave propagation properties can be achieved from MMs for example directional wave propagation, cloaking, negative refraction, collimation, and topological state. In particular, all of these behaviors, attained from elastic passive MMs, work on some specific and rather narrow and fixed frequency bands, that may limit the performance of such MMs. Electroactive metamaterials (EMMs) present a new class of tunable multipurpose structures with the perspective to remove limitations of the passive MMs and provide active, tunable wave propagation control. The active control and manipulation of wave propagation is an on-demand topic in real-time applications [1-3].

Band gap (BG) frequency, a frequency range where no wave propagation exists, is an interesting feature in metamaterials that provide the condition for significant vibration attenuate. There are two mechanisms for creating BG frequency, named Bragg's scattering (BS) and local resonance (LR) [4,5]. The introduction of defects in the perfect structure of metamaterials induces some energy bands inside the band gap range. These band pass frequencies, which are due to the resonance of the defect, create a frequency passage for the propagating waves. Such an idea is able to concentrate energy into a local spot, which is very effective for the design of sensors, frequency filters, and energy harvesters. Employment of such a structure leads to the invention of multi-functional metamaterials with concurrent vibration attenuation and energy concentration. Yet, all of these properties are passive and mainly depend on the practical frequency ranges of BG and defect. Integration of electroactive materials into these structures provides the ability to tune their practical frequencies and remove the limitations due to passive properties [6,7].

Electroactive metastructures constituted as elastic structures with embedded electroactive components serving as the sensors and actuators open new options for the active control of elastic waves and bandgaps [8,9]. In this regard, an external electric circuit connected to such structures and involving tunable resistors, inductors, and capacitors, can modify the effective mechanical properties of the whole structure and, thus, provide an opportunity for adjusting bandgaps. Moreover, the electrical field can be applied through boundary conditions to tune the bandgap properties instead of changing the material or geometry of a heterogeneous structure [10,11]. The employment of piezoelectric materials also introduces modulate propagation and transmission of elastic waves in terms of frequency band and amplitude [12,13]. The active elements in metamaterial structures can be used to design varying density and bulk moduli over the space domain [14]. Piezoelectric phononic metamaterial also has been suggested for modulating mechanical properties and tuning bandgaps in various frequency ranges, particularly in the low-frequency range [15].

In this paper, we propose an electroactive meta-structure with dual objectives: (A) attenuating vibrational waves on the band gap frequencies (B) desining tunable vibrational filter at the resonance frequency of the electric circuit. The passive metamaterial functionalities are

enhanced by connecting electroactive elements to a periodic electric circuit. It is shown, that this electroactive metastructure provides the option to easily tune band gaps and pand passes to either stop or transmit vibrations through the structure.

This paper is organized as follows. In section 2, the structure of the metamaterial model is introduced, and the heterogeneous configurations are presented. The bandgap properties are evaluated in section 3. Then, the impacts of piezoelectricity as well as the external electric circuit on the band gap properties are examined, and the propagation of vibrational waves using the circuit is controlled (section 4). Finally, the conclusions are discussed.

2 METAMATERIAL MODEL

The metamaterial model includes a heterogeneous periodic structure made from a piezoelectric matrix interacting with inclusions as presented in Fig. 1. Two configurations are considered for the heterogeneity named (i) 2-phase configuration: constituted from soft inclusions embedded in the piezoelectric matrix and (ii) 3-phase configuration: rigid inclusions are connected to the matrix through elastic rings.

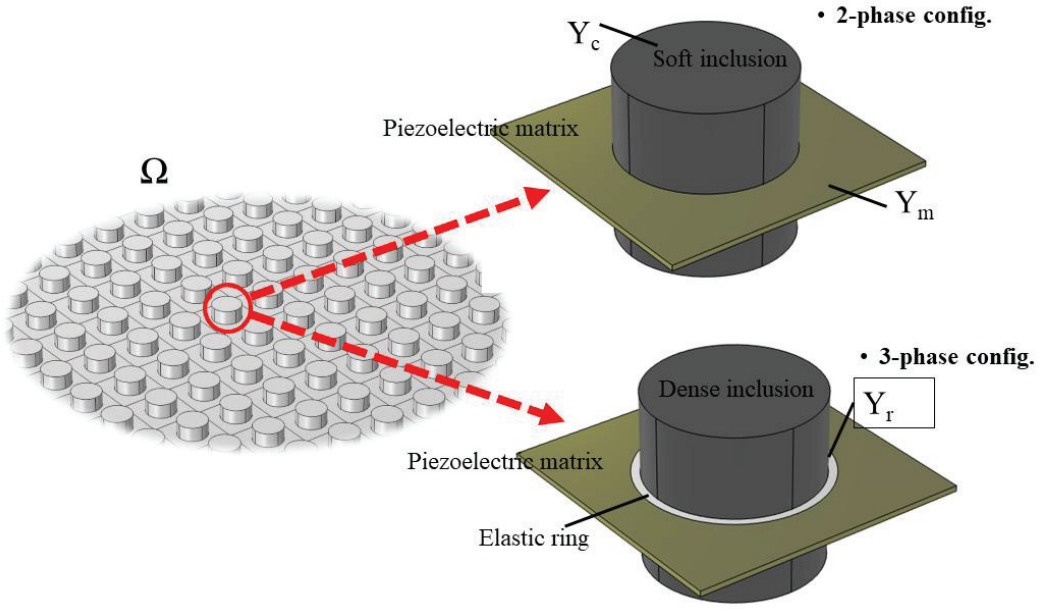

Figure 1: Illustration of the periodic structure and the configurations.

Here we refer to the solid domain as the domain related to inclusions or rings, and we refer to the piezoelectric domain as the domain related to the piezoelectric matrix. Hence, the constitutive laws for piezoelectric and solid domains respectively are:

$$\begin{cases} \boldsymbol{\sigma}(\boldsymbol{u},\phi) = \mathbb{A}\boldsymbol{e}(\boldsymbol{u}) - \boldsymbol{g}^T \cdot \boldsymbol{\nabla}\phi \ \ in \quad \Omega_m, \\ \boldsymbol{D}(\boldsymbol{u},\phi) = \boldsymbol{g} : \boldsymbol{e}(\boldsymbol{u}) + \boldsymbol{k}\boldsymbol{\nabla}\phi \ \ in \quad \Omega_m, \end{cases} \tag{1}$$

$$\boldsymbol{\sigma}(\boldsymbol{u}) = \mathbb{A}\boldsymbol{e}(\boldsymbol{u}) \ \ in \quad \Omega_r \ and \ \Omega_c,$$

where, $\mathbb{A}$ is the elasticity tensor, $\boldsymbol{g}$ is the piezoelectric coupling tensor, $\boldsymbol{g}^T$ is the transpose of $\boldsymbol{g}$, $\boldsymbol{k}$ is the dielectric tensor, and the electric field is the gradient of the electric potential ($\boldsymbol{E} = -\boldsymbol{\nabla}\phi$). Ω_m represents the domain of the piezoelectric medium while Ω_r and Ω_c present the domains of elastic rings and elastic inclusions, respectively. The elastic behavior of the solid domains is presented by the displacement vector $\boldsymbol{u}(\boldsymbol{r},\boldsymbol{t})$ as a function of position vector $\boldsymbol{r}$ and time, and the electro-elastic behavior of the piezoelectric domain is presented by the displacement vector $\boldsymbol{u}(\boldsymbol{r},\boldsymbol{t})$ and the electric potential $\phi(\boldsymbol{r},\boldsymbol{t})$. The equilibrium equations governing the electric and dynamic behavior of the domains are:

$$\begin{cases} \rho\ddot{\boldsymbol{u}} + \boldsymbol{\nabla}\cdot\boldsymbol{\sigma}(\boldsymbol{u},\phi) = \boldsymbol{f} \ \text{ in } \ \Omega \ , \\ -\nabla\cdot\boldsymbol{D}(\boldsymbol{u},\phi) = q \ \text{in} \ \ \Omega \ , \end{cases} \tag{2}$$

where, double dots ($\ddot{}$) stand for the double time derivatives, ρ is the density, $\boldsymbol{f}$ is the volume force and q is the volume charge. The related boundary conditions for Eq. (2) are:

$$\begin{cases} \boldsymbol{\sigma}\cdot\boldsymbol{n} = \boldsymbol{b}, \quad on \ \ \Gamma_\sigma \ , \qquad \boldsymbol{u} = \overline{\boldsymbol{u}} \quad on \ \ \Gamma_u, \\ \boldsymbol{D}\cdot\boldsymbol{n} = \dot{\eta}, \quad on \ \ \Gamma_D \ , \qquad \phi = \overline{\phi} \quad on \ \ \Gamma_\phi, \end{cases} \tag{3}$$

where, $\boldsymbol{b}$ is the prescribed load on the boundary of Γ_σ, $\overline{\boldsymbol{u}}$ is the prescribed displacement on Γ_u, $\dot{\eta}$ is the prescribed charge on Γ_D, $\overline{\phi}$ is the prescribed potential on Γ_ϕ, and $\boldsymbol{n}$ is the normal unit vector. The weak formulation governing the behavior of the system can be achieved from the equilibrium, constitutive, and boundary condition equations in the following form:

Find $(\boldsymbol{u},\phi) \in (\boldsymbol{V_0}(\Omega), \boldsymbol{\Phi_0}(\Omega))$ for all $(\boldsymbol{v},\psi)$ such that:

$$\begin{aligned} \omega^2 \int_\Omega \rho\boldsymbol{u}\cdot\boldsymbol{v} + \int_\Omega \boldsymbol{\sigma}(\boldsymbol{u},\phi) : \boldsymbol{e}(\boldsymbol{v}) &= \int_\Omega \boldsymbol{f}\cdot\boldsymbol{v} \ + \int_{\partial\Omega} (\boldsymbol{n}\cdot\boldsymbol{\sigma})\cdot\boldsymbol{v} \ dS + \int_{\Gamma_\sigma} \boldsymbol{b} \ . \ \boldsymbol{v} \ dS, \\ \int_{\Omega_m} \boldsymbol{D}(\boldsymbol{u},\phi)\cdot\boldsymbol{\nabla}\psi &= \int_\Omega q\psi \ + \sum_K \int_{\Gamma_K} \boldsymbol{D}\cdot\boldsymbol{n}\psi \ dS \ . \end{aligned} \tag{4}$$

3 BAND GAP PROPERTIES

In this section, the band gap diagram is evaluated and presented for the two introduced configurations, i.e., 2-phase and 3-phase configurations. Band gap diagrams are calculated based on Bloch's theory which is for infinite mediums. According to this theory, an infinite medium can be replaced by its representative unit cell, and the infinite situation is applied using periodic boundary conditions. The bandgap properties are calculated for one cell in frequency-wave space $(f, \boldsymbol{k})$, also known as reciprocal space, and the results will be expanded to the whole domain. Based on the theory, every variable can be written as a harmonic function:

$$\boldsymbol{u}(\boldsymbol{r},t) = \tilde{\boldsymbol{u}}(\boldsymbol{r})e^{i(\boldsymbol{k}\cdot\boldsymbol{r}-\omega t)} \tag{5}$$

where $\tilde{\boldsymbol{u}}(\boldsymbol{r})$ is a periodic function with the same periodicity length of the lattice, and $\boldsymbol{k} = \left(k_x, k_y\right)$ is the wave vector. The periodic boundary condition, known as Floquet-Bloch's periodic condition, is applied to the periodic function as:

$$\tilde{\boldsymbol{u}}(\boldsymbol{r} + L_0) = \tilde{\boldsymbol{u}}(\boldsymbol{r})e^{i\boldsymbol{k}L_0} \tag{6}$$

where L_0 is the lattice constant. The band gap diagram is evaluated based on this theory for one unit cell of each configuration. The corresponding Eigen-frequency analysis is solved for each problem by use of COMSOL Multiphysics software.

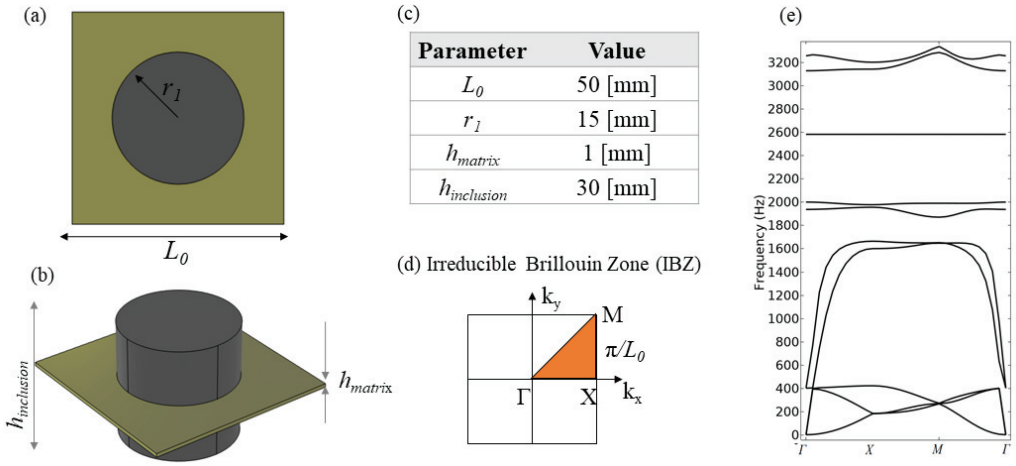

Figure 2: Two-phase configuration (a) top view, (b) 3D view, (c) geometrical parameters, (d) irreducible Brillouin zone, and (e) bandgap diagram.

The unit cell of two-phase configuration, hard-matrix with soft-inclusion, is illustrated in Fig. 2 in 2D and 3D views along with the geometrical parameters and the irreducible Brillion zone (IBZ). The corresponding band gap diagram is illustrated in Fig. 2 (e) over the frequency range of 0-3300 Hz. Three complete bandgaps exist on this frequency range which are from 1663-1936 Hz (1st BG), 1998-2580 Hz (2nd BG), and 2580-3127 Hz (3rd BG).

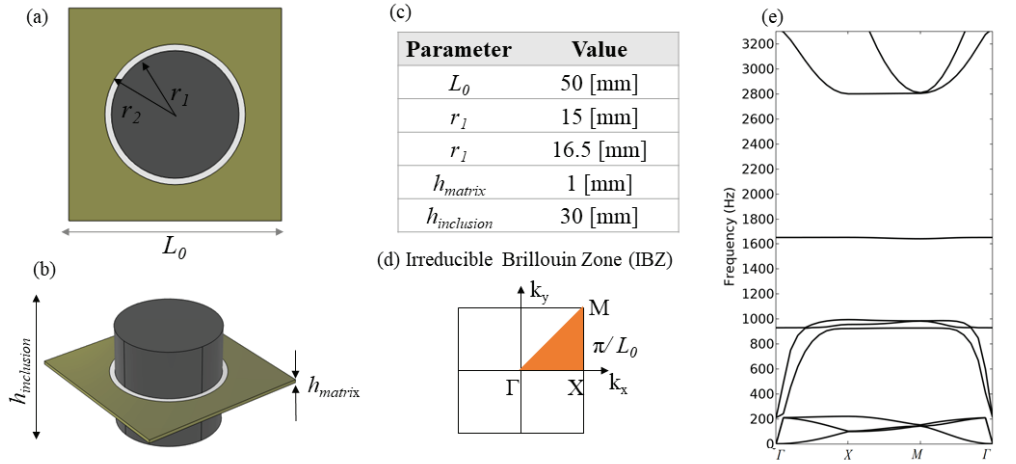

Figure 3: Three-phase configuration (a) top view, (b) 3D view, (c) geometrical parameters, (d) irreducible Brillouin zone, and (e) bandgap diagram.

For the 3-phase configuration, the geometry and parameters of the unit cell are presented in

Fig. 3. The Bandgap diagram is again calculated and plotted along the irreducible Brillouin zone in the figure. In this case, there are two complete band gaps over the frequency range of 0-3300 Hz which are: 993-1640 Hz (1st band gap) and 1651-2800 Hz (2nd band gap).

4 PIEZOELECTRICITY AND VIBRATION PROPAGATION

In this section, we investigate how the introduced structure can attenuate vibrations effectively on the band gap frequencies. Then, the impacts of piezoelectricity and the external electric circuit on the band gap frequencies are illustrated. Moreover, it is shown how the propagation of the vibrational wave is guided using a simple electric circuit.

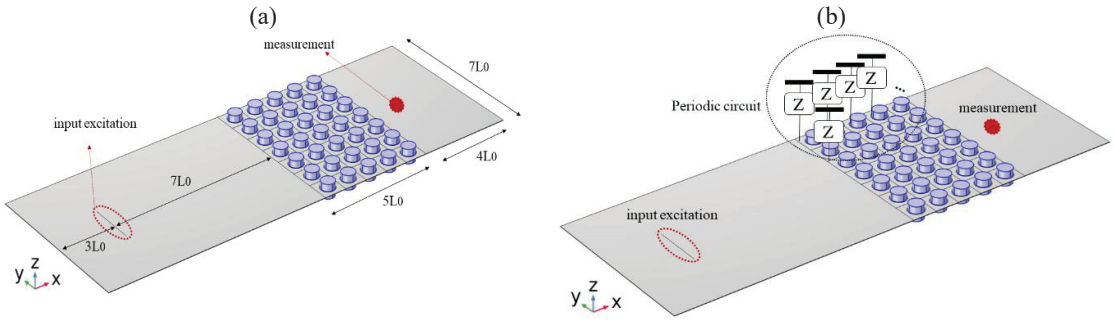

Figure 4: (a) meta-plate structure constructed from periodic unit-cell (b) illustration of the periodic circuit connected to the meta-plate.

To examine these aims, the two-dimensional plate consisting of a heterogeneous segment is used, named the "meta-plate". The heterogeneous segment of the meta-plates contains the 7*5 arrangement of primitive unit-cells including the periodic electric field. A prescribed displacement with the amplitude of 1e-6 [m] is taken as the input excitation and the result is measured on the measurement point. It is noted that the mechanical effect of the electrodes connected to the piezoelectric material is neglected since they are considered to be thin enough. To apply the effect of mechanical damping on the structure, an isotropic loss factor of 1% is considered for all materials.

4.1 Vibration attenuation

The vibration attenuation is investigated by defining the term Transmission (T) as follows

$$T(dB) = 20 \log_{10} \frac{Y_{obs}(f)}{Y_{excit}(f)} \tag{7}$$

while $Y_{obs}(f)$ and $Y_{excit}(f)$ are the frequency responses at the observation (measurement) and excitation points.

The transmission of vibration with respect to the frequency for each configuration (2-phase and 3-phase) is presented in Fig. 5 and the location of bandgaps is shown on the figure. We can

see that there is a significant drop of more than 80 dB on the band gap ranges. This means the vibrational wave is stopped by the phononic segment on the band gaps. The transmission curves show the frequency analysis closely confirms the respective band gap (BG) diagrams.

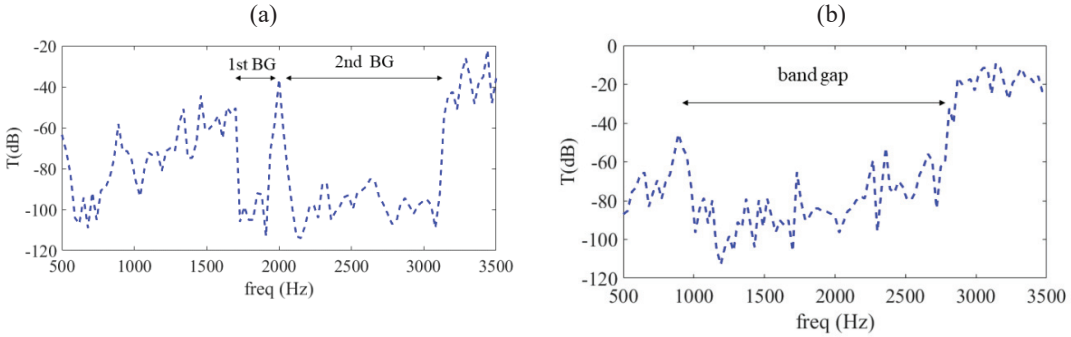

Figure 5: Diagrams of vibration transmission of (a) 2-phase configuration (b) 3-phase configuration.

4.2 Waveguiding by external circuit

In this section, it is shown how the electric circuit can be used to control the dynamic behavior of the system. At first, the effect of the piezoelectric matrix is investigated and compared with the case of the solid matrix. The constitutive law for piezoelectric materials is presented in equation (1). We can see that the coupling tensor g contributes to the system's mechanical properties and overall response. To investigate the impact of this feature on BG characteristics, we compare the BG diagrams of the UC with a pure-elastic matrix and the one with a piezo-elastic matrix. The BG diagram for the pure-elastic is obtained by setting the coupling tensor to zero (g = 0) in equation (1). Fig. 7(c) illustrates the effect of the coupling tensor on BG properties for the 2-phase configuration.

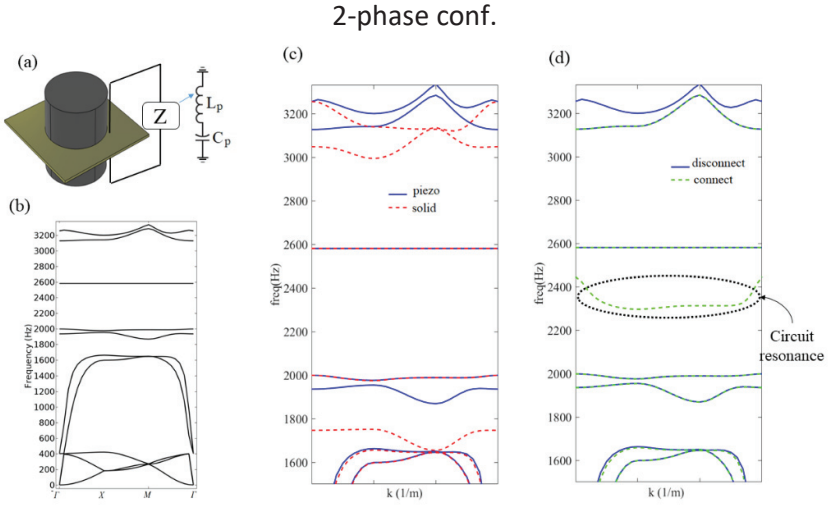

Figure 6: Band gap diagram of the 2-phase unit cell. (d) Comparison between solid matrix and piezoelectric matrix cases and (d) comparison between connected and disconnected circuits.

Secondly, the effect of connecting the piezoelectric matrix to the external electric circuit is investigated. An interesting feature enabled by the external circuit connected to the piezo-matrix is the introduction of a new resonance branch in the BG diagram. A simple circuit containing an inductor in series with the piezoelectric creates this branch. In Fig. 6 (d), the BG diagram for the piezo-matrix connected to this electrical circuit shows the resonance branch. This new tunable resonance branch offers potential applications in wave guiding, which is investigated in the meta-plate later in Fig. 8 for the case of 2-phase config.

In Fig. 7 (c), for the case of 3-phase conf., the impact of the piezoelectric matrix on the BG diagram is investigated and compared with the solid matrix. We can see that the first and second bandgaps are changed. In the case of the piezoelectric matrix, the branches are shifted to higher values, compared to the case of a solid matrix.

The impact of connecting the piezoelectric matrix to the external circuit is illustrated in Fig. 7 (d) for the 3-phase config. The presence of a new branch around the frequency of 1400 Hz can be seen, which is due to the resonance of the electric circuit.

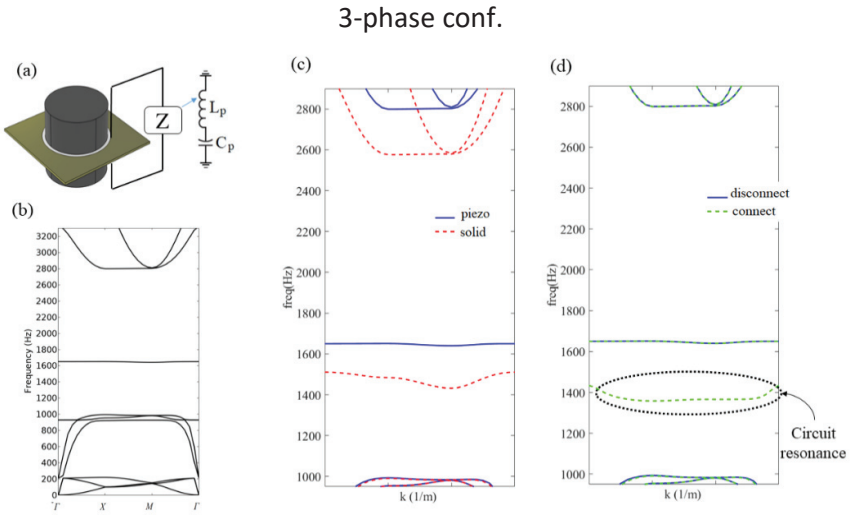

Figure 7: Band gap diagram of the 3-phase unit cell. (d) Comparison between solid matrix and piezoelectric matrix cases and (d) comparison between connected and disconnected circuits.

The electric circuit, known as the shunting circuit, is used to control the propagation of the vibrational wave through the metaplates. This feature is first investigated for the 2-phase metaplate. In Fig. 8 (a), the displacement response for the metaplate is plotted with respect to frequency when the circuit is connected and disconnected. The curve related to the case of the connected circuit shows there is a peak at the frequency of 2355 Hz compared to the case of the disconnected circuit. The surface displacement is plotted at 2355 Hz for the case of the disconnected circuit (Fig. 8 (b)) and for the case of the connected circuit (Fig. 8 (c)). The surface

displacement confirms that, if the circuit is connected, the vibrational wave is propagating through the metaplate at the resonance frequency of the circuit.

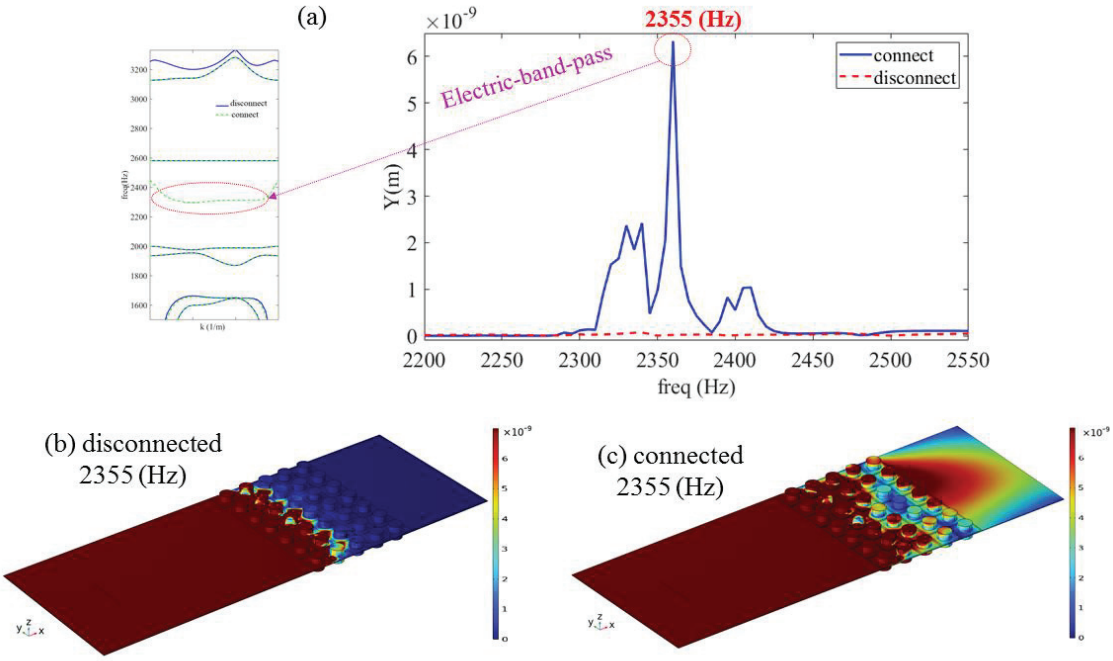

Figure 8: Vibrational waveguiding at the bandpass frequency due to the presence of the electrical circuit. (a) no wave propagation in the case of the disconnected circuit (b) wave propagation in the case of the connected circuit (c) a comparison between the dynamic response at the measurement point for the cases of connected and disconnected circuits (2-phase conf.)

A similar analysis is implemented for the metaplate with the 3-phase unit cell configuration. The frequency response at the measurement point is plotted when the circuit is disconnected and connected. The resonance frequency due to the presence of the electric circuit is 1250 Hz which leads to a peak in the frequency response of the metaplate connected to the periodic electric circuit. The surface displacement is illustrated for the cases of disconnected and connected circuits. It is seen that the vibrational wave propagates at this frequency when the circuit is connected while it completely stops once the circuit is disconnected.

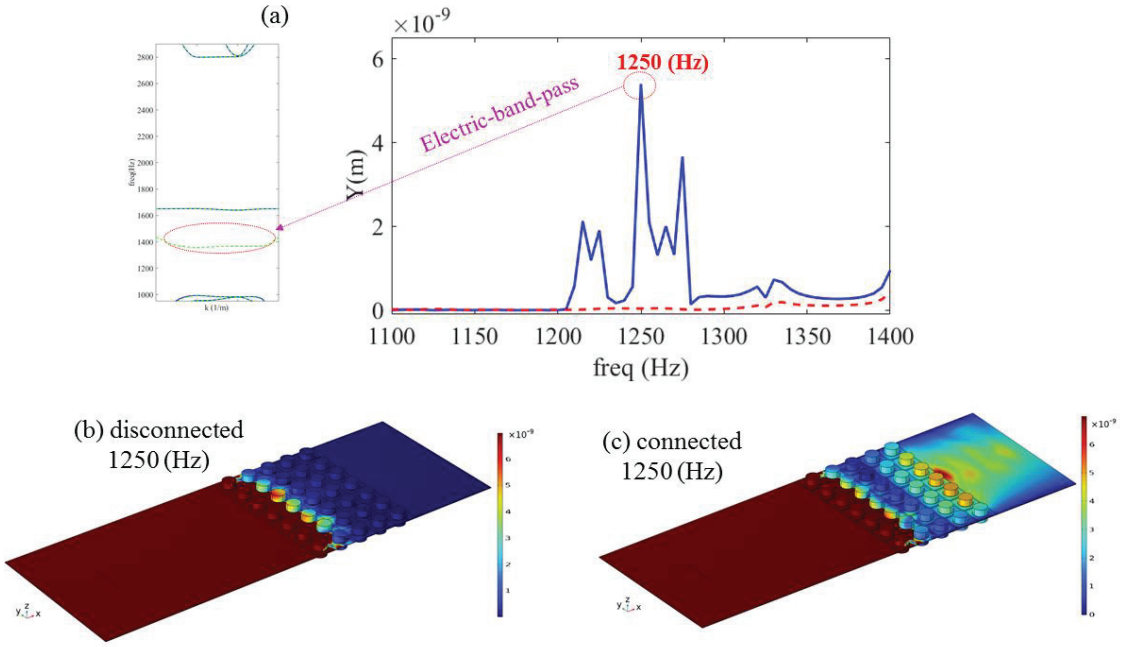

Figure 9: Vibrational waveguiding at the bandpass frequency due to the presence of the electrical circuit. (a) no wave propagation in the case of the disconnected circuit (b) wave propagation in the case of the connected circuit (c) a comparison between the dynamic response at the measurement point for the cases of connected and disconnected circuits (3-phase conf.)

5 CONCLUSIONS

In this paper, an extension to the conventional passive metamaterials was proposed by integrating them with piezoelectric materials. Connecting piezoelectric material to an external circuit provides more options for tuning band gaps and controlling vibrations. The impacts of the external circuit on BG features and vibration propagation were investigated in metaplate with 2-phase and 3-phase unit cell configurations.

It was observed that the presented configurations contain several band gaps over the frequency range of 0-3500 Hz, and effective vibration attenuation occurs on the bandgap frequencies. The presence of the external circuit creates a new branch in the bandgap diagram that is related to the resonance of the circuit. The frequency of this branch was tuned using the electrical properties, the impedance of the inductor in here, of the circuit while the frequency was tuned around 2355 Hz and 1250 Hz for the cases of 2-phase and 3-phase configurations, respectively. The resonance branch introduces a bandpass within the band gap frequency that allows the propagation of vibrational waves at the specific frequency. The presented electroactive metamaterial suggests several applications in designing frequency filters, sensors, and energy harvesting devices.

REFERENCES

[1] Wang, Y. F., Wang, Y. Z., Wu, B., Chen, W., & Wang, Y. S. (2020). Tunable and active phononic crystals and metamaterials. *Applied Mechanics Reviews*, *72*(4), 040801.

[2] Wu, B., Jiang, W., Jiang, J., Zhao, Z., Tang, Y., Zhou, W., & Chen, W. (2024). Wave manipulation in intelligent metamaterials: recent progress and prospects. *Advanced Functional Materials*, 34(29), 2316745.

[3] Hosseinkhani, A., & Rohan, E. (2024). Multi-functional periodically heterogeneous structures for energy harvesting and vibration attenuation-effects of piezoelectricity and shunting circuits. *Smart Materials and Structures*, *33*(11), 115009.

[4] Zeng, Y., Xu, Y., Yang, H., Muzamil, M., Xu, R., Deng, K., ... & Du, Q. (2020). A Matryoshka-like seismic metamaterial with wide band-gap characteristics. *International Journal of Solids and Structures*, 185, (pp. 334-341).

[5] Panahi, E., Hosseinkhani, A., Frangi, A., Younesian, D., & Zega, V. (2022). A novel low-frequency multi-bandgaps metaplate: Genetic algorithm based optimization and experimental validation. *Mechanical Systems and Signal Processing*, 181, 109495.

[6] Jo, S. H. (2024). Electrically controllable behaviors in defective phononic crystals with inductive-resistive circuits. International Journal of Mechanical Sciences, 278, 109485.

[7] Hosseinkhani, A., Ebrahimian, F., Younesian, D., & Moayedizadeh, A. (2022). Defected meta-lattice structures for the enhanced localized vibrational energy harvesting. *Nano Energy*, 100, 107488.

[8] Mansoura, S. A., Maréchal, P., Morvan, B., Hladky-Hennion, A. C., & Dubus, B. (2014). Active control of a piezoelectric phononic crystal using electrical impedance. In *2014 IEEE International Ultrasonics Symposium* (pp. 951-954). IEEE.

[9] Rohan, E., & Miara, B. (2007). Sensitivity analysis of acoustic wave propagation in strongly heterogeneous piezoelectric composite. In *Topics on Mathematics for Smart Systems* (pp. 193-207).

[10] Miao, Z., Li, J., Li, S., & Ma, Q. (2022). Complex band structure of 2D piezoelectric local resonant phononic crystal with finite out-of plane extension. *Applied Sciences*, *12*(14), 7021.

[11] Chen, S. B., Wen, J. H., Yu, D. L., Wang, G., & Wen, X. S. (2011). Band gap control of phononic beam with negative capacitance piezoelectric shunt. *Chinese Physics B*, 20(1), 014301.

[12] Ren, T., Li, F., Chen, Y., Liu, C., & Zhang, C. (2020). Improvement of the band-gap characteristics of active composite laminate metamaterial plates. *Composite Structures*, 254, 112831.

[13] Hsu, J. C. (2012). Switchable frequency gaps in piezoelectric phononic crystal slabs. *Japanese Journal of Applied Physics*, 51(7S), 07GA04.

[14] Akl, W., & Baz, A. (2013). Active acoustic metamaterial with simultaneously programmable density and bulk modulus. *Journal of Vibration and Acoustics*, 135(3), 031001.

[15] Bao, B., Guyomar, D., & Lallart, M. (2016). Electron–phonon metamaterial featuring nonlinear tri-interleaved piezoelectric topologies and its application in low-frequency vibration control. *Smart Materials and Structures*, 25(9), 095010.

XI ECCOMAS Thematic Conference on Smart Structures and Materials - SMART 2025
M. Krommer, M. Nader and M. Schagerl (Eds)

Received: 30 April 2025 / Revised: 31 August 2025 / Accepted: 3 October 2025
© The Author(s) 2025

Eigenfrequency Adaptivity of Locally Resonant Metamaterial Resonators using Piezoelectric Elements with Negative Capacitance Shunts

Stefan Janssen, Gabriel Konda Rodrigues, Leopoldo Pisanelli Rodrigues de Oliveira, Carlos De Marqui Jr., Claus Claeys, Elke Deckers

Abstract. Locally resonant metamaterials (LRMs) have shown exceptional noise and vibration reduction capabilities within targeted frequency ranges. By adding resonant elements onto a flexible host structure on a sub-wavelength scale, free wave propagation can be inhibited in a targeted frequency range, known as a stop band. However, these stop bands are fixed by design, limiting the applicability of LRMs for non-stationary noise and vibration problems. This work explores the addition of piezoelectric elements with negative capacitance shunts onto a beam-shaped resonator to tune the frequency of its first out-of-plane bending mode for application in an LRM context. A coupled electromechanical finite element (FE) model is constructed in COMSOL, with FE matrices exported to MATLAB and connected to negative capacitance shunts in parallel and series configurations. First, the modal electromechanical coupling is numerically calculated for different resonator beam dimensions and three configurations chosen for further study. Eigenfrequency adaptivity using negative capacitance shunts is predicted and experimentally validated. The results highlight the potential of integrating piezoelectric elements to achieve adaptivity in LRM resonators and emphasize the importance of considering the modal electromechanical coupling during the design phase.

Key words: Locally resonant metamaterials, piezoelectric elements, negative capacitance, noise and vibration reduction

Stefan Janssen & Elke Deckers
KU Leuven, Department of Mechanical Engineering, Campus Diepenbeek, Wetenschapspark 27, B-3590 Diepenbeek, Belgium, e-mail: stefan.janssen@kuleuven.be

Stefan Janssen & Claus Claeys & Elke Deckers
Flanders Make@KU Leuven

Gabriel Konda Rodrigues & Leopoldo Pisanelli Rodrigues de Oliveira
University of São Paulo, São Carlos School of Engineering, Department of Mechanical Engineering, 13566-590, São Carlos, Brazil

Carlos De Marqui Jr
University of São Paulo, São Carlos School of Engineering, Department of Aeronautical Engineering, 13566-590, São Carlos, Brazil

Claus Claeys
KU Leuven, Department of Mechanical Engineering, Celestijnenlaan 300, B-3001 Heverlee, Belgium

1 INTRODUCTION

The trend towards lightweight design has driven the search for innovative lightweight noise and vibration solutions, especially in the low-frequency range [1]. In this context, locally resonant metamaterials (LRMs) have emerged as a promising potential solution. By integrating or adding resonant elements onto a flexible host structure on a sub-wavelength scale, a stop band can be achieved [2]. In this stop band, elastic waves are prohibited from travelling freely throughout the host structure, therefore typically leading to a targeted frequency range of high noise and vibration reduction [3]. Despite their potential, conventional LRMs come with several drawbacks that limit their versatility. The stop band width is tied to the resonant mass added, which is constrained in lightweight designs, therefore typically resulting in a narrow stop band. Moreover, the stop band frequency is related to an eigenmode of the resonator which exerts a non-zero net force on the host structure. Once fabricated, the resonator's structural properties are fixed, making the LRM solution less effective for systems subject to dynamic changes in time or frequency, as commonly found in automotive, aerospace and industrial applications.

To overcome these limitations, research has increasingly focused on adaptive metamaterials [4]. Piezoelectric elements with synthetic inductance shunts have been explored for their ability to create tunable stop bands [5, 6]. By modifying the electrical impedance of the shunts, the resonance frequencies of piezoelectric elements can be shifted, allowing for adaptivity in the LRM solution. Integrating a negative capacitance element, typically in parallel or series with a shunt circuit, has been shown to enhance the electromechanical coupling of piezoelectric elements by modifying their effective behavior [7, 8]. The piezoelectric element then acts as an equivalent transducer with altered coupling and stiffness: a parallel configuration increases the open-circuit stiffness, while a series setup decreases the short-circuit stiffness [7]. Even without additional shunt components, this stiffness tuning offers a promising route to adaptive stop band behavior in otherwise purely mechanical LRMs through stiffness control [9, 10, 11]. While the principle of tunability via negative capacitance has been studied, previous research has not fully explored the optimal integration of piezoelectric elements onto elastic resonators for maximum adaptivity. Moreover, experimental realization and validation remains limited. In this study, a piezoelectric element is added to an established beam-shaped elastic resonator design [11, 12, 13, 14]. For a fixed piezoelectric element, modal electromechanical coupling for the first out-of-plane bending mode is numerically calculated across various resonator beam dimensions. From these results, three resonator configurations are selected and eigenfrequency adaptivity simulated for both series and parallel negative capacitance configurations. Finally, the resonators are fabricated and their adaptivity measured in an experimental campaign.

This paper is structured as follows: **Section 2** introduces the beam-shaped resonator. **Section 3** describes the modeling approach, including finite element analysis and negative capacitance implementation. **Section 4** presents the modal electromechanical coupling results, selection of three resonator designs and simulated eigenfrequency shifts. **Section 5** details the fabrication and experimental validation. Finally, **Section 6** summarizes the conclusions.

2 APPLICATION CASE: BEAM-SHAPED RESONATORS

The resonator under investigation is a beam-shaped resonator (Figure 1), commonly used in the context of locally resonant metamaterials (LRMs) [12, 13, 14, 11]. The first out-of-plane bending mode of this type of resonator is known to interact with and generate a stop band for acoustically-relevant bending waves traveling through host structures. For this study, a piezoelectric element (PZT-5J) with fixed dimensions is selected, as it is typically constrained by the manufacturer. In Section 4, two dimensions of the resonator, length (l_{beam}) and height (h_{beam}), are varied to achieve different modal electromechanical couplings for the first out-of-plane bending mode. Other resonator dimensions are provided in Table 1 and are chosen to ensure that the targeted mode remains within the low-frequency range across a wide range of l_{beam} and h_{beam} values and in view of later manufacturing through laser cutting. Polymethyl methacrylate (PMMA) is selected for the beam-shaped resonator with properties used from [14], while the properties of the piezoelectric element (PZT-5J) are used from the COMSOL Multiphysics® material library.

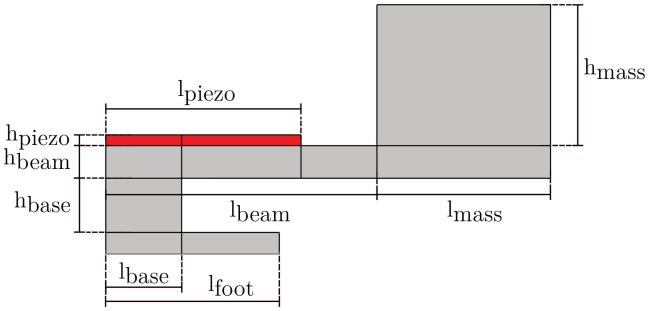

Figure 1: Beam-shaped resonator under study

3 METHODOLOGY

This section briefly outlines the modeling approach used to compute modal electromechanical coupling and predict eigenfrequency adaptivity, following the methodology in [11].

Table 1: Beam-shaped resonator dimensions in [mm].

l_{foot}	l_{base}	l_{beam}	l_{mass}	l_{piezo}	h_{foot}	h_{base}	h_{beam}	h_{mass}	h_{piezo}	w_r
16	7	$21.5-40$	20	21	2	5	$1-10$	20	0.55	6

3.1 Finite element modelling of resonators with piezoelectric patches

The beam-shaped resonator with piezolectric element of Section 2 is constructed and discretized using COMSOL Multiphysics® 6.1. After discretization, the coupled stiffness $\boldsymbol{K}$ and mass matrix $\boldsymbol{M}$ are exported with LiveLink™ for MATLAB®. Following the procedure of [11], the following system of equations is obtained:

$$\begin{bmatrix} \boldsymbol{M}_{uu} & \boldsymbol{0} \\ \boldsymbol{0} & 0 \end{bmatrix} \begin{Bmatrix} \ddot{\boldsymbol{u}} \\ \ddot{v}_p \end{Bmatrix} + \begin{bmatrix} \boldsymbol{H}_{uu} & \boldsymbol{H}_{uv_p} \\ -\boldsymbol{H}_{uv_p}^T & H_{v_pv_p} \end{bmatrix} \begin{Bmatrix} \boldsymbol{u} \\ v_p \end{Bmatrix} = \begin{Bmatrix} \boldsymbol{f} \\ q_p \end{Bmatrix}, \tag{1}$$

where $\boldsymbol{u}$ and $\boldsymbol{v_p}$ equal the displacement and piezoelectric voltage degrees-of-freedom (DOFs), $\boldsymbol{f}$ and q_p the nodal external forces and piezoelectric charge. $\boldsymbol{M}_{uu}$ contains the structural inertia of the structure, $\boldsymbol{H}_{uu}$ the structural stiffness, $\boldsymbol{H}_{uv_p}$ the piezoelectric coupling terms that link $\boldsymbol{u}$ to v_p and $\boldsymbol{H}_{v_pv_p}$ the capacitance at constant strain. From this set of equations, a lumped negative capacitance element can be connected by imposing a relation between v_p and q_p, further detailed in Section 3.3.

3.2 Modal electromechanical coupling evaluation

To explore how the geometry of the piezoelectric component influences the adaptivity of the chosen resonator type, a parametric analysis is carried out on a FE model to calculate the modal electromechanical (EM) coupling. This parameter captures the ratio of electrical energy stored in the piezoelectric elements to the total mechanical strain energy supplied to the structure when the structure is vibrating in a particular eigenmode [15]. The modal EM coupling for the first out-of-plane bending mode of the beam-shaped resonator is calculated through the difference in the eigenfrequencies with the piezoelectric element in open- and short-circuit conditions [16]:

$$EM = \sqrt{\frac{f_{OC}^2 - f_{SC}^2}{f_{SC}^2}} \times 100\%. \tag{2}$$

To this end, a clamped boundary condition is applied at the bottom surface of the resonator's foot and using the FE formulation from Section 3.1, both open- and short-circuit eigenfrequencies are calculated for different lengths and heights of the resonator beam. To identify the first out-of-plane bending mode, the modal effective mass in the out-of-plane direction is evaluated. The modal effective mass represents the portion of mass that effectively resonates within a specific eigenmode of the structure, which will differ from the total mass. Finally, the modal EM coupling is evaluated according to Eq. 2.

3.3 Negative capacitance implementation

The approach from [11] is used to connect a lumped negative capacitance element C_N, where $C_N < 0$, in either a series or parallel configuration (Figure 2 (a,b)). The effect of both configurations is a piezoelectric transducer with an equivalent capacitance and modified electromechanical coupling and stiffness characteristics (Figure 2 (c)). In the parallel configuration, the following set of equations is derived:

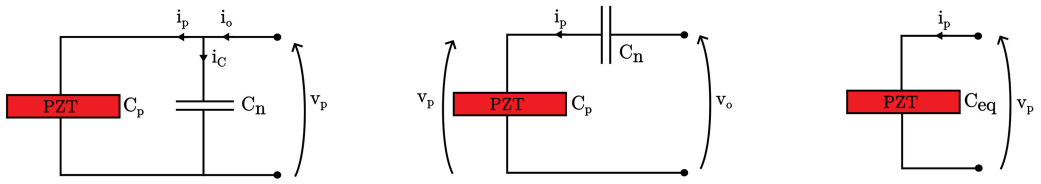

(a) Parallel (b) Series (c) Equivalent

Figure 2: Parallel (a) and Series (b) configurations of negative capacitance shunts. In both cases, the system can be reduced to a system with equivalent capacitance (c).

$$\begin{bmatrix} \boldsymbol{M}_{uu} & \boldsymbol{0} \\ \boldsymbol{0} & 0 \end{bmatrix} \begin{Bmatrix} \ddot{\boldsymbol{u}} \\ \ddot{v}_p \end{Bmatrix} + \begin{bmatrix} \boldsymbol{H}_{uu} & \boldsymbol{H}_{uv_p} \\ -\boldsymbol{H}_{uv_p}^T & H_{v_pv_p} + C_N \end{bmatrix} \begin{Bmatrix} \boldsymbol{u} \\ v_p \end{Bmatrix} = \begin{Bmatrix} \boldsymbol{f} \\ q_o \end{Bmatrix}, \tag{3}$$

while for the series configuration the following set is obtained:

$$\begin{bmatrix} \boldsymbol{M}_{uu} & \boldsymbol{0} \\ \boldsymbol{0} & 0 \end{bmatrix} \begin{Bmatrix} \ddot{\boldsymbol{u}} \\ \ddot{q}_p \end{Bmatrix} + \begin{bmatrix} \boldsymbol{H}_{uu} + \boldsymbol{H}_{uv_p} H_{v_pv_p}^{-1} \boldsymbol{H}_{uv_p}^T & \boldsymbol{H}_{uv_p} H_{v_pv_p}^{-1} \\ H_{v_pv_p}^{-1} \boldsymbol{H}_{uv_p}^T & H_{v_pv_p}^{-1} + C_N^{-1} \end{bmatrix} \begin{Bmatrix} \boldsymbol{u} \\ q_p \end{Bmatrix} = \begin{Bmatrix} \boldsymbol{f} \\ v_o \end{Bmatrix}. \tag{4}$$

Using these assembled mass and stiffness matrices, the eigenfrequencies of the coupled electromechanical system are then computed by solving the eigenvalue problem using the built-in *eigs* function in MATLAB.In the parallel configuration, this means $q_0 = i_0 = 0$ and in the series configuration $v_0 = 0$.

Negative capacitance stability

Since the equivalent capacitance (C_{eq}) of the piezoelectric element connected to a negative capacitance cannot be negative for practical stability reasons, several limits upon C_N are imposed [7]. In the parallel case, the equivalent capacitance is:

$$C_{eq} = C_p + C_N, \tag{5}$$

where C_p is the piezoelectric capacitance. Since $C_N < 0$, the magnitude of the negative capacitance element $|C_N|$ can therefore not be larger than the capacitance of the piezoelectric element C_p. For C_N connected in series, C_{eq} is:

$$C_{eq} = \frac{C_p C_N}{C_P + C_N}. \tag{6}$$

Again to ensure system stability, $|C_N|$ must in this case always be greater than C_p. The capacitance of the piezoelectric element is obtained in COMSOL Multiphysics® by applying a voltage (V) to the piezoelectric element and capturing the electric displacement on the top electrode surface (A) in the normal direction (D_Z):

$$C_P = \frac{1}{V} \int_A D_Z \, dA \tag{7}$$

4 RESONATOR EIGENFREQUENCY ADAPTIVITY SIMULATIONS

This section presents numerical results based on the methodology from Section 3. in Section 4.1 the modal EM coupling for various resonator beam dimensions are shown and three configurations selected. Section 4.2 then evaluates eigenfrequency adaptivity using negative capacitance shunts.

4.1 Modal EM coupling evaluation

The methodology from Section 3.2 is followed, varying the resonator beam length l_{beam} (Figure 1) from $21.5\,mm$, maintaining a minimum gap of $0.5\,mm$ with the piezoelectric element, up to $40\,mm$. The beam height h_{beam} is varied from $1\,mm$, the minimum allowed for laser cutting, up to $10\,mm$.

The resulting modal EM coupling for the first out-of-plane bending mode of the beam-shaped resonator is depicted in Figure 3a. A strong variation can be observed within the chosen parameter range. For a h_{beam} of $3\,mm$ and l_{beam} of $21.5\,mm$, the piezoelectric element is able to exert the most influence to the resonator under beam bending, as obvious from the highest modal EM-coupling. With these dimensions, the highest combination of elastic strain energy within the piezoelectric element and its ability to influence the dynamics of the host structure within the composite piezoelectric/PMMA beam section is observed. When h_{beam} increases or decreases from this optimal value, the piezoelectric element is less able to change the dynamics of this resonator and therefore also a lower eigenfrequency adaptivity with negative capacitance is expected [11]. Likewise, it is clear that a thicker piezoelectric element is not necessarily better to achieve a stronger influence on the dynamics of the resonator. Also, the non-linear and complex nature of the results presented in Figure 3a highlight the importance of performing this analysis before the design of the electromechanical resonator.

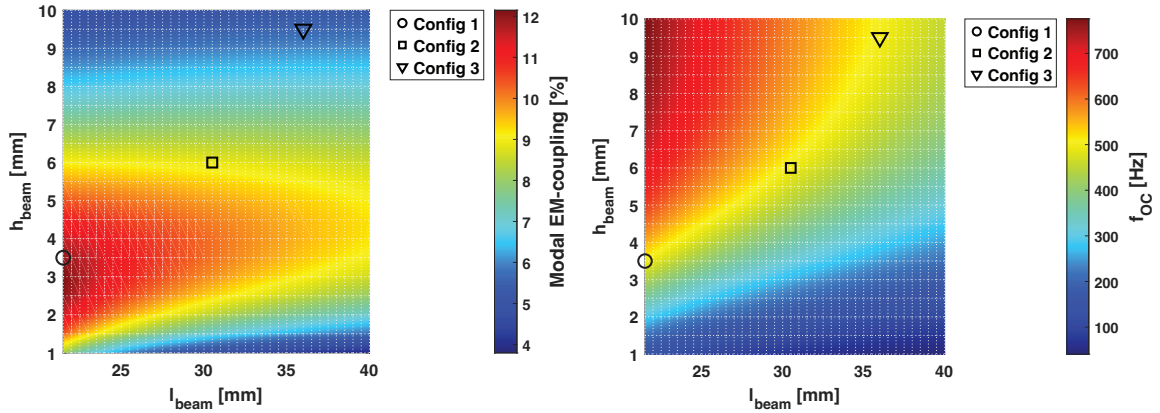

(a) Modal EM-coupling (b) Open-circuit eigenfrequency

Figure 3: Results of parametric study with configurations 1, 2 and 3 marked

Table 2: Parameters of the three selected configurations

Config	$l_{beam}\,[mm]$	$h_{beam}\,[mm]$	$EM\,[\%]$	$f_{OC}\,[Hz]$
1	21.5	3.5	12.0	499.6
2	30.5	6.0	8.90	496.6
3	36.0	9.5	5.65	500.4

Additionally, the open-circuit eigenfrequency of the first out-of-plane bending mode f_{OC} of the resonator is captured and displayed in Figure 3b. To properly compare the effects of the modal EM-coupling to the frequency adaptivity with negative capacitance shunts, three configurations with different modal EM-coupling, however approximately the same f_{OC} are chosen, marked as Config 1, 2 and 3. The dimensions and properties of these configurations are summarized in Table 2.

4.2 Eigenfrequency adaptivity simulations

Using the methodology outlined in Sections 3.1 and 3.3, lumped negative capacitance elements are connected to the piezoelectric element of the three selected configurations in both parallel and series. For the parallel case, as described in Eq. 5, the negative capacitance C_N can be varied from $C_N = 0$ to $C_N = -C_p$, which represents the theoretical stability limit. In the series configuration (Eq. 6), C_N can theoretically range from $C_N = -\infty$ to $C_N = -C_p$, again reaching the same stability limit. In the series case, C_N is varied from $-2C_P$ to $-1C_p$. A step size of $0.01C_N/C_P$ is chosen for both series and parallel simulations.

The results are shown in Figure 4. In both the series and parallel configurations, configuration 1, with the highest modal EM-coupling, exhibits the strongest eigenfrequency adaptivity. Adaptivity increases exponentially as the negative capacitance approaches the theoretical stability limits for all three configurations. However, the greater the modal EM-coupling, the stronger the adaptivity effect, also at points further from the stability limits. This suggests that for practical applications, a high modal EM-coupling is essential.

5 EXPERIMENTAL VALIDATION OF EIGENFREQUENCY ADAPTIVITY

This section first describes the manufacturing of the beam-shaped resonators with integrated piezoelectric elements and the practical implementation of the negative capacitance circuits. Section 5.2 outlines the experimental test setup and Section 5.3 presents the measurements.

5.1 Resonators and negative capacitance circuit realization

The beam-shaped resonators (Config 1, 2 & 3) were fabricated by laser cutting PMMA panels using a Trotec Speedy 100R laser cutter. Piezoelectric plates (PZT-5J, *SMPL21W21T05410*) with dimensions $21 \times 21 \times 0.55\,\mathrm{mm}$ were cut to size using waterjetcutting. Thin copper tape was soldered to the bottom electrodes of the piezoelectric elements using a reflow oven and the

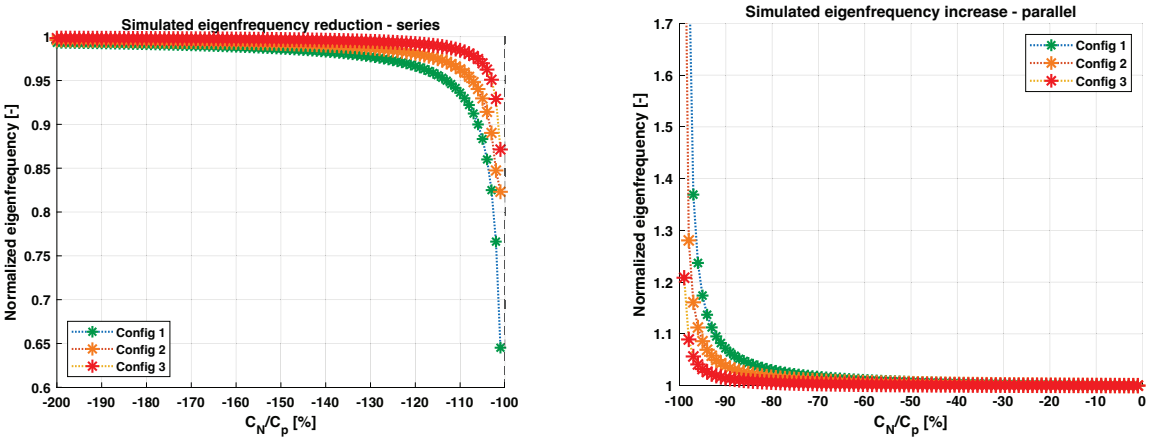

(a) Series C_N (b) Parallel C_N

Figure 4: Eigenfrequency decrease (4a) and increase (4b) adaptivity simulations of configurations 1, 2 & 3

piezoelectric elements were bonded to the PMMA resonator beams with 3M DP460 glue. To ensure good adhesion, custom supports were 3D-printed and a clamp was used to apply pressure for a minimum of six hours. Finally, copper wires were soldered to the top electrodes and to the copper tape to establish electrical connections with the bottom electrodes. The realized resonators are shown in Figure 5.

To implement negative capacitance shunts in practice, active circuits are required. In this work, the circuits from [10] are realized and shown in Figures 6a & 6b for parallel and series configurations, respectively. By using a potentiometer for resistor R_1, the value of the negative capacitance can be tuned according to $C_N = -CR_1/R_2$. Component values for R_1 ($5k\,\Omega$), R_2 ($10k\,\Omega$) and C ($100\,nF$) were chosen to provide sufficient resolution in C_N when adjusting R_1. Also a test was performed with $C = 50\,nF$, however the results yielded equivalent performance. Resistor R_s was experimentally chosen with a potentiometer to provide a small amount of damping and stabilize the circuit in the parallel configuration, while R_p in the series case was chosen high to achieve a high pass filter and stop low frequency signals that can cause bias-current and offset-voltage errors [8]. In both circuits, an operational amplifier of type OP-551 was used.

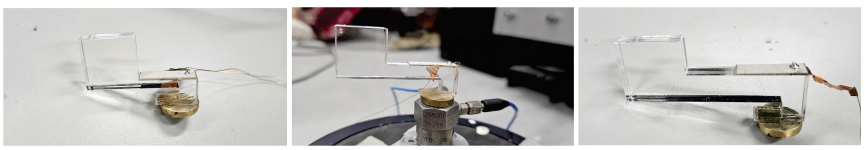

1 2 3

Figure 5: The manufactured beam-shaped resonators (Config 1, 2 and 3)

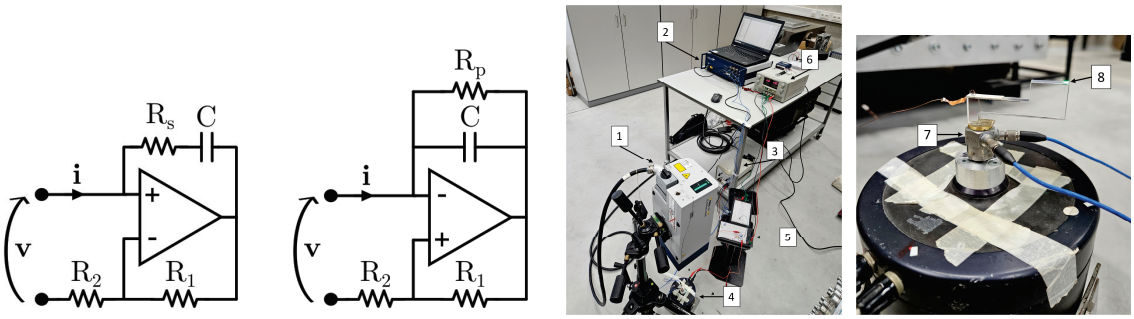

(a) Parallel C_N (b) Series C_N (c) Test set-up (d) Resonator close-up

Figure 6: Schematics of the negative capacitance shunts (a–b) and the experimental test set-up (c–d) used for validating eigenfrequency adaptivity.

5.2 Test set-up

An overview of the experimental set-up is provided in Figures 6c & 6d. The resonators were excited by an electrodynamic shaker (4), driven by a white noise signal up to 1 kHz. A 0.1 V input signal was amplified using a power amplifier (3). The resulting input force of about 200 mN RMS and acceleration were measured with an impedance sensor (7). The tip velocity of the resonator (8) was measured using a Polytec PSV Qtec laser vibrometer (1) and captured with a data acquisition system (2), averaging over 10 measurements. The negative capacitance circuit and the power supply are depicted in (5) and (6), respectively. Frequency response functions (FRFs) of the tip velocity over the input force were measured and recorded for various levels of negative capacitance.

5.3 Experimental validation results

Prior to each test with series and parallel negative capacitance shunts, the capacitance of the piezoelectric elements was measured using a B&K 878B handheld LCR meter. These values fluctuated slightly across configurations and tests, ranging from 4.03 to $4.28\,\mathrm{nF}$. During the experiments, R_1 was gradually adapted to vary the negative capacitance C_N until the system reached instability. At each step, the eigenfrequency of the first out-of-plane bending mode and the corresponding value of C_N were recorded. As the system approaches the theoretical stability limits, the FRFs become increasingly noisy. This behavior is attributed to the voltage and current limitations of the operational amplifiers in the negative capacitance circuits. The onset of instability was defined as the point where the eigenfrequency no longer increased (parallel case) or decreased (series case), indicating circuit saturation and dynamic instability.

The measured open-circuit eigenfrequencies of the manufactured resonators were close to the targeted $500\,Hz$, however not exact. These discrepancies arise due to several factors, i.e. damping is not included in the simulations, small variations in the lasercut geometry, waterjet-cutting of the piezoelectric elements and thickness of the adhesive. To reduce the impact of

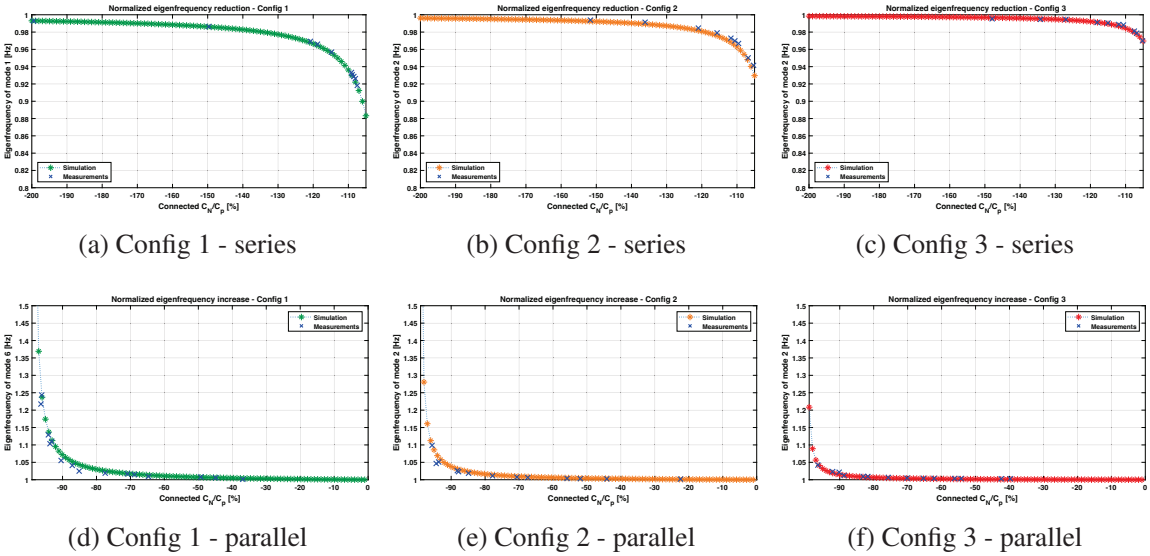

(a) Config 1 - series (b) Config 2 - series (c) Config 3 - series

(d) Config 1 - parallel (e) Config 2 - parallel (f) Config 3 - parallel

Figure 7: Normalized eigenfrequency shift for each configuration comparing simulations and experiments: series (top row) and parallel (bottom row) negative capacitance

this variability and enable a clearer comparison, both experimental and simulation results were normalized with respect to f_{OC} and f_{SC} for the parallel and series configurations, respectively. Figure 7 presents the normalized change in eigenfrequency as a function of C_N, demonstrating excellent agreement between the two. This close match validates both the simulation approach and the practical implementation of the negative capacitance shunting strategy. The maximum experimentally achieved eigenfrequency shifts are summarized in Table 3. As the resonator was removed and remounted between the series and parallel measurements, slight differences occurred in the open- and short-circuit frequencies. Nevertheless, considering the shift relative to f_{SC} in the series case and to f_{OC} in the parallel case, Config 1 showed the best performance, with a maximum reduction of $-8.8\,\%$ and an increase of $24\,\%$, clearly outperforming Configs 2 and 3.

Table 3: Maximum experimentally achieved frequency shifts (Δ) for all configurations.

Config	**Series**					**Parallel**				
	f_{SC} $[Hz]$	f_{OC} $[Hz]$	$\frac{C_N}{C_p}$ max $[\%]$	f_{min} $[Hz]$	$\Delta_{\downarrow}$ $[\%]$	f_{SC} $[Hz]$	f_{OC} $[Hz]$	$\frac{C_N}{C_p}$ max $[\%]$	f_{max} $[Hz]$	$\Delta_{\uparrow}$ $[\%]$
1	477.8	481.3	-107.5	439.1	-8.8	477.8	481.3	-96.1	596.9	$+24.0$
2	507.8	509.8	-105.3	478.1	-6.2	502.2	503.8	-95.6	553.1	$+9.8$
3	529.7	530.3	-105.2	514.1	-3.0	535.6	535.9	-96.4	558.1	$+4.1$

6 CONCLUSIONS

This study presented a comprehensive investigation into the eigenfrequency adaptivity of beam-shaped elastic resonators enhanced with surface-bonded piezoelectric elements connected to negative capacitance shunts. A multi-physical finite element framework was used to systematically explore how variations in beam length and height affect the modal electromechanical (EM) coupling of the first out-of-plane bending mode, which is relevant for stop band creation in metamaterials. Results showed a nonlinear and complex dependence of the modal EM coupling on these parameters, underscoring its importance in resonator design. Three resonator configurations with similar open-circuit eigenfrequencies but varying EM coupling were selected. Simulations demonstrated that stronger EM coupling leads to larger eigenfrequency shifts under both series and parallel negative capacitance shunts. In an experimental campaign, these findings were validated. While absolute eigenfrequencies differed slightly due to fabrication tolerances, normalized results showed excellent agreement with simulations, confirming the accuracy and robustness of the modeling approach. The results highlight the critical role of EM coupling in achieving effective adaptivity. These findings provide a solid foundation for achieving adaptivitity in LRM resonators, enabling noise and vibration control across a broader frequency range. Future research will extend the approach to full metamaterial structures, targeting practical implementation of tunable stop bands for real-world applications.

ACKNOWLEDGMENTS

The research of S. Janssen (fellowship no. 1SHCW24N) is funded by the Research Foundation Flanders (FWO). The Research Foundation Flanders (FWO) and São Paulo Research Foundation - Brazil (FAPESP) are gratefully acknowledged for their support through the bilateral research cooperation project (FWO no. G0F9922N, FAPESP no. 21/05510-3). The authors gratefully acknowledge the São Paulo Research Foundation (FAPESP) (grant no. 2023/00687-8 and 2021/09473-5) and the Research Fund KU Leuven for their support.

REFERENCES

[1] M. I. Hussein, M. J. Leamy, and M. Ruzzene, "Dynamics of phononic materials and structures: Historical origins, recent progress, and future outlook," *Applied Mechanics Reviews*, vol. 66, no. 4, jul 2014.

[2] Z. Liu, X. Zhang, Y. Mao, Y. Y. Zhu, Z. Yang, C. T. Chan, and P. Sheng, "Locally resonant sonic materials," *Science*, vol. 289, no. 5485, pp. 1734–1736, 2000.

[3] C. C. Claeys, K. Vergote, P. Sas, and W. Desmet, "On the potential of tuned resonators to obtain low-frequency vibrational stop bands in periodic panels," *Journal of Sound and Vibration*, vol. 332, no. 6, pp. 1418–1436, 2013.

[4] G. Ji and J. Huber, "Recent progress in acoustic metamaterials and active piezoelectric acoustic metamaterials - A review," *Applied Materials Today*, vol. 26, p. 101260, 2022.

[5] G. K. Rodrigues, M. M. D. Silva, and L. P. D. Oliveira, "Modular modeling approach for fdm printed structures and piezo disks for metamaterial design," *Latin American Journal of Solids and Structures*, vol. 16, 7 2019.

[6] J. A. Mosquera-Sánchez and C. D. Marqui, "Dynamics and wave propagation in nonlinear piezoelectric metastructures," *Nonlinear Dynamics*, vol. 105, pp. 2995–3023, 9 2021.

[7] B. De Marneffe and A. Preumont, "Vibration damping with negative capacitance shunts: theory and experiment," *Smart Materials and Structures*, vol. 17, no. 3, p. 035015, 2008.

[8] M. Berardengo, O. Thomas, C. Giraud-Audine, and S. Manzoni, "Improved resistive shunt by means of negative capacitance: new circuit, performances and multi-mode control," *Smart Materials and Structures*, vol. 25, p. 075033, 6 2016.

[9] Y. Y. Chen, G. L. Huang, and C. T. Sun, "Band Gap Control in an Active Elastic Metamaterial With Negative Capacitance Piezoelectric Shunting," *Journal of Vibration and Acoustics*, vol. 136, no. 6, 2014.

[10] R. Zhu, Y. Y. Chen, M. V. Barnhart, G. K. Hu, C. T. Sun, and G. L. Huang, "Experimental study of an adaptive elastic metamaterial controlled by electric circuits," *Applied Physics Letters*, vol. 108, no. 1, p. 11905, 2016.

[11] S. Janssen, C. S. Schimidt, L. P. R. De Oliveira, C. De Marqui Junior, C. Claeys, and E. Deckers, "On the stop band adaptivity range of locally resonant metamaterial resonators with piezoelectric patches: a case study," *Proceedings of the International Conference on Noise and Vibration Engineering (ISMA) / International Conference on Uncertainty in Structural Dynamics (USD) 2024*, 2024-09-11.

[12] C. Claeys, N. G. Rocha de Melo Filho, L. Van Belle, E. Deckers, and W. Desmet, "Design and validation of metamaterials for multiple structural stop bands in waveguides," *Extreme Mechanics Letters*, vol. 12, pp. 7–22, 2017.

[13] S. Janssen, L. Van Belle, N. G. R. de Melo Filho, W. Desmet, C. Claeys, and E. Deckers, "Improving the noise insulation performance of vibro-acoustic metamaterial panels through multi-resonant design," *Applied Acoustics*, vol. 213, p. 109622, 2023.

[14] L. Van Belle, N. G. Rocha de Melo Filho, M. Clasing Villanueva, C. Claeys, E. Deckers, F. Naets, and W. Desmet, "Fast metamaterial design optimization using reduced order unit cell modeling," *Proceedings of ISMA 2020*, 2020.

[15] M. A. Trindade and A. Benjeddou, "Effective electromechanical coupling coefficients of piezoelectric adaptive structures: Critical evaluation and optimization," *Mechanics of Advanced Materials and Structures*, vol. 16, no. 3, pp. 210–223, 2009.

[16] O. Thomas, J. Ducarne, and J. F. Deü, "Performance of piezoelectric shunts for vibration reduction," *Smart Materials and Structures*, vol. 21, p. 015008, 12 2011.

XI ECCOMAS Thematic Conference on Smart Structures and Materials - SMART 2025
M. Krommer, M. Nader and M. Schagerl (Eds)

Received: 23 April 2025 / Revised: 28 August 2025 / Accepted: 3 October 2025
© The Author(s) 2025

Piezoelectric Patch with Self-Tuning Analogue Shunt Circuit for Vibration Control

Gabriel Konda Rodrigues, Leopoldo Pisanelli Rodrigues de Oliveira, Paolo Gardonio

Abstract. This paper is focused on the design and real-time implementation of a vibration control unit formed by an analogue self-tuning RL-shunt connected to a piezoelectric patch, which can be bonded in batches on thin structures to control the resonant responses of target flexural modes. The tuning is implemented in such a way as the inductance is set to maximise the electric power absorption by the shunt in a given frequency band centered at the resonance frequency of a target flexural mode of the hosting structure. This corresponds to maximising the vibration energy absorption, and thus to reducing the resonant response, of the target flexural mode. The shunt circuit is implemented on a PC-board encompassing a synthetic inductor which is optically coupled to a self-tuning analogue circuit that implements an extremum seeking algorithm to maximise the electric power absorption by the shunt circuit. The paper discusses the vibration control performance produced by multiple shunted patches tuned to control a single or three resonant responses of a thin plate model structure.

Key words: shunted piezoelectric patch, tunable vibration absorber, extremum seeking.

1 INTRODUCTION

Since 1979 when Forward [1] first proposed to use electrically shunted piezoelectric patches to control the vibration of an optical system, many authors have investigated the application of shunted piezoelectric transducers for vibration control of single [2-12] and multiple [13-17] resonant responses of hosting flexible structures. In presence of intrinsic (due to production and installation) and operational (due to temperature and tensioning effects) variations, the implementation of an adaptive shunt is mandatory to have robust smart structures that generate significant vibration control effects [18-22]. In the past, few self-tuning strategies of shunted piezoelectric patches were proposed in the literature [23-26], which, nevertheless, are based on solutions requiring additional monitor sensors. This is particularly critical for hosting structures characterised by complex vibration fields, which can be detected only by distributed transducers or arrays of point sensors [27,28]. Hence, the implementation of a model-free self-tuning system providing a robust adaptation of the shunt parameters without the need of additional sensors would be a desirable solution. In this context, Gardonio *et al*. [29-31] proposed to tune the

Gabriel Konda Rodrigues & Leopoldo De Oliveira
Department of Mechanical Engineering, São Carlos School of Engineering, University of São Paulo, Av. Trabalhador Sancarlense, 400, 13566-590 São Carlos (SP), Brazil,
e-mail: gabriel.konda.rodrigues@usp.br, leopro@sc.usp.br

Paolo Gardonio
Dipartimento Politecnico di Ingegneria e Architettura, Universita degli Studi di Udine, Via delle Scienze 206, 33100 Udine, Italy, e-mail: paolo.gardonio@uniud.it

components of the shunt in such a way as the shunted piezoelectric patch maximises the vibration absorption from the hosting structure. More specifically, they suggested to maximise the time-averaged electric power absorbed by the shunt such that the response of target resonating modes of the structure would be minimised. They showed that the optimal resistance and inductance that maximise this cost function would minimise the total vibration response of the hosting structure due to the target resonant mode. In brief, the local electric power cost function would lead to the minimisation of the response of the hosting structure without the need of extra sensors that detect the actual vibration response of the hosting structure.

This paper presents an experimental study on the design and implementation of a modular piezoelectric patch vibration absorber encompassing an analogue self-tuning shunt, which can be bonded in batches on a flexible structure to control the resonant responses of target low order flexural modes. The self-tuning shunt is composed by shunt and tuning Printed Circuit Boards (PCB), which are optically coupled via a Light Dependent Resistor (LDR) and a Light Emitting Diode (LED). The shunt PCB encompasses a fixed resistor and, in series, a synthetic inductor whose value is controlled by the LDR. The tuning PCB implements an extremum seeking control algorithm that adjust the shunt inductor via the LED in such a way as to maximise the electric power absorption by the shunt itself. The study considers a thin plate model structure equipped with five piezoelectric patches connected to the analogue self-tuning RL shunts, which are set to control the resonant response of the first three flexural modes of the structure. The study is organized into 4 Sections. To start with, Section 2 describes the self-tuning shunted piezoelectric patch vibration absorbers. Then, Section 3 presents experimental results on the online control of the resonant response of a single or multiple flexural modes of the plate structure. Finally, Section 5 summarises the principal conclusions of the paper.

2 PLATE WITH FIVE SELF-TUNING UNITS

Figure 1 shows the plate model structure, which is equipped with 5 shunted Macro Fiber Composite (MFC) piezoelectric patches. As highlighted in Figure 2a, each patch is connected to a series RL shunt with fixed resistance and variable inductance. As shown in [30,31], the tuning of the resistance is less critical and thus was fixed upfront. The inductance was synthesised by the active circuit depicted in Figure 2b, which is based on the gyrator principle, commonly known as Antoniou's inductance [9,32]. The shunt inductance was tuned online with a controller that adapts its value in such a way as to maximise the electric power absorption by the shunt [30,31]. As shown in Figure 1, the plate was fixed to a rigid frame structure and it was excited in bending by a transverse force exerted by a shaker. Also, the plate was equipped with a 3×3 grid of accelerometers to detect online its overall flexural vibration up to 150 Hz.

As shown in Figure 1b, the RL-shunt circuit encompasses a synthetic inductor such that the inductance effect can be adjusted online during operation and the resonance frequency of the shunted piezoelectric patch, that is the frequency where there is maximum vibration energy absorption, can be kept optimally tuned to the resonance of the target mode of the hosting structure, even in presence of significant variations of the dynamic response of the structure and of the shunt itself. The shunt inductance is controlled by a separate board, which implements an extremum seeking control algorithm [33,34] that maximises the vibration power

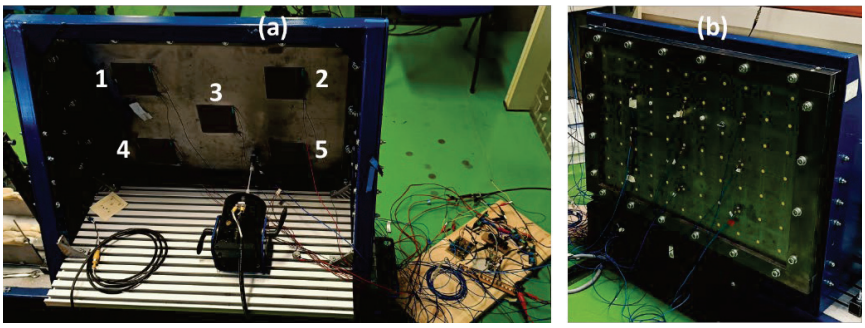

Figure 1: Experimental setup: (a) back of the plate with the piezoelectric patches and shaker force excitation, (b) front of the plate with the 3×3 array of accelerometers.

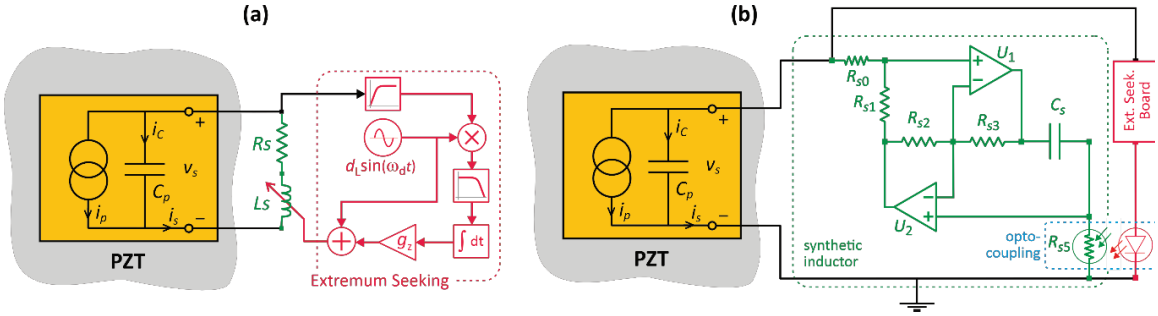

Figure 2: Self tunning shunted piezoelectric patch vibration absorbers: (a) panel with 5 control units, (b) ESC block diagram and (c) synthetic inductance with ESC opto-coupling.

absorption by the shunt [30,31]. As depicted in Figure 2b, the shunt inductance is modulated via the LDR resistor R_{S5}, whose resistance is controlled by the light generated by an LED source in the control board. This solution offers a simple and effective tuning mean, which rather importantly avoids electrical coupling between the shunt and control board itself. This is quite important to avoid the shunt is affected by unwanted electrical noise that could disrupt the vibration control action of the shunted patch or even lead to the generation of vibration noise rather than vibration mitigation.

3 VIBRATION CONTROL PERFORMANCES

The implementation of the self-tuning shunted piezoelectric patches on the plate model structure is now considered. To start with, Subsection 3.1 presents experimental results on the flexural vibration of the plate when the five piezoelectric patches are connected to shunts set to control simultaneously the same resonant response of the structure. More specifically, three cases are presented where the five shunts are tuned to control in turn the responses of the first, second and third flexural modes of the plate, which resonates at $f_{\mathrm{rl}} = 32$ Hz, $f_{\mathrm{r2}} = 49$ Hz, $f_{\mathrm{r3}} = 84$ Hz. Then, Subsection 3.2 presents experimental results on the flexural vibration of the plate when the five shunted piezoelectric patches are clustered into three groups in such a way as to simultaneously control the responses of the first three flexural modes of the plate.

3.1 Single-mode control

The real-time implementation of the self-tuning shunted piezoelectric patches is first investigated assuming all units are set to control the same flexural mode of the plate, which is excited by a white-noise broadband force. More specifically the control of the resonant responses of the first, second and third flexural modes of the panel are considered, which resonate at $\omega_{r1} = 32$ Hz, $\omega_{r2} = 49$ Hz, $\omega_{r3} = 84$ Hz. When the self-tuning shunts are implemented, the dithering signal of the extremum seeking algorithm produces a time-harmonic effect on the vibration response at the dithering frequency ω_d. Hence, the flexural response of

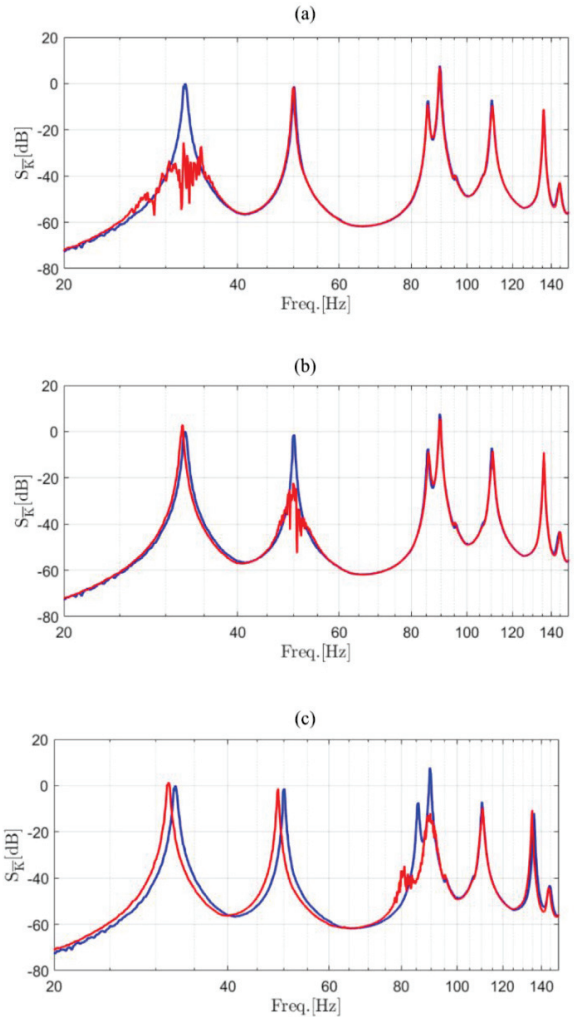

Figure 3: Spectra of the kinetic energy of the plate with the automatic tuning (red) and with the piezoelectric on open circuit (blue) for the (a) first, (b) second, and (c) third flexural modes.

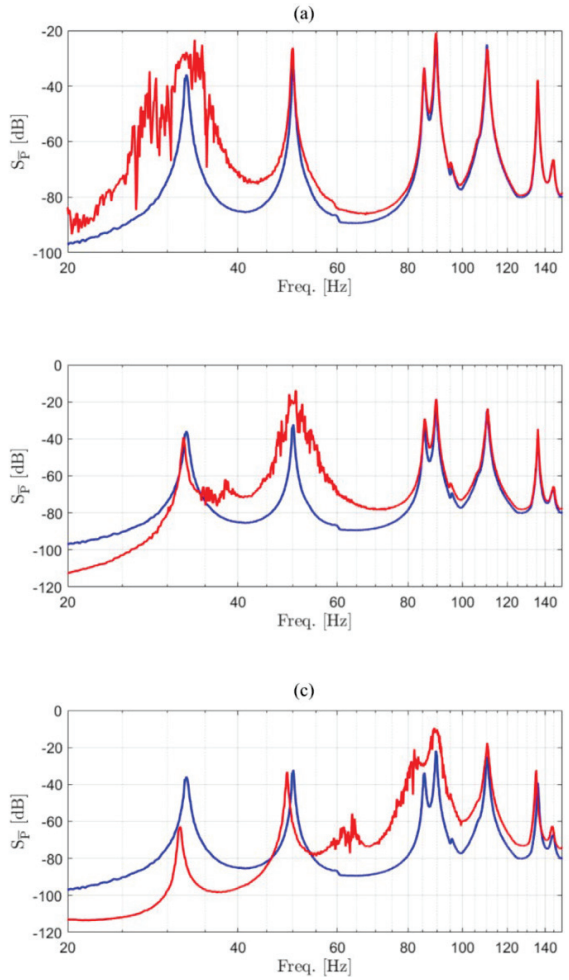

Figure 4: Spectra of the electric power on the central patch with the automatic tuning (red) and with the piezoelectric on open circuit (blue) for the (a) first, (b) second, and (c) third flexural modes.

the plate can be treated as that of a cycle-stationary system such that its response can be conveniently analysed in the frequency domain with spectra. Thus, Figures 3and 4 show the measured power spectral densities (PSD) of the plate flexural kinetic energy and of the electric power absorbed by the shunt connected to centre patch N. 3.

Starting first with the flexural response of the plate, the blue lines in the plots of Figure 3 show the spectra of the spatially averaged flexural response of the plate with the five piezoelectric patches connected to a large resistor that mimics an open circuit. The plots show that in the 20-150 Hz, the plate is characterised by 7 well separated resonance peaks which, as shown in [16], are related to the resonant responses of the first seven flexural modes of the plate with the piezoelectric patches in open-circuit. The red lines show how these spectra are modified when the five shunts are tuned to control in turn the resonant response of respectively

the first, the second and the third resonant modes. The three graphs show quite remarkable reductions of the three resonance peaks. More specifically, the first and third resonance peaks are brought down by 28 dB whereas the second one by 23 dB. The spectra with the shunted patches active look noisier, particularly at the resonance frequency of the target mode. This is the result of the fact that the flexural response of the plate and shunted patches is not fully stationary but is bound to vary cyclically as the shunt inductance is continuously swinged harmonically around the optimal value. The amount of this effect depends on the amplitude of the dithering signal, which nevertheless should not set too small otherwise the adaptation process would be too slow.

Moving to the electric power absorbed by the shunt connected to the patch N. 3 at the centre of the plate, the blue lines in Figure 4 show that, when the patches are connected to a large resistor that mimics an open circuit, as for the flexural vibration, the PSD of the absorbed electric power is characterised by a sequence of resonance peaks. Here, the high levels of flexural vibration are effectively transferred to equally larger level of electric energy, which is absorbed by the large resistor connected to the piezoelectric patch. When the piezoelectric patches are connected to the shunts tuned to control in turn the resonant responses of the first, second and third flexural modes, the spectra show a clear increment of the power absorbed at the resonance peak relative to the target mode. In general, the peak levels of absorbed power are raised by about 10 dB at all three target resonance frequencies. Once more, these experimental results confirm that when the shunt is tuned to maximise the electric power absorbed from the resonating target mode, then the resonant flexural response of the mode itself is effectively lessened.

3.2 Multi-mode control

The implementation of the self-tuning shunted piezoelectric patches is now investigated for the case where they are clustered into three groups to control simultaneously the resonant responses of the first three flexural modes. More specifically, the shunted patch N. 3 at the centre of the plate is set to control the resonant response of the first mode that resonates at $\omega_{\mathrm{r1}} = 32$ Hz. Instead, the diagonal shunted patches N. 1 and 5 are set to control the resonant response of the second mode that resonates at $\omega_{\mathrm{r2}} = 49$ Hz. Finally, diagonal shunted patches N. 2 and 4 are set to control the resonant response of the third mode that resonates at $\omega_{\mathrm{r3}} = 84$ Hz. The graph in Figure 5 shows, in this case too, quite good results with reductions of the three resonance peaks of respectively 18, 14, 7 dB. Also, the graph in Figure 6 shows that now electric power is absorbed at the resonance frequencies of all three target flexural modes.

4 CONCLUSIONS

This work has presented a study on the implementation of a self-contained, model-free, adaptive vibration absorber formed by a piezoelectric patch connected to a self-tuning RL shunt that adapts the inductance in such a way as to maximise the electric power absorption from the resonant response of a target flexural mode of the hosting structure. Two separate analogue circuits have been proposed that implement a RL shunt with tuneable inductance and an extremum seeking algorithm set to maximise the electric power absorption. To minimise noise

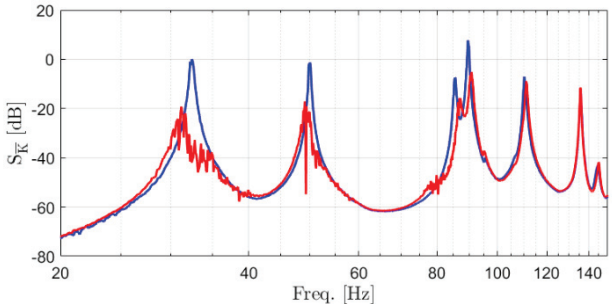

Figure 5: Spectra of the kinetic energy of the plate with the automatic tuning (red) and with the piezoelectric on open circuit (blue) for the multi-modal control on the first third flexural modes.

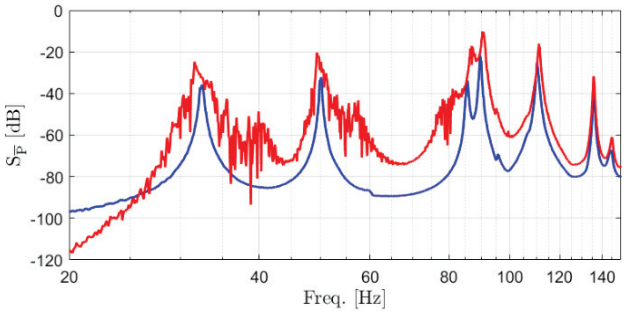

Figure 6: Spectra of the averaged electric power with the automatic tuning (red) and with the piezoelectric on open circuit (blue) for the multi-modal control on the first third flexural modes.

effects, a LDR has been employed to control the inductance in the shunt circuit, which is commanded by the tuning board via a LED. The tuning criterion based on the maximisation of the electric power absorbed by the shunt filtered in a small band centred at the nominal resonance frequency of the target mode with the analogue shunt circuit and extremum seeking tuning circuit has been proven experimentally. Experimental tests have been conducted on a model plate structure equipped with five tuneable shunted piezoelectric patches, which have been set to all control the resonant response of one target mode or have been clustered in three groups to control the resonant response of three modes simultaneously. In the former configuration reductions comprised between 20 and 30 dB were generated at the resonance frequency of the target mode. Instead, in the latter configuration reductions of the order of 10 to 15 dB were generated at the resonance frequencies of the target modes.

ACKNOWLEDGEMENTS

The authors acknowledge the financial support of the São Paulo Research Foundation (FAPESP) grants 23/00687-8 and 18/15894-0; also the Research Foundation - Flanders (FWO) and FAPESP through the bilateral research grant FWO G0F9922N and FAPESP 21/05510-3.

REFERENCES

[1] R. L. Forward, "Electronic damping of vibrations in optical structures" *Appl. Opt.*, vol. 18, pp. 690–697, 1979.
[2] N. W. Hagood and A. von Flotow, "Damping of structural vibrations with piezoelectric materials and passive electrical networks" *J. Sound Vib.*, vol. 146, pp. 243–268, 1991.
[3] S. Y. Wu, "Piezoelectric shunts with parallel RL circuits for structural damping and vibration control" in *Smart Mater. Struct.: Passive Damping and Isolation*, Proc. SPIE, vol. 2720, pp. 259–269, 1996.
[4] J. Høgsberg and S. Krenk, "Balanced calibration of resonant shunt circuits for piezoelectric vibration control" *J. Intell. Mater. Syst. Struct.*, vol. 23, no. 17, 2012. doi: 10.1177/1045389X12455727.
[5] C. H. Park, "Dynamics modelling of beams with shunted piezoelectric elements" *J. Sound Vib.*, vol. 268, pp. 115–129, 2003.
[6] J. Høgsberg and S. Krenk, "Calibration of piezoelectric RL shunts with explicit residual mode correction" *J. Sound Vib*., vol. 386, pp. 65–81, 2017.
[7] J. A. B. Gripp and D. A. Rade, "Vibration and noise control using shunted piezoelectric transducers: A review" *Mech. Syst. Signal Process.*, vol. 112, pp. 359–383, 2018.
[8] O. Nishihara and T. Asami, "Closed-form solutions to the exact optimizations of dynamic vibration absorbers (minimizations of the maximum amplitude magnification factors)" *J. Vib. Acoust.*, vol. 124, pp. 576–582, 2002.
[9] O. Thomas, J. Ducarne, and J.-F. Deü, "Performance of piezoelectric shunts for vibration reduction" *Smart Mater. Struct.*, vol. 21, 015008, 2012.
[10] P. Soltani, G. Kerschen, G. Tondreau, and A. Deraemaeker, "Piezoelectric vibration damping using resonant shunt circuits: an exact solution" *Smart Mater. Struct.*, vol. 23, no. 12, 125014, 2014.
[11] P. Gardonio and D. Casagrande, "Shunted piezoelectric patch vibration absorber on two-dimensional thin structures: Tuning considerations" *J. Sound Vib.*, vol. 395, pp. 26–47, 2017. doi: 10.1016/j.jsv.2017.02.019.
[12] T. Ikegame, K. Takagi, and T. Inoue, "Exact solutions to H_∞ and H_2 optimizations of passive resonant shunt circuit for electromagnetic or piezoelectric shunt damper" *J. Vib. Acoust.*, vol. 141, no. 3, 031015, 2019.
[13] G. K. Rodrigues, M. M. da Silva, and L. P. R. de Oliveira, "Modular modeling approach for FDM printed structures and piezo disks for metamaterial design" *Lat. Am. J. Solids Struct.*, vol. 16, no. 7, 2019. doi: 10.1590/1679-78255310.
[14] L. Y. M. Sampaio, G. K. Rodrigues, J. A. Mosquera-Sánchez, C. De Marqui, and L. P. R. de Oliveira, "Membrane smart metamaterials for unidirectional wave propagation problems" *J. Sound Vib.*, vol. 512, 116374, 2021. doi: 10.1016/j.jsv.2021.116374.
[15] G. Raze, J. Dietrich, and G. Kerschen, "Passive control of multiple structural resonances with piezoelectric vibration absorbers" *J. Sound Vib.*, vol. 515, 116490, 2021. doi: 10.1016/j.jsv.2021.116490.
[16] L. Dal Bo, H. He, P. Gardonio, Y. Li, and J. Z. Jiang, "Design tool for elementary shunts connected to piezoelectric patches set to control multi-resonant flexural vibrations" *J.*

Sound Vib., vol. 520, pp. 1722–1741, 2022. doi: 10.1016/j.jsv.2021.116554.
[17] K. Yamada, H. Matsuhisa, H. Utsuno, and K. Sawada, "Optimum tuning of series and parallel LR circuits for passive vibration suppression using piezoelectric elements" *J. Sound Vib.*, vol. 329, pp. 5036–5057, 2010.
[18] M. Berardengo, A. Cigada, S. Manzoni, and M. Vanali, "Vibration control by means of piezoelectric actuators shunted with LR impedances: Performance and robustness analysis" *Shock Vib.*, vol. 2015, pp. 1–30, 2015.
[19] H. Hanselka, "Adaptronik und Fragen zur Systemzuverlässigkeit" *ATP, Automatisierungstechnische Praxis*, vol. 2, pp. 44–49, 2002.
[20] G. Matten, M. Collet, E. Sadoulet-Reboul, and S. Cogan, "Sensitivity analysis and control of a cantilever beam by means of a shunted piezoelectric patch," in *Proc. 1st Euro-Mediterranean Conf. on Structural Dynamics and Vibroacoustics (MEDYNA 2013)*, Jan. 2013, France, pp. 1–4.
[21] U. Andreaus and M. Porfiri, "Effect of electrical uncertainties on resonant piezoelectric shunting," *J. Intell. Mater. Syst. Struct.*, vol. 18, no. 5, pp. 477–485, 2007.
[22] R. Darleux, B. Lossouarn, and J.-F. Deü, "Passive self-tuning inductor for piezoelectric shunt damping considering temperature variations," *J. Sound Vib.*, vol. 432, pp. 105–118, 2018.
[23] J. J. Hollkamp, T. F. Starchville, and A. Starchville Jr, "A self-tuning piezoelectric vibration absorber" *J. Intell. Mater. Syst. Struct.*, vol. 5, no. 4, pp. 559–566, 1994.
[24] A. J. Fleming and S. R. Moheimani, "Adaptive piezoelectric shunt damping" *Smart Mater. Struct.*, vol. 12, no. 1, 36, 2003. doi: 10.1088/0964-1726/12/1/305.
[25] D. Niederberger, A. Fleming, S. O. R. Moheimani, and M. Morari, "Adaptive multi-mode resonant piezoelectric shunt damping" *Smart Mater. Struct.*, vol. 13, no. 5, pp. 1025–1035, 2004. doi: 10.1088/0964-1726/13/5/007.
[26] J. A. B. Gripp, L. C. S. Góes, O. Heuss, and F. Scinocca, "An adaptive piezoelectric vibration absorber enhanced by a negative capacitance applied to a shell structure" *Smart Mater. Struct.*, vol. 24, 125017, 2015. doi: 10.1088/0964-1726/24/12/125017.
[27] P. Gardonio, Y. S. Lee, S. J. Elliott, and S. Debost, "Analysis and measure of a matched volume velocity sensor and uniform force actuator for active structural acoustic control" *J. Acoust. Soc. Am.*, vol. 110, no. 6, pp. 3025–3031, 2001. doi: 10.1121/1.1412448.
[28] S. Hartono, M. Karsten, and C. Harley, "A piezoelectric array for sensing vibration modal coordinates" *Sensors and Actuators A: Physical*, vol. 93, no. 2, pp. 123–131, 2001. doi: 10.1016/S0924-4247(01)00644-6.
[29] P. Gardonio, M. W. Zientek, and L. Dal Bo, "Panel with self-tuning shunted piezoelectric patches for broadband flexural vibration control" *Mech. Syst. Signal Process.*, vol. 134, 2019.
[30] G. K. Rodrigues, P. Gardonio, L. Dal Bo, and E. Turco, "Piezoelectric patch vibration control unit connected to a self-tuning RL-shunt set to maximise electric power absorption" *J. Sound Vib.*, vol. 536, 117154, 2022. doi: 10.1016/j.jsv.2022.117154.
[31] P. Gardonio, G. K. Rodrigues, L. Dal Bo, and E. Turco, "Extremum seeking online tuning of a piezoelectric vibration absorber based on the maximisation of the shunt electric power

absorption" *Mech. Syst. Signal Process.*, vol. 176, 109171, 2022. doi: 10.1016/j.ymssp.2022.109171.
[32] A. Antoniou, "Gyrators using operational amplifiers" *Electronics Letters*, vol. 3, no. 8, pp. 350–352, 1967.
[33] M. Krstić, "Performance improvement & limitations in extremum seeking control" *Systems and Control Letters*, vol. 39, pp. 313–326, 2000.
[34] D. E. Casagrande, P. Gardonio, and G. K. Rodrigues, "Tonal vibration control with a self-tuning absorber employing the extremum seeking algorithm" *Mech. Syst. Signal Process.*, vol. 211, 111254, 2024. doi: 10.1016/j.ymssp.2024.111254.

XI ECCOMAS Thematic Conference on Smart Structures and Materials - SMART 2025
M. Krommer, M. Nader and M. Schagerl (Eds)

Received: 27 March 2025 / Revised: 7 July 2025 / Accepted: 3 October 2025
© The Author(s) 2025

Embedded Piezoelectric Shear Actuators as Inertial Systems for Vibration Control in Metallic Structures

Sherif Okda, Sneha Rupa Nampally, Mauro Fontana, Sven Herold, Rainer Nordmann, Stephan Rinderknecht, Tobias Melz

Abstract. This paper presents a novel approach to integrate piezoelectric shear actuators into thin metallic structures for active vibration control. Piezoelectric inertial mass actuators operate by utilizing the inertial forces generated by piezoelectric materials under dynamic motion. However, these actuators have several limitations, including the addition of mass to the structure, the need for preload, and high power consumption. Unlike traditional IMAs, the proposed inertial shear actuator is integrated within the thickness of the structure, with the inertial mass effectively extracted from the metallic structure itself, offering several advantages. This integration leads to a significant reduction in weight and size. In addition, the actuator features reduced capacitance, leading to a significant reduction in power consumption, as well as eliminating the need for preload. While piezoelectric shear actuators have been mostly applied to composite structures, this work extends their use to metallic structures. A comprehensive model is developed to characterize the proposed shear actuator concept, and its performance is validated through a simulation on a simple plate structure. Experimental results show a vibration reduction of approximately 34 dB, targeting the first bending mode of the plate.

Key words: Inertial Mass Actuator, Piezoelectric, Active Vibration Control, Smart Structures

1 INTRODUCTION

Active Vibration Control (AVC) systems are superior regarding adaptability and precision compared to passive methods. Their ability to respond in real time allows them to perform optimally in a wide range of operating conditions, making them ideal for many applications where dynamic stability is crucial.

Sherif Okda & Tobias Melz
Technical University of Darmstadt, Research Group System Reliability, Adaptive Structures, and Machine Acoustics (SAM), Otto-Berndt-Str. 2, Darmstadt, 64287, Germany,
e-mail: sherif.okda@sam.tu-darmstadt.de

Sneha Rupa Nampally & Rainer Nordmann & Stephan Rinderknecht
Technical University of Darmstadt, Research Group Mechatronic Systems in Mechanical Engineering (IMS), Otto-Berndt-Str. 2, Darmstadt, 64287, Germany

Mauro Fontana
Powerflex S.R.L, via Campitiello 6, 82030, Limatola, Italy

Sven Herold & Tobias Melz
Fraunhofer LBF, Bartningstraße 47, 64289, Darmstadt, Germany

AVC systems rely on actuators, sensors, and control algorithms to generate forces that counteract vibrations in real time. Inertial Mass Actuators (IMAs) have gained significant attention in vibration control applications because of their unique ability to provide effective vibration suppression without requiring a fixed reaction point. Using the inertia of an internal mass to generate control forces, IMAs are particularly advantageous in applications where traditional reaction-based actuators are impractical.

Various actuator technologies, including piezoelectric, electrodynamic, magnetostrictive, electromagnetic, and dielectric elastomer actuators, have been employed in IMAs. Piezoelectric actuators are distinguished by their high blocking force, superior high-frequency performance, compact size, and reliability. These actuators operate based on the piezoelectric effect, where an applied voltage induces mechanical deformation, enabling precise displacements across a broad frequency range.

Several studies have explored the integration of piezoelectric actuators into IMAs. Herold et al. [1] developed a piezoelectric-driven IMA capable of adjusting resonance frequency through stiffness modification, demonstrating its effectiveness in AVC for lightweight structures. Zhao et al. [2, 3] introduced a novel concept utilizing two piezo-based rotating inertial actuators to suppress structure-borne noise in gearbox systems by intervening early in the transfer path. Further advancements include Cao et al. [4], who proposed a compact inertial piezoelectric rotary actuator with high load capacity, and Deng et al. [5], who developed a bipedal piezoelectric actuator with triple actuation modes, enhancing displacement linearity and load stability. Pan et al. [6] designed a piezoelectric inertial actuator with asymmetric inertial masses capable of operating in both quasi-static and resonant states.

Despite their advantages, traditional IMAs have several limitations, including the increase in system weight, high power consumption, and the need for preload. Additionally, the high capacitance reduces the operating frequency range, making the selection of low-capacitance actuators critical for optimizing energy efficiency and performance in AVC systems.

To address these challenges, this paper proposes an integrated inertial shear actuator with a compact design, low weight, and reduced capacitance. Unlike conventional piezo stack actuators, piezo shear actuators have significantly lower capacitance, which minimizes their power consumption and improves their power efficiency at high frequencies. The proposed design further reduces weight by using a cutout of the mechanical structure as the inertial mass, eliminating the need for additional components. The relationship between power consumption, capacitance, and operating frequency is governed by:

$$I_{max} = U_{pp} \pi f C \tag{1}$$

and the maximum power necessary for this mode of operation is given by:

$$P_{max} = U_{pp}^2 \pi f_{max} C \tag{2}$$

Where I_{max} is the maximum amplifier current, f_{max} is the maximum operating frequency, C is the piezo actuator capacitance, and U_{pp} is the peak-peak drive voltage. It can be observed

that the consumed power relies on the capacitance of the actuator.

While piezo shear actuators are mainly used in positioning stations and composite structures, their application in IMAs remains underexplored. Senthil and Batra [7] developed a 3D state-space solution for laminated plates with embedded shear actuators. Trindade [8] investigated the use of both extension and shear piezoelectric actuators for active vibration control of clamped sandwich beams. His study showed that shear actuators, when embedded in the structure, provide reduced sensitivity to actuator position and improved durability compared to surface-mounted actuators. Baillargeon and Vel [9] experimentally demonstrated vibration suppression in sandwich beams using piezoelectric shear actuators with feedback control. Notably, Zech et al. [10] were the first to employ piezoelectric shear elements in an IMA for high-frequency AVC in planetary gearboxes as an add-on solution, demonstrating effective suppression of dominant vibration orders.

Building on these advancements, this paper presents a novel integrated inertial shear actuator designed for thin metallic structures, targeting localized vibrations in the high-frequency range. The following sections explain the actuator design, modeling, and experimental validation. The work presented in this paper stems from the research project LIVE-I [11].

2 METHODOLOGY

A small setup is constructed to test the new concept, the setup employs a metallic aluminum plate with a piezoelectric shear actuator that is fully integrated within the thickness of the plate. This innovative configuration connects the actuator to an inertial mass that is formed by strategically machining cutouts from the metallic structure itself, thereby eliminating the need for additional mass. The shear actuator has one side fixed to the main structure and the opposing side attached to the integrated inertial mass, as illustrated in Figure 1.

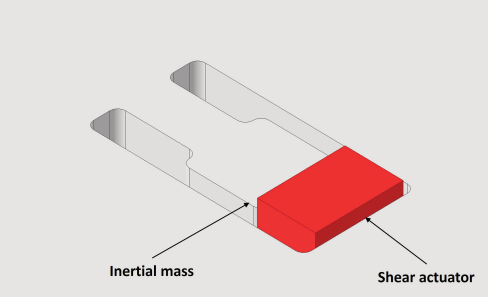

Figure 1: Integrated inertial shear actuator design.

A comprehensive numerical model is developed in MATLAB Simulink to simulate and validate the actuator's vibration control performance. The model incorporates four key components: the mechanical structure, the shear actuator, the inertial mass, and the controller, which employs a Filtered-x Least Mean Square (FxLMS) algorithm. The mechanical structure is simulated using a finite element analysis model conducted in ANSYS, which identifies the structure's modal

characteristics. The modal analysis shows that the first bending mode occurs at 2998 Hz, as shown in Figures 2 and 3.

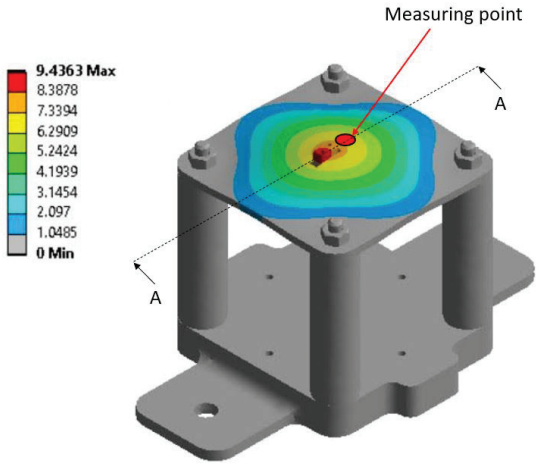

Figure 2: Modal analysis of the test setup.

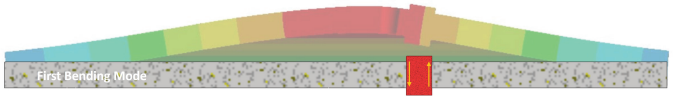

Figure 3: First bending mode (section A-A).

The finite element model is subsequently reduced to its first 22 modes, covering a frequency range up to 12.4 kHz, and converted into state-space representation for integration with the Simulink environment. The state space model has 44 states, having three input force points, which are the excitation point and the shear actuator influence points. In addition, there are three output points, which are the displacement, velocity, and acceleration of the measuring point. The modal damping is estimated and added to the State space matrices.

The mechanical modeling approach follows the framework established by Herold et al., employing alternating impedance and admittance formulations to describe the interaction between the mechanical structure and the piezoelectric actuator. In this representation, the plate structure is characterized by its admittance properties while the shear actuator is modeled as an impedance element. The coupling between these components occurs at discrete connection

points, with the actuator module receiving input voltages and connection point velocities as inputs and generating output forces. The piezoelectric actuator's behavior is implemented using the AdaptroSim™ toolbox from Fraunhofer LBF, which provides an analytical formulation incorporating the actuator's mechanical properties (stiffness and damping) and its electromechanical coupling characteristics. For this initial modeling phase, the electrical interaction between the actuator and power amplifier is simplified by assuming an ideal voltage source, though this aspect may be refined in subsequent development stages.

The model's inputs are the velocities v_1 and v_2 at both ends of the actuator as well as the driving voltage U. The block's outputs are the resulting forces F_1 and F_2 at the corresponding positions. Thus, the transducer is described in terms of impedance in the mechanical domain. The shear actuator is described by the following equation:

$$F_1 = -F_2 = (\frac{k}{s} + d)(v_2 - v_1) + \alpha U \tag{3}$$

The shear actuator stiffness and the coupling factor between the actuator input voltage and output force are determined experimentally. The damping parameter *d* is estimated for the shear actuator module. The excitation force is modeled as an ideal sinusoidal force supplied to the excitation point.

The complete Simulink model, depicted in Figure 4, integrates the reduced-order state-space representation of the plate structure with the shear actuator module, inertial mass, and controller. The power amplifier is modeled as a constant gain.

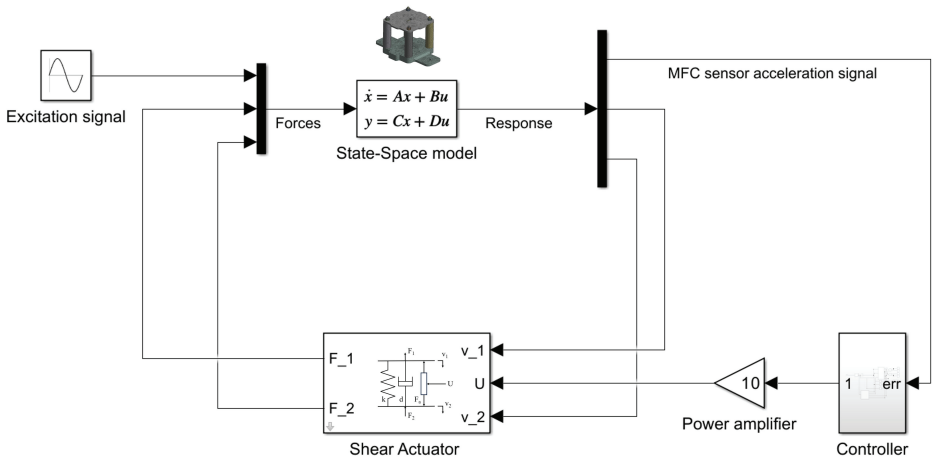

Figure 4: Developed setup Simulink model.

Simulation results demonstrate the system's effectiveness in vibration suppression, achieving approximately 60 dB of attenuation at the the first resonance frequency when subjected to an ideal sinusoidal excitation, as shown in Figure 5.

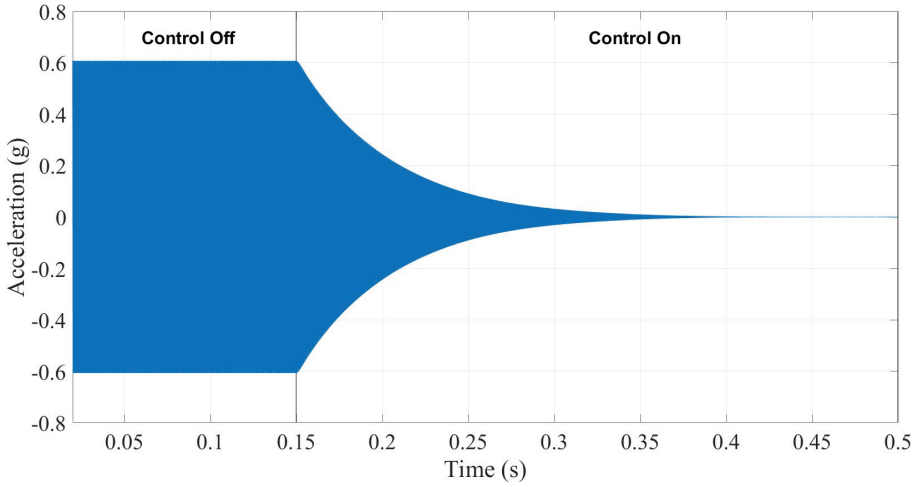

Figure 5: Simulink model acceleration levels before and after control of the shear actuator design.

Upon the completion of model construction and its subsequent successful evaluation, an experimental setup is developed to validate the newly developed concept. A test rig featuring an aluminum alloy plate, the shear actuator of type P-121.01 from Physik Instrumente (PI), an MFC (Macro Fiber Composite) [12] sensor for vibration monitoring, and an additional exciting inertial actuator that acts like a shaker. The test setup is shown in Figure 6. The piezo shear actuator is chosen due to its small size compared to the thickness of the plate, the shear actuator has a low electric capacitance of 1.4 nF. The size of the shear actuator is shown in Figure 7.

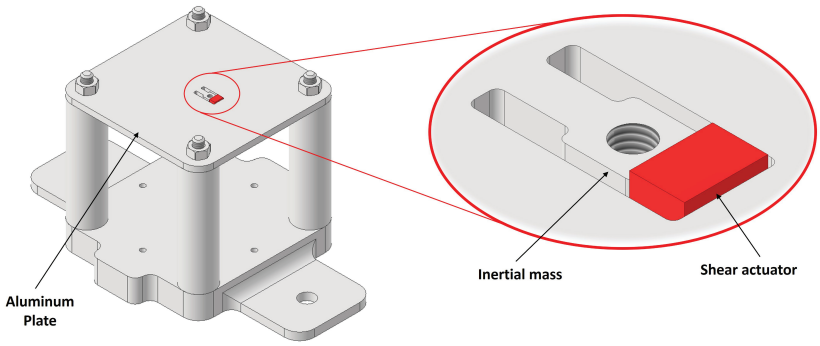

Figure 6: Developed plate structure with the integrated shear actuator design.

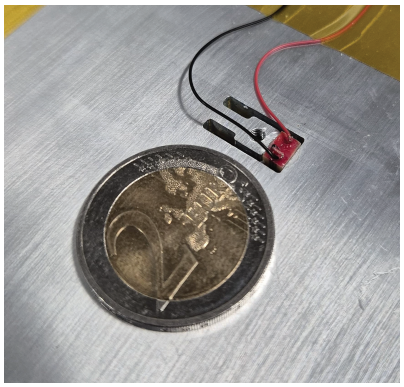

Figure 7: The developed inertial shear actuator size.

3 RESULTS AND DISCUSSION

Following the model evaluation, the test setup is assembled successfully with the integrated shear actuator, as illustrated in Figure 8.

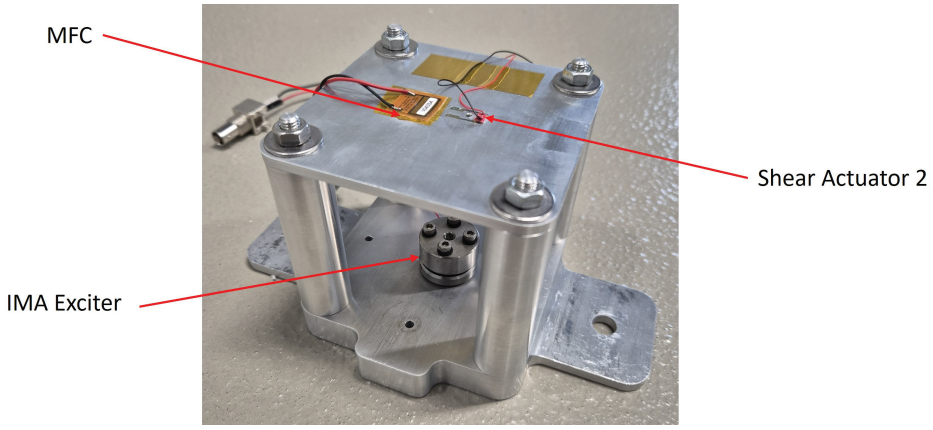

Figure 8: Test setup of the shear actuator utilizing the shear actuator.

The experimental procedure involves exciting the plate to induce its first bending mode and subsequently applying a control signal to the shear actuator. A sine chirp signal is applied at the excitation point to identify the resonant frequencies, revealing a first bending mode at 2990 Hz—closely matching the finite element model prediction of 2998 Hz. Following the resonance identification, a sustained sinusoidal excitation at this frequency is applied to generate steady-state vibrations.

The control system is activated after a 0.15-second initialization period, achieving convergence within 0.2 seconds of engagement. As shown in Figure 9, the time-domain response demonstrates effective vibration suppression of 34 dB reduction in acceleration amplitude.

The experimental results show strong agreement with the Simulink model, confirming the actuator's real-time mode identification and suppression capabilities, Although the achieved 34 dB reduction in vibration amplitude is lower than the 60 dB shown in simulation. This difference is likely due to small misalignments in actuator placement that affect force coupling efficiency, as well as unmodeled damping effects in the physical system. Nevertheless, the 34 dB suppression level proves highly effective for practical implementation, especially considering the actuator's compact dimensions and negligible weight addition, demonstrating the design's viability for real-world vibration control applications.

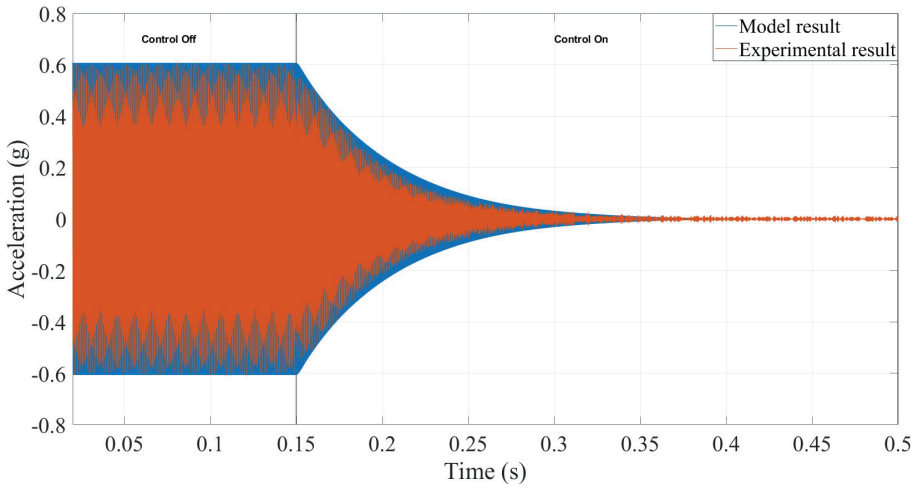

Figure 9: Time domain MFC sensor signal without and with activated control.

4 CONCLUSION

This study presents an innovative concept for integrating a piezoelectric shear actuator directly into a metallic structure, offering significant advantages over traditional IMAs. The newly developed actuator demonstrates better performance through reduced weight, lower power consumption, extended high-frequency operation, and improved structural integration. Numerical modeling in MATLAB Simulink confirmed the actuator's vibration suppression capabilities, which are subsequently validated through experimental testing on a simple plate structure. The system achieved a vibration reduction of 34 dB for the first bending mode of the plate.

The successful validation of the plate structure establishes a strong foundation for further development. Additional investigations should explore sensor dynamics optimization and power amplifier performance characterization to enhance the system modeling accuracy. Future work should also consider long-term reliability testing under operational conditions and potential adaptation for composite-metal hybrid structures to broaden the technology's applicability.

Funding

The work done in this paper is funded by the Marie Sokolowski-Curie Actions - LIVE-I project, which has received funding from the European Union's Horizon 2020 research and innovation program under grant agreement No 860243.

REFERENCES

[1] S. Herold, D. Mayer, T. Melz, and T. Röglin, "Design and test of a piezoelectric inertial mass actuator for active vibration control," *Vibration Engineering and Technology of Machinery: Proceedings of VETOMAC X 2014, held at the University of Manchester, UK, September 9-11, 2014*, pp. 587–597, 2015.

[2] G. Zhao, N. Alujević, B. Depraetere, and P. Sas, "Active structural acoustic control of gear-box systems using a pair of piezo-based rotating inertial actuators," in *7th ECCOMAS Thematic Conference on Smart Structures and Materials SMART 2015*. IDMEC, 2015, pp. 1–16.

[3] G. Zhao, N. Alujević, B. Depraetere, G. Pinte, J. Swevers, and P. Sas, "Experimental study on active structural acoustic control of rotating machinery using rotating piezo-based inertial actuators," *Journal of sound and vibration*, vol. 348, pp. 15–30, 2015.

[4] Y. Cao, Z. Xu, L. You, Y. Wu, and H. Huang, "An inertial piezoelectric actuator with small structure but large loading capacity," *Review of Scientific Instruments*, vol. 92, no. 8, 2021.

[5] J. Deng, W. Wang, S. Zhang, F. Lu, and Y. Liu, "An inertial bipedal piezoelectric actuator with integration of triple actuation modes," *Smart Materials and Structures*, vol. 31, no. 11, p. 115019, 2022.

[6] C. Pan, C. Shi, A. Feng, M. Hu, S. Shu, and H. Xia, "Resonant-type piezoelectric inertial drive mechanism with asymmetric inertial masses," *Review of Scientific Instruments*, vol. 92, no. 1, 2021.

[7] S. S. Vel. and B. R. C., "Exact solution for the cylindrical bending of laminated plates with embedded piezoelectric shear actuators," *Smart Materials and Structures*, vol. 10, p. 240, 4 2001.

[8] M. A. Trindade, "Simultaneous extension and shear piezoelectric actuation for active vibration control of sandwich beams," *Journal of intelligent material systems and structures*, vol. 18, no. 6, pp. 591–600, 2007.

[9] B. P. Baillargeon and S. S. Vel, "Exact solution for the vibration and active damping of composite plates with piezoelectric shear actuators," *Journal of Sound and Vibration*, vol. 282, pp. 781–804, 4 2005.

[10] P. Zech, D. F. Plöger, T. Bartel, T. Röglin, and S. Rinderknecht, “Design of an inertial mass actuator for active vibration control of a planetary gearbox using piezoelectric shear actuator.” In Proceedings of ISMA2018 International Conference on Noise and Vibration Engineering, 2018, pp. 203–215.

[11] H2020. Live-i. [Online]. Available: https://livei.fr/

[12] S. M. GMBH. Macro Fiber Composites - Overview. [Online]. Available: https://www.smart-material.com/fxlms-product-mainV2.html

XI ECCOMAS Thematic Conference on Smart Structures and Materials - SMART 2025
M. Krommer, M. Nader and M. Schagerl (Eds)

Received: 1 April 2025 / Revised: 1 July 2025 / Accepted: 3 October 2025
© The Author(s) 2025

Experimental Calibration of Digital Piezoelectric Shunts: Practical Considerations, Parameter Estimation and Dielectric Losses

Jens Damholt Richardt, Boris Lossouarn, Jan Høgsberg, Jean-François Deü

Abstract. Piezoelectric shunts have been studied extensively over the past decades for vibration mitigation of flexible structures. The admittance of the electrical circuit in a piezoelectric shunt can be synthesized by a digital control unit, commonly referred to as a digital piezoelectric shunt. While the digital control unit requires power (and is therefore semi-active), it allows for a straightforward implementation and adaptation of, in theory, any electrical circuit, making it effective for prototyping. Furthermore, the hardware of the digital shunt allows for a direct measurement of the dynamic capacitance of the piezoelectric transducer by applying a known current and measuring the resulting voltage. All required parameters for calibration of a shunt targeting a single vibration mode can be obtained directly from such capacitance measurements, eliminating the need for additional sensors in the shunt calibration. This study considers practical issues for experimental implementation of digital shunts from capacitance measurements, such as the influence of delay introduced by the digital control unit on the performance of the shunt. Furthermore, it is demonstrated how the performance of a resonant digital shunt is affected by the parallel resistance in the used digital shunt hardware and dielectric losses in the piezoelectric transducer. Corrections for these effects are introduced by modification of the implemented transfer function and their effectiveness is evaluated experimentally for a composite blade.

Key words: Piezoelectric Shunt Damping, Dielectric Loss, Shunt Calibration, Digital Shunt

1 Introduction

Piezoelectric shunt damping has been considered extensively for vibration reduction in flexible structures by connecting an electrical circuit to a piezoelectric transducer embedded in the structure. Resonant shunts are often used for single-mode vibration reduction where an inductor and resistor are tuned to the targeted vibration mode. While allowing effective vibration

Jens Damholt Richardt & Jan Høgsberg
Department of Civil and Mechanical Engineering, Technical University of Denmark, Koppels Alle Building 404, 2800 Kongens Lyngby, Denmark

Boris Lossouarn & Jean-François Deü
Laboratoire de Mecanique des Structures et des Systemes Couples, Conservatoire national des arts et metiers (Cnam), 292 Rue Saint-Martin, 75003 Paris, France

reduction, resonant shunts are sensitive to mistuning [1] and may require large custom inductors with a small series resistance [2]. Experiments are therefore often performed with synthetic inductors [3, 4] or by introducing a synthetic impedance [5, 6].

Synthesizing the electric impedance of the shunt circuit with a synthetic impedance was first considered by Fleming et al. in 2000 [5] by the introduction of a device that prescribes the relationship between the current and voltage between two terminals. While the device can contain either a current or a voltage source, a voltage-controlled current source is typically used to minimize hysteretic nonlinearities of the piezoelectric transducer and because implementation of improper transfer functions, where the order of the numerator is greater than the denominator, is impractical [7]. The desired electrical impedance is then implemented by synthesizing the corresponding admittance by measuring the voltage across the terminals of the piezoelectric transducer and prescribing the current.

The device used to implement a synthetic impedance consists of a digital control unit (DCU) where the desired transfer function is implemented, as well as additional hardware to convert between the input/output of the DCU and the voltage/current at the two terminals of the device. As the impedance relation is governed by the DCU, the device is, in the present paper, referred to as a digital shunt. Following the digital shunt design proposed by Fleming et al. [5], different digital shunt hardware have been applied in the literature, for instance, with the current being generated using the voltage compensation method [6, 8, 9] or based on a Howland current pump [10, 11, 12]. A comparison between a digital shunt based on the voltage compensation method and on the Howland current pump can be found in [10]. One advantage of the Howland current pump is that it allows one of the electrodes of the piezoelectric transducer to be grounded. Other modifications of the digital shunt hardware have been used, for instance, to scale and transform the voltage between the two terminals to the input of the DCU. As demonstrated in [13] and [14], impedance measurements with the digital shunt hardware can be used for the estimation of the modal parameters required for shunt tuning.

While the digital shunt, in theory, allows for the implementation of almost any shunt impedance, care must be taken to obtain an accurate representation of the shunt impedance. In [15], Raze et al. demonstrated the importance of accounting for the delay introduced by the DCU for the stability of the digital shunt. Similarly, the present paper describes practical considerations for the implementation of an accurate digital shunt, observed during experiments conducted in [14].

In Sec. 2, the experimental setup is described for context, and the hardware used for the digital shunt setup is introduced. Next, in Sec. 3, the discretization of the transfer function in the digital control unit is described together with the additional delay introduced by the digital shunt unit. A correction minimizing the influence of delay is then presented using simplified terms to ease the implementation of the correction. The influence of a bias resistance in the digital shunt hardware and dielectric losses in the piezoelectric transducer is briefly discussed in Sec. 4, while conclusions are given in Sec. 5.

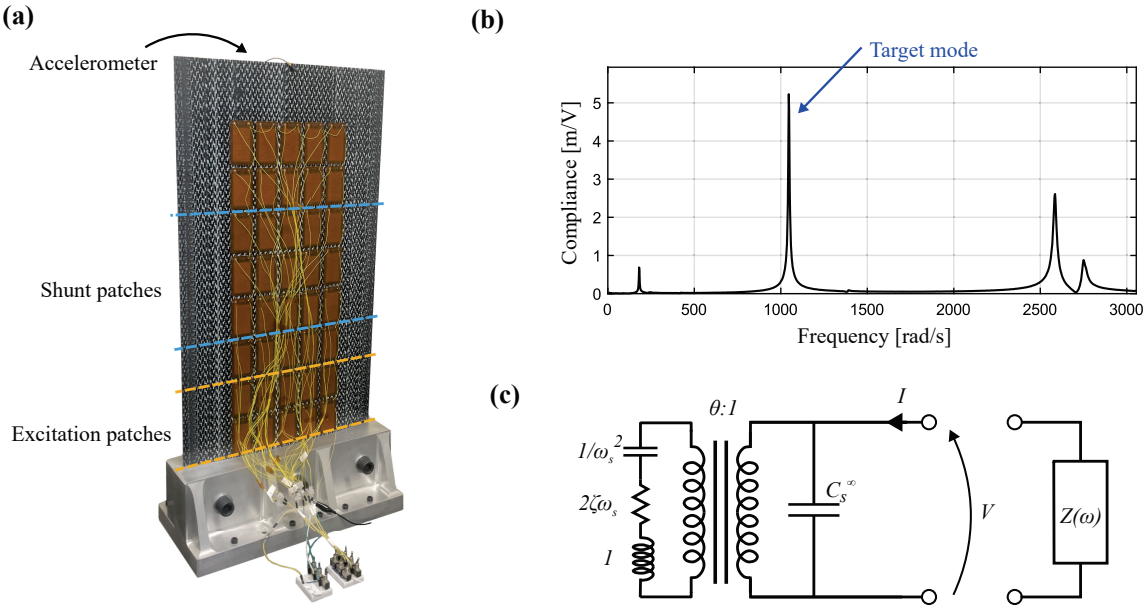

Figure 1: Experimental setup with a composite blade (a), the frequency response function at the top of the blade with the shunt in the OC condition (b), and an equivalent electrical circuit (c) of the targeted vibration mode with $\theta = \omega_s \kappa_s \sqrt{C_s^\infty}$.

2 Experimental setup

This section describes the experimental setup, including the governing equations of the considered electromechanical system and the hardware of the used digital shunt.

2.1 Composite blade

The experimental setup considered in the present paper is the composite blade shown in Fig. 1(a) with 40 piezoelectric patches (DuraAct -P-876.A15, PI Ceramic). One of the electrodes of each patch is grounded, whereby any number of patches can easily be connected in parallel and used as part of a single shunt. The initial analysis is limited to the calibration of a resonant shunt targeting the second bending mode with the short circuit (SC) natural frequency $\omega_s = 1047\ \mathrm{rad/s}$, corresponding to 167 Hz when only the patches highlighted in Fig. 1(a) are used for shunt damping. The frequency response for the displacement at the top of the blade is shown in Fig 1(b) with the shunt patches in the SC condition. A reduced-order model with a single vibration mode is introduced to describe the targeted vibration mode of the structure. For harmonic motion with the angular frequency ω and the modal coordinate r_s, the governing equations are

$$\left(-\omega^2 + 2i\omega\zeta_s\omega_s + \omega_s^2\right) r_s - \omega_s \kappa_s \sqrt{C_s^\infty} V = f_{s,ext} \tag{1}$$

$$i\omega\omega_s \kappa_s \sqrt{C_s^\infty} r_s + i\omega C_s^\infty V = I \tag{2}$$

where V is the voltage across the electrodes of the piezoelectric shunt patches, I is the current at one of the terminals and $f_{s,ext}$ is an external modal load. The modal parameters are defined in accordance to [14], where $\omega_s = 1047\,\mathrm{rad/s}$ and $\zeta_s = 0.0026$ are the natural frequency and damping ratio with SC electrodes, $C_s^\infty = 482\,\mathrm{nF}$ is the modal blocked capacitance, and $\kappa_s = 0.075$ is the effective electromechanical coupling factor (EEMCF). The equivalent electrical circuit to the considered electromechanical system is shown in Fig. 1(c) for $f_{s,ext} = 0$.

Shunting of an electrical circuit with impedance $Z = Z(\omega)$ to the used piezoelectric patches, as illustrated in Fig. 1(c), introduces the relation between voltage and current

$$V = -ZI \tag{3}$$

For a series RL shunt with the resistance R and inductance L, the impedance is

$$Z = i\omega L + R \tag{4}$$

As demonstrated in [14], C_s^∞ and κ_s contain an implicit correction for the existence of residual (non-targeted) vibration modes when used for calibration of a shunt attached to a flexible structure and tuned to target a single vibration mode. In the present paper, the shunt circuit is therefore calibrated directly using the calibration expressions for minimum acceleration amplitude (accelerance) in the frequency response, derived in [16] for a piezoelectric shunt attached to a single-degree-of-freedom (sdof) structure. The optimal inductance and resistance are then

$$L = \frac{1}{C_s^\infty \omega_s^2} \frac{1}{(1+\kappa_s^2)^2} \quad , \quad R = \frac{1}{C_s^\infty \omega_s} \sqrt{\frac{3}{2} \frac{\kappa_s^2}{(1+\kappa_s^2)^3}} \tag{5}$$

For the modal parameters given above, the inductance and resistance are evaluated as $L = 1.87\,\mathrm{H}$ and $R = 181\,\Omega$.

2.2 Digital shunt hardware

In the digital shunt, the impedance Z is synthesized by a two-terminal device with a digital control unit (DCU) and additional hardware converting the input and output signal of the DCU to the voltage and current at the terminals. The present setup uses the digital shunt hardware in [11] with the same components as in [14]. The hardware is shown in Fig. 2(a) with a schematic of the circuit in Fig. 2(b). The circuit contains the two resistors R_c and R_b, as well as two operational amplifiers (OPA445, Texas Instruments) and one instrumental amplifier (AMP03, Analog Devices) powered by a $\pm 15\,\mathrm{V}$ DC power supply. The circuit is based on a modified Howland current pump and is chosen for its simplicity and as it allows one of the electrodes of the piezoelectric transducer to be grounded.

Assuming ideal operational amplifiers, the digital shunt hardware in Fig. 2 introduces the relation between the input voltage V_{in} and output voltage V_{out} of the DCU to the voltage V across the two electrodes of the digital shunt and the current I_p shown in Fig. 2(b) as

$$V = V_{in} \quad , \quad I_p = -\frac{1}{R_c} V_{out} \tag{6}$$

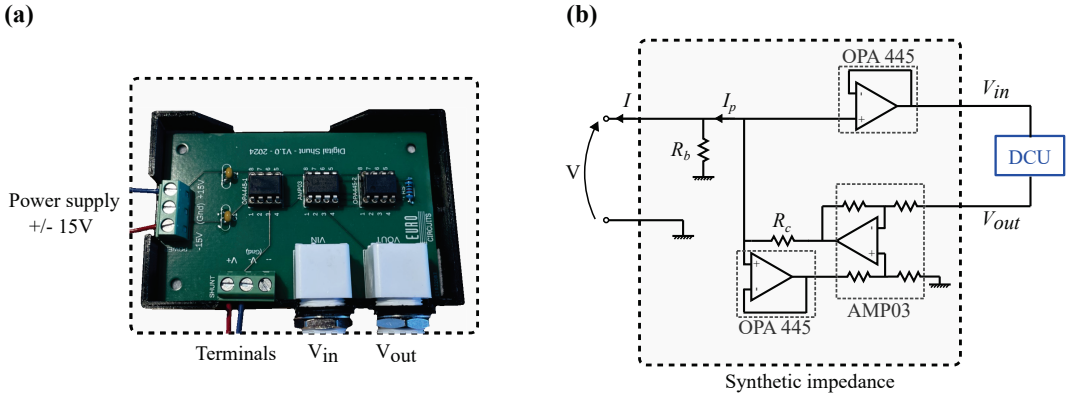

Figure 2: Digital shunt hardware, with an image of the used circuit in (a) and a schematic of the circuit in (b).

The magnitude of the current I_p is limited by the resistor R_c and the maximum output voltage $|V_{DCU,max}| = \max(|V_{out}|)$ of the DCU, such that

$$|I_p| \leq \frac{|V_{DCU,max}|}{R_c} \tag{7}$$

The value of the resistor R_c is then chosen based on the required maximum current $|I_p|$ and the maximum voltage $|V_{DCU,max}|$ of the DCU. For an ideal circuit, the current at the terminal of the digital shunt circuit is only governed by the voltage V_{out}. However, in practice, a resistance R_b must be added to the circuit to remove DC bias current. The current I at the terminal of the digital shunt device is then

$$I = I_p - \frac{1}{R_b}V = -\frac{1}{R_c}V_{out} - \frac{1}{R_b}V_{in} \tag{8}$$

The resistance R_b is chosen to be as large as possible while removing the DC bias current. Using (8), it is possible to account for the influence of R_b when implementing the synthetic impedance by including it in the implemented transfer function. This approach is applied for another digital shunt circuit in [12]. Presently, an alternative approach is used where R_b is considered as part of the inherited resistance of the piezoelectric transducer. The influence of the bias resistance is then accounted for in the calibration of the shunt, see Sec. 4.

Considering R_b as part of the piezoelectric transducer corresponds to letting $I_p = I$, whereby (3) and (6) gives the transfer function of the DCU as

$$V_{out} = \frac{R_c}{Z}V_{in} \tag{9}$$

Using (9), the admittance $1/Z$ of a piezoelectric shunt can then be synthesized with a digital shunt by implementation of the transfer function R_c/Z in the DCU.

In the present experimental setup, a dSpace MicroLab box is used as the DCU, with an input/output voltage range $V_{in} \in [-10, 10]$ V and $V_{out} \in [-10, 10]$ V. The two resistors are

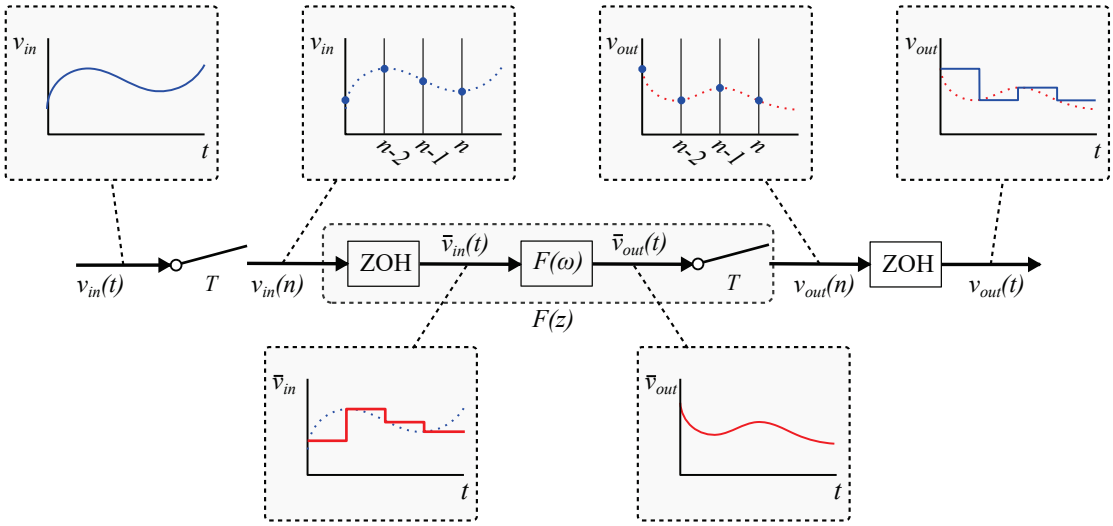

Figure 3: Block diagram of the DCU, with the discrete transfer function $F(z)$ modeled as a ZOH followed by a continuous transfer function $F(\omega)$ and a sampler.

chosen as $R_s = 10\ \mathrm{k\Omega}$ and $R_b = 1\ \mathrm{M\Omega}$. The current I_p is thereby in the range $I_p \in [-1, 1]\ \mathrm{mA}$, while the shunt voltage must be in the range $V \in [-10, 10]\ \mathrm{V}$. For applications where the magnitude of the shunt voltage V exceeds the operational range of the DCU, two additional resistors can be added to the circuit to reduce the input voltage in the DCU, see for instance [12]. Additionally, some DCUs only allow positive voltage in-/output. In [6], this is accounted for by adding a constant voltage offset in the digital shunt circuit.

3 Discretization of transfer function

In Sec. 2.2, the transfer function $R_c/Z(\omega)$ of the DCU is described in the continuous frequency domain. This section considers the required sampling of the DCU and its influence on the accuracy of the synthesized admittance.

3.1 Effect of sampling

Fig. 3 show a block diagram of the DCU, where the continuous time signals of the parameters defined in previous sections are denoted by the corresponding lower-case symbols as a function of time t. Assuming that the analog-to-digital converter can be considered as an ideal sampler with the fixed sample period T, the continuous input signal $v_{in}(t)$ is converted to the sampled signal $v_{in}(n)$ for the sample n. The corresponding sampled output signal $v_{out}(n)$ is then determined by the difference equation that prescribes the current output from past outputs and past/current inputs, illustrated in Fig. 3 by the discrete transfer function $F(z)$. Finally, as the clock frequency of the DCU is significantly higher than the sampling frequency, the digital-to-analog converter that converts the discrete signal $v_{out}(n)$ to a continuous signal $v_{out}(t)$ is considered as a zero-order hold (ZOH) maintaining a constant voltage between each sample.

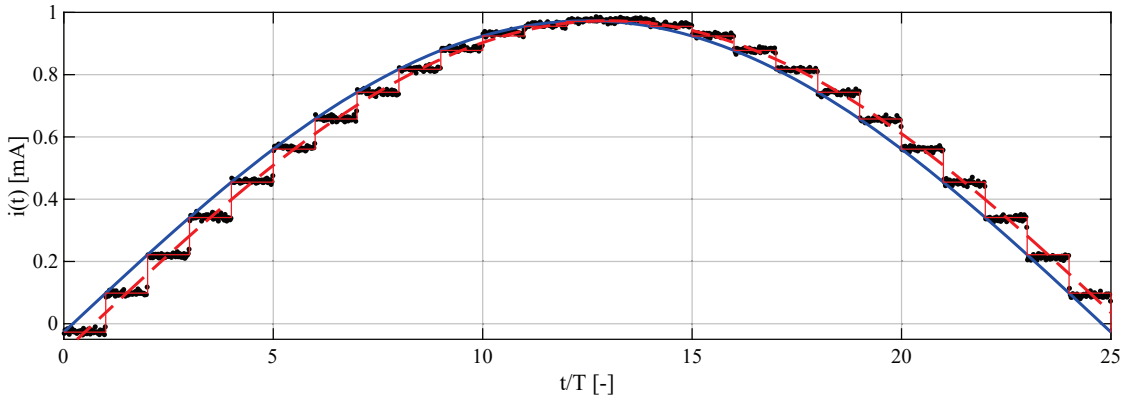

Figure 4: Sine current generated by the digital shunt hardware (black dots) with an ideal sine curve manually fitted to the signal (solid blue), including the ZOH (solid red), and with an ideal phase delay $\tau = T/2$ (dashed red).

As described in [17], the delay associated with the hold is the most important parameter to account for in the implementation of digital control systems. The influence of the ZOH on the output of the digital shunt is demonstrated in Figure 4 showing the current $i(t)$ measured at the terminal of the digital shunt unit (black dots) when a sine function with the amplitude $1\ \mathrm{mA}$ and frequency $200\ \mathrm{Hz}$ is prescribed with a sampling frequency of $10\ \mathrm{kHz}$. A continuous sine function with a frequency of $200\ \mathrm{Hz}$ (solid blue) is manually fitted to the first data point of each sample. It is seen that applying a ZOH (solid red) to the continuous sine function gives a good description of the measured data.

Following [15, 17], the transfer function of a ZOH can be written for a unit impulse as

$$G(\omega) = \frac{1 - \mathrm{e}^{-2i\omega\tau}}{2i\omega\tau} = \mathrm{e}^{-i\omega\tau}\left(\frac{\mathrm{e}^{i\omega\tau} - \mathrm{e}^{-i\omega\tau}}{2i\omega\tau}\right) \approx \mathrm{e}^{-i\omega\tau} \tag{10}$$

where $\tau = T/2$ and a Taylor series of the parenthesis in the second expression is applied to simplify the expression. The Taylor series of the parenthesis is $1 + \frac{1}{6}(i\omega\tau)^2 + \mathcal{O}\left((i\omega\tau)^4\right)$, whereby the error of the approximation is seen to be small for $\omega\tau \ll 1$. The ZOH is then considered as an addition of an ideal delay τ to the continuous signal. For the example in Fig. 4, the delayed signal (dashed red) is seen to give a better description of the measured data compared to the original continuous signal (solid blue).

3.2 Difference equation

The difference equations represented as the discrete transfer function $F(z)$ in Fig. 3, governs the output voltage $v_{out}(n)$ with $v_{in}(n)$ as the input voltage and is used to synthesize the required admittance of the digital shunt. The discrete filter $F(z)$ can be represented as a hold approximating the continuous signal $v_{in}(t)$ from the discrete signal $v_{in}(n)$, i.e. representing the associated continuous filter $F(\omega)$. When the approximating hold is a zero-order hold as in the

full expression in (10), the discrete and continuous filters are related by

$$F(z) = (1 - z^{-1})\mathcal{Z}\left(\frac{F(\omega)}{i\omega}\right) \tag{11}$$

If the continuous filter $F(\omega)$ is defined to synthesize the admittance of a series RL-shunt with the inductance $\hat{L}$ and resistance $\hat{R}$, this leads to

$$F(z) = (1 - z^{-1})\mathcal{Z}\left(\frac{R_c}{i\omega\hat{L} + \hat{R}}\right) = \frac{\frac{R_c}{\hat{R}} - \frac{R_c}{\hat{R}}\mathrm{e}^{-\frac{\hat{R}}{\hat{L}}T}}{z - \mathrm{e}^{-\frac{\hat{R}}{\hat{L}}T}} \approx \frac{\frac{R_c}{\hat{L}}T}{z - (1 - \frac{\hat{R}}{\hat{L}}T)} \tag{12}$$

where the final expression follows from the Taylor series approximation of the exponential function: $\mathrm{e}^{-\hat{R}T/\hat{L}} = 1 - \hat{R}T/\hat{L} + \mathcal{O}((\hat{R}T/\hat{L})^2)$. This simplified discrete transfer function corresponds to applying the forward Euler rule in numerical integration, for which the difference equation implemented in the DCU can be expressed as

$$v_{out}(n) = \left(1 - \frac{\hat{R}}{\hat{L}}T\right)v_{out}(n-1) + \frac{R_c}{\hat{L}}Tv_{in}(n-1) \tag{13}$$

While other more advanced integration methods such as Tustin's method can be applied for the discretization of the continuous transfer function, the forward Euler rule is considered here due to its simplicity. Implementing the difference equation from the full expression in (12) corresponds to using a ZOH discretization.

3.3 Correction for phase delay

This section presents a simplified correction for the delay introduced by the DCU when synthesizing the impedance of a shunt targeting a single vibration mode with the frequency ω_s. The correction has previously been applied in [14]. When the transfer function in (10) for a ZOH is considered as an ideal delay, the Fourier transforms of the continuous signals in Fig. 3 are related by

$$\bar{V}_{in} = V_{in}\mathrm{e}^{-i\omega\tau} \quad , \quad V_{out} = \bar{V}_{out}\mathrm{e}^{-i\omega\tau} \tag{14}$$

From these representations, the relation between the continuous transfer function $F(\omega)$ implemented in the DCU and the ideal transfer function of the shunt $R_c/Z(\omega)$ in (9) is defined as

$$F(\omega) = \frac{\bar{V}_{out}}{\bar{V}_{in}} = \frac{V_{out}\mathrm{e}^{i\omega\tau}}{V_{in}\mathrm{e}^{-i\omega\tau}} = \frac{R_c}{Z(\omega)}\mathrm{e}^{2i\omega\tau} \tag{15}$$

When the transfer function $F(\omega)$ is written on the same form as the ideal transfer function $R_c/Z(\omega)$, the expression in (15) can be used to account for the delay introduced in the digital shunt by letting $\omega = \omega_s$ and defining the parameters in $F(\omega_s)$ such that (15) is satisfied.

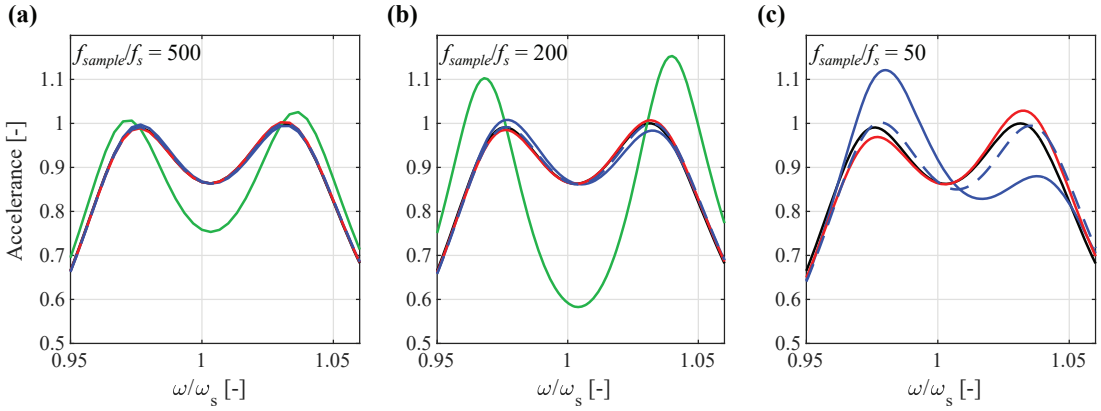

Figure 5: Frequency response with varying ratios between target frequency f_s and sampling frequency f_{sample} in (a), (b), and (c), with a series RL shunt calibrated without correction for delay (solid green), with the proposed correction using forward Euler integration (solid blue) and full ZOH integration (dashed blue), with the correction in [15] using Tustin's method (solid red), and with the analytical continuous transfer function (solid black).

For the series RL-shunt with the inductance L and resistor R, the corrected parameters implemented in the DCU ($\hat{L}$ and $\hat{R}$) are found as

$$\hat{L} = L\cos(2\omega_s\tau) - \frac{R}{\omega_s}\sin(2\omega_s\tau) \tag{16}$$

$$\hat{R} = R\cos(2\omega_s\tau) + \omega_s L\sin(2\omega_s\tau) \tag{17}$$

The effect of the correction in (16)-(17) is illustrated in Fig. 5 for a numerical time simulation of a digital shunt implemented for the reduced order model described in Sec. 2.1. The time simulation is performed at a sampling frequency of 50 MHz, using a digital shunt modelled with a sampling rate of 50 kHz. The natural frequency ω_s of the structure has been modified to give the ratio between the shunt sampling frequency f_{sample} and the targeted frequency $f_s = \omega_s/(2\pi)$ as 500, 200 and 50 in (a), (b) and (c), respectively. The response is shown for a shunt calibration without correction for delay (solid green), for the correction in (16)-(17) with both forward Euler integration (solid blue) and the full ZOH integration in (12) (dashed blue). Finally, a more detailed correction for resonant shunts in [15] is also included (solid red), based on pole matching between the Laplace and discrete domain, and Tustin's method for the discretization of the the transfer function.

While the proposed correction, using either ZOH or Euler integration, is not as accurate as the shunt implementation from [15], a significant improvement compared to the case without correction is still obtained by the proposed correction when the ratio between the sampling and targeted frequency is at least 200. In the conducted experiments for the composite blade, the target frequency was 166 Hz with a sampling frequency of 50 kHz, corresponding to $f_{sample}/f_s \approx 300$ for which the simplified correction with Euler integration is considered sufficiently accurate and thus implemented in [14] because of its simplicity.

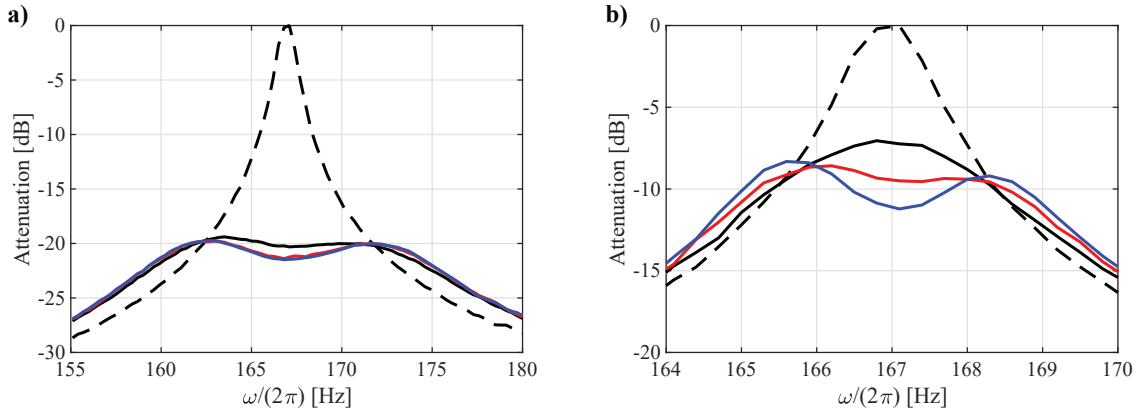

Figure 6: Attenuation of accelerance at the top of the composite blade with an EEMCF of $\kappa_s = 0.074$ in (a) and $\kappa_s = 0.016$ in (b), with response for a shunt in OC condition (dashed black), and with a series RL-shunt calibrated without correction (solid black), with partial correction (solid red) and full correction for losses (solid blue).

4 Bias resistance and dielectric losses

In Sec. 2.2, the bias resistance R_b of the digital shunt hardware is neglected by considering it to be part of the inherited resistance in the piezoelectric transducer. This section briefly describes how the influence of the resistance can be accounted for in the shunt calibration.

The influence of dielectric losses in the piezoelectric transducer on the accuracy of shunt calibration is considered. The dielectric loss is modeled as a hysteresis loss by the introduction of a complex capacitance $\tilde{C}_s^\infty = C_s^\infty(1-i\eta_\varepsilon)$ in the governing equations in (1)-(2). By impedance matching at the targeted frequency ω_s, it can be shown that the inductance L and resistance R of a series RL-shunt can be corrected for the influence of dielectric losses by

$$\frac{L}{\bar{L}} = \frac{1}{\eta_\varepsilon^2\bar{\lambda}^2 + \eta_\varepsilon^2\bar{\rho}^2 - 2\eta_\varepsilon\bar{\rho} + 1} \tag{18}$$

$$\frac{R}{\bar{R}} = \frac{1 - \frac{\eta_\varepsilon}{\bar{\rho}}(\bar{\lambda}^2 + \bar{\rho}^2)}{\eta_\varepsilon^2\bar{\lambda}^2 + \eta_\varepsilon^2\bar{\rho}^2 - 2\eta_\varepsilon\bar{\rho} + 1} \tag{19}$$

where $\bar{L}$ and $\bar{R}$ are the optimal inductance and resistance when dielectric losses are neglected, and $\bar{\lambda} = \omega_s C_s^\infty \bar{L}$, $\bar{\rho} = \omega_s C_s^\infty \bar{R}$. Further papers are in preparation for a deeper insight of the problem, showing that the influence of the corrections in (18)-(19) increases for larger dielectric losses η_ε and small EEMCFs κ_s.

The dielectric loss η_ε can be considered as a frequency-dependent resistor $1/(\omega\eta_\varepsilon C_s^\infty)$ in parallel with the capacitor C_s^∞. The bias resistance of the shunt circuit R_b can then be combined with the inherited dielectric loss of the piezoelectric transducer. When evaluated at the target frequency ω_s, the combined loss is given as

$$\eta = \frac{1}{\omega_s R_b C_s^\infty} + \eta_\varepsilon \tag{20}$$

By letting $\eta_\varepsilon = \eta$ in (18) and (19), the influence of the bias resistance R_b can thus be directly included in the correction for dielectric losses.

The influence of the dielectric losses η_ε and the bias resistance R_b on the tuning of a series RL-shunt attached to the composite blade is demonstrated experimentally in Fig. 6 for the piezoelectric patches in rows 4-6 from the bottom of the blade with $\kappa_s = 0.074$ in (a) and for the patches in row 8 with $\kappa_s = 0.016$ in (b). The frequency response at the top of the blade is shown in Fig. 6 for the shunt in the OC condition (dashed black), for an RL-shunt calibrated without correction for dielectric loss (solid black) and with the correction for dielectric loss in (18)-(19) (solid blue). The ideal response of the shunt is characterized by two peaks of equal magnitude in the frequency response curve. While the magnitudes of the two peaks in Fig. 6 are not exactly identical, the corrected calibration response is substantially more accurate than the calibration neglecting dielectric losses, especially for small EEMCFs.

In the present example, the modal parameters are estimated by modal analysis from impedance measurements using the digital shunt. The bias resistance R_b is thereby directly applied as an inherited parallel resistance and included in the correction for dielectric losses (solid blue). When the bias resistance is removed from the transfer function of the measured impedance, the correction for dielectric losses does not account for the bias resistance (solid red). For low EEMCFs, it is seen that including the bias resistance R_b in the correction for dielectric losses gives a more accurate tuning compared to the case where the bias resistance is neglected.

5 Conclusion

The present paper considers practical design considerations for digital piezoelectric shunts. The importance of accounting for the delay introduced by the digital control unit is illustrated, and a simplified correction based on an ideal delay assumption is shown to be accurate when the ratio between the sample and target frequency is at least 200. Finally, it is demonstrated experimentally that the bias resistance in the digital shunt hardware can be included in the proposed correction for dielectric losses, improving the accuracy of the shunt implementation.

REFERENCES

[1] U. Andreaus and M. Porfiri, “Effect of electrical uncertainties on resonant piezoelectric shunting,” *Journal of Intelligent Material Systems and Structures*, vol. 18, no. 5, pp. 477–485, 2007.

[2] B. Lossouarn, M. Aucejo, J.-F. Deü, and B. Multon, “Design of inductors with high inductance values for resonant piezoelectric damping,” *Sensors and Actuators, A: Physical*, vol. 259, pp. 68–76, 2017.

[3] O. Thomas, J. Ducarne, and J.-F. Deü, “Performance of piezoelectric shunts for vibration reduction,” *Smart Materials and Structures*, vol. 21, 2012.

[4] K. Dekemele, P. Van Torre, and M. Loccufier, “High-voltage synthetic inductor for vibra-

tion damping in resonant piezoelectric shunt," *Journal of Vibration and Control*, vol. 27, 2021.

[5] A. J. Fleming, S. Behrens, and S. O. R. Moheimani, "Synthetic impedance for implementation of piezoelectric shunt-damping circuits," *Electronic Letters*, vol. 36, no. 18, 2000.

[6] G. Raze, A. Jadoul, S. Guichaux, V. Broun, and G. Kerschen, "A digital nonlinear piezoelectric tuned vibration absorber," *Smart Materials and Structures*, vol. 29, 2020.

[7] S. O. R. Moheimani and A. J. Fleming, *Piezoelectric Transducers for Vibration Control and Damping*. Springer, 2006.

[8] G. Matten, M. Collet, S. Cogan, and E. Sadoulet-Reboul, "Synthetic Impedance for Adaptive Piezoelectric Metacomposite," *Procedia Technology*, vol. 15, pp. 84–89, 2014.

[9] J. Nečásek, J. Václavík, and P. Marton, "Digital synthetic impedance for application in vibration damping," *Review of Scientific Instruments*, vol. 87, no. 2, 2016.

[10] J. Nečásek, J. Vaclavik, and P. Marton, "Comparison of analog front-ends for digital synthetic impedance device," *Proceedings of the 2017 IEEE International Workshop of Electronics, Control, Measurement, Signals and their Application to Mechatronics, ECMSM 2017*, 2017.

[11] C. Sugino, M. Ruzzene, and A. Erturk, "Digitally Programmable Resonant Elastic Metamaterials," *Physical Review Applied*, vol. 13, no. 6, p. 1, 2020.

[12] G. Raze, J. Dietrich, B. Lossouarn, and G. Kerschen, "Shunts vs. networks: tuning and comparison of centralized and decentralized piezoelectric vibration absorbers," *Smart Materials and Structures*, vol. 31, 2022.

[13] J. Dietrich, "Vibration Mitigation of Bladed Structures Using Piezoelectric Digital Vibration Absorbers," Ph.D. dissertation, University of Liege, 2023.

[14] J. D. Richardt, B. Lossouarn, J. Høgsberg, and J.-F. Deü, "Sensorless Calibration of Piezoelectric Shunts using Capacitance Measurements," *Smart Materials and Structures*, 2025.

[15] G. Raze, J. Dietrich, and G. Kerschen, "Onset and stabilization of delay-induced instabilities in piezoelectric digital vibration absorbers," *Journal of Intelligent Material Systems and Structures*, vol. 33, no. 16, pp. 2033–2048, 2022.

[16] K. Yamada, H. Matsuhisa, H. Utsuno, and K. Sawada, "Optimum tuning of series and parallel LR circuits for passive vibration suppression using piezoelectric elements," *Journal of Sound and Vibration*, vol. 329, pp. 5036–5057, 2010.

[17] G. F. Franklin, J. D. Powel, and A. Emami-Naeini, *Feedback Control of Dynamic Systems*, 4th ed. Prentice Hall, 2002.

XI ECCOMAS Thematic Conference on Smart Structures and Materials - SMART 2025
M. Krommer, M. Nader and M. Schagerl (Eds)

Received: 28 April 2025 / Revised: 31 August 2025 / Accepted: 3 October 2025
© The Author(s) 2025

A Semi-Active Metastructure System for Vibroacoustic Isolation

Giorgos M. Sarmas, Ilias A. Tsakonas, Dimitris K. Dimitriou, Nikolaos A. Chrysochoidis, Dimitris A. Saravanos, Christoforos S. Rekatsinas

Abstract.
Metastructures have the potential to suppress vibrations by utilizing local resonators tuned to frequencies within a bandwidth near the modal frequencies of the baseline structure. The present vibration suppression mechanism relies on the interaction between the host structure and the local resonators, which act as multiple-tuned mass dampers (TMDs). Unlike a single TMD, multiple TMDs significantly increase the effective frequency range of vibration attenuation, forming a bandgap. Our previous studies [1], [2] demonstrated the effectiveness of a piezoelectric semi-active TMD equipped with an R-L circuit in achieving high and adaptable vibration reduction performance through the judicious selection of the resistive and inductive loads. Building on this foundation, the current work presents a numerical investigation of one-dimensional piezoelectric metastructures. The conceptual framework leverages recent advancements in the 4D printing concept, allowing the development of metastructures equipped with multiple piezoelectric resonators. The numerical models employed in this study encompass simple lumped-mass systems to analyze axial vibrations and beam models to investigate bending vibrations, both incorporating piezoelectric resonators. Each resonator is mechanically tuned to operate at the same modal frequency, and an R-L circuit is connected to its terminals, providing electromechanical coupling capabilities. This integration facilitates the dynamic adjustment of bandgap properties efficiently and effectively. This study aims to investigate the vibration attenuation mechanisms and assess their influence on the structure's steady-state dynamic response by introducing multiple poles and zeros into the electromechanical system. The potential of the current approach, including the ideal number of resonators, the effectiveness of the piezoelectric characteristics, and the influence of circuit parameters, is thoroughly studied.

Key words: piezoelectric resonators, metastructure, tuned mass dampers, bandgap, electromechanical response.

Giorgos Sarmas & Ilias Tsakonas & Dimitris Dimitriou & Nikolaos Chrysochoidis & Dimitris Saravanos
Department of Mechanical and Aeronautical Engineering, University of Patras, Patras University Campus, 26504, Patras, Greece, e-mail: nchr@mech.upatras.gr

Christoforos Rekatsinas
National Center of Scientific Research, Demokritos

1 INTRODUCTION

In modern engineering applications, the need for effective vibration mitigation and vibration-based energy harvesting has become more critical than ever. Unwanted vibrations and noise not only compromise performance but also increase wear, reduce lifespan and raise safety concerns. As a result, various vibration control strategies have been investigated. A well-established approach is the integration of a baseline structure with passive tuned mass dampers (TMDs) or dynamic vibration absorbers (DVAs) [3].While effective, TMDs typically perform well only at a single resonant frequency, making them unsuitable for broadband vibration control. To address this limitation, they have been coupled with piezoelectric [1], [2] and electromagnetic transducers [4], granting them semi-active characteristics. Shunting these transducers with electrical circuits, the vibration attenuation and energy dissipation can be enhanced by leveraging the circuit's dissipative and dynamic properties. Another widely studied approach involves the bonding of piezoelectric patches on the main structure, giving raise into electromechanical coupling and vibration tailoring [5], [6], [7].

Another promising methodology, which is similar, encompasses the periodical placement of locally resonant elements on the vibrating structure, forming what is known as a metastructure. Through careful parametric tuning of these resonant elements, metastructures can introduce frequency bands where vibration transmission is significantly suppressed, the so-called bandgaps or stopbands. Extensive research has been conducted on achieving both single [8], [9] and multiple bandgaps [10] for beam structures. A basic factor in the procedure of incorporating absorbers is their added mass. In this context, conserved-mass approaches and optimized procedures have been explored for axial [11] and bending vibrations [12] to develop lightweight structures with the proper dynamic responses. Another crucial challenge is the synergy between vibration control and energy harvesting. Over the last decade, research on vibration-based energy harvesting has grown significantly, exploring various energy conversion mechanisms, such as electromagnetic and piezoelectric, tailored to specific applications [13], [14].

Building on our group's previous research [1], [2], [15], current work explores the attenuation capabilities of multiple semi-active TMDs on uniform bars and beams for axial and bending vibrations, respectively. The physical model of each TMD consists of a diamond-shaped frame equipped with a piezoelectric stack transducer, modelled as a single-degree-of-freedom system. To achieve the semi-active characteristics, a resistor-inductor (RL) circuit is connected to the terminals of the stack. In this way, the whole system acquires electromechanical behavior, leveraging the dissipative and dynamic characteristics of the circuit. The vibration attenuation performance, as well as the efficiency to create tunable vibration bandgaps, will be studied.

2 DYNAMICS OF PIEZOELECTRIC SATMD

The equation of motion of a passive single-degree-of-freedom TMD is:

$$m_d\ddot{u}_d + c_d\dot{u}_d + k_d u_d = f \tag{1}$$

where $u_d, \dot{u}_d, \ddot{u}_d,$ represent the displacement, velocity, and acceleration responses under the excitation force f. However, for the SATMD, considering that a part of the kinetic energy is converted into electrical at the PZT terminals, the connected spring-damper elements of TMD are replaced with a piezoelectric transducer (PZT), **Figure 1**.

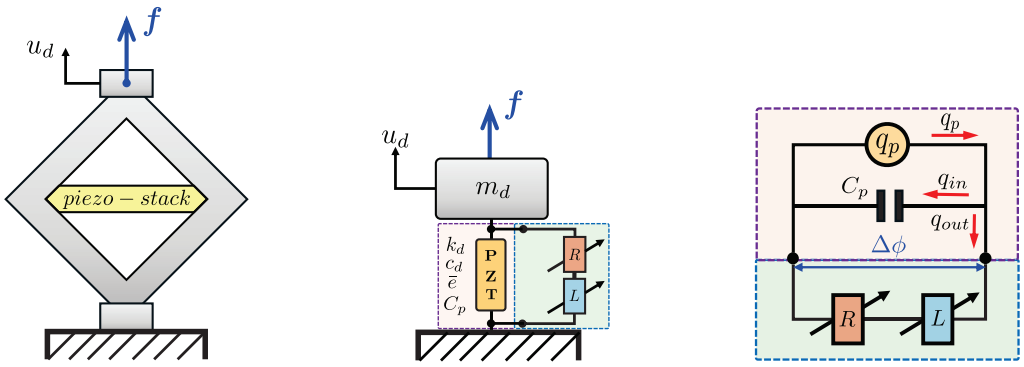

(a) (b) (c)

Figure 1: Modeling of SATMD, (a): Diamond-shaped SATMD, (b): Lumped model, (c): Circuit.

Hence, the equation of motion of the SATMD has the following form:

$$m_d\ddot{u}_d + c_d\dot{u}_d + k_d u_d + \bar{e}\Delta\phi = f \tag{2}$$

With:

$$\begin{cases} f_m = k_d u_d \\ f_e = \bar{e}\Delta\phi \end{cases} \tag{3}$$

Expressing the mechanical f_m and the electrical f_e force generated in the piezoelectric stack [15]. k_d represents the mechanical stiffness of the piezoelectric device, $\bar{e}$ [N/V] stands for the equivalent piezoelectric stress coefficient of the piezoelectric stack, indicating the level of the piezoelectric coupling, and $\Delta\phi$ is the generated voltage due to the direct piezoelectric effect. Examining the electric quantities as presented in **Figure 1**c, a source of electric charge, q_p, is generated from the relative movement of the piezoelectric stack and divided into the one that charges the inherent piezoelectric capacitor, q_{in}, and the one that flows as current in the connected circuit, q_{out}. The equilibrium of electric charges in the circuit is:

$$q_p = q_{in} + q_{out} \tag{4}$$

where:

$$\begin{cases} q_p = \bar{e}u_d \\ q_{in} = C_p\Delta\phi \end{cases} \tag{5}$$

and C_p is the inherent capacitance of the piezoelectric stack. Now we can distinguish between two cases:

Case1: Open Circuit Conditions

If the PZT is in an open-circuit condition ($q_{out} = 0$), this leads only to the charge of the capacitor:

$$q_{in} = q_p \tag{6}$$

and the corresponding equation of motion takes the form:

$$m_d\ddot{u}_d + c_d\dot{u}_d + \left(k_d + \bar{e}^{\,2}/C_p\right)u_d = f \tag{7}$$

The above equation implies that the internal energy of the system is stored in the form of either strain energy in the springs or as electric energy in the piezoelectric element, resulting in a stiffness variation of the system by the piezoelectric coupling term ($\bar{e}^{\,2}/C_p$).

Case2: Shunt Circuit

Shunting the PZT with a resistor and an inductor in series, and applying Kirchhoff's Voltage Law at the respective loops of the circuit, **Figure 1**c:

$$\Delta\phi = L\ddot{q}_{out} + R\dot{q}_{out} = \frac{q_{in}}{C_p} \tag{8}$$

Combining equations (2), (4), and (8), the equations of motion of the shunted SATMD can be written as:

$$\begin{bmatrix} m_d & 0 \\ 0 & L \end{bmatrix}\begin{Bmatrix} \ddot{u}_d \\ \ddot{q}_{out} \end{Bmatrix} + \begin{bmatrix} c_d & 0 \\ 0 & R \end{bmatrix}\begin{Bmatrix} \dot{u}_d \\ \dot{q}_{out} \end{Bmatrix} + \begin{bmatrix} k_p & -\bar{e}/C_p \\ -\bar{e}/C_p & 1/C_p \end{bmatrix}\begin{Bmatrix} u_d \\ q_{out} \end{Bmatrix} = \begin{Bmatrix} f \\ 0 \end{Bmatrix} \tag{9}$$

where $k_p = k_d + \bar{e}^{\,2}/C_p$.

In the above form, one can see that inductance and resistance play the role of phenomenal mass and damping, respectively.

3 DEVELOPMENT OF GLOBAL MATRICES

In the finite element model of the metastructure, the total degrees of freedom (DOFs) consist of (1) the mechanical DOFs of the host structure, (2) the mechanical DOFs of the SATMDs, and (3) the electric DOFs (output electric charges) which arise from the shunted piezoelectric element of each SATMD. Hence, the vector of total DOFs is:

$$\boldsymbol{u_{tot}} = \{\boldsymbol{u}_h, \boldsymbol{u}_d, \boldsymbol{q}\}^{\mathrm{T}}_{(N+2n)\times 1} \tag{10}$$

where N: number of DOFs of the host structure, n: number of SATMDs, $\boldsymbol{u}_h$: mechanical DOFs of the host structure, and $\boldsymbol{u}_d$ & $\boldsymbol{q}$ are the mechanical and electric DOFs of the SATMDs, respectively. For a better understanding of the following procedure, the construction of rod matrices is only presented assuming a single SATMD connected to the 2nd DOF. The addition of multiple SATMDs is similar and easily reproducible. When a SATMD is incorporated into

a host DOF characterized by effective mass m_1, damping c_1 and stiffness k_1, it alters the host DOF dynamics, resulting in a coupled system of equations:

$$\begin{bmatrix} m_1 & 0 & 0 \\ 0 & m_d & 0 \\ 0 & 0 & L \end{bmatrix} \begin{Bmatrix} \ddot{u}_h \\ \ddot{u}_d \\ \ddot{q} \end{Bmatrix} + \begin{bmatrix} c_1 + c_d & -c_d & 0 \\ -c_d & c_d & 0 \\ 0 & 0 & R \end{bmatrix} \begin{Bmatrix} \dot{u}_h \\ \dot{u}_d \\ \dot{q} \end{Bmatrix} + \begin{bmatrix} k_1 + k_p & -k_p & \bar{e}/C_p \\ -k_p & k_p & -\bar{e}/C_p \\ \bar{e}/C_p & -\bar{e}/C_p & 1/C_p \end{bmatrix} \begin{Bmatrix} u_h \\ u_d \\ q \end{Bmatrix} = \begin{Bmatrix} f \\ 0 \\ 0 \end{Bmatrix} \quad (11)$$

where u_h is the host DOF, u_d and q are the mechanical and electric DOFs of the SATMD.

The global unconstrained stiffness matrix of the rod is:

$$[\boldsymbol{K}_0] = \begin{bmatrix} k_0 & -k_0 & 0 & \cdots & 0 \\ -k_0 & 2k_0 & -k_0 & \cdots & 0 \\ 0 & -k_0 & 2k_0 & \cdots & 0 \\ \vdots & \vdots & \vdots & \ddots & -k_0 \\ 0 & 0 & 0 & -k_0 & k_0 \end{bmatrix}_{N\times N} \quad (12)$$

where $k_0 = EA/L_e$, E: Young's modulus, A: cross-section area and L_e the finite element length. The lumped elemental mass matrix is utilized for the lumped rod model, therefore:

$$[\boldsymbol{M}_0] = \text{diag}([m_0, 2m_0, 2m_0, \dots, m_0])_{N\times N} \quad (13)$$

where $m_0 = \rho A L_e/2$, ρ: density.

From Eq. (11) and (12) the whole structure's unconstrained stiffness matrix is:

$$[\boldsymbol{K}] = \begin{bmatrix} k_0 & -k_0 & 0 & \cdots & 0 & 0 & 0 \\ -k_0 & 2k_0 + k_p & -k_0 & \cdots & 0 & -k_p & \bar{e}/C_p \\ 0 & -k_0 & 2k_0 & \cdots & 0 & 0 & 0 \\ \vdots & \vdots & \vdots & \ddots & -k_0 & 0 & 0 \\ 0 & 0 & 0 & -k_0 & k_0 & \vdots & \vdots \\ 0 & -k_p & 0 & 0 & \cdots & k_p & -\bar{e}/C_p \\ 0 & \bar{e}/C_p & 0 & 0 & \cdots & -\bar{e}/C_p & 1/C_p \end{bmatrix}_{(N+2)\times(N+2)} \quad (14)$$

and the mass matrix, Eq. (11) and (13):

$$[\boldsymbol{M}] = diag(\{ m_0, 2m_0, \dots, 2m_0, m_0, m_d, L \}) \quad (15)$$

Rayleigh damping is introduced for the damping matrix of the metastructure, and the steady-state response is calculated via the dynamic stiffness matrix:

$$\boldsymbol{U} = ([\boldsymbol{K}] + j\omega[\boldsymbol{C}] - [\boldsymbol{M}]\omega^2)^{-1}\boldsymbol{F} \quad (16)$$

where $\boldsymbol{U}$: is the complex amplitude vector and $\boldsymbol{F}$: the generalized force vector, $j^2 = -1$.
The outlines represent the contribution of the SATMD dynamics in the already calculated matrices.

4 NUMERICAL CASE STUDIES

Consider a cantilever rod and beam equipped with multiple SATMDs positioned at regular intervals, separated by a distance d, **Figure** 2.

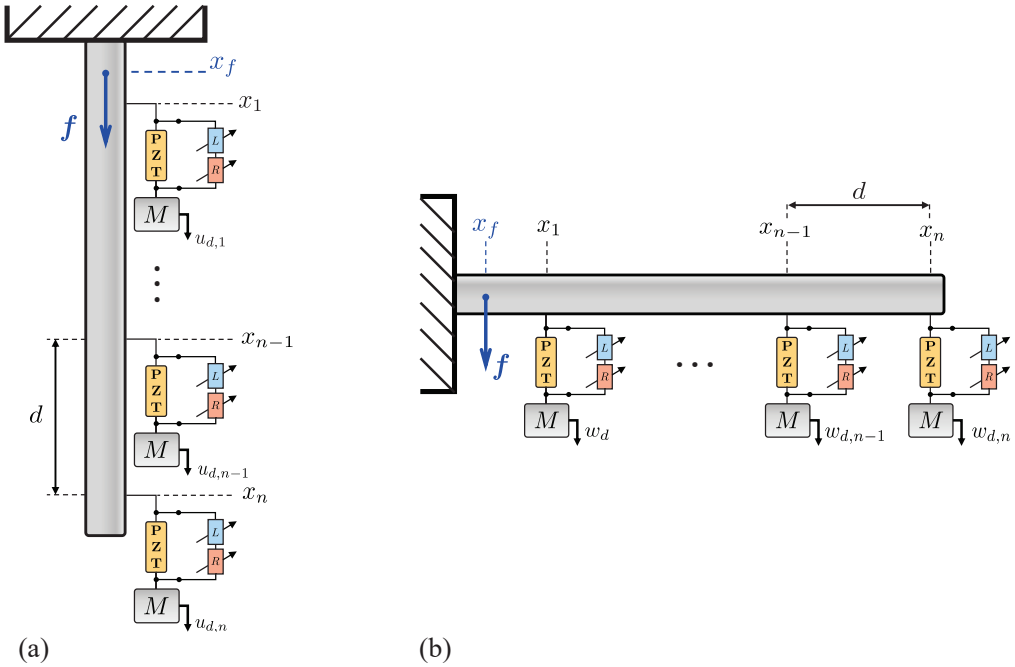

Figure 2: Metastructure models (a): Rod and (b): Beam.

The material properties of the plain structures and the electrical characteristics of commercially available piezoelectrics for the SATMDs are listed in Tables 1 and 2, respectively. The SATMDs are mechanically tuned to the same eigenfrequency for each model, and each unit is shunted to an RL circuit. A harmonic force is applied near the cantilevered end, at $x_f = 0.05$ m. A key parameter in the analysis is the mass ratio:

$$\mu = \frac{\sum_{i=1}^{n} m_{d,i}}{m_{hs}} = \frac{m_{d,tot}}{m_{hs}} \tag{17}$$

where m_{hs} is the host structure mass and $m_{d,tot}$ is the total mass of the absorbers. In this study, the mass ratio is maintained constant, i.e., independent of the number of SATMDs (n). Therefore, $m_{d,i}$ (SATMD mass) and $k_{d,i}$ (SATMD stiffness) must be adjusted appropriately to keep the same SATMD natural frequency as n increases.

Table 1: Geometric and material characteristics of rod and beam

	Length [m]	Height [m]	Width [m]	Young's Modulus [GPa]	Density [kg/m^3]
Rod	1	0.025	0.05	70	2800
Beam	1	0.0167	0.667	70	2800

Table 2: SATMDs characteristics

	$\bar{e}$ [N/V]	C_p [μF]
Rod SATMD	5	2.2
Beam SATMD	0.2	2.2

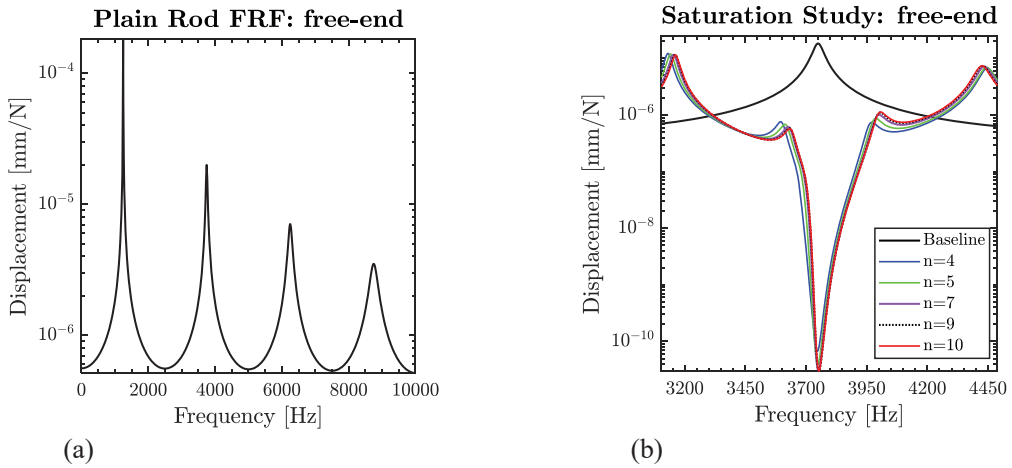

Figure 3: Rod FRFs at its free-end (a): Plain rod, (b): Saturation study at the rod's 2nd mode.

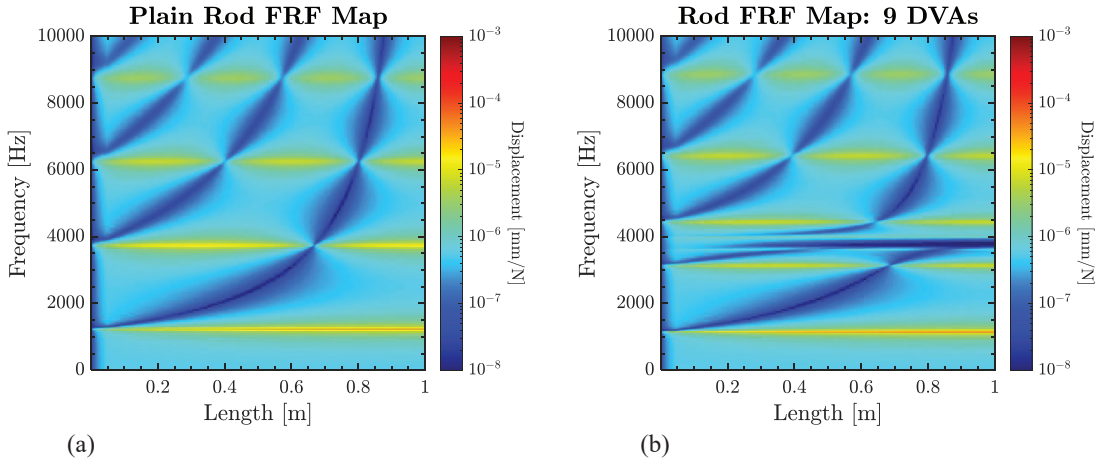

Figure 4: Rod FRF maps, (a): Baseline, (b): Rod with 9 SATMDs.

4.1. Rod with multiple SATMDs

The forced response of the plain rod of **Figure 2**a was simulated at the free end and is presented in **Figure 3**a. This case study aims to suppress the second and third vibration modes. Additionally, introducing the vibration suppression configuration influences the structure's

global dynamic characteristics, which will be investigated to ensure a holistic understanding of the system's performance. Specifically, each of the added SATMDs was tuned at the second mode (3750 Hz) via selecting the appropriate stiffness as the mass ratio μ was set at 0.1. A saturation study is conducted to determine an optimal number of SATMDs [9] and is illustrated in **Figure 3**b.

Based on this study, nine SATMDs were modelled on the rod with $x_1 = 0.285$ m and $d = 0.0894$ m. Aiming to provide a more detailed demonstration of the plain rod's dynamic response **Figure 4**a presents a spatial representation of the FRFs, serving as a baseline reference. On the other hand, **Figure 4**b demonstrates the metastructure's dynamic response. The emergence of an oscillatory bandgap centered around 3750 Hz is obvious, with an estimated bandwidth of 200 Hz and spatial coverage of approximately 0.5 meters. Notably, the bandgap intensity increases with distance from the point of excitation.

Beyond passive tuning, electromechanical coupling is introduced by equipping each SATMD with identical inductors. This generates additional dynamics through electric poles and zeros that arise from the inductors. **Figure 5**a illustrates how the free-end bandgap bandwidth evolves under varying inductance, assuming negligible resistance. Two key effects are observed: (1) the electrically introduced antiresonance creates a new bandgap (right antiresonance zone), passing from higher to lower frequencies while its bandwidth gradually increases, and (2) the mechanical bandgap (left antiresonance zone) is also moving downward in frequency, but its bandwidth progressively decreases. The electric component tends to stabilize in frequency at higher inductance values while the mechanical component gradually diminishes. The reason is that the current flowing through the inductor (for negligible resistance) is:

$$I_{out} = \frac{\Delta\phi}{j\omega L} \to 0 \quad \text{as} \quad L \text{ increases}, \qquad j^2 = -1 \tag{18}$$

This drives the PZT into an open-circuit (OC) condition, decreasing its effective stiffness. These phenomena demonstrate the potential of electromechanical coupling in tuning the bandgap locations and enhancing vibration suppression, providing added flexibility in controlling the system's dynamic response.

The next objective is to suppress vibrations at the free-end corresponding to the third mode, at 6450 Hz, with the set of resonators mechanically tuned at 2nd mode. As shown in **Figure 5**a the right-side antiresonance crosses 6450 Hz when the inductance is approximately 380μH. At this value, two electromechanical bandgaps emerge: one centered at 6450 Hz and another appearing at 3230 Hz. It is evident that the appropriate selection of the connected inductance can tune the desired mechanical bandgap to alternative frequency ranges. The 2nd available tuning parameter is the resistance. In this case, increasing the resistance causes the bandgap to shift toward higher frequencies as higher resistance values gradually drive PZT into OC condition, **Figure 5**b. Interestingly, an optimal resistance, $R = 5\Omega$, yields substantial simultaneous attenuation for both the 2nd and 3rd modes, **Figure 5**c. These results highlight the potential of inductance and resistance regulation as an effective tool for adaptive vibration suppression.

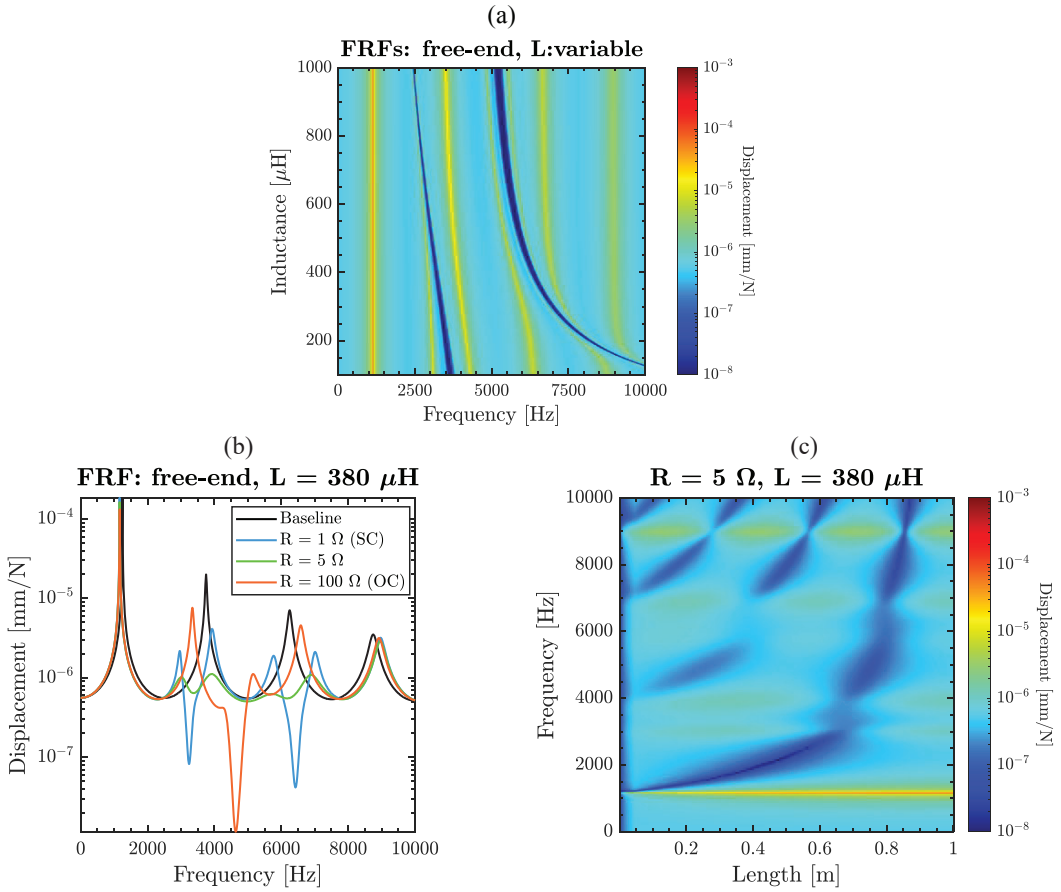

Figure 5: Metastructure Rod FRFs, (a): Frequency-Inductance-Displacement map at rod's free-end, (b): FRFs at rod's free-end with variable resistance, (c): FRF map for whole structure.

4.2. Beam with multiple SATMDs

In the context of the current case study, the oscillatory performance of the beam **Figure 2**b is studied. The dynamic response for the normal displacement of the plain beam at the tip is illustrated in **Figure 6**a, serving as a baseline response. Similar to the rod study case, the objective here is to suppress both the third and fourth natural frequencies at the beam tip. With $\mu = 0.1$, the saturation study determined that eight SATMDs can create a stable mechanical bandgap centered around the 3rd natural frequency at 237 Hz. The 8 SATMDs were positioned with $x_1 = 0.23m$ and $d = 0.11m$. Implementing the SATMDs shifts the fourth natural frequency from 465 to 475 Hz, as observed in **Figure 6**b, while **Figure 6**c demonstrates the variation of electromechanical bandgaps simulated at the beam tip as a function of the connected inductance to the terminals of each SATMD. Based on this analysis, an inductance value of 55 mH is selected to suppress the modal response at 475 Hz effectively.

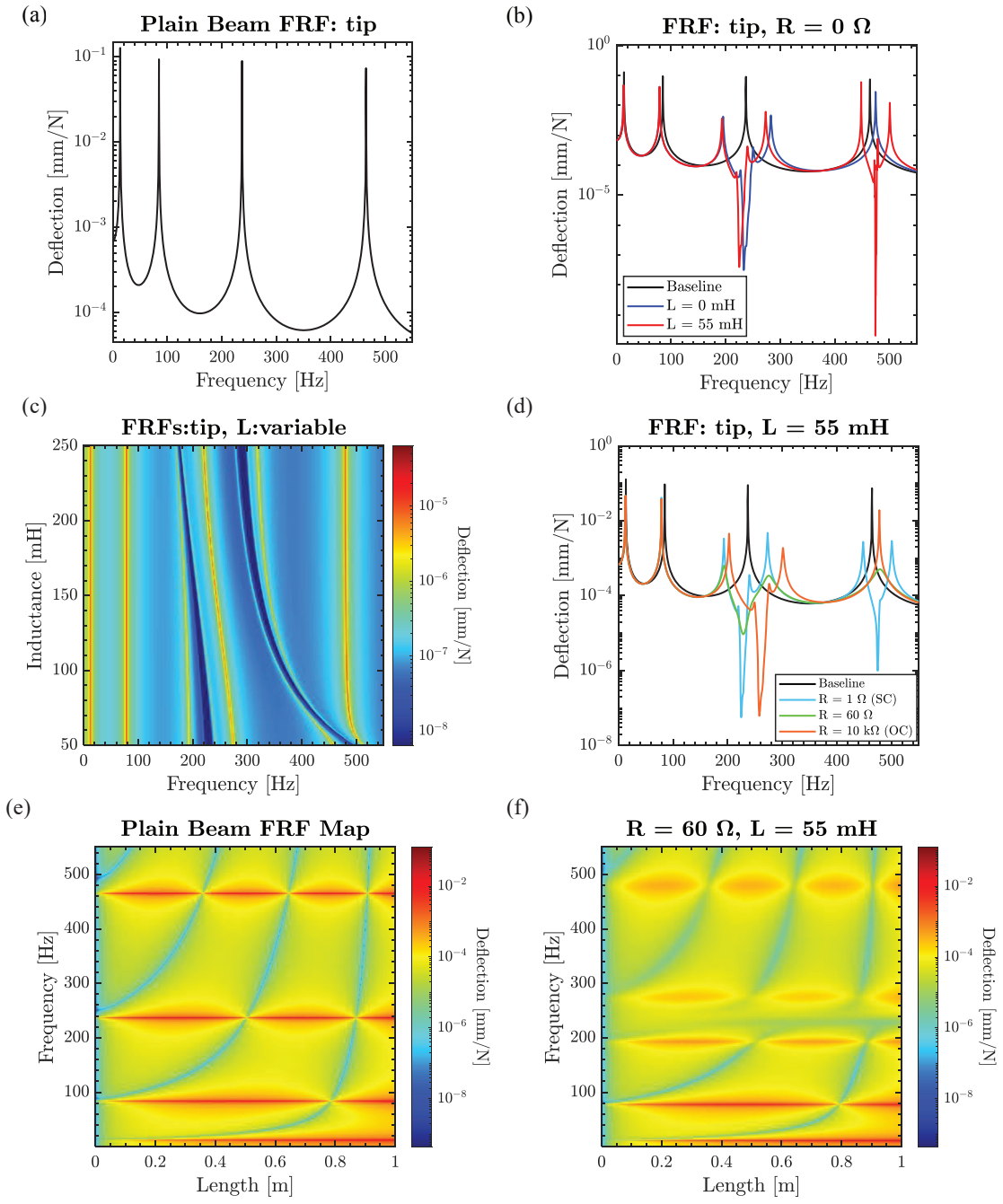

Figure 6: Beam FRFs, (a): Plain beam FRF at the tip, (b): Metabeam FRF at the tip for different inductance values, (c) Metabeam FRF map with variable inductance for the tip, (d) Metabeam FRF at the tip for different resistance values, (e) Plain beam FRF map for whole structure, (f): Metabeam FRF map for whole structure.

With a fixed inductance value, the attention is focused on the connected resistance, selecting three resistance values: $R = 1\Omega$ for SC conditions, $R = 60\,\Omega$ as an optimal value and finally $R = 10k\Omega$ for the OC. For these values, the free end, normal displacement FRFs are presented in **Figure 6**d. Spatial representation of the dynamic response is performed in **Figure 6** e and f correlating the plain beam with the beam equipped with the set of 8 SATMDs, respectively. These figures demonstrate the drastic attenuation achieved across the length of the beam for all the frequency range exceeding the 3rd modal frequency.

5 CONCLUSIONS

This study demonstrated the effectiveness of SATMDs in suppressing targeted vibration modes in beam and rod structures through mechanical and electromechanical tuning. Initially, passive suppression was achieved by aligning the mechanical bandgaps with the targeted natural frequencies. A saturation study confirmed that nine SATMDs were necessary for the rod and eight for the beam, with a 10% mass ratio, ensuring lightweight feasibility. The introduction of electromechanical coupling by integrating an RL circuit into each SATMD, enabled further flexibility in tuning the dynamic response. Inductance variation allowed for the creation and repositioning of additional bandgaps, while resistance regulation provided significant damping effects. The resulting frequency shifts, including the ability to move bandgaps to higher or lower frequencies, highlight the adaptive nature of this approach. In the rod case, the second and third vibration modes were successfully suppressed through appropriate combinations of inductance and resistance, with optimal performance observed at 380 μH and 5 Ω, respectively. Similarly, in the beam case, the third and fourth modes were attenuated, with 55 mH inductance and 60 Ω resistance, providing effective suppression. Overall, the results confirm that electromechanical tuning via multiple SATMDs offers a promising and versatile solution for adaptive vibration control in lightweight structural applications. The method provides precise control over bandgap location and bandwidth, enabling suppression of multiple vibration modes with minimal added mass.

ACKNOWLEDGMENTS

This work is funded by the research project 4D-PIEZOUMME that is implemented in the framework of H.F.R.I call “Basic research Financing (Horizontal support of all Sciences)” under the National Recovery and Resilience Plan “Greece 2.0” funded by the European Union – NextGenerationEU (H.F.R.I. Project Number: 16580).

Further support was provided by the funding program “MEDICUS”, of the University of Patras

REFERENCES

[1] G. M. Chatziathanasiou, N. A. Chrysochoidis, and D. A. Saravanos, “A semi-active shunted piezoelectric tuned mass damper for robust vibration control,” *Journal of Vibration and Control*, vol. 28, no. 21–22, pp. 2969–2983, Nov. 2022, doi: 10.1177/10775463211026487.

[2] G. M. Chatziathanasiou, N. A. Chrysochoidis, C. S. Rekatsinas, and D. A. Saravanos, “A semi-active shunted piezoelectric tuned-mass-damper for multi-modal vibration control of large flexible structures,” *J Sound Vib*, vol. 537, p. 117222, Oct. 2022, doi: 10.1016/j.jsv.2022.117222.

[3] S. Elias and V. Matsagar, "Research developments in vibration control of structures using passive tuned mass dampers," *Annu Rev Control*, vol. 44, pp. 129–156, 2017, doi: 10.1016/j.arcontrol.2017.09.015.

[4] M. Auleley, O. Thomas, C. Giraud-Audine, and H. Mahé, "Enhancement of a dynamic vibration absorber by means of an electromagnetic shunt," *J Intell Mater Syst Struct*, vol. 32, no. 3, pp. 331–354, Feb. 2021, doi: 10.1177/1045389X20957097.

[5] O. Thorp, M. Ruzzene, and A. Baz, "Attenuation and localization of wave propagation in rods with periodic shunted piezoelectric patches," *Smart Mater Struct*, vol. 10, no. 5, pp. 979–989, Oct. 2001, doi: 10.1088/0964-1726/10/5/314.

[6] L. Airoldi and M. Ruzzene, "Wave Propagation Control in Beams Through Periodic Multi-Branch Shunts," *J Intell Mater Syst Struct*, vol. 22, no. 14, pp. 1567–1579, Sep. 2011, doi: 10.1177/1045389X11408372.

[7] S. Manzoni, M. Berardengo, F. Boccuto, and M. Vanali, "Piezoelectric-shunt-based approach for multi-mode adaptive tuned mass dampers," *Mech Syst Signal Process*, vol. 200, p. 110537, Oct. 2023, doi: 10.1016/j.ymssp.2023.110537.

[8] C. Sugino, S. Leadenham, M. Ruzzene, and A. Erturk, "On the mechanism of bandgap formation in locally resonant finite elastic metamaterials," *J Appl Phys*, vol. 120, no. 13, Oct. 2016, doi: 10.1063/1.4963648.

[9] R. Yazbeck, R. Fernandes, J. G. Boyd, D. C. Lagoudas, and S. El-Borgi, "Effect of resonator location and boundary conditions on bandgap formation in a locally resonant beam metastructure," *Mechanics of Advanced Materials and Structures*, pp. 1–10, Jan. 2025, doi: 10.1080/15376494.2025.2452369.

[10] S. El-Borgi, R. Fernandes, P. Rajendran, R. Yazbeck, J. G. Boyd, and D. C. Lagoudas, "Multiple bandgap formation in a locally resonant linear metamaterial beam: Theory and experiments," *J Sound Vib*, vol. 488, p. 115647, Dec. 2020, doi: 10.1016/j.jsv.2020.115647.

[11] K. K. Reichl and D. J. Inman, "Lumped mass model of a 1D metastructure for vibration suppression with no additional mass," *J Sound Vib*, vol. 403, pp. 75–89, Sep. 2017, doi: 10.1016/j.jsv.2017.05.026.

[12] E. E. Basta, M. Ghommem, and S. A. Emam, "Vibration suppression and optimization of conserved-mass metamaterial beam," *Int J Non Linear Mech*, vol. 120, p. 103360, Apr. 2020, doi: 10.1016/j.ijnonlinmec.2019.103360.

[13] Q. Cai and S. Zhu, "The nexus between vibration-based energy harvesting and structural vibration control: A comprehensive review," *Renewable and Sustainable Energy Reviews*, vol. 155, p. 111920, Mar. 2022, doi: 10.1016/j.rser.2021.111920.

[14] M. A. Mangi *et al.*, "Applications of piezoelectric-based sensors, actuators, and energy harvesters," *Sensors and Actuators Reports*, vol. 9, p. 100302, Jun. 2025, doi: 10.1016/j.snr.2025.100302.

[15] G. Chatziathanasiou, "Development and application of a novel semi-active piezoelectric tuned mass damper for robust vibration control of flexible structures with focus on airframe structures," University of Patras, Department of Mechanical Engineering & Aeronautics, Division of Applied Mechanics, Technology of Materials and Biomechanics, Applied Mechanics Laboratory, 2024. doi: 10.12681/eadd/57187.

XI ECCOMAS Thematic Conference on Smart Structures and Materials - SMART 2025
M. Krommer, M. Nader and M. Schagerl (Eds)

Received: 29 April 2025 / Revised: 1 October 2025 / Accepted: 3 October 2025
© The Author(s) 2025

A Nonlinear Piezoelectric Shunt Absorber with 2:1 Internal Resonance and Saturation

Olivier Thomas, Christophe Giraud-Audine, Zein A. Shami

Abstract. We present a theoretical and experimental analysis of a new nonlinear piezoelectric shunt absorber designed to attenuate the vibration of an elastic structure under external excitation. This absorber is formed by connecting the elastic structure, via a piezoelectric patch, to an electrical shunt circuit consisting of a resonant shunt combined in series with a nonlinear voltage component, that includes a quadratic and a cubic components, and with its natural frequency tuned to half that of the target mechanical mode. As a consequence, a two to one internal resonance occurs, generating a strong coupling between the mechanical mode and the electrical mode that leads to the creation of a nonlinear antiresonance that replaces the mechanical resonance of the elastic structure. The antiresonance amplitude is also subjected to a saturation, thus becoming independant of the input amplitude and giving this absorber an advantage over the standard linear absorbers. The presentation will describe the shunt circuit and its optimization, its main nonlinear components, and the use of the normal form theory to adjust the value of the cubic component, necessary to improve the performance of the absorber.

Key words: piezoelectric shunt absorbers, 2:1 internal resonance, normal form, saturation phenomenon, nonlinear vibrations

1 INTRODUCTION

In this article, a nonlinear piezoelectric shunt is considered. The purpose is to reduce the vibrations of an elastic structure thanks to an electromechanical energy transfer between this structure and an electronic circuit, through a piezoelectric transducer. The idea, in contrast to active control strategies [1], is to use the most passive electronic circuit possible, in order to avoid instabilities and to obtain a miniaturized device. As shown by many authors, standard piezoelectric shunts, called resistive and resonant, are the electrical analogues of standard Lanchester and Frahm absorbers [2, 3]. In those cases, the electric circuit is simply a single resistor for the first case, whereas it includes also an inductor for the second case. They work by

Olivier Thomas & Zein A. Shami
Arts et Metiers Institute of Technology, LISPEN, Lille, France
e-mail: olivier.thomas@ensam.eu

Christophe Giraud-Audine
Arts et Metiers Institute of Technology, L2EP, Lille, France

Zein A. Shami
ONERA, Chatillon, France

dissipating the vibration energy, transforming it into heat in the resistor, as well as by generating forces that counteract the vibrations of the structure, using resonant principles.

Whereas those basic working principle are purely linear, electronic circuits offer the freedom to include nonlinearities. As described in the introduction parts of [4, 5, 6, 7], to which the reader is redirected for details, a wide variety of nonlinear phenomena exist and four families of mechanical dampers may be considered. First, the Nonlinear Energy Sinks (NES) family, for which an essential nonlinearity is in use. Their extension to piezoelectric shunt is recent [8, 9]. The second family is based on the Nonlinear Tuned Vibration Absorbers (NLTVA) concept, for which the absorber must be the mirror of the mechanical structure. In the case of a nonlinear primary structure, the absorber is thus also nonlinear and can be made with a piezoelectric shunt [10]. The third family is the one of the Synchronized Switch Dampers (SSD), originaly proposed in [11], based on switching the electromechanical transducer on two distinct shunt impedances, synchronously with the oscillations of the host structure, obtaining significant performance with respect to their linear analogues [12]. Finally, the present article proposes to take advantage of the singular properties of nonlinear couplings thanks to internal resonances. It summarises three complementary contributions of the literature [4, 6, 5, 7], based on a 1:2 internal resonance.

2 BASICS OF A 1:2 INTERNAL RESONANCE

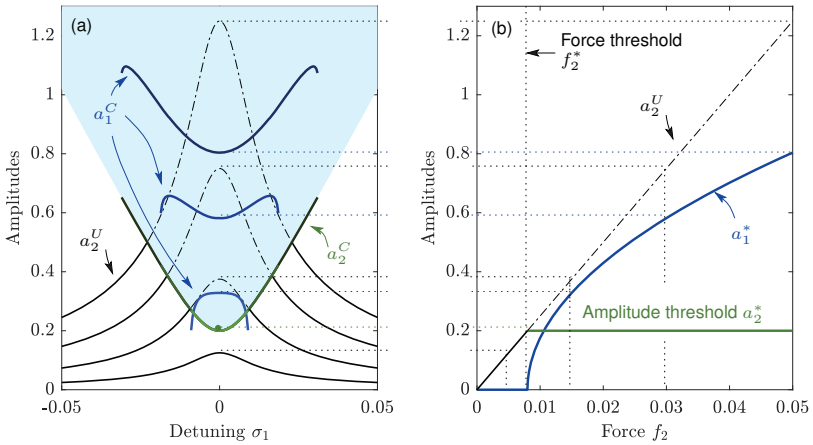

Figure 1: Typical response of Eqs. (1) obtained with the multiple scale method [4]. (a) amplitudes a_1 and a_2 as a function of the detuning $\sigma_1 = \Omega - \omega_2$ for several values of the forcing $f_2 = F \in \{0.005; 0.015; 0.03; 0.05\}$; (b) amplitudes a_1 and a_2 for a forcing at the antiresonance ($\Omega = \omega_2$), as a function of the forcing F. The numerical values are $\alpha_1 = \alpha_2 = 0.1$, $\xi_1 = \xi_2 = 0.005$. Superscript U refers to the uncoupled solution (in black) whereas superscript C refers to the coupled solution (in blue for a_1 and in green for a_2). The blue shaded area depicts the instability region for a_2.

In a nonlinear system, if the ratio of two modal frequencies ω_i and ω_j is a rational number,

namely $q\omega_i \simeq p\omega_j$, $p, q \in \mathbb{N}$, a strong coupling between the two corresponding modes can occur, leading to a particular resonant exchange of energy between the modes, called an internal resonance. In our case, we focus on a 1:2 internal resonance, meaning that two modes of the system fulfills the relation $\omega_2 \simeq 2\omega_1$ between their modal frequencies. To fix the ideas, let us consider the following set of two oscillators coupled by quadratic resonant terms:

$$\ddot{x}_1 + 2\xi_1\omega_1\dot{x}_1 + \omega_1^2 x_1 + \alpha_1 x_1 x_2 = 0, \tag{1a}$$

$$\ddot{x}_2 + 2\xi_2\omega_2\dot{x}_2 + \omega_2^2 x_2 + \alpha_2 x_1^2 = F\cos\Omega t. \tag{1b}$$

where $x_1(t), x_2(t)$ are two unknown functions of time t, $\dot{\diamond} = \mathrm{d}\diamond/\mathrm{d}t$, ω_1, ω_2 are the natural frequencies, ξ_1, ξ_2 are the damping ratio, α_1, α_2 are the coefficients of the quadratic nonlinear terms, F is the forcing amplitude and Ω its angular frequency. We also consider the case for which the natural frequencies are tuned, such that $\omega_2 = 2\omega_1$. With the forcing localised on the second oscillator (the first oscillator is not forced) and around its resonance ($\Omega \simeq \omega_2$), the solution can be approximated by $x_1(t) = a_1\cos(\Omega/2t + \varphi_1)$ and $x_2(t) = a_2\cos(\Omega t + \varphi_2)$, with typical evolutions of the amplitudes (a_1, a_2) as functions on the frequency Ω and the forcing F shown in Fig. 1. Typically, the classical resonant response $a_2 = f(\Omega)$ (denoted a_2^U) of the second oscillator becomes unstable in a region around its resonance, giving birth to a stable coupled response, with an energy transfer to the first oscillator, with a non zero response $a_1^C = f(\Omega)$. Moreover, it is observed that the coupled response of $a_2^C = f(\Omega)$ shows a minimum (at $\Omega = 2\omega_1 = \Omega_2$), in the form of a kind of antiresonance, *which is independent of the forcing amplitude* F, resulting in a *saturation phenomena* above a given threshold, that depends on the damping ξ_2. At this particular antiresonance frequency, all the energy above this threshold is transferred to the first oscillator. Notice that the oscillation frequency of the first (slave) oscillator occurs at $\Omega/2$, half the driving frequency.

The idea of this article is to artificially create this coupling by a nonlinear and resonant electrical circuit tuned at half a resonance of a host mechanical structure, to reduce its acuity using this saturation phenomenon.

3 MODELLING

We consider an arbitrary elastic structure subjected to an external excitation and connected to a shunt circuit via a piezoelectric patch (PE Patch) as shown in Fig. 2. The circuit includes an inductance L which, together with the capacitance C of the PE patch, create an electrical resonator that is tuned at half a target resonance: $\omega_e = 1/\sqrt{LC} \simeq \omega_m/2$, where ω_e and ω_m are the natural frequencies of the electrical resonator and the elastic structure. Then, a resistor R models the electrical losses and a voltage source $V_{\text{nl}} = \beta_q V^2 + \beta_c V^3$ (with V the voltage across the terminals of the PE patch and $\beta_q, \beta_c \in \mathbb{R}$ two gains) is included in the circuit to create the nonlinearity, with quadratic and cubic nonlinear terms, in order to activate a 2:1 internal resonance between the elastic mode at ω_m and the electrical mode at ω_e. In practice, a semi-passive circuit made of operational amplifiers is used [6, 7].

Considering a single mode motion (the displacement $\boldsymbol{U}$ at any point $\boldsymbol{x}$ of the structure is written $\boldsymbol{U}(\boldsymbol{x}, t) = \boldsymbol{\Phi}(\boldsymbol{x})q(t)$, with $\boldsymbol{\Phi}$ the considered mode shape) and following [13], the be-

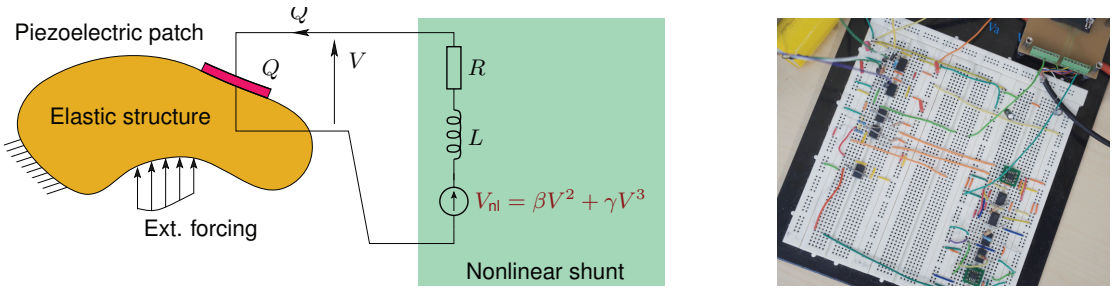

Figure 2: Mechanical structure coupled to a nonlinear shunt circuit and practical implementation

haviour of the system is governed by the pair $(q(t), Q(t))$ of its (mechanical) modal coordinate and the electric charge in the piezoelectric patch, such that:

$$\ddot{q} + 2\xi\omega_m\dot{q} + \omega_m^2 q + \frac{\theta}{mC}Q = \frac{F}{m}\cos\Omega t \tag{2a}$$

$$\ddot{Q} + 2\xi_e\omega_e\dot{Q} + \omega_e^2 Q + \frac{\theta}{LC}q + \frac{V_{\text{nl}}}{L} = 0 \tag{2b}$$

where m, ξ, and F are respectively the modal mass, damping ratio and forcing. θ is the piezoelectric coupling coefficient and C is the effective capacitance of the piezoelectric patch [14]. The electric natural frequency, damping factor and piezoelectric coupling coefficient are:

$$\omega_e = \frac{1}{\sqrt{LC_{\text{pi}}}}, \quad \xi_e = \frac{R}{2}\sqrt{\frac{C_{\text{pi}}}{L}}, \quad \kappa = \frac{\theta}{\omega_m\sqrt{Cm}}. \tag{3}$$

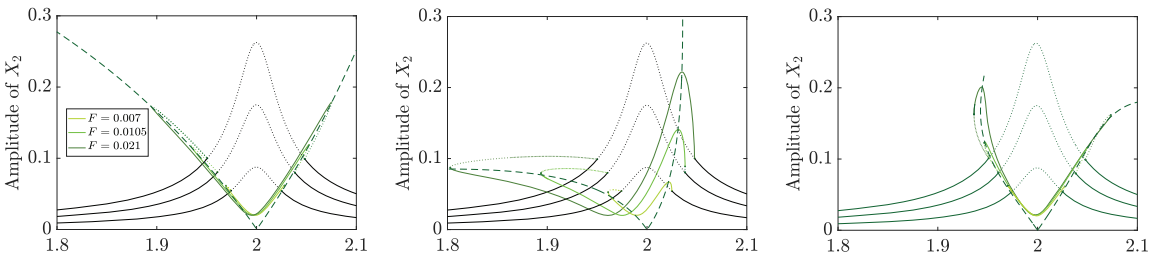

Figure 3: Amplitude of the mechanical oscillator as a function of the forcing frequency Ω. (left) case with only the two resonant quadratic terms of Eq. (1); (middle) case with all quadratic terms (Eq. (2)) without cubic term $\beta_c = 0$ in V_{nl}; (right) case with all quadratic terms (Eq. (2)) with a cubic term correction $\beta_c = 10\beta_q^2/9$ in V_{nl}.

This two degree of freedom nonlinear model (2a,b) can be solved either by numerical continuation methods (we used the software Manlab [15]) or by analytical perturbation methods. This enables to first show that the figure of merit of the system is the term $\xi_e/(\kappa\beta_q)$: thus, increasing

the gain β_q improves the performances and can also counterbalance, in a certain extent, a high ξ_e and a low κ [4].

However, since quadratic terms are to be created, a first choice is to select a quadratic only nonlinear voltage, $V_{\text{nl}} = \beta_q V^2$. As shown in [4], diagonalising the linear part of Eqs. (2a,b) to approach the canonical model (1) leads to create additional quadratic terms in the equations. Whereas the two quadratic terms of Eqs. (1a,b), called resonant terms [16], are responsible of the main features of the energy transfer and notably the saturation phenomena, the effect of the other terms is not negligible as it creates a slight detuning of the antiresonance frequency that depends on the amplitude of the forcing [5] (see Fig. 3(middle)). As shown theoretically in [5] with a second order multiple scale analysis, the effect of these additional unwanted quadratic terms is equivalent to cubic terms in a normal form expansion, such that their effect can be partially cancelled by adding a cubic nonlinearity, such that $V_{\text{nl}} = \beta_q V^2 + \beta_c V^3$, with $\beta_c = 10\beta_q^2/9$. This correction effect is successfully illustrated in Fig. 3(right).

4 EXPERIMENTAL VALIDATION

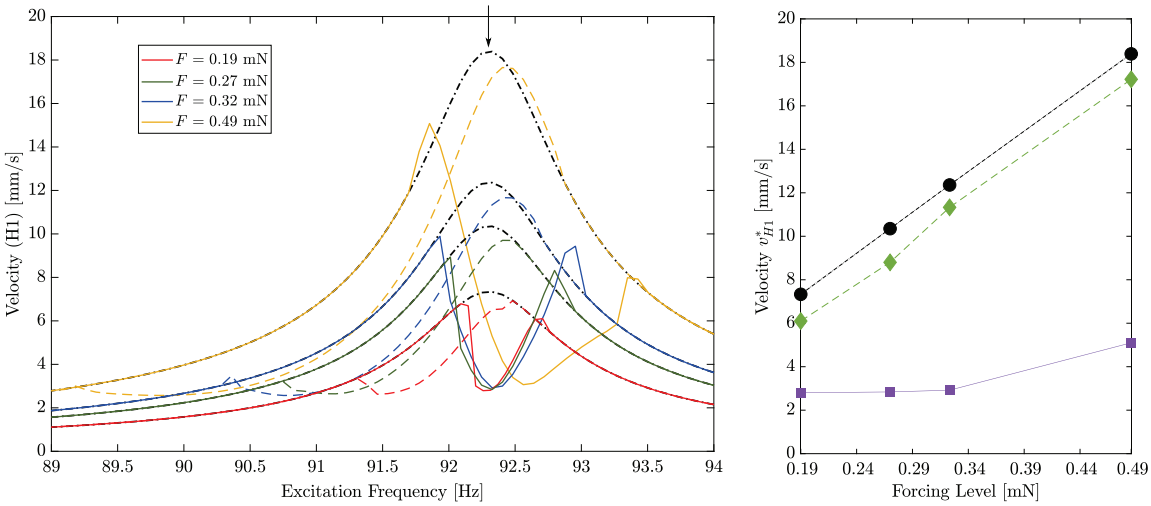

Figure 4: Experimental results; (left) vibration amplitude of the structure as a function of the excitation frequency: '-·-': without shunt; '---': without cubic correction; '—' with cubic correction; (right) vibration amplitude at the antiresonance as a function of the forcing amplitude (black) without shunt; (green) without cubic correction; (purple) with cubic correction.

Experimental validations of the theory exposed in the previous sections are proposed in [6] with a quadratic voltage source and in [7] with an additional cubic term to counterbalance the antiresonance detuning and recover an amplitude saturation. In both cases, the nonlinearities are practically implemented with analog mutipliers. Figure 4 shows experimental results measured on a foil model equipped with a piezoelectric patch (see [7] for details), showing the ability of

the nonlinear shunt to (1) replace a resonance by an antiresonance and (2) to create a saturation at this antiresonance, thanks to the cubic correction.

5 CONCLUSIONS

In this article, the proof of concept of a piezoelectric nonlinear shunt, based on a 1:2 internal resonance, was theoretically and experimentally introduced, with further details present in [4, 5, 6, 7]. The nonlinear circuit implementation was based on operational amplifiers and analog multipliers, that necessitate a power supply. A promising idea, naturally offered by electronic circuits, is to use the (nonlinear) saturation phenomena observed in operational amplifiers or diodes. Pioneering works include the artificial changing of the tuning of a linear resonant shunt thanks to a diode [17], and the design of an efficient NES with a saturated operational amplifier [18]. The former, associated to high inductance passive components [19] is a way of designing efficient fully passive nonlinear shunt circuits.

REFERENCES

[1] A. Preumont, *Vibration Control of Active Structures: An Introduction*. Springer, 2018.

[2] O. Thomas, J. Ducarne, and J.-F. Deü, "Performance of piezoelectric shunts for vibration reduction," *Smart Materials and Structures*, vol. 21, no. 1, p. 015008, Jan. 2012.

[3] M. Auleley, O. Thomas, C. Giraud-Audine, and H. Mahé, "Enhancement of a dynamic vibration absorber by means of an electromagnetic shunt," *Journal of Intelligent Material Systems and Structures*, vol. 32, no. 3, pp. 331–354, Feb. 2021.

[4] Z. A. Shami, C. Giraud-Audine, and O. Thomas, "A nonlinear piezoelectric shunt absorber with a 2:1 internal resonance: Theory," *Mechanical Systems and Signal Processing*, vol. 170, p. 108768, 2022.

[5] Z. A. Shami, Y. Shen, C. Giraud-Audine, C. Touzé, and O. Thomas, "Nonlinear dynamics of coupled oscillators in 1:2 internal resonance: effects of the non-resonant quadratic terms and recovery of the saturation effect," *Meccanica*, vol. 57, pp. 2701–2731, 2022.

[6] Z. A. Shami, C. Giraud-Audine, and O. Thomas, "A nonlinear piezoelectric shunt absorber with 2:1 internal resonance: experimental proof of concept," *Smart Materials and Structures*, vol. 31, p. 035006, 2022.

[7] ——, "Saturation correction for a piezoelectric shunt absorber based on 2:1 internal resonance using a cubic nonlinearity," *Smart Materials and Structures*, vol. 32, p. 055024, 2023.

[8] T. M. P. Silva, M. A. Clementino, C. D. M. Jr., and A. Erturk, "An experimentally validated piezoelectric nonlinear energy sink for wideband vibration attenuation," *Journal of Sound and Vibration*, vol. 437, pp. 68–78, 2018.

[9] K. Dekemele, C. Giraud-Audine, and O. Thomas, "A piezoelectric nonlinear energy sink shunt for vibration damping," *Mechanical Systems and Signal Processing*, vol. 220, p. 111615, 2024.

[10] B. Lossouarn, J.-F. Deü, and G. Kerschen, "A fully passive nonlinear piezoelectric vibration absorber," *Philosophical Transactions of the Royal Society A*, vol. 376, p. 20170142, 2028.

[11] C. Richard, D. Guyomar, D. Audigier, and G. Ching, "Semi-passive damping using continuous switching of a piezoelectric device," in *Proc. of SPIE Smart Structures and Materials Conference: Passive Damping and Isolation*, vol. 3672, 1999, pp. 104–111.

[12] J. Ducarne, O. Thomas, and J.-F. Deü, "Structural vibration reduction by switch shunting of piezoelectric elements: modelling and optimization," *Journal of Intelligent Materials Systems and Structures*, vol. 21, no. 8, pp. 797–816, 2010.

[13] O. Thomas, J.-F. Deü, and J. Ducarne, "Vibration of an elastic structure with shunted piezoelectric patches: efficient finite-element formulation and electromechanical coupling coefficients," *International Journal of Numerical Methods in Engineering*, vol. 80, no. 2, pp. 235–268, 2009.

[14] M. Berardengo, O. Thomas, C. Giraud-Audine, and S. Manzoni, "Improved resistive shunt by means of negative capacitance: new circuit, performances and multi-mode control," *Smart Materials and Structures*, vol. 25, no. 7, p. 075033, 2016.

[15] L. Guillot, A. Lazarus, O. Thomas, C. Vergez, and B. Cochelin, "A purely frequency based floquet-hill formulation for the efficient stability computation of periodic solutions of ordinary differential systems," *Journal of Computational Physics*, vol. 416, p. 109477, 2020.

[16] O. Thomas, "Understanding, computing and identifying the nonlinear dynamics of elastic and piezoelectric structures thanks to nonlinear modes," in *Model Order Reduction for Design, Analysis and Control of Nonlinear Vibratory Systems*, C. Touzé and A. Frangi, Eds. Springer Series CISM courses and lectures, 2025.

[17] Z. A. Shami, C. Giraud-Audine, and O. Thomas, "A nonlinear tunable piezoelectric resonant shunt using a bilinear component: theory and experiment," *Nonlinear Dynamics*, vol. 111, pp. 7105–7136, 2023.

[18] K. Dekemele, C. Giraud-Audine, and O. Thomas, "A nonlinear saturating amplifier circuit for piezoelectric vibration conrol of flexible mechanical systems," in *Proc. of the XIth. ECCOMAS Thematic Conference on Smart Structures and Materials – SMART 2025*, Linz, Asutria, Jul. 2025.

[19] B. Lossouarn, M. Aucejo, J.-F. Deü, and B. Multon, "Design of inductors with high inductance values for resonant piezoelectric damping," *Sensors and Actuators, A: Physical*, vol. 259, pp. 68–76, 2017.

Part III
MS 02 - ADVANCED MODELLING, DESIGN AND TESTING OF SMART COMPOSITE STRUCTURES
Aurelio Araujo, Enrico Zappino

XI ECCOMAS Thematic Conference on Smart Structures and Materials - SMART 2025
M. Krommer, M. Nader and M. Schagerl (Eds)

Received: 28 April 2025 / Revised: 31 August 2025 / Accepted: 5 October 2025
© The Author(s) 2025

Materials informatics approaches for the layering of smart composites

Adrian Ehrenhofer, Thomas Wallmersperger

Abstract. A large variety of active and passive materials can be combined to realize the same function – such as shape adaptation – in a smart composite. Each material offers a unique set of advantages and disadvantages, ranging from activation stimulus and mechanical parameters to environmental impact and costs. Materials informatics comprises a set of computationally powered methods for designing these kinds of composites in a data-driven way. Based on the processing of the material (such as synthesis parameters of a polymer), the material properties (such as the capabilities for active expansion or the elastic modulus) of a material can be predicted. Together with continuum-based models, the performance of a specific application can be evaluated. Furthermore, non-mechanical criteria for the performance can be included. This closes the chain of the well-known Processing→Structure→Property→Performance relations and allows the end-to-end design of active-passive composites.

In the current work, we present the background of every link in the chain – from data sources to composite scale performance parameters – and a realization of this end-to-end design process, which is based on an Artifical Neural Network model for Processing→Property prediction and the Stimulus-Expansion-Model for Property→Performance prediction. For an active mesh setup – i.e., a mesh that is open and breathable in dry state, but becomes water-proof when it is actuated – we demonstrate this end-to-end process in action, which allows the high-throughput screening of material combinations to identify promising candidates for experimental validation.

Key words: Materials Informatics, Data-driven Modeling, Continuum-based Simulation, Smart Structures, Active-Passive Composites

Adrian Ehrenhofer & Thomas Wallmersperger
Institute of Solid Mechanics, Technische Universität Dresden, George-Bähr-Str. 3c, 01159 Dresden, Germany, e-mail: adrian.ehrenhofer@tu-dresden.de

1 Introduction

There are various methods for modeling active behavior of smart composites for designing solutions to engineering challenges, ranging from the molecular scale up to the system scale [1, 2, 3, 4, 5, 6]. These kinds of models are mostly focused on the understanding of physical processes and continuum-based modeling approaches of materials and systems. Methods from *Materials Informatics* leverage high computational power and large amounts of data, while including less physical knowledge of the included processes [7]. Various tools based on this paradigm are available to facilitate the process of material discovery [8, 9, 10]. In the current work, we show how the steps in the Processing→Structure→Property→Performance (PSPP) chain [11] are realized for smart composites, and how Materials Informatics approaches are applied towards an end-to-end design approach for this kind of system.

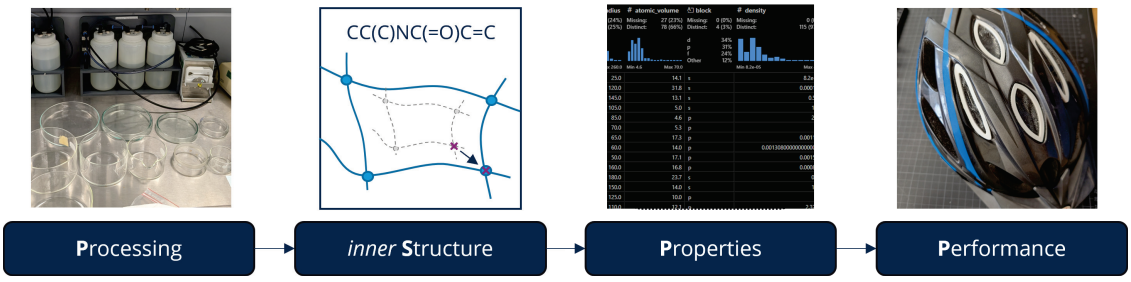

Figure 1: The PSPP-chain for the example of a smart helmet cover according to Ref. [12]. The task of the smart composite is to close the helmet's ventilation openings (to become water-repellent) when it starts raining.

The current work starts with the description of the constituents of the PSPP chain and the description of the specific example from the class of Soft–Hard Active–Passive Embedded Structures (SHAPES) [6] – an automatically rainproofing mesh – which is presented in Figure 1. The different interconnected steps in the PSPP chain are presented in section 2 and details about models that connect the steps are provided. In section 3, data-driven approaches from Materials Informatics to connect the points by leapfrogging specific models, are provided. Finally, the implications of these approaches to the way we design smart composites are discussed in section 4.

2 Constituents of the Processing→Structure→Property→Performance chain for active-passive composite systems

Different active and passive materials can be combined into Soft–Hard Active–Passive Embedded Structures (SHAPES), which can solve engineering challenges [6, 13]. One functional concept is the manipulation of flow/obstruction, which was previously realized, e.g., for switchable particle permeability [14] and for an active mesh [12].

In the current work we will focus on this active mesh application, which solves the following problem: When riding a bike, a helmet is typically not water-resistant, because a high

breathability is beneficial against sweating. When it starts raining, a separate part – a helmet cover – is added against the rain. Our previously presented technology solves this by introducing a hydrogel-coated mesh that will automatically become rain-resistant due to the rainwater [15, 12]. An image of the current prototype of the product is shown in Figure 1.

As a Soft–Hard Active–Passive Embedded Structure (SHAPES), the active mesh comprises a backbone mesh and an active material layer made of a hydrogel. The combination of active and passive component must be adapted to each other to allow this function as a Case I (constrained) expansion behavior (i.e., the backbone mesh is not deformed due to the activation of the hydrogel), as presented in Ref. [16].

The system insofar poses only moderate challenges to the description of active behavior: Upon water contact, the pores either close or they do not. Modeling the maximum expansion of the hygro-responsive hydrogel material is therefore sufficient for an initial design. Only in later steps, additional requirements are included – such as *fast*[1] time behavior, *adequate* elastic modulus, *high* wear resistance, or *adequate* high activation cycle behavior/fatigue behavior.

	2.1 **Processing**	2.2 **Inner Structure**	2.3 **Properties**	2.4 **Performance**
Explanation	Which steps are taken to obtain the material? Which parameters describe these steps?	What is the inner (atomic/molecular) arrangement of the chemical elements inside the material?	Which parameters allow the description of the material's reaction to the stimulus?	Does this fulfill the requirements in the envisioned application?
Smart mesh hydrogel example	Thermally initiated free radical polymerization and cross-linking.	Statistical copolymer with hydrophilic side-groups and low cross-linking density.	Maximum swelling $q_{\max} = \ldots$	Closing of the pores: YES/NO.

Table 1: Explanation of the nodes in the PSPP relationship with the smart mesh example.

This adaptation starts at the level of material choice, synthesis conditions, and additional processing steps. Methods from the field of *Materials Informatics* can be beneficially applied in this context: The so-called fourth paradigm of material science leverages methods from machine learning, high throughput simulations, and multi-parameter optimization with generative approaches [7]. These methods are applied to tackle different complicated relations in the well-known Processing→Structure→Property→Performance chain [11]. The constituents of the chain are presented in Table 1 at the example of the above-mentioned smart helmet cover and a hydrogel material. It must however be noted that this only shows one specific realization: It is one of the characteristics of the PSPP relationships that different processing steps may lead

[1]Please note that these terms in italic are qualitative. In a typical design process, they must be quantified, as discussed in section 2.4.

to the same inner structure, while different inner structures may lead to the same properties, and different properties of a material may also lead to the same performance.

Here, the starting point is the set of parameters of a manufacturing process, which must be adequately represented as numerical values, see section 2.1. This is followed by the inner structure in section 2.2 and the relevant properties of a material that follow from it (see section 2.3). For the final step to the performance of SHAPES – such as the smart helmet cover – specialized continuum models will be introduced, see section 2.4. Please note that, while the current work is mostly focused on modeling approaches, there is always the need for experimental validation of each description approach. Therefore, experimental validation methods are included in the sections, as well.

2.1 Numerical values and embeddings for processing parameters

Processing describes the set of all steps that lead to a material in the smart composite [11]. In the current context, a material is a specific realization of its class: For example, a poly(N-isopropyl acrylamide) hydrogel with specified synthesis conditions is itself a material, while a change in any of these processing parameters leads to a new material (which can however have very similar properties). It can however be disputed if the change of an *insignificant* parameter (e.g., the change of the color of the glass in which the polymerization is performed) still leads to another material. The evaluation whether a processing parameter is significant or not, is itself an important task in the processing parameter definition [17].

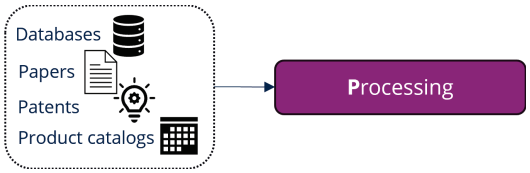

Figure 2: For obtaining processing parameters, there are different types of available resources, which must be carefully considered.

As shown in Figure 2, the input can be obtained from various sources. Both, aspects for general inclusion in material design processes, as in materials informatics approaches, are presented:

- Material data can be obtained from **databases** that provide typical steps that must be performed to obtain a certain material, and the relevant machine parameters. Often, these kinds of databases with experiences are tightly-kept company secrets, especially in the context of Small and Medium Enterprises that heavily depend on this kind of internal know-how, because disclosing them (in the form of papers or patents) would endanger their technology leadership. However, there is also an increasing interest in open source datasets, which are made available online in the context of data science, e.g., on kaggle.com, huggingface.co, or from specific institutions (e.g., materialhub.de which is developed in cooperation with TU Dresden).

- **Scientific publications** that disclose methods (and specific realizations of materials obtained by these methods) can also be a valuable data source. Material scientists and engineers mostly focus their work on answering specific scientific questions and provide data points that are relevant and indicative to their interpretation. This has a profound impact on the available data points in the high-dimensional processing parameter space – especially because negative results are only rarely published [18, 19]. For data-driven methods, the impact of this bias is especially notable.

- When new processing methods are invented in scientific institutions, they are often followed by **Patent** applications. However, even method-focused patents are generally written such that only minimal information is disclosed; their integration into a PSPP workflow must therefore be handled carefully.

- Various forms of **Product catalogs** that are available from suppliers can be a data-source as well. Especially in the context of product design, only obtainable materials are relevant. However, these datasets are also sparse points in the parameter space. In the data-driven context, they can only serve as evaluation points for inference of an already (pre-)trained model.

In the context of data-driven approaches, it must be noted that different platforms have different requirements about how their data can be used: While open datasets include a license (such as the well-known open licenses such as Apache, BSD, GPL, or MIT licenses [20]), it must be retrieved from the terms of usage of a database provider, if – and under which requirements – data scraping for scientific purposes is allowed. Different requirements can include, e.g., a total number of data points that can be extracted, or a number of database queries per time. Further information about the rules of automated access is also provided in a `robots.txt` file, which is present on many websites.

The task of identifying relevant parameters for a material creation process is tedious. In our previous works [17, 21], the processing parameters for different hydrogels were manually gathered and interpreted. Current machine-learning based tools still do not show an adequate performance in handling scientific papers, in which the information is distributed among main text, figures (diagrams, sample images), tables, supplementary materials documents and even self-citations/references to previous works.

Besides the discovery and evaluation of their significance, the adequate representation of the processing steps in numerical values is highly relevant. Different fabrication methods that lead to the same material type – e.g., UV-initiated or thermally initiated polymerization of hydrogels – can be represented by discrete values, as shown in Ref. [17]. However, assigning discrete numbers to different methods does not adequately capture their similarity. This problem can be circumnavigated by applying the concept of embedding spaces that is known from natural language processing, which will be discussed in future works.

2.2 Deciphering the inner structure of a material

The *inner* structure of a material, which is based on the processing, governs the material's behavior [11]. The term *inner* is added to avoid confusion with other definitions of structure in engineering context. This field of materials science is very complex, because the specific arrangement of atoms – e.g., in macro-molecules or crystals – governs their specifics, and the same chemical elements can lead to entirely different materials, which is especially visual in Carbon (graphite, carbon nanotubes, graphene, diamond) and metal complexes.

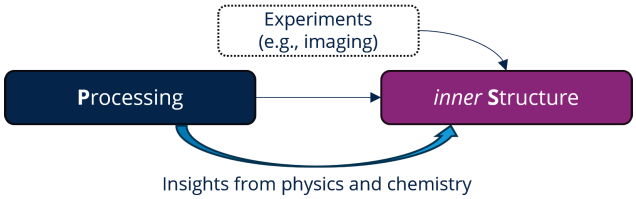

Figure 3: The transition to the inner structure, based on the processing, is performed through a combination of modeling and experimental insights from the fields of physics and chemistry. Some experimental methods, such as microscopic imaging, can give insights into the internal atomic/molecular arrangement of the material.

As shown in Figure 3, materials science provides insights into the inner structure of materials. Models on this scale include specific parameters, such as the cross-linking density or mean chain-length in polymers. Besides the derivation of inner structures based on insights from physicists and chemists, some structural parameters can be measured independently, e.g., with methods from microscopy. Predictive Processing→Structure models can be evaluated in their accuracy with these kinds of experiments. Furthermore, parameters in models that describe the inner structure can be indirectly derived, which we will show in future works.

2.3 Relevant parameters in material models

Based on the identified inner structure, parameters of material models can be derived. In the context of smart structures, these models are mostly on the continuum scale. Please note that even models at the micro-scale, that are later transitioned through computational homogenization approaches [22, 23], are still continuum models. In fact, the choice of the material model (set of constitutive equations) fixes the number of parameters and implicitly assumes their relevance: For example, defining the elastic modulus as a relevant parameter, a linear-elastic behavior with Hooke's model is implicitly assumed, and all limitations of this model apply.

As shown in Figure 4, the transition from inner structure to material properties can be done with specialized approaches, from fully resolved quantum mechanical approaches like, density functional theory [24, 25], over semi-empirical methods like molecular dynamics [26], to statistic models like the Flory-Rehner theory for hydrogel swelling [27].

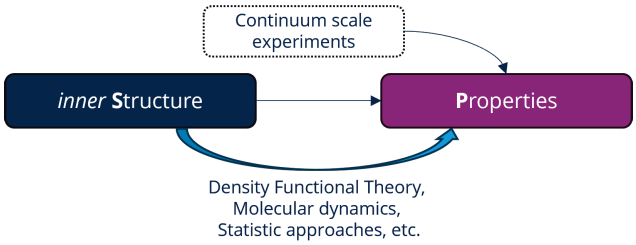

Figure 4: Property parameters, such as the elastic modulus, can be derived based on the known inner structure. The properties that are relevant in the design process are directly connected to the chosen set of constitutive equations (material model). Experimental data for verification of predictions are performed on the continuum scale.

The chosen material model is connected with appropriate experimental methods on the continuum scale: For example, the elastic constants of orthotropic materials require multiple tensile tests of adequately-shaped samples.

2.4 Performance of materials in active-passive setups

The performance of a material in the context of smart composites can only be understood on the application scale and in the work environment. This means that all multi-field influences – from mechanical to thermal and electro-chemical loads – must be considered [4].

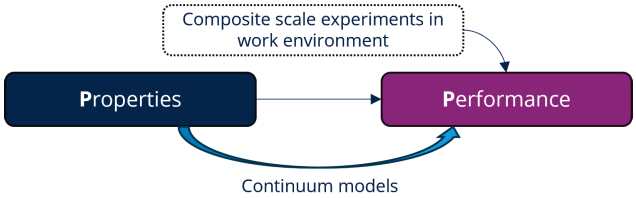

Figure 5: The performance of a material in a specific context can be derived by leveraging continuum models. The predictions can be validated through experiments with the smart composite in its intended work environment.

As specified in Figure 5, continuum models and the complete set of computational methods for solving the set of equations with boundary conditions (e.g., the Finite Element Method) can be leveraged for this step. The ground-truth data for the composite's behavior can be gained from composite scale experiments in the work environment. Please note that the reaction of the smart composite itself can be an adequate experiment: The visible deformation in this kind of systems depends on the properties of active expansion (such as maximum swelling in hydrogels), as well as the mechanical parameters of the material pairing – which is valuable in the context of sensor-actuators (i.e., SHAPES setups that transform a stimulus input into another field, see Ref. [6]).

3 Towards end-to-end design of active-passive composites

The idea of an end-to-end approach – the so-called fourth paradigm of material science [7] – is defined in analogy to the recent developments in natural language processing and machine learning: In various studies, it has been shown that leapfrogging steps in the reasoning chain (i.e., using one blackbox model for the regression of output values based on the input data, instead of applying multiple specialized models) may lead to better outcomes, as long as enough data with sufficiently high quality is available. This has been true, e.g., for Large Language Models, in which concepts of semantic understanding are replaced with the attention mechanism approach. In various other contexts, it has been shown that search and learning provide better outcomes than specialized models [28].

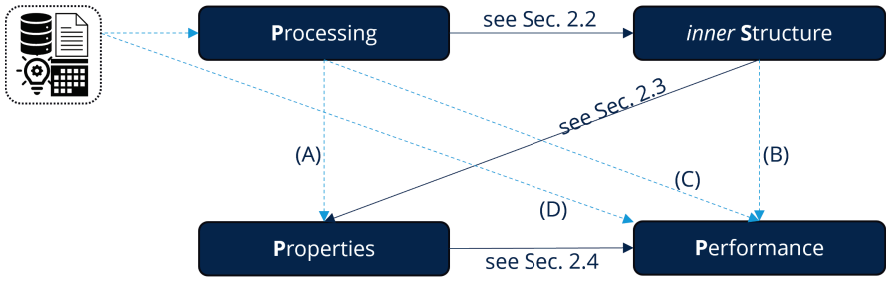

Figure 6: Overview over the possible relations/connections between the constituents of the PSPP chain.

In Figure 6, the classical chain from Figure 1 is rearranged to show all possible connections between the steps:

(A) **Processing→Properties**: Data-driven models that link processing parameters to properties of a specific material model, offer the opportunity to leapfrog the description of the inner structure [29, 17, 21]. They are especially useful for engineers, because they provide material parameters which can be directly added into Finite Element simulation software for specific test cases.

(B) **inner Structure→Performance**: Models of this type can be helpful, when the inner structure of a material can be generated with different processing approaches. This is, e.g., relevant for self-assembly [30] where the inner structure builds itself only in one specific way. Furthermore, certain materials are defined by their inner structure, such as graphene or diamond.

(C) **Processing→Performance**: Starting with well-defined processing parameters, dimension reduction methods such as Autoencoders or Principal Component Analysis can be applied to identify relevant parameters, and a regression to the performance of the material in a specific smart composite can be performed. In comparison to the data-driven Processing→Properties model, there is not sufficient data for this kind of studies in literature yet. Synthetic data from modeling can be used to overcome this obstacle.

(D) **End-to-end**: Models of this type include all steps from newly discovered materials in papers, or new combinations that are gained from databases, to the final performance in a specific environment/setting. A reliable automated workflow for all data source types according to section 2.1 must first be implemented to obtain this kind of end-to-end data, which we will show in future works.

In the context of the smart mesh, an end-to-end approach starting from the synthesis conditions of the hydrogel, can be obtained in the following way: In previous works [29, 17, 21], a Processing→Properties model of type (A) was derived for hydrogels. The feed-forward neural network model relies on well-defined processing parameters and allows the regression of hydrogel swelling curves based on the synthesis parameters. To obtain this model, the training data was first extracted from literature sources, as detailed in section 2.1. The maximum swelling between dry and swollen state can be derived from this kind of model.

The next step, Properties→Performance, can be taken by applying the Stimulus-Expansion-Model (a continuum model according to Ref. [4]). In this approach, the maximum achievable swelling is included in the active expansion term, which is analogous to the thermal expansion term. We provide a software tool [31], which allows the implementation of this behavior into any finite element framework, or analytical description, that includes thermal expansion.

The combination of these approaches allows the design of hydrogels for smart meshes at the level of synthesis conditions and ingredients, as we will show in future works. Furthermore, the Stimulus-Expansion-Model can be leveraged to produce synthetic data for the training of an end-to-end model of type (D).

4 Conclusions and outlook

The current work presents an approach to the end-to-end design of Soft–Hard Active–Passive Embedded Structures (SHAPES). The systems in question are composites consisting of active and passive materials that can be applied as actuators, sensors, or more specific tasks like shape-morphing or controllable obstruction. The well-known concept of PSPP relationships can be applied to these kinds of smart structures. For every step in the chain, specialized models – such as continuum-based models, or molecular dynamics models – can be applied.

Approaches from the realm of Materials Informatics are presented, which replace those specialized models with data-driven blackbox approaches. The required data for different steps of the PSPP chain can be produced as synthetic data with the well-known models, or gained from experiments.

Eventually, an end-to-end approach for designing active-passive composites can be defined: It starts with newly discovered materials – or re-discovered old materials – and their description in scientific works, patents, or databases. The output side is the performance of the material as a part of a smart composite for a specific application and work environment. In this kind of model, computationally expensive search methods, which are only available due to computational scaling, can be leveraged to find optimal solutions. This is exciting because of the opportunities that follow but may also lead to a decline in application of specialized methods in the smart materials community.

REFERENCES

[1] A. Ehrenhofer, P. Bakardjiev, Y. Wang, A. Voigt, U. Marschner, A. Richter, and T. Wallmersperger, "System design and models for active materials," in *2024 Symposium on Design, Test, Integration and Packaging of MEMS/MOEMS (DTIP)*, 2024, pp. 1–6.

[2] D. J. Leo, *Engineering analysis of smart material systems*. John Wiley & Sons, Hoboken, New Jersey, 2007.

[3] P. Gaudenzi, *Smart structures: physical behaviour, mathematical modelling and applications*. John Wiley & Sons, Chichester, United Kingdom, 2009.

[4] A. Ehrenhofer and T. Wallmersperger, "The Stimulus-Expansion-Model for representing arbitrary active behavior in smart materials," *Published online in Acta Mechanica*, 2025.

[5] Y. Bar-Cohen, *Electroactive Polymers as Artificial Muscles: Capabilities, Potentials and Challenges*. American Society of Civil Engineers, Hoboken, New Jersey, USA, 2000, ch. 23, pp. 188–196.

[6] A. Ehrenhofer and T. Wallmersperger, "Soft-Hard Active-Passive Embedded Structures: A review of smart structures with design and modeling guidelines," *Smart Materials and Structures*, vol. 34, no. 3, p. 033005, 2025.

[7] A. Agrawal and A. Choudhary, "Perspective: Materials informatics and big data: Realization of the 'fourth paradigm' of science in materials science," *Apl Materials*, vol. 4, no. 5, p. 053208, 2016.

[8] S. Curtarolo, W. Setyawan, G. L. Hart, M. Jahnatek, R. V. Chepulskii, R. H. Taylor, S. Wang, J. Xue, K. Yang, O. Levy *et al.*, "Aflow: An automatic framework for high-throughput materials discovery," *Computational Materials Science*, vol. 58, pp. 218–226, 2012.

[9] K. Guo, Z. Yang, C.-H. Yu, and M. J. Buehler, "Artificial intelligence and machine learning in design of mechanical materials," *Materials Horizons*, vol. 8, no. 4, pp. 1153–1172, 2021.

[10] S. Diao, Q. Wu, S. Li, G. Xu, X. Ren, L. Tan, G. Jiang, P. Song, and X. Meng, "From synthesis to properties: expanding the horizons of machine learning in nanomaterials research," *Materials Horizons*, 2025.

[11] W. D. Callister Jr, *Materials Science and Engineering: An introduction*. John Wiley & Sons Inc., Hoboken, New Jersey, 2007.

[12] A. Ehrenhofer, A. Mieting, S. Pfeil, J. Mersch, C. Cherif, G. Gerlach, and T. Wallmersperger, "An automatically rainproofing bike helmet through light-sensitive

hydrogel meshes: design, modeling and experiments," in *Proc. SPIE 11587, Electroactive Polymer Actuators and Devices (EAPAD) XXII*, Y. Bar-Cohen, Ed., vol. 11375, International Society for Optics and Photonics. SPIE, 2020, pp. 47 – 58.

[13] A. Ehrenhofer and T. Wallmersperger, "SHAPES_Tables: A living document with a collection of sources for active materials and concepts of soft-hard active-passive embedded structures (SHAPES)," 2025. Available: https://zenodo.org/records/15000565

[14] A. Ehrenhofer, G. Bingel, G. Paschew, M. Tietze, R. Schröder, A. Richter, and T. Wallmersperger, "Permeation Control in Hydrogel-Layered Patterned PET Membranes with Defined Switchable Pore Geometry - Experiments and Numerical Simulation," *Sensors and Actuators B: Chemical*, vol. 232, pp. 499–505, 2016.

[15] S. Binder, A. Ehrenhofer, and A. Mieting, "Stimulus-responsive mesh," U.S. Patent US17/329,371, 2021, submitted on 25 May 2021.

[16] A. Ehrenhofer, "Design of soft and hard active-passive composite beams," *Mechanics of Advanced Materials and Structures*, vol. 30, no. 5, pp. 945–960, 2023.

[17] Y. Wang, T. Wallmersperger, and A. Ehrenhofer, "Prediction of hydrogel swelling states using machine learning methods," *Engineering Reports*, vol. 6, no. 11, p. e12893, 2024.

[18] D. Fanelli, "Negative results are disappearing from most disciplines and countries," *Scientometrics*, vol. 90, no. 3, pp. 891–904, 2012.

[19] F. Strieth-Kalthoff, F. Sandfort, M. Kühnemund, F. R. Schäfer, H. Kuchen, and F. Glorius, "Machine learning for chemical reactivity: the importance of failed experiments," *Angewandte Chemie International Edition*, vol. 61, no. 29, p. e202204647, 2022.

[20] P. M. Smith, "Copyright, contract, and licensing in open source," in *Open Source Law, Policy and Practice*. Oxford University Press, 10 2022.

[21] Y. Wang, T. Wallmersperger, and A. Ehrenhofer, "Application of back propagation neural networks and random forest algorithms in material research of hydrogels," *PAMM*, vol. 23, no. 1, p. e202200278, 2023.

[22] S. Forest, "Homogenization methods and mechanics of generalized continua-part 2," *Theoretical and Applied Mechanics*, vol. 28-29, pp. 113–144, 2002.

[23] J. Yvonnet, *Computational homogenization of heterogeneous materials with finite elements*. Springer, 2019, vol. 258.

[24] P. Sarker, T. Harrington, C. Toher, C. Oses, M. Samiee, J.-P. Maria, D. W. Brenner, K. S. Vecchio, and S. Curtarolo, "High-entropy high-hardness metal carbides discovered by entropy descriptors," *Nature Communications*, vol. 9, no. 1, p. 4980, 2018.

[25] W. E. McMullen and K. F. Freed, “A density functional theory of polymer phase transitions and interfaces,” *The Journal of Chemical Physics*, vol. 92, no. 2, pp. 1413–1426, 1990.

[26] X. Ou, Q. Han, H.-H. Dai, and J. Wang, “Molecular dynamic simulations of the water absorbency of hydrogels,” *Journal of molecular modeling*, vol. 21, pp. 1–10, 2015.

[27] M. Shibayama and T. Tanaka, *Volume phase transition and related phenomena of polymer gels*. Springer, Berlin, Heidelberg, 2005.

[28] R. Sutton, “The bitter lesson,” *Incomplete Ideas (blog)*, vol. 13, no. 1, p. 38, 2019.

[29] Y. Wang, A. Ehrenhofer, and T. Wallmersperger, “Adapting sigmoid functions for hydrogel swelling curve prediction with neural networks,” *PAMM*, vol. 24, no. 2, p. e202400078, 2024.

[30] C. Huang, Q. Zhang, and A. Jákli, “Nematic anisotropic liquid-crystal gels—self-assembled nanocomposites with high electromechanical response,” *Advanced functional materials*, vol. 13, no. 7, pp. 525–529, 2003.

[31] A. Ehrenhofer, “Normalization_Monosensitive: A tool for normalizing active behavior,” May 2023. Available: https://doi.org/10.5281/zenodo.7885801

XI ECCOMAS Thematic Conference on Smart Structures and Materials - SMART 2025
M. Krommer, M. Nader and M. Schagerl (Eds)

Received: 22 April 2025 / Revised: 30 August 2025 / Accepted: 5 October 2025
© The Author(s) 2025

A novel Multistable Sandwich Hinge Design with a Flexible Honeycomb Core

Abhijeet Kumar, Anoop Singh Bagri, Yuvraj Singh, Suranjan Kumar, Subham Sekhar Mandal, Ayan Haldar, Pralay Maiti

Abstract. Deployable structures are essential for applications requiring rapid assembly and compact storage. These structures rely on hinges to enable both deployability and compactness. However, existing composite hinges typically have low bending stiffness and require external forces to remain stable in either the compact or deployed configuration. This limitation can be addressed through the concept of multistability, which can be introduced in anti-symmetric laminates by applying initial curvature. In such composite laminates, a very high snap-through load is required when the laminates become too thick, whereas excessively thin laminates lack the bending stiffness required to support structural loads. This trade-off limits their applicability in morphing or adaptive structures, which require both stability and flexibility. To overcome this challenge, we propose a multistable sandwich composite hinge that balances flexibility with adequate bending stiffness. The hinge consists of a flexible honeycomb core sandwiched between two antisymmetric laminates.

An experimental study has been conducted on anti-symmetric composite hinges made from carbon fibre laminates combined with square and hexagonal honeycomb cores. Specimens with varying core thicknesses have been tested to evaluate snap-through behaviour. The results have shown that increasing the core thickness raises the snap-through load, though the required force has remained significantly lower than that for carbon fibre-only composite hinges. The honeycomb core has enhanced stiffness while retaining flexibility. These findings have been validated through finite element (FE) simulations. This innovative design enables the development of robust deployable systems, such as shelters and bridges, where the thick multistable hinge functions as both a structural and functional component. It establishes a foundation for integrating multistable mechanisms into large-scale, load-bearing applications, advancing adaptive and deployable engineering systems.

Key words: Composite hinge, Multistable, Deployable structure, Snap-through, Sandwich structure

Abhijeet Kumar & Anoop Singh Bagri & Yuvraj Singh & Suranjan Kumar & Ayan Haldar
Department of Civil Engineering, Indian Institute of Technology (BHU) Varanasi, Varanasi, India
e-mail: ayan.civ@itbhu.ac.in

Subham Sekhar Mandal & Pralay Maiti
School of Materials Science and Technology, Indian Institute of Technology (BHU) Varanasi, Varanasi, India

1 INTRODUCTION

Deployable structures play a crucial role in infrastructure applications that require rapid assembly, compact storage, and structural adaptability. These structures are widely used in emergency shelters, and portable bridges because of their ease of deployment. Traditional deployable designs typically incorporate either metallic hinges, which are heavy and susceptible to corrosion, or composite hinges, which often suffer from low bending stiffness and require continuous external forces to maintain their deployed state [1, 2]. These limitations significantly hinder their performance in load-bearing roles and large-scale structural deployments. Multistability in composite laminates offers a promising approach to overcome these challenges by enabling multiple stable configurations without requiring continuous external energy input.
Kebadze et al. [3] investigated bistable prestressed shell structures, demonstrating that specific residual stress distributions induced by plastic bending can result in two stable configurations. They used thin cylindrical shells made of beryllium–copper alloy, which were plastically deformed using a rolling process after age-hardening. The study demonstrated that this process could reliably produce two distinct stable configurations.
Several studies have explored methods to achieve multi-stability in composite laminates to be both load-carrying as well as shape-adaptive [4, 5, 6, 7, 8]. Multistability can be introduced in anti-symmetric laminates through initial curvature as well in unsymmetric laminates by cooling them from curing temperature to room temperature [9, 10]. Iqbal and Pellegrino [9] developed and experimentally characterized bi-stable composite shells capable of large snap-through deformations, showing that geometric curvature and layup asymmetry play a critical role in achieving and controlling bistability in cylindrical shell configurations. Zhao et al. [1] investigated a multistable composite hinge structure combining several laminates. They observed that the multistability of composite hinges can be tailored by connecting two distinct regions—commonly referred to as the patch region and the poly region—which have different thicknesses. Their results demonstrate that the geometrical configuration and the connecting sequence of these regions significantly influence the number of stable states and the associated curvatures of the composite hinge.

Li et al. [11] investigated bistable hybrid symmetric laminates composed of carbon/epoxy layers embedded with a centrally placed metallic strip, demonstrating that the inclusion of the metal strip enhances bistability by increasing the mismatch in thermal expansion and residual stress. Their study showed that such hybridization not only improves curvature control but also broadens the design space for bistable morphing structures. Zhang et al. [12] developed a novel bistable hybrid laminate by embedding asymmetrically placed bimetallic strips into an unsymmetric composite structure composed of T700 carbon/epoxy layers. The integration of bimetallic strips enabled temperature-induced, contactless actuation between two stable states. Experimental and numerical results showed that increasing the thickness and width of

the bimetallic strips enhanced the principal curvature and strengthened the bistable response.

However, a critical trade-off exists: increasing laminate thickness can take a very high load to snap-through [13], while overly thin laminates may lack the necessary bending stiffness for structural applications [14]. This challenge limits their practical application in morphing and adaptive structures.

To address this issue, we propose a novel multistable sandwich composite hinge that balances flexibility with adequate bending stiffness. The hinge consists of a flexible honeycomb core sandwiched between two anti-symmetric multistable laminates. Honeycomb cores are known for their high strength-to-weight ratios and energy absorption capabilities, making them suitable for deployable applications [15, 16]. By integrating honeycomb cores with anti-symmetric multistable laminates, we aim to enhance structural integrity while maintaining reconfigurability.

The manuscript is structured into six sections. Section 1 introduces the motivation, background, and relevant literature on multistable composite hinges. Section 2 discusses the manufacturing and testing process, including the fabrication of square and hexagonal honeycomb cores, the preparation of anti-symmetric laminates using carbon fibres, and the assembly of the composite hinges, followed by the description of the testing setup. Section 3 presents the non-linear finite element analysis using ABAQUS to simulate the snap-through behaviour of the composite hinge. Section 4 presents the results of the snap-through load of the composite hinges with and without honeycomb cores. Section 5 compares the snap-through loads for varying thicknesses of the honeycomb core. Section 6 concludes the study and highlights its implications for deployable structural applications.

2 MANUFACTURING AND TESTING

The specimens are manufactured through different steps. This includes separate 3D printing of honeycomb core (Fig. 1), manufacturing the steel mould, and fabricating the anti-symmetric laminate (Fig. 2), which are discussed in detail in the following sections.

2.1 Honeycomb core

The honeycomb structures in this study (Fig. 1) have been fabricated using Fused Filament Fabrication (FFF) 3D printing with a desktop 3D printer. For the printing process, TPU 95A filament has been selected due to its high flexibility and durability. The filament has a density of $1230\,\mathrm{kg/m^3}$ and a Shore hardness of 95A, making it suitable for applications requiring both elasticity and strength. Mechanical testing has been conducted using a dogbone specimen printed according to ASTM D412, and the elastic modulus has been observed to be approximately 45 MPa. Poisson's ratio has also been calculated and found to be approximately 0.44.

To achieve optimal print quality with minimal voids, the printing parameters have been carefully adjusted. Through preliminary testing, the nozzle temperature has been set to $220\,^{\circ}\mathrm{C}$, while the printing speed has been maintained at $30\,\mathrm{mm/s}$. These settings have been chosen to ensure proper material flow, layer adhesion, and structural integrity of the printed parts. The

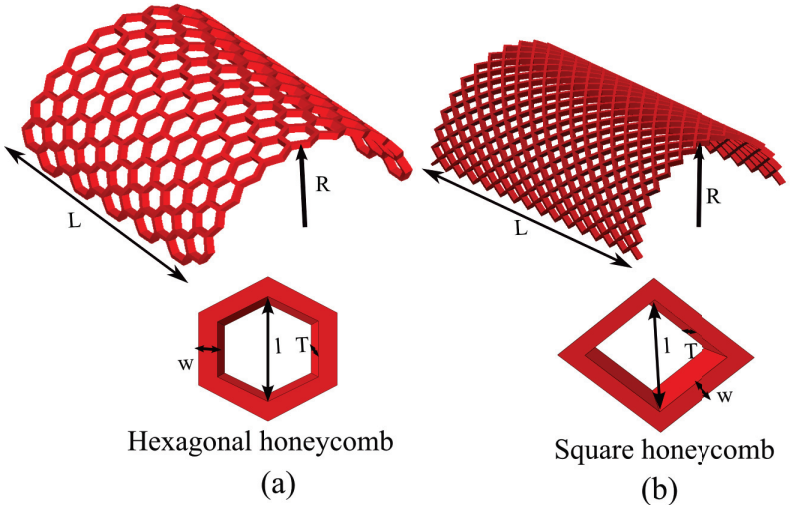

Figure 1: A semi-circular honeycomb core with length L and radius R is shown: (a) Hexagonal core (b) Square core. The unit cell has a length l, with ligament width w and thickness T, respectively.

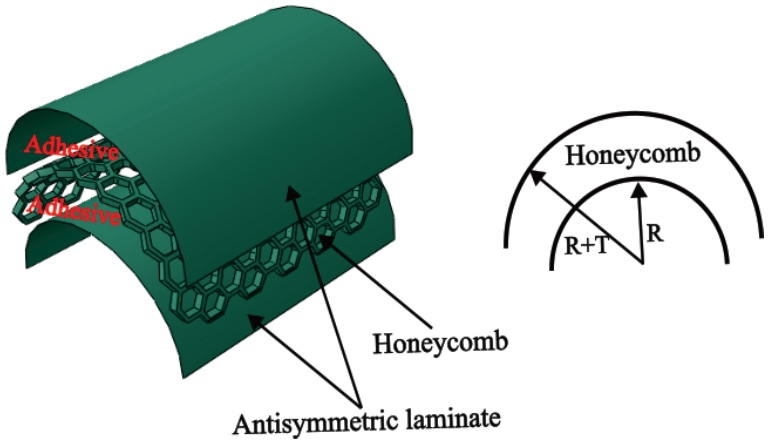

Figure 2: The placement of the honeycomb core inside the anti-symmetric laminate is shown. An adhesive has been used to attach the honeycomb core to the anti-symmetric composite laminate. The radius of the bottom anti-symmetric laminate is R, and the radius of the upper laminate is $R + T$, where T is the thickness of the honeycomb core.

flexibility of TPU 95A allows it to stretch up to three times its original size, making it an excellent choice for applications as a flexible core element of a composite hinge.

Honeycombs with similar dimensions for both hexagonal and square unit cells have been fabricated, where l is the diagonal length of the unit cell, w is the width of the ligament, T is the

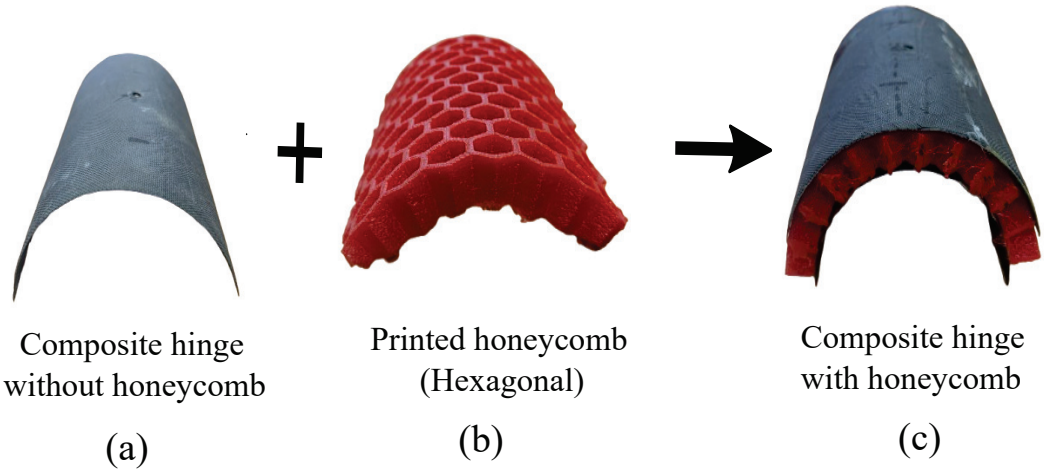

Figure 3: Fabricated samples of composite hinge components: (a) composite hinge without honeycomb core, (b) 3D-printed hexagonal honeycomb core, (c) composite hinge with honeycomb core.

thickness, L is the total length, and R is the radius of the honeycomb core as shown in Fig. 1.

2.2 Composite hinge

A composite hinge has been made using carbon fibre prepreg (Bhor Preg UC 202-A45-38). The composite hinge has been designed as an anti-symmetric laminate (Fig. 3 (a)). The fibre layers have been arranged in a specific sequence of $[45/-45/45/-45]$. The carbon fibre hinge has been cured in an autoclave at $120\,^{\circ}\mathrm{C}$ and approximately 4 bar pressure. This method applies heat and pressure evenly, ensuring a well-bonded, defect-free structure with excellent mechanical properties.

2.3 Composite hinge with honeycomb

A composite hinge with a honeycomb core has been developed by attaching square and hexagonal honeycomb cores to an anti-symmetric composite hinge using polyurethane adhesive, as shown in Fig. 3 (c). The adhesive bonding process has ensured a strong connection between the hinge and the honeycomb structure, enhancing structural integrity. To achieve optimal bonding and mechanical performance, the assembly has been cured for 5-6 hours under controlled conditions. The hinge geometry consists of a bottom hinge with a radius R and an upper hinge with a radius $R+T$, where T is the thickness of the honeycomb core, as given in Fig. 2.



Before experiment (a) After experiment (b)

Figure 4: The experimental setup for mechanical testing of the composite hinge includes a fixture designed to apply a two-point load. The composite hinge is fixed at the centre during the test. A stable configuration is illustrated: (a) Before the load is applied (b) After the load is applied.

2.4 Testing

A universal testing machine (UTM) of Tinus Olsen has been used to apply the load on the composite hinge. The load has been applied at two points while the hinge has been fixed at its centre, as illustrated in Fig. 4. Before loading, the hinge has remained in a stable configuration (Stable shape I), as shown in Fig. 4 (a). After the load has been removed, the hinge has transitioned to another stable configuration (Stable shape II), as depicted in Fig. 4 (b).

3 FINITE ELEMENT

A non-linear finite element analysis has been performed to investigate the bistable behaviour of the composite hinge [17]. A three-dimensional shell model has been developed using the ABAQUS software. The structure has been discretised using S4R elements, which are 4-node doubly curved shell elements suitable for large deformation and non-linear analysis.

A total of 756 shell elements have been used to mesh the geometry, ensuring a balance between computational efficiency and solution accuracy. The boundary conditions have been defined such that the centre of the shell is fixed, while two-point loads have been applied symmetrically along the transverse edges to induce snap-through deformation. Upon application of the snap-through load, the structure has deformed from its first stable configuration (Stable shape I) toward a nearly straight configuration, and has subsequently reached a second stable configuration (Stable shape II), where it has remained even after the load has been removed.

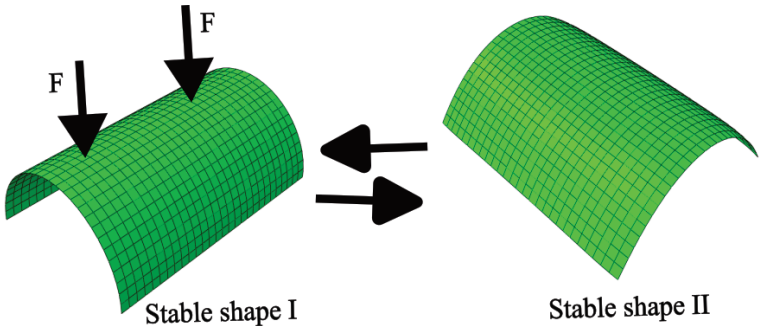

Figure 5: Two stable configurations of anti-symmetric composite laminate (without honeycomb core): Stable shape I and Stable shape II.

Through this simulation setup, two distinct stable configurations—Stable shape I and Stable shape II—have been successfully captured, validating the bistable nature of the structure under applied loading, as shown in Fig. 5.

4 RESULTS

The mechanical testing of the composite hinge with a honeycomb core has been performed. The load-carrying capacity of hinges with hexagonal and square honeycomb cores of different dimensions has been observed. The material properties of anti-symmetric laminate have been given in Table 1.

Table 1: Typical material properties for Carbon/Epoxy [18].

Material	E_1 (GPa)	E_2 (GPa)	G_{12} (GPa)	v_{12}	Ply thickness (m)
Carbon/Epoxy	141	9.6	5.6	0.31	2.0×10^{-4}

4.1 Composite hinge without honeycomb

Initially, a curved antisymmetric composite laminate with 4 and 8 layups is manufactured without honeycomb, with a hinge length of 110 mm and a radius of 35 mm.

It is observed that when a load is applied to the composite hinge initially in Stable shape I (Fig. 4 (a)), the deflection increases progressively with the applied load, as shown in Fig. 6. As the deformation continues, the hinge approaches a nearly flat intermediate configuration (though not perfectly flat). Beyond this point, the applied load begins to decrease gradually, indicating the onset of instability, followed by a sharp drop in load as the structure undergoes a snap-through transition into Stable shape II (Fig. 4 (b))

The limiting load for the four-layup carbon fibre composite hinge has been observed to be 618 N, while for the eight-layup configuration, it has been significantly higher at 4511 N, as shown in Fig. 6 (a) and (b). These results indicate that the load-carrying capacity of composite hinge increases as the number of layups increases.

The experimental results has been validated using finite element (FE) analysis. The limiting load for the four-layup and eight layups has been observed to be 650 N and 4913 N, respectively, which shows a good agreement between FE and experimental results, as shown in Fig. 6.

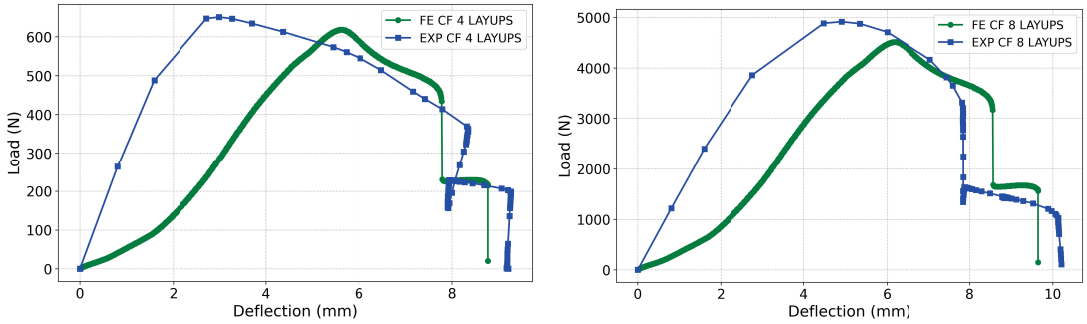

(a) (b)

Figure 6: Load-deflection curve of composite hinge without honeycomb core featuring a length of 110 mm and a radius of 35 mm with : (a) Four layups (b) Eight layups

4.2 Composite hinge with square honeycomb

Experimental testing has been conducted on a composite hinge (four layups) incorporating a square honeycomb core with thicknesses of 5 mm and 10 mm, as shown in Fig. 7 (a) and (b), respectively. The length (l) of the unit cell and width (w) of the ligament are 8 mm and 1.5 mm (Fig. 1), respectively.

The load-deformation behaviour of the composite hinge with honeycomb is similar to that of the composite hinge without honeycomb. The limiting load has been observed to be 1280 N for the 5 mm thick honeycomb core (Fig. 7 (a)) and 2180 N for the 10 mm thick honeycomb core (Fig. 7 (b)). These results indicate that as the core thickness increases, the limiting load also increases.

4.3 Composite hinge with hexagonal honeycomb

Similar to the previous section, a hexagonal honeycomb core has been used in the composite hinge (four layups) with thicknesses of 5 mm and 10 mm, as shown in Fig. 8 (a) and (b), respectively. The values of l and w are 8 mm and 1.5 mm (Fig. 1), respectively.

Experimental testing has shown that the limiting load for the 5 mm thick honeycomb core is 1580 N (Fig. 8 (a)), while for the 10 mm thick honeycomb core, it is 2500 N (Fig. 8 (b)). These results also indicate that as the honeycomb thickness increases, the limiting load-carrying capacity also increases.

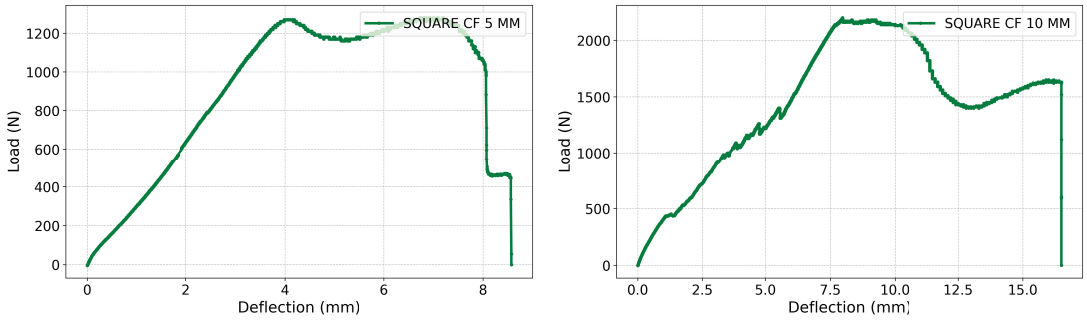

(a) (b)

Figure 7: Load-deflection curve of a carbon fibre composite hinge with a square honeycomb core featuring a length of 110 mm and an internal radius of 35 mm: (a) Honeycomb core with a thickness of 5 mm (b) Honeycomb core with a thickness of 10 mm

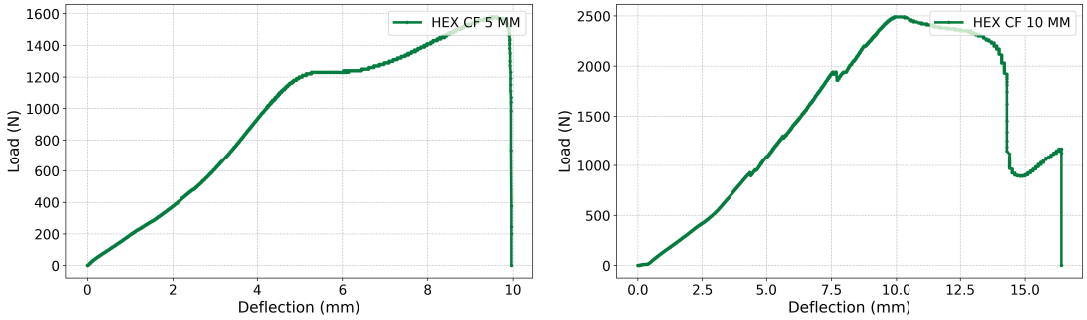

(a) (b)

Figure 8: Load-deflection curve of a carbon fibre composite hinge with a hexagonal honeycomb core featuring a length of 110 mm and an internal radius of 35 mm: (a) Honeycomb core with a thickness of 5 mm (b) Honeycomb core with a thickness of 10 mm

5 OBSERVATIONS

A comparison of snap-through loads for varying thicknesses of square and hexagonal honeycomb cores is presented in Table 2. It is observed that the snap-through load for the hexagonal honeycomb core is higher than that of the square honeycomb core for the same core thickness. This indicates that the snap-through load required for transitioning from Stable shape I to Stable shape II depends not only on the core thickness but also on the geometry of the honeycomb core.

Furthermore, the snap-through load for composite hinges with both square and hexagonal honeycomb cores is higher than that of the 4-layup composite hinge without a core, but lower than that of the 8-layup composite hinge without a core. The limiting load required for snap-

through of the composite hinge with a honeycomb core is 51% lower for the square core and 44.5% lower for the hexagonal core compared to the 8-layup composite hinge without a honeycomb. This suggests that incorporating a honeycomb core enhances the structural stiffness of the hinge while maintaining a degree of flexibility.

Table 2: Snap-through load comparison with and without honeycomb

With honeycomb			Without honeycomb		
	Snap-through load [N]			Snap-through load [N]	
T [mm]	5	10	Layups	4	8
Square	1280	2180	Anti-symmetric laminate	618	4511
Hexagonal	1580	2500	–	–	–

Table 3: Comparison of final internal radius of Stable shape II (R_f) for different honeycomb core thicknesses

T [mm]	5	10
R_i	35	35
R_f	44	51

The final (Stable shape II) internal radius (R_f) has been calculated for square and hexagonal honeycombs with varying thicknesses, as shown in Table 3. It is observed that as the thickness of the honeycomb core increases, the radius (R_f) after snap-through (Stable shape II) also increases. The values of R_f for hexagonal and square honeycombs are observed to be the same for the same thickness (T). The R_f for the composite hinge without a honeycomb core is approximately 41 mm, whereas it is about 44 mm and 51 mm for 5 mm and 10 mm honeycomb core thicknesses, respectively.

6 CONCLUSIONS

An experimental investigation has been carried out on composite hinges developed by attaching anti-symmetric laminates to honeycomb cores. Two different types of honeycomb cores—square and hexagonal—have been tested in combination with anti-symmetric laminates made of carbon fibre.

The results have shown that the snap-through load increases with an increase in the thickness of the honeycomb core, indicating that core thickness significantly influences the bistable behaviour of the structure. Furthermore, it has been observed that hexagonal honeycomb cores

require comparatively more load to induce snap-through than square honeycomb cores, suggesting that core geometry also plays a crucial role in bistability. Interestingly, the snap-through load for the specimen with a honeycomb core (total thickness of 11.6 mm) was lower than that of the composite hinge without a honeycomb core (thickness of 1.6 mm), indicating that the composite hinge with a honeycomb core provides bending stiffness while maintaining flexibility. The final radius after snap-through increased with increasing honeycomb core thickness for both hexagonal and square cores.

To validate these experimental findings of anti-symmetric composite hinge, a non-linear finite element analysis has also been performed, which confirms the observed trends and bistable behaviour. In future work, a finite element analysis of the composite hinge with a honeycomb core may be conducted and validated against experimental results.

The development of this multistable sandwich hinge holds substantial potential for advancing deployable systems in infrastructural and architectural applications. By effectively addressing the trade-off between flexibility and bending stiffness, this work lays the groundwork for incorporating multistable mechanisms into large-scale, load-bearing structures, thereby contributing to the progress of adaptive and deployable engineering systems.

REFERENCES

[1] C. Zhao, X. Lin, B. Wang, J. Zhu, C. Guan, and S. Zhong, "A multistable composite hinge structure," *Thin-Walled Structures*, vol. 198, p. 111709, 2024.

[2] J. Yee and S. Pellegrino, "Composite tube hinges," *Journal of Aerospace Engineering*, vol. 18, no. 4, pp. 224–231, 2005.

[3] E. Kebadze, S. Guest, and S. Pellegrino, "Bistable prestressed shell structures," *International Journal of Solids and Structures*, vol. 41, no. 11-12, pp. 2801–2820, 2004.

[4] A. Kumar and A. Haldar, "Auxetic metamaterial using bistable composite laminates," in *Structural Engineering Convention*. Springer, 2023, pp. 525–533.

[5] A. Haldar, J. Reinoso, E. Jansen, and R. Rolfes, "Thermally induced multistable configurations of variable stiffness composite plates: Semi-analytical and finite element investigation," *Composite Structures*, vol. 183, pp. 161–175, 2018.

[6] A. Kumar and A. Haldar, "Shape-adaptive metamaterials using bistable laminates," in *Asian Conference on Mechanics of Functional Materials and Structures*. Springer, 2022, pp. 205–215.

[7] A. Haldar, R. Groh, E. Jansen, P. M. Weaver, and R. Rolfes, "An efficient semi-analytical framework to tailor snap-through loads in bistable variable stiffness laminates," *International Journal of Solids and Structures*, vol. 195, pp. 91–107, 2020.

[8] A. Haldar, P. Anilkumar, E. Jansen, B. Rao, and R. Rolfes, "Semi-analytical investigations on bistable cross-ply laminates with mfc actuators," *Smart Materials and Structures*, vol. 30, no. 10, p. 105008, 2021.

[9] K. Iqbal and S. Pellegrino, "Bi-stable composite shells," in *41st structures, structural dynamics, and materials conference and exhibit*, 2000, p. 1385.

[10] A. Kumar, A. Haldar, and P. M. Weaver, "An adaptive metastructure concept using bistable composite laminates," *Composite Structures*, vol. 330, p. 117767, 2024.

[11] H. Li, F. Dai, P. Weaver, and S. Du, "Bistable hybrid symmetric laminates," *Composite Structures*, vol. 116, pp. 782–792, 2014.

[12] Z. Zhang, K. Pei, H. Wu, M. Sun, H. Chai, H. Wu, and S. Jiang, "Bistable characteristics of hybrid composite laminates embedded with bimetallic strips," *Composites Science and Technology*, vol. 212, p. 108880, 2021.

[13] S. Phatak, O. J. Myers, S. Li, and G. Fadel, "Defining relationships between geometry and behavior of bistable composite laminates," *Journal of Composite Materials*, vol. 55, no. 22, pp. 3049–3059, 2021.

[14] H. Chen, B. Wang, X. Lin, K. A. Seffen, and S. Zhong, "Folding mechanics of a bistable composite tape-spring for flexible mechanical hinge," *International Journal of Mechanical Sciences*, vol. 272, p. 109188, 2024.

[15] W. Wang, H. Rodrigue, and S.-H. Ahn, "Deployable soft composite structures," *Scientific reports*, vol. 6, no. 1, p. 20869, 2016.

[16] Z. Meng, M. Liu, H. Yan, G. M. Genin, and C. Q. Chen, "Deployable mechanical metamaterials with multistep programmable transformation," *Science Advances*, vol. 8, no. 23, p. eabn5460, 2022.

[17] Z. Zhang, H. Wu, G. Ye, H. Wu, X. He, and G. Chai, "Systematic experimental and numerical study of bistable snap processes for anti-symmetric cylindrical shells," *Composite Structures*, vol. 112, pp. 368–377, 2014.

[18] I. Paliwal and M. Ramji, "An fea-based study on the damage behavior of cfrp hybrid joint under tensile loading," in *Advances in Structural Integrity: Structural Integrity Over Multiple Length Scales*. Springer, 2022, pp. 445–454.

XI ECCOMAS Thematic Conference on Smart Structures and Materials - SMART 2025
M. Krommer, M. Nader and M. Schagerl (Eds)

Received: 27 March 2025 / Revised: 1 September 2025 / Accepted: 5 October 2025
© The Author(s) 2025

Multimodal optimization for effective vibration reduction using passive shunt damping

Pedro A. Magalhaes, Aurelio L. Araujo, Jose F. A. Madeira

Abstract. The presence of vibrations is common in most lightweight engineering applications, with the potential to lead to structural and operational undesired issues. Therefore, vibration control is crucial for reducing excessive oscillation amplitudes, suppressing undesirable resonances, and preventing early fatigue failure of structures and structural elements. In this context, the use of piezoelectric patches to act as controllers on structural panels has been increasingly studied and implemented, being the shunt tuning method one of the most popular approaches. A significant challenge in this scenario is the investigation of optimal patch positioning. In this paper, we developed a model in ANSYS to optimize positioning of patches with the Direct Multisearch (DMS) algorithms. The aim is to determine the optimal patch location based on the electromechanical coupling coefficient (EMCC), with DMS optimizing multiple modes simultaneously to ensure maximum EMCC values. This approach enables the calculation of passive shunt circuits optimal tuning values for electrical resistances and inductances, effectively mitigating vibration issues.

Key words: Piezoelectric materials, Shunt damping, Effective electromechanical coupling coefficient, Direct Search Optimization

1 INTRODUCTION

1.1 Passive Shunt Control

Many engineering optimization problems depend on numerical simulations where derivatives are either unavailable or unreliable, limiting the applicability of gradient-based methods. Derivative-Free Optimization (DFO) methods, particularly directional direct search techniques, offer a robust alternative for handling computationally expensive and black-box functions.

One of the key challenges in engineering structures is vibration control, especially in composite materials widely used in aerospace, automotive, and robotics industries. While these

Pedro Magalhaes & Aurelio Araujo
IDMEC- Instituto de Engenharia Mecanica, Instituto Superior Tecnico, Universidade de Lisboa Av. Rovisco Pais, 1049-001 Lisboa, Portugal, e-mail: aurelio.araujo@tecnico.ulisboa.pt

Jose Madeira
ADM, ISEL, Instituto Politecnico de Lisboa, Rua Conselheiro Emidio Navarro 1, 1959-007 Lisboa, Portugal, e-mail: aguilarmadeira@tecnico.ulisboa.pt

materials offer excellent mechanical properties and reduced weight, they are susceptible to unwanted vibrations, which can lead to structural fatigue and performance degradation. Passive shunt control using piezoelectric patches, coupled with electrical circuits, has emerged as an effective solution, but its efficiency is highly dependent on the optimal placement of the patches. These materials, while offering excellent mechanical properties and reduced weight, are susceptible to unwanted vibrations, which can lead to structural fatigue and reduced performance. Passive shunt control using piezoelectric patches, coupled with electrical circuits, has been widely explored as an effective solution for mitigating vibrations. However, the placement of these patches plays a crucial role in maximizing their efficiency.

This paper investigates the application of directional direct search methods in optimizing the number and placement of piezoelectric patches on a structure to maximize the Effective ElectroMechanical Coupling Coefficient (EMCC), a key performance metric in vibration suppression. A finite element model is developed in ANSYS to simulate the system, and the Direct Multisearch (DMS) algorithm is employed to determine optimal configurations. The results demonstrate the effectiveness of this approach, providing valuable insights into the integration of derivative-free optimization techniques for structural vibration control.

The use of piezoelectric materials to control vibrational energy in multilayer structures has gained significant attention in the literature. Vibration control techniques are generally classified into three types: Passive Control, Active Control, and Hybrid Control. This paper focuses exclusively on the study of passive control.

The initial implementation of passive shunt control using piezoelectric materials connected to resistors and inductors was first explored by [1], where demonstrated how these electrical components could influence the structural response. Building on this, [2] introduced calibration methods for RL series shunt circuits, while [3] expanded the framework by developing techniques for RL parallel shunt circuits. Over the years, more advanced calibration methods have been proposed, such as residual mode correction [4] and approaches incorporating the Effective EMCC [5].

In the context of passive shunt control, the optimal values of electric components, such as resistors and inductors, can be determined through calibration equations based on the EMCC. As highlighted by [6, 7], the EMCC depends not only on the material properties of the piezoceramic patches but also on their placement on the host structure. Consequently, determining the best positions for the patch pairs on the plate structure is crucial, as it directly influences the optimal actuator values and, by extension, the system's ability to reduce vibrations effectively.

Therefore, the main objective of this paper is to identify the optimal positions and number of patch pairs in the plate structure for individual vibrational modes as well as for multimodal phenomena while keeping the patch mass constant. This optimization process is guided by the effective EMCC, ensuring that the positioning leads to the best possible reduction in structural vibrations through passive shunt control.

2 Effective EMCC

Piezoelectric materials possess the property of converting mechanical energy into electrical energy and vice versa. When subjected to mechanical deformation, these materials generate an electrical potential. Conversely, when an electric potential is applied, they induce mechanical deformation in their structure. This relation between the electrical and mechanical domains can be mathematically described through well-established equations, validated and documented in the literature, as summarized in equation (1).

$$\begin{aligned} \boldsymbol{\epsilon} &= \mathbf{S}^E\boldsymbol{\sigma} + \mathbf{d}^T\mathbf{E}_f \\ \mathbf{D} &= \mathbf{d}\boldsymbol{\sigma} + \boldsymbol{\epsilon}^\sigma\mathbf{E}_f \end{aligned} \tag{1}$$

where $\boldsymbol{\sigma}$ is the mechanical stress vector, $\boldsymbol{\epsilon}$ is the mechanical strain vector, $\mathbf{D}$ is the electric displacement vector, $\mathbf{E}_f$ is the electric field vector, $\mathbf{S}^E$ is the compliance matrix, $\mathbf{d}$ is the piezoelectric coupling matrix in strain form and $\boldsymbol{\epsilon}^\sigma$ is the dielectric matrix measured at constant stress.

Considering the complexity of the problem, this paper implemented a finite element approach considering 3D structures. So, rearranging the equation (1) in FE model, it's possible to formulate the equations representing the equilibrium equations for free vibrations, accounting for the piezoelectric effect. These equations can be presented below:

$$\left[\begin{bmatrix} \mathbf{K_{uu}} & \mathbf{K_{u\phi}} \\ \mathbf{K_{u\phi}}^T & \mathbf{K_{\phi\phi}} \end{bmatrix} - \omega^2 \begin{bmatrix} \mathbf{M} & \mathbf{0} \\ \mathbf{0} & \mathbf{0} \end{bmatrix}\right] \begin{Bmatrix} u \\ \phi \end{Bmatrix} = \begin{Bmatrix} \mathbf{0} \\ \mathbf{Q} \end{Bmatrix} \tag{2}$$

where $\mathbf{K_{uu}}$, $\mathbf{K_{u\phi}}$ and $\mathbf{K_{\phi\phi}}$ are the stiffness matrices associated with the mechanical displacements, electromechanical coupling and electric potentials, respectively, $\mathbf{M}$ contains the physical mass associated with the inertia of the plate and piezoelectric patches, $\mathbf{Q}$ is the applied electric charges vector, ω is the circular frequency, $\mathbf{u}$ is the vector of mechanical degrees of freedom and $\boldsymbol{\phi}$ is the vector of electric potentials.

Therefore, as shown in equation (2), the presence of piezoelectric materials affects the natural frequency of the system. Recognizing this, several studies in the literature have developed methods to quantify this influence based on the system's natural frequency. Some approaches make estimates based on a single-mode representation that includes quasi-static effects, referred to as quasi-static EMCC [8] and [9]. Others focus on the effective EMCC, which is determined through both numerical simulations and experimental validation [10] and [11]. As said previously, this paper focus on the effective EMCC, which it can be trivial calculated using finite element method and it allows for an accurate calculation using the following equation, which avoids approximations. The coefficient can thus be calculated as follows:

$$k^2_{e(m)} = \frac{\omega^2_{OC(m)} - \omega^2_{SC(m)}}{\omega^2_{SC(m)}} \tag{3}$$

where $\omega_{OC(m)}$ represents the natural frequency of the m-th mode when the patches are in an open circuit condition, denoted by electric impedance $Z = \infty$, indicating that the electric

charge $\mathbf{Q}$ is equal to zero in eq. (2). Similarly, $\omega_{SC(m)}$ denotes the natural frequency of the m-th mode when the patches are in a short circuit condition, indicated by $Z = 0$, meaning that $\mathbf{Q}$ is not null in eq. (2). These frequencies are derived through finite element analysis of equation (2). It is important to note that the value of $k^2_{e(m)}$ is typically expressed as a percentage.

3 Numerical Implementation

The piezoelectric-plate structure was modeled in ANSYS using an algorithm designed to handle and simulate varying conditions related to the positions of patch pairs, which serve as the primary optimization variable in this study. The program was developed to accommodate the following general inputs: the number of patch pairs and the corresponding coordinates (x, y) for each patch pair.

So, the numerical implementation is structured into three main steps:

3.1 Preprocessing

In this step, all fixed parameters of the problem are defined, including the plate geometry, mesh size, material properties, and element types. The plate geometry is specified as $414 \times 313 \times 1$ mm (Length $\times$ Width $\times$ Thickness), with a fixed mesh size of 3.175 mm. The plate structure is modeled using the SOLID186 3D element with aluminum as the material, while the piezoelectric patches are modeled using the SOLID226 element with PZT-5H [12] as the material. The material properties of PZT-5H are detailed in Table 3.1. With these parameters established, the geometric and finite element models are created.

Table 1: Material properties for PZT-5H.

S^E [$\times 10^{12}$ Pa^{-1}]	d [$\times 10^{-12}$ C/N]	ϵ_R	ρ [kg/m^3]
$S^E_{11} = 16.5$	$d_{31} = -274$	$(\epsilon_R)_{11} = 3130$	7500
$S^E_{12} = -4.78$	$d_{31} = -274$	$(\epsilon_R)_{22} = 3130$	
$S^E_{13} = -8.45$	$d_{33} = 593$	$(\epsilon_R)_{33} = 3400$	
$S^E_{33} = 20.7$	$d_{24} = 741$		
$S^E_{44} = 43.5$	$d_{15} = 741$		
$S^E_{55} = 43.5$			
$S^E_{66} = 42.6$			

Additionally, this step includes defining the interaction between the plate and patch structures. Since the program treats these structures as separate bodies, it is necessary to establish contact surfaces to ensure proper interaction. To achieve this, a node-to-surface contact with a no-separation condition is applied. This ensures that no gaps or relative movements occur at the interface during the simulations, thereby maintaining the structural integrity of the assembly throughout the analysis.

3.2 Solution

The solution involves a modal analysis, with the problem addressed in two different implementations: Short Circuit and Open Circuit. As shown in section 2 and expressed in equation (3), the calculation of the Effective EMCC requires solving the problem for both implementations. The key difference between these two setups lies in the electrical connection: in the Short Circuit case, all electric potentials of the patches are grounded, whereas in the Open Circuit case, the patches are left open, with no electrical connections between the terminals.

3.3 Postprocessing

After solving the problem, the postprocessing phase involves extracting the variables of interest, primarily the natural frequencies. By simulating these two modal solution approaches, it is possible to calculate the natural frequencies for each case. From these frequencies, the Effective EMCC can be determined, which serves as the primary objective of this paper. The goal is to maximize the Effective EMCC by optimizing the patch positions.

4 Patch Pair Distribution

One of the main challenges in solving problems related to structural placement lies in the infinite number of possibilities that can be modeled, as the problem involves a real number domain. Furthermore, another significant challenge is preventing the overlap between structures, as can be present in this paper problem, where patch pairs cannot overlap each other. To tackle these two challenges, it was implemented specific strategies, which will be discussed in the following sections.

4.1 Percentage Position

Although the problem exists in the real domain, it is possible to discretize this continuous domain into a discrete subset, enabling the optimization of patch pair positions within this subset. This approach offers a practical solution since the positions can be optimized with a high level of discretization, progressively refining the position mesh until the solution stabilizes and achieves a desired level of precision.

To implement this discretization, the percentage position approach is an effective method for interpreting the values. By transforming the real domain, which corresponds to the plate area, into a normalized domain ranging from 0 to 1, the positions become easier to analyze and adjust. For instance, in this normalized domain, 0 represents the starting edge of the plate, while 1 represents the opposite edge. The domain is then discretized, starting with an initial increment of 0.1, and gradually refined until achieving sufficient precision. Figure 1 illustrates this transformation, considering an increment of 0.05.

4.2 Overlap Prevention

To prevent cases of overlap, a strategy was implemented to evaluate the distribution of patch pairs before running the ANSYS program. This process involves a script developed in MAT-

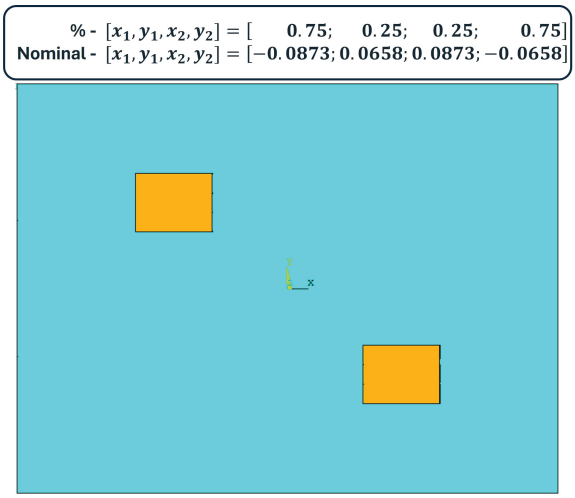

Figure 1: Position transformation between nominal and percentage position.

LAB that verifies the patch pair distribution proposed by the optimization algorithm. Essentially, the optimization algorithm generates a potential optimal solution, which must first be checked for overlaps.

If overlaps are detected in the solution, the overlapping patch pair is removed from the system, reducing the total number of patch pairs to $N-1$, where N is the original quantity of patch pairs. The overlap verification process is then repeated iteratively until no overlaps are found. This ensures that the final configuration is free from overlap issues.

5 Patch Pair Dimension

To evaluate the performance of different numbers of patches in the structure, it is crucial to ensure that the total mass of the patches remains constant, even as the number of patch pairs changes. To achieve this, the system was designed with a fixed total patch area and a defined length-to-width ratio that must be maintained across all configurations and quantities. This ensures that regardless of the number of patch pairs, the geometry of each patch remains consistent, and the total mass stays the same.

By maintaining these parameters, it becomes possible to exclusively assess the impact of the number of patch pairs on the Effective EMCC, isolating it from the influence of varying patch masses. Table 2 presents the patch dimensions for configurations with 1 to 5 patch pairs.

6 Optimization Program

The Direct Multisearch (DMS) multi-objective optimization algorithm, as detailed in [13], was incorporated into this study to address the need for a multi-objective approach. This approach is essential because the optimization problem involves not only maximizing the effective EMCC values but also optimizing the number of patch pairs. Thus, the optimization program

Table 2: Dimensions of each patch in each case.

Pairs of patches	Length [m]	Width [m]	Thickness [m]
1	0.0828	0.0628	0.0005
2	0.0585	0.0444	0.0005
3	0.0478	0.0363	0.0005
4	0.0414	0.0314	0.0005
5	0.0370	0.0281	0.0005

is tasked with maximizing the EMCC for each vibrational mode while simultaneously varying the position and number of patch pairs in the system. In essence, the program aims to solve the following problem:

6.1 Problem Description

The objective is to maximize the effective EMCC for the first 5 vibrational modes while varying the number of patch pairs in the range of 1 to 5. Additionally, the position of each patch pair is optimized within a discretized domain, where the plate's dimensions are normalized to a percentage range from 0 to 1, with a discretization increment of 0.01. Equation (4) formally represents this problem.

$$
\begin{aligned}
&\text{Minimize} \quad F(\mathbf{x}) = \left(-k^2_{e(a)}\,, -N_{pairs}\right) \\
&\text{Where} \\
&\qquad \mathbf{x} = [x_1, y_1, \cdots, x_5, y_5]^T \\
&\text{Subject to} \\
&\qquad x_n \in [0 : \text{increment} : 1, -1] \\
&\qquad y_m \in [0 : \text{increment} : 1, -1] \\
&\text{For } n = 1,2,3,4,5 \\
&\text{For } m = 1,2,3,4,5 \\
&\text{For } a = 1,2,3,4,5
\end{aligned}
\tag{4}
$$

As shown in equation (4), the x and y domains can take on a value of -1. This numerical artifice was introduced by the authors to facilitate the evaluation of different quantities of patch pairs. Specifically, if the optimization program assigns a value of -1 to either the x or y coordinate of a given patch pair, it signifies that this pair is excluded from the system. Consequently, the program can analyze configurations with varying numbers of patch pairs.

This approach also streamlines the overlap prevention process. If an overlap is detected, the program simply assigns a value of -1 to the x or y coordinate of the overlapping patch pair, effectively removing it from the computation. By employing this method, the optimization program ensures that only valid configurations of patch pairs are considered in the analysis.

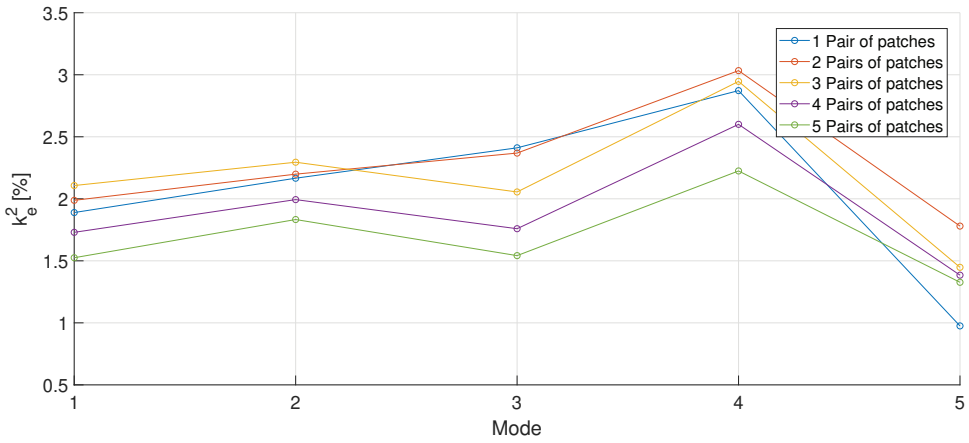

Figure 2: Effective EMCC values at optimal patch pair positions considering up to five patch pairs for the first five vibrational modes.

7 Results and Discussion

The optimization problem described in equation (4) was solved using the DMS program, focusing on the individual analysis of the first five vibrational modes. The maximum Effective EMCC values obtained for each mode are presented in Figure 2, based on the optimal patch pair positions identified for each case.

As observed in Figure 2, implementing two pairs of patches on the plate structure yields a strong performance for nearly all five vibrational modes. In cases where this configuration is not the best, its performance remains close to the optimal solution, making it a practical and effective choice.

Focusing specifically on the configuration with two patch pairs, the optimal positions for each of the first five vibrational modes are illustrated in Figure 3. This configuration demonstrates a consistent balance between performance and simplicity, emphasizing its potential for practical implementation.

As seen in Figure 3, the placement strategy consistently places the patches in regions of maximum deformation, specifically at the peaks and valleys of each vibrational mode, ensuring effective energy coupling. A particularly noteworthy result is observed in the first mode, shown in Figure 3(a). As expected, the patch pairs are positioned near the center of the plate. However, they exhibit a slight offset from the exact center, aligning more closely with the diagonal of the plate. This behavior occurs because the plate is rectangular, and the deformation profile of the first mode is not circular but elliptical. Consequently, the regions of maximum displacement are located along the plate's diagonal rather than precisely at its geometric center.

Furthermore, as observed in Figure 2, when the number of patch pairs increases, it becomes significantly more challenging to position all patches within the peak or valley regions of the vibrational mode near the center. This difficulty arises from two factors: first, the optimization

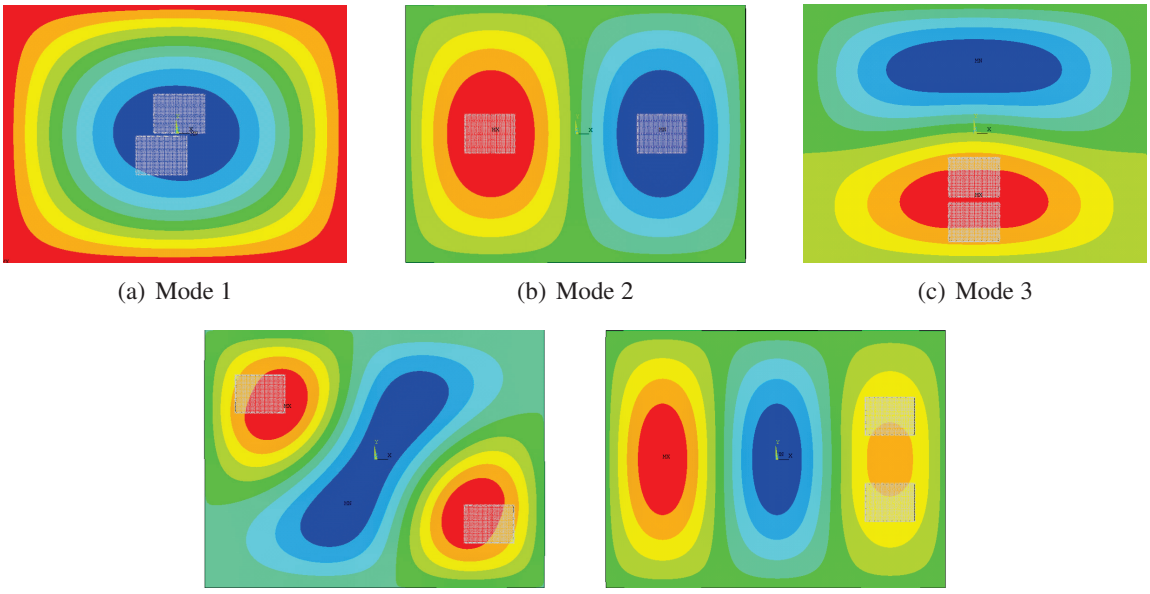

(a) Mode 1 (b) Mode 2 (c) Mode 3

(d) Mode 4 (e) Mode 5

Figure 3: ANSYS plot showing the deformation along the z-axis with two patch pairs implemented at their optimal positions for the first five vibrational modes.

program faces greater complexity in identifying the optimal positions, and second, the available area becomes insufficient to accommodate the total number of patch pairs. Consequently, the growth in the number of patch pairs leads to a decrease in the effective EMCC value.

8 Conclusion

This study highlights the effectiveness of directional direct search methods in optimizing piezoelectric patch placement for passive vibration control, ensuring maximum energy dissipation and vibration suppression. By leveraging the Direct Multisearch (DMS) algorithm, we identified optimal configurations that maximize the Effective ElectroMechanical Coupling Coefficient (EMCC), ensuring improved energy dissipation and vibration suppression.

The results indicate that configurations with two patch pairs consistently achieve a strong balance between performance and practical feasibility, outperforming other setups in most vibrational modes. Additionally, the study demonstrates how numerical modeling using ANSYS, combined with DFO techniques, provides a powerful framework for solving structural optimization problems.

Future research will explore multimodal vibration control, optimizing patch placement for multiple vibrational modes simultaneously. Additionally, further research could focus on real-time adaptive implementations, enabling structures to dynamically adjust piezoelectric patch configurations in response to varying external conditions.

The findings reinforce the potential of derivative-free optimization in structural engineering,

opening new possibilities for adaptive, real-time implementations in aerospace, automotive, and robotics applications. Future research should explore real-time adaptive control strategies, enabling structures to dynamically adjust piezoelectric patch configurations in response to changing operational conditions.

REFERENCES

[1] R. L. Forward, "Electronic damping of vibrations in optical structures," *Applied optics*, vol. 18, no. 5, pp. 690–697, 1979.

[2] N. W. Hagood and A. Von Flotow, "Damping of structural vibrations with piezoelectric materials and passive electrical networks," *Journal of sound and vibration*, vol. 146, no. 2, pp. 243–268, 1991.

[3] S.-y. Wu, "Piezoelectric shunts with a parallel rl circuit for structural damping and vibration control," in *Smart Structures and Materials 1996: Passive Damping and Isolation*, vol. 2720. Spie, 1996, pp. 259–269.

[4] J. Høgsberg and S. Krenk, "Calibration of piezoelectric rl shunts with explicit residual mode correction," *Journal of Sound and Vibration*, vol. 386, pp. 65–81, 2017.

[5] J. F. Toftekær, A. Benjeddou, and J. Høgsberg, "New piezoelectric shunt tuning method based on the effective electromechanical coupling coefficient: validation and 3d implementation," *7th International Symposium on Aircraft Materials*, 2018.

[6] J. F. Toftekær, A. Benjeddou, J. Høgsberg, and S. Krenk, "Optimal piezoelectric resistive–inductive shunt damping of plates with residual mode correction," *Journal of Intelligent Material Systems and Structures*, vol. 29, no. 16, pp. 3346–3370, 2018.

[7] J. F. Toftekær, A. Benjeddou, and J. Høgsberg, "General numerical implementation of a new piezoelectric shunt tuning method based on the effective electromechanical coupling coefficient," *Mechanics of Advanced Materials and Structures*, vol. 27, no. 22, pp. 1908–1922, 2020.

[8] O. Thomas, J.-F. Deü, and J. Ducarne, "Vibrations of an elastic structure with shunted piezoelectric patches: efficient finite element formulation and electromechanical coupling coefficients," *International journal for numerical methods in engineering*, vol. 80, no. 2, pp. 235–268, 2009.

[9] M. Berardengo, O. Thomas, C. Giraud-Audine, and S. Manzoni, "Improved resistive shunt by means of negative capacitance: new circuit, performances and multi-mode control," *Smart Materials and Structures*, vol. 25, no. 7, p. 075033, 2016.

[10] A. F. Ulitko, "Theory of electromechanical energy conversion in nonuniformly deformable piezoceramics," *Soviet Applied Mechanics*, vol. 13, no. 10, pp. 1055–1062, 1977.

[11] S. Chang, N. Rogacheva, and C. Chou, "Analysis of methods for determining electromechanical coupling coefficients of piezoelectric elements," *IEEE Transactions on Ultrasonics, Ferroelectrics, and Frequency Control*, vol. 42, no. 4, pp. 630–640, 1995.

[12] eFunda Portal, "Lead zirconate titanate (pzt-5h)," https://www.efunda.com/materials/piezo/material_data/matdata_output.cfm?Material_ID=PZT-5H, 2024, last accessed: 2024-07-03.

[13] A. L. Custódio, J. A. Madeira, A. I. F. Vaz, and L. N. Vicente, "Direct multisearch for multiobjective optimization," *SIAM Journal on Optimization*, vol. 21, no. 3, pp. 1109–1140, 2011.

XI ECCOMAS Thematic Conference on Smart Structures and Materials - SMART 2025
M. Krommer, M. Nader and M. Schagerl (Eds)

Received: 29 April 2025 / Revised: 8 September 2025 / Accepted: 5 October 2025
© The Author(s) 2025

Integration of piezoelectric transducers in hydrofoils made of composite materials

Antoine Morvan, Boris Lossouarn, Y. Watine, Jean-François Deü

Abstract. Boat appendices, such as hydrofoils, can be subjected to significant dynamic loads during navigation at high Reynolds number ($R_e > 10^5$). The turbulent nature of the flow as well as vortex shedding at the trailing edge generate structural vibrations which couple with the resonant modes of the hydrofoil. These turbulence-induced vibration (TIV) and vortex-induced vibration (VIV) phenomena lead to undesirable structural fatigue and radiated noise, which can be mitigated using piezoelectric shunts. This study considers the integration of piezoelectric transducers in hydrofoils manufactured in composite material made of carbon fiber and epoxy resin. Macro Fiber Composite (MFC) piezoelectric patches can be used to sense and possibly control bending and torsional vibration modes induced by the flow. In this work, two structures are considered: a rectangular plate made of unidirectional plies and a hydrofoil structure with angle-ply layers. The external shape corresponds to a NACA 006 truncated at 80% with a 100 mm chord and 191 mm wingspan. The internal geometries and the arrangement of the composite plies are described for both manufactured structures. In addition, their respective finite element (FE) models are built according to the manufacturing specifications. Attention is paid to the modeling of the piezoelectric transducers and the associated electromechanical coupling. Indeed, the FE models have been created to perform modal analyses of the hydrofoils in air and in water and then optimize coupling factors between the transducer and the structures. This work is part of the HYDRAVIB project, which aims to develop a hydrofoil vibration mitigation systems based on the integration of piezoelectric transducers.

Key words: Hydrofoils, Piezoelectric transducer, Composite materials, Finite element model

Antoine Morvan & Y. Watine
Institut de Recherche de l'Ecole Navale (IRENav), EA 3634 - Ecole Navale, Brest, 29240, France
e-mail: antoine.morvan@ecole-navale.fr

Boris Lossouarn & Jean-François Deü
Conservatoire national des arts et métiers, Laboratoire de Mécanique des Structures et des Systèmes Couplés (LMSSC), 292 rue Saint-Martin,75003 Paris
e-mail: boris.lossouarn@lecnam.net

1 INTRODUCTION

The integration of piezoelectric transducers into mechanical structures is an effective approach for active and passive vibration mitigation. These sensors or actuators convert mechanical energy into electrical energy and vice versa, allowing real-time action on the deformation of the structure. By acting through an appropriate control circuit, piezoelectric transducers can generate forces that oppose vibrations, thereby reducing their amplitude. This technology is particularly relevant in fields such as aerospace and marine [1, 2, 3, 4, 5]

More specifically, this paper explores the integration of piezoelectric transducers in hydrofoils, a critical component in modern naval engineering that enhances the efficiency and stability of vessels by reducing drag and improving lift. With the growing emphasis on lightweight yet durable materials, composite materials have emerged as an ideal solution for hydrofoil construction due to their high strength-to-weight ratios [6, 7, 8]. Incorporating piezoelectric transducers into hydrofoils allows for real-time monitoring of structural health and performance. These transducers can also contribute to active or passive control systems [9] enabling improvement of hydrofoil dynamics response to change operational conditions.

According to Meyer et al. [10], integrating piezoelectric transducers into composite structures is not an easy task. The difficulties lie in the composite manufacturing processes, which can deteriorate the properties of the piezoelectric patch [11]. Nevertheless, the use of composite materials in conjunction with piezoelectric sensors and actuators provide a robust platform for innovative applications.

This paper presents preliminary numerical and experimental investigations around the integration of piezoelectric transducers within hydrofoil structures made of composite materials. In Section 2, the manufacturing process for the selected composite structures is explained and the experimental setup for modal analyses is described. Two structures have been selected: a first simplified foil with parallelepiped geometry and a second complete hydrofoil with NACA geometry. In Section 3, numerical models for modal analyses of the hydrofoils are described. The focus is on modeling the different plies representing the layers of carbon/epoxy composite material and their orientations. This section also presents a comparison between numerical and experimental modal analyses of the two selected structures. The Section 4 deals with the numerical integration of the piezoelectric patch within the two hydrofoils. The coupling factors for the first three natural frequencies are computed. Finally Section 5 provides conclusions and some perspectives.

2 MANUFACTURING OF HYDROFOIL AND EXPERIMENTAL SETUP

In this study, the company AVEL Robotics, based in Lorient (France), was in charge of manufacturing the composite structures. Two composites structures have been produced. The first one is a rectangular parallelepiped with two orientations (0° and 90°) of unidirectional carbon/epoxy layers representing the hydrofoil core. The second one, representing the geometry of a hydrofoil with NACA 006 cross-section truncated at 80% of the chord, is composed of unidirectional carbon/epoxy plies (UD) in the core and ±45° carbon/epoxy plies on the skins. Composite fiber orientations are in relation to the hydrofoil's span axis. For both structures, draping plans and manufacturing process are described in the following section.

2.1 Manufacturing of the core structure

In this section, the manufacturing of the parallelepiped hydrofoil core is described. The dimensions are 246 mm × 100 mm × 0.51 mm.

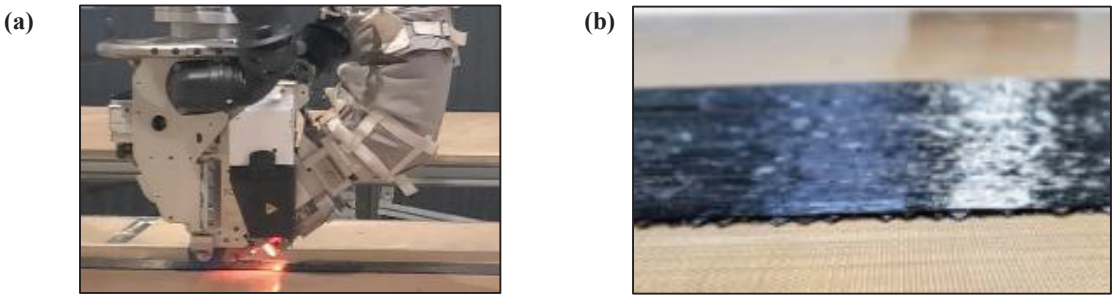

Figure 1 (a) AFP robot spreading carbon/epoxy fiber **(b)** Close view of composite layers during AFP

As seen in Figure 1, the hydrofoil core has been made with Automatic Fiber Placement (AFP) robot. The draping plan is symmetrical with the following stacking sequences $[(0°)_{10}, 90°, (0°)_{10}]$. The hydrofoil core has been cooked at 130 °C in a furnace under pressure at 700 kPa.

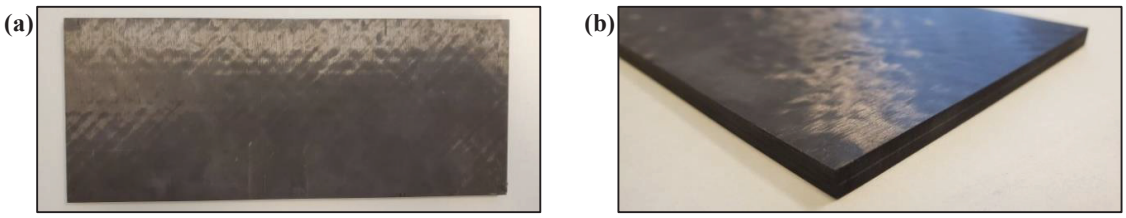

Figure 2 (a) Parallelepiped hydrofoil core sample **(b)** Close view to the cross-section, the grey line in the middle of the section correspond to the UD at 90°

Figure 2 show the manufactured parallelepiped hydrofoil core and a close view to the cross section. Length and width comply with 0.5 mm tolerance. The final stack thickness is approximately 5.14 ± 0.01 mm, so the final thickness of a ply is considered equal to 0.245 mm. Table 1 shows the mechanical properties of the hydrofoil core material provided by the company AVEL Robotics.

Table 1 Mechanical characteristics of the hydrofoil core supplied by the company AVEL Robotics

Modulus [GPa]	E_1	$E_2=E_3$	$G_{12}=G_{13}$	G_{23}	**Poisson Ratio**	$\nu_{12}=\nu_{13}=\nu_{23}$
	125.0	8.4	4.0	3.0		0.37

2.2. Manufacturing of the hydrofoil structure

The manufacture of the NACA 006 hydrofoil, truncated at 80% from the leading edge, as well as the draping plan of the composite material is presented in the following.

The stacking sequence is $[(\pm 45°)_4, (0°)_{10}, 90°, (0°)_{10}, (\pm 45°)_4]$ as shown in Figure 3. To manufacture the full hydrofoil, another parallelepiped hydrofoil core has been made. The hydrofoil core has been processed by CNC milling machine in order to match the geometry of the UD carbon/epoxy part of the hydrofoil (see Figure 4a):

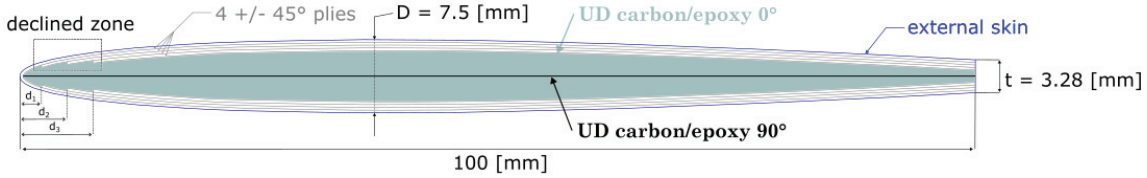

Figure 3 Cross section of draping plan

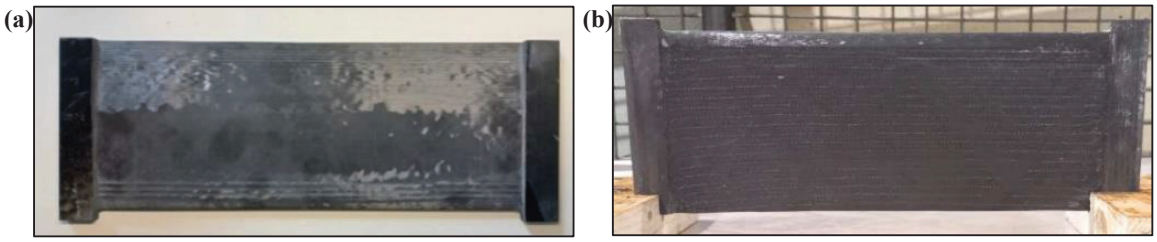

Figure 4 (a) Hydrofoil after CNC machining **(b)** Hydrofoil after wet-draping and cooking

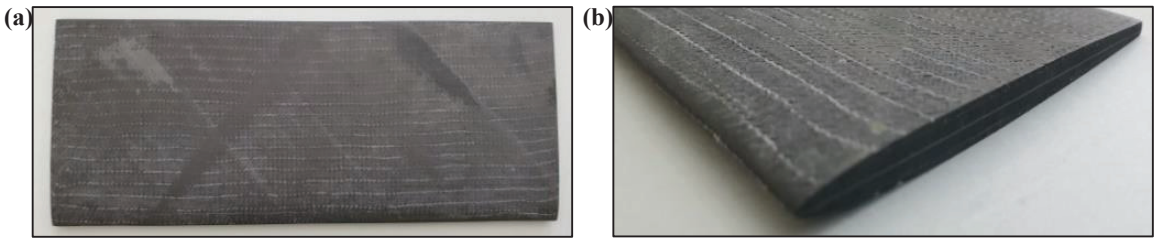

Figure 5 (a) Overview of the hydrofoil **(b)** Close view to the draping

The four plies at ±45° have been draped in wet process (Figure 4b). After AFP draping, skins are slowly vacuum-cooked at 40 °C. Figure 5 presents an overview of the final hydrofoil and a close view to the cross section to visualize the draping plan. The four external layers, cut into two unidirectional layers (Figure 10) have the effect of stiffening the complete hydrofoil in torsion.

2.3 Experimental setup for modal analysis

Two types of modal analysis were carried out: one with free boundary conditions and the other with a clamped edge (Figure 6).

(a) **(b)**

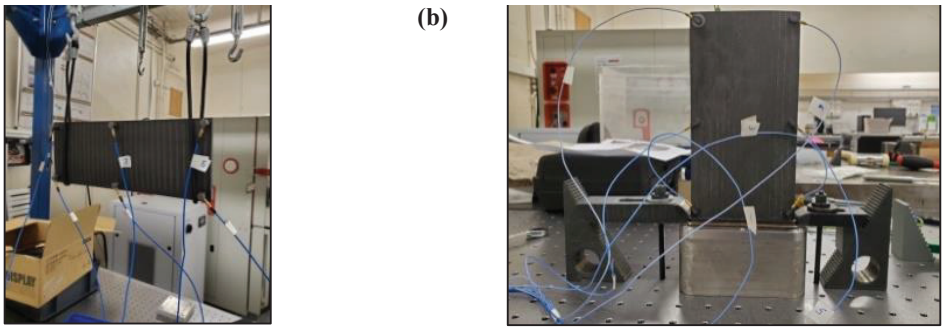

Figure 6 (a) Setup for the hydrofoil core in free boundary conditions **(b)** Setup for the modal analysis of the clamped hydrofoil

For the modal analysis under free boundary conditions, the two composite structures were suspended from three elastic ropes to allow the structure the move in all directions. Six accelerometers were glued along the edges of the structures. Excitation was performed using an impact hammer. The averaged frequency response function (FRF) of the structures has been obtained with the 6 accelerometers data and post processed with the m+p Analyzer software. The eigen-frequencies are determined by analyzing the first three peaks of the FRF. For more information about the experimental modal analysis algorithm used in the frequency domain called "PolyFreq", the reader may refer to (m+p) documentation [12]. The experimental eigen-frequencies along with a comparison to numerical results are provided in the next section.

3 MODELLING OF COMPOSITE HYDROFOILS

3.1 Update of the mechanical properties the hydrofoil core

As described in Section 2, the draping plane is a symmetrical stack of 10 UD at 0°, one UD at 90° and then 10 UD at 0° as shown in Figure 7**.**

(a) **(b)**

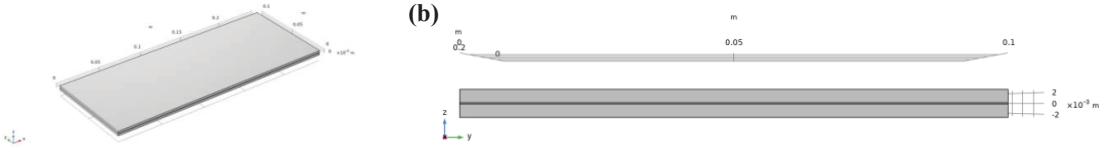

Figure 7 (a) Overview of the foil core geometry **(b)** Close view to the draping of the foil core

The COMSOL Multiphysics structural mechanics module is used to compute eigenmodes of the hydrofoil core in order to compare the results with experimental data. A modal analysis of the hydrofoil core in air is carried out, taking into account the material characteristics supplied by the manufacturer (see Table 1). After mesh convergence of 0.1 Hz tolerance on the first natural frequency, the selected mesh comprises around 70,000 finite elements, i.e about 300,000 degrees of freedom.

Table 2 Comparison of experimental natural frequencies of the hydrofoil core in free boundary conditions and numerical natural frequencies obtained from simulation with raw mechanical parameters

Natural Frequencies	**f_1 [Hz]**	**f_2 [Hz]**	**f_3 [Hz]**
Experimental	379.27	694.58	1024.59
Numerical	352.62	839.98	1095.99
Relative deviation	7.03%	20.9%	6.67%

According to Table 2, numerical results compared to the experimental values shows deviations up to 20.9% which is not satisfactory when considering the material characteristics presented in Table 1. A 5-parameter optimization, representing the transversely isotropic characteristics of the mechanical properties of the materials, is performed by minimizing the function presented in equation (1). The range of mechanical parameters used for the analysis is presented in Table 3.

$$F_{min}(f_{i\,num}, f_{i\,exp}) = \sqrt{|f_{1\,num} - f_{1\,exp}|^2 + |f_{2\,num} - f_{2\,exp}|^2 + |f_{3\,num} - f_{3\,exp}|^2} \quad (1)$$

Table 3 Mechanical parameters used in the analysis varied with step sizes of 1 Pa for the longitudinal Young's modulus, 0.5 Pa for the transverse and shear moduli, and 0.02 for Poisson's ratio

Mechanical parameters	**E_1 [GPa]**	**E_2 [GPa]**	**G_{12} [GPa]**	**ν_{12} [-]**	**ν_{23} [-]**
Range of parameters	{95:150}	{3:9}	{3:8}	{0.20:0.40}	
Optimized Value	100	7.5	4.5	0.22	0.38

After running thousands of COMSOL simulations, a minimum of the F_{min} function has been found with the mechanical parameters presented in Table 3. The most significant parameter is axial Young's E_1, which mainly controls bending stiffness.

Table 4 Comparison between experimental measurements and numerical simulation using optimized mechanical parameters for free modal analysis

Natural Frequencies	**f_1 [Hz]**	**f_2 [Hz]**	**f_3 [Hz]**
Experimental	379.27	694.58	1024.59
Numerical	371.99	697.66	1018.50
Relative deviation	2.01%	0.44%	0.62%

With all the optimized mechanical parameters of the unidirectional carbon/epoxy material, the maximum relative deviation is obtained for the first natural frequencies f_1 and is about 2%. Additionally, Figure 8 shows the first three mode shapes.

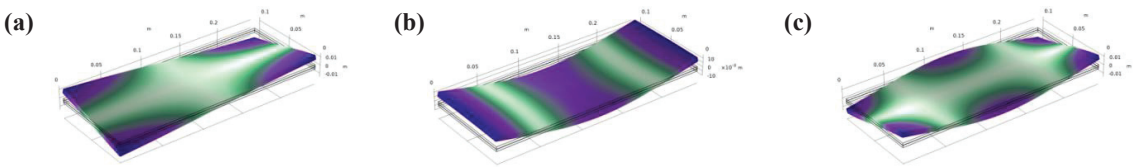

Figure 8 First three eigenmodes for free modal analysis: **(a)** torsion #1, (**b)** bending #1, (**c)** torsion #2

For the mechanical parameters of optimized UD (see Table 3), a further experimental comparison on clamped modal analysis of the hydrofoil core is carried out. The results in terms of relative deviation and modal shapes are presented in Table 5 and Figure 9, respectively

Table 5 First three natural frequencies of the clamped structure: experimental results vs. numerical simulation with optimized parameters

Natural Frequencies	**f_1 [Hz]**	**f_2 [Hz]**	**f_3 [Hz]**
Experimental	146.76	298.18	920.71
Numerical	158.66	305.70	973.51
Relative deviation	8.10%	2.52%	5.73%

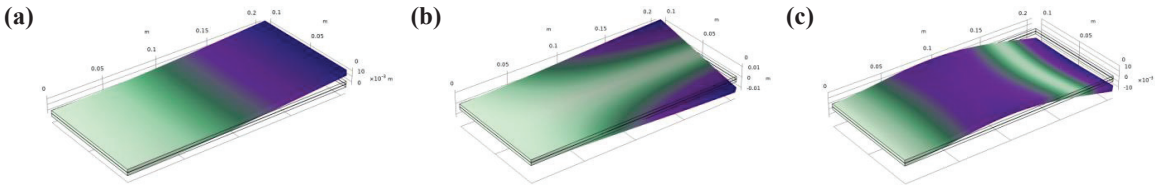

Figure 9 (a) First eigenmode for clamped modal analysis: **(a)** bending #1, (**b)** torsion #1, (**c)** bending #2

For modal analysis with clamped boundary condition, the comparison between numerical and experimental results shows relative deviations up to 8.10% for the first eigenmode of the hydrofoil core. This increase in relative deviations is most likely due to an imperfect clamping condition. The model is therefore stiffer, leading to an increase in numerical frequencies compared with experimental frequencies. Nevertheless, for both comparisons free and clamped, the relative deviations remain less than 10% which is enough for pre-design phases. From now on, the mechanical characteristics retained are the optimized mechanical parameters of UD carbon/epoxy presented in Table 3.

3.2 Full hydrofoil numerical model and comparisons

In this section, the full hydrofoil numerical model build with COMSOL is described. The results in terms of modal analyses are compared to experimental measurements. In terms of modeling, the draping plan presented in Figure 3 is simplified.

Since we do not know the exact 3D mechanical characteristics of the ±45° plies, theses 4 plies are broken down into 2 unidirectional plies at +45° respectively -45°. After mesh convergence on the first natural frequency, similarly to the hydrofoil core a model with 200,000 finite elements model has been selected.

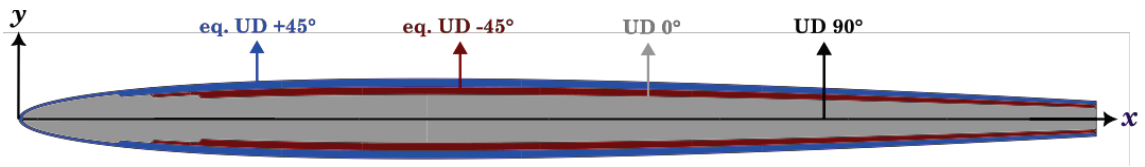

Figure 10 Simplified draping plan with unidirectional material only

Figure 10 shows the simplified draping plan. The blue zone and the red zone represent the domain equivalent to UD +45° and the domain equivalent to UD -45°, respectively. The convenience of this simplification is that each domain represented in the blue and red zones assumes transversely isotropic behavior. In the COMSOL model, all the equivalent UD zones are assumed to have the same mechanical characteristics as those obtained with the optimization loop in section 3.1. Considering this equivalent UD hypothesis, free and clamped modal analyses are compute with COMSOL in order to compare with experimental measurements.

Table 6 Comparison between experimental measurements and numerical simulations for full hydrofoil

Natural Frequencies	**f_1 [Hz]**	**f_2 [Hz]**	**f_3 [Hz]**
Experimental free	578.56	976.27	1583.28
Numerical free	529.06	1027.36	1457.21
Relative deviation free	8.56 %	5.23 %	7.96 %
Experimental clamped	134.09	630.26	862.07
Numerical clamped	149.31	714.96	893.52
Relative deviation clamped	11.35%	13.44%	3.65%

Table 6 presents a comparison in terms of free and clamped eigenmodes between experimental measurements and numerical simulations for the full hydrofoil. This table shows adequate agreement between experimental measurement and experimental data for the free configuration where the relative deviation, lower than 10% is probably due to inaccurate material properties for the ±45° plies. For the clamped comparison, the relative deviations are above 10% for the 1st and 2nd eigen-frequencies. This increase in relative deviations can be explained by the imperfect clamping condition, which will be investigated in further analysis.

4 INTEGRATION OF PIEZOELECTRIC TRANSDUCERS

4.1 MFC transducer modelling

In this section, the modeling of an MFC (Micro Fiber Composite) patch is briefly described. This modeling is based on the work of Watine et al. [9]. Figure 11 shows a MFC transducer with the following dimensions 105 mm × 65 mm × 0.3 mm. Figure 11b shows a simplified representation of the thickness of the MFC patch for numerical modeling.

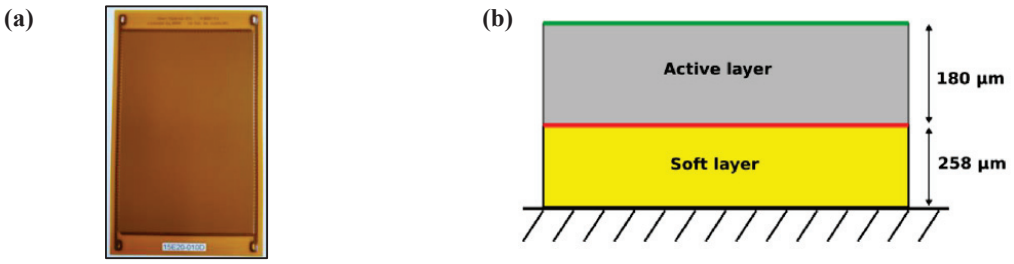

Figure 11 (a) A picture of the MFC patch **(b)** Simplified representation of the patch from [9]

The numerical model of the MFC patch is made in two domains. The soft layer represents the Kapton shell and glue layer. The active layer corresponds to the layer with the piezoelectric fibers. According to [13] the active layer can be modeled as a homogenized orthotropic material. For more information about the mechanical and piezoelectric characteristics of MFC transducers implemented in COMSOL Multiphysics, the reader may refer to [9]

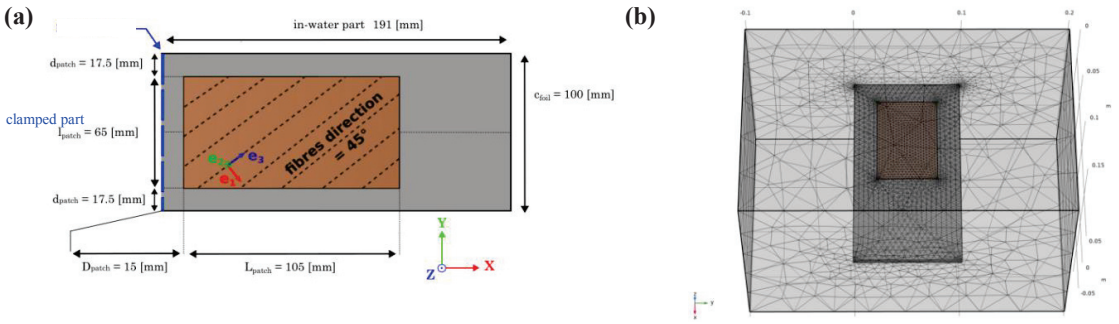

Figure 12 (a) MFC transducer bonded for torsional control [9] **(b)** Mesh of the finite element model for the hydrofoil core with MFC transducers in a water cavity.

The numerical model of the hydrofoils with MFC transducers is used to perform modal analysis. The eigen-frequencies were computed in-water configuration with the transducer in open-circuit and short-circuit. Figure 12a shows the area where the patch is bonded on the hydrofoil and Figure 12b the mesh used for the hydrofoil core with the patch and a water enclosure with the following dimension 300 mm × 193 mm × 100 mm.

4.2 Coupling factor for the core and the full hydrofoil

According to [9], the capability of a piezoelectric shunt to mitigate vibrations is dependent of coupling factors defined by:

$$k_{c\,i} = \sqrt{[f_{oc\,i}^2 - f_{sc\,i}^2]/f_{sc\,i}^2}, i \in [1,2,3] \quad (2)$$

where $f_{oc\ i}$ and $f_{sc\ i}$, are the ith eigen-frequencies when the MFC transducer is open-circuited and short-circuited, respectively. By means of equation (2), coupling factors are computed for the first three eigenmodes considering both hydrofoil structures in water.

The orientations of the MFC fibers for control of torsional modes are 45° (Figure 12a) and 0° for control of bending modes.

Table 7 Eigen-frequencies and coupling factor for the three first modes for the core and the full hydrofoil

Structures	**Natural Frequencies**	**f_1 [Hz]**	**f_2 [Hz]**	**f_3 [Hz]**
Hydrofoil Core	*Short-Circuit*	60.06	160.58	412.90
	Open-Circuit	60.18	161.53	413.55
	Coupling Factor	$k_{c\,1}$ = 6.32%	$k_{c\,2}$ = 10.89%	$k_{c\,3}$ = 5.61%
Full hydrofoil	*Short-Circuit*	55.77	336.26	406.43
	Open-Circuit	56.04	337.54	407.39
	Coupling Factor	$k_{c\,1}$ = 9.85%	$k_{c\,2}$ = 8.73%	$k_{c\,3}$ = 6.88%
Mode Shape		bending #1	torsional #1	bending #2
MFC piezoelectric fibers orientation		0°	45°	0°

Table 7 presents the three coupling factor and the related eigen-frequencies in open- and short-circuit for the hydrofoil core and the full hydrofoil. It shows that the hydrofoil core and the full hydrofoil have comparable values for the first and third eigen-frequencies. However, the second natural frequency is roughly twice as high for the complete hydrofoil as for the hydrofoil core. This is directly related to the composite materials oriented at +45° and -45°. Finally, in accordance with to [9], to obtain significant vibration attenuation, the coupling factor must generally be greater than 5%. Table 7 presents numerical coupling factor always higher than 5% for the hydrofoil core and the full hydrofoil. This result is encouraging for the further application of piezoelectric shunt damping to both bending and torsional modes of composite hydrofoils.

5 CONCLUSION AND DISCUSSION

In this study the manufacturing processes for two composite structures were explained in detail. The first composite structure represents the core of the hydrofoil. The second structure uses the same machined core covered with additional layers of composite skin material. Both of these structures are used in order to compare experimental measurements and numerical simulations in terms of eigen-frequencies. These modals analyses have the aim to better understand the vibratory responses of the composite structures under dynamic excitations.

An update of the mechanical characteristic of the composite material is carried out by using an optimization method. Considering the new mechanical properties of the composite materials, comparisons between experimental measurements and numerical simulations are conducted. For the full core configuration, the agreement between experimental and numerical results is considered satisfactory, with relative deviations below 10%. In the case of the full hydrofoil configuration, the relative deviation remains below 10% for the free boundary conditions, and does not surpass 14% for the clamped boundary conditions. This increase of the relative deviation may be due to the imperfect nature of the clamping condition. This clamping condition will be characterized in a future study.

Nevertheless, these first comparisons are satisfactory for pre-design phases and may partially validate our modelling approach.

MFC transducers have been added to the numerical model in order to compute coupling factors to know the capability of the transducers to mitigate hydrofoil vibrations. After introducing the MFC model, coupling factors are obtained for the core and the full hydrofoil for the three eigen-frequencies. For both structures, couplings factor for the torsional mode and first two bending modes are between 5 and 10%. This is an encouraging result showing the capabilities of the piezoelectric shunt to mitigate vibrations of a composite hydrofoil. The next step in terms of modelling is to integrate two MFC transducers inside the full hydrofoil structure.

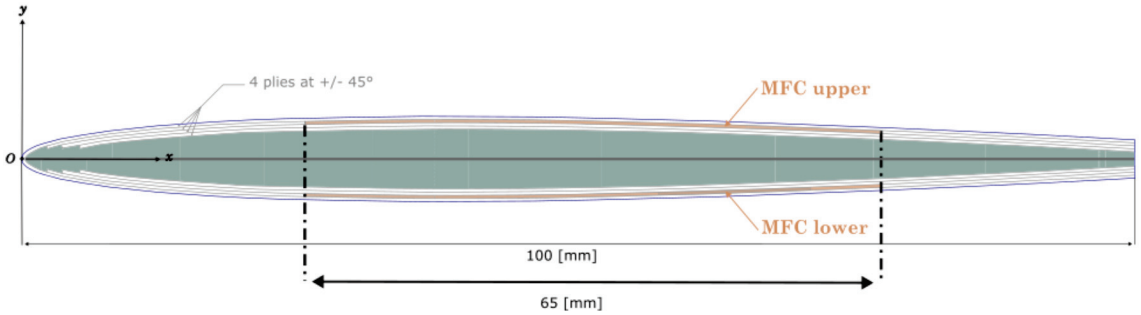

Figure 13 Overview of the two MFC transducer future integrations

Figure 13 shows the future MFC transducer integrations inside the full hydrofoil. On the upper surface, the MFC will control torsion, and on the lower surface, it will control bending. The MFC transducers will be integrated in replacement of a 45° ply. The final step of the work is to perform an in-situ experimental control of the vibrations of the full hydrofoil with the two integrated MFC transducers. To carry out these experimental measurements the hydrodynamic tunnel of the French Naval Academy will be used

ACKNOWLEDGMENTS

The authors would like to express sincere gratitude to the *Agence de l'Innovation de Defense* (AID) and the Agence Nationale de la Recherche (ANR) for the support of the project HYDRAVIB (ANR-22-ASTR-0012).

REFERENCES

[1] S. S. Rao and M. Sunar, "Piezoelectricity and its Use in Disturbance Sensing and Control of Flexible Structures: A Survey", *Appl. Mech. Rev.,* vol. 47, no. 4, pp. 113-123, 1994.

[2] H. Sodano and D. Inman, "A Review of Power Harvesting Using Piezoelectric Materials", *Smart Materials and Structures,* vol. 16, no. 3, 2007.

[3] L. Pernod, B. Lossouarn, J.-A. Astolfi et J.-F. Deü, "Vibration Damping of Marine Lifting Surfaces with Resonant Piezoelectric Shunts", *Journal of Sound and Vibration,* vol. 496, no. 1115921, 2021.

[4] A. Preumont, "Electromagnetic and Piezoelectric Transducers. Vibration Control of Active Structures", *Solid Mechanics and Its Applications,* vol. 179, p. 41–59, 2011.

[5] C. Shee, S. Banerjee, R. Alagirusamy et S. Wazed Ali, "Deployment of piezoelectric transducers for diverse technical applications: A comprehensive review", *Results in Engineering,* vol. 25, no. 1103881, 2025.

[6] S. T. Peters, Handbook of Composites, London: Chapman and Hall, 2nd Edition, 1998.

[7] M. Hyer and S. White, Stress analysis of fiber-reinforced composite materials, DEStech Publications, 2009.

[8] K. K. Chawla, Composite Materials, Springer, 4th Edition, 2019.

[9] Y. Watine, B. Lossouarn, C. Gabillet, J.-A. Astolfi and J.-F. Deü, "Mitigiation of hydrofoil torsional flow induced virbations by resonant piezoelectric shunt, "*Ocean Egineering*", vol. 313, no. 3, 2024.

[10] Y. Meyer, R. Lachat and G. Akhras, "A Review of Manufacturing Techniques of Smart Composite Structures with Embedded Bulk Piezoelectric Transducers", *Smart materials and structures*", vol. 28, no. 5, 2019.

[11] G. Degefa, M. Płaczek and G. Kokot, "The Study of the Influence of Temperature and Low Frequency on the Performance of the Laminated MFC Piezoelectric Energy Harvester", *Applied Sciences MDPI,* vol. 12, no. 23, 2022.

[12] m+p Analyzer: User Manual Revision 5.3, 2020.

[13] A. Deraemeker, H. Nasser, A. Benjeddou and A. Preumont, "Mixing Rules for the Piezoelectric Properties of Macro Fiber Composites,"*Journal of intelligent material systems and structures*", vol. 20, no. 12, pp. 1475-1482, 2009.

XI ECCOMAS Thematic Conference on Smart Structures and Materials - SMART 2025
M. Krommer, M. Nader and M. Schagerl (Eds)

Received: 17 April 2025 / Revised: 2 October 2025 / Accepted: 5 October 2025
© The Author(s) 2025

New finite element for piezoelectric modeling of plates and shells structures

Olivier Polit, Michele D'Ottavio, Philippe Vidal

Abstract. This paper presents a C^0 8-node quadrilateral finite element (FE) for geometrically linear piezoelectric plates/shells. It is based on a high-order kinematics proposed in [1] for the mechanical part. Furthermore, Murakami's ZigZag Function [2] is superimposed for the three displacement components for improving the accuracy for multilayered modeling. The approximation of the electric potential must be able to model piezoelectric patches, and a constant value is considered on each elementary domain while a cubic variation in each layer is used, based on the polynomial expansion given in [3]. A plate/shell FE is finally deduced with nine degrees of freedom (dof) per node for the mechanical part, twelve dofs if the ZigZag functions are included [4] and, for the layerwise description of the piezoelectric behavior, three additional dof per element and per layer are added.

This FE is evaluated on two piezoelectric plate/shell tests including sensor and actuator configurations. The role of electrode segmentation, i.e. the size of equipotential surfaces, on the electro-mechanical response has been also considered.

Key words: Composite structures, finite element, high-order model, Zig-Zag function, piezoelectric patch analysis

1 Introduction

Research and development concerning high-performance structures are very intense since some decades. Structural health monitoring, active vibration damping, and energy harvesting are some examples of possible applications of a multifunctional structural component. Piezoelectric materials permit to convert mechanical and electrical energy at frequency ranges that are most interesting for technical applications such as vibration damping and rapid shape adaptation [5]. Development of theoretical and numerical models for this kind of structures is very important and active. For this purpose and in the framework of two-dimensional plate/shell models, different choices can be made for the mechanical approximation and the following classification is classically admitted for the variation in the thickness direction: (i) Equivalent Single Layer (ESL) models, in which the number of unknowns is independent of the layer

Olivier Polit & Michele D'Ottavio & Philippe Vidal
LEME - Univ. Paris Nanterre, 50 rue de Sèvres, 92410 Ville d'Avray, France
e-mail: olivier.polit@parisnanterre.fr

number; (ii) Layer-Wise (LW) descriptions, for which the number of unknowns and, thus, the computational cost increases with the number of layers. While most developments employ an ESL description for the mechanical behavior, and particularly the First order Shear Deformation Theory (FSDT), a Layer-Wise description is necessary for the piezoelectric approximation to impose electric boundary conditions at each piezoelectric layer interfaces, i.e., the electrodes, within the stack. Inside each piezoelectric layer, the electric potential can be linear, quadratic or higher and a comparison has been proposed in [6].

A review of different approaches is available in [7, 8] and in the framework of the Carrera Unified Formulation (CUF) in [9]. For the FE approximations, a review limited to shell models is also given in [10].

The limitation of the FSDT model is related to the constant transverse displacement hypothesis, inducing no thickness change and the use of the reduced 2D constitutive law. The use of the full 3D constitutive law is an important feature for a consistent representation of complex physical interactions like multi-field coupling. Furthermore, accurate modelling of thick structures needs the transverse normal stress and the 3D constitutive law.

Therefore, a high-order model is chosen with sinus function for the in-plane displacements and quadratic assumption along the thickness of the transverse deflection. Thus, the 3D constitutive law is retained along with a parabolic distribution of the transverse shear strains and a linear variation of the transverse normal strain are recovered. In order to introduce transverse strain discontinuities required to fulfill the interlaminar equilibrium, Murakami's Zig-Zag function (MZZF) [2] is superimposed to the high-order ESL kinematics for the 3 displacement components. Note that MZZF does not depend on the constitutive coefficients and is, hence, attractively simple in conjunction with three-dimensional constitutive laws including multi-field coupling. Based on this kinematics, an 8-node shell Finite Element (FE) is proposed, free of numerical problems such as transverse shear and Poisson lockings, oscillation and spurious mechanics [1]. The approximation of the electric potential must be able to model piezoelectric patches, and a constant value is considered on each elementary domain while a cubic variation in each layer is used, based on the polynomial expansion proposed in [3, 11].

The paper is organized as follows: Section 2 describes the plate problem, the approximations for the displacement and the electric potential and the system to be solved. The resulting FE is evaluated in Section 3 for composite plate and shell, and electrode segmentation modelling is discussed.

2 Description of the plate problem

2.1 Governing equations

Let us consider a plate occupying the domain $\mathcal{V} = \Omega \times [-\frac{e}{2} \leq z \leq \frac{e}{2}]$ in a Cartesian coordinate system $(x_1, x_2, x_3 = z)$. The plate is defined by an arbitrary surface Ω in the (x_1, x_2) plane, located at the midplane for $z = 0$, and by a constant thickness e.

The primary variables are the displacements vector field $\vec{u}(x_1, x_2, z)$ and the scalar electric potential $\phi(x_1, x_2, z)$. $\varepsilon_{ij}(x_1, x_2, z)$ and $\vec{E}(x_1, x_2, z)$ are the strain tensor components and the elec-

tric field vector, respectively, deduced from primary variables by the geometric relations. Furthermore, $\sigma_{ij}(x_1,x_2,z)$ and $\vec{D}(x_1,x_2,z)$ are the conjugated fluxes (stress tensor components and dielectric displacement vector, respectively) obtained from the constitutive equations given in the next subsection.

2.1.1 Constitutive relation

The 3D constitutive equation for a linear piezoelectric material is given by the following set of coupled equations [12] for a layer (k):

$$[\sigma^{(k)}] = [C^{(k)}]\,[\varepsilon^{(k)}] - [e^{(k)}]^T\,[E^{(k)}] \tag{1a}$$

$$[D^{(k)}] = [e^{(k)}]\,[\varepsilon^{(k)}] + [\varepsilon^{(k)}]\,[E^{(k)}] \tag{1b}$$

where we denote by $[C]$ the matrix of elastic stiffness coefficients taken at constant electric field, by $[e]$ the matrix of piezoelectric stress coefficients and by $[\varepsilon]$ the matrix of electric permittivity coefficients taken at constant strain. The explicit form of these matrices can be found in [10] for an orthotropic piezoelectric layer polarized along the thickness direction z. Eq. (1a) expresses the piezoelectric *converse* effect for actuator applications, whereas Eq. (1b) represents the piezoelectric *direct* effect which is exploited in sensor applications. Note that the constitutive law is expressed in the local reference frame associated to each layer.

2.1.2 The weak form of the boundary value problem

The classical piezoelectric variational formulation of [13] is employed in which the primary field variables are the "generalized displacements", i.e. the displacement field, and the electrostatic potential. Using a matrix notation and for admissible virtual displacements $\vec{u}^*$ and electric potential ϕ^* (virtual quantities are denoted by an asterisk), the variational principle is given by:

$$\begin{aligned}\int_{\mathcal{V}} \rho[u^*]^T[\ddot{u}]\,d\mathcal{V} = &-\int_{\mathcal{V}}[\varepsilon(u^*)]^T[\sigma(u,\phi)]\,d\mathcal{V} + \int_{\mathcal{V}}[u^*]^T[f]\,d\mathcal{V} + \int_{\partial\mathcal{V}_F}[u^*]^T[F]\,d\partial\mathcal{V} \\ &+\int_{\mathcal{V}}[E(\phi^*)]^T[D(u,\phi)]\,d\mathcal{V} - \int_{\mathcal{V}} q\,\phi^*\,d\mathcal{V} - \int_{\partial\mathcal{V}_Q} Q\,\phi^*\,d\partial\mathcal{V}\end{aligned} \tag{2}$$

where $[f]$ is the body force vector, $[F]$ the surface force vector applied at $\partial\mathcal{V}_F$, q the volume charge density, Q the surface charge density supplied on $\partial\mathcal{V}_Q$ and ρ is the mass density. Finally, $\varepsilon(u^*)$ and $E(\phi^*)$ are the virtual strain and virtual electric field that satisfy the compatibility gradient equations. In the remainder of this article we will refer only to static problems, for which the left-hand side term is set to zero. Furthermore, body forces and volume charge densities will be discarded ($[f] = [0]$; $q = 0$).

2.2 The mechanical part

2.2.1 The displacement field

Based on the sinus model, see [14], a new plate model which takes into account the transverse normal stress is presented in this section. This extension is based on following developments

- various models for beams, plates and shells based on the refined sinus theory, see [14, 15, 16, 17, 18, 19];
- our previous paper on a 7 parameter model for thermo-mechanical analysis [1].

In the framework of ESL approach, the kinematics of our model is assumed to have the following particular form

$$\left\{\begin{array}{lcl} U_1(x_\alpha,z) &=& u^0{}_1(x_\alpha)+z\,u^1{}_1(x_\alpha)+f(z)\,u^f{}_1(x_\alpha) \\ U_2(x_\alpha,z) &=& u^0{}_2(x_\alpha)+z\,u^1{}_2(x_\alpha)+f(z)\,u^f{}_2(x_\alpha) \\ U_3(x_\alpha,z) &=& u^0{}_3(x_\alpha)+z\,u^1{}_3(x_\alpha)+z^2\,u^2{}_3(x_\alpha) \end{array}\right. \tag{3}$$

where $\alpha \in \{1,2\}$ and $i \in \{1,2,3\}$. In Eq. (3), the superscript is associated to the expansion order in z while the subscript is related to the component of the displacement. Thus, $u^0{}_i$ are the displacements of a point of the reference surface, while $(u^1{}_\alpha, u^f{}_\alpha)$ measure the rotations about the axis $(0,x_\alpha)$ and the warping of the normal transverse fiber, respectively. The functions $u^\alpha{}_3$ permit to have a non-constant deflection for the transverse fiber and allow to have non zero transverse normal stretch. Furthermore, the quadratic assumption for the transverse displacement avoids the occurrence of Poisson (or thickness) locking, see [1].

In the context of the sinus model, we have

$$f(z) = \frac{e}{\pi}\sin\frac{\pi z}{e} \tag{4}$$

It must be noticed that the classical homogeneous sinus model [14] can be recovered from Eq. (3) assuming $u^1{}_\alpha = -u^0{}_{3,\alpha}$, and discarding the unknown functions $u^\alpha{}_3$.

2.2.2 The Murakami's Zig-Zag terms

In order to evaluate the influence of Zig-Zag terms [2] in a high-order ESL model, the following contributions per layer (k) could be added to Eq. (3):

$$\left\{\begin{array}{lcl} U_1{}^{(k)}(x_\alpha,z) &=& Z^{(k)}(z)\,u^z{}_1(x_\alpha) \\ U_2{}^{(k)}(x_\alpha,z) &=& Z^{(k)}(z)\,u^z{}_2(x_\alpha) \\ U_3{}^{(k)}(x_\alpha,z) &=& Z^{(k)}(z)\,u^z{}_3(x_\alpha) \end{array}\right. \tag{5}$$

with

$$Z^{(k)}(z) = (-1)^k\,\zeta_k(z) \quad \text{and} \quad \zeta_k(z) = \frac{2}{e_k}\left(z - \frac{1}{2}(z_k + z_{k+1})\right) \tag{6}$$

where e_k is the thickness of the kth layer while (z_k, z_{k+1}) are the bottom and top coordinates of this layer. It is obvious that $Z^{(k)}(z)$ is a piecewise linear function with bi-unit amplitude for all the layers as we have $\zeta_k(z) \in [-1,1]$. Note that, despite the $Z^{(k)}(z)$ function depends on the layer index inside the stack, the amplitudes ${u^z}_i$ are unique for the whole laminate, i.e., the ESL framework is still preserved.

2.3 The electric part

On each elementary domain Ω_e, the electric potential is assumed to be constant with respect to the mid-surface coordinates. Therefore, no variation with respect to x_α is considered. A cubic layerwise (LW) description is used across the thickness, according to the approximation introduced in [3] and used in [11]: in each layer (k), the electric potential distribution is described by the normal electric field components at the bottom and top surfaces, denoted E_{3b} and E_{3t}, respectively, and the potential difference $\Delta\phi$ between top and bottom surface. Using these dofs, the approximation of the electric potential can be written as:

$$\left[\phi^{(k)}\right] = \left[F_\phi\right] \left[Cst_\phi^{(k)}\right] \left[q_\phi^{e(k)}\right] \tag{7}$$

where the following definitions have been introduced:

$$\left[F_\phi\right] = \left[\begin{array}{cccc} 1 & z & z^2 & z^3 \end{array}\right]; \quad \left[q_\phi^{e(k)}\right]^T = \left[\begin{array}{ccc} {E_{3b}}^{(k)} & \Delta\phi^{(k)} & {E_{3t}}^{(k)} \end{array}\right] \tag{8}$$

and $\left[{Cst_\phi}^{(k)}\right]$ is a (4×3) matrix containing constant coefficients. The electric field vector in each layer $\left[E^{(k)}\right]$ is then obtained as:

$$\left[E^{(k)}\right] = \left[\begin{array}{c} 0 \\ 0 \\ -\phi_{,3}^{(k)} \end{array}\right] = \left[F_E\right] \left[{Cst_E}^{(k)}\right] \left[{q_\phi}^{e(k)}\right] \text{ with } \left[F_E\right] = \left[\begin{array}{ccc} 1 & z & z^2 \end{array}\right] \tag{9}$$

where $\left[{Cst_E}^{(k)}\right]$ is a (3×3) matrix. So, the adopted approximation yields a quadratic transverse electric field across the thickness of each layer.

2.4 The system to be solved

The FE approximations are not detailed here for the sake of brevity and can be found elsewhere [10, 1]. The eight-node quadrilateral finite element is used and classical FE approximation is used for the geometry. A special treatment is used to control the transverse shear locking by using a dedicated interpolation for ${\gamma_{\alpha 3}}^0$ according to the methodology presented in [1]. Note that since the electric potential is assumed to be constant on each elementary domain, there is no need to introduce any FE approximation for this field.

The elementary matrices are then deduced from the bi-dimensional weak form obtained from Eq. (2) upon carrying out the integral along the thickness z. Assembling each elementary

contribution in the global reference frame, the following discrete form of the coupled piezoelectric system is obtained:

$$\begin{bmatrix} [K_{uu}] & [K_{u\phi}] \\ [K_{u\phi}]^T & [K_{\phi\phi}] \end{bmatrix} \begin{bmatrix} [q_u] \\ [q_\phi] \end{bmatrix} = \begin{bmatrix} [L_u] \\ [L_\phi] \end{bmatrix} \tag{10}$$

where $[K_{uu}]$, $[K_{\phi\phi}]$ and $[K_{u\phi}]$ are the global stiffness, dielectric and piezoelectric matrices of the plate, respectively. The mechanical dofs are in the vector $[q_u]$, while the electrical dofs are in the vector $[q_\phi]$ and we have at the elementary level

$$\begin{aligned} [q_u{}^e] &= \left[\begin{array}{ccc|ccc|ccc|ccc} u^0{}_1 & u^0{}_2 & u^0{}_3 & u^1{}_1 & u^1{}_2 & u^1{}_3 & u^f{}_1 & u^f{}_2 & u^2{}_3 & u^z{}_1 & u^z{}_2 & u^z{}_3 \end{array} \right)_{i=1,8} \Big] \\ [q_\phi{}^e] &= \left[\begin{array}{ccc} E_{3b}{}^{(k)} & \Delta\phi^{(k)} & E_{3t}{}^{(k)} \end{array} \right)_{k=1,Nl} \Big] \end{aligned} \tag{11}$$

with Nl the number of layers. From the mechanical point of view, the Zig-Zag dofs can be activated or not: the P9 model corresponds to the case of no Zig-Zag dof, P9Z denotes the model using only in-plane Zig-Zag dof $u^z\alpha$, and P9ZZ denotes the FE with all the Zig-Zag dof $u^z{}_i$. So, the three models P9, P9Z and P9ZZ use 9, 11 and 12 kinematical unknown functions, respectively, and the associated FE have 72, 88, 96 mechanical dofs per element, respectively.

Since the electric potential is assumed constant on each FE, the assembly involves only the approximation along the thickness. A piezoelectric patch comprising several FEs can be defined through the imposition of the equipotential condition between electrodes: the same $\Delta\phi$ is imposed on the piezoelectric layer for all elements belonging to the same patch. From the numerical point of view, this is accomplished through linear homogeneous and non-homogeneous Multi-Point Constraints (MPC) using penalty function method. In the sensor case, an open-circuit configuration is considered and the value is let free and computed by the coupled problem, providing a single value of the potential difference for all the elements constituting the patch.

In Eq. (10), the load vectors $[L_u]$ and $[L_\phi]$ represent the external loading from applied forces and prescribed charges, respectively. Essential boundary conditions (i.e., prescribed displacements and electric potentials) are imposed numerically by a penalty technique. The coupled system is then solved by the classical static condensation procedure for the electrical dof:

$$[q_\phi] = [K_{\phi\phi}]^{-1}([L_\phi] - [K_{u\phi}]^T[q_u]) \tag{12a}$$

which yields the following purely mechanical system with a modified equivalent stiffness matrix:

$$\Big[[K_{uu}] - [K_{u\phi}][K_{\phi\phi}]^{-1}[K_{u\phi}]^T\Big][q_u] = [L_u] - [K_{u\phi}][K_{\phi\phi}]^{-1}[L_\phi] \tag{12b}$$

In the remainder of the paper, $[L_\phi] = [0]$ will be considered.

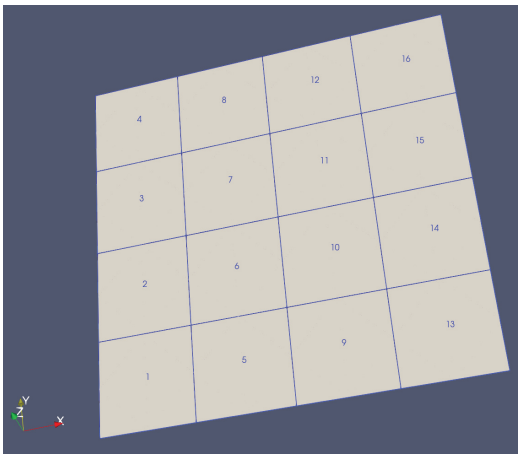

Figure 1: Mesh $N = 4$ and element numbers.

3 Numerical results

3.1 Clamped composite plate

This test is interesting to evaluate the segmentation of a piezoelectric layer using different number of patches. It considers first the response of a cantilever, square, hybrid plate consisting of a laminate sandwiched between two piezoelectric layers, with one edge clamped and other edges free subjected to a uniform pressure load. It has been widely used in the literature [20] and recently re-considered [21] to evaluate the segmentation of the electrode sensor surfaces :

- **geometry** square plate 200×200 mm^2 and total thickness $e = 1.2$ mm,

- **materials** seven-layers $(pz, 45°, -45°, 45°, -45°, pz)$; the outer piezoelectric layers of thickness 0.1 mm are made out of PZT-G1195N material with opposite polarization directions normal to the mid-surface; and four inner layers of graphite/epoxy (T300/976) with thickness $e = 0.25$ mm. The material properties are given in Tab. 1,

- **boundary conditions** clamped at $x_1 = 0$; uniform pressure load p_0; piezoelectric layers can be in sensor configuration ($\Delta\phi$ let free) or in actuator configuration ($\Delta\phi \neq 0$); actuator configuration is considered by imposing $-\Delta\phi$ in the bottom layer and $\Delta\phi$ in the top one,

- **mesh** four regular meshes $N \times N$ are used, with $N \in \{2, 4, 8, 16\}$; Fig. 1 presents the $N = 4$ case.

- **results and locations** transverse displacement at the center tip of the free edge and piezoelectric potential distribution.

Prop.	PZT -G1195N	T300 /976	PZT4	Graphite -epoxy	Prop.	PZT -G1195N	T300 /976	PZT4	Graphite -epoxy
E_1 [GPa]	63.0	150.0	81.3	132.4	e_{15} [C/m^2]			12.72	
E_2 [GPa]	63.0	9.0	81.3	10.8	e_{24} [C/m^2]			12.72	
E_3 [GPa]	63.0	9.0	64.5	10.8	e_{31} [C/m^2]	30.8		-5.2	
ν_{23}	0.30	0.3	0.43	0.49	e_{32} [C/m^2]	30.8		-5.2	
ν_{13}	0.30	0.3	0.43	0.24	e_{33} [C/m^2]	18.5		15.08	
ν_{12}	0.30	0.3	0.33	0.24	ε_{11} [nF]	15.3	ε_0	13.05	ε_0
G_{23} [GPa]	24.2	2.5	25.6	3.6	ε_{22} [nF]	15.3	ε_0	13.05	ε_0
G_{13} [GPa]	24.2	7.1	25.6	5.6	ε_{33} [nF]	15.0	ε_0	11.5	ε_0
G_{12} [GPa]	24.2	7.1	30.6	5.6					

Table 1: Material properties used in the plate and shell problems.

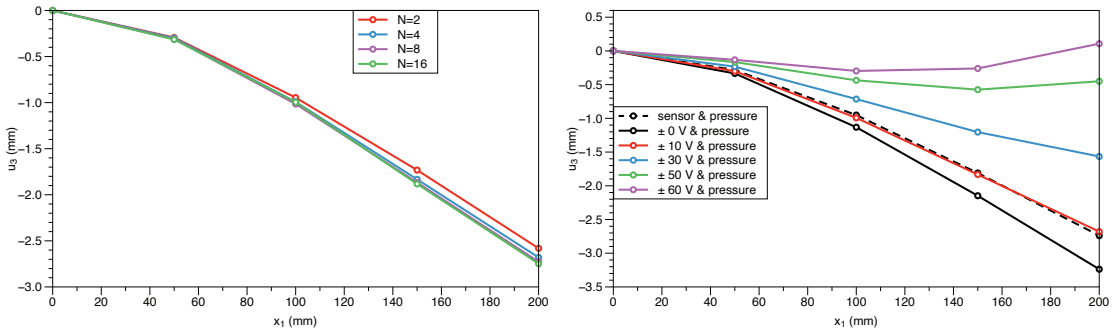

Figure 2: Clamped composite plate: convergence of the transverse displacement along the central line for actuator configuration ($\pm 10V$) (left) and distribution of the transverse displacement under uniform pressure load and variation of the electric potential (right).

Fig. 2 (left) presents the convergence of the transverse displacement of P9 FE, with five values along the central line of the plate, when electric potential load ± 10 V is applied at the bottom and top layers of the plate. The convergence is very fast for the transverse displacement and the mesh $N = 4$ will be used for the following simulations. The actuator effect is presented in Fig. 2 (right) for the shape control of the plate subjected to a uniform pressure load. Increasing the voltage of the actuation induces a decrease of the deflection of the plate. When a voltage of ± 60 V is applied, the transverse displacement at the cantilever's tip becomes slightly positive.

The effect of electrode segmentation is evaluated for the open circuit boundary condition. Fig. 3 reports the output (sensed) voltage at the bottom and top $pz-$layers for 4 different electrode configurations represented by a 4×4 FE mesh: (i) 4×4 electrode grid (i.e., one electrode per FE); (ii) 2×2 electrode grid (i.e., 4 patches, each consisting of 4 FE); (iii) 4 strips of electrodes, segmenting the plate along the x_1 axis in 4 patches covering the whole plate's

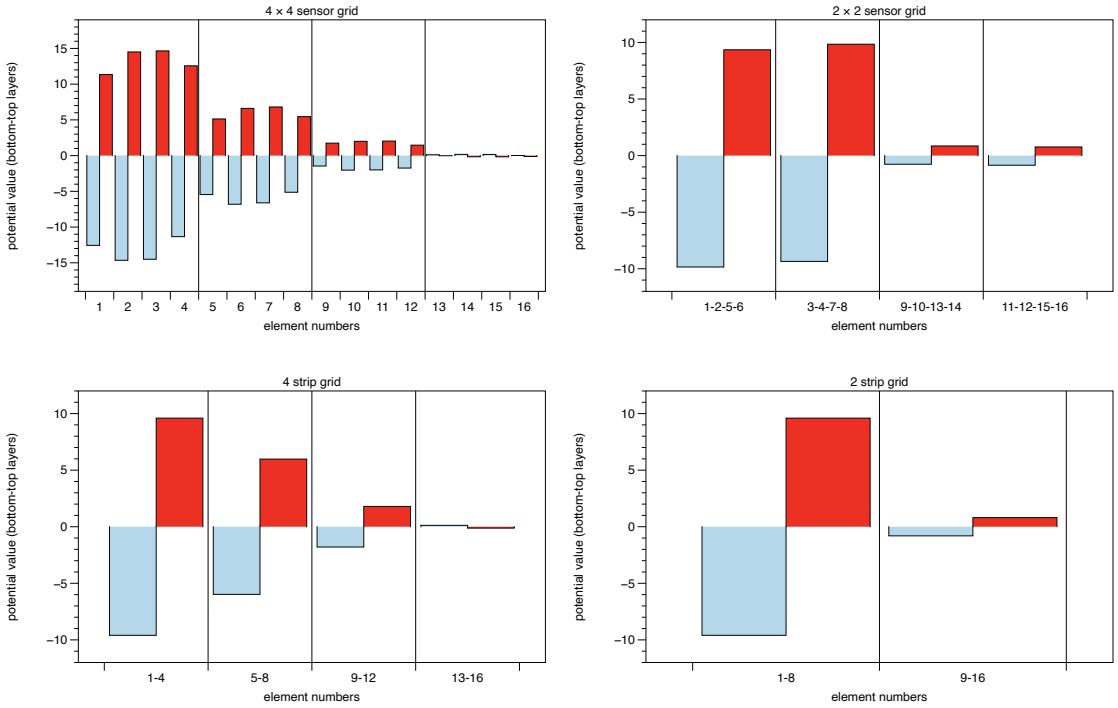

Figure 3: Clamped composite plate: effect of the segmentation of the piezoelectric patches in the sensor configuration for the four different segmentation of the patches.

width; (iv) 2 strips of electrodes, segmenting the plate along the x_1 axis in 2 patches covering the whole plate's width. Note that the employed mesh is illustrated in Fig. 1, where the element numbers can be found that are given in the abscissa of the figures. The results are in agreement with expected values and it can be noticed that the high voltage is located close to the clamped side. As expected, the 2×2 grid gives symmetric results with the same values of the 2 strip grid configuration, as there are no gradients in the (O, x_2) direction. The maximum voltage output (15 V) is obtained with the 4×4 grid; as the electrode size increases, the output voltage drops due to the potential redistribution over the equipotential patch.

3.2 Cylindrical shell panel

A cylindrical shell panel Fig. 4 (left), in the form of a quarter of a complete cylinder, is considered in this last numerical test in order to evaluate the shell FE approach. The problem is as follows [22]:

- geometry cylindrical panel with $R_m = 200$ mm and $e = 2$ mm.

- materials four-layer graphite-epoxy laminate $[0^\circ, 90^\circ]_S$ with a continuous PZT-4 actuator that

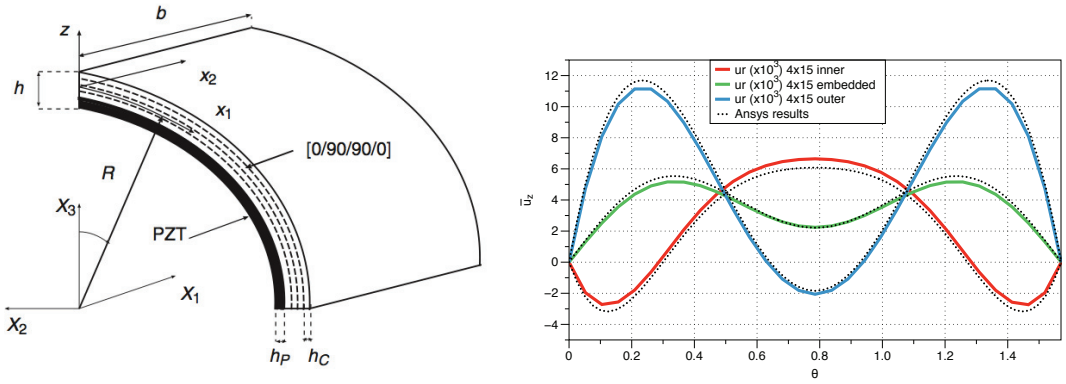

Figure 4: Simply supported cylindrical panel: description of the problem with $pz-$layer bonded at inner surface (left); distributions of the transverse displacement along the central line for the 3 locations of the piezoelectric layer (right).

is either bonded to the shell (at the inner surface or at the outer surface), or embedded at the center of the laminate. Each graphite-epoxy ply is ~~of~~ 0.375 mm thick, and the thickness of the PZT-4 actuator is 0.5 mm. The material properties are given in Tab. 1.

- boundary conditions simply supported on the four edges; the PZT-4 layer is actuated with $\Delta\Phi = 200$ V.

- mesh 4×15 elements (finer discretization along the circumferential direction).

- results and locations deformed shape and distributions of the transverse displacement along the center line of the cylindrical panel.

The distributions of the transverse displacement along the central curvilinear line of the cylindrical panel are presented in Fig. 4 (right). Present results are compared against those obtained by a full 3D simulation carried out with Ansys. The agreement is excellent, which confirms that this shell FE is able to capture the effect of the actuation with a very coarse mesh. In order to highlight the effect of the piezoelectric layer position in the structure, the three deformed shapes are given in Fig. 5. It can be seen that the shell panel curvature is strongly modified by the piezoelectric actuation and that very different shapes are obtained depending on the location of the actuator layer inside the stack.

4 Conclusion

This paper has presented a family of plate and shell FE for piezoelectric composite modelling. A high-order ESL kinematic model is considered that includes the sinus function for the in-plane displacements, a quadratic polynomial expansion for the transverse displacement and Zig-Zag functions for introducing slope discontinuities at layers' interfaces for both, the

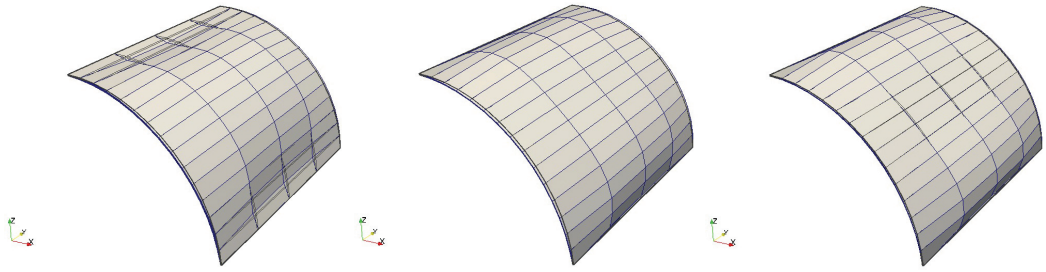

Figure 5: Deformed shapes of simply supported cylindrical panel for 3 different $pz-$layer locations: inner, embedded and outer , from left to right.

in-plane and the transverse displacements. The importance of this Zig-Zag terms was not presented in this short paper but it has been discussed in [4]. A LW cubic approximation is used for the electric potential in order to capture its non-linear distribution induced by the local bending of the piezoelectric layer; the elementary domain is considered as an equipotential surface (constant electric potential).

The element has been assessed through linear static case studies in both sensor and actuator configurations for laminated plates and shells. The role of electrode segmentation, i.e., the size of equipotential surfaces, on the electro-mechanical response has been also evaluated. The results are in good agreement for actuator and sensor configurations. This family of FE, using only 9, up to 12 mechanical dof per node, is very accurate, simple to use, without any numerical problem and could be used for a large range of thin to thick plate and shell problems involving piezoelectric patches or layers.

REFERENCES

[1] O. Polit, P. Vidal, M. D'Ottavio, Robust c^0 high-order plate finite element for thin to very thick structures: mechanical and thermo-mecanical analysis, International Journal for Numerical Methods in Engineering 90 (4) (2012) 429–451, dOI: 10.1002/nme.3328.

[2] H. Murakami, Laminated composite plate theory with improved in-plane response, J. App. Mech. 53 (1986) 661–666.

[3] J. Jiang, D. Li, A new finite element model for piezothermoelastic composite beam, J. Sound Vibr. 306 (2007) 849–864.

[4] O. Polit, M. D'Ottavio, P. Vidal, High-order plate finite elements for smart structure analysis, Composite Structures 151 (2016) 81–90.

[5] I. Chopra, Review of state of art of smart structures and integrated systems, AIAA Journal 40 (2002) 2145–2187.

[6] O. Polit, I. Bruant, Electric potential approximations for an eight node plate finite element, Computers and Structures 84 (22-23) (2006) 1480–1493.

[7] S. Gopinathan, V. Varadan, V. Varadan, A review and critique of theories for piezoelectric laminates, Smart Materials and Structures 9 (1) (2000) 24–48.

[8] R. Gibson, A review of recent research on mechanics of multifunctional composite materials and structures, Compos. Struct. 92 (2010) 2793–2810.

[9] E. Carrera, M. Boscolo, A. Robaldo, Hierarchic multilayered plate elements for coupled multifield problems of piezo- electric adaptive structures: formulation and numerical assessment, Archives of Computational Methods in Engineering 14 (4) (2007) 383–430.

[10] P. Vidal, M. D'Ottavio, M. Ben Thaïer, O. Polit, An efficient shell finite element for the static response of piezoelectric laminates, Journal of Intelligent Material Systems and Structures 22 (7) (2011) 671–690.

[11] S. B. Beheshti-Aval, M. Lezgy-Nazargah, P. Vidal, O. Polit, A refined sinus finite element model for the analysis of piezoelectric-laminated beams, Journal of Intelligent Material Systems and Structures 22 (3) (2011) 203–219.

[12] A. S. 176, IEEE Standard on Piezoelectricity, American National Standard Institute, 1987.

[13] H. Tiersen, Linear Piezoelectric Plate Vibrations, Plenum, New-York, 1969.

[14] M. Touratier, An efficient standard plate theory, Int. J. Eng. Sci. 29 (1991) 901–916.

[15] M. Ganapathi, B. P. Patel, P. Boisse, O. Polit, Flexural loss factors of sandwich and laminated composite beams using linear and nonlinear dynamic analysis, Composites Part B: Engineering 30 (3) (1999) 245–256.

[16] O. Polit, M. Touratier, A multilayered/sandwich triangular finite element applied to linear and non-linear analyses, Composite Structures 58 (1) (2002) 121–128.

[17] F. Dau, O. Polit, M. Touratier, C1 plate and shell finite elements for geometrically nonlinear analysis of multilayered structures, Computers and Structures 84 (19-20) (2006) 1264–1274.

[18] P. Vidal, O. Polit, A thermomechanical finite element for the analysis of rectangular laminated beams, Finite Elements in Analysis and Design 42 (10) (2006) 868–883.

[19] P. Vidal, O. Polit, A family of sinus finite elements for the analysis of rectangular laminated beams, Composite Structures 84 (1) (2008) 56–72.

[20] K. Lam, X. Q. Peng, G. R. Liu, J. N. Reddy, A finite-element model for piezoelectric composite laminates, Smart Mater. Struct. 6 (1997) 583–591.

[21] T. Liu, X. Sun, J. Zheng, L. Wang, Q. Liu, T. Q. Bui, Multi-patch isogeometric analysis for smart plates with distributed piezoelectric patches, Thin-Walled Structures 209 (2025) 112937.

[22] R. Kumar, B. Mishra, S. Jain, Static and dynamic analysis of smart cylindrical shell, Finite Elements in Analysis and Design 45 (2008) 13–24.

XI ECCOMAS Thematic Conference on Smart Structures and Materials - SMART 2025
M. Krommer, M. Nader and M. Schagerl (Eds)

Received: 20 April 2025 / Revised: 29 August 2025 / Accepted: 5 October 2025
© The Author(s) 2025

Advanced Multi-Field Modeling for the Virtual Manufacturing of Layered Structures with Embedded Sensors

Enrico Zappino, Marco Petrolo

Abstract. This study presents a multi-physics modeling framework based on the Carrera Unified Formulation (CUF) within a virtual manufacturing environment to analyze the effects of embedded sensors in composite structures. The proposed layer-wise approach enables high-fidelity representation of the sensor-structure interface, accurately predicting interlaminar stress distributions and residual deformations around the sensor. By incorporating a multi-field electromechanical description, the model enables real-time monitoring of the curing process by tracking capacitance variations, thus providing a direct evaluation of the degree of cure. Furthermore, the framework predicts the development of residual stress fields induced by sensor integration, offering critical insights into local stress concentrations that could affect structural performance. The results highlight the importance of advanced modeling techniques for minimizing stress accumulation and optimizing the integration of sensors. Finally, the study demonstrates how virtual manufacturing environments can improve sensor placement strategies, enhancing the overall reliability and longevity of smart composite structures.

Key words: Embedded Sensors, Structural Health Monitoring, Virtual Manufacturing, Carrera Unified Formulation, Multi-field Model

1 INTRODUCTION

The integration of embedded sensors into composite materials represents a significant advancement in the field of structural health monitoring (SHM), offering enhanced capabilities in damage detection, system diagnostics, and real-time monitoring [1, 2]. However, the inclusion of such sensors introduces challenges during manufacturing, particularly stress concentrations and residual deformations, which can compromise the mechanical integrity of the structures [3].

Enrico Zappino & Marco Petrolo
MUL2 Lab, Department of Mechanical and Aerospace Engineering, Politecnico di Torino, 10129 Turin, Italy
e-mail: enrico.zappino@polito.it,marco.petrolo@polito.it

Composite manufacturing processes involve complex thermal and chemical cycles that induce free strains due to thermal expansion and resin shrinkage. The mismatch of these free strains across material phases and interfaces leads to the development of residual stresses and deformations, particularly significant in curved geometries such as L-shaped laminates [4]. Process-induced deformations, such as spring-in and warpage, are closely linked to the evolution of material properties during cure and the tool-part interaction [5].

Traditional modeling approaches, such as Classical Lamination Theory (CLT) and First-order Shear Deformation Theory (FSDT), are often insufficient to capture through-the-thickness deformations and local effects induced by sensor embedding. To overcome these limitations, the Carrera Unified Formulation (CUF) provides a powerful and versatile modeling framework that allows for refined kinematic descriptions and multi-field coupling [6]. Layer-wise models developed within CUF enable detailed evaluation of interlaminar stresses and localized phenomena without the need for computationally expensive full 3D models [7, 8].

Recent studies have shown that the integration of embedded piezoelectric sensors not only affects the mechanical performance but also alters the electrical response of the structure, such as variations in capacitance [9]. The capacitance change, sensitive to local stress states, offers an additional non-invasive metric for monitoring the structural integrity during and after manufacturing. However, classical models fail to predict this behavior accurately, highlighting the necessity of refined electro-mechanical coupling models [10, 11].

To address these challenges, multi-physics virtual manufacturing frameworks have been proposed, combining thermo-mechanical and electro-mechanical analyses to simulate the manufacturing process of smart composite structures [12, 3]. These frameworks allow for the accurate prediction of residual stresses, spring-in deformations, and sensor performance, enabling optimized sensor placement and manufacturing strategies.

This study builds upon previous efforts and presents an integrated methodology for the virtual manufacturing of layered structures with embedded sensors. By exploiting the capabilities of CUF-based refined models, it aims to provide a high-fidelity prediction of process-induced phenomena, offering insights into the effects of embedded devices on the structural and functional performance of smart composites.

2 ADVANCED NUMERICAL MODEL

The numerical framework employed in this study is based on a refined one-dimensional model developed within the Carrera Unified Formulation (CUF). The approach enables the accurate description of through-the-thickness displacement and stress fields using a layer-wise (LW) expansion.

The three-dimensional displacement field $\mathbf{q} = [u_x, u_y, u_z](x, y, z)$ is approximated by a hierarchical expansion over the beam cross-section, leading to the one-dimensional form:

$$\mathbf{q}(x, y, z) = \mathbf{F}_\tau(x, z)\, \mathbf{q}_\tau(y), \tag{1}$$

where $\mathbf{F}_\tau(x, z)$ are the cross-sectional expansion functions, and $\mathbf{q}_\tau(y)$ are the generalized one-dimensional unknowns.

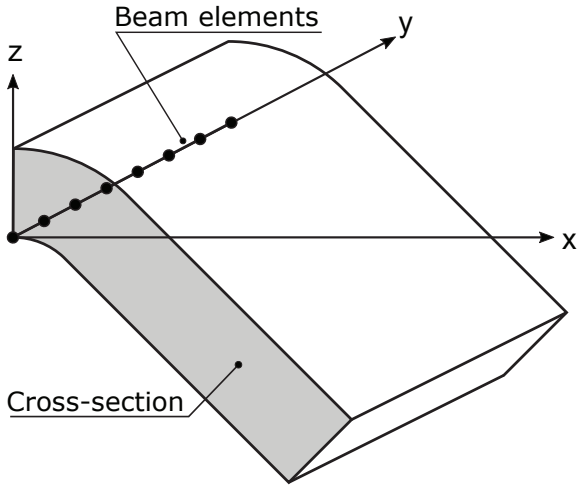

Figure 1: Reference system .

In this work, Lagrange polynomials were used as expansion functions $\mathbf{F}_\tau(x, z)$ to achieve a layer-wise representation of the section.

The finite element discretization along the beam axis y was performed using standard shape functions $N_i(y)$, resulting in the following FEM approximation of the displacement field:

$$\mathbf{q}(x, y, z) = N_i(y)\, \mathbf{F}_\tau(x, z)\, \mathbf{q}_i \tau, \tag{2}$$

where $\mathbf{q}_\tau^i$ are the nodal unknowns associated with the generalized displacements.

The mechanical response of the composite panel during the curing process was modeled using a Cure Hardening Instantaneously Linear Elastic (CHILE) constitutive model, capturing the evolution of the material properties as a function of the degree of cure. The interaction between the composite part and the steel tool was modeled by introducing a shear layer, with a thickness equal to one-tenth of a ply thickness.

The resulting finite element problem was solved through an iterative procedure to account for the curing-dependent material behavior, as schematically illustrated in Figure 2. A fully coupled electro-mecanical model, see [9], has been used to predict the variation of the capacitance in the sensor.

3 NUMERICAL RESULTS

In this section, the main numerical results obtained from the virtual manufacturing simulations are presented. The effects of the embedded sensor on the mechanical response of the composite panel are first analyzed. Subsequently, the evolution of the electrical response during the curing process is investigated through capacitance monitoring. The results aim to validate the proposed modeling strategy and highlight the potential of the developed framework for real-time process tracking and structural performance assessment.

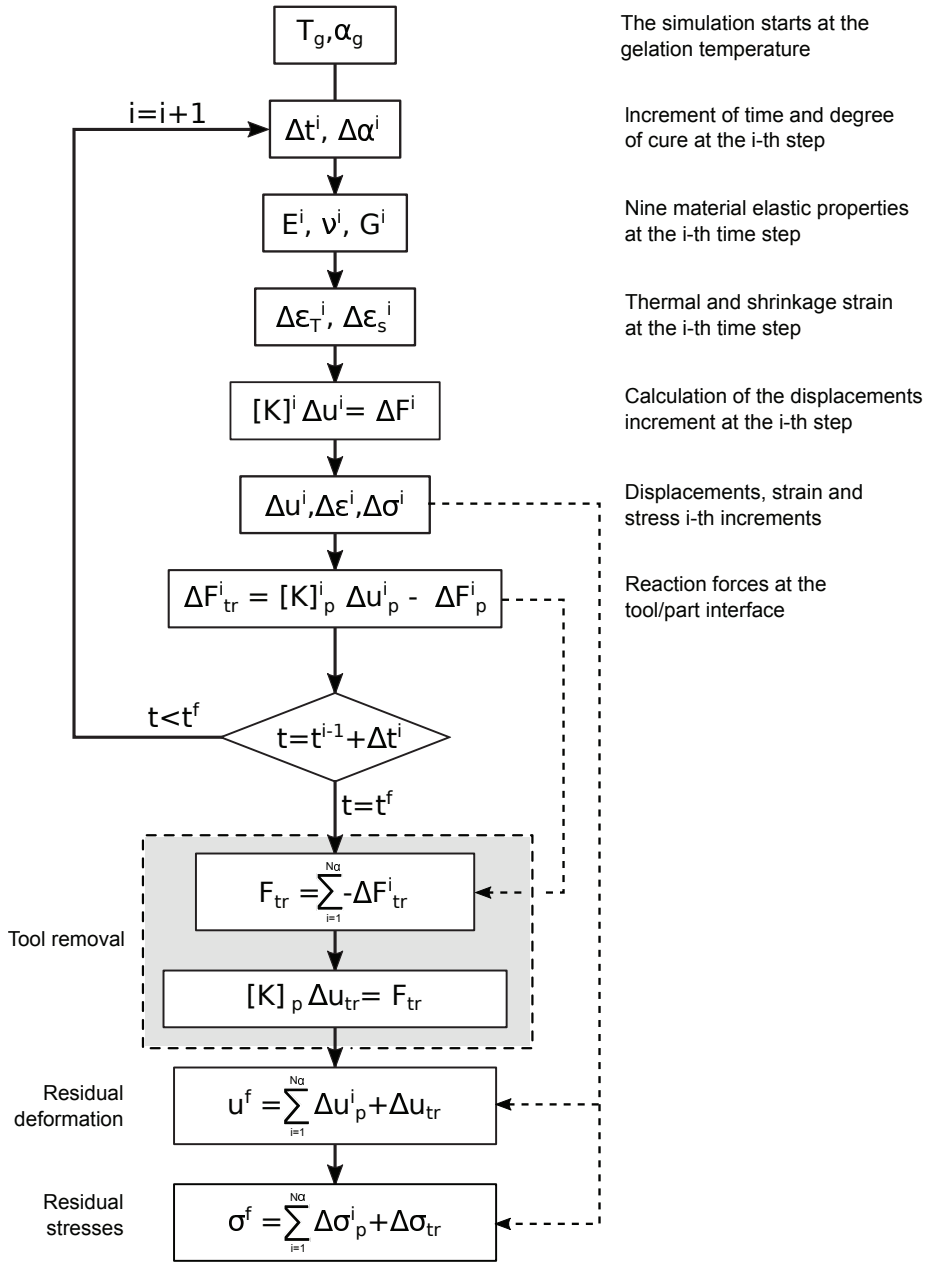

Figure 2: CHILE Numerical solution scheme [4].

Table 1: Mechanical and thermal properties of the steel tool and the ZPT-H5 sensor.

Property	Steel	ZPT-H5
Young's Modulus [GPa]	210	63
Poisson's Ratio [-]	0.30	0.31
Thermal Expansion Coefficient [μm/m°C]	12	3.5
Density [kg/m^3]	7850	7700

3.1 Virtual manufacturing of a composite panel with an embedded sensor

The system under investigation consists of a composite panel made of eight plies of AS4/8552 material, laminated in a symmetric $[0/90/0/90]_s$ stacking sequence. The panel rests on a steel tool with a thickness of 0.01[m], and a shear layer is introduced at the tool-panel interface, with a thickness equal to one-tenth of that of a single composite ply. Two configurations were analyzed: in the first, the panel is free from inclusions; in the second, a ZPT-H5 piezoelectric sensor is embedded at the mid-plane of the laminate. The properties of the materials of the sensor and the tool are reported in Tab. 1 while the properties of the composite material can be found in [4].

The curing cycle considered consists of a single holding phase at 180°C. Detailed information about the curing parameters can be found in the literature [4]. The geometry of the embedded sensor is depicted in Figure 3.

A beam layer-wise model based on Lagrangian expansions was employed to accurately capture the multilayered behavior of the composite panel. Quadratic nine-node elements (Q9) were used to discretize the cross-section of the beam, allowing an accurate representation of the displacement and stress fields across each ply and the embedded sensor. Along the beam axis, a single three-node beam element (B3) was adopted, assuming that the variations along the longitudinal direction, y, can be considered negligible.

Symmetry boundary conditions were imposed at $x = 0$, and at $y = 0$ and $y = 1.667$ mm u_y have been set equal to zero. These constraints exploit the physical and geometrical symmetries of the problem, thus reducing the computational cost while maintaining the accuracy of the simulation.

To assess the impact of the embedded sensor, the displacement fields were evaluated. All results refer to the post-demolding condition. Figure 4 shows the vertical displacement field (u_z), highlighting how the presence of the sensor modifies the shrinkage behavior of the panel, as the piezoelectric material does not undergo significant curing shrinkage.

Figure 5 presents the in-plane displacement field (u_x), revealing that the embedding of the sensor also affects in-plane deformations, particularly at the interface between the composite and the piezoelectric material. A detailed profile of vertical displacements is provided in Figure 6. The value of the vertical displacement has been reported along the thickness of the panel. The negative value is due to the shrinkage od the material due to the curing process. The picture clearly shows that the sensor region does not experience vertical shrinkage.

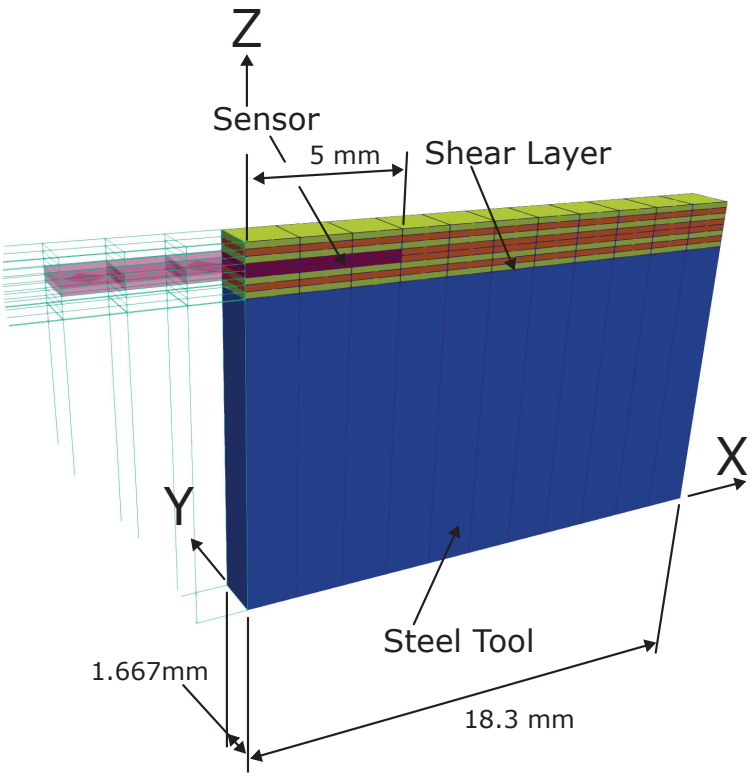

Figure 3: Geometry of the embedded ZPT-H5 sensor within the composite panel.

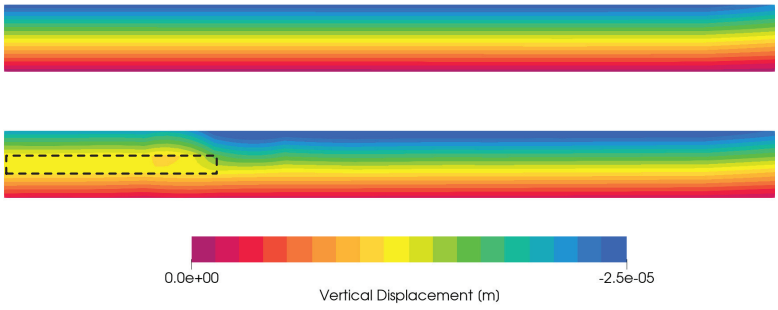

Figure 4: Vertical displacement field u_z: comparison between panel without (top) and with (bottom) embedded sensor.

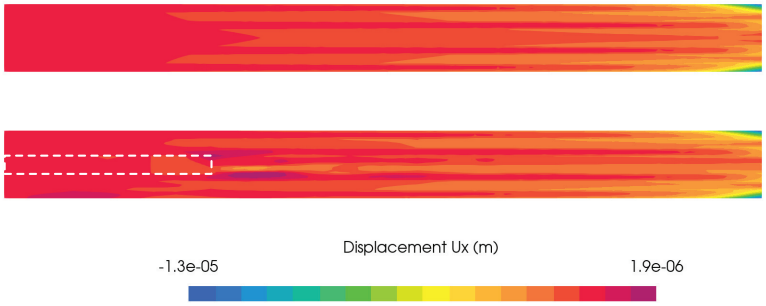

Figure 5: In-plane displacement field u_x: effect of the embedded sensor at the material interface.

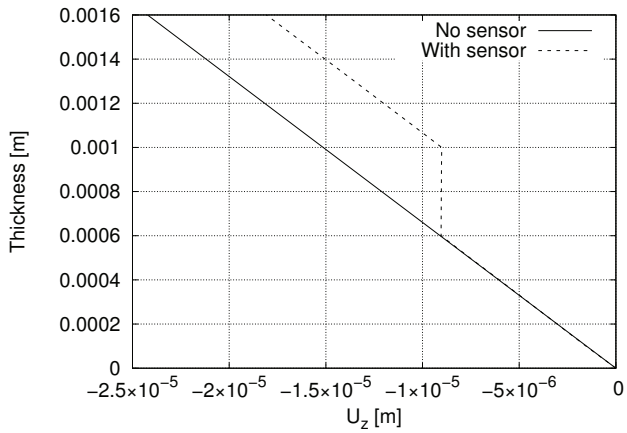

Figure 6: Vertical displacement profile u_z across the panel thickness. The region corresponding to the sensor shows no vertical displacement.

3.2 Real time estimation of the curing process via capacitance monitoring

Following the methodology presented in [9], for the configuration under investigation, the variation of the sensor capacitance was evaluated at each step of the curing process. A potential difference of 1 V was applied across the embedded piezoelectric transducer. In this case, the generated electric charge depends not only on the dielectric properties of the material but also on the mechanical stresses, as the piezoelectric material produces additional electric charges in response to the developing stress field. This surplus of electric charge results in a measurable variation of the sensor capacitance.

Figure 7 illustrates the temporal evolution of the degree of cure and of the transverse elastic modulus E_t. The modulus increases at first for the polimerization process and after $t = 200s$ a second variation of the modulus is due to the cool down phase. In Figure 8, the percentage variation of the capacitance value is reported as a function of the evolving transverse elastic modulus.

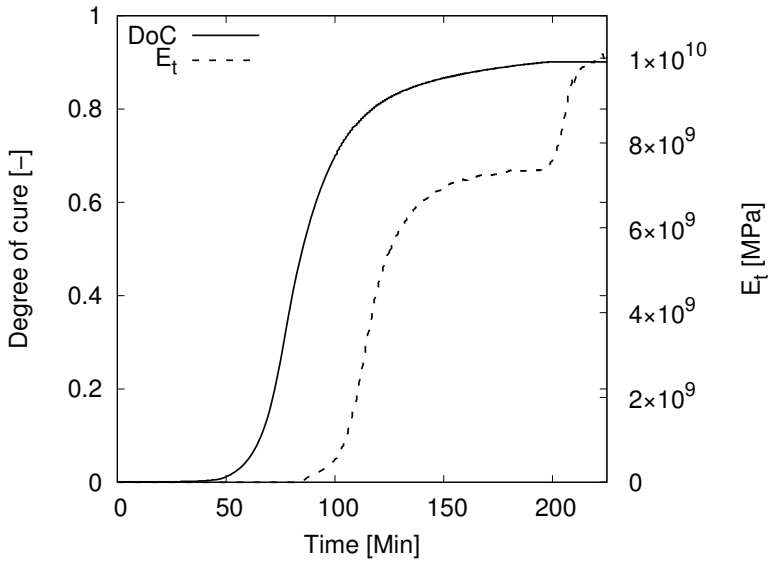

Figure 7: Temporal evolution of the degree of cure and the transverse elastic modulus E_t during the curing process.

The results show that the proposed approach allows an accurate tracking of the curing process. The numerical model adopted is the same described previously, based on a beam layer-wise approach with Lagrangian interpolation functions and quadratic elements for the cross-section discretization.

4 CONCLUSIONS

In this work, an advanced numerical framework based on a layer-wise model developed within the Carrera Unified Formulation (CUF) was employed to simulate the virtual manu-

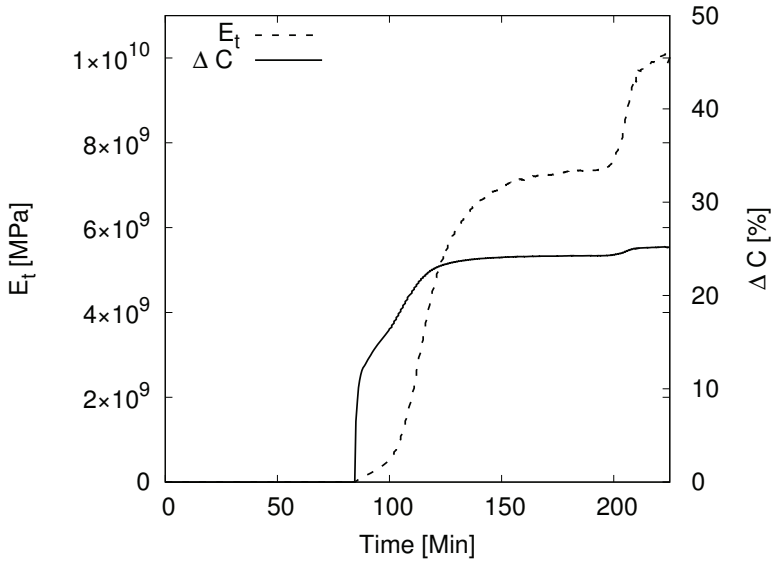

Figure 8: Percentage variation of the sensor capacitance as a function of the transverse elastic modulus E_t.

facturing of composite structures with embedded piezoelectric sensors. The methodology accurately captured the complex interactions between mechanical, thermal, and electrical fields during the curing process. The CHILE constitutive model was used to account for the evolving material properties, while the tool-part interaction was modeled through a dedicated shear layer. Furthermore, a fully coupled electro-mechanical analysis was performed to monitor the evolution of the sensor capacitance throughout the process.

The numerical results demonstrated the significant impact of the embedded sensor on both the mechanical and electrical responses of the structure. The presence of the sensor locally altered the shrinkage behavior, leading to variations in the displacement fields, especially around the sensor region. Moreover, the monitoring of capacitance variations proved to be an effective non-invasive technique to track the curing progression, with a clear correlation observed between the capacitance change and the evolution of the transverse elastic modulus.

Future developments will focus on extending the current framework to more complex geometries and multi-sensor configurations. In addition, the integration of damage initiation and propagation models within the virtual manufacturing environment will allow for a more comprehensive prediction of the long-term structural performance of smart composite structures.

Acknowledgements

This work was supported by the project “An AI-assisted virtual manufacturing approach to mitigate defects in advanced composites” funded by the Italian Minister of Foreign Affairs and INTERNATIONAL COOPERATION (MAECI) [grant number US23GR12].

REFERENCES

[1] A. Alaimo, A. Barracco, A. Milazzo, and C. Orlando, "Structural health monitoring procedure for composite structures through the use of artificial neural networks," *Aerotecnica Missili & Spazio*, vol. 94, no. 1, p. 14–22, Jan. 2015. [Online]. Available: http://dx.doi.org/10.1007/BF03404684

[2] C. Tuloup, W. Harizi, Z. Aboura, Y. Meyer, K. Khellil, and R. Lachat, "On the use of in-situ piezoelectric sensors for the manufacturing and structural health monitoring of polymer-matrix composites: A literature review," *Composite Structures*, vol. 215, p. 127–149, May 2019. [Online]. Available: http://dx.doi.org/10.1016/j.compstruct.2019.02.046

[3] E. Zappino, R. Masia, N. Zobeiry, M. Petrolo, and E. Carrera, "Development of mitigation strategies for process-induced deformations through finite elements," *Mechanics of Advanced Materials and Structures*, vol. 31, no. 28, pp. 11 054–11 066, 2024.

[4] E. Zappino, N. Zobeiry, M. Petrolo, R. Vaziri, E. Carrera, and A. Poursartip, "Analysis of process-induced deformations and residual stresses in curved composite parts considering transverse shear stress and thickness stretching," *Composite Structures*, vol. 241, p. 112057, 2020.

[5] K. Takagaki, S. Minakuchi, and N. Takeda, "Process-induced strain and distortion in curved composites. part i: Development of fiber-optic strain monitoring technique and analytical methods," *Composites Part A: Applied Science and Manufacturing*, vol. 103, pp. 236–251, 2017.

[6] E. Carrera, M. Cinefra, M. Petrolo, and E. Zappino, *Finite element analysis of structures through unified formulation*. John Wiley & Sons, 2014.

[7] E. Carrera and M. Petrolo, "Refined beam elements with only displacement variables and plate/shell capabilities," *Meccanica*, vol. 47, no. 3, pp. 537–556, 2012.

[8] E. Carrera, M. Petrolo, and E. Zappino, "Performance of cuf approach to analyze the structural behavior of slender bodies," *Journal of Structural Engineering*, vol. 138, no. 2, pp. 285–297, 2012.

[9] J. Najd, E. Zappino, E. Carrera, W. Harizi, and Z. Aboura, "A variable kinematic model for the prediction of capacitance variations in embedded pzt sensors," *Journal of Intelligent Material Systems and Structures*, vol. 34, no. 7, p. 811–824, Sep. 2022. [Online]. Available: http://dx.doi.org/10.1177/1045389X221121974

[10] M. N. Ghasemi-Nejhad, R. Russ, and S. Pourjalali, "Manufacturing and testing of active composite panels with embedded piezoelectric sensors and actuators," *Journal*

of Intelligent Material Systems and Structures, vol. 16, no. 4, p. 319–333, Apr. 2005. [Online]. Available: http://dx.doi.org/10.1177/1045389X05050103

[11] S. Shin, B. Zamorano, and N. Elvin, "Comparison of the electromechanical properties of embedded and surface-mounted piezoelectric transducers," *Journal of Intelligent Material Systems and Structures*, vol. 27, no. 20, p. 2837–2850, Jul. 2016. [Online]. Available: http://dx.doi.org/10.1177/1045389X16642299

[12] E. Zappino and E. Carrera, "Advanced modeling of embedded piezo-electric transducers for the health-monitoring of layered structures," *International Journal of Smart and Nano Materials*, vol. 11, no. 4, pp. 325–342, 2020.

Part IV
MS 03 - SYMBIOTIC MECHATRONICS
Manfred Nader, Sven Herold, Alexander Büchner

XI ECCOMAS Thematic Conference on Smart Structures and Materials - SMART 2025
M. Krommer, M. Nader and M. Schagerl (Eds)

Received: 28 March 2025 / Revised: 27 August 2025 / Accepted: 11 October 2025
© The Author(s) 2025

Condition Monitoring of the Human Arterial System by Modal Analysis of Blood Flow Rates

Florian Brunnmayr, Gudrun Mikota, Peter Benedikt, Georg Hagleitner

Abstract. Theoretical modal analysis is performed on a 63 degree of freedom model of the human arterial system and the first six flow rate modes are shown. Afterwards, the system is modified on the upper right arm with a simulated vasoconstriction (stenosis). The resulting first six flow rate modes are compared with the modes of the original system. A test person is then subjected to ultrasound examinations, with and without a pressure cuff applied to the right arm. The resulting ultrasound images are analysed, filtered and Fast Fourier transformed. Individual operational flow rate shapes of the original and modified test subject are extracted from the resulting spectra and displayed. Finally, the operational flow rate shapes are compared among each other and matched with the eigenmodes of the model. The pressure cuff makes a significant difference in both theory and practice so that the modified condition can be monitored by operational flow rate shapes.

Key words: Vibration SHM, Modal Analysis, Medical Engineering, Human Arterial System

1 INTRODUCTION

The human arterial system is a complex network of vessels which conducts a pulsating blood flow excited by the heart. Its dynamic behavior has been modeled at various degrees of refinement [1, 2, 3, 4]. Considering blood inertia and wall elasticity, the vessels can be interpreted as acoustic ducts, where local changes due to aneurysms and stenoses alter the system's dynamics [5]. Modal analysis, both theoretical and experimental, offers a promising approach for non-invasive diagnostic tools, akin to structural health monitoring in engineering.

Florian Brunnmayr & Gudrun Mikota
Institute of Machine Design and Fluid Power, Johannes Kepler University Linz Altenbergerstr. 69, Linz, Austria, e-mail: florian.brunnmayr@jku.at,gudrun.mikota@jku.at

Peter Benedikt
Kepler University Hospital, Medical Faculty of the Johannes Kepler University, Department for Thoracic and Cardiovascular Surgery, Krankenhausstraße 9, Linz, Austria
e-mail: peter.benedikt@kepleruniklinikum.at

Georg Hagleitner
Kepler University Hospital, Medical Faculty of the Johannes Kepler University, Central Radiology Institute, Krankenhausstraße 9, Linz, Austria, e-mail: georg.hagleitner@kepleruniklinikum.at

In this paper, we aim to simulate the effects of arterial stenosis using a pressure cuff. The objective is to investigate the impact of artificially induced narrowing on the dynamic behavior of the arterial system, focusing on changes in modal parameters. By applying the pressure cuff to a specific section of the artery, we simulated a stenosis, effectively altering the physical properties of the vessel at that location.

To detect a change in the arterial system due to the pressure cuff, a reference measurement was made beforehand. In both investigations, an ultrasonic device was employed to measure the blood velocities at multiple points along the arterial tree. From frequency spectra of blood flow rates, operational flow rate shapes were extracted at key frequencies. As a reference, an undamped lumped parameter model of the arterial tree was used to predict natural flow rate modes with and without stenosis. These mode shapes are illustrated and compared with operational flow rate shapes from respective investigations. The effect of the stenosis is thus analyzed in theory and practice.

2 Theoretical modal analysis

An eigenvalue analysis is performed on a 63-degree-of-freedom model of the arterial system [6], see Figure 1a. In analogy with mechanical systems, the discretized model becomes

$$\mathbf{M}_a\,\ddot{\mathbf{q}} + \mathbf{K}_a\,\mathbf{q} = \dot{\mathbf{p}}_{\mathbf{ex}} \tag{1}$$

where $\mathbf{M}_a$ and $\mathbf{K}_a$ denote mass and stiffness matrix, respectively, $\mathbf{q}$ denotes the flow rate vector and $\mathbf{p}_{\mathbf{ex}}$ is the vector of pressure excitation. The boundary conditions are specified such that the heart end is considered open, while the ends of the capillaries are considered closed. The primary focus is on the representation of the flow rate mode shapes, in which the flow rate is constant over each element. For the calculation of flow rate modes, the eigenvalue problem

$$(-\omega^2\mathbf{M}_a + \mathbf{K}_a)\boldsymbol{\Phi} = \mathbf{0} \tag{2}$$

is solved by MATLAB. The first six eigenmodes of the original system are presented in Figure 2. The illustration uses the same grid as the model in Figure 1a, on which the flow rate amplitude is indicated by the line thickness. Red lines indicate a flow direction away from the heart, while blue lines stand for the opposite direction. The highest amplitude of each mode is scaled to a thickness of $25\,\mathrm{pt}$.

For the simulation of stenosis, the diameter of element 48 on the right arm is reduced to 20% of its original value (see Figure 1a). Consequently, the hydraulic capacity decreases, while the hydraulic inductance increases. The eigenvalues are then computed using the updated mass and stiffness matrices. The original system without stenosis is used as a reference for comparison. The first six eigenmodes of the system perturbed by the stenosis are displayed in Figure 3.

3 Discussion of theoretical modes

Figure 2a shows the first flow rate mode at $2.37\,\mathrm{Hz}$ with an antinode at the heart end of the aorta. The legs participate rather than the arms.

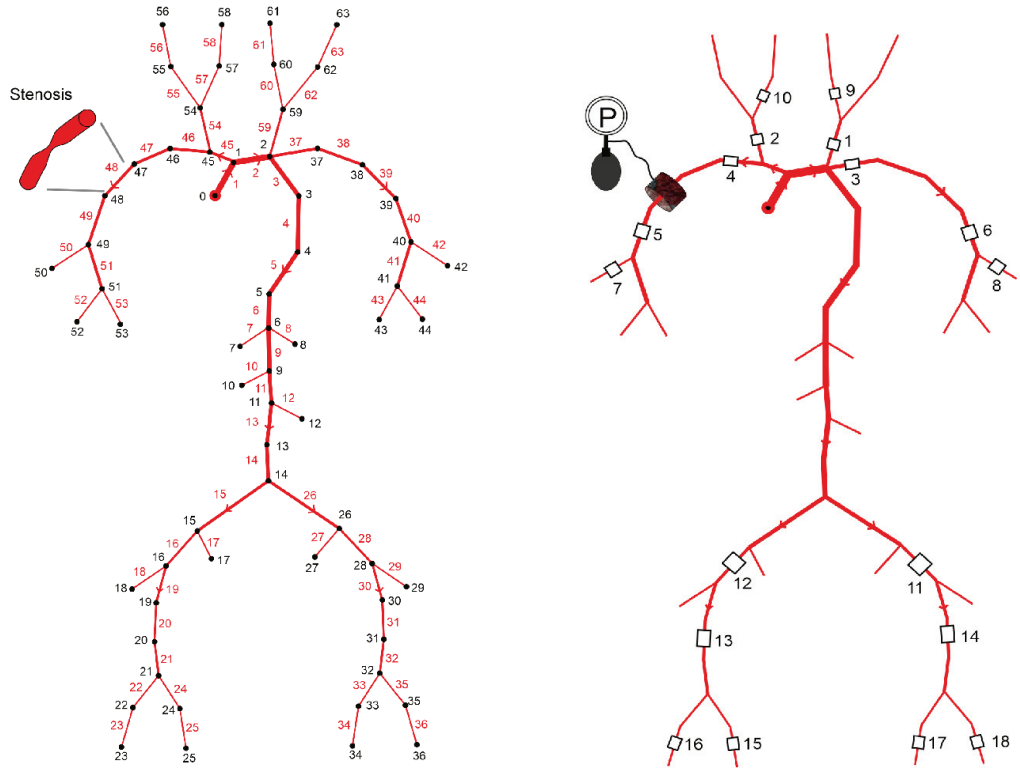

(a) 63 degree-of-freedom model of the arterial tree

(b) Measurement points throughout arterial tree

Figure 1: Arterial tree (left) for theoretical modal analysis and measurement points (right) for experimental investigations

The next flow rate mode appears at $3.62\,\mathrm{Hz}$ with an antinode between the legs (Figure 2b).

Figure 2c shows the third flow rate mode at $3.94\,\mathrm{Hz}$ which concerns the left arm, with an antinode at the heart. The main aorta and other extremities don't participate. A small reversed flow is recognized in the lower body and the legs.

Figure 2d shows the fourth flow rate mode at $4.49\,\mathrm{Hz}$. It has an antinode at the heart and opposite antinodes in the legs with reversed flow. A node occurs in the lower body. The right arm participates slightly.

Figure 2e shows a full wavelength mode at $4.61\,\mathrm{Hz}$ starting at the right arm, leading through the aorta and ending at the legs. The reversed flow in the right arm is caused by the convention of the blood flow direction starting at the heart and ending in the capillaries. The heart aorta hardly participates.

Figure 2f shows a more local mode at $6.02\,\mathrm{Hz}$ were an antinode occurs at the splenic and

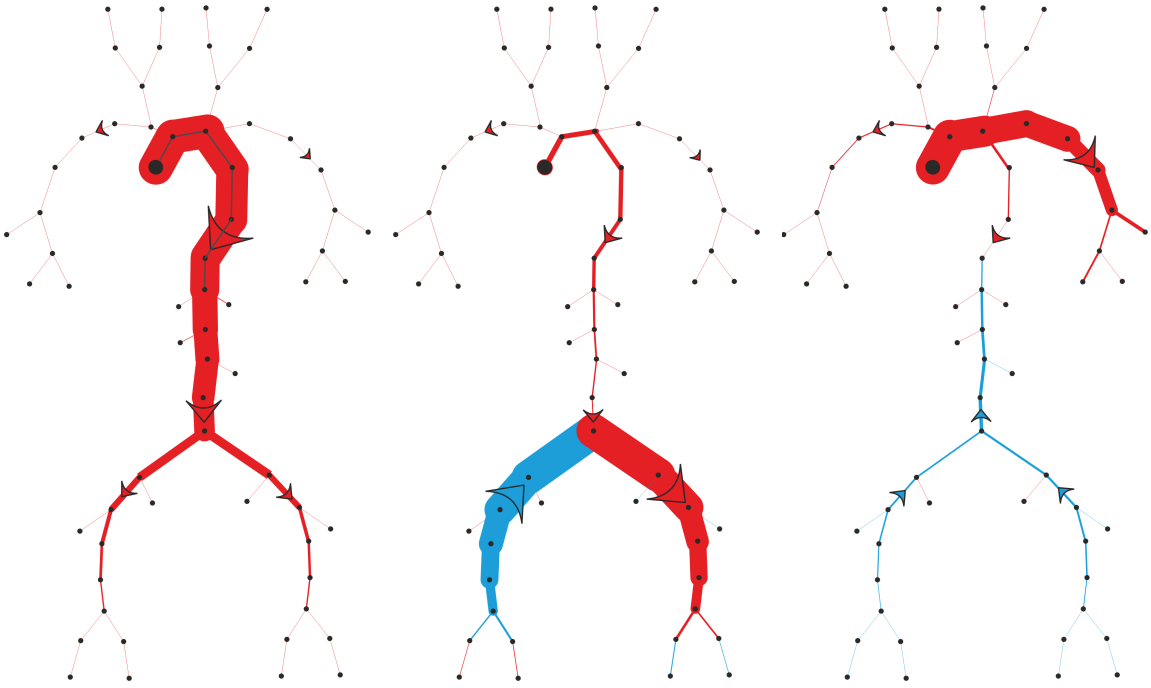

(a) 2.372 Hz (b) 3.618 Hz (c) 3.944 Hz

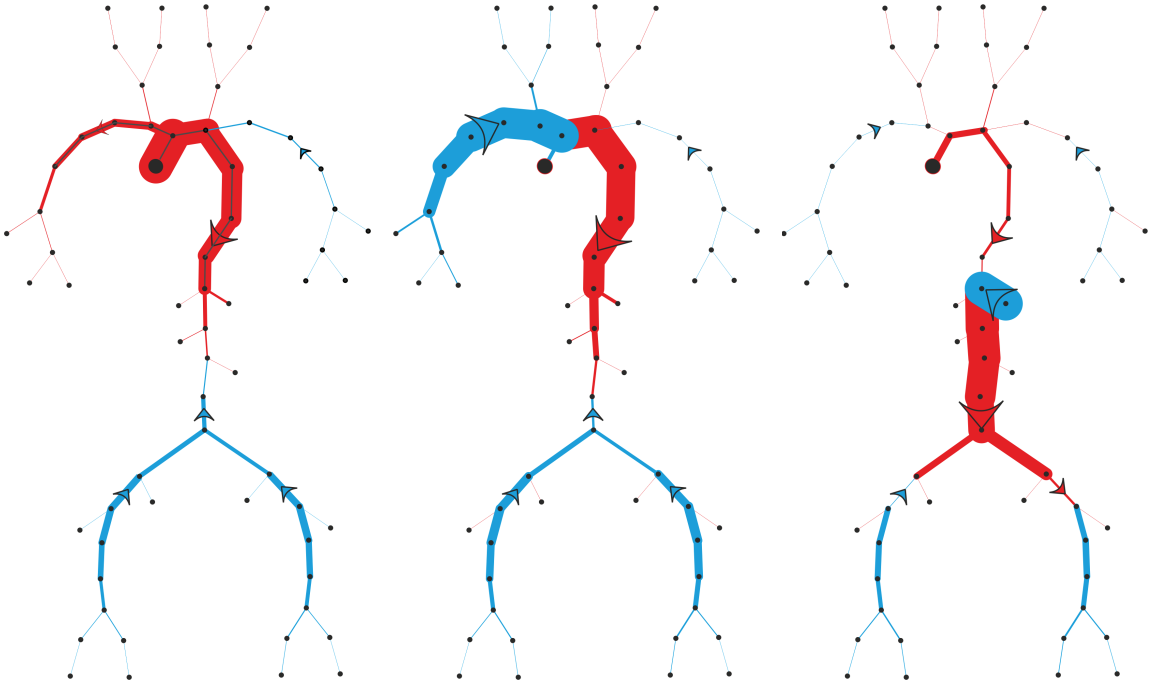

(d) 4.489 Hz (e) 4.607 Hz (f) 6.022 Hz

Figure 2: First six eigenmodes of the original system

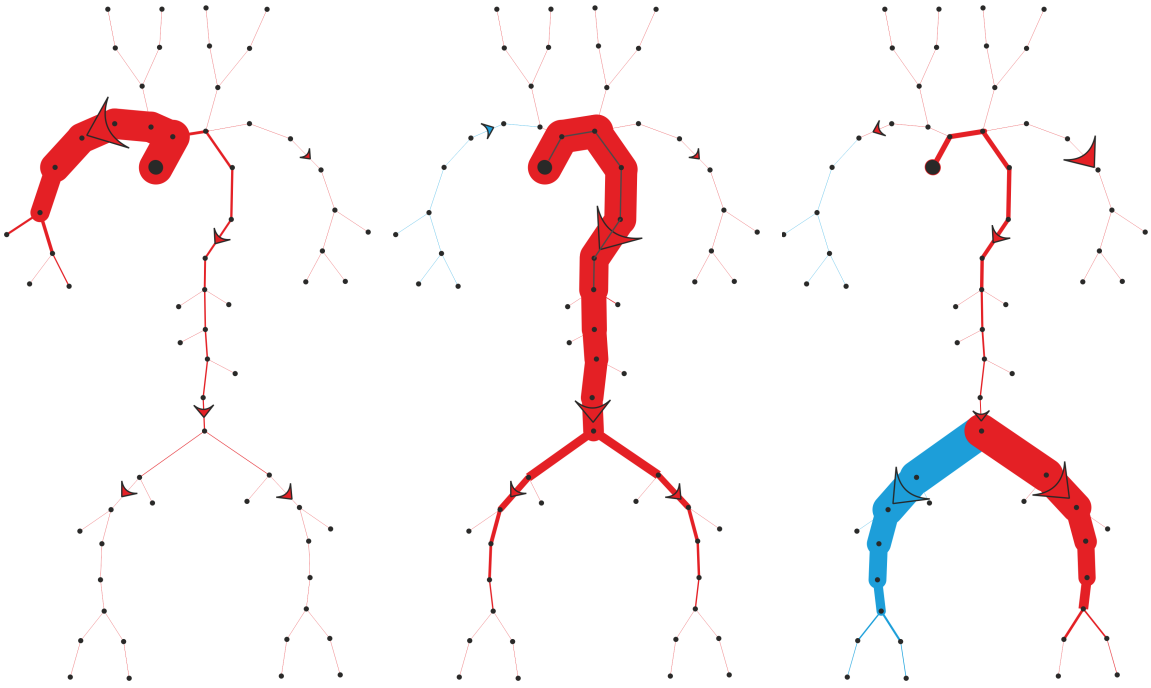

(a) 1.759 Hz (b) 2.372 Hz (c) 3.618 Hz

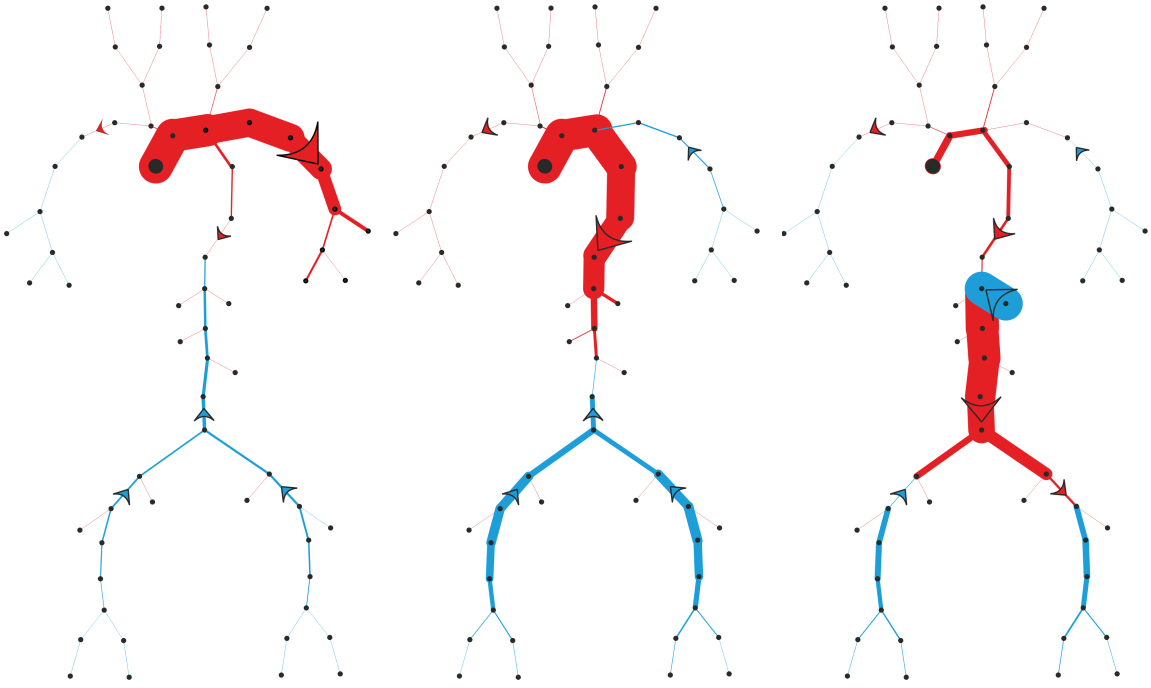

(d) 3.945 Hz (e) 4.517 Hz (f) 6.022 Hz

Figure 3: First six eigenmodes of stenotic system

gastric artery (these two arteries are summarized in element 8). This mode goes through the lower aorta and has an opposite antinode in the lower legs. A node can be detected at the hips.

As for the set of stenotic modes, Figure 3a shows the first flow rate mode at $1.76\,\mathrm{Hz}$ which concerns the right arm with an antinode at the heart. This mode does not occur in the original set of modes.

Figure 3b shows the second flow rate mode at $2.37\,\mathrm{Hz}$ with the same shape as Figure 2a in the original set of modes. No change in frequency is recognized.

Figure 3c shows an antinode between the legs with the same shape as Figure 2b in the original set of modes. As before, no change in frequency is recognized.

Figure 3d shows the fourth flow rate mode at $3.95\,\mathrm{Hz}$ with the same shape as Figure 2c in the original set of modes. No change in frequency is recognized.

Figure 3e shows the fifth flow rate mode at $4.52\,\mathrm{Hz}$ with an antinode in the upper body and a node in the lower body. The legs have an opposite antinode. Compared to Figure 2d the right arm participates no longer. A change in frequency is recognized by $0.03\,\mathrm{Hz}$.

Figure 3f shows the sixth flow rate mode at $6.02\,\mathrm{Hz}$ with the same shape as Figure 2f without any change in frequency. However, the mode in Figure 2e disappeared in the modified mode shape set.

4 Condition monitoring of a test subject

4.1 Test procedure

A 19 year old man, $196\,\mathrm{cm}$ tall and with $100\,\mathrm{kg}$ weight was subjected to several ultrasound examinations as a test subject in order to determine the blood velocities at different points of the arterial system with the aid of pulsed-wave doppler ultrasound (see Figure 1b). First, a reference measurement was performed and the blood velocities were determined and stored in the above sequence. Next, a pressure cuff was placed around the subject's right upper arm and the measurement was repeated. The pressure cuff was equipped with a manometer. After agreement between the test person and the doctors present, the pressure cuff was inflated to a pressure of $p = 105\,\mathrm{mmHg}$ ($140\,\mathrm{mbar}$). The blood pressure in a healthy human body usually fluctuates between a systolic pressure of $120\,\mathrm{mmHg}$ and a diastolic pressure of $80\,\mathrm{mmHg}$. This means that the pressure cuff should cause a clear constriction there.

4.2 Signal processing

The determination of blood flow rates from ultrasound imaging is described in [7]. Individual frames from the ultrasound video file were stitched together to create a continuous panoramic image. A single frame is displayed in Figure 4. From this image, individual sections were cropped based on the electrocardiogram (ECG) line shown in cyan, with a fixed size in pixels. The result is shown in Figure 5a. Noise and distracting artifacts were removed. In the next step, a MATLAB function was used to determine the maximum velocity in the artery (see Figure 5b). For the following step, two assumptions have to be made. The cross-sectional areas of the arteries are assumed to be constant over time and the cross-section of the theoretical model is

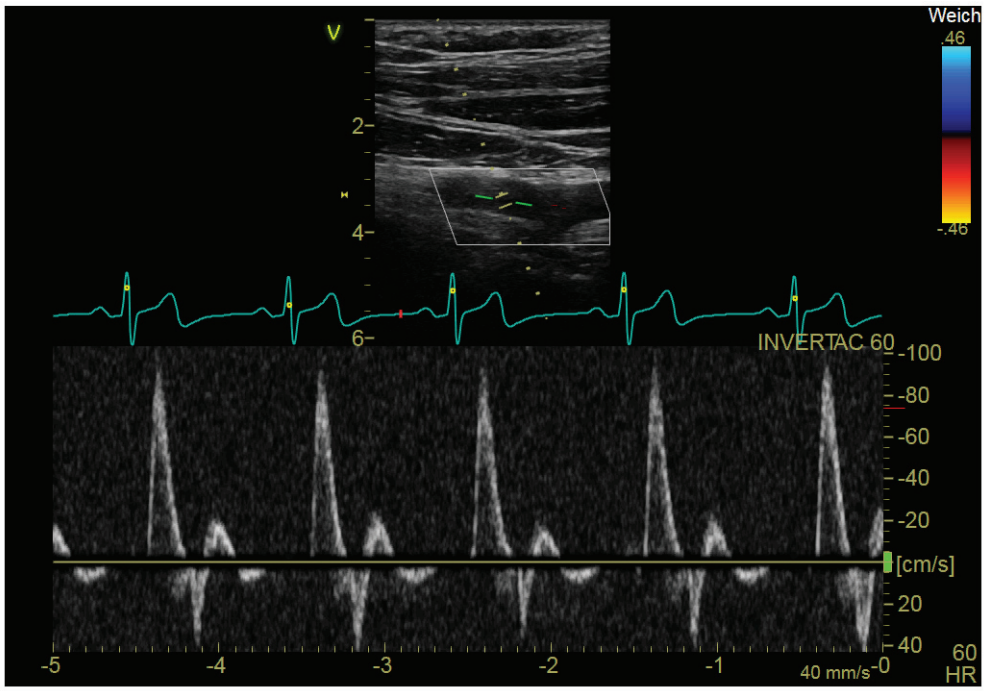

Figure 4: Snapshot from ultrasonic device at measurement point 4

used. By multiplying the velocity by the cross-sectional area of the artery, the velocity profile was converted into a volumetric flow rate q, which is illustrated in Figure 5c.

4.3 Spectra

To analyze the frequency content of the flow rate signal, a Fast Fourier Transform (FFT) was applied. In order to enhance the visual frequency resolution, the signal was zero-padded, effectively increasing its length by a factor of four. This corresponds to a quartering of the frequency domain resolution in the resulting interpolation of the spectrum, which enables a more accurate peak estimation. At least eight of these single signal spectra were then averaged. The resulting spectrum from this signal analysis is shown in Figure 6. The first maximum is located at $0.85\,\mathrm{Hz}$ with amplitude around $8\,\mathrm{ml/s}$ while the second maximum is at $2.29\,\mathrm{Hz}$ with amplitude around $11\,\mathrm{ml/s}$.

5 Discussion of operational flow rate shapes

Operational flow rate shapes are extracted at dominant amplitude maxima in flow rate spectra. The extraction of operational flow rate shapes from spectral data requires the analysis of complex-valued information. For visualization, only the real component of the complex num-

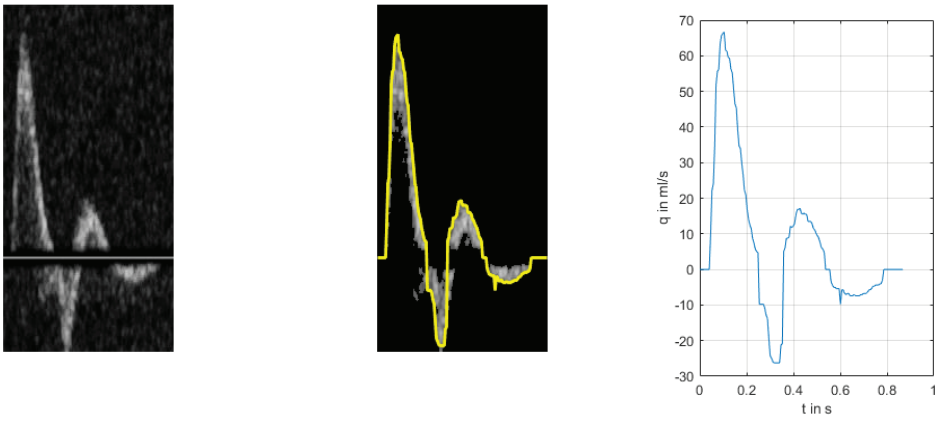

(a) cut-out image (b) image with envelope (c) flow rate

Figure 5: Signal processing of point 4

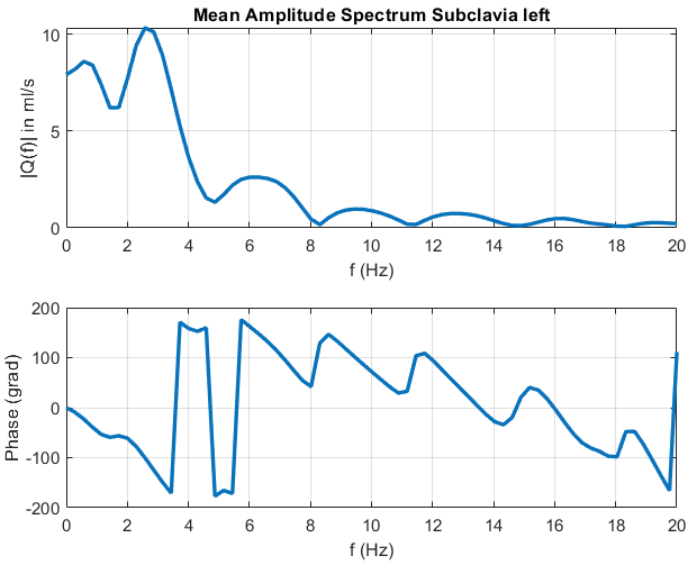

Figure 6: Averaged and four times zero padded flow rate spectrum of point 4

bers is used. This choice simplifies the representation and interpretation of the spectral data. Additionally, the complex-valued elements can be rotated in the complex plane by multiplying them with

$$\tilde{\boldsymbol{\Psi}} = \bar{\boldsymbol{\Psi}} \cdot e^{i \cdot \varphi} \tag{3}$$

where $\tilde{\boldsymbol{\Psi}}$ denotes the rotated operational flow rate shape, $\bar{\boldsymbol{\Psi}}$ denotes the original operational flow rate shape from spectra and φ represents the phase angle. Figures 7 and 8 show the operational flow rate shapes at the points where they could be measured, with neighboring arteries given the same amplitude. Where no measurement could be made, the artery was colored grey.

Figure 7a shows the $0.85\,\mathrm{Hz}$ operational flow rate shape of the test subject with pressure cuff on the right upper arm. In all measured arteries a positive blood flow is recognized, with highest amplitude in the right arm, which is scaled to a real value with $25\,\mathrm{pt}$ thickness. This operational flow rate shape resembles of Figure 3a. All other operational flow rate shapes are shown with real value at the measurement point of highest amplitude and scaled by the same factor.

According to this rule, Figure 7b shows the $2.29\,\mathrm{Hz}$ operational flow rate shape. It looks similar to Figure 7a, with different frequency and slightly reduced amplitudes.

Figure 7c shows the same operational flow rate shape in a $90°$ phase angle. Compared to Figure 7b, overall amplitudes are much smaller. This demonstrates that the shape is nearly real.

Figure 8a shows the $0.85\,\mathrm{Hz}$ operational flow rate shape of the test subject without pressure cuff. Compared to Figure 7a the shape is much more symmetric and the scaling shows that this flow rate shape is less expressed than its counterpart.

Figure 8b shows the operational flow rate shape at $2.29\,\mathrm{Hz}$. In contrast to Figure 7b, symmetry is maintained between the arms and the amplitude in the right arm is reduced.

Figure 8c shows the same operational flow rate shape at $2.29\,\mathrm{Hz}$ in a $90°$ phase angle. Here the legs participate like in Figure 2d. In contrast to the measurement with pressure cuff, this $2.29\,\mathrm{Hz}$ shape is heavily complex.

Theoretical flow rate modes and operational flow rate shapes can only be matched to a limited extent. Physical parameters of the theoretical model were taken from literature and do not necessarily match the parameters of the test subject. Moreover, it should be clarified how close operational flow rate shapes can come to eigenmodes in theory. At a later stage, the Modal Assurance Criterion could be applied for comparing mode shape sets from theory and experiment.

6 Conclusion

As demonstrated, the pressure cuff significantly changed the systems behavior both in theory and practice. Some theoretical eigenmodes dissolve and new modes appear. Operational flow rate shapes, which can be approximated by a superposition of eigenmodes, were also changed by the pressure cuff. This phenomenon could be used to monitor the modified condition.

Future studies should incorporate measurement points along the main aorta to enhance data accuracy and understanding. Damping effects from arterial wall viscoelasticity and fluid viscosity can be considered in future models. High but widely proportional damping is expected so that similar mode shapes should result at lower natural frequencies.

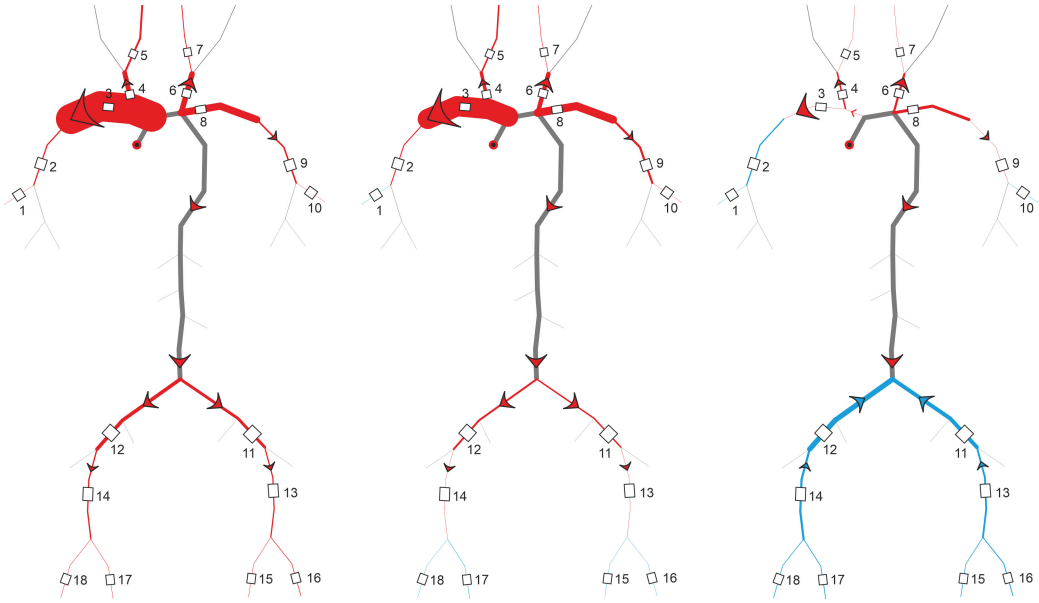

(a) 0.85 Hz (b) 2.29 Hz at $\varphi = 0°$ (c) 2.29 Hz at $\varphi = 90°$

Figure 7: Extracted operational flow rate shapes from modified test subject

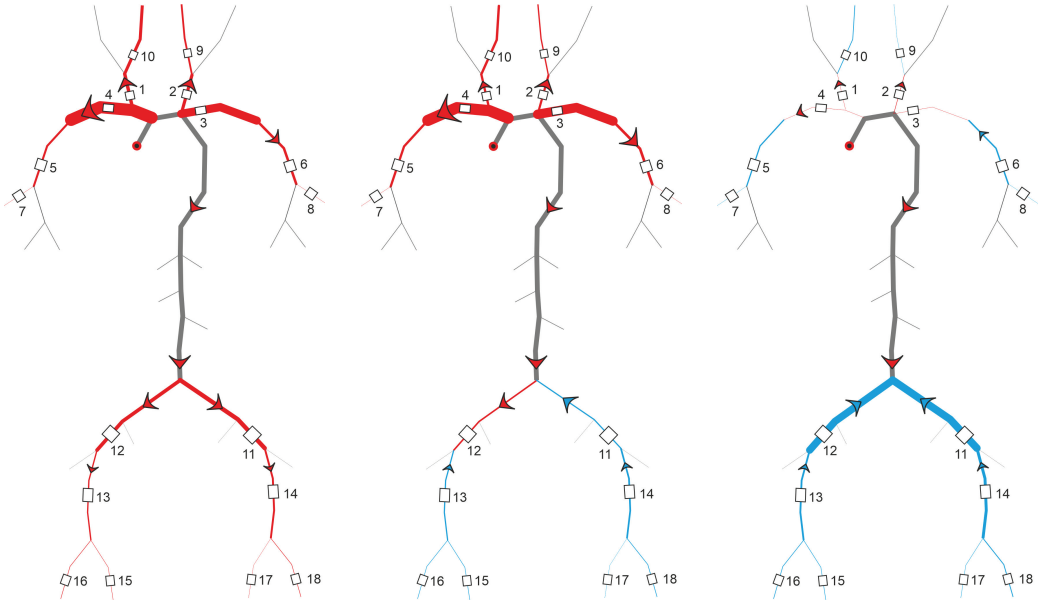

(a) 0.85 Hz (b) 2.29 Hz at $\varphi = 0°$ (c) 2.29 Hz at $\varphi = 90°$

Figure 8: Extracted operational flow rate shapes from original test subject

The findings of this study have potential implications for non-invasive diagnostic techniques, offering a novel approach to identifying and characterizing arterial defects based on their influence on the modal behavior of the arterial system.

Acknowledgements

The authors acknowledge the financial support by the Faculty of Medicine of the Johannes Kepler University Linz through its internal funding programme LIT SeedplusMED Grant Nr. LIT-2022-11-SMED-412. LIT is funded by the State of Upper Austria and the Federal Ministry of Education, Science and Research.

REFERENCES

[1] A. P. Avolio, "Multi-branched model of the human arterial system," *Medical and Biological Engineering and Computing*, vol. 18, pp. 709–718, 1980.

[2] P. Reymond, Y. Bohraus, F. Perren, F. Lazeyras, and N. Stergiopulos, "Validation of a patient-specific one-dimensional model of the systemic arterial tree," *American Journal of Physiology-Heart and Circulatory Physiology*, vol. 301, no. 3, pp. H1173–H1182, 2011.

[3] S. Sherwin, L. Formaggia, J. Peiró, and V. Franke, "Computational modelling of 1d blood flow with variable mechanical properties and its application to the simulation of wave propagation in the human arterial system," *International Journal For Numerical Methods In Fluids*, vol. 43, pp. 673–700, 2003. [Online]. Available: http://dx.doi.org/10.1002/fld.543

[4] Y. T. Kim, J. S. Lee, C. H. Youn, J. S. Choi, and E. B. Shim, "An integrative model of the cardiovascular system coupling heart cellular mechanics with arterial network hemodynamics," *jkms*, vol. 28, no. 8, pp. 1161–1168, 2013. [Online]. Available: http://www.e-sciencecentral.org/articles/?scid=1022031

[5] J. Alastruey, K. H. Parker, and S. J. Sherwin, "Arterial pulse wave haemodynamics," in *11th International Conference on Pressure Surges*. Virtual PiE Led t/a BHR Group, 2012, pp. 401–443.

[6] F. Brunnmayr and G. Mikota, "Theoretical and experimental modal analysis applied to the arterial system of the human body," in *31st edition of the biennal ISMA Conference on Noise and Vibration Engineering*. KU Leuven, Belgium, September 2024, pp. 942–956.

[7] E. Kim, A. Sharma, R. Scissons, D. Dawson, R. Eberhardt, M. Gerhard, J. Hughes, S. Knight, A. Kupinski, G. Mahe, M. Neumyer, P. Poe, R. Shugart, P. Wennberg, D. Williams, and R. Zierler, "Interpretation of peripheral arterial and venous doppler waveforms: A consensus statement from the society for vascular medicine and society for vascular ultrasound," *Journal for Vascular Ultrasound*, vol. 44, pp. 484–506, 07 2020.

XI ECCOMAS Thematic Conference on Smart Structures and Materials - SMART 2025
M. Krommer, M. Nader and M. Schagerl (Eds)

Received: 17 April 2025 / Revised: 27 August 2025 / Accepted: 11 October 2025
© The Author(s) 2025

High Frequency Dipole Magnetic Field For Vacuum Magnetic Birefringence

Dominik Freller, Gerald Jungmayr, Robert Santner, Laura Roberts, Aldo Ejlli, Guido Mueller

Abstract. According to Quantum Electrodynamics (QED), the vacuum consists of fluctuations which under the influence of a strong magnetic field lead to an effect called vacuum magnetic birefringence (VMB). Despite ongoing efforts spanning multiple decades to confirm this QED prediction, VMB has yet to be detected. With previous VMB experiments being limited by a frequency dependent noise source, the use of a high frequency dipole magnetic field brings promising prospects. In this paper, two setups to generate this magnetic field are investigated: a) an oscillating magnetic field produced by an electromagnet; b) a rotating magnetic field generated with a magnetically levitated Halbach array. The objectives include ensuring precise rotor positioning and rotational frequency, minimizing the stator's force impact on the machine bed as well as avoiding any disturbances within the measurement frequency range. The latter arrangement is considered to be more promising as it produces less vibration excitation.
In a symbiotic collaboration, combining the precise metrology of experimental physics and the electromagnetic actuator design of mechatronics, the Linz Center of Mechatronics is commissioning a magnetically levitated, rotating Halbach array permanent magnet, which will be the heart of the VMB experiment in construction at the Max-Planck-Institute for Gravitational Physics in Hanover, Germany.

Key words: SMART 2025, Magnetic Bearing, Electromagnet, Dipole, Vacuum Magnetic Birefringence

Dominik Freller & Gerald Jungmayr & Robert Santner
Linz Center of Mechatronics GmbH Altenbergerstr. 69, A-4040 Linz, Austria
e-mail: dominik.freller@lcm.at

Laura Roberts & Aldo Ejlli & Guido Mueller
Max-Planck-Institut für Gravitationsphysik (Albert-Einstein-Institut) and Leibniz Universität Hannover, Germany, e-mail: aldo.ejlli@aei.mpg.de

Guido Mueller
Department of Physics, University of Florida Gainesville, FL 32611, USA

1 INTRODUCTION

Following the formulation of Quantum Electrodynamics (QED) in the early 1930s, the classical theory of electromagnetic radiation was modified to incorporate the non-linear dynamics of electromagnetic fields. Euler, Kockel, and Heisenberg derived an effective Lagrangian for electrodynamics in vacuum [1, 2, 3], predicting that a vacuum in a magnetic field becomes a birefringent, anisotropic medium. In other words, the refractive indices for light polarized parallel ($n_{\parallel}$) and perpendicular ($n_{\perp}$) to an external magnetic field differ by a tiny amount:

$$\Delta n = n_{\perp} - n_{\parallel} \approx 4 \times 10^{-24}\,\mathrm{T}^{-2} \cdot B^2. \tag{1}$$

where B is the magnetic field strength. This QED effect is known as vacuum magnetic birefringence (VMB), which causes a phase delay, φ, between two orthogonal polarization components of an initially linearly polarized light beam. The phase difference results in the light acquiring a small ellipticity ψ. In the small-angle approximation, one finds:

$$\psi \;=\; \frac{\varphi}{2}\,\sin(2\theta) \;\approx\; \frac{\pi\,\Delta n\,L}{\lambda}\,\sin(2\theta)\;, \tag{2}$$

where L is the length of the magnetic field region traversed by the light, λ is the light's wavelength, and θ is the angle between the polarization direction and the magnetic field. Despite decades of experimental efforts, no direct observation of VMB has been achieved to date because the predicted effect is exceptionally weak.

The PVLAS collaboration performed a detailed noise analysis to identify the dominant factors limiting sensitivity in such birefringence experiments [4]. The results of this study show a clear frequency-dependent sensitivity which rises at lower frequencies, approximately following a $1/f^{\alpha}$ power-law. This behavior is consistent with thermally induced birefringence fluctuations in the cavity mirrors [4, 5]. Incorporating this noise model into the signal expression (Eq. (2)) provides a way to estimate the signal-to-noise ratio (SNR) and thus the achievable experimental sensitivity. In general, the SNR scales with key parameters as:

$$\mathrm{SNR} \propto \left(\frac{B}{1\,\mathrm{T}}\right)^2 \left(\frac{L}{1\,\mathrm{m}}\right) \left(\frac{f}{1\,\mathrm{Hz}}\right)^{\alpha} \left(\frac{T}{1\,\mathrm{s}}\right)^{1/2}, \tag{3}$$

where B is the magnetic field strength, L the interaction length, f the frequency at which the birefringence signal is modulated (typically the magnet rotation or field modulation frequency), and T the total integration time. In this work, we adopt $\alpha \approx 0.8$, consistent with previous experimental findings—see Fig. 2 in [6] and Sec. 6.3.7 of [4]—which report a noise scaling behavior approximately proportional to $1/f^{0.8}$, attributed to thermally driven birefringence noise in the cavity mirrors.

Equation (3) provides a simplified, dimensionless scaling relation that highlights the primary experimental dependencies. For rigorous quantitative comparisons, the complete SNR formulation—including the VMB constant, cavity finesse, laser wavelength, and measured noise amplitude—must be used. While the simplified relation is useful for intuitive assessments and

comparative analyses throughout this work, it does not capture all relevant experimental details and constants required for precise predictions.

Maximizing the SNR while minimizing internal noise is the guiding principle in the design of a VMB experiment. For the magnet system in particular, the following design requirements are established: (i) ability to modulate or rotate the field at high frequency (to move the signal to frequencies with lower noise), (ii) minimal mechanical vibrations, (iii) continuous long-term operation, and (iv) the highest possible field amplitude.

There are two primary methods to modulate the magnetic birefringence signal. In the first method, a static magnetic field or polarisation direction is physically rotated, which means the angle θ in Eq. (2) becomes time-dependent (the field's direction relative to the polarization rotates). In the second method, the field amplitude is varied in time (e.g. $B(t) = B_0 \sin \nu t$ with ν the modulation frequency). Both approaches shift the VMB signal to the chosen modulation frequency $f_{\rm m} = \nu$, but the resulting SNR differs.

In the rotating-field scheme, the full field strength contributes to the birefringence at frequency $f_{\rm m}$. In contrast, a sinusoidally oscillating field yields a birefringence oscillating at 2ν with half the amplitude (since $B^2(t)$ produces a $\sin^2$ term with average $1/2$). As a result, only the time-varying part of B^2 contributes to the detected signal, effectively halving the SNR for the same peak field. Quantitatively, one finds:

$$\mathrm{SNR} = \begin{cases} \left(\dfrac{B}{1\,\mathrm{T}}\right)^2 \left(\dfrac{L}{1\,\mathrm{m}}\right) \left(\dfrac{f_{\rm m}}{1\,\mathrm{Hz}}\right)^{\alpha}, & \text{for a rotating field scheme,} \\ \dfrac{1}{2}\left(\dfrac{B}{1\,\mathrm{T}}\right)^2 \left(\dfrac{L}{1\,\mathrm{m}}\right) \left(\dfrac{f_{\rm m}}{1\,\mathrm{Hz}}\right)^{\alpha}, & \text{for a sinusoidally oscillating field.} \end{cases} \tag{4}$$

Maximizing B, L, and $f_{\rm m}$ (within practical limits) while mitigating mirror noise is therefore crucial for a successful detection of VMB.

1.1 The polarimetry experiment

The magnet designed by LCM serves as the core of a highly sensitive polarimeter for VMB search. A simplified sketch of the polarimeter is shown in Fig. 1, where each of the main components is housed in an ultra-high vacuum (UHV) system. A UHV-compatible tube passes through the magnet, maintaining vacuum continuity between the two optical chambers on either side. A linearly polarized laser beam (prepared by a high-extinction polarizer) is injected into a high-finesse Fabry–Perot cavity that surrounds the magnet. The cavity effectively increases the interaction length of the light with the magnetic field by trapping the beam for many passes.

The light's polarization is modulated at a known frequency by a photoelastic modulator (PEM) to enable heterodyne detection of the tiny birefringence signal. Downstream of the magnet and cavity, an analyzer (a second polarizer) is oriented to extinguish the original polarization component, thereby transmitting only the polarization component induced by birefringence. This emergent light (normally zero in the absence of birefringence) is then detected by a photodiode. We refer to this detector as the extinction photodiode (PDE), while a second photodiode

(PDT) monitors the main transmitted beam for reference. The small intensity measured at the extinction port due to VMB-induced ellipticity is given by:

$$I_{\perp}^{(\mathrm{ell})} \;=\; I_{\parallel}\Big[\,\sigma^2 + \,\eta(t)^2 \;+\; 2\,\eta(t)\,N\,\psi\,\sin(2\vartheta(t)) \;+\; \ldots\Big]\,, \tag{5}$$

where $I_{\parallel}$ is the intensity of the linearly polarized light entering the cavity, $\eta(t)$ describes the modulation imposed by the PEM, and σ^2 is the extinction ratio of the crossed polarisers. The term N is the amplification factor of the optical cavity (proportional to its finesse, representing the effective number of passes through the field), and ψ is the small induced ellipticity as defined in Eq.(2).

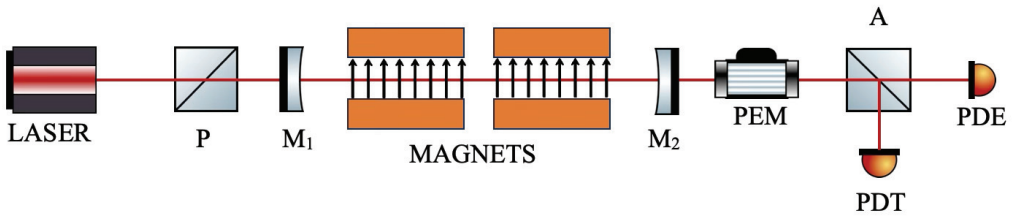

Figure 1: Simplified schematic of the experimental setup. The red line indicates the laser beam path. M_1 and M_2 denote the mirrors of the Fabry–Pérot cavity. PEM is the photoelastic modulator. P is the polarizer, and A (analyzer) is a high-extinction polarizer oriented to separate the orthogonal (S and P) polarization components. PDT and PDE are photodiodes monitoring the transmitted and extinguished beams, respectively. The extinction photodiode (PDE) is sensitive to the small polarization component induced by vacuum magnetic birefringence (VMB).

2 ELECTROMAGNET

As mentioned in the previous section, the VMB-Experiment requires a high-amplitude magnetic field that rotates or oscillates with a certain frequency f. A straightforward method to generate such a rotating field is by utilizing the stator of a three-phase electric machine, as illustrated in Fig. 2. The stator coils can either be designed as concentrated or distributed windings, the former being easier to wind, and the latter achieving more homogeneous fields in the air gap. An alternative approach is shown in Fig. 3, using a toroidal winding scheme that results in a different stator core geometry. These types of coils are particularly easy to wind if a segmented stator core is used. In addition, its air gap field is also very homogeneous. Due to the fact that one side of each coil is close to the outer stator edge, it is assumed that cooling this system is rather simple. However, this topology comes with higher stray fields outside the stator as well as lower magnetic field amplitudes in the air gap compared to the more common solution shown in Fig. 2.

The first calculations indicated that high power losses will occur during operation. To address this, a third topology was developed, specifically designed to facilitate efficient cooling of both the stator core and the copper windings. As depicted in Fig. 4, in contrast to previous systems,

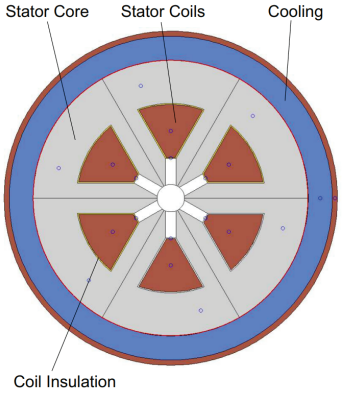

Figure 2: Three-phase system with distributed or concentrated windings.

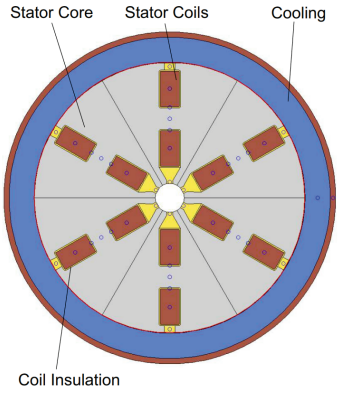

Figure 3: Three-phase system with toroidal winding for improved uniformity.

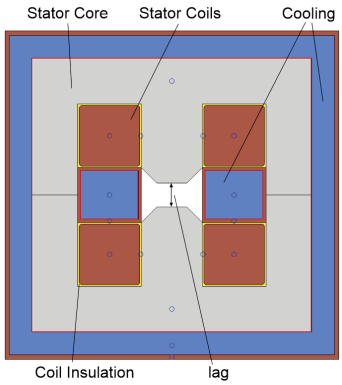

Figure 4: Single-phase system with enhanced cooling.

this solution offers easily accessible space between the coils that can be used for cooling. By horizontally segmenting the stator, water coolant pipes can be easily integrated. The coils of this system would be connected in series to a singular supplying phase, which would also simplify the power supply, as only a single-phase solution would be required. In this case, the magnetic field in the air gap is not rotating as in the three-phase systems, but oscillating along the vertical axis. As a result, the SNR, as described in Eq. 4, is only half as high. This reduction has to be taken into account when comparing the described topologies.

To perform this comparison, 2D magnetic and thermal finite-element simulations were carried out. The software package SyMSpace [7] combines these calculations into one singular workflow, while additionally offering the possibility to perform multi-parameter and multi-objective optimizations using suitable genetic algorithms. In a first step, the magnetic simulation is carried out, and a series of results are calculated. These include the power losses (e.g. eddy-current losses in the stator lamination stack P_{fe} and resistive losses in the copper windings P_{cu}), stator voltages and currents, coil inductances and resistances as well as input and output powers (including total apparent- S, real- P and reactive-powers Q). The losses of the shaft core and winding power, P_{fe} and P_{cu}, are then used to calculate the thermal behavior of the systems, including the coil temperature T_{c}. SyMSpace allows cluster-computing to significantly reduce simulation times. The optimizations mentioned above were then carried out for all three topologies described. The relevant data for the optimizations are collected in Table 1.

The specifications contain the fixed air gap size l_{ag}, the maximum temperature T_{max} that is expected to occur in the copper windings, a fixed stator length l_{fe} as well as an ambient coolant temperature. Parameters include the whole stator geometry, however sizes such as thickness of the outer cooling channel and electrical insulation of the coils are fixed for all systems. Besides minimizing the maximum occuring temperature T_{max} as well as the total losses P_{v}, which are given by

Table 1: Optimization constraints, variation parameters, and objectives

Constraints	Variation Parameters	Objectives
$l_{\text{ag}} = 8\,\text{mm}$	Stator geometry	SNR $\rightarrow$ MAX
$T_{\text{max}} = T_{\text{c}} < 150\,^{\circ}\text{C}$	Oscillation/Rotation frequency	$B_{\text{center}} \rightarrow$ MAX
$l_{\text{fe}} = 400\,\text{mm}$	Coil current density	$T_{\text{max}} \rightarrow$ MIN
$T_{\text{coolant}} = 50\,^{\circ}\text{C}$		$P_{\text{v}} \rightarrow$ MIN

$$P_{\text{v}} = P_{\text{fe}} + P_{\text{cu}}, \tag{6}$$

the SNR given by Eq. 4 and the magnetic field amplitude at the air gap center B_{center} are maximized.

Figure 5 shows the resulting Pareto fronts of the respective topologies. It is obvious that the single-phase solution achieves higher SNR per watt of power loss and thus a higher SNR per degree of temperature increase compared to the other topologies. Furthermore, it enables significantly higher magnetic field values, despite the fact that an oscillating field reaches only half the SNR of a rotating field, as described in Eq. 4. Among the three topologies examined, the three-phase system with toroidal windings depicted in Fig. 3 performs worse. The three-phase stator of Fig. 2 performs better but does not come close to the single-phase system. In addition to the inferior performance of the three-phase systems compared to the single-phase topology, they also require a much larger power supply effort because of the higher number of phases. For these reasons, the single-phase system is considered superior to the other topologies and is therefore the focus of further investigation.

As shown in Table 1, the current density of the coil was used as an optimization parameter instead of the actual current itself so that the optimization can be carried out independently of the winding design (e.g., specifying the number of coil turns N). Therefore, as a next step an exemplary winding design is carried out for a selected design on the Pareto-front. The design was selected so that the maximum temperature is approximately $T_{\text{max}} \approx 130\,^{\circ}\text{C}$, as depicted in Fig. 6. This results in an SNR of 283.8, an air gap field of $B_{\text{center}} = 1.36\,\text{T}$, and total power losses $P_{\text{v}} = 7.3\,\text{kW}$.

By adjusting the number of coil turns N, the corresponding phase voltage and current can be adjusted to match the power-supply specifications. In this example, $N = 3$ is selected to ensure that the RMS voltage remains below $U_{\text{rms}} = 1000\,\text{V}$. The design results are summarized in Table 2.

As shown in Table 2, the required apparent power of this design reaches a very high value of $917\,\text{kVA}$. This is due to the high oscillation frequency of $2\,\text{kHz}$, the large current density

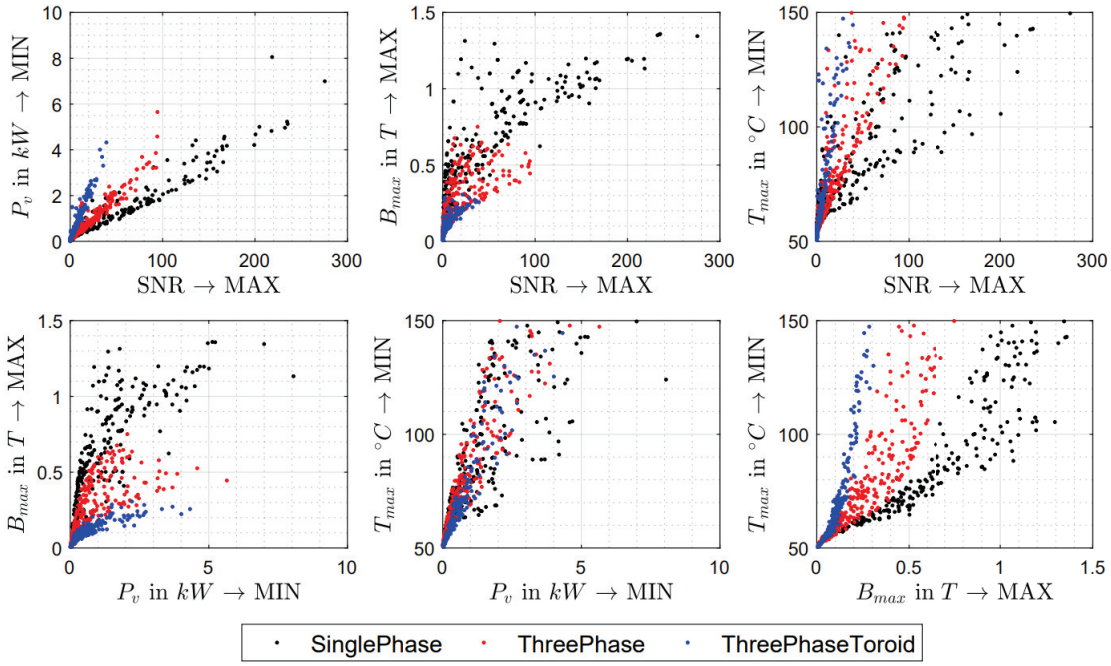

Figure 5: Comparison of optimization Pareto fronts

Table 2: Example winding design for the single-phase system.

Winding Parameters	**Losses**
Oscillation frequency $f = 2\,\mathrm{kHz}$	Iron losses $P_{\mathrm{fe}} = 5.8\,\mathrm{kW}$
Number of turns $N = 3$	Copper losses $P_{\mathrm{cu}} = 1.5\,\mathrm{kW}$
Coil inductance $L = 57\,\mu\mathrm{H}$	Total losses $P_{\mathrm{v}} = 7.3\,\mathrm{kW}$
Coil resistance $R = 1.1\,\mathrm{m\Omega}$	Apparent power $S = 917\,\mathrm{kVA}$
RMS Voltage and Current	**Performance Results**
Voltage $U_{\mathrm{rms}} = 800\,\mathrm{V}$	Air gap field $B_{\mathrm{center}} = 1.36\,\mathrm{T}$
Current $I_{\mathrm{rms}} = 1140\,\mathrm{A}$	Signal-to-noise ratio SNR $= 283.8$
Current density $J_{\mathrm{rms}} = 8.5\,\mathrm{A/mm^2}$	Maximum temperature $T_{\mathrm{max}} = 130\,°\mathrm{C}$

required to generate the high magnetic field in the air gap, as well as the relatively large inductance. Active power losses are relatively low, so a power factor correction circuit (PFC) can be used to minimize the required reactive power, and thus the power supply requirement. Ideally, the supply would therefore only have to deliver the active power losses ($P_{\mathrm{v}} = 7.3\,\mathrm{kW}$)

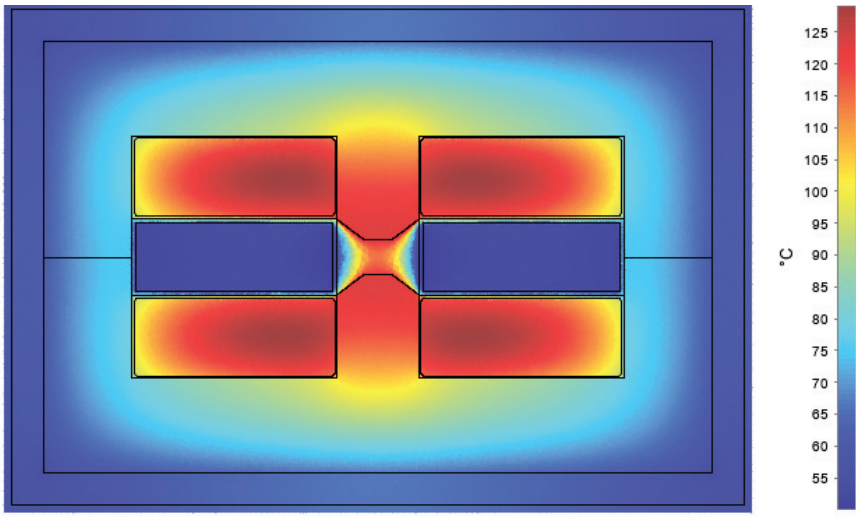

Figure 6: Simulated temperature distribution of the exemplary electromagnet design. The optimization leads to a distribution of the power losses in such a way, that the maximum temperatures in the stator iron and in the windings are approximately the same.

and not the entire apparent power ($S = 917\,\mathrm{kVA}$). However, this would lock the frequency to the specified value, as even a small deviation from this considerably increases the required reactive power if no active compensation is implemented. In addition, the high phase currents would still be present and oscillate between the PFC and the electromagnet, which would cause significant vibrations of the connecting cables and the magnet itself because of magnetostrictive forces. Due to the previously mentioned high demands of the VMB experiment regarding vibrations and noise generation, the next section explores an alternative solution for generating a high-frequency alternating magnetic field using a magnetically levitated Halbach magnet.

3 MAGNETIC BEARING SYSTEM

The topology of the planned magnetic bearing and motor arrangement is shown in Fig. 7. It consists of a cylindrical permanent magnet that is levitated by two radial magnetic bearings. The permanent magnet is designed as a discrete Halbach-array with $n_{\mathrm{seg}} = 16$ tangential segments. This allows high magnetic fields to be generated in the air gap. For a theoretically infinite number of segments, the following applies [8]

$$B_{\mathrm{center}} = B_{\mathrm{r}} \ln \frac{d_{\mathrm{o}}}{d_{\mathrm{i}}}, \tag{7}$$

where B_{r} denotes the remanence field of the permanent magnets. Introducing a finite number of segments naturally reduces this value. The magnets are embedded in a ferromagnetic bandage, which also serves as a return path for the magnetic field of the two radial bearings. The degree of freedom along the horizontal axis is passively stabilized. The levitated Halbach array is rotated by a separate motor next to the magnetic bearings as depicted in Fig. 7. This allows

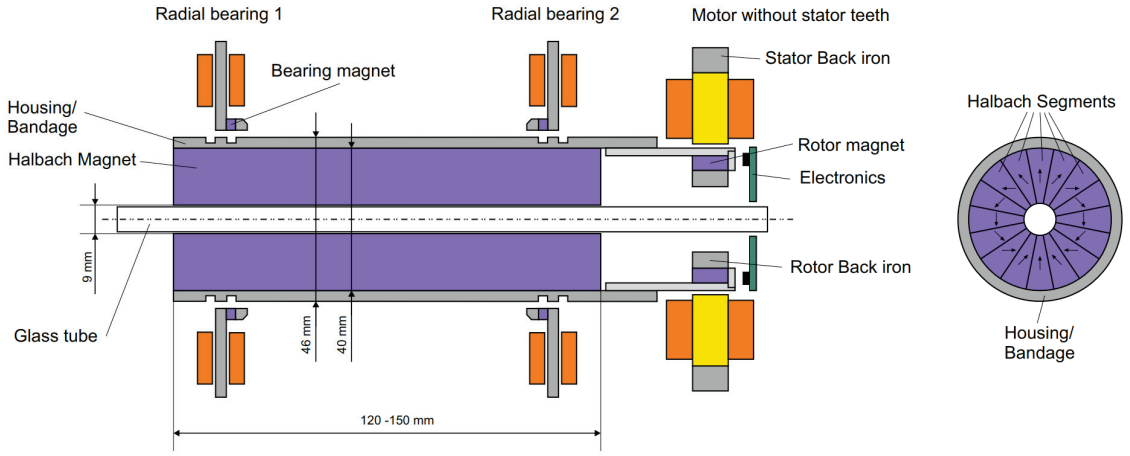

Figure 7: Magnetic bearing setup

for a completely contactless operation without any mechanical friction losses. The only losses that occur are copper losses in the windings of the bearings and the motor, iron losses due to changes in the magnetic field, as well as air friction losses on the outer diameter of the rotating bandage. The geometric parameters are also shown in Fig. 7. Note that the air gap length has increased to $l_{\mathrm{ag}} = 9\,\mathrm{mm}$ compared to Table 1 to achieve greater safety against damage to the glass tube containing the UHV. According to Eq. 7, this results in a maximum air gap field of $B_{\mathrm{center,\,max}} = 1.91\,\mathrm{T}$ with a remanence field of $B_{\mathrm{r}} = 1.28\,\mathrm{T}$. Simulations show that this value is reduced to

$$B_{\mathrm{center}} = 1.77\,\mathrm{T} \tag{8}$$

with $n_{\mathrm{seg}} = 16$ segments. To ensure that the first bending mode frequencies of the Halbach-magnet is far enough away from the rotational f or measurement frequency f_{m}, the magnet length will be in the range of $l_{\mathrm{fe}} = 120\,\mathrm{mm} - 150\,\mathrm{mm}$. In the event of a system crash due to power failure, for example, emergency bearings ensure a safe shutdown without damaging critical components.

Several advantages of the magnetic bearing system over the electromagnet can now be identified. The rotation frequency can be varied as required during operation within the mechanical limits. By using digital signal processors, sophisticated control strategies can be implemented. For example, notch filters to suppress critical noise frequencies or iterative learning control to further improve controller performance during operation. Much lower contained energy, power consumption, and noise generation can be expected. The most significant disadvantage, however, is the high complexity of the overall system.

4 COMPARISON

For a quantitative comparison between the electromagnet and magnetic bearing systems, similar operational parameters are assumed: an interaction length of $l_{\mathrm{fe}} = 150\,\mathrm{mm}$ and a rotational (or oscillating) frequency of $f = 500\,\mathrm{Hz}$. Since the achievable magnetic field amplitude in the air gap is independent of system length, the electromagnet's maximum field amplitude is estimated as $B_{\mathrm{max,\,EM}} = 1.5\,\mathrm{T}$, assuming a maximum operating temperature of $T_{\mathrm{max}} = 150\,^{\circ}\mathrm{C}$ (see bottom right of Fig. 5).

Consequently, the maximum achievable dimensionless SNR for this geometry, using Eq. (4), is

$$\mathrm{SNR}_{\mathrm{max,\,EM}} = \frac{1}{2}\left(\frac{B_{\mathrm{max,\,EM}}}{1\,\mathrm{T}}\right)^2\left(\frac{l_{\mathrm{fe}}}{1\,\mathrm{m}}\right)\left(\frac{f_{\mathrm{m}}}{1\,\mathrm{Hz}}\right)^{\alpha} \approx 42.4, \tag{9}$$

where $f_{\mathrm{m}} = 2f$ is the modulation frequency, and the exponent $\alpha = 0.8$ is consistent with earlier experimental findings [6, 4]. Using Eq. 8, the corresponding value for the magnetic bearing system is

$$\mathrm{SNR}_{\mathrm{MB}} = \left(\frac{B_{\mathrm{center}}}{1\,\mathrm{T}}\right)^2\left(\frac{l_{\mathrm{fe}}}{1\,\mathrm{m}}\right)\left(\frac{f_{\mathrm{m}}}{1\,\mathrm{Hz}}\right)^{\alpha} \approx 118.1, \tag{10}$$

which could still be increased if, for example, a stronger magnet is used. Calculations indicate that the expected power loss and apparent power for an electromagnet of this size are approximately $P_{\mathrm{v,\,EM}} = 900\,\mathrm{W}$ and $S_{\mathrm{EM}} = 100\,\mathrm{kVA}$, respectively. In contrast, for the magnetic bearing system, power losses of less than $P_{\mathrm{v,\,MB}} = 100\,\mathrm{W}$ can be anticipated during operation. Given the comparatively small inductances, the apparent power S_{MB} is expected to be nearly equal to the total power losses $P_{\mathrm{v,\,MB}}$.

5 CONCLUSIONS

As described in Section 4, the magnetic bearing system shows more than double the SNR compared to the electromagnet, considering identical geometric dimensions. In addition, much higher power losses and contained energies are existent in the single-phase electromagnet solution. This would most likely cause inferences incompatible with the VMB-experiment, such as vibration of the lamination stack and the supplying cables. Also the electromagnet requires an appropriate cooling system in order to manage the large power losses. Implementing a PFC circuit would drastically reduce power supply demands, as it would only have to provide the real power losses and not the large apparent powers present during operation. However, this would lock the frequency at a specific value, decreasing the flexibility of the system. Based on all these points, the magnetic bearing system is considered far superior to the electromagnet system and will therefore be pursued further.

6 ACKNOWLEDGEMENTS

This work has been supported by the COMET-K2 Center of the Linz Center of Mechatronics (LCM) funded by the Austrian federal government and the federal state of Upper Austria.

REFERENCES

[1] H. Euler, "Über die Streuung von Licht an Licht nach der Diracschen Theorie, English translation by D. H. Delphenich: *On the scattering of light by light in Dirac's theory*," *Ann. Phys.*, vol. 26, pp. 398–448, 1936. [Online]. Available: http://www.neo-classical-physics.info/uploads/3/4/3/6/34363841/euler_-_scattering_of_light_by_light.pdf

[2] H. Euler and B. Kockel, "Über die streuung von licht an licht nach der diracschen theorie, english translation by d. h. delphenich: *The scattering of light by light in Dirac's theory*," *Naturwiss.*, vol. 23, pp. 246–247, 1935. [Online]. Available: http://www.neo-classical-physics.info/uploads/3/4/3/6/34363841/euler-koeckel_-_scattering_of_light_by_light.pdf

[3] W. Heisenberg and H. Euler, "Folgerungen aus der Diracschen Theorie des Positrons, English translation by W. Korolevski and H. Kleinert: *Consequences of Dirac's theory of positrons*," *Z. Phys.*, vol. 98, pp. 714–732, 1936.

[4] A. Ejlli, F. Della Valle, U. Gastaldi, G. Messineo, R. Pengo, G. Ruoso, and G. Zavattini, "The PVLAS Experiment: A 25 Year Effort to Measure Vacuum Magnetic Birefringence," *Physics Reports*, vol. 871, pp. 1–74, 2020. [Online]. Available: https://doi.org/10.1016/j.physrep.2020.06.001

[5] S.-X. Yang, Y.-P. Zhang, W.-H. Tan, C.-G. Shao, M.-K. Zhou, and S.-Q. Yang, "Study of the birefringence noise in high-finesse ule cavity," *Optics & Laser Technology*, vol. 181, p. 111660, 2025. [Online]. Available: https://www.sciencedirect.com/science/article/pii/S0030399224011186

[6] G. Zavattini, F. Della Valle, A. Ejlli, and G. Ruoso, "A polarisation modulation scheme for measuring vacuum magnetic birefringence with static fields," *Eur. Phys. J. C*, vol. 76, no. 5, p. 294, 2016, [Erratum: Eur.Phys.J.C 77, 873 (2017)].

[7] S. Silber, W. Koppelstätter, G. Weidenholzer, G. Segon, and G. Bramerdorfer, "Reducing development time of electric machines with symspace," in *2018 8th International Electric Drives Production Conference (EDPC)*, 2018, pp. 1–5.

[8] P. Blümler and F. Casanova, *CHAPTER 5: Hardware developments: Halbach magnet arrays*, 01 2016, pp. 133–157.

XI ECCOMAS Thematic Conference on Smart Structures and Materials - SMART 2025
M. Krommer, M. Nader and M. Schagerl (Eds)

Received: 14 April 2025 / Revised: 2 September 2025 / Accepted: 11 October 2025
© The Author(s) 2025

Low Temperature Effects on Guided Wave Structural Health Monitoring Signals

Shankar Galiana Blanch, Bhooshit Patel, Maria Moix-Bonet, Daniel Schmidt, Peter Wierach

Abstract. Structural Health Monitoring (SHM) has become a critical technology for maintaining the safety and performance of high-value structures, particularly those exposed to extreme environments such as cryogenic temperatures. Applications such as hydrogen storage tanks and aerospace components experience mechanical and thermal stresses that can degrade material properties, increase brittleness, and compromise structural integrity. In such conditions, traditional inspection methods may be impractical, whereas SHM provides a reliable means for real-time monitoring and early damage detection.
Among SHM techniques, guided wave (GW) methods are particularly promising for fiber-reinforced polymers, offering long-range coverage and high sensitivity to various defect types. However, GW signals are also sensitive to environmental and operational factors, including temperature, mechanical loads, and surrounding media (e.g., moisture, ice, gas), which can lead to signal variation unrelated to damage. Without proper compensation, these effects may obscure actual damage or result in false positives.
This study investigates the influence of cryogenic temperature and surrounding media on GW signal behavior in a unidirectional carbon fiber-reinforced polymer panel instrumented with co-bonded DuraAct™ piezoceramic transducers. The specimen is subjected to controlled thermal cycling from liquid nitrogen temperature to room temperature, while guided waves are recorded across a wide frequency range.
Results demonstrate distinct temperature and frequency-dependent behavior in both A0 and S0 wave modes. Amplitude and time-of-flight characteristics reveal strong interactions between temperature, transducer performance, and media boundary effects. These findings underscore the importance of environmental compensation in GW-SHM systems and highlight new opportunities for using wave behavior as a dual indicator of both structural health and environmental state.

Key words: Structural Health Monitoring, Low temperatures, DuraAct™, Guided waves.

Shankar Galiana Blanch & Maria Moix-Bonet & Daniel Schmidt & Peter Wierach
Institute of Lightweight Systems, DLR, 35108 Braunschweig, Germany
e-mail: shankar.galiana@dlr.de

Shankar Galiana Blanch & Bhooshit Patel & Peter Wierach
Institut für Polymerwerkstoffe und Kunststofftechnik, TU Clausthal, Clausthal-Zellerfeld, Germany

1. INTRODUCTION

Structural Health Monitoring (SHM) has emerged as a promising technology for ensuring the integrity and safety of complex structures, particularly those operating under extreme environmental conditions. Components such as hydrogen storage tanks and aerospace structures are frequently exposed to cryogenic temperatures, which can adversely affect material properties, leading to increased brittleness and potential structural failures. In such scenarios, traditional inspection methods may be impractical or insufficient, making SHM a crucial tool for early damage detection and life extension of critical assets [1].

Composite materials, especially carbon fiber-reinforced polymers (CFRPs), are extensively used in high-performance applications due to their superior strength-to-weight ratios and adaptability. These materials are prevalent in sectors like aerospace and hydrogen energy, where components often operate under cryogenic conditions [2, 3]. Despite their advantageous properties, CFRPs are susceptible to damage mechanisms such as impact-induced delaminations, fatigue, and environmental degradation, which can compromise structural reliability [4].

Among various SHM techniques, guided wave (GW)-based methods have shown significant promise due to their sensitivity to damage and capability for long-range inspection, particularly in fiber-reinforced composites [5, 6]. Guided waves can propagate over considerable distances with minimal attenuation and are highly responsive to material discontinuities. However, the effectiveness of GW-SHM systems is influenced by external factors, including mechanical loads, ambient temperature, and surrounding media such as moisture or gaseous environments [7, 8].

Temperature effects are especially critical in cryogenic applications, where material properties like stiffness and residual stresses in CFRPs undergo significant changes. These variations can alter wave propagation characteristics, particularly in the transverse direction, where the polymeric matrix plays a dominant role [9]. Moreover, the performance of piezoelectric transducers, such as those based on lead zirconate titanate (PZT), can degrade at low temperatures due to changes in their dielectric and electromechanical properties [10, 11]. This degradation affects the reliability of SHM systems operating in cryogenic environments.

In this context, the present study aims to investigate the response of guided wave signals at cryogenic temperatures using co-bonded DuraAct™ transducers on a unidirectional carbon fiber-reinforced polymer (UD-CFRP) panel. The research focuses on evaluating how temperature and surrounding media influence guided wave propagation and transducer functionality. Measurements are conducted across various temperature states, with and without immersion in liquid nitrogen (LN_2), to analyze signal amplitude and time-of-flight (ToF) behavior comprehensively.

2. MATERIALS AND METHODS

2.1. Specimen configuration

The test specimen used in this study shown in **Figure 1 (a)** consists of a UD-CFRP panel integrated with co-bonded DuraAct™ transducers, to evaluate GW-SHM performance under cryogenic conditions. DuraAct™, developed by PI Ceramic GmbH, is a commercial piezocomposite acousto-ultrasonic transducer. It features a soft PZT piezoceramic (PIC255), placed between metallized electrodes and encapsulated within a polyester fleece-reinforced laminate, providing both electrical insulation and mechanical flexibility. Electrical connectivity is established through two solder points.

The UD-CFRP laminate is fabricated using HexPly® 8552-IM7 prepreg with a $[0]_{18}$ stacking sequence. Each ply has a nominal thickness of 0.125 mm, resulting in a panel measuring 700 mm × 500 mm. Eleven DuraAct™ transducers are strategically positioned on the laminate to establish signal propagation paths in three orientations: along the fiber direction (0°), perpendicular to it (90°), and diagonally (45°). Each path consists of one actuator and two sensors, spaced 157 mm and 222 mm apart, as depicted in **Figure 1 (b)**. After transducer placement, the laminate is autoclave-cured to achieve a final consolidated thickness of approximately 2.25 mm.

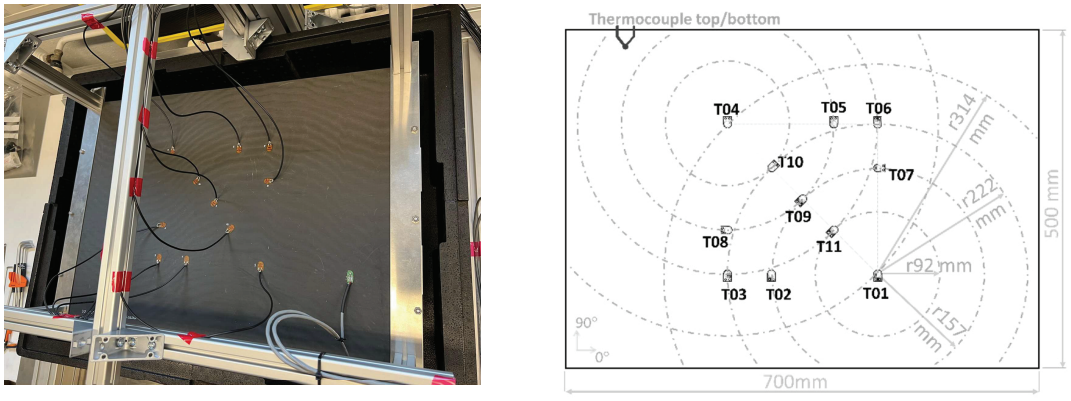

(a) (b)

Figure 1: (a) Schematic of specimen configuration and (b) UD-CFRP panel with transducer network and thermocouples.

2.2. Thermal test set-up

The panel is mounted using aluminum clamps on both sides along the 90° axis and affixed to a lifting mechanism designed for precise vertical translation into and out of a LN_2 bath. This setup ensures the specimen remains perpendicular to the cryogenic liquid surface during immersion and withdrawal.

The transducer network is connected to a PXIe-based guided wave SHM acquisition system provided by National Instruments. Temperature monitoring is achieved using two thermocouples bonded to the top and bottom surfaces of the CFRP panel. The experimental configuration is illustrated in **Figure 2 (a)**.

During testing, the panel is submerged in LN_2 until thermal equilibrium is reached at approximately -197 °C. It is then gradually lifted and allowed to warm to ambient room temperature (~15 °C) under natural convection. Throughout this thermal cycle, guided wave signals are continuously recorded at excitation frequencies from 50 kHz to 250 kHz in 10 kHz increments. A representative temperature profile recorded from the top-surface thermocouple is shown in **Figure 2 (b)**.

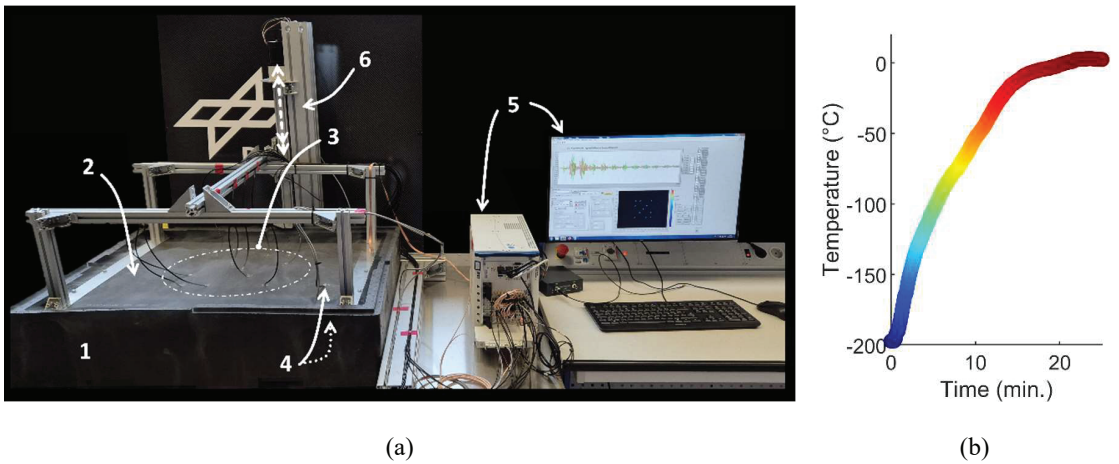

(a) (b)

Figure 2: (a) Experimental setup showing: (1) cryogenic bath, (2) UD-CFRP panel, (3) transducer network, (4) thermocouples, (5) data acquisition system, and (6) lifting mechanism; (b) representative top-surface temperature profile during thermal cycling.

3. RESULTS AND DISCUSSIONS

3.1. GW signal temperature response

For the current study, guided wave excitation was performed using transducer 1 (T1), which generated a five-cycle Hanning-windowed sine burst with a peak voltage of 50 V. The signals acquired along the fiber direction of the UD-CFRP laminate by transducer 2 (T2) were processed through a multi-step chain comprising denoising, cross-talk removal, Hilbert transform-based envelope extraction, and peak estimation for each propagating mode. Maximum signal amplitudes and ToF values were extracted for both the A0 and S0 modes approximations across a frequency sweep from 50 kHz to 250 kHz, in 10 kHz increments, to evaluate dispersion characteristics under varying thermal conditions.

The A0 mode remained identifiable up to 150 kHz. Above this frequency, signal quality degraded due to mode overlap and reflection interference. Conversely, the S0 mode became

discernible only above 100 kHz, as lower-frequency signals produced amplitudes too weak for consistent detection.

Amplitude behavior for the A0 mode depicted in **Figure 3 (a) (c),** followed a non-monotonic trend. As the temperature decreased from room temperature, amplitude initially increased, reaching a maximum near −60 °C. This increase is more pronounced as frequency increases. Below this temperature, amplitude declined sharply as temperature drops till −197°C equally in all frequency range. In contrast, ToF for the A0 mode depicted in **Figure 3 (b) (d),** remained relatively stable below −60 °C, with a slight decrease observed from room temperature to −60 °C.

When analyzing both amplitude and ToF trends together, two distinct behaviors emerge. From room temperature down to −60 °C, the increase in amplitude and decrease in ToF could be attributed to the thermal stiffening of the polymer matrix, reduced viscoelastic damping, and improved wave propagation efficiency. This effect specially affects A0 mode at higher frequencies (>70kHz) and has a lower impact at lower frequencies (<70kHz). However, below −60 °C, this coupling between amplitude and ToF diminishes, that could indicate that the reduction in amplitude is no longer linked to changes in structural wave speed or material dispersion. Instead, this behavior is most plausibly explained by temperature-induced degradation of piezoelectric performance in the DuraAct™ transducers. At cryogenic temperatures, the dielectric constant and piezoelectric coefficients (e.g., $d31$) of the soft PZT decrease substantially, reducing the effectiveness of wave generation and sensing [10, 11], and could result in the observed amplitude losses.

In addition to amplitude trends, the A0 mode also displayed a temperature-dependent shift in its frequency of maximum amplitude. At room temperature, the A0 mode showed a peak response around 65 kHz. As the temperature decreased, this peak shifted upward in frequency, settling near 90 kHz at −197 °C, albeit with diminished amplitude.

For the S0 mode, the amplitude response depicted in **Figure 4 (a) (c)** was distinctly different. Across the frequency spectrum, S0 amplitudes decreased monotonically as temperature dropped. This trend was most pronounced at higher frequencies where amplitudes are higher. Regarding S0 mode ToF depicted in **Figure 4 (b) (d)**, values remained consistent over temperature up to 200kHz where ToF starts to slightly decrease when lowering temperature with higher frequency.

When considering both amplitude and ToF trends together, behavior seems to be consistent to the behavior of A0 mode below −60 °C, where the reduction in amplitude could be explained due to the reduction of electromechanical coupling efficiency of the PZT piezoceramic when decreasing temperatures, rather than propagation-related loss mechanisms. The absence of changes in amplitudes and ToF close to room temperature in line with A0 mode, can be attributed to the S0 mode's dominance in in-plane axial displacements, are less affected by transverse stiffness alterations in unidirectional laminates while A0 mode has a greater influence in the out-of-plane components more dominated by matrix properties changes.

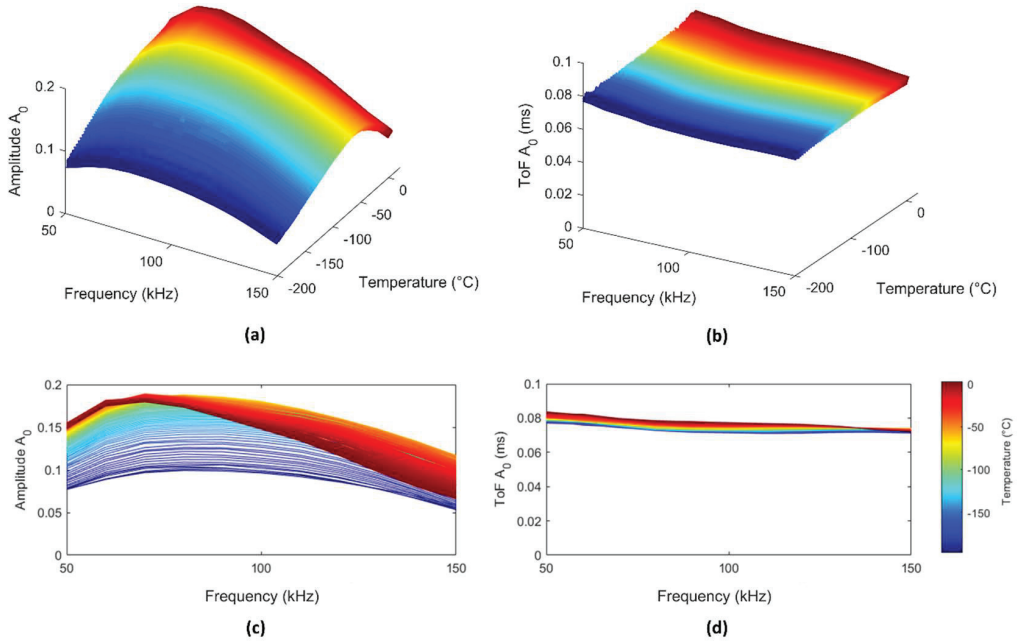

Figure 3: T1 to T2 (a) 3D representation of maximum amplitude spectrum of A0 mode over temperature, (b) 3D representation of ToF spectrum of A0 mode over temperature, (c) 2D representation of maximum amplitude spectrum of A0 mode over temperature and (d) 2D representation of ToF spectrum of A0

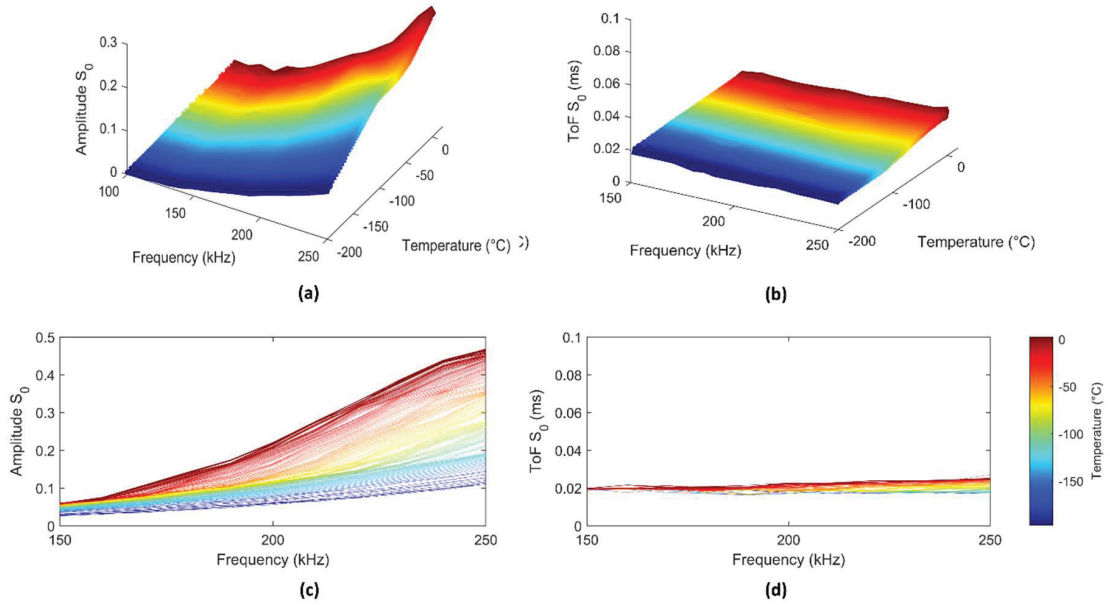

Figure 4: T1 to T2 (a) 3D representation of maximum amplitude spectrum of S0 mode over temperature, (b) 3D representation of ToF spectrum of S0 mode over temperature, (c) 2D representation of maximum amplitude spectrum of S0 mode over temperature and (d) 2D representation of ToF spectrum of S_0 mode over temperature

3.2. GW Adjacent media response

In addition to investigating the influence of temperature on guided wave propagation, this study examined the role of surrounding media, simulating realistic boundary conditions present in cryogenic storage applications, particularly in composite cryotanks containing both liquid and gaseous phases of cryogens. These structures often exhibit heterogeneous thermal environments, with partially submerged components encountering distinct heat transfer mechanisms and physical interactions depending on their immersion depth and phase interface.

To replicate such configurations, three test cases depicted in **Figure 5** were considered using the same UD-CFRP specimen:

- Fully Immersed in LN_2, with both transducer-equipped top and transducer-free bottom surfaces submerged.
- Partially Immersed, where only the bottom surface was in contact with LN_2 and the top remained exposed to gaseous nitrogen (GN_2).
- Fully Emerged, with the entire specimen suspended above the LN_2 bath in a GN_2 environment.

Thermocouple readings confirmed stable thermal gradients across the panel. In the fully immersed case, both surfaces stabilized near -197 °C. In the partially immersed configuration, the bottom surface remained at -197 °C, while the top was slightly warmer at -193 °C. The emerged panel recorded temperatures of approximately -195 °C and -183 °C at the bottom and top surfaces, respectively. These differences, though modest, create asymmetric thermal boundary conditions that can significantly affect guided wave propagation, particularly in anisotropic and multilayered materials like CFRP.

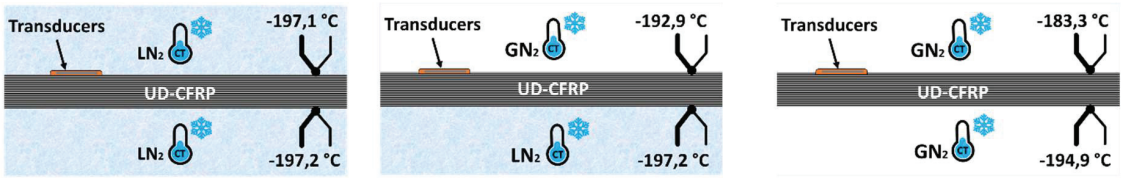

(a) (b) (c)

Figure 5: Schematics of the three configurations: (a) fully immersed, (b) partially immersed, and (c) fully emerged specimen.

Results depicted in **Figure 6** show that for the S0 mode, ToF remained essentially unchanged across all configurations, indicating that its wave speed was largely insensitive to whether the adjacent medium was LN_2 or GN_2. Amplitude showed minor increases in the emerged configuration, likely due to the slightly elevated surface temperatures rather than changes in damping or acoustic impedance. This supports the S0 mode's robustness to external medium effects, as its in-plane displacement profile minimizes interaction with environmental boundaries.

In contrast, the A0 mode displayed more pronounced sensitivity to immersion conditions. Subtle variations in ToF between the immersed and emerged states suggest slight changes in group velocity, potentially influenced by asymmetric boundary stiffness or pressure effects (e.g., hydrostatic pressure in LN_2 versus the lower-density GN_2).

Amplitude variations in the A0 mode were notably larger. Fully immersed conditions consistently produced the lowest amplitudes, while the partially emerged and fully emerged configuration resulted in the highest. This trend can be attributed to several factors:

- Increased acoustic damping in LN_2 due to its higher density and thermal conductivity.
- Acoustic impedance mismatch at the CFRP–LN_2 interface, reducing wave transmission efficiency.
- Reduced transducer coupling efficiency under thermal contraction in LN_2.

Conversely, the GN_2 environment imposes less mechanical constraint and thermal loading, enhancing transducer coupling and signal reception.

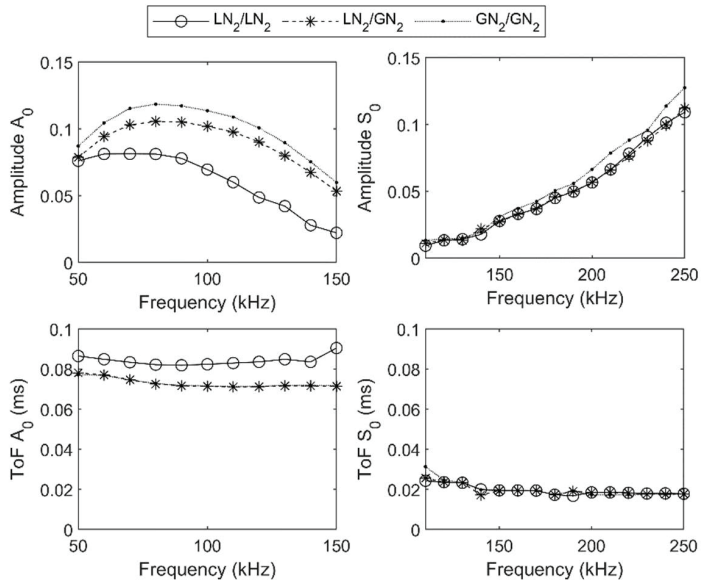

Figure 6: T1 to T2 signal comparison of A0 and S0 mode amplitude and ToF spectra across surrounding media configurations.

4. CONCLUSIONS

This study demonstrates that both cryogenic temperature and immersion state significantly influence guided wave behavior in UD-CFRP panels instrumented with DuraAct™ transducers.

The A0 mode shows strong sensitivity to temperature and immersion conditions, with amplitude increasing to approximately −60 °C that authors hypothesize that could be due to

polymer stiffening and reduced damping, followed by a sharp decrease at r temperatures below −60 °C. This decline is thought to be primarily attributed to cryogenic degradation of piezoelectric performance in the transducers, rather than changes in material dispersion.

In contrast, the S0 mode exhibits stable ToF across all temperature and immersion conditions, following a monotonic amplitude variation over temperature. Authors hypothesize that this consistency could be due to the S0 mode's in-plane displacement nature, which is less influenced by changes in matrix stiffness or external boundary conditions.

Among the two wave modes, ToF measurements proved more robust for SHM in harsh environments, showing minimal sensitivity to electromechanical degradation and environmental variations. Amplitude, while more sensitive, provides valuable early indicators when corrected for environmental effects.

The upward shift in A0 amplitude peak frequency at cryogenic temperatures cannot be explained solely by thermal contraction of the transducer and further studies needs to carry out for a compressive understanding of the temperature effects on the dispersion characteristics and signal acquisition.

Immersion state plays a critical role, particularly for the A0 mode. Fully immersed conditions in LN_2 resulted in the lowest amplitudes. Conversely, emerged configurations yielded stronger signals, highlighting the need to account for surrounding media in SHM interpretations.

These findings have several important implications for SHM system design in cryogenic applications:

- Amplitude-based diagnostics, while sensitive, require environmental compensation and transducer performance tracking.
- ToF measurements provide a more stable diagnostic metric and are better suited for baseline tracking in long-term monitoring.
- Dual-mode strategies, leveraging the A0 mode's amplitude sensitivity alongside the S0 mode's temporal stability, may enhance the detection of early damage while maintaining robust operation across variable cryogenic environments.
- Immersion-sensitive behavior of the A0 mode opens possibilities for environmental sensing, such as liquid level detection or phase change monitoring, offering potential for dual-function SHM systems.

Future work should focus on:

- Developing adaptive signal processing techniques to normalize amplitude variations based on immersion configuration or thermal gradients.
- Exploring multi-frequency fusion of A0 and S0 responses to balance sensitivity and robustness in extreme conditions.

Together, these insights lay the groundwork for more resilient, accurate, and multifunctional SHM systems in next-generation cryogenic structures.

5. REFERENCES

[1] S. P. E. Irving and C. Soutis, *Polymer Composites in the Aerospace Industry*. Cambridge, UK: Woodhead Publishing, 2014.

[2] D. A. McCarville, K. R. Meacham, J. S. McKnight, and J. M. Wood, *Design, Manufacture and Test of Cryotank Components*. Amsterdam: Elsevier, 2018.

[3] R. Talreja and C. V. Singh, *Damage and Failure of Composite Materials*. Cambridge: Cambridge University Press, 2012.

[4] S. Sánchez-Sáez, E. Barbero, R. Zaera, and C. Navarro, "Static behavior of CFRPs at low temperatures," *Compos. Part B*, vol. 33, pp. 383–390, 2002.

[5] C. Boller, F.-K. Chang, and Y. Fujino, Eds., *Encyclopedia of Structural Health Monitoring*. Hoboken, NJ: John Wiley & Sons, Ltd, 2009.

[6] V. Janapati, M. Seaver, S. F. Masri, F.-K. Chang, and M. J. Todd, "Damage detection sensitivity characterization of guided wave SHM," *Struct. Health Monit.*, vol. 15, pp. 143–161, 2016.

[7] B. Eckstein, D. V. Martin, and G. Gollnick, "Environmental effects on guided ultrasonic waves," in *Proc. Eur. Workshop Struct. Health Monit. (EWSHM)*, Nantes, France, 2014.

[8] M. Moix-Bonet, A. Ruiz, and J. M. Serra, "Temperature compensation for damage detection," in *Proc. Eur. Workshop Struct. Health Monit. (EWSHM)*, Manchester, UK, 2018.

[9] S. Sánchez-Sáez, E. Barbero, R. Zaera, and C. Navarro, "Static behavior of CFRPs at low temperatures," *Compos. Part B*, vol. 33, pp. 383–390, 2002.

[10] X. L. Zhang, R. X. Guo, and A. S. Bhalla, "Dielectric and piezoelectric properties of PZT ceramics at low temperatures," *J. Mater. Sci.*, vol. 18, pp. 968–972, 1983.

[11] G. H. Haertling, "Ferroelectric ceramics: History and technology," *J. Am. Ceram. Soc.*, vol. 82, no. 4, pp. 797–818, 1999.

XI ECCOMAS Thematic Conference on Smart Structures and Materials - SMART 2025
M. Krommer, M. Nader and M. Schagerl (Eds)

Received: 22 April 2025 / Revised: 5 October 2025 / Accepted: 11 October 2025
© The Author(s) 2025

A Digital Twin for Vibration and Fault Monitoring in Power Plant Turbogenerators

Hendrik Holzmann, Vincent Rachor, Georg Stoll, Rainer Nordmann, Sven Herold

Abstract. Turbogenerators, consisting of steam turbines and generators, are central components in power plants. The steam turbines transform thermal energy into mechanical energy, causing the rotor to rotate. The generator generates electrical energy through electro-mechanical interactions in the air gap, where energy transfer occurs. When disturbances arise in the electrical generator-grid system, transient torsional vibrations in the shaft train can be induced, potentially reaching significant amplitudes due to the system's low damping. To ensure safe and reliable operation, it is essential to automatically monitor and assess the electro-mechanical interaction processes and the torsional vibrations of the shaft train and to react to faulty operating conditions immediately.
A Digital Twin for monitoring and evaluating torsional vibrations can serve as an effective tool for this purpose. Through theoretical modeling, numerical analysis, and experimental analysis, key tasks such as simulation, validation, and identification can be carried out to operate a Digital Twin. Utilizing a Finite Element Model as a component of the Digital Twin, torsional vibrations can be calculated as either natural vibrations or as forced vibrations resulting from electro-mechanical air gap excitation. During operation, the actual torsional vibrations of the turbogenerator are measured at specific locations using sensors that capture torsional displacements or shear strains.
In this work, a Digital Twin is presented, taking measured vibration data as an input to compare it to the corresponding calculated torsional vibrations. The vibration difference is introduced into a calibration loop of the Digital Twin, in which the actual system parameters of the turbogenerator as well as the actual air gap torque can be identified and adjusted using a sensitivity-based model fitting algorithm. The torsional vibration state of the Turbogenerator at arbitrary locations of the shaft train is evaluated in the time and frequency domain in real time. Furthermore, it is demonstrated to be efficient for the identification and diagnosis of system failures, disturbances and parameter changes (mass, stiffness, damping). The Digital Twin can be used as an online system, running permanently parallel to the real turbogenerator as a monitoring system.

Key words: Digital Twin, Turbogenerator, Model Updating, Failure Detection, Real Time.

Hendrik Holzmann & Vincent Rachor & Georg Stoll & Rainer Nordmann & Sven Herold
Fraunhofer Institute for Structural Durability and System Reliability LBF, Bartningstr. 47, 64289 Darmstadt, Germany, e-mail: hendrik.holzmann@lbf.fraunhofer.de

1 INTRODUCTION

A stable energy supply is fundamental to the functioning of modern societies, underpinning economic development, technological advancement, and overall quality of life. The role of thermal power plants is evolving significantly with the rise in the share of renewable energy sources. As the integration of variable renewables, such as solar and wind energy, increases, thermal power plants are required to operate more flexibly to maintain a stable energy supply. This flexibility is essential for balancing load fluctuations and ensuring that energy demands are met even during periods of low renewable generation. Thermal power plants are increasingly taking on the role of backup facilities, providing essential support during unexpected outages or when renewable generation falls short. This shift necessitates a transformation in how these plants are managed and operated, as they must now be prepared to respond quickly to changes in energy supply and demand. Additionally, market dynamics are shifting as competition between fossil fuels and renewable energy intensifies, leading to new business models for thermal power generation. In summary, as renewable energy continues to grow, thermal power plants must adapt their operational strategies and technologies to thrive in an increasingly renewable-driven energy market. The stable and reliable operation of thermal power plants is crucial for ensuring energy security and operational efficiency. As these facilities play a significant role in meeting the growing energy demands, monitoring their performance and early detection of potential failures becomes imperative. Early identification of issues not only enhances safety for personnel and surrounding communities but also minimizes costly repairs and reduces downtime, thereby sustaining reliable energy production. [1–3]

In recent years, the concept of the Digital Twin has emerged as a valuable tool for advancing the monitoring and management of thermal power plants. By enabling real-time surveillance, a Digital Twin allows for continuous assessment of operational states, thus providing critical insights into the plant's performance by tracking back changes in the observed system behavior to changes to the systems physical parameters [4, 5]. Moreover, it facilitates predictive analytics, enabling simulations of future operational conditions, which aids in proactive maintenance planning. The ability to diagnose errors and identify root causes through a Digital Twin significantly shortens response times to anomalies, enhancing the overall reliability of the facility. Additionally, the integration of data analyses fosters operational optimization, ultimately leading to improved efficiency and power output. Through informed decision-making supported by a Digital Twin, thermal power plants can achieve greater sustainability and economic viability. [6, 7]

This paper will demonstrate the utilization of Digital Twin technology integrating physical models with operational data in thermal power plants, focusing on means of detection and classification of disturbance and failure to support optimal operational decision making.

2 A DIGITAL TWIN FOR CONDITION MONITORING OF TURBOGENERATORS

In the context of power plant operation, the Digital Twin proposed herin is a digital replica of relevant parts of a real system. It operates by comparing sensor data from the real system with predictions from its model (cf. Figure 1). Differences between these observations help identify and update system parameters and operational conditions. Deviations can indicate potential internal failures or external disturbances and can also inform active system controls. Additionally, they can provide recommendations to experts for adjusting operational conditions. Modeling and analysis procedures are crucial for a Digital Twin's functionality. For developing a Digital Twin for turbogenerator torsional vibrations, three key tools are needed: theoretical modeling, numerical analysis, and experimental analysis [8]

Figure 1 (b) illustrates the Digital Twin concept for torsional vibrations of turbogenerators. The real turbogenerator (orange frame) experiences air gap torques (AGT) that cause torsional vibrations. Vibration measurement signals from sensors serve as input data for the Digital Twin (green frame) and are compared to virtual signals calculated by the Digital Twin.

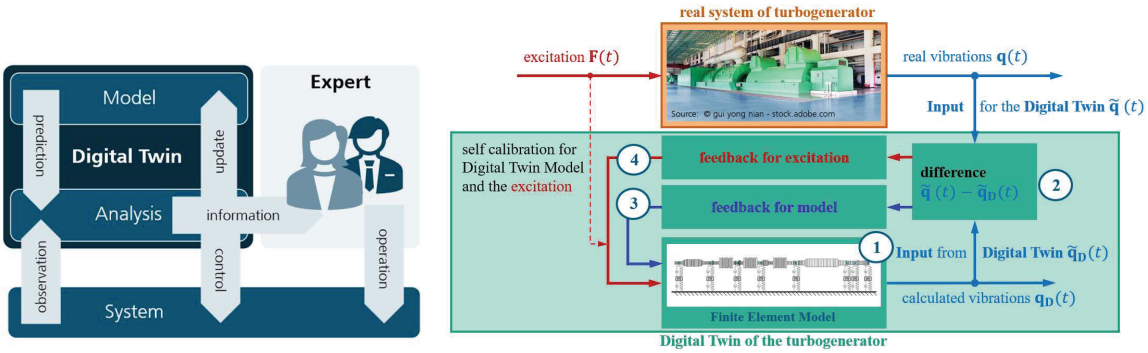

Figure 1: Digital Twin for a system at operation (a) and overview of coexistence of Digital Twin and turbogenerator system (b)

A key component of the Digital Twin is a model of the physical system. In this work, a Finite Element (FE) model (1) is used, that calculates natural and forced torsional vibrations along the shaft. Simulated vibrations at sensor positions are compared to measured data collected from the turbogenerator via a datalogger. The comparison point (2) integrates these two inputs, with forced vibration calculations performed using numerical modal analysis, representing the vibrations as a lumped mass multi-degree-of-freedom (MDOF) system that can be decoupled into a series of single-degree-of-freedom (SDOF) systems. Each SDOF system represents a normal mode of the original system. The differences between the measured and modeled data generate the output of the comparison point, which is fed back into the calibration component of the Digital Twin. This calibration process is divided into two parts: one for adjusting system parameters (3) and another for estimating the airgap torque excitation signal (4). This overall process enables real-time determination of torsional vibrations and derived quantities, such as stresses and torques, at any operational point. In this way, a significant benefit for the real

system is created by providing a simulated insight into every part of interest of the real system.

2.1 Finite Element model

Under the assumption of linear and quasi-stationary behavior of the shaft train structure, the torsional vibrations of the rotor can be simulated using the second order differential equation

$$\boldsymbol{J}\ddot{\boldsymbol{q}}(t) + \boldsymbol{D}\dot{\boldsymbol{q}}(t) + \boldsymbol{K}\boldsymbol{q}(t) = \boldsymbol{M_{el}}(t) \tag{1}$$

including mass ($\boldsymbol{J}$), damping ($\boldsymbol{D}$), and stiffness ($\boldsymbol{K}$) matrices, along with an excitation vector ($\boldsymbol{M_{el}}$) for the AGT. The components used to establish this equation consist of the elements of the shaft train and the attached turbine blades. As depicted in Figure 2, cylindrical elements are used for modeling the shaft train. Their dynamic behavior is described by their moments of inertia, included in the mass matrix $\boldsymbol{M}$, and their torsional stiffness, included in the stiffness matrix $\boldsymbol{K}$.

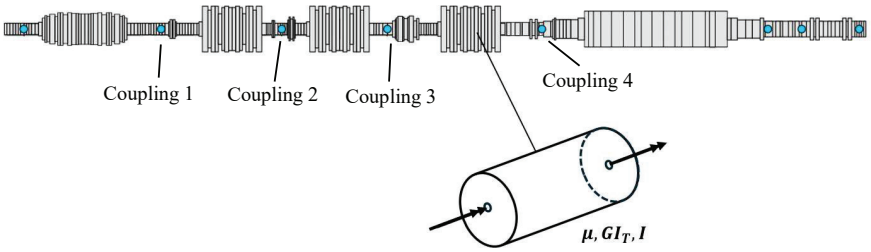

Figure 2: Finite Element Model of the turbogenerator

The turbine blades, which have significant moments of inertia, mainly contribute to the polar moment of inertia terms in the mass matrix $\boldsymbol{J}$. Additionally, the last stage blades in the low-pressure (LP) turbines must be accounted for in the stiffness matrix $\boldsymbol{K}$ as flexible elements. When these blades are coupled with the rotor's torsional vibrations, they are all excited identically in-phase, allowing them to be approximated as a two-degree-of-freedom system comprising two rings with adjusted polar moments of inertia and two torsional springs. As a test case for the Digital Twin, the shaft train of a real thermal Power Plant has been utilized. Initially, the FE Model of this system was employed to determine the dynamic characteristics of a baseline model.

2.2 Calibration of the system parameters

For the established Finite Element (FE) base model, the system matrices $\boldsymbol{J}$ and $\boldsymbol{K}$, along with the natural frequencies ω_i and mode shapes $\boldsymbol{\varphi}_i$, are known. To determine potential parameter changes $\Delta\boldsymbol{J}$ and/or $\Delta\boldsymbol{K}$ from the measured deviations in the torsional natural frequencies compared to the base model, a sensitivity based approach [9] is used. By introducing the eigenvalues $\lambda_i = \omega_i^2$, the eigenvalue problem can be formulated as

$$(\boldsymbol{K} - \lambda_i \boldsymbol{J})\,\boldsymbol{\varphi}_i = \boldsymbol{0} \qquad (i = 1{,}2 \ldots N). \tag{2}$$

For an arbitrary system parameter p_k, representing either mass or stiffness, the partial derivative of the eigenvalue λ_i is defined with respect to this parameter p_k as follows:

$$S_{i,k} = \lambda_{i,k} = \delta(\lambda_i)/\delta(p_k) = \boldsymbol{\varphi}_i^T(-\lambda_i \boldsymbol{J}_k + \boldsymbol{K}_k)\,\boldsymbol{\varphi}_i \tag{3}$$

$S_{i,k}$ represents the sensitivity of the eigenvalue λ_i with respect to the parameter p_k. This sensitivity is calculated using the eigenvector $\boldsymbol{\varphi_i}$ and the derivatives of $\boldsymbol{M}$ and $\boldsymbol{K}$ with respect to p_k. Utilizing these sensitivities, an iterative calibration procedure is implemented to determine parameter changes in the turbogenerator when deviations in the torsional natural frequencies are observed. The dynamic characteristics of the base model, which reflects normal operation, can be derived from the stiffness matrix $\boldsymbol{K}$ and the mass matrix $\boldsymbol{M}$.

This approach allows for the calculation of the torsional natural frequencies ω_j and the corresponding torsional mode shapes $\boldsymbol{\varphi}_i$. The torsional natural frequencies of the automatically updated model and the real system are illustrated in Figure 3.

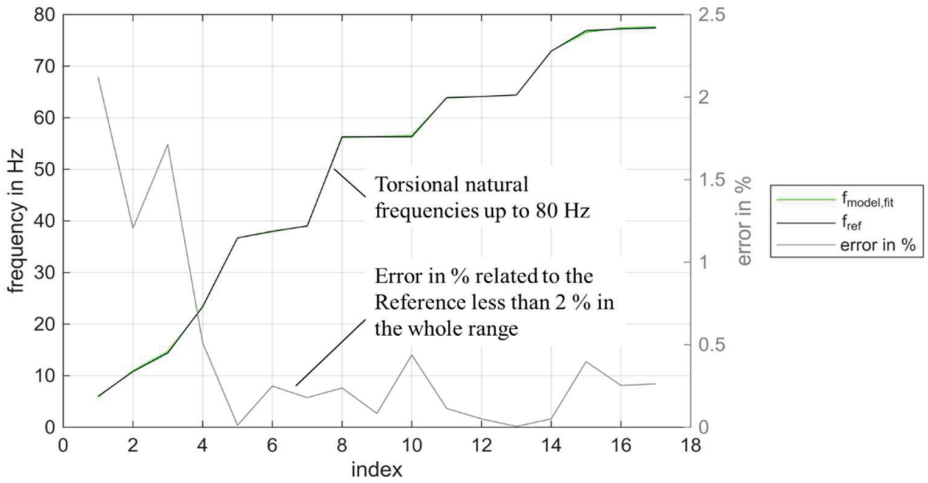

Figure 3: Torsional natural frequencies f_j of turbogenerator up to 80 Hz for the updated model and the real system (updated model and reference graphs on top of each other)

The torsional natural frequencies of the Digital Twin FE Model ($f_{model,fit}$) are compared with reference values (f_{ref}), showing a strong correlation with errors of less than 2%. In conclusion, the FE base model accurately predicts the torsional natural frequencies within the required frequency range. This accuracy is further supported by comparisons with measured torsional natural frequencies from strain spectrum measurements of the turbogenerator during operation (Figure 4) where a good agreement of the first seven eigenfrequency peaks is observed.

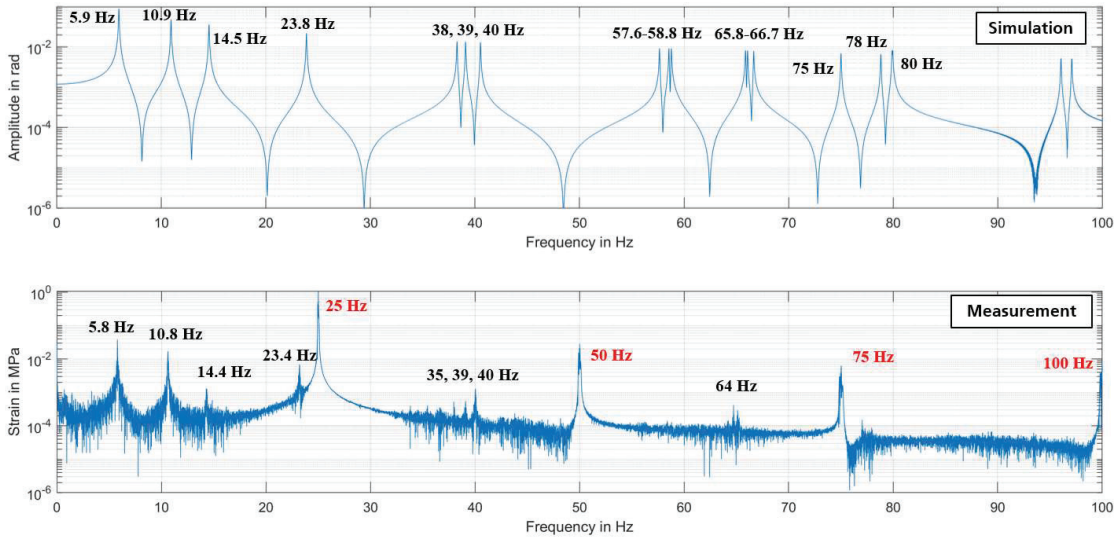

Figure 4: Measured and calculated natural frequencies of the turbogenerator (grid frequency and harmonics shown in red)

3 DEMONSTRATION OF USE-CASES

The digital twin enables condition and fault monitoring of the torsional vibration behaviour. Changes in the torsional vibration of the turbogenerator can be caused either by changes in the system parameters $\Delta \boldsymbol{J}$, $\Delta \boldsymbol{K}$ and $\Delta \boldsymbol{D}$ or by a change in the excitation, e.g. by the AGT. The AGT reflects the interaction between the electric generator and the mechanical shaft system.

3.1 Condition monitoring of the electrical excitation

The continuous calculation and monitoring of the AGT is an effective measure for detecting disturbances in the electrical system, such as a two-phase short circuit, negative sequence current or sub-synchronous resonance. To calculate the AGT (cf. Figure 5), the dynamic shaft torque is determined in the FE base model for each finite element of the turbogenerator in a frequency range between 0 and 100 Hz. This is done assuming a unit excitation of 1 Nm at the generator. The dynamic torsional stresses can be determined from the calculated dynamic shaft torques, in particular for the elements in which the sensors are located. The ratio of the dynamic stresses and the measured stresses of the SSR-sensors describes the acting AGT.

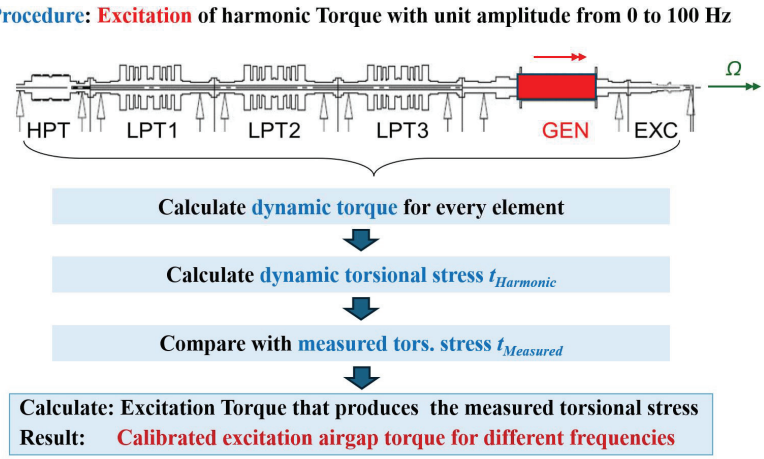

Figure 5: Calibration of the AGT in the Digital Twin

No measurement data of the torsional stresses for the disturbance load excitations were available. Therefore, these data for the electrical moment for the mentioned excitations were created based on existing formulas. This data was introduced as the corresponding moment at the input point of the digital twin. In the case of the two-phase terminal short circuit (equation 4), the AGT identification procedure is tested for an input with and without noise (signal-to-noise ratio of 10 dB).

$$M_e(t) = M_0 + \frac{M_0}{\cos\varphi} \times \frac{1}{x_d'' + x_{TR}} \times \{\sin(\Omega t) - 0{,}5 \times \sin(2\Omega t)\} \tag{4}$$

Figure 6 shows the time signal of the two-phase terminal short-circuit and the AGT calculated from it in the frequency domain. A representation of the AGT in the frequency domain allows a targeted analysis of the existing frequency components, whereby specific disturbances in the grid can be recognised. In this case, the two main frequencies (grid and double grid frequency) can be identified very well. The identification is also successful using noisy signals.

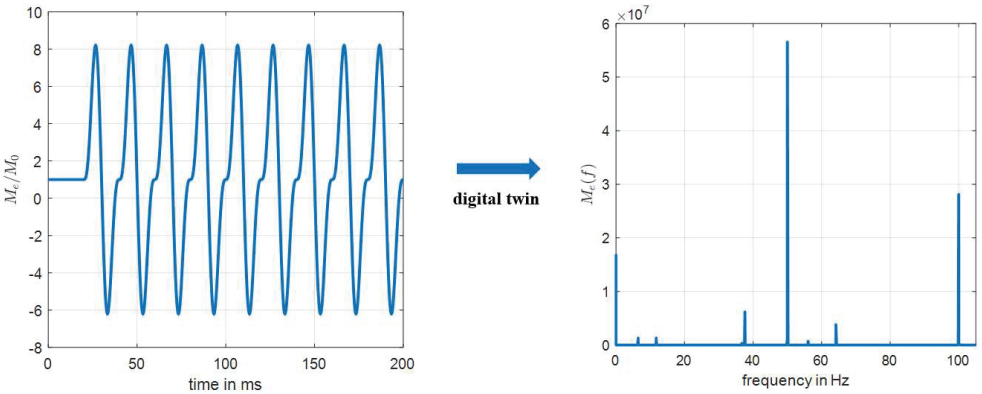

Figure 6: Calibration of the AGT for the case of a two-phase short circuit

3.2 Condition monitoring through attenuation calculation

Continuous monitoring of the modal damping can also be used for condition monitoring. Modal damping consists of mechanical damping (material, steam, blade joints) and electrical damping (generator and grid). In this case, the electrical part is the dominant one. The cause of changes in modal damping during operation of the turbo generator will therefore in most cases be an electrical event, such as a change in power or an event in the grid. In the case of a sub-synchronous resonance event, which can lead to strong changes in the damping, the modal damping can become negative. This means instability for torsional oscillations of the shaft train.

If the torsional natural frequencies in the frequency spectrum are sufficiently far apart, each peak in the frequency response function (FRF) can be interpreted approximately as that of a single-degree-off-freedom system (SDOF system). In this case, the established half-power bandwidth method (HPB method) can be used to determine the modal damping D. The resonance frequency ω_j and the associated maximum value V_{max} can be determined in the FRF of a general SDOF system. The frequency difference $\Delta\omega$ at an amplitude of V_{max}/p results from these values. The modal damping D can then be determined using equation 5. For exact determination of the modal damping, even with noisy measurement signals, this is determined for different parameter values for p.

$$D = \frac{\Delta\omega}{2\omega_j\sqrt{p^2 - 1}} \tag{5}$$

It was shown that this method can be used to calculate the modal damping and changes in the modal damping for the first four natural frequencies accurately. The higher natural frequencies were too little excited and noisy in the measurements.

3.3 Dominant change of one modal damping coefficient: Sub Synchronous Resonance

This application demonstrates the effect of a change in modal damping for the 3rd mode at 14.6 Hz on the system response in both the time and frequency domains, as shown in Figure 7. The modal damping for the base model is identified as $D = 0.1\ \%$ and is subsequently reduced to approximately 20% of its original value. Such a reduction in modal damping could occur, for instance, during a Sub-Synchronous Resonance (SSR) event. The HPB is employed for continuous identification of the actual modal damping values.

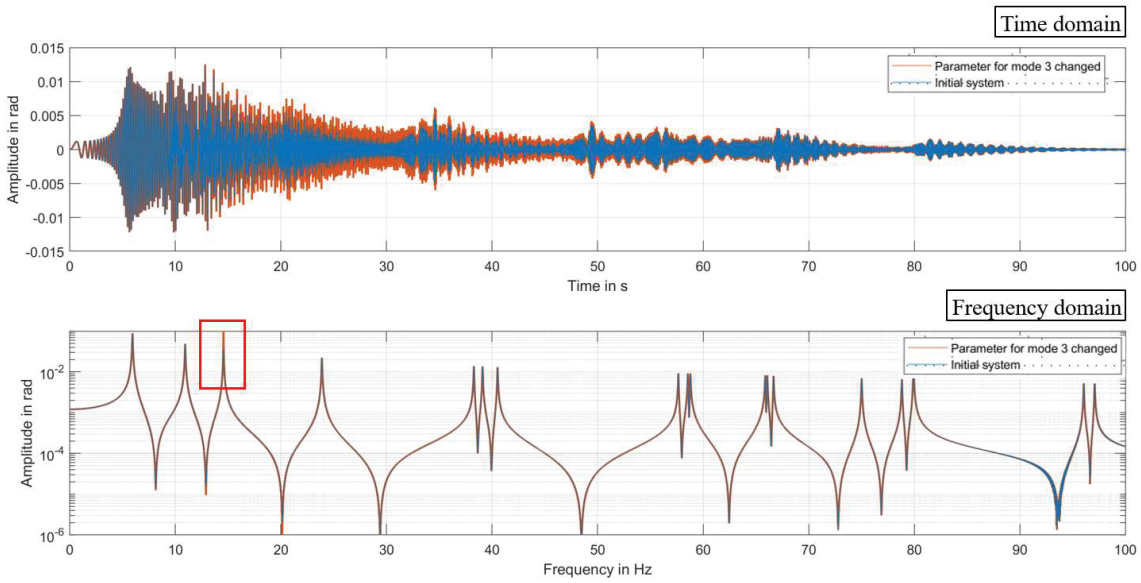

Figure 7: System response in the time and frequency domain due to the changed damping value at the third frequency at 14.6 Hz

3.4 Fault monitoring through natural frequency sensitivity analysis

In this application test, the torsional stiffness of couplings 3 and 4 (see Figure 2) is reduced by 10%, representing a sudden damage. The changes in the torsional natural frequencies for both cases are compared with the spectrum of the system that has the original stiffness values of the couplings.

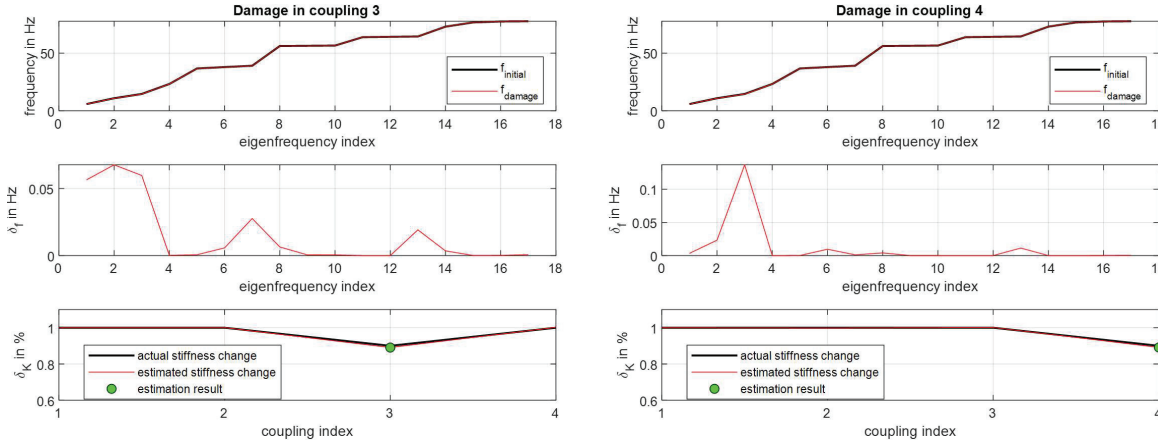

Figure 8: Deviations of Natural Frequencies and Changed Stiffness in Couplings

Using the sensitivity-based calibration procedure, the following results are obtained for each of the two cases: The percentage change in the torsional natural frequencies within the frequency

range of 0 to 100 Hz (as shown in the middle diagrams) indicates the respective influence of coupling stiffness change on the eigenfrequencies and hence sensitivity. The predicted change in coupling stiffness is compared to the actual change in the lower diagram. The highest change is considered by the algorithm as the location of damage. The severity of damage is automatically estimated by this procedure. The results show, that in all cases, the location is predicted correctly and the stiffness change is estimated with an error of less than 1 %. Through the real time prediction, an instant feedback to the power plant operator is performed, allowing for potentially automatic shutdown and early maintenance before additional damage is caused.

4 CONCLUSION / OUTLOOK

In this work, a Digital Twin for turbogenerators was presented, taking measured vibration data as an input to compare it to the corresponding calculated torsional vibrations. The vibration difference is introduced into a calibration loop of the Digital Twin, in which the actual system parameters of the turbogenerator as well as the actual air gap excitation torque can be identified and adjusted. Simple yet fast and effective tools used in this work were a sensitivity-based model updating algorithm as well as the HPB method for damping identification. The torsional vibration state of the Turbogenerator at arbitrary locations of the shaft train was evaluated in the time and frequency domain in real time. Furthermore, it was demonstrated to be efficient for the identification and diagnosis of system failures, disturbances and parameter changes (mass, stiffness, damping). The Digital Twin can be used as an online system, running permanently parallel to the real turbogenerator as a monitoring system. Through this real time functionality, feedback is provided to the power plant operator continuously. This allows for early shutdown and maintenance, hence preventing additional damage to the power plant in case of unforeseen changes of the system state or operating condition. Future studies will focus on more sophisticated model updating algorithms and more complex systems. Online monitoring of a entire power plant systems using the Digital Twin is the final aim of future work.

REFERENCES

[1] S. Chen, P. Liu, and Z. Li, "Low carbon transition pathway of power sector with high penetration of renewable energy," *Renewable and Sustainable Energy Reviews*, vol. 130, p. 109985, 2020, doi: 10.1016/j.rser.2020.109985.

[2] O. Smith, O. Cattell, E. Farcot, R. D. O'Dea, and K. I. Hopcraft, "The effect of renewable energy incorporation on power grid stability and resilience," *Science advances*, vol. 8, no. 9, eabj6734, 2022, doi: 10.1126/sciadv.abj6734.

[3] Y. Zou, Q. Xia, Y. Chi, and Q. Wang, "Enhancing Renewable Energy Accommodation by Coupling Integration Optimization with Flexible Retrofitted Thermal Power Plant," *Applied Sciences*, vol. 14, no. 7, p. 2907, 2024, doi: 10.3390/app14072907.

[4] C. Tamm, "Ein Beitrag zur Modellbildung parametrischer digitaler Zwillinge für schwingungstechnische Anwendungen," Eingereichte Dissertation, TU Darmstadt, Darmstadt, 2020.
[5] C. Tamm, "Efficient and Parametric Digital Twins for System Engineering Applications," in *NAFEMS: Better Products with Model Based Systems Engineering (MBSE) and CAE*, Wiesbaden, Deutschland, 2018, pp. 21–29.
[6] W. Zhang *et al.,* "Build Digital Twins for Smart Upgrading of Thermal Power Plants: A Practical Framework," in *2024 IEEE 4th International Conference on Digital Twins and Parallel Intelligence (DTPI)*, Wuhan, China, Oct. 2024 - Oct. 2024, pp. 625–628.
[7] F. Tao, H. Zhang, A. Liu, and A. Y. C. Nee, "Digital Twin in Industry: State-of-the-Art," *IEEE Trans. Ind. Inf.*, vol. 15, no. 4, pp. 2405–2415, 2019, doi: 10.1109/TII.2018.2873186.
[8] D. J. Ewins, "Exciting vibrations: the role of testing in an era of supercomputers and uncertainties," *Meccanica*, vol. 51, no. 12, pp. 3241–3258, 2016, doi: 10.1007/s11012-016-0576-y.
[9] J. E. Mottershead, M. Link, and M. I. Friswell, "The sensitivity method in finite element model updating: A tutorial," *Mechanical Systems and Signal Processing*, vol. 25, no. 7, pp. 2275–2296, 2011, doi: 10.1016/j.ymssp.2010.10.012.

XI ECCOMAS Thematic Conference on Smart Structures and Materials - SMART 2025
M. Krommer, M. Nader and M. Schagerl (Eds)

Received: 5 May 2025 / Revised: 25 August 2025 / Accepted: 11 October 2025
© The Author(s) 2025

Modeling the Human as a Control Component in Power Tool Systems: A Case Study on Chainsaw Operation

Helena Käppeler, Stefan C. Schlanderer, Edmund Marth, Gerd Bramerdorfer

Abstract. In the operation of power tools, the interaction of the user with the tool and the work piece both play a crucial role, as they define the load for the tool's drive train. It is also highly dependent on the user's response on the system behavior. The way the power tool is used has a significant influence on the optimal design. Furthermore, the type of application can also result in different contributions of the load points and their temporal distribution to the load cycle. For a resource-efficient and user-centered design, it is essential to integrate the human factor into the analysis of the system. While research has predominantly focused on modeling and developing the device, less attention has been paid to understand the human role as a controlling component within this system. A common limitation lies in the lack of realistic models for the human part, preventing a holistic evaluation of the entire system. Furthermore, the acquisition of user-related data, as well as the large number of degrees of freedom, represent a particular challenge in user modeling.

This study investigates the impact of the user behavior on the corresponding machine operating point and work progress over a defined cycle. A battery-powered chainsaw is used in the case study. A model that represents the key interactions between device, application, and user, including their most important characteristics is developed. In this approach, the user is modeled as a controller exhibiting various control variables. The behavior of different persons can be integrated, and their effects on the overall system performance is analyzed. Based on this analysis, recommendations on how to model the human as a controller within this system are proposed. In the future, user-adaptive approaches to device control could be implemented based on knowledge of users' influence. This facilitates a more holistic approach to future power tool development.

Key words: battery-powered chainsaw, human-machine interaction, system modeling

Helena Käppeler & Stefan C. Schlanderer
ANDREAS STIHL AG & Co. KG, Badstraße 115, 71336 Waiblingen, Deutschland
e-mail: helena.kaeppeler@stihl.de

Edmund Marth & Gerd Bramerdorfer
Institute of Electric Drives and Power Electronics, Johannes Kepler University Linz, Linz, Austria

1 INTRODUCTION

Due to the significant influence of the human operator and the use of power tools, the overall performance is strongly dependent on both factors. In particular, human behavior is difficult to evaluate using purely simulation-based approaches. Therefore, this study proposes an initial concept for simulating user behavior during power tool operation, using the chainsaw as a representative example. Based on the insights gained, recommendations for future investigations will be derived.

Investigations considering a system defined by handheld devices with the human as a central subsystem was carried out in 2014 by Matthiesen [1]. Based on the achieved results, it is possible to develop models of user-device interactions. The user, the device, and the load were part of the system under investigation. The study considered the mechanical interactions between the user and an impulse screwdriver during operation.

In another study, Matthiesen [2] investigated the necessity of modeling varying biodynamic responses of the user in test rigs for power tool development, revealing key factors such as user, posture, grip, and feed force. The study showed that different biodynamic responses lead to varying vibration levels, which in turn affect the interactions of the technical subsystems inside the power tool, highlighting the importance of considering these variations in test rig design.

With a focus on efficiency, Uhl et al. [3] investigated the impact of feed and transverse forces on the productivity of hammer drills. For this purpose, 1152 experiments with different variants of drills, drilling tools, and use cases were carried out. All variants showed that the user has a significant influence on productivity, especially with regard to feed force.

In a subsequent analysis, Zimprich [4] analyzed the effect of the feed force on productivity and vibration of a hammer drill. In the set up, a modified hammer drill for constant motor speeds over a wide feed force range was used. Both the feed force and the device speed have a significant impact on productivity.

In the application of the chainsaw, the load caused by cutting wood and the associated work progress are crucial for a comprehensive assessment of the device's performance and efficiency from the user's perspective. There are several studies in literature analyzing the cutting process in wood. A systematic study of the cutting process in wood was reported by Krenke [5]. The study reviewed various approaches to describe the cutting process of wood mathematically in three parts, highlighting the limitations of existing empirical, analytical, statistical, numerical, and semi-empirical methods due to numerous influencing factors. The outcome was a semi-empirical model, as it was the only approach considered to represent the physics.

In [6], is discussed the importance of cutting and disintegration processes for wood and wooden materials, emphasizing the need for optimal process control to meet quality, quantity, energy, tool wear, and emission requirements. It analyzes the cutting process of wood, defining typical kinematic and geometric characteristics for common wood processing methods. There has been no further investigation into the kinematics of the chainsaw. Furthermore, the study presents basic process variables and the qualitative effects of various influencing factors.

Dvoracek [7] presents a novel test method for investigating the cutting process of oak wood.

The study introduces a mathematical model that can be used for process and quality control, contributing to sustainability and machine lifetime, and highlights the importance of factors such as uncut chip thickness and fibre angle for predicting cutting forces. The established model was determined by measurements using a specific cutting tool.

In systems involving humans and machines, there are several aspects that can be examined. A point to consider is the human's function in controlling the system. Several studies have focused on examining and modeling humans as a controller. The research by Mulder [8] introduces a new framework based on Linear Parameter-Varying (LPV) models. With LPV it is possible to mathematically model and identify time-varying, adaptive human control. This capability enables key innovations, such as the creation of human-like automation. The presented framework includes the aspects of feed forward and feedback control, neuro-muscular system effects, learning and adaptation.

More recent work by Mabrok [9] discusses the major directions and challenges in man-machine systems from a control theory perspective with a focus on human modeling in the man-machine system. One part of it was the understanding of the attributes and limitations of the human operator. These limitations include, for example, response delay or threshold limits.

However, there is still a need for modeling a system with consideration of the human factor, the application and the device. Therefore, a deeper understanding of the influence of the human factor on the system is necessary. In order to take these previously unconsidered aspects into account, an approach is presented in which the main components and their interactions are simulated in the context of a chainsaw. In addition, this approach is used to evaluate the influence of humans within the system in order to provide a recommendation for further investigations. The analysis is carried out using a defined load cycle over an entire battery charge. The evaluation focuses on the cut area, the cutting performance, the duration of the cutting process, and the resulting device losses.

2 SYSTEM SIMULATION

To address the question of the significance of how the user influences the machine behavior and the work result, a modular simulation framework is used. The model is implemented in Matlab/Simulink. Particularly important are the modules of the device, the application, and the user. As shown in Figure 1, the approach of modular modeling is also applied at the device level. The fundamental notion of the modular structure of the three primary components has been adapted from [1]. In contrast to the system presented in [1], the interactions between the application and the user are also considered. The interactions between the main components and their modeled effects is outlined in the following chapters for the use case of a chainsaw.

For this study, the STIHL MSA 300 chainsaw was used as the test device. The most significant chainsaw specifications are listed in Table 1.

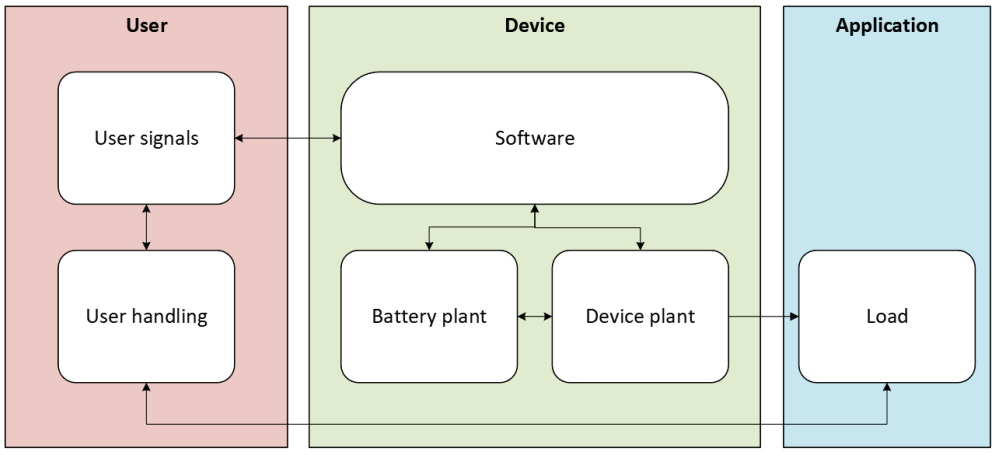

Figure 1: Modular structure of the system under consideration.

Table 1: Technical details of STIHL MSA 300 [10]

Nominal voltage	Power consumption	Power output	System weight	Motor type
36 V	3 kW	2.5 kW	5.4 kg	PMSM

2.1 Device Model

This application focuses on analyzing long-term behavior, for instance the energy losses over a load cycle. Consequently, the individual operating points, rather than the short-term dynamic behavior between these points, are crucial. The operating point, therefore, is defined as the specific speed and torque combination at which the machine is predominantly operated. The device model, as illustrated in Figure 1, has the interface to the user and includes the operating mode information, i.e. eco mode or performance mode and the target speed. The user can specify the target speed by means of a potentiometer. Furthermore, the device model has an interface for load modeling. This is where the information about the load torque and the speed is exchanged.

The product software features simplified modeling, including speed controller, torque, and power limits. The motor control is not included, as the corresponding torque is set directly to the plant model with a time delay. The plant model of the device includes the operating point-dependent losses of the motor, the power electronics losses, and the mechanical drive train losses. Additionally, the speed-dependent no-load losses from the chainsaw's cutting attachment are considered in the model.

The battery is modeled using an equivalent circuit with parameters based on measurements. The dynamic behavior is represented using 2-RC elements. Furthermore, the open-circuit voltage of the cells is dependent on the state of charge. The temperature-dependent behavior is modeled using variable resistances. The thermal characteristics of the battery are modeled with

a thermal network model.

For initial validation, several steady-state operating points were compared to actual measurements. Therefore, the values from the controller were logged with a fully assembled chainsaw, which was not externally loaded by a cut. However, resulting torque losses occur depending on the speed. The simulation model was then fed with the same potentiometer values as input. On average, a deviation of 4.52% for the reference torque was observed.

2.2 Model of the application

Within the application model, two aspects are important for investigating the influence of the user on machine operation. First, it is necessary to determine the load on the drive train of the machine represented by a torque at a given tool speed. It should be noted that this torque depends not only on the tool speed, but also on a number of workpiece-dependent conditions, such as engagement length and wood properties. The cutting process with the main conditions and results is schematically shown in Fig. 2 on the left side. The second relevant aspect is determining the work progress. This serves for a later assessment of the work performed as well as for the definition of a dynamic load cycle. In this case, the work progress is described by the cutting performance P_{cut} and is defined by the ratio of the cut area a_{cut} per time t_{cut}.

$$P_{\mathrm{cut}} = \frac{a_{\mathrm{cut}}}{t_{\mathrm{cut}}} \left[\frac{cm^2}{s} \right] \tag{1}$$

The physical description of the cutting process in wood requires a high effort for parameterization. This fact is applicable not only to the cutting process with a chainsaw, but to processing operations with wood as a material in general. Therefore, a data-based representation is used for this study. The approach applied here is comparable to the work of [4] for drilling machines. In contrast to [4], the focus here is not on determining vibrations dependent on the feed force F_{f}. In the current case, the relationship between the machine's operating point, the feed force, and the resulting cut area per unit time were measured. The model of the application and the model of the machine are linked by the torque T_{cut} and the chain speed v_{chain} , as can be seen in Figure 2.

To generate the data set used for modeling, the possible operating points are controlled in the test bench, and a characteristic map for the operating range is measured. The validity of individual data set is restricted to the specific type of wood, wood shape, and chain-bar combination. This type of measurement is also part of the patent [11]. There, the knowledge about the cutting performance is used to design the battery-powered chainsaw. As shown in Figure 2 on the right, the recorded measurements are then used in the simulation to map the load torque and cutting performance, speed, and feed force dependencies. The data was processed in a way that the engagement length l_{cut} is specified as an input variable in the simulation. For the initial approach, a linear relationship between the number of teeth engaged and the torque or cutting performance was assumed. This allows the simulation to consider varying l_{cut} and thus different cross-sections of the work piece.

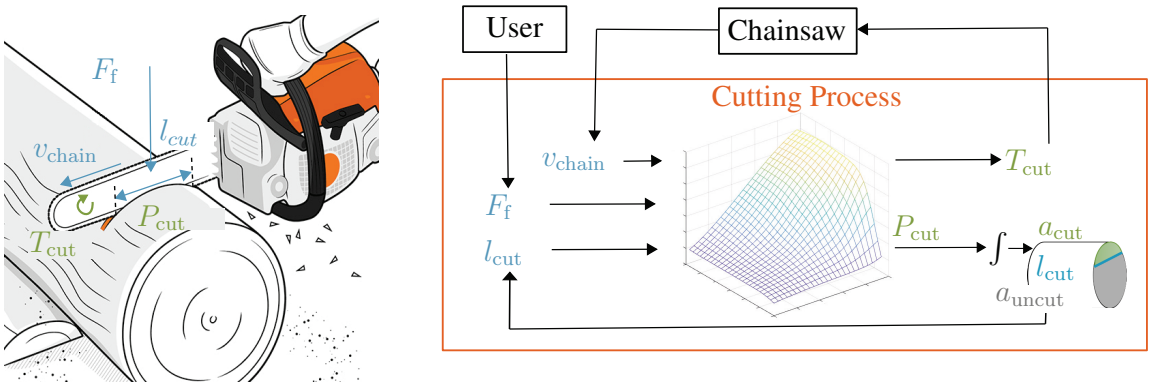

Figure 2: Definition of parameters and modeling of the cutting process.

An advantage of this approach is that typical work processes in the wood industry can now be described and simulated. For this purpose, a sequence of circular cross-sections with varying diameters is defined. In the simulation, l_cut is dynamically calculated based on the cross-section and the resulting a_cut. This context is also illustrated with Figure 2 in the lower right corner. The advantages of this approach is twofold: On the one hand, it leads to a more realistic definition of the load and, on the other hand, it allows the work progress to be assessed.

2.3 Simplified user modeling

This section explores the potential scope of human influence and the methodologies by which it can be modeled. Overall, users have two options to control the machine. On the one hand, they can set the desired speed of the motor using a potentiometer. The machine will attempt to set the desired speed. On the other hand, they can influence the external load by the force used to press the machine to the work piece surface. The actual speed will be at the torque equilibrium regarding external load and the capabilities of the drive train that might depend on surrounding conditions, in particular the temperature. The type and condition of the wood, as described in 2.2, have an additional significant but uncontrollable influence on the load.

In the work processes of cross-cutting, field cutting, or delimbing, the experienced user operates at a maximum desired speed during normal cutting. In other words, the potentiometer is always set to its maximum. The operating point is only determined by the feed force F_f. This conclusion is supported by user reports.

The goal of this operating strategy is to maximize the work progress and thus achieve maximum cutting performance P_cut. Throughout this paper, the term optimal operating point will refer to the operating point with the maximum cutting performance. The assessment of P_cut during the work process is carried out purely subjectively by the user. Trained users are very good at finding the right operating point and therefore also the point with the best performance. They are also good at keeping the machine stable at this operating point, especially for longer cuts. They primarily use the machine's sound as a reference. Due to the speed and therefore the frequency of the motor and the mechanical drive train, the sound is a good indicator for the

machine's operating point. The optimum operating point must be frequently redetermined, as the sound changes due to various factors, such as the type of wood.

In summary, the users have two primary goals. First, they aim to determine the optimal operating point by evaluating the cutting performance P_{cut}. Second, they need to control the chainsaw to ensure it operates consistently at this optimal point. The aim of this analysis is to evaluate the influence of this user behavior to determine whether a more detailed investigation or modeling of the user is necessary. Consequently, the approach of identifying the optimal operating point by the user is neglected. Instead, two different methods are used to determine the feed force F_f delivered by the user. First, different constants F_f are used directly. Second, the optimum operating point is determined based on knowledge of the machines power characteristic. This parameter is determined analytically beforehand and remains constant throughout the series of following simulation. The desired operating point defined by the chain speed is then reached through the application of a controlled feed force. The control is implemented using a PI controller.

The technique presented is capable of modeling two types of user behavior. The understanding of user group behavior is based on long-term experience accumulated within the company. This empirical knowledge has been developed over an extended period through continuous observation. On the one hand, there is the experienced user who can control the optimal operating point. This is modeled through optimal operating point control. The other group of personas consists of unexperienced users. These users do not manage to use the device in the optimal operating point. Therefore, it is assumed here that the user consistently cuts with either a too high or a too low F_f.

2.4 Simulation results

So far, this section was about how the system is modeled. The following section will discuss simulated results, in order to provide a better understanding of the system. Therefore the chainsaw model described in subsection 2.1 with a full battery charge was used. Furthermore the application model explained in subsection 2.2 was used to model the wood to be cut with a circular cross-section. To show the different cutting behavior, two cross-sections with the diameters $d_1 = 30\,cm$ and $d_2 = 3\,cm$ are simulated. The smaller diameter d_2 is typical of the system's behavior during the process of cutting branches. In contrast, d_1 is typical for the process of felling a tree or the act of cutting it in smaller parts. For the purpose of this analysis, the user was modeled using the controlled feed force. This control system sets the optimal operating point, thereby ensuring the maximum achievable cutting performance P_cut during the cutting process.

Figure 3 shows the motor speed, the feed force F_f and the target speed from the user input over time for these two cutting processes. The motor speed serves as an indicator for the chainsaw's operating point at the respective time. While in Figure 3 a) the cutting process of the piece of wood with diameter d_1 is illustrated, Figure 3 b) shows the cutting process for the other piece with diameter d_2.

As seen in Figure 3, during the first phase P.1, the chainsaw accelerates to the target speed. In

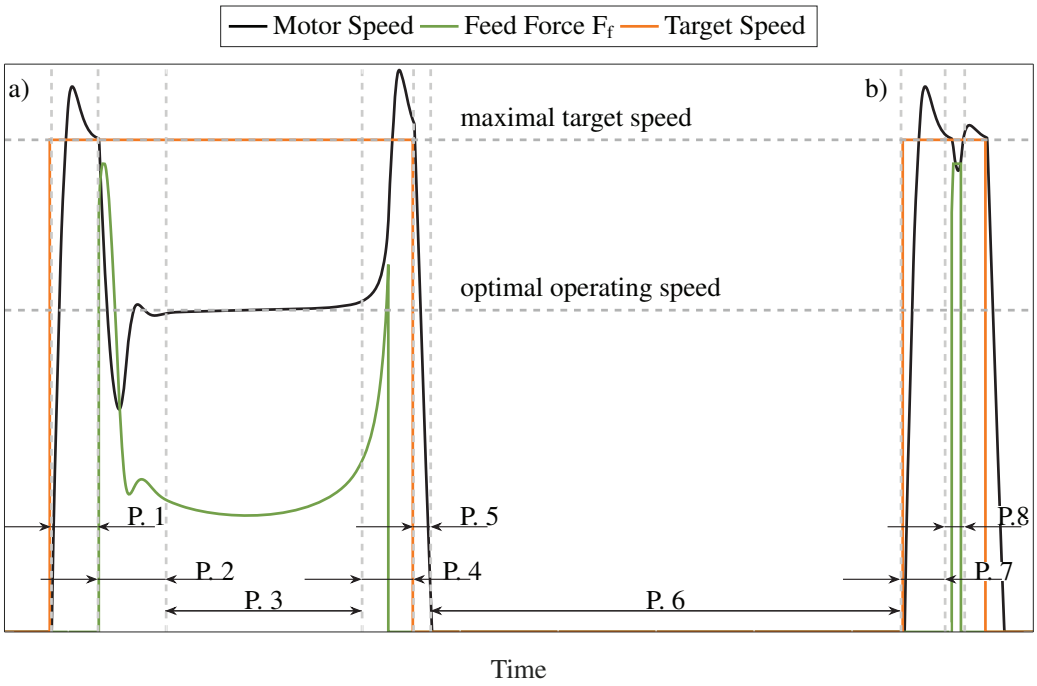

Figure 3: Typical speed profiles of the motor during the cutting process with a diameter of a) $d_1 = 30\,cm$ and b) $d_2 = 3\,cm$.

this case, it is the maximum speed that can be set. Subsequently the cutting process commences to the acceleration process. First, the user model starts by applying the feed force F_f. Consequently, as the feed force F_f and the load increase, the speed decreases. The speed reduction and the adjustment of the optimal operating point take place in phase P.2.

As shown in phase P.3, once the desired operating point is reached, the wood is constantly cut at this operating point. As the engagement length l_cut changes continuously due to the circular cross-section, the feed force applied here must also change continuously. This is the only way to achieve a constant operating point, as demonstrated in P.3.

The end of the cutting process is described in phase P.4. This phase is initialized by the almost completely cut cross-section. Towards the end, the feed force F_f is increased due to the controlled user in order to keep the cutting performance P_cut constant. After finishing the cut of the cross-section, the force is removed from the system. The behavior exhibited at the termination of the cut is attributable to the prevailing user model, which has not yet been adapted. The decreased in load follows an increase in motor speed back to the maximum target speed.

P.5 and P.6 show, due to the end of the cutting process, that the chainsaw is halted because of the absence of a desired target speed set by the user. In the simulation framework, the break time t_break is used to represent the duration of P.6. This time is of particular importance when

considering the temperature of the chainsaw.

Figure 3 b) illustrates the system characteristics of the cutting process of a branch. As expected, the chainsaw acceleration in P.7 is the same as in P.1. While the user model successfully adjusted the desired operating point in P.2, the desired operating point was not reached in P.8. The time in the cutting process is too short and the inertia of the drive train too high to reach the optimal operating point. This behavior is consistent with the findings in real applications.

3 EXPERIMENTS

A set of virtual experiments was specified with the two different user models and different parameters of the models. The reference for later benchmarks used in this study is a predefined load cycle. This cycle includes five cross-cuts of a tree with a trunk diameter of $d_{\mathrm{trunk}} = 30cm$. This is followed by twenty branches, which are simplified to have a round cross-section of $d_{\mathrm{branch}} = 3\,cm$. A break of $t_{\mathrm{break,trunk}} = 10\,s$ is defined between the trunk cuts, and $t_{\mathrm{break,branch}} = 5\,s$ between the branches. During the breaks $t_{\mathrm{break,trunk}}$ and $t_{\mathrm{break,branch}}$, the machine is turned off. Before each cut, the chainsaw is first accelerated to its maximum speed. One second after successful acceleration, the cutting process of the wood cross-section defined by the cycle begins. In order to identify the battery runtime, the simulation keeps running as many load cycles as needed to drain a fully charged battery. The influence of the user is evaluated using the runtime of the battery, the cut area a_{cut}, the cutting performance P_{cut}, and the energy losses of the device. These losses consist of the losses of the battery, the electronics, and the motor. Furthermore the losses of the mechanical drive train are accounted by the power consumption of the fan impeller, and the friction power of the cutting attachment in a load-free state. There is no straightforward method to measure the additional friction losses under load. Therefore, any load-dependent changes are not included when discussing losses in this study. The results are visualized as a percentage difference compared to a reference simulation. The reference simulation uses the aforementioned load cycle and a trained user, who approaches the optimal operating point by the controlled feed force F_{f}. In the previous section, we established that the operating point with the maximum cutting performance is referred to as the optimal operating point.

3.1 User impact

To evaluate the user impact, different types of user control behavior were considered. In addition to the controlled feed force F_{f} for the optimal operating point, three cases with a constant force were compared.

The upper part of Figure 4 shows the development of the speed over time. This demonstrates how the different user models, in combination with the load definition, affect the speed results. While the speed remained constant over a cut when the controlled optimal operating point was approached, it decreased in conjunction with a constant F_{f}. The round cross-section, as delineated in the model, constitutes the underlying rational for this phenomenon. As a result, the engagement length of the bar in the wood changes continuously. With increasing engagement

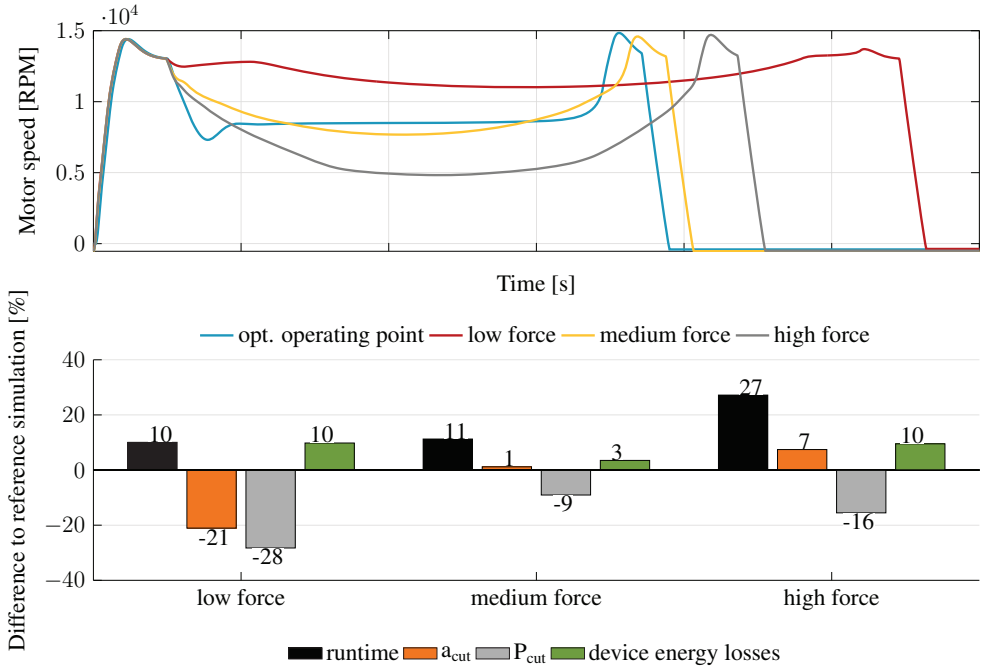

Figure 4: The speed profiles of the motor during the cutting process. Differences in performance indicators relating to the reference simulation with the optimal operating point.

length, the load on the machine also increases resulting in a different operating point and a reduction of the speed.

The lower part of Figure 4 reveals how performance parameters change when the applied feed force does not lead to an operation in the optimal operating point. Overall, it can be seen that on the one hand, the battery run time is shortest due to the high force. On the other hand, the cut area is smallest due to the low force and largest due to the high force. For the reference with the optimal operating point and medium force, the cut area is similar. However, considering the cutting performance P_{cut} being the cut area relative to the cut time, it is apparent that it is the highest for the case with the optimal operating point. This illustrates the aim of the system design optimizing work progress per unit time and confirms that the optimal operating point considering P_{cut} was indeed achieved in the cycle with the user model. If a high force is applied, the machine is operated at a low speed. In this operating point, the device reduced the maximum allowed power. Consequently, the time required for the battery to reach a state of complete discharge will be increased. However, in comparison the cut area a_{cut} increases significantly slower for this operating point. This results in a 16% reduction in cutting performance P_{cut}. Both the cut area and the losses in the device have increased for this user behavior. Although higher losses reduced the available energy for the cutting process, a larger area was still cut. This indicates a higher cutting efficiency at the collective operating point with a consistently

high applied force. Here, efficiency is defined as the ratio of the cut area to the energy input, suggesting that the cutting process becomes more efficient under these conditions.

An additional operating range for an unexperienced user is represented by high speeds with low feed forces. Here, the high speeds result in speed-dependent losses taking up a significantly larger proportion. As a result, this operating range has a longer battery runtime, the cut area is reduced by 21%, following less work is done with more time. As anticipated, this also results in a noticeable decrease in cutting performance, with a total reduction of 28%.

4 CONCLUSION

An approach was presented that can be used to evaluate various influences within the human, machine, and application system in the context of hand-held devices. This approach is also useful for determining important components of the Product Carbon Footprint (PCF) of power tools according to [12] at an early stage. The study has shown that factors influencing the operating point have a significant impact on run time and cutting results. While the machine configuration, such as the motor characteristic curve, the transmission ratio, and the efficiency of the components, can be specified by the manufacturer, its use in practice cannot be controlled, but has a significant influence on the run time and the output. Differences in run time of up to 27% were observed, and cutting results varied by 28%. Depending on the boundary condition of the application, there are different goals. In some cases, the primary objective is the maximization of the cut area, while in others, the focus is on optimizing the cutting performance, i.e. cut area per unit time. The proposed approach can now be utilized to design and optimize new products. The focus here is on an efficient and customer-oriented drive train. However, the modeling of the user has so far been idealized, without considering the influences and behavior of a human. Due to the significant impact, it is recommended to model the behavior more accurately, which will be subject so future studies.

ACKNOWLEDGMENTS

This work has been partly supported by the COMET-K2 Center of the Linz Center of Mechatronics (LCM) funded by the Austrian federal government and the federal state of Upper Austria.

REFERENCES

[1] S. Matthiesen, S. Mangold, T. Bruchmüller, and A.-M. Marko, “The human being as central subsystem in interaction with handheld devices - a problem-oriented approach for the investigation of this interface,” 2014, Conference paper, p. 193 – 204. [Online]. Available: https://publikationen.bibliothek.kit.edu/1000056722

[2] S. Matthiesen, S. Mangold, and T. Bruchmüller, “The influence of variating passive user interactions on power tools in the context of product development,” *Forschung im Ingenieurwesen*, vol. 82, p. 157–168, 06 2018.

[3] M. Uhl, J. H. Robens, M. Gauch, T. Gwosch, and S. Matthiesen, "Does the user behavior effect the productivity of hammer drilling? – analysis of the influences of feed and lateral force," *International Journal of Industrial Ergonomics*, vol. 94, p. 103400, 2023. [Online]. Available: https://www.sciencedirect.com/science/article/pii/S016981412200141X

[4] S. Zimprich, F. Matter, J. Reiser, J. H. Robens, and S. Matthiesen, "The effect of feed force on vibration and productivity in hammer drilling: A machine-independent analysis excluding the effect of motor speed reduction," *International Journal of Industrial Ergonomics*, vol. 98, p. 103524, 2023. [Online]. Available: https://www.sciencedirect.com/science/article/pii/S0169814123001166

[5] T. Krenke, S. Frömel-Frybort, A. Martinez-Conde, and U. Müller, "Internationaler stand zur schnittkraftuntersuchung bei holz - teil 3," *Holztechnologie*, vol. 56, pp. 43–50, 01 2015.

[6] C. Gottlöber, *Cutting and Disintegration of Wood and Wood-Based Materials*. Cham: Springer International Publishing, 2023, pp. 595–677. [Online]. Available: https://doi.org/10.1007/978-3-030-81315-4_12

[7] F. H. Ondrej Dvoracek, Daniel Lechowicz and S. Frybort, "Cutting force analysis of oak for the development of a cutting force model," *Wood Material Science & Engineering*, vol. 17, no. 6, pp. 771–782, 2022. [Online]. Available: https://doi.org/10.1080/17480272.2021.1955296

[8] M. Mulder, D. Pool, D. Abbink, E. Boer, and M. van Paassen, "Fundamental issues in manual control cybernetics," *IFAC-PapersOnLine*, vol. 49, no. 19, pp. 1–6, 2016, 13th IFAC Symposium on Analysis, Design, and Evaluation ofHuman-Machine Systems HMS 2016. [Online]. Available: https://www.sciencedirect.com/science/article/pii/S240589631632016X

[9] M. Mabrok, H. Mohamed, A.-H. Abdel-Aty, and A. Alzahrani, "Human models in human-in-the-loop control systems," *Journal of Intelligent and Fuzzy Systems*, vol. 38, pp. 1–12, 12 2019.

[10] "Akku-Kettensäge MSA 300 - AP-System," www.stihl.de.https://www.stihl.de/de/p/kettensaegen-motorsaegen-akku-kettensaege-msa-300-ap-system-144339, accessed: 2025-03-04.

[11] H. Dr Roßkamp, G. Liebhard, and R. Wichert, "Work device with an electric drive motor: European Patent Office," Patent EP 2 438 808 B1, 2012.

[12] *DIN SPEC 91519 Preparation of an Product Carbon Footprint (PCF) for Power Tools*, 2024.

XI ECCOMAS Thematic Conference on Smart Structures and Materials - SMART 2025
M. Krommer, M. Nader and M. Schagerl (Eds)

Received: 21 April 2025 / Revised: 29 August 2025 / Accepted: 11 October 2025
© The Author(s) 2025

Performance Evaluation of MS-SLAM in Indoor Environments

Daniel Louback S. Lubanco, Ahmed Hashem, Markus Pichler-Scheder, Thomas Schlechter, Reinhard Feger, Andreas Stelzer

Abstract. The wish to achieve more efficient, effective, and sustainable industrial processes has led to an increasing number of mobile robots which seek to autonomously operate in these environments. In order to successfully perform their tasks, e.g., intralogistics of warehouses, these autonomous agents require a highly accurate comprehension of their surroundings. Consequently, exteroceptive sensors are necessary for enabling autonomous mobile robots in industrial settings. Among many sensors that are capable of perceiving the environment, radar stands out because of its robustness to harsh environments, long-range capabilities and energy efficiency. In this work, we evaluate the performance of the multiple input multiple output synthetic aperture radar simultaneous localization and mapping (MS-SLAM) algorithm in indoor conditions. We demonstrate that the MS-SLAM algorithm can be employed in indoor industrial environments, thus enabling mobile robots to perform self-localization, to create a map of the environments, and to navigate autonomously.

Key words: Radar, SLAM, Autonomous Robots

1 INTRODUCTION

Intelligent robots are pivotal components for enabling smart manufacturing [1]. For example, highly autonomous mobile robots in industrial environments, e.g., autonomous guided vehicles (AGVs), enable highly efficient management of inventory and intra-logistics. In order for AGVs to safely, efficiently and effectively move between different places in their working

Daniel Louback S. Lubanco & Thomas Schlechter
University of Applied Sciences Upper Austria, Stelzhamerstr. 23, 4600 Wels, Austria
e-mail: lubanco@ieee.org,thomas.schlechter@ieee.org

Ahmed Hashem & Reinhard Feger & Andreas Stelzer
Institute for Communications Engineering and RF Systems, Johannes Kepler University Altenbergerstr. 69, 4040 Linz, Austria
e-mail: Ahmed.Hashem@jku.at,Reinhard.Feger@jku.at,Andreas.Stelzer@jku.at

Markus Pichler-Scheder
Linz Center of Mechatronics, Altenbergerstr. 69, 4040 Linz, Austria
e-mail: markus.pichler-scheder@lcm.at

environment, it is necessary that they have a reliable representation of their environment as well as an estimation of their localization within that environment.

Consequently, it is necessary to equip AGVs with sensor(s) which can permit mapping and localization. Amid the possible sensors that could enable that, radars are particular attractive to industrial environments due to, e.g., their robustness against harsh environments.

The employment of radars for mapping and localization has been an active topic of research and development [2, 3, 4, 5, 6, 7, 8, 9]. In [4], the multiple input multiple output synthetic aperture radar simultaneous localization and mapping (MS-SLAM) algorithm was proposed. The MS-SLAM algorithm is capable of generating multiple input multiple output (MIMO) synthetic aperture radar (SAR) [10] images of the environment using only radar data and through that performs simultaneous localization and mapping (SLAM).

Whereas in [4] all the evaluations of the MS-SLAM algorithms were performed outdoors, in this paper we perform a qualitative evaluation of the MS-SLAM algorithm in an indoor industrial-like environment. This poses different characteristics for the MIMO-SAR generated image used in the SLAM algorithm when compared to an outdoor environment. When compared to outdoor environments, indoor environments typically consists of MIMO-SAR images with: (1) higher density of strong reflectors due to the large number of metallic components, and higher occlusion levels which can lead to MIMO-SAR images with scarcity of targets in the radar far-field.

This paper is organized as follows: in Section 2 a concise introduction to the MS-SLAM algorithm is provided, followed by an evaluation of the MS-SLAM algorithm in an indoor environment in Section 3. Finally, in Section 4, a conclusion is provided.

2 MS-SLAM

The MS-SLAM algorithm performs SLAM through the pose-graph approach [11]. In this approach, the trajectory of the vehicle is calculated by optimizing a graph in which the nodes are the unknown poses (i.e., the position and orientation) and the edges between the nodes are the constraints (i.e., the estimated relative pose between the nodes). In the context of SLAM, there are at least two types of constraints: (1) odometry constraints and (2) loop-closure constraints.

The steps performed by the MS-SLAM algorithm are:

- estimating ego-velocity through using targets position and radial rate;
- generating a MIMO-SAR image of the environment;
- generating odometry constraints:
  - estimating translation using a robust ego-velocity estimator;
  - estimating rotation using the Radon transformed spectra of pairs of MIMO-SAR images.
- generating loop-closure constraints through the robust Radon radar place-recognition (R^3PR) algorithm;

- optimizing the trajectory using a pose-graph solver, e.g., GTSAM [12];
- generating a map of the traversed region by using the estimated poses and summing the MIMO-SAR images.

The pivotal advantages of MS-SLAM compared to other radar-based SLAM algorithms include:

1. a robust estimator for ego-velocity;
2. radar-only approach for generating MIMO-SAR images;
3. a robust rotation estimator as well as place-recognition algorithm based on the Radon transformed spectra of MIMO-SAR images.

A detailed explanation of each part of the MS-SLAM algorithm as well as thorough evaluation of MS-SLAM with other radar-based SLAM algorithms can be found in [4].

3 EVALUATION



Figure 1: Robotic platform used in our evaluation.

We evaluated the MS-SLAM algorithm by equipping a Clearpath Husky mobile platform with a forward-looking MIMO FMCW radar produced by Inras GmbH. In Figure 1, the robotic platform used in our experiments can be seen. The radar used in our evaluation used 4 transmitter antennas, 16 receiver antennas, center frequency of $77\,\mathrm{GHz}$, bandwidth of $1\,\mathrm{GHz}$, and

maximum unambiguous range of $74.88\,\mathrm{m}$. The mobile robot was remotely controlled and traversed an indoor environment surrounded by industrial machines, e.g., granulate dryers, injection molding machine, and extruder, as well as typical warehouse components, e.g., storage shelves and forklift. Two sequences were acquired in this environment:

- Short: it consisted of traversing a relatively small area with a similar trajectory over 3 loops.
- Long: it consisted of covering a large portion of the available drivable area (which included the region covered in the Short sequence); there was a non-uniform amount of loops, e.g., some regions were visited 2 times, while others were visited 3 times.

The estimated trajectories and maps generated by the MS-SLAM algorithm in the Short and Long sequences can be seen in Figure 2 and 3 respectively. The trajectories, as well as the information of the obstacles in the map agree with the driven trajectory and with the dimensions of the objects within the traversed region. Moreover, in Fig. 3, it is possible to compare some regions in the map with their corresponding optical images. For example, the area which the injection molding machine was located is annotated as "1".

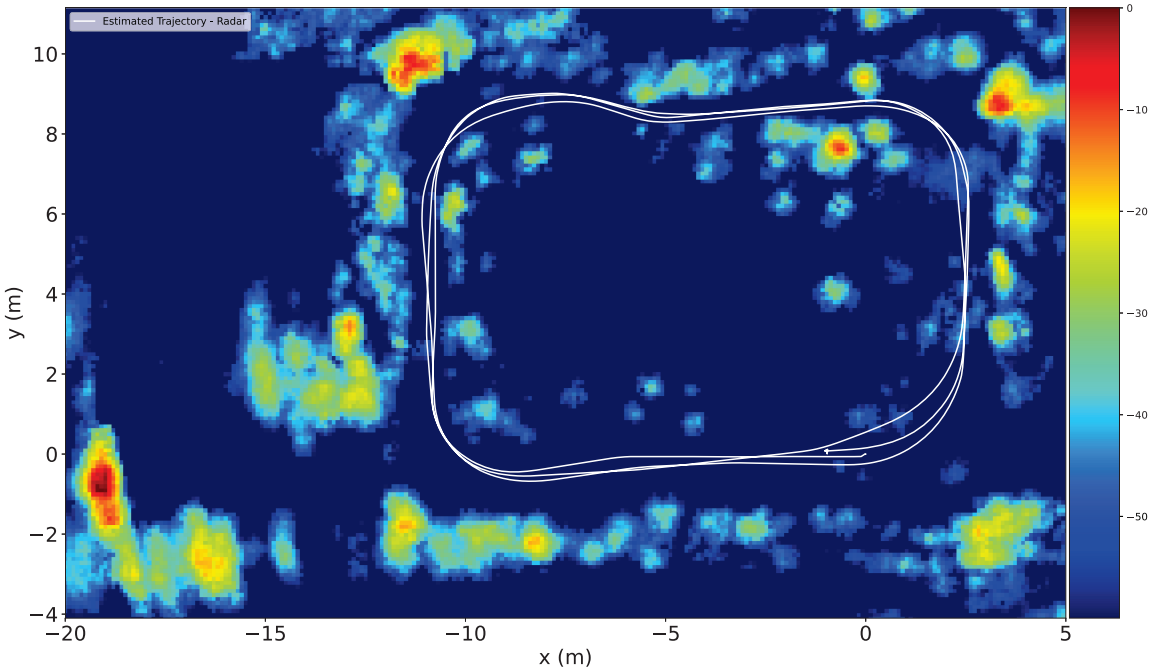

Figure 2: Estimated trajectory and generated map in the Short sequence. The MIMO-SAR map is normalized to the maximum power and in decibels.

4 CONCLUSION

In this paper we demonstrated that the MS-SLAM algorithm can also be employed in indoor industrial environments. Consequently, especially in industrial harsh environments, the MS-SLAM algorithm can be a radar-based SLAM solution for facilitating highly autonomous tasks in smart manufacturing.

5 ACKNOWLEDGMENTS

This work has been supported by the COMET-K2 Center of the Linz Center of Mechatronics (LCM) funded by the Austrian federal government and the federal state of Upper Austria.

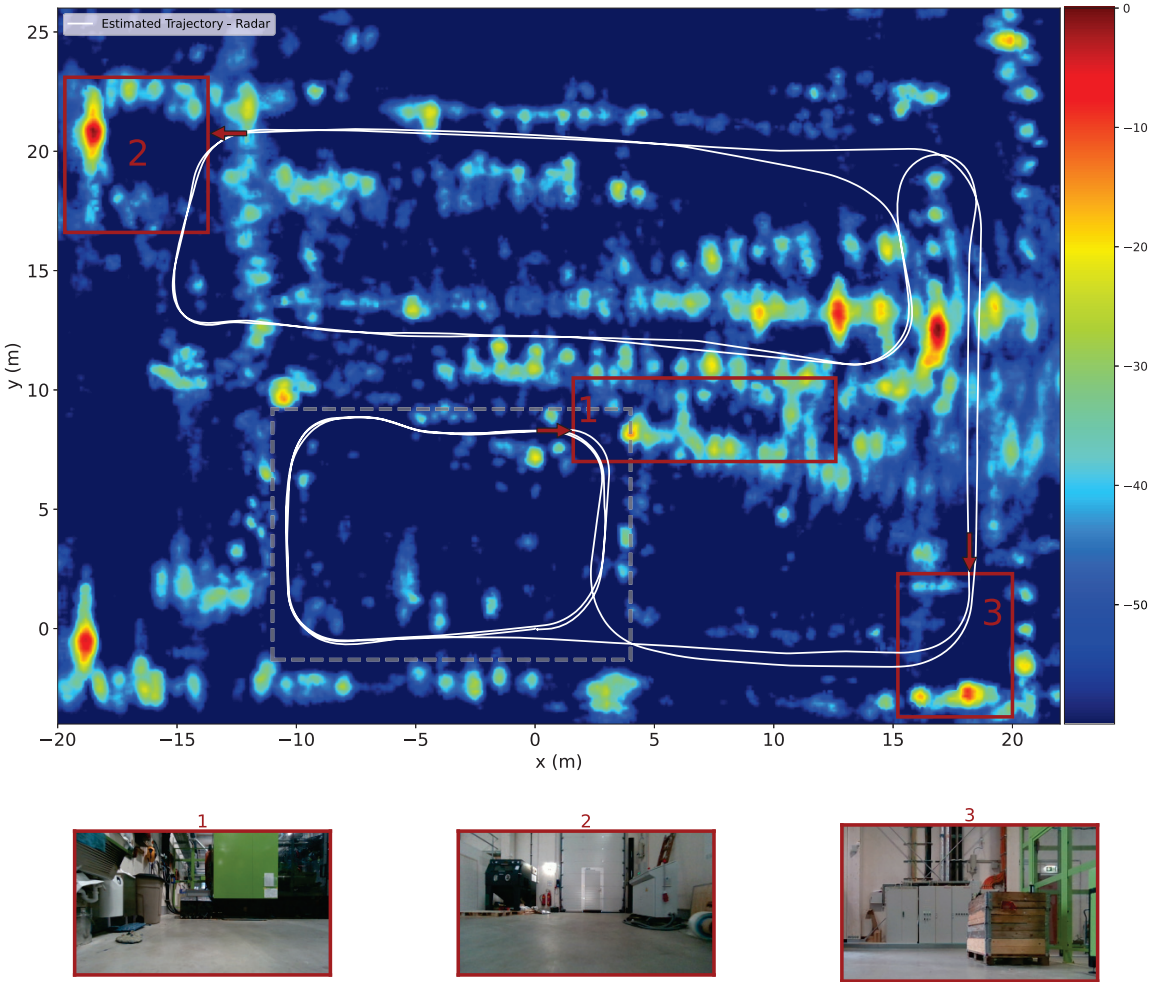

Figure 3: Estimated trajectory and generated map in the Long sequence with annotations. The region inside the gray dashed rectangle corresponds to the region also covered in the Short sequence. The arrows indicate from where the optical images were taken. The MIMO-SAR map is normalized to the maximum power and in decibels.

REFERENCES

[1] M. Soori, R. Dastres, B. Arezoo, and F. Karimi Ghaleh Jough, "Intelligent robotic systems in Industry 4.0: A review," *Journal of Advanced Manufacturing Science and Technology*, pp. 2 024 007 – 0, 2024. [Online]. Available: https://hal.science/hal-04439263

[2] D. Louback da Silva Lubanco, T. Schlechter, M. Pichler-Scheder, and C. Kastl, "Survey on radar odometry," in *Computer Aided Systems Theory – EUROCAST 2022*, R. Moreno-Díaz, F. Pichler, and A. Quesada-Arencibia, Eds. Cham: Springer Nature Switzerland, 2022, pp. 619–625.

[3] D. L. S. Lubanco, A. Hashem, M. Pichler-Scheder, A. Stelzer, R. Feger, and T. Schlechter, "R3o: Robust radon radar odometry," *IEEE Transactions on Intelligent Vehicles*, vol. 9, no. 1, pp. 231–246, 2024.

[4] D. L. S. Lubanco, A. Hashem, M. Pichler-Scheder, T. Schlechter, R. Feger, and A. Stelzer, "Ms-slam: Multiple input multiple output synthetic aperture radar simultaneous localization and mapping," *IEEE Transactions on Intelligent Vehicles*, pp. 1–20, 2024.

[5] ——, "Spatial-radon and doppler aggregated radar odometry," in *2024 21st European Radar Conference (EuRAD)*, 2024, pp. 344–346.

[6] Y. Almalioglu, M. Turan, C. X. Lu, N. Trigoni, and A. Markham, "Milli-rio: Ego-motion estimation with low-cost millimetre-wave radar," *IEEE Sensors Journal*, vol. 21, no. 3, pp. 3314–3323, 2021.

[7] T. Grebner, R. Riekenbrauck, and C. Waldschmidt, "Simultaneous localization and mapping (slam) for synthetic aperture radar (sar) processing in the field of autonomous driving," *IEEE Transactions on Radar Systems*, vol. 2, pp. 47–66, 2024.

[8] D. C. Herraez, M. Zeller, L. Chang, I. Vizzo, M. Heidingsfeld, and C. Stachniss, "Radar-only odometry and mapping for autonomous vehicles," in *2024 IEEE International Conference on Robotics and Automation (ICRA)*, 2024, pp. 10 275–10 282.

[9] Y. E. Ritterbusch, J. Fink, and C. Waldschmidt, "Simultaneous localization and mapping for indoor mobile robots using synthetic aperture radar images," *IEEE Journal of Indoor and Seamless Positioning and Navigation*, vol. 3, pp. 1–12, 2025.

[10] M. Farhadi, R. Feger, J. Fink, T. Wagner, and A. Stelzer, "Combining mimo dbf with automotive synthetic aperture radar imaging and phase error correction," *IEEE Access*, vol. 12, pp. 31 944–31 959, 2024.

[11] G. Grisetti, R. Kümmerle, C. Stachniss, and W. Burgard, "A tutorial on graph-based slam," *IEEE Intelligent Transportation Systems Magazine*, vol. 2, no. 4, pp. 31–43, 2010.

[12] F. Dellaert and G. Contributors, "borglab/gtsam," May 2022.

XI ECCOMAS Thematic Conference on Smart Structures and Materials - SMART 2025
M. Krommer, M. Nader and M. Schagerl (Eds)

Received: 29 April 2025 / Revised: 31 August 2025 / Accepted: 11 October 2025
© The Author(s) 2025

A Comprehensive Review of Prior Art in Bearingless Induction Machine - Part I: Control

Stefan Mallinger, Wolfgang Gruber

Abstract. This paper aims to provide a comprehensive overview of the state of the art in control of bearingless induction machines through a literature review, with the goal of enabling researchers in this field to develop a good overview. This is urgently needed, because the last review of bearingless induction machine research was given back in 2014 [1], and in the meantime, significant improvements in design [2], [3] and control of bearingless induction machines were reported. The actual overview of the technological developments will be provided directly through a diligent review of available publications in this field. The prior art is categorized in two main parts: control (part I) and topology (part II) of bearingless induction machines. Here the various control strategies will be categorized and compated. Most promising control strategies are described in detail.

Key words: bearingless machine, induction machine, bearingless induction machine, active magnetic bearings, controllers, control strategies

1 INTRODUCTION

Based on the concept of magnetic bearings first introduced by Hermann in 1973 [4], the technology of bearingless machines is first proposed in 1988 by Bosch [5]. Since then many different machine topologies have been implemented in a bearingless configuration. In 1991 the first paper of an induction machine has been published by Chiba [6]. Therein, Chiba first describes the operating principles of a bearingless induction machine (BIM). This and following papers determined general advantages of BIMs over permanent magnet excited synchronous machines (PMSM)

- robustness (BIMs are more robust, due to their simpler construction)
- lower maintenance (BIMs need less maintenance due to the lack of mechanical bearings)
- lower cost (easier manufacturing, due to lack of permanent magnets (PMs))

and disadvantages over PMSM

Stefan Mallinger & Wolfgang Gruber
Institute of Electric Drives and Power Electronics, Johannes Kepler University Linz Altenbergerstr. 69, A-4040 Linz, Austria,
e-mail: stefan.mallinger@jku.at

- efficiency (BIMs have a lower efficiency, especially at lower speeds, because the air-gap field needs to be be excited by induced rotor currents, and not PMs)
- control complexity (BIMs with a rotor cage have a control lag because a part of the current in the two-pole radial position control windings is induced into the rotor squirrel cage windings. The radial force is produced by an unbalanced four-pole symmetrical revolving magnetic field with currents of the two-pole windings. Therefore, actual radial force is less than the radial force command, it has a phase delay.)

of BIMs.

This paper is based on an literature study of *IEEE Xplore*® [1] as well as the *magneticbearings.org* [2] database. In preparation for this paper, a total of 115 papers were reviewed, of which 65 were related to the topic of bearingless induction machine control. The content of these papers will be analyzed in this work, while 50 topology related papers will be discussed in the second part of this paper series [7].

The chronological order of the analyzed papers is shown in Fig. 1. Furthermore control themed papers of Fig. 1 are chronologically and thematically sorted in Tab. 1.

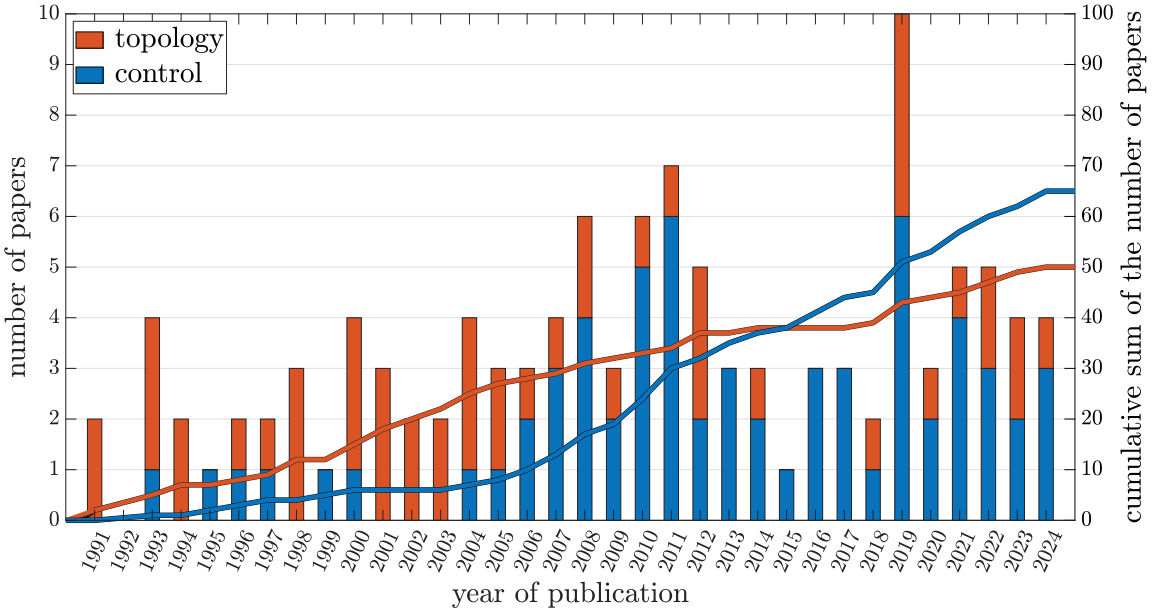

Figure 1: Reviewed papers about bearingless asynchronous machines, categorized by publication year and main subject area: motor control (blue) or topology (red)

[1] https://ieeexplore.ieee.org
[2] https://www.magneticbearings.org

Table 1: Considered papers about control organized by their year of publication, color coded regarding their main control methods and marked for their winding design

(a) Years 1993 - 2010

Year	Papers
1993	[8]
1995	[9]
1996	[10]
1997	[11]
1999	[12]
2000	[13]
2004	[14]
2005	[15]
2006	[16], [17]
2007	[18], [19], [20]
2008	[21], [22], [23], [24]
2009	[25], [26]
2010	[27], [28], [29], [30], [31]

(b) Years 2011 - 2024

Year	Papers
2011	[32], [33], [34], [35], [36], [37]
2012	[38], [39]
2013	[40], [41], [42]
2014	[43], [44]
2015	[45]
2016	[46], [47], [48]
2017	[49], [50], [51]
2018	[52]
2019	[53], [54], [55], [56], [57], [58]
2020	[59], [60]
2021	[61], [62], [63], [64]
2022	[65], [66], [67]
2023	[68], [69]
2024	[70], [71], [72]

(c) Colorcode: color of reference number is main topic, background color is supplementary topic

Color	Nr. of papers	Control method
	8	control related topics
	17	PID control
	8	space vector modulation (SVM)
	4	direct torque control (DTC)
	4	sliding mode observer (SMO)
	3	sensorless control
	8	active disturbance rejection control (ADRC)
	13	air-gap or rotor-flux oriented control (AGFOC or RFOC)
	4	dynamic model and system decoupling control strategies
	3	fuzzy control (FC)
	7	neural network control

(d) Framecode for references

Frame	Nr. of papers	Winding Design
	55	Additional Levitation Winding
	10	Split Winding

2 WINDING DESIGN

There are basically three types of BIM for which control papers have been published. First, a conventional induction machine (IM) with an additional winding to produce levitation forces, which in essence results in a separated winding BIM (papers with this winding type are marked in Tab. 1 with a dashed rectangle). Second, conventional IM with split winding approach, where the phases are split to generate three additional phases (papers with this winding type are marked in Tab. 1 with a black rectangle). And third, multiphase or combined winding BIM exist. As theses are typically presented in combination with new rotor-cage topologies or stator winding schemes, the BIMs with multiphase windings are considered in the second paper of this series.

3 CONTROL RELATED TOPICS

In this category all papers are collected which deal with control related topics but not the motor and bearing control itself. Topics are improved rotor resistance identification [21], vibration suppression [22], [70] or elimination of PWM harmonics for noise reduction [35], [38]. Further topics which are categorized herein are the effect of rotor control on the overall motor efficiency [44], an improved mathematical model for the BIM [72] or a review paper for control methods applied to BIMs with split windings [41].

4 PID CONTROL

First BIMs used the proportional-integral-derivative (PID) controller [8]. These controllers are typically used to control bearing forces and motor speed [11], [15], [67]. Additionally it is also used in subordinate current controllers to impress phase currents in the motor-windings, if only voltage source inverters are available [27], [29], [68].

5 SPACE VECTOR MODULATION

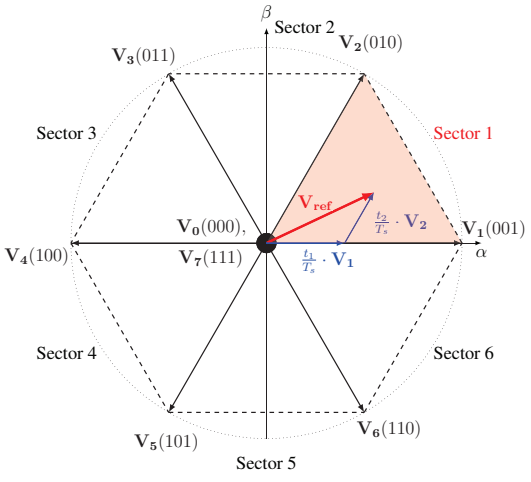

Figure 2: SVM principle with voltages states. Brackets: half-bridge state in binary

Space Vector Modulation (SVM) is a widely used technique in power electronics for controlling three-phase inverters [56]. It aims to generate sinusoidal waveforms for phase voltage and current in a three-phase system, achieving reduced harmonic distortion and higher efficiency. Unlike conventional methods that treat the phases independently, SVM considers the three-phase inverter as a single unit. This methodology represents the three-phase voltages as a rotating vector within a two-dimensional plane, commonly referred to as the $\alpha\beta$-plane. The operation of SVM is based on approximating a desired reference vector $\mathbf{V_{ref}}$, which rotates within the hexagonal boundary of the two-dimensional space. The inverter generates

eight discrete switching states—six active and two zero states [37]. Depending on the location of $\mathbf{V_{ref}}$ within the hexagonal sectors, as shown in Fig. 2, it is decomposed from two adjacent active vectors and, if required, one or two zero vectors. The inverter switches between these states during each control cycle, with the time spent in each state being proportional to the proximity of $\mathbf{V_{ref}}$ to the active vectors. By rapidly switching, SVM synthesizes a smooth, sinusoidal output, while also optimizing the utilization of the DC supply voltage. This principle is used in combination with other control methods in BIMs [28], [30], [37], [53], [57] to drive the inverters of the power electronics.

6 DIRECT TORQUE CONTROL

Typically used in combination with SVM [28], [30], [37]. The operation of direct torque control space vector modulation (DTC-SVM) begins with the estimation of the motor's torque and stator flux, based on voltage and current measurements. These parameters are compared with the desired reference values for torque and flux, and the resulting errors are processed by the controllers. The outputs of these controllers generate the reference voltage vector $\mathbf{V_{ref}}$, which represents the desired state of the motor in terms of torque and flux. Once $\mathbf{V_{ref}}$ is determined, SVM is used to generate the appropriate switching signals for the inverter [58].

7 SLIDING MODE OBSERVER

A Sliding Mode Observer (SMO) is an estimation technique widely employed in dynamic systems for determining unmeasured state variables, such as rotor position or speed [52] in electric machines, especially under conditions involving disturbances and uncertainties. It is recognized for its robustness against system parameter variations, external noise, and modeling inaccuracies, making it well-suited for demanding applications. The design of the SMO is based on the principles of sliding mode control, which utilizes a discontinuous estimation term to drive the error between actual system and observer model to zero [49], [51].

8 SENSORLESS

In this category the few papers are collected, which try to partially control the BIM without rotor angle or speed sensors. The only approach tried in practical implementation [42], [50], [72] was controlling the speed of the BIM without sensors.

9 ACTIVE DISTURBANCE REJECTION CONTROL

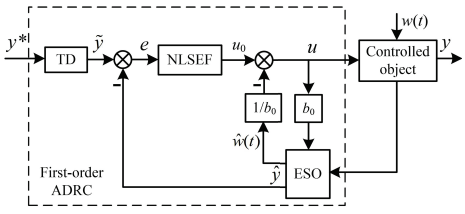

Figure 3: Structure of a ADRC, Source: [60]

Active Disturbance Rejection Control (ADRC) is a method that compensates for disturbances and uncertainties in dynamic systems in real time. Unlike traditional methods relying on precise models, ADRC treats unknown dynamics and external disturbances as generalized disturbances [60], [63], [64]. These are estimated and canceled, ensuring desired performance de-

spite modeling inaccuracies or external perturbations. An ADRC as shown in Fig. 3 uses three components: a tracking differentiator (TD) for smooth reference signals, an extended state observer (ESO) to estimate unmeasured states and disturbances, and a nonlinear state error feedback (NLSEF) to compensate for these disturbances, isolating the system from their effects [58], [65], [66], [69].

10 AIR-GAP OR ROTOR-FLUX ORIENTED CONTROL

Rotor-flux or air-gap oriented control are motor control methods that decouples torque and flux components in the rotor or air-gap reference frame, enabling control similar to DC machines [13], [29], [71]. By aligning the reference frame with the rotor or air-gap flux vector, stator currents are transformed into components that independently regulate flux (direct-axis) and torque (quadrature-axis). Rotor or air-gap flux estimation uses stator voltages, currents, and rotor speed, allowing precise and dynamic control through this decoupling [36], [43].

11 DYNAMIC MODEL AND SYSTEM DECOUPLING CONTROL STRATEGIES

In this category improved dynamic models of the BIM [67] and different methods to decouple the torque and bearing control with α-th order inverse system theory [17], neural network inverse systems [26] or with least squares SVM inverse system theory [53].

12 FUZZY CONTROL

Fuzzy control uses fuzzy logic to handle imprecise, uncertain, or vague information. Unlike traditional control systems that rely on precise mathematical models, fuzzy control mimics human reasoning by using linguistic rules and approximate values to make control decisions [54]. It operates by defining a set of ”if-then” rules based on expert knowledge, where inputs and outputs are represented as fuzzy sets with degrees of membership [40]. These rules are then processed to determine the appropriate control actions. Fuzzy control is particularly useful in complex systems, where precise modeling is difficult [65].

13 NEURAL NETWORK CONTROL

Neural network control uses artificial neural networks to model and manage the behavior of dynamic systems. Neural networks are computational models inspired by the structure and functionality of the human brain, consisting of interconnected layers of nodes (neurons) that process information [24], [25], [40]. In control applications, neural networks are trained using data to approximate the relationship between inputs and outputs of a system, enabling them to learn and adapt to complex, nonlinear, or time-varying dynamics. This approach is particularly effective in situations, where traditional control methods struggle due to the lack of an accurate mathematical model or the presence of uncertainties [42], [45], [46].

14 CONCLUSION AND OUTLOOK

A total of 65 papers on the control of BIMs were reviewed and categorized into various control techniques. Furthermore, this paper highlights recent advancements in BIMs, such

as the use of ADRC to achieve even better control properties, including reduced overshoot, smaller deflections in response to disturbances, and decreased vibrations in the stable rotor [58], [64], [66], [69]. Additionally, progress has been demonstrated in the field of field-oriented controllers, such as the complete decoupling of torque generation and bearing functions for BIMs with squirrel-cage rotors [47], as well as for BIMs with pole-specific rotors cages [71].

Looking forward, the field holds significant potential for innovation, especially in regards to sensorless position control. Future research needs to focus on enhancing efficiency through advanced control strategies and leveraging machine learning or AI techniques, such as neural networks, to enable adaptive and angle sensorless control. Addressing these challenges will drive the development of BIMs and facilitate their adoption in industrial applications.

ACKNOWLEDGMENT

The authors would like to thank R-PODID - Reliable Powerdown for Industrial Drives and for providing essential resources and support.

R-PODID is supported by the Chips Joint Undertaking and its members, including the top-up funding by National Authorities of Italy, Turkey, Portugal, The Netherlands, Czech Republic, Latvia, Greece, and Romania under grant agreement n° 101112338.

References

[1] X. Sun, L. Chen, and Z. Yang, "Overview of Bearingless Induction Motors," *Mathematical Problems in Engineering*, vol. 2014, no. 1, pp. 1–10, 2014.

[2] J. Chen, Y. Fujii, M. W. Johnson, A. Farhan, and E. L. Severson, "Optimal Design of the Bearingless Induction Motor," *IEEE Transactions on Industry Applications*, vol. 57, no. 2, pp. 1375–1388, Mar. 2021.

[3] J. Chen, M. W. Johnson, A. Farhan, Z. Wang, Y. Fujii, and E. L. Severson, "Reduced Axial Length Pole-Specific Rotor for Bearingless Induction Machines," *IEEE Transactions on Energy Conversion*, vol. 37, no. 4, pp. 2285–2297, Dec. 2022.

[4] P. Herman, "A radial active magnetic bearing," London Patent No. 1 478 868, 1973.

[5] R. Bosch, "Development of a bearingless motor," in *Proceedings of the International Conference of Electric Machines (ICEM '88)*, Pisa, Italy, 1988, pp. 373–375.

[6] A. Chiba, D. Power, and M. Rahman, "Characteristics of a bearingless induction motor," *IEEE Transactions on Magnetics*, vol. 27, no. 6, pp. 5199–5201, 1991.

[7] S. Mallinger and W. Gruber, "A Comprehensive Review of Prior Art in Bearingless Induction Machine - Part II: Topology," in *Proceedings of 19th International Symposium on Magnetic Bearings (ISMB19)*, Otsu, Japan, Aug. 2025.

[8] S. Nomura, A. Chiba, F. Nakamura, K. Ikeda, T. Fukao, and M. Rahman, "A radial position control of induction type bearingless motor considering phase delay caused by the rotor squirrel cage," in *Conference Record of the Power Conversion Conference - Yokohama 1993*, Apr. 1993, pp. 438–443.

[9] A. Chiba, D. T. Power, and M. A. Rahman, "Analysis of no-load characteristics of a bearingless induction motor," *IEEE Transactions on Industry Applications*, vol. 31, no. 1, pp. 77–83, Jan. 1995.

[10] R. Furuichi, Y. Aikawa, K. Shimada, Y. Takamoto, A. Chiba, and T. Fukao, "A stable operation of induction type bearingless motor under loaded conditions," in *IAS '96. Conference Record of the 1996 IEEE Industry Applications Conference Thirty-First IAS Annual Meeting*, vol. 1, Oct. 1996, pp. 603–609.

[11] A. Chiba, R. Furuichi, Y. Aikawa, K. Shimada, Y. Takamoto, and T. Fukao, "Stable operation of induction-type bearingless motors under loaded conditions," *IEEE Transactions on Industry Applications*, vol. 33, no. 4, pp. 919–924, Jul. 1997.

[12] T. Suzuki, A. Chiba, M. Azizur Rahman, and T. Fukao, "An airgap flux oriented vector controller for stable magnetic suspension during high torque acceleration in bearingless induction motors," in *Conference Record of the 1999 IEEE Industry Applications Conference. Thirty-Forth IAS Annual Meeting*, vol. 3, Oct. 1999, pp. 1543–1550.

[13] T. Suzuki, A. Chiba, M. Azizur Rahman, and T. Fukao, "An air-gap-flux-oriented vector controller for stable operation of bearingless induction motors," *IEEE Transactions on Industry Applications*, vol. 36, no. 4, pp. 1069–1076, Jul. 2000.

[14] Z. Deng, X. Wang, X. Meng, and Y. Yan, "An Independent Controller of Radial Force Subsystem for Super-High-Speed Bearingless Induction Motors," in *Proceedings of Ninth International Symposium on Magnetic Bearings (ISMB9)*, 2004.

[15] R. Ribeiro, F. Castro, A. Salazar, and A. Maitelli, "A suitable current control strategy for split-phase bearingless three-phase induction machine," in *2005 IEEE 36th Power Electronics Specialists Conference*, Jun. 2005, pp. 701–706.

[16] A. Chiba, T. Fukao, and M. A. Rahman, "Vibration suppression of a flexible shaft with a simplified bearingless induction motor drive," in *Conference Record of the 2006 IEEE Industry Applications Conference Forty-First IAS Annual Meeting*, vol. 2, Oct. 2006, pp. 836–842.

[17] Y. Zhou, H. Zhu, J. Ji, and X. Liu, "Decoupling control for bearingless induction motor with α-th order inverse system theory," in *Proceedings of Tenth International Symposium on Magnetic Bearings (ISMB10)*, 2006.

[18] D. Lei, L. Xianxing, and S. Yuxin, "Decoupling control of the bearingless induction motor based on differential geometry variable-structure method," in *2007 Chinese Control Conference*, Jul. 2007, pp. 17–21.

[19] L. Xianxing, D. Lei, F. Wenjin, and S. Yuxin, "Decoupling control of the 5 degree-of-freedom bearingless induction motor based on α-th order inverse system method," in *2007 Chinese Control Conference*, Jul. 2007, pp. 262–266.

[20] Z. Huangqiu, L. Feng, P. Wei, and S. Xiaodong, "Rotor magnetic field oriented control for bearingless induction motors," in *2007 Chinese Control Conference*, Jul. 2007, 19–22.

[21] A. Chiba, D. Akamatsu, T. Fukao, and M. A. Rahman, "An improved rotor resistance identification method for magnetic field regulation in bearingless induction motor drives," *IEEE Transactions on Industrial Electronics*, vol. 55, no. 2, pp. 852–860, Feb. 2008.

[22] A. Chiba, T. Fukao, and M. A. Rahman, "Vibration suppression of a flexible shaft with a simplified bearingless induction motor drive," *IEEE Transactions on Industry Applications*, vol. 44, no. 3, pp. 745–752, May 2008.

[23] Z. Huangqiu, H. Jianxin, Z. Weixia, P. Wei, and L. Xianxing, "Performance analysis and design of two magnetic flux oriented control systems for bearingless induction motors," in *2008 27th Chinese Control Conference*, Jul. 2008, pp. 145–149.

[24] J. a. de Paiva, A. O. Salazar, A. L. Maitelli, and R. M. Stephan, "Performance Improvement of a Split Winding Bearingless Induction Machine Based on a Neural Network Flux Observer," in *Proceedings of Eleventh International Symposium on Magnetic Bearings (ISMB11)*, 2008.

[25] V. F. Victor, J. a. de Paiva, A. O. Salazar, and A. L. Maitelli, "Performance analysis of a neural flux observer for a bearingless induction machine with divided windings," in *2009 Brazilian Power Electronics Conference*, Sep. 2009, pp. 498–504.

[26] X. Sun, H. Zhu, and T. Zhang, "Dynamic decoupling control for radial position of bearingless induction motor based on neural networks inverse system," in *2009 IEEE 6th International Power Electronics and Motion Control Conference*, May 2009, pp. 602–606.

[27] Q. Li and X. Liu, "Decoupling control of bearingless induction motor based on rotor flux orientation with inverse system theory," in *2010 International Conference on Measuring Technology and Mechatronics Automation*, vol. 1, Mar. 2010, pp. 894–897.

[28] X. Liu and W. Wang, "SVM-DTC control of the bearingless induction motor," in *2010 International Conference on Measuring Technology and Mechatronics Automation*, vol. 3, Mar. 2010, pp. 706–709.

[29] Z. Wang and X. Liu, "An improved rotor flux oriented control system of bearingless induction motors," in *2010 Chinese Control and Decision Conference*, May 2010, pp. 2733–2737.

[30] L. Xianxing and W. Weiran, "DSVM and duty ratio control combined direct torque control for bearingless induction motor," in *2010 Chinese Control and Decision Conference*, May 2010, pp. 2025–2030.

[31] X. Liu, W. Wang, and D. Zhu, "Direct torque control system using space vector modulation for bearingless induction motor based on active disturbance rejection controller," in *Proceedings of the 29th Chinese Control Conference*, Jul. 2010, pp. 3311–3315.

[32] E. F. Rodriguez and J. A. Santisteban, "An improved control system for a split winding bearingless induction motor," *IEEE Transactions on Industrial Electronics*, vol. 58, no. 8, pp. 3401–3408, Aug. 2011.

[33] B. Wenshao, X. Juanya, Y. Lan, and H. Shenghua, "Induction compensation control of bearingless induction motor," in *2011 IEEE International Conference on Mechatronics and Automation*, Aug. 2011, pp. 944–949.

[34] B. Wenshao, Z. Songcan, W. Shanming, and H. Shenghua, "Hardware implement of numerical control system for bearingless induction motor," in *2011 IEEE International Conference on Mechatronics and Automation*, Aug. 2011, pp. 1934–1938.

[35] A. Chiba and J. A. Santisteban, "A PWM harmonics elimination method in simultaneous estimation of magnetic field and displacements in bearingless induction motors," in *2011 IEEE International Electric Machines & Drives Conference (IEMDC)*, May 2011, pp. 1042–1047.

[36] X. Liu, B. Zhu, J. Zheng, and Z. Wang, "Air-gap-flux oriented optimized control of bearingless induction motor," in *Proceedings of the 30th Chinese Control Conference*, Jul. 2011, pp. 3549–3553.

[37] Y. Sun, Y. Mao, X. Liu, and Z. Wang, "The SVM-DTC system of the bearingless induction motor based on model reference adaptive," in *Proceedings of the 30th Chinese Control Conference*, Jul. 2011, pp. 3565–3569.

[38] A. Chiba and J. A. Santisteban, "A PWM harmonics elimination method in simultaneous estimation of magnetic field and displacements in bearingless induction motors," *IEEE Transactions on Industry Applications*, vol. 48, no. 1, pp. 124–131, Jan. 2012.

[39] H. Chen, S. Zhang, and R. Zhang, "Control of rotor radial displacement for bearingless induction motors," in *2012 7th IEEE Conference on Industrial Electronics and Applications (ICIEA)*, Jul. 2012, pp. 1084–1089.

[40] J. S. B. Lopes, A. O. Salazar, and A. L. Maitelli, "Adaptative neuro-fuzzy inference system for estimation of rotor flux of a bearingless induction motor applied to speed control," in *Proceedings of First Brazilian Workshop on Magnetic Bearings (BWMB2013)*, 2013.

[41] J. a. de Paiva, A. O. Salazar, and A. L. Maitelli, "Review of control strategies and model estimation techniques applied to bearingless induction machine with divided winding," in *Proceedings of First Brazilian Workshop on Magnetic Bearings (BWMB2013)*, 2013.

[42] X. Sun, L. Chen, Z. Yang, and H. Zhu, "Speed-sensorless vector control of a bearingless induction motor with artificial neural network inverse speed observer," *IEEE/ASME Transactions on Mechatronics*, vol. 18, no. 4, pp. 1357–1366, Aug. 2013.

[43] L. P. d. S. Salazar, J. Lopes, V. Victor, A. Maitelli, and Andres, "Robust speed controller of a bearingless AC motor type divided winding, based on a conventional squirrel cage induction motor," in *Proceedings of 14th International Symposium on Magnetic Bearings (ISMB14)*, 2014.

[44] A. Sinervo and A. Arkkio, "Rotor radial position control and its effect on the total efficiency of a bearingless induction motor with a cage rotor," *IEEE Transactions on Magnetics*, vol. 50, no. 4, pp. 1–9, Apr. 2014.

[45] W. Bu, Z. Li, X. Wang, and X. Li, "A control method of bearingless induction motor based on neural network," in *2015 IEEE International Conference on Information and Automation*, Aug. 2015, pp. 2252–2257.

[46] J. S. B. Lopes, J. D. Fernandes, F. E. Souza, L. P. Santos, J. A. D. Paiva, and A. O. Salazar, "Using feed-forward back propagation for rotor flux estimation of a bearingless

induction motor applied in the speed vector control," in *Proceedings of 15th International Symposium on Magnetic Bearings (ISMB15)*, 2016.

[47] S. Zhang, L. Liu, S. Wang, Y. Jia, and C. Qie, "Complete control of radial suspension force for bearingless induction motors," in *2016 IEEE 11th Conference on Industrial Electronics and Applications (ICIEA)*, Jun. 2016, pp. 2180–2184.

[48] S. Zhang, L. Liu, Y. Jia, S. Wang, and C. Qie, "Compensation control for radial suspension force in bearingless induction motors," in *2016 IEEE 11th Conference on Industrial Electronics and Applications (ICIEA)*, Jun. 2016, pp. 2185–2189.

[49] Z. Yang, D. Zhang, X. Sun, W. Sun, J. Zhu, and Y. Guo, "Vector control for a bearingless induction motor based on nonsingular terminal sliding mode structure," in *20th International Conference on Electrical Machines and Systems (ICEMS)*, Aug. 2017, pp. 1–5.

[50] W. Sun, Z. Yang, X. Sun, and D. Zhang, "Speed sensorless of a bearingless induction motor based on super-twisting-model reference adaptive system," in *2017 20th International Conference on Electrical Machines and Systems (ICEMS)*, Aug. 2017, pp. 1–5.

[51] Z. Yang, D. Zhang, X. Sun, W. Sun, and L. Chen, "Nonsingular fast terminal sliding mode control for a bearingless induction motor," *IEEE Access*, vol. 5, pp. 16 656–16 664, 2017.

[52] Z. Yang, D. Zhang, X. Sun, and X. Ye, "Adaptive exponential sliding mode control for a bearingless induction motor based on a disturbance observer," *IEEE Access*, vol. 6, pp. 35 425–35 434, 2018.

[53] W. Bu and Z. Li, "LS-SVM inverse system decoupling control strategy of a bearingless induction motor considering stator current dynamics," *IEEE Access*, vol. 7, pp. 132 130–132 139, 2019.

[54] E. A. De Freitas Nunes et al., "Proposal of a fuzzy controller for radial position in a bearingless induction motor," *IEEE Access*, vol. 7, pp. 114 808–114 816, 2019.

[55] X. Sun, H. Zhu, and L. Dang, "Linearization decoupling control of bearingless induction motor based on rotor field oriented control," in *2019 IEEE 3rd Information Technology, Networking, Electronic and Automation Control Conference (ITNEC)*, Mar. 2019, pp. 11–15.

[56] J. Lu, Z. Yang, X. Sun, C. Bao, and X. Chen, "Direct levitation force control for a bearingless induction motor based on model prediction," *IEEE Access*, vol. 7, pp. 65 368–65 378, 2019.

[57] K. Li, G. Cheng, X. Sun, and Z. Yang, "A nonlinear flux linkage model for bearingless induction motor based on GWO-LSSVM," *IEEE Access*, vol. 7, pp. 36 558–36 567, 2019.

[58] K. Li, G. Cheng, X. Sun, D. Zhao, and Z. Yang, "Direct torque and suspension force control for bearingless induction motors based on active disturbance rejection control scheme," *IEEE Access*, vol. 7, pp. 86 989–87 001, 2019.

[59] H. Zhu, Z. Yang, X. Sun, D. Wang, and X. Chen, "Rotor vibration control of a bearingless induction motor based on unbalanced force feed-forward compensation and current compensation," *IEEE Access*, vol. 8, pp. 12 988–12 998, 2020.

[60] Z. Yang, J. Ji, X. Sun, H. Zhu, and Q. Zhao, "Active disturbance rejection control for bearingless induction motor based on hyperbolic tangent tracking differentiator," *IEEE*

Journal of Emerging and Selected Topics in Power Electronics, vol. 8, no. 3, pp. 2623–2633, Sep. 2020.

[61] C. He, H. Xiong, Z. Ding, and L. Wang, "Research on fractional order PID control of bearingless induction motor," in *2021 3rd International Conference on Electrical Engineering and Control Technologies (CEECT)*, Dec. 2021, pp. 109–113.

[62] J. Y. Yang, D. Ming Wang, and Y. J. Ge, "Design and implementation of hardware platform for bearingless induction motor control system," in *2021 IEEE International Conference on Electrical Engineering and Mechatronics Technology (ICEEMT)*, Jul. 2021, pp. 147–150.

[63] Z. Yang, C. Lu, X. Sun, J. Ji, and Q. Ding, "Study on active disturbance rejection control of a bearingless induction motor based on an improved particle swarm optimization–genetic algorithm," *IEEE Transactions on Transportation Electrification*, vol. 7, no. 2, pp. 694–705, Jun. 2021.

[64] W. L. A. Silva, E. R. L. Villarreal, J. M. S. Ferreira, A. O. Salazar, and A. L. Maitelli, "Application of active disturbance rejection control (ADRC) in the radial position control of a bearingless induction machine with split winding," in *Proceedings of 17th International Symposium on Magnetic Bearings (ISMB17)*, 2021.

[65] Z. Yang, J. Jia, X. Sun, and T. Xu, "A fuzzy-ELADRC method for a bearingless induction motor," *IEEE Transactions on Power Electronics*, vol. 37, no. 10, pp. 11 803–11 813, Oct. 2022.

[66] Z. Yang, J. Jia, X. Sun, and T. Xu, "An enhanced linear ADRC strategy for a bearingless induction motor," *IEEE Transactions on Transportation Electrification*, vol. 8, no. 1, pp. 1255–1266, Mar. 2022.

[67] Z. Yang, C. Sun, X. Sun, and Y. Sun, "An improved dynamic model for bearingless induction motor considering rotor eccentricity and load change," *IEEE Transactions on Industrial Electronics*, vol. 69, no. 4, pp. 3439–3448, Apr. 2022.

[68] Q. Ding, Z. Yang, X. Sun, and C. Lu, "Stepless speed regulation study of a wound pole-fixed bearingless induction motor with three windings," *IEEE Transactions on Industrial Electronics*, vol. 70, no. 7, pp. 6724–6734, Jul. 2023.

[69] R. Teixeira, W. Silva, J. Ferreira, J. Paiva, A. Salazar, and A. L. Maitelli, "Practical results of ADRC applied to radial position control of a bearingless induction machine," in *Proceedings of 18th International Symposium on Magnetic Bearings (ISMB18)*, 2023.

[70] X. Ye, X. Tang, K. Xing, H. Wang, J. Yao, and T. Zhang, "Repetitive control for vibration suppression of bearingless induction motor," *IEEE Access*, vol. 12, pp. 60 532–60 540, 2024.

[71] Q. Ding, Z. Yang, X. Sun, and C. Lu, "Accurate modeling and optimal rotor flux control of a bearingless induction motor with the specific pole," *IEEE Transactions on Industrial Electronics*, vol. 71, no. 6, pp. 5553–5563, Jun. 2024.

[72] C. Sun, Z. Yang, X. Sun, and Q. Ding, "An improved mathematical model for speed sensorless control of fixed pole bearingless induction motor," *IEEE Transactions on Industrial Electronics*, vol. 71, no. 2, pp. 1286–1295, Feb. 2024.

XI ECCOMAS Thematic Conference on Smart Structures and Materials - SMART 2025
M. Krommer, M. Nader and M. Schagerl (Eds)

Received: 29 May 2025 / Revised: 14 August 2025 / Accepted: 11 October 2025
© The Author(s) 2025

Assessment of Ecometrics in Engineering Workflows

Hubert Mitterhofer, Stefan Fragner

Abstract. Life cycle assessment is the established method to evaluate ecological impacts of a product or process. In order to consider them in the design process of a product, the article proposes a reduced assessment step (Ecometrics) that can be integrated into the workflow. For the example of electric motors, the effects and possibilities in the design are demonstrated.

Key words: Environmental footprint, engineering workflows, Ecometrics, optimization

1. INTRODUCTION

This paper presents the integration of an ecological assessment within the design process of mechatronic systems such as electric motors. High energy costs, direct costs such as CO_2 taxes [1], and indirect measures such as investment regulations through the European taxonomy [2] are putting price tags on ecological properties like CO_2 emissions, resource depletion or environmental destruction. The preferred method to evaluate these aspects of a product is Life Cycle Assessment (LCA). It is reasonable and justified that such an investigation is carried out by professionals, trained to carry out the assessments according to the current regulatory setting, e.g. the ISO14040 standard. This, however, means that the ecological impacts are typically evaluated post-design.

In case of insufficient ecologic performance, i.e. high environmental impact, the assessment *aposteriori* can have two consequences: Either, the product in design needs to be redesigned, prolonging the time to market, or a fast market entry is valued higher than the ecologic assessment and the product enters the market having a high ecologic footprint. Both consequences are undesirable and require a fast and direct reaction to insufficient ecologic metrics *before* being constrained by finalized designs. It is, therefore, essential to evaluate ecologic metrics continuously and as early as possible in the design phase.

Quantified ecologic considerations in general and LCA in particular are fields that are not present in many engineers' daily working routine. The first part of this publication is, therefore, dedicated to the introduction of the LCA method.

The second part is describing the process of motor simulation and optimization within a multi-physical framework, e.g. SyMSpace® [3], and how the ecologic assessment methods (Ecometrics) have been introduced to that workflow. In the final part, the application of the Ecometrics component is demonstrated for the design optimization of an industrial motor-gearbox system.

Hubert Mitterhofer & Stefan Fragner
Linz Center of Mechatronics, Altenbergerstr. 69, 4040 Linz, Austria
e-mail: hubert.mitterhofer@lcm.at

2. INTRODUCTION TO LCA

For the domain of magnetic bearing systems, the authors have presented the LCA method in [4]. Parts of this introduction shall be repeated here in an adapted form to provide the relevant information and contextualization of the Ecometrics component.

In the year 1995, the authors of the Nordic Council report on Guidelines on Life-Cycle Assessment [5] described the LCA as follows:

"*The LCA methodology evaluates holistically the environmental consequences of a product system or activity, by quantifying the energy and materials used, the wastes released to the environment, and assessing the environmental impacts of those energy, materials and wastes.*"

While the statement was clear and comprehensible, the mentioned "LCA methodology" was diverse. An increasing number of different implementation methods led to the publication of the ISO 14040 standard [6] in 1997 in its first edition to unify this methodology. Later editions followed and in 2020, an amendment was published [7]. ISO 14044 [8] comprises directives and technical specifications, also added later. This unification of the different approaches defines the principles and structure of an LCA to achieve comparability between individual LCA results.

ISO 14040 defines four stages in an LCA.

Figure *1* shows how they are interconnected in the LCA framework. The short descriptions below explain the content of the individual stages. Further guidelines and explanations for the application of ISO 14040 can be found in the literature, e.g. in [9] or [10].

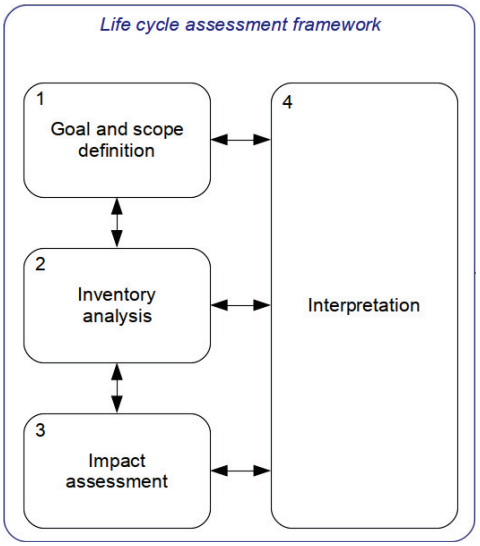

Figure 1: Stages of an LCA according to ISO 14040:2006:1

STAGE 1 – **GOAL AND SCOPE DEFINITION**

The first task of an LCA study is to formulate its goal. Then the functional unit[1] as well as the system boundaries must be defined. Additionally, the handling of (missing) data must be clarified and the required data quality has to be stated. Simply put, Stage 1 specifies what the LCA applies to and why, how, and for whom the LCA is relevant.

STAGE 2 – **LIFE CYCLE INVENTORY (LCI) ANALYSIS**

The inventory analysis deals with the description, acquisition, modelling and calculation of material and energy flows to create an inventory of input/output data. The numerical result

[1] A functional unit is a quantified description of the function of a product that serves as the reference basis for the impact assessment.

contains only input flows from the natural environment und output flows to the natural environment. Materials and pre-products of the technical sphere have to be retraced to get the input streams from the ecosphere. The graphical result of the inventory is the process flow chart which visualizes the system boundaries and enables traceability.

The main part of an LCI analysis is data acquisition. Data can either be measured, calculated, or estimated. Their accuracy influences the quality of the inventory considerably. With the mass and energy balance, the inventory can be validated. Unless every single process is balanced, the data quality is not sufficient.

STAGE 3 – **LIFE CYCLE IMPACT ASSESSMENT (LCIA)**

In the impact assessment stage, the data from the LCI analysis are bundled with regard to their potential environmental impacts to achieve a better understanding of the effects on the natural environment.

The goal is to assess all theoretical environmental impacts and to make them comparable. The combination of scientific-based assessment methods and subjectively generated compare mechanisms leads to an impact assessment consisting of mandatory and optional components. While CO_2 emissions causing global warming are the most dominant environmental influence in today's public perception, there are many different impact categories that may be considered in an LCIA.

There is a wide range of LCIA methods, each defining a certain set of categories and characterization factors. Amongst the most popular methods are ReCiPe [11], IPCC 2013, ILCD 2011 [12], CML 2012 [13], and Cumulative energy demand [14] according to a recent survey [15]. A comprehensive description of the most popular method sets and the included impact categories has been published by Acero et al. in [16]. **Table *1*** shows typical impact categories present in many of the mentioned LCIA methods.

Impact category	Indicator unit
Global warming potential	kg CO_2 equivalent
Stratospheric ozone depletion	kg CFC-11 equivalent
Ecotoxicity for aquatic fresh water	CTUe (comparative toxic unit for ecosystems)
Human Toxicity – cancer effects	CTUh (comparative toxic unit for humans)
Ionising radiation – human health effects	kg U^{235} equivalent (to air)
Acidification potential	mol H+ equivalent or kg SO_2 equivalent
Eutrophication - aquatic	Fresh water: kg P equivalent Marine: kg N equivalent
Land transformation	kg soil organic matter deficit

Table 1: Common LCIA impact categories [19]

STAGE 4 – **INTERPRETATION**

In the fourth and last stage of an LCA study, the results of LCI analysis and the LCIA are compared with the goals defined in the first stage to generate conclusions, limitations, and recommendations. An important part is also the critical review, which is intended to ensure the validity of the study.

3. ECOMETRICS IN MOTOR DESIGN WORKFLOWS

Electric motor design can be considered as a truly mechatronic discipline, requiring knowledge in multiple physical domains. Due to the high number of design degrees of freedom, modern tools offer multi-objective optimization on top of multi-physics simulation [17], which usually consists of electromagnetic, thermal, and mechanical calculations.

The workflow management system SyMSpace offers such design methods, that typically consist of the geometry definition of rotor and stator as initial step. The following definitions cover the winding system, the material allocation, and load scenario definition. Then, multiple simulations are triggered for the individual physical domains including electromagnetic, mechanic, and thermal design. Because the soft magnetic materials in stator and rotor core exhibit nonlinear behavior, these calculations are typically done via finite element analysis (FEA), requiring computation times from several minutes to several hours. The FEA is then followed by the postprocessing phase, where the FEA results are evaluated, additional questions like demagnetization risk or short-circuit behavior are answered and also non-technical calculation steps like production cost models can be executed.

As SyMSpace implements a modular approach, all of the described calculations or simulation steps are available as individual components that can be assembled to a consistent workflow by automatically matching and connecting the outputs and inputs of the consecutive workflow steps. This modular approach allows adding further simulation steps, calculation scripts (e.g. in Python), or models for supplementary analysis, that require inputs which are available at some point of the previous workflow steps.

As stated in Section 2, conducting an LCA requires detailed analysis of the considered product, process or service. It would, therefore, be presumptuous to try to replace this process and automatically deduct a full LCA from the motor design data. However, following a quotation of Arthur Ashe, an American tennis player: "*Start where you are. Use what you have. Do what you can.*", it seems appropriate to deduct as much information regarding the ecologic performance of the design object as possible.

3.1. EMBEDDING ECOMETRICS CALCULATION

The described modular structure of SyMSpace using calculation and analysis components makes it relatively easy to extend a motor design project with an additional component. A typical structure is shown in Figure 2.

3.2. MATERIAL CONSUMPTION

The most obvious ecologic information that can be deducted from a motor design project is the environmental impact based on the material masses used. As marked in Figure 2, the mass data and material definition are automatically linked from the output of the geometry

components within the SyMSpace project to the input of the Ecometrics component. Information on the environmental impact of individual relevant materials such as copper as the dominant conductor material, electric steel sheets, or diverse permanent magnets has been retrieved from the *ecoinvent* [18] database and related literature. If relevant, the masses and respective materials of additional parts such as housings, gears, bearing shields, etc. can be added manually in the *Material Consumption* sub-component.

3.3. ENERGY CONSUMPTION

Other than with passive devices, an electric motor consumes electricity in its use phase, which constitutes a second, important, driver of its environmental impact. To estimate the related impact, the load profile during operation and an electricity generation mix must be specified. As a typical output of the motor simulation, individual efficiency ratings from individual load points are known within the design workflow and can be linked to the input of the Ecometrics component, cf. Figure 2.

3.4. TRANSPORTATION

For also estimating the environmental impacts caused by the transportation of components, an additional sub-component can be used. In this case, the transported masses, the transportation distances and the transportation modes can be selected manually.

3.5. EXECUTION IN WORKFLOW

Upon execution of the workflow, the Ecometrics component receives the inputs from the geometry modules, stator- and rotor components, the load point calculations, etc. With these inputs, the specified environmental impacts according to the chosen impact categories are calculated and depicted as interactive *sunburst* charts with multiple rings as shown in Figure 5 and Figure 6.

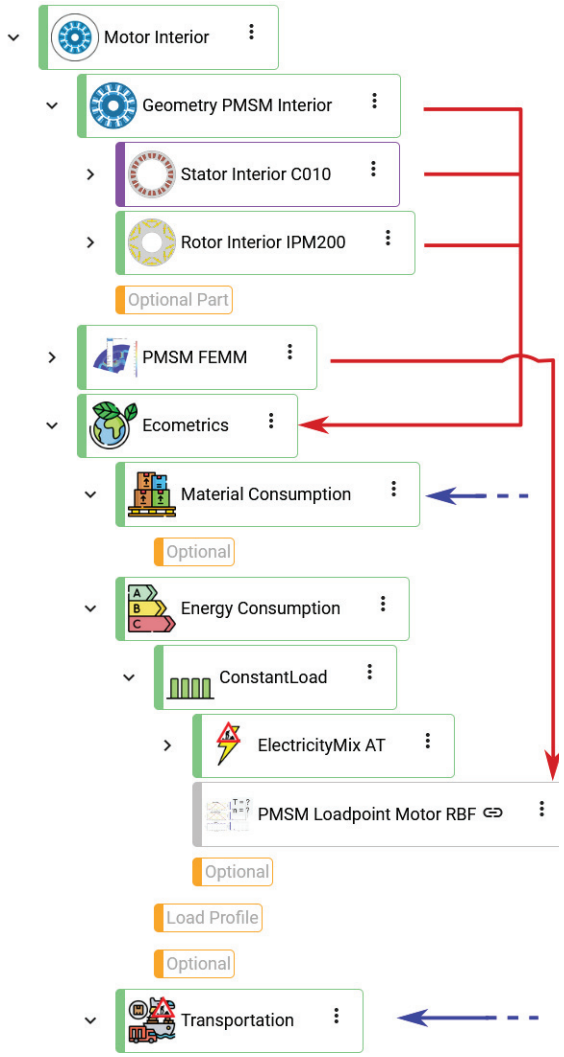

Figure 2: Ecometrics component embedded in a motor design workflow in SyMSpace, red arrows mark automated data flow, blue arrows mark external / manual input possibility

Potentially more relevant than the graphic representation is the quantified outputs for the selected impact categories. This means that, for the first time, an environmental metric can be chosen as optimization criterium along with conventional performance values such as efficiency, power density, or weight in a multi-objective optimization: Environmental considerations, therefore, (co)steer the process and have direct influence on the design outcome.

4. MOTOR DESIGN INCLUDING ENVIRONMENTAL IMPACTS

To demonstrate the use of the Ecometrics component described in Section 3, the optimization of an industrial drive system is presented in this section. The considered system consists of a permanent magnet synchronous machine (PMSM) with rare-earth Neodymium-Iron-Boron (NdFeB) magnets and a two-stage planetary gear. The use case requires that the motor-gear-system is optimized with regard to the environmental impact caused by material and use-phase energy consumption for a given load scenario while maintaining performance.

The motor design workflow was set up in SyMSpace with the newly available Ecometrics component for an existing drive as reference. The nominal data and chosen gear type, holding a definition of gear ratio, gear mass and related gear efficiency, which depends mainly on the number of gear stages, are listed in Table 3.

To fulfill the use case requirements, the workflow was then optimized, setting the required performance parameters and environmental parameters as the optimization targets (Table 2) and allowing the optimization algorithm to adapt a number of geometric variables and the gearbox type.

Variable	Value in reference design
T_n : Nominal torque at gear output	2.64 Nm
n_n: Nominal speed at gear output	350 rpm
type: Gearbox type	1:12
t_{idle}: Yearly standby power time	6760 h
P_{idle}: Standby losses	2.4 W
t_1: Yearly on-time	2000 h

Table 3: Nominal data of reference design

Optimization target
Min(P_v): Total losses
Min($T_{r,cogg,pp}$): Cogging torque at gear output
Min(GWP): Global warming potential
Min(AP): Acidification potential

Table 2: Optimization targets

4.1. OPTIMIZATION

The following optimization process automatically calls the design workflow repeatedly with varying input parameter sets that are generated by a genetic algorithm based on the results of already calculated motor-gear combinations. Referring to evolution, the calculated motors of the optimization are referred to as *individuals*. Using a computation cluster, several thousand individuals are calculated, and the Pareto-optimal results are gathered and displayed in scatter plots as shown in Figure 3.

4.2. COMPARISON OF RESULTS

The optimization viewer within SyMSpace allows browsing, highlighting, and selecting different individuals to choose the desired optimum solution. Due to the consideration of Ecometrics within the design workflow and the optimization process, the environmental performance can also be considered for the final selection. In the presented use case, the chosen individuum has improved in nearly all of the regarded results, cf. Table 4. The resulting geometries of reference and optimized design are depicted in Figure 4. It becomes apparent that the optimization algorithm has mainly driven the design in three directions: Increase of efficiency, reduction of magnet material, and increase of transmission ratio.
A detailed look at the environmental impacts of the motor-gear system in the sunburst charts of Figure 5 and of Figure 6 reveals the reasoning behind:

- The GWP is dominated by the use-phase energy consumption. The center scatter plot of Figure 3 clearly shows this behavior in the direct correlation of GWP and P_V. This is, of course, dependent on the specified use case – in this case the relatively long on-time of 2000 hours per year. Therefore, efficiency was highly prioritized by the optimization algorithm. In case of an, e.g. flap actuator for adjusting an angular valve position twice a day, the material input would likely dominate the GWP and efficiency would be far lower weighted.
- High content of magnet material is a main ingredient for high efficiency in PMSMs. However, magnet material (especially NdFeB and other rare earth magnets) is also the main driver of that share of the acidification potential that can be directly influenced by design[2]. As a look at the motor cross sections in Figure 4 reveals, the optimization algorithm has pushed to minimize magnet mass.
- The push for less magnet mass leads to reduced torque capacity which would cause an efficiency-deteriorating increase in motor currents. The design answer to this is a higher transmission ratio (without increasing the number of gear stages, which would lead to reduced gear efficiency and increased gear mass) which reduces the torque T_l demand and allows achieving the output power by higher motor speed n_l.

[2] The larger part of the acidification potential stems from the energy generation and can only be influenced indirectly through less energy consumption. The choice of energy supply mix usually has the more significant influence but needs to stay constant for result comparability.

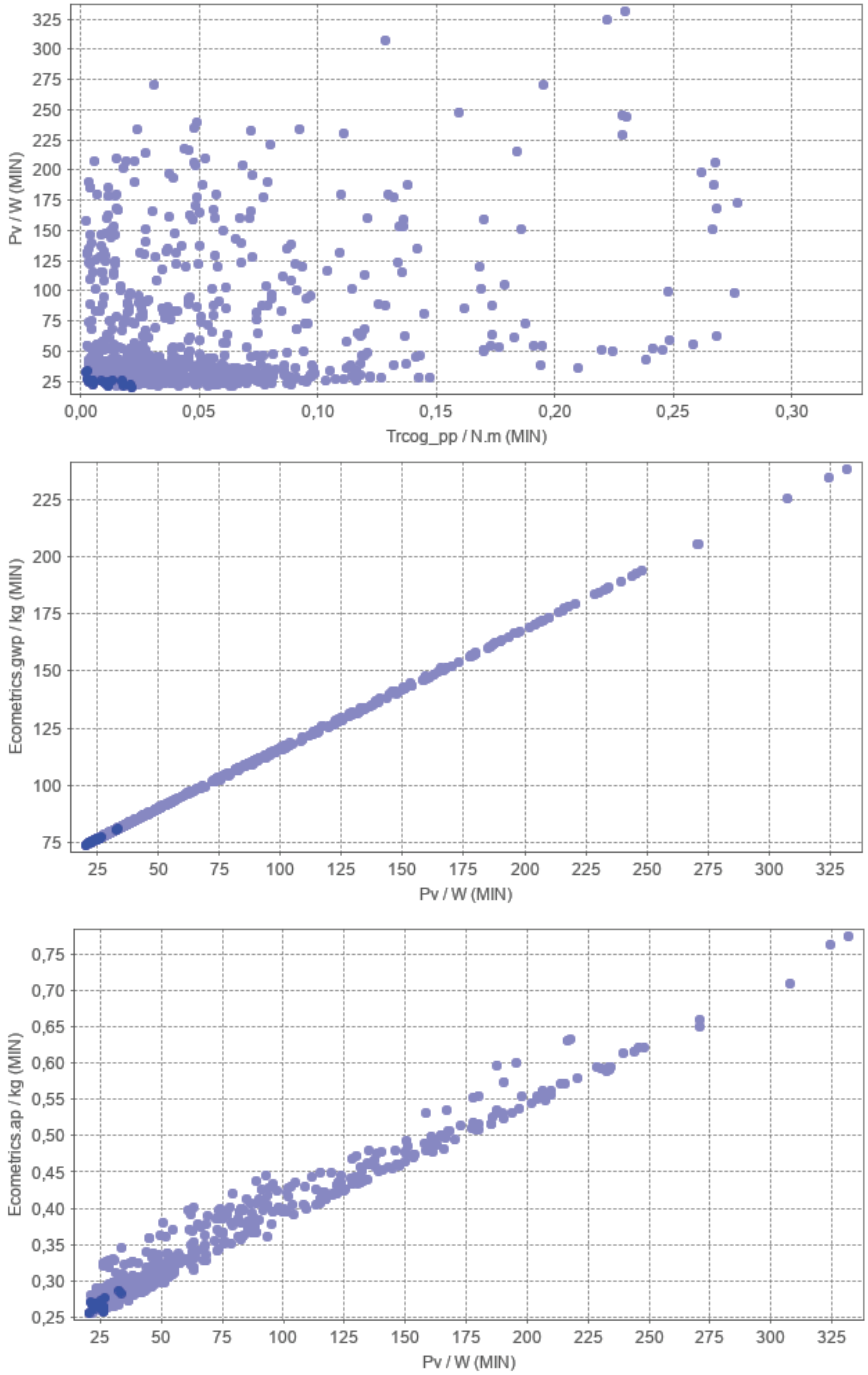

Figure 3: Scatter plots with Pareto-optimal individuals, revealing the different correlations for three optimization targets: Losses over Torque ripple (top), Global warming potential vs. Losses (center), Acidification potential vs. Losses (bottom)

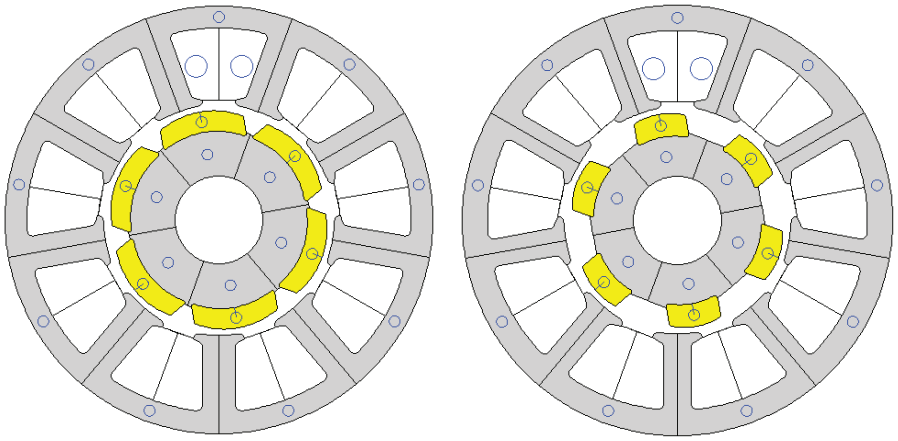

Figure 4: Rotor and stator cross section of reference design (left) and optimized design (right). The yellow permanent magnets have been reduced in volume as they dominantly drive the ecologic footprint.

Variable	Reference design	Optimized design
T_l : Load point motor torque	0.24 Nm	0.14 Nm
n_l: Load point motor speed	4200 rpm	7000 rpm
P_l: Load point motor power	131.6 W	127 W
$T_{r,pp}$: Cogging torque motor	0.011 Nm	0.016 Nm
η: Efficiency	80.2 %	83.1 %
P_v: Losses	26.1 W	21.5 W
type: Gearbox type	1:12	1:20
GWP: Global warming potential	77.6 kg CO_2eq	74.76 kg CO_2eq
AP: Acidification potential	0.32 kg SO_2eq	0.28 kg SO_2eq

Table 4: Comparison of reference and optimized design, both fulfilling nominal requirements

5. SUMMARY & OUTLOOK

The paper argues why the assessment of environmental impacts of products in general and electric motors in the particular example needs to be integrated into the design phase. This demand requires an approach differing from classical LCA which, understandably, is a lengthy process *after* the design or even industrialization phase. The shown Ecometrics component which has been embedded in the motor design tool SyMSpace provides such an integration to the design loop by delivering automatically deducted, quantified impact metrics. The consequential possibility of using these metrics as optimization targets was demonstrated for the use case of an industrial motor-gear system.

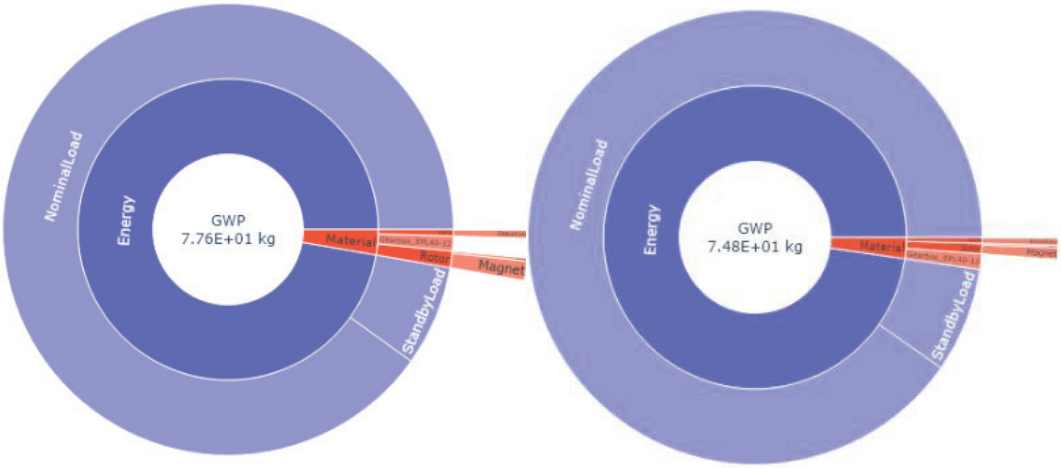

Figure 5: Global warming potential in kg CO_2 equivalent of reference design (left) and optimized design (right), showing the strong dominance of use phase energy (blue) over material impact (red).

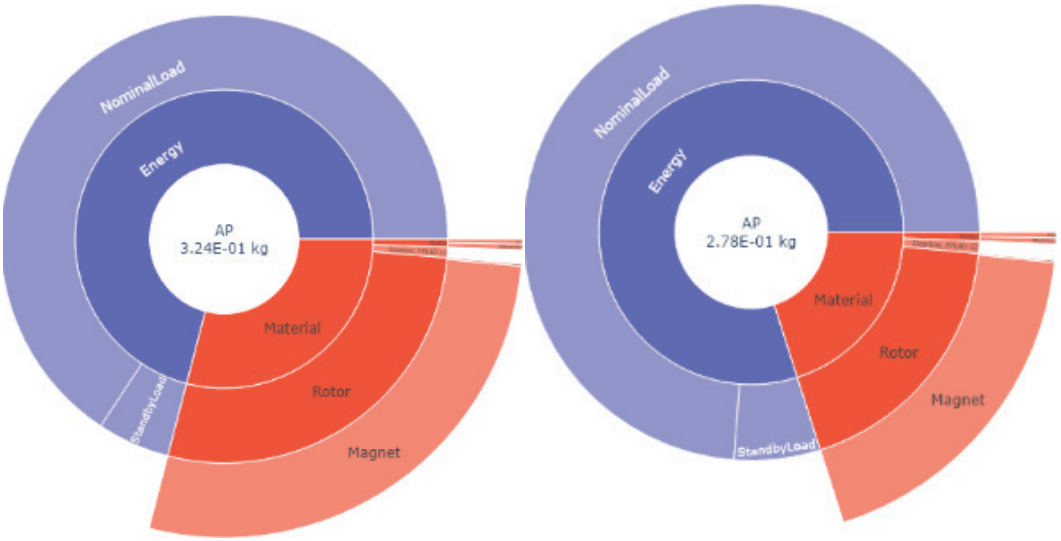

Figure 6: Acidification potential in kg SO_2 equivalent for reference design (left) and optimized design (right), showing the dominance of the magnet in the red material impact section.

The presented Ecometrics component was driven by motor design engineers and is far from being complete – future works in this direction may address the following topics:

- While currently focusing on classical LCA impact categories, future work should also address circularity aspects, such as the suitability for repair, re-use, or high-quality recycling. For instance, the production energy and material usage of stator potting has little influence on the Ecometrics outcome in its current version, however, this step hampers repair and remanufacturing significantly.
- While also raising questions about data quality and reliability of the sources behind, it seems beneficial to automatically access and retrieve inventory data, e.g. on material and process impacts, from inventory databases at execution of the Ecometrics component.
- Eventually, the output of the Ecometrics component is predestined to support the reporting obligations of industry regarding national and international regulatory frameworks. This future step may require specific data evaluation according to individual reporting task requirements.

6. ACKNOWLEDGMENT

This work has been supported by the COMET-K2 Center of the Linz Center of Mechatronics (LCM) funded by the Austrian federal government and the federal state of Upper Austria.

REFERENCES

[1] T. M. Bachmann, „Considering environmental costs of greenhouse gas emissions for setting a CO2 tax: A review.," *Science of The Total Environment,* 2020.

[2] C.-A. Papari, H. Toxopeus, F. Polzin, H. Bulkeley und E. V. Menguzzo, „Can the EU taxonomy for sustainable activities help upscale investments into urban nature-based solutions?," *Environmental Science & Policy 151,* 2024.

[3] „SyMSpace," Linz Center of Mechatronics, 2025. [Online]. Available: https://symspace.lcm.at/, accessed at 04/2025.

[4] H. Mitterhofer und S. Fragner, „Approaches to Efficiency and Life Cycle Assessment of Magnetic Bearing Systems," in *17th International Symposium on Magnetic Bearings*, Rio de Janeiro, 2021.

[5] L.-G. Lindfors, K. Christiansen, L. Hoffman, Y. Virtanen, V. Juntilla, O.-J. Hanssen, A. Ronning, T. Ekvall und G. Finnveden, Nordic Guidelines on Life-Cycle Assessment, Copenhagen: Nordic Council of Ministers, 1995.

[6] ISO 14040:2006-1, Environmental management - life cycle assessment - principles and framework, International Standardization Organization, 2006.

[7] ISO, „ISO 14040:2006/Amd 1:2020 Environmental management — Life cycle assessment — Principles and framework," 2020.

[8] ISO 14044:2006, Environmental management - Life cycle assessment - Requirements and Guidelines, International Standardization Organization, 2006.

[9] I. V. Muralikrishna und V. Manickam, „Life Cycle Assessment," *Environmental Management,* 2017.

[10] W. Klöpffer und B. Grahl, Life Cycle Assessment (LCA): A Guide to Best Practice, ISBN: 978-3-527-32986-1: Whiley, 2014.

[11] National Institute for Public Health and the Environment, Netherlands, „LCIA: the ReCiPe model," [Online]. Available: https://www.rivm.nl/en/life-cycle-assessment-lca/recipe, accessed at 06/2021.

[12] S. Sala, M.-A. Wolf und R. Pant, „Characterisation factors of the ILCD Recommended Life Cycle Impact Assessment methods. Database and supporting information," *European Commission Report EUR25167EN,* 2012.

[13] Universiteit Leiden, „CML-IA Characterisation Factors," 2016. [Online]. Available: https://www.universiteitleiden.nl/en/research/research-output/science/cml-ia-characterisation-factors, accessed at 06/2021.

[14] R. Frischknecht, F. Wyss, S. Knöpfel-Büsser, T. Lützkendorf und M. Balouktsi, „Cumulative energy demand in LCA: the energy harvested approach," *The International Journal of Life Cycle Assessment 20 (7),* 2015.

[15] iPoint GmbH, „Life Cycle Impact Assessment – which are the LCIA indicator sets most widely used by practitioners?," [Online]. Available: https://www.ipoint-systems.com/blog/lcia-indicator/, accessed at 06/2021.

[16] A. P. Acero, C. Rodriguez und A. Ciroth, „LCIA methods - Impact assessment methods in Life Cycle Assessment and their impact categories," 2016. [Online]. Available: https://www.openlca.org/wp-content/uploads/2016/08/LCIA-METHODS-v.1.5.5.pdf, accessed at 06/2021.

[17] S. Silber, W. Koppelstätter, G. Weidenholzer, G. Segon und G. Bramerdorfer, „Reducing development time of electric machines with SyMSpace," *Proceedings 8th International Electric Drives Production Conference,* 2018.

[18] „ecoinvent," [Online]. Available: https://ecoinvent.org/database/, accessed at 04/2025.

[19] H. K. Stranddorf, L. Hoffmann und A. Schmidt, Impact categories, normalisation andweighting in LCA, Danish Ministry of the Environment, 2005.

XI ECCOMAS Thematic Conference on Smart Structures and Materials - SMART 2025
M. Krommer, M. Nader and M. Schagerl (Eds)

Received: 31 March 2025 / Revised: 29 July 2025 / Accepted: 11 October 2025
© The Author(s) 2025

Data acquisition and evaluation for condition monitoring of a cutting tool

Kurt Pichler, Christian Helmel, Gerhard Kaineder, Robert Schlosser, Veronika Putz

Abstract. In this paper, we present the data acquisition and evaluation for the purpose of condition monitoring for a cutting tool in fiberboard processing. To record the measurement data, a modular and distributed measurement and processing system, called DisDAQ, is used. The data recorded in this way is evaluated using machine learning techniques in order to draw conclusions about the wear condition of the cutting tool. For this purpose, a large amount of features from different domains are extracted. Subsequently, the most meaningful features are selected using feature selection techniques. Finally, these features are used to train multivariate regression models of varying complexity. For evaluating the regression models, the root mean square error is used. Tests with various regression methods, various shapes of the target function, and smoothing of the input variables are carried out to obtain the best possible results.

Key words: Data Acquisition, Feature Extraction, Feature Selection, Multivariate Regression, Condition Monitoring

1 INTRODUCTION

In the industrial landscape, ensuring optimal performance and minimizing downtime is crucial. Industries, from manufacturing to energy, are increasingly adopting proactive maintenance strategies to enhance operational efficiency. Condition monitoring and predictive maintenance have become essential tools, transforming maintenance practices and helping organizations prevent potential failures. Traditionally, maintenance was reactive, relying on routine inspections or post-breakdown repairs, leading to unplanned downtime, production losses, and high emergency repair costs. Condition monitoring involves continuous, real-time assessment of industrial assets using sensors, advanced analytics, and machine learning. This approach allows production facilities to collect extensive operational data, monitor critical parameters, and de-

Kurt Pichler & Christian Helmel & Gerhard Kaineder & Leander B. Hörmann & Veronika Putz
Area Sensors & Communication, Linz Center of Mechatronics GmbH Altenberger Straße 69, A-4040 Linz, Austria, e-mail: office@lcm.at

Robert Schlosser
Leitz GmbH & Co. KG, Leitzstraße 80, A-4752 Riedau, Austria, e-mail: office.riedau@leitz.org



Figure 1: New and heavily worn cutting tool

tect early signs of potential failures. Consequently, maintenance teams can make informed decisions and take preventive actions, reducing disruptions and optimizing productivity.

In fiberboard processing, cutting an angled edge is a crucial step performed with a rotating cutting tool. Ensuring the tool's sharpness is essential for producing a clean edge. Therefore, the sharpness must be continuously monitored to replace the tool when it becomes too worn.

Many publications discuss feature extraction and classification for monitoring rotating machines. For example, [1] reviews features for cutting tool fault diagnosis, using methods like support vector machines (SVMs), decision trees, and k-nearest neighbors. In [2], an overview of gearbox fault diagnosis features, assigning them to specific fault types, is provided. The review papers [3, 4] also suggest numerous diagnostic features for condition monitoring of bearings and gears in rotating machinery. Monitoring of a cutting tool by reconstructing the tool's 3D geometry using optical measurements is presented in [5].

In this application-focused paper, we employ established features and machine learning techniques to estimate the condition of a cutting tool based on measured signals. Initially, we extract a set of features from the raw data and use an unsupervised method to distinguish between active cutting and idle states. Subsequently, we estimate tool wear through a supervised approach, selecting the most significant features and utilizing them as inputs for multivariate regression.

The paper is organized as follows: in Section 2, the problem statement is given and the test setup is explained. The data acquisition system is described in detail in Section 3. Section 4 deals with the actual wear estimation approach. Finally, Section 5 provides test results, and in Section 6 conclusions are drawn.

2 PROBLEM STATEMENT AND TEST SETUP

As outlined in the introduction, this paper aims to estimate the wear of a cutting tool used in fiberboard processing by analyzing measurement data from the cutting process. In Fig. 1, a cutting tool in new (left) and heavily worn (right) condition is shown. Traditionally, personnel at the fiberboard processing facility inspect the cutting edge at regular intervals to assess its condition based on the cutting pattern and replace the tool if necessary. This routine inspection consumes resources that could be more urgently utilized elsewhere in the plant. By replacing this manual inspection with continuous condition monitoring of the cutting tool, the workload on employees can be significantly reduced, and the company can operate more efficiently by reallocating these freed-up resources.

The implementation of a robust data acquisition system is crucial in this context. Such a

system enables real-time monitoring and precise measurement of the relevant working parameters of the cutting tool, ensuring timely maintenance and reducing unexpected downtimes. By capturing and analyzing data continuously, the system provides valuable insights that help in optimizing the production process, enhancing tool life, and ultimately improving overall productivity and cost-efficiency. Additionally, a well-designed data acquisition system can integrate with other manufacturing processes, providing a comprehensive overview of the production environment. This integration allows for predictive maintenance, where potential issues are identified and addressed before they lead to significant problems, further minimizing disruptions and maximizing operational efficiency. The ability to collect and analyze large volumes of data also supports continuous improvement initiatives, driving innovation and maintaining a competitive edge in the market.

The modular sensor system DisDAQ (Distributed Data Acquisition and Algorithms Quiver), which can be quickly adapted to a wide range of measurement tasks, was used for test data acquisition. More details will follow in Section 3. The test data were collected during ongoing fiberboard processing. Measurements were continuously recorded over 5 weeks. A new cutting tool was installed at the start of each week. As the tools wore down, product quality decreased by the end of each week but remained acceptable. However, there is no continuous data on the actual wear of the cutting tool (therefore no ground truth of the wear). There is also no information on the different types of fiberboard processed or the machine settings used.

3 DATA ACQUISITION SYSTEM

As mentioned above, the modular data acquisition system called DisDAQ was used to record measurement data. Designed for feasibility studies, initial measurement campaigns, and industrial process monitoring, it offers extensive capabilities for data acquisition and analysis, as well as serving as a runtime environment for real-time data processing algorithms [6]. DisDAQ is a well-tuned software stack based on Kubernetes and Robot Operation System 2 (ROS2) to achieve these goals.

3.1 System Architecture

The overall system architecture is shown in Fig. 2. The DisDAQ system is structured in multiple layers:

Hardware Node Layer: The foundational layer consists of the operating system running on the hardware nodes which is typically Linux and deploying K3s. The hardware nodes can range from single-board computers with ARM64 architecture (e.g., Raspberry Pi) and high-power AMD64 architecture industrial PCs to specialized processing units for embedded AI applications (e.g. NVIDIA Jetson).

K3s Layer: K3s is a certified Kubernetes distribution built for IoT & edge computing [7]. It provides a state-of-the-art, resilient container management framework that enhances DisDAQ's modularity and robustness.

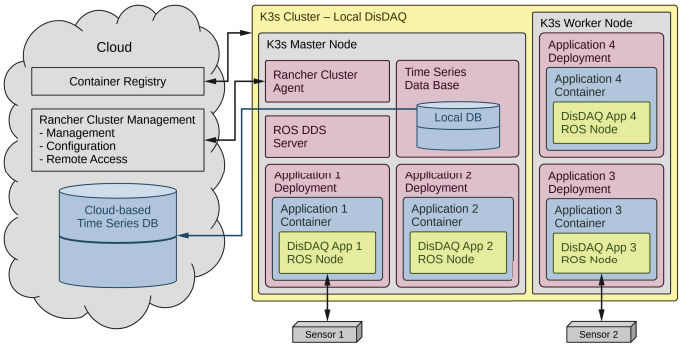

Figure 2: DisDAQ System Architecture

ROS2 Layer: The data transport layer is implemented using ROS2, which is based on DDS (a Data-Centric Publish-Subscribe model for distributed application communication and integration, and an industry standard [8]). ROS2 provides a framework for modularly deploying data-focused applications.

Application Layer: DisDAQ applications use the ROS2 API and client libraries to subscribe to and publish data for their respective purposes (e.g., sensor data acquisition, data processing, real-time algorithms, and more).

3.1.1 System Stack

The DisDAQ stack is maintained as a Helm v3 [9] chart package and includes all necessary tools and configurations. This includes ROS2 configuration for both the ROS2 nodes themselves and the Pods running the ROS2 nodes, enabling inter-container and inter-host communication of ROS2 nodes.

Other tools provided with the DisDAQ stack include a live visualization for ROS data based on Foxglove Studio [10], a JupyterLab environment, cluster and data monitoring tools, and more.

3.1.2 Applications

All DisDAQ applications are also maintained as Helm v3 chart packages. A DisDAQ application contains a containerized application that can range from sensor drivers to simple data processing or demanding machine learning tasks. Each application defines all components needed for its operation, such as local storage, networking configuration, container arguments, cluster services, and container security context.

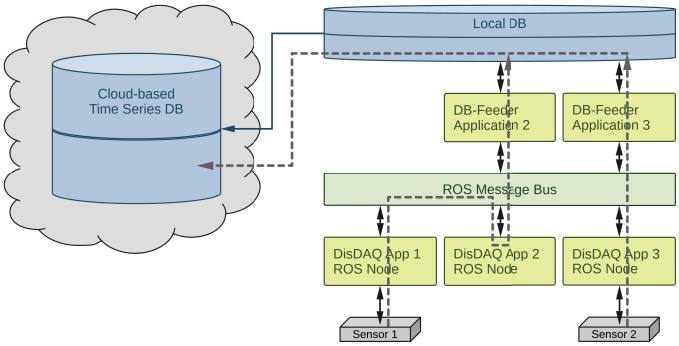

Figure 3: DisDAQ Data Flow

3.1.3 Data-Centric View

DisDAQ components are designed to be modular and independent of each other, connected only through the data they produce and consume. Typically, each DisDAQ instance has a method for storing data, such as a local time-series database or local files like HDF5 [11] files.

Fig. 3 shows an exemplary data flow produced by two sensors. The data from *Sensor 2* is stored directly in a local database via a DB feeder application. The data from *Sensor 1* is processed through an application before being stored in the same local database. The local database is then synced with a cloud-based instance. Data processing applications can vary in type and complexity, including tasks such as statistics, re-sampling, feature detection, and machine learning.

3.2 Application Specific Setup

This section describes the specific setup used in the DisDAQ system for the application at hand. The sensors and actuators configured are tailored to the requirements of the project, ensuring accurate and reliable data acquisition and control.

The setup employed various sensors, including two DAQ units with 8 channels at 2kS/s and 5 channels at 20kS/s, four digital environmental sensors operating at 2S/s, and a Smart Meter capable of measuring up to 50kA at 2S/s. Additionally, the setup featured digital output logic for controlling an external spindle measurement device.

Given the need to gather large amounts of data for developing a feature detection algorithm, some real-time processing alorithms were also deployed. These tasks included re-sampling and restructuring data, as well as tracking the operating status of the plant where the system was installed. The operating status then served as a gate to store data only when production was in session. Additionally, the digital output to control the external spindle measurement device was managed by a calculated state.

For algorithm development purposes, the raw data was stored locally in HDF5 files. Additionally, for visualization and monitoring, downsampled variants of the data were fed into the local time-series database and mirrored to a cloud-based database instance.

4 WEAR ESTIMATION

Some fundamental steps for wear estimation of a cutting tool have already been addressed in [12]. These steps encompass the extraction and selection of appropriate features, the definition of a virtual ground truth, and the regression of this ground truth using the selected features. Since these procedures have been previously detailed, they are only briefly summarized here and not elaborated upon. This part of the paper primarily focuses on the application and comparison of various methods for each of these individual steps.

4.1 Feature extraction and selection

Using the DisDAQ system described in Section 3, the measurement channels *motor current*, *microphone in the exhaust hood*, *microphone in the cutting cabin*, *infrared thermometer at the cutting edge before cutting*, and *infrared thermometer at the cutting edge after cutting* were recorded at a sampling rate of 125 kHz for one minute every 15 minutes. However, production does not run continuously, but is repeatedly interrupted by idle runs or downtimes, for example to change the product. To ensure that only data from active production periods are evaluated, the motor current is used as a simple indicator of cutting activity. If the motor current for an entire one-minute data set exceeds a specified threshold, the data set is considered valid for production analysis. Otherwise, it is discarded.

Statistical and manually engineered features are extracted from all valid datasets. The statistical features include well-known metrics such as mean, median, standard deviation, skewness, and short-time energy. For a comprehensive list of potential features, readers are referred to [1, 2, 13, 14, 15, 16]. In terms of manual feature engineering, measured values from the beginning and end of each week were compared, with an attempt to mathematically quantify visually recognizable differences. For instance, a feature was defined to represent the temperature difference at the cutting edge before and after cutting. The entire set of features is extracted once from each valid one-minute measurement across all channels. Consequently, the one-minute measurement at 125 kHz is represented by a comparatively low-dimensional feature vector. This approach significantly reduces the amount of data to be processed subsequently.

Then, the relevant features for regression are identified using a feature selection filter approach. The data is categorized into three classes: "*beginning of the week (new)*", "*middle of the week (medium wear)*", and "*end of the week (heavy wear)*". Features that effectively differentiate these classes are selected. Given that the condition of the cutting tool can be approximately classified into these three categories using the chosen features, they are considered suitable for wear estimation through regression.

Feature selection is conducted using a forward filter approach [17]. Starting with an empty feature set, features are incrementally added until a predefined number of features or a certain level of information content is achieved. The Dy-Brodley measure [18] serves as the selection criterion. In each step, it maximizes the separation between different classes while minimizing the variance within the same class. The relative change in the Dy-Brodley measure is used as the stopping criterion. If the addition of another feature does not significantly increase the

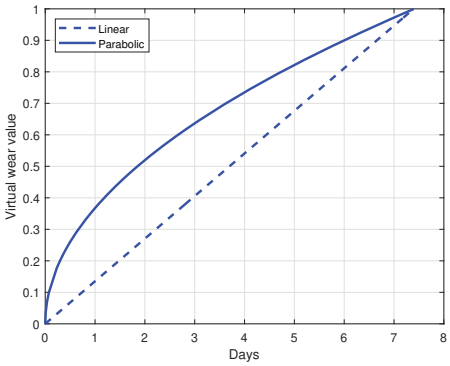

Figure 4: Virtual wear value for linear and parabolic assumption

measure, the feature selection process is stopped.

4.2 Virtual ground truth

As previously mentioned, there is no ground truth regarding the actual condition of the tool. However, a target value is necessary to estimate the tool state using regression. Therefore, a virtual ground truth for the wear is defined, assuming that the wear increases continuously over the course of the week.

Two different approaches are tested for the virtual wear. The first approach assumes a linear progression, starting at the value 0 at the beginning of the week and reaching the value 1 at the end of the week. The value 0 corresponds to the new condition of the tool, while 1 represents the maximum permissible wear at which the tool should be replaced.

The second approach assumes a parabolic progression, reflecting the shape of some of the selected features. This also starts at the value 0 and reaches the value 1 at the end of the week. Exemplary diagrams of the virtual linear and parabolic ground truths are shown in Fig. 4.

In both the linear and parabolic cases, the virtual ground truth does not reach the value 1 exactly after 7 days but slightly later. This is because the longest measurement period with one tool in the present test was slightly longer than 7 days. Therefore, the virtual ground truth was adjusted to reach the value 1 exactly at the end of the longest measurement period.

4.3 Regression

Once the features have been selected and the virtual wear has been defined, multivariate regression models are trained. The features serve as input variables for the regression model, while the virtual wear represents the target variable. Three different regression models of varying complexity are tested for this purpose. In linear regression [19], simple linear combinations of the input features are formed. This method assumes a linear relationship between the input features and the target variable, making it computationally efficient and easy to interpret. The model parameters are estimated by minimizing the sum of squared differences between the

observed and predicted values.

In support vector regression [20] (SVR), a non-linear method is trained using individual support vectors. SVR aims to find a function that deviates from the actual observed values by a value no greater than a specified margin, while simultaneously being as flat as possible. This method is particularly effective in handling high-dimensional data and capturing non-linear relationships.

In kernel regression [21], a sum of (nonlinear) kernel functions is formed using all training samples. This method allows for capturing complex relationships between the input features and the target variable by mapping the input space into a higher-dimensional feature space where linear separability is more likely.

The raw feature curves exhibit a tendency to be quite noisy, which is suboptimal for the inputs of the regression model. Consequently, it is tested whether smoothing the feature curves enhances the quality of the regression. For this purpose, Whittaker's smoother [22] is employed. Whittaker's smoother is a data smoothing technique designed to reduce noise in datasets while preserving important features. It works by fitting a smooth curve to the data using a penalized least squares approach. The method involves balancing the accuracy to the original data with a smoothness constraint, controlled by a smoothing parameter λ. This parameter determines the trade-off between fitting the data closely and achieving a smoother curve.

To evaluate a model's performance, the root mean square error (RMSE) [23] between the virtual ground truth and the prediction is computed. A lower RMSE value indicates a better model approximation. As noted by [23], the RMSE serves as a measure of accuracy, useful for comparing the estimation errors of different models on the same dataset, but not across different datasets due to its scale-dependence. Given that this scenario aligns with the context of this work, the application of RMSE is appropriate.

5 RESULTS

To briefly summarize the variants described in Section 4, the following different methods are now compared to achieve the best possible result for wear estimation: virtual ground truth forms, which include linear (assumes a straight-line relationship) and parabolic (assumes a quadratic relationship) forms; input signal processing, which involves smoothing (reduces noise in the data) and non-smoothing (uses raw data without noise reduction); and regression models, which consist of linear regression (models the relationship as a straight line), SVR (uses support vectors to model the relationship, effective for non-linear data), and kernel regression (uses kernel functions to handle non-linear relationships).

At the beginning, we would like to provide a brief overview of what typical features might look like. For instance, Fig. 5 shows the progression of a randomly selected feature (impulse factor of motor current) over the 5 test weeks. It can be observed that the feature does not exhibit a clear trend in any of the 5 weeks. Therefore, it can be assumed that this feature cannot represent the wear, which increases within each week.

In contrast, Fig. 6 shows the feature spectral spread of motor current selected by the feature selection process. A clear upward trend can be observed over the individual weeks (with the

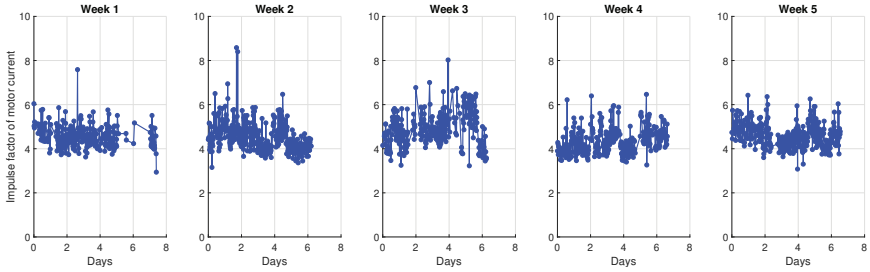

Figure 5: Randomly selected feature (impulse factor of motor current) over the 5 test weeks

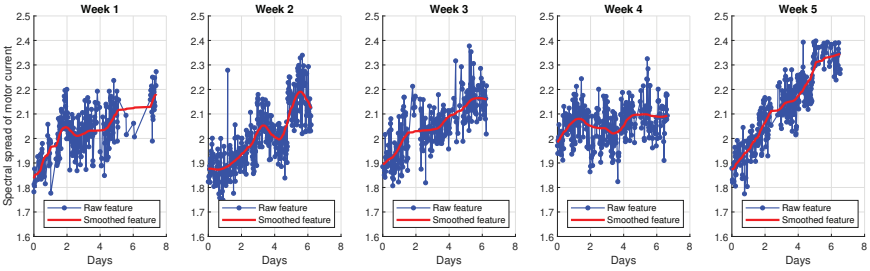

Figure 6: Feature (spectral spread of motor current) selected by the feature selection process

trend being least pronounced in week 4). Additionally, the smoothed trajectory using Whittaker's smoother (with $\lambda = 5$) is shown to provide an impression of how smoothing affects the feature trajectory.

In total, 3 features were selected by the feature selection process, namely the *median value of the temperature difference before and after cutting*, the *spectral spread of the motor current*, and the *median value of the motor current*. These features were used as inputs for the regression models, both in unsmoothed and smoothed form.

To test the regression models, leave-one-week-out cross-validation was used. In this approach, each of the five recorded weeks is once held back for testing, while the model is trained with the other four weeks. An exemplary result is shown in Fig. 7, specifically an SVR model with smoothed inputs and linear ground truth. The virtual ground truth is depicted in blue, and the model output is shown in red. It can be seen that the general trend is well captured. However, it is not yet possible to assess the true performance of the models based on the available data. This is mainly because the ground truth is only an assumption, and the actual tool wear was not determined through regular inspections.

The RMSE values for all tested cases are presented in Fig. 8. In the upper sub-figure, the results for the linear ground truth are displayed, while the lower sub-figure presents the results for the parabolic ground truth. The x-axis represents the regression models used, with non-smoothed and smoothed inputs distinguished by different colors. For the linear ground truth, it is evident that all three models yield similar results with non-smoothed input features. How-

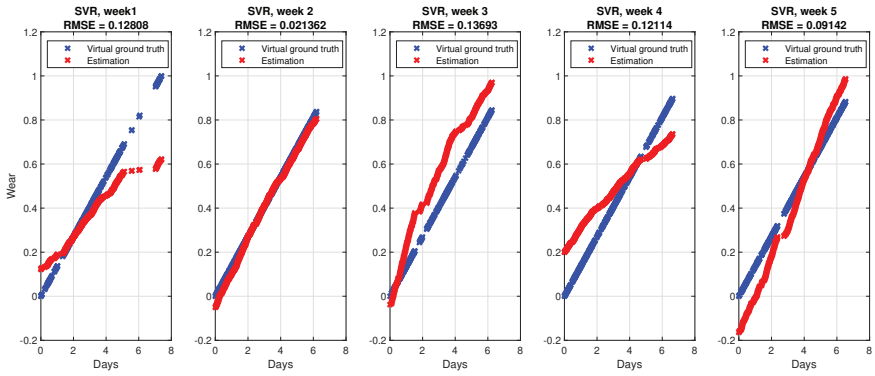

Figure 7: Wear estimation using SVR, smoothed inputs and linear wear

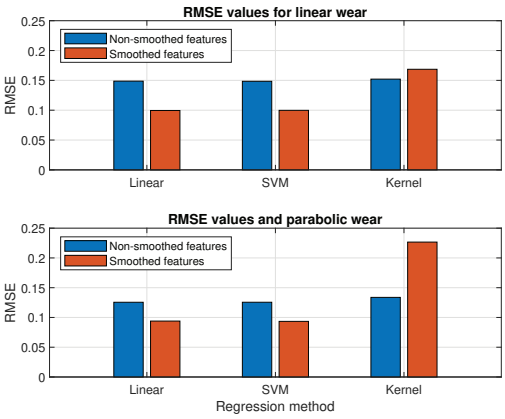

Figure 8: The RMSE values for all tested cases

ever, with smoothed input features, the performance of linear regression and support vector regression improves significantly, whereas the quality of kernel regression deteriorates. A similar trend is observed for the parabolic ground truth. Once again, the different models produce comparable results with non-smoothed features. For smoothed input features, the performance of linear regression and support vector regression increases, while it decreases for kernel regression. Moreover, it is significant to note that the performance discrepancies between linear regression and support vector regression are minimal, regardless of whether the ground truth is linear or parabolic. The only significant drop in performance is observed with kernel regression compared to the other regression methods.

6 CONCLUSIONS

This paper demonstrates the feasibility of modeling cutting tool wear using features derived from measured signals, acquired through a modular and distributed measurement and

processing system. Key features were extracted and selected, followed by training a regression model. Both linear regression and support vector regression yielded similar results, with linear regression preferred for its simplicity. Additionally, smoothing the input features improved the model's performance.

However, further development is needed before the system is ready for practical application. Crucially, additional test data must be collected. Additionally, a valid ground truth for wear, such as through regular tool inspections, is necessary. Different fiberboard types and machine settings should also be considered for the regression model.

ACKNOWLEDGMENT

This work has been supported by the COMET-K2 Center of the Linz Center of Mechatronics (LCM) funded by the Austrian federal government and the federal state of Upper Austria.

REFERENCES

[1] N. R. Tambake, B. B. Deshmukh, and A. D. Patange, "Data driven cutting tool fault diagnosis system using machine learning approach: A review," *Journal of Physics: Conference Series*, vol. 1969, no. 1, 2021.

[2] V. Sharma and A. Parey, "A review of gear fault diagnosis using various condition indicators," *Procedia Engineering*, vol. 144, pp. 253–263, 2016.

[3] D. Wang, K. Tsui, and Q. Mia, "Prognostics and health management: A review of vibration based bearing and gear health indicators," *IEEE Access*, vol. 6, pp. 665–676, 2017.

[4] S. Singh and M. Vishwakarma, "A review of vibration analysis techniques for rotating machines," *International Journal of Engineering Research & Technology*, vol. 4, no. 03, pp. 757–761, 2015.

[5] R. Salaets, V. Sturm, T. Ooijevaar, V. Putz, J. Mayer, and A. Bey-Temsamani, "Optical cutting tool wear monitoring by 3d geometry reconstruction," *PHM Society European Conference*, vol. 7, no. 1, pp. 449–457, 2022.

[6] L. Hörmann, C. Helmel, V. Putz, and C. Kastl, "DisDAQ - A Modular and Distributed Measurement and Processing System for Industrial Process Optimization," in *22. GMA/ITG-Fachtagung Sensoren und Messsysteme*, 01 2024, pp. 510–515.

[7] R. Labs, "K3s - lightweight kubernetes," 2025, version 1.21. [Online]. Available: https://k3s.io/

[8] O. M. Group, "Data distribution service (dds)," version 1.4. [Online]. Available: https://www.omg.org/spec/DDS/

[9] The Helm Authors, "Helm: The kubernetes package manager." [Online]. Available: https://helm.sh/

[10] I. Foxglove Technologies, “Foxglove studio.” [Online]. Available: https://foxglove.dev/product/visualization

[11] S. Koranne, “Hierarchical data format 5: Hdf5,” in *Handbook of Open Source Tools*. Springer, 2011, pp. 191–200.

[12] K. Pichler, M. Huemer, G. Kaineder, R. Schlosser, B. Dorfner, and C. Kastl, “Wear detection for a cutting tool based on feature extraction and multivariate regression,” in *2024 IEEE International Conference on Information Reuse and Integration for Data Science (IRI)*, 2024, pp. 90–95.

[13] L. Barbini, A. Ompusunggu, A. Hillis, J. du Bois, and A. Bartic, “Phase editing as a signal pre-processing step for automated bearing fault detection,” *Mechanical Systems and Signal Processing*, vol. 91, pp. 407–421, jul 2017.

[14] A. Hu, L. Xiang, S. Xu, and J. Lin, “Frequency loss and recovery in rolling bearing fault detection.” *Chinese Journal of Mechanical Engineering*, vol. 32, no. 35, 2019.

[15] M. Jalil, F. A. Butt, and A. Malik, “Short-time energy, magnitude, zero crossing rate and autocorrelation measurement for discriminating voiced and unvoiced segments of speech signals,” in *The International Conference on Technological Advances in Electrical, Electronics and Computer Engineering*, 2013, pp. 208–212.

[16] H. Wang and P. Chen, “Fault diagnosis of centrifugal pump using symptom parameters in frequency domain,” *Agricultural Engineering International: the CIGR Ejournal*, vol. IX, 2007.

[17] I. Guyon and A. Elisseeff, “An introduction to variable and feature selection,” *Journal of Machine Learning Research*, vol. 3, 2003.

[18] J. Dy and C. Brodley, “Feature selection for unsupervised learning,” *Journal of Machine Learning Research*, vol. 5, 2004.

[19] N. R. Draper and H. Smith, *Applied Regression Analysis*. John Wiley & Sons, Inc., 1998.

[20] A. J. Smola and B. Schölkopf”, “A tutorial on support vector regression,” *Statistics and Computing*, vol. 14, pp. 199–222, 2004.

[21] W. Härdle and M. Müller, *Multivariate and Semiparametric Kernel Regression*. Humboldt-Universität zu Berlin, Wirtschaftswissenschaftliche Fakultät, 1997.

[22] P. Eilers, “A perfect smoother,” *Analytical Chemistry*, vol. 75, no. 14, pp. 3631–3636, 2003.

[23] R. J. Hyndman and A. B. Koehler, “Another look at measures of forecast accuracy,” *International Journal of Forecasting*, vol. 22, no. 4, pp. 679–688, 2006.

XI ECCOMAS Thematic Conference on Smart Structures and Materials - SMART 2025
M. Krommer, M. Nader and M. Schagerl (Eds)

Received: 23 April 2025 / Revised: 31 July 2025 / Accepted: 11 October 2025
© The Author(s) 2025

Holistic Simulation Model for optimizing Piezoelectric Bone Conduction Implant with SyMSpace

Alexander Reininger, Lukas Grasböck, Daniel Reischl, Julia Lieber, Armin Stockhammer, Kathrin Sonntag

Abstract. Bone conduction hearing aids and bone conduction implants are a treatment option for conductive hearing damage in the outer and middle ear (conductive hearing loss). In this process, the sound information is transmitted through the skin by means of mechanical vibrations of transducers or directly at the skull bone through bone conduction to the cochlea. The implantation of a hearing aid is a significant intervention in the human body. In order to carry out this procedure in the least invasive way possible, the implants have to be designed to be very small. Implantable bone conduction transducers, which are based on the electrodynamic principle of a linear oscillator, can lead to problematic interactions during examinations in magnetic resonance imaging. Since piezoelectric materials generally have a higher power density than electromechanical components and are insensitive to electromagnetic fields, this article presents a possible piezoelectric alternative. Piezoelectric ceramics exhibit very stiff behavior due to their physical properties. Suitable designs must therefore be considered in order to achieve the desired electrical and mechanical system properties. Due to numerous criteria that can be adjusted and varied, a comprehensive multi-criteria optimization approach is particularly well-suited to achieve an optimal design. This multi-physical optimization is carried out using the software package SyMSpace, as it allows for orchestrating all the inputs and results needed for the different applications in this framework. Starting with the audio processor needed to transmit the voice to the receiver, followed by a re-conversion of the signal for the piezoelectric actuator to convert the electrical signal into a mechanical vibration, the entire workflow is described. Furthermore, the model is validated using measurements and simulations, and the optimization goals and results are illustrated.

Key words: Bone Conduction, Bonebridge, Smart Structures, Multiphysic Simulations, Piezoelectric Systems

Alexander Reininger & Lukas Grasböck & Daniel Reischl
Linz Center of Mechatronics GmbH, Altenbergerstr. 69, A-4040 Linz, Austria
e-mail: alexander.reininger@lcm.at

Julia Lieber & Armin Stockhammer & Kathrin Sonntag
MED-EL Medical Electronics, Fürstenweg 77a, 6020 Innsbruck, Austria

1 INTRODUCTION

The vibrations generated by piezoelectric or electromagnetic actuators can be used to improve hearing in patients with certain types of hearing loss. By converting an electrical signal into a vibration, these actuators in combination with an electronic system, can transmit sound directly through the skull bone to the cochlea, bypassing the outer and middle ear. This process, known as bone conduction, is also utilized in conventional headphones that allow users to hear ambient sounds while listening to music. Bone conduction technology has significant potential for use in hearing rehabilitation devices, particularly those designed to treat conductive or mixed hearing loss. Devices such as the Adhear (MED-EL) model feature an external transducer that stimulates the bone through the skin, providing a more discret and convenient option. In contrast, partially implantable devices incorporate a sealed actuator that directly stimulates the bone, minimizing signal loss caused by skin interference. To minimize the invasiveness of implanting a hearing aid, it is essential that the actuator itself is as compact as possible, yet also capable of delivering high output to ensure optimal hearing performance. However, these two requirements are inherently contradictory. In this particular application, piezoelectric actuators enable the optimization of compact designs with enhanced power density. Furthermore, an implantable hearing aid is not just a simple actuator driven by a constant excitation voltage, but comprises the entire system, including associated electronics, which must be minimized in terms of size and weight to maximize user comfort and convenience. MED-EL's implantable Bonebridge is illustrated in Figure 1. The audio processor transfers the signal via an inductive link to the hearing aid. The actuator itself transmits vibrations directly to the inner ear, thereby bypassing conductive or mixed hearing loss, where sound waves fail to reach the inner ear due to damage of the outer or middle ear.

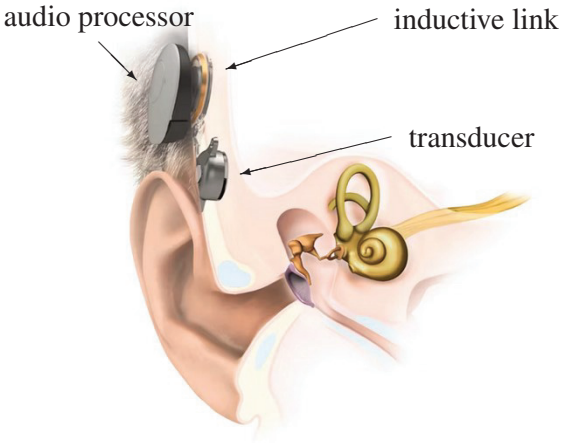

Figure 1: Anatomical illustration of MED-EL Bonebridge system with audio processor, inductive link and electromagnetic transducer BCI 602 [1]

To reconcile all limitations, the entire hearing aid system, encompassing both the mechanical actuator and its electronic components, was simulated using a multiphysical workflow. This approach required the integration of several software tools but allowed for efficient management of interfaces between different software solutions or intermediate calculations within a single workflow. The software tool SyMSpace was chosen to facilitate the integration of multiple simulations and calculations, allowing them to be executed as a single, cohesive workflow. Additionally, SyMSpace facilitates multi-criteria optimization, permitting the identification of the optimal solution that balances competing requirements, such as maximizing output while minimizing installation space.

2 MODELING

The workflow integrates mechanical, electrical, and software components using tools like LTspice [2], FEMM [3] and SyMSpace [4]. This involves designing and simulating the mechanical part, adding electrical components such as piezoelectric elements and sensors, and optimizing the system's behavior with these software tools. The results enables accurate predictions of the system's performance under various conditions, allowing improved design decisions and lowering the amount of prototypes needed. An overview of the workflow is given in Figure 2.

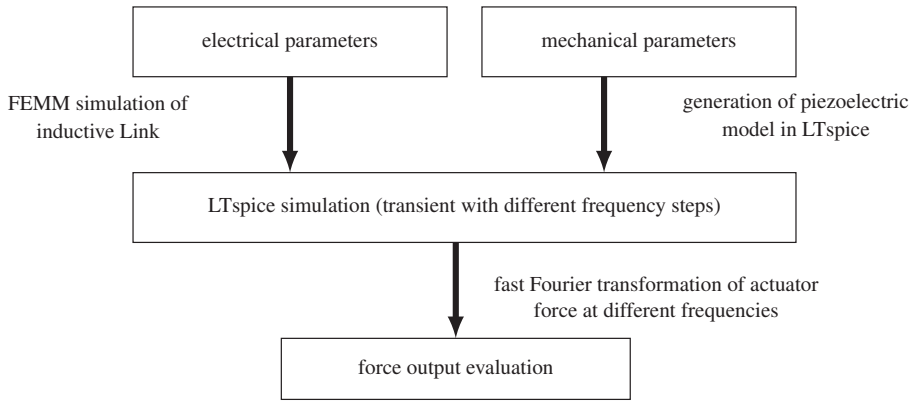

Figure 2: Overview of the simulation workflow

Two parallel workflows are employed in conjunction. On one hand, an analytical formulation of the mechanical model is transformed into a LTspice model, enabling simulation-based analysis. On the other hand, a FEMM (Finite Element Method of Magnetics) model is simulated to predict the performance of the inductive link responsible for transmitting electrical signals, thereby providing essential electrical parameters for the LTspice model. Subsequently, the LTspice model simulates the entire system, encompassing both mechanical and electrical aspects. The output force produced by the actuator serves as a reference point, playing a pivotal role in evaluating the implant's performance. Since a single frequency is insufficient for comprehensive analysis, multiple frequency points are computed, and a FFT (Fast Fourier Transform) is

performed to quantify the force and THD (Total Harmonic Distortion). To comprehensively assess the system's frequency response, a L2-norm is calculated across multiple frequency points.

2.1 Essential Parameters and Constraints

Currently only three implantable, active bone conduction devices are available on the market [5], including MED-EL's electromagnetic BCI 602, COCHLEAR's piezoelectric OSI 200 and OTICON's Sentio Ti. To develop a device that competes with these existing models, it was essential to adhere to their size and design standards. The dimensions used in this work (see Table 1) were chosen to be comparable to those of existing products, falling within the same order of magnitude.

Table 1: Dimensions of the three available active bone conduction implants on the market [1], [6] and [5]

	BCI 602	OSI 200	Sentio Ti
diameter	18.2 mm	31.4 mm	20.0 mm
thickness above the bone	min. 4.1 mm	4.9 mm	min. 2 mm

The dimensions of two of the devices are illustrated in Figure 3, which highlights the significant size differences between the various devices. Notably, as the actuator decreases in size,

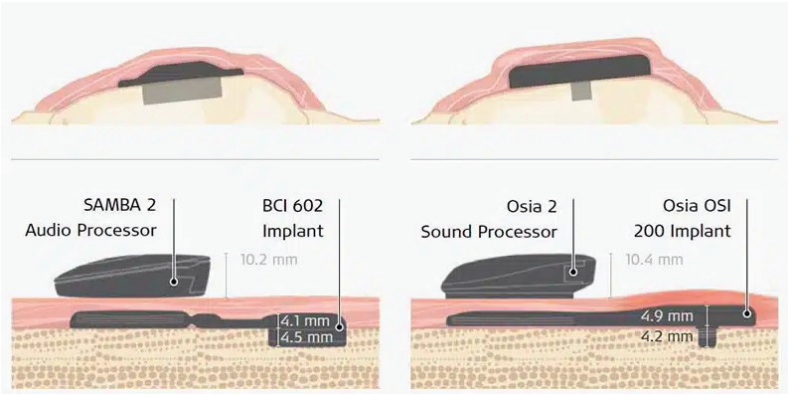

Figure 3: Bone conduction implant profile in comparison [7]

wearing comfort improves. If a significant reduction in height can be achieved while maintaining a constant diameter, skull penetration may be avoided, and the implantation procedure would be substantially simplified. Therefore, minimizing the device's dimensions while maintaining optimal performance was a key consideration throughout this design process.

2.2 Electrical Model

The electrical model was created and simulated using the LTspice simulation software. The electrical model consists of several key components: an audio processor that processes the sound wave into an electrical signal and modulates it onto a carrier, an inductive link that transmits the signal, a demodulator that extracts the useful signal from the carrier signal, and a piezoelectric actuator that converts the electrical signal into mechanical force (Figure 4).

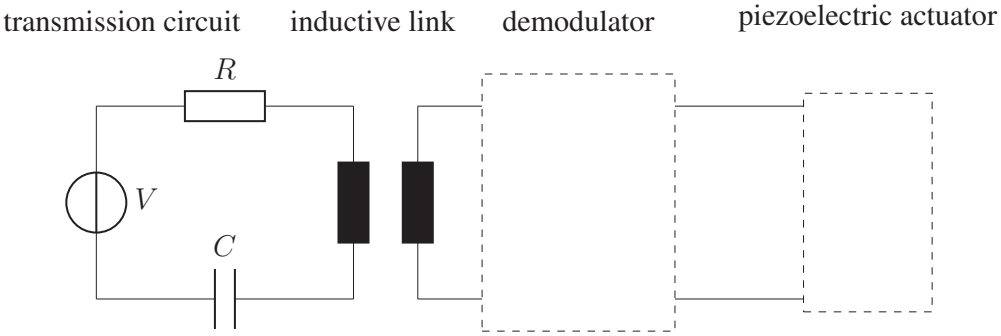

Figure 4: Transmission circuit schematic diagram with demodulator and piezoelectric actuator

The force generated by the actuator serves as the objective function for optimization. Ideally, this force should be maximized to achieve optimal performance. In addition, it is essential to ensure that harmonic distortion remains within acceptable limits during the electrical optimization process. This involves carefully selecting and tuning the components of the demodulator, transmitter, and inductive link to minimize signal degradation and maintain signal fidelity.

2.3 Mechanical Model

The mechanical model comprises three primary components: a piezoceramic assembly, a base mass, and an oscillating mass. This configuration is similar to the structure of the actuator from COCHLEAR's piezoelectric implant (see [8] and [5]). A detailed schematic of the setup used can be seen in Figure 5.

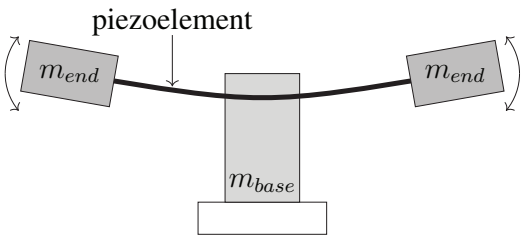

Figure 5: Simplified 2D model of the mechanical structure

The mechanical model was simplified to a 2D representation, allowing a more manageable analysis. The equation of motion was derived, taking into account the specific characteristics of the piezoelectric material. There are two primary formulations of the linear piezoelectric equations: the e-formulation and the d-formulation. The e-formulation can be expressed as [9], [10]:

$$\boldsymbol{\sigma} = \mathbf{C}^E \boldsymbol{\varepsilon} - \mathbf{e}^{\mathrm{T}} \mathbf{E}, \tag{1}$$

$$\mathbf{D} = \mathbf{e}\,\boldsymbol{\varepsilon} + \boldsymbol{\epsilon}^{\varepsilon} \mathbf{E}, \tag{2}$$

including $\mathbf{C}^E$, which represents the elasticity tensor at constant electric field, $\mathbf{e}^{\mathrm{T}}$ which defines the piezoelectric tensor, $\boldsymbol{\epsilon}^{\varepsilon}$ which is the electrical permittivity tensor at constant strain and $\boldsymbol{\varepsilon}$, which denotes the strain vector. The equations take into account the stress vector $\boldsymbol{\sigma}$, dielectric displacement $\mathbf{D}$ and electric field $\mathbf{E}$.
The equation of motion was obtained using the principle of virtual work.

$$\mathbf{M}\ddot{\mathbf{q}}(t) + \mathbf{D}\dot{\mathbf{q}}(t) + \mathbf{K}\mathbf{q}(t) = \mathbf{B}U(t), \tag{3}$$

with $\mathbf{M}$ as the mass matrix, $\mathbf{K}$ as the stiffness matrix, and $\mathbf{BU}(t)$ as the load vector. The electrical voltage is denoted by $U(t)$. The damping matrix $\mathbf{D}$ can be determined using the Rayleigh damping model. The deformation DOF is denoted by $\mathbf{q}(t)$. After converting the equation of motion into a system of first order equations

$$\dot{\mathbf{x}} = \begin{bmatrix} \mathbf{0} & \mathbf{I} & \mathbf{0} \\ -\mathbf{M}^{-1}\mathbf{K} & -\mathbf{M}^{-1}\mathbf{D} & -\mathbf{M}^{-1}\mathbf{B} \\ \mathbf{0} & \mathbf{Q}_w/C_p & \mathbf{0} \end{bmatrix} \mathbf{x} - \begin{bmatrix} 0 \\ 0 \\ -1/C_p \end{bmatrix} i, \tag{4}$$

with i as electric current, C_p as piezoelectric capacity and $\mathbf{I}$ as identity matrix, the equations can be solved in LTspice. The vector $\mathbf{x}$ can be written as follows

$$\mathbf{x} = \begin{bmatrix} w_0 & q_{w1} & q_{w2} & \dot{w}_0 & \dot{q}_{w1} & \dot{q}_{w2} & U \end{bmatrix}^{\mathrm{T}}. \tag{5}$$

The motion of the base mass is given as w_0, while q_{w1} and q_{w2} are the deformation DOF, and U represents the electrical voltage. An integrator subsystem (depicted in Figure 6) is used to solve the system of equations in LTspice. This integrator network represents one row of Equation

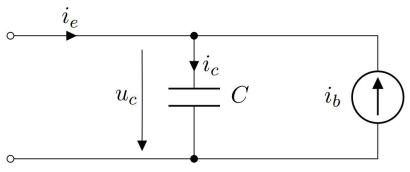

Figure 6: Integrator subsystem in LTspice

4. To solve the entire system, a corresponding set of equations must be constructed to be able to simulate the entire system of equations in Equation 4. The network consists of the external current i_e, the current of the controlled current source i_b and the current through the capacitor i_c (see Figure 6).
A systematic model validation was conducted to ensure accuracy and prepare for subsequent optimization studies. Comparative analyses revealed conformity between the simplified analytical model and FEM simulations with respect to measured data (see Figure 7) This validated model served as a basis for subsequent optimization studies conducted within SyMSpace. In the measurement, additional resonances appeared at approximately $3000\,\mathrm{Hz}$ and $6000\,\mathrm{Hz}$. These resonances are modes, which are not accounted in the simulation model.

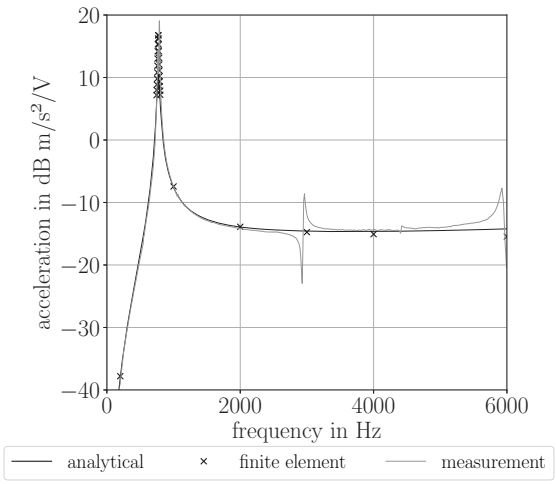

Figure 7: Model validation with FEM and measurement

3 OPTIMIZATION

The next step in automating the design process is to close the optimization loop, as illustrated in Figure 8. A SyMSpace model typically contains fixed parameters, representing a single design or a small set of designs for comparison purposes. To achieve multi-objective optimization, the Optimizer tool (indicated by blue arrows) adjusts the parameters of a SyMSpace model (black arrows). This allows the model to explore various design spaces and identify optimal solutions that meet multiple criteria. The external Optimizer tool, which is part of the SyMSpace platform, modifies the design parameters to maximize or minimize specified cost functions within the SyMSpace model. Several advanced optimization algorithms are available to ensure rapid and reliable convergence. When using the Optimizer tool, any variable within the SyMSpace model can be designated as a design parameter or optimization goal. To prevent excessive iteration and ensure reasonable results, restrictions on the design variables can be applied, and their resolution can be resolved if necessary.

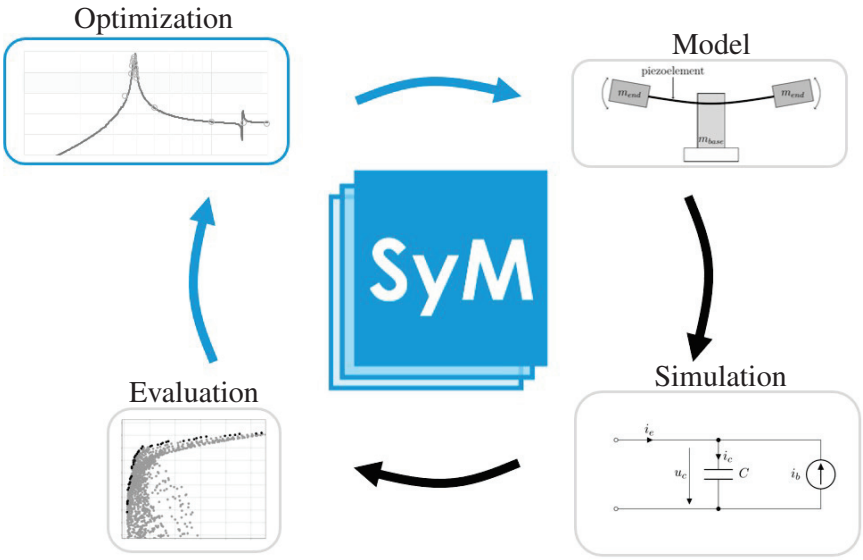

Figure 8: The Optimizer (blue arrows) adjusts the parameters of a SyMSpace model (black arrows) to enable multi-objective optimization.

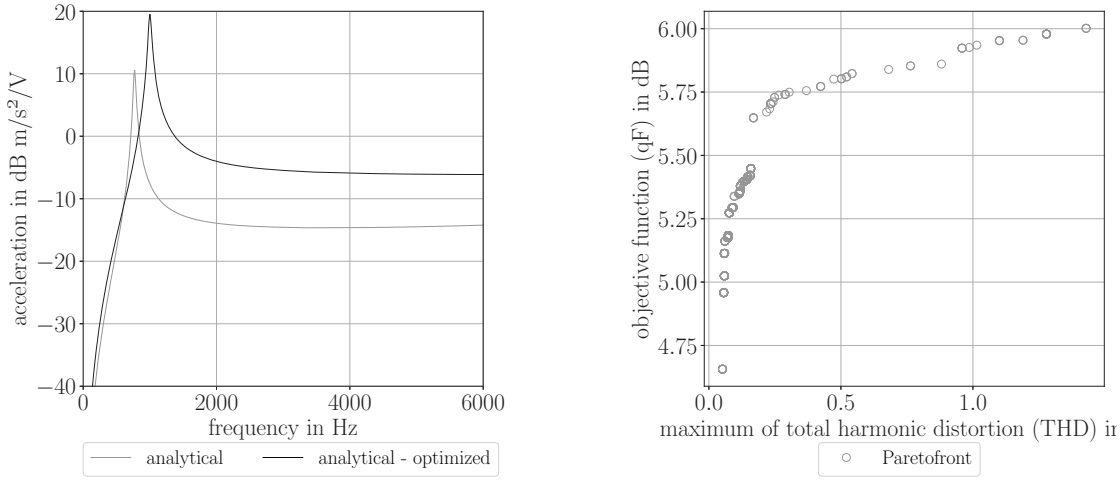

Figure 9: Comparison of measurement, finite element simulation and analytical simulation left, and Pareto front right

Considering the inherently stiff characteristics of piezoelectric elements, it is essential to carefully optimize their geometric configuration to maintain a flat frequency response within the audible range (approximately from 200 Hz to 6000 Hz). The objective is to achieve a

very low first natural frequency while observing a stable plateau above 1000 Hz (illustrated in Figure 9). However, this goal is typically compromised by the trade-off between mechanical compliance and achievable output power, as increased geometric softening leads to decreased output.

The optimization parameters included the entire inductive link structure (primary and secondary coils), the electrical parameters of the demodulator, the dimensions of the piezoelectric element (thickness and length), as well as the endmass (dimensions and its associated weight).

The results of the optimization are depicted in Figure 9, where the Pareto front [11] for the optimized actuator with respect to electrical control is depicted as well as the frequency behavior of the new design. The Pareto frontiers were obtained using the Differential Evolution-based Co-evolutionary Multi-Objective (DECMO) optimization algorithm. A detailed discussion of this algorithm can be found in [12] and [13].

Typically, several individuals from the Pareto front are extracted and their results evaluated in terms of frequency response. However, since the electrical parameters also need to be adjusted based on available parameters, multiple individuals from the Pareto front are selected and manually adapted. Furthermore, a suitable choice of mechanical parameters is made, as well as any necessary adjustments to the end mass, due to discrepancies in CAD geometries. After the adaption, the system is then simulated once more to evaluate the effects of the adjustments. A critical point when dealing with such small structures is the attachment of the end mass and clamping mechanism. Considering the stiffness of the piezoceramic, it becomes apparent that a very stiff clamping setup must be chosen. However, this is not always feasible or can even be impossible for a functional samples, and therefore must be accurately represented in simulation accordingly.

4 CONCLUSIONS AND SUMMARY

A comprehensive workflow for designing and optimizing a piezoelectric actuator was presented, covering design parameters, as well as the challenges associated with such tiny structures. A comparison with a simplified analytical model was shown, and the necessary steps for developing a piezoelectric implant was highlighted. Additionally, an optimized solution for a piezoelectric actuator was proposed.

5 ACKNOWLEDGMENT

This work has been supported by the COMET-K2 Center of the Linz Center of Mechatronics (LCM) funded by the Austrian federal government and the federal state of Upper Austria.

REFERENCES

[1] MED-EL, “Which active bone conduction implant: Bonebridge and osia compared,” https://web.archive.org/web/20241104214217/https://www.medel.com/de-at/hearing-solutions/bonebridge, 2024, accessed: 2024-11-04.

[2] Linear Technology Corporation, Mike Engelhardt, "LTspice: Version IV," https://www.analog.com/en/resources/design-tools-and-calculators/ltspice-simulator.html, 2016.

[3] P. David Meeker, "Femm: Version 4.2," https://www.femm.info/wiki/HomePage, 2019.

[4] Linz Center of Mechatronics GmbH , "Symspace: Version 1.5," https://symspace.lcm.at/, 2020.

[5] D. Reischl, J. Lieber, and T. Lechleitner, "Piezoelectric bone-conduction devices and active middle ear implants - motivation, challenges and promising approaches," in *5. Symposium für Smarte Strukturen und Systeme – 4SMARTS (2024)*, Darmstadt, Germany, 11 2024.

[6] C. Americas and C. C. Inc, "How the osia® system works," https://web.archive.org/web/20240705230427/https://assets.cochlear.com/api/public/content/OSI086-Osia-System-Datasheet.pdf, 2022, accessed: 2024-07-05.

[7] MED-EL, "Which active bone conduction implant: Bonebridge and osia compared," https://web.archive.org/web/20230529190214/https://blog.medel.com/technology/which-active-bone-conduction-implant-bonebridge-and-osia-compared/, 2025, accessed: 2025-01-19.

[8] C. Australia and N. Zealand, "How the osia® system works," https://www.youtube.com/watch?v=-Fl4uhPClOs, 2022, accessed: 2025-03-28.

[9] A. Pechstein, M. Meindlhumer-Schmidthaler, and A. Humer, "New mixed finite elements for the discretization of piezoelectric structures or macro-fiber composites," *Journal of Intelligent Material Systems and Structures*, vol. 29, pp. 3266–3283, 07 2018.

[10] Y. J., *An Introduction to the Theory of Piezoelectricity*. Boston: Kluwer Academic Publishers, Jan. 2005.

[11] C. Zavoianu, G. Bramerdorfer, E. Lughofer, and S. Saminger-Platz, "Multi-objective topology optimization of electrical machine designs using evolutionary algorithms with discrete and real encodings," 01 2018, pp. 331–338.

[12] C. Zavoianu, G. Bramerdorfer, E. Lughofer, S. Silber, W. Amrhein, and E. P. Klement, "Hybridization of multi-objective evolutionary algorithms and artificial neural networks for optimizing the performance of electrical drives," *Engineering Applications of Artificial Intelligence*, vol. 26, pp. 1781–1794, 09 2013.

[13] C. Zavoianu, E. Lughofer, G. Bramerdorfer, W. Amrhein, and E. P. Klement, "Decmo2: a robust hybrid and adaptive multi-objective evolutionary algorithm," *Soft Computing*, vol. 19, 06 2014.

XI ECCOMAS Thematic Conference on Smart Structures and Materials - SMART 2025
M. Krommer, M. Nader and M. Schagerl (Eds)

Received: 3 April 2025 / Revised: 22 August 2025 / Accepted: 11 October 2025
© The Author(s) 2025

Design and Experimental Characterization of Rotatory Magnetorheological Actuators

Thomas Wiener, Christina Offenzeller, Bernhard Jakoby

Abstract. Magnetorheological (MR) fluids are smart materials whose rheological properties can be dynamically changed by applying a magnetic field, offering versatility in engineering and scientific applications. Basically, MR fluids consist of two main components: ferromagnetic particles dispersed in a carrier fluid such as hydrocarbon oil. An actuator design with a waveform boundary shaped (star geometry) rotor will be presented, which improves torque generation. Compared to traditional disk designs, the star geometry introduces additional functional mechanisms, that improve the maximal possible torque. In this study, we compared the two different cross-sections for the central fixed rod in such an actuator. The star contour yielding localized higher fields and the disk contour featuring a virtually constant field distribution over the entire circumference. Both contours were compared for the same mean magnetic field strength. Our results show that the star contour has some improvements over the disk contour. These include the elimination of the previously observed initial fluid activation and improved remanent idling performance. In addition, both actuators showed high robustness in terms of repeatability.

Keywords: Magnetorheological Actuator, Magnetorheological Fluid (MRF), Rotary Actuator, Star Geometry.

1 INTRODUCTION

Magnetorheological (MR) fluids are a class of smart materials with the ability to swiftly change their rheological properties from a fluid-like behavior to a near solid state under the influence of an external magnetic field thus providing the opportunity to realize devices with tunable mechanical properties [1-4]. The two main components, magnetizable particles and a carrier fluid, together with other additives, define the behavior of the fluid [5]. Without a magnetic field, the viscosity of the MR fluid is low. However, when exposed to a magnetic field, the ferromagnetic particles in the fluid align into chain-like structures along the lines of the magnetic field [6]. This increases the fluid's viscosity, thus increasing the shear stress required to sustain a given shear rate [7,8].

Thomas Wiener & Christina Offenzeller
STIWA Advanced Products GmbH, Technologiepark 10, 4851 Gampern, Austria
e-mail: thomas.wiener@stiwa.com

Bernhard Jakoby
Inst. for Microelectronics and Microsensors, Johannes Kepler University Linz, Altenbergerstr. 69, A-4040 Linz, Austria,
e-mail: bernhard.jakoby@jku.at

In an earlier work [9], we identified a generalized demagnetization routine that can degauss the particles but also disperses clusters of particles that have built up during magnetization. At the same time, a so-called shear history [10] or long-term non-stationary behavior [9] was observed in the experimental setup that was used in these studies, where it turned out that as soon as a fresh (unused) MR fluid had been used, a certain residual viscosity could not be eliminated even by these generalized demagnetization routines. As the design of the experimental setup used in [9] may promote segregation of carrier oil and iron particles, this was considered as a possible cause for this effect, which we refer to as *initial activation* and which will also be discussed below.

The aim of our work is to particularly study the impact of the working gap, which is filled with MR fluid, on the performance of a haptic feedback device. We consider rotary actuators such as “hapticore” [11] that are already used in a wide range of applications. Examples include integration into mouse wheels (in a compact design), control of CNC milling machines, and the development of a multi-functional rotary knob for selecting display functions in the automotive sector (e.g. for volume control and navigation, which require different detent functions).

While MR fluid-based actuators are already on the market, comprehensive models for device design are still scarcely available. Current other research work focuses on the response time [12], control performance [13], development of novel designs [14] and analysis of haptic devices based on MR fluids [15,16].

Nam and Ahn were the first to describe a so-called waveform boundary structure in the context of a rotary disk actuator and found that other mechanical effects occur in addition to pure shear stress behavior [17]. Their investigations showed that by introducing an arc waveform boundary structure, the transmittable torque could be increased by up to 600% compared to a classic disk. Mousavi et al. applied a similar structural approach to the development of an artificial knee joint based on a rotary MR fluid actuator. Improved performance was achieved by using the waveform boundary structure [18]. Building on this concept, Saini et al. used an optimization approach to investigate different structural variants in order to identify an optimal geometry. They also concluded that in addition to shear forces, other forces contribute significantly to torque transmission in an arc waveform boundary structure [19].

Common to all the three works is that they use circular arc waveform structures and focus primarily on their modeling and computational analysis. In contrast, the present work investigates a new type of structure that is geometrically different from the previous approaches: Instead of a circular contour, an involute-like structure is used named star geometry [20]. The aim of this design is to improve the flow conditions within the MR fluid gap, to locally concentrate the magnetic flux density and thus to optimize the formation of chain-like particle structures and the resulting force transmission.

The presented structure is implemented in a rotating MR fluid actuator and compared to a classical flat disk structure with respect to several aspects relevant for the use in haptic control elements. The focus is not on numerical simulation or analytical modeling, but on a phenomenological and experimental consideration of the interactions.

2 DESIGN AND MAGNETIC FIELD DISTRIBUTION

The basic design of the actuator, as illustrated in Fig. 1, consists of a radially symmetric rotor which rotates around a stator with the MR fluid in between. The stator (yellow) is a stationary cylinder which also carries the field-generating coil. The rotor (green) rotates around the stator. Both parts are made of free machining steel with appropriate magnetic and mechanic properties. Between the stator and the rotor is the MR fluid chamber (red), which is sealed with a complex rotary seal. The sealing system is a complex unit that acts as a bearing between the rotor and stator. It also reliably confines the MR fluid within the MR chamber throughout its entire service life.

The interaction area, or working gap, is located around the entire circumference at the top and at the bottom of the stator, and $r = 16.56$ mm denotes the radius at the center of the gap at the peaks. The geometrical advantages of the magnetically radial design in Fig. 1 compared to a rheometer design or the horizontal disk from the test setup from [9,21] is that the working gap is located at a position featuring maximum shear rate, yielding maximum impact on the torque.

The magnetic flux is generated by a coil in the stator and runs along the red dashed lines sketched in Fig. 1(a). The magnetic field penetrates the interaction area radially and closes across the rotor.

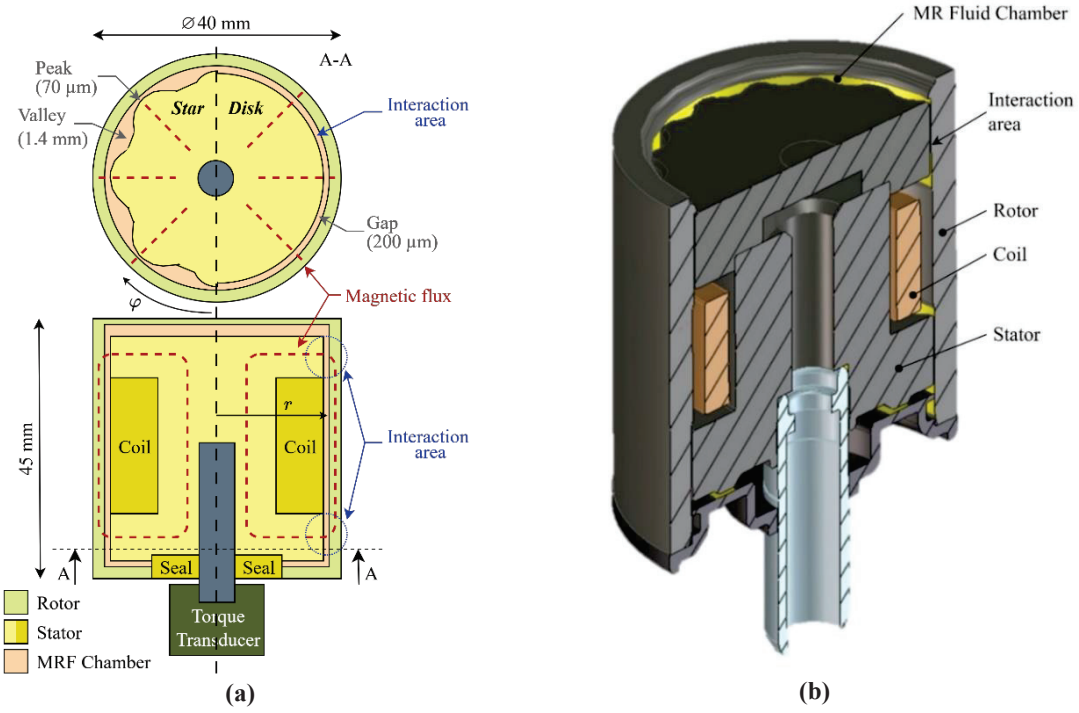

Figure 1: **(a)** Basic design of the rotary actuator with stator, rotor, and MR fluid chamber with star and disk contour (cross section). The coil wires intersect this cross section orthogonally to the drawn plane. For reasons of clarity, the schematic diagram shows the actuator with eight peaks in total. In the measured actuator a total of sixteen peaks are used. **(b)** A 3D representation of half of the actuator is shown with the star contour.

Based on the basic design in Fig. 1, the investigations focus on two different stator designs. First, we measure what we refer to as a *star geometry*, shown on the left upper part of Fig. 1(a). The design of the star contour is the result of calculations and numerous intuitive trial and error attempts to produce an actuator with high braking torque, low idle torque, and a distinct response upon actuation for which a patent has been granted [20]. The geometry is similar to an involute gear wheel with a defined number of teeth (sixteen) referred to as peaks. Between two peaks there is a sufficiently large interdental space (valley), which serves as dead volume (where the magnetic field strengths are minimal) and storage space for the MR fluid but also supports the magnetic flux concentration in the peaks. The gap size, which is the distance between stator and rotor filled with MR fluid, ranges from 70 µm to 1.37 mm, depending on whether it is measured from the peak or the valley of the stator.

Secondly, to have a reference, we have investigated a cylindrical contour with a constant gap size of 200 µm, referred to as *disk*, shown on the right upper part of Fig. 1(a). Both designs were completely filled with MR fluid, resulting in a higher fill volume in the star design due to the associated large interdental space.

The MR fluid is a commercially available fluid of type MRF-140BC, consisting of synthetic oil containing 40% by volume of carbonyl iron particles, and was supplied by LORD Corporation (USA). To ensure uniform particle distribution and to avoid sedimentation, the fluid was thoroughly redispersed before filling the chamber. This was achieved by two-stage mixing: First, the container was placed in a uniaxial mixer for at least two hours to disperse the iron particles. Second, a biaxial shaker was then used to break up potential particle agglomerates by shaking the container for at least 20 minutes. Various methods, including density measurement and visual analysis, were used to verify the manufacturer's specification of 40 vol% iron.

Many models are used to describe the relationship between the magnetic field, the shear rate, and the resulting shear stress. In case of MR fluids, the Bingham model

$$\tau(H) = \tau_0(H) + \eta\dot{\gamma} \tag{1}$$

is a particularly useful model to describe the non-Newtonian behavior, where τ is the shear stress caused from the MR fluid as a function of the yield stress τ_0 (depending on the applied magnetic field strength H), the dynamic viscosity η and the shear rate $\dot{\gamma}$ [2-4].

On the test bench we can only directly measure the torque at a defined coil current. The associated shear stresses particularly in case of the star design are non-uniform, so we decided to compare the measured torques, which are proportional to the shear stress at the outer perimeter of the MR fluid chamber, i.e. the inner surface of the rotating cylinder.

The two configurations (star and disk) share identical components including coils, core material, rotor, and magnetorheological fluid; the only differences are the contour. Due to the different working gaps, distribution of the magnetic field in the gaps differs as well.

Fig. 2 shows the magnetic field distribution calculated using the finite element method (Ansys Maxwell) over the angle for the star contour on the left for a gap filled with uniformly dispersed and non-remanent MRF-140BC. The effect of the four peaks indicated in the geometry shown in Fig. 1(a) can be seen in the calculation where the magnetic field is analyzed at the radius r and is plotted versus the angle. Obviously, field strengths reach a maximum when

the gap thickness is minimal and vice versa. However, at minimal gap size, the star geometry yields pronounced field spikes, with maximum field strengths H_{peak} = 450 kA/m higher than in the valley. The MR fluid therefore experiences regions of alternating (high and low) field strengths. On the right, Fig. 2 shows the associated results for a disk design with a 200 µm gap yielding a uniform angular distribution.

Since the field distributions are distinctly different and the field strength is essential for the force effect in the MR fluid, we decided to compare the two designs for the case that the mean magnetic field along the outer perimeter of the MR fluid chamber is the same by choosing the excitation currents accordingly.

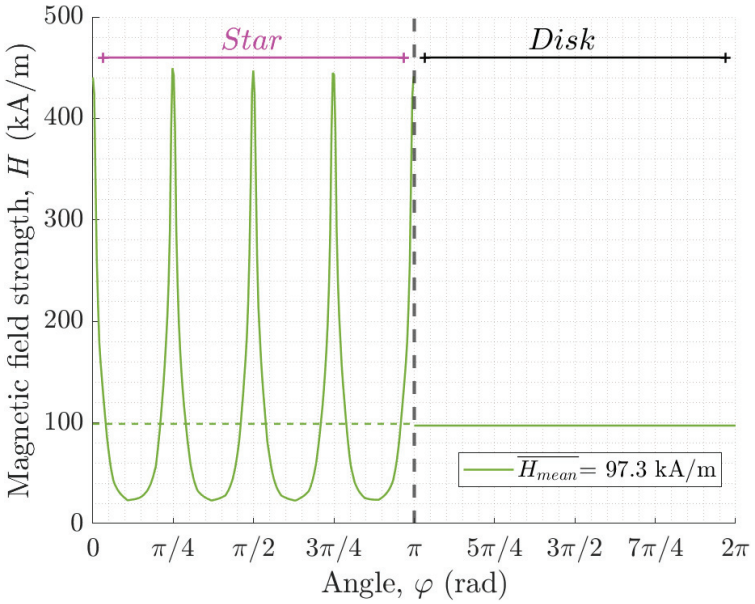

Figure 2: Magnetic field strengths H_{mean} over the angle in the interaction area, calculated using the finite element method. On the left is the result for the star contour with the mean field strength shown as dashed line and on the right the disk contour. Both contours have the same mean magnetic field strengths.

3 RESULTS

A major application of these designs would be a rotary actuator for use in human computer interaction systems. Such a device must be able to realize resistance against mechanical rotation ranging from free rotation (idle) to blocking at an applied maximum torque (barrier). Short detents must also be possible in between to, e.g., simulate the behavior of rotary encoders with detents.

The star contour should improve the performance compared to a classic disk actuator with respect to known issues [9]. Associated improvements include the elimination of the so-called initial fluid activation, reduced power consumption (at equal torques and magnetic high field strengths) and lower remanent idle.

3.1 Initial irreversible fluid activation

In a previous work [9], we observed a so-called initial irreversible fluid activation, where the very first measurement with a new MR fluid resulted in a lower torque (at prescribed angular speed) than in subsequent measurements. This behavior can also be seen in Fig. 3 for the disk actuator: the first measurement (1st) is lower than the second (2nd) and subsequent measurements (not shown here) under the same conditions. Using indirect inductance measurements and a physically inspired model [21], we suggested a possible explanation for this effect at the disk actuator as an accumulation of iron particles in the working gap (i.e. a segregation of the MR fluid).

The star contour does not show this behavior, and the 1st and 2nd (and subsequent) measurements show nearly the same torque curve, as shown in Fig. 3. The reason for the more stable behavior associated with the star design is supposedly related to the small gaps and the neighboring larger fluid pockets (valleys between the peaks) and possibly the associated enforced mixing during rotation. While these speculations are somewhat supported by the inductance measurements, they remain an experimental finding at this stage.

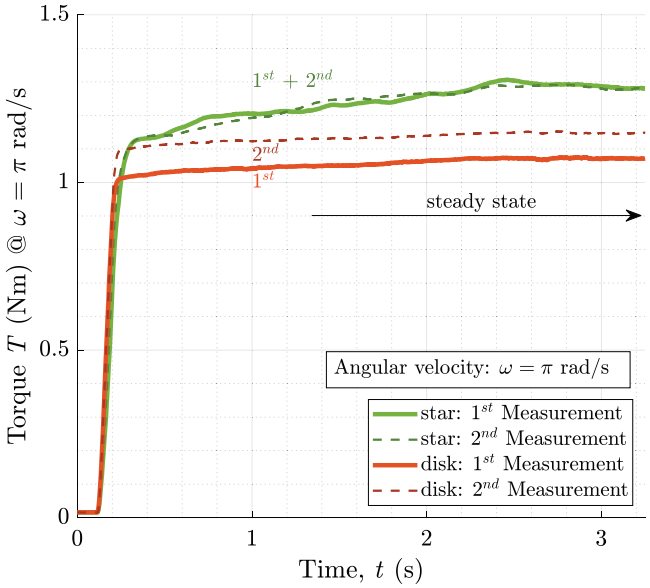

Figure 3: Torque over time for a magnetic field strength of H_{mean} = 97.3 kA/m with 1st and 2nd measurement for a rotational speed of $\omega = \pi$ rad s^{-1}, which corresponds to a shear rate of 234 s^{-1} across the gap of the disk.

3.2 Steady state

In the steady state, when the transients of the switching-on process have decayed (t > 3s), the star contour achieves a higher torque at the same average field strength as the disk contour. However, the power consumption associated with the star design is lower, because for a magnetic field of H_{mean} = 97.3 kA/m, the star contour requires a current of 610 mA while the disk device requires 1000 mA. As a result, the device utilizing the star contour required only 37% of the power associated with the disk design.

3.3 Rise time

The rise time (time required for the torque to change from 10% to 90% of the step level) is the same for disk and star at lower field strengths (not shown here). Fig. 4 shows the rise time for the measured field strength $H_{\text{mean}} = 97.3$ kA/m for both actuator geometries. Initially, the rise time is the same for both, but above 0.3 Nm the disk rises significantly faster than the star. The rise time of the disk is therefore superior to that of the star.

The reason for this seems to be that at low magnetic field strengths, the active surface of the peaks is large enough for sufficient chains and particle cluster to form and for all the flux to flow over them without saturation, so the chains can form quickly. At higher field strengths, the surface across the peak is initially sufficient, but then chains must form outside the active surface of the peak and expand into the valleys, and the chains must also migrate into longer and thicker structures [22,23]. This takes longer because the distance to be bridged is greater and the particles have to be brought up sufficiently from the valleys.

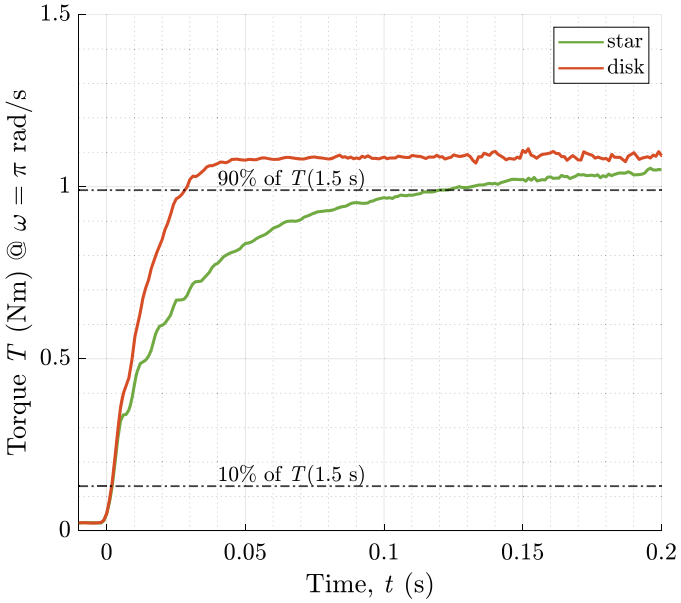

Figure 4: Torque over time curve for a current jump to the same mean magnetic field strength $H_{\text{mean}} = 97.3$ kA/m. For the disk there is a jump from 0 to 1 A, for the star from 0 to 0.6 A respectively.

4. CONCLUSION

We have considered designs for a rotary actuator device, where we introduced a contour (star design) which improves many characteristics compared to a conventional disk cylinder rotatory actuator. In particular, the star actuator requires no initial activation and achieves the higher torque at only 37% of the disk power, which is important for battery powered applications.

ACKNOWLEDGMENT

This project was partially supported by the Austrian Research Promotion Agency (FFG) under the funding code 53106862.

REFERENCES

[1] Rabinow, J. (1948). The Magnetic Fluid Clutch. *Transactions of the American Institute of Electrical Engineers*, **67(2), 1308–1315**. https://doi.org/10.1109/t-aiee.1948.5059821

[2] Chen, D., Song, A., Tian, L., Ouyang, Q. & Xiong, P. (2019). Development of a Multidirectional Controlled Small-Scale Spherical MR Actuator for Haptic Applications. *IEEE/ASME Transactions On Mechatronics*, **24(4), 1597–1607**. https://doi.org/10.1109/tmech.2019.2916099

[3] Shafer, A. S. & Kermani, M. R. (2011). On the Feasibility and Suitability of MR Fluid Clutches in Human-Friendly Manipulators. *IEEE/ASME Transactions On Mechatronics*, **16(6), 1073–1082**. https://doi.org/10.1109/tmech.2010.2074210

[4] Qin, H., Song, A., Gao, Z., Liu, Y. & Jiang, G. (2018). A Multi-Finger Interface with MR Actuators for Haptic Applications. *IEEE Transactions On Haptics*, **11(1), 5–14**. https://doi.org/10.1109/toh.2017.2709321

[5] Carlson, J. D. (2002). What Makes a Good MR Fluid? *Journal of Intelligent Material Systems and Structures*, **13(7–8), 431–435**. https://doi.org/10.1106/104538902028221

[6] Tao, R. (2001b). Super-strong magnetorheological fluids. *Journal of Physics: Condensed Matter*, **13(50), R979–R999**. https://doi.org/10.1088/0953-8984/13/50/202

[7] Rossa, C., Eck, L., Micaelli, A. & Lozada, J. (2014). On a Novel Torque Detection Technique for Magnetorheological Actuators. *IEEE Sensors Journal*, **14(4), 1223–1231**. https://doi.org/10.1109/jsen.2013.2287730

[8] Becnel, A. C., Hu, W. & Wereley, N. M. (2012). Measurement of Magnetorheological Fluid Properties at Shear Rates of up to 25 000 s^{-1}. *IEEE Transactions On Magnetics*, **48(11), 3525–3528**. https://doi.org/10.1109/tmag.2012.2207707

[9] Wiener, T., Offenzeller, C., Martetschläger, D., Wimmer, D., Spirowski, T., & Jakoby, B. (2024). Phenomenological studies on magnetic and mechanical remanence effects in magnetorheological fluids. *Smart Materials and Structures*, **33(4), 045004**. https://doi.org/10.1088/1361-665x/ad2aa7

[10] Shan, L., Chen, K., Zhou, M., Zhang, X., Meng, Y., & Tian, Y. (2015). Shear history effect of magnetorheological fluids. *Smart Materials and Structures*, **24(10)**. https://doi.org/10.1088/0964-1726/24/10/105030

[11] "Hapticore." STIWA. https://www.stiwa.com/en/manufacturing/advanced-products/hapticore (accessed Apr 3, 2025)

[12] Kikuchi, T., Noma, J., Akaiwa, S., & Ueshima, Y. (2015). Response time of magnetorheological fluid–based haptic device. *Journal of Intelligent Material Systems and Structures*, *27***(7), 859–865**. https://doi.org/10.1177/1045389x15596621

[13] Han, Y., Kim, C., & Choi, S. (2008). A magnetorheological fluid-based multifunctional haptic device for vehicular instrument controls. *Smart Materials and Structures*, **18(1), 015002**. https://doi.org/10.1088/0964-1726/18/1/015002

[14] Ryu, S., Koo, J., Yang, T., Pyo, D., Kyung, K., & Kwon, D. (2014). Design, simulation, and testing of a magnetorheological fluid–based haptic actuator for mobile applications. *Journal of Intelligent Material Systems and Structures*, **26(13), 1670–1678**. https://doi.org/10.1177/1045389x14536009

[15] Liu, B., Li, W. H., Kosasih, P. B., & Zhang, X. Z. (2006). Development of an MR-brake-based haptic device. *Smart Materials and Structures*, **15(6), 1960–1966**. https://doi.org/10.1088/0964-1726/15/6/052

[16] Najmaei, N., Kermani, M. R., & Patel, R. V. (2014). Suitability of Small-Scale magnetorheological Fluid-Based clutches in haptic interfaces for improved performance. *IEEE/ASME Transactions on Mechatronics*, ***20*(4), 1863–1874.** https://doi.org/10.1109/tmech.2014.2357447

[17] Nam, T. H., & Ahn, K. K. (2009). A new structure of a magnetorheological brake with the waveform boundary of a rotary disk. *Smart Materials and Structures*, **18(11), 115029**. https://doi.org/10.1088/0964-1726/18/11/115029

[18] Mousavi, S. H., & Sayyaadi, H. (2018). Optimization and testing of a new prototype hybrid MR brake with arc form surface as a prosthetic knee. *IEEE/ASME Transactions on Mechatronics*, **23(3), 1204–1214**. https://doi.org/10.1109/tmech.2018.2820065

[19] Saini, R. S. T., Kumar, H., & Chandramohan, S. (2020). Optimal design of inverted rotary MR brake with waveform boundary using a novel combined magnetostatic approach. *Smart Materials and Structures*, **29(10), 105014**. https://doi.org/10.1088/1361-665x/aba176

[20] Inventus Engineering GmbH & Battlogg, S. (2023). MAGNETORHEOLOGICAL BRAKING DEVICE (Patent No. US2023375052A1). U.S. Patent and Trademark Office. https://worldwide.espacenet.com/patent/search/family/078414622/publication/US2023375052A1?q=pn%3DUS2023375052A1

[21] Wiener, T., Offenzeller, C., Berger, D., & Jakoby, B. (2024). In situ monitoring of the iron content in magnethorheological rotary actuators. *Smart Materials and Structures*, **33(11), 115044**. https://doi.org/10.1088/1361-665x/ad85b4

[22] Jolly, M. R., Bender, J. W., & Mathers, R. T. (1999). Indirect measurements of microstructure development in magnetorheological fluids. *International Journal of Modern Physics B*, **13(14n16), 2036–2043**. https://doi.org/10.1142/s0217979299002113

[23] Kubík, M., Válek, J., Žáček, J., Jeniš, F., Borin, D., Strecker, Z., & Mazůrek, I. (2022). Transient response of magnetorheological fluid on rapid change of magnetic field in shear mode. *Scientific Reports*, **12(1).** https://doi.org/10.1038/s41598-022-14718-5

XI ECCOMAS Thematic Conference on Smart Structures and Materials - SMART 2025
M. Krommer, M. Nader and M. Schagerl (Eds)

Received: 29 April 2025 / Revised: 26 August 2025 / Accepted: 11 October 2025
© The Author(s) 2025

Hotspot Temperature Modeling for the Online Condition Monitoring of PMSMS With Jumble Windings

Daniel Wöckinger, Magdalena Schaber, Gerd Bramerdorfer

Abstract. This paper investigates the relationship between the surface temperature and the hotspot temperature within the jumble windings of a permanent magnet synchronous machine. As a result, an already established hybrid modeling approach that combines experimental data with numerical simulations to accurately predict the thermal behavior of the winding's surface can be used to indicate the hotspot temperature and allow machine utilization up to its material's thermal limits. For studying winding's thermal behavior by numerical analyses, a force-biased algorithm is presented and then validated by experiments to achieve realistic conductor arrangements within the winding cross-sections for two-dimensional thermal finite element simulations. Furthermore, boundary conditions for the numerical simulations are calibrated using empirical data from DC tests, ensuring strong agreement between measured and simulated temperatures. Thus, operating the electric machine at its thermal limits will become possible, allowing for higher utilization.

Key words: Condition Monitoring, Online Temperature Estimation, Virtual Sensor Array

1 INTRODUCTION

The online condition monitoring of electric machines' components becomes more crucial due to increased demands on highly utilized machines and redundant safety monitoring, e.g., controlled derating or emergency stops. Additionally, the machine components' temperatures especially impact the machine's overall lifespan. According to V. M. Montsinger's rule, initially developed for transformer lifetime prediction, a temperature rise of about $8\,^{\circ}\mathrm{C}$ above the limit halves winding's lifetime and, thus, makes accurate temperature monitoring important [2]. Additionally, F. Hoffmann suggests in [6] that exceeding the limit up to $10\,^{\circ}\mathrm{C}$ also reduces an electric machine's lifetime by $50\,\%$ due to Montsinger's rule. Besides observing machine components' temperatures for estimating the machine's lifespan, e.g., the winding and bearing temperature [3], the knowledge about other components' thermal state, e.g., the permanent magnet or, again, the winding, is crucial regarding the machine's operational safety. If the temperature exceeds the material-specific maximum working temperature, the components can lose

Daniel Wöckinger & Magdalena Schaber & Gerd Bramerdorfer
Institute of Electric Drives and Power Electronics, Johannes Kepler University Linz, Altenbergerstr. 69, A-4040 Linz, Austria,
e-mail: daniel.woeckinger@jku.at

their functionality and, thus, reduce the electrical machine's efficiency or cause thermal destruction. Especially the winding of electric machines in outer rotor topology is a critical component, as it typically has the lowest but most sensitive temperature limit regarding thermal destruction due to the relatively low temperature limit of copper lacquer between $125\,^{\circ}\mathrm{C}$ and $200\,^{\circ}\mathrm{C}$. Note that established strategies often focus on the mean winding temperature or consider its surface temperature, e.g., through using sensors [4] and, hence, neglect the existence of a temperature hotspot within the winding. In contrast, an operating point-independent temperature difference is often used as a safety margin between the predicted temperature and the limit. Therefore, the hotspot temperature is estimated to be 8–$10\,^{\circ}\mathrm{C}$ higher than the average winding temperature [5]. Consequently, accurately predicting the hotspot temperature and its localization would allow a more efficient machine operation and help prevent significant lifetime reduction due to overheating the insulation system. However, previous statements are based on studies with machines in a high-power range or transformers, and it is unclear if the results can be applied to motors in the low-power segment. Thus, this study aims to establish a relationship between the typically measured winding's surface temperature and the hotspot temperature for a permanent magnet synchronous machine (PMSM) with an outer rotor used in fans. The thermal modeling of the overall machine is generally challenging due to the complex cooling situation. Additionally, no precisely reproducible winding topology is usually employed for low-price machines. Instead, jumble windings, i.e., windings with randomly distributed conductors in the slot, are typically applied. For this reason, analytical approaches allow only limited insights and necessitate a hybrid modeling approach based on experiments and simplified numerical analyses.

First, the machine, its rated data, and the sensor placement used for determining a data-based thermal model are presented in Section 2. The hybrid thermal modeling approach and the finally used lumped parameter thermal network (LPTN) of the device under test (DUT) are introduced in Section 3. Then, the windings of the DUT are analyzed regarding their thermal connection to the environment, i.e., heat flow paths, and their effective winding characteristics, e.g., the copper fill factor, are identified in Section 4. This provides a solid base for the following numerical analyses in the same section. The numerical simulations allow for determining the spatial temperature distribution within the winding cross-section, including the thermal hotspot and its spatial position. Finally, Section 5 concludes all findings and discusses further investigations.

2 DEVICE UNDER TEST AND SENSOR PLACEMENT

In this section, the machine, its nominal data, and the thermal sensor placement for both the hybrid thermal modeling of the whole machine and the DC thermal tests for simulation calibration discussed later in Section 4 are presented.

2.1 The outer rotor synchronous machine under test

This study focuses on a 3-phase, brushless PMSM with an outer rotor topology, as depicted in Fig. 1a - 1c. It consists of an aluminum-made flange holding the stator, the jumble windings, and the rotor bell with inlaid permanent magnets connected by two ball bearings. The DUT

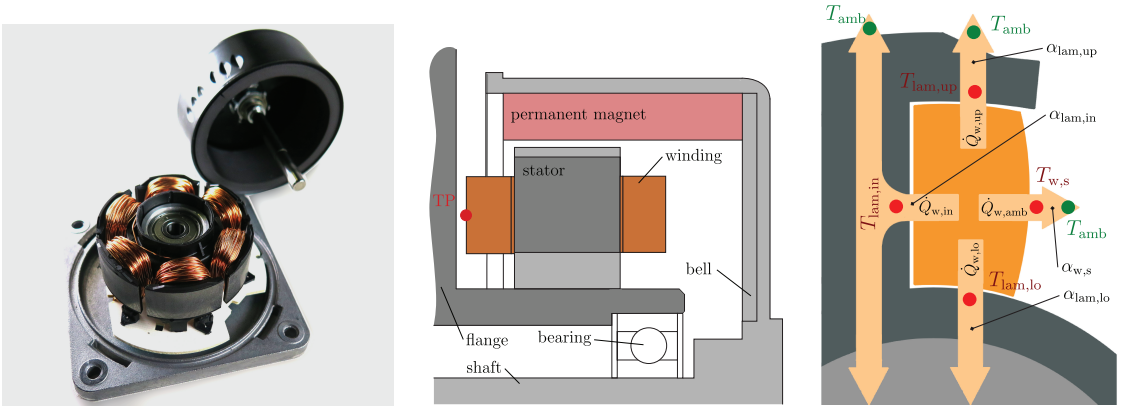

(a) (b) (c)

Figure 1: (a) Photograph of the DUT consisting of a stator carrying the windings and the mounting flange as well as the rotor bell, (b) schematic representation of the motor's longitudinal section with labeled machine components and the test point (TP) for acquiring winding's surface temperature $T_{\mathrm{w,s}}$, and (c) a part of the machine cross-section with one half of a winding and the stator teeth, illustrated heat fluxes and the measurement positions for the DC experiments.

has a rated power of $110\,\mathrm{W}$ at $150\,\mathrm{mNm}$ and operates at a maximum speed of $7100\,\mathrm{rpm}$. Our company partner, ebm-papst St. Georgen GmbH & Co. KG, has provided the machine. Its most important electrical and mechanical characteristics are detailed in Table 1.

Table 1: Characteristic machine data.

Rated DC link voltage	$24\,\mathrm{V}$
Rated DC link current	$5.1\,\mathrm{A}$
Rated speed	$7100\,\mathrm{rpm}$
Rated torque	$150\,\mathrm{mNm}$
Terminal resistance (at $20\,^{\circ}\mathrm{C}$)	$0.49\,\Omega$

Developing a generally valid thermal model for this type of machine, i.e., accurate temperature prediction in the machine's overall operating range, is complex due to the rotating rotor bell. It introduces speed-dependent heat dissipation in the magnetic air gap and affects heat flows. Additionally, a gap of about $4\,\mathrm{mm}$ between the bell and the mounting flange, cf. Fig. 1b further complicates the thermal modeling by facilitating convection influenced by rotor speed and internal temperatures. Finally, specific parameters and material properties are not accurately known. Hence, a hybrid modeling approach, as discussed in [1], is employed to model these thermal characteristics effectively to address these challenges.

2.2 Machine preparation and senor placement

Implementing a data-based or hybrid modeling methodology requires acquiring temperatures at various mechanical and electrical operating points and different ambient conditions to ensure the accuracy and general validity of the resulting model. Therefore, an experimental setup, measurement data acquisition, and the fundamental methodology are detailed in [7]. However, as the sensor is installed after the machine's assembly, a sensor placement within the winding structure is not feasible, restricting measurements to the coil's outer surface. The test point for the winding temperature is shown in Fig. 1b as TP. Typically, one coil of each phase is equipped with a sensor to detect defects or imbalances.

Due to the sensor positioning, the derived thermal model is trained in [7] and improved in [8] to predict the coil's surface, not the hotspot temperature. Nevertheless, this surface temperature $T_{\mathrm{w,s}}$ is commonly interpreted as an estimate of the mean winding temperature T_{w} according to the high thermal conductivity of copper and high copper filling factors reached in high-efficient machines. Usually, this is a significant simplification with limited validity and may lead to overloading the windings at high loads when no sensor is used. Consequently, the hotspot, i.e., the maximum temperature within the winding, is considered as a constant bias, e.g., 8–$10\,^{\circ}\mathrm{C}$ regarding [5], on T_{w}. Therefore, this study focuses on the winding temperature, its spatial distribution, and, thus, the hotspot temperature T_{h} and its position.

The investigations presented in Section 4 are also based on a finite element analysis (FEA) discussed below. In order to guarantee realistic results, the boundary conditions of the FEA are validated through measurement data gained by a simple DC thermal test, i.e., a steady-state test with a DC power supply in the stator windings, cf. [9]. Therefore, three additional temperature sensors to acquire $T_{\mathrm{lam,lo}}$, $T_{\mathrm{lam,in}}$, and $T_{\mathrm{lam,up}}$ are mounted to the stator lamination's front near the winding as illustrated in Fig. 1c enabling together with the ambient temperature a heat flux estimation at various conditions.

3 HYBRID THERMAL MODELING APPROACH

Generally, insulated modeling of the winding temperature T_{w} and, thus, T_{h} and neglecting the residual machine is impossible as T_{w} strongly depends on the entire drive system, including all machine components, the heat transmissions between machine parts, and DUT's environment. A DSP-ready seven-node LPTN of the overall machine is depicted in Fig. 2a allowing the temperature observation of winding's surface $T_{\mathrm{w,s}} = T_{\mathrm{w}}$ assumed to be the average winding temperature, the stator lamination T_{s}, the bearings T_{bi} and T_{bo}, the mounting flange T_{f}, and the rotor bell's outer surface T_{r}. If the machine's geometrical dimensions and material properties are known, the network parameters, i.e., values for thermal capacitors and resistors, can be approximated using analytical equations reported in the literature, see [7] and [10].

The LPTN comprises five constant and five speed-dependent thermal resistances, six heat capacities, and five partly speed-dependent power loss sources, cf.[7] and [8]. The thermal resistances constitute the different heat flow paths inside the machine and, thus, allow for computing the steady-state temperatures while the thermal capacitors model their transient behavior.

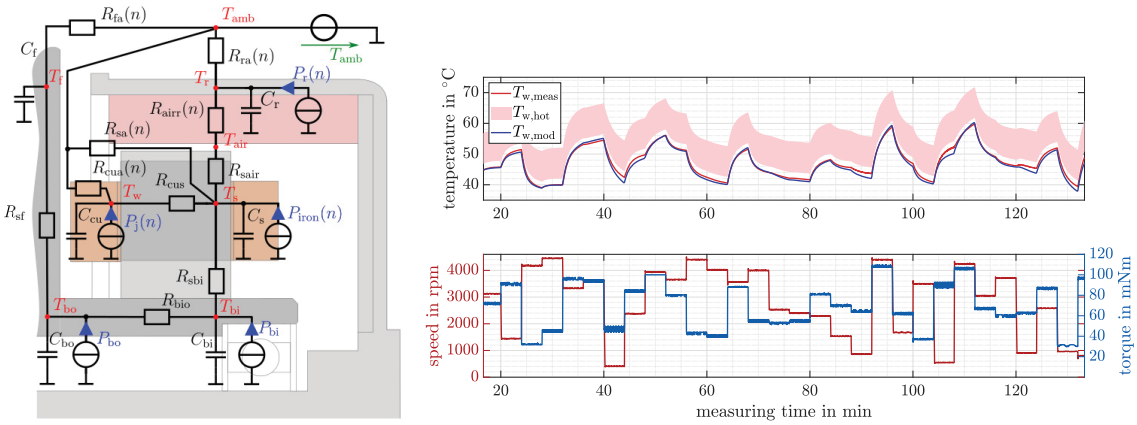

(a) (b)

Figure 2: (a) Lumped parameter thermal network of the DUT, as derived in [7] and enhanced in [8], displayed over the machine's cross-section, and (b) comparison of typical measurement data and the winding temperature prediction of the thermal model.

For considering the complex cooling situation mainly caused by forced convection in the machine's air gaps, e.g., between the stator and rotor or among the bell and flange, the thermal resistances $R_{\mathrm{sair}}(n)$, $R_{\mathrm{sa}}(n)$ and $R_{\mathrm{cua}}(n)$ have to be modeled as speed-dependent. Additionally, the heat transitions from the rotating bell to the environment represented by $R_{\mathrm{ra}}(n)$ and from the mounting flange to the ambient modeled with $R_{\mathrm{fa}}(n)$ show a speed-dependent nature due to the spinning rotor. Thus, the thermal model in Fig. 2a exhibits more than 20 parameters initialized based on the expert's knowledge. However, due to unknown effects, e.g., the assembly gap between the stator and mounting flange and this huge parameter domain, the LPTN's parameters are improved using measurement data and an evolutionary algorithm. According to [7], the optimization process reduces the mean effective temperature error by a factor of 2.3 compared to the first knowledge-based guess and results in an effective temperature error of about $2.5\,\mathrm{K}$ over 134 hours of recorded training and evaluation data.

Figure 2b compares measured and modeled results for a given step-shaped speed-torque profile. The red line in the upper diagram represents the measured winding temperature $T_{\mathrm{w,meas}}$, i.e., at the winding's surface, while the blue line represents the temperature $T_{\mathrm{w,mod}}$ predicted by the LPTN running on the power electronics' signal processor. The light red area spans the 2-$10\,^{\circ}\mathrm{C}$ temperature range on top of $T_{\mathrm{w,meas}}$ as a theoretically possible range for the hotspot temperature as discussed before. Thus, the high prediction accuracy can only partially be utilized because of the unknown correlation between hotspot temperature and surface temperature. In other words, the machine's efficiency could be greatly enhanced if the surface temperature are directly correlated with the hotspot temperature through a mathematical function.

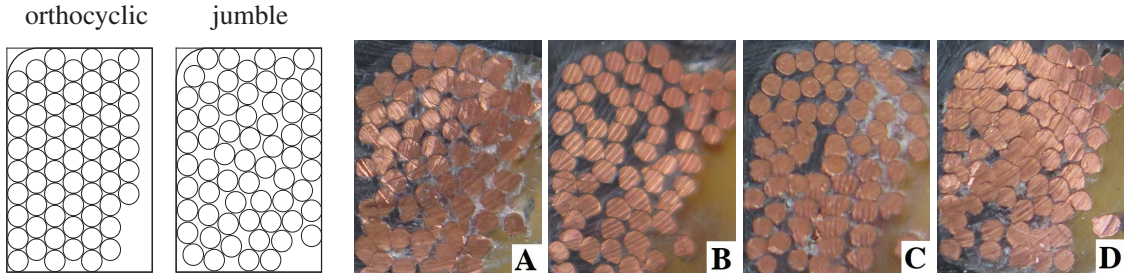

Figure 3: (a) Cross-section comparison of an orthocyclic and a jumble winding within the slot, and (b) a detailed view of four exposed winding distributions positioned similar to Fig. 1c.

4 WINDING TOPOLOGY CHARACTERIZATION

The random nature of the jumble winding's spatial arrangement complicates predicting the relationship between the winding's surface and hotspot temperature. Therefore, four real winding cross sections are studied in Section 4.1 to determine reference values for realistic copper fill factor. Furthermore, Section 4.2 presents an experimental data-driven calibration of the 2D-FEA, enabling statistical analysis of jumble windings' thermal properties in the same section.

4.1 Identification of the copper filling factors as a reference

Different winding types can be employed for electrical drives based on the application's needs. A common measure for winding space utilization is the copper fill factor

$$f_{\mathrm{cu}} = \frac{A_{\mathrm{cu}}}{A_{\mathrm{slot}}}\,, \tag{1}$$

where A_{cu} represents the effective copper cross-sectional area related to the maximum available area A_{slot}. Generally, orthocyclic windings, as illustrated in Fig. 3a on the left, are characterized by carefully arranged conductors placed side by side within the machine's slot to achieve a high copper fill factor, making the winding compact. However, this process is time-consuming and labor-intensive, and thus, it is typically not used for low-cost applications in series production. In contrast, jumble windings, cf. Fig. 3a on the right involves randomly winding the conductors onto the bobbin at high speed, resulting in a lower copper fill factor and, hence, more space requirement for the same number of turns. Fill factors for orthocyclic windings can typically reach up to maximum $f_{\mathrm{cu}} = 0.901$. In contrast, jumble windings have lower and largely varying fill factors in a range of $f_{\mathrm{cu}} = 0.40 - 0.73$ when using round wires. It generally depends on the slot size, the winding method, and conductor shape [11].

Due to the significant variability in the jumble windings' copper fill factor f_{cu} in the DUT, a detailed analysis of its coils is necessary. Therefore, the cross-sections of four windings are analyzed in detail here. The stator is encapsulated in epoxy resin and subsequently milled to

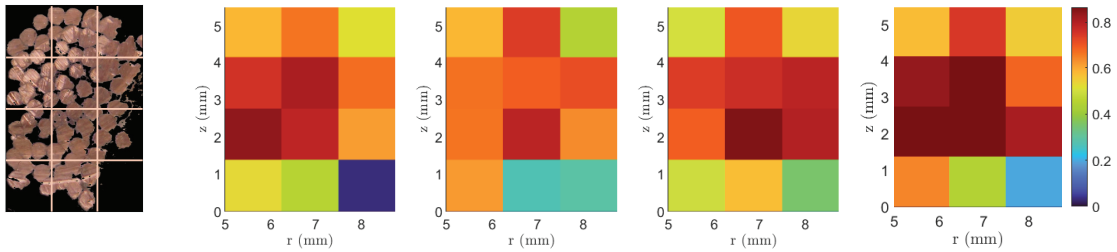

(a) (b) (c) (d) (e)

Figure 4: (a) The masked image of winding A from Fig. 3b showing the winding cross-section divided into 12 zones, and (b)-(e) the local copper fill factors obtained by image processing from the cross-section images of the four exposed windings A-D in Fig. 3b.

expose for winding cross-sections, as illustrated in Fig. 3b. Each winding represents the left coil side similar to Fig. 1c, i.e., with the stator teeth and, hence, the coil's center on its left. The round edge of coil protection is visible in the upper left corner. The images already reveal substantial variations in the arrangement of conductors, as expected. However, for quantifying the spatial distribution of $f_{\mathrm{cu}}(r, z)$ across the winding, segmentation has been employed to divide each winding into a 4x3 matrix representation. This partition is a compromise between spatial resolution and the validity of the determined f_{cu} value. Segments smaller than a conductor's cross-section are impractical. The photographs' RGB values evaluate the area taken by copper. Therefore, the RGB values for copper remain, while all other values are changed to black, as illustrated in Fig. 4a for the winding A. Then, the copper fill factor f_{cu} can be computed by summing up non-black pixels relative to the total number of pixels per segment, cf. (1).

Figures 4b - 4e depict the copper fill factors f_{cu} averaged per segment of the four exposed windings. The results show a denser concentration of wires in the half-height towards images' left corner, i.e., closer to the coil's center, cf. spatial positions between $r = [5\,\mathrm{mm}, 7.5\,\mathrm{mm}]$ and $z = [1.5\,\mathrm{mm}, 4\,\mathrm{mm}]$. This is probably caused by the winding process used. This observation indicates that the fill factor is not uniform across the cross-section but varies spatially as expected. Furthermore, the winding process causes wire deformation, leading to very high f_{cu} values in localized areas, cf. Fig. 3b winding D. A detailed investigation into this variation follows. Due to wire deformation, certain regions achieve a fill factor of $f_{\mathrm{cu}} = 0.84$, which approaches the theoretical maximum of an ideal orthocyclic winding. However, by averaging across all segments and windings, a mean fill factor of $\bar{f}_{\mathrm{cu}} = 0.629$ is obtained, with a standard deviation of $\sigma_{\mathrm{fcu}} = 0.157$, serving as a reference for winding distributions gained by simulation.

4.2 Preparatory work for the numerical simulation

A 2D FEA is applied to analyze the jumble windings' thermal behavior, simplifying the CAD process for the numerical analysis and reducing computational efforts. Additionally, rotational symmetry of the winding geometry, cf. Fig. 1a, is assumed.However, three-dimensional

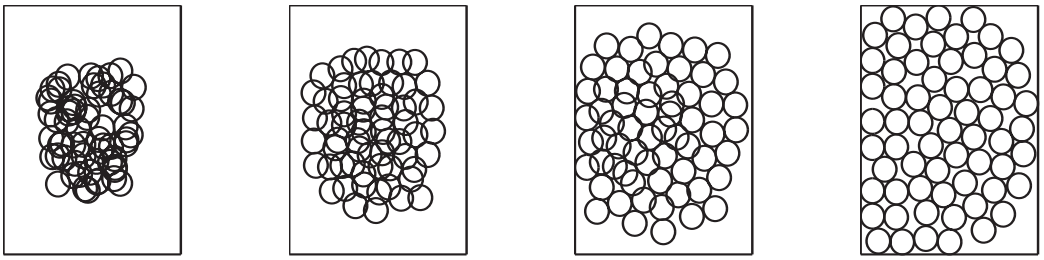

(a) $i = 0$ (b) $i = 12$ (c) $i = 100$ (d) $i = 331$

Figure 5: Actual conductor distribution during the iterative generation of randomly distributed conductors in a winding cross-section at different iteration steps i.

effects, such as the crossing of the windings, cannot be considered in this analysis. The thermal simulation is performed for many winding distributions, specifically 16,000 different spatial configurations and boundary conditions, to ensure statistical significance of the results and capture a realistic geometry-independent impact of local copper fill factor variability.

4.2.1 Generation of jumble windings in 2D FEA

For this, circles representing the conductors must be arranged in an arbitrary area of the slot without overlapping, as illustrated in Fig. 3a. Furthermore, the proposed methodology aims to achieve realistic conductor distributions within a winding cross-section with comparable local copper fill factors as presented in Fig. 4b - 4e.

As illustrated in Fig. 5a, the procedure begins with a random conductor placement around the simulation area's center. Then, a force-biased algorithm systematically eliminates conductor overlaps through iterative position adjustments inspired by mechanical forces, such as gravitational forces. Additionally, the algorithm calculates repulsion forces proportional to the conductors' overlap and shifts all circles until all overlaps resolve completely. In order to reach realistic packing density, the already mentioned repulsion is balanced with an additional attraction force proportional to the conductor's distance, cf. [12], and an external force directed to the upper left corner. Thus, a realistic packing density distribution can be finally reached. Figure 5 visualizes the transition from initial overlapping states to final overlap-free arrangements.

Figure 6a showcases two winding distributions generated by the introduced algorithm, illustrating the variability and randomness in the conductor placement. One disadvantage of the actual approach is that conductor deformation cannot be considered. However, the comparison of segment-wise averaged local copper fill factors found by experiments and depicted in Fig- 6b and the configurations arranged by the algorithm presented in Fig 6c highlights the method's functionality. It shows that the simulated copper fill factors closely match those of the real one, indicating that the algorithm effectively captures the essential characteristics of the winding geometry. Thus, a representative winding geometry can be ensured in the simulation.

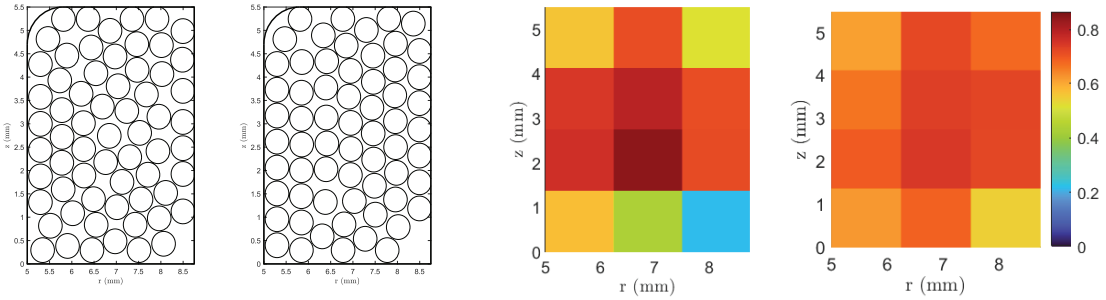

(a) (b) (c)

Figure 6: (a) Two typical conductor configurations of 1,000 arrangements generated by a force-biased algorithm, (b) segment-averaged local copper filling factor f_{cu} from the experiments presented as color density plot, and (c) segment-averaged copper filling factor f_{cu} of all windings generated by the force-biased algorithm illustrated as color density plot.

4.2.2 Data-based identification of equivalent boundary conditions for FEA

An isolated numerical analysis of the winding reduces computational effort if the boundary conditions correctly reflect the residual machine at various operating points. Therefore, an empirical calibration is performed using DC tests. Thermocouples are placed at specific positions on the stator, as shown in Fig. 1c, to record transient temperature profiles at various DC current levels, i.e., $1\,\mathrm{A}$, $2\,\mathrm{A}$, $3\,\mathrm{A}$, and $4\,\mathrm{A}$. The measured temperatures are exemplarily depicted in Fig. 7 and serve as reference data for adjusting the heat transfer coefficients α_i with $i = \{\mathrm{w,s,\,lam,lo,\,lam,in,\,lam,up}\}$ illustrated in Fig. 1c for the 2D FEA. First, they are analytically identified as $\hat{\alpha}_{\mathrm{w,s}} = 5\,\mathrm{W\,m^{-2}\,K^{-1}}$, $\hat{\alpha}_{\mathrm{lam,lo}} = 118\,\mathrm{W\,m^{-2}\,K^{-1}}$, $\hat{\alpha}_{\mathrm{lam,in}} = 90\,\mathrm{W\,m^{-2}\,K^{-1}}$, and $\hat{\alpha}_{\mathrm{lam,up}} = 1104\,\mathrm{W\,m^{-2}\,K^{-1}}$ by calculating an equivalent heat transfer coefficient for the whole heat flux paths. Then, all α_i finally used in FEA are adjusted by a factor f defined as $\alpha_i = f\hat{\alpha}$ to optimally fit the measurement's end temperatures. The factor f is identified by comparing the experimental data with the simulated one using a standard least-squares optimization approach. Note that the simulated temperatures in FEA are spatially averaged for $2\,\mathrm{mm}$ along FEA's boundary contour to consider the sensor's and adhesive's extent. The results are summarized in Tab. 2 and demonstrate strong agreement between measured and simulated temperatures, with deviations of less than $5\,\%$ across the tested current range and high accuracy at $4\,\mathrm{A}$ with only $0.38\,\%$ error. These findings confirm that the calibrated simulation model reliably predicts the thermal behavior of the stator under different operating conditions.

4.3 Numerical analyses of the winding temperature hotspot

After successfully aligning the geometry and boundary conditions with real-world scenarios, 1,000 different conductor configurations generated using the force-biased algorithm are analyzed. This analysis is conducted with *FEMM 4.2* [13] under four different boundary condi-

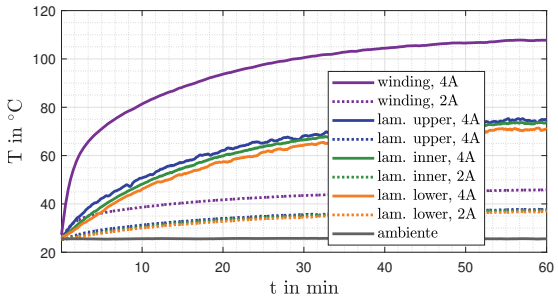

Figure 7: Extract from winding temperature measurements at different currents to determine boundary conditions for calibrating the numerical simulations.

Table 2: Summary of identified boundary condition coefficients f at different DC currents I_s and comparison of the measured and simulated winding surface temperatures T_w.

I_s	f	$T_\mathrm{w,s}$	
		measured	**simulated**
1 A	1.50	30.25 °C	31.84 °C
2 A	1.00	46.55 °C	47.32 °C
3 A	1.00	70.65 °C	71.28 °C
4 A	0.918	109.50 °C	109.08 °C

tions and excitation currents, resulting in 16,000 numerical simulations. Therefore, the conductors are modeled as pure copper. Wire insulation is excluded from thermal analysis by defining it as air due to the identical heat transfer coefficients of air and lacquer, cf. both values are $\alpha = 0.26\,\mathrm{W\,m^{-2}\,K^{-1}}$ [6]. This simplification does not affect simulation accuracy but enhances computational efficiency. The rotation of the rotor bell at different speeds is represented by a variable boundary condition $\alpha_\mathrm{w,s}$, while the other heat transfer coefficients are kept constant.

The numerical simulations reveal an average hotspot temperature of $31.03\,°\mathrm{C} \pm 0.007\,°\mathrm{C}$ at 1 A, $72.92\,°\mathrm{C} \pm 0.0574\,°\mathrm{C}$ at 3 A, and $111.88\,°\mathrm{C} \pm 0.0978\,°\mathrm{C}$ at 4 A, where the given variation represents the 95 % confidence interval. Figure 8a demonstrates the hotspot's spatial positions within the winding cross-section for all simulations, with the averaged location marked as a big cross depending on the boundary condition $\alpha_\mathrm{w,s}$. Generally, the thermal hotspot is located near the surface for low heat transfer coefficients. However, an increasing $\alpha_\mathrm{w,s}$, which correlates with higher rotor speeds, shifts hotspots' spatial location toward the coil center and reduces its temperature, as illustrated in 8b. Therefore, a hotspot detection with a surface-mounted sensor fails at higher speeds. In contrast, in the worst case, i.e., a non-rotating bell, and thus a very low $\alpha_\mathrm{w,s}$, the hotspot is located near the winding surface, allowing an estimate via surface temperature measurement. Figure 8c presents the temperature difference between the surface $T_\mathrm{w,s}$ and winding's hotspot T_h, showing a linear correlation. This behavior is assessed by simulating three additional operating points at 1.5 A, 2.5 A, and 3.5 A. Their temperature prediction results show the same trend as identified by the four load points calibrated by measurement. Based on this result, the hotspot temperature can be calculated via $T_\mathrm{h} = 1.03347 \cdot T_\mathrm{w,s} - 0.801$ independent of the selected boundary conditions as between the two temperature potentials only solid-state heat conduction takes place. For example, at a recorded surface temperature of $100\,°\mathrm{C}$, the hotspot can be assumed to be only $2.5\,°\mathrm{C}$ hotter within a 95 % confinence interval smaller than $\pm 0.1\,°\mathrm{C}$. In other words, the coil's surface temperature of the class B enameled wires is reduced from $130\,°\mathrm{C}$ maximum operating temperature to $\approx 126\,°\mathrm{C}$, and not to $120\,°\mathrm{C}$ as it is the case for the conservative estimation.

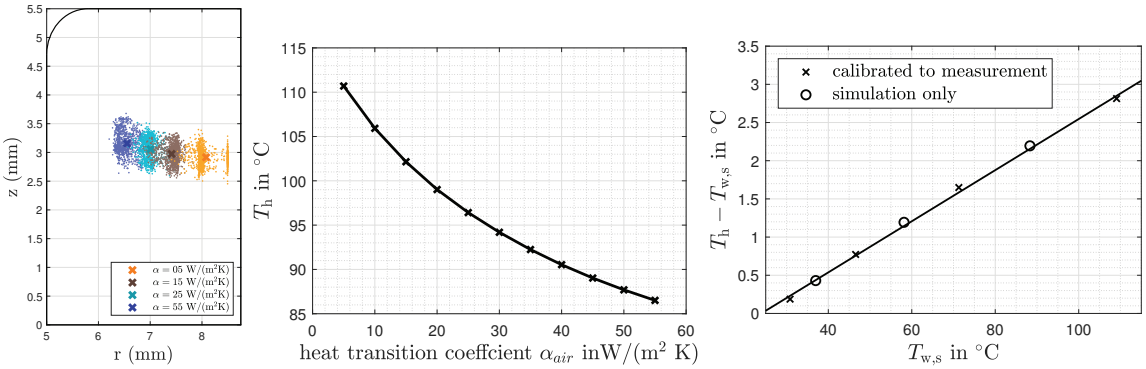

(a) (b) (c)

Figure 8: (a) Spatial positions of the hotspot temperatures within the winding cross-section at various boundary conditions, (b) change in the mean hot spot position when the heat transfer coefficient is increased, and (c) difference between hot spot and winding surface temperature.

5 CONCLUSIONS

The study identifies significant variations in the copper fill factor of jumble windings, with a mean value of $\bar{f}_\mathrm{cu} = 0.629$ and a standard deviation of $\sigma_\mathrm{fcu} = 0.157$. Furthermore, a force-biased algorithm generates realistic conductor arrangements in 2D FEA. The boundary conditions for the numerical simulations are calibrated with empirical DC tests, allowing a surface temperature prediction of jumble windings by less than $5\,\%$. A clear link between the winding's surface and the hotspot temperature of a PMSM could be identified based on numerical simulations. Thus, a hybrid modeling approach trained with surface temperature data of the winding can predict both surface and hotspot temperatures, enhancing motor efficiency and reducing overheating risks. Additionally, the findings suggest that the rules proposed by Z. Gao and F. Hoffmann in [5] and [6] tend to overestimate hotspot temperatures in low power-density machines.

ACKNOWLEDGMENT

This work has been supported by the COMET-K2 "Center for Symbiotic Mechatronics" of the Linz Center of Mechatronics (LCM) funded by the Austrian federal government and the federal state of Upper Austria.

REFERENCES

[1] D. Wockinger, G. Bramerdorfer, S. Drexler, S. Vaschetto, A. Cavagnino, A. Tenconi, W. Amrhein, and F. Jeske, "Measurement-based identification of lumped parameter thermal networks for sub-kw outer rotor pm machines," *IEEE Transactions on Industry Applications*, vol. 59, no. 1, pp. 823–833, Jan. 2023.

[2] V. M. Montsinger, "Abridgment of loading transformers by temperature," *Journal of the A.I.E.E.*, vol. 49, no. 4, pp. 293–297, Apr. 1930.

[3] S. Gupta, "A review of lifespan and aging modelling techniques for electrical machine insulation systems," in *2023 International Conference on Power Energy, Environment & Intelligent Control (PEEIC)*. IEEE, Dec. 2023, pp. 101–105.

[4] O. Wallscheid, "Thermal monitoring of electric motors: State-of-the-art review and future challenges," *IEEE Open Journal of Industry Applications*, vol. 2, pp. 204–223, 2021.

[5] Z. Gao, R. S. Colby, T. G. Habetler, and R. G. Harley, "A model reduction perspective on thermal models for induction machine overload relays," *IEEE Transactions on Industrial Electronics*, vol. 55, no. 10, pp. 3525–3534, Oct. 2008.

[6] F. Hoffmann, M. Halwas, J. Fleischer, and M. Doppelbauer, "Thermal analysis of novel winding structures for the usage in electrical machines," in *2022 International Conference on Electrical Machines (ICEM)*. IEEE, Sep. 2022, pp. 490–495.

[7] D. Wockinger, G. Bramerdorfer, S. Drexler, S. Vaschetto, A. Cavagnino, A. Tenconi, W. Amrhein, and F. Jeske, "Measurement-based optimization of thermal networks for temperature monitoring of outer rotor pm machines," in *2020 IEEE Energy Conversion Congress and Exposition (ECCE)*. IEEE, Oct. 2020, pp. 4261–4268.

[8] D. Wockinger, G. Bramerdorfer, S. Vaschetto, A. Cavagnino, A. Tenconi, W. Amrhein, and F. Jeskey, "Approaches for improving lumped parameter thermal networks for outer rotor spm machines," in *2021 IEEE Energy Conversion Congress and Exposition (ECCE)*. IEEE, Oct. 2021, pp. 3821–3828.

[9] A. Boglietti, M. Cossale, M. Popescu, and D. A. Staton, "Electrical machines thermal model: Advanced calibration techniques," *IEEE Transactions on Industry Applications*, vol. 55, no. 3, pp. 2620–2628, May 2019.

[10] A. Boglietti, A. Cavagnino, M. Lazzari, and A. Pastorelli, "A simplified thermal model for variable speed self cooled industrial induction motor," in *Conference Record of the 2002 IEEE Industry Applications Conference. 37th IAS Annual Meeting (Cat. No.02CH37344)*, ser. IAS-02, vol. 2. IEEE, 2002, pp. 723–730.

[11] J. Hagedorn, F. Sell-Le Blanc, and J. Fleischer, *Handbuch der Wickeltechnik für hocheffiziente Spulen und Motoren*. Springer Berlin Heidelberg, 2016.

[12] W. S. Jodrey and E. M. Tory, "Computer simulation of close random packing of equal spheres," *Physical Review A*, vol. 32, no. 4, pp. 2347–2351, Oct. 1985.

[13] D. C. Meeker, "Finite element method magnetics, version 4.2 (28feb2018 build)," https://www.femm.info, 2018.

Part V

MS 04 - SMART MATERIALS, SENSORS, ACTUATORS AND CONTROL FOR MACHINE ELEMENTS AND ROBOTICS

Thomas Wallmersperger, Markus Vorrath, Karsten Stahl, Eckhard Kirchner

XI ECCOMAS Thematic Conference on Smart Structures and Materials - SMART 2025
M. Krommer, M. Nader and M. Schagerl (Eds)

Received: 31 March 2025 / Revised: 30 August 2025 / Accepted: 9 October 2025
© The Author(s) 2025

Numerical Investigations of the Asymmetric Energy Landscape in Cantilever Bistable Piezoelectric Energy Harvesters

Danish Bashir, P. M. Anilkumar, Ayan Haldar, Sven Scheffler, B. N. Rao, Raimund Rolfes

Abstract. Bistable piezoelectric energy harvesters are widely investigated due to their broadband energy harvesting capabilities. These harvesters can be developed using unsymmetrical composite laminates and flexible piezoelectric materials, such as Macro Fiber Composites (MFCs). Depending on the geometrical parameters and boundary conditions of unsymmetrical composite laminate, such harvesters exhibit symmetric or asymmetric properties in their two stable shapes. In this study, a rectangular bistable composite laminate, attached with an MFC patch and clamped on one side, is investigated, and the asymmetry in its static and dynamic characteristics is quantified. It is observed that a rectangular clamped bistable composite laminate has an asymmetric potential energy landscape, which results in asymmetric stable shapes. To study the asymmetry in the properties of the bistable composite laminate bonded with an MFC, a fully nonlinear finite element (FE) model is employed. Asymmetry in static properties, such as strain energy (SE) and out-of-plane displacement, is evaluated for the bistable laminate with the MFC and compared to the case without MFC patch. Similarly, asymmetry in dynamic properties, such as free vibration characteristics, is analyzed for the bistable laminate bonded with the MFC patch and compared to the laminate without MFC patch. The results show that bonding an MFC patch to one surface reduces the asymmetry in the static and dynamic properties of the clamped rectangular bistable laminate, demonstrating its significance in energy harvesting. Furthermore, a detailed parametric study is conducted by varying the size of the MFC patch to identify the optimal configuration with minimal asymmetry. The findings from this study can be applied to design bistable piezoelectric energy harvesters with reduced asymmetry in static and dynamic properties, enhancing vibration-based piezoelectric energy harvesting performance.

Danish Bashir & B. N. Rao
Structural Engineering Laboratory, Indian Institute of Technology Madras, 600 036 Chennai, India
e-mail: ce21d402@smail.iitm.ac.in

Danish Bashir & P. M. Anilkumar & Sven Scheffler & Raimund Rolfes
Institute of Structural Analysis, Leibniz Universität Hannover, Appelstraße 9A 30167, Hannover, Germany

Ayan Haldar
Department of Civil Engineering, Indian Institute of Technology (BHU), 221005 Varanasi, India

Key words: Asymmetry, Bistable, Finite elements, Piezoelectric, MFC

1 INTRODUCTION

Multistable structures, which can undergo shape transformations while simultaneously bearing loads, have attracted significant research interest due to their diverse engineering applications [1]. These structures are ideal candidates for developing morphing and energy-harvesting applications. Among them, bistable structures represent the simplest form of multistable structures. The cured shapes of unsymmetrical composite laminates serve as a classical example of bistable structures. In the cured shapes of unsymmetrical laminates, bistability is induced by the difference in the coefficients of thermal expansion between the different layers of the unsymmetrical layups. These bistable structures possess two equilibrium shapes and can transition continuously from one to another through a snap-through mechanism. This shape change is accompanied by significant nonlinear deformations, which are rich in dynamics and can be utilized for piezoelectric energy harvesting [2].

Bistable composite laminates exhibit a double-well potential energy landscape, with minima separated by an energy threshold [3]. The nature of this potential energy landscape depends on structural geometry and boundary constraints. A square laminate has a symmetric landscape, yielding identical stable states, while a rectangular laminate creates an asymmetric landscape, leading to distinct curvatures [4]. In addition, the boundary conditions (such as center fixed or edge clamped) also influence the potential energy landscape. Integrating piezoelectric components like Macro Fiber Composites (MFCs) for actuation and energy harvesting applications alters the potential energy distribution, affecting bistable response, snap-through behavior, and dynamics [5]. Symmetric potential energy landscapes benefit morphing applications but may cause undesired cross-well oscillations [6]. In contrast, asymmetric potential energy landscapes enhance wave transmission [7], reduce snap-through force [4], and aid vibration mitigation [8]. However asymmetric potential energy landscape hinder piezoelectric energy harvesting because the system tends to get trapped in the deeper well, reducing transition frequency and energy conversion. Additionally, higher activation energy is required for transitions, limiting energy harvesting at low excitation, while asymmetry causes irregular switching, leading to inconsistent voltage output and lower efficiency [9]. While many studies assume perfectly symmetric potential energy distributions, but generally due to integration to another systems or asymmetric boundary conditions, symmetry in the potential energy landscape gets distorted. Extensive research on bistable energy harvesters (BEHs) has examined how asymmetry in potential energy landscapes affects efficiency. Harne and Wang [10] showed that avoiding asymmetry in bistable energy harvesters composed of weakly bistable systems could potentially provide minor performance benefits. He and Daqaq [11] found that an asymmetric potential energy landscape gives rise to weaker restoring forces, due to which bistable systems suffer reduced power output. Wang et al. [9] confirmed that asymmetry hinders bistable energy harvesters by trapping the system in a deeper well, diminishing cross-well oscillations. Giri et al. [12] showed that tuning

asymmetry can enhance stability and reduce chaos. Recently, Cai and Harne [13] suggested that lowering asymmetry improves snap-through motion and energy conversion abilities.

Bistable structures have gained significant attention in piezoelectric energy harvesting due to their double-well potential energy landscape [14], which enables them to capture ambient vibrations over a broad frequency spectrum. Their bistable nature can be easily achieved, making bistable unsymmetrical composite laminates particularly well-suited for broadband energy harvesting applications. Bistable unsymmetrical composite laminates bonded with MFC patches have been extensively studied under various geometrical shapes and boundary conditions. Square-shaped, center-fixed bistable composite laminates are commonly investigated due to the symmetry in their stable shapes as developed by Arrieta et al. [15]. Later, Betts et al. [16], conducted in-depth studies by characterising different dynamic regimes and optimized output power for energy harvesting. Harris et al. [17] further explored various bistable unsymmetrical composite laminate geometries, introducing an electromechanical coupling model validated through experimental studies. Lee et al. [18] proposed an innovative square-shaped, center-fixed bistable composite laminate composed entirely of MFCs. These studies mainly focused on the centre fixed boundary condition, which restricts the practical application of these harvesters. Rectangular unsymmetrical composite laminates clamped on one side have also been widely investigated. Arrieta et al. [19] developed a broadband piezoelectric energy harvester using rectangular bistable laminates with a cantilever boundary condition. Li et al. [20] examined clamped cantilever boundary conditions in bistable laminates with hybrid parts, commonly known as bistable hybrid symmetric laminates (BHSLs) for vibration control and energy harvesting applications. Dainkun et al. [21] experimentally compared the broadband response of clamped bistable piezoelectric energy harvesters (BPEHs) made of BHSLs with that of their linear counterparts. Liu et al. [22] analyzed the energy harvesting capabilities of clamped BHSLs under wind-induced vibrations. Recently, Boddapati et al. [23] investigated clamped rectangular bistable laminates with MFCs bonded to one side, focusing on energy harvesting under vortex-induced vibrations. These studies primarily examined rectangular bistable laminates or BHSLs with clamped boundary condition, where excitation was applied at the fixed end. While they focused on the energy-harvesting potential of bistable laminates, the influence of the MFC patch on the potential energy landscape of BEH remains unaddressed.

As discussed earlier, a single end-clamped rectangular bistable laminate exhibits an inherently asymmetric potential energy landscape. When such a structure is utilized for energy harvesting, attaching an MFC patch to one side further alters the potential energy distribution, introducing additional asymmetry into an already unbalanced landscape. To the best of the authors' knowledge, no prior study has specifically examined how MFC bonding affects the asymmetric potential energy landscape of a clamped rectangular bistable laminate in the context of energy harvesting. The present study aims to bridge this gap by employing a finite element (FE) modeling approach. A FE framework is developed to predict the stable configurations of a clamped rectangular bistable laminate with an MFC attachment, quantify the induced asymmetry in its

potential energy landscape, and analyze its static and dynamic characteristics. The structure of the manuscript is as follows: Section 2 describes the bistable energy harvester, followed by Section 3, which explains the FE model. A discussion on the verification example is presented in Section 4, followed by a parametric study in Section 5. Finally, concluding remarks are provided in Section 6.

2 BISTABLE ENERGY HARVESTER

Figure 1(a) illustrates a cantilever bistable piezoelectric energy harvester, where a bistable laminate serves as the host structure under external vibrations. The host structure vibrates within one of its stable shapes and can switch between them, producing significant strains that are transferred to the MFC patch and converted into voltage via the piezoelectric effect. Figure 1(b) shows the clamped rectangular bistable laminate consisting of a symmetric lay-up, $[0/0]$, of length L_s and width W_l, and an unsymmetric lay-up, $[0/90]$, of length L_u and width W_l. An MFC patch of length L_m and width W_m is bonded to the top surface at a distance D_m from the clamped edge. Both lay-ups have a thickness t_l, while the MFC patch has a thickness t_m. The symmetric lay-up is crucial for bistability, as an unsymmetric lay-up alone loses bistability under clamped boundary conditions [23].

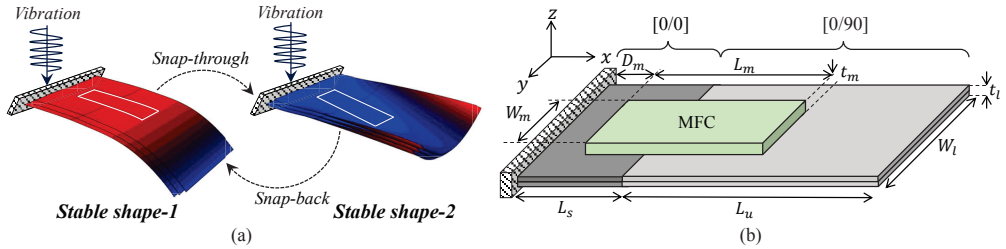

Figure 1: Representation of (a) A cantilever bistable energy harvester under external vibrations (b) Problem definition.

3 FINITE ELEMENT MODEL

A thermomechanically coupled FE model with geometric nonlinearity is formulated using `ABAQUS`. It is used to determine the equilibrium shapes and assess the static and dynamic characteristics of a clamped bistable rectangular laminate with an integrated MFC patch. Both the laminate and the MFC are modeled as linear elastic materials and are discretized using S4R (four-noded quadrilateral) shell elements due to their computational efficiency. A global mesh size of 2.5 mm is selected after a rigorous mesh refinement study. The connection between the symmetric and asymmetric sections of the laminate, as well as the bonding between the MFC and the laminate, is modeled using the `TIE` constraint. The assembled laminate-MFC structure is clamped at the symmetric section. To replicate the curing process, a thermal load of $180°$C is applied uniformly across the structure. Subsequently, the temperature is gradually reduced to room temperature ($20°$C), leading the laminate-MFC system to attain its initial sta-

ble configuration. It is crucial to account for geometric nonlinearities in the simulation; thus, the NLGEOM option remains active throughout the analysis. Since the MFC is also represented using S4R shell elements, its piezoelectric constant is correlated with the coefficient of thermal expansion using the concept of free strain per applied voltage [24]. To transition into the second equilibrium configuration, an equivalent thermal load corresponding to an actuation voltage is introduced at the MFC nodes. The actuation voltage must exceed the critical snap-through threshold for the structure to adopt the alternate stable shape. Given the substantial nonlinear deformations associated with the snap-through event, the NLGEOM setting remains enabled, and artificial damping may be incorporated to facilitate numerical stability. Once snap-through occurs, the applied voltage (modeled as a thermal input) is removed to confirm the stability of the second configuration. Following the determination of both stable states, the LANCOZS eigenvalue solver in ABAQUS is used to compute the fundamental frequencies and associated mode shapes of the laminate-MFC assembly. A schematic representation of the entire simulation framework is illustrated in Figure 2.

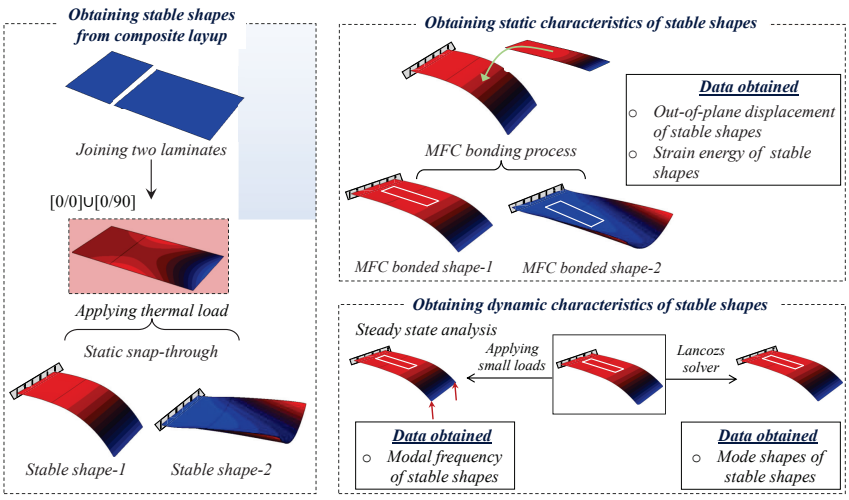

Figure 2: Schematic representation of the steps followed in FE analysis.

4 VERIFICATION EXAMPLE

A rectangular bistable laminate, composed of a symmetric $[0/0]$ and an asymmetric $[0/90]$ layup, with an M8557 MFC patch bonded to its upper surface, is analyzed based on the experimental work of Boddapati et al. [23]. The laminate is clamped along its symmetric section. The MFC patch is positioned on the top surface of the laminate at a distance of $D_m = 27.5$ mm from the clamped boundary. Details regarding the geometric specifications and material properties of both the laminate and MFC patch are provided in Table 1 and 2, respectively.

To examine the influence of MFC patch bonding on the potential energy landscape of a clamped rectangular bistable laminate, along with its static and dynamic behavior, two configurations from the chosen example are considered for further analysis: a rectangular laminate without

Table 1: Geometric properties of lamina and MFC patch [23]

Laminate				MFC		
L_s (mm)	L_u(mm)	W_l (mm)	t_l (mm)	L_m (mm)	W_m (mm)	t_m (mm)
65	125	100	0.24	85	57	0.29

an MFC patch, depicted in Figure 3(a), and a laminate with an MFC patch, illustrated in Figure 3(b).

Table 2: Material properties of lamina and MFC patch [23]

	ρ (kg/m^3)	E_{11} (GPa)	E_{22} (GPa)	G_{12} (GPa)	ν_{12}	α_{11} ($10^{-7}/°$C)	α_{22} ($10^{-6}/°$C)
Lamina (TR50S)	1346	140	9.40	5.00	0.30	-0.18	21.50
MFC (M8557-P1)	5440	27.27	14.76	4.13	0.32	-3.50	0.87

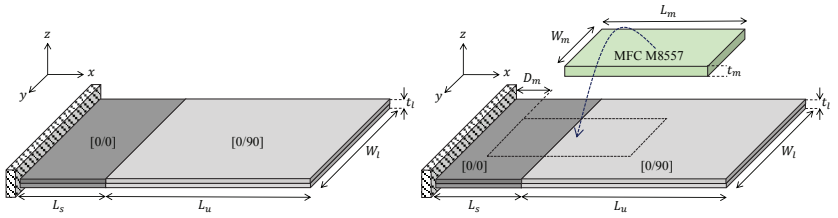

(a) (b)

Figure 3: Schematic representation of selected clamped rectangular bistable laminate: (a) Only laminate, (b) With MFC patch.

4.1 Out-of-plane displacement of the bistable shapes

To compare the out-of-plane displacements of the stable configurations, the parameter τ is introduced, which represents the ratio between the area of the bonded MFC patch and the area of the rectangular bistable laminate. The out-of-plane displacements of the stable configurations obtained at the corners of the free end, both with and without the MFC patch, are summarized in Table 3. Also, the out-of-plane displacement from the FE framework for $\tau = 0.255$ is compared with the study conducted by Boddapati et al. [23] and is found to be in good agreement, confirming the validity of the proposed FE framework. It is evident that without the MFC, the rectangular laminate $(\tau = 0)$, show unequal out-of-plane displacements, in the two stable configurations with a difference of 46.95 mm, which is attributed to the inherent asymmetry in the stable shapes of the clamped rectangular bistable laminate. On the other hand, when the MFC patch is bonded to the top surface of the laminate $(\tau = 0.255)$, there is a substantial reduction in the out-of-plane displacement in both stable shapes, resulting in a reduced absolute difference of 25.33 mm. The decrease in out-of-plane displacement of the stable configurations upon attaching the MFC patch is due to the MFC patch's ability to reduce the natural curvature of the stable shapes. Notably, the reduction in out-of-plane displacement for stable shape 1 after

bonding the MFC patch is 49%, while for stable shape 2, it is 63.64%. The larger reduction in stable shape 2 is attributed to the MFC bending along the shorter side, which provides greater stiffness compared to stable shape 1, where the MFC bends along the longer side, imparting less stiffness. It is also important to note that the absolute difference in the out-of-plane displacement of the stable shapes decreases from 46.95 mm to 25.33 mm with the bonding of the MFC patch. This 46.05% reduction in the out-of-plane displacement difference indicates that the bonding of the MFC patch helps to minimize the asymmetry in the static characteristics of the bistable laminate-MFC assembly.

Table 3: Out-of-plane displacement comparison in two stable shapes of cantilevered bistable laminate with and without MFCs obtained at the corners.

	FE Framework		Boddapati et al. [23]	
Description	Shape-1	Shape-2	Shape-1	Shape-2
$\tau = 0$	59.38	12.43	-	-
$\tau = 0.255$	29.85	4.52	27.00	4.50

4.2 Strain energy of the stable shapes

Table 4 presents the strain energies of the stable shapes for a rectangular bistable laminate without ($\tau = 0$) and with ($\tau = 0.255$) an MFC patch. The strain energy (SE) of stable shapes without the MFC is unequal, confirming the asymmetric potential energy landscape. Bonding the MFC patch to the top surface increases the SE of both shapes due to added stiffness. As the MFC patch alters the curvatures of stable shapes, it makes their stored potential energy unequal, shifting energy levels in the bistable laminate. Without the MFC ($\tau = 0$), the SE difference is 1 mJ, but with the MFC M8557 patch ($\tau = 0.255$), it increases to 3 mJ, amplifying the system's asymmetry.

Table 4: SE comparison of cantilevered bistable laminate with and without MFC patch.

	Strain energy (mJ)		
Description	Shape-1	Shape-2	Difference
$\tau = 0$	72	73	1
$\tau = 0.255$	79	82	3

To gain further insights into what happens to the potential energy landscape of bistable system once MFC is bonded, SE variation during the snap-through process is extracted and plotted for the cases: without MFC patch ($\tau = 0$) and with MFC M8557 patch ($\tau = 0.255$). Figure 4 shows the variation of the SE, where the x axis represents the status of transition from stable shape-1 to stable shape-2 and y axis depicts the SE levels. It is clear that the addition of MFC patch elevates the SE levels of both the stable shapes and also increases the SE difference between them when compared to the case of clamped rectangular bistable laminate with no MFC patch.

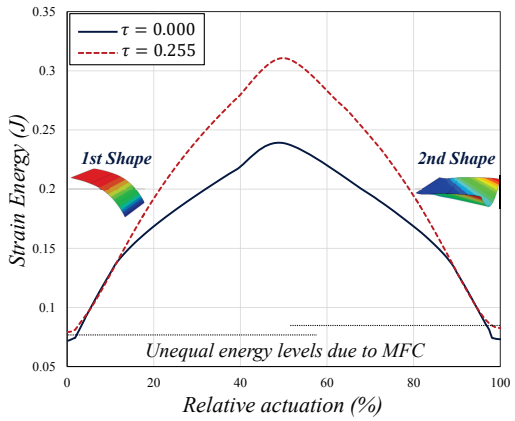

Figure 4: SE versus relative actuation of bistable laminate without MFC ($\tau = 0$) and with MFC M8557 patch ($\tau = 0.255$), showing the induced asymmetry due to attachment of MFC.

4.3 Natural frequency of the stable shapes

To understand the effect of bonding the MFC patch on the dynamic characteristics of the clamped rectangular bistable laminate, a free vibration analysis of the assembly is conducted. Table 5 presents the natural frequencies of the stable shapes for two scenarios: without the MFC patch ($\tau = 0$) and with the MFC M8557 patch ($\tau = 0.255$). From Table 5, it is evident that without the MFC, the two stable shapes of clamped rectangular bistable laminate exhibit unequal frequencies, reflecting the asymmetric nature of their dynamic characteristics. After bonding the MFC patch to one surface of the bistable laminate, the natural frequency of both stable shapes decreases significantly. This is due to the additional inertial effect introduced by the MFC, which reduces the natural frequencies of the stable shapes. However, it is noteworthy that the natural frequency difference between the stable shapes reduces from 98.61 Hz to 64.22 Hz with the addition of the MFC patch. This 34.87% reduction in the frequency difference indicates that the bonding of the MFC patch helps to minimize the asymmetry in the modal characteristics of the bistable laminate-MFC assembly. Reducing the asymmetry in the modal characteristics is highly advantageous for piezoelectric vibrational energy harvesting.

Table 5: Natural frequency comparison of selected bistable laminate with and without MFCs.

Description	Natural frequency (Hz)		
	Shape-1	Shape-2	Difference
$\tau = 0$	37.91	136.52	98.61
$\tau = 0.255$	35.25	99.47	64.22

5 PARAMETRIC STUDIES

In this section, the effect of changing the area of the MFC patch on the induced asymmetry in the static and dynamic characteristics is examined. The length of the MFC patch remains

constant at 85 mm, while its width is varied until the clamped rectangular bistable laminate loses bistability. Figure 5(a) illustrates the variation in the absolute difference in out-of-plane displacement (Δw) of the stable shapes as the area of the MFC patch increases (increasing τ parameter). As discussed in Section 4, bonding the MFC patch helps reduce the asymmetry in the out-of-plane displacement of the stable shapes. This reduction is more pronounced with smaller MFC patches (lower τ values) compared to larger ones (higher τ values). It is important to note that a smaller MFC patch, combined with minimal out-of-plane displacement of the stable shapes, leads to a significant decrease in the harvester's output power. Therefore, the MFC patch size should balance the induced asymmetry in out-of-plane displacement (Δw) with the harvested output power. Figure 5(a) serves as a design chart for selecting an appropriate MFC patch size, ensuring optimal asymmetry in static characteristics without significantly reducing output power. Figure 5(b) shows the variation in the absolute difference in SE (ΔSE) of the stable shapes as the area of the MFC patch increases (increasing τ parameter). As mentioned earlier, bonding the MFC patch increases the SE levels of the stable shapes due to the additional stiffness provided by the MFC. Larger MFC patches significantly raise the SE levels of the stable shapes compared to smaller patches, leading to an increase in the SE difference as the MFC patch size grows (increasing τ parameter), as shown in Figure 5(b). Beyond a certain value of the τ parameter, the assembly loses its bistability.

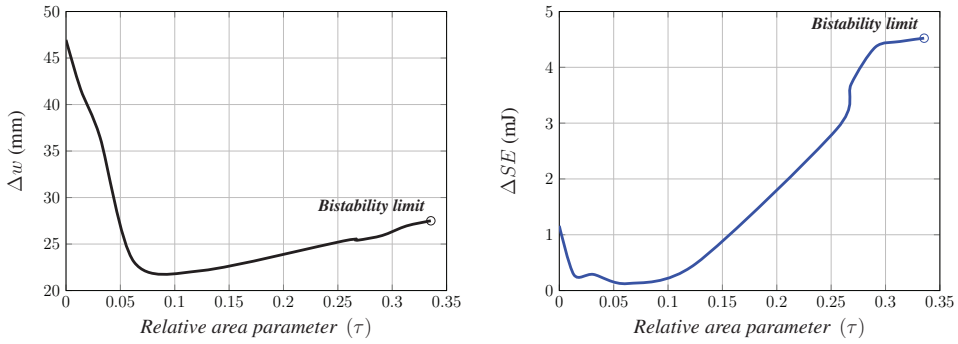

(a) (b)

Figure 5: Change in the (a) out-of-plane displacements, (b) SE difference with the area of MFC patches.

Similarly, the effect of varying the area of the MFC patch on the induced asymmetry in the modal characteristics of the laminate-MFC assembly is analyzed. Figure 6 shows how the absolute difference in natural frequency (Δf) between the stable shapes changes as the area of the MFC patch increases. As discussed in Section 4, bonding the MFC patch lowers the natural frequency of both stable shapes, with this reduction more noticeable with larger MFC patches (higher τ values) compared to smaller patches (lower τ values). As a result, the absolute difference in natural frequency (Δf) between the stable shapes decreases as the MFC patch size increases. This can be used as a design guideline for selecting the optimal size of the MFC patch in developing BEH, ensuring minimal asymmetry in their modal characteristics.

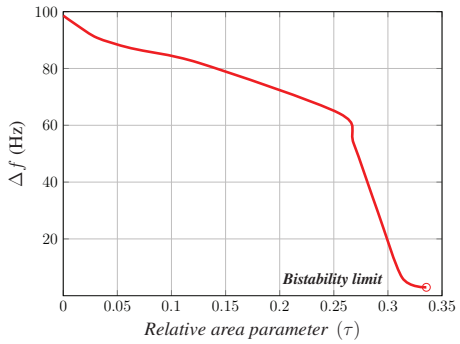

Figure 6: Change in the natural frequency difference with the area of MFC layers.

6 CONCLUSIONS

Bistable rectangular composite laminates exhibit an asymmetric double-well potential energy landscape, leading to asymmetric stable shapes. Consequently, their static and dynamic characteristics also exhibit induced asymmetry. The nature of this potential energy landscape is significantly influenced by the bonding of additional elements like Macro Fiber Composites (MFC) for shape-changing and energy-harvesting applications. This study investigates the effect of MFC bonding on the asymmetric potential energy landscape of a bistable piezoelectric energy harvester (BPEH). A fully nonlinear FE model is employed to quantify asymmetry in the potential energy landscape and the static and dynamic characteristics of BPEH. Results show that bonding an MFC patch alters the asymmetric potential energy levels of the stable shapes in a clamped rectangular bistable laminate-MFC assembly, further increasing the existing asymmetry. However, MFC bonding positively impacts static and dynamic characteristics by reducing asymmetry in out-of-plane displacement (Δw) and natural frequency (Δf), thereby enhancing piezoelectric vibrational energy harvesting. The symmetric static and modal characteristics of the two stable shapes facilitate continuous snap-through transitions under external ambient vibrations. A detailed parametric study explores the effect of MFC patch size on induced asymmetry in the potential energy landscape and static and dynamic characteristics. Increasing the MFC patch size increases the asymmetry in the potential energy landscape, whereas smaller MFC patches more effectively reduce asymmetry in the out-of-plane displacement. Additionally, larger MFC patches decrease asymmetry in modal characteristics. These findings provide a design guideline for selecting MFC patch sizes that minimize asymmetry in the potential energy landscape and static and dynamic characteristics, optimizing piezoelectric vibrational energy harvesting.

REFERENCES

[1] X. Lachenal, S. Daynes, and P. M. Weaver, “Review of morphing concepts and materials for wind turbine blade applications,” *Wind energy*, vol. 16, no. 2, pp. 283–307, 2013.

[2] D. Bashir, P. M. Anilkumar, S. Scheffler, A. Haldar, B. N. Rao, and R. Rolfes, “A review

of the dynamic behavior of thermally induced bistable configurations of unsymmetrical composite laminates and their applications," *Archives of Computational Methods in Engineering*, pp. 1–43, 2024.

[3] A. M. Giri, S. F. Ali, and A. Arockiarajan, "Dynamics of symmetric and asymmetric potential well-based piezoelectric harvesters: A comprehensive review," *Journal of Intelligent Material Systems and Structures*, vol. 32, no. 17, pp. 1881–1947, 2021.

[4] A. P. Kumar, P. M. Anilkumar, A. Haldar, S. Scheffler, E. L. Jansen, B. N. Rao, and R. Rolfes, "Tailoring bistability in unsymmetrical laminates using an additional composite strip," *Thin-Walled Structures*, vol. 168, p. 108212, 2021.

[5] P. M. Anilkumar, S. Scheffler, A. Haldar, E. L. Jansen, B. N. Rao, and R. Rolfes, "Investigations on the dynamic snap-through of MFC bonded self-resetting bistable laminates," *Composite Structures*, vol. 332, p. 117906, 2024.

[6] A. J. Lee, A. Xie, and D. J. Inman, "Suppression of cross-well oscillations for bistable composites through potential well elimination," *Journal of Vibration and Acoustics*, vol. 142, no. 3, p. 031003, 2020.

[7] J. R. Raney, N. Nadkarni, C. Daraio, D. M. Kochmann, J. A. Lewis, and K. Bertoldi, "Stable propagation of mechanical signals in soft media using stored elastic energy," *Proceedings of the National Academy of Sciences*, vol. 113, no. 35, pp. 9722–9727, 2016.

[8] B. Danish, P. M. Anilkumar, and B. N. Rao, "Suppression of cross-well vibrations of a bistable square cross-ply laminate using an additional composite strip," *International Journal of Dynamics and Control*, pp. 1–11, 2023.

[9] W. Wang, J. Cao, C. R. Bowen, and G. Litak, "Multiple solutions of asymmetric potential bistable energy harvesters: numerical simulation and experimental validation," *The European Physical Journal B*, vol. 91, pp. 1–9, 2018.

[10] R. Harne and K. Wang, "Prospects for nonlinear energy harvesting systems designed near the elastic stability limit when driven by colored noise," *Journal of Vibration and Acoustics*, vol. 136, no. 2, p. 021009, 2014.

[11] Q. He and M. F. Daqaq, "Influence of potential function asymmetries on the performance of nonlinear energy harvesters under white noise," in *International Design Engineering Technical Conference*, vol. 46391. ASME, 2014, p. V006T10A060.

[12] A. M. Giri, S. Ali, and A. Arockiarajan, "Influence of asymmetric potential on multiple solutions of the bi-stable piezoelectric harvester," *The European Physical Journal Special Topics*, vol. 231, no. 8, pp. 1443–1464, 2022.

[13] W. Cai and R. L. Harne, "Characterization of challenges in asymmetric nonlinear vibration energy harvesters subjected to realistic excitation," *Journal of Sound and Vibration*, vol. 482, p. 115460, 2020.

[14] R. L. Harne and K. Wang, "A review of the recent research on vibration energy harvesting via bistable systems," *Smart materials and structures*, vol. 22, no. 2, p. 023001, 2013.

[15] A. Arrieta, P. Hagedorn, A. Erturk, and D. J. Inman, "A piezoelectric bistable plate for nonlinear broadband energy harvesting," *Applied Physics Letters*, vol. 97, no. 10, 2010.

[16] D. N. Betts, A. I. Salo, C. R. Bowen, and H. A. Kim, "Characterisation and modelling of the cured shapes of arbitrary layup bistable composite laminates," *Composite Structures*, vol. 92, no. 7, pp. 1694–1700, 2010.

[17] P. Harris, "Bistable laminates for energy harvesting," Ph.D. dissertation, University of Bath, 2017.

[18] A. J. Lee, A. Moosavian, and D. J. Inman, "A piezoelectrically generated bistable laminate for morphing," *Materials Letters*, vol. 190, pp. 123–126, 2017.

[19] A. Arrieta, T. Delpero, A. Bergamini, and P. Ermanni, "Broadband vibration energy harvesting based on cantilevered piezoelectric bi-stable composites," *Applied Physics Letters*, vol. 102, no. 17, 2013.

[20] M. Li, D. Yu, Y. Li, X. Liu, and F. Dai, "A bi-stable device for simultaneous vibration absorption and energy harvesting using bi-stable piezoelectric composite laminate," *Composite Structures*, vol. 314, p. 116971, 2023.

[21] D. Pan, B. Ma, and F. Dai, "Experimental investigation of broadband energy harvesting of a bi-stable composite piezoelectric plate," *Smart Materials and Structures*, vol. 26, no. 3, p. 035045, 2017.

[22] X. Liu, H. Jia, M. Li, Y. Li, Y. Tao, and F. Dai, "Piezoelectric wind energy harvester of bi-stable hybrid symmetric laminates," *Composites Science and Technology*, vol. 242, p. 110198, 2023.

[23] K. Boddapati and A. F. Arrieta, "Structural multistability for multi-speed wind energy harvesting from vortex-induced vibrations," *Smart Materials and Structures*, vol. 33, no. 10, p. 105048, 2024.

[24] P. Portela, P. Camanho, P. Weaver, and I. Bond, "Analysis of morphing, multi stable structures actuated by piezoelectric patches," *Computers & Structures*, vol. 86, no. 3-5, pp. 347–356, 2008.

XI ECCOMAS Thematic Conference on Smart Structures and Materials - SMART 2025
M. Krommer, M. Nader and M. Schagerl (Eds)

Received: 27 March 2025 / Revised: 15 July 2025 / Accepted: 9 October 2025
© The Author(s) 2025

Development of a Shape-Adaptive Robot Gripper using Magnetorheological Fluids and Additively Manufactured Cylinders

Jennifer J. Blöchle, Thomas M. Wendt, Thomas Seifert

Abstract. Manipulating fragile objects of different shapes is a major robotics challenge. This led to the development and investigation of various gripper concepts with different flexible materials. This concept study focuses on the development of a shape-adaptive gripper that uses additively manufactured cylinders with variable heights and Shore hardness to achieve optimal adaptability and gripping force. The cylinders are filled with magnetorheological fluid (MRF), the properties of which are controlled by a standard electromagnet operating at 24 volts and 2 amps. The proposed concept aims to systematically investigate the influence of cylinder height, MRF volume, and material hardness on adaptability and gripping stability. Cylinders of varying heights allow for variations in MRF volume, enabling analysis of the fluid's volumetric behavior under the influence of a magnetic field. The Shore hardness of the additively manufactured structures is incrementally adjusted to optimize the balance between flexibility and structural stability. The electromagnet stimulates the MRF, altering its viscosity and stiffness to enable effective adaptation to various object geometries. The concept combines the properties of flexible materials and active fluids in a modular design, making it relevant for diverse applications such as robotics and automation.

Key words: Magnetorheological fluid (MRF), Smart Structures, Multiphysics Problems, Magnetic Field Distribution, Shape-Adaptive Gripper, Additive Manufacturing

1 INTRODUCTION

The ongoing development of shape-adaptive grippers for the precise manipulation of fragile handling objects with variable geometries represents a central challenge in robotics and automation. The use of magnetorheological fluids (MRF) offers specific advantages in this context, such as rapid, reversible, and contactless changes in viscosity and the resulting stiffness. These properties enable gripper systems to dynamically adapt their mechanical characteristics, which is particularly relevant for handling delicate and geometrically diverse objects [1]. By combining flexible structural elements with actively tunable rheological properties. An adaptive object manipulation can be achieved.

Jennifer J. Blöchle & Thomas M. Wendt & Thomas Seifert
University of Offenburg, 77652 Offenburg, Germany
e-mail: jennifer.bloechle@hs-offenburg.de

Studies highlight the advantages of these systems, particularly in terms of their rapid and reversible adjustment of rheological properties in response to an applied magnetic field. Previous research has examined gripper systems optimized for the manipulation of delicate objects, as well as hybrid concepts that combine pneumatic actuators with MRF to achieve targeted stiffness control [2, 3]. These studies demonstrate the high potential of MRF for adaptive gripping systems and emphasize the need to further optimize relevant design parameters [4].
In this contribution, the magnetic interaction between an external magnetic field and cylindrical thermoplastic polyurethane (TPU) structures filled with magnetorheological fluid is investigated by simulation. The focus is on analyzing the influence of cylinder height and wall thickness on the resulting structural stiffening of the MRF. While MRFs are conventionally used in damping systems under high shear rate conditions, this work concentrates on the low shear regime where the structural reorganisation of the particles under static magnetic field exposure is investigated [2].
The present investigation contributes to this field by analyzing the underlying physical mechanisms governing magnetic field interactions with structured TPU cylinders and magnetorheological fluids. To illustrate the underlying gripper concept, a schematic representation of the system setup is provided in Figure 1.

2 Geometry and Materials

2.1 Geometry

The numerical simulations were carried out using the COMSOL 6.3 Multiphysics software. The simulation model consisted of a commercially available electromagnet, at the pole of which a cylindrical hollow body made of thermoplastic polyurethane was modeled. The wall thickness of the TPU cylinder was varied in a range from 0.2 mm to 1 mm in 0.2 mm steps. The height of the cylinder remained constant at 10 mm to allow a systematic analysis of the geometric influences on the magnetic field distribution. This configuration provides a standardized basis for investigating the interactions between the magnetic field and the MRF as a function of the geometry of the TPU hollow body, see Figure 2.

2.2 MR Fluid

Products considered included RHEOTEC, MRF-210 and MRF-132 DG, all supplied by *Arus MR Tech*. RHEOTEC was chosen due to its high sedimentation stability, response time of less than 10 ms, and controlled viscosity change within the relevant magnetic field range. It also features a homogeneous particle distribution and excellent long-term stability. The decisive factor was the higher iron content, which enables a stronger and more precise reaction to the magnetic field, a decisive aspect for the simulation in the low shear range.
In comparison, MRF-210 and MRF-132 DG exhibited lower iron content. This limited their suitability for the specific application, as the reduced concentration of magnetic particles resulted in a lower achievable change in viscosity and mechanical stiffness under applied magnetic fields.

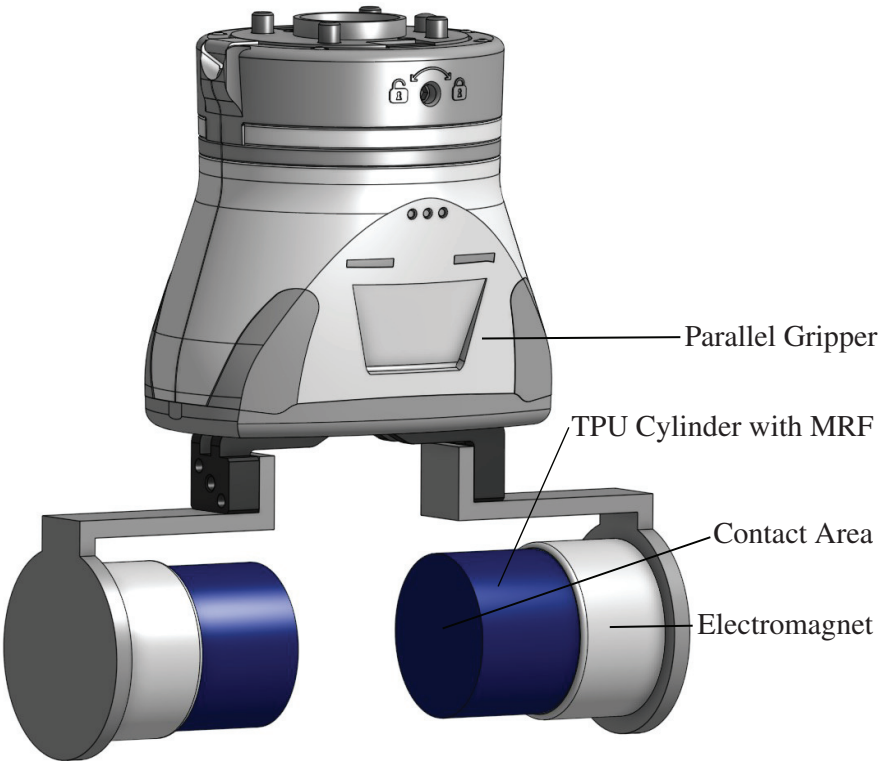

Figure 1: Schematic representation of the underlying gripper concept based on a model sketch using a parallel gripper.

2.3 B-H-Curve

The B-H curve describes the relationship between the magnetic flux density (B) and the magnetic field strength (H), serving as a fundamental basis for modeling magnetorheological materials.
The data points used in the simulation were extracted directly from the datasheet [5] and show a consistent slope in the low-field strength region (see Figure 3). To obtain intermediate values between the known data points, linear interpolation was applied using the following equation:

$$B = B_1 + \frac{(B_2 - B_1)}{(H_2 - H_1)} \cdot (H - H_1) \tag{1}$$

In this context, B_1 and B_2 denote the known magnetic flux densities corresponding to the magnetic field strengths H_1 and H_2, respectively. Linear interpolation was employed to establish a continuous relationship between these discrete data points. This interpolation method is considered appropriate and sufficiently accurate for the intended simulations, as the magnetorheological fluid exhibits an approximately linear behavior in the low shear regime.

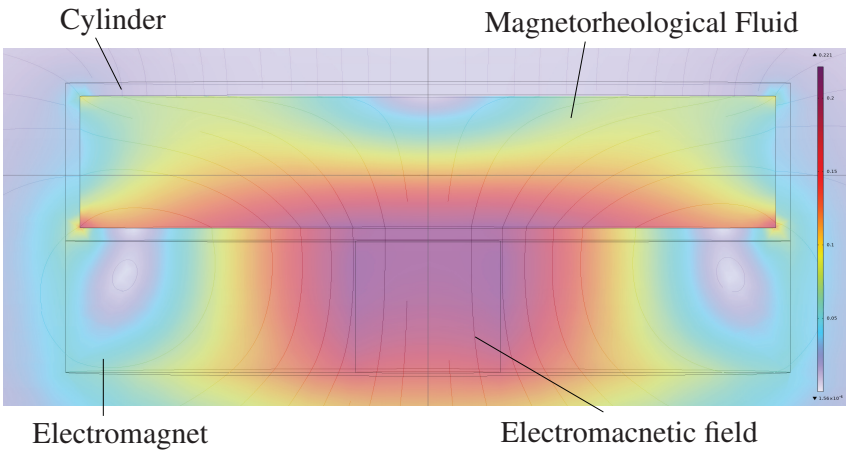

Figure 2: Distribution of the magnetic flux density in an MRF-based setup influenced by an electromagnet. The color scale denotes the magnetic flux density, with red indicating high and blue indicating low field strengths.

2.4 Relative permeability

The experimental analysis of the relative permeability $\mu_r(H)$ shows that it can be described by the function :

$$\mu_r(H) = \mu_{r0} - \left(\frac{H}{H_{\text{ref}}}\right)^n \tag{2}$$

At low field strengths, the initial magnetic behavior of the material is characterized by $\mu_{r0} = 10.89$, which describes its permeability in the unsaturated state. The reference field strength $H_{\text{ref}} = 1118.27\ \text{A/m}$ defines the scaling of the saturation processes and indicates the field strength at which the permeability significantly decreases from its initial value. A lower H_{ref} value is associated with an earlier onset of magnetic saturation, while a higher value reflects a more gradual reduction in permeability. The exponent $n = 0.372$ quantifies the nonlinear reduction of permeability as a function of the magnetic field strength. This function served to verify and quantify the behavior of the B-H curve, providing a mathematical description of how the permeability evolves with increasing magnetic field strength. The derived permeability function can be interpreted as a material-dependent field equation describing the B-H curve. The resulting permeability function (2) is used to validate the B–H behavior and describes the field-dependent evolution of the magnetic properties. It represents a material-specific model for characterizing the nonlinear magnetization process.

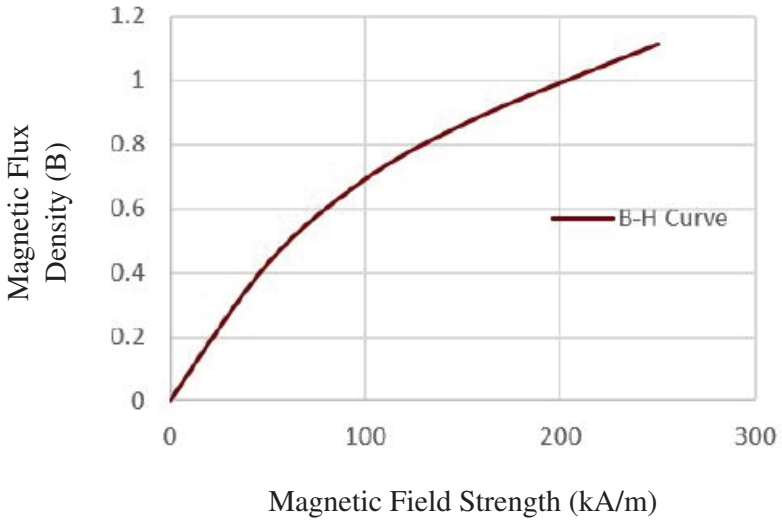

Figure 3: B-H curve for AMT-RHEOTEC+ MRF interpolated in COMSOL

2.5 Thermoplastic Polyurethane

TPU exhibits an elongation at break of up to 500%, high wear resistance under repeated mechanical stress and frictional contact, and dimensional stability within a temperature range of $-40°\mathrm{C}$ to $+80°\mathrm{C}$ [6]. These characteristics ensure reproduction of complex geometries in additive manufacturing. In addition, TPU contributes to reducing weight, material consumption, and production time, while supporting the realization of application-specific designs that can be flexibly adapted to varying requirements [7]. TPU is considered neutral, with a relative permeability of approximately $\mu_r \approx 1$ and negligible magnetic susceptibility.

3 Method of Study and Physics Used in COMSOL

3.1 Simulation Approach

The simulation was conducted as a stationary analysis at the moment of magnetic field activation. A detailed examination of the magnetic field distribution and the magnetic field strength within the magnetorheological fluid was carried out. The complex interaction between the electromagnet, the TPU cylinder, and the MRF was investigated in order to systematically characterize the mutual influences.

3.2 Magnetic Analysis

Ampère's Law was used in COMSOL for the magnetic analysis to accurately calculate the magnetic field distribution within the material. Ampère's law describes the relationship between an electric current and the resulting magnetic field and is expressed in its differential form as:

$$\nabla \times \mathbf{H} = \mathbf{J} \tag{3}$$

$\mathbf{H}$ denotes the magnetic field strength and $\mathbf{J}$ the current density. The magnetic field is generated by an electromagnet operating at 24 volts and 2 amps, with a total of 1,680 turns. These parameters are critical in determining the strength and distribution of the magnetic field generated. The coil wire parameters were defined based on literature data. The electrical conductivity was set to 6×10^7 S/m, and the cross-sectional area to 1×10^{-6} m^2 [8]. These material properties ensure efficient current conduction and allow a simulation of the magnetic field. The resulting magnetic flux density $\mathbf{B}$ is determined by the nonlinear magnetization behavior of the material, which follows the B-H curve. Instead of the linear relation where μ_r is a constant relative permeability:

$$\mathbf{B} = \mu_0 \mu_r \mathbf{H} \tag{4}$$

The magnetic material behavior is described by a nonlinear constitutive relation given by:

$$\mathbf{B} = f(|\mathbf{H}|) \frac{\mathbf{H}}{|\mathbf{H}|} \tag{5}$$

This equation accounts for the nonlinear response of the material to the applied magnetic field strength $\mathbf{H}$. The function $f(|\mathbf{H}|)$ represents the material's B-H curve, ensuring that the dependency of the magnetic flux density $\mathbf{B}$ on the magnitude of $\mathbf{H}$ is accurately captured.
Electrical conductivity was taken into account to capture the interaction between electric current and the magnetic field. The relationship between current density $\mathbf{J}$ and the electric field $\mathbf{E}$ is governed by Ohm's law, which is expressed as:

$$\mathbf{J} = \sigma \mathbf{E} \tag{6}$$

where σ is the scalar electrical conductivity of the material, assuming isotropic electrical behavior of the magnetorheological fluid (MRF). Ampère's law was implemented as a fundamental component of the simulation framework to resolve the magnetic field distribution and its effect on the MRF. This allowed a detailed analysis of the interactions between the electromagnetic field, the material properties of the cylinder, and the MRF filling.

4 Results

The simulation results illustrate the influence of the wall thickness of the additively manufactured TPU cylinders on the magnetic flux density distribution in the magnetorheological fluid (MRF). Figures 4 and 5 depict the magnetic flux density distribution for cylinders with wall thicknesses of 0,2 mm and 1 mm respectively.

- Cylinder with 0.2mm wall thickness (Figure 4): The MRF exhibits a higher magnetic flux density compared to the cylinder with a thicker wall. Due to the shorter distance to the magnetic field source, the field strength within the fluid is increased, leading to a stronger magnetization effect.

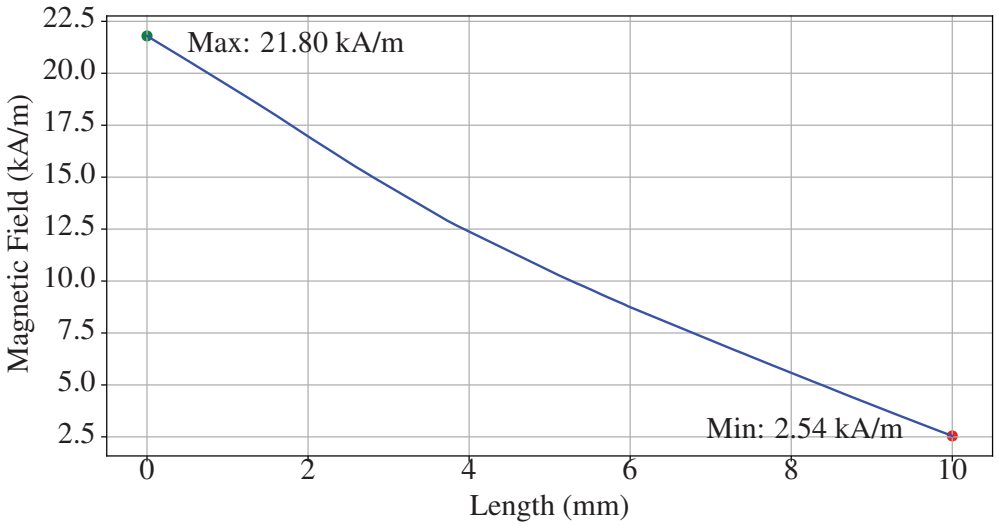

Figure 4: Magnetic field strength in the MRF for TPU wall thickness 0,2 mm

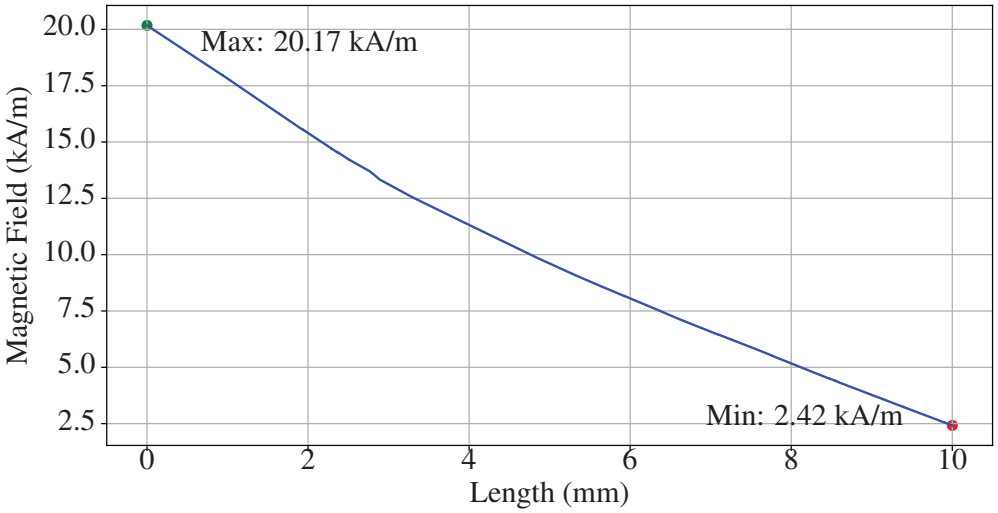

Figure 5: Magnetic field strength in the MRF for TPU wall thickness 1 mm

- Cylinder with 1.0mm wall thickness (Figure 5): In this case, a lower magnetic flux density is observed within the MRF compared to the thinner-walled cylinder. The increased wall thickness results in a greater distance between the MRF and the magnetic field source, reducing the magnetic field strength inside the fluid.

The magnetic flux density directly in front of the TPU surface was set to 200 mT in all simulations. The spatial distribution of the magnetic field is influenced by the geometry of the cylinder, leading to variations in the magnetization of the MRF.

In addition to geometric parameters, the effect of Shore hardness was also evaluated. Variations in the Shore hardness of the TPU did not exhibit any measurable influence on the distribution of the magnetic flux density. Due to its magnetic neutrality—characterized by a relative permeability of approximately $\mu_r \approx 1$ and negligible magnetic susceptibility—changes in mechanical surface properties such as hardness do not affect the propagation of the magnetic field. Consequently, the interaction between the magnetic field and the MRF is predominantly governed by geometrical aspects, particularly the distance to the field source.
This dependence is supported by a field analysis along the cylinder geometry. Figure 6 presents the spatial distribution of the magnetic field strength (in kA/m) and the magnetic flux density (in mT) along the arc length of an MRF-filled cylinder with a wall thickness of 0.2 mm. Both quantities decrease continuously with increasing distance from the electromagnetic source. The flux density decreases from an initial value of 200 mT to below 25 mT, while the magnetic field strength follows a similar trend with a smaller absolute variation. This indicates that the most pronounced magnetization occurs in close proximity to the magnetic field source.

Yield Stress and Magnetic Field Strength

Figure 7 illustrates the yield stress curve of the employed *AMT-RHEOTEC+ MRF* as a function of the magnetic field intensity. The curve confirms that the yield stress increases with rising magnetic field strength. At 50 kA/m, the yield stress is approximately 30 kPa, whereas at 200 kA/m, it exceeds 70 kPa. This shows that the MRF significantly stiffens under magnetization, allowing controlled adjustments in the stiffness of the gripper.
The previously discussed decline in the magnetic field intensity along the cylinder (Figure 7) implies that the yield stress is not uniformly distributed within the MRF volume. In regions with lower field strength, the MRF remains softer, while in areas with high magnetization, it exhibits increased rigidity. This phenomenon could be exploited to create localized stiffness gradients within the gripping element, optimizing adaptability to different object geometries.

5 Discussion

The results indicate that the wall thickness of the TPU cylinder has a significant influence on the magnetic field distribution and, consequently, on the magnetorheological properties of the fluid.

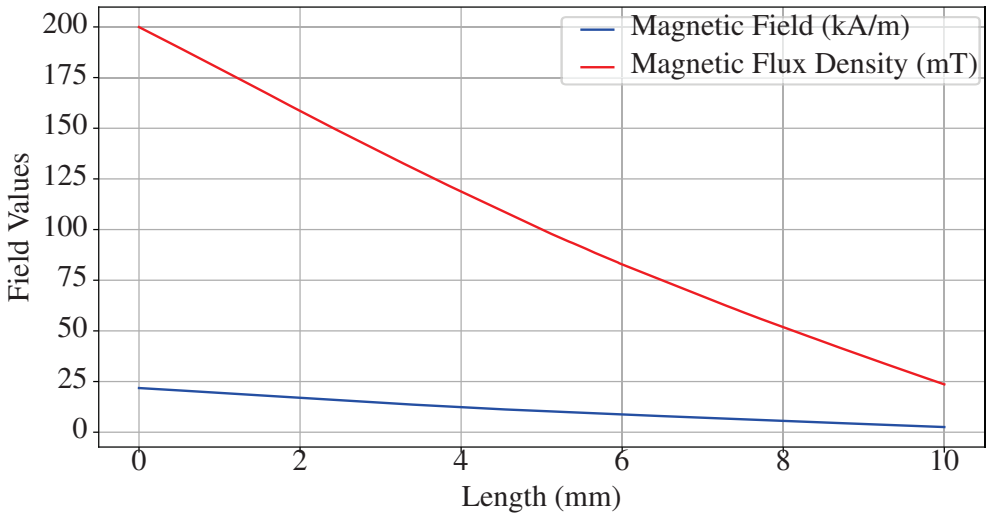

Figure 6: Magnetic field strength in the MRF for TPU wall thickness 0,2 mm

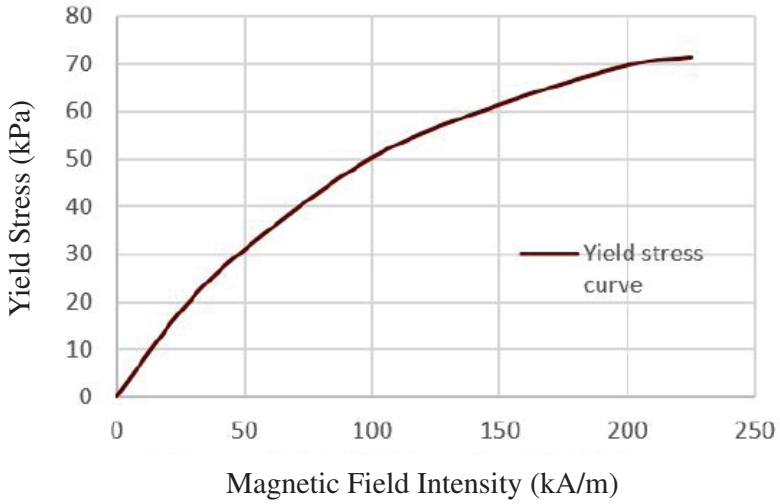

Figure 7: Yield strength vs. magnetic field strength for AMT-RHEOTEC+ MRF

Influence of Wall Thickness on MRF Magnetization

A thinner wall thickness 0.2 mm enhances MRF magnetization due to its proximity to the magnetic field source. This results in a higher field strength within the fluid and a more pronounced increase in viscosity. In contrast, a thicker wall (e.g., 1 mm) increases the distance between the MRF and the magnetic field, thereby reducing the magnetic field strength within the fluid.

Additional Confirmation through the Magnetic Field Distribution Diagram (Figure 6)

The diagram quantitatively demonstrates the decrease in magnetic flux density along the arc length of the cylinder with a 0.2 mm wall thickness. This supports the hypothesis that an increased wall thickness—and thus a greater distance of the MRF from the magnetic field source—leads to reduced magnetization. The activation of the MRF decreases with increasing distance from the magnetic field, directly affecting the adaptability of the gripper.
The observed decrease in magnetic flux density is not solely attributable to the geometric distance from the magnetic field source but is also influenced by the relative permeability μ_r of the MRF. Since μ_r describes a material's ability to conduct a magnetic field, it directly impacts the field distribution within the fluid.
The investigated MRF exhibits a nonlinear dependency of relative permeability on the applied magnetic field strength. This phenomenon implies that, in addition to the diminishing magnetic field intensity with increasing distance from the field source, the material's internal magnetizability is also subject to alteration. A higher relative permeability amplifies the fluid's magnetization, whereas a lower μ_r results in attenuated magnetization.

Relationship with Yield Stress (Figure 7)

The yield stress illustrated in Figure 7 shows that the MRF experiences a significant increase in stiffness at higher magnetic field strengths. The previously discussed decrease in magnetic flux density along the cylinder implies that the MRF in the region farther from the electromagnet exhibits a lower yield stress compared to areas closer to the magnetic field source. This effect can be utilized for optimizing the gripper by selectively generating regions with different stiffness levels to facilitate efficient shape adaptation.

6 Conclusion

This contribution provides insights into the role of TPU cylinder wall thickness in governing the magnetization behavior and mechanical response of MRFs. The results demonstrate that reducing the wall thickness enhances MRF activation due to increased proximity to the magnetic field, whereas increasing the thickness diminishes magnetization and subsequently affects yield stress. These findings have direct implications for the design of MRF-based adaptive systems, particularly in applications requiring controlled stiffness variations, especially in low-shear conditions.
Future research will focus on refining experimental validation, investigating alternative material

compositions, and optimizing structural designs to maximize adaptability and performance in practical applications. Additionally, additive manufacturing technologies could be leveraged to fabricate complex, functionally graded structures with precisely controlled wall thicknesses, enabling further advancements in adaptive gripping systems and other MRF-based applications.

REFERENCES

[1] M. Xu, Y. Liu, J. Li, F. Xu, X. Huang, and X. Yue, "Review of flexible robotic grippers, with a focus on grippers based on magnetorheological materials," *Materials*, vol. 17, no. 19, p. 4858, 2024. [Online]. Available: https://www.mdpi.com/1996-1944/17/19/4858

[2] A. Pettersson, S. Davis, J. O. Gray, T. J. Dodd, and T. Ohlsson, "Design of a magnetorheological robot gripper for handling of delicate food products with varying shapes," vol. 98, no. 3, pp. 332–338, 2010. [Online]. Available: https://www.sciencedirect.com/science/article/pii/S0260877410000130

[3] A. Pagoli, M. Alkhatib, and Y. Mezouar, "A Soft Variable Stiffness Gripper with Magnetorheological Fluids for Robust and Reliable Grasping," *IEEE Robotics and Automation Letters*, vol. 9, no. 5, pp. 4519–4526, May 2024, conference Name: IEEE Robotics and Automation Letters. [Online]. Available: https://ieeexplore.ieee.org/document/10480537?utm_source=chatgpt.com

[4] J. S. Kumar, P. S. Paul, G. Raghunathan, and D. G. Alex, "A review of challenges and solutions in the preparation and use of magnetorheological fluids," *International Journal of Mechanical and Materials Engineering*, vol. 14, no. 1, p. 13, Nov. 2019. [Online]. Available: https://doi.org/10.1186/s40712-019-0109-2

[5] Arus MR Tech, "Technical datasheet: Rheotec magnetorheological fluid," https://arusmrtech.com/wp-content/uploads/2021/11/RHEOTEC.pdf, 2021, accessed Mar. 21, 2025.

[6] G. Abts, *Einführung in die Kautschuktechnologie*. Carl Hanser Verlag GmbH Co KG, Apr. 2021, google-Books-ID: sI4mEAAAQBAJ.

[7] T. Xu, W. Shen, X. Lin, and Y. Xie, "Additively manufactured thermoplastic polyurethane (TPU) mold for concrete casting of complex structure," *Rapid Prototyping Journal*, vol. 28, no. 9, pp. 1717–1730, Apr. 2022.

[8] N. M. Sivaram, K. Sankaranarayanasamy, and J. P. Davim, Eds., *Advances in Manufacturing, Automation, Design and Energy Technologies: Proceedings from ICoFT 2021*, ser. Lecture Notes in Mechanical Engineering. Singapore: Springer Nature Singapore, 2023. [Online]. Available: https://link.springer.com/10.1007/978-981-99-1288-9

XI ECCOMAS Thematic Conference on Smart Structures and Materials - SMART 2025
M. Krommer, M. Nader and M. Schagerl (Eds)

Received: 2 April 2025 / Revised: 28 August 2025 / Accepted: 9 October 2025
© The Author(s) 2025

Experimental investigation of a novel sensor-integrating jaw coupling for data acquisition

Arthur Ewert, Johannes D. M. Menning, Artem Prokopchuk, Thomas Rosenlöcher, E.-F. Markus Vorrath, Thomas Wallmersperger, Berthold Schlecht

Abstract. The demand for high-quality data is continuously increasing across various industries to leverage modern condition monitoring or predictive maintenance techniques. Acquiring and providing such data represents major challenges, particularly when in-situ measurements of gearboxes or interface measurements between a gearbox and a motor are required. To address these challenges, sensor-integrating machine elements that incorporate sensors for data acquisition through a space-neutral approach need to be developed. For the measurement of the transmitted torque, a sensor-integrating jaw coupling was proposed. This coupling measures capacitances resulting from the deformation of integrated dielectric elastomer sensors. A regression model can then be used to approximate the transmitted torque based on the measured capacitances.

The present work focuses on the measured data obtained from the sensor-integrating jaw coupling under varying load conditions. For this reason, the coupling is tested on a test bench with various frequencies and amplitudes. The experimental results are analyzed, and non-linear dependencies between the applied torsion angle and the torque are outlined. Finally, the results of the measurements are discussed based on their repeatability and steps that are necessary to improve the quality of the torque measurement are outlined.

Key words: sensor-integration, jaw coupling, DES, experimental investigation, data acquisition

Arthur Ewert & Thomas Rosenlöcher & Berthold Schlecht
Institute of Machine Elements and Machine Design, Technische Universität Dresden, Münchner Platz 3, 01069 Dresden, Germany, e-mail: arthur.ewert@tu-dresden.de

D. M. Menning & Thomas Wallmersperger
Institute of Solid Mechanics, Technische Universitaät Dresden, George-Bähr-Str. 3c, 01069 Dresden, Germany

Artem Prokopchuk & E.-F. Markus Vorrath
Institute of Semiconductors and Microsystems, Technische Universitaät Dresden, Nöthnitzer Straße 64, 01187 Dresden, Germany

1 INTRODUCTION

Predictive maintenance holds a vast potential in the optimization of maintenance intervals. However, detailed data about the status and previous loads of a machine are necessary to accurately predict the maintenance interval. Acquiring this data is a challenging task, which often requires expensive sensors and redesigns of certain parts. Sensor-integrating machine elements allow a space neutral exchangeability with the original (conventional) machine element. As a result, they enable to reduce the time and costs for the data acquisition substantially. In this context, sensor-integrating machine elements allow an effortless retrofitting of machines for the purpose of data acquisition [1]. A relevant field of application of sensor-integrating machine-elements are flexible couplings, e.g., elastic jaw couplings. Their main task is the transmission of torque between two shafts. Furthermore, they are intended to minimize the restoring forces caused by shaft misalignments due to manufacturing, mounting and dynamic loads. Additionally, they are used to shift the natural frequencies of a drive train due to their low torsional stiffness and high relative damping [2]. For these reasons, elastic jaw couplings are widely used. Hence, they hold a great potential for sensor-integration. A first concept of a sensor-integrating jaw coupling was proposed by Schork et al. [3]. They replaced the majority of a tooth by a metallic bending plate and were able to measure the deformation of a single tooth using a strain gauge. This is achieved at the cost of a high reduction in transmittable torque. Furthermore, several industrial suppliers, e.g., *R+W Antriebselemente GmbH* and *KTR Systems GmbH*, offer sensor-integrating couplings [4, 5]. This highlights the relevance of the topic for academic research and industry. Currently, several sensor-integrating machine elements are developed. A detailed overview of current research is outlined by Kirchner et al. [1].

The available solutions primarily focus on modifying metallic hubs and shafts. Currently, there are no available solutions that integrate sensors into the elastomer parts. The present work therefore presents a novel prototype of the sensor-integrating jaw coupling by only modifying the elastomer gear rim, see Figure 1.

The developed coupling is able to measure the transmitted torque and the temperature of the gear rim. Furthermore, as shown conceptually by Ewert et al. [6], and numerically by Menning et al. [7], the concept enables the measurement of shaft misalignment, in particular radial shaft misalignment. The prototype aims to enable the wireless transmission of measurement data, while maintaining a space neutral retrofitting. A detailed summary of the concept can be found in Ref. [8].

In the present work, experimental results of the novel sensor-integrating jaw coupling are presented. Two experiments were conducted to characterize the sensitivity of the developed prototype in regard to the measured capacitance of the dielectric elastomer sensors at different loading frequencies and amplitudes. Section 2 presents the prototype of the coupling and the test bench for the experimental investigation. Section 3 outlines the testing parameters, followed by the results of the experiments in Section 4. The results are discussed in Section 5 and conclusions are drawn in Section 6.

2 MATERIALS

The developed and measured prototype is presented in Figure 1. The sensor-integrating gear rim has an outer diameter of $d_{\text{outer}} = 65\,\text{mm}$ and is made of thermoplastic polyurethane with a Shore hardness of $92\,\text{Sh(A)}$. The measurement of torque is realized by measuring the deformation of the teeth with dielectric elastomer sensors (DESs). One DES is integrated into every tooth of the gear rim. The measurement electronics are located in the center cavity of the gear rim, see Figure 1.

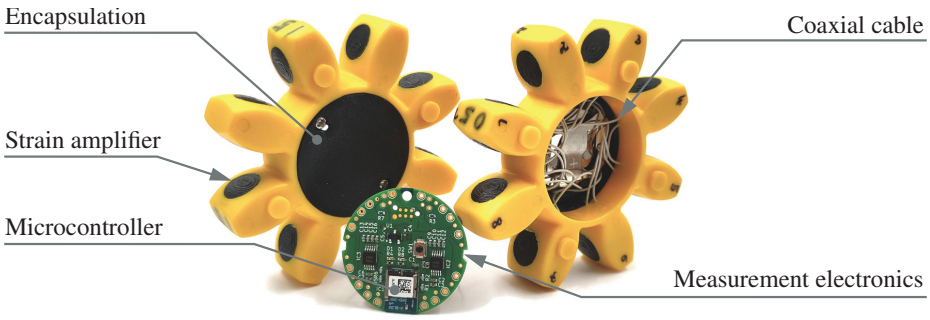

Figure 1: Image of two prototypes of the sensor-integrating gear rim for the jaw coupling and the measurement electronics. The left gear rim is the assembled prototype. The right gear rim is a partially disassembled prototype without the encapsulation. The printed circuit board of the measurement electronics is shown in the center.

DESs are flexible plate capacitors that consist of alternating layers of electrodes and non-conductive elastomer layers used as dielectrics. For a detailed overview of the internal structure and the stack-up of the used DESs refer to Refs. [9, 10]. Mechanical strain amplifiers are used to increase the compression of the DESs in the teeth, thereby increasing the sensitivity of the measurement [11]. The strain amplifiers are 3D printed from polycarbonate. Polycarbonate is chosen based on its high heat deflection temperature of $\vartheta_{\text{deflect}} = 126.0\,°\text{C}$ (ISO 75-2 method A) [12], ensuring the strain amplification over the entire possible operating temperature range of the coupling. A detailed description of the dimensions can be found in preliminary works in Ref. [8]. To enable the electrical connection between the DES and the amplifier, a copper foil pad is glued to each amplifier. This copper foil is soldered to a coaxial wire *9436* made by *Alphawire*. The cable is routed through the tooth into the inner gear rim and soldered to the central electronics, see Figure 1. The measurement electronics are shown in the center of Figure 1. The main element is a BMD-A-R-380 module by *Ublox* with an *nRF52840* microcontroller unit (MCU) made by *Nordic Semiconductors*. The MCU handles the data acquisition with the FDC1004, stores the measurement data and provides the collected data using *Bluetooth low energy* wirelessly to a nearby computer. The capacitances of the DESs are measured using two *FDC1004DGSR* made by *Texas Instruments*. Each FDC1004 measures two DESs for clockwise

and counterclockwise loading of the coupling. Hence, eight DESs can be measured simultaneously. The FDCs are programmed with a measurement rate of $f_{\text{measure}} = 400\,\text{Hz}$. Please note that the prototype was improved on the basis of preliminary works, e.g., [8, 11], by (i) designing new measurement electronics, (ii) using polycarbonate as material for the strain amplifiers with an included strain relief, (iii) software updates and (iv) measuring eight DESs for the first time.

Testing of the sensor-integrating jaw coupling is done on a quasi static servo-hydraulic test bench. The sensor-integrating gear rim is inserted into two hubs. The two hubs are made of aluminum and have four jaws each. Connection of the hubs to the adapter shafts is realized by half shell clamping hubs. The torsion angle is applied through the hydraulic pivot engine and an adapter shaft at the bottom of the test bench. At this position, the torsion angle ϕ is measured. The torsion sensor has a resolution of $0.0025\,\text{deg}$. The sensor-integrating jaw coupling is mechanically connected with the adapter shaft from the pivot engine and a second adapter shaft that is fixed at the top of the test bench. The torque sensor of the test bench is located between the fixed shaft and the test bench. The resolution of the torque sensor is $0.0002\,\text{Nm}$ with a maximum measurement rate of $10\,\text{kHz}$.

3 STUDY DESIGN

Two experiments were conducted to investigate the sensor-integrating jaw coupling. In each test, the applied torsion angle ϕ, the transmitted torque T by the coupling, and the capacitance C of each DES were measured. The capacitance of each DES measured in the relaxed mounted state was used as reference for calculating the capacitive difference ΔC. The sensitivity of each DES is calculated as the quotient of the change in torque and the change in capacitance. Here, the central difference quotient is used, considering 20 measurements points in order to reduce the influence of measurement oscillations. Both tests were carried out with rotational angle control. First, a *cyclic loading* of the coupling was conducted to investigate non-linearities and the sensitivity of the measured capacitances. The coupling was loaded with a frequency of $f_{\text{load}} = 0.25\,\text{Hz}$ and a torsion amplitude of $\phi_{\text{amp}} = 1\,\text{deg}$. Second, a *frequency sweep* with a constant loading amplitude of $\phi_{\text{amp}} = 1\,\text{deg}$ and an increasing loading frequency $0.01\,\text{Hz} \leq f \leq 3\,\text{Hz}$ was conducted. The frequency was increased with one octave per minute, leading to a test time of approximately 250 seconds. The parameters were chosen to mitigate the heating of the coupling. Thus, the stiffness of the coupling was not reduced by an increasing temperature. Within the experimental setting, the odd teeth were loaded during a clockwise rotation, while the even teeth were loaded during a counterclockwise rotation. In the following, the index *cw* (ΔC_{cw}) refers to capacitance changes measured for the odd teeth (clockwise loading), whereas the index *ccw* (ΔC_{ccw}) is used for counterclockwise loading.

4 RESULTS

Figure 2 displays the results of the cyclic loading. The top two graphs show the torsion angle and torque measured from the test bench over time. The bottom two graphs highlight the capacitance of the DES in each tooth. The measurements of the DESs are split based on their loading direction to enhance the visibility.

The acquired measurement data show that the capacitances of the DESs change in accordance to the torsion angle. The capacitances for the clockwise loaded teeth increase with a positive torsion angle, while the capacitances for the counterclockwise loaded teeth increase with a negative torsion angle. A relevant observation is the smaller capacitance of the unloaded teeth in comparison to their reference measurement, resulting in negative capacitance changes. This effect relates to the relief of the pre-tension of the unloaded teeth in comparison to the mounted state. Another notable finding is a small relaxation characteristic observed in the unloaded state of each tooth, excluding the 8th tooth. The results further reveal differences of the maxima and minima of the capacitance change between different DESs. However, the maximal and minimal capacitance changes for a DESs are consistent during the cyclic loading. Except for the measurements of the 8th tooth, which results in a maximal capacitance change of $\Delta C_{\text{max}} \approx 7\,\text{pF}$, the other DESs achieve an average maximum capacitance of approximately $\Delta C_{\text{max}} \approx 10\,\text{pF}$.

For a detailed investigation of the correlation of the measured values, Figure 3 illustrates the experimental results for one load cycle. Figure 3 (a) shows the measured torque T over the applied torsion angle ϕ. The selected load cycle shows the results from the interval $34\,\text{s} \leq t_{\text{load}} \leq 38\,\text{s}$ of the measurement are presented in Figure 2 (a). The results show that a hysteresis is present, indicating a non-linear dependency between torque and torsion angle. Figure 3 (b) shows the torsion angle over the capacitance change of one clockwise (solid line) and one counterclockwise loaded tooth (dotted line), i.e., 3rd and 2nd tooth. The results indicate that during a clockwise rotation ($\phi > 0\,\text{deg}$), the capacitance of the clockwise loaded tooth (solid line) increases. Simultaneously, the capacitance of the counterclockwise tooth (dotted line) decreases until a certain threshold is reached. During the counterclockwise loading ($\phi < 0\,\text{deg}$), the capacitance behavior is vice versa, i.e., the capacitance of the counterclockwise loaded DES increases and the capacitance of the clockwise loaded DES decreases until a certain threshold is reached.

Figure 4 shows the capacitance changes of all DESs for the load cycle, which is shown in Figure 3 (a). In Figure 4 (a) the torsion angle ϕ is visualized over the capacitance change ΔC. Overall, the capacitance changes of the DESs are in good accordance, except for the 8th tooth. Unloading can be detected up to a torsion angle of approximately $\phi \approx \pm 0.25\,\text{deg}$. For torsion angles greater than $|\phi| > 0.25\,\text{deg}$ no change in capacitance of the unloaded teeth can be observed. Furthermore, it can be seen that the measured capacitance follows the torsion angle with nearly no hysteresis. In Figure 4 (b) the torque T is shown over the capacitance change ΔC.

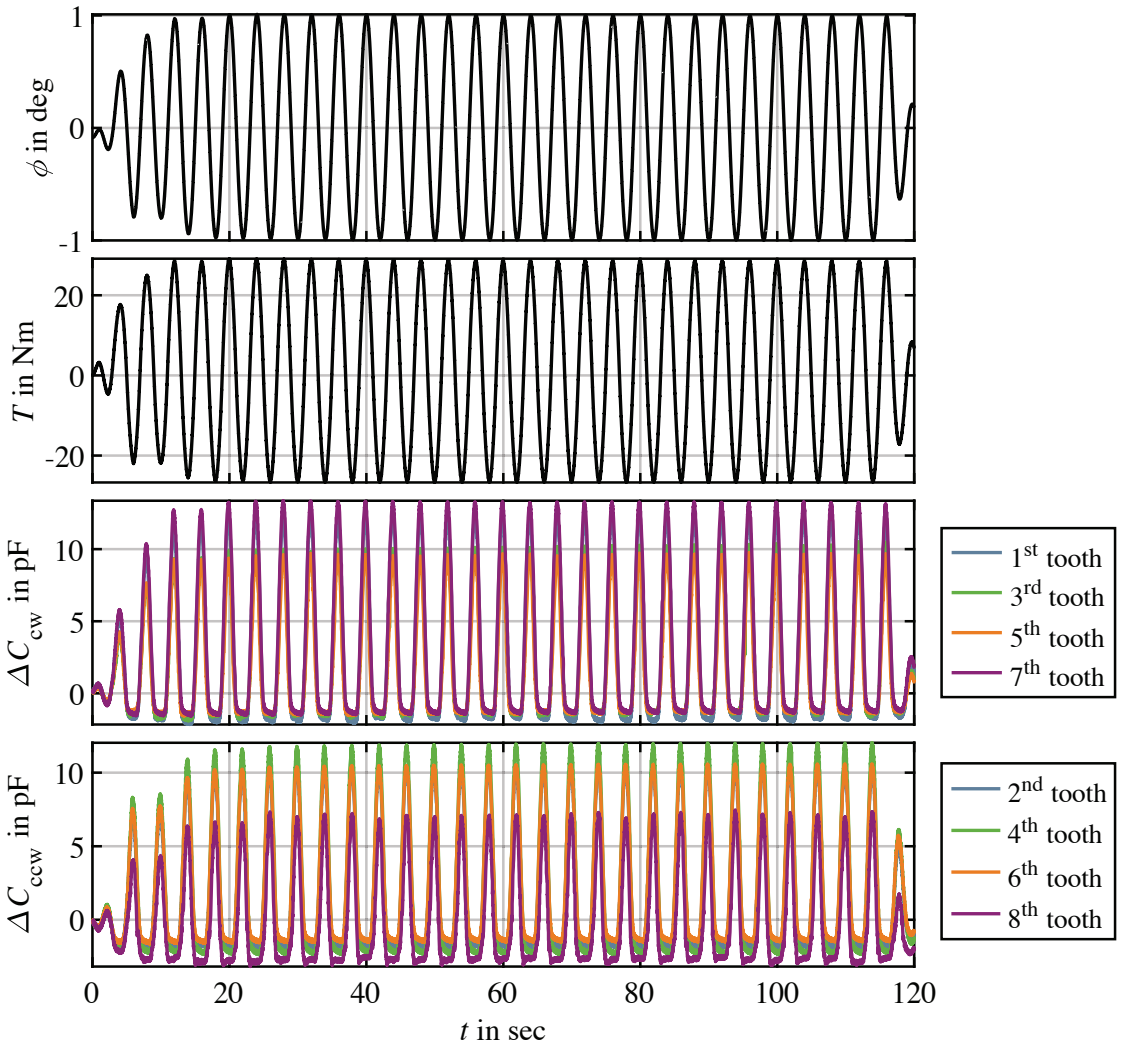

Figure 2: Measurements of the cyclic loading with a frequency of $f_{\text{load}} = 0.25\,\text{Hz}$ and a torsion amplitude of $\phi_{\text{amp}} = 1\,\text{deg}$. From top to bottom, the torsion angle ϕ, torque T, the capacitance change of the clockwise loaded teeth ΔC_{cw} and the capacitance change of the counterclockwise loaded teeth ΔC_{ccw} over the time t are presented.

Considering the loading direction by the sign, the results show that there is a non-linear dependency between the measured changes in capacitance and the measured torque. Furthermore, a closer inspection shows that there is a hysteresis present for each tooth, indicating a non-linear dependency. Since the capacitance change is proportional to the torsion angle, the hysteresis

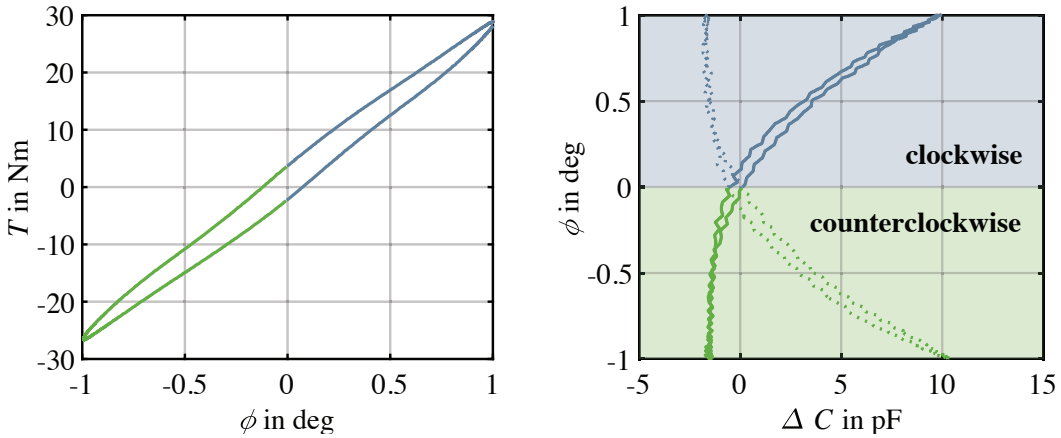

(a) Torque T over torsion angle ϕ for the sensor-integrating jaw coupling.

(b) Torsion angle ϕ over change in capacitance ΔC for a clockwise (sold line) and a counterclockwise (dotted line) loaded tooth.

Figure 3: Schematic analysis of one loading cycle of the sensor-integrating jaw coupling with the data from $34\,\mathrm{s} \leq t_{\mathrm{load}} \leq 38\,\mathrm{s}$. Blue represents clockwise and green counterclockwise loading of the coupling.

that can be seen when visualizing the torque over the torsion angle (see Figure 3 (a)) can also be observed in the visualization of the torque over the capacitance change (see Figure 4 (b)). Additionally, the results show that the gradient in the capacitive difference increases with an increasing absolute torque. This implies larger sensitivities of the DESs for a larger torque.

In order to further analyze the sensitivity of the sensor-integrating jaw coupling, the sensitivity of each DES is calculated at specific torque levels. The results are summarized in Table 1. The capacitance of the unloaded teeth is only changed until the DESs are fully relieved. After that, a further change in the torsion angle does not lead to any further change in the capacitance. To avoid implausible results, i.e., $\pm$ infinity, the sensitivity for these DESs is not taken into account. The results show that the sensitivity increases for an increasing load. This is indicated by smaller values of the sensitivity, which means that for the same change of torque, a higher change in capacitance is observed, c.f. [13]. In addition, fluctuations between the sensitivity of the DESs are present.

The results of the frequency sweep analysis are shown in Figure 5. From top to bottom, the four subplots show the measured torsion angle ϕ, torque T, the capacitance change of the clockwise loaded teeth ΔC_{cw} and the capacitance change of the counterclockwise loaded teeth ΔC_{ccw} over time.

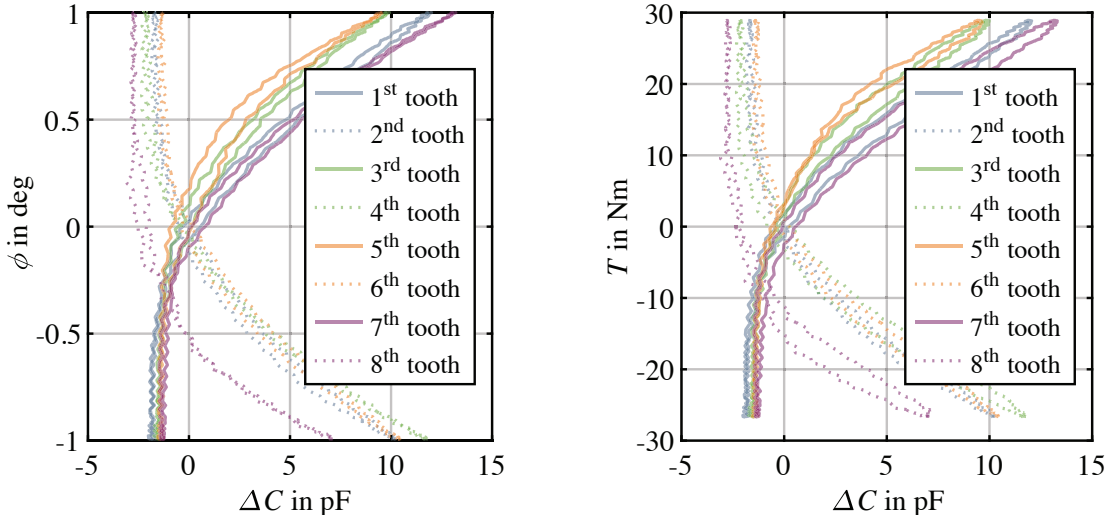

(a) Torsion angle ϕ over change in capacitance ΔC for all teeth.

(b) Torque T over change in capacitance ΔC for all teeth.

Figure 4: Measurements from the DESs over one loading cycle from the loading in Figure 2 ranging from $34\,\text{s} \leq t_{\text{load}} \leq 38\,\text{s}$. The counterclockwise loaded teeth are represented with dashed lines.

Table 1: Sensitivity of each DES in the sensor-integrating gear rim at varying torque from $-25\,\text{Nm} \leq T \leq 25\,\text{Nm}$.

torque	sensitivity clockwise teeth [Nm/pF]				sensitivity counterclockwise teeth [Nm/pF]			
in Nm	1th	3rd	5th	7th	2nd	3rd	6th	8th
-25.0	-	-	-	-	-2.035	-2.435	-2.304	-1.736
-16.6	-	-	-	-	-2.226	-1.846	-2.079	-1.757
-8.3	12.377	13.526	17.613	13.546	-3.173	-2.664	-2.960	-3.934
0.0	4.361	7.856	7.277	4.826	-5.357	-3.979	-4.949	-9.797
8.3	2.903	4.125	5.023	3.123	-15.171	-9.227	-12.278	-26.802
16.6	2.299	2.786	3.238	2.184	-	-	-	-
25.0	1.725	1.657	1.585	1.402	-	-	-	-

With increasing frequency, the transmitted torque increases by approximately $1\,\text{Nm}$. This is due to the viscous behavior of the TPU of the gear rim [2, 13]. However, the measured capacitance peaks decrease with increasing frequency by approximately $0.4\,\text{pF}$. This can have various reasons. For instance, due to the increased loading frequency the capacitance can not

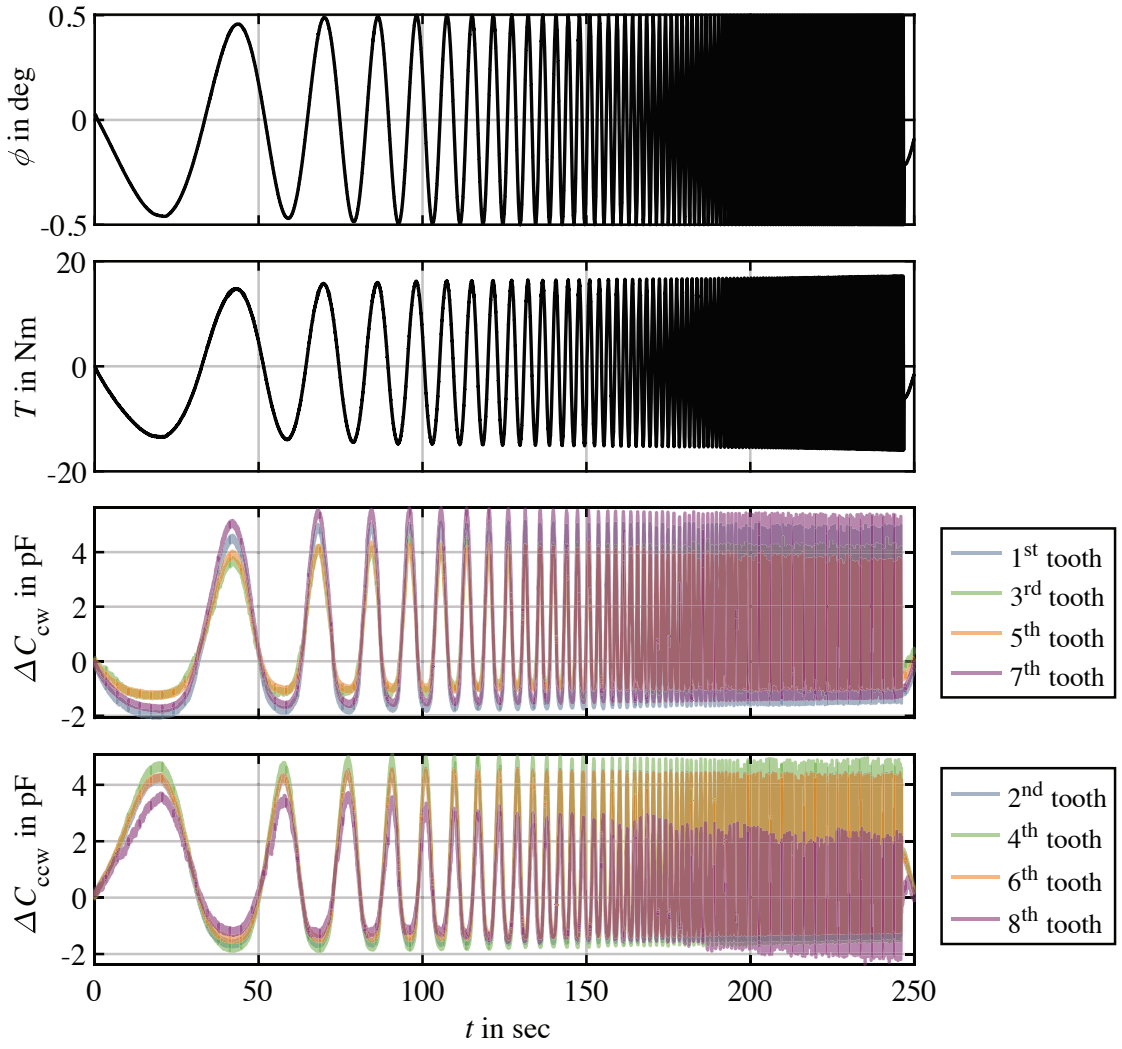

Figure 5: Frequency sweep for the sensor-integrating jaw coupling from $0.01\,\text{Hz} \leq f \leq 3\,\text{Hz}$. The Figure shows the torsion angle ϕ, the torque T, the capacitance change of the clockwise loaded teeth ΔC_{cw} and the capacitance change of the counterclockwise loaded teeth ΔC_{ccw} over time.

be sampled fast enough, which results in a reduced resolution of the load cycle. This hypothesis is supported by the presence of fluctuating values of the peak magnitude of the measured capacitance changes ΔC_{cw} and ΔC_{ccw}, see Figure 5 for $t > 200\,\text{sec}$. In this range, the difference between two peaks reached approximately $0.2\,\text{pF}$. Additionally, the value of the minima in-

creases with increasing frequency. Similar to the results from the cyclic loading, the measured values from the 8th tooth deviate considerably from the other teeth.

5 DISCUSSION

The results show that the developed prototype enables the measurement and wireless transmission of the capacitance of DESs integrated into an elastomer gear rim. The results show a good sensitivity even with small loads, and therefore this measurement concept holds a great potential. The results indicate overall consistency in the measured values for seven out of eight teeth, indicating a reliable reproducibility of data acquisition. However, the reference capacitance, measured in the relaxed mounted state, was slightly different for each DES. This might be related to the overall tolerances on the layer thickness of the DESs and the modified gear rim. These tolerances need to be reduced in order to achieve more consistent results between the DESs. Furthermore, the results indicate that a thorough calibration of each DES will be crucial to apply a regression model for the approximation of the transmitted torque.

The frequency sweep experiments reveal that the capacitance of the DES in the 8th tooth continuously decreased. This was also observed in the cyclic loading, but not as severely. A possible explanation for this drop in the capacitance are micro fractures in the electrode – made of conductive ink – which start to form under load. This can lead to an electrical separation of small parts from the electrode and could reduce the capacitance slightly in each load cycle. However, this drop in capacitance seems to be reversible, as the capacitance returns to its original value after some time in the unloaded state. However, the effect needs to be investigated further in order to properly determine the underlying processes and to develop methods to minimize it.

The conducted experiments show two main non-linearities. Firstly, the hysteresis in the experimental data indicates non-linear visco-elastic material behavior of the gear rim. This also includes the thermal dependency of the material properties, which is out of the scope of the present work. Secondly, the results indicate non-linearities of the DESs, i.e., the non-linear dependence between the measured changes in capacitance and torque. This characteristic can be advantageous, but simultaneously also poses major challenges. On the one hand, the sensitivity at the nominal load is very high, which leads to a good measurement accuracy. On the other hand, this non-linear sensitivity increases the complexity for the measurement of the transmitted torque.

Further investigations are needed to address the observed relaxation in the unloaded state. Currently, it is unclear if this effect occurs due to the fact that the gear rim doesn't fully relax into the unloaded state, or if the DESs do not relax. If the DESs relaxed slower in comparison to the gear rim, they would lose contact to the copper foil on the amplifier. Currently, this can not be observed in the data. However, further studies are necessary to investigate whether the effect can occur at higher frequencies.

6 CONCLUSIONS AND OUTLOOK

The present work presents measurement data from a prototype of a sensor-integrating jaw coupling with a smart gear rim for the acquisition of operating data. The presented gear rim enables the data acquisition by measuring the capacitance of dielectric elastomer sensors, which are integrated into each tooth of the gear rim. The collected data is provided wirelessly via Bluetooth low energy. The coupling was tested in a test bench with a cycling loading and a frequency sweep test. The measured capacitances indicate an excellent correlation with the measured torque and a consistent sensitivity between the DESs. Non-linearities (i) in the used material (thermoplastic polyurethane) of the gear rim and (ii) between the correlation of changes in the capacitance change, and the measured torque were observed. Overall, the results highlight the great potential of the developed prototype of a sensor-integrating gear rim by wirelessly transmitting data during operation. Further studies are needed to address the following research questions in order to enable a reliable measurement of torque: (i) the development and integration of a regression model that can handle the discussed non-linearities, (ii) further investigation of the system under extended possible loading conditions, including increased load frequencies and amplitudes, and (iii) the optimization of tolerances for the internal structure of the DESs and the gear rim to reduce the variations between the DES in the capacitance measurements.

Acknowledgement

The support of the German Science Foundation (DFG) (project numbers: 466661922, 441853410 and 418669083) is gratefully acknowledged.

REFERENCES

[1] E. Kirchner, T. Wallmersperger, T. Gwosch, J. D. M. Menning, J. Peters, R. Breimann, B. Kraus, P. Welzbacher, J. Küchenhof, D. Krause, E. Knoll, M. Otto, B. Muhammedi, S. Seltmann, A. Hasse, G. Schäfer, A. Lohrengel, S. Thielen, Y. Stiemcke, O. Koch, A. Ewert, T. Rosenlöcher, B. Schlecht, A. Prokopchuk, E.-F. M. Henke, F. Herbst, S. Matthiesen, D. Riehl, F. Keil, K. Hofmann, F. Pape, D. Konopka, G. Poll, T. Steppeler, R. Ottermann, F. Dencker, M. C. Wurz, S. Puchtler, T. Baszenski, M. Winnertz, G. Jacobs, B. Lehmann, and K. Stahl, "A review on sensor–integrating machine elements," *Advanced Sensor Research*, vol. 3, no. 4, p. 2300113, 2024.

[2] W. Pampel, *Kupplungen 1 Drehstarre, elastische und drehschwingungsdämpfende Kupplungen*. Berlin: Verlag Technik, 1958.

[3] S. Schork, S. Gramlich, and E. Kirchner, "Entwicklung von Smart Machine Elements – Ansatz einer smarten Ausgleichskupplung," *Design for X*, vol. 27, pp. 181–192, 2016.

[4] R+W Antriebselemente, “Sensortechnik - Zukunft heute erleben,” https://www.rw-kupplungen.de/sensortechnik/, 2023, accessed: 2023-10-23.

[5] KTR Systems GmbH, “MONITEX® BT-drehmomentmessende Kupplungsnabe,” https://www.ktr.com/de/de/produkte/drehmomentsensoren/monitex-bt-drehmomentsensor/, 2023, accessed: 2023-11-02.

[6] A. Ewert, J. D. M. Menning, A. Prokopchuk, T. Rosenlöcher, M. E.-F. Henke, T. Wallmersperger, and B. Schlecht, “SMART MACHINE ELEMENTS – SENSOR-INTEGRATED ELASTOMER COUPLINGS,” *10th ECCOMAS Thematic Conference on Smart Structures and Materials SMART 2023*, pp. 1681–1690, 2023.

[7] J. D. Menning, A. Ewert, A. Prokopchuk, E.-F. M. Vorrath, B. Schlecht, and T. Wallmersperger, “Numerical detection of shaft misalignments using a sensor-integrating jaw coupling,” *PAMM*, p. e202400038, 2024.

[8] A. Ewert, J. D. M. Menning, A. Prokopchuk, T. Rosenlöcher, E.-F. M. Henke, T. Wallmersperger, and B. Schlecht, “Concept of a sensor-integrating jaw coupling for measuring operating data,” *Forschung im Ingenieurwesen*, vol. 88, no. 1, 2024.

[9] A. Prokopchuk, A. Ewert, J. Menning, A. Richter, B. Schlecht, T. Wallmersperger, and E.-F. M. Henke, “Manufacturing of soft capacitive strain sensor based on dielectric elastomer material for an elastic element of a jaw coupling,” *Engineering Research Express*, vol. 6, p. 015493, 2024.

[10] A. Prokopchuk, A. Ewert, D. M. J. Menning, A. Richter, B. Schlecht, T. Wallmersperger, and E.-F. M. Vorrath, “Influence of stacking on the stability of a multi-layer capacitive dielectric elastomer sensor for strain detection,” *Proceedings of SPIE*, vol. 12945, p. 129450Q, 2024.

[11] E.-F. M. Henke, B. Schlecht, and T. Wallmersperger, “Vorrichtung zum Messen von Betriebsgrößen, insbesondere Drehmomenten, in Wellenkupplungen mit Elastomerbauteilen. German Patent Application,” German Patent 10 2022 120 075.2, 2022.

[12] DIN German Institute for Standardization, “DIN EN ISO 75-2:2013 Kunststoffe - Bestimmung der Wärmeformbeständigkeitstemperatur - Teil 2: Kunststoffe und Hartgummi,” Berlin, Wien, Zürich, 2013.

[13] J. D. M. Menning, A. Ewert, A. Prokopchuk, E.-F. M. Vorrath, B. Schlecht, and T. Wallmersperger, “Numerical and experimental investigations of conventional and sensor-integrating jaw couplings of mechanical and electrical behavior,” *Forschung im Ingenieurwesen*, 2025, submitted.

XI ECCOMAS Thematic Conference on Smart Structures and Materials - SMART 2025
M. Krommer, M. Nader and M. Schagerl (Eds)

Received: 29 April 2025 / Revised: 31 August 2025 / Accepted: 9 October 2025
© The Author(s) 2025

Structural Integrated Supercapacitors

Sebastian Geier, Jan Petersen, Peter Wierach

Abstract. The latest developments in all-electric flying either of short-range fixed wings or very short take-off and landing (VTOL) vehicles suffer from the low performance of current available battery technology. Therefore, conventional power supplies such as gasoline or alternative power systems using hydrogen, synthetic fuels and gas turbines are favorized for realization in the next generation aircrafts. Additionally, more and more electrical applications are used within the aircraft. One environmentally driven scientific focus is research on more powerful batteries. However, due to the chemical storage processes their lifetime is limited to 5000-10000 cycles. In contrast, supercapacitors primarily use physical processes for energy storage. These processes are reversible. As result more than 1 million cycles are possible, so that the supercapacitor can be considered as maintenance free. They are ideally suited to being combined with a fiber composite structure. The combination of structure and energy storage results in great opportunities to save weight and volume. Due to high costs this approach is especially interesting for aerospace applications.

The presented approach consists mainly on the integration of a pouch-like supercapacitor component, which is integrated into the lay-up of a fiber reinforced plastic composite using autoclave processing. The supercapacitors are manufactured using two aluminum collectors coated with a layer of 140µm activated carbon, a separator film and an ionic liquid. The aim is to reach high specific power density AND high mechanical stiffness. The whole setup is intensively electro-mechanical characterized. Still there are challenges of minimizing parasitic masses, improving the specific energy and improving the durability. This approach is realized in laboratory scale but also in several full-scale demonstrators successfully tested for space qualification.

Key words: Power composites, Integrated energy devices, Multifunctional materials, Structural integration, Structural battery.

Sebastian Geier & Jan Petersen
Institute of Lightweight Systems, German Aerospace Center, Lilienthalplatz 7, 38108 Braunschweig, Germany
e-mail: sebastian.geier@dlr.de

Peter Wierach
Institute for Polymer Materials and Plastics Technology, Technical University Clausthal, Clausthal, Germany

1 INTRODUCTION

In the aerospace sector, the available energy is not only a decisive factor for the success and duration of a mission, but also a very cost-intensive subsystem. Due to high costs for space applications (5500€/kg [18]) current trends of nano and micro satellites using miniaturized electronics highlight the demand of volume and weight optimized structures. One solution can be the combination of two indispensable subsystems - the satellite structure and the energy system. For an integration of energy devices within the structure, the lifetime of the device is of decisive importance. A battery, as the most common energy device, suffers from their chemical energy storage process via ion diffusion. Batteries degrade within a period of at least 20000 cycles (solid-state battery, 71% of capacity left [35]). In contrast, supercapacitors are a highly efficient type of energy storage in terms of cycle stability. Furthermore, supercapacitors feature some advantages especially for short-term peak power applications, such as robotics, radar, heating and energy conversion. They achieve high specific power densities up to 10-15 kW/kg [1] which is an order of magnitude larger than lithium ion batteries [2]. However, due to the different storage processes, batteries feature higher specific energy density. This is one of the main reasons why batteries are used for applications with demand for constant power. A further advantage of supercapacitors is their ability to be charged within seconds, to manage power peaks and their build-up using sustainable, lightweight and abundant materials such as carbon. Finally, supercapacitors can be discharged completely and show a more robust lifetime behavior even at rough temperature conditions. However, supercapacitors also reveal a temperature-dependent behavior.

Charged within their electrochemical window (EW), supercapacitors show an almost endless lifetime. This characteristic can be explained with their energy storing mechanism. It is mostly based on a physical, reversible electrostatic-induced ion diffusion between charged electrodes. As a result, life cycles of $5 \cdot 10^5 - 3 \cdot 10^6$ without degradation are possible [2, 3]. This freedom from maintenance favors their integration into composites, namely a structural power composite, more than any other energy storage device.

In this field research is done using large specific surface area, such as electrodes made of graphene [4]. Furthermore, µm-thin separators or electrolytes with a wide electrochemical window are investigated. Even the combination of supercapacitors and batteries in a supercabattery [5] are developed and tested. However, this presented approach focuses on the structural integration of supercapacitors into load-bearing structures [6-9]. Especially the lay-up of composites is ideal for the integration of additional functions. For a better understanding of different integration strategies, Adam [10] introduced the *Degree of Integration* (DoI), also shown in figure 1. The DoI represents the level of multifunctionalization of an energy storage device. DoI 0 can be considered as the classical arrangement of two isolated, separated systems. The DoI I means, the structure and energy device are still isolated and separated systems, but the energy storage device is integrated in free spaces of the structure. The DoI II represents, the energy devices are part of the structure, such as layers, integrated thin-films or applied patches. These approaches represent combined components that also work on their own. In this status, the energy devices can already influence the mechanical behavior of the structure positively or

negatively. The DoI reaches higher values when the energy-storing materials substitute structure materials and become small and light. This is the case when neat carbon fibers are used as electrodes, which represents a DoI of III. Here, the whole structure can be used as an energy storing device. Composites are particularly suitable for this task. However, the highest DoI IV can only be reached by functionalizing the microscopic components of a structure, such as the carbon filaments of the carbon fibers or the fiber itself, and by using their specific excellent properties.

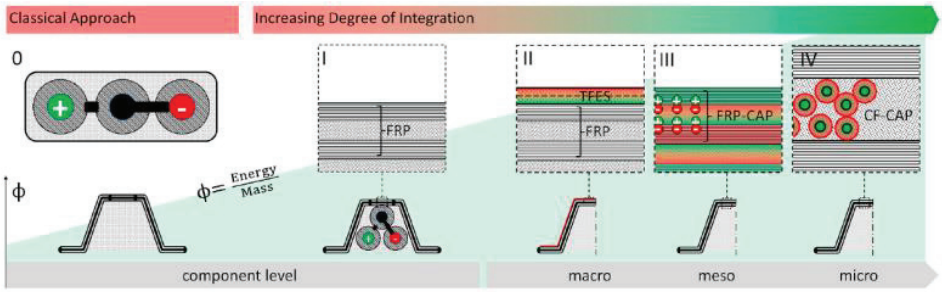

Figure 1: DoI-values 0 to IV, representing different levels of integration [10]

Wetzel [11] started the research on structural power composites 2004 and reported the integration of energy supplies (battery, supercapacitor and fuel cell) and electronic devices into composites for military applications. His thin-film approach already reached a DoI of II to III. Petersen integrated a thin-film supercapacitor (ITFC) into glas fiber reinforced plastics (GFRP) reaching a DoI of II and adding thermal and mechanical sensoric capabilites [12]. An even greater scientific challenge seems to be the single-ply functionalization to reach a DoI of III. Quian [6] and Shirshova [7] developed carbon fabrics which are coated with carbon aerogel for higher specific surfaces. They also developed an electrolytic matrix to build up a structural supercapacitor. Unfortunately, the energy composite shows neither good mechanical properties nor does it have a sufficient electrical performance. According to several researchers [8, 13], the synthesis of a multifunctional matrix combining the two properties, ionic conductivity and stiffness, is the most challenging task. Ciocanel [9] defined theoretically the requirements for such an ideal structural energy storage material. Currently, there are two promising approaches for the multifunctional matrix of structural batteries, a strategy of which can also be applied to supercapacitors. The first approach is the multifunctional matrix, combining ionic conductivity and mechanical stability in the same material. The second approach combines materials consisting of two different phases. The first ionic conductive phase is embedded within a second mechanical loadable structure phase [13-15]. Tu [13] simulated the best multifunctional bi-continuous electrolyte as resin for the composite. A structural battery based on these approaches achieved good mechanical and electrochemical performances [16].

The whole topic is summarized in several review papers [8, 23, 24, 26]. So far only a few full-scale demonstrators are presented, such as a Volvo S80 bootlid demonstrator [25] which never went into series production, a satellite positioning system using high torque wheels (HTW) with 14 integrated supercapacitors [27] and a solar panel with 12 integrated supercapacitors [28, 29] still waiting for their in-orbit tests. However, on the 14th of January

2025 a cube satellite called InnoCube was launched into space carrying a structural battery [37] for tests in orbit. The start-up NOVAC commercially sells structural integrated supercapacitors, based on solid state electrolytes and integration in CFRP [38].
This paper presents insights of the development of integrated supercapacitors within the German Aerospace Center (DLR)-funded projects Peak Power Platform (PPP), Hybrid Solar Energy Storage (HySES) and Decentralized Energy supplied Electrical Propulsion (DEEP).

2 MATERIALS AND PROCESSES

This section gives detailed views on the materials such as electrodes, separators and electrolytes used to build the supercapacitors. Furthermore, the processes of manufacturing and integration are presented.

2.1 Electrodes and collectors

The film supercapacitor consists of a separator membrane with a thickness of 20µm (Celgard 3501-4000M-AS40), which is supplied by the company Celgard, LLC (USA). A SEM picture in figure 2 a) shows the surface of the membrane with slot-like pores of 400-700 nm in length and 30-50 nm in width. The separator film is durable even to handle compression and temperature during the manufacturing. It is on the one hand dense and thick enough to avoid any short circuiting via electrode material passing the pores and on the other hand permeable enough for the comparative large ionic ions to diffuse through the holes.

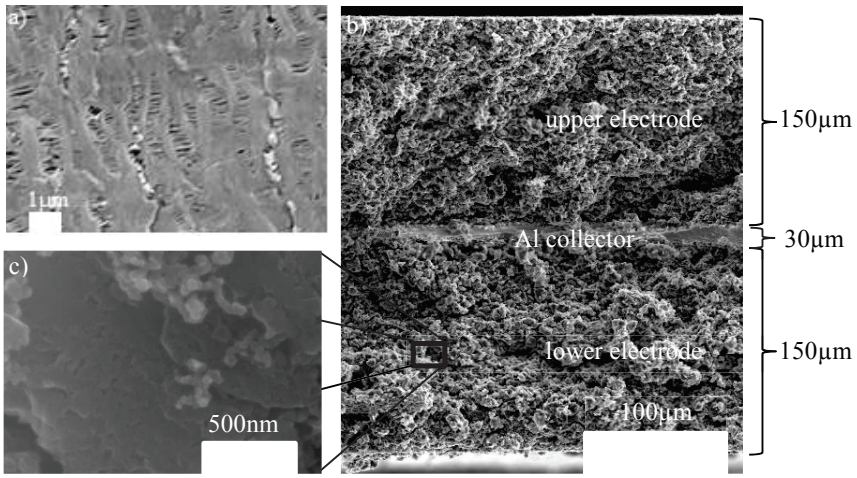

Figure 2: SEM-micrographs of the used material: a) Celgrad separator, b) Skeleton double side electrode, c) Detail of Skeleton electrode

Figure 2 b) shows a cross section of the double-sided electrode and collector. The 30µm thick Al-collector on which electrodes of activated carbon are coated (AC, thickness of 150µm) are customer-tailored produced and supplied by the company Skeleton Technologies GmbH (Estonia, Germany). The SEM picture in figure 2 c) points out details of the cubic agglomerates

of activated carbon (AC) revealing some pores on the even surfaces of the agglomerates. However, a specific pore size cannot be defined. The electrode is coated on both sides of the collector for efficient stacking of the supercapacitor cells.

2.2 Electrolytes

The vacuum-assisted manufacturing process as well as a planned application in space reduces the variety of possible electrolytes dramatically. Typical water-based electrolytes such as sodium chloride have high ion mobility due to their low viscosity, but they vaporize in vacuum as a result of their high vapor pressure (12.28hPa at 5°C-25°C). However, this property is important for space applications. There are several cases in which outgassing materials had caused failures of satellites. Mechanical properties of materials decrease due to outgassing, outgasses might contaminate devices e.g. optics [22], or the outgassing can generate discharge breakdowns in high-voltage devices [22], seriously affecting the performance and reliability of the whole satellite.

In contrast, ionic liquids (ILs) which have very low vapor pressure, offer a wider EW up to 6.1 V [21] referring to the cathodic and anodic window. Actually, here the anodic window of 0V up to +4,5 V is used. Ionic liquids consist of long charged molecules, resulting in higher densities and viscosity, which causes higher internal resistances and therefore slower electrochemical behavior, but higher electrochemical stability.

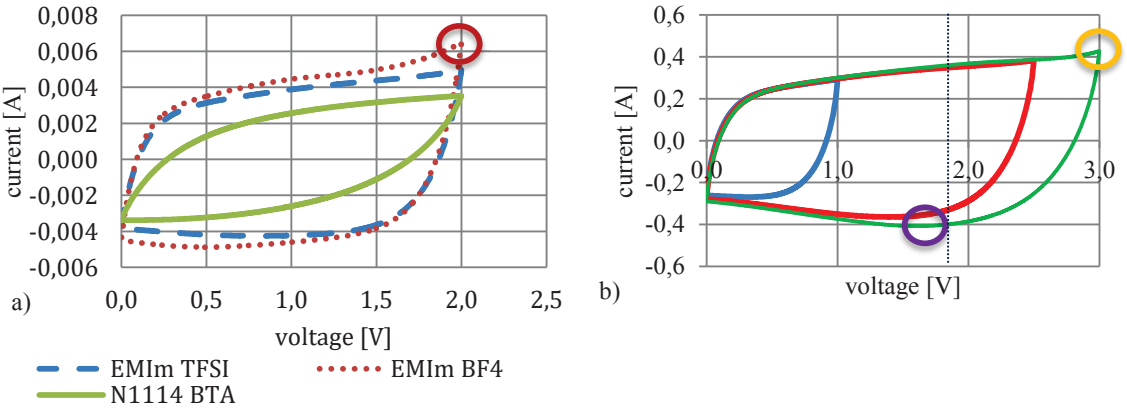

Figure 3: CV-tests of ionic liquids: a) Three different promising ionic liquids in direct comparison at a scan rate of 20 mV/s revealing some current peaks a 2 V for EMIm BF4 (red circle) b) EMIm TFSA at different voltages at a scan rate of 20 mV/s, even reaching 3 V with only a small peak (orange circle)

As shown in earlier publications [28-30], 1-ethyl-3-methylimidazolium bis(trifluoromethylsulfonyl)imide ([EMIm][TFSA], IL-0023-HP) supplied by Iolitec – Ionic Liquids Technologies GmbH, Germany – was chosen as the most promising electrolyte among others (see figure 3 a) dashed blue line). In cycling voltammetry tests (CV) with an EW of 0-+2 V EMIm TFSA showed no current peak along with the highest capacity. This result might be the reason why EMIm TFSA is also used as electrolyte in [1, 8, 9]. Further conducted cyclic voltammetry tests reveal a first small current peak at 3V (fig. 3 b) orange circle) and an increasingly larger counter-peak at +1.7V (fig. 3 b purple circle) on the negative current side

(see figure 3 b) green graph). This results in the definition of a maximum voltage of ≤+3 V. Typically, this maximum voltage should not be used for long cycling as the energy storage would start to degrade earlier. However, space requirements of the European Cooperation for Space Standardization (ECSS, [30]) require a derating of 40% so that safe operations are ensured. In the case of EMIm TFSA 1.8 V would be the maximum operation voltage per supercapacitor (see figure 3 b), pointed black line). Finally, in wetting tests EMIm TFSA is highly compatible with the used electrode and diffuses into its pores.

2.3 Manufacturing and integration processes

The lay-up of the thin-film supercapacitor and a picture of the result is schematically shown in figure 4.

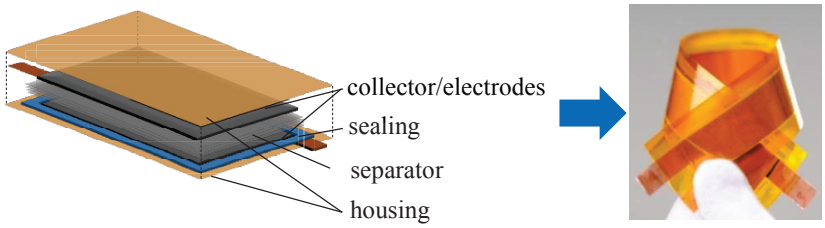

Figure 4: Lay-up of the supercapacitor and its final shape

Two collectors coated with carbon are separated by one layer of separator film. The electrode should be dried before processing to avoid moisture deposition. Furthermore, the electrodes must be sufficiently wetted with IL. The amount of IL on the electrodes is a decisive parameter. On the one hand, an insufficient amount of electrolyte reduces the available ions and as result the serial resistance increases while the capacity drops. On the other hand, too much IL will be pressed out of the capacitor into the composite during manufacturing, which reduces the mechanical properties (e.g. stiffness or strength) of the surrounding resin matrix. Due to the high specific surface area of the electrode and the viscosity of the ionic liquid, a complete wetting needs some time. A diffusion period that is too short results in less wetted electrodes that participate in the electrochemical processes. Furthermore, the remaining IL will reach into the composite, causing delamination during the manufacturing, as it interferes with the curing of the epoxy resin.

The preparation and manufacturing process is done in seven steps. At first the materials have to be stored in a dry atmosphere to avoid the storage of moisture on the surface of the material. For the preparation, the materials have to be cut, wetted with IL and stored for IL-diffusion and drying. In the manufacturing process the prepared materials and the pre-impregnated composite material (Hexply 913, Hexcel Corp., USA) are combined and arranged on a metal tool plate. This lay-up has to be evacuated and prepared for the curing process, which takes place according to the material specifications at 125 °C for 6 hours. Finally, post processing such as drilling, cutting and the cleaning of the contacts has to be done to finalize the power composite.

3 ELECTRO-CHEMICAL TESTING

In this section mechanical and cycling tests of structural integrated supercapacitors are presented.

3.1 Mechanical Tests

The mechanical tests are carried out to prove the integration strategy. For tensile tests a Zwick 1476 test machine (ZwickRoell GmbH & Co KG, Germany) is used, while the four point-bending (4PB) is conducted using a Zwick 1484. For the tensile tests a 100kN load cell (BZ2-MM14760-ZW02, Zwick GmbH & Co KG, Germany), strain gauges (DMS, XY-F/DMS, Höttinger Baldwin Messtechnik GmbH, Germany) and an extensometer (MTS 776, model 632.85, MTS Systems Corporation, USA) is used. The 4PB tests are carried out using a 5kN load cell (type BZ2-MM14760.ZW02, Zwick GmbH & Co KG, Germany) and a linear position sensor (WA 50, type K-WA-U-050-W-32K-K4-F1-2-8-10, Höttinger Baldwin Messtechnik GmbH, Germany). The tensile test results and the setup are shown in figure 5 a), the 4PB results and the setup are presented in figure 5 b).

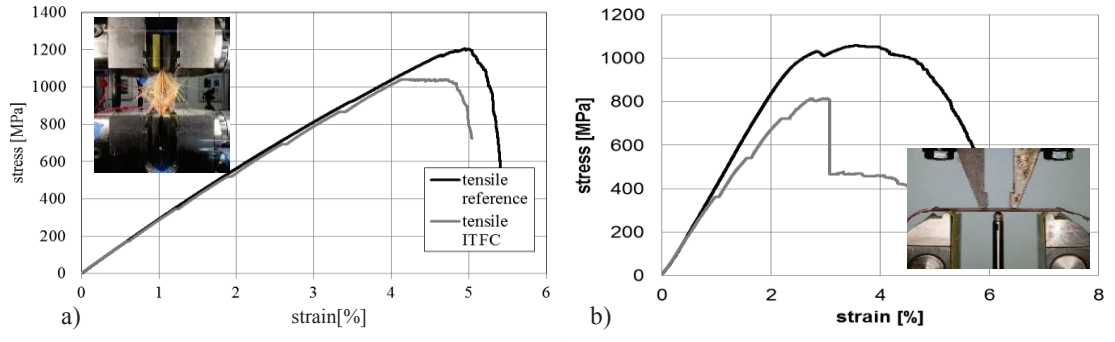

Figure 5: Mechanical tests of composite coupon specimen with integrated supercapacitors: a) Representative tensile test results of a reference specimen and a specimen with ITFC, on the left the test setup is shown. b) Representative 4PB test results of a reference sampe and a sample with ITFC, on the right the test setup is depicted.

The sample size of 4PB tests is 5mm in width, 50mm in length with a thickness of 2 mm. The integration of the supercapacitor is done as an interlayer analogue to the tensile specimens. The size of a tensile specimen is 15mm in width, 240mm in length and thickness of 2 mm.

Within the tensile tests the tensile modulus is reduced by 6% and the tensile strength by 7.8% as result of the ITFC (see figure 5 a). The capacitor has a capacitance of 109mF (0.5V) and is intact until the mechanical failure of the sample (see figure 6 a).

As it can be seen in figure 5 b), the ITFS-sample fails abruptly in the 4PB test due to the collapse of the supercapacitor. The reference sample didn't show this behavior. This failure reduces the flexural strength by 18% and the bending modulus by 12%. The capacitance of the capacitor, shown in figure 6 b), remains at 5mF (0.5V), which does not change until failure. The different capacitances of the capacitors used at the tensile test and 4PB are due to their different sizes. The test results of both tests are summarized in table 1.

Table 1: Overview of mechanical properties and comparison to neat glas fiber composite

value	reference	ITFC	Change [%]
Young's modulus [MPa]	43000	40420	-6
Tensile strength [MPa]	1100	1012	-8
Bending modulus [MPa]	41000	36080	-12
Bending strength [MPa]	1050	861	-18

In situ electrochemical measurement are conducted at steps of constant load every 10.000N for tensile tests and every 250N at bending tests. The tests are performed at 23°C and 50%rh according to the test standard [39-41]. Every test series consists of four samples. The test procedure for both tests is slightly modified. Tests are being paused at constant load levels to characterize the integrated supercapacitor. The cyclic voltammetry is performed with a potentiostat (Zennium, Zahner-Elektrik GmbH & Co. KG, Germany) during the 4th load step. The CV-results are shown in figure 6 a) and b).

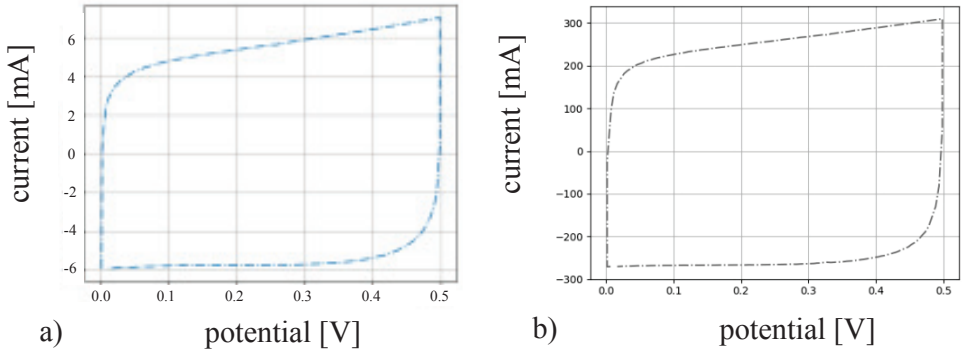

Figure 6: CV results of mechanical tests with different ITFC (therefore different current values) : a) CV using a scan rate of 50mV/s during tensile test b) CV at a scan rate of 50mV/s during 4PB test

3.2 Cycling tests

Figure 7 depicts the capacity of two different integrated SCs, which were cycled up to 10^6 cycles. Both test results show a moderate degradation due to their operation. The blue graph represents the cycling with the comparatively low current of 0.334A, while the red graph reveals the cycling with 2A. As it can be seen, the SC with the lower current still achieves 82% of the first measured capacity. The SC treated with 2A shows 77% of the initial value. However, to evaluate the degradation of a SC, the capacity after some cycles should be considered. In the presented tests, the first measurement was carried out right after the first cycle. If the results are recalculated using the capacity at the second test point (at 10,000 cycles), the degradation only reaches 13% for the SC at 0.334A and 14% for the SC charged with 2A.

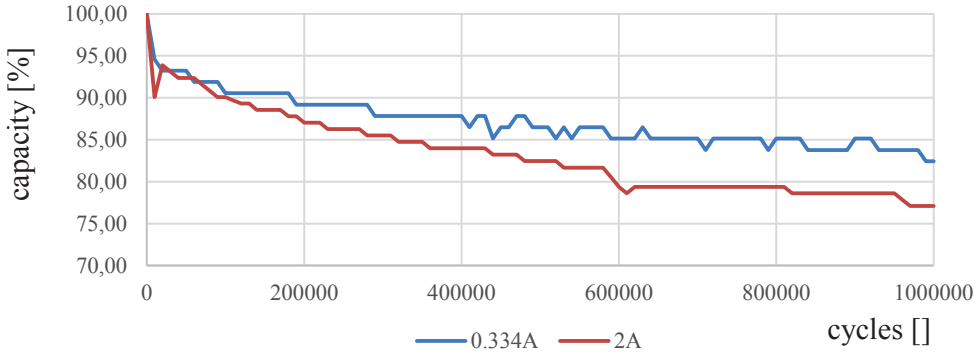

Figure 7: Performance of two integrated SCs during 10^5 cycles at 0.334A with a final capacity of 82% and a second SC cycled at 2A with a final capacity of 77%.

4 CONCLUSION

This paper describes the materials and processes to develop, manufacture and integrate a thin-film supercapacitor into a fiber reinforced composite. Furthermore, coupon specimens were tested mechanically via tensile testing and 4PB tests. It could be shown, that most of the neat mechanical performance (elastic modulus and strength) is still available. However, the 4PB tests appeared to be more critical. As consequence the composites would have to be reinforced, if it is already load tailored. In further tests the cycling stability of the integrated supercapacitors, their main advantage, was tested via cycling tests. It could be demonstrated that these manufactured and integrated ITFCs can reach 10^6 cycles, even with high current of 2A (10x10cm). Lower current will reduce the stress and enhance their lifetime, as the cycling test with 0.334A depicts. So far, all tests reveal the functionality and robustness of this approach. Furthermore, compared with space qualified supercapacitors, volume and weight saving up to 70-80% are possible. In figure 8 three in full-scale realized applications are shown such as the ITFC modified base plate of a high torque wheel (figure 8 a), a multifunctional satellite panel for vibration damping (figure 8 b) and a solar panel with ITFCs in figure 8 c).

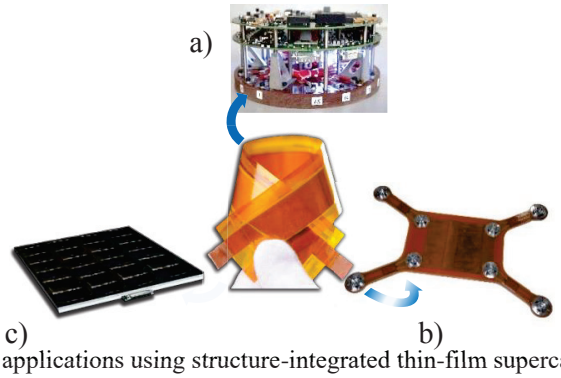

Figure 8: Realized full-scale applications using structure-integrated thin-film supercapacitors : a) 14 ITFCs integrated into the base plate of a high torque wheel [27] b) Multifunctional panel using two ITFCs as power source for vibration cancelling [33] c) Power storing sandwich solar panel [29]

However, in terms of improved lightweight design polymeric ionic liquids could avoid parasitic masses such as the separator and could further increase the mechanical performance of the SCs. An additional advantage of using polymeric electrolytes would be a pre-manufacture quality assessment before integration. As result supercapacitors with low performance can be identified and replaced before integration to avoid performance variations. Specific manufacturing parameters causing varying performances have also to be investigated further for more reliability.

ITFCs might not reach higher levels than DoI II because of their component character, but their robust behavior, their scalability, volume and weight savings in different realized applications (see figure 8) highlights this approach to be a promising candidate for further applications. The lay-up of the ITFC is designed to accommodate varying components such as electrode, ionic liquid or separator as soon as new, more powerful materials are available, enabling higher performances.

AKNOWLEDGEMENTS

This work was part of the DLR-funded project GigaStore. The modified High Torque Wheel was developed within the project Peak Power Platform. Further research is done within the DLR projects Hybrid Solar Energy Storage (HySES) and Multifunctional Satellite Panel and Decentralized Energy Supplied Electrical Propulsion (DEEP), which all deal with integrated supercapacitors within space structures. We would like to acknowledge the funding by the Deutsche Forschungsgemeinschaft (DFG, German Research Foundation) under Germany´s Excellence Strategy – EXC 2163/1 - Sustainable and Energy Efficient Aviation – Project-ID 390881007**.** Tribute has to be paid to Phillip Freytag and Marius Eilenberger for his contribution on this topic.

REFERENCES

[1] Beguin, F., Presser, V., Balducci, A., Frackowiak, E. Carbons and Electrodes for advanced Supercapacitors, 2014, Adv. Mater., 26, 2219-2251.

[2] Wu, Z.-S., Parvez, K., Feng, X., Müllen, K. Graphene-based in-plane micro-supercapacitors with high power and energy densities, 2013, Nature Communications, 4, 2487.

[2] Conway, B. E. Electrochemical Supercapacitors - Scientific Fundamentals and Technological Applications, 1999, Kluwer Academic.

[3] Christen T., Carlen, M. Theory of Ragone plots, 2000, Journal of Power Sources, Vol. 91, pp. 210-216.

[4] Ke, Q., Wang, J., Graphene-based materials for supercapacitor electrodes - A review, 2016, J. Materiomics, Vol. 2, pp. 37-42.

[5] Dubal, D., P., Ayyad, O., Ruiz, V., Gómez-Romero, P. Hybrid energy storage: the merging of battery and supercapacitor chemistries, 2015, Chem. Soc. Rev., 44, pp. 1777-1790.

[6] Qian, H., Kucernak, A. R., Greenhalgh, E. S., Bismarck, A., Shaffer, M. S. P. Multifunctional Structural Supercapacitor Composites Based on Carbon Aerogel Modified High Performance Carbon Fiber Fabric, 2013, Appl. Mater. Interfaces, Vol. 5, 6113-6122.

[7] Shirshova, N., Qian, H., Shaffer, M. S.P., Steinke, J. H.G, Greenhalgh, E. S., Curtis, P. T., Kucernak, A., Bismarck, A., Structural composite supercapacitors, 2013, Composites: Part A, Vol. 46, pp. 96-107.

[8] Asp, L., Greenhalgh, E. S. Structural power composites 2014, Composites Science and Technology, Vol. 101, pp. 41-61.

[9] Ciocanel, C., Browder, C., Simpson, C., Colburn, R. The challenges of achieving good electrical and mechanical properties when making structural supercapacitors, 2013, Proc. of SPIE Vol. 8689, 868917.

[10] Adam, J. T., Liao, G., Petersen, J., Geier, S., Finke, B., Wierach, P., Kwade, A., Wiedemann, M. Multifunctional Composites for Future Energy Storage in Aerospace Structures, 2018, Energies, Vol. 11, 335.

[11] Wetzel, E. D. Reducing Weight: Multifunctional Composites Integrate Power, Communications, and Structure 2004, AMPTIAC Q, Vol. 8, pp. 91–95;

[12] Petersen, J., Kube, A., Geier, S.;,Wierach, P., Structure-Integrated Thin-Film Supercapacitor as a Sensor. Sensors 2022, 22, 6932. https://doi.org/10.3390/s22186932

[13] Tu, V., Asp, L., E., Shirshova, N., Larsson, F., Runesson, K., Jänicke, R. Performance of Bicontinuous Structural Electrolytes, 2020, Multi Funct. Mater., 100124.

[14] Cameron, N. R. High internal phase emulsion templating as a route to well-defined porous polymers, 2005, Polymer Vol. 46 (5), pp. 1439-1449.

[15] Schulze, M., W., McIntosh, L., D., Hillmyer, M., A., Lodge, T., P. High-Modulus, High-Conductivity Nanostructured Polymer Electrolyte Membranes via Polymerization-Induced Phase Separation, Nano Lett. 2014, 14, pp. 122-126.

[16] Johannisson, W., Ihrner, N., Zenkert, D., Johansson, M., Carlstedt, D., Asp, L., E., Sieland, F. Multifunctional performance of a carbon fiber UD lamina electrode for structural batteries, 2018, Comp. Sci. Techno., Vol. 168, pp. 81-87.

[18] Moeller, E. Handbuch der Konstruktionswerkstoffe: Auswahl, 2014, Hanser Verlag, Vol. 2.

[21] Galiński, M, Lewandowski, A.,Stępniak, I. Ionic liquids as electrolytes, 2005, Electrochimica Acta, Vol. 51(26), pp. 5567-5580.

[22] Pope, A.M., Korkut, S., Punckt, C. and Aksay, I.A. Supercapacitor Electrodes Produced through Evaporative Consolidation of Graphene Oxide-Water-Ionic Liquid Gels, 2013, J. Electrochem. Soc., Vol. 160 (10), pp. A1-A8.

[23] Chan, K-Y., Jia, B., Lin, H., Hameed, N., Lee, J-H., Lau, K-T., A Critical Review on Multifunctional Composites as Structural Capacitors for Energy Storage, Composite Structures (2017), doi: https://doi.org/10.1016/j.compstruct.2017.12.072

[24] Kühnelt, H., Beutl, A., Mastropierro, F., Laurin, F., Willrodt, S., Bismarck, A., Guida, M., Romano, F., Structural Batteries for Aeronautic Applications—State of the Art, Research Gaps and Technology Development Needs. Aerospace 2022, Vol 9(7). https://doi.org/10.3390/aerospace9010007

[25] Volvo Car Group. Volvo Car Group Makes Conventional Batteries a Thing of the Past. Available online: https: //www.media.volvocars.com/global/en-gb/media/pressreleases/134235/volvo-car-group-makes-conventional-batteries-athing-of-the-past (accessed on 28 April 2022);

[26] Greenhalgh, S., E., Nguyen, S., Valkova, M., Shirshova, N., Shaffer, M., S., P., Kucernak, A., R., J., A critical review of structural supercapacitors and outlook on future research challenges, Composites Science and Technology 235 (2023) 109968;

[27] Geier, S., Petersen, J., Wierach, P. "Structure Integrated Supercapacitors for Space Applications. Proceedings of the ASME 2019 Conference on Smart Materials, Adaptive Structures and Intelligent Systems. Louisville, Kentucky, USA, 9.–11. September, 2019; https://doi.org/10.1115/SMASIS2019-5687

[28] Geier, S., Petersen, J., Eilenberger, M., Wierach, P. Robust and Powerful Structural Integrated Thin Film Supercapacitors for Lightweight Space Structures, Proceedings of the ASME 2021 Conference on Smart Materials, Adaptive Structures and Intelligent Systems. ASME 2021 Conference on Smart Materials, Adaptive Structures and Intelligent Systems, September 14–15, 2021. V001T05A019.
ASME. https://doi.org/10.1115/SMASIS2021-68349

[29] Geier, S, Petersen, J, & Wierach, P. "Challenges of Upscaling Power Composites for Aerospace Applications." Proceedings of the ASME 2022 Conference on Smart Materials, Dearborn, Michigan, USA. September 12–14, 2022. V001T04A016.
ASME. https://doi.org/10.1115/SMASIS2022-91201

[30] European Cooperation for Space Standardization (ECSS) ECSS-Q-ST-30-11C Rev1 Space Product Assurance Derating – EEE components, 2011.

[33] Montano Rejas, Z., Keimer, R., Geier, S., Lange, M., Mierheim, O., Petersen,J., Pototzky, A., Wolff, J. Design and Manufacturing of a Multifunctional Highly Integrated Satellite Panel Structure, 16th European Conference on Spacecraft Structures, Materials and Environmental Testing, ECSSMET 2021, Braunschweig, Germany, March 23-25, 2021.

[35] Liu, S., Zhou, S., Han, J., Wen, K., Guan, S., Xue, C., Zhang, Z., Xu, B., Lin, Y., Shen, S., Li, L., Nan, C.-W., Super Long-Cycling All-Solid-State Battery with Thin Li6PS5Cl-Based Electrolyte, Advanced Energy Materials, Vol. 12, Issue 25, 2022.

[37] Grzesik, B., Baumann, T., Walter, T., Flederer, F., Sittner, F., Dilger, E., Gläsner, S., Kirchner, J.-L., Tedsen, M., Montenegro, S., Stoll, E., InnoCube- A Wireless Satellite Platform to Demonstrate Innovative Technologies, *Aerospace*, *8*(5), 127, 2021.

[38] Solid-state moldable supercapacitors - NOVAC, 14.04.2025.

[39] DIN EN ISO 14125, Faserverstärkte Kunststoffe – Bestimmung der Biegeeigenschaften, 1998, Beuth Verlag GmbH.

[40] DIN EN ISO 527-4, Kunststoffe - Bestimmung der Zugeigenschaften - Teil4: Prüfbedingungen für isotrop und anisotrop faserverstärkte Kunststoffverbundwerkstoffe, 1997, Beuth Verlag GmbH.

[41] EN 62391-1, Elektrische Doppelschichtfestkondensatoren zur Verwendung in Geräten der Elektronik – Teil 1: Fachgrundnorm, 2006, Electrosuisse.

XI ECCOMAS Thematic Conference on Smart Structures and Materials - SMART 2025
M. Krommer, M. Nader and M. Schagerl (Eds)

Received: 1 April 2025 / Revised: 27 August 2025 / Accepted: 9 October 2025
© The Author(s) 2025

High Load Shape Memory Alloy Actuators: Design, Development and Application in Production Engineering

Andreas Hofer, Kai Thüsing, Kenny Pagel, Welf-Guntram Drossel

Abstract. The ongoing automation, customization, and flexibilization of manufacturing processes requires actuators that can actively influence manufacturing processes besides an increased use of sensors and improved connectivity between production steps and machines. In recent decades, novel actuators based on smart materials have gained importance in various application areas. Shape memory alloys (SMAs), as a prominent class of smart materials, exhibit the highest specific energy density among all solid-state actuation principles and offer exceptional scalability. Here, especially miniaturized SMA actuators are already being used in numerous applications, predominantly with forces up to 10 N. In contrast, this paper provides a comprehensive overview of the design, development and application of novel types of high load (HL)-SMA push-actuators with forces above 1 kN.

Recent advances in SMA actuators are reviewed, while focusing on innovative geometries and integration strategies for SMA components, along with their thermal, mechanical, and fatigue properties. In addition, advanced modeling approaches, such as finite element (FE) and simplified lumped parameter models, are evaluated for their ability to simulate, and optimize actuator dynamics. On top of this potential industrial applications of HL- SMA actuators are explored. Focusing here on where HL-SMA-actuator technology can improve force distribution, streamline adjustment processes, and enhance overall system reliability and performance. Cutting-edge manufacturing methods, including additive manufacturing of SMA components, are also highlighted, demonstrating significantly improved functional properties. Combining efficiency, adaptability, and sustainability, these HL-SMA actuators offer forward-looking solutions for a wide range of industrial applications.

Keywords: Shape Memory Alloys, High Load Actuators, Production Engineering, Machine Tools, Mechatronics, Smart Materials.

Andreas Hofer & Kai Thüsing & Kenny Pagel
Fraunhofer Institute for Machine Tools and Forming Technology IWU, Nöthnitzer Straße 44, 01187 Dresden, Germany, e-mail: andreas.hofer@iwu.fraunhofer.de

Welf-Guntram Drossel
Professorship Adaptronics and Lightweight Design, TU Chemnitz, Reichenhainer Straße 70, 09126 Chemnitz, Germany, e-mail: welf-guntram.drossel@mb.tu-chemnitz.de

1 INTRODUCTION

With the ongoing development toward Industry 4.0, industrial processes are becoming more and more automated and digitalized. This shift aims to increase efficiency, adaptability, and productivity, while enabling economical small-batch production, customization, and predictive maintenance. To achieve this, actuators are essential as they enable the physical manipulation of manufacturing processes, as shown by two examples in section 4, which were calculated based on sensor and model data. Here, especially actuator systems with high actuating forces in the kN range are crucial for several industrial applications. High-load (HL)-actuators based on thermal shape memory alloys (SMA) are most promising where commonly used actuators based on electromechanical, hydraulic, pneumatic, or piezoelectric technologies are limited.

SMAs are able to return their original shape after plastic deformation through thermal activation based on a martensitic phase transformation [1]. This effect enables SMAs to generate mechanical strains and stresses if constrained, with the martensite to austenite transformation. The reversable deformation in the martensite phase is usually achieved by a return spring. SMA actuators offer a high specific energy density, which enables extremely compact actuators and high forces. Thus, SMA are ideal for applications with limited installation space [1, 2]. SMAs have mostly been used as wire actuators in micro and small systems with actuation forces of up to a few Newtons. Large batch examples include pneumatic valves in the automotive industry [3] and optical image stabilization systems in smartphone cameras. The advantages of these systems are their small footprint, low weight and noiseless operation [3, 4]. Due to their excellent scalability, the development of HL- SMA actuators enables to design small actuator systems with high actuation forces for machine and process automation.

In recent years, HL-SMA actuators have already been investigated in several studies and been practically implemented in technical applications. Britz and Motzki investigated in [5] bundles of SMA actuator wires. By connecting 28 SMA wires in parallel they achieved actuator forces up to 1200 N. However, the space requirement is greatly increased by the large installation space required for the clamping elements. Another application is the breaking of rocks as part of geological investigations during space missions [2]. For this purpose, rod or tube actuators made of high-temperature SMAs are manually deformed, inserted into a borehole of the rock sample and subsequently heated. The forces are sufficient to fracture the rock sample. Due to the lack of passive reset elements a manual reset is necessary. Another example are torque tubes to generate torsional motion [6]. Such actuators are used in the aerospace industry for flap actuation, control of process fluids in thermal management systems or in adaptive aerodynamics to adjust wings or intake ducts. The max. torque depends on the geometry and specific operating conditions and can reach 1400 Nm [7].

The actuators presented can only be used for their specific fields of application and the adaptability to production machines is very limited due to installation space, one-way actuation or the type of generated force. Therefore, this paper focuses on HL-SMA push-actuator technology, which is characterized by high actuating forces of more than 1 kN, small space requirements, cyclic operation, simple control, and low acquisition and operating costs.

2 DEVELOPMENT OF HIGH LOAD SMA PUSH-ACTUATORS

2.1 Basic structure of HL-SMA push-actuators

The design of a suitable shape memory component (SMC) is crucial for the development of HL-SMA push-actuators. The selected SMC geometry is strongly dependent on the availability of SMA semi-finished products. Generally, SMAs are available as sheet, strip, rod, tube or wire. Wires are the most common SMA geometry and already used in large quantity in products.

The type of mechanical load (tension, compression, bending, torsion) determines the choice of SMC geometry. To cyclically utilize the shape memory effect (SME), local strains and stresses must remain below a critical threshold. In general, the highest material efficiency can be achieved by applying tensile and compressive loads [8].

While wire actuators are cost effective, they present a challenge for mechanical integration under high load conditions. The space required for clamping SMA wire bundles is disproportionately large compared to the actual actuator volume, as shown in the work of Britz and Motzki [5]. Compression-loaded actuators offer better miniaturization potential, since simple axial clamping eliminates the need for large connecting structures. Figure 1 (left) illustrates a schematic compression-loaded SMA actuator system.

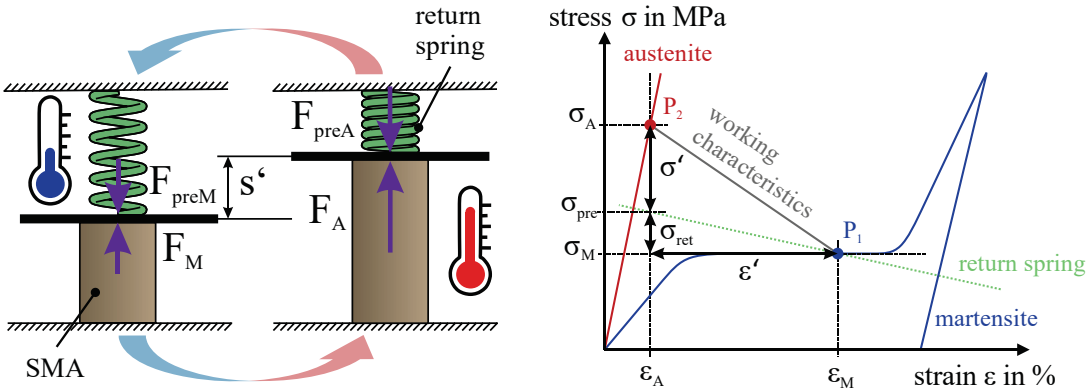

Figure 1: Structure of a compressed SMA actuator (left) and SSD for the design of SMA actuators (right)

2.2 Mechanical design

The mechanical properties of the SMC are critical. Stress-strain diagrams (SSDs) determine these properties in martensitic (low temperature) and austenitic (high temperature) states (see Figure 1, right). The operating points (P1: disabled, P2: enabled) define the usable stroke and force of the actuator. The effective actuator strain ε' is derived from the difference between the SMC strain ε_M in the deactivated (martensitic) state and the strain ε_A in the activated (austenitic) state, as expressed in Equation 1.

$$\varepsilon' = \varepsilon_M - \varepsilon_A \tag{1}$$

Strain must not exceed 2% to achieve more than 10^5 actuation cycles [8]. Higher strain (up to 8%) increases structural degradation, causing actuator shortening if compression-loaded or

elongation and breaking if tension loaded. The effective usable actuator stress σ' is determined by the maximum austenite stress σ_A, the martensite stress σ_M, and the reset stress σ_{ret} of the reset element, as described in Equation 2.

$$\sigma' = \sigma_A - \sigma_M - \sigma_{ret} \tag{2}$$

As a rough design guideline, the maximum stress σ_A of 400 N/mm² should not be exceeded [8]. However, this limit varies depending on the semi-finished product used. Beyond the maximum stress limit, increased functional degradation is observed in the form of a reduction in the SME. This leads to a decrease in the reversible strain of the actuator.

2.3 Miniaturized HL-SMA push-actuators

Figure 2 shows two HL-SMA push-actuators using tubular SMCs. The right-hand design, introduced in [9], is a miniaturized evolution of the earlier concept from [10], integrating the spring return element as a Belleville washer pack inside the SMC to reduce overall package size.

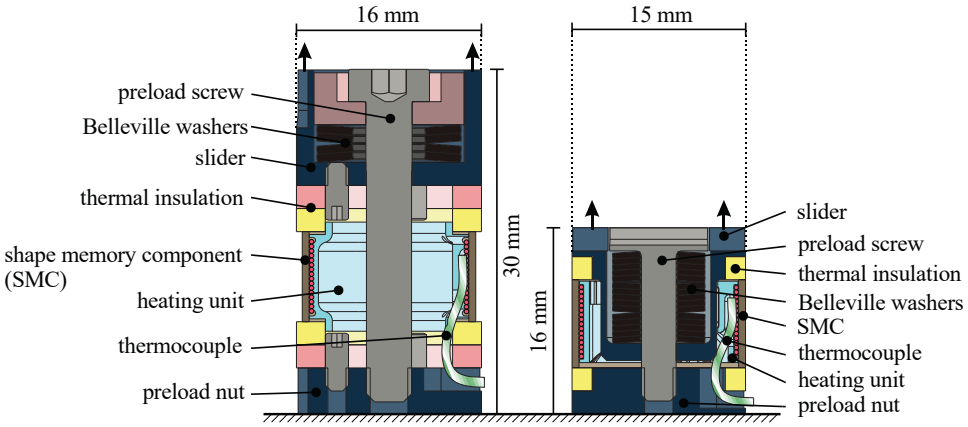

Figure 2: Structure of the HL-SMA push-actuators (left - based on [10], right - based on [9])

Both actuators share identical SMC dimensions: 15 mm outer diameter, 0.6 mm wall thickness, and 7.8 mm height in the austenitic undeformed state. A preload mechanism (slider, screw, nut, pack of Belleville washers) compresses the SMC in the martensitic state with a torque of 2.4±0.1 Nm. The max. cold-state strain ε_M of 2% yields a theoretical displacement of 156 µm, with an actuation force of 8.86 kN at σ_A of 400 MPa. Actuator stroke can be increased to 180 µm for applications with cycling requirements of less than 10^5 cycles [9].

The tubular design allows for the integration of the heating unit and a thermocouple inside the SMC, in addition to improved thermal properties by maximizing the ratio of surface area to SMC volume. The heating unit consists of resistance wire wrapped around a temperature-resistant sleeve, with a thermocouple for temperature control. The ceramic thermal insulation minimizes heat loss to the surrounding components. For more dynamic cooling of the actuator, the ceramic disks can be replaced by discs with higher thermal conductivity. As a result, more energy is lost during heating; however, the surrounding structure acts as a heat sink.

2.4 Thermal design

In [10], the thermal simulation of HL-SMA actuators, using the actuator concept from Figure 2 (left) as an example, is performed using the finite element method (FEM) and a simplified lumped parameter model (LPM). The structure of the LPM used is shown in Figure 3 (left). The LPM simplifies the actuator system into four nodes with thermal capacitance C_i and temperatures ϑ of the actuator components.

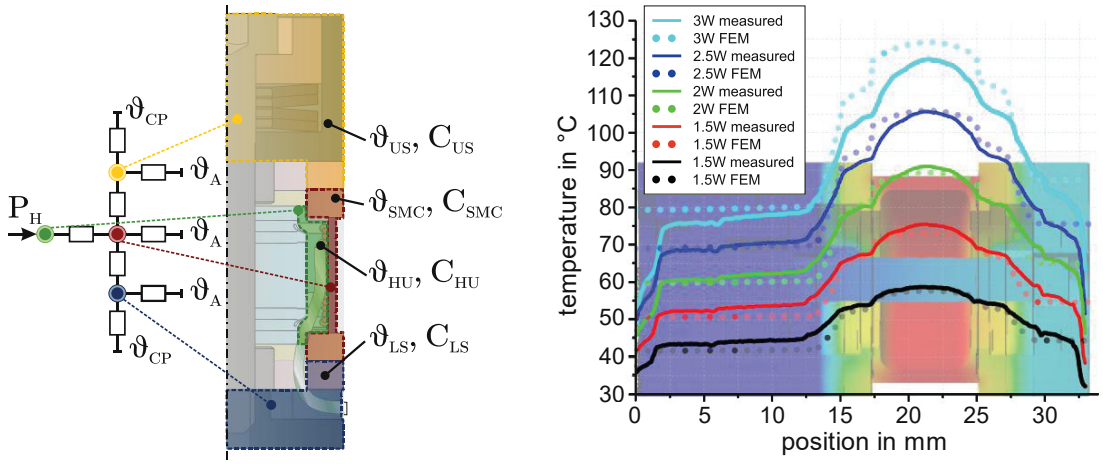

Figure 3: Structure of LPM (left, based on [10]) and comparison of experimental measurements and FEM simulation results (right)

Heat flow between nodes is modeled via thermal resistances $R_{th,ij}$, considering transfer, contact, and boundary effects. The model uses the temperature of the force-introducing planes ϑ_{CP} and ambient temperature ϑ_A as global conditions. The heating power P_H serves as an input parameter, determining the SMC temperature ϑ_{SMC}. FEM simulations provide model parameters based on the actuator geometry and material properties required for the LPM. The FE model describes the spatial temperature distribution and heat flows but requires specific assumptions for simplification due to long computation times. The LPM is a highly simplified model suitable for fast dynamic calculations. Both models have been validated in [10] with experimental data obtained from temperature measurements during the operation of the SMA actuator. Figure 3 (right) shows an exemplary comparison between experimental measurements and the FEM simulation. The validated models enable accurate and efficient thermal prediction, supporting real-time control and early-stage actuator design.

2.5 Control system

HL-SMA push-actuators are controlled by SMC temperature regulation. A resistance heating unit (Figure 4 - left) converts electric power into thermal energy to dynamically heat and activate the SMC. A graphite foil layer minimizes thermal resistance between the SMC and the resistance heating wire and allows friction reduced movement. An electrical heating power of maximum 22.5 W (15 V/1.5 A) is used to activate an HL-SMA push-actuator [11].

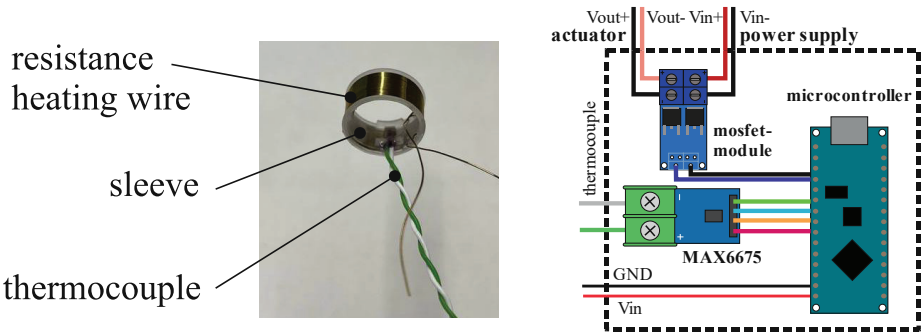

Figure 4: Heating unit (left) and control system (right, based on [11])

Compared to piezoceramic, hydraulic, or electromechanical actuators, SMA actuators require low-cost control electronics. A microcontroller controls the heating power using pulse width modulation (PWM) in conjunction with a MOSFET. A thermocouple measures the SMC temperature as an input to a PID controller that controls the MOSFET. A simplified structure of a control system for HL-SMA actuators based on [11] is shown in Figure 4 (right).

3 PROPERTIES OF HL-SMA PUSH-ACTUATORS

In the following sections, different characteristics of HL-SMA actuators are presented based on the actuator concept of [9]. This miniaturized design is a further development of the concept from [10].

3.1 Mechanical characteristics

This section presents mechanical properties of HL-SMA push-actuators in practical applications. Empirical tests were conducted using a custom-built SMA test bench introduced in [9]. This setup includes a robust steel frame to ensure high overall system stiffness, linear bearings for free movement and minimal friction influences, a load screw for adjustment of various load scenarios, and the option to use a pack of Belleville washers to simulate loads. The measurement system consists of a 20 kN load cell, three eddy current displacement sensors rotated by 120° around the measurement point, and various temperature sensors.

Three load scenarios have been examined, focusing on the resulting actuator displacements and forces. Figure 5 shows the experimentally obtained stroke-temperature behavior of the HL-SMA push-actuator (left) and the corresponding force-stroke diagram (right). The actuator behavior was analyzed under three load conditions: without additional external forces acting on the actuator, under a constant load of 2800±100 N, and with the actuator stroke blocked by the load screw.

When comparing the stroke-temperature behavior of the load scenarios, differences in maximum strokes can be observed. The increased stroke under constant load compared to free stroke is due to higher martensitic strain, as the constant load exceeds the actuator's restoring force. This additional preload on the SMA allows for a larger stroke. To prevent excessive pre-deformation, martensitic stops can be implemented to limit compression in the deactivated state.

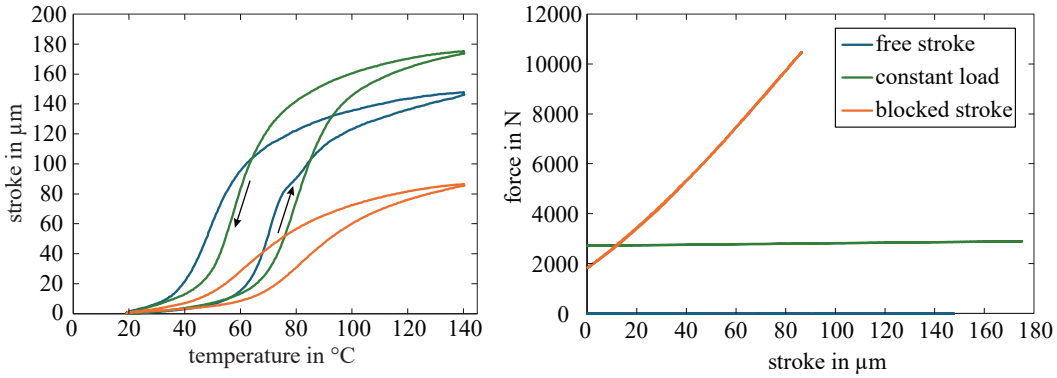

Figure 5: Stroke-temperature behavior (left) and force-stroke behavior (right) of HL-SMA push-actuator

In the blocked stroke scenario, the measured stroke corresponds to the compliance of the load screw. With an initial force of 1.9 kN, the HL-SMA actuator can generate actuating forces of more than 10 kN. The critical stress limit of 400 MPa, as defined in Section 2.2, corresponds to a force of 8.86 kN, which is therefore exceeded. Due to the high slenderness of the SMA cylinder, buckling occurs under such loads, as shown in Figure 6 (center) compared to the unloaded state (Figure 6 - left). This reduces both actuator life and performance by reducing the usable stroke. Buckling can be mitigated by using martensitic stops or limiting the maximum load.

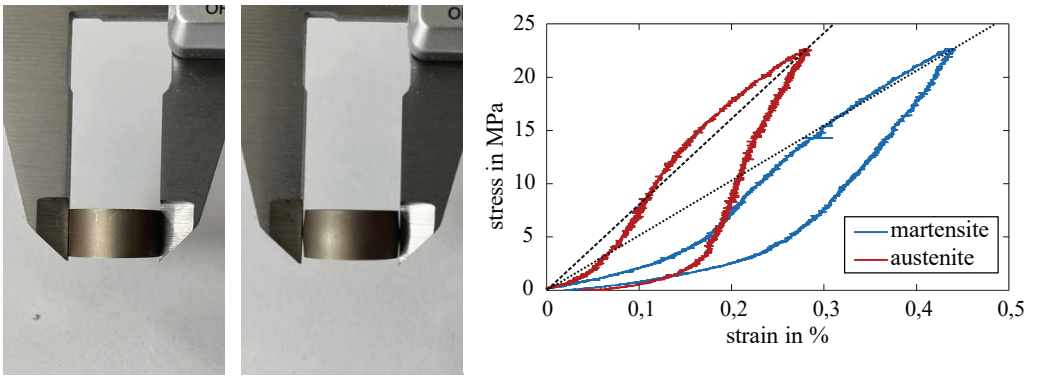

Figure 6: New and bumped SMC (left) and stress-strain-behavior of HL-SMA push-actuator (right)

In addition, higher actuator loads shift the phase transformation temperatures (PTTs) to higher ranges, indicating a stress dependence of the transformation. Consequently, the SMC requires higher temperatures for complete austenitic transformation at high operating loads. To ensure full activation of the SMA actuator during long-term operation, higher activation temperatures must be applied.

To further characterize the HL-SMA push-actuator, tests were performed using a *ZwickRoell* universal tensile-compression testing machine with a maximum force of 20 kN. The stiffness of the entire actuator system was investigated in both the deactivated and activated states. In

addition, the stiffness of the test machine without the actuator was measured, and the data were corrected accordingly. The measurement results for the actuator presented in [9] (⌀15mm × 16mm) are shown in Figure 6 (right).

Due to the phase transformation of the SMC, the actuator has a different average stiffness depending on the activation state: 89.17 N/µm when activated and 57.12 N/µm when deactivated. This variation must be considered when integrating HL-SMA push-actuators into manufacturing machines that require high stiffness.

3.2 Dynamic characteristics

A drawback of SMA actuators compared to other actuation technologies is their limited dynamic performance. Because the SME is thermally driven, actuation speed is limited by thermal inertia and the ability to rapidly heat and cool the material. Due to their much larger volume compared to wire actuators, HL-SMA push actuators have a larger thermal capacity which limits actuation frequency. Using a heating unit is a simple and space-efficient method of activating the HL-SMA push-actuator. However, it has the disadvantage of slow heating dynamics and lack of active cooling. Forced convection with compressed air or the use of fluid-based temperature control can improve dynamic performance.

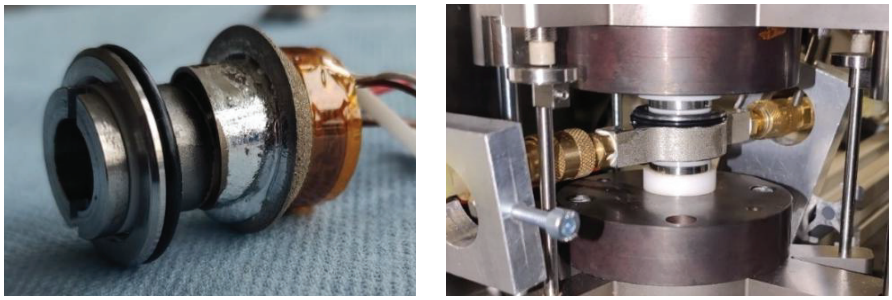

Figure 7: SMA actuator with liquid metal and sleeve (left) and dynamic test setup (right)

Figure 7 shows an example setup using an additively manufactured sleeve with integrated cooling channels. Liquid metal (*Thermal Grizzly Conductonaut*) is used to improve thermal conductivity between the sleeve and the SMC. Hot (90 °C) and cold (5 °C) fluids are alternately pumped through the two connectors of the sleeve. Figure 8 shows the dynamic behavior of different temperature control methods during heating and cooling of the actuator.

The experiments show actuation times (activation and deactivation) of 175 s with a heating unit and free convection, 45 s with a heating unit and forced air cooling using compressed air directed at the SMC, and 4.35 s with fluid-based temperature control, resulting in a maximum switching frequency of 0.23 Hz. The different actuator strokes result from slightly different preload forces. These forces are caused by limited accuracy during preloading due to the preload screw's torque specification.

These dynamic characteristics result in application limitations. HL-SMA actuators are generally not suitable for processes requiring switching frequencies above 1 Hz. In addition, their integration into technical systems becomes more complex and space-consuming when

high dynamics are required due to the need for additional components for fluid-based temperature control or forced convection.

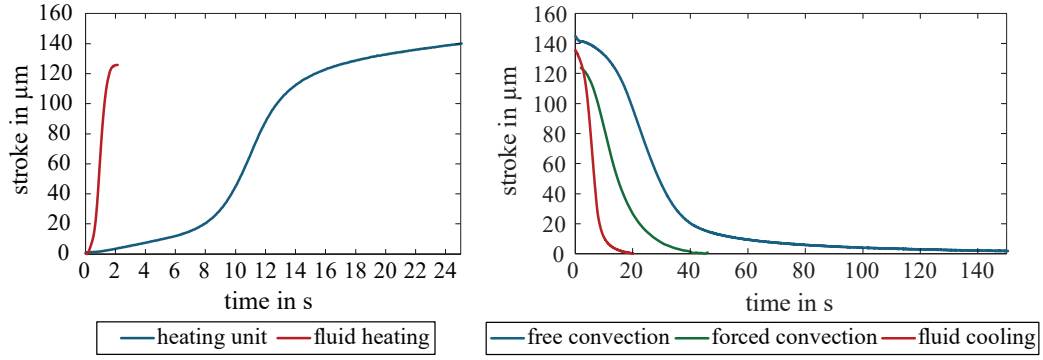

Figure 8: Heating and cooling characteristics with different temperature control methods

3.3 High load shape memory components

To the best of the authors' knowledge, there are currently no commercially available SMA tubular semi-finished products with PTTs for actuation purposes. As a result, hollow cylinders are typically cut from round-hammered ingots, which are intermediate products in SMA wire production and have inferior shape memory properties compared to the final wire product, resulting in reduced actuation performance and efficiency. In addition, manufacturing SMA hollow cylinders from ingots is cost intensive. Due to the poor machinability of SMAs, these cylinders must be cut using electrical discharge machining (EDM), a time-consuming and expensive process.

In [9], additive manufacturing is presented and compared as an alternative to conventional ingot-based SMC manufacturing. The base material was produced by *Ingpuls GmbH* and was a Ni42.5Ti50.0Cu7.5 (at.%) ingot. The additive specimens were produced using the laser powder bed fusion (PBF-LB/M) process. The base material was powder atomized from a Ni45.0Ti50.0Cu5.0 (at.%) ingot, also supplied by *Ingpuls GmbH*.

Figure 9 (left) shows a conventional and an additive manufactured SMC. HL-SMA actuators with conventional and additively manufactured SMCs were evaluated for their degradation behavior, specifically the cyclic stroke reduction and SMC shortening. Actuators with both additive and conventional SMCs were subjected to 10^4 load cycles. Figure 9 (right) shows the stroke-temperature behavior and shows significantly greater degradation and a more pronounced shift of PTTs to higher temperatures for conventionally manufactured SMCs. This highlights the superior stability and performance of additively manufactured SMCs for HL-SMA actuator systems.

A key advantage of additive manufacturing is the increased geometric flexibility in SMC design, which removes the previous constraints imposed by the size limitations of semi-finished products. However, the high costs associated with powder production and the PBF-LB/M process currently limit its feasibility to specialized applications with low production volumes. To improve actuator performance and cost efficiency, future research should focus on

optimizing SMA tubular semi-finished products, refining material processing, and exploring alternative manufacturing technology.

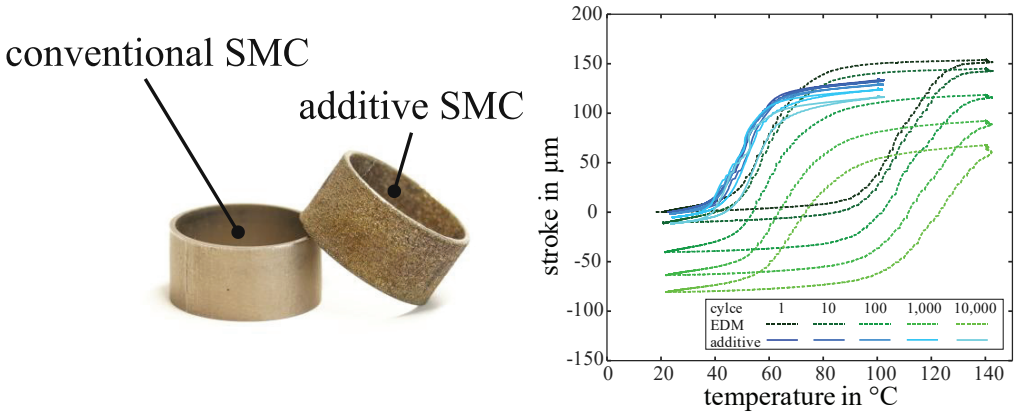

Figure 9: Conventional (EDM) and additive manufactured SMC (left) and comparison of stroke-temperature behavior (right, based on [9])

4 APPLICATIONS

HL-SMA actuators have significant potential to be utilized in production systems due to their advantages: high actuating forces, compact design, long service life, maintenance-free operation, easy integration into existing systems, scalable force and stroke ranges, low energy consumption, and low cost. However, their limited dynamics due to thermal inertia make them particularly suitable for applications requiring slow actuation or holding functions. Two practical applications for HL-SMA actuators are presented below.

In [12], an HL-SMA actuator system is presented for adjusting guide rails during the assembly of a machining center. The goal is to automate the previously time-consuming and costly manual alignment process. The main requirements for the actuators are high forces up to 10 kN, strokes up to 200 µm, and high positioning accuracy. Figure 10 shows the application concept (left) and the developed HL-SMA actuator (right).

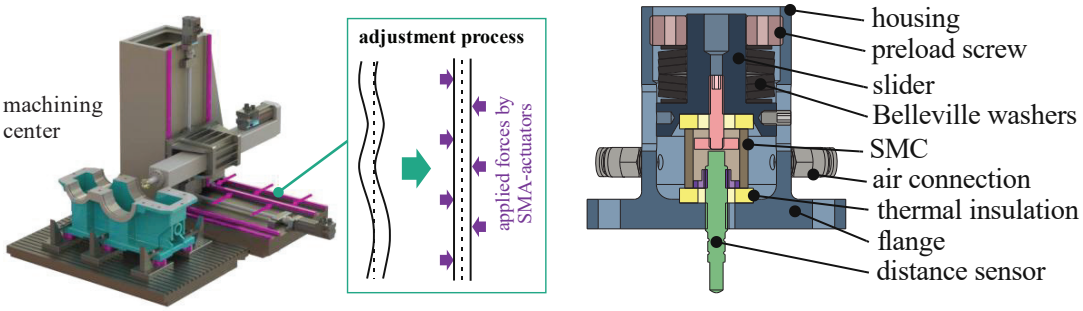

Figure 10: Application concept for automated fine adjustment of guide rails (left) and corresponding HL-SMA actuator concept (right) (based on [12])

Another application field is the use of HL-SMA actuators in deep drawing processes for sheet metal forming. In [11] and [13], a novel active blank holder is presented that allows real-time adjustment of the blank holder force distribution. The aim is to automate the try-out phase and actively compensate for process fluctuations to minimize scrap. Figure 11 shows a sectional view of the active blank holder with an integrated HL-SMA actuator (left) and the measured blank holder force distributions from deep drawing tests without and with the activated actuator array of 16 HL-SMA actuators (right). This demonstrates that the blank holder force distribution on forming tools can be actively controlled using HL-SMA actuators.

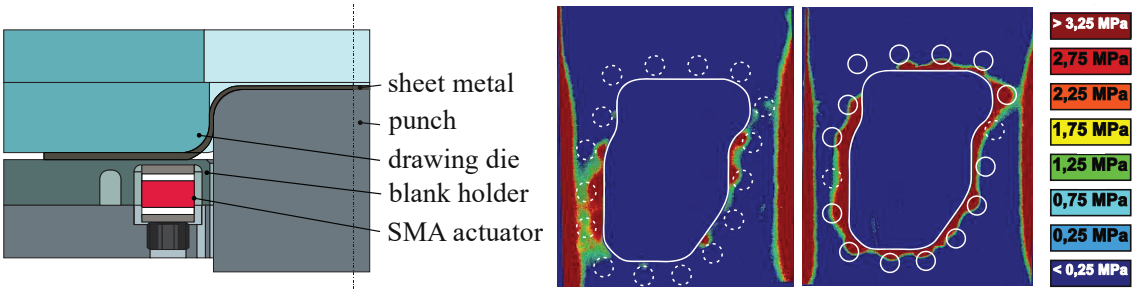

Figure 11: Sectional view of active deep drawing tool (left) and measured blank holder force distribution with deactivated and activated HL-SMA actuator array (right) (based on [13])

11 CONCLUSIONS

High-Load Shape Memory Alloy (HL-SMA) push-actuators provide a compact and efficient solution for industrial applications requiring high force actuation. This paper provides an overview of their development, properties, control strategies and applications. Optimized actuator geometries, improved manufacturing technologies such as additive manufacturing of shape memory components (SMCs), and insights into dynamic and cyclic behavior can improve performance and lifetime.

Experimental investigations have demonstrated actuation forces of more than 10 kN with minimal space requirements using an HL-SMA actuator concept. The scalability of HL-SMA push-actuators make them a suitable alternative to conventional actuators, especially in space-constrained environments. However, their low dynamics limits their use in high-frequency processes. Forced convection or active fluid temperature control can significantly improve dynamics, but at the expense of increased actuator size and cost. The limited stroke of HL-SMA linear actuators (up to 1 mm) makes them ideal for industrial applications such as fine positioning, holding or locking of tools and workpieces.

The application examples presented, including automated guide rail adjustment and adaptive blank holding in deep drawing, highlight their industrial relevance by improving efficiency, reducing manual intervention, and increasing system adaptability.

For large-scale industrial use, further research is needed on SMA tubular stock shapes, optimized SMC geometries to avoid buckling, and control strategies for continuous position and force regulation. By addressing these challenges, HL-SMA actuators will be able to support the next generation of automation and Industry 4.0.

REFERENCES

[1] J. Arias Guadalupe, D. Copaci, D. Del Serrano Cerro, L. Moreno, and D. Blanco, "Efficiency Analysis of SMA-Based Actuators: Possibilities of Configuration According to the Application," *Actuators*, vol. 10, no. 3, p. 63, 2021, doi: 10.3390/ACT10030063.

[2] O. Benafan, R. D. Noebe, and T. J. Halsmer, "Static rock splitters based on high temperature shape memory alloys for planetary explorations," *Acta Astronautica*, vol. 118, pp. 137–157, 2016, doi: 10.1016/j.actaastro.2015.10.009.

[3] J. M. Jani, M. Leary, and A. Subic, "Shape Memory Alloys in Automotive Applications," *AMM*, vol. 663, pp. 248–253, 2014, doi: 10.4028/www.scientific.net/AMM.663.248.

[4] L. Manfredi, Y. Huan, and A. Cuschieri, "Low power consumption mini rotary actuator with SMA wires," *Smart Mater*. Struct., vol. 26, no. 11, p. 115003, 2017, doi: 10.1088/1361-665X/aa8aa4.

[5] R. Britz, and P. Motzki, "Analysis and evaluation of bundled SMA actuator wires," *Sensors and Actuators A: Physical*, vol. 333, p. 113233, 2022, doi: 10.1016/j.sna.2021.113233.

[6] A. P. Jardine, J. D. Bartley-Cho, and J. S. Flanagan, "Improved design and performance of the SMA torque tube for the DARPA Smart Wing program," *Proc. SPIE 3674, Smart Structures and Materials* 1999: Industrial and Commercial Applications of Smart Structures Technologies, July 1999, doi:10.1117/12.351564.

[7] T. Chen, Y. Zhang, S. Qiu, J. Jiang, Q. Zhang, and X. Zhang, "Experiments and Modeling of Machined Spring Rotary Actuators with Shape Memory Alloys," *Materials* (Basel, Switzerland), vol. 15, no. 19, 2022, doi: 10.3390/ma15196674.

[8] S. Langbein, and A. Czechowicz, *Konstruktionspraxis Formgedächtnistechnik*. Wiesbaden: Springer Fachmedien Wiesbaden, 2013, isbn: 978-3-8348-1957-4.

[9] K. Thüsing, A. Hofer, K. Pagel, C. Weck, and W.-G. Drossel, "High Load NiTi Shape Memory Alloy Actuators: A Study of Cyclic Behavior," in ASME 2023 Conference on Smart, 2023, doi: 10.1115/SMASIS2023-110991.

[10] D. Maiwald, T. Trittler, A. Bucht, K. Pagel, and W.-G. Drossel, "Characterization and Modeling of the System Behavior of High Load SMA Actuators," in ASME 2022 Conference on Smart Materials, Adaptive Structures and Intelligent Systems, 2022, doi: 10.1115/SMASIS2022-88892.

[11] A. Hofer, K. Thüsing, K. Pagel, L. Hamm, C. Weck, and W.-G. Drossel, "Optimizing Force Distribution in Deep Drawing Tools Using SMA High Load Actuators," *Proc. ASME 2024 Conference on Smart Materials, Adaptive Structures and Intelligent Systems*, 2024, doi: 10.1115/SMASIS2024-140067.

[12] D. Maiwald, A. Bucht, W. Zorn, and W.-G. Drossel, "Development Approach of Actuators for High Loads Based on Shape Memory Alloys," *Proc. ASME 2020 Conference on Smart Materials, Adaptive Structures and Intelligent Systems*, 2020, doi: 10.1115/SMASIS2020-2232.

[13] A. Hofer, K. Thüsing, K. Pagel, L. Hamm, W.-G. Drossel, “Development of an Active Deep Drawing Tool Based on SMA High Load Actuators,”. in Drossel, WG., Ihlenfeldt, S., Dix, M. (eds) *Production at the Leading Edge of Technology*. WGP 2024. Lecture Notes in Production Engineering. Springer, 2025, doi: 10.1007/978-3-031-86893-1_19.

XI ECCOMAS Thematic Conference on Smart Structures and Materials - SMART 2025
M. Krommer, M. Nader and M. Schagerl (Eds)

Received: 25 March 2025 / Revised: 4 July 2025 / Accepted: 9 October 2025
© The Author(s) 2025

Systematic Conceptualization of Soft Sensors

Florian Koetz, Michel Fett, Eckhard Kirchner

Abstract. Soft sensors are sensors that do not measure measurands or quantities of interest with a physical entity but determine them with the help of an algorithm. They combine aspects of sensor technology with aspects of model-based data evaluation, which requires know-how from various aspects for development and thus makes this considerably more difficult. While the literature already contains initial approaches that support the selection and integration of (physical) sensors or the creation of models, they do not cover all aspects of soft sensors on their own.
For this reason, this article considers the sensor- and model-aspects of soft sensors together. The specific boundary conditions of soft sensors are combined with existing approaches for the systematic development of (physical) sensors and models. From this, a procedure for systematic conceptualization of soft sensors is derived. The resulting procedure combines sensor- and model-aspects of soft sensors and supports their development. The procedure is illustrated using an exemplary use case. Lastly, the differences and commonalities between physical sensors, soft sensors and digital twins are discussed.

Key words: Soft Sensor, Model Fidelity, Sensor Development

Florian Koetz & Michel Fett & Eckhard Kirchner
Institute for Product Development and Machine Elements, Technical University of Darmstadt, 64287 Darmstadt, Germany,
e-mail: florian.koetz@tu-darmstadt.de

1 INTRODUCTION

Within the context of industry 4.0 concepts such as condition monitoring are becoming more relevant. However, in practice these concepts often fail due to the financial and organizational effort needed to integrate sensors into existing systems. Further concepts such as digital twins require additional sensors that complicate development and raise cost. Additionally, some manufacturers of systems are potentially unfamiliar with some measurement principles complicating development. In such an environment the use of soft sensors can be a remedy to some of these problems as it enables the use of a wide variety of sensors that allow a wide range of locations.

The term soft sensor refers to a virtual sensor that uses information from other sensors and combines it with a software-based model. Soft sensors allow a greater freedom in design and retrofitting for a sensing task as long as the model used for interpreting the sensor signal fulfils the requirements of the soft sensor.

However, so far there is no concise sensor selection and integration method for soft sensors that allows the systematic selection, integration and validation of soft sensors. This contribution therefore aims to generate a procedure for the systematic conceptualization of soft sensors. The systematic procedure is then illustrated using an example. The following research questions will be answered:

RQ1: Which steps are necessary to conceptualize soft sensor solutions? Which of these steps can be taken from existing sensor integration approaches and approaches for the conceptualization of digital twins?

RQ2: Which commonality and relationship can be identified between soft sensors, physical sensors and digital twins?

2 MATERIALS AND METHODS

This section introduces the fundamentals required for this article, starting with the basics of soft sensors. Subsequently, a procedure for the selection and integration of (physical) sensors is presented. Finally, the basics of models and initial suggestions for systematic procedures for modeling are outlined.

2.1 Soft Sensors

The term “soft sensor” is a combination of the words “software” and “sensor” and describes a mathematical or statistical model that is used to determine quantities of interest in a measurement task. For this purpose, the model is fed with data from sensors integrated at more easily accessible locations, from which the model determines the quantity of interest [1–4]. It is not necessary for the virtual measuring location to be close to the physical sensors. However, it is necessary that the calculated output variable of the soft sensor $S_{Softsensor}$ and the input

variables of the physical sensors $S_{phyical,i}$ have a relationship that can be expressed in the following form [2, 5]:

$$S_{Softsensor} = f\left(S_{phyical,1}, \dots, S_{phyical,n}\right)$$

There is a distinction between model-based and data-driven soft sensors. Model-based soft sensors describe the behavior of a system with equations that are based on physics and describable effects. Since the behavior of the system are known and described fully, these are referred to as white-box models. One challenge here is that the mechanisms must not only be known, but must also be precisely mathematically describable, which becomes more difficult with an increasing complexity of a system. In comparison, data-driven soft sensors are based on data from the real process. Large amounts of data are required which are processed using various statistical and machine learning approaches. This approach is less transparent, which is why it is also referred to as black-box models. Data-driven soft sensors are easier to implement than model-based soft sensors, which is why they are more widespread today [6, 7].

The creation of soft sensors can be complex, and without the necessary expertise, the full potential cannot be exploited [1, 4]. For this reason, there is already some preliminary work addressing the development of soft sensors, although this work focuses primarily on software-based data processing [1, 3, 6, 7]. Considerations relating to measurement technology which are used for "classic" sensor design are neglected here.

2.2 Procedure for the selection and integration of (physical) sensors

In industrial practice, physical sensors are often selected and integrated pragmatically [8, 9]. This often leads to solutions that work but are not optimal. To address this, Hausman et al. have proposed an eight-step, iterative procedure for the systematic selection and integration of physical sensors. The procedure includes with the clarification of the measurement task and determination of the quantity of interest. The quantity of interest initially describes the quantity about which knowledge is to be obtained. From this, various measurands can then be derived, which are to be measured by the sensors. Additionally, suitable measurement locations and measurement principles must be determined. Once the requirements, measurand, measuring location and measuring principle have been determined, selection criteria for the sensor can be derived and a suitable sensor can be selected. The sensor is then integrated into the system. During the process there is a continuous verification. Finally, the results are validated [9].

2.3 Modeling of physical relationships

According to the general system theory of Stachowiak, models are characterized by the fact that they represent a real system or example. They serve a specific purpose and are limited to the relevant aspects. Details that are less important for the application are neglected [10]. These models can be simple mathematical models like equations that represent the interrelationships, but also more complex simulation models can be realized. In addition to these empirical or

system-based models, there are also data-driven models in the form of machine learning and artificial intelligence, which are trained based on large amounts of data.

These models are often created pragmatically based on experience and system knowledge. However, efforts are also being made to systematize modelling. For example, the SET Level project proposes a procedure for the systematic creation of simulation models. It begins with the analysis of the modeling task and objectives, from which requirements for the models can be derived. Based on this, design specifications for the models are defined and the models are implemented. The quality of the models can be evaluated as part of an application (in this case the execution of a simulation) and a decision can be made as to whether the modeling objectives set at the beginning have been fulfilled [11].

In the context of digital twins, Fett et al. propose a similar procedure for creating models. The process begins with the identification of requirements for the models. Based on this, the model scope is defined, which describes which aspects of the physical relationships are to be modeled and to what level of detail. In contrast, the aspects to be neglected are defined and delimited by a system boundary. In this way, it is determined which behavior is to be modeled. In some cases, this behavior cannot be represented directly by models but must be broken down hierarchically. This creates a model structure with corresponding, detailed sub-models. These must then be implemented individually and then aggregated into a superior super model. During the entire process, continuous verification takes place. Finally, the results are validated [12, 13].

As described above, models never represent their source material to 100%. Depending on their purpose, they focus on some aspects of the source material and neglect other aspects. However, the individual facets of systems are very rarely completely independent of each other, but still influence each other. By neglecting aspects that are apparently irrelevant, there arises a small but existing difference between the model and its source material. This results in uncertainty. It is a central question in modelling which aspects can be neglected in good conscience and which deviations between model and prototype are acceptable. The attempt to replicate every detail of the source material leads to excessively complex models which's accuracy is usually no longer necessary for the original purpose of the model. These issues are discussed extensively in the corresponding literature under the term model fidelity [14–16]. It is a rule of thumb that models should always be as accurate as necessary for the task, but at the same time as simple as possible [13].

3 DERIVIATION OF AN APPROACH FOR THE SYSTEMATIC DESIGN OF SOFT SENSORS

Soft sensors combine aspects of conventional, physical sensors and aspects of model-based data assessment using corresponding algorithms. For this reason, the systematic procedures for sensors or models introduced in the previous section are not directly applicable. Instead, they need to be combined in order to adequately consider the boundary conditions and adequately guide and support the systematic design of soft sensors. In the following, a combination is presented which enables a systematic design of soft sensors

Step 1: Clarification of the measurement task, determination of the quantity of interest and requirements

Similarly to Hausmann et al. [9], the procedure proposed in this article begins by clarifying the measurement task. In particular, the purpose of the soft sensor is considered, in terms of which systems must be fed with which information. This leads to the quantity of interest that the sensor needs to enable knowledge of. In addition, requirements for the sensor parameters must be defined. These can include, accuracy, resolution, measuring range, sampling frequency or susceptibility to errors [17]. There is a large amount of literature [18] on the systematic identification of general requirements in the context of requirement engineering, which can also be used for this procedure.

As the development of the soft sensors and therefore the level of knowledge progresses, requirements are continuously adapted and supplemented. Furthermore, a continuous verification is to be carried out, where the results are checked regarding their fulfillment of the set requirements

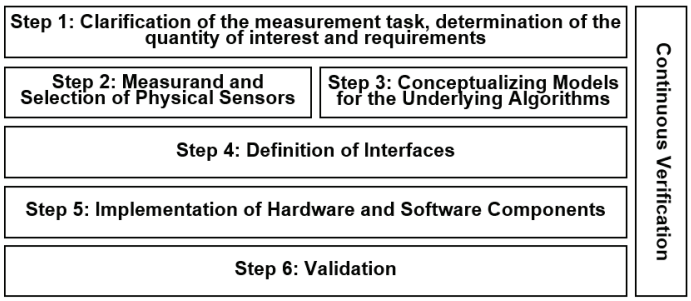

Figure 1 Steps of the procedure for the systematic design of soft sensors

Step 2: Measurand and Selection of Physical Sensors

Although soft sensors determine the quantity of interest or measurand by calculation, they still need data from the system. This data can be obtained from other physical sensors that are installed in the system but not directly at the measurement location. The usability of this data by the soft sensors requires a correlation between the quantities of interest of the soft sensor and the measurands of the installed physical sensors. This correlation results from physical relationships, for example between force and mechanical stress. A systematic consideration of these correlations makes it possible to identify suitable measurands and measurement locations for the physical sensors. It is not always necessary to integrate additional physical sensors into the system for a soft sensor; often sensors that are necessary for the system are already installed and can also be used for the soft sensor. It should also be considered to what extent data from the system control can be used to feed the soft sensor with data.

Step 3: Conceptualizing Models for the Underlying Algorithms

The algorithms of the soft sensors are based on models that describe the relationships between the measurands of the physical sensors and the quantities of interest of the soft sensors. Therefore, the algorithms must always be considered iteratively and in accordance with the

identification of suitable measurands and measurement locations of the physical sensors. It must also be determined to what degree of detail the models on which the soft sensor is based depict these relationships and which influences can be neglected. Depending on the application, there may be a trade-off between the accuracy and reliability of the results of the soft sensor and the effort involved in creating and computing the models.

The models on which the algorithms are based can be implemented differently depending on the application. For simple relationships that have already been empirically investigated and described, the models can be implemented in the form of simple equations. These can be physical formulas or equations for interpolation or extrapolation. More complex relationships may require the use of more sophisticated simulation models or data-based models. For the latter, large amounts of data are required in which the correlations are contained. This data can then be used to create models using machine learning approaches that not only contain these relationships, but also describe them.

Step 4: Definition of Interfaces

The definition of interfaces plays an important role with physical sensors, but it is even more important with soft sensors due to the ability to evaluate data independently. Hardware interfaces such as cables, connectors, computing units or transmitters must be considered. In addition, software interfaces such as communication protocols or data translation must be considered.

On the one hand, interfaces exist between the data sources and the soft sensor. Specifically, the physically installed sensors or the control unit and the models of the evaluation algorithm must be connected. In addition, the interface between the soft sensor and the superordinate system, which processes the data and is the purpose of the sensors, must be considered.

Step 5: Implementation of Hardware and Software Components

The defined interfaces are then implemented in the form of hardware and software components. In particular, the models are embedded in an IT infrastructure and a data transfer is established from the physical sensors or system control to the algorithms and then to the higher-level system. Furthermore, the necessary computing power must also be provided.

Step 6: Validation

The resulting soft sensors are finally tested and validated. This involves checking not only whether the initial requirements are met, but also the extent to which the overall purpose of supplying a system with necessary data is achieved.

4 ILLUSTRATION EXAMPLE

In the following an illustrative example is described to visualize the procedure to implement a soft sensor in systems. The purpose of this simplified example is to identify important points that need to be considered when implementing a soft sensor system. The system used for this purpose consists of a two-step helical gear transmission as shown in Figure 2.

Step 1: Clarification of the measurement task, determination of the quantity of interest and requirements

The measurement task chosen for this illustration example is the measurement of torque in the transmission. Torque sensors are generally expensive and difficult to integrate due to the requirements to the packaging space. For this reason, they are a potential use case for the implementation of soft sensors. The quantity of interest and point of interest result from the clarification of the measurement task which is in this case the torque at the output shaft.

The final measure of Step 1 is to define requirements for the soft sensor development. This is an essential step as it sets the boundaries for the development activities. Furthermore, it is necessary for the continuous verification of the results. To generate requirements, literature offers checklists that help to ensure completeness. Particularly, when previous experience with similar systems is limited, these checklists make building experience easier. Typical requirements for sensor systems contain cost, accuracy, resolution, measurement range, measurement frequency or reaction time and requirements as to the environment the sensor has to be able to withstand such as oil and high temperature.

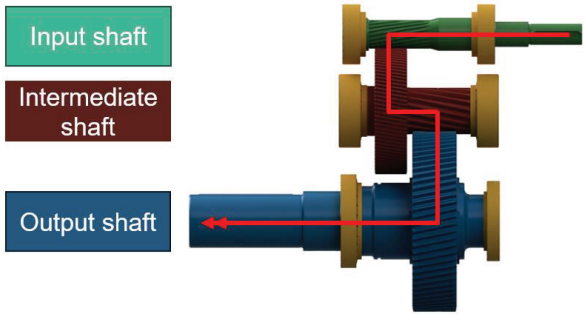

Figure 2: Transmission for the illustration example

Step 2: Measurand and Selection of Physical Sensors

In this step the measurand should be selected. In a typical direct measurement, the quantity of interest equals the measurand. When measuring indirectly or via soft sensor concepts, this is no longer the case and other physical variables are used to calculate the quantity of interest. That requires the measurand and the quantity of interest to be connected by correlation which allows the calculation of the quantity of interest. At this point the distinction between an indirect measurement and a soft sensor is no longer possible as both rely on an algorithm to describe the quantity of interest based on the measurand.

In practice, the identification of all possible measurands that can be used as a soft sensor is difficult as some options are easily missed. One way to approach this topic is by focusing on the dependencies of physical variables as published by Kraus et al. [19]. In his work effect graphs are used to identify common physical laws between the quantity of interest and the measurand. This way a systematic review of all available options in a system can be listed and analyzed based on their suitability for the intended measurement task. In this illustrative

example the measurand is the motor current that can be used to calculate the motor torque. An example measurement principle for motor current is a shunt resistance which is used in this illustration example.

Step 3: Conceptualizing Models for the Underlying Algorithms

To create the white box model that can interpret the measurand, chains of physical dependencies need to be identified. In this case the basic model uses the conservation of power between the input side of the gearbox $P_{mech,input}$ and the electrical input side of the motor P_{el}. The efficiency coefficient η needs to be considered as an important factor for the accuracy of the soft sensor model.

$$P_{el} \cdot \eta_{motor} = P_{mech,input} \tag{1}$$

The selection of effects that the model needs to consider depends on the model fidelity which will be discussed later in this section. The efficiency coefficient is an important factor in that regard as it is a complex value that's difficult to model but needs to be considered if high model fidelity is required. The model in this contribution is simplified and used to show the general modelling steps but not representative of a real high fidelity model.

The goal is to describe a relationship between the variable of interest output torque of the gearbox T_{output} and the measurand motor current I_{motor}. For that purpose, the mechanical input power of the gearbox $P_{mech,input}$ can be described using the input torque T_{input} and the input rotation rate n_{input} for a constant torque.

The electrical power on the motor side P_{el} can be described using the motor current I_{motor} and the motor voltage U_{motor}. If we assume a shunt resistor in series to the motor, the motor current can itself be calculated using the resistance of the shunt R_{shunt} and the voltage of the shunt U_{shunt}.

$$P_{el} = U_{motor} \cdot \frac{U_{shunt}}{R_{shunt}} \tag{2}$$

By combining equations (1) and (2) the input torque T_{input} and the voltages on the electrical side can be expressed according to equation (3).

$$U_{motor} \cdot \frac{U_{shunt}}{R_{shunt}} \cdot \eta_{motor} = T_{input} \cdot n_{input} \cdot 2\pi \tag{3}$$

Then lastly the output torque of the transmission T_{output} can be expressed using the gear ratios of the first and second gear stage i_1 and i_2, the input torque of the transmission T_{input} as well as the efficiency of both gear stages $\eta_{gear,1}$ and $\eta_{gear,2}$. With all previous equations combined, the relationship between the output torque T_{output} and the measured voltages can be expressed according to equation (5).

$$T_{output} = T_{input} \cdot i_1 \cdot i_2 \cdot \eta_{gear,1} \cdot \eta_{gear,2} \tag{4}$$

$$T_{output} = \frac{U_{shunt} \cdot U_{motor} \cdot \eta_{motor} \cdot i_1 \cdot i_2 \cdot \eta_{gear,1} \cdot \eta_{gear,2}}{R_{shunt} \cdot n_{input} \cdot 2\pi} \tag{5}$$

The analytical model created in this section still has several unknown variables that degrade the model fidelity. It can be assumed that values such as the rotation rate n_{input} and the voltages can easily be measured. However, the accuracy of such measurements needs to be kept in mind and a propagation of uncertainty when using multiple sensors need to be considered as this can degrade the performance of the soft sensor system. In addition to the measurement inaccuracies, the inaccuracies of the efficiencies $\eta_{gear,1}$, $\eta_{gear,2}$ and η_{motor} need to be considered. These values are virtually impossible to measure in the field and they are generally dependent on multiple influence factors. Consequently, the modelling of these values is difficult. This degrades the model fidelity.

Generally, the longer the measurement path between measurand and point of interest, the more inefficiencies and variables need to be considered for a model [19, 20]. When measuring vibration or electrical systems additional effects such as other sources of vibration along the measurement path or induced voltages also need to be considered which are difficult to describe fully. This needs to be considered when implementing a soft sensor solution as the cost advantage of soft sensors should not be used up by the accuracy disadvantage of it.

One final consideration about potentially long measurement paths is closely related to the efficiency values. If for example dynamic forces are applied to the gearbox through the output side due to external factors, then the proposed soft sensor system will not be able to detect it. Even a torque measurement at the input side of the gearbox might not detect these forces due to the dampening effects of the friction. It is therefore essential to express a clear measurement objective for a soft sensor system in Step 1 to avoid false assumptions when comparing the potential functions of soft sensor solutions to direct measurement solutions.

The example analytical model shown in this section describes a simple relationship between the measurand and the variable of interest. This is no longer the case when more complex systems are used that have ambiguous effects. Then it is no longer as simple to just observe an effect and clearly identify the cause through a soft sensor model. In this case other modelling types such as empirical models or models based on artificial intelligence can be used. Empirical models are also often used when it's cheaper and quicker to simply measure the relationship between a measurand and a variable of interest. This can help in dealing with unknown variables as multiple unknown variables can be substituted with one measurement plan on test benches.

Step 4: Definition of Interfaces

The definition of interfaces is highly individual and depending on the environment of the sensor system. Interfaces refers to all soft and hardware interfaces related to the system. This includes mechanical connections within the system, electrical connections and interfaces that are necessary for the flow of information. Naturally interfaces occur between hardware

components such as Data Acquisition Devices, control units and other components. Therefore, the interfaces need to be iterated simultaneously with the selection of hardware components.

Step 5: Implementation of Hardware and Software Components and Step 6: Validation
In the final two steps the defined interfaces are implemented and all necessary components are installed. Lastly, the system needs to be validated. Specifically, the validation needs to confirm that the final product is a valid solution for the initially observed problem. It requires the testing of the system in a prototype or in the field.

5 SUMMARY AND OUTLOOK

In this contribution an approach to conceptualize and implement soft sensor systems is discussed and important steps highlighted. The approach is generated by analyzing existing sensor integration approaches and modelling approaches and combines important aspects of both. This answers research question 1. Additionally, an illustration example is used to visualize the steps of the approach.

The conceptualization shows that the model determines the accuracy of the soft sensor to a large degree. It is desirable but generally not possible to describe all variables that need to be considered in a model fully. This is especially important as soft sensors are often suggested as cheaper solutions compared to potentially expensive physical sensors. But soft sensors can require more effort to design due to the necessity to deal with the inaccuracies.

One important aspect of sensor development is that sensor selection and integration methods should provide a complete and thorough analysis of a system and the intended measurement task like the sensor selection and integration approach by Hausmann et al. [9]. According to this approach, possible measurands that can potentially fulfill the measurement task should be identified. From that point the distinction between a soft sensor and an indirect measurement of a physical sensor is no longer clear. Similarly, digital twins can be of varying complexities. In its simplest form the digital twin can be a single model that takes data from one sensor and computes a variable of the system that is not measured. Therefore, the distinction between soft sensors, digital twins and physical sensor is not always possible. Furthermore, the distinction is not always necessary in regard to sensor systems as a sensor integration approach should offer both physical and soft sensors as valid solutions. A restriction to focus on soft sensor and disregarding physical sensor solution restricts the open-minded solution process unnecessarily.

Figure 3 shows a visualization of the relationship between soft sensors, digital twins and physical sensors to answer research question 2. The most basic sensor solution in the form of a physical sensor and a direct measurement gives an unambiguous and simple solution provided that the setup of the sensor itself is robust and the signal processing is chosen such that measuring frequencies, filters etc. match the measuring task [20]. However, it also requires more integration effort as the necessary packaging space has to be made available at the point of interest. A soft sensor solution gives more freedom in choosing where to place the sensor at the cost of an increased modelling effort and more complexity. Additionally, some physical cause effect chains cannot be reversed. The most complex system in Figure 3 is the digital twin which also requires the most modelling effort at the benefit of the greatest freedom in sensor

placement under the prerequisite that the digital twin concept is based on sufficient sensors which facilitate an exchange of real time data [2, 12, 21].

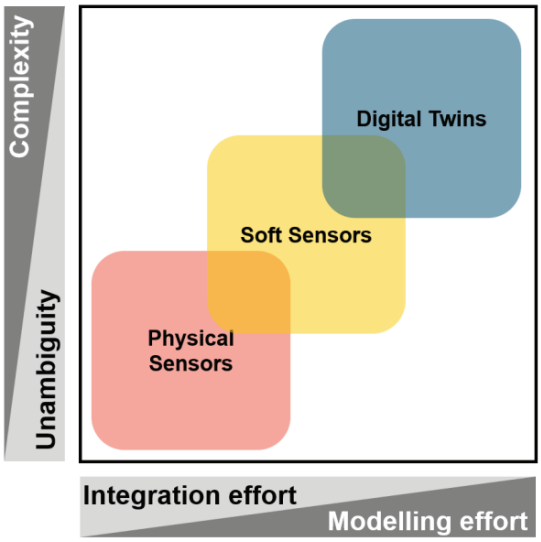

Figure 3: Relationship between physical sensor, soft sensors and digital twins

REFERENCES

[1] Y. Jiang, S. Yin, J. Dong und O. Kaynak, "A Review on Soft Sensors for Monitoring, Control, and Optimization of Industrial Processes," *IEEE Sensors J.*, Jg. 21, Nr. 11, S. 12868–12881, 2021, doi: 10.1109/JSEN.2020.3033153.

[2] M. Fett, E. Turner, R. Breimann und E. Kirchner, "Extension of the system boundary of the Digital Twin onto the sensors of the Physical Twin through the introduction of redundant soft sensors," *Forsch Ingenieurwes*, Jg. 87, Nr. 1, S. 479–488, 2023, doi: 10.1007/s10010-023-00653-y.

[3] K. Fujiwara, M. Kano, S. Hasebe und A. Takinami, "Soft-sensor development using correlation-based just-in-time modeling," *AIChE Journal*, Jg. 55, Nr. 7, S. 1754–1765, 2009, doi: 10.1002/aic.11791.

[4] L. Fortuna, S. Graziani, A. Rizzo und M. G. Xibilia, *Soft Sensors for Monitoring and Control of Industrial Processes*. London: Springer London, 2007.

[5] P. Peniak, K. Rástočný, A. Kanáliková und E. Bubeníková, "Simulation of Virtual Redundant Sensor Models for Safety-Related Applications," *Sensors (Basel, Switzerland)*, Early Access. doi: 10.3390/s22030778.

[6] P. Kadlec, B. Gabrys und S. Strandt, "Data-driven Soft Sensors in the process industry," *Computers & Chemical Engineering*, Jg. 33, Nr. 4, S. 795–814, 2009, doi: 10.1016/j.compchemeng.2008.12.012.

[7] B. Lin, B. Recke, J. K. Knudsen und S. B. Jørgensen, "A systematic approach for soft sensor development," *Computers & Chemical Engineering*, Jg. 31, 5-6, S. 419–425, 2007, doi: 10.1016/j.compchemeng.2006.05.030.

[8] E. Kirchner, G. Martin und S. Vogel, "Sensor Integrating Machine Elements - Key to In-Situ Measurements in Mechanical Engineering," in *Seminario Internacional de Alta Technologia*, Piracicaba, Brasilien, 2018, S. 63–75.
[9] M. Hausmann, L. Häfner und E. Kirchner, "A Procedure Model for the Systematic Sensor Selection and Integration into Technical Systems," *Proc. Des. Soc.*, Jg. 2, S. 445–454, 2022, doi: 10.1017/pds.2022.46.
[10] H. Stachowiak, *Allgemeine Modelltheorie*. Wien, 1973.
[11] H.-M. Heinkel und K. Steinkirchner, "Credible Simulation Process - SET Level Project," 2021. Zugriff am: 1. Januar 2025. [Online]. Verfügbar unter: https://setlevel.de/assets/forschungsergebnisse/Credible-Simulation-Process.pdf
[12] M. Fett, F. Wilking, S. Goetz, E. Kirchner und S. Wartzack, "A Literature Review on the Development and Creation of Digital Twins, Cyber-Physical Systems, and Product-Service Systems," *Sensors (Basel, Switzerland)*, Early Access. doi: 10.3390/s23249786.
[13] M. Fett, F. Wilking, S. Goetz, S. Wartzack und E. Kirchner, "Utilization of RFLP in V-Model methodology for the interdisciplinary development of Digital Twins," *Forsch Ingenieurwes*, Jg. 89, Nr. 1, 2025, doi: 10.1007/s10010-025-00812-3.
[14] R. P. M. Chan, K. A. Stol und C. R. Halkyard, "Review of modelling and control of two-wheeled robots," *Annual Reviews in Control*, Jg. 37, Nr. 1, S. 89–103, 2013, doi: 10.1016/j.arcontrol.2013.03.004.
[15] D. Jones, C. Snider, A. Nassehi, J. Yon und B. Hicks, "Characterising the Digital Twin: A systematic literature review," *CIRP Journal of Manufacturing Science and Technology*, Jg. 29, S. 36–52, 2020, doi: 10.1016/j.cirpj.2020.02.002.
[16] C. Kober, B. N. Algan, M. Fette und J. P. Wulfsberg, "Relations of Digital Twin Fidelity and Benefits: A Design-to-Value Approach," *Procedia CIRP*, Jg. 119, S. 809–815, 2023, doi: 10.1016/j.procir.2023.03.126.
[17] J. Fleischer, B. Klee und Spohrer, Andreas, Merz, Simon, "Leitfaden Sensorik für Industrie 4.0," 2018.
[18] K. Pohl, *Requirements engineering: Fundamentals, principles, and techniques*. Berlin, Heidelberg: Springer, 2010.
[19] B. Kraus, S. Matzke und E. Kirchner, "Utilizing a graph data structure to model physical effects and dependencies between different physical variables for the systematic identification of sensory effects in design elements," in *DS 119: Proceedings of the 33rd Symposium Design for X (DFX2022)*, 22 and Sep. 2022, S. 10, doi: 10.35199/dfx2022.09.
[20] P. Welzbacher, G. Vorwerk-Handing und E. Kirchner, "A CONTROL LIST FOR THE SYSTEMATIC IDENTIFICATION OF DISTURBANCE FACTORS," *Proc. Des. Soc.*, Jg. 1, S. 51–60, 2021, doi: 10.1017/pds.2021.6.
[21] M. Fett, F. Wilking, S. Goetz, E. Kirchner und S. Wartzack, "Sensor selection and integration for Cyber-Physical Systems in context of Digital Twins – A systematic review of requirements," in *2023 18th Annual System of Systems Engineering Conference (SoSe)*, Lille, France, 2023, S. 1–7, doi: 10.1109/SOSE59841.2023.10178669.

XI ECCOMAS Thematic Conference on Smart Structures and Materials - SMART 2025
M. Krommer, M. Nader and M. Schagerl (Eds)

Received: 31 March 2025 / Revised: 28 August 2025 / Accepted: 9 October 2025
© The Author(s) 2025

A Parametric Study on Magnetic Force Effects in Enhancing the Dynamic Response of Vibration Energy Harvester

Kishor Kumar, Amit Tyagi

Abstract

This paper presents an enhanced multi-stable vibration energy harvester (VEH) that integrates a cantilever beam with a tip magnet and three external magnets, operating under the influence of a nonlinear magnetic force. The magnetic force surrounding the harvester tip plays a critical role in influencing the harvester's output response. The magnetic force acting on the beam tip is effectively tuned by carefully selecting key parameters such as the relative gaps between the magnets, the size of the external magnets, and the inclination of the side magnets. This strategic combination of parameter adjustments aims to enhance the power output performance of the multi-stable harvester. The cantilever beam VEH is modelled using Euler-Bernoulli beam theory, and the governing equations of the VEH system are derived through the application of the Euler-Lagrange equations. The nonlinear dynamic behaviour of the VEH system is analysed under low-intensity vibrations of up to 1 g within a low-frequency range (below 22 Hz) using both the method of multiple scales and numerical simulations. The theoretical model is validated through experimental results, which demonstrate that an improved VEH design can be achieved by optimising these parameters. Furthermore, the effects of key parameters such as the relative gap, the volume ratio of external magnets, and the inclination angle of side magnets are comprehensively analysed through experimental studies.

Keywords: Vibration Energy Harvester (VEH), Nonlinear Dynamics, Method of Multiple Scales, Multi-stable.

Nomenclature	
Subscripts h, p, a, b, c,	host beam and piezoelectric beam, magnets A, B, and C
ρ, A, b, h, L	Density, cross-sectional area, width, thickness, length
B_r, $B_{j,a}$, μ_0	Magnetic residual flux density and Magnetic flux density, Permeability of free space
C, ζ, ω_n	Damping coefficient, Damping ratio, Natural frequency of the harvester
C_{11}, Y	Elastic modulus of the piezoelectric and brass beam
$C_p, e_{31}, \varepsilon_{33}$	Capacitance, Coupling constant, and Permittivity constant
M, V, $\vec{\mu}$	Magnetisation vectors, volume of magnets, and Magnetic moment vectors

Kishor Kumar & Amit Tyagi
Department of Mechanical Engineering, Indian Institute of Technology (BHU) Varanasi, India 221005
e-mail: kishorkumar.rs.mec20@itbhu.ac.in

$w(x,t), q(t), v(t)$	Transverse deflection of the harvester beam, Generalised displacement coordinate, Voltage across resistance
R, θ	Load resistance, Coupling coefficient
$\overrightarrow{r_{ab}}, \overrightarrow{r_{ac}}$	Position vectors from magnet A to B and A to C
$r, s, s_1, \theta, \delta$	Vertical distance of magnet C from A, Horizontal distances of magnet B from A, and Horizontal distances of magnet C from A, Slope, inclination angle
$\ddot{y}_b(t)$	Base excitation acceleration

1 INTRODUCTION

Energy harvesting offers a sustainable solution for low-power devices, with vibration energy harvesting (VEH) gaining prominence for converting mechanical vibrations into electricity. Early VEH designs had limited efficiency beyond resonance, leading to innovations like multi-degree-of-freedom systems, frequency up-conversion, magnetic coupling, parametric and internal resonance, and self-tuning mechanisms.

Magnetic coupling is widely utilised in piezoelectric vibration energy harvesters (PVEHs) to modify stiffness and enhance performance. Research has demonstrated that integrating magnetic interactions significantly improves energy harvesting efficiency. Shahruz [1] introduced a magnetic proof mass at the tip of a cantilever beam with nearby attractive permanent magnets, showing that optimal magnetic strength and placement amplify tip vibrations. Repulsive magnetic configurations shift the beam's equilibrium, creating a bi-stable system with two equilibrium points. Stanton et al. [2] confirmed through numerical and experimental studies that bi-stable harvesters with repulsive magnets exhibit an expanded operational frequency range. Similarly, Ferrari et al. [3] demonstrated that coupling a piezoelectric beam converter with permanent magnets enables oscillations between stable states under random vibrations, improving energy harvesting. Al-Ashtari et al. [4] proposed a frequency self-tuning technique, showing that small changes in magnet distance alter the magnetic force, thereby influencing the generated voltage. Cao et al. [5] investigated the nonlinear dynamics of a piezoelectric energy harvester by incorporating external magnets at adjustable angles.

Additional magnets can create multi-stable systems with multiple equilibrium points, allowing harvesters to transition between them under sufficient excitation. Zhou et al. [6] introduced a tri-stable PVEH with three potential wells, demonstrating that tri-stable configurations enable easier snap-through transitions and higher power output over a wider frequency range than bi-stable systems. Leng et al. [7] investigated a tri-stable PVEH under random excitation, using equivalent magnetising current theory to model magnetic forces. Their findings emphasised the importance of optimising system parameters to facilitate large-amplitude inter-well motion, significantly enhancing output voltage. Zhou et al. [8] later introduced a quad-stable PVEH by adjusting three external magnets, showing that this configuration provides a lower threshold energy and a wider frequency bandwidth. Ju et al. [9] extended this concept to a quin-stable PVEH, combining magnetic nonlinearity with mechanical linearity to achieve broadband frequency operation.

Since the magnetic field directly affects the harvester's response, researchers have explored techniques to actively modify it. Chen et al. [10] investigated a bi-stable harvester with a self-decreasing potential barrier, incorporating a spring-magnetic oscillator to regulate magnetic force. Zhang et al. [11] proposed a multi-stable harvester utilising rotatable external magnets to alter potential well characteristics. Yang and Towfighian [12] explored internal resonance by integrating a movable magnet to actively adjust the magnetic field. Mei et al. [13] developed a magnetic-linkage PVEH for effective low-intensity excitation across a wide frequency range using time-varying potential wells. Lan and Qin [14] introduced an additional small magnet between two external magnets, lowering the energy barrier in a bi-stable harvester under random excitation and facilitating snap-through transitions.

The strength of the magnetic field between the tip magnet and external magnets is crucial in determining PVEH output response. Parameters such as the relative spacing, size, and inclination angle of magnets influence field strength. Existing literature has not comprehensively examined their independent effects. This study systematically analyses these parameters to optimise PVEH performance subjected to low-intensity vibrations. Using the Runge-Kutta method and the method of multiple scales, the nonlinear dynamic response of the PVEH is evaluated. Experimental validation confirms the theoretical model and highlights improvements in PVEH efficiency, providing valuable insights for optimising magnetic force parameters in energy harvesting applications.

2 MATHEMATICAL MODELLING OF THE PVEH SYSTEM

The PVEH system consists of a cantilever beam with a piezoelectric patch near its fixed end and a magnetic proof mass (A) at the tip, as shown in Figure 1. Three adjustable external magnets–middle (B) and side (C)–are positioned at varying distances (s, s_1, r) from A. The study analyses how the relative positions, sizes, and orientations of magnets influence performance under low base excitation. Systematic testing across multiple configurations evaluates their combined impact on the harvester's output response.

The cantilever beam harvester is modelled using Euler-Bernoulli beam theory, with governing dynamic equations derived via Euler-Lagrange equations. The simplified electromechanical equations for the PVEH system, as derived in the author's previous work [15], are expressed as follows:

$$M\,\ddot{q}(t) + C\,\dot{q}(t) + K_1 q(t) + K_3 q^{\,3}(t) + K_5 q^{\,5}(t) + \theta\,V(t) + K_{12} q^{\,2}(t)\,V(t) + F_m = -m\,\ddot{y}_b(t) \tag{1}$$

$$\theta \dot{q}(t) + K_{12} q^{\,2}(t)\dot{q}(t) + \frac{V(t)}{R} + C_p\,\dot{V}(t) = 0 \tag{2}$$

M, *C* are equivalent mass and damping, and *K* represents the stiffness coefficient. The presence of nonlinear stiffness terms indicates that nonlinear strain effects are taken into account. The parameters K_{12} and θ characterise the electromechanical coupling within the system equations. The displacement and voltage output are represented by *q(t)* and *V(t)* respectively. C_p, *R* represent the capacitance of the piezoelectric material and resistive load whereas $\ddot{y}_b$ indicates the base excitation.

The magnetic potential energy and the nonlinear repulsive magnetic force F_m due to the interaction of permanent magnets are modelled using the point dipole approach [8], [14], [16].

The magnetic moment vectors for magnets A, B, and C are given in Eq. (1):

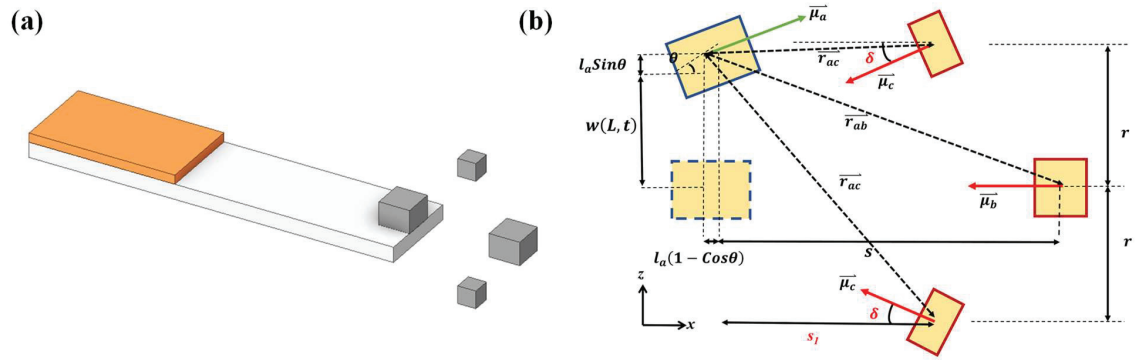

Figure 1: a The PVEH system with additional magnets in geometric configuration, **b** various design configurations of the tip magnet and external magnets

$$\left.\begin{array}{c}\overrightarrow{\mu_a} = \{M_a V_a\, cos\theta,\ M_a V_a\, sin\theta\} \\ \overrightarrow{\mu_b} = \{-M_b V_b\ , 0\} \\ \overrightarrow{\mu_c} = \{-M_c V_c\, cos\delta, -M_c V_c \sin(-\delta)\}\end{array}\right\} \tag{3}$$

The position vectors given by $\overrightarrow{r_{ab}}$ and $\overrightarrow{r_{ac}}$, are expressed as:

$$\overrightarrow{r_{ab}} = \{-s - l_a(1 - cos\theta), w(L,t) + l_a sin\theta\ \}$$

$$\overrightarrow{r_{ac}} = \{-s_1 - l_a(1 - cos\theta), w(L,t) + l_a sin\theta \pm r\} \tag{4}$$

The positive and negative signs indicate the position of side magnets C relative to magnet A. Slope is obtained as follows: $\theta = w'(L,t)$. Magnetisation vector M for the magnets is calculated by dividing the magnetic residual flux density, B_r, by the permeability of free space, μ_0, as: $M = \frac{B_r}{\mu_0}$. The magnetic flux density generated by middle magnet B and side magnets C on magnet A is given by:

$$\overrightarrow{B_{J,a}} = \sum_{j=b,c} -\frac{\mu_0}{4\pi} \nabla \frac{\overrightarrow{\mu_J}.\overrightarrow{r_{a,J}}}{\|\overrightarrow{r_{a,J}}\|_2^3} \tag{5}$$

The magnetic potential energy, U_m, of the specified magnetic configuration is expressed as follows:

$$U_m = \sum_{j=b,c}(-\overrightarrow{B_{J,a}}\,\overrightarrow{\mu_a}) \tag{6}$$

The total magnetic force $\overrightarrow{F_m}$ can be calculated as follows:

$$\overrightarrow{F_m} = -\nabla(U_m) = \sum_{j=b,c} -\frac{\mu_0}{4\pi} \nabla \left(\frac{\overrightarrow{\mu_j}}{\|\overrightarrow{r_{a,j}}\|_2^3} - \frac{3\,\overrightarrow{r_{a,j}}}{\|\overrightarrow{r_{a,j}}\|_2^5} (\overrightarrow{\mu_j}.\overrightarrow{r_{a,j}}) \right) \overrightarrow{\mu_a} \tag{7}$$

The total vertical magnetic force due to all additional magnets on the tip magnet, $F_{m,}$ is approximated by a polynomial expression.

$$F_m = \sum_n K_{nf} q^{\,n}(t) \tag{8}$$

Where n = 1, 3, 5, 7, 9, and 11. The nonlinear magnetic force F_m is substituted in Eq. (1) to obtain the simplified model. The response of the dynamic system exhibiting nonlinearities can be obtained using the analytical approximate method of multiple scales (MMS). The system is defined by the following simplified equations with the introduction of ϵ as a book-keeping parameter.

$$\ddot{q}(t) + \omega_n^2\, q(t) + \epsilon(2\,\omega_n\,\zeta\ \dot{q}(t) + k_3 q^{\,3}(t) + k_5 q^{\,5}(t) + \theta_1\, V(t) + k_{12} q^{\,2}(t)\, V(t) + k_7 q^{\,7}(t) + k_9 q^{\,9}(t) + k_{11} q^{\,11}(t)) + (m/M)\ddot{y}_b(t) = 0$$

$$C_p\, \dot{V}(t) + \frac{V(t)}{R} + (\theta \dot{q}(t) + K_{12} q^{\,2}(t)\dot{q}(t)) = 0 \tag{9}$$

The time scale dependence of the solution is defined to keep the expansion uniformly valid up to O (ϵ^{-j}) as $T_j = \epsilon^j t$. Two-term approximation of the response solution and the time derivatives obtained are given using the following expressions:

$$q(t) = q_0(T_0, T_1) + \epsilon\, q_1(T_0, T_1)$$

$$V(t) = V_0(T_0, T_1) + \epsilon\, V_1(T_0, T_1) \tag{10}$$

$$\frac{d}{dt} = \frac{dT_0}{dt}\frac{\partial}{\partial T_0} + \frac{dT_1}{dt}\frac{\partial}{\partial T_1} + \cdots = D_0 + \epsilon\, D_1 + O(\epsilon^2)$$

$$\frac{d^2}{dt^2} = \frac{d^2}{{dT_0}^2} + 2\,\epsilon \frac{d^2}{\partial T_0 \partial T_1} + \cdots = D_0^2 + 2\,\epsilon\, D_0\, D_1 + O(\epsilon^2) \tag{11}$$

After substituting the solutions from Eq. (10) in Eq. (9) and collecting the coefficients of ϵ, the following equations are obtained.

O (ϵ^0):

$$\frac{\partial^2 q_0}{\partial T_0^2} + \omega_n^2\, q_0 = 0$$

$$C_p \frac{\partial V_0}{\partial T_0} + \frac{V_0}{R} = -(\theta \dot{q_0} + K_{12} q_0^2 \dot{q_0}) \tag{12}$$

O (ϵ^1):

$$\frac{\partial^2 q_1}{\partial T_0^2} + \omega_n^2\, q_1 = 2\zeta\omega_n \frac{\partial q_0}{\partial T_0} + k_3 q_0^3 + k_5 q_0^5 + k_7 q_0^7 + k_9 q_0^9 + k_{11} q_0^{11} + k_{12} q_0^2 V_0 + 2\frac{\partial^2 q_0}{\partial T_0 \partial T_1} + \theta_1 V_0 + f \tag{13}$$

$$C_p \frac{\partial V_1}{\partial T_0} + \frac{V_1}{R} = C_p \frac{\partial V_0}{\partial T_1} + 2K_{12} \frac{\partial q_0}{\partial T_0} q_0 q_1 + K_{12} \frac{\partial q_0}{\partial T_1} {q_0}^2 + K_{12} {q_0}^2 \frac{\partial q_1}{\partial T_0} + \theta \frac{\partial q_0}{\partial T_1} + \theta \frac{\partial q_1}{\partial T_0} \tag{14}$$

The solution of zero-order perturbation given in Eq. (12) can be written as:

$$q_0 = A(T_1) e^{iT_0\omega_n} + \bar{A}(T_1) e^{-iT_0\omega_n} \tag{15}$$

$$V_0 = -\frac{e^{iT_0\omega_n} R\theta\, A(T_1)\omega_n}{-i + RC_p\omega_n} - \frac{e^{3iT_0\omega_n} R\, K_{12} A^3(T_1)\omega_n}{-i + 3RC_p\omega_n} - \frac{e^{iT_0\omega_n} RK_{12} A^2(T_1)\omega_n\, \bar{A}(T_1)}{-i + RC_p\omega_n} + e^{-\frac{T_0}{RC_p}} + cc \tag{16}$$

$$\omega = \omega_n + \epsilon\sigma$$

Where cc represents the complex conjugate of preceding terms and σ represents the detuning parameter. The solutions obtained in Eq. (15) are substituted in Eq. (13) for the solution of the first order. To obtain the bounded solution, the resulting secular terms are eliminated by setting the

coefficient of $e^{-iT_0\omega_n}$ to zero. The solution of amplitude, $A(T_1)$, is obtained by expressing it in polar form as:

$$A(T_1) = \frac{1}{2}a(T_1)e^{i\phi_1(T_1)}$$

$$\bar{A}(T_1) = \frac{1}{2}a(T_1)e^{-i\phi_1(T_1)} \tag{17}$$

Here $a(T_1)$ and $\phi_1(T_1)$ represent the amplitude and phase. To obtain the solution, the real and imaginary parts of the equations are set to zero. Further simplification of these equations is done by rearranging the terms.

$$\frac{1}{2}f\,cos(\gamma(T_1)) + a(T_1)H_7 + a(T_1)^3H_8 + a(T_1)^5H_9 = \omega_n\frac{\partial a(T_1)}{\partial T_1} \tag{18}$$

$$\frac{1}{2}f\,sin\big(\gamma(T_1)\big) + H_1a(T_1) - a(T_1)\omega_n\sigma + a(T_1)^3H_2 + a(T_1)^5H_3 + a(T_1)^7H_4 + H_5a(T_1)^9 + a(T_1)^{11}H_6 = -a(T_1)\omega_n\frac{\partial\gamma(T_1)}{\partial T_1} \tag{19}$$

Where:

$\gamma(T_1) = T_1\sigma - \phi_1(T_1)$, $G_1 = \frac{R}{R^2C_p^2\omega_n^2+1}$, $G_2 = \frac{R}{9R^2C_p^2\omega_n^2+1}$, $H_1 = -\frac{1}{2}\big(G_1\theta\theta_1RC_p\omega_n^2\big)$,

$H_2 = (-\frac{G_1R\theta C_pk_{12}\omega_n^2}{4} + \frac{3}{8}k_3 - \frac{G_1RC_pK_{12}\theta_1\omega_n^2}{8})$, $H_3 = (-\frac{G_1RC_pk_{12}K_{12}\omega_n^2}{16} + \frac{5}{16}k_5 - \frac{3G_2RC_pk_{12}K_{12}\omega_n^2}{32})$, $H_4 = \frac{35}{128}k_7$,

$H_5 = \frac{63k_9}{256}$, $H_6 = \frac{231k_{11}}{1024}$, $H_7 = (-\zeta\omega_n^2 + \frac{1}{2}G_1\theta\theta_1\omega_n)$, $H_8 = \frac{1}{4}G_1\theta k_{12}\omega_n + \frac{1}{8}G_1\theta_1K_{12}\omega_n$,

$H_9 = \frac{1}{16}G_1k_{12}K_{12}\omega_n + \frac{1}{32}G_2k_{12}K_{12}\omega_n$.

To obtain the steady state solution, the terms in Eqs. (18) and (19) are squared and added, then the derivatives of amplitude and phase with respect to time are set to zero, $\frac{\partial a(T_1)}{\partial T_1} = \frac{\partial\gamma(T_1)}{\partial T_1} = 0$. The resulting equation is a polynomial equation of order 11 in a and order 2 in σ.

$$(aH_1 + a^3H_2 + a^5H_3 + a^7H_4 + a^9H_5 + a^{11}H_6 - a\omega_n(\sigma))^2 + (aH_7 + a^3H_8 + a^5H_9)^2 = \frac{1}{2}f^2 \tag{20}$$

The solution of the above equation provides the amplitude and phase of the response solution. To get the stability analysis of the PVEH system, the Jacobian matrix is calculated as follows:

$$J(a,\sigma) = \begin{bmatrix} \frac{H_7+3a^2H_8+5a^4H_9}{\omega_n} & \frac{aH_1+a^3H_2+a^5H_3+a^7H_4+a^9H_5+a^{11}H_6-a\sigma\omega_n}{\omega_n} \\ -\frac{H_1+3a^2H_2+5a^4H_3+7a^6H_4+9a^8H_5+11a^{10}H_6-\sigma\omega_n}{a\omega_n} & \frac{aH_7+a^3H_8+a^5H_9}{a\omega_n} \end{bmatrix} \tag{21}$$

The Jacobian matrix's eigenvalues determine PVEH system stability and bifurcations. The solution is stable if all eigenvalues have negative real parts and unstable if any have a positive real part. These conditions are crucial for analysing bifurcations, where parameter changes alter system response qualitatively. The steady state solution amplitude and voltage can be calculated using Eqs. (15) and (16).

3 THEORETICAL INVESTIGATIONS

Theoretical analysis examines the total potential energy and magnetic force to assess the impact of different geometric configurations. The material properties of the harvester system are listed in Table 1.

Table 1: Material Properties

Parameter	Value
Brass beam properties	
L x b_h x h_h (mm^3)	130 x 20 x 0.5
Elastic modulus of brass beam Y (GPa)	100
Density of brass beam ρ_h (Kg/m^3)	8570
MFC properties	
L_p x b_p x h_p (mm^3)	28 x 14 x 0.3
Elastic modulus C_{11} (GPa)	30.336
Density of MFC beam ρ_p (Kg/m^3)	5440
Coupling constant e_{31} (C/m^2)	-5.16
Permittivity constant ϵ_{33} (F/m)	9.18×10^{-8}
Magnetic properties	
Tip mass M_{tip} (grams)	7.474
Residual magnetic flux density B_r (T)	1.25
Permeability of free space μ_0 (H/m)	$4\pi \times 10^{-7}$

Figure 2 illustrates the potential energy landscape and corresponding magnetic force variations for different system configurations. The first and third rows depict the potential energy distribution, while the second and fourth rows represent the associated nonlinear magnetic force. Figures 2a and 2b analyse the effect of horizontal distance s in the presence of a single middle magnet, V_b = 1000 mm^3. As s decreases from 25 mm to 15 mm, the nonlinear magnetic force intensifies, reaching up to 5 N, strengthening bi-stability. However, this increased force makes inter-well transitions more difficult, requiring higher excitation. Figures 2c and 2d examine the effect of horizontal distances s and s_1 when three external magnets, $V_b = V_c$ = 1000 mm^3, symmetrically surround the tip magnet. As these distances decrease, additional potential wells emerge, and existing wells deepen, with magnetic force reaching approximately 5 N. Figures 2e and 2f investigate the impact of vertical distance r. Reducing r alters the potential well depth and weakens the magnetic force, which remains within 2 N. Figures 2g and 2h investigate the effect of the horizontal distance of side magnets s_1. Decreasing this distance leads to the formation of multiple potential wells, with deeper outer wells at higher potential energy and shallower inner wells at lower potential energy. The magnetic force exhibits weaker nonlinearity at lower amplitudes but becomes strongly nonlinear at higher amplitudes, reaching up to 5 N. Figures 2i and 2j explore the effect of side magnet size. With the middle magnet volume fixed at 648 mm³, increasing side magnet volume from 50 mm³ to 1800 mm³ transitions the system from bi-stable to quad-stable, increasing potential well depth and magnetic force up to 5 N. Figures 2k and 2l assess inclination angle effects while $V_b = V_c$ = 1000 mm^3. Adjusting the angle reshapes potential wells, transitioning the system between bi-stable and multi-stable states. The magnetic force remains below 4 N.

Overall, Figure 2 highlights the crucial role of geometric parameters in shaping energy landscapes and nonlinear interactions, emphasising the importance of tuning these parameters to optimise energy harvesting performance.

Figure 3 presents the potential energy and corresponding magnetic force as a function of amplitude for three different configurations of the PVEH system. The left column shows the potential energy, while the right column illustrates the magnetic force with respect to amplitude.

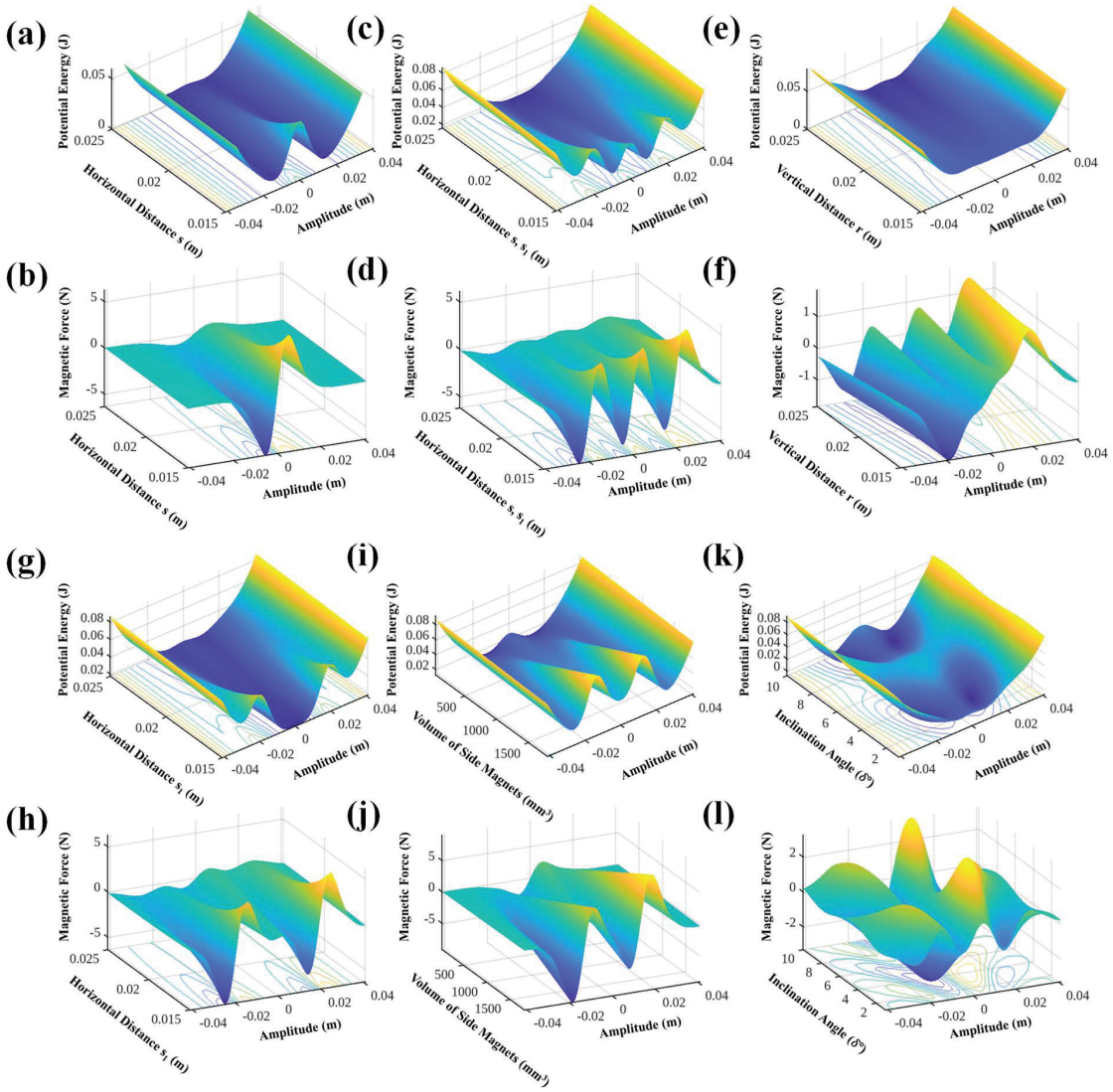

Figure 2: Potential energy and magnetic force with respect to amplitude for configurations **a** bi-stable **c** r = 22 mm **e** s = s_1 = 22 mm **g** s = 22 and r = 22 mm **i** s = 17, r = 15, s_1 = 16 mm, and V_b = 648 mm^3 **k** s = 21, r = 18, and s_1 = 21 mm **b**, **d**, **f**, **h**, **j**, **l** corresponding magnetic force respectively

Figure 3a shows the potential energy profile exhibits a quad-stable behaviour with multiple wells, indicating that the system can operate under multi-stable conditions for configurations s = s_1 = 15

mm and r = 22 mm. The corresponding magnetic force shows an alternating pattern, which suggests strong nonlinear interactions between the magnets. The presence of multiple potential wells allows for large tip displacements under dynamic excitation, which can enhance power generation under sufficient excitation. Figure 3b illustrates that the potential energy profile is relatively shallow and symmetric, suggesting a system with reduced nonlinearity and limited multi-stable behaviour for configurations $s = s_1 = 22$ mm and r = 15 mm. The magnetic force exhibits a smoother variation with amplitude, implying a weaker magnetic influence. Figure 3c indicates the potential energy profile is characterised by a bi-stable nature, with two dominant wells for configurations $s = s_1 = 22$ mm and r = 22 mm. The magnetic force varies gradually, maintaining a moderate level of nonlinearity.

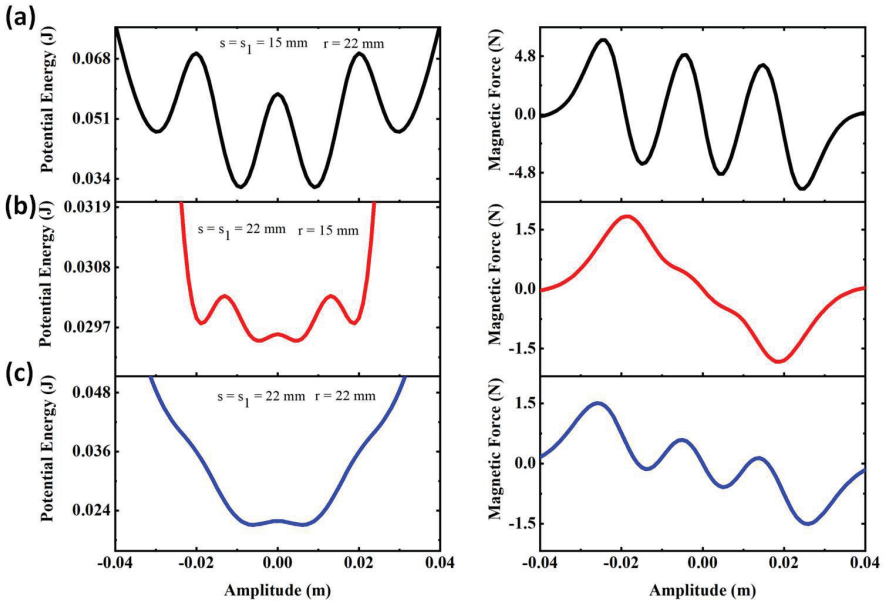

Figure 3: Potential energy function and magnetic force under different configuration types

Nonlinear magnetic interactions play a crucial role in shaping the potential energy landscape and influencing the harvester's performance. For maximising energy harvesting performance, configurations with shallower and multiple potential wells are preferred. These conditions allow the harvester to transition between states efficiently, utilising nonlinear dynamic effects to generate higher power output.

Figure 4 presents the nonlinear frequency response of the system, comparing theoretical predictions with experimental results under 5 m/s² excitation. The plots show tip displacement amplitude versus excitation frequency, demonstrating multi-stable behaviour. The black solid line represents the stable solution branch, while the red dashed line indicates the unstable branch, separated by a saddle-node (SN) bifurcation. Blue dots denote experimental data, highlighting real-world nonlinear effects. Quantitative deviations arise from factors such as structural damping, fabrication imperfections, and environmental noise. The observed jump phenomena, characteristic of nonlinear systems, facilitate inter-well motion, enhancing tip displacement and improving power output. The results confirm that tuning system parameters significantly impact stability, response amplitude, and overall energy harvesting efficiency.

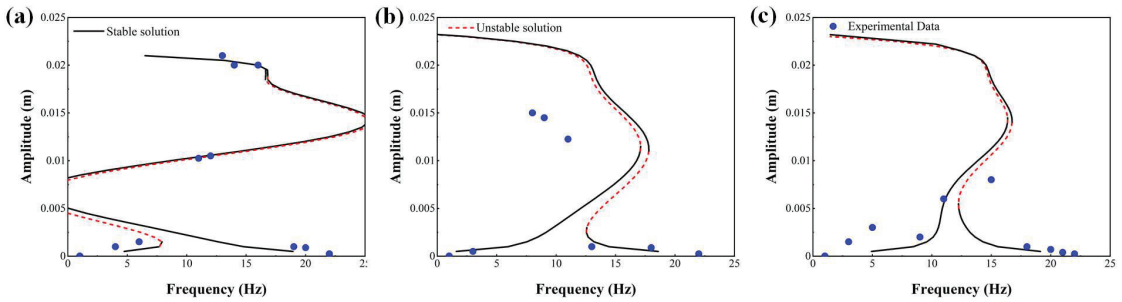

Figure 4: Amplitude vs frequency results obtained by MMS and experimental data for configuration **a** s = s_1 = 15 mm and r = 22 mm, **b** s = s_1 = 22 mm and r = 15 mm, **c** s = s_1 = 22 mm and r = 22 mm

4 EXPERIMENTAL INVESTIGATIONS

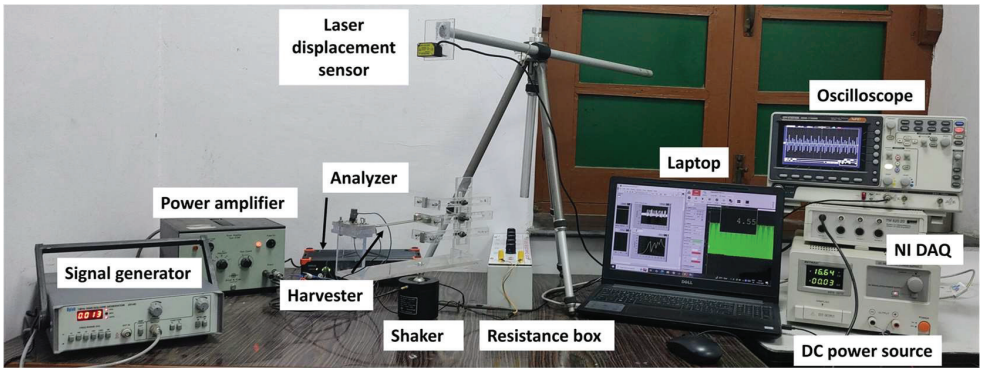

Figure 5: Experimental setup for PVEH

The experimental setup is designed to analyse the output response of a piezoelectric vibration energy harvester (PVEH) system, Figure 5. A signal generator produces an excitation signal, which is amplified using a power amplifier and fed to a shaker that induces controlled vibrations in the harvester. The harvester converts mechanical vibrations into electrical energy, and its response is analysed using multiple instruments. A laser displacement sensor measures the tip displacement, while an oscilloscope captures the voltage output. A resistance box provides a variable resistive load to study power output under different conditions. The NI DAQ collects and transfers experimental data to a laptop, where real-time visualisation and analysis are performed.

5 RESULTS AND DISCUSSION

Figure 6 presents the power output, time response, and phase portraits of the PVEH system under different magnet configurations. The first column shows power output (in mW) as a function of excitation frequency (Hz) for various horizontal (s, s_1) and vertical (r) distances under a 400 kΩ external load. The results indicate that smaller horizontal distances enhance magnetic coupling, leading to higher power generation. The configuration s = s_1=15 mm achieves the highest power (~0.27 mW) around 15–18 Hz for r=22 mm. Increasing s and s_1 (to 18 mm, 22 mm, and 25 mm) reduces peak power but broadens the frequency response. The optimal configuration for r=18 mm (s= s_1 =22 mm) produces the highest peak power (~0.30 mW) near 12–15 Hz. Lower values of r shift resonance to lower frequencies (~10 Hz), emphasising the role of magnetic interactions in

tuning response. The configuration s_1 =25 mm with s=r=22 mm achieves the highest power (~0.27 mW) at 15 Hz, outperforming other setups.

The second and third columns present the experimental time response and phase portraits compared with mathematical simulations. The time response for s = s_1=15 mm, r=22 mm (Figure 6b) exhibits an initial oscillatory motion followed by chaotic behaviour, confirmed by the quad-stable trajectories in Figure 6c. Figure 6e shows intra-well oscillations for s = s_1 = 22 mm, r = 15 mm, indicating higher excitation requirements for inter-well transitions. The phase portrait (Figure 6f) reveals double-well oscillations in shallow wells. Figure 6h exhibits more stable oscillations for s = s_1 =22 mm, r=22 mm, with phase confinement to a single well, indicative of a bi-stable response.

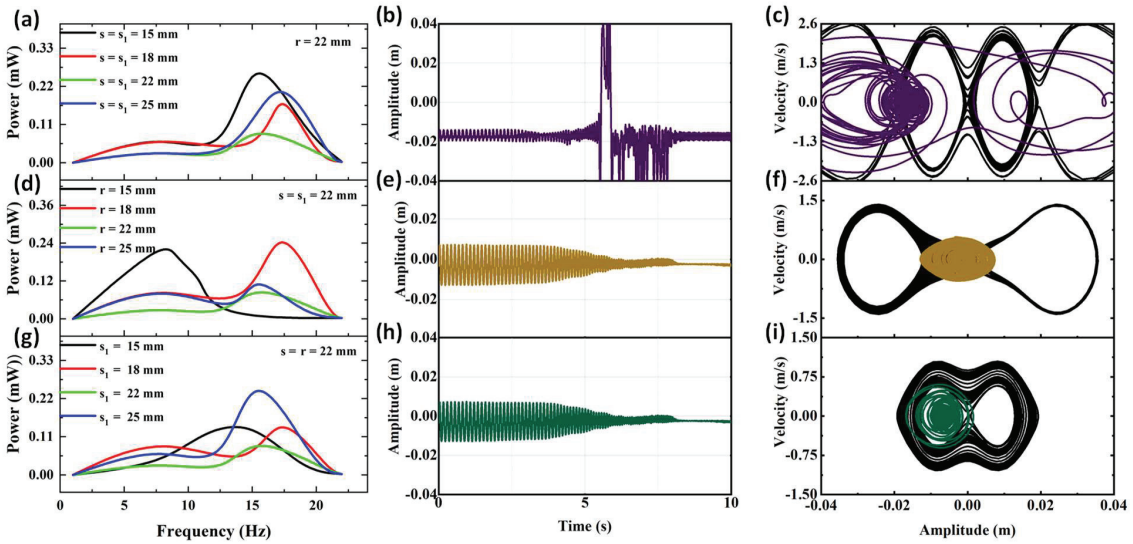

Figure 6: a Power vs frequency, **b** displacement amplitude vs time, **c** phase portraits

Overall, Figure 6 captures quad-stable and bi-stable regimes depending on system parameters, highlighting the nonlinear characteristics of the harvester. Reducing the horizontal distance (s, s_1) enhances peak power output but limits operational frequency range. Optimising vertical distance achieves maximum power. A combination of smaller horizontal distances 's', moderate vertical spacing 'r', and larger horizontal distance 's_1' provides the most efficient energy harvesting configuration.

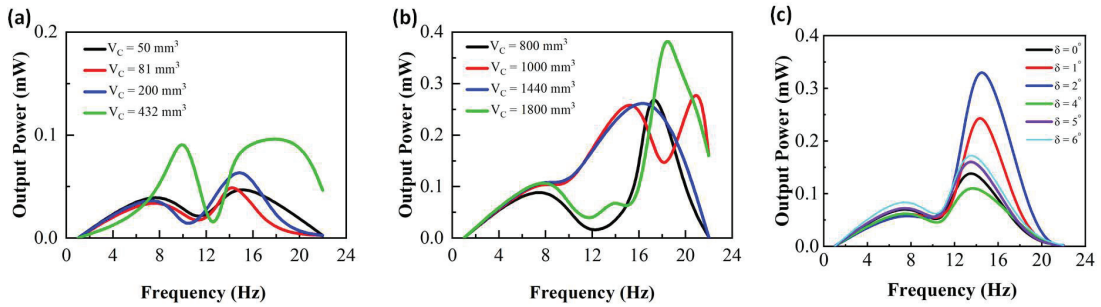

Figure 7: a and **b** Power vs frequency under for a different size of external magnets for relative position s = 17, r = 15, and s_1 = 16 mm and V_b =648 mm³ **c** under different inclination angle for relative position s = 21, r = 18, and s_1 = 21 mm and $V_b = V_c$ = 1000 mm³

Figure 7 illustrates the effect of magnet volume and side magnet inclination on the harvester's output under an upward frequency sweep with a 400 kΩ load. The setup includes a middle magnet at 17 mm (horizontal) and side magnets at 15 mm (vertical) and 16 mm (horizontal). Figure 7a presents power output when side magnets are smaller than the middle magnet (V_b =648 mm³), while Figure 7b shows results for larger side magnets. With smaller side magnets, both frequency response peaks remain nearly equal. However, larger side magnets significantly amplify the secondary peak, enhancing overall performance. Figure 7c examines the effect of inclination angle with the middle magnet at 21 mm (horizontal) and the side magnets at 18 mm (vertical) and 21 mm (horizontal). Increasing the inclination from 0° broadens the frequency range, with the secondary peak (~15 Hz) becoming more pronounced while the primary peak (~8 Hz) remains weaker. The optimal inclination (2°) yields peak power exceeding 0.3 mW between 13–19 Hz. Beyond this, power output initially decreases before increasing again, aligning with potential energy trends where magnet orientation cyclically affects potential well formation.

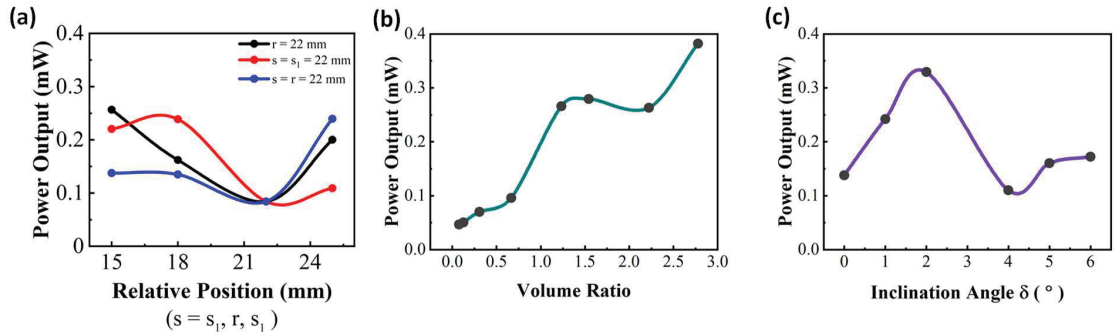

Figure 8: power output vs: **a** relative position **b** volume ratio **c** inclination angle

Figure 8 presents the influence of relative positions (s, r, and s_1), magnet volume ratio (side magnet volume/ middle magnet volume), and inclination angle on the power output of the PVEH system under a 400 kΩ load. Figure 8a shows power output variations for three configuration cases: (i) for r=22 mm (black curve), (ii) for s = s_1 = 22 mm (red curve), and (iii) for s = r =22 mm (blue curve) where the relative position represents the horizontal distances (s = s_1), vertical distance (r), and horizontal distance of side magnets (s_1) respectively. Initially, at 15 mm, all configurations achieve relatively high power, with the r = 22 mm configuration reaching ~0.25 mW. As the

relative position increases toward 21 mm, power output declines to ~0.1 mW for all configurations. Beyond 21 mm, power output rises again. This trend highlights the critical role of magnet positioning in optimising energy harvesting efficiency. Figure 8b explores peak power output as a function of magnet volume ratio for a fixed relative position (s=17 mm, r=15 mm, s_1=16 mm). As the volume ratio increases, peak power also rises. When the ratio exceeds 1, power jumps beyond 0.25 mW and continues increasing, approaching 0.4 mW. Figure 8c examines the effect of inclination angle on peak power for a different relative position (s=21 mm, r=18 mm, s_1 =18 mm). Power initially increases with inclination, reaches a peak, then declines before rising again. This cyclical trend aligns with potential energy variations, demonstrating how inclination influences energy well formation and harvesting performance.

7 CONCLUSIONS

The analysis confirms that magnet positioning, volume ratio, and inclination angle are critical parameters influencing the power output of the PVEH system. Optimal relative placement of magnets enhances energy transfer and improves overall harvesting performance. Similarly, increasing the side-to-middle magnet volume ratio significantly boosts peak power, exceeding 0.25 mW, while appropriate inclination angles further optimise efficiency by reshaping the potential wells.

In conclusion, the findings emphasise the importance of parameter tuning in optimising the harvester's response for improved energy harvesting.

REFERENCES

[1] S. M. Shahruz, "Increasing the efficiency of energy scavengers by magnets," *Journal of Computational and Nonlinear Dynamics*, vol. 3, no. 4, Oct. 2008.

[2] S. C. Stanton, C. C. McGehee, and B. P. Mann, "Nonlinear dynamics for broadband energy harvesting: Investigation of a bistable piezoelectric inertial generator," *Physica D: Nonlinear Phenomena*, vol. 239, no. 10, pp. 640–653, May 2010.

[3] M. Ferrari, V. Ferrari, M. Guizzetti, B. Andò, S. Baglio, and C. Trigona, "Improved energy harvesting from wideband vibrations by nonlinear piezoelectric converters," *Sensors and Actuators, A: Physical*, vol. 162, no. 2, pp. 425–431, 2010.

[4] W. Al-Ashtari, M. Hunstig, T. Hemsel, and W. Sextro, "Frequency tuning of piezoelectric energy harvesters by magnetic force," *Smart Materials and Structures*, vol. 21, no. 3, Mar. 2012.

[5] J. Cao, S. Zhou, D. J. Inman, and J. Lin, "Nonlinear dynamic characteristics of variable inclination magnetically coupled piezoelectric energy harvesters," *Journal of Vibration and Acoustics*, vol. 137, no. 2, 2015.

[6] S. Zhou, J. Cao, D. J. Inman, J. Lin, S. Liu, and Z. Wang, "Broadband tristable energy harvester: Modeling and experiment verification," *Applied Energy*, vol. 133, pp. 33–39, Nov. 2014.

[7] Y. Leng, D. Tan, J. Liu, Y. Zhang, and S. Fan, "Magnetic force analysis and performance of a tri-stable piezoelectric energy harvester under random excitation," *Journal of Sound and Vibration*, vol. 406, pp. 146–160, Oct. 2017.

[8] Z. Zhou, W. Qin, and P. Zhu, "A broadband quad-stable energy harvester and its advantages over bi-stable harvester: Simulation and experiment verification," *Mechanical Systems and Signal Processing*, vol. 84, pp. 158–168, Feb. 2017.

[9] Y. Ju, Y. Li, J. Tan, Z. Zhao, and G. Wang, "Transition mechanism and dynamic behaviors of a multi-stable

piezoelectric energy harvester with magnetic interaction," *Journal of Sound and Vibration*, vol. 501, Jun. 2021.

[10] L. Chen, X. Liao, B. Sun, N. Zhang, and J. Wu, "A numerical-experimental dynamic analysis of high-efficiency and broadband bistable energy harvester with self-decreasing potential barrier effect," *Applied Energy*, vol. 317, Jul. 2022.

[11] Y. Zhang, J. Cao, W. Wang, and W. H. Liao, "Enhanced modeling of nonlinear restoring force in multi-stable energy harvesters," *Journal of Sound and Vibration*, vol. 494, Mar. 2021.

[12] W. Yang and S. Towfighian, "Internal resonance and low frequency vibration energy harvesting," *Smart Materials and Structures*, vol. 26, no. 9, Aug. 2017.

[13] X. Mei *et al.*, "Magnetic-linkage nonlinear piezoelectric energy harvester with time-varying potential wells: Theoretical and experimental investigations," *Mechanical Systems and Signal Processing*, vol. 208, no. November 2023, p. 110998, 2024.

[14] C. Lan and W. Qin, "Enhancing ability of harvesting energy from random vibration by decreasing the potential barrier of bistable harvester," *Mechanical Systems and Signal Processing*, vol. 85, pp. 71–81, Feb. 2017.

[15] K. Kumar and A. Tyagi, "Enhancing the Performance of Piezoelectric Vibration Energy Harvester Through Adjustments in the Geometric Configuration and the Volume of Additional Magnets," *Journal of Vibration Engineering & Technologies*, vol. 6, 2025.

[16] Y. Fan, M. H. Ghayesh, and T. F. Lu, "A broadband magnetically coupled bistable energy harvester via parametric excitation," *Energy Conversion and Management*, vol. 244, Sep. 2021.

XI ECCOMAS Thematic Conference on Smart Structures and Materials - SMART 2025
M. Krommer, M. Nader and M. Schagerl (Eds)

Received: 9 April 2025 / Revised: 15 August 2025 / Accepted: 9 October 2025
© The Author(s) 2025

Numerical Study of the Impact of Manufacturing Deviations on the Performance of a Bi-directional Piezoelectric Motor

Paul Marter, Sascha Eisenträger, Ryan Orszulik, Daniel Juhre

Abstract. Piezoelectric transducers are widely used as actuators due to their high precision, fast response time, and cost-effectiveness. Their advantageous scaling properties make them particularly well-suited for mesoscale applications, bridging the gap between micro-electromechanical systems and large-scale systems. An example of such a mesoscale application is the standing wave planar piezoelectric motor, which consists of a stator with attached piezoelectric transducers, a rotor, and a flat spring, as analyzed in this study. Utilizing the inverse piezoelectric effect, rotational motion is achieved through the frictional contact between the rotor and the three unimorph arms of the stator. For this design, bi-directionality was shown experimentally and numerically depending on the excitation frequency. However, especially in small-scale applications and prototype development, manufacturing deviations caused by manual processes become a serious problem leading to significant changes in the motor characteristics. Here, the finite element method plays an important role in the early stages of the design development process, helping to identify the potential impact of manufacturing deviations on motor performance. Therefore, this study presents a transient numerical model to analyze the motor behavior based on both the undeformed and a uniformly deformed stator geometry. The numerical results are compared with experimental findings, demonstrating that the experimental outcomes can be accurately replicated using the developed numerical motor model.

Key words: piezoelectricity, standing wave motor, finite elements, manufacturing deviations

1 INTRODUCTION

In recent years, practical fabrication and actuation techniques have been developed for large-scale robotic systems utilizing electromagnetic motors and for microscale applications, such

Paul Marter & Sascha Eisenträger & Daniel Juhre
Institute of Materials, Technologies and Mechanics, Otto von Guericke University Magdeburg Universitätsplatz 2, 39106 Magdeburg, Germany, e-mail: paul.marter@ovgu.de

Ryan Orszulik
Lassonde School of Engineering, York University Toronto 4700 Keele Street, Toronto, M3J 1P3, Canada

as micro-electromechanical systems (MEMS), which typically rely on electrostatic actuators. However, the mesoscale at an intermediate size between the micro and macro scale continues to present challenges, as direct adaptations of approaches developed for other length-scales are not always feasible [1]. First, electromagnetic motors are subject to physical scaling effects, primarily governed by the surface-area-to-volume ratio. This ratio influences friction, current density, and heat dissipation, ultimately reducing performance. As a result, designing electromagnetic motors that weigh only a few grams and measure just a few millimeters remains a significant challenge [2]. Second, scaling MEMS technology to centimeter-sized systems while maintaining high energy densities presents additional difficulties. Such scaling demands strong electrostatic fields, requiring extremely high voltage inputs or narrow gaps to work effectively. Piezoelectric material-based actuators are highly suitable at the mesoscale due to their advantageous scaling properties. While they produce limited overall displacements, they offer wide bandwidth, minimal internal friction, and exceptional power density. These characteristics enable rapid and precise motion, making them a compelling choice for various applications [3].

Depending on the application area, different types of piezoelectric motors exist, which can be classified in various ways, typically categorized into quasi-static and resonant types based on the employed dynamics [4, 5]. Resonant-type motors are the most extensively researched actuators in the literature. Furthermore, this motor class can be divided into standing and traveling wave motor designs. Traveling wave motors use multiple driving sources to generate a traveling wave, resulting in elliptical trajectories on the stator surface, which transfer motion via friction. In contrast, standing wave motors rely on single or multiple mode excitations with angled contact points, requiring only a single low-frequency drive source for high torque generation [6].

This paper investigates a planar design of a standing wave-type piezoelectric motor planned to be employed as an actuator for single-gimbal control moment gyroscopes in pico to femto satellites, for example, as shown in [7] for larger satellite applications. The cost-efficient design is created by fabricating the individual components from sheet metal using laser micromachining. Figure 1 depicts the motor's components and structure based on a design proposed by Suzuki et al. [8]. These components include the stator with three arms, the rotor, and the flatspring, all aligned on a fixed shaft. The flatspring limits the rotor's vertical movement by maintaining a particular contact pressure between it and the rotor. A piezoelectric patch is bonded to each arm of the stator to create a unimorph. Utilizing the inverse piezoelectric effect, each stator arm functions as a unimorph bending actuator by applying a voltage. The generated bending motion of the arms leads to contact between the stator and the rotor, which results in the targeted rotational motion of the motor, induced by friction and through the relative tangential movement of the stator and rotor.

Bidirectionality is a pivotal criterion to ensure the broadest possible range of motor applications. Marter et al. [9] demonstrated this key feature of the proposed design experimentally by varying the frequency around the stator resonances (see Fig. 2). Avoiding the need for complex control hardware to achieve bidirectional motion could preserve the motor design's

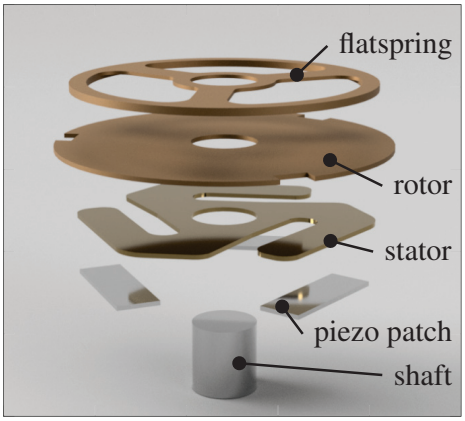

Figure 1: Components of the rotational piezoelectric motor.

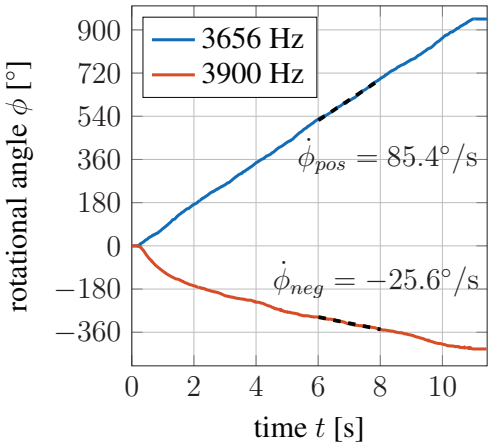

Figure 2: Experimentally determined prototype stator's positive and negative rotational angle.

cost-effectiveness. However, preliminary experiments revealed that prior assumptions regarding the motor's working principle were insufficient for accurately determining the excitation frequencies required for bidirectional operation.

Precise fabrication plays a vital role in maintaining the performance and reliability of smart structures. This is particularly critical for small-scale applications and prototype development, where deviations from manual manufacturing processes can pose significant challenges [10]. As it is impossible to avoid these deviations entirely, addressing them in the modeling is necessary to predict the behavior of smart structures such as the motor discussed in this paper. The finite element method (FEM) is particularly suitable for this purpose [11, 12]. Especially at the mesoscale, numerical models can offer valuable insights that are difficult to obtain through experiments.

The manual assembly process in the prototype stage is assumed to be the primary factor influencing this discrepancy between predicted and observed behavior for the presented motor. In this early phase of the development process, the electrical contacts in the shoulder region of the stator arms (see Fig. 3) are soldered by hand. Despite the utmost care, the introduced thermal energy and applied pressure can plastically deform the stator. This causes an out-of-plane deformation, which is assumed to be the main source of the observed deviations. In the paper at hand, we analyze the performance of the motor by introducing an idealized deformation pattern. Thus, the alteration of the motor characteristics due to this deformation is examined in more detail.

2 NUMERICAL MODEL

To reduce the complexity of the model, only the stator and the rotor are considered in the numerical studies. This avoids the numerically expensive contact analysis between flatspring and rotor. In addition, this arrangement corresponds to the experimental test setup used to generate the results depicted in Fig. 2 and, therefore, does not introduce additional error sources.

While the stator and the rotor can be described by linear isotropic material behavior, orthotropic material behavior is required for the piezo patches made of PZT-5H. An overview of used material parameters is presented in Table 1. An overview of the numerical model is given in Fig. 4. All parts are dominantly discretized using hexahedral elements of the serendipity type with quadratic shape functions and 20 nodes per element. 15446 elements were used for the stator, 3204 for the rotor, and 1980 for the piezo patches, resulting in 314604 degrees of

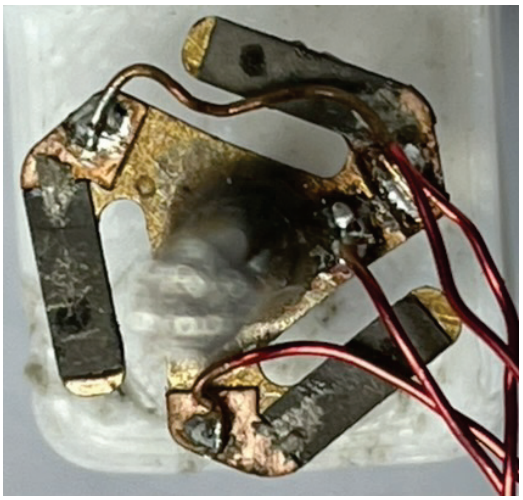

Figure 3: Assembled motor with soldering points on the shoulder parts of the stator.

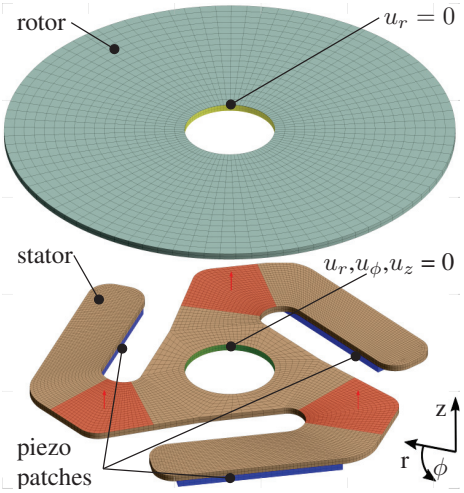

Figure 4: The Numerical model with employed boundary conditions.

Table 1: Mechanical, piezoelectric and electrical material parameters.

	ρ $\mathrm{kg/m^3}$	E_{xx} GPa	E_{yy} GPa	E_{zz} GPa	ν_{xy} –	ν_{yz} –	ν_{xz} –	
Phosphor Bronze	8860	110	-	-	0.359	-	-	
PZT-5H	7700	60.60	60.60	43.81	0.2897	0.5121	0.4082	
	G_{xy} GPa	G_{yz} GPa	G_{yz} GPa	e_{31}	e_{33}	e_{15} $\mathrm{Vm/N \cdot 10^{-3}}$	ε_{33} -	ε_{11} -
PZT-5H	23.47	22.99	22.99	-8.11	28.47	20.87	1434	1704

freedom (DOF). Since two element layers are taken into account for each component, the bending deformation can be represented with sufficient accuracy with solid elements. In addition to the translational DOF, the elements of the piezo patches (highlighted blue in Fig. 4) have an additional voltage DOF. Consequently, a sinusoidal voltage signal can be applied to the bottom surface of each patch while the top surface, contacting the stator, is grounded. The piezoelectric patches and the stator are perfectly bonded, allowing no relative motion in the form of sliding or separation. While the nodes at the inner surface of the rotor (highlighted yellow in Fig. 4) can only translate and rotate along and around the z-axis (fixed in the radial direction), the nodes at the inner surface of the stator (highlighted green in Fig. 4) are entirely clamped. Furthermore, gravity ($g = 9.81\ \mathrm{m/s^2}$) acts in the negative z-direction and a frictional contact based on Coulomb's law ($\mu = 0.1$) is defined between the stator top surface and the rotor bottom surface. To reach the steady state faster in transient analyses and thus reduce the overall simulation time, Rayleigh damping is considered for the stator material. According to Rayleigh's hypothesis, the damping matrix is defined as

$$\mathbf{D} = \alpha\mathbf{M} + \beta\mathbf{K} \tag{1}$$

Here, $\mathbf{D}$, $\mathbf{M}$, and $\mathbf{K}$ denote the damping, mass, and stiffness matrix, respectively. By choosing the Rayleigh coefficients $\alpha = 2243\ 1/\mathrm{s}$ and $\beta = 1.2 \cdot 10^{-6}\ \mathrm{s}$ an artificially high damping ratio of $\zeta = 0.08$ is achieved for the first and third resonance frequencies, whereas the damping ratio for the second resonance is slightly lower. This high damping ratio guarantees that the steady state is reached within ten load cycles (see Fig. 5) without affecting the stator's qualitative characteristics. Due to the high damping, the voltage amplitude must be artificially increased to meet the experimentally identified stator tip amplitudes in the first resonance of approximately $120\ \mu\mathrm{m}$.

3 Idealized manufacturing-induced deformations

In the first step, a static analysis is conducted where pressure is evenly applied on the shoulder parts of the stator arms (see red highlighted areas in Fig. 4), imitating a manual soldering

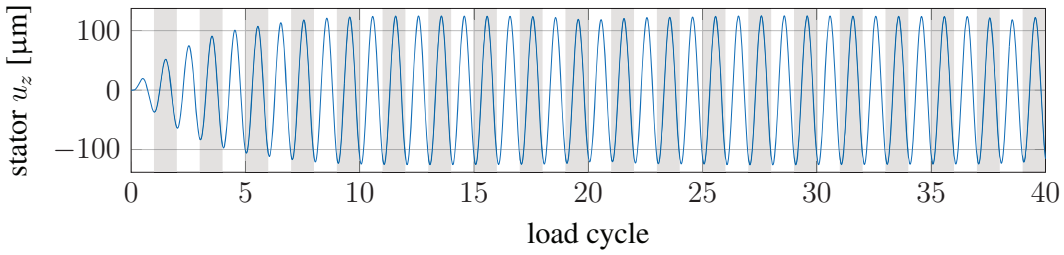

Figure 5: Maximum amplitude development of the vertical stator deformation at the tips of the arms in the first resonance with artificially high damping of $\zeta = 0.08$.

process. The pressure value of $p = 0.1$ MPa correlates to an estimated force of $F = 1$ N on each arm imposed by the soldering iron. This creates a deformation, as shown in Fig. 6, where the shoulder parts are bent upwards in the positive z-direction while the tip parts of the arms are bent downwards. The middle part of the stator around the shaft seat is mainly unaffected by the applied load. As the starting point for the following simulations, the deformed state of the stator is taken as the initial geometry, neglecting the pre-stress caused by the pre-deformation. A key parameter for the motor characteristics and the subsequent evaluation is the vertical displacement difference $\Delta z = z_{\text{init,sho}} - z_{\text{init,tip}}$ of the potential contact regions between the stator and the rotor represented by the tip and the shoulder region of each arm and highlighted in Fig. 6. In the linear elastic case, this difference is directly proportional to the applied pressure and, accordingly, $\Delta z \approx 63.5$ µm.

Due to the motor's resonant operation, the contact regions can be derived directly from the stator's eigenmodes. Figure 7 depicts the first two eigenmodes of the stator resembling typical bending modes, with the largest magnitudes at the tip and the shoulder, respectively. It is important to note that the locations of the areas with the largest magnitudes are independent of the stator's pre-deformation. The contact region between the stator and the rotor can be controlled depending on the motor's chosen excitation frequency. For example, the contact location is forced to occur at the tip region of the stator for an excitation at the first resonance or at the shoulder region for an excitation at the second resonance.

In contrast to the locations of the regions with the highest magnitudes, the pre-deformation affects the node trajectories in the potential contact zones. Figure 8 shows the trajectories of

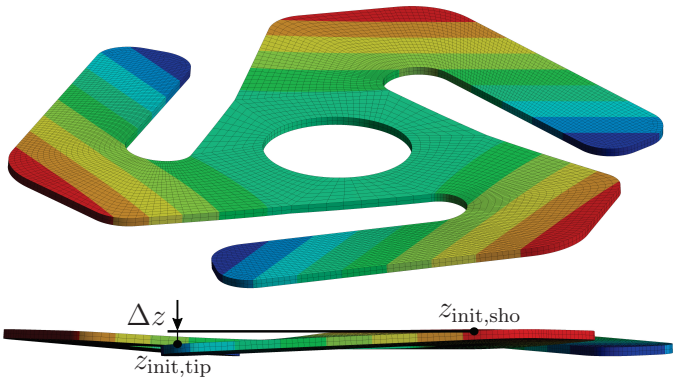

Figure 6: Idealization of the manufacturing-induced pre-deformation of the stator geometry colored by u_z: $u_{z,\max} = 52.8$ µm, $u_{z,\max} = -32.6$ µm.



(a) First eigenmode at 2558 Hz



(b) Second eigenmode at 4814 Hz

Figure 7: Identified eigenmodes of the stator.

potential contact nodes at the tip and the shoulder region in the first resonance with a scaling factor of 150 in the x-y-plane. The dashed line represents the direct connection between the stator's center of gravity (midpoint) and the particular initial location of the contact point (magenta-colored marker) around which the node oscillates during one load cycle in the steady state.

As a result of the out-of-plane deformation, the lateral motion in the x-direction at the tip becomes more pronounced, which is counter-intuitive as we expect the bending eigenmode, where a pure movement in the y-direction would be expected. Even for the undeformed geometry, an apparent lateral motion in the x-direction can be observed, which can be attributed to the stator arm design and the placement of the piezo patch. In this way, an upward bending of the arm results in a negative tangential displacement, consequently leading to a negative rotation direction. Although the trajectories in the shoulder region are less affected by the pre-deformation, the change of lateral motion in the x-direction behaves similarly. The node trajectory is basically a straight line in this region for the first resonance.

4 Harmonic Analysis

The direction of the motor's rotation cannot be found from the contact area location alone. In addition, the phase information of the vertical and tangential contact node trajectories must also be evaluated to predict the rotational direction for different operation points. Therefore, a

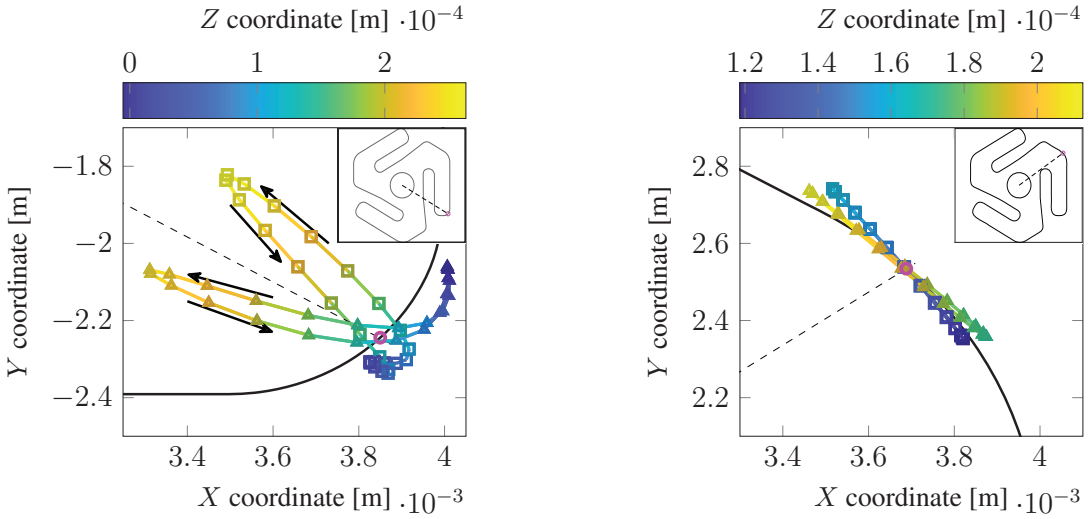

(a) Tip contact region.

(b) Shoulder contact region.

Figure 8: Contact area trajectory of the undeformed (square marks) and the pre-deformed (triangle marks) stator geometry.

harmonic analysis of the stator is used where a harmonic voltage input signal is applied to the piezo patches

$$\mathbf{V}(\mathbf{x}, t) = \hat{\mathbf{V}}(\mathbf{x}) \cdot \sin(\omega t) \tag{2}$$

with the amplitude vector $\hat{\mathbf{V}}(\mathbf{x})$ defined for the nodal coordinates $\mathbf{x}$, to solve the equation system

$$\mathbf{M}\ddot{\mathbf{u}} + \mathbf{D}\dot{\mathbf{u}} + \mathbf{K}\mathbf{u} = \mathbf{f} \tag{3}$$

for several frequencies ω. Here, $\mathbf{u}$ denotes the vector of unknowns (including displacement and electric potential DOFs) and $\mathbf{f}$ the vector of external forces.

A Bode diagram can be created from this analysis, shown in Fig. 9 with the magnitude plot on the left-hand side (Fig. 9a) and the phase plot on the right-hand side (Fig. 9b). The magnitude plot compares the results for the Rayleigh damped system (solid line) and a stator with only material damping ($\mathbf{D} = c/(2\pi\Omega)\mathbf{K}$, with the constant structural damping coefficient c, dashed line). The artificial high damping significantly increases the magnitudes away from the resonances, but the qualitative behavior stays the same. The red curves correspond to the tip region, while the blue curves belong to the shoulder region. By definition, the magnitudes of both regions have a maximum in the resonance at 2555 Hz with the magnitude of the tip being

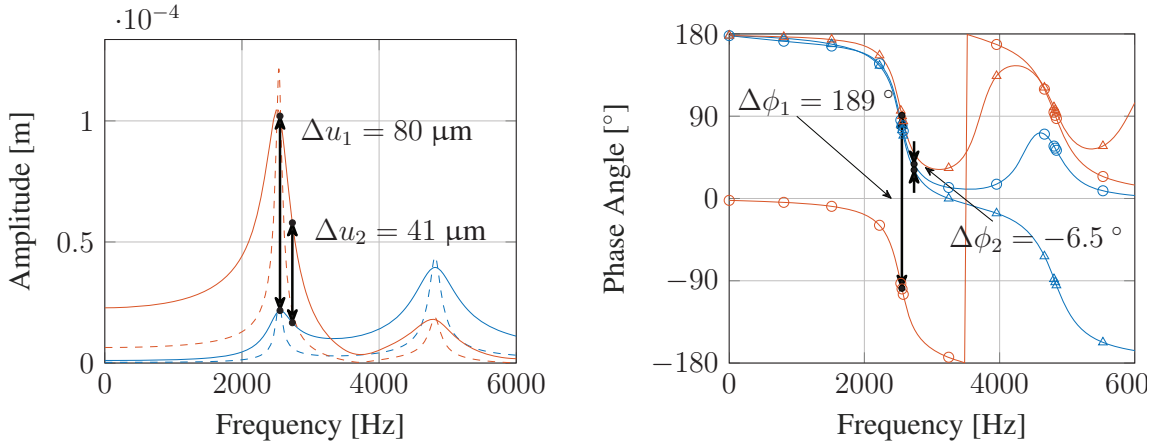

(a) Amplitude

(b) Phase angle

Figure 9: Bode diagram: Frequency response for the amplitude and the phase shift for the tip (red curve) and the shoulder (blue curve) contact regions with Rayleigh damping (solid line) and with a constant structural damping coefficient (dashed line). The phase angle plot shows the vertical (triangle marks) and the tangential (circle marks) displacements for both contact regions. The excitation frequencies for transient simulations are highlighted.

approximately $\Delta u_1 = 80\ \mu\mathrm{m}$ larger than the one of the shoulder region. This value exceeds the initial vertical displacement from the pre-deformation of $\Delta z = 63.5\ \mu\mathrm{m}$. Consequently, with the largest magnitude at the tip, the contact occurs there. For the same frequency, a difference in the phase angle of the tip (red curve) of approximately $\Delta\phi_1 = 189°$ between the vertical displacement (triangles) and the tangential displacement (circles) can be observed in the phase plot (Fig. 9b), meaning that a negative tangential displacement occurs at the time of contact when the vertical displacement is at a maximum. This results in a negative rotational direction, already apparent from Fig. 8a, where the tangential displacement in the x-y-plane has a negative increment toward the vertical displacement maximum.

The magnitude difference between both regions reduces for higher frequencies moving away from the first resonance. At $2735\ \mathrm{Hz}$ for example, the magnitude difference is approximately $\Delta u_2 = 41\ \mu\mathrm{m}$ and therefore smaller than the initial vertical displacement of $\Delta z = 63.5\ \mu\mathrm{m}$ shifting the contact region to the shoulder of the arm. The corresponding phase angles in Fig. 9b for the vertical (triangle) and tangential (circle) displacements of the shoulder regions (blue curve) have a difference of $\Delta\phi_2 = -6.5°$. This phase difference is close to zero, leading to a positive direction of rotation, as the tangential displacement has a positive value at the time of the maximum vertical displacement.

Considering the pre-deformed state of the stator, it is evident that the initial displacement difference Δz of both regions allows a simplified way of controlling the contact region by varying the excitation frequency around the first resonance of the stator. From the the presented results, a key motor characteristic to determine the rotational directions is the phase difference ($\Delta\phi$) between the vertical and tangential displacement at particular contact locations. In this regard, a phase difference of $\Delta\phi \approx 180°$ leads to a negative rotational direction while, in contrast, $\Delta\phi \approx 0°$ results in a positive direction. The proposed methodology works solely in the first resonance, as the initial vertical displacement difference can be overcome only by the resulting magnitude at the tip of the arm. An excitation in the second resonance of the stator would cause a contact location at the shoulder part of the arm, resulting in a negative rotational direction again with a phase difference between tangential and vertical displacement of $\Delta\phi \approx 135°$.

5 Transient Analysis

Implicit transient simulations by the *Hilber-Hughes-Taylor Method* ($\gamma = 0.1$, $\alpha = 0.3025$, $\delta = 0.6$) are carried out for different operation points to account for the frictional contact between the stator and the rotor and investigate its influence on the predicted rotational direction. For this reason the previously discussed excitation frequencies of $2555\ \mathrm{Hz}$ and $2735\ \mathrm{Hz}$ are used corresponding to a resonance excitation and a slightly off-resonance excitation. Figure 10 displays the trajectories and time variations for a representative contact node. Here, vertical and tangential displacements for both excitation frequencies in the predicted contact regions are shown. In addition, the resulting rotational angles over the load cycles are plotted in Fig. 11.

The displacement and voltage curves in Fig. 10b and Fig. 10d are normalized by the highest positive amplitude of each curve. While the qualitative shape of the oscillating trajectory of the tip region is largely unaffected by the contact (see Fig. 10a), the trajectory in the shoulder region is more influenced by the contact, exhibiting a more undulating form (see Fig. 10c).

In both figures, the cross markers highlight the locations where the stator is in contact with the rotor. For the tip region at resonance (2555 Hz), one contact event during one load cycle can be observed when the vertical displacement reaches the maximum (see red curve in Fig. 10b). The hypothesis made from the harmonic analysis can be confirmed, although the phase difference between the vertical and tangential displacement is at $189°$, which is slightly larger than $180°$ as previously determined. In contrast to the tip region, two contact events occur in the shoulder region for the excitation frequency of $2735\ \mathrm{Hz}$, indicating a more distributed contact area (see Fig. 10). This can be explained by the rotor's inertia, which allows several contacts to take place before the stator and rotor separate again. A comparison between the two contact periods indicates that the slope of the first one is positive and larger than that of the second one, which exhibits a negative slope. Thus, the overall rotational angle for excitation at $2735\ \mathrm{Hz}$ evolves positively (see red curve in Fig. 11) as predicted by the harmonic analysis with a phase difference of approximately $0°$.

Figure 11 shows the resulting rotational directions for different operation frequencies of the undeformed and the pre-deformed stator over the first 40 cycles. The rotational angle is plotted over the load cycles to allow a better comparison between the different frequencies. Due to the high computational effort, the overall simulation time for all transient analyses (0.146 s) is two orders of magnitude shorter than the period considered in the experiments (10.5 s) from Fig. 2. However, the same qualitative behavior for the deformed stator can be observed when the positive rotational direction (see red curve in Fig. 11) shows a larger angle and velocity than the negative one (see blue curve in Fig. 11) after the same load cycle number. This shows that the numerical motor model accurately captures the key properties of the manufactured prototypes.

In contrast, operating the undeformed stator achieves only the negative rotational direction. Here, the resulting contact region of either the tip or the shoulder region can only be controlled by the excitation in the first or the second resonance. As shown in Fig. 9b, a phase difference between the vertical and tangential displacement significantly larger than $90°$ exists in not only the first resonance for the tip region but also in the second resonance for the shoulder region, leading to a negative rotation direction for both contact regions when excited in the corresponding resonance frequency. This example highlights again that a targeted pre-deformation of the stator benefits the effect on the bi-directional motor characteristic.

6 SUMMARY AND OUTLOOK

In the present work, a finite element model of a planar bidirectional standing wave-type piezoelectric motor is used to investigate the influence of out-of-plane deformation on the motor characteristics. It is assumed that the deformations are caused by the manual soldering process,

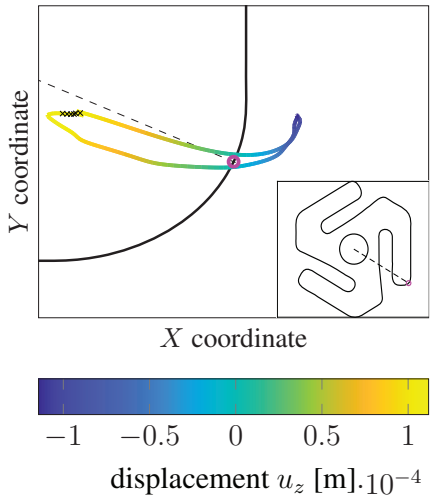

(a) Representative contact node trajectory at 2555 Hz.

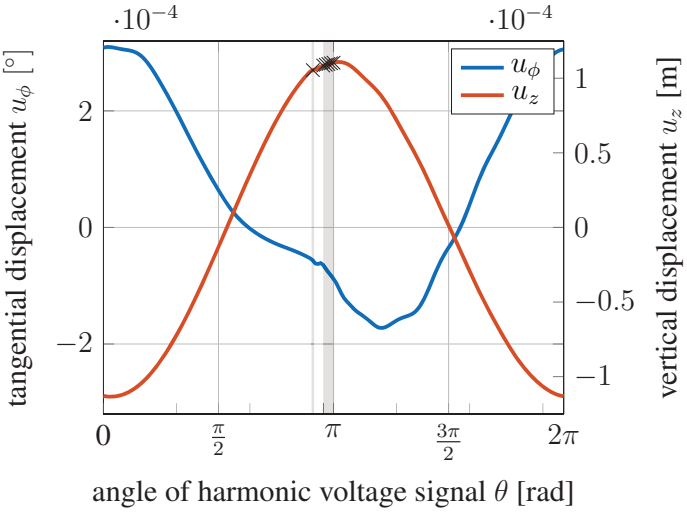

(b) Vertical and tangential displacement of a representative contact node at 2555 Hz.

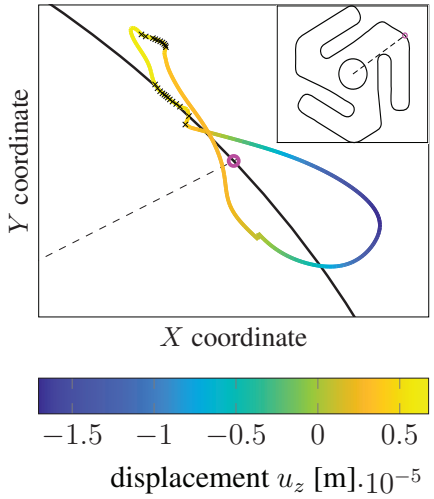

(c) Representative contact node trajectory at 2735 Hz.

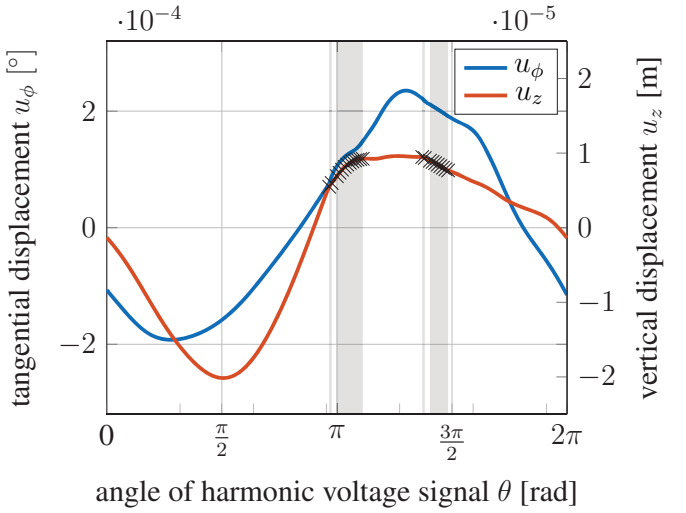

(d) Vertical and tangential displacement of a representative contact node at 2735 Hz.

Figure 10: Contact region and contact node kinematics.

which is the basis for a simplified stator pre-deformation to limit the numerical effort. Various numerical analyses are carried out to characterize the motor behavior. It has been shown that the pre-deformation of the stator has a decisive influence on potential contact points in or near

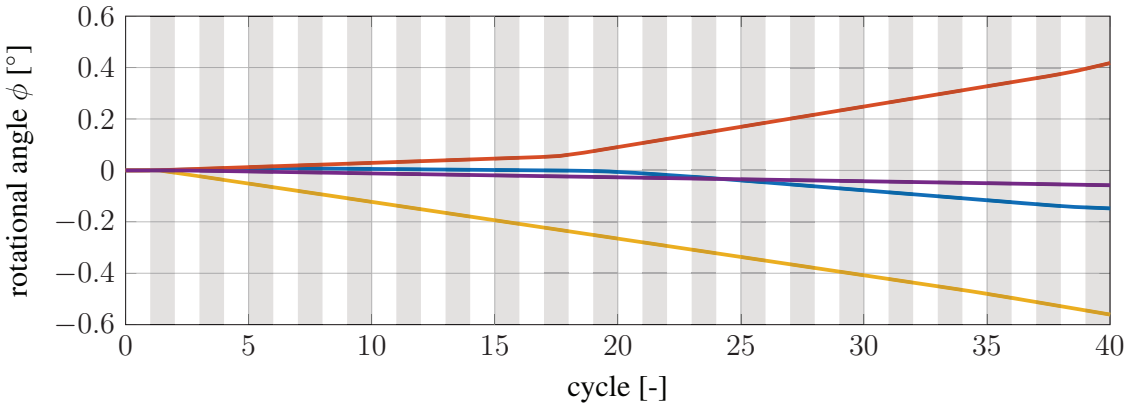

Figure 11: Rotational angles for the undeformed (1st resonance – yellow, 2nd resonance – purple) and the deformed stator geometry (2555 Hz – blue, 2735 Hz – red).

the resonance excitation. However, the phase difference between the tangential and vertical displacement of the respective contact zone is the critical criterion for the resulting direction of rotation. Thus, targeted pre-deformations can be advantageous in controlling the motor, as they allow for more specific control of individual operating points. In future work, the methodology will be applied to the real stator geometry measured by focus variation microscopy and other optical techniques to gain further insights by analyzing the *as-manufactured* geometry.

REFERENCES

[1] R. J. Wood, "The challenge of manufacturing between macro and micro," *American Scientist*, vol. 102, no. 2, p. 124, 2014.

[2] N. T. Jafferis and R. J. Wood, "The delta-motor: A multi-modal, high-speed, flexure-based piezoelectric motor," *Sensors and Actuators A: Physical*, vol. 366, p. 114927, Feb. 2024.

[3] R. R. Orszulik and J. Shan, "Output feedback integral control of piezoelectric actuators considering hysteresis," *Precision Engineering*, vol. 47, pp. 90–96, Jan. 2017.

[4] Y. Peng, Y. Peng, X. Gu, J. Wang, and H. Yu, "A review of long range piezoelectric motors using frequency leveraged method," *Sensors and Actuators A: Physical*, vol. 235, pp. 240–255, Nov. 2015.

[5] X. Gao, J. Yang, J. Wu, X. Xin, Z. Li, X. Yuan, X. Shen, and S. Dong, "Piezoelectric actuators and motors: Materials, designs, and applications," *Advanced Materials Technologies*, vol. 5, no. 1, Nov. 2019.

[6] K. Spanner and B. Koc, "Piezoelectric motors, an overview," *Actuators*, vol. 5, no. 1, p. 6, Feb. 2016.

[7] S. Pan, Z. Xu, and C. Zhao, "A novel single-gimbal control moment gyroscope driven by an ultrasonic motor," *Advances in Mechanical Engineering*, vol. 11, no. 4, Apr. 2019.

[8] Y. Suzuki, K. Tani, and T. Sakuhara, "Development of a new type piezoelectric micromotor," *Sensors and Actuators A: Physical*, vol. 83, no. 1, pp. 244 – 248, 2000.

[9] P. Marter, M. Khramova, F. Duvigneau, R. J. Wood, D. Juhre, and R. Orszulik, "Bidirectional motion of a planar fabricated piezoelectric motor based on unimorph arms," *Sensors and Actuators A: Physical*, p. 115642, Jun. 2024.

[10] D. K.-C. Liu, J. Friend, and L. Yeo, "A brief review of actuation at the micro-scale using electrostatics, electromagnetics and piezoelectric ultrasonics," *Acoustical Science and Technology*, vol. 31, no. 2, pp. 115–123, 2010.

[11] R. Toledo, S. Eisenträger, and R. Orszulik, "Finite element analysis of thermopiezoelectric bimorph actuators considering temperature-dependent piezoelectric strain coefficients," *Acta Mechanica*, vol. 235, no. 12, pp. 7199–7222, Sep. 2024.

[12] C. Jiang, Z. Zhao, D. Lu, Z. Xu, and L. Jin, "Contact analysis and performance evaluation of ring type traveling wave ultrasonic motors based on a surface contact model," *Ultrasonics*, vol. 127, p. 106851, Jan. 2023.

XI ECCOMAS Thematic Conference on Smart Structures and Materials - SMART 2025
M. Krommer, M. Nader and M. Schagerl (Eds)

Received: 28 March 2025 / Revised: 28 August 2025 / Accepted: 9 October 2025
© The Author(s) 2025

Numerical investigation of wear effects on sensor-integrating jaw couplings

Johannes D. M. Menning, Arthur Ewert, Artem Prokopchuk, Berthold Schlecht, E.-F. Markus Vorrath, Thomas Wallmersperger

Abstract. Condition monitoring, which requires extensive sensor data, has gained a lot of interest in recent years. However, the subsequent implementation of sensors into machines can often be difficult or unfeasible due to limitations in the design space. To address this challenge, sensor-integrating machine elements have been developed in which the sensors are directly integrated into the machine elements. In the present work, the possibility to detect the wear of the gear rim of a sensor-integrating jaw coupling is investigated by numerical simulations. The main purpose of the sensor-integrating jaw coupling is to determine the transmitted torque. This is achieved by capacitive dielectric elastomer sensors (DESs), which measure the deformation of the teeth of the gear rim. This allows a regression model to be trained that links a specific deformation to a specific torque.

However, the gear rim wears during use of the coupling, which leads to a change in the stiffness of the coupling. It is therefore crucial to determine the wear in order to be able to accurately determine the transmitted torque over the entire service life.

For this purpose, CAD models of the jaw coupling are modified by removing material of the gear rim teeth. Subsequently, a numerical finite element model is used to investigate the effect of different wear depths on (i) the transmitted torque and (ii) the sensor signal. A hyperviscoelastic material model is used for the gear rim due to the viscoelastic properties of the material, namely thermoplastic polyurethane. The resulting change in capacitance of the DESs due to their deformation is computed in the post-processing. Finally, a functional relationship is determined with which the wear can be detected on the basis of the sensor data available during operation.

Key words: Sensor-integrating machine element, Dielectric elastomers, Modeling, Simulation

D. M. Menning & Thomas Wallmersperger
Institute of Solid Mechanics, Technische Universitaät Dresden, George-Bähr-Str. 3c, 01069 Dresden, Germany
e-mail: johannes.menning@tu-dresden.de

Arthur Ewert & Berthold Schlecht
Institute of Machine Elements and Machine Design, Technische Universität Dresden, Münchner Platz 3, 01069 Dresden, Germany

Artem Prokopchuk & E.-F. Markus Vorrath
Institute of Semiconductors and Microsystems, Technische Universitaät Dresden, Nöthnitzer Straße 64, 01187 Dresden, Germany

1 Introduction

It is often not entirely clear which torques are currently being transmitted in a machine, because measuring torques is not a simple task. To alleviate this problem, the authors have presented a sensor-integrating jaw coupling with which the transmitted torque can be measured, see Ref. [1]. The advantages of sensor-integrating machine elements (SiME) compared to e.g., add-on sensor solutions as well as a general classification of those can be found in the review paper by Kirchner et al. [2]. In an ideal world, the coupling, which consist out of two claw bodies and a gear rim, in which the sensors and the electronics are integrated, would not be altered during use. However, it is known that during use of a jaw coupling the gear rim is subjected to wear. Wear can be distinguished into multiple categories, e.g., abrasion or adhesion. There exist several systems for the classification of wear types [3]. The abrasive wear of the gear rim is mainly caused by the relative movement between the gear rim and the two claw bodies.

In the literature there exist numerous models for simulating wear. Meng and Ludema compared the models between 1957 and 1992 [4]. They categorized them into three main categories (i) empirical models, (ii) models based on mechanical contact, which are often based on the model proposed by Archard [5], and (iii) models in which the employed equations depend on material failure characteristics. For the simulation of the wear rate on ductile materials see e.g., Lian et al. [6] which based their model on Kapoor and Franklin [7]. In their work, an element is considered to be failed, when the accumulated plastic deformation reaches a certain threshold. If now all elements in a layer have failed, the layer is removed and a new layer takes its place. With this, the wear rate can be modeled as the rate with which a new layer moves to the surface to replace the loss. In Martinez et al. [8], the wear resulting from friction on a moving TPU component on steel was simulated. There, the wear rate was modeled using the ABAQUS user subroutine UMESHMOTION.

In the sensor-integrating jaw coupling (SiJC), the deformation of the teeth is measured using dielectric elastomer sensors (DESs) [1]. The manufacturing of these DESs is described in Refs. [9, 10]. These electroactive polymers, which are capable of measuring large deformations and have first been described in Ref. [11], change their electrical resistance [12] and capacitance [13] when subjected to a mechanical load. For the SiJC described in Ewert et al. [1] the change in capacitance is evaluated. For the integration of the DESs into the teeth of the gear rim, stepped boreholes are drilled into each tooth of the gear rim. The gear rim is made of thermoplastic polyurethane (TPU). To increase the deformation of the DESs and thus their sensitivity, a strain amplifier, made of a stiffer material than TPU, is inserted at each end of every DES. An additional advantage of the strain amplifiers is the encapsulation of each DES inside the tooth. A regression model is required to obtain the corresponding torques for the measured capacitances. Due to the viscoelastic material properties of the TPU of the gear rim, cf. Refs. [14, 15], the use of a regression model is necessary. Such a regression model must be able to capture the hysteresis relationship between the capacitance – used as input – and the torque it is intended to predict. For such tasks recurrent neural networks are a promising

candidate, see e.g. Refs. [16, 17]. It is expected that the most influential wear mechanism for the sensor-integrating jaw coupling is abrasion over the whole surface leading to a thinning of the teeth over time. Due to this, the stiffness of the coupling decreases with an increase in wear. This poses a challenge for a future regression model that predicts the torque based on the measured sensor data, as will become clear in the following.

The compression of the gear rim, which is required to transmit a certain torque, increases with increasing wear. Thus, the regression model will predict a too large torque. Therefore, the aim of the present paper is to (i) show the effects of wear using a numerical model and (ii) to derive a method to detect the wear using only the available sensor data of the DESs, in order to ensure that the sensor-integrating gear rim does not need to be replaced once the first effects of wear appear. The knowledge of the present wear can then be integrated into the employed regression model to compensate for the mentioned wear effects. Please note that both the regression model itself and the modeling of the evolution of wear are not part of the present paper.

The present paper is structured as follows. In Section 2 the employed model for the numerical simulation of the effect of wear on the gear rim is presented. After that, the results of the influence of wear on the transmitted torque and on the capacitances are given in Section 3. A simple regression model for quantifying the wear is developed on the basis of the measured capacitances in Section 4. Finally, a conclusion is drawn, and an outlook is given in Section 5.

2 Modeling

For the numerical simulation of the sensor-integrating jaw coupling (SiJC) the finite element method is employed. The coupling is modeled and discretized by the finite element program ABAQUS. Due to the large deformation of the teeth and the viscoelastic material behavior of the TPU a hyper-viscoelastic material model is used for the gear rim. The employed numerical model including (i) the equations in space and time and (ii) the boundary conditions are described in Ref. [18]. The material parameters are taken from Ref. [19]. Furthermore, it is assumed that no shaft misalignments are present. Thus, the use of a quarter model of the coupling is sufficient. To investigate the effect of wear on the characteristics of the SiJC, the CAD model of the gear rim was altered. As a first attempt, the areas, which are constantly in contact with the claw bodies and are thus expected to wear first, were removed, see Figure 1. The investigated depths of the cutout were $[0, 50, 100, 150, 200]\,\mu$m. This simple approach serves to demonstrate the potential of the model in the absence of more precise data. Two wear cases are distinguished in the following. In test case **A**, all teeth have the same wear, which results in a symmetrical weakening of the gear rim. Such a wear is expected to occur if the loading direction of the coupling is frequently changed and therefore all teeth are exposed to the same load during the entire service life. In test case **B** only every second tooth is modified, resulting in an unsymmetrical modification of the gear rim. This is the case if the load direction of the coupling is never or rarely changed due to which only the loaded teeth are exposed to wear.

As described in Ref. [19], the DESs are not explicitly modeled. Instead, the change in distance of their connecting strain amplifiers is evaluated. This change in height Δh is subse-

quently inserted into a quadratic equation which links Δh to a capacitance C. To derive this equation, the DESs were subjected to uniaxial loading–unloading tests using a tensile testing machine, while measuring their capacitance. Due to manufacturing tolerances, the DESs show some slight deviations in their performance. For the sake of simplicity, it is assumed that all DESs behave the same. The parameters from the DES 2 with a height of $h_{\mathrm{DES}} = 5.9\,\mathrm{mm}$ from Ref. [19] were chosen for the computation of the capacitance C of the DESs and are given by

$$C = 15.15\,\frac{\mathrm{pF}}{\mathrm{mm}^2}\Delta h^2 + 16.93\,\frac{\mathrm{pF}}{\mathrm{mm}}\Delta h + 76.12\,\mathrm{pF}\,. \tag{1}$$

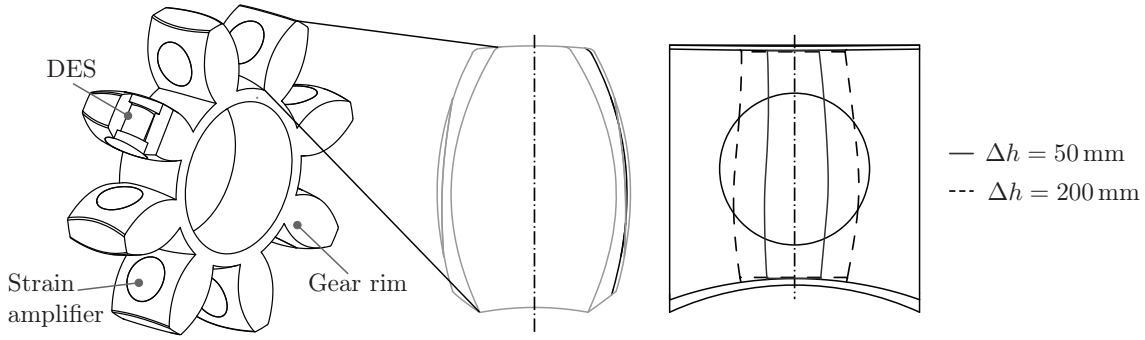

Figure 1: Schematic representation of (i) the sensor-integrated gear rim with a dielectric elastomer sensor (DES) (left), (ii) a single tooth of the gear rim of the sensor-integrating jaw coupling with inserted strain amplifier, side view (middle) and (iii) a front view (right). Additionally, the sections which were removed for modeling the different wear depths are shown, which increase with an increase in the wear depth. During use, the whole area of the tooth, as seen on the right, is in contact with the two claw bodies which are omitted here for a better visibility.

3 Results of the wear simulations

In the present section the influence of wear on the mechanical and electrical results is investigated. In the present work for the numerical simulations a sinusoidal torque load with a frequency of $f = 1\,\mathrm{Hz}$, an amplitude of $\hat{T} = 49\,\mathrm{Nm}$ and a mean value of $\bar{T} = 49\,\mathrm{Nm}$ was applied. This load was chosen as it corresponds to a torque of $T = 98\,\mathrm{Nm}$ for a torsion angle of $\phi = 3.2°$ for a sensor-integrating gear rim without any wear. With jaw couplings, only every second tooth is loaded when a torque is transmitted. Thus, the capacitances of both the loaded and the unloaded teeth are given in the following.

3.1 Symmetrical wear – test case A

The applied loads and the resulting torsion angles for the test case **A** are given in Figure 2, in the two upper diagrams. The different colors correspond to the different investigated wear

depths. In the unloaded state, there is a small preload on the teeth, visible in the peaks of the capacitance of the unloaded tooth C_{unload} for $\phi \approx 0$, see e.g. Ref. [20]. As a result, in the unloaded state of the coupling, all DESs have a capacitance that exceeds their capacitance in the unloaded state C_0. Furthermore, it can be seen that the preload decreases with an increase in wear. This decline is visible in the decrease of C_{unload} for $\phi \approx 0$ and higher wear depths. With a wear of slightly more than $150\,\mu$m, the preload of the tooth has completely disappeared. This leads to numerical difficulties for the unloaded state, as the gear rim is no longer in contact with the two claw bodies. Thus, rigid body movements are theoretically possible. To alleviate this problem, automatic contact stabilization, which introduces a small damping, cf. Ref. [21], was used in the simulations. With an increase of the wear — and thus a thinning of the tooth — the capacitance of the DES in the loaded tooth decreases. This decrease in the tooth thickness leads to a smaller overall deformation of the tooth, see Figure 2.

It could be expected that the strain of a fully unloaded tooth is zero. As a result, the capacitance of the unloaded tooth should be the same for all wear depths. However, due to the viscoelastic material properties of the gear rim material, this is not the case as there is still a small remaining strain. This remaining residual strain decreases with increasing wear depth, as the preload, which is the cause for this strain, decreases as well. Thus, the capacitances of the unloaded tooth in the quarter model do not match for different depths, see Figure 2.

3.2 Unsymmetrical wear – test case B

The applied loads and the resulting torsion angles for the test case **B** are given in Figure 3, in the top two diagrams.

The loading direction was chosen in such a way, that the worn tooth was loaded and the tooth without wear was unloaded. For the unloaded tooth, a drop in capacitance can also be observed at higher wear depths. Initially, it was expected that this drop is the same for all wear depths, as the unloaded tooth was not modified. The reason for this discrepancy for the different wear depths lies in the fact that the torsion angle ϕ does not start from zero but at a small offset, see Figure 3. This is due to the unsymmetrical modification of the gear rim due to which the coupling is slightly rotated after the preload was resolved in the first step. As a result, the loaded tooth is never fully relieved during the entire process.

3.3 Comparison of both test-cases

In Figure 4 the consequences of disregarding wear are shown for both test cases. The slopes of the hysteresis curves, which are due to the viscoelastic material properties of the gear rim, increases with increasing wear. If the amount of wear is not considered, the regression model would predict the torque of the coupling wear-free, i.e., a torque which is too low.

4 Regression of the wear

In this section the regression of the wear based on the capacitance of the DES inside the unloaded tooth is described for both test cases **A** and **B**. The necessity to determine the current

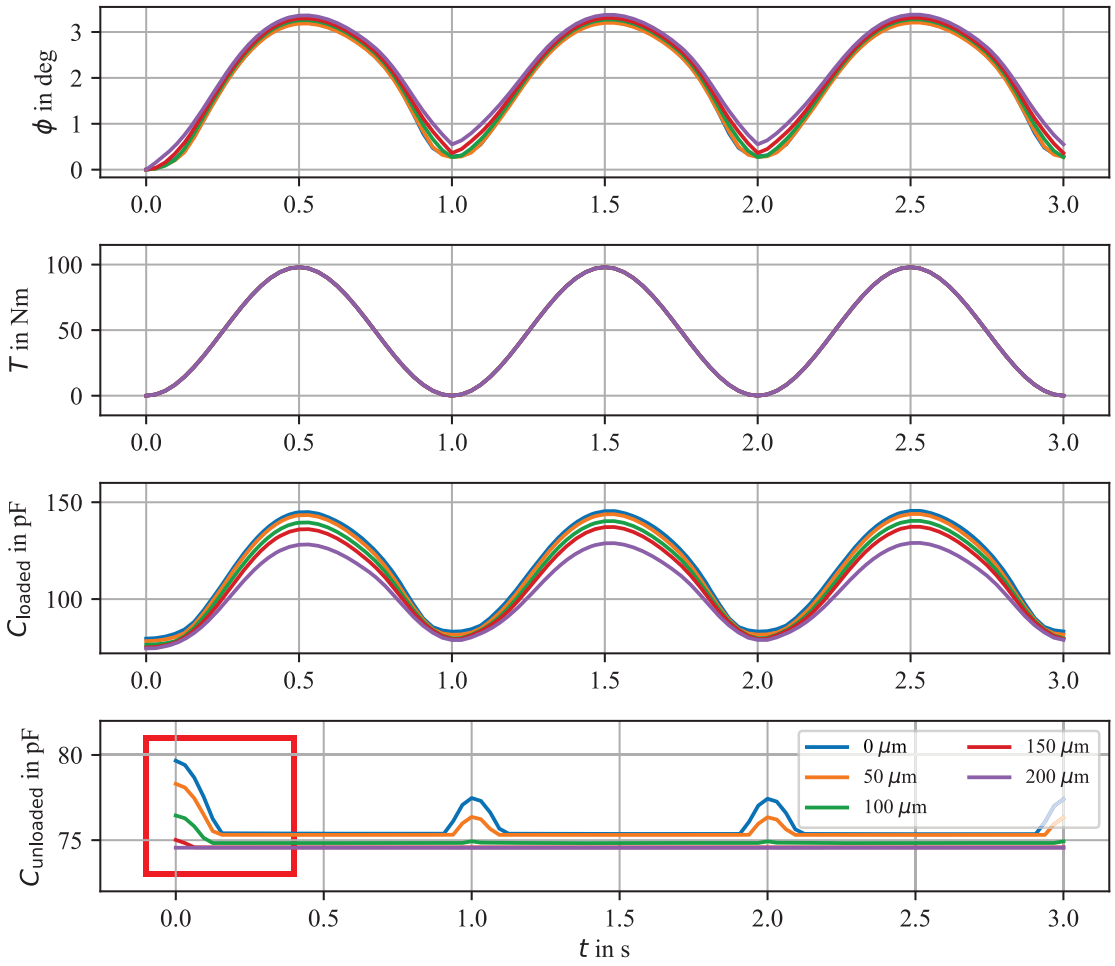

Figure 2: Test case **A**: Applied torsion angle ϕ, resulting torque T and capacitance of the loaded C_{loaded} and unloaded C_{unloaded} tooth versus time t for the investigated wear depths of $[0, 50, 100, 150, 200]$ μm.

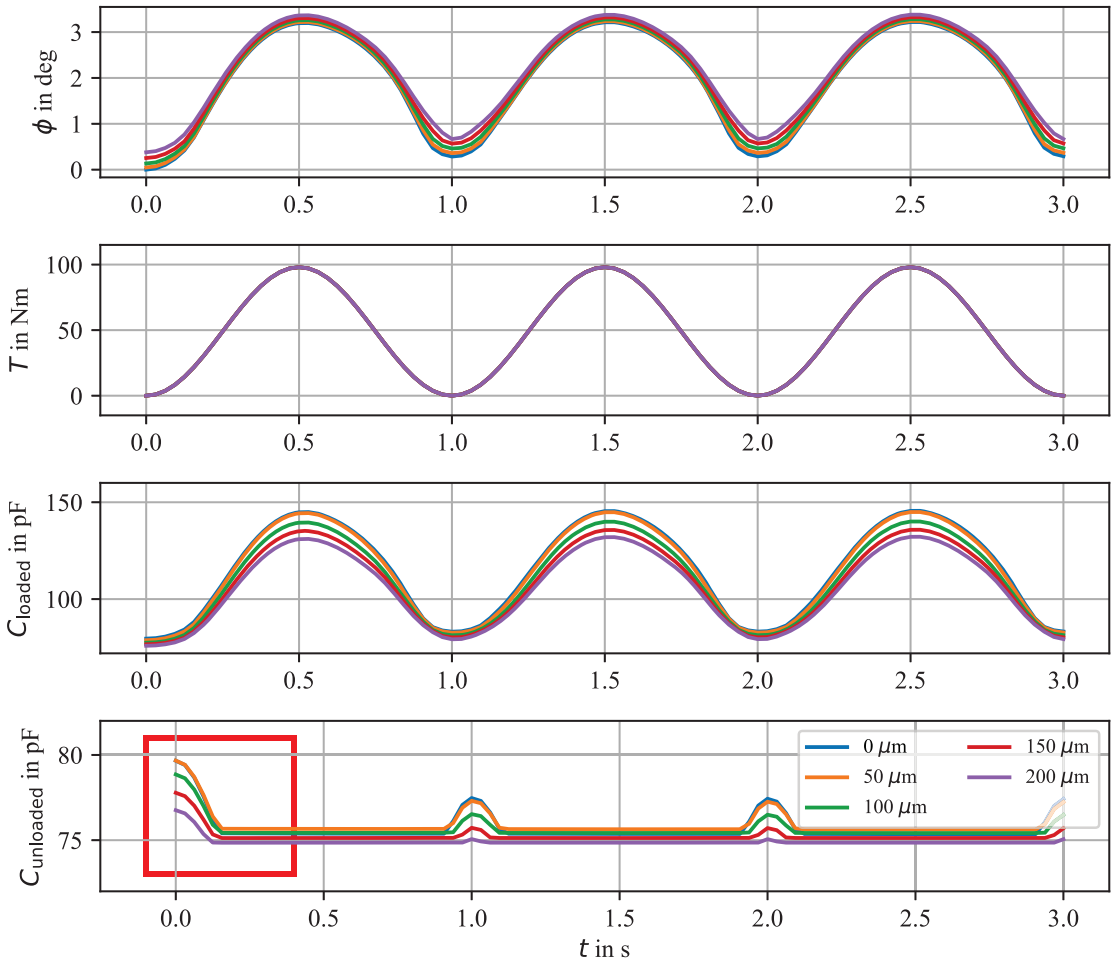

Figure 3: Test case **B**: Applied torsion angle ϕ, resulting torque T and capacitance of the loaded C_{loaded} and unloaded C_{unloaded} tooth versus time t for the investigated wear depths of $[0, 50, 100, 150, 200]$ μm.

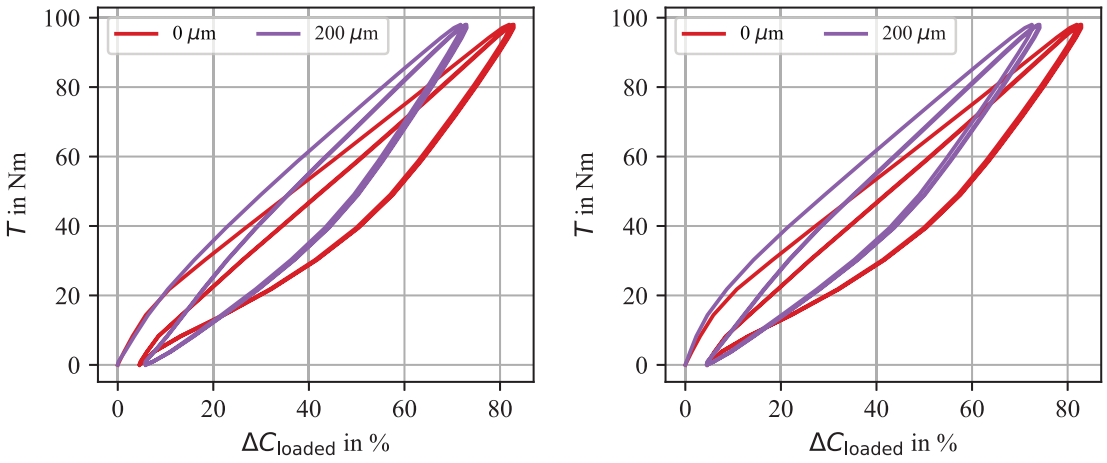

(a) Test case **A** (b) Test case **B**

Figure 4: Torque T versus capacitance of the loaded tooth C_{loaded} for the investigated wear depths of $[0, 200]$ μm for (a) test case **A** and (b) test case **B**.

wear was described in section 1. As will be shown in Section 4.1 and Section 4.2 it is necessary to determine whether a symmetrical or unsymmetrical wear is present. If the loading history is known, it can a priori be determined which of the two test cases will be more prominent. If e.g., the load rotation was never changed during use, it is to be expected that the load case **B** will be present. If this is not known, it can be determined by running a test in which the load direction is changed. If the capacitance of the DESs is different in one load direction than in the other, it is very likely that an unsymmetrical wear is present. Please note that for this it is assumed that the DESs in all teeth are very similar in their characteristics.

4.1 Symmetrical wear – test case A

If a load is applied, every second tooth is loaded and thus compressed, while every other tooth is unloaded, as shown in Figure 2. With increasing wear depths, the influence of the preload and the capacitance difference of the unloaded tooth decreases. To predict the wear, the maximal absolute capacitance difference of the initial drop in capacitance of the unloaded tooth, as shown by the red rectangle in Figure 2, is evaluated. When plotted versus the respective wear of the teeth, an almost linear relationship, up to the intersection with the vertical line for $\Delta C = 0$, can be seen, see Figure 5a. For higher wear depths the capacitance difference is zero and thus constant. It follows that with the proposed method the wear depth can only be determined if the teeth are still subjected to a preload in the unloaded state. For wear depths which exceed this threshold, a determination of the wear using this method is no longer possible, see Figure 5a.

The thus determined linear equation to determine the wear based on the capacitance of the

unloaded tooth reads

$$\text{Wear}_{\text{sym}} = -38.455\,\Delta C_{\text{unloaded}}\frac{\mu\text{m}}{\text{pF}} + 165.081\,\mu\text{m}\,. \tag{2}$$

The equation was derived by using the polyfit function from the python library Numpy which minimizes the squared error between the target and the linear equation.

In this work, numerical studies have shown that it is easier to detect wear if the DESs are slightly larger. The initial drop in capacitance of the unloaded tooth increases with increasing DES height, see Figure 5b. A higher capacitance change results in a more accurate prediction of the wear, provided that the sensitivity of the sensor is assumed to be constant. The larger capacitance change is due to the quadratic nature of eq. (1). A DES with a larger height is, as a result, compressed to a higher degree with the same preload.

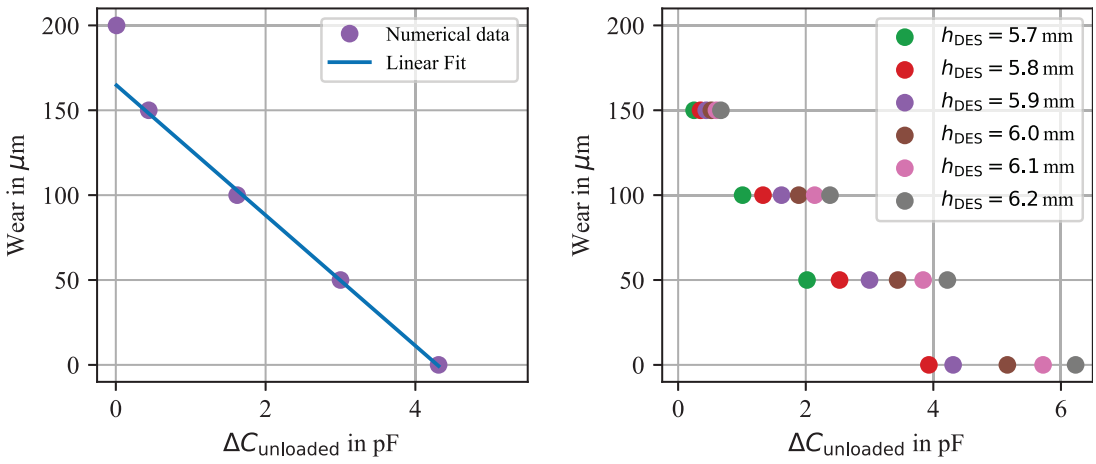

(a) $h_{\text{DES},\,0} = 5.9\,\text{mm}$ (b) $h_{\text{DES},\,0} = 5.7 \ldots 6.2\,\text{mm}$

Figure 5: Test case **A**: Maximal capacitance differences of the unloaded tooth C_{unloaded} for the investigated wear depths of $[0, 50, 100, 150, 200]\,\mu$m for the initial DESs heights $h_{\text{DES},\,0}$.

4.2 Unsymmetrical wear – test case B

A similar approach, as used for test case **A**, is employed for the determination of the wear depths for the case if only every second tooth is subjected to wear. As the unloaded tooth is not subjected to wear, the threshold, up to which the wear depth can be detected, is much higher, see Figure 6a.

The thus determined equation is given by

$$\text{Wear}_{\text{unsym}} = -84.71\,\Delta C_{\text{unloaded}}\frac{\mu\text{m}}{\text{pF}} + 372.64\,\mu\text{m}\,. \tag{3}$$

Similar to test case **A**, larger heights for the DESs are advantageous, as the maximum change in capacitance is higher there, see Figure 6b.

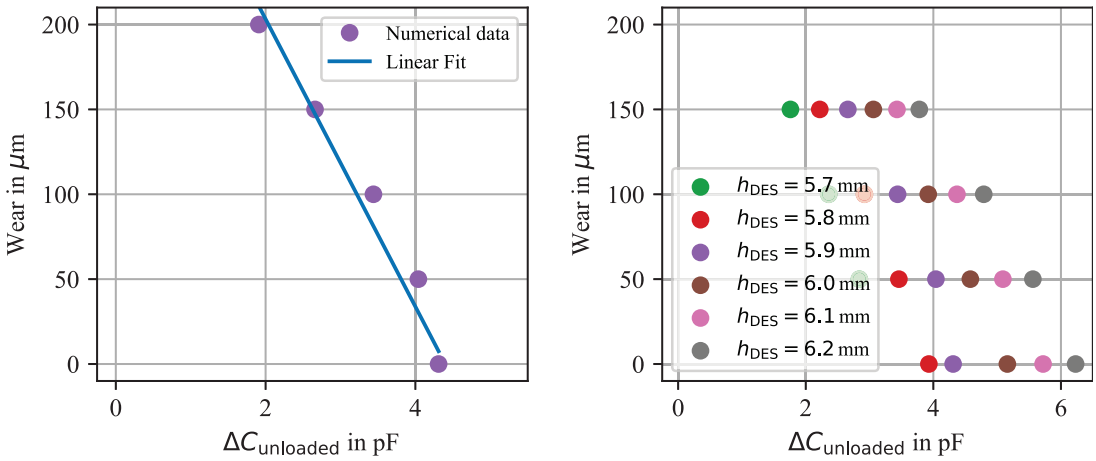

(a) $h_{\text{DES},\,0} = 5.9\,\text{mm}$ (b) $h_{\text{DES},\,0} = 5.7 \ldots 6.2\,\text{mm}$

Figure 6: Test case **B**: Maximal capacitance differences of the unloaded tooth C_{unloaded} for the investigated wear depths of $[0, 50, 100, 150, 200]\,\mu$m for the initial DESs heights $h_{\text{DES},\,0}$.

5 Conclusion and Outlook

In the current work, the influence of wear of the gear rim of a sensor-integrating jaw coupling was investigated. The main purpose of the sensor-integrating coupling is to predict the torque. For this, dielectric elastomer sensors (DESs) were inserted into every tooth of the gear rim. These DESs change their capacitance when a torque is transmitted. Based on the relationship between capacitance and torque, a regression model can be trained, which predicts the torque based on the history of measured capacitances. However, it is important to note that the correlation between torque and capacitance will change if wear is present. Therefore, it is essential to determine the current state of wear.

For this purpose, a numerical model of the sensor-integrating jaw coupling was used in which the geometry of the gear rim was modified with respect to the original geometry. Due to the cyclic symmetry of the jaw coupling, a quarter model was used in the finite element simulation.

In order to investigate the influence of different wear depths, the parts of the teeth which are constantly in contact with the two claw bodies and are thus expected to wear first, were removed.

Due to the nature of a jaw coupling, only every second tooth is loaded if a torque is transmitted while every other tooth is unloaded. In an unloaded and wear-free state, the teeth and thus the DESs are all subjected to a small pre compression. If a torque is transmitted, the unloaded teeth are fully load-free and thus the capacitances of the inserted DESs are minimal.

In the present research, two cases were distinguished. In the test case **A** the wear was modeled on both teeth, resulting in a symmetrical weakening of the gear rim. In the test case **B** only one tooth was modified to account for the wear, resulting in an unsymmetrical weakening of the gear rim. As the wear depth increases, the pre-compression decreases for both test cases. This decrease is reflected in the reduced drop in the capacitance of the unloaded teeth. This circumstance was successfully used to derive an analytical equation for the prediction of the wear for both test cases. Please note that we have assumed here that no shaft misalignments are present, as otherwise all teeth would additionally be subjected to changing loading–unloading conditions due to the rotation of the coupling.

In future research, this wear prediction will be incorporated into a regression model which takes the capacitance changes of the dielectric elastomer sensors as input and predicts the transmitted torque. Additionally, (i) the combination of wear with shaft misalignments and (ii) the superposition of the two test cases **A** and **B**, e.g., some teeth being subjected to a larger wear than the others, are of great interest.

Acknowledgement

The support of the German Science Foundation (DFG) (project numbers: 466661922, 441853410 and 418669083) is gratefully acknowledged.

REFERENCES

[1] A. Ewert, J. D. Menning, A. Prokopchuk, T. Rosenlöcher, E.-F. M. Henke, T. Wallmersperger, and B. Schlecht, "Concept of a sensor-integrating jaw coupling for measuring operating data," *Forschung im Ingenieurwesen*, vol. 88, no. 1, p. 28, 2024.

[2] E. Kirchner, T. Wallmersperger, T. Gwosch, J. D. M. Menning, J. Peters, R. Breimann, B. Kraus, P. Welzbacher, J. Küchenhof, D. Krause, E. Knoll, M. Otto, B. Muhammedi, S. Seltmann, A. Hasse, G. Schäfer, A. Lohrengel, S. Thielen, Y. Stiemcke, O. Koch, A. Ewert, T. Rosenlöcher, B. Schlecht, A. Prokopchuk, E.-F. M. Henke, F. Herbst, S. Matthiesen, D. Riehl, F. Keil, K. Hofmann, F. Pape, D. Konopka, G. Poll, T. Steppeler, R. Ottermann, F. Dencker, M. C. Wurz, S. Puchtler, T. Baszenski, M. Winnertz, G. Jacobs, B. Lehmann, and K. Stahl, "A review on sensor-integrating machine elements," *Advanced Sensor Research*, vol. 3, no. 4, p. 2300113, 2024.

[3] K. Feng, J. Ji, Q. Ni, and M. Beer, "A review of vibration-based gear wear monitoring and prediction techniques," *Mechanical Systems and Signal Processing*, vol. 182, p. 109605, 2023.

[4] H. Meng and K. Ludema, "Wear models and predictive equations: their form and content," *Wear*, vol. 181, pp. 443–457, 1995.

[5] J. Archard, "Contact and rubbing of flat surfaces," *Journal of applied physics*, vol. 24, no. 8, pp. 981–988, 1953.

[6] Q. Lian, G. Deng, A. K. Tieu, H. Li, Z. Liu, X. Wang, and H. Zhu, "Thermo-mechanical coupled finite element analysis of rolling contact fatigue and wear properties of a rail steel under different slip ratios," *Tribology International*, vol. 141, p. 105943, 2020.

[7] A. Kapoor and F. Franklin, "Tribological layers and the wear of ductile materials," *Wear*, vol. 245, no. 1-2, pp. 204–215, 2000.

[8] F. Martínez, M. Canales, S. Izquierdo, M. Jiménez, and M. Martínez, "Finite element implementation and validation of wear modelling in sliding polymer–metal contacts," *Wear*, vol. 284, pp. 52–64, 2012.

[9] A. Prokopchuk, A. Ewert, J. Menning, A. Richter, B. Schlecht, T. Wallmersperger, and E.-F. M. Henke, "Manufacturing of soft capacitive strain sensor based on dielectric elastomer material for an elastic element of a jaw coupling," *Engineering Research Express*, vol. 6, p. 015493, 2024.

[10] A. Prokopchuk, A. Ewert, J. D. M. Menning, A. Richter, B. Schlecht, T. Wallmersperger, and E.-F. M. Henke, "Influence of stacking on the stability of a multi-layer capacitive dielectric elastomer sensor for strain detection," in *Electroactive Polymer Actuators and Devices (EAPAD) XXVI*, J. D. W. Madden, S. S. Seelecke, and A. L. Skov, Eds., vol. 12945, International Society for Optics and Photonics. SPIE, 2024, p. 129450Q.

[11] R. E. Pelrine, R. D. Kornbluh, Q. Pei, and J. S. Eckerle, "Electroactive polymer sensors," Oct. 26 2004, US Patent 6,809,462.

[12] B. O'Brien, J. Thode, I. Anderson, E. Calius, E. Haemmerle, and S. Xie, "Integrated extension sensor based on resistance and voltage measurement for a dielectric elastomer," in *Electroactive Polymer Actuators and Devices (EAPAD) 2007*, vol. 6524. SPIE, 2007, pp. 307–317.

[13] Z. Suo, "Theory of dielectric elastomers," *Acta Mechanica Solida Sinica*, vol. 23, no. 6, pp. 549–578, 2010.

[14] A. Ewert, J. D. Menning, A. Prokopchuk, T. Rosenlöcher, E.-F. M. Vorrath, T. Wallmersperger, and B. Schlecht, "Experimental investigations and material modeling of an elastomer jaw coupling," *Materials Testing*, vol. 66, no. 9, pp. 1425–1438, 2024.

[15] H. J. Qi and M. C. Boyce, "Stress–strain behavior of thermoplastic polyurethanes," *Mechanics of Materials*, vol. 37, no. 8, pp. 817–839, 2005.

[16] H. S. Han, J. Yoon, S. Nam, S. Park, and D. J. Hyun, "A soft ground reaction force sensor system utilizing time-delay recurrent neural network," *IEEE Sensors Journal*, vol. 20, no. 18, pp. 10 851–10 861, 2020.

[17] D. Wu, Y. Zhang, M. Ourak, K. Niu, J. Dankelman, and E. Vander Poorten, "Hysteresis modeling of robotic catheters based on long short-term memory network for improved environment reconstruction," *IEEE Robotics and Automation Letters*, vol. 6, no. 2, pp. 2106–2113, 2021.

[18] J. D. M. Menning, A. Prokopchuk, A. Ewert, B. Schlecht, E.-F. Markus Henke, and T. Wallmersperger, "Dielectric elastomer sensor integrated in a jaw coupling: Modeling and simulation of mechanical and electrical behavior," *Journal of Intelligent Material Systems and Structures*, p. 1045389X241274816, 2024.

[19] J. D. M. Menning, A. Ewert, A. Prokopchuk, E.-F. M. Vorrath, B. Schlecht, and T. Wallmersperger, "Numerical and experimental investigations of conventional and sensor-integrating jaw couplings," *Forschung im Ingenieurwesen*, 2025, accepted.

[20] J. D. Menning, A. Ewert, A. Prokopchuk, B. Schlecht, M. Henke, and T. Wallmersperger, "Finite element based modeling and simulation of an elastomer gear rim," *PAMM*, vol. 23, no. 1, p. e202200141, 2023.

[21] R. J. Boulbes, "Troubleshooting finite-element modeling with abaqus," *Fransa*, vol. 1, p. 439, 2020.

XI ECCOMAS Thematic Conference on Smart Structures and Materials - SMART 2025
M. Krommer, M. Nader and M. Schagerl (Eds)

Received: 30 March 2025 / Revised: 4 September 2025 / Accepted: 9 October 2025
© The Author(s) 2025

Correlation between Temperature Changes and Magnetstriction Effect of Magnetoactive Foam

Nur Azmah Nordin, Nurul Nadia Senin, Saiful Amri Mazlan, Mohd Aidy Faizal Johari, Abdullah Yasser Abd Fatah

Abstract. Magnetorheological (MR) foam has been identified as a promising magnetostrictive material due to its high flexibility in changing dimensions and rapid response to applied magnetic fields. Nevertheless, magnetic moment of MR foam is highly influenced by temperatures, and it may affect the magnetostrictive performance of MR foam. While this has yet to been thoroughly investigated, the study aimed to examine the effects of temperatures and magnetic fields on the magnetostriction of MR foam. Two samples, namely PU foam and MR foam were tested across the temperatures ranging from 25°C to 50°C and under the magnetic fields from 0 to 0.7 T. At the off-state condition (0 T), both samples exhibited a reduction in the dimensions, decreased by approximately 0.03-0.04% as temperature increased from 25°C to 35°C. As the temperature rose from 35°C to 50°C, both samples however expanded, with the dimensions increased by 0.06% and 0.04% for the PU foam and MR foam, respectively. Meanwhile, at the on-state condition (0.1 to 0.7 T), similar trends were observed, with the transition from reduced to expand dimensions occurred at 35°C. This behaviour might be attributed to the polymer matrix's soft-segment and hard-segment dynamics, which were affected at temperature ranges between 25°C-35°C and 35°C-50°C, respectively. These dynamic phenomena caused a negative magnetostriction at lower temperatures and positive

Nur Azmah Nordin & Nurul Nadia Senin & Saiful Amri Mazlan & Mohd Aidy Faizal Johari
Engineering Materials and Structures iKohza, Malaysia-Japan International Institute of Technology, Universiti Teknologi Malaysia Kuala Lumpur, 54100 Kuala Lumpur, Malaysia

Nur Azmah Nordin & Saifal Amri Mazlan
Automotive Development Centre, Institute for Sustainable Transport (IST), Universiti Teknologi Malaysia, 81310 Skudai, Johor, Malaysia

Abdullah Yasser Abd Fatah
Department of Smart Engineering and Advanced Technology, Faculty of Artificial Intelligence, Universiti Teknologi Malaysia, Jalan Sultan Yahya Petra, 54100 Kuala Lumpur, Malaysia

magnetostriction at higher temperatures. In brief, the temperature increased in both PU and MR foams demonstrating a unique pattern of shrinkage, then followed by expansion with the dimensional transition consistently noted at 35°C, for both samples.

Key words: Polyurethane Foam, Magnetoactive Foam; Magnetostriction, Temperatures, Soft-segment, Hard-segment.

1 INTRODUCTION

Magnetostrictive polymer composite (MPC) is a material that has been introduced to overcome the drawbacks and enhance the performance of metal-based magnetostrictive materials which are generally expensive [1–3] and require relatively large magnetic field of more than 1 T to drive greater magnetostriction saturation that is currently up to 0.02% only [1]. MPC consists of magnetically permeable particles which are dispersed in a soft, non-magnetic and elastic polymeric matrix such as polydimethylsiloxane (PDMS) [4], silicone rubber [5] and polyurethane (PU) foam [6–8]. The advantages of MPCs as compared to metal-based magnetostrictive materials are the ability to change dimensions elastically, more flexible, lightweight and produce greater saturation magnetostriction with presence of magnetic field [1], especially at low value of less than 0.5T. PU foam that is incorporated with magnetic particles of carbonyl iron (CIPs), also known as magnetorheological (MR) foam have attracted interest recently due to reduce stiffness [9], low density and high flexibility [2] and high sensitivity to magnetic field [2,10] as compared to other existing MPCs. Besides, nucleation of pores in the matrix phase of MR foam causes a decrease in the resultant Young's modulus, which is in return result the MPC to be more susceptible to elongation [7], thus suitable for magnetostrictive application that require changeable dimensions easily and reversibly. This improved property of MR foam can be further utilized in applications of semi-active adaptive variable-stiffness devices, soft actuators, sensors and artificial muscles [2,11].

However, inducing current to generate magnetic field to the device may generate heat [9,12] that subsequently affect the magnetostriction behavior and performance of the MR foam. In fact, during continuous operation of the system, most devices tend to experience a rise in temperature due to heat dissipation of the components, friction, or heat from the electrical conductance. This phenomenon in return would affect the material that developed for the device as well as its resultant properties. A study on temperature effect of an alloy has reported that the magnetostriction behavior would be changed as temperature increases. In fact, in the study of monolithic Terfenol-D at temperature between -40 to 80°C, the magnetostriction of the material increased from initial temperature of -40 up to 0°C, by ~1.5 x 10^{-3} then significantly dropped in the magnetostriction value, particularly at the temperature of 0°C onwards (to 80°C) by ~0.3 x 10^{-3} reduction [13]. Another study of the galfenol-based alloy, particularly $Fe_{83}Ga_{17}$ has shown that the magnetostrictive effect of the material has constantly decreased as the applied temperature increased, from -50 to 27°C by ~5 x 10^{-3} decrement [14]. A similar decreasing trend has been reported by the $Fe_{0.81}Ga_{0.19}$ alloy in which the magnetostrictive effect of the alloy reduced as the temperature increased from -20 to 80°C, by 45 x 10^{-6} decrement [15].

However, another composition of galfenol-based alloy, specifically $Fe_{65}Ga_{35}$ has stated that the magnetostrictive effect of the material has decreased from -50 to 0°C by ~3 x 10^{-3} but then increased slightly from 0°C to 27°C, by ~1 x 10^{-3} increment [14]. The findings of magnetostrictive effect of the galfenol-based alloys somehow show dependency on its compositions as stated in those previous studies, and the exact phenomenon of the effect with the temperature increment is still rather ambiguous. On the other hand, a study on iron-beryllium (FeBe) alloy has stated that a slight decrement in the magnetostrictive effect of the material as the applied temperature increased from -200 to 50°C, which was about 1.0 x 10^{-3} only [16].

Meanwhile, a study on iron-aluminium-lanthanum alloy, $LaFe_{13-x}Al_x$ (x = 1.8) between the temperature of 0 to 300K (-273°C to 27°C) showed a significant finding in which the magnetostrictive effect increased by 1.8 x 10^{-3} from -273 to -100°C, particularly with the applied magnetic flux density of 12T. However, the magnetostrictive effect dropped by 1.8 x 10^{-3} as the temperature rose from 100 to 27°C and the maximum magnetostrictive effect was obtained at the temperature of -100°C, which was around 2000ppm [17]. This material somehow showed a dependency of magnetostriction to the temperature changes and has a narrow temperature range to obtain the maximum magnetostriction or magnetostrictive effect. Another studies on the cobalt-ferrite, $CoFe_2O_4$ alloy have stated that the magnetostrictive effect of the material decreased by about 1.75 x 10^{-9} for the temperature between -200 to 23°C and the value of the magnetostriction remain unchanged for the temperature that increased to 80°C. Nevertheless, when the Al was added to the alloy; $CoAl_xFe_{2-x}O_4$ (where x=0.2), the magnetostriction was constant at 3 x 10^{-9} for the temperature between -200 to -120°C and then decreased by 1.5 x 10^{-9} when temperature further increased from -120 to 80°C [18] with the temperatures and the findings somehow showed some uniqueness and distinctive from one to one another depending on the presence of cations in the alloy; for example Al^{3+} and Fe^{3+}, composition of the alloying elements such as $Fe_{83}Ga_{17}$ and $Fe_{65}Ga_{35}$, and the range of temperatures investigated. However, detail analysis and mechanism on the changed of the magnetostrictive effect of the alloys with temperatures are still rather limited and not comprehensively being discussed.

On the hand, the effect of temperatures on the MPC materials are also available but limited to magnetorheological investigations. For instance, a study on cis-polybutadiene rubber (BR) that composed with iron particles as main filler has shown a decreasing trend in storage and loss modulus as temperature increased from 20 to 90°C. However, samples that were composed of natural rubber (NR) and iron particles exhibited a decreasing trend in both modulus as temperature rose from 20 to 50°C before both outputs increased as temperature further increased to 90°C [19]. The study has shown a similar trend as in alloy-based materials, but the exact trend of the behaviors is still unclear. In fact, the extend of study towards the magnetostrictive effect of the MPC with temperatures has not yet been discovered and this would become a significant concern to be focused on, especially related to the analysis of decrement and increment trend of magnetostriction with certain temperatures.

Since the study of MPCs, particularly MR foam has advantages on magnetostrictive effect, particularly in soft robotics and sensors technology, the effect of MR foam at different temperatures is crucial to be explored to understand the correlation between the temperatures

and property changes before associating into the applications and products. To address this gap, a study on the effect of temperatures and magnetic fields towards the magnetostriction behavior of MR foams is carried out. In this study, two different samples of PU foams were fabricated that contained 0 wt.% CIPs known as PU foam, and 75 wt.% CIPs known as MR foam. The samples underwent magnetostriction test at room to modest temperatures, 25 to 50ºC and at various magnetic fields ranging from 0 to 0.7T. The change in dimension of both samples, represented as magnetostrictive effect were recorded and analyzed.

2 MATERIALS AND METHODOLOGY

The fabrication of MR foam comprised of foam that acted as a matrix phase, and embedded with magnetic particles as reinforced material. The magnetic particles used in this study were soft magnetic carbonyl iron particles (CIPs), typed-OM with the diameter of 1 to 10 μm was supplied by BASF Corporation, Germany. The flexible polyurethane (PU) foam meanwhile was selected as a matrix material which consist of two component of raw materials which were 4,4′-methylene bis(phenyl isocyanate) (MDI) benzene (Fraction A) and polyether polyols (PPG)-based triol (Fraction B). The raw materials were supplied by Smooth On Inc, USA.

Prior to the fabrication of MR foam, 75wt.% of CIPs was used (75g) to be mixed with the PU foam and the MR foam was prepared via in situ fabrication method. For sample with CIPs content, fraction B was mixed with 75wt.% of CIPs using a mechanical stirrer with 550rpm of speed, at 20seconds. Then, fraction A was added to the mixture and the stirring continued for another 20seconds at the same speed. The final mixture was instantly poured into a mould for the foaming process to take place. At this point, the mixture would begin to slowly expand and solidify. The mixture was left for curing at room temperature, for 24 hours. The same procedure was applied for the fabrication of PU foam sample but the step of adding the CIPs was skipped.

The magnetostriction test was carried out in terms of the length changes of the sample by using a rheometer, modelled MCR302 that was manufactured by Anton Paar. The rheometer is also equipped with temperature controller (Viscotherm, VT2) to induce difference value of heat during the testing. The PU foam and MR foam were cut into a circular shape with a diameter of 20mm and thickness of 1mm for the magnetostriction test as illustrated in Figure 1 and the samples were placed between the upper and lower parallel measuring plates. Magnetic field excitations in the range of 0 to 0.7Tesla (T) were applied to the MR foam by varying the currents from 0 A to 5A, and initial preload of 15N and frequency of 1Hz were set and maintained throughout the testing. Prior to the effect of temperatures on the MR foam during the magnetostriction test, the temperature was increased stepwise starting from 25ºC (room temperature) to 50ºC, by 5ºC increment. Magnetostriction effect of the MR foam was then calculated using equation (1) as shown in the following:

$$\text{Magnetostriction} = 100\% \times (Lf - Li) / Li \quad (1)$$

Where Li and Lf are the length (mm) of the sample in the absence and presence of magnetic field, respectively. The change in the length of the sample was measured based on the gap

difference between the upper and bottom plates, detected by displacement sensor, respective to applied magnetic fields and temperature changes.

3 RESULTS AND DISCUSSION

3.1 Dimension change of PU foam and MR foam at different operating temperatures

Figure 2 shows the dimensional change of PU foam and MR foam in the absence of magnetic field which is also called as the off-state condition, particularly with increasing temperatures from 25 to 50°C. Based on the figure, it can be observed that both PU foam and MR foam exhibited a similar trend as decreased and increased in dimensional change with increasing temperatures. Specifically, with increasing temperatures from 25 to 35°C, both samples have shown a decrease in dimension indicating the shrinkage of the materials by about 0.03-0.04%. However, further increased in temperatures from 35 up to 50°C, the dimensional change possessed a reverse effect as increased, showing the expansion of the foam's dimension with the temperatures. In fact, the expansion of PU foam is slightly larger, about 0.06% increment for temperature up to 50°C. Meanwhile for MR foam, the increment is about 0.04% indicating the denser composite foam to experience the expansion as compared to the unfilled foam (PU foam). The reason for such a phenomenon can be attributed to the presence of magnetic particles of carbonyl iron (CIPs) that has influenced the physical properties of the matrix foam. With presence of the CIPs, the density and stiffness of MR foam has been increased causing its elasticity to be reduced and might restrict the expansion of the material upon induced of temperatures.

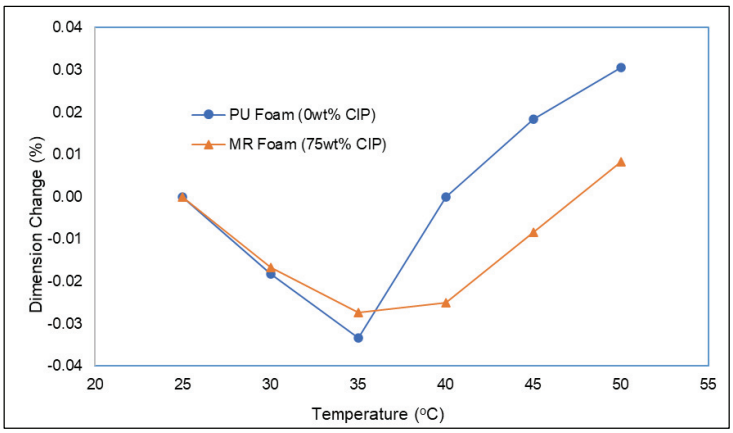

Figure 2. Magnetostriction of PU foam and MR foam at the off-state condition, with increasing temperatures

The phenomenon of decrease and increase in dimension with increased in temperatures at the off-state condition can be related to the structural feature of the polymer matrix. Polyurethane (PU) generally comprised of alternate copolymer of hard segments (HS) which is methylene diphenyl diisocyanate (MDI)-benzene and soft segments (SS) of polypropylene glycol (PPG)-polyols that acts as linkage agent between the hard segments (HS) of the

diisocyanate. This alternate copolymers between the HS and SS in the PU foam are illustrated in Figure 3 (a). In the study conducted by Zhu et al. [21] on the shape memory polyurethane (PU) ionomer has found the endothermic crystalline melting point of SS in the PU was in the range of 20 to 50°C. It is related to the heat absorb that gradually allow melting of the crystalline SS which was subsequently affect the resultant behavior of the material. Respective to current finding as presented in Figure 2, the decrement in magnetostriction at increasing temperature from 25 to 35°C might also be due to the heat consumed by the SS of the MR foam. As heat was absorbed by the SS in the MR foam within the temperature range, the amount of SS that acted as linkages between the HS has reduced and in return causing the material to slightly shrink, as illustrated in Figure 3 (b). Thus, it led to a decrease in the dimensions of the MR foam. In fact, Zharinova et al. [22] also stated that the melting process of some PU segments would cause shrinking of the pores and decreased in the length of the sample.

Then, both PU and MR foams showed an increment in dimension when temperature has further increased from 35 to 50°C. There are two factors that can contribute to this finding. The first one related to the thermal expansion phenomenon of the hard segments (HS) in the PU matrix of both PU and MR foams. A study that introduced a short-range and long-range order of molecular chain of HS has stated that the melting temperature of short-range molecular chain of HS is in the range of 30 – 60°C while 200°C is for the long-range molecular chain of HS [23]. The short-range order of HS has much lower melting temperature as compared to the long-range order thus it responded immediately, but slightly higher than SS. Thus, at this temperature range of 30 - 60°C, the HS is not completely melted yet, but the arrangement has started to loosen due to the short-range molecular chains of HS have been affected. In fact, a study done by Somdee et al. [24] have found that a glass transition temperature, Tg of HS of PU elastomer matrix was in the range of 58 to 70°C. Meanwhile in this study, the increase in magnetostriction of PU and MR foams are noted in between 35 to 50°C. This finding can be related to the looseness or dissociation of short-range of HS from the PU matrix, with increased temperatures. This might cause the remaining or long-range of HS to expand resulting in the increment of the length of the sample, as illustrated in Figure 3 (c). On the other hand, the second factor is related to the CIPs that are presented in the MR foam which might also experience thermal expansion with temperatures. However, the thermal expansion of the metal-based particles is generally ten times lower than the polymer matrix [25] thus, the change is not significant as compared to the polymer-based material. Therefore, the thermal expansion of the PU matrix in both PU and MR foams has a significant effect to expand its length of the materials. Nevertheless, the expansion of the MR foam is quite smaller as compared to the PU foam due to presence of the CIPs in the MR foam that subsequently increased the density of the composite foam.

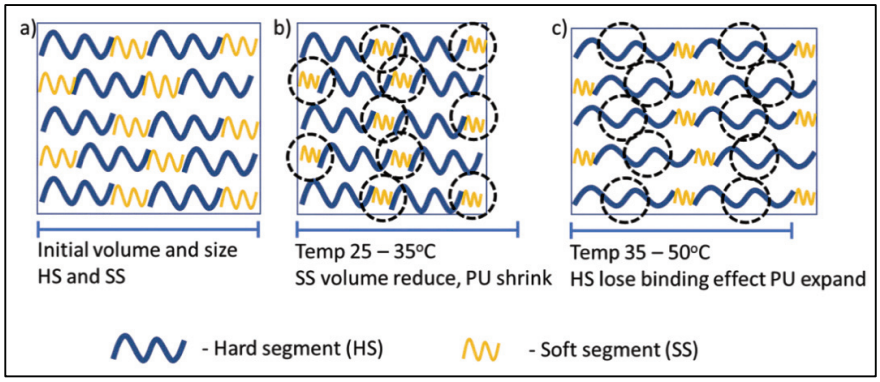

Figure 3. Schematic diagram of PU matrix in the PU foam and MR foam that contained of hard segment (HS) and soft segment (SS) for (a) Initial condition at 25°C, (b) 25 to 35°C and (c) 35 to 50°C

3.2 Magnetostriction of MR foam at different operating temperatures and magnetic fields

Meanwhile, Figure 4 shows the magnetostriction of MR foam at the on-state condition or with magnetic fields from 0 to 0.7 T, for temperatures between 25 to 50°C. It can be observed that the MR foam has experienced positive magnetostriction indicating the expansion of the material with applied magnetic fields. It is due to the magnetostriction experienced by the CIPs as well as the magnetic forces that formed between the particles in the matrix structure that caused the MR foam to expand. In fact, the magnetostriction of MR foam increased with larger value of magnetic fields showing the greater magnetic field strength was induced to the material. In particular, at specific temperature of 50°C, the magnetostriction of MR foam increased from 0.008 to 6.66, 9.67, 11.74, 12.89, 14.22, 15.29 and 15.97% when magnetic fields were applied from 0 to 0.1, 0.2, 0.3, 0.4, 0.5, 0.6 and 0.7T, respectively. However, the increment in magnetostriction of MR foam has reduced with increasing temperatures from 25 to 35°C, but the value has re-increased for the temperature from 40 to 50°C. In fact, the changed of magnetostriction of MR foam with temperatures has been interpreted as in Figure 5, with different magnetic field values. The magnetostriction effect is reversible as shown in Figure A1.

In brief, the trends are similar as in the off-state condition in which the magnetostriction of MR foam decreased for the temperature between 25 to 35°C then, the MR foam re-expanded for the temperature from 35 to 50°C, particularly for all values of magnetic field. Thus, the transition from reduced to increase in magnetostriction of MR foam also occurred at 35°C. Corresponds to previous discussion as in Figure 3, the decreased in magnetostriction of MR foam at the temperature between 25 to 35°C is due to the soft-segment (SS) of PU matrix that has been affected as begin to melt with increasing temperatures, and in return the MR foam was slightly shrink. Although the induced of magnetic fields from 0.1 to 0.7T have improved the magnetostriction of the material, the expansion however reduced with the temperatures. Meanwhile, positive magnetostriction or the expansion of MR foam occurring from temperature 35 to 50°C might be due to the looseness of the short-range molecular chain of HS in the PU matrix that result the long-range molecular chain of HS to expand. Besides, with

applied and increased in magnetic field values, the MR foams experienced greater magnetostrictions causing the longer dimension of the MR foam, attributed to the stronger magnetic forces between the magnetic particles (CIPs) and towards the magnetic fields, that also lead to the change of the pore structure of MR foam.

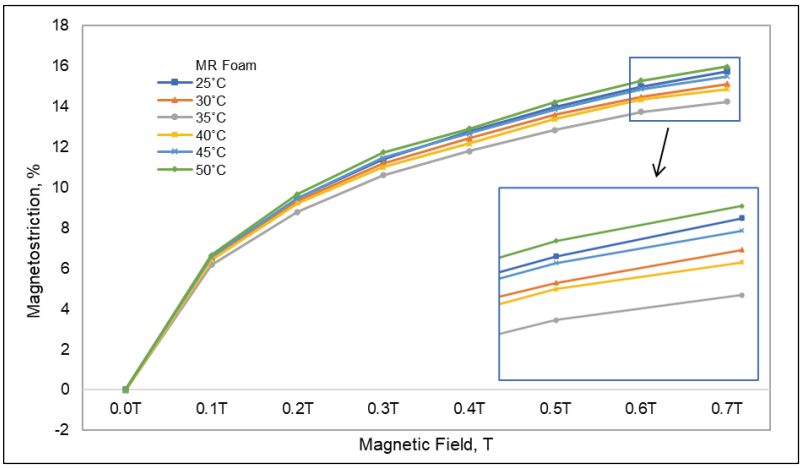

Figure 4. Magnetostriction of MR Foam with increasing magnetic field from 0 to 0.7T, at different temperatures.

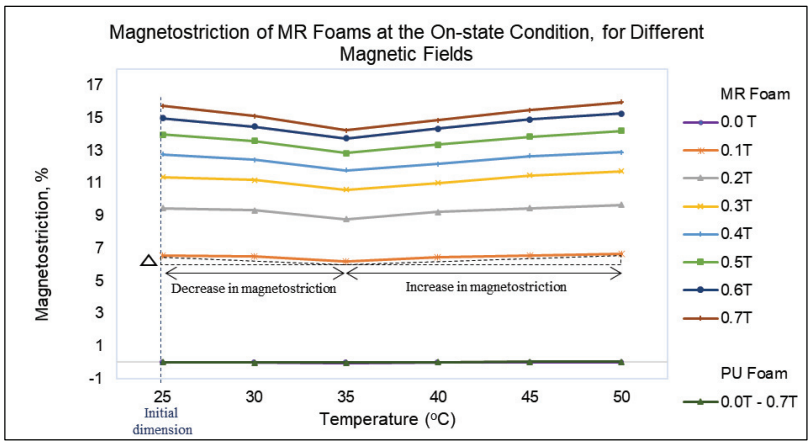

Figure 5. Magnetostriction of PU and MR foams with increasing temperatures from 25 to 50°C, at different magnetic fields (0.0-0.7T).

Table 1. Difference in magnetostriction of MR foams under different temperature ranges, at various magnetic fields.

Magnetic Field (T)	25 to 35°C (Δ Decrease magnetostriction)	35 to 50°C (Δ Increase magnetostriction)
0	0.033	0.064
0.1	0.309	0.333
0.2	0.576	0.888

0.3	0.645	0.922
0.4	0.817	1.254
0.5	0.944	1.380
0.6	0.946	1.543
0.7	1.272	1.739

Meanwhile, Table 1 presents the difference in decreased and increased magnetostriction (Δ) respective to different temperature ranges, with different magnetic fields. The difference for decreased and increased magnetostriction (Δ) also can be illustrated in Figure 5. It shows that the difference in decreased magnetostriction (Δ), particularly for temperature range between 25 - 35°C is getting bigger with increasing magnetic fields, and the trend is similar for the difference in increased magnetostriction (Δ) for temperature between 35 - 50°C indicating the influence of magnetic fields towards the magnetostriction behavior of the MR foam. In general, increasing magnetic fields would increase the magnetization of the magnetic material (CIPs) [26,27]. It is due to the uniform magnetic domains in the CIPs with the strength and direction of magnetic fields. As a result, the magnetostriction of MR foam would be enhanced. Based on Figure 5 as well, although increased in magnetic fields have increased the magnetization effect of the MR foam, the increased in temperatures from 25 to 35°C however, has reduced the magnetostriction of the sample, as difference in decreased magnetostriction (Δ) is getting bigger. Since the effect of temperatures between 25 to 35°C has caused shrinkage of the sample as shown in Figure 2, the induced fields seemed contribute more to the shrinkage effect of the MR foam.

On the other hand, when temperature increased from 35 to 50°C, the magnetostriction of MR foam has further increased especially with more applied magnetic fields. The increased in temperatures might induce greater heat transfer to the MR foam which causes the thermal expansion phenomenon within the material, attributed to the binding effect of the HS of PU foam that has been loosened. Besides, the distance between molecular chains of PU foam also has been increased with the temperature [28] thus, the magnetostriction of MR foam increased. At this temperature ranges as well, the MR foam is observed to expand from the transition point of decreased to increased magnetostriction, particularly at 35°C, then returned to its initial dimension before expanding more to its maximum magnetostriction with further applied temperature up to 50°C. The initial dimension here is referred to the dimension of the MR foam at 25°C and at a specific magnetic field. In addition, at greater magnetic fields, the magnetic forces between the CIPs increased causing the particles in the structure of MR foam to tend to align following the direction of magnetic fields thus, resulting in greater magnetostriction effect. It is susceptible that the attraction between the CIPs with stronger magnetic fields caused the pores structure to slightly elongate resulting in the increment of the dimension of MR foam, in the same direction of magnetic fields, as illustrated in Figure 6. A similar phenomenon of the pore's elongation has been stated in previous study, but it was related to the sounds wave that passed through the MR foam. The absorbed sound is forced to oscillate at the frequency of sound waves that caused the elongation of the pores in the MR foam [29]. In fact, the elongation of pores is also expected due to pressure within the MR foam that increased with temperatures. Nevertheless, more investigation is required to support the hypothesis.

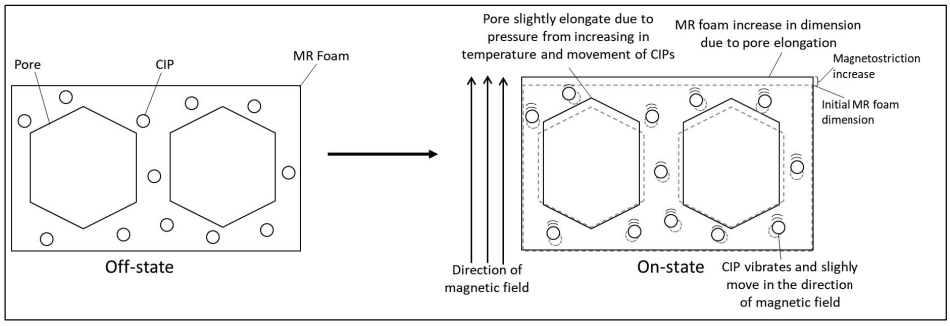

Figure 6. Schematic diagram of pore's elongation with induced of magnetic fields (on-state) that result in the magnetostriction effect of MR foam

4 CONCLUSIONS

In this study, two samples were fabricated which are PU foam and MR foam with 75 wt.% of CIPs. Both samples were tested under different temperatures from 25 to 50°C, with increasing by 5°C stepwise, at off-state and on-state conditions. At the off-state, the increased in temperature from 25 to 35°C caused both PU and MR foams to reduce its dimension by approximately 0.03-0.04% known as negative magnetostriction, before expanding to about 0.06% for PU foam and 0.04% for MR foam when both samples underwent temperature increment from 35 to 50°C. Meanwhile, at the on-state condition for magnetic field ranging from 0.1 to 0.7T, similar patterns were observed since the transition from decreased to increase in magnetostriction occurred at 35°C. In fact, the magnetostriction values are getting bigger with higher applied magnetic fields indicating stronger magnetic forces between the magnetic particles of carbonyl iron (CIPs) which caused the increment of the dimension of MR foam. The decrement in magnetostriction of MR foam at temperature ranges between 25 to 35°C can be related to the soft-segment of the PU matrix that began to reduce meanwhile, re-increased in magnetostriction at temperature between 35 – 50°C was due to the looseness of hard-segment (HS) of PU matrix that resulted in the thermal expansion of the MR foam.

5 ACKNOWLEDGEMENTS

This work was supported by Higher Institution Centre of Excellence (HiCOE) program of Ministry of Higher Education (MOHE) Malaysia under HiCOE Research Grant. The authors also would like to acknowledge the financial support from UTM Fundamental Research Grant (Vot. No. 23H17).

6 REFERENCES

[1] Elhajjar R, Law CT, Pegoretti A. Magnetostrictive Polymer Composites: Recent Advances in Materials, Structures and Properties. Progress in Materials Science, 2018 97: 204–229.
[2] Norhaniza R, Mazlan SA, Ubaidillah, Abdul Aziz SA, Nazmi N, Yunus NA. Enhancement of Sensitivity of Magnetostrictive Foam in Low Magnetic Fields for Sensor Applications. Polymer, 2020 211(123083): 1–10.

[3] Guruswamy S, Srisukhumbowornchai N, Clark AE, Restorff JB, Wun-Fogle M. Strong, Ductile, and Low-Field-Magnetostrictive Alloys Based On Fe-Ga. Scripta Materialia, 2000 43(3): 239–244.
[4] Saveliev D V., Belyaeva IA, Chashin D V., Fetisov LY, Romeis D, Kettl W, et al. Giant Extensional Strain of Magnetoactive Elastomeric Cylinders in Uniform Magnetic Fields. Materials, 2020 13(15): 3297.
[5] Chen L, Gong XL, Jiang WQ, Yao JJ, Deng HX, Li WH. Investigation on Magnetorheological Elastomers Based on Natural Rubber. Journal of Materials Science, 2007 42(14): 5483–5489.
[6] Coquelle E, Bossis G. Magnetostriction and Piezoresistivity in Elastomers Filled with Magnetic Particles. Journal of Advance Science, 2005 17 (1): 132–138.
[7] Bednarek S. The Giant Linear Magnetostriction in Elastic Ferromagnetic Composites within a Porous Matrix. Journal of Magnetism and Magnetic Materials, 2006 301(1): 200–207.
[8] Guan X, Dong X, Ou J. Magnetostrictive Effect of Magnetorheological Elastomer. Journal of Magnetism and Magnetic Materials, 2008 320 (3–4): 158–163.
[9] Zhao Z, Sui X. Temperature Compensation Design and Experiment for a Giant Magnetostrictive Actuator. Nature Research, 2021 11 (251): 1–14.
[10] Li SY, Wang BW, Weng L, Zhou Y, Sun Y, Huang WM. The Effect of Magnetic Field Heat Treatment on Magnetostriction of Terfenol-D 2-2 Composites. Journal of Magnetism and Magnetic Materials, 2008 320 (6): 806–809.
[11] Davino D, D'auria M, Pantani R, Sorrentino L. Reinforced Smart Foams Produced with Time-Profiled Magnetic Fields. Polymers, 2021 13(24): 1–18.
[12] Gao X, Liu Y, Guo H, Yang X. Structural Design of Giant Magnetostrictive Actuator. AIP Advances, 2018 8 (6).
[13] Clark AE, Teter JP, McMasters OD. Magnetostriction "Jumps" in Twinned Tb0.3Dy 0.7Fe1.9. Journal of Applied Physics, 1988 63 (8): 3910–3912.
[14] Cullen JR, Clark AE, Wun-Fogle M, Restorff JB, Lograsso TA. Magnetoelasticity of Fe-Ga and Fe-Al Alloys. Journal of Magnetism and Magnetic Materials, 2001 226 (230): 948–949.
[15] Kellogg RA, Flatau AB, Clark AE, Wun-Fogle M, Lograsso TA. Temperature and Stress Dependencies of the Magnetic and Magnetostrictive Properties of Fe 0.81Ga 0.19. Journal of Applied Physics, 2002 91(10): 7821–7823.
[16] Clark AE, Wun-Fogle M, Restorff JB, Lograsso TA, Petculescu G. Magnetostriction and Elasticity of Body Centered Cubic Fe 100-XBe x Alloys. Journal of Applied Physics, 2004 95(11): 6942–6944.
[17] Wan Y, Xiong Y, Zhang S. Temperature Dependent Dynamic Mechanical Properties of Magnetorheological Elastomers: Experiment and Modeling. Composite Structures, 2018 202: 768–773.
[18] Nlebedim IC, Ranvah N, Melikhov Y, Williams PI, Snyder JE, Moses AJ, et al. Effect of Temperature Variation on the Magnetostrictive Properties of $CoAlxFe_2$-XO_4. Journal of Applied Physics, 2010 107 (9): 44502.
[19] Zhang W, Gong X, Xuan S, Jiang W. Temperature-Dependent Mechanical Properties and Model of Magnetorheological Elastomers. Industrial and Engineering Chemistry Research, 2011 50 (11): 6704–6712.

[20] Pachence JM, Kohn J. Biodegradable Polymers. Principles of Tissue Engineering, 2000 22: 263–277.
[21] Zhu Y, Hu J, Choi KF, Yeung KW, Meng Q, Chen S. Crystallization and Melting Behavior of the Crystalline Soft Segment in a Shape-Memory Polyurethane Ionomer. Journal of Applied Polymer Science, 2007 107 (1): 599–609.
[22] Zharinova E, Heuchel M, Weigel T, Gerber D, Kratz K, Lendlein A. Water-Blown Polyurethane Foams Showing a Reversible Shape-Memory Effect. Polymers, 2016 8 (412): 1–22.
[23] Kandil SH, El-Kholy AE, El-Shirbiny M, El-Sheikh ZR. Thermal Behaviour of Polyurethane for Use in Solar Cell Encapsulation. Solar Energy Materials, 1989 19: 211–219.
[24] Somdee P, Lassú-Kuknyó T, Kónya C, Szabó T, Marossy K. Thermal Analysis of Polyurethane Elastomers Matrix with Different Chain Extender Contents for Thermal Conductive Application. Journal of Thermal Analysis and Calorimetry, 2019 138 (2): 1003–1010.
[25] Radulescu B, Mihalache AM, Hrituc A, Radulescu M, Slatineanu L, Munteanu A, et al. Thermal Expansion of Plastics Used for 3D Printing. Polymers, 2022 14 (15): 1–18.
[26] Feynman RP, Leighton RB, Sands M. The Feynman Lectures on Physics, Mainly Electromagnetism and Matter. vol. 2. New Millenium. New York: Basic Books; 2010.
[27] Krishnan KM. Fundamentals and Applications of Magnetic Materials. 1st ed. United Kingdom: Oxford; 2016.
[28] Gunes IS, Cao F, Jana SC. Effect of Thermal Expansion on Shape Memory Behavior of Polyurethane and Its Nanocomposites. Journal of Polymer Science, Part B: Polymer Physics, 2008 46 (14): 1437–1449.
[29] Muhazeli NS, Nordin NA, Ubaidillah U, Mazlan SA, Aziz SAA, Nazmi N, et al. Magnetic and Tunable Sound Absorption Properties of an In-Situ Prepared Magnetorheological Foam. Materials, 2020 13 (24): 1–16.

XI ECCOMAS Thematic Conference on Smart Structures and Materials - SMART 2025
M. Krommer, M. Nader and M. Schagerl (Eds)

Received: 29 April 2025 / Revised: 6 October 2025 / Accepted: 9 October 2025
© The Author(s) 2025

Bidirectional Evolutionary Structural Optimization for Enhanced Design of SMA Superelastic Structures and Actuators

Sefa Oksuz, Darren Hartl

Abstract. The most important engineering behaviors exhibited by shape memory alloys (SMAs) are superelasticity, which is the ability to fully recover considerable and seemingly permanent deformation when a previously applied load is removed, and the shape memory effect, which allows for recovery of the original shape of an SMA component that has seemingly been permanently deformed given the sufficient application of heat. This shape memory allows actuators to be created with high energy density. Evolutionary structural optimization (ESO) is a heuristic method that maximizes the functional performance of a structure by iterative removal of elements that least contribute to the desired functionality until a predefined volume fraction is satisfied. Further developments have given rise to a more efficient approach: Bi-directional ESO (BESO). This iterative scheme adds and removes elements to achieve continuous load paths and even higher functional performance. In previous studies, two independent BESO optimizations of SMA components were conducted for the austenite and martensite phases, each under constant temperatures, without assuming actuator functionality. In contrast, a new approach described herein directly considers the actuator application by incorporating temperature evolution, allowing for the simultaneous optimization of austenite, martensite, and intermediate phases within a continuous thermo-mechanical cycle. This enables the effective utilization of SMAs in actuator design, making them more suitable for practical applications. Here, the BESO method is used for topology optimization of SMA superelastic structures and actuators with the aim of maximizing volume-specific transformation energy density while accepting definite volume constraints. The thermo-mechanical behavior of SMA actuators is calculated using a phenomenological constitutive model, while the sensitivities are evaluated using the real load method. In the more challenging case of actuators, high temperature loading and subsequent cooling comprise the operational regime (i.e., forward transformation of the component) to be optimized, during which the sensitivity is determined. SMA beam structures and simply supported cubic structures are designed, and their displacement and volume-specific actuation energy density values are evaluated throughout the optimization process. The findings show that our novel approach for the optimization of actuator topologies leads to more energy-dense actuators than those designed by prior (i.e., elastic strain energy-based) methods.

Sefa Oksuz & Darren Hartl
Texas A&M University, Department of Aerospace Engineering College Station, TX 77843, USA
e-mail: sefaoksuz@tamu.edu,darren.hartl@tamu.edu

Key words: Shape Memory Alloy, Bi-Directional Evolutionary Structural Optimization, Actuators

1 INTRODUCTION

Shape memory alloys have attracted considerable attention in recent years owing to rising demands for reliability and functionality across multiple objectives in engineering applications. These unique materials can support significant recoverable inelastic strains associated with a solid-to-solid phase transformation, enabling them to provide both high force and displacements compared to other metals but relatively small compared to mechanical actuators (e.g., hydraulic, pneumatic, screw-driven, etc.) [1]. In parallel with the growing interest in SMAs, topology optimization has become an essential aspect of modern engineering design, driven by the pursuit of superior performance. Over the past several decades, numerous topology optimization approaches have emerged, including the homogenization method [2], the very common Solid Isotropic Material with Penalization (SIMP) method [3, 4], and the level set method [5, 6]. A particularly notable branch of topology optimization is Evolutionary Structural Optimization (ESO), introduced by Xie and Steven [7, 8], which refines a structure toward an optimal layout by iteratively removing low-stress elements. Chu *et al.* [9] subsequently replaced the stress measure with an element-based strain energy criterion, while the BESO framework [10] further extended the purely subtractive ESO method by also permitting the *addition* of previously removed elements in high-stress regions. Later, Huang and Xie [11] showed that soft-kill BESO could be more stable and less sensitive to algorithmic parameters than standard ESO or SIMP, prompting its use in a variety of problems. This has most recently been addressed by Brent et al. [12].

Although topology optimization has been extensively studied, the design of SMA-based topologies remains comparatively underexplored. Early work was hindered by limitations in manufacturing methods, but recent progress in additive manufacturing has expanded the possibilities for SMA structures [13]. One of the first studies to focus on SMAs in a topology optimization setting was by Langelaar *et al.* [14], who examined superelastic behavior in an SMA actuator. More recently, Kang and James [15, 16] introduced a density-based approach that includes both the two-way shape memory effects and superelasticity, later extending it to multi-material SMA systems by incorporating transient heat conduction. Zhu *et al.* [17] applied SIMP to develop high-performance SMA structural designs, while Hou *et al.* [18] proposed a pseudoelastic framework intended to maximize energy dissipation. Most recently, Dong *et al.* [19] implemented a BESO-based topology optimization procedure for SMAs, considering their superelastic response at different constant temperatures and applying multiple constraints (e.g., specified volume fraction, displacement, and fundamental frequency). Their results demonstrated higher computational efficiency compared with SIMP-based methods and revealed uniform mechanical properties combined with substantial deformation capacity.

In this study, a topology optimization model for SMAs is introduced to maximize the volume-specific actuation energy density under fixed volume constraints. To assess its effectiveness, two

topology optimization strategies are compared under thermo-mechanical loading. First, a conventional (i.e., elastic strain energy) BESO procedure is performed on a linearized material domain, and the resulting topology is reanalyzed using an SMA user-defined material subroutine (UMAT) applied to the Abaqus finite element solver, producing baseline force–deflection and temperature–deflection data. Subsequently, a second optimization employs a new UMAT-based BESO method directly, which explicitly accounts for temperature-dependent phase transformations throughout the actuation cycle. Contrasting the force–deflection and temperature–deflection outcomes confirms the validity of the proposed approach. In addition, the UMAT-based SMA topology demonstrates a higher volume-averaged martensite fraction than the linear BESO solution, indicating more efficient actuator performance, as indicated by greater volume-specific actuation energy density. The versatility of the framework is illustrated by applying it to a cantilever beam under both constant-temperature superelastic conditions and varying-temperature actuation scenarios—each using the real load strategy—and by extending it to a three-dimensional simply supported cubic domain, demonstrating its suitability for complex geometries.

2 Theoretical Background

A phenomenological SMA constitutive model by Lagoudas *et al.* [20] is used to capture both superelastic and thermally driven phase transformations. It is implemented in the commercial finite element software *Abaqus* through a UMAT, ensuring accurate updates of the stress tensor, the transformation strain tensor and the scalar martensitic volume fraction (MVF) at each load increment. Table 1 summarizes key SMA parameters used in this work, including the elastic moduli of austenite and martensite (E^A, E^M), zero-stress start and finish transformation temperatures (M_s, M_f, A_s, A_f), Poisson's ratio ν for both phases, and thermal expansion coefficients (α^A, α^M). During each loading step, the UMAT is provided a global estimate for the total strain increment and calculates the transformation strain increment, determines the MVF evolution, and provides the updated stress state to *Abaqus*, all in such a way to expedite convergence of the nonlinear system [20].

Table 1: Representative SMA parameters [19].

Parameter	Value	Parameter	Value
E^A	70 GPa	E^M	60 GPa
M_s	258 K	M_f	233 K
A_s	273 K	A_f	298 K
α^A	$10^{-6}\,\mathrm{K}^{-1}$	α^M	$10^{-6}\,\mathrm{K}^{-1}$
ν	0.3		

Objective Function: From Compliance Minimization to Volume-Specific Actuation Energy Maximization. Conventional linear BESO implementations, such as that of Zuo *et al.* [21] use linear strain-energy-based sensitivity measures to minimize compliance under a pre-defined

volume constraint. In contrast, this new work modifies Zuo's original *Abaqus* BESO code using the results from UMAT (e.g., constitutive model) calculations to maximize actuation energy. Drawing inspiration from Wheeler *et al.* [22] and Chemisky *et al.* [23], the local transformation energy $\Phi^{\text{tr}}_{\text{ener},i}$ of the ith element is defined as:

$$\Phi^{\text{tr}}_{\text{ener},i} = \overline{\sigma}_i \, \overline{\varepsilon}^{\,t}_i, \tag{1}$$

where $\overline{\sigma}$ is the Mises stress and $\overline{\varepsilon}^{\,t}$ is the energetically conjugate Mises transformation strain, both determined incrementally within the UMAT. The global objective is the ratio of total actuation energy to the current number of elements, subject to the prescribed volume constraint:

$$\max_{\{x_i\}} \frac{\sum_{i=1}^{n} \left[\Phi^{\text{tr}}_{\text{ener},i} \, v_i\right]}{\sum_{i=1}^{n} x_i} \quad \text{subject to} \quad \sum_{i=1}^{n} x_i \, v_i \;\leq\; V^*, \tag{2}$$

where $x_i \in \{0, 1\}$ indicates element removal or retention, v_i is the element volume, and V^* is the goal total volume. A BESO scheme is used to maximize the volume-specific transformation energy within this volume limit. At each iteration, local transformation-energy sensitivities $\Phi^{\text{tr}}_{\text{ener},i}$ are computed and sorted. A threshold $\alpha_{\text{threshold}}$, linked to the target volume V_{k+1}, dictates which elements are removed or added. The target volume for each step is updated by [21]

$$V_{k+1} = V_k\big(1 - \text{EVR}\big), \quad (k = 1, 2, 3, \ldots), \tag{3}$$

where EVR is the evolution rate that reduces V_k to V_{k+1}. Once the cumulative volume of the first m elements (in ascending sensitivity order) equals V_{k+1}, the threshold is set to the sensitivity of the m-th element. This removal/addition process continues until convergence in the objective, effectively yielding a topology that maximizes recoverable actuation energy. Because the SMA UMAT is integrated into BESO, both superelastic and shape memory (i.e. actuation) responses are directly incorporated into the sensitivity analysis, progressively evolving SMA structures toward topologies with superior martensite phase transformation performance.

3 NUMERICAL EXAMPLES

In this section, the effectiveness of the proposed UMAT-based BESO framework is illustrated through three representative case studies. In each case, final topologies and martensite distributions are examined for both a conventional (linear) BESO method and a UMAT-based BESO approach. The linear BESO solution considers only compliance minimization under a prescribed volume constraint, with iterative compliance and volume-fraction plots provided to track convergence. By contrast, the UMAT-based approach targets maximum actuation performance, monitored through displacement, volume-specific actuation energy density, and volume fraction. In the first two cases, all these metrics are presented to highlight the design evolution, while the third case serves as a demonstration for more complex 3D structures, focusing on the comparison of pre- and post-optimization topologies. Comparing these scenarios under different loading and temperature conditions underscores the importance of explicitly modeling SMA phase transformations in topology optimization.

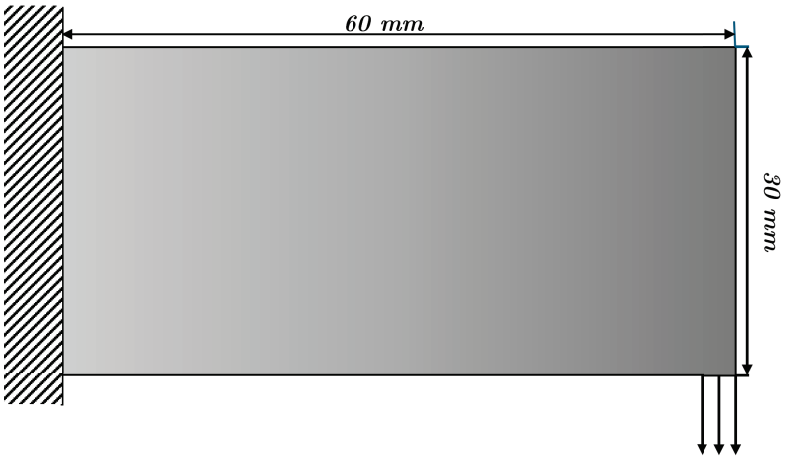

Figure 1: Design domain of the SMA cantilevered structure. This 100% volume domain was reduced to 50% in all examples.

3.1 Case 1: Superelastic Cantilevered Structure

A cantilevered structure measuring $60\times30\times1\,\mathrm{mm}$ (Figure 1) is modeled using solid elements and subjected to a constant tip load of $1500\,\mathrm{N}$ at $273\,\mathrm{K}$ to capture superelastic SMA behavior. A 50% volume-fraction target V^* is imposed, and two topology optimizations are carried out:

1. *Linear BESO*, where only the austenitic elastic modulus is used to compute the local elastic strain energy in each, approximating a purely elastic material using that response to select which elements are kept and which are eliminated. The resulting design is later reanalyzed with the full SMA subroutine to assess superelastic effects.

2. *UMAT-Based BESO*, where phase transformation effects at known constant temperature via Eq. (1) are directly incorporated into the optimization process.

Comparisons of force–deflection curves and martensite distributions illustrate how explicitly modeling transformation phenomena via Eq. (1) can better enforce transformation efficiency in this nonlinear problem. In particular, the UMAT-based approach yields more uniform transformation work energy by promoting more uniform martensitic transformations across all regions.

Results for Case 1

As shown in Figure 2, the linear BESO topology reanalyzed under SMA properties exhibits a comparatively lower martensite volume fraction in high-stress regions, and less uniformly overall, whereas the UMAT-based design achieves a more uniform and higher-density distribution. From the force-deflection curves in Figure 3, the UMAT-based approach is shown to create a structure that creates more energy dissipation. Thus, in the context of superelasticity, the objective defined by Eq. (2) generates a better structure.

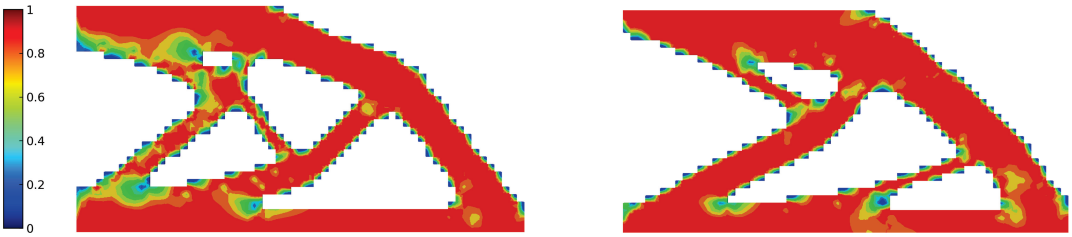

Figure 2: MVF distributions for the linear strain energy-based BESO design (left) and the UMAT-based BESO design (right).

Figure 4 compares the iterative evolution for both methods. Although using a UMAT inevitably introduces additional computational overhead, the number of iterations required for convergence remains similar between the two approaches, which is promising. Notably, the average martensite volume fraction for the linear BESO solution is 0.869, whereas the UMAT-based BESO reaches 0.90, reflecting the more extensive phase transformation afforded by our proposed topological optimization approach. Correspondingly, the average volume-specific actuation energy density for the linear BESO design measures $121.75\,\mathrm{N\,mm}$ per element, while the UMAT-based approach attains $127.21\,\mathrm{N\,mm}$ per element, underscoring the enhanced phase transformation efficiency offered by the UMAT-based design tool.

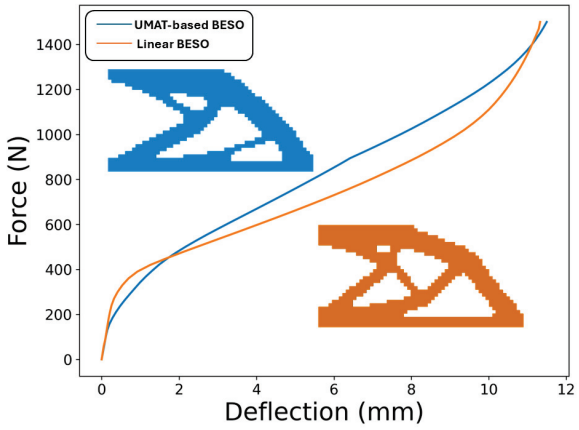

Figure 3: Force-deflection curves for the linear BESO and UMAT-based BESO.

3.2 Case 2: Thermally Driven Cantilever Actuator

Using the same cantilever geometry and a $900\,\mathrm{N}$ distributed load, an actuator scenario is modeled by initially loading the structure at $328\,\mathrm{K}$, followed by cooling to $258\,\mathrm{K}$. A 50% volume-fraction target is imposed on the design. A UMAT-based BESO routine optimizes the topology for this temperature-dependent actuation cycle, generating temperature-deflection

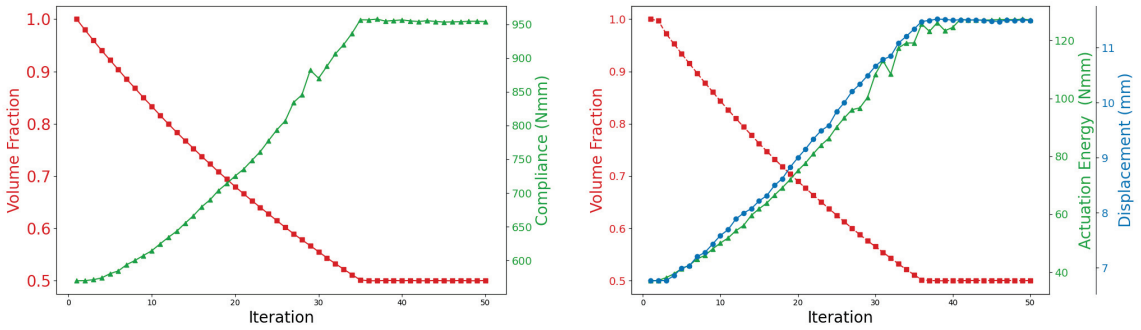

Figure 4: BESO convergence histories for the linear BESO approach (left) and the UMAT-based approach (right).

graphs and martensite distributions. To validate these outcomes, a linear BESO solution is also computed; the resulting form is then reanalyzed within the SMA framework under the same load and temperature conditions used in the UMAT-based optimization case, allowing direct comparisons of transformation-driven performance.

Results for Case 2

Figure 5 compares the linear BESO design (reanalyzed with SMA properties) against the UMAT-optimized topology. The UMAT-based approach again achieves more uniform and thus more volume-efficient martensitic transformation, supporting the finding that direct incorporation of phase-transformation behavior during the optimization leads to improved actuator performance.

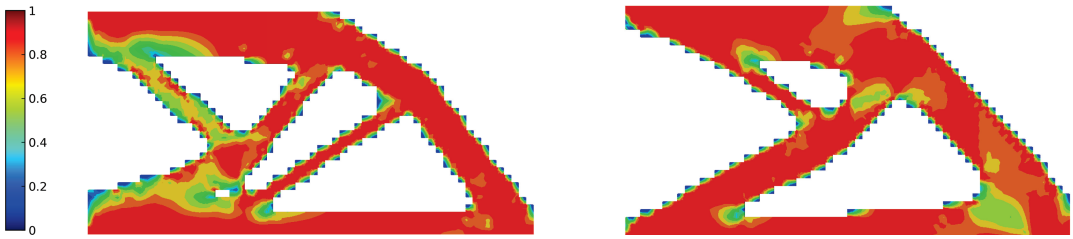

Figure 5: MVF distributions for the linear strain energy-based BESO design (left) and the UMAT-based BESO design (right).

In Figure 6, the linear method converges more rapidly but does not capture displacement or phase fraction accurately, thus offering lower actuation potential when reexamined using SMA properties. In contrast, the UMAT-based actuator optimization shows higher iteration counts to converge, driven by the additional complexity of temperature-dependent phase transitions.

Finally, Figure 7 shows that, although cooling was ended at $259\,\mathrm{K}$ due to convergence concerns for some models, further cooling would yield additional actuation deflection for the UMAT-based design. Although the deflection difference appears modest at this intermediate

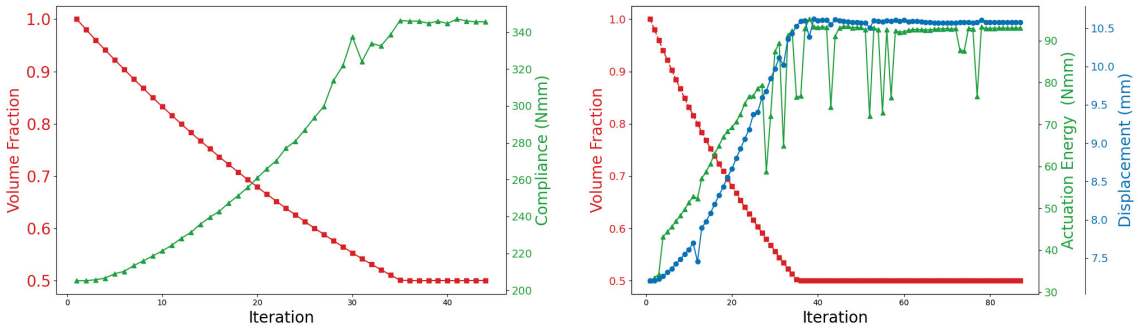

Figure 6: BESO convergence histories for the linear BESO (left) and the UMAT-based (right).

temperature, the UMAT-based approach achieves superior material utilization: the higher and more uniform martensite distribution translates to 14% greater stored transformation energy. In terms of martensite content, the linear BESO solution averages 0.85, whereas the UMAT-based BESO reaches 0.88, indicating a greater phase transformation under the proposed method. Correspondingly, the average volume-specific actuation energy density for the linear BESO design is measured at $81.54\,\mathrm{N\,mm}$, while the UMAT-based approach achieves $93.01\,\mathrm{N\,mm}$, underscoring the higher actuation energy potential of the UMAT-based model.

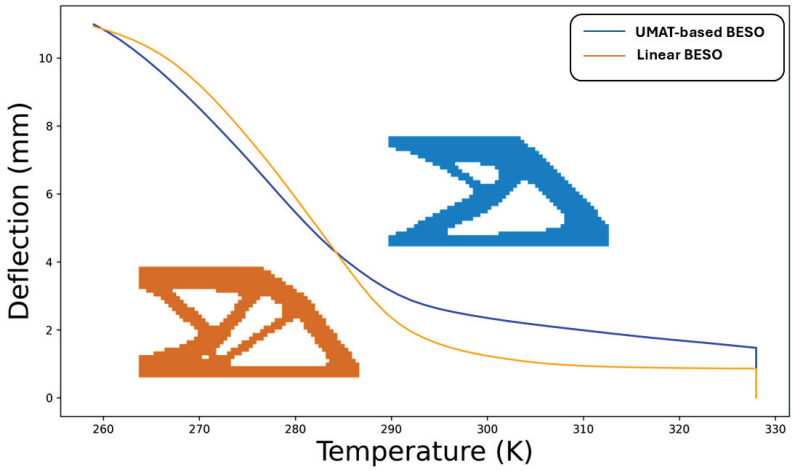

Figure 7: Temperature-deflection curves for the linear BESO and UMAT-based BESO.

3.3 Case 3: Demonstration of a 3D Actuator

A three-dimensional simply supported cubic domain (Figure 8) is subjected to an $8000\,\mathrm{N}$ distributed load, with the same thermal profile of loading at $328\,\mathrm{K}$ followed by cooling to $258\,\mathrm{K}$. A

25% volume-fraction target V^* is specified to demonstrate the adaptability of the UMAT-based BESO framework to more complex (i.e., lower density) geometries. The resulting topology, temperature-deflection response, and martensite distribution show how transformation-based optimization can be applied effectively to intricate three-dimensional domains, providing a pathway to advanced SMA actuator designs.

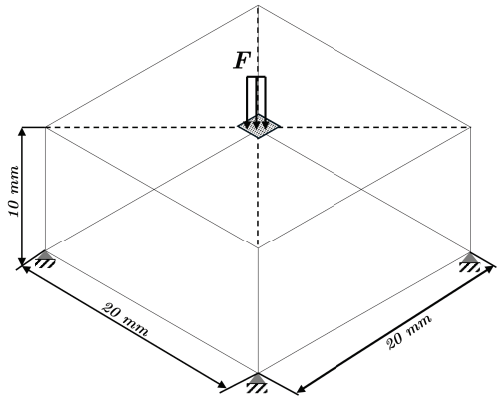

Figure 8: 3D simply supported cube design domain.

Results for Case 3

Figure 9 illustrates the final topology once the volume fraction is reduced to 25% of the initial design. A substantial increase in transformation (indicated by a higher MVF) is observed in critical load-bearing regions, underlining the effectiveness of the UMAT-based BESO method in navigating complex three-dimensional domains. Even at lower volume fractions, the proposed framework exploits thermally driven transformations to maximize actuation performance.

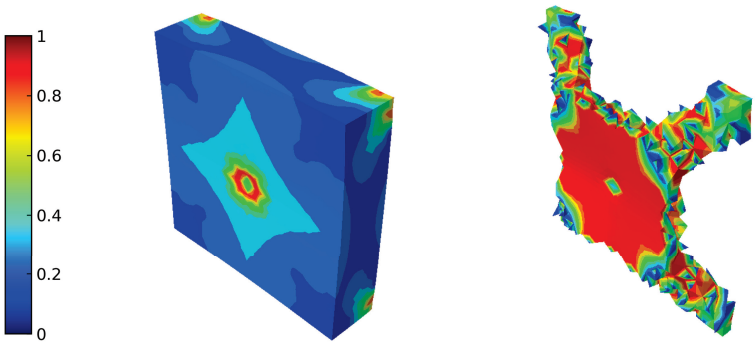

Figure 9: MVF distributions of initial topology (left) and optimized topology (right).

4 CONCLUSIONS

A UMAT-based BESO scheme has been presented for the topology design of SMAs, effectively accounting for both superelastic and thermally driven phase transformations. Numerical examples considering cantilever structures confirm that directly embedding transformation mechanics into the BESO process yields significantly enhanced force-deflection characteristics under constant-temperature loading and superior temperature-deflection responses for actuator scenarios. Extending the framework to a three-dimensional simply supported cubic structure further demonstrates its suitability for complex geometries. By maximizing volume-specific actuation energy within a prescribed volume fraction, the proposed method enables SMAs that achieve uniform, high-density martensite distributions under both constant-temperature superelastic conditions and temperature-varying actuation scenarios, ultimately producing higher actuation energy. This methodology is particularly relevant for aerospace, biomedical, and robotics applications where compact, high-performance actuators are essential. Recent advances in additive manufacturing of NiTi alloys [13] have enabled the fabrication of such complex optimized geometries, further enhancing the practical applicability of this framework.

Future work should investigate the impact of topology optimization on maximum stress distributions, as stress concentrations may affect fatigue life under cyclic loading. Incorporating stress constraints into the BESO framework, extending to multi-objective optimization considering actuation energy, weight, and thermal response time, and experimental validation through additive manufacturing of NiTi structures represent promising research directions.

REFERENCES

[1] D. J. Hartl and D. C. Lagoudas, "Aerospace applications of shape memory alloys," *Proceedings of the Institution of Mechanical Engineers, Part G: Journal of Aerospace Engineering*, vol. 221, no. 4, pp. 535–552, 2007. [Online]. Available: https://doi.org/10.1243/09544100JAERO211

[2] M. P. Bendsøe and N. Kikuchi, "Generating optimal topologies in structural design using a homogenization method," *Computer Methods in Applied Mechanics and Engineering*, vol. 71, no. 2, pp. 197–224, 1988. [Online]. Available: https://www.sciencedirect.com/science/article/pii/0045782588900862

[3] M. P. Bendsøe and O. Sigmund, "Material interpolation schemes in topology optimization," *Archive of Applied Mechanics*, vol. 69, no. 9, pp. 635–654, Nov 1999. [Online]. Available: https://doi.org/10.1007/s004190050248

[4] M. P. Bendsøe and O. Sigmund, *Topology optimization by distribution of isotropic material*. Berlin, Heidelberg: Springer Berlin Heidelberg, 2004, pp. 1–69. [Online]. Available: https://doi.org/10.1007/978-3-662-05086-6_1

[5] G. Allaire, F. Jouve, and A.-M. Toader, "Structural optimization using sensitivity analysis and a level-set method," *Journal of Computational Physics*, vol. 194, no. 1,

pp. 363–393, 2004. [Online]. Available: https://www.sciencedirect.com/science/article/pii/S002199910300487X

[6] M. Yulin and W. Xiaoming, "A level set method for structural topology optimization and its applications," *Advances in Engineering Software*, vol. 35, no. 7, pp. 415–441, 2004. [Online]. Available: https://www.sciencedirect.com/science/article/pii/S0965997804000705

[7] Y. Xie and G. Steven, "A simple evolutionary procedure for structural optimization," *Computers Structures*, vol. 49, no. 5, pp. 885–896, 1993. [Online]. Available: https://www.sciencedirect.com/science/article/pii/004579499390035C

[8] Y. M. Xie and G. P. Steven, *Basic Evolutionary Structural Optimization*. London: Springer London, 1997, pp. 12–29. [Online]. Available: https://doi.org/10.1007/978-1-4471-0985-3_2

[9] D. Chu, Y. Xie, A. Hira, and G. Steven, "Evolutionary structural optimization for problems with stiffness constraints," *Finite Elements in Analysis and Design*, vol. 21, no. 4, pp. 239–251, 1996. [Online]. Available: https://www.sciencedirect.com/science/article/pii/0168874X9500043S

[10] O. M. Querin, G. P. Steven, and Y. M. Xie, "Evolutionary structural optimisation (eso) using a bidirectional algorithm," *Engineering Computations*, vol. 15, no. 8, pp. 1031–1048, Jan 1998. [Online]. Available: https://doi.org/10.1108/02644409810244129

[11] X. Huang and Y.-M. Xie, "A further review of eso type methods for topology optimization," *Structural and Multidisciplinary Optimization*, vol. 41, no. 5, pp. 671–683, May 2010. [Online]. Available: https://doi.org/10.1007/s00158-010-0487-9

[12] B. R. Bielefeldt, D. J. Hartl, and M. H. Kobayashi, *Topology Optimization via L-Systems and Genetic Algorithms: Bioinspired Encoding for Generative Design*. Cambridge University Press, 2025.

[13] E. Farber, J.-N. Zhu, A. Popovich, and V. Popovich, "A review of niti shape memory alloy as a smart material produced by additive manufacturing," *Materials Today: Proceedings*, vol. 30, pp. 761–767, 2020, materials Science: Composites, Alloys and Materials Chemistry. [Online]. Available: https://www.sciencedirect.com/science/article/pii/S2214785320306738

[14] M. Langelaar, G. H. Yoon, Y. Y. Kim, and F. van Keulen, "Topology optimization of planar shape memory alloy thermal actuators using element connectivity parameterization," *International Journal for Numerical Methods in Engineering*, vol. 88, no. 9, pp. 817–840, 2011. [Online]. Available: https://doi.org/10.1002/nme.3199

[15] Z. Kang and K. A. James, "Thermomechanical topology optimization of shape-memory alloy structures using a transient bilevel adjoint method," *International Journal for Numerical Methods in Engineering*, vol. 121, no. 11, pp. 2558–2580, 2020. [Online]. Available: https://doi.org/10.1002/nme.6319

[16] Z. Kang and K. A. James, "Multiphysics design of programmable shape-memory alloy-based smart structures via topology optimization," *Structural and Multidisciplinary Optimization*, vol. 65, no. 1, p. 24, Dec 2021. [Online]. Available: https://doi.org/10.1007/s00158-021-03101-z

[17] Z. Jihong, W. Chang, H. Jie, Y. Kaike, G. Xiaojun, and Z. Weihong, "A topology optimization method for shape memory alloy structures," *Chinese Journal of Computational Mechanics*, 2021.

[18] J. Hou, C. Wei, J. Wang, X. Gu, J. Zhu, and W. Zhang, "Topology optimization for energy dissipation structures based on shape memory alloys," *Structural and Multidisciplinary Optimization*, vol. 66, no. 3, p. 55, Feb 2023. [Online]. Available: https://doi.org/10.1007/s00158-023-03491-2

[19] X. Dong, X. Jiang, P. Li, T. Niu, Y. Wang, and J. Zhang, "Topology optimization structure design of shape memory alloy with multiple constraints," *Journal of Intelligent Material Systems and Structures*, vol. 35, no. 10, pp. 892–906, 2024. [Online]. Available: https://doi.org/10.1177/1045389X241237581

[20] D. Lagoudas, D. Hartl, Y. Chemisky, L. Machado, and P. Popov, "Constitutive model for the numerical analysis of phase transformation in polycrystalline shape memory alloys," *International Journal of Plasticity*, vol. 32-33, pp. 155–183, 2012. [Online]. Available: https://www.sciencedirect.com/science/article/pii/S0749641911001793

[21] Z. H. Zuo and Y. M. Xie, "A simple and compact python code for complex 3d topology optimization," *Advances in Engineering Software*, vol. 85, pp. 1–11, 2015. [Online]. Available: https://www.sciencedirect.com/science/article/pii/S0965997815000241

[22] R. W. Wheeler, D. J. Hartl, Y. Chemisky, and D. C. Lagoudas, "Modeling of thermo-mechanical fatigue and damage in shape memory alloy axial actuators," in *Proc. SPIE 9432, Behavior and Mechanics of Multifunctional Materials and Composites 2015*, vol. 9432. SPIE, 2015, p. 94320K, presented at SPIE Smart Structures and Materials + Nondestructive Evaluation and Health Monitoring 2015, San Diego, California, United States. [Online]. Available: https://doi.org/10.1117/12.2175747

[23] Y. Chemisky, D. J. Hartl, and F. Meraghni, "Three-dimensional constitutive model for structural and functional fatigue of shape memory alloy actuators," *International Journal of Fatigue*, vol. 112, pp. 263–278, 2018. [Online]. Available: https://www.sciencedirect.com/science/article/pii/S0142112318301002

XI ECCOMAS Thematic Conference on Smart Structures and Materials - SMART 2025
M. Krommer, M. Nader and M. Schagerl (Eds)

Received: 31 March 2025 / Revised: 31 July 2025 / Accepted: 9 October 2025
© The Author(s) 2025

Small-Scale Energy Harvesting using Piezoelectric Paints

Ismael Payo, César García-Asensio, José García-Delgado

Abstract. This study explores energy harvesting from vibrational processes using piezoelectric paints, a novel and cost-effective approach to small-scale energy generation. The paint is formulated with an acrylic-based matrix and ceramic powder of lead zirconate titanate (PZT), homogeneously distributed. The primary objective of this research is to identify the operating conditions to maximize the electrical power output of the paint, enabling its application in the development of piezoelectric energy harvesters capable of powering small electronic devices. The paper begins with a theoretical analysis of the piezoelectric properties of the paint, which provides the basis for understanding the sensitivity of the material and the energy harvesting capabilities under mechanical stress. The electrical power output depends on the electromechanical properties of the paint, its geometric dimensions, the frequency and amplitude of the vibration, and the electrical load. In this study, the power output is analyzed as a function of the electrical load. Series and parallel connections of piezoelectric paint energy harvesters are also investigated. Practical experiments involved the design and construction of a prototype to ensure consistent deformation of painted steel substrates, followed by signal conditioning and electrical measurements using specialized equipment. Key findings include the confirmation of the capabilities of the piezoelectric paint, the identification of the electrical load to maximize power output, and the validation of the theoretical model with experimental data for both series and parallel configurations. The results suggest that piezoelectric paints hold significant promise for energy harvesting in remote or hard-to-access locations, such as powering sensors, lighting or signalling devices on structures subject to constant vibration, including bridges and roadways.

Key words: Energy Harvesting, Piezoelectric Paints, Small-Scale Energy Harvesters, Vibrational Processes

1 INTRODUCTION

Energy harvesting from vibrational processes has attracted considerable attention due to its potential for powering small electronic devices, particularly in remote or hard-to-reach areas. Among the various techniques for harvesting energy from mechanical vibrations, piezoelectric

Ismael Payo & César García-Asensio & José García-Delgado
Escuela de Ingeniería Industrial y Aeroespacial, Universidad de Castilla-La Mancha Campus Antigua Fábrica de Armas, 45071 Toledo, Spain
e-mail: ismael.payo@uclm.es

materials have been widely studied and applied due to their ability to convert mechanical energy into electrical energy [1]. Traditional piezoelectric energy harvesters are typically based on bulk piezoelectric crystals or ceramics. However, recent advances have introduced piezoelectric polymer composites as a more versatile and cost-effective alternative for energy harvesting that can be easily integrated into different types of structures [2].

The potential applications of piezoelectric energy harvesting are vast. In addition to powering small electronic devices, piezoelectric energy harvesters can be used in structural health monitoring, where sensors powered by harvested energy can provide real-time data on the condition of infrastructure [3]. Other applications include powering wireless sensor networks [4], wearable electronics [5], and environmental monitoring devices [6].

The efficiency of energy conversion depends on several factors, including material properties, geometric dimensions, frequency and amplitude of vibration [7]. One of the critical aspects in the design of piezoelectric energy harvesters is the determination of the optimum electrical load and the configuration of the harvesters, such as series and parallel connections, to maximize power output [8], [9].

Recent advances in materials science have led to the development of piezoelectric paints, which offer a novel approach to energy harvesting. Piezoelectric paints consist of piezoelectric nanoparticles embedded in a polymer matrix that can be easily applied to various substrates with irregular surfaces. This innovative technology offers several advantages, including flexibility, ease of application, and the ability to cover large areas. Recent studies have highlighted the potential of piezoelectric paints in various applications, including energy harvesting, structural health monitoring and flexible electronics [10]. These advances highlight the importance of enhancing the design and application processes to improve the efficiency of energy harvesting systems.

Our study has shown that when piezoelectric paint harvesters are connected in series, the voltage output increases, while the current remains constant across all devices. In contrast, when the energy harvesters are connected in parallel, the current increases, while the voltage remains constant. Power output has been studied for both series and parallel configurations as a function of electrical load.

Piezoelectric paints represent an exciting advance in energy harvesting technology, offering a lightweight, versatile, and cost-effective solution for small-scale energy harvesting. The study of electrical output, through both theoretical modelling and experimental validation, demonstrates the feasibility of these systems for a range of applications. Piezoelectric paints have the potential to play an important role in the future of energy harvesting.

2 THEORETICAL BASIS

The purpose of this section is to calculate the electrical power output of the piezoelectric paint designed in this study under mechanical stress caused by vibrational processes. Therefore, the direct piezoelectric effect is used in the strain-voltage form of the constitutive equations of

piezoelectricity, given by:

$$\begin{aligned} \varepsilon_{(6\times1)} &= S^{D}_{(6\times6)}\sigma_{(6\times1)} + g^{\mathrm{T}}_{(6\times3)}\, D_{(3\times1)} \\ F_{(3\times1)} &= -g_{(3\times6)}\sigma_{(6\times1)} + (\epsilon^{\sigma})^{-1}_{(3\times3)} D_{(3\times1)} \end{aligned} \tag{1}$$

where ε, σ, D and F are the components of the strain tensor, stress tensor, electric displacement vector and electric field vector, respectively. S is the component of the fourth-order compliance tensor obtained in the absence of electric charge ($D = 0$), g is the component of the third-order piezoelectric coefficient for the strain-voltage form (also known as the piezoelectric voltage coefficient), and ϵ is the component of the permittivity tensor obtained under zero stress ($\sigma = 0$). The mathematical symbol T denotes transposition.

Figure 1 shows a schematic of the piezoelectric paint applied to the substrate (steel plate).

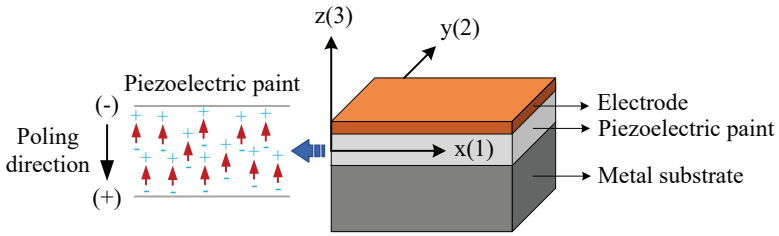

Figure 1: Schematic of the piezoelectric energy harvester.

Considering that: 1) the piezoelectric paint is poled in direction 3, and therefore the electric displacement is only in direction 3, and 2) the substrate is stressed in directions 1 and 2, the second equation of (1) can be written as:

$$F_3 = -g_{31}\,\sigma_1 - g_{32}\,\sigma_2 + \beta_{33}\,D_3 \tag{2}$$

where β is the inverse of the permittivity ϵ. On the other hand, considering the Reissner-Mindlin plate theory, the two-dimensional stress and strain are related by the following equation [11]:

$$\begin{bmatrix}\sigma_1 \\ \sigma_2\end{bmatrix} = \frac{E}{1-\nu^2}\begin{bmatrix}1 & \nu \\ \nu & 1\end{bmatrix}\begin{bmatrix}\varepsilon_1 \\ \varepsilon_2\end{bmatrix} \tag{3}$$

where E is the Young's modulus and ν is the Poisson's ratio of the material. From (2) and (3) and assuming that g_{31} and g_{32} are equal, the following expression is derived:

$$F_3 = \frac{-g_{31}\,E}{1-\nu}(\varepsilon_1 + \varepsilon_2) + \beta_{33}\,D_3 \tag{4}$$

Multiplying the previous equation (4) by the thickness of the piezoelectric material, h, gives:

$$u_o = \frac{-g_{31}\,h\,E}{1-\nu}(\varepsilon_1 + \varepsilon_2) + \beta_{33}\,h\,D_3 \tag{5}$$

where $u_o = F_3\,h$ is the output voltage.

When an electrical load, R, is connected to the piezoelectric material, the electric displacement can be defined as:

$$D_3 = \frac{-1}{A} \int i\, dt \tag{6}$$

where A is the area of the surface of the piezoelectric material covered by the electrode, and the electric current , i, is defined by the formula of Ohm's law:

$$i = \frac{u_o}{R} \tag{7}$$

Substituting (6) in (5) and assuming a simple harmonic deformation, $\varepsilon_1 + \varepsilon_2 = C\, sin(\omega\, t)$, the output voltage can be expressed as:

$$u_o = \frac{-g_{31}\, h\, E}{1-\nu}\, C\, sin(\omega\, t) - \frac{\beta_{33}\, h}{A} \int i\, dt \tag{8}$$

and including (7) into (8), the output voltage can finally be expressed as:

$$u_o = \frac{-g_{31}\, h\, E}{1-\nu}\, C\, sin(\omega\, t) - \frac{\beta_{33}\, h}{A} \int \frac{u_o}{R}\, dt \tag{9}$$

The amplitude of the output voltage can be calculated by solving (9):

$$U_o = \frac{g_{31}\, E\, C\, h\, A\, \omega\, R}{(1-\nu)\sqrt{(\beta_{33}\, h)^2 + (A\, \omega\, R)^2}} \tag{10}$$

On the other hand, the active power generated by the piezoelectric material is calculated using the following equation:

$$P = \frac{U_o^2}{2R} = \frac{(g_{31}\, E\, C\, h\, A\, \omega)^2 R}{2(1-\nu)^2[(\beta_{33}\, h)^2 + (A\, \omega\, R)^2]} \tag{11}$$

The aim is to maximize the power in relation to the electrical load ($\frac{dP}{dR} = 0$):

$$P^m = \frac{(g_{31}\, E\, C)^2\, h\, A\, \omega}{4(1-\nu)^2 \beta_{33}} \tag{12}$$

when the electrical load is:

$$R^m = \frac{\beta_{33}\, h}{A\, \omega} \tag{13}$$

2.1 Series and parallel electrical connections

When designing piezoelectric energy harvesters, it is important to analyze the power supply when multiple harvesters are electrically connected in series and in parallel. Figure 2 shows a schematic of piezoelectric energy harvesters connected in series and in parallel.

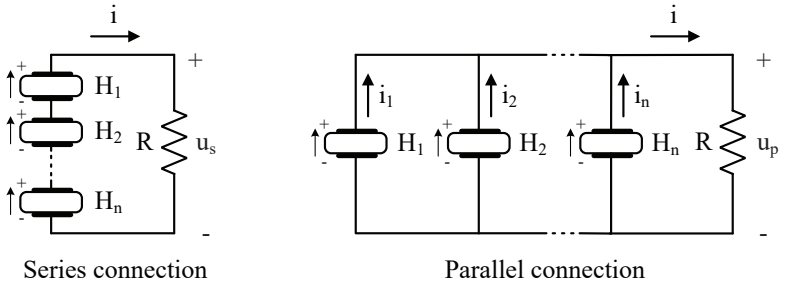

Figure 2: Series and parallel connection of energy harvesters.

When n energy harvesters are connected in series, the load voltage is the sum of the individual voltages of each energy harvester, and the load electric current is the same for all energy harvesters. Assuming identical energy harvesters are subjected to the same harmonic strain, the series voltage is derived from (8):

$$u_s = n\,\frac{-g_{31}\,h\,E}{1-\nu}\,C\,sin(\omega\,t) - n\,\frac{\beta_{33}\,h}{A}\int\frac{u_s}{R}\,dt \tag{14}$$

The amplitude of the series voltage can be calculated by solving (14):

$$U_s = \frac{g_{31}\,E\,C\,n\,h\,A\,\omega\,R}{(1-\nu)\sqrt{(\beta_{33}\,n\,h)^2 + (A\,\omega\,R)^2}} \tag{15}$$

and the active power is:

$$P_s = \frac{(g_{31}\,E\,C\,n\,h\,A\,\omega)^2 R}{2(1-\nu)^2[(\beta_{33}\,n\,h)^2 + (A\,\omega\,R)^2]} \tag{16}$$

The maximum power is:

$$P_s^m = \frac{(g_{31}\,E\,C)^2\,n\,h\,A\,\omega}{4(1-\nu)^2\beta_{33}} \tag{17}$$

when the electrical load is:

$$R_s^m = \frac{\beta_{33}\,n\,h}{A\,\omega} \tag{18}$$

Note that the expressions (15)-(18) are the same as (10)-(13) where h is replaced by $n\,h$.

On the other hand, when n energy harvesters are connected in parallel, the load voltage is the same for all the energy harvesters and the load electric current is the sum of the individual electric currents of each energy harvester. Assuming that identical energy harvesters are subjected to the same harmonic strain, the parallel voltage is derived from (8):

$$u_p = \frac{-g_{31}\,h\,E}{1-\nu}\,C\,sin(\omega\,t) - \frac{\beta_{33}\,h}{A}\int\frac{u_p}{n\,R}\,dt \tag{19}$$

The amplitude of the parallel voltage can be calculated by solving (19):

$$U_p = \frac{g_{31}\,E\,C\,h\,n\,A\,\omega\,R}{(1-\nu)\sqrt{(\beta_{33}\,h)^2 + (n\,A\,\omega\,R)^2}} \tag{20}$$

and the active power is:

$$P_p = \frac{(g_{31}\, E\, C\, h\, n\, A\, \omega)^2 R}{2(1-\nu)^2[(\beta_{33}\, h)^2 + (n\, A\, \omega\, R)^2]} \tag{21}$$

The maximum power is:

$$P_p^m = \frac{(g_{31}\, E\, C)^2\, h\, n\, A\, \omega}{4(1-\nu)^2 \beta_{33}} \tag{22}$$

when the electrical load is:

$$R_p^m = \frac{\beta_{33}\, h}{n\, A\, \omega} \tag{23}$$

Note that the expressions (20)-(23) are the same as (10)-(13) where A is replaced by $n\, A$.

2.2 Normalized expressions

Voltage and power output have been normalized in all cases for better understanding.

The amplitude of the voltage and power for an individual energy harvester was normalized to the maximum value, as a function of the load resistance, which was also normalized to the value that maximizes the power:

$$\frac{U_o}{U_o^m} = \frac{\frac{R}{R^m}}{\sqrt{1 + \left(\frac{R}{R^m}\right)^2}}, \qquad \frac{P}{P^m} = \frac{2\frac{R}{R^m}}{1 + \left(\frac{R}{R^m}\right)^2} \tag{24}$$

The series voltage and power were normalized to the maximum values of the individual energy harvester as a function of the load resistance, which was also normalized to the value that maximizes the power in the individual energy harvesters:

$$\frac{U_s}{U_o^m} = \frac{n\, \frac{R}{R^m}}{\sqrt{n^2 + \left(\frac{R}{R^m}\right)^2}}, \qquad \frac{P_s}{P^m} = \frac{2\, n^2\, \frac{R}{R^m}}{n^2 + \left(\frac{R}{R^m}\right)^2} \tag{25}$$

Following the same procedure with the parallel voltage and power, these are the results:

$$\frac{U_p}{U_o^m} = \frac{n\, \frac{R}{R^m}}{\sqrt{1 + \left(n\, \frac{R}{R^m}\right)^2}}, \qquad \frac{P_p}{P^m} = \frac{2\, n^2\, \frac{R}{R^m}}{1 + \left(n\, \frac{R}{R^m}\right)^2} \tag{26}$$

Note that when n = 1 (one energy harvester), expressions (25) and (26) coincide with (24). Figure 3 shows the voltage and power output when energy harvesters are connected in series and in parallel connections, according to (25) and (26). It can be observed that when some energy harvesters are connected in series, the voltage is the sum of the voltages of each energy harvester (Fig. 3a), where the load current is equal to the current generated by each energy harvester, while when they are connected in parallel the voltage is the same (Fig. 3c), where the load current is the sum of the current generated by each energy harvester. On the other hand, the peak power in both cases is the sum of the peaks of each energy harvester, but whereas in series connection the peak power moves as the load resistance increases (Fig. 3b), in parallel connection the peak power moves as the load resistance decreases (Fig. 3d), according to expressions (18) and (23).

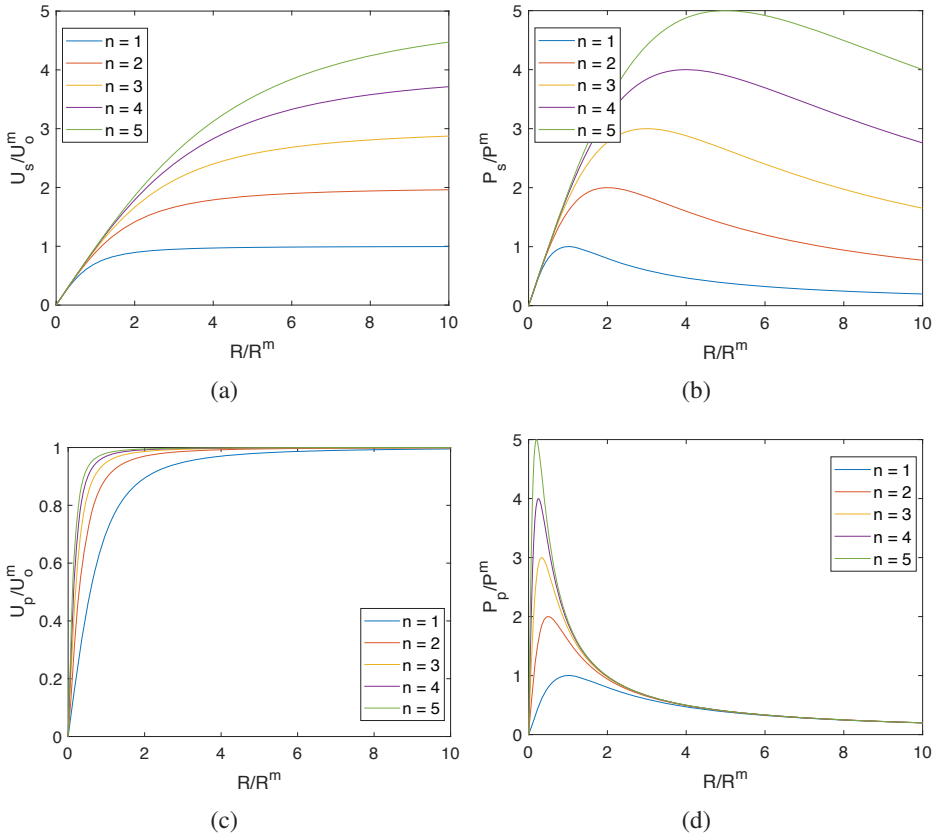

Figure 3: Voltage and power when energy harvesters are connected in series (a and b) and in parallel (c and d).

3 EXPERIMENTAL VALIDATION

3.1 Experimental setup

The piezoelectric energy harvesters designed in this study consist of piezoelectric paint applied on a steel plate. The paint consists of lead zirconate titanate (PZT) powder homogeneously dispersed in an acrylic matrix. The thickness of the paint is controlled by an automatic thickness control device (model K Control Coater, commercialized by the company RK Print) to obtain a wet coating of 60 μm, which is reduced to 36 μm after drying due to the evaporation of volatile components. A layer of silver paint is then added to form the top electrode (20×20 square), which ensures correct electrical conduction with the wire through an adhesive copper tape (Fig. 4a). Note that the bottom electrode is the steel plate (Fig. 4b). Finally, a polarization process is carried out by applying a voltage of 180 V (5 kV/mm) for 30 seconds to improve the piezoelectric capacity of the material. More detailed information on the preparation of the piezoelectric paint can be found in [12]. This procedure guarantees the functionality of the piezoelectric paint energy harvesters for evaluation in experiments. Figure 4c shows some samples of the energy harvesters produced in this study.

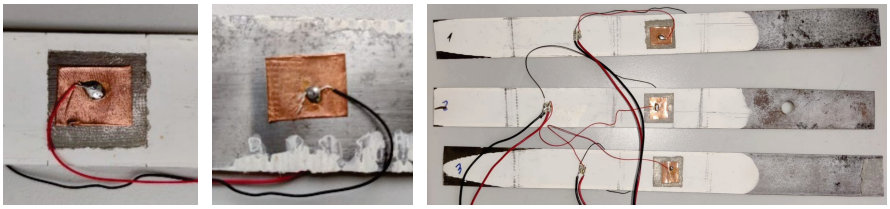

(a) (b) (c)

Figure 4: Parts of the experimental energy harvesters: a) Top electrode; b) Bottom electrode; c) Overview of three different experimental energy harvesters.

These samples were subjected to vibrational processes to analyze the voltage and power output individually and when they were connected in series and in parallel. Figure 5a show a photograph of the experimental setup and Figs. 5b and 5c shows a schematic of the setup for better understanding. The purpose of this design is to ensure uniform strain of the substrate on which the piezoelectric paint energy harvester is placed. The plate is supported at both ends and a shaker (model K2004E01, commercialized by The Modal Shop company) vibrates the plate by means of a U-shaped structure connected to the central area of the plate. This configuration allowed a controlled mechanical load to be applied to the plate, creating a uniform strain in the central area of the plate where the piezoelectric paint was placed, as shown in Fig. 5b. The output voltage generated by the energy harvesters was recorded using an oscilloscope.

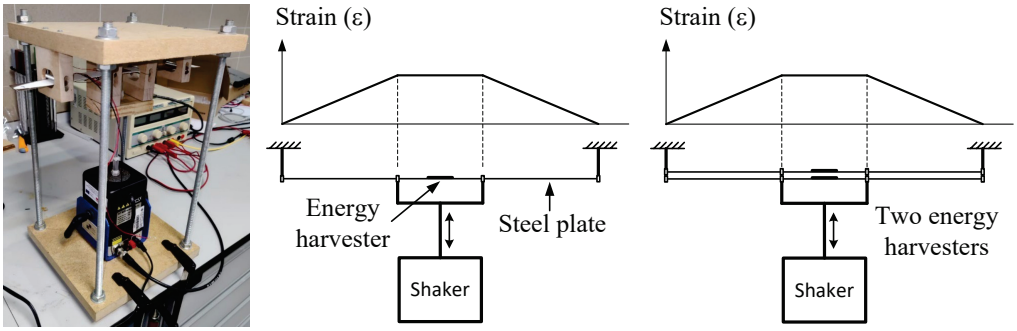

(a) (b) (c)

Figure 5: a) Photo of the test setup; b) Schematic of the test setup for one energy harvester; c) Schematic of the test setup for two energy harvesters.

3.2 Experimental results

One of the preliminary experiments was to evaluate the influence of the oscilloscope on the measurements. For this purpose, the output voltage was recorded with and without the use of a signal conditioning circuit based on an operational amplifier (model TL051, commercialized by the company Texas Instruments) forming an impedance isolator. The results obtained showed a discrepancy in the amplitude of the measured signal, indicating that the electrical input

impedance of the oscilloscope (1 MΩ) is not sufficient to avoid influencing the measurement. This phenomenon highlights the need to use a conditioning circuit (based on an impedance isolator designed with a 1 TΩ input impedance operational amplifier) to reduce the effect of the instrumentation on the data collected.

The vibration frequency was selected to maximize the amplitude of the signal generated. Tests were carried out by varying the frequency from 5 Hz to 30 Hz, and it was observed that the value which maximized the signal amplitude was approximately 20 Hz. Beyond this value, a degradation in the performance of the shaker was observed, which in turn affected the amplitude of the strain imposed on the piezoelectric paint energy harvesters. Furthermore, a structural resonance of the system was identified around 25 Hz, which increased the scatter of the data in this frequency region.

Having established the operating frequency, the relationship between voltage and power was analyzed as a function of the load resistance. The power was calculated from the output voltage as $P = V^2/R$, where R is the load resistance. Voltage measurements were carried out for all cases with varying load resistances up to 10 MΩ. The resulting curves for a single energy harvester (Fig. 6) show a behaviour that is qualitatively similar to that observed in the theoretical analysis, with a maximum power recorded at approximately a load resistance of R^m = 1 MΩ, and a maximum voltage achieved around a load resistance of 4 MΩ, four times R^m. After a detailed analysis, voltage measurements were recorded taking into account small increments of the load resistance up to 2 MΩ corresponding to the range where the voltage changed the most. Ten values were recorded for each load resistance analyzed and the mean ± deviation standard data were calculated as shown in Fig. 6a. For simplicity, only the mean data are shown in the other graphs.

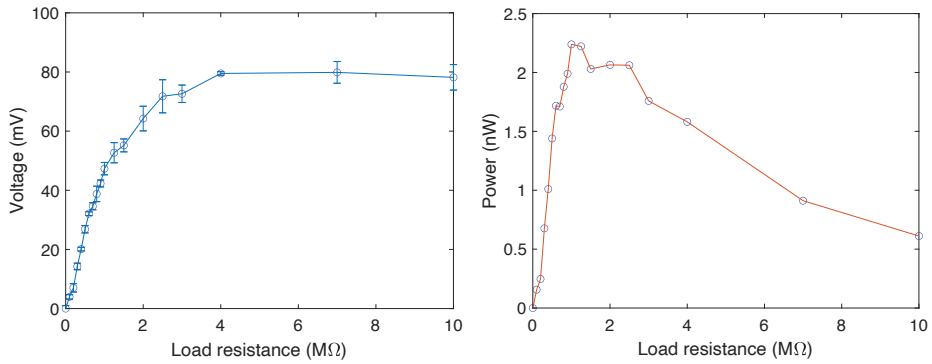

Figure 6: Voltage (a) and power (b) curves of an individual energy harvester.

The behavior of the energy harvesters in series and in parallel configurations was also investigated. First, two energy harvesters were individually analyzed using the configuration of the setup shown in Fig. 5b. Then, the same energy harvesters were connected in series and in parallel using the configuration of the setup shown in Fig. 5c, to ensure the same strain for

both energy harvesters. In the series configuration, the output voltage is less than the sum of the voltages of each energy harvester, which does not exactly match the theoretical analysis. A corresponding increase in the power generated is also observed, but the peak value is greater than the sum of both and does not move with increasing the load resistance as predicted by the theoretical analysis, although the trend is the same. In the parallel configuration, the voltage is similar to one of the energy harvesters voltages, while the peak power is greater than the sum of both. The peak value moves as the load resistance decreases, but not exactly as predicted by the theoretical analysis. These results are consistent with the principles of piezoelectric generator theory, where the series configuration is known to facilitate voltage accumulation, while the parallel configuration is said to enhance current delivery.

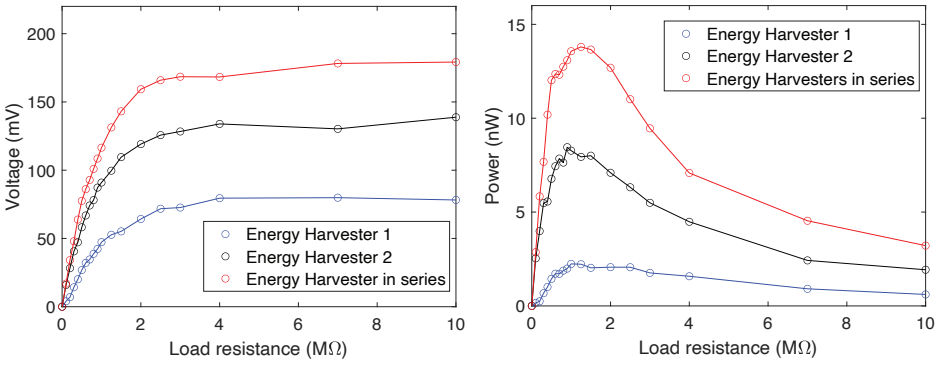

(a) (b)

Figure 7: Voltage (a) and power (b) curves of energy harvesters 1 and 2 and of the series connection

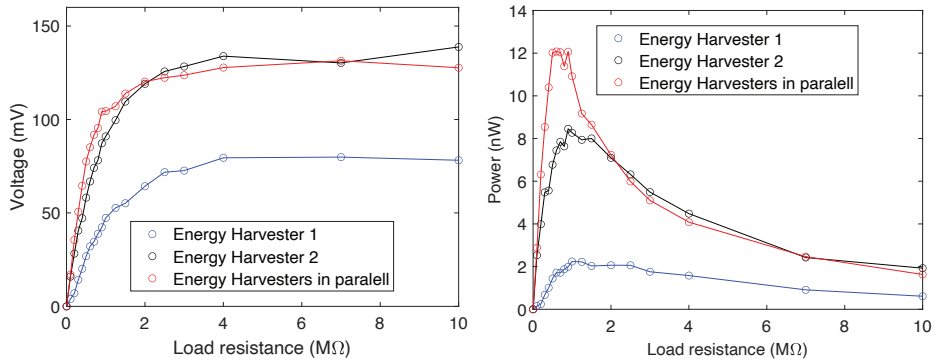

(a) (b)

Figure 8: Voltage (a) and power (b) curves of energy harvesters 1 and 2 and of the parallel connection

In conclusion, the experimental results confirm the expected behavior of the piezoelectric paint energy harvesters, although they also show the presence of small variations with respect to the theoretical analysis. These variations can be attributed to factors such as the uniformity of the paint application, variations in the polarization of the material and the adhesion of the top electrode. The results suggest the possibility of enhancing the design and manufacture of these generators to improve their efficiency in energy recovery applications in vibrating environments.

4 CONCLUSIONS

The present study has demonstrated the feasibility of using piezoelectric paints as an innovative and cost-effective alternative for small-scale energy harvesting from mechanical vibrations. Through the development of a theoretical model and its experimental validation, it has been confirmed that the performance of these devices depends on key factors such as electrical load, connection configuration (series or parallel) and material properties. The experimental results have shown that series connection of the energy harvesters increases the total voltage, while parallel connection promotes current generation, thus validating the principles of piezoelectric theory. It was also found that the value of the electrical load is critical to maximizing power output, highlighting the importance of effective system design for specific applications.

Tests have revealed slight variations in the performance of individual energy harvesters and their connection in series and in parallel, attributable to differences in paint application, polarization process, and electrode adhesion. These results suggest that manufacturing control is a critical aspect of improving device reproducibility and efficiency.

Overall, the results confirm the viability of piezoelectric paints for use in environments where structural vibration energy harvesting can be used to facilitate the operation of autonomous sensors, monitoring systems and low-power electronic devices. Based on the experimental setup described in our study (36 μm thick layer of piezoelectric paint over 4 cm^2 area), the maximum power output recorded for a single harvester was approximately 8 nW. To estimate the surface area required to power specific devices, we can extrapolate linearly from this value. For example: a wireless sensor node with intermittent operation averaging 10 μW would need around 0.5 m^2 of painted surface, and a low-power sensor requiring 100 μW would need approximately 5 m^2. Future studies should focus on optimizing the fabrication process and integrating these energy harvesters into self-sufficient energy systems to maximize their impact in real-world applications.

ACKNOWLEDGMENTS

This study was supported in part by Ministerio de Ciencia e Innovación through the European Union NextGenerationEU under the Advanced Materials programme (PRTR-C17.I1); in part by the project PID2023-151681OB-I00, funded by Ministerio de Ciencia, Innovación y Universidades (MICIU)/Agencia Estatal de Investigación (AEI)/10.13039/501100011033 and by European Regional Development Fund (ERDF), European Union (EU); and in part by the project SBPLY/21/180501/0000135/2, funded by the EU through the ERDF, and the Regional Government of Castilla-La Mancha through Agencia de Investigación e Innovación de Castilla-La Mancha (INNOCAM).

REFERENCES

[1] D. G. Wakshume and M. L. Placzek, “Optimizing piezoelectric energy harvesting from mechanical vibration for electrical efficiency: A comprehensive review,” *Electronics*, vol. 13, no. 5, 2024.

[2] S. Parthasarathy, S. Behera, and S. Moharana, *Piezoelectric Polymer Composites for Energy Harvesting*. Singapore: Springer Nature Singapore, 2024, pp. 533–554.

[3] M. Ju, Z. Dou, J.-W. Li, X. Qiu, B. Shen, D. Zhang, F.-Z. Yao, W. Gong, and K. Wang, "Piezoelectric materials and sensors for structural health monitoring: Fundamental aspects, current status, and future perspectives," *Sensors*, vol. 23, no. 1, 2023.

[4] A. Alhamadani, K. Abood, and T. Ntayeesh, "Design and optimization of piezoelectric energy harvesting systems for enhanced performance in wireless sensor networks," *International Journal of Science and Research Archive*, vol. 12, pp. 568–576, 07 2024.

[5] L. Sun, L. He, G. Yu, X. Zheng, H. Wang, D. Yu, and J. Lin, "Recent developments in wearable piezoelectric energy harvesters," *Review of Scientific Instruments*, vol. 95, no. 4, p. 041501, 04 2024.

[6] V. Kovacova, N. R. Alluri, O. Bouton, J. Polesel, T. Granzow, V. Frick, L. Wassouf, C. S. Cojocaru, G. Feugnet, P. Bondavalli, and E. Defay, "High power piezoelectric energy harvester for a temperature monitoring system," *APL Electronic Devices*, vol. 1, no. 1, p. 016110, 03 2025.

[7] J. D. Boles, J. E. Bonavia, P. L. Acosta, Y. K. Ramadass, J. H. Lang, and D. J. Perreault, "Evaluating piezoelectric materials and vibration modes for power conversion," *IEEE Transactions on Power Electronics*, vol. 37, no. 3, pp. 3374–3390, 2022.

[8] Y. Liao and J. Liang, "Maximum power, optimal load, and impedance analysis of piezoelectric vibration energy harvesters," *Smart Materials and Structures*, vol. 27, no. 7, p. 075053, jun 2018.

[9] K. Dong, L. Jiang, and B. Ding, "Performances investigation of multi-configuration connections in piezoelectric energy harvester," *Journal of Vibration Engineering & Technologies*, 2025.

[10] K. Baidya, A. Roy, and K. Das, "A review of polymer-matrix piezoelectric composite coatings for energy harvesting and smart sensors," *Journal of Coatings Technology and Research*, vol. 21, 09 2023.

[11] S. Timoshenko and S. Woinowsky-Krieger, *Theory of Plates and Shells*. New York: McGraw-Hill, 1959.

[12] I. Payo and J. Hale, "Sensitivity analysis of piezoelectric paint sensors made up of PZT ceramic powder and water-based acrylic polymer," *Sensors and Actuators A: Physical*, vol. 168, no. 1, pp. 77–89, 2011.

Part VI
MS 05 - ADAPTIVE AND COMPLIANT ENGINEERING STRUCTURES

Malte von Scheven, Renate Sachse, Alexander Hasse

XI ECCOMAS Thematic Conference on Smart Structures and Materials - SMART 2025
M. Krommer, M. Nader and M. Schagerl (Eds)

Received: 1 April 2025 / Revised: 25 August 2025 / Accepted: 14 October 2025
© The Author(s) 2025

Stability Analysis of Adaptive Funicular Structures

Andres Felipe Guerra Riaño, Péter L. Várkonyi

Abstract. Inspired by slender plant organs that autonomously respond to external signals, we investigate and extend a recently proposed approach to actively control the shapes of slender structures, restoring and maintaining funicularity through real time shape adaptation under static or slowly varying loads. We investigate a discrete model of cantileverstructures represented as chains of rigid bars with pin joints, nodal loads, and rotary actuators at each joint. These models have multiple funicular configurations, most of which are unstable without shape control. To stabilize these configurations, we implement Proportional-Integral-Derivative (PID) controllers, adjusting the system geometry based on carefully chosen error functions. The controllers use nodal torque values, and allow the system to maintain funicularity without explicitly sensing the load, and computing the target shape. Tuning control parameters is a key issue, as an incorrect selection of controller gains can lead to instability. To address this, the stability of discrete cantilever structures is studied. For the simplest one-degree-of-freedom (DoF) model, the Routh-Hurwitz stability test is used. Then, linear stability analysis is extended to multiple DoF models.

Key words: Funicularity, Shape Adaptation, Structural Control, PID Control, Active Structures, Stability Analysis.

1 INTRODUCTION

Funicular structures carry loads exclusively through axial forces, relying purely on tension and/or compression [1]. Due to the absence of bending moments, funicularity often implies structural efficiency, which is why these structures are typically extremely light.

Tensile funicular structures, such as slender cables, cable networks, and chains, are often highly flexible and automatically adapt their shapes under varying loads to maintain funicularity. In contrast, pure compression structures require sufficient bending stiffness to ensure structural stability. Consequently, they cannot maintain funicularity under load variations, leading to bending moments for time-dependent load distribution. However, for most of their lifetime, these structures experience more favorable load conditions, and small bending moments. This design strategy results in the use of excess material that remains largely unused while also imposing restrictions on architectural freedom [2] and compromising structural efficiency.

Andres Felipe Guerra Riaño & Péter L. Várkonyi
Budapest University of Technology and Economics, Department of Mechanics, Materials and Structures, 1111 Budapest, Hungary
e-mail: guerra.andres@edu.bme.hu,varkonyi.peter@epk.bme.hu

Adaptive structures enable control over structural geometry to achieve various objectives, requiring key components such as sensory feedback on the structure's state, a control policy, and actuators [3]. These features are common in the robot and machine industry. In structural applications, recent research has focused on developing small-scale adaptive structures [4, 5], while large-scale civil engineering applications remain largely unexplored, mainly due to reliability problems [6, 7].

This work investigates structures capable of feedback control and shape adaptation to stabilize compressive funicular shapes, significantly reducing material usage and promoting more sustainable construction. Previous studies on discrete cantilever [8] and arch [9] models demonstrated that by using Proportional-Integral-dDerivative (PID) controllers, rotary actuators at joints, and an innovative error function, one can maintain funicularity. However, careful selection of controller gains is essential to ensure stability of the controlled system.

In this work, the equations of motion for a discrete linear cantilever are presented in Section 2. In Section 3, we review a funicular control strategy that generates torques to maintain structural stability under unpredictable and unmeasurable load variations, with examples of stable and unstable 1-DoF structures. Additionally, linear stability analysis is performed using the Routh-Hurwitz test in Section 4, focusing on the influence of control parameters. Finally, the results are extended to 2- and 3-DoF models.

2 MODEL SETUP

Consider a chain of n weightless, rigid bars with lengths l_i, connected by pin joints equipped with masses m_i. It is assumed that external forces $\mathbf{F}_i$ with components (F_{ix}, F_{iy}) are applied at the joints (Figure 1 (a)). Each pin joint has a rotary actuator, generating torques at the adjacent bars. The point 0 is fixed (square) at the origin, and all other joints move freely (circles).

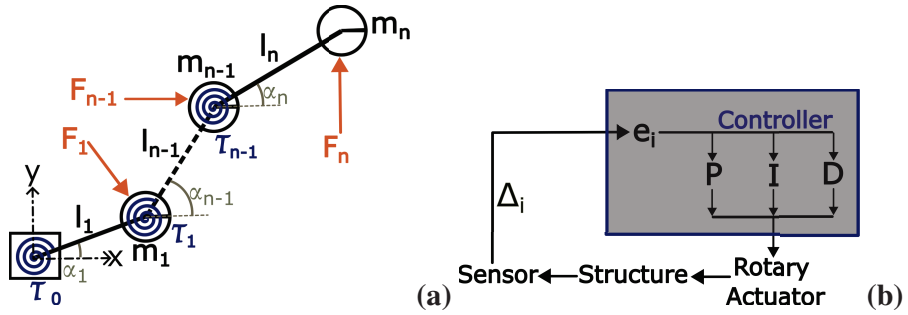

Figure 1: (a)A linear structure composed by n bars with length l_i connected by pin connections with masses m_i. External loads F_i are assumed to be stationary, and rotary actuators producing torques τ_i set the shape of the structure. (b) A closed-loop operation of a PID control system with continuous feedback.

The equations of motion are derived using Lagrangian mechanics as follows.

Let $\mathbf{l} = [l_1, l_2, ..., l_n]^T$, and $\boldsymbol{\alpha} = [\alpha_1, \alpha_2, ..., \alpha_n]^T$ denote vectors composed of bar lengths and rotation angles. Let $\mathbf{L} = diag(\mathbf{l})$. Nodal coordinate differences between adjacent joints can be

calculated as:

$$\mathbf{B}_x = \mathbf{L}\cos(\boldsymbol{\alpha}), \quad \mathbf{B}_y = \mathbf{L}\sin(\boldsymbol{\alpha}) \tag{1}$$

Setting as origin the position of the fixed node ($i = 0$), particles positions R_{xi} and R_{yi} can be calculated using:

$$\mathbf{R}_x^T = \left[R_{x1}, R_{x2}, \cdots, R_{xn}\right], \quad R_{x_i} = \sum_{j=1}^{i} B_{x_j}, \ \forall i = 1, 2, \ldots, n \tag{2}$$

$$\mathbf{R}_y^T = \left[R_{y1}, R_{y2}, \cdots, R_{yn}\right], \quad R_{y_i} = \sum_{j=1}^{i} B_{y_j}, \ \forall i = 1, 2, \ldots, n \tag{3}$$

The particle velocities in each direction can be computed as follows:

$$\mathbf{V}_x = \frac{d}{dt}\mathbf{R}_x, \mathbf{V}_y = \frac{d}{dt}\mathbf{R}_y, \tag{4}$$

The kinetic energy of the system is

$$T = \frac{1}{2}[\mathbf{V}_x^T \mathbf{M} \mathbf{V}_x + \mathbf{V}_y^T \mathbf{M} \mathbf{V}_y] \tag{5}$$

where $\mathbf{M}$ is the diagonal matrix composed of the nodal masses. Besides, by using vectors composed of the external load components $\mathbf{F}_x = [F_{x1}, F_{x2}, ..., F_{xn}]$ and $\mathbf{F}_y = [F_{y1}, F_{y2}, ..., F_{yn}]$, the associated potential energy can be calculated as:

$$P = -\mathbf{F}_x \mathbf{R}_\mathbf{x} - \mathbf{F}_y \mathbf{R}_\mathbf{y} \tag{6}$$

Then, the Lagrangian $\mathcal{L}$ can be computed as:

$$\mathcal{L} = T - P \tag{7}$$

The effect of the torques τ_i produced by the rotary actuators is taken into account by computing the corresponding generalized force. Let $\boldsymbol{\tau} = [\tau_0, \tau_1, ..., \tau_{n-1}]^T$. The corresponding generalized force is $\mathbf{G}\boldsymbol{\tau}$ where $\mathbf{G}$ is an n by n matrix, and its (j, i) entry is given by

$$G_{j,i} = \frac{\partial \Delta_j}{\partial \alpha_i} \tag{8}$$

$$\Delta_0 = \alpha_1 \tag{9}$$

$$\Delta_j = \alpha_{j+1} - \alpha_j \text{ for } 1 \leq j \leq n-1 \tag{10}$$

$$\Delta_n = -\alpha_n \tag{11}$$

Finally, the equations of motion are given by the Euler-Lagrange equation

$$\frac{\partial}{\partial t}\left(\frac{\partial}{\frac{\partial}{\partial t}\boldsymbol{\alpha}}\mathcal{L}\right) = \frac{\partial}{\partial \boldsymbol{\alpha}}\mathcal{L} + \mathbf{G}\boldsymbol{\tau} \tag{12}$$

and they can be expressed as

$$\ddot{\boldsymbol{\alpha}} = \mathbf{A}^{-1} \cdot [\mathbf{G}\boldsymbol{\tau} + \mathbf{b}] \tag{13}$$

The specific expressions for $\mathbf{A}$, $\mathbf{G}$, and $\mathbf{b}$ depend on the model parameters. For example, if $n = 1$, then

$$\mathbf{A} = l_1^2 m_1 \tag{14}$$

$$\mathbf{b} = F_{y1} l_1 \cos(\alpha_1) - F_{x1} l_1 \sin(\alpha_1) \tag{15}$$

$$\mathbf{G} = 1 \tag{16}$$

For $n = 2$, the explicit form of the equations has been given by [8].

3 FUNICULAR SHAPE CONTROL

Values of actuator torques τ_i are determined by PID (Proportional-Integral-Derivative) controllers. Figure 1 (b) illustrates a closed-loop system where a sensor measures data necessary to calculate the error e_i, and a controller responds as

$$\tau_i(t) = \tau_i^p(t) + \tau_i^d(t) + \tau_i^i(t) \tag{17}$$

$$\tau_i(t) = -k_{pi} e_i - k_{di} \dot{e}_i - k_{Ii} \int_0^t e_i(x) dx \tag{18}$$

where τ_i^p is a term proportional to the error function, τ_i^d is proportional to the derivative of the deviation, and an integral term τ_i^i is proportional to the integral of the same quantity over time. In previous studies of discrete cantilevers [8], a shape control policy was developed to keep the system in a funicular state responding to unpredictable loads but sensors can monitor nodal torques constantly. In this case $e_i = \alpha_i(t) - \alpha_{i-1}(t) - \lambda_{0,i}$ is used as the error function by the controllers, where $\lambda_{0,i}$ is an initial guess of the $\alpha_i - \alpha_{i-1}$ value corresponding to the unknown target shape and $\alpha_0 = 0$ by convention. A key observation of the control law is that the integral control term can be understood as a dynamically evolving estimation of the unknown target shape. After some algebraic transformation, PID control can be formulated as

$$\tau_i(t) = -k_{pi}(\alpha_i(t) - \alpha_{i-1}(t) - \lambda_i(t)) - k_{di}(\dot{\alpha}_i(t) - \dot{\alpha}_{i-1}(t)) \tag{19}$$

where $\lambda_i(t))$ is the continuously evolving estimated value of the $\alpha_i - \alpha_{i-1}$ values corresponding to the target shape.

$$\dot{\lambda}_i(t) = \frac{k_{Ii}}{k_{pi}}(\alpha_i(t) - \alpha_{i-1}(t) - \lambda_i(t)). \tag{20}$$

The equations of motion can be rewritten as a set of first-order differential equations in the state vector composed of angles, angular velocities, and torque-free angles:

$$\dot{\mathbf{y}} = \mathbf{h}(\mathbf{y}), \tag{21}$$

$$\mathbf{y} = [\alpha_1, \alpha_2, ..., \alpha_n, \dot{\alpha}_1, \dot{\alpha}_2, ..., \dot{\alpha}_n, \lambda_1, \lambda_2, ..., \lambda_n]^T, \tag{22}$$

$$\mathbf{h}(\mathbf{y}) = \ [\dot{\alpha}_1, \dot{\alpha}_2, ..., \dot{\alpha}_n, \mathbf{A}^{-1} \cdot [\mathbf{G}\boldsymbol{\tau} + \mathbf{b}], \tfrac{k_{I0}}{k_{p0}}(\alpha_1 - \lambda_1), \tfrac{k_{I1}}{k_{p1}}(\alpha_2 - \alpha_1 - \lambda_2), .., \tfrac{k_{In}}{k_{pn}}(\alpha_n - \alpha_{n-1} - \lambda_n) \ ]^T \tag{23}$$

This form will prove useful later when linear stability analysis is performed. Besides, if an initial condition vector

$$\mathbf{y}_0 = [\alpha_{0,1}, \alpha_{0,2}, ..., \alpha_{0,n}, \dot{\alpha}_{0,1}, \dot{\alpha}_{0,2}, ..., \dot{\alpha}_{0,n}, \lambda_{0,1}, \lambda_{0,2}, ..., \lambda_{0,n}]^T \tag{24}$$

is specified, we obtain an initial value problem for the system dynamics, which can be solved through numerical simulation. In the sequel, we use the ode45 solver of Matlab for this purpose.

Consider the simplest case of $n = 1$. For each load, The structure has two possible funicular shapes: one, where the bar is in tension and another where it is in compression. Turning off the actuator's proportional and integral terms allows the structure to achieve a pure tension funicular configuration similar to a passive cable or chain. In addition, we have found that the shape control converges to a purely compressive bar if the sign of the integral gain is negative. In this configuration, the control is necessary to stabilize the system.

As an illustration, we show simulations where the target is to achieve the pure compression funicular shape using an external load vector $\mathbf{F}_1 = [F_{1x}, F_{1y}] = [0, -1]$ and initial condition $y_0 = [\alpha_1, \dot{\alpha}_1, \lambda] = [0, 0, 0]$. The control parameters are $k_{p_0} = 1.1$, $k_{I_0} = -0.01$ and $k_{d_0} = 1$. The results are shown in Figure 2(a), where the initial shape is denoted by a blue continuous line, and a sequence of transient shapes is shown until the system reaches the expected funicular shape, represented by a green continuous line. Nevertheless, if the integral gain is increased further, the system may become unstable, as shown in Figure 2 (b). For this simulation, the controller has an integral parameter $k_{I_0} = -0.1$, and it can be seen how the system fails to achieve funicularity and continues oscillating over time. To understand this phenomenon, we undertake a linear stability analysis to identify conditions of a suitable set of controller parameters.

4 STABILITY ANALYSIS

Eq. 23 is linearized at a funicular state $\mathbf{y}_f$ as:

$$\dot{\mathbf{y}} = \mathbf{h}(\mathbf{y}) = \mathbf{h}(\mathbf{y}_f) + \mathbf{J}_h(\mathbf{y}_f)(\mathbf{y} - \mathbf{y}_f) + \text{higher order terms} \tag{25}$$

where $\mathbf{J}_h(\mathbf{y}_f)$ represents the Jacobian matrix of $\mathbf{h}(\mathbf{y})$ and contains the control gains k_{pi}, k_{di} and k_{Ii}. As the funicular shape ensures equilibrium without torques, $h(\mathbf{y}_f) = 0$, and the high-order terms are neglected. By direct computation we obtain for $n = 1$

$$\mathbf{J}_h(y_h) = \begin{bmatrix} 0 & 1 & 0 \\ -\frac{k_{p0} + F_{x1}\, l_1\, \cos(\alpha_1) + F_{y1}\, l_1\, \sin(\alpha_1)}{{l_1}^2\, m_1} & -\frac{k_{d_0}}{{l_1}^2\, m_1} & \frac{k_{p0}}{{l_1}^2\, m_1} \\ k_{I_0}\, k_{p_0} & 0 & -k_{I_0}\, k_{p_0} \end{bmatrix}. \tag{26}$$

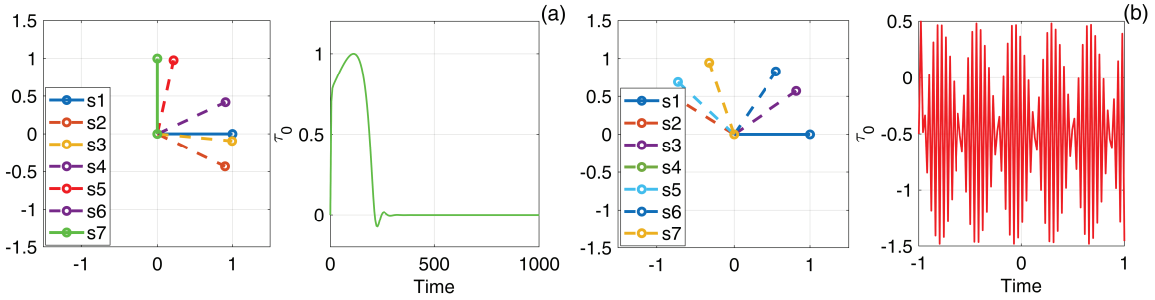

Figure 2: Comparison of shape adaptation times for a one-bar cantilever structure with external load $\hat{F}_1 = [0, -1]$, and two different integral gain values $k_{I_1} = -0.001$ (a) to $k_{I_1} = -0.1$ (b).

To get stability conditions the Routh-Hurwitz stability test is used [10]. First, the coefficients of the characteristic polynomial are:

$$s_1 = 1 \tag{27}$$

$$s_2 = \frac{k_{I0}\, k_{p0}\, m_1\, {l_1}^2 + k_{d0}}{{l_1}^2\, m_1} \tag{28}$$

$$s_3 = \frac{k_{p0} + F_{x1}\, l_1\, \cos(\alpha_1) + F_{y1}\, l_1\, \sin(\alpha_1) + k_{I0}\, k_{d0}\, kp_0}{{l_1}^2\, m_1} \tag{29}$$

$$s_4 = \frac{k_{I0}\, F_{x1}\, k_{p0}\, l_1\, \cos(\alpha_1) + k_{I0}\, F_{y1}\, k_{p0}\, l_1\, \sin(\alpha_1)}{{l_1}^2\, m_1} \tag{30}$$

Then, the Routh array is constructed as

$$r = \begin{bmatrix} s_1 & s_3 \\ s_2 & s_4 \\ \frac{s_2 s_3 - s_1 s_4}{s_2} & 0 \\ s_4 & 0 \end{bmatrix} \tag{31}$$

A necessary and sufficient condition for stability is the absence of sign changes in the first column of eq. (31). Since $s(1) = 1$ is positive, all other coefficients must also be positive. Given that l_i and m_i are always positive, a stable system is characterized by the following conditions:

- Condition 1

$$\frac{k_{I0}\, k_{p0}\, m_1\, {l_1}^2 + k_{d0}}{{l_1}^2\, m_1} > 0 \tag{32}$$

The derivative gain k_{d0} is normally positive in order to dampen oscillations. Then, Condition 1 is always satisfied as long as $k_{I0}k_{p0} > 0$. In the converse case, stability is still possible if $|k_{I0}k_{p0}| < k_{di}$.

- Condition 2

$$\frac{k_{d0}\,k_{p0}+k_{I0}\,{k_{d0}}^2\,k_{p0}+k_{d0}\,F_{x1}\,l_1\,\cos(\alpha_1)+k_{d0}\,F_{y1}\,l_1\,\sin(\alpha_1)+k_{I0}\,{k_{p0}}^2\,{l_1}^2\,m_1+{k_{I0}}^2\,k_{d0}\,{k_{p0}}^2\,{l_1}^2\,m_1}{{l_1}^2\,m_1\left(k_{I0}\,k_{p0}\,m_1\,{l_1}^2+k_{d0}\right)} > 0$$

If $[F_{x1}l_1cos\,(\alpha_1) + F_{y1}l_1sin\,(\alpha_1)]$ and the gain parameters are all positive, condition 2 is satisfied for sure. In case of negative values of k_{I0} and $[F_{x1}l_1cos\,(\alpha_1) + F_{y1}l_1sin\,(\alpha_1)]$, sufficiently large values of proportional gain k_{p0} is needed for stability. An intuitive explanation of this finding is provided by noting that passive structures under compression need sufficient bending stiffness to avoid buckling. In our case, the critical stiffness corresponding to buckling is $k_{p0} = -[F_{x1}l_1cos\,(\alpha_1) + F_{y1}l_1sin\,(\alpha_1)]$.

- Condition 3

$$\frac{k_{I0}\,F_{x1}\,k_{p0}\,l_1\,\cos\,(\alpha_1) + k_{I0}\,F_{y1}\,k_{p0}\,l_1\,\sin\,(\alpha_1)}{{l_1}^2\,m_1} > 0 \tag{33}$$

This condition is equivalent to $sign(k_{I0}k_{p0}) = sign(F_{x1}l_1cos\,(\alpha_1) + F_{y1}l_1sin\,(\alpha_1))$, which explains why the sign of the integral gain determines the funicular shape found by the controller.

Considering the same load, mass and length used in the previous numerical simulations, contour lines relating the three parameters that ensure the linear stability conditions are plotted in Figure 3. In this case, the curved boundary is determined by Condition 2, and the straight boundary by Condition 3. Regions between the two curves indicate linear stability. Additionally, the shape of the curved contour line suggests that there is an optimal value of k_{pi} where the stability boundary in k_{Ii}/k_{pi} reaches its maximum magnitude. Moreover, it can be observed that there is an optimal value of the derivative parameter that allows us to maximize k_{Ii}/k_{pi}.

Similar stability analyses are conducted for the two-bar and three-bar models, focusing on achieving a pure compression funicular shape. Structures have unitary masses and lengths and external forces load vector $\mathbf{F}_i = [F_{ix}, F_{iy}] = [0, -1]$ and initial condition:
$\mathbf{y}_0 = [\alpha_1, ..., \alpha_n, \dot{\alpha}_1, ..., \dot{\alpha}_1, \lambda_1, ..., \lambda_n] = [0, ..., 0, ..., 0, ..., 0]$.

Nevertheless, as the complexity of the structure increases, analytical approaches using the Routh-Hurwitz test become impractical, requiring the numerical calculation of the eigenvalues of the Jacobian matrix to ensure that all of them have negative values. Figure 4 (a) presents the stability analysis for the two-bar model and (b) for the three-bar model. Again, these analyses help to identify controller setup configurations that maximize the magnitude of the integral gain, along with proportional and derivative gain values that ensure stability and shape convergence.

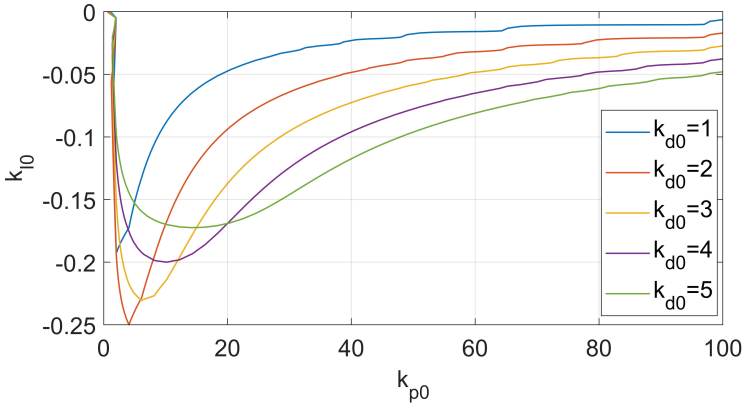

Figure 3: Linear stability analysis of the one bar cantilever example, different integral and proportional parameters are studied, contour lines are shown for five values of differential parameter k_{d_i} for the one bar cantilever example. Regions inside the contour lines correspond to stable systems.

5 CONCLUSIONS

Equations of motion for a discrete chain model with rotary actuators at joints are derived with the goal of maintaining a pure compression configuration. Stability analysis using the Routh-Hurwitz criterion identifies conditions for selecting controller gains that ensure stability. It is assumed that the derivative gain is positive in line with common practice. Then, if the integral gain is negative, its magnitude must remain sufficiently small. Stability is guaranteed when all gain parameters and external force components are positive. However, if the integral gain and external forces are negative, a sufficiently large proportional gain is required to maintain stability. This behavior aligns with the structural requirement of sufficient bending stiffness to prevent buckling, where the critical stiffness threshold is determined by the external force components.

The findings are extended to 2- and 3-degree-of-freedom (DoF) cantilevers, demonstrating similar stability conditions across different configurations. Stability diagrams are provided to illustrate the boundaries between stable and unstable parameter selections, offering practical guidelines for controller tuning. The results show that small negative values of the integral gain, combined with high proportional and sufficient derivative gains, ensure stability.

Additionally, in future works, it is important to analyze the importance of actuator response delay, the presence of additional constraints at supports, and the role of initial conditions in determining convergence to the target shape.

ACKNOWLEDGMENT

This work has been supported by the National Research, Development and Innovation Fund of the Ministry of Culture and Innovation of Hungary under project K143175.

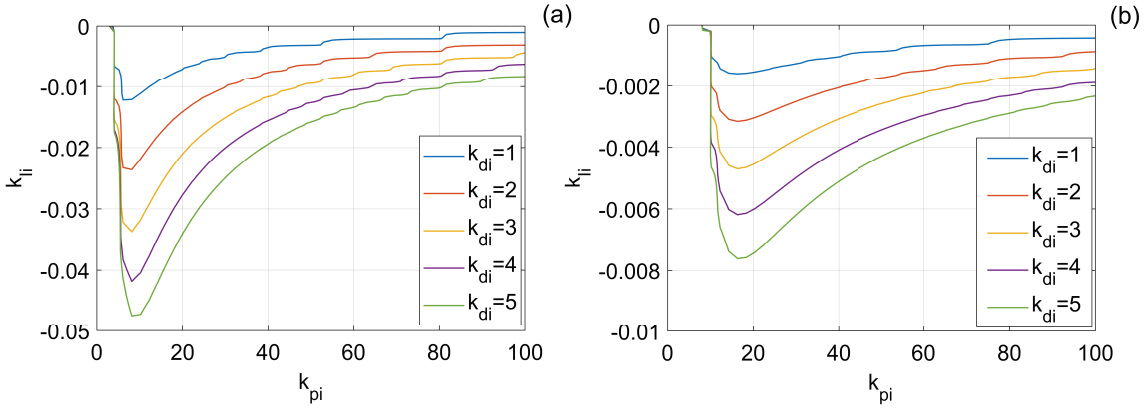

Figure 4: Linear stability analysis for two bar (a) and three bar (b) cantilever structures. Regions inside the contour lines are combinations of control parameters that produce stable funicular adaptation processes

REFERENCES

[1] S. Adriaenssens, P. Block, D. Veenendaal, and C. Williams, *Shell structures for architecture: form finding and optimization*. Routledge, 2014.

[2] G. Senatore, *Designing and Prototyping Adaptive Structures—An Energy-Based Approach Beyond Lightweight Design*. Cham: Springer International Publishing, 2018, pp. 169–189.

[3] C. Honold, H. Binz, D. Roth *et al.*, "Planning and developing adaptive buildings require methodical support," *DS 85-1: Proceedings of NordDesign 2016, Volume 1, Trondheim, Norway, 10th-12th August 2016*, pp. 321–330, 2016.

[4] T. van Manen, S. Janbaz, and A. A. Zadpoor, "Programming the shape-shifting of flat soft matter," *Materials Today*, vol. 21, no. 2, pp. 144–163, 2018.

[5] Z. Zhang, Y. Li, X. Yu, X. Li, H. Wu, H. Wu, S. Jiang, and G. Chai, "Bistable morphing composite structures: A review," *Thin-walled structures*, vol. 142, pp. 74–97, 2019.

[6] D. Efinger, A. Ostertag, M. Dazer, D. Borschewski, S. Albrecht, and B. Bertsche, "Reliability as a key driver for a sustainable design of adaptive load-bearing structures," *Sustainability*, vol. 14, no. 2, p. 895, 2022.

[7] M. Maierhofer and A. Menges, "Towards integrative design processes and computational design tools for the design space exploration of adaptive architectural structures," in *International conference on emerging technologies in architectural design (ICETAD2019)*, 2019.

[8] P. L. Várkonyi and A. F. Guerra Riaño, “Shape control of adaptive funicular structures,” in *10th ECCOMAS Thematic Conference on Smart Structures and Materials*. Patras, Greece: ECCOMAS 2023, 2023.

[9] A. F. Guerra Riaño and P. L. Varkonyi, “Robust funicularity of arches via adaptive shape control,” in *IASS 2024*. Zürich, Switzerlan: IASS 2024, 2024.

[10] M. Rahmani-Andebili, *Feedback Control Systems Analysis and Design*. Springer, 2002.

XI ECCOMAS Thematic Conference on Smart Structures and Materials - SMART 2025
M. Krommer, M. Nader and M. Schagerl (Eds)

Received: 25 June 2025 / Revised: 19 August 2025 / Accepted: 14 October 2025
© The Author(s) 2025

Design of a Thermoresponsive Shading System with shape memory material

Weifeng He, Aniket Pal, Thomas Wortmann, Maria Matheou

Abstract. This paper presents a comparative experimental study of an Adaptive Shading System (ASS) integrating smart material-based actuators to enhance building energy efficiency and visual comfort. 3D-Printed rhomboid façade modules of size 75 cm x 75 cm incorporate Shape Memory Polymers (SMPs) and Shape Memory Alloys (SMAs) in their horizontal axis, allowing folding configurations. This study adopts an integrated design methodology driven by a performance-based approach, employing a closed-loop process that includes material study, SMP geometry design, performance evaluation and prototype fabrication. Feedback from the performance evaluation informs the geometry design and material selection, optimising the shading's overall functionality. Experimental prototypes in scale 1:3 focus on three material-based actuation methods for the Two-Way Shape Memory Effect (TWSME), including a single SMA with a compliant mechanism, dual SMAs and integration of SMA into SMP. The aim is to assess these three methods in terms of responsiveness, such as responsive time and maximal folding angles (based on visual comfort criteria) and energy efficiency. Results indicate that dual SMA-driven solutions are particularly effective for adaptive shading, requiring only 183 J compared to the integration of SMA into SMP which requires 549 J. Additionally, daylight analysis was conducted in the summer and winter solstices at 9:00 am, 12:00 pm and 3:00 pm to evaluate the performance of the proposed adaptive shading installed on an office building with a floor area of 113 m^2 in Stuttgart, Germany. The proposed ASS with dual SMAs offers a TWSME for shape-changing mechanisms aligned with performance-driven architectural goals for sustainable façade design.

Key words: Adaptive Shading System, Daylighting Analysis, Shape Memory Alloy, Shape Memory Polymer, Two-way Shape Memory

Weifeng He & Maria Matheou
Institute for Lightweight Structures and Conceptual Design, University of Stuttgart, Pfaffenwaldring 14, 70569 Stuttgart, Germany
e-mail: weifeng.he@ilek.uni-stuttgart.de,maria.matheou@ilek.uni-stuttgart.de

Aniket Pal
Institute of Applied Mechanics, University of Stuttgart, Pfaffenwaldring 7, 70569 Stuttgart, Germany
e-mail: aniket.pal@mib.uni-stuttgart.de

Thomas Wortmann
Institute for Computational Design and Construction, University of Stuttgart, Keplerstraße 11, 70174 Stuttgart, Germany,
e-mail: thomas.wortmann@icd.uni-stuttgart.de

1 INTRODUCTION

The operations of buildings account for 30% of global final energy consumption and 26% of global energy-related emissions. While energy codes and renewable technologies are advancing, the sector must accelerate its transformation to align with the Net Zero Emissions by 2050 (NZE) scenario, ensuring all new buildings and 20% of the existing stock are zero-carbon-ready by 2030 [1]. Façades are the physical barrier and interface between external environmental conditions and internal comfort requirements. Given their dynamic nature, traditional static façades respond inadequately to climatic changes, failing to address the optimisation issues under dynamic constraints [2]. Hence, dynamic façade systems, capable of altering their properties in response to climatic conditions or seasonal variations, have been developed to meet evolving environmental conditions and occupant needs, thereby enhancing building efficiency continually [3]. These adaptations can be achieved through various actuation methods, broadly categorised into mechanical actuation (i.e. pneumatic and hydraulic) and material-based actuation [4].

Several researchers are looking into the "organic" or biological paradigm of kinetic adaptation, which relies on the material instead of mechanical actuation [4]. For example, a biobased 4D printed humidity-responsive smart structure, which could produce an actuated response (bending) when exposed to changing levels of humidity was developed in [5].

This paper presents a comparative experimental study of an Adaptive Shading System (ASS) integrating smart material-based actuators to enhance building energy efficiency and visual comfort. In this study, three different actuation methods, including a single Shape Memory Alloy (SMA) with a compliant mechanism, dual SMAs and integration of SMA into Shape Memory Polymer (SMP), have been proposed for the Two-Way Shape Memory Effect (TWSME) of the ASS and evaluated their performance in experimental prototypes.

2 INTEGRATED DESIGN METHODOLOGY

The aim of this paper is to design an ASS that can adjust its configurations according to the changing seasons, as shown in Figure 1. The proposed design methodology follows a performance-based approach and is divided into four key phases: Material Study, Geometry Design, Performance Evaluation, and Prototype Fabrication, as illustrated in Figure 2. In the Material Study phase, we explore flexible and shape memory materials through 3D-Printed (3DP) compliant hinges at a scale of 1:7. This phase also integrates SMA actuation with various parameters (Section 3.5). The Geometry Design phase is divided into macro and meso levels. At the macro level, we focus on shape, dimensions and curvature of the hinge.

In contrast, the meso level optimises the 3DP direction, material selection and combinations for actuation. We tested three actuation methods using 1:3 scale prototypes (Section 4.3). The Performance Evaluation phase assesses energy consumption and daylighting, analysing power requirements and illuminance levels at specific times to ensure visual comfort. A prototype built at a scale of 1:5 demonstrates the chosen actuation method.



Figure 1: Outdoor views of the ASS during the summer (left) and the winter solstice (right)

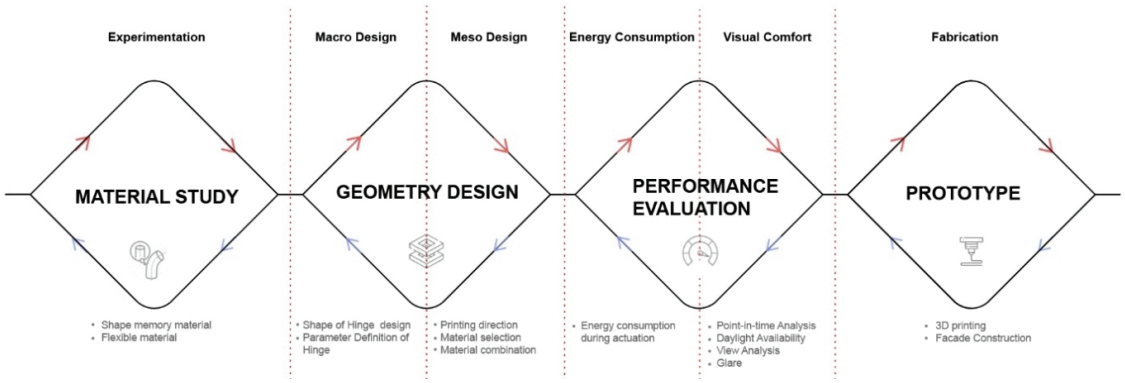

Figure 2: Design methodology of the proposed ASS

2.1 Experimental studies

Three different scales of prototypes were developed in this study. Initially, preliminary 3DP prototypes were created at a 1:7 scale, consisting of a single 10.5 cm x 6 mm strip. These served to explore printing direction, materials and reconfiguration within a simplified framework. Subsequently, façade module prototypes were built at 1:3 and 1:5 scales to investigate material behaviour and system performance further. In the next phase, panels were incorporated to refine the adaptive functionality.

2.2 Simulation study for the daylighting analysis

The daylight analysis was conducted in the summer and winter solstices at 9:00 am, 12:00 pm and 3:00 pm in Stuttgart, Germany, to evaluate the performance of the ASS installed on an office building with a floor area of 113 m^2. The office model is south-oriented, with the south and west elevations fully glazed. The width of the south and west elevations measures 13.64 m and 10.9 m, respectively, while the office height is 3.0 m. All material properties were assigned

accordingly using Climatestudio for Rhino3D [6]. The walls, floor and ceiling have default values for lighting simulations as per the Illuminating Engineering Society Lighting Metrics 83 [7]. The glazing has a visible transmission of 0.546 and a U-Value of 1.05 W/m^{2}K. A white opaque material with a reflectance of 79 % has been assigned to the façade panel.

3 SHAPE MEMORY MATERIALS AND INTEGRATION

3.1 Thermally induced shape-memory effect in polymers

Figure 3 illustrates the shape-memory effect in polymers. At room temperature, the SMP remains in its original shape. When an external force is applied, it deforms, reaching its maximum folding angle while still at room temperature, thereby maintaining a temporary shape. Upon heating to the target temperature (Tg), the polymer chains regain mobility, allowing the material to recover its original shape. Figure 4 shows the transformation process, where the polymer is heated through the current provided by two batteries with 1.5 volts respectively.

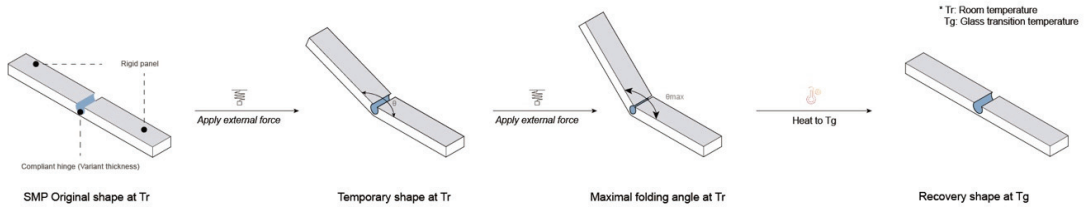

Figure 3: Thermally induced shape-memory effect in polymers

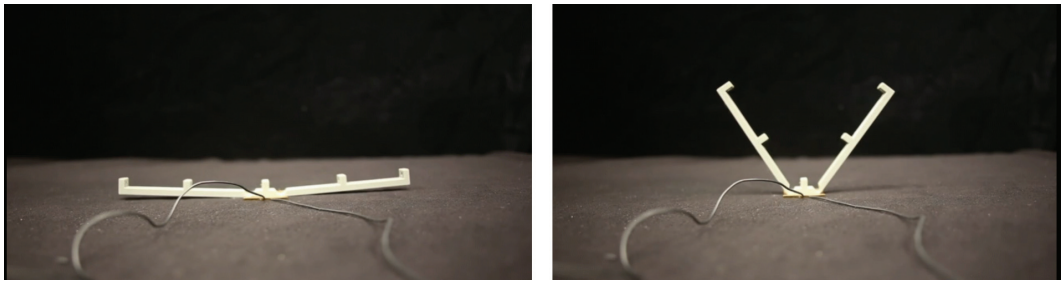

Figure 4: Experiment of shape memory effect with the original shape (left) and deformation after external force (right)

3.2 Shape-memory effect in SMAs

Figure 5 illustrates the shape-memory effect in SMAs. At low temperatures, the SMA remains in its original shape. When an external force is applied, it deforms into a temporary shape, but its internal crystalline structure retains a "memory" of the original form. Upon heating to the target temperature (Tg), the alloy undergoes a phase transformation, allowing it to return to its original shape.

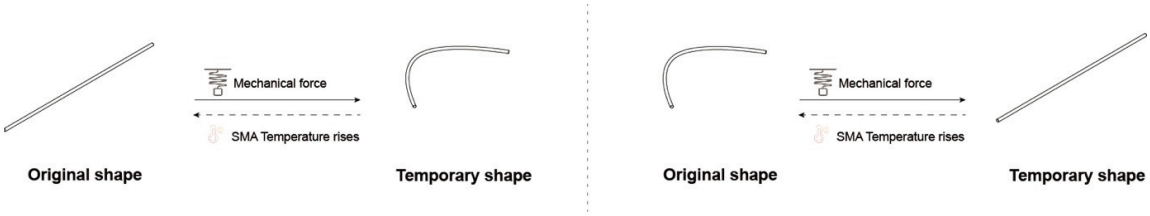

Figure 5: Shape memory effect in SMAs

3.3 Three actuation methods

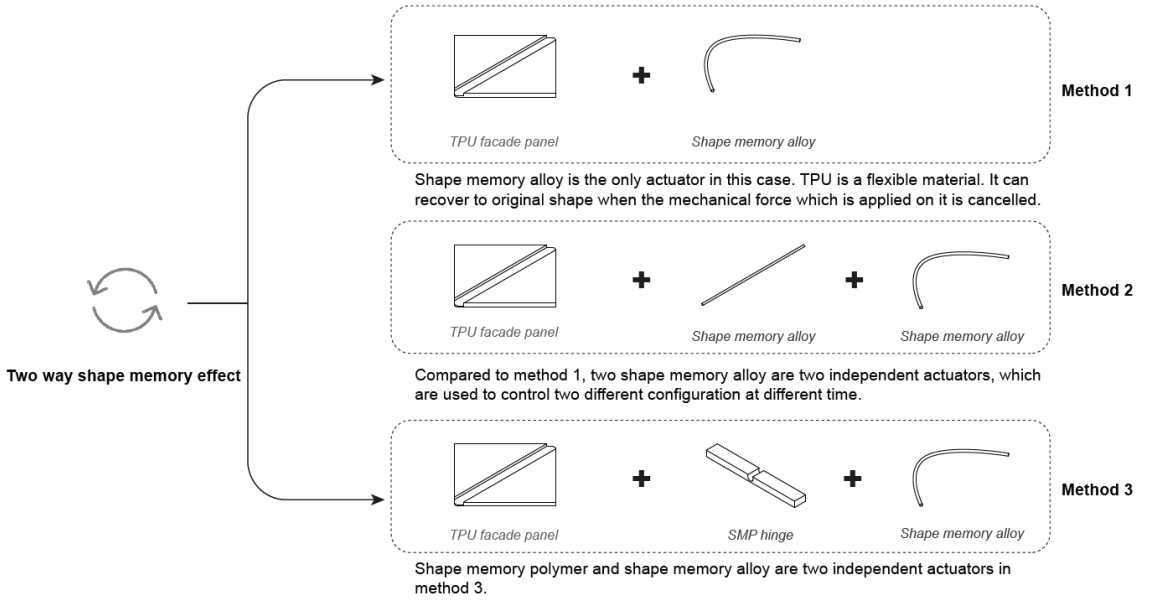

Figure 6: Three actuation methods for two-way shape memory effect

Achieving a TWSME can be realised through innovative material combinations and integration strategies, enabling reversible shape transformations without manual intervention. Figure 6 shows the three actuation methods proposed in this paper, which were evaluated through experimental studies. All experiments utilised a SMA specifically Nitinol alloyed with copper (NiTiCu), with a diameter of 1 mm and a phase change temperature of 60° (+-5). Method 1 integrates a single SMA wire into a Thermoplastic Polyurethane (TPU) façade panel. The SMA is known for its ability to return to a pre-programmed shape, while the TPU offers flexibility, enabling the panel to recover its original shape once the external force is removed. Method 2 integrates two SMAs with distinct original shapes into the flexible façade panel. This dual-SMA system allows for more complex and programmable movements, as each SMA responds differently to temperature changes, thus enhancing adaptability. Method 3 takes a

different approach by integrating an SMA into SMP hinges, which are then combined with the façade panel. This method leverages the simple programmability of SMP.

A comparison of the three different actuation methods will be discussed in Section 4.3. Figure 7 illustrates the principle of the three actuation methods in detail: a) the principle of Compliant Structure (CS) and SMA in Method 1; b) two different pre-programmed (original) shapes of SMA in the dual SMA system; c) the connection between the flexible panel and SMP with SMA in Method 3.

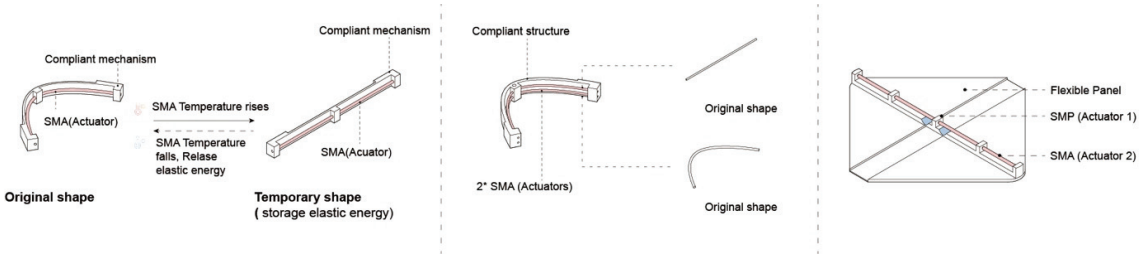

a) b) c)

Figure 7: a) Method 1; b) Method 2; c) Method 3

3.4 Stiffness matrix of three actuation methods

The stiffness relationship among different components is essential for ensuring proper actuation and recovery in an integrated system. In accordance with Hooke's law [8], the stiffness relationship among different components for the three actuation methods is outlined below.

Method 1:

Temporary shape ($_{SMA}^{h}$*:High temperature, CS:Compliant structure*): $K_{SMA}^{h} > K_{CS}$ (1)

Original shape ($_{SMA}^{l}$*: Low temperature*): $K_{SMA}^{l} < K_{CS}$ (2)

Combine (1) and (2): $K_{SMA}^{l} < K_{CS} < K_{SMA}^{h}$ (3)

Method 2:

Temporary shape (SMA as actuator): $K_{SMA1}^{h} > K_{CS} + K_{SMA2}^{l}$ (4)

Original shape: $K_{SMA2}^{h} > K_{CS} + K_{SMA1}^{l}$ (5)

Both SMAs have the same stiffness: $K_{SMA1} = K_{SMA2} = K_{SMA}$ (6)

Combine (5) and (6): $K_{CS} < K_{SMA}^{h} - K_{SMA}^{l}$ (7)

Method 3:

Open configuration (SMA as an actuator, *PA:Panel*): $K_{SMA}^{h} > K_{PA} + K_{SMP}^{l}$ (8)

Closed configuration (SMP as an actuator): $K_{SMP}^{h} + K_{PA} > K_{SMA}^{l}$ (9)

Combine (8) and (9): $K_{SMA}^{h} - K_{SMA1}^{l} < K_{PA} < K_{SMA}^{h} - K_{SMA}^{l}$ (10)

After we get the stiffness relationship among different components, it is necessary to analyse what parameters have an influence on the stiffness of them. The stiffness matrix (K)can simply deconstruct into two parts: Coefficient Matrix(α) and Parameter Matrix(P), as shown below:

$$K = \alpha * P$$

For different components, the stiffness matrices are slightly different:

Method 1 and Method 2:
$K_{SMA} = [a] * [D]$ *(a:coefficient; D: Diameter)*
$K_{CS} = [b \quad c]* [T_{cs} \quad H]^T$ *(b and c: coefficients, T_{cs}: Thickness of the compliant structure, H: Height of the compliant structure)*
Method 3:
$K_{PA} = [d \quad e]* [T_{panel} \quad T_{hinge}]^T$ *(T_{panel} : Thickness of the panel, T_{hinge}: Thickness of the hinge on the panel.*
$K_{SMP} = [f \quad g \quad h] *[T_{SMP_Hinge} \quad T_{joint} \quad H_{SMP}]$ *(T_{SMP_Hinge}: Thickness of SMP hinge, T_{joint}: Thickness of joint part of the SMP hinge, H_{SMP} : Height of SMP hinge)*

3.5 Experimental studies

3.5.1 3DP Compliant hinge

Preliminary experimental studies in scale 1:7 were conducted on a single 3DP strip with different flexure thicknesses to evaluate the stiffness of the compliant hinge made of TPU (Figure 8). By systematically varying these parameters and actuating the integrated SMA with current, the experiments demonstrated how the geometry design of the compliant mechanism influences its folding behaviour and recovery angle.

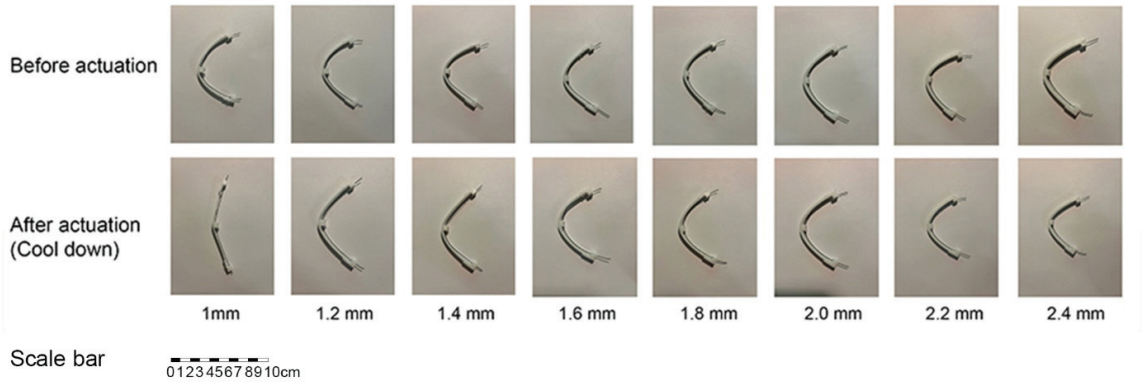

Figure 8: 3DP strips before and after actuation

Table 1 presents the flexure thickness and folding angles of the 3DP strips, which affect the stiffness of the CS during actuation by an integrated actuator, such as an SMA. Thinner flexures enhance actuation but may compromise durability. Flexure properties are also vital during recovery, as they store and release elastic energy to restore the original shape. For instance, a compliant hinge with a flexure thickness of 1.8 mm has the largest transformation angle range, achieving a maximum folding angle of 60° when actuated and a corresponding recovery angle. Experimental results emphasise the importance of balancing flexibility and stiffness for precise and efficient shape reconfiguration.

Table 1: Flexure thicknesses and folding angles

Flexure Thickness (mm)	1	1.2	1.4	1.6	1.8	2.0	2.2	2.4
Maximum folding angle when actuated (°)	175	150	150	145	145	125	120	110
Recover angle without actuation (°)	140	100	95	90	85	80	80	80
Transformable angle range	30	50	45	55	60	45	40	30

3.5.2 3DP façade module

To evaluate the three actuation methods, three 1:3 scale 3DP rhomboid façade prototypes (25 x 25 cm) were fabricated (Figure 9). Each integrates SMPs and SMAs along the horizontal axis, depending on the method. The panel is made of TPU with a different in the compliance hinge material. For single SMA and dual SMA actuation, the hinges are TPU, whereas Polyethylene Terephthalate Glycol (PETG) is used for SMA-SMP integration. PETG, heated by a foil to enhance thermal distribution and reduce actuation time, was selected for its higher stiffness at higher temperatures compared to Polyactic Acid (PLA).

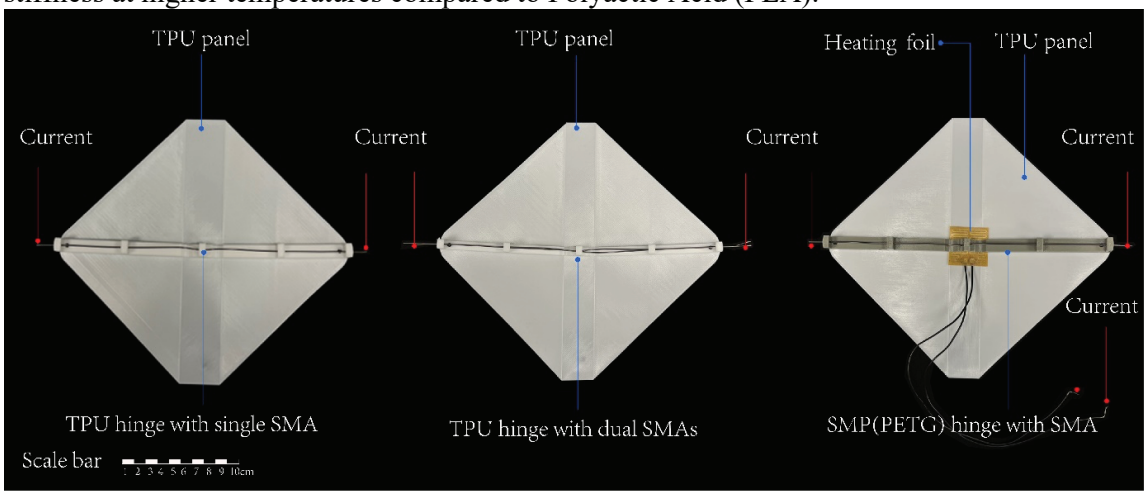

a) b) c)

Figure 9: Prototypes in scale 1:3: a) (1) SMA; b) (2) SMAs; c) SMP + (1) SMA

4 RESULTS AND DISCUSSION

4.1 Performance Evaluation

Figure 10 presents the maximal transformation angles for each façade module across the three actuation methods. Both SMA and SMP are activated by electric current to reach their phase change temperatures. Method 2, using a dual SMA system, shows the fastest reconfiguration at 50s for folding and 48s for recovery, with the largest transformation angle of 60°. Method 3, which integrates SMP and SMA, demonstrates the slowest reconfiguration at 80s for folding and 105s for recovery, with the smallest transformation angle of 45°. Method 1 requires a continuous activation to maintain its deformed state.

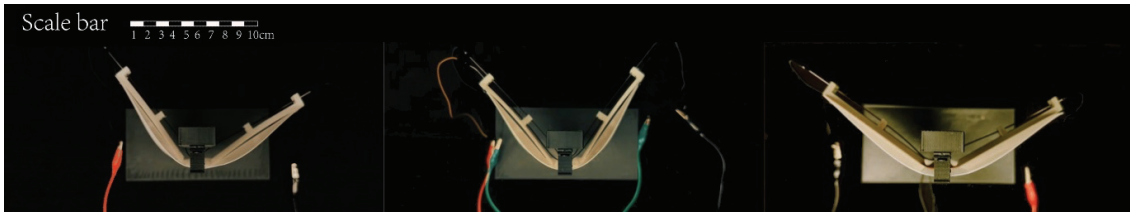

a) b) c)

Figure 10: Folded configuration of the three actuation methods a) Method 1; b) Method 2; c) Method 3

4.2 Daylight Analysis

Figure 11 compares the illuminance levels of a static façade with the proposed ASS. The red dashed lines indicate optimal office lighting levels based on EN 12464 [9]. Results show that the static façade modules admit excessive or insufficient daylight during the seasons. On the other hand, the proposed ASS dynamically adjusts panel angles to improve daylight control. Further analysis on glare and light uniformity shows a need for geometry and material optimisation. Figure 12 illustrates indoor and outdoor visualisations of the ASS for an office room in Stuttgart during the summer and winter solstices.

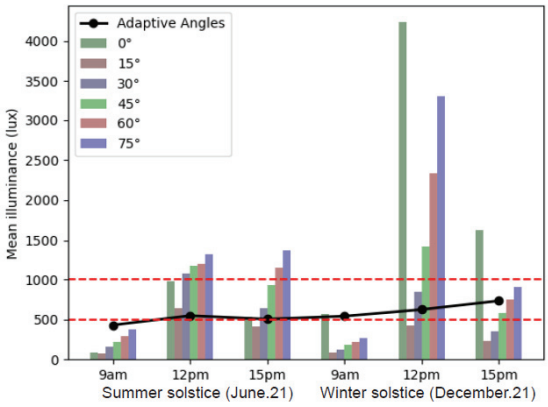

Figure 11: Mean illuminance simulation study of static and adaptive façade

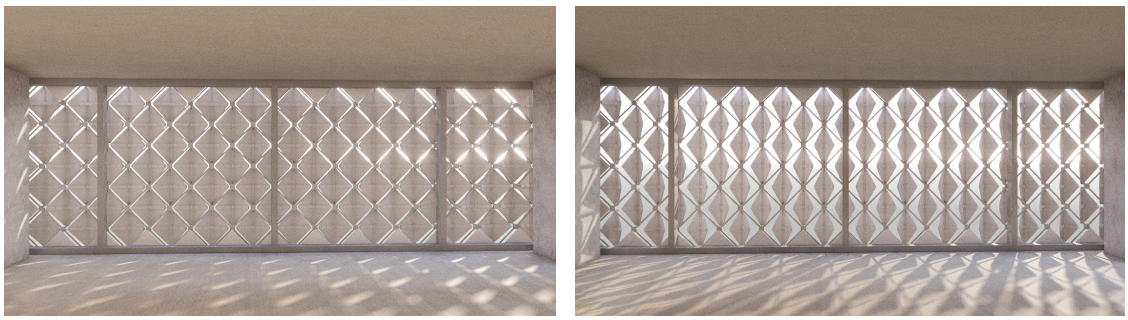

Figure 12: Indoor views of the ASS during summer (left) and the winter solstice (right)

A prototype in scale 1:5 of Method 2 was built with 15 cm x 15 cm panels. The 3DP panels, made of TPU, incorporate two SMAs per panel, as shown in Figure 13.

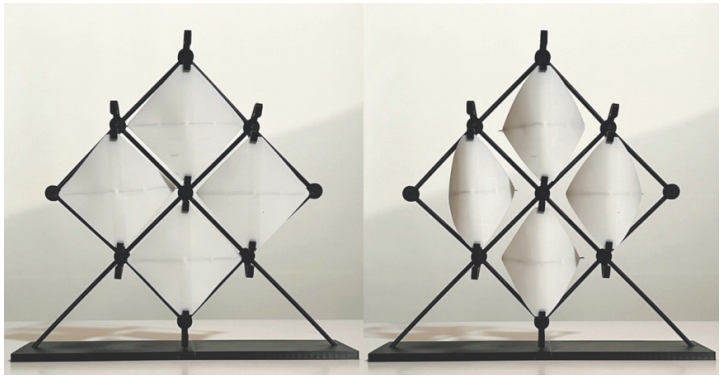

Figure 13: Prototype in scale 1:5 with open (left) and folded configuration (right)

4.3 Discussion

As shown in Table 2, the dual SMA-driven method is the most energy-efficient, requiring only 183 J for folding and recovery, about one-third of the 549 J needed for the SMA-SMP approach. While a single SMA uses only 121 J for folding, its requirement for continuous actuation to maintain fixed positions increases daily energy use. Overall, SMA/SMP-based systems achieve comparable motion to conventional mechanical solutions [10] with substantially lower energy demand, highlighting their potential for energy-efficient adaptive shading.

The comparative assessment of the three actuation methods for achieving the TWSME reveals distinct strengths and limitations, underscoring the adaptability of shape memory materials in reconfigurable systems. Method 1 prioritises simplicity but lacks high holding-energy requirements, Method 2 combines adaptability with low energy consumption, and Method 3 facilitates easier programmability for complex configurations. These differences make each approach suitable for specific functional and design objectives in adaptive façade applications.

This study demonstrates feasibility at prototype scales (1:3, 1:5), but requires further work to refine manufacturing, improve structural durability, and assess long-term performance under real environmental conditions. At the façade scale, optimising SMP-based panel geometry and material properties can improve mechanical strength, lower activation energy, reduce glare, and enhance indoor light uniformity.

Although we used 3DP to prototype different designs of our adaptive shading systems, more effective manufacturing methods can be used for mass production on a real scale. For example, large TPU panels can be produced efficiently using extrusion of injection molding. SMA wires can be used as purchased, similar to those used in this manuscript. The SMP PETG is highly adaptable to various traditional manufacturing processes like die-cut, machining,

thermoforming etc., although 3DP can remain a viable option at larger scales due to the relatively smaller footprint of the SMP part.

Table 2: Evaluation criteria for the three actuation methods

Dimensions for a single façade module	Actuation Method	Actuator [no.]	Actuation	Progra-mmed angle [°]	Transfo-rmation angle [°]	Actua-tion Time [s]	Power [W]	Energy Consumption (W=P*t) [J]
25 x 25 cm	Method 1	(1) SMA	Folding (1 SMA)	80	55	65	1.875	121
	Method 2	(2) SMA	Folding (1 SMA)	80	60	50	1.875	93
			Recovery (2 SMA)	0	5	48	1.875	90
	Method 3	SMP + (1) SMA	Folding (SMA)	80	45	80	1.875	150
			Recovery (SMP)	0	15	105	3.8 (Heating foil)	399

Beyond architectural applications, the thermo-responsiveness of this system can scale down to create wearable applications such as clothes with adaptive ventilation. For such small-scale application, multimaterial 3DP will become the preferred fabrication method, allowing simultaneous printing with two polymers (passively flexible TPU and thermo-responsive PETG) to create monolithic parts for easy integration into fabric. Alternative shape memory polymers, with lower glass transition temperatures such as Poly (vinyl acetate) or PVAc can also be considered as a way of using body temperature to regulate the actuation of the panels, and in turn, the ventilation of the clothes.

5 CONCLUSIONS

This study highlights the effectiveness of dual SMA-driven solutions in enhancing the energy efficiency and adaptability of thermo-responsive shading systems. Compared to single SMA and SMP-SMA integrated designs, the dual SMA approach offers a balanced trade-off between energy consumption and dynamic shape transformation, making it an efficient solution for sustainable architecture. By leveraging the inherent properties of shape memory materials, these systems contribute to responsive façade technologies that optimize daylighting, thermal comfort, and energy consumption in buildings. The findings emphasize the potential of such shading systems to play a crucial role in sustainable building methodologies, aligning with the broader goal of reducing reliance on active energy-intensive climate control solutions. Future work could focus on the scalability and seamless integration of these systems into full-scale architectural projects.

REFERENCES

[1] International Energy Agency, *Buildings,* 2025. [Online]. Available: https://www.iea.org/energy-system/buildings.

[2] D.-K. Bui, T.N. Nguyen, A. Ghazlan, N.-T. Ngo, and T.D. Ngo, "Enhancing building energy efficiency by adaptive façade: a computational optimization approach," *Appl. Energy*, vol. 265, 2020 114797, https://doi.org/10.1016/j.apenergy.2020.114797.

[3] J. Böke, U. Knaack, M. Hemmerling, "Automated adaptive façade functions in practice - case studies on office buildings," *Automation in Construction*. vol. 113, 2020, Art. no. 103113, https://doi.org/10.1016/j.autcon.2020.103113.

[4] B. Kolarevic, V. Parlac, *Building Dynamics: Exploring Architecture of Change*. Routledge, 2016.

[5] Y. Tahouni, T. Cheng, S. Lajewski, J. Benz, C. Bonten, D. Wood, and A. Menges, (2022). "Codesign of biobased Cellulose-Filled filaments and mesostructures for 4D printing humidity responsive smart structures." *3D Printing and Additive Manufacturing*, vol. 10, no. 1, pp. 1–14, 2022 https://doi.org/10.1089/3dp.2022.0061

[6] Solemma, *ClimateStudio*, 2025. [Online]. Available: https://www.solemma.com/climatestudio. [Accessed: 10-Mar-2025].

[7] Illuminating Engineering Society (IES), *Lighting Handbook*, 10th ed. New York, NY, USA: IES, 2011.

[8] R. Hooke, De Potentia Restitutiva, or of Spring. Explaining the Power of Springing Bodies. London, U.K.: John Martyn, Printer to the Royal Society, 1678

[9] European Committee for Standardization, *EN 12464-1: Light and Lighting – Lighting of Workplaces – Indoor Workplaces*, Brussels, Belgium, 2021.

[10] Jeong, M., Rössle, R., Böhm, M., Matheou, M., & Sawodny, O. (2024). Bridging exterior and interior climate: interdisciplinary design of a dual-functional adaptive kinetic façade prototype. Proceedings of the International Conference on Computer-Aided Architectural Design Research in Asia, 1, 435–444. https://doi.org/10.52842/conf.caadria.2024.1.435

Acknowledgments

The project was funded by the Deutsche Forschungsgemeinschaft (DFG, German Research Foundation) under Project-ID 279064222—SFB 1244 and Germany's Excellence Strategy – EXC 2120/1 390831618.

XI ECCOMAS Thematic Conference on Smart Structures and Materials - SMART 2025
M. Krommer, M. Nader and M. Schagerl (Eds)

Received: 23 April 2025 / Revised: 31 August 2025 / Accepted: 14 October 2025
© The Author(s) 2025

Efficient Design of Compliant Mechanisms Using Multi-Objective Optimization

Alexander Humer, Sebastian Platzer

Abstract. Compliant mechanisms achieve motion through elastic deformation. In this work, we address the synthesis of a compliant cross-hinge mechanism capable of large angular strokes while approximating the behavior of an ideal revolute joint. To capture the competing demands of kinematic fidelity, rotational stiffness, and resistance to parasitic motion, we formulate a multi-objective optimization problem based on kinetostatic performance measures. A hybrid design strategy is employed: an efficient beam-based structural model enables extensive exploration of a high-dimensional design space using evolutionary algorithms, followed by fine-tuning with high-fidelity three-dimensional finite element analysis. The resulting Pareto-optimal designs reveal diverse geometric configurations and performance trade-offs.

Key words: Compliant Mechanisms, Large Deformation, Multi-Objective Optimization, Hybrid Structural-Continuum Approach

1 INTRODUCTION

"If something bends to do what it is meant to do, then it is compliant. If the flexibility that allows it to bend also helps it to accomplish something useful, then it is a compliant mechanism", is how Larry Howell describes the essence of compliant mechanisms [1]. Their functionality relies on flexible deformation, which is determined by geometric shapes and material properties.

A *hinge* can arguably be regarded as the quintessential mechanism—embodying the concept of a revolute joint in kinematic terms. Replicating a hinge's functionality using compliant mechanisms first requires identifying its defining characteristics. These characteristics will, in turn, inform the objectives for the synthesis process. At its core, the purpose of a hinge is to allow two bodies to rotate relative to one another about a single common axis. In the ideal case of a perfect hinge, this axis remains fixed with respect to both bodies, and the hinge offers no resistance to rotation, regardless of the amplitude. Conversely, it provides infinite stiffness to all other modes of deformation. These contrasting requirements—flexibility in one direction and rigidity in others—are what makes a hinge a good example for the synthesis of compliant mechanisms based on multi-objective optimization.

Alexander Humer & Sebastian Platzer
Institute of Technical Mechanics, Johannes Kepler University Linz, Altenberger Str. 69, A-4040 Linz, Austria
e-mail: alexander.humer@jku.at

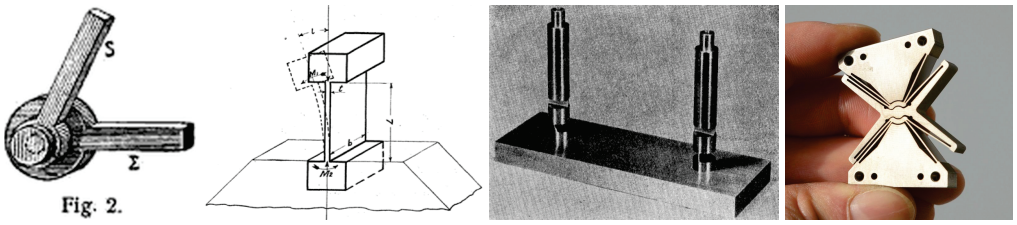

(a) (b) (c) (d)

Figure 1: Different kinds of hinges: Conventional pin-hole realization and compliant mechanisms.

Conventional realizations of revolute joints can be remarkably simple. Consider, for instance, the pairing of a pin and hole as illustrated in Fig. 1 (a) taken from the encyclopedia [2]. Relative rotation is enabled by the frictional sliding between the cylindrical surfaces of the pin and hole. The most fundamental way to join two (ideally rigid) bodies via a compliant element is to connect them using a thin flexible strip, i.e., a *'flexure'*, whose ends are fixed to each link it connects, see Fig.1 (b). The idea of using flexures as connecting elements in machinery is by no means a recent concept. In arguably one of the first articles on design rules for compliant mechanisms, Eastman [3] mentioned wind-tunnel balances of the 19th century using flexure pivots. None of the variants of flexure hinges illustrated in Fig.1 succeeds in reproducing the behavior of a revolute joint from the kinematic point of view. A single slender flexure (b) allows for comparatively large rotations among the connected links. However, the instantaneous axis of rotation shifts significantly as the deformation—or *stroke*—increases. Short flexures (c) exhibit less shift as far as the axis of rotation is concerned. The strength of materials, however, limits their admissible stroke as the flexure's (effective) slenderness decreases. To improve kinematics and increase stiffness, multiple flexures can be integrated within a mechanism as, e.g., in CSEM's 'butterfly-hinge' [4] (d). Its stroke, however, is limited to ±15°.

In a recent survey, Ling et al. [5] have given a comprehensive overview of three decades of research on the kinetostatic and dynamic modeling of compliant mechanisms. The progress in computational methods is reflected in the methodologies, which evolved from engineering beam theories to 3D-finite element analysis. Optimization lies at the heart of any synthesis problem, irrespective of whether conventional rigid-body or compliant mechanisms are concerned. In compliant mechanisms, however, we deal with multiple—typically conflicting—kinematic, static, and dynamic objectives that do not admit globally optimal solutions but demand for compromises. Finite stiffness is a defining property of compliant mechanisms, which demands for a trade-off between a maximum compliance regarding the intended motion and minimal compliance in all orthogonal directions. By employing *multi-objective optimization* methods and the pivotal notion of *Pareto optimality*, we avoid an a priori weighting among objectives, which inevitably introduces bias for certain designs. In what follows, we propose a hybrid two-stage approach to efficiently synthesize mechanisms composed of slender flexures: Structural models provide effective means to capture the global behavior of mechanisms in a first step. In a second step, continuum models allow us to resolve details and fine-tune design variants.

2 CROSS-HINGE GEOMETRY

Our focus lies on mechanisms with *distributed compliance* since we aim at large strokes. To this end, we generalize the well-established two-flexure cross-hinge, a classical design within the field of compliant mechanisms. As opposed to the classical cross-hinge, however, we allow for curved flexures with a preferably general shape, see Fig. 2. In the undeformed configuration, the cross-sections' angle of rotation $\theta^{(i)}$ follows a cubic polynomial in a normalized arc-length coordinate s,

$$\theta^{(i)}(s) = (1-s)\,\theta_0^{(i)} + s\,\theta_1^{(i)} + 4s\,(1-s)\,\theta_2^{(i)} + 4s\,(1-s)\,(2s-1)\,\theta_3^{(i)}, \tag{1}$$

where superscripts $i = 1, 2$ identify the respective flexure of the cross-hinge.

We use hierarchical polynomials inspired by finite-element shape functions, which guarantees that coefficients $\theta_0^{(i)}$ and $\theta_1^{(i)}$ directly correspond to the angles at the terminal points. We assume cross-sections to be initially perpendicular to the flexures' centerlines. The position of the centerline $\boldsymbol{X}^{(i)}$ with respect to some global Cartesian frame, whose origin coincides with the point $s = 0$ of the first flexure, i.e., $\boldsymbol{X}^{(1)}(0) = \boldsymbol{0}$, then follows upon integration of the unit tangent $\boldsymbol{s}^{(i)}$, which is scaled by the length $l^{(i)}$ of the respective flexure,

$$\boldsymbol{X}^{(i)}(s) = \boldsymbol{X}_0^{(i)} + l^{(i)} \int_0^s \boldsymbol{s}^{(i)}(\sigma)\mathrm{d}\sigma, \qquad \boldsymbol{s}^{(i)}(s) = \boldsymbol{e}_x \cos\theta^{(i)}(s) + \boldsymbol{e}_y \sin\theta^{(i)}(s), \tag{2}$$

where $\boldsymbol{X}_0^{(i)}$ denotes the position at $s = 0$. For the sake of simplicity, we assume the cross-sections of the flexures to have rectangular shapes, which remain constant along the centerlines; their widths and heights are denoted by $w^{(i)}$ and $h^{(i)}$, respectively.

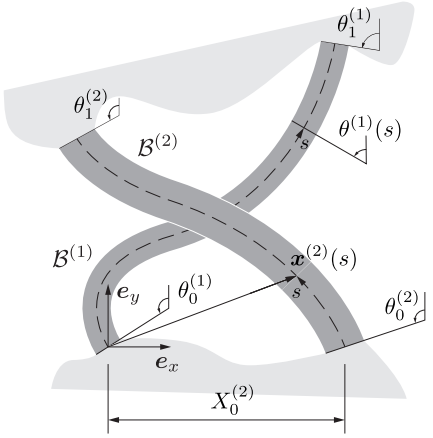

Figure 2: Schematic representation and kinematic description of the shape of the cross-hinge.

Table 1: Admissible ranges of the design variables.

variable	range	variable	range
$\theta_0^{(i)}/1$	$0 \ldots \pi$	$\alpha/1$	$0.5 \ldots 2$
$\theta_1^{(i)}/1$	$-\pi \ldots \pi$	$\beta^{(i)}/1$	$5 \ldots 20$
$\theta_2^{(i)}/1$	$-\pi \ldots \pi$	$\gamma/1$	$0.5 \ldots 2$
$\theta_3^{(i)}/1$	$-\pi \ldots \pi$	$\delta/1$	$0 \ldots 1$

The choice of appropriate design variables plays a crucial role in any synthesis problem, and compliant mechanisms are no exception. To obtain preferably general results, we introduce a

set of non-dimensional similarity parameters as design variables that govern the geometry of the generalized cross-hinge. The coefficients $\theta_1^{(i)}, \dots, \theta_4^{(i)}$, with $i = 1, 2$, represent angles and, hence, are dimensionless by definition. We further introduce the length-ratio α, the respective slendernesses $\beta^{(i)}$ of the flexures, the width-ratio γ, and the horizontal position $X_0^{(2)}$ of the point $s = 0$ of the second flexure, which is scaled by the length $l^{(1)}$ of the first flexure giving a non-dimensional ratio δ:

$$\alpha = \frac{l^{(2)}}{l^{(1)}}, \qquad \beta^{(i)} = \frac{l^{(i)}}{h^{(i)}}, \qquad \gamma = \frac{w^{(2)}}{w^{(1)}}, \qquad \delta = \frac{X_0^{(2)}}{l^{(1)}}. \tag{3}$$

To allow for effective optimization, we need to impose restrictions on the design variables that preclude rotated and mirrored shapes, which behave identical from in terms of objectives which are to be adopted subsequently. For this purpose, we fix the point $\boldsymbol{X}^{(2)}(0) = \boldsymbol{X}_0^{(2)}$ of the second flexure to the y-axis if the global Cartesian frame, i.e., $Y_0^{(2)} = 0$. To avoid reflection symmetries, δ is required to be positive and the angle of the cross-section at $s = 0$ of the first flexure is restricted to the range $\theta_0^{(1)} \in [0, \pi]$ The individual bounds for all 13 design variables as being used in the optimization are listed in Tab. 1. Note that infeasible shapes may occur when randomly sampling from the parameter ranges. In particular, self-intersecting centerlines of the flexures are not admissible and are rejected in the optimization process.

3 PARETO-OPTIMIZATION OF CROSS-HINGE GEOMETRY

In what follows, we assume the body attached to the flexures at $s = 0$ as spatially fixed. The (rigid) body connected to cross-sections $s = 1$ rotates by the angle φ about the z-axis. The operational range (action space) of the cross-hinge is specified as $\varphi \in \mathcal{A} = [0, \pi/2]$.

3.1 Kinetostatic performance measures

In what follows, we formulate the objective functions based on the above characterization of a hinge's nature. Accordingly, we first introduce an appropriate measure to quantify the kinematic deviation of the cross-hinge from an ideal revolute joint. Subsequently, static properties of the cross-hinge, i.e., its compliance with respect to translational motion and the stiffness against rotation are introduced.

Kinematics. The distinguishing feature of a hinge's axis of rotation being stationary relative to the connected body is in the center of attention. Within our approach, we refrain from specifying the actual position of the axis a priori. Instead, we want to minimize the variation of the axis' position relative to connected bodies in the course of motion. For this purpose, we resort to the kinematic concept of centrodes, specifically the *fixed* centrode as the curve described by the instantaneous center of rotation relative to the fixed body. Let $\boldsymbol{x}^{(i)}(s, \varphi)$ denote the position of the centerlines for a prescribed (relative) rotation φ:

$$\boldsymbol{x}^{(i)}(s, \varphi) = \boldsymbol{X}^{(i)}(s) + \boldsymbol{u}^{(i)}(s, \varphi), \qquad \varphi \in \mathcal{A}. \tag{4}$$

We choose the terminal point A of the flexure $i = 1$ as a reference point on the rotating body, whose position as a function of the rotation φ is given by:

$$\boldsymbol{x}_A(\varphi) = \boldsymbol{x}^{(1)}(s = 1, \varphi). \tag{5}$$

Recalling elementary kinematics of rigid bodies, the variation of the current position of A can be expressed in terms of the instantaneous center of rotation $\boldsymbol{x}_c$ as

$$\frac{\partial \boldsymbol{x}_A}{\partial \varphi}\delta\varphi = \delta\varphi \boldsymbol{e}_z \times (\boldsymbol{x}_A - \boldsymbol{x}_c)\,. \tag{6}$$

In the course of the optimation, we increase the prescribed angle φ in discrete steps, which allows us to approximate the fixed centrode $\varphi \mapsto \boldsymbol{x}_c$ replacing the derivative in the above relation by the corresponding difference quotient:

$$\boldsymbol{x}_c \approx \boldsymbol{x}_A + \boldsymbol{e}_z \times \frac{\Delta \boldsymbol{x}_A}{\Delta \varphi}. \tag{7}$$

While we used the arc-length of the centrode in previous studies [6], we propose to use the radius r_c of the smallest circle containing the centrode instead. Although both the length of the centrode and r_c vanish ideally, the latter preserves information on the spatial variation of the axis as the cross-hinge deforms, whereas the former only captures the absolute distance by which the instant center of rotation get displaced.

Translational compliance. An ideal revolute joint is characterized by an infinite stiffness in all directions except for rotational degree of freedom. Even though conventional hinges hardly meet this requirement, the finite stiffness of compliant mechanisms against translational motion is typically significantly smaller. When rotating the cross-hinge in discrete steps, we determine the principal translational compliances of the mechanism in each equilibrium configuration throughout the action space $\mathcal{A}$. The largest of all principal compliances, i.e.,

$$c_{\max} = \max_{j=1,2,\ \varphi \in \mathcal{A}} c_{\mathrm{transl},j}(\varphi), \tag{8}$$

serves as a measure to quantify the finite stiffness (or, much rather, the lack thereof) of the cross-hinge with respect to parasitic loads.

Rotational stiffness. Conversely, we seek for a minimum stiffness against a rotation about the indended axis. In analogy to the translational motion, we consider the maximum rotational stiffness within the action space $\mathcal{A}$ as a measure which is to be minimized by the cross-hinge:

$$k_{\min} = \max_{\varphi \in \mathcal{A}} k_{\mathrm{rot}}(\varphi). \tag{9}$$

To obtain cross-hinge designs that can be easily scaled, we prefer to formulate the objectives as non-dimensional functions of the kinetostatic properties introduced above. For this purpose,

the length of the first flexure serves as a natural choice for the referential length, i.e., $l_{\mathrm{ref}} = l^{(1)}$. To define a referential force, we take the product of Young's modulus with the referential length and the width of the first flexure, i.e., $F_{\mathrm{ref}} = El^{(1)}w^{(1)}$. Accordingly, the set of objective functions is given by

$$\bar{r} = \frac{r_c}{l_{\mathrm{ref}}} = \frac{r_c}{l^{(1)}}, \qquad \bar{c} = \frac{c_{\max}F_{\mathrm{ref}}}{l_{\mathrm{ref}}} = c_{\max}Ew^{(1)}, \qquad \bar{k} = \frac{k_{\min}}{F_{\mathrm{ref}}l_{\mathrm{ref}}} = \frac{k_{\min}}{Ew^{(1)}\left(l^{(1)}\right)^2}, \tag{10}$$

where bars have been added to distinguish non-dimensional quantities. Referring stiffnesses and compliances to the width $w^{(1)}$, we essentially eliminate effects related to the depth of the mechanism z-direction from the objectives. While this makes perfect sense when using (planar) beam theory in the analysis, such effects are certainly present in three-dimensional solid models of compliant mechanisms, as our subsequent results will show.

3.2 Formulation of the optimization problem

The individual performance measures are combined to form a vector-valued objective function:

$$f : X \to Y \subseteq \mathbb{R}^3, \qquad x \mapsto \left(\bar{r}, \bar{c}, \bar{k}\right)^T. \tag{11}$$

In general, a global optimum that minimizes all components of f does not exist. From a mathematical point of view, we are lacking an order relation that allows us to compare two individuals x, x' in the sense $f(x) \leq f(x')$. We adopt the concept of *Pareto-optimality*, which has its roots in economy and, ever since, has successfully been applied to engineering problems [7, 8, 9].

Let x, x' denote two solutions characterized by their respective objective vectors $y = f(x)$, $y' = f(x')$. Solution x *dominates* x' if x is at least as good as x' with respect to all objectives and better than x' with respect to (at least) one objective, i.e.,

$$\forall i \in \{1, \ldots, k\} : \; y_i \leq y'_i \quad \wedge \quad \exists i \in \{1, \ldots, k\} : \; y_i < y'_i. \tag{12}$$

To indicate the Pareto order, the short-hand notation

$$y \prec y', \qquad x \prec_f x' \tag{13}$$

is typically used. The set of all *non-dominated* solutions represents the *Pareto set*,

$$X_P = \{x \in X : \{x' \in X : x' \prec_f x, x \neq x'\} = \emptyset\}; \tag{14}$$

the *Pareto front* is the image of the Pareto set in the objective space, i.e.,

$$Y_P = \{y \in Y : \{y' \in Y : y' \prec y, y \neq y'\} = \emptyset\}. \tag{15}$$

Although the optimization problem is formulated in terms of non-dimensional objectives, their numerical values may differ by several orders of magnitude. We normalize the Pareto front for

the sake of comparability of the individual objectives. To this end, we introduce the concepts of the the *ideal* objective vector and the *nadir* point, respectively,

$$y_{\text{ideal}} = \left(\inf_{x' \in X_P} f_1(x'), \ldots, \inf_{x' \in X_P} f_k(x') \right)^T, \qquad y_{\text{nadir}} = \left(\sup_{x' \in X_P} f_1(x'), \ldots, \sup_{x' \in X_P} f_k(x') \right)^T, \tag{16}$$

which represent the respective lower and upper bounds of the individual objectives over the Pareto set. The (approximations of the) ideal and nadir solutions are used to normalize the Pareto front, i.e.,

$$\tilde{Y}_P = \left\{ \tilde{y}_i = \frac{y_i - y_{\text{ideal}}}{y_{\text{nadir}} - y_{\text{ideal}}} : y_i \in Y_P \right\} \subseteq [0,1]^3, \tag{17}$$

where a tilde has been introduced to indicate normalized objectives subsequently.

3.3 Implementation and solution

The proposed hybrid structural-continuum approach relies two distinct models of the cross-hinge. To approximate the Pareto set by means of evoluationary algorithms, we employ the geometrically exact theory for the planar deformation of shear-deformable beams, which goes back to Reissner [10]. We assume the conventional constitutive relations of structural mechanics, by which cross-sectional stress resultants and generalized strains are related linearly. The absolute value of Young's modulus is not relevant within our non-dimensional framework. Poisson's ratio is set to $\nu = 0.49$ to account for nearly incompressible materials as used in additively manufacturing. Although closed-form solution under concentrated loads do exist, see, e.g., [11, 12], we use a finite-element model based on the formulation of Simo and Vu-Quoc [13]. Each flexure of the cross-hinge is discretized into 30 cubic beam elements. The ends at $s = 0$ are fully constrained; cross-sections at $s = 1$ share three degrees of freedom representing a rigid-body motion. The rotation of $\pi/2$ at $s = 1$ is kinematically imposed in 20 steps. After each step, we compute a Schur complement of the tangent stiffness matrix to determine the stiffnesses with respect to a translational motion of a body attached at $s = 1$, from which the principal compliances follow as inverse of corresponding eigenvalues. The rotational stiffness is obtained by a finite-difference approximation of the reaction moment that occurs in the course of deformation. Welzl's algorithm [14] is used to compute the circumradius of the centrode (7). To distribute the compliance along the flexures, we impose a constraint on the bending strain, which is bound from above by 0.2. A single cross-hinge design can be analyzed within a few tenths of a second. Both SPEA2 [15] and NSGA-II [16] evolutionary algorithms as implemented in the open-source Python package `pymoo` [17] are used to find Pareto-optimal solutions.

Once a sufficient approximation of the Pareto-set is obtained, selected solutions are to be refined using three-dimensional finite-element models of the cross-hinge. Specifically, we employ third-order elements, which almost directly replace the beam elements of the structural model. A nearly incompressible, Neo-Hookean constitutive model governs the stress-response of the flexures. The kinetostatic performance measures are evaluated similarly as for the structural

model. The computational effort to analyze a single cross-hinge design using the high-fidelity model exceeds the structural model by more than 1000 times, which is prohibitively large for evolutionary algorithms. To fine-tune cross-hinge designs, we apply the Nelder-Mead [18] algorithm to a single-objective problem obtained by scalarization. All finite-element models are implemented in the open-source code `Netgen/NGSolve`.

4 RESULTS AND DISCUSSION

4.1 Pareto-optimal solutions

To approximate the Pareto front based on the structural model, we evolve populations of 500 individuals over 1000 generations using SPEA2 and NSGA-II, respectively. It turns out that the algorithms favor different directions of exploration for the present problem. For this reason, we merge the respective Pareto sets, for which a total of 1 000 000 designs has been simulated. Figure 3 shows the approximation of Pareto front, which is a surface in the three-dimensional objective space. Despite the seemingly simple nature of the present problem, the Pareto front has a comparatively complex shape showing several disconnected regions, which already indicate the presence of diverse design variants.

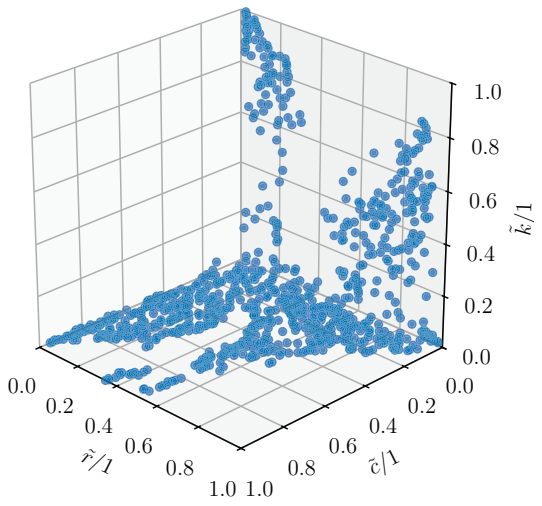

Figure 3: Approximation of the Pareto front comprising 798 individuals.

Projections of the Pareto front onto two-dimensional subspaces spanned by pairs of the objectives are illustrated in Fig. 4. As all objectives are to be minimized, solutions optimal with respect to the respective pairs of lie towards the lower left. The projection onto the $\tilde{c}\tilde{k}$-plane (right) shows a typical trade-off among two conflicting objectives: A smaller rotational stiffness k implies a greater translational compliance c and vice versa. Projections that include the deviation from a hinge's kinematics in terms of the centrode circumradius r, by contrast, show

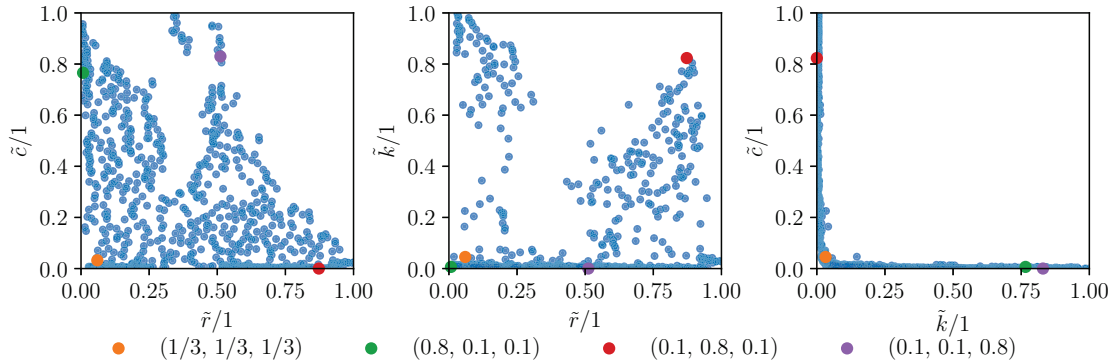

Figure 4: Projections of the Pareto front onto two-dimensional subspaces spanned by pairs of objectives. Colored markers correspond to selected solutions obtained upon uniform and preferential weighting, respectively.

a more complex relationship among the objectives. We find disconnected regions in projections both onto the $\tilde{c}\tilde{r}$-plane (left) and the $\tilde{k}\tilde{r}$-plane (center).

4.2 Multi-criteria decision making

Having approximated the Pareto set, we are only halfway through in multi-objective optimization. We still face the question of how to systematically choose individual soluations from the Pareto set. The field of *multi-criteria decision making* provides us with different approaches, among which we employ the concept of *pseudo-weights* as introduced by [7]. For each solution of the Pareto set $x \in X_P$, a vector of pseudo-weights $w_{\text{pseudo}} \in \mathbb{R}^3$ is computed based on the normalized distance to the worst solution, i.e., the nadir point y_{nadir}, cf. Eq. (16):

$$w_{\text{pseudo},i}(x) = \frac{y_{\text{nadir},i} - f_i(x)}{y_{\text{nadir},i} - y_{\text{ideal},i}} \sum_{j=1}^{3} \frac{y_{\text{nadir},j} - y_{\text{ideal},j}}{y_{\text{nadir},j} - f_j(x)} = \frac{1 - \tilde{f}_i(x)}{\sum_{j=1}^{3} \left(1 - \tilde{f}_j(x)\right)}, \qquad i = 1, \ldots, 3. \tag{18}$$

To make a selection, we choose the particular solution x^* that minimizes the L_1-distance between a preferred (target) weighting $w = (w_r, w_c, w_d)^T$ and the vector of pseudo-weights w_{pseudo}:

$$x^* = \arg\min_{x \in X_P} \sum_{i=1}^{3} |w_{\text{pseudo},i}(x) - w_i|. \tag{19}$$

Note that (pseudo) weights w_i need to be non-negative and sum up to 1, i.e., $\sum_{i=1}^{3} w_i = 1$.

To provide some insight into the diversity within the set of Pareto-optimal cross-hinge designs, we consider four different target weightings: A uniform weighting of $w_i = 1/3$, $i = 1, 2, 3$ is meant to represent what could be referred to as ideal trade-off. Additionally, we consider cross-hinge designs that emphasize one of the objectives over the remaining two by setting $w_i = 0.8$ and $w_j = 0.1$ for all $j \neq i$, where $i, j \in \{1, 2, 3\}$. Figure 5 illustrates the shapes of

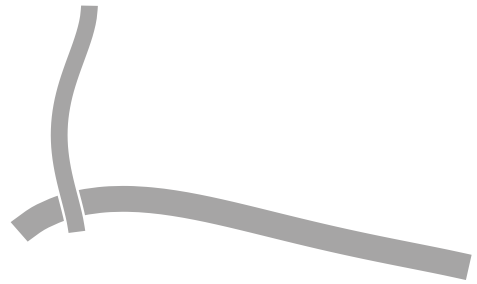

(a) $w = (1/3, 1/3, 1/3)$, $\gamma = 1.947$



(b) $w = (0.8, 0.1, 0.1)$, $\gamma = 0.724$

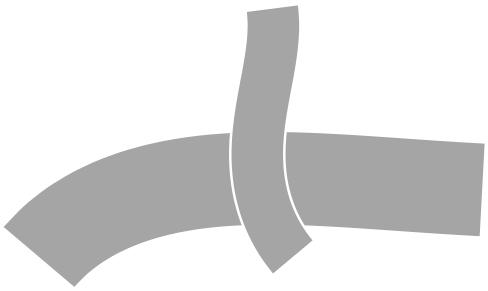

(c) $w = (0.1, 0.8, 0.1)$, $\gamma = 1.961$



(d) $w = (0.1, 0.1, 0.8)$, $\gamma = 0.516$

Figure 5: Schematic representations of cross-hinge geometries corresponding to uniform weighting among objectives (a) and preferred weighting of one of the objectives each (b)-(d).

the flexures corresponding to these weightings; the respective (normalized) objectives are listed in Tab. 2. The location of the specific designs are also highlighted by colored markers in the two-dimensional projections of the Pareto front, see Fig. 4.

Table 2: Selected solutions of the Pareto set: uniform weighting of all objectives and preferred weighting of one of the objectives – target-weights, pseudo-weights and non-dimensional objectives.

target weights	pseudo-weights	$\tilde{r}/1$	$\tilde{c}/1$	$\tilde{k}/1$	shape
(0.333, 0.333, 0.333)	(0.328, 0.338, 0.333)	5.978e−2	3.228e−2	4.534e−2	(a)
(0.800, 0.100, 0.100)	(0.447, 0.105, 0.447)	7.513e−3	7.658e−1	6.467e−3	(b)
(0.100, 0.800, 0.100)	(0.098, 0.767, 0.135)	8.727e−1	1.077e−4	8.234e−1	(c)
(0.100, 0.100, 0.800)	(0.295, 0.103, 0.603)	5.115e−1	8.298e−1	6.610e−5	(d)

The cross-hinge designs show a remarkable variety in shape. The shapes of the (undeformed) axes of the flexures obtained upon uniform weighting (a) show some similarity to the design preferring low translational compliance (c), but the latter design is characterized by much less slender flexures. The cross-hinge design preferring high kinematic accuracy (b) has two strongly

curved, comparatively slender flexures. For a small rotational stiffness (d), the points of the two beams with respect to the ground body almost coincide. All four designs share the property that flexure $\mathcal{B}_2$ has a smaller thickness than $\mathcal{B}_1$.

The numerical results in Tab. 2 show that the individual performance measures vary by several orders of magnitude. It is also remarkable that target weights and pseudo-weights agree well for uniform weights (a) and small translational compliance (c). The mismatch between target and pseudeo-weights suggests that designs with pseudo-weights preferring high kinematic accuracy (b) or low rotational stiffness (d) in the desired extent are not present in the Pareto set.

4.3 Fine-tuning based on three-dimensional model

The structural model has proven as powerful tool to efficiently explore a the high-dimensional design space using evolutionary algorithms. Next, we want to fine-tune the cross-hinge designs using three-dimensional high-fidelity models. As an example, the shape obtained upon uniform weighting of the objectives, cf. Fig. 5 (a), is considered subsequently. For this purpose, we scalarize the objective function using what is referred to as inverse normalization, i.e., the inverted normalized objectives are used as weights. After 200 Nelder-Mead iterations, we obtain the cross-hinge design illustrated in Fig. 6, where the schematic representation is complemented by the three-dimensional finite-element model used in the analysis. For the sake of compara-

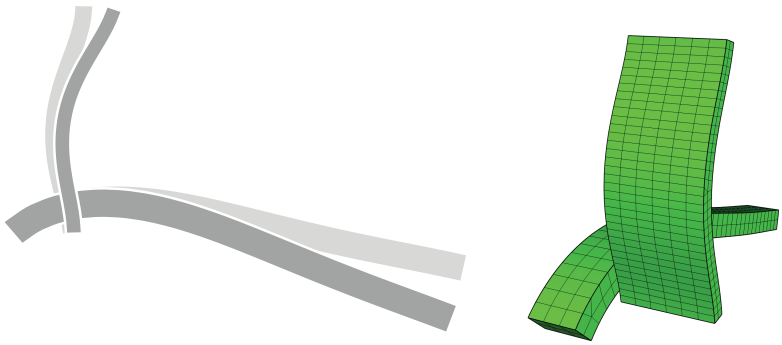

Figure 6: Schematic representation and three-dimensional finite-element model of the fine-tuned cross-hinge.

bility, the original shape obtained from the structural model, which serves as initial solution for the scalar optimization, is included in light gray. Clearly, the original shape of the cross-hinge is mostly preserved; the adaptations through the single objective optimization using the three-dimensional model indeed improve the cross-hinge design with respect to all three objectives, see Tab. 3. The scalarized objective function $\tilde{f}_{\mathrm{scalar}}/1$, which implies a weighting of $w_{\mathrm{SOO}} = (0.240, 0.444, 0.316)^T$, is reduced by almost 20 % in the course of the single-objective optimization based on the high-fidelity model.

Table 3: Comparison of the structural model and the fine-tuned three-dimensional model of the cross-hinge: individual objectives and scalarized objective function.

	$\tilde{r}/1$	$\tilde{c}/1$	$\tilde{k}/1$	$\tilde{f}_{\mathrm{scalar}}/1$
structural model	5.978e−2	3.228e−2	4.534e−2	4.300e−2
high-fidelity model	3.747e−2	3.072e−2	3.948e−2	3.511e−2

5 CONCLUSION

In the present paper, we have addressed the synthesis of compliant mechanisms with distributed compliances for applications characterized by large deformations. A problem as simple as a hinge already provides some intution on the manifold aspect that need to be accounted for, not least from a computational point of view. Considering a generalized cross-hinge described by a set of 13 design variables, we have shown that the framework of multi-objective optimization provides effective means to explore feasible designs. Allowing for trade-offs among the kinetostatic objectives adopting the notion of Pareto-optimality, we have found are great variety of different shapes of the cross-hinge, which is reflected in the complex shape of the Pareto front. We have outlined the concept of pseudo-weights to systematically select individuals from the set of Pareto-optimal solutions. Clearly, computational cost is key when using evolutionary algorithms. For this reason, we have adopted a two-stage approach: Structural models based on the geometrically exact theory for shear-deformable beams have been used in the multi-objective optimization, where hundreds of thousands of variants are simulated efficiently. Subsequently, high-fidelity, high-order finite-element have been employed to further refine and fine-tune cross-hinge designs using scalarized objective functions suited for conventional optimization methods.

REFERENCES

[1] L. L. Howell, *Compliant Mechanisms*. John Wiley & Sons, 2001.

[2] O. Lueger, Ed., *Lexikon der gesamten Technik und ihrer Hilfswissenschaften*, 2nd ed. Stuttgart and Leipzig: Deutsche Verlags-Anstalt, 1904.

[3] F. S. Eastman, "The Design of Flexure Pivots," *Journal of the Aeronautical Sciences*, vol. 5, no. 1, pp. 16–21, 1937.

[4] S. Henein, P. Spanoudakis, S. Droz, L. I. Myklebust, and E. Onillon, "Flexure Pivot for Aerospace Mechanisms," in *Proc. 10th ESMATS*, no. ESA SP-524, 2003, pp. 285–288.

[5] M. Ling, L. L. Howell, J. Cao, and G. Chen, "Kinetostatic and dynamic modeling of flexure-based compliant mechanisms: A survey," *Applied Mechanics Reviews*, vol. 72, no. 3, 2020.

[6] A. Humer, "Design and Optimization of Large-Deformation Compliant Mechanisms," *PAMM*, vol. 18, no. 1, p. e201800469, 2018.

[7] K. Deb, *Multi-Objective Optimization Using Evolutionary Algorithms*. USA: John Wiley & Sons, Inc., 2001.

[8] A. Humer, G. Jungmayr, W. Koppelstätter, M. Schörgenhumer, S. Silber, G. Weidenholzer, and S. Weitzhofer, "Multi-Objective Optimization of Complex Multibody Systems by Coupling HOTINT With MagOpt," vol. Volume 6: 12th International Conference on Multibody Systems, Nonlinear Dynamics, and Control, 2016.

[9] A. Humer, A. Ehrenhofer, T. Wallmersperger, and M. Krommer, "Pareto-optimization of hypodermic needles with respect to flow, buckling and piercing," *Acta Mechanica*, submitted.

[10] E. Reissner, "On one-dimensional finite-strain beam theory: the plane problem," *Zeitschrift für angewandte Mathematik und Physik ZAMP*, vol. 23, no. 5, pp. 795–804, 1972.

[11] A. Humer, "Exact solutions for the buckling and postbuckling of shear-deformable beams," *Acta Mechanica*, vol. 224, no. 7, pp. 1493–1525, 2013.

[12] A. Humer and A. S. Pechstein, "Exact solutions for the buckling and postbuckling of a shear-deformable cantilever subjected to a follower force," *Acta Mechanica*, vol. 230, no. 11, pp. 3889–3907, 2019.

[13] J. C. Simo and L. Vu-Quoc, "On the Dynamics of Flexible Beams Under Large Overall Motions—The Plane Case: Part I," *Journal of Applied Mechanics*, vol. 53, p. 849, 1986.

[14] E. Welzl, "Smallest enclosing disks (balls and ellipsoids)," in *New Results and New Trends in Computer Science*, H. Maurer, Ed. Berlin, Heidelberg: Springer Berlin Heidelberg, 1991, pp. 359–370.

[15] E. Zitzler, M. Laumanns, and L. Thiele, "SPEA2: Improving the strength Pareto evolutionary algorithm," *TIK report*, vol. 103, 2001.

[16] K. Deb, A. Pratap, S. Agarwal, and T. Meyarivan, "A fast and elitist multiobjective genetic algorithm: NSGA-II," *IEEE Transactions on Evolutionary Computation*, vol. 6, no. 2, pp. 182–197, 2002.

[17] J. Blank and K. Deb, "pymoo: Multi-Objective Optimization in Python," *IEEE Access*, vol. 8, pp. 89 497–89 509, 2020.

[18] J. A. Nelder and R. Mead, "A simplex method for function minimization," *The Computer Journal*, vol. 7, no. 4, pp. 308–313, 1965.

XI ECCOMAS Thematic Conference on Smart Structures and Materials - SMART 2025
M. Krommer, M. Nader and M. Schagerl (Eds)

Received: 16 April 2025 / Revised: 27 August 2025 / Accepted: 14 October 2025
© The Author(s) 2025

Proof of Concept for a Damage Localization Strategy in Beams through Stiffness Modulation

Arka P. Reksowardojo, Ann C. Sychterz

Abstract. Vibration-based damage localization methods that rely on relative changes in dynamic characteristics such as eigenfrequencies have been extensively studied. However, such methods have inherent drawbacks, since eigenfrequencies are global metrics that provide limited spatial information. In this work, stiffness modulation as a strategy for damage localization in beams is studied theoretically. A new damage indicator is formulated based on the Laplacian similarity kernels of the eigenfrequency residuals. Results demonstrate that the additional spatial information gained via stiffness modulation can overcome systematic ambiguity stemming from symmetry and reduce reliance on observing multiple eigenmodes.

Key words: Damage Localization, Stiffness Modulation, Adaptive Systems

1 INTRODUCTION

Vibration-based *damage localization* strategies largely rely on the assumption that damage induces changes in eigenfrequencies, mode shapes, and damping ratios [1]. Despite extensive investigations, challenges persist in accurately measuring these parameters, as mode shapes require spatially distributed monitoring and damping ratios are both difficult to quantify and highly sensitive to environmental factors.

Damage localization based on relative changes in eigenfrequencies has been extensively investigated due to the ease of measurement with relatively simple setups. Hu & Liang [2] proposed a crack detection method using eigenfrequency variation functions, establishing a mathematical link between eigenfrequency changes and crack-induced stiffness reductions. Narkis et al. [3] modeled localized damage as a linear reduction in spring stiffness, correlating eigenfrequency changes with stiffness changes at discrete structural nodes. Sha et al. [4] developed a Bayesian framework for the probabilistic interpretation of eigenfrequency variations, thereby improving diagnostic reliability. Previous efforts have not addressed the systematic ambiguity that arises from the inherent symmetry of simply supported beams. In a follow-up work by Sha et al. [5], the eigenfrequency-based approach was complemented with a guided wavefield technique to resolve this ambiguity. However, implementing this complementary technique requires highly specialized testing equipment.

Arka P. Reksowardojo & Ann C. Sychterz
Civil & Environmental Engineering, University of Illinois Urbana-Champaign, 205 N Mathews Ave, Urbana, 61801, IL, USA, e-mail: reksowar@illinois.edu

Adaptive structures are equipped with sensors and actuators to maintain an optimal structural state against changing load conditions through active control [6]. Adaptivity opens new possibilities for damage localization, since actuation-induced changes to the system can provide additional information otherwise not available. The use of adaptivity to enhace system diagnosis has been investigated in tensegrity and truss systems by Adam & Smith [7], Sychterz & Smith [8] and Reksowardojo et al. [9]. Among various adaptation strategies, stiffness modulation has emerged as a promising approach, as demonstrated for vibration control by Nowak et al. [10].

This paper presents a proof-of-concept study on damage localization in beam systems using stiffness modulation, which reduces localization ambiguity by providing additional spatial information. A new damage indicator is developed based on the Laplacian similarity kernels. A case study is given to demonstrate the potential of the proposed strategy.

2 METHODOLOGY

Fig. 1 illustrates two beam systems with stiffness modulation properties. Both systems can be modeled as *parameter-varying systems*, whose dynamics depend on a *scheduling parameter*. A scheduling parameter is a time-varying process that determines the instantaneous dynamics of the system but evolves independently from the system response.

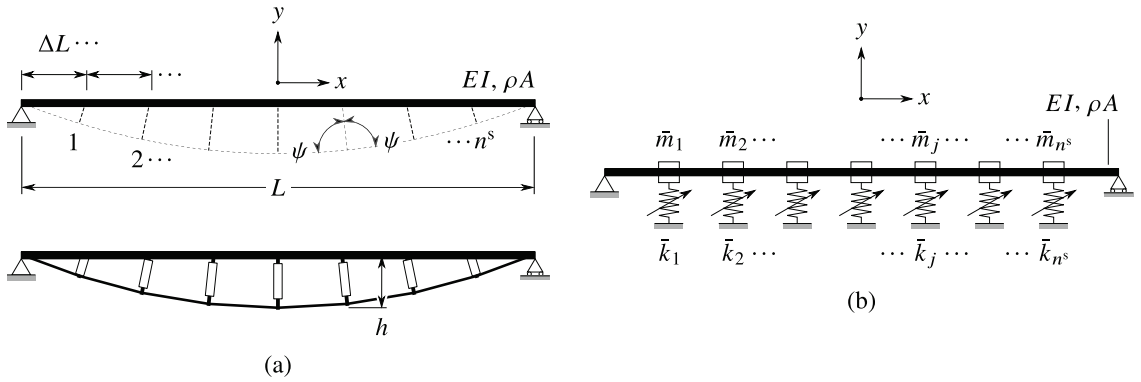

Figure 1: Illustration of beam systems with stiffness modulation properties: (a) a beam equipped with an underdeck adaptive tensioning system, linear actuators are indicated by outlined white boxes, (b) a simplified proof-of-concept model with variable springs and concentrated masses

Fig. 1a depicts a beam with an underdeck adaptive tensioning system. The underdeck cables are deviated by variable length compressive struts that act as intermediate supports. Linear actuators adjust the length of the struts, inducing force equilibrium and second-order effects that increase the stiffness of the system. In this case, the scheduling parameter is the setpoints of the actuators.

As a proof-of-concept, a simplified model consisting of an *Euler–Bernoulli* beam with n^{s} uniformly spaced variable springs and concentrated masses is studied (Fig. 1b). Note that the simplified model is not intended to fully capture the response of a beam with an underdeck

adaptive tensioning system. For example, the effects of geometry changes of the beam induced by the extension of actuators are not considered in the simplified model. In this case $\bar{\mathbf{k}}(\theta) \in \mathbb{R}^{n^{\mathrm{s}}}$ denotes the spring constants, which vary with the parameter θ. According to the assumptions underlying parameter-varying systems, alterations in the dynamics occur only during transitions between parameters. Additionally, the damage localization method in this work does not involve large vibrations. The springs are therefore assumed to behave linearly for a given θ. For better readability, the function notation $\blacksquare(\theta)$ and the k subscript notation in $\blacksquare_{i,k}$ related to θ_k are omitted from the formulations in §2.1–2.2. These notations are included only when the change in the scheduling parameter is of direct significance, as in §2.3. The concentrated masses $\bar{\mathbf{m}} \in \mathbb{R}^{n^{\mathrm{s}}}$ remain constant with respect to θ.

2.1 Dynamics of undamaged system

The equation of motion describing the undamped free vibration of the simplified model shown in Fig. 1b is expressed as a partial differential equation (PDE),

$$\begin{aligned} EI\frac{\partial^4 w(x,t)}{\partial x^4} + \rho A\frac{\partial^2 w(x,t)}{\partial t^2} + \sum_{j=1}^{n^{\mathrm{s}}} \bar{k}_j \delta(x - j\Delta L)\, w(x,t) \\ + \sum_{j=1}^{n^{\mathrm{s}}} \bar{m}_j \delta(x - j\Delta L)\frac{\partial^2 w(x,t)}{\partial t^2} = 0, \end{aligned} \tag{1}$$

where $\Delta L = L/(n^{\mathrm{s}}+1)$ is the distance between consecutive springs and concentrated masses. $\delta(x - j\Delta L)$ denotes the Dirac delta, which is employed to incorporate discontinuities from the elastic effect of the springs $\bar{k}_j$ and the inertial effect of concentrated masses $\bar{m}_j$. The transformation of the PDE in Eq. (1) into ordinary differential equation (ODE) via the method of separation of variables can only be done by splitting the problem into $(n^{\mathrm{s}}+1)$ sub-domains that satisfy:

$$\frac{\mathrm{d}^4\phi_i}{\mathrm{d}x^4} - \beta_i^4\phi_i = 0, \quad \beta_i^4 = \frac{\rho A\omega_i^2}{EI}. \tag{2}$$

This way, the discontinuity terms related to $\bar{k}_j$ and $\bar{m}_j$ vanish and are incorporated as boundary conditions. The general solutions of the resulting ODEs yield the mode shapes of the system in a piecewise harmonic form,

$$\phi_i(x) = \begin{cases} \phi_{i,1}(x) = c_{i,1}\cdot\cosh(\beta_i x) + c_{i,2}\cdot\sinh(\beta_i x) \\ \qquad + c_{i,3}\cdot\cos(\beta_i x) + c_{i,4}\cdot\sin(\beta_i x), & 0 \le x \le \Delta L, \\ \qquad\qquad \vdots & \\ \phi_{i,(n^{\mathrm{s}}+1)}(x) = c_{i,(4n^{\mathrm{s}}+1)}\cdot\cosh(\beta_i x) + c_{i,(4n^{\mathrm{s}}+2)}\cdot\sinh(\beta_i x) \\ \qquad + c_{i,(4n^{\mathrm{s}}+3)}\cdot\cos(\beta_i x) + c_{i,(4n^{\mathrm{s}}+4)}\cdot\sin(\beta_i x), & n^{\mathrm{s}}\Delta L \le x \le L. \end{cases} \tag{3}$$

All functions denoted by i subscript $\blacksquare_i$ can be applied to any finite number of eigenmodes, $\forall i \in \{1,\ldots,n^{\mathrm{f}}\}$. For each eigenmode, there are $4n^{\mathrm{s}}+4$ constants to be determined in Eq. (3).

The enforcement of boundary conditions related to the supports at $x = \{0, L\}$,

$$\phi_{i,1}(0) = 0, \quad \left.\frac{\mathrm{d}^2\phi_{i,1}}{\mathrm{d}x^2}\right|_{x=0} = 0, \quad \phi_{i,(n^s+1)}(L) = 0, \quad \left.\frac{\mathrm{d}^2\phi_{i,(n^s+1)}}{\mathrm{d}x^2}\right|_{x=L} = 0, \tag{4}$$

yields a set of 4 homogeneous equations. Additional boundary conditions related to kinematic continuities at $x = j\Delta L$,

$$\begin{gathered}\phi_{i,j}(j\Delta L) = \phi_{i,(j+1)}(j\Delta L), \quad \left.\frac{\mathrm{d}\phi_{i,j}}{\mathrm{d}x}\right|_{x=j\Delta L} = \left.\frac{\mathrm{d}\phi_{i,(j+1)}}{\mathrm{d}x}\right|_{x=j\Delta L}, \\ \left.\frac{\mathrm{d}^2\phi_{i,j}}{\mathrm{d}x^2}\right|_{x=j\Delta L} = \left.\frac{\mathrm{d}^2\phi_{i,(j+1)}}{\mathrm{d}x^2}\right|_{x=j\Delta L}, \quad \forall j \in \{1,\ldots,n^s\},\end{gathered} \tag{5}$$

as well as those related to shear force discontinuities due to $\bar{k}_j$ and $\bar{m}_j$, also at $x = j\Delta L$,

$$\left.\frac{\mathrm{d}^3\phi_{i,(j+1)}}{\mathrm{d}x^3}\right|_{x=j\Delta L} - \left.\frac{\mathrm{d}^3\phi_{i,j}}{\mathrm{d}x^3}\right|_{x=j\Delta L} = -\eta_{i,j}\cdot\phi_{i,(j+1)}(j\Delta L), \quad \forall j \in \{1,\ldots,n^s\}, \tag{6}$$

with the discontinuity factor $\eta_{i,j}$,

$$\eta_{i,j} = \frac{\bar{k}_j}{EI} - \beta_i^4\frac{\bar{m}_j}{\rho A}, \tag{7}$$

yield an additional set of $4n^s$ homogeneous equations. All $4n^s + 4$ homogeneous equations from Eq. (4–7) are presented in a matrix form as:

$$\mathbf{F}_i\mathbf{c}_i = \mathbf{0}. \tag{8}$$

Since the linear system in Eq. (8) must admit a nontrivial solution for $\mathbf{c}_i \in \mathbb{R}^{(4n^s+4)}$, the matrix $\mathbf{F}_i \in \mathbb{R}^{(4n^s+4)\times(4n^s+4)}$ should be singular, and thus the condition $\det(\mathbf{F}_i) = 0$ yields the required frequency equation to obtain β_i. The resulting frequency equation is transcendental, whose roots β_i, cannot be determined analytically via a finite sequence of algebraic operations. In this case, numerical techniques such as the gridded *Brent–Dekker* algorithm can be used to find the roots. Once β_i is determined, the eigenfrequencies ω_i can be obtained using the relation in Eq. (2). The constants $\mathbf{c}_i$ for Eq. (3) can be obtained as the nontrivial solution of Eq. (8), which corresponds to the basis vector spanning the null space of $\mathbf{F}_i$.

2.2 Eigenfrequency variation function of damaged system

Extending the approach employed by Sha et al. [5], a continuous frequency variation function can be estimated by assuming that the mode shapes of the damaged system are not significantly different from those of undamaged system. Considering the maximum potential and kinetic energy of the vibrating undamaged system,

$$U_i^{\max} = \frac{1}{2}\int_0^L EI\left(\frac{\mathrm{d}^2\phi_i}{\mathrm{d}x^2}\right)^2\mathrm{d}x + \frac{1}{2}\sum_{j=1}^{n^s}\bar{k}_j\cdot\phi_i(j\Delta L)^2, \tag{9}$$

$$T_i^{\max} = \frac{\omega_i^2}{2} \int_0^L \rho A \phi_i^2 \mathrm{d}x + \frac{\omega_i^2}{2} \sum_{j=1}^{n^{\mathrm{s}}} \bar{m}_j \cdot \phi_i (j\Delta L)^2 . \tag{10}$$

The square of the eigenfrequency of the undamaged system can be obtained via Rayleigh quotient of energy conservation,

$$\omega_i^2 = \frac{\int_0^L EI \left(\frac{\mathrm{d}^2\phi_i}{\mathrm{d}x^2}\right)^2 \mathrm{d}x + \sum_{j=1}^{n^{\mathrm{s}}} \bar{k}_j \cdot \phi_i (j\Delta L)^2}{\int_0^L \rho A \phi_i^2 \mathrm{d}x + \sum_{j=1}^{n^{\mathrm{s}}} \bar{m}_j \cdot \phi_i (j\Delta L)^2}. \tag{11}$$

Similarly, the square of the eigenfrequency of the damaged system, for any arbitrary location x and severity γ of damage can be obtained as:

$$\omega_i^{\mathrm{d}}(x,\gamma)^2 = \frac{\int_0^L EI \{1-\gamma\delta(x)\} \left(\frac{\mathrm{d}^2\phi_i}{\mathrm{d}x^2}\right)^2 \mathrm{d}x + \sum_{j=1}^{n^{\mathrm{s}}} \bar{k}_j \cdot \phi_i (j\Delta L)^2}{\int_0^L \rho A \phi_i^2 \mathrm{d}x + \sum_{j=1}^{n^{\mathrm{s}}} \bar{m}_j \cdot \phi_i (j\Delta L)^2}. \tag{12}$$

Note that γ is a notional factor, which takes a value between $0 \le \gamma \le 1$ and reduces EI, the bending rigidity of the beam. The pair of γEI and the Dirac delta is included in Eq. (12) for mathematical convenience. Therefore, the value of γ does not correspond to physically quantifiable properties of damage, such as the width and depth of a crack. By taking the $\omega_i^{\mathrm{d}}(x,\gamma)^2/\omega_i^2$ quotient and making use of the sifting properties of Dirac delta, the *eigenfrequency variation function* $\Delta\omega_i(x,\gamma)$ under damage can be obtained as:

$$\Delta\omega_i(x,\gamma) = \frac{\omega_i - \omega_i^{\mathrm{d}}(x,\gamma)}{\omega_i} = 1 - \sqrt{1 - \frac{\gamma\alpha_i}{\chi_i}} \approx \frac{\gamma\alpha_i}{2\chi_i}, \tag{13}$$

$$\alpha_i = EI \left(\frac{\mathrm{d}^2\phi_i}{\mathrm{d}x^2}\right)^2, \quad \chi_i = \int_0^L EI \left(\frac{\mathrm{d}^2\phi_i}{\mathrm{d}x^2}\right)^2 \mathrm{d}x + \sum_{j=1}^{n^{\mathrm{s}}} \bar{k}_j \cdot \phi_i (j\Delta L)^2 . \tag{14}$$

2.3 Damage localization

For damage localization, a finite number of discrete scheduling parameters $\theta_k, \forall k \in \{1,\ldots,n^{\mathrm{p}}\}$ are employed. Suppose that $\Delta\omega_{i,k}^*$ is the relative changes of eigenfrequency measured via testing, which corresponds to the ith eigenmode and k^{th} scheduling parameter. The unknown location x^* and severity γ^* of damage must satisfy the condition of zero *eigenfrequency residuals*, i.e., deviation between the eigenfrequency variation functions and the measured change of eigenfrequencies,

$$\Delta\omega_{i,k}(x^*,\gamma^*) - \Delta\omega_{i,k}^* = 0. \tag{15}$$

The *damage severity function* $\gamma^0_{i,k}(x)$ given the knowledge of the measured $\Delta\omega^*_{i,k}$ can be obtained by substituting Eq. (13 & 14) into Eq. (15),

$$\gamma^0_{i,k}(x) = \frac{\left\{2\Delta\omega^*_{i,k} - (\Delta\omega^*_{i,k})^2\right\}\chi_{i,k}}{\alpha_{i,k}} \approx \frac{2\Delta\omega^*_{i,k}\chi_{i,k}}{\alpha_{i,k}}. \tag{16}$$

In principle, there exists only a unique pair (x^*, γ^*) that satisfies Eq. (15), independent of the eigenmode or scheduling parameter, which identifies the damage location as the intersection of all $\gamma^0_{i,k}$. The *damage indicator function* $\lambda(x)$ is obtained via the product of *Laplacian similarity kernels* over combinatorial pairs of damage severity functions $\{\gamma^0_{i,k}, \gamma^0_{l,m}\}$,

$$\lambda(x) = \prod_{(i,k),(l,m)\in\binom{S}{2}} e^{-\kappa\left|\gamma^0_{i,k} - \gamma^0_{l,m}\right|}, \tag{17}$$

$$S = \left\{(i,k) \mid i \in \left\{1,\ldots,n^{\mathrm{f}}\right\},\ k \in \{1,\ldots,n^{\mathrm{p}}\}\right\}. \tag{18}$$

Each kernel $e^{-\kappa\left|\gamma^0_{i,k} - \gamma^0_{l,m}\right|}$ gives a value of 1 when the pair $\{\gamma^0_{i,k}, \gamma^0_{l,m}\}$ intersects and decays exponentially to 0 when the pair separates. Since damage severity functions may yield infinitely large values due to singularities around the supports and nodes in the mode shapes, a Laplacian similarity kernel is appropriate since it gives a value of 0 when any of $\{\gamma^0_{i,k}, \gamma^0_{l,m}\}$ has values near ∞. The factor κ determines the rate of exponential decay of the kernels, which can be tuned to account for the uncertainties of the measured $\Delta\omega^*_i$. A larger κ produces sharper, more precise peaks in $\lambda(x)$, at a penalty of lower accuracy that may occur from the uncertainties of the measured $\Delta\omega^*_i$. Generally, with a larger number of available observations ($n^{\mathrm{f}} \cdot n^{\mathrm{p}}$), a smaller decay factor κ can be used.

3 CASE STUDY

A system comprising $n^{\mathrm{s}} = 3$ variable springs (Fig. 1b) is studied. It models a small-scale $L = 2$ m span prototype, which will be constructed entirely of aluminium ($E = 69\times10^9$ N/m^2, $\rho = 2710$ kg/m^3) for subsequent experimental testing. A uniform cross-section is used for the beam, with $I = 6.261\times10^{-8}$ m^4 and $A = 45\times10^{-5}$ m^2. The spring constants and concentrated masses are determined by equivalence with a beam of identical span equipped with a $h = 0.1$ m deep underdeck adaptive tensioning system (Fig. 1a). All struts and cables are assumed to have circular cross-sections with areas of 7.85×10^{-5} and 17.67×10^{-5} m^2, respectively. Based on geometric operations described by Madrazo-Aguirre et al. [11], the default values for spring constants are $\bar{\mathbf{k}}^0 = [17131.4\ \ 27362.2\ \ 17131.4]^{\mathrm{T}}$ N/m. As noted in §2, the springs are assumed to be linear, except during parameter transitions. By considering tributary cable lengths connected to each strut, the equivalent concentrated masses are $\bar{\mathbf{m}} = \bar{\mathbf{m}}^0 = [0.28\ \ 0.29\ \ 0.28]^{\mathrm{T}}$ kg.

3.1 Effects of stiffness modulation

The effects of stiffness modulation on the dynamics of the system are investigated through sequential variations of the spring constants, via multiplying factors of $\mu \in \{1, 5, 10\}$. Fig. 2

presents the mode shapes of the undamaged system $\phi_i(x)$ (Eq. (3)) under variations of $\bar{k}_1$ and $\bar{k}_2$. The effect of varying $\bar{k}_3$ is a mirror image of that of $\bar{k}_1$ and is therefore omitted for brevity. The operator "$\circ$" denotes the Hadamard element-wise product.

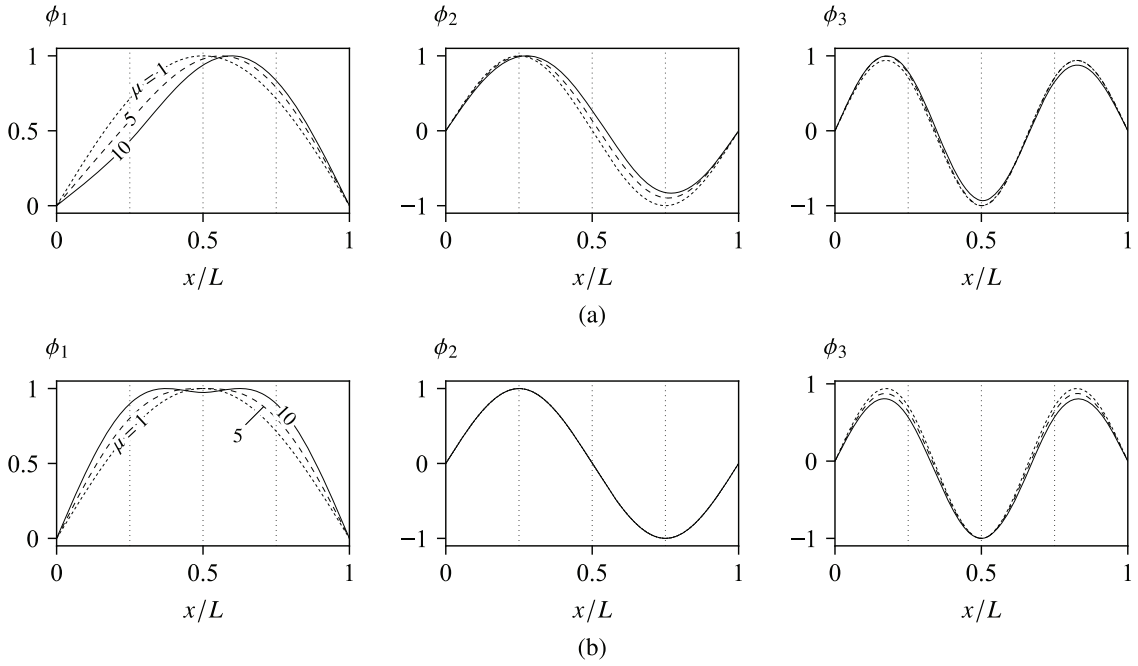

Figure 2: Mode shapes of undamaged system $\phi_i(x)$ under a variation of the stiffness parameters $\forall \mu \in \{1, 5, 10\}$: (a) variation of $\bar{k}_1$, $[\mu \ \ 1 \ \ 1]^{\mathrm{T}} \circ \bar{\mathbf{k}}^0$, (b) variation of $\bar{k}_2$, $[1 \ \ \mu \ \ 1]^{\mathrm{T}} \circ \bar{\mathbf{k}}^0$; locations of variable springs and concentrated masses are indicated by dotted vertical lines ($n^{\mathrm{s}} = 3$)

As shown in Fig. 2a, the effect of increasing $\bar{k}_1$ is most pronounced in the shape of the 1st eigenmode. For $\mu = 10$, a noticeable inflection point with curvature variation appears in proximity of $\bar{k}_1$. Although $\bar{k}_1$ is located near the antinodes of the 2nd and the 3rd eigenmodes, the effect is less pronounced in the corresponding shapes. Similarly, in Fig. 2b, the effect of increasing $\bar{k}_2$ is more significant in the shape of the 1st eigenmode. In this case, curvature variations occur at the midspan, in proximity of $\bar{k}_2$. Since $\bar{k}_2$ is located exactly at the node of the 2nd eigenmode, no effect is observed. *Vice versa*, as $\bar{k}_2$ coincides with the antinode of the 3rd eigenmode, it results in a slight reduction of magnitudes in adjacent locations.

Fig. 3 shows the eigenfrequency variation functions $\Delta\omega_i(x)$ (Eq. (13)), under the variations of $\bar{k}_1$ and $\bar{k}_2$. Note that the notional severity factor is set to unity $\gamma = 1$ in this case. This condition can be interpreted theoretically as a complete loss of bending rigidity EI, over an infinitesimal $\mathrm{d}x$, which is not physically realizable. Therefore, Fig. 3 is presented solely to illustrate the general trend of eigenfrequency variation under the effect of stiffness modulation.

Similarly to observations regarding mode shapes, the effect of increasing $\bar{k}_1$ on the eigenfrequency variation (Fig. 3a) is most pronounced in the 1st eigenmode. Taking $\mu = 10$ as an example, the increase in stiffness results in a reduction in eigenfrequency variation for damage

ocurring near $\bar{k}_1$. In other words, the sensitivity of the eigenfrequency to a damage ocurring in the region is reduced. On the other hand, the variation increases when the location of the damage is sufficiently far from $\bar{k}_1$. In the 2nd eigenmode, increasing stiffness leads to an overall reduction in sensitivity, particularly near $\bar{k}_1$ (Fig. 3b). The effect in the 3rd eigenmode is generally marginal. The effect of increasing $\bar{k}_2$ in the 1st eigenmode results in an overall reduction of eigenfrequency variation in the mid-span. In this case, the variation increases only marginally in the other regions. The effects in the 2nd and 3rd eigenmodes are generally negligible.

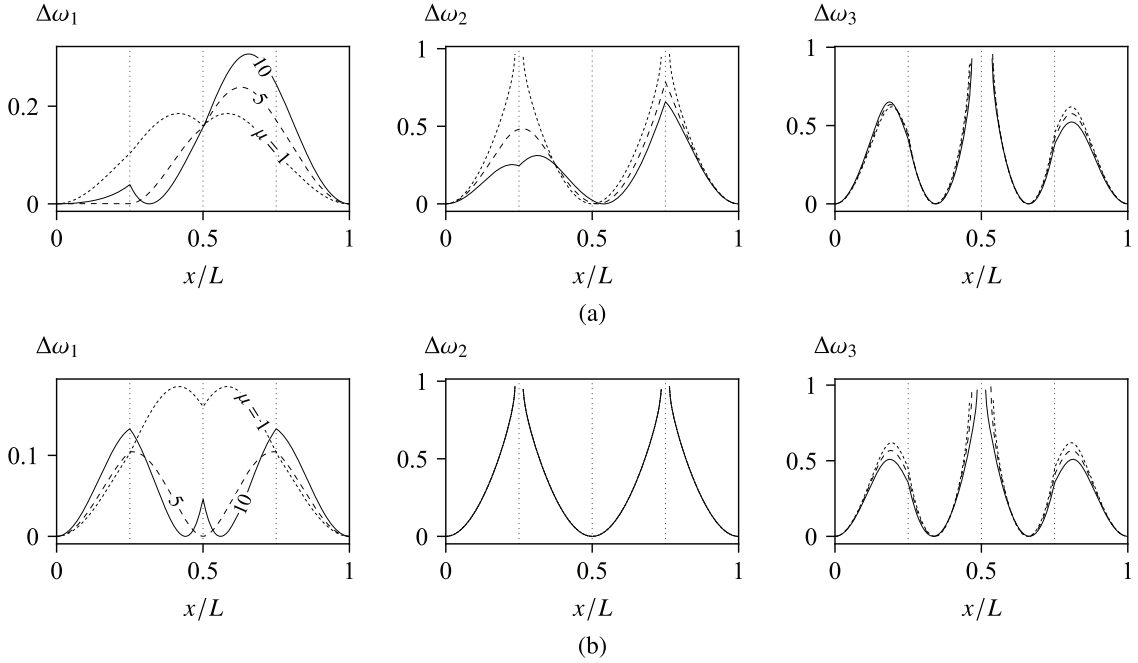

Figure 3: Eigenfrequency variation functions $\Delta\omega_i(x)$ for a notional damage severity of $\gamma = 1$ under a variation of the stiffness parameters $\forall\mu \in \{1, 5, 10\}$: (a) variation of $\bar{k}_1$, $[\mu \ 1 \ 1]^{\mathrm{T}} \circ \bar{\mathbf{k}}^0$, (b) variation of $\bar{k}_2$, $[1 \ \mu \ 1]^{\mathrm{T}} \circ \bar{\mathbf{k}}^0$; locations of variable springs and concentrated masses are indicated by dotted vertical lines ($n^{\mathrm{s}} = 3$)

3.2 Damage localization

The measured relative changes of eigenfrequency $\Delta\omega^*_{i,k}$ are obtained numerically through eigenvalue analyses of a *finite element* (FE) model, which is used in place of experimental testing. The FE model comprises $n^{\mathrm{e}} = 100$ planar frame elements with six degrees of freedom per element. Variable springs and concentrated masses are incorporated by adding $\bar{k}_j$ and $\bar{m}_j$ to the respective diagonal entries of the global stiffness and mass matrices. To simulate damage, the bending rigidity EI of the 30th element is reduced by a factor of 0.4. In this case, the unknown location of the damage is $x^* = 0.295$ m. Note that $\gamma^* \neq 0.4$, since γ is a notional factor that quantifies an infinitesimally small damage. The FE model is used only to obtain $(n^{\mathrm{f}} \cdot n^{\mathrm{p}})$ observations of $\Delta\omega^*_{i,k}$, to replicate the measurement process. All functions required for damage localization are determined analytically through the formulations in §2.1–2.2.

As shown in Table 1, $n^{\mathrm{p}} = 4$ discrete scheduling parameters are considered in the case study; θ_1 for the default configuration, and θ_2 to θ_4 for the sequential perturbation of spring constants by a factor of 1.5. The operator "$\circ$" denotes the Hadamard element-wise product. Table 2 presents a summary of the eigenfrequencies and the respective relative changes obtained via FE simulations.

Table 1: Discrete scheduling parameters and the corresponding spring constants

Parameter, θ_k	Spring constants, $\bar{\mathbf{k}}(\theta_k)$
θ_1	$[1 \;\; 1 \;\; 1]^{\mathrm{T}} \circ \bar{\mathbf{k}}^0$
θ_2	$[1.5 \;\; 1 \;\; 1]^{\mathrm{T}} \circ \bar{\mathbf{k}}^0$
θ_3	$[1 \;\; 1.5 \;\; 1]^{\mathrm{T}} \circ \bar{\mathbf{k}}^0$
θ_4	$[1 \;\; 1 \;\; 1.5]^{\mathrm{T}} \circ \bar{\mathbf{k}}^0$

Fig. 4 presents the eigenfrequency residuals $\Delta\omega_{i,k}(x,\gamma) - \Delta\omega^*_{i,k}$ for all eigenmodes and scheduling parameters, except θ_4 since the effect is a mirror image of that of θ_2. The solid black contour lines represent the damage severity functions $\gamma^*_{i,k}$, which can be interpreted as the cross section of the surface $\Delta\omega_{i,k}(x,\gamma) - \Delta\omega^*_{i,k}$ by an x-γ plane at a level of 0.

Table 2: Summary of eigenfrequencies obtained through FE simulations, in lieu of experimental measurements

Parameter, θ_k	Eigenfreq. undamaged, $\boldsymbol{\omega}_k$ [rad/s]	Eigenfreq. damaged, $\boldsymbol{\omega}^{\mathrm{d}}_k$ [rad/s]	Relative change, $\Delta\boldsymbol{\omega}^*_k$ [%]
θ_1	$[199 \;\; 506 \;\; 1095]^{\mathrm{T}}$	$[199 \;\; 504 \;\; 1094]^{\mathrm{T}}$	$[0.16 \;\; 0.57 \;\; 0.13]^{\mathrm{T}}$
θ_2	$[210 \;\; 516 \;\; 1098]^{\mathrm{T}}$	$[210 \;\; 513 \;\; 1096]^{\mathrm{T}}$	$[0.10 \;\; 0.55 \;\; 0.13]^{\mathrm{T}}$
θ_3	$[233 \;\; 506 \;\; 1103]^{\mathrm{T}}$	$[233 \;\; 504 \;\; 1101]^{\mathrm{T}}$	$[0.14 \;\; 0.57 \;\; 0.13]^{\mathrm{T}}$
θ_4	$[210 \;\; 516 \;\; 1098]^{\mathrm{T}}$	$[210 \;\; 513 \;\; 1096]^{\mathrm{T}}$	$[0.19 \;\; 0.55 \;\; 0.13]^{\mathrm{T}}$

It is evident that variations in θ_k significantly affect $\Delta\omega_{i,k}(x,\gamma) - \Delta\omega^*_{i,k}$, and thereby $\gamma^0_{i,k}$, for the 1st eigenmode. Comparing $\gamma^0_{1,1}$ and $\gamma^0_{1,2}$ (Fig. 4a & b), the perturbation of $\bar{k}_1$ in θ_2 induces asymmetry in $\gamma^0_{1,2}$ with a discontinuity at $\bar{k}_1$. Similarly in $\gamma^0_{1,3}$ (Fig. 4c), the perturbation of $\bar{k}_2$ in θ_3 introduces a discontinuity at $\bar{k}_2$.

Table 3 summarizes the three cases used to compute the damage indicator function λ (Eq. (17)). In Case #1, λ is obtained using all combinatorial pairs of 3 eigenmodes and 4 scheduling parameters. In Case #2, λ is computed using all 3 eigenmodes but only the default scheduling parameter θ_1. Case #3 involves only the 1st eigenmode and all 4 scheduling parameters.

Fig. 5 presents the damage indicator functions $\lambda(x)$ (Eq. (17)) obtained for Case #1–3. In Case #1, the largest peak in λ appears near the unknown damage location x^*, indicating accurate and relatively unambiguous localization. A smaller secondary peak occurs at the the mirrored location relative to the mid-span, i.e., around $L - x^*$. In Case #2, two peaks of nearly identical prominence appear in λ around x^* and $L - x^*$, leading to accurate but highly ambiguous

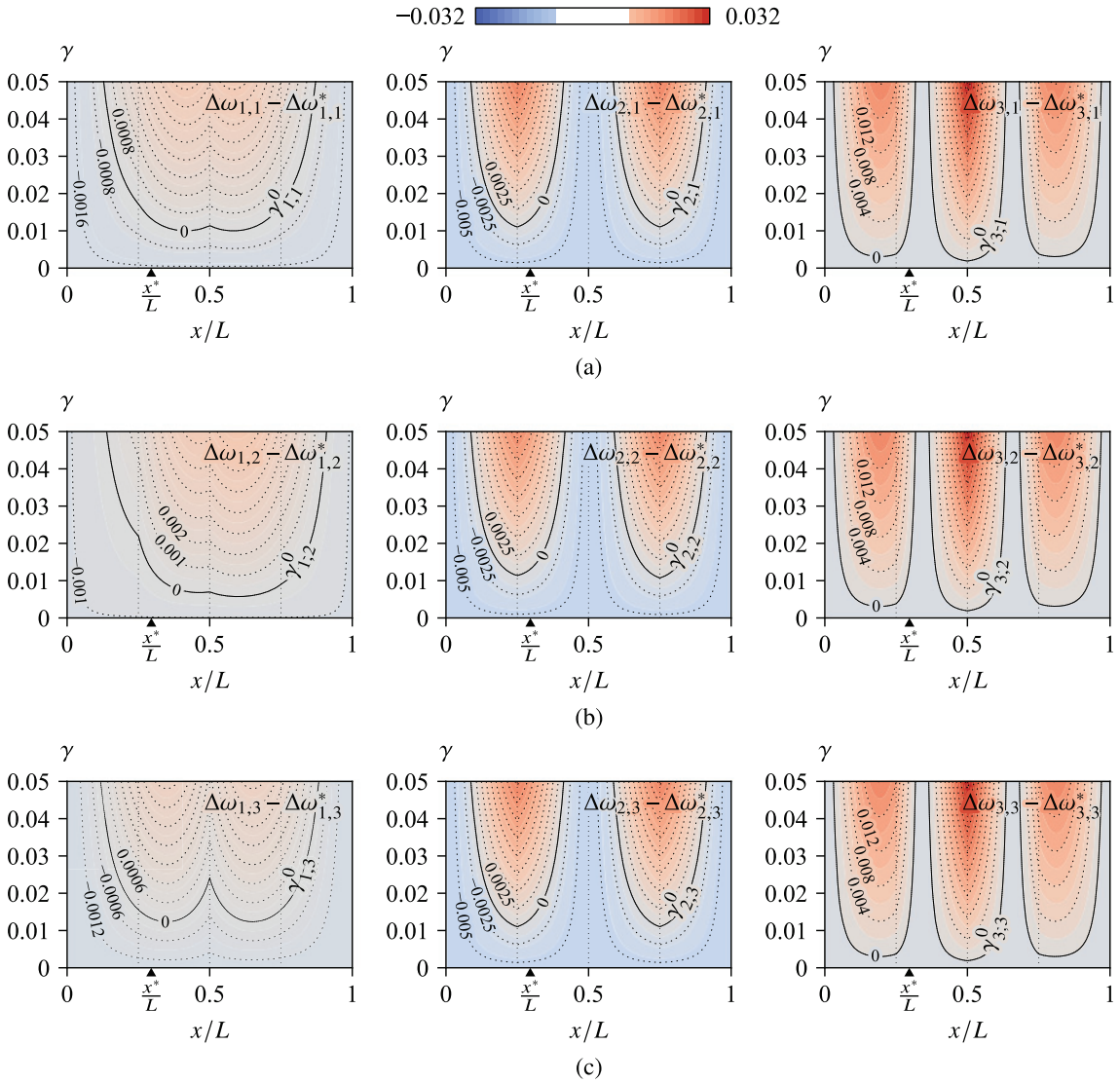

Figure 4: Contour of eigenfrequency residuals $\Delta\omega_{i,k}(x,\gamma) - \Delta\omega^*_{i,k}$, damage severity function $\gamma^0_{i,k}$ in solid black lines: (a) parameter θ_1, (b) parameter θ_2, (c) parameter θ_3; locations of variable springs and concentrated masses are indicated by dotted vertical lines ($n^s = 3$), the unknown location of damage $x^* = 0.295$ m is indicated by a "▲"

localization. Only a single prominent peak appears in Case #3, which indicates accurate and completely unambiguous localization.

As shown in Case #2 and previously demonstrated in [4], due to the symmetry of the system, and thereby the mode shapes, using the default scheduling parameter θ_1 always leads to ambiguous localization. In this case, all observations $\{\gamma^0_{1,1}, \gamma^0_{2,1}, \gamma^0_{3,1}\}$ are symmetric (Fig. 4a), and thus resulting in a mirrored λ (Fig. 5b).

Table 3: Cases of eigenmode and scheduling parameter pairs considered for computing $\lambda(x)$

Case #	n^{f}	n^{p}	$n^{\mathrm{f}} \cdot n^{\mathrm{p}}$	Eigenmode and parameter pairs, S (Eq. (18))
1	3	4	12	$\{(1,1),(2,1),(3,1),(1,2),\ldots,(2,4),(3,4)\}$
2	3	1	3	$\{(1,1),(2,1),(3,1)\}$
3	1	4	4	$\{(1,1),(1,2),(1,3),(1,4)\}$

Case #1 and #3 showcase the potentials of stiffness modulation strategy in providing additional spatial information that would otherwise be unavailable. Considering Case #3, where only $\{\gamma^0_{1,1},\gamma^0_{1,2},\gamma^0_{1,3},\gamma^0_{1,4}\}$ are used, the perturbation of $\bar{k}_1$ in θ_2 and $\bar{k}_3$ in θ_4 introduces a significant asymmetry to $\{\gamma^0_{1,2},\gamma^0_{1,4}\}$ (Fig. 4b; col. 1) out of 4 observations of $\gamma^0_{i,k}$. The predominantly asymmetric observations produce a prominent peak in λ (Fig. 5c). This demonstrates that stiffness modulation can be leveraged not only to mitigate ambiguity, but also to achieve the necessary number of observations for damage localization when measuring higher eigenfrequencies is challenging. In Case #1, a total of 12 observations of $\gamma^0_{i,k}$ are used, with only $\{\gamma^0_{1,2},\gamma^0_{1,4}\}$ showing significant asymmetry (Fig. 4b; col. 1). In this case, the perturbation of $\bar{k}_1$ and $\bar{k}_3$ induced only marginal asymmetry to $\{\gamma^0_{2,2},\gamma^0_{2,4},\gamma^0_{3,2},\gamma^0_{3,4}\}$ (Fig. 4b & c; col. 2 & 3), which results in the smaller secondary peak in λ (Fig. 5b).

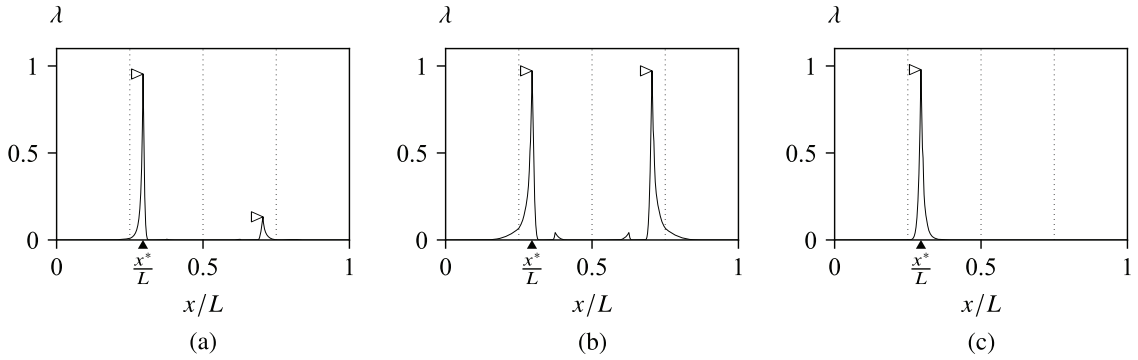

Figure 5: Damage indicator functions $\lambda(x)$: (a) Case #1, $\kappa = 10$, (b) Case #2, $\kappa = 100$, (c) Case #3, $\kappa = 500$; locations of variable springs and concentrated masses are indicated by dotted vertical lines ($n^{\mathrm{s}} = 3$), the unknown location of damage $x^* = 0.295$ m is indicated by a "▲", peaks with a magnitude > 0.1 are indicated by a "▷"

4 CONCLUSIONS

This paper presents a theoretical investigation on a damage localization strategy in beams via stiffness modulation. A new damage indicator based on the Laplacian similarity kernels of the eigenfrequency variation functions is formulated. The results of the case study lead to the following conclusions:

1. A local increase in stiffness reduces eigenfrequency variation nearby while amplifying it in adjacent regions.

2. Stiffness modulation provides additional spatial information to resolve ambiguities from the inherent symmetry of the system.
3. Stiffness modulation can be employed to meet the number of observations required for damage localization when measuring higher eigenfrequencies is challenging.

Future work could investigate methods to identify parameter perturbations that enhance the sensitivity of eigenfrequency variations. For practical applications, future studies should evaluate the effects of sensor noise, ambient noise, and systematic errors arising from modeling assumptions and physical imperfections.

FUNDING

This work was supported by the Deutsche Forschungsgemeinschaft (DFG, German Research Foundation) through the Walter Benjamin Fellowship (Project no. 547150077).

REFERENCES

[1] O. S. Salawu, "Detection of structural damage through changes in frequency: a review," *Engineering structures*, vol. 19, no. 9, pp. 718–723, 1997.

[2] J. Hu and R. Y. Liang, "An integrated approach to detection of cracks using vibration characteristics," *Journal of the Franklin Institute*, vol. 330, no. 5, pp. 841–853, 1993.

[3] Y. Narkis, "Identification of crack location in vibrating simply supported beams," *Journal of sound and vibration*, vol. 172, no. 4, pp. 549–558, 1994.

[4] G. Sha, M. Radzieński, M. Cao, and W. Ostachowicz, "A novel method for single and multiple damage detection in beams using relative natural frequency changes," *Mechanical Systems and Signal Processing*, vol. 132, pp. 335–352, 2019.

[5] G. Sha, W. Xiao, H. Zuo, M. Cao, M. Radzieński, and W. Ostachowicz, "Global-local damage localization and imaging in beam structures using laser-measured natural frequencies and guided wavefields," *Measurement*, vol. 236, p. 115061, 2024.

[6] T. T. Soong, "Active structural control in civil engineering, a state-of-the-art review," *Engineering Structures*, vol. 10, 1988.

[7] B. Adam and I. F. C. Smith, "Self-diagnosis and self-repair of an active tensegrity structure," *Journal of Structural Engineering*, vol. 133, no. 12, pp. 1752–1761, 2007.

[8] A. C. Sychterz and I. F. C. Smith, "Damage mitigation of near-full–scale deployable tensegrity structure through behavior biomimetics," *Journal of structural engineering*, vol. 146, no. 1, p. 04019181, 2020.

[9] A. P. Reksowardojo, G. Senatore, L. Blandini, and I. F. C. Smith, "Application of self-diagnosis and self-repair on a truss prototype that adapts to loading through shape morphing," *Journal of Structural Control and Health Monitoring*, 2025.

[10] A. Nowak, L. F. Campanile, and A. Hasse, "Vibration reduction by stiffness modulation–a theoretical study," *Journal of Sound and Vibration*, vol. 501, p. 116040, 2021.

[11] F. Madrazo-Aguirre, M. A. Wadee, and A. M. Ruiz-Teran, "Non-linear stability of under-deck cable-stayed bridge decks," *International Journal of Non-Linear Mechanics*, vol. 77, pp. 28–40, 2015.

XI ECCOMAS Thematic Conference on Smart Structures and Materials - SMART 2025
M. Krommer, M. Nader and M. Schagerl (Eds)

Received: 29 April 2025 / Revised: 24 June 2025 / Accepted: 14 October 2025
© The Author(s) 2025

Stiffness Adjustment of Compliant Mechanisms via Prestress Considering Large Deformations

Stephanie Seltmann, Alexander Hasse

Abstract. Compliant mechanisms make use of elastic deformations to generate functional deformations, with mechanical work being stored as strain energy in the elastically deformed areas. This leads to restoring forces, which reduce efficiency in many applications. The stiffness of compliant mechanisms, which determines the tendency to generate restoring forces, can be influenced by prestressing forces. The effect of prestressing on stiffness is well-known, but the application points, direction, and amplitude of prestressing forces are typically chosen based on experience. A method has been developed to systematically determine prestressing forces for adjusting stiffness, but it is limited to small deformations. In this work, the method is extended to incorporate large deformations, which are common in real-world applications. Several linearization points are defined within the functional deformations, and optimization is performed for each point. The optimization results in configurations of prestressed truss elements that achieve the desired stiffness. The required prestresses for different deformation levels within a specific deformation range are specified. Thus, in this contribution, a systematic approach is presented, enabling the determination of prestressing forces for large deformations.

Key words: Compliant mechanisms, Prestressing forces, Large deformations, Prestress optimization

1 INTRODUCTION

Compliant mechanisms (CM) use elastic distortions to generate the motions required for their function - so-called functional deformations. In doing so, they transfer mechanical energy, convert forces, convert paths and enable shape adaptation [1]. They thus fulfill the same tasks as conventional mechanisms, in which deformations are caused by the relative movement of rigid load-bearing elements (links) that are coupled to each other via guides or joints.

Due to their monolithic design, CM are particularly interesting in soft robotics [2], in medicine [3] and as micro-electro-mechanical systems (MEMS) [4]. Due to the functional principle of CM, mechanical work is required, which is partially stored as deformation energy

Stephanie Seltmann & Alexander Hasse
Chemnitz University of Technology, Professorship Machine Elements and Product Development, Institute of Design Engineering and Drive Technology, Chemnitz, 09107, Germany, e-mail: alexander.hasse@mb.tu-chemnitz.de

in the elastically deformed areas. The stiffness of the CM determines how much energy is required for a particular deformation and results from the geometry, the boundary conditions and the material used [5]. In many applications, it would be desirable to influence the stiffness in a targeted manner. The stiffness of a CM leads to restoring forces [6], which are only desirable in certain applications, as they can reduce efficiency.

One way of specifically influencing the stiffness of CM is to use prestressing forces. Suitable prestressing can be used to stiffen the CM or make it more flexible. The central effect here is referred to as the stress stiffening effect [5]. The effects of prestressing and the associated change in stiffness have already been extensively researched - especially for bending beams with different boundary conditions [7]. A classic example is the cantilever beam, where an axial compressive force reduces the transverse stiffness, while a tensile force increases it [8]. This effect has also been observed in stability analyses for cartwheel, leaf, and cross-spring hinges [9, 10, 11]. These are solid-state joints, which on the one hand represent the smallest unit in CM, but on the other hand can also be seen as CM themselves.

Prototypical implementations of devices with variable stiffness that use prestressing forces can be found in [12, 13]. The application points, direction and amplitude of the prestressing forces are usually chosen heuristically, relying on intuition and prior experience [8]. The first steps towards systematically and automatable determining prestressing forces were made by MAUSER AND HASSE [8] and MAUSER ET AL. [14], who developed an optimization-based method for adjusting the stiffness of CM. However, it is limited to small deformations, as geometric and material nonlinearities are not considered. For a more realistic description of the behavior of CM in practical applications, both geometric and material nonlinearities must be taken into account. Especially in the case of large deformations, which occur in many applications of soft robotics or adaptive structural engineering, the need for extended modeling becomes clear.

This paper therefore presents an approach that makes it possible to systematically determine and optimize prestressing forces in order to enable a targeted adjustment of stiffness over larger deformation ranges. A central aspect of this approach is the precise determination of the required prestressing dependent on the deformation amplitude of the CM. This leads to a comprehensive and systematic method that can also be used for large deformations.

2 ANALYSIS OF COMPLIANT MECHANISMS

In order to specifically adjust the stiffness of a CM, it is first necessary to determine the general deformation behavior and, in particular, the functional deformations. A deeper understanding of the deformation behavior of CM requires a look at the kinematics of conventional mechanisms. This is based on modeling systems of rigid links and ideal joints, ignoring elastic distortions and undesirable deformations. As a result, the kinematics can be determined purely geometrically and is independent of external forces, which ensures its uniqueness.

Due to the changed functional principle of CM in contrast to conventional mechanisms, the elastic distortions must be taken into account during the analysis. The deformation of the CM therefore always depends on the external forces acting on it, which means that a purely kine-

matic analysis as with the CM is no longer possible and the kinematics can no longer be clearly defined. Arbitrary deformations can also be generated with arbitrary forces, whereas with CM, with idealized modeling, only deformations corresponding to the kinematics are possible.

A CM opposes every possible deformation with stiffnesses and thus restoring forces. In principle, any deformation of the CM is possible, but the stiffnesses opposing these deformations are different. The set of deformations that are only opposed by low stiffnesses, i.e. the functional deformations, is referred to as the natural kinematics of the CM [15]. All other deformations are opposed by higher stiffnesses. To ensure the functionality of a CM under any external forces (as they occur in practice), the amount of undesired deformations must be kept to a minimum. Transverse loads are external forces that cause these deformations, and the precision describes how sensitive the deformations are to such loads. A complete analysis of the precision requires the consideration of all possible transverse loads that can act on the CM [15]. The deformation behavior of a CM to be determined therefore includes both the natural kinematics and the precision. Assuming small deformations, the modal approach presented in [15] is suitable for their determination, which was extended to geometric (large deformations) and material nonlinearities (large distortions) in [16] and is briefly summarized below.

Since CM realize their deformation through elastic distortion, modeling as continuum is required. Theoretically, they have an infinite number of structural degrees of freedom (DoFs), which are discretized to p DoFs for the finite element (FE) analysis. It is assumed that suitable boundary conditions have been selected so that global rigid body motions are suppressed. The tangent stiffness matrices ${}^t\mathbf{K}$ approximate the local deformation behavior at the stationary points ${}^t\mathbf{u}$ and satisfy the static equilibrium there, where ${}^t\mathbf{r}$ are the external forces:

$$ {}^t\mathbf{K}\,{}^t\mathbf{u} = {}^t\mathbf{r}. \tag{1}$$

The variable ${}^t[*]$ identifies all quantities associated with a stationary point. Variables without this parameter are deformation-independent. With the help of ${}^t\mathbf{K}$, the further deformation can be estimated starting from the stationary point by analyzing the eigenbehavior. For this purpose, a special eigenvalue problem of the tangent stiffness matrix is solved:

$$ {}^t\mathbf{K}\,{}^t\boldsymbol{\chi} = {}^t\lambda\,{}^t\boldsymbol{\chi}. \tag{2}$$

Equation (2) allows the determination of p eigenvalues ${}^t\lambda_i$ in ascending order, together with the corresponding orthogonal eigenmodes ${}^t\boldsymbol{\chi}_i,\ i = 1...p$. The first m eigenmodes ${}^t\boldsymbol{\chi}_1\,{}^t\boldsymbol{\chi}_2\,\cdots\,{}^t\boldsymbol{\chi}_m$ are referred to as kinematic eigenmodes and the remaining $p-m$ eigenmodes ${}^t\boldsymbol{\chi}_{m+1}\,{}^t\boldsymbol{\chi}_{m+2}\,\cdots\,{}^t\boldsymbol{\chi}_p$ as parasitic eigenmodes. The parameter m, known as the pseudo-mobility [17], describes the kinematic DoFs of the CM and is comparable to the DoFs of conventional mechanisms.

Assuming that condition

$$ {}^t\boldsymbol{\chi}_i^{\mathrm{T}}\,{}^t\boldsymbol{\chi}_i = 1,\ i = 1...p \tag{3}$$

holds, the following quantities can be designated as primary stiffnesses ${}^tK_{\mathrm{p}i}$ and secondary stiffness ${}^tK_{\mathrm{s}}$ for each stationary point:

$$
\begin{aligned}
{}^{t}K_{\mathrm{p}i}({}^{t}\mathbf{K}) &= {}^{t}\lambda_i = {}^{t}\boldsymbol{\chi}_i^{\mathrm{T}}\,{}^{t}\mathbf{K}\,{}^{t}\boldsymbol{\chi}_i,\ i = 1\ldots m, \\
{}^{t}K_{\mathrm{s}}({}^{t}\mathbf{K}) &= {}^{t}\lambda_{m+1} = {}^{t}\boldsymbol{\chi}_{m+1}^{\mathrm{T}}\,{}^{t}\mathbf{K}\,{}^{t}\boldsymbol{\chi}_{m+1}.
\end{aligned} \tag{4}
$$

The primary stiffnesses correspond to the eigenvalues that are assigned to the kinematic eigenmodes. Similarly, the secondary stiffness in each stationary point results from the eigenvalue of the first parasitic eigenmode, i.e. the eigenvalue at position $m+1$.

The eigenmodes represent the linearized deformations with which the CM can continue to deform starting from the stationary point. The associated eigenvalues indicate the stiffnesses opposite to these deformations and are a measure of the required strain energy [17]. A larger eigenvalue therefore requires more energy for the corresponding deformation. As the ratio between primary and secondary stiffness increases, the tendency of the CM to deform further according to the kinematic eigenmodes increases, as these deformations are energetically more favorable. High precision is achieved if the deformation in the respective stationary point is predominantly composed of the kinematic eigenmodes, which is the case with small primary stiffnesses and a large secondary stiffness. The quotient between secondary stiffness and the largest primary stiffness is referred to as selectivity[1]:

$$
{}^{t}S = {}^{t}\lambda_{m+1}/{}^{t}\lambda_m. \tag{5}
$$

The natural kinematics of a CM with $m = 1$ can be approximated by successively applying the first eigenmode to the displacement vector ${}^{t}\mathbf{u}$ and computing the corresponding tangent stiffness matrices:

$$
{}^{t}\mathbf{K} = \mathbf{K}({}^{t}\mathbf{u}),\ t = 2...n_{\mathrm{s}} \tag{6}
$$

with the incremental update scheme defined as

$$
\begin{aligned}
{}^{1}\mathbf{u} &= \mathbf{0},\ t = 1 \\
{}^{t}\mathbf{u} &= {}^{t-1}\mathbf{u} + \alpha\,{}^{t}\boldsymbol{\chi}_1^{\mathrm{T}},\ t = 2...n_{\mathrm{s}}.
\end{aligned} \tag{7}
$$

To ensure sufficient accuracy, the increment parameter α must be chosen appropriately small. Here, n_{s} denotes the number of incremental steps used to describe the natural kinematics. The value of n_{s} must be chosen based on α such that the resulting total deformation is sufficiently large to cover the desired range of functional deformations. See standard texts on nonlinear elasticity such as [18] for a detailed derivation of $\mathbf{K}({}^{t}\mathbf{u})$.

The selectivity of the CM can be determined from the calculated ${}^{t}\mathbf{u}$ and serves as a measure of precision. A high selectivity means that the structure deforms preferentially along the natural kinematics with minimal energy expenditure, while deviations from this are energetically unfavorable.

3 OPTIMIZATION FORMULATION

Based on the previously determined deformation properties of the non-prestressed CM, the natural kinematics and the tangent stiffness matrices ${}^t\mathbf{K}$ belonging to the functional deformations are known, which were determined under the assumption of large deformations and distortions. By solving the eigenvalue problem (2), the primary and secondary stiffnesses as well as the corresponding eigenmodes are also available. For clarity, the variables ${}^t\mathbf{K}$ and ${}^t\lambda_i$ are hereinafter denoted as ${}^t\mathbf{K}_\mathrm{e}$ and ${}^t\lambda_{\mathrm{e},i}$, while the eigenmodes ${}^t\boldsymbol{\chi}_i$ remain unchanged, as they are assumed to be unaffected by prestress [8].

The following discussion extends the considerations presented in [8, 14] to CM with large deformations and distortions. In selected ${}^t\mathbf{K}_\mathrm{e}$, i.e. certain stationary points, the stiffness can be specifically modified using prestressing elements such as truss elements. An optimization problem can be formulated for each stationary point in order to determine the position of the truss elements and the size of the associated prestress. As a basis for the optimization, it is assumed that the applied prestress slightly affects the deformation at stationary points. Therefore, the change in structural stiffness can be modeled in a linearized manner based on [8, 14].

All n truss elements considered in the subsequent optimization are attached to the CM in the deformation state ${}^t\mathbf{u}$. Since the CM is already in the deformed state, the truss elements are also deformed. A prestress ${}^t\mathbf{N}_\xi,\ \xi = 1 \dots n$ is applied to each truss. This generates a truss force ${}^t p_\xi$, which is directed along the central axis of the deformed truss. Cutting the respective truss element free provides the reaction forces at the nodes of the CM to which the truss element is connected. These forces arise as a result of the applied prestressing and the current geometry of the truss. The resulting truss forces cause a change in deformation ${}^t\Delta\mathbf{u}$ of the overall structure. If this deformation change is small, it can be approximated according to [19] by a linear calculation step instead of an iterative method. Using the tangent stiffness matrix ${}^t\mathbf{K}_\mathrm{e}$ of the non-prestressed CM in the considered stationary point, ${}^t\Delta\mathbf{u}$ can be determined in a linearized way:

$$ {}^t\Delta\mathbf{u} = {}^t\mathbf{K}_\mathrm{e}^{-1}\, {}^t\mathbf{p}. \tag{8} $$

The resulting deformation alters the internal stresses and leads to an adjustment of the structural stiffness, which is captured in the initial stress stiffness matrix ${}^t\mathbf{K}_\mathrm{g}({}^t\Delta\mathbf{u})$. The linearized contribution of each truss to ${}^t\mathbf{K}_\mathrm{g}$ can be determined using classical formulations, such as those described in [18], and added up to the total matrix. In the stress-displacement equations, the stiffness matrix ${}^t\mathbf{K}$ is linearly adjusted by superposition:

$$ {}^t\mathbf{K} = {}^t\mathbf{K}_\mathrm{e} + {}^t\mathbf{K}_\mathrm{g}. \tag{9} $$

Since the resulting reaction forces at the nodes due to the prestressing depend linearly on the applied prestress ${}^t N_\xi$ and (8) is also a linear relationship, the initial stress stiffness matrix ${}^t\mathbf{K}_{\mathrm{g},\xi}({}^t N_\xi)$ generated by the respective truss element scales linearly with the prestress.

The total stiffness matrix of the prestressed CM thus results in:

$$ {}^t\mathbf{K} = {}^t\mathbf{K}_\mathrm{e} + \sum_{\xi=1}^{n} {}^t\mathbf{K}_{\mathrm{g},\xi}(({}^tx_\xi^+ - {}^tx_\xi^-){}^tN_\xi) = {}^t\mathbf{K}_\mathrm{e} + \sum_{\xi=1}^{n} ({}^tx_\xi^+ - {}^tx_\xi^-){}^t\mathbf{K}_{\mathrm{g},\xi}({}^tN_\xi). \tag{10} $$

The expression $({}^tx_\xi^+ - {}^tx_\xi^-)$ describes the effective scaling of the stress component acting on the respective truss element ξ. For this purpose, separate parameters are used for positive $({}^tx_\xi^+)$ and negative $({}^tx_\xi^-)$ scaling, where ${}^tx_\xi^+, {}^tx_\xi^- \in \mathbb{R}_{\geq 0},\ \xi = 1 \dots n$ applies. Due to the assumed linearity, the total stiffness matrix ${}^t\mathbf{K}$ can be represented as a superposition of the unstressed matrix ${}^t\mathbf{K}_\mathrm{e}$ and the scaled contributions ${}^t\mathbf{K}_{\mathrm{g},\xi}({}^tN_\xi)$, whereby these are entered as functions of the respective prestress ${}^tN_\xi$.

By inserting equation (10) into the eigenvalue problem (2) and then transforming it to ${}^t\lambda$, the influence of the prestress on the modal stiffnesses can be expressed as follows:

$$ {}^t\boldsymbol{\chi}_i^\mathrm{T}({}^t\mathbf{K}_\mathrm{e} + \sum_{\xi=1}^{n} ({}^tx_\xi^+ - {}^tx_\xi^-){}^t\mathbf{K}_{\mathrm{g},\xi}({}^tN_\xi)){}^t\boldsymbol{\chi}_i = {}^t\lambda_i,\ i = 1 \dots p. \tag{11} $$

Equation (11) can also be formulated as:

$$ {}^t\lambda_{\mathrm{e},i} + \sum_{\xi=1}^{n} ({}^tx_\xi^+ - {}^tx_\xi^-) \cdot {}^t\lambda_{\mathrm{g},i,\xi} = {}^t\lambda_i,\ i = 1 \dots p \tag{12} $$

$$ \text{with} \quad {}^t\lambda_{\mathrm{e},i} = {}^t\boldsymbol{\chi}_i^\mathrm{T}\, {}^t\mathbf{K}_\mathrm{e}\, {}^t\boldsymbol{\chi}_i, \quad {}^t\lambda_{\mathrm{g},i,\xi} = {}^t\boldsymbol{\chi}_i^\mathrm{T}\, {}^t\mathbf{K}_{\mathrm{g},\xi}({}^tN_\xi)\, {}^t\boldsymbol{\chi}_i. \tag{13} $$

The design variables to be determined are the scaling factors ${}^tx_\xi^+$ and ${}^tx_\xi^-$, which are summarized in a common vector ${}^t\mathbf{x}$. The deformation modes ${}^t\boldsymbol{\chi}_i$ result from the solution of the eigenvalue problem of the non-prestressed CM (2) and remain constant during the optimization. Thus, all terms in equation (11) - with the exception of the design variables ${}^t\mathbf{x}$ - are to be regarded as constant.

The formal representation of the underlying linear optimization problem is based on [14]:

$$ \begin{aligned} \min_{{}^t\mathbf{x}} \quad & f(\mathbf{x}) = \sum_{\xi=1}^{n} \left({}^tx_\xi^+ + {}^tx_\xi^-\right) \\ \text{s.t.} \quad & {}^t\lambda_{\mathrm{d},i} - {}^t\lambda_i({}^t\mathbf{x}) = 0,\ i = 1 \dots m \\ & {}^t\boldsymbol{\chi}_j^\mathrm{T}\, {}^t\Delta\mathbf{u}({}^t\mathbf{x}) = 0,\ j = 1 \dots m + \eta \\ & \beta\, {}^t\lambda_m({}^t\mathbf{x})\, {}^t\lambda_{\mathrm{e},k} - {}^t\lambda_k({}^t\mathbf{x})\, {}^t\lambda_{\mathrm{e},m} \leq 0,\ k = m+1 \dots m + \eta \\ & {}^tx_\xi^+, {}^tx_\xi^- \geq 0 \end{aligned} \tag{14} $$

The aim of the optimization is to minimize the sum of the positive and negative scaling factors in $\mathbf{x}$ - and thus the total applied prestress. The decomposition of the scaling factor into separate non-negative positive and negative components allows the use of linear terms in the objective function, thus avoiding the need to minimize absolute values. This facilitates a linear optimization formulation.

The first constraint ensures that the resulting primary stiffness value ${}^t\lambda_i(\mathbf{x})$ corresponds to a specified target value ${}^t\lambda_{\mathrm{d},i}$. This target value can be defined, for example, as a fraction of the corresponding primary stiffness value ${}^t\lambda_{\mathrm{e},i}$ of the non-prestressed structure.

The second constraint ensures that the prestresses do not activate the first $m+\eta$ deformation modes with the lowest associated eigenvalues. Here, η denotes a user-defined number of additional low-energy deformation modes which, alongside the m kinematic eigenmodes, should remain unaffected by the prestressing. This is particularly relevant to ensure the validity of the assumption that prestressing causes only small changes in the deformation state.

The precision and therefore the selectivity of the CM should also be maintained or improved in the prestressed state. For this purpose, a scaling factor β is introduced in the third constraint, which can be used to specifically adjust the precision: For $\beta = 1$ it is maintained compared to the non-prestressed state, for $\beta > 1$ it is increased.

The objective function (14) and all constraints are linear. The optimization problem is therefore formulated completely linearly. This represents a significant advantage, as linear optimization problems can be solved efficiently and - subject to solvability and boundedness - global optima are guaranteed to be found.

4 IMPLEMENTATION

The first step is to define a structural design for the CM to be optimized. Once this design has been discretized, the natural kinematics are determined step by step by calculating the associated functional deformations. The tangent stiffness matrices ${}^t\mathbf{K}_{\mathrm{e}}$ are calculated for the determined deformations, taking into account large deformations and distortions. The eigenmodes and eigenvalues of ${}^t\mathbf{K}_{\mathrm{e}}$ are then determined for a specified selection of stationary points. Based on this, initial configurations of prestressed truss elements are defined and the corresponding initial stress stiffness matrices are calculated. Based on these values, the modal contributions ${}^t\lambda_{\mathrm{e},i}$ and ${}^t\lambda_{\mathrm{g},i,\xi}$ can be determined.

The optimization problem formulated in (14) can now be solved for the selected stationary points to specifically adjust the stiffness of the CM. After selecting a suitable starting point for the design variables $\mathbf{x}$, the resulting scaling factors and the associated stress vector ${}^t\mathbf{N}$ can be calculated. This makes it possible to evaluate both the objective function and the constraints.

An optimization algorithm is used to iteratively improve the scaling of the prestress; the simplex algorithm is used for this purpose in this work. The Optimization and FE analyses were implemented in MATLAB.

5 USE CASE: CARTWHEEL HINGE

The cartwheel hinge is chosen as use case - a planar CM with pseudo-mobility of $m = 1$, which is characterized by a high selectivity [17]. The underlying geometry and the FE meshing are shown in Figure 1(a). The geometric dimensions are: height $h = 90\,\mathrm{mm}$, length $l = 80\,\mathrm{mm}$, bar thickness $t = 2\,\mathrm{mm}$ and structure depth $b = 80\,\mathrm{mm}$. The material used is steel with a modulus of elasticity of $E = 210\,000\,\mathrm{N/mm^2}$ and a Poisson's ratio of $\nu = 0.3$. Planar 8-node

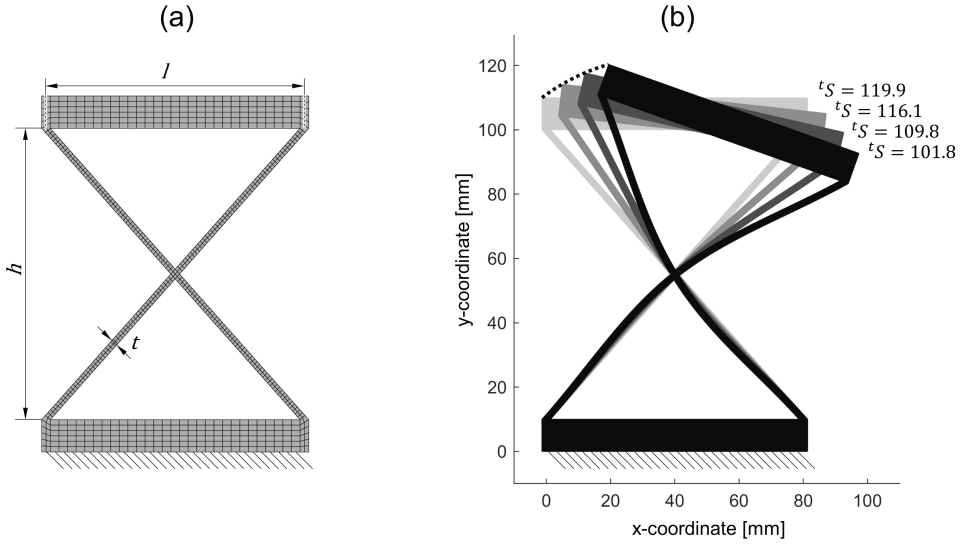

Figure 1: Cartwheel hinge: (a) Boundary conditions and meshing, (b) Natural kinematics

quadrilateral elements are used for the FE simulation. The hinge is fixed clamped as shown.

The natural kinematics is determined for the deformation direction shown in Figure 1(b) with an increment parameter of $\alpha = 0.01$. Since natural kinematics is based on a linearized calculation methodology, such a fine incremental resolution is required to ensure sufficient accuracy of the results. Too coarse a discretization, on the other hand, can lead to unrealistic stress states that are not part of the actual natural kinematics. The calculation is performed step by step over a total of 60 000 increments. Figure 1(b) shows the undeformed initial configuration, the final deformed state after all increments, and two representative intermediate configurations. The corresponding selectivities are also indicated for each deformation state. It can be observed that the selectivities remain consistently high throughout the deformation process. Additionally, the trajectory of a selected point across all computed configurations is illustrated by a dashed line.

The deformations of the natural kinematics are used to determine ${}^t\mathbf{K}_\mathrm{e}$. The structural stiffness is not optimized for all 60 000 steps of the natural kinematics, but only in intervals of 100 steps. This means that a total of 60 independent optimization steps must be performed.

For the optimization, the structure is connected with prestressed truss elements. The prestress of all truss elements is set to ${}^tN = 0.01\,\mathrm{N/mm^2}$. In previous work assuming small deformations and distortions [14, 8], all possible combinations of nodes were connected by truss elements. However, these studies referred to structures with a smaller number of finite elements where beam elements were used. In contrast, a finer parameterization with other finite elements is used here: The FE mesh results in a total of 2 947 nodes. A complete coupling of all nodes would generate about 4.3 million truss elements. Since very short members would hardly be feasible in practical implementation, all members whose length is less than $20\,\mathrm{mm}$ are removed. In addition, only the corner nodes of the finite elements are connected to each other and only corner

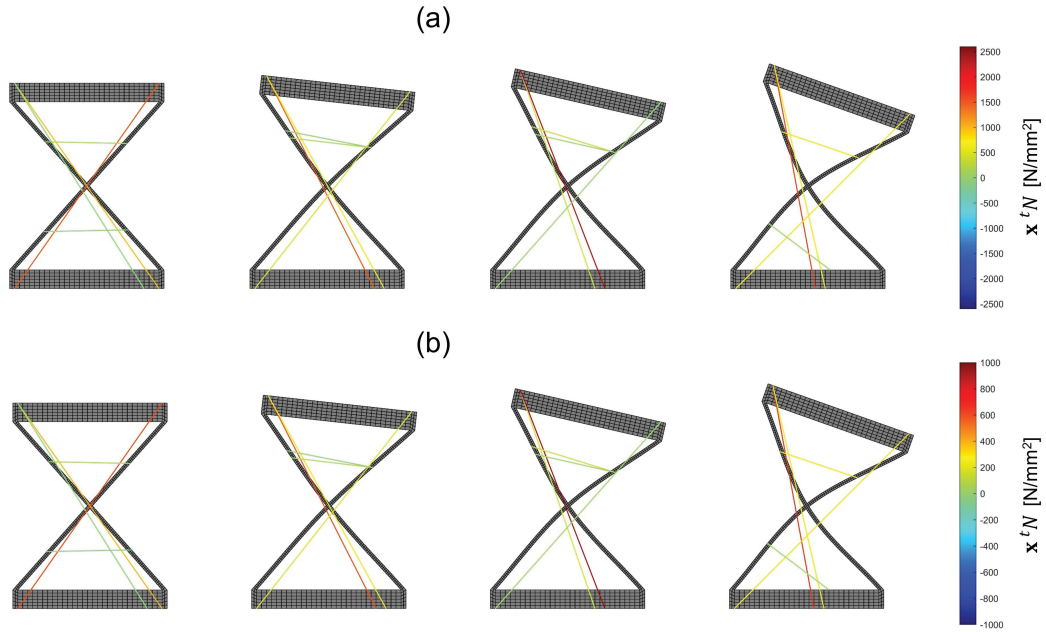

Figure 2: Cartwheel hinge: (a) Solution of optimization 1 for 4 different functional deformations, (b) Solution of optimization 2 for 4 different functional deformations

nodes that are at least 4 mm apart are included. This leaves a total of $11\,561$ truss elements that are taken into account in the optimization. This corresponds to $11\,561 \cdot 2$ design variables.

Two optimizations are carried out. For optimization 1, a target stiffness value of ${}^t\lambda_{\mathrm{d},1} = 0.5\,{}^t\lambda_{\mathrm{e},1}$ is defined for all stationary points, for optimization 2 ${}^t\lambda_{\mathrm{d},1} = 0.8\,{}^t\lambda_{\mathrm{e},1}$. In both cases, the scaling factor $\beta = 1$ is selected so that the precision of the prestressed CM is at least equal to the precision of the non-prestressed CM. The prestress should be determined specifically so that it does not activate any of the first 3 parasitic eigenmodes, i.e. $\eta = 3$ is selected, in accordance with the recommendations in [8, 14].

Figure 2 shows the results of the two optimizations. Subfigure 2(a) displays the positions of the truss elements and the corresponding prestresses for the optimization 1, and subfigure 2(b) for optimization 2. Only truss elements with nonzero prestressing after the optimization are shown for clarity. In both cases, the results are shown exemplarily for the deformations illustrated in Figure 1(b). It can be seen that the basic solutions of both optimizations differ only slightly. The positions of the prestressed truss elements remain unchanged, while the amounts of prestress increase as the target stiffness value decreases. In addition, there are few truss elements with low prestress. These should be specifically reduced or eliminated in future work using a suitable penalty mechanism in the optimization process in order to improve the practical feasibility of the solution.

To validate the results of the optimization, where the influence of the truss elements is linearized, a verification is carried out using nonlinear FE analysis. Therefore, the force dis-

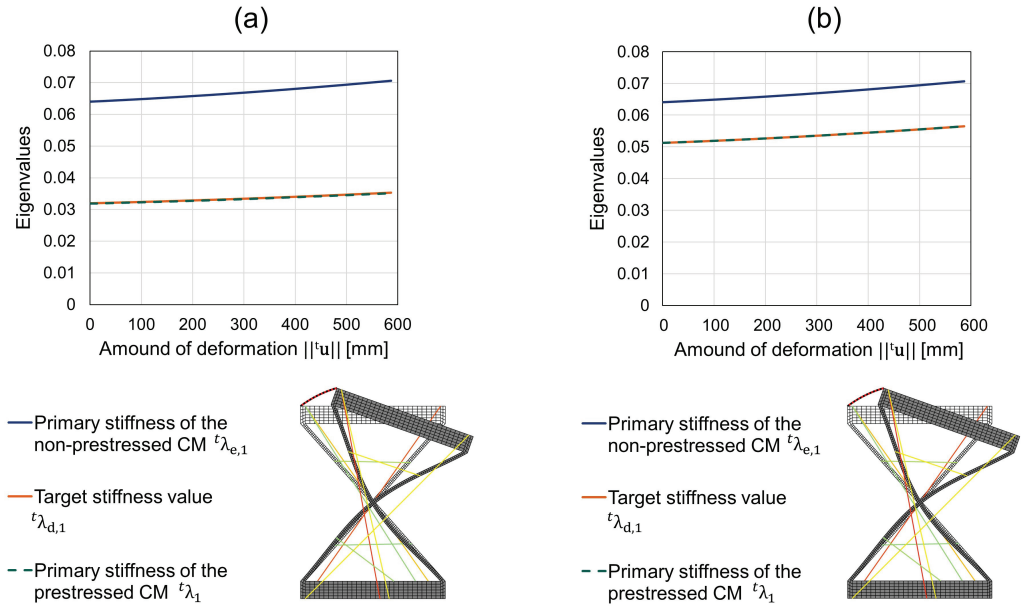

Figure 3: Cartwheel hinge: (a) Validation of optimization 1, (b) Validation of optimization 2

tribution required to generate the deformation corresponding to each optimization step in the non-prestressed state is determined. These equilibrium forces are applied as external loads to induce the corresponding deformation. Once this deformation is achieved, the optimized truss elements are incorporated into the model, and the system is rebalanced by iteratively solving for equilibrium using the Newton-Raphson method.

The validation results for all optimization steps of both optimizations are presented in Figure 3. To investigate how the prestress affects the existing deformation, the deformation curves of a selected point are highlighted in red; the corresponding natural kinematics are shown as black dashed line. The deformation curves show that the introduced prestress only slightly affects the deformations, as required by the second constraint in the optimization.

Additionally, the primary stiffness of the prestressed CM is calculated for all optimization steps. The diagrams in Figure 3 show the original primary stiffnesses, the target stiffnesses, and the primary stiffnesses obtained after optimization across the entire optimized deformation range. Both optimizations resulted in a reduction in primary stiffness with a good approximation to the target stiffness values.

6 CONCLUSIONS

This contribution presents a systematic approach for the determination of prestressing forces in CM considering large deformations for targeted stiffness control. For this purpose, several linearization points are defined within the functional deformations, for each of which an opti-

mization is performed. The optimization provides configurations of prestressed truss elements with which the desired stiffnesses are achieved in the respective state. The required prestressing can be interpolated based on the generated deformation amplitude so that a consistent relationship between the deformation state and the required prestressing can be created. The method is demonstrated using a cartwheel hinge as an example. The results show that both the target stiffnesses for the optimized range of functional deformations can be set via the prestress with a high degree of accuracy.

In future studies, the introduction of suitable penalty mechanisms in the optimization process is planned in order to minimize the number of truss elements used. Furthermore, the dependency of the material parameters of the truss elements on their deformation will be considered and integrated into the optimization process to enhance practical feasibility. The aim is to reduce the currently high control effort through optimized material parameters.

7 ACKNOWLEDGEMENTS

Funded by the Deutsche Forschungsgemeinschaft (DFG, German Research Foundation) – A-posteriori Anpassung der Steifigkeit Nachgiebiger Mechanismen unter Berücksichtigung geometrischer Nichtlinearitäten (project number HA 7893/6-2).

REFERENCES

[1] S. Kirmse, L. F. Campanile, and A. Hasse, “Synthesis of compliant mechanisms with selective compliance – An advanced procedure,” *Mech. Mach. Theory*, vol. 157, p. 104184, 2021.

[2] A. Hasse and K. Mauser, “Poisson Induced Bending Actuator for Soft Robotic Systems,” *Soft Robot.*, vol. 7, no. 2, pp. 155–167, 2020.

[3] S. Kota, K.-J. Lu, Z. Kreiner, B. Trease, J. Arenas, and J. Geiger, “Design and Application of Compliant Mechanisms for Surgical Tools,” *J. Biomech. Eng.*, vol. 127, no. 6, pp. 981–989, 2005.

[4] S. Kota, “Design of compliant mechanisms: Applications to MEMS,” in *Proc. Vol. 3673 Smart Struct. Mater. 1999 Smart Electron. MEMS*, V. K. Varadan, Ed., Newport Beach, CA, 1999, pp. 45–54.

[5] L. L. Howell, *Compliant Mechanisms*. New York: John Wiley & Sons., 2001.

[6] J. C. Hawks, M. B. Colton, and L. L. Howell, “A Variable-Stiffness Straight-Line Compliant Mechanism,” in *Vol. 5A 39th Mech. Robot. Conf.* Boston, Massachusetts, USA: American Society of Mechanical Engineers, 2015, p. V05AT08A011.

[7] W.-F. Chen and E. M. Lui, *Structural Stability - Theory and Implementation*. New York: Elsevier, 1987.

[8] K. Mauser and A. Hasse, "How to prestress compliant mechanisms for a targeted stiffness adjustment," *Smart Mater. Struct.*, vol. 29, no. 8, p. 085021, 2020.

[9] F. S. Eastman, "The Design of Flexure Pivots," *J. Astronaut. Sci.*, vol. 5, no. 1, pp. 16–21, 1937.

[10] J. A. Haringx, "The cross-spring pivot as a constructional element," *Flow Turbul. Combust.*, vol. 1, no. 1, p. 313, 1949.

[11] W. Wittrick, "The Theory of Symmetrical Crossed Flexure Pivots," *Aust. J. Chem.*, vol. 1, no. 2, p. 121, 1948.

[12] Y.-S. Wu and C.-C. Lan, "Design of a linear variable-stiffness mechanism using preloaded bistable beams," in *2014 IEEEASME Int. Conf. Adv. Intell. Mechatron.* Besacon: IEEE, 2014, pp. 605–610.

[13] H. Zhao, D. Han, L. Zhang, and S. Bi, "Design of a stiffness-adjustable compliant linear-motion mechanism," *Precis Eng.*, vol. 48, pp. 305–314, 2017.

[14] K. Mauser, M. Sjarov, A. Nowak, L. F. Campanile, and A. Hasse, "Design and control of actively prestressed compliant mechanisms for variable stiffness actuators," *J. Intell. Mater. Syst. Struct.*, vol. 33, no. 19, pp. 2422–2439, 2022.

[15] L. F. Campanile, S. Kirmse, and A. Hasse, "Accuracy and precision: A new view on kinematic assessment of solid-state hinges and compliant mechanisms," *J. Intell. Mater. Syst. Struct.*, vol. 33, no. 13, pp. 1743–1748, 2022.

[16] S. Seltmann and A. Hasse, "Nonlinear synthesis of compliant mechanisms with selective compliance," 2024.

[17] A. Hasse and L. F. Campanile, "Design of compliant mechanisms with selective compliance," *Smart Mater. Struct.*, vol. 18, no. 11, p. 115016, 2009.

[18] K.-J. Bathe, *Finite-Elemente-Methode*, 2nd ed. Berlin Heidelberg: Springer, 2002.

[19] J. S. Przemieniecki, *Theory of Matrix Structural Analysis*. New York: McGraw-Hill,Inc, 1968.

XI ECCOMAS Thematic Conference on Smart Structures and Materials - SMART 2025
M. Krommer, M. Nader and M. Schagerl (Eds)

Received: 15 May 2025 / Revised: 19 September 2025 / Accepted: 14 October 2025
© The Author(s) 2025

Retrofitting a Tied-Arch Bridge with Adaptive Elements

Axel Trautwein, Amelie Zeller, Spasena Dakova, Christina Tarín, Oliver Sawodny, Manfred Bischoff

Abstract. Bridges are increasingly subjected to higher loads due to growing traffic volumes and the deployment of heavier transportation systems, such as new generations of trains. This case study investigates the extent to which a tied-arch bridge can be retrofitted with active hangers to counteract these increased loads.

A detailed finite element model of the bridge is developed and used to formulate a multi-objective optimization problem. The two competing objectives are to minimize the actuation forces required by the active hangers and to limit the increase in stress within the arch. Additionally, constraints are imposed to ensure that displacement limits are not exceeded, maintaining structural integrity and serviceability.

Key words: Adaptive Structures, Adaptive Bridges, Displacement Control, Stress Control

1 INTRODUCTION

The construction industry is facing increasing pressure due to global population growth, climate-damaging emissions, and the rising scarcity of natural resources. To meet these challenges, innovative approaches are being developed to reduce material consumption and lower the environmental impact of buildings and infrastructure. One promising strategy is the use of adaptive structures—systems that integrate active elements capable of responding to external loadings in real time. By adjusting their mechanical behavior, such as geometry or stiffness, adaptive structures can improve performance and maintain serviceability even when built with significantly reduced material quantities [1].

Since 2017, the Collaborative Research Center 1244 “Adaptive Skins and Structures for the Built Environment of Tomorrow” has been investigating the practical application of adaptive structures through interdisciplinary research. These efforts have demonstrated the feasibility of

Axel Trautwein & Manfred Bischoff
University of Stuttgart, Institute for Structural Mechanics, Pfaffenwaldring 7, 70550 Stuttgart, Germany, e-mail: trautwein@ibb.uni-stuttgart.de

Amelie Zeller & Spasena Dakova & Christina Tarín & Oliver Sawodny
University of Stuttgart, Institute for System Dynamics, Waldburgstr. 17/19, 70563 Stuttgart, Germany, e-mail: amelie.zeller@isys.uni-stuttgart.de

adaptive design strategies and their implementation in experimental buildings. An important milestone is the realisation of the world's first adaptive high-rise building D1244 on the campus of the University of Stuttgart [2].

The concept of using adaptive structures to actively control static deformations and internal forces was initially introduced in [3]. Subsequent research, such as [4], has explored the active mitigation of external influences, particularly vibrations. While vibration control remains also a focus in [5], the work provides a broader perspective by outlining fundamental design principles and a wide range of applications across different engineering disciplines.

Active structural systems in civil engineering are examined in detail in [6], where design strategies demonstrate the potential for substantial reductions in structural mass compared to conventional solutions. A comprehensive overview of the current research landscape and applications of adaptive structures is presented in [7] and [8].

Several studies have already addressed the design of adaptive structures. In addition to structural mass reduction, the minimization of actuation energy has emerged as a key design objective. Research shows that this energy demand can be significantly reduced when actuation is considered as an integral part of the structural design from the beginning. For truss and shell structures this has been investigated in [9, 10, 11, 12, 13].

For Bridges there are two promising approaches for bridges: firstly, the above-mentioned approach should be taken into account in the design for new bridges. For example, various studies have shown that a bridge equipped with an active underslung can ensure mass savings compared to a bridge equipped with a conventional underslung [14, 15, 16]. In [17], the design of a cable-stayed bridge equipped with an active control system is investigated. And secondly, existing bridges that are close to the end of their service life can be retrofitted with active elements to extend their operating life [18]. This is particularly important in Germany, because of the great need to renovate railway bridges. Due to the increasing loads caused by the intercity express (ICE) generation 4, the bridges are suffering from increased displacements and internal forces. Therefore their service life is reducing [19].

This contribution investigates a tied-arch bridge located near Hamburg, shown in Figure 1 As presented in [20], dynamic analyses and on site measurements have revealed that the resulting displacements pose a significant challenge. The present work focuses on the structural-mechanical analysis of the bridge and explores an adaptive retrofit strategy in which the existing hangers are replaced by actuators. For this purpose, a finite element model of the bridge was created. This is presented in Section 2. This numerical model is transformed into different optimization problems in Section 3. The primary objective is to minimize the required actuation effort, while ensuring that stress and displacement limits are not exceeded. This is done under statical conditions. Section 4 concludes this paper.

2 Model setup

Figures 1 shows the analyzed tied-arch bridge. The bridge has 16 hangers and is made of steel. The four corner nodes are simply supported. In order to ensure a linear-elastic analysis, a detailed finite element model of the bridge is created, as shown in Figure 2 and Figure 3.



Figure 1: Railway bridge “EÜ Elbe-Lübeck Kanal” (@Amelie Zeller)

The required material parameters and cross-section values were provided by *DB InfraGo AG*. *Ansys Mechanical APDL 2024* is used as simulation software. The arch and the bridge deck are modeled with beam elements. *BEAM188* is used for this purpose. This corresponds to a two-node linear beam element according to Timoshenko beam theory. The associated regular element size for the beam elements is 10 cm.

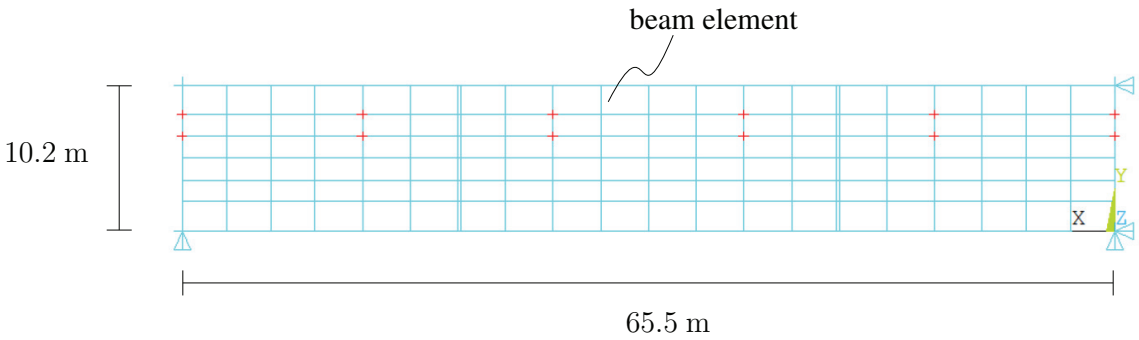

Figure 2: Finite element model of the railway bridge (top view).

Two-node truss elements are used for the hangers. This means that they can only bear normal forces. The used element type is called *LINK180* in *Ansys*. The actuation of the hangers is modeled by using a temperature load case. The necessary actuation force can then be recalculated

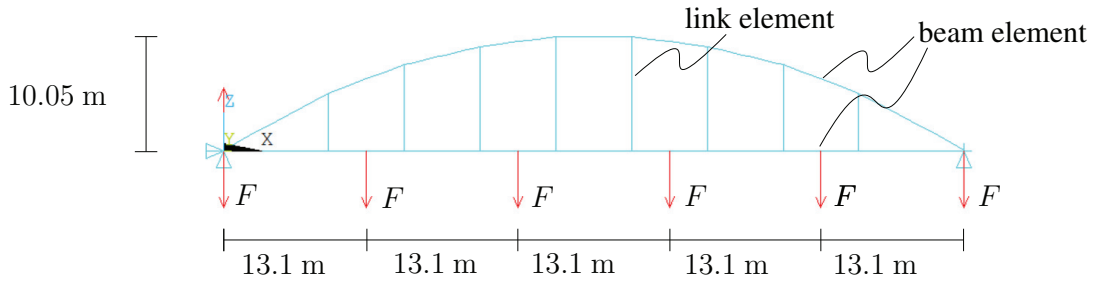

Figure 3: Finite element model of the railway bridge (side view).

by applying the required temperature difference.

Figure 2 and Figure 3 show the applied loads F with a magnitude of 400 kN. These are based on the dimensions and the load applied by the ICE 4 [21].

3 Optimization setup

In a first optimization problem, the maximum actuator force $F_{\max}$ is minimized and the corresponding optimization problem can be formalized as follows:

Minimize
$f(\Delta T_i) = F_{\max}(\Delta T_i)$

Subject to
$g(\Delta T_i) = u_{\max}(\Delta T_i) - 0.038 \text{ m} \leq 0$

Design variables
$\Delta T_i \in \mathbb{R}, \quad \text{for } i \in \{1, 2, \ldots, 16\}$

Only the actuator forces are used as design variables as this is an existing bridge and further structural changes to the bridge would be difficult to implement. The maximum displacement $u_{\max}$ for the nodes of the bridge deck is specified as a constraint. The value of 0.038 m is derived from a reference solution with a load of $F = 300$ kN. The optimization has been implemented using the *Python* package PyAnsys, which enables communication between *Python* and *Ansys*. The constrained optimization problem described is been solved using sequential least squares programming [22]. The optimization process yields the solution of the maximum actuator force of $F_{\max} = 2442$ kN.

As a second approach, the stresses $\sigma_{\max}$ in the arch are now also included in the optimization

problem, since the previous calculation showed a increasing stress in the arch compared to the passive system. For this reason, a multi-criteria optimization problem is defined as follows:

Minimize
$f_1(\Delta T_i) = F_{\max}(\Delta T_i)$
$f_2(\Delta T_i) = \sigma_{\max}(\Delta T_i)$

Subject to
$g(\Delta T_i) = u_{\max}(\Delta T_i) - 0.038\ \mathrm{m} \leq 0$

Design variables
$\Delta T_i \in \mathbb{R}, \quad \text{for } i \in \{1, 2, \ldots, 16\}$

So we have a objective function consisting of the conflicting functions $f_1(\Delta T_i)$ and $f_2(\Delta T_i)$. The problem was solved using the NSGA-II algorithm, as implemented in the *Python* library *pymoo*. *NSGA-II* is particularly well-suited for constrained multi-objective, nonlinear optimization problems due to its efficient non-dominated sorting and diversity preservation mechanisms, detailed information are given in [23]. The optimization was conducted with a population size of 100 individuals over 200 generations. Genetic operators for crossover and mutation were chosen according to or adapted from the default parameters in *pymoo*.

4 Conclusion

For the second optimization problem the result is a Pareto-optimal solution set that reflects the trade-off between mechanical stress and actuation effort. This Pareto front serves as a valuable decision-making basis for further design stages, depending on whether structural load reduction or actuation efficiency is prioritized.

In the Pareto front you can see that a reduction of the stress to about $200\ \frac{\mathrm{N}^2}{\mathrm{mm}}$ is possible, which is up to 20 percent compared to the first optimization problem. This increases the maximum actuator force by 10 percent to $2700\ \mathrm{kN}$. That shows that it is possible to reduce the maximum tension with a moderate increase in actuator force. However, steel has a material strength up to $350\ \frac{\mathrm{N}^2}{\mathrm{mm}}$, in accordance with the guidelines of Eurocode 3 [24]. The stresses in the arch are therefore not crucial for the selected load case. In further work, it would therefore be advantageous to simply incorporate these as boundary conditions in order to reduce the complexity of the optimization problem.

Another important aspect for further work related to this is the following. Often the maximum stresses are not the problem for bridges, but the material fatigue plays a decisive role. It is therefore proposed to carry out a service life analysis for critical points of the bridge, mainly the connections between arch/hanger and bridge deck/hanger. And to subsequently investigate how the service life can be extended by using active hangers.

Funding

The work described in this paper was conducted in the framework of the Collaborative Research Center 1244 "Adaptive Skins and Structures for the Built Environment of Tomorrow", within the projects C07 "Adaption of Bridges: Increasing Durability and Optimizing Stiffness" and B02 "State estimation and optical deformation measurements", funded by the Deutsche Forschungsgemeinschaft (DFG, German Research Foundation) under project number 279064222. The authors are grateful for the generous support. The authors are also thankful to *DB InfraGo AG* for their willingness to provide plans and information on the technical data of the bridge.

REFERENCES

1 W. Sobek, O. Sawodny, M. Bischoff, L. Blandini, M. Böhm, W. Haase, Y. Klett, M. Mahall, S. Weidner, T. Burghardt, P. Leistner, M. Maierhofer, S. Park, G. Reina, D. Roth, and C. Tarín, "Adaptive Hüllen und Strukturen," *Bautechnik*, vol. 98, no. 3, pp. 208–221, 2021. [Online]. Available: https://doi.org/10.1002/bate.202000107

2 L. Blandini, W. Haase, S. Weidner, M. Böhm, T. Burghardt, D. Roth, O. Sawodny, and W. Sobek, "D1244: Design and Construction of the First Adaptive High-Rise Experimental Building," *Frontiers in Built Environment*, vol. 8:814911., 2022. [Online]. Available: https://doi.org/10.3389/fbuil.2022.814911

3 W. Zuk and R. H. Clark, *Kinetic architecture*. New York [u.a.]: Van Nostrand Reinhold, 1970.

4 T. T. Soong and G. D. Manolis, "Active Structures," *Journal of Structural Engineering*, vol. 113, no. 11, pp. 2290–2302, 1987. [Online]. Available: https://doi.org/10.1061/(ASCE)0733-9445(1987)113:11(2290)

5 S. Utku, *Theory of Adaptive Structures: Incorporating Intelligence into Engineered Products*, ser. New Directions in Civil Engineering. Boca Raton: CRC Press, 1998. [Online]. Available: https://doi.org/10.1201/9780203719015

6 H. Domke, *Aktive Tragwerke*. Wiesbaden: VS Verlag für Sozialwissenschaften, 1992. [Online]. Available: https://doi.org/10.1007/978-3-322-85350-9

7 S. Korkmaz, "A review of active structural control: Challenges for engineering informatics," *Computers & Structures*, vol. 89, no. 23-24, pp. 2113–2132, 2011. [Online]. Available: https://doi.org/10.1016/j.compstruc.2011.07.010

8 L. Schwegmann, K. Steffen, and Z. Volkmar, "Adaptive structures in civil engineering – state of the art," *Engineering Computations*, vol. 41, no. 6, pp. 1424–1440, 2024. [Online]. Available: https://doi.org/10.1108/EC-12-2023-0952

9 F. Geiger, J. Gade, M. von Scheven, and M. Bischoff, "Optimal Design of Adaptive Structures vs. Optimal Adaption of Structural Design," *IFAC-PapersOnLine*, vol. 53, no. 2, pp. 8363–8369, 2020. [Online]. Available: https://doi.org/10.1016/j.ifacol.2020.12.1604

10 Y. Wang and G. Senatore, "Design of adaptive structures through energy minimization: Extension to tensegrity," *Structural and Multidisciplinary Optimization*, vol. 64, pp. 1079–1110, 2021. [Online]. Available: https://doi.org/10.1007/s00158-021-02899-y

11 Y. Wang and S. Gennaro, "Minimum energy adaptive structures – All-In-One problem formulation," *Computers & Structures*, vol. 236, p. 106266, 2020. [Online]. Available: https://doi.org/10.1016/j.compstruc.2020.106266

12 A. Trautwein, T. Prokosch, G. Senatore, L. Blandini, and M. Bischoff, "Analytical and Numerical Case Studies on Tailoring Stiffness for the Design of Structures with Displacement Control," *Frontiers in Built Environment*, vol. 9, 2023. [Online]. Available: https://doi.org/10.3389/fbuil.2023.1135117

13 A. Trautwein, T. Prokosch, and M. Bischoff, "A case study on tailoring stiffness for the design of adaptive rib-stiffened slabs," *10th ECCOMAS Thematic Conference on Smart Structures and Materials*, Patras, Greece. 2023. [Online]. Available: https://doi.org/10.7712/150123.9821.444802

14 M. del Mar Corral, L. Todisco, and J. M. Soria, "Design, construction and testing of a smart underdeck cable-stayed footbridge prototype." *Engineering Structures*, vol. 209, 2023. [Online]. Available: https://doi.org/10.1016/j.engstruct.2023.116387

15 A. Zeller, S. Dakova, C. Stein, M. Böhm, G. Senatore, A. P. Reksowardojo, L. Blandini, O. Sawodny, and C. Tarín, "Bridge state and average train axle mass estimation for adaptive railway bridges," *IEEE/ASME Transactions on Mechatronics*, vol. 28, no. 4, pp. 1880–1889, 2023. [Online]. Available: 10.1109/TMECH.2023.3277317

16 A. P. Reksowardojo, G. Senatore, M. Bischoff, and L. Blandini, "Design and control of high-speed railway bridges equipped with an under-deck adaptive tensioning system," *Journal of Sound and Vibration*, vol. 579, p. 118362, 2024. [Online]. Available: https://doi.org/10.1016/j.jsv.2024.118362

17 Z. Zhu, Y. Liu, W. Zheng, and Z. Ren, "A novel high-speed railway large-span cable-stayed bridge with deformation active control function: structural system and control algorithm," *Structure and Infrastructure Engineering*, vol. 0, no. 0, pp. 1–12, 2025. [Online]. Available: https://doi.org/10.1080/15732479.2025.2488379

18 K. A. Canny, G. Senatore, and L. Blandini, "Investigation of retrofit strategies to extend the service life of bridge structures through active control," *Journal of Bridge Engineering*, vol. 30, no. 2, p. 04024109, 2025. [Online]. Available: https://ascelibrary.org/doi/abs/10.1061/JBENF2.BEENG-6925

19 P. Mark and P. Neugebauer, *Erhalt unserer Bausubstanz – zentrale Forschungsaufgabe mit modernen Methoden.* Nordrhein-Westfälische Akademie der Wissenschaften und der Künste (Hrsg.). Verlag Ferdinand Schoeningh. Paderborn, 2014.

20 A. Zeller, S. Dakova, A. Trautwein, M. Böhm, M. Bischoff, O. Sawodny, and C. Tarin., "Vibration damping of adaptive railway bridges: A case study." *IABSE Symposium: Environmentally Friendly Technologies and Structures - Focusing on Sustainable Approaches.*, pp. 1868–1876, Tokyo, Japan. 2025. [Online]. Available: https://doi.org/10.2749/tokyo.2025.1868

21 ICE 4. Accessed: 2025-04-28. [Online]. Available: https://www.bahn.de/service/ueber-uns/zugtypen/ice-4.

22 J. Nocedal and S. J. Wright, *Numerical Optimization*. Springer New York, NY, 2006. [Online]. Available: https://doi.org/10.1007/978-0-387-40065-5

23 K. Deb, A. Pratap, S. Agarwal, and T. Meyarivan, "A fast and elitist multiobjective genetic algorithm: Nsga-ii," *IEEE Transactions on Evolutionary Computation*, vol. 6, no. 2, pp. 182–197, 2002. [Online]. Available: https://doi.org/10.1109/4235.996017

24 *DIN EN 1993-1-1:2010-12, Eurocode 3: Bemessung und Konstruktion von Stahlbauten*, DIN e.V. Std., 2010. [Online]. Available: https://www.eurocode-online.de/de/eurocode-inhalte/eurocode-3

XI ECCOMAS Thematic Conference on Smart Structures and Materials - SMART 2025
M. Krommer, M. Nader and M. Schagerl (Eds)

Received: 31 March 2025 / Revised: 26 August 2025 / Accepted: 14 October 2025
© The Author(s) 2025

Static Shape Control of Slender Structures: An Overview and a Classification of Control Laws

Péter L. Várkonyi, Andres Felipe Guerra Riaño

Abstract. This study explores shape control in kinematic chains of rigid bars, subject to quasi-static external loads. The structural shapes are stabilized by rotary actuators with feedback control at the joints. Classifications based on the number of actuators, and the type of control are presented. The main ideas are illustrated by examples where our goal is to maintain a structural shape capable of balancing the loads via pure compression. The relevance of the classification to engineering applications is highlighted.

Key words: Shape Adaptation, Underactuated Systems, Fully Actuated System, Kinematic Chains, funicularity

1 INTRODUCTION

Robotic arms are typically designed as chains of rigid segments fixed at one endpoint, with the relative rotation angles at the joints set by rotary actuators. The typical tasks of a robotic arm include object manipulation, transportation, and manufacturing. All of these require transition between *prescribed shapes*. For stiff robots, small payloads and relatively slow operation, shape control is straightforward, as the angle of each joint is set directly by an actuator. In contrast, soft robotic arms are operated under a strong influence of *load-induced deformation* and *dynamic vibrations*, and the success of shape control often requires fine tuning of controllers and the management of time delays [1].

Plant roots and shoots are highly similar to soft robotic arms. However in this case, the goal of shape control is adaptation to unpredictable environmental conditions, such as the avoidance of shaded areas (shoots), growth towards local water sources (roots), and clinging to supports (tendrils of climbing plants). These mechanisms are often referred to as *tropism*: plants use simple sensors to detect directional stimuli such as light, touch, or gravity, and they develop internal curvature in response. Tropism is quasi-static, yet often much faster than the growth of plants. [2]. An important challenge of plant tropism is to predict the preferable change of curvature from *limited sensor data*.

Péter L. Várkonyi & Andres Felipe Guerra Riaño
Budapest University of Technology and Economics, Department of Mechanics, Materials and Structures, 1111 Budapest, Hungary, e-mail: guerra.andres@edu.bme.hu,varkonyi.peter@epk.bme.hu

Large-scale, adaptive load-bearing structures are closely related to the previous examples. However the primary purpose of those structures is to resist external loads with limited material usage. Common applications of active control include active vibration suppression [3], earthquake protection [4, 5], and compensation of static deformations, and the optimization of shape for static deformations or resistance against static loads [6].

Structures with shape control are often lightweight (and thus soft), furthermore the direct measurements of time-dependent loads is difficult. Hence, structures with shape adaptation may face the challenges of softness and limited sensor data simultaneously. In addition, the large scale of those structures implies that safety and reliability are also crucial factors. These finding explain why shape control is not very common among civil engineering structures. At the same time, overcoming these challenges has a great potential in reducing the environmental footprint of structures by reduced material usage, hence it is worth exploring.

This study investigates a model problem, first proposed in recent works of the authors [7, 8]. We consider a discrete model consisting of a kinematic chain of rigid bars fixed at one endpoint, whose shapes are stabilized by rotary actuators with feedback control at each joints. The joints are subject to quasi-static loads, and are assumed to have no passive bending stiffness, thus they are stabilized entirely by the actuators. In addition we work under the hypothesis that the load cannot be detected by the sensors. Instead, the load must be inferred from the response of the structure indirectly.

The aim of the actuators is to drive the structure towards a shape where the load is balanced by pure compression of the bars. Structures subject to pure compression and tension are often called funicular, and are known for their exceptional material efficiency [9]. Compressive funicular structures include arches, vaults, and columns. The classical approach to the design of funicular structures is to find an appropriate shape corresponding to their dominant load, and to use bending resistance in order to balance time-dependent components of the load. In contrast, we investigate smart structures, which adapt to time-dependent loads by shape changes, and preserve funicularity, which can further improve material efficiency. As loads are not measurable, the target shape cannot be specified in advance, and it has to be detected by the controller as part of the shape control task.

After presenting the model problem and a general framework of shape control in Section 2, we propose a classification of shape control strategies within this framework in Section 3. Fundamental properties of the strategies are identified, and illustrated by examples. Finally the paper is closed by a discussion of future perspectives.

2 PROBLEM STATEMENT

We investigate a planar model of a chain of n rigid bars of lengths l_i, connected by hinges. The mass and the load of the structure are modeled as lumped masses m_i and forces $\mathbf{F}_i = (F_{i,x}, F_{i,y})$ at the joints. Joint 0 is fixed by a pin support, and the opposite endpoint moves freely. Each joint (except the free end) is equipped with a rotary actuator generating prescribed torques τ_i between the two adjacent components, as well as sensors measuring the relative angles $\alpha_i - \alpha_{i-1}$ of the two components connected by each joint (where $\alpha_0 = 0$ by convention).

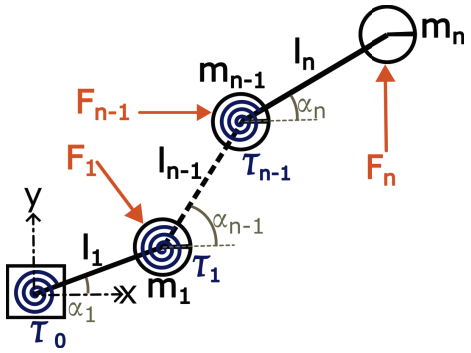

Figure 1: A chain composed of m bars with length l_i connected by pin connections equipped with lumped masses m_i. External loads F_i are assumed to be stationary, and rotary actuators producing torques τ_i in order to set the shape of the structure.

It is straightforward to show, that for each set of loads, such a chain has a unique compressive funicular configuration, which is unstable in the absence of actuation. The dynamic equations of motion can be derived using Lagrange's equation [8]. The equations are of the form

$$\ddot{\boldsymbol{\alpha}} = \mathbf{A}^{-1} \cdot [\mathbf{G}\boldsymbol{\tau} + \mathbf{b}] \tag{1}$$

where dot means derivative with respect to time, $\boldsymbol{\alpha} = [\alpha_1, \alpha_2, .., \alpha_n]^T$, $\boldsymbol{\tau} = [\tau_0, \tau_1, ..., \tau_{n-1}]^T$ (and ^{T} means transpose). The mass matrix $\mathbf{A}$, and the matrix $\mathbf{G}$ composed of column vectors of the generalized representing actuator torques are both of size n by n. The free acceleration vector $\mathbf{b}$ represents the angular accelerations of the bars in the absence of actuation, and is of length n. The exact values of these terms depend on various model parameters. For example, in the case of a chain of 2 bars, we have

$$\mathbf{A} = \begin{bmatrix} l_1^2 m_1 + l_1^2 m_2 & l_1 l_2 m_2 cos(\alpha_1 - \alpha_2) \\ l_1 l_2 m_2 cos(\alpha_1 - \alpha_2) & l_2^2 m_2 \end{bmatrix} \tag{2}$$

$$\mathbf{b} = \begin{bmatrix} -l_1 l_2 m_2 sin(\alpha_1 - \alpha_2)\dot{\alpha_2}^2 + T_1 l_1 \\ l_1 l_2 m_2 sin(\alpha_1 - \alpha_2)\dot{\alpha_1}^2 + T_2 l_2 \end{bmatrix} \tag{3}$$

$$\mathbf{G} = \begin{bmatrix} 1 & -1 \\ 0 & 1 \end{bmatrix}. \tag{4}$$

where the shorthand notation $T_i = \sum_{j=i}^{n}(-F_{j,x} \sin \alpha_i + F_{j,y} \cos \alpha_i)$. has been used.

The funicular shapes correspond to solutions of $T_1 = T_2 = 0$, where the system is in equilibrium with $\boldsymbol{\tau} = 0$. There are altogether 2^n funicular configurations, form which one corresponds to pure compression.

3 CLASSIFICATION OF SHAPE CONTROL STRATEGIES

3.1 General framework

Feedback controllers use sensor data to gain information about the system in question. In our case, the sensor data available to the controller are the relative angles of the adjacent bars,

i.e. the elements of vector

$$\boldsymbol{\Delta} = [\alpha_1, \alpha_2 - \alpha_1, ..., \alpha_n - \alpha_{n-1}]^T.$$

The control action is the set of torques collected in vector $\boldsymbol{\tau}$ (see above). The typical formulation of control strategies assumes that the control action depends on present and/or past values of an error function. A very popular framework of feedback control strategy uses terms proportional to the present value of the error (P control), the first and/or second time derivative of the error (D, and A control), as well as the integral of its past values (I control). In our previous work, we have found that spontaneous stabilization of unspecified funicular shapes is possible using PID control (without A term) and the vector-valued error function $\mathbf{e} = \boldsymbol{\Delta}$, even if the target shape does not correspond to $\boldsymbol{\Delta} = 0$. This apparent contradiction can be resolved by noting that the effect of I control is equivalent to a continuously evolving estimation of the target state, which can be used to find an unspecified target using an inaccurate initial guess.

After some algebraic manipulation, a general formulation of the PID control described above is given by

$$\boldsymbol{\tau} = -\mathbf{K}_P(\boldsymbol{\Delta} - \boldsymbol{\lambda}) - \mathbf{K}_D\dot{\boldsymbol{\Delta}} \tag{5}$$

$$\dot{\boldsymbol{\lambda}} = \mathbf{K}_I(\boldsymbol{\Delta} - \boldsymbol{\lambda}) \tag{6}$$

where the vector

$$\boldsymbol{\lambda} = [\lambda_1, \lambda_2, ..., \lambda_n]^T, \tag{7}$$

can be interpreted as a dynamically evolving estimation of $\boldsymbol{\Delta}$ values corresponding to the funicular shape. The entries of the n-by-n matrices $\mathbf{K}_P$, $\mathbf{K}_D$, $\mathbf{K}_I$ are gain parameters of the controllers. Within this framework, the success of shape control depends on the values of the $3n^2$ gain parameters.

The performance of the controller can be investigated by testing convergence using numerical simulations, however the result depends on the initial state of the simulation, which requires systematic investigation with many initial conditions. Alternatively, the linear stability of the funicular state can be tested by linearization and numerical evaluation of the eigenvalues of the Jacobian matrix. This semi-analytical process is straightforward [10] and provides information about the local behaviour of the controller in a small neighborhood of the target state.

3.2 Local and nonlocal control

In our previous work, as well as in a companion paper of the same authors [11], we investigate the special case when the matrices $\mathbf{K}_P$, $\mathbf{K}_D$, $\mathbf{K}_I$ are diagonal. This means that each actuator is independent: actuator i uses the locally measured Δ_i value as input and its action depends on the internal state variable λ_i. Hence we refer to this case as *local control*. The paper [11] concludes that the compressive shape can be stabilized by appropriately large and positive diagonal values in $\mathbf{K}_P$, positive diagonal values in $\mathbf{K}_D$, and sufficiently small, negative

values in $\mathbf{K}_I$. The potential benefits of adding off-diagonal elements to the gain matrices, i.e. non-local control have not been investigated.

For an illustration, Figure 2 shows a structure with unit masses ($m_1 = m_2 = 1$) and bar lengths ($l_1 = l_2 = 1$) subject to horizontal load $\mathbf{F}_1 = \mathbf{F}_2 = (-1, 0)$ which has a compressive funicular configuration at $\alpha_1 = \alpha_2 = 0$ (unknown for the control system). Initial conditions are set as $y_0 = [\alpha_1, \alpha_2, \dot{\alpha_1}, \dot{\alpha_2}, \bar{\lambda_1}, \bar{\lambda_2}]^T = [\pi/6, \pi/6, 0, 0, \pi/6, 0]^T$. The controller gains are and the simulation shows convergence to the target shape.

$$\mathbf{K}_P = \begin{bmatrix} 5 & 0 \\ 0 & 5 \end{bmatrix}; \mathbf{K}_D = \begin{bmatrix} 1 & 0 \\ 0 & 1 \end{bmatrix}; \mathbf{K}_I = \begin{bmatrix} -0.02 & 0 \\ 0 & -0.02 \end{bmatrix} \tag{8}$$

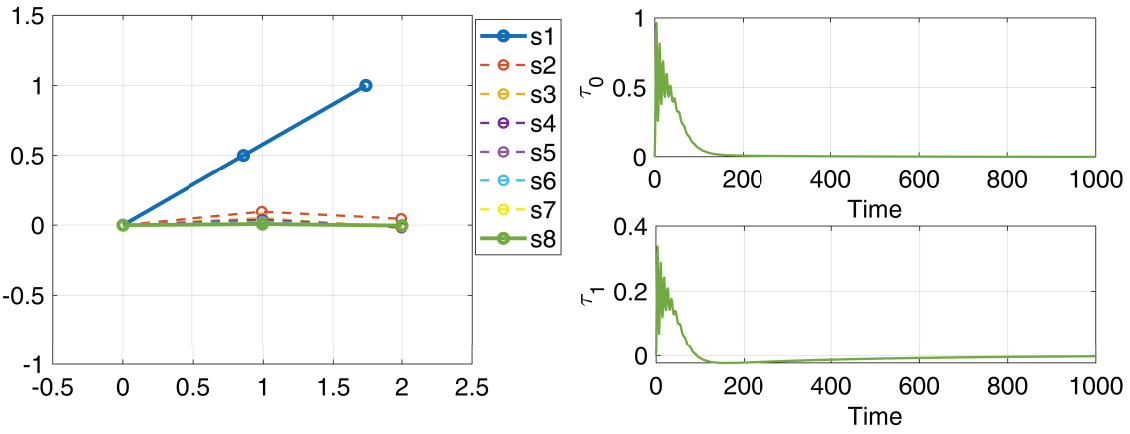

Figure 2: Snapshots of the simulated shape evolution of a 2-degree-of-freedom (2-DOF) fully actuated cantilever with local control, transitioning from initial conditions (blue solid line) to the final configuration (green solid line) (left). On the right, the corresponding torques τ_0 and τ_1 are plotted as functions of time.

3.3 Number of actuators

Previous works on funicular shape control have assumed that all actuators are active. As the system has as many degrees of freedom as the number of actuators, this assumption corresponds to *full actuation* in the terminology of control theory. One can also attempt to stabilize a target state by using less actuators, which gives rise to an *underactuated* system. In general, the stabilization of unstable, underactuated systems is usually considered to be a notoriously difficult task. A popular example of underactuated control is the task of balancing an inverted double pendulum using torques or horizontal displacements at the base [12]. Indeed the balancing task is a special case of our problem, where the external load, and the target shape are specified in advance (both are vertical), and thus PD or PDA controllers without I control suffice.

If we relax the assumption of a known target shape, the addition of I control becomes essential. We made systematic attempts to stabilize the system with $n = 2$ bars using a single actuator

at the base, but our numerical results suggested that local control (even with I control) always fails. However we have been able to find examples, where non-local control ensures linear stability. Figure 3 illustrates the same problem introduced in section 3.2 but now actuation occurs only at node 0, initial conditions are set as $y_0 = [5\pi/180, 5\pi/180, 0, 0, 5\pi/180, 5\pi/180]^T$ and PID control is used with gain parameters:

$$\mathbf{K}_P = \begin{bmatrix} -10 & -25 \\ 0 & 0 \end{bmatrix}; \mathbf{K}_D = \begin{bmatrix} -50 & -25 \\ 0 & 0 \end{bmatrix}; \mathbf{K}_I = \begin{bmatrix} 5 & 0 \\ 0 & 2 \end{bmatrix} \tag{9}$$

The structure possesses linear stability, which is conformed by numerical simulation results. Note that underactuation is reflected by the 0 values in the second rows of $\mathbf{K}_P$ and $\mathbf{K}_D$ ensuring $\tau_1 = 0$.

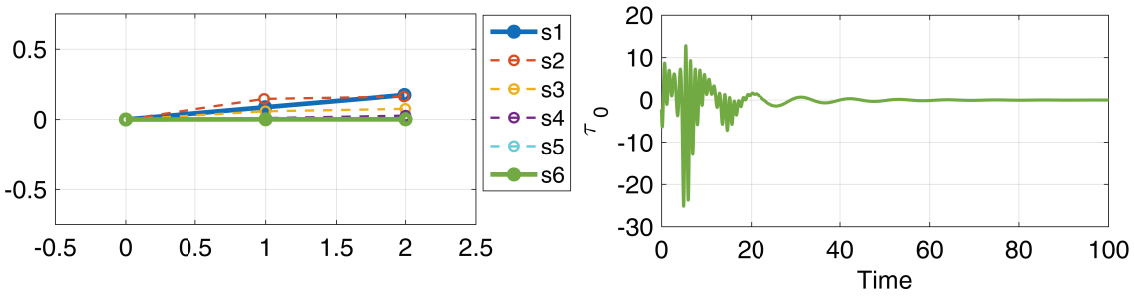

Figure 3: Snapshots of simulated shape evolution towards a pure compression funicular shape of a 2-Dof underactuated cantilever bar with non-local control (left) and torque τ_0 as a function of time (right).

3.4 Energy balance of actuation

We now investigate the mechanical power of the actuator in the case of local control. Firstly, local P control with positive gain parameters is equivalent to the effect of torsional springs with linear torque-angle characteristics. Hence P control in itself is conservative, and acts like a virtual bending stiffness. Similarly, local D control with positive gains is equivalent to torsional dampers with linear torque-angular velocity characteristics at the joints, which are always dissipative. Hence, the crucial role of D control is vibration absorption in this case. Finally, local I control can be understood as a dynamically evolving unstressed angle of the torsional springs mentioned above. It is easy to see that positive integral gains are equivalent to a passive relaxation behavior of those springs, which is dissipative. These findings imply that local control with nonnegative gains in all components is dissipative. It is straightforward to show that for conservative external loads, a dissipative controller cannot stabilize those configurations, which would be unstable without control.

In contrast, local control with positive P and D but negative I gains represents a damped torsional spring with 'anti-relaxation', which is an active behaviour, and which proved succesful in stabilization tasks (see Figure 2 for an example).

The analogy with springs and dampers is not applicable to non-local control, thus the signs of controller gains do not have a simple, intuitive meaning.

4 DISCUSSION

This work investigated shape control of cantilever structures towards an unspecified target, which is a model problem incorporating load-induced deformation, the risk of dynamic instability and the challenge of limited sensor data. We proposed a distinction between fully actuated and underactuated systems, as well as between local and non-local PID control strategies. It has been demonstrated by an example that non-local control has a potential application to the shape control of underactuated structures, where local control appears to fail.

While reducing the number of actuators is certainly a promising direction towards the economical design of smart structures, one needs to asses the added risk and vulnerability carefully. As we have pointed out, local control is equivalent to the application of torsional springs with time-dependent stress-free angles, and torsional dampers. This analogy suggest the use of actual springs and dampers in physical implementations, in which case the tunable stress-free angle is the only remaining active component in the system. This setup is *semi-active*, which means that a carefully designed actuator can preserve partial functionality in the case of power outage, or failure of the active component. Semi-activity is an important step towards safe, and failure tolerant design. According to the authors knowledge, non-local control does not offer the possibility of semi-active implementation. These initial results suggest that further investigation is needed to understand the optimal number of actuators and the best type of control strategy from a structural designer's perspective.

ACKNOWLEDGMENT

This work has been supported by the National Research, Development and Innovation Fund of the Ministry of Culture and Innovation of Hungary under project K143175.

REFERENCES

[1] O. Yasa, Y. Toshimitsu, M. Y. Michelis, L. S. Jones, M. Filippi, T. Buchner, and R. K. Katzschmann, "An overview of soft robotics," *Annual Review of Control, Robotics, and Autonomous Systems*, vol. 6, no. 1, pp. 1–29, 2023.

[2] D. E. Moulton, H. Oliveri, and A. Goriely, "Multiscale integration of environmental stimuli in plant tropism produces complex behaviors," *Proceedings of the National Academy of Sciences*, vol. 117, no. 51, pp. 32 226–32 237, 2020.

[3] S. Weidner, C. Kelleter, P. Sternberg, W. Haase, F. Geiger, T. Burghardt, C. Honold, J. Wagner, M. Böhm, M. Bischoff *et al.*, "The implementation of adaptive elements into an experimental high-rise building," *Steel Construction*, vol. 11, no. 2, pp. 109–117, 2018.

[4] R. Guclu, "Sliding mode and PID control of a structural system against earthquake," *Mathematical and Computer Modelling*, vol. 44, no. 1-2, pp. 210–217, 2006.

[5] N. Djedoui, A. Ounis, and M. Abdeddaim, "Active vibration control for base-isolated structures using a PID controller against earthquakes," *International Journal of Engineering Research in Africa*, vol. 26, pp. 99–110, 2016.

[6] W. Sobek and P. Teuffel, "Adaptive systems in architecture and structural engineering," in *Smart structures and materials 2001: Smart systems for bridges, structures, and highways*, vol. 4330. SPIE, 2001, pp. 36–45.

[7] P. L. Várkonyi and A. F. Guerra Riaño, "From swinging cables to adaptive funicular structures in architecture," in *2022 IEEE 20th Jubilee International Symposium on Intelligent Systems and Informatics (SISY)*. IEEE, 2022, pp. 169–174.

[8] A. F. Guerra Riaño and P. L. Várkonyi, "Shape control of adaptive funicular structures," in *X ECCOMAS Thematic Conference on Smart Structures and Materials SMART 2023*. Eccomas Proceedia, 2023, pp. 679–690.

[9] D. O'Dwyer, "Funicular analysis of masonry vaults," *Computers & Structures*, vol. 73, no. 1-5, pp. 187–197, 1999.

[10] V. I. Arnold, *Ordinary differential equations*. Springer Science & Business Media, 1992.

[11] A. F. Guerra Riaño and P. L. Várkonyi, "Stability analysis of adaptive funicular structures," in *XI ECCOMAS Thematic Conference on Smart Structures and Materials SMART 2025*.

[12] O. Boubaker, "The inverted pendulum benchmark in nonlinear control theory: a survey," *International Journal of Advanced Robotic Systems*, vol. 10, no. 5, p. 233, 2013.

Part VII
MS 06 - FUNCTIONAL AND NON-LINEAR METAMATERIALS

Andrea Bergamini, Bart Van Damme, Nikolaos Karathanasopoulos

XI ECCOMAS Thematic Conference on Smart Structures and Materials - SMART 2025
M. Krommer, M. Nader and M. Schagerl (Eds)

Received: 22 April 2025 / Revised: 15 October 2025 / Accepted: 19 October 2025
© The Author(s) 2025

Electro-Mechanical Coupling in Compliant Dielectric Elements with Bias Voltage

Andrea E. Bergamini, Alexandre Brun d'Arre, Patrick Danner, Dorina Opris, Bart Van Damme

Abstract. Among smart materials, piezoelectric materials occupy a very prominent position for sensing and actuation functions. Combined with simple or more advanced shunts, they are also proposed in various vibration mitigation schemes. In recent work, we have demonstrated the implementation of frequency-dependent stiffness in structural elements, using resonantly shunted piezoelectric devices. However, the selection of available piezoelectric materials is mainly limited to ceramics (with an elastic modulus in the order of $10^{10}Pa$ (e.g. PZT ceramics) and a few polymer materials, with elastic modulus in the range of $10^{9}Pa$ (e.g. PVDF). In both cases, the high mechanical impedance and, consequently, the small dynamic strains limit the application of these materials to stiff structures. In this contribution, we discuss using a bias voltage to polarize dielectric materials and thereby compensate for the lack of spontaneous polarization observed in piezoelectrics. This enables access to materials with a wider range of elastic properties, such as soft elastomers, like poly(dimethylsiloxane). As an example, we present a practical implementation of a silicone rubber membrane used as a highly compliant dynamic converter.

Key words: Smart Structures, Multiphysics Problems, Materials, Computing Methods

1 INTRODUCTION

Energy coupling between the mechanical and electrical domain using smart materials offers a host of possibilities, ranging from strain and vibration sensing to shape morphing and energy harvesting. Piezoelectric materials hold a prominent position in this field, due to their excellent coupling coefficients (e.g. Lead Zirconate Titanate ceramics PZT) and are widely used in applications ranging from consumer goods to precision instruments.

Andrea E. Bergamini & Alexandre Brun d'Arre & Bart Van Damme
Empa-Materials Science and Technology, Acoustics/Noise Control, Ueberlandstrasse 129, CH-8600 Duebendorf, Switzerland, e-mail: andrea.bergamini@empa.ch

Patrick Danner & Dorina Opris
Empa-Materials Science and Technology, Functional Polymers, Ueberlandstrasse 129, CH-8600 Duebendorf, Switzerland

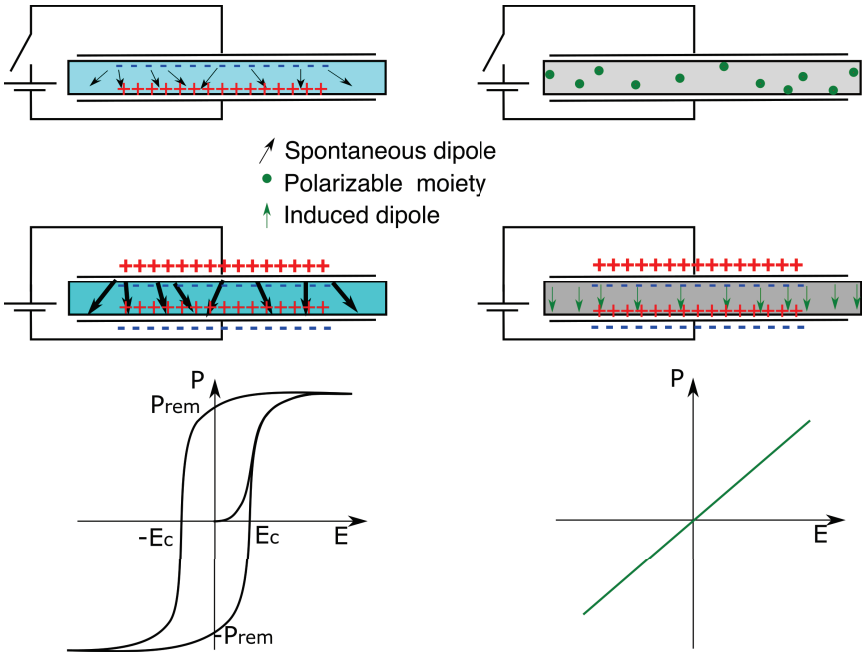

Figure 1: Piezo-electric materials (left) are characterized by the presence of spontaneous dipoles that are oriented during the polarization process. In linear dielectrics (right), dipoles are induced by external fields but are not present in absence of electric fields.

The material properties of ceramic piezoelectrics make them ideal candidates for applications in stiff structures with a high mechanical impedance, where the strains, that the piezoelectric elements are subjected to, are compatible with the modest strain capacity of the materials ($\varepsilon_{failure} \approx 1‰$ [1]). However, in some cases, small impedance values and large strains are desirable. For example coupling acoustic power into electrical circuits or providing frequency dependent stiffness capabilities in the sense of what we presented in recent work [2] to systems subject to large strains would benefit from electromechanical coupling elements with substantially lower elastic modulus E than ceramics ($E_Y \approx 70$ GPa [3]) or engineering polymers, such as PVDF ($E_Y \approx 2.5$ GPa [4]).

While recent efforts [5] have led to the development of piezoelectric elastomers, here we present the use of an external bias voltage to achieve macroscopic polarization of elastomer membranes to realize electromechanical coupling, as a less material-dependent alternative to highly specialized materials. This approach warrants great flexibility in selecting dielectric materials, based on their elastic properties, and allows for tuning the polarization and electromechanical coupling, via the applied bias voltage. Figure 1 shows a conceptual comparison between the spontaneous polarization of ferroelectrics and the polarization from applied bias voltage.

In piezoelectric materials (polarization curve shown in the bottom left of fig1), the spontaneous dipoles observed at $E = 0$ V/m are structurally coupled to the strain of the material, via

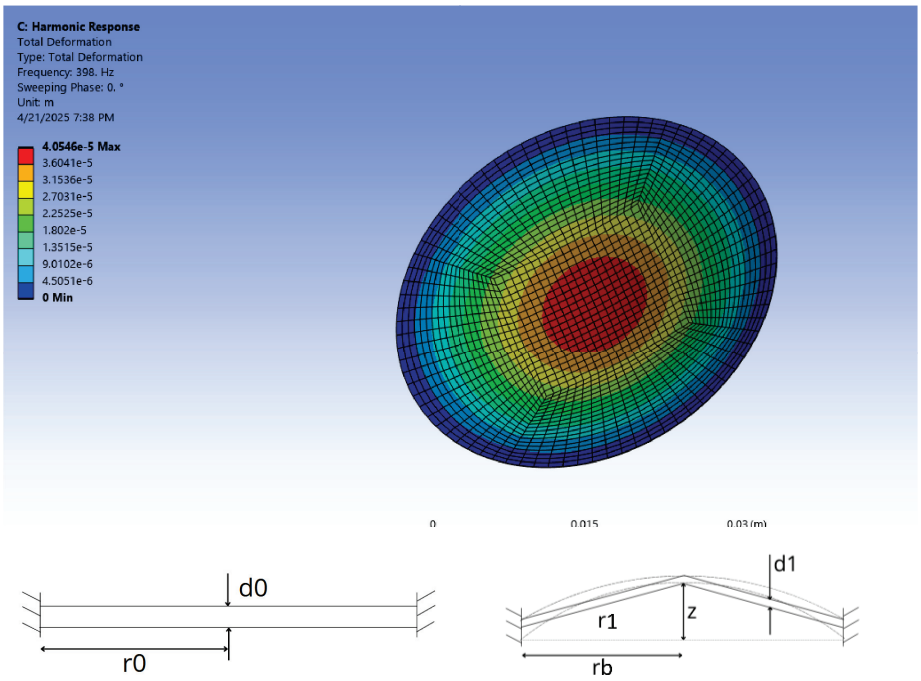

Figure 2: Shape corresponding to the 1st mode of the membrane at a frequency of approximately 308 Hz (top), shown for illustration purposes, only. The change of surface area and thickness, based on the assumption of volume invariance, leads to a variation of the membrane's capacitance.

the distance between the centers of charge in the crystal (such as in the PZT Perovskite structure), making the polarization strain dependent. In a linear dielectric however, no spontaneous polarization is observed. Dipoles can be generated by applying an external field E, as shown in figure 1. In the presence of a bias electric field, the deformation of a compliant dielectric will cause a change of the polarization of the system associated with the change of its capacitance. Consequently, as a harmonic load deforms the dielectric, a current will flow to the electrodes to balance the charges to satisfy $Q(t) = C(t) \cdot V_{bias}$, where $Q(t)$ is the charge accumulated on the electrodes, $C(t)$ is the time variable capacitance of the device, and V_{bias} is the applied bias voltage, see eq. (1).

In this document, we describe models of and experiments on thin, compliant dielectric membranes, subject to a static bias voltage, and their coupling to an acoustic pressure field. The system discussed here is the most basic component of different devices that can be assembled from it: Arrays of membrane elements allow to couple acoustic energy into the electrical domain over larger areas, while stacking compliant membranes are customarily used as stacked transducers [6].

2 MODELLING

The top panel of Figure 2 shows the membrane mode targeted in this work aiming at coupling acoustic power into the the electrical domain. The origin of the coupling is the change of capacitance of the membrane caused by its deformation. Here, we present an approximation of the capacitance variation as a function of the out of plane deflection. The indices in the bottom two panels of figure 2 refer to the following membrane states:

- index 0: undeformed, non-strained membrane, with known radius r_0 and thickness d_0,
- index a: undeformed, strained membrane, with known radius r_a (not shown in Fig2, as essentially identical to the drawing with index $_0$),
- index b: undeformed, strained and clamped membrane, with known radius r_b not shown in Fig2, as essentially identical to the drawing with index $_0$), and
- index 1: deformed, strained and clamped membrane, with known deflection $z(t)$.

The deformed shape of the membrane is approximated as a cone with height $z(t)$. Based on these geometrical quantities and the capacitance C_0, in the undeformed state, the current flowing the electrodes to account for variation of the capacitance is:

$$I_1(t) = 4VC_0\frac{r_a^2}{r_0^4}\left(1+\frac{z(t)^2}{r_b^2}\right)z(t)\frac{dz(t)}{dt} \tag{1}$$

Here, C_0 is the capacitance of the undeformed membrane, V is the applied voltage, and $z(t)$ is the out-of-plane displacement of the center of the membrane. In correspondence with the first vibration mode of the membrane, large displacement amplitudes of the center are expected to cause large capacitance variations.

3 EXPERIMENTS

3.1 Sample Preparation

The preparation of the samples includes the pre-stretching of the membrane, its fixation on an external frame, the application of thin electrodes, and the preparation of connections to the voltage source. The workflow for the preparation is well established and is carried out with tools and materials developed in the laboratory for the purpose. The photographs in figure 3 show the main steps in the preparation of a transducer: 1) The silicone membrane is positioned in the iris device and adhered to the eight movable tabs. 2) The movable tabs are shifted to strain the membrane radially (here shown at the maximum radial displacement). 3) A rigid frame is positioned in contact with the membrane to take up radial stress. 4) After the membrane is fixated on the frame with an adhesive, thin ($\approx 20nm$) gold electrodes are sputtered. Aluminium foil leads were then applied and connected to the two faces.

1)  2) 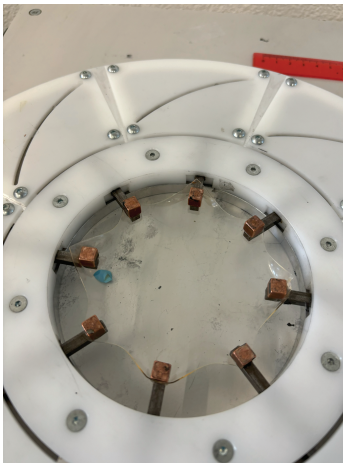 3) 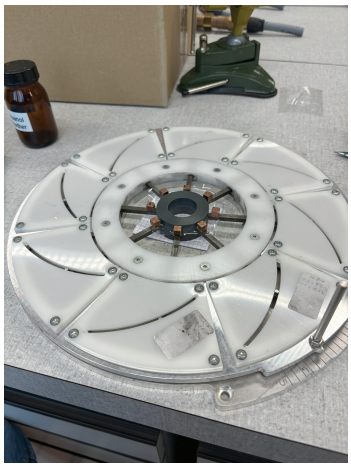

4) 

Figure 3: From top left to bottom: the main phases of the preparation of the elastomer transducers as described in the text.

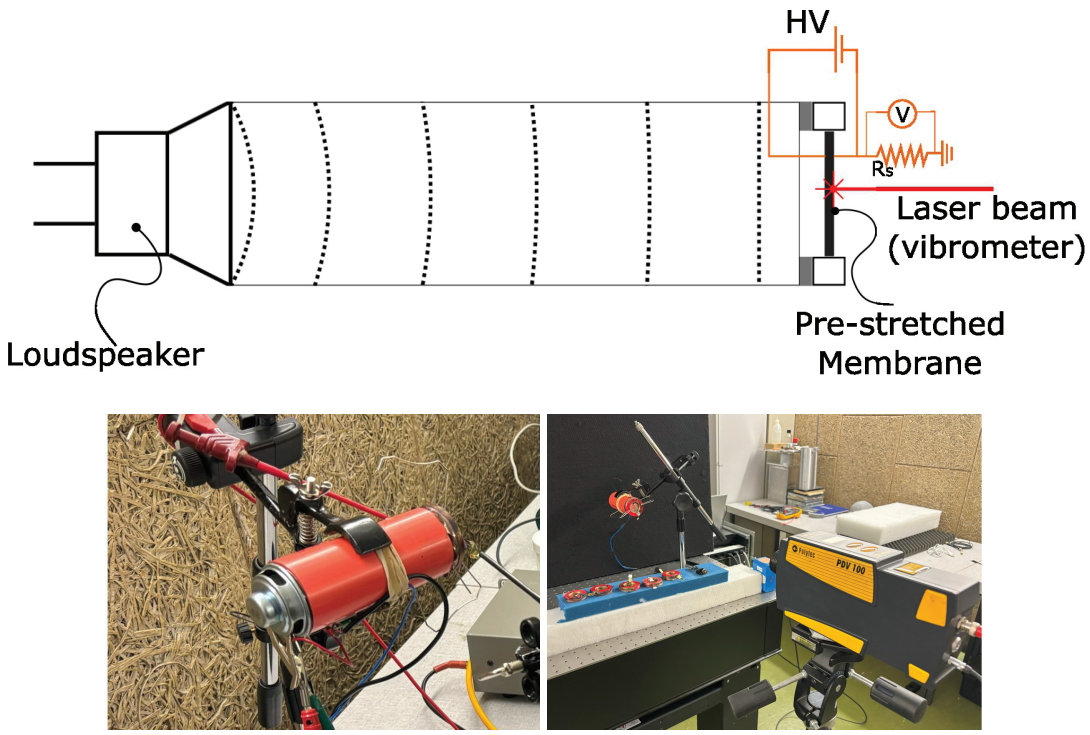

Figure 4: Schematic representation of the test setup (top) and images showing the speaker (bottom left) and a membrane being tested, and the complete setup (bottom right.)

3.2 Test Setup

In the experiments, an acoustic wave was shone onto the membrane from a speaker attached to a 200 mm long polymer tube, as schematically shown in the top of figure 4. The speaker was driven by a Thomann t.amp E400, connected to the analog output of a NI PXI data acquisition system. The membrane under test was positioned at the opposite end of the pipe. A laser Doppler vibrometer (LDV, Polytec PDV-100) was used to monitor the velocity of the center of the membrane. A high voltage power supply (Stanford Research Systems PS350) was connected to the leads to the membrane to apply the necessary bias voltage. A 1 MΩ shunt resistor R_s between the outer electrode and ground was used to measure the capacitance dependent current flowing to the biased membrane.

3.3 Measurements

Tests were performed with a sine sweep signal of 5 s duration spanning the frequency range 0-1200 Hz. Within this range, the frequency response of the speaker and the amplifier were assumed to be linear. No measurement of the acoustic pressure within the tube was carried out. The membrane velocity, recorded with the LDV, the shunt voltage, and the voltage signal driving the speaker were measured with a rate of 20 kS/s. Tests were at various bias voltage

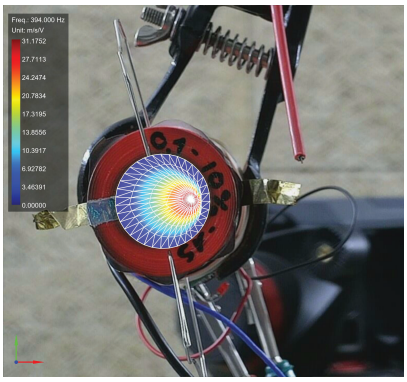

Figure 5: 1st membrane mode of a $100\mu m$ membrane with a 10% pre-stretch, as recorded with a scanning laser vibrometer.

levels ranging from 0 V to 1000 V for membranes with two different levels of pre-stretch, $\varepsilon = 0.1$ and $\varepsilon = 0.2$.

4 RESULTS AND DISCUSSION

The comparison of the model for a 100 μm thickness and a pre-stretch of 10% in radial direction shows a satisfactory match for the first membrane mode, as a comparison of figure 5 (recorded with an Optoscan laser scanning vibrometer) with the shape shown in figure 2.

Figure 6 shows an overview of the quantities measured for the assessment of the electromechanical coupling capability of the biased membranes. From top to bottom: signal driving the loudspeaker in the setup, velocity measured with a single point vibrometer at the center of the membrane, voltage measured over the shunt resistor, shunt-to-driving voltage transfer function.

From these measurements, it is possible to gain some insights into the coupling of acoustic into electrical power in the systems under consideration. Here, we consider two membranes, both prepared with a pre-stretch $\varepsilon = 0.2$ and thickness of 100 μm and 200 μm. In both cases, the bias voltage was varied between 0 V and 1000 V, as indicated in the legends of the respective images.

The top left panel in the respective figures7 and 8 shows the velocity/driving voltage (as a proxy for the acoustic pressure) transfer function. This indicates a clear resonance at approximately 443 Hz and 415 Hz for the membrane with $100\mu m$ and $200\mu m$ thickness, respectively. The transfer functions are essentially identical for all bias voltage values. This indicates that the electric field resulting from the potential applied across the membranes is not sufficient to deform them in an appreciable manner, and consequently affect the membrane tension related to the applied pre-stretch. Assuming a nearly incompressible behavior of the silicone, a radial stretch of 20% leads to a thickness reduction of 30%. Accordingly the field across the 100 μm membrane will be ranging from 0 V/m to 14.4 MV/m, fairly modest values as compared to the fields of the order of 100 MV/m [7] applied to modify the resonant frequency of similar

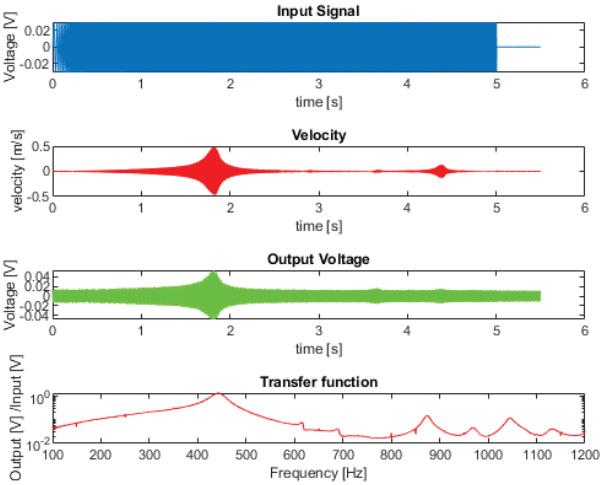

Figure 6: Overview of the measured signals and a transfer function derive from them.

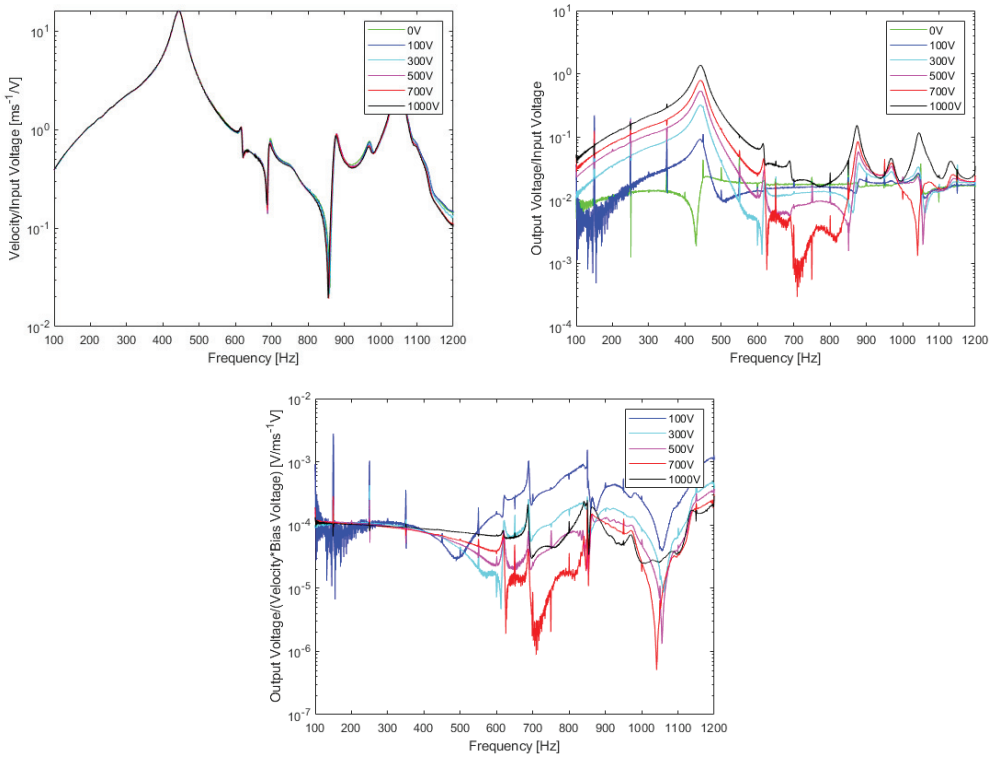

Figure 7: Overview of the measured signals and a transfer function derived from them. Membrane thickness: 100 μm, pre-stretch $\varepsilon = 0.2$

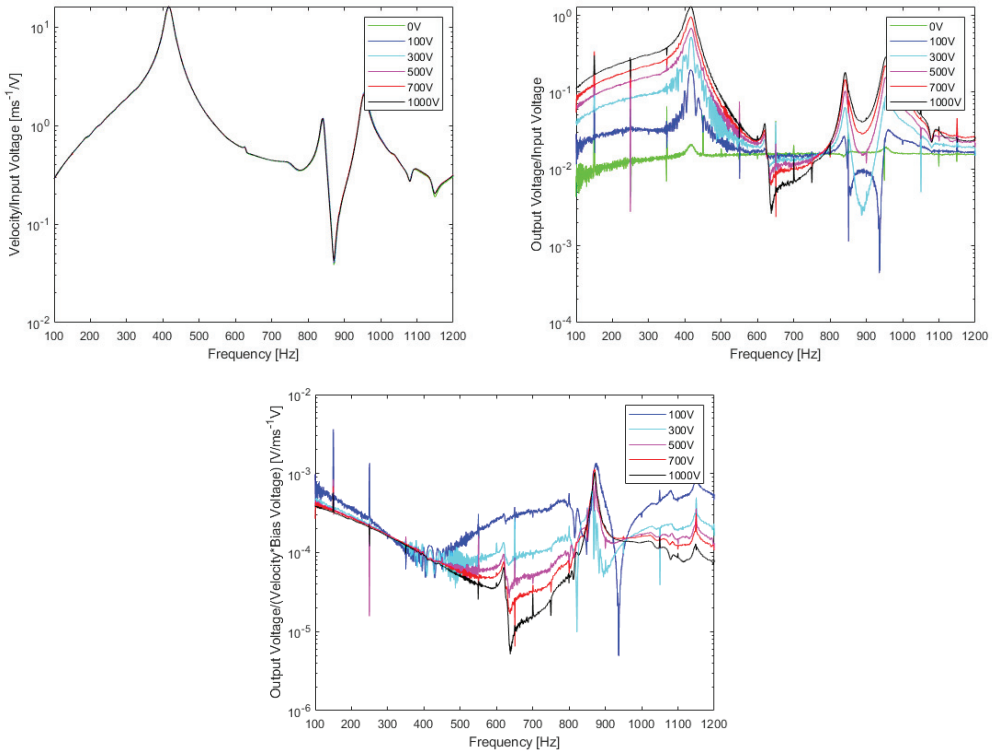

Figure 8: Overview of the measured signals and a transfer function derived from them. Membrane thickness: 200μ m, pre-stretch $\varepsilon = 0.2$

membranes.

The shunt voltage/driving voltage transfer functions shown in the top right plots of the two figures show a clear sensitivity to the applied bias voltage. This observation is compatible with the relation described in (1). The final plots in the two pictures report the measured voltages normalized with the velocity amplitude and the applied voltage. The resulting quantity relates to the straining of the membrane to the voltage measured over the shunt, which is proportional to the current. As the transfer functions for the respective membranes are essentially identical, we can assume that the terms of (1) containing $z(t)$ are not affected by the bias voltage. This is especially the case for the thinner membrane. However, for the thicker membrane, the coupling term shows a frequency dependent behavior.

5 CONCLUSIONS

The experiments described in this work show that the combination of thin dielectrics with an externally applied bias voltage show coupling power between domains similar to a piezoelectric material. However, the mechanism at the base of the observed flow of current are different than in piezoelectric crystals with spontaneous electric dipoles. In the membranes we investigated,

the electric field acting on them was approximately one order of magnitude smaller than the fields typically reported for actuation applications. Hence, the observed coupling did not affect the mechanical response of the system.

In both possible applications outlined in the introduction (meta-surface and stack actuator), the ability to functionalize a soft dielectric material to achieve electromechanical coupling offers new possibilities where stiffer and more brittle materials, such as ceramics (or dielectric polymers, such as PVDF) do not fulfil requirements such as the need to undergo large strains or to match the mechanical impedance to a specific application (e.g. in acoustics). Additionally, the experiments discussed here show the ability to tune the coupling coefficient of the elements by varying the level of applied bias voltage. This additional degree of freedom can be used to adapt the response of smart systems.

REFERENCES

[1] D. Munz, T. Fett, S. Mueller, and G. Thun, "Deformation and strength behavior of a soft pzt ceramic," in *Smart Structures and Materials 1998: Mathematics and Control in Smart Structures*, vol. 3323. SPIE, 1998, pp. 84–95.

[2] B. Van Damme, R. Weber, J. U. Schmied, A. Spierings, and A. Bergamini, "Implementation of tunable frequency-dependent stiffness elements via integrated shunted piezoelectric stacks," *Smart Materials and Structures*, vol. 33, no. 7, p. 075037, 2024.

[3] A. Bouzid, E. Bourim, M. Gabbay, and G. Fantozzi, "Pzt phase diagram determination by measurement of elastic moduli," *Journal of the European Ceramic Society*, vol. 25, no. 13, pp. 3213–3221, 2005.

[4] I. Y. Dmitriev, S. Gladchenko, V. Lavrent'ev, O. Praslova, and G. Elyashevich, "Dependence of the dielectric constant on the structure of extruded polyvinylidene fluoride films," *Russian journal of applied chemistry*, vol. 79, pp. 642–646, 2006.

[5] F. Owusu, T. R. Venkatesan, F. A. Nüesch, R. M. Negri, and D. M. Opris, "How to make elastomers piezoelectric?" *Advanced Materials Technologies*, vol. 8, no. 15, p. 2300099, 2023.

[6] G. Kovacs, L. Düring, S. Michel, and G. Terrasi, "Stacked dielectric elastomer actuator for tensile force transmission," *Sensors and actuators A: Physical*, vol. 155, no. 2, pp. 299–307, 2009.

[7] L. Dong, M. Grissom, and F. T. Fisher, "Application of bias voltage to tune the resonant frequency of membrane-based electroactive polymer energy harvesters," in *Energy Harvesting and Storage: Materials, Devices, and Applications VII*, vol. 9865. SPIE, 2016, pp. 96–110.

XI ECCOMAS Thematic Conference on Smart Structures and Materials - SMART 2025
M. Krommer, M. Nader and M. Schagerl (Eds)

Received: 29 April 2025 / Revised: 14 August 2025 / Accepted: 19 October 2025
© The Author(s) 2025

Metamaterial Inspired Vibration Damping System for Rotors

Ankur Dwivedi, Tanuj Gupta, Bishakh Bhattacharya

Abstract. Considering the key applications of rotors in aerospace, manufacturing industry, and transport systems, this study pertains to the reduction of vibration amplitude in a rotor using mechanical metamaterial-inspired unit cells. We propose a spider-web-based metamaterial unit cell for reducing rotor vibration by shifting the critical speed of a flexible rotor system. This approach is based on investigating the vibration absorption characteristics of the spider-web-based metamaterial unit cell. By integrating this unit cell geometry into a rotor, the metastructure is designed and analyzed numerically, with experimental validation. The metamaterial unit cells facilitate amplitude reduction around their natural frequencies and are influenced by local resonances within the unit cell structure. Using finite element analysis, we simulated the frequency response function of a shaft equipped with the proposed spider-web-based metamaterial unit cell, confirming the effect of these unit cells and resulting in a reduction of vibration amplitude. Further, using a single-point laser displacement sensor, the experiments were conducted by measuring vibration responses at various rotating speeds of the rotor to visualize the amplitude reduction of the metashaft. A comparison of the harmonic response of the shaft and metashaft (shaft-unit cell assembly) is conducted and found to reduce the amplitude of vibration by 40 $\%$.

Key words: Metashaft, Metamaterials, Metastructures, Spider-web, Rotors, Vibration control

1 INTRODUCTION

Vibration in rotating components is a major concern in industries, as it directly affects the performance, safety, and longevity of critical systems like engines, turbines, and rotor assemblies. For instance, aircrafts operate under extreme conditions, where rapid environmental changes and high-speed forces can cause uncontrolled vibrations. It can lead to structural fatigue, reduced efficiency, and, in extreme cases, catastrophic failure of the essential parts. The most dangerous phenomenon related to vibration is resonance, which occurs when the natural frequency of a component aligns with the rotational frequency of the engine. Thus, effective

Ankur Dwivedi & Tanuj Gupta & Bishakh Bhattacharya
Smart Materials, Structures and Systems Laboratory, Department of Mechanical Engineering, Indian Institute of Technology Kanpur, Uttar Pradesh, 208016, India, e-mail: ankudwi@iitk.ac.in

vibration control is essential to ensure the reliability and safety of any rotating mechanical system. To combat these challenges, the aircraft industry employs several strategies for vibration control, such as dynamic balancing, which ensures even weight distribution in rotating components, minimizing imbalances that can cause excessive vibration. However, for flexible rotors, dampers, isolators, and advanced vibration monitoring systems are used to absorb energy and detect early signs of vibration issues. The choice of materials also plays a vital role, with modern engines using materials that offer high fatigue resistance and vibration-dampening properties.

By carefully managing vibrations through design, material selection, and monitoring, the performance, safety, and durability of critical components in rotating systems can be enhanced. In this effort, metamaterials can play a pivotal role as mechanical metamaterials are highly effective in damping vibrations due to their unique ability to manipulate and control elastic waves through structural design rather than material composition alone [1, 2]. Metamaterials have applications in creating invisibility cloaks, super lenses for high-resolution imaging, improved antennas, noise-cancellation technologies, and controlling various types of waves, including electromagnetic, sound, and seismic waves [3, 4]. One key feature of metamaterials is their ability to create bandgaps, which are frequency ranges where elastic waves, including mechanical vibrations, are blocked or significantly reduced [5, 6]. These bandgaps arise from the periodic arrangement of the metamaterial unit cell structures, which interfere with incoming waves in specific ways [7]. When a vibration falls within this frequency range, it is either reflected or absorbed by the metastructure, preventing the transmission of mechanical vibrations. This capability is especially useful in industries where specific vibrations can cause damage or affect performance, such as in buildings, bridges, or machinery.

Mechanical metamaterials-inspired unit cells can act as vibration absorbers in rotor dynamics. Hence, researchers have used metamaterials to mitigate mechanical and sound vibrations. Xu et al. have investigated the vibration characteristics of multi-acoustic metamaterial rotors by incorporating geometrical nonlinearity [8]. Their theoretical and numerical findings provide valuable insights into optimizing rotor designs for improved stability and reduced vibration in rotor systems. In another study, the authors proposed an elastic metamaterial (EM) shaft with discretized arc-shaped rubber layers, which shows excellent low-frequency vibration properties [9]. It was concluded that the proposed EM shaft exhibits much lower band gaps than the corresponding structures with the whole rubber ring. In a similar study, Li et al. numerically investigated the band gap behavior of a novel EM shaft with discretized arc-shaped scattering layers [10]. The dispersion relations and frequency response function (FRF) were calculated by considering multi-layered locally resonant ring oscillators in which soft rubber layers are covered by hard scattering layers. The proposed design produced broader band gaps at much lower frequencies but with $34\ \%$ reduced weight when compared to the conventional multi-layered EM shaft without discretization. Further, the authors also designed an inerter-enhanced meta-shaft to suppress torsional vibrations in a rotor system [11]. By numerical simulations and experiments, the study concluded that compared to traditional absorbers, the inerter-enhanced

meta-shaft is lighter and offers better vibration isolation. In the literature, Ruan et al. examined the wave propagation properties of a spider-web-like hierarchical acoustic metamaterial [12]. Through numerical simulations and theoretical analysis, the authors investigated the impact of the hierarchical designs on acoustic wave propagation. Their findings suggest potential applications in noise reduction, sound insulation, and vibration control in various engineering fields. Inspired by this, we propose a spider-web-based metamaterial unit cell design for damping mechanical vibrations in a rotor system. We numerically simulate the rotor system integrated with spider-web-based metamaterial unit cells and also perform the experiments on a test rig. The following sections provide detailed information about design, numerical simulation, and experimentation on the metashaft rotor system.

2 DESIGN OF THE METASHAFT

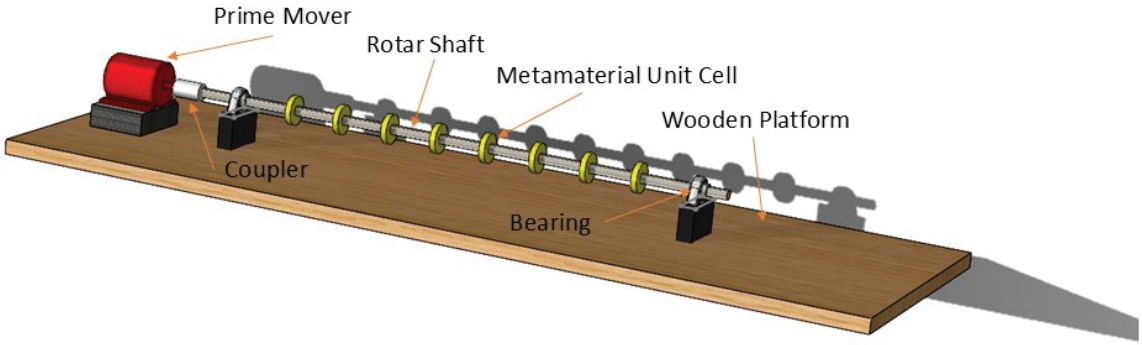

Figure 1: A schematic CAD model of the metashaft depicting the metamaterial-inspired unit cells integrated on a shaft. The metashaft is driven by a prime mover, and the complete system is mounted on a platform.

To investigate the effect of metamaterials-based unit cell integration in a rotor system, we design and fabricate an assembly of a shaft and metamaterial-inspired unit cells (metashaft) and other mountings that can dampen the vibrations of the rotor system during operation. Before proceeding with the physical setup, a detailed CAD model of the assembly is created to finalize the design of each component. As shown in figure 1, it includes the shaft, platform, and metamaterial unit cells, ensuring that all parts fit together properly and function as intended. The CAD model helps in freezing the dimensions and geometries of the components before fabrication.

2.1 Rotor shaft

The tested rotor can be considered as a horizontal slender cylindrical beam with uniformly distributed mass, subjected to forces applied perpendicularly to the axis of the shaft. As per the Euler-Bernoulli beam theory (EBT) assumption, we may consider that any plane cross-section

Table 1: RPM for transverse frequency modes corresponding to different shaft diameters

Shaft Diameter (mm)	Mode 1 (RPM)	Mode 2 (RPM)
10	761	3046
12	1096	4387
14	1492	5971
16	1949	7799
17	**2071**	**8287**
18	2467	9871
20	3046	12187
22	3686	14746
24	4387	17549
26	5148	20596

of a slender beam remains plane and normal to the longitudinal axis during small bending. This assumption simplifies the solution of the equation of motion to extract the natural frequencies and mode shapes of the shaft under study. Following this theory and applying simply supported boundary conditions in the modal solution, provides the natural frequency associated with each normal transverse mode from the below-mentioned expression[13].

$$\omega_b = \beta^2 \sqrt{\frac{EI}{\rho A}} \tag{1}$$

where for the simply supported boundary condition $\beta = \frac{n\pi}{l}$. l is the length of the shaft, n is the mode number, E is the Young's Modulus, I is the moment of inertia, ρ is the density of the shaft material and A is the cross-sectional area. Therefore, the natural frequency in each mode can be calculated for different shaft diameters as compiled in Table 1.

We can plot shaft transverse frequencies for different shaft diameters as depicted in figure 2. This implies that as we increase the diameter of the shaft, the natural frequency in each mode increases. Table 2 shows the parameters for solid and hollow shafts with natural frequencies in different modes. By analyzing the shaft parameters in tables 1 and 2, we choose the solid shaft over the hollow due to the restriction on RPM in experimental testing. As far as material selection is concerned, we select steel over aluminum as the ratio of E over ρ is almost the same. Therefore, for the experimental case study, a mild steel solid shaft of 1000 mm in length and 17 mm in diameter is taken. The material properties of the shaft are chosen, having mass density ρ = 7850 kg/m3, modulus of elasticity E = 200 MPa, and Poisson's ratio ν = 0.3. The diameter of the shaft is chosen as per the RPM constraint up to the first mode natural frequency for experimental testing, and also based on the availability of the prime mover. Based on the shaft diameter, bearings having an inner diameter of 17 mm can be selected with a maximum

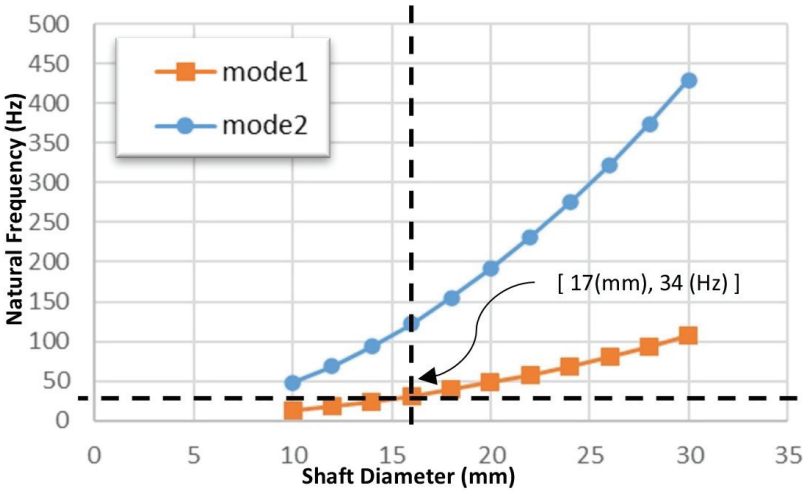

Figure 2: Variation of the modal natural frequency of the shaft with an increase in the diameter.

frictional torque of 0.73 N-m. As the mass of the shaft is 1.78 kg, a DC motor with a minimum power of 160 W and 3000 RPM can be selected based on availability in the market. Apart from the transverse modes, the torsional vibration mode frequencies can be calculated from the following formula

$$\omega_t = \frac{n\pi c}{l} \tag{2}$$

where shear wave speed $(c) = \sqrt{\frac{G}{\rho}}$, n is the mode number and G is the shear modulus.

The first mode of torsion is observed at 1493 Hz for the selected solid shaft specifications above, which is much higher than the first two transverse vibration modes (34 Hz and 138 Hz). Hence, the torsional vibration modes can be ignored in the experiments.

2.2 Design of metamaterial inspired spider-web based unit cell

The metamaterial unit cells used for damping are inspired by spider web structures, designed to mimic the unique ability of the spider web to absorb and dissipate energy. A spider web structure is a natural design known for its strength, flexibility, and efficient force distribution, as shown in the figure 3. Engineers mimic this structure in metamaterials to enhance vibration control. A decrease in the spiral elements reduces the eigen-frequency. Additionally, a decrease in thickness and an increase in outer diameter drastically reduce the eigen-frequency. On tuning these geometric parameters, we reached the optimal parameters to obtain a fundamental frequency close to 34 Hz. As shown in the figure 3a, the number of spiral webs is 4, whereas the number of radial spokes is 8. The inner and outer diameters are 17 mm and 100 mm, respectively. The width of the unit cell is 10 mm, and web thickness is 2 mm. The thickness of the spoke is 1 mm at the center and 10 mm at the outer diameter of the spider unit cell. The

Table 2: Parameters for Solid and Hollow Shafts

(a) Solid Steel Shaft

Parameter	**Unit**	**Value**
Diameter of Shaft	mm	17
Length	mm	1000
Area Moment of Inertia	mm^4	4100
Density	kg/m^3	7850
Area	mm^2	227
Young's Modulus	GPa	210
Frequency with EBT	rad/sec	217
1st mode frequency	Hz	34
1st mode	RPM	2071
2nd mode	RPM	8287

(b) Hollow Steel Shaft

Parameter	**Unit**	**Value**
Outer diameter of Shaft	mm	17
Inner diameter of Shaft	mm	9
Length	mm	1000
Area Moment of Inertia	mm^4	3778
Density	kg/m^3	7850
Area	mm^2	163
Young's Modulus	GPa	210
Frequency with EBT	rad/sec	245
1st mode frequency	Hz	39
1st mode	RPM	2345

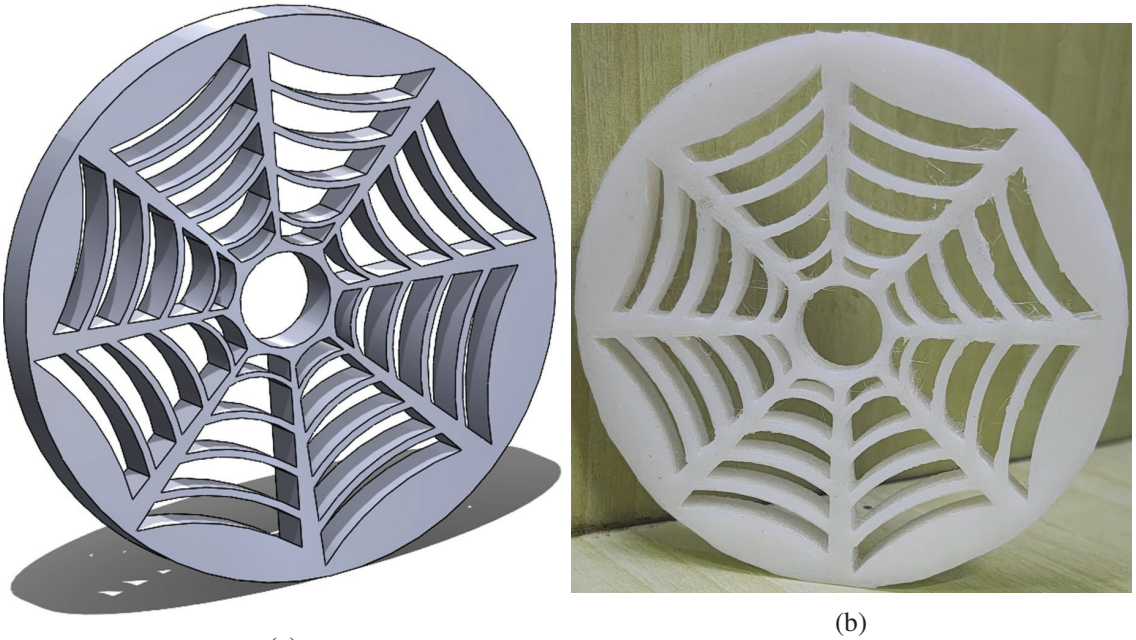

(a) (b)

Figure 3: (a) Spider-web-inspired metamaterial unit cell (b) 3D-Printed spider-web unit cell.

spider-web-inspired metamaterial unit cells are fabricated using 3D printing technology with the plasticized copolyamide thermoplastic elastomer (PCTPE) as portrayed in figure 3b. The material properties of the metamaterial unit cells are selected as follows: mass density ρ = 960

kg/m^3, modulus of elasticity E = 75 MPa, and Poisson's ratio ν = 0.28. The volume of the spider-web metamaterial unit cell is 3.78 $\times 10^{-5}$ m^3, resulting in a unit cell mass of 36.28 g.

3 NUMERICAL ANALYSIS

After the design and material selection for the shaft and spider-web-based metamaterial unit cells, we numerically simulate these in the commercial finite element analysis software.

3.1 Modal analysis of shaft

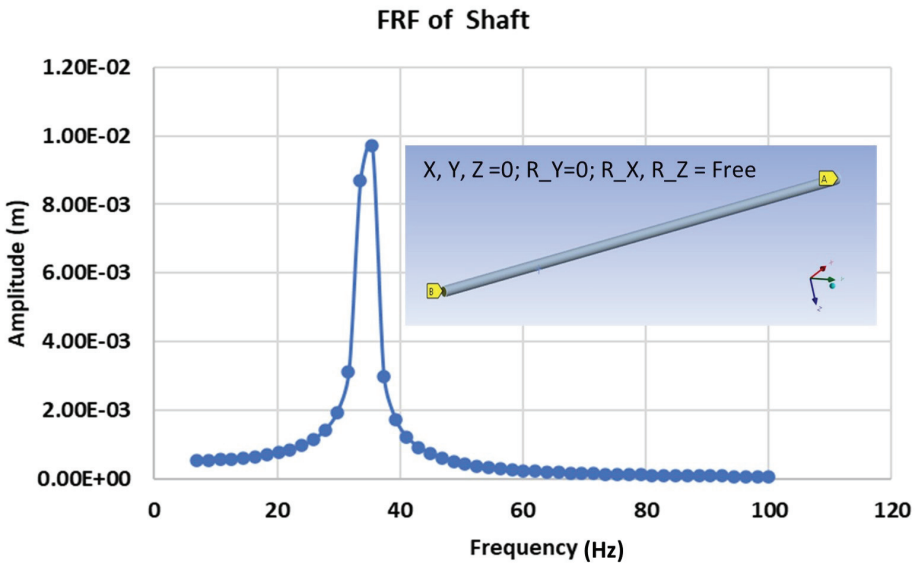

Figure 4: Harmonic analysis of the shaft without the metamaterial unit cells. Geometry and boundary conditions for the modal analysis of the shaft are shown in the panel.

We perform modal analysis of the shaft in Ansys using the structural analysis module. The figure 4 shows the frequency response function (FRF) of the shaft, which shows maximum amplitude at 34 Hz. The simply supported boundary conditions are applied to the shaft as represented in the figure panel. The shaft is free to rotate in the Y-plane only; however, no translational motion is allowed at both ends of the shaft due to bearing mounting. Numerically, through the modal analysis, we obtain natural frequencies in the first and second modes, 34 Hz and 138 Hz, which are consistent with analytical calculations.

3.2 Modal analysis of spider-web inspired metamaterial unit cell

We obtained the fundamental natural frequency of the shaft at 34 Hz numerically and analytically. Hence, now we design the spider-web-based metamaterial unit cell by tweaking the geometric parameters in such a way as to get close to 34 Hz. For modal analysis, the inner

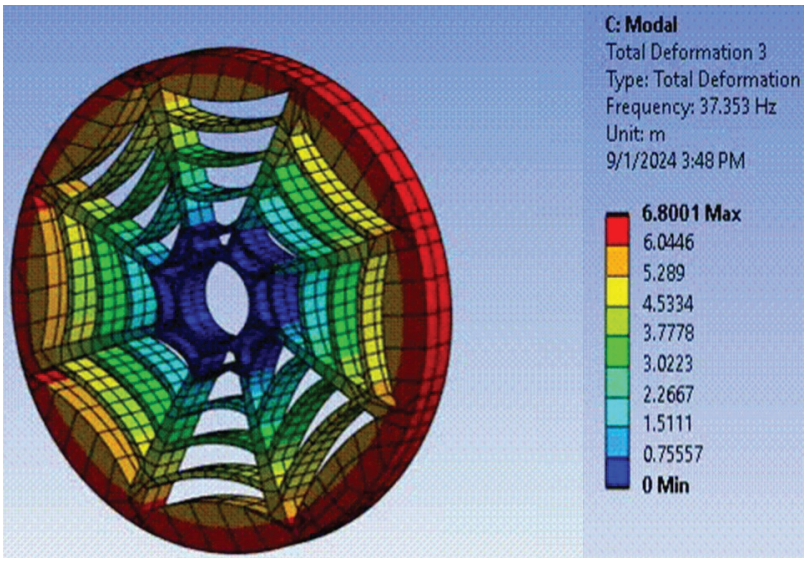

Figure 5: Modal analysis of spider-web inspired metamaterial unit cell.

surface of the spider-web unit cell is fixed. The closest value of the fundamental frequency of the unit cell achieved is 37 Hz, which acts like a tuned mass damper as shown in figure 5.

3.3 Harmonic analysis of shaft integrated with spider-web metamaterial unit cells

The harmonic analysis of the metashaft with spider-web metamaterial unit cells has been performed, as shown in figure 6a. We will integrate spider-web-based metamaterial unit cells on the shaft, as shown in the figure panel. The spider-web unit cells are assembled at equal distances on the shaft. The simply supported boundary conditions at both ends of the metashaft are applied as previously done for the shaft only. Additionally, a 0.73 N-m torque is applied at one end. The figure 6a delineates the FRF of the metashaft as the unit cells are integrated on the shaft. We increased the number of unit cells from one to eight to see the effect of metamaterial unit cells on the vibration of the shaft. With each unit cell weighing 36.28 g, the addition of up to eight unit cells increases the resonator mass to a maximum of 290.30 g on the rotor shaft. Consequently, the ratio of rotor mass to added resonator mass is approximately 1:6. The metashaft with 8-unit cells gave maximum vibration reduction out of all the cases. This effect is clearly visible in Figure 6b, where the midpoint displacement of the simple shaft is compared with that of the metashaft equipped with eight metamaterial-inspired spider-web unit cells.

4 EXPERIMENTAL ANALYSIS

The experimental setup is made to analyze the effectiveness of metamaterial-based damping systems in reducing vibrations in the metashaft rotor. As shown in figure 7, the assembly consists of key components such as the shaft, platform, and spider-web-inspired metamaterial unit cells, which are fabricated with PCTPE material. Additionally, a BLDC motor with

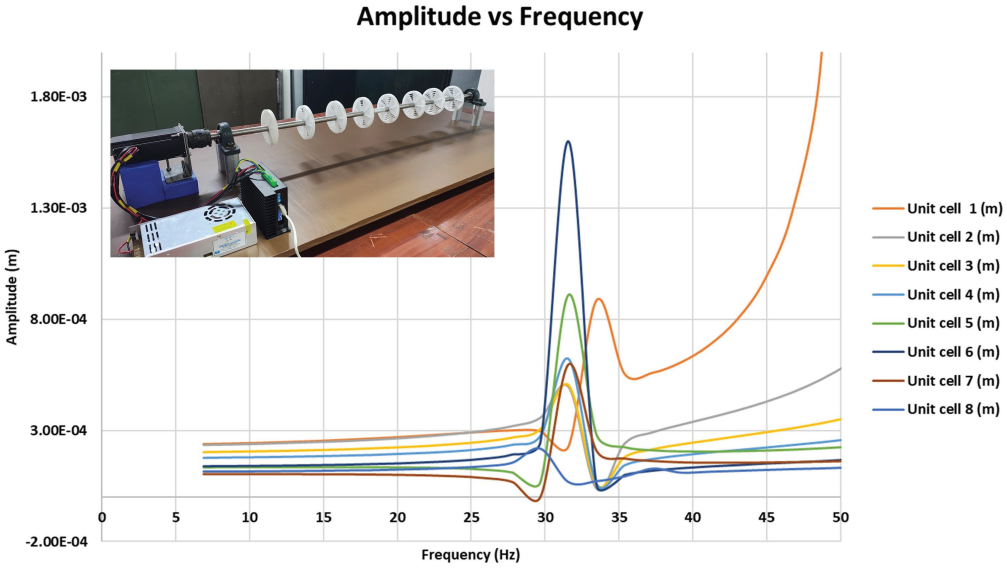

(a)

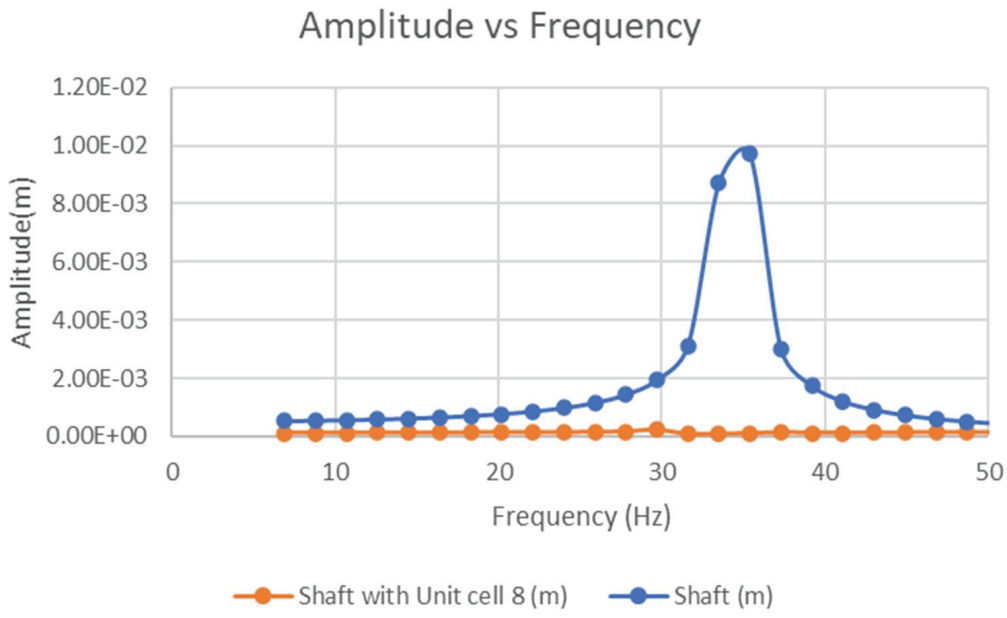

(b)

Figure 6: (a) Harmonic analysis of the metashaft with the integration of metamaterial unit cells. Metashafts with spider-web unit cells are integrated on the shaft, as shown in panel (b). Comparison of the frequency response of the metashaft with 8 unit cells with the shaft alone.

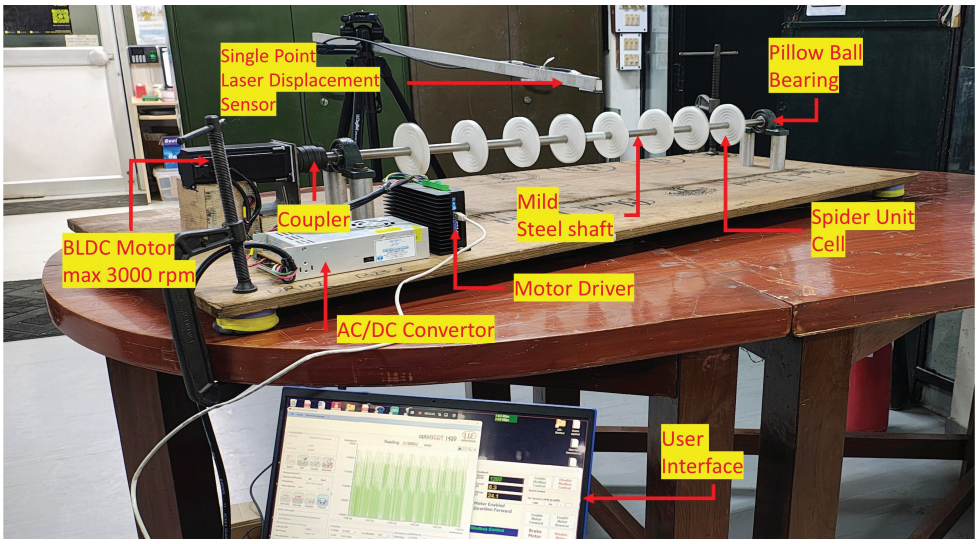

Figure 7: Experimental test rig showing the metashaft integrated with spider-web-based metamaterial unit cells. A BLDC motor with a driver control system rotates the metashaft at variable speeds. The displacement of the metashaft is measured with a single-point laser displacement sensor.

a motor-driver, AC-DC converter, and platform dampers are sourced from the manufacturers. The experimental setup consists of a BLDC motor mounted at one end, which drives a central shaft. The BLDC motor, capable of operating up to 3000 RPM, will be controlled through a motor driver connected to a computer, allowing speed adjustments. Therefore, the motor is responsible for rotating the shaft at different speeds to simulate operating conditions that generate vibrations in the system. The motor speed is controlled using a variable-speed controller (motor-driver) to allow precise adjustments of the rotational speed for experimentation. To ensure the motor runs smoothly at controlled speeds, an AC-DC converter is also used in the setup. It converts the alternating current from the main power supply into direct current, which is then fed to the motor. The shaft is supported by two pillow block bearings on either side, allowing it to rotate freely. The bearings ensure smooth motion and stability, minimizing friction and external interference in vibration measurements. The shaft is connected to the BLDC motor with the help of a spider coupler to transfer the rotational motion from the motor to the shaft.

The 3D printed spider-web-inspired metamaterial unit cells are mounted along the shaft at regular intervals, as shown in figure 7. The unit cell consists of spiral and radial threads, mimicking the layout of a spider-web. These unit cells are designed based on the structural properties of spider webs, which are known for their excellent energy absorption and vibration-damping properties. The entire setup is mounted on a wooden platform equipped with dampers, which absorb residual vibrations from the system and isolate it from external disturbances that could affect the measurements. This platform acts as an isolation base, ensuring that vibrations mea-

sured by the sensor are only due to the operation of the rotor and the behavior of the mounted unit cells.

The vibrations in the rotor system are monitored using a single-point laser displacement sensor, and data is collected at various motor speeds to observe the vibration characteristics and damping performance [14]. The sensor uses laser technology to detect the displacement of the rotor in real-time, offering high-precision data on vibration patterns and peak-to-peak displacement values. The sensor can be strategically placed to monitor the displacement of the shaft at specific points, providing accurate readings of vibration amplitudes. To measure the vibrations of the metashaft rotor during rotation, the single-point laser displacement sensor is positioned at the midpoint of the shaft. The amplitude of the vibration is acquired using the data acquisition tool named ILD1420 DAQ tool, and the speed is controlled using Rhino BLDC drive 6611 software. After completing the experimentation at various speeds, the vi-

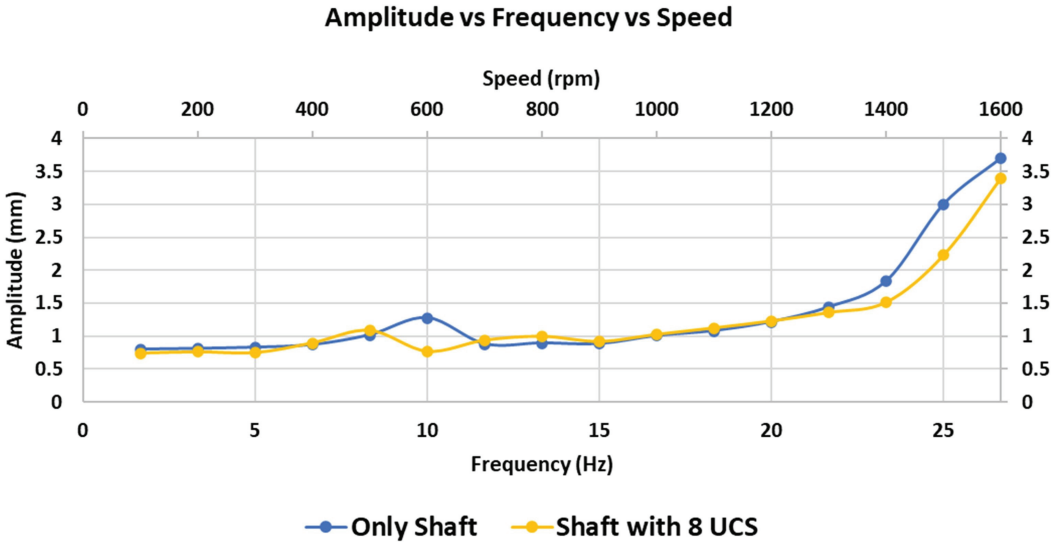

Figure 8: The amplitude variation is shown with frequency and speed for the only shaft and the metashaft integrated with spider web-based unit cells (UCS) assembly.

bration data is plotted to visualize the effect of the spider-web-inspired metamaterial unit cells in damping the mechanical vibrations transmitted to the shaft. The graph is plotted between the amplitude and respective frequency of the metashaft with corresponding RPM as shown in figure 8. The observed fundamental frequency is close to the numerically evaluated frequency, which is around 34 Hz. A decrement in the amplitude of vibration is observed with the addition of spider-web-inspired metamaterial unit cells. The maximum percentage reduction is around 40 at 600 RPM, and at higher frequencies, the reduction is clearly evident, but the experiment cannot be performed beyond 26 Hz (1600 RPM) due to the resonance band.

5 CONCLUSIONS

We proposed a nature-inspired, spider-web-based metamaterial unit cell for reducing rotor vibrations in the metashaft. The approach is founded on an investigation of the vibration absorption characteristics of spider-web-inspired metamaterial unit cells, driven by local resonances inherent to their geometry. Using finite element analysis, we simulated the frequency response function (FRF) of a metashaft rotor system equipped with the proposed unit cells. Experimental validation was performed by measuring vibration amplitudes across various excitation frequencies, with the influence of local resonance on amplitude reduction clearly observed. The experimental results demonstrated up to a 40 $\%$ reduction in the vibration amplitude of the metashaft with the inclusion of eight unit cells on the rotor. These promising results suggest that the application of metamaterials can be extended to rotor dynamics. This can be achieved through the design of innovative, mechanical metamaterial-inspired unit cells that exhibit negative effective properties such as stiffness and mass, arising from local resonance.

ACKNOWLEDGEMENTS

The authors acknowledge the 46th batch of Hindustan Aeronautics Limited (HAL) Trainees and SMSS Lab members for their discussions and assistance in developing the testing setup.

REFERENCES

[1] H. Huang and C. Sun, "Wave attenuation mechanism in an acoustic metamaterial with negative effective mass density," *New Journal of Physics*, vol. 11, no. 1, p. 013003, 2009.

[2] A. Dwivedi, A. Banerjee, and B. Bhattacharya, "Dynamics of piezo-embedded negative stiffness mechanical metamaterials: A study on electromechanical bandgaps," in *ASME International Mechanical Engineering Congress and Exposition*, vol. 84478. American Society of Mechanical Engineers, 2020, p. V001T01A015.

[3] S. Horsley and A. Dwivedi, "Theory of electromagnetic line waves," *Physical Review B*, vol. 108, no. 15, p. 155437, 2023.

[4] A. Dwivedi and S. A. Horsley, "Line waves in elastic metamaterials," in *ASME International Mechanical Engineering Congress and Exposition*, vol. 87684. American Society of Mechanical Engineers, 2023, p. V011T12A013.

[5] S. Sahana, A. Singh, A. Dwivedi, and B. Bhattacharya, "Vibration attenuation in tapered metabeams: Influence of conicity and lattice arrangement on elastic wave dispersion," *Engineering Structures*, vol. 342, p. 120886, 2025.

[6] A. Dwivedi, A. Banerjee, S. Adhikari, and B. Bhattacharya, "Bandgap merging with double-negative metabeam," *Mechanics Research Communications*, vol. 122, p. 103889, 2022.

[7] T. Gupta, A. K. Sharma, A. Dwivedi, V. Gupta, S. Sahana, S. Pathak, A. Awasthi, and B. Bhattacharya, "Ai-driven inverse design of band-tunable mechanical metastructures for tailored vibration mitigation," *arXiv preprint arXiv:2412.12122*, 2024.

[8] Q. Xu, Y. Lv, Z. Liu, H. Yao, and B. Wen, "Vibration characteristics of multi-acoustic metamaterials rotor with geometrical nonlinearity," *Nonlinear Dynamics*, vol. 111, no. 14, pp. 12 817–12 833, 2023.

[9] L. Lixia and C. Anjiang, "Control of the low-frequency vibrations of elastic metamaterial shafts with discretized arc-rubber layers," *Japanese Journal of Applied Physics*, vol. 55, no. 6, p. 067301, 2016.

[10] L. Li, R. Lv, A. Cai, M. Xie, Y. Chen, and G. Huang, "Low-frequency vibration suppression of a multi-layered elastic metamaterial shaft with discretized scatters," *Journal of Physics D: Applied Physics*, vol. 52, no. 5, p. 055105, 2018.

[11] Z. Li, H. Yao, and H. Li, "Application of metamaterial in vibration suppression of rotor system," in *International Conference on Rotor Dynamics*. Springer, 2023, pp. 15–24.

[12] H. Ruan and D. Li, "Wave propagation properties of a spider-web-like hierarchical acoustic metamaterial," *physica status solidi (b)*, vol. 259, no. 12, p. 2200341, 2022.

[13] S. S. Rao and F. F. Yap, *Mechanical vibrations*. Addison-Wesley New York, 1995, vol. 4.

[14] A. Dwivedi, R. K. Munian, B. Bhattacharya, and S. Adhikari, "Bandgap formation mechanism in tacticity inspired elastic mechanical metastructures," *Scientific Reports*, vol. 14, no. 1, p. 24611, 2024.

XI ECCOMAS Thematic Conference on Smart Structures and Materials - SMART 2025
M. Krommer, M. Nader and M. Schagerl (Eds)

Received: 22 April 2025 / Revised: 11 July 2025 / Accepted: 19 October 2025
© The Author(s) 2025

Inverse design of the Acoustic Black Hole Metabeam using Tandem Neural Network

Pratham Khairnar, Ankur Dwivedi, Aman Sengar, Bishakh Bhattacharya

Abstract. Acoustic Black Holes (ABH) provide an effective passive vibration control mechanism by leveraging power-law based thickness variations to decelerate and trap flexural waves. This study focuses on the inverse design of metabeams incorporating multiple symmetric ABH unit cells, optimizing key geometric parameters to achieve targeted energy trapping and broadband attenuation. The spectral element method (SEM) formulation is used to generate a dataset, which is used to train the deep-learning model. As the inverse design problem is of a one-to-many nature, i.e., multiple ABH geometries can yield similar displacement transmissibility, hence direct optimization poses significant challenges. To overcome this, we propose a tandem neural network framework that enforces a one-to-one mapping for stable and deterministic design predictions. In this model, the forward neural network maps ABH geometric parameters to displacement transmissibility values, while the inverse neural network predicts ABH parameters from the transmissibility. This enables rapid evaluation of various design configurations. The effectiveness of this approach is validated by conducting computational evaluations where the predicted ABH geometric parameters are used to calculate the displacement transmissibility values, and then the results are compared with the results obtained from actual ABH-based metabeam geometries. The tandem neural network used is able to achieve high predictive accuracy across various ABH-based metabeam configurations. The model is also able to predict parameters for ABH-based metabeams with a second-order power-law variation that yields a transmissibility curve similar to those obtained from a higher-order power-law based metabeam. Our findings emphasize the potential of deep learning in accelerating the inverse design process while ensuring precision in ABH-based metastructures. Therefore, it can be an efficient solution for optimizing metastructure design in practical applications like vibration damping in mechanical systems, aerospace structures, and civil infrastructure.

Key words: Acoustic Black Hole, Mechanical Metastructure, Inverse Design, Tandem Neural Network, Multilayer perceptron, Modal Assurance Criterion.

Pratham Khairnar & Ankur Dwivedi & Aman Sengar & Bishakh Bhattacharya
Smart Materials, Structures and Systems Laboratory, Department of Mechanical Engineering, Indian Institute of Technology Kanpur, Uttar Pradesh, 208016, India, e-mail: bishakh@iitk.ac.in

1 INTRODUCTION

Metamaterials are engineered materials that have gained the attention of researchers because of their unique properties[1]. These materials tend to show unique properties that are not found in natural materials. One can achieve such novel characteristics by carefully designing the geometry of the unit cell rather than completely relying on the composition of the material. One such category of metamaterials is acoustic black hole (ABH) based mechanical metamaterials. The unit cells of these metamaterials are designed using the power-law based thickness variation for controlling flexural waves in the metastructure [2, 3]. The key advantage of ABH-based mechanical metastructure is that these are efficient in trapping elastic wave energy [4, 5]; thus, they are suitable for applications like passive vibration damping. Additionally, the ABH-based design exhibits a wider bandgap region as compared to existing mechanical metamaterials such as effective negative stiffness [6, 7, 8] and mass [9]. Therefore, ABH-based metastructures and their application in vibration control have gained considerable interest in structural engineering and aerospace engineering because of their vibration attenuation ability.

Advancement in optimization techniques like inverse design plays a significant role in the field of metamaterials. The most recent work on inverse design showed the potential of machine learning algorithms in designing metamaterials, highlighting how data-driven approaches optimize nonlinear mechanical properties, hence minimizing the computational cost and effort in numerical simulations [10]. Another remarkable work on inverse design demonstrated the use of a machine learning-based inverse design framework for spinodoid metamaterials [11]. Their approach includes the use of neural networks, which are trained on parametrized microstructure. This allows rapid prediction of topology without involving expensive and complex phase-field simulations. Further, Wang et al. proposed a metamaterial design framework using variational autoencoders (VAE) [12]. Their framework is used to map the complex microstructure of functionally graded metamaterial systems into latent space. Deng et al. also presented an approach for inverse designing of metamaterials by utilizing the evolution strategy in their neural network [13]. Their method enhanced the design speed and accuracy compared to traditional optimization techniques. Recently, Zang et al. proposed a neural network framework for inverse designing a 3D mixed-size cavity-based acoustic metamaterials for broadband waterborne sound absorption using FEM and deep learning techniques [14]. Therefore, using deep learning algorithms in the inverse design of mechanical metamaterials is a revolutionary move for effectively identifying the ideal configuration while preserving accuracy.

This study focuses on the inverse design of mechanical metastructures with symmetric ABH-based unit cells. Since the inverse design is inherently a one-to-many problem, it implies that multiple geometric configurations can result in similar displacement transmissibility responses. To address this problem, we propose a tandem neural network framework [15] to implement one-to-one mapping for stable and accurate design prediction. The study demonstrates that by using deep learning [16] for the inverse design process, we can speed up the optimization

process of ABH-based metastructures, resulting in high accuracy and efficiency. The purpose of this research is to show the potential of data-driven inverse design methodologies, which can help to advance vibration-damping technologies with applications in aerospace, infrastructure engineering, and other fields that require advanced structural control.

2 METHODOLOGY

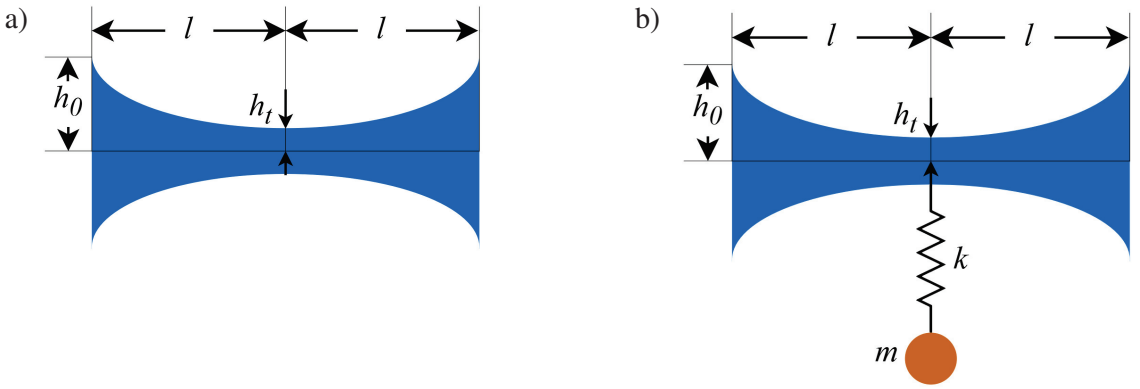

Figure 1: Representative unit cell design of mechanical metastructure having a) Symmetric ABH-based metabeam unit cell b) Symmetric ABH-based metabeam unit cell attached with a discrete local resonator.

In this study, we have chosen the spectral element method (SEM) for numerical modelling, leveraging its accuracy and efficiency in solving elastic wave propagation problems. This serves as the foundation for training and validating the tandem neural network for inverse design. As shown in Figure 1, the design of a symmetric ABH-based metabeam unit cell consists of two sub-units called converging and diverging ABH sub-unit cells. Hence, each sub-unit cell can be modeled as an Euler-Bernoulli beam with two elements and three nodes [17]. Therefore, the governing equation of a simple Euler–Bernoulli beam for a particular frequency ω, where $\omega \in \{\omega_j\}, j = 0, 1, \ldots, n$, can be written as

$$\frac{d^2}{dx^2}\left(EI(x)\frac{d^2W}{dx^2}\right) - \rho A(x)\omega^2 W = 0, \tag{1}$$

Here, the material parameters ρ and E represent the density and Young's modulus of the beam, respectively. $W(x)$ denotes the deflection amplitude at a given frequency. The second moment of area is given by $I(x) = bh(x)^3/12$, where b is the constant width of the beam. Assuming a rectangular cross-section, the area of the beam can be written as $A(x) = bh(x)$. The ABH sections follow a power-law based parabolic thickness variation in the converging ABH section along the x-direction as per the following expression

$$h(x) = 2h_0\left(1 - \frac{x}{x_0}\right)^2 \tag{2}$$

where h_0 is the thickness of the half section of the converging sub-unit cell at $x = 0$ as shown in Figure 1. x_0 is the length, where ideally, taper thickness reaches zero. The length of this portion is $l = (1 - \sqrt{r_0})x_0$, where $r_0 = \frac{h_t}{h_0}$. Here, h_t is the half thickness at the junction between the converging and diverging sections at $x = l$. The exact solution of the converging section [18] corresponding to the parabolic thickness variation can be written as

$$W(x) = a_1 \left(1 - \frac{x}{x_0}\right)^{c_1} + a_2 \left(1 - \frac{x}{x_0}\right)^{c_2} + a_3 \left(1 - \frac{x}{x_0}\right)^{c_3} + a_4 \left(1 - \frac{x}{x_0}\right)^{c_4} \tag{3}$$

where c_1, c_2, c_3, and c_4 are the functions of the particular frequency ω. These can be represented by

$$\begin{aligned} c_1 &= -\frac{3}{2} - \frac{1}{2}\sqrt{17 - 4\sqrt{4+\lambda}}, \quad c_2 = -\frac{3}{2} - \frac{1}{2}\sqrt{17 + 4\sqrt{4+\lambda}}, \\ c_3 &= -\frac{3}{2} + \frac{1}{2}\sqrt{17 - 4\sqrt{4+\lambda}}, \quad c_4 = -\frac{3}{2} + \frac{1}{2}\sqrt{17 + 4\sqrt{4+\lambda}}. \end{aligned} \tag{4}$$

where, $\lambda = 3x_0^4\rho\omega^2/(Eh_0^2)$.
Following similar steps, the solution for the diverging section of the ABH unit cell can be obtained by appropriately modifying Eq. 2. These solutions can be used to form the dynamic stiffness matrix, which is subsequently required to calculate displacement at a point. The displacement transmissibility can be determined using the following formula

$$T = 20 \log \frac{d_{out}}{d_{in}} \tag{5}$$

where d_{out} and d_{in} represent the output and input displacement amplitudes, respectively, and T denotes the transmissibility response.

2.1 Data Generation

The above-discussed SEM-based formulation is implemented in MATLAB for generating the dataset to efficiently model the elastic wave propagation characteristics in an ABH-based metabeam having 8 unit cells. The dataset is characterized by a set of ABH-based metabeam unit-cell parameters, represented as $G = \{G_1, G_2, ..., G_n\}$. The parameters that have been included are ABH sub-unit length (l), tip thickness (h_0), base thickness (h_t), stiffness (k) and mass of resonator (m). The SEM methodology yields the displacement transmissibility response for each configuration of G, which is denoted as $T = \{T(f)|f \in [1, 3000]\,\text{Hz}\}$, showing the frequency-dependent wave attenuation. The vector T consists of 1500 equally spaced elements ranging from 1 Hz to 3000 Hz. The SEM based formulation is implemented in MATLAB to generate a comprehensive dataset consisting of 30,000 data points. Among the 30,000 data points, 28,000 are allocated for training the model, and the remaining 2,000 are utilized as the test dataset. Formulated dataset is denoted by $D = \{(G_i, T_i)\}$. Where G_i and T_i denote the geometric and transmissibility parameters corresponding to the ith data point, respectively. This dataset gives a structured mapping between the ABH parameters and their corresponding transmissibility response.

2.2 Forward Neural Network (FNN)

The forward neural network is designed to approximate the complex mapping between the ABH geometric parameters (G) and transmissibility (T).

$$F_\eta : G \mapsto \boldsymbol{T} \tag{6}$$

Where η represents the trainable parameters of the neural network, which includes weights and biases. The forward neural network is a multilayer perceptron model with nine fully connected layers with increasing neurons. In the suggested neural network architecture, in order to introduce non-linearity, the rectified linear unit (ReLU) activation function is used for hidden layers and linear activation is used for the output layer. To train the model efficiently, the root mean square error (RMSE) is used as the loss function. For this model, the RMSE can be defined as

$$\mathcal{L}_{\text{FNN}} = \sqrt{\frac{1}{N}\sum_{i=1}^{N}\left(T_i - F_\eta(\boldsymbol{G}_i)\right)^2} \tag{7}$$

where, N denotes the total number of data points (samples). For training the FNN, backpropagation algorithm [19] is used, in which gradient of $\mathcal{L}_{FNN}$ with respect to η is computed using automatic differentiation [20] and updated via adaptive moment estimation (Adam) optimizer [21], dynamically adjusting the learning rate for efficient training. To ensure stability during model training, the early stopping mechanism is used. The early stopping mechanism tracks the validation loss and halts model training if no significant change in the validation loss is detected. Additionally, this model also incorporates the use of learning rate reduction on the plateau, which decreases the learning rate by half if the validation loss stays constant for five epochs. This technique effectively leads to better and smoother convergence. As a result, the forward neural network ensures high accuracy and stability during predictions. Thus, FNN successfully captures the intricate relationship between the ABH parameters and displacement transmissibility responses.

2.3 Inverse Neural Network (INN)

Addressing the inverse problem, a new multilayer perceptron model is introduced. The purpose of the model is to map the geometric parameters of ABH from the transmissibility.

$$I_\tau : T \mapsto \boldsymbol{G} \tag{8}$$

where τ represents the trainable parameters of the inverse model.
As the mapping in inverse design is inherently ill-posed and non-unique, there is a need to define a stable and well-regularized architecture. Therefore, a neural network architecture with nine fully connected layers with decreasing neurons is utilized in INN. To ensure model stability and penalize large errors effectively, the mean squared error (MSE) loss function is used, which is defined as

$$\mathcal{L}_{\text{INN}} = \frac{1}{N}\sum_{i=1}^{N}\left(G_i - I_\tau(\boldsymbol{T}_i)\right)^2 \tag{9}$$

Analogous to the forward model, to train the inverse model effectively, the backpropagation algorithm with the Adam optimizer is used to optimize τ, while incorporating early stopping and learning rate reduction on plateau to ensure stability and convergence. This inverse model enhances efficiency in inverse designing ABH-based metabeams, thus improving vibration damping optimization. Figure 2 presents the convergence plot illustrating the variation of the loss function with epochs for both the forward and inverse neural network models.

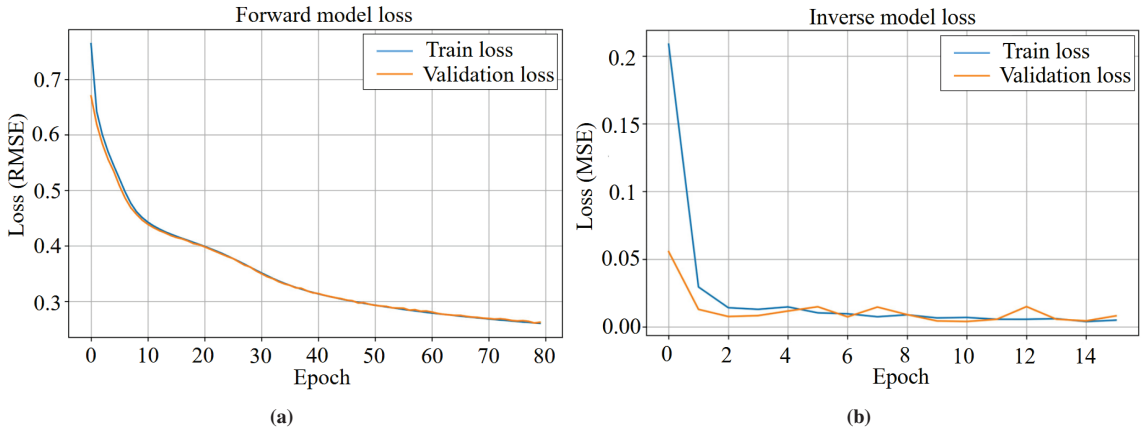

Figure 2: Convergence plot showing the variation of loss function with epochs for forward and inverse neural network models.

2.4 Tandem training and Inverse model optimization

In order to enforce one-to-one mapping between displacement transmissibility (T) and ABH parameters (G), a tandem training approach is utilized. Both the FNN and the INN are used iteratively to optimize the predictions of the inverse model by minimizing the reconstruction or tandem loss function. As shown in figure 3, the tandem training approach consists of two steps. The forward neural network (FNN) is employed to reconstruct displacement transmissibility (T) from ABH parameters (G). Whereas, the inverse neural network (INN) is used sequentially after the FNN to predict ABH parameters (G) from displacement transmissibility (T). The difference between the original parameters and the predicted parameter is captured using a tandem loss function, which is expressed as

$$\mathcal{L}_{\text{tandem}} = \frac{1}{N}\sum_{i=1}^{N}\left(G_i - I_\tau(F_\eta(\boldsymbol{G}_i))\right)^2 \tag{10}$$

The tandem loss is used to update the weights of the inverse model only, while the weights of the forward model remain fixed.

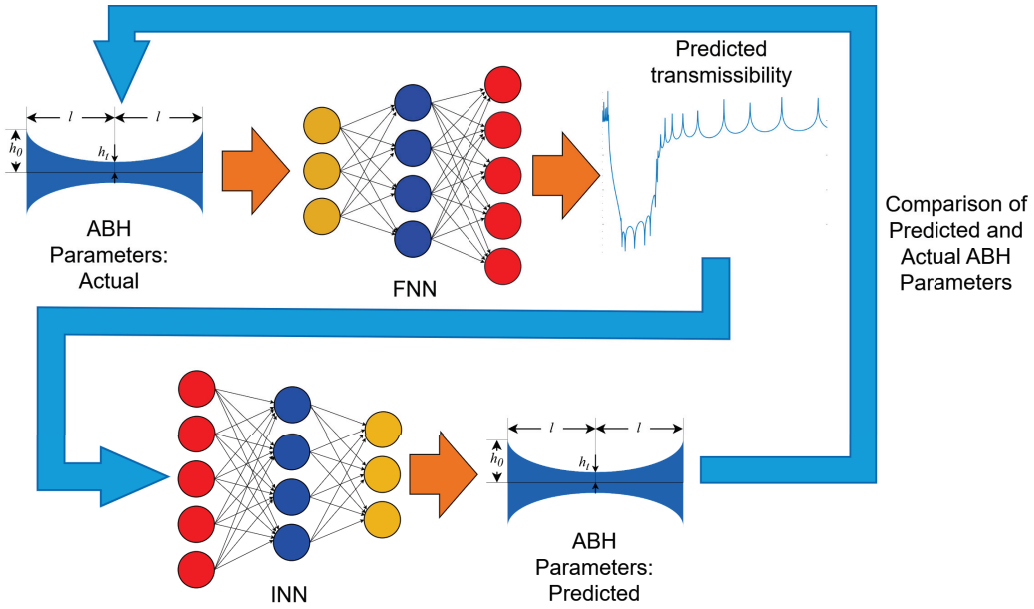

Figure 3: Illustration of a tandem neural network approach by combining forward and inverse neural networks for the transmissibility and ABH-based metabeam unit cell parameter prediction.

Training the INN ensures that the predicted ABH parameters ($\hat{G}$) align with the given ABH parameters (G) for a given displacement transmissibility response. This approach helps in optimizing the determination of ABH parameters for a desired transmissibility response, making the model more robust. Figure 4 shows the convergence of tandem loss with increasing epoch.

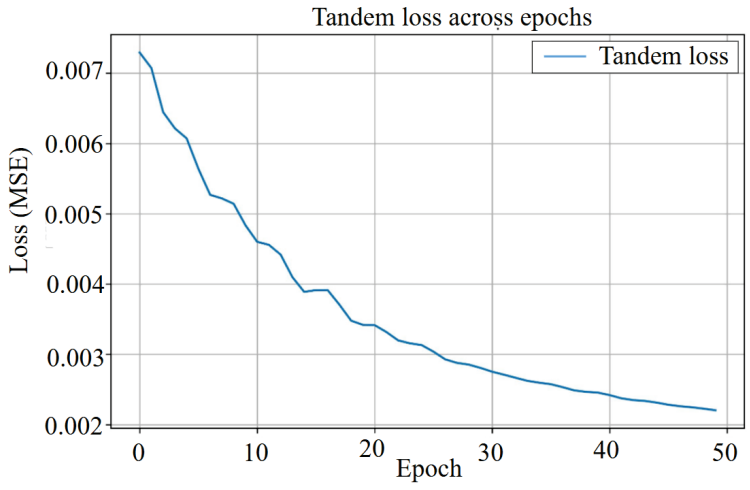

Figure 4: Variation of tandem loss with epochs denoting stable convergence.

3 RESULTS

To check the accuracy of prediction by the model, the modal assurance criterion (MAC) is used, which gives the similarity between two mode shapes [22]. MAC value of one shows that the mode shapes are identical and MAC value of zero shows that there is no correlation between mode shapes. The MAC is calculated based on the similarity between the displacement transmissibility curve derived from the actual parameters and that obtained from the predicted parameters. MAC can be calculated by the following expression

$$MAC = \frac{\left|\{\boldsymbol{T}_A\}^T\{\boldsymbol{T}_P\}\right|^2}{\left(\{\boldsymbol{T}_A\}^T\{\boldsymbol{T}_A\}\right)\left(\{\boldsymbol{T}_P\}^T\{\boldsymbol{T}_P\}\right)} \tag{11}$$

where, T_A is displacement transmissibility from actual ABH parameters and T_P is displacement transmissibility from the predicted ABH parameters.

3.1 Elastic Wave Dispersion in ABH Metabeams using Displacement Transmissibility

Table 1 compares the actual ABH-based metabeam unit cell parameters and the one predicted by the INN model. It is observed that the model can predict the values of ABH-based metabeam unit cell parameters quite well with minimal error. The parameters predicted in this case are ABH unit cell base thickness (h_0), tip thickness (h_t), and ABH sub-unit cell length (l). The dispersion of elastic waves in ABH-based metabeams is shown by calculating displacement transmissibility. As shown in Figure 5, the displacement transmissibility curve for ABH-based metabeam unit cell with different parameters shows strong alignment between the actual and predicted parameters across a frequency range of 1Hz-3000Hz. The MAC values are very close to one, signifying a strong correlation between transmissibility from predicted ABH-based metabeam unit cell parameters and transmissibility from actual parameters. The results confirm that the model is effective in predicting the ABH-based metabeam unit cell parameters.

Table 1: ABH-based metabeam unit cell parameters with actual and predicted values

ABH Parameter	**Case 1**		**Case 2**		**Case 3**		**Case 4**	
	Actual	**Predicted**	**Actual**	**Predicted**	**Actual**	**Predicted**	**Actual**	**Predicted**
h_0 (m)	0.0049	0.004872	0.0035	0.003491	0.0043	0.0043	0.0055	0.00552
h_t (m)	0.0011	0.001103	0.0025	0.002523	0.0024	0.002401	0.0024	0.00239
l (m)	0.028	0.02793	0.023	0.02315	0.03	0.03003	0.028	0.02809

To evaluate the generalization capability of the model, it is tested on ABH-based metabeam profiles following a higher-order power-law variation. The study considers a metabeam with 8 unit cells, with test data generated via finite element simulations using COMSOL Multiphysics.

Table 2 shows the actual ABH-based metabeam unit cell parameters following the 4th and 7th-order power laws, along with their corresponding predicted parameters based on the 2nd order power-law.

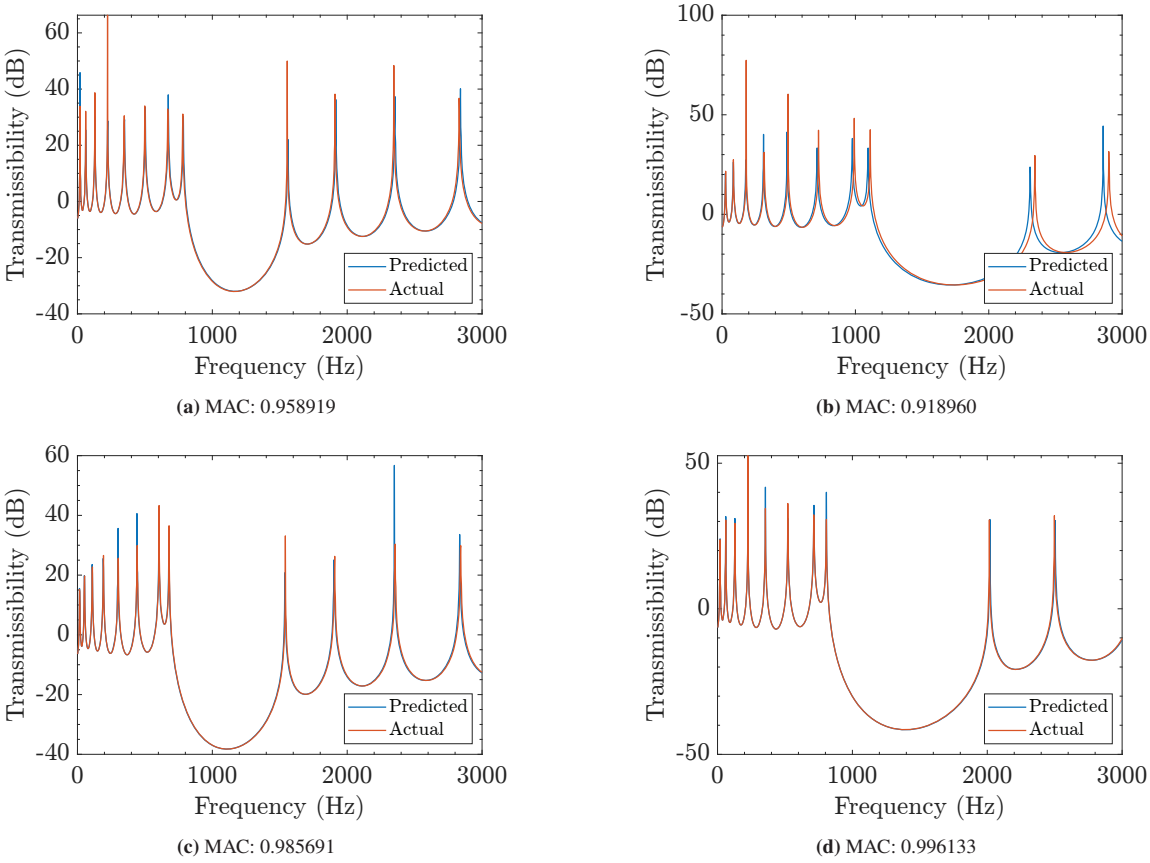

(a) MAC: 0.958919

(b) MAC: 0.918960

(c) MAC: 0.985691

(d) MAC: 0.996133

Figure 5: Comparison of displacement transmissibility between actual parameters and the parameters predicted by the INN model for various ABH-based metabeam with 8 unit cells.

Figure 6 illustrates the performance of the model when tested against 4th and 7th-order power-law profile-based ABH metabeams, respectively. The results show that the model adjusts the predicted parameters such that the displacement transmissibility obtained from a 2nd-order power-law profile-based ABH metabeams closely matches that obtained from higher-order power-law profile-based ABH metabeams. This shows the ability of the model to generalize higher power-law profiles into the 2nd-order power-law profiles.

Table 2: ABH-based metabeam unit cell parameters for higher order profiles and their corresponding predicted values for 2nd order profile

ABH Parameter	4th order power-law		7th order power-law	
	Actual	**Predicted**	**Actual**	**Predicted**
h_0 (m)	0.0065	0.003797	0.008	0.006137
h_t (m)	0.00125	0.001114	0.001	0.001163
l (m)	0.030	0.02599	0.03	0.033351

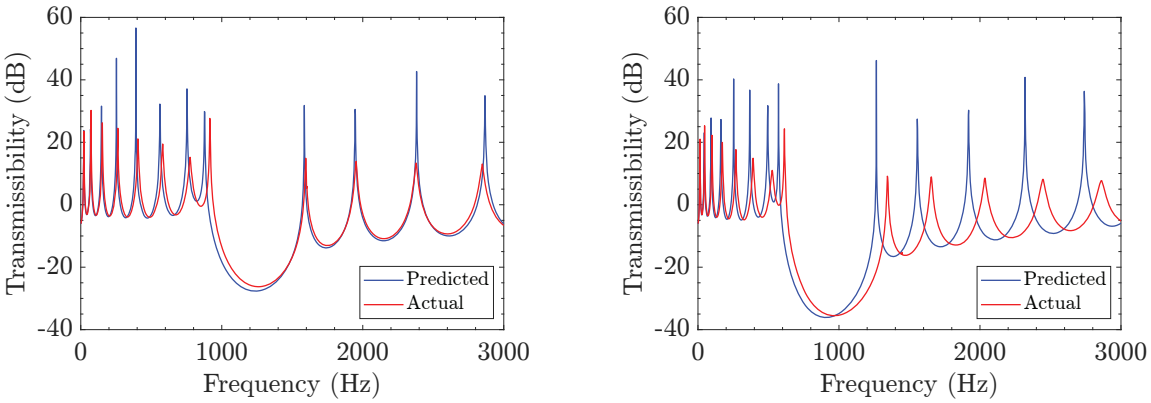

(a) MAC: 0.849096 **(b)** MAC: 0.678285

Figure 6: Comparison of displacement transmissibility of an ABH-based metabeam with 8 unit cells following **a)** the 4th order power-law and its corresponding predicted design for the 2nd order power-law. **b)** the 7th order power-law and its corresponding predicted design for the 2nd order power-law.

3.2 Elastic Wave Dispersion in ABH Metabeams attached with a spring-mass resonator using Displacement Transmissibility

Table 3 shows the actual parameters and the corresponding parameters predicted by the INN model for an ABH-based metabeam unit cell with a resonator attached to it. The parameters predicted in this case are ABH unit cell tip thickness (h_t), base thickness (h_0), ABH sub-unit length (l), stiffness (k) and mass (m) of the resonator. Analysis of the table shows that predicted values by the model fall within a reasonable range. As shown in Figure 7, it can be observed that the displacement transmissibility plot obtained by the actual parameters is quite close to the transmissibility obtained by the predicted parameters. Also, the MAC values signify that the model successfully captures the trend of bandgap for all the cases.

Table 3: ABH-based metabeam unit cell parameters with actual and predicted values for various cases of ABH-based metabeams attached with a resonator

ABH Parameter	Case 1		Case 2		Case 3		Case 4	
	Actual	**Predicted**	**Actual**	**Predicted**	**Actual**	**Predicted**	**Actual**	**Predicted**
k (N/m)	120000	122522	113000	125365	107000	110488	102000	103663
m (kg)	0.028	0.02898	0.024	0.02648	0.046	0.04783	0.047	0.04990
h_0 (m)	0.0062	0.00656	0.0083	0.00818	0.0058	0.00552	0.0065	0.00613
h_t (m)	0.0028	0.00254	0.0022	0.00217	0.0020	0.00215	0.0020	0.00233
l (m)	0.022	0.02254	0.024	0.02373	0.031	0.03064	0.028	0.02707

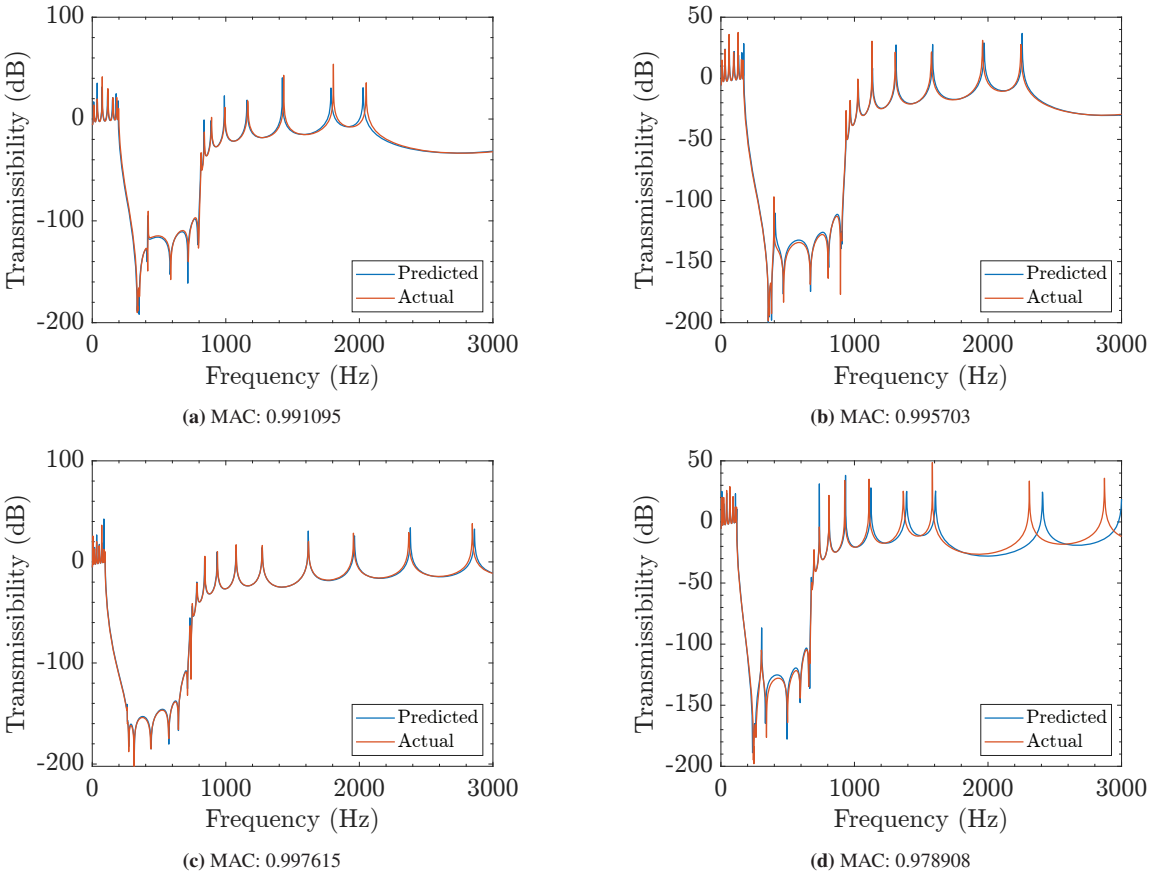

(a) MAC: 0.991095

(b) MAC: 0.995703

(c) MAC: 0.997615

(d) MAC: 0.978908

Figure 7: Comparison of displacement transmissibility between actual parameters and parameters predicted by the INN model for various ABH-based metabeams with 8 unit cells attached with a spring-mass resonator.

4 CONCLUSION

This study highlights the effectiveness of a tandem neural network framework for the inverse design of ABH-based metabeam unit cells. By addressing the one-to-many nature of the inverse design problem, the proposed approach ensures stable and accurate predictions of ABH-based unit cell geometric parameters from the displacement transmissibility responses of the ABH-based metabeams. The results validate the high predictive accuracy of the model for different ABH-based metabeam configurations through comparisons with the spectral element method and finite element simulations using COMSOL multiphysics. Additionally, the study demonstrates the generalization capability of the model by showing its effectiveness in handling ABH-based metabeam configurations with attached resonators. Moreover, the model is capable of predicting second-order ABH profile parameters corresponding to higher-order ABH profiles, which are obtained via finite element simulations using COMSOL Multiphysics. The high value of the modal assurance criterion (MAC) confirms the ability of the model in capturing the key displacement transmissibility characteristics accurately, making it a reliable tool for rapid and precise optimization of ABH-based metastructures. The proposed methodology can be applied in structural vibration control applications in aerospace, civil infrastructure, and mechanical systems. Future research directions may include incorporating rigorous experimental validation, integrating actual material properties into the inverse design framework, and exploring multi-objective optimization strategies.

REFERENCES

[1] A. Dwivedi, R. K. Munian, B. Bhattacharya, and S. Adhikari, "Bandgap formation mechanism in tacticity inspired elastic mechanical metastructures," *Scientific Reports*, vol. 14, no. 1, p. 24611, 2024.

[2] M. Mironov and A. Gladilin, "Vibrational black hole as a matching structure," in *Forum Acusticum*, 2020, pp. 3305–3308.

[3] L. Tang and L. Cheng, "Broadband locally resonant band gaps in periodic beam structures with embedded acoustic black holes," *Journal of Applied Physics*, vol. 121, no. 19, 2017.

[4] M. Mironov, "Propagation of a flexural wave in a plate whose thickness decreases smoothly to zero in a finite interval," *Sov. Phys. Acoust*, vol. 34, no. 3, pp. 318–319, 1988.

[5] A. Dwivedi and S. A. Horsley, "Line waves in elastic metamaterials," in *ASME International Mechanical Engineering Congress and Exposition*, vol. 87684. American Society of Mechanical Engineers, 2023, p. V011T12A013.

[6] A. Dwivedi, A. Banerjee, and B. Bhattacharya, "Simultaneous energy harvesting and vibration attenuation in piezo-embedded negative stiffness metamaterial," *Journal of Intelligent Material Systems and Structures*, vol. 31, no. 8, pp. 1076–1090, 2020.

[7] A. Dwivedi, A. Banerjee, S. Adhikari, and B. Bhattacharya, "Bandgap merging with double-negative metabeam," *Mechanics Research Communications*, vol. 122, p. 103889, 2022.

[8] H. Huang and C. Sun, "Theoretical investigation of the behavior of an acoustic metamaterial with extreme young's modulus," *Journal of the Mechanics and Physics of Solids*, vol. 59, no. 10, pp. 2070–2081, 2011.

[9] A. Dwivedi, A. Banerjee, S. Adhikari, and B. Bhattacharya, "Optimal electromechanical bandgaps in piezo-embedded mechanical metamaterials," *International Journal of Mechanics and Materials in Design*, vol. 17, no. 2, pp. 419–439, 2021.

[10] P. Thakolkaran, M. Espinal, S. Dhulipala, S. Kumar, and C. M. Portela, "Experiment-informed finite-strain inverse design of spinodal metamaterials," *Extreme Mechanics Letters*, vol. 74, p. 102274, 2025.

[11] S. Kumar, S. Tan, L. Zheng, and D. M. Kochmann, "Inverse-designed spinodoid metamaterials," *npj Computational Materials*, vol. 6, no. 1, p. 73, 2020.

[12] L. Wang, Y.-C. Chan, F. Ahmed, Z. Liu, P. Zhu, and W. Chen, "Deep generative modeling for mechanistic-based learning and design of metamaterial systems," *Computer Methods in Applied Mechanics and Engineering*, vol. 372, p. 113377, 2020.

[13] B. Deng, A. Zareei, X. Ding, J. C. Weaver, C. H. Rycroft, and K. Bertoldi, "Inverse design of mechanical metamaterials with target nonlinear response via a neural accelerated evolution strategy," *Advanced Materials*, vol. 34, no. 41, p. 2206238, 2022.

[14] H. Zhang, J. Liu, W. Ma, H. Yang, Y. Wang, H. Yang, H. Zhao, D. Yu, and J. Wen, "Learning to inversely design acoustic metamaterials for enhanced performance," *Acta Mechanica Sinica*, vol. 39, no. 7, p. 722426, 2023.

[15] D. Liu, Y. Tan, E. Khoram, and Z. Yu, "Training deep neural networks for the inverse design of nanophotonic structures," *Acs Photonics*, vol. 5, no. 4, pp. 1365–1369, 2018.

[16] Y. LeCun, Y. Bengio, and G. Hinton, "Deep learning," *nature*, vol. 521, no. 7553, pp. 436–444, 2015.

[17] A. Mondal and S. Murugan, "Flexural wave propagation characteristics of metabeam with simultaneous acoustic black hole and local resonator," *European Journal of Mechanics-A/Solids*, vol. 104, p. 105217, 2024.

[18] J. Y. Lee and W. Jeon, "Exact solution of euler-bernoulli equation for acoustic black holes via generalized hypergeometric differential equation," *Journal of sound and vibration*, vol. 452, pp. 191–204, 2019.

[19] I. Goodfellow, Y. Bengio, A. Courville, and Y. Bengio, *Deep learning*. MIT press Cambridge, 2016, vol. 1, no. 2.

[20] A. Paszke, "Pytorch: An imperative style, high-performance deep learning library," *arXiv preprint arXiv:1912.01703*, 2019.

[21] D. P. Kingma and J. Ba, "Adam: A method for stochastic optimization," *arXiv preprint arXiv:1412.6980*, 2014.

[22] M. Pastor, M. Binda, and T. Harčarik, "Modal assurance criterion," *Procedia Engineering*, vol. 48, pp. 543–548, 2012.

XI ECCOMAS Thematic Conference on Smart Structures and Materials - SMART 2025
M. Krommer, M. Nader and M. Schagerl (Eds)

Received: 29 April 2025 / Revised: 1 September 2025 / Accepted: 19 October 2025
© The Author(s) 2025

Wave Propagation in Phononic Beam Structure with Periodically Varying Cross-Section in Presence of Crack

Subhasish Sarkar, Srinivasan Gopalakrishnan

Abstract. Phononic structures are widely utilised for their exceptional wave propagation characteristics, particularly their bandgap properties. The two fundamental mechanisms for creating bandgaps used in vibration attenuation are Bragg-type bandgaps and locally resonant bandgaps. However, like any other structures, periodic architectures are susceptible to defects over time, which can alter their wave propagation and dynamic behaviuor. In this study, we investigate the bandgap properties of a phononic beam structure with a periodically varying cross-section in the presence of cracks that disrupt periodicity. The dispersion analysis of both intact and damaged structures is performed using the spectral finite element method (SFEM), incorporating Bloch's theorem and the Wittrick-Williams (W-W) algorithm. Exact solutions are employed to derive the dynamic stiffness matrix, making the spectral element method highly accurate while requiring minimal discretization, thus ensuring computational efficiency. A single edge crack in the host beam is modeled on the basis of fracture mechanics principles, and a new dynamic stiffness matrix is formulated for the cracked beam. The effect of cracks on dispersion curves is initially examined using the super-cell method. Finally, frequency response functions (FRFs) are calculated for a finite structure with and without defects to validate the bandgap behaviour of the super-cell. The proposed method can be applied further for damage detection in periodic structures.

Key words: Phononic Crystals, Metamaterials, Bandgaps, Vibration Attenuation, Cracks, Damage Detection

1 INTRODUCTION

Phononic crystals and elastic metamaterials are widely used for their superior and unique wave propagation properties, including bandgaps and wave directionality. Brillouin et al. [1] showed the presence of phononic bandgaps in 1D monoatomic and diatomic chains, while the

Subhasish Sarkar & Srinivasan Gopalakrishnan
Department of Aerospace Engineering, Indian Institute of Science, Bangalore India - 560012
e-mail: subhasishs@iisc.ac.in

elastic wave propagation in 1D periodic structures made up of beam structures was first studied by Mead et al. [2, 3]. Phani et al. [4] later studied the wave propagation properties in 2D lattices with various topologies (square, hexagonal, Kagomé and triangular). Bragg's scattering mechanism, due to destructive interference because of material or geometric discontinuity, is one of the main reasons for the bandgap formation. Another popular and more tunable way to form the bandgap is the local resonance mechanism [5]. The longitudinal, flexural, and torsional wave bandgaps were obtained in the rod[6, 7], beam[8, 9, 10] and shaft [11] structures, respectively, with periodically placed local resonators. Various types of phononic structures have been successfully designed to create bandgaps tailored to specific engineering requirements. Finite phononic structures, in particular, can effectively attenuate the propagation of elastic waves within targeted frequency ranges. However, these structures are prone to damage, particularly the development of cracks over time. The presence of cracks can significantly alter the bandgap characteristics, making it crucial to understand their impact on the bandgap behaviour. The free vibration analysis of cracked beams has been extensively studied, primarily using the finite element method (FEM) [12, 13]. However, the dynamic stiffness method (DSM), particularly when implemented through the Fourier-based spectral finite element method (SFEM), offers a powerful alternative. Since SFEM employs exact shape functions, it provides highly accurate results even at high frequencies, requiring significantly less discretization compared to traditional FEM [14, 15]. The eigenvalue problem arising from the dynamic stiffness method (DSM) is transcendental and non-linear in nature, and can be efficiently solved using the Wittrick-Williams (W-W) algorithm [16, 17].

In this work, a detailed investigation is carried out to examine the effect of a concentrated open-edge crack on the dispersion characteristics of a phononic beam structure featuring a periodically varying cross-section. For the healthy structure, the dispersion analysis of the repeating unit cell is carried out using DSM based on SFEM in conjunction with Bloch's theorem. However, to account for the effect of the crack on the dispersion relation, the super-cell method is employed, which incorporates multiple unit cells along with the cracked unit cell. The bandgap properties obtained are further verified for a finite phononic system using the frequency response functions (FRFs). The effects of various parameters, such as crack depth, crack location within the unit cell, and the position of the cracked unit cell, on the dispersion relation and frequency response functions (FRFs) are also investigated. The methodology proposed here can be further applied to crack localisation and detection in phononic crystals.

2 METHODOLOGY

A healthy phononic beam structure with periodically varying cross-section as shown in Figure 1 is considered. The unit cell length is L_{uc} with two sub-cells, each of length L_A and L_B. The sub-cells have same width B, but differ in height, with values H_A and H_B respectively. Similarly, phononic beam structure with open edge non-propagating cracks and a unit cell with a single crack is shown in Figure 2.

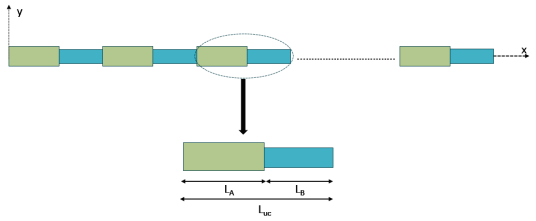

Figure 1: Healthy phononic beam system with unit cell

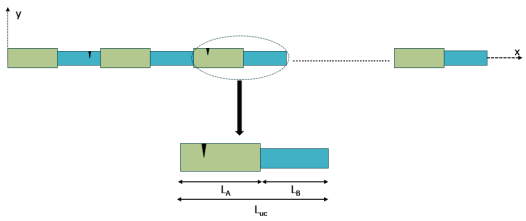

Figure 2: Phononic beam system and unit cell in presence of cracks

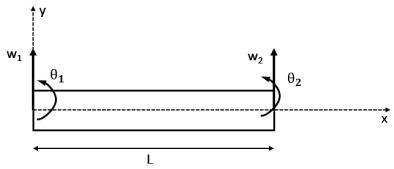

Figure 3: Beam element with nodal degrees of freedom

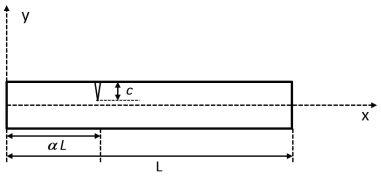

Figure 4: Beam with single open-edge crack

2.1 Dynamic stiffness matrix of healthy beam

The unit cell comprises beam elements, with each beam node having two degrees of freedom (dofs) as shown in Figure 3. The dynamic stiffness formulation of the beam is based on the Timoshenko beam theory for flexural vibration, which includes both shear deformation and rotary inertia.

The governing differential equations for flexural vibration based on Timoshenko theory in the frequency domain are:

$$\begin{aligned} kAG\frac{\partial}{\partial x}\left(\frac{\partial W(x)}{\partial x}-\theta(x)\right)+\omega^2\rho AW(x)=0 \\ EI\frac{\partial^2\theta(x)}{\partial x^2}+kAG\left(\frac{\partial W(x)}{\partial x}-\theta(x)\right)+\rho I\omega^2\theta(x)=0 \end{aligned} \tag{1}$$

where E is Young's modulus, G is shear modulus, A is the cross-section area, ρ is density, k is the shear correction factor, and ω is the angular frequency in rad/sec. The dynamic stiffness formulation for transverse vibration is:

$$\begin{bmatrix} V_1 \\ M_1 \\ V_2 \\ M_2 \end{bmatrix} = \begin{bmatrix} a_1 & a_2 & a_4 & a_5 \\ a_2 & a_3 & -a_5 & a_6 \\ a_4 & -a_5 & a_1 & -a_2 \\ a_5 & a_6 & -a_2 & a_3 \end{bmatrix} \begin{bmatrix} W_1 \\ \theta_1 \\ W_2 \\ \theta_2 \end{bmatrix} \Rightarrow F = K(\omega)U \tag{2}$$

where

$$
\begin{aligned}
a_1 &= R_3\bar{b}^2(\lambda_2+\eta\lambda_1)(cS+\eta sC)/(\lambda_1\lambda_2\delta)\\
a_2 &= R_2k_1\left[(\lambda_1+\eta\lambda_2)sS-(\lambda_2-\eta\lambda_1)(1-cC)\right]/\delta\\
a_3 &= R_1(\lambda_2+\eta\lambda_1)(sC-\eta cS)/\delta\\
a_4 &= -R_3\bar{b}^2(\lambda_2+\eta\lambda_1)(S+\eta s)/(\lambda_1\lambda_2\delta)\\
a_5 &= R_2k_1(\lambda_2+\eta\lambda_1)(C-c)/\delta\\
a_6 &= R_1(\lambda_2+\eta\lambda_1)(\eta S-s)/\delta
\end{aligned}
\tag{3}
$$

with

$$
\begin{aligned}
R_j &= EI/L^j, \quad j=1,2,3\\
s &= sin(\lambda_1), \quad c=cos(\lambda_1), \quad S=sinh(\lambda_2), \quad C=cosh(\lambda_2)\\
\eta &= k_1/k_2, \quad \delta = 2\eta(1-cC)+(1-\eta^2)sS\\
k_1 &= (\lambda_1^2-\bar{b}^2s^2)/\lambda_1, \quad k_2=(\lambda_2^2-\bar{b}^2s^2)/\lambda_2
\end{aligned}
\tag{4}
$$

where

$$
\left.\begin{matrix}\lambda_1\\ \lambda_2\end{matrix}\right\} = \bar{b}\left\{\pm\Delta/2+\left[\Delta^2/4+\left(1-\bar{b}^2r^2s^2\right)/\bar{b}^2\right]^{1/2}\right\}^{1/2} \tag{5}
$$

with

$$
\Delta = r^2+s^2, \quad \bar{b}^2=\frac{\rho A\omega^2L^4}{EI}, \quad r^2=\frac{I}{AL^2}, \quad s^2=\frac{EI}{kAGL^2} \tag{6}
$$

2.2 Dynamic stiffness matrix of cracked beam

A beam with a single non-propagating open-edge crack is shown in Figure 4, where the crack location is defined by the parameter α. The crack model formulated by taking bending, and shear stiffness reduction into account. As shown in Figure 5, the beam is discretized into three elements (a),(b) and (c) of lengths L_a, L_b, and L_c, respectively. L_c represents the cracked cross-sectional length, which is infinitesimally small.

The local flexibility at the location of the crack is related to the stress intensity factor. Using the Castigliano's theorem and the relation between the strain energy release rate and the stress intensity factor, the local flexibility at crack location is obtained assuming plane strain condition for various types of cross-sections. The local flexibility matrix of the crack element (c) is given by:

$$
C = \begin{bmatrix} C_{11} & 0\\ 0 & C_{22}\end{bmatrix} \tag{7}
$$

where

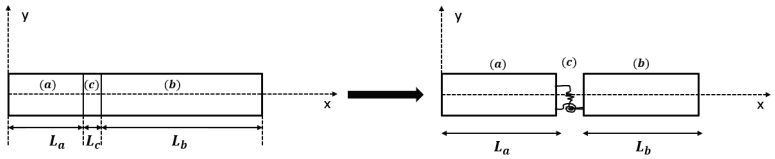

Figure 5: Cracked beam discretisation and its equivalent spring model

$$C_{11} = \frac{(1-\nu^2).F(1,1)}{EB}, \quad C_{22} = \frac{(1-\nu^2).F(2,2)}{EBH^2} \tag{8}$$

where ν is Poisson's ratio, b is the breadth, and h is the height of the rectangular beam cross-section. The dimensionless functions $F(1,1)$ and $F(2,2)$ are given by [13]:

$$\begin{aligned} F(1,1) = e^{\frac{1}{1-\xi}}\big(&- 0.326018 \times 10^{-6}\xi + 1.454954\xi^2 - 1.455784\xi^3 \\ &- 0.421981\xi^4 - 0.279522\xi^5 + 0.455399\xi^6 \\ &- 2.432830\xi^7 + 5.427219\xi^8 - 6.643057\xi^9 + 4.466758\xi^{10}\big) \\ F(2,2) = e^{\frac{1}{1-\xi}}\big(&- 0.219628 \times 10^{-4}\xi + 52.379034\xi^2 - 130.248317\xi^3 \\ &+ 308.442769\xi^4 - 602.445544\xi^5 + 939.044538\xi^6 \\ &- 1310.950293\xi^7 + 1406.523682\xi^8 - 1067.499820\xi^9 + 391.536356\xi^{10}\big) \end{aligned} \tag{9}$$

where $\xi = \frac{c}{H}$ is dimensionless crack depth.

The 4 X 4 stiffness matrix of the cracked element can be obtained as:

$$K_c = \begin{bmatrix} C^{-1} & -C^{-1} \\ -C^{-1} & C^{-1} \end{bmatrix} = \begin{bmatrix} k & -k \\ -k & k \end{bmatrix} \tag{10}$$

Now, the complete DSM of the cracked beam can be obtained by assembling the dynamic stiffness matrices of two beams elements (a) and (b) and a cracked element (c). DSM of elements (a) and (b) are given by:

$$K_a(\omega) = \begin{bmatrix} k_{11}^a & k_{12}^a \\ k_{21}^a & k_{22}^a \end{bmatrix}, \quad K_b(\omega) = \begin{bmatrix} k_{11}^b & k_{12}^b \\ k_{21}^b & k_{22}^b \end{bmatrix} \tag{11}$$

Using Equation (2), and (11), the overall DSM of the cracked beam is obtained as:

$$K_{cracked}(\omega) = \begin{bmatrix} k_{11}^a & k_{12}^a & 0 & 0 \\ k_{21}^a & k_{22}^a + k & -k & 0 \\ 0 & -k & k_{11}^b + k & k_{12}^b \\ 0 & 0 & k_{21}^b & k_{22}^b \end{bmatrix} \tag{12}$$

The DSM for a healthy beam in Equation (2) is a 4 X 4 matrix, whereas the DSM for a beam with single crack in Equation (12) is 8 X 8 matrix.

2.3 Bloch's theorem

When analysing periodic structures, it is not necessary to model the entire infinite structure to study its wave propagation characteristics. By applying Bloch's theorem [1], one can analyse a single unit cell to extract all essential vibrational properties, particularly the bandgap characteristics. For the unit cell illustrated in Figure 1, Bloch's theorem imposes the following periodic boundary condition:

$$u_R = e^{ik_x L_{uc}}.u_L \tag{13}$$

where, u_L and u_R are the generalised displacement vectors at left and right nodes respectively, $k_x \in [-\frac{\pi}{L_{uc}}, \frac{\pi}{L_{uc}}]$ is the wave vector along the first Brillouin zone. Equation (2) and Equation (13) are combined for the unit cell to formulate the final eigenvalue problem.

2.4 Wittrick-Williams algorithm

The dynamic stiffness matrices can now be utilised for eigenfrequency analysis for different scenarios like finite structures with classical and non-classical boundary conditions and periodic structures with Bloch boundary conditions. The eigenfrequency analysis requires that equation $K_{overall}(\omega).U = 0$ be solved by evaluating the zeros of the determinant of $K_{overall}(\omega)$. But the transcendental form of the eigenvalue problem is prone to numerical ill-conditioning and can miss closely spaced natural frequencies. However, this problem can be solved using an efficient and powerful technique called the Wittrick-Williams (W-W) algorithm. Using the Strum sequence property, the W-W algorithm computes the total number of natural frequencies $J(\omega^*)$ below a considered trail frequency ω^* as [16]:

$$J(\omega^*) = J_0(\omega^*) + s\{K_{overall}(\omega^*)\} = \sum_{k=1}^{n_b} J_k(\omega^*) + s\{K_{overall}(\omega^*)\} \tag{14}$$

where $s\{K_{overall}(\omega^*)\}$ is the sign count of the DSM of the overall structure $K_{overall}$, J_k is the number of natural frequencies between 0 and ω^* for k^{th} beam component with its ends fully clamped and n_b is the total number of beam components in the strucutre.

3 RESULTS AND DISCUSSIONS

3.1 Free vibration of a cracked beam

To validate the dynamic stiffness matrix formulation of the cracked beam element, the natural frequencies of a cantilever Timoshenko beam are calculated for various crack locations α and normalised crack depths ξ. Material and geometric properties used for the beam are given in Table 1. The first four natural frequencies for various cases are summarised in Table 2 and compared with the findings of [12], demonstrating a strong agreement.

Table 1: Material and Geometric Properties

Young's Modulus, E	**Density,** ρ	**Poisson's Ratio,** ν	**Length,** L	**Width,** B	**Height,** H
216 GPa	7850 kg/m^3	0.28	0.2 m	0.025 m	0.0078 m

Table 2: Comparison of natural frequencies ω (rad/sec) for different α and ξ values

$\alpha = L_1/L$	ω(rad/sec)	$\xi = c/H = 0.2$		$\xi = c/H = 0.4$	
		Present	*Ref. [12]*	*Present*	*Ref. [12]*
0.2	1	1021.3	1020.1	971.8	966.9
	2	6448.7	6457.4	6445.6	6454.0
	3	17768.5	17872.9	17521.9	17596.5
	4	34021.5	34553.1	32940.5	33100.4
0.4	1	1030.5	1030.1	1008.9	1006.9
	2	6386.2	6389.4	6186.9	6174.5
	3	17740.7	17844.8	17422.7	17499.8
	4	34288.5	34866.9	33960.3	34420.1

3.2 Dispersion Analysis

The unit cell of the phononic beam structure is of length L_{uc} = 0.1m, with $L_A = L_B$ = 0.05m, same width = 0.003m but different heights H_A = 0.005m and H_B = 0.0025m. The same material properties are used for both sub-cells, as listed in Table 1.The dispersion relation ($k_x - \omega$) within the first Brillouin zone for the healthy unit cell is presented in Figure 6, showing the presence of two flexural bandgaps: P1–P2 (601.1–838.8 Hz) and P3–P4 (2665–3806 Hz). The mode shapes associated with the edges of the identified bandgap (P1,P2,P3, and P4) are plotted in Figure 7, highlighting the fundamental vibration modes. The supercell method is commonly employed to investigate the effect of defects on the dispersion relation. The dispersion relation of a supercell, composed of 10 healthy unit cells, is presented in Figure 8. This dispersion relation exhibits band folding within the normalized first Brillouin zone; however, the bandgap region remains invariant, analogous to the results obtained from the individual unit cells.

To investigate the effect of a crack on the dispersion relation and the associated bandgaps, a supercell consisting of $n = 15$ unit cells is considered, with the cracked unit cell positioned at $n_c = 8$. The dimensionless crack depth is $\xi = 0.8$, and the crack is located at $\alpha = 0.5$ from the left end of the unit cell. The dispersion relation of the supercell containing a single cracked

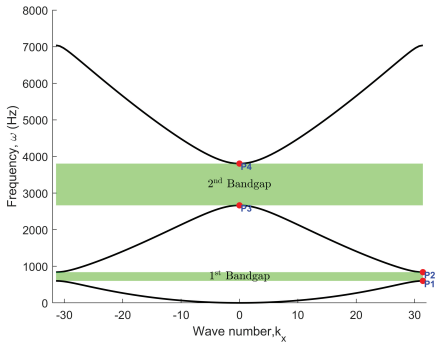

Figure 6: Dispersion curve of a healthy unit cell

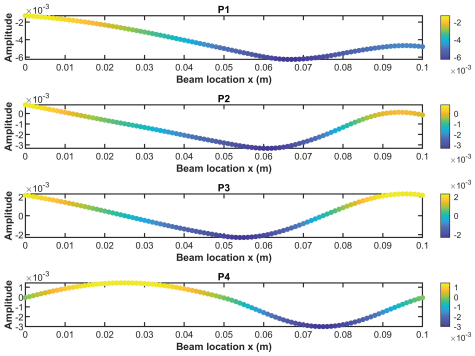

Figure 7: Mode shapes corresponding to points P1, P2, P3 and P4

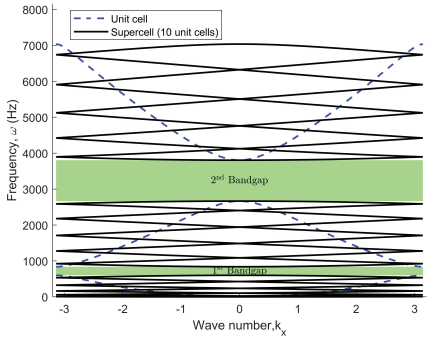

Figure 8: Dispersion curve of a supercell with 10 unit cells

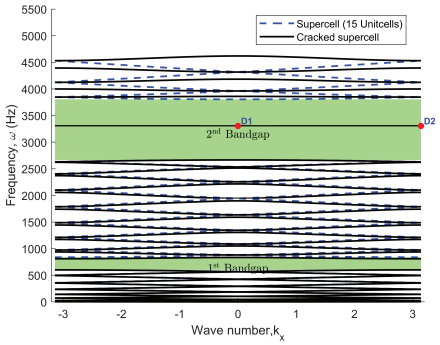

Figure 9: Dispersion curve of a cracked supercell

unit cell is shown in Figure 9. Although minor deviations in the dispersion characteristics are evident due to the introduction of crack-induced periodicity, the primary flexural bandgaps remain largely preserved. Importantly, a flat band appears within the second bandgap at $\omega = 3304$ Hz, signifying the emergence of a localised mode. The mode shapes corresponding to points D1 and D2 on the flat band are presented in Figure 10, clearly illustrating the localised defect modes within the second bandgap.

3.3 Frequency Response Functions

While dispersion relations (k–ω) are characteristic of infinite phononic crystals (PnCs), real-world structures are finite in nature. To validate the effectiveness of the predicted bandgaps, frequency response functions (FRFs) are analysed for a finite periodic structure. The structure consists of 30 unit cells, with a harmonic force (F) applied at the extreme left end (L) of the

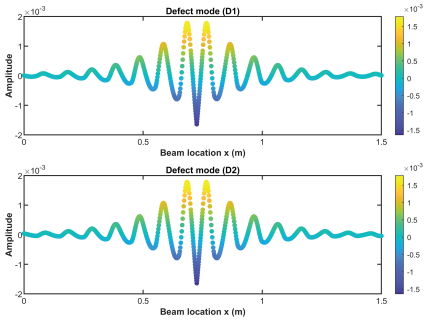

Figure 10: Defect mode shapes corresponding to points D1 and D2

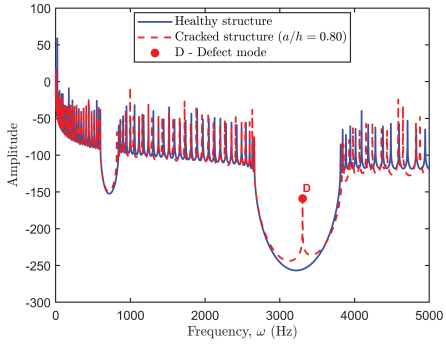

Figure 11: Frequency response function (FRF) for finite periodic structure with and without crack

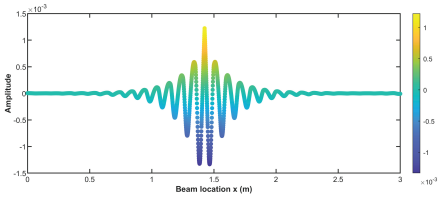

Figure 12: Mode shape corresponding to the point D for finite periodic beam with single crack

beam, and the response (x measured at the extreme right end (R), with the FRF is computed as $20\log(x_R)$ (in dB). Figure 11 presents a comparison of the frequency response functions (FRFs) between the healthy structure and the structure with a cracked unit cell located at $n_c = 15$. The FRF results show two prominent vibration attenuation regions, aligning with the first two bandgap regions identified in the dispersion curve Figure6. However, the FRF of the cracked structure displays a peak 'D' within the second attenuation region, which corresponds to the localised defect mode, as illustrated in Figure 12.

The defect mode observed in the FRF is influenced by several factors, including the crack depth (c), the crack location (α) within the unit cell, and the position of the cracked unit cell (n_c) within the phononic structure. The normalized crack depth (ξ) significantly influences the defect mode, as illustrated in Figure 13. For $\xi = 0.5$, the defect mode is located near the edge of the bandgap. However, as ξ increases, the defect mode shifts towards the center of the bandgap and becomes more distinctly localised. The crack location (α) within the unit cell, however,

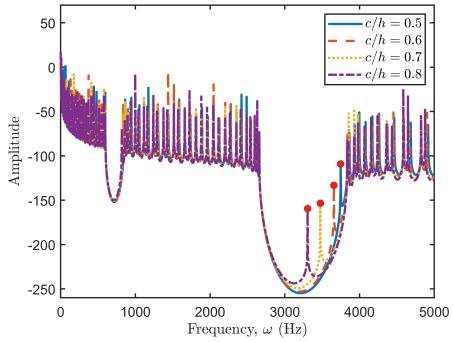

Figure 13: Frequency response function (FRF) for different $\xi = c/h$ values

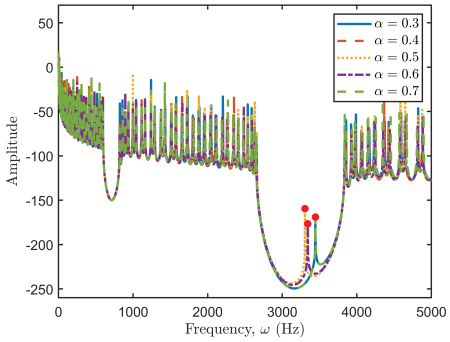

Figure 14: Frequency response function (FRF) with different 'α' values

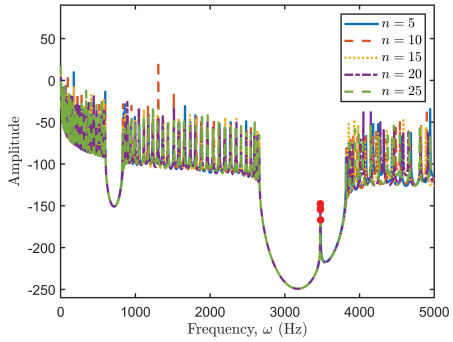

Figure 15: Frequency response function (FRF) with different cracked cell location (n_c)

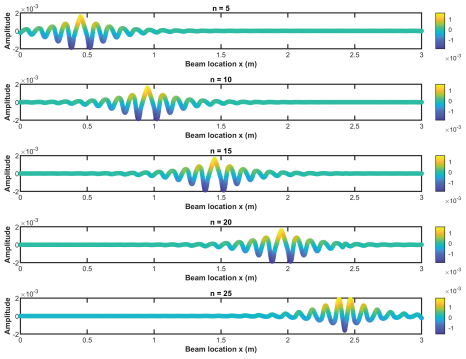

Figure 16: Defect mode shapes corresponding to various cracked cell locations (n_c)

exerts minimal influence on the position of the defect mode, as illustrated in Figure 14.

The position of the cracked unit cell (n_c) within the phononic structure does not affect the FRF, as the position of defect mode in the FRF remains unchanged, as shown in Figure 15. However, to better understand the actual impact of n_c, the shape of the mode corresponding to the defect modes is plotted and compared in Figure 16, which clearly shows that although the defect modes have same frequency but the localisation occurs in the location of the cracked unit cell for different cases of n_c.

4 CONCLUSIONS

In this study, the effect of non-propagating open-edge cracks on the dispersion relation of phononic beam structures is explored. The dynamic stiffness matrix based on the spectral finite element method (SFEM) was utilised in conjunction with Bloch's theorem to compute the dis-

persion relations of the phononic crystal. To incorporate the effect of crack on the bandgaps, the supercell method was utilised. The presence of the crack gives rise to defect modes, which appear within the bandgap regions. Further, the frequency response functions for finite phononic structures are analysed to verify the band structures of infinite phononic crystals. The FRFs demonstrates that the defect mode's position and its localisation are influenced by factor like crack depth, crack location within the unit cell, and the position of cracked unit cell in the phononic structure. Notably, the crack depth has a significant impact on the position of the defect mode, while the location of the cracked unit cell affects its localisation properties. The mode shapes corresponding to the defect modes further confirm the localised nature of these modes. This characteristic of the defect mode can be highly beneficial for crack localisation and detection in phononic structures. The work presented here can be further explored for complex lattice structures with crack elements. Also, the presence of defect modes in the bandgap regions can be used for crack localisation and detection.

REFERENCES

[1] L. n· Brillouin, *Wave Propagation in Periodic Structures: Electric Filters and Crystal Lattices*. Dover, 1953.

[2] D. J. Mead, "Wave propagation and natural modes in periodic systems: I. mono-coupled systems," *Journal of Sound and Vibration*, vol. 40, no. 1, pp. 1–18, 1975.

[3] D. Mead, "Wave propagation and natural modes in periodic systems: Ii. multi-coupled systems, with and without damping," *Journal of Sound and Vibration*, vol. 40, no. 1, pp. 19–39, 1975.

[4] A. S. Phani, J. Woodhouse, and N. Fleck, "Wave propagation in two-dimensional periodic lattices," *The Journal of the Acoustical Society of America*, vol. 119, no. 4, pp. 1995–2005, 2006.

[5] Z. Liu, X. Zhang, Y. Mao, Y. Y. Zhu, Z. Yang, C. T. Chan, and P. Sheng, "Locally resonant sonic materials," *science*, vol. 289, no. 5485, pp. 1734–1736, 2000.

[6] J. Lou, L. He, J. Yang, S. Kitipornchai, and H. Wu, "Wave propagation in viscoelastic phononic crystal rods with internal resonators," *Applied Acoustics*, vol. 141, pp. 382–392, 2018.

[7] E. Nobrega, F. Gautier, A. Pelat, and J. Dos Santos, "Vibration band gaps for elastic metamaterial rods using wave finite element method," *Mechanical Systems and Signal Processing*, vol. 79, pp. 192–202, 2016.

[8] D. Yu, Y. Liu, H. Zhao, G. Wang, and J. Qiu, "Flexural vibration band gaps in euler-bernoulli beams with locally resonant structures with two degrees of freedom," *Physical Review B—Condensed Matter and Materials Physics*, vol. 73, no. 6, p. 064301, 2006.

[9] E. Miranda Jr and J. Dos Santos, "Flexural wave band gaps in multi-resonator elastic metamaterial timoshenko beams," *Wave Motion*, vol. 91, p. 102391, 2019.

[10] S. R. Patro, A. Banerjee, and G. Ramana, "Vibration attenuation characteristics of finite locally resonant meta beam: Theory and experiments," *Engineering Structures*, vol. 278, p. 115506, 2023.

[11] L. Fan, Y. He, X. Chen, and X. Zhao, "Elastic metamaterial shaft with a stack-like resonator for low-frequency vibration isolation," *Journal of Physics D: Applied Physics*, vol. 53, no. 10, p. 105101, 2019.

[12] M. Kisa and J. Brandon, "The effects of closure of cracks on the dynamics of a cracked cantilever beam," *Journal of sound and vibration*, vol. 238, no. 1, pp. 1–18, 2000.

[13] D. Y. Zheng and N. Kessissoglou, "Free vibration analysis of a cracked beam by finite element method," *Journal of Sound and vibration*, vol. 273, no. 3, pp. 457–475, 2004.

[14] J. F. Doyle, *Wave propagation in structures: an FFT-based spectral analysis methodology*. Springer Science & Business Media, 2012.

[15] S. Gopalakrishnan, M. Martin, and J. Doyle, "A matrix methodology for spectral analysis of wave propagation in multiple connected timoshenko beams," *Journal of Sound and Vibration*, vol. 158, no. 1, pp. 11–24, 1992.

[16] W. Wittrick and F. Williams, "A general algorithm for computing natural frequencies of elastic structures," *The Quarterly Journal of Mechanics and Applied Mathematics*, vol. 24, no. 3, pp. 263–284, 1971.

[17] F. Han, D. Dan, W. Cheng, and Z. Jubao, "An improved wittrick-williams algorithm for beam-type structures," *Composite Structures*, vol. 204, pp. 560–566, 2018.

XI ECCOMAS Thematic Conference on Smart Structures and Materials - SMART 2025
M. Krommer, M. Nader and M. Schagerl (Eds)

Received: 31 May 2025 / Revised: 31 August 2025 / Accepted: 19 October 2025
© The Author(s) 2025

On the Global Dynamics of Metaimpactor Lattices using Physics-Enhanced Machine Learning

Rui Zhang, Marcus Haywood-Alexander, Oleg Gendelman, Sami Masri, Eleni Chatzi, Vasilis Dertimanis

Abstract. We introduce the metaimpactor, a metamaterial lattice that leverages impact dampers for enhanced energy dissipation and vibration attenuation. While discontinuous dynamics can be approximated by high-order smooth functions, they fall short in capturing the chaotic behavior and bifurcations of the metaimpactor. To address this, we develop a physics-enhanced machine learning (PEML) framework using sequential Physics-Informed Neural Networks (PINNs) Impact times—unknowns in conventional analysis—are treated as learnable variables, while the dynamics between impacts are solved via PINNs. By embedding physical constraints, the method accurately reconstructs complex, multi-impact responses. We validate the approach on a single-degree-of-freedom system, demonstrating its ability to capture nonsmooth dynamics and sequential impacts. This work lays the foundation for new classes of vibration control devices, with future extensions targeting nonlinear lattices and high-frequency, multi-impact regimes.

Key words: Nonlinear Metamaterials, Vibro–Impact, Physics-Enhanced Machine Learning

1 INTRODUCTION

The mitigation of structural vibrations under dynamic loads, such as earthquakes, remains a critical engineering challenge. Traditional passive dampers, including tuned mass dampers (TMDs) [1, 2], are constrained by narrow operational bandwidths, while active systems [3, 4] face prohibitive costs and energy demands. Recent advancements in metamaterials—artificially

Rui Zhang & Marcus Haywood-Alexander & Eleni Chatzi & Vasilis Dertimanis
Department of Civil, Environmental and Geomatic Engineering, ETH Zürich, Stefano-Franscini-Platz 5, 8093 Zürich, Switzerland, e-mail: rui.zhang@ibk.baug.ethz.ch

Oleg Gendelman
Department of Mechanical Engineering, Technion, Israel Institute of Technology, 3200003 Haifa, Israel, e-mail: ovgend@technion.ac.il

Sami Masri
Department of Civil Engineering, University of Southern California, Los Angeles, CA, 90089-2531, USA, e-mail: masri@usc.edu

structured systems with tailored wave-filtering properties—offer a promising alternative. By leveraging periodic arrangements of resonant unit cells, these systems exhibit frequency bandgap where vibrational energy is attenuated [5, 6]. However, conventional linear metamaterials often suffer from limited bandgap widths and high cutoff frequencies, restricting their applicability to low-frequency structural vibrations.

To address these limitations, nonlinearity has been explored as part of the unit cell design, with solutions including nonlinear resonators, and impact dampers [7, 8]. Impact dampers dissipate energy through momentum exchange during impacts, enabling broadband vibration suppression [9, 10, 11]. While their effectiveness in single-degree-of-freedom systems is well-documented [12, 13], extending these benefits to metamaterial lattices poses significant modeling challenges. The nonsmooth dynamics of impacts, characterized by discontinuous velocity resets and chaotic regimes [14, 15, 16, 17], defy conventional analytical and numerical methods. Traditional solvers, such as Runge-Kutta with event detection, struggle with scalability for large lattices and often require a priori assumptions about impact timing, leading to inaccuracies in predicting bandgaps and energy dissipation.

Modeling the complex, nonsmooth behavior of impact-based systems requires methods that can capture both continuous dynamics and discontinuous events in a unified framework. Physics-Informed Neural Networks (PINNs) offer a promising direction in this regard. By embedding the governing equations and boundary or initial conditions directly into the loss function of a neural network, PINNs enable the solution of forward and inverse problems [18, 19, 20]. This approach has proven effective across diverse applications, including fluid mechanics [21], material modeling [22], contact mechanics [23], nonsmooth dynamical systems [24], and structural dynamics [25]. The use of PINNs for systems with repeated impacts and discontinuous velocity profiles remains a challenging and relatively unexplored area. However, decomposing the learning paradigm into simpler domains has been shown to benefit PINNs; such as with parallel [26] or sequential/recurrent [27] PINNS which reduce the scope of individual training domains.

This work introduces a sequential Physics-Informed Neural Network (PINN) framework for modeling the nonsmooth dynamics of vibro-impact systems with internal impact dampers. Impact times are treated as learnable variables, enabling the network to identify discontinuities directly from the governing physics. Each PINN segment models the response between successive impacts and enforces the dynamics and impact conditions during training. Upon impact, velocities are updated using momentum and restitution laws, and the resulting state initializes the next segment. Chaining these segments yields a complete multi-impact response without requiring explicit event detection. While the framework is designed for nonlinear lattice systems, this study focuses on a single-degree-of-freedom (SDOF) configuration to demonstrate its core mechanisms. This simplified case enables transparent validation and demonstrates the framework's ability to capture nonsmooth dynamics and sequentially identify multiple impacts based on embedded physical constraints. The proposed framework will be further developed for application to full-scale metamaterial lattices, facilitating dispersion analysis and performance validation under high-frequency, multi-impact conditions.

2 PROBLEM DESCRIPTION AND GOVERNING EQUATIONS

2.1 Nonlinear Meta-Impact Lattice

The system under consideration is a nonlinear metamaterial lattice composed of a consecutive arrangement of unit cells, each incorporating an impact damper. The primary objective of this configuration is to reduce the vibrational response of a protected structure through energy dissipation induced by internal impacts. Each unit cell consists of a rigid container of mass m, connected to neighboring cells via springs with stiffness k and damping coefficient c, and housing a free internal mass μ that can translate laterally. The internal mass is allowed to move within a bounded region defined by a clearance D on either side and interacts with the container walls through impact events.

The unit cells are arranged in a chain and elastically connected to each other. The leftmost cell is fixed, while the rightmost cell is attached to a primary oscillator with mass M, stiffness K, and damping C. An external force F is applied to the primary mass. This configuration is illustrated in Figure 1.

Dynamic nonlinearity arises when the relative displacement between the outer mass and the inner mass in a unit cell reaches the clearance limit. At such instances, a discontinuous change in velocity occurs due to impact, introducing complex nonsmooth dynamics that are challenging to model using classical continuous-time approaches.

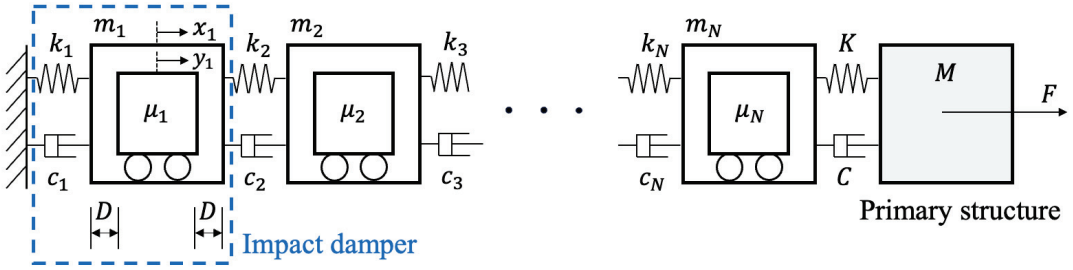

Figure 1: Nonlinear lattice of impact dampers coupled to a primary structure.

2.2 Governing Equations

The global equation of motion for the nonlinear metamaterial lattice coupled to a primary structure can be expressed as:

$$\mathbf{M}\ddot{\mathbf{X}}(t) + \mathbf{C}\dot{\mathbf{X}}(t) + \mathbf{K}\mathbf{X}(t) = \mathbf{F}(t), \tag{1}$$

where $\mathbf{X}(t) \in \mathbb{R}^{N+1}$ is the vector of nodal displacements of the N unit cells and the main structure:

$$\mathbf{X}(t) = \begin{bmatrix} x_1(t) & x_2(t) & \cdots & x_N(t) & X(t) \end{bmatrix}^\top. \tag{2}$$

Here, $x_i(t)$ denotes the displacement of the i-th container mass in the lattice, and $X(t)$ is the displacement of the protected primary mass. The external excitation $\mathbf{F}(t)$ is nonzero only in the last component:

$$\mathbf{F}(t) = \begin{bmatrix} 0 & \cdots & 0 & F(t) \end{bmatrix}^\top. \tag{3}$$

The mass matrix $\mathbf{M}$ is diagonal and expressed as:

$$\mathbf{M} = \text{diag}(m_1, m_2, \ldots, m_N, M). \tag{4}$$

The stiffness matrix $\mathbf{K}$ is tridiagonal and expressed as:

$$\mathbf{K} = \begin{bmatrix} k_1 + k_2 & -k_2 & 0 & \cdots & 0 & 0 \\ -k_2 & k_2 + k_3 & -k_3 & \cdots & 0 & 0 \\ 0 & -k_3 & k_3 + k_4 & \cdots & 0 & 0 \\ \vdots & \vdots & \vdots & \ddots & \vdots & \vdots \\ 0 & 0 & 0 & \cdots & k_N + K & -K \\ 0 & 0 & 0 & \cdots & -K & K \end{bmatrix}. \tag{5}$$

The damping matrix $\mathbf{C}$ is tridiagonal and expressed as:

$$\mathbf{C} = \begin{bmatrix} c_1 + c_2 & -c_2 & 0 & \cdots & 0 & 0 \\ -c_2 & c_2 + c_3 & -c_3 & \cdots & 0 & 0 \\ 0 & -c_3 & c_3 + c_4 & \cdots & 0 & 0 \\ \vdots & \vdots & \vdots & \ddots & \vdots & \vdots \\ 0 & 0 & 0 & \cdots & c_N + C & -C \\ 0 & 0 & 0 & \cdots & -C & C \end{bmatrix}. \tag{6}$$

Each internal mass $y_i(t)$ evolves as:

$$\mu_i \ddot{y}_i(t) = 0, \quad \text{subject to} \quad |x_i(t) - y_i(t)| < D. \tag{7}$$

This formulation governs the structure between impact events. Discontinuities due to impact are handled by conservation laws, detailed in the subsequent sections.

2.3 Impact Conditions

The impact condition is enforced when the displacement gap reaches the clearance:

$$|x_i(t) - y_i(t)| = D, \tag{8}$$

triggering a discontinuous velocity change governed by momentum and restitution laws.

To characterize the discontinuous jump in velocity at impact, we introduce the coefficient of restitution $r \in [0, 1]$, which defines the ratio of relative velocities after and before impact [12]:

$$r = -\frac{\dot{y}_i^+ - \dot{x}_i^+}{\dot{y}_i^- - \dot{x}_i^-}, \tag{9}$$

where $\dot{x}_i^-$ and $\dot{y}_i^-$ are the pre-impact velocities, and $\dot{x}_i^+$, $\dot{y}_i^+$ are the post-impact velocities.

Momentum conservation during the (assumed instantaneous) impact yields:

$$m_i\dot{x}_i^+ + \mu_i\dot{y}_i^+ = m_i\dot{x}_i^- + \mu_i\dot{y}_i^-. \tag{10}$$

Combining Eqs. (9) and (10), the post-impact velocities can be computed using:

$$\begin{bmatrix}\dot{x}_i^+\\ \dot{y}_i^+\end{bmatrix} = \frac{1}{m_i+\mu_i}\begin{bmatrix}m_i - r\mu_i & (1+r)\mu_i\\ (1+r)m_i & \mu_i - rm_i\end{bmatrix}\begin{bmatrix}\dot{x}_i^-\\ \dot{y}_i^-\end{bmatrix}. \tag{11}$$

2.4 Modeling Challenges and Motivations

Modeling impact-based systems poses significant challenges due to the presence of nonsmooth dynamics and discontinuous velocity changes. Traditional event-based solvers require precise impact detection and manual velocity resets, which can become cumbersome and numerically sensitive, especially in systems with multiple impacts or chaotic behavior.

To overcome these limitations, the problem is reformulated using a sequential Physics-Informed Neural Network (PINN) framework that incorporates both the governing equations and impact conditions directly into the training process. The architecture of the proposed sequential PINN framework is detailed in the following section.

3 SEQUENTIAL PHYSICS-INFORMED NEURAL NETWORK FRAMEWORK

3.1 Overview of the Framework

While the proposed sequential PINN framework is formulated with the general goal of modeling nonlinear lattice systems with internal impact dampers, its structure is equally well-suited to single-unit configurations. In this work, a single-degree-of-freedom system is used to demonstrate the key features of the framework—namely, its ability to identify impact times, model nonsmooth dynamics, and reconstruct the system response through modular PINN segments. An overview of the sequential framework is shown in Figure 2.

As shown in Figure 2(a), each PINN cell models the system response between two successive impacts. Figure 2(b) illustrates the internal structure of a PINN cell, at the beginning of each segment, the system state $\mathbf{z}_0 = [x_0, \dot{x}_0, y_0, \dot{y}_0]^\top$ is used as the initial condition. The network takes time $t \in [0, T]$ as input and predicts the displacement of the primary mass $x(t)$. The displacement of the internal mass is defined analytically, based on its initial displacement and velocity, as

$$y(t) = y_0 + \dot{y}_0 t. \tag{12}$$

The neural network $x(t;\theta)$ consists of fully connected layers with `tanh` activation functions, chosen to model smooth dynamics between impacts. The first and second order time derivatives of $x(t)$ are computed using automatic differentiation. The impact time t_{impact} is treated as a learnable scalar variable, optimized during training to satisfy the impact constraint. When an impact occurs, post-impact velocities are computed based on momentum conservation and restitution laws, and the resulting state is passed forward to initialize the next PINN cell.

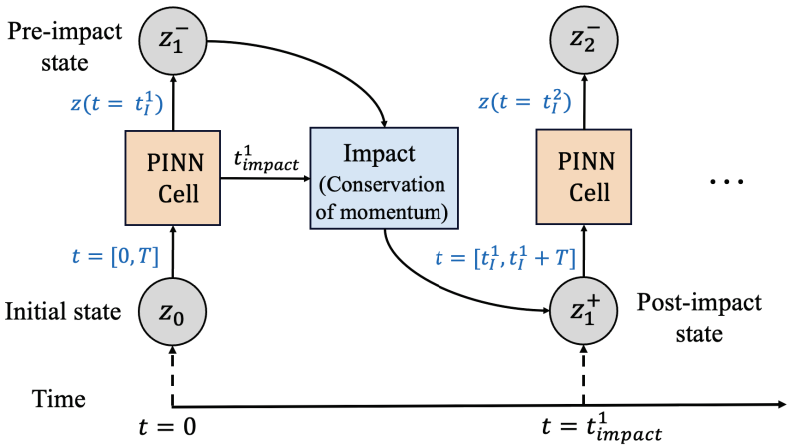

(a) Proposed Sequential PINN framework for modeling impact dampers.

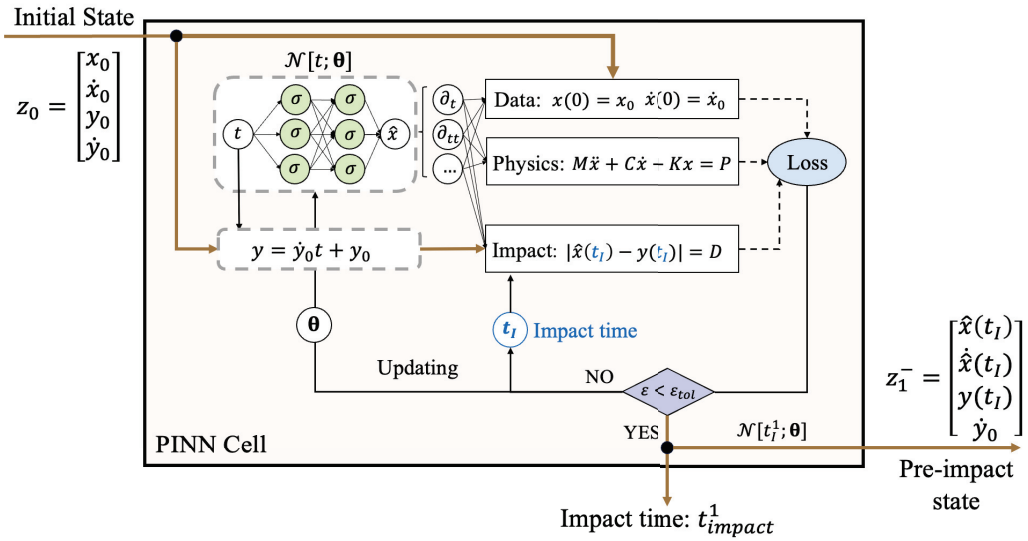

(b) PINN Cell.

Figure 2: (a) Proposed Sequential PINN framework for modeling impact dampers; and (b) PINN Cell.

3.2 Physics-Informed Loss Function

Each PINN cell is trained by minimizing a composite loss function that enforces physical consistency of the solution within its time interval. The total loss is defined as:

$$\mathcal{L}_{\text{total}} = \beta_{\text{IC}}\mathcal{L}_{\text{IC}} + \beta_{\text{ODE}}\mathcal{L}_{\text{ODE}} + \beta_{\text{impact}}\mathcal{L}_{\text{impact}}, \tag{13}$$

where β_{IC}, β_{ODE}, and β_{impact} are weights balancing the convergence rate of each loss term.

The first term, the initial condition loss $\mathcal{L}_{\text{IC}}$, ensures agreement with the known initial displacement and velocity of the primary mass at the start of the interval:

$$\mathcal{L}_{\text{IC}} = \left(x(0) - x_0\right)^2 + \left(\dot{x}(0) - \dot{x}_0\right)^2 . \tag{14}$$

The second term, the ODE residual loss $\mathcal{L}_{\text{ODE}}$, penalizes violations of the governing equation over a set of collocation points $\{t_i\}_{i=1}^{N_r}$:

$$\mathcal{L}_{\text{ODE}} = \frac{1}{N_r} \sum_{i=1}^{N_r} \left(m\ddot{x}(t_i) + c\dot{x}(t_i) + kx(t_i)\right)^2 . \tag{15}$$

The final term, the impact condition loss $\mathcal{L}_{\text{impact}}$, enforces the occurrence of an impact at an unknown time $t = t_{\text{impact}}$. This is achieved by penalizing deviations between the predicted relative displacement and the known clearance D at that instant:

$$\mathcal{L}_{\text{impact}} = \left(|x(t_{\text{impact}}) - y(t_{\text{impact}})| - D\right)^2 . \tag{16}$$

3.3 Determination of the Impact Time and Estimation of the Structural Response

The training procedure minimizes the total loss by jointly optimizing the neural network parameters θ and the impact time variable t_{impact} within each PINN cell. At each training iteration, the network is evaluated at both the collocation points and the current estimate of t_{impact}. The total loss is then computed and backpropagated to update both θ and t_{impact}.

Once trained, the network identifies the corresponding impact time and predicts the displacement $x(t)$, along with its first and second derivatives $\dot{x}(t)$ and $\ddot{x}(t)$. At the estimated impact time, the velocities of the primary and internal masses are updated using conservation of momentum and restitution laws. The resulting post-impact state serves as the initial condition for the subsequent PINN cell.

This procedure is repeated for each impact segment using a sequence of independently trained PINN cells. The full multi-impact response of the system is reconstructed by concatenating the outputs of all segments. To improve convergence and stability, a two-stage training strategy is employed: the loss function is initially minimized using the Adam optimizer with a predefined stopping condition, followed by refinement using the L-BFGS-B algorithm. Pseudocode outlining the proposed sequential PINN framework is provided in Algorithm 1.

4 NUMERICAL RESULTS

4.1 Simulation Setup

To evaluate the performance of the proposed framework, a single impact damper unit cell is considered as a representative test case. The system parameters are defined as follows: primary mass $m = 1\,\text{kg}$, internal mass $\mu = 0.3\,\text{kg}$, spring stiffness $k = 1\,\text{N/m}$, damping coefficient $c = 0\,\text{Ns/m}$, and clearance distance $D = 1\,\text{m}$. The total simulation time is set to $T = 20\,\text{s}$.

The initial conditions are given by $x(0) = 0\,\text{m}$, $\dot{x}(0) = 0\,\text{m/s}$, $y(0) = 0\,\text{m}$, and $\dot{y}(0) = -1\,\text{m/s}$. Both the sequential PINN framework and the event-based reference simulation are initialized with these same conditions to ensure consistency and fairness in the comparison.

Algorithm 1 Sequential PINN Framework for Impact Time and Response Estimation

Require: Initial state $\mathbf{z}_0 = [x_0, \dot{x}_0, y_0, \dot{y}_0]$, parameters m, c, k, μ, D, either number of impacts N_{imp} or final time T

Set $j = 1$, $t_0 = 0$
while (not reached T) **or** (not reached N_{imp}) **do**
  Initialize PINN cell with parameters $\theta^{(j)}$ and learnable $t_{\text{impact}}^{(j)}$
  Sample collocation points in $[t_{j-1}, T]$
  Define loss with initial condition, governing equation, and impact constraints
  Minimize loss using Adam followed by L-BFGS-B
  Estimate $t_{\text{impact}}^{(j)}$ and predict $x^{(j)}(t)$, $\dot{x}^{(j)}(t)$, and $\ddot{x}^{(j)}(t)$ in $[t_{j-1}, t_{\text{impact}}^{(j)}]$
  Apply impact law; update state $\mathbf{z}_j$, set $t_j = t_{\text{impact}}^{(j)}$
  Increment $j \leftarrow j + 1$
end while
return Estimated impact times and full response $x(t)$, $\dot{x}(t)$, $\ddot{x}(t)$, $y(t)$, $\dot{y}(t)$

4.2 Determination of the Impact Times

A key feature of the proposed sequential PINN framework is its ability to discover the impact times through physics-constrained optimization. During training, each impact time $t_{\text{impact}}^{(i)}$ is treated as a learnable scalar variable. The corresponding loss term $\mathcal{L}_{\text{impact}}^{(i)}$ is minimized jointly with the residuals of the governing equations and initial conditions.

Figure 3 illustrates the training convergence of impact time estimates across six successive impacts. Each subplot shows the evolution of $t_{\text{impact}}^{(i)}$ over training iterations. Dashed horizontal lines indicate the reference values computed by the event-based solver. The results demonstrate that the PINN framework reliably converges to accurate impact times that closely match those obtained from the event-based solver.

4.3 Structural Response Estimation

Figures 4(a)–(d) present the structural response predicted by the sequential PINN framework. In all panels, vertical dashed lines indicate the estimated impact times. Figure 4(a) shows the displacement of the primary and internal masses, while Figure 4(b) presents their corresponding velocities. Figure 4(c) plots the relative displacement $x(t) - y(t)$, which captures the onset of impacts as it approaches the clearance threshold. Figure 4(d) illustrates the impulse history, reflecting the momentum exchange resulting from the impacts.

For comparison, impact times are first determined using an event-based method, and the structural response between impacts is then computed analytically from the closed-form solution of the undamped system. As shown in Figure 4(c), the results demonstrate that the sequential PINN framework can accurately reconstruct both the smooth dynamics and nonsmooth impact events of the system.

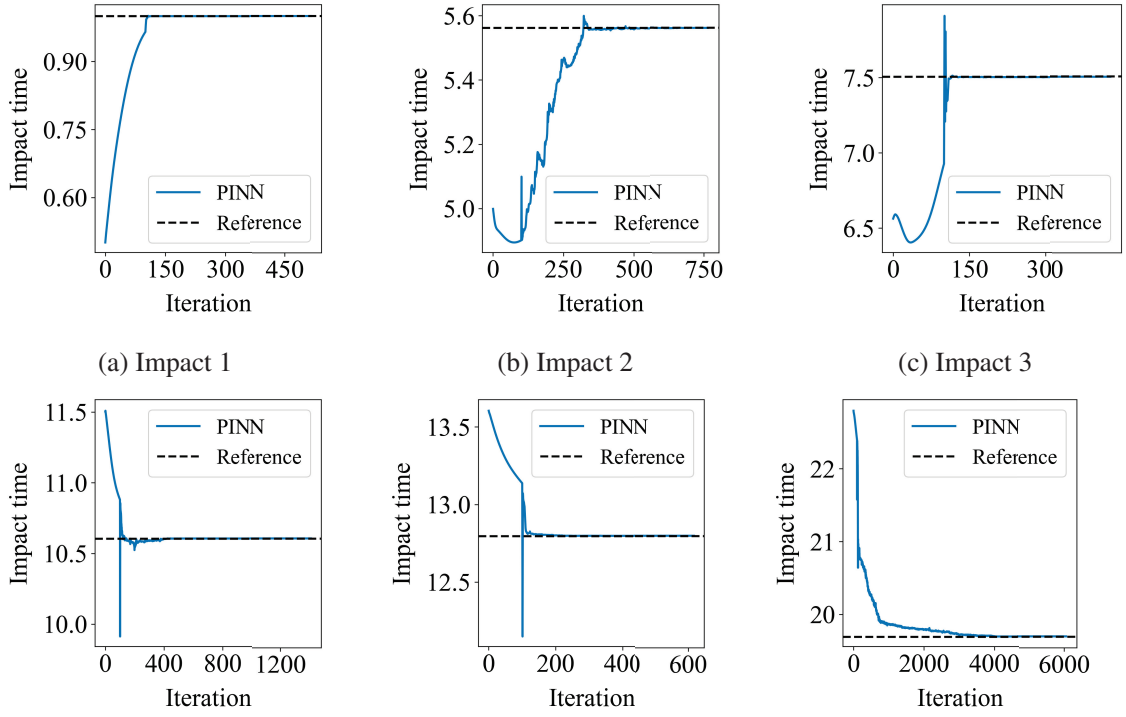

(a) Impact 1 (b) Impact 2 (c) Impact 3

(d) Impact 4 (e) Impact 5 (f) Impact 6

Figure 3: Training convergence of impact time estimation using PINN.

5 CONCLUSION

This work presents a sequential Physics-Informed Neural Network (PINN) framework for modeling the dynamics of vibro-impact systems equipped with internal impact dampers. By embedding both the governing equations and impact constraints into the loss function, the method enables direct learning of nonsmooth dynamics from the underlying physics, without relying on labeled data or explicit event detection. A key feature of the framework is the treatment of impact times as learnable variables, allowing the network to identify discontinuities through physics-constrained optimization.

The structural response is captured by linking multiple PINN segments, each responsible for modeling the system behavior between two consecutive impacts. At each predicted impact, momentum-based velocity updates are applied, and the resulting post-impact state is used to initialize the next segment. This recursive structure provides a modular and physically consistent approach to modeling repeated impact events.

The framework has been validated on a single degree-of-freedom impact damper system. The results demonstrate that the PINN accurately identifies both the impact times and the dynamic response of the system. Future developments will target the extension of this framework

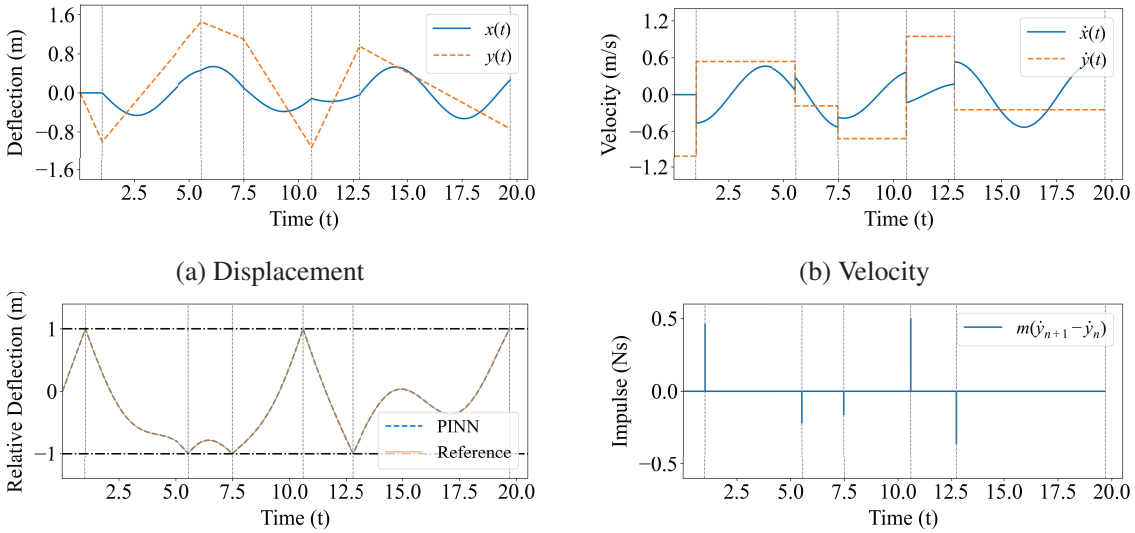

(a) Displacement

(b) Velocity

(c) Relative displacement

(d) Impulse time history

Figure 4: Structural response of the impact damper system predicted by the sequential PINN framework. (a) displacement and (b) velocity of primary and internal masses, (c) relative displacement compared to the reference impact threshold, and (d) impulse time history. Vertical dashed lines indicate impact events.

to lattice systems with many unit cells and more frequent impact events.

REFERENCES

[1] R. Rana and T. T. Soong, "Parametric study and simplified design of tuned mass dampers," *Engineering structures*, vol. 20, no. 3, pp. 193–204, 1998.

[2] S. Elias and V. Matsagar, "Research developments in vibration control of structures using passive tuned mass dampers," *Annual Reviews in Control*, vol. 44, pp. 129–156, 2017.

[3] I. Venanzi, "A review on adaptive methods for structural control," *The Open Civil Engineering Journal*, vol. 10, no. 1, 2016.

[4] W. Yu and S. Thenozhi, *Active structural control with stable fuzzy PID techniques*. Springer, 2016.

[5] M. Sigalas and E. N. Economou, "Band structure of elastic waves in two dimensional systems," *Solid state communications*, vol. 86, no. 3, pp. 141–143, 1993.

[6] M. S. Kushwaha, P. Halevi, G. Martinez, L. Dobrzynski, and B. Djafari-Rouhani, "Theory of acoustic band structure of periodic elastic composites," *Physical Review B*, vol. 49, no. 4, p. 2313, 1994.

[7] V. K. Dertimanis, S. F. Masri, and E. N. Chatzi, "On the vibration attenuation properties of finite periodic lattices of impact dampers," in *9th ECCOMAS Thematic Conference on Smart Structures and Materials (SMART 2019)*, 2019, pp. 1146–1154.

[8] K. A. Chondrogiannis, V. Dertimanis, S. Masri, and E. Chatzi, "Vibration absorption performance of metamaterial lattices consisting of impact dampers," in *EURODYN 2020. Proceedings of the XI International Conference on Structural Dynamics. Volume II*. European Association for Structural Dynamics, 2020, pp. 4139–4149.

[9] S. Masri, "General motion of impact dampers," *The Journal of the Acoustical Society of America*, vol. 47, no. 1B, pp. 229–237, 1970.

[10] S. Masri and T. Caughey, "On the stability of the impact damper," *Journal of Applied Mechanics*, vol. 33, no. 3, pp. 586–592, 1966.

[11] S. Masri and A. Ibrahim, "Response of the impact damper to stationary random excitation," *The Journal of the Acoustical Society of America*, vol. 53, no. 1, pp. 200–211, 1973.

[12] A. F. Vakakis, O. V. Gendelman, L. A. Bergman, D. M. McFarland, G. Kerschen, and Y. S. Lee, *Nonlinear targeted energy transfer in mechanical and structural systems*. Springer Science & Business Media, 2008, vol. 156.

[13] M. Duncan, C. Wassgren, and C. Krousgrill, "The damping performance of a single particle impact damper," *Journal of sound and vibration*, vol. 286, no. 1-2, pp. 123–144, 2005.

[14] O. V. Gendelman, "Modeling of inelastic impacts with the help of smooth-functions," *Chaos, Solitons & Fractals*, vol. 28, no. 2, pp. 522–526, 2006.

[15] R. A. Ibrahim, *Vibro-impact dynamics: modeling, mapping and applications*. Springer Science & Business Media, 2009, vol. 43.

[16] M. Dimentberg and D. Iourtchenko, "Random vibrations with impacts: a review," *Nonlinear Dynamics*, vol. 36, pp. 229–254, 2004.

[17] V. Pilipchuk, "Impact modes in discrete vibrating systems with rigid barriers," *International journal of non-linear mechanics*, vol. 36, no. 6, pp. 999–1012, 2001.

[18] M. Raissi, P. Perdikaris, and G. E. Karniadakis, "Physics-informed neural networks: A deep learning framework for solving forward and inverse problems involving nonlinear partial differential equations," *Journal of Computational physics*, vol. 378, pp. 686–707, 2019.

[19] S. Cuomo, V. S. Di Cola, F. Giampaolo, G. Rozza, M. Raissi, and F. Piccialli, "Scientific machine learning through physics-informed neural networks: Where we are and what's next," *arXiv preprint arXiv:2201.05624*, 2022.

[20] G. E. Karniadakis, I. G. Kevrekidis, L. Lu, P. Perdikaris, S. Wang, and L. Yang, "Physics-informed machine learning," *Nature Reviews Physics*, vol. 3, no. 6, pp. 422–440, 2021.

[21] S. Cai, Z. Mao, Z. Wang, M. Yin, and G. E. Karniadakis, "Physics-informed neural networks (pinns) for fluid mechanics: A review," *Acta Mechanica Sinica*, vol. 37, no. 12, pp. 1727–1738, 2021.

[22] G. P. Pun, R. Batra, R. Ramprasad, and Y. Mishin, "Physically informed artificial neural networks for atomistic modeling of materials," *Nature communications*, vol. 10, no. 1, p. 2339, 2019.

[23] T. Sahin, M. von Danwitz, and A. Popp, "Solving forward and inverse problems of contact mechanics using physics-informed neural networks," *Advanced Modeling and Simulation in Engineering Sciences*, vol. 11, no. 1, p. 11, 2024.

[24] Z. Li, J. Bai, H. Ouyang, S. Martelli, M. Tang, Y. Yang, H. Wei, P. Liu, R. Wei, and Y. Gu, "Physics-informed neural networks for friction-involved nonsmooth dynamics problems," *Nonlinear Dynamics*, vol. 112, no. 9, pp. 7159–7183, 2024.

[25] M. Haywood-Alexander, W. Liu, K. Bacsa, Z. Lai, and E. Chatzi, "Discussing the spectrum of physics-enhanced machine learning: a survey on structural mechanics applications," *Data-Centric Engineering*, vol. 5, p. e30, 2024.

[26] R. Zhang, G. P. Warn, and A. Radlińska, "Physics-informed parallel neural networks with self-adaptive loss weighting for the identification of continuous structural systems," *Computer Methods in Applied Mechanics and Engineering*, vol. 427, p. 117042, 2024.

[27] M. Haywood-Alexander and E. Chatzi, "Physics-informed neural networks for one-step-ahead prediction of dynamical systems," *STRUCTURAL HEALTH MONITORING 2023*, 2023.

Part VIII
MS 07 - RECENT ADVANCES IN NON-LINEAR MODELING AND NUMERICAL METHODS FOR SMART MATERIALS AND STRUCTURES

Alexander Humer, Michael Krommer, Astrid Pechstein

XI ECCOMAS Thematic Conference on Smart Structures and Materials - SMART 2025
M. Krommer, M. Nader and M. Schagerl (Eds)

Received: 29 April 2025 / Revised: 29 August 2025 / Accepted: 22 October 2025
© The Author(s) 2025

Application of Rate-type Variational Formulations and Scalable Linear Solvers to the Thermo-Chemo-Mechanical Modeling of Hydrogels

Akshay B Jeeja, Bjoern Kiefer, Stefan Prüger, Oliver Rheinbach, Friederike Röver

Abstract. In this work, we compare two variational formulations of a chemo-mechanical problem: one as a minimization problem, the other in saddle point form. Our test problem is a mechanically-driven diffusion problem, using a Neo-Hooke energy. Our numerical results demonstrate clear advantages of the minimization approach. We observe experimentally that it yields symmetric positive definite system matrices, allowing the use of the conjugate gradient (CG) method with efficient preconditioning. This leads to noticeably lower computation times compared to GMRES, which is required for the indefinite saddle point system. Additionally, the minimization formulation results in sparser matrices, further reducing computational effort - especially in regimes where sparse direct solvers are still viable. These benefits are expected to extend to parallel domain decomposition methods that rely on sparse direct solvers, locally.

Key words: Variational Methods, Thermo-Chemo-Mechanics, Hydrogels, FROSch

1 INTRODUCTION

Hydrogels are water-swollen three-dimensional polymer networks, that possess a number of favorable properties such as high water absorption capability, tunable mechanical properties, easy functionalization, i.e., gels are sensitive to external stimuli, which makes them very attractive for medical or biomedical applications [1, pp. 453 ff.],[2, 3]. In order to support the development of hydrogel based medical devices like contact lenses, to predict cross-linking kinetics in hydrogels or to simulate the printing of 3D hydrogel scaffolds, a robust and efficient modeling framework is required. In the current contribution, such a modeling framework is based on two variational formulations of a simplified chemo-mechanical boundary value problem, in which the main phenomena of hydrogels are incorporated, namely the mutually coupled

Akshay B Jeeja & Bjoern Kiefer & Stefan Prüger
Technische Universität Bergakademie Freiberg, Institute of Mechanics and Fluid Dynamics, Lampadiusstrasse 4, 09599 Freiberg, Germany, e-mail: stefan.prueger@imfd.tu-freiberg.de

Oliver Rheinbach
Technische Universität Bergakademie Freiberg, Institute of Numerical Mathematics and Optimization, Akademiestrasse 6, 09599 Freiberg, Germany

Oliver Rheinbach & Friederike Röver
Technische Universität Bergakademie Freiberg, University Computing Center (URZ), Bernhard-v.-Cotta Strasse 1, 09599 Freiberg, Germany

solvent diffusion and the swelling-induced deformation of the gel. As the boundary value problem is solved by means of the Finite Element technique, the impact of different iterative solvers and the corresponding preconditioners is examined for the different variational formulations in the sense of a co-design of the model formulation and numerical solvers.

2 VARIATIONAL FORMULATIONS

This contribution employs the variational framework of chemo-mechanics, which couples the mechanical balance relations to mass diffusion, introduced in [4, 5]. In particular, the two dual formulations of mass diffusion, that lead either to a variational minimization or to a variational saddle point structure, are considered and briefly summarized in the subsequent subsections.

2.1 Minimization formulation of the chemo-mechanical problem

The rate-type potential associated with the minimization formulation is introduced as

$$\Pi\left(\dot{\boldsymbol{\varphi}}, \dot{v}, \boldsymbol{J}_v\right) = \int_{\mathcal{B}} \frac{\mathrm{d}}{\mathrm{d}t} \widehat{\psi}\left(\nabla\boldsymbol{\varphi}, v\right) \mathrm{d}V + \int_{\mathcal{B}} \widehat{\phi}\left(\boldsymbol{J}_v; \nabla\boldsymbol{\varphi}, v\right) \mathrm{d}V - P^{\boldsymbol{\varphi}}_{\mathrm{ext}}\left(\dot{\boldsymbol{\varphi}}\right) - P^{\mu}_{\mathrm{ext}}\left(\boldsymbol{J}_v\right) \ . \tag{1}$$

Herein, the specific free-energy function and the dissipation potential are denoted as $\widehat{\psi}$ and $\widehat{\phi}$, respectively. While the energy function depends on the material gradient of the deformation $\nabla\boldsymbol{\varphi}$ and the swelling volume fraction v, the state-dependent dissipation potential is a function of the volume flux $\boldsymbol{J}_v$ and is additionally parameterized by the former two fields. The power of the external forces corresponding to the deformation and the volume flux are given as

$$P^{\boldsymbol{\varphi}}_{\mathrm{ext}}\left(\dot{\boldsymbol{\varphi}}\right) = \int_{\mathcal{B}} \boldsymbol{R}_{\boldsymbol{\varphi}} \cdot \dot{\boldsymbol{\varphi}} \, \mathrm{d}V + \int_{\partial\mathcal{B}^{\boldsymbol{T}}} \bar{\boldsymbol{T}} \cdot \dot{\boldsymbol{\varphi}} \, \mathrm{d}A \qquad P^{\mu}_{\mathrm{ext}}\left(\boldsymbol{J}_v\right) = -\int_{\partial\mathcal{B}^{\mu}} \bar{\mu} \underbrace{\boldsymbol{J}_v \cdot \boldsymbol{N}}_{H_v} \mathrm{d}A \ . \tag{2}$$

in which the body force vector and the prescribed nominal traction vector are denominated as $\boldsymbol{R}_{\boldsymbol{\varphi}}$ and $\bar{\boldsymbol{T}}$, respectively. Furthermore, the prescribed chemical potential and the volume flux projected into the outward normal direction $\boldsymbol{N}$ are called $\bar{\mu}$ and H_v.
Noting that the choice of the volume flux as the primary field in the diffusion problem renders the balance of solute volume

$$\dot{v} = -\operatorname{Div}[\boldsymbol{J}_v] \tag{3}$$

an ordinary differential equation, allowing for the elimination of $\dot{v}$ from Eq. (1) and thus yielding a two-field problem. The deformation and the volume flux field that make the reduced rate-type potential stationary, are determined from

$$\{\dot{\boldsymbol{\varphi}}^{\star}, \boldsymbol{J}_v^{\star}\} = \operatorname{Arg}\left\{ \inf_{\dot{\boldsymbol{\varphi}} \in \mathcal{W}_{\dot{\boldsymbol{\varphi}}}} \inf_{\boldsymbol{J}_v \in \mathcal{W}_{\boldsymbol{J}_v}} \Pi\left(\dot{\boldsymbol{\varphi}}, \boldsymbol{J}_v\right) \right\} \ . \tag{4}$$

The suitable function spaces for the two fields are detailed as

$$\mathcal{W}_{\dot{\boldsymbol{\varphi}}} = \left\{ \dot{\boldsymbol{\varphi}} \in H^1(\mathcal{B}) \mid \dot{\boldsymbol{\varphi}} = \dot{\bar{\boldsymbol{\varphi}}} \text{ on } \partial\mathcal{B}^{\boldsymbol{\varphi}} \right\} \ , \quad \mathcal{W}_{\boldsymbol{J}_v} = \left\{ \boldsymbol{J}_v \in H\left(\operatorname{Div}, \mathcal{B}\right) \mid \boldsymbol{J}_v \cdot \boldsymbol{N} = H_v \text{ on } \partial\mathcal{B}^{H_v} \right\} \tag{5}$$

where both fields have to satisfy the respective Dirichlet boundary conditions along $\partial\mathcal{B}^{\boldsymbol{\varphi}}$ and $\partial\mathcal{B}^{H_v}$. While the deformation field $\dot{\boldsymbol{\varphi}}$ is taken from the standard Sobolev space [6, p. 47f], i.e. the norm of the field and its first partial derivatives are bounded in an integral sense [7, p.136ff.], the choice for the flux field is less restrictive, as it only requires that the norms of the field and its divergence are bounded [6, p.49f]. The conforming choice of finite element ansatz functions is given in Section 3.1.

2.2 Saddle point formulation of the chemo-mechanical problem

As an alternative to the two-field formulation introduced above, the coupled chemo-mechanical problem can also be cast into the three-field variational formulation

$$\Pi^*\left(\dot{\boldsymbol{\varphi}}, \dot{v}, \mu\right) = \int_{\mathcal{B}} \Big[\frac{\mathrm{d}}{\mathrm{d}t}\, \widehat{\psi}(\nabla\boldsymbol{\varphi}, v) - \mu\, \dot{v} - \widehat{\phi}^*(-\nabla\mu; \nabla\boldsymbol{\varphi}, v) \Big]\, \mathrm{d}V - P^{\boldsymbol{\varphi}}_{\mathrm{ext}}\left(\dot{\boldsymbol{\varphi}}\right) - P^{H_v}_{\mathrm{ext}}\left(\mu\right)\ , \quad (6)$$

in which the dissipation potential $\widehat{\phi}$ is replaced by its Legendre transform and the power of the external forces associated with the diffusion problem is redefined as

$$P^{H_v}_{\mathrm{ext}}\left(\mu\right) = \int_{\partial\mathcal{B}^{H_v}} \mu \bar{H}_v \mathrm{d}A\ . \quad (7)$$

The state-dependent dissipation potential $\widehat{\phi}^*$ emerges as a function of the negative material gradient of the scalar chemical potential with an additional parameterization based on the gradient of the deformation and the swelling volume fraction. Furthermore, the role of the chemical potential and the normal component of the volume flux H_v has changed in the sense that $\bar{H}_v$ is now prescribed as a Neumann boundary condition on the $\partial\mathcal{B}^{H_v}$, while the Neumann boundary condition for the minimization formulation is specified in terms of $\bar{\mu}$ on $\partial\mathcal{B}^{\mu}$. Once again, primary fields satisfying the underlying balance equations are determined by demanding that the rate-type potential is stationary.

$$\{\dot{\boldsymbol{\varphi}}^\star, \dot{v}^\star, \mu^\star\} = \mathrm{Arg}\left\{ \inf_{\dot{\boldsymbol{\varphi}}\in\mathcal{W}_{\dot{\boldsymbol{\varphi}}}} \inf_{\dot{v}\in L^2} \sup_{\mu\in\mathcal{W}_\mu} \Pi^*\left(\dot{\boldsymbol{\varphi}}, \dot{v}, \mu\right) \right\} \quad (8)$$

Here, the deformation field as well as the chemical potential are taken from standard Sobolev space as

$$\mathcal{W}_{\dot{\boldsymbol{\varphi}}} = \left\{ \dot{\boldsymbol{\varphi}} \in H^1(\mathcal{B}) \,|\, \dot{\boldsymbol{\varphi}} = \dot{\bar{\boldsymbol{\varphi}}} \text{ on } \partial\mathcal{B}^{\boldsymbol{\varphi}} \right\}\ , \qquad \mathcal{W}_\mu = \left\{ \mu \in H^1(\mathcal{B}) \,|\, \mu = \bar{\mu} \text{ on } \partial\mathcal{B}^{\mu} \right\}\ , \quad (9)$$

where the associated Dirichlet boundary conditions have to be fulfilled on $\partial\mathcal{B}^{\boldsymbol{\varphi}}$ and $\partial\mathcal{B}^{\mu}$. From the inspection of Eq. (8), it turns out that the minimum of Π^* with respect to $\dot{v}$ can be obtained point-wise for given fields $\dot{\boldsymbol{\varphi}}$ and μ. Thus, a reduced form of Eq. (6) can be constructed that only depends on the deformation and the chemical potential, see [4] for further details. The choice of the conforming finite element ansatz functions and the suitable numerical handling of the local condensation of $\dot{v}$ is given in Section 3.1.

2.3 Constitutive functions

The two variational formulations outlined in Section 2.1 and 2.2 introduce only the dependencies of the specific free-energy function and the dissipation potentials and are therefore valid for a large class of materials. However, this contribution focuses on an isotropic, hyperelastic material model for hydrogels that accounts for a strong two-sided coupling between the deformation and the flux field. Regarding the finite strain kinematics, the multiplicative split of the deformation gradient $\mathbf{F}_\mathrm{d} = \mathbf{F} \cdot J_0^{1/3}\mathbf{I}$ is assumed, where $\mathbf{F}_\mathrm{d}$ maps from the initial configuration associated with the dry-state of the hydrogel to the current configuration, while J_0 corresponds to a material parameter that characterizes the volume change stemming from the pre-swelling of the initial configuration. The deformation gradient $\mathbf{F}$ and its determinant J specify the mechanical deformation of the pre-swollen hydrogel. A coupled free-energy function of Neo-Hookean type, suitable for compressible material behavior, is specified relative to the pre-swollen configuration as

$$\widehat{\psi}\left(\nabla\boldsymbol{\varphi}, v\right) = \frac{\gamma}{2J_0}\left[J_0^{2/3}\,\mathbf{F}:\mathbf{F} - 3 - 2\ln\left(JJ_0\right)\right] + \frac{\lambda}{2J_0}\left[JJ_0 - 1 - v\right]^2 + \frac{\alpha}{J_0}\left[v\ln\left(\frac{v}{1+v}\right) + \frac{\chi v}{1+v}\right], \quad (10)$$

in which γ and λ correspond to the shear modulus and the first Lamé constant, while the mixing modulus and the mixing control parameter in the Flory-Rehner type contribution of the energy are denoted as α and χ, respectively. The latter accounts for the mixing of the solvent and the polymer network, where $\chi = 0$ represents an ideal mixture. The scaling factor $\frac{1}{J_0}$ is introduced to enforce the equality of the energy in the initial and the pre-swollen configuration.
The first Piola-Kirchhoff stress and the chemical potential are computed as

$$\mathbf{P} = \frac{\partial\widehat{\psi}}{\partial\mathbf{F}} \overset{(10)}{=} \frac{\gamma}{J_0^{1/3}}\mathbf{F} + \left[\lambda J\left[JJ_0 - 1 - v\right] - \frac{\gamma}{J_0}\right]\mathbf{F}^{-\mathrm{T}} \quad (11)$$

and

$$\mu = \frac{\partial\widehat{\psi}}{\partial v} \overset{(10)}{=} -\frac{\lambda}{J_0}\left[JJ_0 - 1 - v\right] + \frac{\alpha}{J_0}\left[\ln\left(\frac{v}{1+v}\right) + \frac{1}{1+v} + \frac{\chi}{(1+v)^2}\right]. \quad (12)$$

As the undeformed state, i.e. $\mathbf{F} = \mathbf{I}$, is assumed to be stress-free, the swelling volume fraction has to be initialized for a given value of the pre-swollen Jacobian J_0 as

$$v_0 = \frac{\gamma}{\lambda}\left[J_0^{-1/3} - \frac{1}{J_0}\right] + J_0 - 1\,. \quad (13)$$

The state-dependent dissipation potentials corresponding to the minimization and the saddle point formulation are taken as the quadratic forms

$$\widehat{\phi}\left(\boldsymbol{J}_v; \mathbf{C}, v\right) = \frac{1}{2\mathrm{M}v}\mathbf{C}:\left(\boldsymbol{J}_v \otimes \boldsymbol{J}_v\right) \quad \text{and} \quad \widehat{\phi}^*\left(-\nabla\mu; \mathbf{C}, v\right) = \frac{\mathrm{M}v}{2}\mathbf{C}^{-1}:\left(-\nabla\mu \otimes -\nabla\mu\right), \quad (14)$$

which yield the following linear relations between the volume flux and the gradient of the chemical potential, employing the volumetric diffusivity parameter M.

$$-\nabla\mu = \frac{\partial\widehat{\phi}}{\partial\boldsymbol{J}_v} \overset{(14)_1}{=} \frac{1}{\mathrm{M}v}\mathbf{C}\cdot\boldsymbol{J}_v \qquad \text{and} \qquad \boldsymbol{J}_v = \frac{\partial\widehat{\phi^*}}{\partial(-\nabla\mu)} \overset{(14)_2}{=} \mathrm{M}\,v\,\mathbf{C}^{-1}\cdot(-\nabla\mu) \tag{15}$$

The additional dependency on the right Cauchy-Green tensor $\mathbf{C}$ or its inverse, is due to the assumption of an isotropic behavior in the current configuration, which is then pulled back to the pre-swollen configuration by means of Nanson's formula. The material parameters are chosen identical to [8].

3 Implementation

3.1 Implementation of the chemo-mechanical problem in deal.II

The variational formulations described in Section 2 are the same as the formulations in [8]. We use our implementation employing the `deal.II` software library [9] Version 9.5.0. For a more detailed description, we refer to [8, Section 3]. In the following, we denote the minimization formulation as *Min* formulation and the saddle point formulation as *SP* formulation to improve the readability. We examine different combinations of conforming approximations. For the *Min* formulation we consider tri-linear (Q_1) Lagrange ansatz functions for the deformation field and lowest order Raviart-Thomas (RT_0) ansatz functions for the flux field $\boldsymbol{J}_v$. The latter ensures the continuity of the normal trace across the element boundaries. In order to compute the swelling volume fraction, Eq. (3) is integrated numerically by a backward Euler scheme.

We employ Taylor-Hood elements (Q_2Q_1) for the approximation of the primary variables $\boldsymbol{\varphi}$ and μ in the saddle point formulation. In addition, the computation of the swelling volume fraction v is carried out by means of the interior affine trust-region method [10], which strictly ensures its non-negativity. The nonlinear algebraic systems emerging from the finite element discretization are solved by a standard Newton-Raphson scheme in each load increment. The solution of the linear system of equations arising in the Newton iterations is obtained by the iterative minimal residual method (*MINRES*) and the generalized minimal residual method (*GMRES*) method with the splitting preconditioners Jacobi and SSOR [11] using the implementation provided by `deal.II`. We use the default settings for GMRES, therefore the GMRES method employs Gram Schmidt with delayed reorthogonolization [12]. In [8], the limitations of sparse direct linear solvers were already shown for the two variational formulations outlined in Section 2.1 and 2.2. Here, we investigate the performance of iterative methods with simple preconditioners. It is well known that these simple preconditioners used here are not scalable. More advanced, scalable preconditioning methods based on domain decomposition methods [13] will be considered in a next step. In [14], we have already successfully applied the parallel overlapping Schwarz preconditioner FROSch [15] of the Trilinos software library [16] to the *Min* formulation.

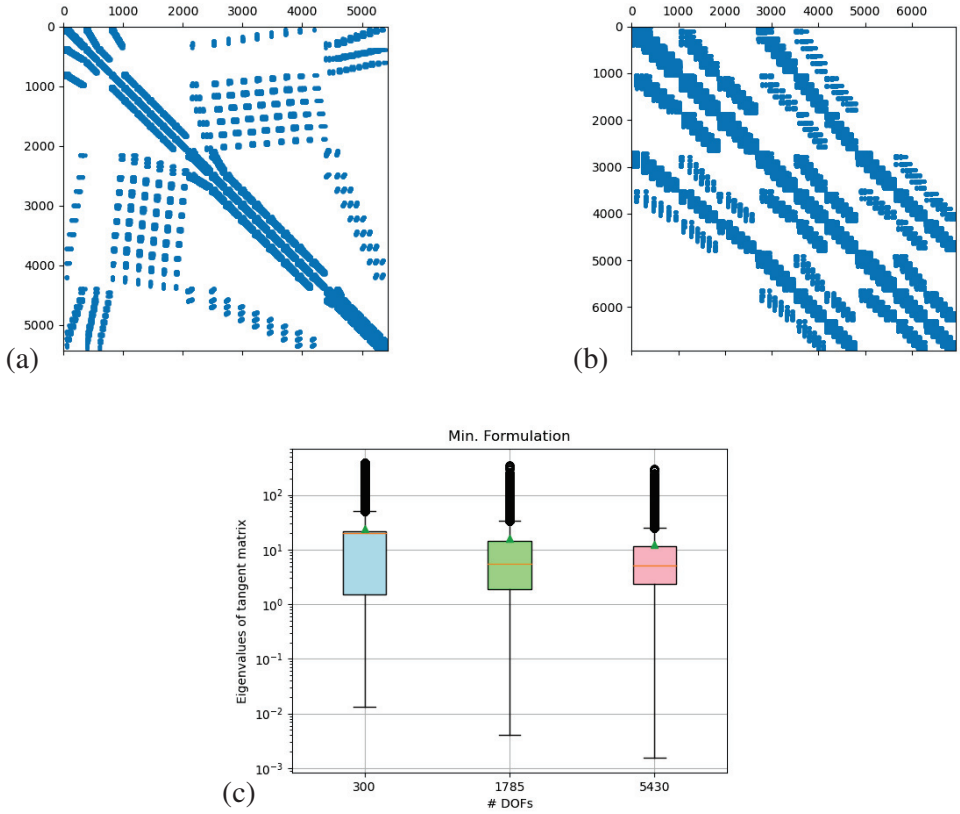

Figure 1: Sparsity pattern of the tangent matrix for the *Min* formulation (a) with 5 430 DOFs and 385 164 non-zero entries and the *SP* formulation (b) with 6 934 DOFs and 1 244 446 non-zero entries. Box plot of the eigenvalues of the tangent stiffness matrices (c) evaluated in the simulation of the mechanically-driven diffusion problem, employing the *Min* formulation, for three different mesh refinements. The smallest eigenvalues are: 0.0131 (300 DOFs), 0.0041 (1785 DOFs), 0.0015 (5430 DOFs).

4 RESULTS

4.1 Comparison of iterative methods in the chemo-mechanical problem

To evaluate the performance of iterative methods for the different variational formulations, we apply our finite element implementation to a mechanically-driven diffusion problem in a cubic domain. The problem considers the indentation of a hydrogel cube with a flat, rigid indenter, where the mechanical stress field leads to a redistribution of the solvent within the sealed domain. It is equivalent to the one described in [8, Section 4]. The same relative stopping criterion of $\|r_k\|/\|r_0\| \leq 10^{-6}$ is used for all iterative solvers, to obtain the solution of the linear system of equations. We set the maximum number of iteration in dependence of the size of the system matrix, such that the maximum number of iterations is four times the number of degrees of freedom. We have observed experimentally that the *Min* formulation yields symmetric posi-

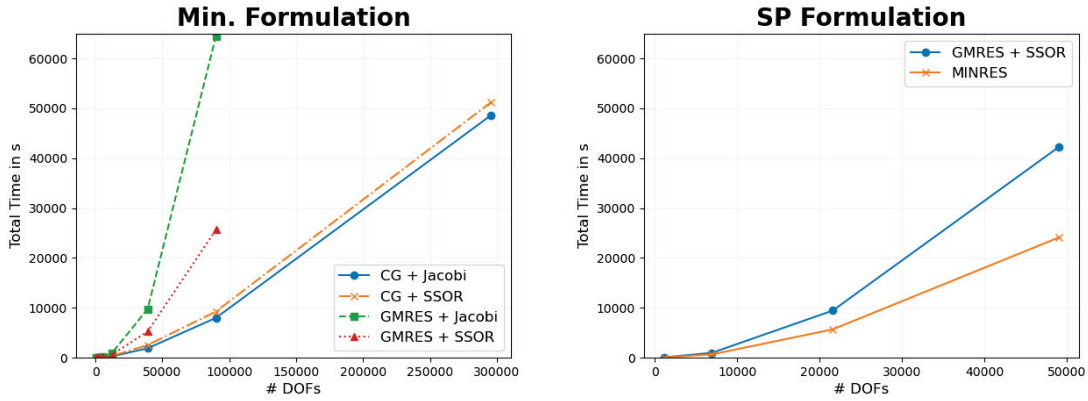

Figure 2: *Total Time* of the calculations performed with $\Delta t = 0.1$ s. Considered are the *Min* formulation (left) with different iterative methods and preconditioner as well as the *SP* formulation (right) employing GMRES with SSOR and MINRES without any preconditioner.

tive definite tangent matrices for our test problem, see Fig. 1(a,c). The smallest eigenvalues are bounded away from zero, which is expected as the boundary value problem does not contain any intrinsic buckling or snap-back/snap-through instabilities. Therefore, we also consider the conjugate gradient (CG) method for this formulation. Note that we have additionally verified the definiteness of all tangents for problem sizes up to 5430 DOFs, using a Cholesky decomposition. In the iterative solvers, the Jacobi and the SSOR preconditioner are employed. In order to obtain a reference for the performance of sparse direct solvers, we also consider the direct solver UMFPACK[17, 18] for both formulations.

The suitability of the iterative solvers in connection with the different preconditioners is first investigated for *Min* formulation. Herein, the relaxation parameter, required for the SSOR preconditioner, is set to $\omega = 0.65$. Considering the average number of linear iterations for the *Min* formulation, it is observed for all methods that the number of iterations increases with increasing number of DOFs, as expected, see Table 1 and Figure 3. However, the CG method, combined with the SSOR preconditioner (CG+SSOR), consistently required the lowest number of iterations. In the subsequent discussion of the computing times, we focus on the *Solver Time*, i.e. the time to solve the linear system in the Newton-Raphson iterations, as it dominates the total time to solution (*Total Time*), except for very small problems. The CG method with the Jacobi preconditioner (CG+Jacobi) is the fastest except for the smallest test case with 300 DOFs, where UMFPACK is faster by 0.01 s. For the SSOR preconditioner, the *Solver Time* is slightly higher compared to CG+Jacobi. However, the slopes by which the *Total Time* is increasing with increasing number of DOFs are similar, compare Figure 2. Overall, the CG method performs better than GMRES with regards to the avg. number of iterations and the *Solver Time*. The higher *Solver Time* for GMRES is due to, both, the higher number of iterations, and of the quadratic complexity in the Arnoldi process. Based on the comparison of the two iterative solvers and the two preconditioners employed for the *Min* formulation, it can be

Minimization Q_1RT_0 60 time steps, Δ t = 0.1 s								
DOFs		300	1785	5430	12 207	39 045	90 075	295 815
Avg #	UMFPACK	-	-	-	-	-	-	-
lin. iter	CG + Jacobi	157	442	726	1053	1777	2577	4250
per Newton step	CG + SSOR	**112**	**242**	**362**	**506**	**818**	**1085**	**1672**
	CG + SSOR †	167	397	601	862	1363	1897	2823
	GMRES + Jacobi	410	1197	2088	3637	8568	18 342	*
	GMRES + SSOR	177	391	542	948	1641	2594	*
	GMRES + SSOR †	309	678	1216	1877	3857	6839	*
Assemble Time	UMFPACK	1.20	9.30	30.70	78.80	250	595	#
	CG + Jacobi	1.18	9.20	30.30	73.60	249	596	2062
	CG + SSOR	1.19	9.20	30.50	73.40	250	599	2068
	CG + SSOR †	1.18	9.20	30.20	73.50	249	596	2064
	GMRES + Jacobi	1.19	9.20	30.60	74.50	259	621	*
	GMRES + SSOR	1.20	9.20	30.40	74	259	616	*
	GMRES + SSOR †	1.22	9.30	31.20	76.40	260	646	*
Solver Time	UMFPACK	**0.72**	12.80	125.60	632	8208	49 210	#
	CG + Jacobi	0.73	**11.20**	**54.60**	**176.80**	**1587**	**7207**	**46 040**
	CG + SSOR	1.13	17.30	79.40	240.60	2198	8492	48 650
	CG + SSOR †	1.67	28	128.70	411.70	3486	14 980	81 470
	GMRES + Jacobi	2.50	41.30	204	779	9444	63 650	*
	GMRES + SSOR	2.15	33.10	136	495.50	4914	24 870	*
	GMRES + SSOR †	3.85	57.30	307.30	996	11 550	68 640	*
Total Time	UMFPACK	4.70	**26.40**	167.80	733	8538	49 970	#
	CG + Jacobi	**3.80**	34.90	**98.40**	**273**	**1909**	**7994**	**48 630**
	CG + SSOR	5.00	33.50	124.70	347	2552	9265	51 240
	CG + SSOR †	4.50	42.60	170.60	509.90	3804	15 740	84 070
	GMRES + Jacobi	5.70	59.20	253	881	9779	64 430	*
	GMRES + SSOR	5.50	48.10	185	597	5259	25 650	*
	GMRES + SSOR †	7.30	71.40	351	1118	11 890	69 460	*
total #	UMFPACK	300	300	**300**	**300**	**301**	**304**	#
Newton steps	CG + Jacobi	300	300	**300**	**300**	**301**	**304**	**312**
	CG + SSOR	300	300	**300**	**300**	**301**	**304**	**312**
	CG + SSOR †	300	300	300	300	301	304	312
	GMRES + Jacobi	300	300	301	304	311	317	*
	GMRES + SSOR	300	300	301	301	311	315	*
	GMRES + SSOR †	307	302	310	310	314	330	*

Table 1: Computation times for the *Min* formulation. Comparison of different (iterative) linear solvers and different levels of grid refinement. The combination of the CG and the GMRES solver with the SSOR preconditioner, marked with †, have a common relaxation parameter of $\omega = 0.18$. For all the entries in the table, indicated by a *, the maximum number of GMRES linear iterations were exceeded, whereas the ones, marked with #, the maximum walltime limit of 96 hours was not sufficient to obtain a solution. We mark the lowest number of linear iterations as well as the fastest *Solver* and *Total time* in bold.

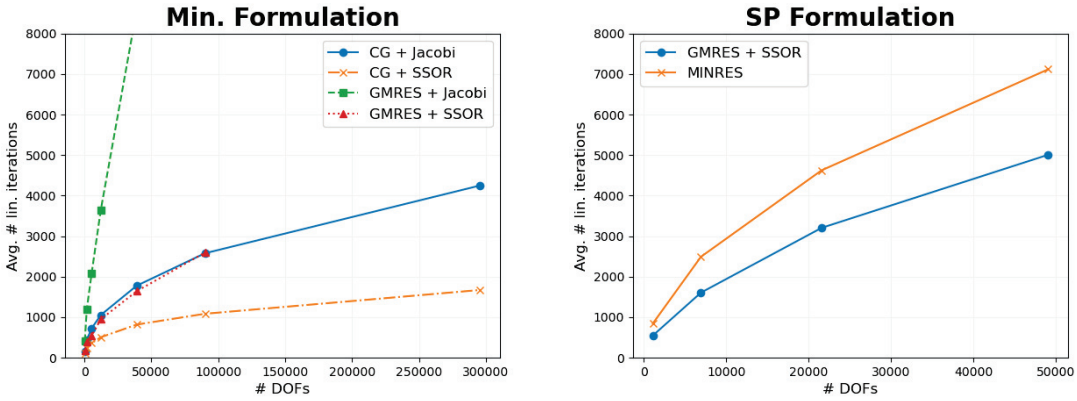

Figure 3: Average number of linear iteration over all Newton steps for the calculations performed with $\Delta t = 0.1$ s. In the *Min* formulation (left) with different iterative methods and preconditioner are considered, while the *SP* formulation (right) employs GMRES with SSOR and MINRES without any preconditioner.

concluded that CG+Jacobi is the most efficient method for this particular problem and the SSOR preconditioner does not reduce the *Solver Time* although the number of linear iterations can be significantly reduced. In contrast to CG, GMRES does not exploit the positive definiteness of the system matrix. Because GMRES builds an orthonormal basis for the Krylov subspace via the Arnoldi process, its computational cost grows with the number of iterations. As the update of the orthogonal basis in one GMRES iteration is computationally more expensive than a single CG iteration, even the application of the SSOR preconditioner, which reduces the number of linear iterations to that of CG, cannot fully compensate the computational overhead. This emphasizes the importance of exploiting known matrix properties when selecting the iterative solution method and the preconditioner.

For the *SP* formulation we consider the direct solver UMFPACK and iterative solvers MINRES and GMRES as the system is symmetric, but indefinite. Employing the simple Jacobi preconditioner in combination with GMRES did not lead to convergence of the iterative solver within the maximum number of linear iterations allowed. In the case of GMRES combined with the SSOR preconditioner, an adjustment of the relaxation parameter to $\omega = 0.18$ was necessary to ensure convergence. In fact, the value has been obtained by systematically varying the relaxation parameter in the range of [0.1,0.2], where the value of $\omega = 0.18$ led to lowest number of linear iterations. Similarly, as in the *Min* formulation, the number of linear iterations increases with increasing problem size. Consequently, the *Solver* and *Total Time* also increase. For the *SP* formulation, for the range of problem sizes considered, UMFPACK is always faster than the iterative methods, but the advantage reduces with the size of the problem. Note that we have considered only problems of modest size for the *SP* formulation. For larger problems, direct solvers will not be applicable anymore. We note that the system matrix in the *SP* formulation possesses a significantly larger number of non-zero entries as the one corresponding to the *Min* formulation, see Fig. 1. We observe that the number of GMRES+SSOR iterations is quite high

Saddle Point Formulation 60 time steps, Δ t = 0.1 s					
DOFs		1093	6934	21 577	49 072
Avg #	UMFPACK	-	-	-	-
lin. iter	MINRES	845	2 490	4 623	7 115
per Newton step	GMRES + SSOR	547	1 607	3 204	5 007
Assembe Time	UMFPACK	**35.20**	**283**	**957**	**2 297**
	MINRES	35.30	286	983	2 319
	GMRES + SSOR	35.30	**283**	961	2 505
Solver Time	UMFPACK	**4.30**	**188**	**1 807**	**14 450**
	MINRES	17.60	386	4 683	21 770
	GMRES + SSOR	38.10	706	8463	39 740
Total Time	UMFPACK	**41.30**	**481**	**2 791**	**16 790**
	MINRES	54.60	681	5 688	24 140
	GMRES + SSOR	75	997	9 448	42 300
total #	UMFPACK	**200**	**201**	**202**	**204**
Newton steps	MINRES	201	**201**	**202**	206
	GMRES + SSOR	201	**201**	**202**	222

Table 2: Computation times for the *SP* formulation. Comparison of direct and iterative linear solvers and different levels of grid refinement. The fastest *Solver* and *Total time* are marked in bold. An additional grid refinement step, yielding 158818 DOFs, has been excluded from the comparison, as the wall time was exceeded for GMRES+SSOR and the condition $\det(\mathbf{F}) > 0$ was violated in a not yet converged Newton iteration for UMFPACK, see [8] for further details on the latter issue.

for the *SP* formulation when compared with the *Min* formulation. As an alternative to GMRES, the MINRES method without a preconditioner is employed to solve the linear system in the *SP* formulation. Due to absence of a preconditioner, the number of linear iterations exceeds even the linear iterations required by GMRES+SSOR. However, for MINRES, the total solution times are still significantly lower, because its computational complexity is comparable to CG and thus yields a much more efficient method than GMRES+SSOR.
In summary, the comparison of the *Min* and *SP* formulation, both yielding a symmetric system matrix, as illustrated in Fig. 1, highlights that the property of being symmetric and positive definite is a significant advantage of the *Min* formulation since the CG method can be applied, leading to faster computation times, see also Fig. 2. When comparing GMRES+SSOR, the *Min* formulation is faster overall; see Tab. 1 and 2. In particular, the *SP* formulation required a *Total Time* of 42 300 s for a medium sized problem with 49 072 DOFs, while the simulations, using the *Min* formulation with 39 045 DOFs, were conducted in a *Total Time* of 5259 s ($\omega = 0.65$) and 11 890 s ($\omega = 0.18$), respectively.

5 CONCLUSIONS

Within the chemo-mechanical modeling framework discussed here, comparing the same problem, but cast either in a minimization formulation or in saddle point form, we observe significant advantages for the minimization problem: As the minimization formulation leads to symmetric positive definite problems, preconditioned CG can be applied, leading to significant gains in computation time compared to GMRES. Moreover, the system matrices are more sparse. As a result, for the range of problem sizes, where sparse direct solvers are still applicable, we see better computation times for the minimization formulation. This will carry over

to parallel domain decomposition methods, where sparse direct solvers are the local computational kernel. We can conclude that the choice of the variational formulation, combined with the suitable discretization, significantly influences the performance.

REFERENCES

[1] M. Abu Jafar Mazumder, H. Sheardown, and A. Al-Ahmed, *Functional Biopolymers*, 1st ed., ser. Polymers and Polymeric Composites: A Reference Series. Springer Cham, 2019.

[2] H. Cao, L. Duan, Y. Zhang, J. Cao, and K. Zhang, "Current hydrogel advances in physicochemical and biological response-driven biomedical application diversity," *Signal Transduct Target Ther*, vol. 6, no. 1, pp. 1–31, Dec. 2021.

[3] T.-C. Ho, C.-C. Chang, H.-P. Chan, T.-W. Chung, C.-W. Shu, K.-P. Chuang, T.-H. Duh, M.-H. Yang, and Y.-C. Tyan, "Hydrogels: Properties and Applications in Biomedicine," *Molecules*, vol. 27, no. 9, p. 2902, May 2022.

[4] L. Böger, A. Nateghi, and C. Miehe, "A minimization principle for deformation-diffusion processes in polymeric hydrogels: Constitutive modeling and FE implementation," *Int J Solids Struct*, vol. 121, pp. 257–274, 2017.

[5] L. Böger, *Saddle-Point and Minimization Principles for Diffusion in Solids : Phase Separation, Swelling and Fracture*. Stuttgart : Institute of Applied Mechanics, 2020.

[6] D. Boffi, F. Brezzi, and M. Fortin, *Mixed Finite Element Methods and Applications*, 1st ed., ser. Springer Series in Computational Mathematics. Berlin, Heidelberg: Springer, 2013, no. 44.

[7] W. Han and B. Reddy, *Plasticity*, 2nd ed. Springer New York, NY, 2013.

[8] A. B. Jeeja, B. Kiefer, S. Prüger, O. Rheinbach, and F. Röver, "Comparison of a minimization and a saddle point formulation of a coupled mechanics-diffusion problem implemented in deal.II," *PAMM*, vol. 25, no. 1, p. e202400188, 2025. [Online]. Available: https://onlinelibrary.wiley.com/doi/abs/10.1002/pamm.202400188

[9] D. Arndt, W. Bangerth, M. Bergbauer, M. Feder, M. Fehling, J. Heinz, T. Heister, L. Heltai, M. Kronbichler, M. Maier, P. Munch, J.-P. Pelteret, B. Turcksin, D. Wells, and S. Zampini, "The deal.II library, version 9.5," *J Numer Math*, vol. 31, no. 3, pp. 231–246, Aug. 2023. [Online]. Available: https://www.degruyter.com/document/doi/10.1515/jnma-2023-0089/html

[10] S. Bellavia and B. Morini, "An interior global method for nonlinear systems with simple bounds," *Optim Method Softw*, vol. 20, no. 4-5, pp. 453–474, Aug. 2005. [Online]. Available: https://doi.org/10.1080/10556780500140516

[11] A. Meister, *Präkonditionierer*. Wiesbaden: Springer Fachmedien Wiesbaden, 2015, pp. 230–255. [Online]. Available: https://doi.org/10.1007/978-3-658-07200-1_5

[12] D. Bielich, J. Langou, S. Thomas, K. Świrydowicz, I. Yamazaki, and E. G. Boman, "Low-synch Gram–Schmidt with delayed reorthogonalization for Krylov solvers," *Parallel Comput*, vol. 112, p. 102940, 2022. [Online]. Available: https://www.sciencedirect.com/science/article/pii/S0167819122000394

[13] A. Toselli and O. Widlund, *Domain decomposition methods—algorithms and theory*, ser. Springer Series in Computational Mathematics. Springer-Verlag, Berlin, 2005, vol. 34. [Online]. Available: https://doi.org/10.1007/b137868

[14] B. Kiefer, S. Prüger, O. Rheinbach, and F. Röver, "Monolithic parallel overlapping Schwarz methods in fully-coupled nonlinear chemo-mechanics problems," *Comput Mech*, vol. 71, no. 4, pp. 765–788, 2023.

[15] A. Heinlein, A. Klawonn, S. Rajamanickam, and O. Rheinbach, "FROSch: A fast and robust overlapping Schwarz domain decomposition preconditioner based on Xpetra in Trilinos," in *Domain Decomposition Methods in Science and Engineering XXV*, R. Haynes, S. MacLachlan, X.-C. Cai, L. Halpern, H. H. Kim, A. Klawonn, and O. Widlund, Eds. Cham: Springer, 2020, pp. 176–184.

[16] T. Trilinos Project Team, *The Trilinos Project Website*.

[17] T. A. Davis and I. S. Duff, "An unsymmetric-pattern multifrontal method for sparse lu factorization," *SIAM J Matrix Anal A*, vol. 18, no. 1, pp. 140–158, 1997. [Online]. Available: https://doi.org/10.1137/S0895479894246905

[18] R. F. Boisvert, T. A. Davis, and I. S. Duff, "A combined unifrontal/multifrontal method for unsymmetric sparse matrices," *ACM Trans Math Softw*, vol. 25, no. 1, p. 1–20, 1999. [Online]. Available: https://doi.org/10.1145/305658.287640

XI ECCOMAS Thematic Conference on Smart Structures and Materials - SMART 2025
M. Krommer, M. Nader and M. Schagerl (Eds)

Received: 11 April 2025 / Revised: 15 September 2025 / Accepted: 22 October 2025
© The Author(s) 2025

Characterization of the Dynamic Behavior of Soft Elastomers Using a Shaker Testbed

Mario Kunzemann, Andreas Brandl, Astrid Pechstein, Alexander Humer

Abstract. Soft elastomers like Ecoflex00-30 are widely used in dielectric actuators, where accurate modeling of both elastic and damping behavior is critical for reliable simulations. This study presents a cost-effective method to characterize the dynamic response of elastomers using a shaker testbed as an alternative to conventional rheometry. A mass is fixed to the top of the Ecoflex specimen and excited harmonically up to a frequency of 900 Hz, while two accelerometers — placed below the specimen and on top of the mass — capture amplitude and phase shifts. Inspired by similar methods in the literature, the proposed setup enables both efficient and affordable material characterization. The viscoelastic behavior is described using a Wiechert model, resulting in a Prony series representation of the complex shear modulus. A frequency-domain finite element model under small-strain assumptions is developed, from which the Prony parameters are identified via least-squares fitting. This approach supports consistent and accurate material characterization across a broad frequency range without the need for expensive rheometric equipment. To validate the parameters, a ball drop experiment is carried out, using a Neo-Hookean potential covering large deformation.

Key words: viscoelasticity, Ecoflex00-30, Prony parameters, shaker testbed, material characterization

1 INTRODUCTION

Soft elastomers are increasingly used in applications such as dielectric actuators (DEA), particularly in soft robotics and sensor technologies. Their versatility and potential are extensively reviewed by Guo [1] and O'Halloran [2]. Accurate modeling of these materials requires capturing both their elastic and damping behavior. While dynamic thermo-mechanical analysis (DTMA) combined with time-temperature superposition (TTSP) theoretically enables frequency-dependent characterization over several decades, its practical use is often limited by high equipment costs, long testing duration, difficult specimen handling and the need to perform tests at multiple controlled temperatures. This highlights the value of direct broadband

Mario Kunzemann & Andreas Brandl & Astrid Pechstein & Alexander Humer
Institute of Technical Mechanics, Johannes Kepler University Linz, Altenbergerstr. 69, A-4040 Linz, Austria
e-mail: mario.kunzemann@jku.at

measurements under constant conditions to reliably extract frequency-dependent properties in a wide frequency range such as shear modulus and damping parameters in an unified approach.

This study proposes a methodology for characterizing the dynamic behavior of soft elastomers using a shaker testbed as an alternative to conventional rheometry. This approach allows for cost-effective measurements within a large frequency range (10 Hz to 900 Hz) and offers a reliable pathway to determine viscoelastic properties. Viscoelastic materials exhibit a combination of elastic and viscous behavior, with their mechanical response depending on both deformation and rate effects. The continuum modeling of viscoelastic materials in general has a long history and is covered in several key monographs such as Lakes [3], Brinson [4] and Tschoegl [5]. Characterization methods typically include stress relaxation, creep tests, or dynamic (thermo-)mechanical analysis (D(T)MA), often performed using rheometers, as in the studies by Liao [6] and Case [7]. While effective, rheometers are costly and limited in frequency range. To overcome these limitations, we adopt a shaker-based testbed for dynamic testing. Similar experimental setups have been reported in the literature. For example, Ilg [8] used a shaker combined with laser triangulation to characterize Ecoflex00-30 up to frequencies of 400 Hz. Huang [9] demonstrated that adding a top mass can improve measurement accuracy within such a testbed. These studies highlight the potential of shaker-based setups as efficient and scalable alternatives for soft material characterization.

In this work, we focus on the soft elastomer Ecoflex00-30 and propose modeling its viscoelastic behavior in the linear regime using a Wiechert model, which is applied exclusively to the experimental setup. For the subsequent ball-drop experiment, the identified parameters are incorporated into a Neo-Hookean potential to account for finite deformations. Under harmonic excitation, this leads to a Prony series representation of the complex Young's modulus. To identify the Prony parameters, a finite element model of the harmonically excited measurement setup is developed. A least-squares fitting procedure is applied to match experimental data with simulation results. The fitted parameters can subsequently be applied in nonlinear finite strain material models, such as the ball drop experiment.

The remainder of this paper is organized as follows: Section 2 introduces the viscoelastic parameters and fundamental quantities used to describe the material behavior. Section 3 details the experimental setup, including specimen fabrication, sensor placement, and the acquisition of dynamic response data. Section 4 outlines the parameter identification using a non-linear least squares approach and verifies the application of the fitted parameters through a ball-drop simulation.

2 VISCOELASTICITY

In this present work we model Ecoflex00-30 as a nearly incompressible viscoelastic elastomer. Since both measurement and simulation are conducted in the small strain regime, a linear viscoelastic model is considered appropriate when reproducing measurement results in a simulation setup. To describe the mechanical behavior, we introduce the displacement vector $\boldsymbol{u}$. For

time-harmonic excitation, the displacement field is represented as $\boldsymbol{u}(\boldsymbol{X},t) = \Re\{\boldsymbol{u}(\boldsymbol{X})e^{j\omega t}\}$, where $\boldsymbol{X}$ is the position vector, ω the excitation frequency, and t the time. The context will clarify whether the full time-dependent displacement $\boldsymbol{u}(\boldsymbol{X},t)$ or its complex amplitude $\boldsymbol{u}(\boldsymbol{X})$ is being considered. The linearized strain tensor $\boldsymbol{\varepsilon}$ is defined as the symmetric part of the displacement gradient,

$$\boldsymbol{\varepsilon} = \frac{1}{2}\left(\nabla\boldsymbol{u} + (\nabla\boldsymbol{u})^{\top}\right). \tag{1}$$

In the case of near-incompressibility, the volume-preserving nature of the viscous strains is typically addressed by decomposing the stress tensor into deviatoric and volumetric components. This leads to the following stress–strain relation,

$$\boldsymbol{\sigma} = \boldsymbol{\sigma}^D + K\,\mathrm{tr}(\boldsymbol{\varepsilon})\mathbf{I}, \qquad \text{with} \qquad \boldsymbol{\sigma}^D = 2\mu\boldsymbol{\varepsilon}^D, \tag{2}$$

where μ is the shear modulus governing the deviatoric response, and K is the bulk modulus associated with volumetric changes. To characterize the viscoelastic behavior of the material, the shear modulus μ is modeled as a frequency-dependent complex quantity, denoted by $\mu^*(\omega)$, capturing both energy storage and dissipation under harmonic excitation.

A suitable representation for this behavior is provided by the Wiechert model, illustrated in Fig. 1. It consists of N Maxwell branches arranged in parallel, where each branch includes a spring with shear modulus μ_i in series with a dashpot defined by a viscosity parameter η_i. Additionally, a single equilibrium spring with shear modulus μ_∞ accounts for the long-term elastic response. The total strain ε is applied uniformly across all branches. In each Maxwell branch, the dashpot accommodates the viscous strain $\varepsilon_{v,i}$, while the corresponding spring responds to the remaining elastic strain $\varepsilon - \varepsilon_{v,i}$.

This uniaxial formulation extends to three dimensions and results in the total strain tensor $\boldsymbol{\varepsilon}$, the viscous strain tensors $\boldsymbol{\varepsilon}_{v,i}$ which are volume-preserving and therefore deviatoric with $\mathrm{tr}\,\boldsymbol{\varepsilon}_{v,i} = 0$ and the elastic remainder given by $\boldsymbol{\varepsilon} - \boldsymbol{\varepsilon}_{v,i}$. The viscosity parameters η_i can alternatively be expressed in terms of the relaxation times τ_i and the shear moduli μ_i, using the relation $\eta_i = 3\mu_i\tau_i$.

The deviatoric part of the stress tensor is composed of the long-term elastic contribution and the sum of the stresses from the Maxwell branches, given by, $\boldsymbol{\sigma}^D = \boldsymbol{\sigma}_\infty + \sum_{i=1}^{N}\boldsymbol{\sigma}_i$. The first part can be defined as $\boldsymbol{\sigma}_\infty = 2\mu_\infty\boldsymbol{\varepsilon}^D$. The second contribution is given by $\boldsymbol{\sigma}_i = 2\mu_i(\boldsymbol{\varepsilon}^D - \boldsymbol{\varepsilon}_{v,i}) = \frac{2}{3}\eta_i\dot{\boldsymbol{\varepsilon}}_{v,i}$. Under time-harmonic excitation, where all fields vary as $e^{j\omega t}$, time derivatives translate to multiplication by $j\omega$. This leads to the frequency domain expression $\boldsymbol{\sigma}_i = \frac{2}{3}\eta_i j\omega\boldsymbol{\varepsilon}_{v,i}$. Combining the two parts results in the following relation in the frequency domain,

$$\boldsymbol{\sigma}^D = 2\mu_\infty\boldsymbol{\varepsilon}^D + \sum_{i=1}^{N} 2\mu_i\frac{\omega^2\tau_i^2 + j\omega\tau_i}{1+\omega^2\tau_i^2}\boldsymbol{\varepsilon}^D. \tag{3}$$

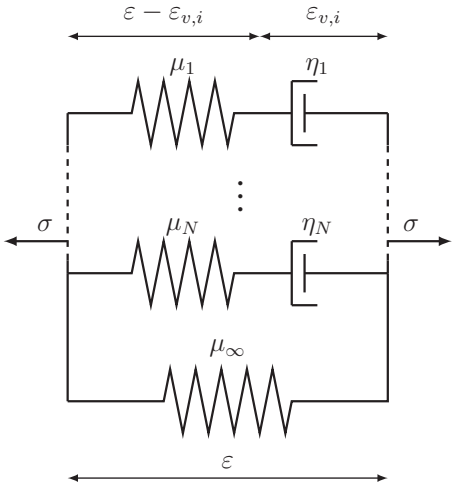

Figure 1: Wiechert model.

The complex shear modulus can be expressed in the frequency domain as a Prony series,

$$\mu^*(\omega) = \mu_\infty + \sum_{i=1}^{N} \frac{\mu_i \tau_i^2 \omega^2}{1 + \tau_i^2 \omega^2} + j \sum_{i=1}^{N} \frac{\mu_i \tau_i \omega}{1 + \tau_i^2 \omega^2}. \tag{4}$$

The parameters μ_∞, μ_i, and τ_i are commonly referred to as the Prony parameters. We obtain the following stress-strain relation for the viscoelastic material in the frequency domain,

$$\boldsymbol{\sigma} = 2\mu^*(\omega)\boldsymbol{\varepsilon}^D + K\,\mathrm{tr}(\boldsymbol{\varepsilon})\mathbf{I}. \tag{5}$$

The bulk modulus K is defined as

$$K = \frac{2\nu\mu_0}{1-2\nu}, \qquad \text{with} \qquad \mu_0 = \mu_\infty + \sum_{i=1}^{N} \mu_i, \tag{6}$$

where ν denotes the Poisson's ratio. To reflect a nearly incompressible behavior of the soft elastomer, we choose $\nu = 0.4999$.

It remains to identify the appropriate values for these Prony parameters based on experimental data to accurately capture the viscoelastic behavior of the material in the model.

3 EXPERIMENT

In this section, we describe the experimental setup used. Rather than employing a rheometer for DTMA, the viscoelastic behavior of the specimen is characterized using a shaker test bed. The shaker is used to apply a harmonic load to the specimen in the vertical direction.

Accelerations are measured both below and above the specimen, allowing the transfer function to be computed and subsequently used to identify the corresponding viscoelastic parameters. This method enables testing over a wide frequency range while being significantly more cost-effective than conventional rheometric approaches.

The experimental setup is illustrated in Fig. 2, providing an overview of the key components used for harmonic excitation and measurement. It consists of the shaker mounting (1), connector discs with glass inlays (2), the Ecoflex00-30 specimen (3), the tuning mass (4) and two accelerometers (5). The specimen, connecting discs, and tuning mass are all cylindrical with a common outer diameter of $d = 100\,\mathrm{mm}$. The sensors are mounted centrally, one between the lower connecting plate and the shaker (sensor A) and the other at the center of the tuning mass (sensor B). In cases where no tuning mass is used, the top sensor is positioned at the center of the upper connecting plate. Due to the viscoelastic behavior of the specimen, the acceleration measured by the upper sensor exhibits an amplitude and phase shift relative to the harmonic excitation signal recorded by the lower sensor. Comparing these signals yields the systems transfer function, capturing both the amplitude and phase response of the setup, which we use to characterize the Prony parameters. To influence the harmonic behavior, we use two options: either adjust the tuning mass placed on top, or modify the specimens geometry by using a specimen with a different height. For this purpose, three different tuning masses (m_T) and two specimen variants ($S1$ and $S2$) are used.

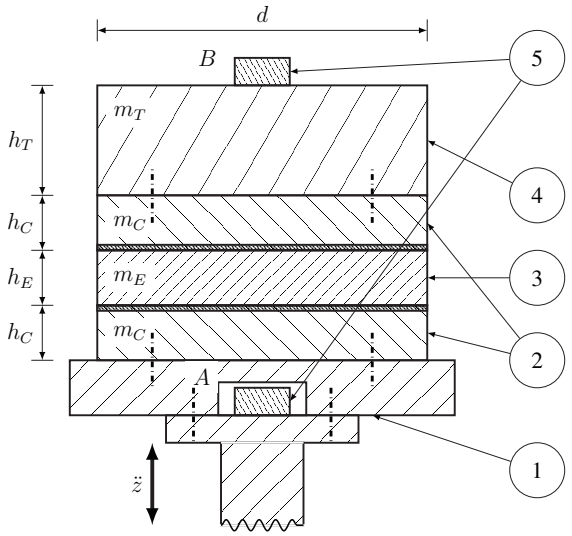

Figure 2: Experimental setup, illustrating the structure of testing sample and showing the position of the two accelerometers.

We use the Tira TV51140 shaker[1], which, under sine control, maintains a constant accelera-

tion amplitude of 0.5 g and supports excitation frequencies up to 900 Hz. The two connecting discs are identical in design and serve two main purposes: facilitating the mounting to both the shaker and the tuning masses, and enabling the casting process of the elastomer specimen. The lower disc is attached to the shaker, while the upper disc allows for the mounting of different tuning masses. The connecting discs are made of aluminum and have a height of 10 mm. For mounting purposes, six symmetrically arranged M6 blind threaded holes are positioned on a bolt circle with a diameter of 80 mm. The elastomer is cast and cured directly between the discs to ensure optimal bonding. However, due to inadequate adhesion between the aluminum and the elastomer near the edges, an additional glass plate was bonded to each connecting disc using a two-component adhesive. This significantly improves adhesion, as the silicone-based elastomer bonds more effectively to glass than to untreated aluminum surfaces. This results in a total height of the connecting discs of 12.3 mm and a mass of 257 g, which includes the aluminum and glass components as well as the adhesive. To facilitate the vacuum casting process, a custom mold was constructed to ensure precise distribution of the material between the discs and to maintain their parallel alignment, resulting in a constant specimen height of 7.9 mm for the first specimen (S1) and 14.8 mm for the second specimen (S2).

The used specimen material, Ecoflex00-30, is a two-component platinum-catalyzed silicone elastomer that is prepared by mixing parts A and B in a specified ratio of 1:1 by weight. The components are thoroughly blended to ensure a homogeneous mixture, then poured into the mold. To remove air bubbles, vacuum degassing is performed before and after pouring. The material then cures at a constant room temperature of 23 °C within a few hours.

The initial test was conducted after the specimen had cured for more than 24 hours. Repeated measurements were conducted over a period of one to two weeks to verify repeatability. The consistent results observed across all tests indicate that the cross-linking process had fully completed. The total weight of the specimen, including the two connector discs, is 576 g for the first setup (S1) and 638 g for the second (S2). Three variants of the tuning mass, all made of steel, are available and differ only in height. Each tuning mass features six through-holes to enable secure mounting onto the connecting discs using appropriate screws. This setup enables eight test configurations, combining either the first or second specimen with four tuning mass conditions: no mass, or a small, medium, or large tuning mass. Screw weights are already accounted for in the tuning mass, while the mass of the sensors (6 g each) is considered negligible.

The total number of measurement datasets is represented by the set $K = \{1, \ldots, 8\}$, where each $k \in K$ denotes a specific test configuration. Table 1 summarizes each setup corresponding to the index k, specifying the tuning mass and specimen height used for each dataset. Due to variations in the screws, the largest tuning mass in the second specimen setup is slightly lighter. The remaining setup parameters, which remain constant across all measurements, are listed in Table 2.

[1] https://www.tira-gmbh.de/fileadmin/inhalte/download/schwingprueftechnik/schwingpruefanlagen/standard/9N_bis_400N/Datenblatt_system_tv_51140_V08.pdf

Table 1: Dataset parameters. The table lists tuning and specimen specifications for each dataset, including tuning mass (m_T) and height (h_T) as well as specimen weight (m_E) and height (h_E).

k	1	2	3	4	5	6	7	8
m_T in g	0	1384	2484	3844	0	1384	2484	3825
h_T in mm	0	22.59	40.55	60.75	0	22.59	40.55	60.75
m_E in g	62	62	62	62	144	144	144	144
h_E in mm	7.9	7.9	7.9	7.9	14.8	14.8	14.8	14.8

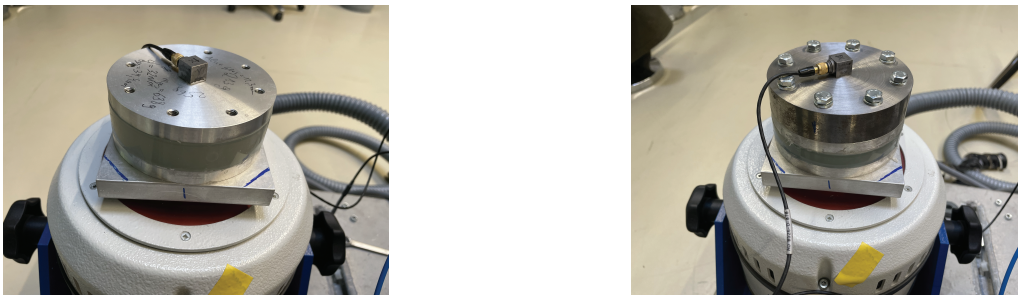

(a) without tuning mass (b) with tuning mass

Figure 3: Experimental setup. The left image shows the configuration without any tuning mass for the first specimen ($k = 1$), while the right image displays the setup with the first tuning mass mounted on the connecting plate ($k = 2$). The location of the top accelerometer is also indicated.

Figure 3 shows the assembled experimental setup, both with and without the tuning mass, as well as the position of the top accelerometer in each case.

Table 2: Setup parameters that remain constant throughout the experiment.

specimen diameter	d	100 mm
connector disc height	h_C	12.3 mm
connector disc mass	m_C	257 g

Two Brüel & Kjær Triaxial 4528-B-001[2] accelerometers were used in the experiment. The experimental setup is controlled and monitored using a Siemens SCADAS Mobile system. Actuation of the shaker is managed by the Syscom Vibcon module, which ensures constant acceleration through a closed-loop feedback controller. Signal acquisition is performed by the VB8-II module, and all measurements are processed and evaluated using Siemens TestLab soft-

[2] https://www.bksv.com/media/doc/bp2451.pdf

ware. The excitation is applied through a logarithmic frequency sweep at a rate of 3 octaves per minute. This results in measurements over a frequency range of 10 Hz to 900 Hz, with a total of 1500 logarithmically distributed sample points per configuration $k \in K$. In each configuration, measurements are taken at discrete frequency points ω_m indexed by $m \in M$, with $M = \{1, \dots, 1500\}$. Since the measurement setup can be considered a linear time-invariant (LTI) system, its behavior can be fully characterized by its transfer function for each configuration.

For each excitation frequency ω_m, the Siemens TestLab software extracts the amplitude A_k and phase ϕ_k of both the input and output acceleration signals via harmonic fitting in each configuration. These fitted quantities are interpreted as complex values in the form $A_k e^{j\phi_k}$. Based on this representation, the input signal $X_{\text{meas},k}(j\omega_m)$ corresponds to the vertical acceleration at the base of the specimen (sensor A), while the output signal $Y_{\text{meas},k}(j\omega_m)$ is the vertical acceleration measured at the top (sensor B). This allows the definition of a complex transfer function for each configuration k as

$$\mathcal{H}_{\text{meas},k}(j\omega_m) = \frac{Y_{\text{meas},k}(j\omega_m)}{X_{\text{meas},k}(j\omega_m)}, \tag{7}$$

capturing both the amplitude ratio and phase difference between the two signals.

Figure 4 presents the recorded measurements in the form of a Bode plot, showing both amplitude and phase responses for the eight different load cases. An increase in tuning mass, as well as an increase in specimen mass, leads to a noticeable shift of the resonance frequency towards lower values, indicating a significant change in the dynamic behavior.

4 FINITE ELEMENT MODEL AND PARAMETER IDENTIFICATION

In this section, we aim to identify the Prony parameters of the viscoelastic material introduced in Section 2. To this end, a finite element model of the experimental setup is developed to compare simulation results with the measurement data presented in Section 3. The parameters are determined by fitting the simulation model, which depends on the Prony parameters, to the experimental datasets using a non-linear least-squares approach. Once identified, the parameters are used in a ball drop simulation to validate the material model under dynamic impact conditions, providing direct insight into the material's damping behavior. The finite element implementation for the identification is carried out using the open-source package *Netgen/NGSolve*[3], and the fitting procedure is performed using a non-linear least-squares routine from the *SciPy* library (Python 3.11). Final validation is conducted in a separate ball drop simulation implemented in *Abaqus*.

To facilitate parameter identification, the Prony parameters are collected into a single parameter vector,

$$\boldsymbol{p} = \left[\mu_\infty, \mu_1, \dots, \mu_N, \tau_1, \dots, \tau_N\right]^\top \in \mathbb{R}^{2N+1}. \tag{8}$$

[3] `https://ngsolve.org`

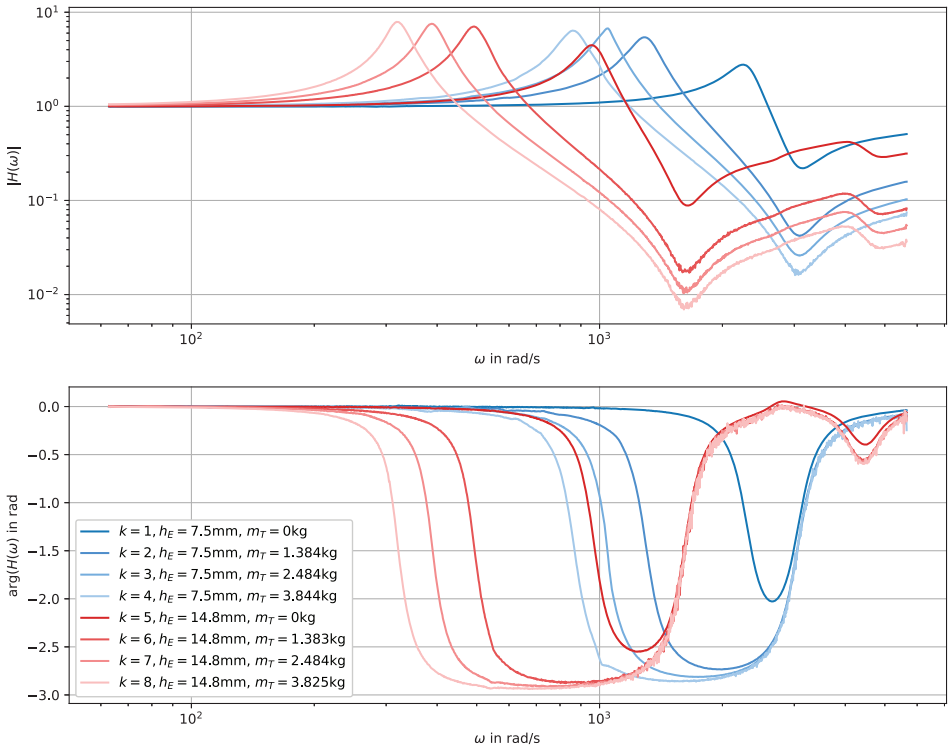

Figure 4: Bode plot of all eight measurement configurations. The data for the first specimen is shown in shades of blue, with lighter tones corresponding to higher tuning masses, while the results for the second specimen are displayed in shades of red.

The dimension of $\boldsymbol{p}$ depends on the selected number of Maxwell elements N, resulting in $2N+1$ parameters to be identified.

For the finite element model, a simplified representation of the experimental setup shown in Fig. 2 is used. As illustrated in Fig. 5, only the components above the specimen are considered, as the shaker motion is directly applied as a boundary condition to the specimen's bottom surface, assuming the lower connecting disc to be rigid. The finite element mesh for the rotationally symmetric model, corresponding to the first specimen without a tuning mass ($k = 1$), consists of 489 fourth-order elements to prevent locking, resulting in 8062 degrees of freedom for the displacement field. The bottom surface of the specimen is constrained to remain fixed in the x and y directions, while a prescribed harmonic displacement is applied in the z direction. The amplitude of the prescribed displacement amplitude is set to 1×10^{-4} m.

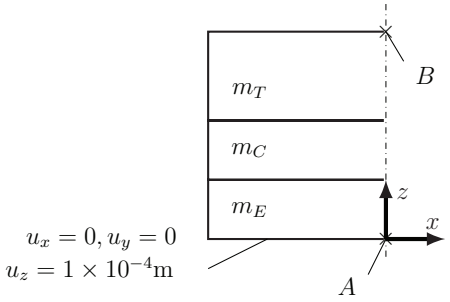

Figure 5: Axisymmetric finite element model.

The two reference points, A and B, are defined as the nodes located at the center of the bottom and top surfaces of the finite element model, respectively, corresponding to the positions of the two accelerometers used in the experiment. In the simulation, the displacement field is solved in the frequency domain under time-harmonic excitation. Since acceleration and displacement are directly related by $\ddot{\boldsymbol{u}}(\boldsymbol{X}) = -\omega^2 \boldsymbol{u}(\boldsymbol{X})$ in this regime, the transfer function can be equivalently defined using displacements. The input $X_{\mathrm{sim},k}(j\omega; \boldsymbol{p})$ refers to the prescribed vertical displacement at the specimen base (point A), while the output $Y_{\mathrm{sim},k}(j\omega; \boldsymbol{p})$ denotes the resulting vertical displacement at the top of the specimen (point B), both depending on the parameter vector $\boldsymbol{p}$. The complex transfer function for the simulation is then given by

$$\mathcal{H}_{\mathrm{sim},k}(j\omega; \boldsymbol{p}) = \frac{Y_{\mathrm{sim},k}(j\omega; \boldsymbol{p})}{X_{\mathrm{sim},k}(j\omega; \boldsymbol{p})}, \tag{9}$$

which applies for any excitation frequency $\omega \geq 0$.

In the next step, the simulation results are compared with the measurements. To this end, an individual subset $\bar{M}_k \subset M$ is selected for each configuration k, prioritizing frequency points that show strong variation or local extrema in the measured transfer function—particularly

around the resonance frequency. This approach also improves computational efficiency, as each frequency point requires solving a finite element problem. The number of selected frequencies $|\bar{M}_k|$ is around ten. Accordingly, at each discrete frequency ω_m with $m \in \bar{M}_k$, the simulated transfer function values are directly compared to the corresponding measured values. The parameter identification is carried out by minimizing the squared magnitude of the difference between the simulated and measured complex transfer functions, evaluated at selected frequency points ω_m for each configuration. This leads to the following least-squares problem,

$$\sum_{k\in K}\sum_{m\in\bar{M}_k}\left(|\mathcal{H}_{\text{sim},k}(j\omega_m;\boldsymbol{p})-\mathcal{H}_{\text{meas},k}(j\omega_m)|^2\right)\rightarrow\min_{\boldsymbol{p}}. \tag{10}$$

Figure 6 presents the results of the fitting procedure for $N = 2$. The fitted Prony parameters for $N = 2$ are summarized in Table 3.

Table 3: Fitted Prony parameters for $N = 2$.

N	μ_∞ in kPa	μ_1 in kPa	μ_2 in kPa	τ_1 in ms	τ_2 in ms
2	39.38	9.49	17.94	1.68	0.1542

To conclude, we validate the identified material parameters using the ball drop experiment. In this test, a steel ball is released from a known height onto a soft elastomer specimen, and the rebound height is measured. The initial drop height, defined as the distance between the ball and the specimen surface, is $h_0 = 155\,\text{mm}$. The ball has a diameter of $d_B = 10\,\text{mm}$, while the specimen measures $d_S = 100\,\text{mm}$ in diameter and $h_S = 8\,\text{mm}$ in height. The damping characteristic is defined by the rebound resilience, defined as $R = h_r/h_0$, where h_r is the rebound height after the first contact. A corresponding finite element simulation was performed using an axisymmetric model in *Abaqus*, incorporating the previously identified Prony parameters using a Neo-Hookean potential for the specimen, while the ball was modeled as a solid steel body. For implementation in *Abaqus*, the instantaneous shear modulus was computed as $\mu_0 = \mu_\infty + \sum_i \mu_i$, from which the Neo-Hookean hyperelastic parameter follows as $C_{10} = \mu_0/2$. The dimensionless Prony coefficients were calculated as $g_i = \mu_i/\mu_0$, and the relaxation times τ_i were used directly. The specimen was discretized using CAX6MH elements. For comparison, measurements were conducted using a high-speed camera to track the ball's trajectory. The results from both the measurements and the *Abaqus* simulations using the parameter set for $N = 2$ are summarized in Table 4. This strong agreement between the simulated and experimental rebound heights highlights the reliability of the fitted parameters and demonstrates the effectiveness of the proposed characterization and modeling approach.

5 CONCLUSIONS

This work presents a robust and cost-effective methodology for the dynamic characterization of soft elastomers using a shaker-based testbed. By modeling the viscoelastic behavior

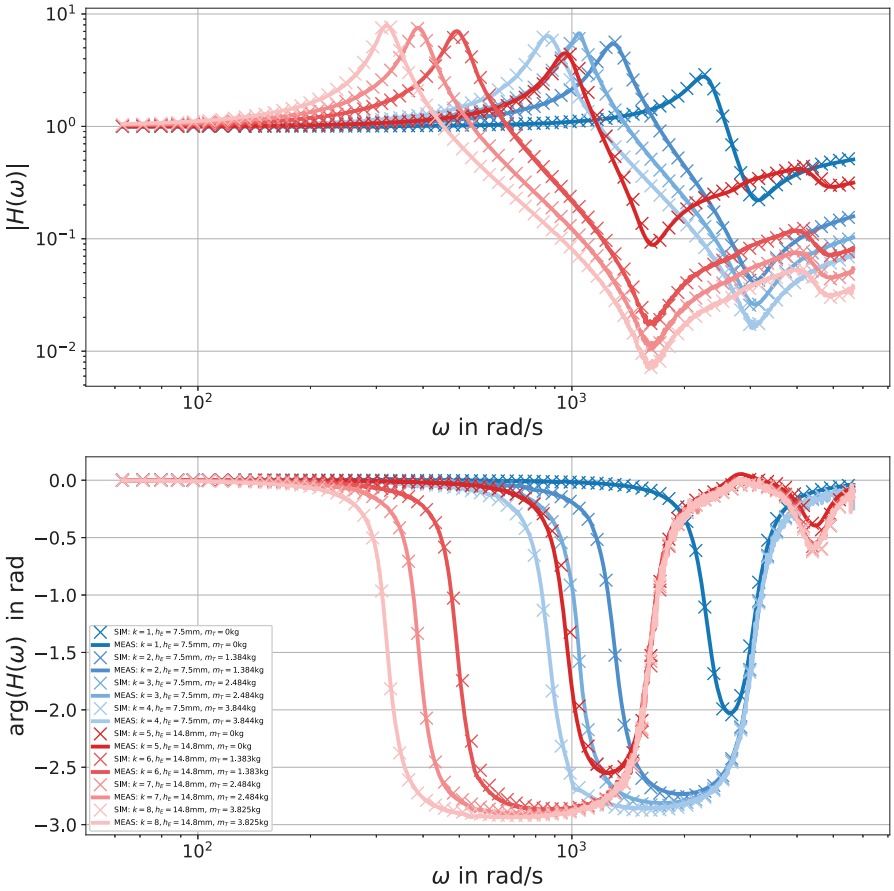

Figure 6: Results of the identification process for $N = 2$. The solid lines represent the measured data from Fig. 4, while the crosses indicate the corresponding finite element model predictions using the identified parameters. A different subset of frequencies $\hat{M}_k \subset M$ was used for the evaluation.

Table 4: Results of the ball drop experiment, comparing the measured rebound height h_r and rebound resilience R with the corresponding simulation outcomes.

	h_r	R
Measurement	$103.5 \pm 1\,\mathrm{mm}$	$\approx 66\,\%$
Simulation $N = 2$	$102.11\,\mathrm{mm}$	$65.88\,\%$

of Ecoflex00-30 with a linear Wiechert model in the linear regime and identifying Prony parameters through frequency-domain finite element simulations, material parameters were obtained without the need for expensive rheometric equipment. The results show strong agreement across different configurations and demonstrate good repeatability. Further validation through a nonlinear ball drop simulation confirms the predictive capability of the identified parameters, suggesting that the proposed approach is well suited for capturing the frequency-dependent behavior of soft elastomers in a broad range of applications.

REFERENCES

[1] Y. Guo, L. Liu, Y. Liu, and J. Leng, "Review of dielectric elastomer actuators and their applications in soft robots," *Advanced Intelligent Systems*, vol. 3, no. 10, p. 2000282, 2021.

[2] A. O'Halloran, F. Omalley, and P. McHugh, "A review on dielectric elastomer actuators, technology, applications, and challenges," *Journal of Applied Physics*, vol. 104, no. 7, 2008.

[3] R. S. Lakes, *Viscoelastic Solids*. CRC PRESS, 1998.

[4] H. F. Brinson and L. C. Brinson, *Polymer Engineering Science and Viscoelasticity - An Introduction*. Berlin, Heidelberg: Springer, 2015.

[5] N. W. Tschoegl, *The phenomenological theory of linear viscoelastic behavior: an introduction*. Springer Science & Business Media, 2012.

[6] Z. Liao, M. Hossain, X. Yao, R. Navaratne, and G. Chagnon, "A comprehensive thermo-viscoelastic experimental investigation of ecoflex polymer," *Polymer Testing*, vol. 86, p. 106478, 2020.

[7] J. C. Case, E. L. White, and R. K. Kramer, "Soft material characterization for robotic applications," *Soft Robotics*, vol. 2, no. 2, pp. 80–87, 2015.

[8] J. Ilg, S. J. Rupitsch, A. Sutor, and R. Lerch, "Determination of dynamic material properties of silicone rubber using one-point measurements and finite element simulations," *IEEE Transactions on Instrumentation and Measurement*, vol. 61, no. 11, pp. 3031–3038, 2012.

[9] J. Huang, Y. Xu, S. Qi, J. Zhou, W. Shi, T. Zhao, and M. Liu, "Ultrahigh energy-dissipation elastomers by precisely tailoring the relaxation of confined polymer fluids," *Nature Communications*, vol. 12, no. 1, p. 3610, 2021.

XI ECCOMAS Thematic Conference on Smart Structures and Materials - SMART 2025
M. Krommer, M. Nader and M. Schagerl (Eds)

Received: 22 April 2025 / Revised: 4 July 2025 / Accepted: 22 October 2025
© The Author(s) 2025

On the Integration of Multiple Load Protocols for Parameter Identification and Calibration of Superelastic Shape Memory Alloy Models Using Artificial Neural Networks

Niklas Lenzen, Florian Kolisch, Sven Klinkel

Abstract. In this study, we present an Artificial Neural Network (ANN) architecture that efficiently identifies all model parameters, while considering multiple load protocols simultaneously. Our approach also addresses the ill-posed nature of the parameter identification problem by implementing a dual-network architecture for training, improving the accuracy of parameter identification. The first part of the dual-network maps stress responses of multiple load protocols to parameters. The second part is a surrogate of the constitutive model and reconstructs the stress responses using the calculated parameters from the first part. To generate training data, we use the constitutive model to simulate stress responses for multiple load protocols with parameters sampled by Latin hypercube sampling. Once trained, the proposed ANN can predict suitable parameter sets for arbitrary compositions and elements of superelastic shape memory alloys (SMA), provided that the parameters are within the sampled space. We validate the proposed method by comparing the numerical results with cyclic stress–strain test data. In conclusion, our method offers an efficient and user-friendly tool for robust parameter identification of superelastic SMA models. It easily integrates multiple load protocols and eliminates the need for expert knowledge and additional training.

Key words: Parameter Identification, Constitutive Modeling, Shape Memory Alloys, Artificial Neural Networks, Inverse Modeling

1 INTRODUCTION

Due to their superior hysteretic energy dissipation and deformation capabilities, superelastic shape memory alloy (SMA) elements are increasingly being incorporated into vibration control devices for civil engineering structures. For the design of SMA-based control devices, accurate constitutive models are required. These models should particularly be able to precisely replicate strain rate-dependent responses such as the uniaxial model proposed by Auricchio et al. [1].

Niklas Lenzen & Florian Kolisch & Sven Klinkel
Chair of Structural Analysis and Dynamics, Department of Civil Engineering, RWTH Aachen University, Mies-van-der-Rohe-Str. 1, 52074 Aachen, Germany, e-mail: lenzen@lbb.rwth-aachen.de

Besides mathematical modeling of SMA, data-driven response modeling techniques, such as *Artificial Neural Networks* (ANNs), have been developed as these can directly learn patterns from data. In their pioneering work, Ozbulut et al. developed an Adaptive Neuro-Fuzzy Inference System to map strain and strain rate inputs to stress responses of SMAs [2]. More recently, Weber et al. successfully modeled the responses of SMA fibers using a *Feedforward Neural Network* (FNN) [3]. To enhance the generalizability, the FNN was trained with a physical constraint. Besides, more advanced architectures, such as *Deep Operator Networks* [4], can be applied for response modeling of SMAs [5]. However, ANN-based response modeling typically requires large amounts of data, which is often not available in desired quality. Thus, in case of low data availability, mathematical modeling approaches are advantageous due to their thermodynamic-consistent framework.

A critical step towards accurate response modeling using mathematical models is the identification of model parameters. Physical parameters, such as the Young's modulus, are typically determined directly through physical experiments, cf. [6]. However, constitutive models also rely on parameters critical to internal calculations, whose relationship with observed responses is often intricate and challenging to interpret. While established calibration methods for SMA models, such as by Meraghni et al. [7], have demonstrated strong capabilities, the evolution of ANNs has brought techniques that offer greater efficiency, especially when modeling highly non-linear relations. Despite their strengths, conventional methods often demand extensive expert knowledge of both the constitutive models and the optimization algorithms, along with access to specialized experimental equipment. This becomes particularly challenging when modeling material responses under dynamic loading conditions, where the large number of model parameters often leads to an ill-posed identification problem.

To efficiently solve these issues, ANNs offer great potential. For SMA models, Helm proposed an FNN-based approach to identify material parameters from stress inputs [8]. As this approach only considered quasi-static loads, several advances were made to apply dynamic loads [9, 10, 11]. However, these methods are specifically designed to predict parameter sets for a specific SMA composition.

In this study, we present an ANN-based method that predicts parameter sets for various SMA compositions without any adjustments of the ANN's trainable parameters. The proposed method enables the ANN to learn the mapping between stress time histories and parameter sets across a broad parameter space, ensuring adaptability and generalizability. Once trained, it provides predictions in near real-time and eliminates the need of expert knowledge for the calibration of SMA models. To ensure robust response modeling across different load scenarios, we integrate multiple load protocols as inputs to the ANN. Moreover, to overcome the ill-posed nature of the identification process, we implement a *dual-network* architecture for the training process, as introduced in [12, 13]. This architecture is inspired by *Autoencoders* [14].

The structure of the paper is as follows. Section 2 introduces the constitutive model used in this work and outlines our ANN-based approach for parameter identification. The results are presented in Section 3, where we examine the training accuracy and demonstrate the application of our method to two distinct SMA compositions. Section 4 summarizes our key findings.

2 METHODOLOGY

2.1 Constitutive model

To demonstrate the performance of the ANN-based parameter identification method, we use the uniaxial constitutive model by Auricchio et al. [1]. The model predicts the stress σ, material temperature T, and martensite volume fraction ξ as functions of the applied strain ε and strain rate $\dot{\varepsilon}$. In this work, the analysis is restricted to wires undergoing uniaxial tensile loading. Accordingly, the free energy is formulated as

$$\psi = \left[(u_A - T\eta_A) - \xi\left(\Delta u - T\Delta\eta\right)\right] + C\left[(T - T_0) - T\ln\frac{T}{T_0}\right] + \frac{1}{2}E(\varepsilon - \varepsilon_l\xi)^2, \tag{1}$$

where u_A is the internal energy of the austenite phase; η_A is the initial entropy of the austenite phase; Δu is the internal energy difference between the austenite and martensite phases; $\Delta\eta$ is the entropy difference between the austenite and martensite phases; C is the heat capacity; T_0 is the ambient/reference temperature; E is the Young's modulus; and ε_l is the maximum inelastic strain at $\xi = 100\%$.

The stress is derived from the free energy as

$$\sigma = \frac{\partial\psi}{\partial\varepsilon} = E\left(\varepsilon - \varepsilon_l\xi\right), \tag{2}$$

where the Young's modulus is defined according to Auricchio and Sacco [15] as a function of the martensite volume fraction to account for a transition between the two phases. It is expressed as

$$E = \frac{E_A E_M}{E_M + \xi\left(E_A - E_M\right)}, \tag{3}$$

where E_A and E_M are constants indicating the respective elastic moduli of the austenite and martensite phases. The heat equation is derived from the *first law of thermodynamics* as

$$\begin{aligned} C\dot{T} &= -\frac{\partial\psi}{\partial\xi}\dot{\xi} + T\frac{\partial^2\psi}{\partial T\partial\varepsilon}\dot{\varepsilon} + T\frac{\partial^2\psi}{\partial T\partial\xi}\dot{\xi} - \gamma(T - T_0) \\ &= \sigma\varepsilon_l\dot{\xi} + \Delta u\dot{\xi} - \gamma(T - T_0), \end{aligned} \tag{4}$$

where γ is the heat convection coefficient. To model the evolution of the martensite fraction ξ, the following first-order differential equations are employed:

$$\mathrm{A} \to \mathrm{M}: \quad \dot{\xi} = \beta^{AM}\left(1 - \xi\right)\frac{\dot{F}}{\left(F - R_f^{AM}\right)^2}\mathcal{H}^{AM}, \tag{5}$$

$$\mathrm{M} \to \mathrm{A}: \quad \dot{\xi} = \beta^{MA}\xi\frac{\dot{F}}{\left(F - R_f^{MA}\right)^2}\mathcal{H}^{MA}, \tag{6}$$

where F is the driving force; $R_f^{AM/MA}$ are the thermo-coupled limit stress levels; $\beta^{AM/MA}$ are the speed parameters controlling the rate effects on the phase transformation; and $\mathcal{H}^{AM/MA}$ are defined as the activation factors. These are expressed as

$$\mathcal{H}^{AM} = \begin{cases} 1 & \text{when } \dot{F} > 0 \text{ and } R_s^{AM} < F < R_f^{AM}, \\ 0 & \text{otherwise,} \end{cases} \tag{7}$$

$$\mathcal{H}^{MA} = \begin{cases} 1 & \text{when } \dot{F} < 0 \text{ and } R_f^{MA} < F < R_s^{MA}, \\ 0 & \text{otherwise,} \end{cases} \tag{8}$$

with

$$F = \sigma - T\frac{\Delta\eta}{\varepsilon_l}, \tag{9}$$

$$R_{s/f}^{AM/MA} = \sigma_{s/f}^{AM/MA} - T_0\frac{\Delta\eta}{\varepsilon_l}, \tag{10}$$

where $\sigma_{s/f}^{AM/MA}$ are the critical stress levels at which phase transformations start/finish.

Accurate identification of these parameters is essential to reliably capture the dynamic response of the material. The large number of model parameters and their direct influence on each other highlights the ill-posed nature of the identification problem. In total, 13 parameters have to be determined.

2.2 ANN-based parameter identification

The constitutive model is represented as $\mathcal{M}\left(\left(\boldsymbol{\varepsilon}, \dot{\boldsymbol{\varepsilon}}\right), \mathbf{p}\right)$, where $\boldsymbol{\varepsilon}$ and $\dot{\boldsymbol{\varepsilon}}$ denote the respective time histories of strain and strain rate. The parameter vector $\mathbf{p}$ contains all material model parameters. Our ANN-based method is designed to integrate multiple stress responses from cyclic tensile stress–strain experiments in the identification process. In this study, to effectively integrate multiple load protocols, we choose *Convolutional Neural Networks* (CNNs). Alternatively, FNNs would also be applicable. The CNN-based method is illustrated in Figure 1.

In a first step, training data is generated using the constitutive model. Therefore, I combinations of parameters $\mathbf{p}_i, \forall i \in \{1 : I\}$ are sampled within a predefined parameter space by the *Latin hypercube sampling* (LHS) [16]. The LHS is selected due to its effectiveness in achieving a balanced exploration of the parameter space, ensuring that samples are both representative and uniformly distributed across defined intervals. To cover all characteristics of the desired SMA specimen, such as strain rate effects and thermomechanical coupling, L load protocols, represented by strain time histories $\boldsymbol{\varepsilon}_j, \forall j \in \{1 : L\}$, are considered. The load protocols should be chosen, such that all desired material phenomena are covered. Thus, we recommend to consider different strain rate loadings and strain amplitudes for the identification process. For training data generation, each parameter sample $\mathbf{p}_i$ is then applied to the constitutive model to generate stress responses $\boldsymbol{\sigma}$ for each of the L load protocols. As a result, the training data set $\mathcal{D} = \left\{\left(\mathbf{p}_i, \left[\boldsymbol{\sigma}_1\, \boldsymbol{\sigma}_2 \ldots \boldsymbol{\sigma}_L\right]_i\right), \forall i \in \{1 : I\}\right\}$ is obtained. To improve training efficiency, the

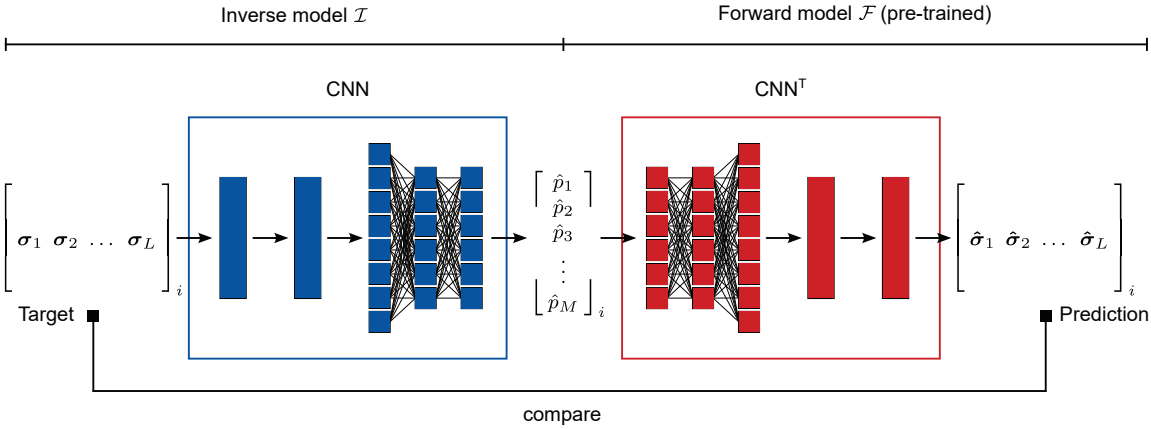

Figure 1: Training phase: The inverse model $\mathcal{I}$ is trained to map stress responses $\boldsymbol{\sigma}$ from L load protocols to parameters $\hat{\mathbf{p}}$. A pretrained forward model $\mathcal{F}$ is attached to reconstruct the stress responses $\boldsymbol{\sigma}$ from the parameter prediction $\hat{\mathbf{p}}$ of the inverse model $\mathcal{I}$. The predicted stress responses $\hat{\boldsymbol{\sigma}}$ are compared with the target stress responses $\boldsymbol{\sigma}$.

data set is normalized using *min–max* normalization. For greater stability against measurement error, *Gaussian noise* is added to the stress responses, with the mean and variance chosen based on the magnitude of the noise in the experimental test data.

Given the inherently ill-posed nature of the inverse problem, directly training an CNN to infer parameters from stress responses often leads to suboptimal results. This is primarily because the CNN may inadvertently penalize valid parameter sets. To mitigate this issue, a dual-network architecture is applied, cf. Figure 1. The training process is structured into two distinct phases. In the initial phase, a forward model $\mathcal{F}$, governed by a set of trainable parameters ω, is optimized to predict stress responses from given parameters, i.e., $\mathcal{F}_\omega : \mathbf{p}_i \rightarrow [\boldsymbol{\sigma}_1\, \boldsymbol{\sigma}_2 \ldots \boldsymbol{\sigma}_L]_i$. The forward model is trained by minimizing a loss function defined as the mean squared error (MSE) between predicted $\mathcal{F}_\omega\,[\mathbf{p}_i]$ and target stress responses $[\boldsymbol{\sigma}_1\, \boldsymbol{\sigma}_2 \ldots \boldsymbol{\sigma}_L]_i$ with respect to the CNN-parameters ω, i.e.,

$$\mathcal{F}_\omega \leftarrow \min_\omega \frac{1}{I} \sum_{i=1}^{I} ||\mathcal{F}_\omega\,[\mathbf{p}_i] - [\boldsymbol{\sigma}_1\, \boldsymbol{\sigma}_2 \ldots \boldsymbol{\sigma}_L]_i\,||^2. \tag{11}$$

Following the training of the forward model, an inverse model $\mathcal{I}$, parameterized by weights and biases θ, is introduced. This model aims to infer the underlying parameters from observed stress responses, i.e., $\mathcal{I}_\theta : [\boldsymbol{\sigma}_1\, \boldsymbol{\sigma}_2 \ldots \boldsymbol{\sigma}_L]_i \rightarrow \mathbf{p}_i$. During the training of the inverse model, the previously trained forward model is employed to reconstruct stress responses using the parameter estimates produced by the inverse network, cf. [12, 13]. Within this architecture, the forward model effectively serves as a differentiable surrogate for the constitutive model. Its integration into the backpropagation process allows for efficient gradient computation via automatic differentiation. As a result, the inverse model is optimized by minimizing the MSE between the reconstructed $\mathcal{F}_\omega\,[\mathcal{I}_\theta\,[[\boldsymbol{\sigma}_1\, \boldsymbol{\sigma}_2 \ldots \boldsymbol{\sigma}_L]_i]]$ and target stress responses $[\boldsymbol{\sigma}_1\, \boldsymbol{\sigma}_2 \ldots \boldsymbol{\sigma}_L]_i$ with respect to the CNN-parameters θ, i.e.,

$$\mathcal{I}_\theta \leftarrow \min_\theta \frac{1}{I} \sum_{i=1}^{I} ||\mathcal{F}_\omega \left[\mathcal{I}_\theta \left[[\boldsymbol{\sigma}_1 \, \boldsymbol{\sigma}_2 \, ... \, \boldsymbol{\sigma}_L]_i\right]\right] - [\boldsymbol{\sigma}_1 \, \boldsymbol{\sigma}_2 \, ... \, \boldsymbol{\sigma}_L]_i \, ||^2. \tag{12}$$

During the training of the inverse model, the CNN-parameters ω of the forward model are held fixed. This ensures that only discrepancies between the reconstructed and target stress responses contribute to the loss, thereby guiding the inverse model's learning process. The dual-network architecture simultaneously reduces dependence on expert knowledge, both in terms of constitutive model formulation and the selection of parameter spaces. By focusing solely on reproducing the target stress responses, the training scheme guarantees that the resulting model effectively captures the material behavior, even if the inferred parameters lack direct physical interpretation. Pretraining of the forward model is essential to enable the inverse model to reliably predict the parameters. Without this step, the inverse model lacks a well-defined mapping between the parameters and the corresponding stress responses, resulting in arbitrary or unstable outputs.

Several additional components are integral to the training process. The hidden layers utilize the *ReLU* activation function in conjunction with the *He initialization* strategy to promote efficient gradient flow and weight scaling [17]. For the inverse model, a sigmoid activation function is applied in the output layer to constrain outputs within the $[0, 1]$ interval, thereby ensuring compatibility with the predefined parameter space. This layer is initialized using the *Glorot initializer* to maintain balanced activation and gradient flow during training [18].

3 RESULTS

3.1 Training

First, we generate training data by using the constitutive model. Therefore, we sample $I = 100 \cdot 10^3$ parameter combinations using the LHS. Depending on the predefined parameter space, the amount of training samples for successful training can vary. Table 1 reports the chosen upper and lower boundaries of the parameter space. To cover a variety of SMA compositions, we choose a broad parameter space. In total, 13 parameters are considered within the identification process. The ambient temperature used in the constitutive model is set to $T_0 = 296.2$ K. To generate stress responses, we use $L = 9$ load protocols, which are reported in Table 2. Each load protocol consists of $J = 1000$ time instants, which are sampled for a time step size $\Delta t = 0.001$ s. For training data generation, we feed the load protocols and the parameter samples through the constitutive model. As a result, we obtain data pairs consisting of parameter samples $\mathbf{p}$ and stress responses $\boldsymbol{\sigma}$, such that the training data set $\mathcal{D} = \{(\mathbf{p}_i, [\boldsymbol{\sigma}_1 \, \boldsymbol{\sigma}_2 \, ... \, \boldsymbol{\sigma}_9]_i), \forall i \in \{1 : 100 \cdot 10^3\}\}$. Moreover, we use additional $\tilde{I} = 20 \cdot 10^3$ data pairs for validation. Before training, the data set is normalized using *min–max normalization*. Furthermore, to enhance the robustness of the CNN prediction, we add *Gaussian noise* with a zero mean and a variance of $1 \cdot 10^{-3}$. This is particularly important as we will be using noisy experimental data for testing.

Table 1: Sample space of the searched parameters. The lower and upper boundaries of the sample space are denoted by min and max.

Parameter		min	max	Unit
Young's moduli	E_A	25,000	40,000	MPa
	E_M	10,000	20,000	MPa
Max. inelastic strain at $\xi = 1$	ε_l	2.0	6.0	%
Critical stress levels	σ_s^{AM}	70	300	MPa
	σ_f^{AM}	350	650	MPa
	σ_s^{MA}	200	350	MPa
	σ_f^{MA}	70	200	MPa
Heat capacity	C	0.1	10.0	MPa K^{-1}
Heat convection coefficient	γ	0	10	-
Internal energy difference	Δu	0	50	MPa
Entropy difference	$\Delta \eta$	0.0	1.0	MPa K^{-1}
Speed parameters	β^{AM}	1	100	-
	β^{MA}	1	100	-

Table 2: Load protocols used for training. Harmonic signals are employed: $\varepsilon = \varepsilon_0 \sin(\Omega t)$, where ε_0 is the strain amplitude and Ω is the excitation frequency. The strain rate amplitude is computed by $\dot{\varepsilon}_0 = \varepsilon_0 \Omega$.

	LP1	LP2	LP3	LP4	LP5	LP6	LP7	LP8	LP9
ε_0 [%]	2	2	2	4	4	4	6	6	6
$\dot{\varepsilon}_0$ [%/s]	6.28	12.57	25.13	12.57	25.13	50.27	18.85	37.70	75.40

The hyperparameters of the dual-network architecture have been optimized by testing various configurations. Table 3 lists all network hyperparameters. To stabilize training and enhance the generalizability, we use *batch normalization* [19]. We trained the forward and inverse models for 2000 epochs with a batch size of $n_b = 1000$. To efficiently optimize the trainable parameters, the *Adam optimizer* [20] is employed with a learning rate of $\eta = 1 \cdot 10^{-3}$.

To determine the accuracy, we calculate the *coefficient of determination* R^2, where we compare the target data of the validation data set with the CNN predictions. Both the forward and inverse models show great accuracy with $R^2_{\mathcal{F}} = 99.90\%$ and $R^2_{\mathcal{I}} = 99.93\%$.

3.2 Experimental validation

To validate the proposed method, we identify constitutive model parameters for two Nitinol wire compositions:

- Sample 1: Ni-55.8%-Ti-43.55% manufactured by SAES Getters S.p.A.

Table 3: Hyperparameters of the inverse $\mathcal{I}$ and forward $\mathcal{F}$ models.

	No. filters	Kernel size	Stride	Padding	No. neurons	Activation
$\mathcal{I}$	2×16	(9,16)	(2,1)	*same*	4×50, 1×13	*ReLU*
$\mathcal{F}$	1×16, 1×1	(9,16)	(2,1)	*same*	1×13, 4×50	*ReLU*

Table 4: Parameter sets $\hat{\mathbf{p}}$ identified from measured cyclic stress responses of the SMA wire samples using the proposed method.

Parameter		Sample 1	Sample 2	Unit
Young's moduli	E_A	24,089	29,980	MPa
	E_M	10,922	12,564	MPa
Max. inelastic strain at $\xi = 1$	ε_l	3.1	2.7	%
Critical stress levels	σ_s^{AM}	203	189	MPa
	σ_f^{AM}	352	370	MPa
	σ_s^{MA}	307	321	MPa
	σ_f^{MA}	171	84	MPa
Heat capacity	C	6.0	3.3	MPa K^{-1}
Heat convection coefficient	γ	0.12	5.1	-
Internal energy difference	Δu	49.20	48.25	MPa
Entropy difference	$\Delta\eta$	0.29	0.19	MPa K^{-1}
Speed parameters	β^{AM}	9.9	6.2	-
	β^{MA}	76.1	70.4	-

- Sample 2: Ni-55.9%-Ti-43.95% manufactured by Baoji Hanz Metal Material Co.

For test data generation, we conducted cyclic tensile stress–strain experiments on wire specimens of length $l = 150$ mm and diameter $d = 0.2$ mm at ambient temperature $T_0 = 296.2$ K, which is consistent with the conditions assumed for training data generation. Moreover, to induce phase transformation at lower strain amplitudes, a pre-stress of $\sigma_0 = 134.9$ MPa was applied. More details on the test setup can be found in [11]. For accurate parameter identification, we measure the experimental stress responses for the same load protocols as used for training, cf. Table 2.

To identify the parameters, the experimental test data is fed into the trained inverse model $\mathcal{I}$ for both alloy compositions separately. The identified parameter sets are listed in Table 4.

Furthermore, we compare the experimental stress–strain data with the estimations calculated by the material model using the identified parameter sets from Table 4. The results for both alloy compositions are plotted in Figures 2 and 3. The calculated responses accurately reconstruct the experimental data, demonstrating the capabilities of our method. Moreover, to evaluate the accuracy of the estimations, we compute the coefficient of determination R^2. The accuracy for

Sample 1 is greater than 88.56%, while Sample 2 reaches an accuracy of greater than 94.80%. It is important to note that the accuracy of our method is limited by the precision of the material model. This can be observed, for example, in the residual deformations that are not considered by the material model.

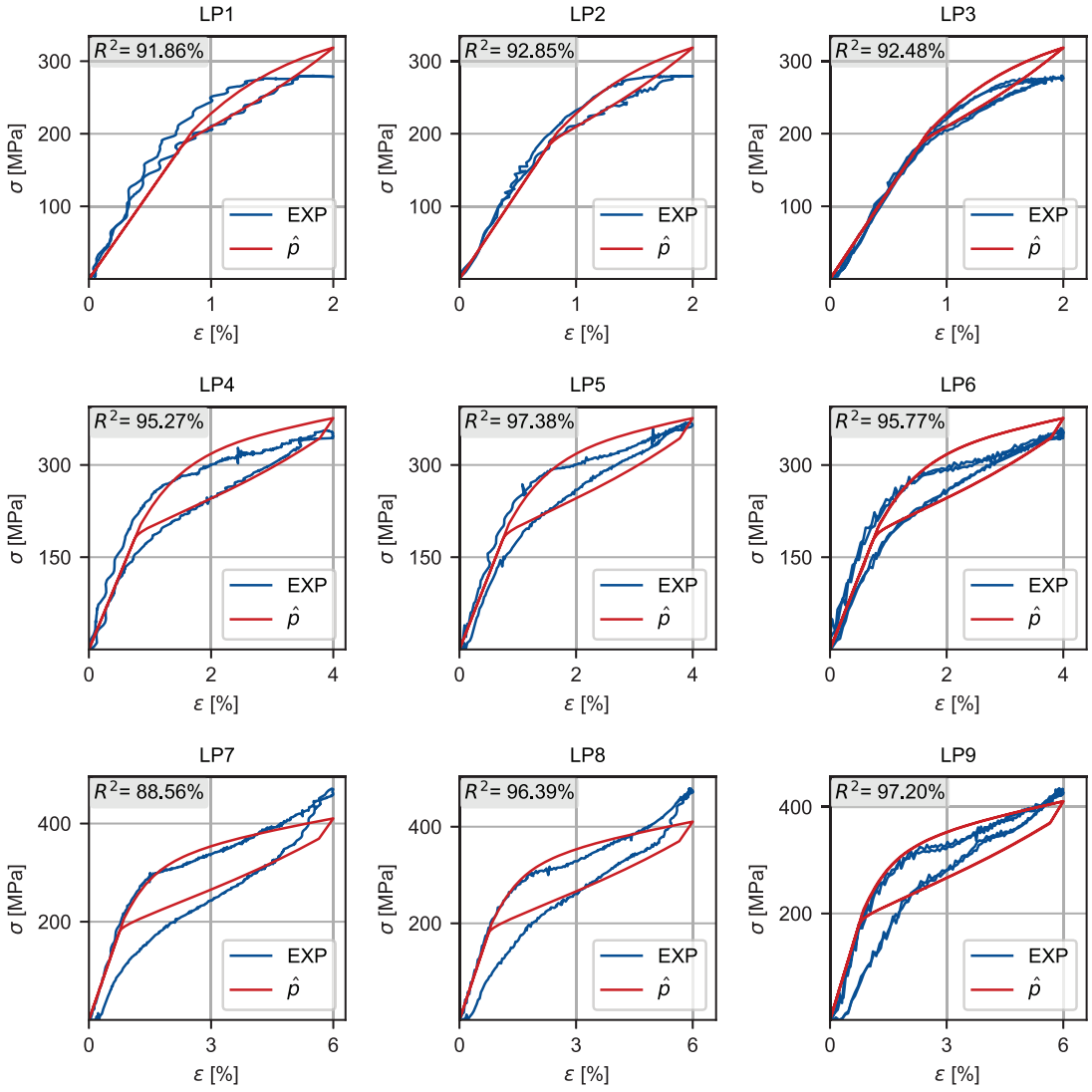

Figure 2: Sample 1: Comparison of the experimentally determined stress–strain responses (EXP) with predictions computed by the constitutive model using parameter set $\hat{\mathbf{p}}$, cf. Table 4.

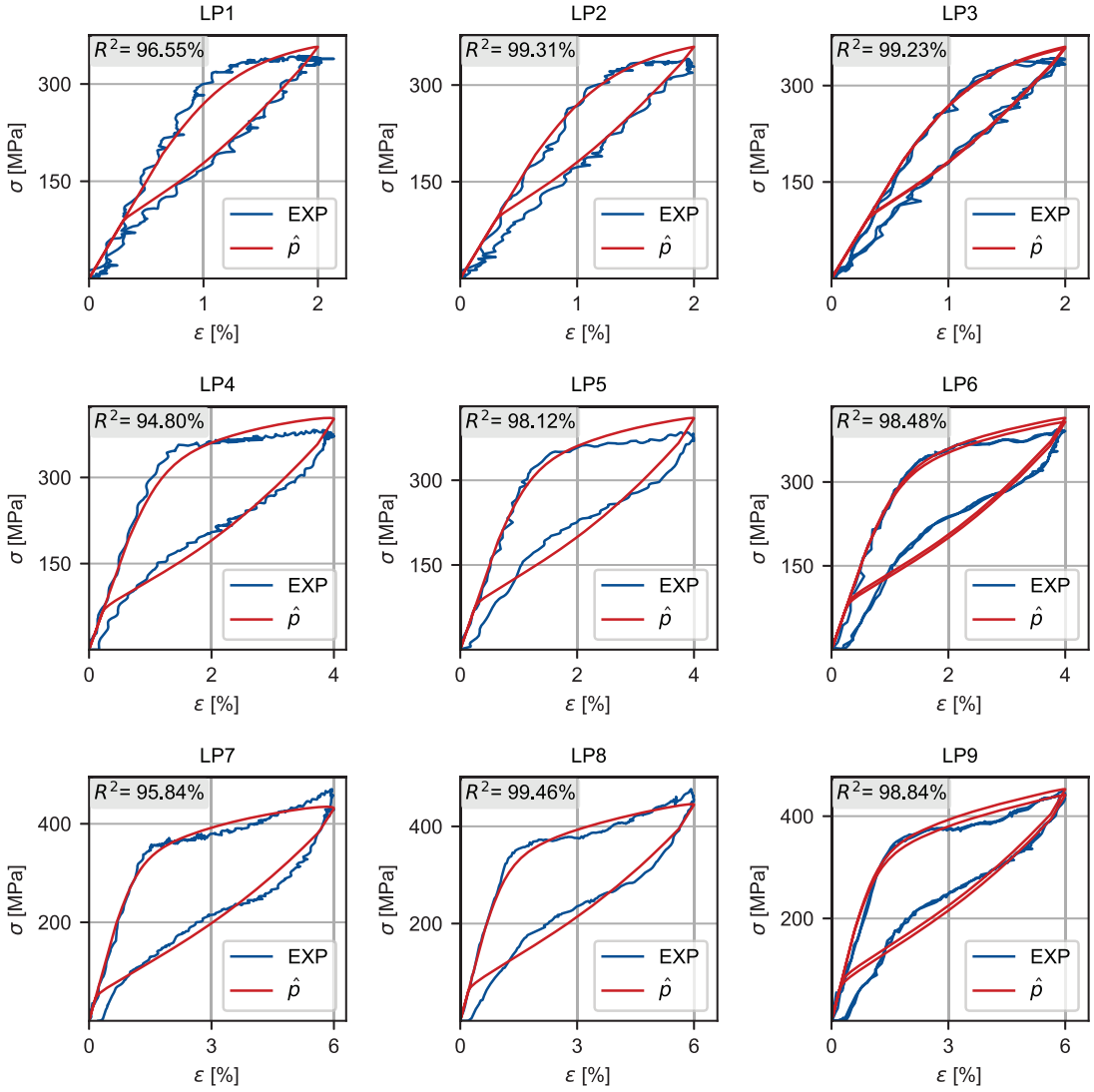

Figure 3: Sample 2: Comparison of the experimentally determined stress–strain responses (EXP) with predictions computed by the constitutive model using parameter set $\hat{\mathbf{p}}$, cf. Table 4.

4 CONCLUSIONS

This paper presented an ANN-based parameter identification method for uniaxial superelastic SMA models subjected to multiple dynamic load protocols. An efficient integration of multiple load protocols has been developed for the parameter identification of constitutive SMA models, ensuring accurate and robust response modeling across a variety of load scenarios. In this study, we used CNNs to efficiently integrate multiple load protocols. To address the ill-posed

nature of the inverse problem, a dual-network architecture was implemented, significantly enhancing the reliability of parameter identification. The CNN prediction accuracy demonstrates the effectiveness of the dual-network architecture, reaching values above $R^2 = 99.90\%$. Moreover, the trained CNN enables near real-time prediction of suitable parameter sets for different SMA compositions, provided the desired parameters lie within the sampled space. In this study, we considered two different SMA compositions for parameter identification. The results underline the high precision of our method, achieving prediction accuracy above $R^2 = 88.56\%$ and $R^2 = 94.80\%$, respectively.

Looking ahead, as the presented method is limited by the accuracy of the constitutive model, further research into more precise material models is required. Consequently, to improve the prediction accuracy of the presented method, additional load protocols should be included in the ANN-based parameter identification process. These additional load protocols should cover all effects present in the material.

REFERENCES

[1] F. Auricchio, D. Fugazza, and R. Desroches, "Rate-dependent thermo-mechanical modelling of superelastic shape-memory alloys for seismic applications," *Journal of Intelligent Material Systems and Structures*, vol. 19, no. 1, pp. 47–61, Feb. 2007.

[2] O. E. Ozbulut, P. N. Roschke, P. Y. Lin, and C. H. Loh, "GA-based optimum design of a shape memory alloy device for seismic response mitigation," *Smart Materials and Structures*, vol. 19, no. 6, p. 065004, Apr. 2010.

[3] P. Weber, W. Wagner, and S. Freitag, "ANN material modeling for SMA fibers enhanced with a physical constraint and its application to FE computations," *Computational Mechanics*, Jan. 2025.

[4] L. Lu, P. Jin, G. Pang, Z. Zhang, and G. E. Karniadakis, "Learning nonlinear operators via deeponet based on the universal approximation theorem of operators," *Nature Machine Intelligence*, vol. 3, no. 3, pp. 218–229, Mar. 2021.

[5] N. Lenzen and O. Altay, "Physics-informed deep operator network for predicting martensite evolution in superelastic shape memory alloys through cyclic tensile tests," *Smart Materials and Structures*, vol. 33, no. 6, p. 065039, May 2024.

[6] F. Auricchio, A. Coda, A. Reali, and M. Urbano, "SMA numerical modeling versus experimental results: Parameter identification and model prediction capabilities," *Journal of Materials Engineering and Performance*, vol. 18, no. 5–6, pp. 649–654, Aug. 2009.

[7] F. Meraghni, Y. Chemisky, B. Piotrowski, R. Echchorfi, N. Bourgeois, and E. Patoor, "Parameter identification of a thermodynamic model for superelastic shape memory alloys using analytical calculation of the sensitivity matrix," *European Journal of Mechanics - A/Solids*, vol. 45, pp. 226–237, May 2014.

[8] D. Helm, "Pseudoelasticity: experimental observations, thermomechanical modeling, and identification of the material parameters," in *Smart Structures and Materials 2004: Active Materials: Behavior and Mechanics*, D. C. Lagoudas, Ed. SPIE, Jul. 2004.

[9] N. Lenzen and O. Altay, "Machine learning enhanced dynamic response modelling of superelastic shape memory alloy wires," *Materials*, vol. 15, no. 1, p. 304, Jan. 2022.

[10] N. Lenzen, S. Klinkel, and O. Altay, "Parameter identification and modeling of superelastic shape memory alloy wires subjected to dynamic loads," in *10th ECCOMAS Thematic Conference on Smart Structures and Materials*, ser. SMART 2023. Dept. of Mechanical Engineering & Aeronautics University of Patras, 2023, pp. 1768–1777.

[11] N. Lenzen and O. Altay, "Feedforward neural network-assisted parameter identification and tuning for uniaxial superelastic shape memory alloy models under dynamic loads," *Journal of Vibration and Control*, Jun. 2024.

[12] Y. Long, J. Ren, Y. Li, and H. Chen, "Inverse design of photonic topological state via machine learning," *Applied Physics Letters*, vol. 114, no. 18, May 2019.

[13] S. Kumar, S. Tan, L. Zheng, and D. M. Kochmann, "Inverse-designed spinodoid metamaterials," *npj Computational Materials*, vol. 6, no. 1, Jun. 2020.

[14] G. E. Hinton and R. R. Salakhutdinov, "Reducing the dimensionality of data with neural networks," *Science*, vol. 313, no. 5786, pp. 504–507, Jul. 2006.

[15] F. Auricchio and E. Sacco, "A one-dimensional model for superelastic shape-memory alloys with different elastic properties between austenite and martensite," *International Journal of Non-Linear Mechanics*, vol. 32, no. 6, pp. 1101–1114, Nov. 1997.

[16] M. D. Mckay, R. J. Beckman, and W. J. Conover, "A comparison of three methods for selecting values of input variables in the analysis of output from a computer code," *Technometrics*, vol. 42, no. 1, pp. 55–61, Feb. 2000.

[17] K. He, X. Zhang, S. Ren, and J. Sun, "Delving deep into rectifiers: Surpassing human-level performance on imagenet classification," in *Proceedings of the IEEE International Conference on Computer Vision (ICCV)*. IEEE, December 2015.

[18] X. Glorot and Y. Bengio, "Understanding the difficulty of training deep feedforward neural networks," in *Proceedings of the thirteenth international conference on artificial intelligence and statistics*. JMLR Workshop and Conference Proceedings, 2010, pp. 249–256.

[19] S. Ioffe and C. Szegedy, "Batch normalization: Accelerating deep network training by reducing internal covariate shift," 2015.

[20] D. P. Kingma and J. Ba, "Adam: A method for stochastic optimization," 2014.

XI ECCOMAS Thematic Conference on Smart Structures and Materials - SMART 2025
M. Krommer, M. Nader and M. Schagerl (Eds)

Received: 3 April 2025 / Revised: 2 September 2025 / Accepted: 22 October 2025
© The Author(s) 2025

Ferroelectric Polarization of bimorph piezoelectric plates - an accurate equivalent single-layer approach

Astrid Pechstein, Alexander Humer, Michael Krommer

Abstract. The aim of the current contribution is the derivation of an equivalent single layer formulation for the evolution of the electric polarization in ferroelectric bimorph plates. Plate or shell models and finite elements for layered piezoelectric devices operated in linear regime are available and prove to be highly accurate. The driving electric field relevant to the evolution of internal polarization, is sensitive to the local stress distribution in the layered medium. Plate or shell formulations, mostly rely on stress resultants such as membrane stress and bending moments. We propose a formulation within a thermodynamically consistent framework based on the Clausius-Duhem inequality. Different variants of reduction from continuum to plate elastic potentials are discussed, and the implications on the driving electric field are analyzed. Numerical examples give evidence of the suitability of a newly proposed variant.

Key words: ferroelectric polarization, Kirchhoff-Love plate, equivalent single layer, ferroelectric bimorph plates

1 INTRODUCTION

When polarizing thin, bimorph ferroelectric plates through the application of high electric fields in two layers independently, the reordering of ferroelectric domains and deformation of single crystals in the electric field leads to out-of-plane deformation of the initially plane structure. The phenomenological modeling of the ferroelectric polarization process using the concept of ferroelectric and piezoelectric strains in a continuum mechanics framework is well understood, see e.g. the extensive article by Kamlah [1], or the works by Miehe and Rosato developing a variational framework [2, 3]. Finite element methods implementing these models using volume elements have been developed simultaneously, see [4] or [3], although at considerable computational cost. Locking effects prevent the usage of flat elements when using classical finite element basis functions. This behavior is remedied in using mixed elements as were developed by Meindlhumer and Pechstein [5, 6], or extend elements from the family of

Astrid Pechstein & Alexander Humer & Michael Krommer
Institute of Technical Mechanics, Johannes Kepler University Linz, Altenbergerstr. 69, A-4040 Linz, Austria
e-mail: astrid.pechstein@jku.at

smart solid shell elements (e.g. as proposed by [7, 8]) to ferroelectric hysteresis. However, the different layers still have to be resolved by layers of finite elements in such a setup.

Whenever thin structures are considered, a dimensional reduction achieved by a transition from continuum to plate or shell theories is of interest, as then thickness as limiting geometric dimension is avoided in discretizations. Plate models and finite elements for layered piezoelectric devices operated in linear regime have long been available and prove to be highly accurate, see e.g. [9, 10].

Ferroelectric polarzation was modeled in a first order shear deformable plate consisting of a single layer [11], where limitations of the approach became apparent in cases where thickness deformation is essential. In a previous contribution [12], we found that as the evolution of ferroelectric polarization in layered plates is concerned, a straightforward reduction of the aforementioned phenomenological material models to a plate theory based on classical deformation measures such as membrane strains and curvature fails.

The present contribution aims at developing an equivalent single-layer plate model, which is capable of predicting the evolution of independent ferroelectric polarization in one or both of the layers, while employing classical Kirchhoff-Love plate theory for the mechanical response. Numerical results show accurate reproduction of the evolution of electric polarization when compared to fully three-dimensional computations at greatly reduced cost.

2 MODELING THE FERROELECTRIC POLARIZATION PROCESS

Let Ω denote the material domain of interest. Considering some material point $\mathcal{P}$, we use its coordinates $\boldsymbol{X} = X_i \boldsymbol{e}_i$ with respect to the inertial frame $(\boldsymbol{e}_1, \boldsymbol{e}_2, \boldsymbol{e}_3)$. Throughout the manuscript, we adopt a notation for tensor analysis as described by Lebedev et al. [13], where the dot denotes the contraction operation, and no symbol is used for the tensor product. Displacement field $\boldsymbol{u}$ and electric potential φ denote the primary kinematic fields. The material derivative $\nabla = \partial/\partial X_i$ is used to define the deformation gradient $\mathbf{F}$, Green strain tensor $\boldsymbol{\varepsilon}$ and material electric field $\boldsymbol{E}$ through

$$\mathbf{F} = \mathbf{I} + (\nabla \boldsymbol{u})^T, \qquad \boldsymbol{\varepsilon} = \frac{1}{2}(\mathbf{F}^T \cdot \mathbf{F} - \mathbf{I}), \qquad \boldsymbol{E} = -\nabla \varphi. \tag{1}$$

In macroscopic models of the ferroelectric polarization process, it is common to introduce the *internal polarization* $\boldsymbol{P}_\mathrm{i}$ as an additional independent unknown field.

In the following, we assume all strains to be small. In this case, an additive split of the total strain $\boldsymbol{\varepsilon}$ into an elastic contribution $\boldsymbol{\varepsilon}_\mathrm{e}$ and an eigenstrain contribution $\boldsymbol{\varepsilon}^*$ is feasible, such that $\boldsymbol{\varepsilon} = \boldsymbol{\varepsilon}_\mathrm{e} + \boldsymbol{\varepsilon}^*$. This eigenstrain again consists of two additive contributions: the ferroelectric polarization strain $\boldsymbol{\varepsilon}^*_\mathrm{f}$ and the reversible piezoelectric strain $\boldsymbol{\varepsilon}^*_\mathrm{p}$.

$$\boldsymbol{\varepsilon} = \boldsymbol{\varepsilon}_\mathrm{e} + \boldsymbol{\varepsilon}^*, \qquad \boldsymbol{\varepsilon}^* = \boldsymbol{\varepsilon}^*_\mathrm{f} + \boldsymbol{\varepsilon}^*_\mathrm{p}. \tag{2}$$

The ferroelectric polarization strain evolves with the internal polarization, similar to an electrostrictive strain. It is modeled in a volume-preserving manner, where saturation strain ε_{sat} and saturation polarization P_{sat} occur as material constants,

$$\boldsymbol{\varepsilon}_{\text{f}}^{*} = \frac{\varepsilon_{\text{sat}}}{P_{\text{sat}}^{2}} \frac{3}{2} \left(\boldsymbol{P}_{\text{i}} \boldsymbol{P}_{\text{i}} - \tfrac{1}{3} (\boldsymbol{P}_{\text{i}} \cdot \boldsymbol{P}_{\text{i}}) \mathbf{I} \right). \tag{3}$$

The piezoelectric strain is modeled in such a way that it grows linearly with the electric field. In its definition, for non-zero internal polarization we use the polarization direction $\boldsymbol{e}_P = \boldsymbol{P}_{\text{i}}/|\boldsymbol{P}_{\text{i}}|$, and the piezoelectric constants d_{33}, d_{31} and d_{15},

$$\boldsymbol{\varepsilon}_{\text{p}}^{*} = \frac{1}{P_{\text{sat}}} \big(d_{33} (\boldsymbol{P}_{\text{i}} \cdot \boldsymbol{E}) \boldsymbol{e}_P \boldsymbol{e}_P + d_{31} (\boldsymbol{P}_{\text{i}} \cdot \boldsymbol{E}) (\mathbf{I} - \boldsymbol{e}_P \boldsymbol{e}_P) + d_{15} \operatorname{sym}(\boldsymbol{E} \cdot (\mathbf{I} - \boldsymbol{e}_P \boldsymbol{e}_P) \cdot \boldsymbol{P}_{\text{i}}) \big). \tag{4}$$

To model the material behavior, we use an approach based on thermodynamics. Let $\mathbf{S}$ denote the second Piola-Kirchhoff stress tensor, and let $\boldsymbol{D}$ be the dielectric displacement vector. For ψ the thermodynamic potential density, the Clausius-Duhem inequality states non-negative dissipation,

$$\mathcal{D} = \mathbf{S} : \dot{\boldsymbol{\varepsilon}} - \boldsymbol{D} \cdot \dot{\boldsymbol{E}} - \dot{\psi} \geq 0, \tag{5}$$

see Eringen and Maugin [14]. In the current contribution, two contributions to the potential $\psi = \psi_{\text{me}} + \psi_{\text{el}}$ are considered; the mechanic free energy ψ_{me} depending on the elastic part of the strain $\boldsymbol{\varepsilon}_{\text{e}}$, and the electric potential ψ_{el} which is deduced from the electric Helmholtz free energy through an Legendre transformation,

$$\psi_{\text{me}} = \mu \boldsymbol{\varepsilon}_{\text{e}} : \boldsymbol{\varepsilon}_{\text{e}} + \frac{\lambda}{2} (\boldsymbol{\varepsilon}_{\text{e}} : \mathbf{I})^2, \qquad \psi_{\text{el}} = \psi_{\text{p}}(|\boldsymbol{P}_{\text{i}}|) - \boldsymbol{P}_{\text{i}} \cdot \boldsymbol{E} - \frac{\epsilon}{2} \boldsymbol{E} \cdot \boldsymbol{E}. \tag{6}$$

Above, the mechanic potential is governed by the Lamé parameters λ and μ describing the isotropic elastic behavior according to a St. Venant-Kirchhoff law. In the electric potential, ϵ denotes the isotropic dielectric permittivity for small electric fields. The polarization potential ψ_{p} determines the evolution and saturation of the internal polarization $\boldsymbol{P}_{\text{i}}$, and depends only on its magnitude. In the current contribution, we present its derivative, characteristic parameters are the polarization susceptiblity χ_{i} and, again, the saturation polarization P_{sat},

$$\psi_{\text{p}}'(p) = -\frac{P_{\text{sat}}}{2\chi_{\text{i}}} (\log(P_{\text{sat}} - p) - \log(P_{\text{sat}} + p)). \tag{7}$$

For modeling the dissipation, we use a dissipation function ϕ depending on the coercive electric field E_c as well as the rate of internal polarization $\dot{\boldsymbol{P}}_{\text{i}}$, such that

$$\mathcal{D} = \frac{\partial \phi}{\partial \dot{\boldsymbol{P}}_{\text{i}}} \cdot \dot{\boldsymbol{P}}_{\text{i}}, \qquad \phi = E_c |\dot{\boldsymbol{P}}_{\text{i}}|. \tag{8}$$

Note that this definition holds in classical sense only for $\dot{\boldsymbol{P}}_\mathrm{i} \neq \boldsymbol{0}$; otherwise sub-differentials must be considered instead of differentiation, which leads to a case distinction discussed in the end of this section (14).

For such a choice as (6) and (8), the Clausius-Duhem inequality (5) can be re-written in the form

$$\left(\mathbf{S} - \frac{\partial \psi}{\partial \boldsymbol{\varepsilon}}\right) \cdot\cdot \dot{\boldsymbol{\varepsilon}} - \left(\boldsymbol{D} + \frac{\partial \psi}{\partial \boldsymbol{E}}\right) \cdot \dot{\boldsymbol{E}} - \left(\frac{\partial \psi}{\partial \boldsymbol{P}_\mathrm{i}} + \frac{\partial \phi}{\partial \dot{\boldsymbol{P}}_\mathrm{i}}\right) \cdot \dot{\boldsymbol{P}}_\mathrm{i} = 0. \tag{9}$$

This leads to the defining relations for the second Piola-Kirchhoff stress, the dielectric displacement vector and the driving electric field

$$\mathbf{S} = \frac{\partial \psi}{\partial \boldsymbol{\varepsilon}}, \qquad \boldsymbol{D} = -\frac{\partial \psi}{\partial \boldsymbol{E}}, \qquad \hat{\boldsymbol{E}} = -\frac{\partial \psi}{\partial \boldsymbol{P}_\mathrm{i}}. \tag{10}$$

One can easily verify the explicit relation for the driving electric field, where it is noted that $\lim_{p\to 0} \psi_\mathrm{p}'(p)/p < \infty$ is essential for the equation below to be well defined,

$$\hat{\boldsymbol{E}} = \mathbf{S} : \frac{\partial \boldsymbol{\varepsilon}^*}{\partial \boldsymbol{P}_\mathrm{i}} - \psi_\mathrm{p}'(|\boldsymbol{P}_\mathrm{i}|) \frac{\boldsymbol{P}_\mathrm{i}}{|\boldsymbol{P}_\mathrm{i}|} + \boldsymbol{E}. \tag{11}$$

The last constitutive relation to be derived from (9) is Biot's equation (see [15] for the original reference, and Rosato and Miehe [3] for the application to ferroelectric media),

$$\hat{\boldsymbol{E}} = \frac{\partial \phi}{\partial \dot{\boldsymbol{P}}_\mathrm{i}}. \tag{12}$$

As the dissipation function is not differentiable at $\dot{\boldsymbol{P}}_\mathrm{i} = \boldsymbol{0}$, Biot's equation (12) has to be considered in the sense of sub-differentials, which leads to the classical evolution conditions for the internal polarization,

$$\text{if } |\dot{\boldsymbol{P}}_\mathrm{i}| = 0 : \qquad |\hat{\boldsymbol{E}}| \leq E_\mathrm{c}, \tag{13}$$

$$\text{else if } |\dot{\boldsymbol{P}}_\mathrm{i}| \neq 0 : \qquad \hat{\boldsymbol{E}} = E_\mathrm{c} \frac{\dot{\boldsymbol{P}}_\mathrm{i}}{|\dot{\boldsymbol{P}}_\mathrm{i}|}. \tag{14}$$

3 AN EQUIVALENT SINGLE-LAYER APPROACH FOR BIMORPH PLATES

We consider the case of a structurally symmetric bimorph plate, with two layers of equal thickness $\frac{t}{2}$ made from ferroelectric material. According to standard notations in plate theories, we assume that the plate mid-surface coincides with the $\boldsymbol{e}_1\boldsymbol{e}_2$ plane, and $\boldsymbol{e}_3$ is the thickness direction. Let Γ be the plate's mid-surface, which is considered as the two-dimensional reference domain in the plate formulation. We use $\boldsymbol{X}_2 = X_1\boldsymbol{e}_1 + X_2\boldsymbol{e}_2$ for points in Γ

and the alias $z = X_3$ for the thickness coordinate for the sake of readability. The two layers are defined on the respective domains $\Omega_{(+)} = \{\boldsymbol{X}_2 + z\boldsymbol{e}_3 : \boldsymbol{X}_2 \in \Gamma, z \in (0, \frac{t}{2})\}$ and $\Omega_{(-)} = \{\boldsymbol{X}_2 + z\boldsymbol{e}_3 : \boldsymbol{X}_2 \in \Gamma, z \in (-\frac{t}{2}, 0)\}$, external and center electrodes are located at Γ, $\Gamma_{(+)} = \Gamma + \frac{t}{2}\boldsymbol{e}_3$ and $\Gamma_{(-)} = \Gamma - \frac{t}{2}\boldsymbol{e}_3$, respectively. Throughout the following, we use $(+)$ and $(-)$ as an index to indicate that the respective quantity is associated to positions $z > 0$ or $z < 0$; e.g. we denote the voltage prescribed at electrodes by

$$\varphi = V_{(+)} \text{ on } \Gamma_{(+)}, \qquad \varphi = V_{(-)} \text{ on } \Gamma_{(-)}, \qquad \varphi = 0 \text{ on } \Gamma. \tag{15}$$

Thus, the center electrode is grounded.

Next, a kinematic reduction of the plate deformation according to Kirchhoff-Love assumptions is performed. A projection to the tangential plane is realized in defining $\mathbf{A} = \mathbf{I} - \boldsymbol{e}_3\boldsymbol{e}_3$. Introducing membrane strain $\mathbf{e}$ and curvature $\boldsymbol{\kappa}$, the in-plane component of the strain tensor $\boldsymbol{\varepsilon}_2 = \mathbf{A} \cdot \boldsymbol{\varepsilon} \cdot \mathbf{A}$ is approximated through

$$\boldsymbol{\varepsilon}_2 = \mathbf{e} + z\boldsymbol{\kappa}. \tag{16}$$

In each of the two layers, internal polarization $\boldsymbol{P}_\mathrm{i}$ and electric field $\boldsymbol{E}$ are assumed constant and orientied in thickness direction. We introduce the scalar-valued electric field $E_{(+)}$ and $E_{(-)}$ as well as the according internal polarization $P_{\mathrm{i},(+)}$ and $P_{\mathrm{i},(-)}$ such that

$$\boldsymbol{E} = E_{(\pm)}\boldsymbol{e}_3 = \mp\frac{2V_{(\pm)}}{t}\boldsymbol{e}_3 \quad \text{and} \quad \boldsymbol{P}_\mathrm{i} = P_{\mathrm{i},(\pm)}\boldsymbol{e}_3 \quad \text{in } \Omega_{(\pm)}. \tag{17}$$

Inserting this assumption into the definition of the eigenstrain component $\boldsymbol{\varepsilon}_2^* = \mathbf{A} \cdot \boldsymbol{\varepsilon}^* \cdot \mathbf{A}$ implies a constant tensor in each layer,

$$\boldsymbol{\varepsilon}_2^* = \varepsilon_{(\pm)}^*\mathbf{A} \quad \text{in } \Omega_{(\pm)}, \text{ with} \quad \varepsilon_{(\pm)}^* = -\frac{\varepsilon_\mathrm{sat}}{2P_\mathrm{sat}^2}P_{\mathrm{i},(\pm)}^2 + d_{31}P_{\mathrm{i},(\pm)}E_{(\pm)}. \tag{18}$$

Thermodynamic potential and dissipation function for the plate formulation are often gained by through-the-thickness integration. For the electric contribution to the potential ψ_el and the dissipation function ϕ, one directly obtains surface potentials,

$$\psi_{\mathrm{el},\Gamma} = \int_{-t/2}^{t/2} \psi_\mathrm{el}\, dz = \frac{t}{2}\sum_{*\in\{+,-\}} \left(\psi_p(|P_{\mathrm{i},(*)}|) - P_{\mathrm{i},(*)}E_{(*)} - \frac{\epsilon}{2}(E_{(*)})^2\right), \tag{19}$$

$$\phi_\Gamma = \int_{-t/2}^{t/2} \phi\, dz = \frac{t}{2}\sum_{*\in\{+,-\}} E_c|\dot{P}_{\mathrm{i},(*)}|. \tag{20}$$

The kinematic assumptions of Kirchhoff-Love theory do not consider an independent thickness deformation. We use the St. Venant-Kirchhoff elastic energy based on plane stress assumptions, which is defined in terms of the in-plane elastic strain $\boldsymbol{\varepsilon}_{\mathrm{e},2}$

$$\hat{\psi}_\mathrm{me} = \frac{E}{2(1+\nu)}\boldsymbol{\varepsilon}_{\mathrm{e},2} : \boldsymbol{\varepsilon}_{\mathrm{e},2} + \frac{E\nu}{2(1-\nu^2)}(\boldsymbol{\varepsilon}_{\mathrm{e},2} : \mathbf{A})^2. \tag{21}$$

Regarding the treatment of eigenstrains in a plate formulation, a common possibility is to reduce the eigenstrain component $\boldsymbol{\varepsilon}_2^*$ to inelastic strain measures. Inelastic membrane strain and curvature can be deduced as mean value and first moment of $\boldsymbol{\varepsilon}_2^*$,

$$\mathbf{e}^* = e^* \mathbf{A}, \qquad e^* = \frac{1}{2}(\varepsilon^*_{(+)} + \varepsilon^*_{(-)}), \tag{22}$$

$$\boldsymbol{\kappa}^* = \kappa^* \mathbf{A}, \qquad \kappa^* = \frac{3}{2t}(\varepsilon^*_{(+)} - \varepsilon^*_{(-)}). \tag{23}$$

Accordingly, we define elastic membrane strain and curvature

$$\mathbf{e}_\mathrm{e} = \mathbf{e} - \mathbf{e}^*, \qquad \boldsymbol{\kappa}_\mathrm{e} = \boldsymbol{\kappa} - \boldsymbol{\kappa}^*. \tag{24}$$

Reduction of St. Venant-Kirchhoff energy density (21) to plate kinematics for an assumed linear distribution of the elastic strain $\boldsymbol{\varepsilon}_{\mathrm{e},2} = \mathbf{e}_\mathrm{e} + z\boldsymbol{\kappa}_\mathrm{e}$ yields

$$\psi^{\text{plate}}_{\text{me},\Gamma} = \int_{-t/2}^{t/2} \hat{\psi}_\text{me}(\mathbf{e}_\mathrm{e} + z\boldsymbol{\kappa}_\mathrm{e})\, dz = t\hat{\psi}_\text{me}(\mathbf{e}_\mathrm{e}) + \frac{t^3}{12}\hat{\psi}_\text{me}(\boldsymbol{\kappa}_\mathrm{e}). \tag{25}$$

We observe that the evolution of internal polarization is not caught correctly in a simulation based on such a plate formulation. To assess the reason for this failure, we define membrane stress $\mathbf{s}$ and moment tensor $\mathbf{m}$ as dual to the plate strain measures $\mathbf{e}$ and $\boldsymbol{\kappa}$, respectively:

$$\mathbf{s} = \frac{\partial \psi^{\text{plate}}_{\text{me},\Gamma}}{\partial \mathbf{e}} = -\frac{\partial \psi^{\text{plate}}_{\text{me},\Gamma}}{\partial \mathbf{e}^*} \tag{26}$$

$$\mathbf{m} = \frac{\partial \psi^{\text{plate}}_{\text{me},\Gamma}}{\partial \boldsymbol{\kappa}} = -\frac{\partial \psi^{\text{plate}}_{\text{me},\Gamma}}{\partial \boldsymbol{\kappa}^*} \tag{27}$$

The driving electric field, or rather voltage, in each layer is formally defined as

$$\begin{aligned} \frac{t}{2}\hat{E}^{\text{plate}}_{(\pm)} &= -\frac{\partial(\psi^{\text{plate}}_{\text{me},\Gamma} + \psi_{\text{el},\Gamma})}{\partial P_{\text{i},(\pm)}} = \mathbf{s} : \mathbf{A}\, \frac{\partial e^*}{\partial P_{\text{i},(\pm)}} + \mathbf{m} : \mathbf{A}\, \frac{\partial \kappa^*}{\partial P_{\text{i},(\pm)}} - \frac{\partial \psi_{\text{el},\Gamma}}{\partial P_{\text{i},(\pm)}} \\ &= \left(\frac{1}{2}\mathbf{s} \pm \frac{3}{2t}\mathbf{m}\right) : \mathbf{A}\frac{\partial \varepsilon^*_{(\pm)}}{\partial P_{\text{i},(\pm)}} - \frac{\partial \psi_{\text{el},\Gamma}}{\partial P_{\text{i},(\pm)}}. \end{aligned} \tag{28}$$

From the above expression we finally obtain the driving field, which we furnish with an additional index *plate* to distinguish it from other choices later,

$$\hat{E}^{\text{plate}}_{(\pm)} = \left(\frac{1}{t}\mathbf{s} \pm \frac{3}{t^2}\mathbf{m}\right) : \mathbf{A}\frac{\partial \varepsilon^*_{(\pm)}}{\partial P_{\text{i},(\pm)}} - \partial\psi'_\text{p}(|P_{\text{i},(\pm)})\frac{P_{\text{i},(\pm)}}{|P_{\text{i},(\pm)}|} + E_{(\pm)}. \tag{29}$$

We compare this expression to the continuum definition of driving electric field in the continuum model (11). Observe that, instead of the second Piola-Kirchhoff tensor $\mathbf{S}$, membrane stress $\mathbf{s}$ and moment tensor $\mathbf{m}$ influence the driving field.

4 AN AUGMENTED EQUIVALENT SINGLE-LAYER APPROACH

The aim is to obtain a more locally relevant approximation of the driving electric field.

In the present case of a constant internal polarization and electric field, we observe that the internal strain ε^* can be represented exactly through the thickness by three parameters, including inelastic membrane strain e^*, curvature κ^* and a further component ξ^*,

$$\varepsilon^*(z) = \begin{cases} \varepsilon^*_{(+)} = e^* + z\kappa^* + (z - t/3)\xi^* & \text{if } z > 0, \\ \varepsilon^*_{(-)} = e^* + z\kappa^* + (z + t/3)\xi^* & \text{if } z < 0. \end{cases} \tag{30}$$

Let us use $(z \mp t/3)$ as a shorthand notation for the piecewise defined function $z \mapsto z - t/3$ if $z > 0$ and $z \mapsto z + t/3$ if $z < 0$. We observe that these thickness distributions 1, z and $(z \mp t/3)$ are orthogonal in the sense that

$$\int_{-t/2}^{t/2} z = 0, \qquad \int_{-t/2}^{t/2} (z \mp t/3) = 0, \qquad \int_{-t/2}^{t/2} z(z \mp t/3) = 0. \tag{31}$$

This implies that ξ^* above can be seen as a generalized higher moment of the distribution ε^*. Its defining equation reads

$$\int_{-t/2}^{t/2} (z \mp t/3)^2 \xi^* \, dz = \int_{-t/2}^{t/2} (z \mp t/3)\varepsilon^* \, dz. \tag{32}$$

For our special choice with two layers of constant inelastic strain, we obtain that the value of the generalized moment ξ^* equals the negative value of curvature,

$$\xi^* = -\kappa^*. \tag{33}$$

One can formally reduce the plane stress elastic energy density taking the additional inelastic strain component into account

$$\psi^{\text{full}}_{\text{me},\Gamma} = \int_{-t/2}^{t/2} \hat{\psi}_{\text{me}}(\mathbf{e} + z\boldsymbol{\kappa} - (e^* + z\kappa^* + (z \mp t/3)\xi^*)\mathbf{A}) \, dz \tag{34}$$

$$= \psi^{\text{plate}}_{\text{me},\Gamma}(\mathbf{e} - \mathbf{e}^*, \boldsymbol{\kappa} - \boldsymbol{\kappa}^*) + \psi_{\text{me,aug},\Gamma}(\xi^*). \tag{35}$$

The splitting above is exact for quadratic potentials such as the plane-stress St. Venant-Kirchhoff energy due to the orthogonality relations (31). The augmentation potential computes as

$$\psi_{\text{me,aug},\Gamma}(\xi^*) = \int_{-t/2}^{t/2} \hat{\psi}_{\text{me}}((z \mp t/3)\xi^*\mathbf{A}) \, dz = \frac{t^3}{36}\hat{\psi}_{\text{me}}(\xi^*\mathbf{A}). \tag{36}$$

Using such an augmentation term in a plate formulation is equivalent to exact integration through the thickness, and an exact representation of the in-plane stress distribution through the thickness.

We observe that there is some flexibility in the choice of the augmentation term. The first formulation neglecting any contribution from the higher moment ξ^* is equivalent to choosing an augmentation potential $\psi^{\text{plate}}_{\text{me,aug},\Gamma}$ as zero,

$$\psi^{\text{plate}}_{\text{me,aug},\Gamma} = 0. \tag{37}$$

The second formulation regarding the additional contribution stemming from ξ^* exactly re-uses the plane stress potential for the definition of the augmentation potential,

$$\psi^{\text{full}}_{\text{me,aug},\Gamma} = \frac{t^3}{36}\hat{\psi}_{\text{me}}(\xi^*\mathbf{A}). \tag{38}$$

We propose a third variant, which performs well in simulations. For the augmentation potential, we propose to use the St. Venant-Kirchhoff model for uni-axial stress states, or Poisson ratio $\nu = 0$. This leads to

$$\psi^{\text{new}}_{\text{me,aug},\Gamma} = \frac{t^3}{36}\frac{E}{2}(\xi^*)^2\mathbf{A} : \mathbf{A}. \tag{39}$$

For all three variants, we use shorthand notation for the total potential including mechanic and electric contribution as well as the augmentation term,

$$\psi^{\text{variant}}_{\Gamma} = \psi^{\text{plate}}_{\text{me},\Gamma} + \psi^{\text{variant}}_{\text{me,aug},\Gamma} + \psi_{\text{el},\Gamma} \quad \text{for variant either } \texttt{plate}, \texttt{full} \text{ or } \texttt{new}. \tag{40}$$

5 IMPLICATIONS ON STRESS AND DRIVING ELECTRIC FIELD

The stress resultants $\mathbf{s}$ and $\mathbf{m}$ are independent of the choice of the augmentation potential, as these quantities depend solely on $\psi_{\text{me},\Gamma}$. As neither the augmentation potential nor the electric contribution contain membrane strain or curvature, one verifies for variant either `plate`, `full` or `new`

$$\mathbf{s} = \frac{\partial \psi^{\text{variant}}_{\Gamma}}{\partial \mathbf{e}} = \frac{\partial \psi^{\text{plate}}_{\text{me},\Gamma}}{\partial \mathbf{e}}, \qquad \mathbf{m} = \frac{\partial \psi^{\text{variant}}_{\Gamma}}{\partial \boldsymbol{\kappa}} = \frac{\partial \psi^{\text{plate}}_{\text{me},\Gamma}}{\partial \boldsymbol{\kappa}}. \tag{41}$$

Thus, the elastic behavior of the plate is independent of the choice of the augmentation potential; only the evolution of internal polarization, and thereby the inelastic strains, is affected.

The evolution equation in the form of Biot's law (12), or the definition of the driving electric field $\hat{\boldsymbol{E}}$ changes for different variants of augmentation. Let us review the impact of the choice of $\psi_{\text{me,aug},\Gamma}$ on the driving electric field.

In case of the direct plate formulation without augmentation $\psi^{\text{plate}}_{\text{me,aug},\Gamma}$, the driving electric field $\hat{E}^{\text{plate}}_{(\pm)}$ has been deduced to include membrane stress $\mathbf{s}$ and moment tensor $\mathbf{m}$, see (29).

Let us now consider the case of the augmentation energy density obeying the original elastic material law, characterized in $\psi^{\text{full}}_{\text{me,aug},\Gamma}$. Then, in view of the exact representation of $\varepsilon^* = e^* + z\kappa^* + (z \mp t/3)\xi^*$ and (34),

$$\frac{t}{2}\hat{E}^{\text{full}}_{(\pm)} = -\frac{\partial \psi^{\text{full}}_{\Gamma}}{\partial P_{\text{i},(\pm)}} \tag{42}$$

$$= \int_{-t/2}^{0} \left(\frac{\partial \hat{\psi}_{\text{me}}}{\partial \boldsymbol{\varepsilon}} \frac{\partial \boldsymbol{\varepsilon}^*}{\partial P_{\text{i},(-)}} - \frac{\partial \psi_{\text{el}}}{\partial P_{\text{i},(-)}} \right) dz + \int_{0}^{t/2} \left(\frac{\partial \hat{\psi}_{\text{me}}}{\partial \boldsymbol{\varepsilon}} \frac{\partial \boldsymbol{\varepsilon}^*}{\partial P_{\text{i},(+)}} + \frac{\partial \psi_{\text{el}}}{\partial P_{\text{i},(+)}} \right) dz. \tag{43}$$

As $\partial \boldsymbol{\varepsilon}^* / \partial P_{\text{i},(\pm)}$ is constant in each layer and zero in the respective non-relevant domain, we see that in each layer integration through the thickness can be replaced by using the respective mean value $\mathbf{S}_{(\pm)}$ of $\mathbf{S}$,

$$\int_{0}^{t/2} \frac{\partial \hat{\psi}_{\text{me}}}{\partial \boldsymbol{\varepsilon}} \frac{\partial \boldsymbol{\varepsilon}^*}{\partial P_{\text{i},(+)}} \, dz = \int_{0}^{t/2} \mathbf{S} : \frac{\partial \boldsymbol{\varepsilon}^*}{\partial P_{\text{i},(+)}} \, dz = \frac{t}{2} (\mathbf{S}_{(+)} : \mathbf{A}) \frac{\partial \varepsilon^*}{\partial P_{\text{i},(+)}}, \tag{44}$$

$$\int_{-t/2}^{0} \frac{\partial \hat{\psi}_{\text{me}}}{\partial \boldsymbol{\varepsilon}} \frac{\partial \boldsymbol{\varepsilon}^*}{\partial P_{\text{i},(-)}} \, dz = \int_{-t/2}^{0} \mathbf{S} : \frac{\partial \boldsymbol{\varepsilon}^*}{\partial P_{\text{i},(-)}} \, dz = \frac{t}{2} (\mathbf{S}_{(-)} : \mathbf{A}) \frac{\partial \varepsilon^*}{\partial P_{\text{i},(+)}}. \tag{45}$$

This implies for the driving field when prescribing the full potential $\psi^{\text{full}}_{\Gamma}$

$$\hat{E}^{\text{full}}_{(\pm)} = (\mathbf{S}_{(\pm)} : \mathbf{A}) \frac{\partial \varepsilon^*_{(\pm)}}{\partial P_{\text{i},(\pm)}} - \psi'_{\text{p}}(|P_{\text{i},(\pm)}|) \frac{P_{\text{i},(\pm)}}{|P_{\text{i},(\pm)}|} + E_{(\pm)}. \tag{46}$$

This indicates a localized driving field using the mean value of in-plane stress through the respective layer. Numerical evidence implies that using the mean stress is not ideal to use in evolution of constant polarization.

For the proposed augmentation term $\psi^{\text{new}}_{\text{me,aug},\Gamma}$, the driving electric field within the two different layers reads

$$\hat{E}^{\text{new}}_{(\pm)} = \left(\frac{1}{t}\mathbf{s} \pm \frac{3}{t^2}\mathbf{m} \right) : \mathbf{A} \frac{\partial \varepsilon^*_{(\pm)}}{\partial P_{\text{i},(\pm)}} + \frac{2}{t} \frac{\partial \psi^{\text{new}}_{\text{me,aug},\Gamma}}{\partial P_{\text{i},(\pm)}} - \partial \psi'_{\text{p}}(|P_{\text{i},(\pm)}) \frac{P_{\text{i},(\pm)}}{|P_{\text{i},(\pm)}|} + E_{(\pm)}. \tag{47}$$

Deriving the potential $\psi^{\text{new}}_{\text{me,aug},\Gamma}$ explicitely in each layer, we see that due to $\xi^* = -\kappa^*$,

$$\frac{\partial \psi^{\text{new}}_{\text{me,aug},\Gamma}}{\partial P_{\text{i},(\pm)}} = \frac{t^3}{36} E \kappa^* (\mathbf{A} : \mathbf{A}) \frac{\partial \kappa^*}{\partial P_{\text{i},(\pm)}}. \tag{48}$$

Inserting the definition of κ^* in terms of the eigenstrain values in both layers $\varepsilon^*_{(+)}$ and $\varepsilon^*_{(-)}$ yields

$$\frac{\partial \psi^{\text{new}}_{\text{me,aug},\Gamma}}{\partial P_{\text{i},(\pm)}} = \pm \frac{Et^2}{24} \kappa^* \mathbf{A} : \mathbf{A} \frac{\partial \varepsilon^*_{(\pm)}}{\partial P_{\text{i},(\pm)}}. \tag{49}$$

This implies for the driving field

$$\hat{E}^{\text{new}}_{(\pm)} = \left(\frac{1}{t}\mathbf{s} \pm \frac{3}{t^2}\mathbf{m} \pm \frac{t}{12} E \boldsymbol{\kappa}^* \right) : \mathbf{A} \frac{\partial \varepsilon^*_{(\pm)}}{\partial P_{\text{i},(\pm)}} - \partial \psi'_{\text{p}}(|P_{\text{i},(\pm)}) \frac{P_{\text{i},(\pm)}}{|P_{\text{i},(\pm)}|} + E_{(\pm)}. \tag{50}$$

In comparison, for $\psi^{\text{full}}_{\text{me,aug},\Gamma}$, we get

$$\hat{E}^{\text{full}}_{(\pm)} = \left(\frac{1}{t}\mathbf{s} \pm \frac{3}{t^2}\mathbf{m} \pm \frac{t}{12} \frac{E}{1-\nu} \boldsymbol{\kappa}^* \right) : \mathbf{A} \frac{\partial \varepsilon^*_{(\pm)}}{\partial P_{\text{i},(\pm)}} - \partial \psi'_{\text{p}}(|P_{\text{i},(\pm)}) \frac{P_{\text{i},(\pm)}}{|P_{\text{i},(\pm)}|} + E_{(\pm)}. \tag{51}$$

Numerical examples presented in the next section reveal that the proposed method employing the driving field (50) yields superior results, where the additional stress contribution $Et/12\boldsymbol{\kappa}^*$ is considered independent of the Poisson ratio.

6 COMPUTATIONAL RESULTS

We consider a circular bimorph plate made from two equally thick layers of PZT. Plate radius and thickness are chosen as $R = 10\,\text{mm}$ and $t = 0.1\,\text{mm}$, respectively. Material constants are taken from [16]. As elastic constants we use Young's modulus $E = 61\,\text{GPa}$ and Poisson ratio $\nu = 0.31$. Piezoelectric constants $d_{31} = -2.74 \times 10^{-10}\,\text{C}\,\text{N}^{-1}$, $d_{33} = 5.48 \times 10^{-10}\,\text{C}\,\text{N}^{-1}$ are used, the d_{15} effect is neglected in the current contribution. The electric permittivity is given by $\epsilon = 2.77 \times 10^{-8}\,\text{C}\,\text{V}^{-1}\,\text{m}^{-1}$, and the susceptibility relevant for the internal polarization is $\chi_i = 1.40 \times 10^{-6}\,\text{C}\,\text{V}^{-1}\,\text{m}^{-1}$. Saturation polarization and saturation strain are assumed as $P_{\text{sat}} = 0.24\,\text{C}\,\text{m}^{-2}$ and $\varepsilon_{\text{sat}} = 9.3 \times 10^{-3}$. Last, the coercive electric field is $E_{\text{c}} = 820 \times 10^3\,\text{V}\,\text{m}^{-1}$.

The circular plate is supported in such a manner that rigid body deformations are constrained in a stress-free manner, the central axis of the disk points in direction of $\boldsymbol{e}_3$ and the central point of the disk is fixed in space. We consider two cases: in a first analysis, cyclic polarization of a single layer is performed, such that hysteresis loops can be detected. In a second, independent analysis, the two layers are polarized in an alternating manner.

In both cases, the internal electrode is grounded, while voltage profiles $V_{(+)}$ and $V_{(-)}$ over time are prescribed at the top and bottom electrode. The mean value of polarization through the two layers is measured. Additionally, the deformation is monitored by tracking the relative vertical displacement of the center point and the outer circumference of the disc. The relevant quantities are

$$P_{\text{i},(\pm)} = \frac{2}{R^2 t \pi} \int_{\Omega_{(\pm)}} \boldsymbol{P}_{\text{i}} \cdot \boldsymbol{e}_3 \, dV, \qquad w = \frac{1}{2Rt\pi} \int_{r=R} \boldsymbol{u} \cdot \boldsymbol{e}_3 \, dA. \tag{52}$$

All simulations are conducted within the open source finite element software package Netgen/NGSolve (see `ngsolve.org`). For comparisons, the axisymmetric problem is solved on a two-dimensional mesh consisting of 1596 second order triangular elements in cylindric coordinates; these results are marked as `3d`. The corresponding plate problem is solved employing low-regularity shell elements introduced by Neunteufel and Schöberl [17, 18] and extended to ferroelectric materials by the authors in [19]. Here, a quarter of the circular plate is resolved by 38 third order elements. The results corresponding to the various choices of augmentation potential are labelled `plate`, `full` and `new`, respectively.

6.1 Polarization of one layer

In the first scenario, only the upper layer is subject to electric loading. The voltage on the top electrode is varied within a range of $V_{(+)} \in [-250\,\mathrm{V}, 250\,\mathrm{V}]$. The corresponding applied electric field amounts to approximately three times the coercive field strength. This gives rise to hysteretic behavior; in Figure 1 the mean value of internal polarization in the top layer $P_{\mathrm{i},(+)}$ is shown, while Figure 2 holds the deflection of the disk's rim w over the applied voltage. All three variants $\psi^{\text{plate}}_{\text{me,aug},\Gamma}$, $\psi^{\text{full}}_{\text{me,aug},\Gamma}$ and $\psi^{\text{new}}_{\text{me,aug},\Gamma}$ for the augmentation term are compared, and labeled accordingly. Classic ferroelectric and butterfly hysteresis behavior are observed. It is observed that when resorting to a classical plate formulation relying on stress resultants only (case `plate`), internal polarization evolves too fast and deflection is overestimated. On the other hand, when using stress mean values in the definition of the driving electric field (case `full`), the evolution of internal polarization is prohibited and deflections are underestimated. For the proposed variant, we get satisfactory results in the dielectric and the butterfly hysteresis loop.

6.2 Alternating polarization of both layers

In the second scenario, both layers are polarized in an alternating manner. The voltage is increased up to $100\,\mathrm{V}$ and then reduced back to zero in the top and bottom layer consecutively. The corresponding electric field of $E_{(\pm)} = 1000\,\mathrm{V\,mm^{-1}}$ is slightly above the coercive field strength of $E_c = 820\,\mathrm{V\,mm^{-1}}$. In a second and third cycle, the voltages are raised up to $150\,\mathrm{V}$ and $200\,\mathrm{V}$ in the same manner. Figure 3 holds the evolution of the observed mean internal polarization in both layers $P_{(\mathrm{i},\pm)}$ over load steps. Clearly, only the proposed variant using $\psi^{\text{new}}_{\text{me,aug},\Gamma}$ is capable of reproducing the evolution of charges in a satisfying manner in this more complex scenario. The same observation is drawn from the evolution of the rim deflection w provided in Figure 4.

REFERENCES

[1] M. Kamlah, "Ferroelectric and ferroelastic piezoceramics – modeling of electromechanical hysteresis phenomena," *Continuum Mechanics and Thermodynamics*, vol. 13, no. 4,

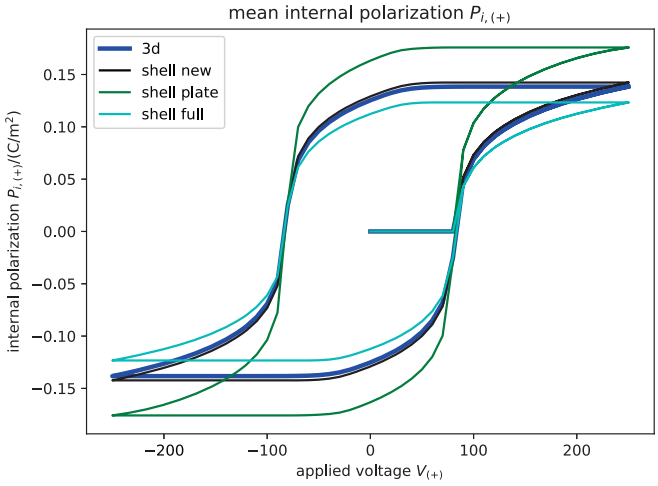

Figure 1: Polarization of one layer: mean internal polarization in layer $P_{\mathrm{i},(+)}$ over applied voltage $V_{(+)}$.

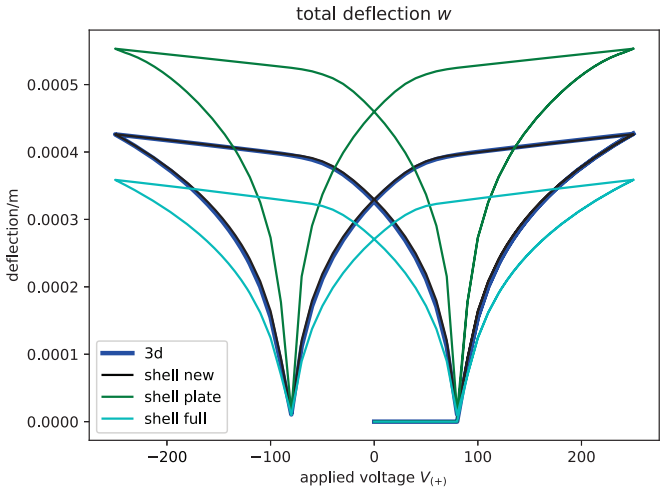

Figure 2: Polarization of one layer: deflection w over applied voltage $V_{(+)}$.

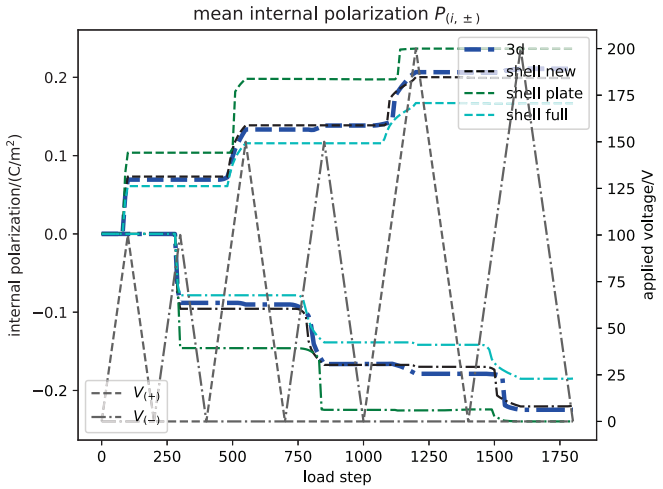

Figure 3: Alternating polarization of both layers: evolution of mean internal polarization in both layers $P_{(\mathrm{i},\pm)}$.

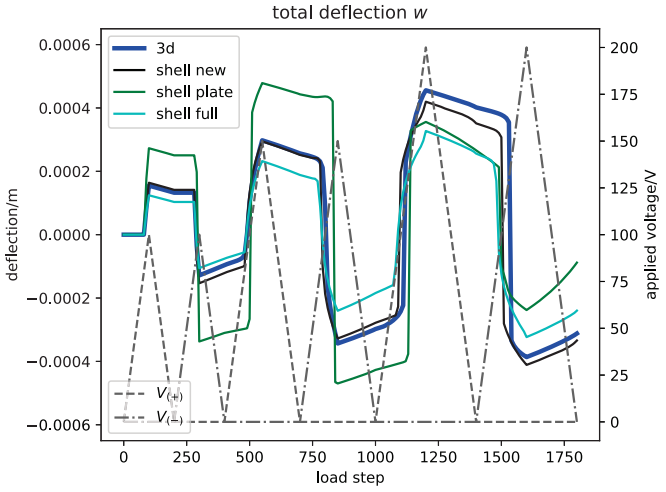

Figure 4: Alternating polarization of both layers: evolution of deflection w.

pp. 219–268, 2001.

[2] C. Miehe and D. Rosato, "A rate-dependent incremental variational formulation of ferroelectricity," *International Journal of Engineering Science*, vol. 49, no. 6, pp. 466–496, 2011.

[3] D. Rosato and C. Miehe, "Dissipative ferroelectricity at finite strains. Variational principles, constitutive assumptions and algorithms," *International Journal of Engineering Science*, vol. 74, pp. 162–189, 2014.

[4] M. Kamlah and U. Böhle, "Finite element analysis of piezoceramic components taking into account ferroelectric hysteresis behavior," *International Journal of Solids and Structures*, vol. 38, no. 4, pp. 605–633, 2001.

[5] A. S. Pechstein, M. Meindlhumer, and A. Humer, "High-order mixed finite elements for an energy-based model of the polarization process in ferroelectric materials," *Journal of Intelligent Material Systems and Structures*, vol. 32, no. 3, pp. 355–368, 2021.

[6] M. Meindlhumer, A. Pechstein, and A. Humer, "Variational inequalities for ferroelectric constitutive modeling," *Journal of Intelligent Material Systems and Structures*, vol. 32, no. 3, pp. 317–330, 2021.

[7] K. Sze and L. Yao, "A hybrid stress ANS solid-shell element and its generalization for smart structure modelling. part I – solid-shell element formulation," *International Journal for Numerical Methods in Engineering*, vol. 48, no. 4, pp. 545–564, 2000.

[8] S. Klinkel and W. Wagner, "A geometrically non-linear piezoelectric solid shell element based on a mixed multi-field variational formulation," *International Journal for Numerical Methods in Engineering*, vol. 65, no. 3, pp. 349–382, 2006.

[9] J. Mitchell and J. Reddy, "A refined hybrid plate theory for composite laminates with piezoelectric laminae," *International Journal of Solids and Structures*, vol. 32, no. 16, pp. 2345–2367, 1995.

[10] D. A. Saravanos and P. R. Heyliger, "Mechanics and computational models for laminated piezoelectric beams, plates, and shells," *Applied Mechanics Reviews*, vol. 52, no. 10, pp. 305–320, 10 1999.

[11] W. Zouari, T. Ben Zineb, and A. Benjeddou, "A fsdt—mitc piezoelectric shell finite element with ferroelectric non-linearity," *Journal of Intelligent Material Systems and Structures*, vol. 20, no. 17, pp. 2055–2075, 2009.

[12] M. Krommer and A. Pechstein, "Nonlinear modeling of ferroelectric plates as electro-elastic surfaces," in *Proceedings of the X ECCOMAS Thematic Conference on Smart Structures and Materials*, N. C. D.A. Saravanos, A. Benjeddou and T. Theodosiou, Eds., 2023, pp. 1962–1973.

[13] L. P. Lebedev, M. J. Cloud, and V. A. Eremeev, *Tensor Analysis with Applications in Mechanics*. New Jersey: World Scientific, 2016.

[14] A. C. Eringen and G. A. Maugin, *Electrodynamics of Continua I: Foundations and Solid Media*. New York, NY: Springer New York, 1990.

[15] M. A. Biot, *Mechanics of incremental deformations*, 1965.

[16] A. S. Pechstein, M. Meindlhumer, A. Humer, and M. Krommer, "Locking free high-order mixed elements for ferroelectric polarization," in *Dynamics and Control of Advanced Structures and Machines: Contributions from the 4th International Workshop, Linz, Austria*. Springer, 2022, pp. 173–186.

[17] M. Neunteufel and J. Schöberl, "The Hellan–Herrmann–Johnson method for nonlinear shells," *Computers & Structures*, vol. 225, p. 106109, 2019.

[18] ——, "The Hellan–Herrmann–Johnson and TDNNS methods for linear and nonlinear shells," *Computers & Structures*, vol. 305, p. 107543, 2024.

[19] A. Pechstein, Y. Vetyukov, and M. Krommer, "Efficient simulation of electromechanical coupling effects in thin shells at large deformations," in *Proceedings of the X ECCOMAS Thematic Conference on Smart Structures and Materials*, N. C. D.A. Saravanos, A. Benjeddou and T. Theodosiou, Eds., 2023, pp. 1950–1961.

Part IX
MS 08 - STRUCTURAL CONTROL AND HEALTH MONITORING

Grzegorz Mikułowski, Olivier Bareille, Łukasz Jankowski

XI ECCOMAS Thematic Conference on Smart Structures and Materials - SMART 2025
M. Krommer, M. Nader and M. Schagerl (Eds)

Received: 21 April 2025 / Revised: 31 August 2025 / Accepted: 25 October 2025
© The Author(s) 2025

A Case Study in Semi-Active Structural Control Based on Multi-Agent Reinforcement Learning

Aleksandra Barbay, Dominik Pisarski, Grzegorz Mikułowski, Bartłomiej Błachowski, Łukasz Jankowski

Abstract: This study applies the machine learning technique of multi-agent reinforcement learning for semi-active structural control. The considered structure is a high-rise shear-type building subjected to seismic excitation, where actuators function as viscous dampers with a controllable level of damping. The problem formulation is inherently nonlinear due to the bilinear nature of the control concept. The analytical derivation of optimal semi-active control solutions is seldom feasible, leading to many practical control algorithms being suboptimal and/or heuristic in their formulation. In the framework proposed here, the control algorithm is developed through interaction with the controlled system by applying actions, observing results, and optimizing effects. For this purpose, a multi-agent reinforcement learning Q-network architecture is employed. Verification is conducted through a numerical experiment, utilizing a finite element model of a structure equipped with a tuned mass damper and a controllable viscous damper. The results demonstrate that the proposed method outperforms a conventional, optimally tuned TMD. This study also includes a comparison of the obtained results with those achieved using the typical single-agent approach. The key contribution is to demonstrate a significant improvement in control performance through the application of a multi-agent policy.

Key words: Structural control, Reinforcement Learning, Multi-agent, Damping, Vibration

1 INTRODUCTION

Recent years have seen significant advances in the field of reinforcement learning (RL), which has been very successful in solving various sequential decision problems in machine learning. Most successful applications of RL, e.g., in games [1], robotics [2], autonomous driving [3], engineering [4], and logistics [5] require the participation of one or more agents, which naturally belongs to the field of multi-agent RL (MARL), which has recently emerged due to advances in single-agent RL techniques. Despite its empirical success, the theoretical foundations of multi-agent approaches are relatively scarce in the literature, especially in the field of structural control. The single-agent approach is more widely researched [6]. This contribution presents research on a collaborative multi-agent control approach of an engineering structure experiencing seismic excitation under increasing levels of measurement noise (0–50%) and compares it to the performance of seven individual agents.

Aleksandra Barbay & Dominik Pisarski & Grzegorz Mikułowski & Bartłomiej Błachowski & Łukasz Jankowski
Institute of Fundamental Technological Research, Polish Academy of Sciences Pawińskiego 5B, 02-106, Warsaw, Poland, e-mail: ajedlins@ippt.pan.pl,ljank@ippt.pan.pl

Vibrations in civil engineering are dangerous and can negatively influence the operation of engineering structures. One of the most dangerous phenomena is an earthquake, which may bring a very destructive range of mechanical vibrations [7]. Buildings experience damage or destruction, with the associated risks for people. Various techniques for structural control and the mitigation of structural vibrations have been investigated. Active methods have high efficiency and are widely used in many industries [8]. Active control requires the generation of external forces, which creates significant power demands. In civil engineering, this demand can become too great to be met during a major seismic event. A typical approach is passive control, which focuses on mitigating vibrations through structural optimization and energy dissipation mechanisms. This approach relies on passive devices such as Tuned Mass Absorbers (TMAs) and Tuned Mass Dampers (TMDs), which are mechanical resonance-based components designed to reduce vibration. These devices take the vibration energy and dissipate it internally, reducing excessive motion. Among the key advantages of TMAs and TMDs is that they do not require altering an existing structure or disrupting its basic functionality, making them an optimal choice for upgrades and troubleshooting. An intermediate solution between the active and passive techniques is semi-active control methods, which focus mainly on dissipating energy rather than generating large external forces. These approaches work by locally adjusting the mechanical properties of specific components, such as modifying viscous damping or stiffness. The generated forces are purely dissipative and opposed to the motion of the structure, large power sources are thus not required, which reduces the risk of instability. Nevertheless, due to their nonlinear nature, deriving optimal control can be analytically complex.

This paper describes research on the use of a semi-active tuned mass damper (TMD) as an actuator and switching control as a structural control strategy. The aim is to improve control quality by using a multi-agent reinforcement learning approach. A TMD is a device installed on structures to reduce mechanical vibrations, consisting of a mass mounted on one or more damped springs [9]. Numerous modifications of the classical TMD approach have been introduced and tested [10]. The effectiveness of the TMD in vibration control can be increased by adjusting several key parameters, such as the mass ratio, the natural frequency ratio between the TMD and the main structure, and the TMD damping ratio. In the case considered here, the TMD is controlled by switching its viscous damping coefficient in an on/off manner (between very low and very high damping). This results in the control signal directly affecting the damping matrix in the equation of motion in a linear manner, which corresponds to bilinear control. Analytical solutions for this type of control are often not available. For open-loop control, a bang-bang strategy is often optimal, which involves switching between two extreme states. In the proposed methodology, the switching points are determined by reinforcement learning (RL) machine learning algorithms. The model learns by interacting with the environment, i.e., through a series of trial and error in a simulated structure subjected to random seismic excitation. The mentioned approach remains novel in the context of using multiple agents. Good results have been achieved in the approach of using a single agent [11]. Also, research is available on the robustness under measurement noise, where the performance was checked in a noisy environment simulating the natural measurement processes [12]. This has shown the potential for further development in this approach, as the evaluation of the model consisted of testing its performance in an environment closer to reality than an ideal

mathematical model. The tests considered here examine the effectiveness of 7 separate agents and a multi-agent voting-based architecture in a range of different levels of measurement noise. The target function quantifies the effectiveness of the control, and it is based on the maximum inter-story displacement and the total energy of the structure. The results show the higher effectiveness of the multi-agent approach as compared to the single-agents operating alone. Applied together, they form an integrated model that allows the structure to be controlled in a more effective way.

2 REINFORCEMENT LEARNING

In contrast to such popular machine learning paradigms as supervised and unsupervised learning, reinforcement learning (RL) is a distinct approach based on sequential decision-making and trial-and-error interactions with the environment [13]. When applied to the adaptive control of highly complex and dynamic systems, the idea appears to be extremely effective. Formally speaking, RL can be defined as a Markov decision process (MDP). Reinforcement learning algorithms encourage the AI agent to explore an optimal decision chain and define "correct behaviour" in the considered environment.

This research explores the potential of reinforcement learning (RL) in improving semi-active structural control. In this study, an RL agent is utilized, which employs a dense artificial neural network to learn and encode the Q-function [14]. Q-learning and DQN [15] are popular RL methods and have been previously applied in multi-agent settings [16]. Q-Learning uses an action-value function under the policy π defined as the following expected value [17]:

$$Q^{\pi}(s, a) = E[R/s^t = s, a^t = a] \tag{1}$$

where R is a total reward received after taking action a in state s and s^t, a^t are the state and action at a specific timestep t. However, this Q function can be rewritten recursively as an expectation over the next state s' and next action a',

$$Q^{\pi}(s, a) = E_{s'}[r(s, a) + \gamma E[Q^{\pi}(s', \pi(s'))]] \tag{2}$$

where $r(s, a)$ is the immediate reward received when taking action a in state s, and γ is a discount factor (between 0 and 1) that controls how much future rewards are valued compared to immediate rewards. The DQN learns the action-value function Q (maximum estimated Q-value for the next state s'), which corresponds with the optimal policy by a loss minimization. The formula below (Loss function of the Deep Q-Network) shows how different the predicted Q-values are from the target y:

$$L(\theta) = E_{s,a}[(Q(s, a/\theta) - y)^2], \quad \text{where} \quad y = r + \gamma \max_{a'} \bar{Q}(s', a'), \tag{3}$$

where y as a target value that follows the Bellman equation, where future rewards are recursively considered. It contains the maximum estimated Q-value for the next state s′. $\bar{Q}$ is a target Q-function with parameters updated periodically with the latest θ to help stabilize learning, where θ are the neural network parameters. Another key element in stabilizing DQN is the use of an experience replay buffer D containing tuples of (s, a, r, s'). By directly applying Q-Learning to multi-agent settings, each agent learns its optimal Q function independently [15].

It is important to note that the approach presented here is inherently probabilistic, as the expected value is drawn from a probability distribution. However, by selecting the maximum value, we effectively transform this method into a deterministic variant [15].

3 MULTI-AGENT REINFORCEMENT LEARNING APPROACH

There are a number of important applications that involve interaction between multiple agents, where emergent behaviour and complexity arise from agents cooperating together. Multi-agent reinforcement learning (MARL) uses a variety of training strategies, often using centralized, decentralized, or hybrid approaches [18]. The training process typically involves the interaction of multiple agents in a shared environment, who learn simultaneously or in sequential phases, however, this approach is not always appropriate for the application.

Centralized MARL is based on agents who are trained together, sharing experiences and learning from each other's experiences. This approach allows agents to learn from the actions and rewards of other agents, which promotes coordinated behaviour and develops cooperative strategies. The centralized approach requires more resources due to shared data and joint policy optimization. The policy example can be a Multi-Agent Deep Deterministic Policy Gradient (MADDPG) – which uses centralized critics during training but decentralized policies during execution [17]. Another example is the QMIX – a value-based approach where a mixing network combines agent-specific Q-values into a global Q-value [19]. The applications of centralized MARL are usually connected with a need for the joint policy of agents (e.g., robotic swarm [20], coordination of multi-drone navigation [21].

In decentralized MARL, each agent learns independently using its observations and rewards without direct access to other agents' information. Each agent optimizes its policy based on its local observations and rewards. The approach is more efficient when dealing with a large number of agents, however, if agents do not have a global knowledge, they might develop conflicting policies. The main examples of policies are: Independent Q-Learning (IQL) – each agent learns its Q-function without considering other agents [22] and Decentralized PPO (Proximal Policy Optimization) – used in environments where agents act independently [23]. Decentralized training is usually used when agents operate in highly dynamic environments (e.g., competitive games, self-driving cars in traffic) and when individual agent policies need to be robust to environmental changes.

Some methods combine centralized and decentralized approaches to balance coordination and scalability. These include: Meta-Learning Strategies [24], where agents learn how to switch between centralized and decentralized modes, and Hierarchical MARL [25], where a central controller guides decentralized agents in complex tasks.

In this contribution, the decentralized MARL approach was used. Agents were trained independently, achieving their own optimal polices over time. Then, they were used in one environment to collaborate and execute the optimal control algorithm with majority voting as a decision strategy.

4 STRUCTURE

Any interaction between the agent and the environment requires continuous feedback from the structure. For testing purposes, it was necessary to create a numerical environment reflecting the nature of the structure and its properties. Due to security reasons, the tests could not be performed on the actual physical structure. As a numerically modeled structure is used, deviations from the physical model are expected. The dynamics of the structure is approximate, and the model's robustness to measurement errors and noise must be taken into account. As shown in [12], the control approach developed here is relatively insensitive to these errors. This contribution also shows how the multi-agent approach manages the measurement noise case. The structure is modeled as a 35-story shear-type building with a single degree of freedom (DOF) per story, equipped with a semi-active TMD at the top. Three areas of measurement are specified as floors 19, 35, and TMD, where the measurements are the displacement and velocity of each pointed floor (Fig. 1).

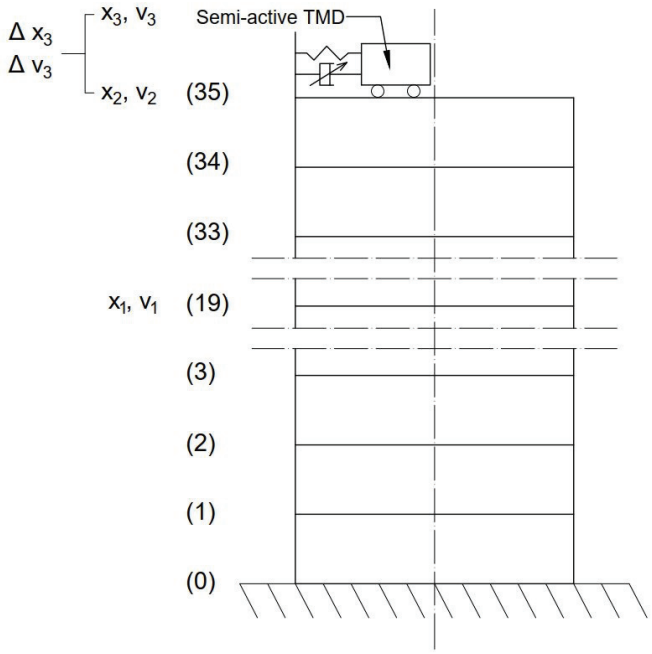

Figure 1: The investigated 35-DOF shear structure with a TMD at the top level

The equation of motion is defined using 36 degrees of freedom (DOF), the seismic excitation being modeled as lateral acceleration, a(t). It is expressed as follows:

$$[M]\{u\} + [C]\{u\} + [K]\{u\} = -[M]\{r\}a(t) \quad (4)$$

The matrices *[M]*, *[C]*, and *[K]* correspond to mass, damping, and stiffness, respectively. The control strategy applied is bang-bang control, which regulates the TMD dashpot by alternating between two extreme states—zero and maximum damping—while *[C]* also considers the inherent damping of the building. A material damping model is used to establish the critical damping ratio for the building's first natural vibration mode without TMD, which is set at 2%. The lateral load distribution is described by a 36-element vector filled with ones. The Tuned Mass Damper (TMD) comprises 3% of the building's total mass. The floor masses and stiffness values are taken from a reference structure mentioned in the literature [26]. The natural frequencies of the structure range from 0.887 Hz to 14.917 Hz.

Artificial intelligence models have a tendency to overfit specific patterns found in the data. To ensure that the model learns to control the structure effectively, the applied excitation must be diverse and cover a broad frequency spectrum, resembling real earthquake scenarios. To avoid the control system adapting to just one ground motion pattern, seismic excitation was modeled as white noise at each time step. The ground acceleration value a(t) was continuously sampled from a uniform distribution centered around zero. The feedback signal employed 6 measurements shown in Fig. 1 (displacements and velocities at floor 19, 35, and the TMD). This approach was used to evaluate the performance of both the control system and the reinforcement learning algorithm.

5 CONTROL WITH AN INDIVIDUAL AND MULTI-AGENT STRATEGY

Each agent receives local observations, including displacement and velocity measurements. Seven agents were trained using observations from 6 sensors (x_1, v_1, x_2, v_2, Δx_3, Δv_3) shown in Fig. 1. The target function quantifies the maximum inter-story displacement and the total energy of the structure, while the reward additionally promotes the restriction of damping control during high relative velocities between the TMD and the top floor. All the considered values are normalized with respect to the same quantities obtained with an optimally tuned passive TMD for the same seismic excitation. Noise levels range from 0% to 50% in 5% increments. When simulating with a multi-agent approach, agents make independent decisions and then apply a majority vote. The simulation phase of each agent is carried out using a dense ANN consisting of an input layer, 2 dense hidden layers (each with 15 neurons), and an output layer. A graphical representation of the ANN is presented in Fig. 2. The activation function used in the neural network is a leaky rectified linear unit (Leaky ReLU). Each test consisted of 1000 test episodes at each noise level. Metrics are the mean target function values for each agent and the multi-agent system and a standard deviation for the multi-agent system.

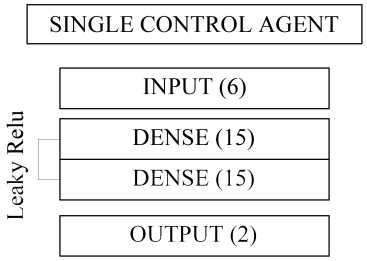

Figure 2: Single RL control agent artificial neural network architecture

7 RESULTS

7.1 Mean target function values across different noise levels

The results plotted in Fig. 3 show the mean target function values across different noise levels:

- The multi-agent architecture consistently achieves better (lower) target function values compared to individual agents, indicating a better performance.
- The standard deviation band (±1σ) of the multi-agent system contains individual agents' results, but the multi-agent approach remains below them, which confirms its effectiveness.
- As noise increases, all systems remain stable, but the multi-agent system consistently outperforms all individual agents.

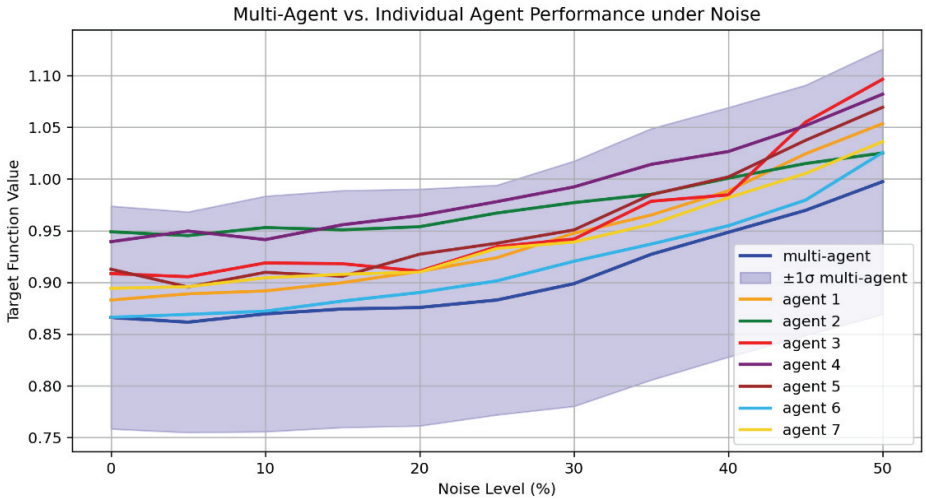

Figure 3: Multi-agent vs. individual agent performance under noise

7.2. Performance distribution of the multi-agent system and individual agents

The box plots in Fig. 4 and Fig. 5 compare the performance distribution of the multi-agent system and individual agents at 0% noise and 50% noise. In Fig. 4, agents' performance distribution for 0% noise level is represented:

- The multi-agent system achieves the lowest median target function value, meaning it outperforms individual agents in a noise-free environment.
- The variance in performance is relatively small, suggesting consistent behaviour.
- Individual agents have their distributions slightly overlapping with the multi-agent system, but all their median values are higher.

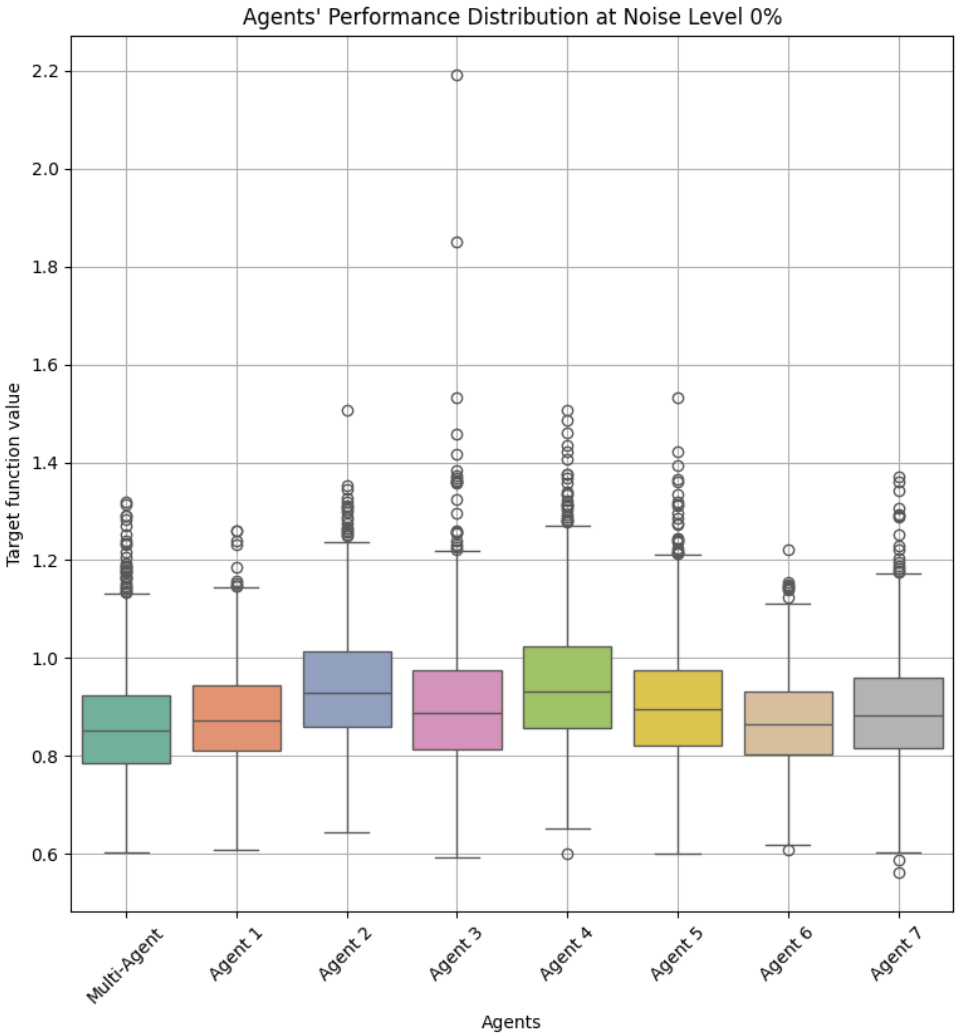

Figure 4: Agents' performance distribution for 0% noise level

In Fig. 5, agents' performance distribution for 50% noise level is represented:

- The multi-agent system maintains its advantage, achieving the lowest median evaluation value.
- The spread of individual agents' performance increases, showing that stability of some agents is lower.
- The multi-agent system remains more stable (less variance), indicating robustness to noise, while some individual agents exhibit high outliers, meaning their performance is getting worse under uncertainty.

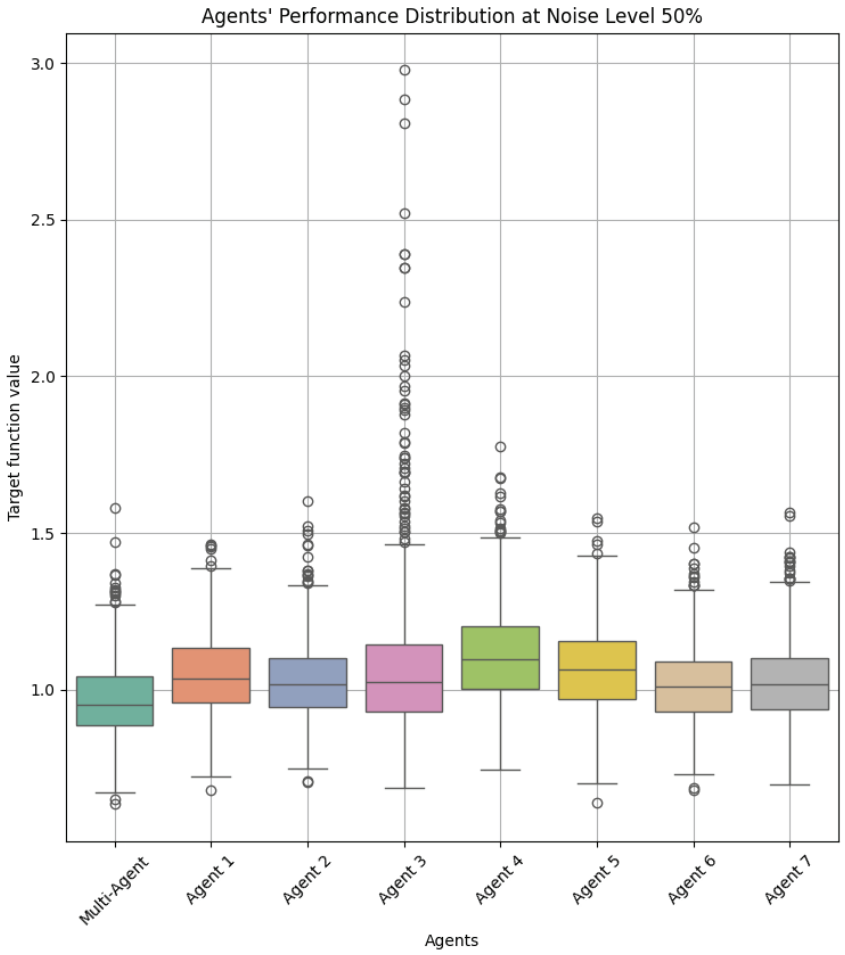

Figure 5: Agents' performance distribution for 50% noise level

8 SUMMARY

The results suggest that the multi-agent approach is both more robust and more effective at optimizing performance across different levels of noise. This study demonstrated that multi-

agent reinforcement learning provides better structural control compared to a single-agent approach. We found that utilizing the combined knowledge of agents improves the control performance, and that the multi-agent system provides more robustness under noise conditions. Future work will explore cooperative learning strategies to further enhance system robustness and adaptability.

ACKNOWLEDGMENT

The authors gratefully acknowledge the support of the National Science Centre, Poland, granted under the grant agreement 2020/39/B/ST8/02615. For the purpose of Open Access, the authors have applied a CC-BY public copyright licence to any Author Accepted Manuscript (AAM) version arising from this submission.

REFERENCES

[1] D. Silver, A. Huang, C.J. Maddison, A. Guez, L. Sifre, G. Van Den Driessche, J. Schrittwieser, I. Antonoglou, V. Panneershelvam, M. Lanctot, et al., "Mastering the game of Go with deep neural networks and tree search," *Nature*, vol. 529, pp. 484-489, 2016.

[2] J. Kober, J.A. Bagnell, and J. Peters, "Reinforcement learning in robotics: A survey," *International Journal of Robotics Research*, vol. 32, no. 11, pp. 1238-1274, 2013.

[3] S. Shalev-Shwartz, S. Shammah, and A. Shashua, "Safe, multi-agent, reinforcement learning for autonomous driving," *arXiv preprint*, arXiv:1610.03295, 2016.

[4] A. Bernard and I.F. Smith, "Reinforcement learning for structural control," *Journal of Computing in Civil Engineering*, vol. 22, no. 2, pp. 133-139, 2008.

[5] B. Rolf, I. Jackson, M. Müller, S. Lang, T. Reggelin, and D. Ivanov, "A review on reinforcement learning algorithms and applications in supply chain management," *International Journal of Production Research*, vol. 61, no. 20, pp. 7151-7179, 2023.

[6] D. Pisarski and Ł. Jankowski, "Reinforcement learning-based control to suppress the transient vibration of semi-active structures subjected to unknown harmonic excitation," *Computer-Aided Civil and Infrastructure Engineering*, vol. 38, no. 12, pp. 1605-1621, 2023.

[7] F. da S. Brandão and L. F. F. Miguel, "Vibration control in buildings under seismic excitation using optimized tuned mass dampers," *Frattura ed Integrità Strutturale*, vol. 54, pp. 66-87, 2020.]

[8] S. Korkmaz, "A review of active structural control: Challenges for engineering informatics," *Computers and Structures*, vol. 89, no. 23-24, pp. 2113-2132, 2011.

[9] J. Ormondroyd and J.P. Den Hartog, "The Theory of the Dynamic Vibration Absorber," *Journal of Fluids Engineering, Transactions of the ASME*, vol. 49-50, no. 2, pp. 021007, 1928.

[10] S. Nagarajaiah and H.-J. Jung, "Smart tuned mass dampers: Recent developments," *Smart Structures and Systems*, vol. 13, no. 2, pp. 173-176, 2014.

[11] A. Jedlińska, D. Pisarski, G. Mikułowski, B. Błachowski, Ł. Jankowski, "Semi-active structural control using viscous dampers and reinforcement learning," In *Proc. of the 10th*

ECCOMAS Thematic Conference on Smart Structures and Materials (SMART), 2023.
[12] A. Jedlińska, D. Pisarski, G. Mikulowski, B. Blachowski, and Ł. Jankowski, "Semi-Active Control of a Shear Building Based on Reinforcement Learning: Robustness to Measurement Noise and Model Error," In *Proc. of the 18th Conference on Computer Science and Intelligence Systems (FedCSIS 2023)*, Warsaw, Poland, 2023, pp. 1007-1010.
[13] R.S. Sutton and A.G. Barto, *Reinforcement Learning: An Introduction*, 2nd ed., MIT Press, 2018.
[14] H. Van Hasselt, A. Guez, and D. Silver, "Deep reinforcement learning with double Q-Learning," In *Proc. of the 30th AAAI Conference on Artificial Intelligence (AAAI 2016)*, Phoenix, AZ, USA, Feb. 12–17, 2016, pp. 2094-2100.
[15] B. Jang, M. Kim, G. Harerimana, and J.W. Kim, "Q-Learning Algorithms: A Comprehensive Classification and Applications," *IEEE Access*, vol. 7, pp. 133653-133667, 2019.
[16] G. Tesauro, "Extending Q-learning to general adaptive multi-agent systems," In *Proc. Advances in Neural Information Processing Systems*, vol. 16, pp. 871-878, 2003.
[17] R. Lowe, Y. Wu, A. Tamar, J. Harb, P. Abbeel, and I. Mordatch, "Multi-agent actor-critic for mixed cooperative-competitive environments," In *Proc. of the 31st Conference on Neural Information Processing Systems (NeurIPS 2017)*, vol. 30, 2017
[18] K. Zhang, Z. Yang, and T. Başar, "Multi-agent reinforcement learning: A selective overview of theories and algorithms," in M.W. Mahoney and R.S. Sutton, Eds., *Handbook of Reinforcement Learning and Control*, vol. 284, pp. 321-384, Springer, 2021.
[19] T. Rashid, M. Samvelyan, C. Schroeder de Witt, G. Farquhar, J. Foerster, and S. Whiteson, "Monotonic value function factorisation for deep multi-agent reinforcement learning," *Journal of Machine Learning Research*, vol. 21, no. 178, pp. 1-51, 2020.
[20] H. Tang, H. Zhang, Z. Shi, X. Chen, W. Ding, and X.-P. Zhang, "Autonomous swarm robot coordination via mean-field control embedding multi-agent reinforcement learning," In *Proc. 2023 IEEE/RSJ International Conference on Intelligent Robots and Systems (IROS)*, Detroit, MI, USA, pp. 8820-8826, 2023.
[21] T. Gavin, S. LacroiX, and M. Bronz, "Multi-agent reinforcement learning based drone guidance for N-view triangulation," In *Proc. 2024 International Conference on Unmanned Aircraft Systems (ICUAS)*, Chania, Crete, Greece, pp. 578–585, 2024.
[22] Z. Zhang and D. Wang, "Adaptive individual Q-learning—A multiagent reinforcement learning method for coordination optimization," *IEEE Transactions on Neural Networks and Learning Systems*, vol. 36, no. 4, pp. 7739-7750, 2025.
[23] J. Liu, F. Li, J. Wang, and H. Han, "Proximal policy optimization based decentralized networked multi-agent reinforcement learning," In *Proc. 2024 IEEE 18th International Conference on Control & Automation (ICCA)*, Reykjavík, Iceland, pp. 839-844, 2024.
[24] Y.Q. Ji, "Application of meta-learning in multi-agent reinforcement learning – A survey," *Trends in Social Sciences and Humanities Research*, 2024. https://doi.org/10.61784/tsshr3075
[25] M. Ibrahim and A. Fayad, "Hierarchical strategies for cooperative multi-agent reinforcement learning," *arXiv Preprint*, arXiv:2212.07397, 2022.
[26] S. Pourzeynali, H.H. Lavasani, and A.H. Modarayi, "Active control of high-rise building

structures using fuzzy logic and genetic algorithms," *Engineering Structures*, vol. 29, no. 3, pp. 346-357, 2007.

XI ECCOMAS Thematic Conference on Smart Structures and Materials - SMART 2025
M. Krommer, M. Nader and M. Schagerl (Eds)

Received: 16 April 2025 / Revised: 28 August 2025 / Accepted: 25 October 2025
© The Author(s) 2025

Verification of a Combined SHM/CM System on a 2.4 MW Wind Turbine

Lukas Bonekemper, Marcel Wiemann, Benedikt Wüllner, Herbert Friedmann, Peter Kraemer

Abstract. In recent years the average yield of the turbines has been steadily rising. With increasing yield and the associated size of a turbine, their monitoring (load and damage monitoring) is becoming increasingly important. Another aspect that has not received as much attention in recent years is the monitoring of factors that reduce the energy yield. It is known, that each turbine has its own behavior, caused for example by manufacturing inaccuracies during production or suboptimal control, which ultimately reduces the service life but not at least the yield of the turbine. The large-scale equipping of each turbine with appropriate sensor technology is costly and very time-consuming. The idea of population monitoring has therefore been the subject of research for several years. The approach used is that fundamentally similar structures exhibit similar behavior under comparable conditions. In this context, the project WEA-produktiv aims to identify yield losses and their causes in a population of wind turbines without additional sensors. Eight identical turbines from a wind farm and a reference turbine are available for testing population monitoring. However, the methodologies to be developed for this require a detailed understanding of the entire system, which was the reason for the additional instrumentation of the reference. For this purpose, the entire drive train and the nacelle as a whole were equipped with sensors for monitoring structural vibrations, strain and torsion measurement. The acquisition of Supervisory Control and Data Acquisition (SCADA) data and additional environmental measurement technology allows operating and environmental conditions (EOC) to be taken into account. In order to be able to reliably develop methods and algorithms based on this measurement data, they must first be validated and checked for plausibility, which is the scope of this paper. Extensive access to the SCADA system provides comparative values for EOCs, for example. By measuring accelerations in the rotor blades, vibrations in the rotor blades can be compared for possible effects on the bending and torsional loads measured on the rotor shaft using strain gauges. Other recent publications resulting from this project document the instrumentation itself as well as the design of a model to simulate time series for the development Structural Health, Condition and Population Monitoring methods.

Lukas Bonekemper & Marcel Wiemann & Benedikt Wüllner & Peter Kraemer
Chair of Mechanics with focus on Structural Health Monitoring (MSHM), University of Siegen, Paul-Bonatz-Straße 9-11, DE-57076 Siegen, Germany, e-mail: lukas.bonekemper@uni-siegen.de

Herbert Friedmann
Wölfel Engineering GmbH & Co. KG, Max-Planck-Str. 15, 97204 Höchberg, Germany
e-mail: friedmann@woelfel.de

Key words: Population Monitoring, SCADA, Onshore Wind Turbine, Condition Monitoring, Structural Health Monitoring, Yield Losses

1 INTRODUCTION

The ongoing transition to renewable energy sources is mainly driven by the rapidly increasing capacity of solar and wind power plants. While new plants make up for the majority of this growth, there is also much potential in optimizing the yield of existing wind plants and wind parks. Each turbine is regulated by its own controller and therefore mostly independent of other turbines. Consequently, local interactions with other turbines in a wind park or other environmental factors are not necessarily taken into account. Also, suboptimal settings of the wind turbine regulator (pitch angle and yaw angle) or mass as well as aerodynamical imbalances can cause yield losses and induce life time consuming vibrations. The research project WEA-produktiv [1] therefore aims to find possible causes of yield losses explicitly by only using existing sensors, e.g. the SCADA system on every turbine, to increase the possible yield of already existing turbines. However, the connection between vibration phenomena and other operational and environmental factors and possible yield losses is not made easily. For this purpose, an extensive measurement system was planned and installed on a 2.4 MW turbine [3] to generate a basis with data starting with rotor blade vibrations and additional sensors throughout the entire drivetrain. This system is supplemented by additional environmental sensors and data acquired by the SCADA system, including timers and status messages. To use this data for algorithm development our system has to be closely examined and validated, which will be the focus of this paper. The first section will explain the main goals of this paper, which are verifying redundant data (e.g. from the SCADA system and from the new measurement system) and a plausibility check for additionally acquired measurement data. Furthermore, some quantities need to be transformed either into a common coordinate system or, if measured indirectly, into the desired unit. The next section gives a quick overview of the available measurement channels and visualizes redundancies and new or additional quantities. Two sections follow in which the aforementioned validation and plausibility check is carried out. This paper concludes with a final resume of the installation and data quality and look out to further use cases in terms of algorithm development in WEA-produktiv as well as future projects and comparisons to simulated wind turbine data [4].

2 GENERAL SPECIFICATIONS

In this section, the objectives of the following analyses will be outlined and explained in more detail. To this end, the later chapters are divided into two main parts: the verification of redundant data sources and the plausibility check of additional or new measured variables. The steps presented here are preceded by a transformation of the data recorded by the various subsystems into a common data format and the conversion of individual measured variables into the desired units or coordinate systems. This step will be presented first as a prerequisite for each analysis.

- Acceleration sensors have been installed at several points on the nacelle [3]. However, the installation positions do not allow consistent alignment of the sensors along a predefined 'global' coordinate system. Therefore, the local axes of the sensors must be converted according to the global axes and inclinations of the local axes must be compensated. The comparable alignment of all sensors achieved in this way facilitates the later data analysis.
- Proximity switches were attached to the gear rims of the rotor and generator shaft, which ultimately realizes a count of the tooth passages. This binary signal must be converted into a speed. The same applies to a signal for registering the blade positions.
- The strain gauge measurements on the rotor shaft are converted into a torsion or bending moment.

The verification of redundant measurement data as a first step is intended to prove the functionality of the system as a basis. This relates in particular to data from the SCADA system, where there are corresponding redundancies due to the environmental sensors installed. In addition, this relatively small number of measured variables is in principle the determining factor for the entire operation of the wind turbine, so the correct and reliable measurement technology is essential. The plausibility checks focusses on newly recorded measured variables that cannot be verified by redundancies. Furthermore, the measuring system offers numerous opportunities to investigate various aspects of wind turbine operation correlated to vibration phenomena and their effects on electricity production with regard to the WEA-produktiv project objectives described above. It is not possible to realize an exhaustive analysis within the scope of this paper, but simple and illustrative examples should provide a first impression.

3 SYSTEM OVERVIEW

Figure 1 serves to illustrate the existing measurement data within the individual measurement system components and their connections to each other. The illustration given here is not complete, but is merely intended to provide an overview of the numerous possibilities for validation and plausibility checks that already exist through the use of very simple methods. Furthermore, the previously described objective of this article, the verification and plausibility check of the measurement system, should become clearer. In the following, the newly installed measurement system will be referred to as "USi system". For this purpose, a color distinction will be made between a direct comparison of measurement data, highlighted by blue arrows, and the calculation of various parameters from the measurement data, illustrated by orange blocks and arrows. These calculated variables can in turn be used for comparison purposes. Environmental conditions in the grey shaded blocks, such as wind speed, temperature and others, are recorded in all subsystems. Direct comparisons and the calculation of statistical parameters are therefore good ways of ensuring that the measurement data is sufficiently consistent. Eigenfrequencies can be calculated from the accelerations of the rotor blades

measured by the ice detection system IDD.Blade [2, 10], which can be compared, for example, with the values determined from an existing Finite Element (FE) model of the rotor blades.

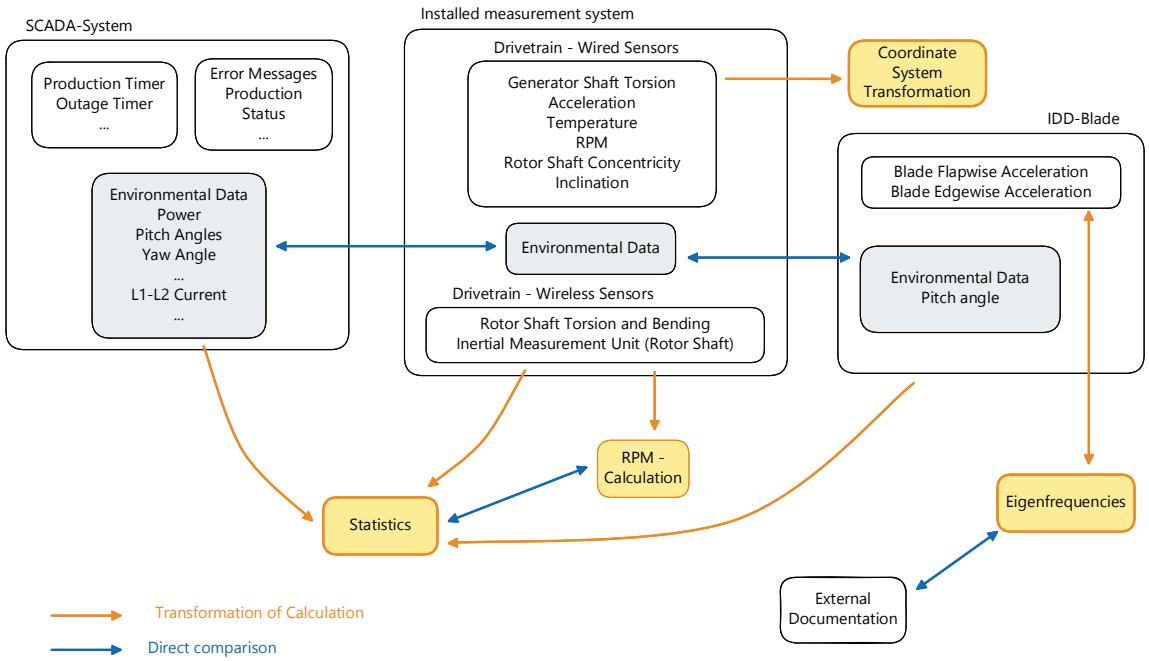

Figure 1: Graph of available sensor groups. Redundancies of several quantities offer ways for data verification, others serve further plausibility check through e.g. signal processing

4 VERIFICATION WITH SCADA

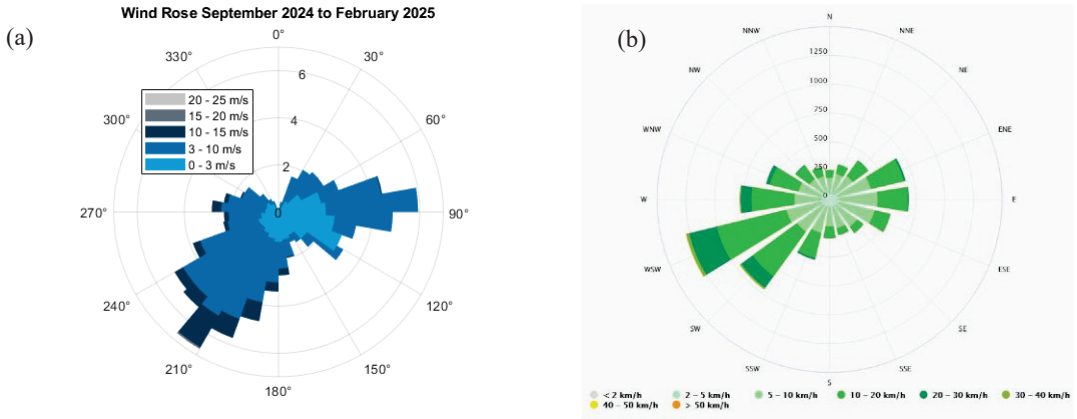

Figure 2: Wind rose from Usi measurements (left) and publicly available model data at the wind turbine location (right) [5]

4.1 Windspeed, Wind direction and Power

The simplest verification options are initially offered by comparing the environmental data recorded by the USi system [3] with that of the SCADA system. Data between September 2024 and February 2025 is available for the SCADA system and public sources are available for the distribution of wind direction during this time [5]. Figure 2(b) shows an example of the data from a weather model compared with measurement data from the period mentioned. Within the scope of expected deviations, good agreement is observed, especially with regard to the main wind direction and wind speeds. If we compare the distribution of wind speeds based solely on the SCADA data from the turbine controller, the typical Weibull distribution [6] is shown in Figure 3(a). The winter period has a slight bias towards higher wind speeds, which is also to be expected. However, a comparison of the winter period between the SCADA data of the turbine and the measurements of the new USi system in Figure 3(b) shows clearer deviations. Figure 4 shows the difference in wind speed according to the SCADA data and the measurement of the USi system using the SCADA data as a reference.

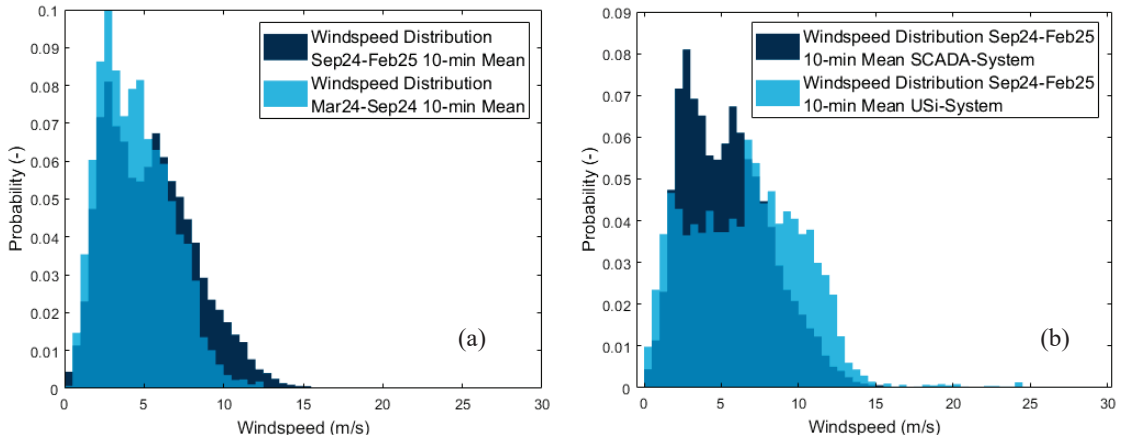

Figure 3: Windspeed distribution from SCADA data comparing summer and winter (left) and comparing SCADA data and Usi system (right)

For lower wind speeds, the deviation is mostly in the range <0.5 m/s, Figure 4(a). It can be seen here that at higher wind speeds a tendency towards greater deviation in the range of up to 1 m/s can occur, Figure 4(b). Possible causes could be mechanical resistance on the part of the cup anemometer, for example, which is particularly noticeable in the measured value in stronger winds. As the USi system uses an ultrasonic anemometer, deviations are entirely plausible. Especially time synchronization was difficult to achieve consistently. After some initial problems the USi system and the SCADA system are in relatively good synchronization, as depicted in Figure 5. Since the SCADA system still uses its own independent time server, occasional differences cannot be entirely avoided, as shown and mentioned in a later section.

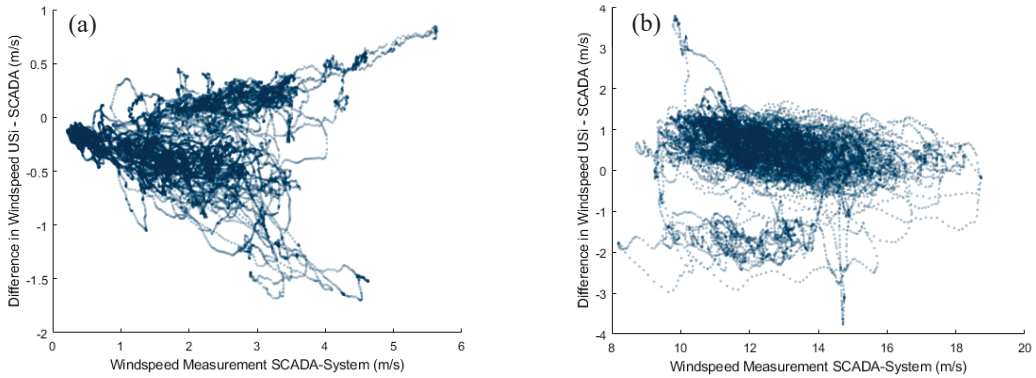

Figure 4: Difference between windspeed recorded by the SCADA system and Usi system (y-axis) plotted against SCADA sstem windspeed as reference. Low windspeeds (left) and high windspeeds (right)

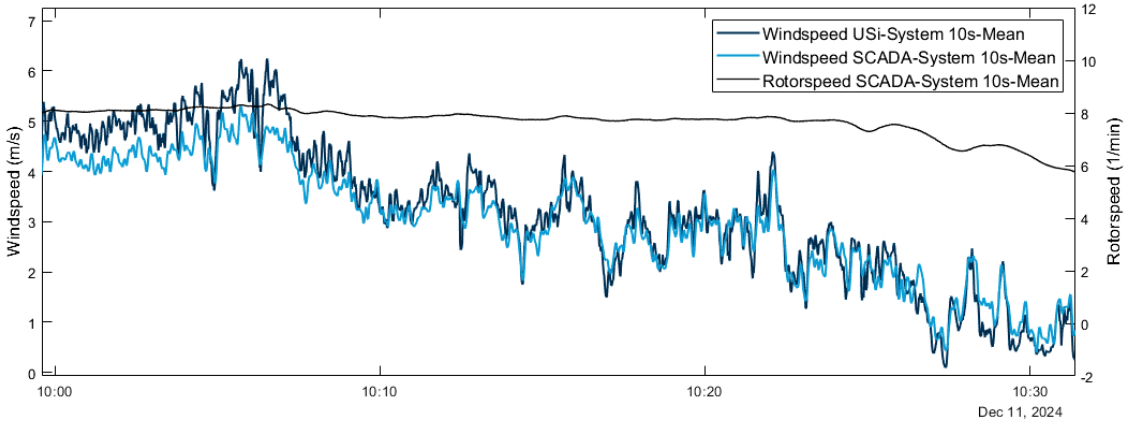

Figure 5: Time synchonization of data from USi system and SCADA system.

With known characteristic values of the turbine according to Table 1, a wind power curve based on both measured wind speeds and the power originating from the SCADA system, each as 10-minute data, can be constructed. Figure 6 shows both wind power curves for the period from September 2024 to February 2025. The previously observed deviation with increasing wind speed becomes clear once again. According to the available documentation, the turbine generates its rated power from a wind speed of approx. 12.5 m/s. The wind speed is measured just behind the rotor plane, so a shift towards lower wind speeds is to be expected. A physically reasonable assumption for the reduction in wind speed directly behind the rotor is around 1 m/s. The wind power curve formed by the USi system enters the constant power range at approx. 11.5 m/s and thus appears to represent a more realistic wind speed curve.

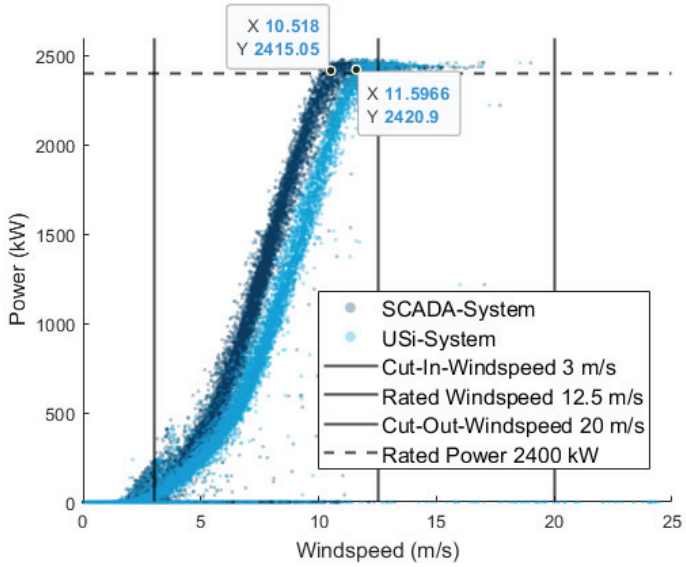

Figure 6: Wind-power-curve. Power measurements based on SCADA system. Windspeeds taken from SCADA and Usi system

Table 1: Some key specifics of wind turbine characteristics

Characteristic	Value
Cut-In Windspeed	3 m/s
Rated Windspeed	12,5 m/s
Cut-Out Windspeed	20 m/s
Rated Power	2400 kW

4.2 Comparing Rotational Speeds

The final example in this section is the speed determination from the data of the USi system. As part of the instrumentation, proximity switches were attached to the gear rims of the rotor and generator shafts, thereby realizing a count of the tooth passages [3]. A rotational speed can thus be reconstructed from the known number of teeth. Figure 7(a) shows an example of such a calculation. Based on the gyroscopic data delivered by the Inertial Measurement Unit (IMU) installed on the rotor shaft, see Figure 7 in [3], a rotational speed can be calculated very easily. Finally, this can be compared with the other variables in Figure 7(b). The speed value of the SCADA system is shown in red as a reference. A counting signal is recorded at both the rotor and generator shafts, and this speed is converted to the rotor speed using the known transmission ratio of the gearbox. This measurement agrees very precisely with the SCADA system in terms of amount. The data from the sprocket of the rotor shaft is incorrect for currently unknown reasons; presumably the incorrect recognition of some teeth results in an offset in the conversion. The data from the IMU, on the other hand, also reproduces the speed very well, despite a very low sampling rate of 4 Hz, which is probably also the cause of the slight offset,

which is only around 0.1 1/min. A final comment should be made on the slight time offset, which is clearly recognizable in Figure 7(a).

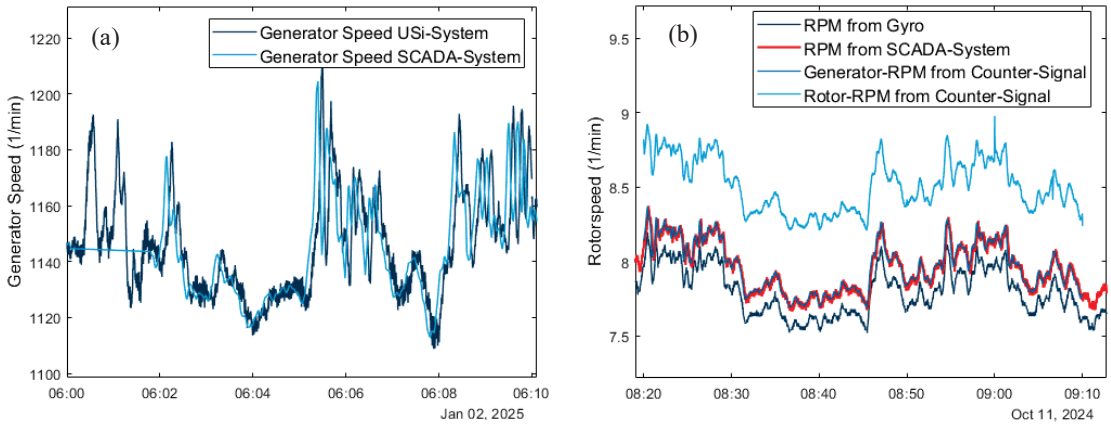

Figure 7: Generator RPM from SCADA system compared to USi system calculation based on proximity sensor (left). Rotor RPM from SCADA system compared to USi system calculation based on proximity sensor, IMU mounted to the rotorshaft and generator rpm divided by gear ratio

An offset of a few seconds occurs both in the previously analyzed data from the environmental sensors and in the speed measurements shown here. The cause of this is difficult to determine. The USi system is PTP-synchronized, while the SCADA system relies on a separate time server, a difference between those two is possible. Another conceivable cause is the internal processes of the SCADA system, possibly with regard to the storage itself; the interface (OPC-XMLDA), which is now considered outdated, may also play a role. Based on the analyses presented as examples in this section, the newly installed system is considered sufficiently reliable to carry out further analyses in the following chapter.

4.2 Calculation of Air Density

Since basically the entire operation of a wind turbine is defined by the environmental conditions and the air density has a considerable effect on operational loads and possible energy yield, an interesting option is to calculate the air density via the environmental sensors USi installed. According to known correlations [7], the ideal gas law initially applies.

$$\rho = \frac{p}{R \cdot T} \tag{1}$$

The gas constant R is generally also dependent on the humidity and temperature. An adapted gas constant R_f takes into account the relative humidity and the saturation vapour pressure for water vapour in humid air.

$$R_f = \frac{R_s}{1 - \left(\varphi \cdot \left(\frac{p_d}{p}\right) \cdot \left(1 - \frac{R_s}{R_d}\right)\right)} \tag{2}$$

The following applies

- Gas constant of water vapor R_d, gas constant of dry air R_S
- Relative humidity φ, saturation vapor pressure of water vapor as a function of temperature $p_d = p_d(T)$, taken from relevant textbooks [8].

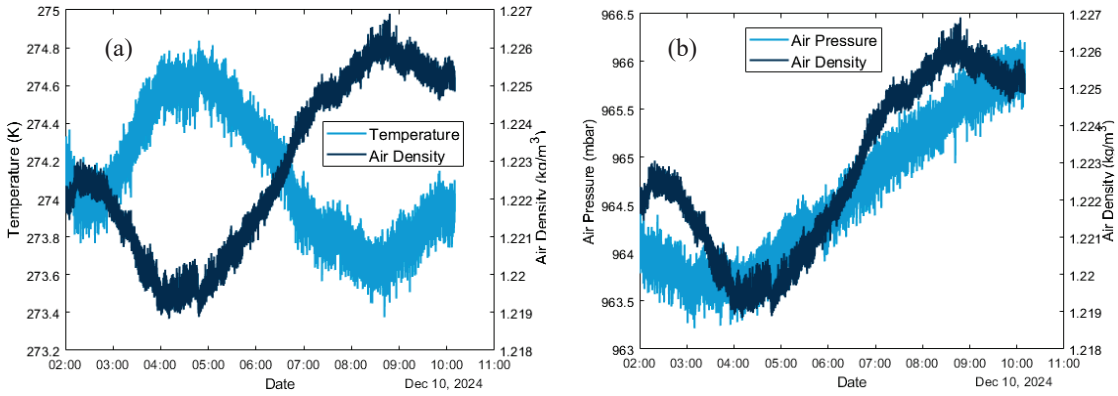

Figure 8: Mean rotorspeed for each time period (top plots) and spectrum of distance sensors (bottom plots, eddy-current-based). Lower RPM (left) just above starting speed of the turbine and higher RPM (right).

Figure 8(a, b) shows the air density calculated from the measured data together with air pressure and temperature. The relations indicated in Eq. (1) are obvious. With calculating the air density, for example turbine performance with regard to the available wind power can be evaluated correctly.

5 PLAUSIBILITY CHECK OF SPECTRAS

5.1 Spectra

We begin by taking a closer look at the spectra of some of the sensors. For this purpose, a period with strong wind is compared with a period of lower speed, see Table 2. The designated directions are based on a nacelle-fixed coordinate system whose x-axis points in the direction of the nacelle, the y-axis is perpendicular to it and the z-axis is orientated upwards. Eddy current sensors are attached next to and below the rotor shaft to measure the distance to the rotor shaft, see Figure 8 in [3]. Figure 9 shows both time periods from Table 2, on the left at low RPM, Figure 9(a).

Table 2: Time periods with higher and lower rotor speed

Time Frame	02. January 2025 06:00-07:00	02. January 2025 10:00-11:20
Mean RPM	11,5 1/min	8 1/min
1P and 3P frequency	0,19 Hz / 0,57 Hz	0,133 Hz / 0,4 Hz

This threshold roughly marks the run-up of the wind turbine. In Figure 9(b) the rotational speed (RPM) is constant at around 11.5 rpm. In its corresponding spectra the blade-passage frequency 1P (Figure 9(a)) and its third 3P harmonic (Figure 9(b)) are clearly visible.

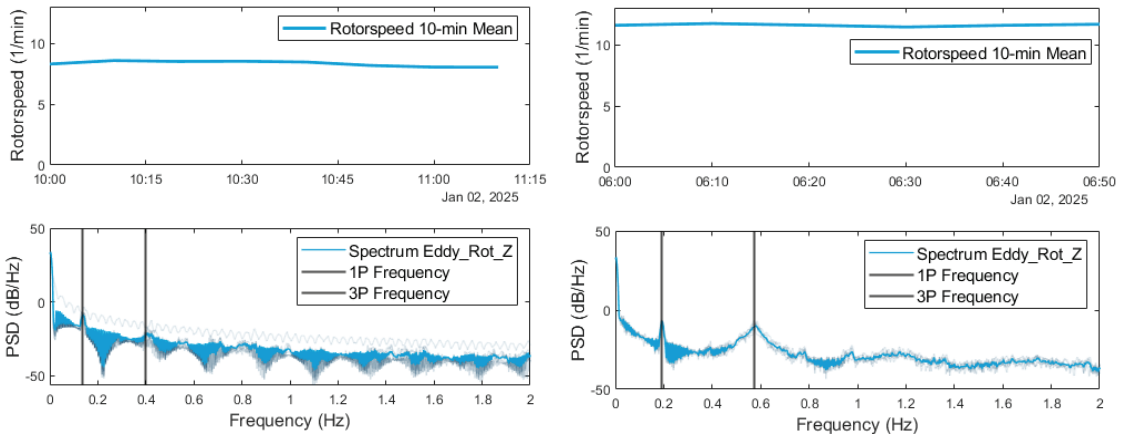

Figure 9: Mean rotorspeed for each time period (top plots) and spectrum of distance sensors (bottom plots, eddy-current-based). Lower RPM (left) just above starting speed of the turbine and higher RPM (right).

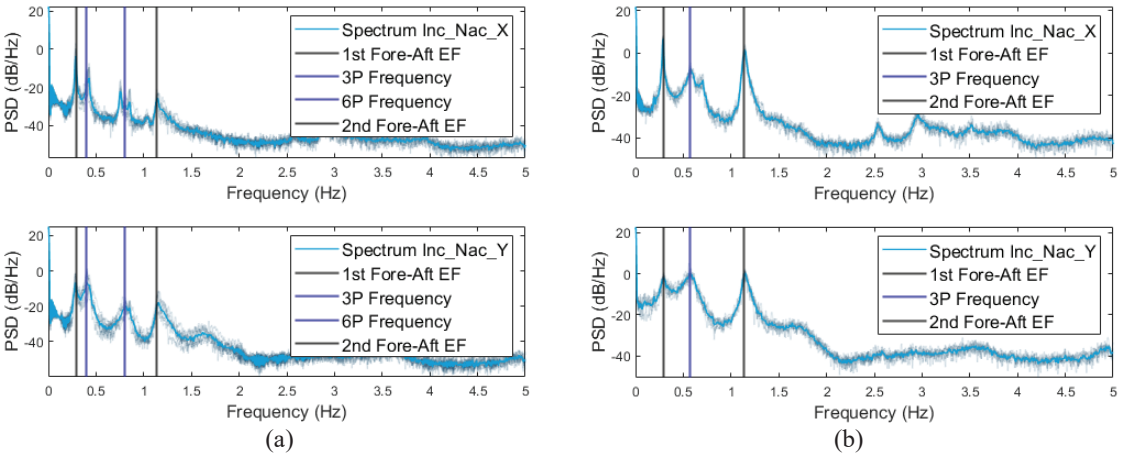

Figure 10: Spectra of inclination sensors in nacelle direcetion (top plot) and perpendicular to the nacelle (bottom plot). Lower RPM (left) just above starting speed / RPM of the turbine and higher RPM (right).

An inclination sensor is installed at the same position, directly below the rotor shaft in the center above the tower, and its spectra for the same time periods are shown in Figure 10. The

results of a model from Bladed (see [4]), which was constructed on the basis of the turbine data available to the authors, serve as a rough orientation for the eigenfrequencies of the tower.

Table 3: Eigenfrequencies based on FE model of the tower

Eigenfrequency	(Hz)	Eigenfrequency	(Hz)
1st Side-Side	0,273	1st Fore-Aft	0,274
2nd Side-Side	1,302	2nd Fore-Aft	1,302
3rd Side-Side	1,319	3rd Fore-Aft	1,49
4th Side-Side	3,91	4th Fore-Aft	3,91

Accordingly, these values should not be considered absolute, but are intended to provide a guide value. This results in eigenfrequencies according to Table 3. The spectra in Figure 10 (a and b) now clearly show the respective 3P frequency, which acts as an excitation on the tower [9].

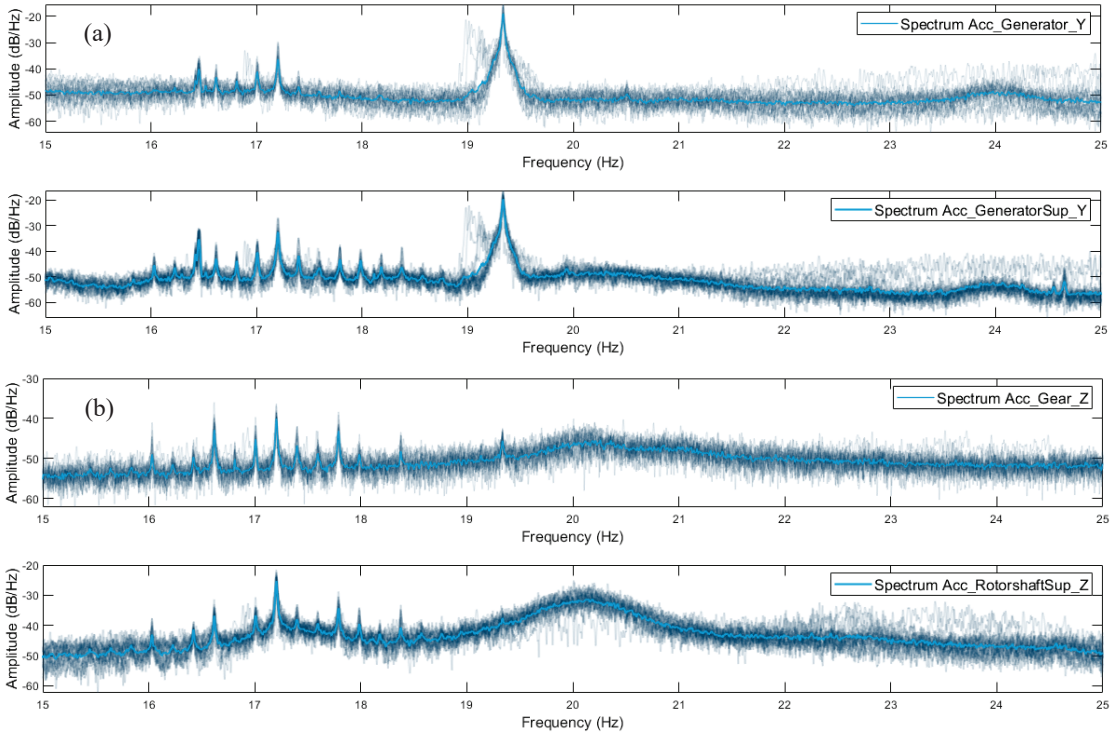

Figure 11: Spectra of acceleration sensors mounted on the generator (top plot in (a)) and directly below the generator (bottom plot in (a)) and spectra of acceleration from sensors mounted on the gearbox (top plot in (b)) and below the rotor shaft (bottom plot in (b))

For the low RPM period (Figure 10(a)), the 6P frequency is 0.8 Hz and is also recognizable. For the period with a higher rotational speed (Figure 10(b)), 6P is 1.14 Hz and coincides with

the peak that presumably belongs to the second eigenfrequency (Fore-Aft, Side-Side), as this also occurs in Figure 10(a) independent of the rotational speed. The deviation from the model value of 1.3 Hz is still relatively small here. Accordingly, the possible excitation of a eigenfrequency can be assumed for the speed range around 11.5 rpm. A final mention is aimed at potential problems occurring during the data analysis process. In Figure 11(a) an example of the spectra of two acceleration sensors are shown, one mounted on the front of the generator casing, the other directly below the generator on the nacelles support structure. In bottom part of Figure 11(a) at around 17,2 Hz a strong peak with approx. 7 harmonics are visible. Figure 11(b) for comparison displays the spectrum of two acceleration sensors, one mounted on top of the gearbox, the other one directly below the rotor shaft. Furthermore, these spectra correspond to the tower axis direction, so no significant signal would be expected. However, the strong peak around 17,2 Hz is again visible together with multiple harmonics. A reason from mechanical point of view for this observation is unknown. It seems more likely to be linked to spurious signals induced in the measurement chain along the signal transmission between sensor and measurement cabinet. This highlights the practical difficulties in real world applications. Although high-quality sensors and shielded cables were used, e.g. cable paths could not be chosen freely. Therefore, signal contamination is hard to prevent entirely. A countermeasure also for future applications could be the inclusion of a dummy-cable along our cable ways just measuring e.g. a known resistance. This would allow at least some compensation of spurious signal components for future measurements.

6 CONCLUSION AND OUTLOOK

The aim of this work, building upon the installation of the new measurement system [3], is to check the plausibility of its acquired data. The new measurement system serves in the project WEA-produktiv to better understand possible causes of yield losses, how these are influenced by environmental and operating conditions and how vibration phenomena from the rotor blades induced in the entire drive train affect the energy yield. An example for a possible approach is described in [11], where the so-called Self-Organizing Map was used to investigate high-dimensional relations between EOCs and energy yield. This and other approaches will be the topic of future research and projects. The plausibility check of the new measurement system was divided into two main steps, where the first step consisted of directly comparing the new measurements to the corresponding data from other sources, e.g. available SCADA. Using mainly environmental quantities like wind speed or wind direction, we showed that the new system does indeed match with other data sources. The second step focused on data acquired exclusively by the new measurement system. Being limited by the available space for this documentation, several spectra from different sensors were compared. Frequencies related to the rotational speed of the rotor and their harmonics, as well as several eigenfrequencies are visible in the spectra across all sensors, underlining the functionality of the measurement system.

7 ACKNOWLEDGEMENT

The authors are grateful for the financial support of this research by the German Federal Ministry for Economic Affairs and Climate Action (Grant number 03EE3074B, Project WEA-produktiv). A particular thanks goes to BürgerEnergie Altertheim for providing the facility as a research platform.

REFERENCES

[1] EnArgus (2022) *Verbundvorhaben: WEA-produktiv - Wind Turbines with Optimized Productivity Through Fleet Monitoring Without Additional Sensors. Funding Code: 03EE3012* [online], [January 14, 2025], https://t1p.de/enargus-weaproduktiv.

[2] Wölfel Wind Systems GmbH & Co. KG (2023) *SHM.Blade - Intelligentes System zur Zustandsüberwachung von Rotorblättern zur Detektion von Strukturschäden, Aerodynamischen Unwuchten sowie Eiserkennung* [online], [January 15, 2025], https://t1p.de/woelfel_iddBlade

[3] Wiemann M, Bonekemper L, Wüllner B, Friedmann H, and Kraemer P (2025) *Development and Implementation of a Combined SHM/CM System to Determine Yield Losses of a 2.4MW Wind Turbine*. Forthcoming. Scheduled for presentation at XI ECCOMAS Thematic Conference on Smart Structures and Materials (SMART 2025), University of Siegen, Germany

[4] Wüllner B, Wiemann M, Bonekemper L, Friedmann H, and Kraemer P (2025) *Simulation of time series of a 2.4 MW wind turbine for the development of CM/SHM methods*. Forthcoming. Scheduled for presentation at XI ECCOMAS Thematic Conference on Smart Structures and Materials (SMART 2025), University of Siegen, Germany

[5] „Simulierte historische Klima- und Wetterdaten für Helmstadt“. meteoblue.com. https://www.meteoblue.com/de/wetter/historyclimate/climatemodelled/helmstadt_deutschland_2906680 (accessed 26.03.2025)

[6] J. A. Carta, P. Ramírez, und S. Velázquez, „A review of wind speed probability distributions used in wind energy analysis“, *Renewable and Sustainable Energy Reviews*, Bd. 13, Nr. 5, S. 933–955, Juni 2009, doi: 10.1016/j.rser.2008.05.005.

[7] W. Wagner, *Lufttechnische Anlagen: Ventilatoren und Ventilatoranlagen*, 2nd ed. in Kamprath-Reihe. Erscheinungsort nicht ermittelbar: Vogel Buchverlag, 2007.

[8] G. Cerbe und G. Wilhelms, *Technische Thermodynamik: Theoretische Grundlagen und praktische Anwendungen*, 17., Überarbeitete Auflage. München: Hanser Verlag, 2013.

[9] P. Kraemer, „Damage diagnosis methods for structural and condition monitoring of offshore wind turbines“, PhD-Thesis, University of Siegen, 2011.

[10] Kraemer, P., Friedmann, H. und Ebert, C., 2015: Vibration-based Ice Detection of Rotor Blades in Wind Turbines—The Industrial Realization of an SHM-System, 10th International Workshop on Structural Health Monitoring, Stanford University, USA, S. 2841-2848.

[11] L. Bonekemper, M. Wiemann, H. Huhn, und P. Kraemer, „Advanced clustering of environmental and operational conditions of an offshore wind turbine using Self-

Organizing Maps“, in *10th ECCOMAS Thematic Conference on Smart Structures and Materials*, Patras, Greece: Dept. of Mechanical Engineering & Aeronautics University of Patras, 2023, S. 873–885. doi: 10.7712/150123.9840.450856.

XI ECCOMAS Thematic Conference on Smart Structures and Materials - SMART 2025
M. Krommer, M. Nader and M. Schagerl (Eds)

Received: 12 May 2025 / Revised: 27 August 2025 / Accepted: 25 October 2025
© The Author(s) 2025

Singularity Detection by K-Space Identification in Plate-like-Structures - Location Index Evaluation

Thomas Brion, Xi Li, Pascal Fossat, Mohamed Ichchou, Olivier Bareille, Abdelmalek Zine

Abstract. This paper presents a method for identifying singularity locations in plate-like structures. The proposed method is based on Algebraic K-Space Identification 2D (AKSI 2D) technique. This method has been validated numerically and experimentally, and its performances have been assessed with respect to other popular k-space identification methods under different uncertainty conditions.

Here, under the algebraic identification framework, the extraction of all properties of the complex k-space in a coherent manner is used for comparison purpose between a reference and disturbed vibrational field. The real part and the imaginary parts convey specific information about the vibrational field disturbances.

A specific subdomain strategy is employed in order to identify the precise location of singularities in plate-like elements. Results are presented on orthotropic plates. The procedure is able to locate singularities. It exhibits that the imaginary part of the identified k-space components gives better contrasted images of the singularities' locations.

Key words: k-space, plate structures, location index, vibration-based technique, SHM

1 INTRODUCTION

This paper is structured as follows. Section 2 presents the formula of the AKSI 2D. Then, Section 3 shows the validation of the proposed method on analytical fields on an example of numerical fields from a homogenised orthotropic 2D metastructure, namely a bi-ribbed plate.

Thomas Brion & Xi Li & Pascal Fossat & Mohamed Ichchou
Ecole Centrale Lyon, LTDS - CNRS UMR 5513, France

Olivier Bareille
INSA Rouen Normandie, Laboratoire de Mécanique de Normandie - CNRS EA 3828, France
e-mail: olivier.bareille@insa-rouen.fr

Abdelmalek Zine
Ecole Centrale Lyon, Institut Camille Jordan - CNRS UMR 5208, France

solved by a finite element method. Section 4 presents the specific strategy which is employed to identify the precise location of singularities. Results are presented on orthotropic plates, before the conclusion of the paper in section 5.

2 ALGEBRAIC K-SPACE IDENTIFICATION 2D: AKSI 2D FORMULAS

In order to later perform the analysis of singularity locations, the Algebraic K-Space Identification technique needs to be thoroughly presented. This is the purpose of this section with a specific emphasis on two-dimensional wavenumber calculations. The theory behind them is mostly inspired by the 1D method proposed by Li et al. [1].

Let U be a displacement field on a two-dimensional bounded domain Ω. In particular, $\Omega \subset [0, L_x] \times [0, L_y]$, $L_x, L_y \in \mathbb{R}^+$. The field is supposed to be known on some points of a subdomain Ω_w of Ω. The simplest case is when the field is known on a regular rectangular grid on Ω_w : (x_i, y_i) where i ranges from 1 to N_x and j ranges from 1 to N_y. From this displacement field, the AKSI 2D method provides a calculation of the wavenumbers in different directions. The first step is to calculate the coefficients γ by solving the system given by Eqn. (1) for numerous pairs of couples of the grid (x_0, y_0) and x, y such that $x_0 < x$ and $y_0 < y$.

The system is solved by a least squares method. The formula of the coefficients ϕ_{ik} needed in this equation is presented in Eqn. (2). In these formulas, n_w is the number of plane waves in the field Eqn. (4). The calculation of ϕ_{ik} needs integration calculations that can be done numerically, such as using the trapezoidal method.

$$\sum_{i=0}^{n_w} \sum_{k=0}^{n_w} \gamma(i,k) \phi_{ik}(x_0, y_0, x, y) = 0, \tag{1}$$

$$\phi_{ik}(x_0, y_0, x, y) = \sum_{j=0}^{n_w} \sum_{l=0}^{n_w} \frac{(-1)^{j+l}(n_w + j)!(n_w + l)!(x - x_0)^{n_w - j}(y - y_0)^{n_w - l}}{j!(i + j)!(n_w - j)!l!(k + l)!(n_w - l)!} \times \int_{y_0}^{y} \int_{x_0}^{x} (y - y_1)^{k+l}(x - x_1)^{i+j} U(x_1, y_1) dx_1 dy_1. \tag{2}$$

From the knowledge of the values of the coefficient γ, the wavenumber is calculated as a root of a defined polynomial equation Eqn. (3). For each direction θ, the wavenumber calculation requires a resolution of Eqn. (3) but with the same coefficients γ.

$$\Psi(K_\theta) = \sum_{l=0}^{2n_w} (-\mathrm{i}K_\theta)^l \left(\sum_{m=\max(0, l-n_w)}^{\min(l, n_w)} \gamma(n_w - l + m, n_w - m) \cos^{l-m}\theta \sin^m \theta \right). \tag{3}$$

3 ANALYTICAL AND NUMERICAL VALIDATIONS

The method is now tested on fields calculated analytically and numerically. This method offers an interesting alternative to popular methods like the IWC [2] and the INCOME [3]. In order to illustrate the performance of the here presented method, an example of an orthotropic plate is used. Further analysis about its efficiency with respect to IWC and INCOME as well as about the robustness to noise and uncertainties can be found in the reference paper from Brion et al. [4]. By the way the following example is taken from it.

3.1 Numerical model of a bidirectional ribbed plate

A bidirectional ribbed plate is a periodic structure, illustrated in Fig. 1, made of a plate to which two perpendicular rows of stiffeners have been added. Since the beam grid of the stiffeners is supposed to be stiffer than the plates put between them, the dynamics of the stiffeners is dominant in the structure. That is why this metastructure presents a multiscale dynamic. The AKSI 2D method is tested on this type of structure to verify its efficiency on complex structures. Boutin et al. [5] have provided an analytical model of the flexural behavior of this type of structure that will serve as a reference. It is a model of an equivalent orthotropic plate obtained from an asymptotic homogenization process.

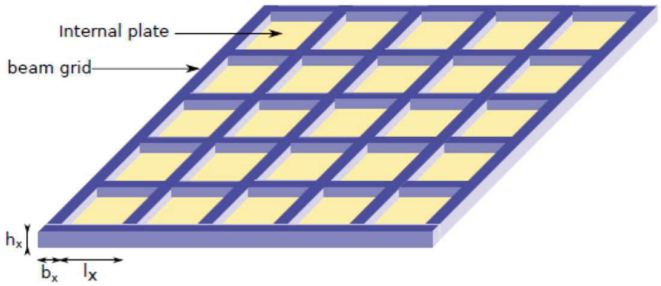

Figure 1: Example of a bidirectional ribbed plate of 5 by 5 cells [4]

This model is a 4th-order partial differential equation which result from the enrichment of an orthotropic plate equivalent to a beam grid, as the stiffeners are dominant compared to the plates in the global dynamics. Let h_j and b_j be respectively the height and the width of the stiffeners of the direction j. j being x or y. l_j is the contact length of the stiffeners with an inner plate. About the mechanical properties of the stiffeners: E_j, ν_j and ρ_j are respectively the Young Modulus, the Poisson ratio and the volume mass. A damping is added as an imaginary part of the Young modulus. η is the damping ratio and $\tilde{E}_j = E_j(1+\mathrm{i}\eta)$. From these parameters, some important quantities can be deduced: the bending inertia I_j, the torsional modulus G_j, the torsional inertia $\mathcal{I}_j$, the linear mass Λ_j and the torsional constant, $\rho_j J_j$.

In addition to these parameters, the properties of the internal plates must be defined. All the

plates have the same properties and are clamped to the beam grid. l_x, l_y are the side lengths and d is the width. E_p is the Young modulus, ν_p the Poisson ratio and ρ_p the volume mass. From these parameters, the following ones are calculated: the surface mass $\Lambda_p^{'} = \rho_p d$, the bending inertia $I_p = d^3/12$ and the modified Young modulus $E_p^{'} = E_p(1+\mathrm{i}\eta)/(1-\nu_p^2)$. With these parameters, the equation of the model of an orthotropic plate equivalent to a bi-ribbed plate proposed is Eqn. (4).

$$\frac{\tilde{E}_x I_x}{l_y}\frac{\partial^4 u}{\partial x^4} + \frac{\tilde{E}_y I_y}{l_x}\frac{\partial^4 u}{\partial y^4} + \left(\frac{G_x \mathcal{I}_x}{l_y} + \frac{G_y \mathcal{I}_y}{l_x}\right)\frac{\partial^4 u}{\partial x^2 \partial y^2} + \omega^2\left(\frac{\rho_y J_y}{l_x}\frac{\partial^2 u}{\partial x^2} + \frac{\rho_x J_x}{l_y}\frac{\partial^2 u}{\partial y^2}\right) + \left(K_{\omega_x}^{bc}\frac{\partial u}{\partial x} + K_{\omega_y}^{bc}\frac{\partial u}{\partial y}\right) = \omega^2\left(\frac{\Lambda_x}{l_y} + \frac{\Lambda_y}{l_x} + \Lambda_p^{'}\langle\phi_\omega^{bc}\rangle\right)u. \tag{4}$$

From Eqn. (4) the analytical dispersion relation is defined by replacing the solution u by a plane wave in the direction θ, $U(x,y)$.

3.2 Numerical simulation and comparison

The stiffeners are supposed to be the same in the x and the y directions and made of aluminum and the plates are made of plexiglass. In addition, a damping of $\eta = 5\%$ is added to the Young modulus as an imaginary part. Table 1 contains the properties of the stiffener and Table 2 contains those of the internal plate.

Table 1: Geometrical and mechanical properties of the beam grid

Parameter	h_x, h_y	b_x, b_y	E_x, E_y	ν_x, ν_y	ρ_x, ρ_y
Value	0.01m	0.01m	69GPa	0.3	2700kg/m^3

Table 2: Geometrical and mechanical properties of the internal plates

Parameter	l_x, l_y	d	E_p	ν_p	ρ_p
Value	0.1m	0.1m	3GPa	0.3	1200kg/m^3

A structure of 20 by 20 cells is considered, with a total side length of $L = 2.21$m. The extremities are clamped, and a point load is applied at the center of the structure. The displacement fields are calculated by solving the analytical equation of the homogenized equivalent orthotropic plate model Eqn. (4) by finite element software. The fields are known on a grid of 91 by 91 regularly spaced points located on a window of side length $L_w = 1.808$m centred on

the entire domain. The frequencies range from 5Hz to 500Hz. The AKSI 2D method is applied to these fields and the extracted wavenumbers are compared with the analytical model. The results extracted by the AKSI 2D are shown in Fig. 2. This figure shows that the wavenumbers are well calculated and match, those of the equivalent orthotropic plate model for most frequencies and directions. The inner resonance at 275Hz is even very well retrieved for both the real and imaginary parts.

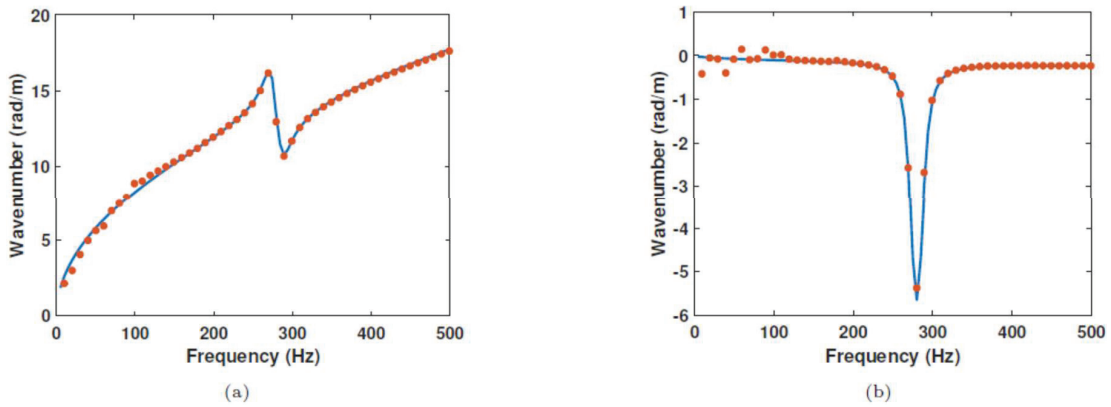

Figure 2: Dispersion relation in the direction 0 rad of the bi-ribbed plate: (a) real part, (b) imaginary part. Analytical model (solid line) and wavenumber calculated with the AKSI 2D (red dots) [4]

4 IDENTIFICATION OF SINGULARITY LOCATION: SUBDOMAIN STRATEGY

This section 4 presents specific subdomain strategy, which is employed in order to identify the precise location of singularities in plate-like elements. Results are presented on orthotropic plates and are inspired from the latest achievements of Brion's PhD thesis [6]. The strategy is based on the variations of the k-space in order to detect singularities and eventually defaults. Even if the impact of the singularities might be very limited on the real part of the wave-number, it is different for the imaginary part. Indeed, this latter is much more sensitive to damping and energy dissipation that can occur when a default is present.

However, for 2D-structures, the k-space-based default detection is made difficult for two reasons: firstly, the wave-numbers depend on the wave-direction of propagation, secondly, the imaginary part is influenced by the reduction of the wave amplitude which is due to both to spatial decay and the material damping. This is the reason why, for damage location, it is necessary to use a recursive protocol based on the evaluation of the k-space variations over subdomains.

4.1 Damage index

The damage index which is used in the study is based on the differences and discrepancies between the wave-numbers. The wave-numbers are evaluated on the structure for N_f frequencies and hence compared to a reference one. The reference can be analytical or experimental. The damage index in Eqn. (5) is based on the discrepancy of either the real part and or the imaginary part of the wave-numbers.

$$Dq_g(k_{\text{measure}}, k_{\text{ref}}) = \sqrt{\frac{1}{N_f N_\theta} \sum_{n=1}^{N_f} \sum_{l=1}^{N_\theta} \left| \frac{g(k_{\text{measure}}(f_n, \theta_l)) - g(k_{\text{ref}}(f_n, \theta_l))}{g(k_{\text{ref}}(f_n, \theta_l))} \right|^2} \tag{5}$$

g is a function which will be thereafter replaced by the expression of the real part of the imaginary part of the wave-number. This index uses values of the k-space over N_f frequencies and N_θ directions.

4.2 Subdomain decomposition

The spatial field is supposed to be known over a regular spatial grid (x_n, y_m) $1 \leq n \leq N_x$, $1 \leq m \leq N_y$. Let N_w be the number of points in a subdomain in the x- or y- direction. Subdomains are hence defined like: $\Omega_{ij} = [x_i, x_i + N_w 1] \times [y_j, y_j + N_w 1]$, with $i \in [1, N_x - N_w + 1]$ and $j \in [1, N_y - N_w + 1]$. We must notice that the sub-domains can be superimposed (Fig. 3) and that N_w must be large enough in order to have a precise solution. Indeed, the sub-domains dimensions shall be large with respect to the wave-lengths.

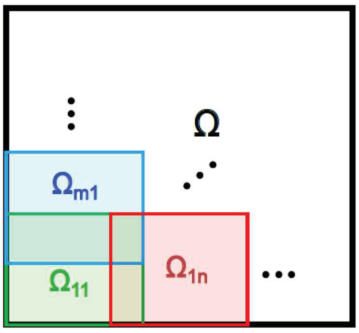

Figure 3: Sub-domain decomposition of the 2D-spatial grid [6]

From this decomposition, we can evaluate the value of the damage index for each one of these subdomains and hence retrieve the ones with the highest values. Since subdomains share locally the same areas, the location of a singularity can be assumed (Fig. 4). From this can be further confirmed by another sub-domain decomposition around only the assumed location of the singularity.

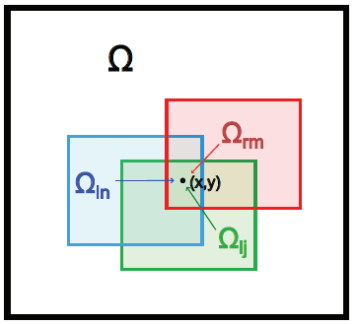

Figure 4: Damage location by damage index comparisons [6]

4.3 Validation on an isotropic plate

In order to simulate a damage on a plate, a finite element model has been designed for a plate with the following characteristics. This is an aluminum simply-supported rectangular plate $L_x = 0.95$m, $L_y = 0.6$m with thickness $d = 0.002$m. The displacement field is calculated of a regular 44 by 55-point grid, within an inner domain of the plates surface $L_{xw} = 0.682$m and $L_{yw} = 0.536$m.

The defect is represented by a hole close to the plates center (radius 1.2mm, 2.4mm, 6mm and 12mm). The frequencies are ranging from 50Hz to 1000Hz with 50Hz steps. From the observation of the displacement field, the damage does not seem to alter the displacement pattern as visible in Fig. 5.

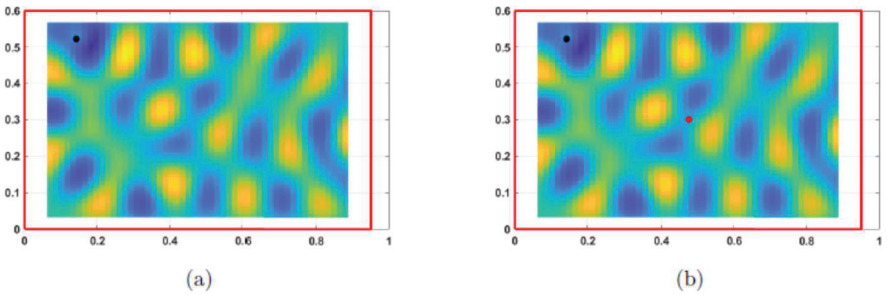

Figure 5: Displacement field at 700Hz, loading location (black dot): (a) without damage and (b) with damage (red dot) [6]

However, when evaluating the damage index over the proposed sub-domain decomposition strategy and by refining cumulating the damage index evaluation for each point of the grid, the damage index distribution is emphasizing some relevant results as visible in Fig. 6. The point load is located on the black dot and the default on the red dot.

Further examples show that the imaginary part seems to be more sensitive and more reliable

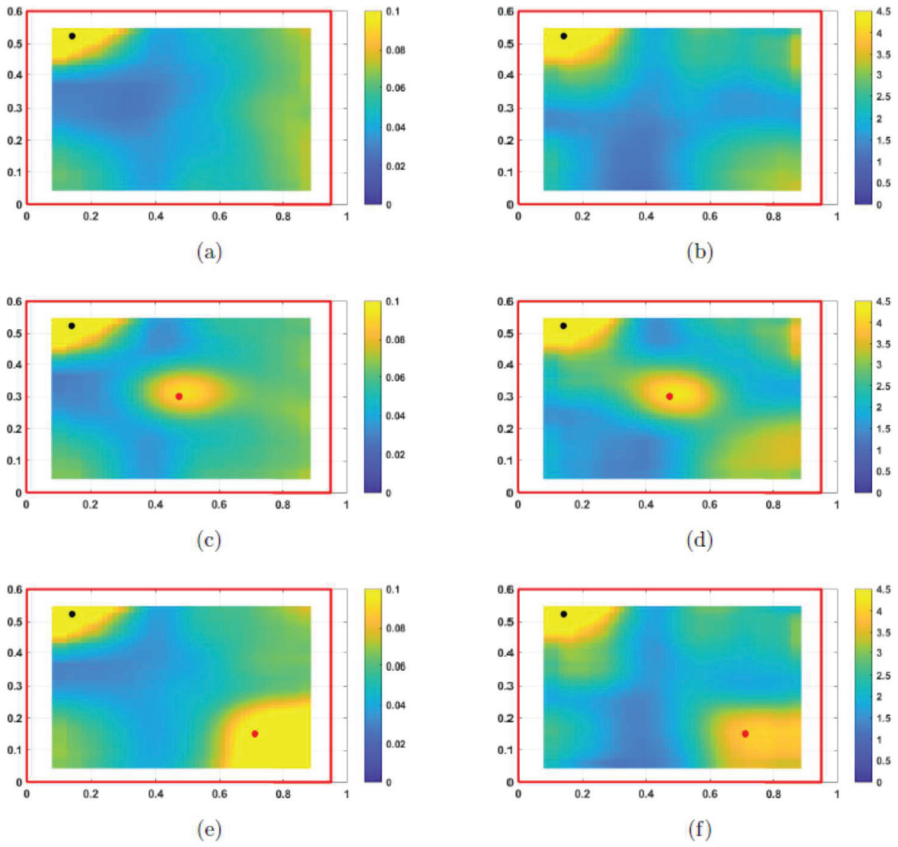

Figure 6: Surface index calculated for a 12mm hole located at red dot: (a), (c) and (e) are calculated for the real part, (b), (d) and (f) for the imaginary part; (a) and (b) are without defaults [6]

in the evaluation of the damage location, as visible in Fig. 7 and in Fig. 8. These last figure also emphasize that the AKSI k-space evaluation method seems to give a better input, as compared to the INCOME one's, to get a better contrasted damage location identification.

5 CONCLUSIONS

In this paper, a new inverse method, the Algebraic K-Space Identification 2D technique (AKSI 2D), is proposed for the extraction of the complex k-space elements from two-dimensiona displacement fields. As compared to other popular 2D k-space techniques, like the IWC and the INCOME, the here-proposed method exhibits interesting performances in terms of efficiency and robustness when computing the complex k-spaces at relatively low frequencies.

This inverse method is then employed at the core of a strategy to identify the location of singularities in a plate-like structure. The strategy is based on a subdomain partition and an

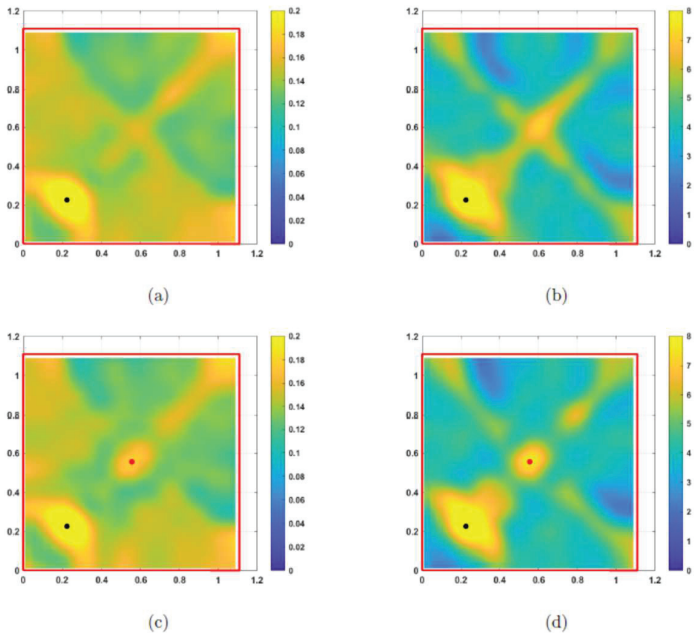

Figure 7: INCOME k-space - Surface index calculated for a 6mm hole located at black dots: (a) and (c) are calculated for the real part, (b) and (d) for the imaginary part; (a) and (b) are without defaults [6]

analysis of the local dispersion curves. A damage index location is here specifically design and give good evaluation about the damage location.

REFERENCES

[1] X. Li, M. Ichchou, A. Zine, C. Droz, N. Bouhaddi, "An algebraic wavenumber identification (awi) technique under stochastic conditions", Mechanical Systems and Signal Processing, vol. 188, pp. 109983, 2023.

[2] J. Berthaut, M. Ichchou, L. Jezequel, "K-space identification of apparent structural behaviour", Journal of Sound Vibration, vol. 280, no. 3-5, pp. 1125–1131, 2005.

[3] R. F. Boukadia, C. Claeys, C. Droz, M. Ichchou, W. Desmet, E. Deckers, "An inverse convolution method for wavenumber extraction (INCOME): formulations and applications", Journal of Sound and Vibration, vol. 520, pp. 116586, 2022.

[4] T. Brion, X. Li, P. Fossat, M. Ichchou, O. Bareille, and A.M. Zine, "Algebraic K-Space Identification 2D technique for the automatic extraction of complex k-space of 2D structures in presence of uncertainty", Mechanical Systems and Signal Processing, vol. 223, pp. 111892, 2025.

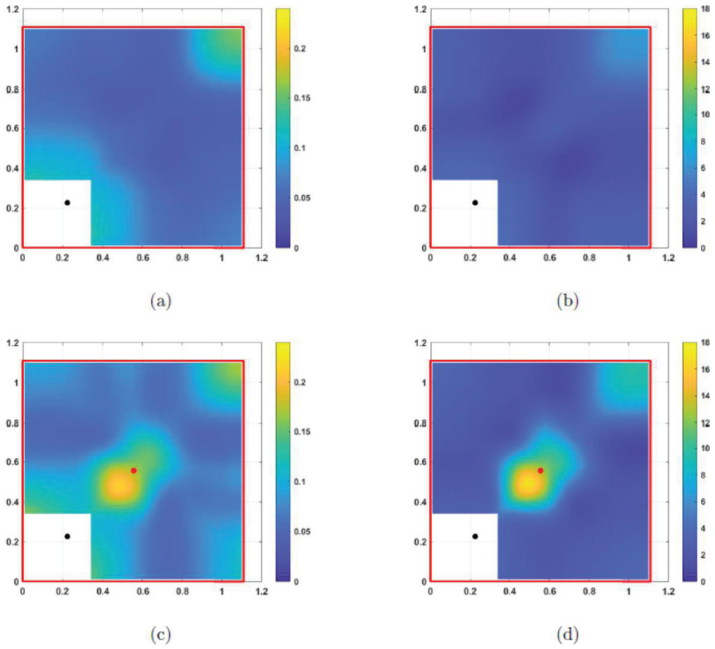

Figure 8: AKSI k-space - Surface index calculated for a 6mm hole located at black dots: (a) and (c) are calculated for the real part, (b) and (d) for the imaginary part; (a) and (b) are without defaults [6]

[5] C. Boutin, P. Fossat, C. Droz, M. Ichchou, ”Dynamics of ribbed plates with inner resonance: analytical homogenized models and experimental validation”, European Journal of Mechanics- A/Solids, vol. 79, pp. 103838, 2020.

[6] T. Brion, ”Suivi de santé structurale sur structures architecturées par techniques en ondes guidées” PhD thesis, Ecole Centrale de Lyon, 2024.

XI ECCOMAS Thematic Conference on Smart Structures and Materials - SMART 2025
M. Krommer, M. Nader and M. Schagerl (Eds)

Received: 22 April 2025 / Revised: 2 July 2025 / Accepted: 25 October 2025
© The Author(s) 2025

Active Control of Vibration Energy Transmission in an Inhomogeneously Damped Plate

Alexander Büchner, Hans Peter Monner

Abstract. The global attenuation of noise in an aircraft cabin for instance, is usually bound to the application of several sensors and actuators on the entire inner structure. However, if there are sharply localized noise and vibration sources in the overall system, the transfer paths from those to the radiating surfaces may be blocked actively. Therefore, by using structural intensity (SI) as a cost function for active control of transferred energy, previous studies show a benefit towards global attenuation of a downstream structure compared to conventional Active Vibration Control using a more centralized set-up of actuators and sensors. These approaches rely on the measurement of SI using finite differences by means of a simple Kirchhoff plate and the assumption of energy transfer mainly by flexural waves. However, these finite differences -approximating local derivatives of displacement- are prone to errors with increasing order of derivatives needed. Hence, a simplification of structural intensity measurement is needed, for the worse of accuracy. Preliminary numerical studies have shown a better attenuation performance than AVC even with simplified methods, especially for inhomogeneously damped structures. Hence, this paper presents the experimental studies on a damped rectangular plate using different sets of sensors and actuators to measure and control structural intensity. A feedforward approach is used for tonal and multi-tonal. Ultimately, the approach is compared to a simple velocity control.

Key words: active control, structural intensity, noise reduction

1 INTRODUCTION

For many applications, noise is still an important topic when it comes to their acceptance. Several approaches have already been researched successfully, however, when it comes to an approach leading to a global noise reduction, the approaches often rely on passive systems with a consequent addition of mass for lower frequency bands. Current active noise reduction systems, being more performant in lower frequency bands, thus, mostly achieve only a local reduction in noise floor. By this, for a global reduction of noise a rather large number of sensors and actuators is required among several positions in the cavity to be calmed. The optimal solution

Alexander Büchner & Hans Peter Monner
German Aerospace Center, Institute for Lightweight Systems, Department of Adaptronics, Lilienthalplatz 7, 38108 Braunschweig, Germany, e-mail: alexander.buechner@dlr.de

would be to physically decouple the noise sources, e.g. vibrating engines. For structural reasons, this is of course not possible. A promising approach, however, poses the active control of transmitted vibrational energy. By designing active systems reducing this energy transmission from its source to the radiating surfaces, a global reduction of noise can be achieved in theory. The structural intensity, i.e. the transmitted vibrational energy through a cross section, proposes a beneficial control target for such a system.

To use structural intensity as such, the measurement has to be possible by means of real-time sensing. In the 1970s the measurement of structural intensity started with the works of Noiseux [1] and Pavić [2], followed by different approaches towards its active control [3, 4, 5]. Preliminary investigation of the author already dealt with the numerical assessment of structural intensity control for flat panels also with different stiffness and damping modifications [e.g. [6, 7]]. Thereby, simplified methods of structural intensity measurements proposed a more performant control target with respect to global downstream attenuation of vibration compared to a simple velocity control (i.e. AVC) for the same number of error estimation positions, especially with the occurrence of traveling waves. Simplified in this case refers to the measures used in order to reduce structural intensity. A detailed explanation is given in section 2. This paper furthermore deals with the experimental comparison of this simplified structural intensity control with an active vibration control approach, i.e. using only single point velocities as control targets. The controller is investigated on a flat non-stiffened aluminum panel with layers of damping applied close to the clamped edges to achieve a partly traveling wave field.

2 STRUCTURAL INTENSITY MEASUREMENT

Structural intensity describes the vibrational energy transmitted per unit area [1]. For a panel element, structural intensity in a single direction can be describes as follows:

$$SI_x = (Q_x \cdot \dot{\eta} + M_{xx} \cdot \omega_x + M_{xy} \cdot \omega_y) \cdot A^{-1} \tag{1}$$

By omitting the cross section itself and only targeting the power flow, the structural intensity depends on the plate elements internal measures (shear force Q_x, bending moment M_{xx} and twisting moment M_{xy}) and the corresponding dynamic measures (normal velocity $\dot{\eta}$ and two rotational velocities ω_x and ω_y), see figure 1.

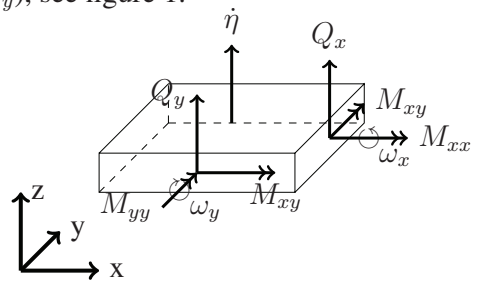

Figure 1: Coordinate system and measures of positive influence line of a plate element: Shear force Q_x, normal velocity $\dot{\eta}$, bending moment M_{xy}, twisting moment M_{xx} and angular velocities ω_y and ω_y

The measurement of he dynamic measures is feasible be applying accelerometers and rotational sensors to the structure. The real-time measurement of the internal measures, however, requires approximation by finite differencing schemes and the knowledge of the plate elements bending stiffness. Hence, this demands the applicability of Kirchhoff plate theory. [1, 2]

As he finite differences required for the theoretically exact estimation of structural intensity for a plate element go up to order three (also with mixed derivatives), this approach is prone to errors considering signal quality and sensor placement. Especially errors in the sensors signal phase amplify with the order of the finite differences. Thus, preliminary numerical studies have shown a better performance using higher order derivatives, but only under perfect conditions. Phase errors due to misplaced sensors, however, reduce the controller performance significantly. A simplified method only uses the dynamic measures as control target. In theory, this also minimizes the structural intensity as a whole. Also, the numerical pre-studies showed better performance compared to AVC.

3 EXPERIMENTAL AND CONTROLLER SETUP

In this paper, an aluminum plate of dimensions $0.8\,\mathrm{m}\ x\ 0.6\,\mathrm{m}$ and a thickness of $2\,\mathrm{mm}$ is clamped on all four sides. Two layers of constrained layer damping tape (type 3M Scotch®2552) are applied on three of the four edges with a width of $0.1\,\mathrm{m}$ each in order to achieve traveling waves in higher frequency bands. A single inertial shaker is applied to induce a disturbance force, whilst four inertial shakers downstream (i.e. in positive x direction) act as control forces. Further downstream, four arrays of accelerometers are applied, deriving the error signals for the controller. The positions of the forces as well as the center of the error sensor arrays can be derived from figure 2.

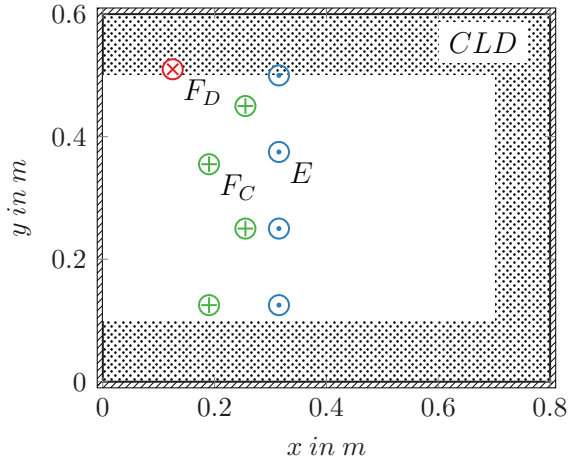

Figure 2: Dimensions and positioning of experimental setup: Rectangular aluminum plate, F_D disturbance force, F_C control forces, E positions of error sensor array center node, CLD area of constrained layer damping application

Each error sensor array consists of four accelerometers (see figure 3 with a spacing $\Delta = 20\,\mathrm{mm}$. Hence, the error signals for the simplified structural intensity control can be derived by averaging for the normal velocity or a finite difference of first order for the two angular velocities - after initial integration of the acceleration signal.

$$\dot{\eta} = \frac{\dot{\eta_1} + \dot{\eta_3}}{2},\ \omega_x = \frac{\dot{\eta_1} - \dot{\eta_3}}{\Delta},\ \omega_y = \frac{\dot{\eta_2} + \dot{\eta_4}}{\Delta} \tag{2}$$

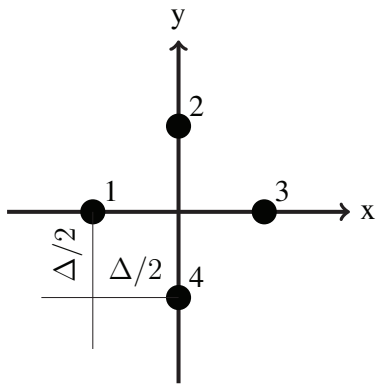

Figure 3: Accelerometer array for approximating SI components by finite differences: 4 query points, $\Delta = 20\,\mathrm{mm}$

For the controller, a complex filtered-xLMS (FxLMS) algorithm is applied as described in Misol [8]. Due to the time invariance of the disturbance, a convergence of the filter towards the optimal solution can be assumed. To make the results comparable, a convergence time of $60\,\mathrm{s}$ for each filter is set. Afterwards, the filter weights are fixed. Four different sets of target functions are investigated: First a simple velocity control targeting the mean velocity signal $\dot{\eta}$ of one sensor per array, second the same for only arrays 1 and 3 (numbering starts at the top in figure 2), third the mean velocities and angular velocities of all of the arrays (i.e. simplified SI) and lastly the simplified SI for arrays 1 and 3. The controller performance is evaluated for four mono-tonal excitations ($188.75\,\mathrm{Hz},\ 390\,\mathrm{Hz},\ 647.5\,\mathrm{Hz}$ and $820\,\mathrm{Hz}$), a multi-tonal excitation (with four dominant frequencies and a broadband noise floor) and a broadband noise band-pass filtered to $20\,\mathrm{Hz}$ to $900\,\mathrm{Hz}$.

Figure 4 shows the general filter scheme. The plant systems P (path from disturbance to error sensors , primary path) and S (path from each of the control shakers to error sensors, secondary path) are identified in a first run by assembling a state-space model based on an incoherent broadband excitation of all shakers. The state-space model S is the fed to the FxLMS. The disturbance exciting voltage is used as the reference signal U_{ref}. The 200 filter weights W are then tuned by the FxLMS algorithm based on the error signal Sig_{res}.

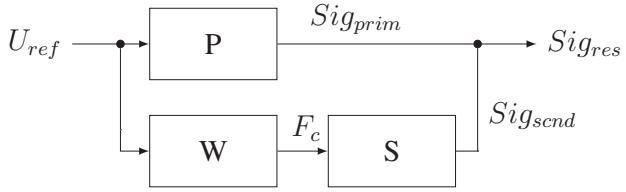

Figure 4: Scheme for feed-forward SI component controller: Reference signal U_{ref}, P primary and S secondary path from reference to SI components Sig_{prim} and Sig_{scnd}, W feed-forward filter, F_c filtered reference signal for secondary actuator input, Sig_{res} sum of primary and secondary SI components

In addition to the accelerometer data, the downstream area of the panel, i.e. behind the error arrays at $x > 0.315\,\mathrm{mm}$, is scanned with a Laser Scanning Vibrometer (LSV) in order to evaluate the global reduction of vibration. Table 1 shows the DSP and prototyping hardware used as well as the signal processing parameters.

Table 1: Sensors, actuators and DSP components

inertial shakers	Visaton EX 45 S
accelerometers	PCB Piezotronics 352A24
low-pass filter	KEMO CardMaster 255G
shaker signal amplifier	custom component
real-time processor/ADC7DAC	dSpace DS1006/DS2004/DS2103
LSV Scanning head	Polytec OFV 055
sampling frequency	$2.56\,\mathrm{kHz}$
frequency resolution	$1.25\,\mathrm{Hz}$
low-pass cut-off frequency	$1\,\mathrm{kHz}$
averaging (LSV)	3 x complex

4 CONTROL RESULTS

The performance of the control approaches is evaluated by the reduction of kinetic energy of the downstream region, exactly speaking the quadratic sum of the velocity amplitudes measured at the query points with the LSV. The total reduction is calculated by the logarithm of the controlled (suffix $ctrl$) and uncontrolled (suffix ref) response:

$$L_\Delta = 10 \cdot \log_{10}\left(\frac{E_{ctrl}}{E_{ref}}\right) \tag{3}$$

Figure 5 shows the total reduction L_Δ for the excitation frequencies (for the mono-tonal excitations) and the total energy for all frequencies for multi-tonal and broadband excitation, respectively. Except for the lowest frequency, the simplified shows a better total attenuation

performance compared to the AVC approaches. For the highest mono-tonal excitation, no control approach could reduce the total vibration, the SI control, however, shows the least reduction. This might be explained by the velocity component leading to an amplification as for the simple AVC, but the angular component, however, slightly reduces this effect. For the remaining excitations, the additional angular component reduction of simple SI control appears to significantly lower the downstream vibration. The comparatively bad performance of SI control for the lowest frequency can be explained by the dominance of the standing waves. In this frequency band, the homogeneous damping of the plate does not affect the vibration significantly, hence the vibration field is mostly consisting of standing waves, which are controllable by only targeting velocity pretty well. However, the reduction of the number of error arrays severely impacts all control approaches. The AVC even leads to an amplification, whilst the simple SI can still reduce the downstream vibration. Again, this can be explained by the additional angular component added to the AVC by simple SI control.

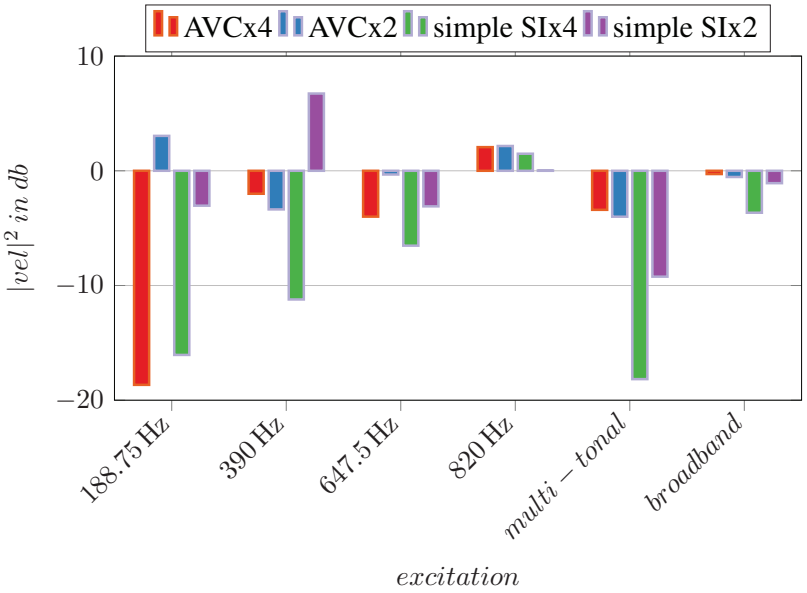

Figure 5: Total downstream reduction of quadratic sum of velocity for tonal, multi-tonal and broadband excitation (sum of all excited frequencies). Control targets: AVCx4 (one velocity from each of the four arrays), simple SIx4 (simplified SI signal from each of the four arrays), AVCx2 (one velocity signal from array 1 and 3), simple SIx2 (simplified SI signal from arrays 1 and 3)

For multi-tonal excitation (see figure 6), both simple SI control configurations can show a comparable or, especially for the non-tonal part, better attenuation compared to the four-array AVC. The AVC with two array positions may only attenuate the first two main frequencies and shows nearly no attenuation for other frequencies.

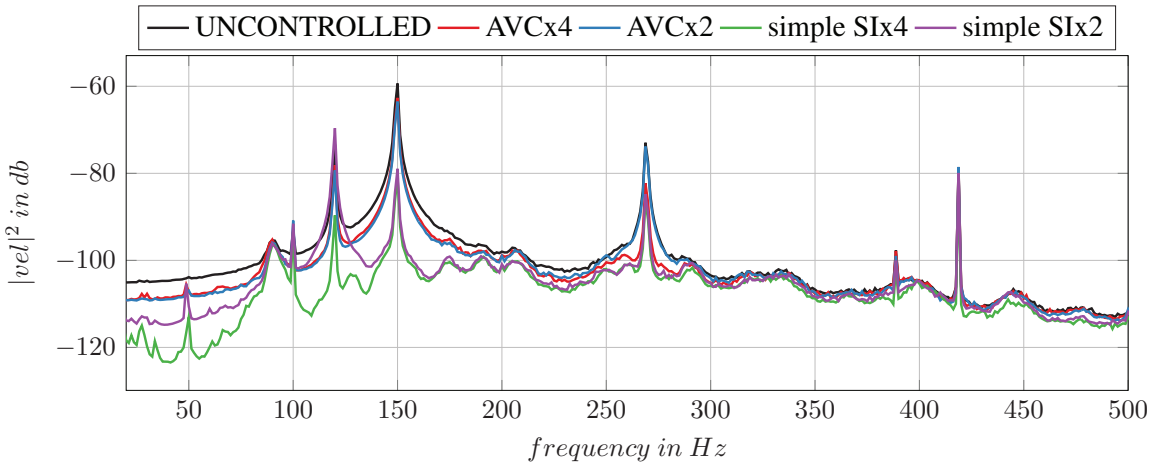

Figure 6: Total downstream quadratic sum of velocity for multi-tonal excitation. Control targets: AVCx4 (one velocity from each of the four arrays), simple SIx4 (simplified SI signal from each of the four arrays), AVCx2 (one velocity signal from array 1 and 3), simple SIx2 (simplified SI signal from arrays 1 and 3)

Figure 7 shows the downstream quadratic velocity amplitude for the entire frequency band measured. For the frequencies above 500 Hz all control targets perform closely with nearly no attenuation. Hence, figure 8 shows a cut-out of the lower frequencies below 500 Hz.

Compared to the baseline, the simple SI control can achieve a better broadband attenuation than the AVC approaches. Especially the four-array SI control shows a significantly better control performance for the downstream vibration. A single frequency with an amplification of vibration at 50 Hz, however, might be explained by disturbances from the power grid running at the same frequencies. Hence, this data point may be excluded from the investigation.

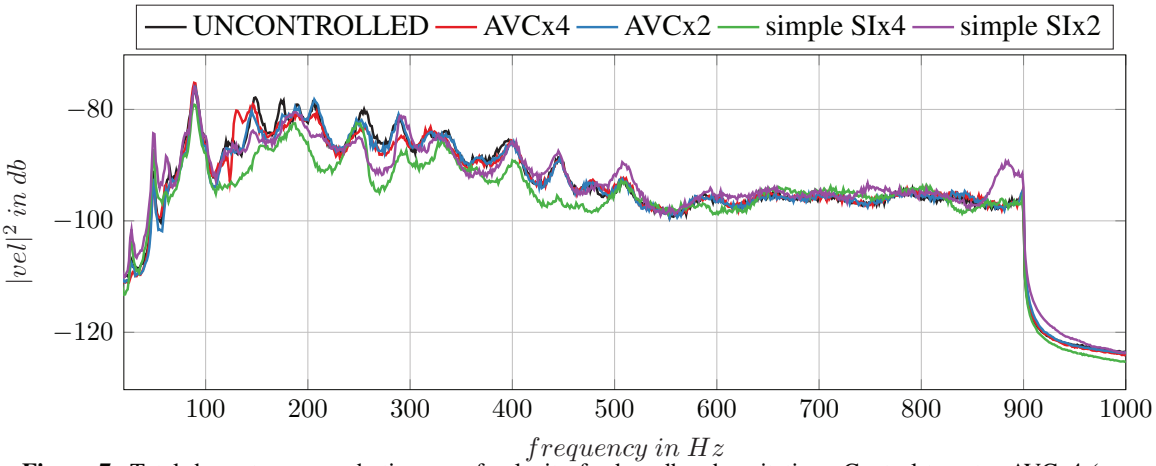

Figure 7: Total downstream quadratic sum of velocity for broadband excitation. Control targets: AVCx4 (one velocity from each of the four arrays), simple SIx4 (simplified SI signal from each of the four arrays), AVCx2 (one velocity signal from array 1 and 3), simple SIx2 (simplified SI signal from arrays 1 and 3)

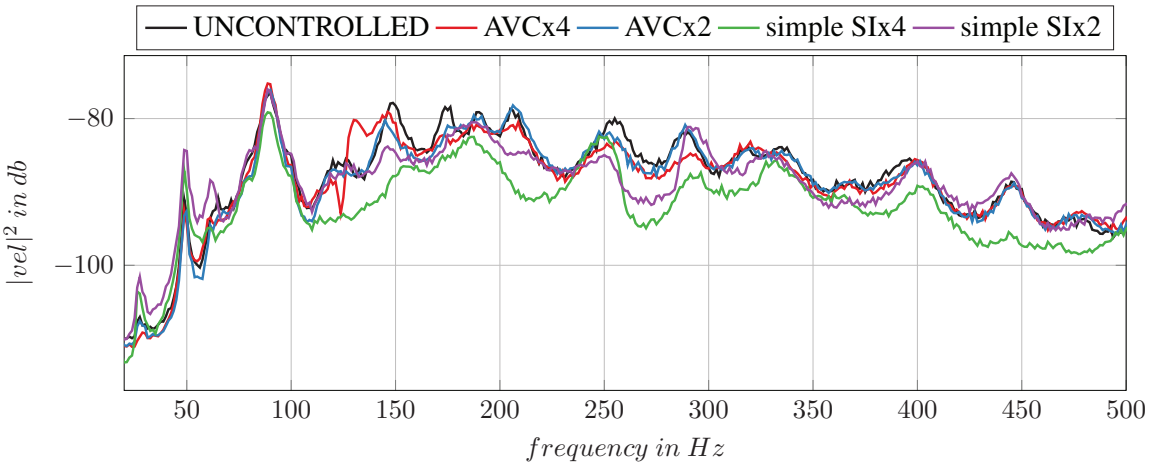

Figure 8: Total downstream quadratic sum of velocity for broadband excitation (zoomed). Control targets: AVCx4 (one velocity from each of the four arrays), simple SIx4 (simplified SI signal from each of the four arrays), AVCx2 (one velocity signal from array 1 and 3), simple SIx2 (simplified SI signal from arrays 1 and 3)

Looking at the 3rd octave bands for a better view of the controller performance, it can be shown that the simple SI control is significantly more performant in frequency bands above $125\,\mathrm{Hz}$. For lower frequencies, SI control seems to lead to an amplification. Thus, these might be explained by the large amplification of the power grid frequency and the double of it as well as an amplitude peak at $27.5\,\mathrm{Hz}$ (of unknown source). For frequencies above $500\,\mathrm{Hz}$, the performance for all control targets decreases. The AVC as well as the simple SI cannot reduce the total downstream vibration anymore, probably due to the higher ratio of traveling waves and the lower wave lengths. Especially the latter interfere with the measurement of SI as the underlying formulae rely on finite differencing. Previous research has shown, that for simple SI measurement the array sensor distance should not exceed about half of the wavelength in order to estimate the amplitude and phase in an acceptable tolerance. For this panel (omitting the damping), this border frequency would calculate to approximately $315\,\mathrm{Hz}$. This correlates to the results shown in this figure, as the performance starts to reduce significantly in this frequency band.

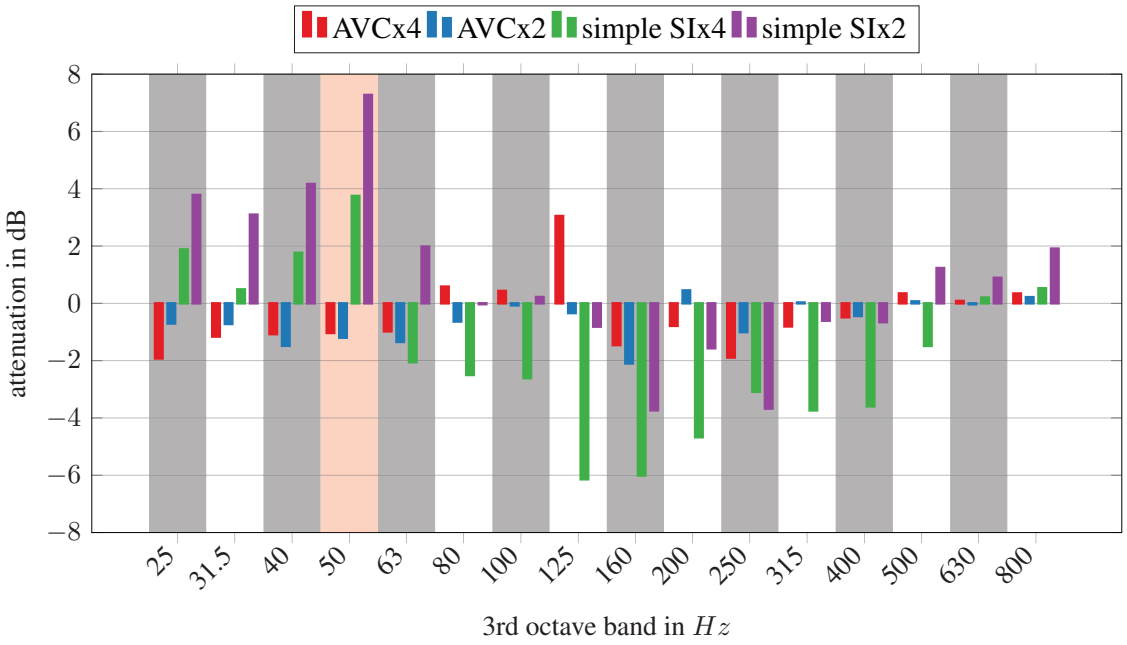

Figure 9: Total downstream reduction of quadratic sum of velocity for broadband excitation (3rd octave bands). Control targets: AVCx4 (one velocity from each of the four arrays), simple SIx4 (simplified SI signal from each of the four arrays), AVCx2 (one velocity signal from array 1 and 3), simple SIx2 (simplified SI signal from arrays 1 and 3). The red bar marks the frequency band of the power grid frequency.

5 CONCLUSION

The results shown in this paper support the numerical pre-investigation on SI control. A simplified approach already achieves greater reduction of downstream vibration compared to AVC with the same amount of actuators and sensor array locations. Especially for the upper frequency bands investigates, SI control performed significantly better, leading to the assumption of better performance for traveling waves, as the numerical investigation already proposed. Further research is necessary, however, to apply these assumptions to more complex structures (e.g. stiffening or bent structures), as these may not apply to the theoretical assumptions made to the approximation of structural intensity.

REFERENCES

[1] D. U. Noiseux, “Measurement of power flow in uniform beams and plates,” *The Journal of the Acoustical Society of America*, vol. 47, no. 1B, pp. 238–247, 1970.

[2] G. Pavić, “Measurement of structure borne wave intensity, part i: Formulation of the methods,” *Journal of Sound and Vibration*, vol. 49, no. 2, pp. 221–230, 1976.

[3] H. Iwamoto and N. Tanaka, "Feedforward control of flexural waves propagating in a rectangular panel," *Journal of Sound and Vibration*, vol. 324, no. 1-2, pp. 1–25, 2009.

[4] B. R. Mace, C. R. Halkyard, and H. M. El-Khatib, "Real-time measurement of wave components and intensity in a beam in the presence of a near field," *Journal of Sound and Vibration*, vol. 286, no. 3, pp. 507–527, 2005.

[5] X. Pan and C. H. Hansen, "Active control of vibratory power transmission along a semi-infinite plate," *Journal of Sound and Vibration*, vol. 184, no. 4, pp. 585–610, 1995.

[6] A. Kokott and H. P. Monner, "Numerische studie zur sensor- und aktuatorplatzierung fur die aktive ausbreitungssteuerung von biegewellen in einer finiten und semi-infiniten isotropen platte," 2021.

[7] A. Kokott, H. P. Monner, and T. Haase, "Numerical investigation towards the control of flexural waves using structural intensity for an active barrier of structure-borne sound," p. 78. [Online]. Available: https://www.spiedigitallibrary.org/conference-proceedings-of-spie/11376/2558100/Numerical-investigation-towards-the-control-of-flexural-waves-using-structural/10.1117/12.2558100.full

[8] M. Misol, "Full-scale experiments on the reduction of propeller-induced aircraft interior noise with active trim panels," *Applied Acoustics*, vol. 159, p. 107086, 2020. [Online]. Available: https://elib.dlr.de/129910/

XI ECCOMAS Thematic Conference on Smart Structures and Materials - SMART 2025
M. Krommer, M. Nader and M. Schagerl (Eds)

Received: 16 April 2025 / Revised: 22 October 2025 / Accepted: 25 October 2025
© The Author(s) 2025

Design and Analysis of a Robust Hybrid Tuned Mass Damper System for Structural Vibration Control: Active Synthesis of Multiple TMD

Simon Chesné, Jonathan Rodriguez

Abstract. The integration of feedback control strategies with tuned mass dampers (TMDs) emerges as an effective method for enhancing their capability to mitigate structural vibrations. These devices offer the significant advantage of being fail-safe, particularly in aeronautical applications. Recently, several control laws associated with hybrid mass dampers have been proposed, targeting specific functionalities such as multi-mode control, sky-hook synthesis, or nonlinear controllers. This study introduces an approach to synthesize specific control laws that ensure system stability. We propose leveraging the analysis of mechanical impedance at the interface to design an equivalent mechanical dynamic behavior. The passivity property of the active device is inherently guaranteed by the existence of such equivalent mechanical system. This concept has been successfully demonstrated in recent works. In this paper, we specifically focus on enhancing the robustness of the closed loop on a highly variable system. To achieve this, the concept of Multiple Tuned Mass Dampers (MTMD) is explored. By employing the initial TMD as an inertial actuator, we generate an active force equivalent to seven parallel TMDs, each optimally tuned. Simulations of the resulting device demonstrate excellent vibration attenuation performance, even under significant variations of the primary structure dynamic response, as changes in the modal frequencies. The robustness and stability margins of the proposed system are analyzed and compared to conventional systems.

Key words: Active Tuned Mass Damper, Multiple Tuned Mass Damper, Electromagnetic actuators

1 INTRODUCTION

Structural vibration control is a crucial challenge in various engineering fields, including civil engineering, aerospace, and mechanical systems in general. Among conventional solutions, Tuned Mass Dampers (TMDs) have proven effective in reducing vibrations. However, their performance is often constrained by sensitivity to parameter variations, structural uncertainties, and the additional mass they introduce.

Simon Chesné & Jonathan Rodriguez
INSA Lyon, CNRS, LaMCoS, UMR5259, 69621 Villeurbanne, France, e-mail: simon.chesne@insa-lyon.fr

To overcome these limitations, hybrid systems that integrate both passive and active components have been developed [1], [2], [3], [4]. Active absorbers enable adaptations of TMD properties, enhancing both efficiency and robustness. These approaches aim to mitigate the shortcomings of conventional TMDs while preserving the advantages of an efficient and stable solution. Research in this area highlights the benefits of active control in improving the robustness and effectiveness of vibration mitigation systems. More recently, nonlinearities have been introduced either in the control law [5] or directly into the mechanical system [6].

Another development in TMD technology is Multi-Tuned Mass Dampers (MTMDs). A major drawback of traditional TMDs is their high sensitivity to detuning, which causes a significant drop in performance outside a narrow frequency range. This phenomenon, known as the frequency detuning effect, also affects MTMDs when all resonators are tuned to the same frequency, as well as resonant metamaterials when they are perfectly periodic. In such cases, the attenuation bandgap is deep but narrow and highly susceptible to uncertainties. One effective strategy to address this issue is to introduce a frequency distribution in MTMDs [7], [8], [9], making them more effective over a broader frequency range and more robust to detuning. These different approaches converge toward the concept of a hybrid system capable of dynamically adjusting its properties to achieve optimized behavior inspired by MTMDs. This approach leverages the adaptability of active control while maintaining the inherent stability of a passive TMD.

This study proposes an innovative strategy to actively synthesize a robust vibration mitigation system inspired by MTMDs. By integrating a passive TMD with a synthesized MTMD configuration, the hybrid system aims to enhance performance and robustness in structural vibration control.

2 Mathematical model of hybrid system

A standard linear hybrid system is illustrated in Fig. 1. It consists of a primary system (denoted as index 1) coupled with a tuned mass damper (TMD, denoted as index 2). The hybridization process involves the addition of an active force controlled by a dedicated unit. Disturbances affecting the primary system may originate from ground motion (X_0) or an external force acting on the primary structure (F_1). The control performance remains consistent regardless of the source of disturbance. In the subsequent analysis, F_1 will primarily be considered.

The equations governing the system's motion are expressed in the Laplace domain as follows:

$$\begin{aligned} s^2 m_1 X_1 = (k_2 + sc_2)(X_2 - X_1) - F_a \\ +F_1 + (k_1 + sc_1)(X_0 - X_1) \end{aligned} \tag{1}$$

$$s^2 m_2 X_2 = (k_2 + sc_2)(X_1 - X_2) + F_a \tag{2}$$

where s is the Laplace variable, m_1 and m_2 are the masses, X_1 and X_2 are their displacements in the Laplace domain, k_1 and k_2 are the stiffness values, and c_1 and c_2 are the mechanical

damping values of the primary system and the TMD. F_a is the active force defined below. The TMDs parameters follow using the equal peak design rules [10]:

$$\omega_2 = \frac{k_2}{m_2} = \frac{k_1}{m_1}\nu \tag{3}$$

with $\nu = 1/(1+\mu)$ and

$$\xi_2 = \frac{c_2}{2\sqrt{k_2 m_2}} = \sqrt{\frac{3\mu}{8(1+\mu)}} \tag{4}$$

where ω_2 is the natural frequency of the TMD, ξ_2 is its damping ratio and μ is the mass ratio (m_2/m_1). For this study, μ is set at 1%, which is representative of the concerned applications. The controller $H(s)$, generating the equivalent mechanical behavior will be defined in the next part. Based on the measurement of the primary system's velocity (as a classical velocity feedback), the resulting active force can be written as follows:

$$F_a(s) = sH(s)X_1(s) \tag{5}$$

3 Active damping: MTMD synthesis

Fig. 2 represents the equivalent mechanical system when the controller is properly tuned to synthesize multiple TMDs. This results in the combination of an optimal passive TMD, initially tuned to damp the host structure, with several additional TMDs having slightly different parameters. There are various strategies to optimize the design of these additional degrees of freedom [7], [8], [9]; however, this is not the main focus of this paper.

In this section, the goal is to use a simple formulation based on the resulting impedance at the interface between the host structure and our new device.

For the analysis developed here, and for sake of simplicity, only damping linked to the hybrid device is considered. This means that the system is analyzed without internal mechanical damping $c_1 = 0$. As previously explained, to ensure fail-safe behavior, the actuator consists of the initial TMD itself, combined with a transduction system (typically a voice coil). Consequently, the standard Direct Velocity Feedback control law exhibits poor stability margins [1] and must be modified.

3.1 Mechanical impedance analysis

As depicted in [3], velocity feedback can be interpreted as an impedance synthesizer. To generate an equivalent MTMD, let's examine the mechanical impedance of a general TMD, written below:

$$Z_{tmd}(s) = \frac{sm_{tmd}(k_{tmd} + sc_{tmd})}{s^2 m_{tmd} + sc_{tmd} + k_{tmd}} \tag{6}$$

In order to be able to generate this behavior we have to consider the dynamic of the transducer, in our case the Hybrid device (indexed 2 in figure 1). The resulting impedance on the

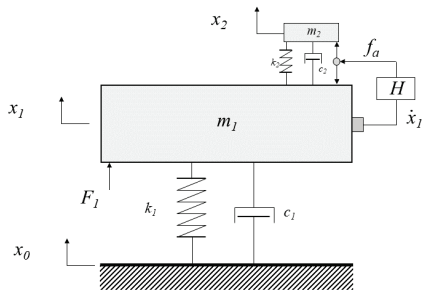

Figure 1: Standard hybrid mass damper using velocity feedback

interface, depending on the control law $H(s)$ can be written:

$$Z_{HMD}(s) = \frac{sm_2(k_2 + sc_2)}{s^2m_2 + sc_2 + k_2} + \frac{s^2m_2}{s^2m_2 + sc_2 + k_2}H(s) \tag{7}$$

3.2 control law design

Using the above equations, it can be understood that to synthesize a new TMD with the properties described in Eq. (6), while using the initial TMD as an actuator, the control law *H* must satisfy the following expression:

$$H(s) = g\left[1 + \frac{c_2}{m_2 s} + \frac{\omega_2^2}{s^2}\right]\frac{sm_{tmd}(k_{tmd} + sc_{tmd})}{s^2m_{tmd} + sc_{tmd} + k_{tmd}} = g\left[1 + \frac{c_2}{m_2 s} + \frac{\omega_2^2}{s^2}\right]Z_{tmd}(s) \tag{8}$$

where *g* is the positive global gain of the control law, which can be interpreted as a mass amplifier. To simplify the following analysis, it will be set to one.

Here, it can be observed that the first part of the control law is intended to cancel the dynamic effect of the initial TMD, which is used as an inertial actuator, to ensure stability.

Considering the linearity of the feedback loop, multiple TMDs can be synthesized in parallel by summing the control laws described above. This leads to:

$$H_{Mtmd}(s) = [1 + \frac{c_2}{m_2 s} + \frac{\omega_2^2}{s^2}]\sum_i Z_{tmd_i}(s) \tag{9}$$

The main challenge now lies in defining the parameters of the various synthesized TMDs, which clearly depend on the context and application. In this study, as a proof of concept, we choose to synthesize six additional TMDs, each with a mass equal to that of the initial real TMD (m_2). The objective is to minimize the H_∞ norm of the frequency response function of the main structure.

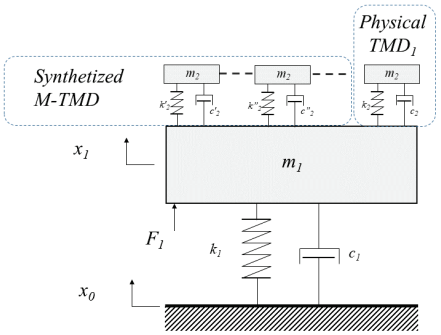

Figure 2: Equivalent mechanical system synthesized by the controller

To achieve this, an optimization function was used to determine the 12 unknown parameters (the six stiffness and six damping values). The *fminsearch* function in MATLAB was employed, to minimize the H_∞ norm of the response, with the algorithm's initial guess simply set to the physical values of the real TMD.

One can underline that one of the main drawback of the proposed system is that the optimization process depends on the gain of the control feedback loop. The optimal parameter distribution may vary depending on this gain. In the illustration provided in this initial study, we remind that the gain is arbitrarily fixed at unity.

3.3 Stability analysis

The introduction of an active system on a tuned damper necessitates a careful analysis of stability as underlined in [11] and [12]. The well-known principle of energy conservation, which holds for all physical systems, states that the variation in stored energy is equal to the sum of external power input and internal power generation [13]. Since the internal mechanical damping values c_1 and c_2 are set to zero, the only internal power generation mechanisms are those associated with the power flow produced by the actuator, which is driven by the controller and its control law $H(s)$. From a stability perspective, the resulting system is passive (or hyperstable) if [13]:

$$Re[G(s)] > 0 \tag{10}$$

where the function $G(s)$ represents this dissipative mechanism generated by the active device. Using eqs (1)-(5), it can be expressed in the Laplace domain as:

$$G(s) = (sX_1)^2 H(s) \left(1 - \frac{X_2}{X_1}\right) \tag{11}$$

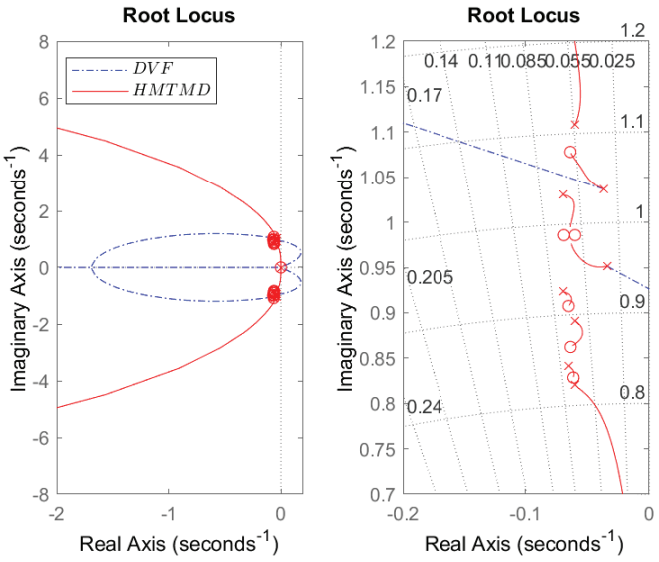

Figure 3: Root Locus for the synthesis of 6 TMDs using the hybrid device (left: Global viex, right: Zoom near the TMDs poles)

Using Eqs. (11) and (8), one can easily demonstrate that Eq. (10) is always satisfied. The extension of this principle to multiple control loops for multiple TMDs is straightforward for linear systems. This stability is illustrated in Fig. 3, which presents the root locus representation of a controller emulating 6 others TMDs. It clearly shows that the controlled poles remain on the left side of the imaginary axis, confirming the stability of the system, contrary to classical DVF controller (in blue in this figure) as demonstrated in [1].

4 Performance

The proposed system aims to reduce vibrations while ensuring robust performance despite variations in the parameters of the supporting structure. The following sections briefly illustrate these aspects.

4.1 Vibration attenuation

Figure 4 shows the frequency response of the supporting structure without a TMD, with a passive TMD, and with the proposed hybrid system. A significant improvement in attenuation performance is observed over a wide frequency range. These performances are equivalent to those achieved with seven optimally tuned passive TMDs. However, the hybrid system requires a mass that is seven times lower than the equivalent passive MTMD. The resulting stability margins are infinite for the gain margin (due to the passivity property of the control law) and a phase margin of $72°$at $1.2rad/s$.

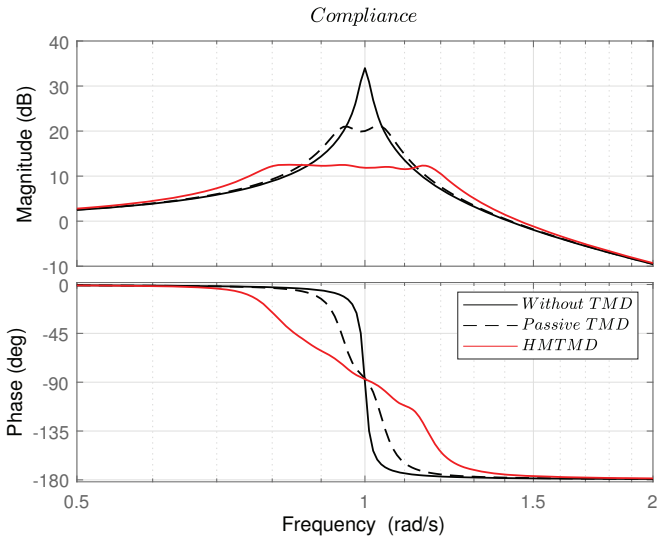

Figure 4: Frequency Response Functions X_1/F_1 of the closed loop system.

4.2 Robustness

Another crucial aspect of control applications, once stability is ensured, is robustness. This refers to the system's ability to maintain equivalent performance even when the environment changes. This is one of the key advantages often highlighted for MTMD. Fundamentally, a change in the environment alters the dynamic properties of the host structure. In such conditions, conventional linear controllers are known to lose performance and, in some cases, even stability. Similarly, passive systems such as TMDs are also susceptible to significant performance degradation. A preliminary approach to assess this aspect is to modify the stiffness of the host structure without updating the controller. A stiffness variation of $\pm 30\%$ is introduced into the model, and the resulting frequency responses are illustrated in Fig. 5.

Without a control device, we can clearly observe a shift in the frequency of the resonance peak. With a passive TMD, performance can be drastically reduced when the initial resonance frequency varies by more than 10%. For the proposed hybrid device, although the nominal performance is naturally reduced, we still achieve an attenuation greater than $10dB$. These results are comparable to those obtained with a network of seven properly tuned passive TMDs. However, we remind that the added mass of the hybrid device remains equivalent to that of just a single TMD. In practice, a better understanding of the uncertainty distribution could help define the controller parameters in a more robust manner.

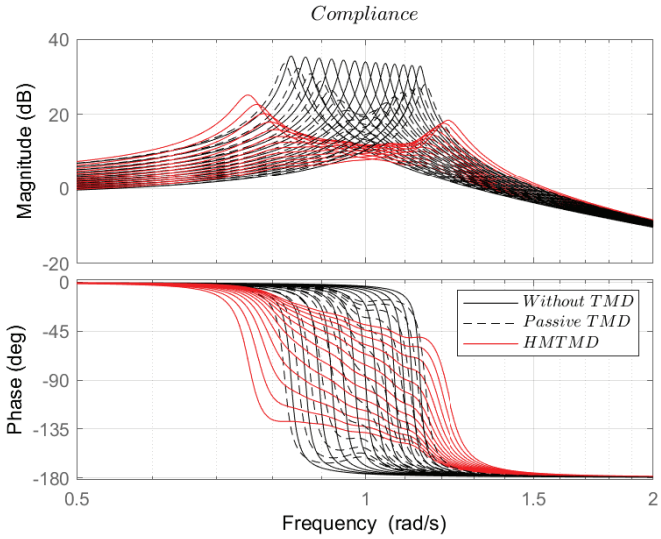

Figure 5: Frequency response X_1/F_1 for stiffness variations ($\pm 30\%$)

5 CONCLUSIONS

This preliminary study illustrates the ability of hybrid mass dampers to control vibrations very efficiently while ensuring fail-safe behavior. It also highlights the relevance of equivalent mechanical impedance analysis in designing controllers to achieve a desired dynamic behavior while ensuring the stability of the resulting system. The synthesis of MTMD appears to be a promising approach to improving the robustness of controllers against system uncertainties or variations. Many aspects are currently under study as tuning optimization or experimental validation. Future research will focus primarily on the optimization step to integrate uncertainty profiles.

REFERENCES

[1] C. Collette and S. Chesne, "Robust hybrid mass damper," *Journal of sound and Vibration*, vol. 375, pp. 19–27, 2016.

[2] S. Chesne and C. Collette, "Experimental validation of fail-safe hybrid mass damper," *Journal of Vibration and Control*, pp. 1–12, 2017.

[3] S. Chesne, "Hybrid skyhook mass damper," *Mechanics and Industries*, vol. 22, no. 49, 2021.

[4] S. Chesné, G. Inquieté, P. Cranga, F. Legrand, and B. Petitjean, "Innovative hybrid mass damper for dual-loop controller," *Mechanical Systems and Signal Processing*, vol. 115,

pp. 514 – 523, 2019. [Online]. Available: http://www.sciencedirect.com/science/article/pii/S0888327018303601

[5] J. Rodriguez, L. Mesny, and S. Chesne, "Sliding mode control for hybrid mass dampers: Experimental analysis on robustness," *Journal of Sound and Vibration*, vol. 575, 2024.

[6] L. Mesny, S. Baguet, and S. Chesne, "An adaptive nonlinear hybrid vibration absorber." *Third International Nonlinear Dynamics Conference (NODYCON 2023)*, vol. Sapienza, Universita di Roma, 2024.

[7] J. Park and D. Reed, "Analysis of uniformly and linearly distributed mass," *Eng. Structures*, vol. 23, no. 7, 2001.

[8] A. Kareem and S. KlineChesne1, "Performance of multiple mass dampers under random loading," *J. Struct. Eng.*, vol. 121, no. 2, 1995.

[9] K. Xu and T. Igusa, "Dynamic characteristics of multiple substructures with closely spaced frequencies," *Earthq. Eng. Struct. Dyn.*, vol. 21, no. 12, 2021.

[10] J. Den Hartog, *Mechnical Vibrations*, 4th ed. Mc Graw-Hill, 1956.

[11] K. Billon, G. Zhao, C. Collette, and S. Chesne, "Hybrid mass damper: theoretical and experimental power flow analysis," *Journal of Vibration and Acoustics*, vol. 144, pp. 1–20, 2022.

[12] N. Alujevic, I. Catipovic, S. Malenica, I. Senjanovic, and N. Vladimir, "Stability, performance and power flow of active u-tube anti-roll tank," *Engineering Structures*, vol. 211, p. 110267, 2020. [Online]. Available: http://www.sciencedirect.com/science/article/pii/S0141029619316864

[13] J. Slotine and W. Li, *Applied non linear control*. Pearson, 1991.

XI ECCOMAS Thematic Conference on Smart Structures and Materials - SMART 2025
M. Krommer, M. Nader and M. Schagerl (Eds)

Received: 28 April 2025 / Revised: 28 August 2025 / Accepted: 25 October 2025
© The Author(s) 2025

Numerical and Experimental Investigation of Novel Control Methods for Self-Adaptive Shock-Absorbers

Cezary Graczykowski, Grzegorz Mikułowski, Rafał Wiszowaty, Michał Niedzielczyk, Rami Faraj

Abstract. This study explores numerically and experimentally innovative control strategies for self-adaptive shock absorbers designed to operate under varying impact conditions. The control problem is addressed with a fundamental constraint – a limited prior knowledge of excitation parameters. To tackle this challenge, state-dependent control methods with progressively enhanced adaptive capabilities are proposed and evaluated numerically. A dedicated experimental setup featuring a pneumatic adaptive shock absorber is developed to ensure validation of the proposed methods and facilitate their comparison. The system incorporates a fast-operating piezoelectric valve with a strain gauge for proportional opening control and enables optimal real-time response to unknown dynamic excitations. The conducted laboratory drop test results confirm the feasibility of the proposed control methods.

Key words: Adaptive Impact Absorption, Self-Adaptive System, Pneumatic Shock Absorber

1 INTRODUCTION

Mechanical impacts are common phenomena encountered in a wide range of systems. To safeguard structures and devices from the detrimental effects of such shocks, impact absorbers have been extensively developed and implemented. Their primary function is to reduce the transmitted loads by absorbing and dissipating the energy of the excitation. Energy absorbing devices are employed in diverse applications, such as vehicle crash protection [1, 2], bicycle suspensions [3], and landing gear systems [4, 5]. In these scenarios, the impact mitigation process occurs within a remarkably short time frame, often just a few to several tens of milliseconds, posing significant practical challenges for control systems. A key limitation arises from the inherent mechanical inertia of actuators, which restricts the operational speed of shock absorbers. However, ongoing rapid advancements in actuator technology, sensor systems, and embedded hardware controllers are paving the way for development of technically feasible shock absorbers designs. The examples include magnetorheological [6, 7] and electrorheological dampers [8],

Cezary Graczykowski & Grzegorz Mikułowski & Rafał Wiszowaty & Michał Niedzielczyk & Rami Faraj
Institute of Fundamental Technological Research, Polish Academy of Sciences, Pawinskiego 5B, 02-106 Warsaw, Poland,
e-mail: cgraczyk@ippt.pan.pl

pneumatic [9, 10] and hydraulic shock absorbers [11, 12] equipped with piezoelectric valves, as well as systems utilizing shape memory alloys [13].

In contrast to typical methods used for impact mitigation, where pre-defined system response is executed using PID controller [14] with feedback from generated force or acceleration [15], the self-adaptive shock-absorbers are equipped with additional path-planning loop [16]. This loop, being simultaneously a basis for self-adaptive performance, enables optimization of the system response in the case of unknown excitation conditions and occurrence of process disturbances. Recently, two different approaches based on kinematic feedback for path-planning process have been developed. In the first method, the measurement of selected state variables allows for maintaining actually optimal system path [17, 18]. The alternative approach is based on the versatile concept Model Predictive Control (MPC) [19], which enables sequential control update and system response optimization at arbitrarily selected control horizon. In the proposed methods, the MPC framework is extended either by conducting repeated identification of process disturbances [20] or by introducing equivalent quantities that account for unknown disturbances and system parameters [21].

The main objective of the paper is to numerically and experimentally validate the performance and robustness of two methods developed for adaptive impact absorption, namely Bi-state HPC method and Continuous HPC method. Both methods are evaluated under impact scenarios involving a wide range of masses and initial velocities of the impacting object. The results from the numerical simulations are confirmed to a large extend by the experimental tests conducted using pneumatic cylinder equipped with piezoelectric valve.

2 CONTROL METHODS FOR ADAPTIVE IMPACT ABSORPTION

A basic example of an impact-absorbing system is a double-chamber (hydraulic or pneumatic) damper subjected to the impact of a rigid object with a given initial velocity (Fig. 1a). The damper contains a fast-operating controllable valve used to regulate fluid flow between the chambers (Fig. 1b) and a system of sensors that measure kinematic and thermodynamic response to impact loading. The system aims to absorb and dissipate impact energy while minimizing reaction force and deceleration of the impacting object. It is designed to operate autonomously and adapt to varying impact conditions. As a self-adaptive system, it provides a high level of robustness against unpredictable impacts and unknown process disturbances.

The proposed control concept assumes online bi-directional exchange of data between the damper and the control system. The signals transmitted from the damper to the control system include piston displacement and deceleration, gas pressures, gas temperatures and actual valve opening. Conversely, the signals transmitted to the damper's valve include required deceleration or required valve opening, and the control voltage supplied to the valve.

The problem of Adaptive Impact Absorption (AIA) is defined here using a state-dependent kinematic formulation that is consistent with fundamental principles governing the operation of self-adaptive systems. The proposed approach involves determining a time-dependent control signal which minimizes the objective function, defined as integral of the difference between the actual impacting object's deceleration $\ddot{x}$ and its currently optimal (required) value $\ddot{x}_{req}$.

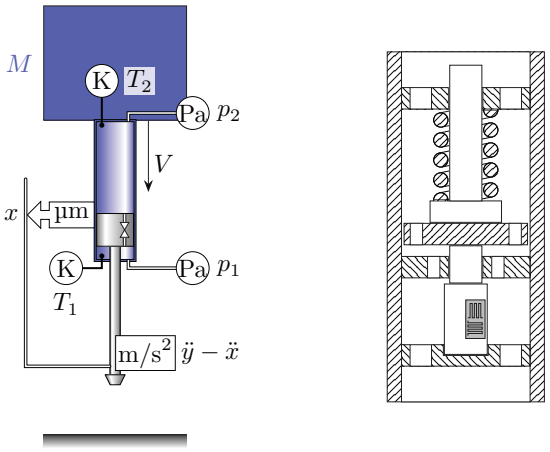

Figure 1: Pneumatic damper with controllable valve under impact excitation

This yields the following dynamic optimization problem:

$$\text{Find } u^* = \underset{u_{\min} \le u(t) \le u_{\max}}{\arg\min} \int_0^{t_{max}} (\ddot{x}(u,t) - \ddot{x}_{req}(u,t))\, dt \tag{1}$$

where u is the searched control signal and t_{max} indicates final time of the process when the impacting object stops. The required impacting object's deceleration $\ddot{x}_{req}$ is determined using the condition of stopping the impacting object using the remaining stroke of the piston $d - x(u,t)$:

$$\ddot{x}_{req} = -\frac{v^2(u,t)}{2(d - x(u,t))} \tag{2}$$

which is called the Kinematic Optimality Condition (KOC). It is assumed that the optimization problem (1) is solved using mathematical model of the considered impact-absorbing system, but without the knowledge about the values of impacting object mass and its initial velocity as well as possible disturbances of the process (e.g. friction forces or fluid leakage).

To address this challenge, two control methods utilizing state-dependent path-tracking (Bi-state Hybrid Prediction Control and Continuous Hybrid Prediction Control) have been developed, Fig. 2. Both methods provide an approximate solution of the dynamic optimization problem (1) by employing different realizations of the path-tracking process.

Specifically, the Bi-state HPC method (Fig. 2) is based on direct tracking of the required deceleration path. In this approach the Path Control Algorithm utilizes KOC to determine the currently optimal deceleration value. This required deceleration is then followed by applying two extreme control signal values, resulting in commutative opening and closing of the valve. In contrast, the Continuous HPC method (Fig. 2) focuses on tracking the required change of valve opening. In this approach, the Path Control Algorithm is followed either by a block enforcing closed valve position (executed at the beginning of the process) or Inverse Dynamics Prediction block, which determines the necessary change of valve opening during the process (executed

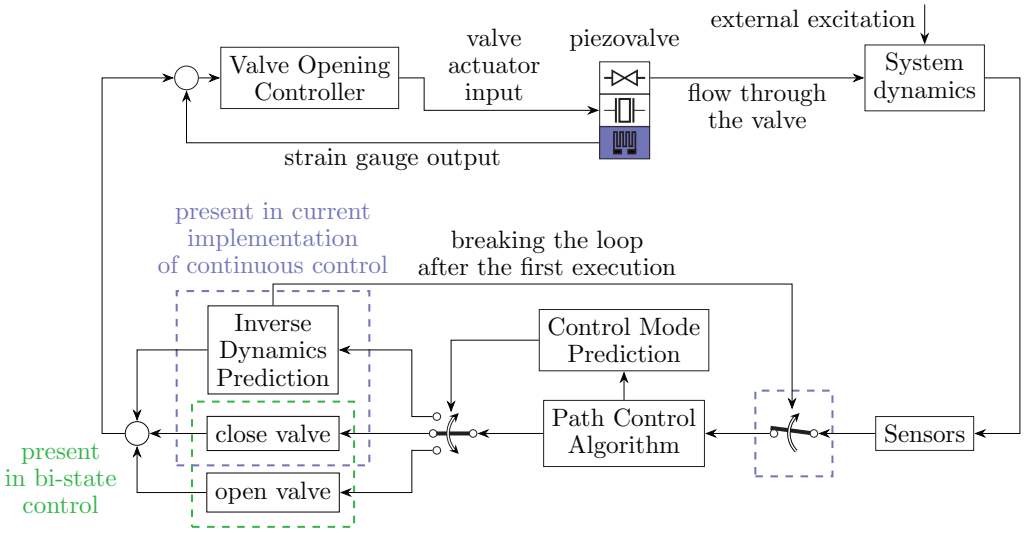

Figure 2: Scheme of Bi-state HPC method and Continuous HPC method

only once when the KOC is satisfied). The required valve opening is further followed using PI controller with feedback from actual deceleration.

3 NUMERICAL INVESTIGATION OF THE CONTROL METHODS

The objective of conducted numerical study is to evaluate the performance of Bi-state and Continuous HPC methods under impact scenarios involving various impacting object masses and initial velocities. The response of the system is computed using a mathematical model based on equations describing the motion of the impacting object, the thermodynamic energy balance, the cotrolled gas flow through the valve and the operation of the control system. The last two equations incorporate the inertial effects related to the gas flow and the valve piston motion.

3.1 Bi-state Hybrid Prediction Control

The baseline case for Bi-state HPC method involves an impact characterised by two parameters: $M = 11.4\,\mathrm{kg}$ and $V_0 = 1.4\,\mathrm{m/s}$. The computed changes of applied control, obtained opening of the valve, required deceleration and obtained deceleration are presented in Fig. 3. In the considered case, the valve's time constant is assumed as $T_0 = 1\,\mathrm{ms}$, which is a typical value for piezoelectric valves. The maximum control signal is $U_m = 200\,\mathrm{V}$ and corresponds to maximum valve's head displacement $d_v^{max} = C = 50\,\mu\mathrm{m}$, which ensures regular fluctuations of the deceleration during the entire process.

The effects of **changing the impacting object mass** (using a scaling factor of 1.5 for both increase and decrease cases) are presented in Fig. 4 The conducted simulations allow to make the following observations:

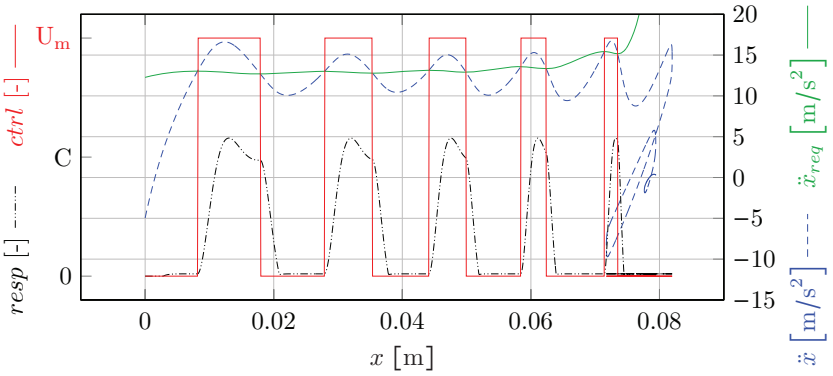

Figure 3: Operation of Bi-state HPC method for $M = 11.4\,\mathrm{kg}$ and $V_0 = 1.4\,\mathrm{m/s}$

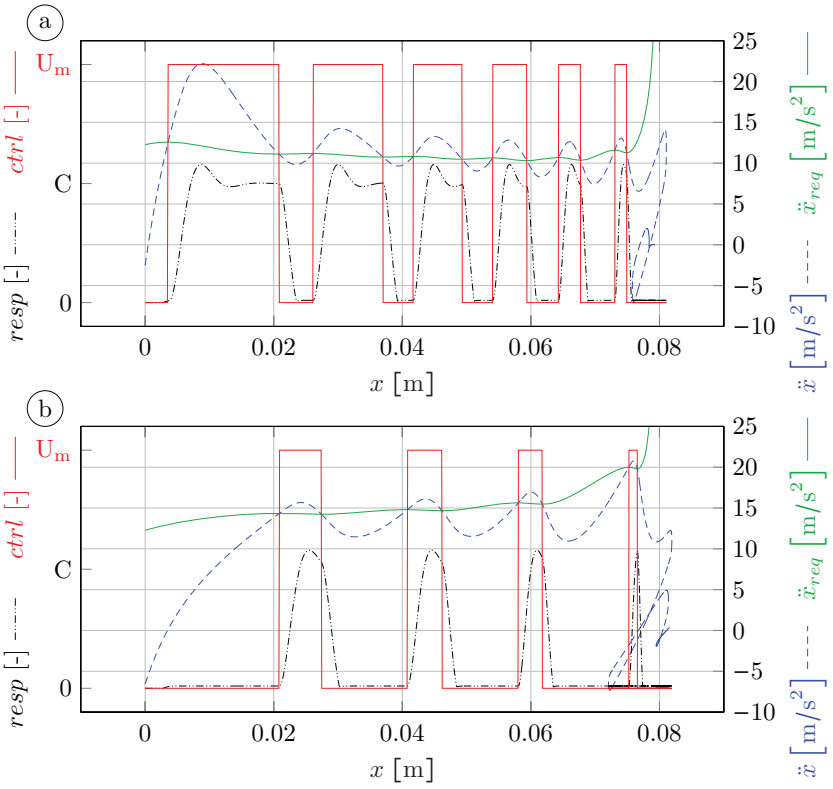

Figure 4: Comparison of Bi-state HPC method operation for small and large mass of the impacting object

- Decreasing the impacting object's mass causes more frequent occurrence of the time intervals when the valve is opened and more frequent fluctuations of deceleration. The gradual decline of the required deceleration corresponds to decrease of both the maximal and minimal deceleration values during the subsequent fluctuations. The peak deceleration occurs at the beginning of the process, during the first valve opening.

- Increasing the impacting object mass leads to fewer occurrences of time intervals when the valve is opened and fewer corresponding fluctuations of deceleration. The gradual raise of required deceleration corresponds to increase of the maximal deceleration value during the subsequent fluctuations. In this case, the peak deceleration appears near the process end, with the magnitude being highly sensitive to the exact mass value.

The example demonstrates that variations in mass value significantly alter the response of the system controlled by Bi-state HPC method. Better performance with more regular fluctuations of deceleration can be achieved by adjusting the maximum valve opening or maximum value of applied control signal. Specifically, for the decreased mass the maximum valve opening has to be enlarged, while for the increased mass the maximum control signal has to be reduced along with precise calibration to current mass value.

The effects of **changing the impacting objects initial velocity** (using a scaling factor of 1.3 for both increase and decrease cases) are depicted in Fig. 5. Although the results of velocity changes are not so evident, the following observations emerge:

- Reduced impacting object velocity results in lower value of the required deceleration (due to modified system kinematics) and significantly more frequent occurrence of time intervals when the valve is open. The largest value of deceleration can occur either at the beginning of the process or at its very end depending on the exact value of impacting object's velocity.

- Increased impacting object velocity leads to higher value of required deceleration and fewer occurrences of time intervals when the valve is open. The largest deceleration typically occurs at the end of the process, with magnitude strongly dependent on impacting object's initial velocity. Moreover, notably larger rebound of the impacting object is observed at the end of the process.

The example shows that variations in impacting object's initial velocity primarily affect the final stage of system response. The occurrence of the final deceleration peak can be prevented by precise tuning of maximum valve opening or maximum control signal, while reducing object rebound often requires change of control strategy at the end of the process.

The entire numerical analysis concerning mass and velocity dependence demonstrates that response of the system controlled by Bi-state HPC method is very sensitive to both these values. Moreover, the adjustment of control parameters aimed at obtaining regular deceleration fluctuations is relatively complicated and its outcomes cannot be easily predicted a priori.

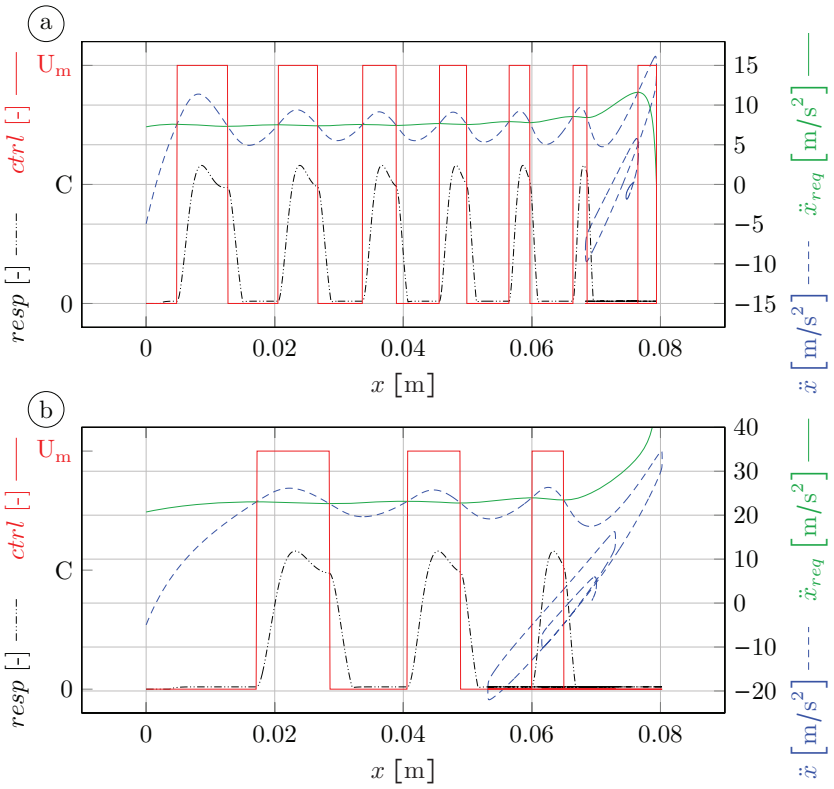

Figure 5: Comparison of Bi-state HPC method operation for small and large velocity of the impacting object

3.2 Continuous Hybrid Prediction Control

For the Continuous HPC method, the baseline case employs the same mass and initial velocity of the impacting object: $M = 11.4\,\mathrm{kg}$ and $V_0 = 1.4\,\mathrm{m/s}$. The valve's time constant is assumed significantly larger than in the Bi-state HPC method ($T_0 = 10\,\mathrm{ms}$) in order to obtain comparable path-tracking precision, while the maximum valve's head displacement is assumed as previously: $d_v^{max} = C = 50\,\mu\mathrm{m}$. The computed changes of applied control, required valve opening, obtained valve opening, required deceleration and obtained deceleration are presented in Fig. 6. The executed control process includes three stages: i) keeping the valve closed to reach the required deceleration, ii) applying the maximum control signal to reach the required valve opening and iii) precise adjustment of the control signal to track the required time-history of valve opening.

The effects of **changing the impacting object mass** (decrease and increase by factor of 1.5) are depicted in Fig. 7, revealing the following observations:

- Decreasing impacting object mass results in shorter initial stage of the process when the valve remains closed and lower value of required constant deceleration (determined using

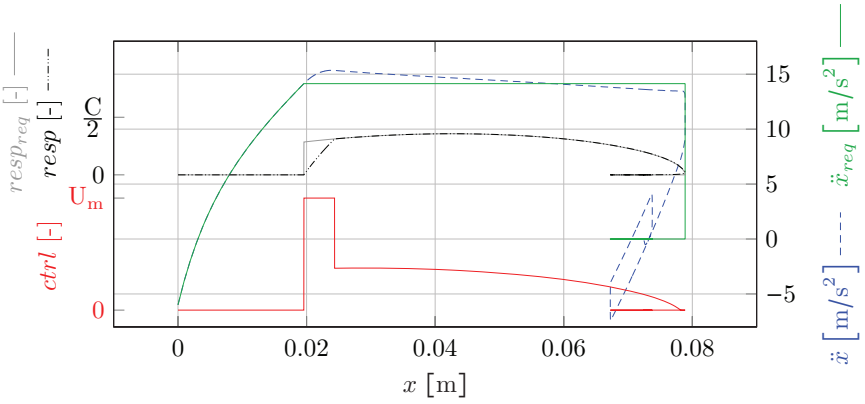

Figure 6: Operation of Continuous HPC method for $M = 11.4\,\mathrm{kg}$ and $V_0 = 1.4\,\mathrm{m/s}$

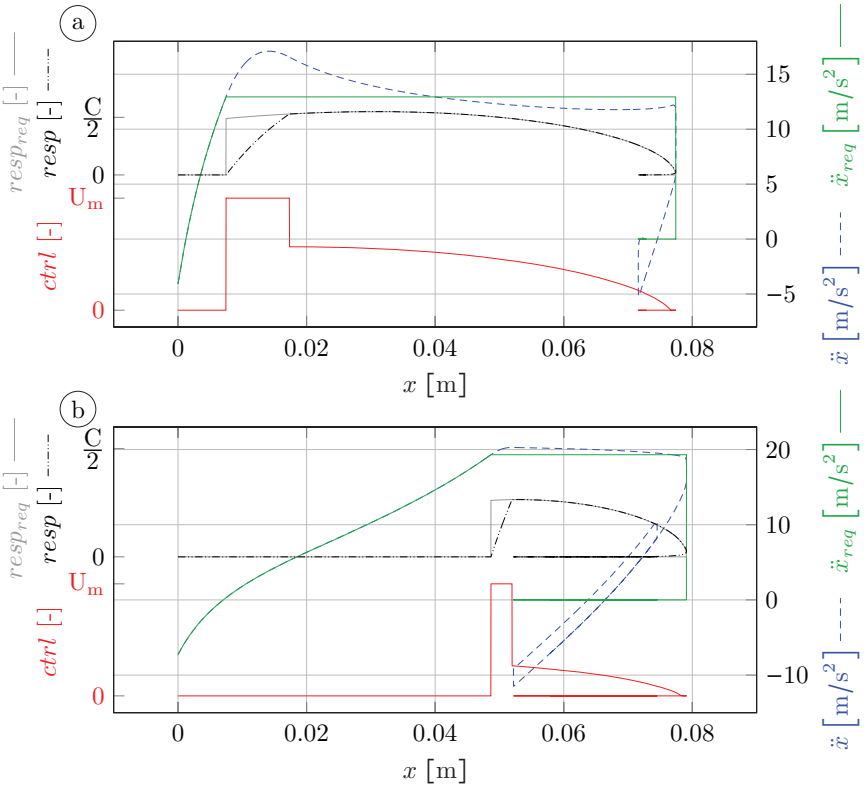

Figure 7: Comparison of Continuous HPC method operation for small and large mass of the impacting object

KOC). The obtained deceleration exceeds the required one at the first part of the control process and drops below it during the second part.

- Increasing impacting object mass leads to longer initial stage with the closed valve and larger value of the required deceleration. The obtained deceleration more closely follows the required one, exceeding it slightly almost during the entire process. Moreover, the rebound of the impacting object substantially increases.

The example shows that change in mass value modifies deceleration path-tracking accuracy and entire performance of the method. The most adverse effects include exceed of the required deceleration for small masses and increased impacting object's rebound for large masses. Both effects can be effectively mitigated by decreasing the value of valve's time constant T_0.

The effects of **changing the impacting object velocity** (decrease and increase by factor of 1.3) show similar trends to those observed in the case of mass modification, i.e.:

- Decreasing the impacting object's initial velocity causes decrease of the required constant deceleration level, which is exceed during the first part of the control process and not reached during the second part.

- Increasing the impacting object velocity results in higher level of required constant deceleration, its slight exceeding during almost the entire process and increase of rebound.

The entire numerical investigation of the Continuous HPC method reveals that despite the use of larger valve's time constant, the path-tracking accuracy is similar or higher than in the Bi-state HPC method. Moreover, the Continuous HPC method is less sensitive to changes of impacting object's mass and its initial velocity. Finally, the adverse effects such as overshoot of the required deceleration (for small masses and velocities) and increased impacting object rebound (for large masses and velocities) can be effectively mitigated by decreasing the valve's time constant. Therefore, the superiority of the Continuous HPC method in adaptation to various impact scenarios is clearly confirmed.

4 EXPERIMENTAL TESTING OF THE CONTROL METHODS

In order to further investigate the performance of the HPC methods and their dependence on the mass and initial velocity of the impacting object, a number of experiments has been conducted. The tests have been carried out in laboratory conditions using uniquely designed pneumatic adaptive absorber (PAA), which consists of a pneumatic cylinder and a piston connected to a single-sided piston rod. Gas transfer between the internal volumes of the cylinder is provided by fast-actuated valve incorporated inside the piston [10]. The valve's actuation mechanism is based on a multilayer piezoelectric actuator, which enables its full opening or closing within $1\,\mathrm{ms}$ timeframe. The actuator is equipped with a strain gauge sensor, which allows for monitoring of its current elongation and computation of the corresponding valve head displacement. Additionally, the investigated absorber is equipped with two pressure sensors

located inside cylinder volumes, two temperature sensors and displacement encoder measuring position of the piston.

The experiments are conducted using a dedicated laboratory drop test stand, which consists of a drop tower and a guided drop cart which carries the tested absorber and a loading mass. The stand is equipped with an encoder to measure cart displacement, an accelerometer mounted at the drop cart and a load sensor at the bottom interface with the ground. The experimental setup enables efficient implementation of Bi-state and Continuous HPC methods, as well as thorough investigation of the dynamic response of the pneumatic absorber under impact loading.

The exemplary experimental results demonstrate the performance of the system with implemented Bi-state HPC method, in which the control signal is switched between two extreme states. The test parameters are set to $M = 8.9\,\mathrm{kg}$ and $V_0 = 1.4\,\mathrm{m/s}$, closely matching those used in the numerical simulation for the decreased impacting object mass. Fig. 8 presents plots of the measured deceleration of the drop cart, the required deceleration (computed online) and the applied control signal. The experimental results indicate that after the deceleration peak at the beginning of the process, the system successfully tracks the required deceleration path and ensures dissipation of the entire impact energy. Moreover, the characteristic deceleration pattern involving the initial peak followed by fluctuations in the later phase closely resembles the numerical results presented in Fig. 4a. Thus, the example validates the applied approach to system modelling and confirms the correctness of the conclusions drawn from the conducted numerical simulations.

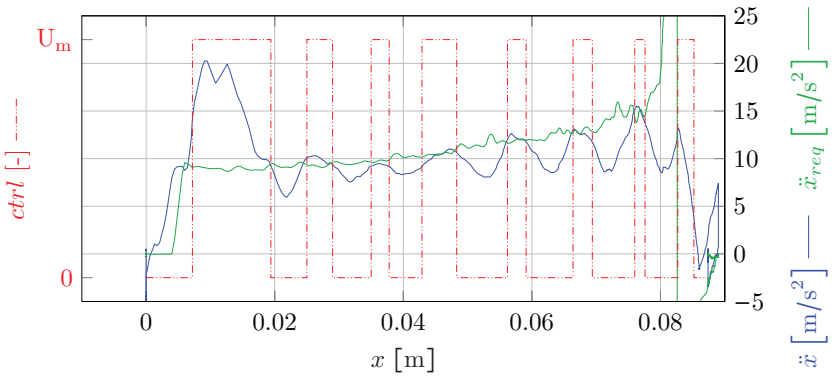

Figure 8: Experimental results of Bi-state HPC operation for $M = 8.9\,\mathrm{kg}$ and $V_0 = 1.4\,\mathrm{m/s}$

5 CONCLUSIONS

The Bi-state HPC and Continuous HPC are two control methods developed for self-adaptive shock absorbers designed to mitigate impact loading. The methods employ different approaches to tracking the required system path (direct tracking of required deceleration and tracking the required valve opening) and use different path-tracking techniques (bi-state control and PI control). The conducted numerical simulations show that Bi-state HPC method performs relatively

well when control system parameters (valve time constant and maximum valve opening) are adjusted to the current impact scenario. However, the path-tracking accuracy deteriorate when the impacting object mass and its initial velocity change, often resulting in a significant exceeding of the required deceleration level.

In contrast, the Continuous HPC method provides efficient tracking of the required system path using a valve with larger time constant and smaller maximum opening. Additionally, the applied path-tracking process demonstrates greater robustness to changes of impacting object mass and its initial velocity, so the method has higher overall adaptation capabilities to diverse impact scenarios. Due to its superiority, the Continuous HPC method constitutes better solution for impact mitigation problems and will be further developed in the future.

REFERENCES

[1] D. Woo, S.-B. Choi, Y. T. Choi, and N. M. Wereley, "Frontal crash mitigation using mr impact damper for controllable bumper," *J. Intell. Mater. Syst. Struct*, vol. 18, no. 12, 2007.

[2] M.-H. Noh and S.-Y. Lee, "Parametric impact performances in a new type crash cushion barrier system using an energy absorption pipe," *Int. J. Crashworthiness*, vol. 25, no. 1, pp. 106–119, 2020.

[3] Y. Chen, W. Chiu, and Y. Chen, "Effect of the shock absorber of the shock absorption benefits for upper arm," in *Mobile and Wireless Technology ICMWT 2018*, K. Kim and K. H., Eds., vol. 513. Singapore: Springer, 2019.

[4] B. Cetinkaya and I. Ozkol, "Evaluation of critical parameters in the design of a trainer aircraft landing gear," in *8th Int. Conf. Mech. Aerosp. Eng. ICMAE 2017*, Prague, Czech Republic, pp. 391–394.

[5] L. Fu, S. Chen, X. Bai, and J. Wang, "Optimal control of aircraft landing gear state feedback based on magneto rheological damper," in *Chinese Control And Decision Conference CCDC 2018*, Shenyang, China, pp. 6673–6676.

[6] C. Han, B.-H. Kang, S.-B. Choi, J. M. Tak, and J.-H. Hwang, "Control of landing efficiency of an aircraft landing gear system with magnetorheological dampers," *J. Aircr.*, vol. 56, pp. 1980–1986, 2019.

[7] M. Makowski and L. Knap, "Reduction of wheel force variations with magnetorheological devices," *Journal of Vibration and Control*, vol. 20, no. 10, pp. 1552–1564, 2014.

[8] H. Du and N. Zhang, "Robust controller design for vehicle semi-active suspensions with electrorheological dampers," in *Proc. of the 48h IEEE Conf. on Decision and Control (CDC) held jointly with 2009 28th Chinese Control Conf.*, Shanghai, China, 2009, pp. 7639–7644.

[9] G. Mikułowski, R. Wiszowaty, and J. Holnicki-Szulc, "Characterization of a piezoelectric valve for an adaptive pneumatic shock absorber," *Smart Materials and Structures*, vol. 22, no. 12, 2013.

[10] G. Mikułowski and R. Wiszowaty, "Pneumatic adaptive absorber: Mathematical modelling with experimental verification," *Mathematical Problems in Engineering*, vol. 2016, no. 7074206, 2016.

[11] L. Knap, M. Makowski, K. Siczek, P. Kubiak, and A. Mrowicki, "Hydraulic vehicle damper controlled by piezoelectric valve," *Sensors*, vol. 23, no. 4, p. 2007, 2023.

[12] L. Knap, C. Graczykowski, and J. Holnicki-Szulc, "Vehicle vibration reduction using hydraulic dampers with piezoelectric valves," *Sensors*, vol. 25, no. 4, p. 1156, 2025.

[13] K. Zhang, S.-T. Cui, Y.-C. Chen, and Z. P. Tang, "Hydraulic shape memory alloy shock absorber: design, analysis, and experiments," *J. Intell. Mater. Syst. Struct.*, vol. 29, p. 1986–1994, 2018.

[14] S. Sivakumar and A. Haran, "Mathematical model and vibration analysis of aircraft with active landing gears," *J. Vib. Control*, vol. 21, no. 2, p. 229–245, 2013.

[15] G. L. Ghiringhelli, "Testing of semi-active landing gear control for a general aviation aircraft," *AIAA J. Aircraft*, vol. 37, p. 606–616, 2000.

[16] C. Graczykowski and R. Faraj, "Development of control systems for fluid-based adaptive impact absorbers," *Mech. Syst. Signal. Process.*, vol. 122, pp. 622–641, 2019.

[17] R. Faraj and C. Graczykowski, "Hybrid prediction control for self-adaptive fluid-based shock-absorbers," *J. Sound Vib.*, vol. 449, p. 427–446, 2019.

[18] R. Faraj, G. Mikułowski, and R. Wiszowaty, "Study on the state-dependent path-tracking for smart pneumatic shock-absorber," *Smart mater. Struct.*, vol. 29, no. 11, 2020.

[19] X. Zeng, G. Li, G. Yin, D. Song, S. Li, and N. Yang, "Model predictive control-based dynamic coordinate strategy for hydraulic hub-motor auxiliary system of a heavy commercial vehicle," *Mech. Syst. Signal Process.*, vol. 101, pp. 97–120, 2018.

[20] C. Graczykowski and R. Faraj, "Identification-based predictive control of semi-active shock-absorbers for adaptive dynamic excitation mitigation," *Meccanica*, vol. 55, pp. 2571–2597, 2020.

[21] ——, "Adaptive impact mitigation based on predictive control with equivalent mass identification," *Sensors*, vol. 23, no. 3, 2023.

XI ECCOMAS Thematic Conference on Smart Structures and Materials - SMART 2025
M. Krommer, M. Nader and M. Schagerl (Eds)

Received: 30 April 2025 / Revised: 4 August 2025 / Accepted: 25 October 2025
© The Author(s) 2025

Localization of Impacts on Thin-Walled Structures by Recurrent Neural Networks: End-to-End Learning from Real-World Data

Alexander Humer, Lukas Grasböck, Ayech Benjeddou

Abstract. Today, machine learning is ubiquitous, and structural health monitoring (SHM) is no exception. Specifically, we address the problem of impact localization on shell-like structures, where knowledge of impact locations aids in assessing structural integrity. Impacts on thin-walled structures excite Lamb waves, which can be measured with piezoelectric sensors. Their dispersive characteristics make it difficult to detect and localize impacts by conventional methods. In the present contribution, we explore the localization of impacts using neural networks. In particular, we propose to use recurrent neural networks (RNNs) to estimate impact positions end-to-end, i.e., directly from sequential sensor data. We deal with comparatively long sequences of thousands of samples, since high sampling rate are needed to accurately capture elastic waves. For this reason, the proposed approach builds upon Gated Recurrent Units (GRUs), which are less prone to vanishing gradients as compared to conventional RNNs. Quality and quantity of data are crucial when training neural networks. Often, synthetic data is used, which inevitably introduces a reality gap. Here, by contrast, we train our networks using physical data from experiments, which requires automation to handle the large number of experiments needed. For this purpose, a robot is used to drop steel balls onto an aluminum plate equipped with piezoceramic sensors. Our results show remarkable accuracy in estimating impact positions, even with a comparatively small dataset.

Key words: Structural Health Monitoring, Impact Localization, Guided Wave Propagation, Recurrent Neural Networks, Robot-Supported Experiments

Alexander Humer
Institute of Technical Mechanics, Johannes Kepler University Linz, Austria, e-mail: alexander.humer@jku.at

Lukas Grasböck
Linz Center of Mechatronics GmbH, Linz, Austria, e-mail: lukas.grasboeck@lcm.at

Ayech Benjeddou
Institut Supérieur de Mécanique de Paris, Saint Ouen, France & Roberval Laboratory, Université de Technologie de Compiègne (UTC), France, e-mail: ayech.benjeddou@isae-supmeca.fr

1 INTRODUCTION

Impact localization on thin-walled structures plays a crucial role in structural health monitoring (SHM) and damage assessment, particularly in aerospace and automotive applications where lightweight and safety-critical components are common. Knowledge of impact locations is essential for assessing structural integrity and detecting potential damage in structures. While this problem has traditionally been approached using blends of physics and data-based methods, recent advances in machine learning have opened new possibilities for more effective solutions, see, e.g., [1].

Mechanical impacts on thin-walled structures generate guided elastic waves—commonly referred to as *Lamb waves* [2], which can be captured using a network of piezoelectric sensors. Accurately determining the location of an impact in such structures, however, remains a challenging task due to the complex propagation characteristics of these waves. Lamb waves are highly dispersive and their behavior is further complicated in non-isotropic materials such as fiber-reinforced polymers, where anisotropy and inhomogeneity introduce additional complexity in wave propagation, see, e.g., [3, 4, 5]. Conventional approaches to impact localization predominantly rely on estimating the time-of-arrival (ToA) of the impact-induced wavefront at several distributed sensors. Classical methods from the field of signal processing include, among several others, continuous wavelet transform, modified energy-ratio and the Akaike information criterion, see, e.g., [6, 7] for an overview. These estimates are then used in triangulation-type algorithms to infer the impact location, see, e.g., [8]. While this methodology has been widely adopted, it typically utilizes only a small portion of the available signal information—namely, the wavefront arrival. The rich signal content that follows, including reflections at structural boundaries and mode conversions, is usually disregarded, despite its potential to enhance localization performance.

Approaches based on different kinds of neural networks can leverage a larger part of the information contained in sensor signals to accurately estimate impact positions. Recent contributions combine fully-connected networks for localization and recurrent structures to reconstruct force histories [9]. Spatio-temporal graph convolutional networks for the localization of impacts on composite plates have been proposed in [10]. The framework of Gaussian processes is used in [11] to account for the inherently probabilistic nature of impact-induced waves in thin-walled structures.

In this work, we propose an alternative approach that aims to exploit the full informational content of the sensor signals by learning to estimate the impact position directly from raw time-series data. In particular, we propose to use *recurrent neural networks* (RNNs) to estimate impact positions *end-to-end*, i.e., directly from *sequential sensor data*. Our central hypothesis is that an end-to-end learning framework can yield more accurate and robust localization results, potentially with fewer sensors than those required in conventional methods. Due to the high sampling rate needed to accurately capture Lamb waves, we deal with comparatively long sequences, which pose a significant challenge when training RNNs. Therefore, we employ more complex network architectures such as Gated Recurrent Units (GRUs) [12], which incorporate

gating mechanisms to manage long-term dependencies more efficiently than standard RNNs.

Quality and quantity of data are crucial when training neural networks. Often, synthetic data is used, which inevitably introduces a reality gap. Here, by contrast, we train our networks using physical data from experiments, which requires automation to handle the large number of experiments needed. For this purpose, a collaborative robot is used to drop steel balls onto an aluminum plate equipped with piezoceramic sensors.

Our results show remarkable accuracy in estimating impact positions, even with a comparatively small dataset. This suggests that the proposed approach effectively leverages the rich information content in Lamb wave signals, potentially offering a more efficient and accurate alternative to conventional impact localization methods.

The present paper is organized as follows: Following this introduction, we briefly outline the network architecture of the proposed estimator. Section 3 introduces the experimental setup for the fully automated generation of training data. The (minimal) data preperation and the training setup are described in Section 4. Results are presented and discussed in Section 5, highlighting the model's performance across different sensor configurations and signal durations. Finally, Section 6 summarizes our findings and outlines directions for future work.

2 METHODOLOGY

2.1 Impact location and sensor signals

The impacts on the plate occur in a target region $T \subset \mathbb{R}^2$. The vector of true positions with respect to some fixed Cartesian frame is denoted by $\boldsymbol{y} = (p_x, p_y)^T \in T$. Let S denote the number of sensors distributed across the structure to be monitored. We assume a fixed sampling rate, i.e., sensors take measurements at equidistant time points t_i, where $i = 1, \ldots, L$. At each time t_i, sensors record signals $x_i^{(j)} \in D$, for $j = 1, \ldots, S$, with D being the range of sensor signals, which are then combined into a vector x_i:

$$\boldsymbol{x}_i = \boldsymbol{x}(t_i) = \left(x^{(1)}(t_i), \ldots, x^{(S)}(t_i)\right)^T \in D \times \ldots \times D \subset \mathbb{R}^S. \tag{1}$$

For notational convenience, sensor signals $\boldsymbol{x}_i$ form the rows of a matrix $\mathbf{X}$,

$$\mathbf{X} = (\boldsymbol{x}_1, \ldots, \boldsymbol{x}_L)^T \in \mathbb{R}^{L \times S}, \tag{2}$$

which represents the complete sensor data over time.

2.2 Model architecture

The proposed location estimator LE is supposed to predict the impact location $\boldsymbol{y}$ from the (temporal) sequence of sensor signals $\mathbf{X}$. In other words, LE maps the (spatio-)temporal patterns in the sensor data to a position in the target region T, which, from a mathematical point of view, translates into

$$LE : \mathbb{R}^{L \times S} \to \mathbb{R}^2 : \quad \mathbf{X} \mapsto \hat{\boldsymbol{y}} = LE(\mathbf{X}), \tag{3}$$

where a hat is introduced for predicted positions. Given the sequential nature of the sensor data $\mathbf{X}$, it is crucial to capture temporal dependencies for accurate predictions. RNNs are a natural choice to represent such an estimator, since, owing to their sequential nature, they are capable of processing variable-length input sequences while maintaining a memory of prior time steps. The memory of an RNN is represented by the hidden state $\boldsymbol{h}_i$, which is computed from the previous hidden state $\boldsymbol{h}_{i-1}$ and the current input $\boldsymbol{x}_i$,

$$\boldsymbol{h}_i = r(\boldsymbol{h}_{i-1}, \boldsymbol{z}_i) \in \mathbb{R}^H, \qquad \boldsymbol{z}_i = \mathbf{W}^{(\mathrm{in})}\boldsymbol{x}_i + \boldsymbol{b}^{(\mathrm{in})}, \qquad \mathbf{W}^{(\mathrm{in})} \in \mathbb{R}^{H\times S},\ \boldsymbol{z}_i, \boldsymbol{b}^{(\mathrm{in})} \in \mathbb{R}^H, \quad (4)$$

where H denotes the dimensionality of the hidden state. Note that we have introduced a linear layer to project the input vector $\boldsymbol{x}_i$ onto a vector $\boldsymbol{z}_i$, which has the same dimension as the hidden state. Following machine learning conventions, $\mathbf{W}^{(\mathrm{in})}$ is referred to as weight-matrix and $\boldsymbol{b}^{(\mathrm{in})}$ denotes the bias vector.

Intuitively, the prediction for the impact location is made once the whole sequence of sensor data has been processed, in our case, by a linear map applied to the final hidden state $\boldsymbol{h}_L$:

$$\hat{\boldsymbol{y}} = \mathbf{W}^{(\mathrm{out})}\boldsymbol{h}_L + \boldsymbol{b}^{(\mathrm{out})}, \qquad \mathbf{W}^{(\mathrm{out})} \in \mathbb{R}^{2\times H}, \boldsymbol{b}^{(\mathrm{out})} \in \mathbb{R}^2. \quad (5)$$

The specific RNN architecture is subject to practical constraints that arise from the particular SHM application of impact monitoring. Lamb waves propagate at comparatively high velocities. For the typical frequencies excited by impacts, the phase velocities of the fundamental anti-symmetric (A_0) mode are 1000 m s^{-1} or higher for the aluminum panel used in our experimental study; see, e.g., [7]. For this reason, high sampling rates are required to capture the propagation of Lamb waves, which implies long sequences of sensor data.

The long input sequences resulting from high sampling rates challenge standard RNNs, which are known to suffer from vanishing gradients when modeling long-term dependencies. GRUs, in contrast, introduce gating mechanisms that control the flow of information to mitigate the problem of vanishing gradients, while maintaining a lower complexity than Long Short-Term Memory (LSTM) [13].

2.3 Loss function and training

The estimator is trained in a supervised manner by minimizing the mean squared error (MSE) between predicted positions $\hat{\boldsymbol{y}}$ and true positions $\boldsymbol{y}$, which serves as natural choice for the loss function. Our initial experiments, however, have shown that the estimator is strongly conditioned to the length of the input sequence if the prediction is made only after the entire sequence has been processed. When training is performed with a fixed sequence length L, the model learns to make accurate predictions only after exactly L time steps, but neither for longer nor for shorter sequences. To address this issue, we modify the training procedure such that the estimator makes intermediate predictions at each time step t_i. By minimizing the loss not only at the end of the sequence, but for every time step, i.e.,

$$\mathrm{MSE} = \frac{1}{L}\sum_{i=1}^{L} \left\|\hat{\boldsymbol{y}}_i - \boldsymbol{y}\right\|^2, \quad (6)$$

the model learns to generalize across variable-length inputs. Using the above loss, we force the estimator to make predictions for every sensor data $\boldsymbol{x}_i$ being processed, so that the length of the training sequence is no longer "learned". This strategy is particularly natural in online monitoring systems, which are meant to provide location estimates continuously, i.e., sample by sample, as new data arrives. That raises the question, of course, what the model predicts prior to the arrival of impact-induced waves at the sensors, i.e., before information on the location of their source becomes is contained in the sensor signals. Initially, the prediction defaults to a mean estimation which reflects the distribution of impact locations in the training data, e.g., the center of the plate if impacts are uniformly distributed.

3 EXPERIMENTAL SETUP

As with any data-driven approach, both the quality and quantity of data are crucial for creating accurate and reliable estimators. Due to the limited availability of real-world data, it has become common practice—particularly in the AI domain—to use synthetic data, especially when training neural networks, which are notorious for their high requirements in terms of data. In physics-related problems, numerical simulation provides effective means to generate synthetic training data, with real-world experiments typically requiring significantly greater expenses. In the present application, however, the situation is different. Owing to the fine temporal and spatial resolution required, simulations of transient Lamb waves that propagate in thin-walled structures are prohibitively demanding in terms of computational efforts to create a reasonable amount of training data. For this reason, physical experiments are key to the realization of the proposed impact localization estimator. As a side effect, we avoid issues related to what is referred to as *reality gap*, i.e., an inevitable modeling error in simulation models.

In the present work, a nearly square aluminum plate measuring $x \times y \times z = 904\,\mathrm{mm} \times 902\,\mathrm{mm} \times 2\,\mathrm{mm}$ serves as an example of a thin-walled structure to be impacted. To capture the propagation of impact-induced waves, eight piezoelectric patch transducers (PI Ceramic P-876.SP1) denoted by S_i, with $i = 1, \ldots, 8$, are bonded to the plate's top surface in a distance of 100 mm from the edges, see Fig. 1 (a). Sensors S_1 – S_4 are placed at the corners of the plate; S_5 – S_8 are located at the centers of the plate's edges. The center positions of the sensors with respect to the global Cartesian frame placed in the upper left corner are listed in Tab. 1. The active area of the patches is 10 mm × 10 mm in size. We want to avoid impacts on or directly

Table 1: Positions of the sensors on the aluminum plate. The coordinates are referring to the centers of the sensor patches.

Coordinates	S_1	S_2	S_3	S_4	S_5	S_6	S_7	S_8
x / mm	100	803	100	803	452	100	803	452
y / mm	100	100	802	802	100	451	451	802

next to the sensors, which is why we leave a margin of 5 mm. The crosshatched region marks the area of potential impacts on the plate. The sensor signals are sampled at 1 MHz using a

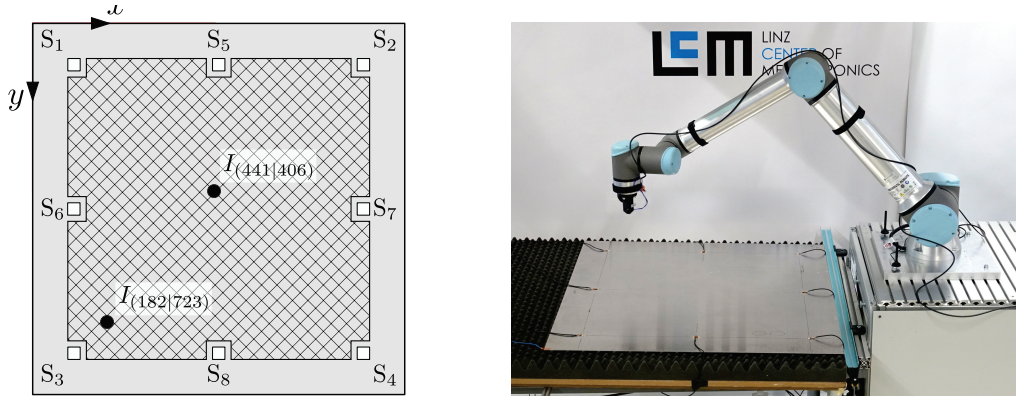

(a) (b)

Figure 1: Experimental setup for impact localization on an aluminum plate: Schematic representation of the plate with the position of the sensors S_j, $j = 1, \ldots, 8$ (a). The crosshatched area indicates the region where impacts are applied. Two example impact positions from the dataset of 5000 impacts are marked as black dots, with their (x, y)-coordinates given in millimeters in parentheses. Picture of the robotic impact test setup used to generate the dataset for training neural networks (b).

National Instruments NI USB-6366 measurement system, which digitizes voltages in the range of ±10 V through a 16-bit analog-to-digital converter, corresponding to an amplitude resolution of 0.31 mV. To protect the data acquisition system from high voltages, a 1:10 probe is used.

To generate a sufficiently large and diverse dataset for training the estimator, a large number of impact events must be recorded. Manual generation of impacts is impractical and prone to inaccuracies in positioning. Therefore, a robotic system is employed to automate the experiments, ensuring precise and repeatable impact locations and enabling efficient collection of high-quality data as needed for training the estimator. For this purpose, a collaborative robot (Universal Robots UR10) is employed, see Fig. 1 (b). An end effector equipped with an electromagnet picks up a steel ball from a designated position and releases it at the precise impact location on the plate. The plate is supported from the bottom by a slightly inclined foam mat (less than 1°), ensuring that, after impact, the ball rolls into a guide rail that returns it to the pickup position, where a magnetic proximity sensor verifies the ball's return before initiating the next drop. The robot operates through a real-time data exchange (RTDE) interface [14].

4 DATA PREPARATION AND TRAINING

Within the present work, balls are dropped from a fixed height of 200 mm onto 5000 random positions sampled from a uniform distribution. Figure 2 shows two representative impacts and the corresponding signals of the corner sensors $\mathrm{S}_1 - \mathrm{S}_4$. The locations of the impacts are shown in Fig. 1. For a rather centered impact (441 mm, 406 mm), sensor signals are relatively similar from a qualitative point of view. The waves excited by the impact arrive at almost the same time

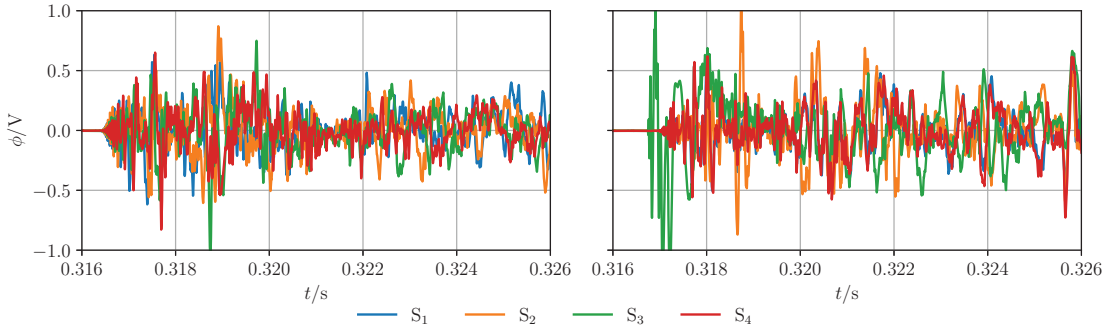

Figure 2: Representative sensor signals: Impacts at a centered position (441 mm, 406 mm) (left) and close to a corner (182 mm, 723 mm) (right).

at the four sensors. For an impact close to a corner (182 mm, 723 mm), the individual sensor signals differ significantly from one another. Unsurprisingly, the sensor closest to the impact (S_3) records waves earlier than the other three sensors. We also note a higher amplitude, since, due to the shorter distance, the waves attenuate less. The peak voltages ϕ are mostly in the range of ±1 V; the maximum voltage occurring in the dataset is 2.21 V. The noise level is three orders of magnitude smaller; we observe constant offsets in the sensor signals of up to 3 mV. Except for a downsampling to 250 kHz, no further processing is applied to the sensor signals.

Measurements are triggered by the robot, which turns off the magnet to drop the steel ball as soon as it reaches the desired position. Between the trigger and the impact on the plate, we see a consistent delay of approximately 316 ms. For efficient training, we do not want to include the entire non-informative pre-impact data. To avoid conditioning the network to a fixed arrival time, we apply a random cropping strategy around the detected signal onset. For each impact, we determine the time t_{th} at which the signal level rises beyond a threshold of 50 mV. We then crop a window of length T from the sensor signals, i.e., $t \in [t_{\mathrm{th}} - t_{\mathrm{shift}}, t_{\mathrm{th}} - t_{\mathrm{shift}} + T]$, where t_{shift} is randomly chosen from the interval $t_{\mathrm{shift}} \in [0.5\,\mathrm{ms}, 2\,\mathrm{ms}]$.

The target positions to be predicted by the estimator are provided in m, which implies that numerical values range from 0.1 to 0.8. No further normalization is applied in what follows. The dataset comprises 4000 impacts for training, 500 for validation (hyperparameter tuning, early stopping) and 500 for testing purposes. The proposed model is implemented in PyTorch [15] and trained on an NVIDIA A30 GPU.

5 RESULTS

The following results aim to demonstrate the feasibility of the proposed end-to-end learning approach for impact localization, rather than to achieve optimal performance through extensive hyperparameter tuning. To this end, we use a baseline model configuration based on empirical estimates that have proven effective in our training experiments. Specifically, the estimator consists of a single GRU layer with an input and hidden size of $H = 32$ ($H = 64$ when using eight sensors). Training is conducted over 5000 episodes using the AdamW optimizer with an

initial learning rate of 1×10^{-2} and a step-wise learning rate decay by a factor of 0.9 every 100 episodes. A fixed batch size of 500 is (mostly) used throughout training; batches are sampled randomly from the training set. Depending on the length T of the crop window, which ranges from 5 ms to 20 ms, the length of the input sequence varies from 1250 to 5000 samples, which is a considerable length in the context of RNNs.

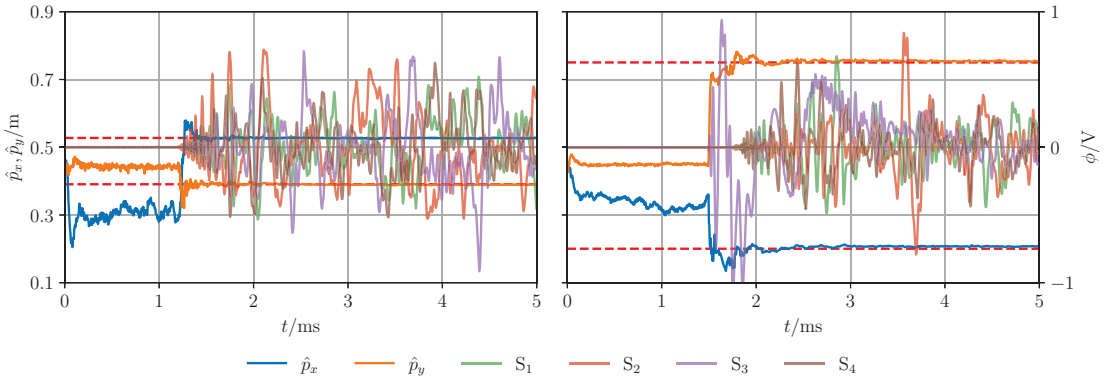

Figure 3: Sequential predictions of impact locations ($S = 4$, $T = 20\,\mathrm{ms}$) for impacts at (527 mm, 391 mm) (left) and (200 mm, 750 mm) (right): Predicted positions $\hat{p}_x$, $\hat{p}_y$ are illustrated along with corresponding input sensor signals $\mathrm{S}_1, \ldots, \mathrm{S}_4$. As long as sensor signals do not contain information on impacts, no meaningful estimates can be made. As impact-induced waves arrive at the sensors, estimated impact locations converge to (and remain at) true positions (red dashed lines).

Figure 3 illustrates the evolution of predicted impact locations $\hat{\boldsymbol{y}}$ over 5 ms as the sensor signals are sequentially processed for two positions of the test set, i.e., (527 mm, 391 mm) (left) and (200 mm, 750 mm) (right), using an estimator trained on $T = 20\,\mathrm{ms}$ sequences recorded by four sensors $\mathrm{S}_1, \ldots, \mathrm{S}_4$. Initially, the sensor signals do not contain any information related to an impact, which is why the predictions fluctuate around seemingly random values. As soon as impact-induced waves arrive at the sensor, the predictions quickly converge to the true positions, which are indicated by red dashed lines, and remain almost constant subsequently. For the second, off-center impact (right), we can observe that the estimator learns to predict impact locations using a single sensor only. Although a sensor signal is only present in S_3 at first, the estimated impact position is already close to the true position before the remaining sensors begin to measure.

Being computed over the entire input sequence, the loss is not an appropriate measure of the estimator's prediction quality. As an intuitive performance metric, we therefore compute the Euclidean distance between the true impact location $\boldsymbol{y}$ and the predicted location $\hat{\boldsymbol{y}}$, which is

averaged over the last $N = 10$ time steps:

$$e = \|\langle\hat{\boldsymbol{y}}\rangle - \boldsymbol{y}\|\,, \qquad \langle\hat{\boldsymbol{y}}\rangle = \frac{1}{N}\sum_{i=L-N}^{L}\hat{\boldsymbol{y}}_i. \tag{7}$$

Figure 4 illustrates the accuracy of our proposed estimator across all impacts in the test set. The true positions of impacts are represented by semi-transparent round markers, while the estimated positions are denoted by crosses. The color coding indicates the Euclidean distance between true and estimated positions, cf. Eq. (7), providing a visual representation of the distribution of the estimation error over the plate structure. For the sake of clarity, the upper limit of the colorbar is set to a value of 25 mm rather than the maximum error in order to emphasize nuances in the variation of the prediction quality. The results are organized in a table where rows correspond to different numbers and configurations of sensors used for prediction, while columns represent different time window lengths, i.e., $T = 5, 10, 20\,\mathrm{ms}$. Specifically, rows in Fig. 4 correspond to: two adjacent sensors $\mathrm{S}_1, \mathrm{S}_2$ in the top row (a)–(c), the four corner sensors S_1 – S_4 in the middle row (d)–(f), and all eight sensors S_1 – S_8 in the bottom row (g)–(i).

When using all eight sensors, the dimensionality of the input per time step increases accordingly. Therefore, the input and hidden size of the GRU cell are both increased to $H = 64$ to account for the larger amount of data that is being processed. For the longest time window ($T = 20\,\mathrm{ms}$), the batch size then has to be reduced for GPU memory constraints; for short windows ($T = 5\,\mathrm{ms}$), we increase the batch size to improve convergence and mitigate overfitting.

Table 2: Impact localization accuracy: Mean error and standard deviation of the position error e for different lengths of the input signals and different numbers of sensors (Note: **bold** values indicate variations from the base model architecture and training setup).

	Sensors	T/ms	L	H	B	mean(e)/mm	std(e)/mm
(a)	1 – 2	5	1250	32	500	9.146	5.845
(b)	1 – 2	10	2500	32	500	7.808	5.445
(c)	1 – 2	20	5000	32	500	6.417	4.945
(d)	1 – 4	5	1250	32	500	8.029	5.263
(e)	1 – 4	10	2500	32	500	6.110	4.941
(f)	1 – 4	20	5000	32	500	5.842	3.941
(g)	1 – 8	5	1250	**64**	**1000**	8.110	5.385
(h)	1 – 8	10	2500	**64**	500	5.902	3.633
(i)	1 – 8	20	5000	**64**	**250**	5.808	3.497

The mean prediction error and its standard deviation over the test set are listed in Tab. 2. Our results reveal a clear and consistent trend: longer input windows generally lead to better localization accuracy. This suggests that the model benefits from later parts of the sensor signals,

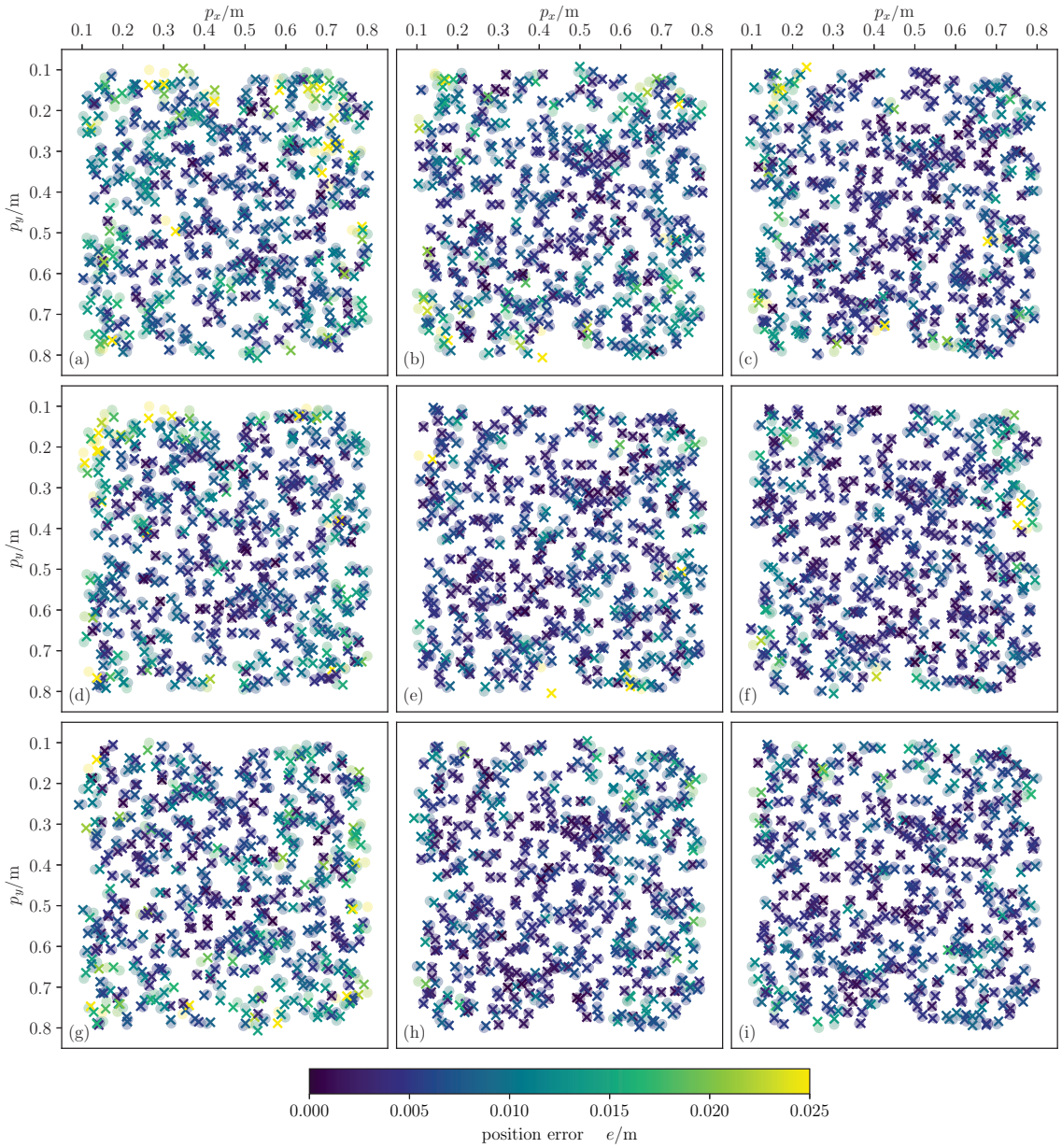

Figure 4: Impact localization accuracy (test set): True positions are indicated by semi-transparent round markers, estimated positions by crosses. Colors respresent the Euclidean distance between true and estimated positions. Rows correspond to the number of sensors used for the prediction ($S = 2, 4, 8$); columns represent different lengths of time windows ($T = 5, 10, 20\,\mathrm{ms}$).

such as reflections and features related to the dispersive nature of Lamb waves, rather than relying solely on the initial wave front. Additionally, using more sensors improves performance, although the gains from increasing the number of sensors from four to eight are relatively modest. Interestingly, even with just two sensors, the estimator is capable of delivering accurate predictions, which is something traditional triangulation approaches typically cannot achieve, since they usually require three sensors at least. We emphasize that the mean position errors are smaller than the dimensions of the piezoelectric patches.

6 CONCLUSION AND OUTLOOK

We presented an end-to-end approach for localizing impacts on thin-walled structures using GRU-based recurrent neural networks. Unlike conventional methods that rely on time-of-arrival estimation, our model learns directly from raw sensor signals and captures both early and late-arriving wave components. Trained entirely on experimental data collected through a robot-assisted setup, the method achieves high localization accuracy—even with a limited dataset and as few as two sensors.

Future work will focus on extending the method to more complex structural scenarios, including composite shells and reinforced structures. We also plan to investigate optimal sensor placement strategies and sensor shapes. Further, we want to explore more advanced network architectures, such as transformers, to further enhance performance of end-to-end impact localization.

REFERENCES

[1] L. Vu-Quoc and A. Humer, "Deep Learning Applied to Computational Mechanics: A Comprehensive Review, State of the Art, and the Classics," *CMES-Computer Modeling in Engineering and Sciences*, vol. 137, no. 2, pp. 1069–1343, 2023.

[2] H. Lamb, "On waves in an elastic plate," *Proceedings of the Royal Society of London. Series A, Containing papers of a mathematical and physical character*, vol. 93, no. 648, pp. 114–128, 1917.

[3] F. Ciampa, M. Meo, and E. Barbieri, "Impact localization in composite structures of arbitrary cross section," *Structural Health Monitoring*, vol. 11, no. 6, pp. 643–655, 2012.

[4] B.-W. Jang, Y.-G. Lee, C.-G. Kim, and C.-Y. Park, "Impact source localization for composite structures under external dynamic loading condition," *Advanced Composite Materials*, vol. 24, no. 4, pp. 359–374, 2015.

[5] D. Xiao, Z. Sharif-Khodaei, and M. Aliabadi, "Hybrid physics-based and data-driven impact localisation for composite laminates," *International Journal of Mechanical Sciences*, vol. 274, p. 109222, 2024.

[6] L. Grasboeck, A. Humer, and A. Benjeddou, "Revisiting multidisciplinary time-of-arrival estimation methods for impact detection on plates," in *Proceedings of the 10th ECCO-*

MAS thematic conference on smart structures and materials, D. Saravanos, A. Benjeddou, N. Chrysochoidis, and T. Theodosiou, Eds., 2023, pp. 107–118.

[7] L. Grasboeck, A. Humer, and A. Benjeddou, "Detection and time-of-arrival estimation of impact-induced waves in composite laminates," *Structural Health Monitoring*, vol. 24, no. 4, pp. 2428–2446, 2025. [Online]. Available: https://doi.org/10.1177/14759217241260848

[8] T. Kundu, "Acoustic source localization," *Ultrasonics*, vol. 54, no. 1, pp. 25–38, 2014.

[9] C. Huang, W. Liao, H. Sun, Y. Wang, and X. Qing, "A hybrid FCN-BiGRU with transfer learning for low-velocity impact identification on aircraft structure," *Smart Materials and Structures*, vol. 32, no. 5, p. 055012, apr 2023.

[10] Z. Zhao and N.-Z. Chen, "Spatial-temporal graph convolutional networks (stgcn) based method for localizing acoustic emission sources in composite panels," *Composite Structures*, vol. 323, p. 117496, 2023.

[11] D. Xiao, Z. Sharif-Khodaei, and M. H. Aliabadi, "Robust impact localisation on composite aerostructures using kernel design and bayesian fusion under environmental and operational uncertainties," 2025. [Online]. Available: https://arxiv.org/abs/2501.18393

[12] K. Cho, B. van Merrienboer, C. Gulcehre, D. Bahdanau, F. Bougares, H. Schwenk, and Y. Bengio, "Learning Phrase Representations using RNN Encoder-Decoder for Statistical Machine Translation," in *Proceedings of the 2014 Conference on Empirical Methods in Natural Language Processing (EMNLP)*, 2014, pp. 1724–1734.

[13] S. Hochreiter and J. Schmidhuber, "Long short-term memory," *Neural Computation*, vol. 9, no. 8, pp. 1735–1780, 1997.

[14] Universal Robots, "Real-Time Data Exchange (RTDE) Guide," 2024.

[15] A. Paszke, S. Gross, F. Massa, A. Lerer, J. Bradbury, G. Chanan, T. Killeen, Z. Lin, N. Gimelshein, L. Antiga, A. Desmaison, A. Köpf, E. Yang, Z. DeVito, M. Raison, A. Tejani, S. Chilamkurthy, B. Steiner, L. Fang, J. Bai, and S. Chintala, "PyTorch: an imperative style, high-performance deep learning library," in *Proceedings of the 33rd International Conference on Neural Information Processing Systems*. Red Hook, NY, USA: Curran Associates Inc., 2019.

XI ECCOMAS Thematic Conference on Smart Structures and Materials - SMART 2025
M. Krommer, M. Nader and M. Schagerl (Eds)

Received: 5 March 2025 / Revised: 15 July 2025 / Accepted: 25 October 2025
© The Author(s) 2025

Unified and Governing Equation for Passive Vibration Control of Buildings via Pole Allocation

Yoshiki Ikeda

Abstract. Pole allocation is applied to a multi-degree-of-freedom stick-shaped shear model with the Kelvin-Voigt/Maxwell damping systems for obtaining new insights into seismic isolation and passive control. As a result, the inverse problem reveals a mathematical equation governing the vibrations of buildings. For seismic isolation, and passive control utilizing a tuned mass damper, interstory viscous dampers or a joint viscous damper, this equation constrains variations in the parameters of control systems by specifying the poles. The equation aids in physically understanding the control effect, and improves the trial-and-error process in the design of passive control. The integration of pole allocation and fixed-point theories directly links structural damping effect with damper capacities. The equation governs dynamic characteristics in earthquake-resistant, seismic isolated and passively controlled structures, playing a significant role in the preliminary design stage.

Key words: Building, Seismic Isolation, Passive Control, Pole Allocation, Governing Equation, Performance-based Design.

1 INTRODUCTION

Pole allocation is consistent with performance-based design, because it assigns control target as natural frequencies and the corresponding damping ratios for a controlled structure. This research obtains new insights into seismic isolation and passive control by applying the pole allocation to a multi-degree-of-freedom (M-DOF) stick-shaped shear model with the Kelvin-Voigt/Maxwell damping systems. As a result, the inverse problem reveals a mathematical equation governing the vibrations of buildings. This equation is expressed in a closed form, and is referred to as the unified and governing equation [1-7]. For seismic isolation, and passive control utilizing a tuned mass damper (TMD), interstory viscous dampers or a joint viscous damper, the equation constrains variations in the control devices' parameters by specifying the poles. In other words, it represents the relationship between the devices' parameters and control effect. The equation aids in physically understanding the control effect, and becomes useful for the preliminary design stage of structural control.

Section 2 introduces the unified and governing equation by applying the pole allocation

Yoshiki Ikeda
Disaster Prevention Research Institute, Kyoto University, Gokasho, Uji, Kyoto 611-0011, Japan
e-mail: ikeda.yoshiki.6r@kyoto-u.ac.jp

method to the M-DOF shear model with the Kelvin-Voigt/Maxwell damping systems [6]. The Maxwell model is utilized to understand the realistic effectiveness of vibration reduction in a building. The model consists of a dashpot and spring in series. The dashpot and spring represent a viscous damper and its joint between the damper and the structural frame, respectively. Subsection 2.1 focuses on interstory viscous damper, and Subsection 2.2 focuses on joint viscous damper. Section 3 describes how the unified equation is utilized in the preliminary design stage of passive control through several applications. Subsection 3.1 reports that the equation is useful for understanding the complex dynamic behavior of interstory seismic isolation using 3-DOF model [1]. Subsection 3.2 proposes a manual optimization for interstory viscous damper based on its minimum joint spring [6]. Subsections 3.3 and 3.4 integrate the unified equation with the classical fixed-point theories for TMD and joint damper, respectively [1, 2, 5]. The integration directly links damping effect with the damper capacities. Subsection 3.5 clarifies difference between the Kelvin-Voigt and Maxwell models in joint damper [7].

2 UNIFIED EQUATION GOVERNING PASSIVE VIBRATION CONTROL

2.1 Interstory viscous damper

Pole allocation is applied to an M-DOF linear model shown in Figure 1 [6]. The figure illustrates a damped building passively controlled by interstory viscous dampers, which are utilizing the Maxwell model.

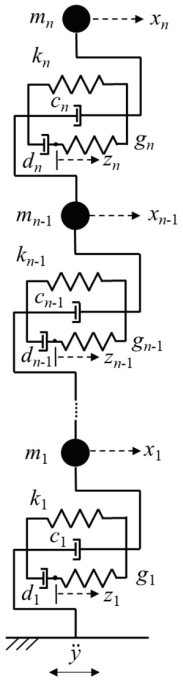

n : total number of lumped masses
m_i : the i-th lumped mass
k_i : shear stiffness in the i-th story
c_i : damping coefficient in parallel to k_i
d_i : damping coefficient of the viscous damper installed in the i-th story in the Maxwell model
g_i : spring of element jointing the viscous damper in the i-th story in the Maxwell model
x_i : displacement of the i-th lumped mass with respect to the base
z_i : displacement relative to the base at a point between d_i and g_i
$\ddot{y}$: ground input acceleration to the building

Figure 1: Building model with Kelvin-Voigt and Maxwell elements for interstory viscous damper

The equations of motion for the model are expressed as follows.

$$M\ddot{x} + C\dot{x} + (K+E)x - Ez = -Me_n\ddot{y} \text{ and } D\dot{z} = F\dot{x} + G(x-z) \tag{1}$$

where,

$$x^T = \{x_n \quad x_{n-1} \quad x_{n-2} \quad \cdots \quad x_2 \quad x_1\} \text{ and } z^T = \{z_n \quad z_{n-1} \quad z_{n-2} \quad \cdots \quad z_2 \quad z_1\} \tag{2}$$

$$M = \begin{bmatrix} m_n & 0 & 0 & \cdots & 0 & 0 \\ 0 & m_{n-1} & 0 & \cdots & 0 & 0 \\ 0 & 0 & m_{n-2} & \cdots & 0 & 0 \\ \vdots & \vdots & \vdots & \ddots & \vdots & \vdots \\ 0 & 0 & 0 & \cdots & m_2 & 0 \\ 0 & 0 & 0 & \cdots & 0 & m_1 \end{bmatrix}, \quad C = \begin{bmatrix} c_n & -c_n & 0 & \cdots & 0 & 0 \\ -c_n & c_n + c_{n-1} & -c_{n-1} & \cdots & 0 & 0 \\ 0 & -c_{n-1} & c_{n-1} + c_{n-2} & \cdots & 0 & 0 \\ \vdots & \vdots & \vdots & \ddots & \vdots & \vdots \\ 0 & 0 & 0 & \cdots & c_3 + c_2 & -c_2 \\ 0 & 0 & 0 & \cdots & -c_2 & c_2 + c_1 \end{bmatrix},$$

$$K = \begin{bmatrix} k_n & -k_n & 0 & \cdots & 0 & 0 \\ -k_n & k_n + k_{n-1} & -k_{n-1} & \cdots & 0 & 0 \\ 0 & -k_{n-1} & k_{n-1} + k_{n-2} & \cdots & 0 & 0 \\ \vdots & \vdots & \vdots & \ddots & \vdots & \vdots \\ 0 & 0 & 0 & \cdots & k_3 + k_2 & -k_2 \\ 0 & 0 & 0 & \cdots & -k_2 & k_2 + k_1 \end{bmatrix}, \quad G = \begin{bmatrix} g_n & 0 & 0 & \cdots & 0 & 0 \\ 0 & g_{n-1} & 0 & \cdots & 0 & 0 \\ 0 & 0 & g_{n-2} & \vdots & 0 & 0 \\ \vdots & \vdots & \vdots & \ddots & \vdots & \vdots \\ 0 & 0 & 0 & \cdots & g_2 & 0 \\ 0 & 0 & 0 & \cdots & 0 & g_1 \end{bmatrix},$$

$$D = \begin{bmatrix} d_n & 0 & 0 & \cdots & 0 & 0 \\ 0 & d_{n-1} & 0 & \cdots & 0 & 0 \\ 0 & 0 & d_{n-2} & \vdots & 0 & 0 \\ \vdots & \vdots & \vdots & \ddots & \vdots & \vdots \\ 0 & 0 & 0 & \cdots & d_2 & 0 \\ 0 & 0 & 0 & \cdots & 0 & d_1 \end{bmatrix}, \quad E = \begin{bmatrix} g_n & 0 & 0 & \cdots & 0 & 0 \\ -g_n & g_{n-1} & 0 & \cdots & 0 & 0 \\ 0 & -g_{n-1} & g_{n-2} & \cdots & 0 & 0 \\ \vdots & \vdots & \vdots & \ddots & \vdots & \vdots \\ 0 & 0 & 0 & \cdots & g_2 & 0 \\ 0 & 0 & 0 & \cdots & -g_2 & g_1 \end{bmatrix}, F = \begin{bmatrix} 0 & d_n & 0 & \cdots & 0 & 0 \\ 0 & 0 & d_{n-1} & \cdots & 0 & 0 \\ 0 & 0 & 0 & \cdots & 0 & 0 \\ \vdots & \vdots & \vdots & \ddots & \vdots & \vdots \\ 0 & 0 & 0 & \cdots & 0 & d_2 \\ 0 & 0 & 0 & \cdots & 0 & 0 \end{bmatrix}$$

$$\text{and } e_n^T = \{1 \quad 1 \quad 1 \quad \cdots \quad 1 \quad 1\} \tag{3}$$

Equations (1) are transformed into the state equation (4).

$$\begin{Bmatrix} \ddot{x} \\ \dot{x} \\ \dot{z} \end{Bmatrix} = \begin{bmatrix} A_{11} & A_{12} & A_{13} \\ I_{n\times n} & O_{n\times n} & O_{n\times n} \\ A_{31} & A_{32} & A_{33} \end{bmatrix} \begin{Bmatrix} \dot{x} \\ x \\ z \end{Bmatrix} + \begin{Bmatrix} e_n \\ o_n \\ o_n \end{Bmatrix} \ddot{y} \tag{4}$$

Where $I_{n\times n}$ is the $n\times n$ unit sub-matrix, $O_{n\times n}$ is the $n\times n$ zero sub-matrix, o_n is the n-dimensional zero vector, and e_n is the n-dimensional vector where each element is a unit. Six sub-matrices A_{11}, A_{12}, A_{13}, A_{31}, A_{32} and A_{33} can be obtained from Equations (3).

By defining s as a pole of the system matrix in Equation (4), the characteristic equation of the system is introduced as a $3n$-dimensional algebraic equation in terms of s. Then, the coefficients of the linear and constant terms for s are introduced as the following equations.

$$\text{The linear term: } (-1)^n \prod_{j=1}^{n} \frac{k_j g_j}{d_j m_j} \sum_{i=1}^{n} \left(\frac{c_i + d_i}{k_i} + \frac{d_i}{g_i} \right) \text{ and the constant term: } (-1)^n \prod_{j=1}^{n} \frac{k_j g_j}{d_j m_j} \tag{5}$$

The pole allocation represents the characteristic equation for control target as Equation (6).

$$\prod_{j=1}^{n}(s^2+2h_j\omega_j s+\omega_j^2)(s+h_{j*}\omega_j)=0 \tag{6}$$

Where ω_j is the natural circular frequency in the j-th mode, h_j is the corresponding damping ratio, and h_{j*} is the damping ratio of the damper. The coefficients of the linear and constant terms for s are introduced as the following equations.

$$\text{The linear term: } \prod_{j=1}^{n}(h_{j*}\omega_j^3)\sum_{i=1}^{n}(\frac{1}{h_{i*}\omega_i}+\frac{2h_i}{\omega_i}) \text{ and the constant term: } \prod_{j=1}^{n}(h_{j*}\omega_j^3) \tag{7}$$

The pole allocation requires Equations (7) align Equations (5).

$$(-1)^n\prod_{j=1}^{n}\frac{k_j g_j}{d_j m_j}\sum_{i=1}^{n}(\frac{c_i+d_i}{k_i}+\frac{d_i}{g_i})=\prod_{j=1}^{n}(h_{j*}\omega_j^3)\sum_{i=1}^{n}(\frac{1}{h_{i*}\omega_i}+\frac{2h_i}{\omega_i}) \tag{8}$$

$$(-1)^n\prod_{j=1}^{n}\frac{k_j g_j}{d_j m_j}=\prod_{j=1}^{n}(h_{j*}\omega_j^3) \tag{9}$$

Dividing Equation (8) by Equation (9) yields Equation (10). In this research, it is called the unified equation governing the model parameters.

$$\sum_{i=1}^{n}(\frac{c_i+d_i}{k_i}+\frac{d_i}{g_i})=\sum_{j=1}^{n}(\frac{1}{h_{j*}\omega_j}+\frac{2h_j}{\omega_j}) \tag{10}$$

When d_i is zero and h_{j*} becomes infinite, the equation can be simplified into the equation only for the Kelvin-Voigt model [3, 4].

2.2 Joint viscous damper

Pole allocation is also applied to a 2.5-DOF linear model shown in Figure 2 [7]. The figure

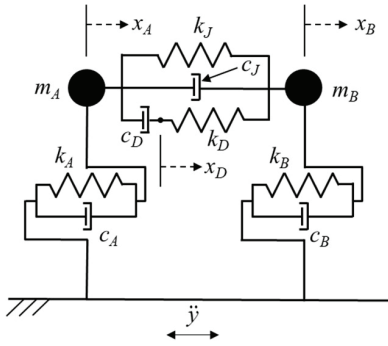

m_A : lumped mass of Building A
k_A : shear stiffness of Building A
c_A : damping coefficient of Building A
m_B : lumped mass of Building B
k_B : shear stiffness of Building B
c_B : damping coefficient of Building B
k_J : joint spring in the Kelvin-Voigt model
c_J : damping coefficient of the damper in the Kelvin-Voigt model
k_D : joint spring in the Maxwell model
c_D : damping coefficient of the damper in the Maxwell model
x_A : displacement of Buildings A relative to the base
x_B : displacement of Buildings B relative to the base
x_D : displacement relative to the base at a point between k_D and c_D

Figure 2: Building model with Kelvin-Voigt and Maxwell elements for joint viscous damper

illustrates two S-DOF damped buildings passively controlled by a viscous joint damper, which is utilizing the Kelvin-Voigt and Maxwell models.

The state equation can be expressed by the following equation.

$$\begin{Bmatrix} \ddot{x}_A \\ \ddot{x}_B \\ \dot{x}_A \\ \dot{x}_B \\ \dot{x}_D \end{Bmatrix} = \begin{bmatrix} -(c_A+c_J)/m_A & c_J/m_A & -(k_A+k_J)/m_A & (k_J+k_D)/m_A & -k_D/m_A \\ c_J/m_B & -(c_B+c_J)/m_B & k_J/m_B & -(k_B+k_J+k_D)/m_B & k_D/m_B \\ 1 & 0 & 0 & 0 & 0 \\ 0 & 1 & 0 & 0 & 0 \\ 1 & 0 & 0 & k_D/c_D & -k_D/c_D \end{bmatrix} \begin{Bmatrix} \dot{x}_A \\ \dot{x}_B \\ x_A \\ x_B \\ x_D \end{Bmatrix} - \begin{Bmatrix} 1 \\ 1 \\ 0 \\ 0 \\ 0 \end{Bmatrix} \ddot{y} \tag{11}$$

When the characteristic equation is introduced from the system matrix in Equation (11), the coefficients of the linear and constant terms for s become the following equations.

$$\text{The linear term: } \{k_D(c_Ak_B+c_Bk_A+c_Ak_J+c_Bk_J+c_Jk_A+c_Jk_B)/c_D+k_Ak_B+k_Bk_J+k_Ak_J+k_Dk_A+k_Dk_B\}/(m_Am_B)$$
$$\text{and the constant term: } k_D(k_Ak_B+k_Bk_J+k_Ak_J)/(c_Dm_Am_B) \tag{12}$$

Similarly to Equation (6), the target characteristic equation is represented as follows.

$$(s^2+2h_1\omega_1 s+\omega_1^2)(s^2+2h_2\omega_2 s+\omega_2^2)(s+h_3\omega_3)=0 \tag{13}$$

Where ω_3 and h_3 are newly defined as the apparent natural circular frequency and damping ratio in the damper's mode. However, the mode is not vibrated. In Equation (13), the coefficients of the linear and constant terms for s become the following equations.

$$\text{The linear term: } \omega_1^2\omega_2^2+2h_3\omega_1\omega_2\omega_3(h_2\omega_1+h_1\omega_2) \text{ and the constant term: } h_3\omega_1^2\omega_2^2\omega_3 \tag{14}$$

The pole allocation requires Equations (14) align Equations (12).

$$\begin{aligned} &\{k_D(c_Ak_B+c_Bk_A+c_Ak_J+c_Bk_J+c_Jk_A+c_Jk_B)/c_D+k_Ak_B+k_Bk_J+k_Ak_J+k_Dk_A+k_Dk_B\}/(m_Am_B) \\ &=\omega_1^2\omega_2^2+2h_3\omega_1\omega_2\omega_3(h_2\omega_1+h_1\omega_2) \end{aligned} \tag{15}$$

$$k_D(k_Ak_B+k_Bk_J+k_Ak_J)/(c_Dm_Am_B)=h_3\omega_1^2\omega_2^2\omega_3 \tag{16}$$

Dividing Equation (15) by Equation (16) yields the unified equation (17).

$$\frac{c_A(k_B+k_J)+c_B(k_A+k_J)+c_J(k_A+k_B)+c_D(k_A+k_B)}{k_Ak_B+k_Bk_J+k_Ak_J}+\frac{c_D}{k_D}=2\left(\frac{h_1}{\omega_1}+\frac{h_2}{\omega_2}\right)+\frac{1}{h_3\omega_3} \tag{17}$$

3 APPLICATIONS TO DESIGN OF PASSIVE CONTROL

3.1 Understanding dynamic behavior of interstory seismic isolation via 3-DOF model

Table 1 indicates three 10-DOF models with the Kelvin-Voigt damping systems: $n=10$, $d_i=0$ and $h_{j*}\to\infty$ in Equation (10). Each model has a 5-DOF lower substructure, a 5-DOF upper substructure, and a interstory where the isolator and damper are installed. The upper substructure includes the isolation story. This model resembles the 10-DOF models applied to investigate the modal coupling between upper and lower substructures [8].

The weight of each lumped mass is 1.0×10^6 kg. The stiffness values from k_1 to k_5 are fixed

Table 1: Stiffness and damping values for three 10-DOF models with interstory isolation [1]

Story	Stiffness k_i (kN/m)			Damping ratio
	Model A	Model B	Model C	
10	310,870	388,340	907,120	2 % in the 2nd mode of the upper substructure including isolation story. Its damping sub-matrix is proportional to the corresponding stiffness matrix.
9	318,720	397,170	914,960	
8	328,520	406,980	921,830	
7	338,330	416,780	931,630	
6 Isolation	12,337			20 % at 0.25 Hz The natural frequency of the upper substructure is fixed as 0.25 Hz when it is assumed to be rigid.
5	1,814,200			2 % at 2.0 Hz The 1st natural frequency of the lower substructure is fixed as 2.0 Hz. Its damping sub-matrix is proportional to the corresponding stiffness matrix.
4	1,853,460			
3	1,902,490			
2	1,961,330			
1	2,010,360			

Table 2: Natural frequencies and damping ratios of 10-DOF models with interstory isolation [1]

Mode	Model A		Model B		Model C	
	Frequency (Hz)	Damping ratio (%)	Frequency (Hz)	Damping ratio (%)	Frequency (Hz)	Damping ratio (%)
1	0.242	17.9	0.243	18.2	0.245	18.7
2	1.830	5.2	1.985	2.0	2.033	6.4
3	1.997	8.0	2.043	10.7	2.992	5.1
4	3.371	5.7	3.756	5.5	5.686	4.5
5	4.636	5.9	5.167	5.9	5.754	7.6

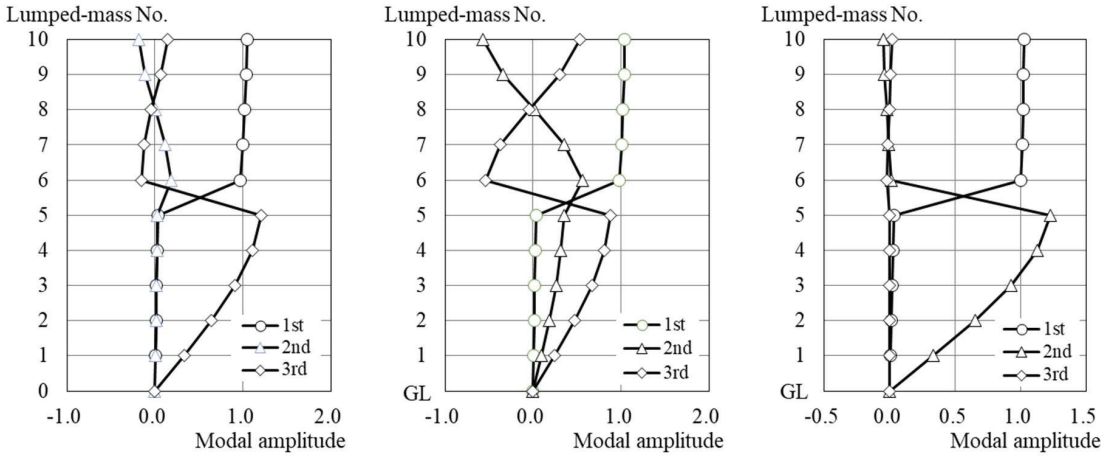

(a) Model A (b) Model B (c) Model C

Figure 3: Modal shapes with excitations' participation factors of 10-DOF models with interstory isolation [1]

such that the 1st natural frequency of the lower substructure is 2.0 Hz. k_6 and c_6 represent the isolator's stiffness and damper damping coefficient, respectively. k_6 is fixed, so that the

natural frequency of the isolator is 0.25 Hz when the upper substructure is assumed to be rigid c_6 is fixed as 3,142 kNs/m, so that the damping ratio of the damper is 20 % under the above rigidity assumption. The damping ratio for the lower substructure is 2 % at 2.0 Hz. Three models are prepared for the upper substructure, so that the 2nd natural frequencies are 1.8 Hz for Model A, 2.0 Hz for Model B, and 3.0 Hz for Model C. A comparison of the three models reveals that the only changeable dynamic property is the ratio of the 2nd natural frequency of the upper substructure to the 1st natural frequency 2.0 Hz of the lower substructure. In the upper substructure, the 1st natural frequency forms the dominant mode in the interstory.

Figure 3 illustrates the lowest three modal shapes with excitations' participation factors, and Table 2 indicates the natural frequencies and damping ratios. Larger interstory drifts are observed in the 1st modes of all the models. In Model B, the modal amplitudes in the 2nd and 3rd modes are larger than those in Model A in the upper substructure, and the 2nd mode stimulates the lower substructure. Table 2 clearly shows that the mode with a small interstory drift cannot accept a high damper capacity in the interstory. This is the so-called modal coupling/interaction problem to be considered in interstory seismic isolation.

Setting $n=3$, $d_i=0$ and $h_{j*}\to\infty$ in Equation (10) leads Equation (18) for a 3-DOF model representing interstory isolation. In general, c_2 in the isolation story is much larger than c_1 and c_3 in the lower and upper substructures, which can neglect c_1 and c_3. For the isolated story, ω_I and h_I are defined as the natural circular frequency and the corresponding damping ratio, respectively, which introduces $\omega_I^2=k_2/(m_2+m_3)$ and $2h_I\omega_I=c_2/(m_2+m_3)$.

$$\frac{c_2}{2k_2}=\frac{h_I}{\omega_I}=\frac{h_1}{\omega_1}+\frac{h_2}{\omega_2}+\frac{h_3}{\omega_3} \tag{18}$$

Even if the lowest three modes in Table 2 are considered, the right side (80.99 %/Hz for Model A, 81.04 %/Hz for Model B, or 81.07 %/Hz for Model C) approximately agrees with the left side (20/0.25 = 80.00 %/Hz) in Equation (18). The equation implies a trade-off relationship between the damping in the 2nd and 3rd modes. The isolator and damper in the isolation interstory constrain the sum of damping ratios in the three vibration modes.

3.2 Design of interstory viscous dampers using minimum joint spring

Figure 4 illustrates a 1.5-DOF model with a viscous damper represented by the Maxwell model. ω_1/ω_0 is the frequency ratio of the controlled model to the uncontrolled one, and h_1 is the target damping ratio in the 1st mode. The minimum joint spring existed when the modal structural damping is constant [6]. By simplifying Equation (10) into Equation (19), the minimum spring can be applied to the model in Figure 1. Then, a damping ratio in the 1st mode is considered in each story, and the equation is the same as that for 1.5-DOF model.

$$\frac{c_i+d_i}{k_i}+\frac{d_i}{g_i}=\frac{1}{h_{1*}\omega_1}+\frac{2h_1}{\omega_1} \tag{19}$$

Now, ω_{01} and h_{01} are defined as the natural circular frequency and damping ratio in the 1st mode of a building before the dampers are installed. ω_1 and h_1 are defined as the natural

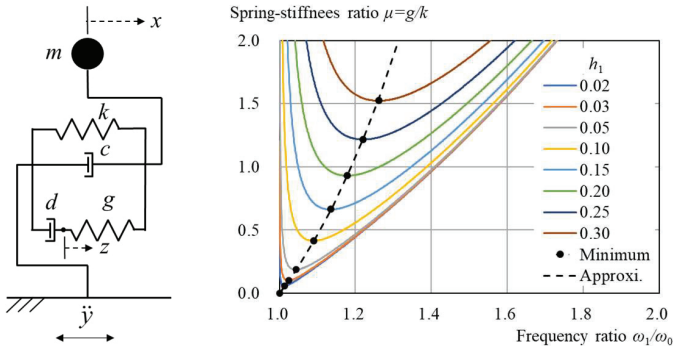

Figure 4: 1.5-DOF model and the minimum joint spring for a viscous damper [6]

Table 3: Structural parameters for 10-DOF model without viscous dampers [6]

Lumped mass no.	Mass m_i (10^3kg)	Story	Stiffness k_i (MN/m)	Damping coefficient c_i (MNs/m)
10	600	10	318.7	1.090
9	450	9	367.7	1.257
8	450	8	441.3	1.509
7	450	7	514.8	1.760
6	470	6	588.4	2.012
5	470	5	656.5	2.347
4	490	4	784.5	2.682
3	510	3	882.6	3.018
2	560	2	980.7	3.353
1	550	1	1078.7	3.688

Table 4: Natural frequencies and modal damping ratios of 10-DOF model without viscous dampers [6]

Mode no.	Natural frequency (Hz)	Damping ratio (%)
1	0.931	1.00
2	2.389	2.57
3	3.887	4.18
4	5.344	5.74
5	6.686	7.18

Table 5: Optimized parameters for dampers represented by Maxwell models [6]

Story	Joint spring g_i (MN/m)	Damper's damping coefficient d_i (MNs/m)
10	125.6	17.98
9	145.0	20.75
8	174.0	24.90
7	203.0	29.05
6	231.9	33.19
5	270.6	38.73
4	309.3	44.26
3	347.9	49.79
2	386.6	55.32
1	425.2	60.86

Table 6: Natural frequencies and modal damping ratios of 10-DOF model with viscous dampers [6]

Mode no.	Natural frequency (Hz)	Damping ratio (%)
1	1.020	10.0
2	2.784	7.5
3	4.573	6.9
4	6.305	7.4
5	7.897	8.1

circular frequency and damping ratio after the dampers are installed. In the optimization, once h_1 is determined, ω_1/ω_{01} is given by Equation (20). Equations (21) provides g_i for the joint spring and d_i for the damping coefficient of dashpot in the Maxwell model in the *i*-th story.

$$\lambda = \omega_1/\omega_{01} = \sqrt{1+2h_1} \text{ and } h_{1*} = 2(h_1 - h_{01}/\lambda)/(\lambda^2-1) \tag{20}$$

$$g_i/k_i = (2h_1h_{1*}+1)\lambda^2 - 2h_{01}h_{1*}\lambda^3 - 1 \text{ and } d_i/g_i = 1/(h_{1*}\omega_1\lambda^2) \tag{21}$$

For an example, Table 3 lists the lumped masses, shear stiffness values, and damping coefficients. The damping matrix is proportional to the stiffness matrix with the damping ratio 1 % for the 1st mode. Table 4 lists the modal information. When h_1 is set as 10 %, ω_1/ω_{01} becomes 1.095 using Equation (20). Table 5 lists g_i and d_i for each viscous damper, and Table 6 shows the modal information for the controlled model. The comparison of Tables 4 and 6 reveals damping effect not only in the 1st mode but also from the 2nd to 5th modes.

3.3 Integration of the unified equation with the fixed-point theory for TMD

When a TMD controls an S-DOF undamped building model, Equation (18) is furthermore simplified for a 2-DOF model into Equation (22).

$$\frac{c_2}{2k_2} = \frac{h_T}{\omega_T} = \frac{h_1}{\omega_1} + \frac{h_2}{\omega_2} \tag{22}$$

Where ω_T and h_T are the natural circular frequency and damping ratio of the TMD, respectively, which introduces $\omega_T^2 = k_2/m_2$ and $2h_T\omega_T = c_2/m_2$. When ω_S ($=\sqrt{k_1/m_1}$) is the natural circular frequency of the S-DOF building and μ ($=m_2/m_1$) is the mass ratio of TMD to building, the fixed-point theory [9] proposes the optimal frequency and damping ratios.

$$\text{The frequency ratio: } \omega_T/\omega_S = 1/(1+\mu) \text{ and the damping ratio: } h_T = \sqrt{3\mu/8/(1+\mu)} \tag{23}$$

The fixed-point theory derives two natural circular frequencies ω_1 and ω_2.

$$\omega_1, \omega_2 = \omega_S\sqrt{\frac{1 \mp \sqrt{\frac{\mu}{2+\mu}}}{1+\mu}} \tag{24}$$

This optimization proposes ω_T for the auxiliary mass and h_T for the damper from μ, while it does not predict the additional damping ratio for the structure directly. The optimization

process does not respond well to the fact that the additional damping is a significant interst in the TMD design. The similar optimizations might design the TMD through trial and error.

When the target damping ratios in both the modes are equal to h ($h = h_1 = h_2$), substituting Equations (23) and (24) into Equation (22) introduces the target h via the Taylor series approximation.

$$h = \sqrt{\frac{3\mu}{4(2+\mu)}} \Big/ \left\{ \sqrt{1-\sqrt{\frac{\mu}{2+\mu}}} + \sqrt{1+\sqrt{\frac{\mu}{2+\mu}}} \right\} \approx \frac{1}{4}\sqrt{\frac{3\mu}{2+\mu}} \Rightarrow \mu = \frac{32h^2}{3-16h^2} \tag{25}$$

Under the optimal tuning by Den Hartog [9], Equation (25) provides the additional damping ratio h via the mass ratio μ. The last equation obtains μ after h is determined as shown in Figure 5(a), and the introduced μ leads ω_T and h_T via Equation (23). The pole allocation for TMD matches the performance-based design.

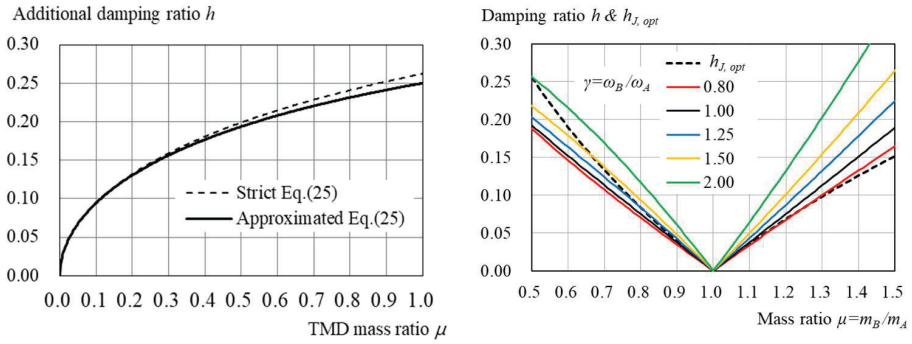

(a) TMD (b) Joint damper

Figure 5: Additional damping ratios via the integration of the unified equation and fixed-point theories [1, 2, 5]

3.4 Integration of the unified equation with the fixed-point theory for joint damper

When a joint damper represented by a dashpot controls two S-DOF undamped adjacent building model, c_A, c_B, c_D and k_J become zero and h_3 become infinite in Equation (17). The equation is simplified into Equation (26).

$$\frac{c_J(k_A+k_B)}{2k_Ak_B} = \frac{h_1}{\omega_1} + \frac{h_2}{\omega_2} \tag{26}$$

By defining μ as m_B/m_A, the fixed-point theory [10] proposes the optimal damping ratio $h_{J,opt}$ for the joint damper as Equation (27) [5].

$$h_{J,opt} = \frac{c_{J,opt}}{2m_B\omega_B} = \frac{|1-\mu|}{4(1+\mu)\sqrt{2(1+\mu)}}\left(2+\mu+\frac{1+2\mu}{\sqrt{\mu}}\right) \tag{27}$$

When ω_A and ω_B are the natural circular frequencies of buildings without a joint damper, the following equations are intoduced via $\omega_A^2 = k_A/m_A$, $\omega_B^2 = k_B/m_B$ and $\gamma = \omega_B/\omega_A$.

$$c_{J,opt} = 2m_B\omega_B h_{J,opt} = 2\mu\gamma m_A\omega_A h_{J,opt} \text{ and } \frac{k_A k_B}{k_A + k_B} = \frac{\mu\gamma^2}{1+\mu\gamma^2} m_A\omega_A^2 \tag{28}$$

Substituting Equations (27) and (28) in Equation (26) and providing two buildings with the same damping ratio ($h = h_1 = h_2$) yield Equation (29). Then, the natural frequencies ω_1 and ω_2 approximately equal ω_A and ω_B, respectively, when both the buildings are connected by only a dashpot. This leads the relationship between $h_{J,opt}$ and h.

$$\frac{1+\mu\gamma^2}{\gamma}\frac{h_{J,opt}}{\omega_A} = h\left(\frac{1}{\omega_A} + \frac{1}{\omega_B}\right) \tag{29}$$

$$h = \frac{1+\mu\gamma^2}{1+\gamma} h_{J,opt} = \frac{(1+\mu\gamma^2)|1-\mu|}{4(1+\gamma)(1+\mu)\sqrt{2(1+\mu)}}\left(2+\mu+\frac{1+2\mu}{\sqrt{\mu}}\right) \tag{30}$$

Based on Equation (30), Figure 5(b) shows that h can be directly estimated from $h_{J,opt}$.

3.5 Difference between Kelvin-Voigt and Maxwell models for Joint Damper

As described in Subsection 3.4, assuming $c_A = c_B = c_D = k_J = 0$ and $h = h_1 = h_2$ in Equation (17) manages only the dashpot c_J in Equation (31). While assuming $c_A = c_B = c_J = k_J = 0$ and $h = h_1 = h_2$ in Equation (17) manages only the Maxwell model in Equation (32).

$$\frac{1}{2}\frac{c_J(k_A + k_B)}{k_A k_B} = h\left(\frac{1}{\omega_1} + \frac{1}{\omega_2}\right) \tag{31}$$

$$\frac{1}{2}\left\{\frac{c_D(k_A + k_B)}{k_A k_B} + \frac{c_D}{k_D}\right\} = h\left(\frac{1}{\omega_1} + \frac{1}{\omega_2}\right) + \frac{1}{2h_3\omega_3} \tag{32}$$

When the relaxation time $\tau = c_D / k_D$ and $c_D / m_B = 2h_D\omega_B$ are newly introduced, the difference between Equations (31) and (32) is expressed as Equations (33) [7].

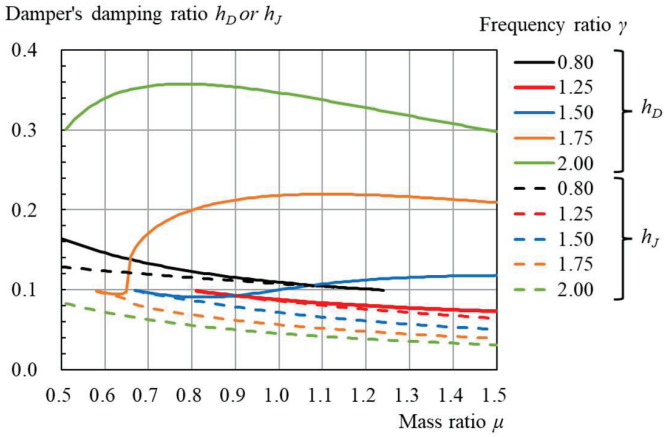

Figure 6: Comparison of two joint dampers' capacities (h =10%, ω_A=2π) [7]

$$(c_D - c_J)\frac{k_A + k_B}{k_A k_B} = \frac{1}{h_3\omega_3} - \tau \;\Rightarrow\; h_D - h_J = \frac{\omega_A \gamma}{2(1+\mu\gamma^2)}\left(\frac{1}{h_3\omega_3} - \tau\right) \tag{33}$$

where,

$$h_3\omega_3 = \{2h(\omega_1 + \omega_2)\omega_A^2\omega_B^2\}/(\omega_1^2\omega_2^2 - \omega_A^2\omega_B^2) \text{ and } \tau = (\omega_A\omega_B/\omega_1\omega_2)^2/h_3\omega_3 \tag{34}$$

ω_1 and ω_2 are obtained from a quintic algebratic equation and the supplemental equation [7].

4 CONCLUSIONS

The introduced unified equation governs dynamic characteristics in earthquake-resistant, seismically isolated and passively controlled structures, playing a significant role in the preliminary design stage of structural control. The advantages are described for interstory seismic isolation, interstory viscous damper, TMD, and joint viscous damper.

ACKNOWLEDGEMENTS

This study was supported by JSPS KAKENHI (Grant No.23K04344). The authors appreciate the financial support received.

REFERENCES

[1] Y. Ikeda, “Fundamental equation based on pole allocation for interstory seismic isolation of buildings”, *Structural Control and Health Monitoring*, vol. 28, no. 3, Mar., 2021. [Online]. Available: https://doi.org/10.1002/stc.2687 [Accessed Feb. 28, 2025].

[2] Y. Matsumoto and Y. Ikeda, “Unified understanding of base seismic isolation, interstory seismic isolation and tuned mass damper for buildings”, *Journal of Structural Engineering*, vol. 68B, Apr., pp. 367-375, 2022 (in Japanese). [Online]. Available: https://doi.org/10.3130/aijjse.68B.0_367 [Accepted Feb. 28, 2025].

[3] Y. Ikeda and Y. Matsumoto, “Unified description of passive vibration control for buildings based on pole allocation applied to three-degree-of-freedom model”, *Structural Control and Health Monitoring*, vol. 29, no. 9, Sep., 2022. [Online]. Available: https://doi.org/10.1002/stc.2995 [Accepted Feb. 28, 2025].

[4] Y. Matsumoto and Y. Ikeda, “Governing equation based on pole allocation for multi-lumped-mass stick-shape shear building model”, *Journal of Structural Engineering*, vol. 69B, Apr., pp. 1-9, 2023. (in Japanese). [Online]. Available: https://doi.org/10.3130/aijjse.69B.0_1 [Accepted Feb. 28, 2025].

[5] Y. Ikeda and Y. Matsumoto, “Pole allocation applied to two buildings connected by joint damper”, *Shock and Vibration*, vol. 2024, Jan., 2024. [Online]. Available: https://doi.org/10.1155/2024/5363146 [Accepted Feb. 28, 2025].

[6] Y. Ikeda and N. Uhara, “Application of pole allocation to optimize passive viscous dampers represented by the Maxwell model”, *Soil Dynamics and Earthquake Engineering*, vol. 188A, Jan., 2025. [Online]. Available: https://doi.org/10.1016/j.soildyn.2024.109037 [Accepted Feb. 28, 2025].

[7] Y. Ikeda, “Pole allocation applied to joint damper represented by the Maxwell Model”, *DPRI Annual Meeting*, Kyoto University, Feb., 2025. [Online]. Available: https://www.dpri.kyoto-u.ac.jp/hapyo/25/pdf/A209.pdf [Accepted Feb. 28, 2025].

[8] M. Kobayashi and T. Koh, “Analytical study of modal coupling effect on mid-story isolation system by eigen value analysis and random vibration analysis”, *Summaries of Technical Papers of Annual Meeting* 2004, *Architectural Institute of Japan*, vol. B-2 (Structure II), pp. 333-334, 2004 (in Japanese).

[9] J.P. Den Hartog, *Mechanical Vibrations*, *4th Edition*, McGraw-Hill Book Company, 1956.

[10] K. Iwanami, K. Suzuki and K. Seto, “Studies of the vibration control method of parallel structures (The method by the theory of P, T, Q)”, *Transactions of the Japan Society of Mechanical Engineers. C*, *Japan Society of Mechanical Engineers*, vol. 52, no. 484, Dec., pp.3063-3072, 1986 (in Japanese). [Online]. Available: https://doi.org/10.1299/kikaic.52.3063 [Accepted Feb. 28, 2025].

XI ECCOMAS Thematic Conference on Smart Structures and Materials - SMART 2025
M. Krommer, M. Nader and M. Schagerl (Eds)

Received: 27 March 2025 / Revised: 8 July 2025 / Accepted: 25 October 2025
© The Author(s) 2025

Extreme Vibration Mitigation and Structural Health Monitoring under Impulse Loads

Mohammad Shamim Miah, Werner Lienhart

Abstract. Vibration induced by dynamic loads are quite common problem in the area of structural engineering. It is obvious that due to the aforementioned problem often structures face serious collapse situation. However, vibration related problems are not so simple to avoid but mitigation is possible. To deal with the vibration mitigation problem, structural health monitoring and control are widely adapted. Hence, it is essential to understand the vibration generated via dynamic loads because extreme vibration may alter the physical properties of the structures. As a result, due to the aforementioned issue structure may struggle to survive. Among many, impulse type dynamic loads are quite dangerous due to their destructive nature within very short-period of time. Therefore, this study has focused on the effect of the impulse type dynamic loads. To do this end, a multi-degree system has been considered and linked with structural controller and impulse loads are applied with different magnitudes. In order to assess the changes of structural parameters, fundamental frequencies, vibrational mode shapes are evaluated. And it is observed that the fundamental dynamical properties of the structure can change due to the variation of the magnitudes of the input excitations.

Key words: Vibration Mitigation, Structural Control, Structural Health Monitoring, Dynamic Loads

1 INTRODUCTION

Civil structures and infrastructures are vulnerable whenever they hit by extreme dynamic loads. Typically, due to the blow of the extreme dynamic loads, it is expected that almost all structures will struggle as a result of vibration. Though there are many vibration mitigation technologies are available in the market but still this topic requires upgradation to improve existing technologies and control mechanisms. Because, the performances of any vibration mitigation and control technology heavily relies on their design strategy, for instance, a passive control device is assumed to be reacting based on the applied action but the control force is not adjustable. In contrary, active, semi-active, hybrid control devices may react and adjust based on the current response of the dynamical system. An overview with benefits and drawbacks of the available vibration control techniques and alternative have been summarised by many

Mohammad Shamim Miah & Werner Lienhart
Institute of Engineering Geodesy and Measurement Systems, Graz University of Technology, 8010 Graz, Austria
e-mail: miah@tugraz.at

[1, 2, 3, 4]. There are many hybrid type vibration mitigation technologies and devices, actually, they are a combination of active and passive [1]. Among them few can be mentioned such as, semi-active [5, 6, 7], tuned liquid damper and active mass damper [8], and active-passive tuned mass [9].

In order to reduce vibration, a tuned liquid damper and a active mass damper have been adopted in [8] for multi-story building. A tuned mass damper type has been adopted in [10] and it shows properly tuned damper parameters can assist to improve the reduction of vibration. An experimental validation of a newly developed tuned mass damper has been conducted in [11] and a reasonable reduction of amplitudes are reported. In [12] has investigated an optimization approach to design tuned mass damper for tall buildings. While tuned mass damper is adopted for offshore structures to reduce excessive vibration in [13]. A robust active control strategy has been studied in [14] and the efficacy of the adopted control approach is reported.

The hybrid type control devices and techniques are also adopted in many structures due to their combined benefits of active and passive as an alternative of either active or passive system. For instance, [15] has studied a mixed vibration control approach by employing H_2/H_∞ to reduce excessive vibration. While a combination of active-passive tuned mass damper has been used to mitigate vibration and excellent performances has been reported [9]. An adaptive approach by using smart materials has been investigated both for structural health monitoring and vibration mitigation purpose [16]. Energy-based control approach for vibration control problems have been adopted by [17, 18]. Both active and passive control systems have been employed and the vibration reduction performance is investigated under seismic loads [19].

Recently, the semi-active type damper has been studied by many authors due to their underlying benefits e.g. such system can be operational during an extreme when electric power is out of reach. For example, a self-tuning fuzzy control approach via the use of magnetorheological (MR) damper is adopted for vibration reduction in [20]. While semi-active (e.g. MR damper) vibration control approach is adopted for suspension type system [21]. Further, a real-time model updating and vibration control approach has been conducted experimentally by employing MR damper in [7]. Semi-active control approach has been adopted for cable stayed bride to mitigate vibration under multi-support excitations in [6]. Both the passive and semi-active techniques have been adopted to reduce the seismic vibration for cable-stayed bridge [5].

It can be summarized from the above discussion that there are many vibration mitigation alternatives for various type of structures for different application goals. One thing is common to all that they all focuses on vibration mitigation problems but almost none of the study explicitly investigated the danger of impulse type dynamic loads. Even though there are many vibration reduction alternatives but still require upgradation and modification because every problem is unique due to considering variables e.g. input excitations, type of structures and so on. Hence, this study has focused into the aforementioned issue to investigate the possibility of an updated optimal vibration control that can be utilized for vibration mitigation under various impulse loads. To do this end, a 10 degree-of- freedom system is adopted and an active control approach is implemented. The performance of the active approach is evaluated by employing the linear quadratic regulator (LQR) control algorithm as control law.

2 PROBLEM STATEMENT AND FORMULATION

A 10 degree-of-freedom (DOF) dynamical system is considered for the investigations of this study that assumed to behave as shear type building. The early mentioned structure has been linked with an active control device. The active damper is assumed to be placed at the 3rd floor level. The control force is estimated via the use of the linear quadratic regulator (LQR). In order to perform simulations, the problem needs to be formulated by deriving the equations of motion (EOM). And later all of those EOMs derived in matrix-vector format as shown in Eq. (1).

$$M\ddot{Z} + C\dot{Z} + MZ(t) = \zeta P(t) \tag{1}$$

where $\ddot{Z}$ is acceleration vector, $\dot{Z}$ is velocity vector, Z is displacement vector, M is mass matrix, C is damping matrix, K is stiffness matrix, ζ is the location control vector (in this study, loads have been applied at all floors level), t represents the time vector, P is the input excitation.

Later, the equations of motion brought into a more compact formulation known as the state-space formulation. There are two governing equations for the state-space formulation, namely, the process and measurement equation. The process equation contains all of the information (i.e., mass, stiffness, damping, external inputs) of the dynamical system, a sample process equation is shown in Eq. (2).

$$x_{k+1} = Ax_k + Bu_k \tag{2}$$

where x is the state vector (contains displacement and velocity vectors) of the system, u is the input vector that consist of both input excitation and control force, A is system matrix that contains mass, stiffness and damping of the system, B is input control matrix, k represents the time instance. While the measurement equation is an accompanying equation that estimates the desired information (e.g. displacements, velocities and accelerations). The measurement equation is given by Eq. (3).

$$y_k = Cx_k + Du_k \tag{3}$$

where y is the output vector, C and D are the measurement and feed-through matrices, correspondingly.

It is mentioned earlier that the control force is estimated by employing the LQR algorithm. In order to estimated the control force a cost function needs to be defined for the problem. The cost function for this problem is described in discrete-form in Eq. (4). The the weight matrices Q and R of the early mentioned cost function needs to follow the following rules: the value of Q must be positive semi-definitive and the R must be positive definitive.

$$J = \sum_{k=0}^{\infty} [x_k^T Q x_k + u_k^T R u_k] \tag{4}$$

where J is the output of the cost function, Q and R are the weight matrices. Herein, the value of the weight factor R is $5e^{-08}$ and the weight factor Q is a 20×20 diagonal matrix with a diagonal element of $5e^2$. Finally, the control force is calculated as described as,

$$u_k = -K^{opt} x_k \tag{5}$$

where K^{opt} is the optimal gain, x is the state vector (contains displacement and velocity vectors).

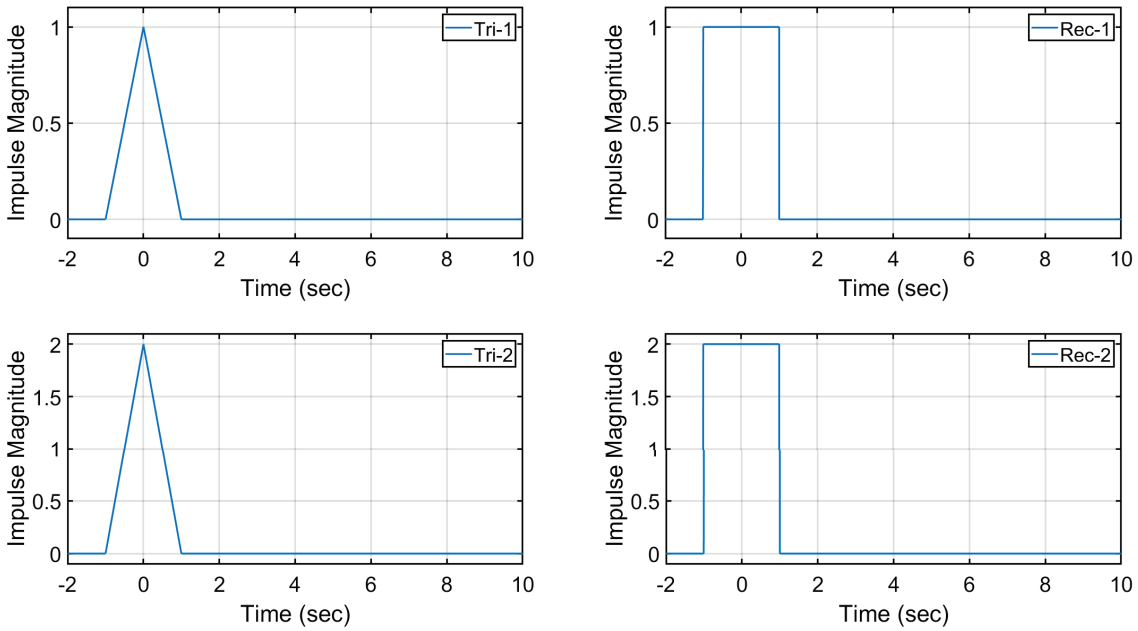

Figure 1: Input excitation

3 RESULTS AND DISCUSSION

As per the goal of this study, the input excitations are considered to be impulse type dynamic loads. The goal here is to create an extreme vulnerable situation due to the destructive nature of the impulse type loads that occur for a very short time with high frequency intensity. Herein, the impulse inputs have been created with a sampling frequency of 5000Hz for a time span of -2 sec to 10 sec. Regarding structural properties, the mass of each floor is assumed to be 44 tons, stiffness constant is about 55×10^4 N/m. The damping matrix is adjusted based on the mass and eigenvalue of the system, where, the diagonal damping components are about 696 N-s/m while the off-diagonal components are 235 N-s/m. It needs to be mentioned that any of the aforementioned structural parameters doesn't have any direct physical meaning as they are selected to perform simulation. The input excitation are applied with different magnitudes to create different destructive scenarios. Specifically, there are four input excitations applied to investigate the controller performance. For all of the control cases the controller parameters remain e.g. controller gain remain same, because controller gain is estimated based on the structural properties. In other words, structure remain same (because the controller gains are estimated based on the structural properties) but different inputs excitations are applied. All the input excitations cases are depicted in Fig. 1. The cases are named as "Tri-1" and "Tri-2" for the triangular pulses, while "Rec-1" and "Rec-2" for the rectangular pulses. Regarding the magnitudes of the aforementioned cases, it needs to be mentioned that "Tri-1" and "Rec-1" have an unit amplitude while "Tri-2" and "Rec-2" have the twice amplitudes of "Tri-1" and

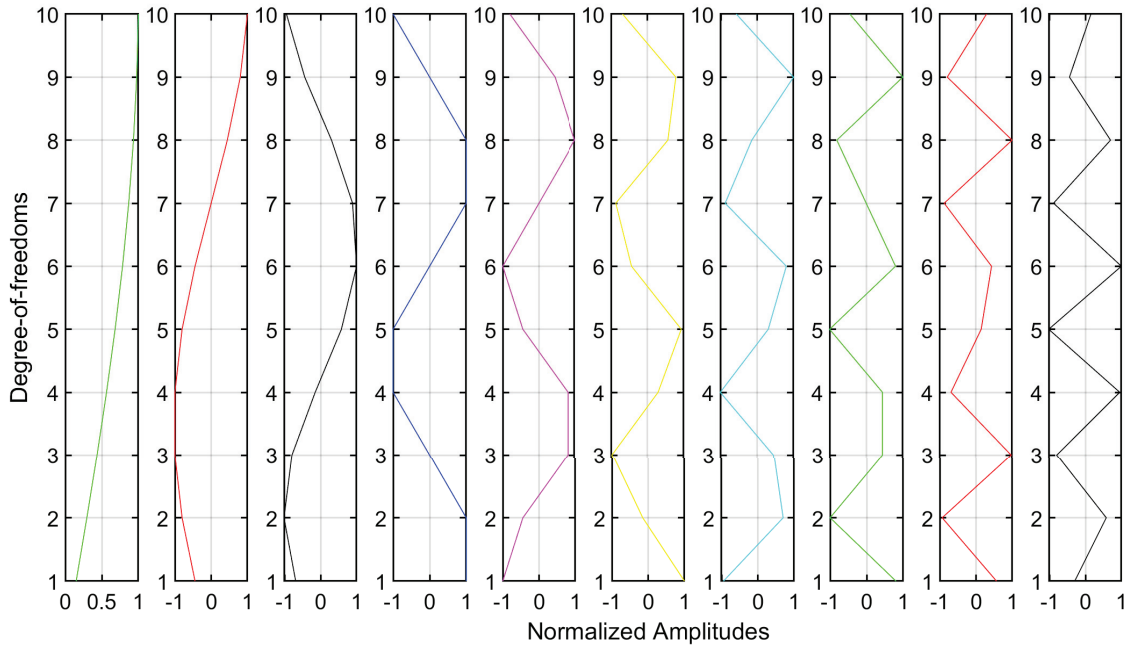

Figure 2: The deflected mode shapes of the uncontrolled structure

"Rec-1". The eigenfrequencies of the uncontrolled system is evaluated and they are 0.27, 0.80, 1.30, 1.78, 2.22, 2.61, 2.94, 3.21, 3.40, 3.52 Hz, accordingly. Further, the mode shapes of the uncontrolled structure has been evaluated and shown in Fig. 2.

In first step, uncontrolled response of the structure is evaluated and compared for all of those four cases e.g. "Tri-1, Tri-2" and "Rec-1, Rec-2". It has been observed that the amplitudes of the displacements have varied with the magnitudes of the input excitations. The displacements of all of the degree-of-freedoms have been compared and presented in Fig. 3 and the unit of the displacements are in "m". For better understanding, in addition to the early mentioned figure, a summary table of the absolute maximum peak displacements values are given in Table 1. The superscripts "'uc' represents the uncontrolled cases and the numbers "1, 2, 3, 4" indicates the input excitations cases. The aforementioned cases are ordered as: Tri-1, Rec-1, Tri-2, Rec-2.

Later, the controlled case for all fours types of input excitations are evaluated and the outcome have been compared with uncontrolled scenarios. In this context, the displacement comparison of "Tri-1" and "Tri-2" are illustrated in Fig. 4 and Fig. 5, respectively. The black lines represents the uncontrolled cases while the dotted-pink lines indicates the respective controlled cases. It is observed that for both triangular impulse cases the uncontrolled amplitudes of have been attenuated significantly.

Further, the comparison of displacement trajectories under "Rec-1" and "Rec-2" have been conducted. And the displacements results are presented Fig. 6 for the "Rec-1" case while the "Rec-2" case has been shown in Fig. 7. Similar to the triangular impulse cases, it is noticed

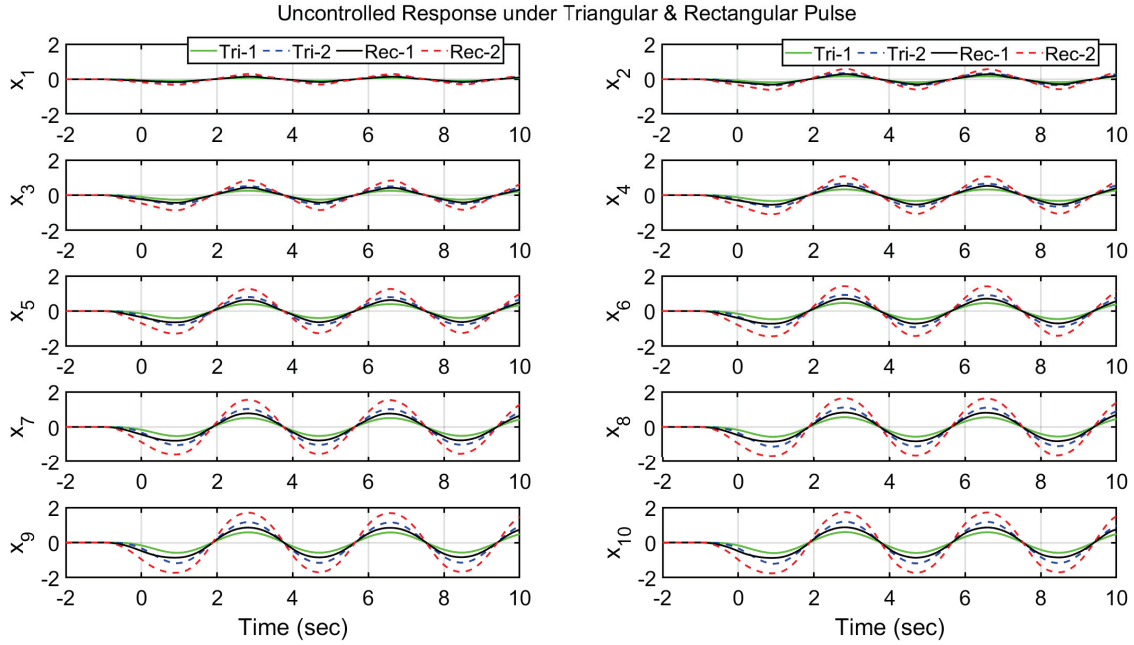

Figure 3: Uncontrolled responses of 1-10 DOFs under triangular and rectangular impulses

Table 1: Summary of the maximum absolute peak displacements for the uncontrolled cases

DOF	d_{max}^{uc1}(m)	d_{max}^{uc2}(m)	d_{max}^{uc3}(m)	d_{max}^{uc4}(m)
1	0.0876	0.1577	0.1752	0.3154
2	0.1732	0.3026	0.3464	0.6052
3	0.2552	0.4316	0.5104	0.8632
4	0.3320	0.5432	0.6639	1.0863
5	0.4020	0.6379	0.8040	1.2758
6	0.4638	0.7171	0.9276	1.4343
7	0.5162	0.7817	1.0324	1.5635
8	0.5578	0.8297	1.1155	1.6594
9	0.5868	0.8610	1.1736	1.7219
10	0.6018	0.8774	1.2036	1.7547

for the rectangular impulse cases the vibration responses have reduced notably. In those figures 6 and 7, the black lines shows the uncontrolled cases while the dotted-blue lines are for the controlled cases.

Finally, the summary of uncontrolled and controlled displacements of all of the floors are given in Table 2. The aforementioned table provides the evidence of the significant attenuation

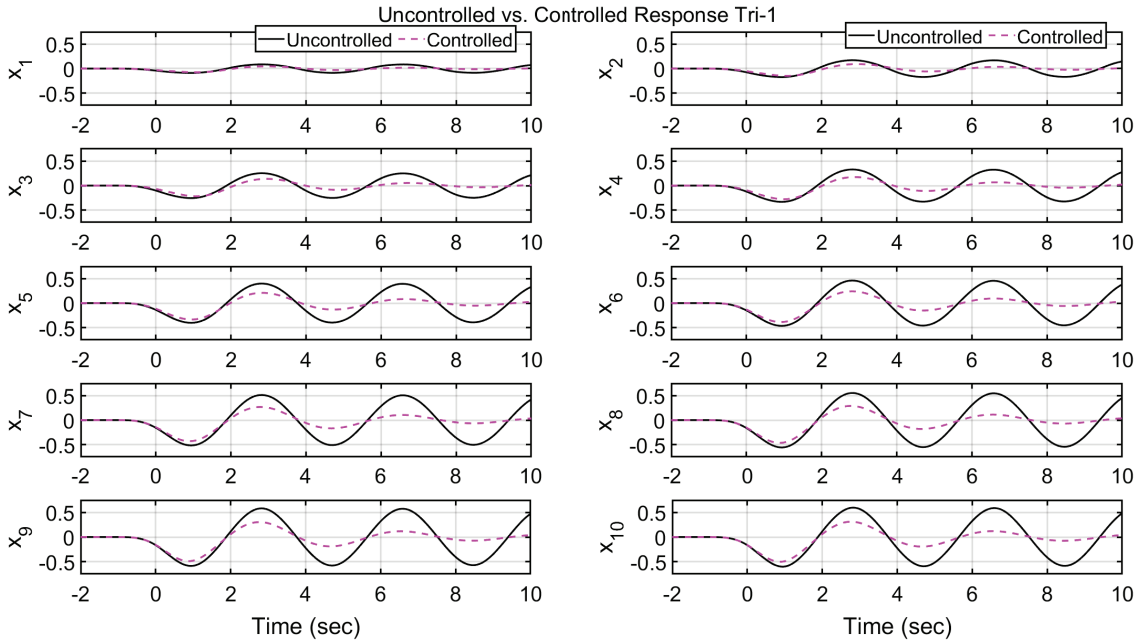

Figure 4: Uncontrolled versus controlled responses of 1-10 DOFs under Tri-1 impulse

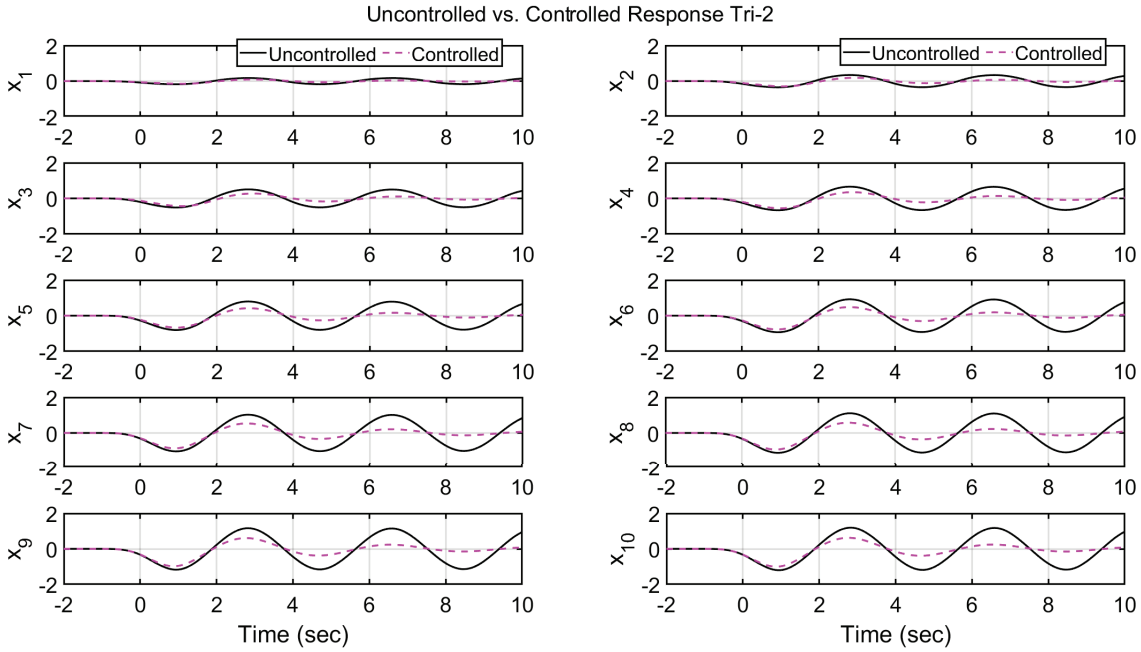

Figure 5: Uncontrolled versus controlled responses of 1-10 DOFs under Tri-2 impulse

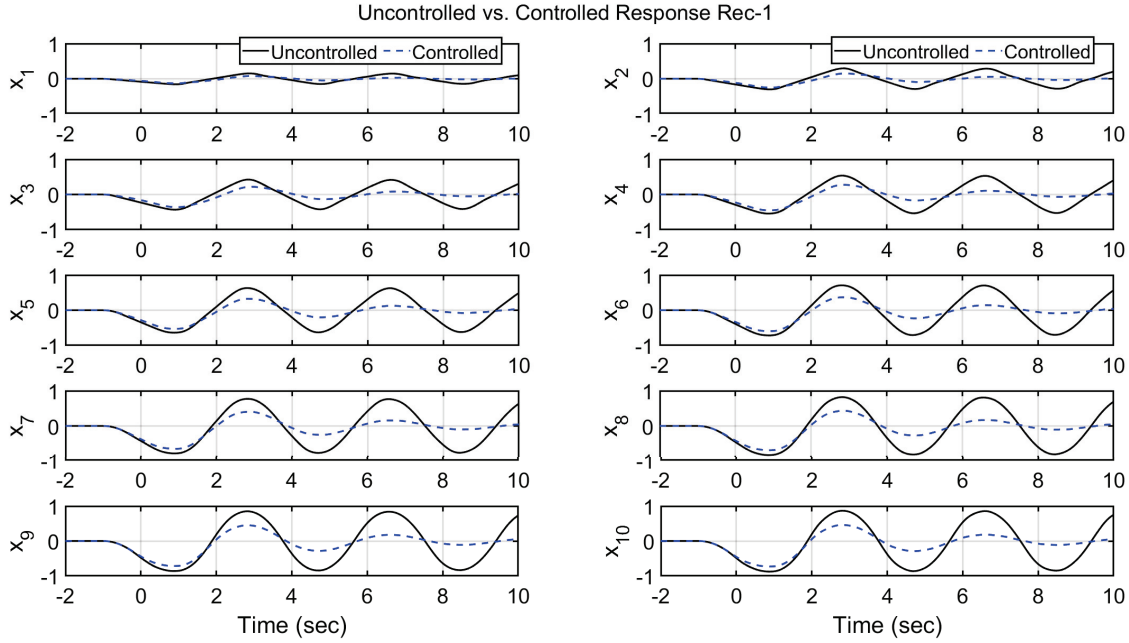

Figure 6: Uncontrolled versus Controlled responses of 1-10 DOFs under Rec-1 impulse

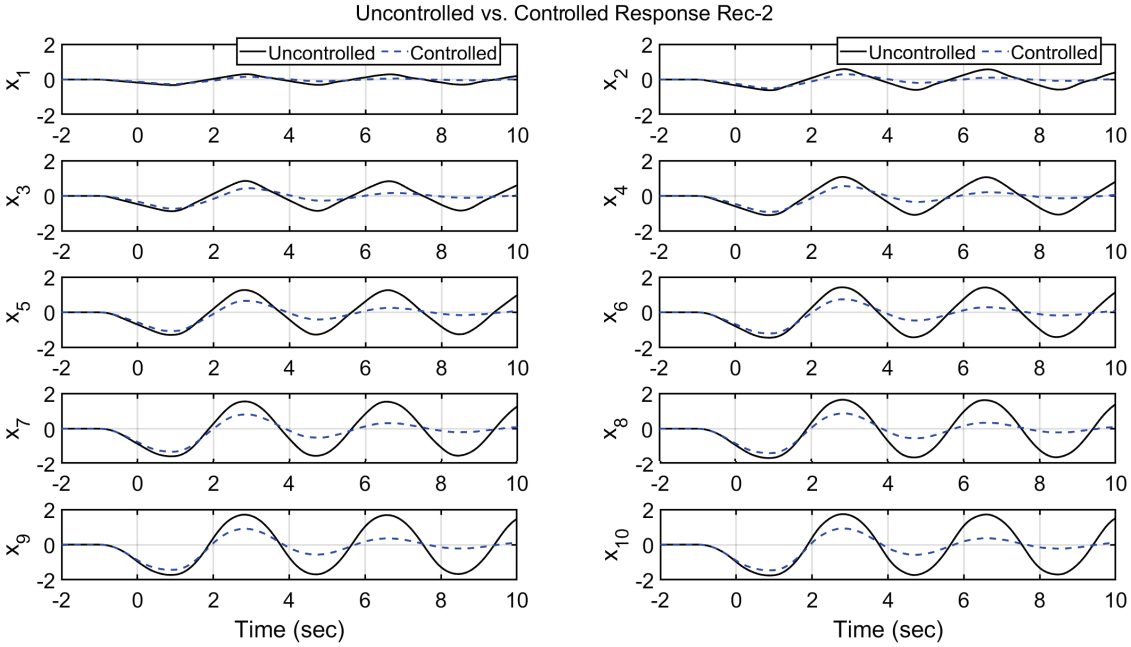

Figure 7: Uncontrolled versus Controlled responses of 1-10 DOFs under Rec-2 impulse

of the uncontrolled responses. As a side note, early mentioned table has the maximum absolute peak displacements value of all degree-of-freedoms. The superscripts “uc” and “c” means the uncontrolled and controlled cases. The input cases are rather ordered as: Tri-1, Rec-1, Tri-2, Rec-2.

Table 2: Summary of the maximum absolute peak displacements for the uncontrolled and controlled cases

DOF	d_{max}^{uc1}(m)	d_{max}^{c1}(m)	d_{max}^{uc2}(m)	d_{max}^{c2}(m)	d_{max}^{uc3}(m)	d_{max}^{c3}(m)	d_{max}^{uc4}(m)	d_{max}^{c4}(m)
1	0.0876	0.0741	0.1577	0.1312	0.1752	0.1483	0.3154	0.2624
2	0.1732	0.1472	0.3026	0.2523	0.3464	0.2945	0.6052	0.5046
3	0.2552	0.2179	0.4316	0.3608	0.5104	0.4358	0.8632	0.7217
4	0.3320	0.2780	0.5432	0.4513	0.6639	0.5559	1.0863	0.9026
5	0.4020	0.3348	0.6379	0.5293	0.8040	0.6695	1.2758	1.0586
6	0.4638	0.3858	0.7171	0.5955	0.9276	0.7716	1.4343	1.1911
7	0.5162	0.4297	0.7817	0.6504	1.0324	0.8594	1.5635	1.3008
8	0.5578	0.4650	0.8297	0.6914	1.1155	0.9300	1.6594	1.3828
9	0.5868	0.4896	0.8610	0.7178	1.1736	0.9793	1.7219	1.4356
10	0.6018	0.5022	0.8774	0.7312	1.2036	1.0044	1.7547	1.4624

4 CONCLUSIONS

This study has investigated the vibration reduction techniques to mitigate the extreme vibration that is generated by impulse type excitations. The destructive nature of such impulse loads are pretty obvious that any structure will struggle to survive, if they are hit by such loads. The investigations are done by considering a 10 degree-of-freedom system under two types of impulse excitations, namely, the triangular and rectangular impulse with two different magnitudes. The controller is employed for all four cases and the active control force is estimated by employing the optimal LQR control algorithm. And the controller gain remain same for all four controlled cases, namely, the Tri-1, Tri-2, Rec-1, and Rec-2. It is observed that the tuned controller is capable of attenuating the uncontrolled vibration peaks quite effectively. This study shows the possibility that properly tuned controller is capable of mitigating extreme vibration even under different input excitations, as often controller parameters require tuning for various reasons. Because it is always a challenge to keep the same controller parameters for different input excitations and gain the optimal performances in terms of vibration mitigation. Further investigations are essential for tall structures to understand the efficacy of studied control approach.

REFERENCES

[1] T. T. Soong and B. F. Spencer, "ACTIVE , SEMI-ACTIVE AND HYBRID CONTROL OF STRUCTURES," in *12th World Conference on Earthquake Engineering*. Auckland, New Zealand: New Zealand Society for Earthquake Engineering, 2000, pp. 1–16.

[2] M. H. El Ouni, M. Abdeddaim, S. Elias, and N. B. Kahla, "Review of Vibration Control Strategies of High-Rise Buildings," p. 8581, nov 2022. [Online]. Available: https://www.mdpi.com/1424-8220/22/21/8581

[3] B. F. Spencer and S. Nagarajaiah, "State of the Art of Structural Control," *Journal of Structural Engineering*, vol. 129, no. 7, pp. 845–856, 2003. [Online]. Available: http://ascelibrary.org/doi/abs/10.1061/(ASCE)0733-9445(2003)129:7(845)%5Cnhttp://ascelibrary.org/doi/abs/10.1061/%28ASCE%290733-9445%282003%29129%3A7%28845%29

[4] J. Connor and S. Laflamme, *Structural Motion Engineering*, 1st ed. Cham: Springer International Publishing, 2014. [Online]. Available: https://link.springer.com/10.1007/978-3-319-06281-5

[5] H. Iemura and M. H. Pradono, "Passive and semi-active seismic response control of a cable-stayed bridge," *Journal of Structural Control*, vol. 9, no. 3, pp. 189–204, dec 2002. [Online]. Available: http://doi.wiley.com/10.1002/stc.12

[6] Z.-B. Dai, J.-Z. Huang, and H.-X. Wang, "Semi-active control of a cable-stayed bridge under multiple-support excitations." *Journal of Zhejiang University. Science*, vol. 5, no. 3, pp. 317–25, mar 2004. [Online]. Available: http://www.ncbi.nlm.nih.gov/pubmed/14727308

[7] M. S. Miah, E. N. Chatzi, V. K. Dertimanis, and F. Weber, "Real-time experimental validation of a novel semi-active control scheme for vibration mitigation," *Structural Control and Health Monitoring*, vol. 24, no. 3, p. e1878, mar 2017. [Online]. Available: http://doi.wiley.com/10.1002/stc.1878

[8] J.-h. Shin, M. K. Kwak, S.-m. Kim, and K.-h. Baek, "Vibration control of multi-story building structure by hybrid control using tuned liquid damper and active mass damper," *Journal of Mechanical Science and Technology*, vol. 34, no. 12, pp. 5005–5015, dec 2020. [Online]. Available: http://link.springer.com/10.1007/s12206-020-1105-4

[9] I. Nishimura, T. Yamada, M. Sakamoto, and T. Kobori, "Control performance of active-passive composite tuned mass damper," *Smart Materials and Structures*, vol. 7, no. 5, p. 637, oct 1998. [Online]. Available: https://dx.doi.org/10.1088/0964-1726/7/5/008

[10] M. S. Miah, "Vibration mitigation of high-rise buildings via tuned mass damper subjected to dynamic loads," *IOP Conference Series: Materials Science and*

Engineering, vol. 1070, no. 1, p. 012031, feb 2021. [Online]. Available: https://iopscience.iop.org/article/10.1088/1757-899X/1070/1/012031

[11] M. S. Miah, M. J. Miah, and M. A. Hossain, "Development and Performance Evaluation of a Novel Translational Tuned Mass Damper," *International Journal of Engineering Research in Africa*, vol. 45, pp. 53–73, nov 2019. [Online]. Available: https://www.scientific.net/JERA.45.53

[12] A. A. Farghaly and M. Salem Ahmed, "Optimum Design of TMD System for Tall Buildings," *ISRN Civil Engineering*, vol. 2012, no. 3, pp. 1–13, aug 2012. [Online]. Available: https://www.hindawi.com/journals/isrn/2012/716469/

[13] Q. Wu, X. Zhao, and R. Zheng, "Experimental Study on a Tuned-Mass Damper of Offshore for Vibration Reduction," *Journal of Physics: Conference Series*, vol. 744, no. 2016, p. 012045, sep 2016. [Online]. Available: https://iopscience.iop.org/article/10.1088/1742-6596/744/1/012045/pdfhttps://iopscience.iop.org/article/10.1088/1742-6596/744/1/012045

[14] S. G. Wang, "Robust active control for uncertain structural systems with acceleration sensors," *Journal of Structural Control*, vol. 10, no. 1, pp. 59–76, 2003.

[15] H. R. Karimi, M. Zapateiro, and N. Luo, "Vibration control of base-isolated structures using mixed H2/H-inf output-feedback control," *Proceedings of the Institution of Mechanical Engineers, Part I: Journal of Systems and Control Engineering*, vol. 223, no. 6, pp. 809–820, sep 2009. [Online]. Available: http://pii.sagepub.com/lookup/doi/10.1243/09596518JSCE730

[16] M.-H. Kim, "Simultaneous Structural Health Monitoring and Vibration Control of Adaptive Structures Using Smart Materials," *Shock and Vibration*, vol. 9, no. 6, pp. 329–339, jan 2002. [Online]. Available: https://onlinelibrary.wiley.com/doi/10.1155/2002/264158

[17] A. Meguenani, V. Padois, J. D. Silva, A. Hoarau, A. Meguenani, V. Padois, J. D. Silva, A. Hoarau, P. B. En, A. Meguenani, V. Padois, J. D. Silva, and A. Hoarau, "Energy based control for safe human-robot physical interaction," in *Springer Proceedings in Advanced Robotics*, 2017, pp. 1–11.

[18] E. Li, Z. Z. Liang, Z. G. Hou, and M. Tan, "Energy-based balance control approach to the ball and beam system," *International Journal of Control*, vol. 82, no. 6, pp. 981–992, 2009.

[19] S. J. Han, P. Tsopelas, and A. Baz, "Active/passive seismic control of structures," *Journal of Earthquake Engineering*, vol. 10, no. 4, pp. 509–526, 2006.

[20] C. M. D. Wilson and M. M. Abdullah, "Structural vibration reduction using self-tuning fuzzy control of magnetorheological dampers," *Bulletin of Earthquake Engineering*, vol. 8, no. 4, pp. 1037–1054, mar 2010. [Online]. Available: http://www.springerlink.com/index/10.1007/s10518-010-9177-7

[21] Y. Shen, M. F. Golnaraghi, and G. R. Heppler, "Semi-active Vibration Control Schemes for Suspension Systems Using Magnetorheological Dampers," *Journal of Vibration and Control*, vol. 12, no. 1, pp. 3–24, jan 2006. [Online]. Available: http://jvc.sagepub.com/cgi/doi/10.1177/1077546306059853https://journals.sagepub.com/doi/10.1177/1077546306059853

XI ECCOMAS Thematic Conference on Smart Structures and Materials - SMART 2025
M. Krommer, M. Nader and M. Schagerl (Eds)

Received: 10 April 2025 / Revised: 1 September 2025 / Accepted: 25 October 2025
© The Author(s) 2025

Vibration attenuation in a semi-passive frame based on reinforcement learning algorithm

Grzegorz Mikułowski, Dominik Pisarski, Błażej Popławski, Łukasz Jankowski

Abstract. This contribution addresses the problem of adaptively tuning the parameters of semi-active devices to mitigate vibrations in structures subjected to unknown periodic excitation. Using a specially designed reinforcement learning algorithm, the semi-active devices adjust their operating parameters to ensure optimal dissipation of vibrational energy. The algorithm incorporates an efficient gradient-based sequence that ensures rapid convergence of the learning process and enables real-time implementation under varying excitation characteristics. The method is experimentally validated on a frame structure equipped with lockable joints, which can be controlled to adjust their stiffness parameters. Since the developed reinforcement learning algorithm incorporates partial knowledge of the structural model, the first part of the work is focused on formulating a simplified numerical model that is easy to identify and scale.

Key words: Vibration attenuation, Reinforcement Learning, Semi-active control, Adaptive structure, Stiffness control

1 INTRODUCTION

Vibrations of engineering structures result from operational or external excitation. Excessive vibration levels endanger integrity and jeopardize the operation of structures and machines. This problem is further exacerbated by the current trend toward cost-effective and lightweight structural design. Mitigation of vibrations is thus the subject of intensive research and development activities [1]. Typical techniques can be categorized into passive, active, and semi-active control approaches. Passive techniques usually employ dedicated dissipative elements and/or rely on structural optimization. A classical passive device is the tuned mass damper (TMD). Low cost, reliability, and design simplicity are the main advantages of these techniques; however, their efficiency is limited in many situations. Active control approaches are effective and widely researched [2], but they rely on actuators that generate large control forces and require significant power supply, which may fail during events such as major earthquakes. Moreover, in the case of a control system malfunction, large control forces can lead to structural instability.

Grzegorz Mikułowski & Dominik Pisarski & Błażej Popławski & Łukasz Jankowski
Institute of Fundamental Technological Research, Polish Academy of Sciences, ul. Pawi´skiego 5B, 02-106 Warszawa, Poland, e-mail: gmikulow@ippt.pan.pl

Semi-active control techniques often combine the advantages of passive and active systems. Instead of generating large external control forces, semi-active actuators modify structural dynamics [3] by affecting local mechanical parameters such as damping, stiffness, or kinematic constraints [4]. They are typically implemented using magnetorheological fluids (in mid- to large-scale applications) or piezoelectric materials (for small-scale control) and may take the form of frictional joints [5] or switched oil dampers [6]. They can be implemented with limited power supply and in a fail-safe manner, while often similarly efficient as active systems. However, the control functions are coupled to the local structural response. The corresponding formulations are thus nonlinear and difficult to solve using classical analytical approaches.

Reinforcement learning (RL) has achieved significant breakthroughs in autonomous control and decision-making, with demonstrated success across a variety of real-world applications, from mastering complex games like chess and Go at superhuman levels [7] to thermal soaring of autonomous gliders [8], robotic swimming via body undulation [9], and self-driving vehicles [10]. Despite RL's success and algorithmic adaptability, its application to structural vibration problems remains limited. Most existing studies focus on active control approaches, often implemented in structures with only a few degrees of freedom. In [11], a deep deterministic policy gradient RL algorithm (DDPG) was used to control a simulated, partially observable six degree of freedom (DOF) shear structure equipped with a force actuator on the first floor. In [12], DDPG was employed to train neural networks for controlling a flexible hinged plate with piezoelectric actuators. Experimental results confirmed that the RL-based control strategy achieved superior stability performance compared to conventional proportional-derivative (PD) control. In [13], the Q-learning RL technique was applied to optimize fuzzy-PD controller parameters for vibration suppression in high-rise buildings. The method was validated under diverse seismic conditions and demonstrated robustness against control loop time delays. In [14], the authors implemented an actor-critic RL algorithm to stabilize a swinging chain at a target position. Their active control approach operated with incomplete state information. While outperformed by model-based analytic solutions, this method presents a viable alternative for scenarios where accurate system modeling is not possible. The application of RL for shape control in active tensegrity structures was suggested in [15]. The algorithm integrated case-based reasoning with error-driven learning, demonstrating both enhanced control precision and reduced computational burden compared to conventional methods. An RL-based algorithm to stabilize free vibrations in semi-active, simply supported beams was developed in [16]. The proposed method optimizes switching controller parameters to adapt to changing excitation force characteristics. A deep Q-network approach (DQN) was used in [17] to mitigate seismic vibrations in a simulated 11-DOF shear structure equipped with an on/off-type semi-active tuned mass damper (TMD). The RL-based control reduced the RMS of the top floor displacements to 75% of that achieved with the same TMD optimally tuned but passive. The same structure was used in [18] to evaluate and confirm the high robustness of the DQN-based semi-active control to model errors and measurement noise. In [19], the neural network of the RL agent was extended to a two-branch configuration with shared features. This architecture enabled simultaneous identification of stiffness-related damage along with semi-active control.

This paper develops an actor-only reinforcement learning algorithm for optimizing the parameters of semi-active actuators installed on a vibrating structure subjected to unknown periodic excitation. First, the control and learning techniques are presented. Then, their performance is verified using a lab-scale frame structure equipped with six semi-active joints that control the effective stiffness of the structure.

2 RL-DRIVEN ACTUATOR PARAMETER ADJUSTMENT

This work studies a class of semi-passive vibrating structures that can be characterized by the ordinary bilinear differential equation:

$$\dot{x}(t) = A\,x(t) + \sum_{i=1}^{m} u_i(t)\,B_i\,x(t) + F(t), \qquad x(0) = x^0. \tag{1}$$

In Eq. (1), the state vector at time t is given by $x(t) = [x_1(t), ..., x_n(t)]^{\mathrm{T}} \in \mathbb{R}^n$, with an initial condition x^0. The parameters $u_1(t), ..., u_m(t)$, where $u_i(t) \in \mathcal{U} \subset \mathbb{R}_+$, are assumed to be piecewise constant and determine the tunable stiffness/damping of the incorporated actuators. The constant matrices A and $B_1, ..., B_m$, each of size $n \times n$, represent the internal subsystem dynamics and the influence of the ith semi-active device, respectively. The excitation force $F(t)$, an $n \times 1$ vector, is assumed to be periodic but unknown.

The aim is to develop a Reinforcement Learning algorithm that tunes the control policy P defined as fixed actuator parameters:

$$P:\ \{u_1, ..., u_m\} \tag{2}$$

to unknown characteristics of the excitation force $F(t)$. The algorithm employs an actor-only framework (Figure 1), utilizing state measurements $x(t)$ over a learning time window T. The algorithm iteratively reduces the value of the following energy-related performance measure:

$$J = \int_{t_0}^{t_0+T} x^{\mathrm{T}}(t)\,Q\,x(t)\,\mathrm{d}t. \tag{3}$$

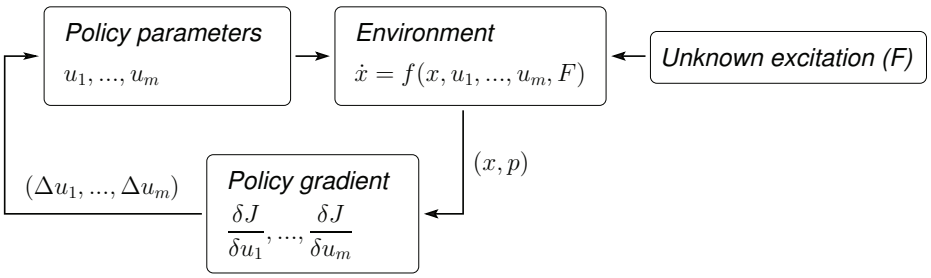

Figure 1: Schematic of Reinforcement Learning-driven actuator parameters (policy parameters) adjustment to unknown excitation forces. The actor's policy is iteratively optimized through interaction with the dynamical system environment. The policy gradients used for updating the policy parameters employ the real-time measurements of system state x and adjoint state p computed by backward integration of the adjoint dynamics (Eq. (6)).

Here, t_0 is a time instant that will be incremented during the adjustment process, while the time window T is selected to be sufficiently large to ensure the decay of transient vibrations, given the assumption of a periodic excitation force F (consistent reduction of the performance measure requires steady-state vibration conditions). The $n \times n$ matrix Q is constant and positive definite. The adjustment of the policy parameters $u_1, ..., u_m$ is based on the gradient descent method:

$$u_i^+ = u_i - \alpha_i \frac{\delta J}{\delta u_i}, \;\; i = 1, ..., m, \;\; \alpha > 0. \tag{4}$$

To compute the derivatives in Eq. (4), we introduce the Hamiltonian H for objective functional defined by Eq. (3) and the dynamical system Eq. (1), assuming that $u_1, ..., u_m$ are constant for $t \in [t_0, t_0 + T]$:

$$H\left(x, p, \{u_i\}_{i=1,...,m}\right) = p^{\mathrm{T}} \left(A\, x + \sum_{i=1}^{m} u_i\, B_i\, x + F \right) - \frac{1}{2} x^{\mathrm{T}}\, Q\, x. \tag{5}$$

The adjoint state $p(t) = [p_1(t), ..., p_n(t)]^{\mathrm{T}} \in \mathbb{R}^n$ satisfies the following differential equation:

$$\dot{p}(t) = -\frac{\partial H}{\partial x} = -A^{\mathrm{T}} p(t) - \sum_{i=1}^{m} u_i\, B_i^{\mathrm{T}} p(t) + Q x(t), \qquad p(t_0 + T) = 0. \tag{6}$$

From Eq. (1) and Eq. (5), the objective functional Eq. (3) can be represented by:

$$J = \int_{t_0}^{t_0+T} \left(p^{\mathrm{T}}\, \dot{x} - H(x, p, \{u_i\}_{i=1,...,m}) \right) \mathrm{d}t. \tag{7}$$

Let the functions $\delta x : [t_0, t_0 + T] \to R^n$ and $\delta p : [t_0, t_0 + T] \to R^n$ denote perturbations of the functions x and p with respect to the infinitesimal changes $\mathrm{d}u_i : R \to R, i = 1, ..., m$ of u_i, respectively. From Eq. (7), it follows that the differential δJ of the objective functional Eq. (3) with respect to perturbations $\delta u_i, i = 1, ..., m$ is given by:

$$\delta J = \int_{t_0}^{t_0+T} \left(-\sum_{i=1}^{m} \frac{\partial H}{\partial u_i}\, \delta u_i - \left(\frac{\partial H}{\partial x} \right)^{\mathrm{T}} \delta x \right) \mathrm{d}t + \int_{t_0}^{t_0+T} \left(p^{\mathrm{T}} \delta \dot{x} + \left(\dot{x} - \frac{\partial H}{\partial p} \right)^{\mathrm{T}} \delta p \right) \mathrm{d}t. \tag{8}$$

The last term in Eq. (8) vanishes, since

$$\dot{x} = \frac{\partial H(x, p, \{u_i\}_{i=1,...,m})}{\partial p}. \tag{9}$$

From the differentiability of the state vector x with respect to t, it follows that:

$$\delta \dot{x} = \frac{\mathrm{d}}{\mathrm{d}t} \left(\delta x \right). \tag{10}$$

Using the assumption given by Eq. (10), we can perform the integration by parts for Eq. (8), which results in

$$\delta J = -\int_{t_0}^{t_0+T} \sum_{i=1}^{m} \frac{\partial H}{\partial u_i}\, \delta u_i \,\mathrm{d}t - \int_{t_0}^{t_0+T} \left(\dot{p} + \frac{\partial H}{\partial x}\right)^{\mathrm{T}} \delta x \,\mathrm{d}t + \left[p^{\mathrm{T}} \delta x\right]_{t_0}^{t_0+T}. \tag{11}$$

From Eq. (1) and Eq. (6), it can be deduced that

$$\dot{p} = -\frac{\partial H}{\partial x}\,, \qquad p(t_0+T) = 0\,, \qquad \delta x(t) = 0, \tag{12}$$

and therefore, the second and the last term in Eq. (11) vanish. As a result, the derivative of the objective functional J with respect to u_i is given by:

$$\frac{\delta J}{\delta u_i} = -\int_{t_0}^{t_0+T} p^{\mathrm{T}}\, B_i\, x \,\mathrm{d}t. \tag{13}$$

To compute the derivatives in Eq. (13), the online algorithm will use the state x, measured by integrated sensors, and the adjoint state p, obtained through backward integration of Eq. (6). Note that the adjoint state dynamical equation does not explicitly depend on the external excitation force F. Instead, the influence of F is embedded in the measured state x. Thus, the adjustment of the policy parameters $u_1, ..., u_m$ is achieved through interaction with the dynamical system, reflecting the core assumption of reinforcement learning techniques.

3 EXPERIMENTAL VERIFICATION

The proposed control approach is verified on a small-scale demonstrator in laboratory conditions. The demonstrator is a cantilever frame structure equipped with 6 semi-active joints, configured in 3 pairs. These joints allow for modification of the local stiffness of the structure by locking and unlocking their angular degrees, which enables control of the bending moments transferred between adjacent components of the structure. The experimental scenario involves forced excitation of the structure with an unknown, varying input. The bandwidth of the harmonic excitation includes the resonant frequency. Compared to the passive case, the results demonstrate that the algorithm efficiently adapts the structural response to the unknown varying excitation and reduces the energy level of the structural response.

4 EXPERIMENTAL DEMONSTRATOR

The experimental object is a cantilever frame subjected to external excitation by an electrodynamic shaker (see Figure 2). The frame consists of two parallel longitudinal segments, each 1.2 m long, connected by transverse beams. It is equipped with six semi-active joints that connect the longitudinal and transverse segments. The joints ensure a passive transfer of planar bending moments between the longitudinal components while enabling controlled moment transfer to the transverse segments. The semi-active elements are organized in 3 pairs, mounted at equal distances of 0.3 m, starting 0.6 m from the fixed end of the frame. Each pair is activated simultaneously, which allows for local modification of structural stiffness.

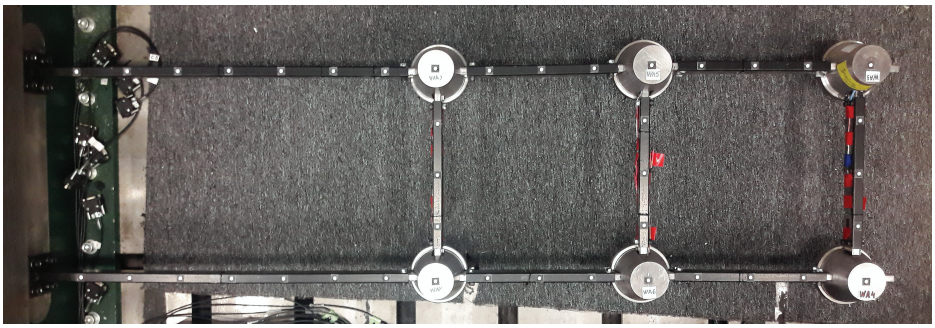

Figure 2: Experimental frame with 3 pairs of semi-actively controlled joints

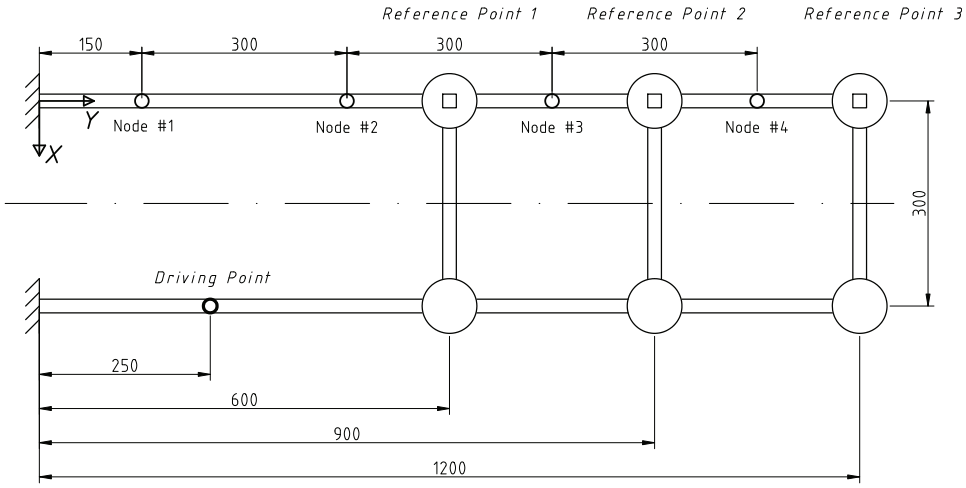

Figure 3: Scheme of the experimental frame setup

4.1 Assumptions

A planar coordinate system is adopted for kinematic analysis of the frame. This choice is determined by the design of the actuators, which implement structural modifications exclusively within the plane of the structure. The OXY coordinate system is shown in Figure 3.

Another assumption is that the demonstration frame structure can be accurately modeled with a 1D Timoshenko beam model. The frame design and its semi-active components emphasize the importance of both bending and shear stress control. The adopted numerical model, based on the Timoshenko beam, accounts for shear effects and their intentional modification. The validity of this assumption is experimentally confirmed by spectral analysis and model validation.

The data acquisition and excitation systems are configured in accordance with the above assumptions. The system is analyzed in-plane, with sensors and the exciter arranged to acquire data in the OXY plane. Displacements are measured for one longitudinal segment of the frame, based on the assumption that the response of the other segment is symmetrical.

4.2 Excitation

The frame is operated under forced vibration conditions. The source of vibrations is a modal shaker connected in the Driving Point and providing excitation in the OX direction, as depicted in Figure 3. The excitation signal depends on the particular task being carried out. First, a downward frequency sweep from 16 Hz down to 6 Hz was utilized for spectral characterization of the object across selected operational states. Next, a predefined signal of a fluctuating frequency was generated to evaluate the self-tuning ability of the proposed control system.

4.3 Data acquisition

The structural response of the frame is acquired using laser sensors divided into two groups. The first group acquires data characterizing the kinematic response in predefined nodes, which serves as input for the controller. The second group monitors the quality of the control process.

The first set of sensors comprises six distance laser sensors (Baumer models 20U2460 and 20U2441), configured to measure displacements with a 10 μm resolution within a 20 mm range. The measuring points are positioned at locations corresponding to all nodes established for numerical analysis. At each node, measurements are taken at two spots to gather displacements along the OX axis, as well as ongoing rotation in the OXY plane. For each node, the state vector includes: displacement along the OX axis, velocity along the OX axis, angle in the OXY plane, and angular velocity in the OXY plane. Data is acquired periodically into sets of 2 s duration at a 1 kS/s rate and used as input for the RL tuning module.

The second set of sensors consists of three distance laser sensors (Baumer model 20I6460; 20 mm range, 10 μm resolution) that measure the displacement of the semi-active joints along the OX direction. The acquired data is used for evaluation of the control process performance.

4.4 Control application

Each semi-active joint pair can be used to modify the local stiffness of the frame. The control system tunes the structure's vibrational response by recognizing the current operating conditions and adjusting the settings to minimize the internal energy of the system. Activating or deactivating the joints affects the spectral response of the structure. Simultaneously, the state of the joints influences the internal damping across the frame.

The application for experimental testing executes the following algorithm during the control procedure: 1. Initialization of the system; 2. Calibration and configuration of the laser sensors; 3. Acquisition of a 2 s data sequence; 4. Data processing and conditioning; 5. Determination and visualization of the quality factor; 6. Formulation of the state vector; 7. Execution of the tuning procedure; 8. Update of the control parameters; 9. Introduction of a predefined delay; 10. Return to point 3. or exit.

5 CHARACTERIZATION OF STRUCTURAL DYNAMICS

In the numerical analysis, the structure is modeled as a 1D Timoshenko beam, with shear effects explicitly considered. The structure exhibits also semi-active functionality that intro-

duces a non-linear behavior into the system. To ensure the predictability of the experimental procedure, precise characterization of the experimental object is necessary. To achieve this, a spectral analysis of the frame was conducted for the following operational states:

1. Pairs 1+2+3 activated;
2. Pair 1 deactivated, Pairs 2+3 activated;
3. Pairs 1+2 deactivated, Pair 3 activated;
4. Pairs 1+2+3 deactivated.

Activation of a semi-active module is interpreted as the state with the ability to transfer bending moments. The investigated set of operational states reveals significant differences in the structural dynamics. These results are necessary for an adequate assessment of the internal energy in the frequency domain.

5.1 Results

The results of the spectral characterization are depicted in Figure 4 as Power Spectral Density (PSD) plots. The plots illustrate the influence of joint activation on the structural response of the frame. The experiment has covered the four operational states described above. Consecutive deactivation of the semi-active pairs decreased the fundamental eigenfrequency. A significant shift is observed when the first pair is deactivated: the frequency is drops from 9.9 Hz to 8.22 Hz, which indicates that the 1st pair of joints has the most substantial impact on the structural dynamics. This can be explained by its proximity to the support, where bending moments are the highest in comparison to the locations of the other pairs. Furhter changes in operational state (deactivating subsequent pairs) resulted in further decreases in the eigenfrequency. Deactivation of both the 1st and 2nd pairs reduced it to 8.08 Hz, while switching all nodes to the low-transfer mode resulted in a 7.97 Hz eigenfrequency. This sequence of eigenfrequency reductions is associated with the corresponding decrease in the bending stiffness of the frame.

Moreover, the examined operational configurations affect the structural damping exhibited by the frame. Similar to stiffness, the damping increases monotonically in the successive operational states. This increase may be the consequence of residual friction present in the semi-active joints in their deactivated state.

The characteristics shown in Figure 4 define the operational range available on the demonstration frame. They reveal that the structural dynamic characteristics can be effectively modified and emphasize the potential for optimal tuning in response to varying excitation.

6 ASSESSMENT OF THE RL CONTROL APPROACH

The developed RL control approach was verified in a series of exemplary trials. To confirm repeatability, the series consisted of 5 samples. The primary assumption for these trials was to subject the frame to an unknown excitation of a fluctuating character. The objective of the tuning algorithm was to adapt the semi-active components of the frame and minimize the amplitude of the vibrational response.

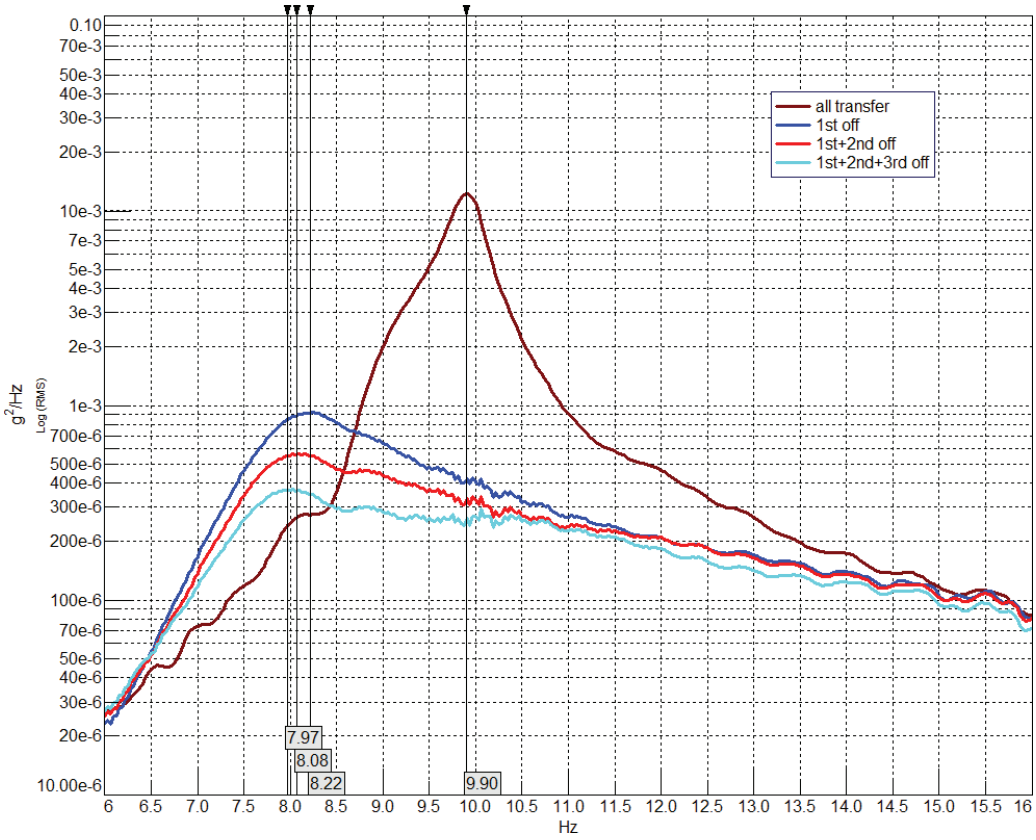

Figure 4: Spectral analysis (PSD functions)

The test demonstrates the self-tuning ability of the system for a stepwise switch of the excitation frequency from 10.5 Hz to 8.3 Hz. Initially, all semi-active joints were deactivated, which corresponds to a suboptimal state. Therefore, the initial response of the frame is characterized by an increased amplitude. Figure 5 depicts the time history of the system operation on four plots. The first plot depicts the excitation frequency as a step function, switching from 10.5 Hz to the target value of 8.3 Hz. The second plot illustrates the time evolution of control parameters related to the three semi-active pairs. It can be observed that the algorithm starts to adjust their values already one iteration after the change in excitation occurs. Since the semi-active pairs provide a bivalent operation while the control parameters are continuous in the range [0,1], a discrimination threshold of 0.7 is applied. The third plot shows the actuator states in time, where a value of 0 indicates low transfer of bending moments (deactivation), and a value of 1 denotes full transfer (activation). The fourth plot presents the RMS of vibration measured in three points of the frame. The RMS serves in this study as an analogue of structural energy, and it is used as a performance measure for quantification of control quality.

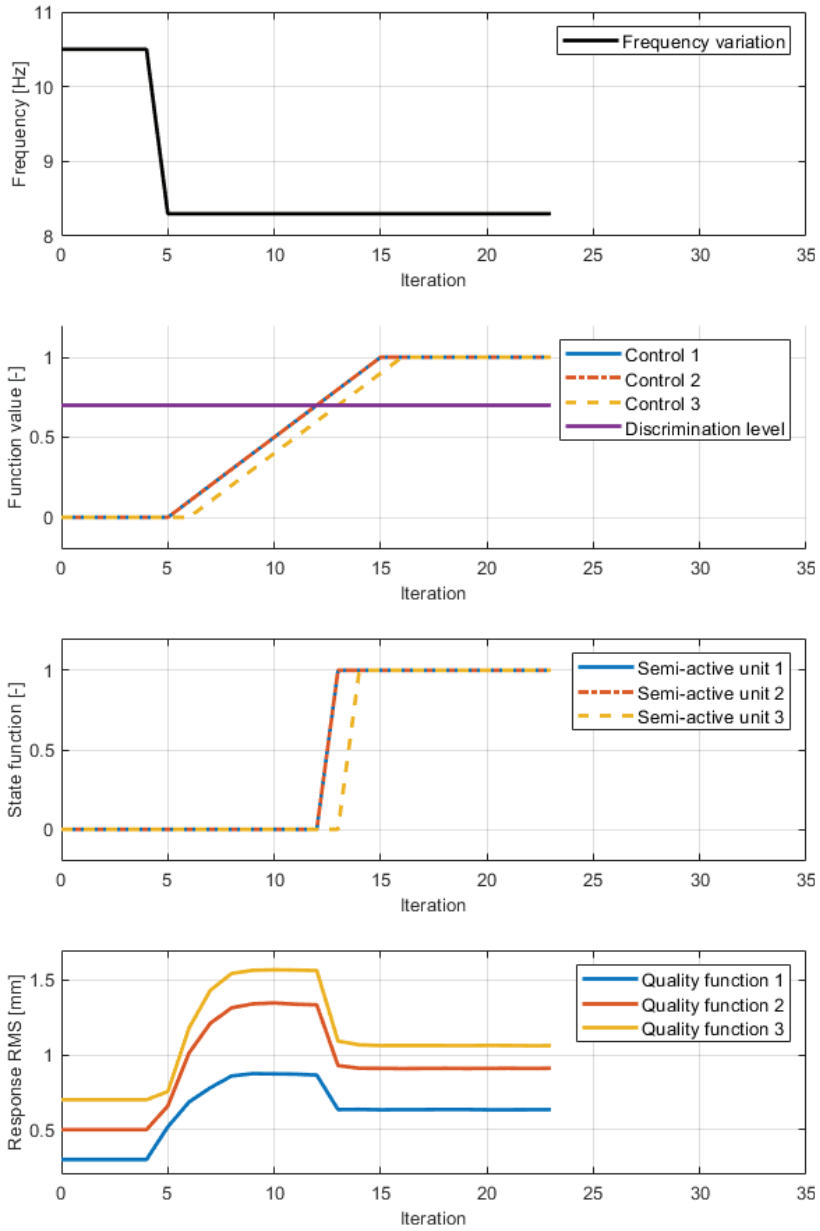

Figure 5: Control algorithm: response of the system to a step frequency decrease

As seen in Figure 5, the stepwise change in excitation frequency triggers an instant reaction of the algorithm and adjustments to the control parameters. The discrimination threshold is crossed at the 12th and 13th iterations, which results in changes of the actuator states. Semi-active unit No. 3 switches its state in the 13th iteration, and a gradual reduction of RMS values can be observed.

7 CONCLUSIONS

This contribution presented preliminary results on vibration control in a frame structure equipped with semi-active members using a reinforcement learning approach. The study confirms the intended effective operation of the system. The algorithm has a potential for tuning the structural response under alternating external excitations and efficiently minimizing the amplitude of the vibration response.

ACKNOWLEDGEMENTS

The authors gratefully acknowledge the support of the National Science Centre, Poland, granted under the grant agreement 2020/39/B/ST8/02615. For the purpose of Open Access, the authors have applied a CC-BY public copyright licence to any Author Accepted Manuscript (AAM) version arising from this submission.

REFERENCES

[1] B. Basu, O. S. Bursi, F. Casciati, S. Casciati, A. E. Del Grosso, M. Domaneschi, L. Faravelli, J. Holnicki-Szulc, H. Irschik, M. Krommer, M. Lepidi, A. Martelli, B. Ozturk, F. Pozo, G. Pujol, Z. Rakicevic, and J. Rodellar, "A European Association for the Control of Structures joint perspective. Recent studies in civil structural control across Europe," *Structural Control and Health Monitoring*, vol. 21, no. 12, pp. 1414–1436, 2014.

[2] S. Korkmaz, "A review of active structural control: challenges for engineering informatics," *Computers & Structures*, vol. 89, no. 23-24, pp. 2113–2132, 2011.

[3] S. Hurlebaus and L. Gaul, "Smart structure dynamics," *Mechanical systems and signal processing*, vol. 20, no. 2, pp. 255–281, 2006.

[4] M. Ostrowski, B. Błachowski, B. Popławski, D. Pisarski, G. Mikułowski, and Ł. Jankowski, "Semi-active modal control of structures with lockable joints: general methodology and applications," *Structural Control and Health Monitoring*, vol. 28, no. 5, p. e2710, 2021.

[5] G. Mikułowski, B. Popławski, and Ł. Jankowski, "Semi-active vibration control based on switchable transfer of bending moments: Study and experimental validation of control performance," *Smart Materials and Structures*, vol. 30, no. 4, p. 045005, 2021.

[6] H. Kurino, J. Tagami, K. Shimizu, and T. Kobori, "Switching oil damper with built-in controller for structural control," *Journal of Structural Engineering*, vol. 129, no. 7, pp. 895–904, 2003.

[7] D. Silver, T. Hubert, J. Schrittwieser, I. Antonoglou, M. Lai, A. Guez, M. Lanctot, L. Sifre, D. Kumaran, T. Graepel, T. Lillicrap, K. Simonyan, and D. Hassabis, "A general reinforcement learning algorithm that masters chess, shogi, and go through self-play," *Science*, vol. 362, no. 6419, p. 1140–1144, 2018.

[8] G. Reddy, A. Celani, T. Sejnowski, and M. Vergassola, "Learning to soar in turbulent environments," *Proceedings of the National Academy of Sciences*, vol. 113, no. 33, pp. E4877–E4884, 2016.

[9] Y. Jiao, F. Ling, S. Heydari, N. Heess, J. Merel, and E. Kanso, "Learning to swim in potential flow," *Physical Review Fluids*, vol. 6, p. 050505, 2021.

[10] H. Shi, Y. Zhou, X. Wang, S. Fu, S. Gong, and B. Ran, "A deep reinforcement learning-based distributed connected automated vehicle control under communication failure," *Computer-Aided Civil and Infrastructure Engineering*, vol. 37(15), pp. 2033–2051, 2022.

[11] Y.-A. Zhang and S. Zhu, "Novel model-free optimal active vibration control strategy based on deep reinforcement learning," *Structural Control and Health Monitoring*, vol. 2023, p. 6770137, 2023.

[12] Z. Qiu, G. Chen, and X. Zhang, "Reinforcement learning vibration control for a flexible hinged plate," *Aerospace Science and Technology*, vol. 118, p. 107056, 2021.

[13] A. Khalatbarisoltani, M. Soleymani, and M. Khodadadi, "Online control of an active seismic system via reinforcement learning," *Structural Control and Health Monitoring*, vol. 26, no. 3, p. e2298, 2019.

[14] C. Dengler and B. Lohmann, "Actor-critic reinforcement learning for the feedback control of a swinging chain," *IFAC Papers*, vol. 51, p. 378–383, 2018.

[15] B. Adam and I. Smith, "Reinforcement learning for structural control," *Journal of Computing in Civil Engineering*, vol. 22, no. 1, pp. 133–139, 2008.

[16] D. Pisarski and Ł. Jankowski, "Reinforcement learning-based control to suppress the transient vibration of semi-active structures subjected to unknown harmonic excitation," *Computer-Aided Civil and Infrastructure Engineering*, vol. 38(12), pp. 1605–1621, 2023.

[17] A. Jedlińska, D. Pisarski, G. Mikułowski, B. Błachowski, and Ł. Jankowski, "Semi-active structural control using viscous dampers and reinforcement learning," in *Proceedings of the 10th ECCOMAS Thematic Conference on Smart Structures and Materials, SMART 2023*, Patras, Greece, July 2023, pp. 589–596.

[18] A. Jedlińska, D. Pisarski, G. Mikułowski, B. Błachowski, and Ł. Jankowski, "Semi-active control of a shear building based on reinforcement learning: Robustness to measurement noise and model error," in *Proceedings of the 18th Conference on Computer Science and Intelligence Systems, FedCSIS 2023*, Warsaw, Poland, September 2023, pp. 1001–1004.

[19] A. Jedlińska, D. Pisarski, G. Mikułowski, B. Błachowski, and Ł. Jankowski, "Damage-aware structural control based on reinforcement learning," in *Proceedings of the 11th European Workshop on Structural Health Monitoring, EWSHM 2024*, Potsdam, Germany, June 2024.

XI ECCOMAS Thematic Conference on Smart Structures and Materials - SMART 2025
M. Krommer, M. Nader and M. Schagerl (Eds)

Received: 29 April 2025 / Revised: 29 August 2025 / Accepted: 25 October 2025
© The Author(s) 2025

Smart Pneumatic Airbag-Type Energy Absorber - Design and Development

Blazej Poplawski, Jan Stoppel, Mariusz Ostrowski, Rafał Wiszowaty, Rami Faraj

Abstract. Large pneumatic airbag-type energy absorbers, such as rescue air cushions, are inherently passive structures. Large size, low stiffness, high displacements during the impact as well as large gas volume enclosed inside the airbag – these are, among others, the biggest obstacles preventing the development of adaptation strategies for these devices. Therefore, their ability to actively adjust their mechanical properties in real-time, based on detected impact parameters, is highly limited. Real-time adaptation seems impossible or extremely challenging to be implemented for such devices. Nevertheless, adaptation of their properties, based on the impact parameters estimations taken before its occurrence, yields promising results.

This study explores the challenges in developing an adaptive pneumatic airbag-type energy absorber. Key aspects include designing an adaptation strategy, implementing the physical adaptation system within the airbag, conducting numerical simulations, experimentally testing the system, and advancing toward full autonomy. Achieving autonomous operation requires several critical steps, primarily the accurate estimation of impact parameters for a falling object. To accomplish this, various methods capable of detecting, tracking, and estimating the object's trajectory must be evaluated, implemented, tested, and compared from multiple perspectives. Promising approaches include radar, lidar, and computer vision, with computational cost being the most crucial factor, as it directly affects processing time. Once an effective impact parameter estimation system is established, it will be integrated with the control system responsible for executing the adaptation strategy, ultimately enabling fully autonomous operation.

Key words: Adaptive Rescue Cushion, Adaptive Airbag, Pneumatic Energy Absorber, Adaptive Impact Absorption, Impact Parameters Estimation

1 INTRODUCTION

Rescue air cushions are intended to safeguard individuals who jump or fall from significant heights. Although their initial use dates back to the 20th century, they represent one of the most recent developments in fall protection systems to gain widespread acceptance among regulatory

Blazej Poplawski & Jan Stoppel & Mariusz Ostrowski & Rafał Wiszowaty & Rami Faraj
Institute of Fundamental Technological Research, Polish Academy of Sciences, ul. Pawi´skiego 5B, 02-106 Warszawa, Poland, e-mail: bpop@ippt.pan.pl

authorities. Despite their long presence, their design has not changed much since the first devices of this type. Their operational principle relies on generating a pneumatic force – similar to that employed in automotive airbags – to decelerate the falling person as gently as possible upon impact. However, practical applications indicate that achieving satisfactory levels of load attenuation and operational safety remains a significant challenge. They are most commonly used in emergency situations, such as evacuation from a burning building or assisting during suicide attempts by jumping from height.

For such a device to be approved for use by qualified safety personnel, such as firefighters, it must undergo a formal certification procedure as stipulated in national standards (e.g. DIN 14151 [1]) or special regulations issued by authorized public administration authorities (e.g. the Polish regulations outlined in [2]). Despite undergoing formal certification procedures, rescue cushions are still regarded as relatively hazardous devices. Consequently, their deployment is recommended only as a last resort, with ladder trucks remaining the preferred method for assisting individuals at risk of falling.

Rescue cushions demonstrate substantially diminished effectiveness when subjected to fall parameters outside their designated operational conditions. This inherent performance degradation justifies their classification as a last-resort intervention in emergency situations. This is also supported by the fact that documented fatalities have occurred during training exercises, where a firefighter died while jumping onto a rescue cushion from relatively low height.

Integration of smart technologies into such structures could significantly improve shock absorption efficiency across diverse impact conditions, representing an important societal benefit. However, all currently available devices of this type remain entirely passive in design. Notably, neither academic nor industrial sectors have demonstrated meaningful progress in this area, leaving the problem of their low efficiency unsolved. Our research so far proved that integrating adaptation mechanisms into these devices is possible and effective [3, 4]. This paper presents a general overview of the impact absorption efficiency of rescue cushions, outlines our findings on potential improvements through the adaptation of their characteristics, and explores the integration of smart functionalities enabling autonomous adjustment of the device.

2 OPERATION PRINCIPLE AND PERFORMANCE IMPROVEMENT

Rescue cushions are, in essence, large-scale airbags whose operating principle relies on the generation of a pneumatic counterforce. This force arises from the rapid compression of air within the cushion upon impact, effectively opposing and dissipating the kinetic energy of a falling individual. Improvement of its energy dissipation effectiveness results in reduction of peak forces transmitted to the body, thereby mitigating the risk of injury. This issue has been acknowledged by German regulatory authorities, who, in the standard specifying the approval criteria for rescue cushions intended for the German market, have stipulated that the maximum accelerative loads transmitted to a person during impact must not exceed 80 g for the head and 60 g for the thorax and pelvis, with these limits applying to durations exceeding 3 ms [1].

Figure 1 illustrates a comparison between the theoretical time profiles of impact force experienced by a falling individual when landing on a conventional rescue air cushion and on

a cushion with improved energy dissipation efficiency. A corresponding comparison in the force–displacement domain is shown in Figure 2.

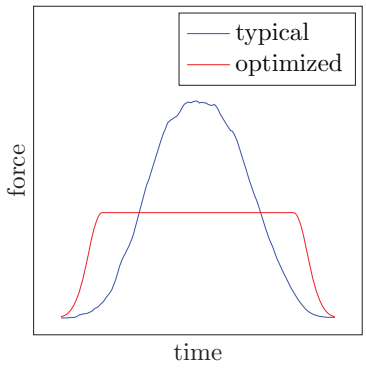

Figure 1: Typical and improved force-time curve during impact

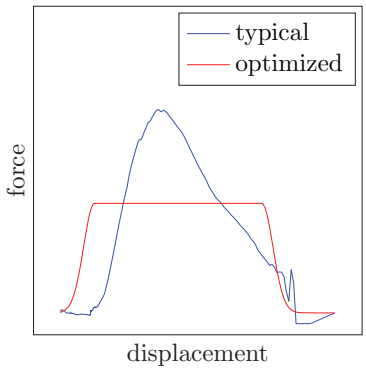

Figure 2: Typical and improved force--displacement curve during impact

The force profiles resulting from impact on a standard rescue cushion typically exhibits a bell-shaped curves, characterized by a pronounced peak. Any proposed improvements should aim to reshape these profiles to more closely resemble the curves labelled ‘optimized’ in the figures, thereby reducing the peak force transmitted to the body. In both cases, the optimized cushion design demonstrates a significant reduction in peak impact force and a broader distribution of force over time or displacement, indicating more effective energy absorption. These characteristics are critical for minimizing injury risk and enhancing the overall safety performance of rescue cushions. Lowering the peak force is critical for minimizing the risk of injury, as it directly decreases the maximum stress experienced by different parts of the human body during deceleration. Ideally, the initial phase of impact would involve the compression of the gas within the airbag without any leakage, allowing for the efficient build-up of internal pressure. Once the force exerted on the falling individual reaches a predefined threshold, a controlled release of gas would commence to maintain a near-constant force plateau, thereby extending the deceleration duration while limiting peak force. Following the completion of the deceleration process – prior to ground contact – the reaction force would rapidly diminish to zero, indicating a safe and complete energy dissipation.

Several factors inherent to the impact dynamics of rescue cushions hinder the achievement of an optimal force-time distribution. The large physical dimensions of the cushion entails a substantial internal gas volume, which in turn requires extensive venting areas to facilitate adequate gas expulsion during impact. This imposes the need for a significant variation in outflow area between the initial pressure build-up phase and the subsequent force plateau phase. Achieving precise real-time control of this gas release would demand highly responsive actuators capable of maintaining accuracy across a wide operational range. Additionally, the use of flexible membrane materials in the construction of the cushion further complicates the continuous control of gas discharge, as such materials may deform unpredictably under dynamic

loading. Compounding these challenges is the short duration of the impact event – typically in the range of 100 to 200 milliseconds – which necessitates extremely rapid and coordinated system response. These constraints significantly limit the feasibility of implementing real-time control mechanisms, as the required precision and response speed are difficult to achieve under the given conditions. Consequently, a more viable approach involves enhancing energy dissipation efficiency through passive means or by pre-adjusting the performance characteristics of the cushion based on estimated impact parameters obtained prior to the event.

3 RESCUE CUSHION DESIGN

Rescue air cushions are conventionally categorized into two principal types: (1) pneumatic-frame systems, which employ an inflated structural frame to maintain cushion shape, and (2) fan-inflated systems, which utilize high-capacity fans to continuously supply air for shape preservation. The typical configurations of both types of rescue cushions are shown in Figure 3. Specifically, the pneumatic-frame variant is depicted in Figure 3a, while the fan-inflated version is illustrated in Figure 3b.



(a) Pneumatic type (b) Fan type

Figure 3: Exemplary rescue air cushions (AI generated)

3.1 PNEUMATIC-FRAME CUSHION

This type of rescue air cushion incorporates a deformable frame structure inflated with compressed air (airtight pneumatic frame), over which a membrane is tensioned to form the airbag. Prior to impact, the internal pressure within the cushion is equal to atmospheric pressure. The

membrane is equipped with discharge orifices/vents that allow air to escape during compression. These orifices are dimensioned to induce choked flow conditions, thereby generating a desirable pressure increase as the cushion deforms. Simultaneously, they are sufficiently large to limit the back-bounce effect from the air cushion. One of the earliest documented references to this type of rescue cushion appears in a patent application by Peter Lorsbach [5]. Since its introduction, the fundamental design has remained largely unchanged.

An advantage of using a pneumatic frame to maintain the shape of the air cushion prior to impact is the possibility of transporting the deployed device, along with the ease and speed of its deployment. The cushion is deployed by filling the frame with compressed gas from a cylinder, after this relatively low time consuming process, the device is ready to absorb a fall. Due to the airtightness of the frame, the device does not require continuous gas supply, which allows for its free relocation within the boundaries of the rescue operation area.

The primary limitation of this design lies in the relatively small top surface area of such rescue cushions. Scaling up the cushion is constrained by the increasing structural demands placed on the frame, as larger dimensions require proportionally greater rigidity to maintain stability. One way to achieve the necessary rigidity is by increasing the internal pressure within the airframe; however, this may exceed the mechanical limits of the materials typically used, potentially necessitating a change to stronger, and often heavier or more expensive, materials. Additionally, enlarging the cushion and its supporting frame leads to a significant rise in the volume of compressed air required for deployment, complicating both storage and operational logistics, as the cylinder with compressed gas, used for filling the pneumatic frame, would be much bigger and heavier. This increase in volume not only extends the deployment time but also adds to the overall weight of the system, thereby reducing portability and limiting its practicality for rapid-response scenarios.

3.2 FAN-INFLATED CUSHION

In fan-inflated rescue cushions, a slight internal overpressure – maintained by the continuous inflow of air from external fans and the regulated outflow through orifices or vents (similar to those used in pneumatic-frame cushions) – allows the structure to retain its shape. This approach facilitates the construction of rescue cushions in virtually any size and reduces the requirement for airtightness, as only a minimal overpressure is needed to maintain its shape. Larger cushion heights significantly enhance impact absorption from higher falls, while increasing the top surface area has been shown to positively influence the psychological comfort of individuals preparing to jump. Consequently, the scalability of fan-inflated systems represents a major advantage over pneumatic-frame designs. However, their primary drawback lies in their stationary nature, due to the necessity of a continuous connection to the air supply system and much greater weight.

As with pneumatic-frame rescue cushions, the fundamental design of fan-inflated systems has remained largely unchanged since their initial development, as documented in John Scurlock's patent application [6].

4 ENERGY ABSORPTION IMPROVEMENT METHODS

As mentioned earlier, passive rescue cushion systems typically produce force-time (force-displacement) profiles with a bell-shaped curve during impact (see Figures 1 and 2). Achieving a force distribution that more closely approximates the optimal profile necessitates the incorporation of adaptive or intelligent/smart features. Such enhancements would enable the system to modify its response characteristics based on pre-estimated impact parameters.

Rescue cushions of pneumatic-frame type may incorporate passive design features aimed at enhancing their energy absorption performance. For instance, one of the earliest patents for such rescue cushions proposed the inclusion of a horizontal bulkhead positioned at mid-height within the cushion, intended to be nearly impermeable to air flow [5]. This internal partition was designed to equalize pressure distribution within the device during impact. In contemporary designs, such bulkheads are still present; however, they typically include large openings that prevent the establishment of significant pressure differences between the upper and lower chambers, thereby limiting their intended function.

In the case of pneumatic-frame rescue cushions, regulating the venting area through adjustable orifices appears to be the most viable approach for achieving adaptive behaviour. The effectiveness of this method has been demonstrated in laboratory-scale experiments [3, 4]. Using this technique, the venting area can be tailored to manually estimated impact parameters by referencing predetermined ”choice surfaces” – surfaces that define the optimal venting area as a function of key parameters, such as impact velocity and the mass of the falling individual, taking into account possible errors in estimates. However, manual estimation of these parameters is prone to significant inaccuracies. To mitigate this, the choice surfaces must incorporate safety margins, which inherently reduces the system’s potential for optimal energy absorption. Moreover, reliance on manual estimation is often viewed by potential operators as risky, as it places a high degree of responsibility on human judgment in critical situations.

Fan-inflated rescue cushions, owing to their operating principle, offer potential for enhancement through the integration of at least two intelligent control features. As with pneumatic-frame systems, one possibility is to regulate the venting area of the outflow orifices (”breathers”) based on estimated impact parameters. Alternatively, the volumetric airflow supplied by the attached fan could be actively controlled to adjust the internal pressure within the airbag. However, this latter approach faces significant limitations. Standard large-scale fan-inflated rescue cushions are certified for use in falls from heights of up to 60 meters. Free-fall duration from such height lasts approximately 3.5 seconds. This time frame is generally insufficient for conventional industrial fans – typically constructed from steel and characterized by high rotational inertia – to achieve meaningful changes in rotational speed, generated airflow and, consequently, built overpressure. Figure 4 illustrates this phenomenon: preliminary tests revealed that the fan supplying gas to the rescue cushion requires approximately 30 seconds to transition from zero to maximum volumetric flow rate, with pressure stabilization occurring after an additional 10-second delay ($\sim$40 seconds total from initiation). This observation further challenges the feasibility of implementing real-time adaptability through fan control. Moreover, the limited

pressure difference achievable by the tested fan presents an additional constraint. Specifically, the fan under investigation was capable of generating an overpressure of approximately 150 Pa (see Figure 5). Range of pressure variation such fans can produce is relatively limited compared to the rapid and substantial pressure changes induced by impact events (see Figure 6 for comparison of pressure levels generated by the fan supplying the airflow and the impact in standard conditions). These limitations favour the use of controllable outflow vents over the regulation of fan operation as a means of adapting the cushion's performance. One possible advantage of fan-inflated rescue cushions is the possibility of placing the venting elements within the duct connecting the fan to the cushion. Since this duct maintains a relatively stable shape during impact, it may offer improved consistency between numerical simulations and experimental results, compared to vents mounted directly on the deformable sidewalls of the cushion.

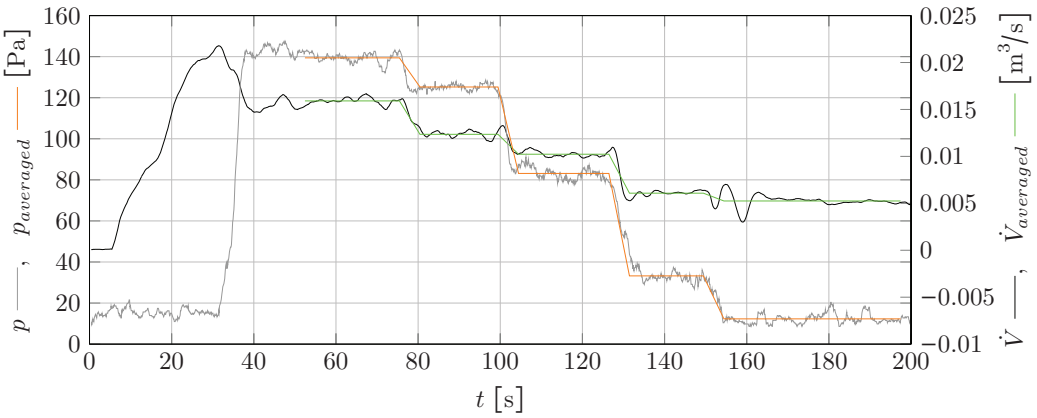

Figure 4: Time histories of internal pressure within the rescue cushion and the volumetric airflow rate generated by the supply fan

5 IMPACT PARAMETERS ESTIMATION SYSTEMS

A remote impact parameters estimation system represents a critical component of an intelligent rescue cushion. It enables the automatic adaptation of the system's performance characteristics, irrespective of the cushion type – whether pneumatic-frame or fan-inflated – as it functions as an independent module. This system can be integrated with adaptive cushions, currently operated manually, by allowing for automatic recognition of impact parameters, thereby eliminating the need for operator input.

Two fundamentally distinct methodological approaches can be identified for remote impact recognition: vision-based and wave-based systems.

Vision-based techniques have gained significant attention in recent years. Numerous methods have been developed for estimating the distance to observed objects, ranging from traditional stereo vision algorithms [7, 8] to more recent monocular vision approaches [9]. A principal limitation of these methods is that depth estimation remains inherently indirect – no

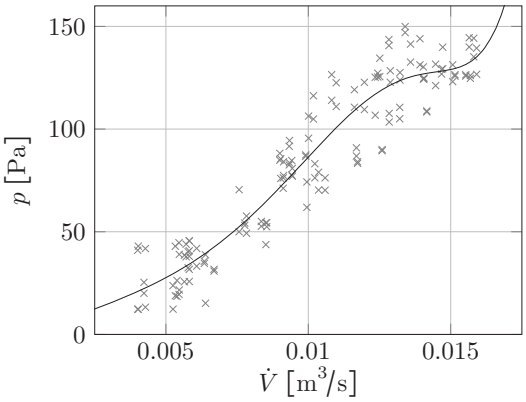

Figure 5: Pressure in the cushion obtained by various volumetric flow rates of the air

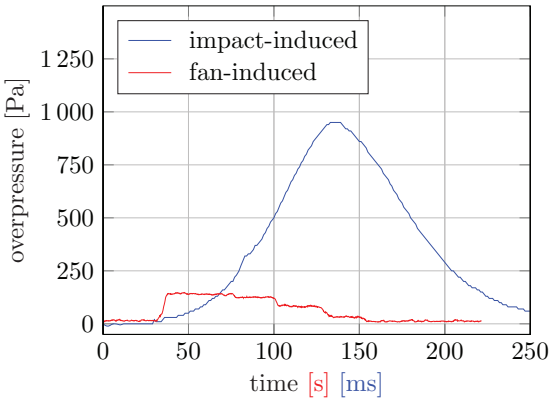

Figure 6: Pressure in the cushion as a result of maximal fan power (red) and impact (blue)

vision-based system can directly measure distance, as the estimation relies on geometric inference or learning-based approximations.

In addition to depth estimation, accurately detecting, classifying, and tracking the object of interest is essential for effective impact parameter recognition. A wide variety of techniques have been developed for this purpose, with deep neural network-based methods currently dominating the field. These can be categorized into two primary classes: single-stage detectors, such as the Single Shot Multibox Detector (SSD) [10], and two-stage detectors, such as Region-based Convolutional Neural Networks (R-CNN) [11]. Historically, two-stage methods offered superior accuracy at the cost of significantly greater computational complexity. However, recent advances in single-stage models have led to notable improvements in both computational efficiency and detection accuracy. Among these, the YOLOv8 framework has demonstrated state-of-the-art performance in object detection and tracking tasks [12].

An alternative class of methodologies, capable of directly measuring the distance to an object of interest, involves the use of wave-based systems comprising wave emitters and receivers. Depending on the nature of the wave employed, these systems can be categorized as ultrasonic, radar, or LiDAR. Ultrasonic devices operate using sound waves, while radar and LiDAR systems utilize electromagnetic waves at differing frequency ranges. Due to the relatively low frequency – and consequently long wavelength – of ultrasound, such systems are generally unsuitable for accurately detecting objects with dimensions comparable to the human body. In contrast, high-frequency radar and LiDAR sensors are highly effective for this application, offering the spatial resolution necessary for precise detection and tracking of human-sized targets.

Both wave-based methodologies – LiDAR and radar – offer distinct advantages and limitations in the context of human body recognition and tracking. The very high frequency of LiDAR, typically in the hundreds of terahertz, enables the detection of small objects due to the inverse relationship between wavelength and object resolution; shorter wavelengths allow for finer spatial discrimination. However, this high frequency also makes LiDAR signals more sus-

ceptible to atmospheric attenuation. Substances such as fog, rain, water vapour, or smoke can significantly absorb or scatter the signal, thereby degrading performance in adverse environmental conditions. In such scenarios, high-frequency radar systems – operating at 24 GHz, 77 GHz, or 79 GHz – present a more robust alternative. Although they offer lower spatial resolution compared to LiDAR, their longer wavelengths enable greater penetration through atmospheric obscurants, making them better suited for reliable operation in challenging environments.

Regardless of the selected approach, these methods offer distinct advantages over computer vision techniques by enabling direct distance measurements and permitting volume estimation of falling objects through methods such as voxelization.

The optimal performance of both methods can be achieved through the application of data fusion techniques.

6 TESTING EQUIPMENT

To reliably evaluate potential enhancements in the energy dissipation performance of rescue cushions, several experimental setups were developed.

The primary and most essential apparatus is the drop tower (see Figure 7a), which enables the simulation of vertical falls from heights of up to 6 meters. Planned modifications to the tower include a mechanism capable of imparting an initial vertical velocity to the falling object, thereby replicating the conditions of falls from greater heights. Additionally, the system will be equipped to introduce horizontal velocity components, enabling the simulation of parabolic trajectories representative of real-world jumping scenarios.

Currently, the test objects being dropped consist of plates and spheres, in accordance with the certification procedures outlined in the DIN standard [1] and relevant Polish regulatory documentation [2]. However, to more accurately replicate the biomechanical response of a human body during impact, a manikin with limited joint mobility is being developed (see Figure 7b). This manikin will be outfitted with a data acquisition system designed to measure accelerations in three critical regions: the head, thorax, and pelvis.

An additional experimental setup was developed for laboratory-scale testing of axial fans. This system was designed in accordance with the ISO standard specifying test methods for industrial fans [13]. It enables the evaluation of fan-inflated rescue cushions constructed at laboratory scale (see Figure 8).

7 CONCLUSIONS

Rescue air cushions play a vital role in public safety; however, they have received limited attention from both academic and industrial communities. Their current energy dissipation capabilities could be significantly enhanced through the integration of intelligent features. An independent system for estimating impact parameters would enable the full automation of adaptive mechanisms incorporated into rescue cushions. This system could be optimized through the fusion of data obtained from computer vision techniques and wave-based sensors such as LiDAR or radar.



(a) Drop tower for testing purposes (b) Dummy imitating a falling person

Figure 7: Drop testing equipment

Although current certification procedures do not require the use of manikins that replicate the biomechanical behaviour of the human body, incorporating such test devices into both experimental and computational studies would be highly advantageous. This is particularly important given that the effectiveness of energy dissipation in rescue cushions is strongly influenced by the specific characteristics of each impact event.

The research campaign undertaken to enhance the energy dissipation characteristics of rescue cushions holds considerable promise for advancing the state of the art in impact mitigation technologies. By improving the performance of these devices, particularly in terms of reducing peak impact forces and adapting to a wider range of fall conditions, the safety and survivability of individuals in emergency scenarios can be significantly increased. In turn, this could lead to meaningful societal benefits, including the reduction of injury severity and fatalities in high-risk situations such as building evacuations or rescue operations. Moreover, from an economic perspective, the widespread deployment of more effective rescue cushions may reduce healthcare costs associated with fall-related injuries and lower the liability risks faced by emergency service providers and building operators.

Continued research and development in this area not only addresses a critical gap in safety technology but also contributes to broader public health and emergency preparedness goals.

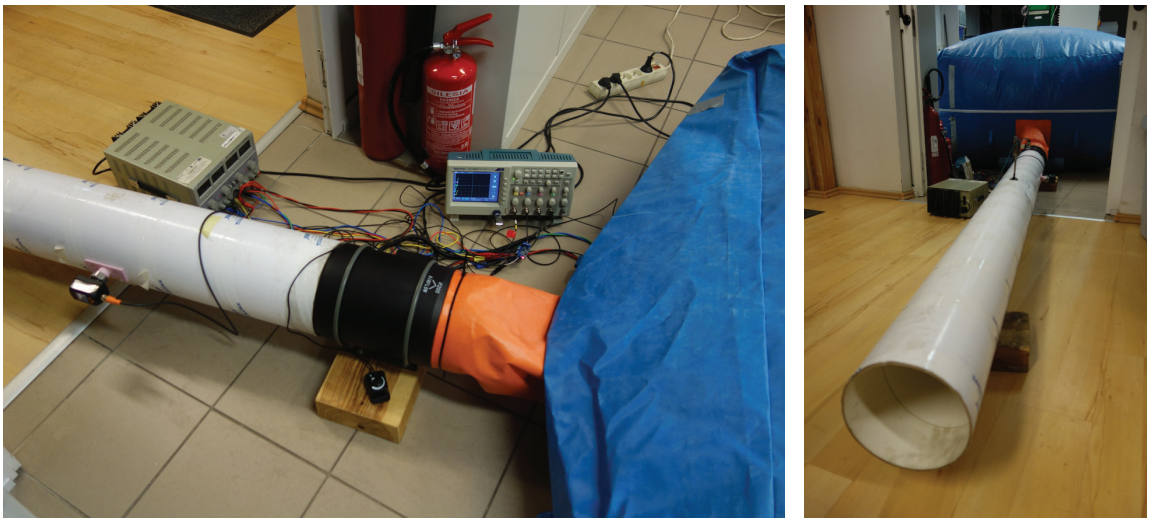

Figure 8: Fan testing equipment

Declaration of Generative AI and AI-assisted technologies in the writing process

During the preparation of this work the authors used DeepL, Google Translate and LLMs in order to correct language, grammar, and punctuation of the text. After using these tools, the authors reviewed and edited the content and take full responsibility for the content of publication.

ACKNOWLEDGMENTS

This research was funded in part by the National Science Centre, Poland (2021/41/N/ST8/04302). For the purpose of Open Access, the authors have applied a CC-BY public copyright license to any Author Accepted Manuscript (AAM) version arising from this submission.

This work was funded in part by The National Centre for Research and Development, Poland (LIDER13/0285/2022), under the programme LIDER. The value of the provided financing is PLN 1,500,000.

REFERENCES

[1] "DIN 14151-3, Sprungrettungsgeräte – Teil 3: Sprungpolster 16 – Anforderungen, Prüfung (in German)," Apr. 2024.

[2] "Rozporzadzenie Ministra Spraw Wewnetrznych i Administracji z dnia 27 kwietnia 2010 r. (in Polish)," Sejm RP, Dz.U. Nr 85, Poz. 553.

[3] R. Faraj, B. Popławski, D. Gabryel, T. Kowalski, and K. Hinc, "Adaptive airbag system for increased evacuation safety," *Engineering Structures*, vol. 270, p. 114853, Nov. 2022. [Online]. Available: https://linkinghub.elsevier.com/retrieve/pii/S0141029622009348

[4] R. Faraj, B. Popławski, D. Gabryel, G. Mikułowski, and R. Wiszowaty, "On optimization of an adaptive pneumatic impact absorber – the innovative rescue cushion," *Bulletin of the Polish Academy of Sciences Technical Sciences*, pp. 153 436–153 436, Feb. 2025. [Online]. Available: https://journals.pan.pl/dlibra/publication/153436/edition/134025/content

[5] P. Lorsbach, "JUMP RESCUE APPARATUS," USA Patent 4,875,548, 1989.

[6] J. T. Scurlock, "INFLATABLE SAFETY CUSHION SYSTEM FOR CONTROLLED DECELERATION FROM FALLS OF GREAT HEIGHT," USA Patent 3,851,730, 1974.

[7] A. Saxena, J. Schulte, and A. Y. Ng, "Depth estimation using monocular and stereo cues," in *Proceedings of the 20th International Joint Conference on Artifical Intelligence*, ser. IJCAI'07. San Francisco, CA, USA: Morgan Kaufmann Publishers Inc., 2007, p. 2197–2203.

[8] J. M. Foley, "Depth, size and distance in stereoscopic vision," *Perception & Psychophysics*, vol. 3, no. 4, pp. 265–274, Jul. 1968. [Online]. Available: http://link.springer.com/10.3758/BF03212742

[9] H. Liu, T. Su, and J. Guo, "Autonomous driving enhanced: a fusion framework integrating LiDAR point clouds with monovision depth-aware transformers for robust object detection," *Engineering Research Express*, vol. 7, no. 1, p. 015414, Mar. 2025. [Online]. Available: https://iopscience.iop.org/article/10.1088/2631-8695/ada7c7

[10] W. Liu, D. Anguelov, D. Erhan, C. Szegedy, S. Reed, C.-Y. Fu, and A. C. Berg, "SSD: Single Shot MultiBox Detector," in *Computer Vision – ECCV 2016*, B. Leibe, J. Matas, N. Sebe, and M. Welling, Eds. Cham: Springer International Publishing, 2016, vol. 9905, pp. 21–37, series Title: Lecture Notes in Computer Science. [Online]. Available: http://link.springer.com/10.1007/978-3-319-46448-0_2

[11] R. Girshick, J. Donahue, T. Darrell, and J. Malik, "Rich Feature Hierarchies for Accurate Object Detection and Semantic Segmentation," in *2014 IEEE Conference on Computer Vision and Pattern Recognition*. Columbus, OH, USA: IEEE, Jun. 2014, pp. 580–587. [Online]. Available: http://ieeexplore.ieee.org/document/6909475/

[12] "YOLOv8: State-of-the-Art Computer Vision Model," https://yolov8.com/, Accessed: 2025-04-10.

[13] "PN-EN ISO 5801:2017-12, Fans - Performance testing using standardized airways (in Polish)," 2017.

XI ECCOMAS Thematic Conference on Smart Structures and Materials - SMART 2025
M. Krommer, M. Nader and M. Schagerl (Eds)

Received: 16 April 2025 / Revised: 27 August 2025 / Accepted: 25 October 2025
© The Author(s) 2025

Development and Implementation of a Combined SHM/CM System to Identify Yield Losses of a 2.4MW Wind Turbine

Marcel Wiemann, Lukas Bonekemper, Benedikt Wüllner, Herbert Friedmann, Peter Kraemer

Abstract. Monitoring of wind turbine critical components has become both obligatory and, in some cases, legally mandated. Due to this, Original Equipment Manufacturers (OEMs) and suppliers have developed and industrialized an extensive portfolio of monitoring systems in recent years. Despite these successful implementations of the before mentioned monitoring concepts, e.g. for ice detection, there remains a need for research and innovative approaches to comprehensively safeguard all critical areas of a wind turbine against damage and suboptimal operation. This paper describes the development and commissioning of an extensive, combined Structural Health Monitoring (SHM) and Condition Monitoring (CM) system for research purposes on a 2.4 MW wind turbine. The resulting measurement data are used primarily to quantify yield losses caused by undesired structural vibrations of rotor blades, the hub, the drivetrain and the nacelle, rather than for damage diagnosis. The already extensively instrumented wind turbine was further equipped with numerous sensor systems. These include telemetry systems for capturing rotational and bending moments of the drivetrain, eddy current sensors for determining the rotor shaft orbit, accelerometers for identifying structural vibrations in supporting structures and rotor blades and meteorological measurement systems for assessing performance-relevant environmental parameters. Additionally, an interface with the turbines control system was established, enabling the synchronous storage and analysis of various operational parameters alongside measurement data. A high-performance 5G connection facilitates the continuous, automated transmission of measurement data and online diagnostics of the connected systems, which are equipped with fail-safe features for self-recovery. The instrumentation was implemented as part of the research project WEA-produktiv, whose long-term objective is to identify yield losses without requiring additional sensor technology. This extensive instrumentation is essential for the deep understanding and identification of significant correlations between measured wind turbine parameters and their impact on

Marcel Wiemann & Lukas Bonekemper & Benedikt Wüllner & Peter Kraemer
Chair of Mechanics with focus on Structural Health Monitoring (MSHM), University of Siegen, Campus Paul Bonatz, 57076 Siegen, Germany, e-mail: marcel.wiemann@uni-siegen.de

Herbert Friedmann
Wölfel Engineering GmbH & Co. KG, Max-Planck-Str. 15, 97204 Höchberg, Germany
e-mail: friedmann@woelfel.de

electricity production.

Key words: Structural Health Monitoring, Condition Monitoring, Yield losses, Imbalances, Drive Train Monitoring, Sensor Faults.

1 INTRODUCTION

CM and SHM systems for wind turbines are in most cases mandatory, either due to legal requirements or insurance regulations. These systems cover a broad range of technical components to ensure the safest possible operation. Typical examples include the continuous monitoring of nacelle vibrations, detecting icing or structural damage in rotor blades [1], and the observation of vibration amplitudes in drivetrain components. This paper presents the development, installation, and commissioning of a SHM/CM system on a 2.4 MW Nordex N117 wind turbine that is already extensively instrumented [2]. While far too complex and expensive for serial application, the system provides valuable insights within the research project WEA-produktiv [3, 4]. The overarching goal of the project is to identify power losses without the use of additional sensor technology, relying solely on SCADA data. However, the elaborate instrumentation described here is initially necessary to establish a meaningful understanding of the relationship between the measured vibration data, SCADA parameters, and power production. The recorded measurement data thus primarily serves to identify yield losses caused by undesired structural vibrations originating, for example, from rotor blades, the hub, the drivetrain or the nacelle. In this context, the instrumented system also serves as a so-called fleet leader. In addition to the intensively instrumented plant, the SCADA data of eight other plants are available, which are then to be analyzed with the findings of the fleet leader as part of the population monitoring. This work is complemented by two further publications focusing on data analysis and turbine simulation in Bladed [5, 6]. The following sections describe the instrumentation process from planning to implementation, addressing the requirements of the measurement system, specific challenges and risks, the integration with the turbine interface, and a detailed analysis of the technical components **[7]**. It is worth noting in this context that, under the terms of a usage agreement, the turbine will remain available to the MSHM working group as a research platform beyond the scope of the current project, meaning that its comprehensive instrumentation will continue to offer significant potential for future research topics and focal areas [8].

2 REQUIREMENT FOR EXTENSIVE INSTRUMENTATION

As outlined in the introduction, the primary purpose of the system is the detection of turbine states that lead to reduced energy yield. In order to identify the aforementioned correlations, the already extensive instrumentation must be further expanded [2]. For instance, essential SCADA parameters related to power generation—such as reactive power, voltage, and current are currently missing, as are simple timers and counters that would enable quantification of operational states. Furthermore, analysis of historical vibration data has revealed that the installed measurement systems do not record data in a time-synchronized manner, which significantly hinders the ability to correlate events such as blade vibrations with the power production. Likewise, rotor-induced vibrations in drivetrain components cannot be adequately captured Key environmental parameters—such as those required to determine air density, wind speed, and wind direction—are accessible only via the turbine's SCADA system and are either sampled at insufficient rates or entirely unavailable for the intended application. These limitations necessitate the establishment of a dedicated turbine interface to capture additional SCADA parameters, implement centralized time synchronization for current and future systems, measure torque and bending moments in drivetrain components, and deploy both a custom environmental monitoring system and a dedicated data transmission solution (via 5G connection).

3 CHALLENGES AND SPECIFIC RISKS FOR THE MEASUREMENT TECHNOLOGY AND PERIPHERALS

The instrumentation requirements directly inform the specifications for the measurement system. The system must be capable of capturing and processing a wide range of sensor data.

Peripheral Requirements

- High-performance 5G connectivity for data transmission and remote access
- Implementation of fail-safe functionalities
    - Self-recovering components and software
- Establishment of a connection to the turbine control system
- Common time base (master clock) for all subsystems

Measurement Technology Requirements

- Torque measurements (generator shaft, rotor shaft)
- Bending moment measurements (rotor shaft)
- Structural vibrations (accelerations and inclinations)
- Temperature monitoring
- Meteorological data (for determining air density, wind direction, and wind speed)
    - Essential for calculating the theoretically achievable power
- Position tracking (rotor shaft, blade positions)

Due to the complexity of the planned system and its integration into a fully operational wind turbine, specific challenges and risks arise that significantly complicate the implementation of the instrumentation and may lead to various complications.

Challenges and Risks

- Extremely limited installation space (existing option platform is fully occupied)
  - Hardly any space available for sensors or the central measurement cabinet
- Antennas on the turbine roof are exposed to wind, weather, and intense vibrations
- External components must be secured with appropriate lightning protection measures
- The existing turbine interface (OPC-XML-DA) is outdated
- Extensive approval processes (to rule out any risk to turbine operation)
- Torque measurement on a fast-rotating generator shaft (1500 RPM)
- Long-term power supply for the rotor shaft telemetry system

4 INSTALLED MEASUREMENT SYSTEM

The following chapter describes the implemented instrumentation, based on relevant subsystems and components, as well as the setbacks and problems during operation and instrumentation. Finally, the planned system expansion is discussed.

4.1 Interface to the SCADA-Server

To achieve the long-term project objective — detecting yield losses without the use of additional sensor systems — it is essential to establish a connection to the turbine's system interface. The parameters currently available or already being recorded are limited to basic environmental data, which are captured and stored via a Modbus system by the project partner Wölfel. Accessing the turbine’s SCADA server through the OPC-XML-DA interface enables the acquisition of over 300 parameters from the wind turbine (See Figure 1). These include a wide range of variables from various subsystems (e.g., condition monitoring system (CMS), PITCH, YAW, etc.) as well as key performance indicators such as active power, reactive power, current, voltage, and power limitations. Additionally, the access to internal timers and counters is possible, allowing for availability assessments since commissioning and, consequently, continuous monitoring of turbine performance. Since the planned IT infrastructure includes a dedicated 5G connection, it must be ensured that this poses no threat to the network of the turbine operator or the OEM. Infiltration of the University of Siegen’s network must not lead to any security risk for the turbine’s operational network. For this reason, a firewall specifically configured by the OEM was implemented to minimize this risk.

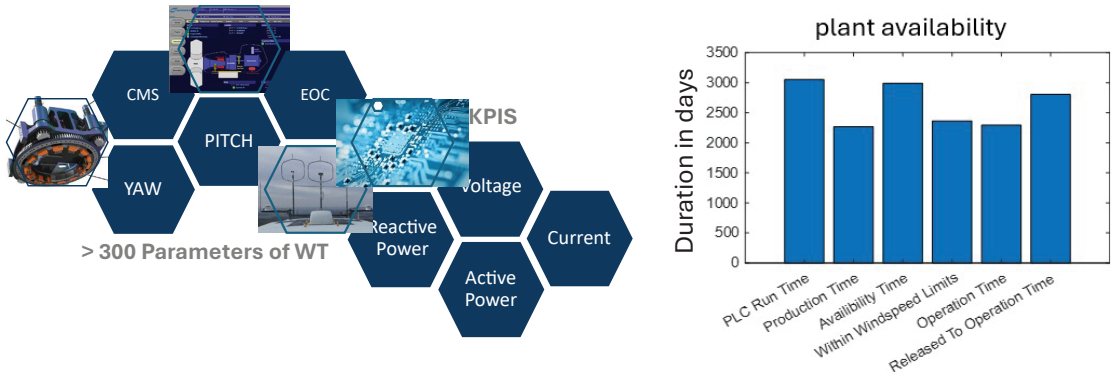

Figure 1: Overview of the possibilities of the OPC-XML-DA interface

4.2 System overview incl. data transmission

The diagram in Figure 2 provides a simplified overview of the planned and partially implemented measurement system, including its peripheral components and infrastructure. Even at the conceptual level, the complexity of the intended installation becomes apparent. Central key components include the IPC, the 5G router, and the time server provided by Hopf Elektronik GmbH. Time synchronization is addressed in detail in a separate chapter. The IPC (industrial computer) is a ruggedized version certified for use in vehicles, making it suitable for withstanding the vibrations typically encountered in wind turbines. It serves as the central hub for collecting measurement data, which is recorded by the Gantner measurement system, the edge base, and the turbine interface. Contrary to earlier concepts [6], no data pre-processing is performed on the IPC. Instead, the collected measurement data is automatically transferred via RSync to a workstation within the University Siegen network, where it is processed and analyzed. Therefore, the reliability of the 5G connection is of critical importance. However, short-term interruptions in connectivity do not pose a significant issue, as the IPC is equipped with sufficient buffer storage.

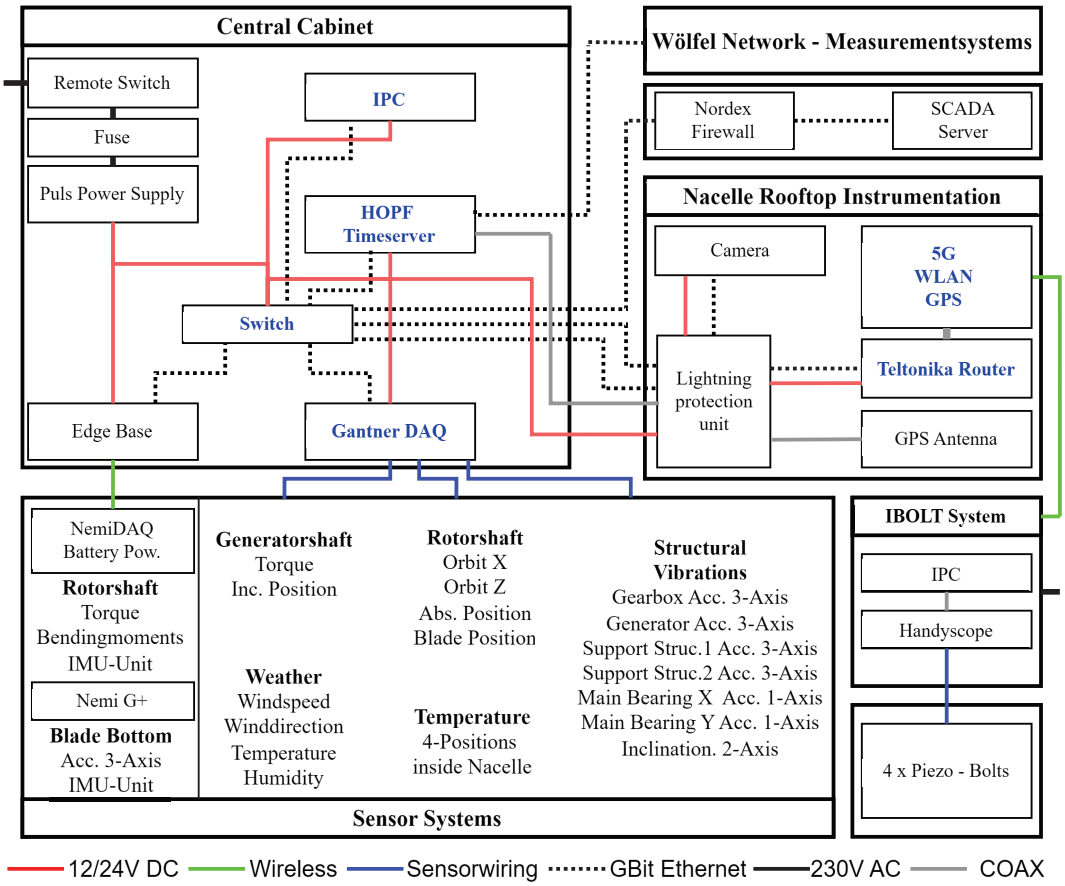

Figure 2: Overview of the implemented instrumentation

4.3 Measuring system – central control cabinet

A large part of the installed sensor system is connected to a central measurement system provided by Gantner. This system consists of a high-performance data acquisition controller and sensor-specific measurement cards. Its modular card-based architecture enables precise tailoring of the system to the instrumentation task at hand. In addition, the central control cabinet houses the evaluation unit for the generator shaft telemetry, power supply, protection systems, the time server, and the IPC. Due to the limited space available, a custom mounting structure had to be designed and integrated into the wind turbine to ensure secure installation of a cabinet of this size. Because of the heat generated by the components, forced ventilation is employed and the cabinet temperature is continuously monitored. The cabinet also provides both network connectivity and power supply for all components. To ensure long-term system availability during extended measurement campaigns, additional safety measures have been implemented. Specifically, it is possible to independently disconnect and restore the power to

system components via two separate subsystems. This functionality allows all components to be recovered from unintended or unforeseen failure states, if necessary. The cabinet weighs approximately 120 kg, which necessitated the use of the turbine's onboard crane for installation.

4.4 Time synchronization via HOPF GPS System

A critical aspect of the implemented instrumentation is the time synchronization of the connected and distributed systems. The system overview shown in Figure 2 represents only a small subset of the measurement systems installed on the turbine. Analysis of historical data has revealed that the recorded measurement data from the various systems are not time-synchronized.



Figure 3: HOPF Timeserver

In the case of simple standalone systems, this issue is usually negligible, as the controllers internal clock is authoritative. However, if data from multiple distributed systems are to be evaluated in a shared context, an appropriate synchronization strategy becomes essential. The installed time server, HOPF 8030 NTS, enables synchronization of a wide range of components (See Figure 3). Synchronization can be performed across two separate networks using the Network Time Protocol (NTP) or the Precision Time Protocol (PTP), or via the hardware-based IRIG-B interface [9]. The achievable accuracies with PTP or IRIG-B are of the order of 50 ns, which allows for advanced signal processing and system identification techniques—such as operational modal analysis—to be applied across different measurement systems. The internal clock of the time server is synchronized via a high-precision GPS signal, which is received by an antenna mounted on the turbine roof. In theory, this also enables highly accurate synchronization across multiple turbines, which could be particularly valuable in the context of population monitoring—for instance, in studies of wake effects [10].

4.5 Sensorics of the roof of the nacelle



Figure 4: Overview of the roof installation - environmental measurement and antenna setup

Despite the challenges associated with external installations on the nacelle roof of a wind turbine, such an installation was indispensable for this project. With a hub height of 141 meters, the system is subject to an increased risk of lightning strikes as well as continuous exposure to strong wind and precipitation. This results in specific requirements regarding the sealing of components and the implementation of appropriate lightning protection measures. The external installation includes a weather station (for measuring wind speed, wind direction, humidity and temperature), antenna systems (5G router, Wi-Fi, 5G antenna), a camera and a dedicated GPS antenna for time synchronization, see Figure 4. To ensure a high-performance and robust 5G connection to the outside world, the decision was made to place both the 5G router and antenna on the roof. This minimizes cable attenuation between the antenna and router, due to the reduced length of the cable. The systems were mechanically mounted on the turbine's instrumentation tube traverse and electrically grounded with great care to ensure safe discharge of electrical surges. All incoming and outgoing connections are equipped with surge protection to safeguard the components located inside the nacelle.

4.6 Sensorics for structural vibrations

The measurement of structural vibrations is a key component of the overall monitoring system, as the influence of undesired oscillations originating from the nacelle, hub, or rotor blades on power production is to be investigated. Therefore, four triaxial MEMS accelerometers have been installed on the generator, the gearbox and their respective support structures, see e.g. Figure 5. Two uniaxial MEMS accelerometers are mounted on the main bearing. In

addition, tower inclination is continuously monitored using a biaxial tilt sensor. A wireless triaxial MEMS accelerometer with an integrated IMU unit is mounted at the blade root of one of the rotor blades. Additional accelerometers provided by the project partner, as well as sensors that are part of the turbine's built-in IDD.Blade and SHM.Blade systems of Wölfel, supply valuable data from all rotor blades [11], [12]. Together, these data sources enable a comprehensive global analysis of structural vibrations.

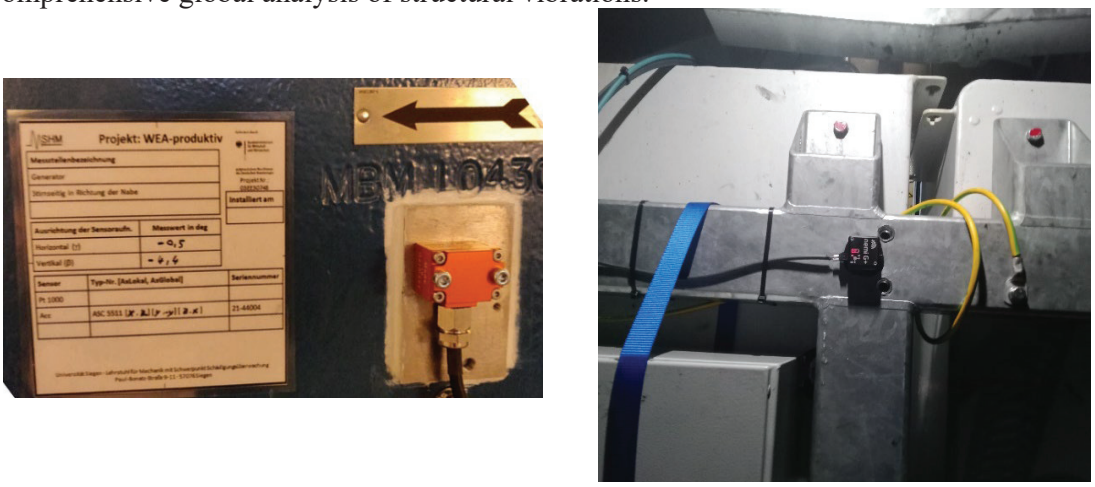

Figure 5: Wired MEMS sensor (left), wireless MEMS sensor (I4M) with attached power supply (right)

4.7 Monitoring of bolted connections

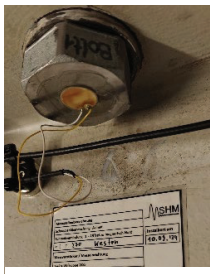

Figure 6: Instrumented screw head

In addition to the project-specific drivetrain instrumentation and the sensor system for structural health monitoring, a system for monitoring bolt preload beneath the azimuth bearing was installed (see Figure 2, bottom right). This system consists of a dedicated IPC for data preprocessing and control of the measurement device (type: Handyscope). Using a custom-developed multiplexer, measurements are performed on four M36x290 bolts to enable continuous monitoring of the preload force. For this purpose, four standard bolts were replaced with instrumented versions and wired accordingly (see Figure 6). The measurement is carried out via a piezoelectric element applied to the bolt head, enabling precise tracking of preload variations over time [13].

4.8 Sensorics for rotor shaft and generator shaft

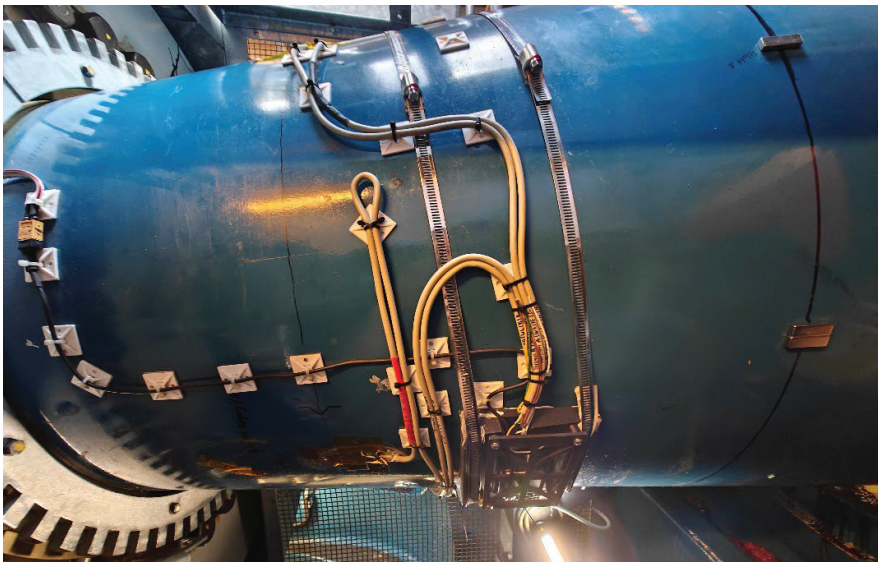

Figure 7: Instrumented rotor shaft



Figure 8: Combination sensor holder

To gain detailed insight into rotor-induced vibrations acting on the drivetrain, the rotor shaft was instrumented with a telemetry system from I4M [14], see Figure 7. The telemetry unit is a low-power device approximately the size of a 2.5-inch hard drive, capable of interfacing with three full-bridge strain gauges and evaluating internal IMU data. The collected data is transmitted wirelessly to the Edge Base, where it becomes available for further processing. In addition to torque, the system also records the bending moments of the rotor shaft. Power supply is provided by custom-built battery packs, which are mounted adjacent to the rotor shaft's encoder ring. At a sampling rate of 125 Hz, this setup allows for a measurement duration of approximately 6–7 months. Beyond the measurement of bending and torsional moments, the rotor shaft orbit is also captured. For this purpose, two eddy current sensors are installed with a 90° offset relative to each other, continuously measuring the distance to the rotor shaft with a precision of 0.01 mm. Combined with proximity switches that scan the encoder ring and a reset function triggered by magnets (visible on the right side in Figure 7), which also detect the passage of the blade relative to the tower, the shaft orbit can be referenced to the shaft's absolute position. To ensure precise measurement, the sensors are mounted in a custom-built, solid sensor bracket bolted beneath the rotor shaft (Figure 8). For reliable long-term monitoring,

it is essential to guarantee that no changes occur to the sensor setup. Therefore, all position-sensitive components are marked with tamper-evident sealant. Any minor change or loosening of nuts or bolts would thus become clearly visible during inspection.

4.9 Setbacks of the installation – lessons learned

Due to the complexity of the system and the implementation of novel technologies by MSHM / University of Siegen, various setbacks and issues were anticipated. The most critical of these are briefly outlined and explained below:

- **5G Router and Connection Stability**
  A key element for the success of the project is the continuous data transfer, realized via a 5G router. To ensure a reliable and stable connection, the router and its antenna were mounted on the nacelle roof. However, an unforeseen complication arose from unexpectedly high vibration amplitudes at the instrumentation support structure. These vibrations caused contact bounce at the SIM card interface, leading to frequent connection losses — particularly during high wind conditions. This issue was resolved by applying a non-conductive grease to the SIM card contacts (to dampen contact bounce) and increasing the contact pressure.
- **Telemetry Unit on the Generator Shaft**
  The telemetry unit from Manner, manufactured in 2000 and mounted on the generator shaft, functioned reliably during laboratory testing. However, on the actual turbine fluctuating temperatures and the system's sensitivity to precise air-gap alignment resulted in only short-term reliable measurements. The root cause was identified as aged electrical components—primarily electrolytic capacitors—which impaired the reliability and electromagnetic robustness of the electronics.
- **Measurement System Configuration and Overload Errors**
  The specific configuration of the measurement setup—including data storage on the IPC, use of an external synchronization source, conversion of measurement data into MATLAB format, integration of wireless sensors, faulty firmware, and continuous recording from over 30 channels (partly at high sampling rates)—led to sporadic overload errors in the central measurement unit. Due to the uniqueness and complexity of the system configuration, identifying the root cause of the issue proved time-consuming, even with support of the manufacturer.
- **Delays in OEM Approval**
  On the organizational side, the planning and approval of the intended instrumentation by the wind turbine OEM took significantly longer than originally anticipated. It is therefore strongly recommended that this aspect be given high priority in future project timelines. One of the main reasons for the delay was the extensive coordination required regarding lightning protection measures.

4.10 Planned system expansion

As part of the planned follow-up project IRoS currently in the application stage, the instrumentation is also to be adapted or extended due to extended project objectives. The expansion of the measurement technology results on the one hand from the research priorities of the follow-up project and on the other hand from the experiences of the WEA-produktiv project. An important focus will be the expansion of the sensor technology in the rotor blades of the turbine, where a system from the company I4M will be used to record local strains and inclinations of the rotor blade during rotation. The data is transmitted wirelessly to the edge base and synchronized with the other measurement data using the common time stamp. In addition, the telemetry system on the generator shaft is to be replaced by a wireless system from I4M. The power supply for the components on the rotor shaft and in future also on the generator shaft is to be converted to a solar solution to ensure permanent battery-independent operation. This effort is not only justified by the project-related objectives, but also due to the long-term planned cooperation with the Wölfel company and the existing research contract with Bürger-Energie Altertheim eG, the operator of the wind turbine.

5 CONCLUSIONS

The instrumentation of the wind turbine described in this paper primarily aims to establish correlations between yield losses and vibration phenomena. As a basis for the overarching objective of identifying yield losses without additional sensors, using only SCADA data. Due to the complexity of the planned and implemented instrumentation, the installation, commissioning and continuous operation was and is a challenge, but in retrospect, apart from the setbacks mentioned, it was a great success. The documentation requirements, ensuring safe plant operation, i.e. ruling out plant hazards and analyzing the historical data took considerably longer than originally planned. The analysis and validation of the measurement data will be carried out in another paper, as well the creation of a digital twin of the instrumented wind turbine to generate EOC-independent measurement and simulation data [5], [6]. Both publications will also be presented at this conference and represent the subsequent work packages in the project plan.

ACKNOWLEDGEMENT

The authors are grateful for the financial support of this research by the German Federal Ministry for Economic Affairs and Climate Action (Grant number 03EE3074B, Project WEA-produktiv). Furthermore, the authors would like to express their gratitude to HOPF Elektronik GmbH for providing the time server and to PULS GmbH for supplying the power supplies. Special thanks go to our project partner Wölfel for the good, reliable, and long-standing collaboration. Additionally, we would like to thank I4M for providing the Edge Base for data acquisition of the wireless sensor system. A particular thanks goes to Bürger-Energie Altertheim for providing the facility as a research platform.

REFERENCES

[1] Wölfel Holding GmbH, "Structural Health Monitoring für Windenergieanlagen – Zustandsüberwachung von Fundament, Turm und Rotorblatt." [Online]. Available: https://www.woelfel.de/branchen/windenergie/structural-health-monitoring.html. [Accessed: Aug. 27, 2025].

[2] H. Friedmann, "Schlussbericht für das Vorhaben Signal-Analyse von Dehnungs- und Schwingungsdaten: Signal-ADS," Wölfel Engineering GmbH + Co. KG, Höchberg, Germany, Apr. 2018.

[3] Projektträger Jülich | Forschungszentrum Jülich GmbH, "Verbundvorhaben: WEA-produktiv." [Online]. Available: https://tinyurl.com/Enargus. [Accessed: Aug. 27, 2025].

[4] H. Friedmann, P. Kraemer, C. Schmidt, L. Bonekemper, and M. Wiemann, "Wind turbines with optimized productivity through fleet monitoring without additional sensor technology," in *Proc. SHM 2023*, 2023, doi: 10.12783/shm2023/36772.

[5] L. Bonekemper, M. Wiemann, B. Wüllner, H. Friedmann, and P. Kraemer, "Verification of a combined SHM/CM system on a 2.4 MW turbine," in *Proc. XI ECCOMAS Thematic Conf. Smart Structures and Materials (SMART 2025)*, 2025. [Forthcoming].

[6] B. Wüllner, M. Wiemann, L. Bonekemper, H. Friedmann, and P. Kraemer, "Simulation of time series of a 2.4 MW wind turbine with Bladed for the development of CM/SHM methods," in *Proc. XI ECCOMAS Thematic Conf. Smart Structures and Materials (SMART 2025)*, 2025.

[7] Verein Deutscher Ingenieure (VDI), "VDI-Richtlinie 3834: Measurement and evaluation of the mechanical vibration of wind turbines and their components – Wind turbines with gearbox," 2015. [Online]. Available: https://www.vdi.de/richtlinien. [Accessed: Aug. 27, 2025].

[8] H. Friedmann, C. Colomer Segura, C. Ebert, A. Nuber, and C. Schmidt, "Structural health monitoring (SHM) as a tool for optimizing the performance of a wind power plant," in *Workshop on Structural Health Monitoring*, 2019, pp. 2758–2766.

[9] Hopf Elektronik GmbH, "Weil jeder Bruchteil einer Sekunde zählt: Die kompakte Form der Netzwerksynchronisation." [Online]. Available: https://www.hopf.com/downloads/brochure/hopf_8030NTS_BR_v0102_de.pdf. [Accessed: Aug. 27, 2025].

[10] H. Friedmann and P. Kraemer, "Vibration-based condition monitoring, structural health monitoring, population monitoring – Approach to a definition of the different concepts by means of practical examples from the field of wind energy," in *Proc. 8th Eur. Workshop on Structural Health Monitoring (EWSHM)*, 2016.

[11] P. Kraemer, H. Friedmann, and C. Ebert, "Vibration-based ice detection of rotor blades in wind turbines—The industrial realization of an SHM-system," *Struct. Health Monit.*, 2015, doi: 10.12783/SHM2015/352.

[12] M. Bülk, F. Lautenschlager, P. Kraemer, C. Ebert, and T. Frese, "Assessment of a vibration-based ice detection system using multi body simulation," [incomplete reference – conference/journal details missing].

[13] A. L. Dreisbach, P. Kraemer, and C. P. Fritzen, "Monitoring of bolted joints with electro-mechanical impedance spectra and acousto-ultrasonics," in *Proc. SHM 2023*, 2023, doi: 10.12783/shm2023/36778.

[14] I4M Technologies GmbH, "Messtechnik, Sensorik und softwaregestützte Datenauswertung zur Digitalisierung von Maschinen,

XI ECCOMAS Thematic Conference on Smart Structures and Materials - SMART 2025
M. Krommer, M. Nader and M. Schagerl (Eds)

Received: 22 April 2025 / Revised: 15 August 2025 / Accepted: 25 October 2025
© The Author(s) 2025

Simulation of time series of a 2.4 MW wind turbine for the development of CM/SHM methods

Benedikt Wüllner, Marcel Wiemann, Lukas Bonekemper, Herbert Friedmann, Peter Kraemer

Abstract. To ensure safe and efficient operation of wind turbines throughout their lifetime, so-called Condition Monitoring (CM) and Structural Health Monitoring (SHM) systems are used. The limited availability of real measurement data in the wind energy sector, measurement errors and the superposition of different operating conditions during measurements complicate the development of methods for these systems. This paper describes the possibility to simulate time series of a wind turbine in order to simplify the development of algorithms for CM and SHM. For this purpose, an entire 2.4 MW turbine is modeled and validated using the aeroelastic simulation program Bladed [1]. As part of the research project WEA-produktiv, it is equipped with a comprehensive, combined SHM/CM research system [2]. One of the most challenging tasks is the modeling of the rotor blades. The corresponding model in Bladed consists of beam elements assembled in the longitudinal direction. To build it, the mechanical properties of a finely meshed finite element model of the real blade are homogenized and reduced to the required few degrees of freedom. The modal parameters of both models show good agreement in a relevant frequency range. Further unknown parameters of the real turbine (e.g. aerodynamic parameters of the blades) are replaced by a reference model from the International Energy Agency [3]. Using the sensor equipment of the real turbine, an error measure between reality and model is defined. For developing SHM and CM methods, analyzing the influence of individual environmental and operating conditions (EOC) on the system's dynamic behavior is important. The control algorithm of wind turbines (WT) is mostly unknown. In order to be able to define all EOC and to be independent of the controller, software is being developed, that allows the generator torque and pitch angle as standard control variables [4] to be specified as input time series in the simulation. The presented work is based on two further publications that deal with the instrumentation of the same turbine [5] and the analysis of its measurement data [6].

Benedikt Wüllner & Marcel Wiemann & Lukas Bonekemper & Peter Kraemer
Chair of Mechanics with focus on Structural Health Monitoring (MSHM), University of Siegen, Campus Paul Bonatz, 57076 Siegen, Germany, e-mail: benedikt.wuellner@uni-siegen.de

Herbert Friedmann
Wölfel Engineering GmbH & Co. KG, Max-Planck-Str. 15, 97204 Höchberg, Germany
e-mail: friedmann@woelfel.de

Key words: Wind Turbine Modeling, Bladed, Simulation, Structural Health Monitoring, Condition Monitoring

1 INTRODUCTION

In most cases, the development of SHM and CM methods is based on measurement data. However, the availability of this data is limited, especially in the field of wind energy; it is subject to measurement errors caused by external influences on the sensors and is limited by the operational conditions of the WT. Furthermore, this data represents the system's response to many superposing complex phenomena, the influence of which cannot be considered separately in retrospect. The results of the research project WEA-produktiv [2] demonstrate the significant effort and challenges associated with the detailed instrumentation of a real turbine. Consequently, this paper deals with the data simulation of a WT, with the aim of facilitating the development of algorithms for SHM/CM. For this purpose, a real 2.4 MW wind turbine from Nordex is modeled in the simulation software Bladed [1]. The model's comparison with the data basis and the real turbine presented here demonstrates the model's usability despite existing deviations. In addition to the model setup, a self developed software extension of Bladed is described which allows the generator torque and pitch angle to be specified as time series in the simulation. This development makes it possible to dispense with the usually unknown controller of real systems. This links the simulation described in this paper to the instrumentation of the same WT as part of the research project WEA-produktiv. The data transfer realized in this project enables the utilization of the generator torque and pitch angle from operation in the simulation, using the aforementioned software. Furthermore, this paper shows that the EOC can be fully defined in the simulation using the developed software. This facilitates the analysis of the influence of individual parameters on system behavior, including efficiency regarding power production and the local stresses. This method will also be employed in the project NOAD [7], which will re-evaluate the lifetime of offshore turbine foundations. This includes analyzing the effects of different EOC on local stresses and thus on the lifetime of the foundations. Thus, the built model and the developed software extension for the specification of time series facilitate the algorithm development in the field of CM/SHM.

2 TURBINE MODEL IN BLADED

The Figure 1 visualizes the simulation process and the relevant model components. The model is exited by a given wind field. This contains information about the spatial distribution, orientation and temporal variation of the velocity vectors. The aerodynamic model is used to calculate the loads on the WT in the next time step based on the relative velocity between the elastic components and the wind (see section 2.2). These serve as external loads on the mechanical model. This model includes all components of the WT: the elastic blades, the elastic tower, the nacelle, the hub, the rotor and the drive train (see section 2.1). The WT's

controller can be specified as external code, so that real controller structures can be used. This option is also used in another context in this paper and is described in chapter 5. The classic control algorithm in power-producing operation, which is also used in the WT considered here, calculates a generator torque or a pitch angle for the next time step based on the current rotor speed. This is explained in more detail in chapter 4. The inertial loads of the elastic components are also taken into account. The mechanical model uses these variables (aerodynamic loads, control variables and inertial loads) of the current time step to calculate the state of the WT in the next time step. This system response is used as input to the aerodynamic model and the controller to recalculate the wind loads and control variables.

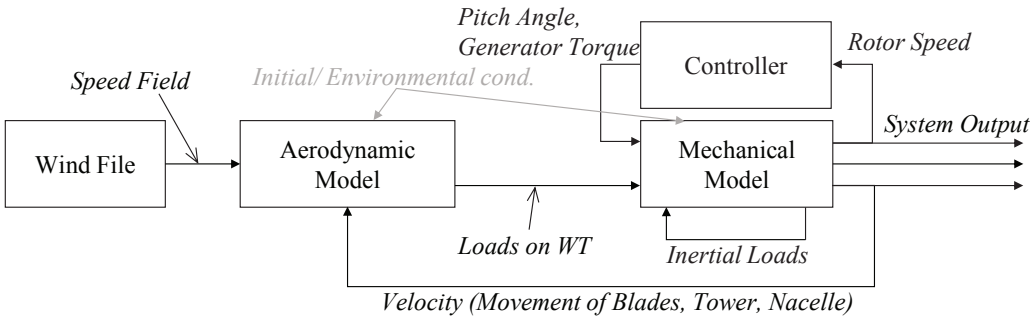

Figure 1: Functionality and procedure of the dynamic simulation in Bladed.

2.1 Mechanical Model

The components of the mechanical model that are relevant to this work are the rotor blades, the tower, the nacelle with hub and the drive train. Figure 2 offers an overview of these components.

The blades and the tower are discretized in the longitudinal direction using the finite element method (FEM). A single element is modeled by a linear shear soft Timoshenko beam with two nodes extended into 3D space. Each node has six degrees of freedom (three translations and three rotations). In addition to bending, shear and torsional stiffness, the rotor blades also have a tensile stiffness for longitudinal elongation. The material and inertia properties vary linearly across the elements. The corresponding limits are defined at the nodes. Detailed descriptions of the modeling of these elastic components can be found in [8]. All the necessary data for the tower are available in tabular form. The substructure is composed of concrete, while the upper segments are made of steel. Due to the homogeneous material and the circular cross-section, the model built is easily possible in Bladed. The interaction between the ground and the tower foundation is limited to a fixed clamping. The rotor blade of the real WT was available as an FE model with smeared material properties. The exact properties and the direction of different

layers are unknown. The calculation of the parameters required for Bladed from this model is described in chapter 3.

The nacelle and the hub are modeled as rigid bodies. The outer dimensions and the weight of these components of the real WT are known. The unknown moments of inertia are replaced by data from a model developed by the National Renewable Energy Laboratory (NREL) in 2019 as part of the "IEA Wind Task 37 on Systems Engineering in Wind Energy" [3]. The mass moments of inertia are scaled using the weight ratio of this model and the real WT.

As illustrated in Figure 2, the drive train considered here consists of the elastic rotor and generator shaft, the gearbox and the generator. A mechanical brake on the generator shaft, for which the parameters are unknown, is also taken into account, but is not shown in the Figure. Again, not all of the parameters required for modeling in Bladed are available for these components and are replaced by values from the NREL plant and scaled accordingly. Detailed information on the models and other options for implementing a wind turbine drive train in Bladed can be found in [9].

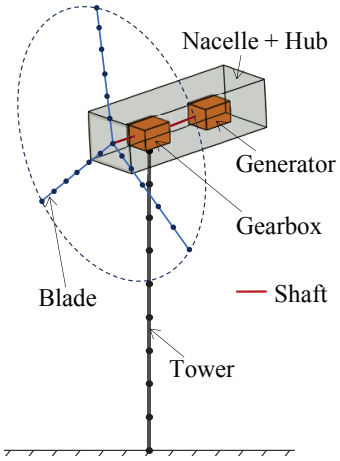

Figure 2: Overview of relevant mechanical components.

2.2 Aerodynamic model

The aerodynamic model is used to calculate the loads acting on the blades as a function of the relative speed between the wind field and the actual blade motion. The most common approach in aeroelastic simulation software such as Bladed is the blade element theory [10]. It is based on the assumption that the flow around the rotor in the radial direction can be divided into multiple independent flow tubes. This concept is illustrated in Figure 3 (left). In other words, the aerodynamic loads on a specific radial section of a rotor blade of width δr are calculated

independently from other sections of the blade. The total loads are calculated by summing over the blade length.

The aerodynamic loads acting on a blade are the lift and drag forces L and D and the aerodynamic moment M, shown in Figure 3 (right). Where u_{rel} is the relative velocity between the airfoil and the flow, α is the angle of attack and c represents the chord length.

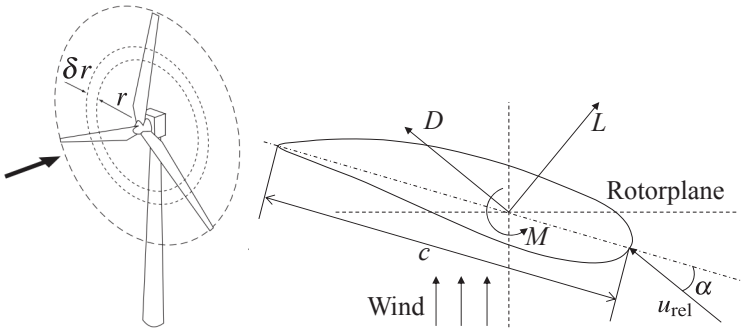

Figure 3: Illustration of the assumptions made in the blade element theory [11]. Left: Separate part of the flow tube. Right: Aerodynamic loads.

Like the drag force, the lift force is generally calculated according to [11] from

$$\delta L \quad = p\, A\, C_{\mathrm{L}} \tag{1}$$

The pressure p results from the dynamic flow conditions around the rotor according to [12] using the Bernoulli equation and A is the area of the blade element exposed to the wind. This general force is adapted to the specific characteristics of the airfoil by multiplying it by the so-called lift, drag and moment coefficients C_{L}, C_{D} and C_{M}. These coefficients are usually determined experimentally and are not known from the real system. They are imported from the NREL reference model described in section 2.1. The effect of deviations between the airfoil properties of the real 2.4 MW plant and the NREL model is demonstrated in chapter 4.

3 MODELING OF THE ROTOR BLADE

The subsequent chapter explains the methodology employed for modeling the rotor blade in Bladed. Firstly, the calculation of the parameters required for Bladed from an FE blade model is explained, without going into details. Finally, a comparison is made between the modal parameters of both models.

The basis for modeling the blades in Bladed is the FE model shown in Figure 4 (left). It is meshed with shell elements and consists of a substantial number of degrees of freedom. The exact material properties, the geometry and the direction of different layers are unknown. In contrast, the rotor blade model in Bladed, as explained in section 2.1 and illustrated in Figure 4 (right), is discretized solely in the longitudinal direction into Timoshenko beam elements

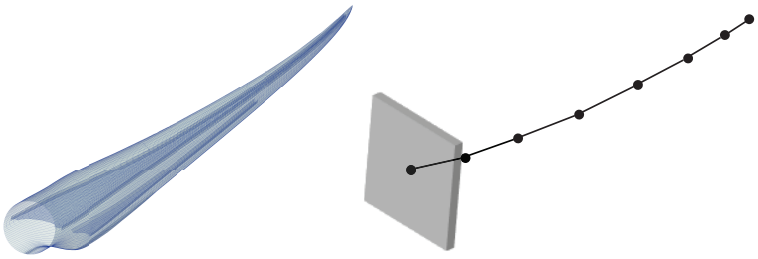

Figure 4: Illustration of the transition from an FE model to the definition of the blades in Bladed. Left: 3D-shell model. Right: Model in Bladed.

with six degrees of freedom per node. The material and inertia parameters must be specified for each node. 13 nodes are used across the longitudinal direction of the blade, as further necessary blade parameters are available at these positions. Further analysis shows that the incorporation of additional nodes does not enhance the outcomes of relevance.

Consequently, these parameters are calculated in two steps: Initially, the finely meshed shell model is discretized coarser in the longitudinal direction of the blade. Only those sections where nodes are present in the Bladed model in Figure 4 (right) are considered. The nodes considered in the shell model are therefore limited to these cross-sections. The behavior of all nodes within a section is then converted into a single node per blade longitudinal position with six degrees of freedom. The shell model is thus first further discretized in the longitudinal direction to a few sections. Finally, the cross-section properties are homogenized to six degrees of freedom. The material parameters for the six degrees of freedom per node are calculated by analyzing static simulations of the shell model. The blade root is clamped, with constant loads acting on the blade tip. The displacements of all nodes within a cross-section are then averaged, thereby yielding an average displacement and inclination for each relevant cross-section, with a known external load. The bending, shear, torsional and tensile stiffnesses are then determined from these values. The mass inertias associated with a cross-section are extracted directly from the FE model. The procedure for calculating the necessary blade parameters, which is only roughly described here, takes up a large part of this work. However, the intention of this paper is not to provide detailed derivations.

The left part of Figure 5 compares the natural frequencies of the first twelve modes of the shell and the Bladed model. This encompasses a frequency spectrum of approx. 10 Hz. It is evident that the higher frequencies exhibit a negligible contribution to the dynamic behavior of the rotor blades, due to their high mass and low stiffness. It can be seen that there exists a discrepancy between the two models, which increases with frequency. The higher natural frequencies of the shell model show that it is generally stiffer. Nevertheless, the extent of the deviations indicates that the dynamic behavior of the two models is only slightly different. Especially the differences of the first seven modes (up to approx. 6 Hz) are small. The reduced stiffness of the Bladed model can be attributed to the omission of coupling terms of the stiffnesses between

individual degrees of freedom. This simplifies the calculation of the stiffness parameters for Bladed and enables a procedure according to [13].

Figure 5 (right) compares the shape of the first twelve modes between both models. The Modal Assurance Criterion (MAC) is analyzed for this purpose. The main diagonal of the Figure compares the related modes of both models based on the natural frequency. A value close to one thus indicates a good match. It can be seen that the first seven modes (up to approx. 6 Hz) are again in very good agreement. High values of the MAC of the off-diagonal elements demonstrate a similarity of the modes of the shell model and Bladed with different natural frequencies. One potential explanation for this observation is that the rotor blade is described by only a small number of degrees of freedom (six per node). With this small number, not all eigenmodes are represented in sufficient detail to recognize the differences between similar modes.

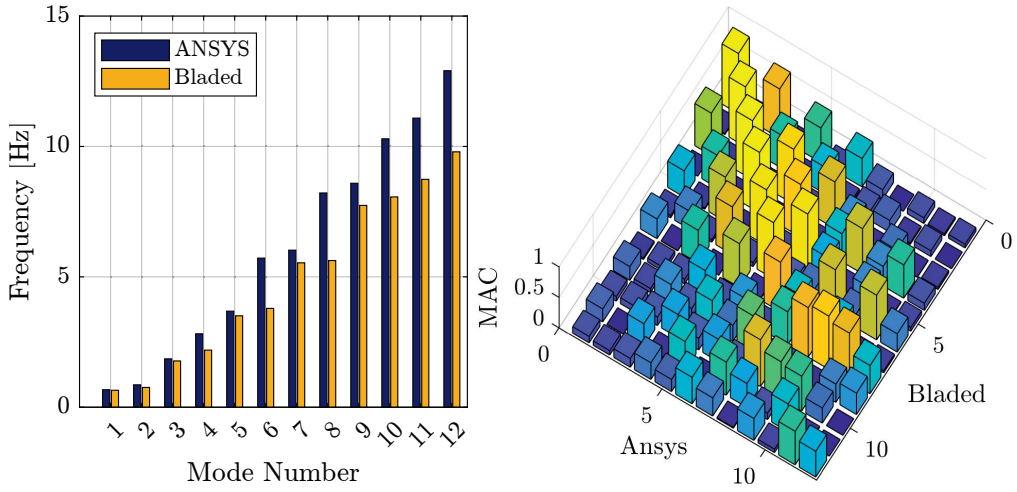

Figure 5: Comparison of modal parameters between the shell and Bladed model. Left: Natural frequencies. Right: MAC.

The analyses demonstrates that both models agree very well in a relevant frequency range up to approx. 6 Hz.

4 COMPARISON OF STEADY-STATE BEHAVIOR BETWEEN THE MODEL AND REALITY

In this chapter, the steady-state behavior of the built Bladed model is compared with measured data from the real 2.4 MW WT. The wind/power curves are considered as an example.

As described in [5], the real WT was equipped with a variety of different measurement technology as part of the project WEA-produktiv. In addition to the self-generated measurement

data, SCADA data is also available. In the case of the wind/power curve simulation, the stationary behavior is compared. Since dynamic effects are not relevant, the measurement data is sampled at 1 Hz and averaged over 30 s intervals that do not overlap. Furthermore, the wind speed measured behind the turbine is converted into the inflow speed far in front of the rotor, assuming a stationary, incompressible flow. The purple curve in the left part of the Figure 6 shows the average electrical power as a function of this wind speed. Each cross represents a 30 s average. In the technical description of the WT, the average inflow speed to reach the nominal power is given as a value of 12.5 $\frac{m}{s}$. This value fits well with the course of the averaged measured values in Figure 6 (left) and confirms the plausibility of the conversion of the wind speed. The nominal power is indicated by the horizontal curve.

The steady-state controller behavior of the real system can be explained on the basis of the purple curve. When a minimum mean wind speed is reached (here 3 $\frac{m}{s}$), the generator is connected to the grid. Below this speed, the system coasts without control. Between the switch-on speed and the nominal operating point, the generator torque is set as the control variable by the controller in such a way as to achieve an optimum ratio between the wind inflow speed and the rotor speed. This maximizes the power absorbed from the wind and thus the efficiency of the system [14]. This is possible because the generator speed of this WT is independent of the grid frequency within a certain range. When the rated electrical power is reached, the generator torque remains constant and the control variable is the pitch angle. The controller adjusts this so that the rated power is not exceeded regardless of the wind speed in order to limit the loads on the WT [4].

Bladed provides the ability to output the steady-state behavior of the model as a function of the wind speed. The operating point corresponding to the speed is calculated on the basis of the defined steady-state control. All elastic components are assumed to be rigid bodies and the wind speed far in front of the rotor is used. This results in the blue curve shown in Figure 6 (left).

It can be seen that the switched-on speed of the turbine and the rated power are in agreement between the model and reality. However, there are deviations in the range between these limits. Here the model rotates with a higher speed for the same wind speed and therefore generates a higher electrical power. This phenomenon can be attributed to the aerodynamic coefficients employed in the model. As outlined in section 2.2, these coefficients influence the loads on the rotor due to the wind and are used from a reference model from NREL [3]. However, it should be noted that the aerofoil cross-sections in the latter are larger than those in the real 2.4 MW wind turbine. A larger cross-section leads to higher wind loads and thus to higher aerodynamic coefficients. Consequently, the wind loads in the Bladed model are overestimated in comparison to reality. For the same wind speed, this results in greater acceleration, leading to higher rotational speed and electrical power output in the model.

The grey markings show mean values in the purple curve of the measurement data. An average value is calculated from all data points within an interval of $+/-0.1$ $\frac{m}{s}$ around the wind

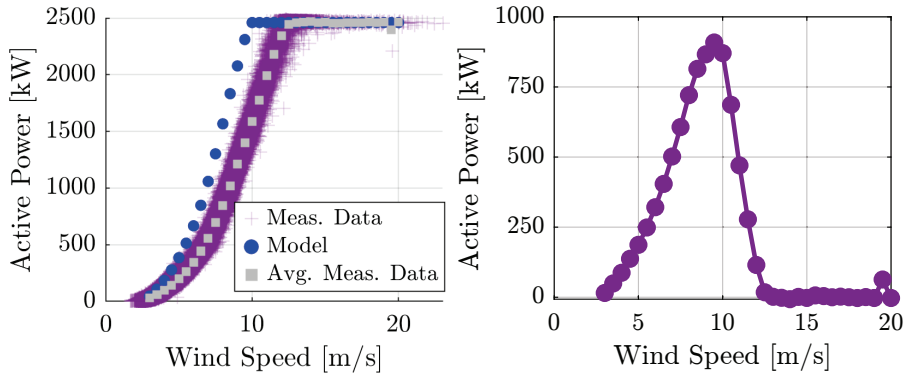

Figure 6: Comparison of the wind/power curve between the model and the real WT. Left: Wind/power curves. Right: Average deviation over wind speed.

speed value used in the Bladed model. The difference between these values and the steady-state model behavior, shown in blue, is the mean deviation of the model from reality as a function of wind speed. This is plotted on the right hand side of the Figure 6. This error measure shows the systematic deviation between the model and reality and relates the model results to the real system. If, for example, the effect of a parameter on the electrical power is analyzed, the effects in the model can be converted into actual changes at the real WT.

5 SPECIFICATION OF TIME SERIES IN THE SIMULATION

In addition to building a model of the real wind turbine for data simulation, a method is being developed as part of this work that allows the generator torque and the pitch angle to be specified as time series in the simulation.

As described in chapter 4, the controller implemented in the real WT specifies the generator torque or the pitch angle as control variables during power production mode. This significantly influences the dynamic behavior and the produced power of the system during operation. The detailed control algorithm is not available due to the importance of the controller for the operating behavior and the system manufacturer's know-how implemented in it. The purpose of the time series specification method developed in this work is, on the one hand, to no longer depend on this unknown controller. This is possible because the control variables (generator torque and pitch angle) are measured and accessible from the operation of the real WT and are specified as time series in the simulation with the help of the mentioned approach. At this point, the present work is based on the realization of the data transmission of measurement and operating data described in [5] as part of the project WEA-produktiv [2].

If a standard controller is used in the simulation, the generator torque and the pitch angle depend on the controller dynamics. The specification as time series with the developed method enables the exact definition of these quantities instead. This is another key advantage of the

mentioned approach, because in conjunction with a known wind field, it facilitates the analysis of a specific operating state of the turbine. This means that the behavior of the WT (e.g. structural vibrations or produced power) can be analyzed in a targeted manner. Due to the defined operating point, the simulation results can also be used as time series for systematic analysis and development of CM and SHM algorithms.

The two aforementioned advantages (the independence from the real controller and the exact definition of the EOC) are also important for the objective of the project NOAD [7]. The simultaneous knowledge of the EOC and the local foundation stresses facilitates the development of algorithms for estimating and predicting the lifetime of offshore WT foundations. The controller of the turbines in the considered wind farm is also unknown, but the generator torque and the pitch angle are accessible. This allows the reproduction and analysis of the real turbine's behavior.

The developed method is based on the ability to integrate the controller as external code into Bladed. The implemented algorithm is executed in each time step in the simulation. In simple terms, the control variables actually calculated by the controller are now read from an external file (e.g. as measurement data). Furthermore, functionalities for simple data specification, error management and the configuration of simulation-ready models have been implemented.

5.1 Application example: Influence of air pressure on local blade loads

As previously outlined, the prescription of the generator torque and the pitch angle as time series results in the full definition of the EOC during simulation. This facilitates the analysis of the effect of an individual parameter on the system's behavior. To illustrate this, the influence of air pressure on the bending moment at the blade root is considered. First, a simulation is carried out at a low barometric pressure of 960 hPa with a PI controller predefined by Bladed to calculate the generator torque and the pitch angle. The bending moment at the blade root around an axis for rotation out of the rotor plane (so-called flapwise direction) is analyzed. In the next step, the control variables used before are specified in a simulation with a higher air pressure of 1020 hPa. Figure 7 shows the described procedure. All other environmental, boundary and initial conditions are identical in both simulations. Thus only the influence of the air pressure becomes clear.

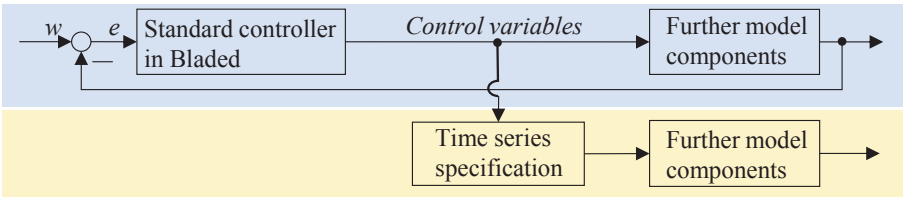

Figure 7: Sequence of the simulation for the exemplary analysis of the influence of the air pressure.

The Figure 8 shows the curves of the bending moment at the blade root when the identical control variables are specified both for an air pressure of 960 hPa and for a higher value of 1020 hPa. It can be seen that increasing the air pressure by 60 hPa results in an average difference in bending moment of approx. 787 kNm. The higher air pressure increases the air density and therefore the wind loads on the rotor. It is important to note that air pressure fluctuations are implicitly compensated by the controller during normal operation of the WT. The above analysis is therefore an example of the effect of air pressure on the load on the WT if the control variables were not adjusted as the pressure increases. In reality, air pressure fluctuations of 60 hPa can occur in a changing weather situation with a change from a low to a high pressure area.

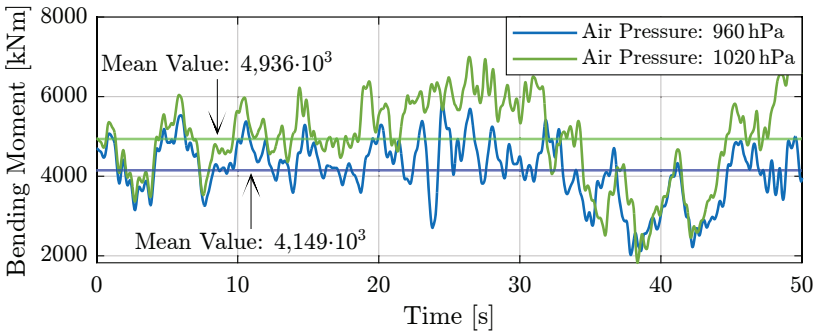

Figure 8: Bending moment at the blade root in flapwise direction at air pressures of 960 hPa and 1020 hPa.

The developed software facilitates the generation of different operating states, enabling the systematic analysis of the effects of isolated parameter manipulation.

6 CONCLUSION

The objective of the presented work is to automatically generate simulation data of a WT for the development of algorithms in the field of SHM/CM. For this purpose, it must be possible to define operating and environmental parameters in order to analyze specific turbine states. A real 2.4 MW Nordex turbine was modeled in the simulation software Bladed. Due to the simple model structure of the rotor blades and the assumptions made when converting a detailed FE model, the dynamic properties of both models match in a sufficiently large frequency range. The aerodynamic airfoil parameters of a NREL reference model used lead to a difference in the steady-state behavior of the Bladed model and the real turbine, which is characterized as function of wind speed. The development of a method for specifying time series in the simulation has enabled the real WT's mostly unknown control algorithm to be rendered redundant. This part of the work is founded on the measurement data transfer and evaluation realized in the project WEA-produktiv. Furthermore, simulations can be carried out under defined EOC

and the effect of individual parameters on the plant dynamics and power production can be analyzed independently. In addition to the achievements presented here, further software has been developed as part of this work, which allows relevant simulation parameters to be defined and several simulations to be carried out automatically, even without experience with Bladed and the direct use of this programme.

In this paper only the influence of air pressure as individual parameter is analyzed as an example. The built model and the developed software extension of Bladed for the specification of time series will be used in the future in various research fields at the chair MSHM at the University of Siegen. The simple and fast simulation of time series of different mechanical and electrical quantities with known EOC makes it possible, for example, to analyze the effects of individual system parameters on the turbines efficiency. This is a part of the objective of the project WEA-produktiv. Furthermore, the research in the field of population monitoring is facilitated, as the simulation enables easy replication of models with different characteristics and EOC. The comparison of these simulations demonstrates, for example, the impact of the modified parameters on lifetime and power production. The effects of different parameters on the stress in the turbine foundation can also be analyzed. In this area in particular, the quantity and quality of measured data is limited. The simultaneous knowledge of the EOC and the local foundation stresses facilitates the development of algorithms for estimating and predicting the lifetime of offshore wind turbines. This objective is being pursued by the project NOAD [7], which is also carried out at the Chair MSHM.

7 ACKNOWLEGEMENT

The authors are grateful for the financial support of this research by the German Federal Ministry for Economic Affairs and Climate Action (grant number 03EE3074B, project WEA-produktiv and grant number 03SX622D, project NOAD). Special thanks go to our project partner Wölfel for the good, reliable, and long-standing collaboration. Additionally, we would like to thank Bürger-Energie Altertheim for providing the wind turbine as a research platform.

REFERENCES

[1] DNV. (2025) Bladed - Wind turbine design and analysis software. [Accessed Mar. 28, 2025]. [Online]. Available: https://www.dnv.com/software/services/bladed/

[2] EnArgus, “Verbundvorhaben: WEA-produktiv - Wind Turbines with Optimized Productivity Through Fleet Monitoring Without Additional Sensors. Funding Code: 03EE3012,” 2022. [Online]. Available: https://t1p.de/enargus-weaproduktiv

[3] P. Bortolotti, H. Canet Tarres, K. Dykes, K. Merz, and L. Sethuraman, “IEA Wind Task 37 on Systems Engineering in Wind Energy - WP2.1 Reference Wind Turbines,” National Renewable Energy Laboratory, Golden CO, USA, Tech. Rep., May 2019.

[4] J. G. Njiri and D. Söffker, "State-of-the-art in wind turbine control: Trends and challenges," *Renewable and Sustainable Energy Reviews*, vol. 60, pp. 377–393, Jul. 2016. [Online]. Available: https://t1p.de/sciencedirect_NjiriJ_WindTurbineControl

[5] M. Wiemann, L. Bonekemper, B. Wüllner, H. Friedmann, and P. Kraemer, "Development and implementation of a combined SHM/CM system to identify yield losses of a 2.4MW wind turbine," in *XI ECCOMAS Thematic Conference on Smart Structures and Materials (SMART 2025)*. University of Siegen, 2025, forthcoming.

[6] L. Bonekemper, M. Wiemann, B. Wüllner, H. Friedmann, and P. Kraemer, "Verification of a combined SHM/CM system on a 2.4MW wind turbine," in *XI ECCOMAS Thematic Conference on Smart Structures and Materials (SMART 2025)*. University of Siegen, 2025, forthcoming.

[7] German Federal Ministry for Economic Affairs and Climate Action, "Verbundvorhaben: NOAD - Re-assessment of offshore foundation structures through an agile design for life-time extension and repowering. Funding Code: 03SX622D," 2022.

[8] DNV. (2025) About the blades. [Accessed Mar. 28, 2025]. [Online]. Available: https://t1p.de/DNV_Bladed_BladesIntroduction

[9] DNV AS. (2024) Generator models. [Accessed Mar. 28, 2025]. [Online]. Available: https://t1p.de/DNV_Bladed_PowerTrain

[10] J. N. Sørensen, *General Momentum Theory for Horizontal Axis Wind Turbines*. Springer International Publishing, 2016.

[11] T. Burton, D. Sharpe, N. Jenkins, and E. Bossanyi, *Wind Energy Handbook*. Wiley, 2001.

[12] S. Pierini, *Oceanic and Atmospheric Fluid Dynamics*, 1st ed. Springer Nature Switzerland, 2025. [Online]. Available: https://t1p.de/springer_PieriniS_FluidDynamics

[13] DNV AS. (2024) Conversion of blade 6x6 matrices to bladed 4.x format. [Accessed Mar. 28, 2025]. [Online]. Available: https://t1p.de/DNV_Bladed_WindIOtoBladed

[14] L. Pao and K. Johnson, *A Tutorial on the Dynamics and Control of Wind Turbines and Wind Farms*. American Control Conference, Jul. 2009.

Part X
MS 09 - ADVANCES IN ACTIVE POLYMERS INNOVATIONS AND APPLICATIONS
Eric Monteiro, Nazih Mechbal, Ingrid Graz

XI ECCOMAS Thematic Conference on Smart Structures and Materials - SMART 2025
M. Krommer, M. Nader and M. Schagerl (Eds)

Received: 24 April 2025 / Revised: 7 September 2025 / Accepted: 10 September 2025
© The Author(s) 2025

Optimization of omnidirectional piezoelectric polymer transducers for high-purity selective excitation of Lamb wave modes

Hao Dong, Pierre Margerit, Marc Rébillat, Mickaël Pruvost, Nazih Mechbal

Abstract. Wave-based structural health monitoring motivates selective excitation of Lamb wave modes by transducer design, which can simplify signal processing and interpretation. While comb array electrodes have been extensively studied for selective excitation, existing tuning methods typically assume uniform width and spacing of the electrodes, thus restricting their performance due to limited tunability. Thanks to advanced printing techniques, the electrodes printed on a flexible P(VDF-*co*-TrFE) piezoelectric substrate can be arbitrarily shaped, opening up the possibility of unprecedented selective performance. This study investigates the numerical optimization of an annular array of electrodes for high-purity Lamb mode selection. The model is based on the experimentally characterized coupling mechanism between the actuator and the host structure. The results demonstrate that globally optimized annular array electrodes can achieve high-purity excitation of either the S_0 or A_0 mode, with a flexible choice of operating frequency.

Key words: Lamb wave, Structural health monitoring, Piezopolymer transducer, Selective excitation, Global optimization

1 INTRODUCTION

Ultrasonic guided waves, especially Lamb waves, are widely used for inspecting large plate-like structural components in structural health monitoring (SHM) applications. A crucial aspect of designing a wave-based SHM system is the development of transducers capable of effective wave excitation and acquisition. The existence of multiple modes propagating at different velocities motivates special efforts in transducer design to enable the selection of a desired mode, which can reduce the need for sophisticated signal processing and ease the interpretation of measured signals. The transducer can comprise multiple independently driven active components [1, 2] or patterned electrodes [3], such as comb array electrodes patterned on a piezoelectric substrate and interdigital transducers (IDTs). The procedure to choose relevant

Hao Dong & Pierre Margerit & Marc Rébillat & Nazih Mechbal
Procédés et Ingénierie en Mécanique et Matériaux (PIMM), UMR 8006, CNRS, Arts et Métiers, CNAM, 75013 Paris, France, e-mail: hao.dong@ensam.eu

Mickaël Pruvost
Centre de recherche de Pierre-Bénite, Arkema, Rue Henri Moissan, 69491 Pierre-Bénite, France

parameters (frequency, geometry, etc.) such that the highest contrast between one desired mode and the other modes is called mode tuning [4, 5, 6]. Conventional tuning methods usually consider periodic arrangements of the electrodes [4, 7], which restricts design flexibility and thus performance. In addition, the design is simply targeted at the best mode contrast at the center frequency of a tone burst input signal, even though it contains rich spectral components. An optimal non-periodic linear IDT for Lamb wave mode-selective acquisition has been recently proposed [8]. An actuator with optimal non-periodic electrodes that eliminates the propagation of a mode wave-packet is promising, which we term as high-purity selective excitation in this work.

The basis of numerical optimization is modeling the structural response of an actuator. Multiphysics models that take full substructure-actuator coupled dynamics into account are accurate but computationally inefficient. Since the actuator applies an external surface traction to the plate, the full-coupled numerical analysis can be simplified into an uncoupled boundary value problem by assuming the surface traction distribution. The latter has analytical solutions and is computationally efficient, which is essential for numerical optimization. Conventional ultrasonic transducers through gel coupling are piston-type and transfer uniform normal traction to the substructure [4, 9]. In comparison, piezoceramic surface-mounted transducers are strain-type, for which a model describing the in-plane traction distribution is proposed based on quasi-static analysis [10, 11]. The model have been further simplified into an ideal bonding solution, also known as the pin-force or line-force models [9, 12]. Another assumption is that the piezoelectric properties of the actuator are constant over the frequency range of interest. This model has been experimentally validated (see e.g. [13, 14]). In comparison, there is not enough discussion and validation in the literature on the simplified models for the piezopolymer actuators, though they have been numerically studied as both piston-type [15, 16] and strain-type transducers [17]. Wilcox et al. [18, 19] model the directional responses of irregular-shaped PVDF IDTs as piston-type transducers based on the superposition of Green's functions, and show excellent agreement with the experiment. Li et al. [7] compare the experimentally measured responses of linear-shaped PVDF IDTs with the normal and shear stress models to conclude the piston-type coupling. Note that these experiments are performed for wave-packets at a few frequencies rather than across a wide frequency range.

In this work, we investigate high-purity selective excitation by an optimized array of concentric annular electrodes patterned on a P(VDF-*co*-TrFE) piezoelectric substrate. Analytical solutions for the normal stress and line-force shear stress models are first presented and validated. The analytical tuning curves are then compared with experimental results to give insights into the coupling mechanisms. In the two-mode low-frequency range, we use the normal stress model to perform optimization. Geometrically simple designs are achieved for nearly perfect elimination of the target fundamental mode. The flexibility of the approach and the role of irregularity are also discussed.

2 Mathematical model

2.1 Assumptions

The piezoelectric actuator is illustrated in Fig. 1. In this work, we consider axisymmetric electrodes that allow omnidirectional excitation, namely, circular or concentric annular electrodes. A pair of identical electrodes are patterned on the top and bottom surfaces of a P(VDF-*co*-TrFE) substrate. The transducer is surface-bonded to a metallic plate through an adhesive layer. The electrodes induce a traction to the plate that generate Lamb waves. Accurate knowl-

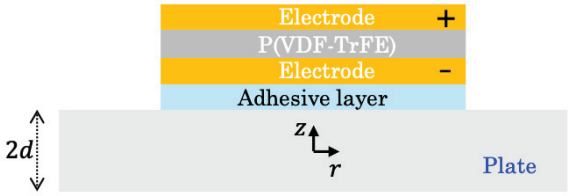

Figure 1: Schematic diagram of the piezoelectric transducer attached to a plate.

edge of this loading distribution needs solving a model that takes into account the full-coupled dynamics of the plate, bonding layer, electrodes, and piezoelectric layer, which can be computationally inefficient so that numerical optimization becomes challenging. Instead, there are two theoretical assumptions of the stress distribution that can simplify the analysis, associated with different underlying coupling mechanisms, as illustrated in Fig. 2. The first one, termed as normal stress model, assumes that a uniform, frequency-independent, out-of-plane stress is distributed over the area covered by the electrode. The second one, termed as line-force model, assumes that uniform in-plane stress is concentrated along the electrode boundaries and points to the normal direction. A complete shear-lag analysis for a circular piezoceramic actuator is referred to [9]. The ideal-bonding condition when the bonding layer is either very thin or very stiff compared to the plate yields the line-force model, in which all the load transfers take place at the surface electrode boundary. Both assumptions allow us to calculate analytically the excited guides wave fields in a common mathematical framework.

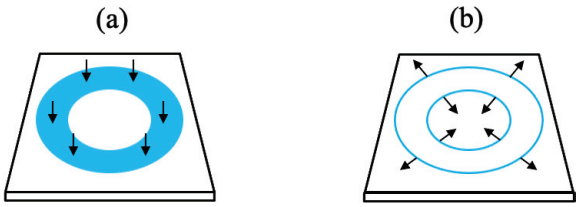

Figure 2: Theoretical assumptions of surface stress distribution: (a) normal stress model (b) pin-force model.

2.2 Integral transform method

The structural response in an isotropic plate induced by each type of the surface loading shown in Fig. 2 can be calculated using the integral transform method. The solving procedure has been detailed in [20]. Here, we summarize the method and solutions. The circular-crested Lamb waves are described in cylindrical coordinates with axisymmetric condition $\partial_\theta = 0$ and vanishing azimuthal displacement component $u_\theta = 0$. Consider the time-harmonic solution $\boldsymbol{U}(r,z,t) = \mathrm{Re}\{\boldsymbol{u}(r,z,\omega)\mathrm{e}^{-\mathrm{i}\omega t}\}$ for an arbitrary axisymmetric loading distribution on the top surface of the plate:

$$\sigma(r,d) = \tau(r),\ \sigma(r,-d) = 0, \tag{1}$$

where σ is a general denotation representing either normal stress σ_{zz} or shear stress σ_{rz}, $d = h/2$ is the half-thickness of the plate, and $\tau(r)$ is an arbitrary function. The Lamb waves are described in terms of two scalar potentials, Φ and H, that satisfy the wave equation in the following form

$$\begin{aligned} &\frac{1}{r}\frac{\partial}{\partial r}\left(r\frac{\partial \Phi}{\partial r}\right) + \frac{\partial^2 \Phi}{\partial z^2} + \frac{\omega^2}{c_\mathrm{p}^2}\Phi = 0, \\ &\frac{\partial}{\partial r}\left[\frac{1}{r}\frac{\partial (rH)}{\partial r}\right] + \frac{\partial^2 H}{\partial z^2} + \frac{\omega^2}{c_\mathrm{s}^2}H = 0, \end{aligned} \tag{2}$$

where $c_\mathrm{p}^2 = (\lambda + 2\mu)/\rho$ and $c_\mathrm{s}^2 = \mu/\rho$ are the longitudinal (pressure) and transverse (shear) wave speeds, λ and μ are Lamé constants, and ρ is the mass density. For each type of loading, the solution steps follow Fig. 3.

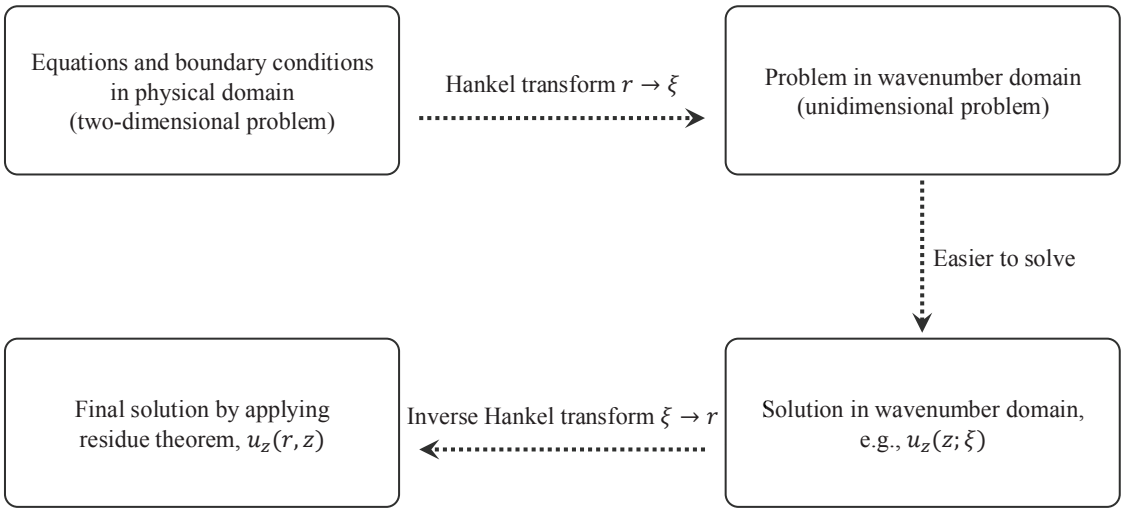

Figure 3: General steps of using the integral transform method for solving the Lamb wave excitation problem.

For either type of loading, the solution of out-of-plane displacement on the top surface can

be written in a general form as a series of modes:

$$u_z(r, z = d) = -\frac{\pi \mathrm{i}}{2\mu}\left[\sum_{i=0}^{\infty}\tilde{\tau}(\xi_i)\frac{N_{\mathrm{S}}(\xi_i)}{D'_{\mathrm{S}}(\xi_i)}\mathrm{H}_0^{(1)}(\xi_i r) + \sum_{j=0}^{\infty}\tilde{\tau}(\xi_j)\frac{N_{\mathrm{A}}(\xi_j)}{D'_{\mathrm{A}}(\xi_j)}\mathrm{H}_0^{(1)}(\xi_j r)\right]. \tag{3}$$

Here, each term represents a Lamb waves mode that is propagating or evanescent. $\{\xi_i\}$ and $\{\xi_j\}$ are the radial wavenumbers of symmetric and anti-symmetric modes at the angular frequency ω, respectively. The expressions $N_{\mathrm{S}}(\xi_i)/D'_{\mathrm{S}}(\xi_i)$ and $N_{\mathrm{A}}(\xi_j)/D'_{\mathrm{A}}(\xi_j)$ are termed modal excitability for the symmetric and anti-symmetric modes, respectively. The denominators are given by:

$$\begin{aligned}
D_{\mathrm{s}}(\xi) &= 4\xi^2\zeta_{\mathrm{p}}\zeta_{\mathrm{s}}\sin\zeta_{\mathrm{p}}d\cos\zeta_{\mathrm{s}}d + (\xi^2-\zeta_{\mathrm{s}}^2)^2\cos\zeta_{\mathrm{p}}d\sin\zeta_{\mathrm{s}}d,\\
D_{\mathrm{A}}(\xi) &= 4\xi^2\zeta_{\mathrm{p}}\zeta_{\mathrm{s}}\cos\zeta_{\mathrm{p}}d\sin\zeta_{\mathrm{s}}d + (\xi^2-\zeta_{\mathrm{s}}^2)^2\sin\zeta_{\mathrm{p}}d\cos\zeta_{\mathrm{s}}d,\\
\zeta_{\mathrm{p}}^2 &= \frac{\omega^2}{c_{\mathrm{p}}^2} - \xi^2,\\
\zeta_{\mathrm{s}}^2 &= \frac{\omega^2}{c_{\mathrm{s}}^2} - \xi^2.
\end{aligned} \tag{4}$$

The symbol $'$ represents derivative with respect to the argument. In fact, $D_{\mathrm{S}} = 0$ and $D_{\mathrm{A}} = 0$ are Rayleigh-Lamb equations, and their roots give the radial wavenumbers $\{\xi_i\}$ and $\{\xi_j\}$ in Eq. (3), respectively. These dispersion relations can be calculated using the method documented in [21]. The numerators for the normal stress loading condition are

$$\begin{aligned}
N_{\mathrm{s}}(\xi) &= \xi\zeta_{\mathrm{p}}(\xi^2+\zeta_{\mathrm{s}}^2)\sin\zeta_{\mathrm{p}}d\sin\zeta_{\mathrm{s}}d,\\
N_{\mathrm{A}}(\xi) &= -\xi\zeta_{\mathrm{p}}(\xi^2+\zeta_{\mathrm{s}}^2)\cos\zeta_{\mathrm{p}}d\cos\zeta_{\mathrm{s}}d,
\end{aligned} \tag{5}$$

and for the shear stress loading condition are

$$\begin{aligned}
N_{\mathrm{s}} &= \xi^2[2\zeta_{\mathrm{p}}\zeta_{\mathrm{s}}\sin\zeta_{\mathrm{p}}d\cos\zeta_{\mathrm{s}}d + (\xi^2-\zeta_{\mathrm{s}}^2)\cos\zeta_{\mathrm{p}}d\sin\zeta_{\mathrm{s}}d],\\
N_{\mathrm{A}} &= \xi^2[2\zeta_{\mathrm{p}}\zeta_{\mathrm{s}}\cos\zeta_{\mathrm{p}}d\sin\zeta_{\mathrm{s}}d + (\xi^2-\zeta_{\mathrm{s}}^2)\sin\zeta_{\mathrm{p}}d\cos\zeta_{\mathrm{s}}d].
\end{aligned} \tag{6}$$

The function $\tilde{\tau}(\xi_i)$ or $\tilde{\tau}(\xi_j)$ is termed source influence. For the normal loading, $\tilde{\tau}(k)$ is the zeroth-order Hankel transform of the distribution function $\tau(r)$,

$$\tilde{\tau}(k) = \int_{-\infty}^{\infty}\tau(r)\mathrm{J}_0(kr)r\mathrm{d}r, \tag{7}$$

with J_0 the Bessel function of first type. For the shear loading, $\tilde{\tau}(k)$ is the first-order Hankel transform of $\tau(r)$,

$$\tilde{\tau}(k) = \int_{-\infty}^{\infty}\tau(r)\mathrm{J}_1(kr)r\mathrm{d}r. \tag{8}$$

$\mathrm{H}_0^{(1)}$ is the zeroth-order Hankel function of first type. If the distance r is much larger than the radial wavenumber $\lambda_r = 2\pi/\xi_r$, $r \gg \lambda_r$, the following asymptotic approximation holds:

$$\mathrm{H}_0^{(1)}(\xi_j r) \approx \sqrt{\frac{2}{\pi \xi_j r}} \mathrm{e}^{\mathrm{i}\left(\xi_j r - \frac{\pi}{4}\right)} \propto \frac{1}{\sqrt{r}}, \tag{9}$$

which indicates cylindrical wavefronts in the far field.

Finally, we present explicit expressions of the source influence for the normal stress and line-force shear stress models from their specific spatial distributions. Consider a circular electrode of radius a and an array of N concentric annular electrodes with outer radii $\{a_i\}$ and inner radii $\{b_i\}$. In the normal stress model, the loading strength takes 1 per unit area, whereas in the line force model, the loading strength takes 1 per unit length. The resulting stress distribution functions $\tau(r)$ and spectra $\tilde{\tau}(k)$ are given in Table 1. It is noteworthy that the source influence spectra of the pressure and line-force models are described by the same order of Bessel functions but differ by an order of wavenumber k.

Table 1: Stress distributions and spectra for axisymmetric electrodes.

Assumption	Normal stress model		Line-force model	
Geometry	Circular	Annular	Circular	Annular
$\tau(r)$	$\begin{cases} 1, r \le a \\ 0, r > a \end{cases}$	$\begin{cases} 1, b_i \le r \le a_i \\ 0, \text{else} \end{cases}$	$\delta(r-a)/r$	$\sum_{i=1}^{N} \left[\delta(r-a_i) - \delta(r-b_i)\right]/r$
$\tilde{\tau}(k)$	$a\mathrm{J}_1(ka)/k$	$\sum_{i=1}^{N} \left[a_i \mathrm{J}_1(ka_i) - b_i \mathrm{J}_1(kb_i)\right]/k$	$a\mathrm{J}_1(ka)$	$\sum_{i=1}^{N} \left[a_i \mathrm{J}_1(ka_i) - b_i \mathrm{J}_1(kb_i)\right]$

2.3 FEM

For verification purpose, the analytical solutions for both normal stress model and line-force model are compared with the finite element method (FEM). The wave fields in an aluminum plate generated by an actuator with two annular electrodes are computed at a single frequency. The parameters are as follows: density of the aluminum $\rho = 2.7 \times 10^3$ kg$\cdot$m^{-3}, Lamé constants of the aluminum $\lambda = 5.74 \times 10^{10}$ and $\mu = 2.61 \times 10^{10}$, thickness of the plate $h = 2$ mm, outer radii of the electrodes $a_1 = 0.5$ cm and $a_2 = 1$ cm, inner radii $b_1 = 0.25$ cm and $b_2 = 0.75$ cm, and frequency $f = 450$ kHz. The FEM solution is obtained using the Solid Mechanics Module of COMSOL Multiphysics. An axisymmetric model is built, with its computation domain truncated by a perfectly matched layer to approximate an infinite extent. For the normal

pressure model, a "boundary load"of 1 Pa is applied to the electrode domain. For the line force model, a "ring load" of 1 N $\cdot$ m^{-1} is applied to each electrode boundary. Comparative results of the real part of the out-of-plane displacement on the top surface Re$[u_z(r, z = d)]$ within the range of the FEM computation domain are shown in Fig. 4. In the FEM results, waves are well damped in the artificial layer. At this frequency, only the fundamental modes, namely S0 and A0 modes, are propagating to the far field. Therefore, in both analytical solutions, we only keep these two modes. In the far-field region $r \gg a_2$, excellent agreement between the analytical and finite element solutions can be observed. It should be noted that the small discrepancies in the near field can be eliminated by taking the evanescent modes into account. Compared to the FEM, the analytical solution gives more physical insights and computationally faster.

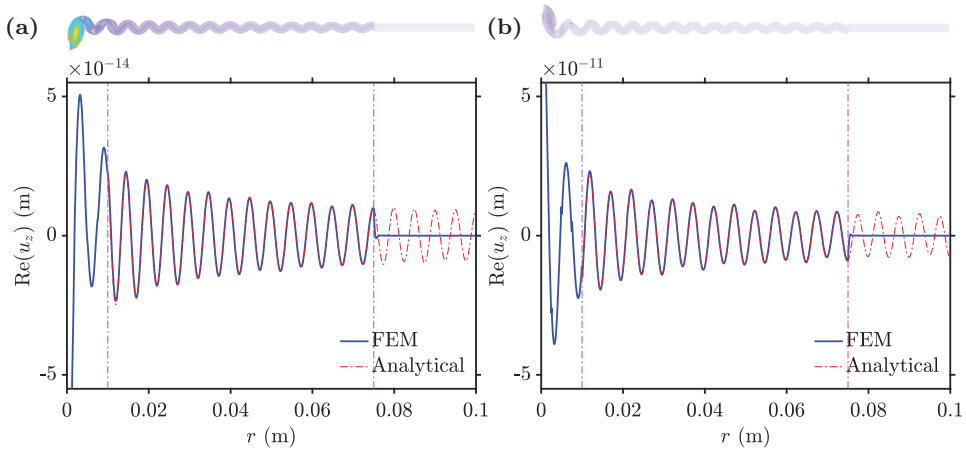

Figure 4: Theoretical displacement fields generated by an actuator with two annular electrodes. A comparison of FEM and analytical results for (a) normal pressure model and (b) line force model. The vertical lines indicate the range of the actuator ($r \leq 0.01$ m) and the perfectly matched layer (0.075 m$\leq r \leq 0.1$ m).

2.4 Model comparison

We now examine the frequency dependence of Eq.(3), namely the behavior of the tuning curves. The displacement magnitude in the far-field can be deduced as

$$|u_z(r, z = d)| = \sqrt{\frac{\pi}{2\xi_r r}} \frac{|\tilde{\tau}(\xi_r)E(\xi_r)|}{d\sqrt{\mu}} \tag{10}$$

where ξ_r is the radial wavenumber for a given mode, $E(\xi_r) = N(\xi_r)d/D'(\xi_r)$ is the corresponding dimensionless modal excitability. The factor

$$A_u(f) = \frac{|\tilde{\tau}(\xi_r)E(\xi_r)|}{\sqrt{\xi_r}} \tag{11}$$

that incorporates all the frequency dependence, is the tuning curve. The Lamb wave dispersion relations $\xi_r(f)$ for the three or four modes are plotted in Fig. 5(a). In this work, we are interested

in the frequency range below the cut-on frequency of the first higher-order symmetric mode (S_1 mode, 2.86 MHz·mm for aluminum). The excitability as a function of frequency-thickness product for the first three modes is shown in Fig. 5(b). The cut-on frequency of the A_1 mode at 1.55MHz·mm distinguishes the behavior of the excitability functions for the two fundamental modes. Below that frequency, the excitability for the A_0 mode decreases monotonically for both the normal and shear traction models, at a similar rate. In the low-frequency limit, the excitability for the normal stress model is much greater. The excitability for the S_0 mode behaves asymptotically as $O(fh)$ and $O[(fh)^2]$ for the normal stress model and shear stress model, respectively. Above that frequency, the excitability for the A_0 mode becomes quite even. The excitability for the S_0 mode, however, exhibits distinct behavior between the models. The normal stress excitability rapidly increases, whereas the shear stress excitability presents a null at 2.20 MHz·mm. According to the analytical expressions given in Table, the source influence spectrum $|\tilde{\tau}(\xi_r)|$ has many zero points and local maximum points, through which mode tuning is possible. The spectra deduced from the normal stress model and line-force model differ only by a factor of the radial wavenumber $k_r(f)$. Consequently, their null frequency points are exactly the same. We exemplify the S0 and A0 mode tuning curves for the simplest case of a circular electrode of radius $a = 2h$, see Figs. 5(c) and 5(d). For the A0 mode, the loading will not change the null frequencies and not significantly shift the maximum frequency points. For the S0 mode, the shear-stress tuning curve has an additional null at 2.2 MHz·mm, this spectral difference is thus crucial to distinguish the loading properties.

3 Experimental measurement of Lamb wave tuning curves

According to the theoretical analysis in Section 2.4, the low-frequency tuning curves for both A_0 and S_0 modes show spectral resemblances between the normal and line-force shear models, while the tuning curves for S_0 mode show notable differences between the models in a particular frequency range. It is thus of essential importance to experimentally measure the tuning curves over a wide frequency range to validate the models at low frequencies, and to identify the model that would provide a better prediction when it comes to higher frequencies.

The time-harmonic wave field on the surface of the plate has more than one wavelength component corresponding to the multiple modes. To separate them, one may project the field over plane waves, namely, transforming the spatial field into two-dimensional wavenumber field. To do so, the out-of-plane velocity field generated by a circular actuator of diameter 22 mm is measured in a finite region $l_x \times l_y$ using the Laser Doppler Vibrometer. The dimension of the scanned region $\sqrt{l_x l_y}$ and the scanning step Δl respectively restricts the biggest and smallest wavelengths that can be resolved. An aluminum plates with dimensions 1 m×1 m×4 mm are measured without applying any absorption treatment on their boundaries. The effect of the near-perfectly reflecting boundaries is known to introduce densely located high-quality-factor resonances into the free-field frequency responses. The mode density is proportional to the longitudinal dimensions of the plate. The input signal is a linear sweep sine signal. The velocity frequency response at each measurement point is obtained by dividing the frequency spectrum of the measured velocity signal by that of the input signal. The wavenumber spectrum is then

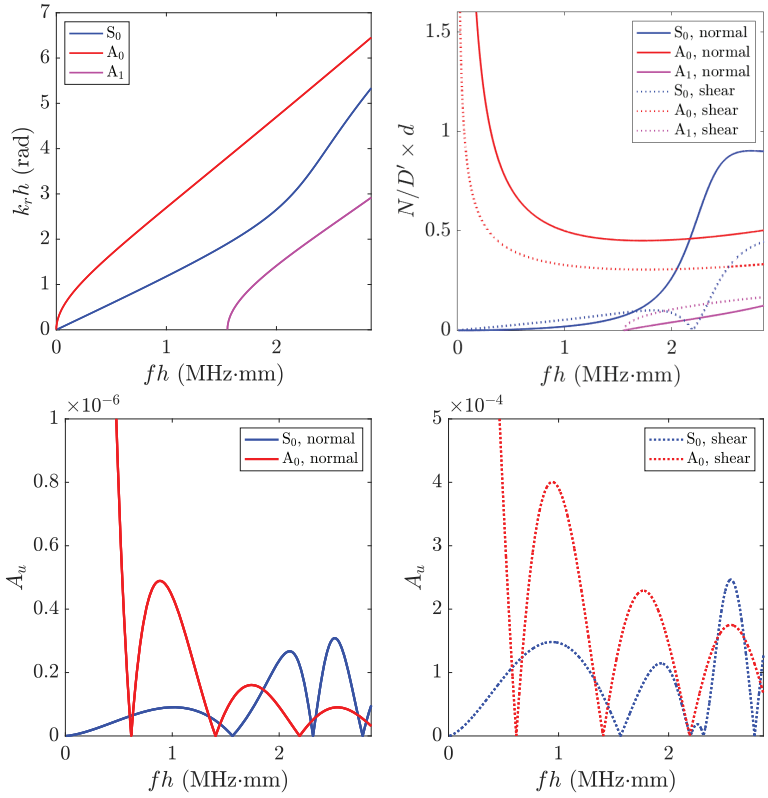

Figure 5: (a) Dispersion curves. (b) Dimensionless excitability. (c) Tuning curves for the normal stress model. (d) Tuning curves for the shear stress model.

calculated by applying two-dimensional spatial Fourier transform to the time-harmonic wave field. The procedure of determining the tuning curves is illustrated in Fig. 6(a). The resonances in frequency domain are first smoothed out by applying moving average to the sequence of two-dimensional spectra. Each individual mode is then selected in the wavenumber domain with a narrow ring-shaped window that is centered about its corresponding wavenumber according to the Rayleigh–Lamb equation. The root-mean-square (rms) value of that mode component within the scanned region is then calculated by averaging the windowed power spectrum. The measured results are compared with the theoretical tuning curve for the velocity $v_z = -\mathrm{i}\omega u_z$:

$$A_v(f) = \frac{|\omega\tilde{\tau}(\xi_r)E(\xi_r)|}{\sqrt{\xi_r}}. \tag{12}$$

The results are shown in Figs. 6(b) and 6(c). Both models predict excellently the null frequency points and global variation trends of the tuning curves. The line-force model agrees better than the normal stress model near the null at 2.2 MHz·mm. In the low-frequency range (less than the cut-off frequency of A_1 mode), the models differ only by a smooth weighting function so both are usable when the input signal is narrow-band.

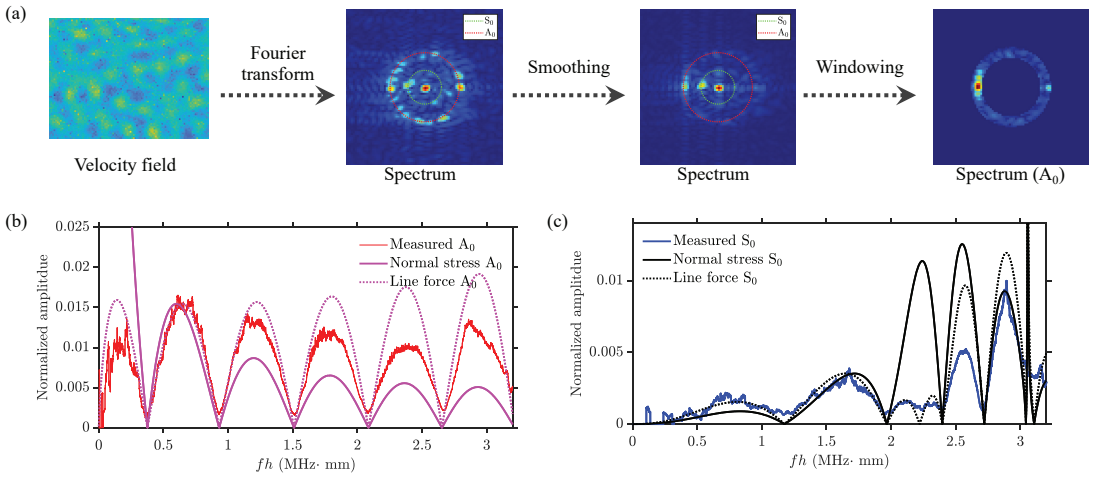

Figure 6: (a) Flowchart of evaluating the tuning curves from measured wave field, exemplified at f =360 kHz. (b)-(c) Comparison of measured and theoretical magnitude responses across a wide frequency range.

4 Optimization

4.1 Formulation

The objective for high-purity selective excitation is to maximize the energy of wave packet of a wanted mode relative to that of an unwanted mode. A tone burst is used as input signal [see Fig. 7(a)]. As shown in Fig. 7(b), the signal has rich frequency components. Therefore, in contrast to the conventional tuning concepts that target simply at the center frequency, in the present work, the objective is to design the annular electrodes such that the continuous wavelength spectral of an unwanted mode is filtered out across the signal frequency band.

To construct the objective function, we begin with the time-domain velocity for a given Lamb wave mode. According to Eq. (3), it writes

$$V_z(r, z = d, t) = \mathrm{Re}\left\{\int_0^\infty -\frac{\pi}{\mu d}\omega\tilde{\tau}(\xi_r)S(\omega)E(\xi_r)\mathrm{H}_0^{(1)}(\xi_r r)\mathrm{e}^{\mathrm{i}\omega t}\mathrm{d}\omega\right\}, \tag{13}$$

where $\xi_r(\omega)$ is the radial wavenumber of the mode, $E(\xi_r) = N(\xi_r)d/D'(\xi_r)$ is the dimensionless modal excitability, and $S(\omega)$ is the Fourier spectrum of the tone burst signal,

$$S(\omega) = \int_0^\infty s(t)\mathrm{e}^{-\mathrm{i}\omega t}\mathrm{d}t. \tag{14}$$

Considering the far-field approximation Eq. (9), the energy of a modal wave packet at distance r can be represented by the following integrated spectral power:

$$W = \frac{\pi}{2\mu^2 d^2 r}\int_0^\infty \left|\omega\tilde{\tau}SE\frac{1}{\sqrt{\xi_r}}\right|^2 \mathrm{d}\omega. \tag{15}$$

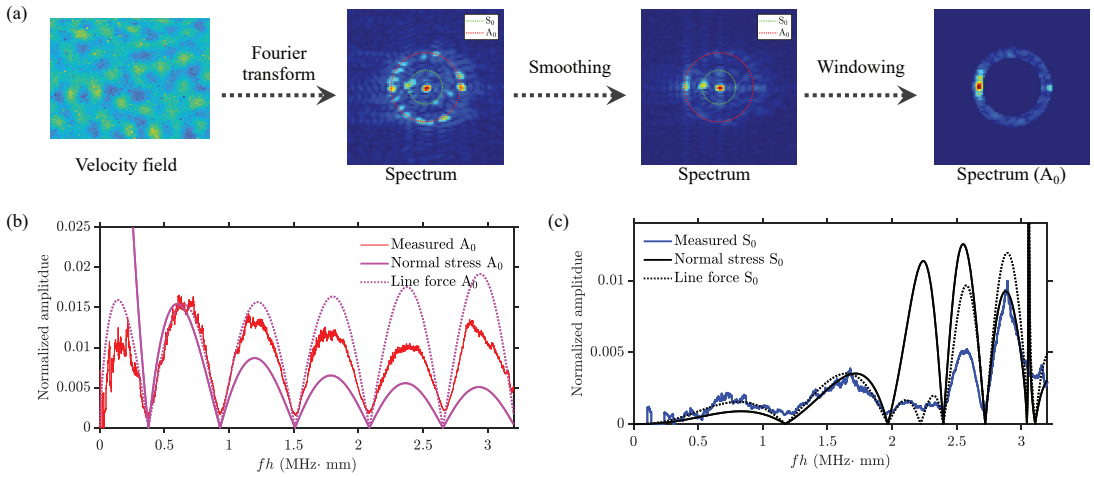

Figure 7: (a) Tone burst signal with 7 cycles and a center frequency of 450 kHz. (b) Spectrum of (a) and -3 dB bandwidth. (c) Schematic diagram of the annular electrodes and design variables.

In the low frequency range where only the two fundamental modes are propagating, the objective function can be defined as

$$J = \frac{W_{\text{mode1}}}{W_{\text{mode2}}} = \frac{\int_0^\infty |\tilde{\tau}_1 SE_1|^2 \omega^2 \xi_1^{-1} \mathrm{d}\omega}{\int_0^\infty |\tilde{\tau}_2 SE_2|^2 \omega^2 \xi_2^{-1} \mathrm{d}\omega}, \tag{16}$$

which is the energy ratio between an unwanted mode 1 and a wanted mode 2, termed as the modal rejection ratio of mode 1. Note that Eq. (16) is independent of the distance r.

As shown in Fig. 7(c), the design variables (represented by the parameter vector $\mathbf{q}$) are the widths of and spacings between the annular electrodes, $q_0, q_1, \ldots, q_M$. During the optimization process, the dimension of the actuator (represented by its outer radius a) and the number of electrodes N_e are fixed. There are $M = 2N_\mathrm{e} - 1$ free variables. These parameters only affect the source influence spectra $\tilde{\tau}$ for mode 1 and mode 2. Therefore, Equation (16) can be regarded as a ratio between two weighted integrals with weight functions $|SE|^2\omega^2\xi^{-1}$.

The optimization problem is formulated as a constrained non-linear minimization problem:

$$\mathbf{q}^* = \arg\min_{\mathbf{q}} J(\mathbf{q}), \text{ subject to } \sum_{i=1}^{M} q_i \leq a \text{ and } q_i \geq 0 \, (i = 1, 2, \ldots, M), \tag{17}$$

The optimization algorithm used to find a global optimal solution is the Global Search approach and is implemented with MATLAB solvers `ga` and `fmincon`. The algorithm starts a local solver from multiple start points sampling multiple basins of attraction and searches thoroughly for a global minimum.

4.2 Numerical results

Optimization experiments are carried out for an actuator of radius $a = 10$ mm mounted on an 2-mm-thickness aluminum plate. The input tone burst signal has seven cycles and a center frequency well below the cut-on frequency of A_1 mode (7.8×10^5 kHz). The design target is selective excitation of either S0 mode or A0 mode. The objective function Eq. (16) is computed using the analytical model presented in Sec. 2.2 and the numerical integral. The weight functions, that is, signal spectrum, dispersion relation, and excitability spectrum for each mode at the quadrature frequency points, are tabulated before the optimization process to accelerate the computation. A periodic electrode distribution with uniform width and spacing $q_0 = q_1 = \ldots = q_M = a/2N_\mathrm{e}$ serves as a reference or conventional design. Optimization experiments are carried out by increasing the number of electrodes from $N_\mathrm{e} = 1$ to find simple arrangements that allow high-purity mode selection.

Optimization results for selective excitation of S0 or A0 mode are shown in Table 2 and Fig. 9. The optimal designs are compared with the reference periodic designs. The optimal

Table 2: Optimization results. The second column represents the mode to be excited. f_c is the center frequency of the input tone burst. J_Ref and J_Opt are the modal rejection ratios of the reference periodic designs and optimal designs, respectively.

No.	Mode	f_c (kHz)	N_e	J_Ref	J_Opt
1	S0	450	2	2×10^3	6×10^{-3}
2	S0	500	2	9×10^2	1×10^{-1}
3	A0	450	2	6×10^{-4}	1×10^{-6}
4	A0	450	4	1×10^{-2}	2×10^{-6}

solutions with only one electrode fail to exhibit satisfactory performance. When the number of electrodes increases to $N_\mathrm{e} = 2$, the optimal solutions exhibit excellent modal selection performance. First, two-electrode optimal designs for selective excitation of S0 mode are discussed. The modal rejection ratios of these two optimized actuators working at different frequencies, 450 kHz and 500 kHz respectively, are significantly reduced compared to the reference design. Their electrode distributions and time-domain modal wave packets at a distance $r = 0.2$ m are compared in Figs. 9(a) and 9(b). For each optimal design, high-purity excitation of S0 mode is manifested in the time-domain signal, accompanied by a significant increase in the wave amplitude compared to the initial design. In addition, these two optimal designs excite S0 wave packet in similar amplitude, despite of their distinct geometry and operating frequency. Next, at the same center frequency as design No. 1, a two-electrode A0-mode-selective design is realized, as shown in the third rows in Table 2 and Fig. 9. Note that the initial electrode distribution is the same as design No. 1, whereas the target of design No. 3 is to eliminate S0 mode. That's

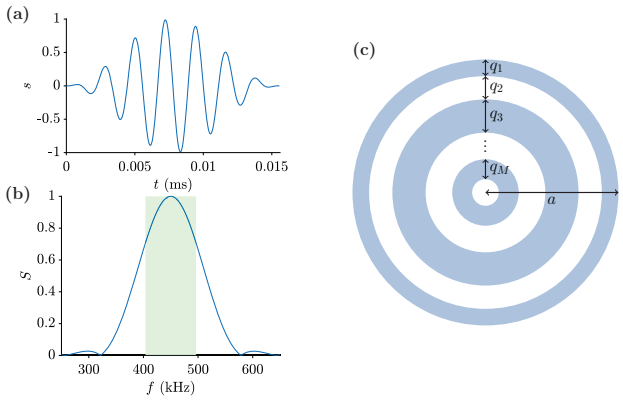

Figure 8: High-purity selective excitation. Comparison of the electrode distribution and time-domain waveform at $r = 0.2$ m of the relevant modes between the reference periodic designs and optimal designs. (a)–(d) correspond to Nos. 1–4 in Table 2, respectively. The velocity has been scaled by an identical factor in these figures.

why the initial objective function value of design No. 3 is reciprocal to that of No. 1. After optimization, this value is decreased by more than two orders of magnitude. In terms of the time domain signal, the S0 mode wave packet vanishes, exhibiting good modal contrast. It should be noted that the wave amplitude for A0 mode for the optimal design is drastically smaller than that for the initial design. A possible cause is the thin annular electrodes in the optimal design and thus relatively small excitation area, which indicates a small magnitude of the source influence spectrum. Nevertheless, this loss in amplitude can be greatly compensated when the number of electrodes increases to $N_\mathrm{e} = 4$, as shown in the last rows in Table 2 and Fig. 9. The optimized modal rejection ratio is comparable to that of the two-electrode design No. 3, while the amplitude of A0 mode increases to a level similar as the S0 mode amplitude in design No. 1 or 2.

The present optimal electrode distributions show noticeable irregularity. In the following, we shed some insights on how the irregularity improves the performance of modal selection and the design flexibility. In conventional linear IDTs, the period of electrodes should be half of the selected wavelength [4], which indicates that given the dimension of the actuator and the number of electrodes, the operating frequency cannot be flexibly chosen. For example, Figure 8(a) shows the source influence spectra $\tilde{\tau}$ for the reference two-electrode design. According to the conventional approach, the nodal frequencies in the S0 and A0 mode spectra are the operating frequencies to which the center frequency of the input signal should be aligned. However, in the present optimization method, the target center frequency needs not to be consistent with the nodal frequencies. In the optimization experiment No. 1, the design objective is to excite S0 mode with a 450-kHz tone burst, whereas this target frequency is distant from any A0 nodal frequencies for the reference two-electrode design. In fact, A0 and S0 modes have similar source influence magnitude at the center frequency of the input signal. After optimization [see Fig. 8(b)], the A0 spectrum exhibits a rejection band owing to gathering of three adjacent nodes, resulting in high-purity excitation of S0 mode. In the optimization experiment No. 4, the design

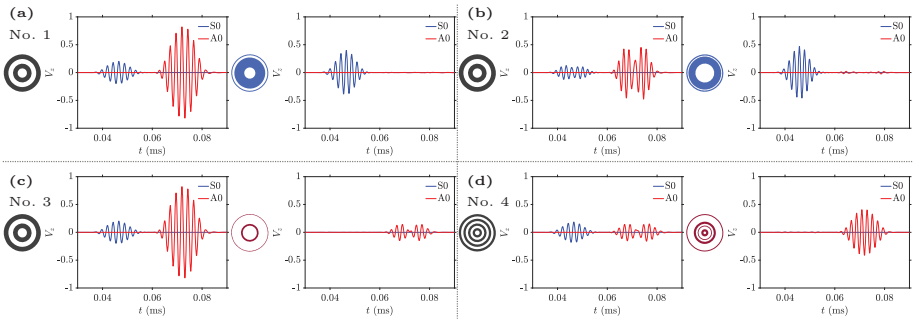

Figure 9: Source influence spectra for (a) reference two-electrode design, (b) optimal design No. 1, (c) reference four-electrode design, and (d) optimal design No. 4. The colored background labels -3 dB bandwidth of a tone burst signal centered at 450 kHz [cf. Fig. 7]. The magnitude has been scaled by an identical factor in these figures.

objective is to excite A0 mode with a 450-kHz tone burst. Although the center frequency is located around an A0 spectral node of the reference four-electrode design [see Fig. 8(c)], the optimization process is still able to gather two adjacent S0 nodes into the signal band to emit A0 mode with high mode contrast [see Fig. 8(d)]. These results indicate remarkable flexibility of the proposed design approach.

5 Conclusion

The effectiveness of analytical models have been validated in terms of predicting the response of surface-mounted P(VDF-*co*-TrFE) piezopolymer transducers. Numerical optimization of annular-array electrodes enables a high modal rejection ratio within compact dimensions. The optimized designs feature a small number of electrodes, resulting in a simple geometry. The introduced irregularity in the electrode distribution leads to the clustering of nodes in the source influence spectrum, effectively forming a rejection band. Additionally, the design frequency of the tone burst signal can be freely selected, independent of the geometric constraints of conventional IDTs of the same size. These findings can be used for high-performance mode-selective transducers in structural health monitoring applications.

REFERENCES

[1] J. Li and J. Rose, "Implementing guided wave mode control by use of a phased transducer array," *IEEE Transactions on Ultrasonics, Ferroelectrics, and Frequency Control*, vol. 48, no. 3, pp. 761–768, 2001.

[2] E. V. Glushkov, N. V. Glushkova, O. V. Kvasha, and R. Lammering, "Selective lamb mode excitation by piezoelectric coaxial ring actuators," *Smart Materials and Structures*, vol. 19, no. 3, p. 035018, feb 2010. [Online]. Available: https://dx.doi.org/10.1088/0964-1726/19/3/035018

[3] M. G. Marilyne Philibert, Kui Yao and C. Soutis, "Lamb waves-based technologies

for structural health monitoring of composite structures for aircraft applications," *European Journal of Materials*, vol. 2, no. 1, pp. 436–474, 2022. [Online]. Available: https://doi.org/10.1080/26889277.2022.2094839

[4] J. L. Rose, *Ultrasonic Guided Waves in Solid Media*. Cambridge University Press, 2014.

[5] V. Giurgiutiu, "Tuned lamb wave excitation and detection with piezoelectric wafer active sensors for structural health monitoring," *Journal of Intelligent Material Systems and Structures*, vol. 16, no. 4, pp. 291–305, 2005. [Online]. Available: https://doi.org/10.1177/1045389X05050106

[6] B. Xu and V. Giurgiutiu, "Single mode tuning effects on lamb wave time reversal with piezoelectric wafer active sensors for structural health monitoring," *Journal of Nondestructive Evaluation*, vol. 26, pp. 123–134, 2007.

[7] Y. Li, K. Wang, W. Feng, H. Wu, Z. Su, and S. Guo, "Insight into excitation and acquisition mechanism and mode control of lamb waves with piezopolymer coating-based array transducers: Analytical and experimental analysis," *Mechanical Systems and Signal Processing*, vol. 178, p. 109330, 2022. [Online]. Available: https://www.sciencedirect.com/science/article/pii/S0888327022004666

[8] J. Li, H. Dong, X. Tian, W. Shi, S. Wang, B. Zhao, and J. Tan, "Optimization and operation of interdigital transducer to improve signal-to-noise ratio," *International Journal of Mechanical Sciences*, vol. 283, p. 109299, 2024. [Online]. Available: https://www.sciencedirect.com/science/article/pii/S0020740324003412

[9] V. Giurgiutiu, "Structural health monitoring with piezoelectric wafer active sensors (second edition)," V. Giurgiutiu, Ed. Oxford: Academic Press, 2014, pp. 395–443. [Online]. Available: https://www.sciencedirect.com/science/article/pii/B9780124186910000083

[10] E. F. Crawley and J. de Luis, "Use of piezoelectric actuators as elements of intelligent structures," *AIAA Journal*, vol. 25, no. 10, pp. 1373–1385, 1987. [Online]. Available: https://doi.org/10.2514/3.9792

[11] E. F. Crawley and E. H. Anderson, "Detailed models of piezoceramic actuation of beams," *Journal of Intelligent Material Systems and Structures*, vol. 1, no. 1, pp. 4–25, 1990. [Online]. Available: https://doi.org/10.1177/1045389X9000100102

[12] V. Giurgiutiu and G. Bottai-Santoni, "Extension of the shear-lag solution for structurally attached ultrasonic active sensors," *AIAA Journal*, vol. 47, no. 8, pp. 1980–1983, 2009. [Online]. Available: https://doi.org/10.2514/1.43946

[13] A. Raghavan and C. E. S. Cesnik, "Finite-dimensional piezoelectric transducer modeling for guided wave based structural health monitoring," *Smart Materials*

and Structures, vol. 14, no. 6, p. 1448, nov 2005. [Online]. Available: https://dx.doi.org/10.1088/0964-1726/14/6/037

[14] L. Li, M. F. Haider, H. Mei, V. Giurgiutiu, and Y. Xia, "Theoretical calculation of circular-crested lamb wave field in single- and multi-layer isotropic plates using the normal mode expansion method," *Structural Health Monitoring*, vol. 19, no. 2, pp. 357–372, 2020. [Online]. Available: https://doi.org/10.1177/1475921719848149

[15] J. Rose, S. Pelts, and M. Quarry, "A comb transducer model for guided wave nde," *Ultrasonics*, vol. 36, no. 1, pp. 163–169, 1998, ultrasonics International 1997. [Online]. Available: https://www.sciencedirect.com/science/article/pii/S0041624X97000425

[16] J. P. Koduru and J. L. Rose, "Time delay controlled annular array transducers for omnidirectional guided wave mode control in plate like structures," *Smart Materials and Structures*, vol. 23, no. 10, p. 105034, sep 2014. [Online]. Available: https://dx.doi.org/10.1088/0964-1726/23/10/105034

[17] B. Lin and V. Giurgiutiu, "Modeling and testing of PZT and PVDF piezoelectric wafer active sensors," *Smart Materials and Structures*, vol. 15, no. 4, p. 1085, jul 2006. [Online]. Available: https://dx.doi.org/10.1088/0964-1726/15/4/022

[18] P. Wilcox, R. Monkhouse, M. Lowe, and P. Cawley, *The Use of Huygens' Principle to Model the Acoustic Field from Interdigital Lamb Wave Transducers*. Boston, MA: Springer US, 1998, pp. 915–922. [Online]. Available: https://doi.org/10.1007/978-1-4615-5339-7_118

[19] P. Wilcox, P. Cawley, and M. Lowe, "Acoustic fields from pvdf interdigital transducers," *IEE Proceedings - Science, Measurement and Technology*, vol. 145, no. 5, pp. 250–259, 1998.

[20] V. Giurgiutiu, *Structural Health Monitoring of Aerospace Composites*. Oxford: Academic Press, 2016. [Online]. Available: https://www.sciencedirect.com/science/article/pii/B9780124096059000064

[21] S. Guo, M. Rebillat, and N. Mechbal, "Dichotomy property of dispersion equation of guided waves propagating in anisotropic composite plates," *Mechanical Systems and Signal Processing*, vol. 164, p. 108212, 2022. [Online]. Available: https://www.sciencedirect.com/science/article/pii/S0888327021005860

XI ECCOMAS Thematic Conference on Smart Structures and Materials - SMART 2025
M. Krommer, M. Nader and M. Schagerl (Eds)

Received: 29 April 2025 / Revised: 7 September 2025 / Accepted: 10 September 2025
© The Author(s) 2025

Characterization of electromechanical properties of Electroactive Polymer Actuators for Soft Robots in mini-invasive surgery

Imane Ferradj, Eric Monteiro, Damien Thuau, Sebastien Roland, Nazih Mechbal

Abstract. In recent decades, soft robots have attracted considerable attention due to their flexibility and ability to adjust stiffness when interacting with the external environment, making them suitable for mini-invasive procedures. These robotic systems require actuators that are both flexible and lightweight, and electroactive polymers (EAPs) have emerged as some of the most promising solutions. Among EAPs, P(VDF-ter-TrFE-ter-CTFE) terpolymers have been extensively studied due to their unique electrostrictive, piezoelectric, and dielectric properties, making them good candidates for actuation. In this work, we established a methodology to evaluate the electromechanical properties of these EAPs, focusing on matching experimental data with an electromechanical model. This model consists of two main parts: the mechanical model, which computes strains due to electrostriction and piezoelectricity, and the electrical model, which models the hysteresis of the electrical displacement. Terpolymers with different amounts of CTFE are modelled to study the effect of this termonomer on the performance of the terpolymers, including the electrostriction and piezoelectric coefficients, as well as other parameters related to electrical displacement.

Key words: Electroactive Polymers, Multiphysics Modelling, electrostriction, hysteresis

Imane Ferradj & Eric Monteiro & Sebastien Roland & Nazih Mechbal
Laboratoire PIMM, Arts et Metiers Institute of Technology, CNRS, CNAM 151 Bd de l'Hopital 75013 Paris, France, e-mail: eric.monteiro@ensam.eu

Damien Thuau
Laboratoire IMS, Université de Bordeaux, CNRS Bordeaux INP/ENSCBP 351 Cours de la Libération 33400 Talence, France, e-mail: dthuau@enscbp.fr

1 Introduction

Recent advances in soft robotics have highlighted the critical need for compliant actuators that combine large deformations with precise control, particularly for mini-invasive surgical applications. While dielectric elastomers and ionic polymers have been widely explored, ferroelectric relaxor polymers based on poly(vinylidene fluoride) (PVDF) terpolymers offer unique advantages including intrinsic electromechanical coupling, scalability, and compatibility with micro-fabrication processes. Among these, P(VDF-*ter*-TrFE-*ter*-CTFE) terpolymers exhibit tunable electroactivity through CTFE content modulation, enabling transition from ferroelectric to relaxor behavior [1]. However, accurately predicting their complex electromechanical response requires models that simultaneously account for nonlinear hysteresis and coupled piezoelectric-electrostrictive effects that are still a challenge.

This work presents a comprehensive experimental and modeling framework to quantify the composition-dependent electromechanical properties of PVDF-based terpolymers. Building upon previous characterization methods [2], we develop a coupled electromechanical model that integrates three key ingredients: (1) a geometrically exact beam formulation capturing large deformations, (2) Separation of piezoelectric (d_{zx}) and electrostrictive (Q_{xz}) contributions, and (3) a hysteresis-aware electrical model parametrized through simultaneous polarization and deflection measurements.

Our experimental methodology employs a novel multi-physics characterization system combining high-speed videometry with synchronized current-voltage measurements, enabling direct correlation between polarization dynamics and mechanical response. We specifically investigate two material systems - a conventional 65/35 VDF/TrFE copolymer and a 66.5/33.5/8.5 VDF/TrFE/CTFE terpolymer - to quantify how CTFE-induced phase transformation affects key parameters including coercive field (E_c), remnant polarization (P_r), and electromechanical coupling coefficients.

The paper is organized as follows: Section 2 details the actuator fabrication process and characterization setup, including our current decomposition method for polarization extraction and optimized digital image correlation for displacement tracking. Section 3 presents the unified electromechanical model, combining a nonlinear Timoshenko beam formulation with Preisach-type hysteresis modeling. Section 4 validates the model against experimental results, revealing the impact of CTFE incorporation.

2 Experimental setup

2.1 Actuator fabrication

Actuators were prepared by screen-printing process, using P(VDF-*co*-TrFE) and P(VDF *ter*-TrFE-*ter*) inks on PEKK substrates, with intermediate annealing steps at 100–110 °C and a final anneal at $T_m - 15\,°\mathrm{C}$ to obtain unimorph devices (active area 4 mm × 10 mm). The complete manufacturing process can be found in [3].

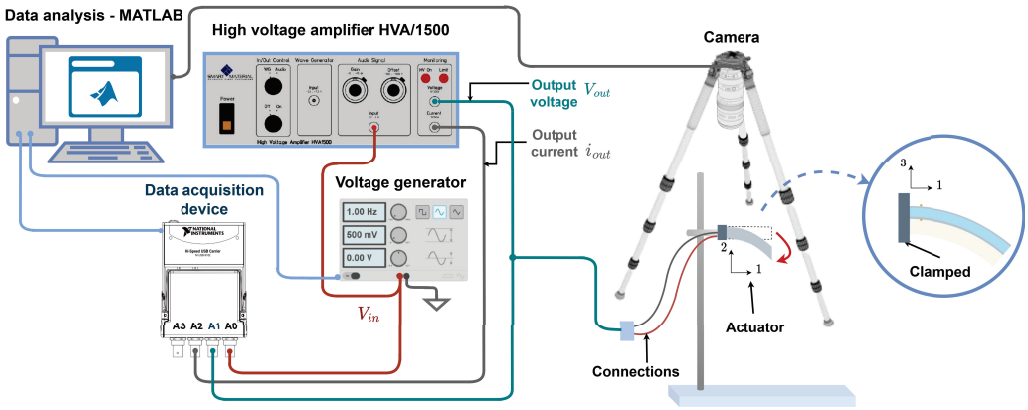

Figure 1: Schematic of the simultaneous electrical and optical characterization setup.

2.2 Experimental characterization system

The ferroelectric polymer actuators were driven by a high-voltage sinusoidal signal generator (Agilent 33220A) and their current response recorded with a Keithley 6517B (100 nA resolution). A Basler usb3 camera (100 fps) captured the macroscale bending (see Fig. 1). All tests were conducted at 25 °C.

2.3 Polarization extraction methodology

The total current can be divided into 3 parts, namely a resistive leakage $I_{\mathrm{i}}(t)$, a capacitive displacement $I_{\mathrm{c}}(t)$ and a ferroelectric contribution $I_{\mathrm{fe}}(t)$, such that

$$I_{\mathrm{total}}(t) \;=\; I_{\mathrm{i}}(t) + I_{\mathrm{c}}(t) + I_{\mathrm{fe}}(t) \tag{1}$$

First, the total current was noise-filtered using Savitzky–Golay filter. The resistive leakage $I_{\mathrm{i}}(t) = V(t)/R_{\mathrm{est}}$ was isolated via linear regression at high voltage and the estimated resistance was about $R_{\mathrm{est}} = 1.7\,\mathrm{M\Omega}$. Then, in a similar way, the capacitive displacement $I_{\mathrm{c}}(t) = C_{\mathrm{est}}\mathrm{d}V(t)/\mathrm{d}t$ was deduced with an estimated capacitance $C_{\mathrm{est}} = 13.5\,\mathrm{nF}$. Finally, the polarization is obtained by integrating the ferroelectric current $I_{\mathrm{fe}}(t)$:

$$P(t) = P(t_{\mathrm{start}}) + \frac{1}{A}\int_{t_{\mathrm{start}}}^{t} I_{\mathrm{fe}}(\tau)\,\mathrm{d}\tau \tag{2}$$

where A is the active area. This workflow is illustrated in Fig. 2 and the obtained polarization depicted in Fig. 3. Note that cycle boundaries were set at $V(t)$ zero-crossings.

2.4 Macroscopic deflection and image processing

A streamlined approach was employed for analyzing actuator deflection. Videos of actuators clamped at one end and driven with sinusoidal voltages were processed using digital image correlation with optimized parameters. The image processing workflow

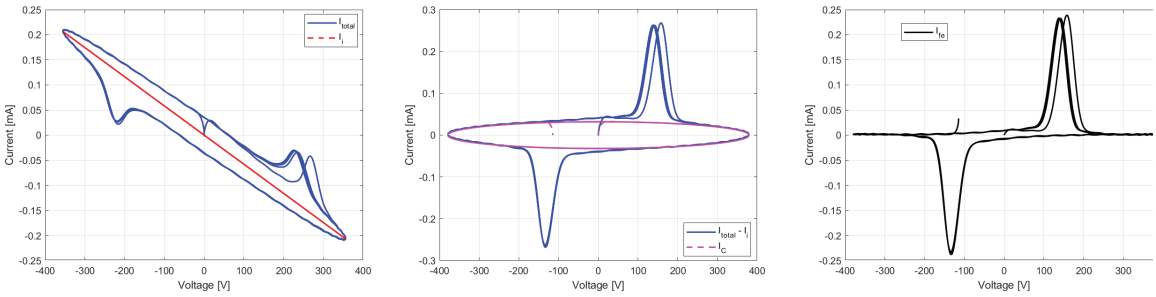

Figure 2: Current-processing workflow: (left) resistive leakage removal; (middle) capacitive displacement removal; (right) final ferroelectric current.

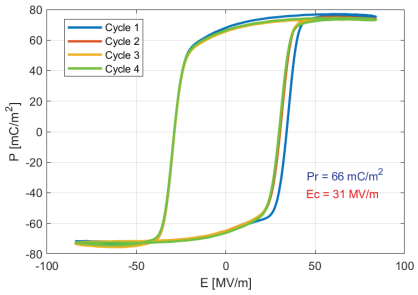

Figure 3: Polarization cycles versus electric field.

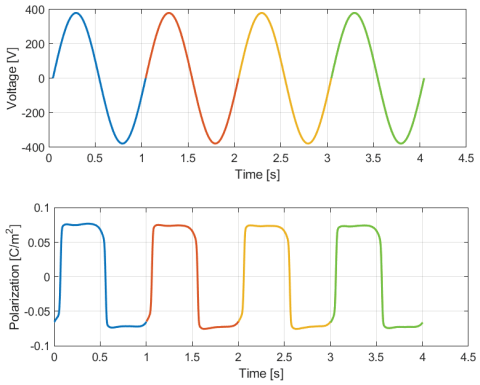

Figure 4: Driving voltage (top) and extracted polarization (bottom) vs. time.

was simplified to focus on essential edge detection and fitting procedures. After spatial calibration, boundary points were efficiently fitted using regularized polynomial optimization. This simplified approach provided accurate deflection measurements while reducing computational complexity.

2.5 Employed actuators – material and geometry

Young's moduli (PEKK substrate $Y_s = 2.9\,\text{GPa}$; PEDOT:PSS electrodes $Y_e = 0.5\,\text{GPa}$) were confirmed by DMA and supplier data. Active layer moduli Y_p were extracted from DMA (5 mm strips, 1 Hz, 0.1 % strain), showing transitions at $-20\,^{\circ}\text{C}$ (glass) and the Curie point, shifting lower with higher CTFE content [4]. Layer thicknesses were measured by SEM cross-sections.

3 Modeling of EAP Actuators for Soft Robots

The modeling of EAP actuators is divided into two main parts: a mechanical model that predicts the deformation of the actuator and an electrical model that describes

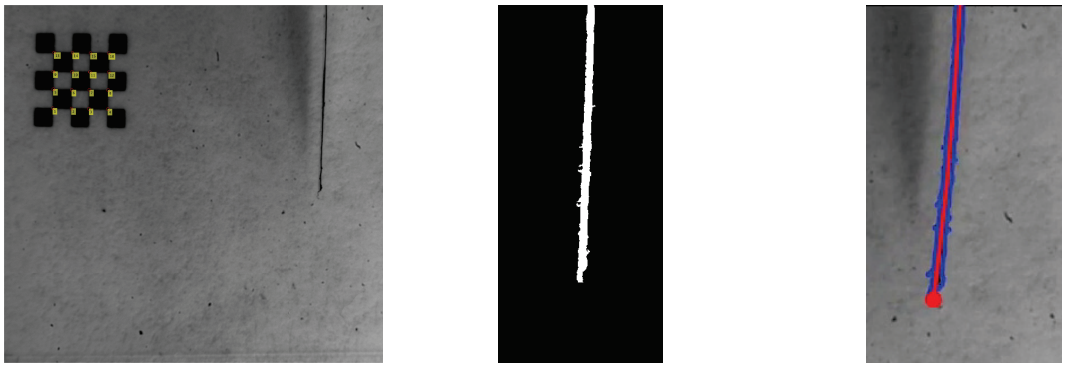

Figure 5: Image-processing workflow for macroscopic deformation: (left) chessboard calibration detection; (middle) texture feature mask; (right) edge tracking and polynomial fit.

Table 1: Active-layer material and geometric properties.

Composition	**Class**	Y_p [GPa]	t_p [μm]
65/35 VDF/TrFE, 0 % CTFE	Copolymer	1.265	4.5
66.5/33.5 VDF/TrFE, 8.5 % CTFE	Terpolymer	0.171	5.0

the behavior of the electric displacement, which can exhibit hysteresis under an applied voltage. This integrated approach allows us to establish a direct relationship between material composition, electrical response, and mechanical output, essential for designing optimized actuators for soft robotic applications.

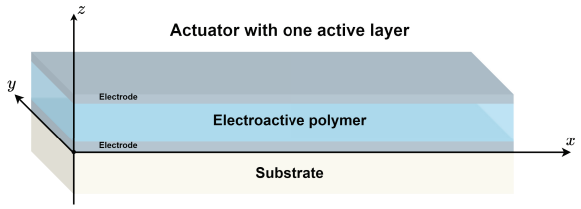

Figure 6: Schematic of the multilayer model.

3.1 Mechanical Model

The employed actuators, depicted in Fig. 6, is modelled as a straight laminated composite cantilever beam of length L with a rectangular cross section. The plies are stacked such that material properties are functions of the z-coordinate. To deal with large deflection and large rotation but small strains, the geometrically exact formulation based on Timoshenko kinematic is used and briefly presented here in 2D. The interested reader

may refer to [5] for more details. Assuming that the cross-section, initially plane, remains plane after deformation and neglecting in-plane deformation of the cross-section, the axial and transverse displacements of any point $M(x,z)$ are defined by:

$$u(x,z,t) = \bar{u}(x,t) - z\sin\left(\psi(x,t)\right) \quad \text{and} \quad v(x,z,t) = \bar{v}(x,t) + z\left(\cos\left(\psi(x,t)\right) - 1\right) \tag{3}$$

where $\bar{u}$ and $\bar{v}$ are the axial and transverse displacements of a centroid while ψ stands for the rotation of the cross section. For the sake of readability, all dependencies are omitted in the following. By means of an ersatz polar decomposition, the non-zero components of the total strain tensor are

$$E_{xx} = (1+\bar{u}')\cos\psi + \bar{v}'\sin\psi - z\psi' - 1 \qquad \text{and} \qquad E_{xy} = -(1+\bar{u}')\sin\psi + \bar{v}'\cos\psi \tag{4}$$

Introducing the axial strain ξ, the shear strain γ and the beam curvature κ, these components reduce to

$$E_{xx} = \xi - z\kappa \qquad \text{and} \qquad E_{xy} = \gamma \tag{5}$$

Assuming small strains and taking into account electromechanical strains ξ_e like thermal expansion strains, the non-zero components of the stress tensor in the i-th layer are given by

$$T_{xx,i} = Y_i\,(E_{xx} - \xi_{e,i}) \qquad \text{and} \qquad T_{xy,i} = G_i\,E_{xy} \tag{6}$$

where Y_i and G_i represent the Young's modulus and the shear modulus of the i-th layer. The electromechanical strain in x-direction is modelled through a combined effect of electrostriction and piezoelectricity such that:

$$\xi_{e,i} = \begin{cases} d_{zx}E_z + Q_{xz}D_z^2 & \text{in active layers} \\ 0 & \text{otherwise} \end{cases} \tag{7}$$

where E_z and D_z represent the electric field and electric displacement in the z-direction, respectively, while ε denotes the permittivity of the active layer. Then, the resultant stresses are computed by integration across the cross-section

$$N = \iint T_{xx}\,dydz\,, \qquad Q = \iint T_{xy}\,dydz \qquad \text{and} \qquad M = \iint z\,T_{xx}\,dydz \tag{8}$$

where N, Q and M stand for the axial force, the shear force and the bending moment respectively. Finally, the equation of motion can be derived from the principal of virtual work as follows

$$\iiint \left(\delta u\rho\ddot{u} + \delta v\rho\ddot{v} + \delta\psi I\ddot{\psi}\right) dxdydz + \int \left(\delta\xi\,N + \delta\gamma\,Q + \delta\kappa\,M\right)\,dx + \int \left(\delta u\,n + \delta v\,q\right)\,dx = 0 \tag{9}$$

where n and q stand for body forces collinear and normal to the neutral axis of the beam respectively while δu, δv and $\delta\psi$ denote the virtual displacements and rotation. This nonlinear equation can't be solved analytically. Here, this equation is solved using standard finite elements with quadratic shape functions using a total Lagrangian approach in tandem with Newmark time integration scheme and Newton-Raphson algorithm.

3.2 Electrical Model

The behavior of the electric displacement in EAP actuators is nonlinear due to the presence of hysteresis. An empirical model is used to describe this behavior. In this model, the total electric displacement D_z is given by

$$D_z = \varepsilon E_z + P_s, \tag{10}$$

where the first term represents the polarization induced by the electric field, and P_s is the spontaneous polarization that occurs naturally in the material and described by

$$P_s = \begin{cases} P_{sat} \tanh\left(\frac{E_z - E_c}{\delta}\right) - P_{offset} & \text{if} \quad dE_z > 0 \\ P_{sat} \tanh\left(\frac{E_z + E_c}{\delta}\right) + P_{offset} & \text{else} \end{cases} \tag{11}$$

where P_{sat} represents the saturation polarization, E_c is the coercive electric field, δ controls the sharpness of the hysteresis curve and P_{offset} closes the gap between both expressions at high electric field [6].

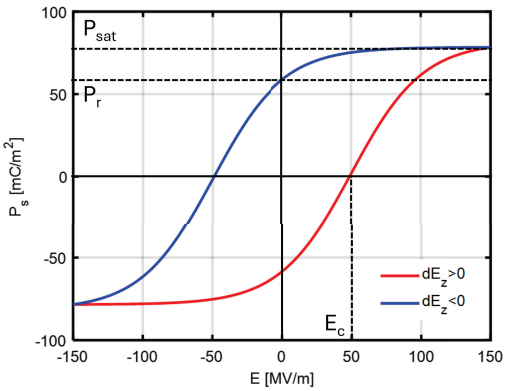

Figure 7: Ferroelectric hysteresis loop.

3.3 Parametric Identification

A concise optimization identifies model parameters by fitting both the D–E hysteresis and tip deflection curves. The single cost function is:

$$J = \frac{1}{2}\left(\frac{||u_{\text{model}} - u_{\text{exp}}||}{||u_{\text{exp}}||} + \frac{||D_{\text{model}} - D_{\text{exp}}||}{||D_{\text{exp}}||}\right) \tag{12}$$

where u is the deflection of the tip and D the electric displacement (model vs. experiment). The parameters to identify include the coercive field E_c, the remnant polarization P_r, the saturation polarization P_{sat}, the permittivity ε and the charge-related coefficients d_{zx} and Q_{xz}.

4 Results and discussion

In this section, the developed methodology is applied to the samples presented in Table 1. Based on actuator deflection and electrical displacement measurements as a function of the applied electric field, the numerical model was tuned to achieve the best fit for both signals. After optimization, the model successfully fits the electromechanical response of both samples although they represent two distinct material behaviors, as shown in Fig. 8 for copolymer and terpolymer samples.

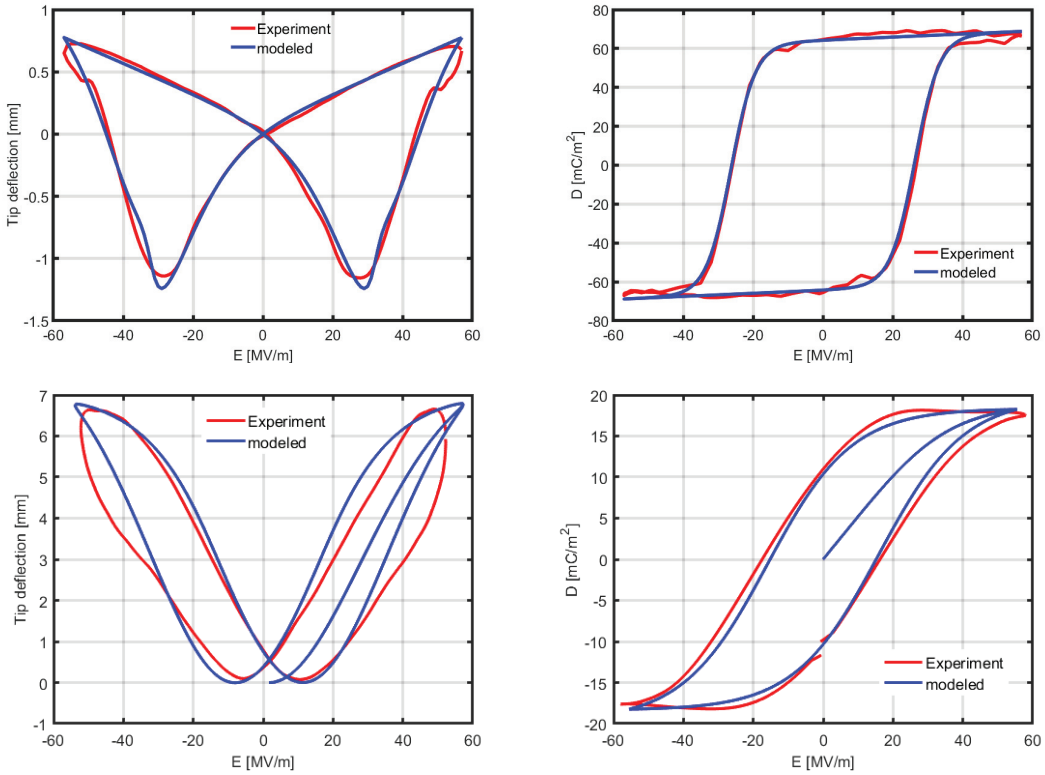

Figure 8: Tip deflection (left) and electric displacement (right) for copolymer sample (top) and terpolymer (bottom).

The presence of CTFE termonomer significantly modifies the electromechanical properties of the material. The addition of 8.5% CTFE in the terpolymer significantly decreases the coercive electric field E_c, remnant polarization P_r and saturation polarization P_{sat}, while simultaneously enhancing the dielectric nature of the material compared to the pure copolymer. These changes directly impact actuator performance, as they determine the operational voltage range and response characteristics of the device. The future soft robot will be composed of multiple EAP strip actuators bonded circumferentially to the

outer surface of endoscope tubes. For electric safety, input voltage must be reduced by increasing the number of active layers and reducing their thickness.

5 Conclusion

This study presents a comprehensive experimental and modeling framework to quantify the composition-dependent electromechanical properties of PVDF-based terpolymers. Our experimental methodology employs a multi-physics characterization system combining high-speed videometry with synchronized current-voltage measurements, enabling direct correlation between polarization dynamics and mechanical response. Through the development of an electromechanical model, we successfully integrated piezoelectric and electrostrictive effects and evaluate their respective contributions independently. This model not only accounts for the non-linear and hysteretic nature of these materials but also provides a deeper insight into the mechanisms driving their actuation under applied electric fields. Finally, the proposed methodology was used to understand how the incorporation of CTFE influences the piezoelectric and electrostrictive properties of P(VDF-*ter*-TrFE) copolymer and P(VDF-*ter*-TrFE-*ter*-CTFE) terpolymer with 8.5% CTFE content.

6 Acknowledgement

This work was conducted within the framework of the Terpolymer Electroactive Actuator for Mini-invasive surgery (TEAM) ANR project, which provides financial support and resources. We extend our warmest thanks to M. Rébillat and P. Margerit for their help in designing the experimental setup and to S. Zanchi for the manufacture of the samples. We also thank F. Domingues Dos Santos and I. Iliopoulos for their helpful discussions.

REFERENCES

[1] P. Lheritier, S. Noel, N. Vaxelaire, F. D. Dos Santos, and E. Defay, "Actuation efficiency of polyvinylidene fluoride-based co-and ter-polymers," *Polymer*, vol. 156, pp. 270–275, 2018.

[2] E. Defaÿ, "Integration of ferroelectric and piezoelectric thin films: concepts and applications for microsystems," 2013.

[3] S. Zanchi, S. Roland, L. Le Goff, D. Thuau, P. Margerit, M. Rebillat, I. Iliopoulos, and S. Tencé-Girault, "Smart actuators based on electroactive fluorinated polymers: relationship between molecular organization and electroactive response," in *10th ECCOMAS Thematic Conference on Smart Structures and Materials*, 2023, pp. 53–63.

[4] F. Bargain, D. Thuau, G. Hadziioannou, F. D. Dos Santos, and S. Tencé-Girault, "Phase diagram of poly (vdf-ter-trfe-ter-ctfe) copolymers: Relationship between crystalline structure and material properties," *Polymer*, vol. 213, p. 123203, 2021.

[5] P. Wriggers, *Nonlinear Finite Element Methods*. Berlin, Heidelberg: Springer, 2008.

[6] J. J. Brondijk, K. Asadi, P. W. Blom, and D. M. De Leeuw, "Physics of organic ferroelectric field-effect transistors," *Journal of Polymer Science Part B: Polymer Physics*, vol. 50, no. 1, pp. 47–54, 2012.

XI ECCOMAS Thematic Conference on Smart Structures and Materials - SMART 2025
M. Krommer, M. Nader and M. Schagerl (Eds)

Received: 29 March 2025 / Revised: 27 August 2025 / Accepted: 10 September 2025
© The Author(s) 2025

Weather-Induced Degradation in Magnetorheological Elastomers: Tropical Climatic Conditions on The Rheological and Mechanical Properties

Mohd Aidy Faizal Johari, Saiful Amri Mazlan, Nur Azmah Nordin, Nur Amirah Farhana Rahimin, Rehnupreya Hentry Viension

Abstract. Integrating advanced materials into engineering has made significant strides in developing innovative applications that support future technologies and enhance human convenience, both in the present and in the coming years. Among these, smart materials like magnetorheological elastomers (MREs) have emerged as promising candidates for replacing traditional materials such as rubber due to their unique ability to alter their mechanical properties in response to external magnetic fields. This capability opens up new possibilities in various fields, from automotive to robotics. Despite these advancements, the full potential of MREs to replace rubber in all its functions remains unfulfilled, particularly when considering their performance in real-world conditions. One critical challenge is their durability and resistance to climatic environmental factors, such as UV radiation, temperature fluctuations, and humidity. These factors can cause significant degradation in the material's mechanical and magnetic properties over time, limiting its long-term functionality. This paper focuses on the degradation of MREs under an outdoor tropical climate and weathering effects. Two types of silicone rubber (SR)-based MREs were developed, containing 70 wt% micron-sized carbonyl iron particles (CIP) and 60 wt% micron-sized electrolyte iron particles (EIP). These samples were exposed to natural weathering conditions for 30 days. The natural weathering process led to significant changes in the material's properties. Mechanical testing, rheological analysis, and morphological evaluation revealed increased storage modulus, indicating enhanced stiffness, while flexibility decreased. These changes suggest that the material became more rigid and less flexible over time due to exposure to environmental conditions, which is important for

Mohd Aidy Faizal Johari & Saiful Amri Mazlan & Nur Azmah Nordin & Nur Amirah Farhana Rahimin & Rehnupreya Hentry Viension
Engineering Material & Structures (eMast) iKohza, Malaysia-Japan International Institute of Technology (MJIIT), Universiti Teknologi Malaysia, 54100 Kuala Lumpur, Malaysia, e-mail: ma.faizal@utm.my

Saiful Amri Mazlan & Nur Azmah Nordin
Automotive Development Centre, Institute for Sustainable Transport (IST), Universiti Teknologi Malaysia, 81310 Skudai, Johor, Malaysia, e-mail: amri.kl@utm.my

understanding its long-term performance and durability. These assessments provided a comprehensive understanding of MRE degradation under prolonged exposure to climatic conditions. Unpredictable climatic variations, particularly variations in weather, may induce uncharacterized behavior in MREs. Investigating these emergent behaviors is essential for optimizing their performance and expanding their applicability in dynamic and complex operational environments.

Key words: Climatic Degradation, Magnetorheological Elastomer, Morphology, Rheology, Smart Materials

1 INTRODUCTION

The study on Magnetorheological Elastomers (MREs) has demonstrated their potential to emerge as a significant smart material in various engineering applications, ranging from vibration control in automotive systems to adaptive structures in advanced industries [1], [2]. As a composite material, MREs consist of magnetic particles embedded within an elastomeric matrix, exhibiting tunable mechanical properties under the influence of a magnetic field. This unique characteristic makes them highly valuable for dynamic response applications [3], [4]. With these capabilities, the automotive sector, in particular, is expected to leverage MREs to develop advanced suspension systems and engine mounts, integrating them into structural components that require adjustable stiffness and damping properties to adapt to existing environmental conditions.

Although the use of MREs is expanding and holds promising benefits, their long-term performance in tropical climates presents significant challenges that remain largely unaddressed and not yet fully understood. Tropical environments are characterized by high temperatures often exceeding 35°C, relative humidity above 80%, and intense ultraviolet (UV) radiation exposure, creating highly aggressive conditions for polymeric materials, including MREs. These environmental factors can trigger complex degradation mechanisms in MREs, potentially compromising their mechanical properties and magnetic responsiveness. The elastomeric matrix in MREs is particularly susceptible to accelerated oxidation and chain scission due to the combined effects of heat and UV exposure, while high humidity levels may affect the interfacial interactions between magnetic particles and the polymer matrix [5].

Recent literatures [6], [7], [8] highlight a critical gap in understanding the degradation mechanisms of MREs under tropical environmental conditions. While previous studies [9], [10], [11], [12], [13] have investigated the effects of temperature and UV exposure on conventional elastomeric materials, comprehensive research on the synergistic impact of natural tropical conditions—including high temperature, humidity, and UV radiation—on MRE performance remains scarce. Existing studies [14], [15], [16] often focus on distinct environmental settings, such as marine or non-tropical climates, which may not fully capture the degradation dynamics specific to tropical regions. Moreover, the implications of these

degradation mechanisms on the magneto-mechanical coupling behavior of MREs, which is essential for their functional performance, are not yet well understood. This knowledge gap hinders the ability to predict long-term reliability and optimize MRE formulations for use in harsh environments. Exploring various particle shapes could offer a potential solution by mitigating the degradation process [17], [18], [19], [20], [21], [22]. While spherical particles are the most commonly used due to their uniformity and ease of dispersion, other shapes, such as ellipsoidal, platelet, rod-like, cubic, and irregular geometries, are less popular but worth investigating. These alternative shapes could influence the stress distribution within the MRE matrix, impact particle-matrix interactions, and potentially enhance durability by altering load transfer mechanisms and reducing localized stress concentrations. Understanding the role of particle morphology in degradation resistance can provide valuable insights for designing more robust MREs suitable for demanding applications.

To bridge this knowledge gap, this study systematically investigates the combined effects of elevated temperature, high humidity, and UV exposure on the degradation mechanisms of MREs, incorporating both spherical and flaky-shaped embedded particles. Additionally, it seeks to quantitatively assess the evolution of mechanical and rheological properties under natural tropical weathering conditions. This study focuses exclusively on the effect of tropical climatic exposure on the rheological and mechanical properties of MREs. Although magneto-mechanical behavior under similar conditions is also of great interest, it lies beyond the scope of this work and will be considered in future investigations. The insights gained from this investigation will serve as a fundamental basis for improving the environmental resilience of MREs and optimizing their performance for advanced applications in tropical climates.

2 METHODOLOGIES

2.1 Sample Preparation

The fabrication of isotropic silicone-based MREs was conducted using a closed-mold method. Two types of MREs were prepared: one incorporating 70 wt.% soft carbonyl iron particles (CIPs) (BASF, Germany) and another with 60 wt.% electrolyte iron particles (EIP) (Industrial Metal Powders Pune, India PVT.LTD), both embedded in a silicone rubber matrix (Nippon Steel Co., Japan). The fabrication process involved mixing iron particles into silicone rubber at 25°C using a mechanical stirrer (200 rpm) until a visually homogeneous dispersion was achieved, followed by the addition of NS625B curing agent (0.1 wt.% for MRE-CIP and 1.5 wt.% for MRE-EIP). The mixtures were then poured into a rectangular aluminum mold (150 mm × 150 mm × 1 mm) and cured for 4 hours. The cured samples were cut into strips (25 mm × 150 mm) and systematically labeled based on exposure duration (0 to 30 days) for weathering studies. For dynamic oscillatory shear testing, circular MRE specimens (20 mm diameter, 1.0–1.3 mm thickness) were prepared using a hollow punch tool. Additionally, mechanical testing was conducted using a tensile testing machine, with samples prepared based on standard test geometry to ensure accurate evaluation of mechanical properties.

2.2 Exposure to Environmental Conditions

The tropical climate exposure was conducted at the Malaysia-Japan International Institute of Technology, Universiti Teknologi Malaysia, Kuala Lumpur, to evaluate the environmental degradation of MRE samples. MRE strips underwent a 30 days exposure following ASTM G7/G7M standards, placed in a caged rack facing south, with periodic retrieval for evaluation. The recorded 24-hour mean temperature was 27.0°C, with 19 rainy days over the period. After retrieval, samples were cleaned with acetone and conditioned at room temperature in a desiccator for 24 hours before further testing. Weather data, including rainfall, humidity, wind speed, and temperature, were obtained from the Malaysian Meteorological Department. In this study, only mean values of temperature, relative humidity, and wind speed during the exposure period are reported. The present study was designed to capture the net effect of tropical exposure, and future work will aim to address this aspect.

2.3 Morphological, Rheological, and Mechanical Analysis

To assess the effects of tropical climate on MRE samples, morphological analysis was conducted using scanning electron microscopy (SEM). SEM Tescan Vega 3 (Brno, Czech Republic) was used to examine the degradation characteristics of aged and unaged samples, including surface defects, discoloration, and structural modifications. Cross-sectional analysis provided insights into particle distribution within the matrix. Before SEM imaging, visually identified degraded areas were cut into 10 mm × 10 mm sections, and a conductive coating was applied using sputter coaters (NS800, Novatic Scientific, Singapore) to minimize charging effects and enhance image quality. Gold and platinum coatings of approximately 1–2 nm was applied to improve resolution.

Rheological testing was conducted using an oscillation parallel plate rheometer (Physica MCR 302, Anton Paar, Austria) to evaluate viscoelastic properties, storage modulus, and the absolute magnetorheological (MR) effect. Circular MRE samples (20 mm diameter, 1 mm thickness) were prepared using a hollow punch and placed between parallel plates, preloaded with a consistent normal force of 5.7 N. Magnetic flux densities from 0 to 0.73T were generated by varying the applied current from 0 to 4A, measured using a Tesla meter. Strain amplitude sweep tests were performed by varying strain from 0.01% to 10% at a constant frequency of 1 Hz. The temperature was maintained at 25°C using a Viscotherm VT2 temperature control unit.

The quasi-static uniaxial tensile properties of the samples were evaluated before and after tropical climate conditions using a universal testing machine (Shimadzu AGX-S, Kyoto, Japan), following ASTM D412. Dumbbell-shaped specimens were precisely cut from the MRE sheets using standardized tensile cutting dies. The tensile tests were conducted at a controlled room temperature of 25°C, with a constant crosshead speed of 50 mm/min.

3 RESULTS AND DISCUSSION

3.1 Morphological Analysis

The SEM image of MRE-CIP before aging in Figure 1(a) reveals a clean and smooth surface, indicating a uniform dispersion of its constituents without significant irregularities. In contrast, the SEM image of MRE-EIP of Figure 1(c) exhibits a slightly rough texture with visible protruding particles on the surface. This roughness can be attributed to the larger surface area of EIP, which enhances matrix-particle interactions. A possible explanation, the increased interaction between the elastomer matrix and EIP particles contributes to greater interfacial adhesion, thereby improving load transfer efficiency and increasing the stiffness of the MRE. However, the presence of protruding particles may also indicate potential stress concentration points, which could influence long-term durability and aging behavior.

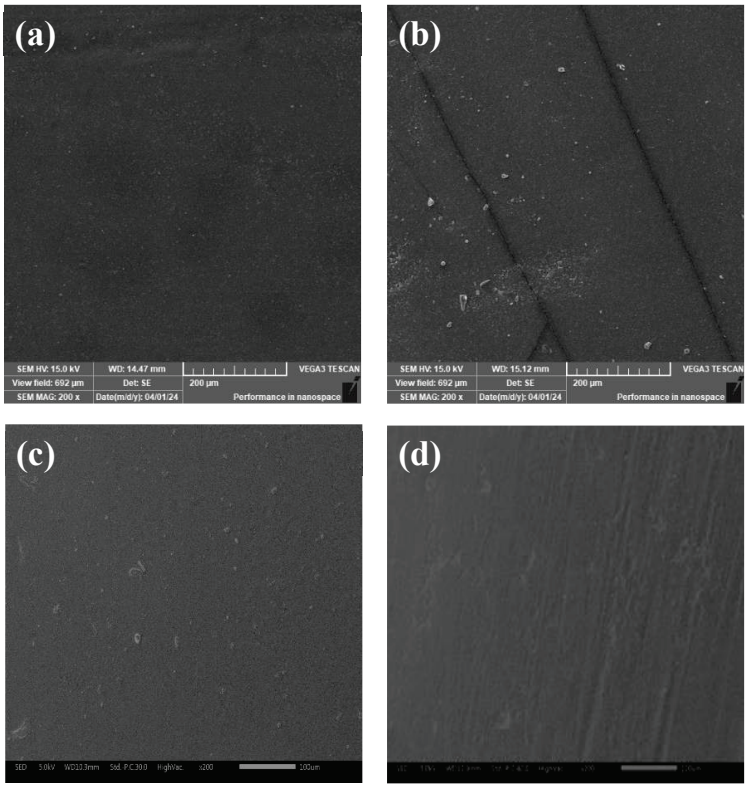

Figure 1: SEM images of (a) unaged MRE-CIP, (b) MRE-CIP after 30 days of exposure, (c) unaged MRE-EIP, and (d) MRE-EIP after 30 days of natural tropical climate aging.

The SEM analysis of the MRE-EIP sample after 30 days (Figure 1(d)) of natural weathering exposure reveals early-stage surface degradation. The micrograph shows a relatively smooth surface with faint linear striations, likely attributed to the stress from environmental exposure. Unlike MRE-CIP samples subjected to prolonged weathering (Figure 1(b)), no significant microcracks, deep voids, or severe surface roughening are observed at this stage. However, subtle textural changes suggest the onset of degradation, potentially influenced by UV radiation, humidity, and temperature fluctuations. UV-induced oxidation of the silicone rubber matrix may have initiated minor surface roughening, while cyclic thermal expansion and contraction could be contributing to the gradual evolution of surface stress. Additionally, prolonged moisture exposure from rainfall may have started affecting the matrix, though no evident water-induced swelling or delamination is detected. These preliminary findings may be attributed to observation that while short-term environmental exposure does not drastically alter the surface morphology, extended exposure may accelerate degradation.

3.2 Rheological Behavior

The graphs in Figure 2 illustrate the variation in the storage modulus of MREs as a function of shear strain under different aging conditions and magnetic stimulation states. The data reveal that the storage modulus decreases with increasing shear strain, a characteristic behavior of viscoelastic materials subjected to deformation. Additionally, aging under a tropical climate has a significant impact on the rheological properties of MREs, as evidenced by the progressive increased in the storage modulus over time. As shown in Figure 2, the samples aged for 15 and 30 days exhibit a higher modulus compared to the unexposed (0-day) samples. This increase may be attributed to surface hardening and possible crosslinking reactions that occur during prolonged exposure to tropical climatic conditions. Such changes can make the material stiffer but potentially less flexible, indicating that aging affects the rheological response of the MREs. Furthermore, the effect of magnetic stimulation is evident, as samples tested under a 5A current, which produced 0.854 T, consistently display a higher storage modulus compared to those without magnetic stimulation (0A) across all aging durations. This suggests that the applied magnetic field enhances the stiffness of the MREs, potentially due to mechanical reinforcement effects that restrict the mobility of the particle in response to the magnetic field within the elastomer matrix. The comparison of both particle types confirms these trends, emphasizing the reliability of the findings. However, a more significant change can be observed in MRE-EIP. Although the unexposed sample has a low storage modulus value, its value increases drastically after exposure to the environment.

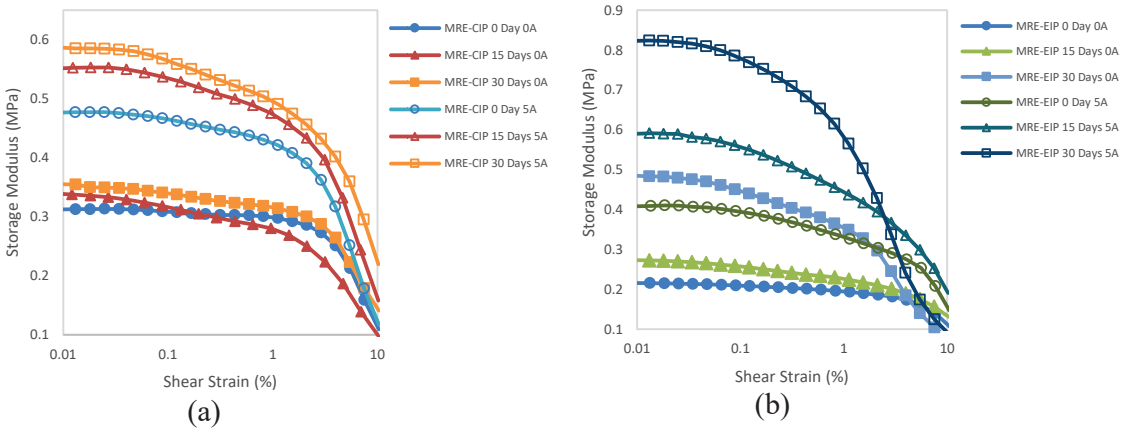

Figure 2: Storage modulus behavior for off-state and on-state at 5A of (a) MRE-CIP and (b) MRE-EIP, after 30 days of exposure to natural tropical climate aging conditions.

The pronounced increase in storage modulus after environmental exposure is more evident in MRE-EIP due to its material composition and susceptibility to environmental factors. This suggests that the higher surface area of the EIP may enhance moisture absorption and particle-matrix interactions, leading to increased stiffness. Additionally, the matrix in MRE-EIP may contain more reactive surface area, making it more prone to oxidation-induced crosslinking when exposed to oxygen, UV light, or heat. These combined mechanisms explain why MRE-EIP exhibits a more significant modulus increase after exposure.

3.3 Tensile Performance

The tensile test results in Figure 3 reveal significant changes in the mechanical behavior of SR and MREs over different aging periods. The Young's modulus at 100% strain increases progressively for both materials, may be attributed to the increased stiffness due to structural modifications such as polymer oxidation, crosslinking, and the evaporation of residual volatiles. In MREs, the modulus enhancement is more pronounced, attributed to stronger matrix-particle interactions that further restrict polymer chain mobility over time. Conversely, the elongation at break decreases with aging, may suggests that signifying a loss of material flexibility. In SR, this reduction is likely caused by polymer oxidation and molecular rearrangements that restrict chain movement. Polymer oxidation is a degradation process in which polymers react with oxygen, leading to structural changes such as additional crosslinking and chain scission. This phenomenon, likely accelerated by environmental exposure and mechanical stress, restricts polymer chain mobility, resulting in increased stiffness and reduced flexibility over time. The effect is more pronounced in MREs, where the presence of particles accelerates embrittlement by further limiting chain mobility. Additionally, particle-matrix detachment and microstructural degradation may contribute to the loss of elasticity and reduced elongation at break in aged

MREs.

A possible explanation is that these findings suggested the trend of the aging-induced trade-off between stiffness and flexibility, where increased stiffness enhances load-bearing capacity but reduces elasticity. This may explain that for the long-term mechanical performance of MREs, particularly in applications requiring durability and adaptive properties. It should be noted that the explanations provided are based on observed trends and previously reported mechanisms. Differences between MRE-CIP and MRE-EIP can be observed in terms of modulus trends, which are linked to the particle morphology and dispersion in the elastomer matrix. As shown in Figure 3, both MRE-CIP and MRE-EIP exhibit an increase in Young's modulus after tropical exposure, although the magnitude of change differs between the two. This difference may be attributed to the distinct particle morphology and dispersion characteristics of CIP and EIP, which influence the stiffness response of the elastomer matrix during aging.

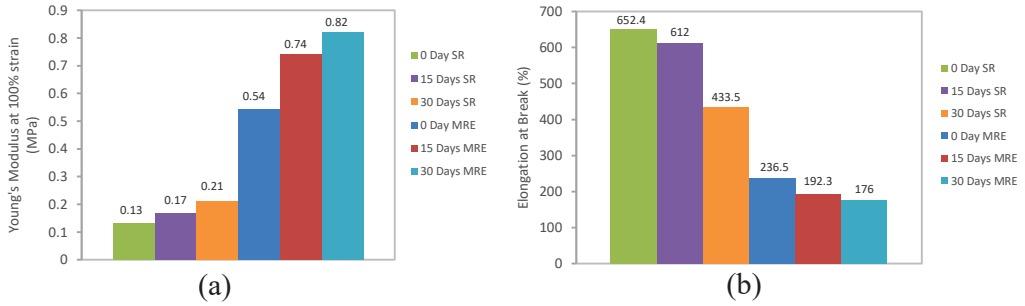

Figure 3: SR and MREs (a) Young's modulus and (b) Elongation at break properties changed after 30 days of exposure to natural tropical climate aging conditions.

4 CONCLUSIONS

This study confirms that MRE, like other rubber-based materials that have been extensively used in various applications, is susceptible to degradation when exposed to environmental conditions, particularly in tropical climates. The tendency for increased hardness after exposure was evident from mechanical and rheological testing, aligning with findings in the literature. This phenomenon is primarily attributed to ultraviolet UV exposure, which promotes cross-linking within the matrix, leading to increased stiffness. However, this hardening effect also contributes to a reduction in elongation at break due to increased brittleness. From a rheological perspective, all samples exhibited an increase in storage modulus, which correlates well with the observed mechanical property changes. This result was expected, as prolonged exposure to high temperatures and solar radiation plays a more dominant role in material degradation, despite the high humidity and frequent rainfall typical of tropical climates. Microstructural observations further support these findings, revealing surface alterations in the exposed

samples. Additionally, MRE with tunable stiffness under magnetic influence demonstrates enhanced properties, as evidenced by rheological evaluations. This characteristic provides a significant advantage over conventional rubber. This study makes a significant contribution to MRE materials research, providing new insights into a topic that has been rarely reported. For future studies, it is recommended to extend the exposure duration to better capture the long-term degradation effects, allowing for a more comprehensive understanding of material deterioration. The present work was limited to the non-magnetic influence of mechanical characterization. Future studies will extend this approach to investigate the influence of tropical climatic conditions on the magnetic and magneto-mechanical properties of MREs, which would provide a more comprehensive understanding of their performance in real environments. Additionally, the development of effective mitigation strategies can be further explored to enhance the durability of MRE under tropical environmental conditions.

ACKNOWLEDGEMENT

This work was supported by the Higher Institution Centre of Excellence (HiCOE) program of the Ministry of Higher Education (MOHE) Malaysia under HiCOE Research Grant and also the Professional Development Research University (PDRU) Special (Vot. No. 07E70).

REFERENCES

[1] S. Kang, K. Choi, J.-D. Nam, and H. Choi, "Magnetorheological Elastomers: Fabrication, Characteristics, and Applications," *Materials*, vol. 13, no. 20, p. 4597, Oct. 2020, doi: 10.3390/ma13204597.

[2] U. Ulusoy, "A Review of Particle Shape Effects on Material Properties for Various Engineering Applications: From Macro to Nanoscale," Jan. 01, 2023, *MDPI*. doi: 10.3390/min13010091.

[3] C. M. M. Model, C. G. Soria-hern, L. M. Palacios-pineda, and A. El, "Investigation of the E ff ect of Carbonyl Iron Micro-Particles on the Mechanical and Rheological Properties of Isotropic and Anisotropic MREs," *Composite Part B*, 2020.

[4] Z. Chen *et al.*, "Investigation of a new metamaterial magnetorheological elastomer isolator with tunable vibration bandgaps," *Mech Syst Signal Process*, vol. 170, no. December 2021, p. 108806, 2022, doi: 10.1016/j.ymssp.2022.108806.

[5] M. Ginic-Markovic, N. R. Choudhury, M. Dimopoulos, and J. G. Matisons, "Weatherability of coated EPDM rubber compound by controlled UV irradiation."

[6] M. A. F. Johari *et al.*, "Unveiling the Influence of natural weathering on the nanomechanical properties of magnetorheological elastomers," *Results in Engineering*, vol. 24, p. 103610, Dec. 2024, doi: 10.1016/j.rineng.2024.103610.

[7] M. A. F. Johari *et al.*, "Natural Weathering Effects on the Mechanical, Rheological, and Morphological Properties of Magnetorheological Elastomer (MRE) in Tropical Climate," *Int J Mol Sci*, vol. 23, p. 9929, 2022, doi: 10.3390/ijms23179929.

[8] M. A. F. Johari *et al.*, "Morphological features of magnetorheological elastomer degradation under a natural weathering environment," *Sci Rep*, vol. 14, no. 1, p. 1155, Jan. 2024, doi: 10.1038/s41598-024-51736-x.

[9] B. Ruellan, J. B. Le Cam, I. Jeanneau, F. Canévet, F. Mortier, and E. Robin, "Fatigue of natural rubber under different temperatures," *Int J Fatigue*, vol. 124, no. June 2018, pp. 544–557, 2019, doi: 10.1016/j.ijfatigue.2018.10.009.

[10] Ç. Yalçınkaya and H. Yazıcı, "Effects of ambient temperature and relative humidity on early-age shrinkage of UHPC with high-volume mineral admixtures," *Constr Build Mater*, vol. 144, pp. 252–259, Jul. 2017, doi: 10.1016/j.conbuildmat.2017.03.198.

[11] R. Chakraborty and B. S. Reddy, "Studies on high temperature vulcanized silicone rubber insulators under arid climatic aging," *IEEE Transactions on Dielectrics and Electrical Insulation*, vol. 24, no. 3, pp. 1751–1760, Jun. 2017, doi: 10.1109/TDEI.2017.006247.

[12] L. Yu, S. Liu, W. Yang, and M. Liu, "Analysis of mechanical properties and mechanism of natural rubber waterstop after aging in low-temperature environment," *Polymers (Basel)*, vol. 13, p. 13132119, Jul. 2021, doi: 10.3390/polym13132119.

[13] A. Boubakri, N. Guermazi, K. Elleuch, and H. F. Ayedi, "Study of UV-aging of thermoplastic polyurethane material," *Materials Science and Engineering A*, vol. 527, no. 7–8, pp. 1649–1654, Mar. 2010, doi: 10.1016/j.msea.2010.01.014.

[14] N. Zaini *et al.*, "Deterioration behavior of aged magnetorheological elastomer under harsh marine environment," *Express Polym Lett*, vol. 18, no. 7, pp. 728–741, 2024, doi: 10.3144/expresspolymlett.2024.54.

[15] M. H. Ahmad Khairi *et al.*, "The effect of salt water ageing on the mechanical and rheological properties of magnetorheological elastomer," *Sci Rep*, vol. 13, no. 1, Dec. 2023, doi: 10.1038/s41598-023-33171-6.

[16] W. Wibowo, B. W. Lenggana, U. Ubaidillah, D. Ariawan, and F. Imaduddin, "Performance Degradation of silicon based magnetorheological elastomer under accelerated weathering treatment," no. December, 2020, doi: 10.20944/preprints202012.0811.v1.

[17] N. L. Burhannuddin *et al.*, "Physicochemical characterization and rheological properties of magnetic elastomers containing different shapes of corroded carbonyl iron particles," *Sci Rep*, vol. 11, no. 1, pp. 1–17, 2021, doi: 10.1038/s41598-020-80539-z.

[18] M. Behrooz, J. Sutrisno, L. Zhang, A. Fuchs, and F. Gordaninejad, "Behavior of magnetorheological elastomers with coated particles," *Smart Mater Struct*, vol. 24, no. 3, p. 35026, 2015, doi: 10.1088/0964-1726/24/3/035026.

[19] M. Cvek, M. Mrlík, M. Ilčíková, J. Mosnáček, L. Münster, and V. Pavlínek, "Synthesis of Silicone Elastomers Containing Silyl-Based Polymer-Grafted Carbonyl Iron Particles: An Efficient Way To Improve Magnetorheological, Damping, and Sensing Performances," *Macromolecules*, vol. 50, no. 5, pp. 2189–2200, Mar. 2017, doi: 10.1021/acs.macromol.6b02041.

[20] E. Burgaz and M. Goksuzoglu, "Effects of magnetic particles and carbon black on structure and properties of magnetorheological elastomers," *Polym Test*, vol. 81, no. November 2019, p. 106233, 2020, doi: 10.1016/j.polymertesting.2019.106233.

[21] Y. Tong, X. Dong, and M. Qi, "Improved tunable range of the field-induced storage modulus by using flower-like particles as the active phase of magnetorheological elastomers," *Soft Matter*, vol. 14, no. 18, pp. 3504–3509, 2018, doi: 10.1039/c8sm00359a.

[22] W. Li *et al.*, "Microstructure and magnetorheological properties of the thermoplastic magnetorheological elastomer composites containing modified carbonyl iron particles and poly(styrene-b-ethylene-ethylenepropylene-b-styrene) matrix," *Smart Mater Struct*, vol. 21, no. 11, Nov. 2012, doi: 10.1088/0964-1726/21/11/115028.

XI ECCOMAS Thematic Conference on Smart Structures and Materials - SMART 2025
M. Krommer, M. Nader and M. Schagerl (Eds)

Received: 28 May 2025 / Revised: 31 August 2025 / Accepted: 10 September 2025
© The Author(s) 2025

An Active Silicone Foam Mat for Medical Applications

Florian Poltschak, Rene Preuer, Ingrid Graz

Abstract. Integrated elastic actuators have recently been discussed in the literature for rehabilitation applications. In most cases, gentle movement is required to either assist the physical movement, massage or vary the pressure on the skin. A well-known solution for the latter application are active anti-decubitus mats used for patients who are forced to remain in bed for long periods of time. While the common pneumatic actuation is regarded as flexible, it suffers from acoustic noise of the air compression. The solution in this paper proposes a mat made from silicon foam with embedded ferromagnetic elements and hence belongs to the class of noiselessly actuated soft actuators. Is is analyzed and modeled in detail how these embedded ferromagnetic pieces behave when positioned on a bed holding actively controllable electromagnetic stator elements. The capability and limit of the generated variable forces are identified. Based on these results a prototype has been built and proves the ability to control the local compression of the silicon foam mat and thus change its stiffness.

Key words: active silicon foam, smart actuator, electromagnetic actuation, noiseless actuation

1 INTRODUCTION

With their inherent softness, elastomer actuators have great potential in the field of rehabilitation [1, 2], in particular, when close contact between a human and an actuator is required. With a plethora of actuation mechanisms ranging from electrical, optical, thermal, magnetical, mechanical [3] stimuli to pneumatics and even explosions [4], these soft actuators show great versatility. To ensure safe operation in proximity or even in contact with the human body, pneumatics are often the first choice of actuation. However, they require bulky and often noisy equipment in the form of a compressor. Therefore, interest in more compact solutions is growing, and dielectric-elastomer (DEA) as well as magneto-elastomer actuators are moving in the focus of interest. DEAs with their need for high voltages in the range of several kV are often

Florian Poltschak
JKU HOERBIGER Research Institute for Smart Actuators Johannes Kepler University Linz, Altenbergerstr. 69, 4040 Linz, Austria, e-mail: florian.poltschak@jku.at

Rene Preuer & Ingrid Graz
Linz School of Education, Johannes Kepler University Linz Altenbergerstr. 69, 4040 Linz, Austria
e-mail: rene.preuer@jku.at

considered less suitable for contact with patients [5, 6], while magneto-elastomer actuators are more user-friendly due to low voltages [5]. To enhance the mechanical response of the elastomers, foams are used instead of bulk materials. Therefore, their stiffness decreases and they become compressible [7].
By adding electrically conducting particles, such as carbon black, these elastomer foams turn into electrically sensitive objects and can be applied as distributed pressure or sensors [8].
It is only a small step from a sensor to an actuator. Adding ferromagnetic particles during the manufacturing process of the foam would result in a foam which can be electromagnetically actuated. Assuming a homogeneous distribution of the ferromagnetic particles, an externally applied magnetic field will result in the mutual attraction of the particles. This consequences two issues: First, the required compressibility of the foam significantly limits the density of the ferromagnetic particles in the foam, and second, the particles and the resulting forces will act along the resulting field lines. Thus, either high magnetic fields are required to generate considerable forces or a different arrangement is required. This led to the idea of embedding ferromagnetic components well known in the field of electromagnetic actuator design into the foam to improve its force capability. A recent study used permanent magnets (PM) and coils to design a soft gripper capable of firmly grasping and lifting parts similar in weight and shape to onions [9].
Our paper develops that idea further to (i) reduce the stray field and (ii) concentrate the ferromagnetic regions to be able to increase and better direct the actuation forces. The first prototype of that approach was developed at our institute and presented in [10]. Now we present the extension to create attractive and repellent forces together with a mathematical analysis of the resulting motion profile of the embedded ferromagnetic flaps.
The paper is organized as follows. First, the actuator principle and the properties of its components are described, and second, the manufacturing process of the silicon foam mat is presented in detail. The next section presents a comprehensive mathematical model to describe the resulting motion profile and analyze its properties and limits. Finally, a prototype is presented that demonstrates the functionality of the proposed system.

2 SILICON FOAM MAT ACTUATION SYSTEM LAYOUT

The proposed system of the actuated silicon foam mat consists of two independent components: The mat and the actuation bed, the mat is put on when actuated. Fig. 1 shows the modular setup of the cross section of the mat with exemplarily three actuated flaps and two end elements. The bed holds the stator of the electromechanical actuator. Both assemblies, the mat and the bed, are not mechanically connected. The mat simply lies on the bed.

2.1 Active Silicon Foam Mat

The considerations of concentrating the ferromagnetic regions in the silicon mat led to the conclusion of integrating solid ferromagnetic pieces made of steel grade 400-TG-179 [11],

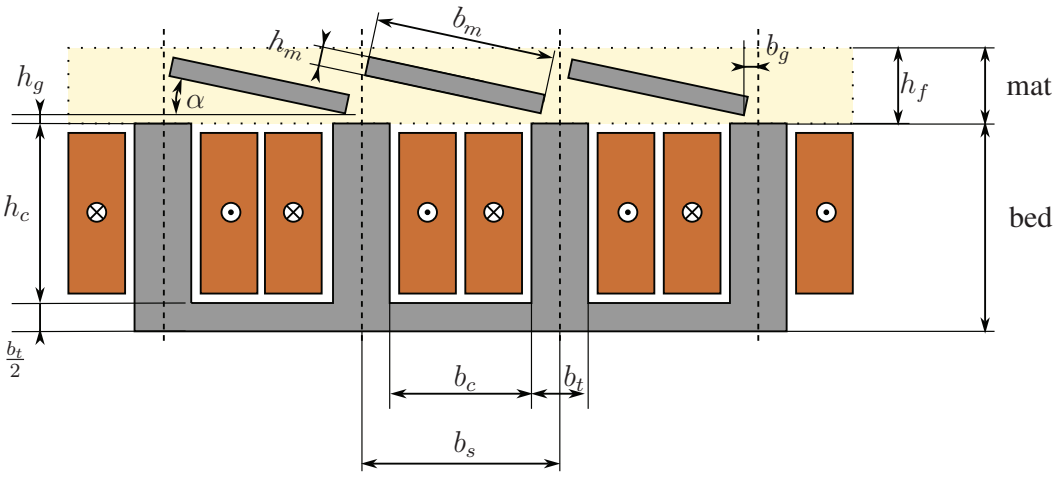

Figure 1: Cross section of the modular actuation system consisting of bed (stator) and silicon foam mat with integrated ferromagnetic flaps (mover).

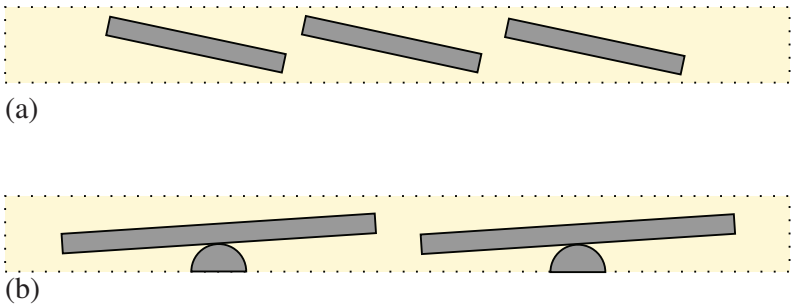

Figure 2: Cross section of two analyzed configurations of the mat (a) able to compress and (b) able to compress and extend. Both are modular and feature only ferromagnetic flaps.

called flaps. Although permanent magnets would have allowed for pushing and pulling forces, the high stray field of this approach ruled out this solution. If pushing forces are required, the second configuration given in Fig. 2 is proposed to be applied.

The silicone foams inspired by their biological counterparts were prepared by template-casting. First, a sugar template was created by mixing store-bought cane sugar (Spar S Budget) in a 100:1 ratio with water. The water sugar mixture was then stirred for 2 min until the sugar particles started to cluster. This sticky sugar-water mixture was then cast into an aluminum mold designed to obtain rectangular flaps. A sawtooth-formed lid was used as the bottom of the mold to press the lower part of the sugar matrix into shape. In a next step, the mold was flipped, the sawtooth bottom was removed, and the ferromagnetic elements (25.5 mm x 100 mm x 2 mm) were placed on the still wet templates until they were covered with another layer of sugar-water mixture. The molds complete with the ferromagnetic plates were then placed in the oven for 12 h at 65 °C to dry and remove all the water. The desiccated sugar templates were ready for

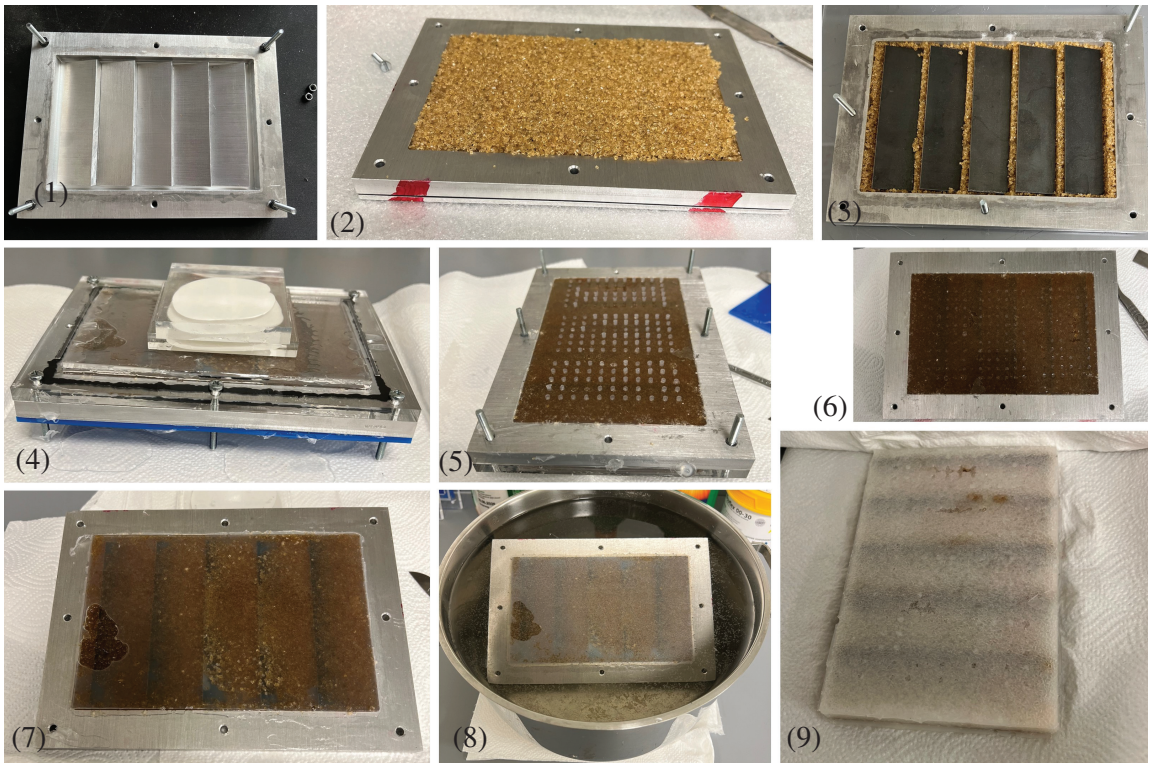

Figure 3: Manufacturing process of the silicon mat with integrated ferromagnetic flaps: (1) Mold with saw-tooth shaped bottom, (2) filling form with sugar, (3) placing flaps, filling (4) top and (5) bottom side with liquid silicon, taking off lid on (6) top and (7) bottom side, (8) dissolving sugar in hot water and (9) drying silicon mat after demolding.

use as a negative matrix for silicone foams.

Silicone elastomer (Ecoflex 00-30) was prepared according to the manufacturer's instructions in a 1:1 mixing ratio and stirred well with a bladeless mixer (Hauschild Speedmixer DAC 400). The silicone was then poured onto the sugar template that was sitting inside rectangular molds. To ensure that the viscous liquid silicone was well inserted into the pores of the template, the molds were first covered with a cover plate and then placed in a desiccator while vacuum was applied. The samples were then pre-cured in an oven at 65 °C for 1 h, before being flipped over and the second side of the template filled with silicone. After compressing with a cover plate, they were cured at 65 °C for 24 h. Subsequently, the template was dissolved in hot water and the foam mats obtained were dried for 12 h at room temperature.

The silicone foams obtained are open-pore foams and exhibit a porosity of approximately 0.6, equivalent to 40 percent of the area comprising the silicone matrix as characterized in scanning electron microscopy (SEM) and micro-computer tomography (µ-CT) images [8].

Fig. 3 shows the manufacturing process of the silicon mat with the embedded ferromagnetic flaps in a picture story.

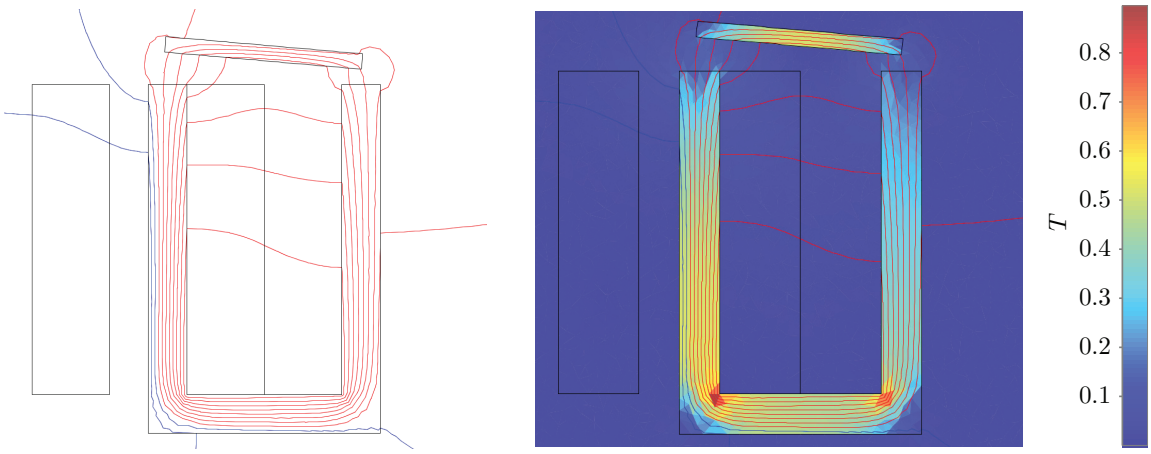

Figure 4: Parameterized FE Model of a single flap used to analyze the electromagnetic behavior. The results given here results from the parameterization of motion: $\alpha = 13°$, $h_g = 2$mm and an excitation current of 900 AWdg.

2.2 Actuation System

The two functional parts of an electromagnetic actuator, the mover and the stator, are here found as mat and bed. The mat is completely passive, while the bed as stator holds the excitation coils. A series of U-shaped stator elements form the yoke and hold the coils. The mat is positioned on the stator in a way that each flap is located on one iron yoke element. Thus, the selected number of elements defines the length of the overall system. The prototype presented has approximately the size of a hand (100 mmx150 mm) and consists of a row of five flaps.

3 MATHEMATICAL MODELING OF FOAM MAT ACTUATION

It is obvious that energizing the coils in Fig. 1 with a current of arbitrary direction will attract the flaps toward the stator and deform the mat. This deformation results in a locally increased stiffness of the mat and is dependent on the chosen current value. The main difference between the mat configurations depicted in Fig. 2 is the bearing situation. While configuration (b) features a distinctive bearing, the flaps in configuration (a) are floating inside the silicon foam. That allows in case (b) for both pushing and pulling forces. However, in the absence of permanent magnets, this requires a mechanical coupling that is realized as seesaw. The attractive forces that lead to the compression of the foam are actively generated, while the counteraction is a passive reaction. Thus, the focus lies on the compression of the foam. Here case (a) is the more general case and for that reason the following analysis concentrates on this mat configuration.

With a horizontal stator surface, the main direction of actuation forces vertical and horizontal forces can be ignored. Thus, mathematical analysis can be reduced to the analysis of one actuation element. To isolate the motion of a single flap, a simple electromagnetic circuit shown in Fig. 4 is sufficient. The parameterization given in Fig. 1 can be split into the geometric parameters given in Tab. 1 and the parameters that define the motion in Tab. 2.

Table 1: Geometric parameters of the system given in Fig. 1.

h_m	height of flap	2 mm
b_m	width of flap	22.5 mm
h_f	mat thickness	12 mm
b_g	horizontal position of flap	2.5 mm
h_c	slot height	40 mm
b_c	slot width	20 mm
b_t	tooth width	10 mm
b_s	element height	30 mm
l_s	element length in the third dimension	100 mm

Table 2: Parameters defining the motion of the system given in Fig. 1.

α	angle of flap	no load value 13 °
h_g	vertical position of flap	no load value 2 mm

3.1 Silicon Form Properties

The basis of the investigation of the compression rate of the foam is a pure silicon foam sample manufactured in the same way as the prototype mat. In a simple compression experiment, the foam sample was loaded with an external force, while the force and the resulting thickness of the foam were measured. The results were transformed into a pressure and the resulting compression rate and are given in Fig. 5. The saturation is reached when the foam is compressed to approximately half of its thickness, which gives a reasonable limit of operation. The area enclosed by the hysteresis allows the estimation of the quasi-static compression losses. The curve is interpolated and used in the model as a compression-related reaction force of the foam.

3.2 Modeling the Foam Reaction Forces

As the flaps of configuration Fig. 4(a) have no classical bearing inside the foam, the actuation forces can move them in the vertical direction and rotate them. In rigid flaps, the electromagnetic force distribution during actuation can be reduced to the resulting force F_y acting vertically and a torque T_{zA} around the lower right corner of the flap, named A. The foam piece under the flap becomes compressed when actuated. Horizontal forces are simulated to be less than 5 % of vertical forces at all operating points and therefore are ignored, as well as the resulting lateral deformation of the foam. The same applies to the other degrees of freedom of a rigid body. The resulting model in Fig. 6 only needs to consider the foam underneath the flap. The vertical foam reaction force can then be calculated as

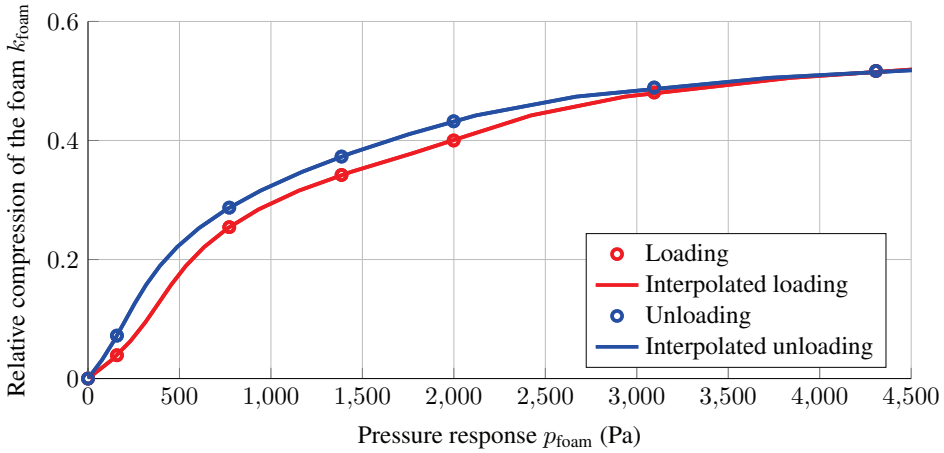

Figure 5: Measured characteristics of the foam under pressure load for loading and unloading.

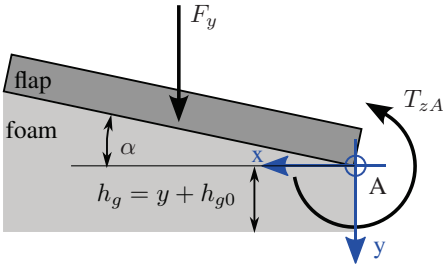

Figure 6: The electromagnetic forces acting on the flap can be reduced to a resulting vertical force F_y and a torque T_{zA} around the point A.

$$F_{y,foam}(\alpha, y) = p_{foam}(k_{foam}(\alpha, y)) l_m b_m \cos(\alpha) \tag{1}$$

with the reaction pressure of the foam resulting from the characteristic in Fig. 5 and the position-dependent compression ratio

$$k_{foam}(\alpha, y) = \text{mean}(k_{foam}(x, \alpha, y), x) \tag{2}$$

giving the mean compression of the foam with respect to the flap dimension in the x-direction calculated from the local compression

$$k_{foam}(x, \alpha, y) = 1 - \frac{h_{g0} + y + x \tan(\alpha)}{h_{g0}}. \tag{3}$$

The resulting torque

$$T_{zA,foam}(\alpha, y) = l_m \int p_{foam}(x, \alpha, y) x \mathrm{d}x \tag{4}$$

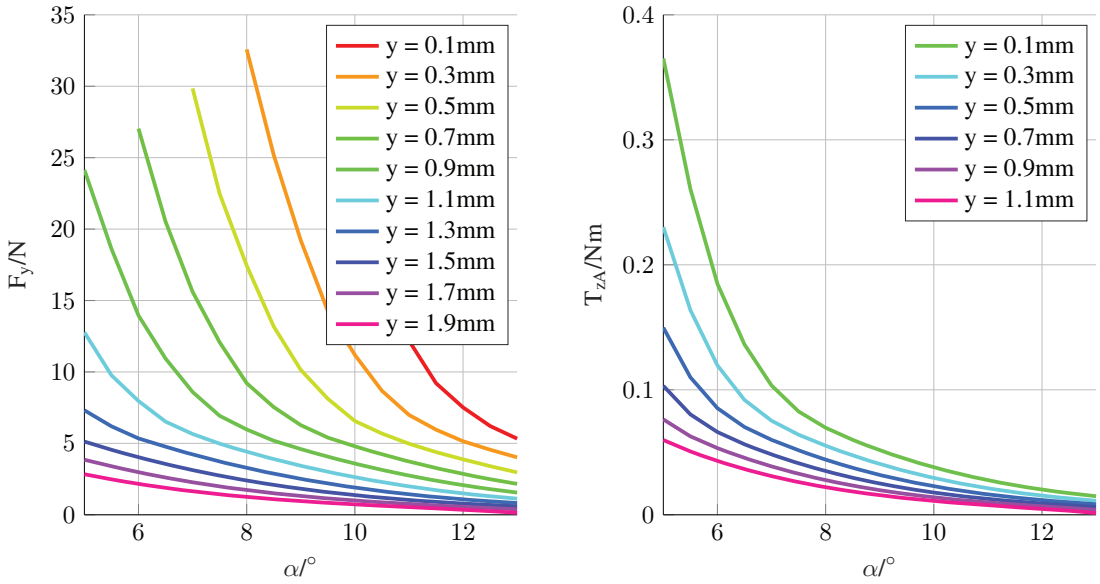

Figure 7: Reaction force F_y and torque $T_{z,A}$ of the foam with respect to the motion coordinates α and y. Values outside the shown range are outside the reasonable area of operation because of saturation of the foam compression. In that range the reaction force equals the applied force without further compression.

integrates the local foam reaction pressure

$$p_{foam}(x, \alpha, y) = p_{foam}(k_{foam}(x, \alpha, y)) \tag{5}$$

with respect to the horizontal coordinate x.

3.3 Simulation of the Actuation forces

To actuate the foam with the resulting characteristics of Fig. 7, the actuator must have the ability to compensate (static) or overcompensate (dynamic) force F_y and torque $T_{z,A}$. Both force components are coupled. Independent control is impossible.
Seen from the perspective of the actuator, its force and torque characteristics is in a similar way coupled but with the excitation current as actuating variable. The electromagnetic circuit of a single flap actuation circuit, given in Fig. 4 was analyzed using the finite element approach with the software package FEMM [12]. Based on the position

$$\mathbf{q} = [\alpha, \mathbf{y}] \tag{6}$$

and the excitation current θ both, the actuation force

$$F_{y,act}(\alpha, y, \theta) \tag{7}$$

and the actuation torque

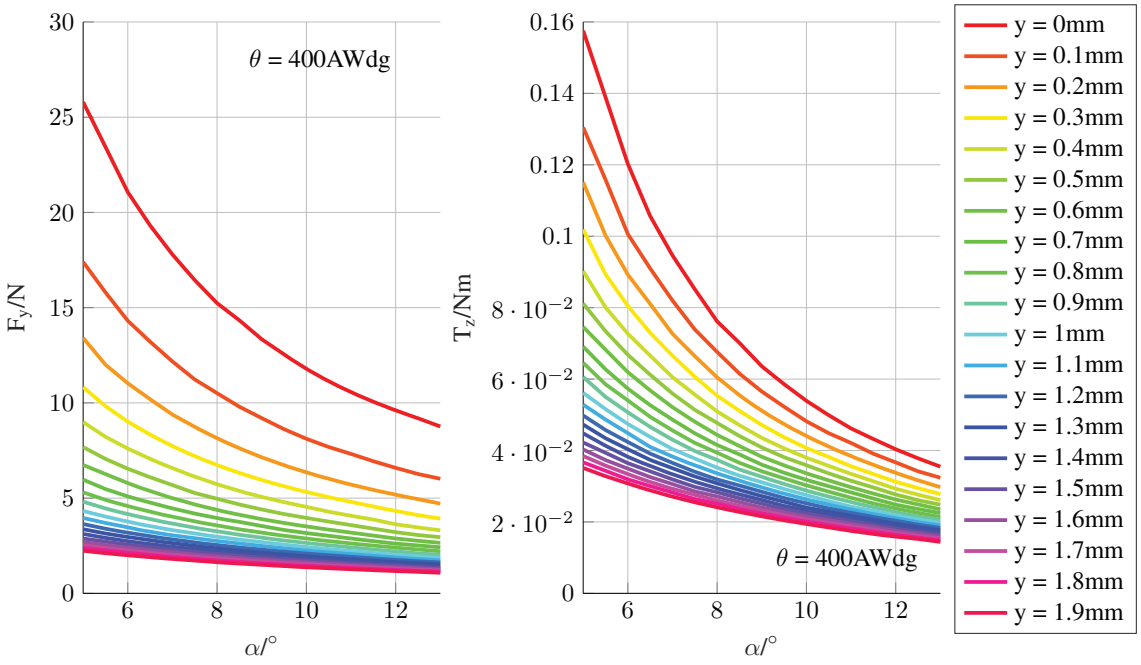

Figure 8: Simulation of the force F_y and the torque $T_{z,A}$ generated by the actuator when energized with an actuation current of 400 AWdg.

$$T_{zA,act}(\alpha, y, \theta) \tag{8}$$

can be calculated. The force components are calculated numerically over the three-dimensional space of position and excitation current. For illustration purposes, the results are given in Fig. 8 for a constant excitation current.

3.4 Calculation of the Flap Movement

Assuming a quasi-static motion, the resulting motion profile (vertical and angular) is found as the solution of the equilibrium

$$F_{y,act}(\alpha, y, \theta) = F_{y,foam}(\alpha, y) \tag{9}$$

$$T_{zA,act}(\alpha, y, \theta) = T_{zA,foam}(\alpha, y) \tag{10}$$

for the current θ. The numerical solution based on the simulated data is given in Fig. 9. When actuated, the flap first begins to rotate from larger to smaller values of α and then simultaneously rotates and vertically compresses the foam. At an angle $\alpha \approx 9°$ the flap moves vertically until the saturation of foam compression is reached in the zone below the point A. If the current is further increased, some more rotation can be achieved until the flap reaches full compression saturation.

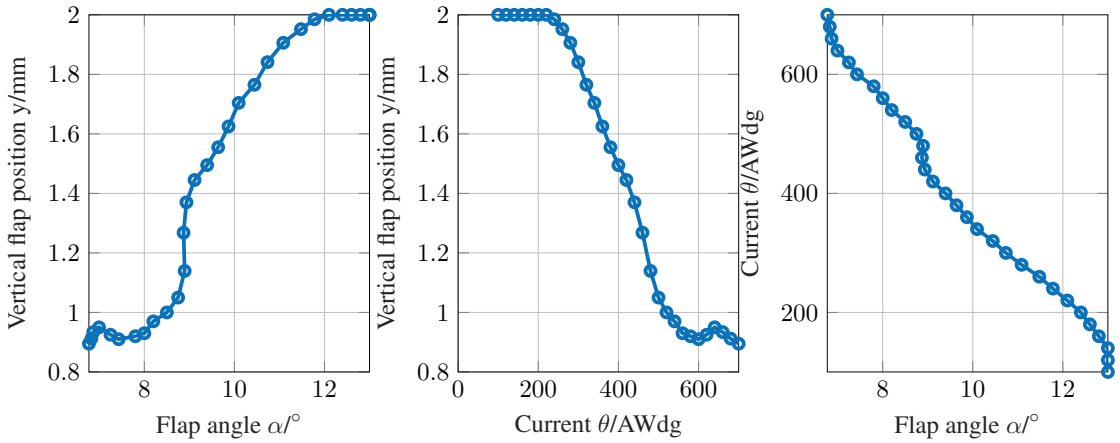

Figure 9: Solution of the resulting quasi-static motion of the flap actuation.

.

4 EXPERIMENTAL EVALUATION

A prototype of the system in Fig. 1 has been manufactured for both mat configurations in Fig. 2 for use with a stator bed with six coils. The embedded flaps have the initial position as specified in Tab. 2. The seesaws embedded in the second mat are twice the size of a single flap of the first mat and have a horizontal initial orientation.

An evaluation of the simulated behavior of the flaps is possible in different ways. First, to validate the simulated motion presented in Fig. 9, the vertical position and the angular tilt of a flap are required. However, the flaps are inseparably united with the foam and an (e.g. laser optical measurement) of the surface will not resemble the results in Fig. 9. A compromise could be a modified system in which spaces are left free on the flap surface to allow direct optical measurement, or the use of sensors that are not sensitive to silicon foam.

A second method would be to evaluate the force and torque calculated and given in Fig. 8. Although this seems to be simpler, as it does not include the foam and can be evaluated on the flaps directly, it would require a specific set-up to precisely position and measure both position (vertical and tilt) as well as forces and torque.

In addition to that, a third method can be thought of that evaluates the feasibility of loading and unloading different zones of a body lying on the mat. This body could, for example, be an array of load cells. However, instead of a quantitative evaluation, the qualitative operation would be evaluated with reference to its intended purpose.

Due to the embedded character, for reasons of simplicity and least influence on the system, only a simple qualitative evaluation is presented here to verify the proposed hypothesis. This includes i) a visual inspection and ii) a sensual impression with a test person's hand positioned on the mat.

Both mats show the expected behavior. A brief summary of the visual impression is given in Fig. 10.

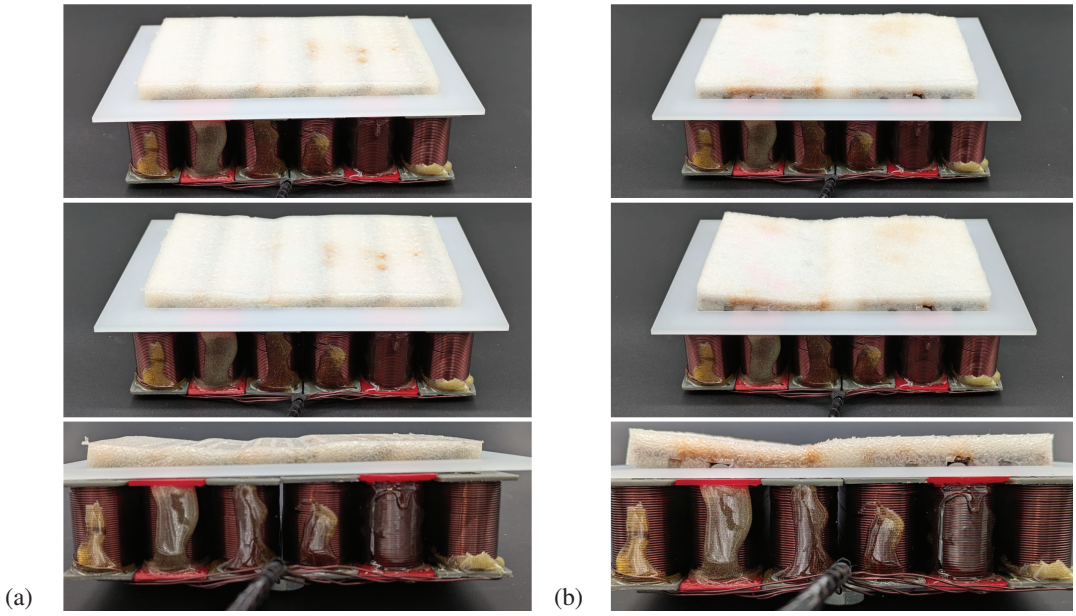

Figure 10: The manufactured prototype with mats with (a) embedded flaps and (b) embedded seesaw-shaped ferromagnetic elements. The top photos show the actuator not powered and the middle and lower ones when two flap resp. one seesaw actuated.

More importantly, when placing one's hand on the mat during actuation, a change of the supported weight distribution can clearly be sensed. The effect remains the same when the hand is pushed with some effort on the mat. From that can already be concluded that the foam parameters as well as actuation forces are in the required range for a full-sized anti-decubitus mat made from an array of elements similar in size to the prototype. Therefore, a detailed evaluation of the forces and positions is not absolutely necessary.

5 CONCLUSIONS

Noiseless actuation of a silicon foam mat can be achieved by embedding ferromagnetic elements into the foam. The embedded rigid elements are the solution to the actuation in a specific region of the foam. Based on the analysis of the compression characteristics of the foam, a model has been derived that allows for calculating the motion of the embedded flaps under the influence of a magnetic field generated by the stator integrated into the bed the mat is put on. This motion profile consists of a combination of vertical and angular movement. The derived characteristics can now be used to generate an arbitrary change in local foam stiffness using integrated flaps or, in addition, an upward motion when using the embedded seesaw elements. The process of prototyping the foam is presented in detail and verifies that manufacturing a silicon mat with embedded ferromagnetic elements is feasible. Finally, the visual and haptic impression when actuated qualitatively validates the results of the mathematical model and shows the concept to be appropriate for medical applications.

REFERENCES

[1] M. Pan, C. Yuan, X. Liang, T. Dong, T. Liu, J. Zhang, J. Zou, H. Yang, and C. Bowen, "Soft Actuators and Robotic Devices for Rehabilitation and Assistance," *Advanced Intelligent Systems*, vol. 4, no. 4, 2022.

[2] M. Li, A. Pal, A. Aghakhani, A. Pena-Francesch, and M. Sitti, "Soft actuators for real-world applications," *Nature reviews. Materials*, vol. 7, pp. 235–249, 2022.

[3] H. Dong, Y. Feng, C. Qiu, and I.-M. Chen, "Construction of Interaction Parallel Manipulator: Towards Rehabilitation Massage," *IEEE/ASME Transactions on Mechatronics*, vol. 28, no. 1, pp. 372–384, 2023.

[4] N. El-Atab, R. B. Mishra, F. Al-Modaf, L. Joharji, A. A. Alsharif, H. Alamoudi, M. Diaz, N. Qaiser, and M. M. Hussain, "Soft Actuators for Soft Robotic Applications: A Review," *Advanced Intelligent Systems*, vol. 2, no. 10, 2020.

[5] H.-J. Chung, A. M. Parsons, and L. Zheng, "Magnetically Controlled Soft Robotics Utilizing Elastomers and Gels in Actuation: A Review," *Advanced Intelligent Systems*, vol. 3, no. 3, 2021.

[6] N. Ebrahimi, C. Bi, D. J. Cappelleri, G. Ciuti, A. T. Conn, D. Faivre, N. Habibi, A. Hošovský, V. Iacovacci, I. S. M. Khalil, V. Magdanz, S. Misra, C. Pawashe, R. Rashidifar, P. E. D. Soto-Rodriguez, Z. Fekete, and A. Jafari, "Magnetic Actuation Methods in Bio/Soft Robotics," *Advanced Functional Materials*, vol. 31, no. 11, 2021.

[7] L. J. Gibson and M. F. Ashby, *Cellular solids: Structure and properties*, 2nd ed., ser. Cambridge solid state science series. Cambridge: Cambridge Univ. Press, 1999.

[8] R. Preuer, J. Sleichrt, D. Kytyr, P. Lindner, U. Cakmak, and I. Graz, "Conductive Open–Cell Silicone Foam for Tunable Damping and Impact Sensing Application," *Macromolecular Materials and Engineering*, vol. 310, no. 4, 2025.

[9] G. Bolanakis and E. Papadopoulos, "Introducing Mag-Nets: Rapidly Bending Electromagnetic Actuators for Self-Contained Soft Robots," *IEEE Robotics and Automation Letters*, vol. 9, no. 6, pp. 5306–5313, 2024.

[10] Maximilian Waismayer, "Entwurf eines Demonstrators zur Smart Foam Aktuierung," Bachelor Thesis, Johannes Kepler University Linz, 2024.

[11] Voestalpine Steel Division, "Steel grade 400-TG-179," *Voestalpine Datasheets*, 2016.

[12] David Meeker, "Finite Element Method Magnetics: Version 4.2," *User's Manual*, 2020.

XI ECCOMAS Thematic Conference on Smart Structures and Materials - SMART 2025
M. Krommer, M. Nader and M. Schagerl (Eds)

Received: 21 May 2025 / Revised: 9 September 2025 / Accepted: 10 September 2025
© The Author(s) 2025

Bioinspired Particle-Filled Silicone Foams for Soft Sensors and Actuators

Rene Preuer, Evrim Burkut, Dan Kytyr, Ingrid Graz

Abstract. Responding to stimuli is a fundamental characteristic of living systems. Inspired by nature, an ultrasoft approach to stimuli-responsive elastomers by fabricating a foam structure filled with particles is presented. Depending on the type of particles used, 1) carbonyl iron (CI)-based magnetoactive materials, and 2) carbon black (CB)-based resistive sensor materials are created. The obtained open-pore silicone foams, produced through template molding, contain varying weight percentages of filler particles rendering them smart: By external mechanical or magnetic stimuli, their elastic moduli can be adjusted and they are able to sense deformations. Their combined mechanical, electrical, and magnetic properties make them interesting materials for simple adjustable dampers. Utilized in conjunction with a pneumatic radial compression actuator they allow adjusting damping properties and impact sensing, inspired by the structure of orange peel.

Key words: elastomer, foam, smart, sensor, magneto-responsive

Rene Preuer & Ingrid Graz
School of Education, Johannes Kepler University, Altenbergerstr. 69, 4040, Linz, Austria
e-mail: ingrid.graz@jku.at

Evrim Burkut
Institute for Polymer Product Engineering, Johannes Kepler University, Altenbergerstr. 69, 4040, Linz, Austria

Dan Kytyr
Department of Biomechanics, Institute of Theoretical and Applied Mechanics, Czech Academy of Sciences, Prosecka 76, 190 00 Prague 9, Czech Republic
e-mail: kytyr@itam.cas.cz

Ingrid Graz
Institute for Biophysics, Johannes Kepler University, Altenbergerstr. 69, 4040, Linz, Austria
e-mail: ingrid.graz@jku.at

1 INTRODUCTION

Foams are fascinating structures found in various natural systems such as wood [1], nuts [2], bone [3], marine sponges [4] or plant tissue called parenchyma [5]. These porous materials consist of open or closed gas- or liquid-filled cells separated by thin solid films, creating lightweight and flexible materials due to their highly structured matrix. Natural foams are present in a wide range of biological contexts, from the microscopic to the macroscopic scale [1], and serve diverse functional roles such as (thermal) insolation, lightweight material, storage and damping. For all these applications engineers take inspiration from nature rebuilding foams with technical materials such as metals [6-9] and polymers [10,11].

Elastomers itself with their inherent network structure resemble foams on the molecular range. Together with their Young's modulus in the range of 0.1-2MPa comparable to many biological materials, this makes them a suitable model system for biologically inspired foams [12-14]. In combination with filler materials in form of conductive or magnetic particles, liquid metals, [15-17], silicone foams can be rendered smart, allowing to expand the properties of the natural foams towards stimuli-responsiveness [18,19,14].

In this paper we have created silicone foams inspired by citrus fruit peel by means of template casting (Figure 1b). Two off-the-shelf polydimethylsiloxane (PDMS) materials, Sylgard 184 and Ecoflex 00-30, were evaluated for their use in creating open pore foams. In order to render the foams stimuli responsive, filler particles were incorporated by blending the PDMS with 1) carbonyl iron particles and 2) carbon black (CB) (Figure 1). The obtained foams were characterized regarding porosity, mechanical, electrical and magneto-responsive properties and evaluated for their use in adjustable dampers. Inspired by the orange and its peel (Figure 1a), a simple proof-of-concept demonstrator for adjustable damping was designed: a pneumatic radial compression actuator (PRCA) served as flavedo, the tough outermost layer of the peel. The CB-silicone foam itself, resembling the albedo, spongy soft layer protecting the fruit flesh of the orange, was placed within the center of the PRCA. Upon actuation of the PRCA, the foam was compressed and evaluated for change in damping behavior. In addition, the CB-silicone foam was evaluated as impact sensor in conjunction with the adjustable damper.

2 PREPARATION OF PARTICLE-FILLED SMART SILICONE FOAMS

The silicone foams inspired by orange peel (Figure 1a) were prepared by means of template-casting of off-the-shelf polydimethylsiloxane (PDMS) Sylgard 184 (DowSil) and Ecoflex 00-30 (Smooth-On) (Figure 1b). The templates serving as negative matrix consisted of fused sugar grains from store-bought sugar. Varying the sugar grain size allows for different sized pores within the foam ranging from granulated or cane sugar with 0.5-1 mm grains down to fine powdered sugar with 0.2 mm grains. This work focusses on templates prepared from cane sugar (SBudget Cane Sugar, Spar). The sugar was mixed in a 100:1 weight% ratio with water and stirred for 2 min until the sugar particles start adhering to one another. The wet sugar mixture was then poured into 3D printed molds. The molds were placed in the oven for 12 h at 65°C for

removing the water. After all water had been removed, the sugar templates were removed from the mold and stored.
The PDMS was prepared according to the manufacturer's instructions in a 10:1 and 1:1 mixing ratio for Sylgard 184 and Ecoflex 00-30, respectively. To render the foams electro- and magnetoactive, the filler particles were added to the uncured PDMS. Figure 1b shows a schematic of the fabrication process.

2.1 Preparation of Resistive Carbon Black-Silicone Foams

For the fabrication of resistive CB-silicone sensor foams, Sylgard 184 (DowSil) was mixed with varying contents of carbon black particles (CB, acetylene, 50% compressed, 99.9+) (ranging from 3.3 wt% to 6.6 wt%) and silicone oil (Elbesil B 50). Silicone oil was required as thinner in a ratio of 10 times the weight percentage (wt%) of carbon black to ensure a mixture with sufficiently low viscosity to be used for mold casting. Also, Ecoflex 00-30 foam samples were investigated. However, when mixed with carbon black and silicone oil, Ecoflex 00-30 samples exhibited extreme softness and would not cure properly. Therefore, only Sylgard 184-carbon black foams were prepared and investigated further.

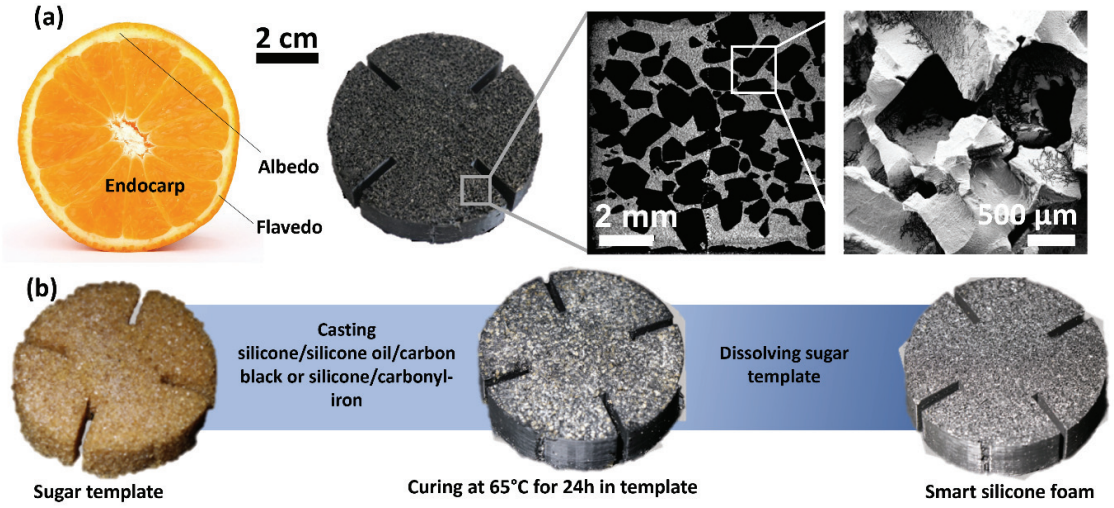

Figure 1: a) Soft smart silicone foams inspired by citrus fruit and their spongy albedo underneath their peel (flavedo) for damping and sensing applications. Porosities and internal open cell foam structures with voids in the range of 1mm depicted with micro-computer tomography (µCT) and scanning electron microscopy (SEM).
(b) Fabrication process of the silicone foams based on a fused sugar template that is used as a mold for silicone-silicone oil-carbon black and silicone-carbonyl iron mixtures. After curing the template is dissolved to release the smart silicone foam. Adapted from [14]

Carbon black (CB) and silicone oil (SO) were weighted and added to the Sylgard 184 subsequently. These CB-SO-silicone mixtures were thoroughly stirred using a bladeless mixer (Hauschild Speedmixer DAC 400) for 1 min (40 s @600 rpm, 20 s @1000 rpm) and then degassed in a desiccator to remove air bubbles. Afterwards, the silicone blend was poured over

the sugar template, which was placed in a mold, ensuring well coverage of the whole template. To remove all air from the template, avoiding areas without silicone, a second desiccation step was performed. Subsequently, the silicone-filled template within the mold was put in the oven for 24 h at 65°C. The silicone-filled template was then submerged in distilled water for 12 h to dissolve the sugar. Afterwards, the foam was placed in a container filled with fresh distilled water for another 12 h to remove any remaining sugar residues. Finally, the foam was dried in an oven at 65°C for 24 h.

2.2 Preparation of Magnetorheological Carbonyl Iron-Silicone Foams

For the fabrication of the magnetorheological silicone foams, round carbonyl iron (CI) particles with 1-2 µm diameter were used. CI powder (Carbonyl iron SQ, BASF) was added in 10% increments starting from 10% up to 40% to Sylgard 184 and Ecoflex 00-30 (prepared according to their manufactuere`s instructions) and thoroughly mixed using a bladeless mixer (Hauschild Speedmixer DAC 400). The silicone-carbonyl iron mixtures were then poured over the sugar template, which were placed into molds. To ensure good insertation into the pores of the template, the molds were placed in the desiccator for 2 min. Afterwards, the samples were cured at 65°C for 24 h. Afterwards, the template was dissolved in hot water and the square CI-silicone foam dried. Subsequently, cylindrical shaped samples with 40 mm diameter (and 20 mm thickeness) were punched out of the foams for further testing.

2.2 Characteristics of Particle-Filled Foams

All obtained silicone foams are open-pore foams, whose mechanical properties can generally be predicted using the Gibson-Ashby model, which establishes a relationship between the properties of a lattice structure and its relative density [20]. Under the assumption of a predominantly bending-dominated behavior of the open-pore foams under compression, the relative modulus, the ratio between modulus of foam and solid is proportional to the squared ratio of the densities of foam and solid. The proportionality coefficient C typically ranges from 0.1 and 4 for bending-dominated open-cell foam lattice structures [21] and was determined to be 0.7 for both pure silicone foams and 0.7 to 1.1 for the CB-silicone foams by measuring their densities and conducting uniaxial compression test using an MTS 852 damper test system (MTS Systems Corporation, Eden Prairie, MN, USA) with a 500 N load cell at a rate of 0.1 mm/s. Experimental results reveal a foam porosity of 0.67 ± 0.013 on average. This is in good alignment with the image analysis of scanning electron microscopy (SEM) and micro-computer tomography (µ-CT) images (Figure 1a, right) where approximately 40% of the area is silicone matrix, equivalent to a porosity of a 0.6.

3 MECHANICAL CHARACTERIZATION OF THE SILICONE FOAMS WITHOUT AND WITH FILLER PARTICLES

Both, the composition and cellular structure of foams, as obvious in various species of citrus fruit [22-24], have significant influence on damping behavior, emphasizing the importance of

considering these factors in designing suitable materials. With the template method, it is feasible to design a plethora of foam structures with different porosity and mechanical properties depending on the silicone elastomer used.
Here, we focus on pure Sylgard 184 and Ecoflex 00-30 foams with porosities of 0.6 as well as foams of the aforementioned silicones filled with carbonyl iron (CI) and carbon black (CB) particles as well as silicone oil as described above.
Damping properties of the as-prepared pure silicone foams and the particle-filled foams were evaluated by means of a simple ball drop test with a steel sphere (diameter = 10 mm, weight = 4.03 g), that was dropped from a drop height of 200 mm and determining the rebound height after impact. The ball drop experiments and the theory for extracting mechanical properties such as Young's modulus and overall damping properties are described elsewhere [12,14].

3.1 Dynamic Mechanical Analysis of Silicone Foams

In addition, the foams were characterized using Dynamic Mechanical Analysis (Bose Corp., ElectroForce Systems Group, MN, USA) (Figure 2). Pure Sylgard and Ecoflex 00-30 foams as well as CI-filled Sylgard and Ecoflex foams were evaluated measuring the storage (E′) and loss moduli (E′′) under sinusoidal compression in a frequency range from 0.3-31.5 Hz with an amplitude of 0.4 N and a mean level of compression of 4 mm. The ratio between E′′ and E′ defines a parameter known as tanδ. tanδ (and E′′) are indicators of damping behaviour, where a higher E′′ indicates better damping characteristics of a material [25]. Typically, silicone foams exhibit tanδ in the range between 0.1 and 0,3, with values ≥ 1 characterizing perfect dampers. Figure 2 a, left shows that the measured E′ and tanδ values for the silicone foam samples without CI powder, with an E′ of approximately 0.1 MPa for Sylgard 184 and approximately 0.01 MPa for the Ecoflex 00-30 samples. With respect to tanδ, Ecoflex 00-30 samples exhibit higher values and better damping properties than those made from Sylgard 184 as is known from literature [12]. This difference triples as the frequency increases. DMA measurements of the CI-silicone foams show, that the addition of CI particles does not have any significant effect on the mechanical properties. In particular for Sylgard 184 foams with 40% CI (depicted in Figure 2a, right) there is no measurable effect on E′ and tanδ. This can be mainly attributed to the initially higher storage modulus, with Sylgard 184 foams being stiffer than their Ecoflex 00-30 counterparts. The latter ones are extremely soft and the addition of 40% carbonyl iron results in a slight stiffening, visible in the decrease of the storage modulus from 0.01 to 0.009 MPa and also a decrease of tanδ of 0.1 from 0.09 to 0.001 at the highest frequency. CI-silicone foams with lesser percentage showed even less changes with respect to unfilled foams of Sylgard 184 and Ecoflex 00-30.

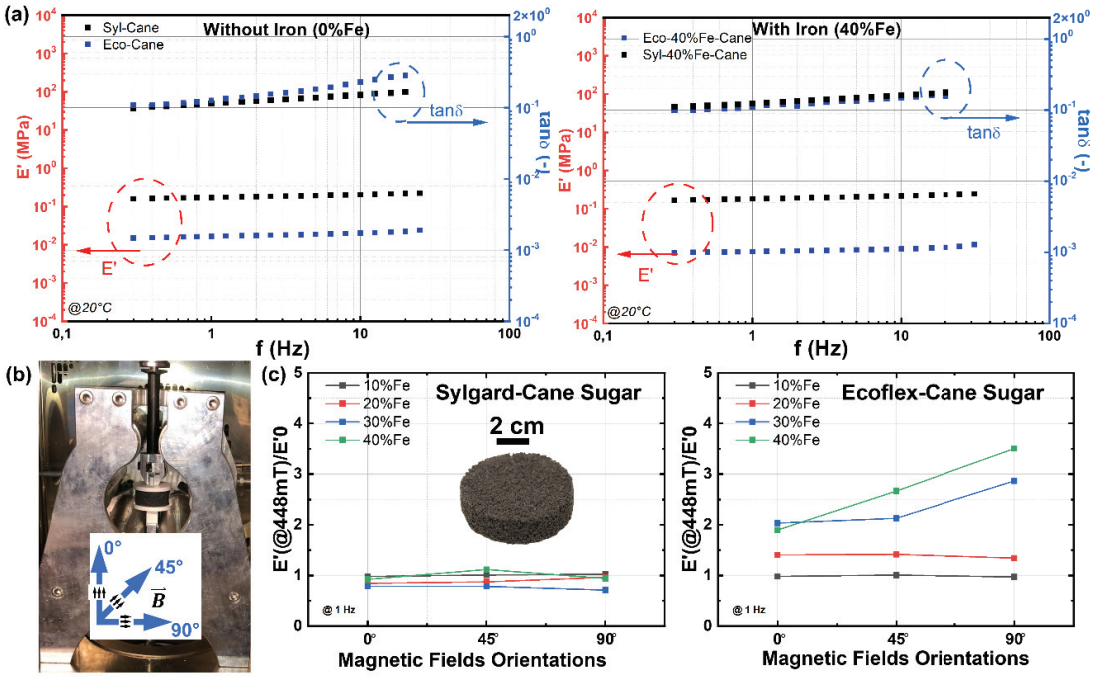

Figure 2: (a) Dynamic mechanical analysis (DMA) of PDMS foams without and with 40% carbonyl iron particles exhibiting that neither Young's modulus (E′) nor tanδ significantly change upon adding the particles. (b) Halbach array magnet setup for DMA measurements allowing to create a homogeneous magnetic field that is either perpendicular (0°), 45° tilted or in the plane of the sample (90°). (c) Effect of the magnetic field orientation on the storage modulus of the 40% CI-filled foams of Sylgard 184 (left) and Ecoflex 00-30 (right).

3.2 Dynamic Mechanical Analysis within magnetic field

To evaluate the effect of the carbonyl iron particles within the foam, the DMA measurements for CI-silicone foams were performed with and without homogeneous magnetic field by using a Halbach array [26] with a magnetic flux density of 448 mT (Fig. 2b). The Halbach array allows testing the CI-silicone foams at different magnetic orientations by adjusting the magnets to 0°, 45° and 90° with regard to the sample. Figure 2b shows the cylindrical CI-silicone foam sample mounted in the DMA within the Halbach array and the adjustable directions of the magnetic field with respect to the sample orientation. The storage modulus (E′) was measured as a function of carbonyl iron content of the foams based on Sylgard 184 (Figure 2c, left) and Ecoflex 00-30 (Figure 2c, right). For Sylgard 184, there is no visible effect on E′ with various magnetic field orientations. This can be explained by the higher stiffness of the overall material. For the much softer Ecoflex 00-30 foams, however, a strong dependency of the storage modulus on the magnetic field orientation is visible, with the largest effect being observed for the 40% CI-silicone foams and a 90° orientation of the magnetic field with respect to the sample.
These results are promising and a proof-of-concept demonstrator for a CI-silicone foam pump inspired by plant roots is currently being evaluated.

4 ELECTRO-MECHANICAL CHARACTERIZATION OF THE CARBON BLACK-SILICONE FOAMS

In addition to the mechanical properties of the CB-silicone foams [14], we investigated their electro-mechanical characteristics, in particular for sensing purposes. The impact of mechanical deformation on the electrical resistivity of the carbon black (CB)-silicone foams was characterized by uniaxial compression tests. A compact table top loading device, as detailed in [27] and illustrated in Figure 3a was used, equipped with load cell LBS200 (Futek, USA) with nominal capacity 2 lbs (= 907.2 g) and conductive copper covered loading plates connected to a resistivity sensor with a nominal resistivity of 22 kΩ. Importantly, due to limitations in electrical measurements, only resistance values < 20 kΩ could be measured. Cylindrical CB-silicone foam test specimen with a diameter of 10 mm and a height of 10 mm and CB contents from 3.3 wt% to 6.6 wt% were characterized [14].

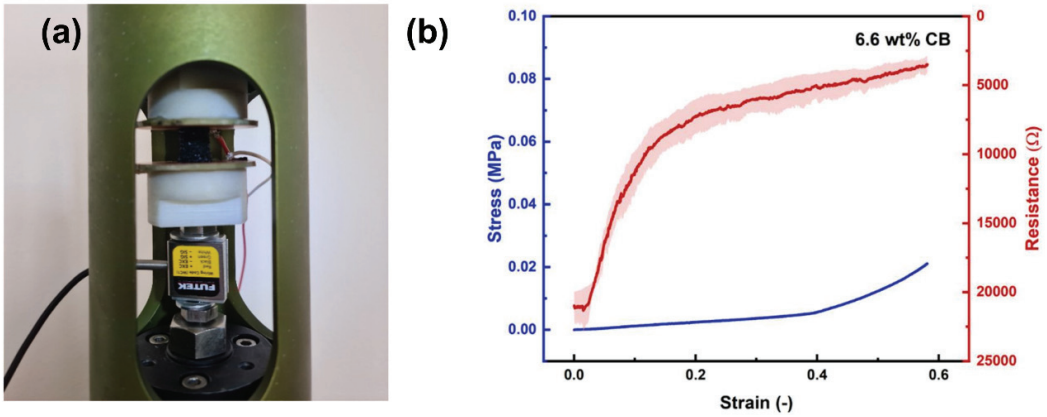

Figure 3: a) Image of loading device [24] for electro-mechanical characterization of CB-silicone foams. b) Stress-strain curve and correlated resistance change of 6.6 wt% CB-silicone foam during compression showing a clear increase in conductivity with increasing stress. Adapted from [14]

Figure 3b shows the stress-strain behavior and resistance change of the 6.6 wt% CB-silicone foam during compression revealing a clear increase in conductivity with stress, resulting in a fourfold decrease in resistance. Despite issues with noise as visible from Figure 3b, the CB-silicone foam hold potential for application in impact detection.

5 PNEUMATIC RADIAL COMPRESSION ACTUATOR FOR ADJUSTABLE DAMPING INSPIRED BY CITRUS FRUIT PEEL

Inspired by the structure-function relationship of citrus fruit (peel) and their ability to sustain impacts from great heights without damage, we have conceived a proof-of-concept demonstrator for adjustable damping. Citrus peel has an outstanding impact resistance due to its hierarchical structure that exhibit a strong resemblance to cellular foams [23,24,28,29]. Figure 1a shows the schematic of typically citrus fruit built-up. On the outside an outer layer

called the flavedo (peel) surrounds the spongy albedo (white layer). These two serve as main protection measures for the endocarp, the soft pulp and juice sacs of the citrus fruit, even from impacts of dropping heights of up to 15 m [23].

5.1 Design and Fabrication of Pneumatic Radial Compression Actuator

We have now replicated the citrus structure: a pneumatic actuated ring structure, the pneumatic radial compression actuator (PRCA) (Figure 4a) served as flavedo, the tough outermost layer of the peel. The PCRA encased the CB-silicone foam (Figure 4b), that resembled the albedo, the spongy soft layer protecting the fruit flesh of the citrus. The PRCA offers a great versatility with respect to design [14] and was entirely fabricated from silicone elastomers. It comprised two main parts: 1) a circular soft casing made from Sylgard 184 (DowSil) and 2) an ultrasoft membrane made of Ecoflex 00–30 (Smooth-On). The outer surface of the soft casing was sealed, while the inner part, housing embedded four cavities, remained exposed. By bonding a thin 1mm membrane to the inner part, four separate airtight compartments were created, enabling inflation with pressurized air and thus pneumatic actuation of the PRCA. Depending on the applied pneumatic pressure, the PRCA was either in a resting state or actuated (Figure 4a). Selecting a PCRA design with four pressurized compartments required the use of a CB-silicone foam with four segments, which are separated by small air gaps as depicted in Figure 4b. Figure 4b also shows that this division allows compression of the CB-silicone foams to various extents, altering their structure and, consequently, their material properties. The PRCA`s inflated compartments transduce the force of the pneumatic pressure onto the foam`s segments, compressing it and reducing the porosity.

5.2 Mechanical Characterization of Pneumatic Radial Compression Actuator

By subjecting the CB-silicone foam to this radial force results in a transition of the foam’s structure from an open cellular configuration to a more bulk-like material, significantly altering the mechanical properties. Figure 4c depicts the force generated by an individual pressurized segment of the PRCA with a size of 51 x 20 mm², evaluated by means of a 50 N force gauge (Alluris FMI-250B5), as a function of the applied pressure ranging from 0 to 0.03 MPa, controlled by pressure regulator (SMC IR1000-F018G-A). As evident from Fig. 4c nearly linear dependency is obtained. Further characterization of the CB-silicone foam in various states of actuation of the PRCA revealed that also its stiffness increased linear with pressure applied to the PRCA. These data provide a solid foundation for using the PRCA in conjunction with the CB-silicone foam for a proof-of-concept demonstrator of an adjustable damper and can be found elsewhere [14].

5.3 Adjustable damping using the Pneumatic Radial Compression Actuator

To test our proof-of-concept citrus fruit peel-demonstrator, ball drop tests were conducted to evaluate the damping performance. For testing the PRCA with the foam in its center was mounted within a custom-made polymethylmethacrylate (PMMA) casing, restricting the deformation of the CB-silicone foam in x-y direction to prevent buckling of the foam during actuation. The ball drop test was conducted by releasing a 10 mm diameter steel sphere from a

drop height of 200 mm onto the uncompressed and compressed foams. The steel sphere was tracked using a high-speed camera (Phantom Miro C110) for drop, impact and rebound height and the imaging data subsequently analyzed through post-processing (Tracker V6.1.3, Physlets). A detailed description of the exact setup and measurement can be found elsewhere [12].

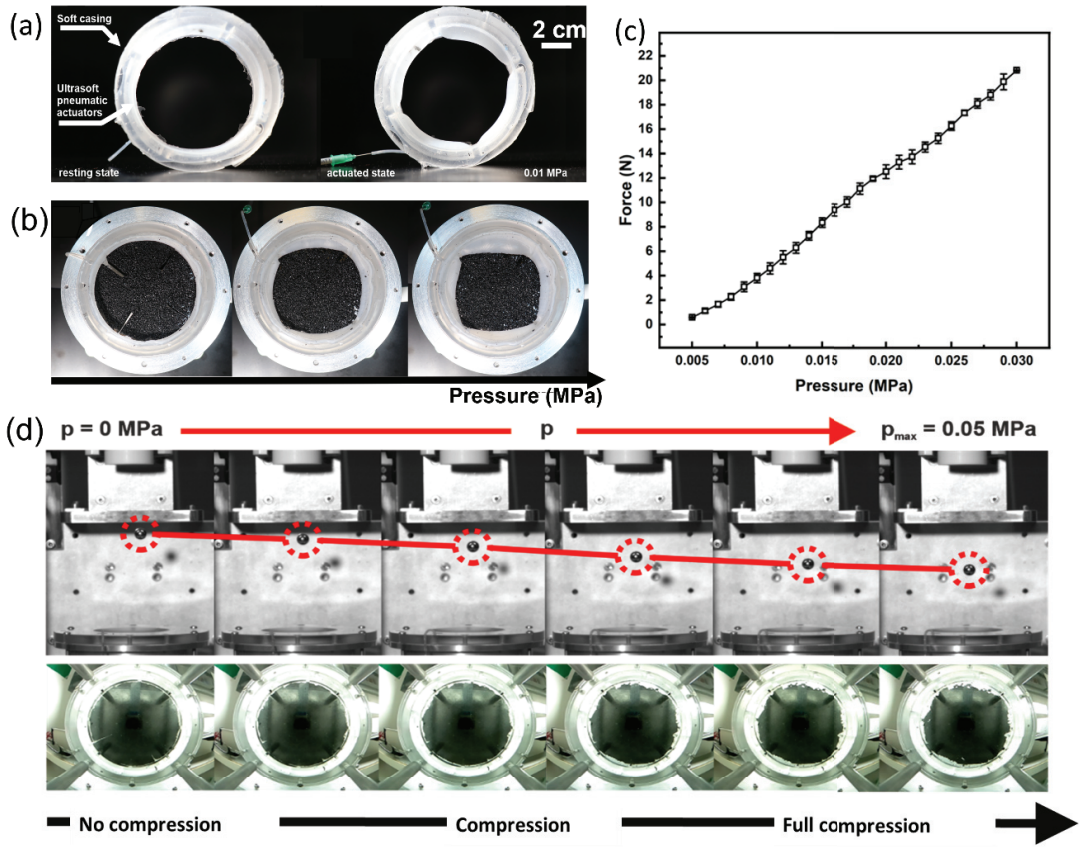

Figure 4: a) Pneumatic radical compression actuator (PRCA) based of silicone ring with 4 individual chambers sealed with a silicone membrane. Upon pressurizing the PRCA each of the 4 chambers was inflated and the membrane was deflected (right). b) PRCA with 4-segmented CB-silicone foam encased in its center. Pressurizing the PRCA resulted in radial compression of the CB-silicone foam (left to right). c) Force generated by a single segment of the PRCA as a function of pressure applied. d) Side view (top) and top view (bottom) of the ball drop test, where a steel sphere (red dotted circle) was released from 200 mm drop height and after impact rebounds. With increasing pressure applied by the PRCA, the foam was compressed and damping improved. Adapted from [14]

Figure 4d, top depicts a side view of the ball drop test for a 6.6 wt% CB-silicone foam within the PRCA with applied pressures ranging from 0-0.05 MPa. The rebound height of the steel sphere (red dotted circle) is depicted as a function of compression of the foam (Figure 4d, bottom). The ratio of drop height to rebound height provides the rebound resilience R, a means

for the damping ability of the foam, with lower R indicating higher energy dissipation and better damping. As visible from the images, with increasing compression, the rebound height and thus R decreased with an almost linear dependence on the pressure. This trend was observed for all foam specimen, with the Ecoflex 00-30 samples without fillers showing the best energy dissipation, closely followed by 6.6 wt% CB-silicone foams. Decreasing the CB-filler content and thus silicone oil content resulted in an increase of the rebound resilience R, independent of the pressure applied within the PRCA. Summarizing, the CB-silicone foams show improved energy dissipation upon compression. The higher energy absorption observed in the radially compressed foam during the sphere drop experiment can be explained on the basis of the characteristic stress–strain response of cellular solids, as described by Gibson and Ashby [20]. Foams exhibit three regimes under compression: (i) an initial linear-elastic region, (ii) a plateau region in which cell walls buckle, collapse, or yield at an almost constant stress, and (iii) a densification region where the stress rises steeply as the cells are compacted. Energy absorption corresponds to the area under the stress–strain curve. Since the plateau regime is long and dissipative, it contributes most significantly to the total absorbed energy.
When the foam is radially pre-compressed prior to impact, the material is effectively shifted into the plateau regime from the very beginning of loading. Consequently, the impact energy from the falling sphere is dissipated immediately by progressive cell collapse, leading to higher energy absorption and reduced elastic rebound. In contrast, an uncompressed foam initially deforms elastically before reaching the plateau stress. During this stage, part of the impact energy is stored elastically and subsequently released, resulting in a lower net energy absorption compared to the pre-compressed case. Thus, the enhanced energy absorption in radially compressed foams arises from their immediate engagement of the plateau collapse mechanism, which maximizes the fraction of impact energy dissipated through plastic deformation rather than elastic storage. It is also noteworthy that the samples with the highest CB-filler content also contained the largest amount of silicone oil, which also has a significant impact on the damping properties, especially under compression. This remains a topic for future research. For more details on the damping properties of the CB-silicone foams with various CB-content look elsewhere [14].

6 CARBON BLACK-SILICONE FOAMS AS IMPACT/INDENTATION SENSORS

To fully exploit the potential of the citrus fruit inspired demonstrator consisting of the PRCA and the CB-silicone foams, we have explored their ability to act as sensor in combination with adjustable damping. Therefore, a 6 wt% CB-silicone foam was mounted within the PRCA and tested for its signal stability when subjected to compression from the PRCA (Figure 5a). The electrical signal was measured using a voltage divider circuit assembled using two multiplexers (CD4051BE) and a USB-6008 data acquisition device (National Instruments). The first multiplexer was configured to switch between multiple precision resistors (low tolerance), with resistance values ranging from 50 Ω to 10 MΩ. These resistors served as the foundation for a custom-designed auto-ranging voltmeter. The second multiplexer (channels 1–4) was connected to electrodes placed on each of the four segments of the CB-silicone foam specimens, enabling the individual measurement of electrical conductivity across each segment. A common

electrode located at the bottom of the foam acted as the ground reference. With Multiplexer 1 connected to a +5 V source through the resistor array, and Multiplexer 2 connected to ground through the foam, measurements were taken across the signal input and output terminals (COM IN and COM OUT) of the multiplexers. To apply periodic mechanical loading, a custom-built setup (Figure 5b) was used, featuring a testing tip attached to a force gauge (Alluris FMI-250B5).

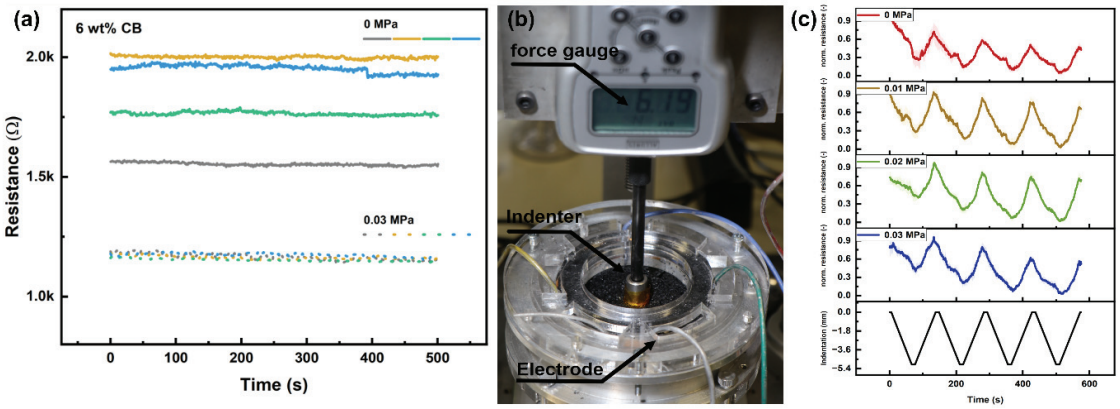

Figure 5: a) Characterization of CB-silicone foam within PRCA as resitive sensor with 4 segments (indicated by the solid yellow, blue, green and grey traces) without actuation/compression and actuated/compressed (with 0.03 MPa pressure applied to the foam) (dotted traces). b) Costum-built indentation setup with force gauge mounted above the PRCA encasing the CB-silicone foam. The CB-silicone foam consisted of 4 segments with each of them represented by an individual electrode and a a common ground counter electrode at the bottom. The obtained signals were measured using a costum-designed voltage divider. Upon indentation of the tip the normalized resistance (as an average signal) was recorded and plotted for various states of compression of the CB-silicone foam by means of pressurizing the PRCA. c) Indentation experiment with normalized resistance, averaged over all four channels, for actuated states ranging from 0 to 0.03 MPa during the loading and unloading cycle plotted versus time. The indentation depth was 5 mm, and the indentation speed was 0.07 mm s−1. Adapted from [14]

The tip indented the foam at a constant rate of 0.07 mm/s to a maximum depth of 5 mm, while simultaneously recording resistance changes in all four segments (as shown in Figure 5a). Kapton tape was used to electrically insulate the indenter tip and prevent interference. The normalized resistance values—averaged across all four channels—are presented in Figure 5b for actuated pressure states ranging from 0 to 0.03 MPa. It is important to note that the indented area in this test (defined by the indenter diameter) was significantly smaller than the total sensor area. In this context, the sensor's response reflects a superposition of both local and long-range compression effects. Specifically, localized indentation causes the foam cells directly beneath the indenter to collapse, while the elastic nature of the material induces stretching in cells located within the same horizontal layer but farther from the contact point. The results demonstrate that the low-resistance 6 wt% CB–silicone foam exhibits high sensitivity to displacement-induced resistance changes. This is evidenced by a sharp and consistent resistance

drop that closely follows the indentation depth and remains largely unaffected by surrounding radial compression (i.e., the actuated pressure state).

7 CONCLUSIONS

In summary, we show that silicone foams due to their inherent softness characterized by a low storage and loss modulus mimic the properties of biological foams. They exhibit a great potential as active or smart materials by addition of stimuli-responsive fillers, in particular magnetic carbonyl iron and conducting carbon black particles. Mechanical, magnetic and electrical characterization reveal their tunability with respect to mechanical properties by compression and application of an external magnetic field as well as their potential as resistive sensors. In particular, the adjustability of the mechanical properties for damping was evaluated by means of external magnetic fields but also the design of a pneumatic radial compression actuator. This actuator in conjunction with the foams acted as a proof-of-concept demonstrator for a citrus fruit inspired adjustable damper. Upon pressurizing the foam was compressed and thus the energy dissipation increased. Combination of the PRCA with the CB-silicone foam even allowed to exploit the sensor properties during various states of actuation. The CB-silicone foam was segmented and showed good stability, sensitivity and was able to detect real-time indentation. Overall, this type of smart silicone foams yields a great potential for a multitude of applications, from damping to sensing but also as porous filter or pump systems that can be actuated by various means of stimuli such as magnetic or pneumatic.

REFERENCES

[1] P. Fratzl and R. Weinkamer, "Nature's hierarchical materials," *Progress in Materials Science*, vol. 52, no. 8, pp. 1263–1334, 2007, doi: 10.1016/j.pmatsci.2007.06.001.

[2] P. Schüler, T. Speck, A. Bührig-Polaczek, and C. Fleck, "Structure-Function Relationships in Macadamia integrifolia Seed Coats – Fundamentals of the Hierarchical Microstructure," *PLOS ONE*, vol. 9, no. 8, p. e102913, 2014, doi: 10.1371/journal.pone.0102913.

[3] E. F. Morgan, G. U. Unnikrishnan, and A. I. Hussein, "Bone Mechanical Properties in Healthy and Diseased States," *Annual Review of Biomedical Engineering*, vol. 20, pp. 119–143, 2018, doi: 10.1146/annurev-bioeng-062117-121139.

[4] E. Martins, H. T. Rapp, J. R. Xavier, G. S. Diogo, R. L. Reis, and T. H. Silva, "Macro and Microstructural Characteristics of North Atlantic Deep-Sea Sponges as Bioinspired Models for Tissue Engineering Scaffolding," *Frontiers in Marine Science*, vol. 7, 2021, doi: 10.3389/fmars.2020.613647.

[5] Z. Zhang, S. Cai, Y. Li, Z. Wang, Y. Long, T. Yu, and Y. Shen, "Mechanical properties of parenchyma-inspired composites," *Composites Science and Technology*, vol. 194, p. 108151, 2020, doi: 10.1016/j.compscitech.2020.108151.

[6] A. Bührig-Polaczek, C. Fleck, T. Speck, P. Schüler, S. F. Fischer, M. Caliaro, and M. Thielen, "Hierarchical biological structures for functional materials design," *Bioinspiration & Biomimetics*, vol. 11, p. 045002, 2016, doi: 10.1088/1748-3190/11/4/045002.

[7] Y. J. Yang, F. S. Han, C. E. Wen, and Y. F. Shu, "Mechanical behavior of porous titanium manufactured by powder metallurgy," *Materials Science and Technology*, vol. 23, pp. 1336–1341, 2007, doi: 10.1179/174328407X213198.

[8] A. Du Plessis et al., "Bioinspired functionally graded lattice structures: A review," *Progress in Materials Science*, vol. 125, p. 100918, 2022, doi: 10.1016/j.pmatsci.2021.100918.

[9] J. Fiocchi, C. A. Biffi, D. Scaccabarozzi, B. Saggin, and A. Tuissi, "Design and testing of auxetic structures made by additive manufacturing for aerospace applications," *Advanced Engineering Materials*, vol. 22, p. 1900722, 2020, doi: 10.1002/adem.201900722.

[10] M. Tomin and Á. Kmetty, "Morphological, mechanical and thermal properties of expanded polypropylene foams modified by different polymer additives," *Journal of Applied Polymer Science*, vol. 139, p. 51714, 2022, doi: 10.1002/app.51714.

[11] D. Eaves, *Handbook of Polymer Foams*. UK: iSmithers Rapra Publishing, 2004.

[12] R. Preuer, C. Emminger, U. Cakmak, and I. Graz, "Material Testing for Physicists: Unraveling the Dissipative Nature of Silicone Elastomers via Ball Drop Testing," *Macromolecular Materials and Engineering*, vol. 309, p. 2400085, 2024, doi: 10.1002/mame.202400085.

[13] D. Li, W. Deng, Z. Jin, J. Hu, Y. Zhao, N. Cao, C. Wan, X. Chen, and P. Yu, "Bioinspired Silicone Rubber Foams With Adjustable Gradient Structures Induced via Temperature Fields," *Journal of Applied Polymer Science*, vol. 142, p. e56765, 2025, doi: 10.1002/app.56765.

[14] R. Preuer, J. Sleichrt, D. Kytyr, P. Lindner, U. Cakmak, and I. Graz, "Conductive Open-Cell Silicone Foam for Tunable Damping and Impact Sensing Application," *Macromolecular Materials and Engineering*, p. 2400273, 2024, doi: 10.1002/mame.202400273.

[15] S. Liang, Y. Li, J. Yang, J. Zhang, C. He, Y. Liu, and X. Zhou, "3D Stretchable, Compressible, and Highly Conductive Metal-Coated Polydimethylsiloxane Sponges," *Advanced Materials Technologies*, vol. 1, p. 1600117, 2016, doi: 10.1002/admt.201600117.

[16] V. Sencadas, C. Tawk, and G. Alici, "Highly Sensitive Soft Foam Sensors to Empower Robotic Systems," *Advanced Materials Technologies*, vol. 4, p. 1900423, 2019, doi: 10.1002/admt.201900423.

[17] J. Yang, D. Tang, J. Ao, T. Ghosh, T. V. Neumann, D. Zhang, Y. Piskarev, T. Yu, V. K. Truong, K. Xie, Y.-C. Lai, Y. Li, and M. D. Dickey, "Ultrasoft Liquid Metal Elastomer Foams with Positive and Negative Piezopermittivity for Tactile Sensing," *Advanced Functional Materials*, vol. 30, p. 2002611, 2020, doi: 10.1002/adfm.202002611.

[18] C. W. Visser, D. N. Amato, J. Mueller, and J. A. Lewis, "Architected Polymer Foams via Direct Bubble Writing," *Advanced Materials*, vol. 31, p. 1904668, 2019, doi: 10.1002/adma.201904668.

[19] S. P. Murali Babu, F. Visentin, A. Sadeghi, A. Mondini, F. Meder, and B. Mazzolai, "Sensorized Foam Actuator with Intrinsic Proprioception and Tunable Stiffness Behavior for Soft Robots," *Advanced Intelligent Systems*, vol. 3, p. 2100022, 2021, doi: 10.1002/aisy.202100022.

[20] L. J. Gibson and M. F. Ashby, *Cellular Solids: Structure and Properties*, 2nd ed. Cambridge, U.K.: Cambridge Univ. Press, 1997.

[21] M. F. Ashby, *Metal Foams: A Design Guide*, Butterworth-Heinemann, Oxford 2000.

[22] L. J. Gibson, "Cellular Solids," *MRS Bulletin*, vol. 28, pp. 270–277, 2003, doi: 10.1557/mrs2003.75.

[23] S. F. Fischer, M. Thielen, R. R. Loprang, R. Seidel, C. Fleck, and T. Speck, "Pummelos as concept generators for biomimetically inspired low weight structures with excellent damping properties," *Advanced Engineering Materials*, vol. 12, no. 12, pp. B658–B663, 2010, doi: 10.1002/adem.201000194.

[24] M. Jentzsch, M.-C. Badstöber, F. Umlas, and T. Speck, "Damage protection in fruits: Comparative analysis of the functional morphology of the fruit peels of five Citrus species via quasi-static compression tests," *Front. Mater.*, vol. 9, Sec. Mechanics of Materials, Dec. 2022. [Online]. Available: https://doi.org/10.3389/fmats.2022.979151.

[25] M. F. Ashby and D. Cebon, "Materials selection in mechanical design," *J. Phys. IV France*, vol. 3, pp. C7-1–C7-9, 1993. [Online]. Available: https://doi.org/10.1051/jp4:1993701.

[26] K. Halbach, "Design of permanent multipole magnets with oriented rare earth cobalt material", Nuclear Instruments and Methods. **169** (1): *1*–10, 1980 [Online]. Available: doi:10.1016/0029-554X(80)90094-4

[27] T. Fíla, J. Šleichrt, D. Kytýř, I. Kumpová, M. Vopálenský, P. Zlámal, V. Rada, D. Vavřík, P. Koudelka, and S. Senck, "Deformation analysis of the spongious sample in simulated physiological conditions based on in-situ compression, 4D computed tomography and fast readout detector," *J. Instrum.*, vol. 13, no. 11, p. C11021, Nov. 2018. [Online]. Available: https://doi.org/10.1088/1748-0221/13/11/C11021.

[28] I. Prabasari, "Peel ultrastructure during developmental stages of Citrus sinensis (L.) Osbeck," *Pelita Teknologi*, vol. 2, no. 1, pp. 1–6, 2014. [Online]. Available: https://doi.org/10.18196/pt.2014.017.1-6.

[29] M. Jentzsch, V. Albiez, T. C. Kardamakis, and T. Speck, "Analysis of the peel structure of different Citrus spp. via light microscopy, SEM and μCT with manual and automatic segmentation," *Soft Matter*, vol. 20, no. 12, pp. 2804–2811, 2024. [Online]. Available: http://dx.doi.org/10.1039/D3SM01511D.

XI ECCOMAS Thematic Conference on Smart Structures and Materials - SMART 2025
M. Krommer, M. Nader and M. Schagerl (Eds)

Received: 23 June 2025 / Revised: 28 August 2025 / Accepted: 10 September 2025
© The Author(s) 2025

Dielectric elastomer actuator-zipping actuator hybrid concept

Rafal Ziembicki, Astrid Pechstein, Alexander Humer, Ingrid Graz

Abstract. Dielectric elastomer actuator (DEA) technology, despite being a well-researched and mature field, has yet to produce practical devices capable of generating forces comparable to pneumatic or hydraulic actuators. The primary challenges lie in the need for extensible electrodes, which limit miniaturization and the generation of higher pressures. Zipping actuation technology, a more recent derivative of DEAs, eliminates the requirement for extensible electrodes but introduces its own limitations, primarily by utilizing only a fraction of the active surface to generate force during the initial phase of actuation. To address these challenges, we propose a novel structure that combines dielectric elastomer actuators with zipping actuators. This architecture employs metallized BOPP foils separated by an elastomer, laser-cut in a trench-like pattern. Together with liquid dielectric filling the spaces between elastomer walls, this structure enables full utilization of the device's active surface throughout the entire contraction process. Proof-of-concept demonstrations with various aspect ratios of the structure showcase the potential of this design, which can be easily miniaturized by a factor of 10 and further enhanced under cleanroom conditions. Additionally, an electro-mechanically coupled finite-element model of the DEA-zipping hybrid is implemented and validated against experimental data. Simulations allow for analyzing sensitivities of the structure, particularly, with respect to geometric dimensions. Thorough understanding of the actuator's response helps to guide both future development of the zipping technology itself and its integration into smart structures.

Key words: Dielectric elastomeric actuators, zipping actuators, elastomers, biaxially oriented polypropylene

Rafal Ziembicki & Ingrid Graz
School of Education, Johannes Kepler University, Altenbergerstr. 69, 4040, Linz, Austria
e-mail: rafal.ziembicki@jku.at

Astrid Pechstein & Alexander Humer
Institute of Technical Mechanics Johannes Kepler University, Altenbergerstr. 69, 4040, Linz, Austria

Ingrid Graz
Institute for Biophysics, Johannes Kepler University, Altenbergerstr. 69, 4040, Linz, Austria
e-mail: ingrid.graz@jku.at

1 INTRODUCTION

With first mentions of dielectric elastomer actuators (DEA) related discoveries going as far as Röntgen's 1880 article [1] and more advanced studies starting around 1990s [2] DEAs are a well-established field with meaningful achievements. However the promise of implementing those into wearable exoskeletons still seems to be a far-fetched idea. One of the major challenges in DEA technology is the compliant electrode, which not only complicates manufacturing but also limits miniaturization, a crucial factor in maximizing the electric breakdown field. Examples include carbon/metal particle-elastomer composites [3, 4], conductive polymers [5], and ionogels [6]. While these materials share similar casting techniques with elastomer dielectric, allowing for reliable and repeatable thicknesses down to tens of microns, miniaturizing DEAs to this scale results in nearly half of the structure consisting of non-contracting electrodes. Other types of electrodes like carbon grease/powder/nanotubes [7, 8, 9], silver nanowires [10] and microcracked metal films [11] suffer from decreasing conductivity with expansion or pose technological and economic challenges. Additionally, all of those variants create difficulties in forming a reliable interface between the expanding electrode surface and the stiff terminal of an exoskeleton. A more recent concept with roots in DEA's technologies is zipping actuation [12, 13, 14]. Here elastomeric dielectric is replaced by liquid dielectric in a thin polymer film shell with electrodes on its outside. While this design eliminates the need for compliant electrodes, it introduces a significant limitation: the actuation force is generated mainly in the current zipping region due to uneven electric fields [15]. This results in inefficient utilization of the active surface, preventing the actuator from reaching its full potential. To address these challenges, we propose a hybrid approach that tailors the dielectric structure to work with inextensible electrodes. Our design consists of an array of silicone walls separated by a liquid dielectric and sandwiched between metallized polymer films. This configuration eliminates issues associated with compliant electrodes in DEAs while enabling more uniform distances between the electrodes and thus equalizing electric field distribution across the entire active surface, improving actuation efficiency.

2 ACTUATOR STRUCTURE AND MANUFACTURING

2.1 Architecture and materials

The architecture of the actuator consists of multiple stacked layers (Figure 1A), similarly to already existing DEA stacks. In this article we focus on manufacturing and characterization of a singular layer presented on Figure 1B. Each individual layer is composed of 20 μm BOPP foil with magnetron sputtered platinum electrode on one of its side (estimated thickness of 3.5 nm) and an array of silicone rubber walls prepared from commercial 50 μm Elastosil 2030 silicone film (Wacker Chemie) with Young Modulus of ~ 0.99 MPa. Periodic stacking of such a structure can form a full scale actuator. In this preliminary setup we test a device consisting only of the following (in order from the bottom): BOPP (metalized on top), silicone rubber walls with liquid dielectric (corn oil) in between, BOPP (metalized on top). Detailed dimensions of particular architecture elements are presented on Figure 1C. The basic working principle of

this setup is as follows: when a high voltage is applied between two separated electrodes, opposite charges accumulate, generating an attractive electrostatic force. Since the BOPP layer is incompressible, the silicone walls deform under this force due to the presence of free spaces between them. To enhance the dielectric breakdown strength within these voids, corn oil is used as a filler. The device currently operates as an open system, partially submerged in the dielectric liquid. Due to the combined effects of dielectrophoretic and capillary forces, corn oil penetrates the trenches and remains confined within them.

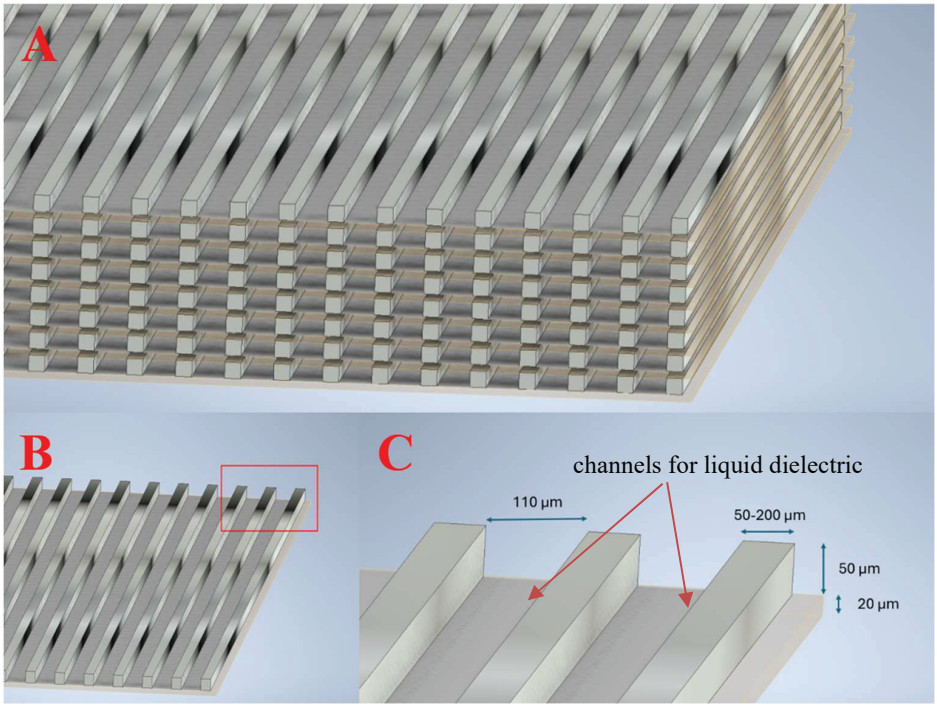

Figure 1: Theoretical structure of the actuator consisting of many (A) and a singular (B) layers. (C) Detailed dimensions of PDMS walls bonded to one side (top side) metalized BOPP.

2.2 Manufacturing

Manufacturing process consists of: (1) Platinum magnetron sputtering through a custom made mask on the outer side of the BOPP film roll. (2) Laser cutting a trench pattern in the Elastosil 2030 film on its plastic carrier. (3) Cleaning of the patterned silicone with general-purpose adhesive tape, rinsing with isopropanol and cutting out the desired testing shape from the sheet using a razor blade. (4) Two minute treatment of the inner side of the BOPP film roll (the one without electrode) using a 2% volume water solution of MPTMS and (5) subsequent 30 second cold atmospheric plasma jet treatment of inner side of BOPP film roll and patterned Elastosil 2030 film on its plastic carrier, followed by (6) clamping both surfaces together and placing them in a 65°C oven overnight. (7) Separation of the plastic carrier from silicone pattern glued to BOPP foil. (8) Two minute treatment of the outer side of the BOPP film roll (the one

with the electrode) using a 2% volume water solution of MPTMS and (9) subsequent 30 second cold atmospheric plasma jet treatment of outer side of BOPP film roll and patterned Elastosil 2030 film glued to BOPP, followed by (10) clamping both surfaces together and placing them in a 65°C oven overnight. As tested by us the same bonding technique can be employed to stack multiple layers in one actuator as well as connect to polymer / metal interface. This can serve as a means of connecting the actuator to attachment points, a crucial feature for real life application, often neglected and ignored in other designs.

2.3 Laser patterning

To create the trench pattern in a 50 μm PDMS film a commercial CO_2 laser (Trotec speedy 360) with a wavelength of 10.6 μm and maximum power output of 120 W was used. Highly useful feature of this system – sonar technology allowed us to precisely and repeatedly focus laser beam on the surface of the processed Elastosil 2030 film. Through trial and error, we deduced that the best parameters that allow to minimize laser cut width, but at the same time grant reliable cut through the thickness of the film are: power of 1.4 % - 1.68 W and velocity of 0.5 % - 17.75 mm/s. Using these parameters, we were able to create cuts with a diameter of 110 ± 10 μm, separating silicone structures with width of 50, 100 and 200 ± 10 μm (Figure 2) and thickness of 50 μm dictated by film. This manufacturing method is simple, but has its drawbacks, namely large amounts of dust created (Figure 2D), not ideally rectangular cross section of the trench and not sufficient precision to go down in size. Dust accumulation on the sample was partially prevented by connecting a running vacuum cleaner tube close to the sample, immobilized with magnets.

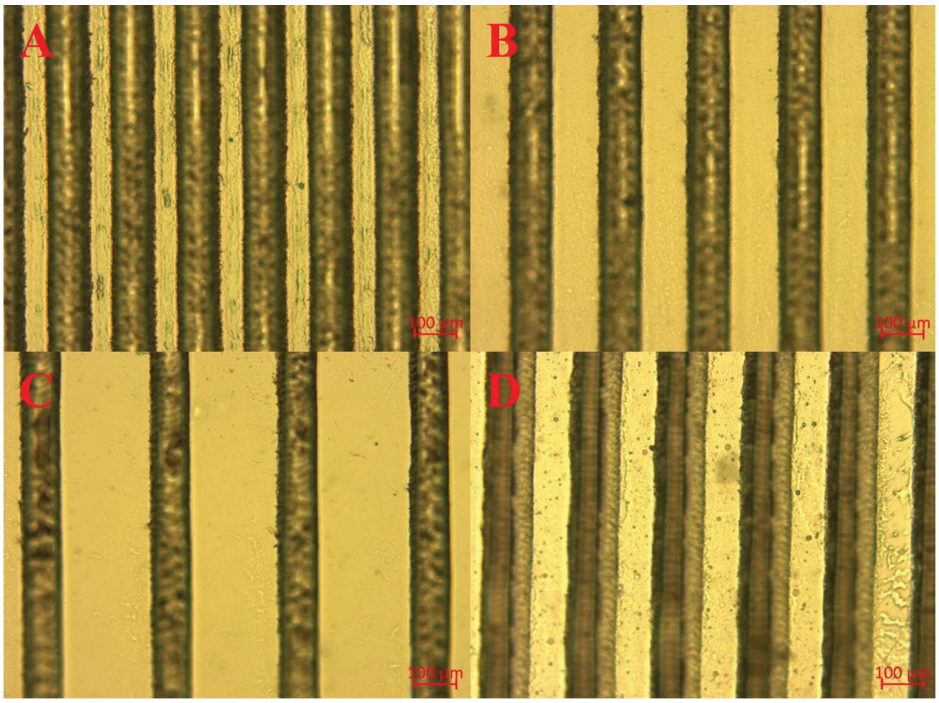

Figure 2: Patterned Elastosil 2030 50 micrometer film with PDMS walls of 50 (A), 100 (B) and 200 (C) micrometers. (D) Dust buildup resulting from the lack of an active dust removal system

3 MEASUREMENTS METHODOLOGY

In order to measure response of the proposed structure to the electric input, we prepared a system comprising of a laser displacement sensor (ILD1900-6LL, Micro-Epsilon), a finely polished steel weight with diameter of 0.7 cm placed on the test sample, a 2 mm clear PMMA cover between the sensor and weight and a CNC machined stand holding all parts (Figure 3). The purpose of the steel weight, generating 1kPa of pressure, is to hold the sample down and move together with its contractions. This allows to reliably measure changes in distance between the top of the weight and laser displacement sensor, representing actuator movement. Due to the explosive nature of the test, a PMMA cover was necessary to protect the sensor from fire and mechanical damage. By our estimates, this resulted in aproximately 10% increase in the measured displacement, using principle of geometrical optics through a plane-parallel transparent plate.

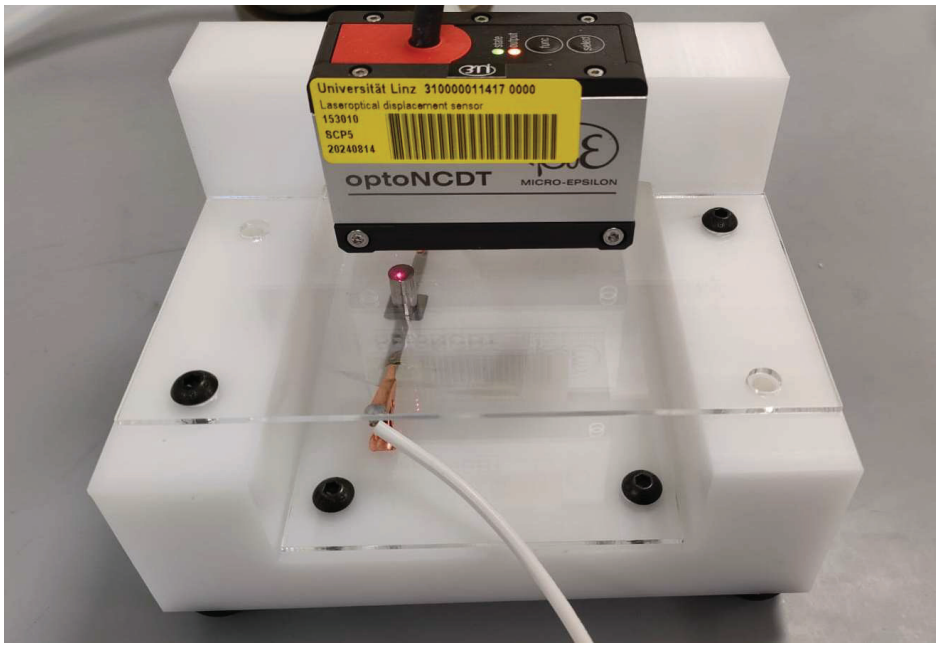

Figure 3: Test sample, pinned down by a steel weight, positioned under the laser displacement sensor.

Testing sample was placed under the sensor and a corn oil serving as liquid dielectric was applied on one side of the trench pattern entry. Through capillary forces liquid filled the device and an additional amount of it was placed around both sides to ensure full immersion. Subsequently the device was connected to a high voltage amplifier (20/20c-hs, Trek) with an input from a wave function generator (DG1022, Rigol). We used two functions to test the samples: a simple step function starting from 8 kV with increments of 0.5 kV every 2 s (Figure 4 – dashed lines), and a more complicated cyclic function with 4 cycles for each voltage step (Figures 5-7 – dashed lines).

4 RESULTS AND DISCUSSION

Most of the samples characterized with a breakdown voltage of 12 ± 1 kV. The electrodes proved to be a vulnerability in this design due to their relatively high resistance and possibly weak adhesion to the BOPP, which together led to a local electrode evaporation. This in turn led to arcing on the surface of electrodes and deviation of the actuating voltage from the one supplied. Due to crude manufacturing methods, samples with the wall width of 50 μm regularly exhibited an odd, irregular behavior (Figure 7), suggesting that bonding processes might be at least partially unsuccessful. Due to this fact results of 50 μm wall structure are not presented on figure 4.

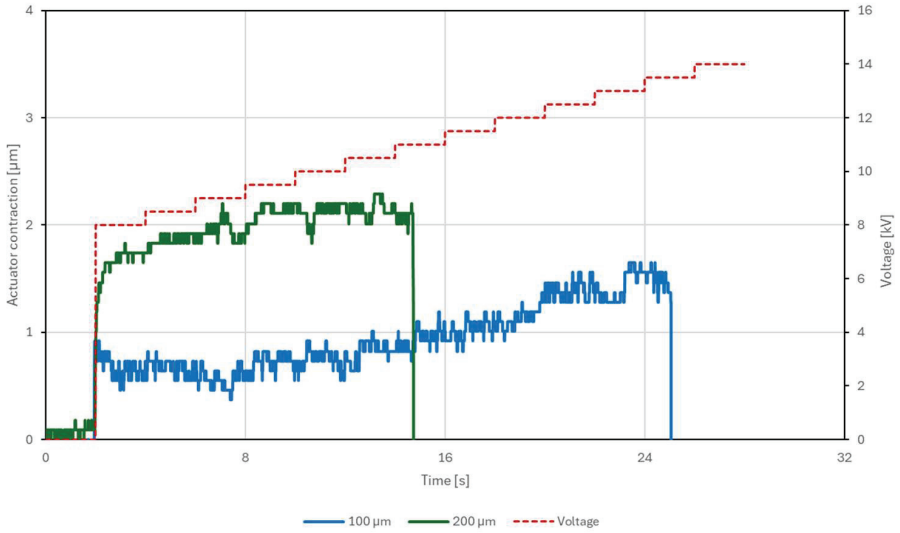

Figure 4: Actuator displacement under step voltage function.

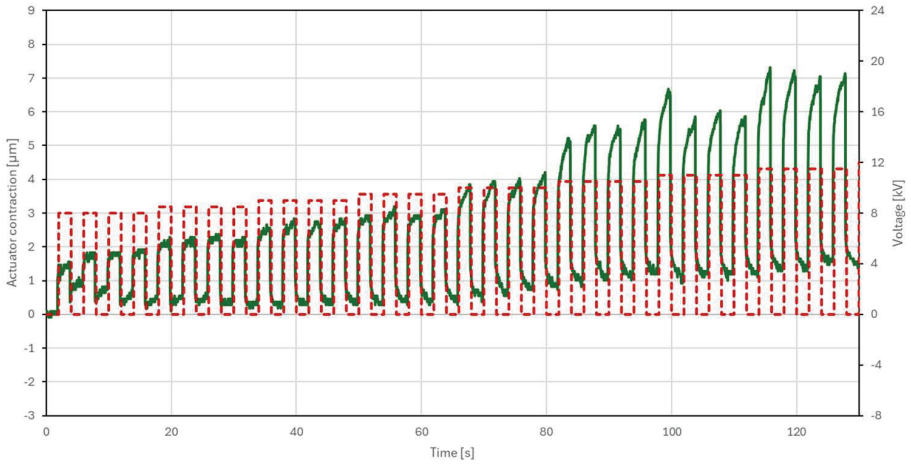

Figure 5 200 microns wall structure under cyclic voltage function.

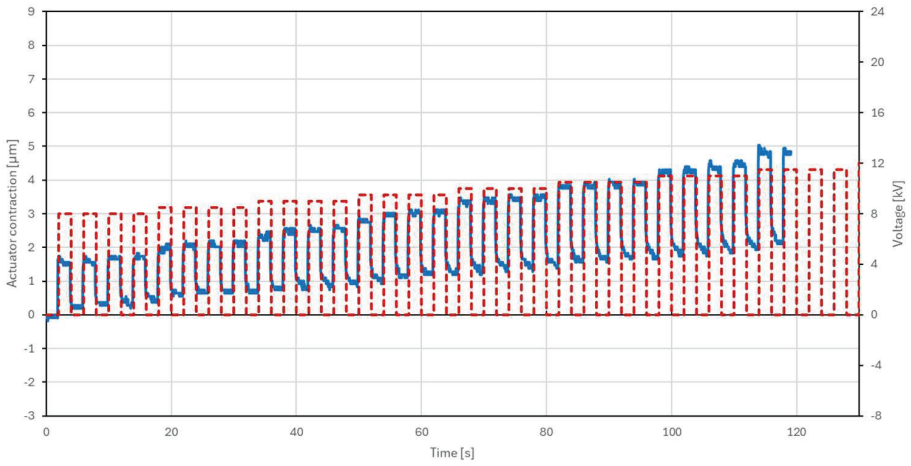

Figure 6: 100 microns wall structure under cyclic voltage function.

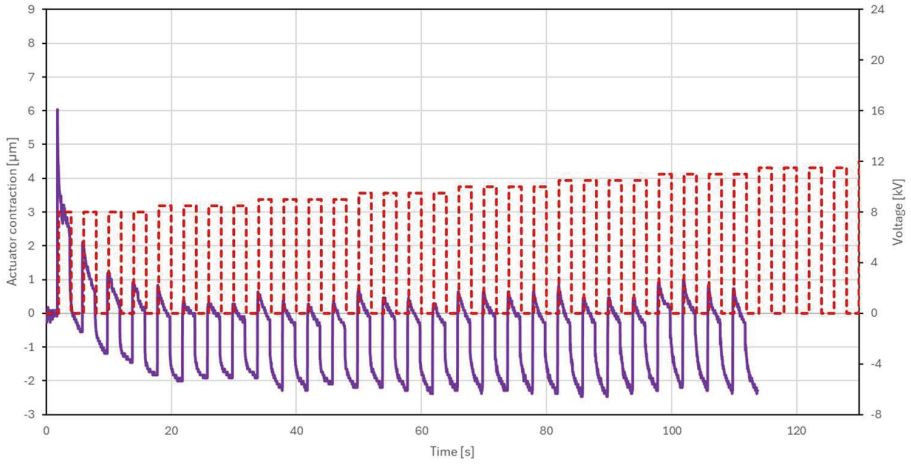

Figure 7: 50 microns wall structure under cyclic voltage function.

Additionally we observe that results obtained using different voltage waves differ significantly, even though they end at a similar breakdown voltage. This might be associated with charge accumulation effects, which can be seen through the shift of the zero actuation level in Figures 5 and 6, but requires further testing. One attempt to overcome charge accumulation, undertaken by us, was reversing polarity between every actuation cycle, but this resulted in reduced breakdown strength and an increased electrode failure rate. Nevertheless, this work reached an actuation of up to 9% with a relatively stiff silicone rubber (E~0.99 MPa) and laid ground for further research. In order to improve upon encountered problems, we plan to use off-the-shelf, already metalized BOPP film with even smaller thickness and electrical resistance. This should improve electrode reliability and further miniaturize the structure. Another planned change is the manufacturing method of patterned PDMS. Based on the recent reports, LCD 3D printers

appear as a cost-effective alternative, which using UV curable silicone should allow for downsized and much cleaner processes. Properties optimization of UV-curable silicone rubber is already in progress and should allow for use of softer silicone, leading to higher contractions.

5 ELECTRO-MECHANICALLY COUPLED FEM ANALYSIS

To further explore the potential of the proposed DEA-zipping concept, we conduct numerical experiments by means of electro-mechanically coupled finite-element models. Owing to the specific combination of materials, this is by no means a trivial task. The Young's moduli of the silicone rubber and the BOPP film ($E = 1500$ MPa, $\nu = 0.42$) differ by orders of magnitude. The liquid dielectric is supposed to have no (mechanical) influence on the elastomer, since the device operates as an open system, so we face the typical challenges of modeling free-space in electro-mechanically coupled problems of structures subjected to large deformations.

In the numerical analysis, we adopt plane-strain assumptions, where the out-of-plane direction is aligned with the walls of the actuator. To model a stack of layers, we employ periodic boundary conditions for the displacement field at the top and bottom of the computational domain. Symmetry conditions are prescribed at the left and right boundaries. Hence, the unit cell comprises half of the elastomer wall, half of the channel containing the dielectric and two halves of the BOPP layers (Figure 8). For the sake of simplicity, electrodes are represented by equipotential conditions at the top and bottom boundaries, which correspond to the center of the actual BOPP layers. The deviation in the electric field from the actual setup, however, can safely be assumed to be negligible.

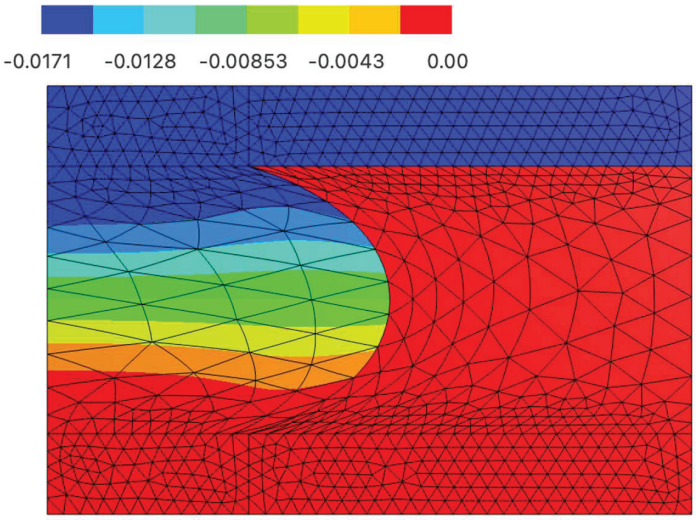

Figure 8: Finite-element model of the DEA actuator: deformed state of a unit cell with 50 microns walls at a voltage of 12 kV. The contours represent the displacement in height direction.

For the silicone elastomer, we use an incompressible Neo-Hookean model; the stress response of the BOPP layers is governed by the St. Venant-Kirchhoff potential. The liquid

dielectric is supposed to be displaced by the deformed elastomer without any resistance. Conventionally, free space is approximated as a very soft elastic solid. For the present problem, however, where we already face a material pairing of significantly different stiffnesses, and where the computational domain gets strongly distorted, such approach has proven infeasible. For this reason, we used an iterative procedure in which the mechanical field within the liquid domain is neglected in a first step, before a linear-elastic surrogate problem is solved in a second step to update the mesh in the liquid domain using the deformation of the rubber and the BOPP layers as kinematic boundary conditions. We use cubic, nodal-based shape-functions for the displacement field and the electric potential; Taylor-Hood elements that approximate the pressure field with one order less than the displacements are adopted for the incompressible elastomer.

Figure 9 (left) shows the displacement u_{top} of the top BOPP film (normalized by the height of the unit cell h_{layer}) as a function of the applied voltage for different wall widths ranging from 50 µm to 200 µm. The simulation results confirm that the contraction of the actuator layer increases as the width of the elastomer walls is decreased. In Figure 9 (right), the top displacement at the maximum voltage of 12 kV is illustrated as a function of the width of the elastomer walls w_{elast}.

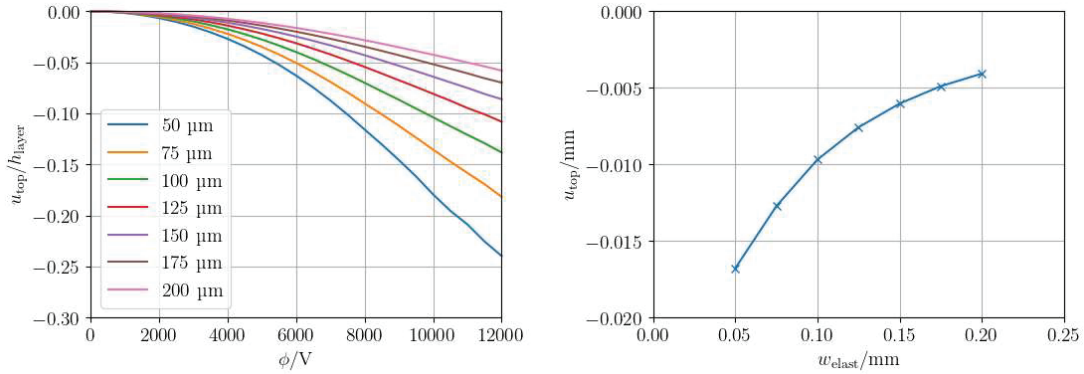

Figure 9: Finite-element model of the DEA actuator: contraction of a unit cell as a function of the voltage for different widths of the elastomer walls (left); contraction at 12 kV as a function of the wall width (right).

6 CONCLUSIONS

This study demonstrates a novel DEA-zipping hybrid actuator, successfully addressing the limitations of both traditional DEAs and zipping actuators. By employing metallized BOPP foils, structured elastomer film, and a liquid dielectric, we allow more efficient utilization of the active surface, leading to improved performance. Experimental validation confirms the feasibility of the proposed design, with actuation contraction reaching 9%, whereas finite element modeling offers further insight into its geometric optimization. While promising, electrode resistance and adhesion, bonding technology and charge accumulation effects remain challenges that must be addressed to enhance reliability and longevity. Future work will explore commercially metalized BOPP films for improved electrode stability and alternative

manufacturing techniques, such as LCD 3D printing, to refine the elastomer structure with higher precision and cleanliness. These developments are expected to facilitate further miniaturization and integration into practical high-force soft actuators, bringing DEA-zipping technology closer to real-world applications in robotics, adaptive structures, and next-generation smart materials.

REFERENCES

[1] W. C. Röntgen, "Ueber die durch Electricität bewirkten Form- und Volumenänderungen von dielectrischen Körpern," Annalen der Physik, vol. 247, no. 13, pp. 771–786, Jan. 1880, doi: 10.1002/andp.18802471304.

[2] R. Pelrine and R. Kornbluh, "INTRODUCTION: HISTORY OF DIELECTRIC ELASTOMER ACTUATORS," in Dielectric Elastomers as Electromechanical Transducers, Elsevier, 2008, pp. xi–xiii. doi: 10.1016/B978-0-08-047488-5.00031-9.

[3] M. Bozlar et al., "Dielectric elastomer actuators with elastomeric electrodes," Appl. Phys. Lett., vol. 101, no. 9, p. 091907, Aug. 2012, doi: 10.1063/1.4748114.

[4] S. Rosset, P. Dubois, M. Niklaus, and H. R. Shea, "Large stroke miniaturized dielectric elastomer actuators," in TRANSDUCERS 2009 - 2009 International Solid-State Sensors, Actuators and Microsystems Conference, Denver, CO, USA: IEEE, Jun. 2009, pp. 2401–2404. doi: 10.1109/SENSOR.2009.5285428.

[5] E. Kim et al., "A Transparent, Patternable, and Stretchable Conducting Polymer Solid Electrode for Dielectric Elastomer Actuators," Adv Funct Materials, vol. 35, no. 1, p. 2411880, Jan. 2025, doi: 10.1002/adfm.202411880.

[6] C. Keplinger, J.-Y. Sun, C. C. Foo, P. Rothemund, G. M. Whitesides, and Z. Suo, "Stretchable, Transparent, Ionic Conductors," Science, vol. 341, no. 6149, pp. 984–987, Aug. 2013, doi: 10.1126/science.1240228.

[7] R. Pelrine, R. Kornbluh, Q. Pei, and J. Joseph, "High-Speed Electrically Actuated Elastomers with Strain Greater Than 100%," Science, vol. 287, no. 5454, pp. 836–839, Feb. 2000, doi: 10.1126/science.287.5454.836.

[8] S. Rosset and H. R. Shea, "Flexible and stretchable electrodes for dielectric elastomer actuators," Appl. Phys. A, vol. 110, no. 2, pp. 281–307, Feb. 2013, doi: 10.1007/s00339-012-7402-8.

[9] L. Hu, W. Yuan, P. Brochu, G. Gruner, and Q. Pei, "Highly stretchable, conductive, and transparent nanotube thin films," Applied Physics Letters, vol. 94, no. 16, p. 161108, Apr. 2009, doi: 10.1063/1.3114463.

[10] W. Hu, X. Niu, L. Li, S. Yun, Z. Yu, and Q. Pei, "Intrinsically stretchable transparent electrodes based on silver-nanowire–crosslinked-polyacrylate composites," Nanotechnology, vol. 23, no. 34, p. 344002, Aug. 2012, doi: 10.1088/0957-4484/23/34/344002.

[11] S. P. Lacour, S. Wagner, Z. Huang, and Z. Suo, "Stretchable gold conductors on elastomeric substrates," Applied Physics Letters, vol. 82, no. 15, pp. 2404–2406, Apr. 2003, doi: 10.1063/1.1565683.

[12] P. Gebbers, C. Grätzel, L. Maffli, C. Stamm, and H. Shea, "Zipping it up: DEAs

independent of the elastomer's electric breakdown field," presented at the SPIE Smart Structures and Materials + Nondestructive Evaluation and Health Monitoring, Y. Bar-Cohen, Ed., San Diego, California, Apr. 2012, p. 83402P. doi: 10.1117/12.915020.

[13] L. Maffli, S. Rosset, and H. R. Shea, "Zipping dielectric elastomer actuators: characterization, design and modeling," Smart Mater. Struct., vol. 22, no. 10, p. 104013, Oct. 2013, doi: 10.1088/0964-1726/22/10/104013.

[14] N. Kellaris, V. G. Venkata, P. Rothemund, and C. Keplinger, "An analytical model for the design of Peano-HASEL actuators with drastically improved performance," Extreme Mechanics Letters, vol. 29, p. 100449, May 2019, doi: 10.1016/j.eml.2019.100449.

[15] M. Taghavi, T. Helps, and J. Rossiter, "Electro-ribbon actuators and electro-origami robots," Sci. Robot., vol. 3, no. 25, p. eaau9795, Dec. 2018, doi: 10.1126/scirobotics.aau9795.

Part XI
SS 01 - STRUCTURAL HEALTH MONITORING SYSTEMS FOR FIBER COMPOSITE AND HYBRID STRUCTURES

Kai-Uwe Schröder, Tobias Schalm, Martin Schagerl, Christoph Kralovec

XI ECCOMAS Thematic Conference on Smart Structures and Materials - SMART 2025
M. Krommer, M. Nader and M. Schagerl (Eds)

Received: 7 May 2025 / Revised: 1 August 2025 / Accepted: 3 September 2025
© The Author(s) 2025

Guided Wave-Based Damage Monitoring of Pinned Hybrid Composite-Titanium Joints

Christoph Humer, Christoph Kralovec, Andreas Dengg, Martin Schagerl

Abstract. In this paper, the damage state of a pinned hybrid composite-titanium joint is monitored using ultrasonic guided waves. This hybrid structure consists of an additively manufactured titanium and a carbon-fiber composite joint part in a single-lap shear configuration. In the overlap region on the titanium part an array of pins is manufactured that protrude into the composite material to additionally reinforce the joint's strength and damage tolerance. The specimens are tested under quasi-static tension loading, with measurement pauses at various load levels, until failure. For each of these load levels, a guided wave measurement is performed. For excitation and sensing of the guided waves piezoelectric transducers are used. These transducers are placed on both the composite and the titanium adherend, distant to the joint region, including one centrally positioned in the overlap region. By analyzing the measured guided wave signals along different paths between these three transducers, the damage state of this single-lap shear joint is monitored. The correlation coefficient deviation (CCD) and the root-mean square deviation (RMSD) metrics are evaluated as damage indicators to predict the degradation of the joint. It is shown, that typical damages for this type of joint, i.e. cracks occurring at the overlap ends, can be detected by these guided wave-based damage indicators. For validation, the length of these cracks are additionally measured by a digital image correlation (DIC) system. The presented results demonstrate high correlation between the DIC-measured crack lengths and the analyzed guided wave-based damage indicators.

Key words: Hybrid structures, Guided waves, Structural health monitoring, Pin-reinforced joint, Composite-metal joint

1 INTRODUCTION

Modern lightweight structures, such as civil aircraft, are composed of numerous interconnected subcomponents and structural elements. Traditionally, these components are joined using mechanical fasteners like rivets and bolts. However, the increasing use of high-performance composite structures has led to a broader adoption of adhesive bonding due to its weight-saving potential and favorable load distribution characteristics. Despite these advantages, adhesive

Christoph Humer & Christoph Kralovec & Andreas Dengg & Martin Schagerl
Institute of Structural Lightweight Design, Johannes Kepler University Linz, Altenbergerstr. 69, A-4040 Linz, Austria, e-mail: christoph.humer@jku.at

joints suffer from several limitations including sensitivity to manufacturing quality, challenges in inspection or limited damage tolerance. This necessitates the continued use of mechanical fasteners to ensure fail-safe behavior and, with it, the designs often remain conservative with excess weight and reduced cost-efficiency.

To address the challenging inspectability of adhesive joints, different structural health monitoring (SHM) approaches have been proposed [1, 2]. These SHM methods allow an automated in-situ assessment of the structural integrity by detecting damage initiation and progression in such advanced joints. The implementation of an SHM system enables the usage of damage-tolerant design philosophies that can reduce weight while maintaining safety and reliability.

Current aircraft configurations increasingly employ a multi-material approach, where carbon fiber reinforced polymer (CFRP) composites are favored for their superior strength-to-weight ratio. Nevertheless, certain components, e.g. load-introduction elements or doorframes, are still made from metallic materials like aluminum or titanium alloys. This necessitates the development of reliable joining methods for hybrid metal-composite structures. Therefore, several enhancements for adhesive bonding have been investigated, such as advanced surface treatment and mechanical interlocking feature, to improve joint strength and damage tolerance [3]. In particular, mechanical interlocking elements have demonstrated significant improvements in static strength, fatigue resistance, and damage tolerance of bonded joints [4]. Recent advancements in additive manufacturing technologies, particularly laser powder bed fusion [5], enable the production of complex metal components from high-performance aerospace titanium alloys. This opens up new possibilities for hybrid joint designs, allowing the integration of geometrically intricate interlocking features, i.e. pins, directly into metallic joining partners. These pins can be used in a co-curing process, where they penetrate the composite part before curing. This eliminates the need for additional adhesives by solely relying on the composite matrix as bonding medium, which simplifies manufacturing while reducing mass and bond line thickness [6].

Although promising, the pinned hybrid design introduces challenges, such as more demanding tooling requirements and the use of matrix materials that may not match the performance of dedicated adhesive films in terms of strength and damage tolerance [7]. These challenges have hindered the implementation of such pinned hybrid metal-composite joints in current aircraft structures despite their demonstrated potential. Kralovec et al. [8] have validated the mechanical effectiveness of such designs in resisting both static and cyclic loads. Digital image correlation (DIC) measurements and fracture surface analysis have confirmed characteristic failure modes and crack arresting capabilities of pin arrays. However, monitoring the onset and progression of damage remains critical to ensure the structural reliability of such joints in service.

The present experimental study investigates guided wave-based SHM as a promising approach for monitoring the damage state of pinned hybrid titanium-CFRP single-lap-shear (SLS) joints under quasi-static tensile loading. Ultrasonic guided waves are sensitive to typical damage mechanisms, i.e. cracks at the overlap regions, and damage indicators are derived from the measured signals. The effectiveness of this method is assessed by correlating these damage indicators with DIC-measured crack length.

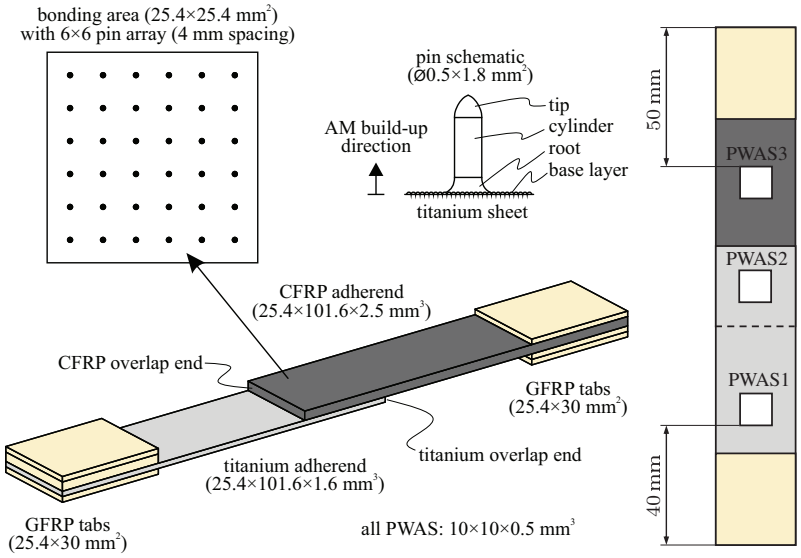

Figure 1: Schematic of pinned hybrid titanium-CFRP SLS specimen with PWAS positions [8]

2 EXPERIMENT

In this section, the SLS test specimen, the experimental setup, the data acquisition and processing methods are explained. Detailed information on the materials and manufacturing process are provided in Refs. [8, 9], and is only shortly summarized herein for conciseness of the paper.

2.1 Test specimen

The SLS specimens used in this study are based on ASTM D5868 [10]. A schematic of the specimen geometry and sensor positions is shown in Fig. 1. The metallic joint partner is additively manufactured from industrial grade Ti-6Al-4V using laser powder bed fusion [5] with a 6×6 pin array (4 mm spacing) in the overlap region. The epoxy resin based CFRP adherend consists of six plies 5-harness (5H) satin weave fabric in a symmetrical layup $[0°/+45°/0°]_S$. The pins in the overlap region are incorporated in the pre-impregnated CFRP layers in a hand layup building process. After co-curing in an autoclave the samples are cut to final dimensions and alignment tabs made from glass fiber reinforced polymer are bonded to the ends to ensure aligned clamping conditions.

Each SLS specimen is equipped with 3 piezoelectric wafer active sensors (PWAS) made from PIC255 material [11]. The PWAS have dimensions of $10 \times 10 \times 0.5\,\text{mm}^3$ and feature wrap around contacts for electrical connection. As illustrated in Fig. 1, PWAS2 is centrally positioned in overlap region on the titanium joint partner. PWAS1 and PWAS3 are located on the same side of the specimen at positions outside the overlap region. Their slight asymmetric positioning result from additional different sensors (not shown and utilized in this study) installed on the

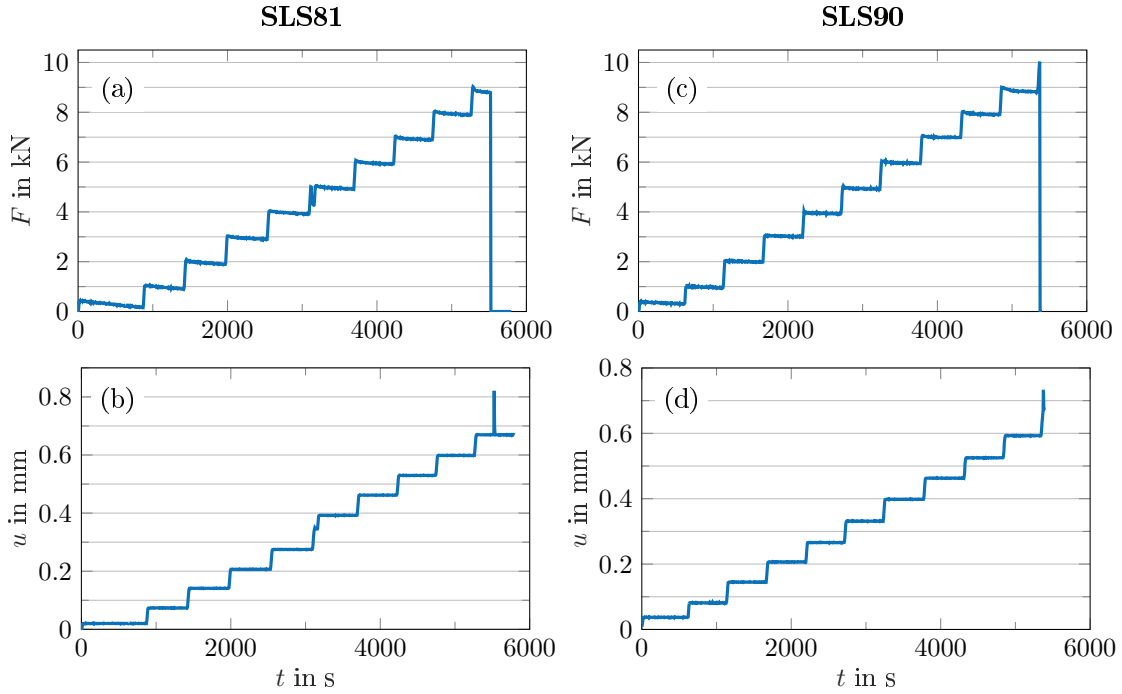

Figure 2: Test rig data for quasi-static loading: (a) force and (b) displacement of the SLS81 specimen with 9 measurement pauses; (c) force and (d) displacement of the SLS90 specimen with 10 measurement pauses

specimen. However, one lateral surface of the specimen is additionally coated with a random speckle pattern in the overlap region for optical strain measurements using a DIC system.

2.2 Experimental setup

Two SLS specimens, designated SLS81 and SLS90, were tested under quasi-static loading in a servo-hydraulic test rig. The specimens were clamped by hydraulic grips at both ends and loaded in longitudinal direction. Crosshead displacements and forces were recorded continuously throughout the test, see Fig. 2. The load was increased slowly until failure, where the guided wave measurements were performed during measurement pauses at defined load levels. The static loads at ultimate failure were $9.0\,\mathrm{kN}$ and $10.04\,\mathrm{kN}$ with nine and ten measurement pauses for the specimens SLS81 and SLS90, respectively. During each measurement pause, a switching unit automatically cycled actuator and sensor roles among the three PWAS. Hence, the signals for all different paths can be analyzed. The excitation signal from the actuator was provided from an arbitrary function generator and consisted of a 5-period sine function windowed by a Von-Hann window with an amplitude of $9\,\mathrm{V}$, see Fig. 3 (a). Two subsequent measurements with frequencies of $280\,\mathrm{kHz}$ and $315\,\mathrm{kHz}$ were performed. The voltage signals of all three PWAS were measured by an oscilloscope with a sampling rate of $125\,\mathrm{MHz}$ for a total time of $1\,\mathrm{ms}$, i.e. $n = 125000$ time points. Additionally, baseline measurements in the

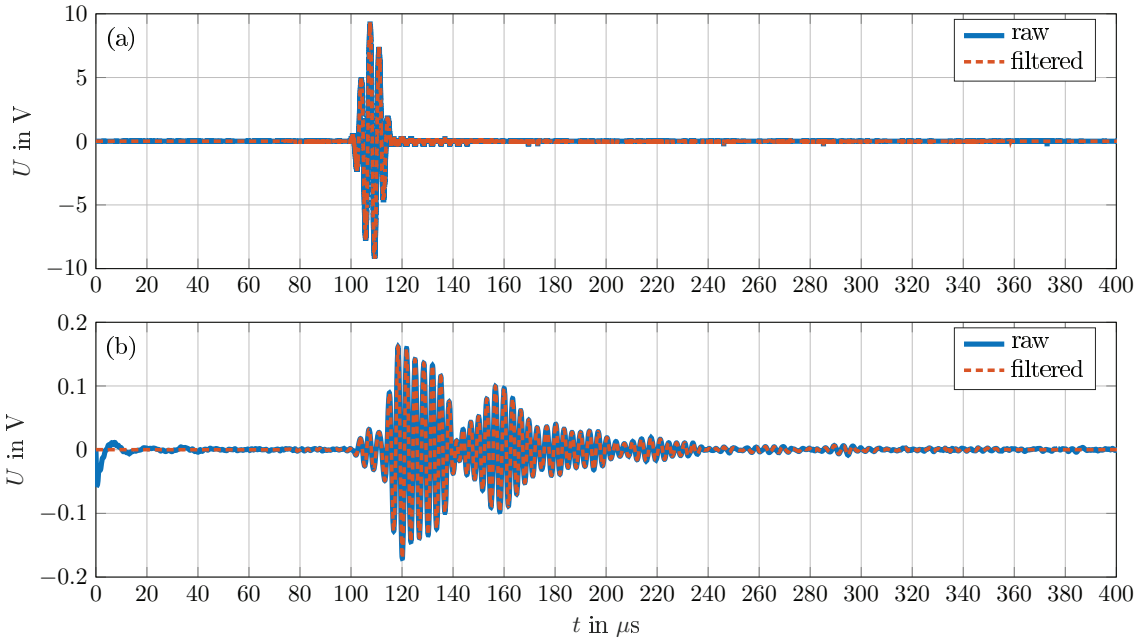

Figure 3: Raw and filtered guided wave signals for specimen SLS81 at the third measurement pause (2 kN) with an excitation frequency of $f = 280$ kHz: (a) actuator voltage (PWAS1) and (b) sensor voltage (PWAS2)

pristine and unloaded condition were carried out.

A 2-dimensional DIC system using a single digital camera with adequate lighting is utilized to optically measure the crack lengths on a single lateral surface of the specimen.

2.3 Data processing

The raw voltage signals acquired from the PWAS are processed in three main steps, i.e. time history tapering, bandpass filtering and damage metric calculation.

First, the relevant part of the time-domain signal, between $t = 80\,\mu$s and $t = 350\,\mu$s, is isolated using a raised cosine filter with a rise time of $10\,\mu$s, as described in Ref. [12]. This step reduces the influence of unwanted signals originating from the hydraulic test rig or electromagnetic interference, as illustrated in Fig. 3 (b).

Subsequently, a bandpass filter with cut-off frequencies of 20 kHz and 800 kHz is applied to filter both low-frequency structural vibrations, e.g. from the test rig, and high-frequency measurement noise. An example of the raw and filtered guided wave signals for specimen SLS81 at the third measurement pause (2 kN) is shown in Fig. 3.

After these data cleansing steps, the root-mean square deviation (RMSD)

$$\mathrm{RMSD} = \sqrt{\frac{1}{n}\sum_{i=1}^{n}\left(U_{\mathrm{prist}}(t_i) - U_{\mathrm{dam}}(t_i)\right)^2} \tag{1}$$

is calculated where $U_{\text{prist}}(t_i)$ and $U_{\text{dam}}(t_i)$ denote the sensor voltages at time steps t_i in the pristine and damaged states, respectively, and n is the total number of time points. The scalar RMSD metric quantifies the quadratic mean of the differences between the two time signals. Furthermore, the correlation coefficient deviation (CCD)

$$\text{CCD} = 1 - \frac{1}{n}\sum_{i=1}^{n}\frac{(U_{\text{prist}}(t_i) - \bar{U}_{\text{prist}})(U_{\text{dam}}(t_i) - \bar{U}_{\text{dam}})}{s_{\text{prist}}s_{\text{dam}}} \tag{2}$$

is evaluated as damage metric, where $\bar{U}_{\text{prist}}$ and $\bar{U}_{\text{dam}}$ are the mean values and s_{prist} and s_{dam} are the standard deviations of the pristine and damaged signals, respectively. The CCD metric measures the loss of correlation between the two time signals due to damage.

Both RMSD and CCD metrics are evaluated for the measured guided wave signals at each measurement pause throughout the quasi-static loading tests.

3 DISCUSSION

In this section the sensitivity of the selected CCD and RMSD metrics as damage indicators to monitor the structural health of the pinned hybrid titanium-CFRP joint are analyzed. In Fig. 4 the development of these metrics for specimen SLS90 across all actuator-sensor paths and at two excitation frequencies ($280\,$kHz and $315\,$kHz) are illustrated. Generally, both the CCD and RMSD metrics are sensitive for damages in the overlap region of the adherends. The trend of both indicators with increasing mechanical loading is rather consistent and well interpretable for both excitation frequencies. Notably, the guided wave measurements at $315\,$kHz often produce slightly higher metric values, particularly for the CCD metric, compared to those at $280\,$kHz. This may indicate that higher frequencies tend to enhance sensitivity due to shorter wavelength and improved interaction characteristics with damages. Generally, guided wave characteristics, e.g. amplitude or wavelength, are highly frequency dependent and their excitability is influenced by both the specimen and PWAS properties [13]. Thus, indiscriminate increase in excitation frequency may not improve sensitivity and could introduce opposing trends. However, measurements for a pair of PWAS using alternating actuator-sensor roles yield closely matching results for both metrics, indicating linearity and reversibility of the guided wave measurements. It is to say, that the measurement file for the excitation frequency $f = 280\,$kHz at the second measurement pause for the path between actuator PWAS1 and sensor PWAS2 was corrupted and could not be evaluated.

For the initial two measurements, the CCD metric shows no discernible changes, consistent with the expectation that the specimen is undamaged at these loads. In contrast, the values of the RMSD metric indicate a change to the pristine measurement, while the results remain in comparable size for these measurements. For the third measurement pause at a load level of $2\,$kN all evaluated measurements show a slight increase for both metrics. This might indicate early deterioration in the joint region although there are no visible damages on the lateral surface observed by the DIC system. The results for these DIC measurements of specimen SLS90 are depicted in Fig. 5. As a crack propagates into a DIC evaluation subset, the bonded surfaces separate from

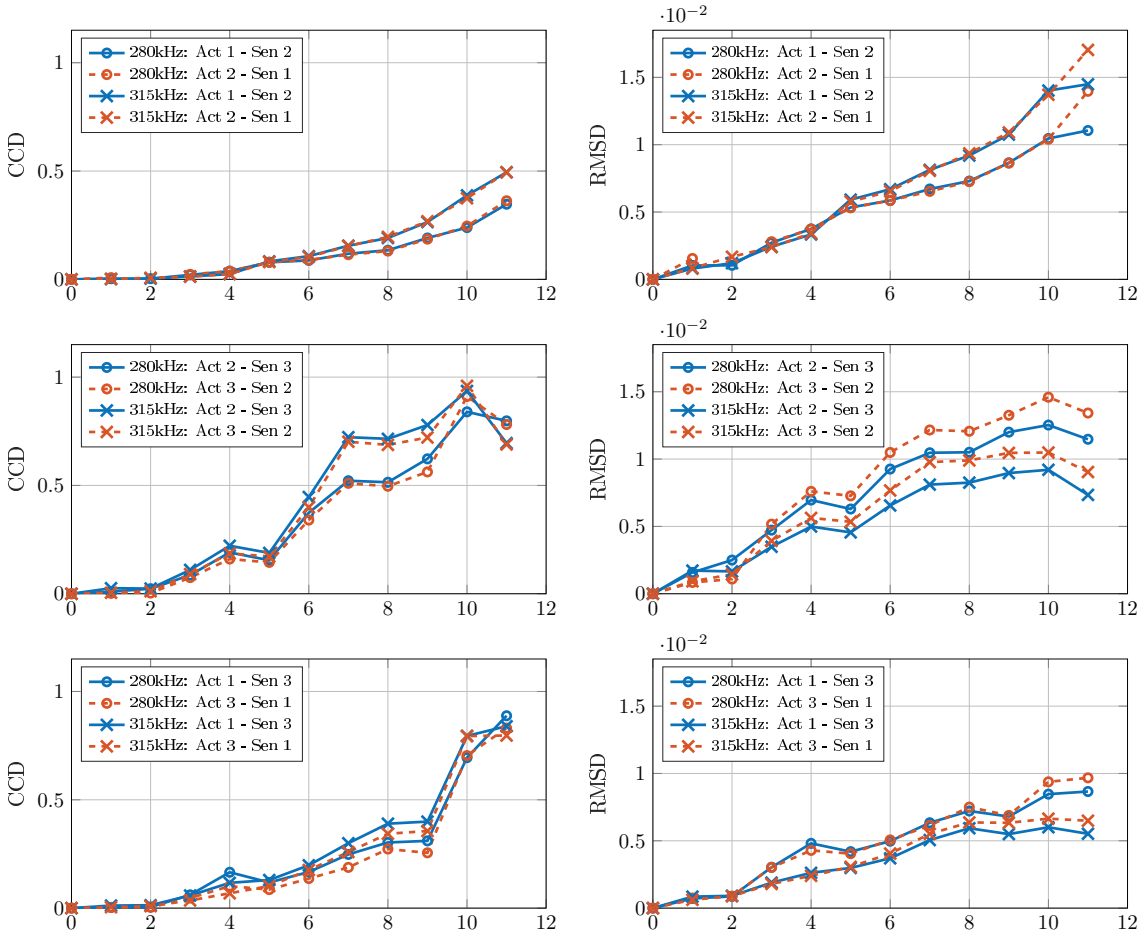

Figure 4: Specimen SLS90: Comparison of CCD and RMSD metrics for 11 load levels in all actuator-sensor paths at excitation frequencies 280 kHz and 315 kHz

each other and open primarily due to joint rotation. The DIC evaluation algorithm interprets this as a pronounced strain concentration with very high strain values, which serves as a highly sensitive indicator of crack presence and growth [8]. Hence, the analysis of the principal strains in the overlap region enables an automated estimation of the crack lengths. Although the DIC system captures crack growth only on the lateral surface of the overlap region, while the guided wave signals are affected by material deterioration throughout the entire overlap area, the estimated surface crack length might serve as an indicator of the overall damage state of the joint. However, the damage evaluation thresholds are determined by analyzing the load-normalized local principal strains along the bond line. Initially, this normalized strain distribution exhibits only minor changes as the load increases. An abrupt and disproportionate deviation from the initial strain distribution is considered indicative for damage initiation, which is additionally validated by visual inspection during testing. The principal strain threshold for damage onset

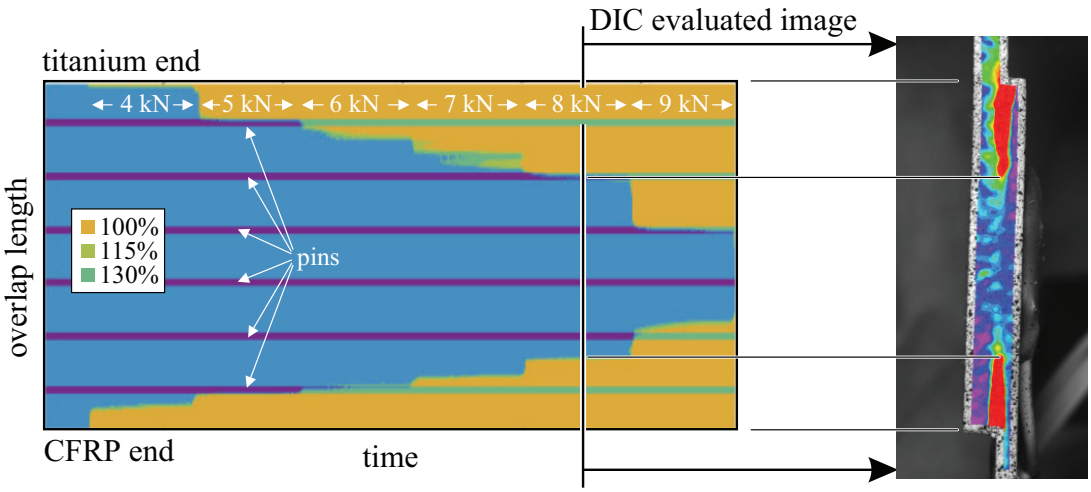

Figure 5: Crack propagation over load cycles for the SLS90 specimen evaluated by DIC principal strain thresholds. In the damage propagation plots the color shading highlights areas where the strain exceeds 100%, 115%, and 130% of the threshold. In the DIC image the color shading represents the principal strain (red: values exceed threshold)

is manually selected for each specimen between the highest strain value observed immediately before and after the abrupt strain deviation. Further details can be found in [8]. However, the sensitivity of the estimated crack length on the selected threshold value is negligibly small, as depicted in Fig. 5, where a 30% increase of the threshold value results in a crack length increase less than 1 mm.

The first cracks on the lateral surface are detected at a load level of 4 kN, where the crack length at the CFRP overlap end is significantly larger in comparison to the titanium end. With increasing load, the damaged area expands as indicated by the growing regions exceeding the principal strain thresholds. Notably, the pins in the overlap region act as effective crack arrestors, i.e. the crack propagation is significantly slowed down by the reinforcement of the pins. This can be clearly seen in Fig. 5 at the load level of 5 kN, where the cracks stop exactly at the pins location. This demonstrates the improved damage tolerance of this design.

The provided temporal and spatial information of the crack propagation in both overlap ends allow to interpret the presented guided wave-based damage indicators. Overall, these DIC-evaluated crack lengths correlate with the trend of the CCD and RMSD metric values. This confirms the physical relevance of these guided-wave based damage indicators and their high potential to detect damage progression in real time. For instance, the load increase from 8 to 9 kN results in a rapid crack propagation by 4 mm (the spacing between the rows of pins) only on the titanium overlap end, see Fig. 5. This once again clearly demonstrate the reinforcement effect of the pins that efficiently slow down the propagation of the cracks. However, this sharp rise in damage size can also be found in the results of the CCD and RMSD metrics in Fig. 4,

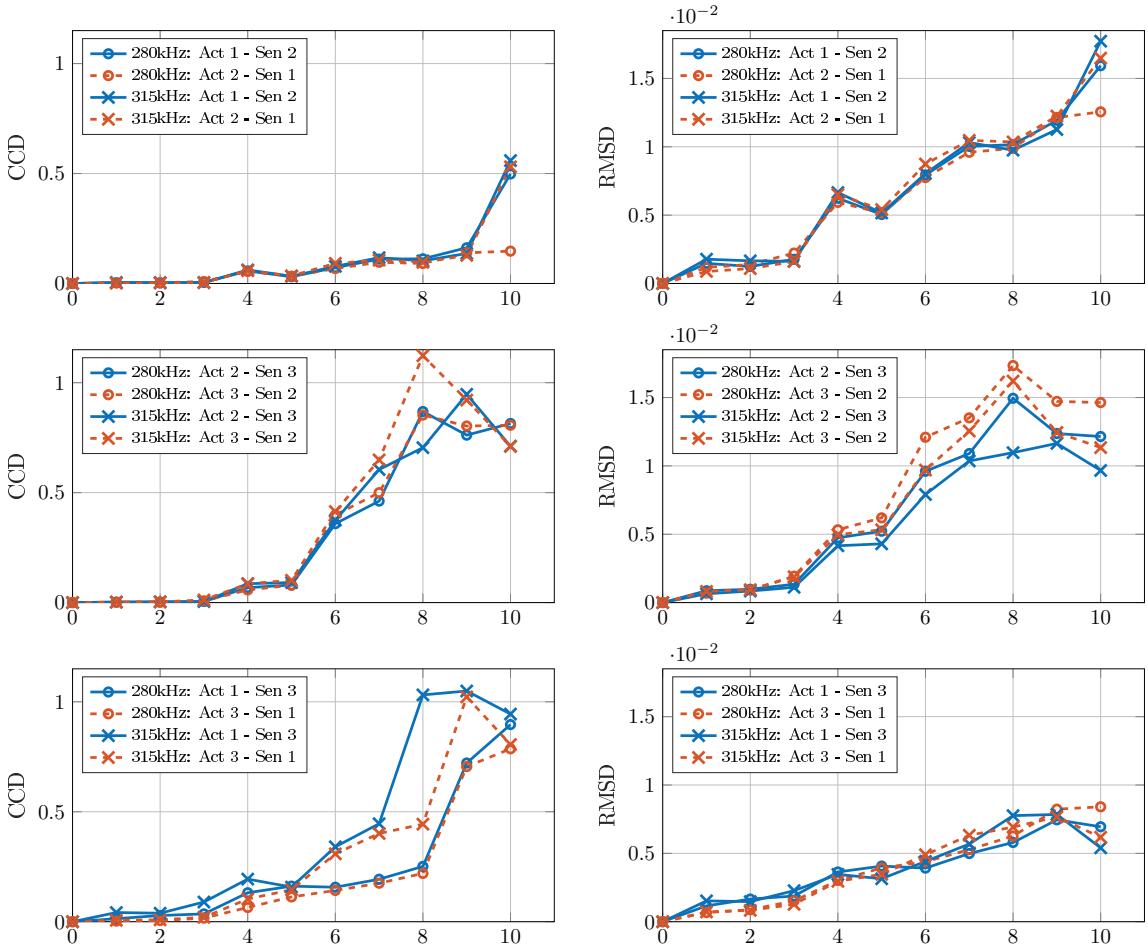

Figure 6: Specimen SLS81: Comparison of CCD and RMSD metrics for 10 load levels in all actuator-sensor paths at excitation frequencies 280 kHz and 315 kHz

where the values between measurement nine and ten increase. It can be seen, that the differences in the measurement path between PWAS1 and PWAS2, which directly covers the titanium overlap end, increases stronger than the results for the path PWAS2-PWAS3. The measurements using PWAS1 and PWAS3 show an increasing trend as well.

Comparable results are found for the second specimen SLS81, see Fig. 6. Both CCD and RMSD values remain relatively stable during the initial load steps, with significant deviations appearing only after the third measurement pause. This delayed response compared to SLS90 indicate specimen-specific differences in damage initiation, likely attributable to inherent material or manufacturing variabilities. For statistical validation more than two specimens would have to be tested. However, both metrics exhibit decreasing or relatively constant values between the fourth and fifths measurement pauses, corresponding to a load increase from 3 to

4 kN, across most actuator-sensor paths. Interestingly, these outliers can be observed for both specimens, see Fig. 4. For specimen SLS90, the DIC system observes the onset of crack propagation, i.e. damage initiation, on the lateral surface exactly for these load steps (see Fig. 5). This counterintuitive behavior could not be reasonably explained.

The specimen SLS81 failed during the tenth measurement pause at a constant load level of 9 kN, see Fig. 2 (a). This shows that the cracks also propagates during the measurement pauses with constant mechanical loading and not only during load increase. Consequently, the damage size may change while switching in between the different excitation frequencies and actuator-sensor paths. However, the final measurements for both specimens were conducted after ultimate structural failure, i.e. the adherends were completely separated but remained in physical contact due to being held in place by the mounting devices of the hydraulic test rig. For these final measurements the results of both metrics diverge, i.e. some showing increases and others decreases, likely due to unstable or highly variable contact conditions. Overall, the trend between both specimens remain consistent, with the same actuator-sensor paths and excitation frequencies exhibiting higher sensitivity. The coherence of these results across two separate specimens underscores the robustness and repeatability of the guided wave-based SHM approach.

4 CONCLUSIONS

This experimental study presents a guided wave-based SHM approach for pinned hybrid titanium-CFRP joints. The results show high sensitivity to damage initiation and progression of the CCD and RMSD metrics as reliable damage indicators. The correlation of both metrics with optical DIC measurements strengthens the validity of the method, while the high consistency across different propagation paths and frequencies until ultimate failure is shown. The guided wave measurements at 315 kHz often yield slightly higher metric values than those at 280 kHz, indicating marginally better sensitivity at higher frequencies. These findings highlight the potential of guided waves-based SHM for in-situ monitoring of advanced composite–metal hybrid structures and demonstrate the enhanced damage tolerance of the pinned joint design.

References

[1] G. M. F. Ramalho, A. M. Lopes, and L. F. M. Silva, “Structural health monitoring of adhesive joints using Lamb waves: A review,” *Structural Control and Health Monitoring*, vol. 29, no. 1, 2022.

[2] A. S. Lim, Z. R. Melrose, E. T. Thostenson, and T.-W. Chou, “Damage sensing of adhesively-bonded hybrid composite/steel joints using carbon nanotubes,” *Composites Science and Technology*, vol. 71, no. 9, pp. 1183–1189, 2011.

[3] M. Löbbecke, T. J. Bayerbasi, M. Bartsch, and J. Haubrich, “Role of surface structures on long term stability of adhesive joints between Ti–15V–3Cr–3Sn–3Al and polyether-ether-ketone,” *International Journal of Adhesion and Adhesives*, vol. 120, p. 103282, 2023.

[4] S. Stelzer, S. Ucsnik, and G. Pinter, "Strength and damage tolerance of composite–composite joints with steel and titanium through the thickness reinforcements," *Composites Part A: Applied Science and Manufacturing*, vol. 88, pp. 39–47, 2016.

[5] B. Dutta and F. H. Froes, "The Additive Manufacturing of Titanium Alloys." Butterworth-Heinemann, 2016.

[6] M. A. Wahab, *Joining composites with adhesives: Theory and applications*. Destech Publications, Inc., 2016.

[7] A. P. Vassilopoulos, *Fatigue and Fracture of Adhesively-Bonded Composite Joints*. Elsevier, 2015.

[8] C. Kralovec, A. Dengg, M. Schagerl, A. Schiller, C. Bisagni, M. Loebbecke, J. Haubrich, and R. Hanelt, "Static strength and fatigue life of pinned hybrid titanium-composite single-lap-shear joints," *Composite Structures*, vol. 354, p. 118765, 2025.

[9] A. Dengg, C. Kralovec, and M. Schagerl, "Damage monitoring of pinned hybrid composite–titanium joints using direct current electrical resistance measurement," *Composite Structures*, vol. 334, p. 117972, 2024.

[10] "Astm d5868-01: Standard test Method for Lap Shear Adhesion for Fiber Reinforced Plastic (FRP) Bonding," 2014.

[11] PI Ceramic GmbH, "PI Piezoelectric Ceramic products catalog," available online: https://www.piceramic.com/ (accessed on 20 March 2025). [Online]. Available: https://www.piceramic.com/

[12] C. Humer, S. Höll, C. Kralovec, and M. Schagerl, "Scattered Ultrasonic Guided Waves Characterized by Wave Damage Interaction Coefficients: Numerical and Experimental Investigations," *Sensors*, vol. 22, no. 17, p. 6403, 2022.

[13] V. Giurgiutiu, *Structural health monitoring with piezoelectric wafer active sensors*, 2nd ed. Amsterdam: Elsevier Academic Press, 2014.

XI ECCOMAS Thematic Conference on Smart Structures and Materials - SMART 2025
M. Krommer, M. Nader and M. Schagerl (Eds)

Received: 29 April 2025 / Revised: 16 July 2025 / Accepted: 3 September 2025
© The Author(s) 2025

Model- and a-priori knowledge-based acoustic emission data fusion for atmospheric corrosion identification on aluminum aircraft structures

Christoph Kralovec, Thomas Erlinger, Christoph Humer, Martin Schagerl

Abstract. Composite materials, such as carbon fiber reinforced polymer, are increasingly being used for structural components in the aircraft industry due to their lightweighting potential. However, metal parts are still advantageous for locations with complex and varying stress states or high surface pressures. Therefore, metal-composite joints are required for optimal material utilization. This comes with other challenges. In addition to increased complexity of failure mechanisms and damage tolerance issues, corrosion accelerated by different electrochemical potentials can also degrade the structure. The use of titanium as the metal adherend solves this corrosion problem, but is expensive. Aluminum is more economical but susceptible to corrosion. Corrosion prevention measures, such as coating, may allow the use of aluminum, but uncertainties remain. This is especially true since efficient and early corrosion damage monitoring methods are lacking, both for non-destructive testing and structural health monitoring, as degradation typically depends on the corrosion type and is initially small and hidden. This paper presents recent results towards a novel data fusion concept for the detection, localization, quantification and typification of atmospheric aluminum corrosion. The concept uses a-priori knowledge of the structure, acoustic emission features and their fused visualization for corrosion imaging through model-based localization. Results on the influence of AE time history and signal characteristics on atmospheric corrosion imaging and evaluation are discussed.

Key words: Atmospheric corrosion, Metal-composite joints, Corrosion identification, Acoustic emission, Data fusion

1 INTRODUCTION

The growing demand for lightweight structures in the aerospace industry has led to the widespread adoption of composite materials, particularly carbon fiber reinforced polymers, due to their high specific strength and stiffness. Despite these advantages, metal components remain indispensable in areas subjected to complex and varying stress states or high surface pressures,

Christoph Kralovec & Thomas Erlinger & Christoph Humer & Martin Schagerl
Institute of Structural Lightweight Design, Johannes Kepler University Linz, Altenbergerstr. 69, A-4040 Linz, Austria, e-mail: christoph.kralovec@jku.at

where their isotropic and reliable properties offer clear benefits. Consequently, hybrid joints combining metals and composites are increasingly employed to exploit the strengths of both material classes [1]. However, the combination of dissimilar materials introduces significant challenges. In addition to the complexity of mechanical failure mechanisms and reduced damage tolerance, galvanic corrosion becomes a critical concern, particularly when materials with differing electrochemical potentials are joined. Titanium is often selected as the metallic component in such joints due to its corrosion resistance, but its high cost limits widespread application. In contrast, aluminum offers an economical alternative with favorable mechanical properties, yet it is highly susceptible to corrosion. To enable the broader use of composite-metal components, protective coatings and maintenance strategies with respect to corrosion damage monitoring are essential. Today, scheduled inspections and clear protocols on how to determine corrosion are used to control corrosion during operational downtime [2]. These controls still rely widely on visual inspection, as non-destructive testing (NDT) and structural health monitoring (SHM) techniques are expensive and often insensitive to the initial, localized, and hidden nature of corrosion damage and therefore inadequate. Furthermore, the available NDT and SHM methods lack a differentiation of corrosion types, but the type of corrosion is a major factor in the deterioration of the structural strength. These limitations emphasize the need for continuous corrosion damage monitoring methods that can be integrated into a structure's operation and which are capable of detecting and identifying corrosion processes and their detrimental effects at an early stage.

Many SHM methods have been investigated for corrosion damage monitoring [3, 4]. Among these, the acoustic emission (AE) method is readily demonstrated for the detection of different types of corrosion of aluminum alloys [5, 6]. The AE method is a passive method. It uses piezoelectric transducers that are attached to the structure of interest, to continuously measure acoustic waves that are emitted by potential sources of degradation, like e.g., crack formation or corrosion processes. This sensitivity to the process of degradation itself makes it a very potential candidate for monitoring the early stages of corrosion damage, when structural damage is very small and therefore difficult to detect. While AE is well established for steel corrosion detection in industrial applications such as pipeline and storage tank monitoring in the oil and gas sector and in reinforced concrete structures, its industrial application for atmospheric corrosion, and in particular aluminum corrosion, is lacking.

A recent study by the authors demonstrated the suitability of AE for the detection of atmospheric corrosion (i.e., small amounts of electrolyte on the surface due to variable relative humidity) in thin-walled AA2024-T351 structures [7]. However, despite these promising results, numerous open tasks remain on the way to an AE-based evaluation method that can provide information on the presence, i.e., separation from noise is required, and severity, i.e., localization, quantification and typification is required, of corrosion damage. To address this gap, recently an AE-based SHM concept for the full identification of atmospheric corrosion damage was proposed by the authors [8]. This paper summarizes the latest results on the way to the concept's realization and gives a brief outlook on the work still to be done.

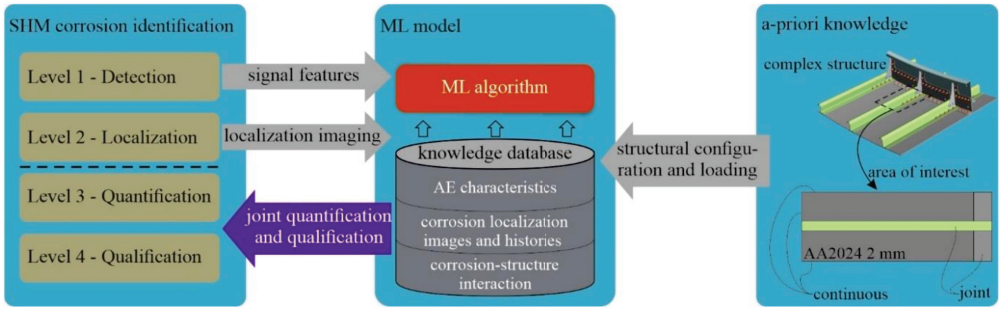

Figure 1: SHM concept for corrosion damage identification based on time and frequency domain signal features, AE source localization-based imaging, and the a-priori knowledge of the structural configuration and loading [8, reprint].

2 CORROSION DAMAGE MONITORING CONCEPT AND BASIC IDEAS

The objective of the SHM concept for corrosion damage monitoring is the complete identification, i.e., level 1: detection, level 2: localization, level 3: quantification, and level 4: typification, of atmospheric corrosion damage in thin-walled aluminum aircraft structures by the AE method. The concept has been proposed in [8] and is presented in Figure 1. The concept requires a sufficient number of transducers to enable AE source localization. Furthermore, setting up a knowledge database is a prerequisite. The proposed corrosion evaluation process can be separated into the following main steps and its basic ideas:

1. Filtering the AE signals received at individual transducers from the ambient noise for efficient data evaluation according to the state of the art by AE features, like e.g., rise-time and counts [9].

2. Evaluation of event evidence and relevance through model-based signal correlation and source localization of single event signals received at multiple transducers. The basic ideas are that (i) signals received at different transducers that can be correlated by a physical model are evidential, and (ii) signals from sources outside the area of interest are not relevant.

3. Corrosion imaging by spatial fusion of one or more features of multiple events received from multiple transducers over discrete time intervals for corrosion evaluation. The basic ideas are that (i) model-based localization reduces random errors by fusing time-frequency domain data from multiple transducers, (ii) spatial cumulation of AE source localizations over discrete time intervals suppresses irrelevant events and highlights true corrosion sites, and (iii) accurate localization results allow conclusions about the type and extent of a potential corrosion damage.

4. Evaluation of corrosion type and quantity by machine learning (ML) models for full corrosion identification. The basic idea is that the training by (i) labeled AE signal characteristics, (ii) labeled corrosion images, and (iii) probabilities for the occurrence of corrosion

types and locations for a given structure (corrosive loads, materials, material combinations and geometric features), enables the ML-based typification and quantification of corrosion damage.

These basic ideas are addressed by the authors in ongoing research. Recent results are presented and discussed with respect to the realization of corrosion identification.

3 IMPROVED AE SOURCE LOCATION THROUGH MODEL-BASED EVALUATION

The presented SHM concept for corrosion damage identification depends strongly on the quality of the AE-based corrosion visualizations. Consequently, the accurate localization of AE signal sources (i.e., AE emitting events), which is used to create the corrosion images, is crucial for the concept. Today's localization methods typically suffer from numerous sources of systematic and random errors. Among these, the estimation of the signal time-of-arrival (TOA) is one of the most critical due to the high wave velocities in the considered aluminum aircraft structures [10]. This is particularly true for AE signals of low signal-to-noise ratios (SNR), which are typical for SHM applications and are highly expected for low energy signals from atmospheric corrosion [7]. Therefore, the authors introduced a novel model-based AE source localization method, that fuses time-frequency domain data from all involved transducers by means of the frequency dependent velocity of elastic guided waves in thin-walled structures. For localization, (i) a grid of possible AE source locations i is defined around a meaningful starting point, (ii) for every grid location i, transducer j and discrete frequency f_k the TOA $t_{\mathrm{OA}}(i, j, t_0, f_k)$ of the AE signal is calculated by the unknown event time t_0 and the model-based computed time-of-flight, and (iii) these forward computed TOAs are best fitted to the measured and continuous wavelet transformed transducer signals by

$$\hat{i} = \arg\max_{i,t_0} \sum_{j=1}^{n_\mathrm{T}} \sum_{k=1}^{n_\mathrm{f}} \left| W(t_{\mathrm{OA}}(i, j, t_0, f_k), f_k) \right| \quad \text{with} \;\; i = 1 \ldots m \,, \tag{1}$$

where n_T is the number of transducers, n_f is the number of considered discrete frequencies, m is the number of defined grid positions, and $W(t_{\mathrm{OA}}(i, j, t_0, f_k), f_k)$ are the wavelet coefficients of the measured signal for the forward calculated $t_{\mathrm{OA}}(i, j, t_0, f_k)$. The result is the most probable AE signal source location grid point $\hat{i}$. Thus, unlike other localization algorithms, the proposed method uses the frequency dependent signal maximums for localization, which is believed to be more robust for low SNR. The method is computationally much more costly than other state of the art localization methods and in its current state its accuracy is limited by the discretization of the used grid of possible AE source locations. However, as demonstrated in [11] by means of pencil lead break tests at known locations on a large aluminum plate that was equipped with piezoelectric wafer active sensors (PWAS) as transducers, the localization results are significantly improved compared to a standard triangulation method with Akaike information criterion (AIC) TOA estimator (average factor 2.2 and average factor 2.4 when the transducer sensitivity is additionally considered). For more details, please see [11]. This improved localization accuracy was also evident for very recent results on the same large aluminum plate but with

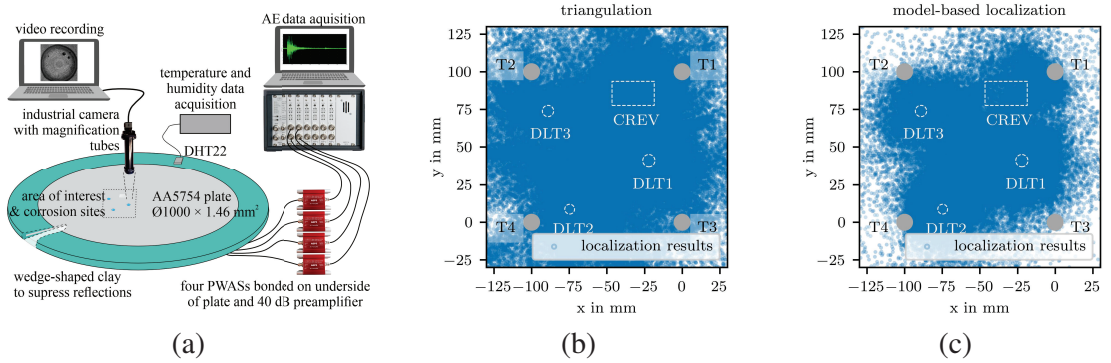

Figure 2: (a) Experimental setup, (b) AIC-based TOA estimation-based triangulation, and (c) model-based localization results with transducer positions T1-4 and corrosion sites DLT1/2/3 and CREV [12, reprint]

local corrosion sites, triggered by 0.05 mL droplets (DLT) of a 50 g/L sodium chloride (NaCl) solution at four defined sites and at different times [12]. Figure 2a shows the employed experimental setup, which was located in a laboratory environment. The NaCl droplets used to trigger corrosion were repeatedly applied, dried and re-wetted by controlled atmospheric humidity over 150 hours according to a predefined protocol (see [12]). Visual inspection after the corroding procedure revealed relevant corrosion only at the NaCl triggered sites. The AE acquisition was based on time-domain thresholds. After pre-filtering of, e.g., electrical interferences, 987,090 valid events remained and their sources were localized. Figure 2b presents the scatter plot of the localization results around the corrosion sites (DLT1/2/3 and CREV) with triangulation and an AIC-based TOA estimation. The AE sources are clustered at the corrosion sites but the scatter of the results is very large. The same applies for the AE source scatter plot generated based on the proposed model-based localization approach (grid size of $40\times40\,\mathrm{mm}^2$ and grid discretization of $0.5\times0.5\,\mathrm{mm}^2$ used; triangulation results are used as starting points), presented in Figure 2c. However, the model-based localizations are much less (approx. 60 % less), as signals that did not correlate well within the search grid were filtered out. The remaining model-based localizations scatter much less around the corrosion sites than the triangulation-based localizations. This demonstrates the value of the proposed model-based localization method and the capability of the AE method to detect and localize atmospheric corrosion on aluminum aircraft structures. Furthermore, the model used for localization can be improved and adapted to more complex structures by considering, e.g., signal amplitudes and phases, boundary reflections or inhomogeneous and anisotropic structural properties. However, for evaluation of the quantity and type of corrosion, a further analysis is required.

4 CORROSION IMAGING THROUGH SPATIAL FUSION OF AE EVENTS

Corrosion imaging by spatial fusion of localized AE events using heatmaps is a very efficient method to visualize AE activity, and thus, corrosion activity hotspots. It also suppresses random localization errors and dispensable events. Figure 3ab present the corrosion image of the whole

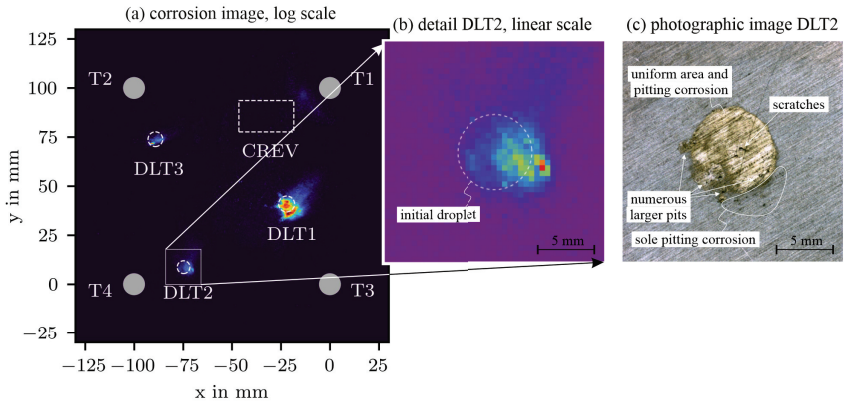

Figure 3: (a) AE-energy-based corrosion image of whole area of interest, (b) AE-energy-based corrosion image of DLT2, and (c) photographic image of DLT2 [12].

area of interest and an exemplary detail plot of DLT2. For visualization, the spatial distribution of the AE energy is represented as heatmap. The AE source energy at the found grid point locations $\hat{i}$ is model-based estimated by

$$E_{\hat{i}} = \frac{1}{n_\mathrm{T}} \sum_{j=1}^{n_\mathrm{T}} \frac{E_j}{r_j} \,, \tag{2}$$

where r_j is the radial transducer to AE-source grid location distance and E_j the AE-energy calculated at every transducer j. The estimated source energies are summed up into $0.5 \times 0.5\,\mathrm{mm}^2$ bins. Thereby, it can be shown that the energy of considered AE signals strongly focus on the NaCl triggered corrosion sites. Similar is found by photographic images of the cleaned corrosion sites after the experiment (rinsed with distilled water, cleaned with isopropyl alcohol and etched with nitric acid). Figure 3c shows the photographic image taken of DLT2 after the cleaning (scaled to the same area as the corrosion image detail). The corroded area (indicated by the light discoloration of the surface) of the photographic image at DLT2 and the area of increased AE-energy shown in the detail plot of the corrosion image correlate very well. However, in the distribution of energy, the AE-based corrosion image shows differences. Most of the AE-energy is allocated at the lower right boundary and partly outside of the initial DLT2. In addition, there are a number of hotspots in the AE-based corrosion image of DLT2 that are neither clearly distinguishable nor easy to assign in the photographic image. However, having a closer look to the photographic image in Figure 3c, small black dots can be found inside and outside the initial droplet area, indicating pitting corrosion. These are mainly concentrated at the lower boundary of the initial droplet, and thus, correlate well with the identified AE-energy hotspots. Remaining deviations in the location of these hotspots are within the range of localization accuracy and it is assumed that they are at least partly due to systematic localization errors [11]. Thus, pitting corrosion appears to be predominant at this site or at least to cause higher energy AE events.

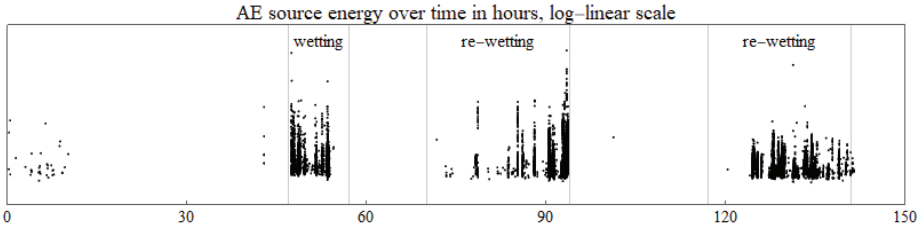

Figure 4: AE source energy allocated to DLT2 over time

5 FEATURE AND TIME DISCRETE CORROSION IMAGING

Time discrete corrosion images are believed to enable the evaluation of the time history of a corrosion site. Furthermore, corrosion type specific features could be used to create higher dimensional images that enable a better differentiation between the corrosion types involved. It is expected that crack propagation dominated corrosion types such as stress corrosion cracking and corrosion fatigue can be easily separated from purely chemical process driven corrosion types such as uniform area and pitting corrosion. However, literature results on the feature-based separation of AE-signals from uniform area and pitting corrosion of passivated steel seem promising to also differentiate between such corrosion types [5]. For further analysis of the AE data collected by the experimental setup presented in Figure 2a, signal features, like e.g., peak amplitude, rise time, duration, were plotted over time. Figure 4 shows exemplarily the source energy of the hits allocated to the location of DLT2 over time. Besides a small number of events, all hits are allocated in the periods of wet conditions at DLT2. Furthermore, no AE signals are detected in the early times of the re-wetting periods. This clearly shows the previously reported requirement of sufficient electrolyte on the surface to measure AE activity [7]. However, for further analysis, the corrosion images for the time intervals of the three wet periods are calculated and presented in Figure 5. Additionally, numerous typical AE signal feature combinations are plotted below the corresponding corrosion images. The time discretization into the three wet phases highlights new AE activity hotspots compared to Figure 3b, thereby demonstrating that time discretization provides more information on the corrosive process. A finding that was also reported in [12] for fixed time intervals of 0.5 hours. There, numerous additional AE activity hotspots were revealed compared to corrosion images that cumulate the energy over the whole experiment and exemplarily presented for DLT1. However, a meaningful clustering of AE events and their assignment to specific corrosion effects is still an open question. This question could not be solved with the application of advanced cluster algorithms, like e.g., k-means clustering and t-distributed stochastic neighbor embedding, that were fed by different combinations of the signal features presented in Figure 5. And also the manual trial-and-error imaging of visually slightly outstanding clusters (cf. Figure 5 duration over amplitude and rise time over amplitude) did not reveal relevant changes in the corrosion visualization. A more meaningful correlation of signals could be found by using the hit rate for signal clustering.

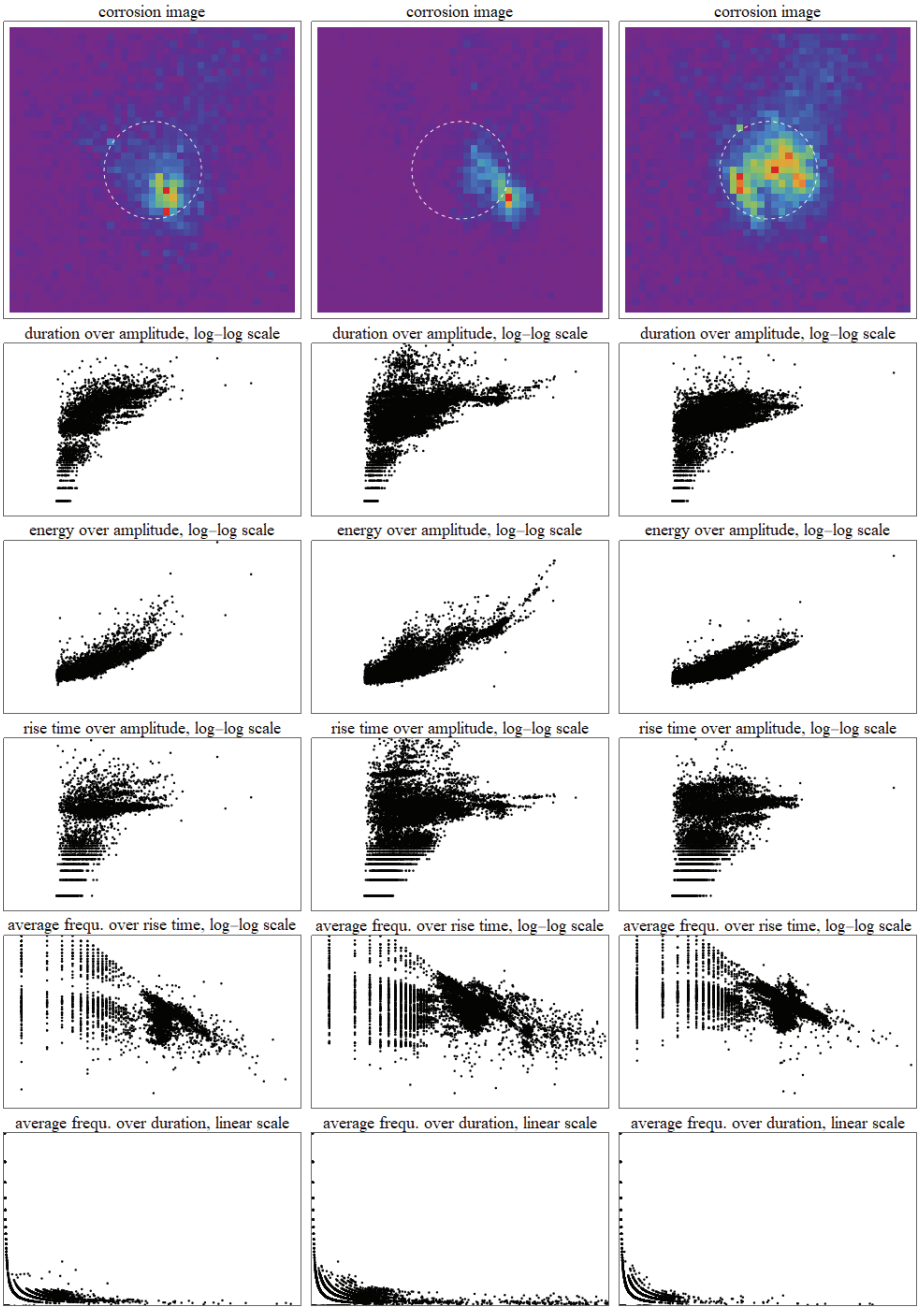

(a) 47-57 hours (b) 70-94 hours (c) 117-141 hours

Figure 5: Corrosion images of DLT2 and plots of different signal feature combinations, evaluated for the three periods of wet conditions, (a) wetting by NaCl droplet, (b) first, and (c) second re-wetting by high atmospheric humidity

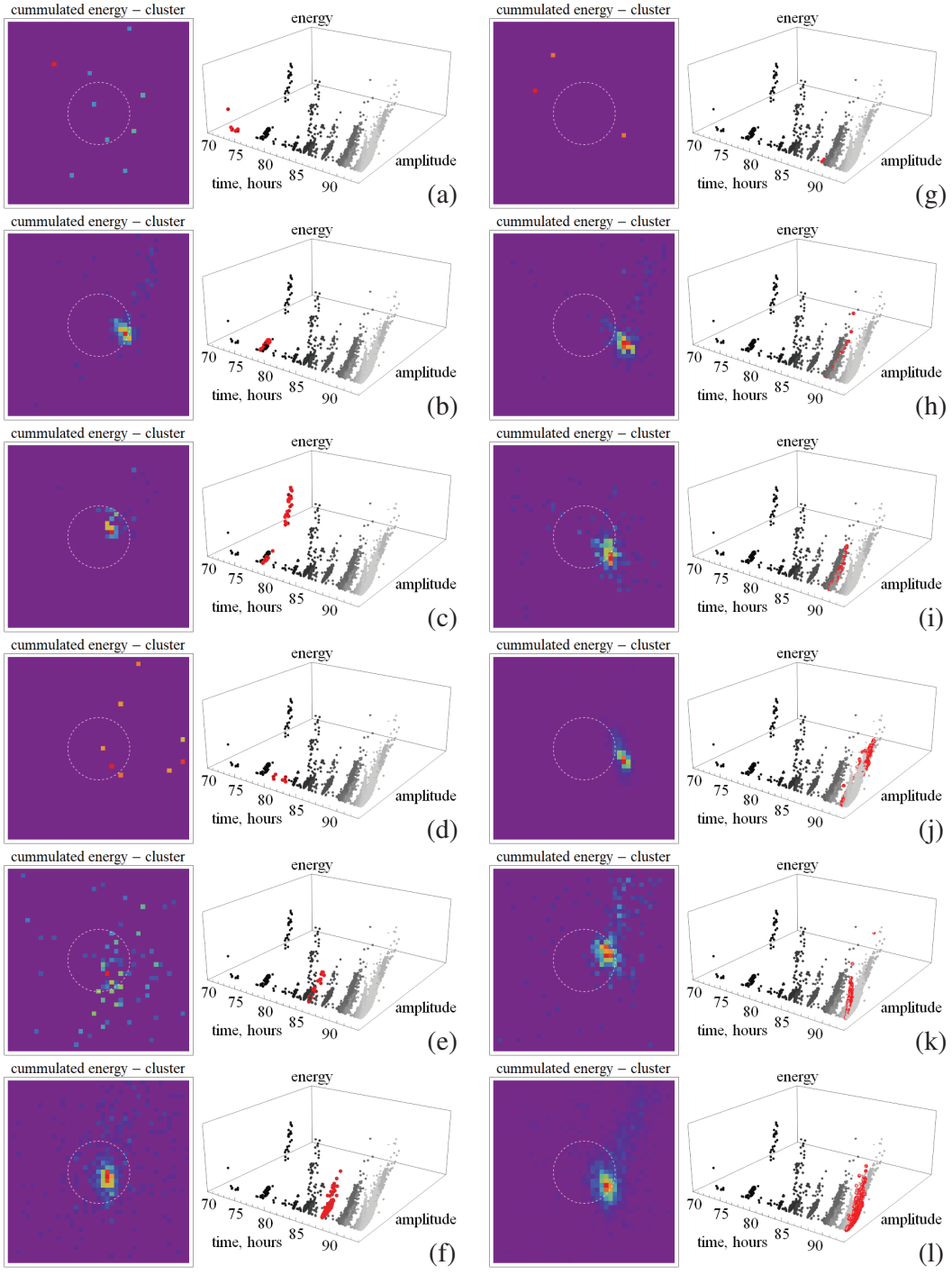

Figure 6: Corrosion images of hit clusters and corresponding energy over amplitude and time plot (linear scale) for first re-wetting period; grayscale indicates found clusters; red indicates signals used for the corrosion image

As visible in Figure 4, the number of hits per time continuously changes between phases of high and low hit rates. The "ClusteringComponents" algorithm of *Wolfram Mathematica 12.0* was used to identify hit clusters. The number of clusters was set to 66, which is the value of peaks found in a hit histogram (60 seconds bin size). The cumulation of the found hit clusters to AE-energy-based corrosion images shows that the signal sources are spatially close to each other. Figure 6 presents some examples of clusters with, (i) low hit rate and energy resulting in poor spatial correlation (cf. Figure 6adeg), and (ii) high hit rate and energy resulting in good spatial correlation (cf. Figure 6bcfhijkl), found at DLT2 through the period of the first re-wetting. The spatial cumulation of the signals is particularly good for high hit rates, and thus, large clusters. These also feature large signal amplitudes and energies. Low hit rate clusters often show signal source location scatter over the whole area of interest. This variation of the hit rate over time suggests that the observed corrosion initiates, propagates and expires again at various locations within the NaCl affected area. A finding that fits well to the atmospheric corrosion kinematics reported in [13] for a 99.9 % pure aluminum, where pit nucleation, growth and death are found to be a typical lifecycle and that one of its driving factors is the amount of electrolyte on the metal surface. Furthermore, the high energy clusters are predominantly found in the region where more pits are found and more electrolyte was observed visually during the experiment (cf. Figure 3 and also results for droplet 1 in [12]). In total this hit rate-based clustering approach identified 18 clusters with high and spatially localized AE activity. However, a direct assignment of visual pits to AE activity hotspots is not possible due to the number of pits and the given AE localization accuracy [11]. Nevertheless, pitting is highly expected to be the dominating source of the measured AE signals.

6 CONCLUSIONS

This article briefly presents an AE-based SHM concept for the full identification (up to SHM level 4) of atmospheric corrosion damage of aluminum alloys and the latest research results on the way to its realization. The concept uses model-based data fusion for signal filtering and accurate localization of AE sources for detailed visual representations of local corrosion sites. Furthermore, the concept takes advantage of the repetitive nature of the processes that drive corrosion to highlight relevant corrosion hotspots in these AE-based images of corrosion. Results from two different experimental setups show a significant accuracy increase by using the model-based AE source localization over standard methods. It is experimentally shown that this accuracy increase allows generating detailed AE-based images of local atmospheric corrosion sites. Particularly, the analysis of the corrosion time history is demonstrated to be of high value to separate different involved corrosion hotspots. Results suggest that very localized corrosion (like a pit) initiates, grows and dies in the interplay with the occurrence of electrolyte. This can be used to cluster related AE signals by the hit rate. The evaluated corrosion site is uniformly corroded over the whole area subjected to the NaCl solution and features numerous visually observable pits. Comparison of AE-based and photographic images of the corrosion sites suggest that the analyzed signals are mainly driven by very local corrosion processes, i.e., the formation of pits. Analyzed signal features do not allow comprehensive conclusions

on different corrosion types. Thus, it is highly expected that the measured AE signals are dominated by a single corrosion type, i.e., pitting.

However, further experimental analysis is required to clarify if the measured AE signals can be directly assigned to pitting or if there was uniform area corrosion involved and also to quantify the corrosion, e.g., by estimation of the volumetric loss. Nevertheless, it is expected that ML models trained on corrosion signal features and images of known corrosion sites, together with a priori knowledge of probable corrosion types and locations of the structure of interest, will already allow a probability-based identification of the damage at a corrosion site. However, this is left for future research.

REFERENCES

[1] C. Kralovec, A. Dengg, M. Schagerl, A. Schiller, C. Bisagni, M. Loebbecke, J. Haubrich, and R. Hanelt, "Static strength and fatigue life of pinned hybrid titanium-composite single-lap-shear joints," *Composite Structures*, vol. 354, p. 118765, 2025. [Online]. Available: https://doi.org/10.1016/j.compstruct.2024.118765

[2] Civil Aviation Authority, "CAP1570 corrosion and inspection of general aviation aircraft," 2017. [Online]. Available: https://www.caa.co.uk/publication/download/16188

[3] G. D. Davis, C. M. Dacres, and L. Krebs, "Eis-based in-situ sensor for the early detection of coatings degradation and substrate corrosion," in *Proceedings of the 55th annual Corrosion Conference, Orlando, Florida, USA*, ser. NACE CORROSION, 2000, pp. NACE–00 275. [Online]. Available: https://onepetro.org/NACECORR/proceedings-pdf/CORR00/All-CORR00/NACE-00275/1915555/nace-00275.pdf

[4] L. Fan and Y. Bao, "Review of fiber optic sensors for corrosion monitoring in reinforced concrete," *Cement and Concrete Composites*, vol. 120, p. 104029, 2021. [Online]. Available: https://doi.org/10.1016/j.cemconcomp.2021.1040290

[5] C. Jirarungsatian and A. Prateepasen, "Pitting and uniform corrosion source recognition using acoustic emission parameters," *Corrosion Science*, vol. 52, no. 1, pp. 187–197, 2010. [Online]. Available: https://doi.org/10.1016/j.corsci.2009.09.001

[6] F. Bellenger, H. Mazille, and H. Idrissi, "Use of acoustic emission technique for the early detection of aluminum alloys exfoliation corrosion," *NDT & E International*, vol. 35, no. 6, pp. 385–392, 2002. [Online]. Available: https://www.sciencedirect.com/science/article/pii/S0963869502000117

[7] T. Erlinger, C. Kralovec, and M. Schagerl, "Monitoring of Atmospheric Corrosion of Aircraft Aluminum Alloy AA2024 by Acoustic Emission Measurements," *Applied Sciences*, vol. 13, no. 1, 2022. [Online]. Available: https://doi.org/10.3390/app13010370

[8] T. Erlinger, C. Kralovec and M. Schagerl, "Acoustic emission-based structural health monitoring concept for corrosion of aluminum aircraft structures," in *Proceedings of the 35th European and 10th International Conference on Acoustic Emission Testing EWGAE 35 ICAE 10, Slovenia, Ljubljana*, ser. e-Journal of Nondestructive Testing (eJNDT), NDT.net, Ed., vol. 28, 2023. [Online]. Available: https://doi.org/10.58286/27628

[9] M. G. Sause, *In situ monitoring of fiber-reinforced composites: theory, basic concepts, methods, and applications*, ser. Springer Series in Material Science. Springer, 2016, vol. 242.

[10] S. Kalafat and M. G. Sause, "Acoustic emission source localization by artificial neural networks," *Structural Health Monitoring*, vol. 14, no. 6, pp. 633–647, 2015.

[11] T. Erlinger, C. Kralovec-Rödhammer, C. Humer, and M. Schagerl, "Impact of Model Knowledge on Acoustic Emission Source Localization Accuracy," in *Proceedings of the 36th Conference of the European Working Group on Acoustic Emission (EWGAE 2024), Potsdam, Germany*, ser. e-Journal of Nondestructive Testing (eJNDT) ISSN 1435-4934, NDT.net, Ed., vol. 29, 2024. [Online]. Available: https://doi.org/10.58286/30262

[12] T. Erlinger, C. Kralovec, M. Schagerl, and M. Ostermann, "Acoustic emission based corrosion imaging as a possible method for identification of localized atmospheric corrosion of aluminum structures," *Preprints*, 2025. [Online]. Available: https://doi.org/10.20944/preprints202504.2493.v1

[13] P. J. Noell, E. J. Schindelholz, and M. A. Melia, "Revealing the growth kinetics of atmospheric corrosion pitting in aluminum via in situ microtomography," *npj Materials Degradation*, vol. 4, no. 1, p. 32, 2020. [Online]. Available: https://doi.org/10.1038/s41529-020-00136-3

XI ECCOMAS Thematic Conference on Smart Structures and Materials - SMART 2025
M. Krommer, M. Nader and M. Schagerl (Eds)

Received: 28 March 2025 / Revised: 27 August 2025 / Accepted: 3 September 2025
© The Author(s) 2025

Optimized Placement of Distributed Optic Fiber Sensors for Structural Health Monitoring via the Modified Constitutive Relation Error

José Andrés Pérez Orozco, Ludovic Chamoin, Julien Cortial, Maya de Buhan, Bruno Soulier

Abstract. In Structural Health Monitoring (SHM), sensor integration within materials is crucial. This paper introduces an Optimal Sensor Placement method using the modified Constitutive Relation Error (mCRE) functional. Unlike classical functionals, mCRE searches for structural parameters alongside mechanical fields, leveraging measured data and physical knowledge without further assumptions. The approach integrates mCRE with Bayesian inference to create a new Fisher Information Matrix (FIM) sensitive to updated parameters. The study emphasizes Distributed Optical Fiber Sensors for their embedded sensing capability, high spatial accuracy, and lightweight nature, providing near 1D full-field data. These fibers are modeled with B-Splines, and their placement is optimized using Differential Evolution considering constraints like fiber length and curvature. The methodology is validated using a linear elastic material benchmark, outperforming traditional FIM techniques.

Key words: Optimal Sensor Placement, Fisher Information Matrix, Structural Health Monitoring, Inverse Problems, Modified Constitutive Relation Error, B-Splines Representation

1 INTRODUCTION

Structural Health Monitoring (SHM) combined with data assimilation is increasingly used to assess structural integrity via onboard sensors [1]. This work focuses on a crucial factor in SHM, namely, optimal sensor placement [2, 3, 4, 5], to ensure that the most informative data is collected. Among various sensor types, Distributed Optical Fiber Sensors (DOFS) have gained interest due to their spatial accuracy, lightweight nature, and ability to provide near-continuous strain data [6]. Unlike discrete sensors, DOFS integrate all sensing points along a single fiber, requiring novel placement strategies.

José Andrés Pérez Orozco & Julien Cortial & Maya de Buhan
Safran Tech, Digital Sciences & Technologies Rue des Jeunes Bois, Châteaufort, 78114 Magny-Les-Hameaux, France, e-mail: jose-andres.perez-orozco@safrangroup.com

José Andrés Pérez Orozco & Ludovic Chamoin & Bruno Soulier
Université Paris Saclay, CentraleSupélec, ENS Paris-Saclay, CNRS, LMPS, 4 avenue des Sciences, Gif-sur-Yvette, 91190, France

Two of the popular DOFS technologies include Rayleigh backscattering and Fiber Bragg grating. Both measure the mechanical strain with great accuracy, but Rayleigh naturally provides near-continuous data, whereas Bragg grating requires physical modifications at sensing locations. Rayleigh is limited to $\sim$100m, while Bragg grating can span multiple kilometers [7]. Most sensor placement methods involve selecting locations from a candidate set, with differences in cost functions and optimization techniques [6]. However, DOFS pose unique challenges since a single fiber must be optimally routed. Few studies address this challenge; for instance: Li et al. [6] used genetic algorithms to optimize fiber layout using NURBS and maximizing the integration of a weighted functional of strain measures over the optic fiber length. Others works focused on modal shape reconstruction [2] and impact damage detection [8].

Fisher Information Matrix (FIM)-based criteria [9, 10] are widely used for sensor optimization, with common metrics including trace (A-optimality) [5] and determinant (D-optimality) [4, 3]. This work introduces a modified FIM (mFIM) tailored to the modified Constitutive Relation Error (mCRE), a robust inverse problem framework in structural mechanics. The mCRE offers improved convexity [11, 12] and noise resilience [13, 14, 15], yet its use to define various sensor placement metrics remain unexplored, except for recent work by Diaz et al. in the domain of low-frequency dynamics [16].

Here, the determinant of the mFIM is used to optimize DOFS placement via differential evolution, with constraints on length and curvature. B-Splines model the fiber path, and numerical tests show that the mFIM outperforms traditional FIM, enhancing robustness to noise, misalignment, and modeling bias. The paper is structured as follows: Section 2 introduces inverse problems, covering stochastic solution approaches and their connection to Fisher Information-based sensor performance metrics. Section 3 presents the modified Constitutive Relation Error (mCRE) and its associated Fisher Information Matrix. Given the focus on optic fiber sensors, Section 4 outlines key considerations for their optimization. Finally, Section 5 showcases test results for 2D linear orthotropic elasticity cases.

2 Classical sensor performance metrics based on Fisher Information

2.1 Basics on inverse problems

In computational mechanics, inverse problems determine unknown input parameters $\theta \in \mathbb{R}^p, p \in \mathbb{N}$ from limited, noisy observations $X_{obs} \in \mathbb{R}^{N_S}$. However, these observations differ from model predictions due to measurement noise (ω_{obs}) or modelling errors (ω_{mod}):

$$X_{obs} = \Pi X(\theta_{real}) + \omega_{obs} + \omega_{mod} \tag{1}$$

where Π is an interpolation matrix to extract information at the sensor locations. Inverse problems can be solved deterministically or stochastically. The latter approach is preferred as it naturally accounts for parameter uncertainties. Bayesian inference provides a probabilistic framework for this objective:

$$\pi(\theta|X_{obs}) \propto \pi(X_{obs}|\theta)\pi_0(\theta) \tag{2}$$

where $\pi_0(\theta)$ is the prior distribution, $\pi(X_{obs}|\theta)$ is the likelihood distribution, and $\pi(\theta|X_{obs})$ is the updated or posterior probability density function on θ after taking observations into account (and the solution to the inverse problem). Considering Gaussian distributions, $\pi_0(\theta)$ and $\pi(X_{obs}|\theta)$ have the form:

$$\pi_0(\theta) \propto exp\left[-\frac{1}{2}(\theta-\theta_0)^T\Sigma_0^{-1}(\theta-\theta_0)\right] \tag{3}$$

$$\pi(X_{obs}|\theta) \propto exp\left[-\frac{1}{2}(X_{obs}-\Pi X(\theta))^T[\Sigma_{mod}+\Sigma_{obs}]^{-1}(X_{obs}-\Pi X(\theta))\right] \tag{4}$$

where θ_0 contains *a priori* parameter values, and Σ_0, Σ_{mod} and Σ_{obs} respectively denote the prior, model, and observation covariance matrices.

2.2 Fisher Information Matrix and optimal sensor placement

The optimal sensor placement problem aims to minimize uncertainty in identified parameters of an inverse problem. This uncertainty can be directly assessed using the parameter covariance matrix or, more commonly, the Fisher Information Matrix (FIM). The FIM quantifies the amount of information that a random variable contains about a given parameter, and its inverse provides the Cramér-Rao lower bound on the parameter covariance matrix [9]. This implies that a higher Fisher Information leads to lower uncertainty in parameter estimates. As a result, scalar performance metrics derived from the FIM are widely used, particularly the maximization of its determinant (D-optimality) [4, 2, 10, 17].

The FIM is computed as the covariance of the score, the gradient of the log-likelihood distribution with respect to θ [9]:

$$FIM = \mathbb{E}\left[\left(\frac{\partial log\pi(X_{obs}|\theta)}{\partial\theta}\right)^T\left(\frac{\partial log\pi(X_{obs}|\theta)}{\partial\theta}\right)\Bigg|_{\theta_{opt}}\right] \tag{5}$$

In this context, $\mathbb{E}$ denotes the mathematical expectation. Alternatively, if the Hessian of the log-likelihood is available, it yields [18]:

$$FIM = -\mathbb{E}\left[\frac{\partial^2 log\pi(X_{obs}|\theta)}{\partial\theta^2}\Bigg|_{\theta_{opt}}\right] \tag{6}$$

It is then clear that the Hessian of the log likelihood plays a big role in the uncertainty quantification for parameter identification. Intuitively, in the case of one parameter, a high curvature in the distribution around the identified parameter translates to a lower variance. For a Gaussian likelihood (4), if the modelling errors are disregarded, and assuming uncorrelated observation errors with equal variance σ^2_{obs}, the FIM is given by the following expression:

$$FIM = \frac{1}{\sigma^2_{obs}}\left(\Pi\frac{\partial X(\theta)}{\partial\theta}\right)^T\left(\Pi\frac{\partial X(\theta)}{\partial\theta}\right)\Bigg|_{\theta_{opt}} \tag{7}$$

It is important to note that this matrix only depends on the sensor locations, as Π extracts information only at the observation points. A sensor configuration that maximizes the FIM's determinant ensures that all principal directions of the FIM have a high information content, making it less sensitive to slight variations in the observation values, and leading to more precise parameter estimate. These variations may result from noise in the measurement instrument or small displacements of the sensors relative to their theoretically optimal positions.

3 The modified Constitutive Relation Error

In structural mechanics, the forward problem determines the displacement field u typically approximated by a finite element solution u_h while the inverse problem estimates constitutive parameters θ. Among various inverse approaches, the modified Constitutive Relation Error (mCRE) stands out for its convexity properties [11, 12] and robustness to noise [13, 14, 15]. Extending the Constitutive Relation Error (CRE) [19], the mCRE balances model confidence with experimental data U_{obs}, forming a hybrid framework for parameter identification.

In the context of linear elasticity and following a discretization with the finite element method, the discretized CRE reads:

$$\mathcal{E}^{2^h}_{CRE}(\hat{U},\hat{V};\theta) = \frac{1}{2}(\hat{U}-\hat{V})^T\mathbb{K}(\hat{U}-\hat{V}) \tag{8}$$

where $(\hat{U},\hat{V})$ represents a pair of kinetically and statically admissible solutions. The CRE (8), quantitatively reflects the confidence on modeling, and is commonly referred in the literature to as the distance to model. Extending this, the mCRE [20, 21] introduces a data-driven regularization term referred to as the distance to data:

$$\mathcal{E}^{2^h}_{mCRE}(\hat{U},\hat{V};\theta) = \underbrace{\mathcal{E}^{2^h}_{CRE}(\hat{U},\hat{V};\theta)}_{\text{Distance to model}} + \underbrace{\frac{\alpha}{2}\left(\Pi\hat{U}-U_{obs}\right)^T\mathbb{G}_{obs}\left(\Pi\hat{U}-U_{obs}\right)}_{\text{Distance to data}} \tag{9}$$

where $\mathbb{G}_{obs}$ scales measurement errors, and α balances model fidelity against data fit. The optimal θ minimizes this functional:

$$\theta_{opt} = \underset{\theta}{\operatorname{argmin}}\left[\min_{(\hat{U},\hat{V})} \quad \mathcal{E}^{2^h}_{mCRE}(\hat{U},\hat{V};\theta)\right] \tag{10}$$

This optimization problem is solved iteratively: first, $(\hat{U},\hat{V})$ are determined through the following saddle point conditions:

$$\begin{aligned}(\alpha(\Pi^T\mathbb{G}_{obs}\Pi)+\mathbb{K})\hat{U} &= \alpha(\Pi^T\mathbb{G}_{obs})U_{obs}+F\\ \mathbb{K}\hat{V} &= F\\ \hat{V} &= \hat{U}+\Lambda\end{aligned} \tag{11}$$

where Λ is a Lagrange multiplier, and then θ is updated using convex minimization techniques [21]. It is emphasized that $\hat{U}$ is a hybrid quantity, based on the model and the experimental data.

3.1 Stochastic interpretation

To relate the mCRE and the Fisher Information Matrix, a Bayesian interpretation of the mCRE is needed, which was developed by Deraemaeker and Ladevèze [22]. Within this framework, the mCRE-based likelihood distribution reads:

$$\pi(U_{obs}|\theta) \propto exp\left[-\frac{1}{2}\left(\Pi\hat{U} - U_{obs}\right)^T \Sigma_{obs}^{-1}\left(\Pi\hat{U} - U_{obs}\right) - \frac{1}{2\alpha}(\hat{U}-\hat{V})^T\mathbb{K}(\hat{U}-\hat{V})\right] \quad (12)$$

This distribution is visibly more complex than the one previously mentioned in (4). However, no assumption on the modelling error covariance (Σ_{mod}) has to be made since the modelling error is already integrated in the distribution. When $\mathbb{G}_{obs} = \Sigma_{obs}^{-1}$ and considering a uniform prior defined in the interval $\theta \in [a,b]$, we get:

$$\pi(\theta|U_{obs}) \propto \begin{cases} \pi(U_{obs}|\theta) \propto exp\left[-\frac{1}{\alpha}\mathcal{E}_{mCRE}^2\right] & \theta \in [a,b] \\ 0 \quad \theta \notin [a,b] \end{cases} \quad (13)$$

The interval of the prior can even be $\theta \in [-\infty, \infty]$. In this case, maximum *a posteriori* estimator of (13) equals the maximum *likelihood* estimator of (12) and corresponds to the minimizer of the deterministic cost function of the mCRE (10)[21].

3.2 FIM based on the mCRE

With the theory behind the mCRE established, attention can now be directed to its Fisher Information Matrix, referred to as the modified FIM (mFIM) to distinguish it from earlier developments. Following the classical FIM formulation (5) poses a computational challenge: its expectation involves third and fourth moments (skewness and kurtosis), which are difficult to evaluate. This complexity becomes particularly problematic when maximizing the determinant of the modified FIM using a stochastic optimization algorithm like differential evolution, as it requires numerous matrix computations. To overcome this issue, the second derivative formulation of the FIM (6) is employed, leading to:

$$mFIM = \frac{1}{\alpha}\left(\hat{U}^{0^T}\frac{\partial\mathbb{K}}{\partial\theta}\frac{\partial\hat{U}^0}{\partial\theta} - \hat{V}^T\frac{\partial\mathbb{K}}{\partial\theta}\frac{\partial\hat{V}}{\partial\theta}\bigg|_{\theta_{opt}}\right) \quad (14)$$

Here, the zero superscript in $\hat{U}^0$ refers to the constant portion of $\hat{U}$. Parallels can be drawn between the modified Fisher Information Matrix (mFIM) (14) and the original Fisher Information Matrix (FIM) (7), as both quantify sensitivity with respect to θ. However, while traditional

methods rely on local evaluations at sensor positions using the projection matrix Π, the mFIM instead evaluates global quantities by incorporating the complete fields $\hat{U}$ and $\hat{V}$, along with their sensitivities to θ. This distinction is directly tied to the nature of the mCRE admissible fields, which are data enriched as seen in (11).

4 Optimization problem

FIM based sensor placement strategies can be generalized for various types of sensors, but additional considerations are needed for optic fiber sensors. These sensors measure strain along their longitudinal direction at N_S positions, and while optimizing the coordinates and orientations of each sensing point is possible, it becomes impractical when N_S can reach thousands, especially in Rayleigh Backscattering fibers, which provide near-continuous data [7].

To address this, the fiber's shape is parameterized using B-Splines, significantly reducing the number of optimization variables. Uniform B-Splines require only $N \ll N_S$ control polygon coordinates to define the curve. Considering that CP is a vector containing the control polygon coordinates, the optimization problem thus reads:

$$\begin{aligned} CP_{opt} &= \underset{CP}{\operatorname{argmin}} -det(\mathbf{M}) \quad M \in [FIM, mFIM] \\ &s.t. \\ \text{Fiber length constraint: } & L \leq L_{Lim} \\ \text{Curvature radius constraint: } & C \geq C_{Lim} \end{aligned} \tag{15}$$

To solve (15) using a differential evolution algorithm, the following cost (or fitness) function is introduced:

$$f = -det(\mathbf{M}) \times k^{-max\left(\frac{L}{L_{lim}}, 1\right)+1} \times k^{-max\left(\frac{C_{lim}}{C}, 1\right)+1} \tag{16}$$

where k is a constant that determines the severity of the penalization, determined empirically to a value of 4 during this work.

5 Sensor placement results

The mFIM (14) serves as an uncertainty indicator in inverse problems using the mCRE. Its effectiveness as a sensor performance metric is now evaluated against the classical FIM (7) using a simple mechanical test case, a 2D plate subjected to a tensile load (Figure 1). The plate is made of a linear, homogeneous, orthotropic material. The plate is subjected to a tensile load, with material properties defined as: Young's moduli $E_1 = E_2 = 1$ Pa, Poisson's ratio $\mu = 0.3$. A tensile load of 0.01 Pa is applied as a Neumann boundary condition on Γ_{N1}, while zero displacement is imposed on Γ_D. Measurement noise is set at 5% to compute $\mathbb{G}_{obs}$.

These constitutive parameters lead to a displacement equivalent to that obtained using an isotropic constitutive law, but the sensitivity of the Young modulus in each direction can be evaluated independently. Setting the same value for E_1 and E_2 ensures that the sensitivity fields

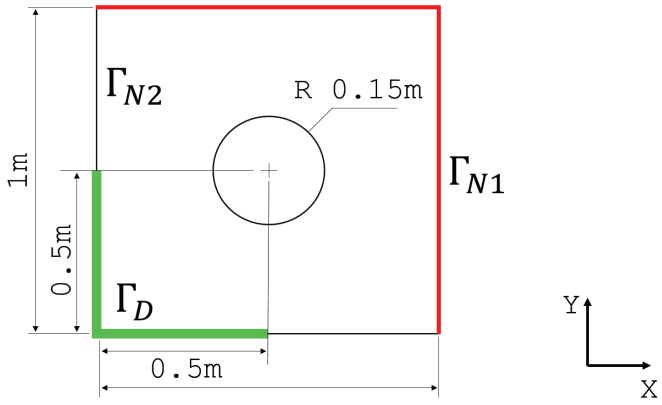

Figure 1: Boundary conditions for the orthotropic case

remain of comparable magnitude, thereby avoiding a bias in the sensor placement towards the identification of a single parameter. The influence of different ratios between E_1 and E_2 on the optimal fiber sensor configuration was analyzed in [23]. The magnitude of the displacement sensibilities ($\partial U/\partial\theta, \theta \in [E_1, E_2]$) can be seen in Figure 2.

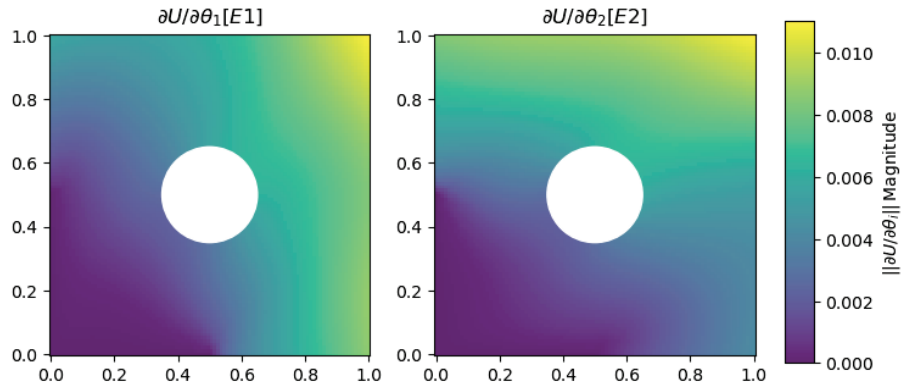

Figure 2: Displacement sensibility with respect to E_1 and E_2

The objective now is to determine the optimal placement of the fiber sensor for the simultaneous identification of E_1 and E_2 using the mCRE approach. The optic fiber is constrained to start on Γ_D, with a maximum length of 3.5m and a minimum curvature radius of 0.01m. The optimization problem is solved using a differential evolution algorithm with a Sobol-distributed initial population, 1000 iterations, a recombination probability of 0.7, and a mutation factor varying between 1.1 and 1.9 (empirically determined, as is typical for global optimization algorithms).

The final shapes that result from the optimization process using the FIM and the mFIM and

the posterior distributions obtained with each sensor configuration are shown in Figure 3. The modified FIM yields a superior sensor configuration for the mCRE, providing lower variance in the identified parameter, which we can verify numerically through the Hessian of the mCRE. The relative improvement is included in Table 1.

As shown in [23], the classical FIM tends to maximize parameter sensitivity along the fiber path, which explains the presence of multiple loops or clusters in regions of high sensitivity. In contrast, the mFIM accounts for global structural quantities and, rather than enhancing local sensitivity, it aims to minimize the overall magnitude of the global sensitivity of the hybrid field associated with the mCRE ($\partial\hat{U}/\partial\theta$).

This intuition can be clarified through two limiting cases. First, when $\partial\hat{U}/\partial\theta \to 0$, the hybrid field becomes insensitive to the parameter, which corresponds to a scenario where observation values are prescribed throughout the structure, achievable when $\alpha \to \infty$ and sensors are densely distributed everywhere. Second, when $\partial\hat{U}/\partial\theta \to \partial U/\partial\theta$, the hybrid field coincides with the physical field due to the absence of observational data, either because no sensors are placed or $\alpha = 0$.

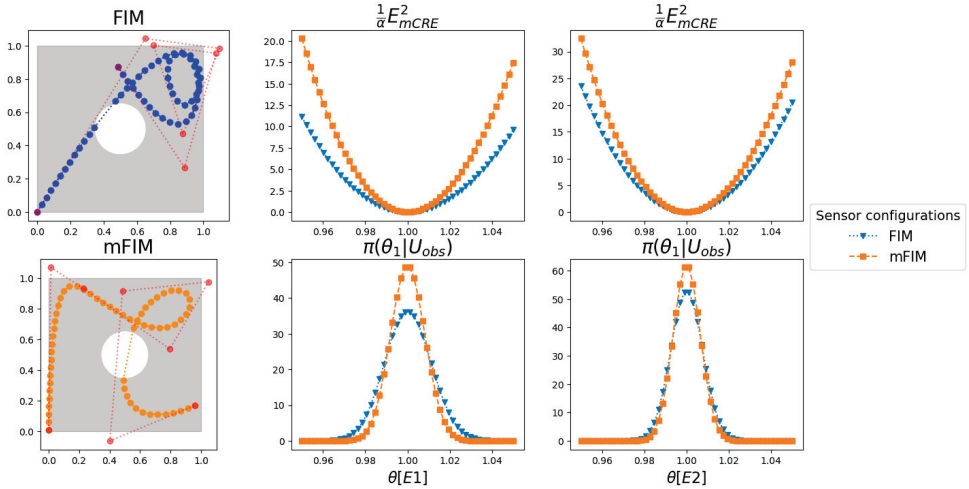

Figure 3: mCRE and posterior distribution curves

Table 1: Improvement in Hessian of the mCRE (compared to the sensor configuration obtained using the FIM)

Improvement using mFIM	
E_1	E_2
45 %	27 %

5.1 Introduction of modeling error

So far, the data has been generated numerically by adding Gaussian noise to the finite element response. However, the mCRE allows incorporating modeling errors, such as discretization errors or deviations in the constitutive law. To account for discretization errors, two different meshes are used: a coarse mesh for the model and a finer mesh, better suited to capture stress concentrations near the hole, for generating the data (Figure 4). The noise level remains at 5%.

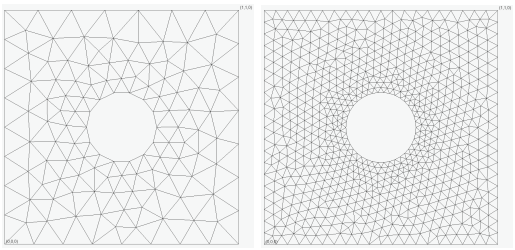

Figure 4: Coarse mesh used for the model and fine mesh used to generate the data

Figure 5 compares the optimized sensor placements using FIM and mFIM, along with their corresponding posterior distributions. The fiber configuration optimized using the classical FIM remains unchanged, as it does not account for modeling errors. In contrast, the modified FIM once again yields a superior sensor placement for the mCRE, effectively reducing the variance in the identified parameters. This improvement, quantified via the Hessian of the mCRE, is detailed in Table 2. Notably, the optimal parameter estimate is no longer centered at 1, as the model is now fitted using a coarser mesh. However, the mFIM successfully identifies a sensor configuration that shifts the estimate closer to the true value of 1.

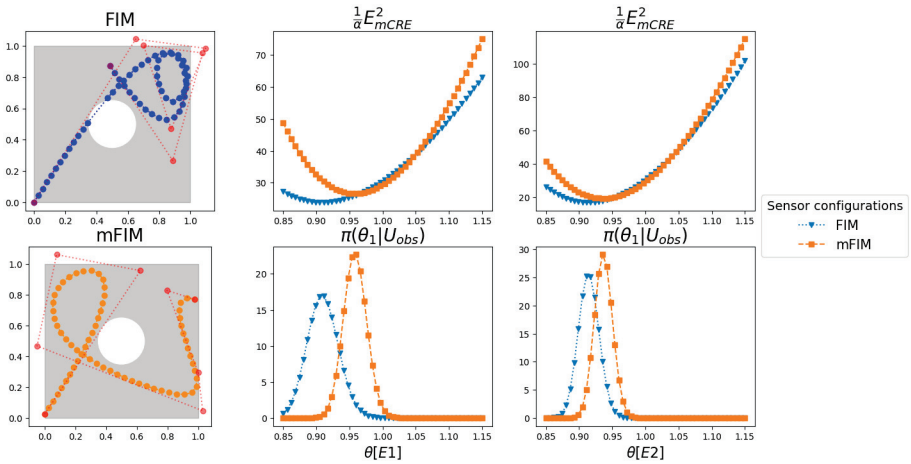

Figure 5: mCRE and posterior distribution curves

Table 2: Improvement in Hessian of the mCRE using different meshes (compared to the sensor configuration obtained using the FIM)

Improvement using mFIM	
E_1	E_2
34 %	17 %

6 Conclusions

This work leads to several key conclusions. For parameterizing the optical fiber in a 2D plane, B-Splines prove efficient, requiring only control point coordinates—unlike other methods [8, 2], which also demand derivative values for interpolation.

For optimal sensor placement, metrics based on the Fisher Information Matrix (FIM) are reliable, as they directly relate to the variance of identified parameters and depend on sensor configuration. The modified FIM (mFIM), introduced in this work (see Eq. 14), serves as a tailored performance indicator for the modified Constitutive Relation Error (mCRE). It also allows direct integration of modeling errors and measurement noise into the placement strategy. While the classical FIM is a local indicator, the mFIM captures the global sensitivity of the mCRE fields.

The main drawback of the mFIM is the computational cost of evaluating the admissible fields $\hat{U}$ for each sensor configuration. However, this can be mitigated through parallelizable optimization algorithms like differential evolution, model order reduction techniques, and improvements in solving the underlying linear systems. For instance, isolating sensor-dependent terms via the Sherman-Morrison-Woodbury formula [24] offers a promising direction. These aspects are subjects of ongoing research.

While this study focused on the theoretical and numerical foundations of the mFIM for sensor placement, future work will explore its application to real-world composite monitoring for damage detection. This includes addressing physical constraints such as manufacturing variability and sensor integration during layup, as well as defining operational limits, e.g., maximum detectable damage size, strain resolution, and sensor survivability, to enable a full SHM solution for advanced composite structures.

REFERENCES

[1] C. R. Farrar and K. Worden, "An introduction to structural health monitoring," *Philosophical Transactions of the Royal Society A: Mathematical, Physical and Engineering Sciences*, vol. 365, no. 1851, pp. 303–315, 2007.

[2] G. Cazzulani, M. Chieppi, A. Colombo, and P. Pennacchi, "Optimal sensor placement for continuous optical fiber sensors," in *Sensors and Smart Structures Technologies for Civil, Mechanical, and Aerospace Systems 2018*, vol. 10598. SPIE, 2018, pp. 970–981.

[3] C. Papadimitriou, "Optimal sensor placement methodology for parametric identification of structural systems," *Journal of sound and vibration*, vol. 278, no. 4-5, pp. 923–947, 2004.

[4] D. C. Kammer and M. L. Tinker, "Optimal placement of triaxial accelerometers for modal vibration tests," *Mechanical systems and signal processing*, vol. 18, no. 1, pp. 29–41, 2004.

[5] F. E. Udwadia, "Methodology for optimum sensor locations for parameter identification in dynamic systems," *Journal of engineering mechanics*, vol. 120, no. 2, pp. 368–390, 1994.

[6] J. Li, R. K. Kapania, and W. B. Spillman Jr, "Placement optimization of distributed-sensing fiber optic sensors using genetic algorithms," *AIAA journal*, vol. 46, no. 4, pp. 824–836, 2008.

[7] L. Chamoin, S. Farahbakhsh, and M. Poncelet, "An educational review on distributed optic fiber sensing based on rayleigh backscattering for damage tracking and structural health monitoring," *Measurement Science and Technology*, vol. 33, no. 12, p. 124008, 2022.

[8] S. Ameduri, M. Ciminello, I. Dimino, A. Concilio, A. Catignani, and R. Mancinelli, "Distributed sensor placement optimization for computer aided structural health monitoring," *Archive of Mechanical Engineering*, vol. 66, no. 1, pp. 111–127, 2019.

[9] J. A. Sharp, A. P. Browning, K. Burrage, and M. J. Simpson, "Parameter estimation and uncertainty quantification using information geometry," *Journal of the Royal Society Interface*, vol. 19, no. 189, p. 20210940, 2022.

[10] G. F. Gomes, S. S. da Cunha, P. da Silva Lopes Alexandrino, B. Silva de Sousa, and A. C. Ancelotti, "Sensor placement optimization applied to laminated composite plates under vibration," *Structural and Multidisciplinary Optimization*, vol. 58, pp. 2099–2118, 2018.

[11] W. Aquino and M. Bonnet, "Analysis of the error in constitutive equation approach for time-harmonic elasticity imaging," *SIAM Journal on Applied Mathematics*, vol. 79, no. 3, pp. 822–849, 2019.

[12] S. Andrieux, "Bregman divergences for physically informed discrepancy measures for learning and computation in thermomechanics," *Comptes Rendus. Mécanique*, vol. 351, no. G1, pp. 59–81, 2023.

[13] P. Feissel and O. Allix, "Modified constitutive relation error identification strategy for transient dynamics with corrupted data: The elastic case," *Computer methods in applied mechanics and engineering*, vol. 196, no. 13-16, pp. 1968–1983, 2007.

[14] P.-E. Charbonnel, P. Ladevèze, F. Louf, and C. Le Noach, "A robust cre-based approach for model updating using in situ measurements," *Computers & Structures*, vol. 129, pp. 63–73, 2013.

[15] P. Ladevèze and D. Leguillon, "Error estimate procedure in the finite element method and applications," *SIAM Journal on Numerical Analysis*, vol. 20, no. 3, pp. 485–509, 1983.

[16] M. Diaz, P.-É. Charbonnel, and L. Chamoin, "Merging experimental design and structural identification around the concept of modified constitutive relation error in low-frequency dynamics for enhanced structural monitoring," *Mechanical Systems and Signal Processing*, vol. 197, p. 110371, 2023.

[17] G. F. Gomes, F. A. de Almeida, P. da Silva Lopes Alexandrino, S. S. da Cunha, B. S. de Sousa, and A. C. Ancelotti, "A multiobjective sensor placement optimization for shm systems considering fisher information matrix and mode shape interpolation," *Engineering with Computers*, vol. 35, pp. 519–535, 2019.

[18] E. L. Lehmann and G. Casella, *Theory of point estimation*. Springer Science & Business Media, 2006.

[19] P. Ladevèze and L. Chamoin, "The constitutive relation error method: A general verification tool," *Verifying Calculations-Forty Years On: An Overview of Classical Verification Techniques for FEM Simulations*, pp. 59–94, 2016.

[20] P. Ladevèze and A. Chouaki, "Application of a posteriori error estimation for structural model updating," *Inverse problems*, vol. 15, no. 1, p. 49, 1999.

[21] H. N. Nguyen, "Nouvelles strategies numeriques pour identification robuste, coherente et efficace de modeles a partir de mesures de champs," Ph.D. dissertation, Universite Paris-Saclay, 2021.

[22] A. Deraemaeker, P. Ladevèze, and T. Romeuf, "Model validation in the presence of uncertain experimental data," *Engineering computations*, vol. 21, no. 8, pp. 808–833, 2004.

[23] J. A. P. Orozco, L. Chamoin, J. Cortial, M. de Buhan, and B. Soulier, "Optimal placement of distributed optic fiber sensors with the modified constitutive relation error," *Mechanical Systems and Signal Processing*, vol. 238, p. 113206, 2025.

[24] B. Marchand, L. Chamoin, and C. Rey, "Parameter identification and model updating in the context of nonlinear mechanical behaviors using a unified formulation of the modified constitutive relation error concept," *Computer Methods in Applied Mechanics and Engineering*, vol. 345, pp. 1094–1113, 2019.

XI ECCOMAS Thematic Conference on Smart Structures and Materials - SMART 2025
M. Krommer, M. Nader and M. Schagerl (Eds)

Received: 22 April 2025 / Revised: 29 August 2025 / Accepted: 3 September 2025
© The Author(s) 2025

Lessons Learned in Developing a Convolutional Neural Network to Identify Damage Modes in Type-IV Composite Overwrapped Pressure Vessels

Finja Carlotta Rentzsch Holm, Tobias Schalm, Finn Eggers, Kai-Uwe Schröder

Abstract. Fiber composite structures are susceptible to various difficult-to-predict damage modes, including delamination, matrix cracking, and fiber breakage. The reliable identification of both, damage mode and location within the composite presents a distinctly complex challenge in Structural Health Monitoring. This work explores this challenge using Composite Overwrapped Pressure Vessels (COPVs) with surface-strain monitoring as a case study. Thereby, Convolutional Neural Networks (CNNs) are utilised for damage localisation and identification as they are particularly suited to process the emergent grid-like sensor data and to match a deviation in the surface-strain field to the corresponding damage states. The surface strain data used for supervised learning in this study is extracted from a finite element model for both an undamaged reference state and various damage conditions. These damage conditions consist of fibre breakage and matrix cracking, which are numerically modelled for different damage sizes and relative positions along the tank's main axis. The CNN used in this work is based on the U-Net architecture first introduced by Ronneberger et al. This study discusses the key lessons learned during the development of the CNN, including the choice of input data, suitable network architectures, training strategies, the impact of sensor spacing on performance, and challenges related to repeatability and generalisability.

Key words: Convolutional Neural Networks (CNNs), Smart Structures, Damage State Identification, Structural Health Monitoring (SHM), Hydrogen Pressure Vessels, Composite Overwrapped Pressure Vessels (COPVs)

1 INTRODUCTION

According to the European Green Deal [1], carbon neutrality within the EU shall be achieved by 2050. Renewable hydrogen is considered an essential energy vector towards decarbonisation of the transportation sector. In addition to production, transportation and utilization, hydrogen storage represents a critical link to the industrial chain for hydrogen energy production. Regarding hydrogen storage equipment and fuel cell vehicles, high-pressure storage tanks for gaseous

Finja Carlotta Rentzsch Holm & Tobias Schalm & Finn Eggers & Kai-Uwe Schröder
Institute of Structural Mechanics and Lightweight Design, RWTH Aachen University, Wüllnerstraße 7, 52062 Aachen, Germany, e-mail: finja.carlotta.rentzsch.holm@rwth-aachen.de

hydrogen have prevailed over solid- and liquid-state based methods. In gaseous hydrogen storage, Type IV Composite Overwrapped Pressure Vessels (COPVs) continuously gain popularity due to superior mass storage efficiency of composite structures in comparison with those made of metallic alloys [2]. However, manufacturing costs will have to be reduced significantly to make hydrogen-powered road, water, and air vehicles competitive and to achieve the necessary economies of scale for broad market penetration. One cost driver is material costs, especially the carbon composite used in Type IV COPVs [3]. As a result of uncertainties related to the material properties, manufacturing and potentially in-service loads, COPVs tend to be overdimensioned. In this context, in-service Structural Health Monitoring (SHM) has the potential to greatly increase the confidence in COPVs, ultimately enabling lighter designs. Furthermore, SHM can help to transfer from a *Safe-Life (no damage during lifetime)* design philosophy to a *Fail Safe* and *Damage Tolerance* philosophy, improving efficiency while retaining or even improving reliability and safety when compared to a traditional Safe-Life philosophy. [4, 5, 6, 7]

Common SHM measurement concepts include strain-based, vibration-based and ultrasound-based methods. Strain-based methods are typically employed for static or quasi-static load conditions and based on the idea, that damage locally redirects the load path, leading to a measurable strain redistribution [5]. Common strain sensor technologies include electrical strain gauges and fiber optic sensors. For COPV monitoring, fiber optic sensors are particularly well suited as they can be easily embedded during the winding process. With multiple sensor positions integrated in a single optical fiber, fiber optic sensors also require significantly less cabling effort than strain gauges. Multiple works found in published literature have leveraged strain-sensing based on fiber optic sensors for health or load monitoring of Type IV COPVs [8, 9, 10, 11].

When analysing strain data, Artificial Neural Networks (ANNs) offer a potent tool to handle the complexity arising from the structure itself and its various possible damage modes, as well as uncertainties related to manufacturing, material properties, and loading conditions. This work describes an approach for damage detection, localization and identification based on Convolutional Neural Networks (CNNs) and the lessons learned during implementation.

2 THEORETICAL FOUNDATIONS

CNNs are a subset of ANNs and designed to process grid-structured input data with strong spatial dependencies (e.g. image data). For this work, CNNs with a U-Net architecture are utilized. The U-Net architecture was first presented by Ronneberger et al. [12] and originally developed for biomedical image analysis. The generalized architecture of a U-Net is depicted in Figure 1. It features a distinctive U-shaped structure comprising an encoder (contracting path), a bottleneck, and a decoder (expanding path). The encoder extracts hierarchical features through convolutional layers and max-pooling, reducing spatial dimensions while increasing feature depth. The bottleneck serves as a compressed representation of the input, capturing essential high-level features. The decoder then reconstructs the image using transposed convolutions (upsampling layers) to restore spatial resolution while refining segmentation details. A key feature of U-Net are its skip connections, which directly link corresponding layers in the

encoder and decoder, preserving fine-grained spatial information lost during downsampling.

U-Net architectures are particularly well-suited for classification tasks that require spatial localization within the output map—in this study, the precise position and extent of damage. Their ability to efficiently propagate features across layers while preserving spatial context makes them a powerful tool for image-based classification tasks. This work extends the application of U-Nets to pixel-like surface strain data, demonstrating their potential for accurate damage detection and localization in composite structures. [12]

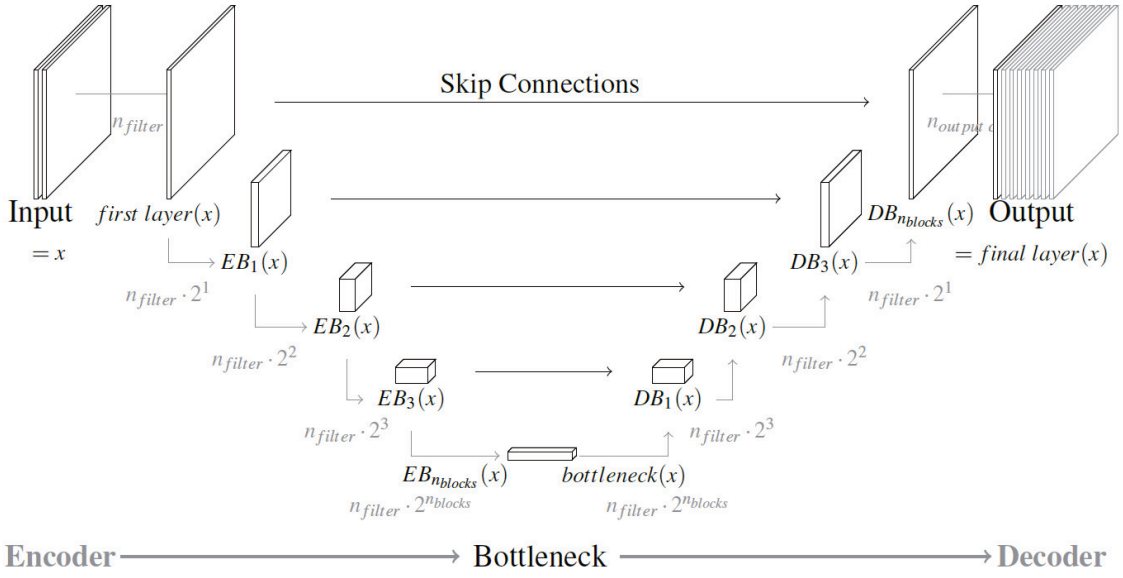

Figure 1: Generalized U-Net architecture based on Ronneberger et al. [12].

3 DEVELOPED METHOD

In this work, CNNs based on a U-Net-architecture are used for damage detection, localization and identification in Type IV hydrogen pressure vessels. Within this section, the input data, general methodology of the approach and constraints imposed by in-service applications are presented and discussed.

3.1 Input data

To generate the input data used to train the CNN, a reference COPV is modelled using the Finite Element Method (FEM). It shall be noted, that the geometry, material and layup used in this study does not correspond to any validated tank design as information about commercially used designs generally may not be disclosed. Therefore, the authors have selected approximate outer dimensions as seen in tank designs for personal mobility and compressed hydrogen transport

applications, which are illustrated in Figure 2. The corresponding layup and material properties found in published literature are listed in Tables 1 and 2. The layer thickness provided in Table 2 is approximated using netting theory for a burst pressure of 1580 bar [13]. Fiber and matrix damage is modelled by reducing elastic material properties in the specified area according to Table 1. To reduce computational effort, it was assumed that the tank is symmetric in all three spacial directions (effectively modelling one-eigth of the tank) and only damage in the cylindrical section is considered. It is ensured that the area of influence of the stress redistribution caused by the investigated damage modes does not extend to the symmetry-boundaries in the FEM model.

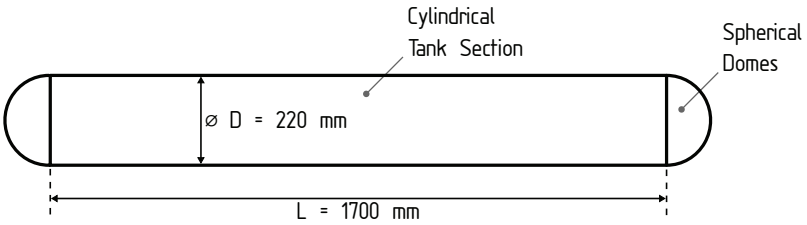

Figure 2: Tank geometry used to generate the input data, based on tank designs found in personal mobility and compressed hydrogen transport applications.

Table 1: Material properties of composite materials for the reference state, matrix damage and fibre damage according to [14, 13]. (The Elastic Modulus E_i and the Shear Modulus G_i is provided in [MPa], the Poisson Ratio ν_{ij} is dimensionless. The subscript 1 denotes the fiber direction.)

	E_1	E_2	E_3	ν_{12}	ν_{13}	ν_{23}	G_{12}	G_{13}	G_{23}
Undamaged	160000	7420	7420	0.28	0.28	0.3	3710	4790	3710
Factor of reduction in case of damage:									
Matrix damage	1	0.1	0.1	1	1	0.1	1	1	0.1
Fibre damage	0.1	1	1	0.1	0.1	1	0.1	0.1	1

The surface-strain data of the cylindrical section of the eight-symmetric tank serves as input for training as illustrated in Figure 3. Matrix cracking or fibre breakage at different relative axial positions, layers and diameters are applied to each tank. The damage properties are generated randomly based on predefined boundaries. The surface strain data is read for 1000 damaged tank models as well as the undamaged reference tank model. A threshold value of $\epsilon_{th} = 10^{-5}$ is introduced to accomodate the assumption that lower strains are not measurable in practical application. All strains below ϵ_{th} are set to zero, effectively excluding these values and the

Table 2: Layer configuration of the composite hydrogen pressure vessel adapted from [15].

layer	0	1	2	3	4	5
thickness $[mm]$	2.50	1.75	1.75	1.75	1.75	2.50
angle $[^\circ]$	89	$\pm$ 22.1	$\pm$ 37.5	$\pm$ 22.1	$\pm$ 37.5	89

information contained within from the training process. To prevent overfitting, the dataset is augmented. Each damage is positioned along the circumferential centerline of the simulated tank segment. As the tanks are assumed to be rotationally symmetric, the input and target data is shifted in circumferential direction to generate augmented data. 100 random circumferential shifts between -45 ° and 45 ° are performed on each damaged tank simulation resulting in a dataset of 53 100 input and target tensors.

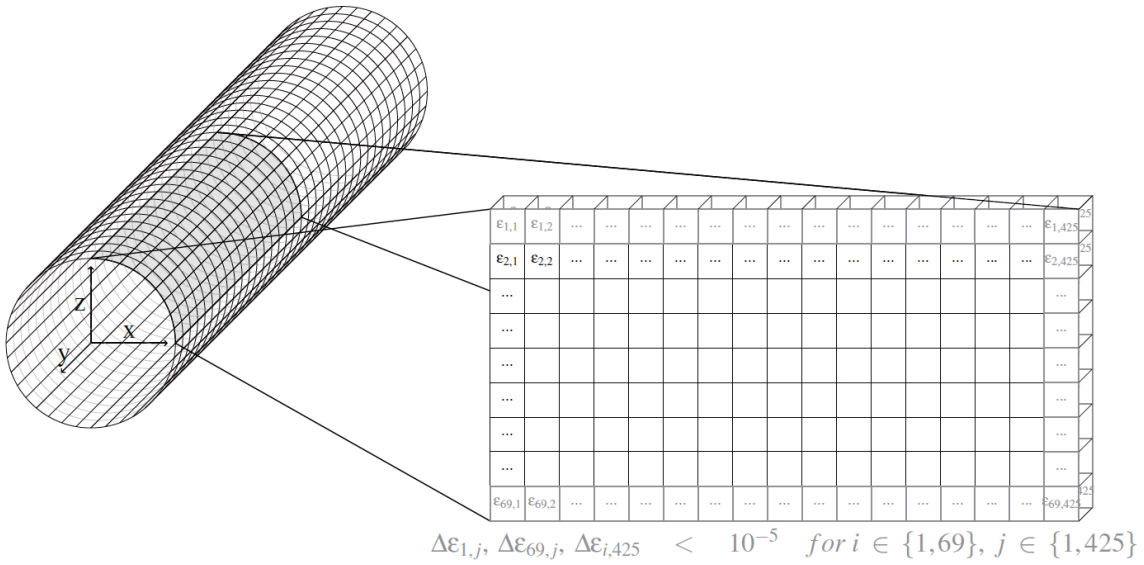

Figure 3: Computation of input data by means of an FEM tank model. The cylindrical section of the FEM model is illustrated, whereby the surface strain data in longitudinal and circumferential direction is extracted for one eight-symmetric tank section.

Adequate data preprocessing can speed up the training process of ANNs, reduce network complexity and increase generalisability [16]. Data with varying scales can cause instabilities during training ANNs and must be adjusted to match the range of values expected by the input layer ($[-1, 1]$ or $[0, 1]$). For this work, z-score-normalisation is used for the input data. The z-score is a measure of how far a value deviates from the mean value of the data. Using z-index based standardization results is particularly suitable for normally distributed data. [16, 17]

The input data that is extracted from the numerical simulation is a tensor of dimension $[2 \times 69 \times 425]$: 2 strain values (deviation of the longitudinal and circumferential strain) are provided for all surface-elements of the modelled cylindrical tank section (69 in circumferential direction and 425 in longitudinal direction). The tank is discretized in 6 different layers, and it is assumed that fiber and matrix damage may occur in the inner five layers, thus focusing on damage not easily spotted in visual inspection. In order to detect both, fiber and matrix damage, in the 5 relevant layers, 10 output maps of size $[69 \times 425]$ need to be predicted. This results in an output size of $[10 \times 69 \times 425]$ with each output channel corresponding to a combination of damage type and layer. Damaged elements are labelled as 1 and undamaged elements are labelled as 0 in the channel corresponding to the respective damage type and layer. Label smoothing is used, adjusting the labels in close vicinity to the modelled damage. Label smoothing improves generalisability and accuracy of deep learning models [18]. Hard targets result in higher true logits and great differences between false logits. Therefore, using hard labels (i.e. assigning each element a binary value for damage / no damage), undamaged elements adjacent to damaged regions would be treated the same as undamaged elements far from damaged regions. Soft labels are introduced for target tensors between damaged and undamaged elements. Undamaged elements that are located at a distance of d ($d \in [1, 16]$) from the damaged element are assigned values $\frac{1}{2^d}$. Exemplary input, target and output data is visualized in Figure 4 for matrix damage in layer 3.

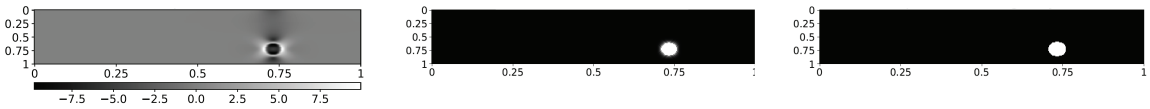

Figure 4: Exemplary training data and results. Left: Input (Surface strain deviation in fiber direction $\Delta\epsilon_1$), Middle: Target map (only for the channel corresponding to matrix damage in layer 3), Right: Output map (only for the channel corresponding to matrix damage in layer 3)

3.2 Approach for damage assessment in COPVs

During the first stage, training, validation and testing datasets are selected. The input and target dataset is randomly divided into training, validation and testing data with shares of 70 %, 10 % and 20 %, respectively. The next step is preprocessing of the input data and the creation of target data. This involves computing the strain deviation from the reference state, z-score-normalisation according to Equation **??**, and the introduction of the aforementioned soft labels to the target data. Subsequently, different candidate topologies are generated and trained. The candidate topologies are created based on the general U-Net architecture illustrated in Figure 1. The encoder part is build up with n_{blocks} Encoder Blocks (EBs) that each contain n_{layer} convolutional layers and ReLU activation functions, batch normalisation, and max-pooling. The bottleneck has the highest degree of abstraction in relation to features of the data and incorporates multiple convolutional layers and ReLU activation functions. This is followed by the decoder block that is build up with n_{blocks} Decoder Blocks (DBs) that each contain n_{layer} ReLU

activation functions and convolutional layers, batch normalisation and ReLU activation analogous to the encoder. While the encoder reduces the dimensions of the data by applying maximum pooling, the decoder increases the dimensions to restore the original dimensions of the data by applying a transposed convolutional layer. The number of blocks n_{blocks} for the U-Net varies between 2 and 5 while the number of filters n_{filter} in the first block varies between 2 and 16. The number of EBs and DBs is determined by n_{blocks} and defines the degree to which the spatial dimensions of the input are compressed, indicating the level of abstraction applied to the input. n_{filter} indicates the range of features the network can learn. Skip connections are added between EBs and DBs to compensate for information loss during decoding and to improve feature integration [19]. Based on the network depth (n_{blocks}), zero-padding is performed on the input and target data to ensure equal dimensions for the skip connections of the U-Net architecture. Therefore, the data is expanded with columns and rows of zeros to match the required dimensions. The best network topology is chosen based on the final validation error. The process of creating and training new candidate topologies is repeated until the validation error is sufficiently small [20]. For the loss function used in training, the Intersection over Union (IoU) is chosen. The IoU loss L_{IoU} is a suitable loss function for binary classification, in particular object detection or semantic segmentation. The IoU loss L_{IoU} is based on the overlap between the predicted segmentation mask and the ground truth mask and is calculated according to Equation 1 [21]. TP amounts to the number of damaged elements predicted as damaged, while FP amounts to the number of undamaged elements predicted as damaged. Accordingly, FN describes the number of damaged elements that is predicted as undamaged.

$$L_{IoU} = 1 - \frac{TP}{TP + FP + FN} \tag{1}$$

During training, numerical instability is adressed by implementing ReLU activation, batch normalisation as well as gradient normalisation and gradient clipping at a threshold value of 1. Furthermore, the AdamW (Adam with decoupled weight decay) optimizer is applied showing superior performance for (over-parameterized) Deep Convolutional Neural Networks (DCNNs) compared to the Adam optimizer. Finally, learning rate scheduling is implemented based on a starting learning rate of 10^{-4} that is reduced by $10\,\%$ if the validation loss fails to improve for five consecutive epochs until a minimum learning rate of 10^{-6} is reached. High learning rates speed up the initial training process, whereas lower learning rates are favored in later stages to ensure stable model convergence. [22, 23, 24]

3.3 Initial results for damage detection and localization in COPVs based on a numerical test case

The progression of the validation loss function for different network topologies during training is depicted in Figure 5. The (expected) difference in performance after repeating the training for a model is referred to as *churn*. Churn can be attributed to different sources of randomness such as parameter initialisation and mini-batch ordering [25, 26]. On average, network performance improves with an increasing number of filters (see Figure 5). The IoU values calculated

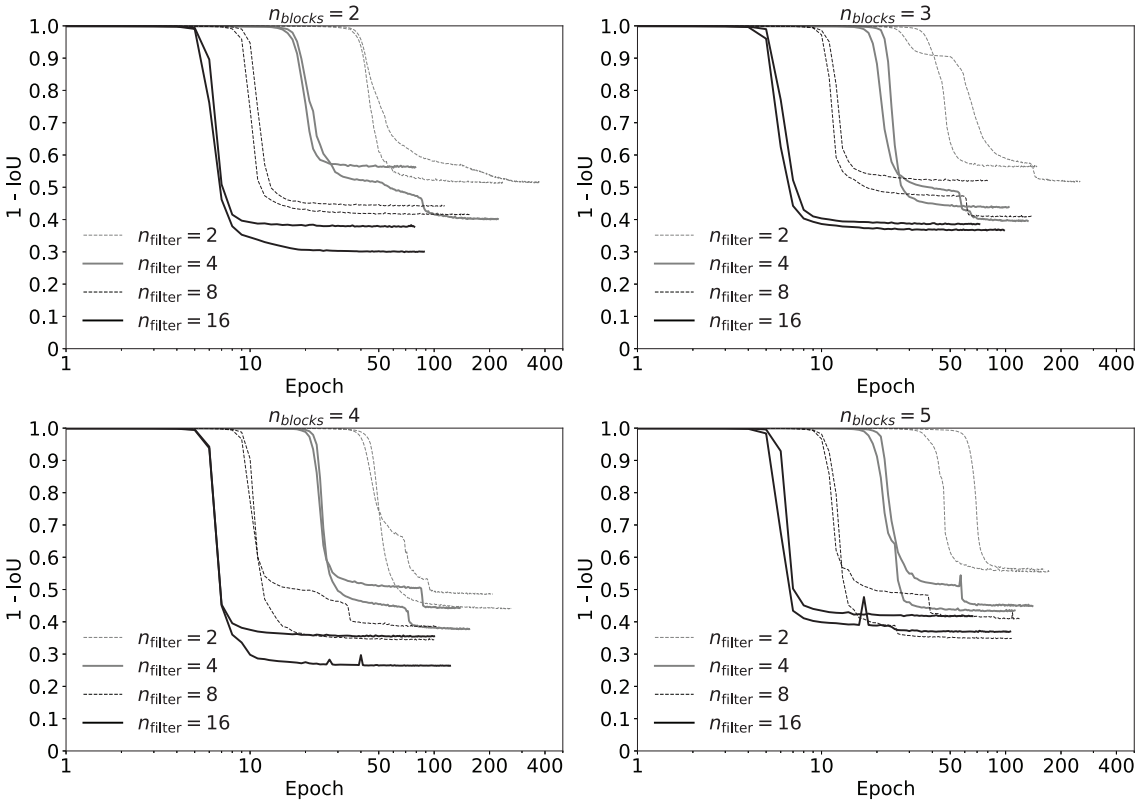

Figure 5: Progression of the validation loss function over training epochs for different network topologies.

based on the validation and training data are sufficiently similar to conclude good generalisability and to indicate that the network was not overfitted on the training data. Measured by IoU, a network topology with $n_{blocks} = 4$ and $n_{filter} = 16$ represents the best model with a maximum IoU of 69.132 % on the validation data and 69.131 % on the training data. For this network topology, 93.198 % of the damaged elements are detected (corresponding to the Recall) and the Precision amounts to 74.815 %. Therefore, 25.185 % of the predicted damaged elements are actually undamaged. This data can be interpreted as follows: Generally, damage is detected, localized (position along the tank surface and damage depth), and identified (matrix or fiber damage) very well based on the numerical input data. However, a common overestimation of the damage size leads to a lower IoU value.

3.4 Investigating constraints imposed by in-service applications

So far, the presented proof-of-concept was conducted in a rather academic nature. Some steps have been undertaken to simulate a more realistic SHM scenario. It has already been considered that strain values below 10 microstrain cannot be accurately measured. When introducing random noise of ± 10 microstrain and using the network trained on ideal data for the

evaluation, the IoU drops to 58.4 % with a Recall (also referred to as True-Positive Rate (TPR)) of 84.4 % and a Precision of 78.6 %. This shows good generalizability of the algorithm. By including random noise in the training, it is expected that these values can be improved. Even if trained on only one damage mode at a time, the approach works well if multiple damage modes are present in the tank. 10260 modified tanks are created by randomly adding corresponding input and target values of 5 tanks from the complete input dataset. With multiple damage modes present in the investigated tank section, the network exhibits an IoU of 63.0 %, a Recall of 86.7 % and a Precision of 71.7 %.

Furthermore, it must be considered that the surface strain is most likely measured using FBGs. FBGs generally can only measure strain in one direction. However, including only the hoop strain of the outermost layer in the training process does not lead to a decrease of IoU, Recall or Precision. As such, the in-service health monitoring is viable if only relying on one strain direction. It must be further considered that sensors are spatially distributed on the tank surface with a larger spacing than the element size used in the FE-analysis (approx. 2 mm). This was modelled by reducing the size of the input data. As expected, the IoU decreases with increasing sensor distance. This decrease in performance can be partially circumvented by training a second CNN to reconstruct the missing strain data from numerical simulation and applying the CNN used for damage detection to the reconstructed data, see Figure 6.

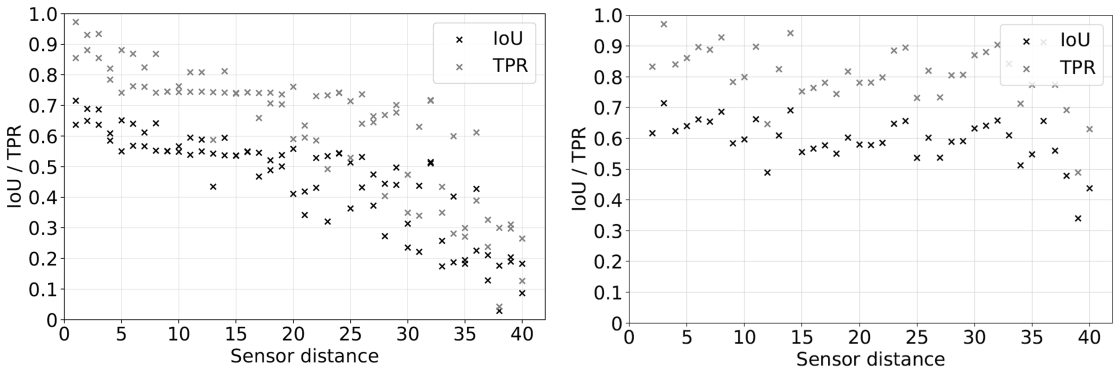

Figure 6: IoU loss in dependence on sensor distance for validation data without data reconstruction (left) and with the dual-CNN data reconstruction approach (right).

4 LESSONS LEARNED AND FUTURE WORK

The implementation of CNNs based on the U-Net architecture for damage detection, localization, and identification in Composite Overwrapped Pressure Vessels has provided several key insights. Firstly, the U-Net-based CNNs proved to be highly effective in accurately identifying and localizing damage within COPVs in a numerical test case. The network's ability to process spatially structured sensor data enables reliable mapping of deviations in the surface-strain field to underlying damage states. However, the damage size is commonly overestimated. Secondly,

it was observed that assessing only the longitudinal strain, which corresponds to utilizing a single sensor per sensing position in a real-world application, does not result in a significant reduction in performance for the numerical test-case. Furthermore, introducing a separate data reconstruction algorithm can enhance the CNN's performance when larger sensor distances are used. This technique mitigates the loss of spatial resolution due to sparse sensor placement, thereby preserving the network's ability to accurately infer damage characteristics even under suboptimal sensing conditions. Lastly, the results demonstrate good generalizability of the trained CNNs towards the presence of multiple damages. These findings underscore the potential of CNN-based approaches for damage identification in composite structures and provide valuable guidance for future experimental implementations and optimizations.

While the current study demonstrates promising results, several key areas for future research remain. Firstly, the repeatability of the CNN training shall be improved by adapting the loss-function and introducing soft labels encompassing multiple layers. Another crucial step towards improving the robustness of the CNN is the integration of manufacturing and load uncertainties as well as sensor noise within the numerical test case. Furthermore, a more realistic tank design will be used to generate training data. Additionally, extending the training dataset to include delaminations as a damage mode will provide a more comprehensive approach to SHM in COPVs. Lastly, the damage models shall be improved based on actual damage observed in CFRP-overwrapped pressure vessels during testing and service. It can be expected, that these steps greatly improve robustness and applicability of the approach.

REFERENCES

[1] E. Commission, "The european green deal. Communication from the commission to the european parliament, the european council, the council, the european economic and social committee and the committee of the regions," 2019.

[2] G. Chi, S. Xu, D. Yu, Z. Wang, Z. He, K. Wang, and Q. Zhou, "A brief review of structural health monitoring based on flexible sensing technology for hydrogen storage tank," *International Journal of Hydrogen Energy*, vol. 80, pp. 980–998, 2024.

[3] H. Yumiya, M. Kizaki, and H. Asai, "Toyota fuel cell system (TFCS)," *World Electric Vehicle Journal*, vol. 7, no. 1, pp. 85–92, 2015.

[4] C. Viechtbauer and K.-U. Schröder, "Structural health control - a comprehensive concept for observation and assessment of damages," *13th Mechatronics Forum International Conference*, 2012.

[5] A. Preisler, "Efficient damage detection and assessment based on structural damage indicators," Ph.D. dissertation, RWTH Aachen University, 2019.

[6] D. F. Braga, S. Tavares, L. F. da Silva, P. Moreira, and P. M. de Castro, "Advanced design for lightweight structures: Review and prospects," *Progress in Aerospace Sciences*, vol. 69, pp. 29–39, 2014.

[7] H. Rocha, P. Antunes, U. Lafont, and J. P. Nunes, "Processing and structural health monitoring of a composite overwrapped pressure vessel for hydrogen storage," *Structural Health Monitoring*, vol. 23, no. 4, pp. 2391–2406, 2024.

[8] G. Souza and Tarpani, "Using OBR for pressure monitoring and BVID detection in type IV composite overwrapped pressure vessels," *Journal of Composite Materials*, vol. 55, no. 3, pp. 423–436, 2021.

[9] P. Gasior, M. Malesa, J. Kaleta, M. Kujawińska, K. Malowany, and R. Rybczyński, "Application of complementary optical methods for strain investigation in composite high pressure vessel," *Composite Structures*, vol. 203, no. 9, 2018.

[10] I. G. Tapeinos, A. Rajabzadeh, D. S. Zarouchas, M. Stief, R. M. Groves, S. Koussios, and R. Benedictus, "Evaluation of the mechanical performance of a composite multi-cell tank for cryogenic storage: Part II – experimental assessment," *International Journal of Hydrogen Energy*, vol. 44, no. 7, 2019.

[11] W. Jiang, M. Liang, M. Schiebel, S. Zaremba, and K. Drechsler, "Development of machine learning based classifier for the pressure test result prediction of type IV composite overwrapped pressure vessels," *International Journal of Hydrogen Energy*, vol. 58, no. 36, 2024.

[12] O. Ronneberger, P. Fischer, and T. Brox, "U-net: Convolutional networks for biomedical image segmentation," in *Medical Image Computing and Computer-Assisted Intervention – MICCAI*, N. Navab, J. Hornegger, W. M. Wells, and A. F. Frangi, Eds. Springer, 2015, pp. 234–241.

[13] Z. Hu, M. H. Chen, l. Zu, X. Jia, A. Shen, Q. Yang, and K. Xu, "Investigation on failure behaviors of 70 MPa type IV carbon fiber overwound hydrogen storage vessels," *Composite Structures*, vol. 259, 2021.

[14] W. Li, H. Lv, L. Zhang, P. He, and C. Zhang, "Experiment, simulation, optimization design, and damage detection of composite shell of hydrogen storage vessel - A review," *Reinforced Plastics and Composites*, vol. 42, pp. 507–536, 2023.

[15] C. Hopmann, N. Magura, R. Müller, D. Schneider, and K. Fischer, "Impact of winding parameters on the fiber bandwidth in the cylindrical area of a hydrogen pressure vessel for generating a digital twin," *Polymer Composites*, pp. 1–13, 2022.

[16] L. Yu, W. Shouyang, and K. K. Lai, "An integrated data preparation scheme for neural network data analysis," *IEEE Transactions on Knowledge and data engineering*, vol. 18, no. 2, pp. 217–230, 2006.

[17] C. Vercellis, *Business Intelligence: Data Mining and Optimization for Decision Making*. John Wiley and Sons Ltd, 2009.

[18] R. Müller, S. Kornblith, and G. Hinton, "When does label smoothing help?" *33rd Conference on Neural Information Processing Systems*, 2019.

[19] Y. Ji, H. Zhang, Z. Zhang, and M. Liu, "CNN-based encoder-decoder networks for salient object detection: A comprehensive review and recent advances," *Information Sciences*, vol. 546, pp. 835–857, 2021.

[20] I. Nunes da Silva, D. Hernane Spatti, R. Andrade Flauzino, L. H. Bartocci Liboni, and S. F. dos Reis Alves, *Artificial Neural Networks*. Springer, 2017.

[21] J. R. Terven, D. M. Cordova-Esparza, A. Ramirez-Pedraza, E. A. Chavez-Urbiola, and J. A. Romero-Gonzalez, "Loss functions and metrics in deep learning," *arXiv preprint*, 2023.

[22] C. C. Aggarwal, "Neural networks and deep learning," 2018.

[23] M. A. Nielsen, "Neural networks and deep learning," 2015.

[24] S. Norouzi and M. R. Ebrahimi, "A survey on proposed methods to address adam optimizer deficiencies," *Department of Electrical and Computer Engineering, University of Toronto*, 2019.

[25] F. Renard, S. Guedria, N. de Palma, and N. Vuillerme, "Variability and reproducibility in deep learning for medical image segmentation," *Scientific Reports, nature research*, vol. 10, 2020.

[26] S. Bhojanapalli, K. Wilber, A. Veit, A. S. Rawat, S. Kim, A. Menon, and S. Kumar, "On the reproducibility of neural network predictions," *arXiv*, 2021.

ACKNOWLEDGEMENT

The project on which this contribution is based was funded by the Federal Ministry of Digital and Transport (Bundesministerium für Digitales und Verkehr) of the German government under the funding code 03B11024. The authors are responsible for the content of this publication. We are grateful for Battenberg Robotic GmbH's partnership in this work.

XI ECCOMAS Thematic Conference on Smart Structures and Materials - SMART 2025
M. Krommer, M. Nader and M. Schagerl (Eds)

Received: 22 April 2025 / Revised: 29 August 2025 / Accepted: 3 September 2025
© The Author(s) 2025

Robotically Automated Tap Testing for Damage Detection in Filament-Wound CFRP Tubes

Tobias Schalm, Linus Wermert, Kai-Uwe Schröder

Abstract. Non-destructive testing (NDT) can greatly benefit the reliability of safety-critical engineering structures throughout their lifecycle. Possible applications include in-line or end-of-line quality control during manufacturing, in-service health monitoring, and re-certification (e.g. in a circular economy context). One long-established method is tap testing, where defects are identified by changes in the acoustic response to a localised impact. This study investigates the robotic automation of tap testing for filament-wound carbon fiber reinforced polymer (CFRP) tubes with barely visible impact damage. An industrial robot equipped with an instrumented modal hammer is used to perform automated sweeps along the specimens. The recorded hammer force signal is shown to contain clear indicators of local damage, enabling detection and localisation without the need for additional sensors such as microphones or vibrometers. The observed correlation between changes in contact stiffness and the attenuation of higher-frequency modes confirms the physical basis of classical tap testing while providing a traceable, automatable measurement signal. The results demonstrate the potential of robotically automated tap testing as a cost-effective and scalable NDT approach for thin-walled composite structures.

Key words: Non-Destructive Testing (NDT), Robotic Tap Testing, Impact Damage Detection, Automated Quality Assurance

1 INTRODUCTION AND MOTIVATION

The tap test is a well-established and widely used non-destructive test. It is particularly well suited for inspecting laminated structures, honeycomb panels, and bonded joints. Traditionally, the test involves an operator manually tapping the surface of a structure with a coin and listening for changes in the emerging sound to identify defects. Regions containing damage are often described as sounding “dead”, providing a qualitative indication of structural anomalies. Despite its widespread use, the test has historically relied on subjective interpretation based on

Tobias Schalm & Linus Wermert & Kai-Uwe Schröder
Institute of Structural Mechanics and Lightweight Design, RWTH Aachen University, Wüllnerstraße 7, 52062 Aachen, Germany, e-mail: tobias.schalm@sla.rwth-aachen.de

the operator's expertise [1]. Recent advancements in published literature aim to enhance the robustness and objectivity of classical tap testing by incorporating additional parameters — such as tap force magnitude and contact duration — and integrating this data with acoustic measurements [2, 3, 4, 5]. Industrialised applications include the Electronic Digital Tap Hammer developed by the Boeing Company and licensed to WichiTech [6], the MITSUI Woodpecker and the Computer-Aided Tap Tester (CATT) developed by the Iowa State University [3, 7]. The robustness and efficiency of tap testing applications can be further improved by exploiting the precision and the automation potential of robotic systems [8, 9]. In addition, artificial neural networks enable the transition from simple binary damage identification (i.e., damage/no damage) to more advanced analyses, including the classification of damage modes and estimation of damage depth [5]. Contributing to ongoing advancements in tap testing, this study aims to demonstrate the viability of robotically automated tap testing for impact damage detection in thin-walled filament-wound composite structures. Impact damage is of particular interest in the non-destructive evaluation of CFRP components, as their low interlaminar strength and lack of plastic deformation make them especially susceptible to this form of damage. Additionally, impact damage in CFRP components is often located sub-surface and barely visible during a visual inspection [10].

2 THEORETICAL FOUNDATIONS

As previously introduced, damage is traditionally identified in tap testing by listening to the sound produced by a localised impact of a coin or hammer. The audible sound is generated when the oscillations of the tapped structure are transmitted into the surrounding air. Skilled operators can recognise damaged areas by the "deadness" or "dullness" of this sound, suggesting that the acoustic response lacks higher-frequency content. The audible sound is predominantly composed of frequencies corresponding to the natural modes of the structure and encompasses local modes (localised oscillation around the tap-position, directly excited by the impact force) as well as the global natural oscillation modes of the structure [4]. The composition of the structural dynamic response (i.e. the natural oscillation modes excited by the tap) can be directly correlated to the width, height and general shape of the tap pulse itself [1]. Generally, the width or duration of the pulse determines the frequency spectrum of the structural dynamic response while the height and shape influence the amplitude of the spectrum [11]. According to Cawley [1, 12], a simplified model, where the local stiffness of contact between the structure and impactor k_c is modelled as a linear spring element and the impacting hammer or coin is modelled as a body of mass m_i, is suitable to explain the underlying physical effects of the tap-test. Geometric non-linearities due to large deflection under impact and non-linearities associated with Hertzian contact modelling are neglected in this model. Following these assumptions and further assuming a quasi-static structural response [13], the impact duration τ (and therefore the width of the tap pulse) is governed by the following equation:

$$\tau = \pi \sqrt{\frac{m_i}{k_c}}. \tag{1}$$

The maximum force exerted on the structure is given by:

$$F = \frac{k_c \, v \, \tau}{\pi}, \tag{2}$$

where v is the velocity of the impactor right before the impact [1, 12]. While the impactor mass is only dependent on the hammer design, the contact stiffness is influenced by the material properties of the structure and the impactor. Structural damage in the specimen reduces the contact stiffness, thereby influencing both the duration of the impact and the maximum force, which are observable in the hammer signal.

Characteristic tap force signals for damaged and undamaged regions are qualitatively depicted in Figure 1. Generally, a lower contact stiffness results in a longer impact duration and a lower force amplitude of the pulse.

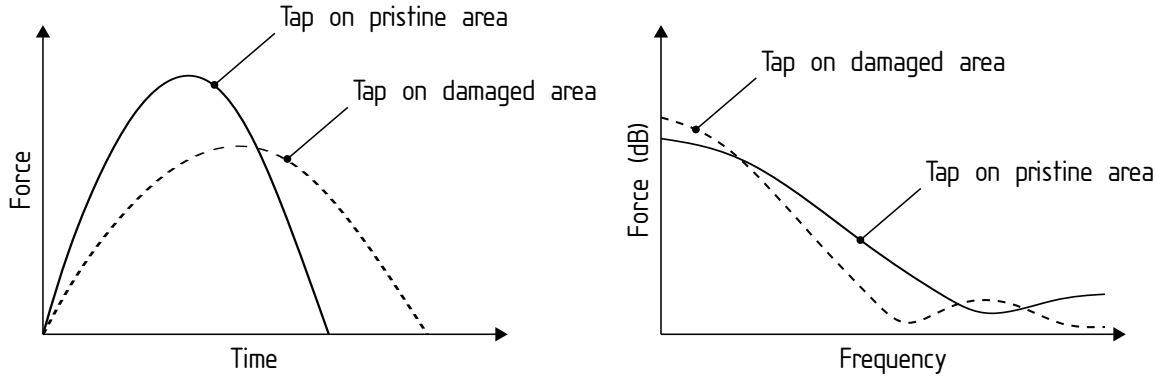

Figure 1: Characteristic tap pulse for damaged and undamaged regions (left) and corresponding FFT signal in the frequency domain (right) [1].

A Fast Fourier Transform (FFT) of the hammer signals at damaged and undamaged positions reveals that the frequency spectrum is altered. Characteristically, the amplitude of the force input falls off more quickly with increasing frequency for damaged areas than when tapping an undamaged area, ultimately resulting in the "dead" sound observed by the operator [1]. It may be concluded that the shift in the audible sound can be observed in the force signal of the hammer without loss of information if the natural modes of oscillation of the structure are known and the damage has sufficient influence on the contact stiffness between the hammer and the structure. This approach greatly simplifies the NDT-setup as no additional measurement equipment (e.g. a microphone or laser vibrometer) is required. Examples for the successful

exploitation of this phenomenon are damage detection in wind turbine blades [5] and concrete used in infrastructure [14]. While the analysis of the tap force data presents a simple and efficient approach to assess structural damage in close vicinity to the tapped surface, it becomes less reliable with increasing damage depth. In such cases, the fusion of the force data with acoustic measurement is beneficial [4]. As the impact damage investigated in this study is generally located close to the surface, the focus of the presented analysis lies on the tap force signal.

3 APPROACH TO AUTOMATIC TAP-HAMMER-TESTING

In this study, filament-wound CFRP pipes are investigated for impact damage detection using automatic tap-hammer-testing enabled by an automatic modal hammer and an industrial robot. The investigated filament-wound CFRP pipes feature an outer diameter of 40 mm, a wall thickness of 1 mm and a length of 500 mm. The $\pm 55°$-layup is manufactured from Toray T 700 carbon fiber and a SIKA CR 141 matrix. In total, five pipes were damaged using a drop tower with an impact mass of 1507 g and a hemispherical steel tip with a diameter of 10 mm. The impact position along the longitudinal direction a as well as the drop height h were varied. Examples for the resulting damage conditions are depicted in Figure 2.

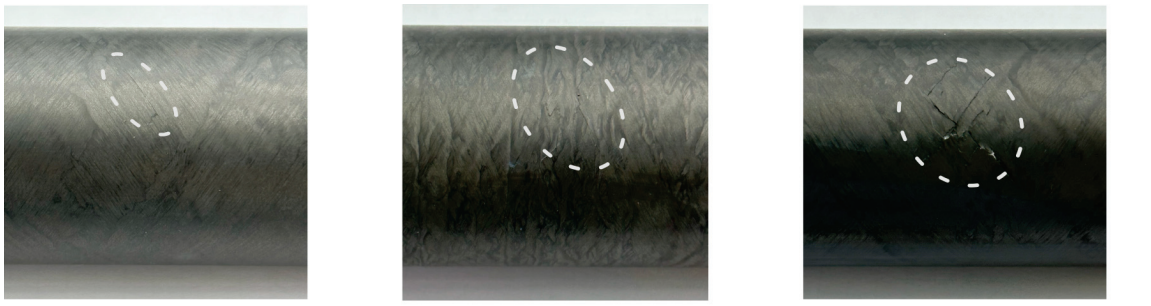

Figure 2: Damage modes and corresponding impact parameters.

A test stand for automatic tap-hammer-testing was set up at Battenberg ROBOTIC GmbH & Co. KG (`www.battenberg-robotic.com`). The test setup consists of three main components, which are depicted in Figure 3: a Mitsubishi Electric MELFA industrial robot, a NV-TECH SAM 1 automatic modal hammer, and a filament-wound CFRP-pipe fixated at both ends. The automatic modal hammer is attached to the industrial robot and aligned in a way that the hard metal tip taps the top of the filament-wound CFRP pipe. During measurement, a sweep is performed in the longitudinal direction of the pipe as depicted in Figure 4. The tip of

the modal hammer is equipped with a force sensor by PCB Piezotronics. The sensor signal is processed at a sampling rate of 250 kHz.

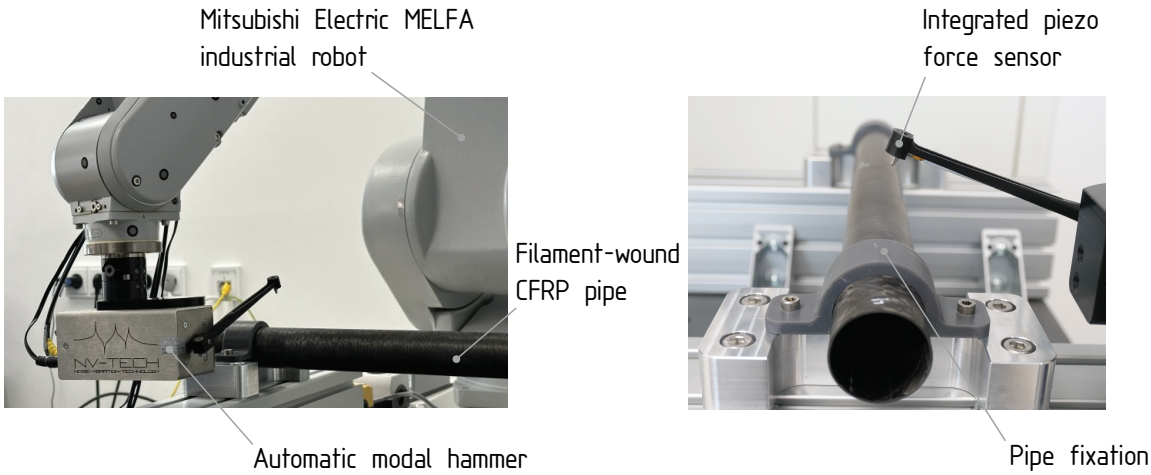

Figure 3: Test setup at Battenberg ROBOTIC GmbH & Co. KG for automatic tap-hammer-testing of filament-wound CFRP pipes.

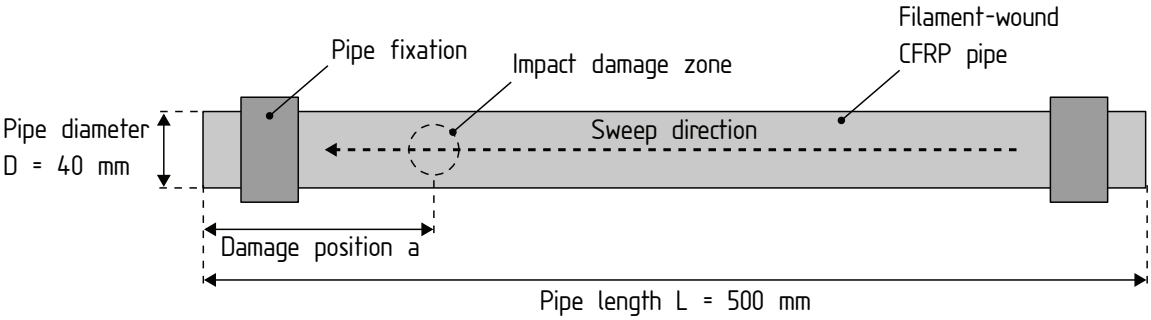

Figure 4: Sweep direction chosen for the automatic tap-hammer-testing.

4 INTERPRETATION OF THE TAP-HAMMER-SIGNAL

Figures 5 and 6 show the hammer contact force at different positions along pipes 1 and 2 when performing a sweep in longitudinal direction. The impact damage is clearly identifiable in the hammer force signal. This can be attributed to the fact that fiber and matrix cracking in the damage region lead to a lower effective elastic modulus of the contact pair (local Hertzian compliance), a lower bending stiffness of the tapped region (global compliance), and potentially

additional damping in the damaged region [12, 13, 15]. Even if the impact damage in pipe 1 is barely visible, the area of influence detectable in the hammer signal is 13 mm, measured between the first and last peak below a threshold of 25 N. The area of influence for the impact damage in pipe 2 is approximately 16.5 mm (using a threshold value of 23 N due to the lower baseline force amplitude).

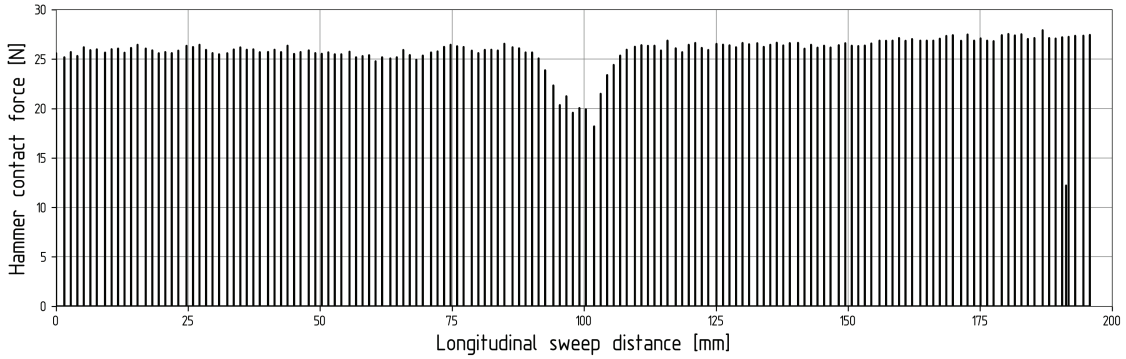

Figure 5: Maximum hammer contact force measured during a longitudinal sweep of pipe 1.

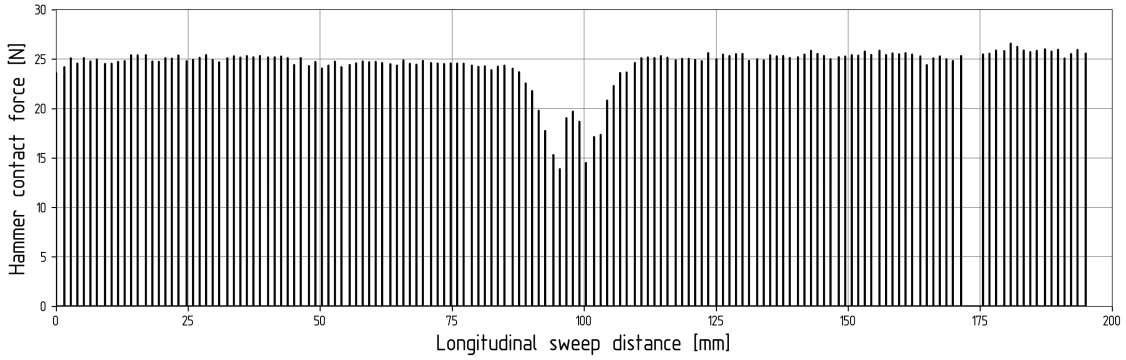

Figure 6: Maximum hammer contact force measured during a longitudinal sweep of pipe 2.

The hammer force signal over the time of contact is depicted in Figure 7 for an undamaged reference position and the position of lowest apparent contact stiffness in the damaged regions of pipes 1 and 2. The time of contact τ between the hammer tip and the pipe is in the order of tenths of a millisecond. Rearranging Equation 1, the contact duration can be used to compute the apparent contact stiffness as described in Equation 3 [14]. Using this equation, a maximum decrease of apparent contact stiffness in the impact area of 58% and 75% is computed for pipes 1 and 2, respectively.

$$k_c \propto \frac{1}{\tau^2} \tag{3}$$

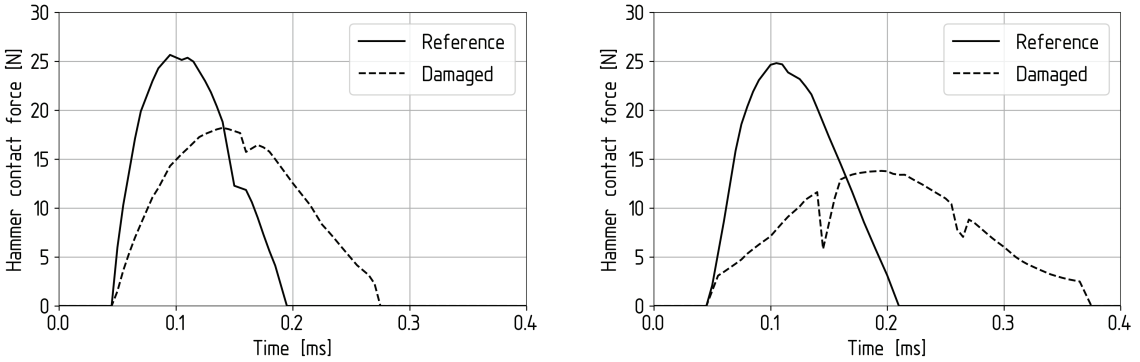

Figure 7: Contact force signals for pipe 1 (left) and pipe 2 (right) for a reference position and the position of lowest apparent contact stiffness in the damaged area.

In addition to the tap hammer signal, the structural dynamic response following excitation from the impact hammer was recorded using a Polytec PSV-500-3D Scanning Vibrometer (see Figure 8). As previously introduced, the spectrum of natural modes excited in the structure that ultimately produces the audible sound observed during traditional tap testing directly correlates with the force spectrum of the hammer pulse in the frequency domain. This effect is visualised in Figures 8 and 9, where the FFT of the hammer signal shows a clear decrease of magnitude towards the frequency range observed in the structural dynamic response (4.5 to 7 kHz). This observation further underlines that the information contained in the audible sound emerging during traditional tap testing of thin-walled filament-wound composites for impact damage can be reconstructed from the tap hammer signal. This observation ultimately enables a cost-effective robotic automation of the tap test for thin-walled composites without the need to rely on further measuring equipment such as microphones or a laser vibrometer.

5 LESSONS LEARNED AND FUTURE WORK

This study showed that robotically automated tap testing is an efficient approach to assess barely visible impact damage in thin-walled composites. Thereby, the amplitude of the hammer force signal presents a simple metric to identify damage areas. It has been highlighted how the information contained in the acoustic signal traditionally relied on in tap testing is reflected in the hammer force signal. Therefore, robotically automated tap testing based on the hammer force signal offers better traceability than classical coin tap testing without loss of information. Expanding upon the sole identification of damaged areas as shown in this study, future

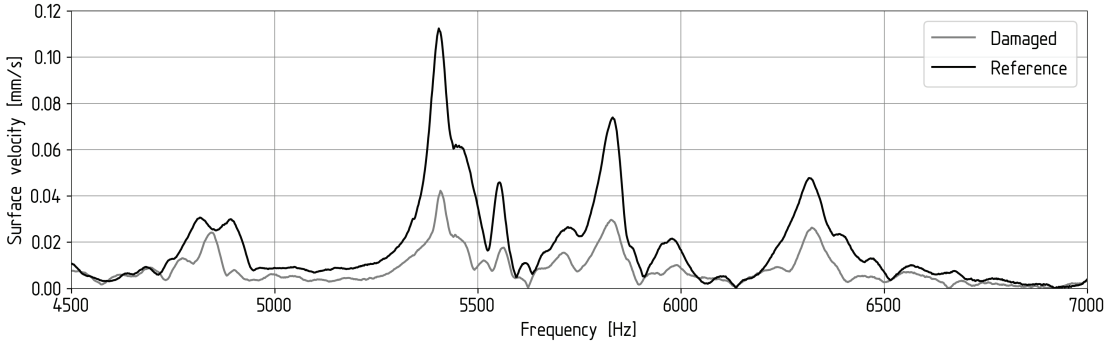

Figure 8: Structural dynamic response of pipe 3 in the frequency-domain when excited using the modal hammer at the damage position (grey line) and at a reference position (black line).

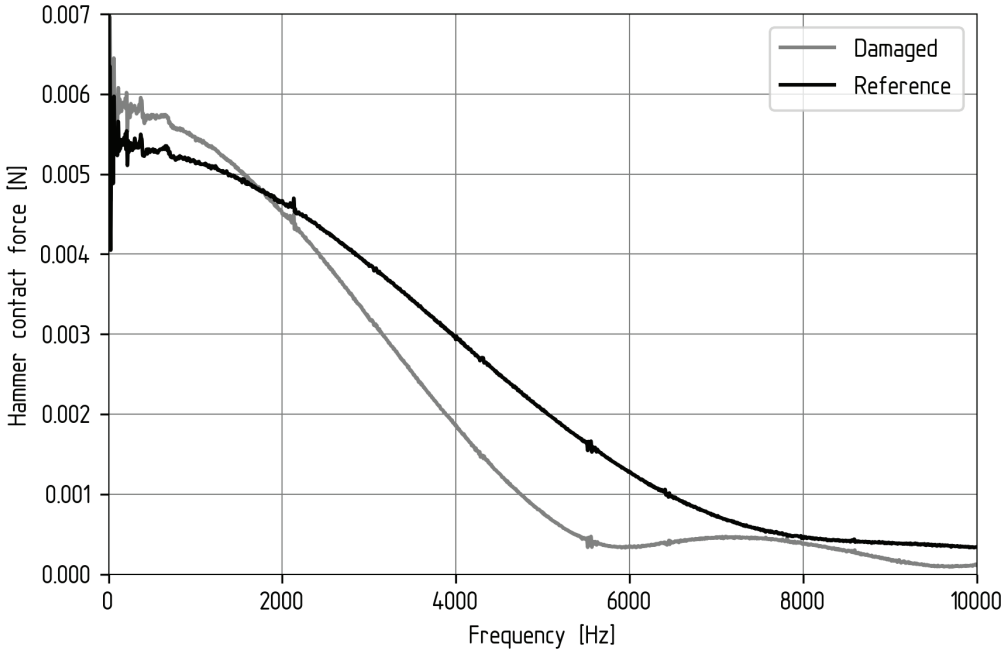

Figure 9: Fast Fourier Transformation of the hammer signal when impacting a damaged region (grey line) and reference position (black line) of pipe 3. The signal shows a reduced excitation of higher-frequency modes as visualised in Figure 8.

work will focus on the development of sophisticated algorithms to provide information about damage mode, depth, and the consequence for the remaining useful life of the structure. Furthermore, advanced evaluation algorithms are required to differentiate between variation in the force signals related to manufacturing-related thickness variations or the general morphology of the structure (e.g. stiffeners beneath the surface) and actual defects. As previously mentioned, a major limitation of the approach employed in this study is that it is only reliable for damages located close to the tapped surface. The apparent contact stiffness measured via the force-time signal is unaffected by defects at depth within the component. This may limit the applicability of the presented approach for thick-walled composites such as carbon-fiber-overwrapped hydrogen pressure vessels. Information about damage in thick-walled composites may be reconstructed by fusing force data with acoustic measurements [4].

ACKNOWLEDGEMENT

The project on which this contribution is based was funded by the Federal Ministry of Digital and Transport (Bundesministerium für Digitales und Verkehr) of the German government under the funding code 03B11024. The authors are responsible for the content of this publication. We are grateful for Battenberg Robotic GmbH's partnership in this work.

REFERENCES

[1] P. Cawley and R. D. Adams, "The mechanics of the coin-tap method of non-destructive testing," *Journal of Sound and Vibration*, vol. 122, no. 2, 1988.

[2] Y. Li, J. Zhang, J. Zhao, and J. Hu, "Research on intelligent tap testing of aviation composite material," in *Proceedings of the 2016 International Conference on Advanced Materials Science and Environmental Engineering*. Paris, France: Atlantis Press, 2016.

[3] J. Gryzagoridis and D. Findeis, "Tap testing of composites benchmarked with digital shearography," *Insight - Non-Destructive Testing and Condition Monitoring*, vol. 56, no. 1, 2014.

[4] A. Poole and N. Hartley, "Force and sound data fusion for enhanced tap testing scanning of composites," *IEEE Access*, vol. 11, no. 5, 2023.

[5] J. C. S. Queiroz, Y. T. B. Santos, I. C. da Silva, and C. T. T. Farias, "Damage detection in composite materials using tap test technique and neural networks," *Journal of Nondestructive Evaluation*, vol. 40, no. 1, 2021.

[6] G. E. Georgeson, S. Lea, and J. Hansen, "Electronic tap hammer for composite damage assessment," ser. SPIE Proceedings, R. D. Rempt and A. L. Broz, Eds. SPIE, 1996.

[7] D. Hsu, "Nondestructive inspection of composite structures: Methods and practice," in *17th World Conference on Nondestructive Testing*, vol. 13, no. 11, Shanghai, China, 2008. [Online]. Available: https://www.ndt.net/?id=6753

[8] R. Nasimi, S. Atcitty, D. Thompson, J. Murillo, M. Ball, J. Stormont, and F. Moreu, "Use of remote structural tap testing devices deployed via ground vehicle for health monitoring of transportation infrastructure," *Sensors (Basel, Switzerland)*, vol. 22, no. 4, 2022.

[9] Y. Nishimura, H. Mochiyama, and T. Yamaguchi, "Propeller-type wall-climbing robot for visual and hammering inspection of concrete surfaces," *IEEE Access*, vol. 12, no. 2, 2024.

[10] N. L. Hancox, "An overview of the impact behaviour of fibre-reinforced composites," in *Impact Behaviour of Fibre-Reinforced Composite Materials and Structures*. Elsevier, 2000, vol. 6.

[11] A. W. Phillips and R. J. Allemang, "Frequency response function estimation," in *Handbook of Experimental Structural Dynamics*, R. Allemang and P. Avitabile, Eds. New York, NY: Springer New York, 2022, vol. 3.

[12] P. Cawley, "A high frequency coin-tap method of non-destructive testing," *Mechanical Systems and Signal Processing*, vol. 5, no. 1, 1991.

[13] S. Abrate, *Impact Engineering of Composite Structures: CISM Courses and Lectures, vol. 526*. Vienna: Springer Vienna, 2011, vol. 526.

[14] K. Shoda, J. Y. L. Kasahara, Q. An, and A. Yamashita, "Defect detection in concrete structures based on characteristics of hammer reaction force and apparent stiffness of concrete," *IEEE Access*, vol. 13, 2025.

[15] R. Chandra, S. Singh, and K. Gupta, "Damping studies in fiber-reinforced composites – a review," *Composite Structures*, vol. 46, no. 1, 1999.

XI ECCOMAS Thematic Conference on Smart Structures and Materials - SMART 2025
M. Krommer, M. Nader and M. Schagerl (Eds)

Received: 4 March 2025 / Revised: 3 July 2025 / Accepted: 3 September 2025
© The Author(s) 2025

A hybrid Piezo / Temperature Sensor for Production and Structural Health Monitoring of Composite Structures - development and lessons learned

Michael Scheerer, Zoltan Simon, Michael Marischler, Bernhard Rittenschober

Abstract. Within this paper, the authors present an overview of the different development steps of a hybrid piezo / temperature sensor and lessons learned out of validation of the sensor performance during production of the composite parts by resin transfer moulding and the detection of defects during usage. For production monitoring the change of the electro-mechanical impedance of the piezo during resin infusion and curing was taken as measure for the flow front arrival and indication of the degree of cure. The ability of the co-cured sensors for damage detection and localization either by Acoustic Emission or ultrasonic guided waves was assessed on different relevant composite parts.

Key words: Structural Health Monitoring, Piezo, EM impedance, Acoustic Emission, Guided Waves, Composites, Process monitoring.

1 INTRODUCTION

To bring the advantages of fibre reinforced polymers – high specific strength and stiffness – into applications where mass production is essential e.g. specific aircraft parts such as stringers or frames, automated manufacturing techniques must replace the widespread manual production. Depending on the part to be manufactured, infusion methods like Resin Transfer Moulding (RTM) are such automated production techniques. The most important steps in the production of complex composite parts by resin infusion are to reach a full impregnation of the dry pre-form and to guarantee a full curing of the resin in the form. Therefore, the control of process parameters like flow front propagation and determination of the degree of cure are important to produce high-quality parts. Currently process monitoring in RTM processes are done by temperature sensors, pressure sensors, dielectric sensors or conventional ultrasonic sensors for the monitoring of the flow front and the determination of the degree of cure which

Michael Scheerer & Zoltan Simon & Michael Marischler
Mechanical Testing, Simulation and NDT Group, Aerospace & Advanced Composites GmbH Wiener Neustadt, Austria,
e-mail: michael.scheerer@aac-research.at

Bernhard Rittenschober
Research & Development, ALPEX Technologies GmbH, Mils, Austria
e-mail: bernhard.rittenschober@alpex-tec.com

are mostly integrated directly in the mould [1, 2, 3]. To be able to monitor the structural integrity during use (Structural Health Monitoring - SHM), further types of sensors such as piezo sensors, which are mainly glued to surface of the structure are under investigation [4, 5, 6]. Fibre optic sensors such as fibre Bragg grating sensors were used for process monitoring. These sensors will remain in the part and can be used for structural health monitoring [7]. A critical aspect is the ingress / egress point from the part and the connection of the fibre optic sensors.

Within the last years the authors developed a novel hybrid multi-functional piezo / temperature sensor concept for flow front, cure and SHM of composite parts thus allowing monitoring of the production and the usage with the same sensor type. The sensor performance and the overall monitoring concept were validated on different composite parts like flat plates, a passenger aircraft (PAX) door edge-member and a hollow composite aircraft part. [8, 9, 10, 11]. In the following chapters an overview of the different development steps of the sensor and lessons learned out of validation of the sensor performance.

2 OVERALL MONITORING CONCEPT

Figure 1 shows the overall process and structural health-monitoring concept. In the first step the piezo sensors are placed at pre-defined positions in the mould. Then the dry preform will be placed in the mould. During the production process (infusion and curing) the impedance spectra are measured over time and the change of the spectra – e.g. the resonance frequency – was used to determine flow front arrival and the hardening of the resin and subsequent the degree of cure. When the curing cycle has been finished and the mould is cooled back to room temperature, the part together with the co-cured sensors will be de-moulded. The co-cured piezo transducers are then ready to be used as sensors and / or actuators of passive (Acoustic Emission - AE) and / or active (Guided Ultrasonic Waves) SHM system, where the temperature sensors are used to account for temperature effects.

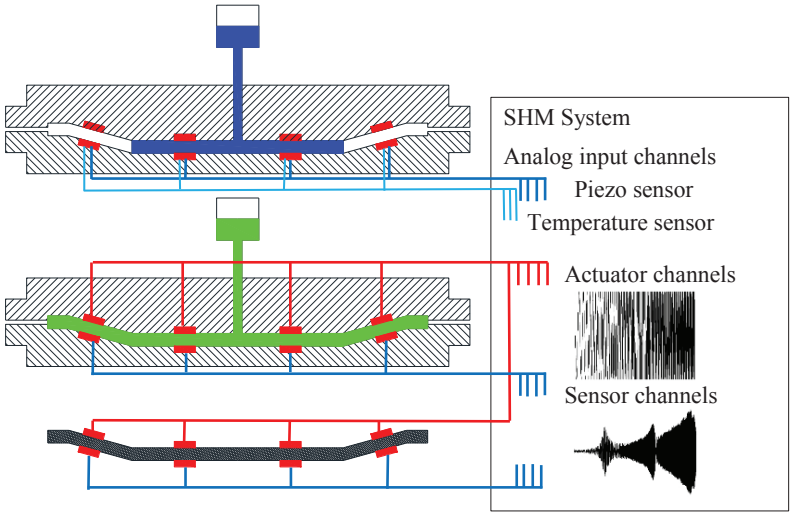

Figure 1: Illustration of the working principle of the integrated process and structural health monitoring system.

2.1 Sensor designs and hardware

The design of the sensor is mainly driven by the production process. The following aspects were considered: the sensor including connector and wiring must operate at temperatures up to 180°C (curing temperature of the resin), the mould with the mounted sensors must be vacuum tight (evacuation of the closed mould cavity prior to resin infusion) and the sensor must be robust to survive the demoulding process. Figure 2 shows the 1st and 2nd generation of sensors.

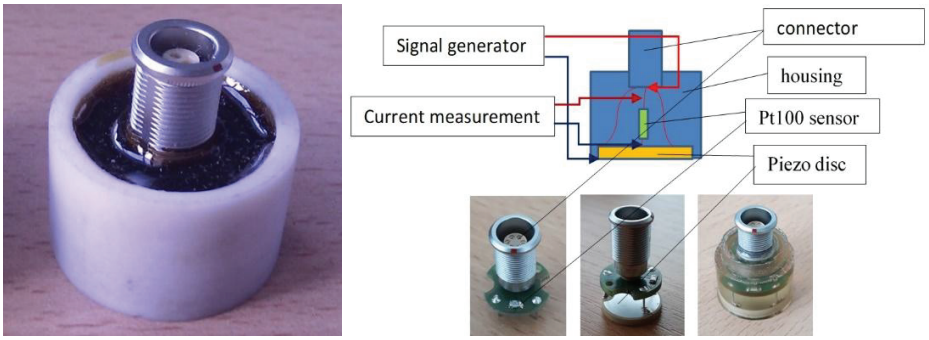

Figure 2: 1st generation - pure piezo (left) and 2nd generation piezo / temperature sensor (right)

The 1st generation sensor consists of a piezo disc of 15 mm diameter and 2 mm thickness with wrapped around electrodes connected to co-axial connecter embedded in epoxy resin cylinder. The whole assembly is embedded in PTFE cylindrical ring, used to tighten the sensor in the RTM mould. The 1st generation sensor system requires two different data acquisition units for process monitoring (impedance analyser) and SHM (AE system with signal actuator card), where the measurement of the impedance spectra for cure monitoring using a conventional impedance analyser took rather long time leading to a low time resolution of the monitoring of the production process.

The concept of the 2nd generation sensor was inspired by the work of [12], where the impedance of a piezo sensor was determined out of the measured response of a resistor in series to the piezo sensor actuated by a frequency modulated chirp signal. The developed multi-functional sensor shown in figure 2 (right) consists of the same piezo disc as the 1st generation sensor. The upper electrode is connected to a Pt100 temperature sensor, used as shunt resistor, soldered to a circuit board that also host the connector. The piezo – Pt100 assembly is embedded in an epoxy housing (diameter of 20 mm and height of 10 mm). To measure the impedance of the piezo a signal generator is connected to the ground electrode of the piezo and the Pt100 temperature sensor. For actuation, a frequency swept chirp signal with a starting frequency of 0 kHz and end frequency of 600 kHz with flat frequency response [12] is used. The response voltage over the PT100 was measured and out of the FFT of the voltage response, the admittance of the piezo sensor is determined (see figure 3).

For data collection a LCR meter type 7600 from Quadtech for the measurement of the electrical impedance of the sensors during curing (only in case of 1st generation sensors) and a combined active/passive SHM system consisting of two 4 channel acoustic emission cards (type

PCI-DISP-4 from PAC), one switchable arbitrary waveform generator card (type: ARB-1410 from PAC) for the actuation of burst signals in up to 4 actuators was used.

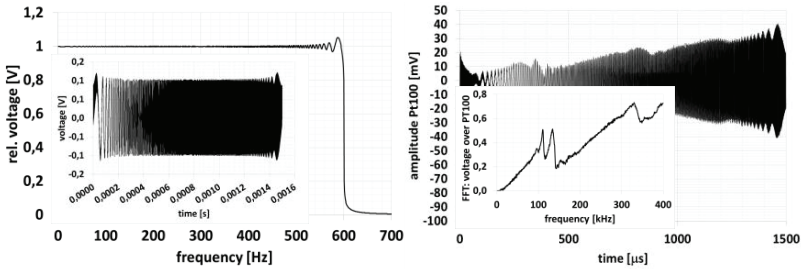

Figure 3: Actuation signal with FFT of the actuation signal (left side) and typical measured voltage signal and FFT of the voltage signal over the Pt100 sensor.

The comparison of both measurement methods – classical via impedance analyser and by chirp actuation – for a typical soldered piezo-pt100 assembly and a sensor shown in figure 2 are in very good agreement.

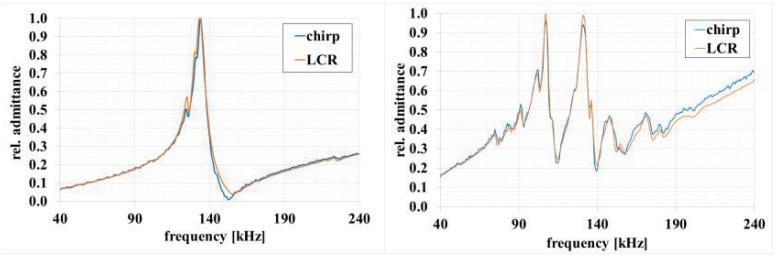

Figure 4: Comparison between both measurement methods for a typical soldered piezo-pt100 assembly (left) and a sensor (right)

3 INVESTIGATED COMPOSITE PARTS

For the validation of the sensor performance for process and structural health monitoring three different composite parts shown in figure 5 were selected: a pax door edge-member with integrated 1st generation pure piezo sensors, a flat composite plate and a hollow composite aircraft part with integrated 2nd generation piezo / temperature sensors.

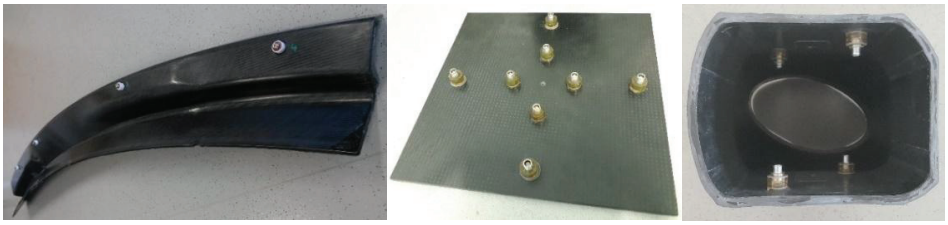

Figure 5: Composite parts for sensor validation: pax door edge-member with integrated 1st generation piezo sensors, flat plate and hollow aircraft part with integrated 2nd generation piezo / temperature sensors.

4 VALIDATION OF 1ST GEN. SENSOR ON A PAX DOOR EDGEMEMBER

4.1 Production process

Resin infusion of the preform was done in a temperature-controlled mould placed inside a press with an injection facility from Tartler at a maximum injection pressure of 5 bar and a constant temperature of 55°C. The following production steps were performed: placement of 4 piezo sensors in mould, placement of the preform in mould, closing of mould and heat up to 55°C, connection of the injection facility and heat up of the resin to 55°C, evacuation of mould, resin injection, closure of vents and inlet point and curing at 85°C for 8 hours with online cure monitoring, cooling of the mould and demoulding of the part.

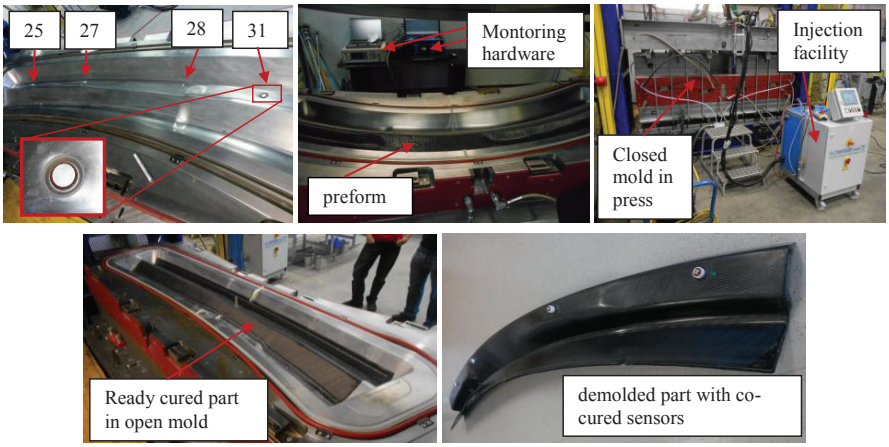

Figure 6: Production steps: sensors (25, 27, 28, 31) mounted in mould, preform in mould (measurement equipment connected), closed mould with infusion facility, open mould with part, part with co-cured sensors

4.2 Cure Monitoring

Once the infusion has been finalized the mould was heated to 85°C and the impedance spectra of sensor 31 were measured in a frequency range between 140 kHz and 200 kHz every 90s. Figure 7 shows the change of the impedance spectra and change of the impedance at 1st anti-resonance frequency and change of the anti-resonance frequency during curing.

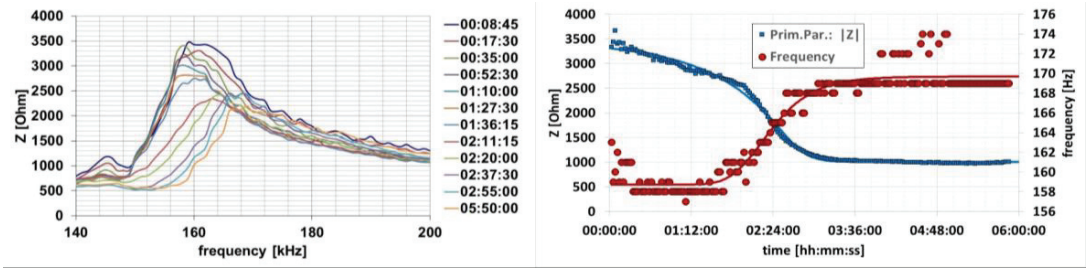

Figure 7: Change of the impedance spectra and the change of the impedance at anti-resonance frequency and the change of the anti-resonance frequency during the time of curing measured by sensor 31

Figure 7 clearly illustrates the change in the impedance spectra around the first radial anti-resonance frequency. Totally the impedance at first radial anti-resonance frequency change from 3.5 kΩ to around 1 kΩ during curing and the anti-resonance frequency change from 158 kHz to around 170 kHz. In addition, once curing has been finished both parameters are stable over time indicating the finalization of the curing process.

4.3 Wave propagation

For validation of the co-cured transducers for SHM each transducer was used as actuator and sensor. For actuation 3-sin burst signals at centre frequencies between 20 kHz and 300 kHz were used. Prior to the measurement of the wave propagation the group velocities of the different guided wave modes were calculated using the software DISPERSE. Figure 8 shows the calculated group velocities and the measured response of sensors 25, 27 and 28 due to the actuation of transducer 31 at 40 and 80 kHz.

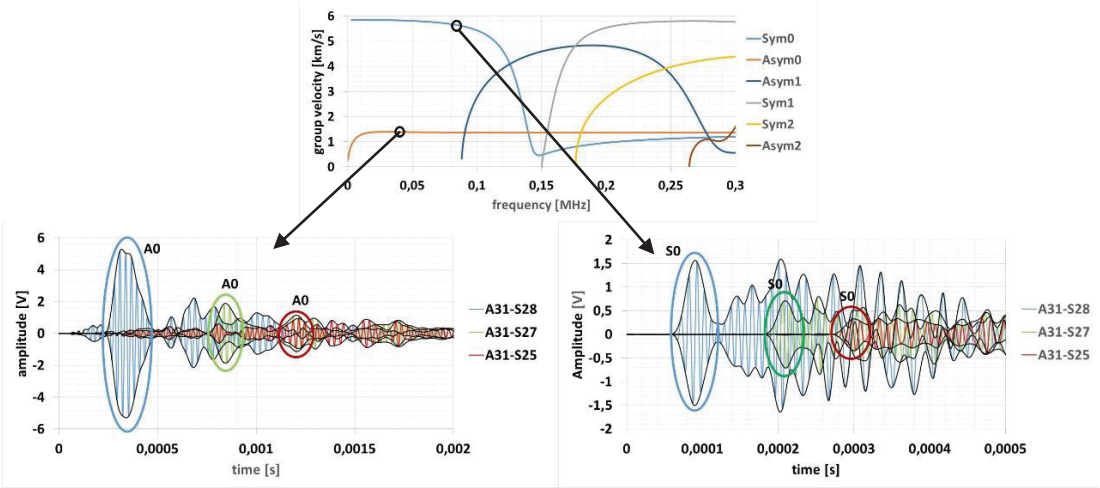

Figure 8: Calculated group velocities (top) and the measured response of sensors 25, 27 and 28 due to the actuation of transducer 31 at 40 kHz (bottom left) and 80 kHz (bottom right).

Only the S0 and the A0 mode is present below the cut of frequency of 85 kHz. At 40 kHz the A0 mode and at 80 kHz the S0 mode is dominant. The measured arrival times for the S0 mode at all sensors correspond well with the predictions made with DISPERSE (5670 m/s for the S0 mode at 80 kHz), where the measured group velocity for the A0 mode of 1250 m/s is somewhat lower compared to the calculations (1400 m/s).

5 VALIDATION OF 2ND GEN. SENSOR BEHAVIOUR ON A FLAT PLATE

For validation of the 2nd generation sensor a composite plate of 350 x 350 mm² with 9 layers of non-crimp fabric (NCF) with a quasi-isotropic fibre architecture $[0/90/45/-45]_s$ and a total thickness of 7.8 mm was produced. Eight piezo-temperature sensors were placed in the lower part of the mould as shown in figure 9 (left side). Sensors labelled T1 to T4 show the position

of the sensors used for temperature monitoring and sensors labelled Ch1 to Ch4 show the position of the sensors used for flow front and cure monitoring by the measurement of the admittance during production. Prior to the production of the plate an infiltration simulation was performed with the Finite Element (FE) software PAM-RTM to determine the infiltration time (middle of figure 9) and the expected arrival time at the sensor locations Ch1 to Ch4 of the flow front during infiltration.

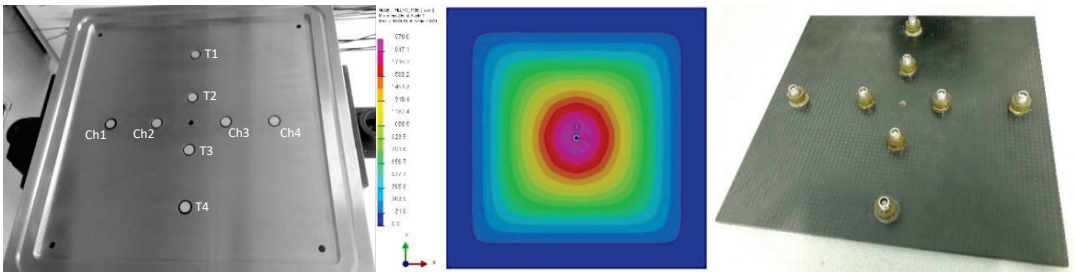

Figure 9: Left side: lower part of the production mould with the mounted sensors for temperature (T1 – T4) middle: flow front and cure monitoring (Ch1 – Ch4) during production and right side infiltration time out of the PAM RTM Simulation.

5.1 Process Monitoring

During the production of the plate the propagation of the flow front and the degree of cure after successful impregnation of the dry preform were determined. The temperatures on 4 positions (T1-T4) and the admittance of the sensors on 4 further positions (Ch1 – Ch4) were measured with a sample rate of 1 Hz. To illustrate the transient behaviour during the whole production step, the peak frequency of the 1st resonance was extracted out of the admittance data. The evolution of the temperatures (T1 – T4) and the peak frequencies of the 4 other sensors (Ch1 – Ch2) are shown in figure 10.

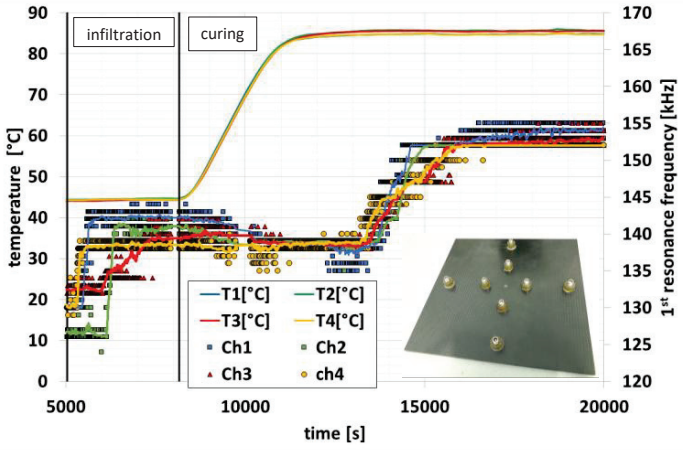

Figure 10: Evolution of the temperatures (T1 – T4) and the peak frequencies of the 4 other sensors (Ch1 – Ch2).

The left part in figure 10 (between 5000 s and 8000 s) shows the period of infiltration and the remaining part (above 8000 s) show the period of curing. The temperature signals indicate a very homogeneous temperature distribution during the whole process. During infusion the steep increases of the frequency for different times of the sensors indicating the different arrival times of the flow front – first for the outermost sensors Ch1 and Ch4 followed by the inner sensors Ch3 and Ch4. During curing all 4 sensors show an increase of the resonance frequency indicating the starting of cure at around 13200 s (1 hour and 23 min after the start of the curing cycle). A stable resonance frequency was reached after around 2 hours and 15 min indicating the completion of the curing step. As the transient behaviour for all 4 distributed sensors are similar, a homogenous curing of the part can be assumed. The measurement of the change of the 1st radial resonance frequency of the developed sensor over time is very well suited to trace the position of the flow front during infiltration and the degree of cure during curing of the part.

5.2 Guided Waves

For guided wave actuation 3-sine burst signals with centre frequencies of 40 kHz and 80 kHz were used to assess the suitability of the developed sensor for the detection of simulated defects under variable temperature conditions. Artificial damages in shape of added mass (weight of 170g / diameter of 25 mm) were placed on several positions on the plate. The baseline of the plate was measured at different temperatures ranging from 22°C to 60°C. For the measurement of the ultrasonic response each co-cured transducer was used as actuator and sensor leading to 8 x 7 matrix of actuator - sensor combinations. Figure 11 shows the measured response of sensor Ch4 due to the actuation of sensor T1 at different temperatures and after the application of the simulated damage. In addition, the residuals between the different baselines and the damage and the best suited baseline is shown in the lower part of figure 11.

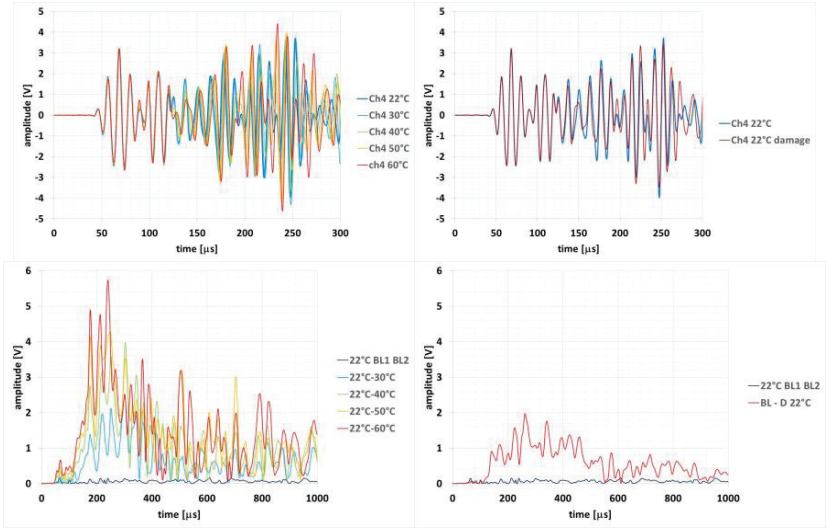

Figure 11: Measured response of sensor Ch4 due to actuation of sensor T1 at different temperatures and after the application of the simulated damage (top) and residuals between the different baselines and the damage and the best suited baseline (bottom).

Due to the change of temperature the signals were stretched in time – the higher the temperature the higher the stretching – indicating a change of group velocity. In addition, the amplitudes change due to a change of the damping in the material. In case of the simulated damage the signal position remains nearly unchanged, and the major change was observed in the amplitude caused by the absorption of the wave by the simulated damage. When the best baseline (baseline with the closest temperature to the damage measurement) was used, the damage could be clearly detected (much higher residuals compared to the residuals from two baselines at similar temperature – bottom left of figure 11). In case of a temperature difference of about 8°C the residuals between the two baselines already reach the same level as the residuals between the intact and damaged plate making it very difficult to discriminate between temperature effects or potential damages.

All raw data have been fed in near field sparse array beam forming algorithm described in more detail in [5]. Figure 12 show the colour coded images of the localized damages using this beam forming algorithm and the data of the 40 kHz (top) and 80 kHz (bottom) measurement assuming a group velocity of 1250 m/s of dominant A0 mode for beam forming using the best baseline (left). The middle and right part of figure 12 show results when a baseline is taken at 30°C with and without temperature compensation by frequency shift algorithms [12].

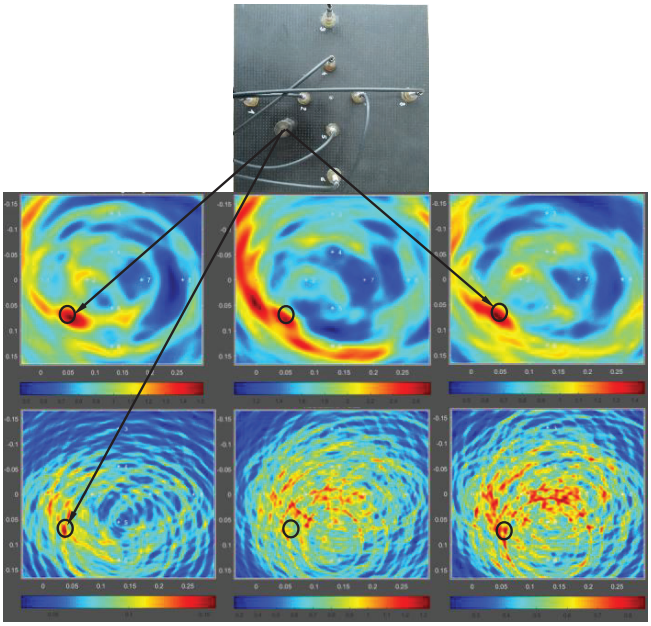

Figure 12: Colour coded images of the localized damages using a sparse array beam forming algorithm, top: 40kHz, best baseline (left), baseline @ 30°C (middle), temperature compensated baseline @ 30°C bottom: 80kHz, best baseline (left), baseline @ 30°C (middle), temperature compensated baseline @ 30°C.

The simulated damage could be detected and located (red coloured region) for both actuation frequencies at 40 kHz and 80 kHz when using the best baseline (left part of figure 12). In case the baseline was assessed at 30° it is still possible to locate the damage in case of 40 kHz, but

additional false positives appear. In case of 80 kHz actuation a clear damage detection and location is not possible (middle pare of figure 12). When a temperature compensation algorithm based on a frequency shift [12] was applied it was possible to achieve nearly similar results for the case of 40 kHz using the best baseline. In case of 80 kHz actuation the results could be improved but the appearance of several false positives makes a clear damage detection and localization extremely difficult. Such observations are in line with previous works [12] were the effect of temperature on damage detection increase with the temperature difference and the actuation frequency indicating the importance of knowledge of the temperature during damage assessment.

6 2ND GENERATION SENSOR BEHAVIOUR ON A HOLLOW AIRCRAFT PART

Finally, the ability of the developed sensor for detection and localization of acoustic emission signals was assessed on the hollow aircraft part shown in figure 5.

6.1 Wave propagation

Figure 13 top left shows the position of the sensors in an unwind view of the quasi-cylindrical part of the component. Each sensor was actuated with a 3-sin burst signal between 30 kHz and 200 kHz and the response of all other sensors, including the additional used piezo active waver sensors of type smart layer from Acellent glued at the same positions on the opposite side of the part were captured. The response of the co-cured sensor is like the smart layer sensor, where to amplitude of the co-cured sensor is higher. One can clearly see the faster symmetric mode followed by the asymmetric mode (top left of figure 13). For each actuator - sensor combination the propagation velocity of the quickest symmetric mode was measured (bottom left of figure 13 for e.g. actuator 1) and evaluated against the propagation angle relative to the circumference of the part. Due to the anisotropic stiffness of the part, the propagation velocity strongly varies with the propagation direction. As approximation the wave front was assumed to be an ellipse with the fastest and lowest velocity of 8000 m/s and 3500 m/s respectively.

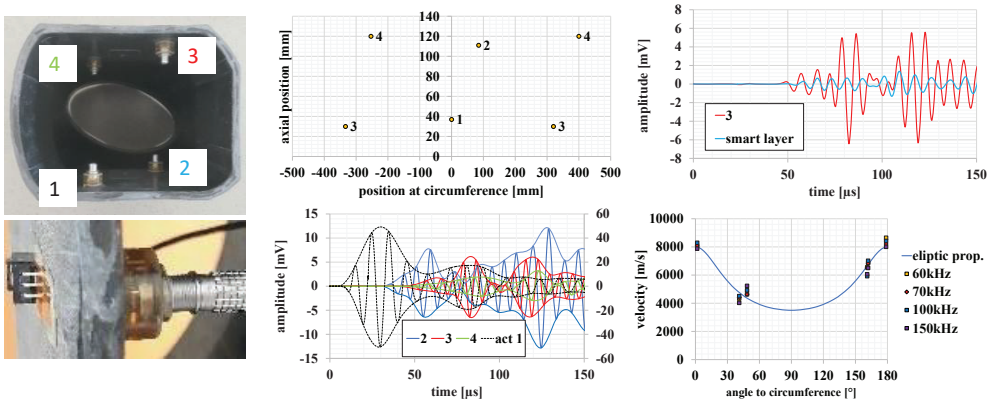

Figure 13: Position of the sensors (top, left), the response of sensor 3 and the smart layer sensor due to actuation of sensor 1 (top right), the response of sensor 2, 3 and 4 due to actuation of sensor 1 (bottom left) and the propagation velocity of the fastest mode as function of the propagation direction (bottom right)

6.3 Acoustic Emission

To prove the ability of the co-cured sensors for detection and localization of AE events two different types of AE events were introduced: 3-sin bursts between 30 and 200 kHz introduced by the smart layer sensors (position of the co-cured sensors) and pencil breaks between the co-cured sensors. Event localization was done by a standard cylindric algorithm, where the arrival time was determined by 1st threshold crossing. To be able to account for the elliptic wave front the dimensions in y-axis were increased by a factor of 8000/3500. All 3-sin burst signals with frequencies higher than 90 kHz can be localized (left side of figure 14: green dots smart layer above sensor 1, red dots: sensor 2 and yellow dots: sensor 3). At lower frequencies the amplitude of the quicker symmetric mode was below the threshold for at least one of the sensors leading to wrong localization values. All pencil lead breaks (Hsu Nielson source) can be located (right side of figure 3: green dots: between sensor 1-2, red dots between sensor 2-3, yellow dots between sensor 3-4 and blue dots between 1-4).

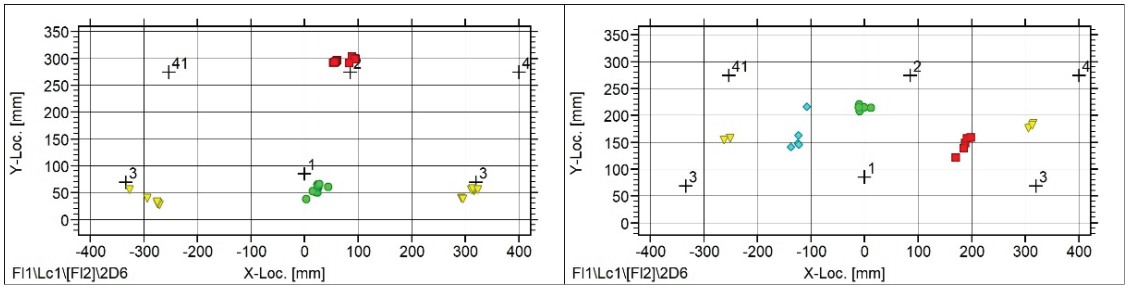

Figure 14: Location of simulated AE events: 3-sin bursts (left side), pencil breaks (right side)

7 CONCLUSIONS

A novel multifunctional piezo-temperature sensor to be used in an integrated process and structural health-monitoring concept for composite parts made by resin transfer moulding has been successfully validated on different composite parts in a laboratory environment. The developed transducers were very well suited to monitor the different production steps during resin infusion and curing – flow front propagation and resin curing – by tracking the change of the 1st resonance frequency of the piezo sensor. The integrated Pt 100 sensor was very well suited as temperature dependent shunt resistor for impedance-based process and cure monitoring.

After the production all transducers were co-cured to the part demonstrating the ability of the developed transducers to be used in infusion production processes. The co-cured transducers were very well suited to be used as actuators and/or sensors of an active guided wave or passive acoustic emission based SHM system. Simulated defects can be detected and located by passive acoustic emission and guided waves using the information of the guided wave propagation properties and the temperature information of the Pt100 sensor for temperature compensation.

REFERENCES

[1] A. Aktas, S.W. Boyd, R.A. Shenoi, “Monitoring and simulation of the vacuum infusion process”, Proc. of the 19th ICCM (2013), pp. 4913
[2] I. Partridge and G. Maistros, ‘Dielectric Cure Monitoring for Process Control’, Chapter 17, Vol. 5, Encyclopaedia of Composite Materials (2001), Elsevier Science, London, page 413.
[3] N. Liebers, D. Stefaniak, M. Kleineberg, M. Wiedemann, „Sensor guided cure processes – a study of productivity and quality optimization potential”, Proc. of the 19th ICCM (2013), pp. 2321.
[3] V. Giurgiutiu “Structural Health Monitoring with Piezoelectric waver active sensors”. Academic Press, 2008.
[4] C. Boller, F-K. Chang, Y. Fujino “Encyclopedia of Structural Health Monitoring”. John Wiley & Sons Ltd., 2009
[5] M. Scheerer, A. Peldszus, M. Stadtschnitzer, R. Wagner “Modern Acoustic NDT Methods for the off- and online Detection of Damages in Composite Aeronautic Structures”. Proc. 3rd IALCCE, Vienna, Austria, pp. 1430–1437, 2012.
[6] T. Kosaka, A. Matsumoto, T. Kajikawa, M. Koike, K. Kusukawa, “Process monitoring of CFRP laminates by embedded fiber optic sensors”, Proc. of the 19th ICCM (2013), pp. 1121
[7] M. Scheerer, Z. Simon, M. Marischler, T. Roser, B. Rittenschober, „Validation testing of an integrated process and structural health monitoring system based on piezoelectric sensors on a PAX door edgemember made by RTM”, Proc. of the 8th. EWSHM, 05.-08.07.2016, Bilboa, Spain
[8] M. Scheerer, Z. Simon, M. Marischler, B. Rittenschober, „Validation of a multifunctional hybrid piezo / temperature sensor for process and structural health monitoring of CFRP structures”, Proc. of the 9th EWSHM, 10.-13.07.2018, Manchester, UK.
[9] M. Scheerer, Z. Simon, M. Marischler, B. Rittenschober, „Influence of Production and Environmental Parameters on the behavior of hybrid Piezo / Temperature Sensors for Production and Structural Health Monitoring of Composite Structures”, Proc. of the 12th IWSHM, 10.-12.09.2023, Stanford, USA.
[10] M. Scheerer, Z. Simon, M. Marischler, D. Kampenhuber, M. Hatzenbichler, “Validation of a piezo based integrated process and SHM system on hollow composite aircraft part made by vacuum infusion using a 3d printed smart mold”, Proc. of the 14th IWSHM, 11.-13.09.2023, Stanford, USA.
[11] B. Xu, V. Giurgiutiu, “A Low-Cost and Field Portable Electromechanical (E/M) Impedance Analyzer for Active Structural Health Monitoring”, Proc. of the 5th. Int. Workshop on Structural Health Monitoring, September 15.-17.09.2005, Stanford, USA
[12] M. Scheerer, D. Lager: “Validation of Temperature Compensation Techniques for Impact Damage Detection and Localization Using Ultrasonic Sparse Arrays”, Proc. of the 7th European Workshop on Structural Health Monitoring, July 2014, Nantes, France

Part XII
SS 02 - SHM-INFORMED STRATEGIES AND THEIR USE FOR LIFETIME EXTENSION OF STRUCTURES

Luis David Avendaño-Valencia, Stefano Manzoni

XI ECCOMAS Thematic Conference on Smart Structures and Materials - SMART 2025
M. Krommer, M. Nader and M. Schagerl (Eds)

Received: 9 April 2025 / Revised: 5 September 2025 / Accepted: 7 September 2025
© The Author(s) 2025

Damage Detection and Filtering of EOV Effects by Monitoring Piezoelectric Coupling

Marta Berardengo, Matteo Brambilla, Stefano Manzoni

Abstract. This paper describes an innovative structural health monitoring approach for smart structures where piezoelectric elements are present and connected to the primary system to be monitored. The approach requires to measure and monitor the piezoelectric coupling trend for different modes of the system. Indeed, this quantity is shown to be sensitive to damage presence and its location, lowly affected by environmental (mainly thermal) and operational variability (which is an important point in structural health monitoring applications), and easy to be estimated. This makes the proposed approach reliable, robust and less expensive compared to already available structural health monitoring methods based on the use of piezoelectric elements (e.g., electromechanical impedance approaches).

Numerical simulations are employed to highlight the capability of the newly proposed method to detect a damage and its location. Then, the final part of the paper proves the reliability of the approach by means of experimental tests on two different structures: a cantilever beam and a truss, using either piezoelectric patches or stacks. During the tests, particular attention was devoted to environmental variability effects, and the experimental activity confirms that the proposed structural health monitoring method shows larger sensitivity to damage presence than to environmental variability effects.

Key words: Structural health monitoring, Damage detection, Smart structure, Piezoelectric element, EOV, Piezoelectric shunt

1 INTRODUCTION

The use of piezoelectric elements in systems and structures can be exploited for many different purposes, such as vibration control (e.g., [1]), energy harvesting (e.g., [2]), micro positioning. Structures equipped with these materials (smart structures, e.g., [3, 4]) can thus show

Marta Berardengo
Department of Mechanical, Energy, Management and Transportation Engineering, Universitá degli Studi di Genova, Via all'Opera Pia, 15a - 16145 Genoa, Italy, e-mail: marta.berardengo@unige.it

Matteo Brambilla & Stefano Manzoni
Department of Mechanical Engineering, Politecnico di Milano, Via La Masa, 1 - 20156 Milan, Italy
e-mail: stefano.manzoni@polimi.it

specific advanced features which are possible because of the double piezoelectric effects: direct effect which implies that mechanical strain is converted in voltage at the electrodes of the piezoelectric element (used to build sensors), and inverse effect which implies that a voltage applied to the electrodes generates a mechanical strain (employed for designing actuators).

The aim of this paper is to show that the presence of this double effect can be exploited for developing a new approach for structural health monitoring (SHM) for smart structures based on piezoelectric elements.

The paper is structured as follows: Section 2 introduces the proposed damage feature and its advantages, as well as a related damage index, then Section 3 discusses some numerical simulations on a beam, and, finally, Section 4 presents experimental tests validating the newly proposed approach. The main aim of this paper is to summarise some of the most important results discussed in [5].

2 DAMAGE FEATURE AND INDEX

When piezoelectric elements (either patches or stacks) are connected to a structure, the dynamics of both the mechanical and electrical parts of the system can be described by means of modal coordinates [6, 7, 8]. These equations are function of a parameter named modal electromechanical coupling factor (MEMCF) k_i, which describes the efficiency of the energy transfer between the electrical part of the system (for the considered piezoelectric element) and the considered i-th mode and vice versa.

The value of k_i depends on different features of the coupled system, such as geometry, material properties, etc. However, the main parameter affecting the value of k_i is the trend of the mode shape at the boundaries of the piezoelectric element [9]. This means that a change of the $|k_i|$ value is expected in case a damage occurs in the structure and it is able to affect the corresponding mode shape at the boundaries of the considered piezoelectric element [5]. Therefore, $|k_i|$ can be seen as a damage feature, and here its main advantages are discussed. Before this, it is important to explain how the value of $|k_i|$ can be estimated. Even if analytical formulations exist for k_i as function of either physical [10] or modal [11] quantities, the easiest way to estimate $|k_i|$ is by using the following formulation:

$$|k_i| \simeq \sqrt{\frac{\hat{\omega}_i^2 - \omega_i^2}{\omega_i^2}} \tag{1}$$

where ω_i is the i-th eigenfrequency with the piezoelectric element short-circuited, while $\hat{\omega}_i$ is the i-th eigenfrequency with the piezoelectric element open-circuited. The value of $\hat{\omega}_i$ is always larger than that of ω_i because of a stiffening effect related to the electromechanical behaviour of the piezoelectric element [6]. When different piezoelectric element are present in the structure, ω_i and $\hat{\omega}_i$ for a given piezoelectric element are determined keeping all the other piezoelectric elements short-circuited. Thus, the value of $|k_i|$ can be obtained both numerically or experimentally by determining eigenfrequency values.

Therefore, if one performs two modal analyses (one with the considered piezoelectric ele-

ment short-circuited and open-circuited for the other), the $|k_i|$ values of many modes can be estimated. Repeating this estimation at different times, the possible rise of a damage can be discovered. As a damage index, the following quantity s_p is proposed in [5]:

$$s_p = \sum_{i=h}^{q} |(|k_{i,p}| - |k_{i,p,\mathrm{u}}|)| \tag{2}$$

where the subscript p indicates that the index is computed for the generic p-th piezoelectric element in the structure and $k_{i,p,\mathrm{u}}$ is related to the undamaged (or reference) structure condition. Furthermore, h and q indicate the generic h-th and q-th modes (with $h < q$), respectively.

The proposed approach allows using piezoelectric elements already present in the structure also for SHM purposes. Such an approach can be somehow categorized among SHM methods based on the estimation of mode shapes or related quantities (e.g., [12, 13]), but with the significant advantage that mode shape estimation can be avoided and substituted with eigenfrequency estimation which is a much simpler approach. Furthermore, this allows avoiding common problems in mode shape identification, such as noise effects and need for dense sensor mesh.

The use of $|k_i|$ as damage feature provides also another important advantage. Indeed, it has been demonstrated in [5] that it shows low sensitivity to environmental and operational variability (EOV). As for the robustness to environmental effects, this can be explained considering Eq. (1), where a ratio of eigenfrequencies is present. Even if ω_i and $\hat{\omega}_i$ change differently in response to environmental changes, their changes are expected to be close and this implies low sensitivity of the value of $|k_i|$ to environmental variations. Furthermore, operational changes (e.g., change of external excitation) are expected not to change the value of $|k_i|$ because eigenfrequency values are not related to operational conditions (unless significant non-linearity arises). This makes the proposed approach robust also to operational variability. The evidenced robustness to EOV makes the proposed method easier to be applied compared to other existing approaches based on piezoelectric elements (e.g., electromechanical impedance methods [14]).

A possible difficulty in using the proposed damage feature and index is related to uncertainty in estimations of small value of $|k_i|$ (i.e., when ω_i and $\hat{\omega}_i$ are close in frequency). This problem can be overcome by shunting a negative capacitance (since a negative capacitance does not exist in nature, it is built by using tailored electrical circuits [15]) to the considered piezoelectric element. Indeed, as explained in [5], this makes farther and farther the short- and open-circuit eigenfrequency, thus artificially increasing the value of $|k_i|$. The artificially increased MEMCF value is referred to as $\tilde{k}_i$, with $|\tilde{k}_i| > |k_i|$.

3 NUMERICAL SIMULATIONS

Here, some simulations are described in order to show that s_p is a reliable index for damage detection and that it is even able to provide information about damage location when more than one piezoelectric element are present on the structure. The considered structure is an aluminum clamped-clamped beam (length 770 mm, thickness 1 mm) equipped with five piezoelectric

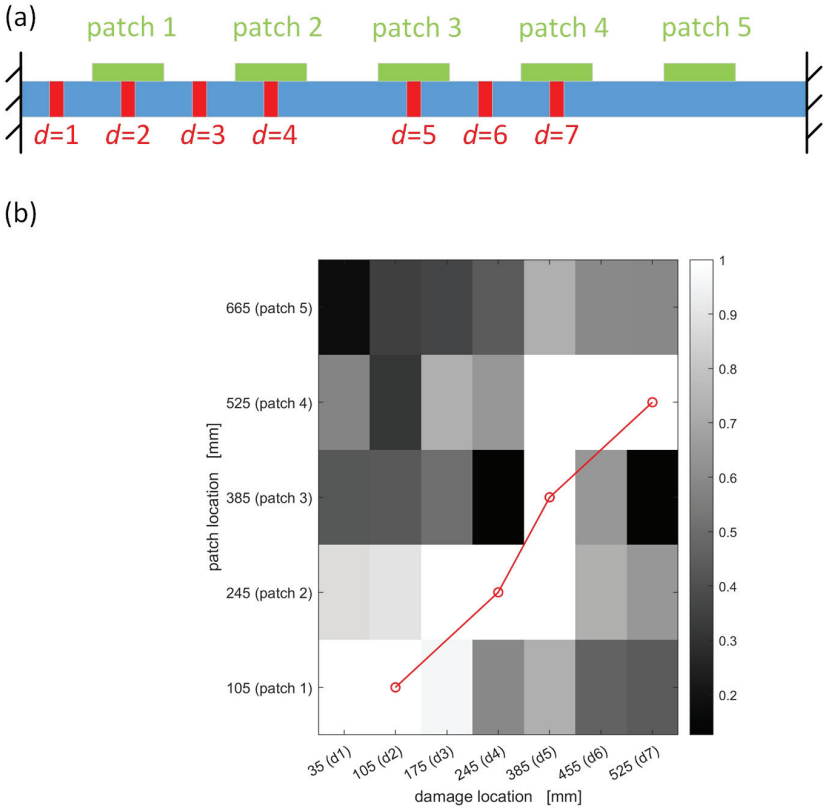

Figure 1: Schematic of the clamped-clamped beam with patch and damage locations (a) and value of $\bar{s}_p$ (b).

patches (material PIC151, length 70 mm, thickness 0.5 mm). Damage is simulated by decreasing of 70% the Young's modulus of the beam in five locations (see Fig. 1a). A single damage is considered in each simulation (i.e., damage is not present in more than one location in a given simulation). For each simulation, the s_p value is computed for all the patches considering the vertical bending modes from the fifth to the fifteenth.

Figure 1b shows the value of $\bar{s}_p$ ($\bar{s}_p$ is a normalised version of s_p such that it is equal to 1 for the patch having the highest s_p value for the considered damage location). It is evident that the value of $\bar{s}_p$ is able to evidence the presence of the damage and its value result high (i.e., close to 1) for the patches close to the considered damage, implying the capability of giving information about damage location. Many more simulations and details are available in [5].

4 EXPERIMENTAL TESTS

This section discusses some tests carried out on two different structures: (i) a cantilever aluminum beam equipped with piezoelectric patches and (ii) a truss structure equipped with

Table 1: Locations of the brick and of the patches.

	position of the center of the considered element from the constraint of the cantilever beam [mm]
patch 1	105.0
patch 2	385.0
brick location deA	47.5
brick location deB	105.0
brick location deD	302.5
brick location deE	347.5

piezoelectric stacks. Details about these structures can be found in [5].

Here, few tests are discussed. The reader can refer to [5] for many more tests.

4.1 Test with the beam

The cantilever beam is made from aluminum and has length of 700 mm and thickness of 1 mm. Two piezoelectric patches (material PIC151, length 70 mm and thickness 0.5 mm) are used for damage detection. The beam is excited with a non-contact electromagnetic actuator providing random disturbance and eigenfrequencies are identified with modified Ibrahim time-domain method [16] applied to response measurements (collected with a non-contact laser vibrometer). Here, two test types are presented.

The first is a test where it is shown that the effect of temperature slightly affect the $|k_i|$ values compared to damage. Damage is simulated here by adding a small brick bonded to the beam in different positions (see Fig. 2 and Table 1).



Figure 2: Picture (a) and schematic (b) of the cantilever beam with patches and brick locations.

The second is a test where s_p (considering five bending modes, excitation between 350 and 900 Hz approximately) is computed for the two patches. Since repetitions of calculation of s_p

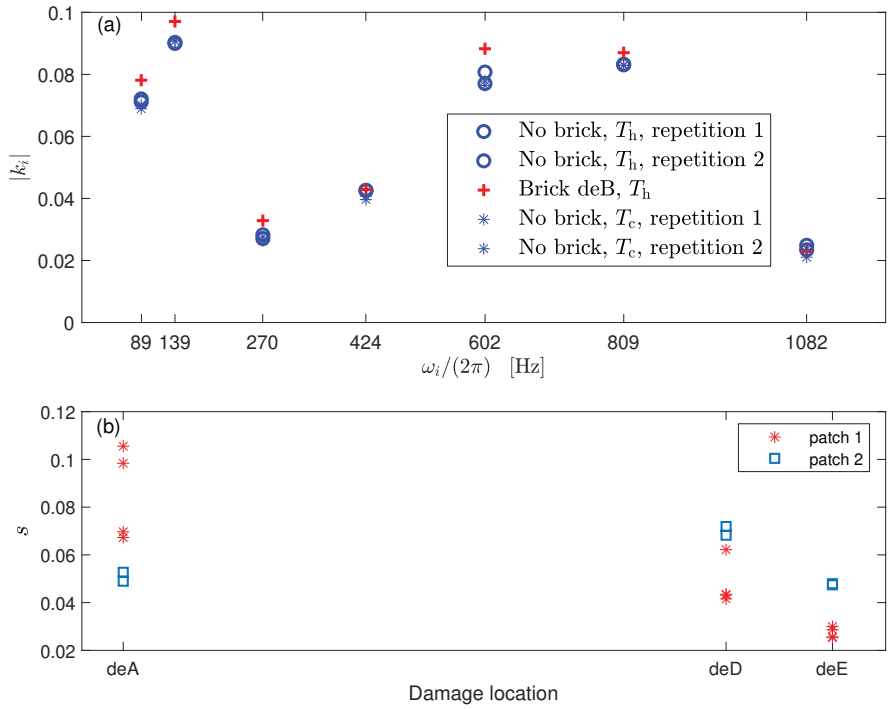

Figure 3: Trend of $|k_i|$ for patch 1 and for some modes defined through the corresponding eigenfrequency ω_i (with all the patches short-circuited) for different temperatures (T_h=300.15 K and T_c=288.15 K) and with brick in position deB (a) and s_p value (calculated on five bending modes) for the two patches as function of the position of the brick (b). See Table 1 for the locations of the brick and of the patches.

without damage showed values below 0.03 for both the patches, Figure 3b shows that damage is always detected at least by a patch for the three locations where the brick was bonded. Furthermore, the patch closest to the considered brick location always shows the largest s_p value, implying the possibility to give indications on damage location (see Table 1).

4.2 Test with the truss structure

Here, a steel truss structure (height of 1 m) with three main pillars is considered (see Fig. 4a). Two piezoelectric stacks are placed at the base of the truss. The truss is excited with a non-contact electromagnetic actuator providing random disturbance and eigenfrequencies are identified with modified Ibrahim time-domain method [16] applied to response measurements (collected with an accelerometer).

The damage is obtained making two small cuts on one of the main pillars approximately 20 cm far from the stacks. A negative capacitance was connected to both the stacks in order

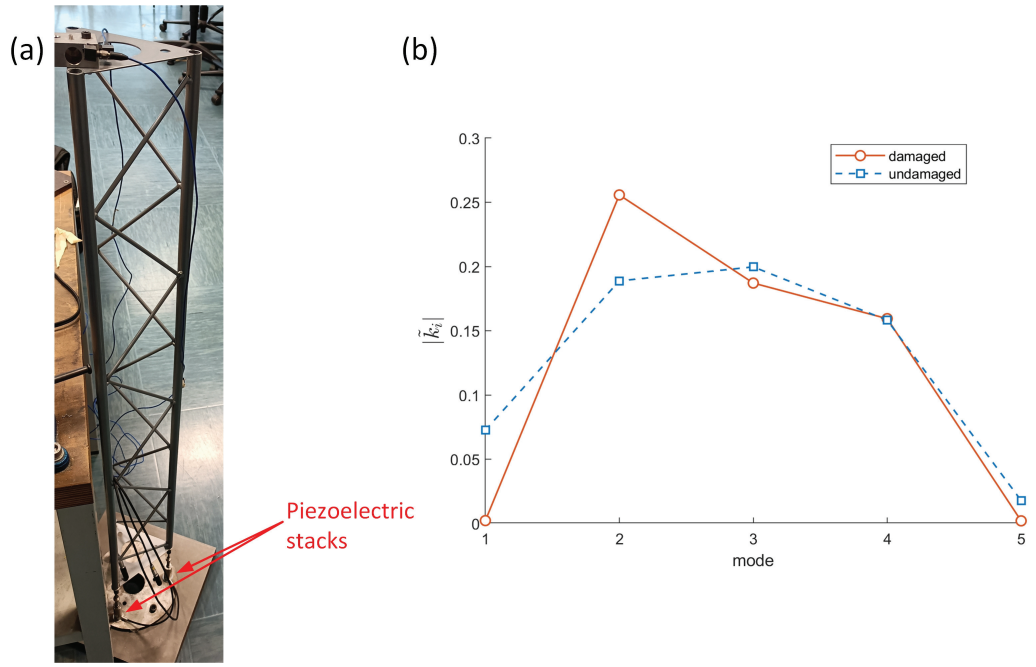

Figure 4: Truss set-up (a) and trend of $|\tilde{k}_i|$ for the considered modes with and without damage for one of the two stacks.

to increase the coupling values because of the initial small values of $|k_i|$ for various modes. The $|\tilde{k}_i|$ values of five bending modes (below 400 Hz) were estimated before and after the cuts. Figure 4b shows that it is easy to detect the damage (significant changes of the $|\tilde{k}_i|$ values of the first two monitored modes) also in a real condition with a real slight damage.

5 CONCLUSION

This paper has dealt with a new approach for damage detection in structures equipped with piezoelectric elements. The damage feature is the MEMCF, which measure the coupling between a given mode and the electrical part of the system. The use of MEMCF as damage feature allows for a low sensitivity to EOV and ease of estimation of the chosen damage index. The proposed approach has been tested on two different structures with good results, paving the way for further developments and opening to the use in the context of real structures.

ACKNOWLEDGMENTS

This research has been supported by the project ”CHIMERA? - is there a CHance that Indexes and Measurements of the energy conversion Efficiency Reveal system Alterations?” funded by the European Union – Next Generation EU, M4C2 I1.1, through Progetti di Rilevante Interesse Nazionale (PRIN) 2022, grant n. 20225PKHWJ (CUP: D53D23003060006).

REFERENCES

[1] P. Gardonio and G. K. Rodrigues, "Shunted piezoelectric patch adaptive vibration absorber set to maximise electric power absorption: A comparison between parallel and series rl-shunts," *JVC/Journal of Vibration and Control*, vol. 31, no. 1-2, p. 37 – 50, 2025.

[2] L. Dal Bo, P. Gardonio, and E. Turco, "Analysis and scaling study of vibration energy harvesting with reactive electromagnetic and piezoelectric transducers," *Journal of Sound and Vibration*, vol. 484, 2020, 115510.

[3] B. Zhou, F. Thouverez, and L. D., "Vibration reduction of mistuned bladed disks by passive piezoelectric shunt damping techniques," *AIAA Journal*, vol. 52, pp. 1194–1206, 2014.

[4] Y. Zhong, X. Ma, J. Yuan, and Z. Zhang, "Electromechanical modelling and vibration control analysis of cyclic symmetric structures with a piezoelectric vibration absorber," *JVC/Journal of Vibration and Control*, 2024, in press.

[5] M. Berardengo, M. Brambilla, A. Codina, N. Schena, and S. Manzoni, "Piezoelectric coupling as a feature sensitive to structural alterations," *Mechanical Systems and Signal Processing*, vol. 224, 2025, 112012.

[6] O. Thomas, J. Ducarne, and J. De$\ddot{u}$, "Performance of piezoelectric shunts for vibration reduction," *Smart Materials and Structures*, vol. 21, no. 1, 2012, 015008.

[7] M. Berardengo, S. Manzoni, J. Høgsberg, and M. Vanali, "Vibration control with piezoelectric elements: The indirect measurement of the modal capacitance and coupling factor," *Mechanical Systems and Signal Processing*, vol. 151, 2021, 107350.

[8] J. D. Richardt, B. Lossouarn, J. Høgsberg, and J.-F. Deü, "Calibration of multiple shunted piezoelectric transducers with correction for residual modes and shunt interactions," *JVC/Journal of Vibration and Control*, vol. 31, no. 1-2, p. 24 – 36, 2025.

[9] S. Moheimani and A. Fleming, *Piezoelectric Transducers for Vibration Control and Damping*. Springer-Verlag, 2006.

[10] J. Ducarne, O. Thomas, and J. De$\ddot{u}$, "Placement and dimension optimization of shunted piezoelectric patches for vibration reduction," *Journal of Sound and Vibration*, vol. 331, no. 14, pp. 3286–3303, 2012.

[11] M. Berardengo, O. Thomas, C. Giraud-Audine, and S. Manzoni, "Improved resistive shunt by means of negative capacitance: new circuit, performances and multi mode control," *Smart Materials and Structures*, vol. 25, 2016, 075033.

[12] D. Dessi and G. Camerlengo, "Damage identification techniques via modal curvature analysis: Overview and comparison," *Mechanical Systems and Signal Processing*, vol. 52-53, no. 1, pp. 181–205, 2015.

[13] M. D. Ulriksen and L. Damkilde, "Structural damage localization by outlier analysis of signal-processed mode shapes - Analytical and experimental validation," *Mechanical Systems and Signal Processing*, vol. 68-69, pp. 1–14, 2016.

[14] V. Giurgiutiu, *Structural health monitoring of aerospace composites*. Academic Press, 2016.

[15] M. Berardengo, S. Manzoni, O. Thomas, C. Giraud-Audine, L. Drago, S. Marelli, and M. Vanali, "The reduction of operational amplifier electrical outputs to improve piezoelectric shunts with negative capacitance," *Journal of Sound and Vibration*, vol. 506, 2021, 116163.

[16] A. Brandt, *Noise and Vibration Analysis – Signal Analysis and Experimental Procedures - 2nd edition*. Wiley, 2023.

XI ECCOMAS Thematic Conference on Smart Structures and Materials - SMART 2025
M. Krommer, M. Nader and M. Schagerl (Eds)

Received: 22 April 2025 / Revised: 27 August 2025 / Accepted: 7 September 2025
© The Author(s) 2025

Vibration-Based Robust Detection of Gear Incipient Faults under Different Speeds and Loads via a Cloud of Functional Models

Dimitrios M. Bourdalos, John S. Sakellariou

Abstract. The detection of incipient faults in a gearbox operating under different speeds and loads is investigated based on a novel unsupervised statistical time series method using a limited set of vibration signals from a single accelerometer. The method employs a cloud of Vector Functionally Pooled AutoRegressive (VFP–AR) models for the representation of the healthy gearbox dynamics at any speed and load within the considered ranges. Their estimation is achieved using vibration signals from the healthy gearbox after a specific angular resampling procedure removing the shaft speed fluctuations. The method's performance is systematically assessed through thousands of experiments on a single-stage spur gearbox, considering two levels of incipient single-tooth pinion faults under 41 distinct rotating speeds and 4 load levels. The results demonstrate near-perfect fault detection, even under speeds and loads not encountered in training, while the method outperforms a conventional multiple-model AR based alternative.

Key words: Spur Gear Faults, Gearbox, Vibration-based Fault Detection, Functional Models, Statistical Time Series Methods, Different Speeds and Loads

1 INTRODUCTION

The reliability of mechanical systems in industrial applications heavily depends on the health of gearboxes, which are essential for torque transmission and speed regulation. Early detection of gear faults is crucial for preventing unexpected and extensive failures, thus minimizing maintenance costs, reducing downtime and ensuring reliability [1]. Vibration-based Condition Monitoring (CM) approaches have become increasingly popular due to their capability to continuously assess machine health in real time without requiring operational downtime. However, in various industrial applications significant challenges arise from the need for variable operating conditions (OCs), such as different rotating speeds and loads, as well as the presence of measurement noise and other uncertainties. These factors may mislead a CM system and degrade diagnostic accuracy, making fault detection in gearboxes a particularly demanding task.

Dimitrios M. Bourdalos & John S. Sakellariou
Stochastic Mechanical Systems Automation (SMSA) Laboratory, Department of Mechanical Engineering and Aeronautics, University of Patras 26504 Patras, Greece
e-mail: dimitrios.bourdalos@upnet.gr

This necessitates the development of robust methodologies capable of maintaining high detection performance under varying OCs and uncertainty[1].

Vibration-based methods for fault detection under varying conditions in rotating machinery may be categorized as: *non-parametric* and *parametric*. Non-parametric methods are based on features extracted from the vibration signals, such as the signal's RMS, kurtosis, crest factor and so on in the time domain, or spectral energy features in the frequency domain, or time-frequency representations (e.g. spectrogram) to characterize gearbox health [2, 3]. Furthermore, signal decomposition methods, including Wavelet Packet Decomposition (WPD) and Empirical Mode Decomposition (EMD), have been employed to enhance feature extraction by isolating fault-related signal components [2, 4, 5, 6, 7]. The extracted features are often used as inputs to machine learning classifiers such as Support Vector Machines (SVMs) [3] or k-Nearest Neighbors (k-NN) [4], while Deep Neural Networks have also been explored for automating feature extraction [8, 9, 10]. Despite their effectiveness, such approaches generally require extensive labeled datasets encompassing both healthy and faulty conditions, which may not always be available in practice. Furthermore, their performance often depends on prior knowledge of the specific fault types considered and their effects on the vibration characteristics of the signals.

In contrast, *parametric* methods tackle the problem by initially applying filtering and noise reduction techniques, such as the well known Time Synchronous Averaging. Then, parametric AutoRegressive with eXogenous input (ARX) type models are employed to represent the system's underlying dynamics. Fault detection is then performed through residual analysis, where deviations from the expected model behavior are assessed using statistical moments like variance and kurtosis. Various parametric models including AutoRegressive (AR) [11, 12], ARX [13], and Vector AR [14, 15], have been explored for detecting gear faults. However, these studies focus only on load variations while assuming a constant rotating speed and are typically assessed with run-to-failure experiments, with no emphasis on early-stage fault detection.

It is important to highlight that the effectiveness of incipient fault detection using both categories of methods has, so far, been assessed under a restricted set of differetn OCs. In contrast, the challenge of fault detection across a broad range of speeds and loads that change simultaneously remains largely unexplored. This gap is particularly significant, as variations in both speed and load typically occur concurrently in industrial applications.

The *goal* of this study is the examination of the potential for unsupervised detection of incipient single-tooth spur gear fault under different speeds and loads through an extension of a recently presented statistical time series method [16, 17]. The extension includes the use of Vector Functionally Pooled (VFP) models of the AR type, instead of scalar ones, incorporating thus both rotating speed and load. In addition, to address the challenges mentioned above and achieve accurate modeling of the gearbox dynamics under different loads within a continuous and wide range of speeds, the concept of employing a 'cloud' of VFP models representing the healthy dynamics is adopted and combined with the angular resampling of the vibration signals via the Computed Order Tracking approach [18, pp. 148–151]. Each VFP model of the cloud may have a different structure and functional subspace covering a specific sub-range of rotating speeds, while accounting for the effects of all considered loads on the dynamics. The VFP

models are estimated using vibration signals from a single accelerometer, acquired from a sample of the considered speeds (in each specific range) and loads with the healthy gearbox. Fault detection is performed through an optimization framework that explores the consistency of the currently available vibration signal with the VFP models of the 'healthy cloud'. The method's performance is systematically assessed through thousands of experiments with a single-stage spur gearbox operating under 41 different rotating speeds and 4 different loads. Two levels of an incipient fault at the base of a single pinion tooth are considered. The results and comparisons with an alternative method, which is based on multiple conventional AR models, are presented via scatter type plots of the fault detection characteristic quantity and a confusion matrix [19].

2 THE EXPERIMENTAL PROCEDURE

2.1 Gearbox, gear fault scenarios, and measurements

The experimental set-up (Fig. 1) consists of a single-stage spur gearbox driven by an AC electric motor and loaded by a DC motor. The gearbox features a pinion with 17 teeth and a gear with 34 teeth. The drive motor operates at 41 distinct speeds, ranging from 15 Hz (1200 rpm) to 25 Hz (1500 rpm) in increments of 0.25 Hz (15 rpm), regulated by a standard variable frequency drive (inverter). The load motor operates as a generator, allowing adjustable loading conditions for the gearbox. Four different load scenarios are implemented: For Load 0, the load motor is detached from the gearbox. For Load 1, the load motor is attached to the gearbox but remains unloaded (no devices are connected to the generator's outputs). In Load 2, the load motor is attached to the gearbox and a 500-watt device is connected. Finally, in Load 3, the load motor is attached to the gearbox with a 1000-watt device connected. An incipient fault is introduced at the base of a single pinion tooth in the gearbox using a standard Dremel-type cutting tool. The fault scenarios are implemented via two distinct severity levels each defined as a percentage of the total tooth face width (w) affected (see Fig. 1). The first level corresponds

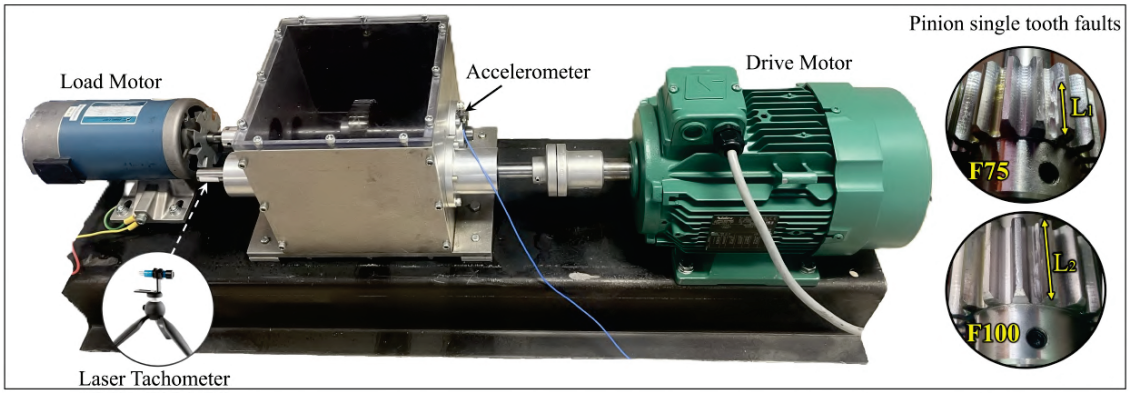

Figure 1: The experimental set-up: Photo of the gearbox including the sensors (accelerometer and tachometer) locations and the pinion single-tooth fault scenarios $F75$ and $F100$.

Table 1: Details on the vibration signals used for the training and assessment of the fault detection methods.

Gearbox state	Rotating speed (Hz)	Load	No. of signals per speed & load	No. of signals per state
Training Phase				
Healthy (H)	$\{15, 16, \ldots, 25\}$	$\{0, 1, 3\}$	1	33
Inspection Phase				
H / $F75$ / $F100$	$\{15, 15.25, \ldots, 25\}$	$\{0, 1, 2, 3\}$	15	7 380
Sampling frequency: $f_s = 10\ 240$ Hz; Signal length: $N = 51\ 200$ samples (5 s); Frequency bandwidth: $BW = [0 - 5\ 120]$ Hz; Total No. of signals = 7 413				

to 75% of the tooth face width affected ($L_1 = 0.75w$) while the second to 100% ($L_2 = w$). It is worth noting that the faults have been introduced on the gears inside the gearbox without disassembly, thus avoiding additional uncertainties.

The vibration signals (details in Table 1) are acquired using a single accelerometer placed on the ball bearing housing of the secondary shaft (see Fig. 1), with a sample frequency of $f_s = 10\ 240$ Hz. Additionally, a laser tachometer measures the rotating speed of the drive motor. A total of 7 413 signals are recorded, with only 33 of them (0.45% of the complete dataset) from the healthy gearbox to be employed for the training of the fault detection method. The remaining 7 380 signals (99.55%) are exclusively used in the inspection phase for the method's assessment and comparison.

2.2 Effects of different operating conditions and incipient faults on the vibration signals

The effects of the different rotating speeds, loads, and gear faults on the vibration signals are initially studied in the time domain using standard features, commonly employed for fault detection in rotating machinery [4]. These include signal RMS, peak, kurtosis and crest factor and are obtained from 164 vibration signals per health state with each corresponding to a unique combination of rotating speed and load level. Their values are presented in Fig. 2, where distinct colors and markers denote the different health states, while the x-axis indicates the signal number and the y-axis the corresponding feature value. As shown, the feature values for both faulty and healthy states exhibit significant overlap, highlighting the challenge of detecting incipient faults in the considered problem.

Furthermore, the effects of the different rotating speeds, loads, and faults are investigated in the order domain by constructing order spectrum zones via the Fast Fourier Transform (FFT). These zones are obtained using the above mentioned 164 angular vibration signals associated with each health state. The signals angular resampling is performed based on order tracking with a common frequency for all considered rotating speeds; refer to Section 3.1 for further details. The spectrum zones of the healthy state with those of the two fault scenarios 75% ($F75$) and 100% ($F100$) are compared in Figs. 3(a) and (b), respectively. Evidently, fault detection proves to be particularly challenging, as the variations in rotating speeds and loads influence the healthy dynamics in a way that obscures the fault-induced effects, causing the faulty spectrum

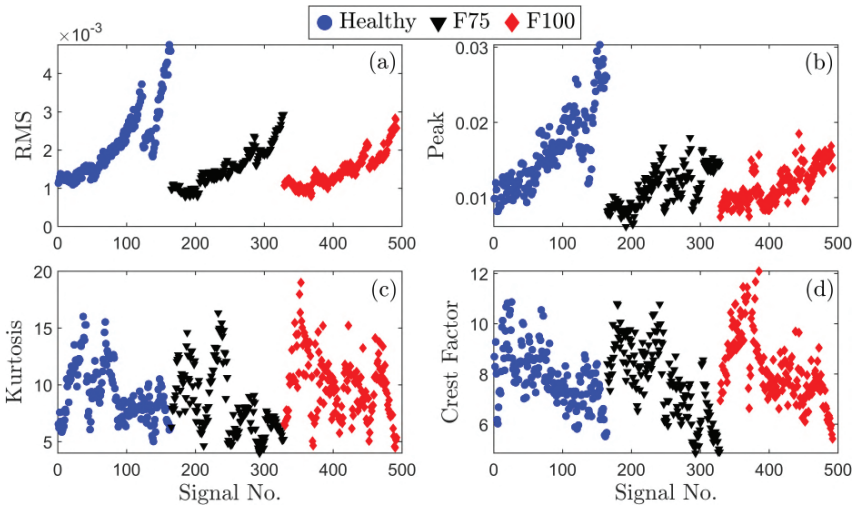

Figure 2: Time domain features corresponding to the Healthy and Faulty ($F75$ and $F100$) states under all 41 speeds and 4 loads: (a) RMS, (b) Peak, (c) Kurtosis, and (d) Crest Factor. Each color indicates a different health state; 492 signals per subplot: 164 per health state, 1 per speed and load combination.

zones to almost entirely overlap with the healthy ones within the considered bandwidth.

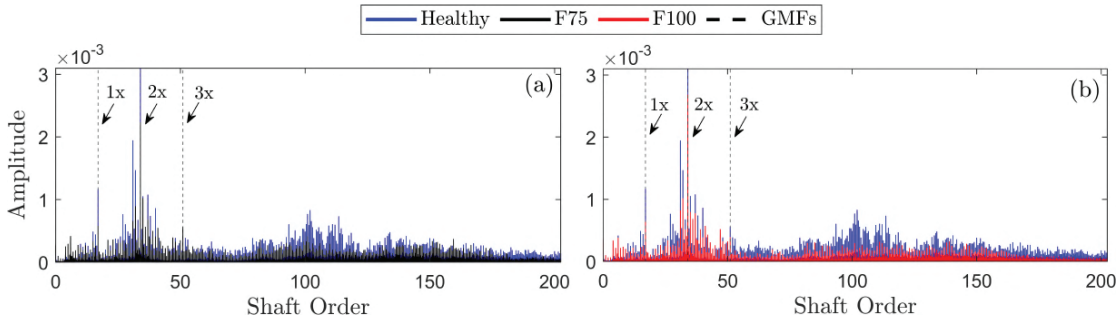

Figure 3: Order spectrum zones based on Fast Fourier Transform (FFT) amplitude estimates using a single angular vibration signal from each rotating speed and load (84 angular signals for each health state): (a) Healthy vs fault $F75$, (b) Healthy vs fault $F100$; The black dashed lines represent Gear Meshing Frequencies (GMFs).

3 THE VFP-AR MODEL CLOUD BASED FAULT DETECTION METHODOLOGY

The fault detection methodology consists of two phases: a *Training phase* and an *Inspection phase*. The *Training phase* operates offline and includes angular resampling of the vibration signals for different nominally constant rotating speeds (Section 3.1), as well as the identification of the VFP–AR 'cloud' of models representing the healthy gearbox dynamics (Section 3.2). The *Inspection phase* is performed in real-time and involves fault detection based on the VFP–AR model cloud (Section 3.3).

3.1 Angular resampling for different nominally constant rotating speeds

The first step of the methodology involves angular resampling of vibration signals based on Computed Order Tracking [20] using the tachometer signal in order to eliminate non synchronous frequency modulation in the time domain signals. This modulation arises primarily due to fluctuations in shaft speed, even when the machinery inverter is set at a nominally constant speed [20]. Based on this and to retain all frequency content up to the Nyquist limit as obtained in the time domain, the sampling frequency in the angular domain (or θ-domain) is selected as $f_s^\theta = f_s/\omega$, where f_s denotes the sampling frequency in the time domain and ω the nominal rotating speed measured in revolutions per second (rev/s). However, the different f_s^θ per rotating speed prevents the gearbox dynamics modelling in a unified way across all different rotating speeds, as a single, common, f_s^θ should be adopted. The selection of this frequency is dictated by the maximum rotating speed ω_{max} of the machinery, resulting in an operational bandwidth of $[0, \frac{f_s}{2\cdot\omega_{max}}]$ in θ-domain. Based on this, it is evident that for any speed $\omega < \omega_{max}$, the resulting frequency bandwidth in time domain should include frequencies in the range $[0, \frac{f_s^\theta}{2} \times \omega]$ Hz, which is narrower than the original measurement bandwidth that extends up to $f_s/2$ Hz. This indicates the need for low-pass filtering of all vibration signals at any $\omega < \omega_{max}$ before angular resampling, using a cut-off frequency of $\frac{f_s^\theta}{2} \times \omega$, in order to avoid signal distortion due to aliasing.

As part of this filtering process, higher-frequency components are lost, especially as rotating speed decreases. To limit this loss of information, the ratio between the maximum and minimum speeds should be constrained within a practical range [18, pp. 156–159]. Thus, n adjacent sub-ranges that cover the entire considered range of rotating speeds are selected in this study, determined based on the highest frequency component that must be retained in each range. This step is crucial to the presented methodology, as it allows the modelling of the gearbox dynamics through a 'cloud' of Functionally Pooled models, as described in the following.

3.2 VFP-AR model based gearbox dynamics identification

Once the n adjacent speed sub-ranges have been determined, the objective of this step of the methodology is the modelling of the healthy gearbox dynamics at any speed $\omega \in [\omega^i_{min},\ \omega^i_{max}]$ $(i = 1, \ldots, n)$ and load $l \in [l_{min}, l_{max}]$ for each range using a Vector Functionally Pooled AutoRegressive (VFP-AR) model [21]. Thus, a 'cloud' of n VFP-AR models, collectively representing the healthy gearbox dynamics for the entire considered speed range and all loads, is estimated, with each model expressed in θ-domain as follows (a functional argument in brackets $[\,\cdot\,]$ designates function of an integer variable; a lowercase boldface symbol represents vector):

$$y_{\boldsymbol{k}}[\theta] + \sum_{i=1}^{n_a} a_i(\boldsymbol{k}) \cdot y_{\boldsymbol{k}}[\theta - i] = e_{\boldsymbol{k}}[\theta] \tag{1}$$

$$a_i(\boldsymbol{k}) = \sum_{j=1}^{p} a_{i,j} \cdot G_j(\boldsymbol{k}), \quad e_{\boldsymbol{k}}[\theta] \sim \text{iid}\, \mathcal{N}\left(0, \sigma_e^2(\boldsymbol{k})\right), \quad \boldsymbol{k} \in \mathbb{R}^2 \tag{2}$$

with $y_{\boldsymbol{k}}[\theta]$ designating the angular vibration signal, $\theta\,(=\ 1,\ \ldots\ ,N)$ equispaced samples after angular resampling, n_a the AR model order, $e_{\boldsymbol{k}}[\theta]$ model residual signal, while iid stands for independent and identically distributed, and $\mathcal{N}(\cdot,\cdot)$ for normal (Gaussian) distribution with the indicated mean and variance. The operating parameter vector $\boldsymbol{k}$ is defined as $\boldsymbol{k} = [\omega_v\ l_m]^T \equiv \boldsymbol{k}_{v,m}$, where $v = 1,\ldots,M_1$ and $m = 1,\ldots,M_2$, with M_1 the number of different speeds within a sub-range and M_2 the number of different loads.

Based on Eq. (2), the AR parameters $a_i(\boldsymbol{k})$ are functions of $\boldsymbol{k}$ belonging to a p-dimensional functional subspace spanned by the (mutually independent) functions $G_1(\boldsymbol{k}), G_2(\boldsymbol{k}),\ldots,G_p(\boldsymbol{k})$ (functional basis). The latter are bivariate (two variables) orthogonal polynomials forming a functional basis. VFP-AR model identification includes: (i) determination of the VFP–AR model order na and its functional subspace dimensionality p for a given basis function family (orthogonal polynomials such Legendre, Chebyshev may be equivalently used) using a Genetic Algorithm (GA) for the minimization of the Bayesian Information Criterion (BIC), (ii) model validation via testing of the obtained model residual signals whiteness hypothesis and, (iii) model estimation based on Ordinary Least Squares (OLS) with data pooling [21] using $M_3 = M_1 \times M_2$ vibration signals from the healthy gearbox. It is noted that each VFP-AR model of the 'Healthy Cloud' may have a different AR oder and functional subspace.

3.3 VFP-AR model based fault detection

Once a new vibration signal $y_u[t]$ is acquired from the gearbox under unknown health state and load, it is initially angularly resampled as previously described using the corresponding tachometer signal, yielding $y_u[\theta]$. Subsequently and based on the machinery rotating speed, $y_u[\theta]$ is driven through the VFP-AR(n_a) model from the 'Healthy Cloud' corresponding to the speed range in which the current speed belongs, and Eq. (1) is written as:

$$y_u[\theta] + \sum_{i=1}^{n_a} a_i(\boldsymbol{k}_{\omega,l}) \cdot y_u[\theta - i] = e_u[\theta, \boldsymbol{k}_{\omega,l}] \tag{3}$$

where the load in $\boldsymbol{k}_{\omega,l}$ is unknown. If $y_u[\theta]$ originates from the healthy machinery under any of the considered loads, this signal will be consistent with the employed VFP-AR model. This consistency is examined through the estimation of the load in $\boldsymbol{k}_{\omega,l}$ based on the following Non-linear Least Squares (NLS) estimator:

$$\widehat{l}_u = \arg\min_{l\in K} \sum_{\theta=1}^{N} e_u^2[\theta, \boldsymbol{k}_{\omega,l}], \quad \widehat{\sigma}^2_{e_u} = \frac{1}{N}\sum_{\theta=1}^{N} e_u^2[\theta, \boldsymbol{k}_{\omega,\widehat{l}_u}] \tag{4}$$

with $e_u[\theta, \boldsymbol{k}_{\omega,l}]$ provided by Eq. (3) and $K = [l_{\min}, l_{\max}]$ the range of the examined loads into which the machinery normally operates. If the current dynamics originates from the healthy gearbox then $e_u[\theta, \boldsymbol{k}_{\omega,\widehat{l}_u}]$ should be a white (uncorrelated) signal which may be examined via any typical whiteness testing procedure; herein the Pena-Rodriguez D statistic which follows a standard normal distribution for a white sequence [22] is employed. If $e_u[\theta, \boldsymbol{k}_{\omega,\widehat{l}_u}]$ is white this means that $y_u[\theta]$ originates from the healthy gearbox operating under $\boldsymbol{k} = [\omega\ \widehat{l}_u]^T$ speed and

load, otherwise the gearbox is declared as faulty. It is noted that in case of a healthy declaration, an interval estimate of the current operating load may also be provided to the user [23].

4 EXPERIMENTAL RESULTS

The considered rotating speed range of $[15, 25]$ rev/s is divided into $n = 2$ adjacent sub-ranges, $[15, 20]$ rev/s and $[20, 25]$ rev/s, as described in section 3.1. Based on the maximum speeds of these ranges, the corresponding angular resampling frequencies are $f_s^\theta = 512$ samples/rev for the first sub-range and $f_s^\theta = 409$ samples/rev for the second. Furthermore, a Chebyshev type II low-pass filter is applied to the vibration signals of all considered $\omega < 20$ in the first range and $\omega < 25$ in the second, before angular resampling, avoiding signals aliasing.

Consequently, the healthy gearbox dynamics within the continuous rotating speed $[15, 25]$ rev/s and load level $[0, 4]$ ranges, is represented by a 'Healthy Cloud' consisting of $n = 2$ VFP–AR models, estimated using the 33 acceleration signals of the baseline that correspond to a sample of rotating speeds and load levels from the considered ranges (see Table 1). All estimation details are shown in Table 2.

The performance of the VFP-AR model cloud fault detection method is assessed in the inspection phase based on $2\ 460$ signals from the healthy gearbox and $2\ 460$ from each fault scenario, with the gearbox operating under 41 different speeds and 4 different load levels (see Table 1). The tachometer signal is also acquired during each vibration measurement in this phase, while the health state of the gearbox and the load level is considered as completely unknown. The D statistic values of the method for all considered inspection phase signals (7 380) are presented in Fig. 4. Based on these, it is evident that signals corresponding to the healthy gearbox are almost fully separated from those obtained from the considered faults indicating

Table 2: Estimation details for the cloud of VFP-AR models.

Model No.	Speed range (rev/s)	f_s^θ (samples/rev)	Model	Samples Per Parameter	Condition Number
1	$[15, 20]$	512	VFP–AR(250)$_{13}$	211.85	$1.44 \cdot 10^5$
2	$[20, 25]$	409	VFP–AR(250)$_{11}$	261.07	$4.87 \cdot 10^5$

Estimation method: Ordinary Least Squares

Functional subspace dimensionality determination based on Genetic Algorithm: population = 100, elite count = 20, crossover fraction = 0.7, maximum number of generations = 1000, Tolerance of the objective function = 10^{-10}.

Functional basis: bivariate Shifted Legendre polynomials:

$\mathcal{G}^1 = \big[G_{0,0}(\boldsymbol{k}),\ G_{0,1}(\boldsymbol{k}),\ G_{0,2}(\boldsymbol{k}),\ G_{0,3}(\boldsymbol{k}),\ G_{0,4}(\boldsymbol{k}),\ G_{1,0}(\boldsymbol{k}),\ G_{1,1}(\boldsymbol{k}),\ G_{1,2}(\boldsymbol{k}),\ G_{1,3}(\boldsymbol{k}),\ G_{2,0}(\boldsymbol{k}),\ G_{2,2}(\boldsymbol{k}),\ G_{3,2}(\boldsymbol{k}),\ G_{3,3}(\boldsymbol{k})\big]$

$\mathcal{G}^2 = \big[G_{0,0}(\boldsymbol{k}),\ G_{0,1}(\boldsymbol{k}),\ G_{0,2}(\boldsymbol{k}),\ G_{0,3}(\boldsymbol{k}),\ G_{0,4}(\boldsymbol{k}),\ G_{1,0}(\boldsymbol{k}),\ G_{1,1}(\boldsymbol{k}),\ G_{1,2}(\boldsymbol{k}), G_{1,4}(\boldsymbol{k}),\ G_{2,1}(\boldsymbol{k}),\ G_{3,3}(\boldsymbol{k})\big]$

$G_{i,j}(\boldsymbol{k})$: bivariate orthogonal polynomial of total degree $i + j$, obtained as tensor product from two univariate polynomials $G_i(x_1)$, $G_j(x_2)$ of degrees i, j, respectively.

nearly-perfect fault detection performance.

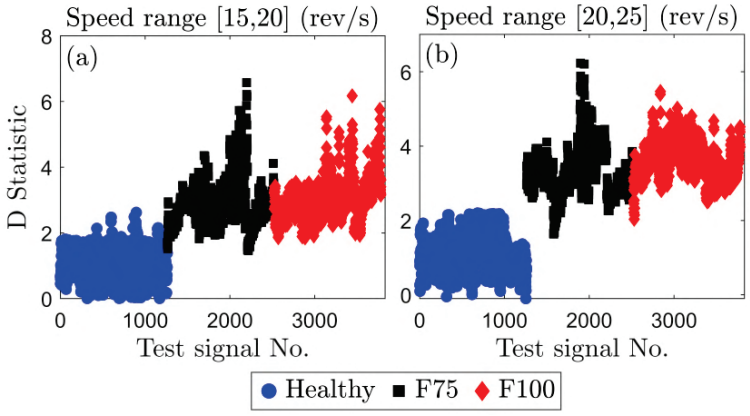

Figure 4: Fault detection results via the Pena-Rodriguez D statistic of the VFP-AR model cloud methodology: (a) $1st$ sub-range of speeds $[15, 20]$ (rev/s) and (b) $2nd$ sub-range of speeds $[20, 25]$ (rev/s); 7 380 signals including 41 rotating speeds and 4 load levels (inspection phase).

Finally, a comparison with the Multiple Model AutoRegressive (MM-AR) method [24], is presented. This method represents the healthy gearbox dynamics through a set of multiple AutoRegressive (AR) models, each associated with a distinct rotating speed and load level. During the training phase, AR models of the same order $n_a = 250$, are individually identified based on the 33 signals of the healthy gearbox (Table 1). In the inspection phase, a new AR model of the same order is estimated based on a fresh vibration signal from the gearbox under unknown health state and load. This model's similarity to the healthy reference models is quantified via the Mahalanobis distance. If it remains below a predetermined (in training phase) threshold, the gearbox condition is classified as healthy otherwise as faulty.

The fault detection results are comparatively presented in Fig. 5 via a typical Confusion Matrix. In the upper left 2×2 submatrix, each column represents a true health state and each row an estimated state. The i,j-th cell shows the ratio of the actual i-th state signals that were misclassified as the j-th state. Correct classifications appear on the diagonal, while errors are off-diagonal. The rightmost column reports the percentages of correctly (green) and incorrectly (red) classified signals within each predicted class, whereas the bottom row gives these percentages relative to the actual health state. Finally, the bottom-right cell summarizes the overall correct detection (green) and false alarm (red) rates; for a more detailed description, see [25].

Evidently, the VFP–AR model cloud method's nearly-perfect results are verified, underlying the detection of the healthy state (H) for 99.0% of the considered test cases, with an impressively low false alarm ratio of 1.0%. Furthermore, it accurately detects the considered incipient faults (F: stands for both fault scenarios) at 98.6%, resulting in an overall detection rate of 98.7% (rightmost bottom cell). Moreover, its superiority over the MM-AR based method is evident, which achieves a lower rate of 86.5%. This pinpoints the limitation of the MM–AR based method to operate at different values of rotating speeds and loads other than those used for its

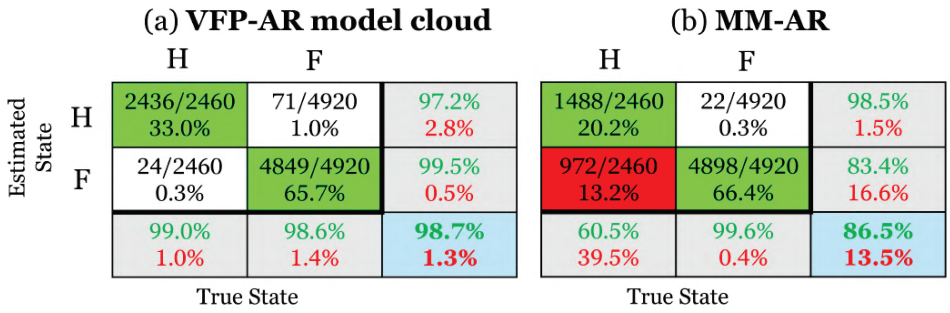

Figure 5: Fault detection comparative assessment via confusion matrices: (a) the VFP-AR model cloud method and (b) the MM-AR method (correct classifications indicated by green – misclassifications by red; 7 380 inspection signals).

training. This happens as the MM–AR based method approximates the healthy dynamics using distinct AR models in contrast to the VFP–AR model cloud based method where the healthy dynamics is modelled for any value within the continuous ranges of the considered OCs.

5 CONCLUSIONS

The robust detection of two severity levels of incipient single-tooth gear fault in a gearbox operating under 41 distinct rotating speeds and 4 distinct load levels has been explored using an unsupervised vibration-based statistical time series methodology. This methodology relies on angular vibration signals and a cloud of Vector Functionally Pooled AR (VFP–AR) models that represent the healthy gearbox dynamics at any rotating speed and load within the range of interest. Fault detection is performed through an optimization framework that assesses the consistency of the current vibration signal with the models in the cloud.

Based on the fault detection results obtained from 7 380 experiments, it is concluded that:

(i) The method achieves nearly perfect fault detection, with a 98.7% detection rate and only 1.3% false alarms, outperforming an alternative MM–AR based method.

(ii) The method can detect incipient faults without prior knowledge of their nature or their effects on specific vibration characteristics. This is achieved using only 33 vibration signals (0.45% of the entire database) for its training, collected from the healthy gearbox for a sample of speeds and loads from the considered ranges.

Acknowledgements

This research work was supported by the Hellenic Foundation for Research and Innovation (HFRI) under the 4th Call for HFRI PhD Fellowships (Fellowship Number 10820).

REFERENCES

[1] K. Feng, J. Ji, Q. Ni, and M. Beer, “A review of vibration-based gear wear monitoring and prediction techniques,” *Mechanical Systems and Signal Processing*, vol. 182, p. 109605, 2023.

[2] Y. Lei, M. J. Zuo, Z. He, and Y. Zi, "A multidimensional hybrid intelligent method for gear fault diagnosis," *Expert Systems with Applications*, vol. 37, no. 2, pp. 1419–1430, 2010.

[3] J. Xie, L. Zhang, L. Duan, and J. Wang, "On cross-domain feature fusion in gearbox fault diagnosis under various operating conditions based on transfer component analysis," in *Proc. IEEE International Conference on Prognostics and Health Management*, Ottawa, Canada, 2016.

[4] D. Wang, "K-nearest neighbors based methods for identification of different gear crack levels under different motor speeds and loads: Revisited," *Mechanical Systems and Signal Processing*, vol. 70, pp. 201–208, 2016.

[5] S. Guo, T. Yang, H. Hua, and J. Cao, "Coupling fault diagnosis of wind turbine gearbox based on multitask parallel convolutional neural networks with overall information," *Renewable Energy*, vol. 178, pp. 639–650, 2021.

[6] P. Boškoski and D. Juričić, "Fault detection of mechanical drives under variable operating conditions based on wavelet packet rényi entropy signatures," *Mechanical Systems and Signal Processing*, vol. 31, pp. 369–381, 2012.

[7] X. Wan, D. Wang, P. Tse, G. Xu, and Q. Zhang, "A critical study of different dimensionality reduction methods for gear crack degradation assessment under different operating conditions," *Measurement*, vol. 78, pp. 138–150, 2016.

[8] J. Koutsoupakis, P. Seventekidis, and D. Giagopoulos, "Machine learning based condition monitoring for gear transmission systems using data generated by optimal multibody dynamics models," *Mechanical Systems and Signal Processing*, vol. 190, p. 110130, 2023.

[9] W. Lu, B. Liang, Y. Cheng, D. Meng, J. Yang, and T. Zhang, "Deep model based domain adaptation for fault diagnosis," *IEEE Transactions on Industrial Electronics*, vol. 64, no. 3, pp. 2296–2305, 2017.

[10] M. Zhang, W. Lu, J. Yang, D. Wang, and L. Bin, "Domain adaptation with multilayer adversarial learning for fault diagnosis of gearbox under multiple operating conditions," in *2019 Prognostics and System Health Management Conference (PHM-Qingdao)*, 2019, pp. 1–6.

[11] W. Wang and A. Wong, "Autoregressive model-based gear fault diagnosis," *Journal of Vibration and Acoustics*, vol. 124, pp. 172–179, 2002.

[12] Y. Zhan and C. Mechefske, "Robust detection of gearbox deterioration using compromised autoregressive modeling and kolmogorov-smirnov test statistic. part ii: Experiment and application," *Mechanical Systems and Signal Processing*, vol. 21, no. 5, pp. 1983–2011, 2007.

[13] M. Yang and V. Makis, "Arx model-based gearbox fault detection and localization under varying load conditions," *Journal of Sound and Vibration*, vol. 329, no. 24, pp. 5209–5221, 2010.

[14] C. Lin and V. Makis, "Application of vector time series modeling and t-squared control

chart to detect early gearbox deterioration," *International Journal of Performability Engineering*, vol. 10, p. 105, 2014.

[15] X. Li, H. Zuo, P. Hao, Y. Su, H. Liu, and C. Xue, "Early fault detection of gearbox using tsa and var model considering load variation," in *2021 Global Reliability and Prognostics and Health Management (PHM-Nanjing)*, 2021, pp. 1–6.

[16] D. Bourdalos, I. Iliopoulos, and J. Sakellariou, "On the detection of incipient faults in rotating machinery under different operating speeds using unsupervised vibration-based statistical time series methods," *Lecture Notes in Civil Engineering LNCE*, vol. 254, pp. 287–296, 2023.

[17] D. Bourdalos and J. Sakellariou, "Vibration-based unsupervised detection of common faults in rotating machinery under varying operating speeds," in *Proc. Surveillance, Vibrations, Shock and Noise*, Toulouse, France, Jul. 2023.

[18] R. B. Randall, *Vibration-Based Condition Monitoring: Industrial, Automotive and Aerospace Applications*, second edition ed. John Wiley & Sons, Ltd, 2021.

[19] C. M. Bishop, *Pattern Recognition and Machine Learning*. Springer Science + Business Media, 2006.

[20] H. Endo and R. Randall, "Enhancement of autoregressive model based gear tooth fault detection technique by the use of minimum entropy deconvolution filter," *Mechanical Systems and Signal Processing*, vol. 21, no. 2, pp. 906–919, 2007.

[21] J. Sakellariou and S. Fassois, "Functionally pooled models for the global identification of stochastic systems under different pseudo-static operating conditions," *Mechanical Systems and Signal Processing*, vol. 72, pp. 785–807, 2016.

[22] T. C. Aravanis, J. Sakellariou, and S. Fassois, "A stochastic functional model based method for random vibration based robust fault detection under variable non-mameasurable operating conditions with application to railway vehicle suspensions," *Journal of Sound and Vibration*, vol. 466, p. 115006, 2020.

[23] J. Sakellariou and S. Fassois, "Vibration based fault detection and identification in an aircraft skeleton structure via a stochastic functional model based method," *Mechanical Systems and Signal Processing*, vol. 22, no. 3, pp. 557–573, 2008.

[24] K. Vamvoudakis-Stefanou, J. Sakellariou, and S. Fassois, "Vibration-based damage detection for a population of nominally identical structures: Unsupervised multiple model (mm) statistical time series type methods," *Mechanical Systems and Signal Processing*, vol. 111, pp. 149–171, 2018.

[25] J. Korolis, D. Bourdalos, and J. Sakellariou, "Machine learning-based damage diagnosis in floating wind turbines using vibration signals: A lab-scale study under different wind speeds and directions," *Sensors*, vol. 25, no. 4, 2025.

XI ECCOMAS Thematic Conference on Smart Structures and Materials - SMART 2025
M. Krommer, M. Nader and M. Schagerl (Eds)

Received: 29 March 2025 / Revised: 1 September 2025 / Accepted: 7 September 2025
© The Author(s) 2025

Modeling and damage detection in systems with multiple operational regimes through a Bayesian Multi-Model time series approach

Casper Aaskov Drangsfeldt, Luis David Avendaño-Valencia, Marie Lützen

Abstract. Vibration-based Structural Health Monitoring (SHM) has been extensively studied for decades; however, developing robust algorithms is challenging when the underlying system operates under multiple operational regimes. The dynamic characteristics of these systems are observed as multiple discrete regimes, each with a significant effect on the vibration response features, which likewise appear as multiple discrete regimes in the feature space. Hence, the development of practical SHM algorithms requires appropriate modeling of the system across operational regimes. To address this challenge, this study proposes a Bayesian Multi-model approach for damage detection. The approach utilizes time-series models for each operating regime, with the Bayesian framework constructing probability distribution models based on available data. During the inspection phase, a time-series model is fitted to newly acquired data and compared against established reference models. The closest match provides an indication of the current operating regime, while deviations serve as an damage indicator. To demonstrate this approach, a Finite Element (FE) model simulating an output shaft on a ship is used, subjected to three distinct axial load states to represent different operational regimes. Results show that the Multi-model approach can detect propagating damage at an early stage, precisely accounting for operational variability. Therefore, the proposed Multi-model effectively improves the reliability of damage detection in systems with changing operational conditions.

Key words: Structural Health Monitoring, Bayesian Autoregressive Models, Operational Variability, Damage Detection, Hamiltonian Monte Carlo

1 INTRODUCTION

The concept of damage detection of a system can be simplified to the process of comparing measurable quantities, referred to as *Damage Sensitive Features* (DSFs), to a baseline representing the expected behaviour of these DSFs under healthy conditions. Deviations from this

Casper Aaskov Drangsfeldt & Luis David Avendaño-Valencia & Marie Lützen
Institute of Mechanical and Electrical Engineering, University of Southern Denmark, Campusvej 55, 5230 Odense, Denmark, e-mail: sdu@sdu.dk

baseline are then used as damage indicators [1]. However, when the dynamic characteristics change, DSFs can be altered in ways similar to damage. If the changing dynamic characteristics of a system can be described through multiple operating regimes, each with unique dynamic characteristics, one approach is to define an expected behaviour of the DSFs for each operating regime. By doing so, the process of damage detection is extended. First, DSFs are extracted at a given time. Then, the operating regime which the system is operating in at the given time is classified. Lastly, the extracted DSFs are compared with the expected behaviour for the classified operating regime.

For a system in which operation is divided into multiple regimes, accurately classifying the current operating regime is crucial, as the DSFs must be compared to a baseline with similar dynamic characteristics. An approach proposed in [2] utilizes the *Gaussian Mixture Model Random Coefficient* (GMM-RC) to predict various damage scenarios in a wind turbine based on the *GMM-RC Marginal Likelihood* (GMM-RC-ML) which is analogous to classifying operating regimes. Another approach proposed in [3] employs a *Switching Vector AutoRegressive* (SVAR) model to mitigate the effects of environmental variability in both simulated and experimental setups of a building. In this approach, the full range of measured environmental parameters is divided into distinct regimes, analogous to operating regimes. Then, an AR model is used to describe the expected behaviour of each regime. In [4], a methodology is proposed for detecting small levels of structural degradation in railway suspensions subjected to various travelling speeds. The methodology establishes a Multiple Model framework, where the dynamics of the system are modeled for different operational conditions using *Transmittance Function* AR with *eXogenous* input (TF-ARX) models. When new data is obtained, a new TF-ARX model is fitted. The Kullback-Leibler divergence is then used as a distance measure between the newly fitted TF-ARX model and those in the Multiple Model. If the smallest deviation between the new model and the models in the Multiple Model exceeds a predefined threshold, it suggests the presence of structural degradation in the railway suspension. Approaches such as the SVAR model in [3] and the Multiple Model framework in [4] leverages the chosen features for both classification and further analysis, ensuring that the classification reflects the actual analysis. This is advantageous since it focuses on factors influencing the problem itself rather than on variations in operating conditions from a different perspective.

Defining the expected behaviour of DSFs under healthy conditions is crucial for ensuring statistical robustness and reliability. If the system operates under significant variability, the behaviour of DSFs will also vary accordingly. Furthermore, precise classification is essential for comparing DSFs of an unknown structural state with their expected behaviour under similar dynamic characteristics. Therefore, an approach which leverages DSFs for both classification and damage detection ensures that the classification reflects the varying dynamic characteristics. Moreover, it simplifies the process of ensuring statistical robustness and reliability by using the same DSFs for both purposes, rather than relying on separate feature sets.

This study aims to develop a Bayesian Multi-model approach for damage detection under

varying operating regimes. The proposed framework establishes individual time-series models for the vibration response characteristics at specific operating regimes. Then, a Bayesian formulation is utilized to construct probability distributions for each regime based on available data, where a *Hamiltonian Monte Carlo* (HMC) approach is employed to optimize the parameters and hyperparameters of the Bayesian model. During the inspection phase, new data is analyzed by fitting a time-series model and comparing it against the established reference models. The closest match identifies the current operating regime, while deviations indicate potential structural damage. To demonstrate the approach, a *Finite Element* (FE) model simulating an output shaft on a ship, connecting an engine to a transmission, is used. The shaft is modeled with coupled axial and lateral degrees of freedom to capture realistic interactions between axial loading and transverse displacement. Three distinct axial load states (low, medium, and high) represent different operational regimes. Then, *Autoregressive* (AR) models are fitted to time-series from each load state using HMC, and the resulting Multi-model framework is applied for damage detection.

2 METHODS

The methodology of the proposed Multi-model for a system with varying operating regimes is illustrated in Fig. 1. Given a discrete time-series of finite length, $y[t]$, DSFs are estimated to represent the unknown structural state of the system, denoted as $\boldsymbol{\Theta}_u$. Next, $\boldsymbol{\Theta}_u$ is compared to every instance within the reference model, $\mathcal{M}$, which contains multiple sets of DSFs for each operating regime, representing the system's healthy structural state. The closest match determines the operating regime active at the time $\boldsymbol{\Theta}_u$ was estimated. Finally, the deviation from the closest match is used to assess potential damage.

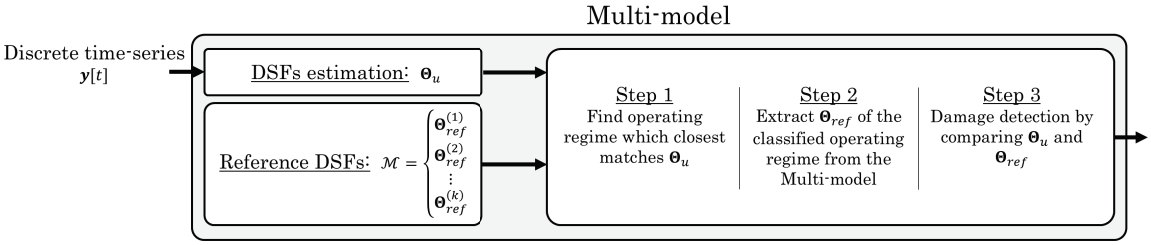

Figure 1: Flowchart of the proposed Multi-model.

The methods included in the Multi-model approach comprises estimation of the chosen DSFs and Step 1-3 as shown in Fig. 1. Therefore, the following section first details *Autoregressive modeling* (Sec. 2.1) and then AR model estimation using *Hamiltonian Monte Carlo* (Sec. 2.2). The parameters of an AR model then constitute DSFs. Lastly, the structure of the *Multi-model approach* (Sec. 2.3) is detailed, including the reference model $\mathcal{M}$ and Steps 1–3 in Fig. 1.

2.1 Autoregressive modeling

AR models are a class of statistical models used to generate a parameterized representation of discrete time-series data. In an AR model, the current value of the discrete time-series is expressed as a linear combination of its previous values and a stochastic error term. Mathematically, an AR model is defined as:

$$y[t] = -\sum_{i=1}^{n_a} a_i \cdot y[t-i] + w[t], \quad w[t] \sim NID(0, \sigma_w^2) \tag{1}$$

where $w[t]$ is *Normally and Independently Distributed* (NID) with zero mean and variance σ_w^2. This term is referred to as the *innovations* which account for the part of the discrete time-series that cannot be predicted from its previous values. The model order, n_a, determines the number of time lags included to predict future values [1]. The AR model can be written compactly as:

$$y[t] = \boldsymbol{\Phi}^T[t] \cdot \boldsymbol{\theta} + w[t], \quad \text{with} \quad \boldsymbol{\Phi}[t] = \begin{bmatrix} y[t-1] \\ y[t-2] \\ \cdots \\ y[t-n_a] \end{bmatrix} \quad \text{and} \quad \boldsymbol{\theta} = \begin{bmatrix} a_1 \\ a_2 \\ \cdots \\ a_{n_a} \end{bmatrix} \tag{2}$$

where $\boldsymbol{\Phi}$ is the design matrix and $\boldsymbol{\theta}$ is the AR parameter vector.

The model parameters, $\boldsymbol{\theta}$ and σ_w^2, are modeled as random variables conditioned on the operating regimes. Applying Bayes' theorem, the inference problem for an AR model in each operating regime is written as:

$$p\left(\boldsymbol{\theta}, \sigma_w^2 | \boldsymbol{y}, \boldsymbol{\Phi}\right) = \frac{p\left(\boldsymbol{y}|\boldsymbol{\Phi}, \boldsymbol{\theta}, \sigma_w^2\right) p\left(\boldsymbol{\theta}|\sigma_w^2\right) p\left(\sigma_w^2\right)}{p\left(\boldsymbol{y}|\boldsymbol{\Phi}\right)} \tag{3}$$

where $\boldsymbol{y}$ and $\boldsymbol{\Phi}$ represent the observations and the lagged observations respectively. Computation of the posterior $p\left(\boldsymbol{\theta}, \sigma_w^2 | \boldsymbol{y}, \boldsymbol{\Phi}\right)$ can be challenging and sometimes impossible. Therefore, the posterior is often estimated using numerical methods, such as HMC.

2.2 Hamiltonian Monte Carlo

HMC is a method derived from *Markov Chain Monte Carlo* (MCMC) simulations, where a sequence of dependent samples is generated to approximate the posterior distribution. Starting from an initial sample drawn from the parameter space, a trajectory based on the curvature in the parameter space is followed to generate a new sample. This process continues until the parameter space has been explored sufficiently.

Following the HMC approach to approximate the posterior in Eq. (3), the posterior is augmented with an independent momentum distribution, $p\left(\boldsymbol{\Theta}, \boldsymbol{\phi} | \boldsymbol{y}, \boldsymbol{\Phi}\right) = p(\boldsymbol{\phi}) p(\boldsymbol{\Theta} | \boldsymbol{y}, \boldsymbol{\Phi})$, where $\boldsymbol{\Theta} = \{\boldsymbol{\theta}, \sigma_w^2\}$ is referred to as the position in the parameter space, and $\boldsymbol{\phi}$ is the momentum.

The momentum dimension matches that of the latent variables, and its distribution is typically chosen as a multivariate normal, $\boldsymbol{\phi} \sim \mathcal{N}(0, \boldsymbol{\Sigma})$. The concept of augmenting the true posterior with a momentum origins from Hamiltonian mechanics, where the total energy of the *system* can be described as:

$$H(\boldsymbol{\Theta}, \boldsymbol{\phi}) = U(\boldsymbol{\Theta}) + K(\boldsymbol{\phi}) \tag{4}$$

Here, the potential energy of the system corresponds to the negative log-posterior and the kinetic energy relates to the momentum distribution, both described as:

$$U(\boldsymbol{\Theta}) = -\log p(\boldsymbol{\Theta}|\boldsymbol{y}, \boldsymbol{\Phi}), \quad K(\boldsymbol{\phi}) = \frac{1}{2}\boldsymbol{\phi}^T \boldsymbol{\Sigma}^{-1} \boldsymbol{\phi} \tag{5}$$

where $U(\boldsymbol{\Theta})$ represents the 'height' in the parameter space, with areas of high probability density corresponding to greater potential energy. The kinetic energy, $K(\boldsymbol{\phi})$, represents the 'speed' of movement through the parameter space. The trajectory through the parameter space to draw new samples is then governed by Hamiltonian dynamics. Here, leapfrog integration is often utilized to discretize the trajectories in time [5].

The leapfrog integration alternately updates the position $\boldsymbol{\Theta}$ and momentum $\boldsymbol{\phi}$ over L steps, referred to as leapfrog steps, with each step scaled by the stepsize ϵ. After L steps, the new position $\boldsymbol{\Theta}$ represents a potential new sample in the parameter space. Before accepting this new position, an accept-reject step is performed. The acceptance ratio is computed as:

$$r = \frac{p(\boldsymbol{\Theta}^*|\boldsymbol{y}, \boldsymbol{\Phi})p(\boldsymbol{\phi}^*)}{p(\boldsymbol{\Theta}^{t-1}|\boldsymbol{y}, \boldsymbol{\Phi})p(\boldsymbol{\phi}^{t-1})} \tag{6}$$

where $\boldsymbol{\Theta}^*$ and $\boldsymbol{\phi}^*$ are the position and momentum obtained after performing the leapfrog integration, and $\boldsymbol{\Theta}^{t-1}$ and $\boldsymbol{\phi}^{t-1}$ are the position and momentum before the leapfrog integration. The new position $\boldsymbol{\Theta}^{t-1}$ is then set as:

$$\boldsymbol{\Theta}^t = \begin{cases} \boldsymbol{\Theta}^* & \text{with probability } \min(r, 1) \\ \boldsymbol{\Theta}^{t-1} & \text{otherwise} \end{cases} \tag{7}$$

This process of drawing a new sample of $\boldsymbol{\Theta}$ is repeated iteratively until N_s accepted samples of $\boldsymbol{\Theta}$ sufficiently resemble the true posterior. The result of the simulation is an approximation of the posterior with N_s samples, $\hat{p}(\boldsymbol{\Theta}|\boldsymbol{y}, \boldsymbol{\Phi})$ where $\boldsymbol{\Theta} \in \mathbb{R}^{N_s \times (n_a+1)}$.

In general, the simulation starts at an initial position $\boldsymbol{\Theta}_0$ and a random momentum drawn from its distribution. From this starting point, the leapfrog integration is performed with L steps to propose a new position, thereby a new sample. If the new position is accepted, the simulation proceeds from this updated position; otherwise, it resumes from the previous position. Independent if the position is updated, $\boldsymbol{\phi}$ is resampled. The parameters of the HMC approach are either tuned manually or adjusted using adaptive methods [5].

2.3 Multi-model approach

Defining the Multi-model requires multiple datasets of the system in a healthy state across all regimes to capture the full variability in DSFs under healthy conditions. Therefore, given the ith subset of data while operating in the kth regime, the posterior $p(\boldsymbol{\Theta}|\boldsymbol{\mathcal{D}}_i^{(k)})$ is approximated with N_s samples where the ith subset of data is denoted as $\boldsymbol{\mathcal{D}}_i^{(k)} = \{\boldsymbol{y}_i^{(k)}, \boldsymbol{\Phi}_i^{(k)}\}$. Then, the Multi-model can be written as:

$$\boldsymbol{\mathcal{M}} = \begin{cases} \hat{p}(\boldsymbol{\Theta}|\boldsymbol{\mathcal{D}}_1^{(1)}) & \hat{p}(\boldsymbol{\Theta}|\boldsymbol{\mathcal{D}}_2^{(1)}) & \cdots & \hat{p}(\boldsymbol{\Theta}|\boldsymbol{\mathcal{D}}_{N_1}^{(1)}) \\ \hat{p}(\boldsymbol{\Theta}|\boldsymbol{\mathcal{D}}_1^{(2)}) & \hat{p}(\boldsymbol{\Theta}|\boldsymbol{\mathcal{D}}_2^{(2)}) & \cdots & \hat{p}(\boldsymbol{\Theta}|\boldsymbol{\mathcal{D}}_{N_2}^{(2)}) \\ \vdots & & & \\ \hat{p}(\boldsymbol{\Theta}|\boldsymbol{\mathcal{D}}_1^{(k)}) & \hat{p}(\boldsymbol{\Theta}|\boldsymbol{\mathcal{D}}_2^{(k)}) & \cdots & \hat{p}(\boldsymbol{\Theta}|\boldsymbol{\mathcal{D}}_{N_k}^{(k)}) \end{cases} \tag{8}$$

where N_1, N_2, and N_k denote the number of data subsets available for each operating regime.

Once the Multi-model is defined , the first step is to classify the operating regime of the system given a new set of DSFs, $\hat{p}(\boldsymbol{\Theta}|\boldsymbol{\mathcal{D}}_u)$ where u denotes that the structural state of the system is unknown. The classification is performed by comparing the parameters $\boldsymbol{\Theta}_u$ in $\hat{p}(\boldsymbol{\Theta}|\boldsymbol{\mathcal{D}}_u)$ to each reference $\boldsymbol{\Theta}_i^{(k)}$ in $\hat{p}(\boldsymbol{\Theta}|\boldsymbol{\mathcal{D}}_i^{(k)})$ in the Multi-model. First, the squared difference between $\boldsymbol{\Theta}_u$ and each reference $\boldsymbol{\Theta}_i^{(k)}$ in the Multi-model is computed and summed across all N_k:

$$\log p(k|\boldsymbol{\Theta}_u, \boldsymbol{\Theta}^{(k)}) = -\frac{1}{N_k} \sum_{i=1}^{N_k} (\boldsymbol{\Theta}_u - \boldsymbol{\Theta}_i^{(k)})^2 \tag{9}$$

where $\log p(k|\boldsymbol{\Theta}_u, \boldsymbol{\Theta}^{(k)})$ represents the log-likelihood of the system being in the kth operating regime while $\boldsymbol{\Theta}_u$ was estimated. Then, the probability of the system operating under regime k is obtained by averaging the log-likelihoods across all references:

$$P_k = \frac{\exp\left(-\frac{1}{N_k}\sum_{i=1}^{N_k}(\boldsymbol{\Theta}_u - \boldsymbol{\Theta}_i^{(k)})^2\right)}{\sum_j \exp\left(-\frac{1}{N_j}\sum_{i=1}^{N_j}(\boldsymbol{\Theta}_u - \boldsymbol{\Theta}_i^{(j)})^2\right)} \tag{10}$$

where P_k represents the probability that the system is operating under regime k. Finally, the regime with the highest probability is selected as the predicted operating regime.

Subsequently, the probability of the predicted operating regime serves as a damage indicator. If $\boldsymbol{\Theta}_u$ exactly matches one of $\boldsymbol{\Theta}_i$ within the Multi-model, the probability P_k equals 1. Conversely, if $\boldsymbol{\Theta}_u$ deviates from its closest match, the probability P_k will be less than 1. Therefore, the damage detection process of the Multi-model approach is defined as:

$$\text{Healthy if:} \quad |\log P_k| \leq \vartheta \quad \text{or} \quad \text{Damaged if:} \quad |\log P_k| > \vartheta \tag{11}$$

where ϑ is a predefined threshold that determines the acceptable level of deviation.

3 CASE STUDY - DAMAGE DETECTION OF A SHAFT

The proposed Multi-model approach is applied to a simply case where the system response is simulated from a FE model. The FE model shown in Fig. 2 represents an output shaft of a Volvo IPS, which connects an engine to a transmission on a ship, transferring torque down to the propellers. The shaft is modeled as simply supported at both ends, as the connections to the engine and transmission are cardan joints. Furthermore, the connection between the shaft and the transmission can vary slightly, since the transmission is clamped to the hull of the ship using rubber mounts, allowing for some movement. This slight movement subjects the shaft to varying levels of axial loading F, depending on the operational conditions. As a result, the dynamic characteristics change over time. This justifies the use of the Multi-model approach for damage detection, as the changing dynamic characteristics are likely to alter the system response in ways similar to damage.

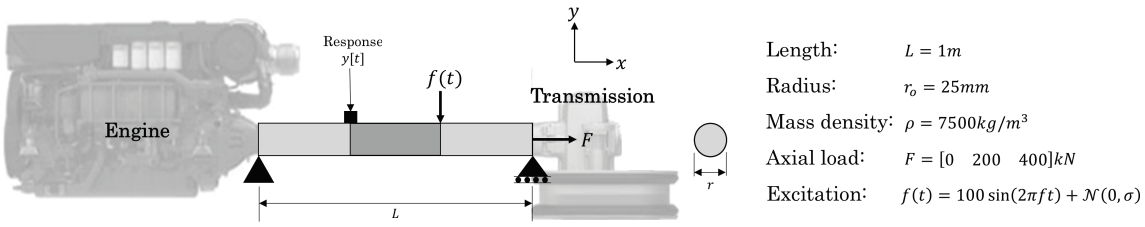

Figure 2: Simply supported beam with 3 elements subjected to transverse and axial loading.

The following details first the formulation of the FE model and the system response simulation in Sec. 3.1. Then, the modeling process of the Multi-model is detailed in Sec. 3.2.

3.1 Finite element formulation and simulation

The FE model in Fig. 2 is subjected to three levels of constant axial load F and modeled using 3 Euler-Bernoulli elements, each with element stiffness matrix defined as:

$$\boldsymbol{K}_e = \frac{EI}{l_e^3}\begin{bmatrix} 12 & 6l_e & -12 & 6l_e \\ 6l_e & 4l_e^2 & -6l_e & 2l_e^2 \\ -12 & -6l_e & 12 & -6l_e \\ 6l_e & 2l_e^2 & -6l_e & 4l_e^2 \end{bmatrix} + \frac{F}{30l_e}\begin{bmatrix} 36 & 3l_e & -36 & 3l_e \\ 3l_e & 4l_e^2 & -3l_e & -l_e^2 \\ -36 & -3l_e & 36 & -3l_e \\ 3l_e & -l_e^2 & -3l_e & 4l_e^2 \end{bmatrix} \tag{12}$$

and element mass matrix defined as [6]:

$$\boldsymbol{M}_e = \frac{\rho A l_e}{420}\begin{bmatrix} 156 & 22l_e & 54 & -13l_e \\ 22l_e & 4l_e^2 & 13l_e & -3l_e^2 \\ 54 & 13l_e & 156 & -22l_2 \\ -13l_e & -3l_e^2 & -22l_e & 4l_e^2 \end{bmatrix} \tag{13}$$

where $l_e = L/3$ is the length of each element, E is the Young's modulus, I is the moment of inertia, ρ is the mass density, A is the cross-sectional area, and F is the axial load. These parameters are given in Fig. 2 and are chosen as a rough representation of a real setup. In total, this yields a global stiffness, $\boldsymbol{K}$, and mass matrix, $\boldsymbol{M}$, with sizes 8×8. In addition, proportional damping is used modeled as:

$$\boldsymbol{C} = \alpha \boldsymbol{M} + \beta \boldsymbol{K} \tag{14}$$

where $\alpha = 10$ and $\beta = 10^{-6}$. Furthermore, the shaft is excited in a single DOF by a harmonic transverse force, $f(t)$ in Fig. 2 where $f = 10Hz$ and $\sigma = 5$. Lastly, the first and last transverse DOF are eliminated due to boundary conditions, reducing the system matrices to 6×6.

To simulate a system that transition through multiple operating regimes, a *Hidden Markov Model* (HMM) is used with the transition probability matrix:

$$\boldsymbol{A} = \begin{bmatrix} 0.85 & 0.15 & 0 \\ 0.1 & 0.8 & 0.1 \\ 0 & 0.15 & 0.85 \end{bmatrix} \tag{15}$$

This structure constrains the load sequence, ensuring that the system cannot move directly from the lowest to the highest level. Then, using the HMM, a total of 400 transitions are generated, with each segment maintaining a minimum stationary period of 5 seconds before a transition occurs in the load sequence.

The system response simulation is through a discrete state-space representation, as detailed in [7], with a sampling rate of $f_s = 4000$Hz. Additionally, damage is introduced after 900 seconds in the element marked as dark gray at the shaft in Fig. 2. Here, the element stiffness is gradually reduced from 0% to 5% over a period of 1100 seconds. During the simulation, the temperature increases linearly from 20^oC to 40^oC over the first 500 seconds, then remains stable for the next 1500 seconds. For this, the Young's modulus is modeled as temperature dependent defined roughly as $E(t) = -\frac{1}{20}\text{GPa}/^o\text{C} \cdot t + 210\text{GPa}$. This is shown at the top of Fig. 3, along with the temperature profile. The load sequence and simulated system response are also shown. Additionally, the onset of damage is indicated by a black line.

The simulation yields a subset of data when the model is undamaged, $\boldsymbol{Y}_H$ and a subset of data after the damage have been introduction, $\boldsymbol{Y}_D$:

$$\boldsymbol{Y}_H \in \mathbb{R}^{5f_s \times 180} \quad \& \quad \boldsymbol{Y}_D \in \mathbb{R}^{5f_s \times 220} \tag{16}$$

where 85% of the 180 subsets in $\boldsymbol{Y}_H$ are randomly chosen for training. The remaining 15% of subsets in $\boldsymbol{Y}_H$ and $\boldsymbol{Y}_D$ is used for testing.

3.2 Modeling process

The modeling framework of the Multi-model approach is structured into three key stages: *AR Model Selection*, *AR Model Estimation*, and *Constructing the Multi-model*.

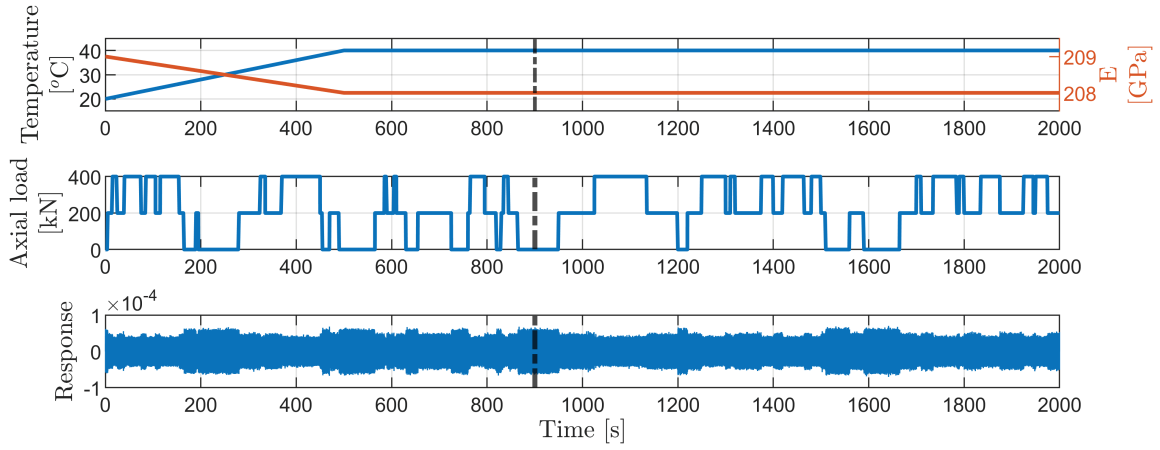

Figure 3: The system response simulation.

AR Model selection involves defining a suitable model order, n_a in Eq. (1) and setting the priors in the Bayesian inference problem in Eq. (3), along with defining a likelihood distribution. The first selection is the model order which is set to 20. This selection was based on a deterministic assessment, where the *Residual Sum of Squares over Series Sum of Squares* and the *Bayesian Informative Criterion* was evaluated for an increasing n_a while $\boldsymbol{\Theta}$ was estimated using *Least Square* (LS) estimation. The next selection is the priors and likelihood distribution. The likelihood is assumed to follow a Gaussian distribution as $p(\boldsymbol{y}|\boldsymbol{\Phi}, \boldsymbol{\theta}, \sigma_w^2) \sim N(\boldsymbol{\Phi}^T\boldsymbol{\theta}, \sigma_w^2)$. The prior distribution of the parameter vector $\boldsymbol{\theta}$ is assumed to follow a Gaussian distribution as $p(\boldsymbol{\theta}|\sigma_w^2) \sim N(\hat{\boldsymbol{\theta}}_{LS}, \sigma_w^2 \boldsymbol{I}_{n_a \times n_a})$ where $\hat{\boldsymbol{\theta}}_{LS}$ is a LS estimate of the parameters. Lastly, the prior distribution of σ_w^2 is assumed to follow an Inverse-Gamma distribution as $p(\sigma_w^2) \sim IG(2, 1)$.

AR Model estimation comprises the HMC simulation to approximate the posterior $p(\boldsymbol{\Theta}|\boldsymbol{\mathcal{D}}_i)$ given each subset in $\boldsymbol{Y}_H$ and $\boldsymbol{Y}_D$ in Eq. (16). Here, the number of accepted samples N_s to approximate the $p(\boldsymbol{\Theta}|\boldsymbol{\mathcal{D}}_i)$ is set to 5000. The remaining parameters of the HMC simulation, namely the variance of the momentum $\boldsymbol{\Sigma}$, the number of leapfrog steps L, and the step size ϵ, are tuned adaptively for each simulation.

Constructing the Multi-model involves using the estimated posteriors from the training subsets to build the Multi-model in Eq. (8). As a result, the Multi-model consists of 153 estimated posteriors, with the number of estimated posteriors for the first operating regime, N_1, being 50, while N_2 and N_3 holds 60 and 43, respectively. The posteriors are estimated both during the temperature increase and after, ensuring that the Multi-model accurately represents the system response under healthy conditions.

4 RESULTS

After the establishment of the Multi-model to represent the system response under healthy conditions, the damage detection process is tested and evaluated. For each subset in both $\boldsymbol{Y}_H$ and $\boldsymbol{Y}_D$, the parameter $\boldsymbol{\Theta}_u$ in the approximated posterior $\hat{p}(\boldsymbol{\Theta}|\boldsymbol{\mathcal{D}}_i)$ are compared with the Multi-model following Eq. (10) where the damage evaluation follows Eq. (11). The process is continued for $i \in [1, 2, \ldots, 400]$, where the damage detection for each classified operating regime is shown in Fig. 4. Here, the regions marked as *Training* comprise the approximated posteriors used to construct the Multi-model, meaning that $\boldsymbol{\Theta}_u$ matches itself within the Multi-model with a probability of 100%. The regions marked as *Testing* contain the approximated posteriors for the 15% subsets in Y_H, which are used to define the threshold ϑ in Eq. (11). This threshold is determined such that the *True Negative* (TN) rate is 100%. The regions marked as *Damaged* contain the subsets in Y_D after damage has been introduced into the simulated system response. However, only the indices exceeding the threshold ϑ indicate instances where the Multi-model successfully detects the damage.

Given the introduced threshold for a TN rate of 100%, it can be determined the level of damage introduced possible to detect by the Multi-model. For the first operating regime, the possible level of damage to detect is a stiffness reduction of ∼1.4%. For the second and third regime, the level is ∼1.5% and ∼0.7% respectively. In total, the damage detection following the Multi-model approach have a *True Positive* (TP) rate of 78.6% while the TN rate is 100%.

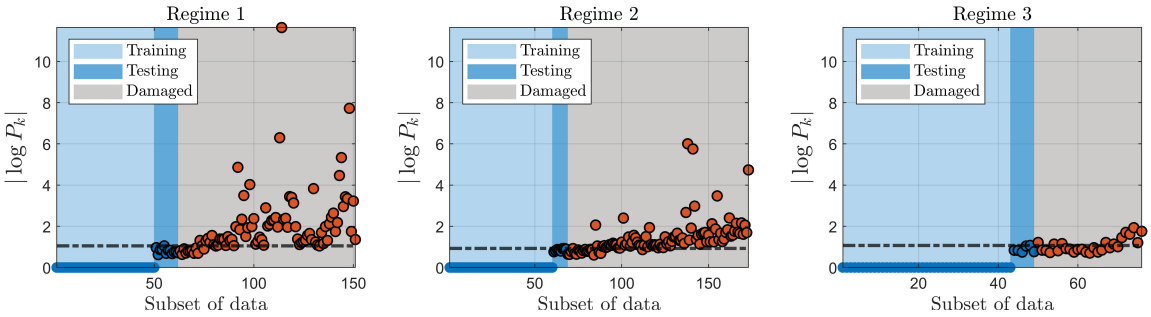

Figure 4: Damage detection following the Multi-model approach.

5 DISCUSSION

An FE model was used to simulate the system response, representing a real-case scenario where the dynamic characteristics of a system change over time. While the simple FE model provides only a rough representation of an output shaft between an engine and transmission, with geometrical dimensions that may not closely resemble any real case, the simulated response captures the changing dynamic characteristics observed in measured data. Additionally,

while the axial loading may not perfectly match real-case conditions, measured data from an actual system exhibit even greater fluctuations between operating regimes. Lastly, the load sequence consists of stationary periods of at least 5 seconds, which is rapid compared to real-case scenarios. However, the system response of a real case would likely extend over a longer duration. Overall, despite its simplicity, it is assumed that the FE model and its simulated system response provide a sufficient proof of concept for evaluating the Multi-model approach.

To represent each data subset with a duration of 5 seconds, an AR model was used, with its parameters treated as random variables and subsequently used as DSFs. While AR models directly reflect the dynamic characteristics of a system, the dimension of the model can be significant. In this controlled simulation, a large dimension is not necessary; however, in a real-case system, the dimension is likely more significant to capture complex dynamics of such system. If so, estimating the posterior could be computationally expensive, thus limiting the practical use of the proposed method if not addressed. However, dimensionality reduction methods, such as *Principle Component Analysis*, could be used, where an AR model is fitted to the features extracted from the reduction method's output, rather than directly on the time-series.

Another aspect to consider regarding the computational cost is the approximated posteriors used to define the Multi-model. In this case, an AR model was fitted to 5 seconds of data, thus resulting in a total of 153 approximated posteriors in the Multi-model. If applied to a real-case system where data for a longer duration is available, the dimension is most likely too significant. In a real-case scenario, it must be considered whether fewer AR models would be sufficient or if the time duration used for each AR model could be increased while still maintaining an accurate representation of the system. Also, having AR models in the Multi-model represent the system under different environmental conditions may prove challenging if not addressed. While varying environmental conditions influence structural dynamics in ways similar to damage, it is crucial to determine whether this also holds for the parameters of the AR models. If so, mitigation approaches must be implemented to improve damage detectability.

The damage detection approach of the proposed Multi-model is computationally inexpensive since P_k is used for both classification and as a damage indicator. Despite being a simple measure of damage, the TP rate and the level of detectable damage were sufficient. However, there may be potential for improvement. In Fig. 4, it is observed that the testing subsets do not perfectly match the approximated posteriors in the Multi-model, resulting in the early stages of damage propagation not being detected. This issue could be addressed either by improving the Multi-model's ability to represent the system more accurately or by refining the damage detection approach to account for variability in the Multi-model.

6 CONCLUSION

A Multi-model methodology was proposed for damage detection in systems with time-varying operations, where the operation can be described through multiple operating regimes. The Multi-model leverages the same features for both classification between the regimes and

for DSFs, enhancing robustness, as classification relies on the same parameters, which could otherwise challenge damage detection. The proposed Multi-model was tested on a simulated system response of a simple FE model representing a shaft connecting an engine to a transmission, subjected to three levels of axial loading. During the simulation, damage propagation was introduced to investigate the lowest detectable level of damage by the proposed Multi-model. With a conservative threshold for damage detection, resulting in a TN rate of 100%, the TP rate was found to be 78.6%. The lowest detectable damage level was a reduction in element stiffness of around 1%. Despite limitations such as high computational cost and accurate representation of the system in real-case scenarios, potential improvements were discussed. Overall, the Multi-model showed promising results and great potential, positioning it for testing on more complex systems in real-world applications.

REFERENCES

[1] C. R. Farrar and K. Worden, *Structural health monitoring: a machine learning perspective*. Wiley, 2013.

[2] L. D. Avendaño-Valencia and S. D. Fassois, "Damage/fault diagnosis in an operating wind turbine under uncertainty via a vibration response gaussian mixture random coefficient model based framework," *Mechanical Systems and Signal Processing*, vol. 91, pp. 326–353, 2017.

[3] A. Liu, L. Wang, L. Bornn, and C. Farrar, "Robust structural health monitoring under environmental and operational uncertainty with switching state-space autoregressive models," *Structural Health Monitoring*, vol. 18, no. 2, pp. 435–453, 2019.

[4] G. Vlachospyros, S. D. Fassois, and J. S. Sakellariou, "On-board vibration-based robust and unsupervised degradation detection in railway suspensions under various travelling speeds via a multiple model framework," *Vehicle System Dynamics*, vol. 62, no. 6, pp. 1446–1470, 2024.

[5] A. Gelman, *Bayesian data analysis*, 3rd ed. CRC Press, 2014.

[6] R. D. Cook and R. D. Cook, *Concepts and applications of finite element analysis*, 4th ed. Wiley, 2002.

[7] Z. Gajic, *Linear dynamic systems and signals*. Prentice Hall/Pearson Education, 2003.

XI ECCOMAS Thematic Conference on Smart Structures and Materials - SMART 2025
M. Krommer, M. Nader and M. Schagerl (Eds)

Received: 23 April 2025 / Revised: 26 August 2025 / Accepted: 7 September 2025
© The Author(s) 2025

A Deep Neural Network Framework for the Prediction of Ice Mass Accumulation on Wind Turbine Blades

Paola Guevara, Jawad Fayaz, Rodrigo Astroza

Abstract. The growing trend in the use of renewable energy to reduce carbon emissions has driven the installation of wind turbines in cold-climate regions, where ice formation on the blades, the most susceptible structural components, creates challenges in energy production and operational continuity. This highlights the need to monitor and quantify ice formations to control de-icing systems and implement efficient solutions. This study addresses the issue by presenting an approach that uses acceleration signals recorded on the blades as input for a deep learning model based on convolutional neural networks (CNN). Fifty tests were conducted on a blade of a 5-kW wind turbine at five different rotational speeds in a mock-up system, simulating realistic ice mass distributions based on historical environmental variation data and ice accumulation equations for aerodynamic profiles. Acceleration time series, rotational speed, and temperature captured by the data acquisition system are used as input for the CNN-based model, which is trained through random hyperparameter search and cross-validation to ensure robustness and generalization. The results show that the model accurately predicts the ice mass accumulated on the blades, achieving a fit with an R-squared of 0.99, a MAPE of 0.5%, and a RMSE of approximately 6.0, both for training data (80%) and testing data (20%). The model effectively accounts for variations in rotational speed and temperature, maintaining relative errors below 4% across all cases. These predictive capabilities enable the model to be applicable in de-icing systems under real conditions, directly integrating structural monitoring data without intermediate procedures.

Paola Guevara & Rodrigo Astroza
Facultad de Ingeniería y Ciencias Aplicadas, Universidad de los Andes Las Condes, 12455 Santiago, Chile
e-mail: pmguevara@miuandes.cl

Jawad Fayaz
Department of Computer Science, University of Exeter, Stocker Rd, Exeter EX4 4PY, UK
e-mail: j.fayaz@exeter.ac.uk

1 INTRODUCTION

The continuous operation of wind turbines under adverse conditions remains one of the main challenges for the global expansion of wind energy. This issue is particularly relevant in cold climates, where energy production is generally higher due to increased air density as temperatures drop [1]. Consequently, the deployment of wind farms in cold regions has grown significantly, currently representing nearly 30% of the global installed capacity [2]. However, in extremely cold environments, ice formation on the blades, components that are directly exposed and highly vulnerable to atmospheric conditions, can lead to critical operational problems. Ice causes surface erosion, which alters the aerodynamic geometry of the blades and can reduce power generation by up to 40% [3]. Moreover, ice accumulation is often uneven, inducing mass imbalance and rotor instability [4].

As a response, structural health monitoring (SHM) systems have been developed to interpret sensor signals in real time and infer the structural behavior of the turbine, enabling coordination of de-icing systems to prevent excessive deformation or unexpected shutdowns. However, ice formation is influenced by both environmental conditions and the geometry of the exposed surfaces [5]. Therefore, effective integration of SHM and de-icing systems requires a thorough understanding of ice mass distribution patterns along the blades. This need becomes even more critical in extreme conditions, where sensor measurements may present error rates between 30% and 60% [6]. The literature presents several approaches aimed at improving de-icing and anti-icing systems, including modeling of ice formation based on the blade's aerodynamic profile [7], [8], [9], and wind tunnel experiments under controlled atmospheric conditions that consider different types of ice formation depending on temperature [10], [11]. Recent studies have simulated ice masses concentrated at the tip of the blade, the area of greatest accumulation, using SHM instrumentation for detection [12]. However, under real-world conditions, ice tends to form along the entire blade. In this context, some works have used camera systems and pixel-based methodologies to observe and quantify ice thickness on the leading edge and its relationship with energy production losses [1], [13]. For applications in continuous monitoring environments, machine learning techniques have been incorporated into ice prediction and damage detection. Artificial neural networks (ANN) have been used to estimate ice mass from modal parameters [14], and deep neural networks (DNN) have been applied to detect ice mass based on changes in natural frequencies identified under experimental condition [15], [16]. While these studies have shown promising results, they generally do not consider realistic ice distributions in their experimental procedures. On the other hand, some approaches using real data have relied on SCADA information processed with convolutional neural networks (CNN) [17], sensor data in recurrent neural networks (RNN), WaveletLSTM architectures, GRUs for faster training, or GCNNs for ice detection [18], [19]. However, many of these models focus only on detecting the phenomenon and rely on intermediate steps such as modal identification, which limits their applicability in real-time monitoring systems.

In this context, the present study proposes a deep learning model based on convolutional neural networks (CNN), given their ability to capture local spatial features from time-series

data. The model is trained using experimental data collected from a real blade subjected to 50 realistic ice mass distributions derived from physical icing equations and historical climatological data from real environments. The main contribution of this work lies, on the one hand, in the integration of realistic ice formation conditions through a controlled experimental procedure, and on the other, in the development of a predictive CNN-based methodology that directly uses operational time-series data to accurately estimate the total ice mass on the blade, with relative errors below 4%. This approach avoids the need for intermediate steps such as modal identification, facilitating future implementation in real-time continuous monitoring systems.

2 EXPERIMENTAL DESIGN

The experimental tests were based on modeling the ice mass distributions on wind turbine blades using empirical aerodynamic profile equations derived from historical data.

2.1 Ice accretion

The accretion of ice on a blade is calculated using equation (1) from the ice mass rate on the surface of a cylinder [20]:

$$\dot{M} = \dot{h} \cdot A \cdot \rho_{ice} \tag{1}$$

$\dot{M}$ is in $[g \cdot s^{-1}]$, A is the contact area between the ice and the cylindrical surface in $[m^2]$; ρ_{ice} is the ice density for the condition of ice (for rime ice $\rho_{ice} \approx 0.88[g \cdot m^{-3}]$ and glaze ice $\rho_{ice} \approx 0.90[g \cdot m^{-3}]$ [21]). The term $\dot{h}$ corresponds to the ice thickness growth rate $[m \cdot s^{-1}]$ and is given by equation (2).

$$\dot{h} = \frac{E \cdot LWC \cdot U \cdot F}{\rho_{ice}} \tag{2}$$

U is the relative wind speed $[m \cdot s^{-1}]$, determined from the rotational speed of the turbine (Ω $[rpm]$) and varies along the blade length—being higher near the tip and lower near the root. LWC $[g \cdot m^{-3}]$ denotes the liquid water content, which can be estimated from meteorological data by applying the cloud liquid water mixing ratio under sub-zero conditions, along with air density [22]. The freezing fraction F, a non-dimensional coefficient between 0 and 1, indicates the portion of impinging water that freezes upon contact. A value of $F = 1.0$, associated with rime ice, signifies complete freezing and is linked to low temperatures under the defined LWC conditions [20].

The collection efficiency E quantifies the proportion of liquid water droplets that, upon impacting a surface, effectively adhere and contribute to ice accretion. This parameter is primarily influenced by the droplet size and is calculated according to equation (3) [23]:

$$E = \frac{St^2}{(St + 0.7)^2} \tag{3}$$

The Stokes number (St) is given by equation (4):

$$St = \frac{U \cdot MVD^2 \cdot p_w}{9 \cdot \mu_a \cdot d_c} \tag{4}$$

Where MVD is the cloud droplet medium volume diameter, which typically ranges from 15 μm to 20 μm in winter stratiform clouds [24]; in this study, a value of 18 μm is used as a representative estimate. p_w is the density of water in $[g \cdot m^{-3}]$, μ_a is the dynamic viscosity of air in $[Pa \cdot s]$ calculated according to Sutherland's Law [25]. The variable d_c represents the cylinder diameter, which depends on the airfoil geometry of the blade.

The main input parameters for ice formation are derived from real data obtained in a previous research [3], which analyzed 32 years of climate data for ice formation in Quebec, Canada. This analysis categorized four average severity levels of events, as shown in Table 1; light, moderate, severe, and extreme according to LWC, temperature, and exposure duration.

Table 1: Properties of icing accretion and corresponding severity classes [3]

LWC $[g/m^3]$	T [°C]	Time[h]	Severity classes
0.36	-23.0	1.50	extreme
0.20	-13.5	2.60	severe
0.07	-5.0	7.50	moderate
0.04	-3.0	13.20	light

The blade geometry used to construct the ice mass distributions corresponds to a 2.4-meter-long blade with a mass of 12 kg, belonging to a 5-kW wind turbine designed to reach rotational speeds of up to 220 rpm. Based on these parameters and the governing equations, the distributions shown in Figure 1 were developed.

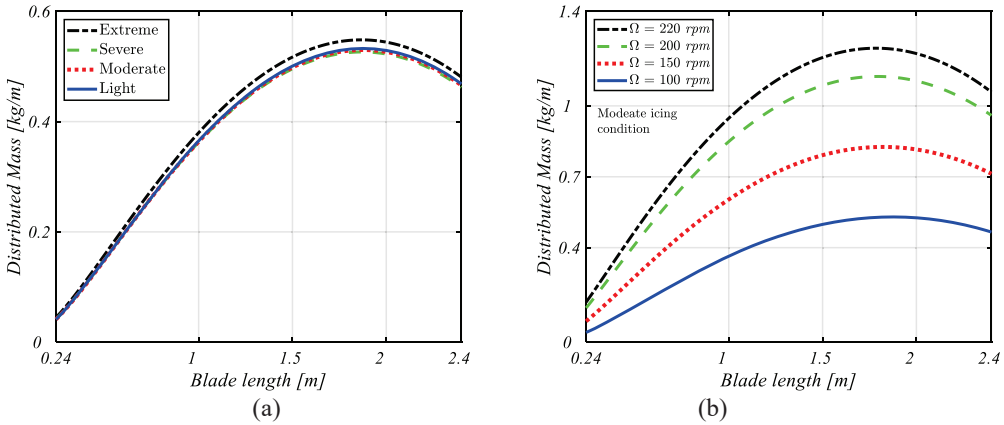

Figure 1: (a) Icing severity classes computed at 100 rpm. (b) Moderate icing condition evaluated across different rotational speeds.

As illustrated in Figure 1a, when comparing different severity levels under the same rotational speed, the curves tend to follow a similar distribution pattern. The general trend indicates an increase in ice thickness toward the blade tip [11]. However, due to the rise in relative airspeed along the blade and the reduction in chord length in the same direction, the pattern of accumulated ice mass varies according to environmental conditions, exposure time, and turbine operating parameters. For the complete exposure times defined in Table 1, the distribution tends to show a higher concentration of ice mass between 60% and 80% of the total blade length. This effect is consistent with increased LWC, which is directly influenced by temperature. Additionally, Figure 1b underscores the relevance of rotational speed as a critical parameter influencing ice accumulation. Under identical environmental conditions, higher rotational speeds result in a notable increase in the mass of ice adhered to the blade. At lower rotational speeds, the accumulation is relatively uniform along the blade span, whereas at higher speeds, the ice deposition tends to shift progressively toward the blade tip.

Based on the variations in ice distribution and in order to capture the full range of conditions outlined in Table 1, intermediate values are interpolated using a variation of 0.01 g/m³ in LWC, while maintaining its relationship with exposure time and the temperature associated with the event. The Ω is considered to vary between 100 and 220 rpm in all cases, as this is the operational range of the turbine model used in the experimental setup.

Under these parameters, 1000 random combinations of the primary variables: LWC, exposure time, temperature, and Ω, are randomly generated to construct the ice mass distribution curves. A uniform probability distribution is applied to ensure balanced sampling across the entire range of input variables. From the total set of generated combinations, 50 representative samples were selected for experimental analysis, as detailed in Table 2. These samples include cases with low ice mass accumulation, starting from 20.8 grams, and span up to 1878 grams, which corresponds to the severe icing condition. This upper limit represents an approximate 15% increase in the blade's original mass due to ice accretion.

Table 2: Trails of ice mass distributions considered in the testing protocol.

Trial	Icing conditions					Application distance in the wind turbine blade (m)										Actual total mass (g)
	LWC $\left(g/m^3\right)$	T (°C)	Exposure time (h)	Ω (rpm)	Theoretical total mass (g)	0.24	0.38	0.61	0.85	1.08	1.32	1.56	1.8	2.04	2.28	
						Mass along the blade (g)										
							P1	P2	P3	P4	P5	P6	P7	P8	P9	
1	0.34	-21.71	0.02	174.00	20.8	0.0	0.5	1.5	2.0	2.5	2.5	3.0	3.0	3.0	2.5	**20.5**
2	0.23	-15.38	0.04	152.00	24.0	0.0	1.0	1.5	2.0	3.0	3.0	3.5	3.5	3.5	3.0	**24.0**
3	0.24	-15.84	0.04	183.00	31.0	0.0	1.0	2.0	3.0	3.5	4.0	4.5	4.5	4.5	4.0	**31.0**
4	0.05	-3.42	0.31	129.00	33.3	0.0	1.0	2.0	3.0	4.0	4.5	5.0	5.0	5.0	4.5	**34.0**
5	0.20	-13.61	0.06	200.00	42.7	0.0	1.5	3.0	4.1	4.9	5.6	6.0	6.2	6.0	5.6	**42.9**
6	0.33	-21.00	0.15	120.00	98.7	0.0	3.0	5.9	9.0	11.1	13.0	14.1	14.6	14.5	13.6	**98.8**
⋮	⋮	⋮	⋮	⋮	⋮	⋮	⋮	⋮	⋮	⋮	⋮	⋮	⋮	⋮	⋮	⋮
48	0.30	-19.21	1.88	183.00	1821.1	0.0	62.0	119.1	169.9	210.7	240.0	258.1	264.0	257.8	239.4	**1,821.0**
49	0.09	-6.50	6.16	190.00	1858.5	0.0	63.2	121.6	173.4	215.0	245.2	263.5	269.4	263.1	244.3	**1,858.7**
50	0.11	-7.91	4.70	204.00	1877.4	0.0	65.5	124.5	176.3	217.7	247.4	265.2	271.0	264.2	245.3	**1,877.1**

2.2 Experimental program

The experiments were carried out on a mock-up wind turbine with a 3 m tower and a 1 HP motor connected to a variable-frequency drive to simulate rotation. Three 2.4 m blades, resembling those of a 5-kW turbine, were attached to a rotating hub. Each blade had a strip of three synchronized triaxial accelerometers, secured with silicone glue and helicopter tape. The sensors were connected to an ESP32-based data acquisition device and a temperature sensor located at the rotor center. Data were collected every 20 minutes, with 10 minutes of vibration measurements at 200 Hz in both edgewise (X) and flapwise (Z) directions, followed by 10 minutes of transmission. The measurements were conducted under five different rotational speeds (ω), simulating continuous turbine operation under ice mass conditions. Nine mass application points were established for experimentation as shown in Figure 2, and their corresponding masses are presented in Table 2 according to the sampled distributions, these points were distributed along the leading edge of the blade at intervals of approximately 0.24 m, except at the root and tip, where the application points were placed 0.38 m from the rotor hub and 0.12 m from the blade tip, respectively. The experimental masses were physically implemented to match the analytical ice distributions. For this purpose, small masses (0.5, 1, 1.5, 2, and 2.5 grams) were fabricated using 3D-printed components, while larger masses were simulated using 5 g and 10 g lead pieces. All masses were placed on the leading edge of the blade, specifically between 10% and 20% of the chord length, which corresponds to the typical ice accretion zone observed under real atmospheric icing conditions [10], [27]. These mass distributions aim to preserve the shape of the analytical ice accretion profiles while ensuring consistent sensor positioning across all trials.

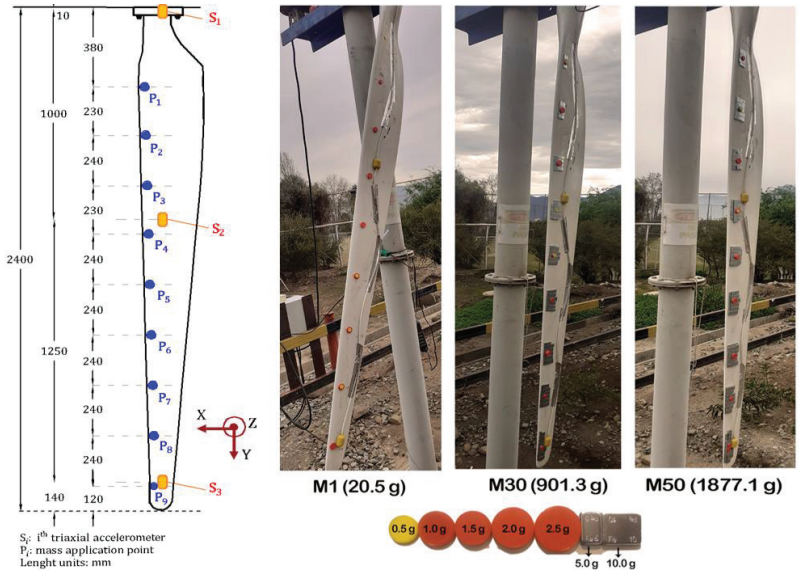

Figure 2: Mass distribution along the blade during testing, including the types of applied masses.

2.3 Experimental data

Since fifty ice mass conditions were tested under five rotational speeds, with three measurements conducted per condition, the resulting dataset comprises 750 entries. Each entry contains acceleration data recorded in both the flapwise (a_z) and edgewise (a_x) directions from the three sensors installed on the blade. The X component exhibited less influence on the blade response to mass adhesion, whereas the Z direction represented the dominant component, as the applied loads act directly within this plane, corresponding to the most deformation, prone side of the blade. Figure 3a displays the FFT of the a_z signal from the first trial and the sensor located at the blade tip for each of the five rotational speeds, where the average values (ω_1 to ω_5) are identified at approximately 14, 23, 30, 38, and 47 rpm, respectively. Figure 3b shows that each rotational speed is associated with 150 datasets. The variation remains within ±1 rpm for speeds below 30 rpm and within ±2 rpm for higher speeds, confirming the stability and control of the experimental setup. As for temperature (T), Figure 3b also shows that the experimental range extends from 5 °C to 30 °C across all conditions, with average values consistently remaining between 15 °C and 20 °C for each rotational speed. This variability results from the continuous execution of tests throughout the day, with two mass distributions evaluated daily and approximately five hours of data acquisition per distribution, conducted under naturally fluctuating environmental conditions. Nevertheless, the three repeated measurements for each case exhibit temperature variations within ±1 °C, supporting reliable and consistent comparisons.

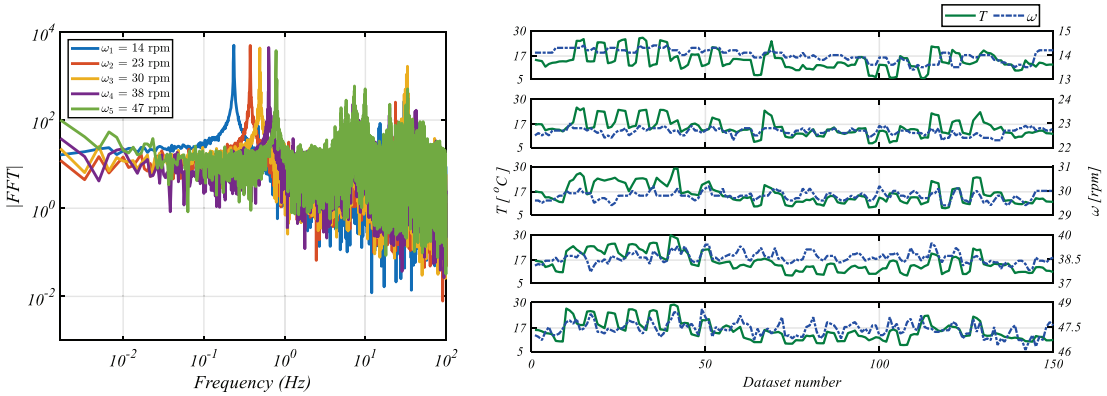

(a) (b)

Figure 3: (a) Logarithmic FFT of measurement 1 at five rotational speeds in the flapwise direction at the blade tip; (b) Variation of experimental temperature and rotational speed.

4 PREDICTIVE MODEL

The predictive model used in this study is based on convolutional neural networks (CNN) due to their suitability for time-series applications and their ability to capture subtle local spatial features. CNNs are designed to identify relationships between temporal inputs and scalar

variables, enabling accurate mass estimation. The experimental data used for the model were randomly split, allocating 80% (600 samples) for training and 20% (150 samples) for testing. This ensured that the full range of tested mass configurations and environmental conditions was adequately represented, supporting variability and generalization in the model. As shown in Figure 4, the model architecture receives four inputs: two time-series signals, a_2 and a_3, which represent the combination of orthogonal acceleration components (edgewise and flapwise) from sensors 2 and 3 located at the mid-span and tip of the blade, respectively; and two scalar variables, experimental rotational speed and temperature. Data from sensor 1, positioned at the blade root, were excluded due to its lower sensitivity to mass changes, as most mass accumulation occurs near the outer blade sections where the other sensors are located. Given that data were sampled at 200 Hz over 10 minutes, the total dataset contains 90 million values for a_2 and a_3. To reduce data size while preserving key information, a rolling mean was applied every 200 points. Additionally, ω and T were standardized by subtracting their mean and dividing by the standard deviation to optimize their use as model inputs. The model's target variable is the logarithm of the accumulated ice mass MM, which helps reduce variance and improve training stability.

The proposed CNN includes a 1D convolutional layer (Conv1D) with 32 filters and a kernel size of 3, followed by a max pooling layer (pool size = 2), a flatten layer, and five dense layers with 256, 213, 177, 32, and 16 neurons, respectively, all using ReLU activation. The output layer contains a single neuron with linear activation. Model optimization was conducted using random grid search. The following hyperparameters were explored: number of layers (3 to 20), neurons per layer (32 to 512), optimizers (Adam, Nadam, SGD), activation functions (ReLU, tanh, sigmoid), loss functions (heteroscedastic, weighted MSE, MSE), kernel sizes (2 to 10), filter counts (32 to 128), pooling window sizes (2 to 10), batch sizes (32 to 128), and training for up to 1000 epochs. Early stopping was applied, halting training if validation loss did not improve by at least 0.01% over 10 consecutive epochs. The final model was selected based on cross-validation performance, ensuring robust and generalizable predictions.

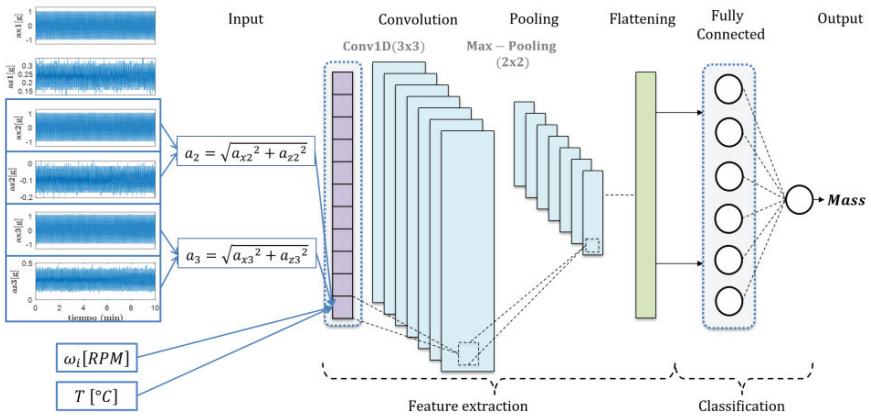

Figure 4: Predictive model diagram

5 RESULTS

The performance of the CNN-based model was evaluated by comparing the predicted and actual mass values, using the mean absolute percentage error (MAPE), the root mean squared error (RMSE), and the coefficient of determination (R^2) as evaluation metrics. The model demonstrated high accuracy, with R^2 values of 0.996 and 0.994 for the training and testing sets, respectively, and a MAPE of approximately 0.5% in both cases. The overall RMSE was 5.64 for training and 5.79 for testing.

The model's residuals remained below 4% across all mass ranges, with higher values observed for larger masses. However, the overall average residual was around 2%. To assess variability related to rotational speed and temperature during the experimental phase, relative residuals were analyzed and are shown in Figure 5a and Figure 55b. In both cases, the residuals stayed below 4%, with the highest values occurring at intermediate speeds, while most predictions showed residuals below 1%. Regarding temperature, another influential variable, relative residuals were analyzed across five intervals ranging from 5 °C to 30 °C. Although some dispersion was observed at mid-range temperatures, with residuals reaching up to 3%, the average residual in each interval remained close to zero. Additionally, most predictions from both the training and testing sets showed relative residuals under 1%, confirming the robustness of the model under environmental variability during experimentation.

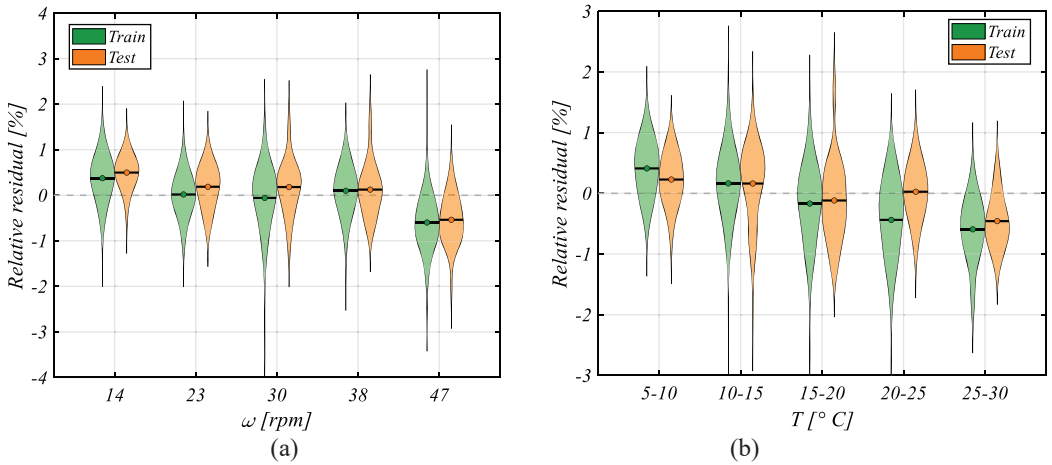

Figure 5: Relative residuals of predicted mass, grouped by (a) rotational speed and (b) temperature intervals

6 CONCLUSIONS

The experimental methodology developed in this study, which applied realistic ice mass distributions on a wind turbine blade under controlled conditions, represents a novel approach to studying ice formation during operation. This strategy enabled the collection of dynamic vibration data representative of icing scenarios, facilitating the development of a deep learning

model with potential for transferability to real-world applications. The convolutional neural network (CNN)-based model proved effective in capturing subtle variations in acceleration signals and predicting ice mass with high accuracy, even under fluctuating environmental conditions such as temperature changes between 5 °C and 30 °C. The model achieved a root mean squared error (RMSE) of 5.64 for training and 5.79 for testing, with a mean absolute percentage error (MAPE) below 1% and a relative error per mass under 4%. A strong correlation between predicted and reference values was confirmed by a coefficient of determination of $R^2 = 0.99$. These results support the feasibility of applying this modeling approach to real-time monitoring systems. However, limitations remain, as the tests were conducted under fixed rotational speeds and with ice formation data based on a specific regional database. Future work should incorporate broader datasets, including different ice types and variable operational conditions, to strengthen model generalizability and practical implementation.

ACKNOWLEDGMENTS

The authors would like to acknowledge the financial support from the Chilean National Research and Development Agency (ANID) through projects FONDECYT Regular 1240503 and FOVI 230030. Paola Guevara acknowledges the financial support from ANID grant Doctorado Nacional #21220456.

REFERENCES

[1] L. Shu *et al.*, “Study of ice accretion feature and power characteristics of wind turbines at natural icing environment,” *Cold Reg Sci Technol*, vol. 147, pp. 45–54, Mar. 2018, doi: 10.1016/j.coldregions.2018.01.006.

[2] L. Gao and H. Hu, “Wind turbine icing characteristics and icing-induced power losses to utility-scale wind turbines,” *Proceedings of the National Academy of Sciences*, vol. 118, no. 42, Oct. 2021, doi: 10.1073/pnas.2111461118.

[3] F. Lamraoui, G. Fortin, R. Benoit, J. Perron, and C. Masson, “Atmospheric icing impact on wind turbine production,” *Cold Reg Sci Technol*, vol. 100, pp. 36–49, Apr. 2014, doi: 10.1016/j.coldregions.2013.12.008.

[4] Y. Chen and D. T. Griffith, “Blade mass imbalance identification and estimation for three-bladed wind turbine rotor based on modal analysis,” *Mech Syst Signal Process*, vol. 197, p. 110341, Aug. 2023, doi: 10.1016/j.ymssp.2023.110341.

[5] D. Al. Katsaprakakis, N. Papadakis, and I. Ntintakis, “A Comprehensive Analysis of Wind Turbine Blade Damage,” *Energies (Basel)*, vol. 14, no. 18, p. 5974, Sep. 2021, doi: 10.3390/en14185974.

[6] A. Ilinca, “Analysis and Mitigation of Icing Effects on Wind Turbines,” in *Wind Turbines*, I. Al-Bahadly, Ed., InTech, 2011. doi: 10.5772/15484.

[7] S. Gantasala, J.-C. Luneno, and J.-O. Aidanpää, "Influence of Icing on the Modal Behavior of Wind Turbine Blades," *Energies (Basel)*, vol. 9, no. 11, p. 862, Oct. 2016, doi: 10.3390/en9110862.

[8] O. Yirtici, S. Ozgen, and I. H. Tuncer, "Predictions of ice formations on wind turbine blades and power production losses due to icing," *Wind Energy*, vol. 22, no. 7, pp. 945–958, Jul. 2019, doi: 10.1002/we.2333.

[9] M. Abbadi, I. Mussa, Y. Lin, and J. Wang, "Preliminary Analysis of Ice Accretion Prediction on Wind Turbine Blades," in *AIAA Scitech 2020 Forum*, Reston, Virginia: American Institute of Aeronautics and Astronautics, Jan. 2020. doi: 10.2514/6.2020-0619.

[10] Y. Zhang, W. Guo, Y. Li, H. Chi, P. Zhao, and K. Tagawa, "An experimental study of icing distribution on a symmetrical airfoil for wind turbine blade in the offshore environmental condition," *Ocean Engineering*, vol. 273, p. 113960, Apr. 2023, doi: 10.1016/j.oceaneng.2023.113960.

[11] Z. Mu, W. Guo, Y. Li, and K. Tagawa, "Wind tunnel test of ice accretion on blade airfoil for wind turbine under offshore atmospheric condition," *Renew Energy*, vol. 209, pp. 42–52, Jun. 2023, doi: 10.1016/j.renene.2023.03.126.

[12] J. Simon *et al.*, "Embedded radar networks for damage detection in wind turbine blades: validation in a full-scale fatigue test," *Struct Health Monit*, vol. 22, no. 6, pp. 4252–4263, Nov. 2023, doi: 10.1177/14759217231152815.

[13] Q. Hu *et al.*, "A method for measuring ice thickness of wind turbine blades based on edge detection," *Cold Reg Sci Technol*, vol. 192, p. 103398, Dec. 2021, doi: 10.1016/j.coldregions.2021.103398.

[14] F. Li *et al.*, "Icing condition prediction of wind turbine blade by using artificial neural network based on modal frequency," *Cold Reg Sci Technol*, vol. 194, p. 103467, Feb. 2022, doi: 10.1016/j.coldregions.2021.103467.

[15] S. Gantasala, J.-C. Luneno, and J.-O. Aidanpää, "Investigating How an Artificial Neural Network Model Can Be Used to Detect Added Mass on a Non-Rotating Beam Using Its Natural Frequencies: A Possible Application for Wind Turbine Blade Ice Detection," *Energies (Basel)*, vol. 10, no. 2, p. 184, Feb. 2017, doi: 10.3390/en10020184.

[16] S. Gantasala, J.-C. Luneno, and J.-O. Aidanpää, "Identification of ice mass accumulated on wind turbine blades using its natural frequencies," *Wind Engineering*, vol. 42, no. 1, pp. 66–84, Feb. 2018, doi: 10.1177/0309524X17723207.

[17] M. Kreutz *et al.*, "Ice prediction for wind turbine rotor blades with time series data and a deep learning approach," *Cold Reg Sci Technol*, vol. 206, p. 103741, Feb. 2023, doi: 10.1016/j.coldregions.2022.103741.

[18] W. Tian, X. Cheng, F. Shi, G. Li, S. Chen, and H. Zhang, "Gated Convolutional Neural Network for Wind Turbine Blade Icing Detection," in *2022 IEEE International Conference on Real-time Computing and Robotics (RCAR)*, IEEE, Jul. 2022, pp. 186–191. doi: 10.1109/RCAR54675.2022.9872273.

[19] X. Wang, Z. Zheng, G. Jiang, Q. He, and P. Xie, "Detecting Wind Turbine Blade Icing with a Multiscale Long Short-Term Memory Network," *Energies (Basel)*, vol. 15, no. 8, p. 2864, Apr. 2022, doi: 10.3390/en15082864.

[20] B. L. MESSINGER, "Equilibrium Temperature of an Unheated Icing Surface as a Function of Air Speed," *Journal of the Aeronautical Sciences*, vol. 20, no. 1, pp. 29–42, Jan. 1953, doi: 10.2514/8.2520.

[21] Y. Liu, L. J. Bond, and H. Hu, "Ultrasonic-Attenuation-Based Technique for Ice Characterization Pertinent to Aircraft Icing Phenomena," *AIAA Journal*, vol. 55, no. 5, pp. 1602–1609, May 2017, doi: 10.2514/1.J055500.

[22] F. Lamraoui, G. Fortin, R. Benoit, J. Perron, and C. Masson, "Atmospheric icing severity: Quantification and mapping," *Atmos Res*, vol. 128, pp. 57–75, Jul. 2013, doi: 10.1016/j.atmosres.2013.03.005.

[23] W. H. Walton and A. Woolcock, "The suppression of airborne dust by water spray," *Int J Air Pollut*, vol. 3, pp. 129–153, Oct. 1960.

[24] S. G. Cober, G. A. Isaac, and J. W. Strapp, "Aircraft Icing Measurements in East Coast Winter Storms," *Journal of Applied Meteorology*, vol. 34, no. 1, pp. 88–100, Jan. 1995, doi: 10.1175/1520-0450-34.1.88.

[25] W. Sutherland, "The viscosity of gases and molecular force," *The London, Edinburgh, and Dublin Philosophical Magazine and Journal of Science*, vol. 36, no. 223, pp. 507–531, Dec. 1893, doi: 10.1080/14786449308620508.

[26] L. Gao, T. Tao, Y. Liu, and H. Hu, "A field study of ice accretion and its effects on the power production of utility-scale wind turbines," *Renew Energy*, vol. 167, pp. 917–928, Apr. 2021, doi: 10.1016/j.renene.2020.12.014.

[27] A. Yousuf, J. Y. Jin, P. Sokolov, and M. S. Virk, "Study of ice accretion on wind turbine blade profiles using thermal infrared imaging," *Wind Engineering*, vol. 45, no. 4, pp. 872–883, Aug. 2021, doi: 10.1177/0309524X20933948.

XI ECCOMAS Thematic Conference on Smart Structures and Materials - SMART 2025
M. Krommer, M. Nader and M. Schagerl (Eds)

Received: 14 May 2025 / Revised: 25 August 2025 / Accepted: 7 September 2025
© The Author(s) 2025

Monitoring-based Identification of Corrosion in Steel Structures

Yasemin Kurtis, Antonina Kosikova, Konstantinos Vlachas, Rosalba Ferrari, Andrew W. Smyth, Eleni Chatzi

Abstract. *Over the service lifetime of a structure, corrosion in steel components progressively deteriorates their load-bearing capacity and compromises overall structural safety. Despite its substantial impact on structural performance, research on corrosion progression and its long-term effects remains limited. Most existing studies focus on corrosion incidents in reinforced concrete bars and steel cables, while effective methods for corrosion detection in steel members, such as girders and other structural elements are scarce. This study presents a methodology for detection and quantification of corrosion-induced damage in large-span steel structural components. The proposed approach leverages measured strain data from the monitored structure and employs a probabilistic framework to model and assess the progression of corrosion over time. Corrosion localization is achieved via use of a data-driven indicator, relying on transmittance functions, which are inferred from pairwise strain measurements at locations within the structure. To address the challenge of limited sensor measurements, a Gaussian Process Regression (GPR) model is employed to predict strains at unmeasured locations. The method is validated through numerical simulations employing a high-fidelity finite element model of a steel bridge.*

Key words: Corrosion in Steel Structures, Structural Health Monitoring, Finite Element Model

Yasemin Kurtis & Konstantinos Vlachas & Eleni Chatzi
Department of Civil, Environmental and Geomatic, ETH Zurich, Zürich, 8092, Switzerland
e-mail: ykurtis@studnet.ethz.ch

Antonina Kosikova & Andrew W. Smyth
Civil Engineering and Engineering Mechanics, Columbia University, New-York, NY, 10027-6699, U.S.A.
e-mail: ak4967@columbia.edu

Rosalba Ferrari
Department of Engineering and Applied Sciences, University of Bergamo, Dalmine, BG, 24044, Italy
e-mail: rosalba.ferrari@unibg.it

1 INTRODUCTION

Steel bridges constitute essential components of transportation infrastructure systems but are inherently prone to corrosion-induced degradation, which progressively diminishes structural capacity and incurs significant maintenance expenditures. Conventional inspection techniques, including visual assessment and non-destructive evaluation (NDE) methods such as ultrasonic testing and eddy current inspection, exhibit fundamental limitations in sensitivity and spatial resolution, particularly when applied to the early detection of corrosion in regions characterized by complex geometrical configurations [1, 2]. Advanced image-based inspection techniques, such as infrared thermography, enhance corrosion detection capabilities, but their efficacy remains limited in regions that are difficult to access [3]. Vibration-based monitoring provides an automated framework for continuous, long-term assessment of structural integrity [4]. This approach relies on identifying alterations in the dynamic response of a structure, such as reductions in stiffness and changes in damping behavior, as indirect indicators of damage. However, the assessment is often limited to identifying updated modal parameters, such as natural frequencies or mode shapes, with respect to a reference state, without explicitly linking these changes to specific physical deterioration mechanisms. In particular, the relationship between corrosion-induced material loss and the consequent reduction in structural stiffness in steel systems remains insufficiently explored, despite stiffness degradation being a primary contributor to structural failure in these structures. Existing studies are primarily focused on evaluating the impact of corrosion on structural behavior and performance characteristics, rather than providing methodologies for real-time quantification of the corrosion severity [5, 6]. Furthermore, much of the existing literature concentrates specifically on reinforced concrete elements and steel cables, while steel girders and arch structures remain underinvestigated in the context of corrosion-induced stiffness degradation [7, 8]. Consequently, a significant gap remains in the real-time monitoring and quantification of corrosion progression for the in-service steel structures. This study aims to address this gap through a strain-based probabilistic framework capable of identifying both the location and severity of corrosion in steel structures, based on analysis of the strain measurements. The proposed methodology comprises three key stages: First, damage localization is achieved using transmittance functions, which capture alterations in the strain response to identify affected regions. Second, strain prediction at uninstrumented locations is performed using Gaussian Process Regression (GPR), a probabilistic machine learning technique that reconstructs strain fields based on measurements from a sparse sensor network. Finally, the depth of corrosion is estimated through an inverse problem, where the maximum likelihood estimate (MLE) is used to determine the most probable depth of corrosion penetration based on strain measurements. The methodology is validated through numerical simulations using a high-fidelity finite element method (FEM) model of the Paderno d'Adda Bridge, as illustrated in Figure 1. The proposed approach is systematically tested under both uniform and pitting corrosion scenarios, assessing its capability to accurately localize damaged regions and quantify corrosion penetration depth across varying damage conditions.

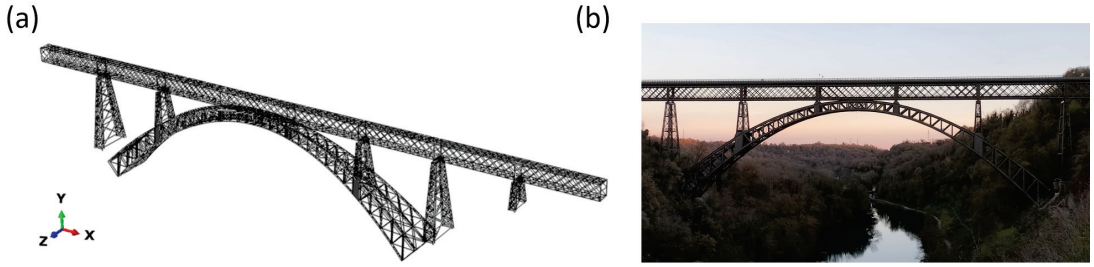

Figure 1: *(a) Finite Element Model. (b) Paderno d'Adda Bridge.*

2 DESCRIPTION OF THE MODEL

The FEM model of the Paderno d'Adda Bridge, originally developed in [9], was used in this study. The model, assembled in Abaqus using Euler-Bernoulli beam elements, represents the bridge's truss frame including the parabolic arch, piers, and upper girder deck. Geometric and boundary condition data were obtained from original design drawings archived in the Archivio Storico Nazionale di Torino. Built-in constraints were applied at the arch shoulders and pier bases, with roller supports at the upper beam bearings. The model comprises 5,337 beam elements and 12,794 nodes, resulting in 13,444 degrees of freedom. In this study, uniform material properties were assigned to the main structural components. A Young's modulus of 204 GPa and a Poisson's ratio of 0.30 were used for all components, while the mass density varied: 8.19 g/cm^3 for the arch, 14.5 g/cm^3 for the girders, and 1.03 g/cm^3 for the piles.

To simulate operational conditions, a dynamic train load was applied following the approach proposed in [10]. It was implemented as a repeating sequence of one second unloaded and one second loaded conditions, using concentrated forces of 19.27 kN at each girder node, determined based on historical loading conditions [11]. This type of loading represents an idealized, periodic train-passing scenario. While it does not reflect exact axle passage intervals, it allows for studying the structure's response to alternating loads under consistent timing. Strain data were collected at 100 Hz during 20 seconds of loading and 80 seconds of free vibration. To simulate structural degradation, both uniform and pitting corrosion cases were simulated in the FEM model. The arch and girder elements were selected for analysis due to their increased exposure to environmental stressors, such as proximity to the water surface, and their susceptibility to high strain concentrations resulting from cyclic traffic loading [12], [13]. Uniform corrosion is modeled as a distributed reduction in T-beam flange thickness over extensive regions of the upper and lower arch chords, representing generalized material degradation resulting from prolonged corrosive exposure [14]. Pitting corrosion was modeled as a series of localized cross-sectional reductions confined to 5 cm-wide regions near girder joints. These regions were chosen to reflect areas of increased vulnerability, such as joints and welds, where corrosion is often initiated and accelerated due to crevice effects, moisture retention, and stress concentration. The simulated pits represent localized material degradation, capturing the irregular and severe nature of pitting typically observed in in-service steel structures [6, 15].

3 METHODOLOGY

3.1 Damage Location Identification

The adopted damage localization approach is based on the use of transmittance functions as a data-driven indicator to identify the corroded regions. The transmittance function (TF) $T_{ij}^{\epsilon}(\omega)$ is defined as the ratio of the cross-spectral density (CSD) over the power spectral density (PSD) at the reference location [16]:

$$T_{ij}^{\epsilon}(\omega) = \frac{G_{ij}^{\epsilon}(\omega)}{G_{jj}^{\epsilon}(\omega)} \tag{1}$$

where $G_{ij}^{\epsilon}(\omega)$ is the CSD function of the strains between locations i and j, and $G_{jj}^{\epsilon}(\omega)$ is the PSD of the strains at location j. This formulation allows for capturing the dynamic relationship between strain responses, making it an effective output-only indicator for structural condition assessment [16]. To enhance sensitivity to damage, the TF is computed within an isolated frequency band corresponding to the natural frequencies of the bridge, as shown in Figure 2(a). The analysis is based exclusively on strain data recorded during the structure's free vibration response after the train passing. To quantify changes in the TF between the healthy and corroded states, a Damage Indicator (DI) is employed, following the formulation introduced in [17]. While originally developed for transmissibility functions, the DI is here adapted to assess strain-based TF variations associated with corrosion-induced damage and defined as:

$$DI_{ij} = \frac{\int_{\omega_1}^{\omega_2} |T_{ij}^{h}(\omega) - T_{ij}^{d}(\omega)| \mathrm{d}\omega}{\int_{\omega_1}^{\omega_2} |T_{ij}^{h}(\omega)| \mathrm{d}\omega} \tag{2}$$

where $T_{ij}^{h}(\omega)$ is the TF for the healthy and $T_{ij}^{d}(\omega)$ the TF for the damaged state, and $[\omega_1, \omega_2]$ corresponds to the selected frequency band.

3.2 Strain predictions at unmeasured locations

To address the common constraint of limited sensor availability in real-world monitoring systems, the proposed methodology incorporates GPR to predict strain values at uninstrumented locations. The strains of the healthy (undamaged) state of the bridge are computed from the calibrated FEM model, providing a comprehensive baseline. For the corroded state, strain measurements are restricted to a subset of locations corresponding to installed sensors, simulating sparse spatial coverage. The GPR model was trained on healthy-state strain data, using sensor node strains as input features and strains at unmeasured locations as output. Training involved maximizing the likelihood under a multivariate normal distribution, given by:

$$P(\epsilon_{\text{obs}}(t)|X) = N\big(\epsilon_{\text{obs}}(t) \mid X, K(X, X'; \boldsymbol{\theta})\big), \quad \text{with} \quad \boldsymbol{\theta} = \left[\sigma_l^2, \sigma_f^2, \sigma_n^2\right] \tag{3}$$

where $\epsilon_{\text{obs}}(t)$ is the vector of observed strain values at the selected node, extracted from the calibrated FEM model in the healthy state, which corresponds to the unmeasured location in the

monitored real-world structure and X is the matrix of input data corresponding to the observed strains at reference nodes in the healthy state. The $K(X, X'; \boldsymbol{\theta})$ is the kernel-covariance matrix of the training inputs where $\boldsymbol{\theta}$ denotes the vector of kernel hyperparameters: length scale, signal variance and noise variance. The trained model was then employed to predict unmeasured strain values at the corroded element as:

$$\epsilon_{\text{obs}}(t^*) = K(X^*, X'; \hat{\boldsymbol{\theta}}) \left[K(X, X'; \hat{\boldsymbol{\theta}})\right]^{-1} \epsilon_{\text{obs}}(t) \tag{4}$$

where $K(X^*, X'; \hat{\boldsymbol{\theta}})$ is the covariance matrix between the new inputs X^* (strains at the reference nodes in the corroded structure) and the training inputs X with $\hat{\boldsymbol{\theta}}$ being the optimal kernel function parameters learned during the training step. The Matérn 3/2 kernel, combined with a stationary kernel to account for measurement noise, was selected as the most suitable candidate based on preliminary analysis of strain cross-correlation functions. This composite kernel is defined as:

$$k(x_i, x_j \mid \boldsymbol{\theta}) = \sigma_f^2 \left(1 + \sqrt{3}\frac{r_{ij}}{\sigma_l^2}\right) \exp\left(-\sqrt{3}\frac{r_{ij}}{\sigma_l^2}\right) + {\sigma_n}^2 I, \tag{5}$$

where r_{ij} is the Euclidean distance between the locations x_i and x_j; the ${\hat{\sigma_n}}^2$ represents the measurement noise variance and I is an identity matrix.

3.3 Corrosion Depth Estimation

Once strain time histories are obtained at both measured and predicted locations, an inverse problem is formulated to estimate the severity of corrosion by quantifying the depth of material penetration. This formulation enables the characterization of corrosion intensity based on deviations from the expected structural response. The observed strain values correspond to the measured data at the sensor locations in the corroded state obtained from the FEM model. The predicted strain values are derived from a force-based strain formulation of a linear system subjected to both axial and bending effects, while incorporating changes in cross-sectional properties and the moment of inertia as a function of corrosion depth d. The relationship is expressed as:

$$\epsilon_{\text{pred}}(t; d) = \frac{F(t)}{EA(d)} + \frac{c(d)M(t)}{EI(d)} \tag{6}$$

where $F(t)$ and $M(t)$ denote the axial force and bending moment as functions of time, extracted from a calibrated FEM model; E is the Young's modulus of the material; $c(d)$ is the distance to the element neutral axis; $A(d)$ is the cross-sectional area, and $I(d)$ is the moment of inertia —expressed as functions of the corrosion depth penetration d. For this study, Bayes' theorem with a non-informative prior was employed as :

$$P(d \mid \{\epsilon_{\text{obs}}(t)\}) \propto P(\{\epsilon_{\text{obs}}(t)\} \mid d) \tag{7}$$

By systematically evaluating the strain response for a range of potential corrosion depths, the method identifies the depth value that maximizes the likelihood of the observed data. The posterior probability $P(d \mid \{\epsilon_{\text{obs}}(t)\})$ of the corrosion depth is considered to be proportional to the likelihood $P(\{\epsilon_{\text{obs}}(t)\} \mid d)$ of the observed strain time-history given the corrosion depth d. Assuming independent and identically distributed (i.i.d.) measurements, the likelihood is formulated as:

$$P(\{\epsilon_{\text{obs}}(t)\} \mid d) = \prod_{t=0}^{N} \frac{1}{\sqrt{2\pi\sigma^2}} \exp\left(-\frac{(\epsilon_{\text{obs}}(t) - \epsilon_{\text{pred}}(t;d))^2}{2\sigma^2}\right) \tag{8}$$

where $\epsilon_{\text{obs}}(t)$ represents the observed strain at time t; $\epsilon_{\text{pred}}(t;d)$ is the predicted strain-time history, estimated according to Eq.(6), the σ^2 is the variance of the time-history of the residuals between $\epsilon_{\text{obs}}(t)$ and $\epsilon_{\text{pred}}(t;d)$, and N corresponding to the size of the datasets. Given the simplified strain formulation, discrepancies between the predicted and measured strain values may arise due to modeling assumptions inherent in the FEM representation. To account for such discrepancies, a modeling error term is incorporated into the formulation, ensuring a more robust and reliable estimation of corrosion severity. This error is computed as the difference between the measured and predicted strains in the healthy state and is assumed to remain constant when propagated to the corroded state.

It is important to emphasize that the adoption of a probabilistic approach, rather than direct estimation of corrosion depth from observed strain, facilitates the quantification of epistemic uncertainty, or degree of belief, in the inferred values. This enhances the framework's applicability to structural health monitoring by providing confidence bounds on the estimated corrosion severity. However, the method relies heavily on the following two assumptions. First, it presumes that loading conditions remain consistent between the healthy and corroded states. In this study, a single train passage is employed as the representative loading scenario. Second, it assumes that the structure exhibits linear elastic behavior, wherein axial strains are linearly proportional to axial forces, and bending strains are linearly proportional to bending moments, in accordance with Hooke's Law.

4 METHODOLOGY APPLICATION

The following section demonstrates the application of the proposed strain-based methodology on the FEM model of the Paderno d'Adda Bridge. Initial evaluations were performed for two severe cases: a 25 *mm* bottom flange reduction representing uniform corrosion, and a 31 *mm* reduction representing pitting corrosion. The methodology's was further assessed under realistic conditions, accounting for prediction uncertainty and measurement noise. Finally, sensitivity to varying corrosion severities is examined.

4.1 Damage Location Identification

Damage location identification was performed using the transmittance-based DI for both uniform and pitting corrosion cases. The frequency band used for the TF computation is

illustrated in Figure 2(a). The sensor locations are presented in Figure 2(b). The DI was computed for multiple possible combinations of sensors and the corresponding evaluation is presented in Figures 2(c),(d).

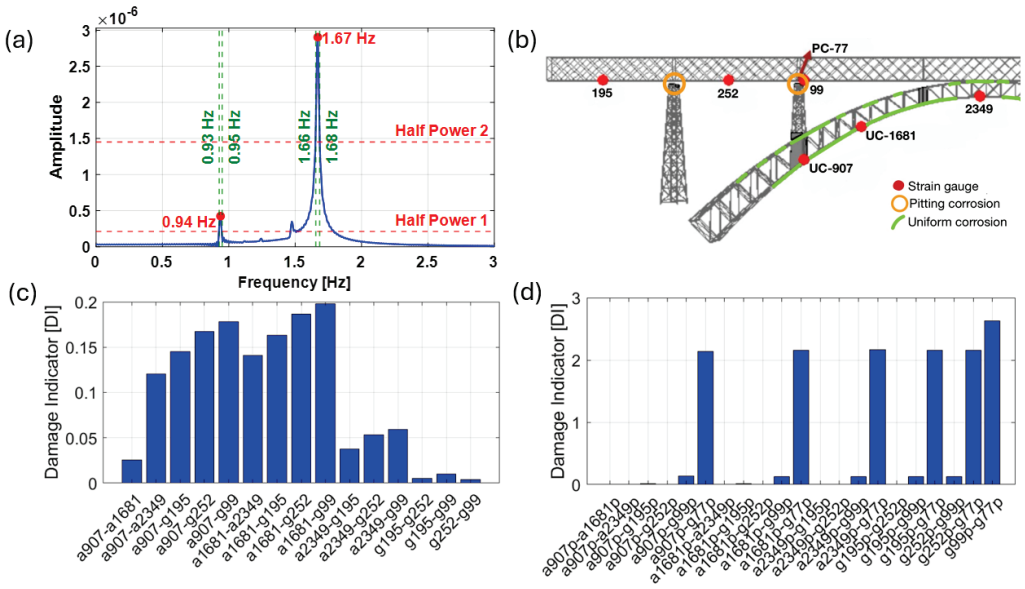

Figure 2: *(a) Frequency band determination. (b) Sensor locations. Sensors placed within the uniform corrosion zone are labeled with the prefix 'UC', while those located in pitting corrosion zones are denoted by 'PC'. (c) DI-values for uniform corrosion. Node combinations are labeled using structural prefixes: 'a' indicate nodes on the arch and 'g' for the girder. (d) DI-values for pitting corrosion. The same prefix convention applies as in (c), with the additional suffix 'p' indicating nodes subjected to pitting corrosion.*

For uniform corrosion, the computed DI values indicate that all sensor combinations involving only the girder nodes exhibit low values, suggesting that the girder remains in a healthy condition. Similarly, combinations between girder nodes and the uncorroded arch node 2349 yield low DI values, indicating that node 2349 is in a healthy state. In contrast, sensor combinations involving either node 907 or node 1681 show significantly higher DI values, suggesting that these locations are likely damaged. Additionally, the DI value between nodes 907 and 1681 remains low, implying that, while both nodes are affected by corrosion, their transmittance remains unchanged. This behavior suggests a similar level of degradation at both nodes and in the surrounding area, indicating that the damage likely extends between the two sensor locations. These results demonstrate that transmittance analysis successfully localizes damage by identifying areas with significant changes in strain response. However, in practical applications, where the exact damage location is unknown, the consistently low DI across girder sensors would indicate that the girder is largely unaffected. This would shift the focus to the arch as the

primary area of concern. Furthermore, the broader distribution of high DI values indicates that uniform corrosion affects a wider region of the structure, rather than being limited to specific locations. In contrast, the DI values for pitting corrosion, reveal a highly localized response. The highest DI is observed at PC-77, which is positioned directly within the pitting corrosion region. A smaller increase in DI is detected at sensor 99, which is located near the pit, while all other sensor locations exhibit negligible DI values. This pattern indicates that the transmittance changes are concentrated around the pit, with minimal impact on the surrounding structure. This localized response is consistent with the expected behavior of pitting corrosion, which generates highly concentrated stress variations. In contrast, the uniform corrosion case exhibits a broad spatial distribution of elevated DI values. The stark difference in DI distribution profiles, broad and diffuse for uniform corrosion versus sharply localized for pitting corrosion, underscores the potential of transmittance-based analysis to differentiate between corrosion types affecting structural elements.

4.2 Estimation of the corrosion depths at measured locations

Following the identification of the corrosion location, the severity of the damage can be subsequently estimated through the probabilistic framework. For the uniform case, the method accurately identifies corrosion depths close to the actual value of 25 *mm* for node 1681 within the damaged area (Figure 3(a)), particularly, the estimation has a relative error of 2.04%. For node 2349, located in the uncorroded region, the method infers a negative value as the corrosion depth (Figure 3(b)). Although this result may seem counterintuitive, it reflects forces redistribution due to adjacent damage, effectively indicating nearby corrosion, while confirming that the node itself remains healthy.

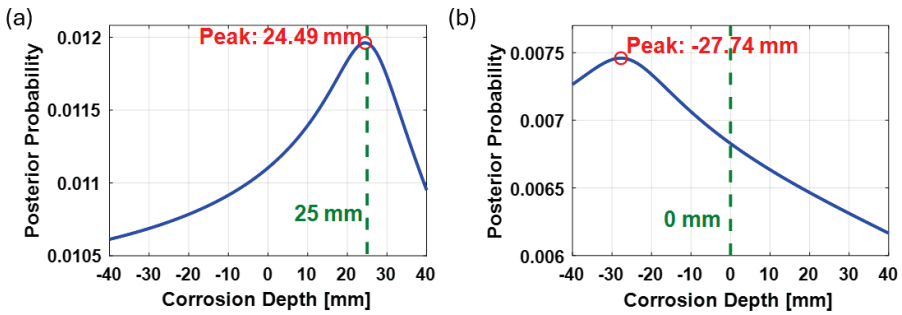

Figure 3: *Uniform corrosion: (a) 1681 (corroded). (b) 2349 (uncorroded).*

The results for the pitting corrosion depth identification are presented in Figure 4. Node 77 is located directly at the pit, while node 99 is located nearby in the uncorroded area. For node 77 the estimated corrosion depth slightly overestimates the actual depth corresponding to a relative error of 14.74%. At node 99, the method effectively indicating a corrosion depth near zero and captures the likelihood of the absence of corrosion at this location.

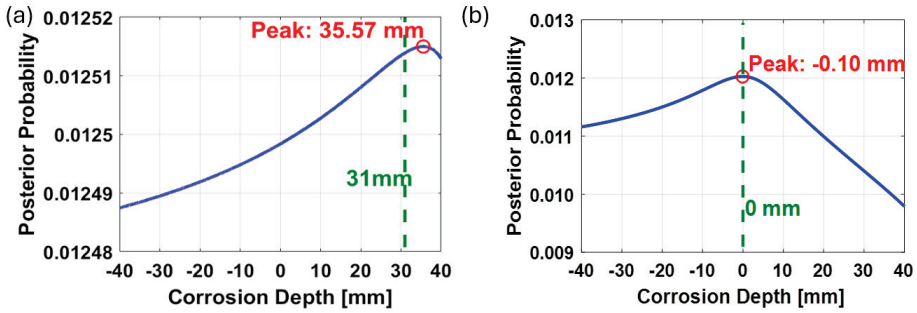

Figure 4: *Pitting corrosion: (a) 77 (corroded). (b) 99 (uncorroded).*

4.3 Estimation of the corrosion depths at unmeasured locations

To evaluate the affect of predicted strains for corrosion depth identification, Node 1447 was selected for analysis. This node lies within the corroded region identified through transmittance analysis but was not instrumented with a sensor, thereby allowing assessment of the method's performance using strain values inferred through GPR using two measured neighboring nodes as the input features (Figure 6(a)). The predicted strains for node 1447 are plotted against the reference FEM strains in Figure 5(a) and the uncertainty of the predictions is shown in a magnified window in Figure 5(b).

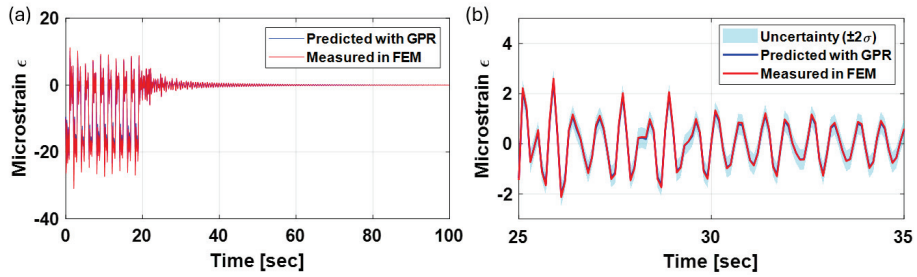

Figure 5: *(a) GPR predicted strain-time history. (b) Uncertainty quantification.*

To quantify the influence of strain prediction under different instrumental conditions, three cases were considered. First, a reference case was established by using FEM strain data for both healthy and corroded states, treating the node as if it was measured directly. In the second scenario, FEM strain data from two reference nodes was used for the healthy state, while GPR was applied to predict corroded-state strains at the unmeasured node. Finally, the measurements noise was added to the reference nodes strain time-histories used for the GPR predictions. The noise was introduced as Gaussian White Noise, equivalent to 10% of the root mean square (RMS) of the measured strain signals.

The results, shown in Figure 6, indicate that while the method allows us to successfully detect corrosion at the unmeasured location, the accuracy decreases. The relative error in the estimation

of the depth of corrosion increases from 5.96% when using FEM strains to 12.84% with GPR predicted strains, which underscores the method's sensitivity to the accuracy of strain data. The introduction of noise further increases the estimation error by approximately 2%, highlighting the compounding effect of measurement noise and prediction errors. Despite these challenges, the method provides corrosion depth estimates close to the actual values, demonstrating its applicability for real-world scenarios.

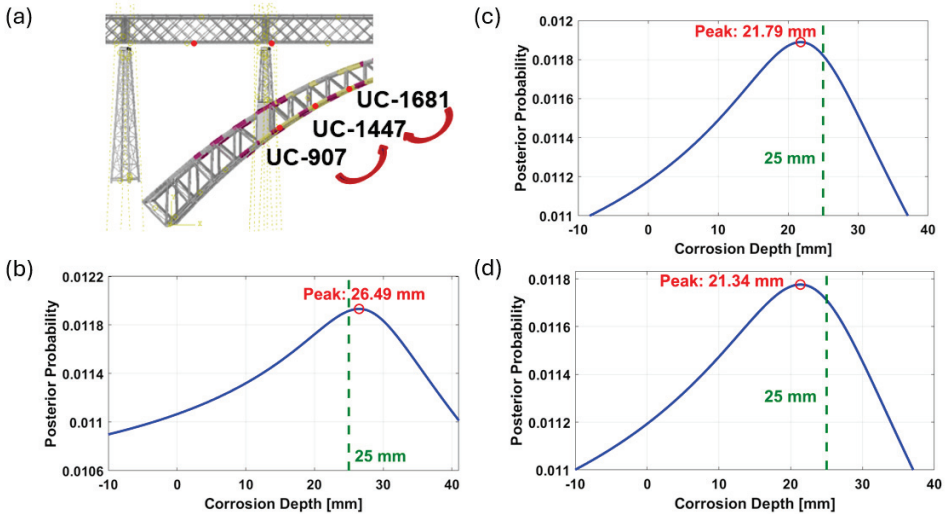

Figure 6: *(a) Unmeasured location (node 1447), and the neighboring locations (nodes 907 and 1681) used for the GPR prediction. Prefix 'UC' stands for uniform corrosion. (b) 1447-Measured. (c) 1447-Predicted. (d) 1447-Predicted based on the noisy strain measurements.*

4.4 Sensitivity to different corrosion stages

To realistically model corrosion, its progression over time must be considered. The corrosion loss for unprotected steel is typically described by an exponential function. Based on the bridge location in Lombardy, Italy, the corrosion is assumed to follow a low degradation rate:

$$C = C_A t^{C_B} = 0.034 t^{0.65} \tag{9}$$

where C is the average corrosion penetration in mm, t is the exposure time in years and C_A, C_B are environment-dependent parameters. For the first 12 years, the corrosion rate is set to zero, accounting for protective coatings delaying material loss [12]. The accumulated section loss (Figure 7(b)) is derived from the time-dependent corrosion rate (Figure 7(a)). Initially, a section loss of 25 mm, corresponding to 100 years, was implemented to assess the methodology. To further evaluate its performance under different levels of material deterioration, additional uniform corrosion stages were introduced, corresponding to section losses of 8 mm at 50 years, 15 mm at 75 years, and 35 mm at 125 years. The results are shown in Figure 7(c).

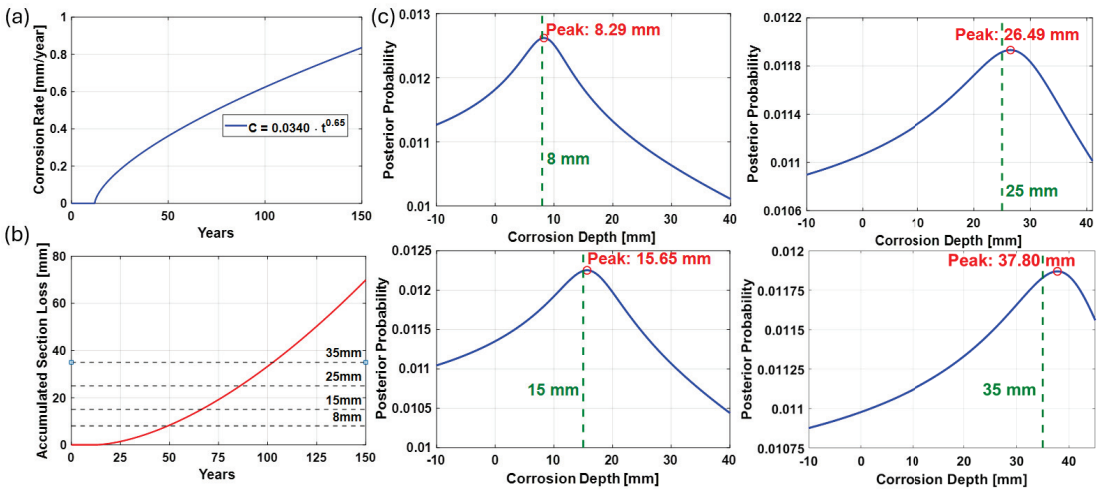

Figure 7: *(a) Corrosion Rate. (b) Accumulated Section loss. (c) Depth Estimation node 1447 for different corrosion stages.*

5 CONCLUSION

This study introduces a strain-based methodology for the detection and quantification of corrosion in steel structures, demonstrated through a case study on a steel arch bridge. The proposed approach effectively identified damage locations and estimated corrosion depths for both uniform and pitting corrosion scenarios. The findings highlight the method's sensitivity to different stages of corrosion, the accuracy of strain prediction at uninstrumented locations, and the influence of measurement noise on the reliability of corrosion assessment. Future work will focus on incorporating force redistribution effects and stiffness degradation to relax the assumption of identical internal forces in healthy and corroded states, thereby enhancing the method's applicability and robustness for real-world structural health monitoring.

REFERENCES

[1] D. Xu, W. Zhang, L. Han, X. Liu, and W. Hu, "Application of Sensor Path Weighting RAPID Algorithm on Pitting Corrosion Monitoring of Aluminum Plate," *Mater.*, vol. 15, no. 11, 2022. [Online]. Available: https://www.mdpi.com/1996-1944/15/11/3887

[2] V. Vasagar, M. K. Hassan, A. M. Abdullah, A. V. Karre, B. Chen, K. Kim, N. Al-Qahtani, and T. Cai, "Non-Destructive Techniques for Corrosion Detection: A Review," *Corros. Eng. Sci. Technol.*, vol. 59, no. 1, pp. 56–85, 2024. [Online]. Available: https://doi.org/10.1177/1478422X241229621

[3] H. J. Lim, S. Hwang, H. Kim, and H. Sohn, "Steel Bridge Corrosion Inspection With Combined Vision and Thermographic Images," *Struct. Health Monit.*, vol. 20, no. 6, pp. 3424–3435, 2021. [Online]. Available: https://doi.org/10.1177/1475921721989407

[4] O. Avci, O. Abdeljaber, S. Kiranyaz, M. Hussein, M. Gabbouj, and D. J. Inman, "A Review of Vibration-Based Damage Detection in Civil Structures: From Traditional Methods to Machine

Learning and Deep Learning Applications," *Mech. Syst. Signal Process.*, vol. 147, p. 107077, 2021. [Online]. Available: https://www.sciencedirect.com/science/article/pii/S0888327020304635

[5] I.-T. Kim, D. K. Dao, Y.-S. Jeong, J. Huh, and J.-H. Ahn, "Effect of Corrosion on the Tension Behavior of Painted Structural Steel Members," *J. Constr. Steel Res.*, vol. 133, pp. 256–268, 2017. [Online]. Available: https://www.sciencedirect.com/science/article/pii/S0143974X1730158X

[6] S. Guo, R. Si, Q. Dai, Z. You, Y. Ma, and J. Wang, "A Critical Review of Corrosion Development and Rust Removal Techniques on the Structural/Environmental Performance of Corroded Steel Bridges," *J. Clean. Prod.*, vol. 233, pp. 126–146, 2019. [Online]. Available: https://www.sciencedirect.com/science/article/pii/S0959652619319766

[7] K. Andisheh, A. Scott, and A. Palermo, "Modeling the Influence of Pitting Corrosion on the Mechanical Properties of Steel Reinforcement," *Mater. Corros.*, vol. 67, no. 11, pp. 1220–1234, 2016. [Online]. Available: https://onlinelibrary.wiley.com/doi/abs/10.1002/maco.201508795

[8] M. J. D. Sloane, R. Betti, G. Marconi, A. L. Hong, and D. Khazem, "Experimental Analysis of a Nondestructive Corrosion Monitoring System for Main Cables of Suspension Bridges," *J. Bridge Eng.*, vol. 18, no. 7, pp. 653–662, 2013. [Online]. Available: https://ascelibrary.org/doi/abs/10.1061/%28ASCE%29BE.1943-5592.0000399

[9] R. Ferrari, G. Cocchetti, and E. Rizzi, "Reference structural investigation on a 19th-century arch iron bridge loyal to design-stage conditions," *International Journal of Architectural Heritage*, vol. 14, no. 10, pp. 1425–1455, 2020. [Online]. Available: https://doi.org/10.1080/15583058.2019.1613453

[10] Z. Zhang, B. Zeng, C. Dai, and W. He, "Study on Structural Service Performance of Heavy-Haul Railway Tunnel with Voided Base," *Adv. Civ. Eng.*, vol. 2018, no. 1, p. 3510979, 2018. [Online]. Available: https://doi.org/10.1155/2018/3510979

[11] R. Ferrari, M. Facheris, and E. Rizzi, "Structural Analysis of the Paderno d'Adda Bridge (Italy, 1889)," *Adv. Mater. Res.*, vol. 133-134, pp. 459–465, 2010. [Online]. Available: https://doi.org/10.4028/www.scientific.net/AMR.133-134.459

[12] W. Zhang and H. Yuan, "Corrosion Fatigue Effects on Life Estimation of Deteriorated Bridges under Vehicle Impacts," *Eng. Struct.*, vol. 71, pp. 128–136, 2014. [Online]. Available: https://www.sciencedirect.com/science/article/pii/S014102961400217X

[13] N. E. A. Nassar, "Corrosion in Marine and Offshore Steel Structures: Classification and Overview," *Int. J. Adv. Eng. Sci. Appl.*, vol. 3, no. 1, p. 7–11, 2022. [Online]. Available: https://www.londontechpress.co.uk/index.php/ijaesa/article/view/80

[14] Y. Sharifi, "Uniform Corrosion Wastage Effects on the Load-Carrying Capacity of Damaged Steel Beams," *Adv. Steel Constr.*, vol. 8, no. 2, pp. 153–167, 2012. [Online]. Available: https://api.semanticscholar.org/CorpusID:252275722

[15] J. R. Galvele, "Pitting Corrosion," in *Corrosion: Aqueous Processes and Passive Films*, ser. Treatise on Materials Science and Technology, J. C. Scully, Ed. Elsevier, 1983, vol. 23, pp. 1–57. [Online]. Available: https://www.sciencedirect.com/science/article/pii/B9780126336702500061

[16] A. G. Poulimenos and J. S. Sakellariou, "A transmittance-based methodology for damage detection under uncertainty: An application to a set of composite beams with manufacturing variability subject to impact damage and varying operating conditions," *Struct. Health Monit.*, vol. 18, no. 1, pp. 318–333, 2018. [Online]. Available: https://doi.org/10.1177/1475921718779190

[17] S. Chesné and A. Deraemaeker, "Damage Localization Using Transmissibility Functions: A Critical Review," *Mech. Syst. Signal Process.*, vol. 38, no. 2, pp. 569–584, 2013. [Online]. Available: https://www.sciencedirect.com/science/article/pii/S0888327013000745

XI ECCOMAS Thematic Conference on Smart Structures and Materials - SMART 2025
M. Krommer, M. Nader and M. Schagerl (Eds)

Received: 21 April 2025 / Revised: 29 August 2025 / Accepted: 7 September 2025
© The Author(s) 2025

A Frequency-Domain Framework for Sensor Fault Diagnosis in Vibration-Based SHM: Application to a Population of Composite Aerostructures under Operational Uncertainity

Ioannis E. Saramantas, Ilias A. Iliopoulos, Sampetai S. Koen, John S. Sakellariou, Spilios D. Fassois, Dimitrios N. Serpanos

Abstract. Reliable sensor fault diagnosis is critical for high performance vibration-based Structural Health Monitoring (SHM) where a network of accelerometers is typically used. The problem is compounded when SHM is performed for a population of nominally identical composite aerostructures where manufacturing and operational uncertainty may not only significantly affect the vibration measurements and obscure early-stage structural faults but also render sensor fault detection unreliable. Building on a recently introduced frequency-domain framework for fault detection in a single vibration sensor, this study presents an extension of the employed methodology for sensor fault diagnosis including, beyond detection, sensor fault type identification and faulty sensor isolation from the network. The methodology is based on indices constructed using the sensors' Multiple Coherence, as well as the Transmittance Functions (TFs) obtained from a Multiple-Input Single-Output TF AutoRegressive with eXogenous (MISO-TF-ARX) input model. The performance of the methodology is assessed through thousands of test cases using acceleration signals from a network of 3 sensors obtained from an Abaqus-based finite element model of a composite beam under population-induced, temperature and excitation variability. The results show an overall fault detection accuracy of 98.16%, with fault type identification rates of 88.23%, 94.32%, and 95.06% for bias, gain and precision degradation faults, respectively, while faulty sensors are overall isolated for the 92.54% of the considered test cases.

Key words: Sensor Fault Diagnosis, Vibration-based SHM, Operational Uncertainty, Population of Composite Aerostructures, Statistical Time Series Methods

Ioannis E. Saramantas & Ilias A. Iliopoulos & Sampetai S. Koen & John S. Sakellariou & Spilios D. Fassois
University of Patras, Department of Mechanical Engineering & Aeronautics, Stochastic Mechanical Systems & Automation (SMSA) Laboratory, 26504 Patras, Greece, e-mail: jsar@upatras.gr

Dimitrios N. Serpanos
Computer Technology Institute and Press "Diophantus" & Industrial Systems of Institute (ISI) ATHENA, 265 04 Patras, Greece, e-mail: serpanos@ece.upatras.gr

1 INTRODUCTION

Sensor fault diagnosis, which includes fault detection, type identification, and isolation of the faulty sensor from the network, is critical for ensuring the high effectiveness and reliability of a vibration-based SHM system that typically employs a network of accelerometers [1]. A bias, gain or other types of sensor fault may mislead the SHM system and significantly increase the false alarms rate. This issue becomes highly challenging when similar sensor networks are installed in a fleet of aircraft for SHM of a population of nominally identical composite aerostructures. The uncertainty in the measurements due to variability in manufacturing, environmental and operating in-flight conditions, may obscure corresponding effects from early stage sensor faults, and thus degrade the SHM system's diagnosis performance.

Based on the type of the employed modelling of the healthy sensor network, the current methods addressing the problem may be classified as *'single-sensor'* or *'multi-sensor'*.

Single-sensor methods use one model per sensor of the network representing its healthy state. Cumulative Sum Control Chart (CUSUM) [2] based methods have been employed for detecting drift in displacement measurements. Deep learning-based methods, including Convolutional Neural Networks (CNN) [3] and Stochastic Gated Recurrent Neural Networks (SG-RNN) [4], have been used for the supervised detection and type identification of a broader range of sensor faults such as bias, gain, and precision degradation in acceleration measurements under uncertainty due to measurement noise.

On the other hand, *multi-sensor methods* relying on the statistical correlations among vibration responses from different sensors of the network, aim to construct a single model that represents the healthy state of the entire network. Methods based on variants of the Principal Component Analysis (PCA) [5, 6] and Independent Component Analysis (ICA) [7] have been extensively utilized for the detection and identification of bias, drift, and gain in acceleration and displacement measurements under operational uncertainty and measurement noise. Alternatively, variants of the Minimum Mean Square Error (MMSE)-based approach [8] have been used for the identification of bias, drift, gain, and precision degradation faults in acceleration measurements of a sensors network. The distinction between sensor faults and temperature effects has been addressed through PCA-based dimensionality reduction of the log-likelihood ratio [9]. In the same context, a virtual sensor may be developed based on a Multi-Layer Backpropagation Neural Network (MLP), trained to represent the healthy state of each sensor in the network by utilizing measurements from all sensors [10]. Sensor fault detection for acceleration measurements is achieved examining deviations on the residuals between the actual sensors output and the corresponding virtual sensor predictions. Deviations in the form of residuals have also been used for sensor fault detection in strain measurements using AutoRegressive with eXogenous inputs (ARX) stochastic models to sensor pairs [11]. While such an approach has shown effectiveness in detecting sensor drift, bias, spikes, precision degradation, and exponential sensor faults, it is challenged in selecting the optimal sensor pairs within the network. The interdependencies among measurements from different sensors may inhibit accurate modelling, while ensuring robustness to variability caused by multi-acting, variable, excitations remains a

significant challenge.

However, there are several limitations in the above studies: (a) typically, only a single uncertainty factor, such as temperature, noise, or excitation, is considered; (b) the achievable performance remains sensitive to multi-acting excitation conditions and variability in the excitation profile; (c) the methods' performance evaluation is often not systematic, frequently based on limited measurements from faulty sensors within the network; (d) the considered sensor faults cause substantial deviations in time-domain responses that are not representative of those observed under realistic fault conditions.

To address these limitations, a novel, robust to varying environmental and multi-acting excitation conditions, frequency-domain framework for sensor fault detection and type identification in a single accelerometer that is used for SHM in a population of composite aerostructures has been recently presented by some of the present authors in [12]. This framework is based on appropriate indices founded on Transmittance Functions (TFs), as obtained from a Multiple-Input Single-Output Transmittance Function AutoRegressive with eXogenous (MISO-TF-ARX) input model, and Multiple Coherence function, which ensure independence from, and thus robustness to, multi-acting excitation conditions and variability in the excitation profile.

The present study aims at extending the above frequency-domain framework for fault diagnosis in a network of multiple sensors employed for SHM, and assessing its effectiveness by addressing the following key research questions:

- Is it possible to reliably detect a fault at any sensor of the network with high accuracy, under the presence of significant uncertainty caused by manufacturing, temperature and multi-acting excitation variability?
- To what extent can the framework correctly identify the type of sensor fault (Bias, Gain, or Precision Degradation) and accurately isolate the faulty sensor within the network?

The postulated framework is assessed using acceleration signals from a three sensors network implemented through a finite element model of a composite UAV tail boom. The model represents the healthy dynamics of the aerostructure under significant uncertainty caused by population-induced manufacturing variability, temperature fluctuations and different excitation profiles. Bias, Gain, and Precision Degradation sensor faults are investigated, each applied at three different magnitudes to any sensor of the network. This results in a total of 27 fault scenarios, 135 test cases per sensor state (healthy, three magnitudes for each fault type), yielding a total of $3\,645$ test cases. The results are provided in terms of correct classification rates for all levels (detection, type identification, isolation) of sensor fault diagnosis.

2 THE FREQUENCY-DOMAIN FRAMEWORK FOR AUTOMATED MULTIPLE SENSOR FAULT DIAGNOSIS

2.1 The fault diagnosis characteristic quantities

Given a network of m accelerometers installed on the considered structure, a total of m Multiple Coherence (MC) functions are obtained. In each MC function a distinct accelerometer

acts as the output while the remaining ones as pseudo-inputs. The MC function for the s-th accelerometer when this is considered as the output is given by:

$$\gamma^2_{y_s|\mathbf{x}_s}(f) = \frac{S^*_{y_s\mathbf{x}_s}(f) \cdot S^{-1}_{\mathbf{x}_k\mathbf{x}_s}(f) \cdot S_{y_s\mathbf{x}_s}(f)}{S_{y_sy_s}(f)} \tag{1}$$

where $\mathbf{x}_s = [y_1[t], \ldots, y_{s-1}[t], y_{s+1}[t], \ldots, y_m[t]]^T$ is the $(m-1)$-dimensional pseudo-input vector, excluding the s-th sensor, and $S_{y_s\mathbf{x}_s}$, $S_{\mathbf{x}_s\mathbf{x}_s}$, and $S_{y_sy_s}$ represent the Cross and Auto Power Spectral Densities (CPSD and PSD) of the vibration signals (see details in [12]. The MC function is the characteristic quantity that is used for the diagnosis of sensor precision degradation as described in the next subsection, while the Transmittance Functions (TFs) of a stochastic MISO-TF AutoRegressive with eXogenous (MISO-TF-ARX) model of orders n_a, n_b are employed for the diagnosis of sensor bias and gain fault for each sensor. The general form of the MISO-TF-ARX model is [12]:

$$y_s[t] + \sum_{i=1}^{n_a} a_i^s \cdot y_s[t-i] = \sum_{\substack{j=1 \\ j\neq s}}^{m-1} \sum_{i=1}^{n_b} b_i^{j,s} \cdot y_j[t-i] + w_s[t], \quad w_s[t] \sim \text{i.i.d. } \mathcal{N}(0, \sigma_w^2) \tag{2}$$

where $t = 1, ..., N$ represents the discrete-time normalized by the sampling period T_s, $w_s[t]$ the model residual signal, i.i.d. stands for independent and identically distributed, and $\mathcal{N}(0, \sigma_w^2)$ indicates normal (Gaussian) distribution with zero mean and variance σ_w^2. a_i^s $(i = 1, \ldots, na)$ indicate the parameters of the model AutoRegressive (AR) part for the s-th sensor (used as output), while $b_i^{j,s}$ with $i = 1, \ldots, nb$ and $j = 1, \ldots, m-1$ the corresponding parameters of the eXogenous (X) part associated with the pseudo-inputs. Using the backshift operator $\mathcal{B}$ ($\mathcal{B}^j \cdot x[t] = x[t-j]$), the model is rewritten as:

$$A^s(\mathcal{B}) \cdot y_s[t] = \sum_{\substack{j=1 \\ j\neq s}}^{m-1} B^{j,s}(\mathcal{B}) \cdot y_j[t] + w_s[t] \tag{3}$$

$$\text{where} \quad A^s(\mathcal{B}) \triangleq 1 + a_1^s \cdot \mathcal{B} + \cdots + a_{n_a}^s \cdot \mathcal{B}^{n_a}, \quad B^{j,s}(\mathcal{B}) \triangleq b_1^{j,s} \cdot \mathcal{B} + \cdots + b_{n_b}^{j,s} \cdot \mathcal{B}^{n_b} \tag{4}$$

Based on the above, the following transmittance functions may be obtained:

$$TF_{j,s}(\mathcal{B}) = \frac{B^{j,s}(\mathcal{B})}{A^s(\mathcal{B})}, \quad j \neq s, \quad s = 1, \ldots, m. \tag{5}$$

The model parameter vector corresponding when each sensor is used as output is estimated using Ordinary Least Squares [13, pp. 204-205]:

$$\boldsymbol{\theta}_s := [a_1^s \ldots a_{n_a}^s \vdots b_1^1 \ldots b_{n_b}^1 \vdots b_1^{m-1,s} \ldots b_{n_b}^{m-1,s}]^T. \tag{6}$$

while model orders n_a and n_b selection and validation are based on a standard identification procedure, based on the minimization of the Bayesian Information Criterion (BIC) and Residual to Series Sum of Squares (RSS/SSS), as well as residual whiteness testing [13, pp. 505-514].

2.2 Sensor Fault Diagnosis

2.2.1 Baseline phase

During the baseline phase, a set of vibration signals from the m sensors are obtained from the considered structure under healthy sensor state. These signals are used for the estimation of the m MC functions and the $(m-1)$ Transmittance Functions derived from the corresponding m MISO-TF-ARX(n_a,n_b) models. Subsequently, the following indices are computed for each sensor ($s = 1, \ldots, m$), within properly selected frequency ranges $[f_{\min}^{\mathcal{FT}}, f_{\max}^{\mathcal{FT}}]$ Hz wherein the effects of each fault type $\mathcal{FT}$, ($\mathcal{FT} = B$ for Bias fault, $\mathcal{FT} = G$ for Gain fault, $\mathcal{FT} = PD$ for Precision Degradation) are expected to be evident ($j = 1, \ldots, m-1$, $j \neq s$):

$$\mathcal{F}_{j,s}^{B} = \sum_{f=f_{\min}^{B}}^{f_{\max}^{B}} \Big| \|TF_{j,s}(f+\delta f)\| - \|TF_{j,s}(f)\| \Big|, \quad \mathcal{F}_{j,s}^{G} = \int_{f_{\min}^{G}}^{f_{\max}^{G}} \|TF_{j,s}(f)\|\, df \tag{7}$$

$$\mathcal{F}_{s}^{PD} = \int_{f_{\min}^{PD}}^{f_{\max}^{PD}} \gamma_{y_s|\mathbf{x}_s}^{2}(f)\, df \tag{8}$$

where $\|\cdot\|$ stands for magnitude of the Transmittance function and δf denotes a selected increment in frequency. For each sensor $s = 1, \ldots, m$ serving as the output, a low $l_L^{\mathcal{FT}}$ and a high threshold $l_H^{\mathcal{FT}}$ are determined for each of the above indices. Thus, different ranges $R_{j,s}^{B}$ and $R_{j,s}^{G}$ are determined for the indices used to detect sensor bias and gain, respectively, within which the indices should lie under healthy state, while the range R_{s}^{PD} is determined for precision degradation.

It is noted that $\mathcal{F}_{j,s}^{B}$ detects the slope change in the low-frequency range induced by the bias-related offset in the DC gain, $\mathcal{F}_{j,s}^{G}$ the overall variation (increase or decrease) of the TF magnitude in the considered bandwidth due to gain variations, and $\mathcal{F}_{s}^{PD}$ the coherence reduction arising from increased measurement noise.

2.2.2 Inspection Phase

Sensor fault detection. During the inspection phase and once a new set of signals is available from the considered structure under unknown sensor state, the indices of Equations (7) and (8) are determined and their values are examined if they lie in the corresponding ranges from the Baseline phase through the following hypothesis testing:

$$\begin{array}{lll} \mathcal{H}_0: & \mathcal{F}_{j,s}^{\mathcal{B}} \in R_{j,s}^{B} \text{ and } \mathcal{F}_{j,s}^{\mathcal{G}} \in R_{j,s}^{G} \text{ and } \mathcal{F}_{s}^{PD} \in R_{s}^{PD},\ \forall j,s & \text{Healthy Sensors} \\ \mathcal{H}_1: & \text{Else} & \text{At least one sensor is faulty} \end{array} \tag{9}$$

Sensor fault type identification and isolation. Once a sensor fault has been detected, the identification of its type is achieved through the following rule :

$$\begin{array}{llll} \text{If:} & \text{any of } \mathcal{F}_{j,s}^{B} \notin R_{j,s}^{B} \text{ and } \mathcal{F}_{j,s}^{G} \in R_{j,s}^{G} \text{ and } \mathcal{F}_{s}^{PD} \in R_{s}^{PD},\ \forall j,s & \rightarrow & \text{Bias Fault} \\ \text{If:} & \text{any of } \mathcal{F}_{j,s}^{G} \notin R_{j,s}^{G} \text{ and } \mathcal{F}_{j,s}^{B} \in R_{j,s}^{B} \text{ and } \mathcal{F}_{s}^{PD} \in R_{s}^{PD},\ \forall j,s & \rightarrow & \text{Gain Fault} \\ \text{If:} & \text{any of } \mathcal{F}_{s}^{PD} \notin R_{s}^{PD},\ \forall s & \rightarrow & \text{Precision Degradation} \end{array} \tag{10}$$

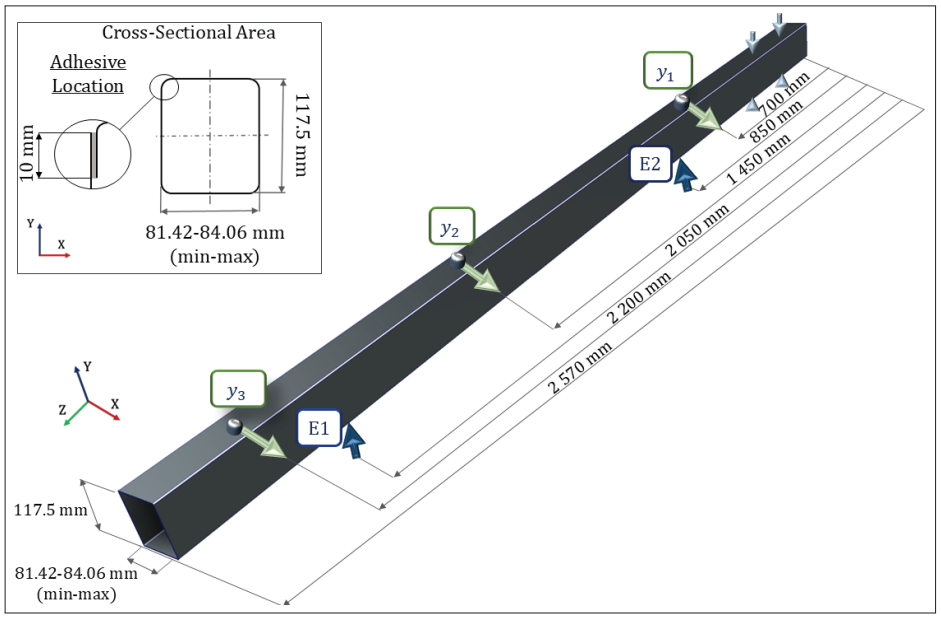

Figure 1: Schematic representation of the finite element representation of the UAV tail boom, the excitation positions ($E1$, $E2$) and the acceleration sensors y_1 /y_2 /y_3.

Fault isolation is achieved simultaneously through the above procedure. In particular, if the fault is of the bias or gain type, then *all* of the corresponding indices, where the faulty sensor participates either as pseudo-input j or output s, will lie outside its range defined during the baseline phase. In the case of precision degradation fault type, the sensor s that yields the minimum value of $\mathcal{F}_s^{PD}$ is isolated as the faulty from the network.

3 THE COMPOSITE AEROSTRUCTURE, THE UNCERTAINTY FACTORS AND THI SENSOR FAULTS

3.1 The finite element representing the healthy dynamics of the composite aerostructure

A bonded spar model of a UAV tail boom, consisting of two C-shaped carbon-epoxy webs and two skins of varying thickness bonded with adhesive to form a closed rectangular beam (see Figure 1), has been implemented in Abaqus using a finite element (FE) model. The structure has nominal dimensions of $2\,570 \times 82.74(\pm 1.32) \times 117.5$ mm, with a ply thickness of 0.22 mm per lamina, and material properties under the healthy state and nominal temperature ($T = 20\,^{\circ}$C) are provided in Table 1. Quad shell elements have been used for the webs and skin, and brick elements for the adhesive, with mesh sizes of 5×5.136 mm and $5 \times 0.2 \times 0.588$ mm, respectively, totaling approximately $187\,098$ elements and $150\,383$ nodes. The structure is considered under fixed-free boundary conditions, with bolts placed at 20 mm and 313 mm from the edge to simulate fuselage attachment.

The acceleration measurements have been acquired in the transverse direction near the root (y_1), center (y_2), and tip (y_3) under multi-acting vertical excitation (E_1 and E_2). The excitation

Table 1: Experimentally measured temperature dependence of the material properties for the nominal composite aerostructure under healthy state.

T (°C)	**Carbon Epoxy**				**Adhesive**	**Damping**
	E_{11} (GPa)	E_{22} (GPa)	G_{12} (GPa)	ν_{12}	G_{12} (GPa)	ζ (%)
-40	58.0	58.0	4.27	0.08	0.584	0.80
20	57.8	56.2	3.87	0.07	0.393	0.48
60	57.9	57.9	3.38	0.07	0.147	1.34

For each simulation, a temperature $T \sim U[-50, 70]$ °C is generated; the corresponding material properties are obtained via quadratic interpolation of the above values at each generated T.

signals have been discretized at an initial sampling frequency of $f_s = 40\,000$ Hz and subsequently filtered using a low-pass Chebyshev Type II filter; $f_{stop} = 2\,000$ Hz (cut-off), order $n = 24$. The Mode Superposition method has been employed, incorporating all modes within the frequency range of $[0, 2\,000]$ Hz. A constant time step of $\Delta t = 2.5 \times 10^{-5}$ s (integration frequency: $f_{\text{int}} = 40\,000$ Hz) has been used, yielding an initial signal length of $100\,000$ samples. The response signals have subsequently been resampled at $f_s = 4\,000$ Hz, resulting in a final signal length of $N = 10\,000$ samples with duration of 2.5 s.

3.2 The uncertainty factors

The performance and robustness of the sensor fault diagnosis frequency-domain framework is investigated under multiple uncertainty factors that affect the obtained acceleration measurements. These factors include: (i) operating temperature variability in the range of $[-50, 70]$ °C, (ii) manufacturing variability affecting skin and adhesive material properties, and (iii) varying excitation profiles due to different operational states and multi-acting excitations.

The variability of the material properties due to temperature uncertainty – including the longitudinal modulus (E_{11}), transverse modulus (E_{22}), and in-plane shear modulus (G_{12}) of the carbon-epoxy (webs and skin), the shear modulus (G_{12}) of the adhesive, and the damping ratio (ζ) – is modelled using temperature samples drawn from uniform distributions within the range $[-50, 70]$ °C (see details in [14]). These samples are then used for quadratic interpolation of the corresponding material properties based on their experimentally measured temperature dependence for the nominal structure and damping [14], as provided in Table 1.

For each considered temperature sample, manufacturing variability is further implemented via three uniform distributions within the range $[-10, 10]\%$. These distributions are applied to the longitudinal, transverse, and shear moduli (E_{11}, E_{22}, G_{12}) of the skin, as well as to the shear modulus (G_{12}) of the adhesive so as each numerical experiment has a unique realization.

In addition, each member is subjected to one of the two multi-acting excitation profiles: P1, a band-limited white noise within $[0, 2\,000]$ Hz; P2, a colored noise generated via an Auto-Regressive (AR) model of order $n = 6$, incorporating engine effects (see details in [14]). Distinct seed numbers are assigned for noise generation at each excitation point to ensure variabil-

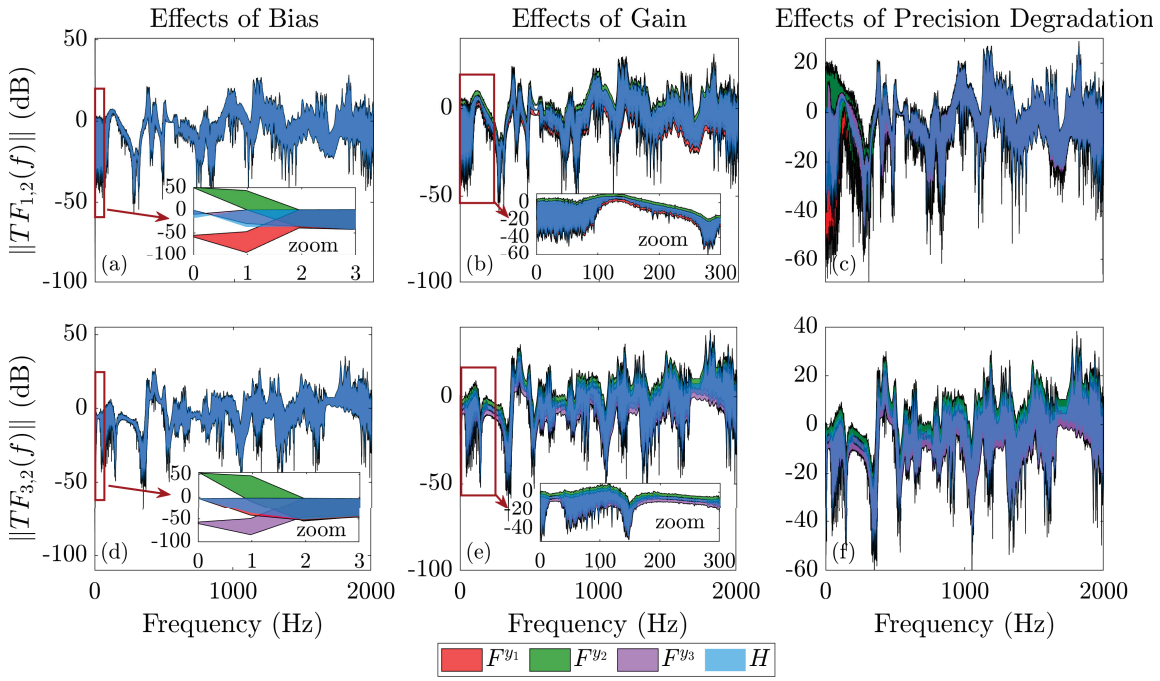

Figure 2: Welch-based MISO-TF envelope magnitude estimates using the sensor y_2 as output and y_1, y_3 as pseudo-inputs. (a) – (c) $TF_{1,2}$ and (d) – (f) $TF_{3,2}$ including healthy sensors (blue envelopes) and the small magnitude of the considered faults in sensor y_1 (red envelopes), y_2 (green envelopes) and y_3 (purple envelopes); Healthy sensors: 135 test cases, Faulty sensors: 135 test cases per fault type, Excitation profiles: both P1 and P2 are used.

ity, with all signals filtered to the above frequency bandwidth using a low-pass Chebyshev Type II filter. The robustness of the framework under excitation profile uncertainty is achieved with measurements obtained under P1 profile in the Baseline phase, while both P1 and P2 profiles are used in the Inspection phase.

3.3 The sensor faults and their effects on the signals

Three distinct sensor fault types, as defined in [8, 12], are considered in this study: (i) Bias (B), (ii) Gain (G), and (iii) Precision Degradation (PD). Each fault persists over the entire duration of the measured signal ($N = 10\,000$ samples). For each fault type, three fault magnitudes ($\mathcal{FM}$) are implemented: Small (S), Medium (M), and Large (L).

In particular, the Bias fault in the measurement is implemented via the equation $y_B[t] = y[t] + \alpha\sigma_y$, where α denotes the fault magnitude that takes the values of 2%, 5%, and 10% corresponding to Small, Medium, and Large, respectively, and σ_y is the standard deviation of the measurement under the healthy sensor state. Gain fault is implemented via the $y_G[t] = \alpha y[t]$, where α takes values of 0.7 (S), 1.4 (M), and 0.5 (L). For Precision Degradation faults, the expression $y_{PD}[t] = y[t] + e[t]$ is used, where $e[t]$ represents the sensor noise that is $e[t] \sim \mathcal{N}(0, \sigma_e^2)$, while the noise-to-signal ratio (NSR) is set to 2% (S), 5% (M), and 10% (L). In

Table 2: Sets of vibration signals used in the baseline and inspection phases.

Sensor State	# of Beams under Manuf. Variab.	# of Temperatures under $P1/P2$	# of Signal Sets under $P1/P2$	# of Signal Sets per $\mathcal{FM}^*$
Baseline Phase				
Healthy	9	$12/0$	$108/0$	–
Inspection Phase				
Healthy (H)	9	$10/5$	$90/45$	–
Faulty$^\diamond$ (F^{y_i})	9	$10/5$	$90/45$	135

$^\diamond$: $\mathcal{FM} = S/M/L$ fault magnitude; *: Faulty sensor $i = 1/2/3$ under fault type $B/G/PD$

Total # of inspection test cases: $135/3\,645$ under healthy/faulty sensor state (135 per sensor, fault type and magnitude).

total, 9 faults are considered, each applied to any of the three sensors network, which results in 27 distinct fault scenarios.

Non-parametric Welch-based magnitude estimates of the MISO TFs [15] $TF_{1,2}$ and $TF_{3,2}$ under all uncertainty factors, are provided in Figure 2 using sensor y_2 as the output. In particular the TFs of the healthy (H) sensors state are depicted, along with those affected by the small sensor faults on each of the three sensors y_1, y_2 and y_3, designated as F^{y_1}, F^{y_2} and F^{y_3}, respectively. Based on these graphs, the following observations are made: (a) the effects of the uncertainty factors on the measured dynamics under the healthy sensor state lead in a significant overlap between the healthy and faulty sensors conditions, indicating a challenging sensor fault detection problem; (b) the impact of bias fault is evident only within the frequency range of $[0, 2]$ Hz, highlighting the need for accelerometers capable of accurate measurements in this range; (c) the weak effects of the considered gain and precision degradation small faults are shown in almost the entire range of $[0, 2\,000]$ Hz; (d) the faults in sensor y_2 (used as output) affect the magnitude of both TFs. On the other hand, when a sensor fault affects any of the pseudo-inputs (y_1 and y_3 in this figure), the impact is limited only to the TF where the sensor contributes. For instance, in Figures 2(a), (d) the corresponding faults in y_3 and y_1 are not evident. All the above points underscore the significant challenges involved in sensor fault diagnosis under combined uncertainty.

4 SENSOR NETWORK FAULT DIAGNOSIS RESULTS

Baseline phase. The training of the postulated frequency-domain framework is conducted using $n = 108$ sets of vibration response signals obtained from the considered three sensors network. The signals are collected from 9 randomly selected healthy aerostructures within the population. The operating conditions vary, as previously mentioned, including different excitation realizations of profile P1 and 12 randomly chosen temperature conditions as shown in Table 2. Based on these, 3×108 MISO–TF–ARX(200,200) models of Equation (2) and 3×108 MC functions of Equation (1) (one model/function per sensor) are estimated. The Welch method with Hamming window of $4\,096$ samples and 90% overlap is used for the MC functions. The indices of Equations (7), (8) are then obtained. Based on these, the ranges

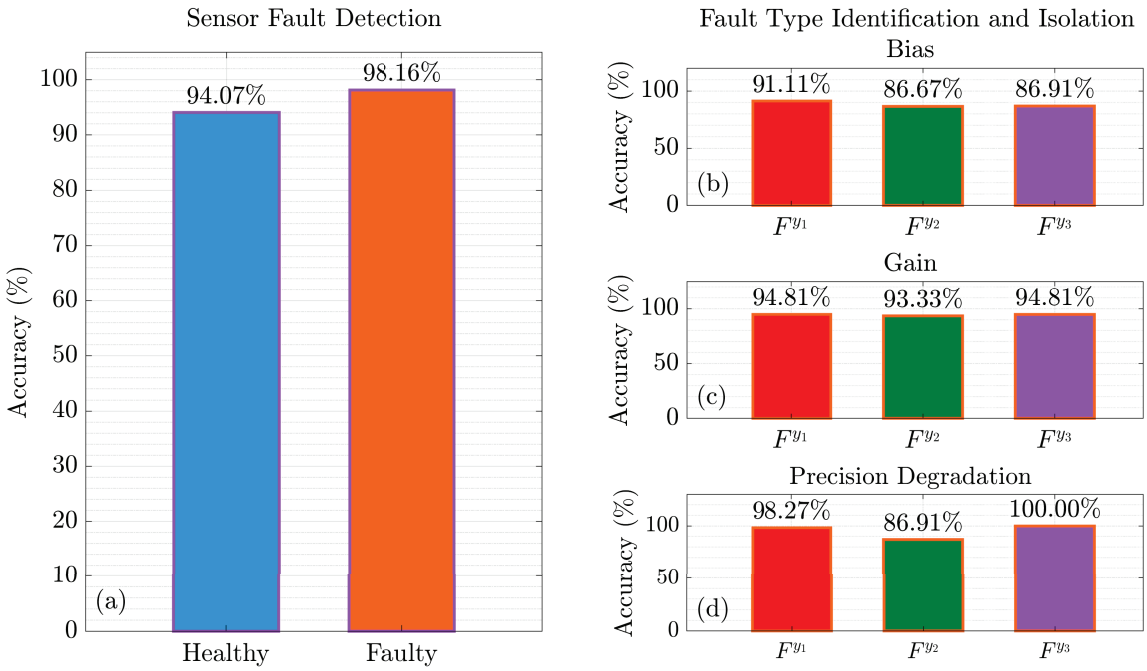

Figure 3: Sensor fault diagnosis results (inspection phase) in terms of correct classification rate (Accuracy). These results are based on 135 test cases under healthy sensor state and $405/405/405$ test cases per faulty sensor $y_1/y_2/y_3$ under Bias/Gain/Precision Degradation; $135/3\,645$ test cases under healthy/faulty sensor state in total.

$[f_{min}^{\mathcal{FT}}, f_{max}^{\mathcal{FT}}]$ are determined for each considered sensor fault type as: $[f_{\text{min}}^{B}, f_{\text{max}}^{B}] = [0.07, 0.15]$ Hz using $\delta f = 0.01$ Hz, $[f_{\text{min}}^{G}, f_{\text{max}}^{G}] = [0.07, 300]$ Hz and $[f_{\text{min}}^{PD}, f_{\text{max}}^{PD}] = [87, 140]$ Hz. Based on the lower and upper thresholds $[l_L^{\mathcal{FT}}, l_H^{\mathcal{FT}}]$ of the indices within the above frequency ranges, the $R_{j,s}^{B}, R_{j,s}^{G}, R_{s}^{PD}$ ranges are determined as described in Section 2.2.1 by using each sensor in the network as output with the remaining sensors used as pseudo-inputs in each case.

Inspection phase. The assessment of the postulated framework is conducted using additional vibration response (see Table 2) signal sets obtained from 9 healthy aerostructures not included in the Baseline phase. Each structure is subjected to 10 randomly selected temperature conditions and both excitation profiles P1 and P2, resulting in $90/45$ simulations under P1/P2, respectively. Each simulation in this phase is considered under both healthy sensor state and each of the 27 sensor fault scenarios, resulting in $135/3\,645$ inspection test cases (Table 2) under healthy/faulty sensor states, respectively. Classification accuracy rates are then computed to assess the performance of the frequency-domain framework in terms of sensor fault detection, type identification, and faulty sensor isolation.

The sensor fault diagnosis results are provided in Figure 3. In particular, *sensor fault detection* (Figure 3(a)) leads to 94.07% of correct classification for the considered healthy and 98.16% for the faulty sensor test cases, indicating very good performance. Regarding *sensor fault type identification and isolation* results and following the procedure of Section 2.2.2 where sensor fault type identification and isolation is simultaneously achieved, the method achieves

similarly very good results. Based on Figure 3(b) the average correct fault type identification rate for the Bias fault is 88.23%, while this rate is 94.32% for Gain and 95.06% for Precision Degradation. On the other hand, based on the left part (red bars) of Figures 3(b)-(d), the average correct fault isolation rate for sensor y_1 is 94.73%, while this rate is 88.97% (green bars) and 93.91% (purple bars) for sensors y_2 and y_3, respectively, leading to a remarkable overall sensor fault isolation of 92.54%.

5 CONCLUSIONS

The study's main conclusions, in response to the questions outlined in the introduction, may be summarized as follows:

- Despite the presence of significant uncertainty, a high fault detection rate has been achieved by the postulated frequency-domain framework with accuracy rates of 94.07% and 98.16% for the healthy and faulty sensor states, respectively.
- High accuracy has been also achieved in fault type identification, with classification rates of 88.23%, 94.32%, and 95.06% for Bias, Gain, and Precision Degradation faults, respectively. The postulated framework has demonstrated strong capability in isolating the faulty sensor in the network, with an overall isolation accuracy of 92.54%.

ACKNOWLEDGMENTS

The research work was supported by the Hellenic Foundation for Research and Innovation (HFRI) under the 2nd Call for HFRI's Research Projects to Support Faculty Members & Researchers (Project Number: 4012).

REFERENCES

[1] T.-H. Yi, H.-B. Huang, and H.-N. Li, "Development of sensor validation methodologies for structural health monitoring: A comprehensive review," *Measurement*, vol. 109, pp. 200–214, Oct. 2017. [Online]. Available: https://linkinghub.elsevier.com/retrieve/pii/S0263224117303718

[2] T.-H. Yi, H.-N. Li, G. Song, and Q. Guo, "Detection of Shifts in GPS Measurements for a Long-Span Bridge Using CUSUM Chart," *International Journal of Structural Stability and Dynamics*, vol. 16, no. 04, p. 1640024, May 2016. [Online]. Available: https://www.worldscientific.com/doi/abs/10.1142/S0219455416400241

[3] Y. Luo, L. Wang, X. Guo, J. Zheng, F. Liao, and Z. Guo, "Structural Damage Identification Based on Convolutional Neural Network Group Considering the Sensor Fault," *KSCE Journal of Civil Engineering*, vol. 27, no. 8, pp. 3403–3417, Aug. 2023. [Online]. Available: https://link.springer.com/10.1007/s12205-023-0683-y

[4] B. Liu, Q. Xu, J. Chen, J. Li, and M. Wang, "A New Framework for Isolating Sensor Failures and Structural Damage in Noisy Environments Based on Stacked Gated

Recurrent Unit Neural Networks," *Buildings*, vol. 12, no. 8, p. 1286, Aug. 2022. [Online]. Available: https://www.mdpi.com/2075-5309/12/8/1286

[5] R. Sharifi, Y. Kim, and R. Langari, "Sensor fault isolation and detection of smart structures," *Smart Materials and Structures*, vol. 19, no. 10, p. 105001, Oct. 2010. [Online]. Available: https://iopscience.iop.org/article/10.1088/0964-1726/19/10/105001

[6] A. R. M. Rao, V. Kasireddy, N. Gopalakrishnan, and K. Lakshmi, "Sensor fault detection in structural health monitoring using null subspace–based approach," *Journal of Intelligent Material Systems and Structures*, vol. 26, no. 2, pp. 172–185, Jan. 2015. [Online]. Available: http://journals.sagepub.com/doi/10.1177/1045389X14522534

[7] M. R. Hernandez-Garcia and S. F. Masri, "Application of statistical monitoring using latent-variable techniques for detection of faults in sensor networks," *Journal of Intelligent Material Systems and Structures*, vol. 25, no. 2, pp. 121–136, Jan. 2014. [Online]. Available: http://journals.sagepub.com/doi/10.1177/1045389X13479182

[8] J. Kullaa, "Detection, identification, and quantification of sensor fault in a sensor network," *Mechanical Systems and Signal Processing*, vol. 40, no. 1, pp. 208–221, Oct. 2013. [Online]. Available: https://linkinghub.elsevier.com/retrieve/pii/S0888327013002057

[9] ——, "Distinguishing between sensor fault, structural damage, and environmental or operational effects in structural health monitoring," *Mechanical Systems and Signal Processing*, vol. 25, no. 8, pp. 2976–2989, Nov. 2011. [Online]. Available: https://linkinghub.elsevier.com/retrieve/pii/S0888327011002196

[10] K. Smarsly and K. H. Law, "Decentralized fault detection and isolation in wireless structural health monitoring systems using analytical redundancy," *Advances in Engineering Software*, vol. 73, pp. 1–10, Jul. 2014. [Online]. Available: https://linkinghub.elsevier.com/retrieve/pii/S0965997814000453

[11] C. Lo, J. P. Lynch, and M. Liu, "Distributed Reference-Free Fault Detection Method for Autonomous Wireless Sensor Networks," *IEEE Sensors Journal*, vol. 13, no. 5, pp. 2009–2019, May 2013. [Online]. Available: http://ieeexplore.ieee.org/document/6428590/

[12] I. E. Saramantas, S. D. Fassois, J. S. Sakellariou, I. Iliopoulos, and D. N. Serpanos, "Sensor fault detection and identification for robust SHM in a population of composite aerostructures under varying excitation and temperature," in *Proceedings of the International Conference on Noise and Vibration Engineering*, Leuven, Belgium, 2024.

[13] L. Ljung, *System Identification: Theory for the User*, 2nd ed. Upper Saddle River, NJ: Prentice Hall, 1999.

[14] I. E. Saramantas, P. E. Konis, I. M. Kriatsiotis, Y. Ofir, I. Kressel, P. E. Spiliotopoulos, F. T. Fera, J. S. Sakellariou, S. D. Fassois, F. Giannopoulos, C. Spandonidis, M. Tur, and Z. Tzioridis, "An Exploratory Study on Data-Driven Vibration Based Damage Detection and Characterization for a Population of Composite Aerostructures," *Journal of Physics: Conference Series*, vol. 2647, no. 18, p. 182029, Jun. 2024. [Online]. Available: https://iopscience.iop.org/article/10.1088/1742-6596/2647/18/182029

[15] J. S. Bendat and A. G. Piersol, *Random Data: Analysis and Measurement Procedures*, 2nd ed. New York: John Wiley & Sons, 1986.

XI ECCOMAS Thematic Conference on Smart Structures and Materials - SMART 2025
M. Krommer, M. Nader and M. Schagerl (Eds)

Received: 29 March 2025 / Revised: 25 August 2025 / Accepted: 7 September 2025
© The Author(s) 2025

Performance of Frequency-Based Fatigue Methods Using Realistic Power Spectral Densities

Jack Rahbek Steengaard, Luis David Avendaño-Valencia, Marie Lützen, Mikkel Løvenskjold Larsen

Abstract. Traditionally, fatigue assessments are performed in the time-domain using well-established rainflow counting procedures to obtain the stress cycles experienced by the material. Due to improved computational costs, frequency-based fatigue methods present attractive alternatives. These methods utilize the power spectral densities of stress signals to assess the fatigue performance. Multiple studies have developed new methods or compared existing methods. However, these studies are based on spectra, which do not always represent real spectra. This study presents an overview of the spectrum types used in the literature on frequency-based fatigue. In addition, simple structural systems subjected to random loading are defined and their response spectra are analyzed using the Dirlik and Zhao-Baker methods. The results are compared to the results of rainflow counting on simulated time-series. The results show that the fatigue damages are accurately predicted, but the stress range distributions are not, except for narrowband spectra.

Key words: Frequency-Based Fatigue, Spectral Methods, Power Spectral Densities

1 INTRODUCTION

Structures subjected to time-varying loads are at risk of fatigue failure due to the formation and growth of cracks. When a crack grows to a certain critical size, sudden fracture of the material will occur [1]. Due to the sudden nature of the failure, the fatigue phenomenon has been studied to avoid failure and the resulting consequences.

In most applications, the fatigue loading has variable amplitude, and the stress range varies over time [2]. In this case, a counting method is utilized for determining the number of cycles

Jack Rahbek Steengaard & Luis David Avendaño-Valencia & Marie Lützen & Mikkel Løvenskjold Larsen
Department of Mechanical and Electrical Engineering, University of Southern Denmark, Campusvej 55, 5230 Odense M, Denmark, e-mail: jars@sdu.dk

Jack Rahbek Steengaard & Mikkel Løvenskjold Larsen
Kverneland Group Kerteminde A/S, Taarupstrandvej 25, 5300 Kerteminde, Denmark

and their corresponding stress range. A damage accumulation method is then to be used together with an S-N curve to determine the fatigue life. Rainflow counting and Palmgren-Miner damage accumulation [3, 4] have been established as the standard for fatigue assessment since they provide results in good agreement with experiments [5, 6, 7].

Rainflow counting considers the time-series of a stress signal to identify the stress cycles. The time-series must be sufficiently long to capture the stress range distribution accurately [8]. However, it is computationally demanding to generate time-series and apply a rainflow counting algorithm to long time-series. The computational cost becomes significant for large structures where multiple exposed locations of the structure need to be analyzed. Frequency-based methods arise as an alternative, where fatigue assessment is made using the power spectral density (PSD), which reduces the computational cost. Moreover, PSDs are well suited to describe random signals [9] such as the stress signal of randomly excited structures in operation.

Multiple frequency-based fatigue methods have been proposed in the literature. The development and comparisons of these methods have been made based on PSDs and corresponding time-series simulations. However, most of these PSDs do not represent realistic spectra, except for a few cases using offshore [7] or automotive spectra [6, 10]. Thus, this poses the question of whether or not the methods perform sufficiently well for response PSDs of randomly loaded structural dynamics systems. The present study gives an overview of spectrum types used in the literature on frequency-based fatigue. Furthermore, simple structural dynamics systems subjected to random excitation are defined, and the performance of selected frequency-based fatigue methods is examined for the stress response PSDs compared to rainflow counting on simulated time-series.

2 SPECTRUM TYPES

Due to the complexity of the rainflow counting algorithms, no relationship between the PSD and the rainflow stress range distribution is available [11, 12]. Thus, all methods correlating the PSD to the rainflow stress range distribution or the corresponding fatigue damage rely on approximations and best-fit expressions relating spectral parameters to simulated time-series results [7, 13, 14, 15]. Since these time-series are generated based on given PSDs, the performance of the methods depends, to some extent, on the PSDs used for the development. Similarly, comparisons of frequency-based fatigue methods investigate how close the results of the methods come to the results of simulated time-series [6, 7, 8, 10, 11, 14, 15, 16]. These results also depend on the spectrum types used in the comparison for the time-series simulations. For this reason, the PSDs should be as close as possible to the real spectra that the methods are intended to be used for.

Figure 1 shows sketches of the spectrum types used in the literature investigated in this paper. Table 1 provides an overview of the spectrum types used in the considered references. The development part of Table 1 shows the spectrum types used for developing the frequency-based fatigue method presented in a given reference. The comparison part of Table 1 shows the

spectrum types used in the comparative study performed in a given reference. Some references are included in both the development and the comparison part of the table since these references present the development of a method and perform a comparison with other methods [7, 14, 15]. For some of these references, the comparison uses other PSDs than those used for developing the presented method [7, 15]. In many cases, the same PSDs are reused for other studies, which is the case for [11, 14, 15], [8, 13], [6, 16], and the automotive spectra of [6, 10]. As seen from Table 1, most PSDs are rectangular (R) or triangular (T) in shape, which is often a simplification of real spectra. Some of the triangular bimodal (T2) spectra of [6] and the rectangular one modal (R1) spectra of [10] have background noise, which is modeled by a minimum amount of frequency content over all frequencies. The only realistic spectra are the automotive spectra (A) used in [6, 10] and the offshore spectra (S1 and S2) of [7]. The other smooth (S) spectra are defined in some other way. The smooth spectra of [11, 14, 15] are defined with a parabolic shape [14], and the smooth spectra of [8, 13] are obtained by a combination of two band pass filters [13]. In short, few spectra used in the literature on frequency-based fatigue are based on realistic stress processes.

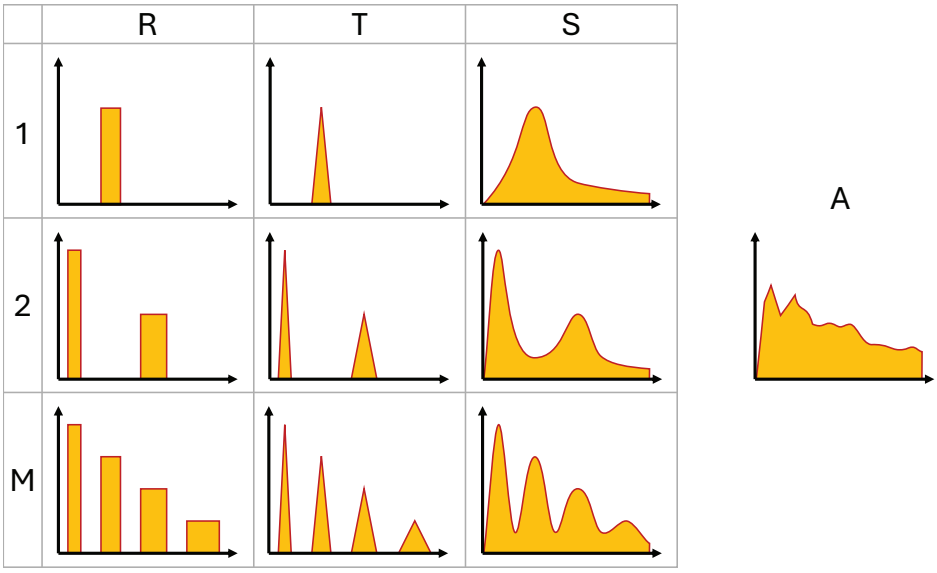

Figure 1: Sketches of spectrum types used in the considered literature. R = rectangular, T = triangular, S = smooth, 1 = one modal, 2 = bimodal, M = multimodal, A = automotive.

3 STRUCTURAL DYNAMICS

Structural systems of masses, dampers, and springs are defined to obtain stress spectra from simple vibrating structures. A one degree of freedom (DOF) system and a two DOF system are

Table 1: Overview of spectrum types used in the considered literature.

	Reference	R1	R2	RM	T1	T2	TM	S1	S2	SM	A
Development	Benasciutti2005 [14]		X			X			X		
	Dirlik1985 [13]		X						X		
	Park2014 [15]		X			X			X		
	Zhao1992 [7]	X	X	X		X		X	X		
Comparison	Benasciutti2005 [14]		X			X			X		
	Benasciutti2006 [11]		X			X			X		
	Larsen2015 [16]	X			X	X	X				
	Mrsnik2013 [6]	X			X	X	X				X
	Park2014 [15]		X								
	Quigley2016 [8]		X						X		
	Zhao1992 [7]	X	X	X		X		X	X		
	Zorman2023 [10]	X	X	X							X

defined and illustrated in Figure 2. For simplicity, the force, F, is defined as white noise with a variance of $1\ N^2$ and frequency content up to $50\ Hz$. The maximum frequency content is set to $50\ Hz$ because the frequency response functions (FRFs) have very low values at this frequency compared to the resonance frequencies.

The deflection FRFs of the systems can be defined according to [17]. The force in the springs can be found from the deflection by Hooke's law, and by considering the springs as bar elements with a cross-sectional area of A, the stress FRFs for the normal stresses in the springs can be expressed by Equation 1. The stress response PSD can then be found by Equation 2.

$$H_\sigma(\omega) = \frac{k}{A} \cdot \mathbf{C_d} \cdot \left(-\omega^2 \mathbf{M} + i\omega \mathbf{C} + \mathbf{K}\right)^{-1} \cdot \mathbf{G} \tag{1}$$

$$G_{\sigma\sigma}(\omega) = |H_\sigma(\omega)|^2 \cdot G_{FF}(\omega) \tag{2}$$

Where $H_\sigma(\omega)$ is the FRF describing the stress in a selected spring, ω is the angular frequency, k is the spring stiffness of the selected spring, $\mathbf{C_d}$ is the output vector used to obtain the stress in the selected spring, $\mathbf{M}$ is the mass matrix, i is the imaginary unit, $\mathbf{C}$ is the damping matrix, $\mathbf{K}$ is the stiffness matrix, $\mathbf{G}$ is the input-coupling vector, $G_{\sigma\sigma}(\omega)$ is the (one-sided) PSD of the stress, and $G_{FF}(\omega)$ is the (one-sided) PSD of the input force.

For the two DOF system, the upper spring is considered, in which case $\mathbf{C_d} = \begin{bmatrix} 1 & 0 \end{bmatrix}$ and $\mathbf{G} = \begin{bmatrix} 1 & 0 \end{bmatrix}^T$, and for the one DOF system, they are equal to one. In this study, the following system parameter values have been used: mass $m_0 = 100\ kg$, damping $c = 10\ kg/s$, spring stiffness $k = 10^6 N/m$, and cross-sectional area $A = 10^{-6}\ m^2$.

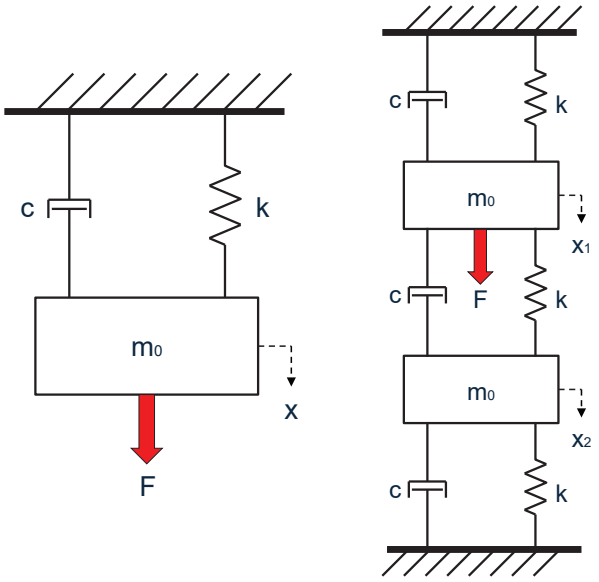

Figure 2: Structural systems used to define stress processes. Left: one DOF system. Right: two DOFs system.

4 TIME-SERIES SIMULATIONS

Having defined the stress response PSDs, the frequency-based fatigue methods can be applied. However, time-based results are also desired for comparison with the frequency-based results. A stress time-series can be simulated from a stress PSD by utilizing Equation 3 [18].

$$\sigma(t) = \sum_{j=1}^{J} [2G_{\sigma\sigma}(\omega_j)\Delta\omega]^{1/2} \cos(\omega_j t + \psi_j) \tag{3}$$

Where $\sigma(t)$ is the stress time-series for the discrete time, t, evaluated at regular intervals ($t = j\Delta t$ where $j = 1, 2, ...J$) with a time step of $\Delta t = \frac{2\pi}{\omega_s}$, ω_s being the angular sampling frequency. ω_j is the angular frequency of the j'th angular frequency bin, $\Delta\omega$ is the width of the angular frequency bins (assuming equal width of all bins), J is the number of time samples, which in this study is chosen to be 500.000, and ψ_j is a random phase angle with a value in the interval $[0, 2\pi]$. ψ_j takes a different random value for each angular frequency bin j.

When using Equation 3, the sampling frequency should be at least ten times the peak frequency content in the spectrum to achieve a converged fatigue damage [8]. This is ensured by using a sampling frequency for the simulated time-series of ten times the maximum frequency content, which is higher than the peak frequency content. Furthermore, the discretization of ω must match the sampling frequency chosen. For a given number of time samples, this is ensured

by having an angular frequency bin width, or step size, given by Equation 4 [13].

$$\Delta\omega = \omega_s / J \tag{4}$$

The simulated time-series can be verified by determining their PSDs. Figure 3 shows the PSDs of the structural systems (Figure 2) and the PSDs of the simulated time-series. The PSDs of the simulated time-series are found by Welch's method using the Hanning window with $50\ \%$ overlap and the biggest possible blocksize, which ensures at least 10 averages [9].

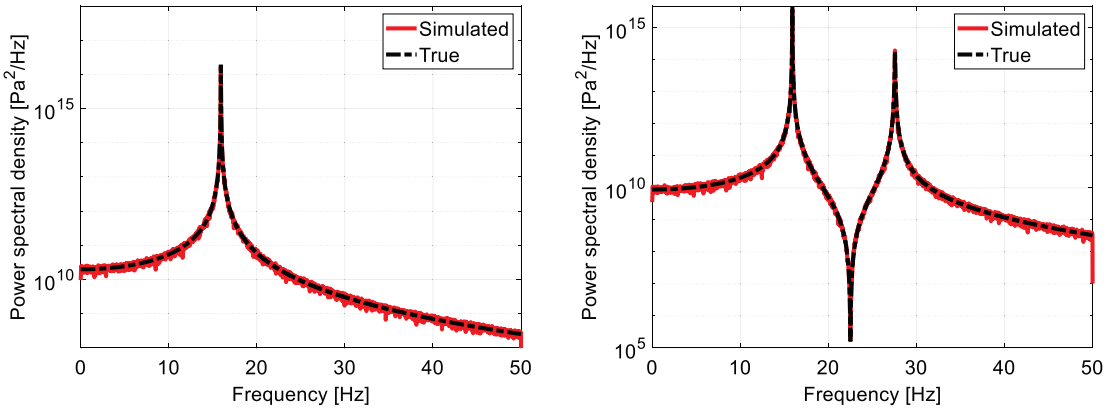

Figure 3: System PSDs (true) and simulated time-series PSDs. Left: one DOF system. Right: two DOF system.

The process of simulating time-series using Equation 3 is inherently random due to the random phase angle, ψ_j. Thus, multiple simulations need to be performed such that averages of the time-based fatigue results can be obtained, which are considered the correct time-based results. Similar to the study in [10], 20 simulations are made in this study.

5 TIME-SERIES FATIGUE DAMAGE

The fatigue damages of the simulated time-series are found by the three-point rainflow counting algorithm described in [19] and subsequent use of the Palmgren-Miner damage accumulation rule expressed by Equation 5 [3, 4].

$$D = \sum_j \frac{n_j}{N_j} \tag{5}$$

Where D is the (accumulated) fatigue damage, n_j is the number of cycles at a given stress range, and N_j is the fatigue life, in number of cycles, at the given stress range indicated by j.

To calculate the fatigue damage from Equation 5, the fatigue life at a given stress range, σ_r, must be found from the S-N curve. The choice of S-N curve is not a focus in this study.

For simplicity, a FAT90 S-N curve with a single slope is used. The S-N curve is described by Equation 6, where a slope, m, of 3 is used, and the fatigue capacity for stress ranges, C_r, can be found from a point on the curve, which for a FAT90 S-N curve is defined by $N = 2 \cdot 10^6$ and $\sigma_r = 90\ MPa$.

$$N \cdot \sigma_r^m = C_r \tag{6}$$

6 FREQUENCY-BASED FATIGUE METHODS

Several concepts from the theory of random processes are utilized in the frequency-based fatigue methods. The relevant quantities for a random stress process are defined based on the moments, M_j, of its PSD, which are given by Equation 7 [14].

$$M_j = \int_0^\infty \omega^j \cdot G_{\sigma\sigma}(\omega)\, d\omega \tag{7}$$

The variance of the stress process is equal to the zeroth moment of the PSD. Thus, the standard deviation, σ_{std}, is given by Equation 8.

$$\sigma_{std} = \sqrt{M_0} \tag{8}$$

The expected peak rate, ν_p, can be found by Equation 9.

$$\nu_p = \frac{1}{2\pi}\sqrt{\frac{M_4}{M_2}} \tag{9}$$

Furthermore, the bandwidth parameters, α_j, given by Equation 10 are utilized. The second bandwidth parameter is commonly called the irregularity factor, I, and is given by Equation 11.

$$\alpha_j = \frac{M_j}{\sqrt{M_0 M_{2j}}} \tag{10}$$

$$I = \alpha_2 = \frac{M_2}{\sqrt{M_0 M_4}} \tag{11}$$

For this study, two frequency-based fatigue methods have been selected for the analysis. These are the Dirlik (DK) and Zhao-Baker (ZB) methods. These two methods have been chosen since they have been developed to provide the rainflow stress range distribution based on a given PSD. Most methods provide only a damage value, but having the rainflow stress range distribution enables an additional comparison than merely comparing the damage values. Furthermore, these two methods have been shown to be accurate, and they are recommended by other studies [6, 11]. The methods are presented below.

Dirlik's method [13] expresses the rainflow stress range probability density function (PDF), p, by a sum of an exponential function, a Rayleigh function with variable Rayleigh parameter, and a standard Rayleigh function, Equation 12.

$$p_{DK}(\sigma_r) = \frac{1}{2\sigma_{std}} \left[c_1 \frac{1}{Q_2} e^{-\frac{Z}{Q_2}} + c_2 \frac{Z}{Q_1^2} e^{-\frac{Z^2}{2Q_1^2}} + c_3 Z e^{-\frac{Z^2}{2}} \right] \tag{12}$$

Where Z is a normalized stress range variable given by Equation 13, and the parameters, c_1, c_2, c_3, Q_1, and Q_2 are given by Equations 14 to 18, which use a "normalized mean frequency" given by Equation 19.

$$Z = \frac{\sigma_r}{2\sigma_{std}} \tag{13}$$

$$c_1 = \frac{2\left(x_M - I^2\right)}{1 + I^2} \tag{14}$$

$$Q_1 = \frac{I - x_M - c_1^2}{1 - I - c_1 + c_1^2} \tag{15}$$

$$c_2 = \frac{1 - I - c_1 + c_1^2}{1 - Q_1} \tag{16}$$

$$c_3 = 1 - c_1 - c_2 \tag{17}$$

$$Q_2 = \frac{1.25\left(I - c_3 - c_2 Q_1\right)}{c_1} \tag{18}$$

$$x_M = \frac{M_1}{M_0} \sqrt{\frac{M_2}{M_4}} \tag{19}$$

The Zhao-Baker method [7] expresses the rainflow stress range PDF as a linear combination of a Weibull and a Rayleigh distribution, Equation 20.

$$p_{ZB}(\sigma_r) = \frac{1}{2\sigma_{std}} \left[w\alpha\beta Z^{\beta-1} e^{-\alpha Z^\beta} + (1-w) Z e^{-0.5Z^2} \right] \tag{20}$$

Where w is a weighting factor given by Equation 21, and α and β are Weibull parameters, which both are to be positive. β is given by Equation 22, and there are two expressions for α, which create two versions of the Zhao-Baker method, denoted ZB1 and ZB2. α can either be found by Equation 23 or by solving Equations 24 and 25. Notes on solving Equations 24 and 25 are given in [7].

$$w = \frac{1 - I}{1 - \sqrt{\frac{2}{\pi}} \Gamma\left(1 + \frac{1}{\beta}\right) \alpha^{-1/\beta}} \tag{21}$$

$$\beta = \begin{cases} 1.1 & for \quad I < 0.9 \\ 1.1 + 9.0(I - 0.9) & for \quad I > 0.9 \end{cases} \tag{22}$$

$$\alpha_{ZB1} = 8.0 - 7.0I \tag{23}$$

$$\lambda = \begin{cases} -0.4154 + 1.392\alpha_{0.75} & for \quad \alpha_{0.75} > 0.5 \\ 0.28 & for \quad \alpha_{0.75} \leq 0.5 \end{cases} \tag{24}$$

$$\Gamma\left(1 + \frac{3}{\beta}\right)(1 - I)\delta^3 + 3\Gamma\left(1 + \frac{1}{\beta}\right)(\lambda I - 1)\delta + 3\sqrt{\frac{\pi}{2}}I(1 - \lambda) = 0 \tag{25}$$

Where Γ denotes the gamma function, and δ is given by Equation 26.

$$\delta = \alpha_{ZB2}^{-1/\beta} \tag{26}$$

When the stress range PDF is obtained, the damage can be calculated by Equation 27. Equation 27 is a probabilistic reformulation of the Palmgren-Miner damage accumulation (Equation 5) for a single slope S-N curve [20].

$$D = \nu_p T C_r^{-1} \int_0^\infty \sigma_r^m p(\sigma_r)\, d\sigma_r \tag{27}$$

Where $T = J\Delta t$ is the total time subjected to the stress described by the given PSD.

Recommendations for numeric integration of Equation 27 can be found in [8].

7 RESULTS

The damage values obtained for the time-series simulations and the frequency-based fatigue methods are given in Table 2. Furthermore, the relative errors in damage, compared to the time-based damages, are given for the frequency-based methods.

Table 2: Fatigue damage results.

	1DOF		2DOF	
Method	Damage	Rel. error	Damage	Rel. error
Time	$3.715 \cdot 10^{-3}$		$5.702 \cdot 10^{-4}$	
DK	$3.706 \cdot 10^{-3}$	$-0.23\ \%$	$5.786 \cdot 10^{-4}$	$1.47\ \%$
ZB1	$3.703 \cdot 10^{-3}$	$-0.30\ \%$	$5.652 \cdot 10^{-4}$	$-0.86\ \%$
ZB2	$3.580 \cdot 10^{-3}$	$-3.63\ \%$	$5.709 \cdot 10^{-4}$	$0.13\ \%$

The rainflow stress range distributions from the time-series simulations and the rainflow stress range PDFs from the frequency-based methods are shown in Figures 4 and 5. Figure 4 shows the results for the one DOF system, and Figure 5 shows the two DOF system results.

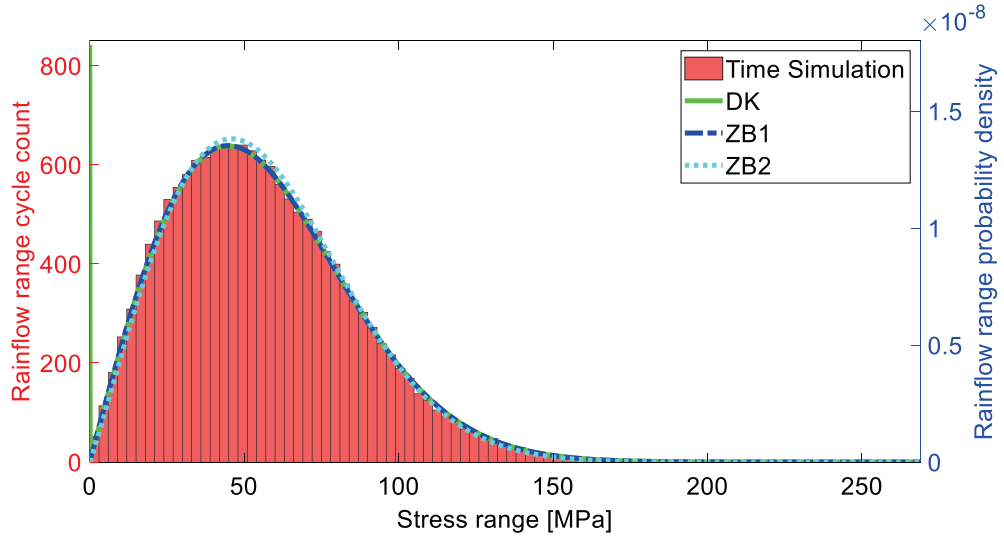

Figure 4: Rainflow stress range distribution and PDFs for the one DOF system. The DK graph is difficult to see because it is behind the ZB1 graph as they are in almost perfect agreement.

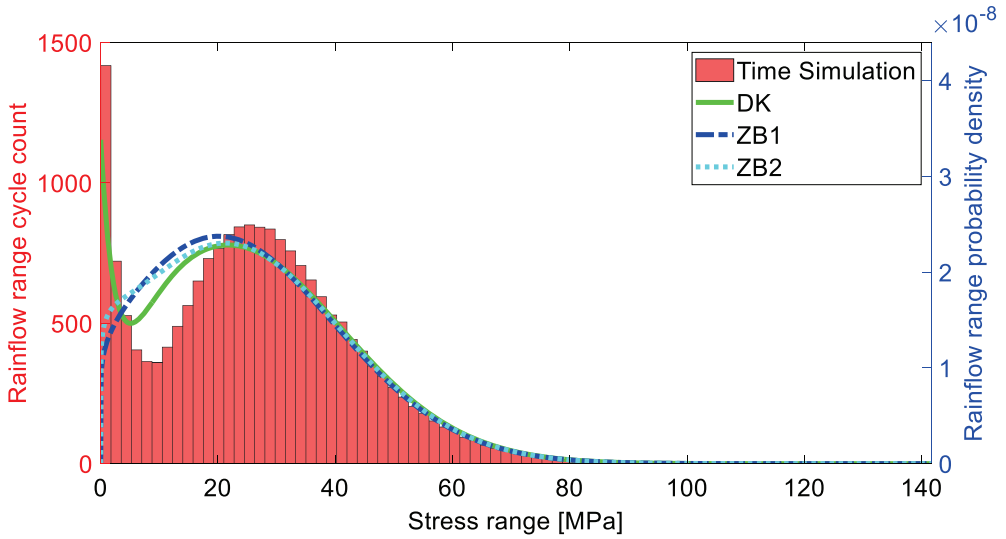

Figure 5: Rainflow stress range distribution and PDFs for the two DOF system.

8 DISCUSSION

The damage errors of the frequency-based fatigue methods are all relatively small, see Table 2. Thus, the methods seem to provide good fatigue results for structural vibration spectra.

However, the stress range distribution can only be accurately predicted for the one modal spectrum of the one DOF system, see Figure 4. This seems reasonable since an analytical solution for the stress range distribution is available for narrowband stress processes, which is the case for the one DOF system. For a narrowband stress process, the stress ranges are Rayleigh distributed [7]. For the bimodal spectrum of the two DOF system, the Dirlik method seems to come closer to the time-based stress range distribution, at least for the low stress ranges, see Figure 5. However, the accuracy at low stress ranges is insignificant for the damage because these stress ranges only have a small damage contribution. Therefore, the methods may still provide good damage estimates if the stress range distribution is accurately predicted for the stress ranges with the largest damage contribution.

9 CONCLUSIONS

In this paper, an overview of the spectrum types used in a set of the literature on frequency-based fatigue is provided. It is shown that only a few realistic spectra are used in the literature, and most are simple spectra, which do not resemble any real spectra. Two simple structural systems are defined to obtain stress response power spectral densities of randomly excited vibrating structures. Stress time-series are simulated to obtain time-based results for fatigue damage and stress range distribution. Furthermore, fatigue damages and stress range probability density functions are calculated using two frequency-based fatigue methods, namely the Dirlik and Zhao-Baker methods. The results show that the damage estimates of the frequency-based methods are relatively close to the damages estimated using a time-based method, with the highest error being $3.6\ \%$. Moreover, it is shown for this study that the stress range distribution can only be predicted accurately for a narrowband stress spectrum. For the bimodal spectrum of the two degrees of freedom system, the stress range distribution is not accurately described by the frequency-based methods. However, mainly the low stress ranges are not predicted accurately, and since these have small damage contributions, the damage estimates are still accurate for the considered cases.

REFERENCES

[1] R. L. Norton, *Machine Design - An Integrated Approach*, 5th ed. Pearson Education, 2014.

[2] D. S. Paraforos, H. W. Griepentrog, S. G. Vougioukas, and D. Kortenbruck, “Fatigue life assessment of a four-rotor swather based on rainflow cycle counting,” *Biosystems Engineering*, vol. 127, pp. 1–10, 2014.

[3] A. Palmgren, “Die lebensdauer von kugellagern,” *Zeitschrift des Vereins Deutscher Ingenieure*, vol. 68, p. 339–341, 1924.

[4] M. A. Miner, “Cumulative damage in fatigue,” *Journal of Applied Mechanics*, vol. 12, pp. 159–164, 1945.

[5] I. Rychlik, "Note on cycle counts in irregular loads," *Fatigue & Fracture of Engineering Materials & Structures*, vol. 16, no. 4, pp. 377–390, Apr. 1993.
[6] M. Mršnik, J. Slavič, and M. Boltežar, "Frequency-domain methods for a vibration-fatigue-life estimation – application to real data," *International Journal of Fatigue*, vol. 47, pp. 8–17, Feb. 2013.
[7] W. Zhao and M. Baker, "On the probability density function of rainflow stress range for stationary gaussian processes," *International Journal of Fatigue*, vol. 14, no. 2, pp. 121–135, Mar. 1992.
[8] J. P. Quigley, Y.-L. Lee, and L. Wang, "Review and assessment of frequency-based fatigue damage models," *SAE International Journal of Materials and Manufacturing*, vol. 9, no. 3, pp. 565–577, Apr. 2016.
[9] A. Brandt, *Noise and vibration analysis*. Chichester: Wiley, 2011.
[10] A. Zorman, J. Slavič, and M. Boltežar, "Vibration fatigue by spectral methods—a review with open-source support," *Mechanical Systems and Signal Processing*, vol. 190, p. 110149, May 2023.
[11] D. Benasciutti and R. Tovo, "Comparison of spectral methods for fatigue analysis of broad-band gaussian random processes," *Probabilistic Engineering Mechanics*, vol. 21, no. 4, pp. 287–299, Oct. 2006.
[12] C. Ronchei, S. Vantadori, A. Carpinteri, I. Iturrioz, R. I. Rodrigues, D. Scorza, and A. Zanichelli, "A frequency-domain approach for damage detection in welded structures," *Fatigue & Fracture of Engineering Materials & Structures*, vol. 44, no. 4, pp. 1134–1148, Jan. 2021.
[13] T. Dirlik, "Application of computers in fatigue analysis," phdthesis, University of Warwick, 1985.
[14] D. Benasciutti and R. Tovo, "Spectral methods for lifetime prediction under wide-band stationary random processes," *International Journal of Fatigue*, vol. 27, no. 8, pp. 867–877, Aug. 2005.
[15] J.-B. Park, J. Choung, and K.-S. Kim, "A new fatigue prediction model for marine structures subject to wide band stress process," *Ocean Engineering*, vol. 76, pp. 144–151, Jan. 2014.
[16] C. E. Larsen and T. Irvine, "A review of spectral methods for variable amplitude fatigue prediction and new results," *Procedia Engineering*, vol. 101, pp. 243–250, 2015.
[17] S. S. Rao, *Mechanical Vibrations*, sixth edition in SI units, global ed. Pearson, 2018.
[18] J.-N. Yang, "Simulation of random envelope processes," *Journal of Sound and Vibration*, vol. 21, no. 1, pp. 73–85, Mar. 1972.
[19] "ASTM E1049-85(2017), standard practices for cycle counting in fatigue analysis," American Society for Testing and Materials, Tech. Rep., 2017.
[20] T. Dirlik and D. Benasciutti, "Dirlik and Tovo-Benasciutti spectral methods in vibration fatigue: A review with a historical perspective," *Metals*, vol. 11, no. 9, p. 1333, Aug. 2021.

Part XIII
SS 03 - VIBRATION CONTROL THROUGH MULTIPHYSICS MATERIALS

Paolo Gardonio, Stefano Manzoni, Emiliano Rustighi

XI ECCOMAS Thematic Conference on Smart Structures and Materials - SMART 2025
M. Krommer, M. Nader and M. Schagerl (Eds)

Received: 27 March 2025 / Revised: 1 August 2025 / Accepted: 10 September 2025
© The Author(s) 2025

An Investigation of Structural Stress in Active Acoustic Black Holes

Jordan Cheer, Archie Keys

Abstract. Acoustic Black Holes (ABHs) are structural features that enable a notable level of vibration control by introducing a spatial variation in either the thickness or material properites of a structure, leading to a significant reduction in the wave speed and resultingly an increase in the efficiency of an applied damping treatment. There are two key potential limitations associated with ABHs – firstly, due to the focusing of structural waves into the ABH feature they can increase the structural stresses; and secondly, their performance at low frequencies is limited by the size of the ABH feature. It has previously been shown that through the integration of active control it is possible to enhance the low-frequency performance of ABHs, however, the effect that this has on the resulting stress has not been previously explored. This paper presents an investigation into the change in structural stress due to the integration of active control into an ABH terminated beam. A feedforward wave-based controller is utilised, which aims to minimise the wave reflected from the ABH termination using a piezoelectric patch actuator attached to the ABH feature. This demonstrates that a conventional active ABH introduces a significant stress enhancement and, therefore, a modified control strategy is explored in which the stress measured in the ABH is included in the cost function being minimised.

Key words: Active vibration control, Acoustic Black Holes, Structural Stress, Smart Structures

1 INTRODUCTION

High performing lightweight vibration control treatments are critical to a variety of industrial applications, including the automotive, aerospace, rail and maritime sectors. Since the observation of the Acoustic Black Hole (ABH) effect in structures with a decreasing thickness profile in the late 1980s [1], so-called ABHs have been extensively explored, as reviewed by Pelat et al [2]. ABHs are most commonly realised as structural features that are designed to control flexural waves and this is now classicaly realised by introducing a power-law decreasing thickness profile into a structure [1], as shown in

Jordan Cheer & Archie Keys
Institute of Sound and Vibration Research, University of Southampton, Highfield Campus, SO17 1BJ, Southampton, UK, e-mail: j.cheer@soton.ac.uk

Figure 1 for a beam. This smooth impedance change results in a gradual decrease in the flexural wave speed and a corresponding decrease in its wavelength, which has now been widely shown to improve the efficacy of an applied damping layer [3, 4] and allow the ABH to offer an extremely high level of vibration control.

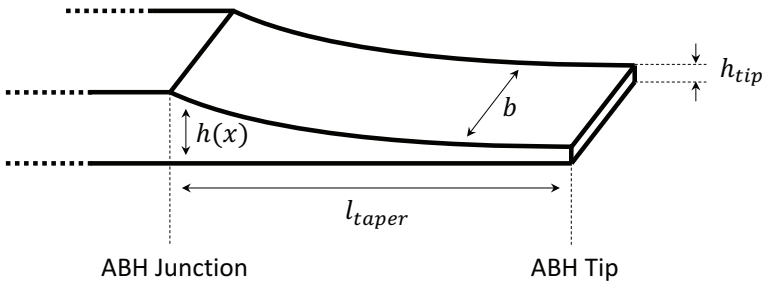

Figure 1: Diagram of a geometric ABH applied as a beam termination.

A wide variety of different ABH designs have been proposed, including extension to a two-dimensional design that can be embedded into plate-like structures [5], spiral ABHs that reduce the space required by the ABH taper [6], and multimaterial designs [7, 8]. In all of these cases the behaviour of the ABH can be tuned by modifiying the impedance, which in the geometrical ABH case can be controlled via the tip height, h_{tip}, taper length, l_{taper}, and taper profile, $h(x)$, as shown in Figure 1. Although these designs can be variously optimised [9] or tuned [10] to achieve broadband vibration control, the low frequency performance is essentially limited by the length of the ABH. It has been shown for both beam [11] and plate [12] applications that this low-frequency limitation can be overcome by incorporating active control into the ABH. In the beam case, the active ABH has been realised by applying a piezoelectric patch actuator to the ABH taper and driving this via either feedforward [12] or feedback [13] control stategies to control the reflected wave component. This has been shown to achieve very wideband control of the reflected wave and, interestingly, offer either a significant increase in performance or a significant reduction in the required electrical power compared to an equivalent active control system applied to a constant thickness beam.

Although geometric ABHs have been shown to offer significant levels of vibration control performance in both passive and active configurations, the thinness of the structure can pose issues in terms of the structural strength [15] and it has also been shown for passive ABHs that the wave focusing that is inherent to the ABH effect leads to stress concentration in the ABH taper due to high amplitude bending [14]. This can lead to a reduced useful life of the ABH structure and limit its application to practical engineering problems. This problem has been quite thoroughly explored for passive ABHs in beams [14], and modified ABH designs to reduce the stress have been proposed [16], however, an analysis of the stress in active ABHs has not been explored. This paper therefore ad-

dresses this gap by exploring through an experimental implementation of an active ABH terminating a beam, the influence of active control on the stress in the ABH taper. In the first instance, the previously proposed active ABH strategy is explored, which attempts to minimise the wave reflected from the active ABH beam termatinion, before an alternative control stategy is proposed in which the active ABH is driven instead to minimise the stress in the ABH taper. The paper is structured as follows: Section 2 describes the physical active ABH system realisation, Section 3 describes the two control strategies being considered, Section 4 presents the performance of the active ABH configurations in terms of the reflected wave and the stress in the ABH taper and Section 5 draws conclusions.

2 ACTIVE ABH SYSTEM DESCRIPTION

To investigate the behaviour of an active ABH system, the setup shown in Figures 2 and 3 has been implemented. The geometrical parameters defining the beam section and ABH taper are defined in Table 1. The ABH terminated beam was attached directly to a shaker, which provides the primary disturbance, and the control force is applied by a piezoelectric patch actuator attached to the flat side of the ABH termination to avoid applying a pre-stress to the actuator. A PI ceramic P-876.A11 actuator has been used, which has dimensions of 61 mm×31 mm and it has been positioned centrally across the width of the ABH and aligned with the tip to maximise the available bending force. The stress in the ABH taper has been measured using a strain gauge, which is applied to the curved side of the ABH taper and centred with resepct to both the length and the width of the taper. A Techni Measure PFL-30-11 strain gauge has been utilised, which has active dimensions of 30 mm×2.3 mm. This strain gauage has been selected so that the active area covers the main stress concentration region in the ABH due to bending, which has been identified via numerical simulations not reported here. The response of the beam has been measured using a pair of accelerometers, which are separated by a distance of $\Delta_x = 2$ cm, with their centre point being located 21 cm from the primary disturbance. All system responses have been measured at a sample rate of 24 kHz, with antialiasing and reconstruction filters set to 10 kHz.

Parameter	Symbol	Value
Beam thickness	h_0	10 mm
Beam length	l_{beam}	300 mm
Beam width	b	40 mm
ABH taper length	l_{ABH}	70 mm
ABH power law	μ	4
ABH tip height	h_{tip}	0.6 mm

Table 1: The geometrical parameters defining the geometry of the geometrical ABH shown in Figure 1.

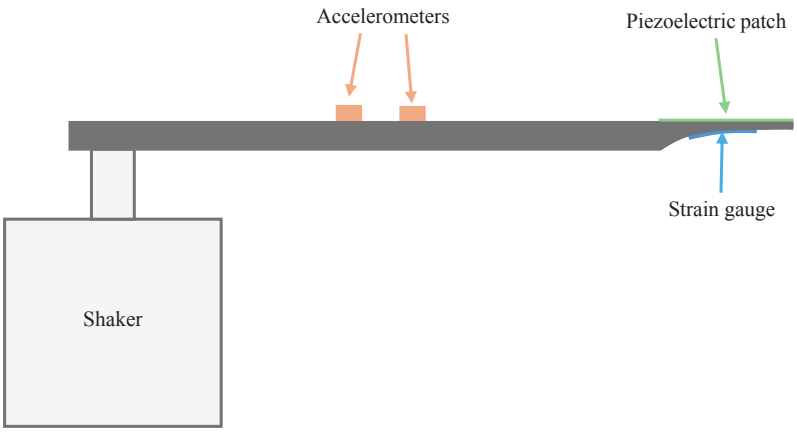

Figure 2: Diagram showing the experimental setup including two accelerometers mounted on the beam section, a piezoelectric patch actuator mounted on the flat side of the ABH termination and a strain gauage mounted on the tapered side of the ABH termination. The primary excitation is provided by a separate shaker to which the beam is mounted.

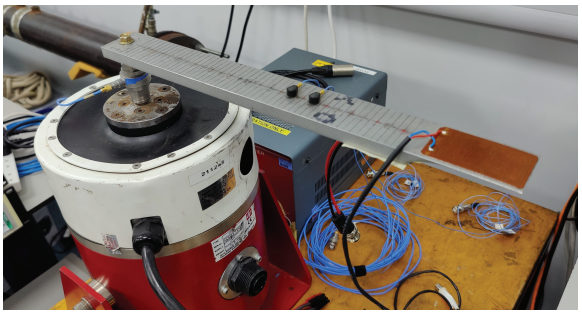

Figure 3: Photograph of the physical realisation of the system described in Figure 2.

3 CONTROL STRATEGIES

Active vibration control has been applied to a wide variety of structures using an even larger variety of control strategies. In the context of an ABH terminating a beam, the overall objective is generally to minimse the reflection from the end of the beam in order to realise an anechoic termination and thus supress the excitation of beam modes. An active anechoic termination applied to a uniform thickness beam has previously been developed in [17] and this strategy has been applied to an active ABH in [11]. This control strategy is first summarised in the following section, before an alternative control strategy is proposed which instead aims to reduce the stress in the ABH taper.

3.1 Reflection Control Strategy

The control strategy used to minimise the reflection from the end of the beam has been previously described in [11] and is outlined by the block diagram presented in Figure 4. From this block diagram it can be seen that this is a feedforward control strategy, where it is assumed for simplicity that the reference signal, $x(n)$, is provided directly from the primary excitation and the broadband controller, $\mathbf{w}$, is either adapted or optimised to minimise the reflected wave component, $e_{\phi^-}(n)$. It would be possible, and required in some practical installations, to instead utilise the incident wave component, $e_{\phi^+}(n)$, as the reference signal, although this complicates the controller design somewhat.

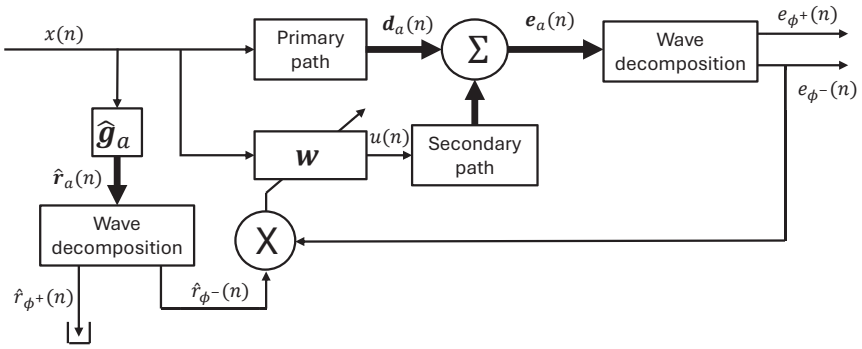

Figure 4: Block diagram showing the wave-based reflection control strategy [11].

In order to realise the feedforward control system shown in Figure 4, it is first necessary to decompose the vibration of the structure into the incident and reflected wave components. This can be achieved using the wave decompoisiton strategy outlined in [17, 11] which uses a pair of closely spaced accelerometers. This assumes that the accelerometer array is sufficiently far from any structural excitations or impedance changes, such as the tapering thickness profile in the ABH terminated beam, such that any evanescent wave

components will be small in magnitude compared to the travelling wave terms so that they can be neglected; the implications and limitations of this assumption are discussed in more detail in [11]. Following this approach, the incident and reflected wave components can be expressed in the frequency domain as

$$\begin{bmatrix} \phi^+(\omega) \\ \phi^-(\omega) \end{bmatrix} = \begin{bmatrix} H_1(\omega) & H_2(\omega) \\ H_2(\omega) & H_1(\omega) \end{bmatrix} \begin{bmatrix} A_1(\omega) \\ A_2(\omega) \end{bmatrix}, \tag{1}$$

where ω is the angular frequency, $A_1(\omega)$ and $A_2(\omega)$ are the complex amplitudes of the acceleration measured by the two accelerometers attached to the uniform beam section, and $H_1(\omega)$ and $H_2(\omega)$ are given by

$$H_1(\omega) = -\frac{1}{4\omega}\left(\frac{1}{\sin k_f \Delta_x/2} + \frac{i}{\cos k_f \Delta_x/2}\right) \tag{2}$$

$$H_2(\omega) = \frac{1}{4\omega}\left(\frac{1}{\sin k_f \Delta_x/2} - \frac{i}{\cos k_f \Delta_x/2}\right), \tag{3}$$

where k_f is the flexural wavenumber of the uniform beam section of the structure. In order to realise a broadband control solution, it is necessary to approximate the frequency domain wave decomposition operators, $H_1(\omega)$ and $H_2(\omega)$, using broadband filters, which can be achieved by inverse Fourier transformation and application of a modelling delay [18] to provide Finite Impulse Response (FIR) filters, $\mathbf{h}_1$ and $\mathbf{h}_2$. The incident and reflected wave components can then be expressed in the time domain as

$$\begin{bmatrix} \phi^+(n) \\ \phi^-(n) \end{bmatrix} = \begin{bmatrix} \mathbf{h}_1 & \mathbf{h}_2 \\ \mathbf{h}_2 & \mathbf{h}_1 \end{bmatrix} * \begin{bmatrix} a_1(n) \\ a_2(n) \end{bmatrix}, \tag{4}$$

where $a_1(n)$ and $a_2(n)$ are the outputs of each of the accelerometers at the nth time step.

The aim of the wave-based reflection controller is to minimise the cost function given as

$$J_{\phi^-} = \mathbf{E}\big[e^2_{\phi^-}(n)\big] + \beta \mathbf{w}^T \mathbf{w}, \tag{5}$$

where the first term relates to the magnitude squared reflected wave amplitude and the second term is proportional to the control effort, with the regularisation parameter β determining the weighting of the second term in the cost function. The error signal used in this cost function is given as

$$e_{\phi^-}(n) = \mathbf{h}_2^T \mathbf{e}_1(n) + \mathbf{h}_1^T \mathbf{e}_2(n), \tag{6}$$

where $\mathbf{h}_1$ and $\mathbf{h}_2$ are the wave decomposition FIR filters, each with I_h coefficients and $\mathbf{e}_1(n)$ and $\mathbf{e}_2(n)$ are the vectors comprising of the current and past samples of the error signals measured at the two accelerometers. This cost function can either be minimised

adaptively using the widely employed Filtered-reference Least Mean Squares (FxLMS) algorithm, or the optimal vector of control filter coefficients can be calculated directly as described in detail in [11]. The optimal control filter that minimises the cost function given by equation 5 is given as

$$\mathbf{w}_{\phi^-}^{(opt)} = -\big\{\mathbf{E}\big[\mathbf{r}_{\phi^-}(n)\mathbf{r}_{\phi^-}^T(n)\big] + \beta\mathbf{I}\big\}^{-1}\mathbf{E}\big[\mathbf{r}_{\phi^-}(n)d_{\phi^-}(n)\big], \tag{7}$$

where $\mathbf{E}$ is the expectation operator, $d_{\phi^-}(n)$ is the disturbance signal corresponding to the negative travelling wave and $\mathbf{r}_{\phi^-}(n)$ is the is the vector of current and past samples of the reference signal filtered by the secondary path, or plant response, between the control actuator and the negative propagating wave error signal.

3.2 Stress Control Strategy

As noted in Section 1, ABHs tend to exhibit high levels of stress concentration due to the wave focusing effect and the inherently thin structure when realised using geometrical tapering [14]. Although passive approaches to reducing the stress in ABHs have been explored [16], the interest here is to evaluate whether an active ABH can be utilised to reduce the stress in the ABH taper. To this end, instead of driving the control actuator to minimise the reflected wave, a new cost function can be defined as

$$J_\sigma = \mathbf{E}\big[e_\sigma^2(n)\big] + \beta\mathbf{w}^T\mathbf{w}, \tag{8}$$

where $e_\sigma(n)$ is the error signal measured by the strain gauge applied to the ABH taper as shown in Figure 2. In this case, the control block diagram is shown in Figure 5 which can again utilise the FxLMS algorithm, or the optimal vector of filter coefficients that minimises the cost function defined by equation 8 can be written as

$$\mathbf{w}_{\sigma}^{(opt)} = -\big\{\mathbf{E}\big[\mathbf{r}_{\sigma}(n)\mathbf{r}_{\sigma}^T(n)\big] + \beta\mathbf{I}\big\}^{-1}\mathbf{E}\big[\mathbf{r}_{\sigma}(n)d(n)_{\sigma}\big], \tag{9}$$

where $d_\sigma(n)$ is the disturbance signal measured by the strain gauge and $\mathbf{r}_\sigma(n)$ is the is the vector of current and past samples of the reference signal filtered by the secondary path, or plant response, between the control actuator and the strain gauge.

4 ACTIVE ABH CONTROL PERFORMANCE

To evaluate the performance of the two active control strategies described in Section 3, the measured primary and secondary path responses of the active ABH system shown in Figure 3 have been used to calculate the optimal control filters according to equations 7 and 9 for the reflection and stress control strategies respectively. The two control strategies are then evaluated via offline simulations using the measured responses. The reflection coefficient is calculated as

$$R(\omega) = \left|\frac{\phi_-(\omega)}{\phi_+(\omega)}\right| \tag{10}$$

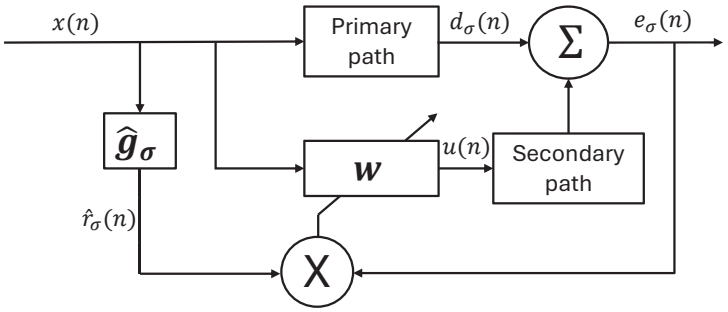

Figure 5: Block diagram showing the stress control strategy.

where $\phi_+(\omega)$ and $\phi_-(\omega)$ are the positive and negative travelling waves respectively, which can be calculated using the wave decomposition described in Section 3.1 for the uncontrolled case using the disturbance signals, d_1 and d_2, or the error signals, e_1 and e_2, for the corresponding controller. The stress in the taper is measured using the attached strain gauage, as shown in Figures 2 and 3, with the stress under control being calculated assuming linear superposition in the frequency domain as

$$e_\sigma(\omega) = d_\sigma(\omega) + g_\sigma(\omega)u(\omega), \tag{11}$$

where $g_\sigma(\omega)$ is the secondary path response between the piezo actuator and the strain gauage and $u(\omega)$ is the control signal generated by passing the reference signal through the corresponding optimal control filter for each control straetgy.

Figure 6 shows the reflection coefficient over frequency for the ABH terminated beam without control (black line) and with both the optimal reflection controller (red line) and the optimal stress controller (blue line). It is first worthwhile noting the characteristic reflection coefficient response of the passive ABH beam termination, which shows a general decrease in reflection with increasing frequency, but also exhibits dips in the reflection coefficient over frequency that correspond to modes of the ABH [10]. It is also worth highlighting that the passive ABH performance is already quite significant compared to an uniform thickness beam with an equivalent damping layer applied, which would have a reflection coefficient close to unity across the presented bandwidth, as previously shown in [11] for example. In the case of the reflection controller, as previous reported in [11], a significant decrease in the reflection coefficient across the presented bandwith is shown, corresponding to an effective increase in the absorption provided by the beam termination. There is some difficulty in achieving control at very low frequencies, which can be related to the low frequency limit of the piezoelectric actuator utilised, and would need to be addressed by selection of an alternative actuator or actuation approach. In the case of the stress controller, it can be seen that the reflection coefficient remains largely unchanged compared to the passive case.

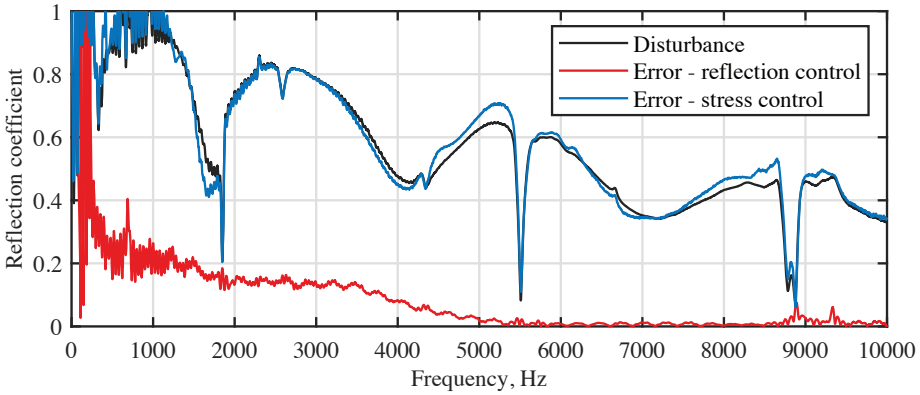

Figure 6: Reflection coefficient plotted over frequency for the ABH terminated beam without control (black line), with reflection control (red line) and with stress control (blue line).

Figure 7 shows the stress measured in the ABH taper without control (black) and with both the optimal reflection controller (red line) and the optimal stress controller (blue line). In this case it can be seen that the reflection control straetgy results in a significant increase in the stress across the whole of the presented bandwidth, except at a narrowband notch at around 8.8 kHz, which can be related to the high reflection control performance already achieved by the passive ABH at this frequency as shown in Figure 6. This is an important result as it demonstrates for the first time the trade-off that is paid for achieving high levels of reflection control using the active ABH termination and motivates the exploration of the active stress control strategy proposed here. The results presented in Figure 7 for the stress controller show a significant reduction in the stress in the ABH taper across the full frequency range presented compared to both the passive ABH and the active ABH using reflection control. This result suggests that the stress control approach could significantly extend the structural life of the ABH taper, although this is at the expense of the augmented reflection control provided by the active ABH termination using reflection control. It is also worth observing that this level of reduction in the ABH stress is significantly greater than that achieved via passive measures, as previously described in [16], but requires the addition of the piezoelectric actuator, strain gauage and controller. It is also interesting to note that the results presented here are consistent with previous work that explored the trade-off between controlling the reflected wave and the acceleration in the ABH taper using a weighted feedback control strategy [13]. However, in that case the stress was not directly observed and the controller required both the taper vibration and the reflected wave to be available whereas the strategy proposed here is potentially able to operate with a local control loop between the piezoelectric actuator and the strain gauage.

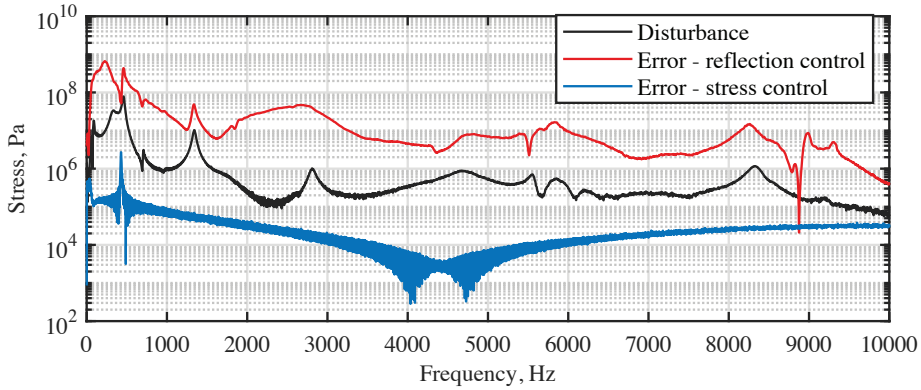

Figure 7: Stress plotted over frequency for the ABH terminated beam without control (black line), with reflection control (red line) and with stress control (blue line).

5 CONCLUSIONS

This paper has presented an investigation into the effect of actively controlling a geometric ABH terminating a beam on the stress in the ABH taper. An experimental implementation of an active ABH has been realised and the measured responses utilised to simulate the performance of two active control straetgies. In the first instance, the reflection control strategy that has previously been applied to ABHs has been explored and it has been shown that although significant levels of reflected wave control are achieved, this approach significantly enhances the stress in the ABH taper. To potentially overcome this increase in stress, an alternative control strategy is proposed that directly minimises the stress measured using a strain gauage attached to the ABH taper. In this case, a significant broadband reduction in stress is achieved, potentially providing a large increase in the structural life of the ABH taper, but the reflection coefficient performance in this case is equivalent to the passive ABH. This work demonstrates a clear trade-off between controlling the absorption provided by an active ABH beam termination and the resulting stress in the ABH taper. The two strategies offer the potential for designers to achieve one of these objectives depending on the requirements of the intended application. Due to the consistent architectures of the two control straetgies, depending on the importance of vibration control or structural life, it would be possible for control to switch between the two strategies. Future work will explore whether a trade-off between reflection control and stress control can be achieved by utilising a modified cost function and in the case of the stress control strategy a local feedback control approach may also be a convenient design approach.

ACKNOWLEDGEMENTS

This work was partially supported by the Intelligent Structures for Low Noise Environments (ISLNE) EPSRC Prosperity Partnership (EP/S03661X/1) and partially by the

Department of Science, Innovation and Technology (DSIT) and the Royal Academy of Engineering under the Research Chairs and Senior Research Fellowships programme.

REFERENCES

[1] Mironov MA (1988) Propagation of a flexural wave in a plate whose thickness decreases smoothly to zero in a finite interval. Sov. Phys. Acoust, 34(3), 318-319.

[2] Pelat A, Gautier F, Conlon F C and Semperlotti F (2020) The acoustic black hole: A review of theory and applications. Journal of Sound and Vibration. 476, 115316.

[3] Krylov VV (2004) New type of vibration dampers utilising the effect of acoustic 'black holes'. Acta Acustica united with Acustica, 90(5), 830-837.

[4] Krylov VV, and Tilman FJBS (2004) Acoustic 'black holes' for flexural waves as effective vibration dampers. Journal of sound and vibration, 274(3-5), 605-619.

[5] Krylov, V. V. (2007). Propagation of plate bending waves in the vicinity of one-and two-dimensional acoustic 'black holes'. ECCOMAS Thematic Conference on Computational Methods Rethymno, Crete, Greece.

[6] Lee, J. Y., and Jeon, W. (2017). Vibration damping using a spiral acoustic black hole. The Journal of the Acoustical Society of America, 141(3), 1437-1445.

[7] Austin, B., Cheer, J., and Bastola, A. (2022, August). Design of a multi-material acoustic black hole. In Proceedings of 2022 International Congress on Noise Control Engineering, INTER-NOISE2022.

[8] Austin, B., Cheer, J., and Bastola, A. (2023, December). Experimental validation of a multi-material acoustic black hole. In Proceedings of Meetings on Acoustics (Vol. 52, No. 1). AIP Publishing.

[9] McCormick C A and Shepherd M R 2020 Design optimization and performance comparison of three styles of one-dimensional acoustic black hole vibration absorbers J. Sound Vib. 470 115164

[10] Hook K, Cheer J, and Daley S (2019). A parametric study of an acoustic black hole on a beam. The Journal of the Acoustical Society of America, 145(6), 3488-3498.

[11] Cheer J, Hook K, and Daley S. (2021) Active feedforward control of flexural waves in an Acoustic Black Hole terminated beam. Smart Materials and Structures, 30(3), 035003.

[12] Hook K, Cheer J, and Daley S. (2022). Control of vibration in a plate using active acoustic black holes. Smart Materials and Structures, 31(3), 035033.

[13] Hook K, Daley S., and Cheer J (2022). Active control of an acoustic black hole using a feedback strategy.Journal of Sound and Vibration, 528, 116895.

[14] Keys A, and Cheer J (2024, October). A parametric study of dynamic stress in acoustic black holes. In INTER-NOISE and NOISE-CON Congress and Conference Proceedings (Vol. 270, No. 3, pp. 8410-8421). Institute of Noise Control Engineering.

[15] Zhou, T., Tang, L., Ji, H., Qiu, J., and Cheng, L. (2017). Dynamic and static properties of double-layered compound acoustic black hole structures. International Journal of Applied Mechanics, 9(05), 1750074.

[16] Keys A, and Cheer J. (2024, September). Optimisation of a modified acoustic black hole profilefor the reduction of dynamic stress. In ISMA2024 Proceedings.

[17] Rustighi, E., Mace, B. R., and Ferguson, N. S. (2011). An adaptive anechoic termination for active vibration control. Journal of Vibration and Control, 17(13), 2066-2078.

[18] Mace, B. R., and Halkyard, C. R. (2000). Time domain estimation of response and intensity in beams using wave decomposition and reconstruction. Journal of Sound and Vibration, 230(3), 561-589.

XI ECCOMAS Thematic Conference on Smart Structures and Materials - SMART 2025
M. Krommer, M. Nader and M. Schagerl (Eds)

Received: 1 April 2025 / Revised: 29 August 2025 / Accepted: 10 September 2025
© The Author(s) 2025

Morphing Aircraft Wing Structure for the Application of 3D Shock Control Bumps

Sven Christian Künnecke, Martin Radestock, Hans Peter Monner

Abstract. The increasing demand for efficient and adaptable aircraft designs leads to the development of morphing structures, which can alter their shape in response to changing flight conditions. In this study, the design of a hybrid wing skin structure made of a fiber composite laminate and an elastomer is described. The primary goal is to develop a shape-variable structure that can be actively transformed into a shock control bump. As conventional aircraft operate at transonic speeds, a shockwave forms on the wing upper side, leading to wave drag and increased overall drag. Introducing a shock control bump aims to reduce the shock‘s intensity, thereby mitigating its detrimental effects on drag. In contrast to former structural studies, this bump has a three-dimensional (3D) shape, and thus, the morphing skin section is mounted on all sides. Consequently, the shape-variable structure is designed to allow such complex deformations. A comprehensive sensitivity study is conducted, exploring the impact of composite as well as elastomer design parameters. The results of this study reveal a structural feasible wing skin design that can be deformed to a 3D shock control bump. The proposed design demonstrates potential for application in real-world aircraft designs, offering a promising solution for mitigating transonic shock effects on wing performance and reducing overall drag.

Key words: Morphing aircraft structure, adaptive aircraft, morphing wing, shape-variable fiber composite, transonic shock control, hybrid structure

1 INTRODUCTION

The aviation sector is driven by the pressing need to meet European sustainability targets. In light of goals such as the European Green Deal [1] or the Flightpath 2050 [2], the industry is increasingly focused on minimizing its carbon footprint, with particular attention given to reducing fuel consumption and greenhouse gas emissions. Consequently, there is a growing recognition that innovative technologies must play a central role in ensuring that aviation reduces its environmental impact. One promising technological approach in this context is the

Sven Christian Künnecke & Martin Radestock & Hans Peter Monner
German Aerospace Center (DLR), Institute of Lightweight Systems, Lilienthalplatz 7, 38108 Braunschweig, Germany, e-mail: Sven.Kuennecke@DLR.de

development of advanced morphing structures for aircraft, which offer the potential for significant aerodynamic improvements. Morphing components, such as droop noses, trailing edges, and spoilers [3, 4, 5, 6, 7, 8, 9], can adjust their shape in response to changing flight conditions, thereby optimizing performance throughout different phases of flight. Morphing concepts have been the subject of numerous studies, where Barbarino et al. (2011) [10] provide a comprehensive review.

A particularly critical challenge in modern commercial aviation is handling the aerodynamic effects of transonic flow. During cruise, most conventional transport aircraft experience transonic conditions, where the airflow over the wing reaches speeds close to the speed of sound, resulting in the formation of a transonic shock wave. This shock induces wave drag, which contributes to a significant increase in fuel consumption [11, 12] and can even lead to undesirable aerodynamic phenomena, such as buffet [13, 14]. The need for strategies to mitigate the adverse effects of this shock is, therefore, a central concern in the pursuit of more fuel-efficient and environmentally friendly aircraft.

One of the most widely studied concepts for mitigating transonic shocks is the use of shock control bumps (SCBs), which were first introduced by Ashill et al. (1992) [15]. SCBs are devices placed on the surface of an aircraft wing in the vicinity of the shock, designed to influence the flow field and lower the shock strength. By altering the pressure distribution over the wing, these bumps can reduce wave drag [11, 12, 16] and even delay the buffet onset [11, 13, 14, 17], leading to improved aerodynamic performance. An extensive review on SCBs has been conducted by Bruce and Colliss (2015) [18]. For further details especially regarding the aerodynamic effects of these devices, the reader is referred to this paper.

Besides two-dimensional (2D) SCBs [11, 12, 14, 16, 18], 3D bumps have been investigated in recent years [13, 17, 18, 19, 20, 21]. According to [18], 2D bumps often exhibit poor off-design performance, whereas 3D SCBs can be applied to a broader operational range since they maintain their effectiveness over wider ranges of Mach numbers and angles of attack. The desirable so-called λ-shock structure is generated by both, 2D and 3D SCBs. However, a decay

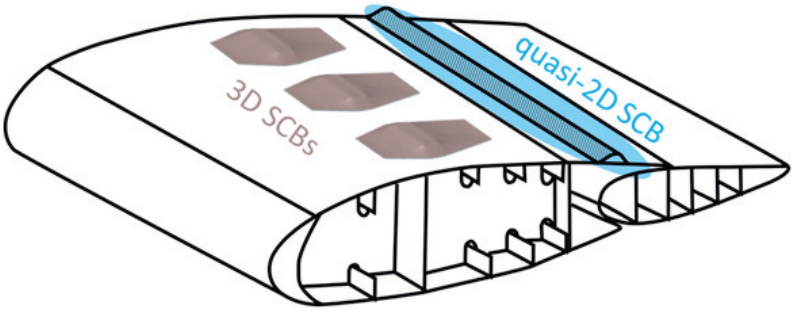

Figure 1: Exemplary illustration of an quasi-2D SCB and 3D SCBs on an aircraft wing without consideration of a specific shock position

in spanwise direction is visible for the 3D variants. According to Ogawa et al. (2008) [19], this spanwise decay of the shock structure is gradual and can be compensated by placing adjacent 3D bumps in such a way that overlapping shock structures are formed. This can lead to a quasi-2D shock structure and thus mitigate potential negative effects of the finite 3D devices. An exemplary illustration of 2D and 3D SCBs is depicted in figure 1.

To provide clarity of terminology related to 2D and 3D SCBs, "infinite" is referring to 2D bumps that are considered over the entire span of an infinite wing. In other words, this is a theoretical construct. Previous studies utilize structural pre-bends on morphing spoilers [8, 9, 22] or pressurized chambers [5, 6, 7] to form an SCB over the entire spoiler span. Since the bump shape is maintained on the spoiler tips, these SCBs are categorized as "quasi-2D" because they are not truly infinite due to their restriction withing the spoiler geometries, but are also not entirely finite in the sense of 3D SCBs.

Rigid SCBs remain fixed in position and shape, as they are permanently attached to the wing. Such devices would not be able to adapt to the dynamic conditions of flight. Fixed bumps could potentially lead to an increase in drag under off-design conditions, such as during takeoff and landing or when they are not optimally positioned relative to the shock location. This is why already in the project EUROSHOCK II [11] adaptive bumps have aerodynamically been investigated.

In recent years, studies on structural designs of morphing SCBs have been conducted. Several of these are summarized by Künnecke et al. (2021) [23]. Besides the above mentioned SCB concepts on morphing spoilers, flexible plates have been investigated that are installed above a cavity on the wing upper side [21, 24]. These plates can be passively deformed by aerodynamic pressure and further supported by actuators to create either 2D or 3D SCBs. However, these structural concepts are limited in producing complex 3D shapes but primarily yield hill-like bumps with smooth transitions between bump shape and the surrounding wing surface.

In this work, a complex 3D SCB shape is investigated which poses challenges in terms of structural design, especially on the flanks of the bump. While a quasi-2D bump on a morphing spoiler can be realized by using a sliding contact on the trailing edge flap due to the free spoiler chordwise end [8, 9, 22], a 3D bump has a finite span and thus, all side edges are fixed. Consequently, large deformations on a small area are necessary to deploy the SCB. Such high strains that become necessary for the formation of 3D bumps cannot be handled with a pure fiber composite structure. Therefore, in this work, a hybrid skin concept that combines elastomer and fiberglass materials is developed and the structural design is simulated in finite element analyses.

2 FINITE ELEMENT ANALYSIS

A finite element analysis (FEA) model is set up in ANSYS Workbench. For this purpose, a parametric computer-aided design (CAD) model has been created. This geometry is imported into the ANSYS Workbench environment and a script-based interface for automatically building

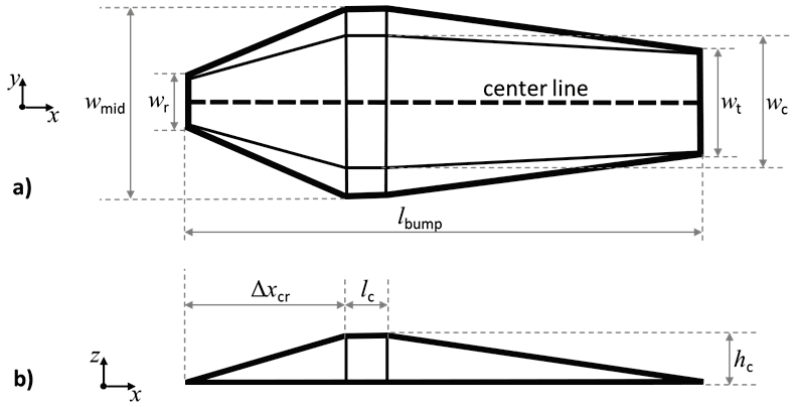

Figure 2: Parametrization in top view a) and side view b) of the 3D SCB for performance increase via wave drag reduction based on [17]

the structural model using the ANSYS tools ACP-Pre and Mechanical is developed.

The 3D SCB parametrization that serves as target shape in this work has been taken from Mayer at al. (2018) [17]. The considered bump shape is applied for the performance-optimized configuration, thus leading to wave drag reduction. This parametrization of the 3D performance bump is depicted in figure 2.

The prescribed parameters in [17] are summarized in table 1. Since the structural design of the morphing skin for such a 3D bump is the focus of this work, the parameters given in table 1 are taken as target values an not changed. These values are given in percent of the wing chord length (%c) at the respective spanwise section.

Mayer et al. [17] investigate two design points, which result in different optimized values of the bump parameters for both cases. In this work, the parameters of the design point which leads to the highest bump in [17] are considered. Consequently, a bump height (h_c) of 1.15%c is taken as target height. The corresponding distance from the bump leading edge to the beginning of the crest plateau (Δx_{cr}) is determined from the parameters in [17] and amount to 8.8%c. For details about the aerodynamic conditions on which the parameters in table 1 are based on, the reader is referred to [17].

Table 1: Parameters of a 3D performance SCB based on [17]

l_{bump}	l_c	w_r	w_{mid}	w_c	w_t	Δx_{cr}	h_c
25%c	3%c	6%c	10%c	6%c	6%c	8.8%c	1.15%c

2.1 Material models

In previous studies on morphing spoilers [8, 9, 22], a flexible glass-fiber reinforced polymer (GFRP) ply-stacking has been implemented which is based on [25]. However, such a spoiler structure is design for a quasi-2D SCB with a free downstream bump end that is equal to the spoiler trailing edge. In a 3D bump design, all sides of the flexible bump are fixed in a comparatively stiff surrounding wing skin structure, thus requiring the morphing skin to handle the deformations and strains itself. Due to the high deformations that occur over a small area, resulting in large strains, it is not possible to realize a pure GFRP structure. Therefore, a hybrid structural design has been defined, consisting of GFRP and an elastomer. This elastomer is an ethylene propylene diene monomer (EPDM), a synthetic rubber that can endure large strains of several hundred percent [26], while the max. strains for GFRP are about single-digit percent.

Table 2: Material properties of GFRP and EPDM based on [25, 27, 28]

Material	Properties	Material model in FEA
EPDM	G_0 = 1.9 MPa d = 1·10^{-9} Pa^{-1}	Hyperelastic (Neo-Hooke)
GFRP	$E_{\parallel}$ = 42 000 MPa $E_{\perp}$ = 15 000 MPa $G_{\parallel,\perp}$ = 5 600 MPa $\nu_{\parallel,\perp}$ = 0.26	Linear elastic

E: Young's modulus; G: Shear modulus; G_0: Initial shear modulus; d: Incompressibility parameter; ν: Poisson's ratio

The resulting EPDM strains are expected to be comparatively large which is why a hyperelastic material model is utilized. Vasista et al. [27] tune the EPDM material parameters in ANSYS according to the results in [28] with the Neo-Hookean incompressible hyperelastic material model. The material properties used in this modeling are presented in table 2, based on the works of [27, 28] for EPDM and [25] for GFRP. Regarding EPDM, the physical relation of the incompressibility parameter d and the initial bulk modulus K is $K = 2/d$. Furthermore, since this work represents an early stage of the design, the values of G and ν for GFRP are not divided into parallel and perpendicular to the fiber orientation. However, in future studies, more detailed material parameters will be applied.

2.2 Setup of the FEA

As stated above, the FEA is build in ANSYS Workbench and the CAD model generation as well as the FE model generation is automatized. To facilitate sufficiently large deformations on the bump leading edge and trailing edge regions, EPDM is incorporated at these areas, extending

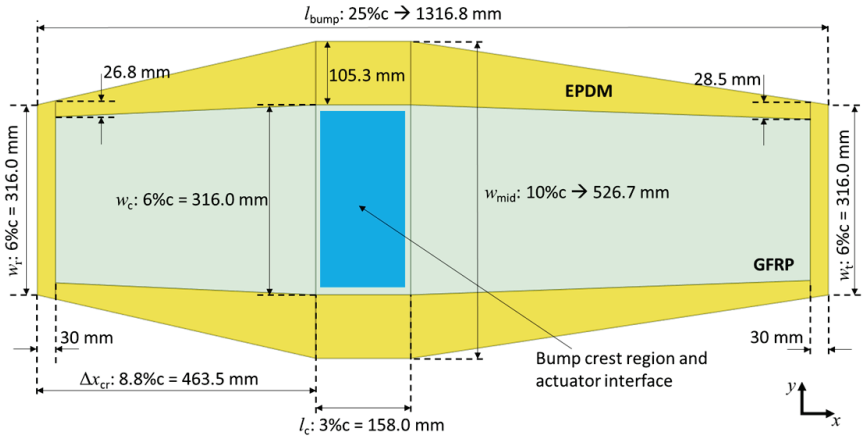

Figure 3: Top view of the 3D SCB model with EPDM (orange) and overall GFRP sections (light green) and GFRP interface for an actuator (blue), considered wing section chord length of 5 267 mm

30 mm in chordwise direction (x-direction). In addition, the bump side flanks are also made of EPDM, whereas the middle region is made of GFRP. This is depicted in figure 3.

The force respectively the displacement boundary condition to move the bump crest face (actuator interface) upwards can be set to different desired values of h_c. The underlying wing section has a chord length (c) of 5 267 mm. Thus, for the largest bump height in [17] of 1.15%c, the displacement condition is set to 60.6 mm. The outer edges of the EPDM have fixed boundary conditions, while an effective cruise pressure of -10 000 Pa is applied. This pressure represents an aerodynamic trade-off between lift and wave drag.

2.3 FEA simulation results for bump deployment

In the FEA, the GFRP thickness (t_{GFRP}) as well as the EPDM thickness (t_{EPDM}) are varied. The values of these studies are given in table 3. The initial baseline configuration of the morphing SCB structure is composed of t_{EPDM} = 30 mm and t_{GFRP} = 3 mm. The ply stacking is based on [25] with a single ply thickness of 0.125 mm. However, the 90° layer in the neutral axis which is present in [25] is neglected, in order to achieve an isotropic laminate stacking.

Table 3: Material thicknesses of the sensitivity studies

Parameter	Thicknesses (mm)
t_{GFRP}	3, 4, 5
t_{EPDM}	10, 20, 30, 40, 50

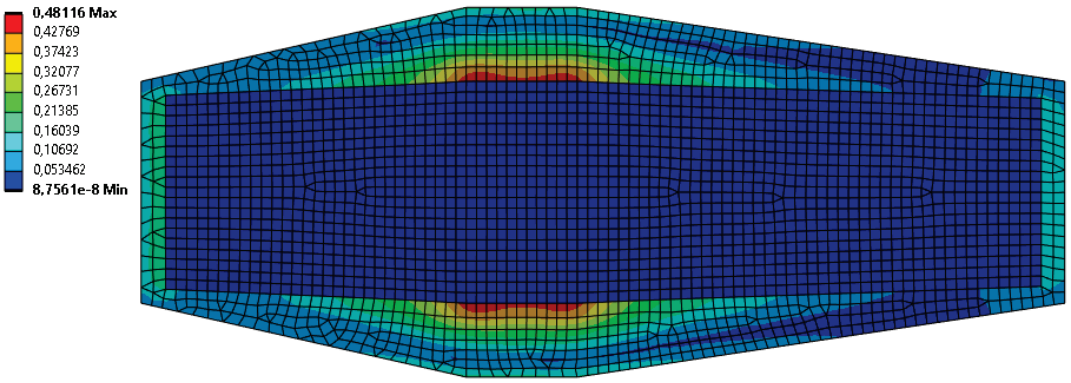

Figure 4: Top view of resulting equivalent von Mises strains (mm/mm) of EPDM and GFRP for 60.6 mm displacement (h_c = 1.15%c) and -10 000 Pa aerodynamic pressure load, t_{GFRP} = 3 mm, t_{EPDM} = 30 mm

In a first simulation of the baseline design, the displacement condition is set to the bump height of h_c = 1.15%c which corresponds to 60.6 mm. The resulting max. von Mises strains inside the GFRP reach 1.75% while the main deformation is covered by the EPDM which is strained by 48.12%. The combined strain results of EPDM and GFRP are depicted in figure 4, while the pure GFRP strain results can be found in figure 5. The results of all studies are summarized in table 4 at the end of chapter 2.5.

In light of extensive prior experience working with the GFRP used in this study, it is known that a maximum strain value of approximately 1% can be considered acceptable for this composite material. Upon examination of the GFRP results in figure 5 the comparatively high strains of about 1.75% are limited to the corners of the actuator interface. In contrast, the remaining structure displayes significantly lower strains. As such, reducing the corner strains is recommended for future work to ensure that the acceptable strain level of 1% is maintained. The overall structural concept, however, is deemed acceptable at this stage of design given these findings.

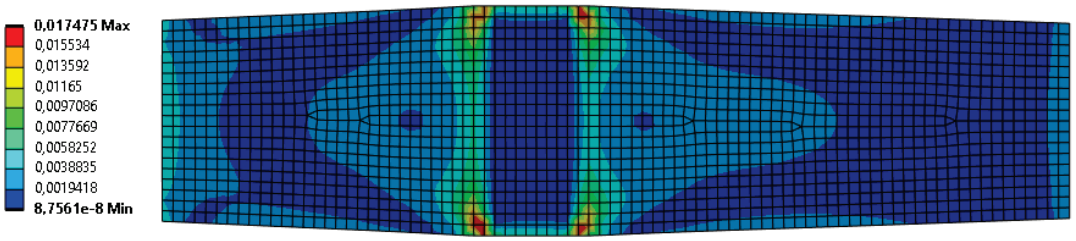

Figure 5: Top view of resulting equivalent von Mises strains (mm/mm) of the GFRP bump structure for 60.6 mm displacement (h_c = 1.15%c) and -10 000 Pa aerodynamic pressure load, t_{GFRP} = 3 mm, t_{EPDM} = 30 mm (EPDM is not shown)

Subsequently, t_{GFRP} is increased to 4 mm respectively 5 mm, while t_{EPDM} stays at 30 mm. The results in table 4 reveal that as the GFRP becomes thicker and consequently stiffer, the GFRP strains decrease but the EPDM strains increase. Taking into account all the studies carried out in this work, the maximum EPDM strains are 49.39% for the configuration with t_{GFRP} = 5 mm and t_{EPDM} = 30 mm.

Although EPDM can handle the resulting max. strains of approximately 50%, it is important to note that the Neo-Hookean material model is only valid for tensile strains up to 30-40% [29]. For larger strains, an alternative hyperelastic material model like the Odgen model may be more appropriate [30]. Therefore, it is recommended that the material model be revised or that the EPDM strains be reduced for future work to ensure accurate simulation results.

To investigate the impact of a smaller bump on the structural results, an additional simulation is performed with only 39.5 mm actuator interface z-displacement. This corresponds to h_c = 0.75%c since this height is also mentioned by Mayer et al. [17], even if not for the same design point and hence a slightly different SCB parametrization. However, for this smaller bump with t_{GFRP} = 3 mm and t_{EPDM} = 30 mm, the GFRP strains reach only 1.12% at the actuator interface corners and the EPDM is strained by only 29.01%.

2.4 FEA simulation results for clean cruise

As previously stated, when a flexible structure is subjected to aerodynamic pressure, it deforms. The challenge for morphing aircraft applications lies in designing a structure that is flexible enough to accommodate large deformations caused by actuation while being rigid enough to withstand operational loads. One important operating mode for such structures is the cruise with retracted bump, which maintains the clean airfoil shape. To achieve this, it is necessary to limit the contour deviations of the morphing skin due to cruise pressure to below 1 mm. To analyze this case, the actuator displacement is set to 0 mm, and the bump structure is loaded with

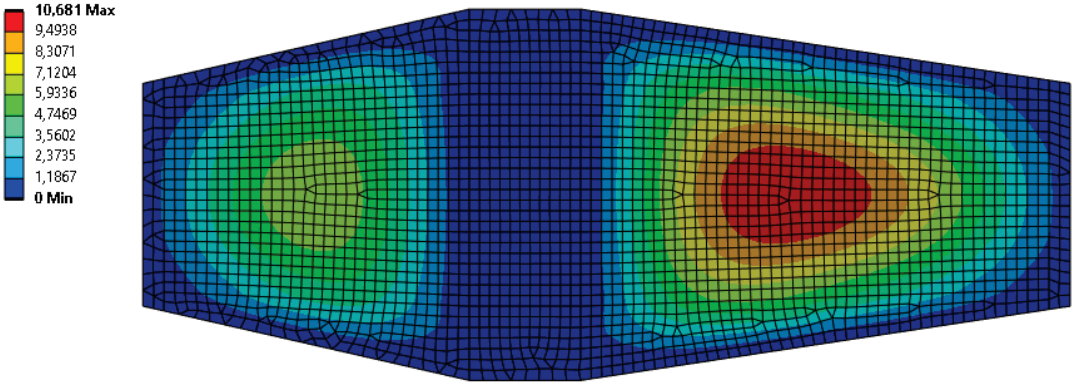

Figure 6: Top view of resulting deformations (mm) for 0 mm actuator interface displacement and -10 000 Pa aerodynamic pressure load, t_{GFRP} = 3 mm, t_{EPDM} = 30 mm

the previously mentioned average cruise pressure of -10 000 Pa. The deformation results for skin with 3 mm GFRP and 30 mm EPDM are shown in figure 6. They reveal a large deformation of approximately 10.7 mm of the morphing skin downstream of the actuator interface.

To see the effect of the EPDM thickness on aerodynamically-induced deformations, a sensitivity study is carried out for a constant GFRP thickness of 3 mm. Secondly, the GFRP thickness is varied for a constant EPDM thickness of 30 mm. The results of these two studies are depicted in figure 7. In this figure, the deformed center line is displayed. As depicted in figure 3, the major share of the center line belongs to the GFRP structure, while only 30 mm (in the x-direction) at the bump leading and trailing edges consist of EPDM.

The results shown in figure 7 emphasize a distinct influence of the EPDM thickness on the contour deviations. However, as t_{EPDM} increases, its impact on the contour deviations decreases. Thus, the relative differences of the deformations with t_{EPDM} of 30, 40 and 50 mm show minor divergences compared to the other EPDM thicknesses from 10 to 30 mm. Furthermore, the deformations in the downstream region are of same magnitude between the two configurations with t_{GFRP} = 3 mm and t_{EPDM} = 40 mm and the one with t_{GFRP} = 4 mm and t_{EPDM} = 30 mm. A similar behavior is observed in the downstream region for t_{GFRP} = 5 mm with t_{EPDM} = 30 mm and t_{GFRP} = 3 mm with t_{EPDM} = 50 mm. These findings suggest that designers have the flexibility to achieve comparable results using various combinations of GFRP and EPDM thicknesses.

However, even for the thickest simulated GFRP structure (t_{GFRP} = 5 mm, t_{EPDM} = 30 mm) the z-deformations respectively contour deviations are 3.8 mm upstream and 7.0 mm downstream of the actuator interface. Consequently, a new approach has to be considered to decrease the contour deviations in clean configuration below the target of 1 mm.

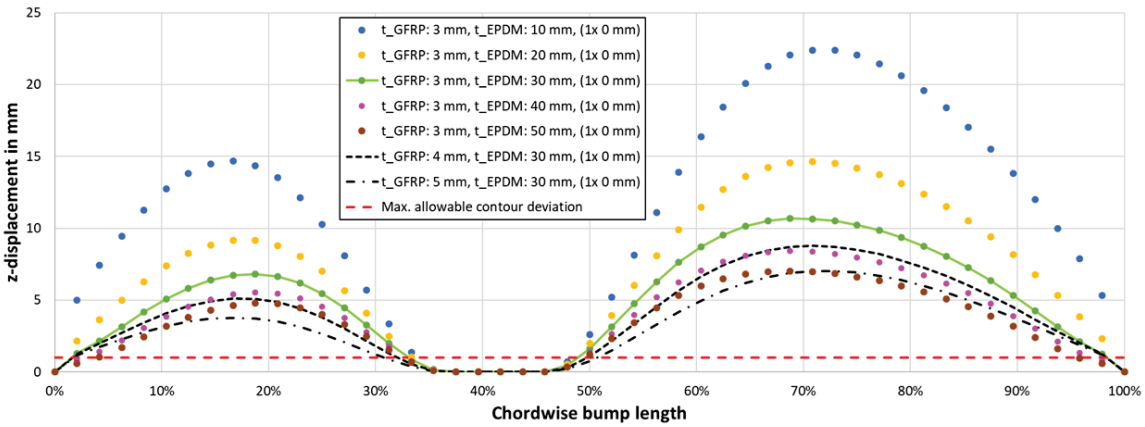

Figure 7: Deformations in z-direction of the center line (mm) for varying EPDM thicknesses, with 0 mm actuator displacement and -10 000 Pa aerodynamic pressure load

2.5 Additional actuators

Due to this fact, that the aerodynamic cruise pressure deforms the morphing structure too much a solution must be found to overcome this drawback. One approach could be to actively control the pressure below the flexible bump structure as already done in [5, 6, 7, 21, 24]. Another idea is to implement several actuation points upstream and downstream of the bump crest face. A similar approach can be found in [3, 4]. Additional actuators could be used not only to change the bump crest position in chordwise direction, but also to achieve an improved shape control on the bump upstream ramp and downstream tail. However, in the following study, the additional actuator interfaces are used to hold the structure down against aerodynamic loads.

In figure 8, the baseline configuration (t_{GFRP} = 3 mm, t_{EPDM} = 30 mm) is further equipped with one respectively two additional actuators (displacement conditions of 0 mm) downstream of the main bump crest actuator interface (Act. 1). Furthermore, a fourth actuator is placed on the upstream ramp. The results reveal that with the implementation of a second actuator downstream of the main actuator, the largest deformation due to the aerodynamic pressure occurs on the upstream ramp. Consequently, the maximum deformations of the simulations with two and three actuators are identical (6.8 mm) as shown in table 4. Only with the addition of an actuator on the upstream ramp, it is possible to reduce these deformations.

Figure 8 clearly shows that more actuators reduce the contour deviations of the skin under aerodynamic loading, as expected. With four actuator interfaces, the center line contour deviations under aerodynamic loading are less than 1 mm, compared to the clean, unloaded wing shape. Nevertheless, the center line plot in figure 8 gives mainly an impression of the GFRP deformations, while the largest shares of EPDM are implemented on the bump side flanks. Therefore, figure 9 depicts the overall deformations, including these EPDM regions for the four-actuator configuration.

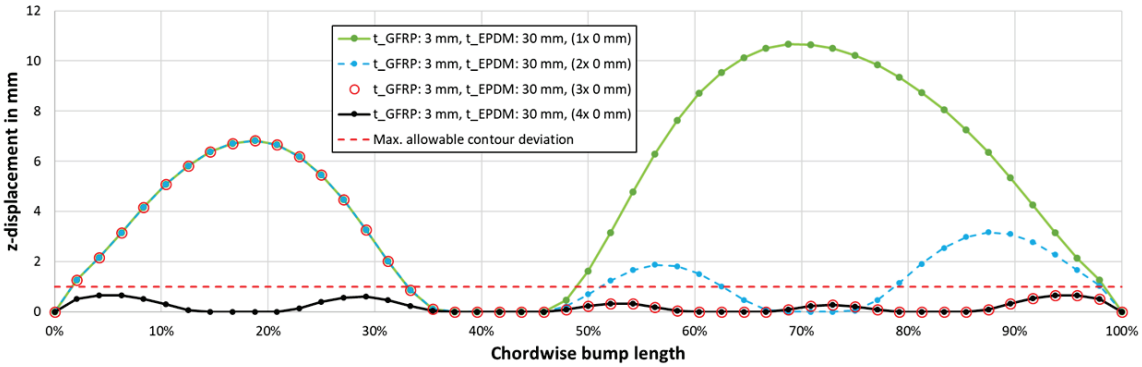

Figure 8: Deformations (mm) in z-direction of the center line with 0 mm displacement at up to four actuator interfaces, with -10 000 Pa aerodynamic pressure load, t_{GFRP} = 3 mm, t_{EPDM} = 30 mm

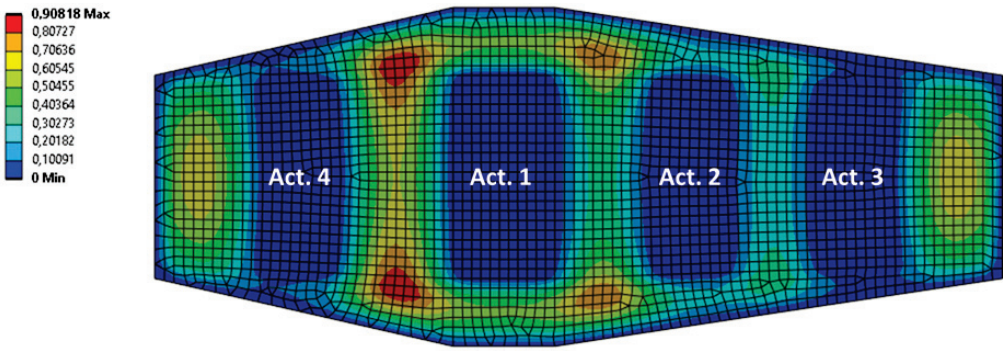

Figure 9: Top view of the total deformations (mm) with 0 mm displacement at four actuator interfaces for -10 000 Pa aerodynamic pressure load, t_{GFRP} = 3 mm, t_{EPDM} = 30 mm

These results show maximum deformations of about 0.9 mm on the side flanks close to the main actuator interface. Even in these highly flexible EPDM regions, deformations due to aerodynamic pressure loading in clean configuration remain within the contour limit of 1 mm.

In table 4, not only the resulting deformations and strains of the morphing structure are presented, but also the actuator forces. A positive value indicates that the main actuator has to push the structure in positive z-direction to deploy the SCB. Negative values represent a pulling

Table 4: FEA results of deformations, strains and actuator forces for an aerodynamic pressure load of -10 000 Pa, t_{EPDM} = 30 mm

Simulation Setup			Results						
t_{GFRP} (mm)	Act. displ. (mm)	Bump height (%c)	Max. deform. (mm)	Max. GFRP strain	Max. EPDM strain	Act. 1 force (N)	Act. 2 force (N)	Act. 3 force (N)	Act. 4 force (N)
3	21.0	0.40	21.1	0.61%	14.46%	1 332	-	-	-
3	39.5	0.75	39.5	1.12%	29.01%	6 891	-	-	-
3	60.6	1.15	60.6	1.75%	48.12%	17 430	-	-	-
4	60.6	1.15	60.6	1.55%	48.91%	18 928	-	-	-
5	60.6	1.15	60.6	1.42%	49.39%	20 473	-	-	-
3	1x 0	-	10.7	0.21%	6.55%	-1 892	-	-	-
3	2x 0	-	6.8	0.18%	5.13%	-2 120	-2 247	-	-
3	3x 0	-	6.8	0.18%	5.13%	-1 829	-972	-852	-
3	4x 0	-	0.9	0.08%	1.08%	-1 325	-972	-853	-1 015

t: thickness (in z-direction); GFRP: glass-fiber reinforced polymer; EPDM: ethylene propylene diene monomer; Act.: actuator; displ.: displacement; deform.: deformation; FEA: finite element analysis

force required to hold the structure in clean configuration against the aerodynamic pressure. The forces to deploy the bump with a height of h_c = 1.15%c are comparatively large. However, since the installation space beneath the skin is limited, the actuators should be minimized in size, which in general corresponds to lower forces. Therefore, thinner GFRP laminates are recommended to reduce actuator loads during bump deployment. Additionally, reducing the bump height from 1.15%c (corresponding to a deformation of 60.6 mm) to 0.75%c (resulting in a displacement of 39.5 mm) would lead to distinctly smaller strains and actuator forces. Furthermore, when the bump height is reduced to 0.40%c (corresponding to 21 mm), the force of actuator 1 amounts only to 1.3 kN. This comparatively small force arises primarily because most of the deformation is caused by aerodynamic pressure. Hence, if in future work an aero-structural SCB optimization is realized the bump height could be reduced to values that are still aerodynamically efficient, and at the same time leading to actuator forces and structural loads that stay in acceptable magnitudes.

3 CONCLUSION AND OUTLOOK

In this work, a novel structural design of a morphing 3D shock control bump has been introduced. By combining fiberglass composite laminates with regions of highly flexible elastomer, large deformations are enabled. While the middle region of the bump structure is made of GFRP, the side flanks as well as small regions at the bump leading and trailing edges are composed of EPDM. Three different GFRP thicknesses (3 mm, 4 mm and 5 mm) have been investigated through finite element analyses, with the EPDM thickness varying from 10 mm to 50 mm. The morphing structure is loaded with a suction pressure of -10 000 Pa representing aerodynamic loading during cruise. While displacement conditions correspond to actuators in current simulations, detailed actuator designs should be investigated in future work.

In addition to the bump deployment, the focus of this works lies on the clean configuration with retracted bump. Since one single actuator has been found to be not sufficient to hold the morphing structure against aerodynamic loading in acceptable limits of the contour deviations, the application of up to four actuators is investigated. For the baseline structure, which has thicknesses of 3 mm GFRP and 30 mm EPDM, four actuators would lead to contour deviations of less than 1 mm during cruise. Future designs may incorporate varying GFRP thicknesses along the bump chord to achieve sufficient stiffness, potentially requiring only one additional downstream actuator. Conversely, employing multiple actuators could enhance contour accuracy and facilitate the use of comparatively thin GFRP structures.

In future work, the morphing concept will be explored by using several actuators to vary the bump crest location in chordwise direction, enabling adaptation to changes in transonic shock position. The GFRP strain concentrations on the four corners of the actuator interface will be reduced, e.g. by implementing an elliptical shape of the interface, or by locally optimizing the structural design. More detailed structural analyses considering laminate failure criteria are planned. Additionally, the bump flank angles should be evaluated with respect to aerodynamic

targets. Moreover, not only the max. contour deviations but also the waviness should be taken into consideration. Furthermore, a comprehensive actuator design study will be conducted in conjunction with evaluating the available design space. This includes the analysis of whether the aerodynamic pressure alone could be sufficient to lift the flexible skin and form an accurate bump shape. If so, only an actuation to pull the bump down to clean configuration would be required. Finally, the precise placement of the SCB will presumably necessitate its implementation between the wing spars, requiring a redesign of the load-bearing upper wing skin.

4 ACKNOWLEDGMENT

This work is part of the DLR project LamTA. Special thanks go to Thomas Kilian for consulting in aerodynamic questions and Srinivas Vasista regarding morphing structures.

References

[1] K. Hainsch, L. Göke, C. Kemfert, P.-Y. Oei, and C. V. Hirschhausen, "European green deal: Using ambitious climate targets and renewable energy to climb out of the economic crisis," *DIW Weekly Report*, vol. 10, pp. 303–310, 2020. [Online]. Available: https://doi.org/10.18723/DIW_DWR:2020-28-1

[2] A. Krein and G. Williams, "Flightpath 2050: Europe's vision for aeronautics," in *Innovation for Sustainable Aviation in a Global Environment: Proceedings of the Sixth European Aeronautics Days*, D. Knörzer and J. Szodruch, Eds., vol. 30, 2012, pp. 63–71, Madrid, Spain. [Online]. Available: https://doi.org/10.3233/978-1-61499-063-5-63

[3] T. Bein, H. Hanselka, and E. Breitbach, "An adaptive spoiler to control the transonic shock," *Smart Materials and Structures*, vol. 9, no. 2, pp. 141–148, 04 2000. [Online]. Available: https://www.doi.org/10.1088/0964-1726/9/2/303

[4] L. F. Campanile, R. Keimer, and E. J. Breitbach, "The "fish-mouth" actuator: Design issues and test results," *Journal of Intelligent Material Systems and Structures*, vol. 15, no. 9, pp. 711–719, 09 2004. [Online]. Available: https://www.doi.org/10.1177/1045389X04044452

[5] M. Kintscher, N. Alves de Sousa, H. P. Monner, and M. Wiedemann, "Generation of a shock control bump by pressurized chambers," in *26th International Conference on Adaptive Structures and Technologies (ICAST2015)*, 10 2015, Kobe, Japan. [Online]. Available: https://elib.dlr.de/100017/

[6] N. B. L. Alves de Sousa, "Design of an adaptive shock control bump using pressurized chambers - structural realization, actuation and integration," 06 2017, Master's thesis, University Técnico Lisboa. [Online]. Available: https://fenix.tecnico.ulisboa.pt/cursos/meaer/dissertacao/283828618790088

[7] N. Alves de Sousa, M. Kintscher, and A. Suleman, "Morphing of an adaptive shock control bump using pressurized chambers," *Journal of Intelligent Material Systems and Structures*, 06 2020. [Online]. Available: https://www.doi.org/10.1177/1045389X20932214

[8] S. C. Künnecke, M. Schäfer, A. Goerttler, A. Waldmann, S. Vasista, and J. Riemenschneider, "CONCEPT OF A MORPHING SHOCK CONTROL BUMP SPOILER WITH TWO ACTUATORS," in *10th ECCOMAS Thematic Conference on Smart Structures and Materials*. Dept. of Mechanical Engineering & Aeronautics University of Patras, 07 2023, pp. 291–302, Patras, Greece. [Online]. Available: https://www.doi.org/10.7712/150123.9786.441212

[9] S. C. Künnecke, J. Riemenschneider, and H. P. Monner, "Adaptive shock control bump with shape memory alloy wires on a morphing spoiler," in *ASME 2024 Conference on Smart Materials, Adaptive Structures and Intelligent Systems*, 09 2024, V001T04A003, Atlanta, Georgia, USA. [Online]. Available: https://www.doi.org/10.1115/SMASIS2024-139102

[10] S. Barbarino, O. Bilgen, R. M. Ajaj, M. I. Friswell, and D. J. Inman, "A review of morphing aircraft," *Journal of Intelligent Material Systems and Structures*, vol. 22, no. 9, pp. 823–877, 06 2011. [Online]. Available: https://doi.org/10.1177/1045389X11414084

[11] E. Stanewsky, "Aerodynamic benefits of adaptive wing technology," *Aerospace Science and Technology*, vol. 4, no. 7, pp. 439–452, 10 2000. [Online]. Available: https://doi.org/10.1016/S1270-9638(00)01069-5

[12] A. Goerttler, "Aerodynamic design of shock control bumps on a transport aircraft wing considering structural constraints," in *AIAA SCITECH 2024 Forum*. American Institute of Aeronautics and Astronautics, 01 2024, Orlando, FL. [Online]. Available: https://doi.org/10.2514/6.2024-2133

[13] J. P. Eastwood and J. P. Jarrett, "Toward designing with three-dimensional bumps for lift/drag improvement and buffet alleviation," *AIAA Journal*, vol. 50, no. 12, pp. 2882–2898, 12 2012. [Online]. Available: https://arc.aiaa.org/doi/10.2514/1.J051740

[14] A. Waldmann, J. Müller, A. Goerttler, and T. Lutz, "Shock control bumps for buffet onset delay on sections of a wing with hybrid laminar flow control," in *New Results in Numerical and Experimental Fluid Mechanics XIV*, A. Dillmann, G. Heller, E. Krämer, C. Wagner, and J. Weiss, Eds. Springer Nature Switzerland, 2024, vol. 154, pp. 693–703. [Online]. Available: https://doi.org/10.1007/978-3-031-40482-5_65

[15] P. R. Ashill, J. L. Fulker, and A. Shires, "A novel technique for controlling shock strength of laminar-flow aerofoil sections," in *First European Forum on Laminar Flow Technology*, 03 1992, pp. 175–183, Hamburg, Germany.

[16] A. Goerttler, S. C. Künnecke, and C. Sabater, "Aerodynamic design of shock control bumps considering structural constraints," in *New Results in Numerical and Experimental Fluid Mechanics XIV*, A. Dillmann, G. Heller, E. Krämer, C. Wagner, and J. Weiss, Eds. Springer Nature Switzerland, 2024, vol. 154, pp. 671–681. [Online]. Available: https://doi.org/10.1007/978-3-031-40482-5_63

[17] R. Mayer, T. Lutz, and E. Krämer, "Numerical study on the ability of shock control bumps for buffet control," *AIAA Journal*, vol. 56, no. 5, pp. 1978–1987, 05 2018. [Online]. Available: https://doi.org/10.2514/1.J056737

[18] P. J. K. Bruce and S. P. Colliss, "Review of research into shock control bumps," *Shock Waves*, vol. 25, no. 5, pp. 451–471, 09 2015. [Online]. Available: https://doi.org/10.1007/s00193-014-0533-4

[19] H. Ogawa, H. Babinsky, M. Pätzold, and T. Lutz, "Shock-wave/boundary-layer interaction control using three-dimensional bumps for transonic wings," *AIAA Journal*, vol. 46, no. 6, pp. 1442–1452, 06 2008. [Online]. Available: https://doi.org/10.2514/1.32049

[20] O. Rhodes and M. Santer, "Structural optimization of a morphing shock control bump," in *52nd AIAA/ASME/ASCE/AHS/ASC Structures, Structural Dynamics and Materials Conference*, vol. AIAA 2011-2129. American Institute of Aeronautics and Astronautics, 04 2011, pp. 6039–6056, Denver, Colorado, USA,. [Online]. Available: https://doi.org/10.2514/6.2011-2129

[21] M. Gramola, P. J. Bruce, and M. Santer, "Passive control of 3d adaptive shock control bumps using a sealed cavity," *Journal of Fluids and Structures*, vol. 112, p. 103580, 07 2022. [Online]. Available: https://doi.org/10.1016/j.jfluidstructs.2022.103580

[22] M. Kintscher, J. Riemenschneider, H.-P. Monner, and M. Wiedemann, "Structural concept of an adaptive shock control bump spoiler," *CEAS Aeronautical Journal*, vol. 12, no. 3, pp. 509–518, 08 2021. [Online]. Available: https://www.doi.org/10.1007/s13272-021-00507-9

[23] S. C. Künnecke, S. Vasista, J. Riemenschneider, R. Keimer, and M. Kintscher, "Review of adaptive shock control systems," *Applied Sciences*, vol. 11, no. 2, p. 817, 01 2021. [Online]. Available: https://doi.org/10.3390/app11020817

[24] E. R. Jinks, P. J. Bruce, and M. J. Santer, "The use of actuated flexible plates for adaptive shock control bumps," in *53rd AIAA Aerospace Sciences Meeting*, ser. AIAA SciTech Forum. American Institute of Aeronautics and Astronautics, 01 2015, Kissimmee, Florida, USA. [Online]. Available: https://doi.org/10.2514/6.2015-1241

[25] S. Vasista, F. Nolte, H. P. Monner, P. Horst, and M. Burnazzi, "Three-dimensional design of a large-displacement morphing wing droop nose device," *Journal of Intelligent Material Systems and Structures*, vol. 29, no. 16, pp. 3222–3241, 09 2018. [Online]. Available: https://www.doi.org/10.1177/1045389X18770863

[26] M. Radestock, A. Falken, J. Riemenschneider, and M. Kintscher, "Hybrid skin design of the transition region between morphing wing and fixed wing," in *Proceedings of the ASME 2018 Conference on Smart Materials, Adaptive Structures and Intelligent Systems. Volume 1: Development and Characterization of Multifunctional Materials; Modeling, Simulation, and Control of Adaptive Systems; Integrated System Design and Implementation.*, 09 2018, V001T04A013, San Antonio, Texas, USA. [Online]. Available: https://www.doi.org/10.1115/SMASIS2018-7976

[27] S. Vasista, F. Nolte, M. Schäfer, and J. Riemenschneider, "Design and manufacture of a fluid-actuated morphing winglet trailing edge control surface," in *ASME 2022 Conference on Smart Materials, Adaptive Structures and Intelligent Systems (SMASIS)*, 09 2022, V001T04A013, Dearborn, Michigan, USA. [Online]. Available: https://www.doi.org/10.1115/SMASIS2022-91054

[28] K. Jacobi, "Aufbau einer regelung für die verformung von morphenden flügelhinterkanten," 2021, Master's thesis, Otto-von-Guericke-Universität, Magdeburg, Germany. [Online]. Available: https://elib.dlr.de/146878/

[29] ANSYS Inc., "ANSYS mechanical advanced nonlinear materials - hyperelasticity - appendix 4a," 03 2017. [Online]. Available: https://innovationspace.ansys.com/courses/wp-content/uploads/sites/5/2024/01/8_Modulus-vs-Strain-data.pdf

[30] B. Kim, S. B. Lee, J. Lee, S. Cho, H. Park, S. Yeom, and S. H. Park, "A comparison among Neo-Hookean model, Mooney-Rivlin model, and Ogden model for chloroprene rubber," *International Journal of Precision Engineering and Manufacturing*, vol. 13, no. 5, pp. 759–764, 05 2012. [Online]. Available: https://www.doi.org/10.1007/s12541-012-0099-y

XI ECCOMAS Thematic Conference on Smart Structures and Materials - SMART 2025
M. Krommer, M. Nader and M. Schagerl (Eds)

Received: 14 April 2025 / Revised: 8 September 2025 / Accepted: 10 September 2025
© The Author(s) 2025

Multi-Frequency Adaptive Tuned Mass Dampers Through Intelligent Materials

Stefano Manzoni, Marta Berardengo, Francescantonio Lucá

Abstract. Tuned mass dampers are well-known systems used for lowering vibrations of a primary system. Although they are effective and reliable, their main drawback is related to the need of a perfect tuning between the dynamic features of the tuned mass damper and the primary system. When mistuning occurs (e.g., due to thermal shifts), the attenuation performance worsens. To solve this issue, adaptive tuned mass dampers, able to change their dynamic features and recover the tuned condition, have been proposed in the literature. One of the most promising approaches is the use of intelligent materials to make tuned mass dampers adaptive, since often this choice allows obtaining the adaptation with lightweight and simple layouts. Some examples are related to piezoelectric-based and shape memory alloy-based adaptive tuned mass dampers. This paper aims at showing how it is possible to adapt different eigenfrequencies of a tuned mass damper at the same time with a given level of independence. More in detail, it will be shown that N tuned mass damper eigenfrequencies can be adapted by using N (or more) elements of intelligent materials fixed to the primary structure and shunting them with proper electric impedances. The paper treats in detail the example of piezoelectric patches but it also underlines that other materials (e.g., magnetostrictive elements) can be used following the same logical approach and the same mathematical treatment. In the discussed case of piezoelectric elements, each of them will be shunted with a capacitance (one capacitance for each patch; each capacitance can be either positive or negative). Experiments carried out on a beam equipped with two piezoelectric patches are presented to confirm the feasibility and reliability of the proposed method.

Key words: Multi-frequency, Adaptive, Tuned mass damper, Vibration, Vibration control

Stefano Manzoni & Francescantonio Lucá
Department of Mechanical Engineering, Politecnico di Milano, Via La Masa, 1 - 20156 Milan, Italy
e-mail: stefano.manzoni@polimi.it

Marta Berardengo
Department of Mechanical, Energy, Management and Transportation Engineering, Universitá degli Studi di Genova, Via all'Opera Pia, 15a - 16145 Genoa, Italy, e-mail: marta.berardengo@unige.it

1 INTRODUCTION

Tuned mass dampers (TMD) are widely used systems for lowering vibrations of primary systems. Even if they are very effective when their dynamics is properly tuned on the dynamics of the primary system, they suffer of possible mistuning which significantly worsens the attenuation performance. Mistuning can occur when, as an example, thermal shifts change the dynamics of either the primary system or the TMD (or both).

To avoid mistuning, different types of adaptive TMDs (ATMD) are proposed in the literature using many different possible approaches (e.g., [1, 2, 3, 4, 5]). Most of the ATMDs are such that they can change their eigenfrequency in order to recover tuning when needed.

Among the possible approaches for making TMDs adaptive, the use of smart materials is gaining more and more attention because of their advantageous features, such as lightweight ease of use, limited cost. Different examples are available in the literature using, e.g., shape memory alloys [6, 7, 8, 9], piezoelectric elements [10, 11, 12, 13, 14, 15, 16, 17, 18] and magneto-rheological elements [19, 20].

This paper will show that when a mechanical structure (named here host structure) is coupled to two (or more) elements made from any intelligent material, it is possible to tune the eigenfrequency of two (or more) modes of the host structure at the same time with a certain degree of independence, thus obtaining a multi-frequency (or multi-resonant) ATMD. Therefore, the ATMD is made from the host structure and the coupled elements of intelligent material. The basic requirement is that the considered intelligent material shows both direct and inverse effect so that it is possible to define the so called modal coupling factor k_i (where the subscript i indicates the coupling factor is related to the i-th mode) for all the modes of the structure. This k_i is a non-dimensional measure of the efficiency of the energy conversion between the intelligent material and the i-th mode of the structure and vice versa.

There exist different types of intelligent materials with a double effect, such as piezoelectric elements [21] and magnetostrictive elements [22]. Nevertheless, also other physical phenomena involving a double effect can be used, such as in the case of, e.g., electro-magnetic devices [23]. In all these cases, it is possible to define k_i thanks to the presence of the double effect and this feature makes all these cases fine for developing multi-frequency ATMDs. This paper will use as example the case of piezoelectric elements but, as evidenced in the paper, the key parameters are the k_i of two (or more) modes and, therefore, the discussion can be considered valid also for other intelligent materials.

The paper is structured as follows: Section 2 will explain how the multi-frequency ATMD can be developed and how its degree of independence in tuning different eigenfrequencies is obtained, while Section 3 presents the tests carried out on a set-up to show the effectiveness of the approach.

2 THE MULTI-FREQUENCY ATMD

A multi-frequency ATMD can be built using piezoelectric elements employing, as an example, a cantilever beam of, e.g., steel, and bonding two (or more) piezoelectric patches in

Table 1: Values used for simulations aimed at showing the effects of α_p and β_p on the r_i values.

$\lvert k_{i=1,p=1}\rvert$	$\lvert k_{i=1,p=2}\rvert$	$\lvert k_{i=2,p=1}\rvert$	$\lvert k_{i=2,p=2}\rvert$	$C_{i=1,p=1}$ [nF]	$C_{i=1,p=2}$ [nF]	$C_{\infty,p=1}$ [nF]	$C_{\infty,p=2}$ [nF]
0.244	0.096	0.072	0.184	79.82	83.66	57.03	58.71

different locations along the beam. In the discussion here, two patches will be used.

According to [24], the i-th eigenfrequency can be shifted from ω_i to $\omega_{i,\text{new}}$ by shunting two capacitances to the two patches, one for each patch. The capacitances can be either positive (i.e., physical capacitances) or negative (i.e., simulated by using circuits based on operational amplifiers [25] since they do not exist in nature as physical components). It is noticed that ω_i is the i-th eigenfrequency with both the patches short-circuited. The relation between ω_i and $\omega_{i,\text{new}}$ is [24]:

$$\omega_{i,\text{new}}^2 = \omega_i^2 \left[1 + \frac{k_{i,p=1}^2}{(C_{\text{a},p=1}/C_{i,p=1}) + 1} + \frac{k_{i,p=2}^2}{(C_{\text{a},p=2}/C_{i,p=2}) + 1}\right] \tag{1}$$

where the subscript p indicates either piezoelectric element 1 or 2, $C_{i,p}$ is the modal capacitance of the p-th patch at the i-th mode (see [26] for the way to estimate this quantity) and $C_{\text{a},p}$ is the capacitance shunted to the p-th patch. Equation (1) can be also rearranged to express $C_{\text{a},p}$ as function of $\omega_{i,\text{new}}$ [24].

It is noticed that the $|k_{i,p}|$ value can be estimated as [21]:

$$|k_{i,p}| = \sqrt{\frac{\hat{\omega}_{i,p}^2 - \omega_i^2}{\omega_i^2}} \tag{2}$$

where $\hat{\omega}_{i,p}$ is the i-th eigenfrequency with all the patches short-circuited, exception made for the p-th patch which is open-circuited.

Equation (1) evidences that, having two shunt capacitances, it is possible to set the value of two $\omega_{i,\text{new}}$ values. Using three patches, it will be thus possible to set the value of three eigenfrequencies, etc. Considering again the example of two patches, Eq. (1) also suggests that, to have good independence in moving the value of the two considered eigenfrequencies, the best choice is to have either $|k_{i=1,p=1}|$ and $|k_{i=2,p=2}|$ large, and $|k_{i=1,p=2}|$ and $|k_{i=2,p=1}|$ small, or $|k_{i=1,p=2}|$ and $|k_{i=2,p=1}|$ large, and $|k_{i=1,p=1}|$ and $|k_{i=2,p=2}|$ small.

When the shunt capacitances are positive, the system is always stable, while, when negative capacitances are employed, stability must be checked. Four different stable configurations (named conf1 to conf4) exist [24]:

1.
$$C_{\text{a},p=1} < -C_{0,p=1}, \quad C_{\text{a},p=2} < -C_{i=1,p=2}(1 + k_{i=1,p=2}^2 X_{i=1,p=1}) \tag{3}$$

2.
$$C_{\text{a},p=1} > -C_{\infty,p=1}, \quad C_{\text{a},p=2} > -C_{\infty,p=2} \tag{4}$$

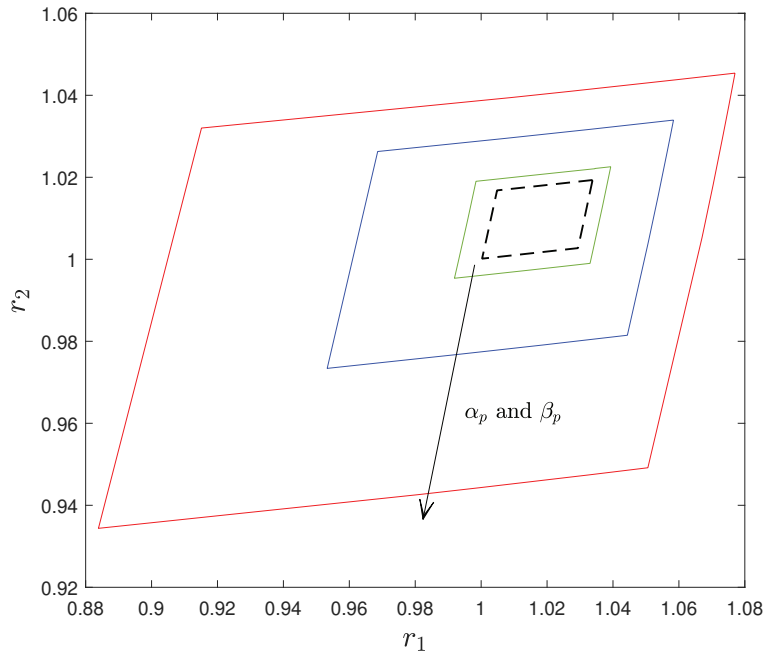

Figure 1: Resulting (r_1, r_2) areas (areas contained in the parallelograms) for different maximum values of α_p and β_p for the system of Table 1. Here, the maximum values for α_p and β_p are: 0.2, 0.6, 0.8 (solid lines in the plot). Furthermore, the case where only positive capacitances are used for shunting the two piezoelectric patches (i.e., $\beta_{p=1} \leq 0$ and $\beta_{p=2} \leq 0$) is also shown by means of a dashed line.

3.

$$C_{\mathrm{a},p=1} > -C_{\infty,p=1}, \quad C_{\mathrm{a},p=2} < -C_{0,p=2} \tag{5}$$

4.

$$C_{\mathrm{a},p=1} < -C_{0,p=1}, \quad C_{\mathrm{a},p=2} > -C_{\infty,p=2} \tag{6}$$

where:

$$X_{i=1,p=1} = \frac{C_{\mathrm{a},p=1} + C_{i=1,p=1}}{C_{\mathrm{a},p=1} + C_{0,p=1}} = \frac{C_{\mathrm{a},p=1} + C_{i=1,p=1}}{C_{\mathrm{a},p=1} + C_{i=1,p=1}(1 + k^2_{i=1,p=1})} \tag{7}$$

and $C_{0,p}$ is the value of the piezoelectric capacitance at the null frequency for the p-th piezoelectric patch ($C_{0,p} = C_{i=1,p}(1+k^2_{i=1,p})$ [25]). Finally, $C_{\infty,p}$ is the capacitance at constant strain for the p-th patch.

Defining:

$$\alpha_p = -C_{0,p}/C_{\mathrm{a},p}, \quad C_{\mathrm{a},p} < -C_{0,p} \tag{8}$$

$$\beta_p = C_{\mathrm{a},p}/(-C_{\infty,p}), \quad C_{\mathrm{a},p} > -C_{\infty,p} \tag{9}$$

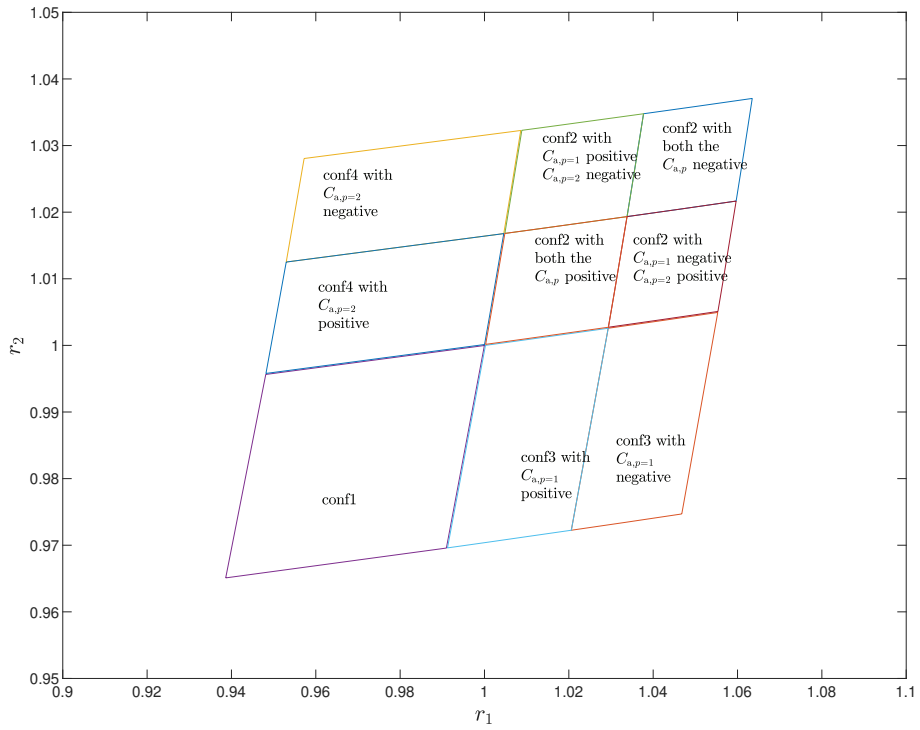

Figure 2: Resulting (r_1, r_2) areas (areas contained in the parallelograms) for different stable configurations of the shunt capacitances.

stability is assured when these two parameters are smaller than 1. Actually, when conf1 is used, according to Eq. (3), the actual stability limit is different from $-C_{0,p}$ for one of the two patches. However, for the sake of simplicity, here the stability limit is approximated to $-C_{0,p}$ for both the NCs connected to the patches.

The use of negative capacitances allows enlarging the achievable frequency changes. As an example, for a system having the features reported in Table 1, Fig. 1 shows that increasing the maximum possible value of α_p and β_p allows having wider and wider possible shifts of the two considered eigenfrequencies. In the figure, r_i expresses the following quantity:

$$r_i = \omega_{i,\text{new}}/\omega_i \tag{10}$$

Furthermore, Fig. 2 shows how the different shut configurations allows moving in different areas of the (r_1, r_2) plane.

The whole discussion can be replicated for other structures equipped, e.g., with electromagnetic devices or magnetostrictive elements, allowing to build ATMDs relying on different physical principles and intelligent materials. In these cases, the shunting elements would be

Table 2: Values of $|k_{i,p}|$, α_p and β_p for the tests. The values of $|k_{i,p}|$ were measured every time before each test for a better accuracy.

Test ID	$\lvert k_{i=1,p=1}\rvert$	$\lvert k_{i=1,p=2}\rvert$	$\lvert k_{i=2,p=1}\rvert$	$\lvert k_{i=2,p=2}\rvert$	$\alpha_{p=1}$ $\beta_{p=1}$	$\alpha_{p=2}$ $\beta_{p=2}$
T1	0.242	0.090	0.057	0.188	$\beta_{p=1}$=-1.14	$\alpha_{p=2}$=0.81
T2	0.242	0.094	0.066	0.186	$\beta_{p=1}$=0.69	$\alpha_{p=2}$=0.70
T3	0.242	0.094	0.071	0.184	$\beta_{p=1}$=0.45	$\beta_{p=2}$=0.57
T4	0.242	0.094	0.066	0.186	$\alpha_{p=1}$=0.66	$\alpha_{p=2}$=0.58

inductances.

3 EXPERIMENTS

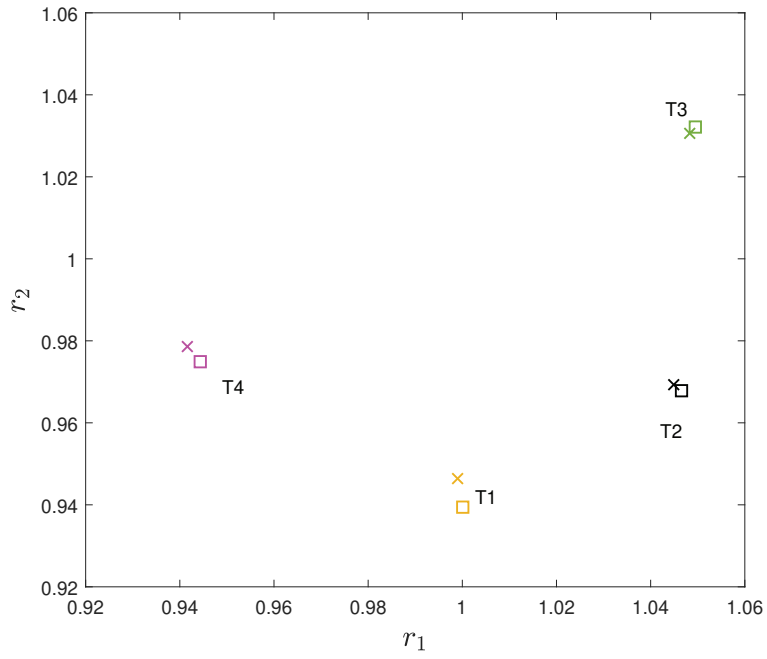

Figure 3: Experimental (x) and theoretical (□) results in terms of r_1 and r_2 values for the tests in Table 2.

In this section, few tests carried out on a cantilever beam equipped with two piezoelectric patches are discussed to show the reliability and feasibility of the proposed principle and treatment. The measured $\omega_i/(2\pi)$ of the first two bending modes of the beam were 22.2 and 124.5 Hz. Table 2 describes the tests considered here. Figure 3 shows that the theoretical expectation for the value of r_i is always close to the obtained experimental value. Many more tests and analyses are available in [24].

4 CONCLUSION

This paper has dealt with an approach for developing multi-frequency ATMDs able to shift two (or more) of its eigenfrequency with a given level of independence. This is obtained by using two (or more) elements made from intelligent material coupled to a mechanical system. The intelligent material used must show both direct and inverse effects.

Some experimental tests carried out on a cantilever beam equipped with two piezoelectric patches have confirmed that the approach is successful and good match was obtained with the theoretical expectations.

REFERENCES

[1] P. Gardonio, L. Ortis, E. Rustighi, C. Malacarne, and M. Perini, "Multi-resonant tva formed by a tree of deflated composite beams with core structured fabrics," *Smart Materials and Structures*, vol. 34, no. 1, 2025, 015039.

[2] P. Gardonio, E. Turco, A. Kras, L. Dal Bo, and D. E. Casagrande, "Semi-active vibration control unit tuned to maximise electric power dissipation," *Journal of Sound and Vibration*, vol. 499, 2021, 116000.

[3] L. Wang, S. Nagarajaiah, Y. Zhou, and W. Shi, "Experimental study on adaptive-passive tuned mass damper with variable stiffness for vertical human-induced vibration control," *Engineering Structures*, vol. 280, 2023, 115714.

[4] Z. H. Wang, Y. W. Xu, H. Gao, Z. Q. Chen, K. Xu, and S. B. Zhao, "Vibration control of a stay cable with a rotary electromagnetic inertial mass damper," *Smart Structures and Systems*, vol. 23, no. 6, p. 627 – 639, 2019.

[5] N. Carpineto, W. Lacarbonara, and F. Vestroni, "Hysteretic tuned mass dampers for structural vibration mitigation," *Journal of Sound and Vibration*, vol. 333, no. 5, p. 1302 – 1318, 2014.

[6] S. Manzoni, A. Argentino, F. Lucà, M. Berardengo, and M. Vanali, "Sma-based adaptive tuned mass dampers: Analysis and comparison," *Mechanical Systems and Signal Processing*, vol. 186, 2023, 109883.

[7] M. Berardengo, G. Della Porta, S. Manzoni, and M. Vanali, "A multi-modal adaptive tuned mass damper based on shape memory alloys," *Journal of Intelligent Material Systems and Structures*, vol. 30, no. 4, pp. 536–555, 2019.

[8] M. A. Savi, A. S. De Paula, and D. C. Lagoudas, "Numerical Investigation of an Adaptive Vibration Absorber Using Shape Memory Alloys," *Journal of Intelligent Material Systems and Structures*, vol. 22, no. 1, pp. 67–80, 2010.

[9] E. Rustighi, M. J. Brennan, and B. R. Mace, "A shape memory alloy adaptive tuned vibration absorber: design and implementation," *Smart Materials and Structures*, vol. 14, no. 1, pp. 19–28, 2005.

[10] G. M. Chatziathanasiou, N. A. Chrysochoidis, C. S. Rekatsinas, and D. A. Saravanos, "A semi-active shunted piezoelectric tuned-mass-damper for multi-modal vibration control of large flexible structures," *Journal of Sound and Vibration*, vol. 537, 2022, 117222.

[11] G. M. Chatziathanasiou, N. A. Chrysochoidis, and D. A. Saravanos, "A semi-active shunted piezoelectric tuned mass damper for robust vibration control," *Journal of Vibration and Control*, vol. 28, no. 21-22, p. 2969–2983, 2022.

[12] P. Gardonio, M. Zientek, and L. Dal Bo, "Panel with self-tuning shunted piezoelectric patches for broadband flexural vibration control," *Mechanical Systems and Signal Processing*, vol. 134, 2019, 106299.

[13] P. Gardonio, G. K. Rodrigues, L. Dal Bo, and E. Turco, "Extremum seeking online tuning of a piezoelectric vibration absorber based on the maximisation of the shunt electric power absorption," *Mechanical Systems and Signal Processing*, vol. 176, 2022, 109171.

[14] G. K. Rodrigues, P. Gardonio, L. Dal Bo, and E. Turco, "Piezoelectric patch vibration control unit connected to a self-tuning rl-shunt set to maximise electric power absorption," *Journal of Sound and Vibration*, vol. 536, 2022, 117154.

[15] D. E. Casagrande, P. Gardonio, and G. K. Rodrigues, "Tonal vibration control with a self-tuning absorber employing the extremum seeking algorithm," *Mechanical Systems and Signal Processing*, vol. 211, 2024, 111254.

[16] O. Heuss, R. Solloum, D. Mayer, and T. Melz, "Tuning of a vibration absorber with shunted piezoelectric transducers," *Archive of Applied Mechanics*, vol. 86, pp. 1715–1732, 2016.

[17] M. Lallart, L. Yan, Y.-C. Wu, and D. Guyomar, "Electromechanical semi-passive nonlinear tuned mass damper for efficient vibration damping," *Journal of Sound and Vibration*, vol. 332, no. 22, pp. 5696–5709, 2013.

[18] C. L. Davis and G. A. Lesieutre, "Actively tuned solid-state vibration absorber using capacitive shunting of piezoelectric stiffness," *Journal of Sound and Vibration*, vol. 232, no. 3, pp. 601–617, 2000.

[19] Y.-W. Xu, Z.-D. Xu, R.-L. Zhao, Z.-H. Wang, Y. Li, and C. Zhu, "Multimode vibration control of stay cables using pseudo negative stiffness mr damping system," *Journal of Intelligent Material Systems and Structures*, vol. 34, no. 14, p. 1617–1632, 2023.

[20] F. Weber, C. Boston, and M. Maślanka, "An adaptive tuned mass damper based on the emulation of positive and negative stiffness with an MR damper," *Smart Materials and Structures*, vol. 20, no. 1, 2011, 015012.

[21] O. Thomas, J. Ducarne, and J. De$\ddot{u}$, "Performance of piezoelectric shunts for vibration reduction," *Smart Materials and Structures*, vol. 21, no. 1, 2012, 015008.

[22] M. Berardengo, M. Mercato, and S. Manzoni, "Magnetostrictive shunt for vibration control and isolation: model, characteristics and similarities with piezoelectric shunt," *Smart Materials and Structures*, vol. 34, no. 1, 2025, 015043.

[23] M. Auleley, O. Thomas, C. Giraud-Audine, and H. Mahé, "Enhancement of a dynamic vibration absorber by means of an electromagnetic shunt," *Journal of Intelligent Material Systems and Structures*, vol. 32, no. 3, p. 331 – 354, 2021.

[24] S. Manzoni, M. Berardengo, F. Boccuto, and M. Vanali, "Piezoelectric-shunt-based approach for multi-mode adaptive tuned mass dampers," *Mechanical Systems and Signal Processing*, vol. 200, 2023, 110537.

[25] M. Berardengo, O. Thomas, C. Giraud-Audine, and S. Manzoni, "Improved resistive shunt by means of negative capacitance: new circuit, performances and multi mode control," *Smart Materials and Structures*, vol. 25, 2016, 075033.

[26] M. Berardengo, S. Manzoni, J. Høgsberg, and M. Vanali, "Vibration control with piezoelectric elements: The indirect measurement of the modal capacitance and coupling factor," *Mechanical Systems and Signal Processing*, vol. 151, 2021, 107350.

XI ECCOMAS Thematic Conference on Smart Structures and Materials - SMART 2025
M. Krommer, M. Nader and M. Schagerl (Eds)

Received: 31 March 2025 / Revised: 29 August 2025 / Accepted: 10 September 2025
© The Author(s) 2025

Self-Tuning Vibration Absorber Made With In-Vacuo Structured Fabrics

Lisa Ortis, Daniel Casagrande, Paolo Gardonio, Emiliano Rustighi, Ciro Malacarne, Matteo Perini

Abstract. This paper presents a study on the design and implementation of a self-tuning beam-like vibration absorber. The beam element is fixed to a middle post and it is made by a core structured fabric encased in a deflated plastic bag. The bending stiffness of this beam can be suitably varied by modulating the vacuum in the bag. In this way the resonant response of its flapping vibration resembles the dynamics of a mass-spring-damper absorber, whose fundamental resonance frequency can be duly adjusted by varying the level of vacuum in the bag. The paper presents an extensive experimental analysis of the tuning features and vibration control performance generated by a prototype absorber, which is fixed on a plate hosting structure excited by a broadband random disturbance. Two tuning principles are investigated: the first relies on the so-called "global cost function" given by the minimisation of the plate total flexural kinetic energy; the second relies on the so-called "local cost function", which is based on the maximization of the vibration power absorbed by the flapping vibration of the beam-like element of the absorber.

Key words: Tuneable Vibration Absorber, Adaptive Absorber, Self-Tuning, Structured Fabrics, In-vacuo structures.

1 INTRODUCTION

Traditionally and up to 1980s, mostly passive control strategies were used to control the structure-borne and air-borne noise of lightweight structures. But as the need to reduce the

Lisa Ortis & Paolo Gardonio
Dipartimento Politecnico di Ingegneria e Architettura, Universitá degli Studi di Udine, Via delle Scienze 206, 33100 Udine, Italy, e-mail: lisa.ortis@uniud.it

Daniel Casagrande
Instituto de Ciencias de la Ingeniería, Universidad de O'Higgins, Libertador O'Higgins 611, 2820000, Rancagua, Chile, e-mail: daniel.casagrande@uoh.cl

Emiliano Rustighi
Dipartimento di Ingegneria Industriale, Universitá degli Studi di Trento, Via Sommarive 9, 38123 Povo, Italy
e-mail: emiliano.rustighi@unitn.it

Ciro Malacarne & Matteo Perini
ProM Facility, Trentino Sviluppo S.p.A., Via Fortunato Zeni 8, 38068 Rovereto, Italy
e-mail: ciro.malacarne@trentinosviluppo.it

ecological impact of machineries, in terms of raw materials and energy consumption, progressively increased over time, the vibration response and sound radiation of these machineries also changed. The increasing stiffness to mass ratio of the newer materiales leads to two effects: the acoustic wavelentgh and the flexural wavelength coincide at lower frequencies [1]; and the low modal overlap frequency band of the flexural response is extended to higher frequencies [2], [3]. There is then, a increment of the structure- and air-borne sound-radiation in an extended low-frequency band in which passive control strategies are less effective, unless heavy vibration and insulation treatments are employed [4], [5], [6]. This led to the development of active and semi-active control strategies [7], [8], [9], [10], [11], [12]. Active control systems, mostly used in the transportation sector can generate large vibration reductions even when the dynamic response of the hosting structure undergo large changes, but they are more complex and costly [13], [14], [15]. Semi-active vibration control systems on the other hand, can deliver good performances even for significant changes in the structural response and are less complex and costly [10], [12].

Tuneable vibration absorbers (TVAs) have been widely studied and implemented extensively during the last century [16], [17], [18], [19]. These are usually composed of a seismic mass fixed on an elastic suspension [19], [20], [21], [22]. Three parameters are crucial to achieve good performances controlling the resonant response of a flexural mode of a structure: the position of the TVA, its natural frequency and its damping. The TVA should be mounted in an antinodal point of the target mode, the natural frequency of the TVA should be about the same as the target mode and its damping should be set to maximise the vibration absorption [3], [23]. Many studies have been conducted to propose tuning laws that find optimal values for the stiffness and damping of a TVA mounted on a simple structure [17], [18], [19], [24], [25], [26], [27], [28], [29], [30], [31]. Typical values for the seismic mass are in the range of 5% to 15% of the mass of the hosting structure and for the damping factor of the TVA, which usually is not so critical, are between 0.1 and 0.2. On the other hand, the natural frequency of the TVA, which is related to its mass and stiffness, should be finely tuned in the vicinity of the frequency of the target mode [31].

This paper presents experimental results of a prototype TVA attached to a thin plate structure to control the resonant response of a target flexural mode when it is being excited by a broadband random disturbance. The TVA is composed of in-vacuo structured fabrics contained in an airtight plastic film enclosure. The stiffness of the prototype can be tuned by modifying the pressure inside the plastic bag. The structured fabric is a regular network of 3D printed interlocked hollowed trusslike rigid particles [32], [33], similar to medieval chain armours and is manufactured using a 3D printer [34], [35]. When air is drawn out of the bag, the pressure generated by the deflated plastic film forces the particles to jam [36], [37], [38], [39], [40], [40], [41]. The coated fabric now behaves as a rigid body, whose stiffness is proportional to the vacuum pressure [32], [33]. The dynamic of the prototype resembles that of a classical mass-spring-damper absorber with tuneable fundamental resonance frequency [42], [43] using a vacuum controller to reach the stiffness value required for a properly tuned TVA. Two control laws are implemented to tune the TVA to control the resonant response of the first flexural mode of a plate model structure: a “global cost function”, which is set to minimise the time-averaged total flexural kinetic energy of the plate; and a “local cost function”, which is set to

maximise the time-averaged vibration power absorbed by the TVA [23], [31]. To minimise the response of a target mode, the two cost functions are derived with reference to the kinetic energy and vibration power functions filtered in a small frequency band centred at the resonance frequency of the target mode.

The paper is structured in five sections. Section two describes the experimental set-up and the proposed prototype TVA. Section three introduces the global and local tuning cost functions. Section four presents a comprehensive experimental analysis of the vibration control performance of a single TVA, tuned to target the first mode, on the flexural response of the structure excited by a random disturbance. This analysis gives insights on the effect of the proposed TVA on the power absorption of the TVA and on the flexural kinetic energy of the structure. Finally, section five reports the conclussion of this study.

2 PLATE WITH THE IN-VACUO STRUCTURED FABRIC TVA

Figure 1a,b shows the model structure used to investigate the tuning and vibration control performance features of a TVA composed by a beam-like in-vacuo element fixed to plate. The plate is made of steel and has dimension $L_x \times L_y = 668 \times 443$ mm and thickness $h_p = 1.8$ mm. As can be seen in Figure 1c, the plate is excited by a transverse point force exerted by a shaker at position $x_f = 0.245L_x$, $y_f = 0105L_y$ and is equipped with one TVA at position $x_{TVA} = 0.455L_x$, $y_{TVA} = 0.300L_y$. The post of the TVA is fixed to the plate via an impedance head to measure the force and velocity at the base of the TVA, which have been used to derive the vibration power absorbed by the TVA. Also, the stinger of the shaker is fixed to the plate via a force cell used to measure the reference force excitation employed in the experiments.

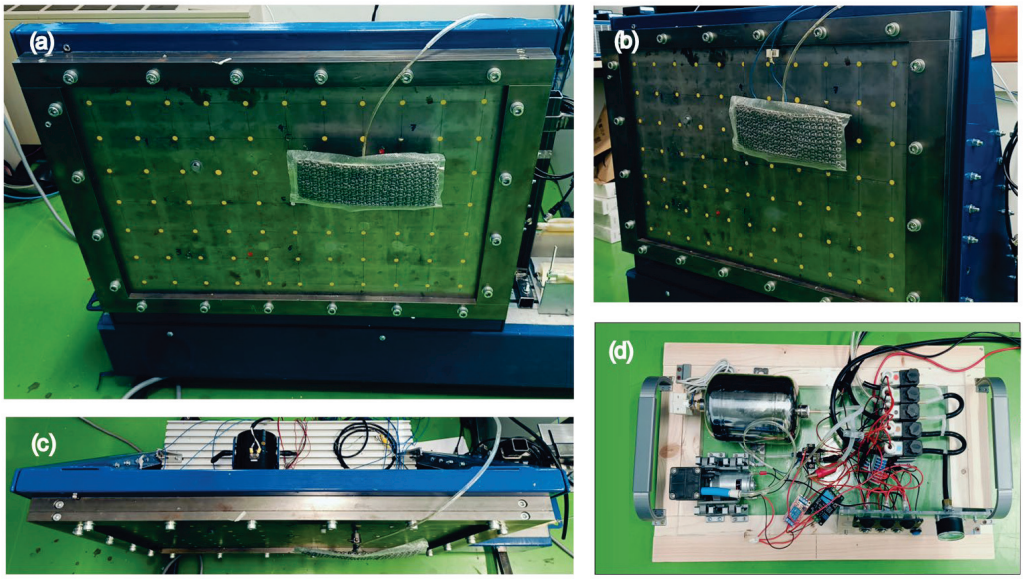

Figure 1: Experimental setup: (a) front and (b) lateral views of the plate with the beam-like vibration absorber made with the in-vacuo structured fabric; (c) top view of the plate and shaker that generates the force excitation; (d) vacuum control plant.

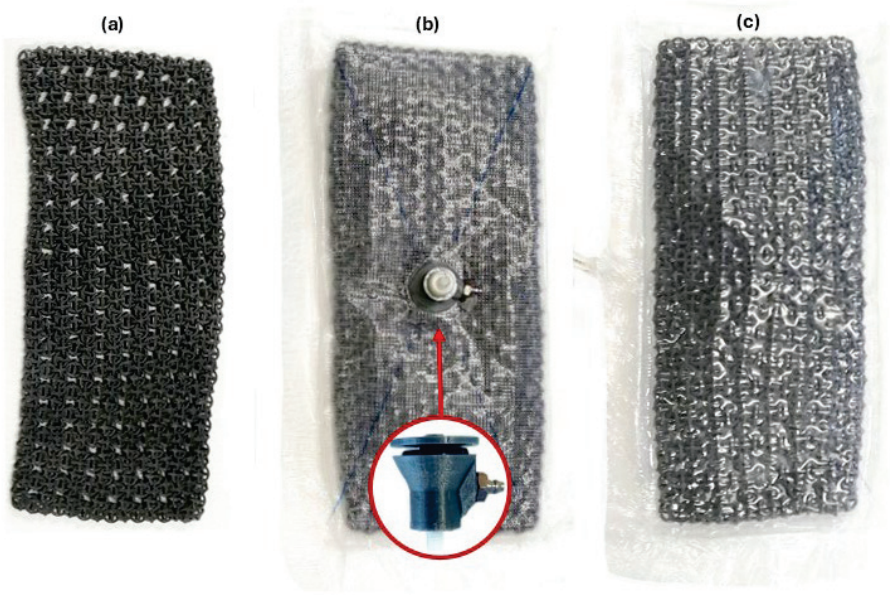

Figure 2: (a) Core fabric made of spherical-octahedral particles. (b) Bottom view of the deflated beam-like structure core fabric encased on a sealed plastic skin equipped with a post-vacuum junction in the middle. (c) Top view of the deflated beam-like structure.

As shown in Figure 2, the TVA is formed by a beam-like composite structure encompassing a core structured fabric and a sealed plastic skin, which is fixed in the middle to a post that works as vacuum junction too (Figure 2b). The core fabric is formed by interlocked rigid truss-like hollowed particles with spherical-octahedral shape [33]. This material shows a fluidlike state due to the mobility of the loosely interlocked grains (Figure 2a). However, when it is enclosed in the vacuum bag, the uniform pressure exerted by the plastic skin forces the truss-like hollowed grains to jam and lock such that the whole composite beam becomes solid (Figure 2c) [36], [37], [38], [39], [40], [41], [44]. At the grain scale, the jamming of the truss-like hollowed particles is characterized by compressive friction [36], [37], [38] that arise both at convex and non-convex contact surfaces (e.g. see page 241 - graph 3c,d in Ref. [32] and Ref. [40], [45], [46]). Nevertheless, at the larger scale of the composite beam, the convex and non-convex contacts generate resistances to compression and to traction respectively [32], which are essential to develop a resistance to bending. For instance, the four-point bending tests presented in Ref. [33] showed that the bending stiffness of a beam-like specimens like that used to fabricate the TVA for this study can be increased by about 40% by raising the vacuum pressure from 20 kPa to 80 kPa. Also, Ref. [43] showed that when the specimens are equipped with a middle post, the vibration of the base post produces a fundamental flapping vibration mode of the beam structure whose resonance frequency can be raised by about 20% when the vacuum pressure is brought up from 5 kPa to 80 kPa.

Ref. [47] showed that this flapping vibration mode resembles the dynamic response of classical vibration absorbers, which can be modelled in terms of a base and a seismic mass

connected via a spring and damper in parallel. Indeed, the spectrum of the absorber base impedance Frequency Response Function (FRF) is characterised by a resonance peak at the fundamental resonance frequency due to the flapping vibration of beam-like element, such that, at this frequency, the absorber effectively drains vibration energy from the hosting structure.

3 GLOBAL AND LOCAL TUNING COST FUNCTIONS

Two tuning laws are investigated in this study. The first relies on a global cost function that accounts for the time-average of the total flexural kinetic energy of the panel, whereas the second is based on a local cost function given by the vibration power absorbed by the TVA. To focus the control on the resonant response of a target *r*-th mode, the two functions are filtered in a small frequency band $\Delta\omega$ centred at the *r*-th flexural resonance frequency of the plate. Here, the two cost functions have been derived first in the frequency domain and then integrated over the small frequency band $\Delta\omega$. For instance, the spectrum of the time-averaged total flexural kinetic energy of the plate has been derived with the following expression:

$$\bar{K}(\omega) = \frac{1}{T}\int_0^T \int_S \frac{1}{2}\rho h \dot{w}(x,y,t)^2 dS\, dt \cong \frac{M}{4}\sum_{\mathrm{n}=1}^{\mathrm{N}} |Y_{\mathrm{n}}(\omega)|^2 F^2. \tag{1}$$

Also, the time-averaged vibration power absorbed by the TVA has been derived from the following formula:

$$\bar{P}(\omega) = \frac{1}{T}\int_0^T f_a(t)\dot{w}_a(t)dt \cong \frac{1}{2}\mathrm{Re}\{T_a^*(\omega)Y_{\mathrm{a}}(\omega)\}F^2, \tag{2}$$

The two cost functions were then averaged in the $\Delta\omega_r$ frequency band centred at the *r*-th flexural resonance frequency of the plate, such that:

$$\bar{K}_r = \frac{\Delta\omega_r}{N_c}\sum_{i=1}^{N_c} \bar{K}(\omega_i), \tag{4}$$

$$\bar{P}_r = \frac{\Delta\omega_r}{N_c}\sum_{i=1}^{N_c} \bar{P}(\omega_i)\ . \tag{5}$$

Here N_c is the number of samples of the kinetic energy and power spectra in the frequency band $\Delta\omega_r$ and ω_i is the frequency at the *i*-th sample. Also, in Eqs. (1), (2), T is the period of the time-harmonic vibration, $(\ )^*$ indicates the complex conjugate and ρ, h, S, M are respectively the density, thickness, surface area and mass of the plate. Also, $Y_{\mathrm{n}}(\omega) = \dot{w}_n(\omega)/f(\omega)$, $Y_{\mathrm{a}}(\omega) = \dot{w}_a(\omega)/f(\omega)$ are the mobility FRFs measured respectively between the $N = 9$ accelerometers and shaker force cell and between the TVA impedance head and the shaker force cell. Moreover, $T_{\mathrm{a}}(\omega) = f_a(\omega)/f(\omega)$ is the force transmissibility FRF measured between the TVA impedance head and the shaker force cell. Here $\dot{w}_n(\omega)$, $\dot{w}_a(\omega)$ $f_a(\omega)$ and $f(\omega)$ are the complex amplitudes of the time-harmonic velocities and forces defined in the following complex forms $\dot{w}_n(\omega) = \mathrm{Re}\{\dot{w}_n(\omega)\exp(j\omega t)\}$, $\dot{w}_a(\omega) = \mathrm{Re}\{\dot{w}_a(\omega)\exp(j\omega t)\}$, $f_a(t) = \mathrm{Re}\{f_a(\omega)\exp(j\omega t)\}$ and $f(t) = \mathrm{Re}\{f(\omega)\exp(j\omega t)\}$, where $j = \sqrt{-1}$ and ω is the circular frequency. Finally, $F = |f(\omega)|$ is the amplitude of the force excitation exerted by the shaker. The global cost function has been

used as a reference metric to identify the optimal tuning of the TVA that guarantees the control of the overall flexural response of the plate at the *r*-th flexural resonance frequency. Instead, the local cost function has been considered as a practical metric that can be easily measured at the TVA position and thus used to tune online the TVA.

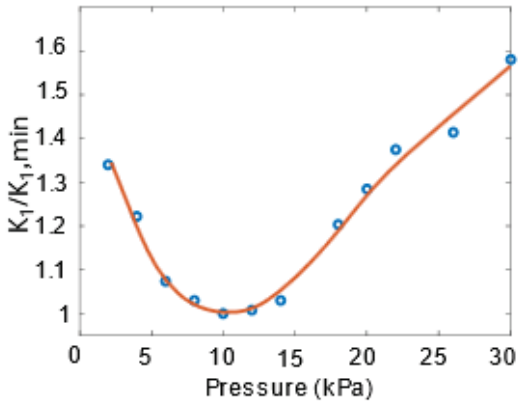

Figure 3: Normalised time-averaged total flexural energy of the panel with the vibration absorber filtered in a small band centred at the first flexural resonance frequency of the panel with respect to the vacuum pressure in the beam-like element of the absorber.

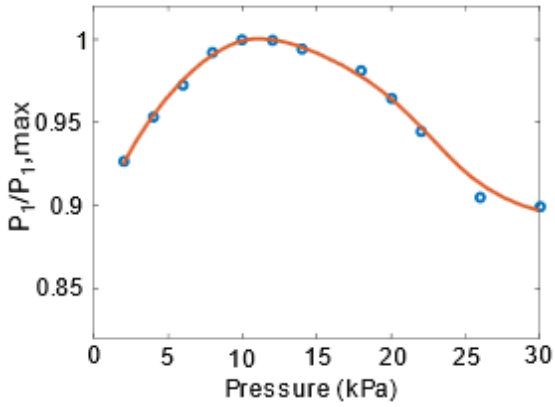

Figure 4: Normalised time-averaged electric power absorbed by the vibration absorber mounted on the panel filtered in a small band centred at the first flexural resonance frequency of the panel with respect to the vacuum pressure in the in the beam-like element of the absorber.

Figures 3, 4 show the two cost functions with reference to the resonant response of the first flexural mode such that $\omega_1 = 32$ Hz and $\Delta\omega_1 = 14$ Hz. The graph in Figure 3 shows that, the time-averaged kinetic energy, that is the spatially averaged flexural response, is characterised

by an inverted bell shape with a minimum for a vacuum pressure of 10 kPa. In parallel, the graph in Figure 4 shows that the time-averaged vibration power absorbed by the TVA is characterised by a bell shape whose maximum is at the same vacuum pressure of 10 kPa. Hence, as found in Ref. [23], the TVA can be swiftly tuned simply by setting the vacuum pressure in the beam element of the TVA to maximise the vibration power absorbed by the TVA itself. This is a rather important finding, since it provides a way to tune online the TVA without the need to measure the overall flexural vibration of the hosting structure; in this case of the plate. This finding complies with similar outcomes obtained for TVA made with a shunted coil-magnet seismic transducer [23] and with a shunted piezoelectric transducer [48], [49]. Indeed it is expected that, as proposed in [48], [49] the self-tuning can be conveniently implemented with a model-free extremum seeking control algorithm [50], [51], [52], [53], [54].

4 SPECTRA OF VIBRATION RESPONSE AND POWER ABSORBED

The spatially averaged flexural vibration of the plate and the vibration absorbed by the TVA are now analysed in the frequency domain with respect to the spectrum of the plate flexural kinetic energy and the spectrum of the vibration power absorbed by the TVA, which were defined in Eqs. (1), (2). The black line in Figure 5a shows that, in the 20 to 150 Hz frequency range, the spectrum of the flexural kinetic energy of the panel without TVA is characterised by 7 resonance peaks, which are well separated from each other. Hence, at each frequency, the response is controlled by the resonant response of a specific flexural mode of the plate. The blue line shows that, when the plate is equipped with the TVA set to maximise the vibration power absorption in the $\Delta\omega_1 = 14$ Hz bandwidth centred at the nominal resonance frequency of the first flexural mode, $\omega_1 = 32$ Hz, the first resonance peak is replaced by the typical double peaks generated by vibration absorbers. The two peaks have equal amplitude, which indicates the TVA is optimally tuned [17], [18], [19], [20], [21], [22]. Indeed, the amplitude of the two peaks is about 18 dB lower than that of the single peak for the plain panel.

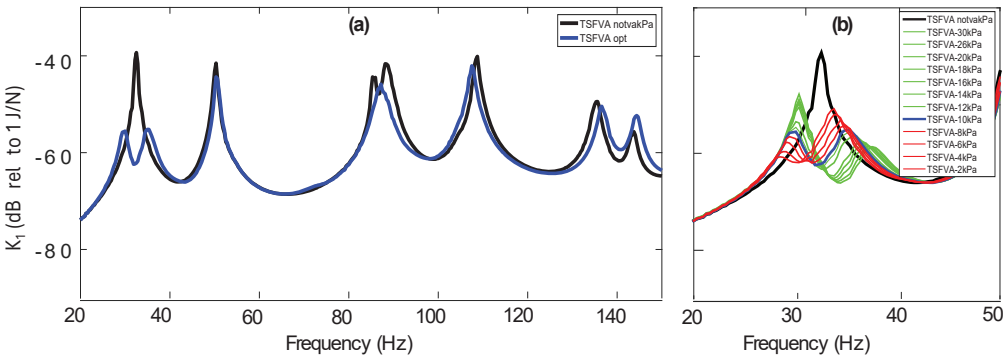

Figure 5: (a) Time-averaged total flexural kinetic energy of the plate (black line) and plate with the vibration absorber optimally tuned (blue line). (b) Magnified plot in the vicinity of the target resonance frequency for the cases where the vibration absorber is under-tuned (green lines), optimally tuned (blue line) and over-tuned (red lines)

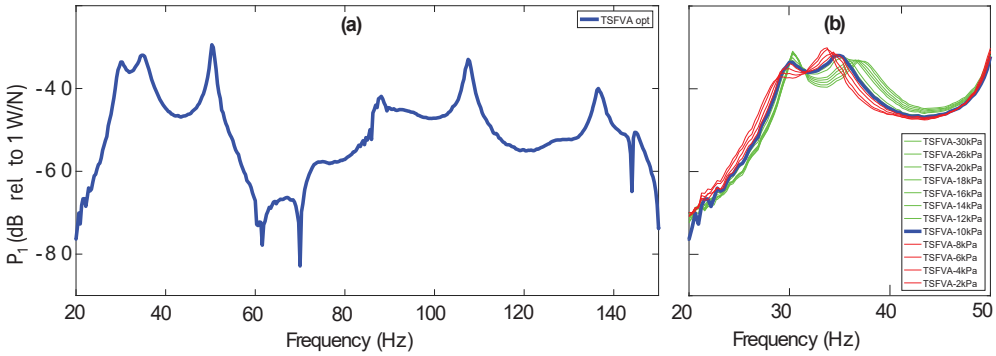

Figure 6: (a) Time-averaged vibration power absorbed by the optimally tuned vibration absorber mounted on the plate (blue line). (b) Magnified plot in the vicinity of the target resonance frequency for the cases where the vibration absorber is under-tuned (green lines), optimally tuned (blue line) and over-tuned (red lines)

The blue line in Figure 6a shows that the spectrum of the vibration power absorbed by the TVA has a wide-band pick centred at $\omega_1 = 32$ Hz, which is characterised by two apices. This confirms that indeed there is a significant vibration absorption effect from the resonant response of the first flexural mode of the plate. The spectrum shows narrowband peaks at the higher resonance frequencies of the plate, indicating significant vibration absorptions at these frequencies too. As discussed in Ref. [47], the dynamic response of the TVA made with the in-vacuo beam element can be modelled in terms of a base and seismic mass which are connected via a spring and damper. At the fundamental resonance frequency, the two masses are characterised by large counter-vibrations such that damper effectively "pumps" vibration energy from the base vibration. At higher frequencies above the fundamental resonance frequency, the seismic mass vibrates progressively less and becomes a sort of sky-hook reference. Hence the damper still produces an energy pumping effect, which however is controlled only by the motion of the base mass and thus it is bound to be relatively large at resonance frequencies of the hosting structure only. This explains why, there is a somewhat large vibration absorption at higher resonance frequencies of the plate structure. Indeed, the large resonant vibrations enhance the vibration of the base mass such that the damper effectively absorbs energy.

To conclude these analyses, the graphs in Figure 5b and 6b show the magnified spectra of the flexural kinetic energy and vibration power absorption in the vicinity of the first resonance frequency. Here the spectra are reported for the cases where the vibration absorber is under-tuned (green lines), optimally tuned (blue line) and over-tuned (red lines). The graphs clearly show how the optimally tuned TVA produces the equal amplitude double peak effect, whereas the under-tuned TVA is characterised by a small-large pair of peaks and the over-tuned TVA is characterised by a large-small pair of peaks [47].

5 CONCLUSIONS

This paper has studied the tuning and vibration control effects of a beam-like TVA made with a beam element mounted to a middle post, which is formed by a structured fabric encased in a deflated plastic bag. Two tuning principles have been investigated, which rely on a "global cost function" given by the minimisation of the plate total flexural kinetic energy, and a "local cost function", based on the maximization of the vibration power absorbed by the TVA. The study has shown that the global cost function is characterised by an inverse bell shape whereas the local cost function has a bell shape with respect to the vacuum pressure in the in the beam-like element of the TVA. The minimum and maximum values of the two functions occur at the same level of vacuum. Hence the local cost function can be effectively used to tune the absorber without the need of complex sensing arrangements that detect the vibration of the whole hosting structure. The study has also demonstrated that the proposed TVA can generate reductions of the order of 18 dB of the resonance peak of the target mode.

ACKNOWLEDGEMENTS

This work was funded by the European Union under NextGenerationEU. PRIN 2022 Prot. n. 20223X5S37_001.

REFERENCES

[1] F. J. Fahy and P. Gardonio, *Sound and Structural Vibration*. Oxford: Academic Press, 2007.

[2] R. S. Langley and F. J. Fahy, "High-frequency structural vibration," in *Fundamentals of Noise and Vibration*, F. J. Fahy and J. Walker, Eds., London: E. & F.N. Spon, 1998, pp. 490–529.

[3] P. Gardonio and E. Turco, "Tuning of vibration absorbers and Helmholtz resonators based on modal density/overlap parameters of distributed mechanical and acoustic systems," *Journal of Sound and Vibration*, vol. 451, pp. 32–70, Jul. 2019, doi: 10.1016/j.jsv.2019.03.015.

[4] D. Thompson, *Fundamentals of Sound and Vibration*. CRC Press, 2015.

[5] J. P. Arenas and M. J. Crocker, "Recent trends in porous sound-absorbing materials," *J. Sound Vib.*, vol. 44, pp. 12–17, 2010.

[6] M. J. Brennan and N. S. Ferguson, "Vibration control," in *Advanced Applications in Acoustics, Noise and Vibration*, First., F. Fahy and J. Walker, Eds., London: CRC Press, 2004, p. 656.

[7] C. R. Fuller, S. J. Elliott, and P. A. Nelson, *Active Control of Vibration*. Academic, 1996.

[8] R. L. Clark, W. R. Saunders, and G. P. Gibbs, *Adaptive Structures (1st ed.)*. New York: John Wiley and Sons Inc., 1998.

[9] S. J. Elliot, *Signal processing for active control*. London: Academic Press, 2000.

[10] S. O. R. Moheimani and A. J. Fleming, *Piezoelectric transducers for vibration control and damping*. in Advances in industrial control. London: Springer, 2006.

[11] C. Hansen, S. Snyder, X. Qiu, L. Brooks, and D. Moreau, *Active Control of Noise and Vibration*. CRC Press, 2012.

[12] A. Preumont, *Vibration control of active structures (3rd ed.)*. Berlin: Springer-Verlag, 2011.
[13] P. Gardonio, "Review of active techniques for aerospace vibro-acoustic control," *J. Aircr.*, vol. 39, pp. 206–14, 2002, doi: 10.2514/2.2934.
[14] S. J. Elliott, "A review of active noise and vibration control in road vehicles," 2008.
[15] P. Gardonio, *Active Noise Control 293 in Encyclopedia of Aerospace Engineering*. Wiley, 2010.
[16] H. Frahm, "Device for damping vibrations of bodies," US989958A
[17] J. Ormondroyd and J. P. Den Hartog, "The theory of the dynamic vibration absorber," *ASME Journal of Applied Mechanics*, vol. 50, pp. 9–22, 1928.
[18] J. E. Brock, "A note on the damped vibration absorber," *J. Appl. Mech.*, vol. 3, p. A284, 1946, doi: 10.1115/1.4009588.
[19] J. P. Den Hartog, *Mechanical vibrations*. in Dover books on engineering. New York: Dover Publications, 1985.
[20] J. B. Hunt, *Dynamic vibration absorbers*. London: Mechanical Engineering Publications, 1979.
[21] D. J. Inman, *Engineering Vibration*, vol. vol 621. Prentice-Hall, 1994.
[22] D. J. Mead, *Passive vibration control*. Chichester: John Wiley & sons, 2000.
[23] P. Gardonio, E. Turco, A. Kras, L. D. Bo, and D. Casagrande, "Semi-active vibration control unit tuned to maximise electric power dissipation," *Journal of Sound and Vibration*, vol. 499, p. 116000, May 2021, doi: 10.1016/j.jsv.2021.116000.
[24] S. H. Crandall and W. D. Mark, *Random vibration in mechanical systems*. New York: Academic Press, 1963. Accessed: Mar. 29, 2021. [Online]. Available: http://books.google.com/books?id=Q6JRAAAAMAAJ
[25] Y. Iwata, "On the construction of the dynamic vibration absorber," *Jpn. Soc. Mech. Eng.*, vol. 820, pp. 150–2, 1982.
[26] J. Q. Sun, M. R. Jolly, and M. A. Norris, "Passive, Adaptive and Active Tuned Vibration Absorbers—A Survey," *Journal of Vibration and Acoustics*, vol. 117, no. B, pp. 234–242, Jun. 1995, doi: 10.1115/1.2838668.
[27] O. Nishihara and T. Asami, "Closed-Form Solutions to the Exact Optimizations of Dynamic Vibration Absorbers (Minimizations of the Maximum Amplitude Magnification Factors)," *Journal of Vibration and Acoustics*, vol. 124, no. 4, pp. 576–582, Oct. 2002, doi: 10.1115/1.1500335.
[28] S. Krenk, "Frequency analysis of the tuned mass damper," *J. Appl. Mech.*, vol. 72, pp. 936–42, 2005, doi: 10.1115/1.2062867.
[29] P. Bisegna and G. Caruso, "Closed-form formulas for the optimal pole-based design of tuned mass dampers," *J. Sound Vib.*, vol. 331, pp. 2291–314, 2012, doi: 10.1016/j.jsv.2012.01.005.
[30] S. Krenk and J. Høgsberg, "Equal modal damping design for a family of resonant vibration control formats," *J. Vib. Control*, vol. 19, pp. 1294–315, 2012, doi: 10.1177/1077546312446796.

[31] M. Zilletti, S. J. Elliott, and E. Rustighi, "Optimisation of dynamic vibration absorbers to minimise kinetic energy and maximise internal power dissipation," *Journal of Sound and Vibration*, vol. 331, no. 18, pp. 4093–4100, Aug. 2012, doi: 10.1016/j.jsv.2012.04.023.
[32] Y. Wang, L. Li, D. Hofmann, J. E. Andrade, and C. Daraio, "Structured fabrics with tunable mechanical properties," *Nature*, vol. 596, pp. 238–43, 2021, doi: 10.1038/s41586-021-03698-7.
[33] E. Rustighi, P. Gardonio, S. Baldini, C. Malacarne, and M. Perini, "Vibration response of in-vacuo tuneable structured fabrics," *J. Vib. Control*, 2024, doi: 10.1177/10775463241245251.
[34] J. Engel and C. Liu, "Creation of a metallic micromachined chain mail fabric," *J. Micromech. Microeng.*, vol. 17, pp. 551–6, 2007, doi: 10.1088/0960-1317/17/3/018.
[35] M. A. Wijnhovena and A. Moskvin, "Digital replication and reconstruction of mail armour," *J. Cult. Herit.*, vol. 45, pp. 221–33, 2020, doi: 10.1016/j.culher.2020.04.010.
[36] A. J. Liu and S. R. Nagel, "Jamming is not just cool anymore," *Nature*, vol. 396, pp. 21–22, 1998, doi: 10.1038/23819.
[37] D. Levine, *Jamming and Rheology: Constrained Dynamics on Microscopic and Macroscopic Scales*. CRC Press Taylor & Francis Group, 2001.
[38] J. Liu and S. R. Nagel, *Jamming and Rheology: Constrained Dynamics on Microscopic and Macroscopic Scales*. Taylor & Francis, 2001.
[39] C. S. O'Hern and L. E. Silbert, "Jamming at zero temperature and zero applied stress: the epitome of disorder"," *Phys. Rev. E*, vol. 68, 2003, doi: 10.1103/PhysRevE.68.011306.
[40] R. P. Behringer and B. Chakraborty, "The physics of jamming for granular materials: a review," *Rep. Prog. Phys.*, vol. 82, 2018, doi: 10.1088/1361-6633/aadc3c.
[41] H. Jaeger, "Celebrating Soft Matter's 10th anniversary: toward jamming by design," *Soft Matter*, vol. 11, p. 12, 2015, doi: 10.1039/C4SM01923G.
[42] J. C. Snowdon and M. A. Nobile, "Beamlike dynamic vibration absorbers," *Acustica*, vol. 44, pp. 98–108, 1980.
[43] P. Gardonio, E. Rustigh, S. Baldini, C. Malacarne, and M. Perini, "In-vacuo adaptive beam element for vibration control," *Mech. Syst. Signal Process.*, vol. 224, 2025, doi: 10.1016/j.ymssp.2024.112089.
[44] D. Bi, J. Zhang, B. Chakraborty, and R. P. Behringer, "Jamming by shear," *Nature*, vol. 480, pp. 355–8, 2011, doi: 10.1038/nature10667.
[45] A. V. Dyskin, Y. Estrin, A. J. Kanel-Belov, and E. Pasternak, "A new concept in design of materials and structures: assemblies of interlocked tetrahedron-shaped elements," *Scr. Mater.*, vol. 44, pp. 2689–94, 2001, doi: 10.1016/S1359-6462(01)00968-X.
[46] A. V. Dyskin, E. Pasternak, and Y. Estrin, "Mortarless structures based on topological interlocking," *Front. Struct. Civ. Eng.*, vol. 6, pp. 188–97, 2012, doi: 10.1007/s11709-012-0156-8.
[47] P. Gardonio, L. Ortis, E. Rustighi, C. Malacarne, and M. Perini, "Multi-resonant TVA formed by a tree of deflated composite beams with core structured fabrics," *Smart Mater. Struct.*, vol. 34, no. 1, p. 015039, Jan. 2025, doi: 10.1088/1361-665X/ad9c07.
[48] G. Konda Rodrigues, P. Gardonio, L. Dal Bo, and E. Turco, "Piezoelectric patch vibration control unit connected to a self-tuning RL-shunt set to maximise electric power

absorption," *Journal of Sound and Vibration*, vol. 536, p. 117154, Oct. 2022, doi: 10.1016/j.jsv.2022.117154.

[49] P. Gardonio, G. Konda Rodrigues, L. Dal Bo, and E. Turco, "Extremum seeking online tuning of a piezoelectric vibration absorber based on the maximisation of the shunt electric power absorption," *Mechanical Systems and Signal Processing*, vol. 176, p. 109171, Aug. 2022, doi: 10.1016/j.ymssp.2022.109171.

[50] I. S. Morosanov, "Method of extremum control," *Automatic and remote control*, vol. 18, pp. 1077–1092, 1957.

[51] I. I. Ostrovskii, "Extremum regulation," *Automatic and remote control*, vol. 18, p. 1957, 907 900.

[52] M. Krstić and H.-H. Wang, "Stability of extremum seeking feedback for general nonlinear dynamic systems," *Automatica*, vol. 36, no. 4, pp. 595–601, Apr. 2000, doi: 10.1016/S0005-1098(99)00183-1.

[53] M. Krstić, "Performance improvement and limitations in extremum seeking control," *Systems & Control Letters*, vol. 39, no. 5, pp. 313–326, Apr. 2000, doi: 10.1016/S0167-6911(99)00111-5.

[54] D. E. Casagrande, P. Gardonio, and G. Konda Rodrigues, "Tonal vibration control with a self-tuning absorber employing the extremum seeking algorithm," *Mechanical Systems and Signal Processing*, vol. 211, p. 111254, Apr. 2024, doi: 10.1016/j.ymssp.2024.111254.

XI ECCOMAS Thematic Conference on Smart Structures and Materials - SMART 2025
M. Krommer, M. Nader and M. Schagerl (Eds)

Received: 2 April 2025 / Revised: 28 August 2025 / Accepted: 10 September 2025
© The Author(s) 2025

A Modeling Study of Elastic Properties of Structured Fabrics under Vacuum Pressure

Emiliano Rustighi, Davide Raffaele, Paolo Gardonio, Ciro Malacarne, Matteo Perini

Abstract. Structured fabrics are compliant, engineered textile materials that can be designed using interlinked truss-like grain elements. Examples include traditional knitted sheets and chainmail armours, which are characterised by negligible bending stiffness in their unconfined state. Recent research, however, has shown that when subjected to confinement pressure, these structures exhibit increased stiffness, transforming them into cohesive structural materials and structures. This unique behaviour enables the development of lightweight, tuneable, and adaptive fabrics for a range of advanced applications, including wearable exoskeletons, haptic systems, and devices for passive and semi-active vibration and noise control, such as tuneable vibration absorbers. In this study, we present a homogenized physical model that describes the variation in elastic properties of in-vacuo structured fabrics with confinement pressure. Inspired by models for granular media, the proposed improved approach incorporates the effects of grain geometry. The model is then applied to predict the resonant response of finite beam structures. Predictions are validated through experimental results, demonstrating the model's capability to capture the mechanical adaption of the in-vacuo structured fabrics with confinement pressure.

Key words: In-vacuo structured fabrics, homogenized elastic properties

Emiliano Rustighi & Davide Raffaele
Dipartimento di Ingegneria Industriale, Universitá degli Studi di Trento, Via Sommarive 9, 38123 Povo, Italy
e-mail: emiliano.rustighi@unitn.it

Paolo Gardonio
Dipartimento Politecnico di Ingegneria e Architettura, Universitá degli Studi di Udine, Via delle Scienze 206, 33100 Udine, Italy, e-mail: paolo.gardonio@uniud.it

Ciro Malacarne & Matteo Perini
ProM Facility, Trentino Sviluppo S.p.A., Via Fortunato Zeni 8, 38068 Rovereto, Italy
e-mail: ciro.malacarne@trentinosviluppo.it

1 INTRODUCTION

Traditional knitted fabrics are made from continuous flexible materials, such as fibres or wires which are interlaced to form two- or three-dimensional fabrics [1]. While 3D woven fabrics offer enhanced structural integrity, they still present a large compliance and they are not yet usable for engineering applications. Recent digital fabrication techniques, such as 3D printing and computational modelling, have enabled the creation of complex textile geometries with tailored mechanical responses [2, 3]. In particular, structured fabrics are composed of a network of rigid elements linked together in an established pattern, similar to medieval chain armour made by linkages of metal rings. These structures show quite a loose bending stiffness at ambient pressure. Imposing a confinement pressure on structured fabrics augments their bending stiffness. These are referred to as tunable structured fabrics (TSF) due to the capability of adjusting their bending stiffness through varying the applied confinement pressure.

A breakthrough in TSF was demonstrated by Wang et al. [4], who developed layered chain mail sheets composed of interlocking 3D particles. These fabrics exhibit dramatic stiffness modulation, up to a 25-fold increase, when subjected to external pressure, transitioning from a flexible state to a rigid, jammed configuration. Discrete-element simulations further revealed that such systems follow a jamming phase transition akin to conventional granular media, but with enhanced tunability due to their designed microstructures.

Recent studies have demonstrated the potential of tunable structured fabrics in adaptive mechanical systems, particularly for vibration mitigation and dynamic stiffness control. Rustighi et al. [5, 6] explored how vacuum-induced jamming in 3D-printed chain mails alters bending stiffness and damping properties, with experimental characterization under four- and six-point bending setups. The study revealed that compressive frictional forces and geometric interlocking significantly enhance stiffness, positioning these materials favourably in Ashby diagrams for lightweight adaptive applications. Building on this, the dynamic response of beam-like specimens with single- and multi-layered fabrics was investigated, showing that vacuum pressure effectively tunes bending stiffness and consequently resonance frequencies, though energy dissipation remained low due to minimal inter-particle friction post-jamming.

Further applications to vibration mitigation were introduced by Gardonio et al. [7], who developed an adaptive beam element with hollow truss-like particles, functioning as a tunable vibration absorber (TVA) via vacuum-modulated flapping modes. The study highlighted the role of particle geometry and stacking layers in defining tunable bandwidths, with non-convex contacts enabling broader stiffness ranges. Similarly, they proposed a multi-resonant TVA using vacuum-jammed structured fabrics [8]. The absorber, composed of a tree of deflated composite beams, demonstrated a tunable frequency band of 8 Hz (5–80 kPa vacuum), reducing plate vibrations by 10–20 dB. Together, these works underscore the versatility of structured fabrics in real-time adaptive systems, bridging granular jamming physics with practical vibration control solutions.

The concept of jamming, where disordered systems transition from fluid-like to solid-like states under compression or shear, has been extensively studied in granular and soft matter

physics [9, 10]. Frictionless soft spheres, for instance, exhibit an isostatic (marginally stable) state at the jamming point, where mechanical properties scale with the distance to this critical transition [9]. Recent work has extended this understanding to frictional and non-spherical particles, demonstrating that contact number and packing geometry play crucial roles in determining jamming behaviour [10]. The basic principles underlying the modelling of granular materials can significantly aid in the understanding of tuneable structured materials. Consequently, within the scope of this paper, we present a physical model aimed at elucidating the relationship between varying levels of confinement pressure and the material's stiffness.

2 TUNEABLE STRUCTURED FABRICS

2.1 Geometry of the Structured Fabric

The structured fabric design draws inspiration from medieval chain mail, where individual rigid structures are linked to form flexible garments. These fabrics are characterized by the geometry of the rigid base element, i.e. the grain, and the lattice arrangement of these elements. Figure 1 depicts the rendering of the base element and its connections to other elements within the fabric. The base elements feature a truss structure composed of curved beams arranged to create an octahedral sphere. They are connected in a lattice formation. Each element is a closed structure, produced and interconnected through rapid prototyping, as detailed in the subsequent section, thereby eliminating discontinuities from welding, gluing, or plastic deformation. Although previous research by the authors has examined various grain shapes, only the rounded octahedral sphere shape was analyzed in this instance, as its smooth exterior provides more consistent contact between grains. The rounded octahedral shape was explored in four distinct dimensions, as shown in Figure 1. Two outer diameters, $D = 6$ mm and $D = 10$ mm, along with two truss thickness d, $d/D = 0.1$ and $d/D = 0.15$, were investigated.

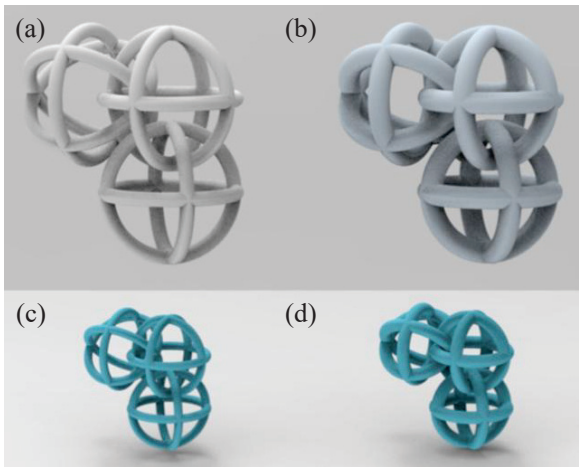

Figure 1: Rounded octahedral structured fabrics of different geometrical ratios: (a) $D = 10$ mm, $d = 0.10D$, (b) $D = 10$ mm, $d = 0.15D$, (c) $D = 6$ mm, $d = 0.10D$ and (d) $D = 6$ mm, $d = 0.15D$

2.2 Manufacturing and assembling

Structured fabrics were produced using Nylon PA12 through the HP Multi Jet Fusion (MJF) technology, a prevalent 3D printing method known for creating highly precise and durable components. MJF 3D printing is a part of the additive manufacturing technology that incorporates powder bed fusion, eliminating the need for support structures and intricate post-processing. During printing, any empty spaces are filled with unused powder, making MJF prints self-supporting. MJF excels in fabricating complex designs, permitting parts consolidation and intricate interconnected geometries, which pose challenges for other technologies. MJF allows for printing in ultra-thin layers, approximately 80 microns, resulting in low porosity and high density, providing excellent resolution and dimensional accuracy. The MJF 3D printing process produces highly isotropic parts with consistent strength across all directions. The printer used was a HP Jet Fusion 3D 4200, which has a build volume of $380 \times 284 \times 380$ mm. The samples were manufactured with extensions of about 20×8 cm. Table 1 presents the precise dimensions of each sample employed in the study. According to the supplier's data, the Nylon PA12 used for the realization of the samples has a tensile elasticity modulus of about 1800 MPa, and a part density of about 1.01 g/cm^3.

The 3D-printed fabrics are also assembled inside an airtight vacuum bag in order to obtain TSF. In this study, vacuum bags (commonly used for food preservation) have been used to wrap one or multiple layers of the prototyped structured fabrics. Up to five layers have been overlapped in this study. Thermal sealing techniques have been employed to close off the open edges, while butyl tape has been applied to ensure an airtight fit at the junction with the vacuum pipe. Consequently, a diaphragm vacuum pump (KNF NEUBERGER UN726 TTP) was linked to the vacuum bag through a pneumatic conduit, incorporating a pneumatic valve and an analogue vacuum gauge.

2.3 Vibration Response of Tuneable Structured Fabrics

Each sample has been constrained as a beam in a simply supported configuration. The clamps were covered with thin layers of foam, in order to optimize the contact surface area between the clamps and to have an accurate specimen placement within the setup. A shaker applied excitation to the sample's midspan through a metal bar connection. A Modal Shop shaker model 2004E with a SmartAmp^{TM} Series 2100E21 amplifier provided the excitation, while a PCB Piezotronics 288D01 impedance head measured the point receptance at the excitation location. Figure 2(a) illustrates the clamping and excitation arrangement for the TSF samples. Testing was conducted under six varying confinement pressures: 5, 10, 20, 40, 60, and 80 kPa. Figure 2(b) depicts the model which has been used to analyse the testing configuration. The sample fabric can be viewed as a homogeneous, uniform beam with simply supported ends, with a harmonic force applied at its midspan via a bar which is modeled as an additional point mass m.

The measured receptances for the sample fabrics with grains with $D = 10$mm and $D/d = 0.15$ are depicted in Figure 2(c). The analysis shows that, within the relevant frequency range,

Table 1: Dimensions and weight of the TSF samples

Shape	Layer	Weight[g]	Length[cm]	Width [cm]	Depth[cm]
$D = 6$ mm	1	9.17	19	6.5	0.6
$d/D = 0.1$	2	18.34	19.5	6.5	1
	3	27.51	20	7	1.5
	4	36.68	20	7	2
	5	45.85	20.5	7	2.5
$D = 6$ mm	1	25.6	23.0	8.0	0.60
$d/D = 0.15$	2	51.2	22.0	9.5	1.25
	3	76.8	22.0	9.5	1.75
	4	102.4	22.5	9.5	2.25
	5	128	23.0	9.5	2.50
$D = 10$ mm	1	18.35	22.5	7.5	1
$d/D = 0.1$	2	36.7	22.5	7.5	1.75
	3	55.05	23	7.25	2.5
	4	73.4	23	7.5	3.25
	5	91.75	23	7.5	4
$D = 10$ mm	1	41.1	22.5	7.75	1
$d/D = 0.15$	2	74	19.5	9	1.75
	3	111	20.5	8.5	2.5
	4	148	21.75	8	3.25
	5	165.5	23	7.75	4

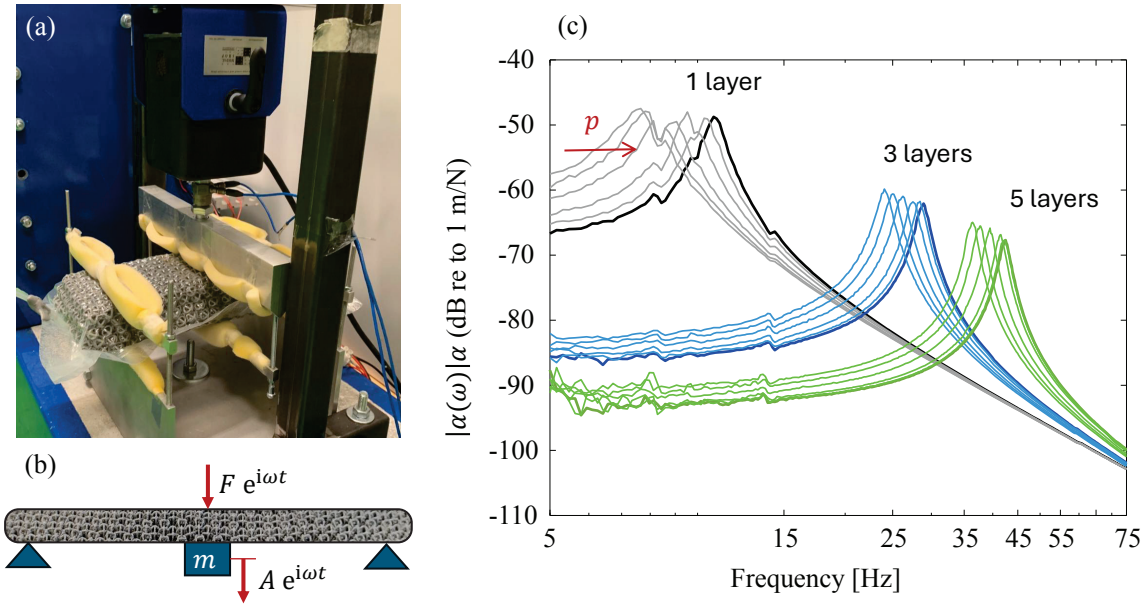

Figure 2: Experimental setup (a), equivalent model (b) and exemplary mobility responses of samples with $D = 10$mm and $D/d = 0.15$ (c)

the system behaves as a single degree-of-freedom system. The confinement pressure modifies the effective Young's modulus of the structured fabrics, i.e. an increase in the confinement pressure p raises the resonant frequency.

3 MODEL OF THE VACUUM CONTROLLED RESPONSE

This section proposes a model illustrating the relationship between Young's modulus and confinement pressure. The subsequent section outlines the sphere-pack model as sourced from soil dynamics literature. The following subsection modifies the soil model for application to the TSF, while the concluding subsection evaluates the model against experimental data.

3.1 The soil sphere-pack model

To explain the dependence of the macroscale Young's modulus on the confinement pressure, a sphere-pack model that makes use of the Hertz theory can be considered [11]. This model encompasses an elementary volume made of identical spheres lined up in rows parallel to the coordinate axes, as depicted in Figure 3(a). Utilizing Hertzian contact theory [12], the stiffness of contact among two perfectly elastic spheres is formulated as

$$k_c(F) = \left[\frac{3\,E_s^2}{8(1-\nu_s^2)^2}\right]^{1/3} D^{1/3} F^{1/3} \tag{1}$$

where E_s and ν_s denote the Young's modulus and Poisson's ratio of the sphere material, D reflects the spheres'diameter, and F represents the force causing their contact. The stiffness

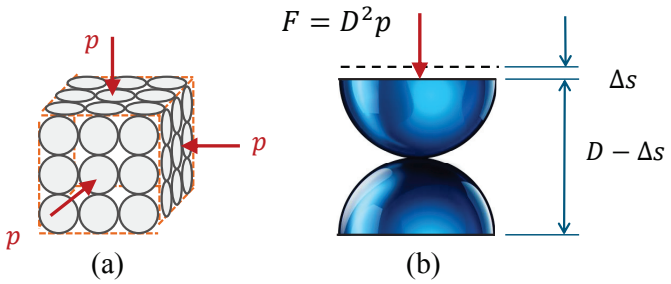

Figure 3: The soil sphere-pack model with all grain disposed in a lattice and confined by the pressure p (a) and the contact between two spheres in the elementary cell of dimension $D \times D \times D$

is evidently force-dependent in a nonlinear fashion, following a cubic root stiffening pattern. The authors suggest that this phenomenon underlies the macroscopic effect of confinement pressure-induced stiffening in a vacuum. They argue that inter-grain frictional forces are not responsible for alterations in the vibrational response, as relative sliding is minimal with small displacements. This aligns with results from a previous study which showed an absence of variation in damping ratio with confinement pressure [6].

Assuming pressure impacts the elementary cell of an equivalent isotropic, homogeneous material, modeled as a cube with side length D, the correlation between contact force F and confinement pressure p is expressed by

$$F = D^2\, p. \tag{2}$$

The compressional stiffness for a basic cube with side length D is described by $k_c = ED$, where E represents the effective Young's modulus. Consequently, the expression for the elastic modulus is derived as follows:

$$E(p) = \frac{k_c}{D} = \left[\frac{3\, E_s^2}{8(1-\nu_s^2)^2}\right]^{1/3} p^{1/3}. \tag{3}$$

The soil sphere-pack model yields a nonlinear correlation between the effective Young's modulus E and the cubic root of the confinement pressure, $p^{1/3}$. The model is also independent of the grains geometry. In fact, the grain diameter D and the truss thickness d do not appear in Equation (3).

3.2 The rigid truss-like sphere-pack model

The previous model can be adapted to TSF by considering that the contact happens between two curved beams. Equation (1) can be modified to consider the contact as occurring between two convex surfaces with a double curvature given by the diameter of the grain D and the diameter of the trusses d. Using an approximated expression for the contact curvature, the contact stiffness can be expressed as

$$k_c(F) = \left[\frac{3\, E_s^2}{4(1-\nu_s^2)^2}\right]^{1/3} \left(\frac{1}{D} + \frac{1}{d}\right)^{-1/3} F^{1/3}. \tag{4}$$

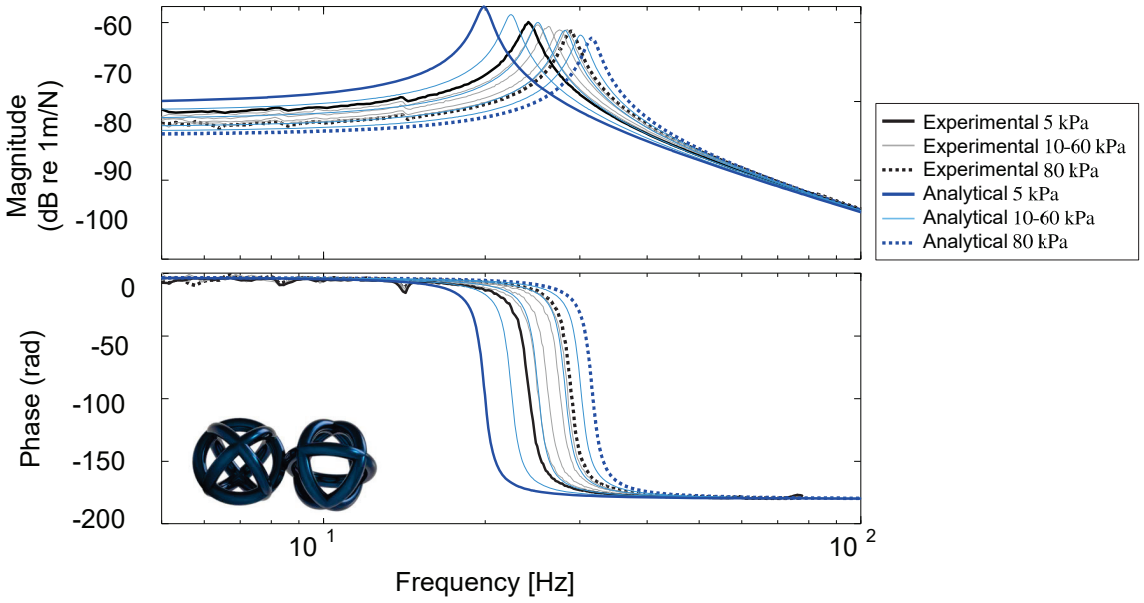

Figure 4: Measured and simulated point receptance of the sample made with five layers of the tuneable structured fabric with $D = 10$ mm and $d/D = 0.10$

Subsequently, the effective Young's modulus is determined as

$$E(p) = \frac{k_c}{D} = \left[\frac{3\,E_s^2}{8(1-\nu_s^2)^2}\right]^{1/3} \left(1 + \frac{D}{d}\right)^{-1/3} p^{1/3}. \tag{5}$$

The final evaluation of Young's modulus serves as a basis for calculating the point mobility of a simply supported beam excited at its midpoint under confinement pressures of 5, 10, 20, 40, 60, and 80 kPa. The outcomes derived from the model for a specimen with five layers, where $D = 10$ mm and $d/D = 0.1$, are presented in Figure 4 alongside the empirical results. In this configuration, there is a notable correspondence, though the model slightly over-predicts the stiffness variation with confinement pressure compared to empirical observations.

Figure 5 provides a comparison of resonant frequency shifts from both experimental measurements and the rigid-truss sphere-pack model. Concerning the average natural frequency, the model effectively delineates the stiffness variation with confinement pressure, displaying high precision for structured materials with $d/D = 0.1$, while underestimating shifts in the central resonant frequency for those with $d/D = 0.15$. As for the bar sizes and thereby the tuneability range, the model accurately represents TSF with smaller grains ($D = 6$ mm) but overestimates the adaptability range for larger grains ($D = 10$ mm).

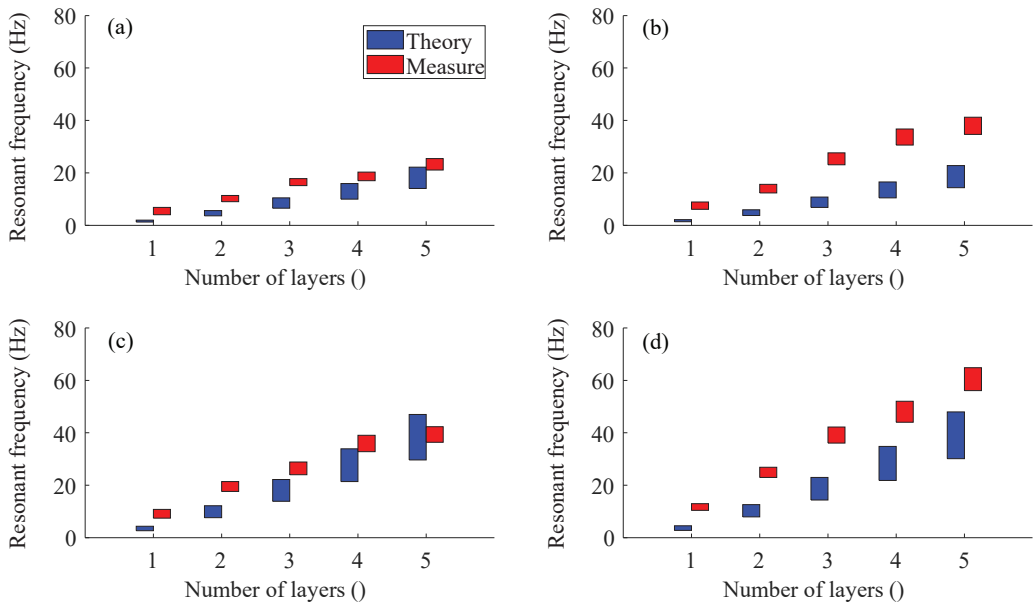

Figure 5: Measured and simulated ranges of resonant frequency tuneability for confinement pressure from 5 to 80 kPa: (a) $D = 6$ mm, $d = 0.10D$, (b) $D = 6$ mm, $d = 0.15D$, (c) $D = 10$ mm, $d = 0.10D$ and (d) $D = 10$ mm, $d = 0.15D$

4 CONCLUSIONS

A homogenized physical model that describes the variation in elastic properties of in-vacuo structured fabrics with confinement pressure has been presented. The model incorporates the effects of grain geometry and contact topology. The proposed approach has been applied to predict the resonant response of finite beam structures realized with tunable structured fabrics. Predictions have been validated through experimental results, demonstrating the model's capability to capture the mechanical adaptation of the structured fabrics. The relationship between Young's modulus and the cubic root of the confinement pressure is derived, displaying high precision for structured materials with $D = 6$ mm, while underestimating shifts in the central resonance frequency for those with $d/D = 0.15$. This research provides a scientific understanding of the adaptability of tuneable structured fabrics, suggesting an initial strategy toward the engineering of granular jamming mechanics for effective vibration control applications.

ACKNOWLEDGEMENTS

Funded by the European Union - Next Generation EU, Mission 4, Component 2 - CUP E53D23002640006.

REFERENCES

[1] X. Chen, L. W. Taylor, and L.-J. Tsai, "An overview on fabrication of three-dimensional woven textile preforms for composites," *Textile Research Journal*, vol. 81, no. 9, pp. 932–944, 2011.

[2] K. Chatterjee and T. K. Ghosh, "3d printing of textiles: potential roadmap to printing with fibers," *Advanced Materials*, vol. 32, no. 4, p. 1902086, 2020.

[3] M. A. Wijnhoven and A. Moskvin, "Digital replication and reconstruction of mail armour," *Journal of Cultural Heritage*, vol. 45, pp. 221–233, 2020.

[4] Y. Wang, L. Li, D. Hofmann, J. E. Andrade, and C. Daraio, "Structured fabrics with tunable mechanical properties," *Nature*, vol. 596, no. 7871, pp. 238–243, 2021.

[5] E. Rustighi, P. Gardonio, S. Baldini, C. Malacarne, and M. Perini, "Material characterisation of deflated structured fabrics," *Aerotecnica Missili & Spazio*, 2024. [Online]. Available: https://doi.org/10.1007/s42496-024-00228-2

[6] E. Rustighi, P. Gardonio, S. Baldini, C. Malacarne, and M. Perini, "Vibration response of in-vacuo tuneable structured fabrics," *Journal of Vibration and Control*, vol. 31, no. 1-2, pp. 4–23, 2025. [Online]. Available: https://doi.org/10.1177/10775463241245251

[7] P. Gardonio, L. Ortis, E. Rustighi, C. Malacarne, and M. Perini, "Multi-resonant tva formed by a tree of deflated composite beams with core structured fabrics," *Smart Materials and Structures*, vol. 34, no. 1, p. 015039, dec 2024. [Online]. Available: https://dx.doi.org/10.1088/1361-665X/ad9c07

[8] P. Gardonio, E. Rustighi, S. Baldini, C. Malacarne, and M. Perini, "In-vacuo adaptive beam element for vibration control," *Mechanical Systems and Signal Processing*, vol. 224, p. 112089, 2025. [Online]. Available: https://www.sciencedirect.com/science/article/pii/S0888327024009877

[9] M. van Hecke, "Jamming of soft particles: geometry, mechanics, scaling and isostaticity," *Journal of Physics: Condensed Matter*, vol. 22, no. 3, p. 033101, 2009.

[10] R. P. Behringer and B. Chakraborty, "The physics of jamming for granular materials: a review," *Reports on Progress in Physics*, vol. 82, no. 1, p. 012601, 2018.

[11] J. E. White, *Underground sound: Application of seismic waves*. Elsevier, 1983.

[12] V. L. Popov *et al.*, *Contact mechanics and friction*. Springer, 2010.

XI ECCOMAS Thematic Conference on Smart Structures and Materials - SMART 2025
M. Krommer, M. Nader and M. Schagerl (Eds)

Received: 22 April 2025 / Revised: 31 August 2025 / Accepted: 10 September 2025
© The Author(s) 2025

Bending Performance of Polymer Auxetic to Non-Auxetic Lattice Gradient Beams

Neeraj Sharma, Kshitij Kumar Yadav

Abstract. Mechanical metamaterials have exceptional mechanical properties and tunable responses. Among these, auxetic metamaterials, characterized by a negative Poisson's ratio, exhibit superior energy absorption, enhanced fracture toughness, and increased shear modulus. Their ability to undergo self-densification under compression makes them particularly suitable for energy absorption applications. However, in bending scenarios, where both compression and tension zones co exist, auxetic architectures alone are insufficient to effectively counteract the combined effects of compression and tension. Incorporating non-auxetic architectures in the tension zones has been demonstrated to significantly enhance the mechanical performance of lattice beams. This study investigates the synergistic combination of auxetic and non-auxetic designs to optimize the mechanical properties of lattice structures under bending loads. The integration of auxetic and non-auxetic designs is essential to address the varying load conditions along the depth of the cross-section. To achieve this, a gradient-based approach is employed, transitioning the architecture from auxetic at the top to non-auxetic at the bottom of the lattice beam. Results demonstrate that these gradient beams exhibit superior mechanical performance compared to beams with purely auxetic, non-auxetic, or cubic lattice configurations. The findings of this study provide valuable insights for the design of robust lattice beams with potential applications in impact absorption, biomedical engineering, and other advanced fields.

Key words: Auxetic Lattice, Meta-material, Bending Performance, Energy Absorption

1 INTRODUCTION

Metamaterials are a new class of engineered materials that exhibit mechanical properties not typically found in conventional materials [1, 2]. One notable example is auxetic metamaterials, which display a negative Poisson's ratio [3, 4, 5]. Traditionally, the high cost and complexity of large-scale production limited the use of metamaterials in practical applications. However, recent advancements in additive manufacturing technologies have significantly improved the ability to design and fabricate complex material structures across various length scales, from

Neeraj Sharma & Kshitij Kumar Yadav
Indian Institute of Technology (BHU), Varanasi, U.P., India e-mail: neerajsharma.rs.civ22@iitbhu.ac.in

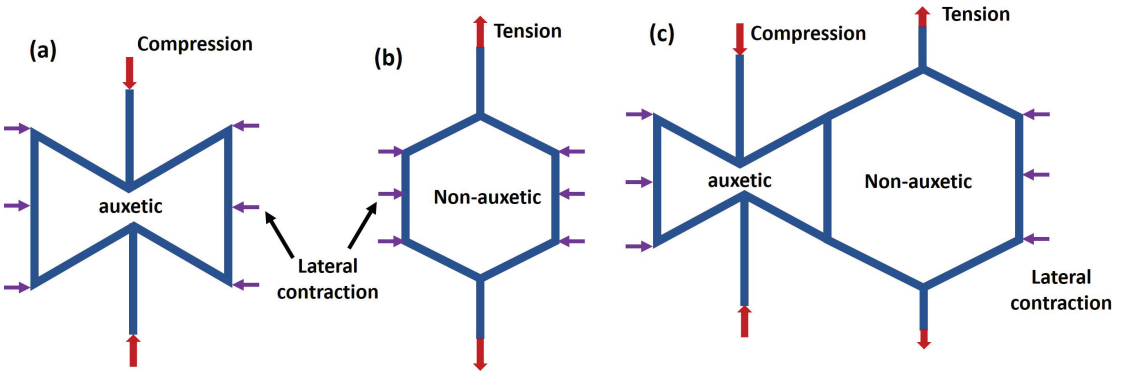

Figure 1: (a) Re-entrant auxetic architecture undergoing contraction under compression, (b) non-auxetic architecture contracting under tension, and (c) gradient architecture composed of both auxetic and non-auxetic unit cells.

nanometers to millimeters [6, 7, 8, 9, 10, 11]. Auxetic materials, due to their negative Poisson's ratio, demonstrate exceptional properties such as high impact resistance [12, 13, 14], high shear modulus [15], excellent energy absorption [16, 17, 18], and increased fracture toughness [19]. These characteristics make them promising candidates for a wide range of applications, including aerospace [20], biomedical devices [21, 22], smart sensors [23], and protective equipment [24].

Re-entrant auxetic lattices, characterized by their bending-dominated deformation behavior, have demonstrated outstanding specific energy absorption capabilities under compressive loading conditions. This enhanced performance is primarily due to the unique mechanism of self-densification that occurs when these structures are subjected to axial loads. Unlike conventional materials, auxetic lattices contract laterally when compressed, which promotes densification of the structure and leads to a substantial increase in energy absorption per unit weight of structure. Due to these advantageous properties, re-entrant auxetic lattices are increasingly being employed as core materials in sandwich panel configurations. When integrated between two face sheets, these lattices contribute to the development of lightweight structural panels with high specific energy absorption. Such panels are particularly beneficial in applications where weight reduction and impact resistance are critical, such as in aerospace structures, automotive crash protection systems, and protective gear. The ability to tailor mechanical behavior through lattice geometry further enhances the versatility and application potential of re-entrant auxetic metamaterials in advanced engineering systems.

While auxetic lattices have proven highly effective in energy absorption under compressive loading, their performance is not equally efficient in structural members subjected to combined loading conditions, such as bending. In purely compressive scenarios, the negative Poisson's ratio behavior of auxetic lattices enables significant self-densification, resulting in high specific energy absorption. However, in bending-dominated components such as beams both tensile and compressive zones develop across the depth of the cross-section. Under such conditions, the auxetic lattices alone are not sufficient to optimize energy absorption performance, particularly

in the tensile regions. To address this limitation, non-auxetic lattice architectures play a crucial role in the tensile zones of the structure shown in Figure 1. Non-auxetic materials, which expand laterally under tensile loading, can better accommodate the mechanical demands in these regions. Therefore, a combined use of auxetic and non-auxetic lattice configurations is essential to effectively manage the varying stress states induced by bending.

In this study, we propose and implement a gradient lattice design that transitions from auxetic to non-auxetic architectures along the depth of the structural cross-section. This gradient-based approach is aimed at enhancing the overall energy absorption characteristics of the lattice structure under uni-directional loading conditions. However, under reversed loading, the response may not be as advantageous, since the auxetic side would be subjected to tension while the non-auxetic side would experience compression. By tailoring the lattice geometry to match the local stress environment, the structure can achieve improved mechanical performance and energy efficiency, making it suitable for applications that require both lightweight and high resilience, such as protective panels and structural components in transportation and defense sectors.

2 Materials and methods

2.1 Gradient lattice design

In the present study, a re-entrant auxetic lattice architecture, previously investigated by [25, 26], has been adopted as the basis for the lattice design. This configuration features two characteristic angles within each unit cell, as shown in Figure 2(a), the green region highlights the characteristic angle of $75°$, while the white regions indicate the characteristic angle of $82.5°$.

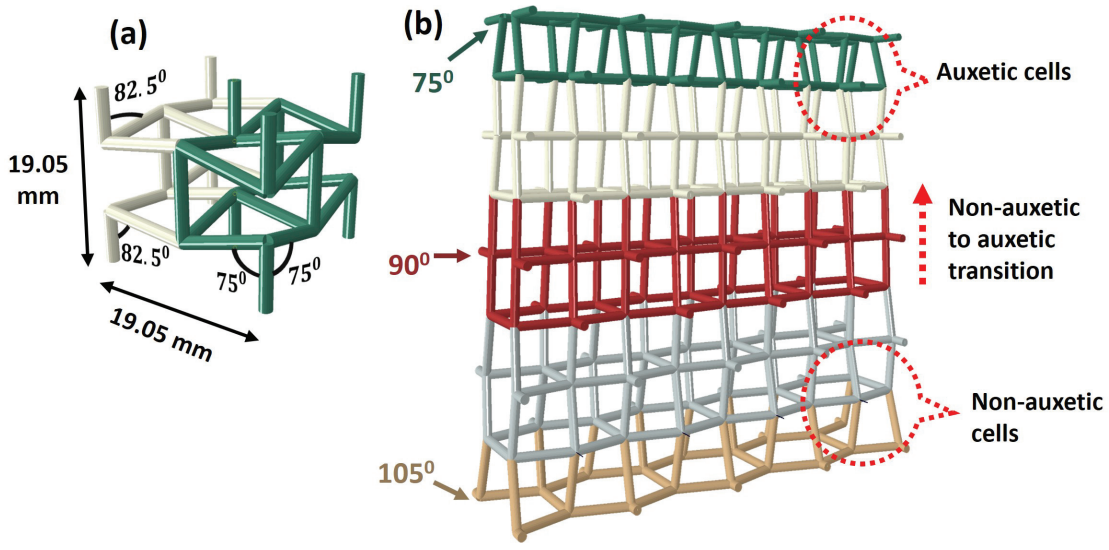

Figure 2: Geometry of the lattice unit cell and beam: (a) transitioning unit cell used in the gradient design, and (b) unit cell layer arrangement in the auxetic to non-auxetic gradient beam.

A 4×4 lattice arrangement was selected for the analysis, illustrated in Figure 2(b). A total of three gradient beams were selected, with angle ranges of $75°$–$105°$, $80°$–$100°$, and $85°$–$95°$. The angle ranges were randomly selected while ensuring the criterion that no two horizontal struts intersect with each other. The thickness of the lattice struts was adjusted to maintain a volume ratio of 5%. To study the response under combined loading conditions, the 4×4 lattice was divided into two zones: the lower 4×2 region consisting of non-auxetic unit cells, and the upper 4×2 region composed of auxetic unit cells. This gradation enables the structure to better accommodate both tension and compression along its depth.

2.2 Finite element modeling and analysis

The bending performance of the lattice beams was evaluated using finite element analysis (FEA) conducted in Abaqus/Explicit [27]. The numerical model was first validated against both experimental data and finite element results reported by [25], achieving an accuracy within 1%. The material used in the simulation is steel, with properties including a density of 7800 kg/m³, a Young's modulus (E) of 200 GPa, and a Poisson's ratio (μ) of 0.3. The plastic behavior of the steel was modeled by assigning yield stresses at different plastic strain levels: 1000 MPa at zero plastic strain, 1100 MPa at a plastic strain of 0.16, and 150 MPa at a plastic strain of 0.2.

The auxetic lattice was modeled using linear Timoshenko beam elements (B31) to capture both bending and shear deformations. A four-point bending setup was employed in accordance with ASTM C1609 standards. The simulation was performed under displacement-controlled loading, where a total displacement of 60mm was applied through discrete rigid pads located at the top surface of the beam. These loading pads were spaced at one-third of the total beam length. Support pads at the bottom were placed such that a clear distance of 26.3mm was maintained from each outer edge of the beam. With a unit cell length of 19.05mm, a total of 14 unit cells were arranged longitudinally, resulting in an overall lattice beam length of 266.7mm.

3 Results and Discussion

This section discusses the findings of the effective Young's modulus and Poisson's ratio of gradient unit cells, along with the four-point bending characteristics of gradient lattice beams.

3.1 Unit cell analysis

The effective Young's modulus and Poisson ratio of the bare unit cell were calculated using the finite element method with Abaqus/Standard. The base properties of the lattice material, i.e., steel, were taken as $E = 200$ GPa and Poisson ratio $\mu = 0.3$, as referenced in [25].

$$\mu = -\frac{\epsilon^t}{\epsilon^l} \tag{1}$$

where ϵ^t is a transverse strain and ϵ^l is a longitudinal strain. Each bare unit cell utilized 6700 beam elements (B31). The effective elastic modulus E_{22} and Poisson ratios μ_x and μ_z were evaluated by applying a 0.1 displacement in the Y direction, as shown in Figure 3 (a). All

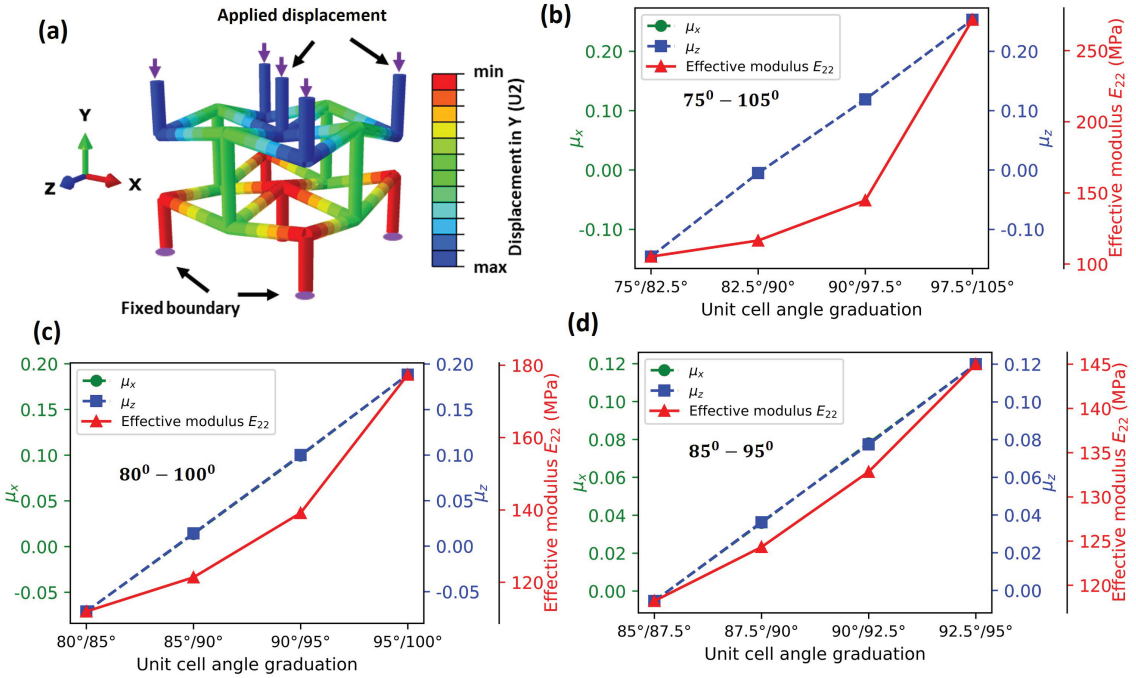

Figure 3: Unit cell analysis: (a) boundary and loading conditions applied to the unit cell model, (b) simulation results for the $75°$–$105°$ gradient unit cell, (c) results for the $80°$–$100°$ gradient unit cell, and (d) results for the $85°$–$105°$ gradient unit cell.

properties were evaluated within the linear elastic region, and material, as well as geometric nonlinearities, were ignored.

Since the unit cells are not symmetric, i.e., there is a gradual transition of angle within cells, such as $7.5°$, $5°$, and $2.5°$ for transitions of $75°/105°$, $80°/100°$, and $85°/95°$, respectively, thus the Poisson ratio in the X and Z directions is not the same. However, it can be observed in Figures 3(b), (c), and (d) that the difference in the Poisson ratio is very small, ranging from 0.25% to 6.4%. Furthermore, it can be noted that in two-angle unit cells, the maximum negative Poisson ratio is observed for angles range $75°/82.5°$, which are away from the $90°$ mark. As the cell angles approach $90°$, the cells become cubic with almost zero Poisson ratio, transitioning to non-auxetic with positive Poisson ratio. Maximum extremums are observed in the $75° - 105°$ transition (refer to Figure 3(b)), while the minimum extremum is seen in the $85° - 95°$ transition. Furthermore, the results have indicated that the uniaxial effective modulus E_{22} for auxetic cells has lower values and increases as cells transition to non-auxetic.

3.2 Bending of gradient lattice beams

The results from the four-point bending tests conducted on both purely auxetic and gradient lattice beams reveal significant differences in mechanical performance. Among the tested con-

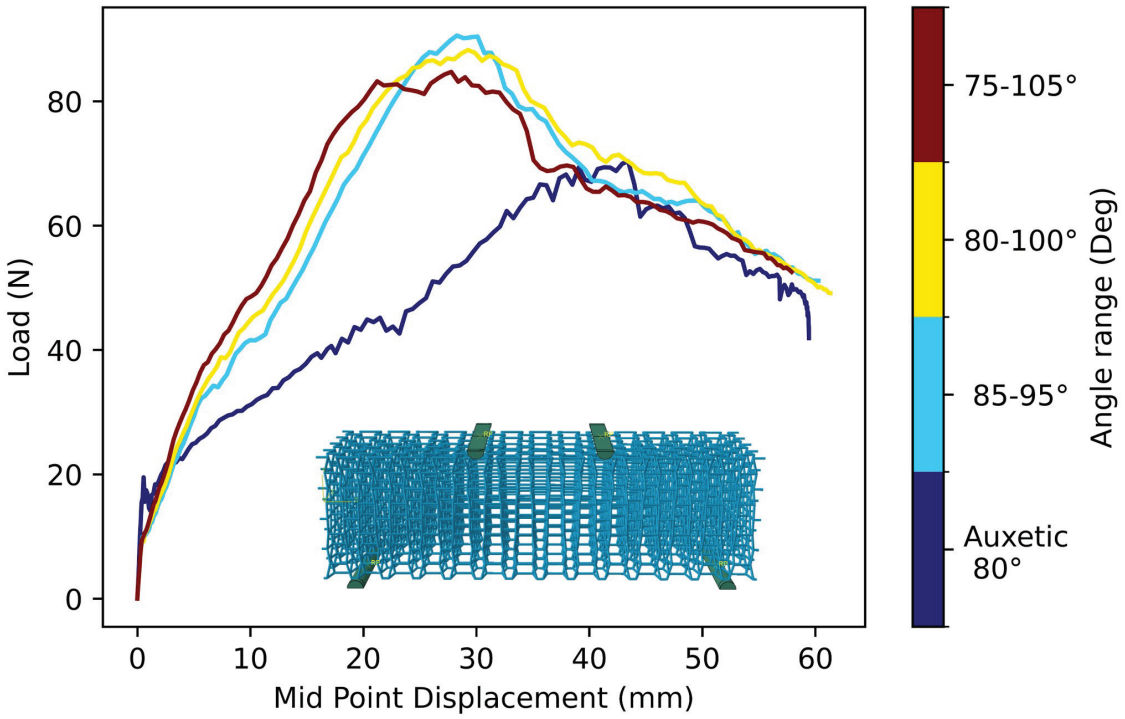

Figure 4: Load–displacement curves from four-point bending analysis for purely auxetic and gradient lattice beams.

figurations, gradient beams with transition angles of $85°$–$95°$, $75°$–$105°$, and $80°$–$100°$ demonstrated notably higher load-carrying capacities compared to the purely auxetic beams designed with a uniform angle of $80°$. The gradient configuration transitioning from $75°$ at the bottom (non-auxetic region) to $105°$ at the top (auxetic region) exhibited the highest stiffness during the initial loading phase, maintaining superior rigidity up to the peak load. This suggests that the broader gradient range provides a more efficient distribution of load and deformation along the depth of the beam, enhancing the structural performance under bending. At the peak load, however, all gradient beams exhibited a similar response, with maximum load capacities approximately 25% higher than that of the purely auxetic lattice beam as shown in Figure 4. This enhancement in performance highlights the effectiveness of introducing a gradient in unit cell geometry to optimize the mechanical behavior of lattice beams under complex loading conditions.

The specific energy absorption (SEA) was evaluated as the area under the load–displacement curve obtained from the four-point bending tests. As shown in Figure 4, the SEA values for the gradient lattice beams are consistently higher than those of the purely auxetic lattice beam. Among the gradient configurations, all demonstrated comparable SEA performance; however, the gradient beam with a transition angle of $80°$–$100°$ exhibited the highest SEA. This configu-

ration achieved a 34.5% increase in SEA compared to the purely auxetic lattice beam, indicating its superior capacity for energy absorption under bending loads as shown in Figure 4.

4 CONCLUSIONS

Gradient lattice beams exhibit superior mechanical performance compared to purely auxetic beams, with up to 25% higher peak load-carrying capacity, demonstrating the effectiveness of combining auxetic and non-auxetic architectures in bending-dominated structures. The specific energy absorption (SEA) is significantly enhanced in gradient configurations, with the $80°$–$100°$ gradient achieving the highest SEA 34.5% greater than that of purely auxetic beams highlighting the potential of geometric gradation for improved energy dissipation.

REFERENCES

[1] M. Askari, D. A. Hutchins, P. J. Thomas, L. Astolfi, R. L. Watson, M. Abdi, M. Ricci, S. Laureti, L. Nie, S. Freear *et al.*, "Additive manufacturing of metamaterials: A review," *Additive Manufacturing*, vol. 36, p. 101562, 2020.

[2] J. P. Turpin, J. A. Bossard, K. L. Morgan, D. H. Werner, P. L. Werner *et al.*, "Reconfigurable and tunable metamaterials: a review of the theory and applications," *International Journal of Antennas and Propagation*, vol. 2014, 2014.

[3] X. Ren, R. Das, P. Tran, T. D. Ngo, and Y. M. Xie, "Auxetic metamaterials and structures: a review," *Smart materials and structures*, vol. 27, no. 2, p. 023001, 2018.

[4] J. K. Wilt, C. Yang, and G. X. Gu, "Accelerating auxetic metamaterial design with deep learning," *Advanced Engineering Materials*, vol. 22, no. 5, p. 1901266, 2020.

[5] X. Cheng, Y. Zhang, X. Ren, D. Han, W. Jiang, X. G. Zhang, H. C. Luo, and Y. M. Xie, "Design and mechanical characteristics of auxetic metamaterial with tunable stiffness," *International Journal of Mechanical Sciences*, vol. 223, p. 107286, 2022.

[6] K. Wang, Y.-H. Chang, Y. Chen, C. Zhang, and B. Wang, "Designable dual-material auxetic metamaterials using three-dimensional printing," *Materials & Design*, vol. 67, pp. 159–164, 2015.

[7] K. Meena and S. Singamneni, "A new auxetic structure with significantly reduced stress concentration effects," *Materials & Design*, vol. 173, p. 107779, 2019.

[8] H. Veisi and A. Farrokhabadi, "Investigation of the equivalent material properties and failure stress of the re-entrant composite lattice structures using an analytical model," *Composite Structures*, vol. 257, p. 113161, 2021.

[9] K. Günaydın, G. Sala, H. S. Türkmen, and A. M. Grande, "Failure analysis of auxetic lattice structures under crush load," *Procedia Structural Integrity*, vol. 35, pp. 237–246, 2022.

[10] L. Yang, O. Harrysson, H. West, and D. Cormier, "Mechanical properties of 3d re-entrant honeycomb auxetic structures realized via additive manufacturing," *International Journal of Solids and Structures*, vol. 69, pp. 475–490, 2015.

[11] J. Schwerdtfeger, F. Wein, G. Leugering, R. Singer, C. Körner, M. Stingl, and F. Schury, "Design of auxetic structures via mathematical optimization," *Advanced materials*, vol. 23, no. 22-23, pp. 2650–2654, 2011.

[12] T. Li, F. Liu, and L. Wang, "Enhancing indentation and impact resistance in auxetic composite materials," *Composites Part B: Engineering*, vol. 198, p. 108229, 2020.

[13] F. Usta, H. S. Türkmen, and F. Scarpa, "Low-velocity impact resistance of composite sandwich panels with various types of auxetic and non-auxetic core structures," *Thin-Walled Structures*, vol. 163, p. 107738, 2021.

[14] G. Imbalzano, S. Linforth, T. D. Ngo, P. V. S. Lee, and P. Tran, "Blast resistance of auxetic and honeycomb sandwich panels: Comparisons and parametric designs," *Composite Structures*, vol. 183, pp. 242–261, 2018.

[15] N. Novak, O. Duncan, T. Allen, A. Alderson, M. Vesenjak, and Z. Ren, "Shear modulus of conventional and auxetic open-cell foam," *Mechanics of Materials*, vol. 157, p. 103818, 2021.

[16] J. Zhang, G. Lu, and Z. You, "Large deformation and energy absorption of additively manufactured auxetic materials and structures: A review," *Composites Part B: Engineering*, vol. 201, p. 108340, 2020.

[17] N. K. Choudhry, B. Panda, and S. Kumar, "Enhanced energy absorption performance of 3d printed 2d auxetic lattices," *Thin-Walled Structures*, vol. 186, p. 110650, 2023.

[18] M. B. Francisco, J. L. J. Pereira, G. A. Oliver, L. R. Roque da Silva, S. S. Cunha Jr, and G. F. Gomes, "A review on the energy absorption response and structural applications of auxetic structures," *Mechanics of Advanced Materials and Structures*, vol. 29, no. 27, pp. 5823–5842, 2022.

[19] J. Choi and R. Lakes, "Fracture toughness of re-entrant foam materials with a negative poisson's ratio: experiment and analysis," *International Journal of fracture*, vol. 80, pp. 73–83, 1996.

[20] Q. Liu, "Literature review: materials with negative poisson's ratios and potential applications to aerospace and defence," 2006.

[21] W. Wu, X. Song, J. Liang, R. Xia, G. Qian, and D. Fang, "Mechanical properties of anti-tetrachiral auxetic stents," *Composite Structures*, vol. 185, pp. 381–392, 2018.

[22] M. Mir, M. N. Ali, J. Sami, and U. Ansari, "Review of mechanics and applications of auxetic structures," *Advances in Materials Science and Engineering*, vol. 2014, 2014.

[23] S. Dong and H. Hu, "Sensors based on auxetic materials and structures: A review," *Materials*, vol. 16, no. 9, p. 3603, 2023.

[24] B. R. Krishnan, A. N. Biswas, K. A. Kumar, and P. R. Sreekanth, "Auxetic structure metamaterial for crash safety of sports helmet," *Materials Today: Proceedings*, vol. 56, pp. 1043–1049, 2022.

[25] G. Tzortzinis, A. Gross, and S. Gerasimidis, "Auxetic boosting of confinement in mortar by 3d reentrant truss lattices for next generation steel reinforced concrete members," *Extreme Mechanics Letters*, vol. 52, p. 101681, 2022.

[26] T. Vitalis, A. Gross, G. Tzortzinis, B. Schagen, and S. Gerasimidis, "Enhancing mortar composite matrices with three-dimensional auxetic truss lattice materials for reinforced concrete structures," *Construction and Building Materials*, vol. 457, p. 139165, 2024.

[27] ABAQUS, "Abaqus theory guide," *United States of America: SIMULIA INC*, 2018.

Part XIV
SS 04 - SMART AND SUSTAINABLE SENSOR TECHNOLOGIES USING CELLULOSIC AND WOOD SUBSTRATES

Arunjunai Raj Mahendran, Martin Riegler, Claudia Pretschuh

XI ECCOMAS Thematic Conference on Smart Structures and Materials - SMART 2025
M. Krommer, M. Nader and M. Schagerl (Eds)

Received: 7 April 2025 / Revised: 14 July 2025 / Accepted: 15 September 2025
© The Author(s) 2025

Prospects and challenges of monitoring moisture uptake in wood samples with acoustic emissions

Mehieddine Derbas, Alexander Schneider, Martin Riegler

The demand on wood buildings has lately increased [1], and is now seen as one of the many ways that can reduce the CO_2 emissions associated with the construction sector [2]. Some challenges associated with wood remain, as wood is a natural material that reacts to the environmental conditions, such as temperature and humidity [3]. The use of large timber panels in wood construction poses problems in identifying and localizing moisture uptake due to the presence of excessive humidity. Moisture content changes are known to affect the way acoustic emission (AE) waves travel through wood [4].

In the present study, the potential for detecting moisture uptake in wood using an AE sensor was explored. A dried sample was placed in a climate-controlled room under norm conditions (65% RH, 20 °C), where moisture uptake was expected to occur due to ambient humidity. The experiment lasted for nearly three days, as it was conducted over the weekend to minimize interference from other users of the climate room. To confirm moisture uptake, weight was measured using a precision scale, and the dimensions of the cross-section were monitored with a high-resolution digital camera, tracking the area, width, and thickness of the sample.

The results indicate a promising correlation between moisture uptake and AE features. Although this correlation was evident in the present case, further studies are needed to assess the feasibility of such a system and to establish a robust and reproducible framework for such a structural health monitoring application.

1 INTRODUCTION

Structural health monitoring (SHM) is a popular tool that can be used to ensure the safe and optimal operation of buildings or machines. This is typically done by measuring data over time, with sensors that are already embedded in the substrate that needs to be monitored [5].

Mehieddine Derbas & Alexander Schneider & Martin Riegler
Wood K plus - Competence Center for Wood Composites & Wood Chemistry, Kompetenzzentrum Holz GmbH, Altenberger Str. 69, 4040 Linz, Austria, e-mail: m.derbas@wood-kplus.at

Mehieddine Derbas & Alexander Schneider & Martin Riegler
Institute of Wood Technology and Renewable Materials, BOKU-University of Natural Resources and Life Sciences, 3430 Tulln, Austria

The increasing trend of using solid wood and wood-based products in construction offer significant benefits for lowering CO_2 emissions [2]. However, the hygroscopic nature of wood makes the usage of wood in buildings unpredictable [6]. To amend this, SHM can be applied in the wood-based construction industry, with the aim of the early detection and exclusion of any sources of damage [7].

Sensor selection for SHM is an important step, and is largely dictated by the engineering requirements in terms of capabilities, feasibility, and cost [8]. AE is one candidate measurand that can be used to monitor wooden structures. It is already known that the wood species, geometry, fiber angles, temperature and moisture content influence AE [4]. Recent studies have also studied AE wave speed in relation to a set of already known moisture content levels. Here, a clear linear correlation ($R^2 = 0.97$) can be seen between the dampening of AE energy and moisture content, possibly due to the higher density in wet samples [9]. Furthermore, the propagation velocity could be modelled as an exponential decay function ($R^2 = 0.93$) with moisture content as an independent variable [9]. Such a system would require at least two AE sensors and a source. This leaves a gap for investigating systems with one AE sensor and the changes of the substrate, such as cracks, that act as an AE source.

In this work, the possibility of employing a single AE sensor to monitor moisture uptake in wood samples was investigated, with weight and swelling as validation measurands that can be compared with AE features. While strong correlations were observed between AE features and the validation measurands, challenges remain in data interpretation, suggesting the need for further investigation.

2 MATERIALS

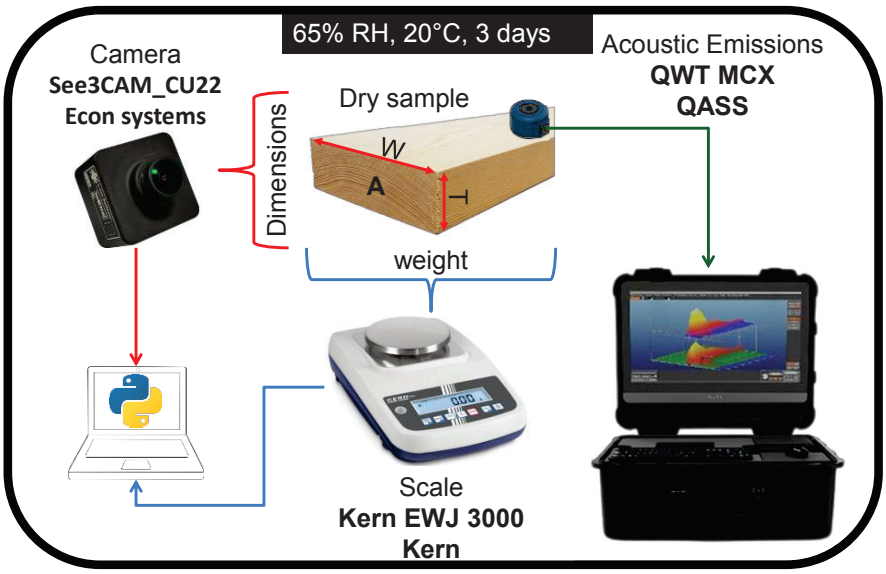

Figure 1: Experimental setup

To test the hypothesis of measuring moisture uptake by AE, a spruce sample (L100xW150XT40mm) was dried at 103°C until mass stability (Figure 1). To measure the weight of the sample, a precision scale was used (EWJ 3000, Kern & Sohn GmbH, Albstadt, Germany). An image was taken every time a weight measurement was executed, with the help of a 2-megapixel USB camera (See3CAM CU20, e-con Systems, Chennai, India). These measurements were automated with a python script. Here, the OpenCV python library was used to connect to the camera and to automatically take images. For the scale, serial commands were sent with an RS232 cable which was connected to the scale. The sampling time was set to 5 minutes.

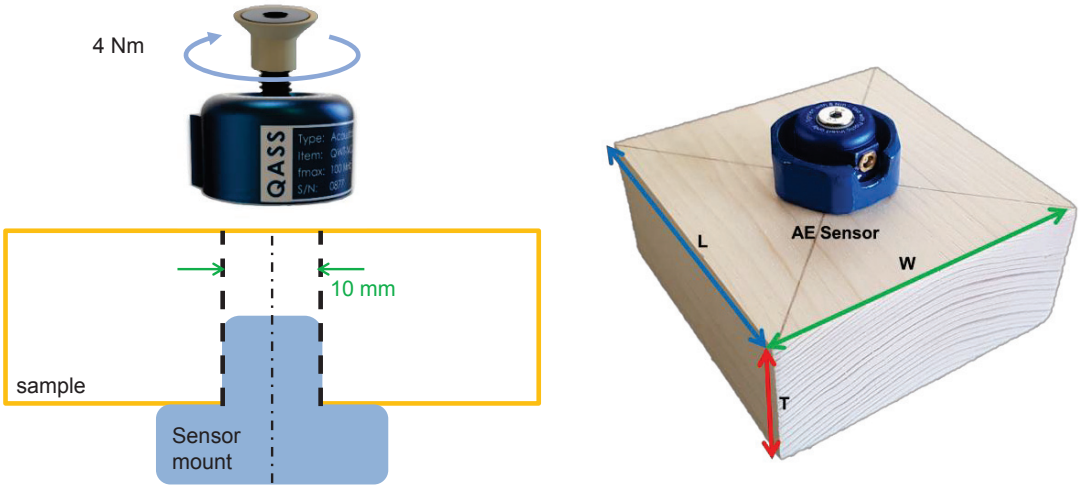

Figure 2: Setup of the AE sensor (left) and real life photo (right)

The AE were measured by the QWT MCX piezo-electric AE sensor (QASS GmbH, Wetter, Germany). To mount the sensor, the sample was drilled in the middle with a 10 mm bit. The sensor mount was also drilled and threaded to accommodate an M5 bolt (Figure 2). The sensor was attached to the mount with a torque wrench at 4 Nm. The signal was recorded by an acquisition from the same manufacturer, after being amplified with a pre-amp and sampled at 800 kHz. Here, the amplification was set at maximum and no filtering was enabled. The experiment was run over the weekend to avoid any interferences, and the duration of the experiment was 67 hours. After exporting and processing, all data was re-sampled to get structured data that can be compared record-wise.

While the experiment was done only once, multiple pre-tests were executed to guarantee a reproducible setup and for the programming of the measurement scripts.

3 METHODS

3.1. Image processing

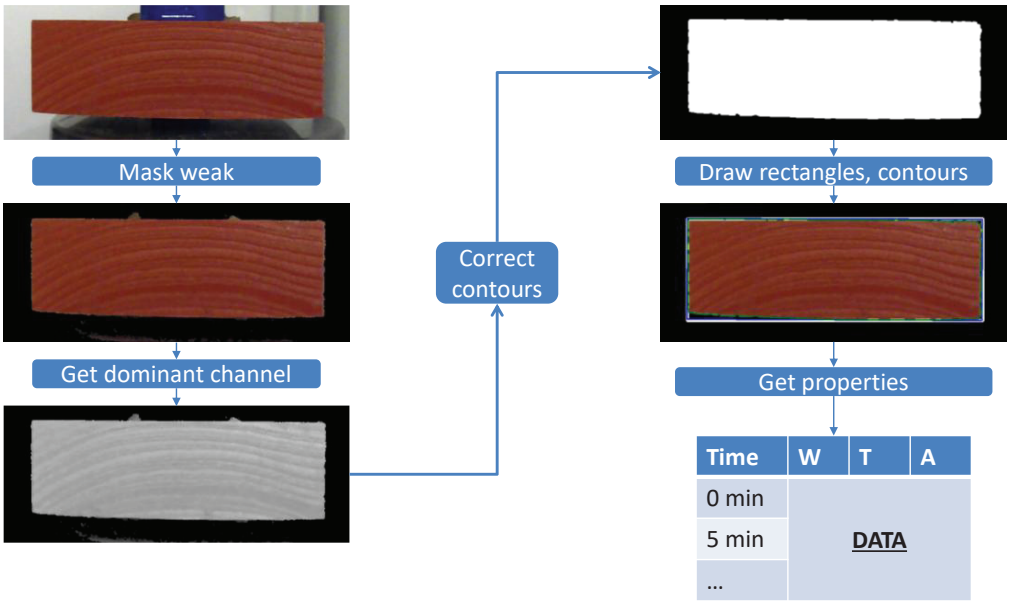

Figure 3: Image processing steps

To facilitate the segmentation of the board from the background, the sample was spray painted in red. The steps that lead to the desired outcome are listed as follows (Figure 3):

- Generating a mask where pixels are dominantly red and applying it to the original image with a bitwise AND operator;
- Applying a contour detection on the red channel;
- Getting the properties of the contour, such as area.

3.2. Acoustic emissions signal processing

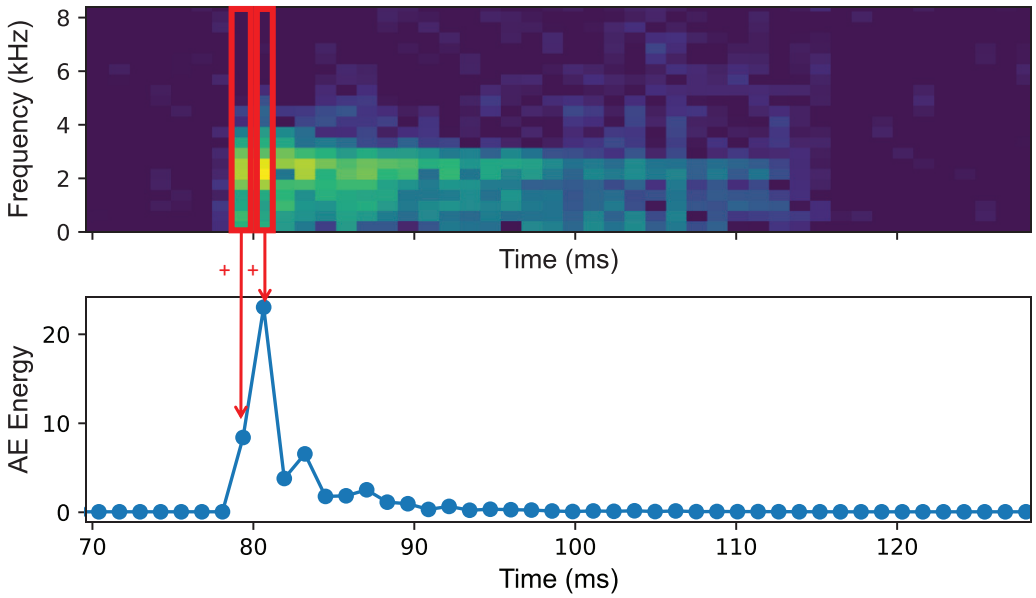

Figure 4: Representation of an AE pulse in the time-frequency domain (top) and after energy calculation (bottom)

The raw data collected during this experiment amounted to approximately 3 TB. To facilitate data export, energy calculations can be done with the proprietary acquisition system (QASS GmbH). In this process, a time window is defined, within which the amplitudes of each frequency are summed up. This method significantly down-samples the data to around 2 GB, making it possible to export it as a more manageable file size (Figure 4).

Two features were calculated from the energy file:

- AE median: in a sliding window, the median of the energy values was taken as an indicator of the swelling of the sample.
- AE cumulative peak count: after applying a peak detection based on z-score peak transformation with the upper threshold being defined as the median with 6 standard deviations. Here, it might be possible to detect pattern changes due to the occurrence of peaks in the signal, which could reflect cracks [10].

4 RESULTS

Weight data confirms that a total percentage change of 4.57% increase took place as a result of placing the dry sample in the humid environment (65% RH). This change was fast at the beginning of the first day, and gradually started to increase linearly over time for the remainder of the experiment that lasted around 3 days (Figure 5).

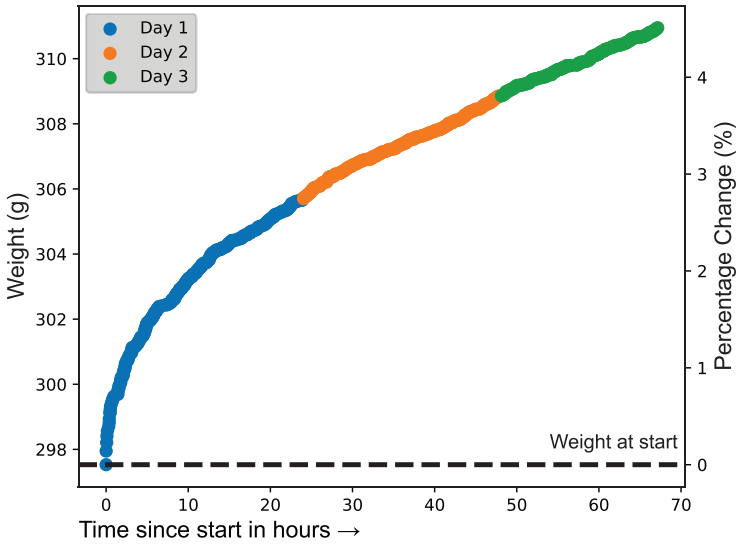

Figure 5: Weight of sample over the duration of the experiment

This trend was similarly seen in the swelling of the sample, characterized with the increase in the area of the cross-section (Figure 6). These measurements were rather noisy and will be improved by using a higher resolution camera or by placing the camera nearer to the surface.

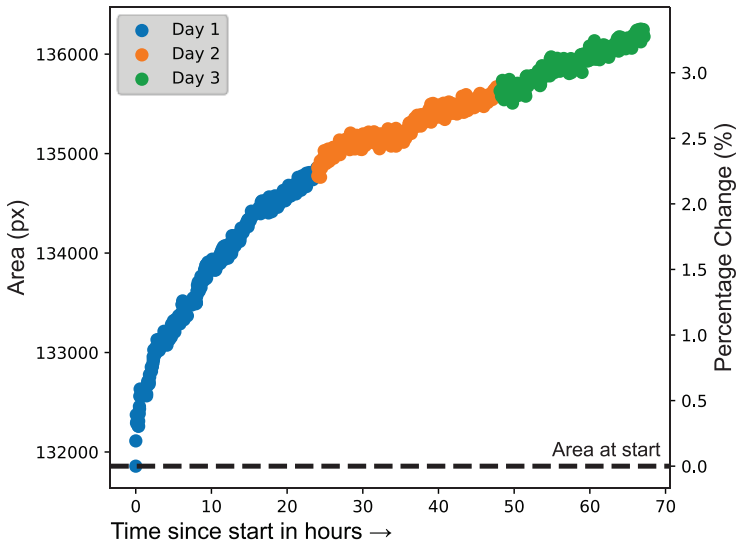

Figure 6: Area of sample over the duration of the experiment

When scattered against each other, the area increase and the weight increase correlate almost perfectly with a coefficient of determination of 0.99 (Figure 7). Given this correlation and the fact that the area is noisier than the weight, the latter will be used in the comparison with the AE features.

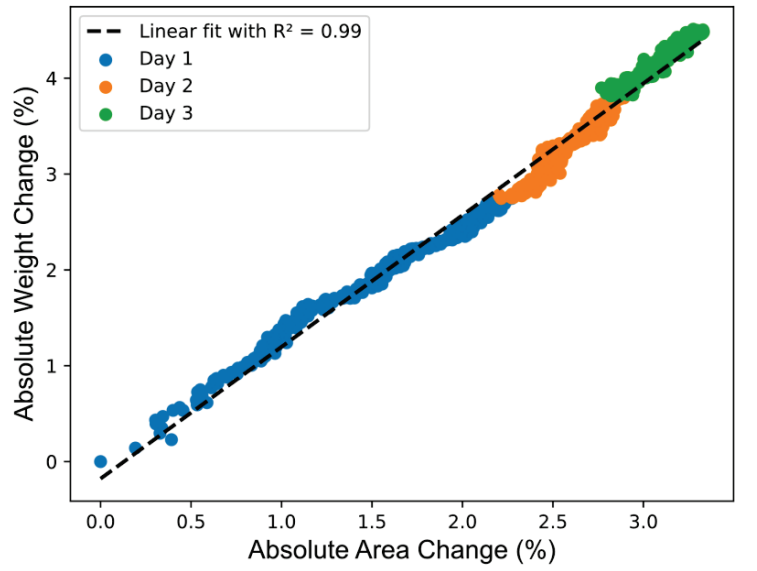

Figure 7: Correlation between weight and area

The AE median feature, which should reflect the base noise of the AE, had a steady increase similar to weight or area measurands (Figure 8). This can be mainly explained by the swelling of the board: as the thickness of the board increases, more tension is applied between the sensor (on the top) and the sensor mount (on the bottom), amplifying the response of the piezo-electric AE sensor.

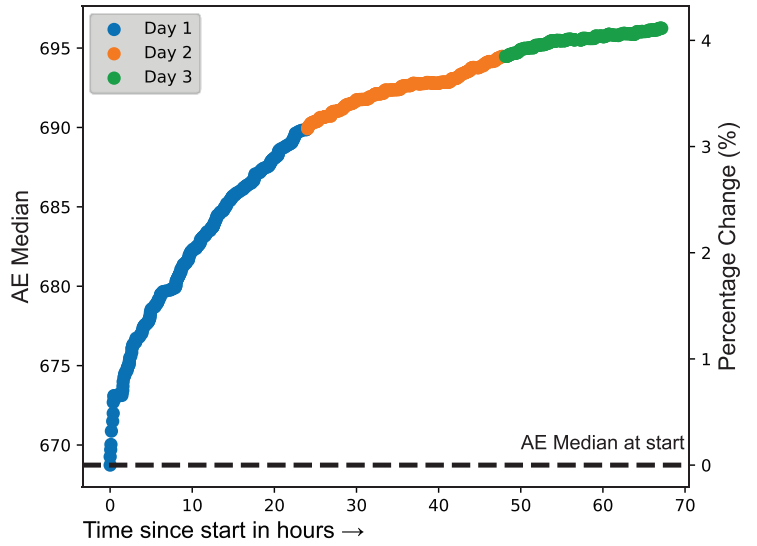

Figure 8: AE median

When plotting the AE median against the weight in a scatter plot (Figure 9), a clear association can be noticed, with high correlation coefficients ($R = 0.98; R^2 = 0.96$). However, some patterns can be seen throughout the experiment:

- During the first hour, the AE median increases more rapidly than the weight.
- After the initial hour, a linear relationship between the AE median and weight is observed, lasting until 24 hours into the experiment.
- Between 24 and 48 hours, another linear relationship emerges, but with a lower slope. This indicates that the rate of increase in AE median has slowed compared to the change in weight.
- Finally, from 48 hours until the end of the experiment, the slope between the AE median and weight suddenly decreases one more time.

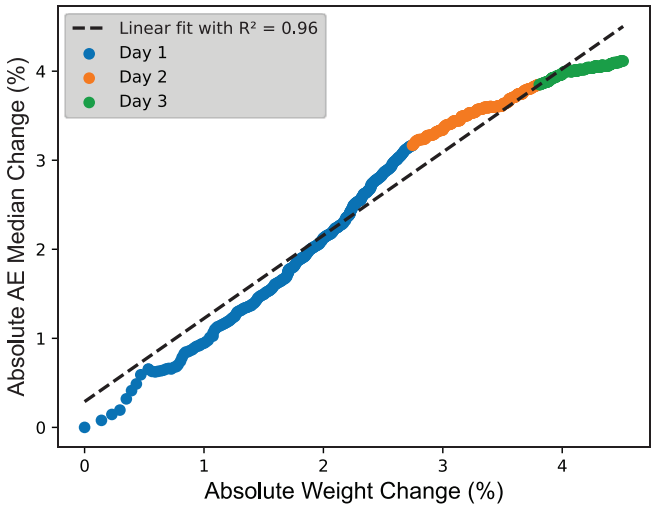

Figure 9: Correlation between AE median and weight

The increase of pre-tension between the surface of the substrate and the sensor was also reflected in the cumulative peak count (Figure 10). For the first 10 hours, a clear linear trend is observed in the cumulative peak count, indicating a steady rate of peaks over time. However, at the 10-hour mark, a noticeable change in behaviour occurs, with a more rapid increase in peaks. This accelerated trend levels off until the 48-hour mark, when another sharp increase in peaks is observed that might origin from plastic deformations of the sample.

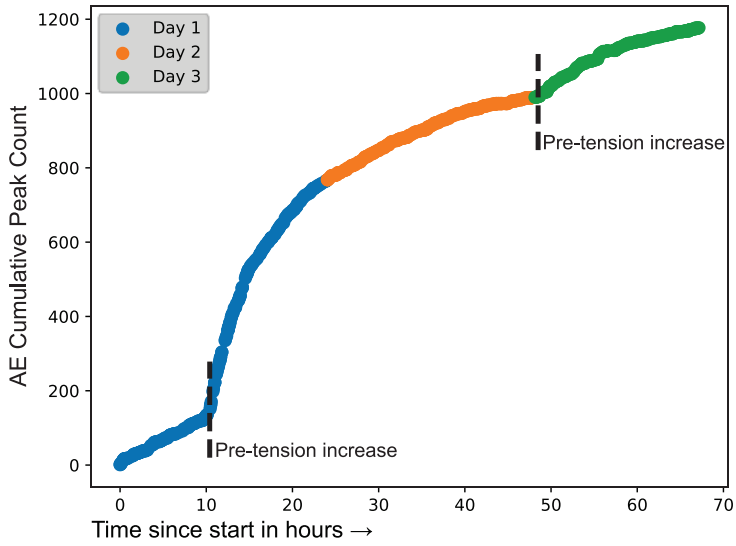

Figure 10: AE cumulative peak count

Interpreting the current data suggests that moisture uptake leads to swelling, which in turn drives changes in AE features, rather than moisture uptake directly influencing AE. This indicates that the swelling itself may be the primary factor affecting the AE response. To minimize the increase in pre-tension between the wood surface and the sensor mount, further exploration of alternative coupling methods is necessary.

5 CONCLUSION

In the presented work, the possibility of monitoring moisture uptake in wood samples by means of an Acoustic Emission (AE) sensor was discussed. The sample was dried at 103 °C until mass stability and can therefore be considered completely dry. The sample was then placed in a climatized room, where it would absorb moisture from the humid air in the environment. The sample was monitored by a camera to measure swelling and a precision scale to measure weight increase. Most importantly, an AE sensor was mounted on the sample and monitored for the duration of 3 days.

The observations from the scale and the camera confirm that the sample underwent moisture uptake, as the weight of the sample increased by 4.51% and the swelling by 3.27%. Correlating the weight increase with the area increase over time shows a near-perfect 1:1 correlation.

The AE energy was exported from the acquisition system and two features were calculated. The AE median, which reflects the base noise of the sensor, was found to correlate well with the weight and area. After peak detection, the cumulative number of peaks was plotted over time, indicating potential plastic deformation resulting from the substrate being pressed against the sensor and its' mount.

Further studies and repetitions are required to investigate these findings, as they are currently limited to a very specific use-case executed in a lab-like environment. Additionally, reproducing this experiment under real-life noise interference would better represent the technical challenges that remain to be solved.

REFERENCES

[1] A. Bahrami and S. M. P. Rashid, "Sustainable Development of Recent High-Rise Timber Buildings," 2024, pp. 1-16.

[2] J. Nässén, F. Hedenus, S. Karlsson, and J. Holmberg, "Concrete vs. wood in buildings – An energy system approach," *Building and Environment,* vol. 51, pp. 361–369, 05/01 2012, doi: 10.1016/j.buildenv.2011.11.011.

[3] E. E. Thybring and M. Fredriksson, "Wood and Moisture," in *Springer Handbook of Wood Science and Technology*, P. Niemz, A. Teischinger, and D. Sandberg Eds. Cham: Springer International Publishing, 2023, pp. 355-397.

[4] V. Nasir, S. Ayanleye, S. Kazemirad, F. Sassani, and S. Adamopoulos, "Acoustic emission monitoring of wood materials and timber structures: A critical review," *Construction and Building Materials,* vol. 350, p. 128877, 2022/10/03/ 2022, doi: https://doi.org/10.1016/j.conbuildmat.2022.128877.

[5] B. Chapuis, "Introduction to Structural Health Monitoring," in *Sensors, Algorithms and Applications for Structural Health Monitoring: IIW Seminar on SHM, 2015*, B. Chapuis and E. Sjerve Eds. Cham: Springer International Publishing, 2018, pp. 1-11.

[6] J. M. Dinwoodie, "Timber—a review of the structure-mechanical property relationship," *Journal of Microscopy,* vol. 104, no. 1, pp. 3-32, 1975/05/01 1975, doi: https://doi.org/10.1111/j.1365-2818.1975.tb04002.x.

[7] E. L. Schmidt, M. Riggio, P. F. Laleicke, A. R. Barbosa, and K. Van Den Wymelenberg, "How monitoring CLT buildings can remove market barriers and support designers in North America: an introduction to preliminary environmental studies," *Rev. Port. Eng. Estrut,* vol. 3, pp. 41-47, 2018.

[8] S. Kessler and S. Spearing, "Selection of Materials and Sensors for Health Monitoring of Composite Structures," *MRS Proceedings,* vol. 785, 01/01 2003, doi: 10.1557/PROC-785-D11.1.

[9] X. Li, S. Ju, T. Luo, and M. Li, "Effect of moisture content on propagation characteristics of acoustic emission signal of Pinus massoniana Lamb," *European Journal of Wood and Wood Products,* vol. 78, no. 1, pp. 185-191, 2020/01/01 2020, doi: 10.1007/s00107-019-01478-9.

[10] E. N. Landis, "Acoustic Emissions in Wood," in *Acoustic Emission Testing: Basics for Research - Applications in Civil Engineering*, C. Grosse and M. Ohtsu Eds. Berlin, Heidelberg: Springer Berlin Heidelberg, 2008, pp. 311-322.

XI ECCOMAS Thematic Conference on Smart Structures and Materials - SMART 2025
M. Krommer, M. Nader and M. Schagerl (Eds)

Received: 3 April 2025 / Revised: 22 July 2025 / Accepted: 15 September 2025
© The Author(s) 2025

Real-Time Cure Monitoring of Thermoset Resin Using Printed Paper Sensors

Nitin Gupta, Günter Wuzella, Arunjunai Raj Mahendran, Martin Kaltenbrunner

Abstract. The curing kinetics of the epoxy resin was studied in dynamic temperature conditions using dielectric analysis (DEA) and differential scanning calorimetry (DSC). The study compared the non-isothermal conversion curves obtained from both techniques. The average enthalpy of the curing was determined to be approximately 280 J/g. Moreover, it was observed that the reaction follows an autocatalytic behavior as the activation energy reduces with an increase in the degree of cure. A good correlation between DEA and DSC was observed during the heating ramp from 40-120°C. Further research on how the different additives affect resin curing can be done using techniques like DEA, DSC, Fourier-transform infrared spectroscopy, and rheology to see the correlation between all methods for the same conditions.

Key words: Smart process monitoring, Dielectric analysis, Paper sensors, DSC, Composites.

1 INTRODUCTION

Thermoset resin is utilized by many industries, such as aerospace (for fuselage materials) [1], energy (for generators and insulation products) [2], electronics, and sporting goods (snowboards, badminton rackets, racing cars, and bicycles) [3]. These resins have properties like dimensional stability, chemical resistance against corrosion, and excellent thermal and mechanical properties, making them interesting for all these applications [4]. The information on the curing behavior of these resin systems is crucial, as it impacts product performance and economics [5]. Therefore, the manufacturer must investigate this behavior to get the best outcomes in every possible way. During the curing of the resin, a steric polymer network forms, which changes different properties of the resin that should be detected. Many authors investigated the behavior of epoxy systems in detail [6], [7], [8], [9], [10], [11], [12], [13], [14], [15], [16], [17], [18]. The curing reaction of bisphenol-based epoxy with an amine hardener involves nucleophilic ring-opening of the epoxy by the amine, forming a highly cross-linked thermoset network [19]. This results in a durable, chemically resistant polymer with strong adhesion and thermal stability. The effects of this polymerization can be observed by thermal (such as DSC) or dielectric characterization (such as DEA) of the material. As they are entirely

Nitin Gupta & Günter Wuzella & Arunjunai Raj Mahendran
Competence Center for Wood Composites and Wood Chemistry, Wood K Plus, Klagenfurter Str. 87-89, 9300 St. Veit an der Glan, Austria, e-mail: n.gupta@wood-kplus.at

Nitin Gupta & Martin Kaltenbrunner
Division of Soft Matter Physics, Institute of Experimental Physics, Johannes Kepler University Linz, Linz, Austria

different characterizations, information on different parameters is obtained from them, but cure conversion can be calculated easily, which helps correlate the different techniques. The correlation of the isothermal cure conversion from these characterizations has already been done in the literature [5], [20].

This study used DEA and DSC in dynamic temperature conditions to characterize bisphenol-based epoxy with an amine hardener. The information on curing behavior was interpreted by DSC data. The non-isothermal conversion curves from both techniques were compared. Paper sensors were used in this study to provide details on the conductivity variation during DEA. The insights from this study might help industries working with resin-based composites.

2 MATERIAL AND METHODS

Bisphenol-based epoxy resin was used for the analysis. The proportion of resin and hardener was 10:4 by weight. Uni-directional glass fiber reinforcement (220 g/m^2) was used for the reinforcement. The impregnation of the fibers was carried out manually, with the fibers being hand-laminated with resin through rollers. The length and breadth of the rectangular samples were 30 cm and 6 cm, respectively. A total of 2 fiber layers were used for every individual experiment. The interdigitated electrode paper sensors were used for the DEA and sandwiched between the fiber layers. The electrode length and spacing of the paper sensor was 300*300 µm. Samples taken from freshly mixed resin and hardener were analyzed in three non-isothermal experiments (HR 5, 10, and 15 °C/min from 30 °C up to 200 °C) with a Mettler-Toledo (Greifensee, Switzerland) 822e DSC. The curing kinetics was studied using the Mettler Toledo DSC software according to Vyazovkin's method. The DEA measurements were conducted using a dielectric analyzer from Novocontrol Technologies (Germany). A sinusoidal AC voltage at 10000 Hz was applied between the electrodes to generate an electric field. In the hot press, 5 bar pressure was used for the measurements.

3 RESULTS AND DISCUSSION

The temperature and curing data (by DSC and DEA) are presented in this section.

3.1 Thermal characterization using DSC

From the heat flow data by DSC, it was inferred that the reaction starts at a very low temperature. The average enthalpy of the reaction was approximately 280 J/g. The activation energy (Eα) is plotted as a function of cure in **Figure 1**. The figure shows that the Eα slowly decreases as the degree of cure increases. This decrease in the Eα might be due to the autocatalytic effect in the curing process. The difference between the maximum and minimum Eα is 16.29 kJ/mol. In the study performed by Hardis et al., this difference was only 3.57 kJ/mol [17].

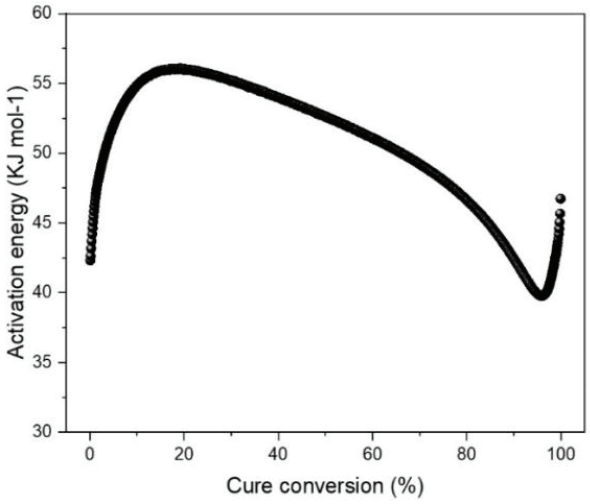

Figure 1: Eα variation with cure conversion of epoxy resin

3.2 Dielectric characterization

For the DEA, the samples were pressed in the hot press. The set temperature conditions in the press were as follows:

Initial temperature: 40°C
Heating ramp: 40-120°C (within 960 seconds or 5°C/minute)
Constant temperature: 240 seconds
Cooling ramp: 120-40°C (within 300 seconds or 16°C/minute)

The set temperature and the actual temperature of the resin might be different hence, the temperature was simultaneously measured using a K-type thermocouple. In **Figure 2,** the measured temperature data is shown during the curing. It can be seen that the temperature at the start of the curing process is 27°C compared to the set temperature of 40°C. This difference is because the thermocouple is inside the glass fibers and takes some time to reach the set temperature. After this point, the temperature increases and reaches the set temperature of 120°C at 5°C/min. Then, it remains constant at 120°C for 240 seconds and decreases afterward. It can be observed that the temperature does not reach the set temperature of 40°C at the end of the process, whereas it only reaches 85°C. This means that the temperature inside the glass fiber was still relatively higher than the set temperature.

The conductivity data during the curing is also shown in **Figure 2**. It can be seen that the conductivity increases till 230 seconds, and then it starts decreasing. After approximately 500 seconds, it is saturated and does not change afterward. The initial increment in the conductivity is due to both the temperature influence on the sensor and the curing of the resin, as the process is not isothermal but a heating ramp. As the temperature increases due to the heating ramp, the

temperature influence is dominant before 230 seconds; hence, the conductivity increase was observed. The curing effect dominates at the highest conductivity point, and the conductivity starts decreasing, representing the curing reaction.

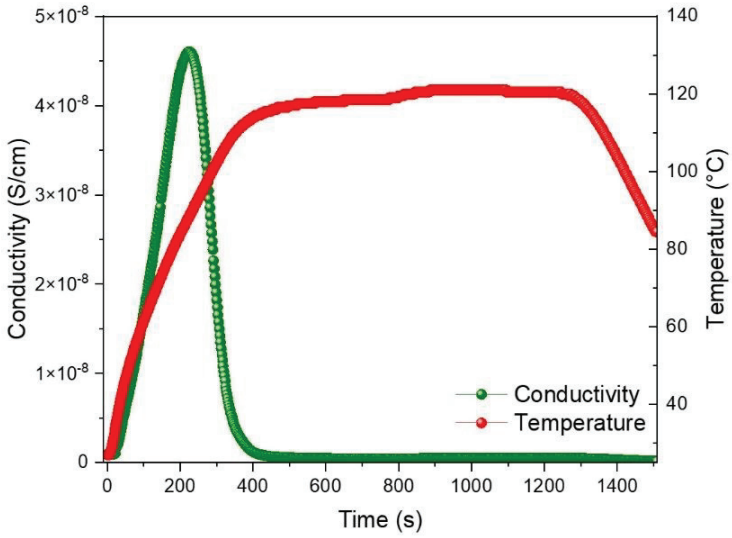

Figure 2: Measured temperature and conductivity during the curing of the epoxy resin

During the curing reaction, the polymer chains get crosslinked with each other and make the three-dimensional network. In the case of epoxy resin with amine hardeners, generally, C-N, C-O, -C-O-C- and N-H bonds form, which result in the cured network [19], [21]. Due to this network formation, the ion mobility gets restricted, and material conductivity is reduced. After the curing completion, the conductivity becomes constant and shows no further changes in the material.

3.3 Correlation of thermal and dielectric characterization of epoxy resin

By the DSC characterization, the heat flow information from/to the material is generally received with respect to temperature, a heating ramp from 30 to 200°C in this case. Meanwhile, by DEA, the material's conductivity information is obtained for the given temperature program, which is a heating ramp from 40 to 120 °C. There is no physical significance in comparing these parameters (heat flow and conductivity). However, the conversion curves can be produced by integrating and normalizing the data, which can be compared.

Figure 3 compares the non-isothermal conversion curves from DEA and DSC at 5°C/minute. To produce non-isothermal conversion curves, only the data during the heating phase (30–120 °C in DSC and 40–120 °C in DEA) was used. This approach was chosen because, in DEA, the temperature either remained constant or decreased after the initial heating ramp, whereas in DSC, heating was continued up to 200 °C. Both conversion curves showed an S-shape curve (the conversion rate is slow at the start and end of curing but very pronounced during the curing reaction). It is visible from the graph that up to 90% cure the DEA and DSC

results correlated very well, but after that, there are insignificant differences between 90< α <100. Our previous study also showed a good correlation of isothermal conversion curves from DEA and DSC for phenol-formaldehyde-impregnated paper [5].

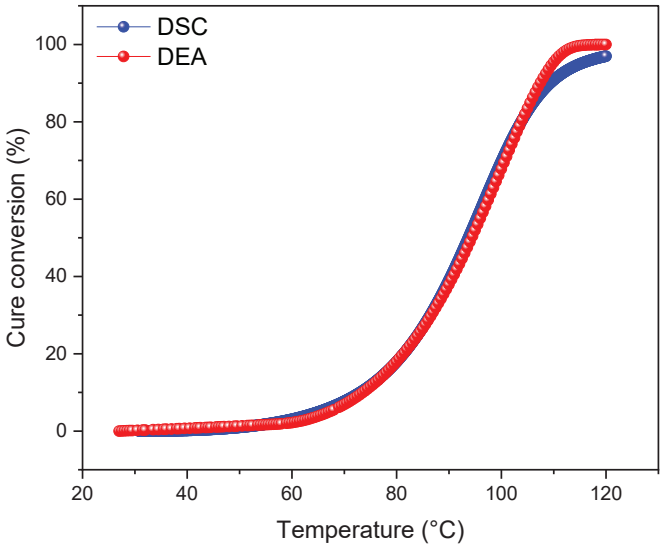

Figure 3: Non-isothermal conversion curves from DSC and DEA

4 Conclusion

The bisphenol-based epoxy with amine hardener was characterized by thermal (DSC) and dielectric (DEA) characterization. From DSC, it was found that Eα slowly decreases as the degree of cure increases, which shows the autocatalytic effect during the curing process. From DEA, the information on the variation of conductivity was received. Moreover, the non-isothermal conversion curves were produced using both techniques and compared. It was determined that the non-isothermal DEA and DSC cure conversion curves correlated very well up to 90% cure, but after that, there were some insignificant differences between 90< α <100 observed. Considering the good correlation of the isothermal (previous study) and non-isothermal conversion (current study), DEA seems to be a good candidate for obtaining information on the cure kinetics of resin. Further research on how the different additives affect resin curing can be done using techniques like DSC, DEA, FTIR, and rheology to see the correlation between all methods for the same conditions.

5 Acknowledgements and funding details

The authors would like to thank Kompetenzzentrum Holz GmbH, Austria, for providing a research facility for doing the research work. This work is a part of “Intelligent, integrated and impregnated cellulose based sensors for reliable bio-based structures (i3Sense)” project funded by the Austrian Research Promotion Agency (FFG), Grant number 888361.

REFERENCES

[1] I. Hirota, S. ichi Takeda, and T. Ogasawara, "Evaluation of thermosetting resin curing using a tilted fiber Bragg grating," *Compos Part A Appl Sci Manuf*, vol. 158, Jul. 2022, doi: 10.1016/j.compositesa.2022.106956.

[2] C. Di Mauro, A. Genua, and A. Mija, "Fully bio-based reprocessable thermosetting resins based on epoxidized vegetable oils cured with itaconic acid," *Ind Crops Prod*, vol. 185, Oct. 2022, doi: 10.1016/j.indcrop.2022.115116.

[3] A. Jahandideh and K. Muthukumarappan, "Star-shaped lactic acid based systems and their thermosetting resins; synthesis, characterization, potential opportunities and drawbacks," Feb. 01, 2017, *Elsevier Ltd*. doi: 10.1016/j.eurpolymj.2016.12.035.

[4] R. Haney, R. H. Kollarigowda, L. Wiegart, and S. Ramakrishnan, "Surface-Functionalized Cellulose Nanocrystals as Nanofillers for Crosslinking Processes: Implications for Thermosetting Resins," *ACS Appl Nano Mater*, vol. 5, no. 2, pp. 1891–1901, Feb. 2022, doi: 10.1021/acsanm.1c03508.

[5] N. Gupta, A. R. Mahendran, S. Weiss, and M. Khalifa, "Thermal curing behavior of phenol formaldehyde resin-impregnated paper evaluated using DSC and dielectric analysis," *J Therm Anal Calorim*, 2024, doi: 10.1007/s10973-023-12843-5.

[6] H. Cai *et al.*, "Curing kinetics study of epoxy resin/flexible amine toughness systems by dynamic and isothermal DSC," *Thermochim Acta*, vol. 473, no. 1–2, pp. 101–105, Jul. 2008, doi: 10.1016/J.TCA.2008.04.012.

[7] N. Saba and M. Jawaid, "Epoxy resin based hybrid polymer composites," in *Hybrid Polymer Composite Materials: Properties and Characterisation*, Elsevier Inc., 2017, pp. 57–82. doi: 10.1016/B978-0-08-100787-7.00003-2.

[8] T. Hoshino, Y. Okamoto, A. Yamamoto, and H. Masunaga, "Heterogeneous dynamics in the curing process of epoxy resins," *Sci Rep*, vol. 11, no. 1, Dec. 2021, doi: 10.1038/s41598-021-89155-x.

[9] F. Ferdosian, Y. Zhang, Z. Yuan, M. Anderson, and C. (Charles) Xu, "Curing kinetics and mechanical properties of bio-based epoxy composites comprising lignin-based epoxy resins," *Eur Polym J*, vol. 82, pp. 153–165, Sep. 2016, doi: 10.1016/j.eurpolymj.2016.07.014.

[10] F. Ferdosian, Y. Zhang, Z. Yuan, M. Anderson, and C. (Charles) Xu, "Curing kinetics and mechanical properties of bio-based epoxy composites comprising lignin-based epoxy resins," *Eur Polym J*, vol. 82, pp. 153–165, Sep. 2016, doi: 10.1016/j.eurpolymj.2016.07.014.

[11] C. Zhang *et al.*, "On the Dielectric Relaxation Characteristics of Epoxy Resins under Different Aging Conditions," in *Proceedings of the 2024 IEEE 5th International Conference on Dielectrics, ICD 2024*, Institute of Electrical and Electronics Engineers Inc., 2024. doi: 10.1109/ICD59037.2024.10613011.

[12] T. Aziz *et al.*, "The epoxy resin system: function and role of curing agents," Jan. 01, 2024, *Springer*. doi: 10.1007/s42823-023-00547-7.

[13] E. Butta, A. Livi, C. Levita, and P. A. Rolla, "Dielectric Analysis of an Epoxy Resin during Cross-Linking," *J Polym Sci B Polym Phys*, vol. 33, 1995, doi: 10.1002/polb.1995.090331610.

[14] S.-N. Lee, Y.-H. Liao, P.-T. Huang, and J.-L. Lee, "Dielectric Behavior of Epoxy Resin During Cure: A Vector Voltage Study," *Polym Eng Sci*, vol. 30, no. 4, pp. 219–227, 1990, doi: 10.1002/pen.760300405.

[15] G. Mashouf Roudsari, A. K. Mohanty, and M. Misra, "Study of the curing kinetics of epoxy resins with biobased hardener and epoxidized soybean oil," *ACS Sustain Chem Eng*, vol. 2, no. 9, pp. 2111–2116, Sep. 2014, doi: 10.1021/sc500176z.

[16] Z. Wu, Q. Chen, D. Liu, J. Fan, Q. Zhang, and W. Chen, "In situ monitoring of epoxy resin curing process: Using glass transition as a bridge," *Polym Test*, vol. 117, Jan. 2023, doi: 10.1016/j.polymertesting.2022.107871.

[17] R. Hardis, J. L. P. Jessop, F. E. Peters, and M. R. Kessler, "Cure kinetics characterization and monitoring of an epoxy resin using DSC, Raman spectroscopy, and DEA," *Compos Part A Appl Sci Manuf*, vol. 49, pp. 100–108, 2013, doi: 10.1016/j.compositesa.2013.01.021.

[18] M. Zolghadr, M. J. Zohuriaan-Mehr, A. Shakeri, and A. Salimi, "Epoxy resin modification by reactive bio-based furan derivatives: Curing kinetics and mechanical properties," *Thermochim Acta*, vol. 673, pp. 147–157, Mar. 2019, doi: 10.1016/j.tca.2019.01.025.

[19] X. Liu, P. Lan, and N. Lin, "Curing reactions of epoxy powder coatings in perspectives of chemical mechanisms and strategies," Feb. 01, 2025, *Elsevier B.V.* doi: 10.1016/j.porgcoat.2024.108956.

[20] J. Chen and M. Hojjati, "Microdielectric analysis and curing kinetics of an epoxy resin system," *Polym Eng Sci*, vol. 47, no. 2, pp. 150–158, 2007, doi: 10.1002/pen.20687.

[21] H. Yamasaki and S. Morita, "Identification of the epoxy curing mechanism under isothermal conditions by thermal analysis and infrared spectroscopy," *J Mol Struct*, vol. 1069, no. 1, pp. 164–170, Jul. 2014, doi: 10.1016/j.molstruc.2014.01.037.

XI ECCOMAS Thematic Conference on Smart Structures and Materials - SMART 2025
M. Krommer, M. Nader and M. Schagerl (Eds)

Received: 14 April 2025 / Revised: 31 July 2025 / Accepted: 15 September 2025
© The Author(s) 2025

Porous Smart Paper Sensors for Structural Health Monitoring in Composites

Christian Koren, Arunjunai Raj Mahendran

Abstract. Detecting cracks or structural damage is essential for effective structural health monitoring. Conventional approaches often rely on embedded sensors within composite materials to identify and locate damage; however, many existing sensor substrates are non-biodegradable, raising environmental concerns. As a result, growing attention is being directed toward sustainable alternatives. In this work, we investigate printed porous paper–based sensors for crack detection and localization. These biodegradable sensors were integrated into both glass fiber and natural fiber composite reinforcements. Electrical resistance was continuously monitored during bending and drop ball impact tests to validate damage detection through resistance variations. The results show that even small cracks lead to pronounced increases in sensor resistance due to partial electrode disruption, whereas extensive cracking can cause complete signal loss resulting from severe electrode failure. The printed paper sensors offer a versatile, easily integrable solution for composite structures or surface application, while providing the added environmental benefit of a biodegradable substrate—a feature largely absent in current sensor technologies. Their incorporation into safety-relevant components can be achieved without introducing noticeable structural impairments. In addition to enabling real-time structural health monitoring, the sensors allow precise localization of deformation and assessment of load distribution. Their low manufacturing cost further supports their suitability for large-scale production of damage detection systems.

Key words: Crack detection, Paper sensor, Printable Electronics, Composites.

1 INTRODUCTION

For natural fiber-reinforced plastics (NFRP) to become established, the other components, in addition to bio-based resin and hardener systems, must also be sustainable and meet the required characteristics [1]. From an economic point of view, conventional materials continue to be glass fiber reinforced plastics (GFRP) on the one hand or carbon fiber reinforced plastics (CFRP) in high-tech applications or for high loads. As the automotive and construction industries continue to move toward sustainability in times of a global climate crisis, and recycling plays a significant role in many areas, NFRP will also continue to move into the focus of economically relevant areas. The technical values are comparable to those of glass fiber, although there are differences in production and processing [2]. The advantages over conventionally used materials are essential for establishing sustainable fiber composite structures. On the one hand, there is the ecological advantage of using renewable raw materials, the biodegradability, and the low CO_2 footprint generated during production [3]. On the other hand, natural fibers offer good mechanical stability, absorb vibrations better than conventional

Christian Koren & Arunjunai Raj Mahendran
Wood-K Plus, Kompetenzzentrum Holz GmbH, Area Wood & Paper Surface Technologies, Klagenfurterstr. 87-89, A-9300 St. Veit an der Glan, Austria, e-mail: c.koren@wood-kplus.at

GFRP, and are usually more elastic than brittle glass fibers [4]. Regionality should also not be ignored in the case of long transport routes, although natural fibers can be produced in Europe. For this reason, we also see great potential for sustainable paper-based sensors and their application and integration in the respective materials.

Paper-based sensors have the great advantage of adaptability and integration without significant changes in layer thickness on the workpiece [5]. Comparable resistance sensors, which are made entirely of plastic, can only be placed on the surface or at locations specifically intended for their use, where they form a local elevation of millimeters. In contrast, the paper sensors investigated have a layer thickness of a few micromillimeters and can be applied to the surface retrospectively or integrated into the manufacturing process.

The sensors discussed in this research work deal with fracture-induced crack propagation and crack detection in fiber composites. The sensors are also best represented here because crack detection and propagation can be represented particularly well in transparent GFRP. We have chosen a unique curve design based on local crack propagation due to an impact. This curve design - the Hilbert curve - is a space-filling curve to recognize possible cracks in all orientation directions [6]. Since a crack in a fiber composite structure - a multilayer composite consisting of different orientation directions - propagates in the direction of loading, this design can detect the crack with a very high probability. The only important thing is that the sensor must also be in the crack area. Many previous papers have been published on this topic, but they mostly concern the structural construction sector or are connected with concrete as a base material. Sensors made from a renewable material offer a new basis for research here.

2 MATERIALS AND METHODS

2.1 SENSOR FABRICATION AND MATERIAL SELECTION

In order to identify a suitable material system for embedded strain sensing, various substrate materials and conductive printing techniques were systematically evaluated. The selection criteria included printability, electrical conductivity, mechanical flexibility, compatibility with composite processing, and stability during lamination.

Among the tested combinations, a lightweight paper substrate (22 g/m²) in combination with a silver-based conductive ink demonstrated the most reliable performance for the intended application (**Figure 1a**). The paper provided sufficient mechanical flexibility and conformability during composite processing, while maintaining dimensional stability. The silver ink ensured high electrical conductivity and good adhesion to the paper substrate, resulting in reproducible and stable sensor signals.

The sensor structures were fabricated by printing conductive tracks onto the 22 g/m² paper using silver ink. After curing the conductive ink according to the manufacturer’s specifications, the electrical continuity and baseline resistance of each sensor were verified before integration into the composite laminates.

2.2 COMPOSITE LAMINATE MANUFACTURING AND SENSOR INTEGRATION

Three-layer composite laminates were manufactured to evaluate the structural and sensing performance of the embedded paper-based sensors. The printed paper-based sensors were positioned between the fabric layers before resin infusion/impregnation (**Figure 1b**). Special care was taken to ensure:

- Proper alignment of the sensor within the laminate,
- Avoidance of wrinkling or folding of the paper substrate,
- Reliable electrical contact routing to the laminate edge.

The lamination process was carried out under controlled pressure and temperature conditions to ensure full impregnation of the reinforcement layers while preventing damage to the printed conductive tracks. After curing, the composite panels were demolded and conditioned at ambient laboratory conditions before mechanical testing.

2.3 FLEXURAL TESTING OF COMPOSITE

To evaluate the electromechanical response of the embedded sensors under mechanical loading, bending tests were performed using a universal testing machine. The bending configuration was designed to simulate a gradually increasing structural load, enabling the investigation of sensor behavior under continuous mechanical stress.

The crosshead (traverse) speed was set to 4 mm/min to generate a steadily increasing load over time. This quasi-static loading condition allowed for precise monitoring of resistance changes in correlation with the applied mechanical deformation.

Each test cycle consisted of: A continuous load increase for 2 minutes, an instantaneous unloading phase, during which the applied load was rapidly removed.

This procedure enabled the assessment of: Sensor sensitivity under progressive strain, Signal stability during sustained loading, Reversibility of the electrical response after unloading, and potential hysteresis or signal drift effects.

To ensure statistical reliability and evaluate position-dependent behavior, the test was repeated three times per sample. In each repetition, the load application point varied systematically:

- Center of the specimen,
- Position above the left sensor,
- Position above the right sensor.

This alternating loading configuration allowed the investigation of localized strain detection capability and the spatial resolution of the embedded sensors.

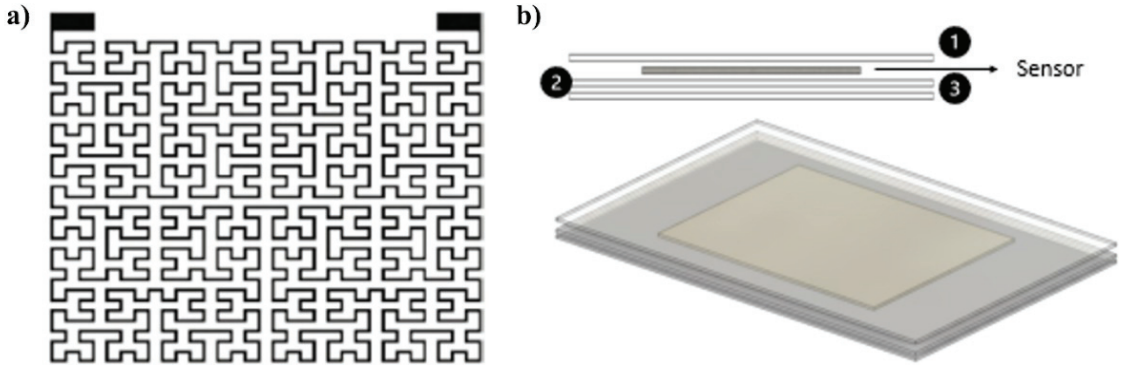

Figure 1: a) Sensor design 100 x 80mm, and b) Schematic illustration of the embedded sensor

Different materials and techniques were tested for the sensor production, but a combination of a 22 g/m^2 paper and silver ink proved the most suitable combination for our test purposes. Three-layer laminates made of glass and natural fiber were produced, and the sensors were laminated between the outer and inner fabric layers

The test on the bending machine simulates a load that ramps up over time. This test should show how the sensors behave under continuous stress. To achieve this, the traverse speed was set to 4 mm/min. After 2 minutes, the load was taken off the sample. This test was performed 3 times per sample, where the position of the load alternated between the middle, on the left sensor, and the right sensor.

3 RESULTS AND DISCUSSION

3.1 ELECTROMECHANICAL RESPONSE UNDER FLEXURAL LOADING

The functional performance of the embedded paper-based sensors was first evaluated under quasi-static flexural loading. During bending, the composite specimen experiences tensile stresses on one side and compressive stresses on the opposite side. Since the sensor was positioned in the tensile region of the laminate, mechanical deformation directly affected the conductive silver tracks printed on the paper substrate.

As shown in **Figure 2**, the electrical resistance increased gradually with increasing applied load. This behavior is consistent with strain-induced elongation of the conductive paths, resulting in an increased electrical path length and a reduction of effective cross-sectional area. The observed monotonic increase in resistance demonstrates a stable and reproducible electromechanical coupling between structural deformation and sensor response.

The linear trend observed in the initial loading regime indicates elastic deformation of both the composite structure and the paper-based sensor. Upon instantaneous unloading after 2 minutes, the resistance partially returned toward its initial value, confirming reversible behavior within the elastic range. Minor deviations between loading and unloading curves suggest slight viscoelastic effects of the paper substrate or microstructural rearrangements within the conductive ink layer.

These results confirm that the embedded sensor enables continuous structural health monitoring under mechanical stress and is capable of detecting gradual strain evolution before structural failure occurs.

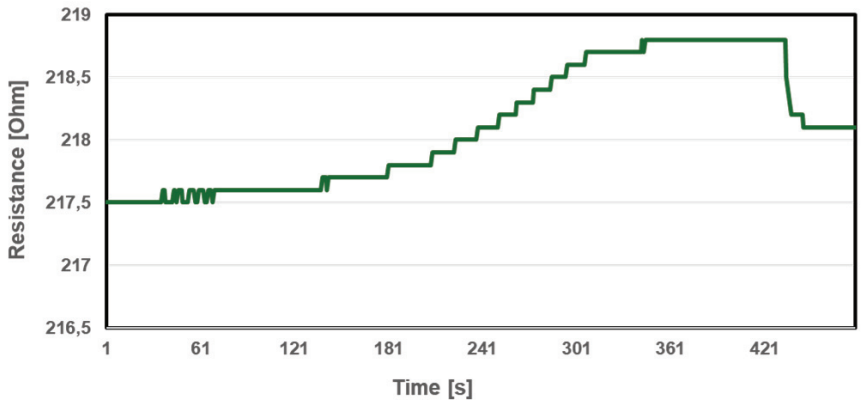

Figure 2: Change in resistance with respect to the applied load during flexural testing

3.2 DAMAGE DETECTION VIA DROP BALL IMPACT TESTING

To investigate the capability of the sensor system to detect sudden and localized damage, drop ball impact tests were performed. This method introduces controlled impact energy, leading to local matrix cracking, fiber–matrix debonding, and permanent indentation of the composite surface.

Following impact, visible dents were observed on the specimen surface. Correspondingly, the electrical resistance increased to a new permanent value compared to the initial baseline resistance. Unlike the reversible response observed during elastic flexural loading, the resistance change after impact remained elevated, indicating permanent structural deformation or microstructural damage within the laminate.

Figure 3 illustrates the permanent resistance shift after impacts from four different drop heights. A clear correlation between impact severity and resistance increase was observed. Higher drop heights resulted in greater resistance changes, which can be attributed to increased damage extent and crack propagation within the laminate.

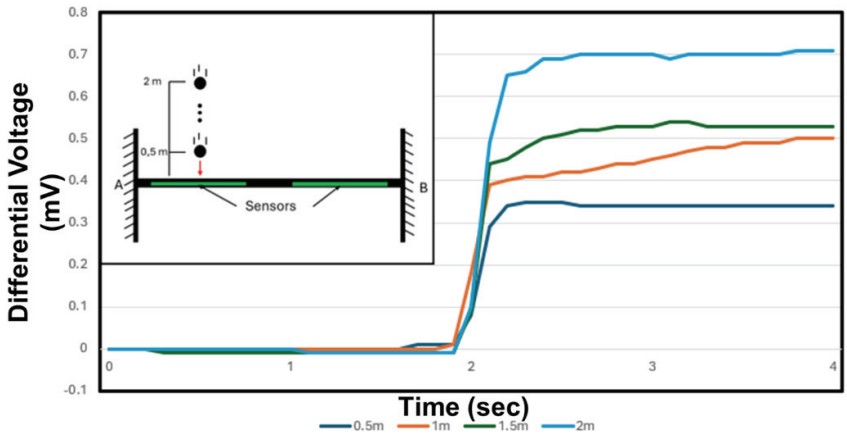

Figure 3: Permanent resistance change after the drop ball impact test

When the impact energy exceeded the structural load-bearing capacity, a catastrophic fracture occurred. In these cases, complete electrical signal loss was observed due to disruption of the conductive pathways. This abrupt signal interruption can therefore serve as a clear indicator of structural failure.

3.3 SENSITIVITY TO MINOR SURFACE INDENTATIONS

Beyond macroscopic dents, the detection of small surface indentations and subcritical damage is essential for early-stage structural health monitoring. Conventional two-point resistance measurements were sufficient to detect noticeable deformation; however, to enhance sensitivity for small resistance variations in the millivolt range, a Wheatstone quarter-bridge configuration was implemented (**Figure 4**).

Due to the low voltage differences generated by minor deformation, an Arduino-based data acquisition system equipped with multiple HX711 amplifier modules was used. The HX711 modules provide high-resolution analog-to-digital conversion, enabling precise detection of small voltage variations. The raw digital output values were converted into voltage signals for analysis.

Impacts on the underlying embedded sensors resulted in measurable millivolt-level changes.

The implemented setup allowed four simultaneous measurements, enabling spatially resolved monitoring across the laminate.

The Wheatstone bridge configuration significantly enhanced detection sensitivity and allowed visualization of even small surface indentations that were not immediately visible to the naked eye. This demonstrates the suitability of the system for early damage detection and progressive monitoring.

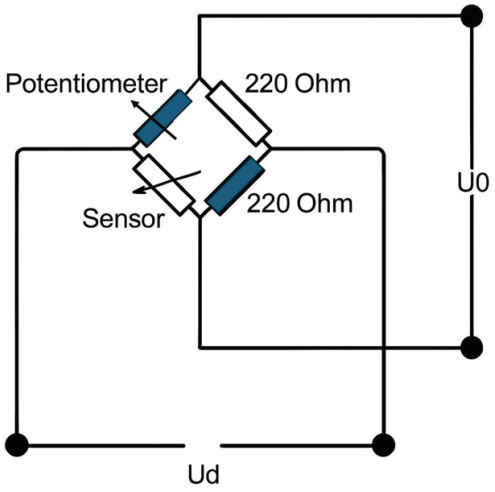

Figure 4: The circuit diagram of the Wheatstone quarter bridge

3.4 CORRELATION BETWEEN MECHANICAL DAMAGE AND ELECTRICAL SIGNAL

The overall results demonstrate a clear correlation between mechanical loading conditions and electrical resistance changes: Gradual and reversible resistance increase due to elastic deformation, Permanent resistance shift due to plastic deformation or internal damage, Abrupt signal loss due to structural fracture.

This hierarchical signal behavior enables differentiation between elastic loading, progressive damage accumulation, and catastrophic failure.

The integration of paper-based printed sensors into hybrid composite laminates therefore provides a lightweight, low-cost, and structurally integrated solution for real-time structural health monitoring. The results confirm that the developed sensor system is capable of detecting both continuous strain evolution and impact-induced damage, while maintaining compatibility with composite manufacturing processes.

4 CONCLUSIONS

This study demonstrates the successful integration of paper-based printed silver sensors into hybrid glass–natural fiber composite laminates for structural health monitoring applications. The experimental results reveal a clear and systematic correlation between mechanical loading conditions and electrical resistance variations of the embedded sensors.

Under quasi-static flexural loading, a gradual and reversible increase in resistance was observed, corresponding to elastic deformation of the composite structure. Impact-induced damage resulted in a permanent shift in resistance, indicating plastic deformation and internal

microstructural damage. In cases of catastrophic structural failure, abrupt signal loss occurred due to disruption of the conductive pathways.

This hierarchical signal response enables clear differentiation between elastic deformation, progressive damage accumulation, and complete structural fracture. Such differentiation is essential for reliable real-time condition monitoring and early damage detection in composite structures.

Furthermore, the implemented Wheatstone bridge configuration combined with Arduino-based signal acquisition demonstrated sufficient sensitivity to detect even minor surface indentations and millivolt-level resistance changes. This highlights the suitability of the system for both global strain monitoring and localized damage detection.

Overall, the presented approach provides a lightweight, cost-effective, and manufacturing-compatible sensing solution. The compatibility of the paper-based sensor with standard composite processing techniques, combined with its reliable electromechanical response, underlines its potential for scalable implementation in smart and sustainable composite structures.

REFERENCES

[1] S. H. Kamarudin *et al.*, "A Review on Natural Fiber Reinforced Polymer Composites (NFRPC) for Sustainable Industrial Applications," Sep. 01, 2022, *MDPI*. doi: 10.3390/polym14173698.

[2] Y. Wu, C. Xia, L. Cai, A. C. Garcia, and S. Q. Shi, "Development of natural fiber-reinforced composite with comparable mechanical properties and reduced energy consumption and environmental impacts for replacing automotive glass-fiber sheet molding compound," *J Clean Prod*, vol. 184, pp. 92–100, May 2018, doi: 10.1016/j.jclepro.2018.02.257.

[3] M. Pervaiz and M. M. Sain, "Carbon storage potential in natural fiber composites," *Resour Conserv Recycl*, vol. 39, no. 4, pp. 325–340, Nov. 2003, doi: 10.1016/S0921-3449(02)00173-8.

[4] A. D. Nugraha, M. I. Nuryanta, L. Sean, K. Budiman, M. Kusni, and M. A. Muflikhun, "Recent Progress on Natural Fibers Mixed with CFRP and GFRP: Properties, Characteristics, and Failure Behaviour," Dec. 01, 2022, *MDPI*. doi: 10.3390/polym14235138.

[5] J. H. Hsiao, Y. T. Tsao, C. Y. Yang, and C. M. Cheng, "Design, application, and integration of paper-based sensors with the Internet of Things," in *Chemical, Gas, and Biosensors for Internet of Things and Related Applications*, Elsevier, 2019, pp. 13–26. doi: 10.1016/B978-0-12-815409-0.00002-4.

[6] S. H. Nair, A. Sinha, and L. Vachhani, "Hilbert's Space-filling Curve for Regions with Holes," IEEE, 2018. doi: 10.1109/CDC.2017.8263684.

XI ECCOMAS Thematic Conference on Smart Structures and Materials - SMART 2025
M. Krommer, M. Nader and M. Schagerl (Eds)

Received: 23 April 2025 / Revised: 3 September 2025 / Accepted: 15 September 2025
© The Author(s) 2025

Exploring the applicability of printed sensors for deformation detection in wooden laminates

Sebastian Platzer, Astrid Pechstein, Alexander Humer, Michael Krommer

Abstract. This work focuses on the applicability of printed sensors for deformation measurement in wooden laminates. A framework is presented, in which mechanic deformations are superimposed to the electric field equations, thus allowing to estimate impedance at different deformation states. Depending on the position of the sensor with respect to the laminate's thickness coordinate, different deformation measures can be captured. We analyze a setup where two sensors are placed symmetrically around the laminate's mid-surface, and show that the in-plane strain and curvature can be related to the change of impedance. Our findings provide insight concerning the capabilities of printed sensors in practical applications for structural health monitoring and real-time deformation detection.

Key words: Smart Structures, Printed Sensors, Integrated Sensors, Bio-Based Structures

1 INTRODUCTION

Detection of local deformations, such as the in-plane strain or curvature, is an important task in structural health monitoring. In [1, 2], Stockinger and co-workers designed impedance sensors printed on paper to monitor the drying and cross-linking process during the gluing of wood. These paper sensors were integrated within the layer of glue, such that they remain within the laminate after dry-pressing. Electric impedance in a frequency range from 10 Hz to 1 MHz was measured, and a distinct relation between capacity and conductivity on the one hand, and the state of cross-linking in the glue on the other hand, was found. In the final state, impedance was dominated by the electric capacity of the sensor, which is, in turn, influenced by electric permittivity of wood and glue, as well as the geometry of the sensor.

While the focus of this study is on the applicability of printed sensors for deformation detection in glued laminated wood, the underlying sensing technology offers broad potential across various fields. These include structural health monitoring in civil engineering – such as in bridges, historical timber buildings, or composite materials – where real-time deformation detection is critical for safety and maintenance. In the automotive and aerospace industries, printed deformation sensors could be integrated into lightweight composite structures to detect stress or

Sebastian Platzer & Astrid Pechstein & Alexander Humer & Michael Krommer
Institute of Technical Mechanics, Johannes Kepler University Linz, Altenbergerstr. 69, A-4040 Linz, Austria
e-mail: sebastian.platzer@jku.at

fatigue. The versatility and low-cost nature of printed electronics make them particularly suitable for applications requiring distributed sensing over large or geometrically complex surfaces.

In the current contribution, we explore the applicability of such sensors to detect deformations in laminates throughout their life-cycle. Deformations of the structure will inevitably lead to a change in the sensor geometries, which result in a change of capacity of the sensor. We model the influence of such a deformation through the deformation gradient in a mathematically consistent manner. Deformations for various load cases are pre-computed and then prescribed in impedance computations. First results show a correlation between change in capacity and in-plane strain in direction orthogonal to the interdigitated sensor electrodes. If two sensors are positioned away from the laminate's mid-plane, in-plane strain and curvature can be recovered from changes in capacity.

2 STRUCTURAL SETUP FOR NUMERICAL EXPERIMENTS

To explore the applicability of printed sensors for deformation detection in wooden laminates, a series of numerical experiments were performed on glued-laminated timber (glulam) beams under various loading conditions. Two integrated sensors were embedded within the adhesive layers of the laminated structure, as illustrated in Fig. 1, to measure strain quantities such as the in-plane strain or the mean curvature.

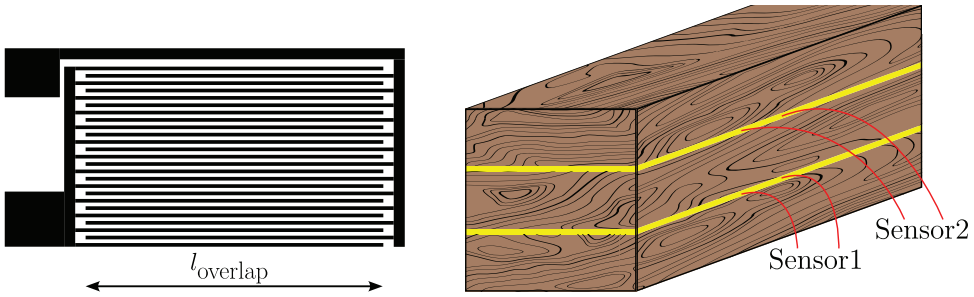

Figure 1: Sensor design (as described in [1]) and the wooden structure (glulam beam) with two integrated, paper-based sensors in the glue layers.

Within this setup, we use the impedance sensor *Sen-PZ1*, where the electrode gap and electrode width are both 0.3 mm, and the electrode overlap length is $l_{\text{overlap}} = 24.3\,\text{mm}$. This configuration is consistent with the setup used in the wood glue curing experiment described in [2].

2.1 Mechanical modeling

To analyze the mechanical response of the glulam beam with integrated sensors, we employ a simplified mechanical model assuming both, the wood and adhesive layers, as isotropic materials characterized by their respective Young's modulus E and Poisson's ratio ν. Although this

assumption is idealized, it offers a practical approach for capturing the primary deformation characteristics under applied loads. This simplification ensures a straightforward, yet sufficiently accurate, estimation of usability, enabling an initial evaluation of sensor performance in detecting deformation.

To model the electric output of the sensor in laminates depending on the deformation state, it is necessary to distinguish between *material coordinates* $\boldsymbol{X}$ describing the position of a material point in reference configuration, and *spatial coordinates* $\boldsymbol{x}$ for the spatial position of the material point after deformation. The displacement field is commonly denoted as $\boldsymbol{u} = \boldsymbol{x} - \boldsymbol{X}$, and the deformation gradient is $\mathbf{F} = (\nabla_{\boldsymbol{X}} \boldsymbol{u})^T + \mathbf{I}$. Note that the nabla operator $\nabla_{\boldsymbol{X}} = \partial/\partial_{X_i}$ is to be understood as differentiation with respect to material coordinates.

The material behavior is governed by the St. Venant-Kirchhoff model, which represents the simplest form of elastic behavior applicable to finite deformations at small strain. The strain energy density Ψ of the St. Venant-Kirchhoff model is a quadratic form in the Green strain tensor $\mathbf{E} = \frac{1}{2}(\mathbf{F}^T \cdot \mathbf{F} - \mathbf{I})$ and is given by

$$\Psi = \frac{1}{2}\lambda(\operatorname{tr}\mathbf{E})^2 + \mu \operatorname{tr}\mathbf{E}^2. \tag{1}$$

Above, λ and μ are the Lamé parameters, which are related to Young's modulus E and the Poisson ration ν as

$$\lambda = \frac{E\nu}{(1+\nu)(1-2\nu)} \quad \text{and} \quad \mu = \frac{E}{2(1+\nu)}. \tag{2}$$

Without going into further details of this formulation, we refer interested readers to [3] for more information.

2.2 Electrical modeling

To analyze the response of the printed sensors integrated in the adhesive layers, we model their electrical behavior in the electrostatic regime, assuming negligible contribution from the rate of the magnetic field intesity $\dot{\boldsymbol{B}} \simeq \mathbf{0}$. This assumption is justified as measurements are usually taken at frequencies from 10 Hz to 1 MHz. We assume the electrodes to be perfectly conductive and of zero thickness. The electric current density consists of both Ohm's current and dielectric displacement currents. Assuming linear relationships specified through the electric permittivity $\varepsilon = \varepsilon_r \varepsilon_0$ and specific conductivity σ implies the relation

$$\boldsymbol{j} = \sigma \boldsymbol{e} + \varepsilon_r \varepsilon_0 \dot{\boldsymbol{e}}, \tag{3}$$

where $\varepsilon_0 = 8.841\,87 \times 10^{-12}\,\mathrm{A\,s\,V^{-1}\,m^{-1}}$ is the permittivity of vacuum. For harmonic excitations at a fixed frequency ω, this behavior is modeled in the frequency domain employing a complex permittivity

$$\boldsymbol{j} = (\sigma + i\omega\varepsilon_r\varepsilon_0)\boldsymbol{e} = i\omega\hat{\varepsilon}\boldsymbol{e}, \tag{4}$$

where we use the two parameter model for $\hat{\varepsilon}$

$$\hat{\varepsilon} = \varepsilon_0 \varepsilon_r + \frac{\sigma}{i\omega}. \tag{5}$$

Faraday's law ($\nabla_{\boldsymbol{x}} \times \boldsymbol{e} = \boldsymbol{0}$) implies the existence of an electric potential, $\boldsymbol{e} = -\nabla_{\boldsymbol{x}} \phi$. Note that here derivatives are to be understood with respect to spatial coordinates. By transformation, the *spatial electric field* $\boldsymbol{e}$ can, however, be related to the *material electric field* $\boldsymbol{E}$,

$$\boldsymbol{E} = \boldsymbol{e} \cdot \mathbf{F}, \qquad \text{with} \qquad \boldsymbol{E} = -\nabla_{\boldsymbol{X}} \phi. \tag{6}$$

Conservation of charge is also stated with respect to spatial coordinates, and can be transformed to material coordinates using the Piola transformation,

$$\operatorname{div}_{\boldsymbol{x}} \boldsymbol{j} = 0, \qquad \text{transforms to} \qquad \operatorname{div}_{\boldsymbol{X}} \boldsymbol{J} = 0 \qquad \text{for} \qquad \boldsymbol{J} = (\det \mathbf{F}) \mathbf{F}^{-1} \cdot \boldsymbol{j}. \tag{7}$$

Inserting the definition of the material electric field (6) and the constitutive relation (4) leads to a partial differential equation for the material electric field,

$$\operatorname{div}_{\boldsymbol{X}} (i\omega \hat{\varepsilon} (\det \mathbf{F}) \mathbf{F}^{-1} \cdot \mathbf{F}^{-T} \cdot \boldsymbol{E}) = 0. \tag{8}$$

Note that the above equation describes the electric field equation in electrostatic regime at a given state of deformation which is characterized through its deformation gradient $\mathbf{F}$. All quantities refer to material quantities, therefore simulations can always be carried out in the reference configuration; $\mathbf{F} = \mathbf{I}$ holds for the case of no deformation.

To determine the impedance of the sensor at a given frequency, a harmonic excitation potential of 1 V is applied at one of the electrodes, while the other one is grounded. Let Γ_{el} denote the surface of this electrode in reference configuration, while γ_{el} shall describe its surface after deformation. In experiments, amplitude and phase of the (complex) electric current J are measured at this electrode. In simulations, this current is represented integrating the normal jump in electric current $[\boldsymbol{j} \cdot \boldsymbol{n}]$ across the electrode surface. The vector normal to the deformed electrode surface $\boldsymbol{n}$ and its counterpart $\boldsymbol{N}$ normal to the electrode's reference surface are related by Nanson's formula,

$$\boldsymbol{n} = \frac{\mathbf{F}^{-T} \cdot \boldsymbol{N}}{|\mathbf{F}^{-T} \cdot \boldsymbol{N}|}. \tag{9}$$

Thus, the total current J can be evaluated via

$$J = \int_{\gamma_{el}} [\boldsymbol{j} \cdot \boldsymbol{n}] \, ds = \int_{\Gamma_{el}} [\boldsymbol{J} \cdot \boldsymbol{N}] \, dS. \tag{10}$$

The impedance $|Z|$ is then given as the ratio $|Z| = \frac{1\,\mathrm{V}}{J}$. For a comprehensive explanation, we point interested readers to [4, 5].

It is important to note that electromechanical coupling effects are not fully considered in this model, as the mechanical and electrical problems are analyzed consecutively. First, deformation is computed from the mechanical model, which is then prescribed in the electrical model. Corresponding finite element models were set up in the open-source finite element package *Netgen/NGSolve* (see `ngsolve.org`). Numerical experiments were conducted to estimate the applicability of sensors of type *Sen-PZ1* for deformation detection in wood laminates.

3 NUMERICAL EXPERIMENTS

For the experiments described here, we employ a two-dimensional model to reduce computational costs, assuming plane strain conditions. The 25 fingers of each individual sensor are positioned in the center of the adhesive layers. The height of the wooden boards is considered to be 10 mm, while the adhesive layer has a thickness of 0.2 mm. The total length of the structure is assumed to be $w = 0.4\,\mathrm{m}$. The material properties are provided in Table 1. It should be noted that the mechanical properties of both wood and adhesive vary significantly. For this initial study, we have selected reasonable values. The previously described approach for calculating the sensor's impedance is modified by accounting for the electrode length and provides the following relationship for the two-dimensional plane model:

$$|Z| = \frac{1\,\mathrm{V}}{l_{\mathrm{overlap}} J}. \tag{11}$$

We analyze the change in impedance at a fixed frequency of $f = 10\,\mathrm{kHz}$ by comparing the sensor's impedance in the reference (undeformed) and deformed configurations. The change in impedance is given by $\Delta Z = |Z_{\mathrm{def}}| - |Z_0|$, where we use $|Z_0|$ for the impedance in the undefomed configuration.

Table 1: Material properties of wood [6] and glue [7] used in the numerical experiments. The parameters on the top characterize the mechanical response and the parameters on the bottom the electrical behavior.

E_{Wood}	E_{Glue}	ν_{Wood}	ν_{Glue}
$11\,000\,\mathrm{MPa}$	$3400\,\mathrm{MPa}$	0.3	0.4
σ_{Wood}	σ_{Glue}	$\varepsilon_{r,\mathrm{Wood}}$	$\varepsilon_{r,\mathrm{Glue}}$
$1 \times 10^{-10}\,\mathrm{S\,m^{-1}}$	$5 \times 10^{-9}\,\mathrm{S\,m^{-1}}$	8	1.1

The structure consists of three wooden boards, forming two adhesive layers, each containing a printed sensor. The finite element mesh for this two-dimensional plane model comprises 51 695 second-order elements, resulting in 207 258 degrees of freedom for the displacement and 102 929 degrees of freedom for the electric potential. Also worth mentioning, is that the high number of elements is necessary due to the resolution of the relatively small electrodes. It should be noted, however, that the number of degrees of freedom varies slightly due to different boundary conditions, which are not further discussed.

3.1 Numerical sensor calibration for pure elongation

As a first example, the sensor output for the case of pure elongation is observed, to calibrate the sensor for this mode of deformation. We examine the wooden laminate subjected to a tensile or compressive load $q_0 \boldsymbol{e}_X$ applied at the right hand boundary, while the left hand boundary is clamped, as shown in Fig. 2.

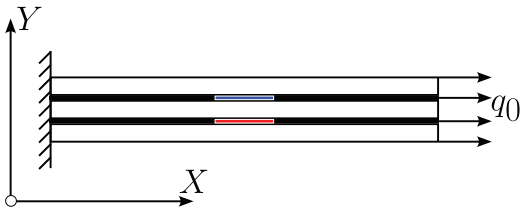

Figure 2: Setup of the structure for pure elongation.

In Fig. 3, the relative change of impedance of the two sensors is illustrated as a function of the line averaged displacement $\boldsymbol{u}$ in X-direction, represented by $\bar{u}_X$, at the right end. As expected, both sensors exhibit identical behavior due to their identical strain state. As a result, the relative change in the individual impedance values is the same, resulting in a zero difference, while their sum corresponds to twice the value of each sensor. Consequently, the sum of sensor signals can be used to monitor elongation. In the current experiment, a change in impedance by $-3.59\,\%$ indicates a nominal extension by $2\,\%$.

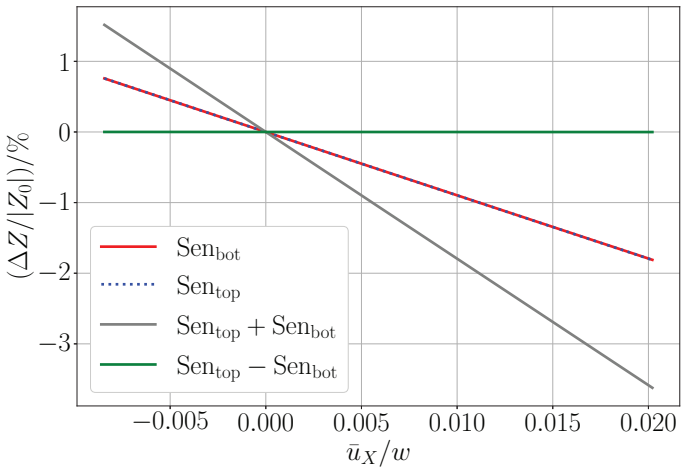

Figure 3: Results for tensile/compressive loading showing the relative change of the impedance over the mean displacement $\bar{u}_X$.

3.2 Numerical sensor calibration for pure bending

In the second example, we examine the previously mentioned structure under pure bending conditions, to assess the usability of sensor signals to detect bending deformation. The displacements at the left and right ends are prescribed as $\tilde{u}$ and $\tilde{u}^*$, respectively, as shown in Fig. 4. Additionally, an extra degree of freedom (${u_X}^{(1)}$) is introduced for the displacement in X-direction to ensure a pure bending loading state.

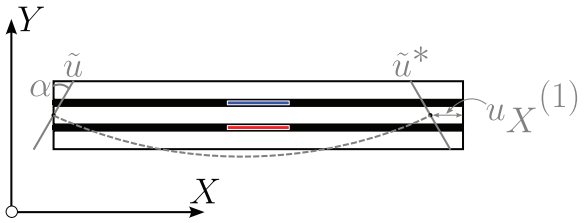

Figure 4: Setup of the structure under pure bending.

For this example, we also examine the relative change in impedance of both sensors, but this time as a function of the curvature κ of the central beam fiber of the structure, as illustrated in Fig. 5. The curvature κ is determined based on the angle at both ends of the beam and the length of the central fiber, which, in the case of pure bending, remains constant during deformation. We can easily calculate the radius of curvature as $r = w/(2\alpha)$, where α denotes the angle as shown in Fig. 4. Ultimately, we can simply take the reciprocal of this radius to find the curvature as $\kappa = 1/r$.

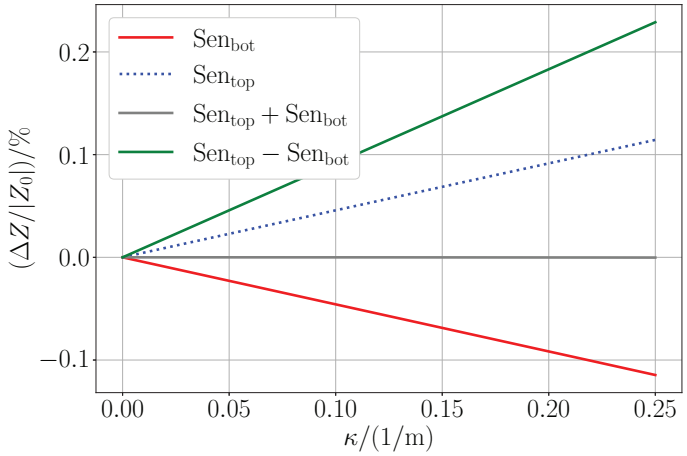

Figure 5: Results of the difference in impedance over the curvature κ.

Under pure bending conditions, the sensors exhibit impedance changes of equal magnitude but opposite sign. As a result, unlike the previous case, the sum of the impedance changes

vanishes, while their difference results in a value twice the magnitude of the individual changes. Consequently, the difference of sensor signals can be used to monitor curvature. In the current experiment, a (relative) change of the difference in impedance by 0.092 % indicates a nominal curvature of 0.1 m^{-1}.

3.3 General loading

In the third and final example, we analyze the same structure, but with both ends clamped while applying a distributed force $q_0 \boldsymbol{e}_Y$ on the top surface of the glulam beam, as shown in Fig. 6.

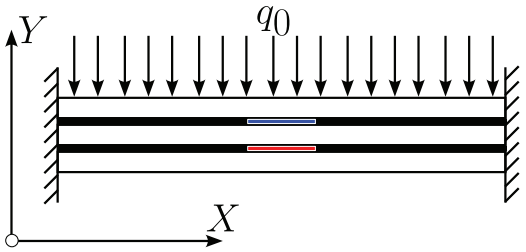

Figure 6: Setup of the structure for the analysis of a general deformation state.

From Fig. 7 below, which illustrates the relative impedance change of the sensors as a function of the length change of the central beam fiber (l/w), one immediately notices the differences compared to the two previous experiments. In this general deformation state, neither the sum nor the difference of the relative impedance changes vanishes.

On the right side of Fig. 7, the change in length of the central beam fiber in the sensor area, as well as the average curvature in this region, is shown. The calculated dashed lines were obtained by applying proportionality factors from the calibration examples. For completeness, the explicit formulation of this computation is presented below.

$$\bar{\kappa}_{\mathrm{Sen}} = 108.696\,\mathrm{m}^{-1} \left(\frac{\Delta Z_{\mathrm{top}}}{Z_{0,\mathrm{top}}} - \frac{\Delta Z_{\mathrm{bot}}}{Z_{0,\mathrm{bot}}} \right) \tag{12}$$

$$\Delta l_{\mathrm{Sen}} / l_{0,\mathrm{Sen}} = -0.557 \left(\frac{\Delta Z_{\mathrm{top}}}{Z_{0,\mathrm{top}}} + \frac{\Delta Z_{\mathrm{bot}}}{Z_{0,\mathrm{bot}}} \right) \tag{13}$$

In the range of small strains ($\Delta l_{\mathrm{Sen}} / l_{0,\mathrm{Sen}} < 0.5$), we achieve a good approximation of the experimental results. For larger deformations, however, the deviation becomes more pronounced, particularly in the case of curvature. It is important to note that the experimental results represent an averaged curvature within the sensor region, which can only be approximated. Therefore, the observed deviation is not unexpected. However, to directly infer the deformation state from the sensor signals, further tests with more complex and realistic material models would be necessary to determine the proportionality constants between the changes in electrical properties and the mechanical deformation state for more complex loading conditions.

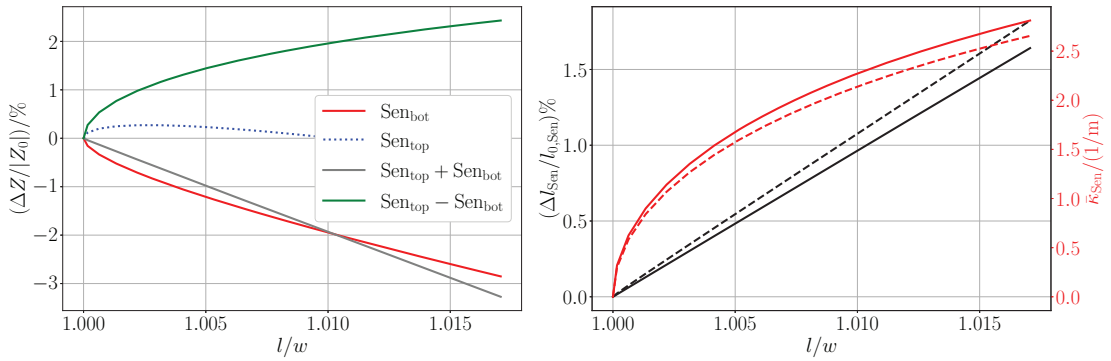

Figure 7: Results of the difference in impedance over the change in length of the central beam fibre (l) on the left hand side as well as the change of length and the curvature of the central beam fiber in the sensor area on the right hand side.

4 CONCLUSION

This study demonstrates the feasibility of using printed impedance sensors for detecting deformations in wooden laminates. By analyzing changes in sensor capacity under different loading conditions – such as tension, compression, and pure bending – we establish a correlation between impedance changes and the mechanical deformation state. Furthermore, when two sensors are positioned away from the laminate's mid-plane, both in-plane strain and curvature can be determined. These findings suggest that impedance-based sensing offers a promising approach for monitoring the structural health of laminated wood components throughout their lifecycle. Future work could focus on refining sensor designs, improving sensitivity, and validating these findings through experimental studies on full-scale glulam beams.

5 FUNDING

This work is a part of "Intelligent, integrated and impregnated cellulose based sensors for reliable bio-based structures (i3Sense)" project funded by the Austrian Research Promotion Agency (FFG).

REFERENCES

[1] T. Stockinger, B. Liedl, M. Steiner, R. Schwödiauer, F. Padinger, S. Bauer, M. Kaltenbrunner, and U. Müller, "Printed sensors on paper and wood — the frugal way of in-line detection to characterize the crosslinking behaviour of water-based glues," *Sensors and Actuators B: Chemical*, vol. 324, p. 128750, 2020. [Online]. Available: https://www.sciencedirect.com/science/article/pii/S0925400520310972

[2] T. Stockinger, D. Wirthl, G. Mao, M. Drack, R. Pruckner, S. Demchyshyn, M. Steiner, F. Egger, U. Müller, R. Schwödiauer, S. Bauer, N. Arnold, and M. Kaltenbrunner, "iSens: A fiber-based, highly permeable and imperceptible sensor

design," *Advanced Materials*, vol. 33, no. 37, p. 2102736, 2021. [Online]. Available: https://advanced.onlinelibrary.wiley.com/doi/abs/10.1002/adma.202102736

[3] P. Wriggers, *Nonlinear finite element methods*. Berlin, Heidelberg: Springer Berlin, Heidelberg, 2008.

[4] P. Monk, *Finite Element Methods for Maxwell's Equations*. Oxford: Oxford University Press, 2003.

[5] A. C. Eringen and G. A. Maugin, *Electrodynamics of continua I: foundations and solid media*. Springer, New York, 1991.

[6] D. Kretschmann, "Mechanical properties of wood," *Wood handbook: wood as an engineering material: chapter 5. Centennial ed. General technical report FPL; GTR-190. Madison, WI: US Dept. of Agriculture, Forest Service, Forest Products Laboratory, 2010: p. 5.1-5.46.*, vol. 190, pp. 5–1, 2010.

[7] F. Stoeckel, J. Konnerth, and W. Gindl-Altmutter, "Mechanical properties of adhesives for bonding wood—a review," *International Journal of Adhesion and Adhesives*, vol. 45, pp. 32–41, 2013.

XI ECCOMAS Thematic Conference on Smart Structures and Materials - SMART 2025
M. Krommer, M. Nader and M. Schagerl (Eds)

Received: 22 April 2025 / Revised: 25 August 2025 / Accepted: 15 September 2025
© The Author(s) 2025

New Approaches to Sensor Fabrication on Wooden Substrates and Cellulosic Paper

Claudia Pretschuh, Arunjunai Raj Mahendran

Abstract. Quality monitoring of composite products and especially of wooden composites requires the development of low-cost and stable sensors, which are prepared or applied directly on surfaces, in glue joints, or on thin carrier substrates. Smart wooden surfaces, the "internet-of-things", the request for complete process monitoring and the development of flexible paper electronics, are the main drivers in this research field. Recently, screen-printing or physical vapor deposition methods have been successfully developed for such approaches. In this review, we present innovative and new sensor fabrication methods on wood and cellulosic substrates, developed and used within the i³ sense project.

Key words: New fabrication techniques, conducting materials, wood, cellulosic paper, sensing, health monitoring of composites.

1 INTRODUCTION

Electrically conductive materials are smart functional materials that enable the construction of conductive structures and thus represent the basic materials in the field of sensors and electronics. The preparation of electrically conductive components is a crucial aspect of manufacturing a wide array of devices from everyday electronics to advanced power systems. The trend in this area is not only to establish more cost-effective materials and processes, but also to include more flexible processes like additive manufacturing and to consider sustainable aspects, such as bio-based and degradable thin substrates to reduce waste and metal consumption during fabrication. Furthermore, the approach to completely new, innovative and simpler manufacturing methods and the approach to produce either degradable or better recyclable electronics are in the foreground.

Conducting traces on wood are of interest either to insert microelectronics and to enable smart wooden surfaces for any connected devices in smart buildings, or to sense and monitor processing conditions during the production of glued wooden composites [1] or to detect the occurring moisture in wooden panels. Cellulosic thin paper, however, is used as well as a very flexible sensor substrate [2], which can be inserted in a composite already during their fabrication process. Such sensors can be used for in-situ detection of strain or load condition and so-called structural health monitoring of composites.

Claudia Pretschuh & Arunjunai Raj Mahendran
Wood K plus, Kompetenzzentrum Holz GmbH, Altenberger Str. 69, 4040, Linz, Austria
e-mail: c.pretschuh@wood-kplus.at

Smart materials used for conducting traces need to be not only sufficiently electrically conductive and homogenous, but they must also present a good adherence to the sensor substrate and solderability, so that a chemically and thermally stable and durable connection is obtained. Depending on the final application, either fine traces or large areas are required. New innovative fabrication methods could be advantageous through higher flexibility in production, the use of low-cost processes or the reduction of energy use, material use and waste. Furthermore, providing solutions for recycling strategies can be an important benefit.

The use of alternative substrates like bioplastics, paper or natural fibers for electronics is still in the R&D phase. The maturity substrates in the market are glass fiber composites or polyimide foils. And to generate more sustainable products, one can use either improved substrates or new processing methods.

Common methods for preparing electronic components are mainly photochemical preparations, copper plating and coatings with copper [3]. At present, etching, plating and stamping are mainly used. Methods which can be used for alternative substrates are printing and deposition. Printing methods can be divided into screen printing and digital inkjet printing. Screen printing is a fast and industrially used method for e.g. preparing commercial papers. But it has drawbacks: the sieve has a fixed geometrical design, so the method is not flexible, and any design change is expensive; high amounts of cleaning agents and silver inks are in addition required. Challenges for inkjet printing are the required specialized nanoparticle-based inks and the need for smooth sensor substrates. Vapor deposition methods are used to prepare thin and stable metallic films on a substrate by using special environments in processing chambers, like vacuum, high temperature or plasma.

Recently, screen-printing and physical vapor deposition methods have been successfully developed for such approaches on wood and on cellulosic paper [1, 4, 5].

In this review, we present innovative and new sensor fabrication methods on wood and cellulosic substrates including the following:

(a) laser-induced graphitization on modified wood surfaces for moisture detection,
(b) the preparation of conductive particleboards for sensing humidity, temperature and load,
(c) and the development of suitable conductive thermoplastic filaments for extrusion-based Fused Deposition Modeling (FDM printing) on very thin cellulosic papers to detect strain in laminated composites.

For each fabrication approach, different manufacturing challenges are shown and discussed in detail. New solutions, using modified materials are provided and the benefits of these fabrication methods regarding their application are given.

2 LASER INDUCED GRAPHITIZATION ON MODIFIED WOOD SURFACES

Wood is biochemically composed of lignin, cellulose, and hemicelluloses. It is a well-known process that carbon structures can be formed from these reactants through thermal treatment. This can be exploited through the so-called laser-induced process to generate electronics even directly on wood surfaces. Only a few processes are known in the research literature that already perform such laser-induced graphitization processes directly on the wooden surface:

- Edberg at al. [6] coated spruce wood with a water-based ink containing lignin and cellulose polymers. A CO_2 laser was subsequently used to produce interdigitated carbon electrodes from the ink coating. The prepared sensor showed a linear change in resistance for different humidity levels - between 40% and 80% relative humidity.
- Dreimol et al. [7, 8] showed in their approach of iron-catalyzed laser-induced graphitization (IC-LIG), the use of an iron-tannic acid ink for their pre-treatment process.
- Lengger et al. [9] investigated the suitability for direct conversion of typical European and Asian woods into laser-induced graphene (LIG), without pre-treatment. The ability to produce LIG on untreated, natural wood under ambient atmosphere was favoured overall by a high density, as well as a high soluble lignin content. Softwoods like spruce were not suitable in their study.
- Lee and Kim et al. [10] report femtosecond laser direct writing of LIG patterns on arbitrary natural woods, thereby using a photoconversion process for LIG instead of irradiating infrared CO2 laser.

It is further known that phenolic condensation resins, such as Novolaks and Resoles, are comparatively well carbonizable and graphitizable, especially due to their aromatic structures. Wu and Hu et al. [11] presented 2018 that a phenolic resin is a promising precursor of LIG on PET films. Paixao and Araujo et al. [12] successfully used CO_2 laser-scribing on phenolic paper, as a type of low-cost substrate to prepare electrochemical devices.

2.1 Materials & Methods

In these following presented approaches, both a Novolak and two different Resol systems were used for the pretreatment of wooden surfaces, which subsequently resulted in the preparation of electrically conductive lines and 2 resistive sensors by using the LIG process.

All laser-induced graphitization (LIG) tests carried out here were performed using a CO_2 laser cutter Trotec Speedy300 flexx. Spruce wood was pre-dried and coated with different types of Novolac resin and laser parameters have been varied (Fig. 1a).

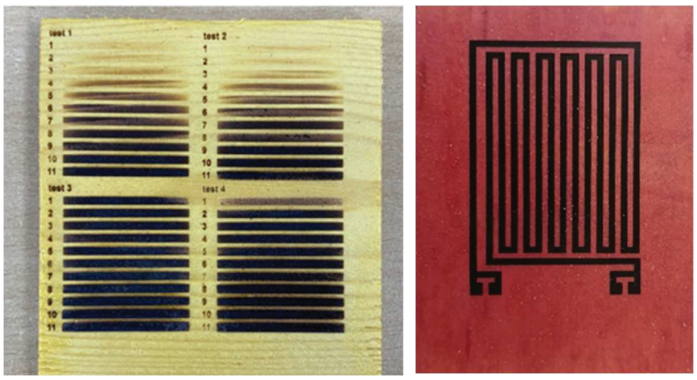

Figure 1: LIG tests on Novolac Resin treated spruce wood (a:left) and a resistive sensor prepared by LIG on PF coated spruce wood (b:right)

The Novolac Resin type was provided by Prefere Resins Germany GmbH and used as a solution in Ethanol. Hexamethylenetetramine was added for cross-linking, after application on the wooden surface it was cured at 130°C. The final applied solid resin content was 61 g/m². The obtained resistance of the optimized lasered lines was even below 0.4 kΩ.

For the second approach, a Phenol formaldehyde resin (PF) and a Lignin Phenol formaldehyde resin (LPF) were prepared. The solution was applied on a pre-dried spruce wood and cured at 130°C. The subsequent laser engraving process was also improved, when the longest lines were parallel with the grain of the wood. On selected samples, a resistive meander structured sensor was prepared (Fig. 1b).

2.2 Testing and Validation

For measuring the temperature response, PF and LPF samples were placed into a climate chamber at 50% relative humidity and the temperature was varied. For analyzing the response to moisture, the climate chamber was set to 25°C and with starting at 25% moisture content, every 30 minutes the relative humidity was increased by 10%. Especially LPF pre-treated samples showed a well correlation of the measured resistance with increasing temperature (Fig. 2a). A quite higher change in resistance was measured for PF samples and LPF samples due to the varied relative humidity (Fig. 2b).

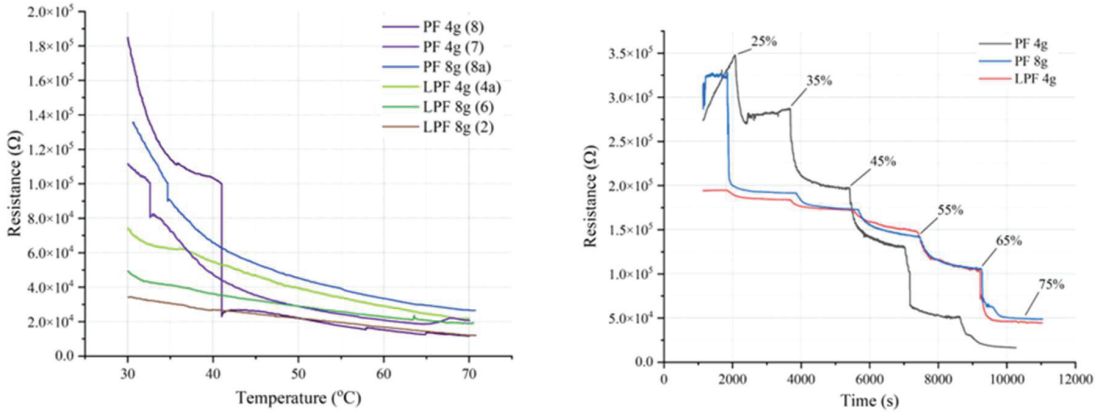

Figure 2: Resistance of sensors prepared by LIG on PF or LPF resin coated spruce wood – in response to the temperature (a: left) and in response to varied relative humidity (b: right)

2.3 Challenge

However, a main challenge for the application of LIG prepared sensors, is the low stability of the graphene layer on the wooden substrate. Optical microscope images are presenting the carbon line before testing (Fig. 3a) and after thermal treatment (Fig. 3b). Thereby, protective layers would be potentially required in further applications, as well as capacitive sensor types.

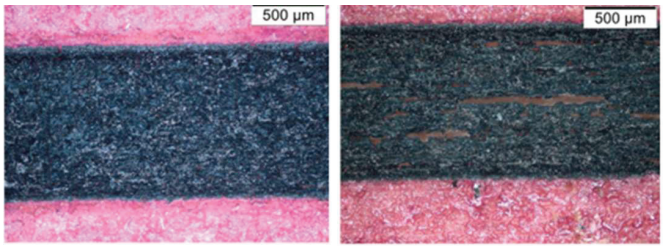

Figure 3: Carbon layer of a LIG sensor, prepared from PF coated sample: before testing (a: left) and ablation of the carbon after thermal treatment in the climate chamber (b: right)

3 CONDUCTIVE PARTICLEBOARDS FOR SENSING HUMIDITY, TEMPERATURE AND LOAD

Although there is existing research available on improving the electrical conductivity of wood-based panels [13, 14, 15, 16], their potential for use as sensors was shown for the first time in detail by Kocoglu and Pretschuh et al. [17] last year. For this purpose, single-layer particle boards were produced by hot pressing using conductive carbon black (CB) and carbon fibers (CF) as conductive fillers.

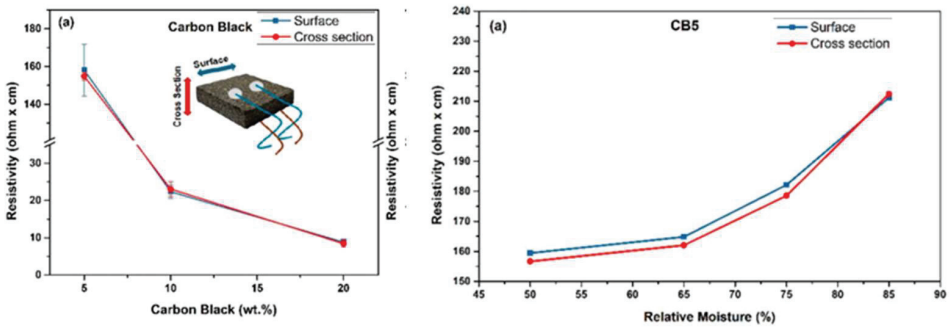

Figure 4: Conductance of CB filled conductive wood-panels (left) and change in resistance due to increase in relative humidity, measured in a climate chamber (right) [17]

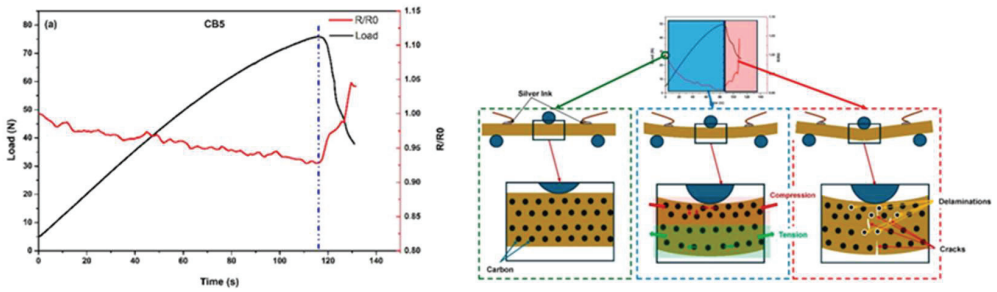

Figure 5: Change of resistance of CB filled conductive wood-panel due to load during 3-point bending test (left), for the phase of compression and after occurring of cracks (see explanation at right-side) [17]

The conductive wood panels were sensitive as well to moisture (Fig.4) and pressure (Fig. 5). In addition, a wooden panel containing a higher amount of CF demonstrated reproducible PTC behavior, see Fig. 6. The measured CF sample showed a decrease of resistance at around 85°C, which can be related to water vaporization from the moisture inside the wood chips.

In future applications, conductive panels could be potentially designed as thin and very low-cost moisture sensors, for crack detection, or as temperature sensors. They can be easily applied on other wooden composite products.

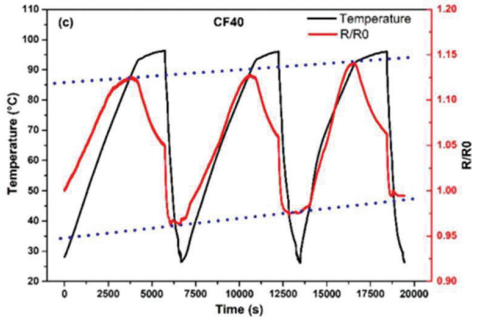

Figure 6: Change of resistance of CF filled conductive wood-panel due to a cyclic temperature change [17]

5 TAILOR-MADE CONDUCTIVE THERMOPLASTIC FILAMENTS FOR EXTRUSION-BASED FDM PRINTED STRAIN SENSING IN THERMOSET COMPOSITES

For a successful embedding of sensors into thermoset composites, it can be advantageous to develop thin and flexible sensors. Therefore, thin cellulosic papers are very suitable substrates. Considering the need for sustainable production, additive manufacturing techniques are also emerging to allow freedom in the design of sensor structures. While relatively new in the field of electronics, 3D printing is becoming more available for specialized applications. In the presented approach, extrusion based FDM printing is applied for the development of thin strain sensors on cellulosic paper. Currently, only a few extruded filament types for printing of electrically sufficient conductive materials are available on the market [18]. The requirements for such filaments include sufficient processability, high and reliable electrical conductivity, and sufficient chemical and thermal stability of the printed conductive structures.

The specialized development of conductive filaments for sensor-based applications on thermoset composites include the following steps: twin screw compounding of a thermoplastic polymer with conductive carbon fillers, filament extrusion, 3D printing of a resistive sensor on cellulosic paper, fixation on a composite and sensor validation during several loading cycles.

Thermoplastic matrix PA12 was compounded with different conductive fillers (different types of conductive carbon black, ENSACO) by using a parallel, co-rotating twin-screw compounder. For the filament extrusion, a conical, counter-rotating twin screw extruder is used in combination with a melt pump. The filament passes through a water bath to cool down the filament temperature and to maintain its diameter at 1.75 mm, which is controlled after the

cooling step. In the subsequent step, the filament is wound onto a spool (Fig. 7). During the FDM printing at a Prusa i3 MK3S onto very thin cellulosic paper, the printing parameters like extrusion and bed temperatures, layer height, extrusion width and printing speed have been optimized.



Figure 7: Winding of extruded filament and FDM printed sensor structure on cellulosic papers

In contrast to commercial TPU or PLA based filaments, the developed PA12-based 3D printed sensors responded successfully after the lamination process with epoxy resins on a fiberboard (Fig. 8). This improved chemical and thermal stability is derived from the change to a polyamide matrix material. During flexural load, the baseline decreased during the first 5 cycles and stayed constant afterwards.

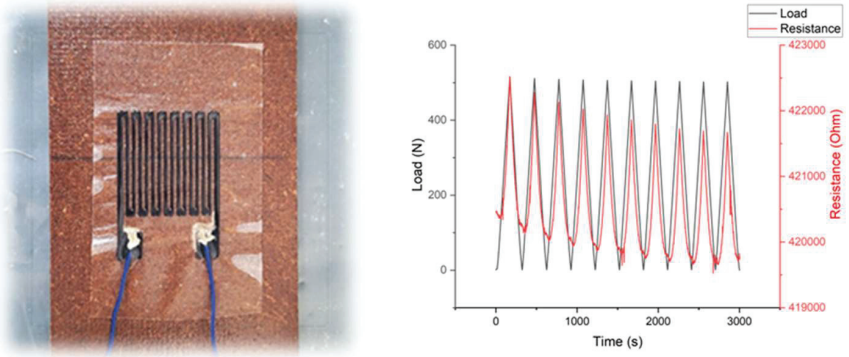

Figure 8: 3D printed paper-based sensor, laminated with epoxy resins on a fiberboard (left) and tested during 3-point flexural test (PA12-30% ENSACO 250G filled)

Such easily printable and sufficient electrically conductive filaments can be used as a low-cost solution for the preparation of 3D FDM printed stable sensors. Potentially, the printing of different sensor types can be carried out in the future by using fully biobased and biodegradable thermoplastic materials. Conductive carbon-based fillers could be available as well from different plant based or recycled precursor materials.

11 CONCLUSIONS

Simple fabrication techniques for sensors on alternative low-cost and biodegradable substrates are highly promising. New approaches for sustainable electronics can include wood surfaces, conductive wooden panels or thin cellulosic paper as substrates and as well innovative fabrication methods will be a focus in the future. Such new preparation methods will increase their market share due to different advantages: easy and simple low-cost processing, potential solutions to reduce waste, use of non-harmful materials, avoiding cleaning agents and the mining of silver. Potential applications include smart wooden surfaces, online monitoring of product quality or processing parameters and flexible paper-based electronics. Laser-induced graphitization, conductive wood-based panels or 3D FDM printing can be successful possibilities to establish new production processes in the field of sensorics and electronics. R&D steps in higher TRL levels will be required to develop promising and subsequently market-ready prototypes. Laser-induced graphitization on wood would be highly promising for humidity or temperature sensors, which are established directly on pre-treated wooden surfaces. In contrast, conductive wood-based panels could be an approach for the preparation of low-cost sensors, which are applied externally on a product, e.g. for moisture or crack detection. For the requirement of very thin, but flexible sensors, we consider the development of 3D printed paper-based sensors.

ACKNOWLEDGEMENT

For the part of laser-induced graphitization, many thanks go to our Bachelor student Ned Cope for the preparation of the samples during his Thesis; and as well to our technician Melanie Steiner for impregnating wood surfaces and to my colleague Franz Zeppetzauer for the preparation method of PF and LPF resins. We thank also Michael Hüttenberger and the JKU SoMAP departement for their help and improvements during the laser process.

For the part of conductive wooden panels, many thanks go to our colleague Mrs. Beste Kocoglu who prepared these results during her PhD thesis.

For the part of conductive filaments for the 3D FDM printing process many thanks go to our Master student Debasish Tamuli who performed a part of this work during his thesis; and as well to our colleagues Melanie Steiner for 3D printings and sensor validation; as well as to Mrs. Beste Kocoglu for data preparation and to Konrad Wipplinger for performing the compounding and extrusion process.

All these studies are part of the COMET Module i³ Sense project: the Exploration of intelligent, integrated and impregnated cellulose-based sensors for load-bearing materials in construction, automotive, and sports industries. I³ Sense is a COMET Module within the COMET – Competence Centers for Excellent Technologies Program and funded by BMK, BMAW. COMET is managed by FFG.

REFERENCES

[1] F. Egger, D. Schiller, T. Stockinger, C. Pretschuh, U. Müller and M. Kaltenbrunner, “Direct Fabrication of Electronic Circuits on Wooden Surfaces.” Advanced Sensor Research, vol.3, no.7, 2024.

Available: https://advanced.onlinelibrary.wiley.com/doi/full/10.1002/adsr.202400010

[2] T. Stockinger, M. Steiner, F. Egger, F. Padinger, R. Schwodiauer, D. Wilmer, A.R. Mahendran, M. Kaltenbrunner, U. Müller, "High porous, ultra-thin paper sensors − An option for successful sensor integration." Sensors & Actuators: A. Physical, vol. 350, 2023. Available: https://www.sciencedirect.com/science/article/abs/pii/S0924424722007336

[3] R. Melentiev, A. Yudhanto, R. Tao, T. Vuchkov, G. Lubineau, "Metallization of polymers and composites: State-of-the-art approaches." Materials & Design, vol. 221, September, 2022. https://www.sciencedirect.com/science/article/pii/S0264127522005809

[4] T. Stockinger, B. Liedl, M. Steiner, R. Schwodiauer, F. Padinger, S. Bauer, M. Kaltenbrunner, U. Müller, "Printed sensors on paper and wood — The frugal way of in-line detection to characterize the crosslinking behaviour of water-based glues", Sensors & Actuators: B. Chemical, vol. 324, 2020.

Available: https://www.sciencedirect.com/science/article/abs/pii/S0925400520310972

[5] T. Stockinger, D. Wirthl, G. Mao, M. Drack, R. Pruckner, S. Demchyshyn, M. Steiner, F. Egger, U. Müller, R. Schwödiauer, S. Bauer, N. Arnold and M. Kaltenbrunner, "iSens: A Fiber-Based, Highly Permeable and Imperceptible Sensor Design." Research Article, Advanced Materials, 2021.

Available: https://advanced.onlinelibrary.wiley.com/doi/full/10.1002/adma.202102736

[6] M. Y. Mulla, P. Isacsson, I. Dobryden, V. Beni, E. Östmark, K. Håkansson and J. Edberg, "Bio-Graphene Sensors for Monitoring Moisture Levels in Wood and Ambient Environment", Research Article, Global Challenges, vol. 7, 2023.

Available: https://onlinelibrary.wiley.com/doi/full/10.1002/gch2.202200235

[7] C.H. Dreimol, H. Guo, M. Ritter, T. Keplinger, Y. Ding, R. Günther, E. Poloni, I. Burgert and G. Panzarasa, "Sustainable wood electronics by iron-catalyzed laser-induced graphitization for large-scale applications." Nature Communications, vol.13, 2022. Available: https://www.nature.com/articles/s41467-022-31283-7

[8] C.H. Dreimol, R. Kürsteiner, M. Ritter, A. Parrilli, J. Edberg, J. Garemark, S. Stucki, W. Yan, S. Tinello, G. Panzarasa and I. Burgert, "Iron-Catalyzed Laser-Induced Graphitization – Multiscale Analysis of the Structural Evolution and Underlying Mechanism", Research Article, Small Journal, vol.20, 2024.

Available: https://onlinelibrary.wiley.com/doi/full/10.1002/smll.202405558

[9] S. K. Lengger, L. Neumaier, J. Kosel, "Laser-induced graphene formation on different wood species: enhancement of electronic performance by intrinsic features of certain types of wood." 2023. Available at SSRN: https://ssrn.com/abstract=4634972 or http://dx.doi.org/10.2139/ssrn.4634972

[10] T.-S. D. Le, S. Park, J. An, P. S. Lee and Y.-J. Kim, "Ultrafast Laser Pulses Enable One-Step Graphene Patterning on Woods and Leaves for Green Electronics", Full Paper, Adv. Funct. Mater., vol. 29, 2019.

Available: https://advanced.onlinelibrary.wiley.com/doi/abs/10.1002/adfm.201902771

[11] Z. Zhang, M. Song, J. Hao, K. Wu, C. Li, C. Hu, "Visible light laser-induced graphene from phenolic resin: "A new approach for directly writing graphene-based electrochemical devices on various substrates." Carbon, vol. 127, 2018. Available: https://www.sciencedirect.com/science/article/abs/pii/S000862231731117X

[12] L. F. Mendes, A. de Siervo, W. Reis de Araujo, T. R. L. C. Paixao, "Reagentless fabrication of a porous graphene-like electrochemical device from phenolic paper using laser-scribing." Carbon, vol. 159, 2020.
Available: https://www.sciencedirect.com/science/article/abs/pii/S0008622319312515
[13] M. Rezanezhad, A, Shalbafan, H. Thoemen. "Development of Electrically Conductive Wood-Based Composites Using Carbon Nets." Polym. Compos., vol.45, 2024. https://4spepublications.onlinelibrary.wiley.com/doi/10.1002/pc.27899
[14] X. Zhu and L. Sun, L. "Multiscale analysis on electrical properties of carbon fiber-reinforced wood composites." BioResources. Vol.10, no. 2, 2015. Multiscale analysis on electrical properties of carbon fiber-reinforced wood composites :: BioResources
[15] J. Hou, J., F. Fu, K. Lu, and L. Chen. "Highly conductive fiberboards made with carbon and wood fibers." BioRes, vol. 10, no. 4, 2015.
Available at: https://bioresources.cnr.ncsu.edu/resources/highly-conductive-fiberboards-made-with-carbon-and-wood-fibers/
[16] C. Tschannen, A. Shalbafan, H. Thoemen. "Development of an Electrically Conductive MDF Panel—Evaluation of Carbon Content and Resin Type." Polymers, vol. 15, 2023. https://www.mdpi.com/2073-4360/15/4/912
[17] O.B. Kocoglu, C. Pretschuh, C. Unterweger, M. Kodal and G. Ozkoc, "Development of Electrically Conductive Wood-based Panels for Sensor Applications." Polymers, vol.16, no.21: p. 3026, 2024. Available: https://www.mdpi.com/2073-4360/16/21/3026
[18] H. Watschke, K. Hilbig and T. Vietor, "Design and Characterization of Electrically Conductive Structures Additively Manufactured by Material Extrusion." Article in Applied Sciences, Vol. 9, 2019. Available: https://www.mdpi.com/2076-3417/9/4/779

XI ECCOMAS Thematic Conference on Smart Structures and Materials - SMART 2025
M. Krommer, M. Nader and M. Schagerl (Eds)

Received: 28 April 2025 / Revised: 12 September 2025 / Accepted: 15 September 2025
© The Author(s) 2025

Simulation of Surface Energy to Identify Optimum Laser Parameters for LIG on Wood

Martin Riegler, Mehieddine Derbas, Christian Hueber

Abstract In a living tree, the hygroscopic behavior of wood is a prerequisite for transporting water via capillary forces to the treetop. However, in the case of using wood as a construction material for buildings, this hygroscopic behavior is undesired as the uptake of water in wood, promotes the growth of fungi that destroys wood cell walls and causes a loss in load-bearing capacity. Thus, it is crucial to monitor moisture in wood construction in the course of a structural health monitoring system, using e.g. sensors. Conventional sensors for real-time monitoring operate either local or if incorporated into the engineered wood product, serve as foreign body and predetermined breaking point. In the present study, the idea is to use material inherent sensing properties of wood to detect moisture uptake by a change in electrical resistance. As untreated wood has very low electrical conductivity, the wood surface needs to be functionalized by e.g. Laser Induced Graphitization (LIG). Most of the recent studies that have investigated LIG on wood, used a pretreatment of the wood surface to achieve sufficient conversion of lignocellulose into electrically conductive carbon black and graphene (e.g. [1]). One study used a UV femtosecond laser without pretreatment of wood surfaces to achieve sheet resistance values of 10 Ω/sq at a writing speed of 10 mm/s [2]. The authors suggested an optimum range and combination of laser parameters for generating LIG.
The aim of the present study was to develop a simulation model for identifying the optimum settings for a CO_2 laser that generates LIG on wood surfaces without any pretreatment. The used CO_2 laser had a wavelength of 10.6 µm, which is more compatible to organic materials and enables higher feed speeds than femtosecond laser devices. To find the optimum range of parameters, the energy impinging on the wood surface was simulated using different laser parameters. In the simulation, parameters such as the laser feed speed, z-offset (defocus), laser frequency and laser power were considered. The simulations revealed, that the number of overlapping laser beams considerably increases below the laser radius. The z-offset of e.g. 25 mm causes six times more overlaps than a z-offset of 0 mm. Below a feed speed of 0.1%, the resulting energy on the surface of samples already dramatically decreases, whereas the laser power shows a positive linear correlation with the energy on samples.
Within upcoming empirical investigations, the simulation model will help to identify the optimum laser parameters for generating high quality LIG on untreated wood surfaces.

Key words: CO_2 Laser, Parameter Study, Graphene, Theoretical Model

Martin Riegler & Mehieddine Derbas & Christian Hueber
Wood K plus - Competence Centre for Wood Composites and Wood Chemistry, Konrad Lorenz Str. 24, 3430 Tulln, Austria, e-mail: m.riegler@wood-kplus.at

Martin Riegler
Institute of Wood Technology and Renewable Materials, BOKU-University of Natural Resources and Life Sciences, Vienna, 3430 Tulln, Austria

1 INTRODUCTION

Wood has been an essential construction material for centuries due to its sustainability, strength, and adaptability. However, its hygroscopic and anisotropic nature presents challenges, particularly in structural applications where moisture absorption can lead to degradation, fungal growth, and a reduction in mechanical integrity. As a result, monitoring moisture levels in wood is critical for ensuring the longevity and safety of wooden structures. Traditional sensor-based monitoring systems often require components embedded into the wooden construction elements, which may compromise the mechanical properties of engineered wood or create weak points within the structure.

An alternative to sensor component embedded additively to the structure is to use wood's material as a sensor by itself, that allows sensing the materials characteristics. A promising technique is laser-induced graphitization (LIG), which converts lignocellulosic surfaces into conductive graphene-like materials through localized laser heating. Unlike conventional methods that rely on embedded electronics, LIG offers a scalable, and sustainable solution for integrating electrical conductivity into wood [3]. This technology has shown potential for various applications, including moisture sensing [4], smart home devices, and flexible bioelectronics, making it a valuable tool for structural health monitoring and smart materials [1, 5].

Despite its advantages, optimizing LIG for untreated wood remains a challenge due to the complexity of laser-material interactions. The efficiency of graphitization is governed by multiple interdependent parameters, such as laser power, feed speed, z-offset (defocus) or frequency [3]. The low thermal conductivity of wood (~0.2 Wm-1K-1)) may lead to uneven heat distribution, causing thermal degradation, mechanical stress, and inconsistent electrical conductivity [1]. Moreover, the lignin content of wood significantly influences the graphitization process, with higher lignin concentrations yielding improved conductivity and structural stability [3]. Previous studies have attempted to improve LIG through chemical pre-treatments, inert gas environments, and alternative laser sources, such as femtosecond lasers [1, 4, 6, 7]. The present work serves as pre-study for generating LIG on wood using a CO2 laser without pre-treatments of the samples.

To achieve LIG without pretreatment, laser parameters need to be perfectly optimized. As a basis for this optimization, the resulting energy and the number of overlaps of laser beams on the sample could by simulated, using the Gaussian Beam Theory [8].

The aim of the present study was to simulate the theoretical resulting energy on samples as well as the number of overlapping laser beams at varying laser parameters such as laser power, frequency, feed speed and z-offset. This optimum set values of the laser parameters will in future be used to enhance the quality of LIG on untreated wood using a CO_2 laser cutter at maximum feed speeds, to ensure scalability to large construction elements.

2 MATERIAL AND METHODS

2.1 Theorical assumptions for simulation

To computationally simulate the lasering process, the laser beam itself is crucial. Here, the Gaussian Beam Theory [8] was taken, where the beam intensity can be modelled with a gaussian distribution (equations 1 to 4 and Figure 1).

$$I_{(r)} = I_0 e^{-2\left(\frac{r}{w_{(z)}}\right)^2} \quad (1)$$

$$I_0 = \frac{2P}{\pi w_{(z)}^2} \quad (2)$$

$$w_{(z)} = w_0 \sqrt{1 + \left(\frac{z}{z_R}\right)^2} \quad (3)$$

$$z_R = \pi \frac{w_0^2}{\lambda} \quad (4)$$

Where:

- r is the radial distance from the centre of the beam;
- I is the intensity of the laser at r;
- I_0 is the peak intensity at the centre of the beam;
- P is the power of the laser;
- z is the offset in z-direction from the beam waist;
- z_R is the Rayleigh length of the laser beam;
- w is the radius of the laser beam at a certain offset z;
- w_0 is the radius of the laser beam at the beam waist (given by the manufacturer of the laser);
- λ is the wavelength of the laser (10.6 µm for CO_2 lasers).

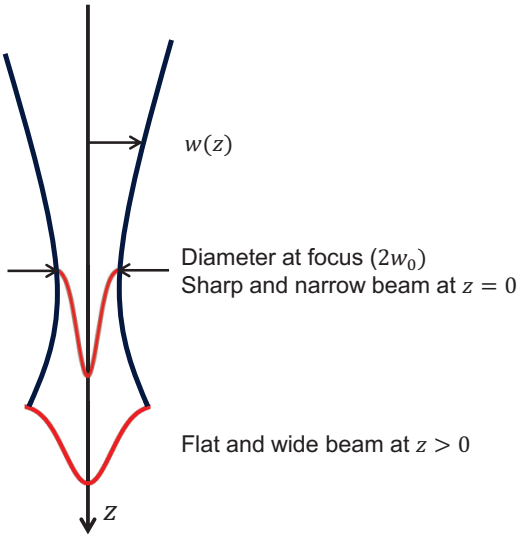

Figure 1: Schematic depiction of a gaussian laser beam with resulting intensities (red curves) at different z

2.2 Parameters for simulation

In addition to modelling the laser beam itself, the process of lasering a sample at a specific speed and frequency is needed. For this analysis, the number of laser pulses along a lasered line needs to be determined, which is a result of the selected feed speed, laser pulse frequency, and raster density. In the current study, parameters were defined that are closely linked to the laser cutter Speedy 360 from Trotec with an 80 W CO_2 laser source.

The defined raster density was 1,000 DPI, the duty cycle was 50%, the feed speed was given in percentage of the maximum feed speed of 3.550 mm/s, the laser power was defined in percentage of the maximum power of the laser source of 80 W, the laser wavelength was 0.0106 mm, the laser beam diameter at beam waist was 0.24 mm.

To get the number of laser pulses *(N)* on a line, the length of a lasered line *(L)*, the feed speed (V_f) and the number of pulses per second, which is the frequency *(f)*, are needed (equation 5).

$$N = \frac{L}{V_f} f \tag{5}$$

The travel distance between laser pulses (d) was calculated by dividing the feed speed (V_f) by the frequency *(f)* (equation 6). The number of overlapping laser beams (n) per laser radius $w_{(z)}$ was calculated according to equation 7. Finally, the surface energy (E) was calculated according to equation 8.

$$d = \frac{V_f}{f} \tag{6}$$

$$n = N \frac{w_{(z)}}{L} \tag{7}$$

$$E = \frac{I}{2f} \tag{8}$$

To simplify the simulation, it was assumed that the pulses occur equidistantly on the line, and that the power of each pulse is identical and instantaneous. Furthermore, only the 1-D calculations were taken, to minimize the computational time. Here, the cross-section with the highest power, which crosses the center of the laser, was used to calculate the energy on the lasered surface.

The simulation was realized in Python 3.12.

3 RESULTS AND DISCUSSION

The energy as well as the size of the laser beam is highly affected by the chosen offset value z (Figure 2). The maximum energy value in the beam drops by 95.5% (0.266 µJ to 0.012 µJ) when using a z of 5 mm instead of full focus (z = 0 mm). Additionally, the full width at half-maximum (FWHM) of the beam increases by 370.6% (z = 5 mm) compared to the full-focus beam (z = 0 mm).

To simulate the energy on the surface of samples to be lasered, the laser power, frequency, feed speed and z-offset were considered as input parameters. To highlight the effect of the input parameters, Figure 3 depicts an example of four different combinations of feed speed and frequency at a laser power of 100%. With low frequency (e.g. 1,000 Hz) and high feed speed (e.g. 100%), the amount of overlap between the laser pulses is minimal, which results in clearly separable gaussian distributions. With high frequency (e.g. 10,000 Hz) and low feed speed (e.g. 50%), the overlap between the laser pulses results in an energy plateau. This effect becomes clearly visible by looking at the zoomed in representation of the version “low speed” and “high frequency” (Figure 4).

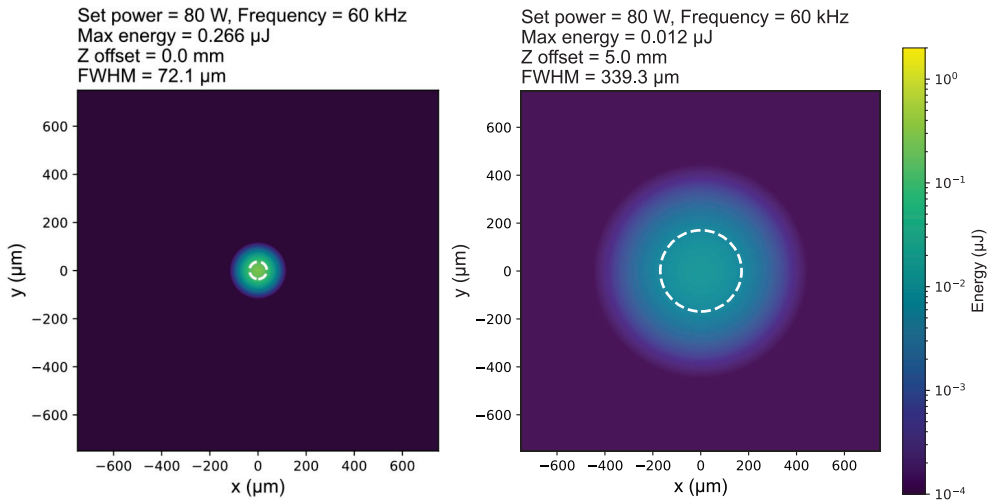

Figure 2: Energy and size of laser beam at different z-offsets

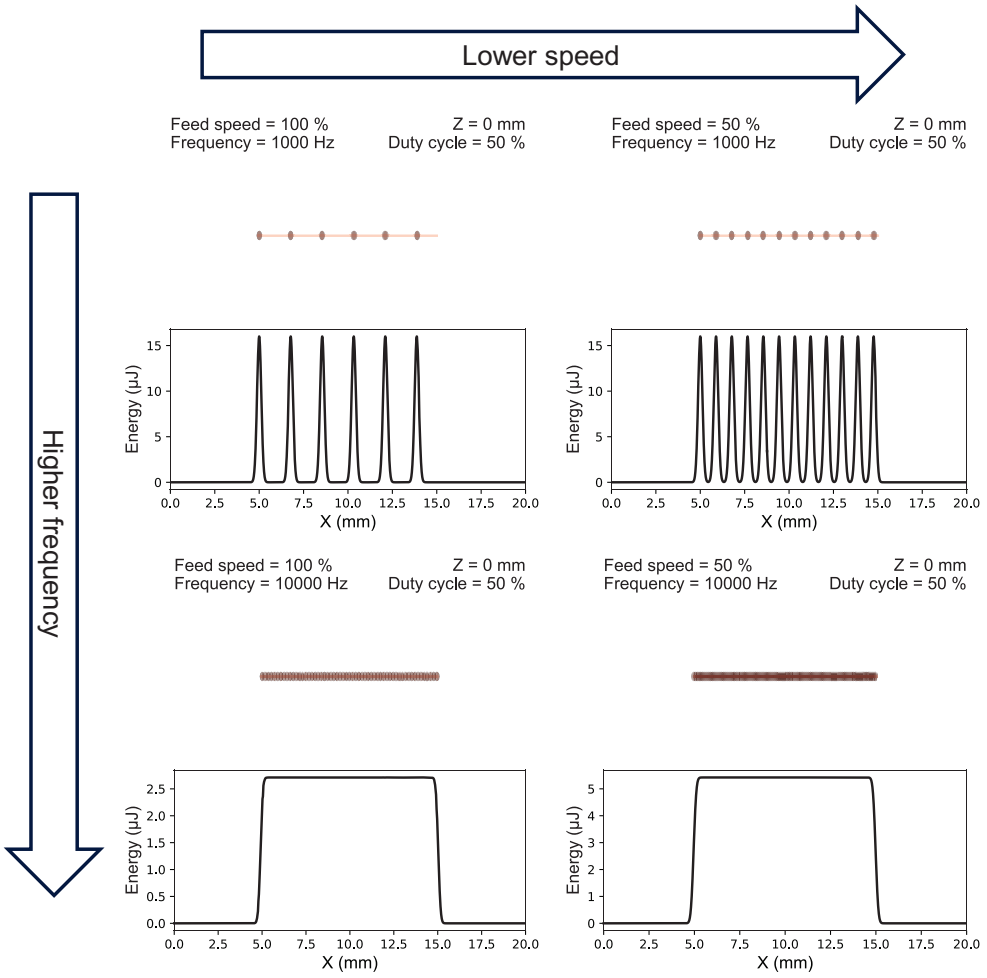

Figure 3: Simulation of energy on sample based on feed speed and frequency at 100% laser power

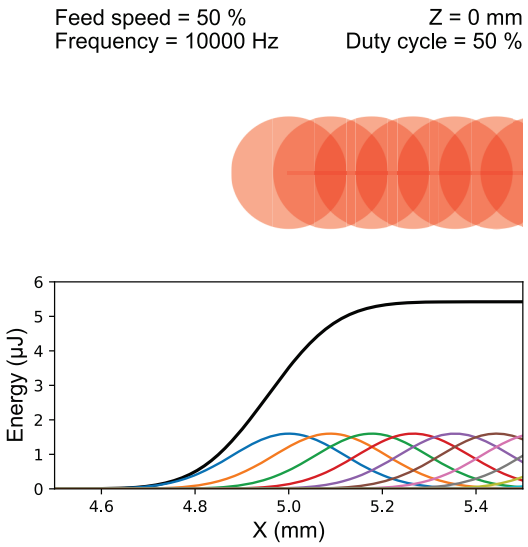

Figure 4: Zoomed in representation of the resulting energy on sample (black line) due to overlaps of laser pulses (colored lines) at low feed speed (50%) and high frequency (10,000 Hz)

The number of overlapping laser beams (n) per laser radius $w_{(z)}$ is highly pronounced at low travel distances between laser pulses (d), especially at travel distances below the laser radius $w_{(z)}$ (Figure 5). The number of overlaps per $w_{(z)}$ (n) highly correlates ($R^2 = 0.9999$) with the travel distance according to a power function. A z-offset of e.g. 25 mm increases n six-fold (e.g. one overlap at travel distance 0.12 mm with z=0 mm and six overlaps with z=25 mm).

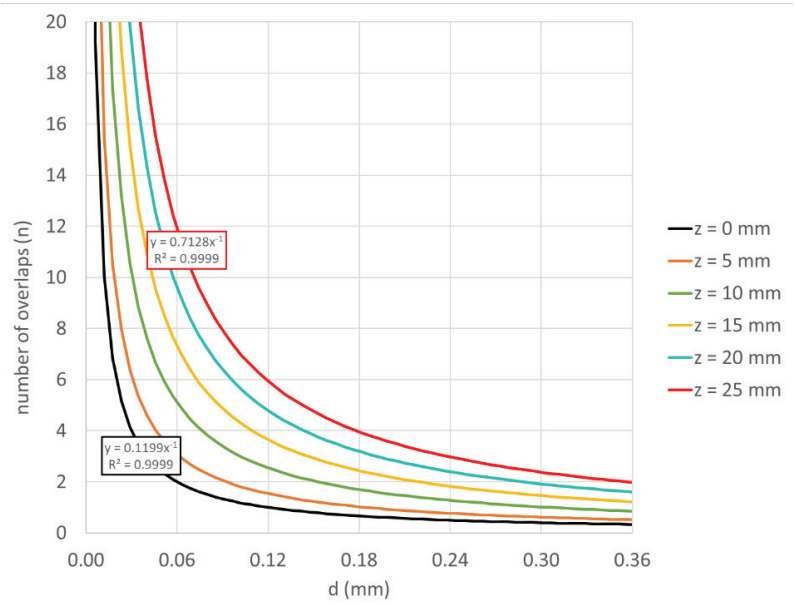

Figure 5: Number of overlaps per $w_{(z)}$ (n) over travel distance (d) at different z-offsets

Pretests with the laser cutter revealed that high frequency and high z-offset values enhance LIG formation on wood surfaces, which seems to be caused by the strongly increasing number of overlaps at travel distances below the radius of the laser beam. To simulate the resulting total energy on the surface of samples, different feed speeds and laser powers were studied (Figure 6, left). It was noticed that the total energy increases linearly with laser power, while it inversely correlated with feed speed, showing a sharp drop already above 0.1% feed speed.

To increase feed speed at the same resulting energy on the sample, a threshold (0.8 µJ – 1.2 µJ) for the total energy was defined. The resulting laser parameter combinations of feed speed and laser power are depicted in the right diagram of Figure 6 in yellow as binary representation.

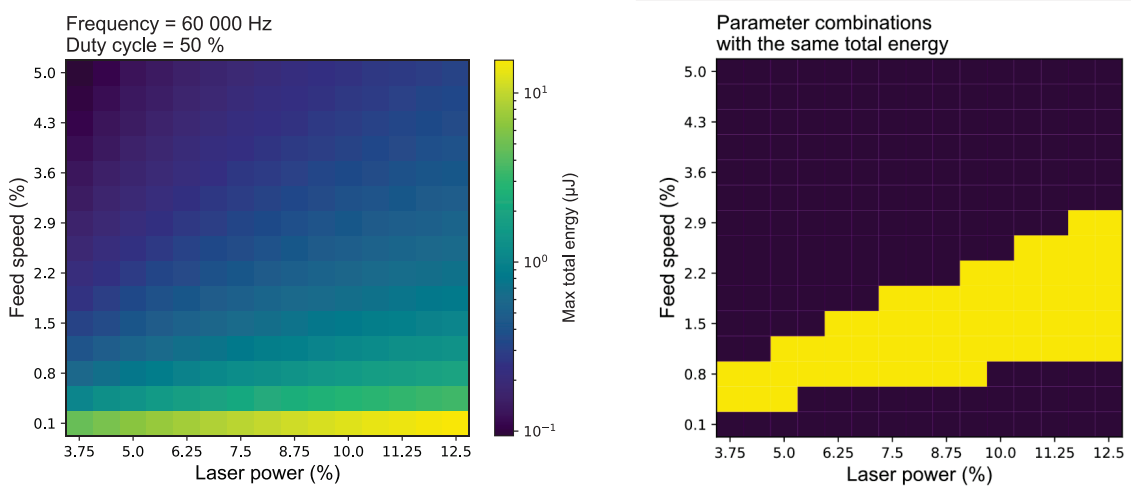

Figure 6: Maximum total energy on sample based on laser power and feed speed (left) and representation of combinations of laser power and feed speed with the same total energy (right)

4 CONCLUSION

Resulting surface energies on samples could be successfully simulated by using the fundamental principle of the gaussian beam theory. Within the simulation, the effects of varying laser parameters such as laser power, feed speed, frequency and z-offset on the resulting energies on samples were investigated. Here, it could be observed that an increase of the z-offset from 0 mm to 25 mm caused six overlaps of laser beams at a travel distance of 0.12 mm (equals to laser radius at beam waist). Additionally, the number of overlaps drastically increased at travel distances below 0.12 mm. The resulting total energy on the sample increases linearly with laser power and decreases with feed speed sharply already above 0.1% feed speed.

This simulation is highly valuable for defining set values for the upcoming empirical laser parameter study. In especially, already carried out pretests will be extended based on the simulation results and favorable ranges identified to generate LIG on untreated wood samples.

REFERENCES

[1] C. H. Dreimol *et al.*, "Sustainable wood electronics by iron-catalyzed laser-induced graphitization for large-scale applications," *Nature Communications,* vol. 13, no. 1, p. 3680, 2022/06/27 2022, doi: 10.1038/s41467-022-31283-7.

[2] T.-S. D. Le, S. Park, J. An, P. S. Lee, and Y.-J. Kim, "Ultrafast Laser Pulses Enable One-Step Graphene Patterning on Woods and Leaves for Green Electronics," *Advanced Functional Materials,* vol. 29, no. 33, p. 1902771, 2019/08/01 2019, doi: https://doi.org/10.1002/adfm.201902771.

[3] Y. Chyan, R. Ye, Y. Li, S. P. Singh, C. J. Arnusch, and J. M. Tour, "Laser-Induced Graphene by Multiple Lasing: Toward Electronics on Cloth, Paper, and Food," *ACS Nano,* vol. 12, no. 3, pp. 2176-2183, 2018/03/27 2018, doi: 10.1021/acsnano.7b08539.

[4] M. Y. Mulla *et al.*, "Bio-Graphene Sensors for Monitoring Moisture Levels in Wood and Ambient Environment," *Global Challenges,* vol. 7, no. 4, p. 2200235, 2023/04/01 2023, doi: https://doi.org/10.1002/gch2.202200235.

[5] H. K. Nam *et al.*, "Smart Wooden Home Enabled by Direct-Written Laser-Induced Graphene," *Advanced Materials Technologies,* vol. 8, no. 9, p. 2201952, 2023/05/01 2023, doi: https://doi.org/10.1002/admt.202201952.

[6] R. Ye *et al.*, "Laser-Induced Graphene Formation on Wood," *Advanced Materials,* vol. 29, no. 37, p. 1702211, 2017/10/01 2017, doi: https://doi.org/10.1002/adma.201702211.

[7] S. Nath *et al.*, "CO2 laser interactions with wood tissues during single pulse laser-incision," *Optics & Laser Technology,* vol. 126, p. 106069, 2020/06/01/ 2020, doi: https://doi.org/10.1016/j.optlastec.2020.106069.

[8] B. E. A. Saleh and M. C. Teich, "Beam Optics," in *Fundamentals of Photonics*, J. W. Goodman, B. E. A. Saleh, and M. C. Teich Eds., 1991, pp. 80-107.

XI ECCOMAS Thematic Conference on Smart Structures and Materials - SMART 2025
M. Krommer, M. Nader and M. Schagerl (Eds)

Received: 24 April 2025 / Revised: 13 September 2025 / Accepted: 15 September 2025
© The Author(s) 2025

Enhancing the Properties of Smart Sustainable Materials Through Atmospheric Plasma Deposition of Bio-Based Coatings

Judith Sinic, Christoph Jocham, Arunjunai Raj Mahendran, Kamal Baba, François Loyer, Nicolas Boscher

Abstract. Presently, the emphasis on environmental sustainability is directed towards minimizing the ecological impact of human activities and advocating for the efficient utilization of natural resources. In the pursuit of enhancing sustainability in industrial coatings, our investigation utilized ultrasonic nebulization, liquid-assisted and vapor deposition in conjunction with atmospheric plasma polymerization. Bio-based coating formulations as monomer precursors were applied to natural fiber reinforcement and paper substrates to augment properties, such as improving interfacial adhesion, hydrophobicity for the release function, barrier properties against oxygen and water vapor transmission and antimicrobial activity. Characterization techniques, including FTIR, HR-MS, profilometry, were employed to assess chemical composition and thicknesses of the deposited coatings, SEM studies were conducted to observe morphological features. Contact angle measurements were carried out for the investigation of hydrophilic / hydrophobic behavior, and bending tests were scrutinized for mechanical properties of reinforced composites. For barrier papers and release liners, oxygen and water vapor transmission rates and release functions were tested. The feasibility study aimed to comprehend how the deposition of nanosized particles on porous or renewable substrates could enhance the macroscopic behavior of the substrate. The applications primarily target the composite and paper industries, aiming to replace conventional thick coatings with relatively thin coatings. While the results indicated an improvement in the properties of the modified substrate, optimization is required before considering complete substitution for conventional pretreatment or wet coating techniques. Additionally, the developed coatings show potential for sensor applications, where their tailored surface properties could enhance sensitivity and functionality in various sensing technologies.

Key words: Sustainable materials, Plasma deposition, Bio-based coatings, Functionalization

Judith Sinic & Christoph Jocham & Arunjunai Raj Mahendran
Wood K plus - Kompetenzzentrum Holz GmbH, Area Wood & Paper Surface Technologies, A-9300 St. Veit an der Glan, Austria, e-mail: j.sinic@wood-kplus.at

Kamal Baba & François Loyer & Nicolas Boscher
Luxembourg Institute of Science and Technology (LIST), L-4362 Esch-sur-Alzette, Luxembourg

1 INTRODUCTION

Research on reducing the ecological impact of industrial processes and maximizing the use of renewable resources has been prompted by the growing emphasis on environmental sustainability on a global scale. The traditional petroleum-based formulations used in the coatings industry, in particular, have given way to bio-based substitutes that are more environmentally friendly and consistent with the circular economy [1], [2]. The use of solvent-based formulations or thick polymer layers in traditional coating techniques presents problems with waste production, emissions of volatile organic compounds (VOCs), and processing that requires a lot of energy [3]. As a result, there has been a lot of interest in creating effective and sustainable deposition techniques for bio-based coatings.

In this work, we investigated the use of atmospheric plasma polymerization in conjunction with advanced coating techniques such as liquid-assisted, vapor deposition, and ultrasonic nebulization. These techniques lower waste and material consumption while enabling the creation of uniform, ultra-thin coatings with customized functions. Bio-based monomer precursors were applied to natural fiber reinforcements and paper substrates to enhance interfacial adhesion, hydrophobicity, barrier properties, and antimicrobial activity that are key attributes for applications in composite materials and the paper industry.

To evaluate the coatings' chemical makeup and thickness, characterization methods including Fourier-transform infrared spectroscopy (FTIR), high-resolution mass spectrometry (HR-MS), and profilometry were used. While bending tests and contact angle measurements assessed mechanical and hydrophobic qualities, respectively, scanning electron microscopy (SEM) provided information on morphological features. The functional enhancements made possible by the deposition techniques were further confirmed by an analysis of the oxygen and water vapor transmission rates for barrier papers. Determining how nanoscale coatings can improve the macroscopic behavior of porous or renewable substrates in order to substitute high-performance layers for traditional thick coatings with relatively thin coating, was a key goal of this study. The results indicate that although notable enhancements in substrate characteristics were attained, additional refinement is necessary to fully replace traditional wet coating methods. Moreover, the developed coatings show promise for sensor applications, where their engineered surface properties may enhance functionality and sensitivity in a range of sensing technologies [4]. By leveraging innovative deposition methods and bio-based precursors, this study contributes to the ongoing transition toward sustainable coatings, offering solutions that balance performance with environmental responsibility.

2 MATERIALS AND METHODS

The renewable precursor vanillyl alcohol methacrylate (VAM) was synthesized from vanillyl alcohol following the procedure outlined below. 30 g of vanillyl alcohol (VA), 60 g of methacrylic anhydride, and 0.2 g of DMAP (dimethyl aminopyridine) were added to a round-bottom flask equipped with a thermometer and a magnetic stirrer set at 200 rpm. The reaction mixture was purged with nitrogen for 20 minutes and then allowed to react at 45°C for four

days. Following the reaction, the mixture was diluted with a blend of ethyl acetate and dichloromethane, then purified using a 3% sodium bicarbonate solution and water. Finally, the solvents were removed by distillation.

The reinforcement nanocrystalline cellulose (NCC) were modified according to the adopted procedure from the reference [5]. NCC were dried in an oven at 90 °C for 1 hour and then functionalized with (3-chloropropyl) trimethoxy silane (CPTMS). Subsequently a mixture of ethanol and water (75:25, 300 ml Et:100 ml H_2O) was prepared and mixed with a magnetic stirrer (300 rpm) for 5 minutes. 2g of CNC particles was first added to the solution and after their dispersion 2g of CPTMS was added afterwards. The mixture was left to mix for two hours (300 rpm). After two hours, the solution was poured in a dish and left over the night in an oven at 70°C to evaporate the solvent.

The plasma-polymer coatings were grown using an atmospheric pressure dielectric barrier discharge plasma set-up described in previous works [6], [7]. The plasma was generated by a 10 kHz, 8 kV sinusoidal generator (SOFTAL 7010R) using Argon (Ar) as plasma gas with a flow of 20 l min^{-1} and a power ranging from 50 to 200 W. Silicon or paper substrates (Barrier paper 60g) were coated with the monomers (VAM) or a suspension of VAM containing 1 w. % of reinforced NCC using a 120 kHz ultrasonic atomizing nozzle (Sono-Tek), fed by a syringe pump (10 µl min^{-1}) and shaped into a 10 cm wide fan spray using an impact spray shaper supplied with 20 l min^{-1} of N_2. Substrates were mounted on a variable-speed moving stage. The spray-curing cycle was repeated 100 times at a stage speed of 50 mm s^{-1} to reach coating thicknesses in the range of several micrometers.

FTIR spectra were acquired using a Bruker Vertex 70 spectrometer with a DTGS detector. Transmission mode was used for coatings on silicon wafers, otherwise ATR mode was used. All spectra were recorded from 4000 to 400 cm^{-1} at 4 cm^{-1} resolution under nitrogen purge. To evaluate the effect of plasma on the polymerization, the degree of double bond conversion was determined by means of FTIR using Equation (1) by calculating the ratios between the vinyl $A_{C=C}$ band intensity against the carbonyl $A_{C=O}$ bands for the monomer and polymer layers. These ratios are then compared to obtain the degree of conversion (DC).

$$DC\ (\%) = \left(1 - \frac{(A_{c=c}/A_{c=o})_t}{(A_{c=c}/A_{c=o})_0}\right) \times 100 \quad (1)$$

Matrix-assisted laser desorption/ionization high-resolution mass spectra (MALDI-HRMS) measurements were performed on an AP-MALDI PDF+ ion source from MassTech, Inc. coupled to an LTQ/Orbitrap Elite from Thermo Scientific. α-Cyano-4-hydroxycinnamic acid diluted in THF (10 mg l^{-1}) was used as the matrix. A total of 0.1 µl of the matrix was then spotted on the thin films to form a co-crystal with the soluble part of the film when the THF evaporated. Due to the numerous side peaks resulting from the plasma side-mechanisms, the relevant peaks corresponding to oligomeric repetitions were isolated for better depiction.

Scanning electron microscopy (SEM) images were obtained using a Hitachi SU-70 FE-SEM.

To prevent distortions caused by charge effects, the samples were coated with a 5 nm thick platinum film under vacuum conditions prior to SEM observations.

3 RESULTS AND DISCUSSIONS

The synthesized vanillyl alcohol methacrylate (VAM) monomer was initially characterized using Fourier-transform infrared spectroscopy (FTIR), which confirmed the successful incorporation of the methacrylate group. To further analyze the surface modification of nanocrystalline cellulose (NCC), X-ray photoelectron spectroscopy (XPS) was employed (Figure 1). The XPS survey spectrum revealed characteristic peaks of oxygen (26.4% at 533.0 eV) and carbon (48.3% at 286.0 eV), which are consistent with the chemical structure of cellulose and the modifying agent CPTMS.

Importantly, successful surface functionalization was evidenced by the appearance of chlorine (14.2% at 201.0 eV) and silicon (11.0% at 103.0 eV) signals, indicating effective grafting of CPTMS onto NCC. For comparison, [8] reported only 4.06% silicon content when modifying cellulose nanocrystals with 3-aminopropyltriethoxysilane. This comparison highlights the efficiency of the applied silanization process, which yielded a substantial proportion of modified hydroxyl groups available for further reaction.

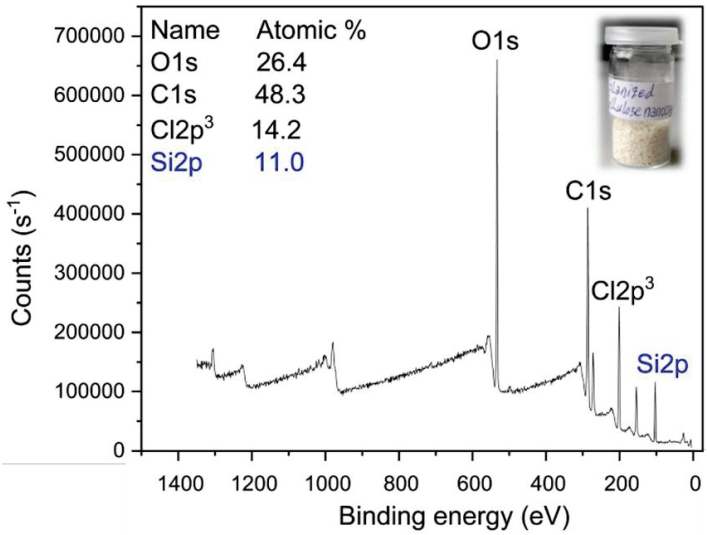

Figure 1: XPS spectrum of CPTMS-modified nanocrystalline cellulose

3.1 Plasma Polymerization and Characterization of VAM

To evaluate the conversion of VAM into a polymer layer, FTIR analysis was carried out following plasma polymerization at different power levels (Figure 2). Key functional group transitions were monitored in the 1600–1800 cm^{-1} region. The carbonyl (C=O) stretching band was observed at 1714 cm^{-1}, and the vinyl (C=C) stretching band at 1633 cm^{-1}. Residual peaks from the monomer synthesis (MAA and MA) appeared at 1782 cm^{-1} and 1693 cm^{-1}, respectively.

In plasma-treated samples, the vinyl band at 1633 cm^{-1} showed a significant reduction, indicating effective polymerization. Additionally, the carbonyl band shifted to a higher wavenumber (1724 cm^{-1}), suggesting free-radical-induced crosslinking of the methacrylate groups. The near disappearance of the MAA and MA peaks suggests their decomposition or evaporation during plasma exposure.

The degree of conversion (DC) of double bonds was calculated from FTIR spectra as the ratio of the C=C and C=O bands. Plasma powers of 50, 100, and 200 W resulted in DC values of 76%, 77%, and 79%, respectively, indicating that even at lower plasma powers, high polymerization efficiency was achieved. The slight increase in DC at higher power reflects improved fragmentation and radical formation, which enhances crosslinking.

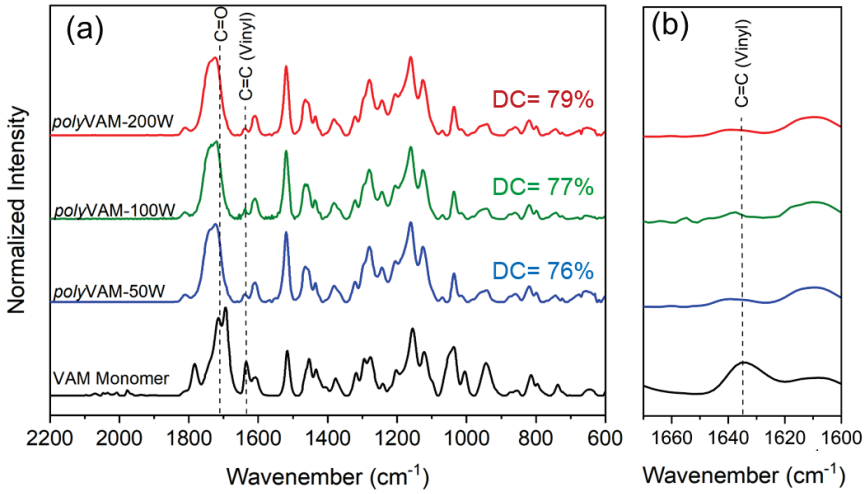

Figure 2: FTIR spectra comparing VAM monomer and plasma-polymerized films at different powers

3.2 Molecular Characterization via MALDI-HRMS

Matrix-assisted laser desorption/ionization high-resolution mass spectrometry (MALDI-HRMS) was used to identify the molecular structure of the resulting polymers (Figure 3). The spectra revealed oligomers composed of mono- and di-methacrylated vanillyl alcohol (mono-VAM and di-VAM) repeating units. At 50 W plasma power, the oligomers consisted of up to three mono-VAM and four di-VAM units. At 100 W, longer chains were formed (up to six mono-VAM and seven di-VAM), while at 200 W, a higher incorporation of di-VAM (eight units) and fewer mono-VAM (four units) was observed. These findings suggest that plasma power influences not only polymer chain length but also the balance between mono- and di-functional incorporation, with 100 W offering a well-balanced structure.

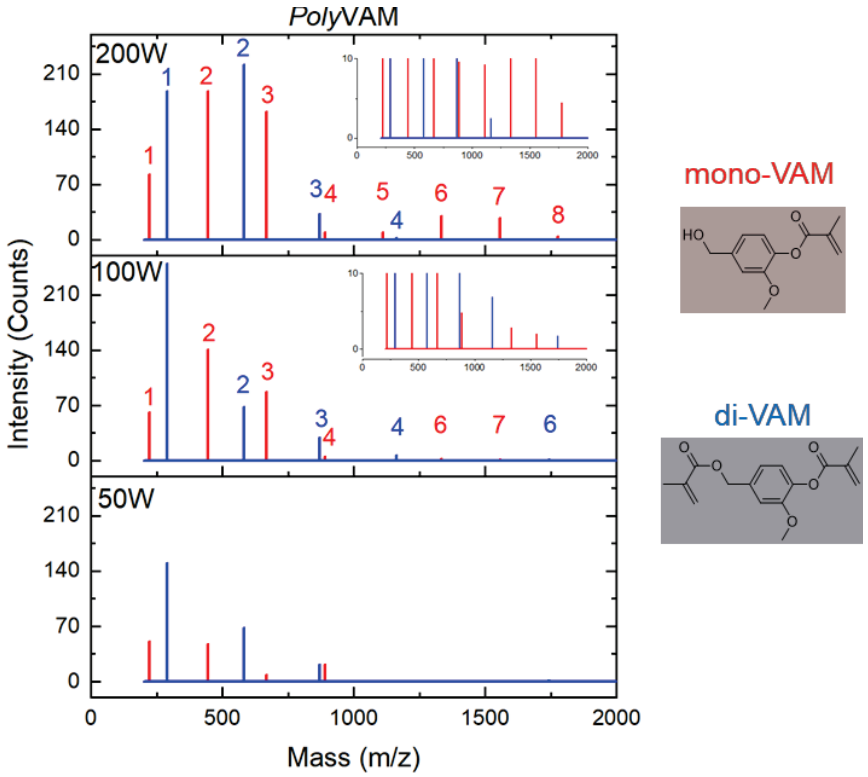

Figure 3: MALDI-HRMS spectra showing mono- and di-VAM oligomer distributions under varying plasma conditions

3.3 Coating Performance and Barrier Properties

Based on polymerization and structural analysis, a plasma power of 100 W was selected as the optimal condition for coating VAM and NCC formulations onto paper substrates. A film thickness of approximately 3 µm was achieved after 100 deposition cycles.

Water vapor transmission rate (WVTR) testing revealed that uncoated paper had a high WVTR of ~350 g m^{-2} day^{-1} (Figure 4). Coating with plasma-polymerized VAM significantly reduced the WVTR to ~70 g m^{-2} day^{-1}, demonstrating the formation of an effective barrier layer. Surprisingly, the incorporation of NCC into the VAM matrix resulted in a slightly increased WVTR (~90 g m^{-2} day^{-1}). This may be attributed to poor dispersion or incompatibility between NCC and the polymer matrix, possibly leading to microstructural defects and compromised barrier performance.

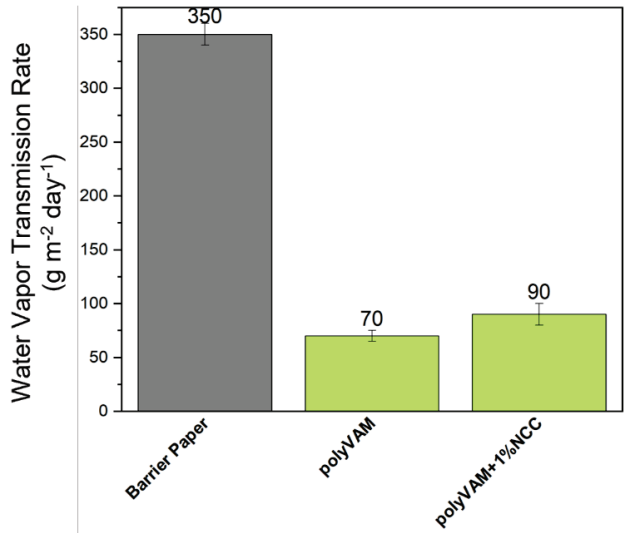

Figure 4: Water Vapor Transmission Rate (WVTR) values of paper samples: uncoated, VAM-coated, and VAM/NCC-coated

4 CONCLUSIONS

The synthesized VAM monomer was successfully polymerized using plasma polymerization, with FTIR and MALDI-HRMS confirming efficient conversion and oligomer formation. An optimal plasma power of 100 W provided balanced incorporation of mono- and di-functional units, ensuring effective crosslinking. Coating the VAM polymer onto paper significantly improved its barrier properties, although the addition of NCC did not enhance performance as expected, likely due to dispersion or compatibility issues. These findings demonstrate the potential of plasma-polymerized VAM as a bio-based coating material for moisture-sensitive applications, with further optimization needed for composite formulations involving nanocellulose.

REFERENCES

[1] J. G. Rosenboom, R. Langer, and G. Traverso, “Bioplastics for a circular economy,” *Nature Reviews Materials 2022 7:2*, vol. 7, no. 2, pp. 117–137, Jan. 2022, doi: 10.1038/s41578-021-00407-8.

[2] A. Gandini, “Furan Monomers and their Polymers: Synthesis, Properties and Applications,” in *Biopolymers - New Materials for Sustainable Films and Coatings*, John Wiley & Sons, Ltd, 2011, pp. 179–209. doi: 10.1002/9781119994312.CH9.

[3] Y. Ding, W. Qu, S. Niu, M. Liang, W. Qiang, and Z. Hong, “Factors Influencing the Spatial Difference in Household Energy Consumption in China,” *Sustainability 2016, Vol. 8, Page 1285*, vol. 8, no. 12, p. 1285, Dec. 2016, doi: 10.3390/SU8121285.

[4] Y. Bai, Z. Jing, B. Zhang, Y. Pan, Q. Wang, and X. Duan, “Recyclable Wearable Sensor Based on Tough, Self-Healing, Adhesive Polyurethane Elastomer for Human Motion

Monitoring," *ACS Appl Polym Mater*, vol. 5, no. 10, pp. 8720–8734, Oct. 2023, doi: 10.1021/ACSAPM.3C01893/SUPPL_FILE/AP3C01893_SI_001.PDF.

[5] L. Manhooei, B. Mehdinejadiani, and S. M. Amininasab, "Cellulose nanocrystal modified with 3-chloro propyl trimethoxysilane: a new bio-adsorbent for nitrate removal from water," *Water and Environment Journal*, vol. 34, no. S1, pp. 50–60, Dec. 2020, doi: 10.1111/WEJ.12503.

[6] J. B. Chemin, D. Del Frari, H. Ghahramanzadehasl, K. Baba, R. Leturcq, and N. D. Boscher, "Atmospheric plasma deposition of conductive and corrosion-resistant composite coatings for proton exchange membrane fuel cell bipolar plates," *Plasma Processes and Polymers*, vol. 20, no. 8, p. 2300056, Aug. 2023, doi: 10.1002/PPAP.202300056.

[7] N. D. Boscher, P. Choquet, D. Duday, and S. Verdier, "Advantages of a Pulsed Electrical Excitation Mode on the Corrosion Performance of Organosilicon Thin Films Deposited on Aluminium Foil by Atmospheric Pressure Dielectric Barrier Discharge," *Plasma Processes and Polymers*, vol. 7, no. 2, pp. 163–171, Feb. 2010, doi: 10.1002/PPAP.200900094.

[8] H. Khanjanzadeh *et al.*, "Surface chemical functionalization of cellulose nanocrystals by 3-aminopropyltriethoxysilane," *Int J Biol Macromol*, vol. 106, pp. 1288–1296, Jan. 2018, doi: 10.1016/J.IJBIOMAC.2017.08.136.

Part XV
SS 05 - SMART AND ARCHITECTED COMPOSITES AND STRUCTURES
Wael Zaki, Marwan El-Rich

XI ECCOMAS Thematic Conference on Smart Structures and Materials - SMART 2025
M. Krommer, M. Nader and M. Schagerl (Eds)

Received: 27 March 2025 / Revised: 30 August 2025 / Accepted: 20 September 2025
© The Author(s) 2025

Characterization of Electrically Conductive Polymers Integrated in Additively Manufactured Parts for Sensing

Giorgio De Pasquale, Ferdinando Ursi

Abstract. Additive Manufacturing (AM) technologies enable the layer-by-layer fabrication of complex geometries with advantages such as cost-effectiveness, waste reduction, and design flexibility. Among polymer-based AM techniques, fused deposition modeling (FDM) is widely used due to its affordability and ease of use. The demand for high-performance materials has led to the development of polymer matrix composites (PMCs), including conductive polymer composites (CPCs), which integrate electrically conductive fillers within a polymeric matrix. CPCs, particularly those with carbon-based fillers, offer promising applications in sensing devices and 3D-printed electronics.
This study investigates commercial CPCs for strain sensing applications, focusing on the impact of sensor track width and temperature on functional performance. Two CPCs are analyzed: a graphite-filled TPU-based CPC (Fili) and a carbon-black-filled TPU-based CPC (FilaFlex Conductive). The materials are co-printed on PLA-based substrates using a dual-extruder FDM process. Tensile tests reveal that graphite-filled CPCs exhibit a strong linear piezoresistive response, while carbon-black-filled CPCs show lower strain sensitivity. Additionally, thermal characterization demonstrates that both CPCs exhibit a positive temperature coefficient (PTC), though matrix-filler interactions influences their response at higher temperatures.
The results indicate that graphite-based CPCs are suitable for strain sensing due to their linear piezoresistive behavior, while carbon-black-filled CPCs maintain electrical stability under mechanical deformation. These findings provide valuable insights for selecting CPCs in sensor applications and highlight the need for further studies on repeatability and strain limits.

Key words: Conductive polymer composites (CPCs), Nanomaterials, Additive Manufacturing, Sensors, IoT.

1 INTRODUCTION

Additive manufacturing (AM) technologies encompass all methods capable of creating objects by building them layer by layer. These technologies offer several advantages, including the ability to produce complex geometries, cost-effectiveness, waste reduction, and design flexibility. However, they also present challenges such as the frequent need for post-processing, design inaccuracies, and a limited selection of available materials [1], [2].

Giorgio De Pasquale & Ferdinando Ursi
Smart Structures and Systems Lab, Politecnico di Torino, Department of Mechanical and Aerospace Engineering, 10129 Torino, Italy. e-mail: giorgio.depasquale@polito.it

During the printing process, the bonding mechanism between layers depends on both the material class (e.g., metal, polymer, or ceramic) and the form of the raw material or feedstock (e.g., powder, liquid, filament, or pellet). AM technologies are widely used across various industries, including medical, manufacturing, aerospace, and automotive sectors showing also. Metals and alloys are commonly employed in applications requiring load-bearing capabilities, heat resistance, or thermal management, thanks to their superior mechanical and thermal properties [3].

Among the new trends regarding the AM technology, efforts also focus on the development of metamaterials [4], [5], [6] and the integration of AM processes with existing methods, such as combining metal AM with carbon composite processes [7], [8], [9], [10] or the integration of sensors in AM components [11]. On the other hand, the primary limitation of metal-based AM is the relatively high cost, which led to the increasing popularity of polymer-based AM, despite its relatively lower mechanical performance. Among polymer-based AM techniques, fused deposition modeling (FDM) is the most widely adopted due to its cost-effectiveness, accessibility to feedstocks, and ease of use. The FDM process involves the extrusion of molten thermoplastic material through a heated nozzle. Traditionally, materials such as polylactic acid (PLA) and acrylonitrile-butadiene-styrene (ABS) are commonly used. However, the growing demand for high-performance materials has led to the development of the new feedstock class of polymer matrix composites (PMC) [12]. In PMCs, the mixing of a polymeric matrix with a filler material enhances the material properties. While the polymeric matrix provides the material with good extrudability, the filler material enhances one or more of the material properties.

Carbon-fiber-reinforced-polymers (CFRP) is one of the most relevant PMC in which the use of continuous carbon fibers as filler material results in a significant increase in mechanical properties that at times may compete with the one of metal parts [13], [14]. In the last years, relevant efforts have been spent in the exploration of conductive polymer composites (CPCs), a class of materials in which the matrix is the structural component and the filler, who exhibits electrically conductive properties, is the functional part. Polymeric matrices are classified in hydrogels, synthetic polymers, natural rubber and synthetic rubber; the fillers are classified in carbon-based, metallic, emerging materials and intrinsically conductive polymers [15]. The CPCs based on carbon and metallic fillers are also referred to as conductive polymer nanocomposites because they are dispersed in the matrix in the form of nanoparticles (NPs) [16], [17]. Even though the metal nanoparticles such as gold, silver or copper NPs noticeably enhance the CPCs electrical properties, they are generally expensive and often cause clogging during the deposition process [18]. The carbon-based NPs deployed in CPCs can be distinguished in carbon black (CB), carbon nanotubes (CNTs) and graphite particles (GPs), characterized by a different aspect ratio and sometime referred to as 0D, 1D and 2D NPs, respectively [18], [19], [20].

The electrical conduction in the CPC is described by the percolation theory, in which the electrical charges move from one nanoparticle to another when they are in contact or very close. Hence, the percolation occur when the volume content of the filler in the CPC is higher than the percolation threshold [20], [21]. The percolation threshold depends on a number of filler parameters including the aspect ratio, the filler size and the filler size distribution [18].

Nowadays, despite CPCs are treated with several processes including inkjet, aerosol jet printing (AJP) and electrohydrodynamic jet printing (EHD), the most simple AM technology to process CPCs is the FDM because it shows less clogging issues [22]. CPCs find wide application in several fields such as automotive, aerospace [23], biomedicine [24], [25], shielding [26], sensing devices [27], [28], [29], [30] and, more generally, in the 3D-printed electronics.

The interconnection between components, a cornerstone of the internet of things (IoT), and the increasing demand for data to train artificial intelligence (AI) models are relevant aspects. In this context, the widespread adoption of this class of materials offers a significant opportunity to address the growing need for data.

In literature, many studies have been reported on the enhancement of the electrical properties of CPCs. However, the development of custom-tailored materials is often complex, challenging to replicate, and requires meticulous manufacturing processes [31]. Additionally, the limited number of CPC's producers rarely provide information on their suitability as sensing materials. To the best of the authors' knowledge, no prior study has specifically investigated this aspect. The experimental characterization of commercial CPCs can therefore provide valuable insights, enabling informed material selection, both for the design of new CPCs and for their procurement. This research aims to introduce and analyze key parameters of selected commercial carbon-based CPCs for strain sensing applications, while also examining how the thickness of the sensing device affects its functional performance. Additionally, the pyro resistive response of the CPCs is investigated to establish the impact of temperature on its sensing performances.

2 SAMPLES AND TESTS DESCRIPTION

2.1 Materials

Literature emphasizes that stretchability, or the ability to generate large strain values, is a key factor for strain sensing. One major challenge associated to stretchability is the decohesion between the sensing material and the substrate. To improve the stretchability of the sensor, the sensing structure is co-printed with the specimen using a double extruder, ensuring it stays securely attached to the substrate during testing.

Polymeric matrices known for their excellent stretchability include hydrogel, SEBS, PDMS, and Ecoflex, with TPU being the most affordable and widely used option [32].

The CPCs selected for characterization are:

- "Fili" – a TPU-based CPC filled with graphite particles, manufactured by AIMPLAS Technological Institute of Plastics.
- "FilaFlex Conductive" – a TPU-based CPC filled with carbon black (CB), manufactured by Recreus Industries.

The substrate used for the CPCs in this study is a dog-bone specimen compliant with the ASTM D638 Type V standard, made from PLA Pro1 white by BASF.

2.2 Specimens preparation

The sample batch is manufactured with the double extruder FDM printer UltiMaker S5. Connecting the CPC to the measurement apparatus with silver inks is a consolidated operation observed in several studies [31], [33]. However, these inks require careful handling, making them unsuitable for long-term applications. To address this limitation, a more reliable connection method is proposed, based on the embedding of copper electrodes using a stop-and-resume technique during the printing process, ensuring a stable sensor connection.

The geometry of the sensing device and substrate is designed in SolidWorks and then exported as an STL file to the UltiMaker Cura Enterprise slicer software. This software not only allows for setting the printing parameters but also enables precise placement of the sensor and electrodes within the substrate material.

Additionally, this study examines the impact of sensing track width on the sensing properties of CPCs. To evaluate this, CPC-based sensors are printed with three layers of CPC material at widths of 0.4 mm, 0.8 mm, and 1.6 mm.

To assess the tensile behavior of the substrate material, three specimens without CPC are prepared for tensile testing. Furthermore, for each CPC and sensor trace width combination, three specimens are produced for piezoresistive characterization, along with an additional specimen designated for pyro resistive characterization.

2.3 Tensile characterization

The tensile test (Figure 1.a), is performed using the INSTRON 8801 universal testing machine under strain rate control conditions at a rate of 1 mm/min. Before testing, the cross-section of the narrowed section of the specimens is measured at three points using a vernier caliper.

The applied load is measured with a 100 kN load cell, while strain is recorded using the uniaxial dynamic extensometer. Since the investigation focuses on the behavior of CPC within the elastic deformation range of the substrate, the test imposes a load range of 0–400 N.

Strain and load signals are acquired by the cRIO-9054 DAQ system, which also records the resistance signal generated by the CPC. The DAQ system synchronizes all signals at a sampling frequency of 100 Hz and transfers the data to a PC for storage and post-processing.

Post-processing is carried out using MATLAB to assess the impact of co-printing the sensor within the dog-bone specimen on the tensile elastic modulus (E), or Young's modulus, of the material in the elastic deformation field, defined as:

$$E = \sigma/\varepsilon \tag{1}$$

where σ [MPa] represents the normal stress induced in the tensile specimen due to the applied load, and ε [-] denotes the strain experienced by the specimen as a result of this load.

The strain sensing properties of the CPC are then evaluated by determining their sensitivity to strain, quantified through the strain sensitivity or gauge factor (GF), along with the coefficient of determination (R^2), which indicates the correlation between the experimental data and a linear regression model. The gauge factor is

$$GF=\frac{\Delta R/R_0}{\varepsilon} \quad (2)$$

where R_0 [$k\Omega$] represents the electrical resistance of the CPC before starting the tensile test and ΔR [$k\Omega$] represents the change in electrical resistance due to the applied load. The coefficient of determination is

$$R^2=1-\frac{\sum_{i=1}^{n}(Y_i-\widehat{Y}_i)^2}{\sum_{i=1}^{n}(Y_i-\overline{Y})^2} \quad (3)$$

where Y refers to the experimental data, $\widehat{Y}$ refers to the linear regression model and $\overline{Y}$ refers to the mean value of all the experimental data.

2.4 Thermal characterization

The thermal test (Figure 1.b) is conducted using a feedback controlled heating plate. In literature, thermal investigations reach up to 50 °C[34], thus some it may result useful to assess the thermal behaviour of CPCs under more severe conditions. The applied thermal profile consists in heating the specimens up to the nominal temperature of 140° for 5 hours. Afterward, the heating platform is turned off and the electrical behavior of the CPC during the cooling is sampled for 1 hour.

During the thermal test, the actual temperature on the heating platform, recorded with a K-type thermocouple, and the electrical resistance of the CPC are synchronized and sampled at 100 Hz with the cRIO-9054 DAQ system. The gathered data are sent to the PC and processed on MATLAB.

The output of the test are the thermos-electric characteristics of examined CPCs with track width of 0.4 mm, 0.8 mm and 1.6 mm and the quantification of the degree of thermal hysteresis (H_T) during the test:

$$H_T = |A_H - A_C|/A_H \quad (4)$$

where A_H and A_C represents the area under the heating and cooling path.

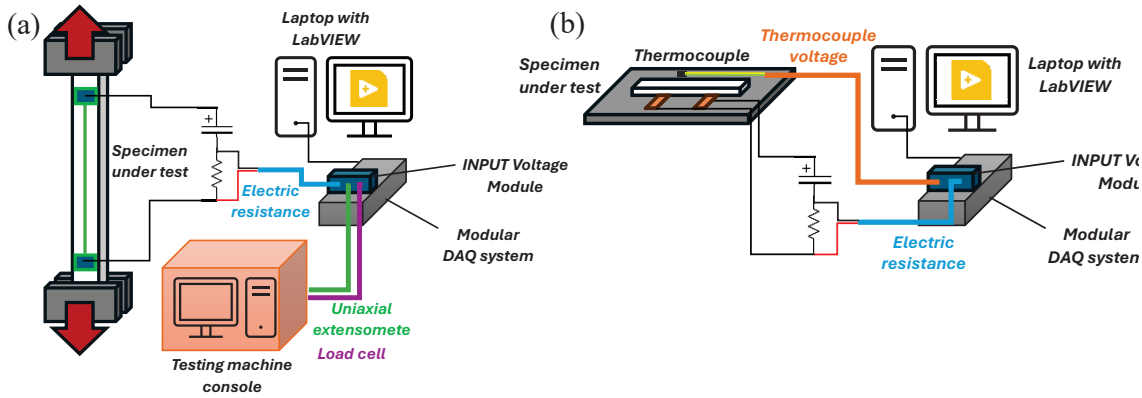

Figure 1: Visual representation of the tensile characterization (a) and thermal characterization (b) experimental setup.

3 RESULTS AND DISCUSSION

3.1 Tensile characterization

The computation of the elastic modulus, based on equation (1), reveals that integrating the sensing apparatus into the substrate affects its tensile response in the elastic region. When the integrated track is small, the elastic modulus significantly increases, regardless of the CPC. This trend is attributed to the surrounding sensor area being reinforced by a wall contour, which contributes to the overall stiffness of the printed part [35]. However, as the CPC cross-section increases, the elastic modulus decreases for both CPCs due to the replacement of the substrate material with more compliant materials. The more pronounced drop in the elastic modulus for FilaFlex Conductive can be attributed to the CB filler's lower load transfer capability compared to the graphite particles in Fili.

Regardless of the sensing track width, Fili exhibits a linear relationship with strain (Figure 2.a), whereas FilaFlex Conductive, as also reported by other authors [36], displays an inconsistent piezoresistive response (Figure 2.b).

The sensing parameters, calculated using equations (2) and (3) and summarized in Table 2, show that Fili demonstrates strong strain-sensing capabilities, with a strain sensitivity exceeding 100 and a coefficient of determination above 0.90. Additionally, increasing the sensing track width further enhances these metrics.

Conversely, FilaFlex Conductive exhibits poor strain-sensing properties, characterized by low strain sensitivity and non-linearity. This behavior is attributed to the aspect ratio of the filler material. Fili contains graphite, which gradually lose contact during matrix deformation due to relative slipping between particles. In contrast, CB, undergoes less predictable changes in particle network percolation during deformation. This comparison highlights that Fili filament provides a sensing material with a linear piezoresistive response, while FilaFlex Conductive is better suited for electronic applications where maintaining electrical properties despite mechanical deformation is crucial. However, the variability in the measured gauge factor limits its potential for large-scale applications.

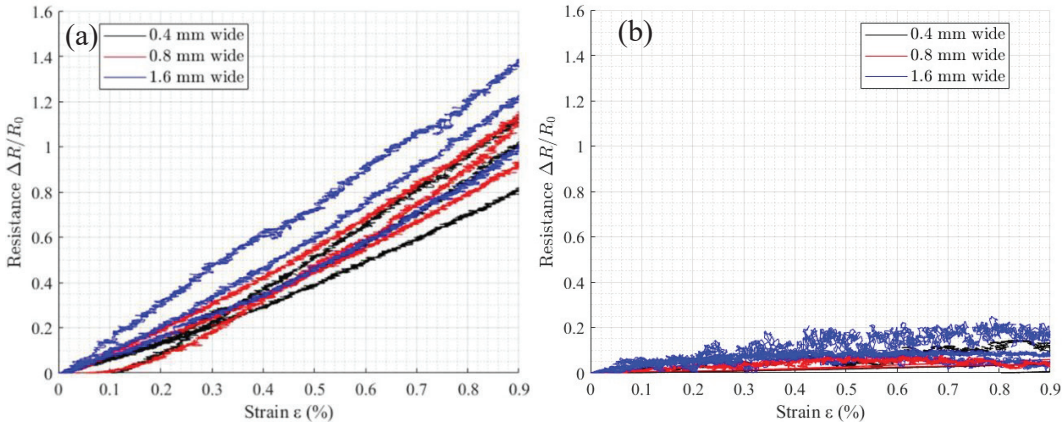

Figure 2: Piezoresistive response of Fili (a) and FilaFlex Conductive (b).

Table 1: Young's modulus of the dog-bone specimens.

Track width (mm)	Young's modulus E (MPa)		
	Fili	FilaFlex Conductive	Without CPCs
0.4	2296	2261	2196
0.8	2202	2058	
1.6	2150	2000	

Table 2: Strain sensing metrics of the CPCs.

Track width (mm)	Strain Gauge GF (-)		Coefficient of determination R^2 (-)	
	Fili	FilaFlex Conductive	Fili	FilaFlex Conductive
0.4	117	6	0.96	0.72
0.8	122	4	0.96	0.69
1.6	130	2	0.97	0.16

3.2 Thermal characterization

The pyroresistive response of the CPCs during a heating cycle, as shown in Figure 3, reveals distinct relationships between resistance and temperature, both influenced by the type of nanofiller used.

Fili exhibits a proportional increase in resistance as temperature rises (Figure 3.a). This behavior, known in the literature as a positive temperature coefficient (PTC) effect and in CPCs is due to the matrix thermal expansion [20], [37] , follows a linear trend up to 50°C, after which the CPC experiences a resistance drop. During cooling, the resistance increases again, ultimately leading to a permanent change in electrical resistance at the end of the test.

In contrast, FilaFlex Conductive (Figure 3.b) also demonstrates a PTC effect, with an initial plateau followed by a linear increase in resistance up to 90°C. Similar to Fili, the resistance then drops. However, unlike Fili, FilaFlex Conductive continues to experience a resistance drop during cooling, suggesting that CB particles enhance their conductivity properties after the heat cycle.

These pyroresistive behaviors can be attributed to differences in the aspect ratio of the fillers and, more specifically, to the filler-matrix interactions, as permanent matrix deformations lead to lasting alterations in sensing characteristics [20]. The test results indicate that when using graphite-filled CPCs for sensing applications, operating temperature must be carefully considered, as exceeding 50°C may alter sensing properties. In contrast, CB-filled CPCs exhibit improved conductivity after the heating cycle, suggesting that controlled heat exposure could serve as a strategy to enhance the resistance properties of this material class.

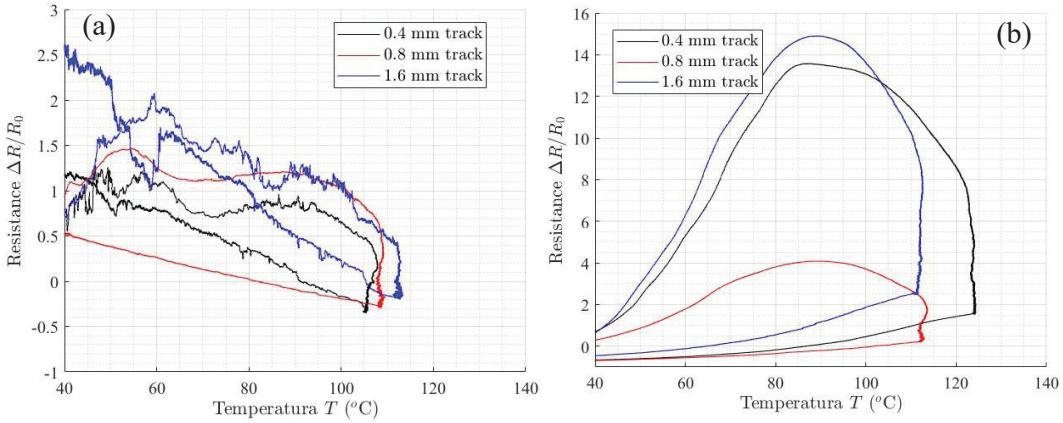

Figure 3: Pyroresistive response of Fili (a) and FilaFlex Conductive (b) with a 1.6 mm sensing track.

The hysteretic observed in Figure 3 over the heat cycle and formalized with the equation (4) are reported in Table 3.

Table 3: Thermal hysteresis of the CPCs.

Track width (mm)	Thermal hysteresis H_T (-)	
	Fili	FilaFlex Conductive
0.4	0.257	0.891
0.8	0.514	0.826
1.6	0.189	0.850

The thermal hysteresis aligns with the curve in Figure 3 as the CB-based CPC (FilaFlex Conductive) exhibits a stable hysteresis of approximately 0.85, while the graphite-based CPC (Fili) shows more variability. However, no clear scale effect is observed with increasing track width. This trend can be attributed to the significant influence of process variability on the final properties of the CPC.

4 CONCLUSIONS

The analysis conducted has emphasized several important aspects, detailed below.

- Embedding the sensor within the component to be monitored, or more generally into the substrate, alters the tensile properties of the final component. This factor must be carefully considered during the design phase of the sensor section.
- The aspect ratio of the filler significantly affects both the piezoresistive and pyroelectric response of CPCs. The study revealed that graphite-based CPCs demonstrate a strong piezoresistive response, whereas CB-based CPCs (carbon black) exhibit low sensitivity to applied deformation. These behaviors can be crucial in applications where correlating or decorrelating electrical resistance with mechanical strain is required. As with traditional strain gauges, the effect of temperature on resistance must be carefully considered to ensure that the operating temperature does not cause permanent

alterations in the sensor's resistive response.

- The pyroresistive response indicates that both carbon-based CPCs exhibit a positive temperature coefficient (PTC). However, at high temperatures, the matrix-filler interactions affect this relationship. The CB-based CPC demonstrates more stable behavior compared to the graphite-filled counterpart. It is important to note that up to 50°C, graphite-based conductive materials maintain a proportional pyroresistive response.
- The findings confirm that commercial CPCs can be effectively used for suitable strain sensing. When comparing graphite-filled and CB-filled CPCs, the former provides a linear piezoresistive response, making it well-suited for strain sensing applications, while the latter shows low piezoresistive sensitivity, making it preferable for applications where minimizing sensitivity to deformation is desired.
  Depending on the filler used, high temperatures may cause a permanent decrease in electrical resistance, revealing potential strategies for enhancing CPC performance.

In conclusion, the choice of filler plays a crucial role in determining the sensor's properties. Therefore, during CPC selection or design, a thorough evaluation of the filler material is essential.
A comprehensive analysis of the lifetime of resettable sensors is beyond the scope of this study; however, it remains a crucial area for future research. Further investigation into CPC sensing properties should prioritize examining the repeatability of piezoresistive and pyroelectric responses, as well as identifying the maximum strain range where linear correlations hold.

5 FUNDING

This paper was funded by the Horizon Europe grant "HORIZON-CL4-2022-RESILIENCE-01", Project MIMOSA (Project 101091826).

REFERENCES

[1] P. Awasthi and S. S. Banerjee, "Fused deposition modeling of thermoplastic elastomeric materials: Challenges and opportunities," *Addit Manuf*, vol. 46, p. 102177, Oct. 2021, doi: 10.1016/J.ADDMA.2021.102177.

[2] M. Askari *et al.*, "Additive manufacturing of metamaterials: A review," *Addit Manuf*, vol. 36, p. 101562, Dec. 2020, doi: 10.1016/J.ADDMA.2020.101562.

[3] M. Srivastava *et al.*, "Additive manufacturing of Titanium alloy for aerospace applications: Insights into the process, microstructure, and mechanical properties," *Appl Mater Today*, vol. 41, p. 102481, Dec. 2024, doi: 10.1016/J.APMT.2024.102481.

[4] Z. Zeng *et al.*, "Additive manufacturing of metallic metamaterials with enhanced mechanical properties enabled by microstructural and structural design," *Int J Mach Tools Manuf*, vol. 199, p. 104172, Jun. 2024, doi: 10.1016/J.IJMACHTOOLS.2024.104172.

[5] X. Wu, H. Yan, Y. Zhou, P. Zhang, Q. Lu, and H. Shi, "Review of additive manufactured metallic metamaterials: Design, fabrication, property and application," *Opt Laser Technol*, vol. 182, p. 112066, Apr. 2025, doi: 10.1016/J.OPTLASTEC.2024.112066.

[6] S. Dai, K. Zhu, S. Wang, and Z. Deng, "Additively manufactured materials: A critical review on their anisotropic mechanical properties and modeling methods," *J Manuf Process*, vol. 141, pp. 789–814, May 2025, doi: 10.1016/J.JMAPRO.2025.02.038.

[7] G. De Pasquale and A. Coluccia, "Modeling and Experimental Validation of CFRP–Metal Joints Utilizing 3D Additively Manufactured Anchors," *J Manuf Sci Eng*, vol. 145, no. 11, Aug. 2023, doi: 10.1115/1.4063110.

[8] G. De Pasquale, F. Enes Altunok, and F. Ursi, "Investigation of the Mechanical Strength of CFRP with Co-Cured Additively Manufactured Metal Inserts," *Procedia Structural Integrity*, vol. 47, pp. 573–578, Jan. 2023, doi: 10.1016/J.PROSTR.2023.07.067.

[9] F. E. Altunok and G. De Pasquale, "Numerical Cohesive Zone Modeling (CZM) of Self-Anchoring AM Metal-CFRP joints," *Frattura ed Integrità Strutturale*, vol. 18, no. 68, pp. 280–295, Apr. 2024, doi: 10.3221/IGF-ESIS.68.19.

[10] G. De Pasquale and F. E. Altunok, "Multiphase modeling of matrix/fiber-related damaging mechanism in multimaterial additively manufactured joints with 3D interlocking," *Eng Fail Anal*, vol. 170, Mar. 2025, doi: 10.1016/J.ENGFAILANAL.2025.109272.

[11] G. De Pasquale, "THERMAL MONITORING OF BRAKING SYSTEMS USING METAL AM CALIPERS WITH INTEGRATED SENSORS," pp. 434–445, Sep. 2023, doi: 10.7712/150123.9798.445855.

[12] X. Wang, M. Jiang, Z. Zhou, J. Gou, and D. Hui, "3D printing of polymer matrix composites: A review and prospective," *Compos B Eng*, vol. 110, pp. 442–458, Feb. 2017, doi: 10.1016/J.COMPOSITESB.2016.11.034.

[13] A. Sola and A. Trinchi, "The need for fused deposition modeling of composite materials," *Fused Deposition Modeling of Composite Materials*, pp. 39–89, Jan. 2023, doi: 10.1016/B978-0-323-98823-0.00004-4.

[14] G. De Pasquale and F. Ursi, "Multi-material fittings with carbon fiber reinforcement from AM process: design and characterization," in *3rd Int. Symp. on Industrial Engineering and Automation (ISIEA)*, Bolzano (Italy), Jun. 2024.

[15] H. T. Tazwar, M. F. Antora, I. Nowroj, and A. Bin Rashid, "Conductive Polymer Composites in Soft Robotics, Flexible Sensors and Energy Storage: Fabrication, Applications and Challenges," *Biosens Bioelectron X*, p. 100597, Feb. 2025, doi: 10.1016/J.BIOSX.2025.100597.

[16] K. R. Ryan, M. P. Down, N. J. Hurst, E. M. Keefe, and C. E. Banks, "Additive manufacturing (3D printing) of electrically conductive polymers and polymer nanocomposites and their applications," *eScience*, vol. 2, no. 4, pp. 365–381, Jul. 2022, doi: 10.1016/J.ESCI.2022.07.003.

[17] M. N. Khatun *et al.*, "Sensors based on polymer nanomaterials," *Sensory Polymers*, pp. 391–428, Jan. 2024, doi: 10.1016/B978-0-443-13394-7.00010-0.

[18] D. Pejak Simunec and A. Sola, "Emerging Research in Conductive Materials for Fused Filament Fabrication: A Critical Review," *Adv Eng Mater*, vol. 24, no. 7, p. 2101476, Jul. 2022, doi: 10.1002/ADEM.202101476.

[19] A. C. Ezika, H. C. Oyeoka, C. C. Obi, S. C. Ugwu, and M. E. Ibenta, "Enhancing the mechanical and electrical properties of polymers using graphene," *Polymers and Two-Dimensional Nanocomposites*, pp. 209–261, Jan. 2025, doi: 10.1016/B978-0-443-14131-7.00009-2.

[20] A. del Bosque, X. F. Sánchez-Romate, M. Sánchez, and A. Ureña, "Toward flexible piezoresistive strain sensors based on polymer nanocomposites: a review on fundamentals, performance, and applications," *Nanotechnology*, vol. 35, no. 29, p. 292003, Jul. 2024, doi: 10.1088/1361-6528/ad3e87.

[21] Z. Wang, J. Zhang, and G. J. Weng, "Modeling the percolation behavior of conductive particles/insulating polymer-based composites with equivalent circuit of resistance," *Polymer (Guildf)*, p. 128262, Mar. 2025, doi: 10.1016/J.POLYMER.2025.128262.

[22] H. W. Tan, Y. Y. C. Choong, C. N. Kuo, H. Y. Low, and C. K. Chua, "3D printed electronics: Processes, materials and future trends," *Prog Mater Sci*, vol. 127, p. 100945, Jun. 2022, doi: 10.1016/J.PMATSCI.2022.100945.

[23] A. H. Alami *et al.*, "Additive manufacturing in the aerospace and automotive industries: Recent trends and role in achieving sustainable development goals," *Ain Shams Engineering Journal*, vol. 14, no. 11, p. 102516, Nov. 2023, doi: 10.1016/J.ASEJ.2023.102516.

[24] N. H. Solangi, R. R. Karri, N. M. Mubarak, and S. A. Mazari, "Mechanism of polymer composite-based nanomaterial for biomedical applications," *Advanced Industrial and Engineering Polymer Research*, vol. 7, no. 1, pp. 1–19, Jan. 2024, doi: 10.1016/J.AIEPR.2023.09.002.

[25] H. Wang *et al.*, "Comprehensive Study of Mechanical, Electrical and Biological Properties of Conductive Polymer Composites for Medical Applications through Additive Manufacturing," 2024, doi: 10.3390/polym16182625.

[26] Y. Mamunya *et al.*, "Influence of conductive nano- and microfiller distribution on electrical conductivity and EMI shielding properties of polymer/carbon composites," *Compos Sci Technol*, vol. 170, pp. 51–59, Jan. 2019, doi: 10.1016/J.COMPSCITECH.2018.11.037.

[27] R. Mutlu, D. Singh, C. Tawk, and E. Sariyildiz, "A 3D-Printed Soft Haptic Device with Built-in Force Sensing Delivering Bio-Mimicked Feedback," 2023, doi: 10.3390/biomimetics8010127.

[28] X. Xosé Fernández Sánchez-Romate, A. Del Bosque García, M. Sánchez, and A. Ureñ, "Electrical Transport Mechanisms in Graphene Nanoplatelet Doped Polydimethylsiloxane and Application to Ultrasensitive Temperature Sensors," *Cite This: ACS Appl. Mater. Interfaces*, vol. 15, 2023, doi: 10.1021/acsami.2c22162.

[29] S. Bhandari, Krishnanand, S. Roy, A. Singh, and M. Taufik, "Design and fabrication of accelerometer sensor using fused filament fabrication technique," *Progress in Additive Manufacturing*, 2024, doi: 10.1007/s40964-024-00762-2.

[30] C. Chen *et al.*, "Next-generation health monitoring: The role of nanomaterials in 3D-printed wearable devices," *Materials Today*, Mar. 2025, doi: 10.1016/J.MATTOD.2025.03.005.

[31] J. Han, Z. Li, S. Kong, S. Tang, D. Feng, and B. Li, "Wide-response-range and high-sensitivity piezoresistive sensors with triple periodic minimal surface (TPMS) structures for wearable human-computer interaction systems," *Compos B Eng*, vol. 287, p. 111840, Dec. 2024, doi: 10.1016/J.COMPOSITESB.2024.111840.

[32] H. Yi, S. Wang, S. Mei, and Z. Li, "Conductive polymer composites for resistive flexible strain sensors," *Polymer (Guildf)*, vol. 307, p. 127286, Jul. 2024, doi: 10.1016/J.POLYMER.2024.127286.

[33] S. Stankevich *et al.*, "Electrical Resistivity of 3D-Printed Polymer Elements," *Polymers 2023, Vol. 15, Page 2988*, vol. 15, no. 14, p. 2988, Jul. 2023, doi: 10.3390/POLYM15142988.

[34] M. A. Ragolia, A. Di Nisio, A. M. Lanzolla, G. Percoco, M. Scarpetta, and G. Stano, "Thermal Characterization of Electrical Resistance of 3D printed sensors," *Conference Record - IEEE Instrumentation and Measurement Technology Conference*, vol. 2021-May, May 2021, doi: 10.1109/I2MTC50364.2021.9459968.

[35] A. Gómez-Ortega, S. Piedra, G. C. Mondragón-Rodríguez, and N. Camacho, "Dependence of the mechanical properties of nylon-carbon fiber composite on the FDM printing parameters," *Compos Part A Appl Sci Manuf*, vol. 186, p. 108419, Nov. 2024, doi: 10.1016/J.COMPOSITESA.2024.108419.

[36] M. F. Rabbi and V. Chalivendra, "Strain and damage sensing in additively manufactured CB/ABS polymer composites," *Polym Test*, vol. 90, p. 106688, Oct. 2020, doi: 10.1016/J.POLYMERTESTING.2020.106688.

[37] J. Cañada and L. F. Velásquez-García, "Semiconductor-free, monolithically 3D-printed logic gates and resettable fuses," *Virtual Phys Prototyp*, vol. 19, no. 1, Dec. 2024, doi: 10.1080/17452759.2024.2404157.

XI ECCOMAS Thematic Conference on Smart Structures and Materials - SMART 2025
M. Krommer, M. Nader and M. Schagerl (Eds)

Received: 26 March 2025 / Revised: 10 July 2025 / Accepted: 20 September 2025
© The Author(s) 2025

Integration of Shape Memory Alloy Wires into Additive Fabricated Structures for Robotic Grippers

Alexander Dierle, Thomas M. Wendt, Thomas Seifert

Abstract. The integration of shape memory alloys (SMA) with additive manufacturing enables novel approaches for robotic gripper applications. This study introduces a method for embedding SMA wires into 3D-printed structures using fused filament fabrication (FFF). The resulting bending behavior is analytically described, numerically simulated, and experimentally validated. The results demonstrate a strong correlation with theoretical predictions, with deviations primarily attributed to manufacturing tolerances and material interactions.

Key words: Shape Memory Alloy, Smart Structures, Robotic Gripper, Structural Integration, Simulation, additive Manufacturing

1 INTRODUCTION

Shape memory alloys (SMAs) are increasingly applied in robotics and automation [1]. Their thermo-mechanical properties, particularly the reversible, diffusionless martensite-austenite phase transformation, enable controlled actuator movements and offer an alternative to electric motors and pneumatic systems [1].

Market analyses predict an annual growth rate of 13.4% by 2031 [2], with increasing relevance in biomedical applications, robotics, and microelectromechanical systems (MEMS). A 2024 patent landscape analysis indicates a significant increase in patent applications for shape memory materials over the past two decades, with a 71.5% rise between 2010 and 2020, highlighting growing interest and continuous innovation in this field [3]. A key driver in robotics is the compact and lightweight design of SMAs [1]. Their high energy density enables integrated drives for gripping systems, particularly in miniaturized and micro-robotic applications [1].

The fabrication of structurally integrated SMA actuators is constrained by conventional methods. Shape memory actuators, such as those developed by Compactive [4] or described in dissertations by Hübler and Nissle [5, 6], require shaping elements such as casting molds. As a result, generative designs remain limited. While additive manufacturing approaches exist (see [7]), challenges include high material costs, variability in material properties, and limited long-term stability and fatigue resistance.

Alexander Dierle & Thomas M. Wendt & Thomas Seifert
Offenburg University of Applied Sciences, Badstraße 24, 77652 Offenburg, Germany
e-mail: alexander.dierle@hs-offenburg.de

In this paper, the combination of additive manufacturing with conventionally produced SMAs is explored for the development of a novel SMA actuator. The methodology is described, and the actuator's motion behavior is analyzed analytically, numerically, and experimentally.

2 STATE OF THE ART

In this chapter, the state of the art in the field of shape memory alloys and additive manufacturing is presented.

2.1 Shape Memory Alloys

SMAs are "smart" materials that function not only as actuators but also as sensors [1]. Their shape memory effect is based on a crystallographically reversible, diffusionless martensite-austenite phase transformation [1]. Depending on temperature or mechanical stress, the alloy exists in the martensitic phase, the austenitic phase, or as a phase mixture, leading to changes in stiffness and shape [1, 8]. A reversible shape change during heating and cooling is referred to as the two-way effect, where the material "remembers" both its high- and low-temperature shapes [1]. The cycle of this transformation is illustrated in Fig. 1.

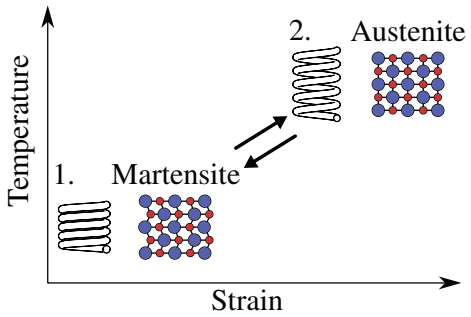

Figure 1: Sketch of the Two-Way Effect (Adapted from [9])

Initially, the SMA is in a fully martensitic structure (see Fig. 1, 1.) [1]. Upon heating beyond a specific temperature (Austenite-Start Temperature), the phase transformation to austenite begins [1]. Once the Austenite-Finish Temperature is reached, the microstructure and the associated shape transformation to the high-temperature position are complete (see Fig. 1, 2.) [1]. Enabling a shape change during the reverse transformation to the martensitic state requires training [1]. This involves thermomechanical treatments that generate microstresses in the austenite phase and promote a preferred orientation for twin martensite formation [1]. When the alloy cools down, the transformation back to martensite starts after the temperature falls below the martensite start temperature and is complete when the martensite finish temperature is reached. (see Fig. 1, 1.) [1]. A challenge of this process is that the reverse transformation from austenite to martensite, and the associated intrinsic deformation, does not perform significant mechanical work [1].

If the reverse transformation is assisted by an external deforming force, an extrinsic two-way effect is present [1]. This force is typically applied using a bias spring [1]. The spring force must not be too large to avoid unnecessarily reducing the actuator's performance [1]. Both the intrinsic and extrinsic effects are suitable for actuator applications [1]. Since mechanical work is often required during the reverse transformation, the intrinsic effect plays a minor role [1]. The extrinsic two-way effect offers higher cyclic stability and a greater contribution to the overall effect [1].

The shape memory effect occurs in several alloy types, but from a technical perspective, nickel-titanium and certain copper-based alloys are the most significant [1, 8]. Nickel-titanium alloys dominate the market with a share of approximately 95% [1]. Their advantages are their mechanical properties. They offer the largest actuation strain among SMAs and exhibit resistance to high temperatures and mechanical stress [8]. Additionally, their biocompatibility makes them particularly suitable for medical applications [8].

2.2 Additive Manufacturing

Additive manufacturing encompasses various processes in which components are produced by pointwise or layerwise material deposition without the need for product-specific tools [10]. Depending on the physical principle, such as extrusion or selective melting, different materials, including polymers, can be processed [10]. One of the most widely used technologies is the extrusion-based Fused Filament Fabrication (FFF) process, which has held the largest market share in 3D printing since 2011 due to its high flexibility and cost efficiency [10]. In the FFF process, filament is fed into an extrusion nozzle, where it is melted and deposited layer by layer through the movement of either the print bed or the nozzle [10]. An innovative application is four-dimensional printing (4DP), where an additional functional dimension is introduced through smart materials [11]. This enables prints with active patterns that respond to external stimuli such as electrical activation or heating [11]. Shape memory alloys are an example of such materials, with over 60% of these structures being fabricated using the FFF process [10].

3 SMA INTEGRATION IN 3D-PRINTED STRUCTURES

The integration of shape memory alloys (SMA) into 3D-printed structures presents several challenges. One key aspect is the positioning of the SMA wire to ensure that its contraction induces a targeted deformation of the structure. In this case, a two-way SMA wire is used, which contracts by approximately 3% (see Table 2, $\epsilon^{tr,max}$). The wire form was chosen due to its ease of handling and good integrability into structures. The wire is fixed at both ends of the actuator and additionally secured with metal/plastic adhesive, ensuring stable positioning above the neutral axis of the structure. Upon activation, its contraction forces the structure to bend (see Fig. 2), resembling the behavior like a bimetal strip. Due to the restoring force of the structure, this represents an extrinsic two-way effect. This principle was chosen because the actuator potential is most efficiently utilized under tensile load [6].

The activation temperature of the SMA wire was set to 57 °C as an optimal compromise be-

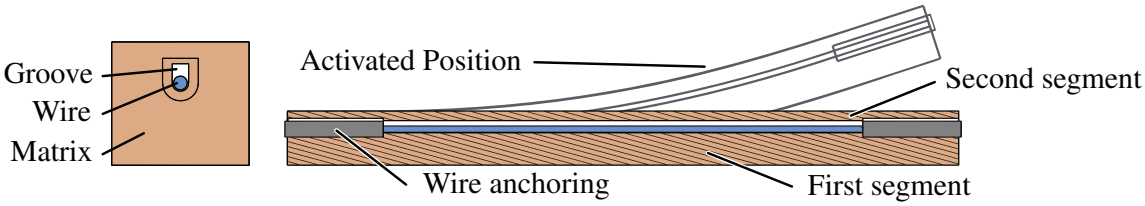

Figure 2: Sketch of the 3D-printed actuator

tween preventing unintended activation due to ambient temperatures and ensuring compatibility with the 3D-printed structure. There are areas of application in the pharmaceuticals, electrical engineering, or the food industry due to the capability of SMA actuators for clean rooms and the possibility of sensitive gripping [12]. Cleanroom conditions, such as those in pharmaceutical and microelectronics manufacturing, maintain a stable temperature of 22 °C ± 0.5 °C, allowing precise prediction of the temperature-dependent closing and opening behavior of the gripper [13]. Possible applications include handling pharmaceuticals, where room temperatures must not exceed 25 °C to ensure drug efficacy [14].

The embedding material is the Ultrafuse TPU (Shore hardness 85A) from BASF, which is thermally stable up to 114 °C [15]. Compared to PLA (Shore 84D) and PETG (Shore 76D) [16, 17], TPU offers higher thermal resistance and lower stiffness. This increases the effective usable gripper force and the deflection of the actuator.

The actuator is manufactured using the FFF process. The 3D model is converted into printable G-code via a slicer. The key parameters are listed in Table 1.

Table 1: 3D printing hardware, software, and parameters of the 3D-printed matrix

Printing parameters	**Value**
3D-Printer, Slicer	Prusa MINI+, PrusaSlicer 2.9.1
Nozzle temperature (First-layer, Subsequent-layer)	225 °C, 220 °C
Bed temperature, cooling fan	40 °C, 20%
Infill, pattern	100%, linear
Printing speed (First-layer, Infill)	140 mm/s, 20 mm/s
Nozzle diameter, Layer height	0.4 mm, 0.2 mm

The printing is paused after completing the first segment to integrate the wire into the matrix (see Fig. 2, groove for the wire). Once the wire is secured within the first segment, the second segment is printed. No activation of the wire occurs during printing, as the nozzle and filament temperatures are insufficient to induce the phase transformation. This is attributed to the rapid cooling of the filament immediately after extrusion. Studies with PLA indicate a 50% temperature drop upon exiting the nozzle [18]. In the event of the bed temperature significantly exceeding the Austenite-Start Temperature of the SMA wire, the wire will be activated.

4 ANALYTICAL DESCRIPTION

The bending of the actuator is analytically described based on a combined beam-column element using shear-rigid Euler–Bernoulli beam theory, e.g. [19]. Fig. 3 illustrates the composite cross-section of the beam consisting of the TPU matrix and the SMA wire, showing the relevant variables.

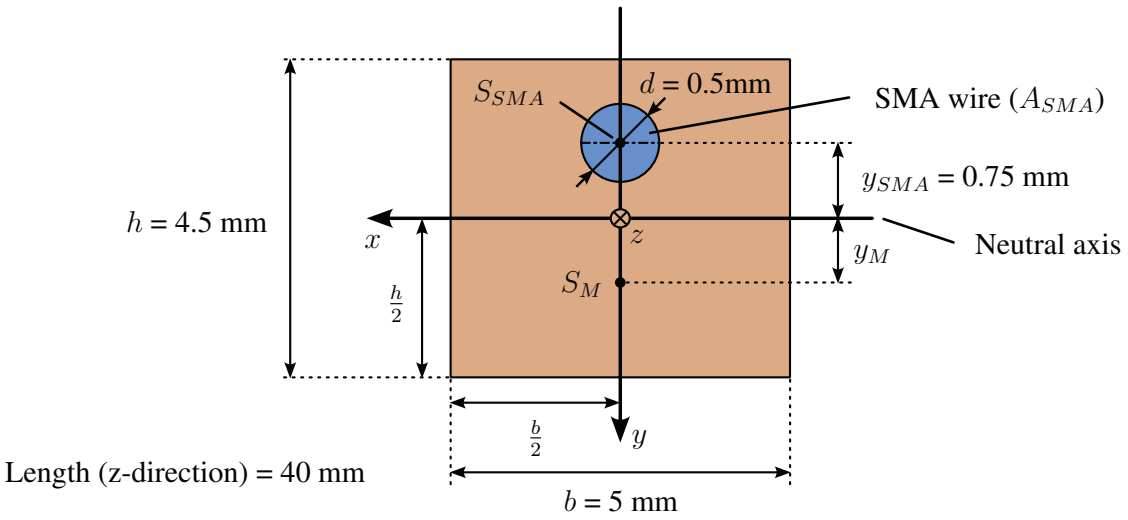

Figure 3: Sketch of the cross-section with the relevant variables

For the calculation of the deflection of the composite beam-column element, the following section properties are required and determined using standard results for composite areas with simple geometries (i.e., a circle for the wire and a rectangle for the total cross-section):

- the area of the SMA wire $A_{SMA} = \pi d^2/4$ and the matrix $A_M = bh - A_{SMA}$,
- the moment of area of the SMA wire $S_{x_{SMA}} = -y_{SMA} A_{SMA}$ and the matrix $S_{x_M} = y_M A_M = y_{SMA} A_{SMA}$ with respect to the x-axis,
- the moment of inertia of the SMA wire $I_{x_{SMA}} = \pi d^4/64 + y_{SMA}^2 A_{SMA}$ and the matrix $I_{x_M} = bh^3/12 - I_{x_{SMA}}$ with respect to the x-axis.

An ideal, rigid connection between the matrix and the SMA wire is assumed. Consequently, both the matrix and the SMA wires experience the same displacement w_0 and the same cross-sectional rotation angle $\partial v/\partial z$ (Fig. 4). Hence, the total displacement $w(y, z)$ in z-direction is calculated as follows:

$$w(y,z) = w_0(z) + \underbrace{w_1(y,z)}_{-\frac{\partial v}{\partial z} y}. \tag{1}$$

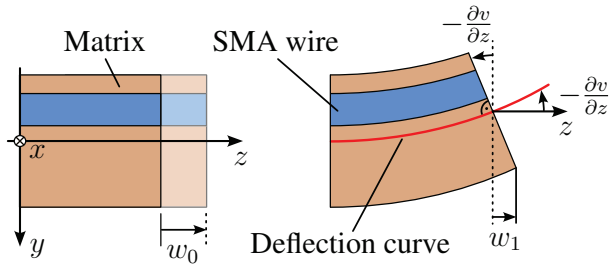

Figure 4: Sketch of the kinematics of the composite beam-column element: homogeneous deformation due to tension/compression (left) and inhomogeneous deformation due to bending (right)

The total strain $\epsilon(y,z)$ is calculated using the partial derivative of the displacement:

$$\epsilon(y,z) = \underbrace{\frac{\partial w_0}{\partial z}}_{\epsilon_0(z)} - \underbrace{\frac{\partial^2 v}{\partial z^2}}_{\kappa_0(z)} y. \tag{2}$$

ϵ_0 is the strain due to a homogeneous tensile compressive deformation (column) and κ_0 is the curvature due to bending (beam).

The total strain consists of elastic (ϵ^{el}), thermal (ϵ^{th}), and transformation induced (ϵ^{tr}) strain. Solving for the elastic strain gives the following expression:

$$\epsilon^{el}(x,y,z) = \epsilon(y,z) - \underbrace{\alpha^{th}(x,y)\Delta T(y,z)}_{\epsilon^{th}(x,y,z)} - \epsilon^{tr}(x,y,z). \tag{3}$$

α^{th} is the coefficient of thermal expansion and corresponds, depending on the spatial location in the section, to the value of the SMA wire (α^{th}_{SMA}) or the matrix (α^{th}_{M}). ΔT is the temperature change referred to an initial temperature.

The normal force in a cross-section is obtained by integrating the normal stress σ over the entire cross-sectional area A:

$$N^{me}(z) = \int_A \sigma(x,y,z)\, dA = \int_{A_M} E_M \epsilon^{el}(x,y,z)\, dA + \int_{A_{SMA}} E_{SMA}\epsilon^{el}(x,y,z)\, dA. \tag{4}$$

E_M and E_{SMA} are Young's modulus of the matrix and the SMA wire, respectively. Insertion of equations (2) and (3) and integration yields

$$\begin{aligned} N^{me} = {} & \underbrace{(E_M A_M + E_{SMA} A_{SMA})}_{D_{11}} \epsilon_0 - \underbrace{(E_M S_{x_M} + E_{SMA} S_{x_{SMA}})}_{-D_{12}} \kappa_0 \\ & \underbrace{- E_M \alpha^{th}_M \int_{A_M} \Delta T(y)\, dA - E_{SMA}\alpha^{th}_{SMA} A_{SMA} \Delta T_{SMA}}_{N^{th}} - \underbrace{E_{SMA} A_{SMA} \epsilon^{tr}}_{N^{tr}}. \end{aligned} \tag{5}$$

Therein, constant temperature change ΔT_{SMA} and constant transformation strain ϵ^{tr} in the section of the SMA wire is assumed.

The bending moment is calculated using the same principle, yielding

$$\begin{aligned} M^{me} = &\underbrace{\left(E_M S_{x_M} + E_{SMA} S_{x_{SMA}}\right)}_{D_{21}} \epsilon_0 - \underbrace{\left(E_M I_{x_M} + E_{SMA} I_{x_{SMA}}\right)}_{-D_{22}} \kappa_0 \\ &\underbrace{- E_M \alpha_M^{th} \int_{A_M} \Delta T(y) y \, dA - E_{SMA} \alpha_{SMA}^{th} S_{x_{SMA}} \Delta T_{SMA}}_{M^{th}} - \underbrace{E_{SMA} S_{x_{SMA}} \epsilon^{tr}}_{M^{tr}}. \end{aligned} \tag{6}$$

From these results, the stiffness matrix can be determined, describing the relationship between normal force N^{me}, bending moment Mme, strain ϵ_0 and curvature κ_0. Solving for ϵ_0 and κ_0 yields:

$$\begin{bmatrix} \epsilon_0 \\ \kappa_0 \end{bmatrix} = \begin{bmatrix} D_{11} & D_{12} \\ D_{21} & D_{22} \end{bmatrix}^{-1} \begin{bmatrix} N^{me} + N^{th} + N^{tr} \\ M^{me} + M^{th} + M^{tr} \end{bmatrix}. \tag{7}$$

By double integration of the curvature, the deflection of the actuator is obtained:

$$v(z) = \iint \kappa_0 \, dz + C_1 z + C_2. \tag{8}$$

Given the boundary conditions on the clamped side, $v(0) = 0$ and $\partial v / \partial z(0) = 0$, the integration constants C_1 and C_2 are zero. In this work, thermal expansion is neglected as thermal expansion of the TPU matrix is considered negligibly small, especially compared to the SMA-induced transformation, where the wire contracts by approximately 3% (see Table 2, $\epsilon^{tr,max}$). Furthermore, since no external loads are applied, N^{me} and Mme are zero. Therefore, bending results solely from the transformation of the SMA and κ_0 is constant, resulting in the deflection curve

$$v(z) = \frac{1}{2} \kappa_0 z^2. \tag{9}$$

5 SIMULATION

The simulation is conducted in COMSOL Multiphysics using the SMA material model. For phase transformation, the Lagoudas model and the Souza-Auricchio model are available [20]. While the Souza-Auricchio model is phenomenological, the Lagoudas model accounts for the microstructure of the SMA [21]. The Lagoudas model provides a more accurate description of mechanical processes but requires more parameters and computation time [22, 21]. Because the focus here is primarily on precise modeling, the Lagoudas model is used. A detailed model description can be found in the COMSOL documentation [20]. As the two-way effect is not directly implemented in COMSOL, it is represented via thermal expansion. The wire length contracts maximally when the martensite fraction (ξ) reaches 0%:

$$\epsilon^{tr}(\xi) = (1 - \xi) \epsilon^{tr,max}. \tag{10}$$

The Electromagnetic Heating module in COMSOL Multiphysics is used for the simulation of heating. The temperature distribution in the wire and the resulting phase transformation are computed given the applied electrical current. The simulation is performed as a time-dependent study with a fully coupled solver. Once the complete transformation from martensite to austenite is achieved, the simulation is terminated. A physics-controlled mesh with normal detail level is used, and its quality is verified based on skewness. The simulation at the moment of complete transformation is shown in Fig. 5.

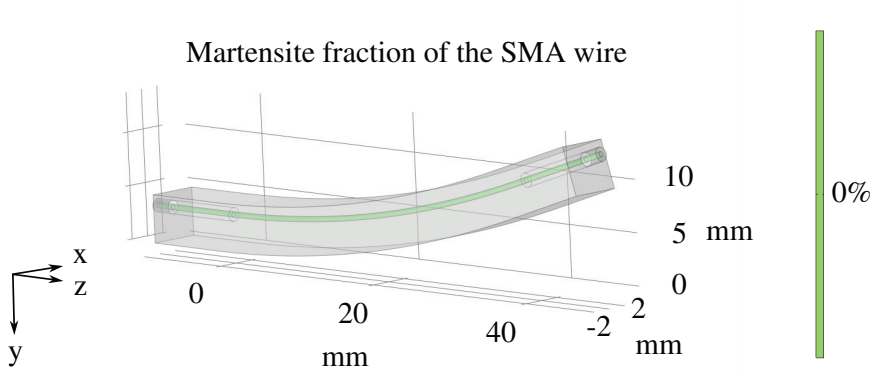

Figure 5: COMSOL simulation of the martensite fraction of the SMA wire at complete transformation to austenite

Since the thermal expansion of the wire diameter is significantly smaller than the wire contraction, it is neglected. Heat transfer from the wire to the structure, as well as the temperature behavior of the contacts and contact resistances, are also not considered. The TPU structure is assumed to be an ideal insulator. These simplifications are made because only the maximum strain of the wire is relevant, while the temporal evolution of the bending and the temperature distribution in the structure are not.

6 RESULTS

The calculated, simulated, and experimentally determined bending curves are shown in Fig. 6. The key parameters to calculate the curves are listed in Table 2. The experimentally determined points represent the average value from five measurements from five different actuators, conducted at 5 mm intervals along the actuator at an ambient temperature of 22 °C. The difference between the top surface of the actuator in its resting and activated states was measured. The measurements were conducted at 60-second intervals to allow the wire to fully cool down. The standard deviation of the measurements was 0.04 mm, indicating a reproducible measurement. The wire was supplied with 3 A for 2.5 s, as it had reached a steady state at this point, with no further measurable contraction or bending. Only the region where the wire can contract was analyzed. Because the wire is crimped at the anchor points, no contraction occurs in these areas, restricting the analyzed length to the 40 mm wire segment.

Table 2: Material parameter Nitinol/ TPU 85A

Material parameter	Nitinol	TPU 85A	Reference
Reference temperature	22 °C	22 °C	meas.
Poisson's ratio (ν)	0.33	0.45	[23], [24]
Density (ρ)	6450 kg/m^3	1114 kg/m^3	[23], [15]
Young's modulus (E)	Martensite: 28 GPa Austenite: 78 GPa	20 MPa	[23], [15]
Maximum transformation strain ($\epsilon^{tr,max}$)	-0.0325 (-3.25%)	-	meas.
Martensite start/ finish temp. (M_s/ M_f)	66.42 °C/ 45.67 °C	-	[23]
Austenite start/ finish temp. (A_s/ A_f)	56.99 °C/ 74.48 °C	-	[23]
Thermal conductivity (k)	18 W/(m · K)	-	[25]
Electrical conductivity (γ_{el})	$1 \cdot 10^6$ S/m	-	[25]

In the COMSOL simulation, the actuator's top surface is also used to represent the bending curve, ensuring comparability with the experimental results. As before, only the wire segment between the anchor points is analyzed. The bending curve of the analytical solution is independent of the observation point in the y-direction under the given assumptions. Therefore, no further adjustments are required for comparability.

In the plot of the deflection curve in Fig. 6, the y-axis represents the deflection in mm, while the x-axis corresponds to the position along the actuator length (z-axis). The origin is set immediately after the wire exits the crimping, and the 40-mm mark is just before it enters the crimping (see Fig 2). For both the simulation and the measurement, the actuator is shown at its maximum displacement after the complete phase transformation to austenite. In the analytical solution, the maximum transformation strain is used.

The root mean squared error (RMSE) is calculated to quantify the model deviations. The mean squared deviation between the analytical model and the experiment is 0.09 mm, corresponding to a relative difference of 3.69%. The RMSE between the simulation and the experiment is 0.20 mm or 8.21%. The deviation between the analytical solution and the simulation is 0.17 mm, corresponding to 6.79%. The standard deviation between the five actuators is ±0.27 mm across all measurement points, increasing from zero to a maximum of ±0.50 mm at a z-value of 35 mm.

7 DISCUSSION

The deviations between the analytical and simulated solutions from the experimental results and the variation among the five tested actuators can be attributed to the manufacturing process. Due to the FFF 3D printing tolerance of approximately ±0.2 mm – resulting from material properties, calibration, and printing settings – constructive tolerances must be considered. The wire is also manually placed into the structure, and the slicing process of the small structure contributes to inaccuracies. A reproducible and secure embedding of the wire requires accounting for the 0.7 mm gap shown in Fig. 2. Ignoring this gap could lead to wire displacement due

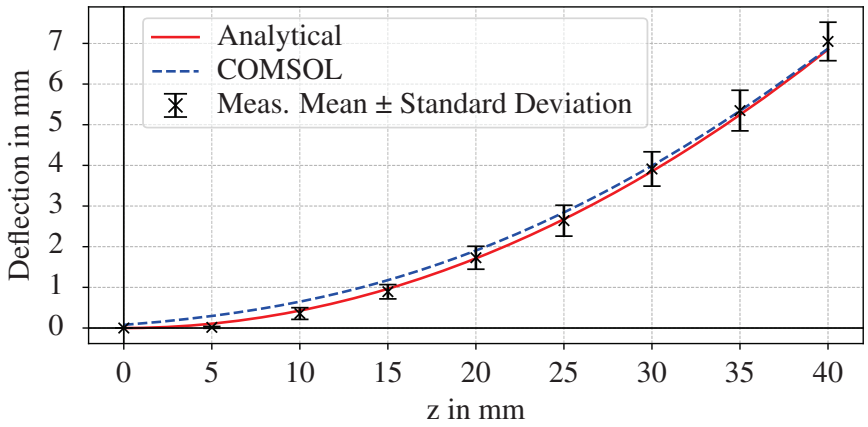

Figure 6: Analytically (absolute value), numerically, and experimentally determined bending curve in the z-direction, referenced to the top surface of the actuator

to its slight deformability in the martensitic state and the movement of the print bed.

The bond between TPU and Nitinol wire is weak, meaning the wire does not adhere or remain positioned ideally as assumed in the models. Since the wire remains movable within the structure and is only fixed at the anchor points, the standard deviation between the five actuators in the bending curve increases with rising z-values. The reason for this is the dependence of the bending behavior on the wire placement.

The discrepancy between the analytical and simulated calculations can be explained by boundary conditions. While the simulation considers the entire actuator, the analytical solution focuses only on the active section, resulting in different constraints. Additionally, in the simulation, the strain is not directly prescribed but rather determined through Joule heating of the wire. The temperature distribution is not homogeneous, which also influences the bending behavior.

8 CONCLUSION AND FUTURE WORK

Using the FFF printing process, an SMA wire can be embedded into a structure. While activation by the hot extrusion nozzle does not take place, the print bed temperature is a critical factor. If the bed temperature exceeds the activation temperature of the wire significantly, unintended activation may set in during the printing process.

The analytical solution, based on a combined beam-column element, predicts the bending curve with an RMSE of 0.09 mm. The COMSOL simulation deviates due to differing boundary conditions, such as Joule heating, resulting in an RMSE of 0.20 mm. Since the wire is not perfectly bonded to the filament as assumed in the models and there is some clearance between the wire and the 3D-printed structure, deviations from the measured values arise.

Future work will focus on improving the bond between the wire and the structure to eliminate

movement within the structure. Additionally, the findings will be extended to multiple wires and different 3D printing materials to further validate the results.

REFERENCES

[1] S. Langbein and A. Czechowicz, *Formgedächtnistechnik: Entwickeln, Testen und Anwenden*. Springer Fachmedien.

[2] Metastat Insight and Technologies Pvt. Ltd. Shape memory alloy market size & share report by 2031. [Online]. Available: https://www.metastatinsight.com/report/shape-memory-alloy-market

[3] D. Ben Zakou. Patentlandschaftsanalyse – formgedächtnismaterialien. [Online]. Available: https://www.questel.com/de/resourcehub/patent-landscape-analysis-shape-memory-materials/

[4] CompActive GmbH. CompActive bending actuator. [Online]. Available: https://www.compactive.de/

[5] S. Nissle, *Zur Kraftübertagung zwischen NiTi-Formgedächtnislegierungen und Faserkunststoffverbunden in aktiven Hybridstrukturen*, ser. IVW - Schriftenreihe. Institut für Verbundwerkstoffe GmbH, vol. 137.

[6] M. Hübler, *Methodik zur Auslegung und Herstellung von aktiven SMA-FKV-Hybridverbunden*. Technische Universität Kaiserslautern.

[7] S. Ahmad, A. W. Hashmi, J. Singh, K. Arora, Y. Tian, F. Iqbal, M. Al-Dossari, and M. Khan, "Innovations in additive manufacturing of shape memory alloys: Alloys, microstructures, treatments, applications," vol. 32.

[8] A. Hein, *Auslegung und Entwurf adaptiver Strukturen und Systeme mit Formgedächtnislegierungen*. Stuttgart : Institut für Konstruktionstechnik und Technisches Design.

[9] I. Özkul, M. Kurgun, E. Kalay, C. Aksu Canbay, and K. Aldas, "Shape memory alloys phenomena: classification of the shape memory alloys production techniques and application fields," vol. 134.

[10] M. Kumke, *Methodisches Konstruieren von additiv gefertigten Bauteilen*. Springer Fachmedien.

[11] S. Junk, H. Einloth, and D. Velten, "A methodical approach to product development in 4d printing using smart materials," in *Progress in Digital and Physical Manufacturing*. Springer International Publishing, pp. 130–137.

[12] M. Kohl, *Entwicklung von Mikroaktoren aus Formgedächtnislegierungen*. Forschungszentrum Karlsruhe, no. 6718.

[13] L. Gail and U. Gommel, *Reinraumtechnik*, ser. VDI-Buch. Springer.

[14] S. Dicheva-Radev, "Arzneimittel und hitze: Temperaturempfindlichkeit und richtige aufbewahrung von arzneimitteln," vol. 47, no. 3, pp. 71–74.

[15] BASF 3D Printing Solutions BV, "Technisches datenblatt für ultrafuse TPU 85a."

[16] UltiMaker, "Ultimaker PLA technical data sheet." [Online]. Available: https://um-support-files.ultimaker.com/materials/2.85mm/tds/PLA/Ultimaker-PLA-TDS-v5.00.pdf

[17] UltiMaker, "Ultimaker PETG technical data sheet." [Online]. Available: https://um-support-files.ultimaker.com/materials/2.85mm/tds/PETG/Ultimaker-PETG-TDS-v1.00.pdf

[18] C.-Y. Lee and C.-Y. Liu, "The influence of forced-air cooling on a 3d printed PLA part manufactured by fused filament fabrication," vol. 25, pp. 196–203. [Online]. Available: https://www.sciencedirect.com/science/article/pii/S2214860418306924

[19] O. A. Bauchau and J. I. Craig, "Euler-bernoulli beam theory," in *Structural Analysis*, O. A. Bauchau and J. I. Craig, Eds. Springer Netherlands, pp. 173–221. [Online]. Available: https://doi.org/10.1007/978-90-481-2516-6_5

[20] COMSOL Inc. Shape memory alloy. [Online]. Available: https://doc.comsol.com/5.5/doc/com.comsol.help.sme/sme_ug_theory.06.33.html#3685019

[21] T. Stocker, "Untersuchung des einflusses von gestaltung und werkstoff auf die dauerfestigkeit und kraftübertragung in nickel-titan brackets."

[22] J. G. Boyd and D. C. Lagoudas, "A thermodynamical constitutive model for shape memory materials. part i. the monolithic shape memory alloy," vol. 12, no. 6, pp. 805–842. [Online]. Available: https://www.sciencedirect.com/science/article/pii/S0749641996000307

[23] R. Rajagopalan, A. J. Petruska, and H. David, "Design of bi-state shape memory material composite soft actuator," vol. 11, no. 3.

[24] Y.-X. Xu and J.-Y. Juang, "Measurement of nonlinear poisson's ratio of thermoplastic polyurethanes under cyclic softening using 2d digital image correlation," vol. 13, no. 9, p. 1498. [Online]. Available: https://pmc.ncbi.nlm.nih.gov/articles/PMC8125632/

[25] JM Medical, "Nitinol properties," Nitinol Actuators, Sep. 2017. [Online]. Available: https://nitinolactuators.com/nitinol-properties

XI ECCOMAS Thematic Conference on Smart Structures and Materials - SMART 2025
M. Krommer, M. Nader and M. Schagerl (Eds)

Received: 13 March 2025 / Revised: 1 July 2025 / Accepted: 20 September 2025
© The Author(s) 2025

Numerical Prediction of Effective Functional Behavior of Mg-NiTi Strut-Architected Interpenetrating Phase Composites

Shahzaib Ilyas, Marwan El-Rich, Mohamad Khalil, Wael Zaki

Abstract
Improving both stiffness and strength and damping capability in metals is critical, but it is a challenging task since both qualities conflict with each other. This study conducted a numerical study to investigate the effective mechanical behavior of Mg-NiTi composites with bi-continuous interpenetrating phase architecture. An in-house UMAT subroutine constitutive model is utilized to incorporate functional behaviors of the superelastic NiTi SMA phase. These smart architected IPCs are modelled as RVEs where a unit-cell method is used to reduce the computational cost, while the functional behavior of the complete composite is assessed using the volumetric homogenization technique under periodic boundary conditions. The composite exhibits a unique combination of mechanical properties with improved stiffness and excellent strain recovery behavior that is unexpected from magnesium material and its alloys. The effective elastic stiffnesses are influenced by reinforcement morphology, which varies monotonically with NiTi SMA concentration. Moreover, Mg-NiTi IPCs exhibit an exponential strain recovery behavior, with the concentration of NiTi indicating good damping capability without compromising the stiffness of the magnesium material. Moreover, the power-law fitting parameters predict stretching-dominated behavior for each loading state. These exceptional responses highlight the potential of such smart composites for structural, including vibration absorption, and biomedical, including implants.

Key words: Shape Memory Alloys, Smart Materials, Interpenetrating Phase Composites, Finite Element Analysis, Lattice Structures.

1 INTRODUCTION

Nitinol (NiTi) is a well-known intermetallic shape memory alloy (SMA) that can exhibit both shape memory and superelastic functional properties. The functional response of NiTi SMAs

Shahzaib Ilyas & Marwan El-Rich & Mohamad Khalil & Wael Zaki
Mechanical and Nuclear Engineering Department, Khalifa University of Science and Technology, Main Campus, 127788 Abu Dhabi, UAE, e-mail: wael.zaki@ku.ac.ae

is due to their capacity to undergo thermos-mechanically induced microstructural solid-phase transitions [1-3]. Contrarily, magnesium and its alloys are distinguished from other metallic materials by their high specific strength and stiffness, which are strength and stiffness normalized by density [4, 5]. Mg has superior damping qualities, outperforming most metals due to its ease of twinning, dislocation mobility, and weak dislocation pinning at defects or impurities [6-8].

The applications, however, associated with magnesium are limited by their poor strength at both ambient and increased temperatures, as well as lesser ductility when compared to steels and aluminium alloys. Strengthening magnesium while retaining its high damping capability remains a challenge, as conventional strengthening methods frequently degrade damping performance [2, 6, 9]. Furthermore, like other engineered materials, magnesium alloys and composites cannot restore their original shape and mechanical integrity after inelastic deformation or damage. Achieving shape memory or self-recovery in Mg-based materials might increase their endurance, which can allow for the creation of smart materials with sophisticated functions that could have potential advantages for biomedical and vibration-damping applications [7].

To overcome this restriction related to magnesium and its alloys, we numerically investigated and characterized the mechanical properties of interpenetrating phase composites (IPCs) with dual-phase bi-continuous architecture, where NiTi SMA is modelled with strut lattice as reinforcement phase, while magnesium is the matrix phase. These Mg-NiTi IPCs can provide high strength, attributed to the superelastic nature of NiTi and larger strain recovery due to the SME of NiTi SMA without compromising the lightweight and damping properties of Pure Mg. Furthermore, preserving the structural integrity and continuity of the NiTi material inside the composite can boost strength efficiency and strain recovery during unloading [7].

This study presents a proof-of-concept for quantitatively analyzing the functional behavior (elastic moduli, strain recovery, and phase transformation) of NiTi-reinforced IPCs under various loading conditions. To incorporate NiTi SMA, an in-house built Fortran subroutine is used in the finite element program *Abaqus*, while the Mg phase material data is obtained from the literature. In this article, Section 2 will focus on the material and methodology, with an emphasis on the 3D CAD design of the composite, the constitutive model for NiTi SMA, and the effective homogenization technique. The results and discussion will be presented in Section 3, followed by the conclusion in Section 4.

2 METHODOLOGY AND MATERIAL

2.1 DESIGN OF STRUT LATTICE AND ITS COMPLEMENTARY PHASE

The dual-phase strut-architected IPCs considered in this study are modelled, discretized, and numerically analysed using modern software. First, the unit cell for the Kelvin-cell (K) strut architecture unit-cell model for strut architecture is created using *nTopology* software. The process starts with the creation of an implicit body, followed by surface meshing with a feature size of 0.2 mm. Then the second phase is created by using a Boolean operation where the K-stut lattice is subtracted from a dense cube, resulting in a second porous phase. This method

allows the development of cellular structures with exact control over both geometric aspects and material distribution. Figure 1(a)-(c) illustrates the K-strut phase, its complementary structure, and the complete K-IPC. The interconnectivity pattern of the K-strut with IPC can be visualized in Figure 1(d). The interconnectivity pattern between the strut and its complementary phase significantly influences the overall effective response of the composite and varies from one topology to another.

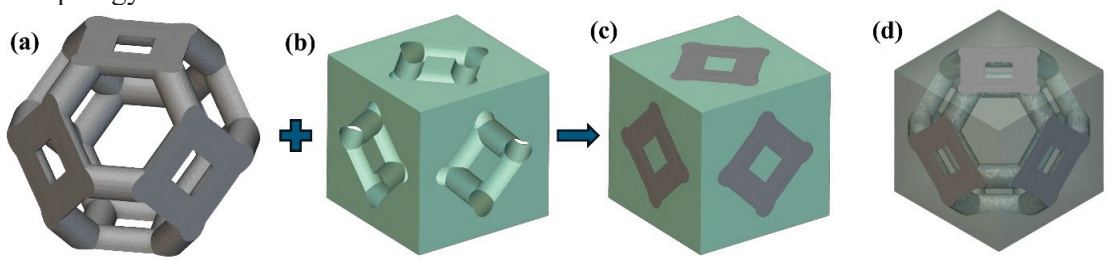

Figure 1: 3D CAD model of the K-strut interpenetrating phase composite (IPC): (a) Kelvin-cell (K) strut lattice structure, (b) corresponding secondary phase of the composite, (c) complete K-strut architected IPC, and (d) IPC with transparent secondary phase to visualize the interconnectivity of the architected phase within the composite.

2.2 THE ZM MODEL FOR NITI SMA

A user-defined subroutine material model [2, 10, 11] has been used that includes the constitutive relationships for NiTi SMA by integrating a time-discrete version to describe the dense NiTi material characteristics. Within the frame of the ZM model, the stress-strain behaviours of NiTi are addressed as follows:

$$\boldsymbol{\sigma} = \boldsymbol{K} : (\boldsymbol{\varepsilon} - \mathrm{z}\boldsymbol{\varepsilon}_{tr}) \tag{1}$$

Where $\boldsymbol{\sigma}$ is the stress tensor, $\boldsymbol{K}$ is the equivalent stiffness of NiTi, $\boldsymbol{\varepsilon}$ is the total applied strain, z is the volume fraction of martensite, and $\boldsymbol{\varepsilon_{tr}}$ Is the local inelastic strain due to detwinning and reorientation of the martensitic phase. The equivalent stiffness $\boldsymbol{K}$ is given in terms of the elastic stiffnesses of austenite ($\boldsymbol{K}_A$) and martensite ($\boldsymbol{K}_M$) that are mathematically correlated:

$$\boldsymbol{K} = [z\boldsymbol{K}_M^{-1} + (1-z)\boldsymbol{K}_A^{-1}]^{-1}. \tag{2}$$

The validation of the ZM NiTi SMA numerical model with experimental data has been performed in preceding work [2, 11], which makes a reliable choice for investigating the behaviors of the NiTi SMA core of the IPC samples considered in this work. Furthermore, the UMAT model requires fourteen input material parameters defining the loading-unloading stress-strain behavior for dense non-linear NiTi and is listed in Table 1. These dense NiTi material parameters are derived from experimental tests cited by Zaki and Momin [2]. Meanwhile, the dense material parameters for the second pure Mg phase material are sourced from the literature [12], with a Young's modulus of 31.06 MPa and a Poisson's ratio of 0.33, respectively.

Table 1: Dense material parameters for superelastic NiTi SMA phase [2]

NiTi SMA Parameter Values			
E_A	61,500 MPa	a	6.89 MPa
E_M	24,000 MPa	b	6.9 MPa
v	0.3	ε^o	0.04
γ	110 MPa	G	4.66 MPa
α	2,750 MPa	β	5,500 MPa
$\xi_{\delta\hat{E}}$	0.4381MPa/℃	k	2.49 MPa
A_f^o	40 ℃	-	-

2.3 FINITE ELEMENT MODELLING AND EFFECTIVE HOMOGENIZATION TECHNIQUE

Both the K-strut and its second phase are meshed with 3D 10-noded tetrahedral elements in *Altair Hypermesh,* which is equivalent to C3D10 in *Abaqus* v16.3 software. The average number of mesh elements is approximately 120,000, with an element size of 0.2 mm in each case. An effective mesh convergence has been found when the number of elements is greater than 50,000 for single-unit cell lattice structures [13]. Furthermore, tetrahedral mesh optimization is performed in *Hypermesh* to further enhance the mesh quality and eliminate unwanted elements that could lead to stress concentrations. The finite element pre-processing is carried out in *Abaqus v2022* Finite element analyses are carried out in *Abaqus* v2022 under displacement-controlled loadings. The perfect "tie" constraint inhibits the relative motion between the two phases.

The finite element simulations are conducted on a high-performance computing (HPC) facility provided by Khalifa University, where 30 cores are utilized on a single node on the high-performance workstation. Additionally, to reduce the computational cost, the representative volume element (RVE) approach [13] with a single unit-cell method under the influence of periodic boundary conditions is a verified approach reported in various literature [14, 15]. The unit-cell size of the IPC is 1 mm × 1 mm × 1 mm, and the volumetric fraction of NiTi SMA in the IPC ranges from 15% to 40%, with increments at 15%, 20%, 25%, 35%, and 40%. Furthermore, the homogenization technique extracts the effective response of the complete structure from the RVE, where the effective stress is evaluated by using the following correlation:

$$\overline{\boldsymbol{\sigma}} = \frac{\int_A dF}{\int_A dA} = \sum_i^N F_i^R \tag{3}$$

Where $\overline{\boldsymbol{\sigma}}$ represents the effective stress (uniaxial, hydrostatic, or shear) that depends on the loading circumstances, N represents the total number of nodes on which displacement is applied, and A and V represents the geometric parameters with cross-sectional area and volume,

respectively. Here, F_i^R corresponds to the average reaction force, which was computed on the faces where the displacement is applied and then divided by the cross-sectional area A to extract the effective stress of the IPCs.

To compute the evolution of martensite during the phase transformation of NiTi SMA lattice phases, the effective martensite volumetric fraction (z^*) is computed, that arises from a solution-dependent variable (SDV1) from the ZM UMAT subroutine model, providing the phase transformation of TPMS/strut SMA functional phase. The z^* is computed from the following relationship:

$$z^* = \frac{1}{V}\int_V z\, dV \tag{4}$$

2.4 ANALYTICAL BOUNDS FOR ELASTIC STIFFNESS

The effective elastic properties for strut-architected TPMS-IPCs are estimated with two well-known analytical models that include Weiner, alternatively known as Ruess and Voigt [16], and Hashin–Shtrikman [17]. Weiner bounds are a consequence of solving the boundary value problem of a random medium while assuming a homogeneous material, and can be represented as:

$$\sum_{m=1}^{n}\left(\frac{\phi_m}{E_m}\right)^{-1} \leq E^* \leq \sum_{m=1}^{n}\phi_m E_m \tag{5}$$

Where ϕ_m is the volumetric fraction of the strut and its second phase, E_m corresponds to the Young's modulus of dense NiTi and Mg materials and E^* is the effective stiffness (uniaxial, shear, and hydrostatic) of the complete composite. As dual-phase IPCs are considered in this study, this provides $n = 2$. On the other hand, Hashin–Shtrikman (HS) bounds are tighter and more accurate than the rule of mixture, and the governing relations for the bounds are presented in [16].

3 RESULTS AND DISCUSSIONS

Starting with the elastic behaviour of the composite, Figure 2 presents the effective elastic moduli (uniaxial, shear, and hydrostatic) of all NiTi SMA strut-architected IPCs for three loading conditions against the volumetric fraction of reinforcement material. To offer a comparative assessment, the effective elastic characteristics are normalized against the dense stiffness of NiTi SMA. This will provide an improvement in the stiffness of the composite with the inclusion of NiTi material within the composite. The overall elastic stiffness results in an increase in elastic stiffness with increasing volumetric fraction of NiTi for all loads. Among analytical bounds, Weiner perfectly predicts and bounds the effective moduli where the response is almost in the middle of the bounds, except during hydrostatic loads. The hydrostatic modulus (Figure 2(c)) for Mg-NiTi IPCs is more closely aligned with the Weiner lower bound, especially at higher volumetric fractions. Contrarily, regarding HS bounds, the model overpredicts the effective response of the IPCs during the hydrostatic loading case. This indicates that the HS limitations are inadequate for predicting the effective response of Mg-

NiTi IPC during hydrostatic loading conditions. Furthermore, the composite exhibited comparatively softer behaviour during hydrostatic loading as indicated by the effective moduli that are closer to the lower bound. Thus, such a combination of materials is suggested to apply in the case of uniaxial and shear loading scenarios.

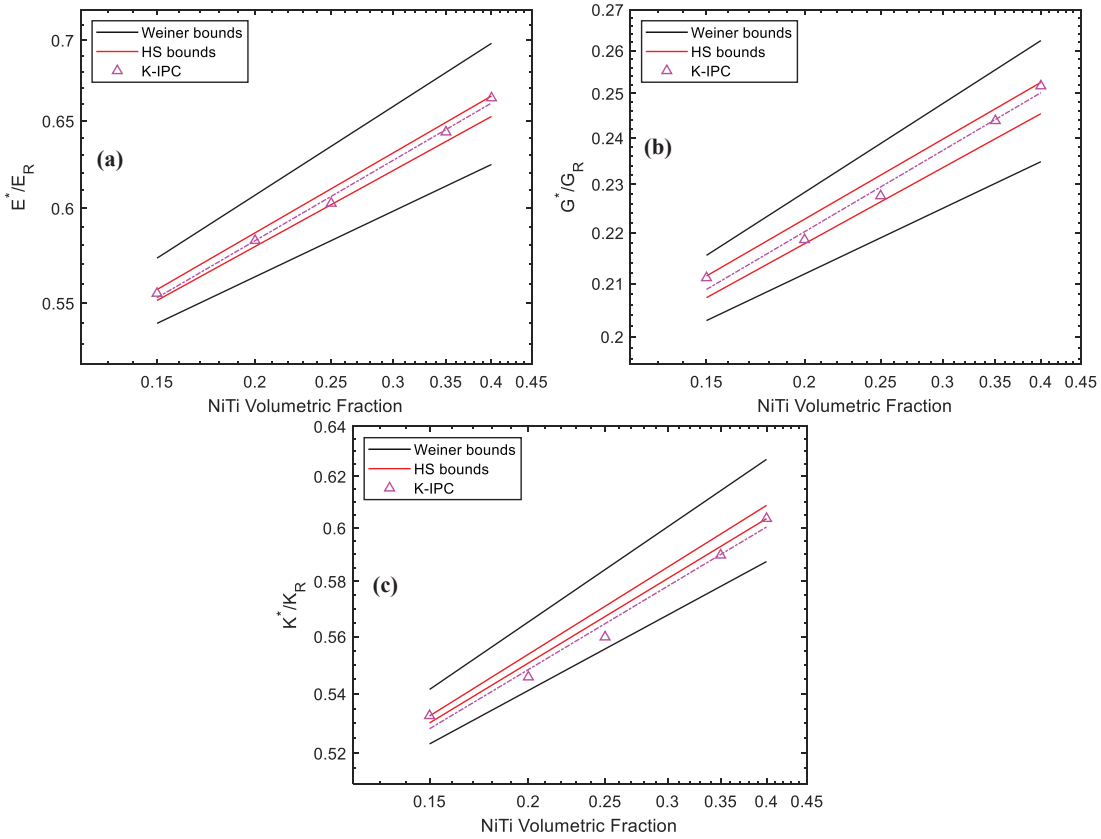

Figure 2: Influence of volumetric fraction of NiTi microstructure on the effective normalized elastic stiffnesses for Mg-NiTi IPCs: (a) uniaxial, (b) shear, and (c) hydrostatic

The phase transformation of NiTi SMA lattice structure within IPCs corresponds to the austenite-to-martensite shifting of the SMA with the application of load. This phase transformation is studied by analysing the change in martensite concentration that corresponds to the martensite volumetric fraction (z^*) with the application of an applied uniaxial load and presented in Figure 3(a). It was observed that an increase in NiTi concentration results in a steeper slope in the z^*-strain curve during the austenite-to-martensite transition zone, indicating a faster and more abrupt phase transition from austenite to martensite. For instance, the 40% NiTi strut lattice exhibits a steeper and more abrupt transition than the 15% or even 20% variants. Moreover, Figure 3(b) presents the effective strain recovery for Mg-NiTi IPC, which shows an exponentially increasing trend in recovering the overall strain with increasing concentration of NiTi material within the composite. This can be attributed to the shape memory

effect of NiTi material that returns the maximum possible amount of strain during unloading of the composite. This is the primary advantage for Mg and its alloys to integrate with NiTi SMA, which will not only enhance the damping capability but also without compromising the strength of the magnesium.

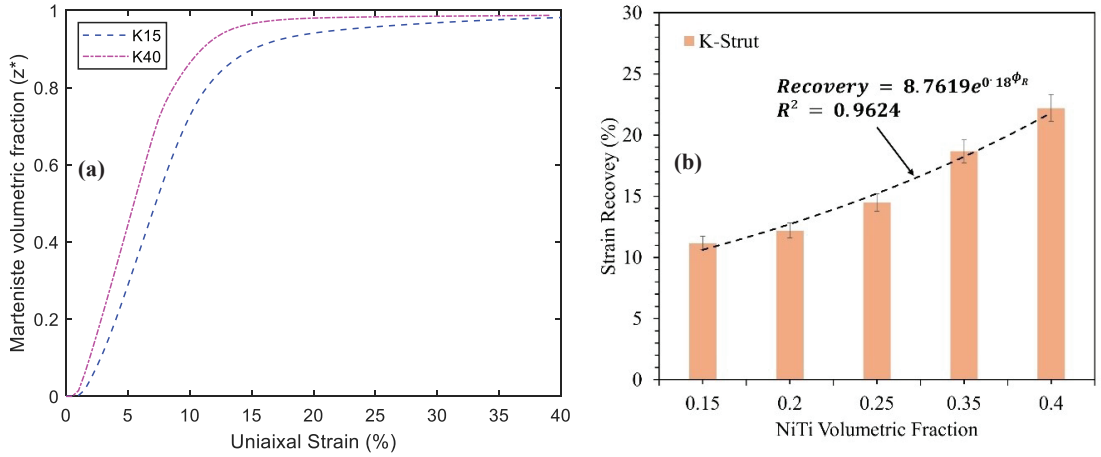

Figure 3: Influence of volumetric fraction on (a) Effective martensite volumetric fraction (z^*) with respect to uniaxial load, and (b) strain recovery behavior for Mg-NiTi IPCs

Figure 4 presents the contour plots illustrating the austenite-to-martensite transformation in a K-strut lattice structure under uniaxial loading. The blue color represents the austenite phase, the red color highlights the martensite phase, and the intermediate colors indicate the transition zone from austenite to martensite.

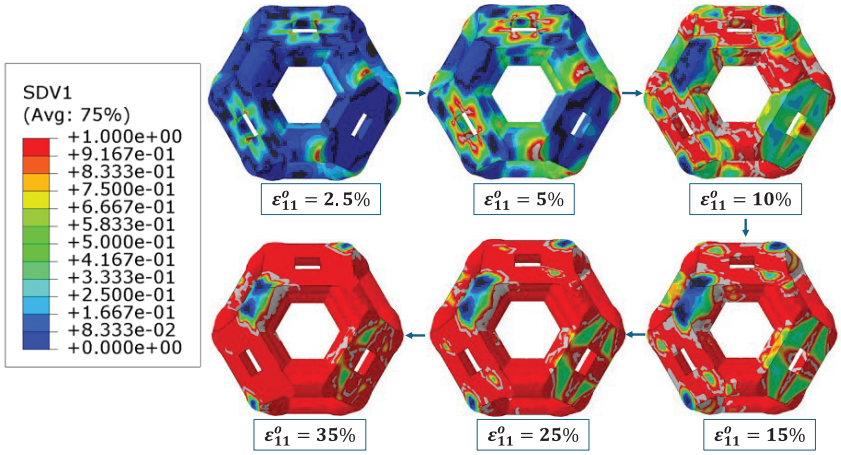

Figure 4: Austenite-to-Martensite phase transformation contours of K-rut NiTi SMA phase against uniaxial strain.

At lower strains, the transformation initiates at the corners of the strut lattice, making them critical zones during phase transformation. This is followed by a transformation in the strut

arms, which are bounded by the Mg secondary phase. Notably, the interface region between the Mg and NiTi phases experiences higher stress, which triggers the phase transformation and facilitates its propagation throughout the structure. The von Mises stress contours are presented in Figure 5, which indicates high stress regions around the strut lattice, especially at the corners. These high-stress regions indicate regions across struts that are prone to crack initiation and debonding.

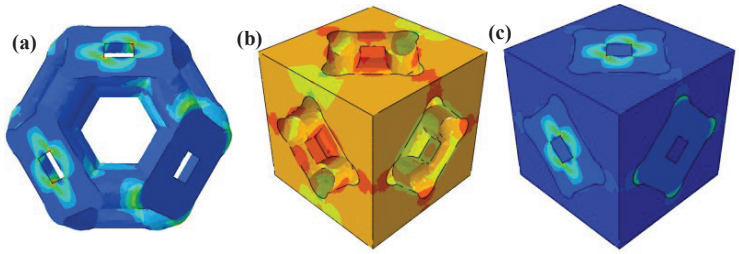

Figure 5: von-Mises contours: (a) NiTi Kelvin cell foam, (b) Mg complementary phase, and (c) Mg-NiTi IPC at 20% volumetric fraction of NiTi material.

Table 2 indicates the power-law fitting parameters that describe the deformation mechanism of the K-Strut IPC, indicating a stretching-dominated response ($n = 1$) across all loading scenarios. The primary reason for this is that the Kelvin cell strut lattice structure is symmetric in all three perpendicular directions, exhibiting strong resistance to bending, which drives the overall effective response to be stretching-dominated rather than bending-dominated. Furthermore, the exponential strain recovery, driven by the NiTi phase change, emphasizes the critical role of strain recovery in increasing the stiffness and functional behaviour of the composites.

Table 2: Fitting parameters for elastic moduli and strain recovery for Mg-NiTi IPC.

K-Strut IPC	Elastic modulus, E^* [MPa]		Shear modulus, G^* [MPa]		Bulk modulus, K^* [MPa]		Strain Recovery (%)	
Expression	$\left\|\frac{E^*}{E_R}\right\| = a\emptyset_R^n + \frac{E_M}{E_R}$		$\left\|\frac{G^*}{E_R}\right\| = a\emptyset_R^n + \frac{G_M}{E_R}$		$\left\|\frac{K^*}{E_R}\right\| = a\emptyset_R^n + \frac{K_M}{E_R}$		$ae^{n\phi_R}$	
Fitting parameters	a	n	a	n	a	n	a	n
Values	0.4401	1.1089	0.1696	1.0988	0.2959	1.0931	8.7619	0.18

4 CONCLUSIONS

In summary, this study numerically investigates the functional behaviour of dual-phase interpenetrating phase composites (IPCs) where the reinforcement phase comprises of smart nitinol (NiTi) core that is embedded in elastoplastic magnesium as the second phase. K-strut lattices are considered here to model the NiTi SMA reinforcement phase, where a UMAT subroutine model is used to incorporate the constitutive model for the SMA phase. A representative volume element (RVE) with a unit-cell method is used, where periodic boundary

conditions and effective homogenization techniques are employed to analyze the functional behavior of IPCs.

- The effective performance of the composite provides improvement in elastic stiffness and displays exponential strain recovery, making them suitable for vibration absorption and biomedical applications.
- Integrating NiTi SMA with magnesium significantly enhances the effective stiffness of the composite.
- Regarding analytical bounds, Weiner analytical model perfectly predicts and bounds the stiffness of the composite. However, the Hashin–Shtrikman (HS) bound is tighter than Weiner and overpredicts the effective properties during hydrostatic loads.
- The volumetric fraction of NiTi SMA significantly influences the phase transformation behavior of the lattice structure.
- The effective strain recovery for Mg-NiTi IPC exhibits exceptional results, showing an exponentially increasing trend with the concentration of NiTi. This behavior can be attributed to the shape memory effect of NiTi material and is not expected from magnesium alone.
- The power-law fitting parameters indicate a stretching-dominated response across all loading scenarios, primarily due to the Kelvin cell architecture's high bending resistance.

5 ACKNOWLEDGEMENT

This research was funded by Khalifa University of Science and Technology through the Sandooq-Al-Watan grant under KU-EXT-SWARD-2023-8434000527.

REFERENCES

[1] A. N. Alagha, S. Hussain, and W. Zaki, "Additive manufacturing of shape memory alloys: A review with emphasis on powder bed systems," *Materials & Design,* vol. 204, p. 109654, 2021/06/01/ 2021, doi: https://doi.org/10.1016/j.matdes.2021.109654.

[2] W. Zaki and Z. Moumni, "A three-dimensional model of the thermomechanical behavior of shape memory alloys," *Journal of the Mechanics and Physics of Solids,* vol. 55, no. 11, pp. 2455-2490, 2007/11/01/ 2007, doi: https://doi.org/10.1016/j.jmps.2007.03.012.

[3] S. Ilyas, R. K. Abu Al-Rub, B. El-Khasawneh, and W. Zaki, "Numerical Prediction of the Effective Mechanical Behavior of Interpenetrating Phase Composites Comprising Architected Nitinol Cores," presented at the Smart Materials, Adaptive Structures, and Inelligent Systems, USA, 2023. [Online]. Available: https://doi.org/10.1115/SMASIS2023-111103.

[4] S. R. Agnew, "Wrought magnesium: A 21st century outlook," *JOM,* vol. 56, no. 5, pp. 20-21, 2004/05/01 2004, doi: https://doi.org/10.1007/s11837-004-0120-8.

[5] T. M. Pollock, "Weight Loss with Magnesium Alloys," *Science,* vol. 328, no. 5981, pp. 986-987, 2010/05/21 2010, doi: https://doi.org/10.1126/science.1182848.

[6] Y. Cui *et al.*, "Enhanced damping capacity of magnesium alloys by tensile twin boundaries," *Scripta Materialia,* vol. 101, pp. 8-11, 2015/05/01/ 2015, doi: https://doi.org/10.1016/j.scriptamat.2015.01.002.

[7] M. Zhang *et al.*, "3D printed Mg-NiTi interpenetrating-phase composites with high strength, damping capacity, and energy absorption efficiency," *Science Advances,* vol. 6, no. 19, p. eaba5581, 2020, doi: 10.1126/sciadv.aba5581.

[8] K. Sugimoto, K. Niiya, T. Okamoto, and K. Kishitake, "A Study of Damping Capacity in Magnesium Alloys," *Transactions of the Japan Institute of Metals,* vol. 18, no. 3, pp. 277-288, 1977, doi: https://doi.org/10.2320/matertrans1960.18.277.

[9] R. Schaller, "Metal matrix composites, a smart choice for high damping materials," *Journal of Alloys and Compounds,* vol. 355, no. 1, pp. 131-135, 2003/06/30/ 2003, doi: https://doi.org/10.1016/S0925-8388(03)00239-1.

[10] W. Zaki, "An approach to modeling tensile–compressive asymmetry for martensitic shape memory alloys," *Smart Materials and Structures,* vol. 19, no. 2, p. 025009, 2010/01/14 2010, doi: https://doi.org/10.1088/0964-1726/19/2/025009.

[11] J. Wang, Z. Moumni, W. Zhang, Y. Xu, and W. Zaki, "A 3D finite-strain-based constitutive model for shape memory alloys accounting for thermomechanical coupling and martensite reorientation," *Smart Materials and Structures,* vol. 26, no. 6, p. 065006, 2017/05/02 2017, doi: https://doi.org/10.1088/1361-665X/aa6c17.

[12] U. Ali, "Numerical modeling of failure in magnesium alloys under axial compression and bending for crashworthiness applications," University of Waterloo, 2012.

[13] N. V. Viet, W. Waheed, A. Alazzam, and W. Zaki, "Effective compressive behavior of functionally graded TPMS titanium implants with ingrown cortical or trabecular bone," *Composite Structures,* vol. 303, p. 116288, 2023/01/01/ 2023, doi: https://doi.org/10.1016/j.compstruct.2022.116288.

[14] K. Krishnan, D.-W. Lee, M. Al Teneji, and R. K. Abu Al-Rub, "Effective stiffness, strength, buckling and anisotropy of foams based on nine unique triple periodic minimal surfaces," *International Journal of Solids and Structures,* vol. 238, p. 111418, 2022/03/01/ 2022, doi: https://doi.org/10.1016/j.ijsolstr.2021.111418.

[15] K. Abu Al-Rub Rashid, D.-W. Lee, A. Khan Kamran, and N. Palazotto Anthony, "Effective Anisotropic Elastic and Plastic Yield Properties of Periodic Foams Derived from Triply Periodic Schoen's I-WP Minimal Surface," *Journal of Engineering Mechanics,* vol. 146, no. 5, p. 04020030, 2020/05/01 2020, doi: https://doi.org/10.1061/(ASCE)EM.1943-7889.0001759.

[16] D. Gross and T. Seelig, "Micromechanics and homogenization," in *Fracture Mechanics: With an Introduction to Micromechanics*, D. Gross and T. Seelig Eds. Berlin, Heidelberg: Springer Berlin Heidelberg, 2011, pp. 229-299.

[17] Z. Hashin and S. Shtrikman, "A variational approach to the theory of the elastic behaviour of multiphase materials," *Journal of the Mechanics and Physics of Solids,* vol. 11, no. 2, pp. 127-140, 1963/03/01/ 1963, doi: https://doi.org/10.1016/0022-5096(63)90060-7.

XI ECCOMAS Thematic Conference on Smart Structures and Materials - SMART 2025
M. Krommer, M. Nader and M. Schagerl (Eds)

Received: 30 March 2025 / Revised: 31 August 2025 / Accepted: 20 September 2025
© The Author(s) 2025

Effect of topological hybridization on the elastic isotropy of three-dimensional lattice metamaterials

Mohamed M. Naji, Rashid K. Abu Al-Rub, Imad Barsoum, Wael Zaki

Abstract. Three-dimensional (3D) lattice metamaterials, derived from triply periodic minimal surfaces (TPMS), or plate lattices, exhibit tuneable mechanical properties, with their elastic anisotropy and stiffness governed by their underlying topology. In this study, the effect of topological hybridization on the elastic isotropy of TPMS-based lattice structures are explored. Specifically, hybrid lattices formed by combining Diamond and Simple Cubic (DSC) as well as Primitive and Simple Cubic (SPSC) architectures are investigated. Finite element simulations are conducted to analyze the directional elastic moduli and visualize the elastic surfaces. The results indicate that the extent of isotropy is strongly dependent on the parent lattice topologies, with certain hybrid configurations failing to resolve anisotropy while still enhancing stiffness compared to their parent structures. This suggests that hybridization enables a tailored approach to mechanical property optimization. Additionally, we compare the isotropy of hybrid structures to their constituent topologies, providing further insight into the trade-offs and advantages of geometric blending. These findings contribute to the rational design of architected materials for load-bearing and multifunctional applications.

Key words: Metamaterials, Isotropy, Triply Periodic Minimal Surfaces, Hybrid lattices.

1 INTRODUCTION

Three-dimensional (3D) lattice metamaterials, particularly those derived from triply periodic minimal surfaces (TPMS), have gained significant attention due to their tunable mechanical properties and structural efficiency [1–7]. These metamaterials offer a unique combination of high strength-to-weight ratio, isotropic or anisotropic behavior, and energy absorption capabilities, making them ideal for various engineering applications, including aerospace, biomedical implants, and lightweight structural components [8–15].

While TPMS-based architectures exhibit promising mechanical properties, the elastic anisotropy of sheet-based TPMS such as the Diamond (D) and Schwarz-Primitive (SP) remains

Mohamed M. Naji & Rashid K. Abu Al-Rub & Imad Barsoum & Wael Zaki
Mechanical and Nuclear Engineering Department, Khalifa University of Science and Technology, 127788 Abu Dhabi, UAE, e-mail: wael.zaki@ku.ac.ae

Mohamed M. Naji & Rashid K. Abu Al-Rub & Imad Barsoum & Wael Zaki
Advanced Digital & Additive Manufacturing (ADAM) Group, Khalifa University of Science and Technology, 127788 Abu Dhabi, United Arab Emirates

a key limitation in certain applications requiring uniform mechanical response. To address this, topological hybridization, a strategy that blends two distinct lattice topologies, has been proposed as a means of enhancing mechanical performance and achieving improved isotropy. However, the influence of such hybridization on the elastic properties and anisotropy of TPMS lattices remains underexplored.

This study investigates the effect of topological hybridization on the elastic isotropy of TPMS-based lattice structures. In this study, the Simple Cubic (SC) plate lattice was selected for hybridization due to its superior stiffness and significant contribution to the load-bearing capacity of hybrid materials [2,3,16–18]. Two hybrid lattice configurations, Diamond-Simple Cubic (DSC) and Primitive-Simple Cubic (SPSC), are analyzed. Finite element simulations are conducted to evaluate the directional elastic moduli, isotropy, and stiffness of these hybrid structures. The results provide insight into the trade-offs between stiffness enhancement and anisotropy reduction, contributing to the rational design of architected materials for load-bearing and multifunctional applications.

2 MATERIALS AND METHODS

2.1 Topological Design

The TPMS topologies considered in this study, being the Schwarz-Primitive and Diamond minimal surfaces, are generated using their respective mathematical formulations. These surfaces are defined by level-set functions, which describe the implicit surfaces where a scalar field remains constant. These iso-surfaces correspond to specific iso-values known as the level-set parameter c. The mathematical expressions for the selected TPMS topologies are given by:

$$\phi_{SP} \equiv \cos x + \cos y + \cos z = c \tag{1}$$

$$\phi_{D} \equiv \cos x \cos y \cos z - \sin x \sin y \sin z = c \tag{2}$$

where $x = 2\pi X/L_x$, $y = 2\pi Y/L_y$, and $z = 2\pi Z/L_z$, in which L_x, L_y, L_z represent the unit cell sizes in the X, Y, and Z directions in Cartesian coordinates [1]. The level-set constant c controls the offsetting of the level-set surface from the zero value (i.e. $\phi = 0$), where the zero value results in minimal surfaces that are equally split into subdomains of equal volumes. This formulation ensures that each TPMS unit cell tessellates periodically in three-dimensional space. The level-set expressions in Eqs. (1-2) are incorporated in the MSLattice software [19], which was utilized in this study to generate the TPMS lattices with sheet networks. The generated TPMS unit cells can then be utilized in construction of the hybrid plate-TPMS lattice, achieved by structurally integrating the SC plate lattice with TPMS architectures, portrayed in Figure 1. In this study, the parent and resultant hybrid lattices are fixed at 20% relative density, with a unit cell size of 1 mm. The relative density of the parent SC and TPMS lattices were controlled by adjusting the wall thicknesses, in which the SC plate-lattice features a 0.072 mm wall thickness, adjusted using SolidWorks commercial software, and the sheet-based P and D lattices contain feature sizes of 0.0987 mm and 0.055 mm, respectively.

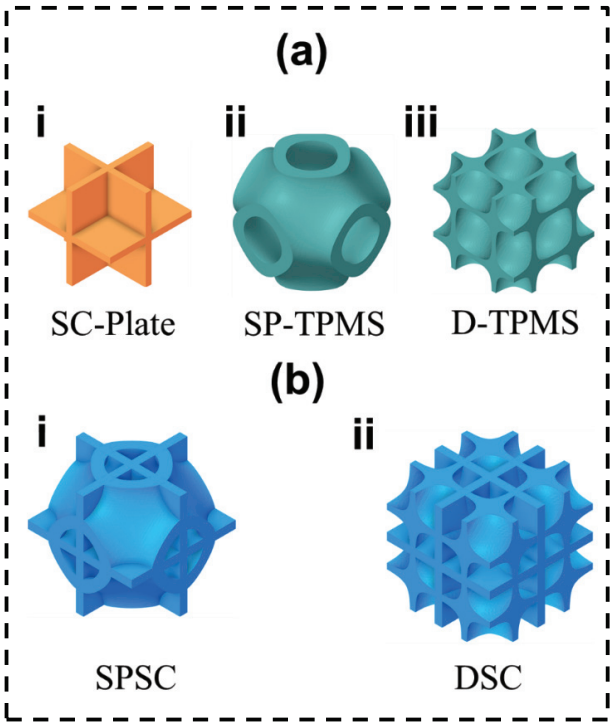

Figure 1 Unit cells of (a) (i) the elementary SC-plate and sheet-based TPMS (ii) SP and (iii) D lattices, and (b) the hybrid SC-TPMS (i) SPSC and (ii) DSC lattice metamaterials

2.2 Finite element methods

To determine the effective elastic properties, appropriate linear elastic constitutive relations that accurately represent the effective properties are necessary to be established first. Considering that the designed sheet-TPMS and hybrid unit cells preserve cubic symmetry, the macroscopic elasticity relation, in Voigt notation form, can be reduced to

$$\begin{bmatrix}\sigma_{11}\\ \sigma_{22}\\ \sigma_{33}\\ \sigma_{23}\\ \sigma_{12}\\ \sigma_{13}\end{bmatrix}=\begin{bmatrix}C_{11} & C_{12} & C_{12} & 0 & 0 & 0\\ & C_{11} & C_{12} & 0 & 0 & 0\\ & & C_{11} & 0 & 0 & 0\\ & \text{sym} & & C_{44} & 0 & 0\\ & & & & C_{44} & 0\\ & & & & & C_{44}\end{bmatrix}\begin{bmatrix}\varepsilon_{11}\\ \varepsilon_{22}\\ \varepsilon_{33}\\ 2\varepsilon_{23}\\ 2\varepsilon_{12}\\ 2\varepsilon_{23}\end{bmatrix} \tag{3}$$

where σ_{ij}, C_{ij}, and ε_{ij} represent the stress, stiffness, and strain components, respectively. This is specifically accomplished using Hill's approximation [20], in which equivalent isotropic material parameters are utilized to represent the macroscopic elastic properties of polycrystalline materials. Hill's approximation serves as a representative modulus, aligning with the modulus value achieved through material testing in any direction when the material exhibits complete isotropy. For the calculation of elastic properties, encompassing

homogenized (or effective) Young's (E^H), shear (G^H), and bulk (B^H) moduli, the following expressions can be obtained using Hill's approximation as

$$B^H=\frac{B^V+B^R}{2} \tag{4}$$

$$G^H=\frac{G^V+G^R}{2} \tag{5}$$

$$E^H=\frac{9B^HG^H}{3B^H+G^H} \tag{6}$$

where superscripts ^{V} and ^{R} represent the Voigt and Reuss upper and lower bounds, respectively. In the context of a 3D representation of elastic properties, the well-known Voigt and Reuss shear and bulk moduli bounds can be determined using the components of C_{ij} and be reduced, due to cubic symmetry, as illustrated by the following equations [21–23]:

$$B^V=\frac{C_{11}+2C_{12}}{3} \tag{7}$$

$$G^V=\frac{C_{11}-C_{12}+3C_{44}}{5} \tag{8}$$

$$B^R=\frac{F}{3C_{11}^2++3C_{12}^2-6C_{11}C_{12}} \tag{9}$$

$$G^R=15/\left[\frac{4\left(2C_{11}^2+C_{11}C_{12}+C_{11}^2+C_{11}C_{12}+C_{11}C_{12}-2C_{12}^2\right)}{F}+\frac{9}{C_{44}}\right] \tag{10}$$

$$F=C_{11}^3+2C_{12}^3-3C_{11}C_{12}^2 \tag{11}$$

The Reuss and Voigt bounds for shear and bulk moduli are also essential for determining the anisotropy of the cellular metamaterial, which can be assessed through using the Ranganathan and Ostoja-Starzewski elastic universal anisotropic index (A^U), expressed as [23,24]:

$$A^U=5\frac{G^V}{G^R}+\frac{B^V}{B^R}-6\geq 0 \tag{12}$$

It can be inferred from the above equations that in the case of a perfect isotropic behavior, where the Voigt and Reuss bounds for shear and bulk moduli would converge, the anisotropy index A^U values yield to 0.

Finite element analysis is then employed using the Abaqus/Standard 2023 commercial software. The generated TPMS and hybrid unit cells were first imported into Abaqus, which had previously been meshed using Hypermesh software, incorporating quadratic tetrahedral elements of type C3D10 (per Abaqus element notion), as tetrahedron elements are geometrically versatile and known to adequately define such complex shapes [25], as shown in Figure 2. Subsequently, the material model was defined with the assumption of isotropic behavior of the base material, where the constituent solid part of the cellular metamaterial possesses $E = 70$ GPa and $v_s = 0.3$ (i.e., assuming $AlSi_{10}Mg$ as the base material). However, the determined elastic properties will be normalized by the elastic properties of the base material, making the results independent of the selected base solid material. The elastic properties (E_1, G_{12}, v_{12}, B) were determined individually through the application of the mixed boundary conditions detailed in Table 1 [23], where x_i, u_i, $\boldsymbol{e}_i$, and t_i are Cartesian coordinates, displacements, unit direction vectors and traction force vectors, respectively, in $i = 1,2,3$ directions, while λ determines the magnitude of the applied displacement. The elastic moduli were obtained by computing the required force to cause the applied displacement. This relationship was converted to a stress-strain response, from which the elastic moduli were determined. These elastic components can then be utilized to obtain the materials constants that constitute the stiffness matrix $[C_{ij}]$, that are essential for Eqs. (3)-(12).

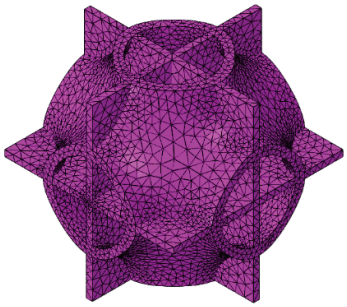

Figure 2 An example of a FEM mesh for the *hybrid SPSC* cellular metamaterial using *quadratic* tetrahedral elements.

Table 1 Applied mixed boundary conditions for elastic moduli calculations of cubic symmetry materials.

Modulus	x_1=0	x_1=L	x_2=0	x_2=L	x_3=0	x_3=L
E_1=E_2=E_3	u_1=0	u_1=λ$\mathbf{e_1}$	u_2=0	t_2=0	u_3=0	t_3=0
G_{12}=G_{13}=G_{23}	u_2=0	u_2=λ$\mathbf{e_2}$	u_1=0	u_1=0	u_3=0	u_3=0
	u_3=0	u_3=0	u_3=0	u_3=0		
B	u_1=0	u_1=λ$\mathbf{e_1}$	u_2=0	u_2=λ$\mathbf{e_2}$	u_3=0	u_3=λ$\mathbf{e_3}$

3 RESULTS AND DISCUSSIONS

This analysis involves the investigation of the SPSC and DSC hybrid lattices, aiming to find the normalized Hill's Young's (E/E_s), shear (G/G_s), and bulk (B/B_s) moduli, in addition to the

universal anisotropy index A^U, at a total relative density of 20%. These values are compared with the elastic properties' values of the parent lattices, as presented in Table 2.

Table 2 Normalized elastic moduli values of the elementary and hybrid lattices and their universal anisotropy index values

	Hill's Approximation			
	B/Bs	G/Gs	E/Es	A^U
SC	0.071	0.040	0.101	0.757
SP	0.065	0.028	0.073	1.126
D	0.067	0.030	0.077	0.116
SPSC	0.067	0.036	0.092	0.040
DSC	0.069	0.036	0.091	0.354

Generally, the incorporation of SC onto the TPMS sheets causes an improvement in Young's and bulk moduli. These observations are also supported by the normalized elastic anisotropy polar plots exhibited in Figure 3, in which Figure 3 (a) displays the anisotropy plot of the elementary lattices, while Figure 3 (b) portray the anisotropy polar plot of the hybrid SPSC and DSC lattices.

The plus-like shape of the SC polar plot in Figure 3 (a) indicates a severely anisotropic composition. The D-TPMS sheet lattice displays a less intense anisotropy configuration with similar soft and stiff directions. The polar plot of the SP indicates dominant stiffness in the diagonal directions compared to the axial direction, thereby also depicting an anisotropic composition. It can be denoted the DSC outperforms the SPSC in terms of maximum stiffness, with more anisotropic compositions, however.

4 CONCLUSIONS

This study explores the role of topological hybridization in improving the elastic isotropy of TPMS-based lattice metamaterials. Through finite element simulations, the hybrid Diamond-Simple Cubic (DSC) and Primitive-Simple Cubic (SPSC) lattices were evaluated for their elastic properties. Key findings include:

- Hybridization significantly influences both stiffness and anisotropy, with SPSC lattices achieving elastic isotropy, while DSC lattice demonstrates superior stiffness but retain higher anisotropy.
- The addition of SC elements to TPMS lattices generally enhances Young's modulus and bulk modulus, with the extent of improvement depending on the parent lattice configurations.

These results demonstrate that strategic hybridization of lattice topologies enables tailored mechanical properties, balancing stiffness and isotropy for various engineering applications. Future work may extend this study by incorporating experimental validation and further topologies to refine the design of hybrid metamaterials.

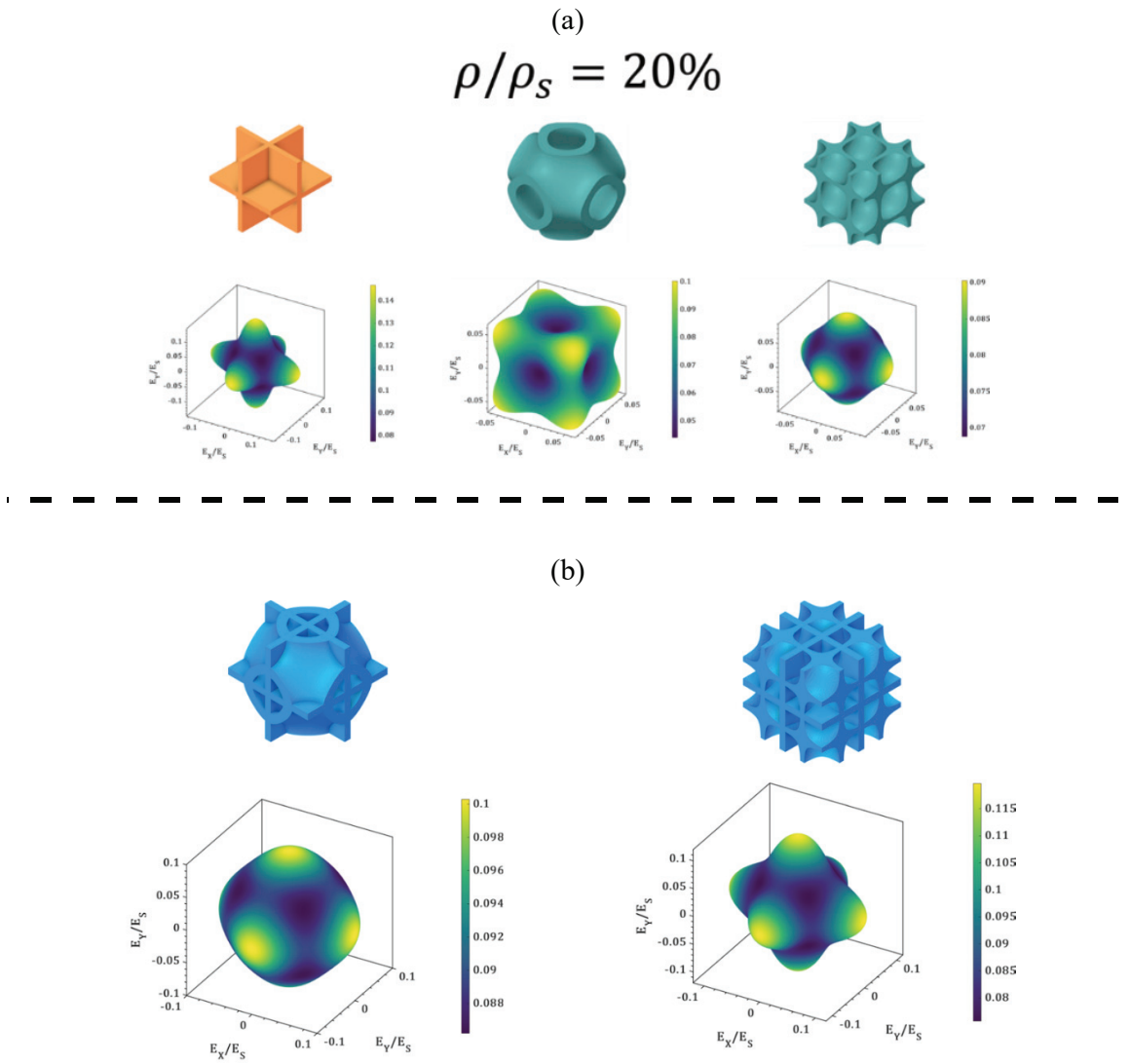

Figure 3 Polar anisotropy plots with normalized modulus values at 20% relative density of (a) the elementary lattices, (b) SPSC, and DSC.

REFERENCES

[1] O. Al-Ketan, R.K. Abu Al-Rub, Multifunctional Mechanical Metamaterials Based on Triply Periodic Minimal Surface Lattices, Adv Eng Mater 21 (2019) 1900524. https://doi.org/10.1002/adem.201900524.

[2] T. Tancogne-Dejean, M. Diamantopoulou, M.B. Gorji, C. Bonatti, D. Mohr, 3D Plate-Lattices: An Emerging Class of Low-Density Metamaterial Exhibiting Optimal Isotropic

Stiffness, Advanced Materials 30 (2018) 1803334. https://doi.org/10.1002/adma.201803334.
[3] Z. Chen, Y.M. Xie, X. Wu, Z. Wang, Q. Li, S. Zhou, On hybrid cellular materials based on triply periodic minimal surfaces with extreme mechanical properties, Mater Des 183 (2019) 108109. https://doi.org/10.1016/J.MATDES.2019.108109.
[4] A. Cebrian Carcavilla, W. Zaki, Effective Superelastic Domains of Schwarz Primitive Shape Memory Alloy Lattices Subjected to Cyclic Loading, Adv Eng Mater 25 (2023) 2300432. https://doi.org/https://doi.org/10.1002/adem.202300432.
[5] A.N. Alagha, V. Nguyen, W. Zaki, Effective phase transformation behavior of NiTi triply periodic minimal surface architectures, J Intell Mater Syst Struct 34 (2022) 672–695. https://doi.org/10.1177/1045389X221115704.
[6] N. V Viet, N. Karathanasopoulos, W. Zaki, Mechanical attributes and wave propagation characteristics of TPMS lattice structures, Mechanics of Materials 172 (2022) 104363. https://doi.org/https://doi.org/10.1016/j.mechmat.2022.104363.
[7] V.V. Nguyen, W. Waqas, A. Anas, Z. Wael, A Deep Artificial Neural Network Model for Predicting the Mechanical Behavior of Triply Periodic Minimal Surfaces under Damage Loading, J Eng Mech 150 (2024) 04024040. https://doi.org/10.1061/JENMDT.EMENG-7511.
[8] W.H. Qi, M.P. Wang, Size and shape dependent melting temperature of metallic nanoparticles, Mater Chem Phys 88 (2004) 280–284. https://doi.org/https://doi.org/10.1016/j.matchemphys.2004.04.026.
[9] O.H. Hassoon, M. Tarfaoui, A. El Malki Alaoui, A. El Moumen, Experimental and numerical investigation on the dynamic response of sandwich composite panels under hydrodynamic slamming loads, Compos Struct 178 (2017) 297–307. https://doi.org/https://doi.org/10.1016/j.compstruct.2017.07.014.
[10] J. Feng, B. Liu, Z. Lin, J. Fu, Isotropic octet-truss lattice structure design and anisotropy control strategies for implant application, Mater Des 203 (2021) 109595. https://doi.org/https://doi.org/10.1016/j.matdes.2021.109595.
[11] S. Yin, H. Chen, Y. Wu, Y. Li, J. Xu, Introducing composite lattice core sandwich structure as an alternative proposal for engine hood, Compos Struct 201 (2018) 131–140. https://doi.org/https://doi.org/10.1016/j.compstruct.2018.06.038.
[12] C.B. Niutta, R. Ciardiello, F. Berto, D.S. Paolino, A. Tridello, On the influence of Additive Manufacturing defects on the energy absorption capability of a lattice structure, Procedia Structural Integrity 42 (2022) 1449–1457. https://doi.org/https://doi.org/10.1016/j.prostr.2022.12.185.
[13] G. Palomba, G. Epasto, L. Sutherland, V. Crupi, Aluminium honeycomb sandwich as a design alternative for lightweight marine structures, Ships and Offshore Structures 17 (2022) 2355–2366. https://doi.org/10.1080/17445302.2021.1996109.
[14] N. V Viet, W. Zaki, On exploration of directional extreme mechanical attributes and energy absorption of bending-dominated and buckling-induced negative Poisson's ratio metamaterials, Compos Struct 349–350 (2024) 118460. https://doi.org/https://doi.org/10.1016/j.compstruct.2024.118460.

[15] N. Van Viet, M. El-Rich, W. Zaki, Multidirectional mechanical properties of functionally graded triply periodic minimal surfaces for bone tissue engineering applications, Compos Struct 363 (2025) 119054. https://doi.org/https://doi.org/10.1016/j.compstruct.2025.119054.
[16] J. Noronha, J. Dash, J. Rogers, M. Leary, M. Brandt, M. Qian, Titanium Multi-Topology Metamaterials with Exceptional Strength, Advanced Materials 36 (2024) 2308715. https://doi.org/https://doi.org/10.1002/adma.202308715.
[17] J.B. Berger, H.N.G. Wadley, R.M. McMeeking, Mechanical metamaterials at the theoretical limit of isotropic elastic stiffness, Nature 543 (2017) 533–537. https://doi.org/10.1038/nature21075.
[18] Y. Liu, Y. Wang, H. Ren, Z. Meng, X. Chen, Z. Li, L. Wang, W. Chen, Y. Wang, J. Du, Ultrastiff metamaterials generated through a multilayer strategy and topology optimization, Nat Commun 15 (2024) 2984. https://doi.org/10.1038/s41467-024-47089-8.
[19] O. Al-Ketan, R.K. Abu Al-Rub, MSLattice: A free software for generating uniform and graded lattices based on triply periodic minimal surfaces, Material Design & Processing Communications 3 (2021) e205. https://doi.org/https://doi.org/10.1002/mdp2.205.
[20] R. Hill, The Elastic Behaviour of a Crystalline Aggregate, Proceedings of the Physical Society. Section A 65 (1952) 349–354. https://doi.org/10.1088/0370-1298/65/5/307.
[21] A. Reuss, Berechnung der Fließgrenze von Mischkristallen auf Grund der Plastizitätsbedingung für Einkristalle ., ZAMM - Journal of Applied Mathematics and Mechanics / Zeitschrift Für Angewandte Mathematik Und Mechanik 9 (1929) 49–58. https://doi.org/https://doi.org/10.1002/zamm.19290090104.
[22] A.E.H. T., (1) Lehrbuch der Kristallphysik (mit Ausschluss der Kristalloptik) (2) Leçons de Cristallographie (3) Die Kristallgruppen nebst ihren Beziehungen zu den Raumgittern, Nature 86 (1911) 544–546. https://doi.org/10.1038/086544a0.
[23] O. Al-Ketan, D.W. Lee, R.K. Abu Al-Rub, Mechanical properties of additively-manufactured sheet-based gyroidal stochastic cellular materials, Addit Manuf 48 (2021). https://doi.org/10.1016/j.addma.2021.102418.
[24] S.I. Ranganathan, M. Ostoja-Starzewski, Universal elastic anisotropy index, Phys Rev Lett 101 (2008). https://doi.org/10.1103/PhysRevLett.101.055504.
[25] F. Cheng, S.-M. Kim, J.N. Reddy, R.K. Abu Al-Rub, Modeling of elastoplastic behavior of stainless-steel/bronze interpenetrating phase composites with damage evolution, Int J Plast 61 (2014) 94–111. https://doi.org/https://doi.org/10.1016/j.ijplas.2014.05.001.

Part XVI
SS 06 - SMART STRUCTURES AND SENSING TECHNOLOGIES FOR REAL-TIME MONITORING

Mehdi Ghommem, Abdessattar Abdelkefi

XI ECCOMAS Thematic Conference on Smart Structures and Materials - SMART 2025
M. Krommer, M. Nader and M. Schagerl (Eds)

Received: 24 March 2025 / Revised: 6 August 2025 / Accepted: 27 September 2025
© The Author(s) 2025

Explainable sensor fault diagnosis for structural health monitoring

Heba Al-Nasser, Kosmas Dragos, Kay Smarsly

Abstract. Sensor faults in structural health monitoring (SHM) systems create significant challenges for maintaining infrastructure safety and operational efficiency. Faults, e.g. caused by sensor aging and environmental conditions, may result in inaccurate monitoring data and unreliable diagnostics. Artificial neural network (ANN) models utilizing time-series data have been proven powerful in diagnosing sensor faults in SHM systems, leveraging the ability of ANN models to analyze complex patterns within large datasets. However, the lack of transparency in – generally – black-box ANN models limits trust and usability, creating barriers to the widespread adoption of ANN models for sensor fault diagnosis. In particular, typical ANN decision-making processes lack explainability and interpretability, thus preventing end-users from confidently relying on ANN-based solutions for SHM applications. To overcome the aforementioned limitation, this study introduces an explainable sensor fault diagnosis (ESFD) approach, drawing from the field of explainable artificial intelligence (XAI), whose application in the context of SHM has been scarce. The ESFD approach essentially consists of a time-series-based ANN concept, designed to enhance the explainability and interpretability of sensor fault diagnosis in SHM by incorporating XAI methods that provide insights into decision-making processes. The ESFD approach is validated using SHM data from a pedestrian bridge for identifying combined sensor faults. The performance of the ESFD approach is assessed using XAI evaluation metrics, including "sufficiency" as a faithfulness metric. The results from the validation tests demonstrate that the ESFD approach improves the explainability and interpretability of time-series-based ANN models for sensor fault diagnosis in SHM. This advancement is expected to support the development of explainable and autonomous SHM systems. Future research will focus on decentralizing the ESFD approach for explainable, real-time decision-making to enhance scalability and reduce computational overhead.

Key words: Explainable artificial intelligence (XAI), structural health monitoring (SHM), sensor fault diagnosis, combined sensor faults, layer-wise relevance propagation (LRP), XAI evaluation metrics.

Heba Al-Nasser & Kosmas Dragos & Kay Smarsly
Institute of Digital and Autonomous Construction, Hamburg University of Technology, Blohmstraße 15, 21079, Hamburg, Germany, e-mail: heba.al-nasser@tuhh.de

1 INTRODUCTION

Aging civil infrastructure requires efficient maintenance to prevent structural failures and ensure public safety [1]. In this direction, structural health monitoring (SHM) has been facilitating the assessment of structural conditions using sensor networks [2]. However, sensor faults arising from various causes, such as aging, environmental conditions, or hardware malfunctions, may compromise the reliability of SHM data, resulting in poor maintenance decisions [3]. The unfavorable effects of sensor faults have paved the way for sensor fault diagnosis (FD) in an attempt to provide accurate inputs, enabling precise structural condition assessment and sustainable maintenance.

SHM of civil infrastructure progressively has been relying on artificial intelligence (AI), and, in turn, the accuracy of AI models highly depends on reliable sensor data [4]. This dependency highlights the need for robust sensor FD to provide accurate inputs, ensuring trustworthy and effective AI-driven structural condition assessment [5]. In this direction, integrating sensor FD into AI-based SHM strategies serves to provide the robustness necessary for ensuring the long-term resilience of civil infrastructure.

Sensor FD in SHM systems has largely relied on artificial neural networks, which offer efficiency in pattern recognition within time-series data [6]. Despite the notable performance in pattern recognition, artificial neural network (ANN) models are often regarded as black-box models, due to the lack of transparency in the inner mechanisms of the models that influence the model predictions. This lack of transparency hinders practitioners from fully trusting model predictions when making decisions on maintenance actions [7]. The lack of transparency becomes particularly demanding when combined sensor faults occur simultaneously at individual sensors, characterized by patterns hardly detectable by ANN models, which render sensor FD more challenging and exacerbate the mistrust of practitioners in the ANN model predictions [8].

Several studies have investigated the capability of ANN models to improve accuracy in sensor FD for SHM systems. For instance, an Internet of Things (IoT)-based ANN architecture has been proposed to diagnose sensor faults in decentralized SHM systems [9]. Another study has used principal component analysis with convolutional neural networks to separate sensor faults from structural anomalies in offshore SHM systems [10]. Moreover, an adaptive ANN-based approach has been reported for diagnosing concurrent sensor faults across multiple sensors [11].

The transparency of the inner mechanisms of ANN models that influence the model predictions remains a critical challenge, as acknowledged in recent research. The low likelihood of widely adopting ANN models for SHM purposes, due to ANN model predictions being hardly comprehensible has been highlighted in [13]. Furthermore, challenges of black-box AI models have been highlighted in [14], emphasizing that the inability to provide transparent prediction explanations leads to skepticism for adoption in real-world applications. A survey reported in [15] has called for decision-making frameworks that allow stakeholders to understand and audit ANN model predictions. Referred to as “explainability”, attributing the predictions of ANN models to specific patterns detected in time-series data may enhance trust in FD predictions, thus enabling the adoption of AI models in real-world SHM applications for

sensor FD [12].

To address the aforementioned challenges, transparent ANN models for sensor FD in SHM are required, leveraging recent trends towards explainable artificial intelligence (XAI). This paper proposes a methodology that incorporates XAI into sensor FD. Specifically, drawing from applications in several disciplines [16, 17, 18], an explainable sensor fault diagnosis (ESFD) methodology is proposed, aiming to enhance transparency and trust in ANN model predictions used for sensor FD in SHM applications. The ESFD methodology integrates the layer-wise relevance propagation (LRP) method into ANN models for identifying combined sensor faults, while ensuring that the ANN model predictions are comprehensible to users. Validation of the ESFD methodology is conducted using real-world SHM data recorded from a pedestrian bridge exhibiting combined sensor faults. The reliability of the explanations is assessed with XAI evaluation metrics; in particular, sufficiency is employed as a faithfulness evaluation metric to verify that LRP-derived explanations correspond to actual fault patterns.

The remainder of the paper is structured as follows: Section 2 introduces the ESFD methodology, including the LRP method for explainability and sufficiency for evaluation. Section 3 describes the implementation and validation of the ESFD methodology in an ANN model for identifying combined sensor faults on a pedestrian bridge. Section 4 presents and discusses the LRP explainability results and the sufficiency evaluation results. Finally, the paper concludes with a summary of the contributions and an outlook on future work.

2 THE EXPLAINABLE SENSOR FAULT DIAGNOSIS METHODOLOGY

The ESFD methodology is presented in this section. First, an overview of the methodology is provided, followed by a brief description of the layer-wise relevance propagation (LRP), used to obtain explanations of ANN model outcomes, and the sufficiency (SUFF), employed as a faithfulness metric.

The ESFD methodology is built upon the identification of combined sensor faults, which is a critical aspect often overlooked in conventional FD methods [8]. The ESFD methodology is composed of the following components:

- **ANN training**: Artificial neural network models are developed and trained to identify combined sensor faults using time-series SHM data recorded from monitored structures. This study builds upon pre-trained ANN models developed and validated in previous experiments [8]. The focus is placed on enhancing the explainability and trustworthiness of the pre-trained ANN models without altering the training process.
- **Explainability using LRP**: To enhance explainability and transparency of ANN predictions, the LRP method is applied. LRP assigns a relevance score to each sensor, representing the contribution of each sensor to the predictions, thereby, increasing transparency.
- **Evaluation metrics using SUFF**: The faithfulness of the explanations is validated by the SUFF metric, employed to verify the degree to which the outputs of the ANN models are derived from the most appropriate patterns captured in the time-series data.

The explainability (LRP) and evaluation metrics (SUFF) components are illuminated in the following subsections.

2.1 Overview of the explainability using LRP

The LRP method boosts explainability for sensor FD by revealing the sensors contributing most to the predictions of the ANN models. The ANN models receive time-series data as inputs from multiple sensors, and the LRP method assigns a relevance score to each sensor, indicating the contribution of the sensors to the predictions [19]. The LRP relevance scores are computed as follows:

$$R_j = \sum_k \left(\frac{z_{jk}}{\sum_j z_{jk}} \right) R_k , \tag{1}$$

where R_j denotes the relevance score of neuron j in one layer of the ANN model, R_k denotes the relevance score of neuron k in the next layer, and z_{jk} denotes the contribution of neuron j to neuron k. By back-propagating the prediction relevance scores to the inputs, the LRP method checks whether the ANN model assigns higher relevance to the sensor contributing the most to the classification prediction. In case of fault occurrence, the highest relevance score is expected to be assigned to the faulty sensor, whereas in non-faulty conditions, relevance is evenly distributed among the sensors.

2.2 Overview of the evaluation metrics using SUFF

The XAI faithfulness evaluation metrics assess how accurately the explanations reflect the true reasoning behind ANN model predictions [20]. Among the faithfulness evaluation metrics, the sufficiency metric measures whether the most relevant "feature", i.e. pattern within time-series data of a faulty sensor, provides sufficient information for the ANN model to yield accurate identification predictions. SUFF quantifies the extent to which the prediction probability of the ANN model changes when retaining only the most relevant feature, as recognized by the LRP method. Low SUFF values indicate high faithfulness, which reflects high reliance on the sensors that are actually faulty. The SUFF metric is calculated as follows:

$$\text{SUFF} = \frac{1}{|B|} \sum_{q \in B} \left[p_{c(x)}(x) - p_{c(x)}\left(x_{q:}\%\right) \right], \tag{2}$$

where $p_{c(x)}$ represents the initial prediction probability of the fault class c, $p_{c(x)}(x_{q:}\%)$ represents the prediction probability after retaining only the most relevant features q, and B represents the complete set of features. Using SUFF in the ESFD methodology ensures that LRP-based explanations accurately capture the reasoning of the ANN model predictions in combined sensor fault identification, enhancing trust in AI-driven SHM. The following section describes the implementation and validation of the ESFD methodology using real-world SHM data from a pedestrian bridge.

3 IMPLEMENTATION AND VALIDATION OF THE ESFD METHODOLOGY

The ESFD methodology is applied to pre-trained long short-term memory (LSTM) models validated using time-series data from a pedestrian bridge in Thessaloniki, Greece. As this study builds on previous work [8], which details the experimental setup and model training, only a brief summary is provided here. The bridge is instrumented with four accelerometers (S1–S4), and combined sensor faults have been synthetically injected into predefined windows of the data. The LSTM models, previously validated for identification of combined sensor faults in [8], are used here to implement the LRP and SUFF algorithms, followed by validation tests.

3.1 Implementation of the ESFD methodology

The implementation of the proposed ESFD methodology involves devising algorithms both for LRP and SUFF. In what follows, the development of algorithms for the aforementioned components is described.

3.1.1 Implementation of the explainability using LRP

The relevance scores, assigned to each sensor in accordance with LRP, are propagated from layer to layer in reverse order, i.e. starting from the output layer back to the input layer, while keeping relevance across all layers. The steps to employ LRP are described in Algorithm 1.

Algorithm 1: Pseudocode to employ LRP

```
Input: Time-series sensor data, pre-trained LSTM models
Output: Relevance scores for each sensor
Predict faults by pre-trained LSTM models
Initialize relevance in the output layer
For each layer from output to input do
        Propagate relevance to previous layer
        Accumulate relevance for each sensor
End for
Average relevance scores for all time steps
Return mean relevance scores for all sensors
```

3.1.2 Implementation of the evaluation metrics using SUFF

As illustrated in the pseudocode shown in Algorithm 2, the calculation of SUFF scores is conducted by comparing prediction probabilities corresponding to original inputs with prediction probabilities obtained from modified inputs where only the most relevant sensor is retained while neglecting less relevant sensors. When only the most relevant sensor is retained, stable predictions imply high faithfulness and corresponding dependence on meaningful input patterns. The applicability of the two algorithms is demonstrated in the validation tests, shown in the next subsection. The results of the tests corroborate the effectiveness of the ESFD methodology using real-world SHM data.

Algorithm 2: Pseudocode to employ SUFF

```
Input: Time-series sensor data, pre-trained LSTM models,
   relevance scores
Output: SUFF scores for each sensor
Predict faults by pre-trained LSTM models
Identify the most relevant sensor by LRP
Retain only the most relevant sensor
Predict output from the most relevant sensor
Calculate SUFF original minus reduced predictions
Average SUFF for all time steps
Return mean SUFF scores for all sensors
```

3.2 Validation of the ESFD methodology

The pedestrian bridge, used for the validation tests, is located in Thessaloniki, Greece. The tests setup includes an SHM system with four accelerometers (S1, S2, S3, and S4), recording time-series data influenced by environmental conditions and pedestrian traffic [8]. Four LSTM models (M1, M2, M3, and M4) have been developed in previous experiments, each model corresponding to an individual accelerometer. Experiments from previous work have hypothesized that only one accelerometer in each LSTM model exhibits combined sensor faults, while other accelerometers remain non-faulty. For instance, S1 is the faulty accelerometer in M1, S2 is faulty in M2, S3 is faulty in M3, and S4 is faulty in M4. The time-series data from the four accelerometers form the inputs to the LSTM models and to the validation of the ESFD methodology with emphasis on enhancing explainability and evaluating faithfulness of the explanations.

Each LSTM model is fed time-series data from each of the four accelerometers, processed sequentially at each time step. The input order follows the sequence S1, S2, S3, S4 for each time step, keeping a consistent temporal flow. All LSTM models maintain hidden states that get updated sequentially while processing the data of each accelerometer, influencing the contribution of each accelerometer to the identification prediction. Due to the sequential flow, the first input (S1) noticeably impacts the initial hidden state, influencing all subsequent layers, while the last input (S4) updates the hidden state at the end of the sequence with minimal influence on previous layers. The output layer then generates the identification prediction based on the final hidden state with cumulative influence of each input in the sequence. Once the LSTM models have generated identification predictions, LRP is applied to assign relevance scores to each accelerometer, determining which accelerometer contributes the most to the fault identification prediction. To evaluate the faithfulness of the explanations, the SUFF metric is computed by comparing relevance scores before and after masking the less relevant accelerometers, verifying whether the predictions truly rely on the most influential features. The following section presents and discusses the results achieved from the validation tests.

4 RESULTS AND DISCUSSION

In this section, the results of validating the ESFD methodology on the pre-trained LSTM models with time-series data from the Thessaloniki bridge are presented. First, the relevance scores by LRP and the faithfulness evaluation scores by SUFF are shown, followed by a discussion on the results.

4.1 LRP explainability results

Figure 1 illustrates the mean relevance scores for all accelerometers across the four LSTM models (M1 to M4). S1 is assigned the highest relevance score in M1, indicating the presence of combined sensor faults in S1. Similarly, M2, M3, and M4 identify S2, S3, and S4, respectively, as the most relevant accelerometers. In all LSTM models, the faulty accelerometer is always assigned the highest relevance scores, affirming the effectiveness of the LRP method in allocating relevance to the faulty patterns. Moreover, the non-faulty accelerometers exhibit consistent patterns, harmonically adhering to the order: S1 > S2 > S3 > S4 in all models. This order follows the temporal sequence of inputs, in which S1 appears first, then S2, S3, and finally S4. The order consistency suggests that the relevance scores are influenced by the LSTM sequential memory mechanism, which naturally places more emphasis on earlier inputs in the sequence. Nevertheless, the faulty accelerometer consistently receives the highest relevance score, providing accurate fault identification. The sequential order effect only influences the ranking of non-faulty accelerometers after the faulty accelerometer has been correctly identified. The results are further elaborated upon in the discussion section.

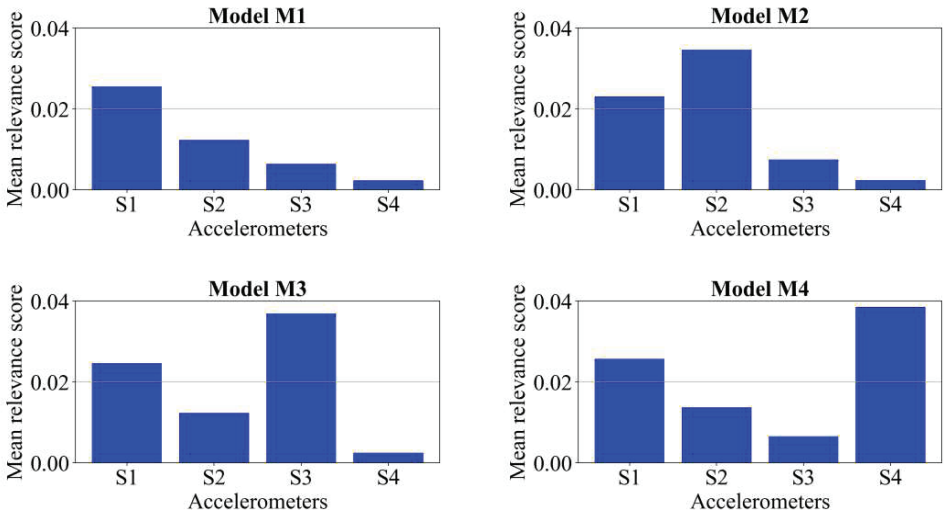

Figure 1: LRP results – Mean relevance scores distributed among the accelerometers (S1-S4) across the four LSTM models (M1-M4). Each subplot shows one model.

4.2 SUFF evaluation results

Figure 2 depicts the SUFF scores for all accelerometers across the four LSTM models by retaining the accelerometer with the highest relevance score, while masking the three non-faulty accelerometers. As observed, the faulty accelerometer is consistently assigned the lowest SUFF score in all models, indicating high faithfulness of the LRP explanations. This observation is in favor of the ESFD methodology as the models appropriately depend on the faulty accelerometer to make predictions. Furthermore, consistent patterns are observed among the non-faulty accelerometers in the SUFF scores, with the same order observed as in the relevance scores: S1 > S2 > S3 > S4. This order captures the temporal sequence of inputs, confirming the influence of the LSTM sequential memory mechanism over both relevance and SUFF scores.

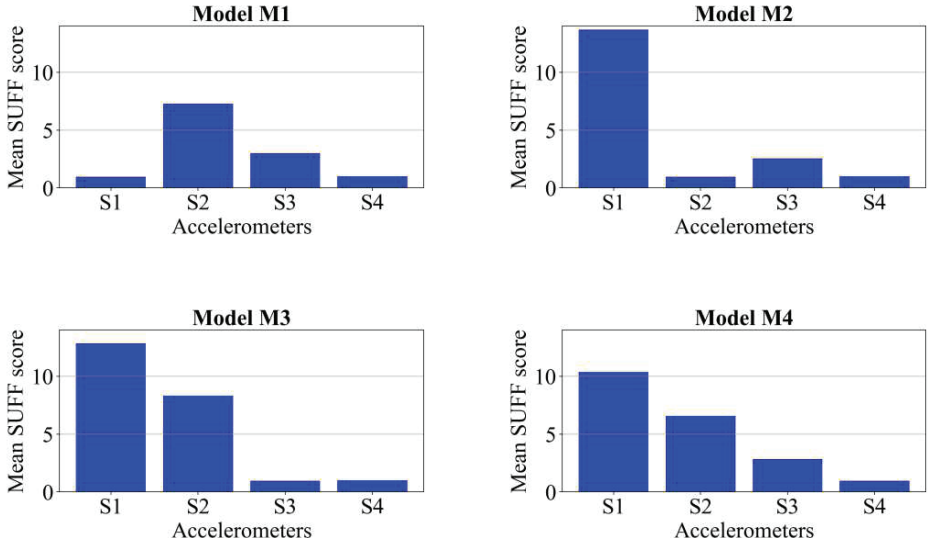

Figure 2: SUFF results – Mean SUFF scores distributed among the accelerometers (S1-S4) across the four LSTM models (M1-M4). Each subplot shows one model.

In summary, the results confirm the effectiveness of the ESFD methodology in accurately identifying combined sensor faults while providing transparent and reliable explanations. Robustness in ordering the non-faulty accelerometers in both relevance and SUFF scores emphasizes the importance of temporal sequencing in the prediction process adopted by the LSTM models. Discussion of the patterns observed is provided in the following section, offering perspective on temporal dependencies affecting the relevance and SUFF scores.

4.2 Discussion

The findings of this study demonstrate that the ESFD methodology is capable of identifying the faulty accelerometers correctly by continuously assigning the faulty accelerometers the maximum relevance and minimum SUFF scores. Additionally, consistent patterns among the non-faulty accelerometers reveal the impact of temporal sequence on the relevance and SUFF

scores. Specifically, the order observed in the non-faulty accelerometers (S1 > S2 > S3 > S4) for both scores (relevance and SUFF) is indicative of the effect of the LSTM sequential memory mechanism, which naturally assigns greater significance to earlier inputs over subsequent inputs. As the initial input, S1 contributes most to the hidden states of the LSTM model and, therefore, has the highest relevance and SUFF scores, while S4, as the final input, contributes the least, with the lowest relevance and SUFF scores when being non-faulty.

The consistent order illustrates the effect of both fault patterns and temporal sequence of inputs, highlighting the important role of input placement in assigning relevance and faithfulness scores. The results underscore the need to consider the LSTM model sequential memory mechanisms on interpreting predictions so as to obtain enhanced transparency and trustworthiness in ANN-based sensor fault diagnosis.

5 SUMMARY AND CONCLUSIONS

Transparency limitations in traditional ANN models, which, in spite of accurate performance, hinder trustworthiness and deployment in SHM applications, have been addressed in this study. In particular, although ANN models have proven to be effective in sensor FD, XAI integration into sensor FD is still scarce, especially for the identification of combined sensor faults. This study has proposed the ESFD methodology, which enhances explainability by LRP and evaluates faithfulness of the explanations by the SUFF metric. The ESFD methodology has been validated on pre-trained LSTM models with real-world SHM data from a pedestrian bridge, with focus on identifying combined sensor faults. LRP explanations have been evaluated by SUFF and have improved the transparency and reliability of ANN-based sensor fault diagnosis. The results have confirmed that the ESFD methodology provides transparency without affecting the fault identification performance. For future work, local explanations will be investigated by considering time steps as features – rather than sensors – to achieve enriched transparency and reliability in SHM sensor fault diagnosis. Additionally, future work will explore the robustness of the ESFD methodology under more realistic and complex conditions, including overlapping faulty sensors.

ACKNOWLEDGMENTS

The authors gratefully acknowledge the support offered by the German Research Foundation (DFG) under grants SM 281/17-1 and SM 281/33-1. Any opinions, findings, conclusions, or recommendations expressed in this paper are those of the authors and do not necessarily reflect the views of DFG.

REFERENCES

[1] Kim H., Seong Y., Han J., Kwon S., and Kim C. (2023). Demonstrating the test procedure for preventive maintenance of aging concrete bridges. Infrastructures, 8(3), 54.

[2] Smarsly K. and Petryna Y. (2014). A decentralized approach towards autonomous fault detection in wireless structural health monitoring systems. In: Proc. of the 7th European Workshop on Structural Health Monitoring, EWSHM 2014. Nantes, France, July 08, 2014.

[3] Yu X., Fu Y., Li J., Mao J., Hoang T., and Wang H. (2024). Recent advances in wireless

sensor networks for structural health monitoring of civil infrastructure. Journal of Infrastructure Intelligence and Resilience, 3(1), 100066.
[4] Smarsly K., Lehner K., and Hartmann D. (2007). Structural health monitoring based on artificial intelligence techniques. In: Proceedings of the International Workshop on Computing in Civil Engineering., IWSHM 2007. Pittsburgh, PA, USA, July 27,2007.
[5] Lydakis E., Koss H., Brincker R., and Amador S. D. R. (2024). Data-driven sensor fault diagnosis for vibration-based structural health monitoring under ambient excitation. Measurement Journal, 237(2024), 115232.
[6] Peralta J. J., Fritz H., Dragos K., and Smarsly K. (2021). Sensor fault diagnosis coupling deep learning and wavelet transforms. In: Proceedings of the 13th International Workshop on Structural Health Monitoring: Enabling Next-Generation SHM for Cyber-Physical Systems, IWSHM 2021. Stanford, USA, March 15, 2022.
[7] Wan S., Guan S., and Tang Y. (2024). Advancing bridge structural health monitoring: Insights into knowledge-driven and data-driven approaches. Journal of Data Science and Intelligent Systems, 2(3), pp. 1-15.
[8] Al-Nasser H., Al-Zuriqat T., Dragos K., Chillón Geck C., and Smarsly K. (2024). Identification of combined sensor faults in structural health monitoring systems. Smart Materials and Structures, 33(8), 085026.
[9] Chillón Geck C., Al-Zuriqat T., Elmoursi M., Dragos K., and Smarsly K. (2024). AIoT-enabled decenetralized sensor fault diagnosis for structural health monitoring. In: Proceedings of the 11th European Workshop on Structural Health Monitoring (EWSHM 2024), Potsdam, Germany, June 10, 2024.
[10] Jiangiang M., Shan C., and Cheng C. (2025). Sensor fault diagnosis using principal component analysis and convolutional neural network for offshore structural health monitoring. Measurement: Sensors, 2024, 101465.
[11] Al-Zuriqat T., Chillón Geck C., Dragos K., and Smarsly K. (2023). Adaptive fault diagnosis for simultaneous sensor faults in structural health monitoring systems. Infrastructures, 8(3), 39.
[12] Hu M., Avval S. S. P., He J., Yue N., and Groves R. M. (2025). Explainable artificial intelligence study on bolt loosening detection using Lamb waves. Mechanical Systems and Signal Processing, 225(2025), 112285.
[13] Chen Q., Cao J., and Zhu S. (2023). Data-driven monitoring and predictive maintenance for engineering structures: Technologies, implementation challenges, and future directions. IEEE Internet of Things Journal, 10(16), pp. 14527-14551.
[14] Qin Y., Su C., Chu D., Zhang J., and Song J. (2023). A review of application of machine learning in storm surge problems. Journal of Marine Science and Engineering, 11(9), 1729.
[15] Bhadauria P. K. S. (2024). Comprehensive review of AI and ML tools for earthquake damage assessment and retrofitting strategies. Earth Science Informatics, 17(5), pp. 3945-3962.
[16 Chaddad A., Peng J., Xu J., and Bouridane A. (2023). Survey of explainable AI techniques in healthcare. Sensors, 23(2), 634.
[17] Weber P., Carl K. V., and Hinz O. (2024). Applications of explainable artificial intelligence in finance – A systematic review of finance, information systems, and computer science literature. Management Review Quarterly, 74(2), pp. 867-907.

[18] Rjoub G., Bentaher J., Abdel Wahab O., Mizouni R., Song A., Cohen R., Otrok H., and Mourad A. (2023). A survey on explainable artificial intelligence for cybersecurity. IEEE Transactions on Network and Service Management, 20(4), pp. 5115-5140.
[19] Montavon G., Binder A., Lapuschkin S., Samek W., and Müller K. R. (2019). Layer-wise relevance propagation: An overview. In: Explainable AI: Interpreting, explaining and visualizing deep learning, Samek W., Montavon A., Vedaldi A., Hansen L. K., and Müller K. R., Eds. Cham, Switzerland: Springer, 2019, pp. 193-209.
[20] Chan C. S., Kong H., and Liang G. (2022). A comparative study of faithfulness metrics for model interpretability methods. In: Proceedings of the 60th Annual Meeting of the Association for Computational Linguistics, Dublin, Ireland, May 22, 2022.

XI ECCOMAS Thematic Conference on Smart Structures and Materials - SMART 2025
M. Krommer, M. Nader and M. Schagerl (Eds)

Received: 21 April 2025 / Revised: 28 August 2025 / Accepted: 27 September 2025
© The Author(s) 2025

A Machine Learning Framework for Predicting Moisture Effects on Active Sensory Piezoelectric Flax Composite Laminates

Vassilis Gkatsis, Antigoni Barouni, Nikolaos A. Chrysochoidis, Georgios Giannakopoulos, Christoforos S. Rekatsinas

Abstract. The increasing use of Flax Fiber-Reinforced Composites (FFRCs) in sustainable engineering applications—particularly in marine environments—demands a deeper understanding of their long-term performance under environmental exposure. In this context, our previous study [1] experimentally investigated how absorbed moisture affects active sensory wave propagation in flax composite laminates. Significant alterations were observed in key signal characteristics, including Time of Flight (ToF), amplitude, and dispersion behavior. Building upon this prior work, the current study extends pitch-and-catch experiments using piezoelectric devices to assess the degradation of mechanical properties over time due to moisture uptake. The experimental campaign includes systematic measurements of stiffness degradation, thickness swelling, and mass gain, which are used to quantify the extent of environmental deterioration in FFRCs. These degradation metrics are then used as inputs to machine learning regression models that aim to predict stiffness loss and dispersion characteristics as functions of moisture uptake. The models are trained on time-resolved experimental data encompassing both moisture diffusion and mechanical response, achieving high accuracy in correlating active-sensory features with material degradation. The proposed methodology establishes a predictive framework for designing environmentally resilient FFRCs with online structural health monitoring capabilities. This work offers valuable insights into moisture-induced degradation mechanisms and contributes to the development of smart, bio-based composite materials for sustainable engineering applications.

Key words: Piezoelectrics, Flax composites, Sustainable composites, Machine Learning, Predictive Modeling

Vassilis Gkatsis
Department of Informatics and Telecommunications, National and Kapodistrian University of Athens, Greece
e-mail: vgkatsis@di.uoa.gr

Antigoni Barouni
Portsmouth Centre for Advanced Materials and Manufacturing (PCAMM), University of Portsmouth, UK
e-mail: antigoni.barouni@port.ac.uk

Nikolaos A. Chrysochoidis
Department of Mechanical and Aeronautical Engineering, University of Patras, Patras, Greece
e-mail: xrysoxoidis@upatras.gr

Georgios Giannakopoulos & Christoforos S. Rekatsinas
Institute of Informatics and Telecommunications, National Center of Scientific Research, Demokritos, Greece
e-mail: ggianna@iit.demokritos.gr,crek@iit.demokritos.gr

1 INTRODUCTION

Flax fiber–reinforced polymer (FFRP) composites are emerging as sustainable alternatives to glass-fiber composites in sectors like marine and wind energy. They offer low density and high specific stiffness, with successful use reported in automotive and boat structures [2]. Studies have even explored replacing glass with flax in small wind turbine blades, showing comparable performance and reduced environmental footprint [3], [4]. However, a well-known drawback of flax/epoxy laminates is their sensitivity to moisture. Flax's hydrophilic lignocellulosic fibers absorb water, leading to fiber swelling, micro-cracking at fiber–matrix interfaces, and overall composite property degradation [5]. Upon water uptake, flax composites can suffer severe stiffness loss – *e.g.*, a >50% drop in Young's modulus within days of immersion has been observed [6]. Likewise, moisture causes reductions in strength and fracture toughness [7] as the weakened fiber/matrix bonding promotes fiber breakage and pull-out under load [8]. Hybridizing flax with glass or carbon fibers can improve moisture resistance [9], [10], but at the cost of full biodegradability. Given the marine environment's constant exposure to humidity, there is clear motivation to monitor moisture-induced damage in flax composites to ensure long-term durability.

Non-destructive evaluation (NDE) techniques are being investigated as maintenance tools to track environmental degradation in natural-fiber composites. In particular, ultrasonic wave methods (using piezoelectric transducers) have been widely used for damage detection in conventional composites [11], [12], [13] . Their use as moisture damage indicators, however, has been limited. Only a few studies in the last decade address this gap for flax composites [14]. For example, El-Sabbagh *et al.* showed that ultrasonic longitudinal wave velocity in flax/PP laminates decreases with increasing fiber moisture content, correlating with reduced composite rigidity [15], [16]. Petrone (2018) carried out one of the first Lamb wave dispersion experiments on flax laminates, mapping how flax/polyethylene panels transmit guided waves across frequencies [17]. These foundational studies suggest that wave speed and attenuation are sensitive to the internal state of flax composites.

Recent work has started leveraging minimal piezoelectric sensor setups (pitch–catch configurations) to quantify such changes under environmental aging. Tsitsas et al. [1] conducted water-immersion aging of flax/epoxy panels instrumented with just a few surface-mounted piezoelectric wafers. They tracked ultrasonic wave propagation over time and found measurable shifts in wave velocity and signal attenuation as the laminates absorbed moisture, up to saturation. This demonstrates that guided wave speed/attenuation can serve as proxies for stiffness loss during hygrothermal ageing. Similarly, Cinquin *et al.* showed in synthetic composites that the low-frequency Lamb wave (A_0 mode) attenuation increases systematically with moisture content, providing a gauge for moisture levels [18].

Beyond purely hygroscopic effects, guided waves have also been used to monitor mechanical degradation in flax composites. Hana *et al.* (2024) examined static and fatigue loading of flax/epoxy laminates by measuring changes in Lamb wave velocities, successfully correlating wave speed reductions to fatigue-induced damage accumulation [19]. In the context of wind energy, Mat Daud *et al.* embedded piezo-sensors in a flax fiber composite wind turbine blade and demonstrated that damage detection (here, induced by a simulated lightning strike) was as feasible as in a traditional glass-fiber blade [20]. Their comparative study concluded that

flax/epoxy could be a viable replacement for glass in blades without losing structural health monitoring (SHM) capability [21]. These studies consistently use only one or a few transducers in a pitch–catch arrangement to send and receive waves, making the techniques practical for in-situ monitoring.

The above efforts highlight a nascent opportunity: integrating **machine learning (ML)** with piezoelectric sensing to predict material properties or the damage state of flax composites. While still emerging, there are promising examples. Czigány's acoustic emission work showed that moisture-aged flax composites produce higher-amplitude AE signals during cracking [22], hinting that signal features carry signatures of moisture damage. Modern data-driven approaches can amplify such insights. For instance, researchers have combined acoustic emission data with deep learning to predict the remaining useful life of flax/epoxy specimens under creep loads [23]. Others report successful automated classification of composite fatigue damage using learned features from Lamb wave signals [24]. In addition, ML has been leveraged to address the environmental degradation of composites. Liu *et al.* (2022) developed an XGBoost (extreme gradient boosting) model to predict the residual tensile strength and Young's modulus of pultruded FRP composites after exposure to water, humidity, and alkaline environments [25]. Another relevant direction is using artificial neural networks (ANNs) for property prediction in aged natural-fiber composites. Nasri *et al.* (2024) recently demonstrated an ANN (multi-layer perceptron) model to assess tensile strength and impact energy of flax/polypropylene biocomposites after UV-aging [26]. In summary, the literature reveals the potential of utilizing machine learning to predict composite mechanical properties under various conditions, including those affected by moisture-induced degradation. Prior studies on flax fiber composites and analogous materials have utilized techniques ranging from linear regression and SVR to decision tree ensembles and MLP neural networks [27].

However, no prior work has focused on using guided wave data to infer stiffness or moisture content in flax fiber laminates directly. This gap in the literature – limited studies applying advanced signal analysis or ML to natural-fiber composite monitoring – represents an opportunity for the present work. By employing a minimal network of piezoelectric sensors and training predictive models on wave speed, time-of-flight, or attenuation features, it is possible to achieve a **real-time assessment of moisture-induced mechanical degradation** in flax-reinforced structures. This approach addresses the sustainability goals (using plant-based materials) and the durability assurance needed for marine and wind energy applications.

2 MATERIALS AND METHODS

2.1 Specimen fabrication

Seven flax/epoxy composite panels were fabricated using non-woven flax fabric impregnated with EL2 epoxy resin (EasyComposites, UK) via hand lay-up and compression molding. Each panel consisted of four fabric layers, which were hot-pressed at 70°C and 100 kN, followed by post-curing in an oven at 80°C for two hours. The final panels measured 200 × 150 mm² and were approximately 3 mm thick, with ~30 wt% fiber content (Figure 1).

2.2 Water immersion

After fabrication, the panels were sealed around the edges with two-part epoxy glue, in order to ensure no moisture would be absorbed from the edges during the immersion of the panels in

the water. In this way, only the top and bottom surfaces will be responsible for absorbing moisture, thereby simulating an actual marine application of flax laminated composites. Six (6) panels were fabricated and immersed in a water tank for different total immersion durations, to facilitate the mechanical testing after these time intervals, namely PF24, PF90, PF180, PF270, PF360 and PF528, as well as a panel PF0, which was the reference panel that was kept dry for comparison purposes. The weight and the average thickness of the final panels were measured and are presented in Table 1.



Figure 1 Flax reinforced panel straight after fabrication, in dry condition.

Table 1 Measured weight of final panels

Plate No.:	PF0	PF24	PF90	PF180	PF270	PF360	PF528
Description	Dry panel	24 hrs immersion	90 hrs immersion	180 hrs immersion	270 hrs immersion	360 hrs immersion	528 hrs immersion
Weight (gr)	135.18	109.56	112.51	101.97	119.38	111.64	121.50
Thickness (mm)	3.70	3.55	3.29	3.05	3.49	3.30	3.45

For the moisture absorption test, the panels PF24 to PF528 were immersed in a container of de-ionised water at a room temperature of 23 ± 1℃, as specified in the ASTM D570 standard. The panels were removed from the container every 24 hours, their surface was dried with absorbent cloth, and measurements of their mass and thickness were taken before they were returned to the water tank. At equal intervals of 90 hours, the panels were sequentially taken out of the container and were cut into tensile samples, according to ASTM D3039 for tensile testing. The total immersion time for the last panel was 528 hours, ensuring that the saturation conditions of the material had been reached. The percentage of gained mass due to water absorption was calculated according to the formula:

$$M(\%) = \frac{M_t - M_0}{M_0} \times 100 \quad (1)$$

where $M(\%)$ is the moisture uptake in percentage, M_t is the weight of the specimen at a given time of the water immersion, and M_0 is the initial weight of the specimen under dry conditions.

2.3 Tensile testing

Tensile tests were carried out according to ASTM D3039 standard using a Zwick/Roell Z30 testing machine equipped with a 30 kN load cell. The tests were conducted by controlling the

displacement using a crosshead speed of $2\,mm/min$ and the Young's modulus (E), the ultimate tensile strength (σ_{UTS}) and the strain at break were determined. Five specimens were used for each water absorption stage and a representative photo of panel PF90 is shown in Figure 2, before and after the tensile testing.

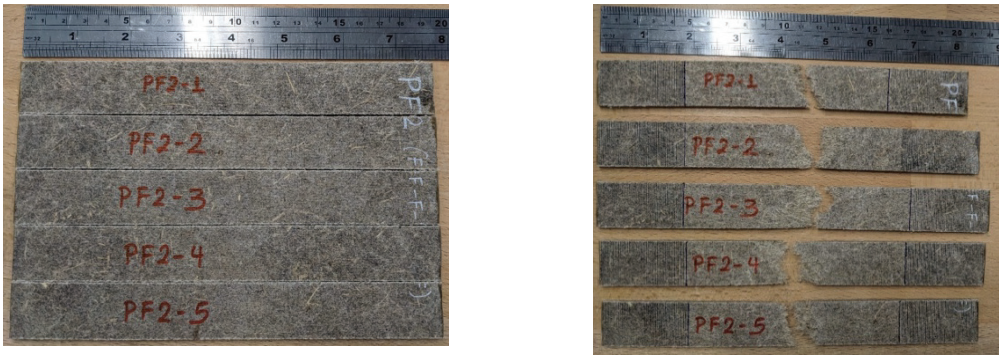

(a) (b)

Figure 2 Five tensile samples cut out of panel PF90 after the water immersion for 90 hours (a) samples before tensile testing; (b) samples after tensile testing.

2.4 Effect of water absorption in wave propagation

Based on the experimental procedure outlined previously, Figure 3 illustrates the increase in thickness and mass for each one of the immersed panels over time spent in immersion. It is evident that after approximately 500 hours of immersion, the curve has nearly plateaued, indicating that the water absorption process is essentially complete.

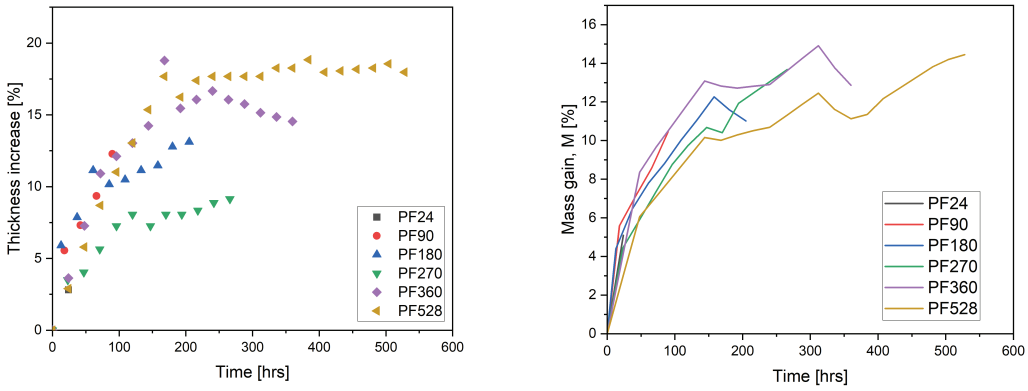

a) b)

Figure 3. (a) Thickness and (b) mass increase (%) as a function of the immersion time.

Each point on the curve of Figure 3 (a) and (b) represents an interval in the immersion procedure, during which a complete set of measurements was acquired. The initial phase of the experimental campaign aimed to investigate how moisture influences the pitch and catch wave propagation between the piezoelectric elements bonded to the plate surface. In order to evaluate the impact of water uptake, a distinct excitation frequency was chosen, at 130 kHz, based on the calculated dispersion characteristics [28]. More specifically, an excitation frequency at 130

kHz exhibits less dispersive characteristics while the group velocities of the two existing modes, A_0 and S_0, are easily distinct (Figure 4).

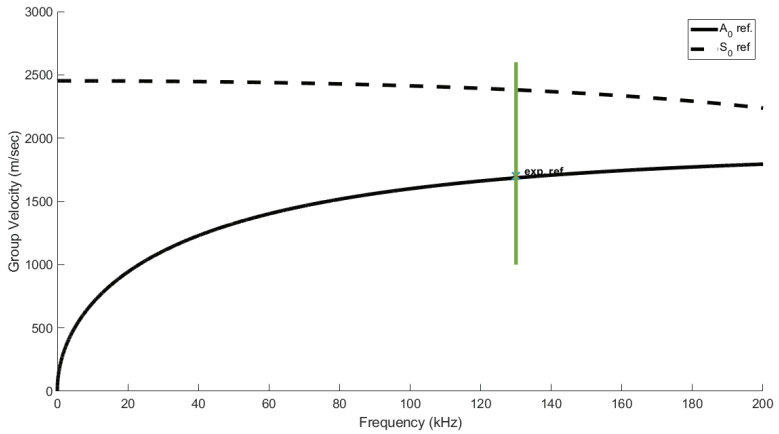

Figure 4. Dispersion characteristics of the fabricated material/laminate of 3mm thickness; group velocity vs frequency.

For the experimental procedure, a set of four rectangular piezoelectric wafers (PZT) was bonded on each panel's surface, in an arrangement as presented in Figure 5, [1]. Each PZT was a square with an edge of 12.7 mm and a thickness of 1 mm. The selection of the piezoelectric wafers' dimensions was based on the dispersion curves demonstrated in Figure 4.

Figure 6 depicts the time response of the sensor voltage and for the actuation-sensing pair 3-4 for each panel used in the study (Figure 5). It is evident from the measurements that the sensor signal undergoes significant distortion due to moisture absorption. Both the amplitude and the time of flight (ToF) are affected, with reductions in amplitude and increases in time of flight observed. This trend intensifies with more extended immersion periods.

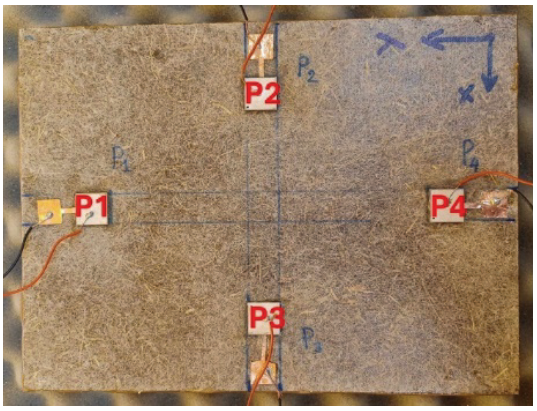

Figure 5. Composite plate equipped with a set of four square piezoelectrics.

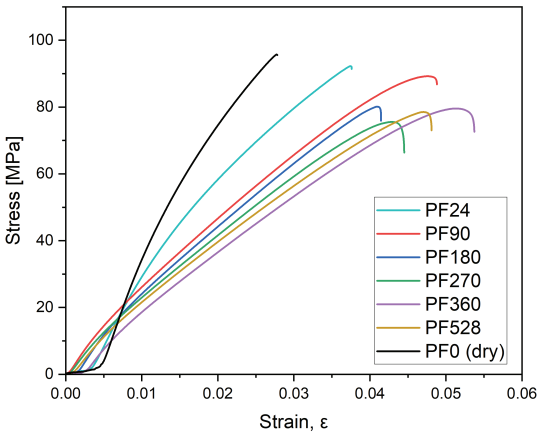

Figure 6. Stress-strain curves derived from tensile testing experiments for each wet and dry panel.

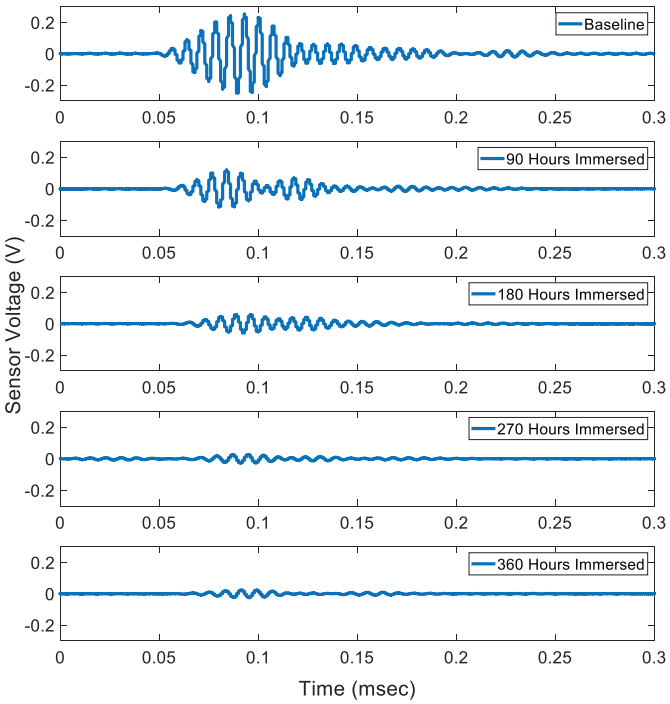

Figure 7. Time response of the sensory voltage for P3 operating as actuator and P4 as sensor. Each plot from the top to the bottom represents a different immersion period starting from the dry baseline condition. Actuation signal set at 130KHz.

A comparison of the stress-strain curves for each wet panel, as well as for the benchmark dry panel (PF0), is given in Figure 7. It is evident that the water uptake from the flax fibres has led to the degradation of the tensile properties and the rate of change of each curve. This is further enhanced by the microstructural degradation mechanisms that take place as the water molecules permeate inside the flax fibres and the composite structure by a diffusion mechanism [29].

As the material is in its dry phase, following the water immersion, the composite material experiences a desorption of water, leading to shrinkage of the flax fibres and, therefore, to local debonding of the flax fibres from the polymer matrix, as evidenced by the morphology of the dry and wet samples (90hrs) through scanning electron microscopy (SEM) images (Figure 8). The variation of the Young's modulus is significant with the minimum water immersion time, due to the hydrophilic nature of the flax fibres and their increase in moisture uptake by the flax/matrix interface. The dry panel PF0 exhibits the highest stiffness of 6.48 GPa, with the panel immersed only for 24 hrs (PF24) demonstrating a drop of 34.8% in the Young's modulus and the rest of the panels showing a similar drop compared to the dry panel of 62% on average. This is the reason for moving forward by developing ML models capable of providing critical information regarding the mechanical characteristics of flax-fiber reinforced structures in critical environments.

In the next section, we demonstrate the Young's modulus inference utilising a minimal number of measurements and relatively simple ML models.

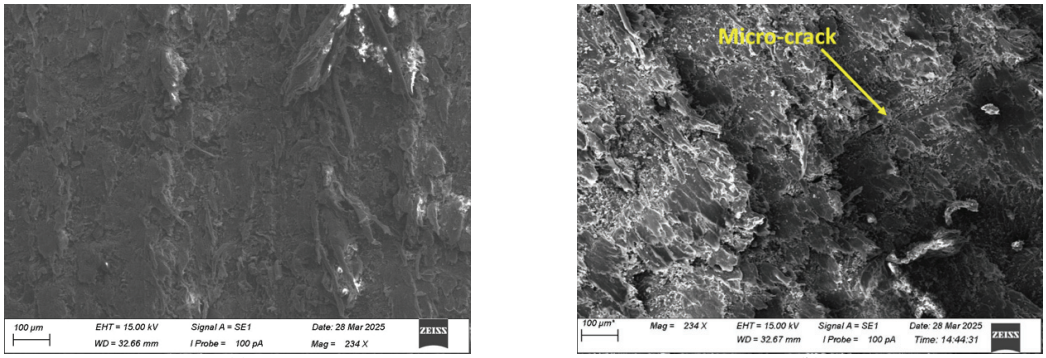

(a) (b)

Figure 8. SEM images of composite (a) dry panel, (b) panel immersed in water for 90 hours.

3 RESULTS

3.1 Predictive modelling utilizing ML algorithms

For the ML experiments, we used six models, ranging from simpler to more complex ones. These are *Linear Regressor, Stochastic Gradient Descent, Support Vector Machines, Decision Trees, Random Forest, and XGBoost predictors*. We have also selected two dummy regressors to be used as a baseline for comparison. These are, the dummy mean and dummy median regressors, which consistently predict the mean and median of the data distribution, respectively.

Table 2 Measured weight of final panels

Hours Underwater	0	90	180	270	360
Weight (gr)	121.5	129.35	132.66	135.2	135.02
Thickness (mm)	3.45	3.63	3.95	4.06	4.08
Youngs Modulus (GPa)	6.479	3.269	2.757	2.774	2.185
Group Velocity Speed (m/sec)	1.70	1.61	1.50	1.34	1.30

As mentioned above, we conducted our prediction evaluations with limited data, namely the five measurements of the panel shown in Table 2. Due to this limitation in numbers, we could not use a proper train–test split of our data, and hence we used the Leave-one-Out technique, which means that we iterated five times over the whole dataset and at each iteration, we kept one measurement as a test set and the remaining four as a train set.

For the evaluation of the models, we have selected Mean Absolute Error (MAE) as the measure, which is defined as:

$$MAE = \frac{1}{n} \times \sum |y_{i,pred} - y_{i,true}| \quad (2)$$

where $y_{i,pred}$ is the predicted value, $y_{i,\ true}$ is the true target value, and n is the number of predictions. This metric has been selected due to its clarity in measuring the model's efficiency and its simplicity in explanation and comparison with baselines.

We have conducted two inference experiments. In the first step, we use Hours Underwater and Group Velocity Speed as features, and we predict the target values of Weight, Thickness, and Young's Modulus. The MAE scores of these results can be seen in Table 3. In the second experiment, we have used Weight and Group velocity speed as independent variables to predict Young's Modulus, and the results are shown in Table 4. We also provide the MAE scores of the dummy regressors in Table 5, utilizing the same features as training with the respective inference experiments.

Table 3 MAE scores of inference models using Hours Underwater and Group Velocity Speed as features.

Model	Linear Regressor	Stochastic Gradient Descent	Support Vector Machines	Decision Trees	Random Forest	XGBoost
Weight (gr)	8.613	3.65	4.204	3.874	**3.401**	4.346
Thickness (mm)	**0.078**	0.344	0.194	0.118	0.127	0.162
Youngs Modulus (GPa)	3.751	1.48	**1.081**	1.622	1.337	1.507

Table 4 Mean Absolute Error scores of inference models using Weight and Group Velocity Speed as features.

Model	Linear Regressor	Stochastic Gradient Descent	Support Vector Machines	Decision Trees	Random Forest	XGBoost
Youngs Modulus (GPA)	1.186	1.134	1.081	1.523	**1.035**	1.619

Table 5 MAE scores of dummy models using Hours Underwater and Group Velocity Speed as features.

Model	Dummy Mean	Dummy Median
Weight (gr)	5.321	5.103
Thickness (mm)	0.238	0.303
Youngs Modulus (GPa)	1.493	1.111

Before interpreting the results, it is important to acknowledge the limitations posed by the small dataset. Overfitting is likely, and model generalization is constrained. Nevertheless, several insights can still be drawn.

In **Experiment 1**, predictions for **Weight** and **Thickness** achieved lower MAE scores than the dummy regressors. Notably, the **Linear Regressor** achieved the lowest error in Thickness prediction, suggesting a likely linear relationship between features and thickness response. Additionally, the prediction errors were small relative to the actual value ranges shown in Table 2, indicating model sensitivity to underlying trends.

In contrast, predicting **Young's Modulus** proved more challenging. The regressors' performance was comparable to that of the baseline models, suggesting that the models were unable to extract meaningful patterns from the limited data. The lowest MAE achieved in this task corresponds to 16.7% and 49.5% of the maximum (6.479 GPa) and minimum (2.189 GPa) values of the target property, respectively, a non-trivial error range.

These findings suggest that, although preliminary trends can be observed from limited data, a more comprehensive and diverse dataset is necessary for robust inference of complex

properties, such as Young's Modulus. Nonetheless, the results demonstrate the **potential** of machine learning for efficient, data-driven property prediction in flax composites when paired with smart sensing.

3.2 Feedback of ML predictions and forecasting of Group Velocity

This section presents the integration of machine learning (ML) predictions into a high-fidelity numerical simulation framework to assess wave propagation behavior in water-immersed flax fiber-reinforced composite laminates. The scope of this work is to establish a predictive loop, where ML-inferred mechanical properties—specifically, Young's modulus, thickness, and effective density—are fed into a physics-based model to forecast the resulting group velocities of guided waves. This approach bridges data-driven prediction with mechanistic simulation, enabling structural behavior to be anticipated under varying environmental conditions.

The numerical tool used here is based on the time-domain spectral element framework developed in previous work by Rekatsinas and Saravanos [30], which models the coupled electromechanical response of composite plates with embedded piezoelectric transducers. This high-order model allows the simulation of transient wave propagation generated by active sensing configurations, including pitch-and-catch arrangements typical in structural health monitoring (SHM) systems.

To replicate the experimental protocol described in our earlier study [1], we modeled the actuation of a piezoelectric wafer bonded on the surface of the composite plate. The simulation emulated the propagation of guided waves to a point 45 mm away, matching the experimental measurement position where waveforms were captured using a Laser Doppler Vibrometer (LDV). For each hydration state of the panel, the ML-predicted Young's modulus and thickness were directly incorporated into the numerical tool. The corresponding density was computed via the rule of mixtures, accounting for water content estimated from the measured mass gain. Specifically, the mass increase due to water uptake was used to estimate the water volume fraction, which was then used to calculate the updated composite density based on its revised mass and volume.

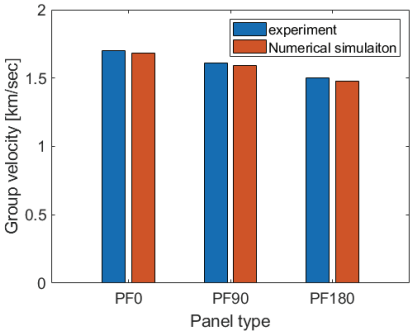

Figure 9 Experimental versus numerically calculated group velocity utilizing the predictive capabilities of ML algorithms

Following this data integration step, a series of numerical simulations were conducted, each corresponding to a different moisture exposure time. For each simulation, the group velocity was calculated by dividing the fixed propagation distance (45 mm) by the simulated time-of-flight. These predicted group velocities are presented in Figure 9, alongside the experimentally measured counterparts. The comparison reveals strong agreement between simulation and experiment, indicating that the ML-inferred material parameters, when combined with a high-fidelity numerical solver, can accurately forecast guided wave behavior in environmentally aged flax laminates. While minor discrepancies are observed, particularly at higher moisture contents, these can be attributed to factors such as local inhomogeneities, imperfect boundary conditions, and the limitations of data-driven inference in capturing highly nonlinear degradation effects.

Nonetheless, the results demonstrate the powerful synergy between machine learning and physics-based modeling.

By combining the predictive capacity of trained regressors with advanced spectral element simulation and High-Performance Computing (HPC), it becomes possible to emulate real-world operational conditions and anticipate wave propagation dynamics in smart natural fiber composites. This integrated methodology opens the door to digital twin frameworks for moisture-sensitive structures, where evolving environmental exposure is continuously monitored and simulated.

CONCLUSIONS

This study presented a hybrid experimental–computational framework for predicting moisture-induced degradation in flax fiber-reinforced composites (FFRCs) using minimal piezoelectric sensing and machine learning regression models. By leveraging changes in guided wave features, such as time-of-flight and amplitude, alongside simple geometric and mass measurements, the methodology enabled the inference of key mechanical properties, notably Young's modulus, during progressive water immersion.

Despite the limitations of a small dataset, several regression models, particularly XGBoost and Support Vector Machines, captured meaningful trends in material degradation. These findings highlight the feasibility of combining active sensing with ML algorithms for effective structural health monitoring of bio-based composites. To further validate the predictive accuracy of the inferred properties, high-fidelity numerical simulations were performed, showing strong correlation with experimental wave propagation results.

Minor discrepancies between simulation and measurement, however, underscore the inherent limitations of purely data-driven models, especially in data-scarce regimes. As a promising direction, future work will explore the development of **physics-informed machine learning (PIML)** frameworks, in which governing physical principles (e.g., wave dispersion, conservation laws, or damage evolution) are embedded directly into the learning process. This integration is expected to improve generalization, reduce data dependency, and enhance robustness, ultimately enabling real-time, closed-loop monitoring and forecasting for smart composite structures in demanding environments such as marine applications and wind turbine blades.

ACKNOWLEDGEMENTS

This work was supported by the European Union's Horizon 2020 research and innovation program, NOUS project under grant agreement **101135927**

REFERENCES

[1] P. Tsitsas, C. Rekatsinas, A. Barouni, and N. Chrysochoidis, "Effect of moisture on the sensing capabilities of piezoelectric actuator/sensor pairs on flax fibre reinforced composite laminates," *e-Journal of Nondestructive Testing*, vol. 29, no. 7, Jul. 2024, doi: 10.58286/29771.

[2] A. Moudood, A. Rahman, A. Öchsner, M. Islam, and G. Francucci, "Flax fiber and its composites: An overview of water and moisture absorption impact on their performance,"

Journal of Reinforced Plastics and Composites, vol. 38, no. 7, pp. 323–339, Apr. 2019, doi: 10.1177/0731684418818893.

[3] D. U. Shah, P. J. Schubel, and M. J. Clifford, "Can flax replace E-glass in structural composites? A small wind turbine blade case study," *Compos B Eng*, vol. 52, pp. 172–181, Sep. 2013, doi: 10.1016/j.compositesb.2013.04.027.

[4] K. Pender, K. Bacharoudis, F. Romoli, P. Greaves, and J. Fuller, "Feasibility of Natural Fibre Usage for Wind Turbine Blade Components: A Structural and Environmental Assessment," *Sustainability*, vol. 16, no. 13, p. 5533, Jun. 2024, doi: 10.3390/su16135533.

[5] C. A. Fuentes *et al.*, "Effect of humidity during manufacturing on the interfacial strength of non-pre-dried flax fibre/unsaturated polyester composites," *Compos Part A Appl Sci Manuf*, vol. 84, pp. 209–215, May 2016, doi: 10.1016/j.compositesa.2016.01.023.

[6] F. K. Sodoke, L. Toubal, and L. Laperrière, "Hygrothermal effects on fatigue behavior of quasi-isotropic flax/epoxy composites using principal component analysis," *J Mater Sci*, vol. 51, no. 24, pp. 10793–10805, Dec. 2016, doi: 10.1007/s10853-016-0291-z.

[7] F. A. Almansour, H. N. Dhakal, and Z. Y. Zhang, "Effect of water absorption on Mode I interlaminar fracture toughness of flax/basalt reinforced vinyl ester hybrid composites," *Compos Struct*, vol. 168, pp. 813–825, May 2017, doi: 10.1016/j.compstruct.2017.02.081.

[8] D. Scida, M. Assarar, C. Poilâne, and R. Ayad, "Influence of hygrothermal ageing on the damage mechanisms of flax-fibre reinforced epoxy composite," *Compos B Eng*, vol. 48, pp. 51–58, May 2013, doi: 10.1016/j.compositesb.2012.12.010.

[9] K. Jarukumjorn and N. Suppakarn, "Effect of glass fiber hybridization on properties of sisal fiber–polypropylene composites," *Compos B Eng*, vol. 40, no. 7, pp. 623–627, Oct. 2009, doi: 10.1016/j.compositesb.2009.04.007.

[10] A. K. Barouni and H. N. Dhakal, "Damage investigation and assessment due to low-velocity impact on flax/glass hybrid composite plates," *Compos Struct*, vol. 226, p. 111224, Oct. 2019, doi: 10.1016/j.compstruct.2019.111224.

[11] C. S. Rekatsinas, N. A. Chrysochoidis, and D. A. Saravanos, "Investigation of critical delamination characteristics in composite plates combining cubic spline piezo-layerwise mechanics and time domain spectral finite elements," *Wave Motion*, vol. 106, p. 102752, Nov. 2021, doi: 10.1016/j.wavemoti.2021.102752.

[12] N. A. Chrysochoidis, A. K. Barouni, and D. A. Saravanos, "Delamination detection in composites using wave modulation spectroscopy with a novel active nonlinear acousto-ultrasonic piezoelectric sensor," *J Intell Mater Syst Struct*, vol. 22, no. 18, pp. 2193–2206, Dec. 2011, doi: 10.1177/1045389X11428363.

[13] N. A. Chrysochoidis, T. T. Assimakopoulou, and D. A. Saravanos, "Nonlinear wave structural health monitoring method using an active nonlinear piezoceramic sensor for matrix cracking detection in composites," *J Intell Mater Syst Struct*, vol. 26, no. 15, pp. 2108–2120, Oct. 2015, doi: 10.1177/1045389X14549865.

[14] A. K. Barouni and C. S. Rekatsinas, "Study on the Propagation of Stress Waves in Natural Fiber Composite Strips," *Journal of Composites Science*, vol. 5, no. 1, p. 34, Jan. 2021, doi: 10.3390/jcs5010034.

[15] A. El-Sabbagh, L. Steuernagel, and G. Ziegmann, "Characterisation of flax polypropylene composites using ultrasonic longitudinal sound wave technique," *Compos B Eng*, vol. 45, no. 1, pp. 1164–1172, Feb. 2013, doi: 10.1016/j.compositesb.2012.06.010.

[16] A. El-Sabbagh, L. Steuernagel, and G. Ziegmann, "Ultrasonic testing of natural fibre polymer composites: effect of fibre content, humidity, stress on sound speed and comparison to glass fibre polymer composites," *Polymer Bulletin*, vol. 70, no. 2, pp. 371–390, Feb. 2013, doi: 10.1007/s00289-012-0797-8.

[17] G. Petrone, "Dispersion curves for a natural fibre composite panel: Experimental and numerical investigation," *Aerosp Sci Technol*, vol. 82–83, pp. 304–311, Nov. 2018, doi: 10.1016/j.ast.2018.08.029.

[18] M. Cinquin, M. Castaings, B. Hosten, P. Brassier, and P. Pérès, "Monitoring of the moisture content in carbon-epoxy plates using Lamb waves," *NDT & E International*, vol. 38, no. 1, pp. 37–44, Jan. 2005, doi: 10.1016/j.ndteint.2004.06.006.

[19] D. Hana *et al.*, "Behavior monitoring of flax fiber reinforced composites by guided waves," *International Journal of Damage Mechanics*, Aug. 2024, doi: 10.1177/10567895241275365.

[20] S. Z. Mat Daud, F. Mustapha, and Z. Adzis, "Lightning strike evaluation on composite and biocomposite vertical-axis wind turbine blade using structural health monitoring approach," *J Intell Mater Syst Struct*, vol. 29, no. 17, pp. 3444–3455, Oct. 2018, doi: 10.1177/1045389X17754259.

[21] "Structural Health Monitoring of Biocomposites, Fibre-Reinforced Composites." Accessed: Mar. 26, 2025. [Online]. Available: https://books.google.gr/books?hl=el&lr=&id=7Jp7DwAAQBAJ&oi=fnd&pg=PP1&ots=Ubj8h4InXr&sig=ohf_w-Qkgu4UlSGjtosiClgrxjo&redir_esc=y#v=onepage&q&f=false

[22] T. Czigany, "An Acoustic Emission Study of Flax Fiber-Reinforced Polypropylene Composites," *J Compos Mater*, vol. 38, no. 9, pp. 769–778, May 2004, doi: 10.1177/0021998304042481.

[23] J. Hao, M. Rupp, S. V. Lomov, C. A. Fuentes, and A. W. Van Vuure, "Remaining useful life prediction of flax fibre biocomposites under creep load by acoustic emission and deep learning," *Compos Part A Appl Sci Manuf*, vol. 188, p. 108572, Jan. 2025, doi: 10.1016/j.compositesa.2024.108572.

[24] H. Lee, H. J. Lim, T. Skinner, A. Chattopadhyay, and A. Hall, "Automated fatigue damage detection and classification technique for composite structures using Lamb waves and deep autoencoder," *Mech Syst Signal Process*, vol. 163, p. 108148, Jan. 2022, doi: 10.1016/j.ymssp.2021.108148.

[25] T. Sadat, "Machine Learning-Assisted Tensile Modulus Prediction for Flax Fiber/Shape Memory Epoxy Hygromorph Composites," *Applied Mechanics*, vol. 4, no. 2, pp. 752–762, Jun. 2023, doi: 10.3390/applmech4020038.

[26] K. Nasri and L. Toubal, "Artificial Neural Network Approach for Assessing Mechanical Properties and Impact Performance of Natural-Fiber Composites Exposed to UV Radiation," *Polymers (Basel)*, vol. 16, no. 4, p. 538, Feb. 2024, doi: 10.3390/polym16040538.

[27] M. V. Pathan *et al.*, "Predictions of the mechanical properties of unidirectional fibre composites by supervised machine learning," *Sci Rep*, vol. 9, no. 1, p. 13964, Sep. 2019, doi: 10.1038/s41598-019-50144-w.

[28] C. S. Rekatsinas, C. V. Nastos, T. C. Theodosiou, and D. A. Saravanos, "A time-domain high-order spectral finite element for the simulation of symmetric and anti-symmetric guided waves in laminated composite strips," *Wave Motion*, vol. 53, pp. 1–19, Mar. 2015, doi: 10.1016/j.wavemoti.2014.11.001.

[29] V. Fiore *et al.*, "On the response of flax fiber reinforced composites under salt-fog/dry conditions: Reversible and irreversible performances degradation," *Compos B Eng*, vol. 230, p. 109535, Feb. 2022, doi: 10.1016/j.compositesb.2021.109535.

[30] C. S. Rekatsinas and D. A. Saravanos, "A cubic spline layerwise time domain spectral FE for guided wave simulation in laminated composite plate structures with physically modeled active piezoelectric sensors," *Int J Solids Struct*, vol. 124, pp. 176–191, Oct. 2017, doi: 10.1016/j.ijsolstr.2017.06.031.

XI ECCOMAS Thematic Conference on Smart Structures and Materials - SMART 2025
M. Krommer, M. Nader and M. Schagerl (Eds)

Received: 25 April 2025 / Revised: 25 September 2025 / Accepted: 27 September 2025
© The Author(s) 2025

In-situ Monitoring of Electrochemically Generated μm-sized Corrosion Pits Growth in Aluminum Thin Plates using Lamb Waves

Cyril Nicard, Marc Rébillat, Olivier Devos, Mohamed El May, Nazih Mechbal

Abstract. Corrosion is a major threat in the aeronautic industry, both in terms of safety and cost. Efficient and cost affordable solutions for corrosion monitoring are thus needed. Ultrasonic Lamb Waves (LW) are very efficient for corrosion monitoring and can be made cost effective and versatile if emitted and received by a sparse array of piezoelectric elements (PZT). A LW solution relying on a sparse PZT array and allowing to monitor µm-sized corrosion pit growth on aluminum thin plates is here proposed and evaluated. Experimentally, the corrosion pit size is electrochemically controlled by both the imposed electrical potential after a localized coating defect has been generated. In parallel, the corrosion pit growth is monitored in-situ every 10 seconds by sending and measuring LW using a sparse array of 4 PZTs bonded to the back of the aluminum thin plate enduring corrosion. As a ground truth information, the corrosion pit volume is estimated as the dissolved volume balancing the electronic charges exchanged during corrosion. Measured LW signals are then post-processed in order to compute a large collection of synthetic damage indexes (DIs). After dimension reduction steps, obtained DI values correlates extremely well with the corrosion pit radius. Using a linear model relating those DI values to corrosion pit radius, it is demonstrated that corrosion pits can be reliably detected and their upcoming size extrapolated. LW managed by a sparse PZT array thus appears to be reliable and efficient to monitor growth of µm-sized corrosion pits growth on aluminum thin plates.

Key words: ultrasonic guided waves, corrosion pit, structural health monitoring, aluminum

1 INTRODUCTION

Corrosion within metallic structures can render an aircraft un-airworthy by weakening structural components, roughening the outer surface, loosening fasteners, hastening cracking, and facilitating the entry of water into electronic fixtures. Anticipating corrosive conditions ahead of time can lead to significant cost savings and less aircraft downtime [1]. In order to limit corrosion issues, a typical aeronautic structure is made of qualified aluminium alloys protected from the environment by treating the surface with adequate coatings. It is generally expected that the protective surface is perfectly flawless over the whole structure. But on a large structure undergoing everyday service this cannot be the case. Impact damage during service life is a common occurrence of coating failure. Damage during maintenance (tools and split

Cyril Nicard & Olivier Devos & Mohamed El May
PIMM - ENSAM/CNAM/CNRS, 151 Boulevard de l'Hopital, 75013 Paris, France

Cyril Nicard & Marc Rébillat & Nazih Mechbal
I2M - University of Bordeaux / CNRS / Arts et Métiers Institute, Esplanade Arts et Métiers, 33400 Talence, France

fluids) can also occur as well as paint cracking at high stress points around joints. From these initial premises, corrosion pits can start and threaten the integrity of the structure at a global level, thus motivating the need for in-situ pitting corrosion monitoring technologies.

Industrially speaking, an ideal corrosion monitoring technology should allow to monitor large-scale structures, to automate measurements, to detect corrosion pits from their premises, and to exhibit a high correlation between sensors measurements and the size and locations of corroded areas. Although various effective non-destructive testing (NDT) methods have been developed to monitor corrosion, they remain limited in their ability to detect and assess corrosion premises and to reliably size a given corrosion damage. Moving from planned maintenance to condition based maintenance (CBM), *i.e.* maintenance only when necessary, seems mandatory to solve these issues. Monitoring in real time and autonomously the health state of structures is thus of high interest in this context. Such a process is referred to as Structural Health Monitoring (SHM) [2, 3]. To achieve this goal, structures become *"smart"* in the sense that they are equipped with sensors, actuators, and algorithms that allow them to state autonomously regarding their own health. There is thus a real need for a large scale, automated, sensitive, low cost and embedded technology to develop corrosion monitoring SHM methodologies of aluminum aeronautic parts.

Ultrasonic technologies relying on Lamb Waves (LW) have been shown to be extremely sensitive to corrosion damage [4, 5] and can be easily automated thanks to permanently embedded piezoelectric elements (PZT) networks [6]. In the present work, the focus is thus put on corrosion monitoring methods based on LW and applied experimentally to plate-like structures. LW inspection methods based on sparse PZT transducers arrays are the most suitable from a practical point of view but have never been validated on small corrosion pits realistic of actual corrosion in aluminum ($\simeq$10 μm in radius) but rather on large generalized corrosion areas (in cm). In a previous work, the authors demonstrated that such an approach is however possible for steel thin plates [7] and associated experimental data have been made available in open access online [8]. The purpose is here to extend this approach to aluminum thin plates.

An option to achieve localized corrosion on aluminium thin plate samples is to protect their surface with a varnish, coat, or paint and to artificially generate a small damage in the protective layer for the pit to develop under control electrochemistry. This method has thus been use here and adapted to fit requirements imposed by the simultaneous presence of a sparse PZT arrays managing LW emission and reception.

The objective of this paper is thus first to introduce an experimental setup allowing to control electrochemically the growth of a μm-sized corrosion pit on a coated aluminium thin plate sample and to simultaneously monitor it in situ by means of LW emitted and received using a sparse array of PZT transducers. It will secondly be demonstrated that such measurements can be post-processed to compute damage indexes (DIs) that, after dimension reduction, correlate very well with actual corrosion pit radius as estimated electrochemically and allow to predict its upcoming size.

3 ELECTROCHEMICALLY CONTROLLED µm-SIZED CORROSION PITS GENERATION AND IN SITU ULTRASONIC LAMB WAVES MONITORING

3.1 Experimental samples

The experimental specimen is a 1.5 mm thick aluminum plate with dimensions of 80 mm by 125 mm. Four PZT transducers (Noliac NCE51, Ø10 mm × 1 mm) are bonded to the plate at specific geometrical positions, as shown in *Figure 1* [Left]. When selecting these positions, care was taken to break symmetry in the layout of the sparse array and to avoid placing the transducers too close to the plate edges in order to reduce Lamb wave reflections. Each transducer is connected to a 150 mm coaxial cable, which is brazed to the element to optimize the signal-to-noise ratio and allow for both the transmission and reception of Lamb waves. The PZTs are bonded to the plate following Cedrat Technologies' recommended bonding procedure. *Figure 1* [Right] shows the rear face of the aluminum plate. The front face (the one subject to corrosion) has been coated with an acrylic protective varnish (Electrolube), except for a 0.4 mm hole drilled at the center of the surface. This hole was manually created to locally damage the varnish while minimizing impact on the underlying aluminum.

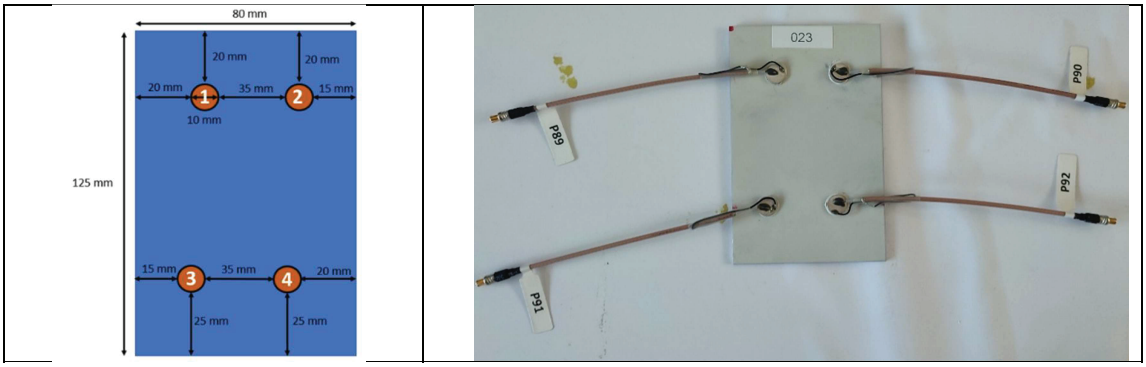

Figure 1: Experimental steel sample under study. [Left] Position of the PZTs composing the sparse network. [Right] Back face of the sample with the 4 bonded PZTs.

3.2 Electrochemical experimental setup

A dedicated electrochemical cell (see Figure 2 [Left]) was designed and 3D printed using PETG filament for the purposes of the experiment. The cell measures 96 mm × 60 mm × 48 mm and holds approximately 150 mL of electrolyte. Its geometry also allows for direct optical microscopic observation of the steel surface using a Keyence VH-Z50L long working distance objective. An overview of the complete experimental setup, along with detailed components, is shown in Figure 2 [Right].

To carry out the corrosion experiments, a standard three-electrode configuration is employed. The working electrode (WE) is the aluminium 2024 sample plate, the counter electrode (CE) is a 20 mm × 20 mm platinum wire mesh, and the reference electrode (RE) is a silver/silver chloride electrode (Ag/AgCl). The CE and RE are inserted into the cell from the top, while the aluminium sample (WE) is mounted at the bottom of the cell using an adaptor

and an O-ring. This setup ensures water tightness while avoiding any contact or mechanical stress on the PZT transducers. The electrodes are connected to a VersaSTAT 3F (Ametek) potentiostat, which manages the electrochemical control and measurements.

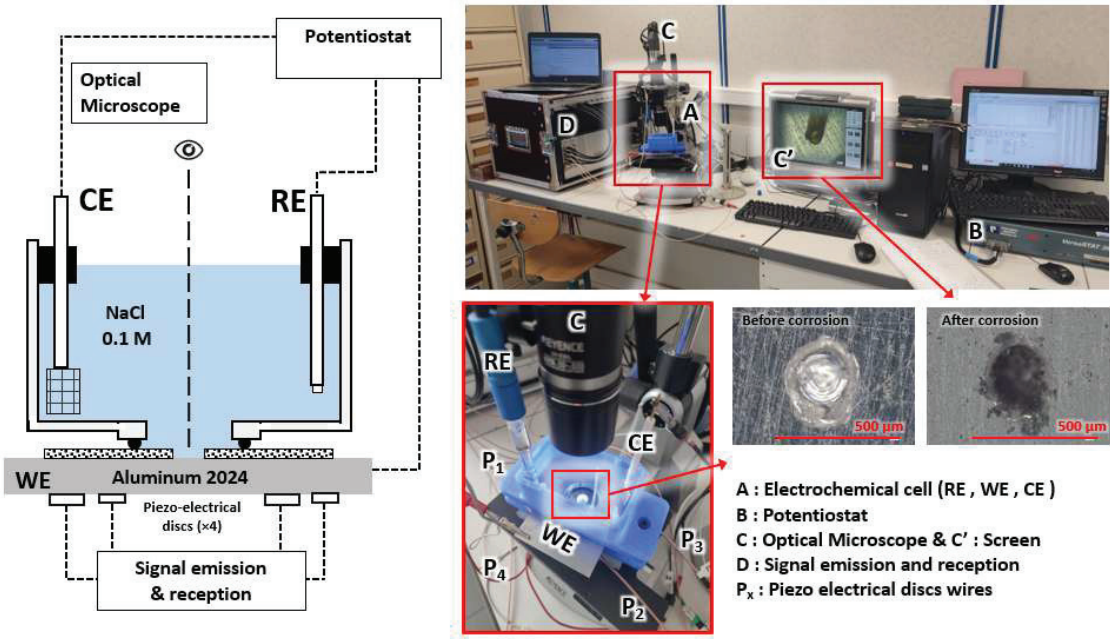

Figure 2: [Left] Schematic of experimental set up and [Right] Pictures of experimental setup with zooms on the specific equipment's details in the text.

3.3 Controlled generation of localized corrosion damage

To induce corrosion damage, preliminary experiments were conducted to determine the appropriate experimental conditions. The open-circuit potential (OCP) of our Aluminium 2024 sample was measured at -620 mV vs Ag/AgCl. Based on this, two different potentials were selected to induce corrosion damage: P1 = -700 mV vs Ag/AgCl, and P2 = -200 mV vs Ag/AgCl. These correspond to the passive and active dissolution regions, respectively, of Al 2024 in a 0.1 M NaCl solution.

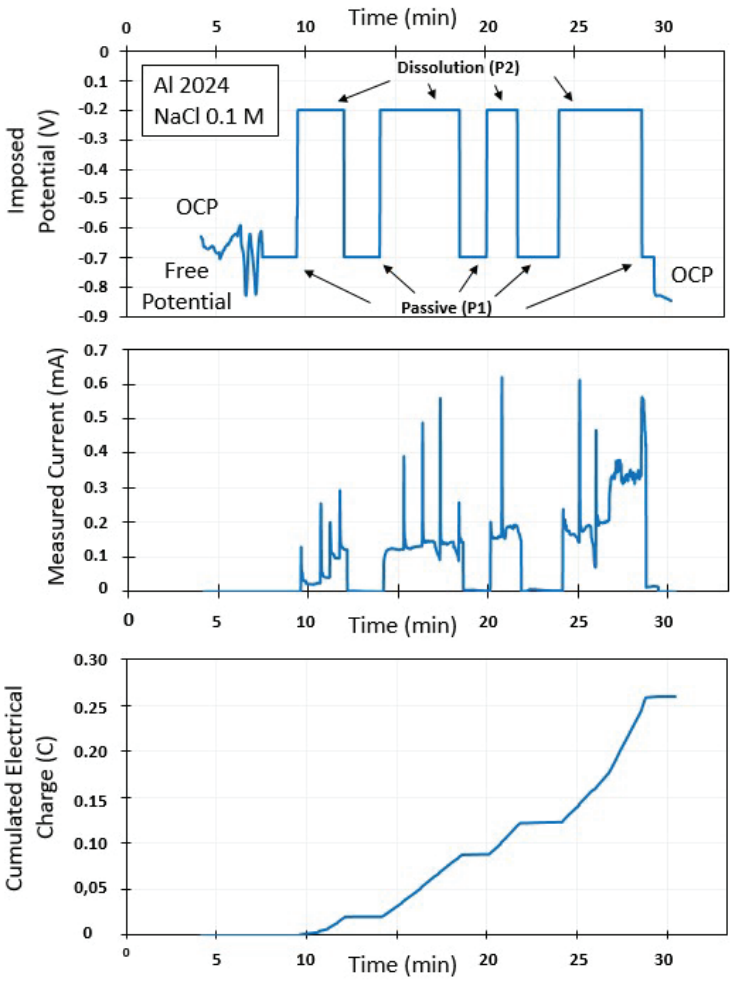

Figure 3: Experimental measurement for localised corrosion on Al 2024. Those figures display the imposed potential, measured current and cumulated electric charge.

To establish a relationship between the electrical charge exchanged during corrosion and the resulting damage size, a coefficient called the "dissolution ratio" D_r (in $mm^3 \cdot C^{-1}$) is defined as follows:

$$D_r = \frac{V}{Q} \qquad \textit{Eq. 1}$$

where V is the volume of the corrosion pit formed by the dissolution of aluminum, and Q is the total charge exchanged.

Preliminary tests revealed a linear relationship between the exchanged charge Q and the pit volume V, within our experimental range. This indicates that D_r can be considered a constant under the given conditions, regardless of the pit radius. The measured value is : $D_r = 20.1 \times 10^{-3}$ mm3·C−1.

Assuming a hemispherical shape for the corrosion pit, an estimate of the pit radius r_e can be obtained using the following equation:

$$r_e = \sqrt[3]{\frac{3QD_r}{2\pi}} \qquad Eq.\ 2$$

where Q is the cumulative charge (in coulombs) measured over time. The evolution of radius along with time as computed from the measured cumulative charge is shown in *Figure 4*.

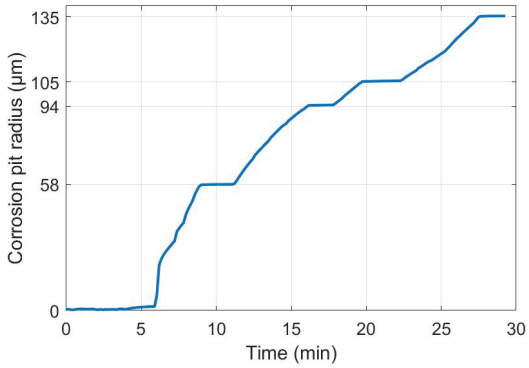

Figure 4: Corrosion pit radius evolution with time during the experiment calculated from cumulated charge in Figure 3.

3.4 In-situ ultrasonic Lamb waves measurements

During the corrosion experiment, LW are being emitted and received by the sparse array of 4 PZTs bonded at the back face of the aluminium sample (see *Figure 1* [Middle]). The system used for LW management is provided by Cedrat Technologies and can be seen in *Figure 5*.

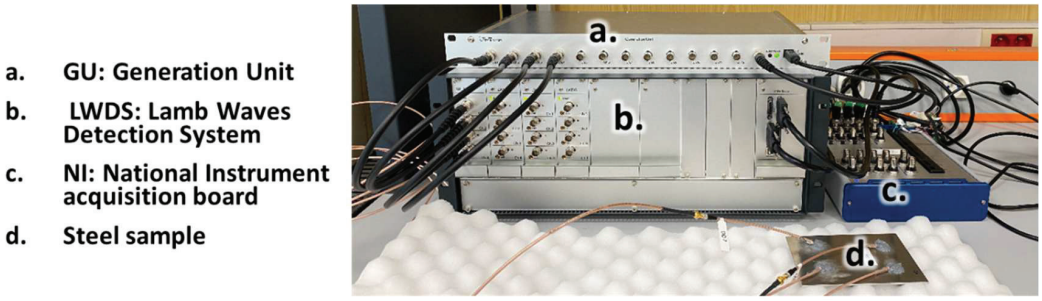

Figure 5: Overview of Cedrat Technologies LW management system.

The LW management system is made up of three blocks: the Generation Unit (GU) generates the signals to be sent for each channel and that can manage simultaneously up to 12 channels. The Lamb Waves Detection System (LWDS) can contain up to 16 independent channels. For each channel, the LWDS has a power amplifier (±15V, 1A) allowing to drive the PZT with a bandwidth larger than 1MHz, and a switching system allowing to toggle between emitting (pulse mode) and receiving (echo mode). Resulting signals are then acquired with a 2 MHz sampling frequency by a National Instrument (NI) acquisition board. Here, only 4 channels of the GU, the LWDS and the NI systems are being used. A custom MATLAB script configures

in a round robin fashion one PZT in actuator mode (pulse mode) and the three others in sensing mode (echo mode) before performing the acquisition. The PZT in pulse mode will generate a Lamb wave at a central frequency of 200 kHz and the other ones will receive the resulting LW that will then be measured by the NI interface. The time required to collect ($\simeq 50$ ms) and store ($\simeq 9.5$ s) the signals for the 4 PZT is around 10 seconds. Measurements are run constantly during the corrosion process and thus one measurement is available roughly every 10 seconds during the corrosion pits growth. Precise time stamps associated with each measurement are also stored.

4 DAMAGE SIZE ESTIMATION FROM LAMB WAVES MEASUREMENTS

4.1 Denoising of raw Lamb waves signals

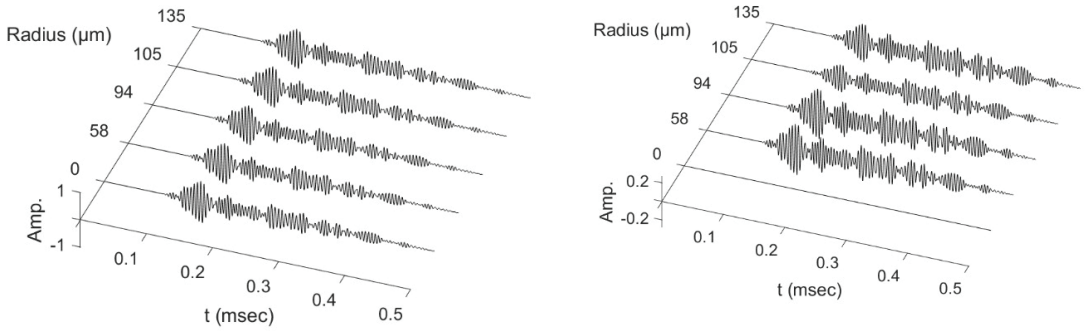

Figure 6: Example of LW signals measured on the path going from PZT 1 (actuator) to PZT 2 (sensor) for the first [left], and the difference between damaged signals and the reference one [right] for various radius of corrosion pits.

As pre-processing steps, the measured LW signals are first denoised by means of a discrete wavelet transform up to the order 4 using the *"db40"* wavelet. Those signals are then filtered around their excitation frequency $f_0 = 200$ kHz using a continuous wavelet transformation based on *"morlet"* wavelets and with a scale resolution equal to 20. The objective of this pre-processing step is to perform a band pass filtering around the excitation frequency by means of wavelets in order to limit the influence of experimental noise. The scale parameter can be sought as an image of the bandwidth of the retained bandpass filter over the frequency range of interest. The diaphonic part present in the measured signals (*i.e.* the copy of the input signals that appears on the measured signal due to electromagnetic couplings in wires) has been eliminated based on the knowledge of the geometrical positions of the PZT and of the estimated waves propagation speed in the material.

Examples of LW signals measured on the path going from PZT 1 (actuator) to PZT 2 (sensor) (see *Figure 1* [left]) for various radius of the corrosion pits are shown in *Figure 6*. The differences between the Lamb waves signals collected in the healthy condition (with a radius equals to 0 µm) and the ones collected at various corrosion states (with a radius larger than 0 µm) are also shown. This confirms that the diffraction generated signals are of small amplitude,

but still exists and can be experimentally observed.

4.2 Damage indexes computation

After LW signals have been denoised for all available actuator-sensor paths, signals are compared together one by one through the computation of a set of 40 Damage Indexes (DI) that have been previously designed for damage monitoring purposes using LWs [9]. These DIs can be categorized depending on the feature of the signal that they target to describe (energy, amplitude, time of flight, or statistical properties among others). One DI is computed from two signals that one would like to compare. Typically one signal in a healthy or reference state is compared to another in a damage state. However, as it has been previously shown, the signals due to the corrosion pit may be of small amplitude and thus corrupted by noise. In order to mitigate that issue, Lamb waves measurements are repeated several times when it is possible (here in the healthy reference state and when the injection is stopped and thus the corrosion pit radius steady). Consequently, instead of having one value of a DI, several values associated with its probability density function are available. Illustrative DIs histograms (namely cross-correlation [CC] and standard deviation [STD]) for the reference and corrosion cases corresponding to intermediary corrosion pits radius values for the path *"Actuator 1 - Sensor 3"* are plotted in *Figure 7*. From this figure it can be seen that irrespectively to the considered experiment or to the considered DI, a global increase is observed along with the corrosion pit radius growth. Furthermore, it can also be seen that the DIs distribution for a given case is relatively spread around its mean value meaning that the effect of noise is somewhat important here and should be considered. This is in agreement with the previously observed small effect of corrosion pits on the measured LW signals. This furthermore demonstrates the effective experimental sensibility of the LW based proposed approach to µm-sized corrosion pits.

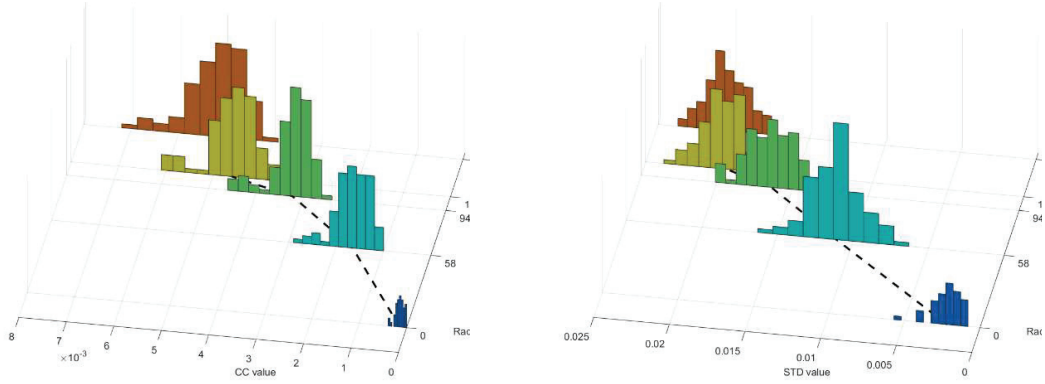

Figure 7: Example of the evolutions with corrosion radius size of DIs computed for the first experiment : [Left] CC and [Right] STD for the path PZT 1 to PZT 3.

A second way to compute DIs consists in processing incoming LW measurements acquired sequentially each $\simeq 10$ s and not to group them as previously by constant corrosion pit radius values. A first measurement is taken as a reference and then all the upcoming measurements are compared to this reference one and associated DIs computed. In that case, the obtained DIs

thus constitute temporal series evolving with time along with the damage radius .The correlation of some DIs (namely cross-correlation [CC] and standard deviation [STD]) with corrosion pit radius for the path *"Actuator 1 - Sensor 3"* are plotted on *Figure 8*. The plateaus associated with each state corresponding to a stop in the corrosion process can clearly be seen on this figure. The correlation quality between the DIs and the corrosion pit radius can be evaluated using the R^2 coefficient denoting the goodness of fit: a value close to one indicates a very good correlation and a value close to zero a very bad one. From this figure, it can thus be seen that whatever the considered DIs, an excellent correlation between DI values and corrosion pit radius is observed.

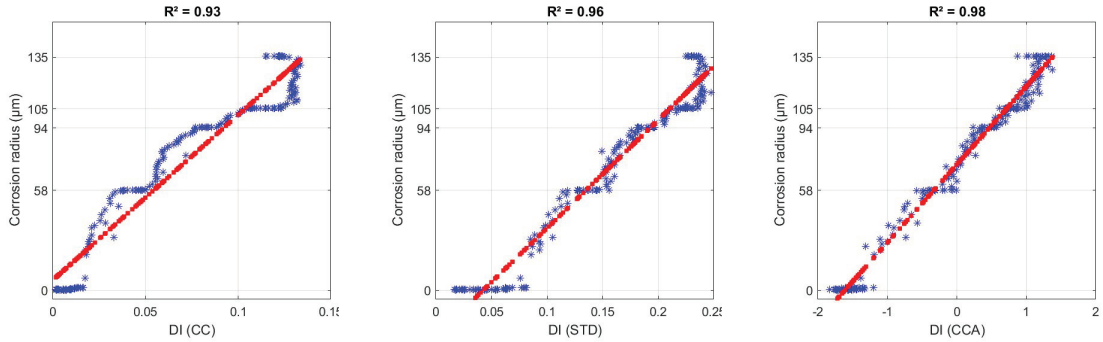

Figure 8: Example of the correlation with corrosion radius size of DIs CC [Left] and STD [Middle] and optimized DIs CCA [Right] for the path PZT 1 to PZT 3.

4.3 Dimension reduction

It is then necessary to be able to reduce the dimension of this set of informative DIs in order to filter out as many variability effects as possible and to keep the most information possible regarding corrosion pit sizes. As a first dimension reduction step, the DIs are averaged spatially for all paths available over the structure to be monitored. What has been chosen here is just to sum out the damage indexes obtained for all the paths in order to obtain 40 global damage indexes denoted DI_G. As a second dimension reduction step, the 40 DI_G that have been computed previously can be processed in order to compute a single DI being the most informative possible. In order to achieve this goal, Canonical Correlation Analysis (CCA) [10, 11, 12] that seek for a lower dimensional space optimizing discrimination has been retained. The CCA approach looks for the linear combination of DIs that maximizes the correlation between projected input and output data. In this way, CCA can conveniently deal with directions of the input or output spaces that present very high correlation. Consequently, after spatially integrating data over the whole structure, a second dimension reduction operation is achieved from a DI space having 40 dimensions to a reduced mono-dimensional space using CCA and makes use of both the 40 DI_G and the corresponding corrosion pit sizes (as CCA is a supervised method) for learning. The optimal DI computed using spatial aggregation and CCA is plotted in *Figure 8* [Right] and it can be seen that such a dimension reduction step indeed increases the correlation between DIs and corrosion pit radius.

4.4 Damage size extrapolation

Finally, the last step of the SHM process investigated here consists in being able to quantify corrosion pits size given only the measured LW signals or equivalently the DIs after the reduction dimension steps. What is more precisely targeted here is to achieve corrosion pits size extrapolation, *i.e.* to predict upcoming larger corrosion pit damage size on the basis of information acquired only on smaller corrosion pits. It is a two steps extrapolation process. As a first step, a linear model relating the corrosion pit radius to the reduced dimension DI is being learnt. This linear model is learnt only from small damage radii. Then, during the extrapolation step, DIs are computed for signals measured with larger values of corrosion radii. Finally, by inverting the linear model relating the DI value with the corrosion pit radii, it is then possible to infer the actual damage radii from the reduced dimension DI and thus to predict it. More details regarding those steps are provided in the following.

In practice, according to the linear correlation demonstrated between the reduced dimension DI and the corrosion pit radius, a linear model relating the reduced dimension $DI(r)$ to the actual damage size r is first learnt only on small damages with radii lying between 0 and r_{min}:

$$DI(r) = \mu_0 + \alpha r, \qquad r \in [0, r_{min}] \qquad Eq.\ 3$$

The estimated corrosion pit damage size $\hat{r}$ is then computed from $DI(r)$ by inverting the previously learnt linear model for larger corrosion pit radii lying between r_{min} and r_{max} as follows:

$$\hat{r} = \frac{DI(r) - \mu_0}{\alpha}, \qquad r \in [r_{min}, r_{max}] \qquad Eq.\ 4$$

The only parameter in that corrosion pit size extrapolation method is related with the range of radii $[0, r_{min}]$ used for learning and can be set up as a percentage value of r_{max}. In order to filter out rapid estimation variations, estimated radii are averaged over 3 values (i.e. over 30 seconds) using a moving average algorithm. It should be noticed that performing extrapolation is particularly challenging and that classically damage quantification algorithms encountered in SHM only perform interpolation, i.e. damage size prediction inside the range where the learning phase has been achieved [13].

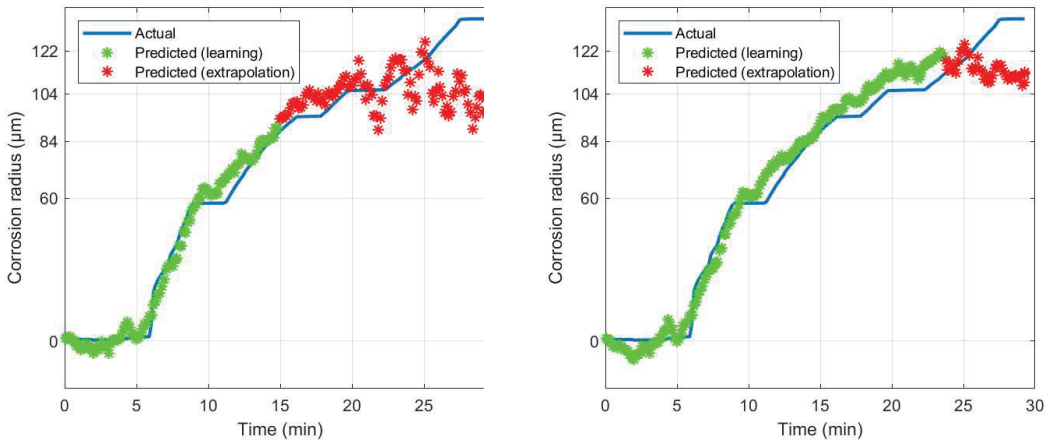

Figure 9: Corrosion pit radius extrapolation for the first experiment and for various learning rates (50% [left] and 80% [right])

Results of corrosion pit radius extrapolation for the first and second experiments and for various learning rates of 50% and 80% are shown in *Figure 9*. It can be seen that whatever the selected learning rate, the learning is correctly achieved (i.e. the green dots are lying close to the blue line) but the extrapolation has a tendency to underestimate the actual corrosion pit radius. This tendency for overestimation remains even when the learning rate is increasing. In conclusion, it can be stated that obtained results are always satisfying in the learning phase and that in the extrapolation phase results are conservative. Nevertheless, such results remains acceptable in practice from an industrial perspective. In terms of maintenance, what is interesting here is to be able to learn DI evolution from small corrosion pit damages that do not impart safety, and from this learning to be able to issue a warning signal when the monitored damage crosses a predefined safety threshold.

5 CONCLUSION

Corrosion is a major threat in the aeronautic industry, both in terms of safety and cost. Efficient, versatile, and cost affordable solutions for corrosion monitoring are thus needed. Ultrasonic Lamb Waves (LW) appear as very efficient for corrosion monitoring and can be made cost effective and versatile if emitted and received by a sparse array of piezoelectric elements (PZT). A LW solution relying on a sparse PZT array and allowing to monitor µm-sized corrosion pit growth on aluminium thin plate is here evaluated. Experimentally, the corrosion pit size is electrochemically controlled by both the imposed electrical potential after locally damaging the coating at the desired pit location. In parallel, the corrosion pit growth is monitored in-situ every 10 seconds by sending and measuring LW using a sparse array of 4 PZTs bonded to the back of the steel plate enduring corrosion. As a ground truth information, the corrosion pit volume is estimated as the dissolved volume balancing the electronic charges exchanged during corrosion. Measured LW signals are then post-processed in order to compute a collection of synthetic damage indexes (DIs). After dimension reduction steps, obtained DI values correlates extremely well with the corrosion pit radius. Using a linear model relating those DI values to corrosion pit radius, it is demonstrated that for corrosion pit from 30 µm to 150 µm, their upcoming size can be extrapolated in a conservative manner. LW managed by a sparse PZT array thus appears to be reliable and efficient to monitor growth of µm-sized corrosion pits on aluminium plates. If embedded in aeronautical structure, such an approach could be a versatile and cost-effective alternative to actual non-destructive maintenance procedures that are both time and manpower consuming.

REFERENCES

[1] S. Benavides, Corrosion control in the aerospace industry, Elsevier, 2009.

[2] D. Balageas, C.-P. Fritzen et A. Güemes, Structural health monitoring, vol. 493, Wiley Online Library, 2006.

[3] C. R. Farrar et K. Worden, «An introduction to structural health monitoring,» *Philosophical Transactions of the Royal Society of London A: Mathematical, Physical and Engineering Sciences,* vol. 365, pp. 303-315, 2007.

[4] C. Jirarungsatian and A. Prateepasen, "Pitting and uniform corrosion source recognition using acoustic emission parameters," *Corrosion Science,* vol. 52, pp. 187-197, 2010.

[5] P. Kudela, M. Radzienski, W. Ostachowicz and Z. Yang, "Structural Health Monitoring system based on a concept of Lamb wave focusing by the piezoelectric array," *Mechanical Systems and Signal Processing,* vol. 108, pp. 21-32, 2018.

[6] S. Grondel, C. Delebarre, J. Assaad, J.-P. Dupuis and L. Reithler, "Fatigue crack monitoring of riveted aluminium strap joints by Lamb wave analysis and acoustic emission measurement techniques," *Ndt & E International,* vol. 35, pp. 137-146, 2002.

[7] C. Nicard, M. D. O. Rébillat, M. El May, F. Letellier, S. Dubent, M. Thomachot, M. Fournier, P. Masse et N. Mechbal, «In-situ monitoring of µm-sized electrochemically generated corrosion pits using Lamb Waves managed by a sparse array of piezoelectric transducers,» *Ultrasonics,* p. In Press, 2024.

[8] «https://zenodo.org/records/14193336,» [En ligne].

[9] A. Rahbari, M. Rébillat, N. Mechbal et S. Canu, «Unsupervised damage clustering in complex aeronautical composite structures monitored by Lamb waves: An inductive approach,» *Engineering Applications of Artificial Intelligence,* vol. 97, p. 104099, 2021.

[10] R. Rosipal, L. J. Trejo et B. Matthews, «Kernel PLS-SVC for linear and nonlinear classification,» chez *Proceedings of the 20th International Conference on Machine Learning (ICML-03)*, 2003.

[11] R. Rosipal et N. Krämer, «Overview and recent advances in partial least squares,» chez *International Statistical and Optimization Perspectives Workshop" Subspace, Latent Structure and Feature Selection"*, 2005.

[12] J. Arenas-Garcia, K. B. Petersen, G. Camps-Valls et L. K. Hansen, «Kernel multivariate analysis framework for supervised subspace learning: A tutorial on linear and kernel multivariate methods,» *IEEE Signal Processing Magazine,* vol. 30, pp. 16-29, 2013.

[13] W. Briand, «Lamb waves based active sparse tomography for damage size quantification in composite structures: data-driven and parameter inversion methods,» 2022.

XI ECCOMAS Thematic Conference on Smart Structures and Materials - SMART 2025
M. Krommer, M. Nader and M. Schagerl (Eds)

Received: 22 April 2025 / Revised: 29 August 2025 / Accepted: 27 September 2025
© The Author(s) 2025

Damage Localization and Quantification Using Meta-Lens for Signal Enhancement

Jiahui Shi, Gabriele Cazzulani, Claudio Sbarufatti

Abstract. In wave-based structural health monitoring (SHM), signal comparison is critical in identifying abnormalities associated with damage. However, the signal difference becomes hard to distinguish particularly for minute damage due to minimal changes in the signal, making conventional damage detection methods often struggle with low sensitivity and accuracy. A meta-lens capable of wave focusing offers a promising solution by enhancing backscattered waves, thereby improving signal comparison. This paper presents a damage identification scheme using meta-lenses to amplify the backscattered waves, thereby improving signal comparison and sensitivity to damage. The identification of a single damage feature (either position or damage length) using a single meta-lens is first presented. The sensor arrangement is discussed first to highlight the superiority of the meta-lens in the signal enhancement. Upon the selected sensor arrangement, the sensitivity of the signal with the damage features is compared in the cases with and without the meta-lens. A dual-meta-lens set up is then proposed, enabling damage localization in a two-dimensional region. This approach significantly improves the sensitivity in detecting damage features, offering a promising solution for identifying minute damage.

Key words: Structural Health Monitoring, Metamaterial, Lamb Wave, Damage Identification.

1 INTRODUCTION

The structural components of modern aircraft operate under increasingly demanding conditions, making them susceptible to fatigue, cracking, and corrosion. Undetected defects may escalate into serious safety threats [1]. To ensure structural integrity and predict service

Jiahui Shi & Gabriele Cazzulani & Claudio Sbarufatti
Department of Mechanical Engineering, Politecnico di Milano, Via la masa, 1, Milan, Italy
e-mail: jiahui.shi@polimi.it

life, continuous monitoring has become essential, giving rise to Structural Health Monitoring (SHM), which enables real-time assessment of structural conditions. Among various SHM techniques, such as vibration-based, resistance-based, and guided wave-based methods, the latter has gained wide attention for its long-range propagation and high sensitivity to minor damage [2]. Guided wave-based Structural Health Monitoring (GWSHM) typically employs passive or active monitoring, both strategies rely on analyzing changes in wave propagation characteristics [3]. The accuracy of damage detection critically depends on clearly distinguishing damage signatures within wave propagation changes.

In practical testing, signals typically include two components: the target structural response and unwanted noise from environmental factors [4], boundary reflections [5], or circuitry interference [6]. Improving signal detectability requires either suppressing noise or amplifying the desired signal. Meta-structures, composed of periodic unit cells with engineered properties, can manipulate wave behavior through refraction [7], filtering [8], and focusing [9]. While filtering-based designs improve signal clarity by blocking noise-associated frequencies [10,11], their effectiveness is limited when the damage-induced signal itself is weak, such as in early stage or remote damage.

Meta-lens, a class of meta-structure for wave focusing [12,13], offers a solution by concentrating wave energy at specific locations. Prior research has demonstrated wave focusing in Lamb [14], bulk [15], and shell waves [16] using meta-lens. Typically, sensors positioned at the focal points capture these amplified signals, with simulations showing energy amplification exceeding tenfold in some cases [17]. Such amplification is particularly beneficial in energy harvesting applications, where signal maximization is a primary goal.

However, GWSHM requires signal enhancement strategies that differ from those used in energy harvesting. In damage detection, the crucial information is contained not within the actuator-generated wave itself but in the portion modified by structural damage. Detection typically involves comparing signals, either against baseline references or through baseline-free approaches. The received signals comprise two distinct components: the direct actuator-generated wave and the damage-modulated wave. Because damage severity correlates strongly with the modulated signal component, effective detection requires distinguishing these components. Ideally, an optimized method would selectively amplify only the damage-related component while preserving the original signal characteristics. However, existing meta-lens designs amplify both components indiscriminately, causing the subtle damage information to remain hidden within the amplified response. Consequently, isolating minor signal variations indicative of defects is challenging, highlighting the need to refine meta-lens configurations to enhance selective sensitivity to damage signals.

This paper introduces an innovative strategy that integrates the meta-lens with the optimized sensor configuration to enhance the detection of damage-related signals. Specifically, Section 2 details the design of a gradient-index (GRIN) meta-lens for Lamb wave focusing. Section 3 explores its performance in enhancing reflected wave signals for quantifying and localizing damage. Furthermore, damage quantification and localization performance are systematically assessed under various damage scenarios. Finally, Section 4 expands this concept into a dual-meta-lens configuration, realizing the two-dimensional damage localization by analyzing the relative energy and arrival-time differences of signals at strategically placed sensors.

2 META-LENS DESIGN

Signal comparison is fundamental to damage detection, and a greater contrast between signals improves the accuracy of defect identification. This section outlines the development of a meta-lens designed for wave focusing. Various types of meta-lenses have been explored for this purpose, each utilizing distinct physical mechanisms, including GRIN lenses, resonant meta-lenses, bandgap-based lenses, and transformation acoustic lenses. Among these options, the GRIN meta-lens is selected in this study for its suitability in damage detection applications. Compared to the other designs, it offers lower reflection losses and a relatively straightforward implementation, making it an effective choice for enhancing wave focusing on structural health monitoring.

In designing a GRIN meta-lens, the choice of an appropriate refractive index distribution plays a pivotal role in determining its focusing efficiency. For a meta-lens that is symmetric along the y-direction and follows a hyperbolic secant distribution of unit cells, the corresponding mathematical formulation is expressed as:

$$n(y)=n_0 \mathrm{sech}(\alpha y) \tag{1}$$

here n(y) denotes the refractive index of the unit cell at a specific position y, while n_0 epresents the refractive index at the symmetric center of the meta-lens. The parameter α, known as the gradient coefficient, plays a key role in determining the focal length, which is governed by the following relationship $f = \pi / 2\alpha$, in which f is the focal length. As described by Snell's law, when a wave transitions between two media with different velocities, its direction changes due to the phenomenon of refraction. Thus, if the wave velocity can be modified to make the refractive index distributes as Eq. (1), the waves are to be focused at the designed focal point.

In summary, the GRIN meta-lens design involves analyzing the dispersion characteristics of the unit cell to determine its effective refractive index, followed by tuning its geometry, material properties, or filling ratio to control wave velocity. A suitable index distribution is then selected to guide wave focusing. Finally, the design is refined to ensure the actual index profile closely matches the target distribution for optimal lens performance.

3 SENSITICITY ANALYSIS WITH SINGLE META-LENS

In the present investigation, an aluminum plate with dimensions $600\times400\times1.5\mathrm{mm}^3$ is adopted as the monitored structure. The wave characteristics within the aluminum plate are analyzed using the Wave Finite Element Method (WFEM), due to its notable advantages of high computational accuracy and efficiency. The analysis is conducted with a mesh resolution of at least 8 mesh elements per wavelength. The A0 wave is taken as an example of behaving as the detection wave, and the strategy for signal enhancing by a single meta-lens is discussed in this section.

3.1 Meta-lens for A0 wave focusing

To effectively amplify actuator-generated wave signals, a meta-lens is integrated along the wave propagation route. According to the principles outlined previously, the initial step in meta-lens design involves obtaining dispersion characteristics from a properly chosen unit cell.

Specifically, for in-situ SHM, the meta-lens should feature compact geometry and minimal added mass to avoid adversely affecting the structure's fundamental properties. Moreover, the unit cell design must allow for convenient tuning of the group velocity through geometric modifications. This implies that the wave number should vary noticeably within the operational frequency range, ensuring high sensitivity to geometric parameter adjustments.

Based on the above considerations, a resonant oscillator-based unit cell, composed of a high-density polyethylene (HDPE) film and a stainless-steel disk (1 mm height, 4 mm diameter), is proposed (Figure 1(a)). Dispersion analysis, shown in Figure 1(b) reveals significant sensitivity of the A0 wave's velocity to disk-height changes, particularly near the chosen working frequency of 30 kHz, which is below the resonance frequency (~50 kHz) to avoid excessive energy localization. At 30 kHz, disk heights are precisely adjusted to achieve the desired refractive index distribution along the y-axis as Eq.(1). According to the Huygens-Fresnel principle, the focusing performance, such as quality, range, and resolution, is influenced by the meta-lens dimensions. A wider lens concentrates more energy but may suffer from diffraction-induced degradation, while lens length (x-axis) controls wave veering, a short length limits phase modulation. To ensure effective focusing and ease of fabrication, the lens is limited to 10 columns. Based on these considerations, the final disk heights are chosen as 1 mm (y=0 mm), 0.97 mm (y=±5 mm), 0.86 mm (y=±10 mm), 0.66 mm (y=±15 mm), and 0.33 mm (y=±20 mm), with a theoretical focal length of L=50 mm. The final meta-lens comprises 7 rows and 9 columns of unit cells, with disk height varying along y-axis and periodic repetition along x-axis (Figure 1(c)).

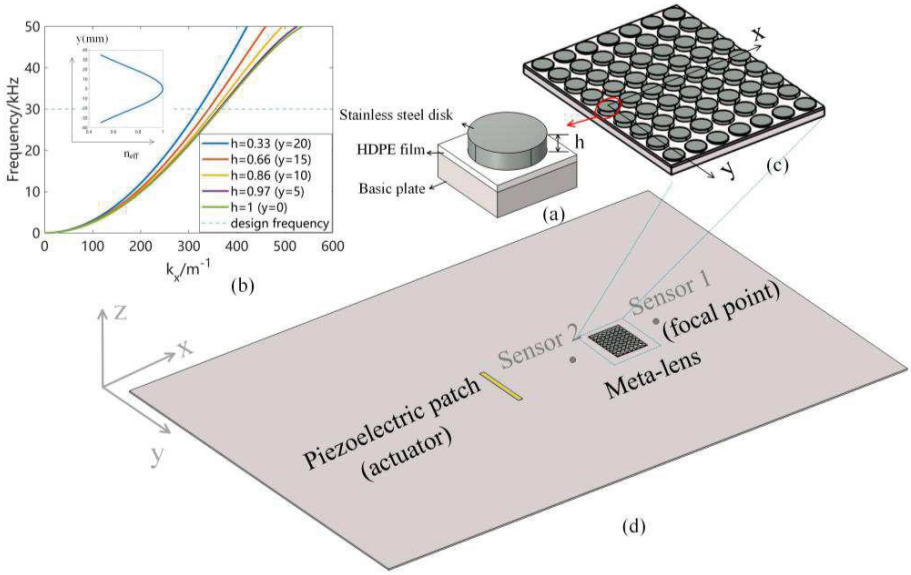

Figure 1: Unit cell (a), dispersion curve of the unit cell with different pillar heights (b), meta-lens composed of 7 rows and 9 columns (c), and meta-lens on the aluminum plate (d)

Figure 1(d) illustrates the simulation setup, where a rectangular actuator on the plate

generates Lamb waves using a five-cycle tone burst centered at 30 kHz. Its shape promotes horizontal wave propagation and minimizes vertical dispersion. Simulations are conducted in COMSOL Multiphysics, with a mesh size of 2 mm to ensure at least eight elements per 16 mm A0 wavelength. Non-reflecting boundaries are applied on all edges to eliminate reflections and isolate wave behavior, despite their absence in real structures.

Two sensors are placed on the plate: one at the focal point (x = 55 mm, y = 0) and the other symmetrically opposite the meta-lens (x = –15 mm, y = 0), as shown in Figure 1(d). The wave-focusing performance of the meta-lens is demonstrated in Figure 2(a), by observing the out-of-plane displacement field at 2.1×10^{-4}s. After excitation, the wave first reaches Sensor 2, then passes through the meta-lens and focuses onto Sensor 1. As shown in Figure 2(b), Sensor 2 records identical signals with and without the meta-lens, confirming no prior interaction with the lens. In contrast, Sensor 1 shows a 1.55 times amplitude increase due to wave focusing.

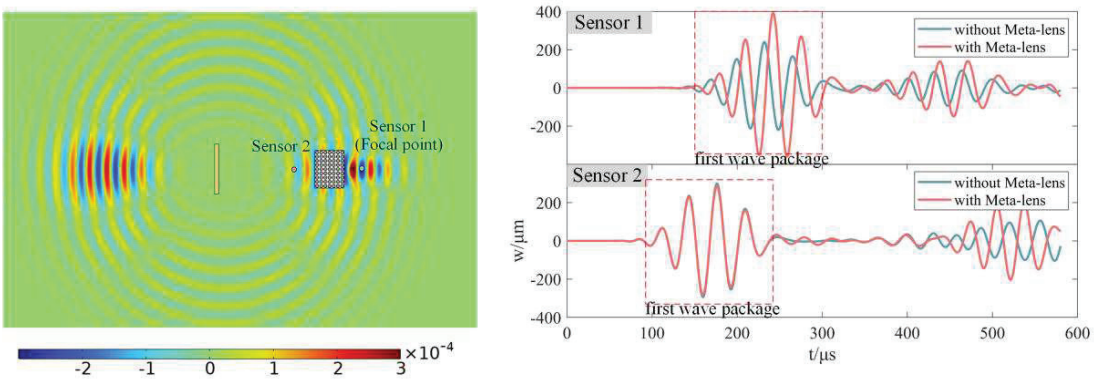

(a) (b)

Figure 2: Out-of-plane displacement (mm) of the upper surface of the plate at 2.1×10^{-4}s (a), and signals obtained from Sensor 1 and Sensor 2 (b)

3.2 Sensor strategy and comparative analysis

To evaluate how damage influences the wave signal, a 12.5 mm × 1.34 mm rectangular through-hole is introduced at x=50mm, y=0, as shown in Figure 3(a). When the wave encounters this damage, part of the waves transmits through the damage and arrive at Sensor 1, as the green arrow shows, while partial waves propagate back toward the meta-lens, as the blue arrow shows, undergoing additional focusing due to the lens's symmetric design. Consequently, a secondary focal point, which is at Sensor 2, forms symmetrically opposite the original one, placing at Sensor 1. Figure 3(b) and (c) illustrates the signals collected at both sensors with and without the meta-lens. The red dot indicates the theoretical arrival time, and the dashed box highlights the wave packet to be concerned. For Sensor 1, the signal passes directly through the damage and shows only a slight amplitude reduction. Introducing the meta-lens leads to a similar response, except for two key differences: the initial wave packet experiences a 10 μs delay due to phase modulation by the meta-lens, and the higher amplitude of the signal. While

the meta-lens increases the overall wave energy, it does not significantly enhance the contrast between the damaged and undamaged signals, which are 76 μm without lens and 73 μm with lens, indicating limited sensitivity to damage at this position.

In contrast, Sensor 2 captures the backscattered wave that has undergone two stages of amplification: once during initial focusing and again after being reflected by the damage. This dual enhancement yields a significantly larger amplitude difference between damaged and baseline signals, which are 76 μm and 108 μm, respectively, clearly demonstrating the meta-lens's ability to amplify damage-specific features.

These results suggest that while Sensor 1 benefits from general signal enhancement, it lacks selectivity for damage-induced changes. Sensor 2, positioned at the symmetric focal point, offers superior sensitivity and contrast, making it the preferred choice for reliable damage detection in meta-lens-based SHM systems.

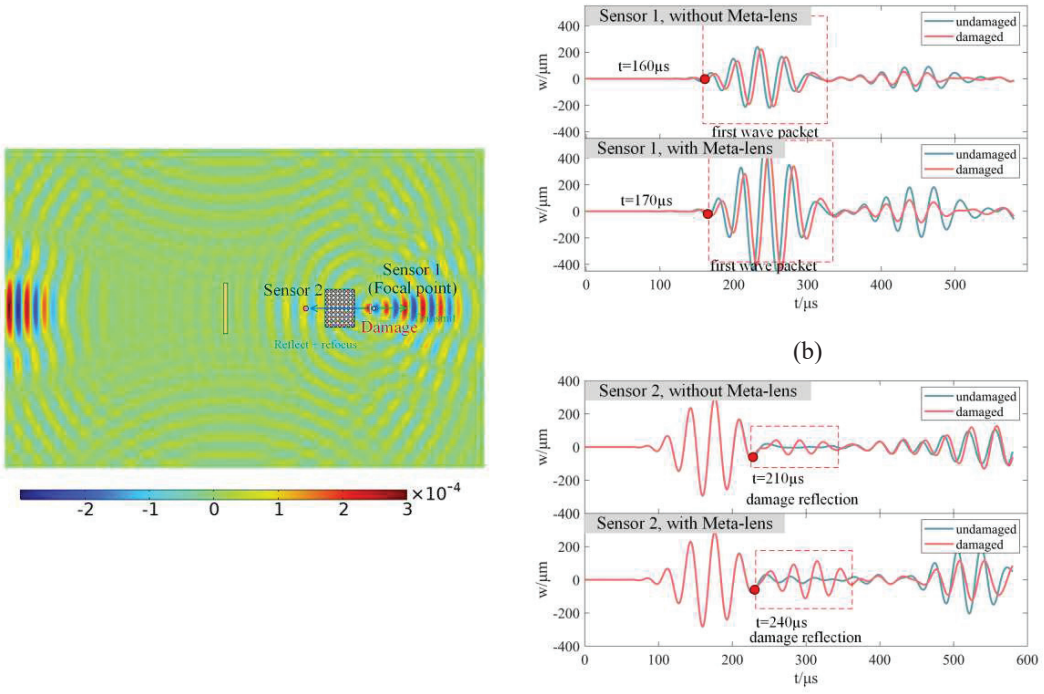

Figure 3: Out-of-plane displacement at 3×10^{-4}s (a), and signals from Sensor 1 (a) and Sensor 2 (b) without and with meta-lens

3.3 Damage identification

This section evaluates the practical effectiveness of the meta-lens-enhanced detection strategy using Sensor 2 under realistic conditions with varied damage characteristics. Two

representative cases are analyzed: (1) through-hole defects of different sizes, and (2) surface-mounted mass blocks placed at varying positions. Simulations systematically assess the method's ability to amplify damage-related signals and distinguish them clearly from baseline conditions. The analysis specifically highlights the meta-lens's capability in enhancing the sensitivity toward different damage geometries and locations while maintaining baseline signal consistency.

3.3.1 Damage quantification

In simulations, rectangular through-hole defects of varying lengths (5–20 mm, increments of 2.5 mm) and constant width (1.7 mm) are introduced at the focal point. Fig. 14 illustrates that the amplitude difference at Sensor 2 increases with defect length, as larger defects reflect more wave energy, which the meta-lens subsequently refocuses. Specifically, at the maximum damage length (20 mm), the meta-lens achieves approximately twofold signal amplification. Additionally, the amplitude contrast between different damage sizes is notably enhanced by the meta-lens, highlighting its capability to significantly improve damage-size discrimination compared to scenarios without enhancement.

To better quantify the observed signal differences, the Damage Index (DI),

$$sigDiffRMS = \sqrt{\frac{\int_0^T (f_s - f_b)^2 \, dt}{\int_0^T (f_b)^2 \, dt}} \tag{2}$$

defined as the root-mean-square difference between the sensor signal and the baseline, is calculated within the time window covering the backscattered wave packet. As shown in Figure 5(a), the DI increases with damage length and shows significantly higher contrast when the meta-lens is applied, highlighting its effectiveness in improving damage quantification sensitivity.

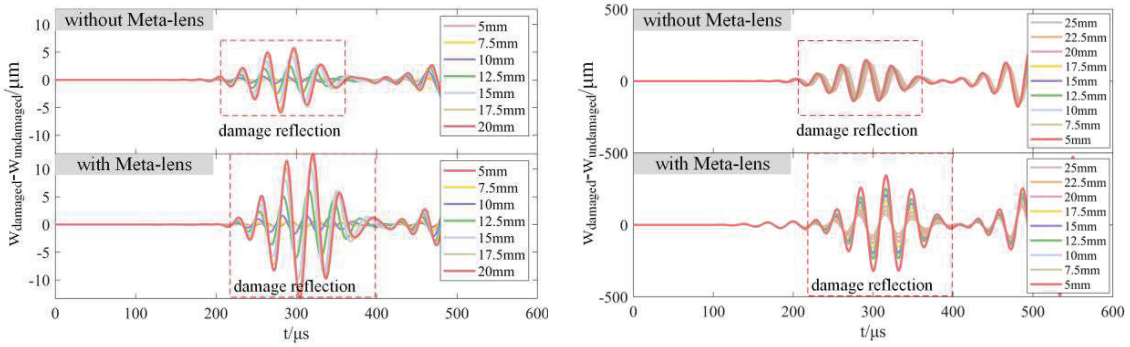

Figure 4: Signals from Sensor 1 and Sensor 2 with different damage lengths (a) and different locations (b)

3.3.2 Damage localization

To examine the ability to identify damage locations, a $12.5\times3.5\times3\text{mm}^3$ stainless-steel mass block is utilized to simulate structural damage instead of a through-hole. The block's vertical position is varied from $x=55\text{mm}, y=5\text{mm}$ to $x=55\text{mm}, y=25\text{mm}$ at intervals of 2.5 mm. As shown in Figure 4(b), signals without the meta-lens exhibit minimal changes across all positions However, with the meta-lens, damage detectability improves significantly because the wave energy distribution peaks along the focal axis and declines rapidly away from it. Thus, as the block moves away from the focal axis, from y = 5 mm to y = 25 mm, fewer reflected waves are produced, resulting in lower signal amplitudes at Sensor 2. This demonstrates the effectiveness of meta-lens in spatially localizing damage based on amplitude differences.

Similarly, Figure 5(b) illustrates how the DI varies with the vertical position of the damage. Without the meta-lens, the DI remains nearly constant, while with the meta-lens, it exhibits a clear monotonic trend, enabling position-based damage characterization. These results confirm the enhanced detectability of the damage when the traditional method for damage identification is used in conjunction with wave-focusing structures.

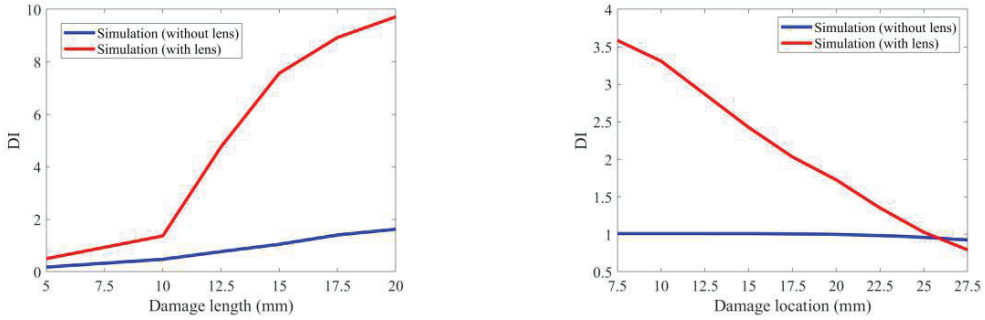

(a) (b)

Figure 5: DI value as damage length changes (a), and location changes (b)

4 DUAL-META-LENS STRATEGY

The capability of a single meta-lens to focus reflected signals and identify damage is verified in Section 3. Once either the size or location of the damage is known, the other can be determined by calculating the corresponding DI. However, in many practical cases, neither the damage location nor size is known in advance, necessitating additional information. Besides, the damage identification is an inverse problem, which might suffer for ill-posedness if no sufficient input information is passed as input for inference. This can be achieved by incorporating more than one sensor and comparing the acquired signals. In this section, a configuration consisting of two meta-lenses arranged in parallel along the vertical axis forming an extended meta-lens is introduced into the base plate, as illustrated in Figure 6. Both meta-lenses are identical to the one designed in Section 2. A $135\times5\text{mm}^2$ actuator is placed 120 mm

away from the lens array to ensure the generation of parallel incident waves. This dual-lens configuration results in two focal points, labeled FP1 and FP2 in Figure 6, which displays a zoomed-in view of the out-of-plane displacement near the meta-lenses at 2.1×10^{-4}s . Two sensors (Sensor 1 and Sensor 2) are positioned symmetrically with respect to these focal points. As discussed in Section 3, the signals collected by Sensors 1 and 2 experience double enhancement, indicating strong potential for damage detection.

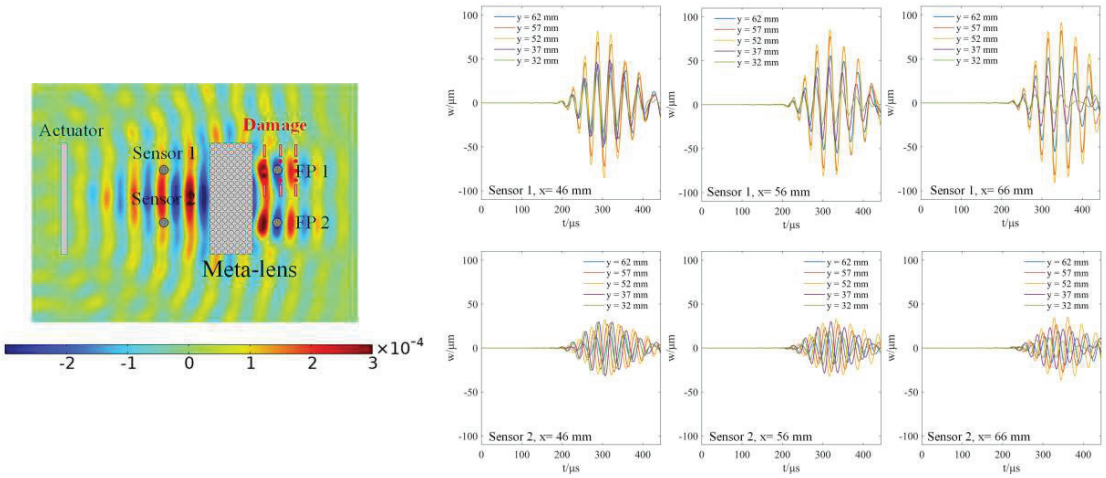

(a) (b)

Figure 6: Out-of-plane displacement (mm) at 2.1×10^{-4}s , with dual meta-lenses (a), and signals from Sensor 1 when the damage moves along x = 46 mm, x = 56 mm, x = 66 mm, and signals from Sensor 2 when the damage moves along x = 46 mm, x = 56 mm, and x = 66 mm (b)

4.1 Signals under damaged case

A $12.5\times1.34\text{mm}^2$ through hole is introduced into the plate at three horizontal positions x = 46 mm, x = 56 mm, and x = 66 mm, and its vertical position is varied from y = 62 mm to y = 32 mm, to simulate damage moving from above to below the upper meta-lens. Similar to the single-lens case, the reflected waves are re-focused by the meta-lens, and the resulting signals at Sensor 1 and Sensor 2 vary depending on the damage position due to the non-uniform energy distribution. As shown in Figure 6, when the damage is near the focal point FP1 y=52 mm, both sensors record the highest amplitudes. As the damage moves away from this point, the signal amplitudes gradually decrease. Sensor 1 consistently records higher amplitudes when the damage is closer to the upper lens, while the amplitudes at Sensor 1 and Sensor 2 become similar when the damage is located lower, due to the symmetry of the configuration. As illustrated in Section 3.3, different damage locations result in distinct signal amplitudes and Time of Flight (ToF) values due to varying wave propagation paths. However, the relationship between these features and the damage location cannot be easily captured using simple analytical functions. Therefore, a machine learning-based damage localization approach is

introduced in the next section due to its superior capability in modeling such complex mappings

4.2 Damage localization

The primary objective of the damage localization task is to establish a mapping between the extracted signal features and the spatial coordinates (x, y) of the damage. To this end, Bayesian inference and Gaussian Process Regression (GPR) are employed, benefiting from their effectiveness in small-sample scenarios and their ability to quantify prediction uncertainty. As illustrated in Figure 7, the red dots represent the training samples, while the yellow cross markers denote the testing samples located at x = 50 mm, y = 43.25mm, x = 58 mm, y = 55.25 mm, x = 62 mm, y = 60.25 mm, and x = 62 mm, y = 36.25 mm. To account for practical noise in signal acquisition, white noise is added to the signals from Sensor 1 and Sensor 2 with signal-to-noise ratios (SNRs) of 10, 50, and 100. The raw sensor signals are analyzed using the continuous wavelet transform (CWT), implemented via a filter bank with a sampling frequency of f_s = 1 MHz over a frequency range of 24 – 36 kHz. For each signal, two key features are extracted: the Time of Flight (ToF), defined as the time corresponding to the peak magnitude of the wavelet coefficient |CWT| within the selected frequency band, representing the arrival time of the main wave packet; and the maximum amplitude, defined as the global maximum of |CWT| across the entire time-frequency domain, indicating the strength of the received signal. These features are extracted from both sensors, yielding four scalar inputs: ToF_1, Amp_1, ToF_2, and Amp_2, which are used as inputs to the regression model. The damage region spanning x = 46–66 mm and y = 30–65 mm is discretized into a 100×100 uniform grid for localization.

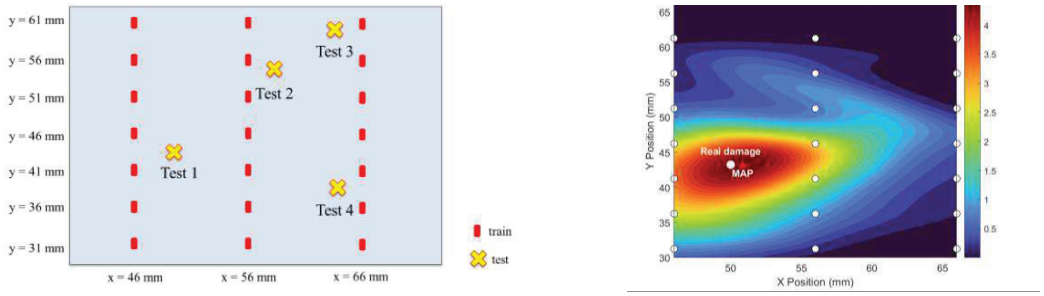

(a) (b)

Figure 7: Training set and testing set in the GPR (a), and the prediction of Test 1 (b)

A multi-output GPR model is constructed to map the four-dimensional feature vector to the corresponding damage coordinates (x,y). The model uses a pure quadratic basis function and a squared exponential kernel, achieving low mean squared error (MSE) under K-fold cross-validation. This approach effectively captures the nonlinear relationship between signal features and damage location and provides predictive uncertainty estimates that are further incorporated into Bayesian inference. As shown in Figure 7(b), the predicted position for Test 1, indicated by a red star, corresponds to the location with the highest posterior probability. The actual damage location is marked by a white dot and labeled as ‘Real damage’, with a

localization error of 1.2 mm, defined as the Euclidean distance between the predicted and true locations. In Figure 8, the horizontal axis represents different test scenarios (Test 1–4), while the vertical axis shows the mean localization errors averaged over 50 independent noise realizations. The dark-blue bars correspond to the predictions without the meta-lens, and light-blue bars represent the results with the meta-lens. This comparison highlights the effectiveness of the meta-lens in improving localization accuracy. By enhancing signal characteristics and amplifying the variations caused by different damage positions, the meta-lens contributes to both detectability and localization sensitivity, demonstrating its functional role in SHM.

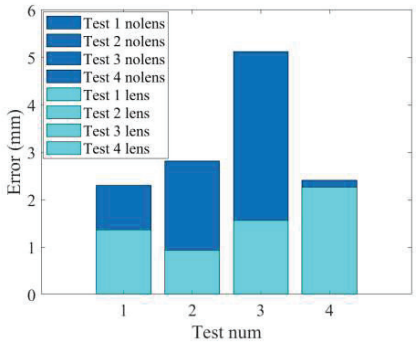

Figure 8: Mean errors of 50 times of prediction of the four test points

5. CONCLUSION

In summary, this study demonstrates the capability of a meta-lens to enhance Lamb wave signals for effective damage detection and localization. A single meta-lens is designed on an aluminum plate to amplify backscattered waves, thereby enabling the correlation between the DI and both damage length and position. Different sensor strategies are evaluated, with the optimal arrangement identified at the reflected focal point, where the double-enhanced signal is captured without affecting the baseline. By selectively amplifying damage-related components and redistributing wave energy, damage identification becomes more straightforward. The proposed DI exhibits a monotonic and more sensitive relationship with damage properties. To further improve localization accuracy and eliminate dependence on prior damage size information, a dual-meta-lens configuration is introduced. By placing sensors at the two focal points, the upper edge of the damage is estimated through joint analysis of the signal features and Bayesian inference over candidate locations. The use of the meta-lens not only amplifies relevant wave components but also enhances the variability of features across different damage positions, enabling more accurate localization using stronger and more informative signals.

REFERENCES

[1] V. R. Gharehbaghi, E. Noroozinejad Farsangi, M. Noori, *et al.*, "A critical review on structural health monitoring: Definitions, methods, and perspectives," *Arch. Comput. Methods Eng.*, vol. 29, no. 4, pp. 2209–2235, 2022.

[2] W. Fan and P. Qiao, "Vibration-based damage identification methods: A review and comparative study," *Struct. Health Monit.*, vol. 10, no. 1, pp. 83–111, 2011.

[3] M. Mitra and S. Gopalakrishnan, "Guided wave based structural health monitoring: A review," *Smart Mater. Struct.*, vol. 25, no. 5, p. 053001, 2016.

[4] S. V. Vaseghi, *Advanced Digital Signal Processing and Noise Reduction*, 4th ed. Chichester, U.K.: Wiley, 2008.

[5] G. Dobie, A. Spencer, K. Burnham, *et al.*, "Simulation of ultrasonic Lamb wave generation, propagation and detection for a reconfigurable air coupled scanner," *Ultrasonics*, vol. 51, no. 3, pp. 258–269, 2011.

[6] S. W. Smith, *Digital Signal Processing: A Practical Guide for Engineers and Scientists*, Burlington, MA, USA: Newnes, 2003.

[7] S. Liu, Z. Ma, J. Pei, *et al.*, "A review of anomalous refractive and reflective metasurfaces," *Nanotechnol. Precis. Eng.*, vol. 5, no. 2, 202.

[8] X. Fang, W. Lacarbonara, and L. Cheng, "Advances in nonlinear acoustic/elastic metamaterials and metastructures," *Nonlinear Dyn.*, pp. 1–28, 2024.

[9] G. Lee, S. J. Lee, J. Rho, *et al.*, "Acoustic and mechanical metamaterials for energy harvesting and self-powered sensing applications," *Mater. Today Energy*, vol. 37, p. 101387, 2023.

[10] Y. Tian, Y. Shen, D. Rao, and W. Xu, "Enhanced identifiability of nonlinear ultrasonic superharmonics for crack detection using an aluminum-lead composite bandgap meta-surface," in *Proc. SPIE Health Monitoring of Structural and Biological Systems XIII*, vol. 10972, pp. 408–414, 2019.

[11] M. Kabir, A. Mostavi, and D. Ozevin, "Noise isolation with phononic crystals to enhance fatigue crack growth detection using acoustic emission," *J. Civil Struct. Health Monit.*, vol. 8, pp. 529–542, 2018.

[12] J. Zhao, B. Bonello, and O. Boyko, "Focusing of the lowest-order antisymmetric Lamb mode behind a gradient-index acoustic metalens with local resonators," *Phys. Rev. B*, vol. 93, no. 17, p. 174306, 2016.

[13] A. Zareei, A. Darabi, M. J. Leamy, *et al.*, "Continuous profile flexural GRIN lens: Focusing and harvesting flexural waves," *Appl. Phys. Lett.*, vol. 112, no. 2, 2018.

[14] S. Tol, F. L. Degertekin, and A. Erturk, "3D-printed phononic crystal lens for elastic wave focusing and energy harvesting," *Addit. Manuf.*, vol. 29, p. 100780, 2019.

[15] K. K. Amireddy, K. Balasubramaniam, and P. Rajagopal, "Holey-structured metamaterial lens for subwavelength resolution in ultrasonic characterization of metallic components," *Appl. Phys. Lett.*, vol. 108, no. 22, 2016.

[16] G. Okudan, H. Danawe, D. Ozevin, *et al.*, "Torsional wave focusing in cylindrical structures with the conformal gradient-index phononic crystal lens," *J. Appl. Phys.*, vol. 129, no. 17, 2021.

[17] Y. Jin, W. Wang, A. Khelif, *et al.*, "Elastic metasurfaces for deep and robust subwavelength focusing and imaging," *Phys. Rev. Appl.*, vol. 15, no. 2, p. 024005, 2021.

XI ECCOMAS Thematic Conference on Smart Structures and Materials - SMART 2025
M. Krommer, M. Nader and M. Schagerl (Eds)

Received: 30 March 2025 / Revised: 29 August 2025 / Accepted: 27 September 2025
© The Author(s) 2025

On the Use of Piezoelectric Flags for Fluid Flow Sensing

Dheeraj Tripathi, Mehdi Ghommem, Abdessattar Abdelkefi, Lotfi Romdhane

Abstract. Piezoelectric flags, widely studied for energy harvesting, provide a robust and self-powered alternative for remote sensing due to their simplicity and ability to operate without specific alignment with the flow direction. To that end, we propose a flow sensing framework using flexible piezoelectric flags. A Macro-Fiber Composite (MFC) patch is attached to a thin steel flag to generate electrical signals through piezoelectric coupling. Wind tunnel tests are performed on this piezoelectric flag in controlled conditions for a flow speed range of 5.0 - 9.0 m/s and an angle of attack (AoA) range of 0° - 15°. The piezoelectric flag exhibits rich dynamic behavior, demonstrating sensitivity to both flow speed and AoA. Dynamic features like root mean square voltage (V_{rms}) and signal frequency show a nonlinear dependence on flow speed as well as AoA, establishing the basis for the proposed framework. A deep neural-network is trained on V_{rms} and frequency data at various speeds and AoA. The model shows a good accuracy with coefficient of determination (R^2) close to 0.95 for the test data.

Key words: Flow sensing, MFC, Neural network, Aeroelastic flutter, Piezoelectric flag

1 INTRODUCTION

Existing flow-sensing devices, such as anemometers and ultrasonic sensors, require external power sources and often face limitations related to durability and directional sensitivity. These challenges make them unsuitable for remote and autonomous applications, such as gas pipes, air-conditioning systems and unmanned aerial vehicle (UAV) control. Flow sensing in confined spaces and remote environments presents challenges due to the need for a continuous power supply and uninterrupted monitoring. Aeroelastic structures that exhibit self-induced flutter offer a viable alternative, as they can operate independently without an external power source.

Dheeraj Tripathi & Mehdi Ghommem & Lotfi Romdhane
Mechanical Engineering, American University of Sharjah, Sharjah, UAE, e-mail: dtripathi@aus.edu

Abdessattar Abdelkefi
Department of Mechanical and Aerospace Engineering, New Mexico State University, USA
e-mail: abdu@nmsu.edu

These structures harness mechanical vibration energy from the ambient flow, eliminating the need for a continuous power supply and can be integrated into highly confined spaces. They also offer significant flexibility in size, allowing them to be tailored for specific application requirements.

Thin flexible structures, such as flags or sheets, undergo flutter when subjected to critical flow speeds [1, 2]. This aeroelastic flutter manifests as sustained limit cycle oscillations (LCOs) due to the inherent nonlinear nature of fluid-structure interaction. Fluttering flags or sheets equipped with electro-mechanical couplings like piezoelectric or triboelectric coupling can offer dual functionality, acting as flow sensors while simultaneously harvesting energy. While the flutter of thin flexible structures has been extensively explored in the context of energy harvesting [3, 4, 5, 6, 7], its potential for sensing applications remains relatively underexplored. The electro-mechanical responses from self sustained LCOs induced by ambient flow can be directly correlated with flow characteristics such as velocity, wind direction and turbulence intensity. This dual functionality eliminates the need for an external power source, making them suitable for remote and autonomous sensing applications. For instance, Fuh et al. [8] developed a self-sustained flow sensing system using polymeric piezoelectric polyvinylidene fluoride nano/microfibers, demonstrating the feasibility of piezoelectric materials in flow sensing. Wang et al. [9] introduced a flag-based triboelectric nanogenerator for self-powered flow sensing.

Typically available flow measurement instruments, such as anemometers and ultrasonic sensors, require continuous monitoring and are direction-specific. This means they must be properly aligned with the flow direction to ensure accurate flow speed measurements. In contrast, fluttering flags offer a promising alternative, as they can operate at various alignments with the flow while exhibiting dynamic characteristics that depend on the angle of attack (AoA) [10]. This feature presents an opportunity to explore the potential of flow-induced oscillating flags for simultaneous flow speed and AoA sensing by exploiting the voltage signals generated by a fluttering piezoelectric flag (piezo-flag) as indicators of flow parameters. To this end, a piezo-flag-based sensing system is developed in this study for flow speed and AoA measurement. We employ a deep neural network for flow speed and AoA prediction. Given the limited dataset, neural networks have demonstrated better performance compared to other conventional approaches such as linear regression and support vector regression [11]. Hence a feedforward neural network is trained on wind tunnel test data and subsequently evaluated. The remainder of the paper is organized as follows: Section 2 describes the methodology for experimental data acquisition and the data-driven sensing framework. Section 3 presents the results and discussion, including flow speed and AoA sensing. Finally, Section 4 summarizes the key findings.

2 METHODOLOGY

The study is conducted in two stages. The first stage involves data acquisition from wind tunnel experiments, while the second focuses on developing a neural network-based framework for predicting flow speed and AoA, trained using the experimental data. The overall workflow is summarized in Fig. 1. The wind tunnel tests are performed on a piezo-flag, capturing flow speed, voltage, and displacement data. The acquired data is post-processed to extract key

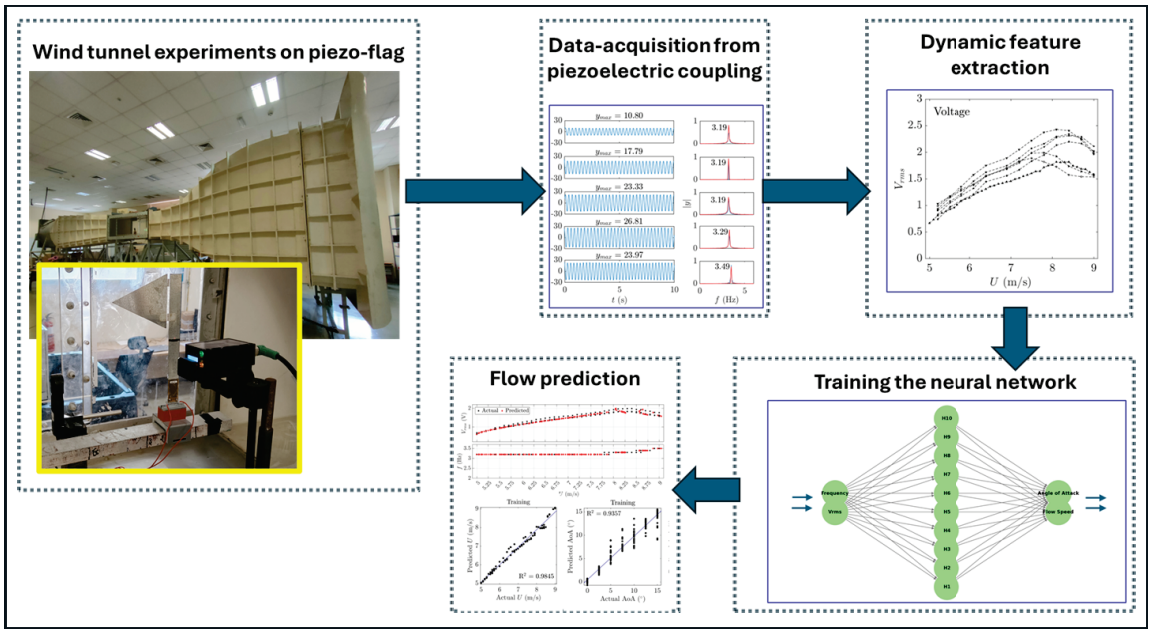

Figure 1: Framework for flow sensing using dynamic responses of a piezo-flag.

dynamic features, including frequency components, estimated using the fast Fourier transform (FFT). These features are then utilized to train the neural network. Finally, the predictive capability of the trained model for flow speed and AoA is validated and tested. The wind tunnel used in this study is a low-speed, open-type facility at the American University of Sharjah, with a test section measuring 0.75 m × 0.9 m × 1.8 m. The experimental setup consists of a piezo-flag, which is a cantilevered steel beam with an attached triangular flag. The piezo-flag comprises a 0.3 mm thick steel beam with dimensions 20 cm × 2 cm, vertically fixed at its base. The free end carries a triangular shaped steel flag (0.3 mm thick, 8 cm base, and 8 cm height), connected to the beam via nylon hinges in an L-configuration. This triangular flag design facilitates lower flutter onset speeds and higher oscillation amplitudes [12], making it well-suited for piezoelectric voltage generation over a broad range of flow speeds. At the base of the beam, a macro fiber composite (MFC) piezoelectric patch (M2814-P2MFC, Manufact.: *Smart Material Corp.*) is deposited. The MFC is a P2-type, operating via the d_{31} effect, commonly used for energy harvesting applications [13]. The active area of the patch is 28 mm × 14 mm. As the flag undergoes self-induced flutter beyond a critical speed, the MFC generates an open-circuit voltage $V(t)$, which is recorded using a *PicoScope (2000 Series)*. The root mean square (RMS) voltage is computed as $V_{rms} = \sqrt{1/T \int_0^T v^2(t)dt}$. In addition to voltage signals, displacement signals $y(t)$ from the flag's bending oscillations are recorded to assess the coherence between flag vibrations and the piezoelectric output voltage. These oscillations are measured using a *Baumer-OM70* laser displacement sensor. The natural frequency of the flag, determined from

wind-off free vibration tests, is 3.25 Hz for the first bending mode, with negligible torsional vibrations in both wind-off and wind-on conditions. Flow speed inside the test section is measured using a *Vernier* anemometer positioned near the flag, with a measurement tolerance of ± 0.3 m/s for flow speeds up to 12.0 m/s. To ensure repeatability, the coefficient of variation (CoV) from five repeated trials is evaluated, yielding: $< 5\%$ for V_{rms} measurements, $< 3\%$ for bending amplitude measurements, and $< 1.5\%$ for flutter speed measurements. Further details on the experimental setup are available in our previous studies [12, 2].

The data is acquired for a flow speed range of 5.0–9.0 m/s. Note that, 5.0 m/s is the minimum flow speed at which flutter occurs in the flag. Subsequent to the data acquisition from the wind tunnel experiments, key dynamic features such as frequency and V_{rms} are extracted and used as inputs for a feed-forward neural network. The network is implemented using MATLAB's *feedforwardnet* toolbox [14]. The dataset is composed of six trials, with four trials used for training and one trial for validation. Finally, the trained model is tested using the unseen data from the sixth trial to assess its predictive performance. The network employs a sigmoid activation function (logsig) for the hidden layers and a linear activation function (purelin) for the output layer. The mean squared error (MSE) is used as the loss function, and the Levenberg-Marquardt optimization algorithm [15] is implemented to minimize the error.

3 RESULTS AND DISCUSSION

The study is conducted in two parts: the first focuses on flow speed measurement at zero AoA, while the second examines AoA estimation at different flow speeds. Together, these two parts constitute the proposed sensing framework.

3.1 FLOW SENSING

The experiments are conducted with the piezo-flag positioned at zero angle of attack, ensuring alignment parallel to the test section windows. The flow speed is varied with a small increment of 0.1 m/s. Flutter is observed in the piezo-flag within the flow speed range of 5.0–9.0 m/s, although a mechanical perturbation is required to initiate oscillations at 5.0 m/s due to the subcritical bifurcation behavior of the flag [12]. Alternatively, flutter at such low speeds can be triggered by introducing flow modifications [2]. However, this study focuses solely on streamlined flow conditions, and such effects are not considered.

The simultaneous voltage (V) and bending oscillation (y) responses are shown in Fig. 2. The V_{rms} gradually increases from 0.73 V to 1.93 V as the flow speed increases from 5.0 to 9.0 m/s, while the maximum bending amplitude (y_{max}) ranges from 10.80 mm to 26.81 mm in this flow speed range. Both the voltage and displacement signals remain periodic across the tested range, showing a single dominant frequency of oscillation. The flutter frequency gradually increases with flow speed while remaining close to the flag's bending natural frequency. FFT analysis of the aeroelastic and piezoelectric responses in Fig. 2 shows that the dominant peak shifts from 3.19 Hz at 5 m/s to 3.49 Hz at 9 m/s. This gradual rise in the dominant frequency is attributed to the combined effect of positive aerodynamic stiffness and negative aerodynamic damping with

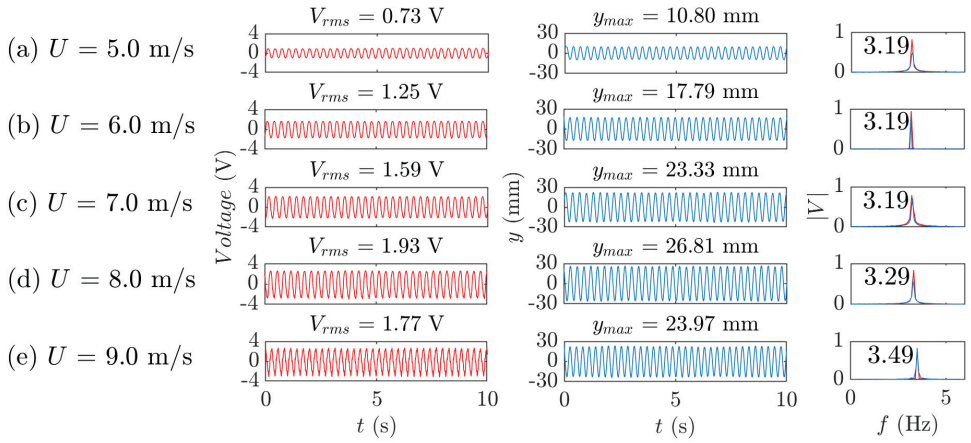

Figure 2: Voltage and aeroelastic responses of the piezo-flag at 0° AoA.

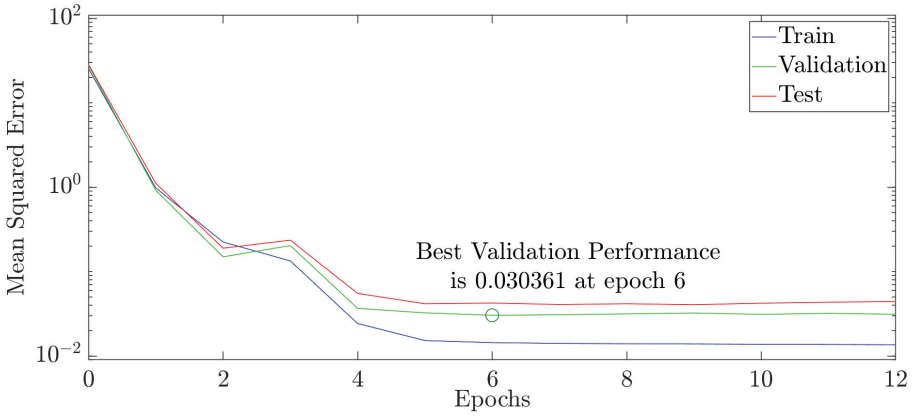

Figure 3: The mean squared error loss in flow speed prediction model.

increasing flow speed, consistent with observations across aeroelastic systems [16].

For flow sensing, periodic signals are preferred over chaotic or aperiodic ones, as the latter exhibit unpredictable long-term behavior, whereas periodic signals have a well-defined and stable long-term response. The dominant frequency of both the electrical and aeroelastic signals remains perfectly aligned across the entire flow speed range, indicating robust electromechanical coupling. This alignment suggests that the system can be reliably used for accurate flow prediction.

Four trials of experimental data, covering a flow speed range from 5.0 to 9.0 m/s with 0.1 m/s increments, are used to train a feed-forward neural network. The network consists of one input and one output layer, with three hidden layers containing 20, 15, and 10 neurons, respectively. The mean squared error (MSE) is used as the loss function for optimization. Its variation over

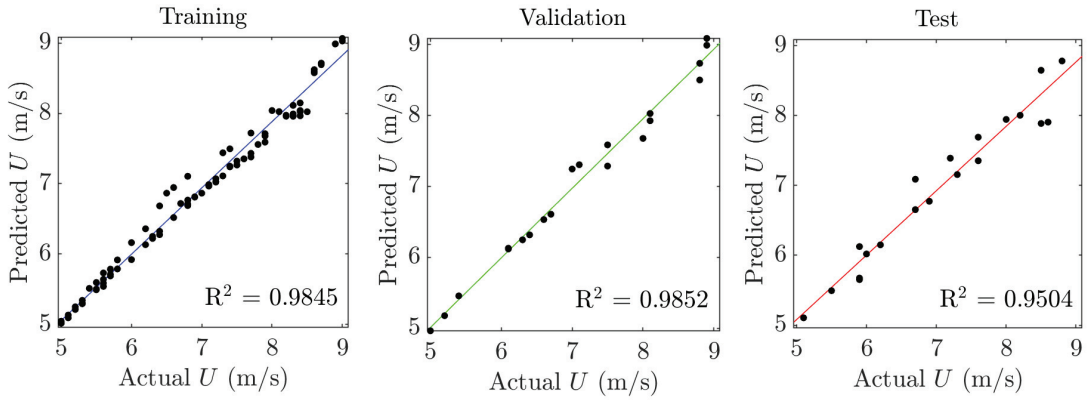

Figure 4: Regression plots of training, validation and test data for flow speed sensing.

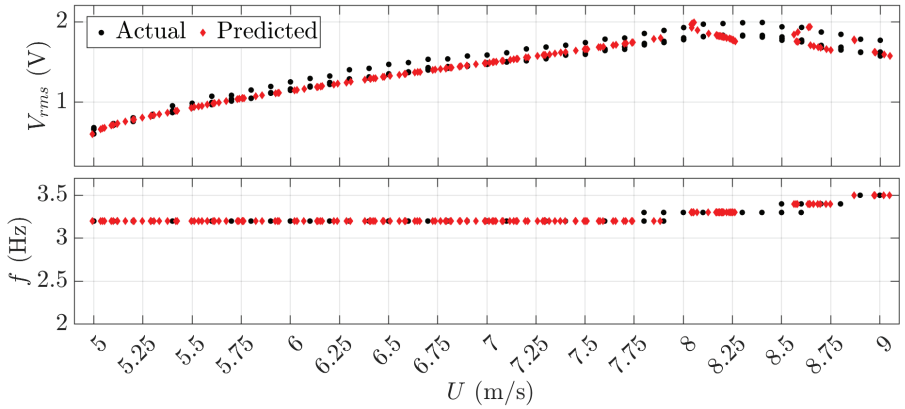

Figure 5: Actual vs predicted speed.

12 epochs is shown in Fig. 3. The minimum loss is observed at the sixth epoch, with an MSE close to 0.03.

The regression plots for training, validation, and testing are shown in Fig.4. The coefficient of determination (R^2) is used as a quantitative marker for accuracy. For training, R^2 is 0.9845. The fifth trial, used for validation, shows good accuracy, with an R^2 value of 0.9852. Finally, the unseen sixth trial is used to test the network, yielding an R^2 value of 0.9504. The predicted flow speeds from the sixth trial are plotted against the actual data from the first four trials in Fig.5, showing the variation of V_{rms} and frequency with flow speed. It can be seen that the predicted speeds closely match the actual values. A slight variation between 8.2 and 8.5 m/s in actual versus predicted values is observed, which can be attributed to the nonlinearity associated with the V_{rms} versus flow speed trend in this range. This discrepancy could be minimized with a larger dataset in this specific range.

3.2 ANGLE OF ATTACK SENSING

In the second part of the study, the angle of attack (AoA) is varied along with the flow speed. The AoA ranges from 0 to 15 degrees in increments of 2.5 degrees, while the flow speed varies from 5.2 to 9.0 m/s in steps of 0.3 m/s, resulting in a large dataset. The variation of V_{rms} and the dominant signal frequency with flow speed at different AoA values is shown in Fig. 6. The variation of V_{rms} with AoA is highly nonlinear, initially increasing up to 7.5 degrees before decreasing. With respect to flow speed also, V_{rms} exhibits nonlinear behavior, increasing linearly up to a peak value at a certain speed and then decreasing linearly. In contrast, the dominant frequency remains within a narrow range across all AoA and flow speed conditions. A deep neural network, structured similarly to the one used for flow speed prediction, is trained with four trials of data for each of the seven AoA values. Each trial consists of V_{rms} and frequency values for flow speeds 5.2 - 9.0 m/s with 0.3 m/s increments. The model is subsequently validated and tested using one additional trial each.

The MSE loss for training, validation and test is shown in Fig.7 over 22 epochs. The best validation performance is observed at 16th epoch with MSE close to 1.37. Note that this MSE is higher than that observed for flow speed validation model. The corresponding regression plots are shown in Fig. 8. For training, the R^2 value is observed as 0.9357 from the four trials, while for validation and testing the R^2 is found as 0.9407 and 0.9545 respectively, obtained from the fifth and sixth trials. Here both the MSE and R^2 values are lower than those observed during the flow measurements at zero AoA. This demands future studies incorporating a larger number of trials with more refined AoA data to improve prediction accuracy.

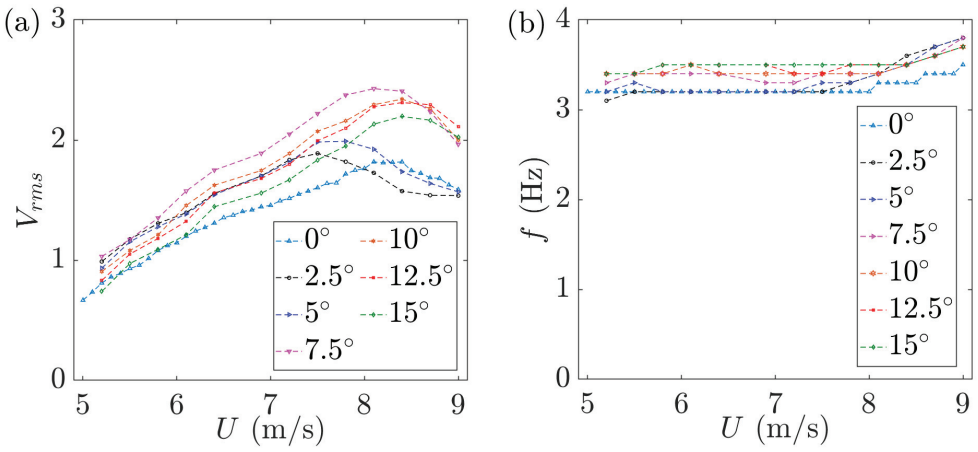

Figure 6: Variation of V_{rms} and signal frequency of the piezo-flag with flow speed at different AoA.

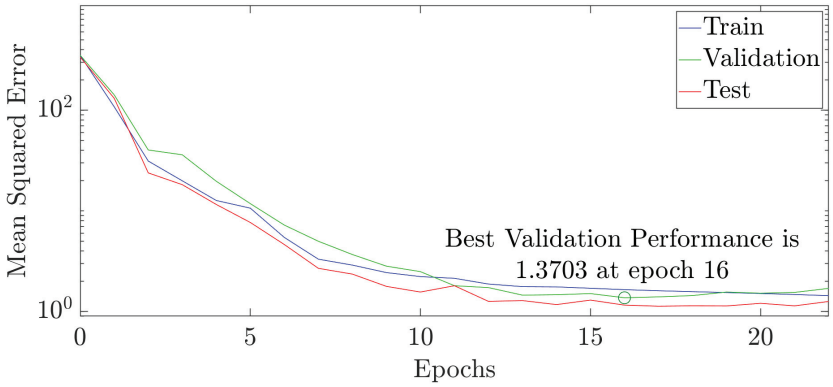

Figure 7: The mean squared error loss in AoA prediction model.

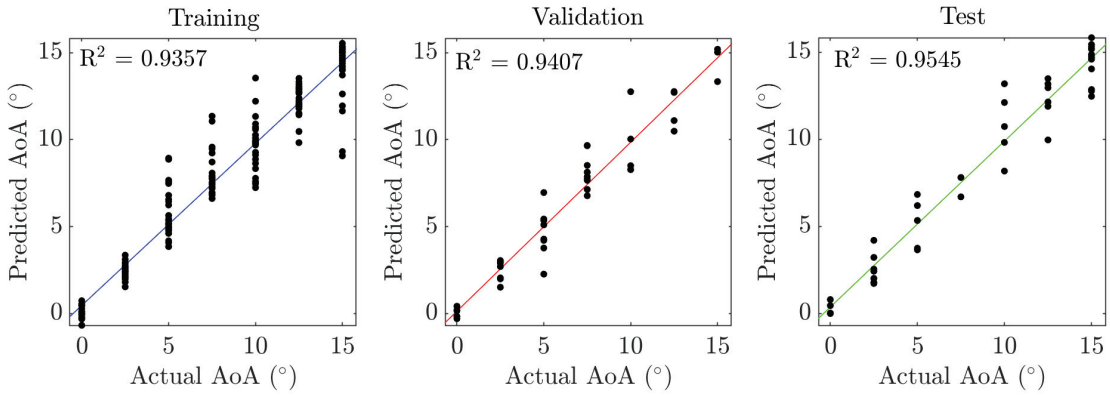

Figure 8: Regression plots of training, validation and test data for AoA sensing..

4 CONCLUSIONS

This study proposes a data-driven dual sensing framework for flow speed and direction measurement. Wind tunnel experiments are conducted to collect data over a flow speed range of 5.0–9.0 m/s and an angle of attack (AoA) range of (0 - 15 °). The experimental data provides voltage signals, from which dynamic features such as V_{rms} and signal frequency are extracted to develop the sensing framework. The acquired data from multiple trials is used to train a feedforward neural network with three hidden layers. For flow speed prediction, the network achieves an R^2 value above 0.98 for training and validation and approximately 0.95 for testing. For AoA prediction, the model demonstrates an R^2 value close to 0.94 for training and validation and 0.95 for testing. Overall, this study establishes a foundation for dual sensing in flow measurement applications such as UAVs, gas pipelines, and air supply systems. The self-powering capability of these sensors provides avenues for developing fully passive sensors that

can operate independently of an external power source. Future work can extend this approach to a broader range of speeds and refined flow conditions to enhance precision.

REFERENCES

[1] D. Kumar, K. Poddar, and S. Kumar, "The effect of aspect ratio and mass ratio on the flow-induced flutter of a thin flexible sheet," *Physics of Fluids*, vol. 36, no. 11, 2024.

[2] D. Tripathi, M. Ghommem, A. Abdelkefi, L. Romdhane, and G. C. Bourantas, "Dynamic aeroelastic response of a slender triangular flag behind bluff bodies of varying shapes," *Journal of Fluids and Structures*, vol. 133, p. 104269, 2025.

[3] S. Orrego, K. Shoele, A. Ruas, K. Doran, B. Caggiano, R. Mittal, and S. H. Kang, "Harvesting ambient wind energy with an inverted piezoelectric flag," *Applied energy*, vol. 194, pp. 212–222, 2017.

[4] M. Eugeni, H. Elahi, F. Fune, L. Lampani, F. Mastroddi, G. P. Romano, and P. Gaudenzi, "Numerical and experimental investigation of piezoelectric energy harvester based on flag-flutter," *Aerospace Science and Technology*, vol. 97, p. 105634, 2020.

[5] A. Mujtaba, U. Latif, E. Uddin, M. Y. Younis, M. Sajid, Z. Ali, and A. Abdelkefi, "Hydrodynamic energy harvesting analysis of two piezoelectric tandem flags under influence of upstream body's wakes," *Applied Energy*, vol. 282, p. 116173, 2021.

[6] Y. Zhang, S.-C. Fu, K. C. Chan, D.-M. Shin, and C. Y. Chao, "Boosting power output of flutter-driven triboelectric nanogenerator by flexible flagpole," *Nano Energy*, vol. 88, p. 106284, 2021.

[7] U. Latif, E. H. Dowell, E. Uddin, M. Younis, and H. Frisch, "Comparative analysis of flag based energy harvester undergoing extraneous induced excitation," *Energy*, vol. 295, p. 130995, 2024.

[8] Y.-K. Fuh, P.-C. Chen, Z.-M. Huang, and H.-C. Ho, "Self-powered sensing elements based on direct-write, highly flexible piezoelectric polymeric nano/microfibers," *Nano Energy*, vol. 11, pp. 671–677, 2015.

[9] Y. Wang, E. Yang, T. Chen, J. Wang, Z. Hu, J. Mi, X. Pan, and M. Xu, "A novel humidity resisting and wind direction adapting flag-type triboelectric nanogenerator for wind energy harvesting and speed sensing," *Nano Energy*, vol. 78, p. 105279, 2020.

[10] J. Cossé, J. Sader, D. Kim, C. H. Cerdeira, and M. Gharib, "The effect of aspect ratio and angle of attack on the transition regions of the inverted flag instability," in *Pressure Vessels and Piping Conference*, vol. 46018. American Society of Mechanical Engineers, 2014, p. V004T04A046.

[11] M. Ghommem, V. Puzyrev, R. Sabouni, and F. Najar, "Deep learning for gas sensing using mofs coated weakly-coupled microbeams," *Applied Mathematical Modelling*, vol. 105, pp. 711–728, 2022.

[12] D. Tripathi, M. Ghommem, A. Abdelkefi, L. Romdhane, and G. C. Bourantas, "Analysis of flutter dynamics in thin flexible flags under streamlined and vortex-induced flows," *Physics of Fluids*, vol. 36, no. 12, 2024.

[13] T. P. Daue, J. Kunzmann, and A. Schönecker, "Energy harvesting systems using piezoelectric macro fiber composites," in *IEEE International Symposium on Electrets (ISE13), paper*, vol. 27, 2008.

[14] MathWorks, "Feedforward neural network," 2025, [accessed 30-Mar-2025]. [Online]. Available: https://www.mathworks.com/help/deeplearning/ref/feedforwardnet.html

[15] A. Ranganathan, "The levenberg-marquardt algorithm," *Tutoral on LM algorithm*, vol. 11, no. 1, pp. 101–110, 2004.

[16] D. Tripathi, R. Shreenivas, C. Bose, S. Mondal, and J. Venkatramani, "Experimental investigation on the synchronization characteristics of a pitch-plunge aeroelastic system exhibiting stall flutter," *Chaos: An Interdisciplinary Journal of Nonlinear Science*, vol. 32, no. 7, 2022.

Part XVII
GS - GENERAL SESSIONS
Michael Krommer, Manfred Nader, Martin Schagerl

XI ECCOMAS Thematic Conference on Smart Structures and Materials - SMART 2025
M. Krommer, M. Nader and M. Schagerl (Eds)

Received: 31 March 2025 / Revised: 27 August 2025 / Accepted: 4 November 2025
© The Author(s) 2025

Finite Element Modelling and Experimental Validation of Endovascular Nitinol Stents: A Pathway to Additive Manufacturing Optimization

Alberto Bellelli, Farzaneh Hoseini, Luke Mizzi, Andrea Spaggiari

Abstract. Nitinol (NiTi) is renowned for its unique properties, such as superelastic behaviour, which make it particularly suitable for medical devices, including endovascular stents. This study focuses on the modelling, simulation, and experimental testing of self-expanding NiTi stents, with the aim of exploring new strategies for design optimization enabled by additive manufacturing (AM). By combining AM with advanced numerical simulations, complex and customised stent geometries can be developed, overcoming the limitations of conventional manufacturing techniques and enabling improved fabrication processes and performance assessment. An integrated experimental–computational approach is adopted to characterize the mechanical response of a commercial self-expanding NiTi stent used as a case study. In particular, two key mechanical performance metrics are considered: bending compliance and crush resistance. Material parameters are identified by adapting a literature-based constitutive framework through a fitting procedure that combines experimental testing and finite element modelling in Abaqus. The calibrated model is then employed to propose alternative stent designs compatible with additive manufacturing constraints. The results provide valuable insight into the mechanical behavior of self-expanding stents and highlight the potential of additive manufacturing as an effective tool for stent performance optimization.

Keywords: Self-expanding stent, Nitinol, Finite element modelling, additive manufacturing.

1 INTRODUCTION

Endovascular stents are a specific class of stent primarily used to treat vascular pathologies, excluding coronary conditions. This study focuses on the prominent category of endovascular stents: self-expanding (SX) Nitinol (NiTi) stents [1]. SX stents are engineered to expand upon deployment within the vessel autonomously, leveraging the inherent superelastic properties of NiTi. These stents are crimped onto a delivery system housed within a sheath and positioned accordingly. Upon release from the delivery system, the sheath is removed, allowing the stent to expand until it contacts the vessel wall, exerting outward pressure to maintain vessel patency. SX stents are intended for permanent placement, providing long-term support, preventing vessel recoil, and ensuring sustained patency. [2].

Before SX stent insertion, angioplasty or other vessel preparation techniques may be employed for several reasons: to dilate narrowed arteries at the lesion site, facilitate optimal stent positioning and deployment, debulk atherosclerotic plaque to create space for stent placement, and mitigate the risk of complications. This preparatory step is especially critical in

Alberto Bellelli & Farzaneh Hoseini & Luke Mizzi & Andrea Spaggiari
Department of Engineering Sciences and Methods, University of Modena and Reggio Emilia, Via Amendola 2-42122 Reggio Emilia, Italy, e-mail: andrea.spaggiari@unimore.it

cases involving calcified lesions or tortuous vessels. Frequently, SX stents necessitate post-dilation balloon angioplasty to achieve full expansion and proper apposition against the arterial wall.

The defining feature of these devices is their material properties, which allow for significant recoverable deformation (up to 5-8%) compared to other metals, an essential characteristic for accommodating physiological movements. [3]. The stent must maintain vessel openness while exerting sufficient force in position, possess adequate stiffness to prevent recoil, and be capable of substantial radial compression for endovascular insertion. Furthermore, it should exhibit flexibility to navigate vessel curvatures and resist fatigue loading. [4]. These mechanical requirements, alongside clinical considerations not addressed in this analysis, render the design of SX stents complex and an excellent candidate for optimization through modern manufacturing techniques. The traditional manufacturing method for these devices is the laser ablation of NiTi tubes of very thin thickness. [5], obtaining a very fine net structure with a large part of the material wasted in the process. The use of additive manufacturing provides an alternative as a net-shape method to save material, and moreover, it opens the possibility to tailor the stent dimension to the patient's needs [6], [7], [8]. This possibility is crucial to increase the efficacy of the device, which must be oversized on the artery diameter to ensure a certain degree of pressure on the vessel wall. Having only off-the-shelf dimensions for the stent diameter, forces the surgeon to operate a trade-off choice between high oversizing (which could lead to inflammation) and low oversizing (which could lead to recoiling of the vessel) [9]. The use of ordered or auxetic disordered metamaterial structures may help in improving the performance of these devices, especially in terms of foreshortening after deployment.

This work aims at evaluating and optimizing the performance of an SX NiTi stent in terms of the main mechanical figures of merit, considering aspects of its performance linked to the physiological behavior and to its manufacturing with additive manufacturing techniques.

2 MATERIALS AND METHODS

The mechanical specifications important for an SX stent heavily depend on its deployment inside the vessel and on the superelastic curve of the material. A good explanation of the deployment is described in [10], **Figure 1** shows a schematic to clarify this point by showing normalized radial forces (N/mm) on the stent and on the vessel, with respect to their diameters (mm), in three phases of stent deployment. The blue line depicts the initial crimping of the stent, from a completely uncrimped stent (initial stent diameter, D_{si} , no radial force on it (point **A)**, to a crimped state (minimum diameter D_{sc} , point **B**). This force, which reaches its maximum in point B, is the radial resistive force (**RRF**). Upon release from the sheath, the stent expands until it encounters the inner wall of the vessel at point **C**. From this point the force on the vessel increases until the stent and the vessel find a first equilibrium diameter, D_e (point **D**). Further expansion is then possible through balloon angioplasty, extending the stent to point **E**, which in turn causes the vessel to expand to the same diameter (point **E'**). Following balloon deflation, compressive force from the vessel is exerted on the stent, causing it to recoil to the diameter D'_e at point **F** due to typical stress strain curve of NiTi. This point provides the final equilibrium in the force displacement diagrams and gives one of the crucial parameters of the stent, the so-called chronic outward force (**COF**). Other important mechanical parameters of the stent are the crush resistance (**CR**) and the bending compliance (**BC**). The first is linked to its ability to sustain load when compressed radially and while the second is fundamental since having a compliant stent makes it easier to deploy and capable of sustaining larger physiological movement.

This four main mechanical figures of merits of a SX NiTi stent are in partial conflict, as already reported in [11], especially increasing the compliance lowers the RRF and the CR so the optimal structure which can be pursued in this investigation finds a trade-off between these four parameters, which are investigated through numerical finite element analyses and once a solution is found the capability of AM can be exploited to prototype the structure.

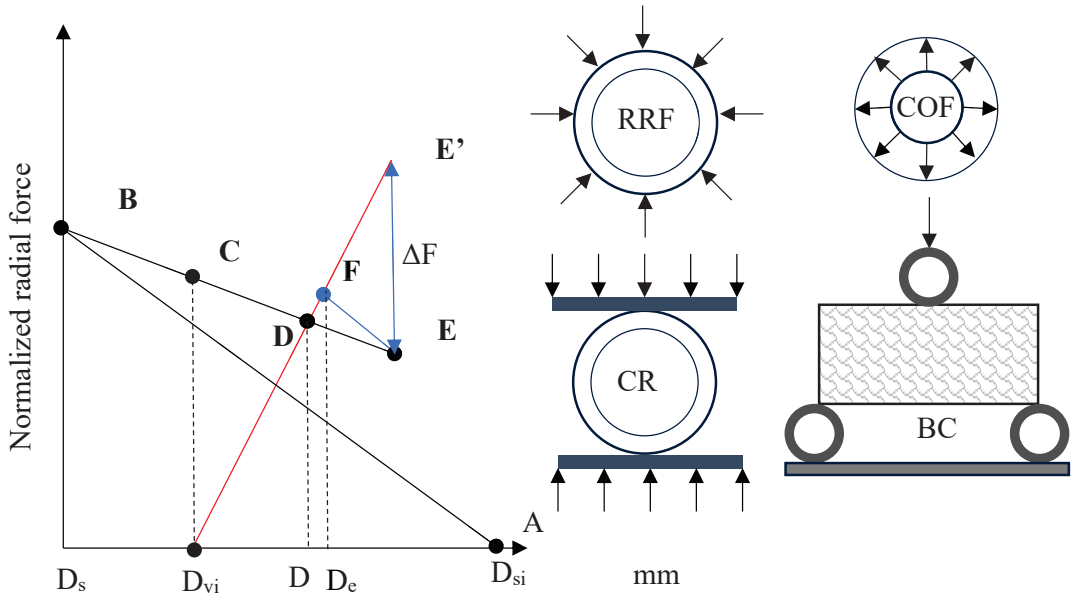

Figure 1: Stent deployment mechanics on the left and schematic representation of COF, RRF, CR and BC on the right

To estimate the behavior of a realistic solution for the stent parametric analysis, a commercial stent was analyzed in detail. The Scitech SOLARIS is a flexible self-expanding endograft, comprised of a thin PTFE membrane encapsulating a Nitinol stent structure, used in the peripheral district [12]. The device has been engineered to provide a higher multidirectional resistance force, high compliance, balanced radial force and low shortening rate. Due to some problems linked to the unexpected rupture of this device when deployed in the popliteal district [13] we envision the need for a structured analysis and optimization of this product, even though the methodology is general and can be applied to each commercial stent. First, a detailed analysis of Solaris stent is carried out by using both microscopy and mechanical tests; then a digital twin is created through the CAD Solidworks, and a series of Finite Elements simulations are carried out to mimic the real structure behavior. The material model, which is a Souza-Auricchio superelastic model already present in the software, is fitted on the experimental curves, and a parametric numerical analysis is carried out to optimize the system, envisioning possible application of AM technology as a printing methodology.

3.1 Experimental tests of the stent

The shape of the stent, which has a nominal diameter of 8 mm and a nominal length of 40 mm, is modeled using Solidworks. The model implemented in the CAD is fully parametric and, through a set of equations, allows fast and coherent change of the structure. The stent has a

modular structure, and the representative unit is depicted in Figure 2a. The dimensions of the stent were measured experimentally using an optical microscope for the smallest details, as reported in Figure 2b-c.



(a) (b) (c)

Figure 2: CAD model of the representative unit cell of the stent (a) and details of the external (b) and internal curvature radii (c).

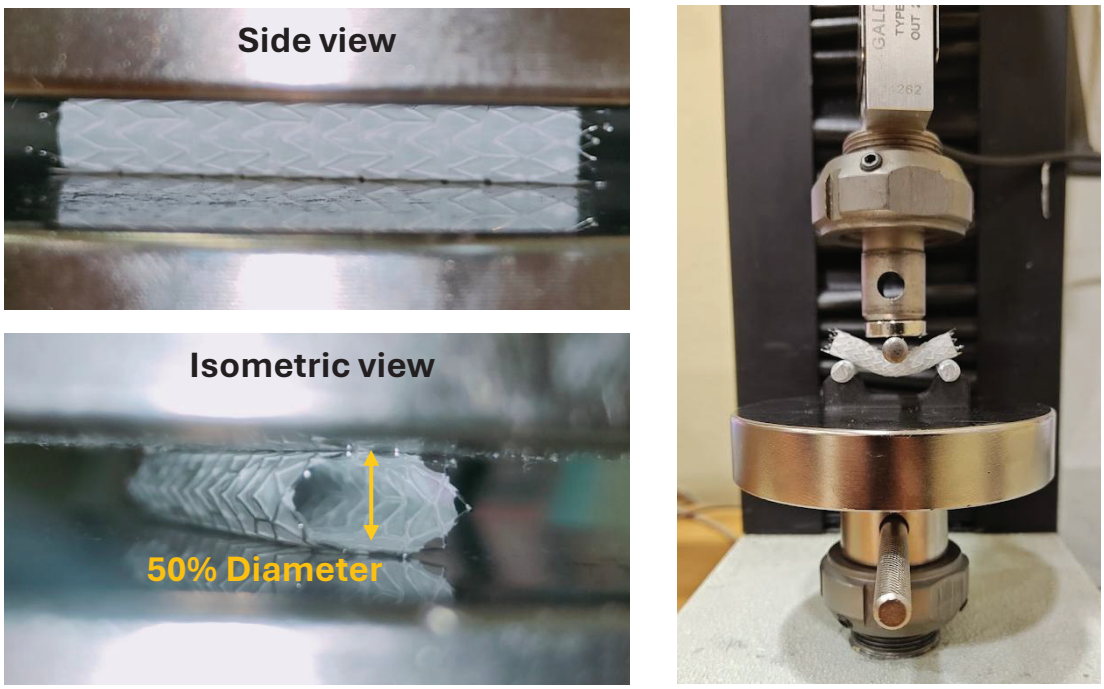

(a) (b)

Figure 3: Crush resistance close-up photo of the stent under compression (a) and three-point bending (b) test set-up.

The stent has a strut thickness of 0.22 mm and a strut width of 0.14 mm, while there are three closed cells per ring, and each ring is connected to the adjacent ones with three axial struts.

Two experimental tests were conducted using a uniaxial tensile machine (Galdabini SUN 500). The test reproduces the CR condition and the BC test as prescribed by the standards. The first one is vertical compression between two rigid plates up the 50% of the diameter reduction

(Figure 3a), while the second one is a three-point bending on 8 mm rollers with a vertical displacement of 6.5 mm (Figure 3b).

3.2 Numerical model fit of the experimental results

The numerical model is based on the geometry already shown in Figure 2a. The real stent has three radiopaque tantalum marks in the ends which are not added to the model since they do not change the system behavior. The stent is modeled using shells in Abaqus software, with linear formulation (S4). The first model resembles the experimental test for BC and CR and they were used to fit the material model parameters. A Souza-Auricchio superelastic material model fitting procedure was used to retrieve the parameter reported in Table 1.

The mesh has at least 5 elements in the strut width, and, after a converging procedure, we set the average element dimension at 0.025 mm. Thanks to the shell approach, the model counts only around 200k nodes, and it takes a reasonable time to run. The comparison between the experimental results and the numerical fit is reported in Figure 4a for the CR test, where the force is provided in N/mm to be independent of the stent length and in Figure 4b for the BC test, where it is not possible to scale the force.

Table 1: Material parameters used in the simulation with Abaqus superelastic model

Parameter	Symbol	Value	Parameter	Symbol	Value
Austenite Elastic Modulus, MPa	E_A	69000	Start of transf. loading stress, MPa	σ_{ST_L}	240
Austenite Poisson's ratio	ν_A	0.3	End of transf. loading stress, MPa	σ_{E_L}	310
Martensite Elastic Modulus, MPa	E_M	22000	Start of transf. unloading stress, MPa	σ_{ST_U}	180
Martensite Poisson's ratio	ν_M	0.3	End of transf. unloading stress, MPa	σ_{E_U}	120
Transformation strain	ε_L	0.04	Start of transf. stress in compression, MPa	σ_{ST_C}	330

3 NUMERICAL RESULTS

The results shown in Figure 4 confirm that the proposed material model provides good agreement with the experimental results. Therefore, a parametric analysis is carried out to find out the influence of the main geometrical parameters on the system behavior in terms of CR and BC, while RRF and COF will be considered in future studies.

3.2 Crush Resistance

The crush resistance numerical results provide not only the force but also an estimate of the stresses occurring in the stent. The parametric analysis considered the following values for the thickness of the strut: 0.198, 0.220, 0.242 mm and 0.112, 0.120 and 0.132 mm for the width. The combination of these values leads to 9 configurations for each of the outputs considered. The numerical set-up of the model is the same as in paragraph 3.2. The stress contour map is provided in Figure 5, where it is possible to note that the material reaches the stress plateau and completely transforms in almost all the struts, which is something expected in a destructive test. In terms of force by unit length, as shown in the chart of Figure 6, the effect of the width is stronger compared to the thickness in increasing the CR figures of merit.

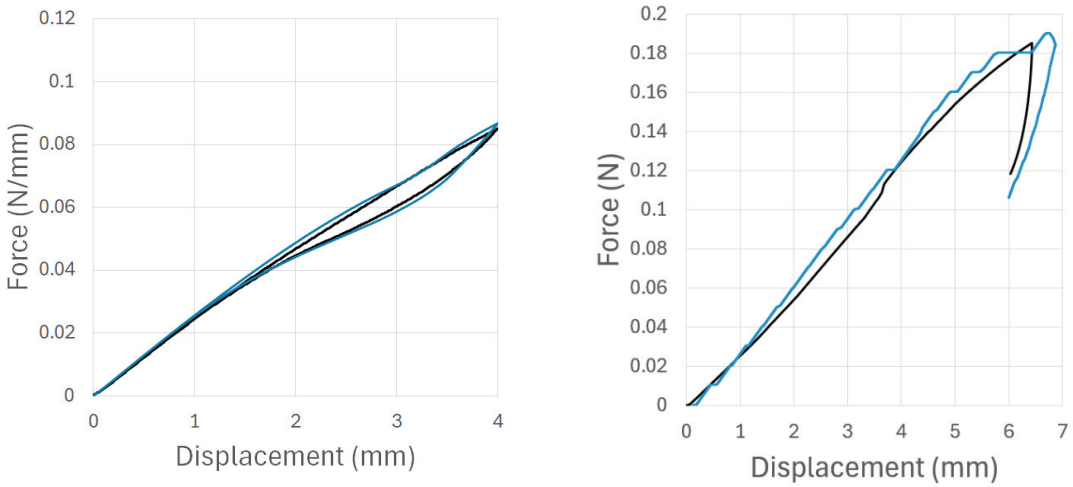

(a) (b)

Figure 4: Experimental curves (blue) and numerical curves (black) for CR (a) and BC (b) tests.

3.2 Bending Compliance

The bending compliance of a stent is crucial to allow the surgeon an easy endovascular deployment, even in districts where the vessels are particularly complex, such as the popliteal or carotid ones. The numerical set-up of the three-point bending model is the same as in paragraph 3.2. The bending compliance numerical results provide not only force but also an estimate of the stresses occurring in the stent when subjected to the biomechanical force due to the gait or the patient motion. The parametric analysis considered the following values for the thickness of the strut: 0.198, 0.220, 0.242 mm and, 0.120, 0.132 and 0.144 mm for the width.

It must be noted that these values are different from the CR tests, only the exact width of the real device (0.120 mm) is kept as the previous design. The lower value (0.122 mm) is too small to be obtained through AM, and it greatly lowers the CR, while the upper value (0.168 mm) has been found to be too high to provide adequate compliance in some preliminary studies, not reported here for the sake of brevity. The stress contour map of the stent undergoing a three-point bending with a 4 mm central displacement is provided in Figure 7, where it is possible to note that the material reaches the stress plateau and completely transforms in all the central struts, while it is unloaded in the rest of the stent. The most stressed region, reported in the magnified view of Figure 7, presents stress above 700 MPa and strains around 6-7%, which is close to the material limit fatigue properties [14] and could explain the disappointing results found in [13]. The results of the analysis in terms of force force-deflection diagram carried out for this figure of merits is reported in Figure 8.

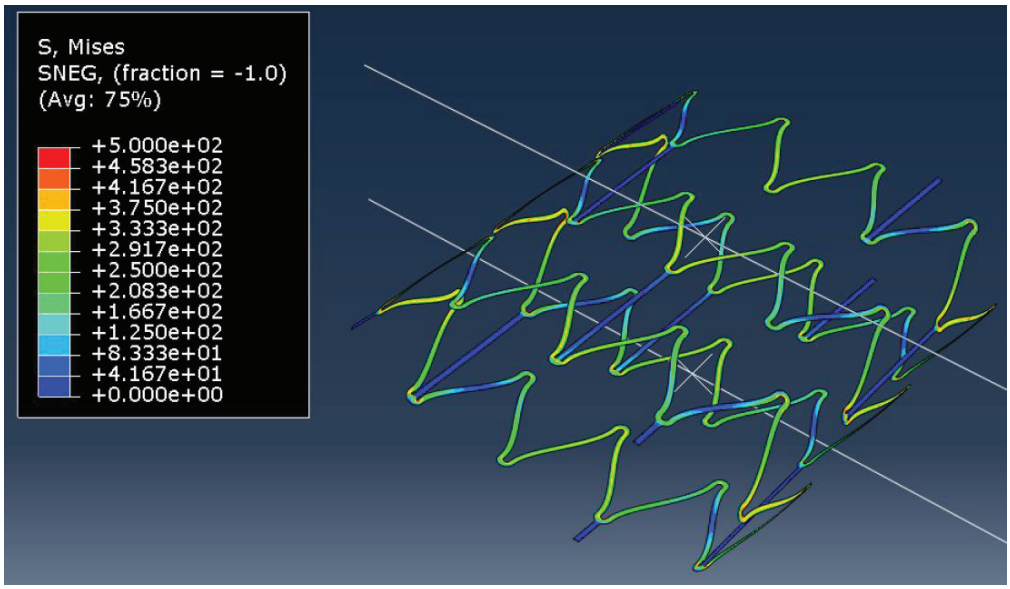

Figure 5: Equivalent stress contour of the stent at maximum deflection, upper limit 500 MPa.

4 DISCUSSION

The CR and BC tests clearly show that both the strut width and thickness play a role in the system behavior and the use of additive manufacturing techniques could lead to an optimization of the system. The influence of the strut width is particularly important in increasing the CR, while the thickness seems to play a crucial role in changing the BC. The optimal combination of these two variables could lead to a stent that can provide enough support when compressed while remaining flexible enough to be deployed endovascularly with enough ease. Another interesting parameter which could be extracted from Figure 6 is the radial crush stiffness, which is closely related to the RRF and it is reported in Table 2 along with the maximum values of the absolute CR force and the bending compliance. Further studies will expand the search toward the optimum values to effectively increase the mechanical performance of a stent without compromising its deployment behaviour.

Additive Manufacturing of NiTi Stents: Opportunities and Challenges

Laser-based powder bed fusion (LB-PBF) has emerged as a groundbreaking method for producing nickel-titanium (NiTi) stents. The main advantages of this technique are the following.

- Patient-specific customization, obtained through the creation of stents tailored to individual anatomies using 3D models derived from CT or MRI scans;
- Material Efficiency, since LB-PBF is a net shape method and the unused powder can be reused with very low waste;
- Functional Performance: obtained through customization of the shape and dimensions of the stent based on the patient's needs, including the possibility of treating bifurcations and complex shapes of the vessel [15].

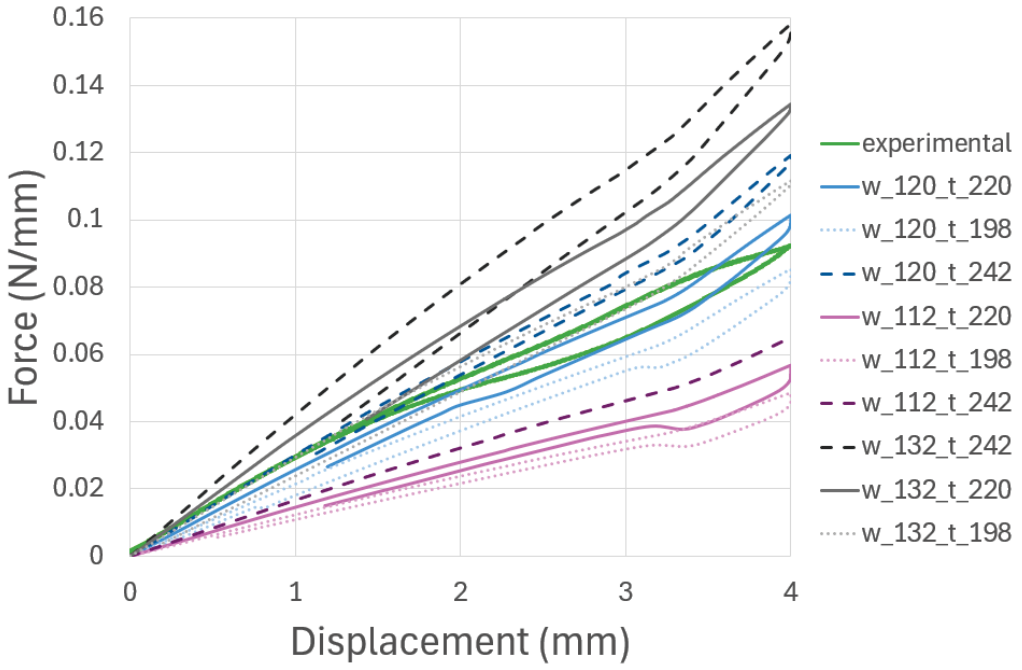

Figure 6: CR force for all the configurations considered.

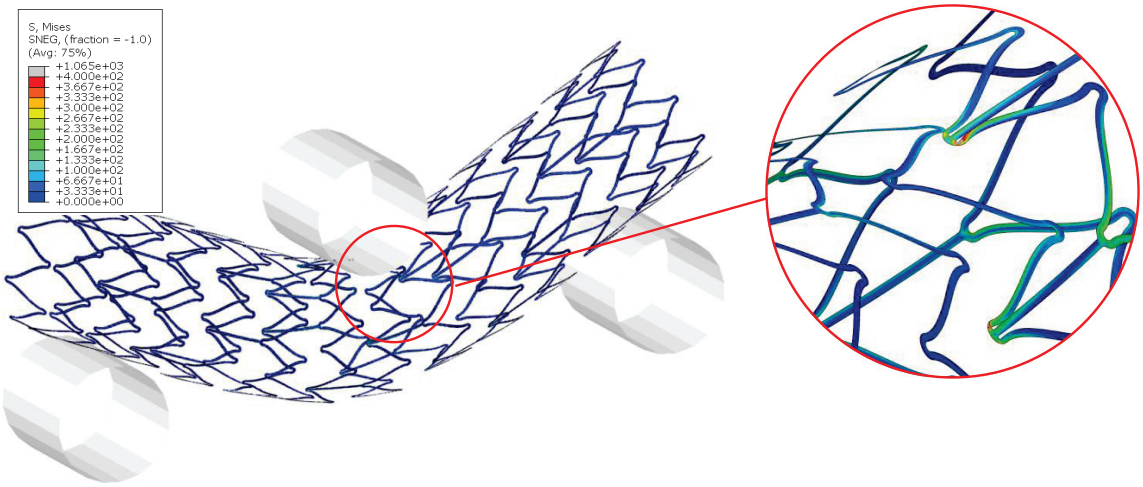

Figure 7: Stress contour of the equivalent stress at maximum bending and detail of the most stressed struts, in the magnified circle within grey the region above 400 MPa.

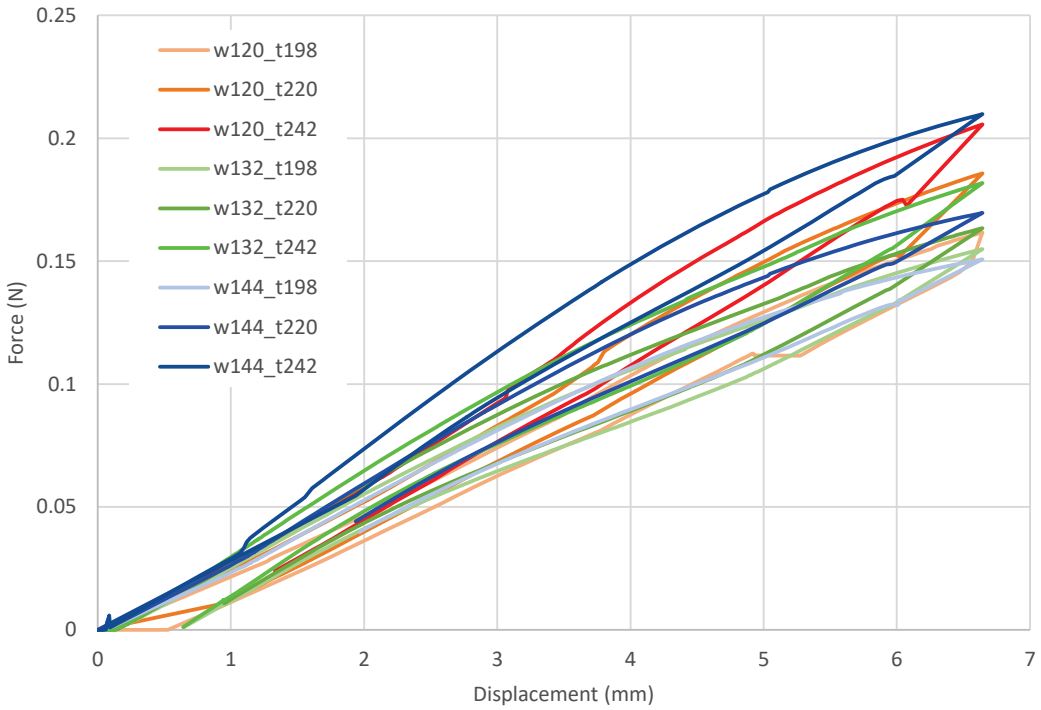

Figure 8: Force–deflection chart for the parametric condition considered. Reddish curve for 0.120 mm width, greenish curves for 0.132 mm and bluish curve for 0.144 mm width.

These advantages are balanced by some open challenges, such as surface quality and dimensional precision, a major concern, especially since strut thicknesses (100–500 μm) are similar to the size of NiTi powder particles (10–60 μm) and the laser beam diameter. Etching and electropolishing are needed as a post-process. [5], [7]. Moreover, the composition of the alloy can be affected by the process, the high-energy laser can evaporate nickel during melting, shifting the phase transformation temperatures. Residual stress, porosity and slight anisotropic behavior are side effects which can be effectively controlled by post-heat and pressure treatment. [16]. The strongest open challenge is related to the supports and the design constraints. [17], which are present also with this technology and limits the possibility of the designer, especially due to the need of a self-supporting lattice in most cases. The findings of this study could help in making the right decision and support the designer of the structure with quantitative information.

Table 2: Results of the CR and BC simulations in terms of Max absolute force, crush stiffness and bending compliance

w	t	Max Force (N)	Crush stiffness (N/mm)	Bending compliance (mm/N)
112	198	0.5667	0.1417	-
112	220	0.6620	0.1655	-
112	242	0.7587	0.1897	-

120	198	0.9888	0.2472	41.092
120	220	1.1743	0.2936	35.777
120	242	1.3800	0.3450	32.308
132	198	-	-	42.894
132	220	-	-	40.659
132	242	-	-	36.551
144	198	-	-	44.072
144	220	-	-	39.166
144	242	-	-	31.663
168	198	1.2834	0.3208	-
168	220	1.5457	0.3864	-
168	242	1.8197	0.4549	-

5 CONCLUSIONS

This work studies NiTi stents for endovascular applications. This study explores the potential of combining additive manufacturing (AM) with advanced simulations to optimize the stent design by focusing on specific figures of merit. The results show that integrating experimental and computational methods can lead to enhanced fabrication processes and more effective performance evaluations, particularly in terms of bending stiffness and crush resistance. This study shows that the strut width has a stronger influence on the CR than the strut width on the BC, while future studies will integrate these findings also with the effect on RRF and COF. By leveraging these values, the study provides valuable insights into stent mechanical responses and highlights the potential for optimizing stent design through AM, offering improved performance compared to traditional methods. AM holds transformative potential for NiTi stents, but overcoming its technical limitations requires interdisciplinary collaboration across materials science, biomechanics, and clinical medicine.

REFERENCES

[1] A. R. Pelton, “Nitinol fatigue: A review of microstructures and mechanisms,” *J Mater Eng Perform*, vol. 20, no. 4–5, pp. 613–617, 2011, doi: 10.1007/s11665-011-9864-9.

[2] A. Kapoor, N. Jepson, N. W. Bressloff, P. H. Loh, T. Ray, and S. Beier, “The road to the ideal stent: A review of stent design optimisation methods, findings, and opportunities,” *Mater Des*, vol. 237, p. 112556, Jan. 2024, doi: 10.1016/J.MATDES.2023.112556.

[3] Funakubo, *Shape Memory Alloys*. Boca Raton, Florida, USA: CRC Press, 1987.

[4] S. W. Robertson, “On the mechanical properties and microstructure of Nitinol for biomedical stent applications,” PhD thesis, University of California, Berkeley, 2006.

[5] J. Dong, M. Pacella, Y. Liu, and L. Zhao, “Surface engineering and the application of laser-based processes to stents - A review of the latest development,” *Bioact Mater*, vol. 10, pp. 159–184, Apr. 2022, doi: 10.1016/J.BIOACTMAT.2021.08.023.

[6] A. Lantada *et al.*, “Additive Manufacturing of Nitinol for Smart Personalized Medical Devices: Current Capabilities and Challenges,” Scitepress, Feb. 2024, pp. 123–134. doi: 10.5220/0012363900003657.

[7] O. M. McGee *et al.*, “An investigation into patient-specific 3D printed titanium stents and

the use of etching to overcome Selective Laser Melting design constraints," *J Mech Behav Biomed Mater*, vol. 134, p. 105388, Oct. 2022, doi: 10.1016/J.JMBBM.2022.105388.

[8] P. Jamshidi *et al.*, "Development, characterisation, and modelling of processability of nitinol stents using laser powder bed fusion," *J Alloys Compd*, vol. 909, p. 164681, Jul. 2022, doi: 10.1016/J.JALLCOM.2022.164681.

[9] M. Bernini *et al.*, "Oversizing of self-expanding Nitinol vascular stents – A biomechanical investigation in the superficial femoral artery," *J Mech Behav Biomed Mater*, vol. 132, p. 105259, Aug. 2022, doi: 10.1016/J.JMBBM.2022.105259.

[10] T. W. Duerig and M. Wholey, "A comparison of balloon- and self-expanding stents," *Minimally Invasive Therapy & Allied Technologies*, vol. 11, no. 4, pp. 173–178, Aug. 2002, doi: 10.1080/136457002760273386.

[11] F. Hoseini, A. Bellelli, L. Mizzi, F. Pecoraro, and A. Spaggiari, "Self-expanding Nitinol stents for endovascular peripheral applications: A review," *Mater Today Commun*, vol. 41, p. 111042, Dec. 2024, doi: 10.1016/j.mtcomm.2024.111042.

[12] L. de O. Harduin *et al.*, "Safety and efficacy of a new covered stent in hemodialysis vascular access outflow stenosis: A Brazilian multicenter retrospective study," *Journal of Vascular Access*, 2024, doi: 10.1177/11297298231226259/ASSET/EBEF75CA-CCC9-4041-8898-76ADEAC51EFE/ASSETS/IMAGES/LARGE/10.1177_11297298231226259-FIG3.JPG.

[13] E. M. Marone, C. Brioschi, C. Barra, and L. F. Rinaldi, "Disappointing results of popliteal aneurysm endovascular treatment with a new self-expandable covered stent," *Asian Cardiovasc Thorac Ann*, vol. 32, no. 4, pp. 227–230, May 2024, doi: 10.1177/02184923241251887.

[14] S. W. Robertson, A. R. Pelton, and R. O. Ritchie, "Mechanical fatigue and fracture of Nitinol," *International Materials Reviews*, vol. 57, no. 1, pp. 1–37, 2012, doi: 10.1179/1743280411Y.0000000009.

[15] V. Finazzi, F. Berti, R. J. Guillory, L. Petrini, B. Previtali, and A. G. Demir, "Patient-specific cardiovascular superelastic NiTi stents produced by laser powder bed fusion," in *Procedia CIRP*, Elsevier B.V., 2022, pp. 244–248. doi: 10.1016/j.procir.2022.06.044.

[16] M. Somireddy and A. Czekanski, "Anisotropic material behavior of 3D printed composite structures – Material extrusion additive manufacturing," *Mater Des*, vol. 195, p. 108953, Oct. 2020, doi: 10.1016/J.MATDES.2020.108953.

[17] V. Finazzi *et al.*, "Design Rules for Producing Cardiovascular Stents by Selective Laser Melting: Geometrical Constraints and Opportunities," *Procedia Structural Integrity*, vol. 15, pp. 16–23, Jan. 2019, doi: 10.1016/J.PROSTR.2019.07.004.

ACKNOWLEDGEMENTS

We acknowledge the financial support of the Italian Ministry of University and Research (MUR), funded by the European Union – NextGenerationEU– Project Title GIFTED - 20228AZTYB – CUP E53D23002810006.

XI ECCOMAS Thematic Conference on Smart Structures and Materials - SMART 2025
M. Krommer, M. Nader and M. Schagerl (Eds)

Received: 15 April 2025 / Revised: 2 July 2025 / Accepted: 4 November 2025
© The Author(s) 2025

Prototype of a cable-actuated lightweight canopy system installed with thin-film photovoltaics

Eftychios G. Christoforou, Eleftherios G. Vourkos, Panayiota Dimitriou, Rafaela Agathokleous, Andreas Müller, Marios C. Phocas

Abstract. The development of energy efficient and sustainable open public spaces may be achieved using elements that combine shading with renewable energy production. Towards that direction an adaptive lightweight canopy structure with integrated photovoltaic modules is currently considered. The system comprises an array of plates whose orientation can be controlled. The plates are installed with thin-film photovoltaic elements, and their purpose is twofold. They can track the motion of the sun towards optimizing the integrated PV system performance, while also providing shading in the area underneath. The modules are suspended on a horizontal tensioned cable net. A system of actuation cables is incorporated to adjust the orientation of the modules, which are endowed with 2 degrees-of-freedom. Their orientation can be adjusted simultaneously while remaining parallel to each other. The two available motions are decoupled and only two actuators suffice for the system reconfigurations. The design aims at reduced weight, structural and technical simplicity, modularity and minimum number of actuators. A small-scale prototype has been developed to verify the applicability and the effectiveness of the approach, while resolving practical implementation issues.

Key words: Adaptive Structures, Reconfigurable Architecture, Photovoltaics Integration, Canopy Structure, Cable Actuation

1. INTRODUCTION

Given an ongoing increase of urban density and the emerging need for sustainability of the built environment, the employment of renewable energy mechanisms within urban areas as well as their performance improvement becomes significant. Of relevance are city-integrated solar technologies, which offer a clean power alternative and mitigate the impacts of climate change [1]. Photovoltaics (PV) have been extensively exploited in recent years and their use is expected to further increase within the cities [2]. Photovoltaic systems are typically installed on building roofs and on the ground due to the heavy weight of traditional silicon-based photovoltaic

Eftychios G. Christoforou & Eleftherios G. Vourkos & Rafaela Agathokleous
Department of Mechanical and Manufacturing Engineering, University of Cyprus, 1 Panepistimiou Ave, 2109 Nicosia, Cyprus, e-mail: e.christoforou@ucy.ac.cy

Panayiota Dimitriou & Marios C. Phocas
Department of Architecture, University of Cyprus, 75 Kallipoleos St., 1678 Nicosia, Cyprus
e-mail: mcphocas@ucy.ac.cy

Andreas Müller
Institute of Robotics, Johannes Kepler University Linz, Altenberger Straße 69, 4040 Linz, Austria
e-mail: a.mueller@jku.at

modules and the high energy production that characterizes them [3]. Less often, photovoltaic systems are installed on civil structures in free landscapes or public spaces within cities.

Towards maximizing solar energy production, specially designed mechanical devices supporting the PV modules are often used to provide automatic readjustment of their orientation to maintain a perpendicular position relative to the incoming solar radiation [4]. The devices may have one or two degrees-of-freedom (DOF) [5, 6] and their mechanical components are described in [7]. Despite their effectiveness and the mature state of these technologies, their applications remain limited, due to the high construction, operation and maintenance costs of the supporting structures and motion mechanisms [8-10].

A promising alternative within the scope of adaptive systems integrated with photovoltaic modules are structures capable of transforming their shape towards adjusting the orientation of the PV panels. Such transformable structures include tensegrity, scissor-like, linkages and origami inspired systems. These have been mainly applied at the level of the primary or building envelope structure [11]. Further reduction of the self-weight of adaptive systems with integrated PV technologies is possible through implementation of thin-film photovoltaic modules, such as Cu(In, Ga)Se2 (CIGS). They achieve similar efficiencies to traditional silicon-based modules, while having further advantages arising from shape flexibility and embodied energy [12, 13].

A precedent of an adaptive photovoltaics structure is the proposed design of a modular flower-shaped shading system with integrated PV panels acting as covering for public spaces [14]. The system is supported on a spatial truss and its motion resembles the opening of the petals of a flower. This modular structure can be placed on the ground or on a single mast. Another design concept of a transformable skylight tensegrity system of six units with sliding photovoltaic modules is presented in [15]. The actuation of the system is based on connecting cables of adjustable length. Finally, a tensegrity membrane roof structure with integrated photovoltaic modules supported on rotating masts in the span direction is described in [16]. Actuation of the system is provided by continuous control cables that interconnect the masts below the membrane level. Further examples of thin-film photovoltaics applications in adaptive structures can be found in [17, 18].

In response to contemporary architectural needs, a novel canopy system is presented, a small-scale prototype of which is currently under development. The general concept of the system is shown in Figure 1. This overhead roof structure comprises an array of shading elements installed with thin-film PV modules. The orientation of the elements can be actively controlled to maximize the overall performance of the PV system, but also to adjust the shading conditions in the area underneath. The former is realized by tracking the sun motion towards minimizing the angle of incidence between the incoming sunlight and the photovoltaic panels. The system operation can be optimized to satisfy these requirements, while prioritizing their importance. It belongs to the category of dual axis azimuth-altitude trackers, which reorient the PV surface and it has several unique features. It is characterized by structural simplicity, low manufacturing and operation costs, and it is subject to a simple actuation and control method. It is a lightweight system using modular components, which can be readily installed on existing or new structures. The parametric digital design of this canopy system was presented in [19].

The paper is structured as follows. In Section 2 the kinematics concept is introduced, and the design approach is described. The prototype in scale 1:5 together with its structural and mechanical details are presented in Section 3, followed by the description of testing, verification and evaluation of its operation in Section 4. Finally, the conclusions are presented together with a brief reference to future work.

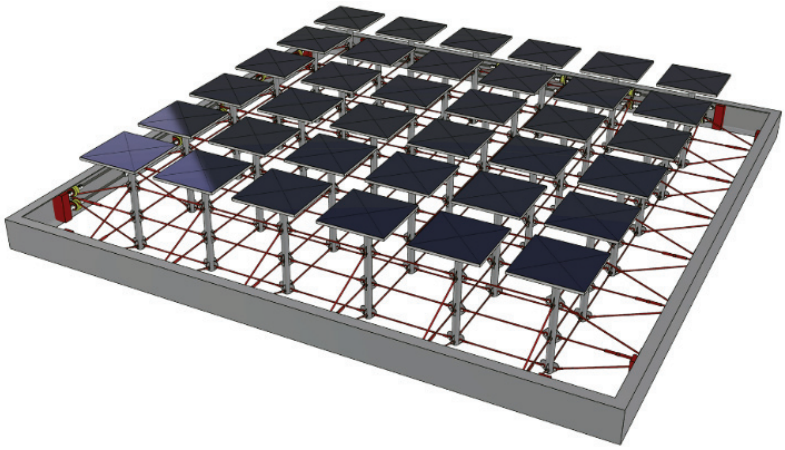

Figure 1. The proposed PV canopy concept.

2. DESIGN CONCEPT

The aim of the proposed adaptive canopy system installed with thin-film photovoltaic modules is to upgrade public spaces through the production of solar energy and the provision of shading underneath. At the current stage, the emphasis is on the structural system design, implementation and evaluation of the kinematics configuration, as well as the actuation and control concepts.

The backbone of the adaptive canopy system is a horizontal rectangular structural frame, which can be supported on four columns at the corners, at the required height. The frame surrounds the PV/shading elements array, which comprises thin rectangular plates installed with the PV modules over their top surface, as depicted in Figure 1. Each plate is mounted on a corresponding mast, which is supported on a spherical joint allowing for its orientation to be adjusted. The basic kinematics concept is represented schematically in Figure 2, corresponding to one system rotation. The spatial arrangement of the cables net (see Figure 1) allows for the same method to apply separately in relation to each individual DOF of the system.

The array of spherical joints is supported by a fixed cables net stretched over the horizontal structural frame. Orientation adjustments are implemented by a dedicated system of actuation cables. It comprises a longitudinal and transverse system of cables, interconnecting the PV masts along their top and bottom edges. For each row/column of the masts array, the corresponding control cables pass through a set of pulleys forming a closed loop. One of the pulleys is passive and its purpose is to redirect the cable, while the other is active. On the active pulley (rotated by an electric motor) the two cable edges are wound in opposite directions, so that while the pulley rotates, an equal length of the cable is pulled and simultaneously released from each side. This arrangement ensures that the PV plates always remain parallel to each other, while their azimuth and altitude angles are adjusted simultaneously.

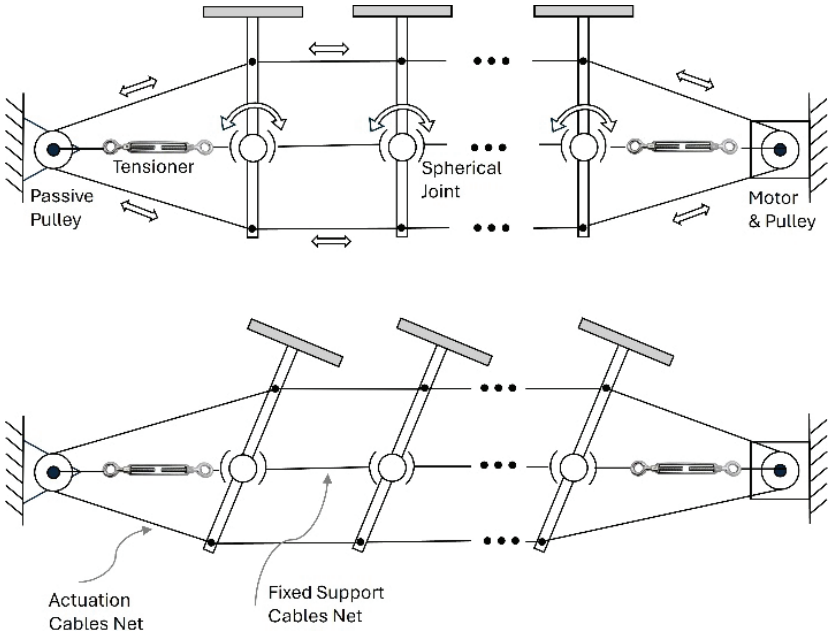

Figure 2. Kinematics concept of the canopy system corresponding to each individual DOF. Top: system at the zero (vertical) position, Bottom: system at an adjusted (inclined) position.

The spacing between the spherical joints over the fixed cables net (i.e., the spacing between the masts' grid) is selected based on two considerations: (a) Avoid collisions between neighboring plates but also prevent the PV system from shading itself. (b) Minimize the gaps between the neighboring plates to maximize sun protection in the area underneath.

As part of the small-scale prototype design, a systematic analysis of its kinematics was undertaken including simulations with 3D motion design software. The kinematic constraints were imposed using appropriate design mates between the model components. The PV masts were modelled as rigid bars and the prestressed cables connecting the masts (fixed support cables and control cables) were also modelled as fixed-length rigid bars. The simulation studies provided useful insights regarding the system design and control.

3. PROTOTYPE DEVELOPMENT

The design of the structural and control members as well as their interconnections, is based on modularity principles to allow interchangeability of the components, as well as ease of assembly and disassembly. A primary objective of the design has been the reduction of the number of actuators required for transformability, and low structural self-weight. A small-scale model of the prototype structure has been implemented in scale 1:5. The support cable net is anchored on a welded 1.3m×1.3m square frame manufactured using a C-channel steel beam (80mm×45mm×7mm), as shown in Figure 3. A total number of 36 masts were included, arranged in a symmetric 6×6 array. The masts were manufactured from aluminum tubes of 10mm outer diameter, the total height of each mast is 23cm and the size of each PV mounting plate is 12cm×12cm. The distance between the actuation cables along the length of each mast is 14cm.

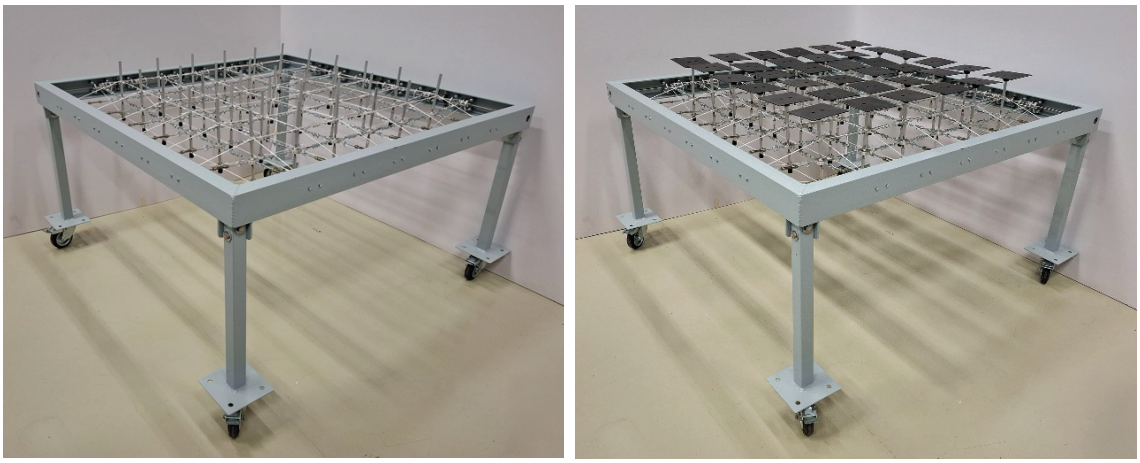

Figure 3. Prototype of the proposed canopy system. Right: basic system with the support and actuation cables. Right: PV/shading plates installed on masts.

The horizontal cables net is prestressed to support the weight of the spherical joints (see Figure 4), the masts and the PV modules, but also resist the moments developed at the spherical joints due to friction while rotating (which is minimal). Turnbuckle wire tensioners are used to adjust the prestress. The spherical joint assemblies allow rotation of the masts by ±55°.

Control cables (see Figure 4) are combined with a system of actuated pulleys and one of passive pulleys, forming a closed loop. For each actuated DOF of the system, actuation cables need to be simultaneously pulled and released by the same amount. For this purpose, each cable is appropriately wound (in opposite directions) around a corresponding actuation pulley, as shown in Figure 5.

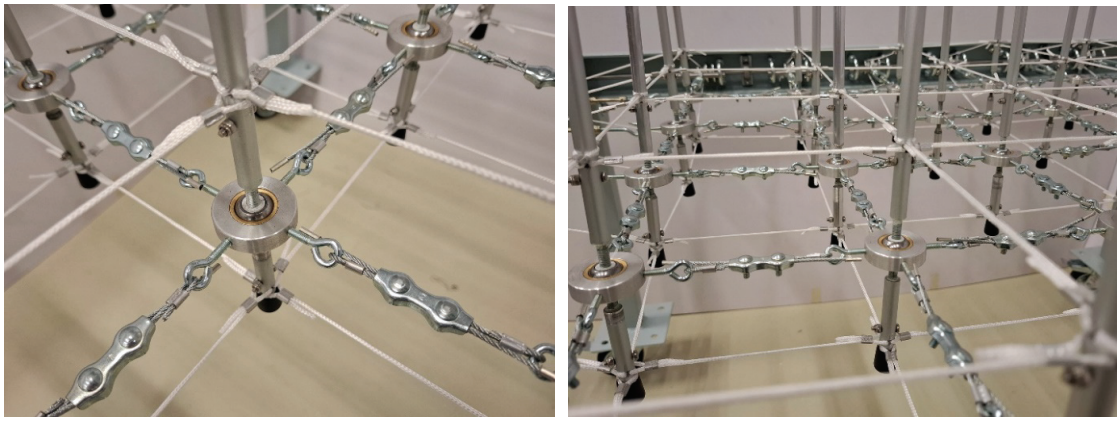

Figure 4. Spherical joints and PV module masts installed on the horizontal prestressed support cable net. The prestressed actuation cables connect to the PV masts on either side of the spherical joints body.

The actuation pulleys are installed on two separate shafts, corresponding to each DOF of the system. Each shaft is attached to the inside of the surrounding structural frame and is supported on pillow block spherical bearing units (see Figure 5). At one end the shaft connects via a flexible coupler to the corresponding actuator (geared DC motor). This allows for all the control cables corresponding to the same DOF to be simultaneously pulled and released by the same amount. This arrangement simplifies the actuation system and facilitates motion planning as well as the implementation of a solar tracker servo system.

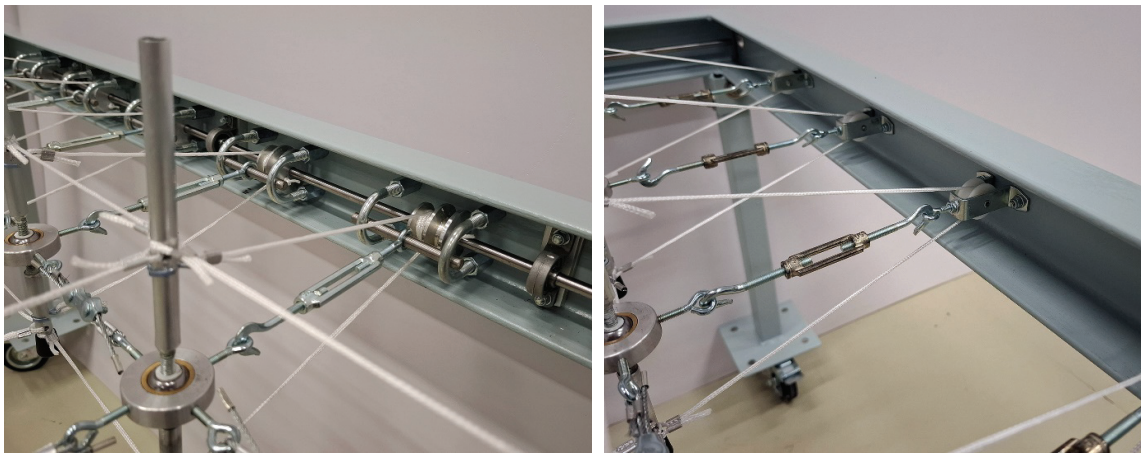

Figure 5. Actuation cables net. Left: actuation shaft/pulleys system.
Right: passive pulleys system.

The PV support/shading elements were 3D-printed (using PLA - Polylactic Acid material) and can be installed on the mast's top edge, as shown in Figure 6. They have a flat top surface for the installation of the PV modules, which will be used for the experimental evaluation of the energy performance of the PV system.

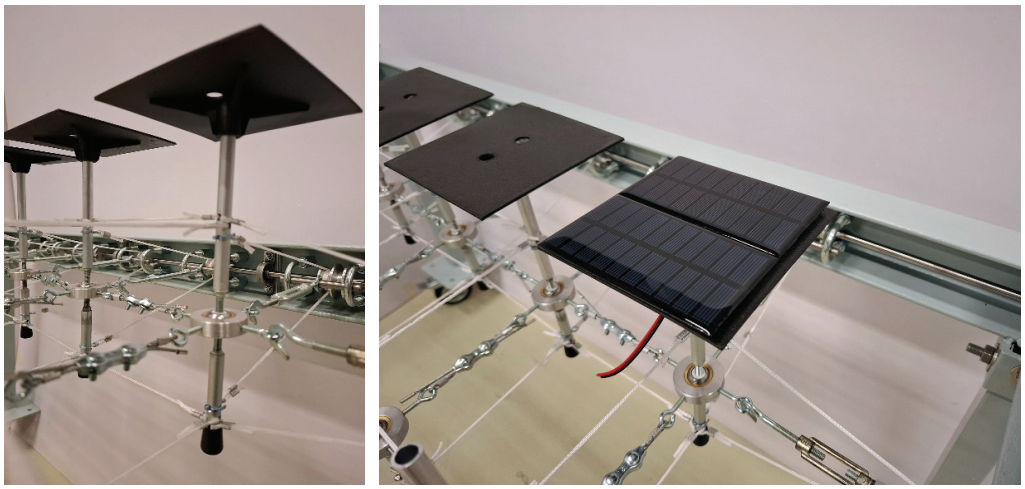

Figure 6. PV/shading elements installed on masts.

The system is currently controlled using simple control hardware (based on an Arduino microcontroller board). For the initial testing of the system a manual interface with a two-axis joystick connected to the motors control system has been implemented to control the system orientation. Eventually, the system motions will be programmed based on the sun tracking requirements. Sun-tracking may involve a servo system with sensory feedback, date-and-time-based algorithms, or a combination of the two. Continuous real time tracking of the sun motion is possible but adjustments in discrete steps at fixed time intervals may be preferable towards minimizing the energy usage corresponding to the system reconfigurations. Other considerations may include avoidance of unnecessary adjustments and waste of energy for reconfigurations during cloudy periods.

4. INITIAL PROTOTYPE TESTING AND EVALUATION

The developed prototype system was tested to evaluate its kinematics behaviour and the structural and mechanical efficiency of the actual implementation. It was confirmed that while actuation shafts are rotated, the masts and the installed plates move parallel to each other, as required. Motion is evenly transferred along the elements in both directions across the array. Of particular importance is to maintain the required prestress in the actuation cables. The two available motions were confirmed to be decoupled, as it was expected. The system can effectively adjust the orientation of its elements in both the azimuth and altitude orientations combined, as shown in the examples of Figure 7. This initial testing shows that a solar tracking servo control system can be readily installed on the system for autonomous operation and optimal efficiency. The system is ready to support the planned field testing towards evaluating its energy efficiency and shading performance.



Figure 7. System testing showing different postures of the canopy plates system while adjusting its azimuth-altitude orientation.

5. CONCLUSIONS AND FUTURE WORK

The prototype of a lightweight structural system with thin-film photovoltaic modules has been presented, which is characterized by structural and control simplicity. It provides flexibility and a minimum number of actuators, as required for adjusting the orientation of the photovoltaic modules to better harvest the solar input. It is well-suited for a canopy system in

open public spaces, combining shading and improved PV performance. The system may also be adjusted for installation as a facade on a building envelope at a vertical position, without affecting its kinematics. The system prototype has been constructed to verify its feasibility and examine its kinematics. Various structural and actuation details have been resolved constituting a significant step towards full-scale architectural implementation.

Future plans include the installation of PV modules on the plates above the masts, before proceeding with energy efficiency studies to evaluate performance improvements given its sun tracking capability, along with its shading efficiency. The implementation of a solar tracking servo system will be considered together with optimal path planning. Then, work will continue towards a full-scale implementation of the proposed canopy system. Importantly, beyond the interesting engineering aspects involved, the operation of the adaptive canopy system is expected to provide unique aesthetic effects.

ACKNOWLEDGMENTS

This work was supported by the University of Cyprus grant AUCPH-2023.

REFERENCES

[1] A. Shah, "Solar cells and modules," *Springer Series in Materials Science*, *SSMATERIALS*, *301, Springer Nature*, 2020.

[2] D. J. Sailor, J. Anand, and R. R. King, "Photovoltaics in the built environment: a critical review," *Energy & Buildings*, vol. 253, pp. 111479, 2021.

[3] H. Gholami, "A holistic multi-criteria assessment of solar energy utilization on urban surfaces," *Energies*, vol. 17, no. 21, p. 5328, 2024.

[4] C. Lee, P. Chou, C. Chiang, and C. Lin, "Sun tracking systems: a review," *Sensors*, vol. 9, no. 5, pp. 3875-3890, 2009.

[5] V. Sumathi, R. Jayapragash, A. Bakshi, and P. K. Akella, "Solar tracking methods to maximize PV system output – a review of the methods adopted in recent decade," *Renewable and Sustainable Energy Reviews*, vol. 74, pp. 130-138, 2017.

[6] A. Z. Hafez, A. M. Yousef, and N. M. Harag, "Solar tracking systems: technologies and trackers drive types – a review," *Renewable and Sustainable Energy Reviews*, vol. 91, pp. 754-782, 2018.

[7] Z. Kvasznicza, and G. Elmer, "Optimizing solar tracking systems for solar cells," In Proc. The 4th Serbian–Hungarian joint symposium on intelligent systems, 2006.

[8] D. Prasad, and M. Snow, *Designing with Solar Power: A Source Book for Building Integrated Photovoltaics*. Earthscan, 2013.

[9] A. P. Gonzalo, A. P. Marugán, and F. P. G. Márquez, "Survey of maintenance management for photovoltaic power systems," *Renewable and Sustainable Energy Reviews*, vol. 134, p. 110347, 2020.

[10] A. Saxena, R. Kumar, A. A. Sagade, D. B. Singh, V. V. Tyagi, E. Cuce, and V. Goel, "A state-of-art review on photovoltaic systems: design, performance, and progress," *Process Safety and Environmental Protection*, vol. 190, pp. 1324-1354, 2024.

[11] M. C. Phocas, M. Matheou, and W. Haase, "Transformable building structures in architectural engineering education," *Architecture, Structures and Construction*, vol. 2, 183-198, 2022.

[12] P. Jayathissa, M. Jansen, N. Heeren, Z. Nagy, and A. Schlueter, "Life cycle assessment of dynamic building integrated photovoltaics," *Solar Energy Materials and Solar Cells*, vol. 156, pp. 75-82, 2016.
[13] P. Reinhard, A. Chirila, P. Blosch, F. Pianezzi, S. Nishiwaki, S. Buechelers, and A. N. Tiwari, "Review of progress toward 20 % efficiency flexible CIGS solar cells and manufacturing issues of solar modules," *IEEE Journal of Photovoltaics*, vol. 3, no. 1, pp. 572-580, 2013.
[14] F. Minelli, D. D'Agostino, M. Migliozzi, F. Minichiello, and P. D'Agostino, "PhloVer: a modular and integrated tracking photovoltaic shading device for sustainable large urban spaces—preliminary study and prototyping," Energies, vol. 16, no. 15, p. 5786, 2023.
[15] M. Fox, "Kinetic architectural systems design," in *Transportable Environments, Book 2*, R. Kronenberg, Ed., Abingdon: Taylor & Francis, 2003.
[16] A. D. C. Pronk, H. Buskes, L. S. Klerk, and P. Koelewijn, "Kinegrity: the kinetic transformation of a tensegrity," In Proc. IASS-SLTE 2014 Symposium, Shells, Membranes and Spatial Structures: Footprints, Brasilia, 2014.
[17] M. C. Phocas, E. G. Christoforou, C. Theokli, and K. Petrou, "Reconfigurable linkage structures and photovoltaics integration," *Building Engineering*, vol. 43, pp. 103201-1 – 103201-12, 2021.
[18] M. C. Phocas, E. G. Christoforou, M. Matheou, and P. Dimitriou, "Concept analysis of an adaptive building envelope with thin-film photovoltaic modules," *Energy and Buildings*, vol. 311, pp. 114150-1 – 114150-13, 2024.
[19] G. Tryfonos, M. C. Phocas, E. G. Christoforou, and M., Matheou, "Generative design and fabrication in the development of an adaptive canopy system with thin-film photovoltaics," In Proc. 42nd eCAADe International Conference 2024, vol. 1, 2024, pp. 439-446.

XI ECCOMAS Thematic Conference on Smart Structures and Materials - SMART 2025
M. Krommer, M. Nader and M. Schagerl (Eds)

Received: 22 April 2025 / Revised: 29 August 2025 / Accepted: 4 November 2025
© The Author(s) 2025

Design of a morphing winglet trailing edge with fluid actuation - Design process and experimental results

Ralf Keimer, Michael Schäfer, Srinivas Vasista

Abstract. Integrating active control surface technology into aircraft wings with confined spaces is challenging. It would be beneficially to do so to enable more efficient wing designs for e.g. load alleviation. This paper details a winglet trailing edge surface composed of fluid actuated morphing unit structures (FAMoUS) that enable control surface deflections under the corresponding aerodynamic hinge moments.

The design of the FAMoUS actuators is comprised of elastomer and metallic stiffeners, which under internal pressure from a fluid exert displacement and force and thus output work. Combining these unit structures in a bimorph setup a trailing edge control surface is build, which is structural and actuating part at the same time.

The structural dimensioning of a demonstrator with 1 m span-width is shown, based on a finite element analyses consisting of detailed tuned material parameters obtained from testing on the individual unit structure tests as well as the inclusion of hydrostatic fluid elements to determine effective stiffnesses from the pressure-volume relationship between the housing structure and internal fluid.

The process of choosing a suitable actuating system including the feedback control and hydraulic systems is presented.

Finally experimental results of tests are presented, starting with calibration of the feedback system with an external measurement, also clarifying deflection uniformity along the span of the demonstrator. Deflection performance and deflection rate are discussed and compared with the predictions from the finite element analyses. The findings are discussed and contextualized. A summary of the results is given and an outlook on the way forward is presented.

Key words: Morphing winglet, Hdyraulic systems, Flight Control

Ralf Keimer & Srinivas Vasista
DLR - German Aerospace Center, Institute of Lightweight Systems Lilienthalplatz 7, 38108 Braunschweig, Germany
e-mail: ralf.keimer@dlr.de

Michael Schäfer
DLR - German Aerospace Center, Institute of Flight Systems Lilienthalplatz 7, 38108 Braunschweig, Germany
e-mail: michael.schaefer@dlr.de

1 Introduction

1.1 FAMoUS Principle

The design of the morphing winglet trailing edge is based on fluid actuated morphing unit structures. Those unit-structures are comprised of a combination of an elastomer with aluminium stiffening material enclosing a pressure cell. Increasinng the pressure of such a cell is resulting in an elongation of the orthotropic part as shown in figure 1. Combining two unit-structures in a bimorph configuration lead to a bending movement which is the setup used for the trailing edge. The pressure change in the cavity of can either be done by pneumatic or hydraulic means and previous works have shown that this fluid actuated morphing unit structures can fullfill deflection and stiffness requirements [1, 2].

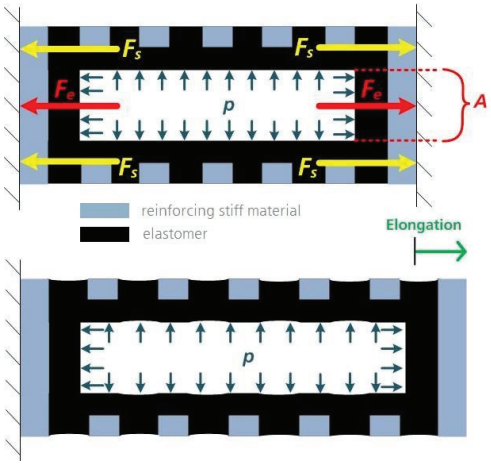

Figure 1: Principle of pressure cells

1.2 Morphing Winglet Trailing Edge Demonstrator

A winglet reduces drag but increases load on the wing. In order to reduce the weight a load reduction is desirable. Active load reduction can be achieved with a winglet tab, i.e. a control surface at the trailing edge of the winglet. A morphing structure, being a control-surface with a continuous deflection, promises to have higher change in lift for a given deflection angle than a conventional control surface according to [3, 4] which together with the confined space at the winglet motivates building a demonstrator for a morphing winglet tab using the FAMoUS principle.

The goal for this demonstrator is to raise technology readiness level to TRL 3. In table 1 some requirements for the design are listed. The demonstrator is designed to have a spanwise dimension of nearly 1 m (as shown in figure 2) and is also taking into account the system design to actuate it.

Table 1: Requirements for trailing edge

	1st Priority		2nd Priority
Function	High Speed Performance	Maneuver Load Alleviation	Gust Load Alleviation
Deflection Range	± 10°	± 15°	± 15°
Deflection Speed	10°/s	20°/s	80°/s
Position Accuracy	± 0.1° Rationale: Ensure device position compliant with aerodynamic tolerance		
Design Assumption	Either 2 actuators or 1 actuator and damper Rationale: Avoiding flutter in case of failure		

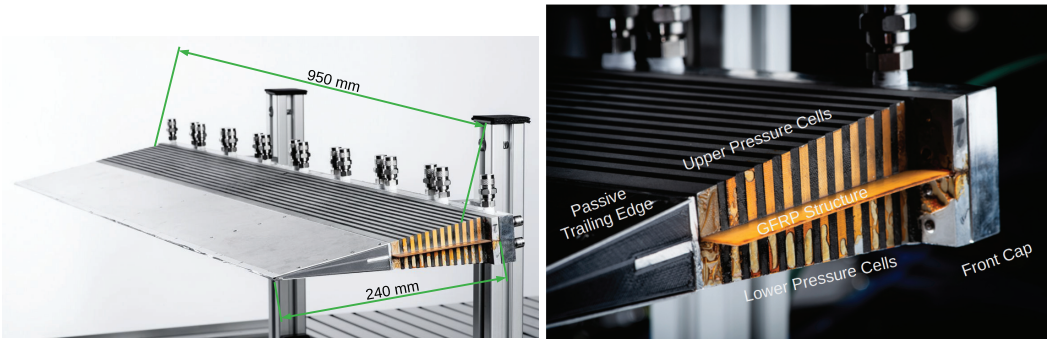

Figure 2: Structural part of demonstrator

2 Design and Manufacturing

2.1 Structural Design

For the structural design a standard aviation aluminium AL7505 combined with an ethylene propylene diene monomer rubber (EPDM) AA6CFZ from Kraiburg is chosen. The bimorph structure is further complemented with an glas-fibre reinforced plastic (GFRP) structure placed in the neutral axes to enforce bending without elongation of the trailing edge. The final setup can be seen in the right of figure 2.

In order to predict performance with a finite element calculation, previous tests are used to tune the hyperelastic material model describing the EPDM as reported in [5, 6]. In order to reduce overall weight not the whole length of the winglet tab is pressurized. In figure 3 results are shown predicting 11° deflection at 14 bar differential pressure between upper and lower pressure cells which equals 0.79°/bar deflection.

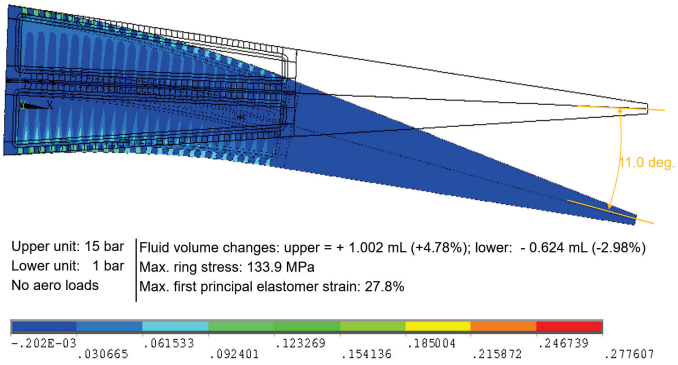

Figure 3: FE Result, color indicating strain in EPDM

2.2 Manufacturing

Manufacturing the 1 m demonstrator is done by building 8 subassemblies individually, i.e. 4 upper and 4 lower pressure cell parts, and combine them later to the full length structural part as shown in figure 4. The steps for manufacturing are:

- Manufacturing aluminium parts of 4 mm thickness with all cutouts
- Stack aluminium parts with EPDM and vulcanised
- Assemble upper and lower pressure cells and mill EPDM from the cavities
- Combine upper and lower cells with GFRP sheet (figure 4 right hand side)
- Mill outer shape of demonstrator

Some prototype parts expose leaking, leading to integration of EPDM-bladders as shown in left side of figure 5 to ensure leak tightness of the pressurized cells. The finished morphing part of the demonstrator is depicted in figure 5 with the pressurized cavities indicated as active while the other cavities are marked as passive.

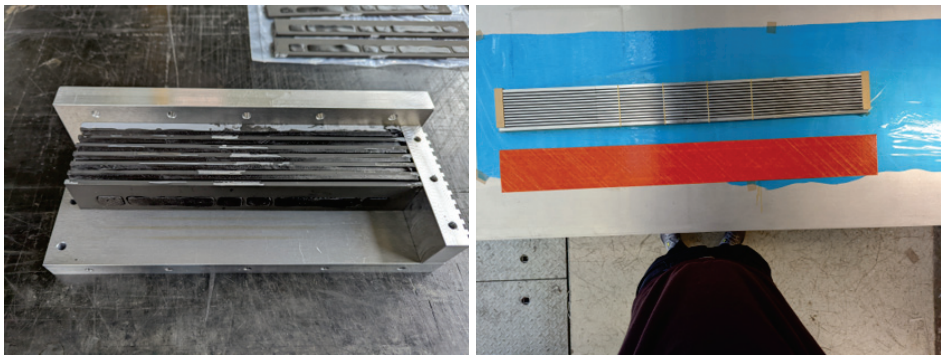

Figure 4: Manufacturing



Figure 5: Left: EPDM-bladders for leak tightness, Right: Active and passive cavities

2.3 System Design

The pressure cells can in principle be driven by pneumatic or hydraulic systems. For the 1 m demonstrator a hydraulic system is chosen as elucidated in [7]. The design and dimensioning of this hydraulic system is discussed in [8]. The setup used in the demonstrator is based on a electro hydrostatic actuator (EHA) as shown on the left side of figure 7. Central to this system is a bidirectional pump driven by an electric motor which is moving fluid volume between upper and lower pressure cells thus establishing a differential pressure. A second pump ensures that all pressure cells are at least pressured to 3 bar through the check valves connected to the line depicted in green. Relieve valves connected to the red line bleed pressure exceeding 17 bar back to the tank. Due to the non-linear elastic behavior of the EPDM structure, sensors must be used that enable the direct measurement of the deflection angle for position control. These sensors are alternatively based on strain-gages or fibre-bragg grating based as shown in figure 6.

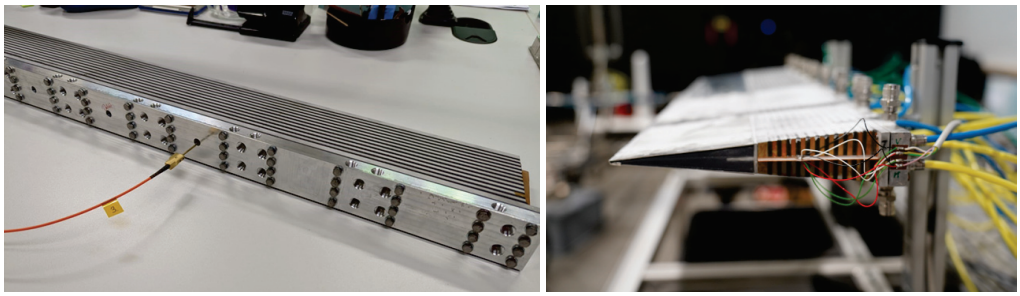

Figure 6: Feedback sensors (Left: Fibre-bragg sensor, Right: Strain-gage)

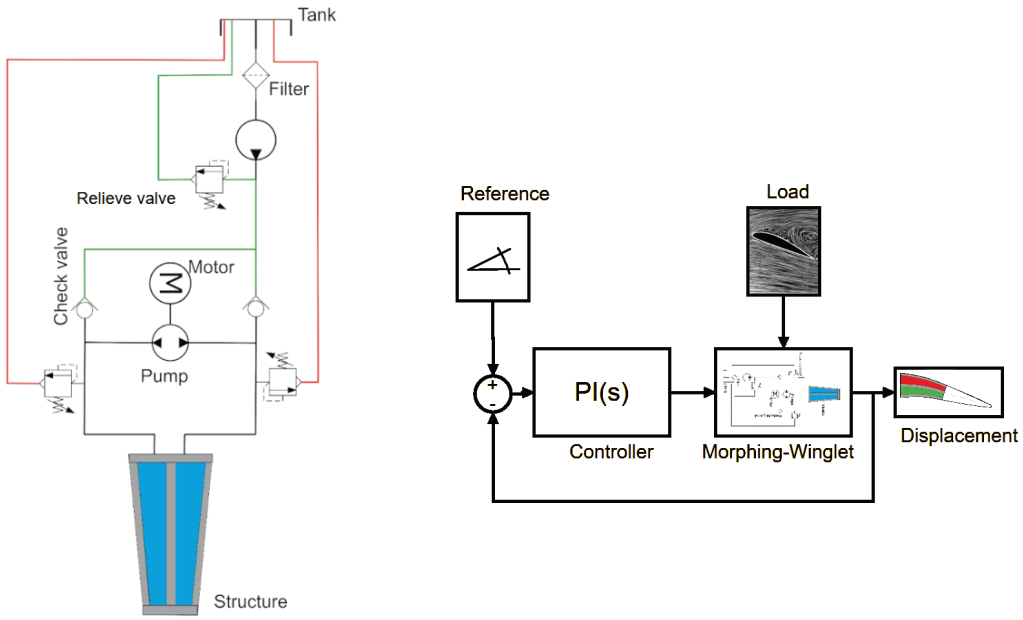

Figure 7: System architecture (Left: Electro hydrostatic actuator, Right: Control-loop)

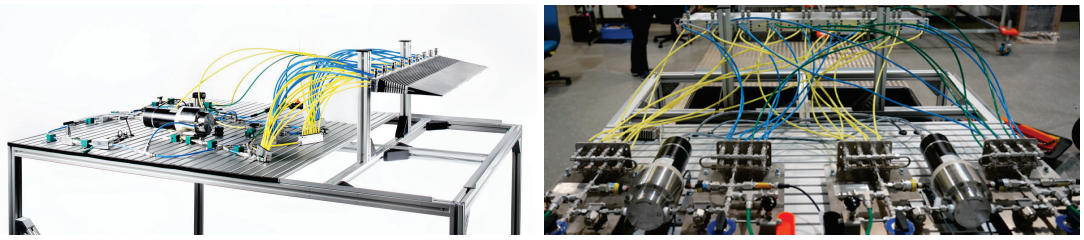

Figure 8: Demonstrator (Left: Single EHA system, Right: Second EHA system for redundancy)

3 Experimental Data

The experiments are designed to achieve multiple goals:

1. Calibration of the feedback sensors, to ensure position control is based on correct angles of deflection.
2. Verification of the design model.
3. Showing that assumption of the actuation being a one degree of freedom system is correct. As the system architecture is designed to have just one control value (i.e the differential pressure between upper and lower pressure cells), the whole demonstrator is supposed to have uniform deflection.
4. Measuring performance of the demonstrator regarding speed and accuracy according to

requirements (see table 1).

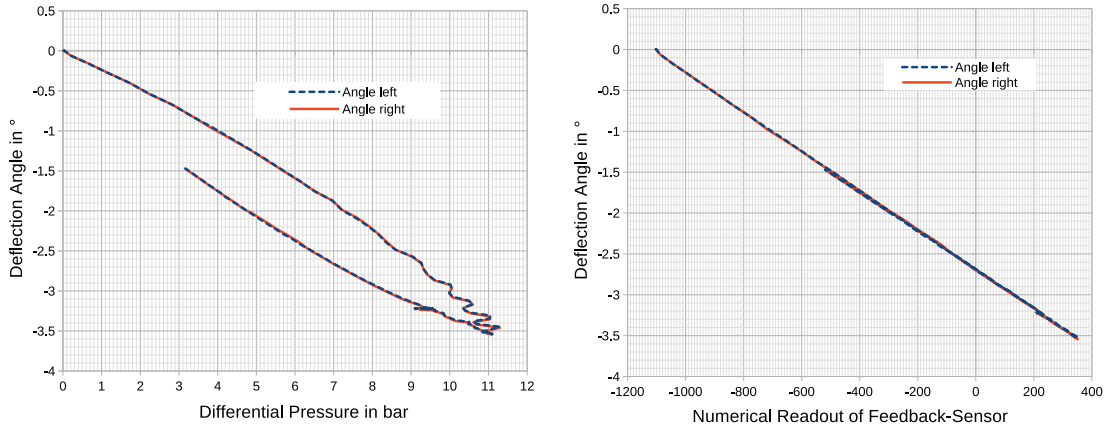

Figure 9: Measured Displacement (Left: Angle over Pressure, Right: Angle over Raw Sensor Readout)

A photogrammetry system is used to externally measure displacements of the demonstrator. Two cordwise cuts along the demonstrator are evaluated for the deflection angle.

The externally measured displacement angle versus the differential pressure of upper and lower pressure cells is shown on the left side of figure 9, clearly showing the non-linearity between pressure and displacement caused by the EPDM material. The right hand side of the figure displays displacement angle versus measured values of the internal sensor, exhibiting linear correlation between both signals. This measurement is used to calibrate the control loop.

In both plots of figure 9 the two externally measured displacements are identical, indicating that the morphing tab is deflecting uniformly, thus supporting the assumption of just needing one control value.

As it is mentioned in section 2.1 the finite element model predicted 0.79°/bar deflection rate. Looking into figure 9 we see a deflection of 3.5° at 11 bar which corresponds to 0.32°/bar, which is just 40% of the predicted value. Looking into the discrepancies two causes are found:

1. Looking at the left side of figure 5 bladders are shown that ensure leak-tightness. These bladders decrease the cross section of the pressure cells, so that the force is reduced 30%. Taking this into account the measured value is 58% of the calculated.
2. Looking on the right side of figure 5 the active and passive parts are shown. Due to problems with manufacturing the ratio between active and passive parts is changed from 46.4% as calculated to 27% as build. Correcting the calculation with this aspect the measured value reaches 95% of the prediction. This is deemed to be a sufficiently accurate prediction to validate the used model.

In order to test for accuracy of the system, the trailing edge is loaded and unloaded with an added weight; the resulting deflection over time is given in figure 10 on the left side for open-loop condition, on the right side for closed loop control. As can be seen the accuracy of $\pm 0.1°$ is reached for the closed loop setup.

The deflection speed is evaluated to be about the order of magnitude required for high-speed performance but inadequate for maneuver load alleviation or gust alleviation as shown on the left side of figure 11. That seems to be caused by the driver for the electric pump not actually delivering the needed current and thus torque for shifting the fluid volume between the pressure cells (see right hand side of figure 11).

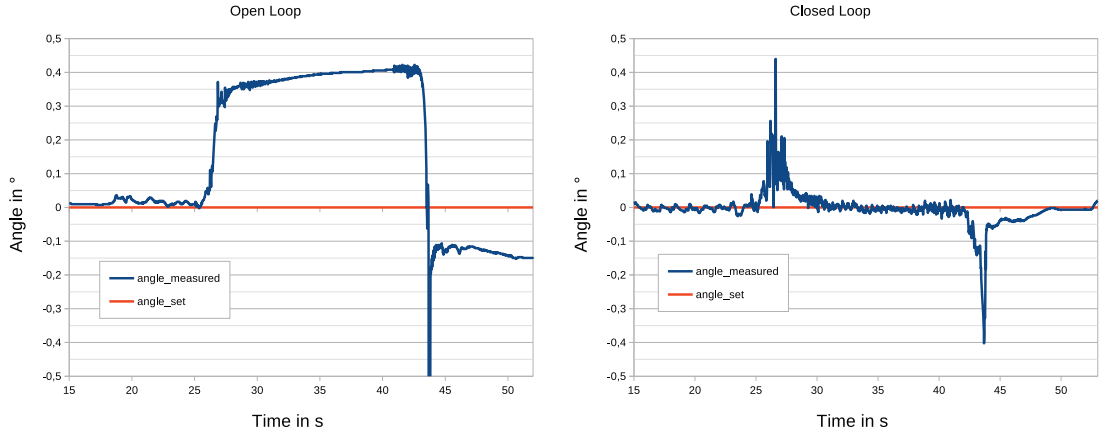

Figure 10: Accuracy of displacement with Disturbance (Left: Open loop, Right: Closed loop)

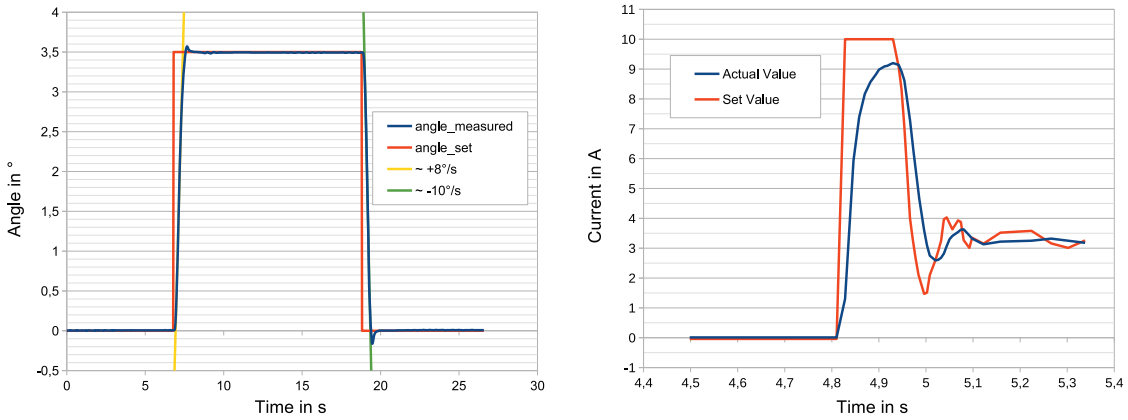

Figure 11: Left: Speed of displacement, Right: Current set value versus actual value

4 Conclusion

A 1 m spanwidth demonstrator is designed, manufactured and tested, including morphing hardware, sensors, redundant hydraulic actuation system and a control system.

The performed tests show the feasibility to use the FAMoUS principle to build a morphing winglet tab. The deflection size and control accuracy requirements are met and the design model is valid after the mentioned corrections. Regarding deflection rates the minimum requirements are met, while the higher deflection rates for load- and gust-alleviation can not be achieved with the current setup.

Summarizing the performed work, it can be stated that TRL 3 is reached, thus meeting the main objective of the experiments.

Furthermore future fields of research to achieve higher TRL are identified: A deeper understanding of dynamic behavior of the pressure cells has to be assessed, especially separating control-parameters and material properties as cause for lower dynamic performance of the system. The testing should address simulated aero-loads and a wider temperature range, as the current test are solely done at room temperature.

Regarding structural design and consequently the manufacturing process a reduction of manufacturing complexity as well as weight optimization should be investigated in more detail, especially addressing observed failure-modes (e.g. as occasional leakage) and aspects of repairability.

Acknowledgment

The work presented in this paper was supported by the Clean Sky 2 Joint Undertaking (JU) with Reference-Nr. 724558 (MANTA – 'Movables for Next Generation Aircraft') and 887240 (AEROMO2 – 'Towards the application of Morphing Movables in Aerostructures'). The JU is financed by the Horizon 2020 program of the European Union.

REFERENCES

[1] S. Vasista, J. Riemenschneider, T. Mendrock, and H. P. Monner, "Pressure-driven Morphing Devices for 3D Shape Changes with Multiple Degrees-of-freedom," in *ASME 2018 Conferene on Smart Materials, Adaptive Structures and Intelligent Systems, SMASIS 2018, Volume 1*, 2018. [Online]. Available: https://elib.dlr.de/124348/

[2] *Integration of Actuators by Additive Layer Manufacturing*, ser. Smart Materials, Adaptive Structures and Intelligent Systems, vol. Volume 2: Modeling, Simulation and Control of Adaptive Systems; Integrated System Design and Implementation; Structural Health Monitoring, 09 2017. [Online]. Available: https://doi.org/10.1115/SMASIS2017-3764

[3] A. Wildschek, S. Storm, M. Herring, D. Drezga, V. Korian, and O. Roock, "Design, Optimization, Testing, Verification, and Validation of the Wingtip Active Trailing Edge," in *Smart Intelligent Aircraft Structures (SARISTU)*, P. C. Wölcken and M. Papadopoulos, Eds. Cham: Springer International Publishing, 2016, pp. 219–255. [Online]. Available: https://doi.org/10.1007/978-3-319-22413-8_12

[4] I. Dimino, F. Gallorini, M. Palmieri, and G. Pispola, "Electromechanical Actuation for Morphing Winglets," *Actuators*, vol. 8, no. 2, p. 42, May 2019. [Online]. Available: http://dx.doi.org/10.3390/act8020042

[5] H. P. Monner, S. Vasista, M. Titze, J. Riemenschneider, C. Contaldi, M. Sahin, K. Jacobi, M. Schäfer, O. Bertram, M. Y. Meddaikar, F. Nolte, P. Horst, A. Wankhade, and R. Evenblij, "Recent Developments on Fluid Actuated Morphing Unit Structures (FAMoUS)," in *ICAST 2021*, Oktober 2021. [Online]. Available: https://elib.dlr.de/145404/

[6] S. Vasista, F. Nolte, M. Schäfer, and J. Riemenschneider, "Design and Manufacture of a Fluid-Actuated Morphing Winglet Trailing Edge Control Surface," in *ASME Turbo Expo 2022: Turbomachinery Technical Conference and Exposition, GT 2022*, 2022. [Online]. Available: https://elib.dlr.de/193223/

[7] M. Schäfer, A. Schäfer, and O. Bertram, "Preliminary Design of Hydraulic and Pneumatic System Architectures for a Morphing Flight Control Structure," *SAE Technical Papers*, September 2019. [Online]. Available: https://doi.org/10.4271/2019-01-1916

[8] M. Schäfer, O. Bertram, S. Vasista, and D. Seer, "Systementwicklung für eine formvariable Struktur an der Flügelhinterkante," in *SMARTE STRUKTUREN UND SYSTEME - TAGUNGSBAND DES 4SMARTS-SYMPOSIUMS 2022*, ser. TAGUNGSBAND DES 4SMARTS-SYMPOSIUMS, M. Wiedemann and T. Melz, Eds. Deutsches Zentrum für Luft- und Raumfahrt e.V., Oktober 2022, pp. 45–54. [Online]. Available: https://elib.dlr.de/189698/

XI ECCOMAS Thematic Conference on Smart Structures and Materials - SMART 2025
M. Krommer, M. Nader and M. Schagerl (Eds)

Received: 18 April 2025 / Revised: 27 August 2025 / Accepted: 4 November 2025
© The Author(s) 2025

A Time Series Global Model Method for Random Vibration Modeling and Generation in Rotating Machinery under any Operating Speed

Xenofon D. Konstantinou, Dimitrios M. Bourdalos, Kyriakos Kritikakos, John S. Sakellariou, Spilios D. Fassois, Josef Koutsoupakis, George Karyofyllas, Dimitrios Giagopoulos

Abstract. A statistical time series global method for random vibration surrogate modeling and signal generation is postulated. Motivated by the mixed spectra nature of the signals, the method is based on a Linear Parameter Varying Generalized AutoRegressive (LPV-GAR) type statistical representation, which, unlike current Neural Network type methods, offers small model size, low complexity, identification simplicity, transparency, and physical interpretability. The LPV nature of the model, employing the rotational speed as scheduling variable, allows, for the first time, for effective signal generation under any speed within an admissible range. The method's effectiveness is assessed via Monte Carlo experiments using a physics-based ADAMS-built high-fidelity drivetrain model and proper signal similarity metrics. The postulated method's performance is superior to those reported in the literature on similar problems, while the importance of using GAR models over simpler AR alternatives is also demonstrated.

Key words: Rotating Machinery, Surrogate models, Data-Driven Random Vibration Signal Generation, Time Series Methods, Generalized AutoRegressive models, Linear Parameter Varying models

1 INTRODUCTION

Over the past decades, data-driven surrogate modeling for the generation of random vibration signals has gained significant attention in the context of design, dynamical analysis, and fault diagnosis in engineering systems and structures [1]. The motivation for this stems from the need for replacing elaborate, large-scale, and expensive physics-based simulations, or actual physical experiments, by small-scale and inexpensive simulations under various Operating

Xenofon D. Konstantinou & Dimitrios M. Bourdalos & Kyriakos Kritikakos & John S. Sakellariou & Spilios D. Fassois
Stochastic Mechanical Systems & Automation (SMSA) Laboratory, Department of Mechanical Engineering & Aeronautics, University of Patras, 26504 Patras, Greece e-mail: xkonstantinou@ac.upatras.gr

Josef Koutsoupakis & George Karyofyllas & Dimitrios Giagopoulos
Machine Dynamics Laboratory (MDL), Department of Mechanical Engineering, Aristotle University of Thessaloniki, Thessaloniki GR54124, Greece, e-mail: jkoutsoup@auth.gr

Conditions (OCs) and real-world scenarios, including faulty conditions [2, 1]. This is important for rotating machinery too, where physics-based models are often characterized by large size and high complexity, and physical experiments under varying OCs (such as rotational speeds and loads) or faulty conditions are typically difficult and expensive [3].

Current data-driven signal generation surrogate models for complex rotating machinery systems (such as gearboxes) are mainly based on specialized Neural Network (NN) architectures, such as Generative Adversarial Networks (GANs) [4, 5, 6, 7, 8, 9] and Variational AutoEncoders (VAEs) [10, 11]. Yet, these models are characterized by their own limitations, including dependence on a number of user-defined hyperparameters (typically more than 8, with their selection often requiring expert knowledge), size and complexity still considered relatively high, tuning requiring intensive computational procedures, and also lack of transparency and interpretability (as their weights cannot be directly associated with the underlying physical system dynamics, such as Gear Meshing Frequencies, GMFs) [12]. An additional important drawback is their inability to operate properly and generate high-fidelity random vibration signals under OCs (such as rotational speed) not specifically used during training [3].

In order to overcome these drawbacks and limitations, the present study takes a different approach and aims at exploring statistical times series methods for effectively tackling the problem. Motivated by the *mixed spectra* nature (consisting of cyclic components, associated with the GMFs, and a rational counterpart associated with the structural dynamics and transmission path effects [13]) characterizing random vibration signals in rotating machinery, the study postulates the use of Generalized AutoRegressive (GAR) representations [14]. Moreover, a Linear Parameter Varying (LPV) structure is additionally imposed on them - with the rotational speed being the *scheduling variable* - in order to provide a *global* LPV-GAR model model capable of representing the random vibration signal under *any admissible* rotational speed within a prespecified range. The postulated global LPV-GAR model thus features small size, low complexity, identification simplicity, transparency, and physical interpretability.

The postulated LPV-GAR method for random vibration signal modeling and signal generation in rotating machinery is then assessed via a physics-based, ADAMS-built [15], high-fidelity drivetrain model, with the similarity between generated and reference (ADAMS-generated) vibration signals quantified by the Cosine Similarity (CS) and the Pearson Correlation Coefficient (PCC) metrics [16]. The achievable performance (in terms of both metrics) is compared to that reported in the literature for similar problems, whereas the importance of resorting on GAR models (versus their simpler AR counterparts that are commonly used in rotating machinery [17, pp. 180–183]) is also considered.

The rest of the paper is organized as follows: The precise problem statement is presented in section 2, while the postulated LPV-GAR model-based method is introduced in section 3. Details on the physics-based simulation model and the Monte Carlo numerical experiments are provided in section 4, and performance assessment in section 5. Concluding remarks are finally summarized in section 6.

2 PRECISE PROBLEM STATEMENT

The problem may be stated as follows: Given M angularly sampled N-sample-long training vibration signals $y_{\Omega_1}[k], \ldots, y_{\Omega_M}[k]$ ($k = 1, 2, \ldots, N$; with k designating equispaced samples characterized by angular sampling frequency f_s^{θ}), with each signal obtained under a specific (fixed and known) *training* rotational speed Ω_i ($i = 1, \ldots, L$; $L \leqslant M$) with $\Omega_i \in [\Omega_{min},\ \Omega_{max}] \subset \Re^+$, do the following:

(a) Obtain a proper stochastic global model $\mathcal{M}_\Omega$ properly representing a random vibration signal under *any* rotational speed $\Omega \in [\Omega_{min},\ \Omega_{max}]$ (*Training Phase*), and,

(b) Generate random vibration signal realizations under *any* rotational speed $\Omega \in [\Omega_{min},\ \Omega_{max}]$ (*Signal Generation Phase*).

Remark: The training vibration signals are typically obtained via angular resampling of corresponding time-domain counterparts.

3 THE DATA-DRIVEN SIGNAL GENERATION METHOD

The method is based on the Generalized AutoRegressive (GAR) model structure [14] capable of representing both cyclic components and a component characterized by a rational (AR) PSD. The former ones are to represent the cyclic frequencies – such as Gear Meshing Frequencies (GMFs) and their sidebands – while the latter one to represent the part of the signal associated with the structural dynamics, transmission path effects, and other sources [13].

For any specific rotational speed Ω the model is of the form:

$$y_\Omega[k] = \sum_{i=1}^{d} \left[A_i(\Omega)\sin(2\pi f_i k) + B_i(\Omega)\cos(2\pi f_i k)\right] + \frac{1}{a(\mathcal{B},\Omega)} e_\Omega[k] \tag{1a}$$

$$a(\mathcal{B},\Omega) := 1 + a_1(\Omega)\mathcal{B} + a_2(\Omega)\mathcal{B}^2 + \ldots a_n(\Omega)\mathcal{B}^n \tag{1b}$$

$$e_\Omega[k] \sim \textit{i.i.d}\, \mathcal{N}(0, \sigma_e^2(\Omega)) \tag{1c}$$

with $y_\Omega[k]$ designating the angularly resampled vibration signal and $e_\Omega[k]$ the model innovations - which, as indicated, is a Gaussian *i.i.d.* (identically independently distributed) zero-mean signal with variance $\sigma_e^2(\Omega)$. f_i the i-th cyclical frequency (order) normalized by the angular resampling frequency f_s^{θ}, $A_i(\Omega)$ and $B_i(\Omega)$ ($i = 1, \ldots, d$) the cyclical component amplitudes, and $\alpha(\mathcal{B},\Omega)$ the AR polynomial with $\mathcal{B}$ representing the backshift operator $\mathcal{B}^i \cdot y_\Omega[k] = y_\Omega[k-i]$.

With proper manipulation, the model of Equation 1 may be re-written as[1]:

$$y_\Omega[k] = \sum_{i=1}^{d} \left[A_i(\Omega)\sin(2\pi f_i k) + B_i(\Omega)\cos(2\pi f_i k)\right] + \sum_{j=1}^{n} a_j(\Omega) y_\Omega[k-j] + e_\Omega[k] \tag{2}$$

[1]Note that the cyclical component amplitudes are not identical to those in Equation 1; yet for simplicity the same symbols are maintained.

with $e_\Omega[k]$ as before. This is subsequently designated as a GAR(n, d) model, with n designating the AR order and d the number of cyclical components.

Based on the above GAR model structure pertaining to a specific rotational speed Ω, a global model capable of representing a random vibration signal under *any* rotational speed $\Omega \in [\Omega_{min},\ \Omega_{max}]$ may be employed. Such a model may be thought of as interpolating the individual (local) GAR(n, d) models using polynomial interpolation to generate a global Linear Parameter Varying (LPV) GAR model that may be designated as LPV-GAR$(n, d)_p$ model, with p designating the polynomial degree. This model is then of the form:

$$y_\Omega[k] = \underbrace{\sum_{i=1}^{d} [A_i(\Omega)\sin(2\pi f_i k) + B_i(\Omega)\cos(2\pi f_i k)]}_{\text{Cyclical component}} + \underbrace{\sum_{j=1}^{n} a_j(\Omega) y_\Omega[k-j]}_{\text{Rational component}} + e_\Omega[k] \tag{3a}$$

$$e_\Omega[k] \sim i.i.d\ N(0, \sigma_e^2(\Omega)) \tag{3b}$$

$$A_i(\Omega) = \sum_{l=0}^{p} A_{i,l} \cdot \Omega^l, \quad B_i(\Omega) = \sum_{l=0}^{p} B_{i,l} \cdot \Omega^l \tag{3c}$$

$$a_j(\Omega) = \sum_{l=0}^{p} a_{j,l} \cdot \Omega^l, \quad \sigma_e(\Omega) = \sum_{l=0}^{p} \sigma_{e,l} \cdot \Omega^l \tag{3d}$$

$$\Omega \in [\Omega_{min}, \Omega_{max}] \subset \mathbb{R}^+ \tag{3e}$$

with $A_{i,l}$, $B_{i,l}$, $a_{j,l}$ and $\sigma_{e,l}$ designating the indicated polynomial coefficients (projection coefficients, with $i = 1, \ldots, d$; $j = 1, \ldots, n$; $l = 0, \ldots, p$).

The *Training Phase* of the proposed signal generation method, which includes the identification of the LPV-GAR$(n, d)_p$ model, is based on M training vibration signals acquired at specific rotational speeds Ω_i ($i = 1, \ldots, L$; $L \leqslant M$), as described in section 2, and consists of four steps as indicated below.

Step 1: Angular Resampling. The time-domain vibration signals are initially angularly resampled via the Computed Order Tracking method [17, pp. 148–151]. This resampling removes non synchronous frequency modulation caused by minor shaft speed fluctuations, which are present even when the nominal speed is constant [17, pp. 148–151]. In order to ensure a common resampling frequency f_s^θ within the considered operational range $[\Omega_{min},\ \Omega_{max}]$, $f_s^\theta = f_s/\Omega_{max}$, where f_s is the time-domain sampling frequency and Ω_{max} the maximum speed (in rev/s). For speeds Ω below Ω_{max}, the bandwidth exceeds the Nyquist limit ($f_s^\theta/2$), causing aliasing which indicates the need for low-pass filtering at $(f_s^\theta/2) \times \Omega$ cut-off frequency [18].

Step 2: Determination of the cyclical frequencies (orders) of the sinusoidal part of the local GAR models. This stage involves the selection of a subset of frequencies (orders) for the cyclical component of the employed local GAR models. Thus, a set of $\bar{d}$ cyclical frequencies (orders) $\mathcal{F}_\Omega^{in} := \{f_1, \ldots, f_{\bar{d}}\}$, including Gear Meshing Frequencies (GMFs) along with a selected num-

ber of their harmonics and sidebands, is initially determined for all L training phase operational speeds $\Omega_1, \ldots, \Omega_L$. Subsequently, for each training speed Ω_i ($i = 1, \ldots, L$), a subset $\mathcal{F}_{\Omega_i}$ is determined by eliminating the frequencies of $\mathcal{F}_{\Omega}^{in}$ that are not manifested in the corresponding signal $y_{\Omega_i}[k]$[2]. This is achieved by applying the Least Absolute Shrinkage and Selection Operator (LASSO) method only for the cyclical component of each local GAR model (as indicated in [19]) as follows[3]:

$$\widehat{\boldsymbol{\theta}}(\Omega_i) := \arg\min_{\boldsymbol{\theta}(\Omega_i)} \left\{ \frac{1}{2N} \sum_{k=1}^{N} \left[y_{\Omega_i}[k] - \boldsymbol{\phi}^T[k] \cdot \boldsymbol{\theta}(\Omega_i) \right]^2 + \lambda \sum_{j=1}^{2\bar{d}} |\theta_j(\Omega_i)| \right\} \tag{4}$$

with:

$$\boldsymbol{\phi}[k] := \left[\sin(2\pi f_1 k) \ldots \sin(2\pi f_{\bar{d}} k) \vdots \cos(2\pi f_1 k) \ldots \cos(2\pi f_{\bar{d}} k) \right]^T_{[2\bar{d}\times 1]},$$

$$\boldsymbol{\theta}(\Omega_i) := \left[A_1(\Omega_i) \ldots A_{\bar{d}}(\Omega_i) \vdots B_1(\Omega_i) \ldots B_{\bar{d}}(\Omega_i) \right]^T_{[2\bar{d}\times 1]}$$

and λ is the regularization factor, a design parameter of the method. Its value is selected by evaluating the following Bayesian criterion [14] over a set of distinct candidate values of λ:

$$\text{Bayesian Criterion} := (N-n) \ln \widehat{\sigma}_e^2(\Omega_i) + (n + 1 + 2\bar{d}) \ln \frac{N}{2\pi} \tag{5}$$

where $n = 0$, as the AR component is omitted in Equation 4. The LASSO solution is obtained using the Coordinate Descent Algorithm [20].

Based on this procedure, the set $\mathcal{F}_{\Omega_i}$ for each training speed Ω_i is obtained as follows:

$$\mathcal{F}_{\Omega_i} = \left\{ \text{all } \Omega_i \in \mathcal{F}_{\Omega}^{in} \mid \max_{j=1,\ldots,\bar{d}} \{A_j(\Omega_i), B_j(\Omega_i)\} > \delta \right\} \tag{6}$$

with $\delta > 0$ designating a user-defined small positive number (threshold above which an estimated amplitude is considered to be non-zero; design parameter).

The set $\mathcal{F}$ of all (d) cyclical frequencies (orders) kept in the final LPV-GAR model of Equation 3 includes all those kept for any individual model, that is:

$$\mathcal{F} := \bigcup_{i=1,\ldots,L} \mathcal{F}_{\Omega_i} \tag{7}$$

Step 3: Identification of the local GAR models. Based on the subset of cyclical frequencies (orders) $\mathcal{F}$ selected in the previous stage, the local GAR models are identified using Ordinary Least Squares (OLS) [21, pp. 204-205]. The AR order n (design parameter) is determined based on the Bayesian criterion[4] given in Equation 5, with $\bar{d}$ substituted by d.

[2] If more than one training signal is available per speed ($M > L$), one signal is selected to be used in Step 2.

[3] Estimators/estimates are indicated via a hat and column-vectors/matrices via bold-face lower/upper case symbols.

[4] The final AR order n is determined as the mean value suggested by the criterion over all M training signals.

Step 4: Determination of the LPV-GAR model. Once the identification of the local GAR models is completed, their parameters are interpolated using standard polynomials, yielding the coefficients $A_{i,l}$, $B_{i,l}$, $a_{j,l}$, and $\sigma_{e,l}$ in Equations 3c and 3d. This leads to the determination of the LPV-GAR model, as defined in Equation 3. The polynomial order p is a design parameter of the method and is selected as the value at which the mean squared error reaches a plateau.

Once the above modeling procedure is completed, the LPV-GAR model may be used for the accurate generation of random vibration signal realizations (*Signal Generation Phase*) for any rotational speed $\Omega \in [\Omega_{min}, \Omega_{max}]$. This is achieved by substituting $e_{\Omega}[k]$ in Equation 3 with a randomly generated Gaussian white noise characterized by zero mean and variance $\sigma_e^2(\Omega)$.

4 THE ROTATING MACHINERY MULTI-BODY DYNAMICS MODEL AND THE MONTE CARLO NUMERICAL EXPERIMENTS

A high-fidelity Multi-body Dynamics (MBD) drivetrain model is developed employing the ADAMS software [15]. The 152 degree-of-freedom (DoFs) drivetrain model, is comprised of two gearboxes, that is a planetary and a two-stage gearbox. The planetary gearbox consists of a sun gear, a ring gear which is stationary, and four planet gears mounted on the carrier, as shown in Figure 1. The gears and shaft are modeled as rigid bodies, while the two gearboxes are modeled as flexible bodies. Motion is introduced via the sun gear's inlet shaft and transmitted through the carrier to the two-stage gearbox, which consists of four gears, with the pinion mounted on the carrier. The shafts mounted to the gearboxes, and the bolts fixing the gearboxes to the ground are modeled as bushings, taking into account the bearings' stiffness and preload conditions in the physical counterpart. The gears are assumed to be fixed to their respective shafts, and gear contact forces are modeled explicitly for each gear pair considering an impact

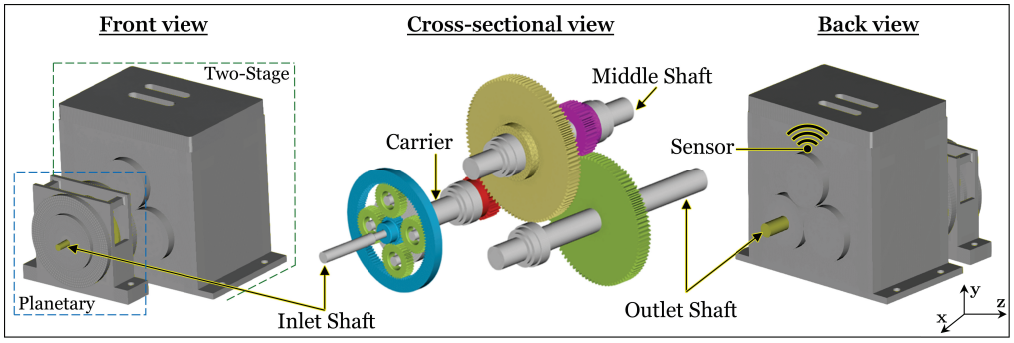

Figure 1: The MBD model of the experimental gear drivetrain, comprising a planetary gearbox with a 28-tooth sun gear, four planet gears (each with 36 teeth), and a stationary 100-tooth ring gear, followed by a two-stage gearbox consisting of a 29-tooth pinion, a 100-tooth gear, and a 36-tooth gear mounted on the middle shaft, along with a 90-tooth gear on the output shaft. A sensor (accelerometer) is positioned on the casing of the middle shaft bearing at the rear side of the gearbox.

force formulation with Hertzian contact stiffness [22], allowing for accurate meshing force estimation.

The MBD model parameters are fine-tuned through an optimization process using experiments from the physical counterpart. This is based on the Covariance Matrix Adaptation Evolution Strategy (CMAES), selected for its ability to effectively improve the fidelity of highly complex and nonlinear models [23]. For each Monte Carlo numerical experiment, a lateral (y) acceleration signal is measured using a single sensor mounted on the casing of the middle shaft bearing, as shown in Figure 1. The sampling frequency is $f_s = 10\,240$ Hz, while the signal length is $N = 40\,960$ samples (4 s).

5 PERFORMANCE ASSESSMENT OF THE SIGNAL GENERATION METHOD

The performance of the proposed LPV-GAR model-based signal generation method is comprehensively assessed using two quality indices: The Pearson Correlation Coefficient (PCC), and Cosine Similarity (CS) which quantify the similarity (D) between the generated signals ($y_\Omega[k]$) and the reference signals ($x_\Omega[k]$) obtained from MBD simulations (see section 4). These are defined as follows [16]:

$$\text{Pearson Correlation Coefficient (angular domain):} \quad D(\dot{\boldsymbol{y}}_\Omega, \dot{\boldsymbol{x}}_\Omega) := \frac{\dot{\boldsymbol{y}}_\Omega^T \cdot \dot{\boldsymbol{x}}_\Omega}{\|\dot{\boldsymbol{y}}_\Omega\| \cdot \|\dot{\boldsymbol{x}}_\Omega\|} \times 100\% \quad (8)$$

$$\text{Cosine Similarity (frequency domain):} \quad D(\tilde{\boldsymbol{y}}_\Omega, \tilde{\boldsymbol{x}}_\Omega) := \frac{\tilde{\boldsymbol{y}}_\Omega^T \cdot \tilde{\boldsymbol{x}}_\Omega}{\|\tilde{\boldsymbol{y}}_\Omega\| \cdot \|\tilde{\boldsymbol{x}}_\Omega\|} \times 100\% \quad (9)$$

with $\dot{\boldsymbol{y}}_\Omega$, $\dot{\boldsymbol{x}}_\Omega$ denoting sample-mean-corrected versions of the vectors $\boldsymbol{y}_\Omega := [y_\Omega[1], \ldots, y_\Omega[N]]^T$ and $\boldsymbol{x}_\Omega := [x_\Omega[1], \ldots, x_\Omega[N]]^T$ containing all signal samples, $\tilde{\boldsymbol{y}}_\Omega$, $\tilde{\boldsymbol{x}}_\Omega$ their (uncorrected) counterparts containing their $N/2$ DFT magnitudes, and $\|\cdot\|$ the Euclidean norm.

The importance of employing GAR models over the simpler and commonly used AR alternatives is also explored via a corresponding LPV-AR$(n)_p$ alternative representation. All details on the vibration signals used in the *Training Phase* and the *Signal Generation Phase* are summarized in Table 1.

5.1 The Training Phase

The selected design parameters and estimation details for the proposed (LPV-GAR) and the alternative (LPV-AR) model-based signal generation methods are summarized in Table 2.

5.2 The Signal Generation Phase - Performance Assessment

The previously identified LPV-GAR$(100, 266)_3$ and LPV-AR$(1280)_3$ models are now employed to generate 20 random vibration signal realizations for each of the 11 rotational speeds specified in Table 1. This results in a total of 220 generated signals, which are directly compared with the corresponding reference (real) signals obtained from the MBD simulations.

The average DFT amplitude over all 20 LPV-GAR$(100, 266)_3$ and LPV-AR$(1280)_3$ model-based generated realizations for an indicative non-training speed (1 110 rpm) is presented in

Table 1: Details on the vibration signals used in the Training and Signal Generation Phases.

Phase	Rotational Speed (rpm)	#Speeds	#Signals/Speed	Total #Signals
Training	$\{900, 960, \ldots, 1\,200\}$ (step of 60 rpm)	6	1	$6^{(a)}$
Signal Generation	$\{900, 930, \ldots, 1\,200\}^{(c)}$ (step of 30 rpm)	11	20	220
Resampling frequency: $f_s^\theta = 2\,340$ (samples/rev)$^{(b)}$; Signal length: $N = 30\,420$ samples.				

$^{(a)}$Each training signal corresponds to a distinct speed, hence $M = L = 6$.
$^{(b)}$Given the planetary gearbox ratio of approximately 4.57, the maximum rotational speed of the carrier shaft is $\Omega_{max} = 4.38$ rev/s.
$^{(c)}$The non-training speeds are: $\{930, 990, 1\,050, 1\,110, 1\,170\}$ rpm.

Table 2: Details on design parameter selection.

Model	Design Parameter	Search Interval	Selected Value
LPV-GAR$^{(a)}$	AR order (n)	$[10, 1\,500]$	100
	Polynomial order (p)$^{(b)}$	$[1, 5]$	3
	LASSO tuning parameter (λ)	$[10^{-4}, 10^{-2}]$	$2.35 \times 10^{-3}{}^{(c)}$
LPV-AR	AR order (n)	$[10, 1\,500]$	1 280
	Polynomial order (p)$^{(b)}$	$[1, 5]$	3

$^{(a)}$The design parameter δ has been selected equal to 10^{-4}.
$^{(b)}$All polynomial coefficients up to degree p are included.
$^{(c)}$Corresponding to $d = 266$ cyclical frequencies. The initial set $\mathcal{F}_\Omega^{in}$ comprises $\bar{d} = 416$ cyclical frequencies, including all GMFs, their harmonics, and associated sidebands.

Figure 2 and directly compared with that of the reference signals obtained from the MBD simulations. Evidently, the close agreement between the average DFT of the LPV-GAR model-based generated signals and that of the reference signals demonstrates the high accuracy of the proposed signal generation method. This performance is clearly superior to that of the alternative LPV-AR model-based method, as it fails to accurately reproduce certain cyclical frequencies (orders), either omitting them entirely or generating them with incorrect amplitudes (see Figure 2(b)).

The cumulative results, over all Generation Phase speeds and signals, are presented in Figure 3 in terms of sample mean values of the PCC and CS similarity metrics for the LPV-GAR$(100, 266)_3$ and LPV-AR$(1280)_3$ model-based methods. It is evident that the LPV-GAR model-based generation method outperforms its LPV-AR counterpart. As expected, the performance of both methods deteriorates at speeds not included in the Training Phase (non-training speeds). This deterioration is more evident in the PCC metric (angular domain), indicating a phase mismatch between the generated and reference signals, an issue that has also been reported in the literature [5]. It is important to note that the achievable performance is superior to the best results reported in the literature for similar problems, in which the PCC reaches 85.4%

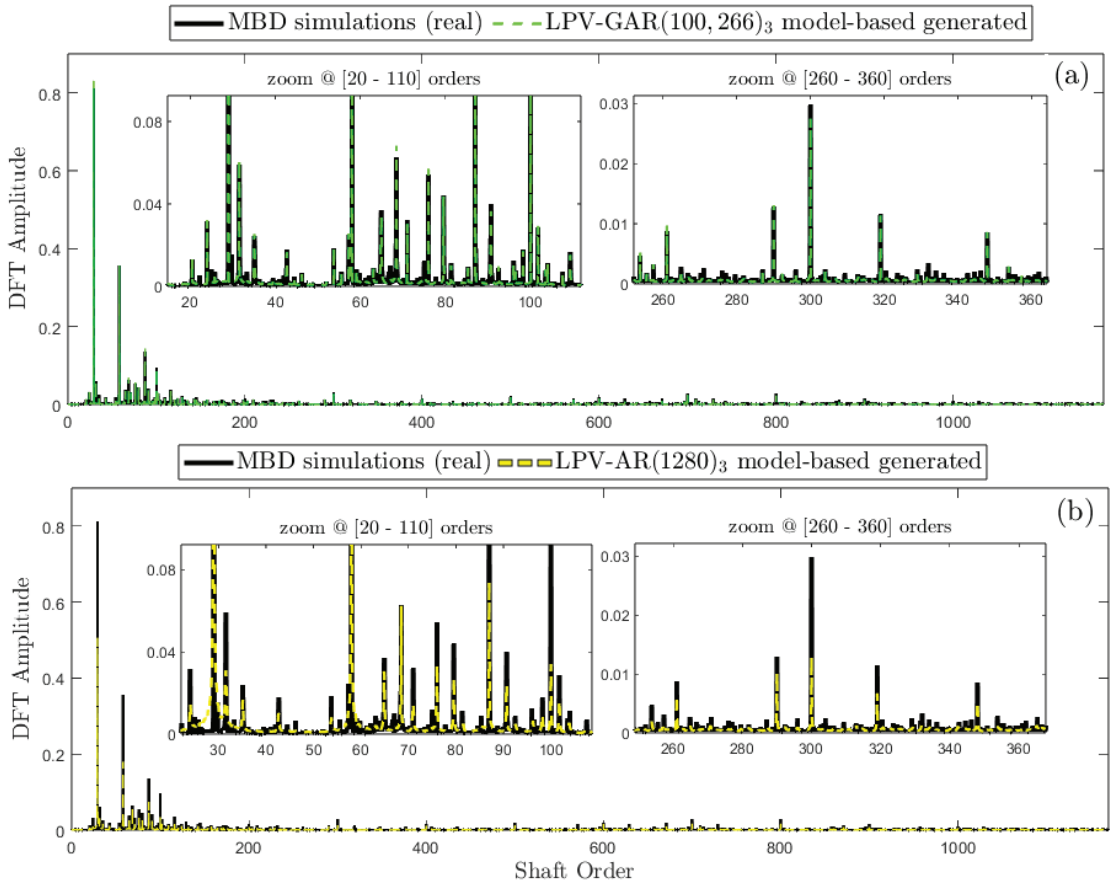

Figure 2: Random vibration signal generation performance for a non-training rotational speed (1 110 rpm): Average DFT magnitude of 20 generated signals (green or yellow) versus that of the actual MBD-provided signal (black): Signal generation based on (a) the LPV–GAR$(100, 266)_3$ model (in green), and (b) the LPV–AR$(1280)_3$ model (in yellow).

[24] and the CS 92.2% [4] under operating conditions (such as rotational speeds and loads) included in the Training Phase, while PCC drops to 10% [5] for non-training conditions.

6 CONCLUDING REMARKS

A statistical time series global method for random vibration surrogate modeling and signal generation has been postulated and comprehensively assessed. Motivated by the mixed spectral nature of the signals, the method is based on a Linear Parameter Varying Generalized AutoRegressive (LPV-GAR) statistical representation. By employing the rotational speed as a scheduling variable, it enables, for the first time, effective signal generation under any speed

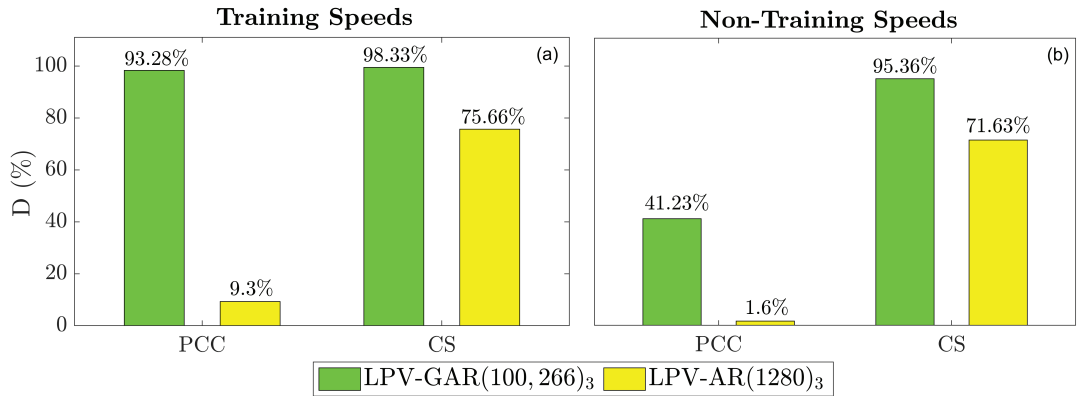

Figure 3: Random vibration signal generation overall performance assessment in terms of sample mean values of the PCC and CS similarity metrics for the LPV-GAR$(100, 266)_3$ (in green) and LPV-AR$(1280)_3$ (in yellow) model-based methods for (a) all training speeds (left subplot) and (b) all non-training speeds (right subplot). [The mean values of the 120 Generation Phase signals corresponding to the 6 training speeds and the 100 signals corresponding to the 5 non-training speeds (20 signals per speed) are presented; details in Table 1.]

within an admissible range.

The postulated method has been systematically assessed via a physics-based, ADAMS-built, high-fidelity drivetrain model, with the similarity between generated and reference (ADAMS-generated) vibration signals quantified by the CS and the PCC metrics. The achievable performance (in terms of both metrics) is compared to that reported in the literature for similar problems, whereas the importance of resorting on GAR models (versus their simpler AR counterparts) is also examined.

The main conclusions drawn from the study may be summarized as follows:

1. The LPV-GAR model-based signal generation method demonstrates high performance, providing high-fidelity signals for any rotational speed within the operational range, even for speeds not employed during training.
2. The achievable performance is superior to that of the alternative LPV-AR model-based method and the best results reported in the literature for similar problems. Unlike current Neural Network type methods, the proposed method offers small size, low complexity, identification simplicity, transparency, and physical interpretability.
3. The employed GAR models offer enhanced model parsimony and identification accuracy compared to the simpler AR counterparts that are commonly used in rotating machinery [17, pp. 180–183].

Acknowledgment

This study has been carried out as part of the ‘EEDRIVEN’ project implemented in the framework of the H.F.R.I. call ‘Basic Research Financing (Horizontal support of all Sciences)’

under the National Recovery and Resilience Plan ‘Greece 2.0’ funded by the European Union – NextGenerationEU (H.F.R.I. Project Number: 16381).

REFERENCES

[1] J. Kudela and R. Matousek, “Recent advances and applications of surrogate models for finite element method computations: a review,” *Soft Computing*, vol. 26, no. 24, pp. 13 709–13 733, Dec 2022.

[2] T. Pan, J. Chen, T. Zhang, S. Liu, S. He, and H. Lv, “Generative adversarial network in mechanical fault diagnosis under small sample: A systematic review on applications and future perspectives,” *ISA Transactions*, vol. 128, pp. 1–10, 2022.

[3] Z. Ju, Y. Chen, Y. Qiang, X. Chen, C. Ju, and J. Yang, “A systematic review of data augmentation methods for intelligent fault diagnosis of rotating machinery under limited data conditions,” *Measurement Science and Technology*, vol. 35, no. 12, p. 122004, 2024.

[4] T. Zheng, L. Song, J. Wang, W. Teng, X. Xu, and C. Ma, “Data synthesis using dual discriminator conditional generative adversarial networks for imbalanced fault diagnosis of rolling bearings,” *Measurement*, vol. 158, p. 107741, 2020.

[5] T. Zhang, J. Chen, J. Xie, and T. Pan, “Sasln: Signals augmented self-taught learning networks for mechanical fault diagnosis under small sample condition,” *IEEE Transactions on Instrumentation and Measurement*, vol. 70, pp. 1–11, 2021.

[6] Y. Liao, R. Huang, J. Li, Z. Chen, and W. Li, “Deep semisupervised domain generalization network for rotary machinery fault diagnosis under variable speed,” *IEEE Transactions on Instrumentation and Measurement*, vol. 69, no. 10, pp. 8064–8075, 2020.

[7] Z. Li, T. Zheng, Y. Wang, Z. Cao, Z. Guo, and H. Fu, “A novel method for imbalanced fault diagnosis of rotating machinery based on generative adversarial networks,” *IEEE Transactions on Instrumentation and Measurement*, vol. 70, pp. 1–17, 2021.

[8] J. Luo, J. Huang, and H. Li, “A case study of conditional deep convolutional generative adversarial networks in machine fault diagnosis,” *Journal of Intelligent Manufacturing*, vol. 32, no. 2, pp. 407–425, 2021.

[9] R. Wang, Z. Chen, and W. Li, “Gradient flow-based meta generative adversarial network for data augmentation in fault diagnosis,” *Applied Soft Computing*, vol. 142, p. 110313, 2023.

[10] Y. Liu, H. Jiang, R. Yao, and H. Zhu, “Interpretable data-augmented adversarial variational autoencoder with sequential attention for imbalanced fault diagnosis,” *Journal of Manufacturing Systems*, vol. 71, pp. 342–359, 2023.

[11] Z. Zhao, Y. Xu, J. Zhang, R. Zhao, Z. Chen, and Y. Jiao, “A semi-supervised gaussian mixture variational autoencoder method for few-shot fine-grained fault diagnosis,” *Neural Networks*, vol. 178, p. 106482, 2024.

[12] D. Neupane, M. R. Bouadjenek, R. Dazeley, and S. Aryal, "Data-driven machinery fault diagnosis: A comprehensive review," *Neurocomputing*, vol. 627, p. 129588, 2025.

[13] Y. Chen, M. Rao, K. Feng, and M. J. Zuo, "Physics-informed LSTM hyperparameters selection for gearbox fault detection," *Mechanical Systems and Signal Processing*, vol. 171, p. 108907, 2022.

[14] C. Chatterjee, R. Kashyap, and G. Boray, "Estimation of close sinusoids in colored noise and model discrimination," *IEEE Transactions on Acoustics, Speech, and Signal Processing*, vol. 35, no. 3, pp. 328–337, 1987.

[15] Hexagon, "Adams: Multibody dynamics simulation software," 2025, accessed: 2025-04-02.

[16] A. S. Shirkhorshidi, S. Aghabozorgi, and T. Y. Wah, "A comparison study on similarity and dissimilarity measures in clustering continuous data," *PLoS ONE*, vol. 10, no. 12, p. e0144059, 2015.

[17] R. Randall, *Vibration-Based Condition Monitoring: Industrial, Automotive and Aerospace Applications*. Hoboken, NJ: John Wiley & Sons, Ltd, 2021.

[18] D. Bourdalos and J. Sakellariou, "Vibration-based robust detection of gear incipient faults under different speeds and loads via a cloud of functional models," in *Proceedings of the 11th ECCOMAS Thematic Conference on Smart Structures and Materials (SMART 2025)*, Linz, Austria, July 2025.

[19] T. Li, *Time Series with Mixed Spectra*. Taylor & Francis, 2014, ch. 5.4, pp. 133–135.

[20] J. H. Friedman, T. Hastie, and R. Tibshirani, "Regularization paths for generalized linear models via coordinate descent," *Journal of Statistical Software*, vol. 33, no. 1, p. 1–22, 2010.

[21] L. Ljung, *System Identification: Theory for the User*, 2nd ed. Prentice Hall PTR, 1999.

[22] J. Koutsoupakis, D. Giagopoulos, and I. Chatziparasidis, "AI-based condition monitoring on mechanical systems using multibody dynamics models," *Engineering Applications of Artificial Intelligence*, vol. 123, p. 106467, 2023.

[23] J. Koutsoupakis, P. Seventekidis, and D. Giagopoulos, "Machine learning based condition monitoring for gear transmission systems using data generated by optimal multibody dynamics models," *Mechanical Systems and Signal Processing*, vol. 190, p. 110130, 2023.

[24] Q. Guo, Y. Li, Y. Liu, S. Gao, and Y. Song, "Data augmentation for intelligent mechanical fault diagnosis based on local shared multiple-generator gan," *IEEE Sensors Journal*, vol. 22, no. 10, pp. 9598–9609, 2022.

XI ECCOMAS Thematic Conference on Smart Structures and Materials - SMART 2025
M. Krommer, M. Nader and M. Schagerl (Eds)

Received: 22 April 2025 / Revised: 27 August 2025 / Accepted: 4 November 2025
© The Author(s) 2025

Multiphysics Modelling of an Active Coupled Helmholtz-Resonator-Cantilever Sound Absorber

Felix Langfeldt

Abstract. Helmholtz-resonators (HRs) are widely used in acoustics for the absorption of low-frequency sound. Owing to their resonant behavior, the sound absorption of HRs is only effective in narrow frequency bands. This limits the applicability of HRs to addressing tonal noise sources or isolated acoustic room modes which do not change over time. In Hoppen *et al.*, *J. Sound Vib.* 559 (2023), 117747, it was shown that by vibro-acoustically coupling a HR with a carefully tuned resonant cantilever (CL) beam that is embedded in the walls surrounding the HR cavity, a more broadband sound absorption can be achieved without changing the mass or size of the HR. This makes Helmholtz-resonator-cantilever (HRCL) sound absorbers ideal for applications in low-frequency noise control problems which have strict constraints on the mass and size of acoustic treatments (e.g., in aircraft cabins or cars).

Another advantage of HRCL sound absorbers is that the vibro-acoustics coupling between HR and CL can be exploited to create an active sound absorber by mechanically actuating the CL. This enables the use of different active control strategies, e.g. to increase the bandwidth of the HRCL absorber or adaptively change the HRCL resonance frequencies to track time-varying tonal noise sources. This contribution explores the multiphysical modelling of an active HRCL absorber concept with a macro-fiber composite (MFC) piezoelectric actuator attached to the CL. A simulation model, based on the finite element method (FEM), is developed, which includes a detailed model of the acoustical, mechanical, and piezoelectric domains and their mutual couplings. The FEM model is validated using impedance tube measurements of a 3D printed HRCL prototype with a MFC actuator. The FEM model is then used to explore the physical behavior of the active HRCL concept and evaluate the performance of basic active control approaches that can be used for the realization of smart HRCL-based sound absorbers.

Key words: Sound absorption, Multiphysics, Vibro-acoustics, Piezoelectric, Finite element method

Felix Langfeldt
Institute of Sound and Vibration Research, University of Southampton, University Road, Southampton SO17 1BJ, United Kingdom, e-mail: F.Langfeldt@soton.ac.uk

1 INTRODUCTION

Helmholtz-resonators (HRs) are acoustic resonators which can be modelled as an equivalent mechanical single degree-of-freedom (DOF) resonator consisting of a spring, a mass, and a damper. In HR, the spring is acoustically formed by a rigidly enclosed cavity (i.e., a well-defined fluid volume) that is connected via a narrow neck (i.e., an acoustic waveguide with dimensions much smaller than the acoustic wavelength, like a narrow cylindrical tube) to the exterior acoustic environment. The fluid inside the neck acts as both the mass and the damping mechanism (through thermoviscous losses in the boundary layer of the oscillating fluid in the neck) in the analog mechanical resonator representation. The resonance frequency f_{HR} is a key characteristic of a HR. For a HR with a straight prismatic neck of cross-sectional area S_{n} and length l_{n}, the resonance frequency is given by

$$f_{\mathrm{HR}} = \frac{c_0}{2\pi}\sqrt{\frac{S_{\mathrm{n}}}{l_{\mathrm{n,eff}} V_{\mathrm{HR}}}}, \tag{1}$$

where c_0 is the speed of sound, V_{HR} is the cavity volume, and $l_{\mathrm{n,eff}}$ is the effective neck length, which is slightly larger than the physical neck length l_{n} due to the entrainment of additional fluid from outside the neck.

HRs are used in many different acoustical applications. Historically, HRs have been widely used as sound absorbers in room acoustics or as silencers in duct systems [1]. More recently, the tunability of HRs (via Eq. (1)) opened up new ways of advanced sound wave manipulation, for example as acoustic metamaterials with negative bulk modulus [2, 3] or to slow down sound waves for controlling combustion instabilities [4]. However, a major shortcoming of HRs in most of these applications is their narrow bandwidth, which is a direct consequence of their resonance-driven behavior. Thus, recent research efforts have focused on developing new HR concepts with increased bandwidth, for example by arranging HR with different resonance frequencies in parallel [5] or cascading HR in series [6] to achieve more broadband sound absorption. Hoppen *et al.* [7] proposed a new HR concept in which the neck is a U-shaped narrow slit, creating a cantilever beam embedded within the cover of the HR. This cantilever exhibits a structural resonance that is coupled to the acoustic resonance of the HR via the acoustic pressure in the cavity. The acoustic and structural resonances of this Helmholtz-resonator-cantilever (HRCL) resonator form a coupled 2-DOF system with two resonance frequencies that can be tuned, for example, to achieve an enhanced bandwidth. A key advantage of the HRCL resonator over other higher-bandwidth HR concepts is that the increased bandwidth is achieved without increasing the volume or mass of the resonator, making HRCL resonators a better choice for applications in which the volume and mass of acoustic treatments are highly constrained.

Despite the additional degree of freedom, the sound absorption bandwidth of HRCL resonators is still very limited. To mitigate this, Kehrbaum and Langfeldt [8] explored the use of a thin and flexible macro-fiber composite (MFC) piezoelectric actuator attached to the cantilever of a HRCL resonator, turning it into an active sound absorber with minimum impact on the HRCL's overall mass and volume. The scoping study in Ref. [8] focused on the design

and basic test of an active HRCL experimental test sample manufactured using 3D printing. The present contribution builds upon this work, aiming at the accurate modelling of the active HRCL resonator using the finite element method (FEM), taking into account the complex multiphysical coupling between the acoustic fields (including thermoviscous effects in the narrow slit), the structural vibration, and the piezoelectric coupling in the MFC. Section 2 provides a description of the FEM model and validates the simulation model using the experimental results obtained with the test sample from Ref. [8]. Section 3 uses the HRCL simulation model to analyze the sound absorption properties of the active HRCL resonator in different active control configurations. Finally, Section 4 provides a summary and the conclusions of this work.

2 NUMERICAL MODEL

2.1 Acoustic and structure modelling

Fig. 1(a) shows an illustration of the geometry of the active HRCL resonator studied here, including the key dimensions. Table 1 lists the geometrical parameters values of the HRCL resonator used for the experimental validation. As shown in Fig. 1(a), the symmetry of the resonator enables the use of a symmetry boundary condition in the xz-plane, reducing the size of the numerical model by half. The other boundary conditions are illustrated in Fig. 1(c): The bottom boundary of the resonator structure was fixed and the side boundaries were unconstrained. The HRCL structure was modelled as a linear elastic material (polylactic acid, PLA) with a Young's modulus of $E_{\mathrm{PLA}} = 3.5\,\mathrm{GPa}$, Poisson's ratio $\nu_{\mathrm{PLA}} = 0.36$, density $\rho_{\mathrm{PLA}} = 1240\,\mathrm{kg\,m^{-3}}$, and

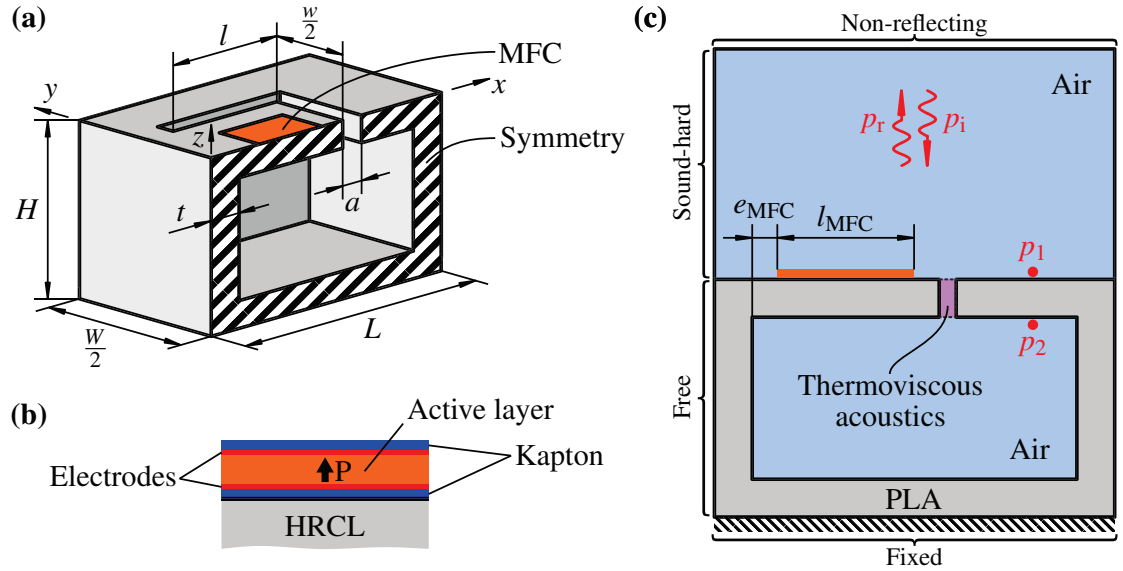

Figure 1: Illustration of the numerical model of the active HRCL resonator. (a) Geometry and dimensions of the resonator; (b) Layers used in the multi-layered shell model of the MFC; (c) Cross-section of the numerical model of the HRCL, including material definitions and boundary conditions.

Table 1: Geometry parameters of the HRCL resonator used for the experimental validation.

H	L	W	t	l	w	a	l_{MFC}	w_{MFC}	e_{MFC}
29.5	75	65	3.5	38	20	0.64	28	14	4
mm	mm	mm	mm	mm	mm	mm	mm	mm	mm

loss factor $\eta_{\mathrm{PLA}} = 0.03$. The fluid inside the cavity and neck of the resonator as well as outside of the resonator was modelled as air, with a speed of sound of $c_0 = 343\,\mathrm{m\,s^{-1}}$, density $\rho_0 = 1.2\,\mathrm{kg\,m^{-3}}$, and dynamic viscosity $\eta_0 = 18.1\,\mu\mathrm{Pa\,s}$. The exterior fluid domain represents a sound-hard walled rectangular waveguide with the same cross section as the resonator and is terminated by a non-reflecting boundary. The fluid inside the neck is modelled using the fully linearised Navier-Stokes equations, taking into account the thermal and viscous losses from boundary layer effects in the narrow slit. All other fluid domains (the cavity and the exterior fluid) are modelled using the lossless wave equation. Full vibro-acoustic coupling is established in all air-PLA interfaces. This includes the continuity of both wall-normal and tangential velocities at the fluid-structure interfaces in the thermoviscous domain, where strong oscillations of the tip of the cantilever are expected to significantly affect the damping of acoustic waves inside the neck.

The simulations are performed in the frequency domain and the resonator is acoustically excited using a normally incident plane acoustic wave with amplitude p_{i}. To obtain the absorption coefficient α, the (complex) amplitude of the reflected sound wave p_{r} is evaluated at the non-reflecting boundary and α is calculated according to

$$\alpha = 1 - \left| \frac{p_{\mathrm{r}}}{p_{\mathrm{i}}} \right|^2 . \tag{2}$$

2.2 Actuator modelling

The actuator is modelled as a multi-layered shell consisting of five layers (see Fig. 1(b)): The first layer is a 40 µm thick Kapton layer, followed by a 18 µm thick layer representing the electrode. The middle layer is the active layer consisting of a homogenized 180 µm thick piezoelectric material. The fourth and fifth layers are another electrode layer and Kapton layer, respectively. The transversely isotropic elastic material properties for all three material types used in the layers are summarized in Table 2. These values are based on the mixing rule values for d_{31}-MFCs provided by Deraemaeker *et al.* [9]. For the density, a homogenized value of $4450\,\mathrm{kg\,m^{-3}}$ was used in all layers. The piezoelectric coupling between the mechanical and electrostatic fields within the active layer is established using a piezoelectric material model with the piezoelectric coefficients d_{31} and d_{32} as well as the relative permittivity $\varepsilon_{r,33}$ given in Table 2. The arrow in Fig. 1(b) indicates the direction of the polarisation of the piezoelectric material. The actuator voltage v_{act} is applied to the top electrode in the multi-layered MFC model and the bottom electrode is set as ground.

Table 2: Material parameters used for the multi-layered shell model of the MFC actuator.

Material	E_1	E_2	ν_{12}	ν_{23}	G_{12}	d_{31}	d_{32}	$\varepsilon_{r,33}$	Rotation[a]
Kapton	2.8	2.8	0.3	0.3	1.08	—	—	—	0
Electrode	30.3	3.8	0.3	0.31	1.46	—	—	—	90
Active layer	16.98	47.17	0.395	0.387	6.06	-183	-153	1600	0
	GPa	GPa	—	—	GPa	$\mathrm{pm\,V^{-1}}$	$\mathrm{pm\,V^{-1}}$	—	°

[a] In-plane rotation angle of the axis 1 with respect to the global y-axis. In the notation for the transversely isotropic material model, axis 1 corresponds to the axis normal to the isotropy plane of the material.

For the mechanical coupling between the MFC and the HRCL cantilever structure, the deformation of the bottom boundary of the first layer in the MFC model is constrained to be equal to the deformation of the HRCL solid structure within all boundary elements shared between the MFC and the HRCL structure. This essentially models the MFC as a cladding on the HRCL and also takes into account the offset between the mid-plane of the MFC layer and the surface of the HRCL as well as the deformation of the cantilever when a voltage is applied to the MFC.

2.3 Discretization

The FEM model of the HRCL was discretized using three-dimensional quadratic elements. Fig. 2 provides an overview of the element sizes used in the structural and acoustical domains. The HRCL walls were discretized with a swept mesh using a maximum element size of $t/3$ to ensure at least three elements in the through-thickness direction of the HRCL structure. In the slit, the element size was reduced to $a/3$ in the wall-normal direction, so that the thermoviscous boundary layer within the slit was sufficiently resolved. In the acoustic domains

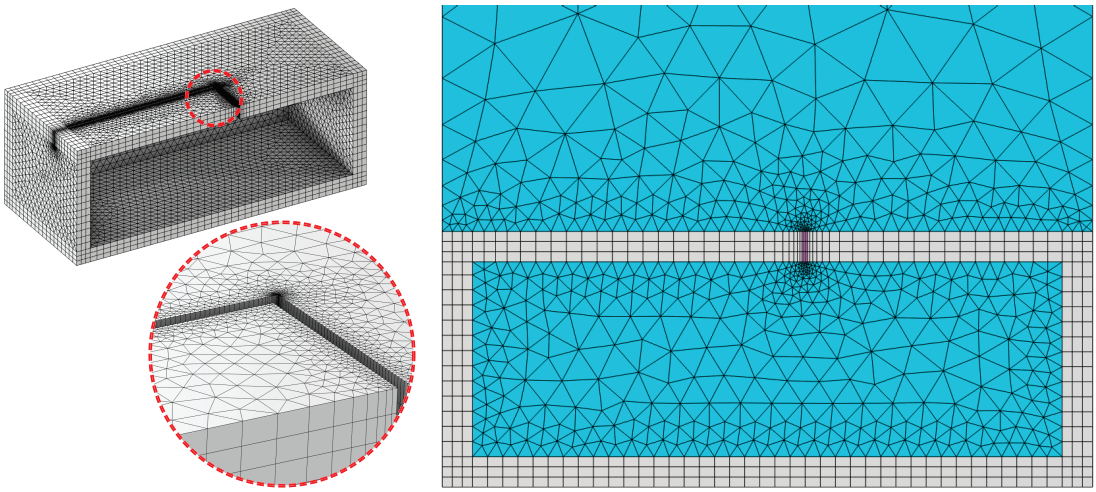

Figure 2: Illustration of the mesh used for the discretization of the HRCL simulation model.

covering the HRCL cavity and the waveguide, the maximum element size was set to 56.7 mm in order to achieve at least six elements per wavelength throughout the frequency range of interest (100 Hz to 1000 Hz). Lastly, the shell elements representing the MFC were discretized using two through-thickness mesh elements per shell layer, i.e. ten through-thickness elements in total.

2.4 Model validation

To validate the simulation model of the HRCL, the purely passive behavior of the HRCL is considered first by comparing the simulated sound absorption coefficient to measured values with the electrical terminals of the actuator shorted ($v_{\mathrm{act}} = 0$). For the measurements, the HRCL test sample (see Fig. 3(a)) was mounted at the end of a circular impedance tube with a diameter of 100 mm. The sound absorption coefficient α was measured according to ISO 10534-2 (two-microphone method). Since the experiment used a circular impedance tube with a cross-sectional area bigger than the area of the HRCL resonator, the simulation model is adapted for this validation study to have a circular waveguide with the same diameter as in the experiment. To take into account the sound absorption introduced by the part of the circular sample holder not covered by the HRCL sample, an impedance boundary condition with a boundary impedance of $1.11\rho_0 c_0$ is included.

Fig. 3(b) shows the measured and simulated absorption coefficients for the passive HRCL resonator with the MFC attached to the cantilever. Generally, the agreement between experiment and FEM simulation is very good. Two sound absorption peaks can be observed: The first peak at 540 Hz corresponds to the resonance frequency of the cantilever. The second peak at 600 Hz with almost perfect absorption is the Helmholtz resonance frequency f_{HR}. At lower frequencies, some discrepancies between the simulations and the measurements can be observed, which could be attributable to the sample holder not being perfectly rigid in the experiments and thus leaking sound energy out of the impedance tube at lower frequencies. The overall very good agreement between the FEM model and the experiments in the vicinity of the two absorption peaks, however, indicates that the passive behavior of the active HRCL resonator is very well captured by the model.

To validate the modelling of the coupled actuator and HRCL system, the plant response of the active HRCL was also measured in the impedance tube. This was done by applying a voltage signal to the actuator electrical terminals and measuring the resulting radiated pressure p_{r}. The plant response measurement and simulation results are shown in Fig. 3(c) (magnitude) and Fig. 3(d) (phase angle), with p_{r} normalized to a unit voltage input. In Fig. 3(c) it can be seen that the magnitude of the pressure radiated by the active HRCL peaks around the cantilever resonance frequency (540 Hz) and then rolls off towards higher frequencies. The peak caused by the Helmholtz resonance is much more damped than the cantilever resonance and therefore is not visible as a distinct second peak in the plant response. However, the approximately 2π change in phase (see Fig. 3(d)) reveals that two resonances are governing the plant response in this frequency range. In general, both plots show that the simulation model agrees very well with the measured plant response, in both the magnitude and the phase. Only at very

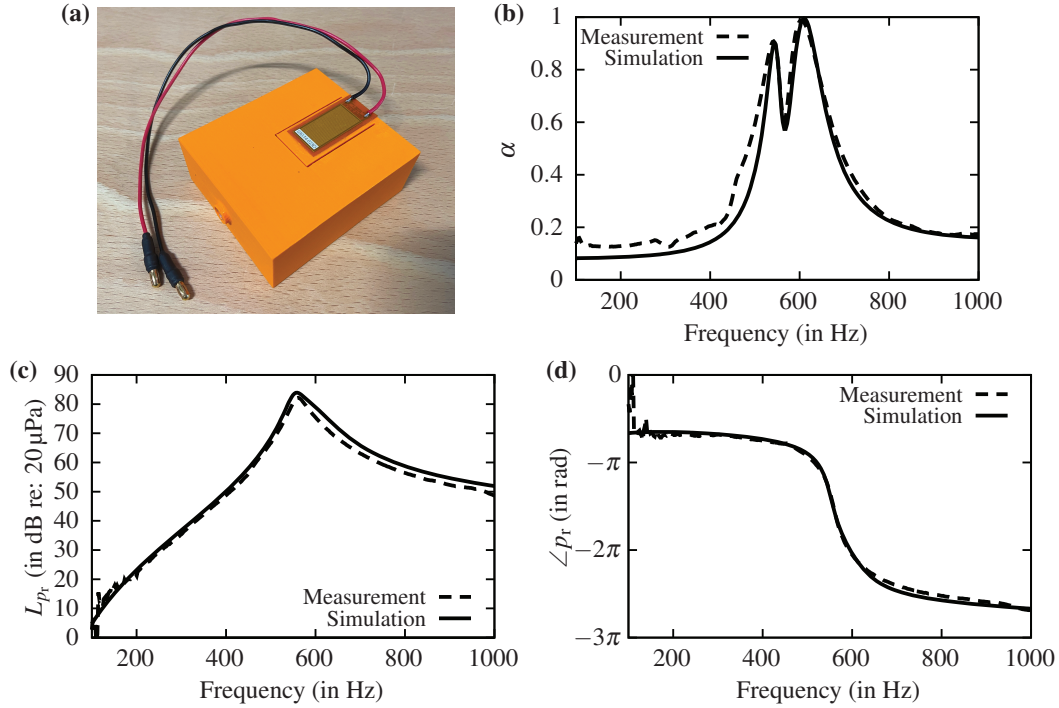

Figure 3: (a) Photograph of the active HRCL resonator test sample. (b) Comparison of the measured and simulated passive sound absorption coefficient of the HRCL resonator. (c)–(d) Comparison of the measured and simulated magnitude and phase angle of the sound pressure p_r radiated by the active HRCL resonator for a unit voltage applied to the actuator (plant response).

low frequencies some differences become visible which are due to noise in the measurements because the radiated sound pressure levels become very low in this frequency range.

3 ABSORPTION CONTROL DESIGN

With the now validated numerical model of the active HRCL resonator different active control strategies can be explored to modify the sound absorption of the HRCL resonator. In this section, two control strategies will be investigated: A simple pressure feedback, enabling the tuning of the HRCL resonance frequencies and impedance-based control, enabling more broadband sound absorption. In both cases, the control strategy will be explained and the stability of the approach analysed using the Nyquist criterion. Then, the control laws will be implemented in the FEM model of the active HRCL to simulate the sound absorption coefficient of the closed-loop system.

3.1 Pressure feedback

In this simple control approach, which was introduced briefly in Ref. [8], the actuator voltage signal v_{act} is proportional to the pressure inside the HRCL cavity p_2:

$$v_{\mathrm{act}} = K_p p_2. \tag{3}$$

To investigate the stability of this control approach, Fig. 4(a) shows the Nyquist diagram of the simulated active HRCL plant response p_2/v_{act} with a control gain of $K_p = -0.25\,\mathrm{V\,Pa^{-1}}$. In the simulation model, the pressure p_2 was extracted using a point probe located at the top boundary of the cavity (see Fig. 1(c)). The Nyquist curve does not encircle the $(-1,0)$ point, indicating that the system is stable for $-0.25\,\mathrm{V\,Pa^{-1}} \leq K_p \leq 0\,\mathrm{V\,Pa^{-1}}$. For positive K_p, the system is stable for much higher gain values, because the Nyquist curve will be rotated around the origin by 180° in this case.

As an example, Fig. 4(b) shows the simulated sound absorption curves for $K_p = -0.25$, 0, and $5\,\mathrm{V\,Pa^{-1}}$. The results show that for positive gain values the two absorption peaks are shifted further apart. At $K_p = 5\,\mathrm{V\,Pa^{-1}}$, the cantilever resonance frequency reduces to 430 Hz (from 540 Hz) and the HR resonance frequency increases to 790 Hz (from 610 Hz). The relative change of the two resonance frequencies (with respect to the passive HRCL) is almost the same ($\pm 25 \ldots 30\%$). When negative gain values are used, the two absorption peaks move closer to each other. For the $K_p = -0.2\,\mathrm{V\,Pa^{-1}}$ example shown in Fig. 4(b), the peaks have shifted to be so close to each other that a strong absorption dip is formed in between, resulting in negative sound absorption within a narrow frequency band. The negative absorption results from constructive interference between the (passively) reflected sound wave and the (actively) radiated sound wave from the cantilever, leading to more sound energy being reflected than being incident and, consequently, to negative absorption. This negative absorption could also be the reason why for negative gain values the instability threshold is very low compared to positive gains.

In summary, these results show that cavity pressure feedback can be used to control the

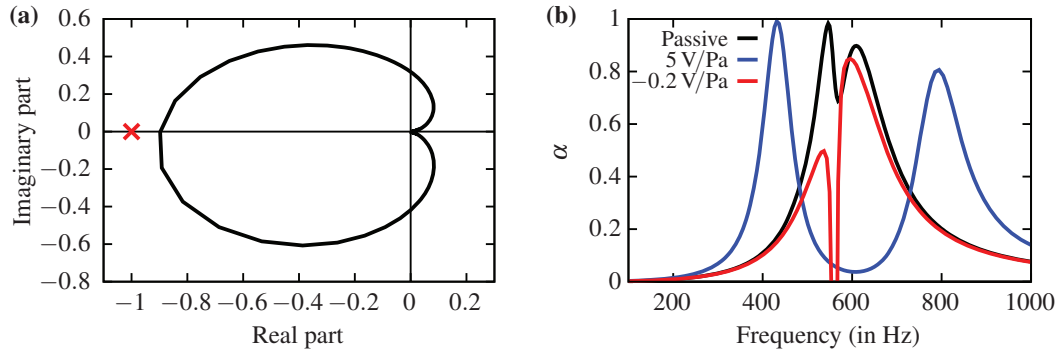

Figure 4: (a) Simulated Nyquist plot of the plant response at p_2 for a feedback gain of $K_p = -0.25\,\mathrm{V\,Pa^{-1}}$. (b) Simulated sound absorption coefficient of the active HRCL resonator with cavity pressure feedback.

spacing between the absorption peaks in the sound absorption spectrum. This could be useful to track the frequencies of tonal noise sources, e.g. using an electronically controllable gain. However, this approach does not result in more broadband absorption of the HRCL, which would be desirable in a wider range of noise control applications.

3.2 Impedance control

This approach aims at directly controlling the acoustic impedance Z_A of the HRCL resonator to achieve a target impedance Z_T, which can, for example, be tailored towards a more broadband absorption performance compared to what can be achieved with the simple cavity pressure feedback. Since the acoustic impedance of the HRCL is given by $Z_\mathrm{A} = p_1/Q_1$, where Q_1 is the volume velocity of the HRCL neck and cantilever combined, a control approaching using p_1 and Q_1 as inputs to the controller could achieve impedance control of the HRCL. While p_1 can be measured using a microphone on the top of the HRCL (see Fig. 1(c)), measuring Q_1 directly is not straightforward. However, the pressure p_2 inside the cavity can be used to estimate Q_1, because in the long-wavelength limit p_2 and Q_1 are related via the acoustic compliance of the cavity: $p_2 = Q_1/(sC_A)$, with the Laplace variable s. Therefore, an error signal ε for the impedance control can be defined as follows

$$\varepsilon = p_1 - Z_\mathrm{T} Q_1 \approx p_1 - Z_\mathrm{T} C_\mathrm{A} \frac{s}{\frac{s}{\omega_\mathrm{c}} + 1} p_2, \tag{4}$$

where the derivative part of ε is band-limited up to a cut-off frequency of $\omega_\mathrm{c}/(2\pi) = 2000\,\mathrm{Hz}$. Passing this error signal through a controller H, the actuator input results in

$$v_\mathrm{act} = H\varepsilon. \tag{5}$$

For simplicity, a proportional-integral-derivative (PID) controller is assumed here, with H given by

$$H = K_\mathrm{PID}\left(1 + \frac{1}{T_\mathrm{i} s} + T_\mathrm{d} \frac{s}{\frac{s}{\omega_\mathrm{c}} + 1}\right), \tag{6}$$

where K_PID is the controller gain, T_i the integration time constant, and T_d the derivative time constant.

As an example, the following PID controller parameters were used to investigate the performance of the PID-based impedance control approach for the active HRCL: $K_\mathrm{PID} = 40\,\mathrm{V\,Pa^{-1}}$, $T_\mathrm{i} = -38.3\,\mu\mathrm{s}$, and $T_\mathrm{d} = -1.36\,\mathrm{ms}$. The acoustic compliance of the cavity was calculated as $C_\mathrm{A} = V_\mathrm{HR}/(\rho_0 c_0^2) = 0.63\,\mathrm{mm^3\,Pa^{-1}}$, where $V_\mathrm{HR} = 88.7\,\mathrm{cm^3}$ is the cavity volume of the HRCL, and the target impedance was set to $Z_\mathrm{T} = \rho_0 c_0/(LW)$, aiming at broadband perfect sound absorption. Fig. 5(a) shows the simulated Nyquist plot for this control configuration, with a zoomed-in view around the $(-1,0)$ point shown in Fig. 5(b). It can be seen that the Nyquist curve does not encircle the $(-1,0)$ point and the control is therefore stable. The corresponding sound absorption coefficient, obtained by implementing the proposed impedance control law

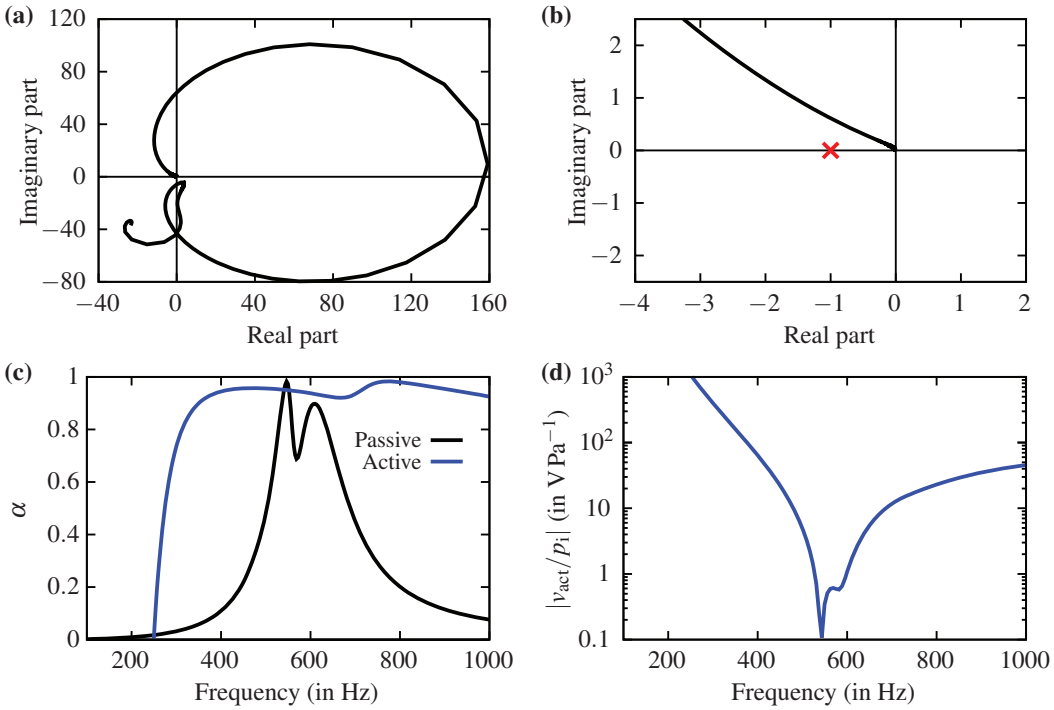

Figure 5: Simulation results for the active HRCL resonator with impedance control. (a) Nyquist plot. (b) Zoomed-in view of the Nyquist plot around the $(-1,0)$ point. (b) Sound absorption coefficient. (d) Control effort.

in the HRCL simulation model, is shown in Fig. 5(c). The control approach indeed yields a much more broadband sound absorption performance, with α well above 80 % for frequencies larger than 300 Hz. At lower frequencies, however, the absorption coefficient becomes negative, which is similar to what was already observed in the negative pressure feedback case (Fig. 4(b)). In the impedance control case considered here, this negative absorption is possibly related to the fact that the control authority of the active HRCL at low frequencies is very low (see the plant response results in Fig. 3(c)) and the PID controller is not able to cancel the (passively) reflected sound wave. Instead, the active HRCL radiates a sound wave that has a larger amplitude than the passively reflected wave, leading to an amplification of the reflected sound. The control effort plotted in Fig. 5(d) also highlights the inefficiency of the HRCL at frequencies below 300 Hz, where control voltages of more than 100 V are required for incident pressure amplitudes of 1 Pa (= 91 dB). For the given MFC actuator, the rated voltage range is −60 V to 360 V, which could therefore be easily exceeded at low frequencies, even at moderate sound pressure levels.

Despite these issues at very low frequencies, the results using the numerical HRCL resonator model show that stable broadband sound absorption can be achieved with an impedance-based control approach. The PID controller used here is very basic and was not designed to avoid negative absorption coefficients or high control voltages in the low frequency range. Possi-

ble alterations of the control approach could be explored to avoid these issues. For example, high-pass filters could be applied to limit the control output and reduce or even eliminate the amplification of the reflected sound at low frequencies. Alternatively, a frequency-dependent target impedance Z_T could be defined, which takes into account the poor absorption (mainly due to the compliance-driven impedance) of the passive HRCL resonator and focuses on achieving high sound absorption values at frequencies around or higher than the CL and HR resonance frequencies. Finally, the numerical HRCL resonator model proposed in this work can also be readily used to investigate the effect of changing the geometry or material parameters of the HRCL design on its impedance control performance. This could include, for example, the use of multiple MFC actuators (to achieve more control authority) or tuning the HRCL resonator to have the CL and HR resonance frequencies more spread apart, so that the plant response does not exhibit a strong, single peak (as in Fig. 3(c)), but two separate peaks with a relatively flat band between the peaks.

4 CONCLUSIONS

This contribution presented a multiphysics FEM simulation model of an active HRCL resonator, which includes coupled acoustic, thermoviscous acoustic, structural, and piezoelectric effects. The model was validated using impedance tube measurements of the passive sound absorption of the HRCL resonator and the radiated sound pressure resulting from a voltage signal applied to the MFC actuator attached to the HRCL resonator. The results from the simulation model agreed very well with the experimental data and the validated HRCL model was then used to explore two active control approaches aiming at modifying the sound absorption of the HRCL resonator: The first approach was a simple proportional feedback of the pressure inside the HRCL cavity, which resulted in a spreading of the two sound absorption peaks that could be controlled based on the gain value used in the proportional feedback controller. The second control approach aimed at controlling the acoustic impedance of the HRCL resonator by measuring the pressure in front of the HRCL and inside the cavity and using these values to estimate the acoustic impedance. Using a PID controller designed to control the HRCL impedance to be equal to the characteristic impedance, broadband sound absorption well above 80 % could be demonstrated. However, the example active HRCL design investigated here also suffered from negative sound absorption and high control effort at lower frequencies, which should be avoided in practical applications.

The simulation model proposed in this work will form the basis for the future development of advanced active HRCL resonator designs, that, for example, achieve high broadband sound absorption without the issues of negative absorption or high control effort. This model allows for rapid design iterations, e.g. using reduced-order models that can be implemented in SIMULINK to investigate more complex control configurations. Additionally, the model enables the investigation of the performance of the active HRCL resonator in situations that are difficult to implement experimentally, e.g. oblique incidence of sound waves or multi-celled arrays of active HRCL resonators, forming large smart sound absorbing panels that can be used in applications that require flexible and efficient control of sound, especially at low frequencies.

REFERENCES

[1] H. V. Fuchs, *Applied Acoustics: Concepts, Absorbers, and Silencers for Acoustical Comfort and Noise Control*. Berlin Heidelberg: Springer, 2013.

[2] S. A. Cummer, J. Christensen, and A. Alù, "Controlling sound with acoustic metamaterials," *Nature Reviews Materials*, vol. 1, no. 3, p. 16 001, Feb. 16, 2016.

[3] X. Hu, K.-M. Ho, C. T. Chan, and J. Zi, "Homogenization of acoustic metamaterials of Helmholtz resonators in fluid," *Physical Review B*, vol. 77, no. 17, p. 172 301, May 1, 2008.

[4] R. Martin, K. Pandey, B. Schuermans, and N. Noiray, "Phase-cancellation of velocity oscillations in a flow duct using a slow-sound metamaterial," *Journal of Sound and Vibration*, vol. 596, p. 118 774, Feb. 5, 2025.

[5] N. Jiménez, V. Romero-García, V. Pagneux, and J.-P. Groby, "Rainbow-trapping absorbers: Broadband, perfect and asymmetric sound absorption by subwavelength panels for transmission problems," *Scientific Reports*, vol. 7, no. 1, p. 13 595, 1 Oct. 19, 2017.

[6] C. Cai and C. M. Mak, "Acoustic performance of different Helmholtz resonator array configurations," *Applied Acoustics*, vol. 130, pp. 204–209, Jan. 2018.

[7] H. Hoppen, F. Langfeldt, W. Gleine, and O. von Estorff, "Helmholtz resonator with two resonance frequencies by coupling with a mechanical resonator," *Journal of Sound and Vibration*, vol. 559, p. 117 747, Sep. 1, 2023.

[8] R. Kehrbaum and F. Langfeldt, "Auslegung eines additiv gefertigten Helmholtz-Resonators mit aktiv angesteuertem Biegebalken," in *Proceedings of DAGA 2024*, Hannover, 2024, pp. 79–82.

[9] A. Deraemaeker, H. Nasser, A. Benjeddou, and A. Preumont, "Mixing Rules for the Piezoelectric Properties of Macro Fiber Composites," *Journal of Intelligent Material Systems and Structures*, vol. 20, no. 12, pp. 1475–1482, 2009.

XI ECCOMAS Thematic Conference on Smart Structures and Materials - SMART 2025
M. Krommer, M. Nader and M. Schagerl (Eds)

Received: 29 April 2025 / Revised: 1 November 2025 / Accepted: 4 November 2025
© The Author(s) 2025

Development of a Tow-steered Composite Design Tool for Morphing Applications

Jared Lilly, Darren Hartl

Abstract. Fiber-reinforced composites (FRC) provide a high strength, low weight material option that is used in many different fields including aerospace, sporting equipment, and ballistic armor. Many design studies consider a FRC laminate made of stacked layers (i.e., plies) where reinforcing fibers are aligned parallel to one another in the plane of a ply. To optimize such laminates, the orientations of each ply layer are iteratively updated until a goal composite layup is found. Ply orientation-focused optimization is sufficient for many applications such as in the design of a stiffened panel or of a morphing panel with zero Gaussian curvature (i.e., simple bending and twisting adaptivity). However, additional challenges arise when adaptive components must bend in multiple directions. We hypothesize that local stress concentrations caused by non-zero Gaussian curvature deformations can be mitigated by considering curvilinear fiber-reinforced (i.e., tow-steered) composites. A design space that captures the parameterization of a tow-steered composite must consider the local fiber tow direction and local fiber volume fraction at every point in the composite and thus is large and potentially intractable for optimization. This work introduces a method to derive both local fiber orientation and local fiber volume fraction from a parameterized governing vector field. Local fiber tow directions are computed using the arctangent of the components of the governing vector field. Fiber volume fraction is found by requiring that all fiber tows begin and end at a boundary (i.e., fiber tow continuity). Locally enforcing the fiber tow continuity constraint is accomplished by requiring that the divergence of the product of a predefined vector field and an unknown scalar field be equal to zero everywhere. The unknown scalar field is taken to represent the varying fiber tow density (i.e., fiber volume fraction) throughout the domain. Finite element method (FEM) is implemented to solve for the unknown fiber volume fraction. The fiber volume fraction and the local fiber tow direction are then used in conjunction with an established homogenization method (e.g., rule of mixtures, Mori-Tanaka method, numerical homogenization techniques) to determine the effective spatially varying structural scale constitutive response of the tow-steered composite. A case study presented includes maximization of stiffness in a composite panel, a common objective in tow-steered composite design, and the matching of a goal deformed shape, an objective in the design of geometrically adaptive aerostructures.

Key words: Tow-steered Composites, Design Tool, Morphing Structures

Jared Lilly & Darren Hartl
Department of Aerospace Engineering, Texas A&M University, College Station, Texas, USA
e-mail: jplilly25@tamu.edu

1 INTRODUCTION

Morphing aerospace structures have been shown to provide operational benefits such as improved flight efficiency in hypersonic vehicles, reduced noise levels due to sonic boom propagation from supersonic aircraft, and improved thermal management on space vehicles [1, 2, 3]. For general aerospace design, stiff and light materials are desired to minimize the total weight of the system. Composites reinforced with straight fibers are a leading material system candidate, but they typically do not have high strain-to-yield limits, thus lacking an important characteristic of shape-adaptive structures. The idea of incorporating curvilinear reinforcing fibers in composites has been extensively researched and shown to be advantageous in relieving stress concentrations in static load cases. We hypothesize that steering the fiber paths will reduce stress concentrations that arise in morphing structures. To investigate the capabilities of tow-steered composites, a continuum field representation of the local variations in the tow-steered composite properties is required to formulate a structural scale constitutive response of the composite. Both the local fiber orientation and the local fiber volume fraction must be known to derive the spatially varying constitutive response. This work seeks to explore the capabilities of using tow-steered composites in morphing applications by developing a field representation of the composite where both the local fiber orientation and the local fiber volume fraction are derived.

There have been three main approaches used to define the spatially varying fiber orientation in literature: 1) trajectorial fiber reinforcement, 2) functionally-derived fiber orientations, and 3) vector field formulated fiber orientations. Trajectorial fiber reinforcement methods iteratively align the fiber orientations with the maximum principal stress directions [4, 5, 6, 7]. Functionally-derived fiber orientations assume a variation of fiber angle throughout the domain (e.g., linear variation, quadratic variation, variations derived from level set functions [8, 9, 10, 11, 12, 13, 14]). Vector field formulations derive fiber orientations from the ratio of vector field components [15, 16, 17]. In all three representations, the local fiber orientations are determined and used to compute the structural scale constitutive response,

$$\boldsymbol{\mathcal{C}}(\theta(\mathbf{x})) = \big[\boldsymbol{Q}^T(\theta(\mathbf{x})) \otimes \boldsymbol{Q}^T(\theta(\mathbf{x}))\big]\boldsymbol{\mathcal{C}}^o\big[\boldsymbol{Q}(\theta(\mathbf{x})) \otimes \boldsymbol{Q}(\theta(\mathbf{x}))\big], \tag{1}$$

where $\boldsymbol{\mathcal{C}}(\theta(\mathbf{x}))$ is the spatially varying structural scale stiffness tensor, $\boldsymbol{\mathcal{C}}^o$ is the local homogenized stiffness tensor, $\boldsymbol{Q}(\theta(\mathbf{x}))$ is the rotation tensor, and $\theta(\mathbf{x})$ is the local fiber orientation at a material point $\mathbf{x}$ [18].

Only [15] considers the variation of fiber density throughout the composite. Specifically, the spacing between fiber tape paths is used to predict the presence of gaps and/or overlaps. This method does not consider local variations in the fiber volume fraction. Therefore, this work develops a method to solve for a continuum field representation of the fiber volume fraction in a tow-steered composite and demonstrates its importance in an aerospace-motivated morphing structures case study.

2 METHODOLOGY

2.1 Field Representation of Composite Properties

In this work, spatially varying composite properties (local fiber orientation and local fiber volume fraction) are derived from a governing vector field,

$$\mathbf{F}(\mathbf{x};\boldsymbol{\xi}) = \begin{Bmatrix} \mathrm{F}_1(\mathbf{x};\boldsymbol{\xi}) \\ \mathrm{F}_2(\mathbf{x};\boldsymbol{\xi}) \end{Bmatrix}. \tag{2}$$

where $\mathbf{x}$ is a material point in the composite, $\boldsymbol{\xi}$ is a vector of variables that parameterize the vector field, and F_1 and F_2 are the $x-$ and $y-$components of the vector field. The general vector field form in equation 2 is used to derive the local fiber orientation and the local fiber volume fraction.

Local Fiber Orientation

The local fiber orientation, $\theta(\mathbf{x})$, is defined analytically throughout the composite by,

$$\theta(\mathbf{x}) = \arctan\left(\frac{\mathrm{F}_2(\mathbf{x};\boldsymbol{\xi})}{\mathrm{F}_1(\mathbf{x};\boldsymbol{\xi})}\right). \tag{3}$$

Figure 1 shows a notional composite domain where curvilinear fiber paths are defined by a vector field ($\mathbf{F} = \left[\frac{x}{\sqrt{x^2+y^2}}, \frac{-y}{\sqrt{x^2+y^2}}\right]^{\mathrm{T}}$). The vector field is plotted at 20 points spaced evenly throughout the domain. A single field line, a line generated by tracking the path of a particle as it moves through the vector field, is plotted to visualize the change in orientation throughout the domain.

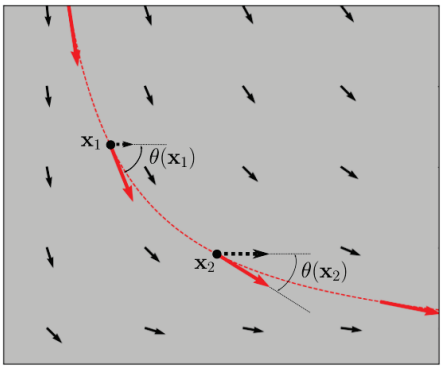

Figure 1: Example vector field to show the change in local fiber orientation along a field line in the composite.

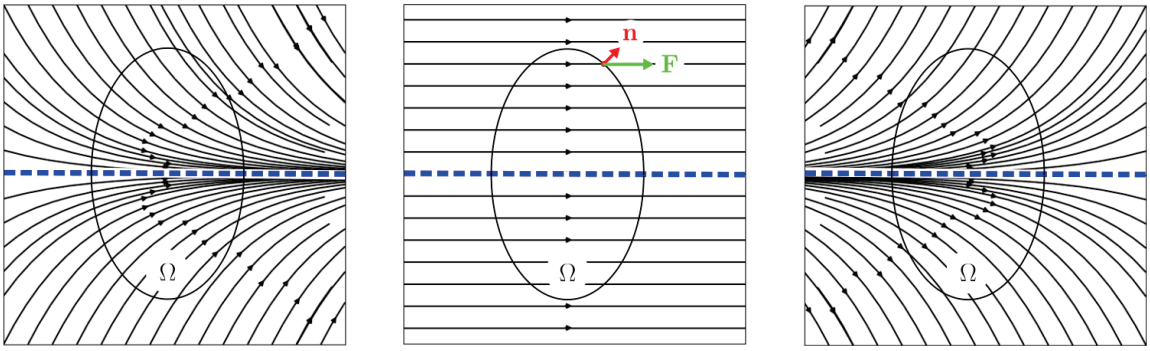

Figure 2: Converging (left), uniform (center), and diverging (right) field lines representing notional fiber paths.

Local Fiber Volume Fraction

Determining the spatially varying fiber volume fraction cannot be done analytically as in equation 3 for the local fiber orientation. Further, the governing vector field representation used does not define explicit fiber paths; therefore, computing the fiber volume fraction from geometry is not possible without additional assumptions (e.g., total number of fibers or tows in the domain, size and shape of the fibers/tows). A new method is proposed where the local fiber volume fraction is derived by introducing a *fiber continuity* constraint in the composite ply domain.

Consider a finite volume, Ω, drawn over three composite ply domains where field lines represent three different sets of notional fiber paths as shown in figure 2. Integrating the flux of the vector field around the finite volume is representative of computing the total mass of fibers that enter and leave the domain. Mathematically, the total flux is written as,

$$\Phi_{\mathbf{F}} = \oint_{\partial\Omega} \mathbf{F} \cdot \mathbf{n} dS, \tag{4}$$

where $\Phi_{\mathbf{F}}$ is the total flux of the vector field into the finite volume Ω, $\partial\Omega$ is the boundary of the finite volume, $\mathbf{n}$ is the outward facing normal of the finite volume, and dS is the differential element on $\partial\Omega$.

As written, there is no constraint on the vector field, $\mathbf{F}$; therefore, there is also no constraint on the flux, $\Phi_{\mathbf{F}}$. In a composite, fibers should be continuous throughout a ply and only begin or end at the edges. Fibers beginning or ending at the edges corresponds to requiring that the flux of the vector field into and out of a finite domain to equal zero in the absence of internal sources or sinks. To enforce the continuity requirement, a scalar field is introduced into equation 4 and the total flux is set equal to zero,

$$\Phi_{v\mathbf{F}} = \oint_{\partial\Omega} v(\mathbf{F} \cdot \mathbf{n}) dS = 0 \tag{5}$$

where v is the scalar field which represents the normalized local fiber volume fraction, and $\Phi_{v\mathbf{F}}$ is the flux of the product of v and $\mathbf{F}$. Equation 5 defines a global constraint on the composite ply domain. To enforce that the fibers are continuous throughout the domain, a local constraint is derived by shrinking the finite volume down to a point,

$$\lim_{V\to 0}\frac{1}{|V|}\Phi_{v\mathbf{F}} = \lim_{V\to 0}\frac{1}{|V|}\oint_{\partial\Omega} v(\mathbf{F}\cdot\mathbf{n})dS \equiv \nabla\cdot(v\mathbf{F}) = 0 \tag{6}$$

where $(\nabla\cdot)$ is the divergence operator [19].

The normalized local fiber volume fraction computed by solving the partial differential equation (PDE) in equation 6 is not restricted to manufacturing limits. Therefore, to ensure that the fiber volume fraction field is manufacturable, the field v computed from equation 6 must be mapped to be within manufacturing limits. In this work, linear interpolation between v and a chosen set of manufacturing limits is used,

$$\frac{v - v_{\min}}{v_{\max} - v_{\min}} = \frac{v_f - v_{f,\min}}{v_{f,\max} - v_{f,\min}} \tag{7}$$

where $v_{\min}$ and $v_{\max}$ are the minimum and maximum values of the normalized local fiber volume fraction v, and $v_{f,\min}$ and $v_{f,\max}$ are the minimum and maximum fiber volume fractions that a machine is capable of achieving during manufacturing.

Structural Scale Constitutive Relations

Local material orientations from equation 3 and the spatially varying fiber volume fraction from equation 7 are used to define the spatially varying constitutive response at the structural scale. To derive the constitutive response, equation 1 is modified,

$$\boldsymbol{\mathcal{C}}(\theta(\mathbf{x}), v_f(\mathbf{x})) = \big[\boldsymbol{Q}^T(\theta(\mathbf{x})) \otimes \boldsymbol{Q}^T(\theta(\mathbf{x}))\big]\boldsymbol{\mathcal{C}}^o(v_f(\mathbf{x}))\big[\boldsymbol{Q}(\theta(\mathbf{x})) \otimes \boldsymbol{Q}(\theta(\mathbf{x}))\big] \tag{8}$$

where $\boldsymbol{\mathcal{C}}^o(v_f(\mathbf{x}))$ is the local homogenized constitutive response which now also depends on the local fiber volume fraction.

2.2 Design Workflow of Tow-steered Composites

The derivation of a structural scale constitutive response from a given set of parameterized variables is outlined in figure 3. Before the iterative portion of the design process, the material system (i.e., matrix material and fiber material), the local homogenization scheme (e.g., rule of mixtures, Mori-Tanaka method), and general parameterized vector field must be defined. In the preprocessing stage, the local homogenization scheme is used to define how the locally homogenized constitutive response depends on the local fiber volume fraction. Once chosen, designs with different curvilinear fiber architectures can be iteratively explored and compared.

Within the iterative design process, composite properties are first derived using equations 3 and 6-7. Since the vector field is defined analytically everywhere in the domain, the local fiber

orientation is also defined analytically in the domain. The analytical equation describing the local fiber orientation is passed to the analysis module. Next, the normalized spatially varying fiber volume fraction, v, is computed by enforcing the *fiber continuity* constraint. In this work, the open-source FEM solver FreeFEM is used to solve the first-order PDE shown in equation 6 [20]. Equation 7 is then used to map the normalized fiber volume fraction values to be within manufacturing limits of a chosen fiber laying machine. The resulting spatially varying fiber volume fraction is passed as a field to the analysis module.

In the structural analysis module, the spatially varying composite properties are used to define the structural scale constitutive response as stated in equation 8. The finite element analysis (FEA) software suite, Abaqus is used to complete the structural analyses of the tow-steered composites [21]. Defining the structural scale constitutive response in Abaqus is accomplished in three steps: 1) inputting the local fiber volume fraction as a predefined field, 2) defining the field dependence of local material properties on the local fiber volume fraction, and 3) defining the spatially varying local fiber orientation. For the first step, a predefined field is created in the "Loads" module. The field is defined using a "Mapped field" expression where a set of local fiber volume fraction values are imported from the composite properties module. Next, the elastic material properties are specified using the "Engineering Constants" drop-down option (i.e., $E_1, E_2, E_3, \nu_{12}, \nu_{13}, \nu_{23}, G_{12}, G_{13}, G_{23}$). The "Number of field variables" box is set to one to allow specification of the material constant values as a function of the local fiber volume fraction (i.e., the predefined field discussed in step 1). Material property dependence on the local fiber volume fraction is imported from the preprocessing stage. With the local fiber volume fraction defined everywhere, and the dependence of material properties on the local fiber volume fraction specified, the variation in the local homogenized constitutive response, $\boldsymbol{\mathcal{C}^o}(v_f(\mathbf{x}))$, can now be computed. In the third step, the spatially varying local fiber orientation is defined using the user subroutine, ORIENT. The ORIENT user subroutine is written in a Fortran file that is executed by Abaqus prior to the structural analysis. In the ORIENT file, the parameterized vector field is pre-programmed so that updates to the parameter values modify the vector field output. Lastly, the composite is analyzed and the results are post processed. In an iterative loop, the parameter values would be updated and the process would repeat starting from the 'Fiber path representation module'.

3 CASE STUDY

In morphing aerospace applications, the structure must resist aerodynamic loads and enable shape adaptivity to match goal configurations. A case study that explores the competing load-carrying and shape-adaptivity requirements is studied herein in which a one meter by one meter square plate reinforced with curvilinear fibers is analyzed. For a given fiber path distribution, the composite plate is analyzed under a pressure load representing the dynamic pressure experienced in flight, and a specified displacement representing the required change in shape of a morphed configuration. In the first analysis, the pressure load is $\bar{P} = 15$ kPa, a notional value representative of the dynamic pressure seen in flight. The edges of the plate at $x = 0$ m and $x = 1$ m are fixed ($u_1 = u_2 = u_3 = \phi_1 = \phi_2 = \phi_3 = 0$; where u_i is the ith translational

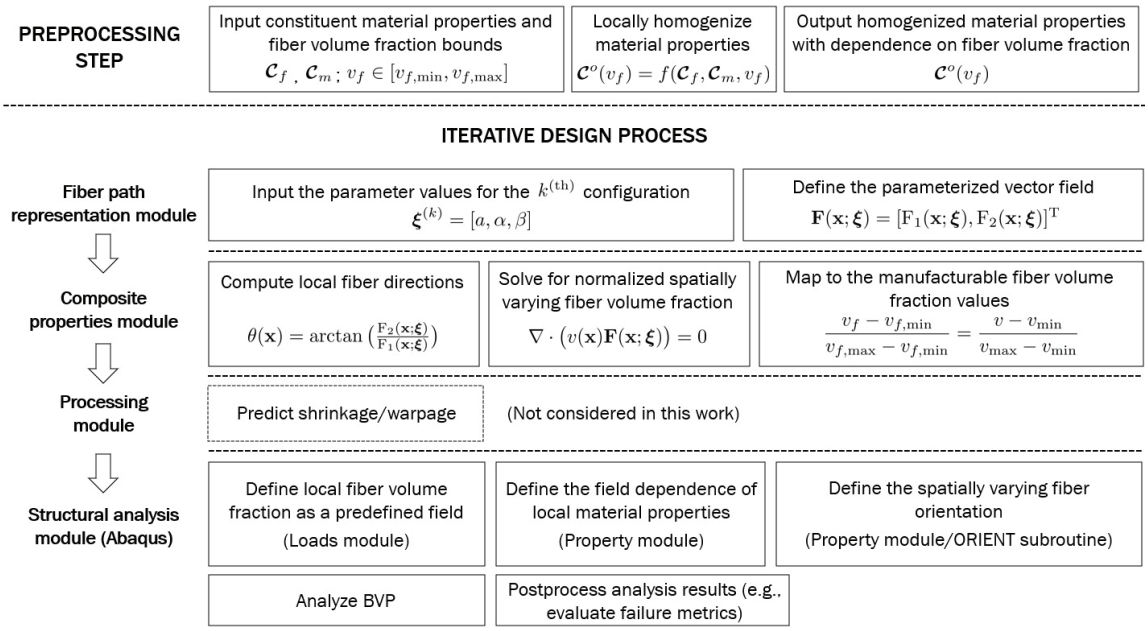

Figure 3: Overview of the workflow followed to analyze tow-steered composites in Abaqus where both the local fiber orientation and the local fiber volume fraction vary throughout the ply.

degree of freedom and ϕ_j is the jth rotational degree of freedom). In the second analysis, the prescribed displacement is $\bar{u}_3(x, y) = 0.1x\cos(\pi y)$ m and is applied over the entire surface. The edge of the plate at $x = 0$ m is fixed. Schematics of each boundary value problem (BVP) are shown in figure 4. The plate in each analysis is modeled using linear, reduced-integration shell elements (S4R element type in Abaqus) in a 3D modeling space.

In this work, the composite plate is limited to a single-ply configuration to test the capabilities of the tools developed. Future work will extend this case study to consider a composite laminate with multiple ply.

3.1 Vector Field Representation

A vector field representing diverging fibers is chosen for this case study. The governing vector field is parameterized,

$$\mathbf{F} = \begin{Bmatrix} a \\ x^{\alpha} y^{\beta} \end{Bmatrix}, \tag{9}$$

where $a \in [0.25, 3.0]$, $\alpha \in [1.0, 3.0]$, and $\beta \in [1.0, 3.0]$ are the three parameters varied in this study. In enforcing the *fiber continuity* constraint in equation 6, the fiber volume fraction should only vary with changes in the local direction of the vector field and not the magnitude.

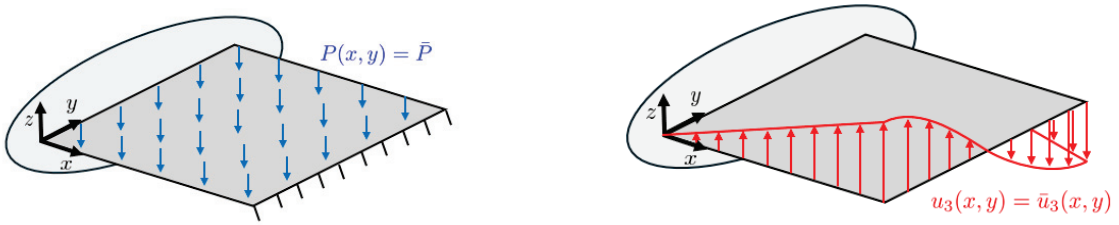

Figure 4: Schematics of boundary value problems seen in morphing aerospace structures where the structure must not fail under a dynamic pressure load (left) and a prescribed displacement (right).

To ensure this property, the vector field is normalized,

$$\hat{\mathbf{F}} = \frac{\mathbf{F}}{|\mathbf{F}|} = \frac{1}{\sqrt{1 + (x^\alpha y^\beta)^2}} \begin{Bmatrix} a \\ x^\alpha y^\beta \end{Bmatrix}, \tag{10}$$

and now the *fiber continuity* constraint reads,

$$\nabla \cdot (v\hat{\mathbf{F}}) = 0. \tag{11}$$

3.2 Material System and Local Homogenization

The material system used in this case study is a fiber-reinforced composite material made of BSL914C epoxy and T300 carbon fibers (material properties of the constituents can be found in [22]). Local homogenization of the fiber-reinforced composite material is accomplished using the rule of mixtures for the modulus along the fiber direction, inverse rule of mixtures for the modulus transverse to the fibers and the out-of-plane shear moduli, and the Halpsin-Tsai equations for the in-plane shear modulus [23]. The locally homogenized properties for the minimum (25%) and maximum (60%) fiber volume fractions (V_f) are listed in table 1.

Table 1: Homogenized material properties of the carbon fiber-reinforced epoxy composite.

Property	Minimum $V_f = 25\%$	Maximum $V_f = 60\%$
E_{11} (GPa)	60.5	140
E_{22} (GPa)	6.75	10.6
ν_{12}	0.2	0.2
G_{12} (GPa)	2.51	5.14
G_{13} (GPa)	1.91	3.22
G_{23} (GPa)	1.91	3.22

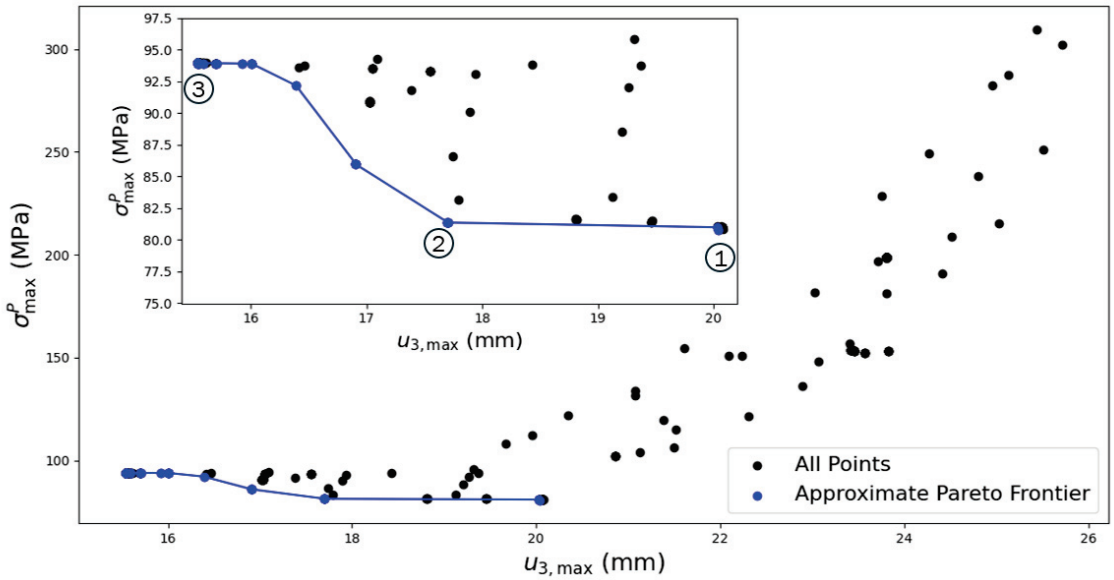

Figure 5: Analysis of single ply configurations with curvilinear fibers offer a design space that spans the competing objective space of morphing aerospace structures.

3.3 Results

The results of a Latin hypercube sampling (LHS) of 45 configurations and multiple gradient-based optimization processes are shown in figure 5. The maximum absolute value of the displacement from the pressure BVP is plotted on the abscissa and the maximum principal stress value from the displacement BVP is plotted on the ordinate. For this case study, the optimal configuration is located in the lower-left corner (i.e., minimizing the displacement due to the dynamic pressure load and minimizing the maximum principal stress value due to the morphing the structure into the adaptive configuration). Currently optimal configurations are plotted in blue and connected to show an approximate Pareto frontier of the objective space. The design space explored highlights the capability of composites reinforced with curvilinear fibers to provide benefits in morphing aerospace applications where both shape adaptivity and load-carrying capabilities are required.

Three resulting fiber orientations and fiber volume fraction distributions are plotted in figure 6. From configuration 1 to configuration 3, the fiber orientations straighten in the horizontal direction. The fiber volume fraction does not vary significantly between the three configurations. The straightening of fiber orientations decreases the maximum displacement but increases the maximum principal stress. This result is to be expected as a ply with horizontal fibers would minimize the displacement in the pressure BVP but would not provide favorable load paths in the displacement BVP.

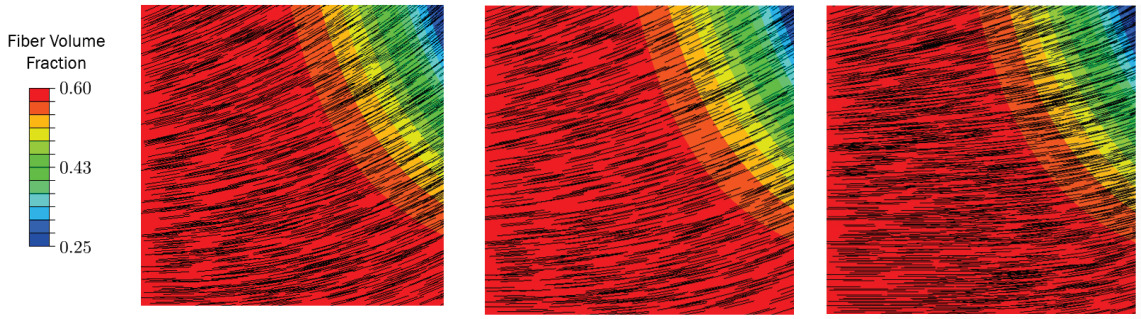

(a) Configuration 1 (b) Configuration 2 (c) Configuration 3

Figure 6: Fiber orientations and fiber volume fractions from three configurations on the approximate Pareto frontier.

4 CONCLUSION

In this work, the use of tow-steered composite materials in morphing aerospace applications was explored. A method to compute the spatially varying fiber volume fraction in the ply of a composite with curvilinear fibers was formulated. A case study of a single-ply composite configuration was presented to test the capabilities of the developed tools; specifically, the incorporation of the spatially varying fiber volume fraction. Results indicate that composites reinforced with curvilinear fibers can provide a tradespace of shape adaptive and load-carrying configurations, two critical requirements of morphing aerospace structures. Future work will consider the design of a morphing aerospace component that uses a composite laminate reinforced with curvilinear fibers. Each ply will have an independent set of design variables that describe the spatially varying fiber orientations and subsequent spatially varying fiber volume fractions.

5 ACKNOWLEDGMENTS

Funding for this research was provided by an Applied Research for the Advancement of S&T Priorities Program award. The authors acknowledge the support of Charis Lin, George Jefferson, Kaitlin Detwiler, and Matthew Dickerson of the Air Force Research Laboratory. The authors also acknowledge Yalchin Efendiev, Xin Liu, Matthias Maier, and Jordan Hoffart of the Department of Mathematics at Texas A&M University for insightful discussions regarding the solution of the partial differential equation used to determine the spatially varying fiber volume fraction.

REFERENCES

[1] A. A. Phoenix, J. R. Maxwell, and G. B. Goodwin, “Morphing high-temperature surfaces for shapeable hypersonic waverider vehicles,” in *Smart Materials, Adaptive Structures and Intelligent Systems*, vol. 58264. American Society of Mechanical Engineers, 2017,

p. V002T03A012.

[2] K. Datta and D. Lagoudas, "Adaptive aerostructures for revolutionary civil supersonic transportation," *NASA TechPort*, 2021.

[3] C. L. Bertagne, T. J. Cognata, R. B. Sheth, C. E. Dinsmore, and D. J. Hartl, "Testing and analysis of a morphing radiator concept for thermal control of crewed space vehicles," *Applied Thermal Engineering*, vol. 124, pp. 986–1002, 2017.

[4] A. A. G. Cooper, *Trajectorial fiber reinforcement of composite structures*. Washington University in St. Louis, 1972.

[5] M. Hyer and R. Charette, "Innovative design of composite structures: use of curvilinear fiber format to improve structural efficiency," Tech. Rep., 1987.

[6] M. W. Hyer and H. Lee, "The use of curvilinear fiber format to improve buckling resistance of composite plates with central circular holes," *Composite structures*, vol. 18, no. 3, pp. 239–261, 1991.

[7] S. Setoodeh and Z. Gürdal, "Design of composite layers with curvilinear fiber paths using cellular automata," in *44th AIAA/ASME/ASCE/AHS/ASC Structures, Structural Dynamics, and Materials Conference*, 2003, p. 2003.

[8] A. S. Tam and T. G. Gutowski, "The kinematics for forming ideal aligned fibre composites into complex shapes," *Composites Manufacturing*, vol. 1, no. 4, pp. 219–228, 1990.

[9] Z. Guerdal and R. Olmedo, "Composite laminates with spatially varying fiber orientations-'variable stiffness panel concept'," in *33rd structures, structural dynamics and materials conference*, 1992, p. 2472.

[10] B. F. Tatting, Z. Gürdal, and D. Jegley, "Design and manufacture of elastically tailored tow placed plates," Tech. Rep., 2002.

[11] C. Lopes, Z. Gürdal, and P. Camanho, "Variable-stiffness composite panels: Buckling and first-ply failure improvements over straight-fibre laminates," *Computers & Structures*, vol. 86, no. 9, pp. 897–907, 2008.

[12] C. Waldhart, "Analysis of tow-placed, variable-stiffness laminates," Ph.D. dissertation, Virginia Tech, 1996.

[13] A. A. Vijayachandran and A. M. Waas, "Minimizing stress concentrations using steered fiberpaths and incorporating realistic manufacturing signatures," *International Journal of Non-Linear Mechanics*, vol. 146, p. 104160, 2022.

[14] Y. Tian, T. Shi, and Q. Xia, "A parametric level set method for the optimization of composite structures with curvilinear fibers," *Computer Methods in Applied Mechanics and Engineering*, vol. 388, p. 114236, 2022.

[15] T. R. Brooks and J. R. Martins, "On manufacturing constraints for tow-steered composite design optimization," *Composite structures*, vol. 204, pp. 548–559, 2018.

[16] C. Luo, F. Ferrari, and J. K. Guest, "Design optimization of advanced tow-steered composites with manufacturing constraints," *Composites Part B: Engineering*, vol. 284, p. 111739, 2024.

[17] T. Shafighfard, E. Demir, and M. Yildiz, "Design of fiber-reinforced variable-stiffness composites for different open-hole geometries with fiber continuity and curvature constraints," *Composite Structures*, vol. 226, p. 111280, 2019.

[18] W. M. Lai, D. Rubin, and E. Krempl, *Introduction to continuum mechanics*. Butterworth-Heinemann, 2009.

[19] J. Stewart, *Calculus: Early vectors*. Brooks/Cole, 1999.

[20] F. Hecht, "New development in freefem++," *J. Numer. Math.*, vol. 20, no. 3-4, pp. 251–265, 2012. [Online]. Available: https://freefem.org/

[21] Dassault Systèmes, *Abaqus Analysis User's Guide*, Dassault Systèmes Simulia Corp., Providence, RI, 2024, available at https://help.3ds.com.

[22] P. D. Soden, M. J. Hinton, and A. S. Kaddour, "Lamina properties, lay-up configurations and loading conditions for a range of fibre reinforced composite laminates," in *Failure criteria in fibre-reinforced-polymer composites*. Elsevier, 2004, pp. 30–51.

[23] J. H. Affdl and J. Kardos, "The halpin-tsai equations: a review," *Polymer Engineering & Science*, vol. 16, no. 5, pp. 344–352, 1976.

XI ECCOMAS Thematic Conference on Smart Structures and Materials - SMART 2025
M. Krommer, M. Nader and M. Schagerl (Eds)

Received: 18 April 2025 / Revised: 28 August 2025 / Accepted: 4 November 2025
© The Author(s) 2025

Wave Propagation Analysis of Sigmoid Functionally Graded Square lattice Structures Using Dynamic Stiffness Method and Wittrick-Williams Algorithm

Mudit Mishra, Sandeep Kumar

Abstract. This study investigates in-plane wave propagation in square lattice structures with Sigmoid-Functionally Graded Material (S-FGM) cell elements using Bloch's theorem. Timoshenko Beam theory models the cell elements, with the sigmoid function representing material property variation along the beam thickness. The dynamic stiffness method and Wittrick-Williams algorithm are employed for the analysis. Three approaches are considered: the first assigns a uniform power law index to all elements, the second uses different power law indices for each element, and the third approach maintains a uniform power law index but assigns unique cross-sectional shapes to each element. The results show that the third approach, with distinct cross-sectional shapes, significantly influences the band gap properties of S-FGM SL structures. Findings are validated with finite element method (FEM) simulations and COMSOL Multiphysics, confirming the accuracy of the results. The study emphasizes the importance of heterogeneous material properties for optimizing wave propagation behavior in engineering applications.

Key words: Sigmoid-Functionally graded material, Dynamic stiffness method, Wave propagation, Square Lattice, Wittrick-William algorithm

1 INTRODUCTION

Honeycomb systems are widely used in aerospace, automotive, and structural engineering due to their periodicity and versatile applications. Formed by repeating unit cells of beams or rods, they can use functionally graded materials (FGMs) [1], for tailored mechanical, thermal, and acoustic properties. Common designs include square and hexagonal [2], re-entrant [3] and kagome lattice [4]. Square lattice (SL) structures exhibit high in-plane stiffness and strength due to their regular geometry and uniform distribution of forces. This unique property enhances load-bearing capacity, structural stability, and resistance to deformation, making SL structures highly valuable in various engineering and material science applications.

Mudit Mishra & Sandeep Kumar
Department of Mechanical Engineering, Indian Institute of Technology (BHU) Varanasi, 221005, India
e-mail: muditmishra.rs.mec20@itbhu.ac.in

Wave propagation in cellular systems has garnered significant attention due to their ability to filter and guide waves. A key feature is the bandgap phenomenon, which blocks wave propagation in specific frequency ranges. Various studies have examined wave behavior in honeycomb lattices. Ruzzenne et al.[5] studied wave beaming and directional effects in re-entrant and hexagonal lattices, while Farzbod et al. [6] compared force treatment methods in lattices, aligning their findings with Langley's work. Phani et al. [4] used finite element methods to analyze band structures, and Gonella et al.[7] investigated dispersion, velocities, and band structures. Leamy [2] included joint inertia in lattice dynamics. However, wave behavior in sigmoid functionally graded (S-FG) lattices remains underexplored, presenting opportunities for tailoring wave propagation properties.

In all the above literature's, Finite Element Method (FEM) was consistently employed. However, a notable drawback of FEM is its reliance on extensive mesh refinement during analysis to achieve precise outcomes. This inevitably prolongs computational time, especially in analyzing dynamic response within mid to high frequency ranges. Moreover, the FE formulation may yield poorly conditioned matrices, potentially leading to numerical singularities.

To overcome the aforementioned challenges, researchers commonly utilize analytical methods to simulate the behavior of unit cells. The dynamic stiffness method (DSM), also known as the spectral element method (SEM), is an analytical modeling technique that allows for the representation of the complete deformation of a system across the entire frequency spectrum using a minimal number of degrees of freedom (DoFs) [8]. Xiang Liu et al. [9] presented the dynamic stiffness (DS) formulation for analyzing wave propagation in re-entrant and hexagonal honeycomb systems. Their study demonstrated how various primitive unit cell configurations affect dispersion curves and iso-frequency contours. However, a primary challenge associated with the DSM is solving the DS matrix. Many researchers opt for the Wittrick-Williams (W-W) [10] algorithm to address this issue, as it is known for its efficiency, reliability, and accuracy in providing eigen-solutions.

Although wave propagation in square lattice (SL) systems has been widely studied, the combination of SL configurations with S-FG materials remains largely unexplored. This study addresses this gap by examining wave propagation behavior in S-FG SL structure using the DSM integrated with the W-W algorithm. To ensure accuracy and reliability, the outcomes are verified against FEM simulations and COMSOL Multiphysics analyses. This approach provides new uunderstanding of the dynamic characteristics of S-FG SL structures.

2 DYNAMIC STIFFNESS FORMULATION OF S-FG SQUARE 2D LATTICE SYSTEMS

The unit cell method is employed to analyze dynamic response in S-FG SL by predicting the behavior of a single unit cell. S-FG Timoshenko beam elements are used, and the DSM is applied to formulate dynamic stiffness matrices, as detailed below.

2.1 Conventions and Principles in Lattice Geometry Notation

This paper thoroughly examines the wave transmission response of S-FG SL systems, illustrated in FIGURE 1 (a). The meticulous assembly of S-FG SL units forms the complete honeycomb structure along predefined directions, represented by lattice basis vectors denoted as e_i (where i = 1,2 as shown in FIGURE 1 (b)). The intersection points of these square unit lattice geometries are referred to as lattice points.

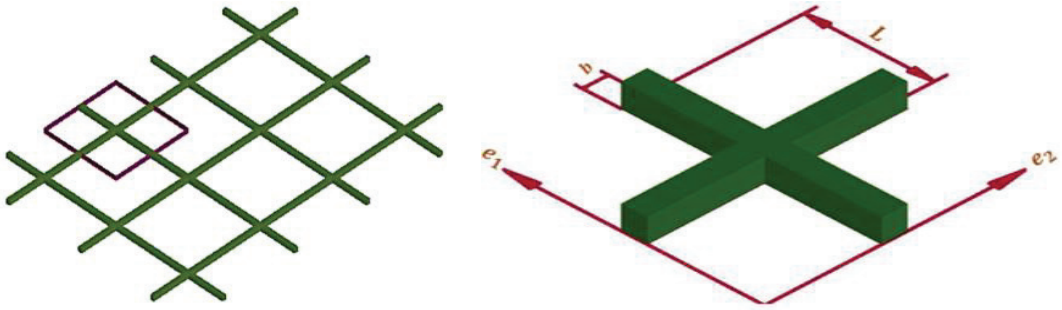

(a) (b)

FIGURE 1. (a) S-FG SL structure, (b) Fundamental unit cells for SL structure, accompanied by descriptions of their lattice geometry. Furthermore, the direct lattice basis vectors, indicated as e_1 and e_2 are illustrated to provide a clearer understanding.

The lattice and reciprocal lattice basis vectors for the square structure are illustrated in FIGURE 2. The irreducible Brillouin zone, its sections, and high-symmetry points are highlighted, aiding in the analysis of lattice symmetry and reciprocal relationships.

Square ($\theta = 0^\circ$)	
Direct Lattice Vector	$e_1 = L_c\,\hat{i}$ $e_2 = L_c\,\hat{j}$
Reciprocal Lattice Vector	$e_1^{\Re} = (\pi/L_c)\,\hat{i}$ $e_2^{\Re} = (\pi/L_c)\,\hat{j}$

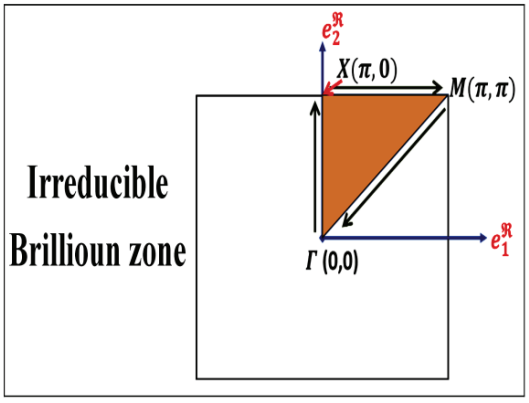

(a) (b)

FIGURE 2. (a) Direct and reciprocal lattice vectors of the SL **(b)** Irreducible Brillouin zone with the coordinates of the high-symmetry points.

2.2 Effective Material Properties of FG Beams

Functionally graded materials (FGMs) feature gradually varying properties, modeled using mathematical functions. This study employs a sigmoid function to analyze volume fraction variations in FG hexagon honeycomb structures.
In the sigmoid law mathematical model, the volume fraction can be represented by a combination of two power-law functions.

$$V_f^1(t) = 1 - \frac{1}{2}\left(\frac{h/2 - z}{h/2}\right)^p \text{ for } 0 \le z \le \frac{h}{2},$$
$$V_f^2(t) = \frac{1}{2}\left(\frac{h/2 + z}{h/2}\right)^p \text{ for } -\frac{h}{2} \le z \le 0. \quad (1)$$

Where h is thickness of the S-FG beam and p is exponent of material gradient.
By employing the rule of mixture, one can compute the material properties of the S-FGM.

$$E_{FG} = V_f^1(t)E_c + (1 - V_f^1(t))E_m \text{ for } 0 \le z \le \frac{h}{2},$$
$$E_{FG} = V_f^2(t)E_c + (1 - V_f^2(t))E_m \text{for } -\frac{h}{2} \le z \le 0. \quad (2)$$

And

$$\rho_{FG} = V_f^1(t)\rho_c + (1 - V_f^1(t))\rho_m \text{ for } 0 \le z \le \frac{h}{2},$$
$$\rho_{FG} = V_f^2(t)\rho_c + (1 - V_f^2(t))\rho_m \text{for } -\frac{h}{2} \le z \le 0. \quad (3)$$

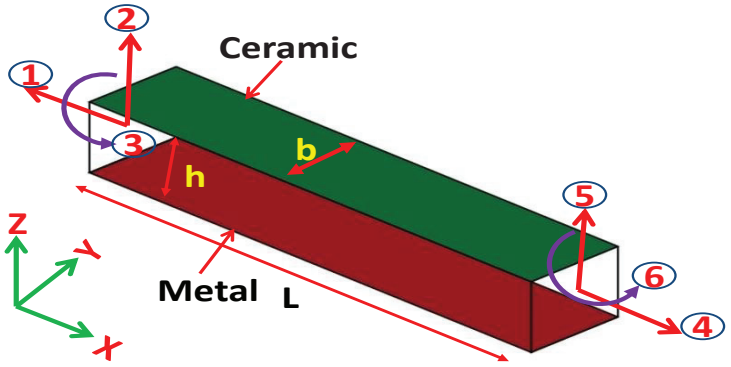

FIGURE 3. Functionally graded material beam element with three degrees of freedom namely axial deformation (1 & 4), transverse deformation (2 & 5) and rotation (3 & 6)

2.3 Dynamic Stiffness Formulation of Unit Cell

The DSM is a reliable approach for precisely determining the eigenvalues and eigenvectors of structures that resemble slender, beam-like elements arranged in two-dimensional frame-like configurations. In this study, instead of examining the entire lattice structure, the focus is on the behavior of an individual unit cell from a 2D periodic lattice. This unit cell is composed of beams, with each node exhibiting three degrees of freedom (DoFs): axial, flexural, and shear

deformations, as shown in FIGURE 3. To create the dynamic stiffness model for the unit cell, classical theory is applied for axial vibrations, while the Timoshenko beam theory (TBT) is used for bending vibrations.

The governing differential equation for axial free vibration in an S-FG beam is supported

$$\rho_z \omega^2 U(x) + E_z \frac{d^2U(x)}{dx^2} = 0 \tag{4}$$

Where

$$\rho_z = \int_{-\frac{h}{2}}^{\frac{h}{2}} \rho_{FG} b dz = \frac{bh((2-2^p+p)\rho_c + (2^p+p)\rho_m)}{2(1+p)} \tag{5}$$

$$E_z = \int_{-\frac{h}{2}}^{\frac{h}{2}} E_{FG} b dz = \frac{bh(E_c\,(2-2^p+p) + E_m(2^p+p))}{2(1+p)} \tag{6}$$

The DS matrix for the axial vibration of the Timoshenko S-FG beam element [9] can be represented by utilizing the above governing differential equation (5)

$$\begin{bmatrix} N_1 \\ N_2 \end{bmatrix} = \begin{bmatrix} a_1 & a_2 \\ a_2 & a_1 \end{bmatrix} \begin{bmatrix} U_1 \\ U_2 \end{bmatrix} \tag{7}$$

Where

$$a_1 = E_e \lambda_a cot\,(\lambda_a L); a_2 = -E_e \lambda_a cosec\,(\lambda_a L) \tag{8}$$

Where L is length of Beam and $\lambda_a = \sqrt{\frac{\rho_e\,\omega^2}{E_e}}$

The differential equation that governs the free vibration of bending in a S-FG beam is as follows:

$$\begin{aligned} kG_z \frac{d}{dx}\left(\frac{dW}{dx} - \theta\right) + \omega^2 \rho_z W = 0 \\ J_z \frac{d^2\theta}{dx^2} + kG_e\left(\frac{dW}{dx} - \theta\right) + M_z \omega^2 \theta = 0 \end{aligned} \tag{9}$$

Where

$$\begin{aligned} J_z &= \int_A E(z)(z - z_0\,)^2\, dA \\ &= \frac{1}{96(2+p)^2(3+p)\left(E_c(2-2^p+p) + E_m(2^p+p)\right)} b({E_m}^2(34^{2+p} \\ &+ p^2(7+p(4+p)) + 2^{2+p}p(34+7p(4+p))) + 2E_cE_m(-34^{2+p} \\ &+ 136p + 149p^2 + 56p^3 + 7p^4 - 32^{2+p}(-8+p(2+p(4+p)))) \\ &+ {E_c}^2(48(-2+2^p)^2 + p(176+63p+12p^2+p^3 - 2^{2+p}(22+p(4 \\ &+ p))))) \end{aligned} \tag{10}$$

$$
\begin{aligned}
&M_z \\
&= \int_A \rho(z)(z - z_0)^2\, dA \\
&= \frac{1}{96(2+p)^2(3+p)(Ec(2-2^p+p)+Em(2^p+p))^2} bh^3(2EcEm((2^p \\
&+ p)(48(-2+2^p)^2 + p(176+63p+12p^2+p^3-2^{2+p}(22+p(4+p))))\rho c - (-2 \\
&+ 2^p - p)(34^{2+p} + p^2(7+p(4+p)) + 2^{2+p}p(34+7p(4+p)))\rho m) \\
&+ Em^2((-34^{2+p}(-2+2^p) + p(4^{1+p}(-14+p(4+p)) + 2^p(192 - p(103+37p(4 \\
&+ p))) + p(258+p(283+p(106+13p)))))\rho c + (2^p+p)(34^{2+p} + p^2(7+p(4 \\
&+ p)) + 2^{2+p}p(34+7p(4+p)))\rho m) + Ec^2(-(-2+2^p-p)(48(-2+2^p)^2 + p(176 \\
&+ 63p + 12p^2 + p^3 - 2^{2+p}(22+p(4+p))))\rho c + 32^{4+p}(-2+2^p)^2\rho m + p(352 \\
&+ 692p + 459p^2 + 128p^3 + 13p^4 + 4^{1+p}(-2+7p(4+p)) - 2^p(160 + p(513 \\
&+ 7p(36+5p))))\rho m))
\end{aligned}
\tag{11}
$$

Where $z_0 = \frac{\int_{-\frac{h}{2}}^{\frac{h}{2}} \mathrm{E_{FG}} z b dz}{\int_{-\frac{h}{2}}^{\frac{h}{2}} \mathrm{E_{FG}} b dz} = -\frac{(Ec-Em)hp(3-2^{1+p}+p)}{4(2+p)(Ec(2-2^p+p)+Em(2^p+p))}$ is the neutral axis of S-FG beam

The DS matrix for the bending vibration of the Timoshenko S-FG beam element [9] can be represented by utilizing the above governing differential equation (9)

$$
\begin{bmatrix} V_1 \\ M_1 \\ V_2 \\ M_2 \end{bmatrix} = \begin{bmatrix} d_1 & d_2 & d_4 & d_5 \\ & d_3 & -d_5 & d_6 \\ & \vdots & d_1 & -d_2 \\ sym & \vdots & & d_3 \end{bmatrix} \begin{bmatrix} W_1 \\ \Theta_1 \\ W_2 \\ \Theta_2 \end{bmatrix} \tag{12}
$$

Where

$$
\begin{gathered}
d_1 = R_3\bar{b}^2(\lambda_2+\eta\lambda_1)(cS+\eta sC)/(\lambda_1\lambda_2\delta) \\
d_2 = R_2k_1[(\lambda_1+\eta\lambda_2)sS - (\lambda_2-\eta\lambda_1)(1-cC)]/\delta \\
d_4 = -R_3\bar{b}^2(\lambda_2+\eta\lambda_1)(S+\eta s)/(\lambda_1\lambda_2\delta) \\
d_5 = R_2k_1(\lambda_2+\eta\lambda_1)(C-c)/\delta \\
d_6 = R_1(\lambda_2+\eta\lambda_1)(\eta S - s)/\delta
\end{gathered} \tag{13}
$$

With

$$
\begin{gathered}
W_j = E_e/L^j, j = 1,2,3 \\
s = sin\ \lambda_1, c = cos\ \lambda_1, S = sinh\ \lambda_2, C = cosh\ \lambda_2 \\
k_1 = \left(\lambda_1^2 - \bar{b}^2s^2\right)/\lambda_1, k_2 = \left(\lambda_2^2 + \bar{b}^2s^2\right)/\lambda_2
\end{gathered} \tag{14}
$$

Where

$$
\left.\begin{matrix}\lambda_1 \\ \lambda_2\end{matrix}\right\} = \bar{b}\left\{\pm\Delta/2 + \left[\Delta^2/4 + \left(1-\bar{b}^2r^2s^2\right)/\bar{b}^2\right]^{1/2}\right\}^{1/2} \tag{15}
$$

With

$$
\Delta = r^2 + s^2, \bar{b}^2 = \frac{\rho_e\omega^2L^4}{E_e}, r^2 = \frac{I_e}{AL^2}, s^2 = \frac{J_e}{kG_eL^2} \tag{16}
$$

I_z is the moment of inertia of S-FG beam about neutral axis and is given by

$$I_z = \int_A (z - z_0)^2 \, dA = \frac{1}{48(2+p)^2\left(E_c(2-2^p+p)+E_m(2^p+p)\right)^2} bh^3(64{E_c}^2 + 128{E_c}^2 p + 64E_cE_m p + 123{E_c}^2 p^2 + 42E_cE_m p^2 + 43{E_m}^2 p^2 + 50{E_c}^2 p^3 + 12E_cE_m p^3 + 34{E_m}^2 p^3 + 7{E_c}^2 p^4 + 2E_cE_m p^4 + 7{E_m}^2 p^4 + 4^{2+p}(E_c - E_m)^2(1+p+p^2) - 2^{2+p}(E_c - E_m)(-E_m p(-8+p+p^2) + E_c(16+p(24+p(21+5p)))))) \quad (17)$$

By combining axial and bending stiffness matrices the elemental DS matrix of S-FG beam can be expressed as

$$\boldsymbol{K}^e(\omega) = \begin{bmatrix} a_1 & 0 & 0 & a_2 & 0 & 0 \\ 0 & d_1 & d_2 & 0 & d_4 & d_5 \\ 0 & d_2 & d_3 & 0 & -d_5 & d_6 \\ a_2 & 0 & 0 & a_1 & 0 & 0 \\ 0 & d_4 & -d_5 & 0 & d_1 & -d_2 \\ 0 & d_5 & d_6 & 0 & -d_2 & d_3 \end{bmatrix} \quad (18)$$

The first step involves converting the above DS matrix into global coordinates. Following this, the overall DS matrix of the unit cell, denoted as $K^O(\omega)$, can be derived by integrating the DS matrices of each element along the lattice directions. The processes of matrix assembly and coordinate transformation in the DSM closely resemble those in the FEM. Ultimately; the overall DS matrix for the entire unit cell is subjected to periodic boundary conditions (PBCs) through the use of Bloch's theorem. The specific procedure for applying these conditions is explained in detail in the following sections.

3 ENFORCEMENT OF PERIODIC BOUNDARY CONDITION

After getting overall DS matrix the Floquet-Bloch theorem [6] has been utilized to impose PBCs. The procedure to apply the theorem is shown for S-FG SL in FIGURE 4. The image below illustrates the unit cell of SL, including four Timoshenko beams with five nodes (four external and one internal).. The external nodes can be further categorized into output (q_2 and q_4) and input nodes (q_1 and q_3) and. The Floquet-Bloch theorem states that the displacement vector of output nodes may be expressed in relation to the displacements of input nodes as follows:

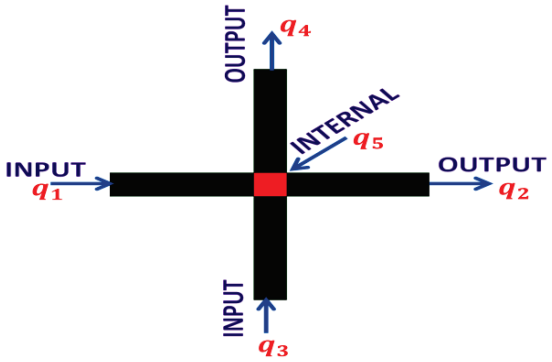

FIGURE 4. S-FG SL unit cell in 2D with designated Output, Input and Internal nodes

$$q_2 = e^{-i\ß_1} q_1 \qquad (19)$$
$$q_4 = e^{-i\ß_2} q_3$$

The wavenumbers β_1 and β_2 correspond to direction along along the basis vectors of the SL in reciprocal space. Equation (19) allows us to formulate the generalized displacement vector for the S-FG square unit cell as

$$q_u = T_b(\beta_1, \beta_2)\widetilde{q_{ul}} \qquad (20)$$

Where over all displacement vector $q_u = [q_1, q_2, q_3, q_{4,} q_5]$, independent displacement components in unit cell $\widetilde{q_{ul}} = [q_1, q_3, q_5]$ and matrix $T_b(\varepsilon_1, \varepsilon_2)$ is given by

$$T_b(\ß_1, \ß_2) = \begin{bmatrix} I & 0 & 0 \\ e^{-i\ß_1} I & 0 & 0 \\ 0 & I & 0 \\ 0 & e^{-i\ß_2} I & 0 \\ 0 & 0 & I \end{bmatrix} \qquad (21)$$

The overall DS matrix after the application of PBCs is given by

$$K^O(\omega, \beta_1, \beta_2) = T_b^H(\beta_1, \beta_2).K^O(\omega).T_b(\beta_1, \beta_2) \qquad (22)$$

Where $T_b^H(\beta_1, \beta_2)$ is the harmonic conjugate of the matrix $T_b(\beta_1, \beta_2)$.

3.1 Witttrick-William Algorithm

The overall DS Matrix $K^O(\omega, \beta_1, \beta_2)$ is highly complicated, having transcendental functions of ω, β_1 and β_2 ,that make it a challenging nonlinear eigenvalue problem. To overcome this, researchers [8-10] often turn to the Wittrick-Williams algorithm, a sophisticated method that takes use of Sturm sequences. What makes this algorithm impressive is its dual capability: it consistently maintains high accuracy while operating with remarkable efficiency. This combination not only ensures precise solutions but also significantly reduces the time required to tackle intricate problems. For brevity, the algorithm is not presented here; readers are referred to Reference [11] for the full implementation of the W–W algorithm.

4 RESULTS AND DISCUSSIONS

This section utilizes the DSM to explore the wave propagation behavior of S-FG SL. A MATLAB code has been developed to execute the DSM formulation and the previously discussed W-W algorithm. These calculations are carried out on a computer with a CPU running at 8.00 GB of RAM and 3.00 GHz. TABLE 1 details the parameters related to the geometry and material properties of the S-FGM beam.

TABLE 1. Material and geometric characteristics of the S-FG beam

Material Properties			
	Density ***(kg/m^3)***	***Poission's Ratio***	***Young's Modulus*** ***(GPa)***
Aluminium	2702	0.3	72
Alumina	3960	0.3	380
Geometric Properties			
	Length	Depth	Width
	0.25 m	0.0125 m	0.0125 m

4.1 Band Structure Validation of the S-FG Square Lattice

To verify the MATLAB code and DSM formulation, a comparative study is performed, focusing specifically on the dispersion curves of the S-FG SL structure. The dispersion curve of the S-FG SL is also calculated using COMSOL Multiphysics software and FEM. In the FEM model, each beam in the S-FG SL unit cell is modeled with 30 elements, totaling 90 components for the entire unit cell. The COMSOL Multiphysics model employs a solid representation with total 4 components and a fine mesh to depict the S-FG SL unit cell. FIGURE 5 illustrates the results obtained from all three methods.

In FIGURE 5 it is evident that the dispersion branches from all three approaches completely align for the lower modes. However, for higher modes, the dispersion curves calculated by the FEM consistently show higher values compared to those obtained by the DSM approach, which might be because of fundamental discretization inaccuracies in FEM. In contrast, the curves from COMSOL sometimes exceed those from DSM and sometimes fall below. This variability can be attributed to COMSOL's use of a FE solid model, which introduces combined effects of discretization errors and differences between solid and beam models. Moreover, the COMSOL model considers the geometric neutral surface, whereas FEM and DSM use the physical neutral surface, potentially leading to higher errors in the COMSOL results.

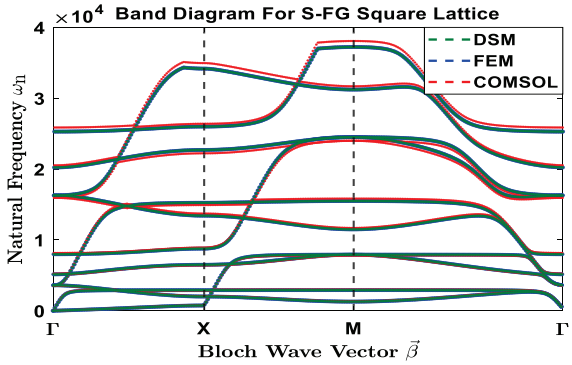

FIGURE 5. The first ten dispersion curve for S-FG SL structure calculated by DSM, FEM, COMSOL (h = L/15 and p = 5)

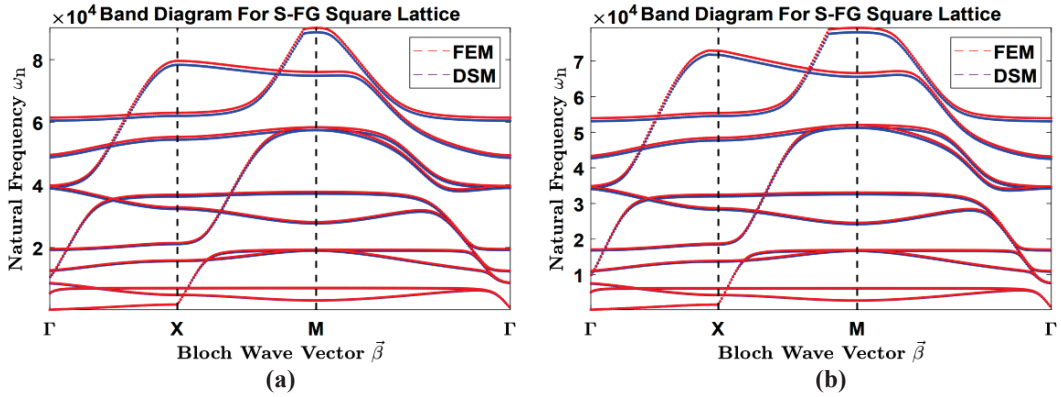

FIGURE 6. Band diagram of S-FG SL with h = L/15 and (a) $p = 0$ (b) $p = 2$

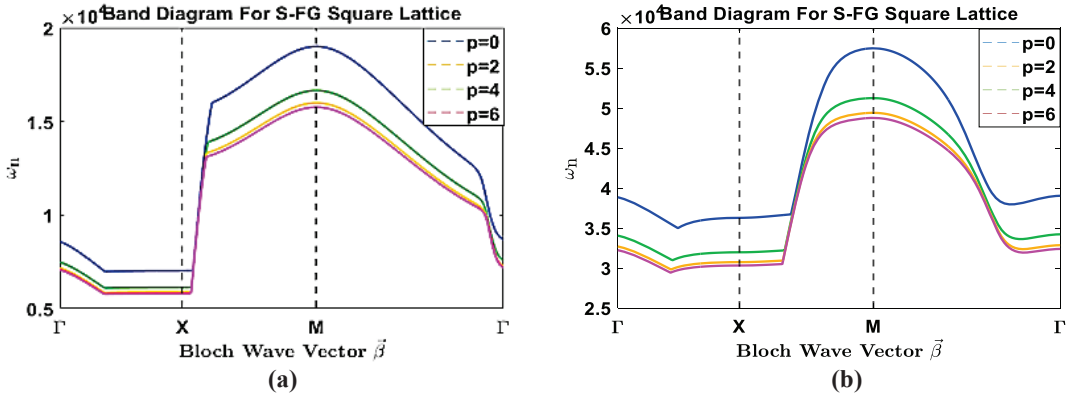

FIGURE 7. Impact of variation in power law gradient index on (a) the 3rd mode and (b) the 7th mode band diagrams of the S-FG SL with h = L/15**.**

The dispersion curves of the first 10 modes of the S-FG SL are shown in FIGURE 6 for material gradient indices (p) of p = 1 and p = 10. The dispersion branches are calculated using the DSM (shown in blue) and verified with FEM (shown in red). From FIGURE 6, it is evident that while the general shape of the dispersion branches retains uniformity across both power law indices, there is a clear reduction in the frequency magnitude of all modes in FIGURE 6 (b) compared to FIGURE 6 (a). This suggests that varying the index (p) impacts the scaling of the dispersion curve of the S-FG SL.

In FIGURE 7, the dispersion curves for the 3rd and 7th branch of dispersion diagram of the S-FG SL are depicted across a range of power law indices. This figure illustrates that with higher power law indices, the curves for both branches shift downwards, suggesting a reduction in the frequency magnitude. The decrease in frequency magnitude can be attributed to the greater proportion of metallic components present within the S-FG beams at higher power law indices. Increase in the metallic volume fraction results in reduced density and stiffness, which consequently lowers the frequency magnitude. Furthermore, it becomes apparent that the distance between the curves narrows with higher values of *p*.

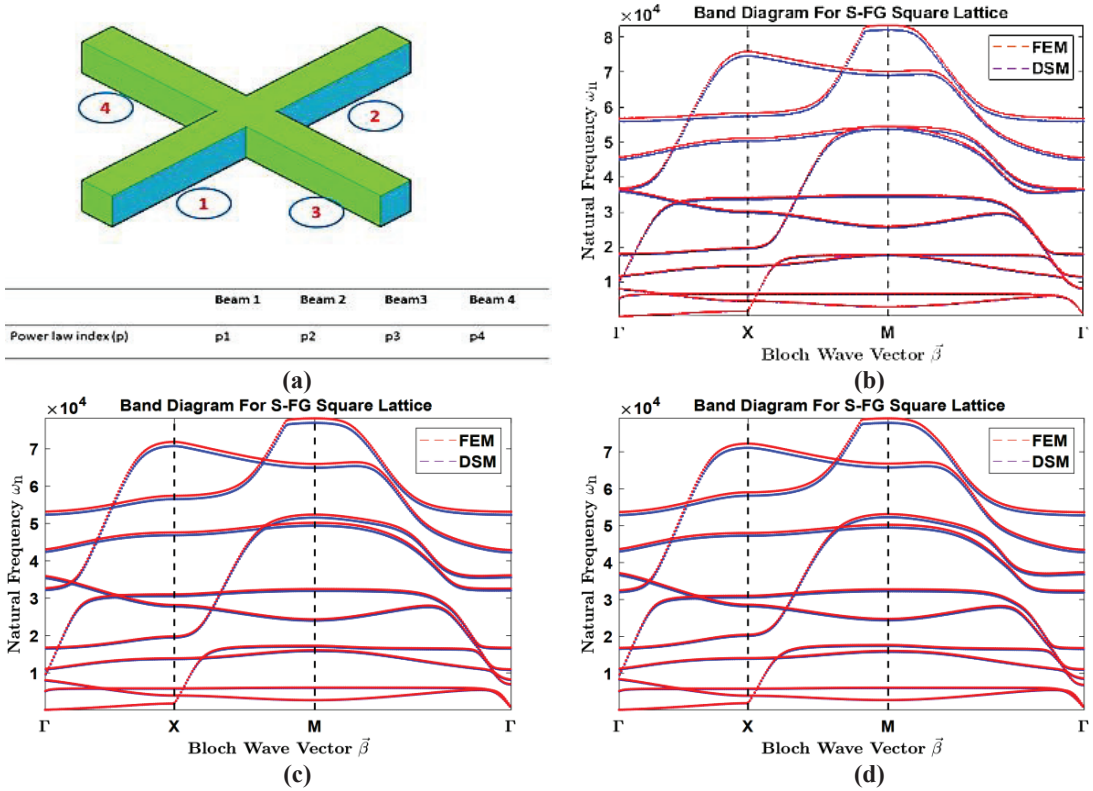

FIGURE 8. (a) Geometry of the FG SL with a table specifying the material gradient index (p) for each beam element within the unit cell. **(b)** Band diagram for a uniformly graded lattice with p1 = p2 = p3 = p4 = 1 **(c)** Band diagram for a lattice with graded indices p1 = 1, p2 = 2, p3 = 4, p4 = 8 **(d)** Band diagram for a lattice with graded indices p1 = 1, p2 = 1, p3 = 4, p4 = 10

The dispersion curves for the S-FG SL structure have been calculated and are shown in FIGURE 8. In this lattice, each element within the unit cell has a distinct power law index. Interestingly, despite this variation in the power law indices, there is no noticeable impact on the dispersion curves. They remain unchanged, indicating that the distinct power law indices do not affect the overall dispersion characteristics. However, only a few variations are shown here for the sake of brevity. It is possible that other variations, not included in this presentation, could lead to the opening of band gaps in the dispersion curves.

FIGURE 9 illustrates the band structure of an S-FG SL with elements of varying cross-sectional shapes. The diagram reveals the emergence of an additional bandgap (yellow region), likely resulting from increased reflection and interference at the junctions where the cross-sectional dimensions of the elements differ. These variations in cross-section seem to create disturbances that contribute to the formation of the new bandgap.

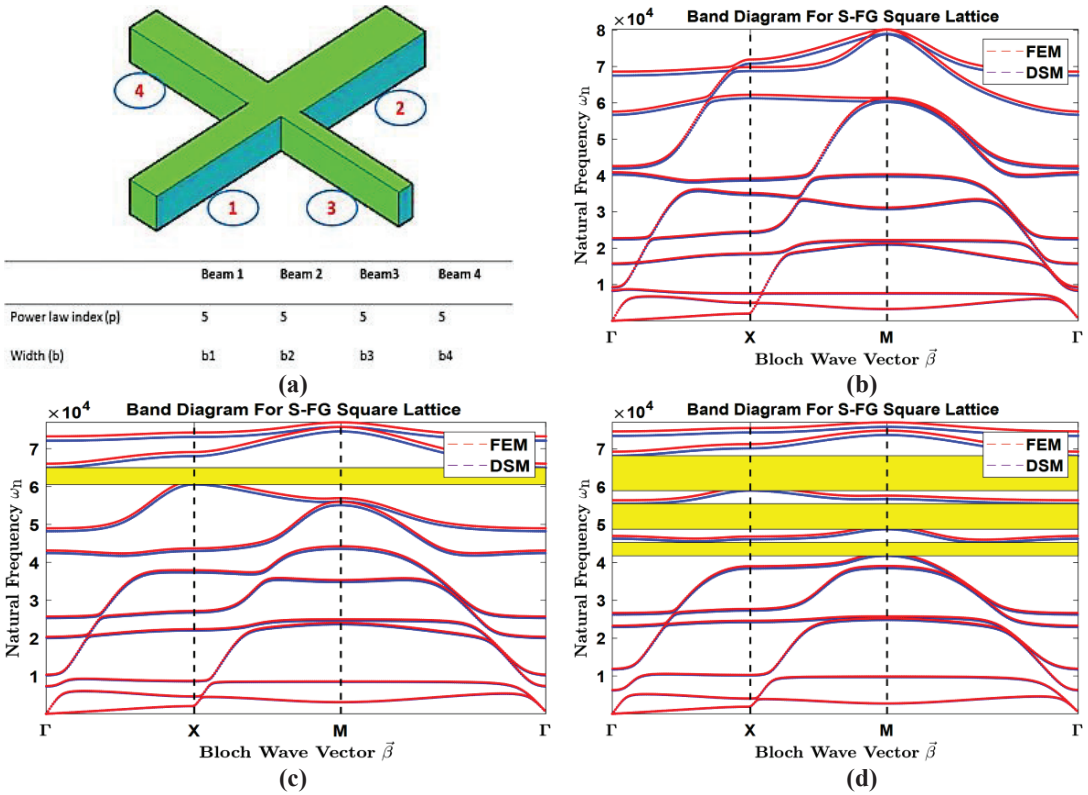

FIGURE 9. (a) Geometry of the FG SL with a table listing the material gradient index (p) and beam widths within the unit cell. (b) Band diagram for the lattice with beam widths b1 = k, b2 = 1.5k, b3 = 1k, b4 = 1.5k (c) Band diagram for the lattice with b1 = k, b2 = 2k, b3 = 1k, b4 = 2k (d) Band diagram for the lattice with b1 = 1 k, b2 = 2.5k, b3 = k, b4 = 2.5k, where $k = L/10$ and $L = 0.125\ m$.

5 CONCLUSION

Wave propagation in S-FG SL structures is investigated using the exact DSM. The impact of the power law index (p) and cross-sectional geometry on dispersion behavior are analyzed. It is observed that increasing p reduces wave frequency, emphasizing the connection between material composition and wave dynamics. Graphical analysis is used to demonstrate how adjusting p tailors dispersion properties for specific applications. Band gaps are formed by introducing variations in p or cross-sectional geometries within unit cells, highlighting the importance of material and geometric design in controlling wave-guiding and filtering functionalities in honeycomb structures.

References

1. M. Mishra, C.K. Srivastav, and S. Kumar, "Free vibration analysis using dynamic stiffness method and first-order shear deformation theory for a functionally graded material plate," Mater Today Proc **98**, 7–15 (2024).
2. M.J. Leamy, "Exact wave-based Bloch analysis procedure for investigating wave propagation in two-dimensional periodic lattices," J Sound Vib **331**(7), 1580–1596 (2012).
3. S. Mukherjee, Fabrizio Scarpa, and S. Gopalakrishnan, "Phononic band gap design in honeycomb lattice with combinations of auxetic and conventional core," Smart Mater Struct **25**(5), 054011 (2016).
4. A.S. Phani, J. Woodhouse, and N.A. Fleck, "Wave propagation in two-dimensional periodic lattices," J Acoust Soc Am **119**(4), 1995–2005 (2006).
5. M. Ruzzene, F. Scarpa, and F. Soranna, "Wave beaming effects in two-dimensional cellular structures," Smart Mater Struct **12**(3), 363–372 (2003).
6. F. Farzbod, and M.J. Leamy, "The treatment of forces in Bloch analysis," J Sound Vib **325**(3), 545–551 (2009).
7. S. Gonella, and M. Ruzzene, "Analysis of in-plane wave propagation in hexagonal and re-entrant lattices," J Sound Vib **312**(1–2), 125–139 (2008).
8. X. Liu, C. Sun, J. Ranjan Banerjee, H.-C. Dan, and L. Chang, "An exact dynamic stiffness method for multibody systems consisting of beams and rigid-bodies," Mech Syst Signal Process **150**, 107264 (2021).
9. X. Liu, Z. Lu, S. Adhikari, Y. Li, and J.R. Banerjee, "Exact wave propagation analysis of lattice structures based on the dynamic stiffness method and the Wittrick–Williams algorithm," Mech Syst Signal Process **174**, 109044 (2022).
10. W.H. WITTRICK, and F.W. WILLIAMS, "A GENERAL ALGORITHM FOR COMPUTING NATURAL FREQUENCIES OF ELASTIC STRUCTURES," Q J Mech Appl Math **24**(3), 263–284 (1971).
11. M. Mishra and S. Kumar, "Analysis of Wave Propagation in Functionally Graded Square Lattice Structures Using the Dynamic Stiffness Method Combined with the Wittrick–Williams Algorithm," *Iranian Journal of Science and Technology, Transactions of Mechanical Engineering*, pp. 1–25, 2025.

XI ECCOMAS Thematic Conference on Smart Structures and Materials - SMART 2025
M. Krommer, M. Nader and M. Schagerl (Eds)

Received: 17 April 2025 / Revised: 28 August 2025 / Accepted: 4 November 2025
© The Author(s) 2025

Lightweight 3D Auxetic Metamaterials

Luke Mizzi, Krzysztof K. Dudek, Mandy Leconte, Andrea Frassineti, Andrea Spaggiari, Gwen Ulliac, Muamer Kadic

Abstract. Auxetic metamaterials are characterised by a number of anomalous and useful properties which make them suitable for a wide variety of niche applications in the biodmedical, personal protection and aerospace industries. Besides possessing a negative Poisson's ratio, the other mechanical properties of these systems such as Young's modulus can be tailored as a function of the geometry along with other relevant characteristics including void volume fraction and stress concentration factors. In this work, we have taken two classes of 3D auxetic metamaterials, namely rotating cubes and rotating octahedra, and, through the introduction of hierarchical truss networks inspired by cubic crystal lattices, improved the stiffness/density ratio of these architectures while maintaining their original negative Poisson's ratio and rotation-based deformation mechanism. The new hierarchical geometries were analysed using a wide ranging parametric Finite Element run on a variety of systems followed by experimental tests on macro- and micro-scale prototypes produced by stereolithography additive manufacturing. The results obtained showed that it is possible to significantly reduce the density of these 3D auxetic systems (by almost 90% in most cases) as well as lower the localised stress concentration factors, thereby increasing the strain tolernace of these systems, while retaining auxeticity and an appreciable level of overall stiffness.

Key words: Auxetics, Metamaterials, Lightweight Systems, Crystal Lattice Geometries

Luke Mizzi & Mandy Leconte & Andrea Frassineti & Andrea Spaggiari
Department of Sciences and Methods for Engineering, University of Modena and Reggio Emilia, Reggio Emilia, Italy

Krzysztof K. Dudek
Institute of Physics, University of Zielona Gora, ul. Szafrana 4a, Zielona Gora 65-069, Poland

Krzysztof K. Dudek & Gwen Ulliac & Muamer Kadic
Institut FEMTO-ST, CNRS, Université Bourgogne Franche-Comté, Besançon 25030, France

1 INTRODUCTION

Auxetic metamaterials are a class of architectured materials which have the ability to exhibit a negative Poisson's ratio. This "negative" property imparts other useful characteristics such as the ability to adopt dome-shaped curvature, enhanced energy absorption and impact resistance as well as unusual acoustic and photonic phenomena. Auxeticity arises primarily from the structure of the material and a wide range of geometries which give rise to deformation mechanisms which are conducive to auxetic behaviour have been identified in the literature. These, all of which confer auxeticity independent of the scale, include re-entrant systems[1], rotating unit modes[2], chiral honeycombs[3], [4] and origami folds[5]. These classes of auxetic metamaterials are typically used to form periodic, tessellatable structures incorporating highly symmetric or asymmetric configurations which have the ability to exhibit an extremely wide range of mechanical properties which may be tailored as a function of the geometric parameters that define the architecture.

Besides the Poisson's ratio, another mechanical property which is of great interest in the design of auxetic metamaterials is the stiffness, i.e. Young's modulus. Being inherently highly deformable structures with a significant volume void fraction, auxetic metamaterials are characterised by a relatively low stiffness[6] which can make their implementation in load-bearing applications challenging. This disadvantage can be offset through the utilisation of an extremely stiff constituent material and/or densification of the structure, however these factors also introduce new complications related to the large localised stress concentrations at the most highly deformable regions of the metamaterial unit cell, which can lead to small-strain failure, and a large increase in weight. These problems highlight the delicate balancing act between strain tolerance, stiffness and metamaterial density (i.e. void-volume fraction), which must be respected when designing these systems.

One potential solution to this problem could be the introduction of hierarchy. Hierarchical materials are structured materials which contain a structure within a structure, with each hierarchical level ideally contributing to the functionality of the global architecture[7]. In the case of auxetic metamaterials, hierarchy is most commonly used to impart enhanced versatility (i.e. a more extensive range of mechanical properties) to the original structure[8], [9], [10]. It can also be used, however, to enhance the stiffness/density ratio of auxetic metamaterials through the introduction of an internal architecture which increases the porosity of the system, but retains a relatively high level of stiffness[11], [12], [13]. This may be achieved through smart design which allows for an optimisation of this ratio by introducing truss-based systems which in typical engineering applications are utilised as structural reinforcements[14], [15]. Some examples of this are shown in Figure 1 below, where typical 2D re-entrant, rotating unit mode and chiral auxetic metamaterials are converted into truss-based hierarchical systems. This structural alteration results in a significant drop in volume fraction (between 70-90%), however the effective Young's modulus is reduced by considerably less, hence improving the stiffness/density ratio of these metamaterial systems.

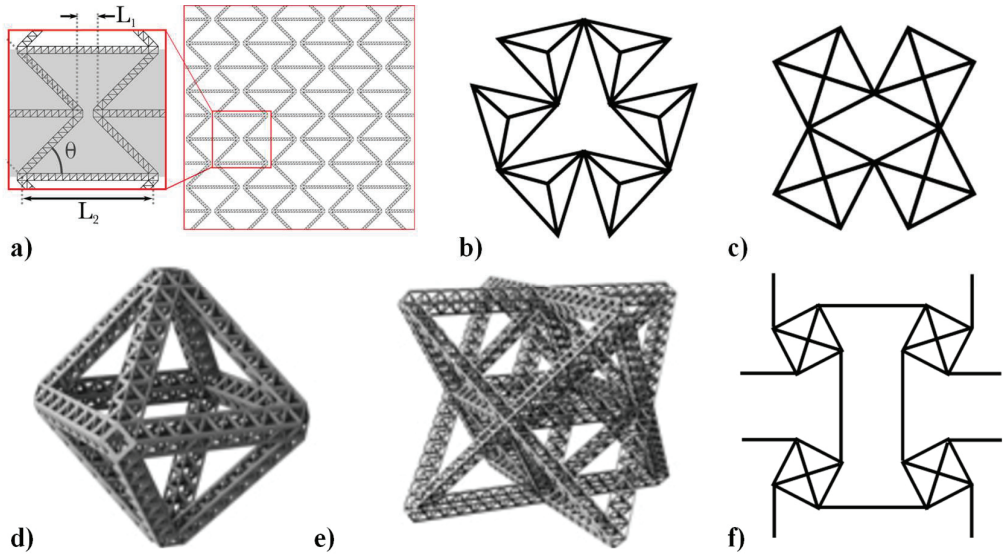

Figure 1: Hierarchical metamaterials formed through the introduction of truss-based ligament systems: a) a reinforced re-entrant honeycomb system, triangular truss-based rotating triangle systems (b), rotating square (c) and anti-tetrachiral honeycomb (f) and two non-auxetic octet-reinforced hierarchical architectures (d and e)[13]**.**

In this work we have extended this concept from 2D architectures to 3D auxetic systems: namely the rotating cube[16] and rotating octahedron systems. Truss-based architectures based on crystalline cubic and octahedral lattice structures were introduced to replace the solid rotating block of material resulting in a final material volume fraction of 4-8% compared to the original of 20-40%. The stiffness of the new hierarchical metamaterial geometries also decreased however if the correct choice of geometric parameters is made, then the stiffness/density ratio of these systems can be improved. A wide ranging Finite Element parametric analysis was carried out to analyse these systems followed by experimental tests on stereolithography 3D-printed prototypes.

2 METHODOLOGY

The two original 3D metamaterial geometries considered in this work are shown in Figure 2 below along with their hierarchical counterparts. Both these systems are anisotropic metamaterials with the potential to exhibit a wide range of Poisson's ratios and Young's moduli. They are geometrically characterised by a small set of independent variables, namely: l, the side length of the rotating unit, r, the radial interconnection region thickness and also the cross-sectional radius thickness of the cylindrical ligaments in the hierarchical systems and finally, θ and ϕ which represent in the angular rotations in the xy- and xz-planes respectively.

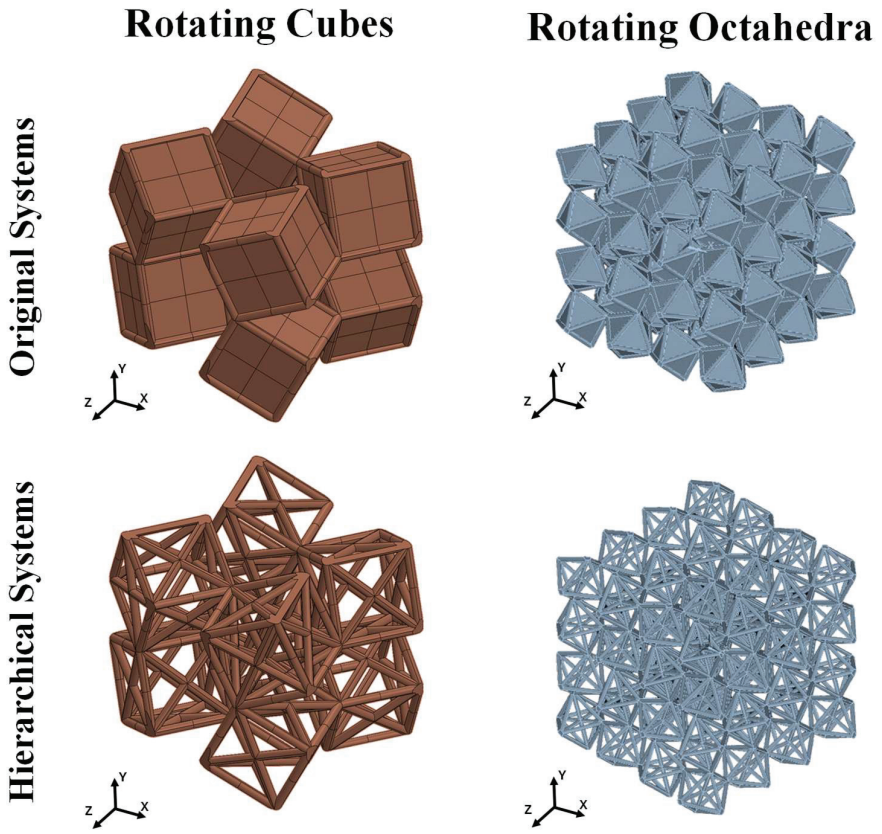

Figure 2: Illustration of the original rotating cubes and rotating octahedra systems and their hierarchical counterparts.

The main objective of the hierarchical arrangement is to reduce the material volume fraction of the system whilst retaining the original rotating deformation mechanism, and hence, auxetic behaviour, along with a considerable level of structural stiffness. In view of this, the choice of arrangement of ligaments was made on the basis of obtaining a stretch-dominated geometry within the rotating unit system. Following preliminary studies involving a number of different configurations, the following were chosen: the Face-Centered Cubic (FCC) arrangement in the case of the rotating cube system and a Body-Centered Cubic-inspired Octahedral (BCCO) configuration for the rotating octahedron system.

In order to analyse the mechanical properties of these systems, Finite Element simulations were carried out on a number of original and hierarchical geometries. The systems were simulated under periodic boundary conditions and subjected to uniaxial loading in the *x*-, *y*- and *z*-directions separately. Since the representative unit cells of all configurations are characterised by three axes of mirror symmetry aligned directly with the three principal on-

axis loading directions, periodicity was induced through the use of axial symmetry-based loading conditions on $1/8^{th}$ of a typical representative element[17]. This means that in each case only one rotating unit block was simulated (shown in Figure 3), significantly reducing the computational time of each simulation run. Periodicity was induced as follows: first, the nodes on the leftmost, bottom-most and innermost edges were constrained using roller fixes in the x, y and z-directions respectively. Then, the nodes in the opposite edges were constrained to undergo identical displacements in the x-, y- and z-directions, respectively. Finally, depending on whether a compressive load was applied in the x-, y- or z-direction, an imposed displacement was applied on the rightmost, uppermost or outermost edge nodes of the system. An illustration of these boundary conditions is shown in Figure 3.

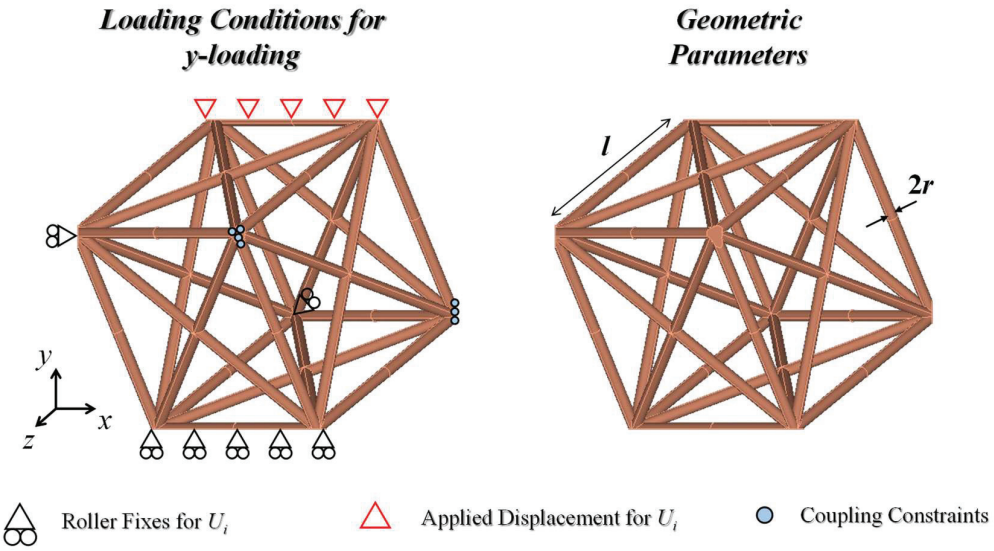

Figure 3: Schematic showing the boundary conditions used to enact periodicity in a single cubic unit and the geometric parameters *l* and *r*. The angles θ and ϕ which correspond to the rotations are not shown. The same set of parameters was used for the rotating octahedera systems.

In order to analyse the mechanical properties of these systems, a range of structures were simulated. The parameter l was kept constant at 20 mm for all structures, while the parameter r was varied from 0.5 to 2 mm in steps of 0.25 mm (i.e. r/l ratio range considered was from 0.025 to 0.1 in steps of 0.0125). The angles θ and ϕ were also varied between 5° to 85° for the rotating cubes systems while for the rotating octahedra (which have different geometric limits), θ was varied from 5° to 85° whereas ϕ was changed between 5° and 40°. The linear elastic material properties of tough resin were utilized as constituent material for each simulation, $\nu = 0.35$ and $E = 4$ GPa.

Following the parametric finite element simulations, a few 3D-printed prototypes were fabricated and tested in order to validate the numerical results. Utilising stereolithography additive manufacturing with a Formlabs 3D-printer, a hierarchical macroscale rotating octahedron system was constructed and subjected to uniaxial compressive loading tests using a tensile loading machine. The experiment was recorded by camera and the frames of the images were subsequently analysed using Digital Image Correlation (DIC) point-tracking analysis to measure the axial and transverse strains and obtain the Poisson's ratio. In the case of the rotating cube systems, a hierarchical FCC system was also realised and tested. Using a Nanoscribe stereolithography 3D printer, a microscale 5x5x5 system was constructed and tested *in-situ* under uniaxial compressive loading utilising a large indenter. The Poisson's ratio was also measured using DIC techniques. The additively-manufactured systems are shown in Figure 4.

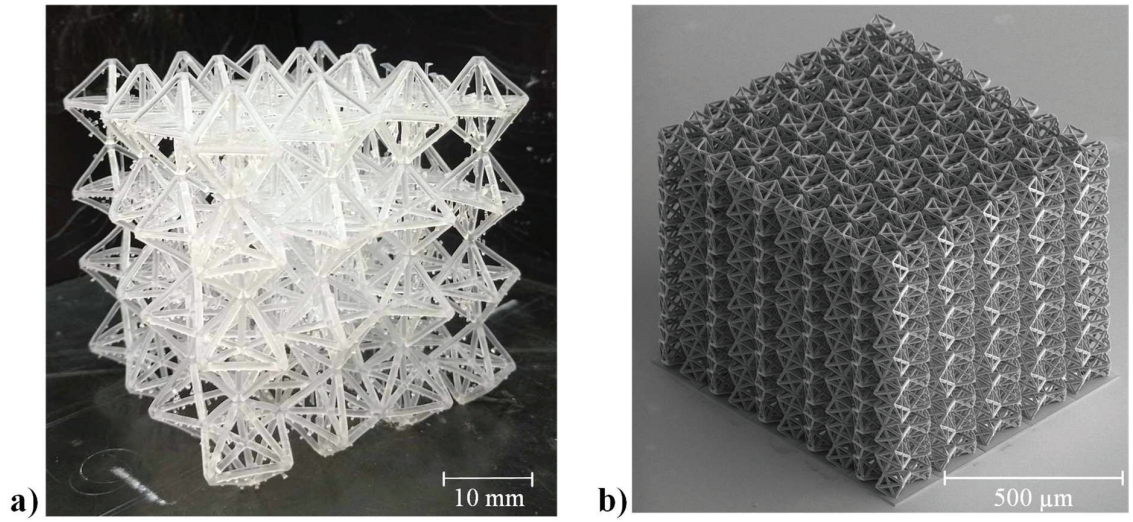

Figure 4: a) Macroscale hierarchical rotating octahedera system and b) microscale hierarchical rotating cube system[18]**. Both structures were produced using stereolithography additive manufacturing.**

3 RESULTS AND DISCUSSION

A representative sample of the results obtained for the Poisson's ratios and effective Young's moduli of the simulated systems are shown in Figures 5 and 6. It is evident that these systems have the potential to exhibit an extremely wide range of Poisson's ratios and that they are highly anisotropic. It is also evident that the introduction of hierarchy does not influence considerably the Poisson's ratios of these structures with both hierarchical and non-hierarchical structures exhibiting similar trends. The main difference is the stiffness, which drops considerably once hierarchy is introduced.

In Figure 5, a set of results for rotating cube structures with ϕ = 30° are presented. It is evident that the Poisson's ratio depends highly on the loading direction, with certain configurations showing both positive and negative Poisson's ratios. The lowest Poisson's ratio was ν_{xz} for both hierarchical and non-hierarchical systems and was -3.2 and -3.7 respectively. In general, the systems with the thinnest ligaments/interconnecting regions displayed the most auxetic behaviour. In terms of effective Young's moduli, the differences between hierarchical and non-hierarchical systems were most pronounced for systems with large *r*/*l* ratios with the original rotating cube systems being on average four times stiffer than the FCC hierarchical systems. The differences were less pronounced for thin ligament systems.

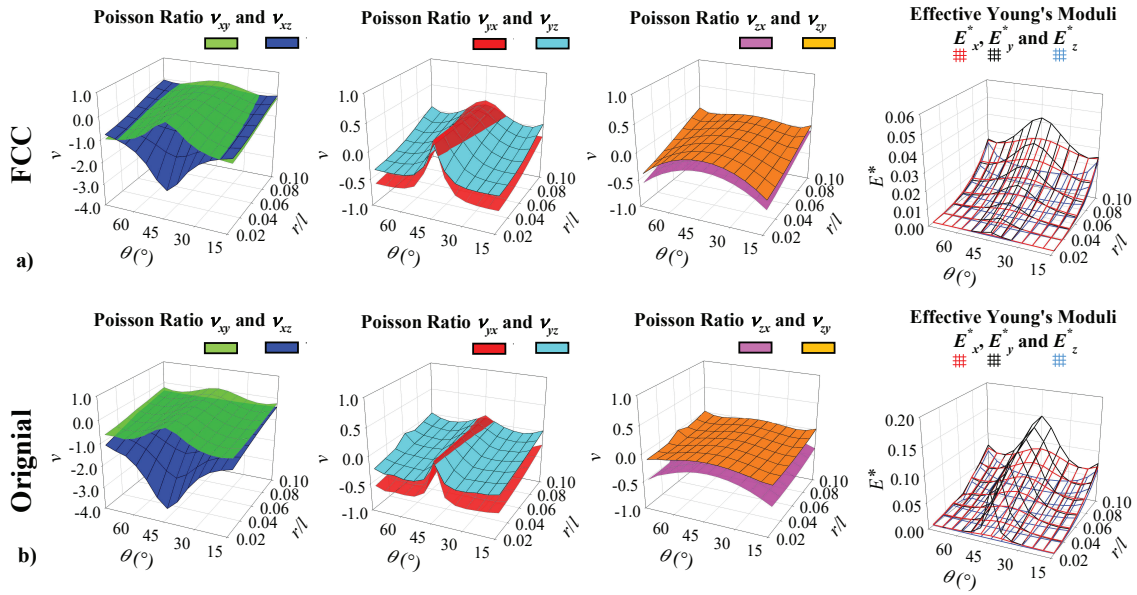

Figure 5: Plots showing how the Poisson's ratios and Young's moduli vary for the a) FCC hierarchical systems and b) the original rotating cubes metamaterials. The results presented here are the systems with a fixed parameter ϕ of 30° while *r*/*l* ratio and θ are varied.

Similar observations were found in the rotating octahedra simulation set (shown in Figure 6). In this case the results are presented with a fixed *r*/*l* ratio of 0.025, with the parameters ϕ and θ varied. The minimum Poisson's ratio obtained was -1.8 and was reached by both hierarchical and non-hierarchical systems. Interestingly, it appears as though in this specific case, more configurations possessing a negative Poisson's ratio were obtained from the hierarchical systems than with the original metamaterial structure. In terms of effective Young's moduli, again, the hierarchical systems are considerably less stiff than the original systems.

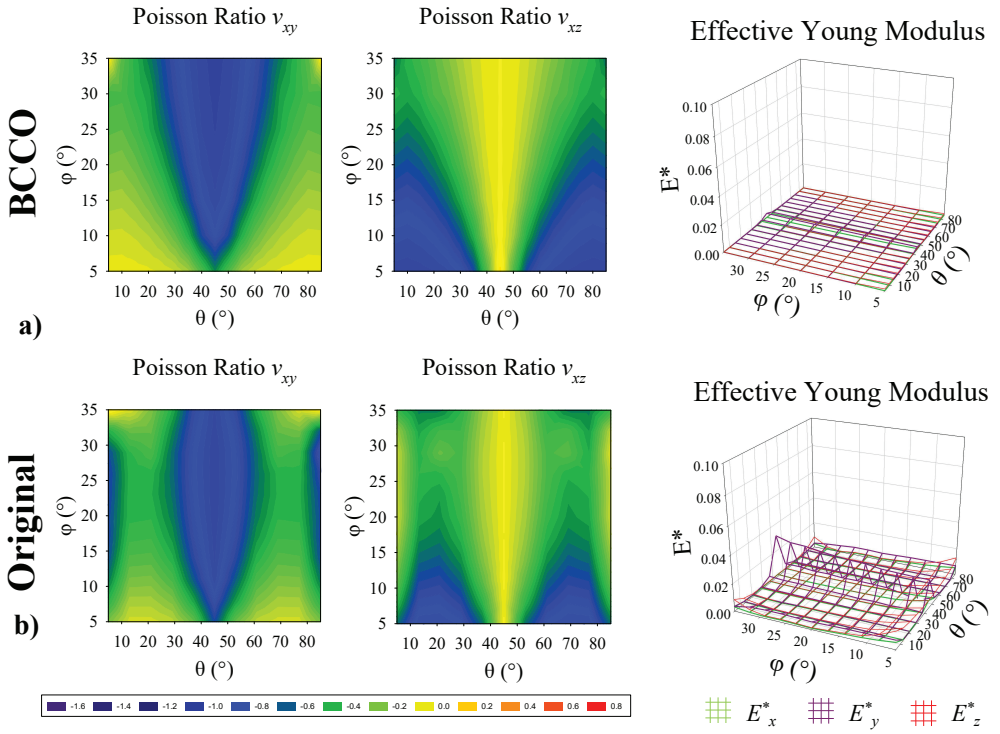

Figure 6: Plots showing how the Poisson's ratios and Young's moduli vary for the a) BCCO hierarchical systems and b) the original rotating octahedra metamaterials. The results presented here are the systems with a fixed parameter $r/l = 0.025$ while ϕ and θ are varied.

The auxeticity of these new hierarchical structures was also confirmed by the experimental tests on the 3D-printed prototypes. The FCC rotating cube system, shown in Figure 7a, exhibits a nearly constant Poisson's ratio of -0.4 over a compressive strain range of 0.08 while the BCCO system, shown in Figure 7b possesses a Poisson's ratio of -1 over a similar strain range.

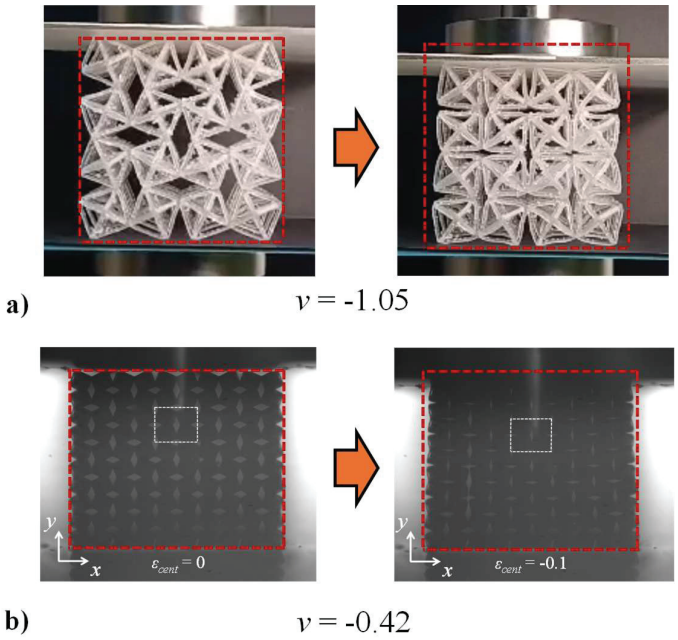

Figure 7: Images of the experimental compressive loading tests in the *y*-direction for the a) BCCO rotating system and b) FCC rotating cube system[18]**. The Poisson's ratio was measured using DIC analyses.**

The results presented in this work highlight how the introduction of truss-based hierarchy may be used to alter the stiffness and volume fraction of 3D rotating unit metamaterials without considerably altering their auxetic characteristics and overall deformation mechanism. This means that one can customize these two properties independently of Poisson's ratio which could lead to the future design of lightweight 3D metamaterial systems based on these architectures.

4 CONCLUSIONS

In this work, two new 3D hierarchical auxetic metamaterial systems were designed and analysed. The new systems are based on truss architectures inspired by cubic crystalline networks and result in a significant reduction of material volume fraction whilst retaining the original auxetic characteristics of the basic rotating cubes and octahedra metamaterial systems. The mechanical properties of these systems were analysed using a parametric finite element simulation run and experimental tests on 3D-printed prototypes and a comparative analysis was also carried out with respect to their non-hierarchical counterparts. The results obtained show that this promising class of mechanical metamaterial systems can achieve auxeticity in spite of the structural modifications and allow for the tunability of stiffness and volume fraction independently of Poisson's ratio characteristics.

REFERENCES

[1] I. G. Masters and K. E. Evans, "Models for the elastic deformation of honeycombs," *Compos Struct*, vol. 35, pp. 403–422, 1996.

[2] J. N. Grima and K. E. Evans, "Auxetic behavior from rotating squares," *J Mater Sci Lett*, vol. 19, pp. 1563–1565, 2000.

[3] D. Prall and R. S. Lakes, "Properties of a chiral honeycomb with a Poisson's ratio of -1," *Int. J. Mech. Sci*, vol. 39, no. 3, pp. 305–314, 1997.

[4] L. Mizzi and A. Spaggiari, "Chiralisation of Euclidean polygonal tessellations for the design of new auxetic metamaterials," *Mechanics of Materials*, vol. 153, Feb. 2021, doi: 10.1016/j.mechmat.2020.103698.

[5] J. L. Silverberg *et al.*, "Using origami design principles to fold reprogrammable mechanical metamaterials."

[6] L. Mizzi, A. Sorrentino, A. Spaggiari, and D. Castagnetti, "A comparison between rotating squares and anti-tetrachiral systems: Influence of ligaments on the multi-axial mechanical response," *Proc Inst Mech Eng C J Mech Eng Sci*, vol. 235, no. 24, pp. 7759–7773, Dec. 2021, doi: 10.1177/09544062211043145.

[7] R. S. Lakes, "Materials with structural hierarchy," *Nature*, vol. 361, pp. 511–515, 1993.

[8] R. Gatt *et al.*, "Hierarchical Auxetic Mechanical Metamaterials," *Sci Rep*, vol. 5, Feb. 2015, doi: 10.1038/srep08395.

[9] K. K. Dudek *et al.*, "Micro-scale graded mechanical metamaterials exhibiting versatile Poisson's ratio," *Compos Struct*, vol. 319, Sep. 2023, doi: 10.1016/j.compstruct.2023.117151.

[10] K. K. Dudek, J. A. I. Martínez, G. Ulliac, and M. Kadic, "Micro-Scale Auxetic Hierarchical Mechanical Metamaterials for Shape Morphing," *Advanced Materials*, vol. 34, no. 14, Apr. 2022, doi: 10.1002/adma.202110115.

[11] L. Mizzi and A. Spaggiari, "Lightweight mechanical metamaterials designed using hierarchical truss elements," *Smart Mater Struct*, vol. 29, no. 10, Oct. 2020, doi: 10.1088/1361-665X/aba53c.

[12] D. Rayneau-Kirkhope, "Stiff auxetics: Hierarchy as a route to stiff, strong lattice based auxetic meta-materials," *Sci Rep*, vol. 8, no. 1, Dec. 2018, doi: 10.1038/s41598-018-30822-x.

[13] L. R. Meza, A. J. Zelhofer, N. Clarke, A. J. Mateos, D. M. Kochmann, and J. R. Greer, "Resilient 3D hierarchical architected metamaterials," *Proc Natl Acad Sci U S A*, vol. 112, no. 37, pp. 11502–11507, Sep. 2015, doi: 10.1073/pnas.1509120112.

[14] E. Dragoni and V. Ciace, "Mechanical design and modelling of lightweight additively manufactured lattice structures evolved from regular three-dimensional tessellations," *Proc Inst Mech Eng C J Mech Eng Sci*, vol. 235, no. 10, pp. 1759–1773, 2019.

[15] E. Turco, I. Giorgio, A. Misra, and F. Dell'Isola, "King post truss as amotif for internal structure of (meta)material with controlled elastic properties," *R Soc Open Sci*, vol. 4, no. 10, Oct. 2017, doi: 10.1098/rsos.171153.

[16] D. Attard and J. N. Grima, "A three-dimensional rotating rigid units network exhibiting negative Poisson's ratios," *Physica Status Solidi B*, vol. 249, no. 7, pp. 1330–1338, 2012.
[17] L. Mizzi, D. Attard, R. Gatt, K. K. Dudek, B. Ellul, and J. N. Grima, "Implementation of periodic boundary conditions for loading of mechanical metamaterials and other complex geometric microstructures using finite element analysis," *Eng Comput*, vol. 37, no. 3, pp. 1765–1779, Jul. 2021, doi: 10.1007/s00366-019-00910-1.
[18] L. Mizzi, K. K. Dudek, A. Frasinetti, A. Spaggiari, G. Ulliac, and M. Kadic, "Lightweight 3D Hierarchical Metamaterial Microlattices," *Advanced Science*, 2025.

XI ECCOMAS Thematic Conference on Smart Structures and Materials - SMART 2025
M. Krommer, M. Nader and M. Schagerl (Eds)

Received: 31 March 2025 / Revised: 1 November 2025 / Accepted: 4 November 2025
© The Author(s) 2025

Auxetic Mechanical Metamaterials Designed using Missing/Added Ribs in Hexagonal Tessellation

Reza Moghimimonfared, Andrea Spaggiari, Luke Mizzi

Abstract. Auxetic mechanical metamaterials are a subclass of metamaterials that exhibit a negative Poisson's ratio. These materials contract laterally under compressive loading and expand globally under tensile loading. This unique behavior arises from their geometry rather than their composition. This study focuses on designing novel structures by adding and/or removing ribs from a hexagonal tessellation with trigonal rotational symmetry to assess the auxetic behavior of the resulting structures through parametric finite element simulations. The original hexagonal tessellation consists of three consecutive pairs of equal side lengths arranged such that each pair of identical lengths is joined at an internal angle of 120°, while the three remaining angles of the hexagon, formed between the unequal side lengths, can vary according to geometrical constraints. Parametric finite element simulations showed the original hexagonal tessellations with trigonal rotational symmetry have the potential to exhibit a limited range of auxetic properties, with a Poisson's ratio ranging from -0.22 to +1. To obtain a higher level of auxeticity, three design strategies were applied to the original hexagon to create new tessellations: deleting one pair of equal side lengths of the hexagon; deleting another pair of equal side lengths of the hexagon while simultaneously adding its corresponding diagonal; and deleting two pairs of equal side lengths of the hexagon while simultaneously adding one diagonal from these two deleted pairs to the original hexagon. The results of the finite element simulations showed that these newly designed structures can exhibit the maximum level of auxeticity in 2D space, i.e., with a Poisson's ratio ranging from -1 to +1.

Key words: Metamaterial, Auxetic, Poisson's Ratio, Hexagonal Tessellations, Parametric Finite Element Simulation.

1 INTRODUCTION

Mechanical metamaterials are a category of artificially designed materials that display unusual behaviors rarely observed in nature. These distinctive properties originate from their structural design rather than their material composition[1]. Studies on mechanical metamaterials primarily focus on systems exhibiting uncommon mechanical properties, particularly those with negative or zero values. These properties include three key elastic constants—Young's modulus

Reza Moghimimonfared & Andrea Spaggiari & Luke Mizzi
Department of Engineering Sciences and Methods, University of Modena and Reggio Emilia, Via Amendola 2- 42122 Reggio Emilia, Italy, e-mail: 338267@studenti.unimore.it

(E), shear modulus (G), and bulk modulus (K)—along with a dimensionless parameter known as Poisson's ratio (v)[2].

A specific subclass of these materials, known as auxetic metamaterials, is characterized by a negative Poisson's ratio. Unlike conventional materials with a positive Poisson's ratio, auxetic materials expand laterally when stretched and contract globally under compression [3, 4]. This unique behavior enhances their resistance to indentation and improves their ability to absorb energy[5]. Additionally, it contributes to their synclastic out-of-plane deformation. These advantageous properties make auxetic metamaterials highly suitable for specialized applications, including biomedical implants such as endovascular stents, as well as protective gear and sports equipment that require lightweight materials with high energy absorption capabilities for impact protection.

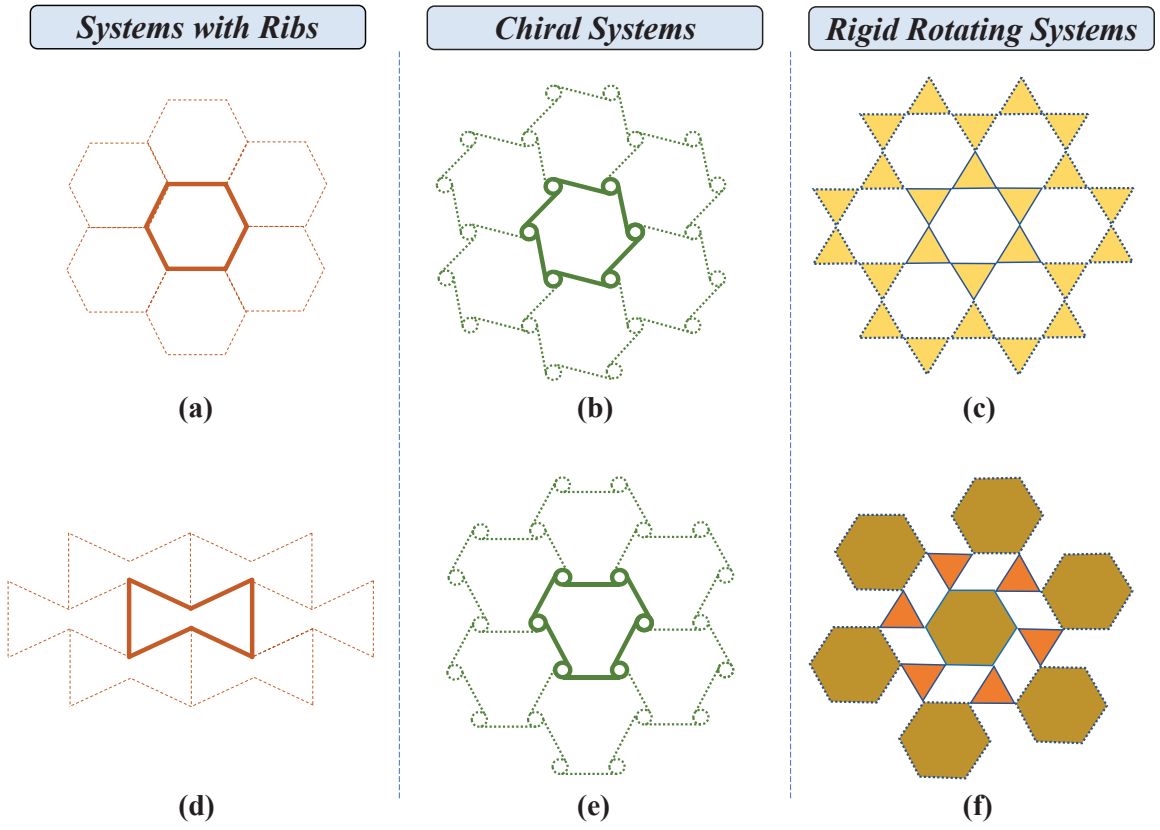

Figure 1. Designing metamaterials using the hexagonal shapes in systems with ribs, chiral structures, and rigid rotating units. a) Regular hexagon, (b) Trichiral, (c) Triangle rotating unit, (d) Re-entrant, (e) Anti-trichiral, and (f) Hexagon-triangle rotating units.

Re-entrant structures [6, 7], chiral honeycombs [8, 9], rigid rotating units [10] are three major categories of auxetic metamaterials. These classifications encompass a variety of symmetric and asymmetric structures, which are periodically arranged in either two-dimensional or three-dimensional space. Many of these configurations are derived from hexagonal tessellations that can be seen in Figure 1. For instance, re-entrant hexagonal honeycombs (see Figure 1d) consist of concave hexagonal cells with two inward-facing angles. The Poisson's ratio of such structures can be adjusted based on the re-entrancy angle. Systems with a positive internal angle (convex honeycombs, see Figure 1a) exhibit a positive Poisson's ratio, whereas those with a negative internal angle (concave honeycombs) display auxetic properties. Similarly, hexagonal cell geometries are commonly found in both rotating unit (see Figure 1c and f) and chiral systems (see Figure 1b and e). A notable example of the former is the fully-opened state of the rotating triangle system. In the case of chiral honeycombs, trichiral and anti-trichiral configurations are both based on hexagonal tessellations. The mechanical characteristics of these auxetic systems can be significantly modified by altering their geometric parameters, allowing them to achieve a broad range of Poisson's ratios, from positive values to large negative ones.

Although extensive research has been conducted on the mechanical properties of hexagon-based structures, such as those depicted in Figure 1, many other configurations remain unexplored. From a geometric perspective, three distinct types of monohedral hexagonal tessellations can be created in two-dimensional space, referred to as Type I, Type II, and Type III (as shown in Figure 2). Each of these tessellations possesses unique symmetry characteristics, offering a vast yet largely unexamined design space for metamaterials and their potential to exhibit auxetic behavior.

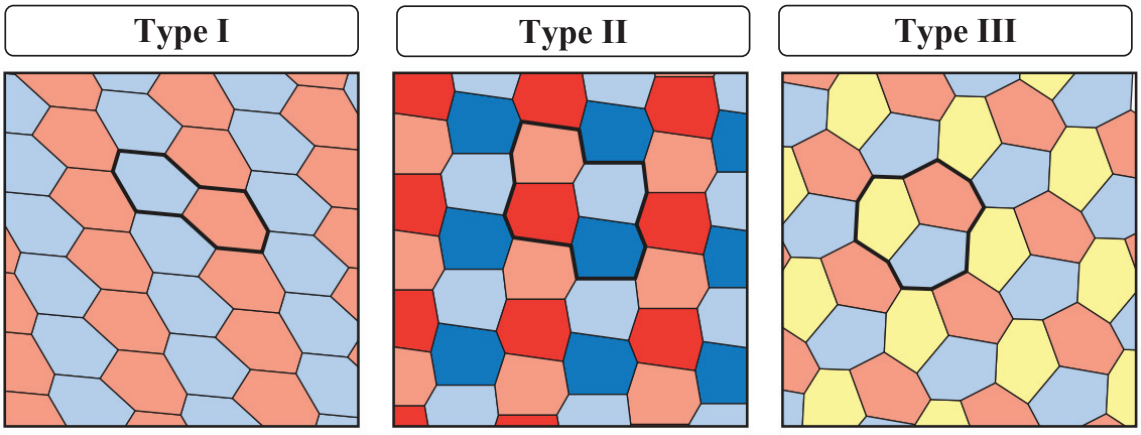

Figure 2. Three main types of monohedral hexagonal tessellation [11].

With this in mind, this study aims to fill this gap in the existing research by conducting FEM simulations on these hexagonal systems and some of their derivatives. In particular, we focus

on the Type III tessellation, which exhibits in-plane trigonal rotational symmetry and lacks a mirror-symmetry axis—an uncommon property among auxetic metamaterial tessellations. This specific tessellation was selected because its symmetry properties are expected to induce transverse isotropy, in contrast to Type I and Type II tessellations, which are likely to exhibit anisotropy. To further explore these properties, we examined three distinct Type III hexagonal tessellations with previously analyzed mechanical propertie [12]. Building on these, we designed new tessellations by modifying the selected hexagons to investigate and compare their mechanical properties with those of their original geometries. The primary objective is to assess the mechanical properties and deformation behavior of these newly designed tessellations, exploring the influence of geometric parameters and identifying configurations that exhibit auxetic behavior. To achieve this, we conducted linear Finite Element (FE) simulations on all the newly designed structures.

2 METHODOLOGY AND DESIGN APPROACH

In this section, first, the design approach used to create novel tessellations by modifying an original hexagonal shape with trigonal rotational symmetry through the addition or removal of ribs was described. Then, the Finite Element method, incorporating periodic boundary conditions to simulate and analyze the mechanical properties of the designed tessellations, was discussed. Finally, the mechanical properties of these newly developed structures were compared with those of their original hexagonal configurations. In the following, the design approaches and methodology employed in this study are discussed in detail.

2.1 Design the new structures using the Type III hexagon

As stated previously, the geometrical features and mechanical properties (Poisson's ratio and Young's modulus) of Type III of the hexagonal tessellations system was investigated in [12] in detail. The hexagon consists of consecutive pairs of sides: one with length i (AB and BC), one with length j (EF and FA), and one with length k (CD and DE). The interior angle between these pairs of sides must be 120°, while the remaining interior angles may vary (i.e., the angles between the sides with lengths i and j, j and k, and k and i). A sample of this hexagon system with geometrical features including its trigonal rotational symmetry and tessellability is depicted in Figure 3.

The three novel configurations designed in this study, named Design I, Design II, and Design III, are derived from the aforementioned original hexagonal shape and can be seen in Figure 4. Design I structures were created by removing both sides of the original hexagon with length i. This alteration reshapes the hexagon into an open-ended shape with four sides. However, after trigonal rotational symmetry, the initial monohedral hexagonal tessellation is transformed into a monohedral dodecagonal tessellation (see Figure 4b). Design II structures were generated by eliminating both sides of the original hexagon with length j and introducing a diagonal that connects these two sides. These adjustments reshape the hexagon into a pentagon. However, after trigonal rotational symmetry, the initial monohedral hexagonal tessellation transforms into

a dihedral tessellation composed of both pentagons and triangles (see Figure 4c). Design III structures were formed by removing four sides of the hexagon with lengths i and j, while introducing a diagonal that connects two sides of j within the original hexagon (see Figure 4d). These modifications reshape the hexagon into an open-ended three-sided structure. However, after trigonal rotational symmetry, the initial monohedral hexagonal tessellation is transformed into a dihedral tessellation comprising a nonagon and a triangle.

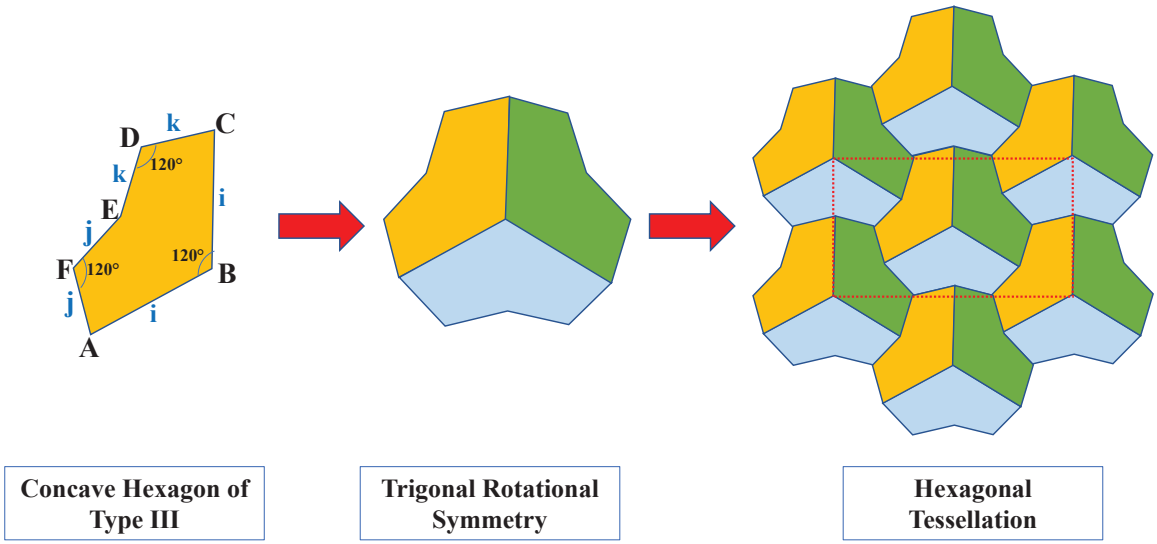

Figure 3. A sample of a Type III (concave) hexagon, along with its trigonal rotational symmetry and tessellation.

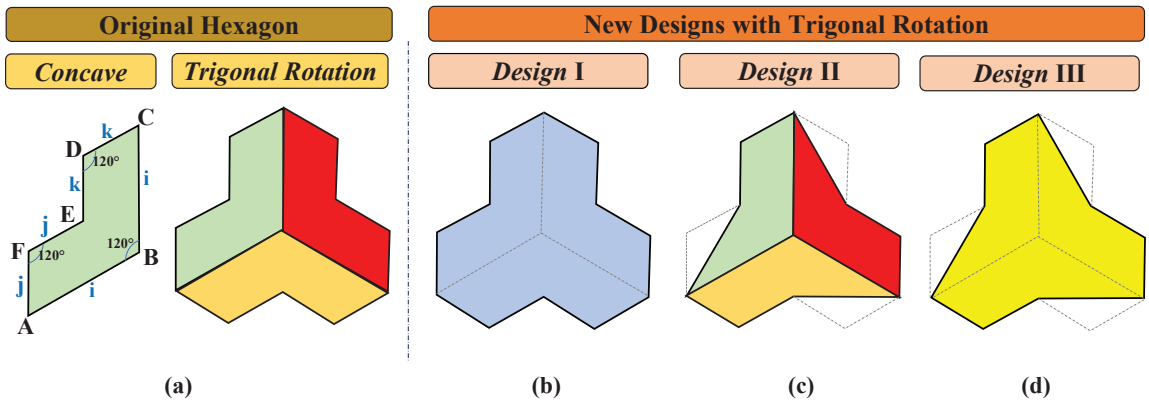

Figure 4. A schematic shape for the original hexagonal shape and the newly designed structures based on the original one. a) A concave hexagon with its trigonal rotational symmetry, b) Design I: structure was created by removing both sides of the original hexagon with lengths i, c) Design II: structure was generated by eliminating both sides of the original hexagon with length j and introducing a diagonal that connects these two sides, and d) Design III: structure was formed by removing four sides of the hexagon with lengths i and j, while introducing a diagonal that connects two sides of j within the original hexagon.

2.2 Finite Element analysis by implementation of periodic boundary conditions

In this study, the ANSYS 16 (Mechanical APDL) multiphysics finite element software was employed to design the new structures and conduct numerical simulations to evaluate their Poisson's ratio and Young's modulus. The structures were meshed using BEAM189 elements with a rectangular cross-section. Simulations were performed on single representative unit cells (RUCs) under general periodic boundary conditions, which will be discussed in the following section. The dimensions of the rectangular RUC, defined by lengths Lx and Ly (as illustrated in Figure 5), can be expressed as a function of the side lengths of the original hexagon—i, j, and k—as follows [13]:

$$L_x = \sqrt{i^2 + k^2 - 2ik\cos\left(\arccos\left(\frac{i^2 + k^2 - j^2}{2ik}\right) + \frac{\pi}{3}\right)} + \sqrt{i^2 + j^2 - 2ij\cos\left(\arccos\left(\frac{i^2 + j^2 - k^2}{2ij}\right) + \frac{\pi}{3}\right)} + \sqrt{j^2 + k^2 - 2jk\cos\left(\arccos\left(\frac{j^2 + k^2 - i^2}{2jk}\right) + \frac{\pi}{3}\right)} \quad (1)$$

$$L_y = L_x \tan\left(\frac{\pi}{6}\right) \quad (2)$$

The BEAM189 element is derived from Timoshenko beam theory, which considers shear deformation effects, making it ideal for analyzing beams that are slender to moderately thick. This element is a quadratic beam with three nodes, where each node has six degrees of freedom by default, including three for translation and three for rotation. The material properties were defined based on the linear isotropic behavior of Onyx® Nylon [14], with a Young's modulus of 1 GPa and a Poisson's ratio of 0.3.

As there is no axis of mirror symmetry for the geometry of the current study, the implementation of specific constraint equations was necessary to simulate the systems under periodic boundary conditions. These equations pair the displacement and rotational degrees of freedom of corresponding nodes on opposite edges of the rectangular RUCs. These equations should guarantee that the deformation on one edge is mirrored on the corresponding opposing side. The rotation of each pair of corresponding nodes on the opposite edges have to be equal. Moreover, Since the simulated systems are 2D structures, both transitional and rotational

movements should be restricted into the plane and any out-of-plane movements should be blocked through definition of extra equations for all of the nodes of the RUC.

In this work, we analysed three systems with the following combinations of geometric parameters: the first structure ($i = 24$, $j = 16$, $k = 8$) , the second structure ($i = 24$, $j = 12$, $k = 12$), and the third structure ($i = 24$, $j = 30$, $k = 6$). For each set of structures the original hexagonal tessellation, Design I, Design II and Design III configurations were analysed under uniaxial loading conditions and the effective Young's moduli and Poisson's ratios were extracted.

3 RESULTS AND DISCUSSION

The deformation behavior and mechanical properties of the original hexagon with combination side lengths of $i = 24$, $j = 16$, and $k = 8$ (the first structure), and the three newly designed structures are depicted in Figure 5. The Poisson's ratio and effective Young's modulus for each configuration is presented below their respective deformed shapes. The original hexagonal structure exhibits a Poisson's ratio of zero, indicating that it neither expands nor contracts laterally when subjected to deformation. In contrast, the three novel designs demonstrate varying degrees of auxetic behavior. Design I has a Poisson's ratio of +0.38, meaning it exhibits conventional material behavior with a slight lateral contraction under axial tension. Design II, on the other hand, has a significantly negative Poisson's ratio of −0.61, making it the most auxetic among the three new as well as the original structures. Similarly, Design III also shows auxetic behavior, with a Poisson's ratio of −0.50, though slightly less pronounced than that of Design II. In addition to Poisson's ratio, the effective Young's modulus of each structure is also different. The effective Young's modulus is defined as the ratio of the resulting Young's modulus of each system obtained from the FE simulation to the predefined Young's modulus of the material. Among the four structures, Design II has the highest effective Young's modulus, indicating that it is the stiffest among the new designs while also showing strong auxetic behavior. Design III follows closely with a slightly lower Young's modulus. In contrast, the original hexagonal structure has a significantly lower Young's modulus, showing that its stiffness is reduced compared to Designs II and III. The lowest Young's modulus is observed in Design I, making it the most compliant structure.

The comparison of the Poisson's ratios and Young's moduli for the second ($i = 24$, $j = 12$, $k = 12$) and third ($i = 24$, $j = 30$, $k = 6$) hexagonal tessellations with their newly designed systems is also presented in Table 1. For both structures, Design I exhibited higher Poisson's ratios and lower effective Young's moduli compared to the original hexagonal structure, while Designs II and III exhibited the opposite behaviour—that is, lower Poisson's ratios (which are negative for both) and higher effective Young's moduli. In addition, Design I has the highest Poisson's ratio and the lowest Young's modulus, while Design II has the lowest Poisson's ratio (indicating the highest auxetic behavior) at nearly -1, along with the highest Young's modulus.

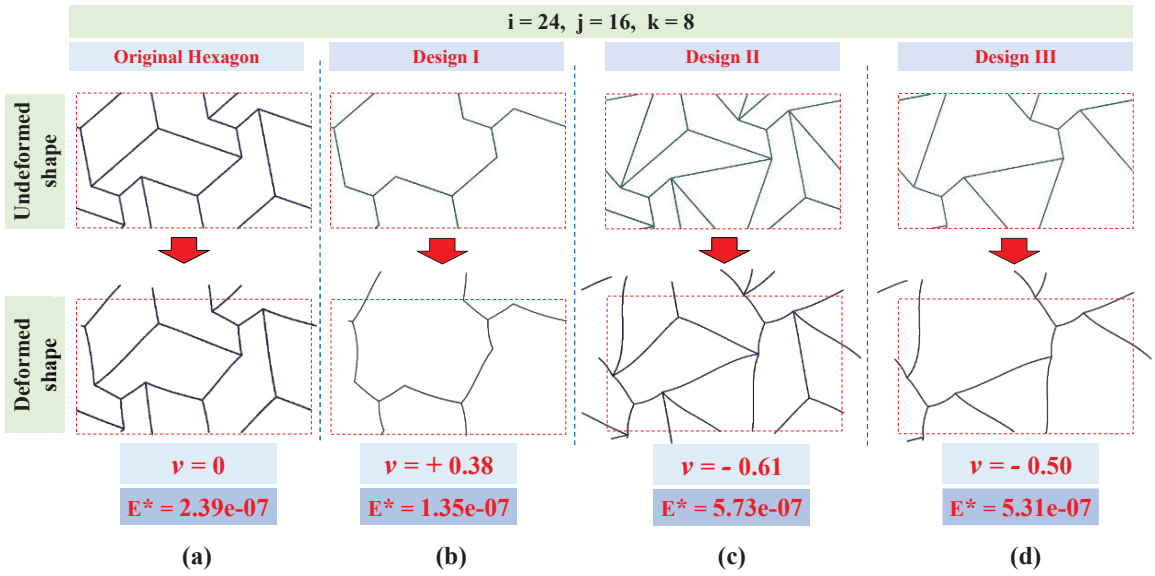

Figure 5. The comparison of deformation behavior and mechanical properties between the original hexagon and the three derivative designs considered in this study: a) the original hexagonal tessellation with trigonal rotational symmetry, b) Design I: structure was created by removing both sides of the original hexagon with lengths *i*, c) Design II: structure was generated by eliminating both sides of the original hexagon with length *j* and introducing a diagonal that connects these two sides, and d) Design III: structure was formed by removing four sides of the hexagon with lengths *i* and *j*, while introducing a diagonal that connects two sides of *j* within the original hexagon.

Table 1. The comparison of the mechanical properties between two configurations and their newly developed designs.

Side lengths	***i* = 24, *j* = 12, *k* = 12**				***i* = 24, *j* = 30, *k* = 6**			
Design / Property	Original Hex.	Deign I	Deign II	Deign III	Original Hex.	Deign I	Deign II	Deign III
ν	-0.22	+0.23	-0.41	-0.26	+0.49	+0.61	-0.999	-0.999
E^*(×e-07)	2.04	1.27	3.38	2.94	1.55	0.48	15.5	11.5

4 CONCLUSION

This study explores the deformation behavior and mechanical properties of three newly designed modified tessellations compared to the original hexagonal structure. Although the

original hexagonal tessellations with trigonal rotational symmetry have the potential to exhibit a limited range of auxetic properties, with a Poisson's ratio ranging from -0.22 to +1, the results show that the newly designed structures exhibit varying degrees of auxetic behavior, with Poisson's ratios ranging from positive values to significantly negative ones, (i.e., -1). Overall, these designs have the potential to demonstrate enhanced stiffness when compared to the original structure whilst retaining the transverse isotropy imparted by their symmetry characteristics. Notably, Design II showcases the most significant auxetic effect with a potential to exhibit a Poisson's ratio nearing -1, while Design III also demonstrates similar auxetic properties, though to a lesser degree in some cases. Design I, on the other hand, behaves more conventionally with a positive Poisson's ratio. In terms of stiffness, Design II stands out by achieving the highest effective Young's modulus, indicating that it is the stiffest structure among the four. This demonstrates that structures which are simulataneously stiff and auxetic can be achieved through smart design. Design I on the other hand exhibited the lowest effective Young's modulus among all four structures, indicating that it is the most compliant and deformable. These findings highlight the potential of these tessellations for the realization of structures with tailored mechanical characteristics suited for specific engineering applications, where a combination of auxeticity and considerable load-bearing capacity is required.

REFERENCES

[1] Bertoldi K, Vitelli V, Christensen J, et al. Flexible mechanical metamaterials. *Nat Rev Mater* 2017; 2: 17066.

[2] Yu X, Zhou J, Liang H, et al. Mechanical metamaterials associated with stiffness, rigidity and compressibility: A brief review. *Prog Mater Sci* 2018; 94: 114–173.

[3] Lakes R. Foam structures with a negative Poisson's ratio. *Science* 1987; 235: 1038–1040.

[4] Evans KE, Nkansah MA, Hutchinson IJ, et al. Molecular network design. *Nature* 1991; 353: 124–124.

[5] Li T, Liu F, Wang L. Enhancing indentation and impact resistance in auxetic composite materials. *Compos Part B Eng* 2020; 198: 108229.

[6] Evans KE, Alderson A, Christian FR. Auxetic two-dimensional polymer networks. An example of tailoring geometry for specific mechanical properties. *J Chem Soc Faraday Trans* 1995; 91: 2671.

[7] Mustahsan F, Khan SZ, Zaidi AA, et al. Re-Entrant Honeycomb Auxetic Structure with Enhanced Directional Properties. *Materials* 2022; 15: 8022.

[8] Prall D, Lakes RS. Properties of a chiral honeycomb with a Poisson's ratio of -1. *Int J Mech Sci* 1997; 39: 305–314.

[9] Mizzi L, Grasselli L, Spaggiari A, et al. Design of isotropic 2D chiral metamaterials based on monohedral pentagonal tessellations. *Thin-Walled Struct* 2023; 187: 110739.

[10] Grima JN, Evans KE. Auxetic behavior from rotating squares. *J Mater Sci Lett* 2000; 19: 1563–1565.

[11] Fathauer R. *Tessellations: mathematics, art, and recreation*. Boca Raton: CRC Press, 2021.

[12] Moghimimonfared R, Spaggiari A, Grasselli L, et al. Hexagonal Tessellation-Based Mechanical Metamaterials. Epub ahead of print 2025. DOI: dx.doi.org/10.2139/ssrn.5193531.

[13] Mizzi L, Grasselli L, Spaggiari A. Clockwise vs anti-clockwise chiral metamaterials: Influence of base tessellation symmetry and rotational direction of chiralisation on mechanical properties. *Thin-Walled Struct* 2024; 205: 112381.

[14] Data sheet for Onyx material, https://markforged.com/it/materials/plastics/onyx (accessed 13 March 2025).

XI ECCOMAS Thematic Conference on Smart Structures and Materials - SMART 2025
M. Krommer, M. Nader and M. Schagerl (Eds)

Received: 8 April 2025 / Revised: 26 August 2025 / Accepted: 4 November 2025
© The Author(s) 2025

Magnetometer-based Particle Filter with enhanced velocity input for GPS-independent navigation of UAV

Dominik Pisarski, Rami Faraj, Robert Konowrocki, Błażej Popławski, Łukasz Jankowski

Abstract. The contribution presents an original method for accurate positioning of an unmanned aerial vehicle (UAV) operating in GPS-denied environment, where GNSS signals may be jammed or spoofed. The proposed approach uses Particle Filtering with an enhanced velocity propagation model to estimate the UAV's position within a magnetic anomaly field. The velocity is estimated based on data fusion of kinematic measurements from an Inertial Measurement Unit (IMU) and magnetic field readings from a scalar magnetometer, which are compared with a magnetic anomaly map. Magnetic field measurements are incorporated at two stages. First, the rate of change of the magnetic field along the UAV's trajectory is introduced into the propagation model using the Bayesian inference to fuse IMU and magnetometer data for a more accurate velocity estimation. Second, measured magnetic field values are compared with the anomaly map to recalculate the particle weights and refine the position estimate. The proposed method was validated using in-flight data. The UAV positioning error was significantly reduced. The results confirm the effectiveness of the proposed and emphasize the high performance of the Particle Filter with enhanced velocity propagation model compared to traditional dead reckoning navigation.

Key words: Magnetic Anomaly Navigation, Unmanned Aerial Vehicle, Particle Filter, Sensor Fusion, Bayesian Inference

1 INTRODUCTION

The accuracy of GNSS-based navigation is degraded in environments with limited or intermittent access to GNSS signal, such as tunnels and dense urban areas. Additionally, GNSS navigation becomes impossible in cases of intentional jamming or spoofing. The need for robust solutions and countermeasures is particularly critical in UAV navigation, where encoders commonly used in robotics cannot be applied, and traditional dead reckoning based on inertial measurements is insufficient. Many types of approaches were developed to ensure reliable navigation under these conditions.

Dominik Pisarski & Rami Faraj & Robert Konowrocki & Błażej Popławski & Łukasz Jankowski
Institute of Fundamental Technological Research, Polish Academy of Sciences, Pawińskiego 5B, 02-106 Warsaw, Poland, e-mail: rfaraj@ippt.pan.pl

A common method is real-time analysis of terrain features, implemented in vision-based navigation systems. These systems offer relatively high spatial accuracy, which makes them a popular alternative to inertial navigation systems (INS) [1, 2]. However, vision-based methods struggle or fail in environments with few reference points or no reference points at all. This includes navigation over flat deserts, water reservoirs, or dense forests. Additionally, even if vision-based are cost-effective in terms of hardware elements, they face significant limitations related to high computational demands, dependency on lighting conditions, reduced accuracy at high flight altitudes, and vulnerability to common adverse weather conditions such as rain, fog, dust, and snow [3].

As an alternative to vision-based systems, some of recently developed navigation approaches employ measurements of crustal anomalies of the Earth's magnetic field. These magnetic anomalies exhibit significant variability across most environments, including over open water and other visually uniform terrains. This variability and insensitivity to weather conditions makes them a reliable reference for positioning. Furthermore, commercially available magnetic sensors are lightweight and compact, which makes them well-suited for integration into ultralight UAV platforms in hardware terms.

Various techniques and methods have been developed for magnetic positioning, dependent on the characteristics of the intended deployment environment. For indoor applications, SLAM (Simultaneous Localization and Mapping) techniques are commonly applied. Intended for robotic applications, they aim to map the ambient magnetic field, while simultaneously positioning the robot within the mapped environment [4]. To effectively fuse inertial and magnetometric data, SLAM techniques often rely on Particle Filtering [5] or Kalman filters [6]. The feasibility of these approaches has been demonstrated in numerous publications. For example, an extended Kalman filter was used in [7] to reduce noise in measurements of magnetic field gradient for positioning of a foot-mounted IMU/magnetometric system. In [8], an extended Kalman filter was used to fuse data coming from a magnetometer and an IMU installed on a ship model and in a foot-mounted sensor. In [9], a magnetic map-matching algorithm based on sequential batch fusion was proposed for stable and fast indoor localization. In [10], a Bayesian data fusion algorithm was developed for improving the positioning accuracy based on IMU data and magnetometric measurements. Besides indoor implementations, researchers have also extensively explored magnetic anomaly-based navigation systems for outdoor environments, particularly airborne systems. In [11, 12], an airborne magnetic anomaly navigation was developed. For accurate measurements of the magnetic field, scalar sensors are often used. The position drift, typical for navigation systems based on inertial data only, is usually addressed using map-matching techniques. Accuracies within tens of meters were achieved for over hour-long flights [13]. More recently, machine learning techniques have been successfully applied for in-flight navigation based on magnetic anomalies [14].

This contribution considers magnetic anomaly-based navigation intended for aerial applications. Particle Filter is used as a well-established core methodology for positioning. The original element proposed here is the velocity-enhanced propagation model used within the Particle Filter. Unlike traditional approaches relying solely on IMU-based velocity, the pro-

posed method integrates onboard magnetometric measurements and fuses them with inertial data using Bayesian inference to enhance velocity estimation. Below, the general architecture of the system is introduced, followed by the basic mathematical formulas. Thereupon, the proposed method is validated using in-flight data collected with a Vertical Take-off and Landing (VTOL) platform and a scalar magnetometer on-board, tested in an autonomous flight over a designated water area.

2 SYSTEM ARCHITECTURE

UAV position is estimated using an approach based on Particle Filter. The measured magnetic field values, the IMU-provided inertial measurements, and the magnetic anomaly map are used as an input. A general scheme of the system architecture is presented in Fig. 1. Measurements of the magnetic field are utilized twice during the Particle Filter procedure:

1. At the particle re-sampling stage, magnetometer readings are compared with the map of magnetic anomalies, and only particles more aligned with the actual measurements are retained. This is a typical use of magnetometric measurements in magnetic navigation.

2. At the particle propagation stage, magnetometric measurements are used to correct the IMU-based velocity. This fusion of magnetic and inertial data is performed based on Bayesian inference within the block "Velocity Estimation Module" in Fig. 1, and the result is an enhanced particle propagation model. This is the actual novelty of the presented approach.

The related formal mathematical formulas are discussed in the subsequent section. The following assumptions are necessary to ensure the proper operation of the proposed system:

- the velocity drift estimated based on IMU alone is sufficiently small,
- a sufficiently accurate map of magnetic anomalies is available,
- the magnetic anomaly field is sufficiently smooth (continuous spatial derivatives),
- the magnetic anomaly field does not change in time,
- the magnetometric measurements are of a sufficient accuracy to reliably estimate the time derivative of the magnetic anomaly field.

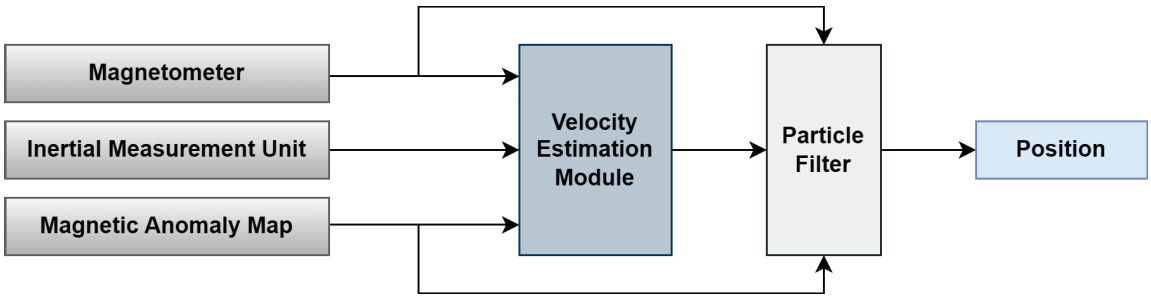

Figure 1: Architecture of the proposed positioning system based on Particle Filter and magnetic anomaly measurements.

3 Particle Filter based on inertial/magnetic data fusion

3.1 Particle Filter procedure

The Particle Filter is a widely used procedure. The distribution p of state X_t at time t is iteratively estimated based on the observation o_t:

$$p(X_t|o_t) = \sum_{i=1}^{N_t} w_t^i \, \delta(X_t - \mathbf{x}_t^i), \tag{1}$$

where N_t is the number of particles at time t, δ is the Dirac delta function, $\mathbf{x}_t^1, ..., \mathbf{x}_t^{N_t}$ are particle locations, and $w_t^1, ..., w_t^{N_t}$ represent their weights. In typical implementations, the the distribution $p(X_t|o_t)$ is computed in the three following steps:

Step 1: Compute the weights w_t^i, $i = 1, ..., N_t$, which should be proportional to the measurement likelihood $p(o_t|X_t)$.

Step 2: Re-sample the particles: discard the particles with lower significance and generate new particles based on the measurement likelihood $p(o_t|X_t)$.

Step 3: Update particle positions to time $t + 1$ based on the propagation model.

3.2 Propagation model and velocity correction based on magnetometric measurements

In applications to positioning systems, the state X_t represents the position, and in the system considered here, the observation o_t is the measured magnetic field. Step 3 makes involves the propagation model, and the propagation model requires estimated velocity of the UAV. The velocity is usually obtained by integrating IMU-sourced acceleration and thus susceptible to substantial drift in time. In the propagation model proposed here, velocity $\mathbf{V}_t$ is modeled probabilistically as a 2D Gaussian random variable, and its IMU-based estimation is corrected using magnetometric measurements and Bayesian framework. Step 3 consists of two updates (position and velocity), and it is performed in the three following substeps:

Step 3.1: (*Position update*) The particle location is updated using the expected value of the velocity in the current time step, $\boldsymbol{\mu}_{\mathbf{V}_t} = \mathbb{E}[\mathbf{V}_t]$:

$$\mathbf{x}_{t+1} = \mathbf{x}_t + \Delta t \, \boldsymbol{\mu}_{\mathbf{V}_t},$$

where Δt is the time increment. This formula corresponds to the Euler's numerical integration scheme, and it allows the location update to be decoupled from the velocity update.

Step 3.2: (*Initial velocity correction*) The last-step velocity $\mathbf{V}_t$ is shifted by the velocity update $\Delta\mathbf{V}_{t+1}^{\text{IMU}}$ provided by the IMU to obtain $\bar{\mathbf{V}}_{t+1} = \mathbf{V}_t + \Delta\mathbf{V}_{t+1}^{\text{IMU}}$. This is then fused with the current-step IMU-based velocity $\mathbf{V}_{t+1}^{\text{IMU}}$ into a temporary random variable $\mathbf{W}_{t+1}$. Assuming independence of the involved random variables,

$$\mathbf{W}_{t+1} \sim \mathcal{N}\left(\boldsymbol{\mu}_{\mathbf{W}_{t+1}}, \boldsymbol{\Sigma}_{\mathbf{W}_{t+1}}\right),$$

where

$$\boldsymbol{\Sigma}_{\mathbf{W}_{t+1}} = \mathrm{Cov}[\mathbf{W}_{t+1}] = \left(\boldsymbol{\Sigma}^{-1}_{\bar{\mathbf{V}}_{t+1}} + \boldsymbol{\Sigma}^{-1}_{\mathbf{V}^{\mathrm{IMU}}_{t+1}}\right)^{-1},$$
$$\boldsymbol{\mu}_{\mathbf{W}_{t+1}} = \mathbb{E}[\mathbf{W}_{t+1}] = \boldsymbol{\Sigma}_{\mathbf{W}_{t+1}}\left(\boldsymbol{\Sigma}^{-1}_{\bar{\mathbf{V}}_{t+1}}\boldsymbol{\mu}_{\bar{\mathbf{V}}_{t}t+1} + \boldsymbol{\Sigma}^{-1}_{\mathbf{V}^{\mathrm{IMU}}_{t+1}}\boldsymbol{\mu}_{\mathbf{V}^{\mathrm{IMU}}_{t+1}}\right).$$

Step 3.3: (*Final velocity correction*) The temporary random variable $\mathbf{W}_{t+1}$ is fused with information provided by the time derivative G_{t+1} of the magnetic field into the final velocity $\mathbf{V}_{t+1}$. The time derivative of the magnetic field is modeled as an independent 1D Gaussian random variable, $G_{t+1} \sim \mathcal{N}(g_{t+1}, \sigma^2_{\mathrm{G}})$, and estimated in flight using magnetometric measurements. The final velocity $\mathbf{V}_{t+1}$ is then normally distributed,

$$\mathbf{V}_{t+1} \sim \mathcal{N}\left(\boldsymbol{\mu}_{\mathbf{V}_{t+1}}, \boldsymbol{\Sigma}_{\mathbf{V}_{t+1}}\right),$$

and

$$\boldsymbol{\Sigma}_{\mathbf{V}_{t+1}} = \mathrm{Cov}[\mathbf{V}_{t+1}] = \left(\boldsymbol{\Sigma}^{-1}_{\mathbf{W}_{t+1}} + \frac{\nabla M(\mathbf{x}_{t+1})\left(\nabla M(\mathbf{x}_{t+1})\right)^{\mathrm{T}}}{\sigma^2_{\mathrm{G}}}\right)^{-1}, \tag{2}$$

$$\boldsymbol{\mu}_{\mathbf{V}_{t+1}} = \mathbb{E}[\mathbf{V}_{t+1}] = \boldsymbol{\mu}_{\mathbf{W}_{t+1}} + \frac{g_{t+1} - \boldsymbol{\mu}^{\mathrm{T}}_{\mathbf{W}_{t+1}}\nabla M(\mathbf{x}_{t+1})}{\sigma^2_{\mathrm{G}}}\boldsymbol{\Sigma}_{\mathbf{V}_{t+1}}\nabla M(\mathbf{x}_{t+1}), \tag{3}$$

where $\mathbf{x}_{t+1}$ denotes the particle location updated in Step 3.1 and $M(\cdot)$ is the magnetic anomaly map.

The output from Step 3 consist of the updated position $\mathbf{x}_{t+1}$ and the corrected velocity $\mathbf{V}_{t+1}$.

4 Field validation

4.1 UAV platform

The proposed method was tested a VTOL (Vertical Take-Off and Landing) aircraft shown in Fig. 2. The UAV was equipped with a magnetometer system with high-precision scalar cesium units (Geometrics MFAM). To ensure reliable magnetic field measurements and mitigate disturbances, the system had to be calibrated to take into account two factors:

1. Aircraft orientation. First, ground-based measurements with a non-magnetic tripod were collected. Then, an artificial neural network was employed to approximate the disturbance in function of yaw, pitch, and roll angles. Finally, the disturbances estimated this way were subtracted in flight from the magnetic field measurements.

2. Solar activity. An additional ground magnetometer was employed to monitor solar activity and account for the associated fluctuations of the magnetic field.



Figure 2: VTOL aircraft used for validation. The magnetometer system was installed on the nose.

4.2 Magnetic map generation

After calibration, the magnetometer system was used to map the area extending between longitudes 16.64–16.69 deg and latitudes 54.565–54.586 deg. Carefully designed flight paths were used to ensure complete coverage of the area, the desired resolution and precision. The resulting magnetic map (Fig. 3) was generated using Bayesian regression, as described in [10]. The discrepancy between the collected magnetic measurements and the map was 0.12 nT on average.

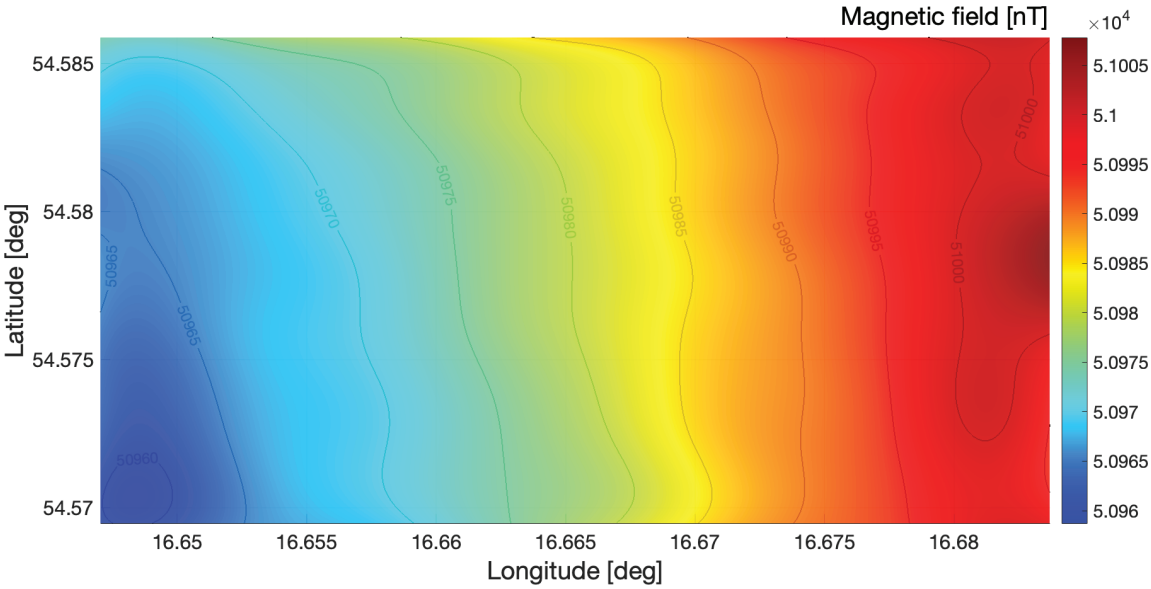

Figure 3: Map of the magnetic field generated using the collected measurements and Bayesian regression.

4.3 Test flight trajectory and Particle Filter procedure

The test flight trajectory, shown in yellow in Fig. 6, was defined using a number waypoints. The total duration of the test flight was 500 s. The IMU-based results included a deterministic velocity drift, which linearly increased with time and resulted at the end of the flight in the position error of 417.7 m. The Particle Filter procedure was started at $t = 50$ s. The initial number of particles was 100, and they were normally distributed around the estimated initial position with the standard deviation of 10^{-4} deg. The Particle Filter calculations were repeated every second, so that the time step $\Delta t = 1$ s.

Step 1: In each update $t \geq 50$, the weights were computed in Step 1 of the Particle Filter procedure by means of a Gaussian function with its argument being the difference between the measured magnetic reading o_t and the value read from the magnetic field map at the particle's location.

Step 2: During the resampling process in Step 2, particles with their normalized weights below 0.9 were discarded. New particles were then generated by sampling from a Gaussian distribution centered around the remaining particles with the standard deviation equal to $3 \cdot 10^{-5}$ deg. Throughout all time steps, the total number of particles, initially equal to 100, was kept between 50 and 200.

Step 3: The time derivative of the magnetic field, used by Eq. (3) in Step 3.3 (velocity correction), was computed using the increment of the collected magnetic measurements: $g_{t+1} = (o_{t+1} - o_t)/\Delta t$. The standard deviation σ_{G}, required in Eqs. (2) and (3)), represented the estimation error of the time derivative g_{t+1}. Its value was selected to correspond to the magnetic field measurement error, so that $\sigma_{\mathrm{G}}^2 = 0.5$ nT^2/s^2.

4.4 Results and discussion

For a comprehensive evaluation of positioning accuracy, the Particle Filter procedure was used both with and without the proposed velocity correction (that is, using only the uncorrected IMU-based velocity or correcting it using magnetometric measurements). In each case, a total of 100 test trajectories were computed. The resulting accuracies are plotted in Fig. 4 (for the uncorrected IMU-based velocity) and in Fig. 5 (for the corrected velocity).

In the initial phase of the flight (for $t < 150$ s), the average positioning errors suggest similar performance for both methods, as the errors obtained for the uncorrected and corrected velocities are comparable. A more significant divergence occurs for $t > 250$ s, with the average positioning error for the uncorrected velocity increasing up to 80.7 m at $t = 486$ s. In contrast, implementation of the proposed velocity correction substantially reduces the average positioning error, which remains consistently below 20.0 m for $t > 215$ s. The maximum error in this case occurs at time $t = 212$ s and equals 30.3 m, which is 62.4% lower than the maximum error obtained using the uncorrected IMU-based velocity. Moreover, with the proposed velocity correction, the total variation in positioning error is significantly reduced. These conclusions are confirmed by the visual analysis of trajectories obtained with both positioning methods, see

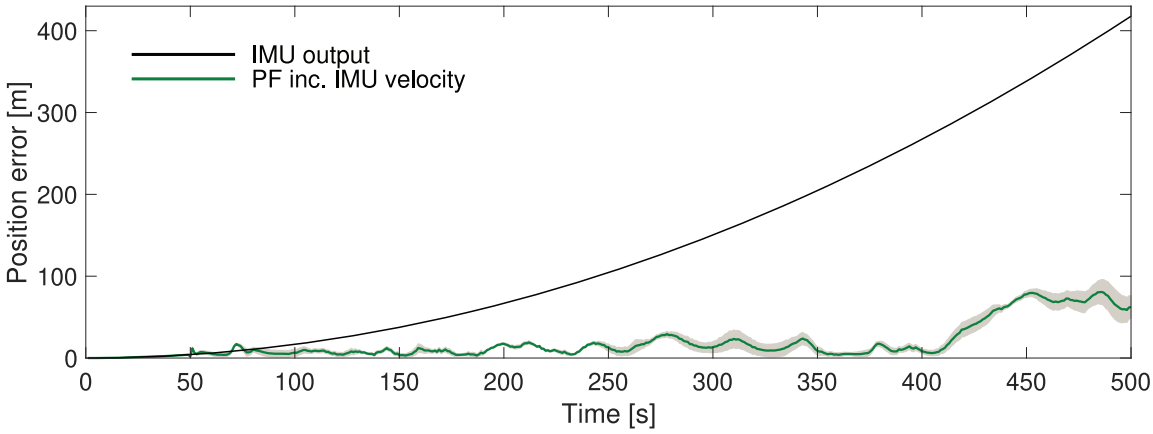

Figure 4: Positioning accuracy of Particle Filter using propagation model with uncorrected IMU-based velocity: mean position errors from 100 simulations (green line) with $\pm 1\sigma$ band (gray area). The reference (black line) corresponds to the position error obtained using inertial data only.

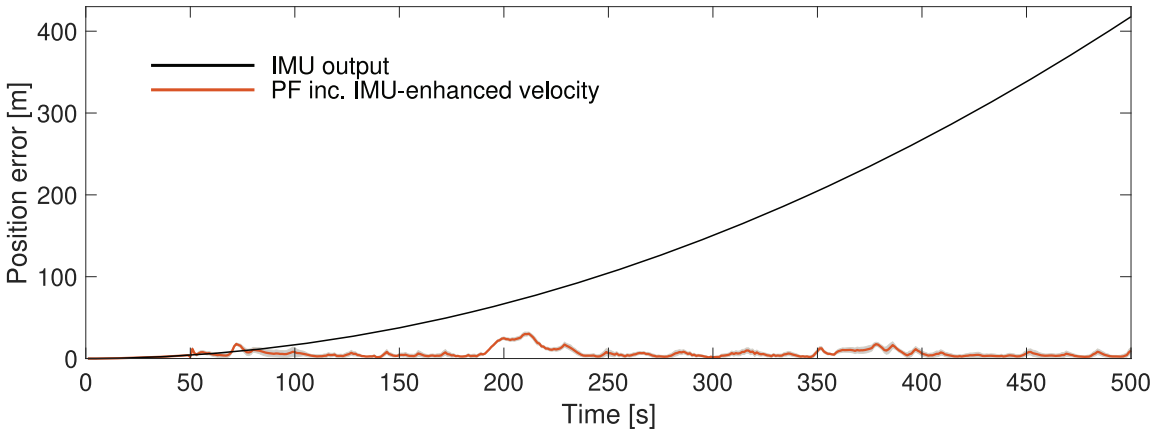

Figure 5: Positioning accuracy of Particle Filter using propagation model with corrected velocity (proposed fusion of inertial and magnetic measurements): mean position errors from 100 simulations (orange line) with $\pm 1\sigma$ band (gray area). The reference (black line) corresponds to the position error obtained using inertial data only.

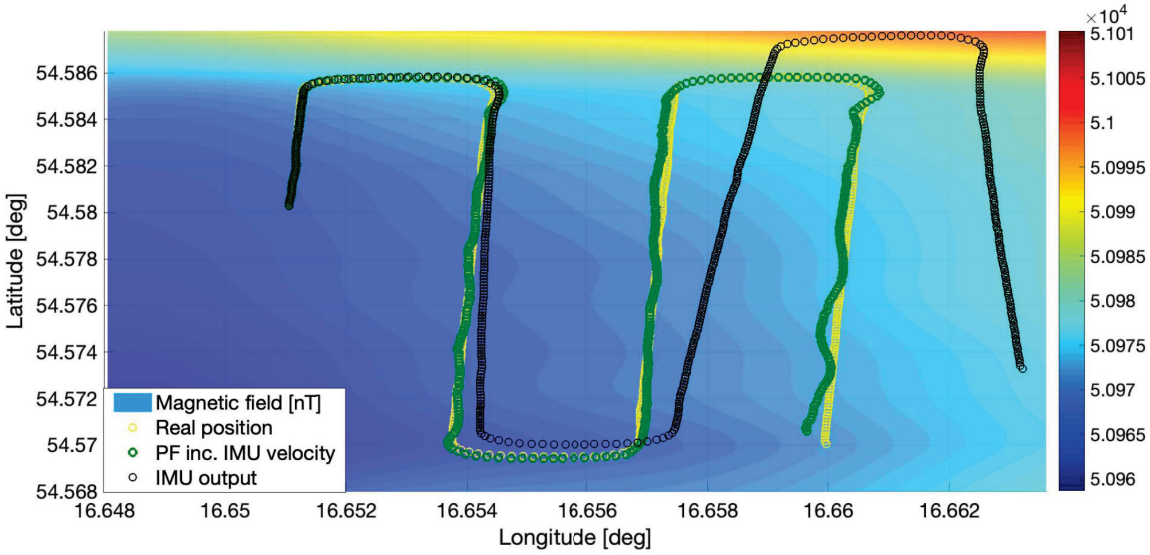

Figure 6: Trajectories obtained using the evaluated positioning methods. The trajectory shown for the Particle Filter with uncorrected IMU-based velocity is randomly selected from the 100 performed simulations.

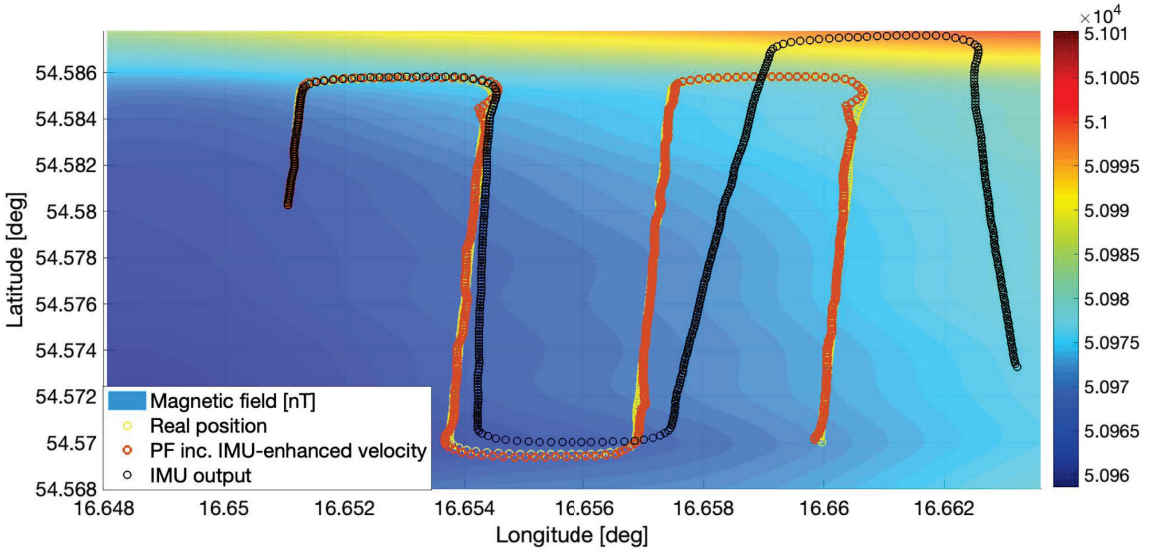

Figure 7: Trajectories obtained using the evaluated positioning methods. The trajectory shown for the Particle Filter with corrected IMU-based velocity (inertial/magnetic data fusion) is randomly selected from the 100 performed simulations.

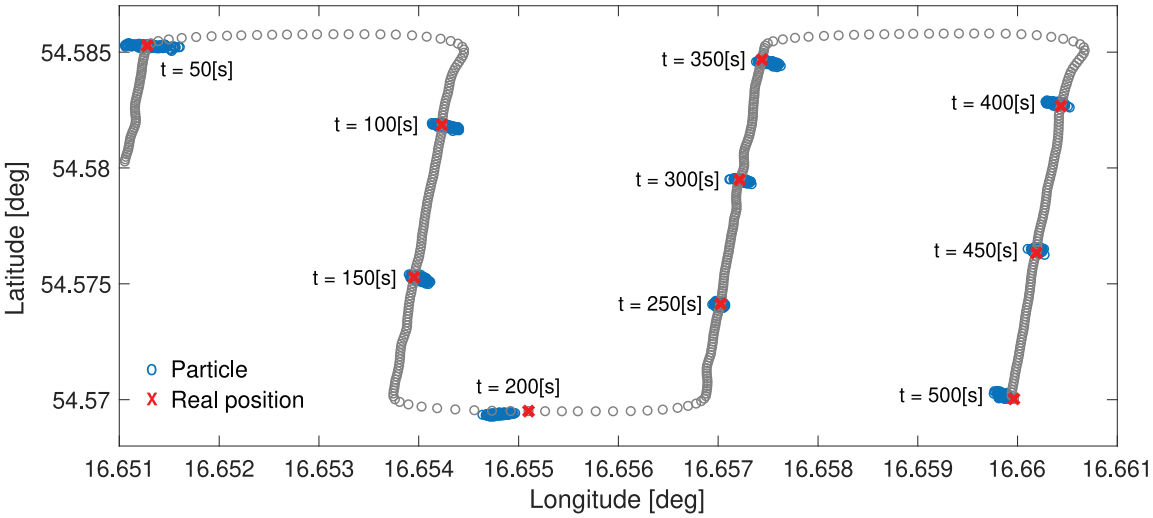

Figure 8: Particle distributions computed every 50 s by the Particle Filter with the corrected velocity (inertial/magnetic data fusion). The real reference trajectory is marked with gray circles. The red crosses indicate the actual UAV positions in the considered time steps. The particle distributions correspond to a simulation randomly selected from the set of 100 performed simulations.

Figs. 6 and 7. The evolution of particle distributions, sampled every 50 s, is illustrated in Fig. 8. These distributions are internally used by the Particle Filter procedure with the proposed inertial/magnetic data fusion and velocity correction. Their general characteristics stay consistent throughout the entire flight. As a result, the estimated position and UAV trajectory are smoother, which can be beneficial for the operation of the autopilot system.

5 Conclusion

This contribution presents an original method for UAV positioning in GNSS-denied environments. The approach is based on Particle Filter, and the measurements of the magnetic anomaly field are integrated at two stages. First, in the *propagation model stage*, velocity—typically derived from inertial measurements only—is additionally corrected using in-flight magnetometric measurements. This fusion of inertial and magnetic information is performed using the Bayesian formalism. Second, at the *position estimation stage*, the posterior distribution generated within the Particle Filter is computed by comparing magnetometric measurements with the magnetic field map, where the particles with the highest discrepancy are discarded.

The developed method was validated in a test flight using a VTOL-type UAV platform equipped with high-precision cesium magnetometers. In comparison to a typical approach based on IMU-only velocity, the proposed data fusion and velocity correction significantly reduced positioning errors and resulted in a smoother and more accurate estimated trajectory.

Acknowledgements

This research was funded by the National Centre for Research and Development (NCBR), Poland, under the grant agreement DOB-SZAFIR/01/B/018/04/2021.

REFERENCES

[1] Y. Lu, Z. Xue, G. S. Xia, and L. Zhang, "A survey on vision-based UAV navigation," *Geo-Spatial Information*, vol. 21, no. 1, pp. 21–32, 2018.

[2] A. V. R. Katkuri, H. Madan, N. Khatri, A. S. H. Abdul-Qawy, and K. S. Patnaik, "Autonomous UAV navigation using deep learning-based computer vision frameworks: A systematic literature review," *Array*, vol. 23, p. 100361, 2024.

[3] C. Zhu, M. Meurer, and C. Günther, "Integrity of visual navigation—developments, challenges, and prospects," *NAVIGATION: Journal of the Institute of Navigation*, vol. 69, no. 2, p. navi.518, 2022.

[4] G. Ouyang and K. Abed-Meraim, "A survey of magnetic-field-based indoor localization," *Electronics*, vol. 11, no. 6, p. 864, 2022.

[5] X. Wang, C. Zhang, F. Liu, Y. Dong, and X. Xu, "Exponentially weighted particle filter for simultaneous localization and mapping based on magnetic field measurements," *IEEE Transactions on Instrumentation and Measurement*, vol. 66, no. 7, pp. 1658–1667, 2017.

[6] J. Aulinas, Y. R. Pétillot, J. Salvi, and X. Lladó, "The SLAM problem: a survey," in *Artificial Intelligence Research and Development*, ser. Frontiers in Artificial Intelligence and Applications. IOS Press, 2008, vol. 184, pp. 363–371.

[7] M. Zmitri, H. Fourati, and C. Prieur, "Magnetic field gradient-based EKF for velocity estimation in indoor navigation," *Sensors*, vol. 20, p. 5726, 2020.

[8] V. F., R. Helmons, and M. Kok, "An extended kalman filter for magnetic field SLAM using Gaussian process regression," *Sensors*, vol. 22, p. 2833, 2022.

[9] Y. H. Kim, H. J. Kim, J. H. Lee, S. H. Kang, E. J. Kim, and J. W. Song, "Sequential batch fusion magnetic anomaly navigation for a low-cost indoor mobile robot," *Measurement*, vol. 213, p. 112706, 2023.

[10] Ł.. Jankowski, D. Pisarski, R. Konowrocki, B. Popławski, and R. Faraj, "Efficient real-time positioning using Bayesian analysis and magnetic anomaly field," *Measurement*, vol. 233, p. 114738, 2024.

[11] A. Canciani and J. Raquet, "Absolute positioning using the Earth's magnetic anomaly field," *NAVIGATION: Journal of the Institute of Navigation*, vol. 63, no. 2, pp. 111–126, 2016.

[12] A. Canciani and J. Raquet, "Airborne magnetic anomaly navigation," *IEEE Transactions on Aerospace and Electronic Systems*, vol. 53, no. 1, pp. 67–80, 2017.

[13] T. N. Lee and A. J. Canciani, "MagSLAM: Aerial simultaneous localization and mapping using Earth's magnetic anomaly field," *Navigation*, vol. 67, no. 1, pp. 95–107, 2020.

[14] A. Gnadt, *Machine Learning-Enhanced Magnetic Calibration for Airborne Magnetic Anomaly Navigation*, San Diego, CA, USA, January 2022.

XI ECCOMAS Thematic Conference on Smart Structures and Materials - SMART 2025
M. Krommer, M. Nader and M. Schagerl (Eds)

Received: 31 March 2025 / Revised: 27 August 2025 / Accepted: 4 November 2025
© The Author(s) 2025

A stationary return mapping scheme for the simulation of elastic-plastic bending of axially moving structures with non-material finite elements

Jakob Scheidl, Stefan Ramsauer

Abstract. Finite element simulations of elastic-plastic forming processes typically rely on some variant of the established return mapping scheme, to obtain a both statically and plastically admissible state for a given load increment. Arbitrary-Lagrangian-Eulerian (ALE) methods make use of a non-material kinematic parametrisation of finite element variables to facilitate the simulation of continuous forming processes that feature axially moving continua. The resolution of variables at spatially fixed points gives rise to advection problems for the plastic variables in account for their downstream transport with the material particles through the non-material mesh. An enhanced return mapping scheme is devised for the time-saving computation of steady-state operation. It is based on a consistent inclusion of the plastic state advection into the corrector step of the iterative algorithm. Plasticity in the numerical examples, which mimic elastic-plastic bending of axially moving thin-walled structures, is treated with condensed models of structural plasticity. Performance and utility of the proposed scheme are verified in comparison to an established time-driven (transient) algorithm.

Key words: Metal plasticity, Axially moving structures, ALE, Finite elements, Predictor corrector method

1 Introduction

Advanced numerical techniques are required to allow for a both accurate and time-efficient simulation of continuous metal forming processes. Here, we consider bending problems of axially moving structures. Such problems feature moving thin continua that are transported through an open control domain and sustain persistent plastic deformations along the way. Finite elements in mixed Eulerian–Lagrangian kinematic formulation allow for a more efficient numerical treatment of problems featuring axially moving structures, see [1] or [2] in the context of sheet metal roll forming. Such models utilize spatial (Eulerian) coordinates for the parametrisation of primary fields, which leads to a partial decoupling of the material particle motion from the deformation of the finite element mesh. The major benefits in comparison

Jakob Scheidl & Stefan Ramsauer
Institute of Mechanics and Mechatronics, TU Wien, Getreidemarkt 9, 1060 Wien, Austria, e-mail: jakob.scheidl@tuwien.ac.at

to purely Lagrangian methods with respect to forming processes are the ability to use appropriately refined meshes in the elastic-plastic regions as well as the more accurate and simpler contact resolution [3]. Plastic deformations on the other hand travel with the material particles, which gives rise to advection problems in the mixed parametrisation. The classic way of treating elastic-plastic problems of moving continua is known as *operator-split method* [4], which features a quasistatic Lagrangian step to obtain a statically and plastically admissible equilibrium state followed by a Eulerian step to account for the material transport in downstream direction.

The test cases considered here are geometrically linear continuous elastic-plastic bending of an axially moving beam and an axially moving plate. Mixed Eulerian–Lagrangian beam and plate finite element models are devised for the numerical solution using different variants of elastic-plastic return mapping schemes [5]. The beam problem has already been considered in [6], where the basics of a novel solution algorithm to compute stationary solutions of bending-dominant forming processes are discussed for the first time. The algorithm shall be referred to as *Streamline Integration in Space*, or SIS in brief, in contrast to the established *Streamline Integration in Time* (henceforth SIT) that originates from the classic operator-split method. The names of both algorithms relate to the adopted solution strategy of integrating the plastic advection problem along the trajectories of material particles ("streamlines"). Provided that plastic states are sampled at finite element integration points of a regular mesh, the method of streamline integration is particularly convenient to use, as the integration points naturally align with the particle trajectories.

Often times in simulation practice the stationary state of operation is of primary interest. For these cases, the SIS is both more time-efficient and convenient to use than the SIT, because it employs an incremental strategy that yields a sequence of practically relevant steady-state solutions. The SIS originates from a "stationary" reformulation of plastic evolution laws that allows for a modification of the corrector step as part of an enhanced elastic-plastic return mapping scheme. Consequently, the Eulerian transport step and the condition of stationary operation can be fully incorporated in the predictor-corrector scheme. Numerical results obtained for both the SIS and the SIT demonstrate correspondence of the two methods as well as the efficiency of the SIS for the simulation of steady states. Simplified structural plasticity models, which employ modified laws of plasticity in terms of stress resultants and structural strain measures, are taken from [6] for the beam and [7] for the plate to further increase computational efficiency.

2 Problem statement

The strong similarity of the beam bending and plate bending test cases considered in Section 4 and Section 5 facilitates a generic problem statement that applies to each of the benchmark examples alike. As depicted in Figure 1, the basic setup features a thin structure that is transported through an open control domain $0 \leq x \leq \ell$ at some constant material transport rate v and subjected to transverse forces that induce elastic-plastic bending deformations. The rate of transport v is assumed to be low such that inertia effects may be disregarded (quasistatic treatment). Linear beam or plate theory govern the kinematics of the structure under the usual prerequisites: Kirchhoff's kinematic assumption and small transverse deflections (ge-

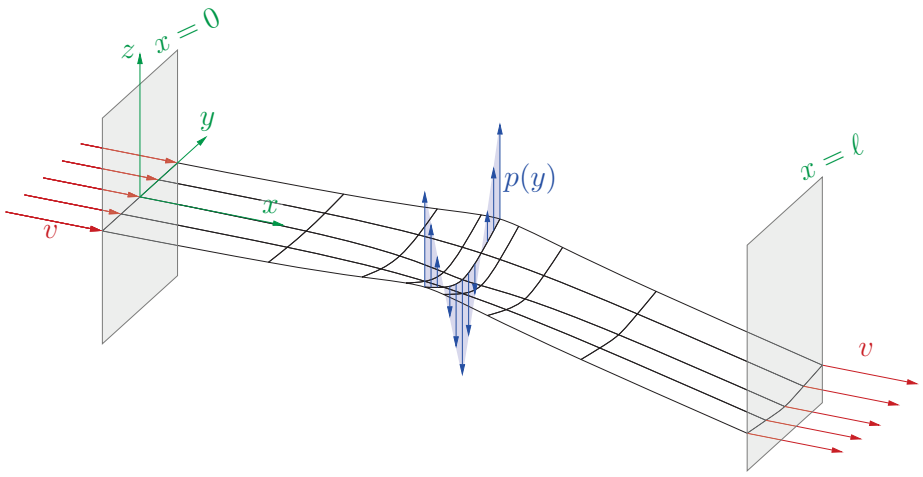

Figure 1: Problem setup for elastic-plastic bending of a thin, axially moving structure; geometrically linear beam and plate models will be considered.

ometrically linear theory). The material behaviour of the underlying continuum is linear elastic ideal plastic, but simplified stress-resultant plasticity models are employed to resolve persistent plastic deformations entirely on the structural level. Such structural plasticity models rest on an appropriate re-formulation of the governing laws of plasticity in terms of structural field variables, namely: bending moments and curvature strains, see [7].

The governing system for static, linear elastic bending of the structure constitutes the basis of the mechanical models. It suffices to compute deformed configurations in purely elastic loading scenarios. Higher load magnitudes induce plastic deformations that travel downstream with the material particles. In these cases, the system of equations is complemented by the plastic constitutive laws and the kinematic relations of material transport.

The field of transverse deflections w in z-direction of the Cartesian reference frame, depicted in Figure 1, fully describes the deformed configuration of the structure. The actual spatial parametrisation depends on the geometric dimension of the structure at hand: $w = w(x,t)$ for the one-dimensional beam or $w = w(x,y,t)$ for the two-dimensional plate. The variational problem to determine the deformed configuration in terms of the primary field w reads:

$$\delta V^{\Sigma}[w] = \int_{\Omega} (\delta U + \delta W) \mathrm{d}\Omega = 0. \tag{1}$$

Hence, quasistatic equilibria are calculated as stationary values of the total potential energy V^{Σ}, which features an integration of the elastic strain energy density U and the potential of conservative external forces W; the domain of integration Ω corresponds to the active material volume currently residing in the open control domain.

In the framework of the geometrically linear theory, the total bending strains κ are directly obtained from the displacement field w:

$$\kappa = \nabla\nabla w, \tag{2}$$

where ∇ serves as a placeholder for the appropriate differential operator, i.e.: the above expression simply reduces to $\kappa = w''$ for the beam, but yields a 2D-tensor $\boldsymbol{\kappa}$ in case of the plate. In a general elastic-plastic state, only the elastic part of the curvature strains κ_e contributes to the strain energy density $U = U(\kappa_e)$ and thus determines the bending moment:

$$M = \frac{\partial U}{\partial \kappa_e}. \tag{3}$$

Naturally, this expression returns M as a scalar for the beam and as a planar tensor for the plate. The notion of elastic strains is necessitated by the possible occurrence of plastic deformations and further motivates an additive decomposition of the total curvature strain increments:

$$\dot{\kappa} = \dot{\kappa}_e + \dot{\kappa}_p, \tag{4}$$

where the incremental dot denotes the total change at a given material particle. This kind of additive decomposition of material strain increments is a common feature of continuum-based small strain plasticity models [5]. The fact that (4) is written in terms of the structural strain measures exemplifies the transition to the aforementioned structural plasticity model.

The structural plasticity model is taken from [7], where elastic-plastic bending solutions of plates are considered as reference load cases; see [8] for an augmentation to incorporate membrane effects. The yield criterion for pure bending features a scalar comparison of the actual bending moment and the yield moment

$$F = f(M) - k_M(A_p)^2 \leq 0, \tag{5}$$

where the current yield moment k_M depends on the plastic work A_p previously done to the material particle. The function $k_M(A_p)$ practically accomplishes the transition to the purely structural model by emulating the through-the-thickness plastification as a kind of isotropic work hardening behaviour. The distinction of elastic and elastic-plastic states is conveniently summarised with complementary Kuhn-Tucker conditions:

$$F \leq 0, \quad \dot{\lambda} \geq 0, \quad \dot{\lambda} F = 0, \tag{6}$$

which introduces the non-negative increments of the consistency parameter $\dot{\lambda}$ that determines the magnitude of plastic flow in the evolution laws for the plastic variables:

$$\dot{\kappa}_p = \dot{\lambda} \frac{\partial f}{\partial M}, \quad \dot{A}_p = M \dot{\kappa}_p. \tag{7}$$

Both the associated flow rule for $\dot{\kappa}_p$ as well as the evolution law for the plastic dissipation $\dot{A}_p$ closely resemble classic metal plasticity theory [9].

So far, no attention has been paid to the axial transport of the structure through the open control domain, as depicted in Figure 1. In particular, the evolution laws of structural plasticity have been stated for material increments $\{\dot{\lambda}, \dot{\kappa}_p, \dot{A}_p\}$, i.e.: changes of plastic variables that the

axially moving particles sustain. Since boundary conditions and external loadings are applied at spatially fixed positions, a mixed Eulerian–Lagrangian kinematic approach is advisable to avoid common deficiencies of purely Lagrangian models in problems of moving structures. This is easily achieved by utilizing the spatial x-coordinate for parametrisation; it is immediately connected to the material arc coordinate s through the prescribed material transport rate v:

$$s = x - vt \tag{8}$$

In the current geometrically linear setting, derivatives with respect to s and x are interchangeable and from the total time derivative $\dot{s} = 0$ we further conclude that $\dot{x} = v$. The plastic variables are treated as functions of x as well, and, correspondingly, their total changes in time feature a convective and a local time derivative at fixed x:

$$\dot{\kappa}_p = v\kappa' - \partial_t \kappa, \quad \dot{A}_p = vA_p' - \partial_t A_p, \tag{9}$$

The respective derivatives on the right-hand side are denoted by a prime and the operator ∂_t, which expands to $\partial_t = \partial/\partial t|_{x=\text{const.}}$. Evidently, the resolution of plastic variables at fixed Eulerian coordinates x leads to an advection problem for the downstream transport of plastic variables, whose material increments are governed by the plastic evolution laws (7).

The typical strategy to simulate this process is known as "operator-split method" [4], which features an alternation of Lagrangian and Eulerian steps: First, a quasistatic statically and plastically admissible equilibrium is computed in the Lagrangian step, which yields new deformed variables and material plastic increments $\{\dot{\kappa}_p, \dot{A}_p\}$ that are further transported downstream according to (9) during the second, Eulerian phase. As simulation time progresses, the transient process gradually approaches a stationary state that is identified by vanishing spatial changes of the primary fields, which is particularly significant for the plastic variables:

$$\partial_t \kappa|_{\text{stationary}} = (\dot{\kappa}_p - v\kappa')|_{\text{stationary}} = 0, \quad \partial_t A_p|_{\text{stationary}} = (\dot{A}_p - vA_p')\Big|_{\text{stationary}} = 0. \tag{10}$$

Thus, the material particle increments equal the convected increments in case of steady state operation. The primary goal of the following section is to use this knowledge in the development of an improved algorithm that allows for a more efficient computation of stationary states as compared to the established operator-split method.

3 Elastic-plastic return mapping schemes for non-material finite elements

Non-material finite element models with shape functions based on cubic Hermitian polynomials are used for the spatial discretisation of the transverse deflection w in all considered problems. Since the specifics of these implementations are not essential here, we refer to previously published works on this subject [1, 10]. The finite element variables for the approximation of the deflection w and the plastic fields $\{\lambda, \kappa_p, A_p\}$ are collected in the matrices $\boldsymbol{q}$ and $\boldsymbol{p}$, respectively. Gaussian quadrature rules are employed to compute the total potential as a sum of

finite element contributions, which is why $\boldsymbol{q}$ holds the finite element nodal variables, whereas $\boldsymbol{p}$ contains integration point samples of the plastic variables $\{\lambda, \kappa_p, A_p\}$.

Currently, our primary concern is the discussion of the plastic sub-routines that are required to accomplish the following two tasks:

- Take a predicted solution for $\boldsymbol{q}$ satisfying equilibrium (1) and compute increments of plastic variables $\dot{\boldsymbol{p}}$ according to the plastic evolution laws (iterative Lagrangian step).
- Take the material plastic increments $\dot{\boldsymbol{p}}$ and solve the advection problem (9) in accordance with the spatial resolution of plastic variables $\boldsymbol{p}$ (Eulerian step).

As visualised in Figure 1, the finite element models feature regular meshes such that the element edges are in perfect alignment with the spatial Cartesian coordinates. Consequently the integration points are also arranged along straight lines parallel to the x-axis. As these lines coincide with trajectories of material particles, we shall refer to them as streamlines. The corresponding numerical schemes of integrating the plastic advection problem are known as streamline integration methods [6]. Here, we distinguish the *Streamline Integration in Time* (SIT) that is based on the established operator-split and the *Streamline Integration in Space* (SIS) that incorporates the Eulerian transport step in an augmented corrector routine in an attempt to compute stationary solutions more effectively.

3.1 Streamline Integration in Time (SIT)

Figure 2 (a) provides a flowchart of the SIT algorithm. Its primary elements reflect the two-stage solution process of the operator-split method, i.e.: fixed-point equilibrium iterations with an elastic predictor and a plastic corrector followed by the transport of plastic variables through the spatially fixed mesh. The equilibrium iteration is called return mapping as the material plastic increments $\dot{\boldsymbol{p}}$ are obtained from a closest point projection back onto the yield surface. This way, predicted states that would violate the yield criterion (5) due to $F(\boldsymbol{q}, \boldsymbol{p}) > 0$ are forced back onto the yield surface, thus fulfilling the consistency condition $F = 0$. After successful completion of the return mapping loop, the Eulerian transport phase is initiated with a new deformed state $\boldsymbol{q}$ and material plastic increments $\dot{\boldsymbol{p}}$. These values enter an explicit forward in time backwards in space finite difference scheme to solve the plastic advection problems for each streamline. The finite difference discretization of the plastic variables along a streamline in accordance with the original equation (9) reads:

$$ {}^{t}\Delta\boldsymbol{p}(x_i) = \left(\dot{\boldsymbol{p}}(x_i) - v \, \frac{\boldsymbol{p}(x_i) - \boldsymbol{p}(x_{i-1})}{x_i - x_{i-1}} \right) \Delta t, \tag{11} $$

where the symbol ${}^{t}\Delta$ is introduced to emphasize that ${}^{t}\Delta\boldsymbol{p}$ is a Eulerian increment. The points x_{i-1} and x_i denote the axial coordinates of two subsequent integration points along the streamline. Note that integration point distances $\Delta x_i = x_i - x_{i-1}$ are not constant even for equidistant finite element meshes due to the specific spacing of the Gauss points in the normalised coordinate domain. Numerical stability of the explicit scheme effectively limits the ratio $v\Delta t/\Delta x_i$ and thus the time step Δt.

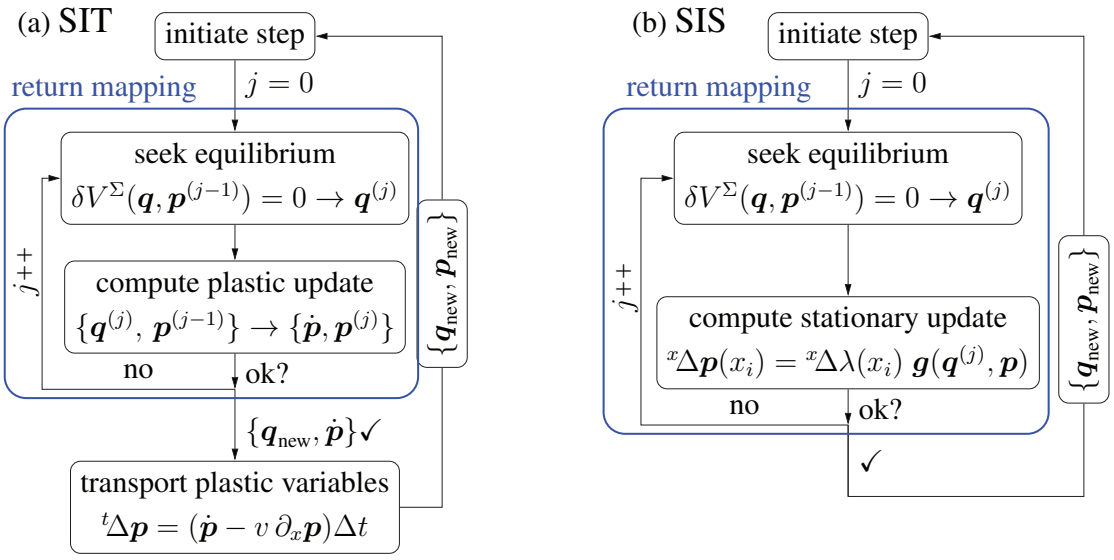

Figure 2: (a) Flowchart of the SIT: the finite difference in (11) for the spatial derivative of $\boldsymbol{p}$ with respect to x is abbreviated with $\partial_x\boldsymbol{p}$; (b) Flowchart of the SIS: a finite difference integration of the steady-state initial value problems for the plastic variables is performed at the corrector stage of a modified return mapping algorithm.

3.2 Streamline Integration in Space (SIS)

The primary distinctive feature of the SIS, as visualised in the flowchart of Figure 2 (b), is the incorporation of the advective transport in a modified corrector step of the return mapping algorithm. Consequently, the step-wise solutions of a given load history for the elastic-plastic bending problems is a sequence of stationary states, which is a particularly convenient feature when conducting parameter studies.

The basic idea behind the SIS algorithm is to replace material plastic increments with spatial derivatives owing to the condition of stationary operation, as stated in (10) and rewritten here in terms of $\boldsymbol{p}$:

$$\dot{\boldsymbol{p}} = v\boldsymbol{p}'. \tag{12}$$

This result allows for a convenient reformulation of the plastic evolution laws (7) as ordinary differential equations in the axial coordinate x:

$$\kappa_p' = \lambda' \frac{\partial f}{\partial M}, \quad A_p' = M\kappa_p', \tag{13}$$

together with corresponding Kuhn-Tucker conditions to govern yielding along a streamline:

$$F \leq 0, \quad \lambda' \geq 0, \quad \lambda' F = 0. \tag{14}$$

Since no plastic deformations occur unless $\lambda' > 0$, the scalar consistency factor λ can be considered to be the driving force for yielding, which is exemplified by the proportionality $\boldsymbol{p}' \propto \lambda'$

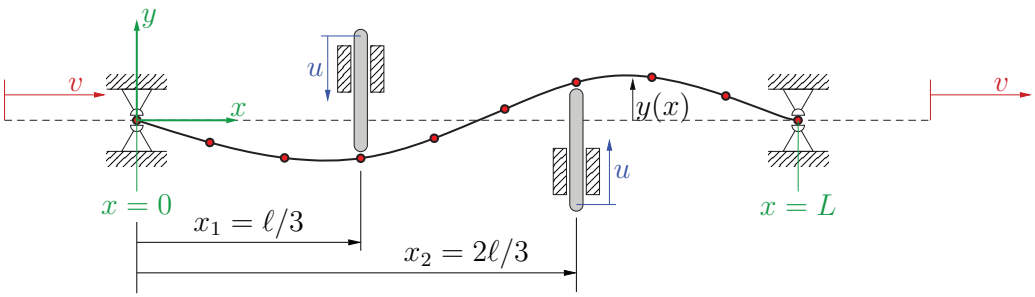

Figure 3: Elastic-plastic bending of an axially moving Euler–Bernoulli beam.

in the ODE system:

$$\boldsymbol{p}' = \lambda' \, \boldsymbol{g}(\boldsymbol{q}, \boldsymbol{p}). \tag{15}$$

Within the loop of predictor corrector iterations, the inhomogeneity $\boldsymbol{g}(\boldsymbol{q}, \boldsymbol{p})$ depends on both the predicted deformed state $\boldsymbol{q}$ as well as the current estimate for the plastic variables. The corresponding finite difference discretization, which may be explicit or implicit depending on how $\boldsymbol{g}$ is evaluated, reads:

$$^{x}\Delta\boldsymbol{p}(x_i) = {}^{x}\Delta\lambda(x_i) \, \boldsymbol{g}(\boldsymbol{q}, \boldsymbol{p}), \tag{16}$$

where ${}^{x}\Delta\boldsymbol{p}$, in contrast to ${}^{t}\Delta\boldsymbol{p}$, denotes stationary (convective) plastic increments that the material point sustains as it travels the distance of two adjacent integration points Δx_i. Observe that the SIS does not require a time step Δt and is also mesh independent in the sense that the integration point spacings Δx_i do not enter this formula. To close the system of equations, the increments ${}^{x}\Delta\lambda$ are computed from the consistency condition $F = 0$ to achieve the projection of plastic states onto the current yield surface.

4 Stationary elastic-plastic bending of an axially moving beam

Consider the elastic-plastic bending problem of an axially moving Euler–Bernoulli beam depicted in Figure 3. As the structure passes through the open domain $0 \leq x \leq L$ at constant rate v, it experiences bending and counter-bending by two vertically deflected rigid stamps at spatially fixed positions. The contact is assumed to be frictionless and the stamps only induce transverse forces. Simply supported boundary conditions at the entry and exit of the control domain are chosen to ensure moment-free and thus yield-free boundaries.

This problem has been studied previously in [6] with a slightly less matured version of the SIS algorithm. The basic parameter set is unchanged, but a higher maximum stamp deflection $u_{\max}$ is considered to obtain plastic regions of significant extent in the final stationary state. We refer to [6] for the explicit expression of the structural plasticity law $k_M(A_p)$ and here merely repeat the basic parameter specifications (SI-units are implied): The beam has total length $\ell = 1$, a rectangular cross-section with thickness $h = 0.01$ and width $H = 0.05$. The stamps are placed at $x_1 = \ell/3$ and $x_2 = 2\ell/3$ and displaced simultaneously up to $u_{\max} = 0.025$. The linear elastic, ideal plastic material has Young's modulus $E = 210 \times 10^9$ and yield strength $\sigma_f = 260 \times 10^6$.

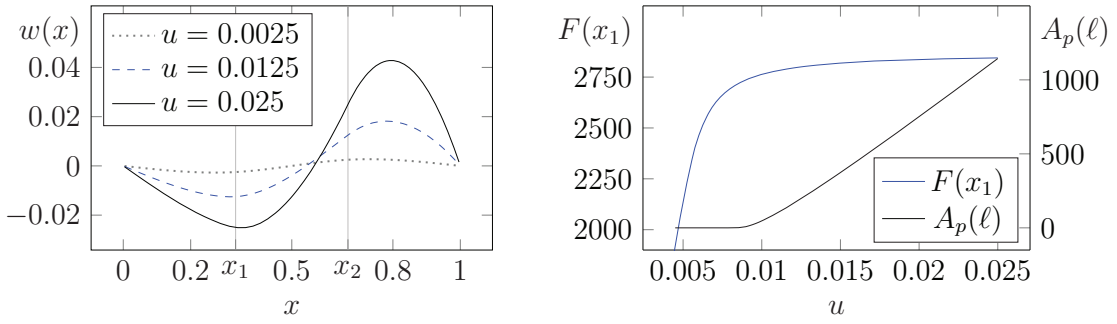

Figure 4: Visualisation of a SIS parameter study featuring: w at different stamp deflection levels (left) as well as the evolution of the forming force at the left stamp $F(x_1)$ and the accumulated plastic work $A_p(\ell)$ at the exit (right).

Δt	$A_p(\ell)$	$\epsilon[A_p]$	$F(x_1)$	$\epsilon[F(x_1)]$	$F(x_2)$	$\epsilon[F(x_2)]$
5.00×10^{-2}	1243	8.59 %	−2892	1.41 %	2918	2.57 %
2.50×10^{-2}	1221	6.68 %	−2896	1.56 %	2919	2.64 %
1.25×10^{-2}	1199	4.81 %	−2901	1.73 %	2922	2.74 %
6.25×10^{-3}	1162	1.54 %	−2875	0.82 %	2866	0.78 %
SIS	1144		−2852		2844	

Table 1: Correspondence of SIT and SIS results as the time step of the SIT simulations is decreased.

The SIS yields a sequence of stationary solutions as the deflection of the stamps is gradually increased up to the final level $u_{\max}$, which is a particularly convenient feature when studying parameter dependencies. To demonstrate these capabilities, Figure 4 depicts evolutions of the bending deflections w, of the forming force at the first stamp $F(x_1)$ and of the accumulated plastic work at the exit $A_p(\ell)$. These results were obtained with an equidistant mesh of $n = 18$ finite elements. As loading progresses the local extrema of w exhibit a significant shift in downstream direction. The degressive nature of the forming force $F(x_1)$ is clearly related to the "plastic softening" of the cross-section as the yield moment slowly approaches its limit value; the accumulated plastic work grows accordingly.

Finally, in addition to the results already published in [6], the results of a comparative study between the two algorithms are collected in Table 1. It presents final values of different SIT simulations with decreasing time step size in comparison to a reference SIS simulation. The same mesh of $n = 18$ elements was used and the material transport rate for the SIT was specified as $v = 0.2$. Total simulation time for the SIT was $t_{\max} = 20$, which means that four times the material length ℓ is transported through the control domain; at this point, practically no transient effects remain. We present values for the accumulated plastic work per unit reference length A_p evaluated at $x = \ell$ as well as the forming forces induced by the stamps at positions x_1 and x_2. Furthermore, the persistent relative deviations, computed as $\epsilon[\alpha] = (\alpha_{\text{SIT}}/\alpha_{\text{SIS}} - 1)$

for each variable $\alpha = \{A_p(\ell), F(x_1), F(x_2)\}$, are given in percent as well. The solutions tend towards each other as the time step Δt is decreased, which comes at the price of increased simulation times for the SIT. Regarding computational efficiency, the final simulation with $\Delta t = 6.25 \times 10^{-3}$ took about an hour on a regular PC, whereas the SIS reference solution was obtained in less than two minutes on the same hardware. The substantial duration of the time-driven simulation is a consequence of the high load magnitude that induces plastic states close to limit yield, as evidenced by the almost horizontal tangent of the forming force depicted in Figure 4.

5 Stationary elastic-plastic bending of an axially moving plate

The plate bending problem is visualised in Figure 1. Kinematic constraints at the boundaries of the control domain resemble a cantilever with material flowing through in axial direction: the plate is clamped at $x = 0$, enters the domain in a fully undeformed planar state and leaves the domain at a free end. An external, self-equilibrated line load acts at the center of the domain $x = \ell/2$. We refer to [7] for the specific set of governing equations for the primary fields, which are now treated as functions of x, y and t.

With the intent to compare the SIT and SIS algorithms, exemplary computations are carried out with the following parameter set (again implying SI-units): The plate has a width of $H = 0.5$, a thickness of $h = 0.01$ and the control volume length is $\ell = 2$. The elastic ideal-plastic material is characterized by a Youngs Modulus of $E = 210 \times 10^9$, a Poisson ratio of $\nu = 0.3$ and a yield strength of $\sigma_f = 250 \times 10^6$. The lateral line load is imposed at $x = \ell/2$ and chosen to be triangular, with peak values of $\pm P$ in the center and at the edges, respectively. The load factor P is incrementally increased up to $P_{max} = 280 \times 10^3$. The set of numerical parameters for the SIT simulations comprises: the material transport rate $v = 0.2$ and the time step $\Delta t = 0.1$. The load increases linearly and reaches its peak value P_{max} at time $t = 2$. The simulation, however, proceeds until $t = 20$ to ensure that transient effects have vanished almost entirely.

As depicted in Figure 5, the plate mesh is refined in axial direction to achieve a better resolution close to the line load at $x = \ell/2$. The simulation frames on the left depict the deformed finite element mesh with an overlay of the plastic work distribution $A_p(x, y, t)$ at different time instances. The sequence clearly demonstrates the transient behaviour simulated by the SIT algorithm: After initiating the computation, the external loading soon induces plastic deformations that are further transported downstream in x-direction. Since the peak load is already reached at $t = 2$, about $90\,\%$ of the simulation time are just spent to wait for transient effects to wear off. In total, the computation on a conventional office PC takes 20 minutes with the SIT and only 8 seconds with the SIS. Additionally, the poor ratio of $v\Delta t/\Delta x_{min} \approx 1$ means that the advection problem is simulated with low accuracy. This causes a persistent deviation of approximately $\epsilon[A_p(\ell, y = 0)] = 4\,\%$, which refers to the final value of the plastic work distribution on the center line of the plate $A_p(x, y = 0, t_{\max})$ as depicted on the right of Figure 5. These plots also visualise the transient evolution of this distribution as simulation time progresses.

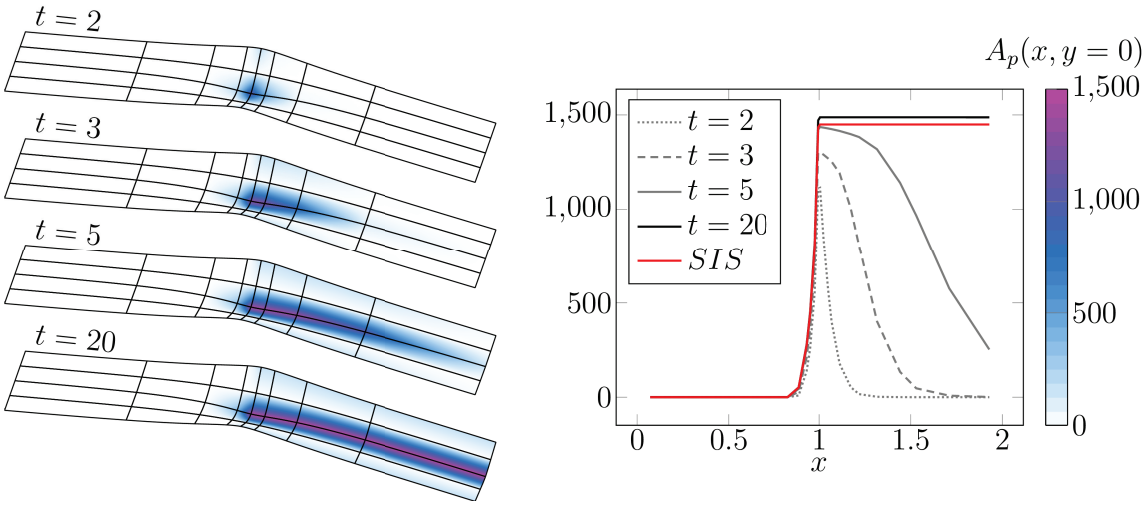

Figure 5: SIT and SIS algorithm applied to benchmark plate problem: The left column depicts the deformed configurations obtained by SIT for time instances $t = 2, 3, 5$ and 20. The right column shows the respective plastic dissipation A_p for each integration point on the central streamline.

6 Conclusion

Different algorithms have been considered to solve the plastic advection problem in mixed Eulerian–Lagrangian finite element models for continuous bending operations of axially moving structures. The benchmark cases comprise geometrically linear bending for an axially moving Euler–Bernoulli beam and an axially moving plate. The algorithm called *Streamline Integration in Space* proves to be very efficient for the computation of steady-state solutions. It utilizes a transformation of plastic evolution laws that holds in case of stationary operation to modify the corrector step of an elastic-plastic return mapping scheme. Simulation results obtained with a standard method referred to as *Streamline Integration in Time* yield corresponding results at significantly higher computational cost.

Acknowledgement: The support by the Austrian Research Promotion Agency (FFG) is gratefully acknowledged; FFG project number: 914865.

REFERENCES

[1] Y. Vetyukov, P. G. Gruber, and M. Krommer, "Nonlinear model of an axially moving plate in a mixed Eulerian–Lagrangian framework," *Acta Mechanica*, vol. 227, no. 10, pp. 2831–2842, 2016.

[2] E. Kocbay, J. Scheidl, F. Riegler, M. Leonhartsberger, M. Lamprecht, and Y. Vetyukov, "Mixed Eulerian–Lagrangian modeling of sheet metal roll forming," *Thin-Walled Structures*, vol. 186, p. 110662, 2023.

[3] Y. Crutzen, R. Boman, L. Papeleux, and J.-P. Ponthot, "Lagrangian and arbitrary Lagrangian Eulerian simulations of complex roll-forming processes," *Comptes Rendus Mécanique*, vol. 344, no. 4, pp. 251–266, 2016, computational simulation of manufacturing processes.

[4] P. M. Pinsky, M. Ortiz, and R. L. Taylor, "Operator split methods in the numerical solution of the finite deformation elastoplastic dynamic problem," *Computers & Structures*, vol. 17, no. 3, pp. 345–359, 1983. [Online]. Available: https://www.sciencedirect.com/science/article/pii/0045794983901268

[5] J. Simo, "Numerical analysis and simulation of plasticity," in *Numerical Methods for Solids (Part 3) Numerical Methods for Fluids (Part 1)*, ser. Handbook of Numerical Analysis. Elsevier, 1998, vol. 6, pp. 183–499. [Online]. Available: https://www.sciencedirect.com/science/article/pii/S1570865998800094

[6] J. Scheidl, "A Stationary Streamline Integration Algorithm for Elastic-Plastic Bending of an Axially Moving Beam," in *Proceedings of the Fifteenth International Conference on Computational Structures Technology*, P. Iványi, J. Kruis, and B. Topping, Eds. Civil-Comp Press, Edinburgh, UK, 2024.

[7] E. Kocbay and Y. Vetyukov, "Stress resultant plasticity for plate bending in the context of roll forming of sheet metal," *International Journal for Numerical Methods in Engineering*, vol. 122, no. 18, pp. 5144–5168, 2021.

[8] E. Kocbay, J. Scheidl, F. Schwarzinger, and Y. Vetyukov, "An enhanced stress resultant plasticity model for shell structures with application in sheet metal roll forming," *The International Journal of Advanced Manufacturing Technology*, vol. 130, no. 1, pp. 781–798, Jan 2024.

[9] J. Lubliner, *Plasticity theory*. Dover Publications, Inc., 2008.

[10] Y. Vetyukov, "Non-material finite element modelling of large vibrations of axially moving strings and beams," *Journal of Sound and Vibration*, vol. 414, pp. 299–317, 2018. [Online]. Available: https://www.sciencedirect.com/science/article/pii/S0022460X17307824

XI ECCOMAS Thematic Conference on Smart Structures and Materials - SMART 2025
M. Krommer, M. Nader and M. Schagerl (Eds)

Received: 20 March 2025 / Revised: 25 August 2025 / Accepted: 4 November 2025
© The Author(s) 2025

Test results of HyTEM a Morphing Trailing edge Demonstrator

Jan Tikalsky, Martin Radestock

Abstract.

The aviation industry's biggest challenge is transitioning to climate neutrality by reducing reliance on fossil fuels. As a result, aerodynamic efficiency has become the primary focus of future aircraft designs.
Morphing trailing edges can improve lift-to-drag ratios, particularly in off-design conditions. However, current solutions often require slitting the wing's pressure side, resulting in gaps that negatively impact aerodynamic performance. To address this issue, a novel approach uses a compliant mechanism in the trailing edge, driven by a conventional kinematic system.
A demonstrator was manufactured and tested, showing good correlation between analytical and finite element calculations. However, initial operation revealed softening due to the Mullins effect, causing deviations from predicted static loads. Fatigue testing based on flight data showed slow crack propagation, meeting aviation requirements.
The pre-design methods used have proven suitable, and the system's crack behavior meets aviation standards. As next step a new demonstrator will be developed to investigate spanwise differentiation of the hyperelastic trailing edge morphing (HyTEM) system. The HyTEM system will be implemented on the unmanned aerial system (UAS) PROTEUS platform and undergo flight tests to evaluate improvements in lift-to-drag ratios achieved through morphing trailing edges.
Key words: Morphing, Wing, Trailing Edge, HyTEM

Jan Tikalsky & Martin Radestock
Institute of Lightweight Systems, German Aerospace Center (DLR), Lilienthalplatz 7, Braunschweig, Germany
e-mail: jan.tikalsky@dlr.de

1 INTRODUCTION

Trailing Edge Morphing (TEM) has been extensively researched over the years, but none of these technologies have been adopted for use in commercial aircraft. However, research conducted in the late 1980s and early 1990s by [1–3] demonstrated that camber morphing can achieve benefits of up to 20% on fighter-type aircraft.

Transonic passenger aircraft were also investigated in the 80s and 90s (see [4, 5]), with studies suggesting a potential increase in lift-to-drag ratio (L/D) by 2-3% when using variable camber on Fowler flaps. Further research by Vale et al. [6] showed that spanwise camber morphing can offer an additional 2% improvement in L/D.

Despite this promising research, only a handful of TEM designs have been tested in flight to date [7]. These designs are subject to stringent requirements for load-bearing and flexibility, which necessitates the use of heavy actuators and sophisticated kinematics. This complexity results in increased manufacturing costs, maintenance expenses, and safety assessments.

This paper presents a new design principle for implementing a camber-variable morphing system, known as Hyperelastic Trailing Edge Morphing (HyTEM). The concept will be introduced first, followed by a description of Demonstrator A. The third section will focus on static testing of the Demonstrator and compare theoretical predictions with test results. Followed by a description of a Cyclic fatigue test and its results.

1.1.Hyperelastic Trailing Edge Bonding Concept

The biggest challenge for morphing designs is the wing skin, which undergoes changes in length due to deformation. This results in large internal loads, making it essential to develop a solution that can mitigate these loads.

To address this issue, Figure 1 shows a stiff and continuous skin (15,16) which are bonded elastically (17) at the skin connection between pressure and suction side. This allows a seamless transition of the profile surface into the deformable area without material changes throughout the profile body.

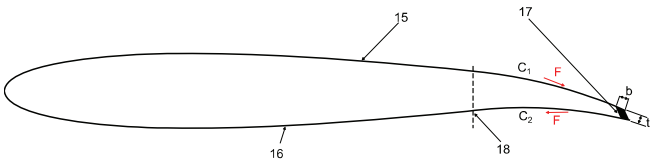

Figure 1: HyTEM Wingsection Concept [8]

The connection between the trailing edge is achieved through a compliant joint made from hyper-elastic adhesive Sika-Pro3 (surface 17 in Figure 1).

This design enables the integration of variable shape trailing edges into conventional composite airfoil designs while maintaining step-free transitions and minimizing gaps. Moreover, it is feasible to have the variable shape area start at different chord length on the upper and lower sides via stiffness differences, allowing to tilt the hinge line (18).

Figure 1 also shows the connection line (18) between the fixed and flexible region of the airfoil.

Due to its high elasticity at the trailing edge, the cross-section of the Flexible area exhibits torsional softness, enabling the curvature of the profile to generate differentiated deflections along the span. Figure 2 shows a sketch where the cross-sections at root and tip deflect downwards, while the middle cross-section deflects upwards.

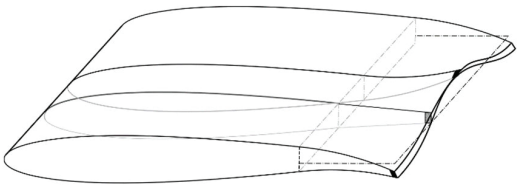

Figure 2: HyTEM spanwise differential excitation [9]

The spanwise differentiation can then be utilized to optimize lift distribution depending on the flight operation point, offering an aerodynamic potential to reduce total drag. One objective of DLR's ongoing project MorphAIR [10] is to develop and test such a spanwise differential morphing concept using an unmanned aerial system (UAS). This approach aims to minimize drag by manipulating the shape of the wing.

Due to the nature of this system, strain energy increases with deformation (displacement) of the trailing edge. The HyTEM is designed as a multifunctional lifting surface to replace ailerons and flaps. This requires fast movements around zero deflection to mimic aileron properties and overcome large as well as slow movements while being deployed as a flap.

To minimize the weight of the actuator, a non-linear transmission is required. A direct transition in the neutral position and a small transmission ratio in the deployed position are necessary to achieve this goal. Figure 3 shows the kinematic with a rotational actuation as scheme.

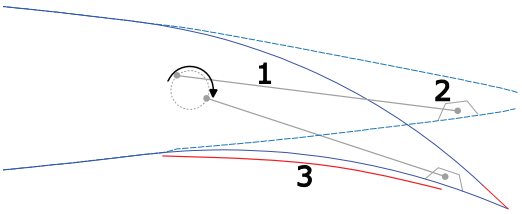

Figure 3: HyTEM Kinematic concept [9]

The kinematic concept for HyTEM involves an excentre attached to a rotary actuator, which is hinged to a pushrod (1). The pushrod itself is hinged to a load introduction bracket close to the trailing edge. This design aims to unload area 3 from compressing loads, thereby avoiding buckling and reducing skin bending Stiffness, which in turn reduces strain energy required for system operation.

For more details, refer to [11] , which proposed a demonstrator description.

1.2.Demonstrator Setup

The concept is intended to fly on the UAS Proteus to investigate performance increases. A demonstrator according to the Proteus design has been developed and fabricated. The most challenging area of the UAS is the close-to-root section, where flaps will be extended maximally. Additionally, aileron functionality is incorporated in this region. Figure 4 shows the Proteus fuselage with the right wing. The cut section is the selected airfoil geometry for the demonstrator in full-scale.

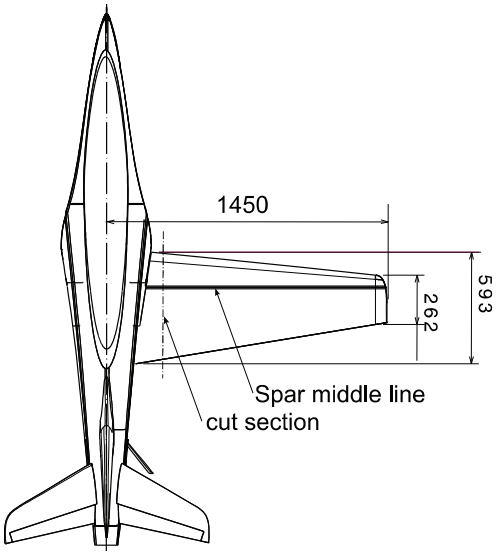

Figure 4: Demonstrator A wing cut section [9]

For simplification purposes, the profile at the trailing edge is replaced by flat plates and do not represent the airfoil curvature. These plates are attached to the main spar. Figure 5 shows the CAD model of the demonstrator cross-section with simplified plates, spar, actuator and pushrod for actuation. Also, the airfoil geometry is plotted over the CAD model in order to give an impression of the deviation for the trailing edge simplification.

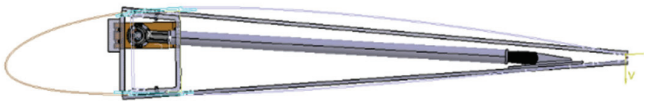

Figure 5: CAD model of the Demonstrator A and cross section of the airfoil [9]

The top view in Figure 6 gives the impression of the 100mm span segment of the demonstrator. Furthermore, this figure show the actuator positioning in orange, because it is not parallel to the spar middle line, which poses a problem for the actuator alignment in the final wing. In the demonstrator A design, the actuator is tilted to accommodate this issue.



Figure 6: Top view of demonstrator A with actuator in orange [9]

The main dimensions of demonstrator A can be found in Figure 7, and additional properties such as skin layup are presented in [11].

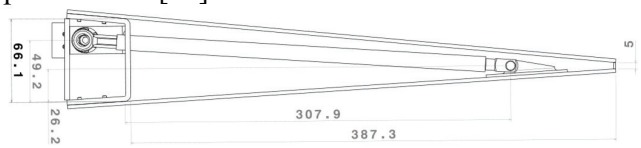

Figure 7: Side view with dimensions [9]

A loadcell has been installed in the pushrod to enable direct force measurements. The demonstrator is prepared for testing, with a bracket installation shown in Figure 8. A small distance between the pushrod and upper skin can be recognized.

Figure 8 is a detailed photo of demonstrator A rear end with the bracket. The tests with demonstrator A will be performed also with masses on the Pressure side of the demonstrator. This allows easier investigations of a flap deflection behavior and the reaction to loads. A small distance (no contact) between Pushrod and upper skin can be recognized.

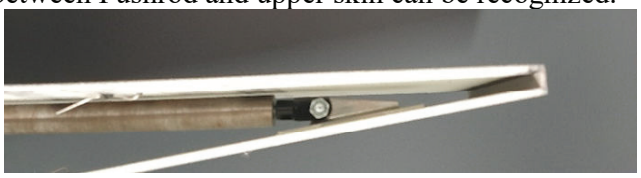

Figure 8: Detailed photo of Demonstrator A with bracket on upper side

Two configurations have been tested. Configuration 1 has a actuator rotational angle of Φ_0 90 degree and Configuration 2 has a Φ_0 of 138 degree, where the angle definition is shown in Figure 9.

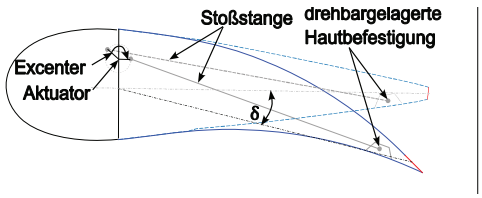

Figure 9: kinematics definition

1.3.Static tests

Within this section focuses on the validation of the FEM as well as analytical model of the system. In a first step the demonstrator in configuration 1 has been 3d scanned with an ATOS

system in undeformed and deformed condition (Figure 10). This system scans the surface with stereographic cameras and an optical fringe pattern.



Figure 10: ATOS Measurement setup

These scanned surfaces were compared to the original CAD design and the results from the deformed FEM calculations shown in Figure 11.

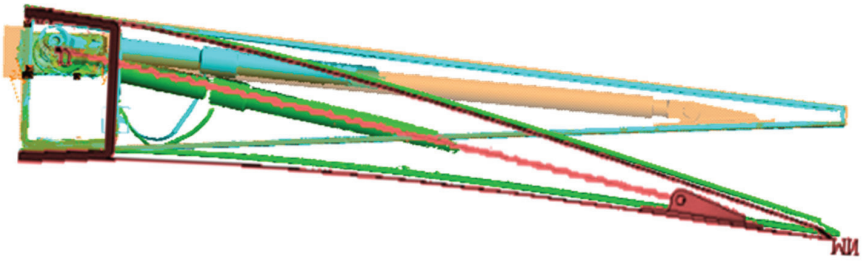

Figure 11: ATOS measurement in deflected position (green) compared to CAD model (orange) and ATOS measurement in undeflected position (turquoise) compared to FE Model (Red)

Good correlation was observed between the experimental data and the analytical predictions. The maximum deviation of deformation is by 1,3% between the measured deformation and the predicted deformation by FE model.

Another focus lies on predicting the pushrod load at the excentre position without external loads. An experiment was performed using configuration 2, where a slow sine movement of the excentre between -45° and +50° was carried out. Pushrod forces and excentre positions where recorded.

Figure 12 shows the overlay of deformed and undeformed Demonstrator.

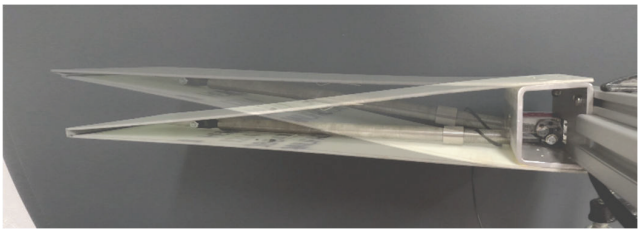

Figure 12: Demonstrator Static measurement without external loads Config. [-45° - 50°]

Figure 13 shows the measurements, the FEM and the analytically predicted pushrod forces in dependence of the excentre position. A hysteresis of the measured pushrod loads can be found in the measurements. This hysteresis can be explained by viscoelastic material behavior in the hyperelastic adhesion.

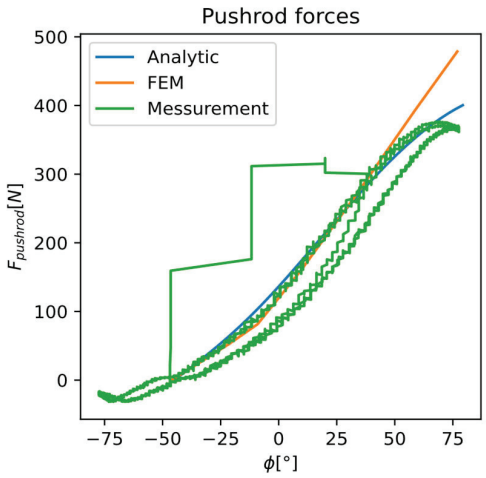

Figure 13: Pushrod measurement over excentre position without external loads

Good correlation between FE predictions and measurement (deviation <4%) was found within this range -45° to +50°, but the FE solution overestimated the pushrod loads for higher angles. In contrast, the analytical solution showed a high correlation between -46° and +60°.

Figure 13 shows the predicted pushrod force over flap deflection, revealing that for small deformations, FEM predicts smaller loads than measured, whereas higher deformations show the opposite trend. The analytical prediction is quasi-linear due to its geometrical and material simplifications.

In case that the analytical solution approximates the measurement data more precise then the FE results, the comparison indicates that the material properties of the adhesive used in this test case are not accurately captured. The analytical material model is conducted from coupon tests to extract linearized material properties. Further characterization on nonlinear Neo Hookean Material properties is needed to improve the FEM accuracy. However, the comparison between measurement, numerical solution and analytical approach show a usable application for first estimation of the Hytem concept in the design process.

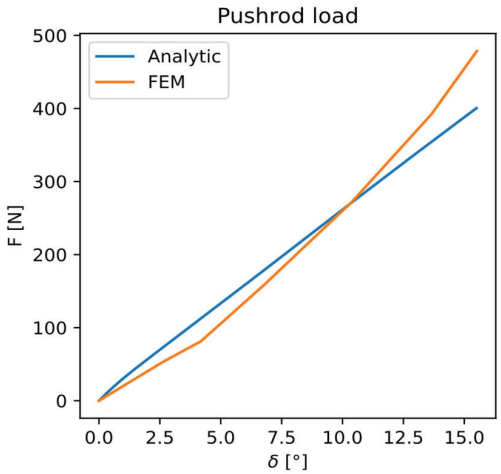

Figure 14: Pushrod forces over flap deflection

Figure 15 shows the actuator and predicted moment over the rotational angle, highlighting that the measurement data may be too coarse for use in flight measurements. This can be attributed to the friction of installed gears, which limits the precision of the actuator internal measurement results. An application scenario for tracking the push rod forces is a health monitoring system for the adhesive. Due to the coarse data such a monitoring system seems to be to inaccurate.

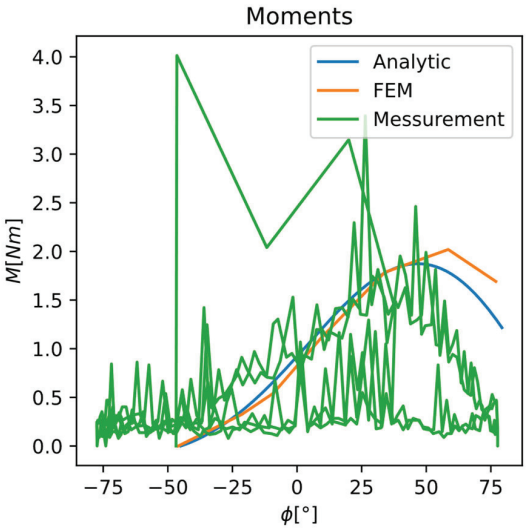

Figure 15: Actuator Moment over angle

2 FATIGUE STRENGTH TEST

The cyclic tests follow a similar structure to static tests. Photos were taken at the end of each cycle to assess crack growth. Before starting the fatigue strength test, 12 cycles were conducted to calibrate the measuring system and CAN-BUS, as well as perform earlier mentioned static tests. The focus is on damage growth, ensuring suitability for flight testing.

To investigate operational stability, a load spectrum from Proteus flights was determined instead of a single-stage test procedure. Figure 16 shows a test cycle including portions mimicking take-off and landing. The morphing trailing edge will be used as multifunctional system so that the cycles are prepared to represent flaperon behavior. For limiting test times ailerons deflections are multiplied by 5 to generate a conservative estimate of maximum load on the wing's root.

The load spectrums amplitude increases at the start (0-35 seconds) and end due to landing (318-360 seconds) flaps and reduced speed. Additionally, control inputs for course correction can be observed in cruise flight (35-318 seconds). This procedure provides a conservative estimate, as no flight test data are available yet. For the fatigue test the load spectrum is repeated until break of the adhesive.

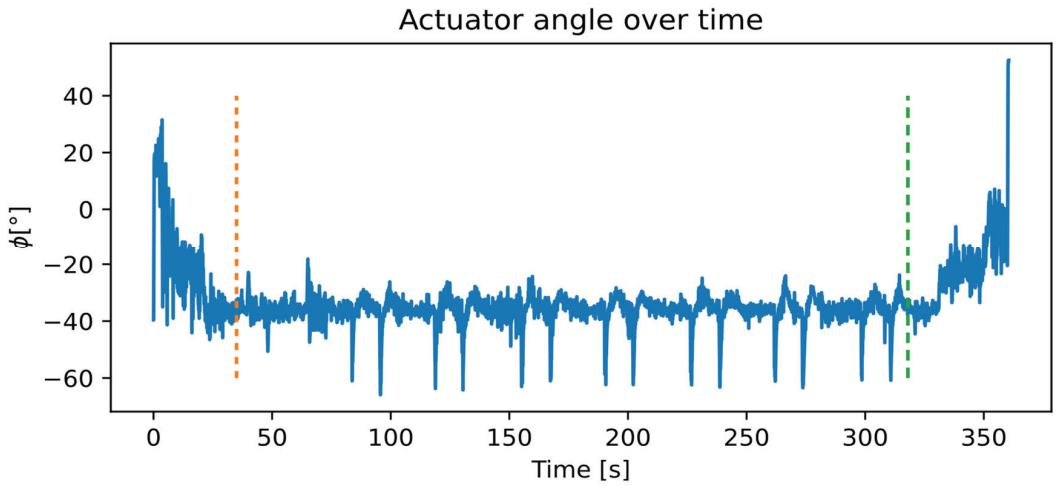

Figure 16: Assumed load Collective

Figure 17 shows the measured pushrod force at sequence time 360s per sequence. The curve declines throughout the investigation. Sample photos (A-F) are presented in Figure 20-25 to observe crack initiation and growth.

At the beginning of the test (Point A), no macro cracks can be detected. The first crack appears at Point B (16.6% of lifetime), consistently growing until Point C (71.3% of lifetime). After Point C, new cracks emerge and grow to Point D (~80% of lifetime). The forces decline steadily up to this point. However, after 80%, the bonding degradation accelerates.

Even if an early crack occurs, the system can still be qualified for flight testing. Cracks in the adhesive can be easily detected and repaired if needed. Between the first crack initiation(B)

and accelerated bonding degradation (D) is about 60% of lifetime to identify and repair the crack. Even after (D) 20% of cycles has been performed before fatal fraction.

The load collectives can then be derived using the measurement data from later flights, resulting in a more accurate determination of actual service life using a higher number of tests and geometries.

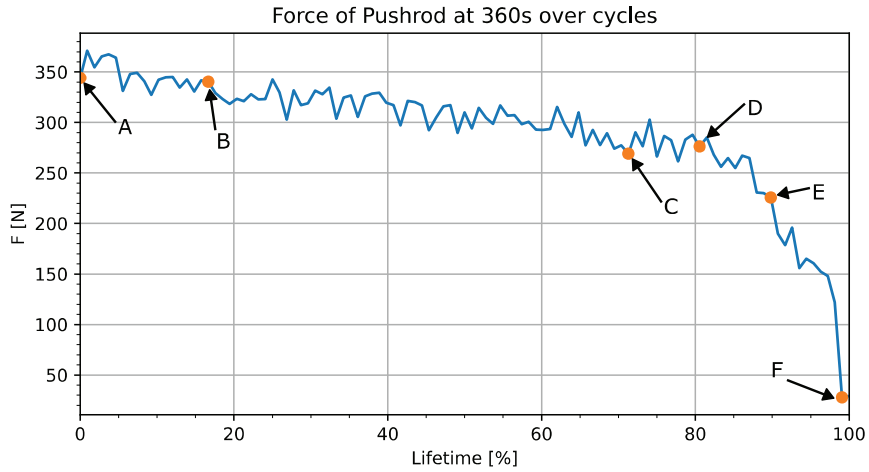

Figure 17: Pushrod force over cycles at 360s sequence time

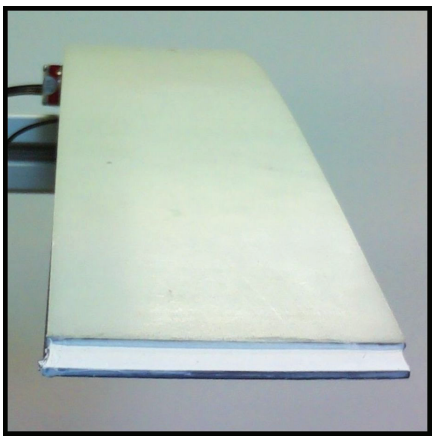

Figure 18: Point A 0%

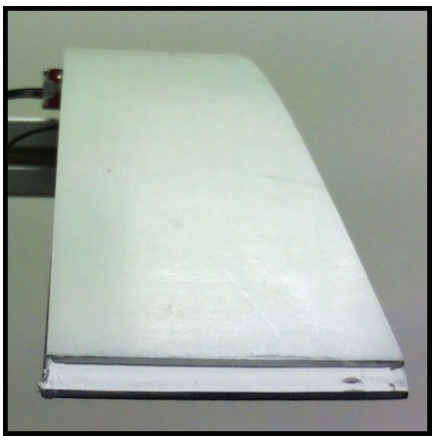

Figure 21: Point D 80,6%

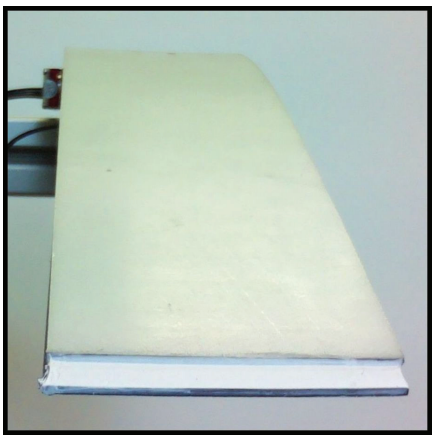

Figure 19: Point B 16,6%

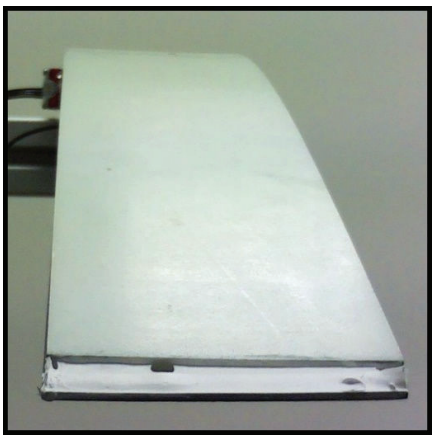

Figure 22: Point E 89,8%

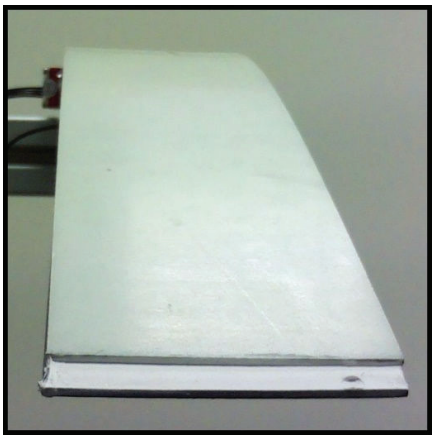

Figure 20: Point C 71,3%

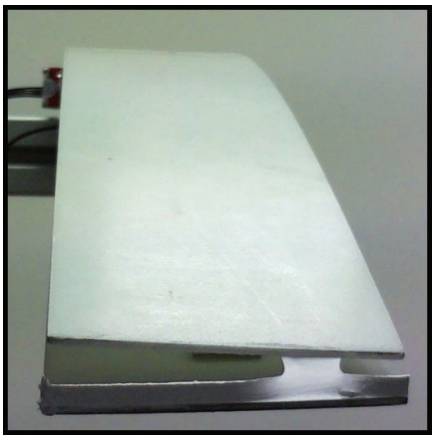

Figure 23: Point F 99%

3 SUMMARY AND OUTLOOK

This work demonstrated the suitability of HYTEM for flight testing through the construction, static and cyclic testing of a HYTEM-based demonstrator A. The results showed that both analytical and Finite Element (FE) modeling provided excellent predictions for static loads on the pushrod and overall deformation. Therefore, these methodologies can be used to assess the design of an hyperelastic trailing edge morphing concept.

Furthermore, slow crack growth was observed in the cyclic tests, which is a crucial indicator of failure-relevant cracks. This finding ensures that such cracks can be detected and repaired during pre-flight inspections, enhancing safety.

Looking ahead, cyclic Test sequence has to be adopted using flight test data. The cyclic tests have to be repeated and analyzed to conduct a more precise lifetime. Using the actual sudden increased degradation could open the possibility to establish a self-monitoring method.

The following demonstrator B with 5 actuator stations and spanwise differentiated deflections will be investigated concerning load interactions. Following this, HYTEM will be integrated into a morphing wing for the MorphAIR project and undergo flight testing, marking an important milestone in its development.

References

[1] AFWAL-TR-88-3082, ed., AFTI/F-111 Mission Adaptive Wing Briefing to industry. Final Report, 1988.
[2] John W. Smith, wilton P. Lock, Gordon A. Payne, “Variable-Camber Systemsintegration and Operational Performance of the AFTI/F-111 Mission Adaptive Wing: NASA Technical Memorandum 4370,” NASA Technical Memorandum 4370, 1992.
[3] Sheryll Goecke Powers, Lannie D. Webb, Edward L. Friend, William a. Lokos, “Flight Tests Results From a Supercritical Mission Adaptive Wing With Smoth Variable camber: NASA Technical Memorandum 4415,” NASa Technical Memorandum, No. 4415, 1992.
[4] Greff, “Stand der Aerodynamik-Arbeiten zum FFE-Vorhaben "Funktion des Intelligenten Flügels" (Status of aerodynamic works for FFE "Function Of Intelligent Wings"),” 21 Jan. 1991.
[5] “SIP-Projekt: Flügel Variabler Wölbung (Wing Of Variable Chamber),” TK 62/099/92, 10.1992.
[6] do Vale, J. L., Afonso, F., Lau, F., and Suleman, A., “Span Morphing Concept: An Overview,” Morphing Wing Technologies, Elsevier, 2018, pp. 125–144.
[7] Barbarino, S., Bilgen, O., Ajaj, R. M., Friswell, M. I., and Inman, D. J., “A Review of Morphing Aircraft,” Journal of Intelligent Material Systems and Structures; Vol. 22, No. 9, 2011, pp. 823–877. doi: 10.1177/1045389X11414084.
[8] Jan Tikalsky, elastische Hinterkantenverklebung(Elastic Trailing edge Bonding), DE 10 2023 117 337 B3, 30.06.2023.
[9] Jan Tikalsky, “HYTEM DEMONSTARTOR: DESIGN AND ANALYSIS OF A MORPHING TRAILING EDGE DEMONSTRATOR USING HYPERELASTIC ADHESIVE,” ASME SMASIS 2024 [online], Vol. 2024; SMASIS2024-140049, https://doi.org/10.1115/SMASIS2024-140049, [retrieved 30 January 2025].
[10] M.Radestock, DLR UAS TEST PLATFORM FOR MORPHING WINGS, Austin (TX), USA, September 2023.
[11] Jan Tikalsky, “Morphing Compliant Trailingedge Skin Concept,” 09/2023.

Index

Abd Fatah, Abdullah Yasser, 565
Abdelkefi, Abdessattar, 1429
Abu Al-Rub, Rashid K., 1367
Agathokleous, Rafaela, 1453
Al-Nasser, Heba, 1379
Amandolese, Xavier, 137
Anilkumar, P. M., 451
Araujo, Aurelio, 263
Arthur Haudeville, 137
Astroza, Rodrigo, 1145
Audrain, Pascal, 113
Avendaño-Valencia, Luis David, 1133, 1183

Büchner, Alexander, 837
Błachowski, Bartłomiej, 801
Baba, Kamal, 1323
Bagri, Anoop Singh, 251
Barbay, Aleksandra, 801
Bareille, Olivier, 827
Barouni, Antigoni, 1391
Barsoum, Imad, 1367
Bashir, Danish, 451
Bellelli, Alberto, 1441
Benedikt, Peter, 315
Benjeddou, Ayech, 3, 33, 149, 869
Berardengo, Marta, 1111, 1225
Bergamini, Andrea E., 681
Bhattacharya, Bishakh, 691, 705
Bischoff, Manfred, 663
Blöchle, Jennifer J., 463
Bonekemper, Lukas, 813, 929, 943
Boscher, Nicolas, 1323
Bourdalos, Dimitrios M., 1121, 1473
Brambilla, Matteo, 1111
Bramerdorfer, Gerd, 361, 437
Brandl, Andreas, 757
Brion, Thomas, 827
Brun d'Arre, Alexandre, 681
Brunnmayr, Florian, 315
Burkut, Evrim, 1009

Carrera, Erasmo, 45
Casagrande, Daniel, 1235
Cazzulani, Gabriele, 1417
Chamoin, Ludovic, 1063
Chatzi, Eleni, 731, 1157
Cheer, Jordan, 1197
Chesné, Simon, 93, 847
Christoforou, Eftychios G., 1453
Chrysochoidis, Nikolaos A., 217, 1391
Claeys, Claus, 173
Collet, Manuel, 93
Cortial, Julien, 1063

D'Ottavio, Michele, 287
Dakova, Spasena, 663
Danner, Patrick, 681
Daraki, Maria-Styliani, 69
de Buhan, Maya, 1063
De Marqui Jr., Carlos, 173
de Oliveira, Leopoldo Pisanelli Rodrigues, 173, 185
De Pasquale, Giorgio, 1333
Deü, Jean-François, 113, 205, 275
Deckers, Elke, 173
Dekemele, Kevin, 81
Dengg, Andreas, 1039
Derbas, Mehieddine, 1269, 1315
Dertimanis, Vasilis, 731
Devos, Olivier, 1405
Dierle, Alexander, 1345
Dimitriou, Dimitris K., 217
Dimitriou, Panayiota, 1453
Dong, Hao, 959
Dragos, Kosmas, 1379
Drangsfeldt, Casper Aaskov , 1133
Drossel, Welf-Guntram, 499
Dudek, Krzysztof K., 1523
Dwivedi, Ankur, 691, 705

Eggers, Finn, 1075
Ehrenhofer, Adrian, 239
Eisenträger, Sascha, 537
Ejlli, Aldo, 327
El May, Mohamed, 1405
El-Rich, Marwan, 1357
Erlinger, Thomas, 1051

Ewert, Arthur, 475, 551

Faraj, Rami, 857, 1545
Fassois, Spilios D., 1169, 1473
Fayaz, Jawad, 1145
Febvre, Maryne, 93
Feger, Reinhard, 373
Ferradj, Imane, 975
Ferrari, Rosalba, 1157
Fett, Michel, 511
Fontana, Mauro, 195
Fossat, Pascal, 827
Foutsitzi, Georgia A., 69
Fragner, Stefan, 393
Frassineti, Andrea, 1523
Freller, Dominik, 327
Friedmann, Herbert, 813, 929, 943
Furtmüller, Thomas, 125

Galiana Blanch, Shankar, 339
García-Asensio, César, 589
García-Delgado, José, 589
Gardonio, Paolo, 185, 1235, 1247
Geier, Sebastian, 487
Gendelman, Oleg, 731
Gerald Jungmayr, Gerald, 327
Ghommem, Mehdi, 1429
Giagopoulos, Dimitrios, 1473
Giannakopoulos, Georgios, 1391
Giraud-Audine, Christophe, 81, 137, 229
Gkatsis, Vassilis, 1391
Gopalakrishnan, Srinivasan, 719
Graczykowski, Cezary, 857
Grasböck, Lukas, 417, 869
Graz, Ingrid, 997, 1009, 1025
Gruber, Wolfgang, 381
Guerra Riaño, Andres Felipe, 603, 671
Guevara, Paola, 1145
Gupta, Nitin, 1279
Gupta, Tanuj, 691

Hörmann, Leander B., 405
Høgsberg, Jan, 149, 205
Hagleitner, Georg, 315
Haldar, Ayan, 251, 451
Hartl, Darren, 577, 1497
Hashem, Ahmed, 373
Hasse, Alexander, 651
Haywood-Alexander, Marcus, 731
He, Weifeng, 613
Helmel, Christian, 405
Hentry Viension, Rehnupreya, 985
Herold, Sven, 195, 349
Hofer, Andreas, 499
Holzmann, Hendrik, 349
Hoseini, Farzaneh, 1441
Hosseinkhani, Ali, 161
Hueber, Christian, 1315
Humer, Alexander, 625, 757, 783, 869, 1025, 1295
Humer, Christoph, 1039, 1051

Ichchou, Mohamed, 827
Ikeda, Yoshiki, 881
Iliopoulos, Ilias A., 1169
Ilyas, Shahzaib, 1357

Jakoby, Bernhard, 427
Jankowski, Łukasz, 801, 905, 917, 1545
Janssen, Stefan, 173
Jeeja, Akshay B., 745
Jocham, Christoph, 1323
Johari, Mohd Aidy Faizal, 565, 985
Juhre, Daniel, 537

Käppeler, Helena, 361
Künnecke, Sven Christian, 1209
Kadic, Muamer, 1523
Kaineder, Gerhard, 405
Kaltenbrunner, Martin, 1279
Karyofyllas, George, 1473
Keimer, Ralf, 1463
Keys, Archie, 1197
Khairnar, Pratham, 705
Khalil, Mohamad, 1357
Kiefer, Bjoern, 745
Kirchner, Eckhard, 511
Klinkel, Sven, 771
Koen, Sampetai S., 1169
Koetz, Florian, 511
Kolisch, Florian, 771
Konda Rodrigues, Gabriel, 173, 185
Konowrocki, Robert, 1545
Konstantinou, Xenofon D., 1473
Koren, Christian, 1287
Kosikova, Antonina, 1157
Koutsoupakis, Josef, 1473
Kraemer, Peter, 813, 929, 943
Kralovec, Christoph, 1039, 1051
Kritikakos, Kyriakos, 1473
Krommer, Michael, 783, 1295
Kudela, Paweł, 23
Kumar, Abhijeet, 251
Kumar, Kishor, 523
Kumar, Sandeep, 1509
Kumar, Suranjan, 251
Kunzemann, Mario, 757
Kurtis, Yasemin, 1157
Kytyr, Dan, 1009

Lützen, Marie, 1133, 1183
Langfeldt, Felix, 1485
Larsen, Mikkel Løvenskjold, 1183
Leconte, Mandy , 1523
Lenzen, Niklas, 771
Li, Xi, 827
Lieber, Julia, 417
Lienhart, Werner, 893
Lilly, Jared, 1497
Lossouarn, Boris, 113, 137, 205, 275
Loyer, François, 1323
Lubanco, Daniel Louback S., 373

Lucá, Francescantonio, 1225

Müller, Andreas, 1453
Madeira, Jose F. A., 263
Magalhaes, Pedro A., 263
Mahendran, Arunjunai Raj, 1279, 1287, 1305, 1323
Maiti, Pralay, 251
Malacarne, Ciro, 1235, 1247
Mallinger, Stefan, 381
Mandal, Subham Sekhar, 251
Manzoni, Stefano, 1111, 1225
Marakakis, Konstantinos, 69
Margerit, Pierre, 959
Marios C. Phocas, 1453
Marischler, Michael, 1097
Marter, Paul, 537
Marth, Edmund, 361
Masri, Sami, 731
Matheou, Maria, 613
Mazlan, Saiful Amri, 565, 985
Mechbal, Nazih, 959, 975, 1405
Melz, Tobias, 195
Menning, Johannes D. M., 475, 551
Miah, Mohammad Shamim, 893
Mikota, Gudrun, 315
Mikułowski, Grzegorz, 801, 857, 905
Mishra, Mudit, 1509
Mishra, Sourava Prasad, 23
Mitterhofer, Hubert, 393
Mizzi, Luke, 1441, 1523, 1535
Moghimimonfared, Reza, 1535
Moix-Bonet, Maria, 339
Monner, Hans Peter, 837, 1209
Monteiro, Eric, 975
Morvan, Antoine, 275
Mueller, Guido, 327

Naji, Mohamed M. , 1367
Nampally, Sneha Rupa, 195
Nicard, Cyril, 1405
Niedzielczyk, Michał, 857
Nielsen, Carl Johan G., 15
Nordin, Nur Azmah, 565, 985
Nordmann, Rainer, 195, 349

Offenzeller, Christina, 427
Okda, Sherif, 195
Oksuz, Sefa, 577
Opris, Dorina, 681
Orszulik, Ryan, 537
Ortis, Lisa, 1235
Ostachowicz, Wiesław, 23
Ostrowski, Mariusz , 917

Pérez Orozco, José Andrés, 1063
Pagel, Kenny , 499
Pal, Aniket, 613
Patel, Bhooshit, 339
Payo, Ismael, 589
Pechstein, Astrid, 757, 783, 1025, 1295
Pedersen, Niels Leergaard, 149
Perini, Matteo, 1235, 1247
Petersen, Jan, 487
Petrolo, Marco, 301
Pichler, Kurt, 405
Pichler-Scheder, Markus, 373
Pierre Flament, 113
Pisarski, Dominik, 801, 905, 1545
Platzer, Sebastian, 625, 1295
Polit, Olivier, 287
Poltschak, Florian, 997
Popławski, Błażej, 905, 917, 1545
Prüger, Stefan, 745
Pretschuh, Claudia, 1305
Preuer, Rene, 997, 1009
Preumont, André, 15
Prokopchuk, Artem, 475, 551
Pruvost, Mickäel, 959
Putz, Veronika, 405

Queste, Adrien, 137

Röver, Friederike, 745
Rébillat, Marc, 959
Rachor, Vincent, 349
Radestock, Martin, 1209, 1569
Raffaele, Davide, 1247
Rahimin, Nur Amirah Farhana, 985
Ramond, Éric, 113
Ramsauer, Stefan, 1557
Rao, B. N., 451
Rebillat, Marc, 1405
Reininger, Alexander, 417
Reischl, Daniel, 417
Rekatsinas, Christoforos S., 217, 1391
Reksowardojo, Arka P., 639
Rentzsch Holm, Finja Carlotta, 1075
Rheinbach, Oliver, 745
Richardt, Jens Damholt, 205
Riegler, Martin, 1269, 1315
Rinderknecht, Stephan, 195
Rittenschober, Bernhard, 1097
Roberts, Laura, 327
Rodrigues, Gonçalo, 15
Rodriguez, Jonathan, 93, 847
Rohan, Eduard, 161
Roland, Sebastien, 975
Rolfes, Raimund, 451
Romdhane, Lotfi, 1429
Rosenlöcher, Thomas, 475
Rustighi, Emiliano, 1235, 1247

Sadeqi, Amirali, 149
Sakellariou, John S., 1121, 1169, 1473
Santner, Robert, 327
Saramantas, Ioannis E., 1169
Saravanos, Dimitris A., 217
Sarkar, Subhasish, 719
Sarmas, Giorgos M., 217
Sawodny, Oliver, 663

Sbarufatti, Claudio, 1417
Scano, Daniele, 45
Schäfer, Michael, 1463
Schaber, Magdalena, 437
Schagerl, Martin, 1039, 1051
Schalm, Tobias, 1075, 1087
Scheerer, Michael, 1097
Scheffler, Sven , 451
Scheidl, Jakob, 1557
Schlanderer, Stefan C., 361
Schlecht, Berthold, 475, 551
Schlechter, Thomas, 373
Schlosser, Robert, 405
Schmidt, Daniel, 339
Schneider, Alexander, 1269
Schröder, Kai-Uwe, 1075, 1087
Seifert, Thomas, 463, 1345
Seltmann, Stephanie, 651
Sengar, Aman, 705
Senin, Nurul Nadia, 565
Serpanos, Dimitrios N., 1169
Shami, Zein A., 229
Sharma, Neeraj, 1257
Shi, Jiahui, 1417
Simon, Zoltan, 1097
Singh, Yuvraj, 251
Sinic, Judith, 1323
Smarianaki, Aikaterini, 69
Smarsly, Kay, 1379
Smyth, Andrew W., 1157
Sonntag, Kathrin, 417
Soulier, Bruno, 1063
Spaggiari, Andrea, 1441, 1523, 1535
Stavroulakis, Georgios E. , 69
Steengaard, Jack Rahbek, 1183
Stelzer, Andreas , 373
Stockhammer, Armin, 417
Stoll, Georg, 349
Stoppel, Jan, 917
Sychterz, Ann C., 639

Tarín, Christina, 663
Thüsing, Kai, 499
Thomas, Olivier, 81, 137, 229
Thuau, Damien, 975
Tikalsky, Jan, 1569
Trautwein, Axel, 663
Trindade, Marcelo A., 3, 33
Tripathi, Dheeraj, 1429
Tsakonas, Ilias A., 217
Tyagi, Amit, 523

Ulliac, Gwen, 1523
Ursi, Ferdinando, 1333

Várkonyi, Péter L., 603, 671
Van Damme, Bart, 681
Vasista, Srinivas, 1463
Vidal, Philippe, 287
Vlachas, Konstantinos, 1157
Vorrath, E.-F. Markus, 475, 551
Vourkos, Eleftherios G., 1453

Wöckinger, Daniel, 437
Wüllner, Benedikt, 813, 929, 943
Wallmersperger, Thomas, 239, 475, 551
Watine, Y., 275
Wendt, Thomas M., 463, 1345
Wermert, Linus, 1087
Wiemann, Marcel, 813, 929, 943
Wiener, Thomas, 427
Wierach, Peter, 339, 487
Wiszowaty, Rafał, 857, 917
Wortmann, Thomas, 613
Wuzella, Günter, 1279

Yadav, Kshitij Kumar, 1257

Zaki, Wael, 1357, 1367
Zappino, Enrico, 45, 301
Zeller, Amelie, 663
Zhang, Rui, 731
Ziembicki, Rafal, 1025
Zine, Abdelmalek, 827